International Solar Energy Society

ISES Solar World Congress 2015

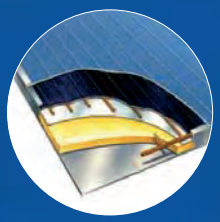

November 8 - 12, 2015
Daegu, Korea

Conference Proceedings

Organized by ISES International Solar Energy Society

Hosted by 사단법인 한국태양에너지학회 THE KOREAN SOLAR ENERGY SOCIETY

Proceedings of the ISES Solar World Conference 2015

Edited by
Dr. Manuel Romero, Vice President of ISES
Solar World Congress 2015, Co-Chair of Scientific Committee

Dr. Taebeom Seo, President of KSES
Solar World Congress 2015, Co-Chair of Scientific Committee

Dr. David Renné, ISES President
Solar World Congress 2015, Chair of Organizing Committee

International Solar Energy Society
Wiesentalstr 50
79115 Freiburg
Germany

Tel + 49 761 45906 – 0
Fax + 49 761 45906 – 99
Email hq@ises.org
Web http://www.ises.org

ISBN 978-3-981 4659-5-2

Produced by
International Solar Energy Society

Notice

The International Solar Energy Society, the Korean Solar Energy Society nor any one of the supporters or sponsors of the ISES Solar World Congress 2015 makes any warranty, express or implied, or accepts legal liability or responsibility for the accuracy, completeness or usefulness of any information, apparatus, product or process disclosed, or represents that its use would not infringe privately on rights of others. The contents of articles express the opinion of the authors and are not necessarily endorsed by the International Solar Energy Society, the Korean Solar Energy Society or by any of the supporters or sponsors of the ISES Solar World Congress 2015. The International Solar Energy Society and the Korean Solar Energy Society do not necessarily condone the politics, political affiliation and opinions of the authors or their sponsors.

Disclaimer

We cannot assume any liability for the content of external pages. The operators of those linked pages are solely responsible for their content. We make every reasonable effort to ensure that the content of this web site is kept up to date, and that it is accurate and complete. Nevertheless, the possibility of errors cannot be entirely ruled out. We do not give any warranty regarding the timeliness, accuracy or completeness of material published on this web site, and disclaim all liability for (material or non-material) loss or damage incurred by third parties arising from the use of content obtained from the web site.

ISES Solar World Congress 2015 Proclamation

Achieving the Renewable Energy Transformation

The International Solar Energy Society is committed to accelerating the transformation of the global energy system to 100% renewable energy for all, used wisely and efficiently. This transformation is necessary for the long, and short, term health and wellbeing of our planet and our people. We know this goal is technically and economically achievable and we know the challenges this entails. The renewable energy movement needs a strong, unified voice to accelerate this transformation, and ISES is expanding its mission to be this voice. To do this, ISES will continue to grow its strong core of solar energy and related renewable energy and environmental professionals, essential for the technical foundations of the movement. In addition ISES will expand its partnership building and outreach with like-minded groups and individuals who can help strengthen the movement through their support. Future ISES events, webinars, publications, participation in global decision making, and other outreach activities will continue to provide the highest quality information on solar energy, and through collaboration with its growing partnership base, address the other wide range of issues central to achieving a 100% renewable energy world.

The Congress brought together a wide range of contributors to the renewable energy movement. Hundreds of participants from 58 countries presented recent developments in solar technologies, and latest updates on financing, policies, access and public support around the world. Young professionals joined with long time solar energy mentors to enrich the discussion of challenges and opportunities for making a difference in all of these areas. The Congress provided an excellent environment for fruitful collaboration and planning, and resulted in the affirmation that we can and will attain the needed energy transformation.

ISES Solar World Congress 2015 participants at the closing ceremony

Welcome of KSES

It is a great pleasure and honor for us to welcome you to the Solar World Congress 2015 which will be held on November 8 to 12, 2015 at EXCO, Daegu, Korea. We aim to help you accomplish ISES's objectives of developing and expanding renewable energy technologies throughout the world.

The Solar World Congress in 2015 would provide an excellent opportunity for renewable energy experts and companies from many nations to meet their colleagues, and offer visitors a chance to discover and enjoy Korean culture during your stay. Based on our successful experience of hosting the SWC1997 in Korea, we expect to achieve outstanding results through the Solar World Congress in 2015, encouraging international colleagues to develop and deploy the renewable energy technologies in the world.

Besides thought-provoking academic challenges and discussions, SWC 2015 also offers a lovely time to enjoy Korea through diverse social programs featuring Korean history, culture and natural scenery.

Korea boasts an enticing blend of modern and traditional culture, warm hospitality and collection of tempting food. In particular, Daegu has been designated as solar city, in recognition of its efforts to apply the renewable energy technology into their daily life.

We assure you that this congress will be an academically enriching, socially enjoyable, and truly memorable experience for all the delegates and their guests.

Thank you.

Prof. Kwang Hwan Choi, President
The Korean Solar Energy Society

Welcome of ISES

The International Solar Energy Society is pleased to welcome you to the ISES Solar World Congress in beautiful Daegu, Korea, 8-12 November, 2015. The Congress is hosted by the Korean Solar Energy Society. SWC 2015 continues a long tradition of connecting the renewable energy research and academic community with decision makers, financiers, and practitioners. The Congress will provide the most up-to-date information on renewable energy technology trends and breakthroughs, global and regional policies, and market opportunities. The Congress will feature a broad spectrum of technical presentations on the latest renewable energy developments, plenary and keynote addresses from global experts, workshops and discussion forums, and a variety of networking and social events.

ISES is committed to achieving the vision of 100% renewable energy for all, used efficiently and wisely. Achieving such a vision will require a transformation of our energy system, addressing technology developments, innovative financing, political will, and, most important, community acceptance of these transformative technologies. In addition, for this vision to become a reality, we must address gender engagement, community involvement, and public education. SWC 2015 offers many examples of progress in all of these areas, as well as addressing the challenges that remain.

I wish you a successful Solar World Congress 2015 and hope that you have a fruitful and enjoyable experience, and are able to meet old friends and colleagues and make many new important contacts to support your work.

Dr. David Renné, President
International Solar Energy Society

Committees

Co-Chairs

· Dave Renné	President ISES
· Kwang Hwan Choi	President KSES

International Organising Committee

· Dave Renné	President ISES
· Kwang Hwan Choi	President KSES
· Taebeom Seo	Former President KSES
· Manuel Romero	Vice-President ISES
· Jennifer McIntosh	Head of Secretariat ISES

Local Organising Committee

· Chair : Yongheack Kang	Director, Korea Institute of Energy Research
· Booseop Nam	CEO, Korea Energy News
· Sang-Yang Noh	President, New and Renewable Energy Center
· Hyungjin Kim	President, Green Energy Institute
· Changhyung Park	Associate President, Korea New and Renewable Energy Association
· Jajoong Kook	Associate President, Korea Photovoltaic Industry Association
· Wonyong Lee	Director, Korea Institute of Energy Research
· Jongdal Kim	Professor, Kyungpook National University
· Taebeom Seo	Professor, Inha University
· Doo Sam Song	Progessor, Sungkyunkwan University
· Seung Ho Yoo	Professor, Korea University
· Jun-Tae Kim	Professor, Kongju National University
· Gihwan Kang	Ph.D, korea Institute of Energy Research
· Donggun Lim	Professor, Korea National University of Transportation
· Hyun-Goo Kim	Ph.D, korea Institute of Energy Research
· Ju-Yeop Choi	Professor, KwangWoon University
· In Soo Cha	Professor, DongShin University
· Jeong-Bae Kim	Professor, Korea National University of Transportation
· Jae-Han Lim	Professor, Ewha Womans University
· Eung-Jik Lee	Professor, Semyung University
· Jung-Ha Hwang	Professor, Kyungpook national University
· Sun Jin Yun	Ph.D, Electronics and Telecommunications Research Institute

Scientific Committee

Co-Chairs

- Manuel Romero — Vice-President ISES
- Taebeom Seo — Former President KSES

Theme Chairs

- Solar Buildings and Architecture
  - Maria Wall — Lund University, Sweden
  - Haruki Sato — Keio University, Japan

- Resource Assessment and Energy Meteorology
  - John Boland — UNISA, Australia
  - Hyun-Goo Kim — Korea Institute of Energy Research, Korea

- Renewable Electricity Technologies: Photovoltaics
  - Nicola Romeo — University Parma, Italy
  - Jae-Ho Yun — Korea Institute of Energy Research, Korea

- Renewable Electricity Technologies: CSP, Biomass, Geothermal, Wind, Hydro, Ocean & Other
  - José González-Aguilar — IMDEA Energy, Spain
  - Zhifeng Wang — IEE Chinese Academy of Sciences, China

- Solar Heating and Cooling: Fundamentals & Applications
  - Andreas Häberle — Fraunhofer Chile Research Foundation, CSET, Chile
  - Jie Ji — University of Science and Technology of China, China

- Solar Energy and Society
  - Paulette Middleton — Panorama Pathways, USA
  - Guofeng Yuan — IEE Chinese Academy of Sciences, China

- Energy Storage
  - Luisa F. Cabeza — GREA, University of Lleida, Spain
  - Hong-Soo Kim — Korea Institute of Energy Research, Korea

- Renewable Energy Grid Integration & Distribution
  - Christof Wittwer — Fraunhofer Institute for Solar Energy Systems ISE, Germany
  - Yong-Hwan Chun — Hongik University, Korea

- Off-Grid & Rural Energy Access
  - Ajay Chandak — SSVPS BSD COE, India
  - Jangho Lee — Kunsan University, Korea

- Clean Transportation Technologies & Strategies
  - Scotte Elliot — Mid-Ohio Regional Planning Commission, USA
  - Xuhui Wen — IEE Chinese Academy of Sciences, China

Committee Members

· Arancibia-Bulnes Camilo	UNAM, Mexico
· Bai Fengwu	IEE-Academy of Sciences, China
· Bajare Diana	Riga Technical University, Latvia
· Barthelmie Rebecca	Cornell University, USA
· Bellan SelvanI	MDEA Energy, Spain
· Beltan Liliana	Texas A&M University, USA
· Bernardo Ricardo	Lund University, Sweden
· Blanc Philippe	Mines-Paristech, France
· Bosio Alessio	Università degli Studi di Parma, Italy
· Brunner Christoph	AEE, Austria
· Bruno Frank	University South Australia, Australia
· Castro Manuel	UNED, Spain
· Chandra Laltu	IIT Jodhpur, India
· Charalambides Alexandros	Cyprus University of Technology, Cyprus
· Chiu Ningwei Justin	KTH, Sweden
· Collares-Pereira Manuel	University Evora, Portugal
· Dai Yanjun	Jiao Tong University, China
· David Mathieu	Reunion University, France
· Epstein Michael	Weizmann Institute, Israel
· Erb Dave	University of North Carolina Asheville, USA
· Esbensen Torben	Esbensen Consulting, Denmark
· Escobar Rodrigo	Pontifici Universidad Católica, Chile
· Fan Janhua	DTU, Denmark
· Ana Inés	University of Barcelona, Spain
· Gracia Alvaro de	University of Antofagasta, Chile
· Grant Ian	Bureau of Meteorology, Australia
· Gutierrez Andrea	University of Antofagasta, Chile
· Han Gui Young	Seonggyunkwan University, Korea
· Hasager Charlotte	Technical University of Denmark. Denmark
· He Wei	University of Science and Technology of China. China
· Holm Dieter	Soltrain, South Africa
· Horvat Miljana	Ryerson University, Canada
· Jaeger-Waldau Arnulf	European Commission DG JRC, Ispra Italy
· Jiang Jiuchun	Jiao Tong University, China
· Julia Enrique	University Jaume I, Spain
· Kanters Jouri	Lund University, Sweden
· Kato Yukitaka	Titech, Japan

· Kay Merlinde	Univ. New South Wales, Australia
· Kim Jonggyu	KIER, Korea
· Kleissl Jan	University California San Diego, USA
· Kodama Tatsuya	Niigata University, Japan
· Kramer Korbinian	ISE Fraunhofer, Germany
· Kumar Satpathy Rabindra	Trina Solar, India
· Kuznik FredericI	NSA Lyon, France
· Lamberts Roberto	Universidade Federal de Santa Catarina, Brazil
· Lauret Philippe	Reunion University, France
· Li Xin	IEE-Academy of Sciences, China
· Lim Donggun	Korea University of Transportation, Korea
· Liu Qibin	IET-Academy of Sciences, China
· Luna de Abreu Samuel	Instituto Federal de Santa Catarina, Brazil
· Marano Vincenzo	University of Salerno, Italy
· Martin Viktoria	KTH, Sweden
· Martinez Diego	Qatar Environment and Energy Research Institute, Qatar
· Martínez-Moll Víctor	University Balearic Islands, Spain
· Matsumoto Yasuhiro	CINVESTAV, Mexico
· Negrò Macado Wilson	Universidade Federal do Pará, Brazil
· Neti Sudhakar	Lehigh University, USA
· Oliphant Monica	Consultant, Australia
· Paksoy Halime	Çukurova University, Turkey
· Pei Gang	University of Science and Technology, China
· Pérez Manuel	Universidad de Almeria, Spain
· Pinheiro Vaz Jerson Rogério	Universidade Federal do Pará, Brazil
· Pisello Anna Laura	CRBNET, Italy
· Probst Maria	EPFL, Switzerland
· Rajagopal Surabhi	Selco Foundation, India
· Remund Jan	Meteotest, Switzerland
· Renné David	ISES/Dave Renné Renewables, USA
· Roeb Martin	DLR, Germany
· Ruivo Celestino	University Algarve, Portugal
· Sakai Koji	Meiji University, Japan
· Scognamiglio Alessandra	ENEA, Italy
· Simone Marilena de	Università della Calabria, Italy
· Stapleton Geoff	Global Sustainable Energy Solutions, Australia
· Suh Ae-Suk	Hydro-meteorological Cooperation Center, Korea

· Tao Hel	EA/SHC ExCo, China
· Tavares PinhoJoão	Universidade federal do Pará, Brazil
· Tawada Yoshihisa	Osaka University, Japan
· Tivari Ayodhya	EMPA, Switzerland
· Ueda Yuzuru	Tokyo University of Science, Japan
· Ushak Svetlana	University of Antofagasta, Chile
· Vajen Klaus	University Kassel, Germany
· Valenzuela Loreto	CIEMAT, Spain
· Vallvé Xavier	Trama Tecnoambiental, Spain
· Vela Nieves	CIEMAT, Spain
· Wald Lucian	Mines-Paristech, France
· Wang Ruzhu	Jiao Tong University, China
· Wang Jin	The Ohio State University, USA
· Wang Lifang	IEE-Academy of Sciences, China
· Wilbert Stefan	DLR, Germany
· Xu Honghua	IEE-Academy of Sciences, China
· Yang Tae-Hyun	KIER, Korea
· Yoon Jongho	Hanbat University, Korea
· Zahnd Alex	RIDS-Nepal, Nepal
· Zarzalejo Luis F.	CIEMAT, Spain
· Zhang Lixi	Northwestern Polytechnical University, China
· Zhang Xiaosong	Southeast China University. China
· Zheng Hongfei	Beijing Institute of Technology, China
· Zhou Rongwei	China Meteorological Administration, China

Congress Themes and Topics

Theme 1: Solar Buildings and Architecture

Solar Architecture and Building Integration
Building Material and Components
Net Zero Energy Buildings
Advanced HVAC
Daylighting
Rational Use of Energy in Buildings
Other issues related to Solar Buildings

Theme 2 : Resource Assessment and Energy Meteorology

Solar Radiation Availability and Variability
Renewable Energy Resource Assessment
Theoretical, Technical and Economic Potentials
Resource Forecasting
Instrumentation and Tools
Other issues related to energy meteorology and resource assessment

Theme 3: Renewable Electricity Technologies: Photovoltaics

PV Cells, Materials and Components
Advanced Materials and Concepts
Design, Operation and Performance of PV Systems
Balance of Plant Components
Grid-integrated PV
Thin Film Solar Cells
Concentrating PV
Other issues related to PV fundamentals and technologies

Theme 4: Renewable Electricity Technologies: CSP, Biomass, Geothermal, Wind, Hydro, Ocean & Other

Solar concentration fundamentals and optical engineering heat transfer, materials and components
Solar Thermal Electricity Systems
Solar Detoxification and Photo-catalytic Processes
Biomass Energy, Geothermal & Other thermal Renewables
Wind Energy, Ocean Energy, Hydro and other direct conversion renewables
Other issues related to renewable thermal electricity
Solar Fuels and Chemicals

Theme 5: Solar Heating and Cooling: Fundamentals & Applications

Solar Collectors (including Thermal-PV collectors)
Testing, Certification and Quality Assessment, Simulation and Engineering Tools
Solar Domestic Hot Water and Combisystems
Solar District Heating and Cooling
Solar Heat for Industrial and Commercial Applications
Solar Distillation and Solar Thermal Desalination
Solar and Heat Pump Systems
Solar Cooling and Air Conditioning

Theme 6 : Solar Energy and Society

Strategies and Policies
International Renewable Energy Review
Solar Cities
Development of Community Renewable Energy Projects
Education and Training
Workforce Development
Gender and energy

Theme 7 : Energy Storage

Electrical Storage, Pumped Hydro and Mechanical Storage
High Temperature Thermal Energy Storage
Low-Medium Temperature Thermal Storage
Energy Storage in Buildings
Novel storage concepts

Theme 8 : Renewable Energy Grid Integration & Distribution

Grid integration of variable renewable energy systems
Automation and control
Smart Grids strategies including smart metering
Active Demand-Side Management
Communications & Data

Theme 9 : Off-Grid & Rural Energy Access

Electrical and Thermal Energy Supply
Small Wind and Small Hydro Power
Micro power and hybrid systems
Energy Access and Security
Expansion of RE in developing countries, off-grid systems
Solar Cooking and Clean Cook Stoves
Solar Food Processing, including crop drying

Theme 10 : Clean Transportation Technologies & Strategies

Renewable Energy in transport sector
Solar powered vehicles
Transport electrification and integration of Renewable Energy
Hydrogen vehicles
Policy, planning and economics

Program at a glance (1)

TIME	Sun (Nov 8)	Mon (Nov 9)					Tue (Nov 10)					
8:00		REGISTRATION DESK & AUTHOR PRESENTATION UPLOAD OPENS (8:00, Lobby 3F)					REGISTRATION DESK & AUTHOR PRESENTATION UPLOAD OPENS (8:00, Lobby 3F)					
		TECHNICAL SESSIONS AND FORUMS (9:00 - 10:30)					**TECHNICAL SESSIONS AND FORUMS (8:30 - 10:00)**					
9:00		**TS09-1 (320-B)**	**TS09-2 (323)**	**TS09-3 (321-A)**	**TS09-4 (322)**	**Forum 1 (321-B)**	**TS10-1 (321-B)**	**TS10-2 (322)**	**TS10-3 (321-A)**	**TS10-4 (324)**	**Forum 4 (323)**	
		Solar Buildings and Architecture	Resource Assessment and Energy Meteorology	Energy Storage	Renewable Electricity Technologies: CSP, Biomass, Geothermal, Wind, Hydro, Ocean & Other	ISES Futures: New Directions, New Opportunities	Renewable Electricity Technologies: CSP, Biomass, Geothermal, Wind, Hydro, Ocean & Other	Solar Heating and Cooling: Fundamentals & Applications	Energy Storage	Renewable Electricity Technologies: Photovoltaics	Public Acceptance and Achieving 100% RE Forum	
10:00		COFFEE BREAK (10:30-11:00)					COFFEE BREAK 10:00 - 10:30					
11:00	REGISTRATION OPEN	**OPENING CEREMONY (11:00 - 12:30, Rm. 325)** Welcome from ISES President, KSES President, National & Local Dignitaries					**PLENARY SESSION (10:30 - 12:30, Rm. 325)** Implementing the Renewable Energy Transformation					
12:00		LUNCH and POSTER VIEWING (12:30 - 13:30)					LUNCH and POSTER VIEWING 12:30-13:30					
13:00		**POSTER Presentations (13:30 - 14:15)**				**Forum 2 (13:30 - 15:00)**	**POSTER Presentations (13:30 - 14:15)**					
		P1-1 (324)	**P1-2 (321-B)**	**P1-3 (322)**	**P1-4 (321-A)**	**Forum 2 (323)**	**P2-1 (324)**	**P2-2 (322)**	**P2-3 (320-B)**	**P2-4 (321-B)**	**P2-5 (323)**	
14:00		Renewable Electricity Technologies: Photovoltaics	Solar Energy and Society	Solar Heating and Cooling: Fundamentals & Applications	Renewable Energy Grid Integration & Distribution, Clean Transportation Technologies & Strategies, and Off-Grid & Rural Energy Access	Photovoltaic Technology and Market: Current Status and Future Prospects	Renewable Electricity Technologies: Photovoltaics	Solar Heating and Cooling: Fundamentals & Applications	Solar Buildings and Architecture	Renewable Electricity Technologies: CSP, Biomass, Geothermal, Wind, Hydro, Ocean & Other	Resource Assessment and Energy Meteorology	
15:00		POSTER Viewing with Authors & COFFEE BREAK (14:15 - 15:30)					POSTER Viewing with Authors & COFFEE BREAK (14:15-15:30)					
		KEYNOTE SPEECHES (15:30 - 16:00)					**KEYNOTE SPEECHES (15:30 - 16:00)**					
16:00		**KS09-1 (324)**		**KS09-1 (323)**		**KS09-1 (322)**	**KS10-1 (324)**		**KS10-1 (323)**		**KS10-1 (322)**	
		High Penetration of PV in Electricity Grids		Issues and Opportunities for Solar Heating and Cooling		Electrifying Remote Outer Island Households in the Republic of the Marshall Islands	Increasing Future Application Potential of Solar Energy		High-Temperature Thermochemical Hydrogen Production Using a Solar Concentrating System		Resource Assessment & Energy Meteorology	
		BREAK (16:00 - 16:15)					BREAK 16:00 - 16:15					
		TECHNICAL SESSIONS AND FORUMS (16:15 - 17:30)					**TECHNICAL SESSIONS AND FORUMS (16:15 - 17:30)**					
17:00	**YOUNG ISES GET-TOGETHER** (17:00 - 18:30 Rm. 322)	**TS09-5 (322)**	**TS09-6 (321-A)**	**TS09-7 (323)**	**Forum 3 (321-B)**		**TS10-5 (323)**	**TS10-6 (322)**	**TS10-7 (321-B)**	**TS10-8 (324)**	**Forum 5 (325)**	
		Solar Heating and Cooling in Buildings	Advances in Rural and Off-Grid Renewable Energy Access	Resource Assessment and Energy Meteorology	International Solar Cities Initiative (ISCI)		Resource Assessment and Energy Meteorology	Solar Heating and Cooling: Fundamentals & Applications	Renewable Electricity Technologies: CSP, Biomass, Geothermal, Wind, Hydro, Ocean & Other	Renewable Electricity Technologies: Photovoltaics	How to get Published in a Scientific Journal: Editorial and Publisher Perspectives	
18:00	**WELCOME RECEPTION** (18:30 - 20:00 Lobby, 5F)						BREAK					
							ISES Annual General Meeting (17:45 - 18:15, Rm. 325)					
							FARRINGTON DANIELS LECTURE by Prof. Richard Perez (18:15 - 19:00, Rm. 325)					
19:00							**HAPPY HOUR/RECEPTION (19:00, Lobby, 5F)**					

APEC WORKSHOP : Experiences and plans to double RE Utlization by 20130 in APEC Region

Program at a glance (2)

TIME	Wed (Nov 11)						Thu (Nov 12)					Fri (Nov 13)
8:00	REGISTRATION DESK & AUTHOR PRESENTATION UPLOAD OPENS (8:00, Lobby 3F)						REGISTRATION DESK & AUTHOR PRESENTATION UPLOAD OPENS (8:00, Lobby 3F)					
	TECHNICAL SESSIONS AND FORUMS (8:30 - 10:00)						**TECHNICAL SESSIONS AND FORUMS (8:30 - 10:00)**					
9:00	**TS11-1 (323)**	**TS11-2 (322)**	**TS11-3 (321-A)**	**TS11-4 (324)**	**Forum 6 (321-B)**		**TS12-1 (320-B)**	**TS12-2 (321-A)**	**TS12-3 (320-A)**	**T12-4 (321-B)**	**TS12-5 (324)**	
	Resource Assessment and Energy Meteorology	Solar Heating and Cooling: Fundamentals & Applications	Energy Storage	Renewable Electricity Technologies: Photovoltaics	Solar Thermal Electricity: Technology and Market Development Forum		Solar Buildings and Architecture	Renewable Energy Grid Integration & Distribution	Off-Grid & Rural Energy Access	Solar Energy and Society	Solar Heating and Cooling: Fundamentals & Applications	
10:00	COFFEE BREAK 10:00 - 10:30						COFFEE BREAK 10:00 - 10:30					
	PLENARY SESSION (10:30 - 12:30, Rm. 325) Global Market and Technology Perspectives						**PLENARY SESSION (10:30 - 12:30, Rm. 325)** Developments in the Asia-Pacific Region					
11:00												
12:00	LUNCH and POSTER VIEWING 12:30 - 13:30						LUNCH and POSTER VIEWING 12:30 - 13:30					
13:00	**POSTER Presentations (13:30 - 14:15)**						**CLOSING CEREMONY (13:30 - 15:30, Rm. 325)** Theme Summairs,Congress Proclamation & Closing Remarks					
	P3-1 (324)	**P3-2 (322)**	**P3-3 (321-B)**	**P3-4 (321-A)**	**P3-5 (323)**							
14:00	Renewable Electricity Technologies: Photovoltaics	Solar Heating and Cooling: Fundamentals & Applications	Renewable Electricity Technologies: CSP, Biomass, Geothermal, Wind, Hydro, Ocean & Other	Energy Storage	Resource Assessment and Energy Meteorology							
15:00	POSTER Viewing with Authors & COFFEE BREAK (14:15 - 15:30)											
	KEYNOTE SPEECHES (15:30 - 16:00)											
16:00	**KS11-1 (324)**		**KS11-1 (323)**		**KS11-1 (322)**							
	Energy and Architecture: The Solar Integration Challenge		Dust and Soiling of Solar Devices: History, Status, and Expectations (Is there a "Holy Grail" Solution?)		Renewable Electricity Technologies / CSP (TBD)							
	BREAK 16:00 - 16:15											
	TECHNICAL SESSIONS AND FORUMS (16:15 - 17:30)											
17:00	**TS11-5 (324)**	**TS11-6 (321-A)**	**TS11-7 (322)**	**TS11-8 (321-B)**	**Forum 7 (323)**							
	Renewable Electricity Technologies: Photovoltaics	Solar Energy and Society	Solar Heating and Cooling: Fundamentals & Applications	Renewable Electricity Technologies: CSP, Biomass, Geothermal, Wind, Hydro, Ocean & Other	Renewable Energy Resource Assessment and Mapping							
18:00												
	CONFERENCE DINNER AND AWARDS CEREMONY (19:00 - 21:00, Hotel Inter Burgo EXCO (Iris Hall))											
19:00												

APEC WORKSHOP : Experiences and plans to double RE Utilization by 20130 in APEC Region

EXCURSIONS

ISES Solar World Congress 2015

Sponsors and Supporters

We thank our Sponsors, Exhibitors and Partners

Sponsors and Exhibitors

K water

Hukseflux Thermal Sensors

KOREA TOURISM ORGANIZATION

KOFST 1966 THE KOREAN FEDERATION OF SCIENCE AND TECHNOLOGY SOCIETIES

Colorful DAEGU

dcvb DAEGU Convention & Visitors Bureau

Media Partners

Global Information

ELSEVIER

www.solarthermalworld.org

SUN & WIND ENERGY

PVTECH

european energyinnovation

Plant Automation -Technology.com™

Table of Contents

Solar Buildings and Architecture

Resource Assessment and Energy Meteorology

Renewable Electricity Technologies: Photovoltaics

Renewable Electricity Technologies: CSP, Biomass, Geothermal, Wind, Hydro, Ocean & Other

Solar Heating and Cooling: Fundamentals & Applications

Solar Energy and Society

Energy Storage

Renewable Energy Grid Integration & DistributionTheme

Off-Grid & Rural Energy Access

Clean Transportation Technologies & Strategies

Solar Buildings and Architecture

ISES International Solar Energy Society

Conference Proceedings

Solar World Congress 2015

Daegu, Korea, 08 – 12 November 2015

Evaluation of a Facade Integrated Concentrating Solar Collector System

Piratheepan Mahendran[1], and Timothy Anderson[1]

[1]Auckland University of Technology, Auckland, New Zealand

Abstract

The use of building integrated photovoltaic/thermal (BIPVT) collector modules is one of the most effective ways to harness the solar energy within the building environment. Using static reflectors along with BIPVT absorbers may be a cost effective way to utilize these in façade applications. In order to precisely predict the overall performance of such building integrated façade collectors it is crucial to develop a mathematical model that represents such systems. As such, a mathematical model was developed to describe the performance of a façade integrated BIPVT solar concentrator system and subsequently this was validated with a physical prototype.

Using the validated model, a sensitivity analysis was performed to determine the design parameters that significantly influence the efficiency of the collector. It was shown that key parameters such as tube spacing and thermal conductivity between the solar cell and the absorber have a significant effect on the overall efficiency while mass flow rate does not have any significant effect on the overall performance.

Keywords: *building integrated photovoltaic/thermal, façade, concentrator, BIPVT*

1. Introduction

Energy consumption in the built environment accounts for nearly one third of the global energy demand (IEA 2011). A significant portion of this could be met through onsite energy generation utilising solar energy, while intelligent building design practices and incorporating solar energy systems within the building envelope are two solutions that could reduce the long term energy costs and reduce environmental impacts. However, traditional solar energy systems such as photovoltaic panels or solar thermal collectors retrofitted onto buildings after they have been built may result in poor aesthetics and sub-optimal energy outputs. Therefore, integration of combined photovoltaic/solar thermal collectors into a buildings fabric could give greater opportunity for the use of renewable energy technologies in buildings.

Generating thermal and electrical energy simultaneously from solar irradiation using photovoltaic/thermal (PV/T) systems is an area of research that has received significant attention in recent years (Ibrahim et al. 2014, Fudholi et al. 2014, Tripanagnostopoulos 2012). However, there have been relatively few attempts to utilize such systems with low concentration ratio concentrating systems to increase the radiation incident on the PV/T absorber, and even fewer that incorporate such systems into the fabric of a building. A significant advantage of low concentration reflectors is that they do not need to track the sun making them ideal for integration into a building's facade, though by doing this they will have a lower acceptance angle range compared with tracking collectors (Rabl 1976). Despite this disadvantage, low concentration ratio collectors offer the advantage of collecting diffuse radiation as well as the beam component (Petter et al. 2012). This increases the possibility of using the traditional Si solar cells with less need for precise optics.

In 2002 Tripanagnostopoulos et al (2002) analysed PV/T combined collectors incorporating low concentration ratio booster reflectors with a view to achieving high combined efficiency. In a parallel study, (Tselepis and Tripanagnostopoulos 2002) performed a life cycle assessment of the combined collector and concluded that they were more cost competitive, had a shorter payback time and less environmental impact than that of standalone PV panels. As such, the combination of low concentration ratio reflective elements along with hybrid absorbers may further improve the cost competitiveness of the system by increasing the radiation on the absorber plate.

doi:10.18086/swc.2015.08.01 Available at http://proceedings.ises.org

Despite the work showing the benefits of using reflectors with PV/T absorbers, there are few studies that have investigated systems with a static reflector combined with a hybrid absorber plate for façade applications. A study by Gajbert, et al. (2007) found that low concentration ratio PV/T modules have advantages over traditional modules and proposed a PV/T collector with a parabolic reflector. However there appears to be few active attempts to utilise concentrating BIPVT systems, and a lack of detail in describing their combined thermal/electrical performances.

In light of this, this study examines the performance of a façade integrated solar collector that incorporates a flat reflective element with a view to increasing the radiation on a photovoltaic/thermal (PV/T) absorber plate, as shown in Figure 1.

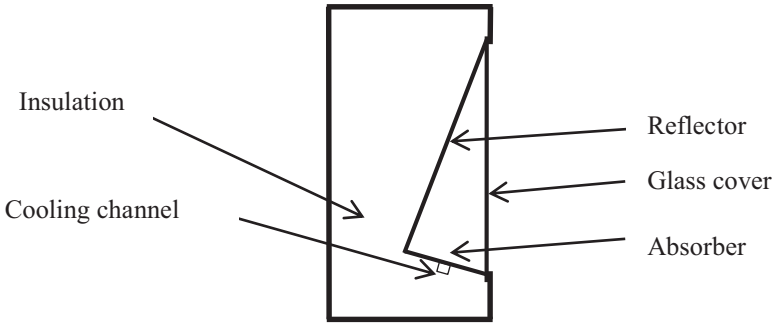

Fig. 1: Façade Integrated Concentrator

2. Mathematical model

In order analyse the performance of the proposed façade integrated collector, a one dimensional steady state thermal model was developed. A simplified thermal resistance network as shown in Figure 2 was used to undertake a heat balance of the absorber plate.

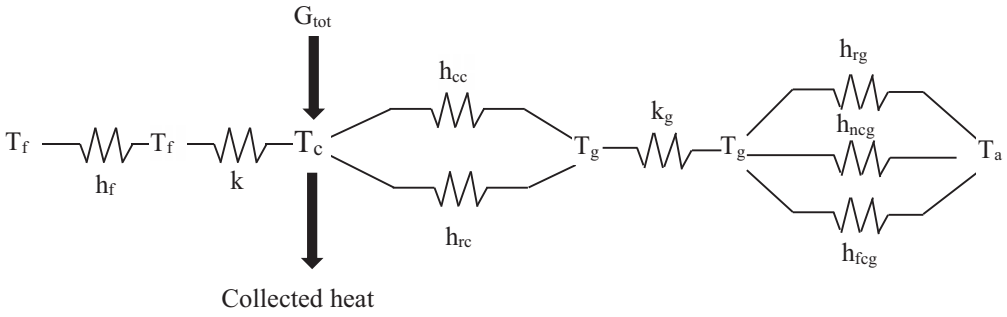

Fig. 2: Simple thermal network of the proposed module

For a typical solar thermal collector, the useful thermal energy gain Q can be determined from equation 1.

$$Q = AF_R[(\tau\alpha)_{PV}G - U_L(T_i - T_a)] \quad \text{(eq. 1)}$$

This equation can be further modified, as shown in equation 2, to incorporate the concentration ratio C of the proposed low concentration collector.

$$Q = AF_R[(\tau\alpha)_{PV}G.C - U_L(T_i - T_a)] \quad \text{(eq. 2)}$$

Here Q is given by a function of absorber area (A), heat removal factor (F_r), the transmittance-absorptance product for the photovoltaic absorber ($\tau\alpha_{PV}$), the solar radiation (G), the concentration ratio (C), the overall heat loss coefficient (U_L) and the temperature difference between inlet and the ambient temperature.

In practice it is not possible to cover the whole absorber module with photovoltaic cells, hence equation 2 can be further modified to include a packing factor (S) and the transmittance-absorptance product of the thermal absorber and the PV material, as shown in equation 3.

$$Q = S\left[AF_R[(\tau\alpha)_{PV}G.C - U_L(T_i - T_a)]\right] + (1-S)\left[AF_R[(\tau\alpha)_T G.C - U_L(T_i - T_a)]\right] \quad \text{(eq. 3)}$$

The ratio of the heat collected against the irradiation falling on the absorber plate gives the thermal efficiency of the collector as shown in equation 4

$$\eta_{thermal} = F_R[S(\tau\alpha)_{PV} + (1-S)(\tau\alpha)_T] - F_R U_L \frac{(T_i - T_a)}{GC} \quad \text{(eq. 4)}$$

Following on from this, to determine the optical concentration ratio in terms of the radiation reaching the absorber, equation 5 can be used (Kostic L et al. 2010).

$$C = {}^{G_{tot}}/_{G_{net}} \quad \text{(eq. 5)}$$

Where G_{tot} is the sum of the radiation directly falling on the absorber G_{dir} and the radiation from the reflector G_{ref} on the absorber, while G_{net} is the amount of radiation received by a horizontal absorber alone without the reflector. By incorporating the reflectance ρ_{Al} of the reflector, C can be expressed as equation 6

$$C = \frac{G_{dir} + \rho_{Al} G_{ref}}{G_{tot}} \quad \text{(eq. 6)}$$

Now from the work of Piratheepan and Anderson (2014), and basic geometry, the relationship for the average optical concentration ratio C for the proposed collector can then be expressed by equation 7. Where α is the elevation angle of the sun and the γ is the inclination angle of absorber relative to the horizontal.

$$\mathrm{C} = \begin{cases} \left[\frac{\cos(\alpha+\gamma)(\tan(\alpha+\gamma)+\tan\gamma)}{Sin\ \alpha}\right]\rho_{Al} + \frac{1}{\cos\gamma} & \alpha < (90-2\gamma) \\ \left[\frac{\cos(\alpha+\gamma)(3+\tan\gamma)}{Sin\ \alpha}\right]\rho_{Al} + \frac{1}{\cos\gamma} & (90-2\gamma) < \alpha < (90-\gamma) \\ \frac{sin(\alpha+\gamma)(1-3tan(\alpha+\gamma-90))(tan(\alpha-(90-\gamma)))}{sin\ \alpha} & (90-\gamma) < \alpha < 90 \end{cases} \quad \text{(eq. 7)}$$

Furthermore, the collector heat removal efficiency factor (F_r) can be expressed in terms of heat loss coefficient (U_L), mass flow rate (m) and the collector efficiency factor (F') as given by equation 8.

$$F_r = \frac{mC_p}{A}\left[1 - exp^{-\frac{AU_L F'}{mC_p}}\right] \quad \text{(eq. 8)}$$

The collector efficiency factor (F') can be calculated using equation 9 in terms of its fin efficiency factor F.

$$F' = \frac{1/U_L}{\left[\frac{1}{U_L[d+(w-d)F]} + \frac{1}{wh_{PVA}} + \frac{1}{\pi d h_{fl}}\right]} \quad \text{(eq. 9)}$$

Here h_{PVA} accounts for the bond resistance between the PV cell and the absorber plate as shown by (Zondag et al. 2002). The forced convection heat transfer coefficient (h_{fl}) in the cooling tube can be determined from equation 10.

$$h_{fl} = \frac{Nu * k_{fl}}{d} \quad \text{(eq. 10)}$$

Where k_{fl} is the conductivity of the fluid at the mean temperature and Nu is the Nusselt number that can be determined from any number of relationships for forced convective heat transfer in a tube, in this study the Gnielinski (Cengel 2007) correlation was used.

In order to calculate the fin efficiency factor F, it is necessary to calculate the coefficient (M) that accounts for the overall thermal conductivity and the thickness of the PV/T absorber plate as given by equation 11 in terms of overall thermal loss coefficient U_L.

$$M = \sqrt{\frac{U_L}{K_{abs}L_{abs} + K_{PV}L_{PV}}} \quad \text{(eq. 11)}$$

As such, the modified fin efficiency F can be calculated using equation 12, where w is the tube spacing and d is the hydraulic diameter of the tube.

$$F = \frac{tanh\left[\frac{M(w-d)}{2}\right]}{\frac{M(w-d)}{2}} \quad \text{(eq. 12)}$$

In the determination of M in equation 9, the overall thermal loss coefficient U_L is the sum of the heat losses via top, rear and edge of the collector as given by equation 13.

$$U_L = U_{top} + U_{rear} + U_{edge} \quad \text{(eq. 13)}$$

As the rear heat loss and edge losses are mainly through the insulation, the rear loss coefficient U_{rear} and the edge loss coefficient U_{edge} can be determined from Fouriers Law.

However, in the determination of the top losses the glazing on the proposed collector, as shown in Figure 1, is not parallel to the absorber plate. Recently though (Piratheepan et al. 2014) showed that the natural convection heat loss in an air filled enclosure such as this could be predicted by equation 14, where b is the breadth of the absorber and h is the height of the reflector.

$$Nu = 0.67Ra^{0.36}(b/h)^{1.75} \quad \text{(eq. 14)}$$

This can subsequently be rearranged to determine the value of the natural convection heat transfer coefficient h_{cc} inside the concentrator enclosure

To estimate the radiation heat transfer coefficient inside the concentrator h_{rc} the enclosure was assumed to be a two-surface enclosure consisting of the absorber plate and the glazing by assuming the reflector is adiabatic. Hence the expression of the h_{rc} can be written in terms of area of the absorber plate (A), area of the glazing (A_g), the view factor (F_{cg}) from the absorber to the glazing, and the emittance of absorber plate and the glazing ε_p and ε_g, as expressed in Equation 15.

$$h_{rc} = \frac{\sigma(T_{pm}^4 - T_g^4)}{\left(\frac{1-\varepsilon_c}{A\varepsilon_c}\right)+\left(\frac{1}{AF_{cg}}\right)+\left(\frac{1-\varepsilon_g}{A_g\varepsilon_g}\right)} \quad \text{(eq. 15)}$$

Where T_{pm} and T_g are the mean plate temperature and the internal glazing temperature of the collector respectively.

The view factor F_{cg} can be deduced from equation 16 in terms of enclosure dimensions

$$F_{cg} = \frac{2b}{b\left(1+\frac{1}{\sin\beta}\right)-h} \quad \text{(eq. 16)}$$

Subsequently, the heat loss through the glass cover can be calculated using the heat transfer coefficient of the glass k_g internal glazing temperature T_g and external glazing temperature T_g'.

Now, the external heat loss from the glazed cover is the sum of the radiation, natural and the forced convection heat losses. As majority of the collector faces the ambient environment, it was assumed that the glass cover radiated heat to the surroundings with an ambient temperature T_a. Hence, the radiation heat transfer coefficient from the glazing h_{rcg} can be expressed in terms of external glazing temperature T_g' and the ambient temperature T_a as shown in equation 17

$$h_{rcg} = \sigma\varepsilon_g(T_g'^2 + T_a^2)(T_g' + T_a) \quad \text{(eq. 17)}$$

Furthermore, the losses due to natural and forced convection also must be taken in to account. The forced convection heat transfer coefficient h_{fcg} will be a function of velocity of the wind, an approximation of which can be expressed by equation 18, where v is the wind velocity.

$$h_{fcg} = 4.214 + 3.575V \quad \text{(eq. 18)}$$

The natural heat transfer coefficient h_{ncg} can be expressed by equation 19

$$h_{ncg} = 1.78(T_{g'} - T_a)^{1/3} \quad \text{(eq. 19)}$$

Using this approximation it is possible to calculate the overall convection heat transfer coefficient h_c by

integrating both forced and natural heat transfer coefficient using equation 20 (Eicker 2006)

$$h_c = \left(h_{fcg}^3 + h_{ncg}^3\right)^{1/3} \quad \text{(eq. 20)}$$

In summary; the combination of heat losses and the total useful energy extracted, considering the energy balance of the collector, mean the thermal efficiency of the façade integrated collector can be established.

Now in examining the electrical performance of the system, one trade-off of using silicon solar cells under concentrated radiation is that their efficiency degrades with the temperature increase. Hence it is essential to express the electrical efficiency in terms of the temperature of the absorber plate.

The electrical efficiency of the solar cell can be determined by firstly determining the power generated by the cell at its maximum power point, as given by equation 21.

$$P = I_{mp} V_{mp} \quad \text{(eq. 21)}$$

This can also be expressed in terms of fill factor (*FF*) and the open circuit voltage V_{oc} and short circuit current I_{oc} as shown in equation 22.

$$P = FF\ I_{sc} V_{oc} \quad \text{(eq. 22)}$$

However, V_{oc} and *FF* decrease significantly with increased temperature, while short circuit current increases marginally with the temperature (Zondag 2008). Taking this into account using equation 23 (Dubey et al. 2013) gives a good approximation of the electrical efficiency of a photovoltaic cells under various temperatures given that the nominal operating cell temperature (*NOCT*) and the temperature coefficient (β) and the efficiency of the cell at *NOCT* conditions are known from the manufacturer's datasheet.

$$\eta_e = \eta_{NOCT}(1 - \beta(T_{pm} - NOCT)) \quad \text{(eq. 23)}$$

for typical crystalline Si modules β can be assumed as 0.004 (Notton et al. 2005).

When the packing factor *S* is taken in to account, the electrical efficiency of the collector on a relative area basis η_{elect} can be expressed by equation 24.

$$\eta_{elect} = \eta_{NOCT}\left(1 - \beta\left(T_{pm} - NOCT\right)\right) * S \quad \text{(eq. 24)}$$

By combining equation 4 and equation 2 the combined efficiency η_{tot} of the collector can be calculated from equation 25.

$$\eta_{tot} = \eta_{thermal} + \eta_{elect} \quad \text{(eq. 25)}$$

3. Experimental testing and results

In order to validate the mathematical model and findings derived from its use, it is necessary to compare the outcome with an experimental model. As there is no standard method for testing photovoltaic/thermal hybrid modules it was decided use a standard steady state test method similar to the one describing the thermal performance of glazed liquid heating collectors given in AS/NZS 2535.1 (2007). As such, an experimental testing system was constructed on the roof of Auckland University of Technology's School of Engineering building, facing true north. In doing this, T-type thermocouples were used to measure the inlet and the outlet of the coolant as well as the ambient temperature. A cup anemometer and a wind vane were mounted adjacent to the collector to measure the wind speed and direction. Finally, a Delta-T SPN1 type sunshine pyranometer was used to measure the beam and diffuse radiation. For the electrical output, the voltage and current were measured simultaneously while keeping the system loaded at maximum power point.

Now, fabrication of the façade collector involves three main parts; the PV/T absorber, the reflector and the insulation elements including the glass cover. For this work the finned tube absorber plate was fabricated from a 1.2 m length of 2 mm aluminium painted matte black, with two absorbers mounted in series. A 10 mm square aluminium tube was attached to the back of each absorber using a thermally conductive adhesive to act as the

cooling channel. Square tube was used as it provides a larger contact surface between the absorber plate and the cooling tube, thus improving the fin efficiency. Each absorber plate was then fitted with a custom made string of seven 150 mm crystalline solar cells connected in series and bonded to the absorber using a silicone conformal coating. This thin layer of clear conformal coating protects the cells under extreme environmental and climatic condition and insulates the rear wiring of the solar cells when the absorber is exposed to the concentrated radiation. Reflector was prepared by attaching a silver metalized film on an aluminum sheet.

Due to the practical issues associated with integrating the façade integrated collector into an actual building façade, two vertical "wall" sections were fabricated to mount the concentrators. Each wall was packed with mineral wool insulation (R2.8) to insulate the rear of the concentrator, and replicate a building façade, while the front surface was glazed using a low-iron glass cover. A schematic representation of the combined collector test system is shown in figure 3.

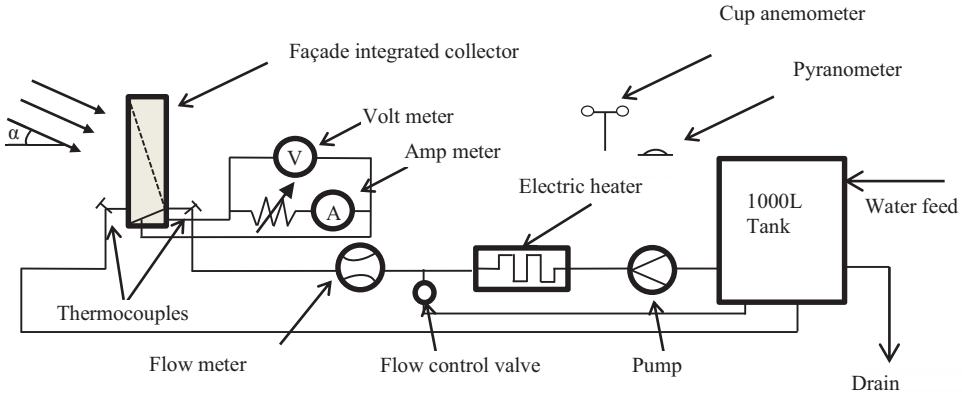

Fig. 3: Experimental test rig and the circuit diagram for electrical measurements

In summary, the design parameters of the prototype collector tested here are given in table 1.

Table. 1: Physical characteristics of experimental prototype

Parameter	Symbol	Value	Unit
System flow rate	m	$1.33X10^{-5}$	m^3/S
Collector length	L	2.4	m
Collector breath	b	0.2	m
Reflector height	h	0.6	m
Collector area	A	0.48	m^2
PV Transmit/apsorpt	$\tau\alpha_{PV}$	0.78 (De Vries 1998)	-
Thermal Transm/apsorpt	$\tau\alpha_T$	0.925 (Anderson et al. 2009)	-
Absorber thickness	L_{abs}	0.002	m
PV thickness	L_{PV}	0.0004	m
PV conductivity	K_{PV}	130	W/mK
Tube hydraulic diameter	d	0.0088	m
Tube spacing	w	0.2	m
Cell-absorber Quasi heat transfer coefficient	h_{PVA}	45	W/m^2K
Insulation conductance	k_{ins}	0.045	W/mK
Back insulation thickness	L_{ins}	0.1	m

Edge insulation thickness	L_{edge}	0.025	m
Absorber conductivity	K_{abs}	130	W/mK
Packing factor	S	0.7	-
Conductance of glass	k_g	0.9	W/mK
Reflectance of silver metalized film	ρ_{Al}	0.9	-

3.1 Experimental results and model validation

To validate the mathematical model several sets of readings were taken from the test rig under various solar elevation angles and input temperatures. These were taken when the sun was near solar noon, such that the effect of shading, due to the design of mounting enclosure, was minimised. As shown in figure 4 the mathematical model incorporating with new heat transfer relationships for the concentrator, as well as the concentration ratio, is capable of predicting the performance with good accuracy.

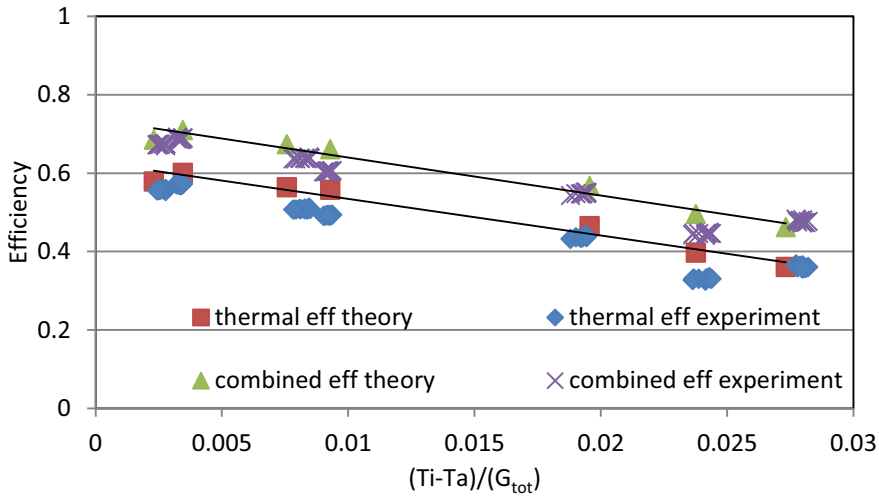

Fig. 4: Experimental and theoretical efficiencies of façade integrated collector

3.2 Modelling Results

Now in table 1, there are number parameters which can be modified to improve the performance of the collector. Hence, having validated the mathematical model it was used to perform a sensitivity analysis on the system. In this study, only one design variable was varied at a time and the effect of that particular parameter on the efficiency was observed. This allows us to determine the design variables that are critical in terms of efficiency of the system and its design.

In the concentrator it is likely that high temperatures will be achieved and so there is a need for improved cooling. Heat transfer in the cooling channel is a function of Reynold's number and thus varying the flow rate may have the effect on the overall efficiency of the collector. However as shown on figure 5, the efficiency of the collector does not significantly improve with the increased fluid flow rate. The slight increase in efficiency can be attributed to an increase in the turbulence in the system increasing the heat transfer marginally. Furthermore, a reduction in temperature will increase the electrical efficiency marginally though the pumping power required to achieve this may offset any gains by doing this.

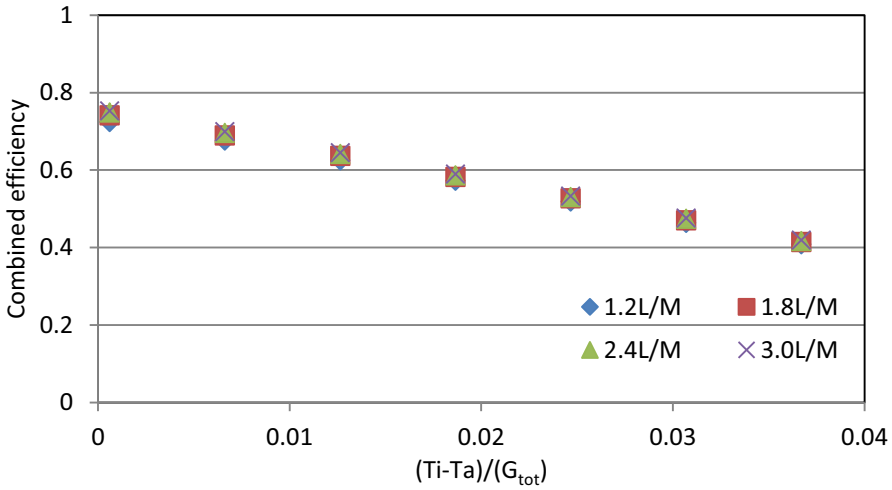

Fig. 5: Combined efficiency by varying flow rate

Another means of improving the efficiency could be to reduce the width of the absorber for a single tube, or by decreasing the spacing between adjacent tubes in systems with multiple cooling tubes. As shown in figure 6, this will increase the efficiency significantly. This can be explained by the fact that an increase in the number of tubes across the absorber plate improves the fin efficiency and thus increases the performance of the collector. However it can be seen that, at higher *(Ti-Ta)/G*C* values they tend to converge. This suggest that although decreasing the tube spacing increases the efficiency initially, there are other factors which will decrease the efficiency at higher *(Ti-Ta)/G*C*.

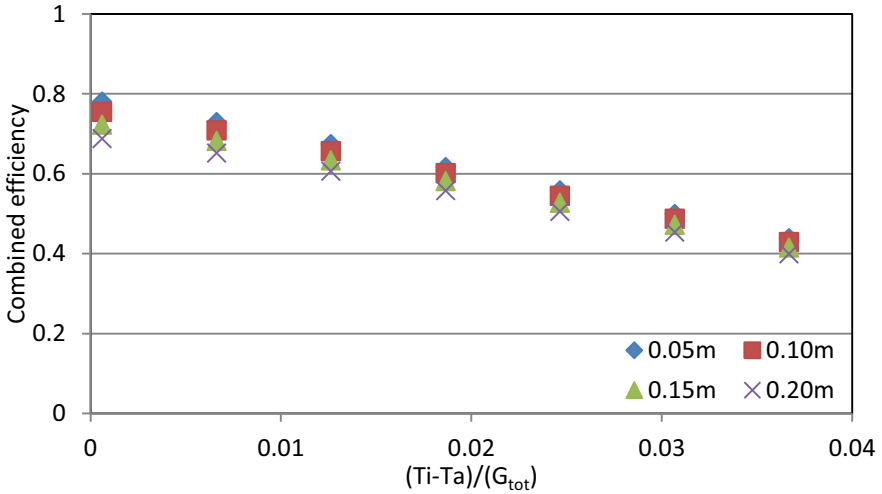

Fig. 6: Combined efficiency by varying tube spacing

Further, the combined efficiency of the collector could be also improved by improving the heat transfer coefficient between the solar cells and the thermal absorber. Unlike a thermal collector that has a bond resistance between the tube and absorber (Duffie and Beckman 2006), a "quasi" heat transfer coefficient, with a value of 45W/m^{2}K, between the PV cells and the absorber plate is used (Zondag et al. 2002). Based on this Anderson et al (2009) stated that this thermal conductance might be improved by means introducing a thermally conductive adhesive. Following on from this recommendation, it can be seen in figure 7, that when the heat transfer coefficient is doubled from 30W/m^{2}K to 60W/m^{2}K the efficiency is improved by approximately 10%.

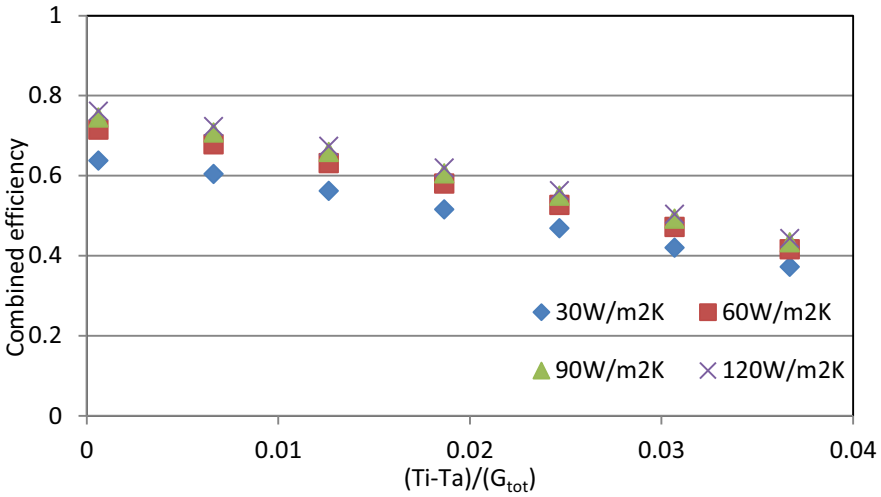

Fig. 7: Combined efficiency by varying cell to absorber heat transfer coefficient

4. Conclusion

From the results, it was shown that the mathematical model incorporated with the heat transfer empirical relationships presented in this paper was able to predict the performance of the particular system. Further, from the sensitivity analysis, there are number of conclusions that can be drawn. Firstly, increasing the flowrate in the cooling tubes appears to offer little benefit with respect to increasing the efficiency of the collector.

However, the combined efficiency of the collector can be improved by increasing the number of cooling channels across the absorber plate though this may not be economical. Hence increasing the number tubes has to be considered as a trade-off between the efficiency and the cost of the collector. Finally, improved thermal contact between the solar cells and the thermal absorber will increase the efficiency dramatically and appears to offer significant potential in improving the performance of the façade integrated BIPVT solar concentrator system.

5. References

Anderson, T. N., Duke, M., Morrison, G.L and Carson, J. K. 2009 Performance of a building integrated photovoltaic/thermal (BIPVT) solar collector. Solar Energy, Vol 83, pp. 445-455.

AS/NZS 2535.1, 2007. Test methods for solar collectors. Part 1: thermal performance of glazed liquid heating collectors including pressure drop. Standards Australia, Homebush.

Cengel, Y. A. 2007. Heat and mass transfer: a practical approach,3rd ed.,McGraw-Hill,Boston.

De Vries, D.W., 1998. Design of a photovoltaic/Thermal Combi-panel, PhD Thesis. Eindhoven University.

Dubey, S., Sarvaiya, J. N and Seshadri B. 2013 Temperature Dependent Photovoltaic (PV) Efficiency and Its Effect on PV Production in the World – A Review. Energy Procedia, Vol 33, pp. 311-321.

Duffie, J. A and Beckman W. A. 2006. Solar Engineering of Thermal Processes. In Solar Engineering of Thermal Processes, Wiley, New York.

Eicker, U. 2006. Solar technologies for buildings. John Wiley & Sons, Chichester.

Gajbert, H., Hall, M and Karlsson, B., 2007, Optimisation of reflector and module geometries for stationary, low-concentrating, facade-integrated photovoltaic systems, Solar Energy Materials and Solar Cells, Vol. 91, pp. 1788-1799.

Fudholi, A., Sopian, K. Yazdi., M. H. Ruslan., M. H. Ibrahim A and Kazem H. A. 2014. Performance analysis of photovoltaic thermal (PVT) water collectors. Energy Conversion and Management, Vol 78, pp 641-651.

Ibrahim, A., Fudholi, A., Sopian, K., Othman M. Y and Ruslan M. H. (2014) Efficiencies and improvement potential of building integrated photovoltaic thermal (BIPVT) system. Energy Conversion and Management, Vol 77**,** pp 527-534.

IEA, International energy agency 2011. Solar energy perspectives: OECD/IEA, France.

Kostic, L.T.,Pavlovic,T.M and Pavlovic Z.T (2010) Optimal edsign of orientation of PV/T collector with reflectors. Applied Energy, Vol 87, pp 3023-3029.

Krauter, S.C.W 2006. Solar electric power generation. Heidelberg: Springer-Verlag.

Notton, G., Cristofari, C., Mattei., M and Poggi P 2005, Modelling of a double-glass photovoltaic module using finite differences. Applied Thermal Engineering,Vol 25**,** pp 2854-2877.

Petter, B., Breivik, C., and Drolsum R 2012, Building integrated photovoltaic products: A state-of-the-art review and future research opportunities. Solar Energy Materials and Solar Cells, Vol 100**,** pp 69-96.

Piratheepan, M. and Anderson, T. N 2014, Experimental evaluation of low concentration collectors for façade applications.Proceedings of the 52nd Annual Australian Solar Council Scintific Conference, Melbourne, May 2014.

Piratheepan, M., Anderson T. N and Saiful S., 2014, Experimental Evaluation of Natural Heat Transfer in Façade Integrated Triangular Enclosures. Proccedings of the 1st Annual Asia-Pacific Solar Research Conference, Sydney, October 2014

Rabl, A. 1976. Comparison of solar concentrators. Solar Energy, Vol 18**,** pp 93-111.

Tripanagnostopoulos, Y. 2012, Photovoltaic/thermal solar collectors. In Comprehensive Renewable Energy, Vol 3, pp 255-300. Elsevier Oxford.

Tripanagnostopoulos, Y., Nousia, T., Souliotis., M and Yianoulis, P. 2002, Hybrid photovoltaic/thermal solar systems. Solar Energy, Vol 72**,** pp 217-234.

Tselepis, S. & Tripanagnostopoulos Y. 2002, Economic analysis of hybrid photovoltaic/thermal solar systems and comparison with standard PV modules. In Proceedings of the international conference PV in Europe, Rome, October 2012.

Zondag, H. A., 2008 Flat-plate PV-Thermal collectors and systems: A review. Renewable and Sustainable Energy Reviews, Vol 12**,** pp 891-959.

Zondag, H., De Vries, D., Van Helden, W., Van Zolingen R and Van Steenhoven A., (2002) The thermal and electrical yield of a PV-thermal collector. Solar Energy, Vol 72**,** pp 113-128.

Potential energy savings from a semi-transparent solar cell window system for code-compliant residential buildings in hot and humid climates

Sung Lok Do[1,*] and Juan-Carlos Baltazar [2]

[1] Department of Building and Plant Engineering, Hanbat National University, Daejeon, South Korea

[2] Department of Architecture, Texas A&M University, College Station, Texas, United States

Abstract

A semi-transparent solar cell window system is one of the most recent building integrated PV window technologies (i.e., BIPV window). This type of BIPV window systems can generate photovoltaic electric energy and can be designed to admit a specific amount of natural light and/or view to an indoor space. This study evaluates potential energy benefits of integrate semi-transparent solar cell windows on a 2009 International Energy Conservation Code (IECC) code-compliant residential building in a hot and humid climate. The energy analysis is based on a whole-building simulation model with a DOE-2.1e, which include a BIPV window module specially made for this study. The study analyzed peak demand, energy use, and electricity production from each orientation (east-, west-, south-, and north-facing). As a result, the south-facing window showed the greatest potential to generate electric power and to reduce building loads and system energy use. In comparison to the code-compliant base-case model, the BIPV windows provided noticeable energy savings about 12-21% in annual site energy use.

Keywords: *Building integrated PV, Energy simulation, Residential building, International Energy Conservation Code, DOE-2.1e simulation program*

1. Introduction

Hot and humid climates demand significant electricity for cooling. In 2001, Texas implemented the Texas Emissions Reduction Plan (TERP) program that aims to diminish the pollution in the state by energy efficiency and renewable energy measures. To lower pollution to generate electricity from fossil fuels, Texas has been utilizing applications of renewable energy resources for both power plants and buildings.

As one of the efforts to reduce pollution, Texas has built renewable energy plants to generate electricity from eco-friendly fuel resources (e.g., mainly wind, solar, and biomass) (Haberl et al., 2014). Texas is one of the largest renewable energy producers in the United States (US), leading the nation in wind-powered generation capacity with over 14,000 megawatts (EIA, 2015; Haberl et al., 2015).

In addition to these efforts, other renewable energy applications to buildings (e.g., photovoltaic, PV, technology integrated into buildings) have been used to reduce the building's energy demands due to onsite power generation, and it resulted in reducing energy demands on power plant (Haberl et al., 2014; NREL, 2015). Recently, an interest in a semi-transparent solar cell window system (i.e., a building integrated photovoltaic (BIPV) window) has increased worldwide (bccResearch, 2011; DOE, 2015b; Kang et al., 2013; Sivanandan, 2009; SNE, 2011) because the these solar cell windows generate electricity without constructing additional PV structures on a building envelop and also provide natural light transmission (Kang et al., 2013; Lee et al., 2014; Li et al., 2009; Yoon et al., 2011). Due to these features, building designers and engineers may use the BIPV windows to generate electricity and to create unique daylighting features in building façades (e.g., window and sunroof), which at the same time reduce unwanted cooling load and glare associated with architectural glazing (Li et al., 2009).

In the US, a new residential construction must comply with a residential building energy code for its energy certificate. A number of residential building energy codes and standards (e.g., IECC, ASHRAE Standard 90.2, California Title 24, etc.) have been developed and adopted. In the US residential sector, the IECC is widely adopted as the state energy code in approximately 40 of the 50 US states (DOE, 2015c). Since January 2012, Texas has adopted the 2009 IECC (ICC, 2009) even though newer versions of IECC (i.e., 2012 and 2015 IECC) are available (DOE, 2015a; SECO, 2015). The aim of this study is to evaluate the potential effects of implementing semi-transparent solar cell windows on a residential building that complies with the adopted state energy conservation code (i.e., 2009 IECC) and is located in a hot and humid climate.

doi:10.18086/swc.2015.08.02 Available at http://proceedings.ises.org

2. Semi-transparent solar cell windows

A semi-transparent solar cell window system (BIPV window) is one of many of the PV technology applications to buildings. The BIPV window system can generate photovoltaic electric energy, and can be designed to admit a specific amount of natural light and/or view to an indoor space (Yoon et al., 2011; DOE, 2015a, 2015c; SECO, 2015). In comparison to the conventional PV cells, it has several advantages: ease-to-manufacture due to no need for vacuum processes, capability to be colorable and transparent, applicability to flexible thin structure, and light weight (Miyazaki et al., 2005).

To calculate the electricity generation from the BIPV window, the PV efficiency (η) is determined as the fraction between the maximum power which a solar cell can convert from absorbed light to electrical energy (P_{max}) and the incident power (P_{in}). This study used Eq. (1) and Eq. (2) for the efficiency calculation, which are basic solar cell efficiency equations (Duffie and Beckman, 2013; Servaites et al., 2009; Sze and Ng, 2006). The degradation of the solar cell efficiency due to the increased cell temperature in operation was not considered in this study.

$$FF = \frac{V_{MP} \cdot I_{MP}}{V_{OC} \cdot I_{SC}} \quad \text{(eq. 1)}$$

$$\eta = \frac{P_{max}}{P_{in}} = \frac{V_{MP} \cdot I_{MP}}{P_{in}} = \frac{V_{OC} \cdot I_{SC} \cdot FF}{P_{in}} \quad \text{(eq. 2)}$$

where P_{max} is the maximum power (W), FF is the fill factor to determines the maximum power from a solar cell, V_{MP} is the maximum power voltage (V), I_{MP} is the maximum power current (A), V_{OC} is the open-circuit voltage (V), I_{SC} is the short-circuit current (A), η is the PV efficiency, and P_{in} is the incident power (W), which is based on 1 kW m^{-2} for the efficiency calculations. The BIPV window electric power generation is estimate using Eq. (3) (Chae et al., 2014; Corrao and Morini, 2012; Duffie and Beckman, 2013; Servaites et al., 2009; Sze and Ng, 2006).

$$P = \eta \cdot A \cdot G \quad \text{(eq. 3)}$$

where P is the generated electricity from a BIPV window (W), A is the BIPV window surface area (m^2), and G is the global irradiance on a BIPV window surface (W m^{-2}).

3. Semi-transparent solar cell windows

To evaluate the potential energy benefits from implementing the BIPV windows instead of conventional windows, this study simulates a 2009 IECC code-compliant residential building. The simulations are conducted under a hot and humid climate; this study selects the city of Houston, the Climate Zone 2 classified in IECC. The overall research methodology is briefly presented in Fig. 1.

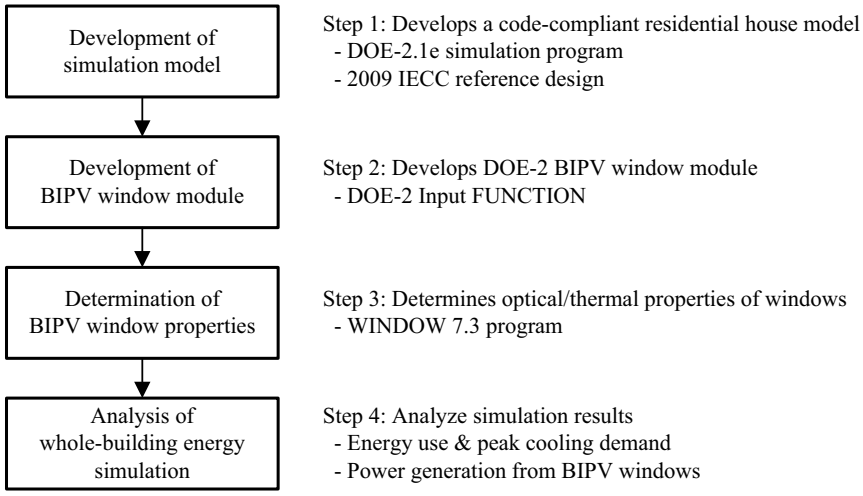

Fig. 1: Diagram of overall research methodology

In order to develop a code-compliant residential base-case simulation model, the requirements as defined in Chapter 4 of the 2009 IECC were referenced (ICC, 2009); the input parameter values such as envelope insulation, window area, and system efficiency were determined according to the code requirements (Do and Haberl, 2015). The developed base-case model (see Fig. 2) had a simplified structure with a rectangular geometry, flat roof, and

no attic space; they are a single-story, single-family, south-facing and detached house that has 232 m^2 of floor area and a 2.4 m floor-to-ceiling height without a plenum. For this study, the base-case model was modified to have five interior thermal zones, including east, west, south, north, and core. The base-case model used a double-pane window with a bronze-tinted glass. The window area on each exterior wall was determined using a 15% window-to-floor ratio (WFR), which was equivalent to a 23.4% window-to-wall ratio (WWR) for the base-case. In addition, this study used the Residential System (RESYS) in the DOE-2.1e program (DOE2, 2015) for a typical residential air-source heat pump system. The simulations for this study were performed using Typical Meteorological Year version 3 (TMY3) weather file.

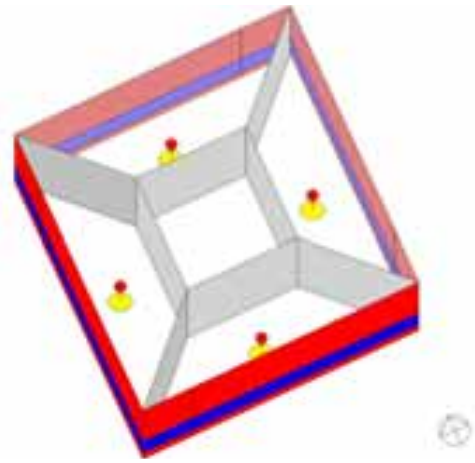

Fig. 2 (a)

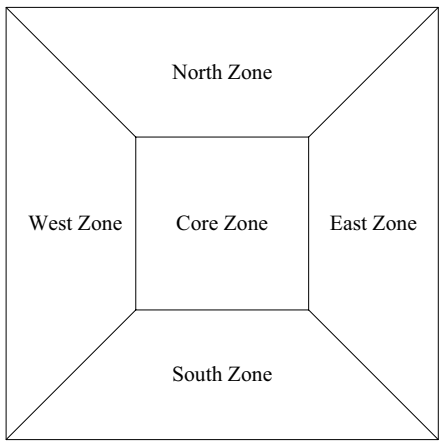

Fig. 2 (b)

Fig. 2: View of the base-case simulation model: (a) exterior 3D view; and (b) interior thermal zoning

In order to calculate the electricity power generated from BIPV windows on each exterior wall, the BIPV window module was developed using the DOE-2 input FUNCTION commands, which can be written in the Building Description Language (BDL) input file without debugging the DOE-2.1e program (LBL, 1993). The BIPV input FUNCTION commands collects the incident solar radiation on each outside window surface for each hour of the run period, and calculates hourly electric power generation from each BIPV window. The results of the calculated hourly electricity generation are separately saved as an output file.

In order to add the calculation of the BIPV window power generation into the DOE-2.1e calculation algorithm, the BIPV input FUNCTION commands were written in the LOADS section of the input BDL file. This study selected three types of the BIPV transparency: 40%, 20%, and 10%. The electrical performances of the selected BIPV types were obtained from the published data (Episolar, 2015). Table 1 presents the BIPV properties for the electrical performances.

Table 1. Electrical performance properties of the selected BIPVs

BIPV	Transparency (%)	Nominal Power (W)	Voc (V)	Isc (A)	Vmp (V)	Imp (A)	Pin (W)	Fill Factor -	Efficiency (%)
Type I	40	48	116	0.59	87	0.55	720	0.6992	6.65
Type II	20	64	116	0.78	87	0.73	720	0.7019	8.82
Type III	10	72	116	0.88	87	0.82	720	0.6989	9.91

The base-case window had a double-pane unit consisting of two layers of glasses, and the two layers were separated by an air gap. To evaluate the thermal performance of the window glass, three glass properties are required as the simulation input parameters: glass conductance (i.e., U-factor), shading coefficient (SC), and visible transmittance (T_{vis}). These input parameters were estimated using the WINDOW 7.3 program which is a windows and daylighting software developed by Lawrence Berkeley National Laboratory (LBNL) (LBNL, 2015). Using the glass library data in the WINDOW 7.3 program, the thermal and optical properties of the glasses used for the base-case and BIPV windows were determined. Table 2 presents the details of the window input parameter values used for performing DOE-2.1e building energy simulations.

Table 2. Defined window input parameters for simulations

DOE-2 Input Parameters	Base-Case	BIPV			Note
		Type I	TYPE II	Type III	
GLASS-CONDUCTANCE (W/m^{2}K)	2.699	2.603	2.412	2.308	Glass conductance
SHADING-COEF	0.574	0.422	0.253	0.182	Shading coefficient
VIS-TRANS	0.468	0.359	0.183	0.091	Visible transmittance

To implement a daylight-dimming system in simulations, this study used the existing daylighting calculation in DOE-2.1e. One reference point at which daylight illuminance levels were to be calculated was used for each exterior thermal zone (i.e., east, west, south, and north zones); it was assumed that a photocell controls the electric lighting system that responds to the light levels at the specified reference point. In simulations, the desired minimum lighting level (i.e., illuminance set point) was defined as 323 lux (30 fc), assuming a general ambient lighting level for a residential building. The lighting reference point was located at the middle of each space with 0.8 m (2.5 ft) height.

4. Semi-transparent solar cell windows

4.1. Power generation from BIPV windows

The electricity power generated from the BIPV window on each exterior wall was evaluated using the developed BIPV window module. Fig. 3 presents the estimation of the electric power generation from the BIPV Type II windows for different orientations.

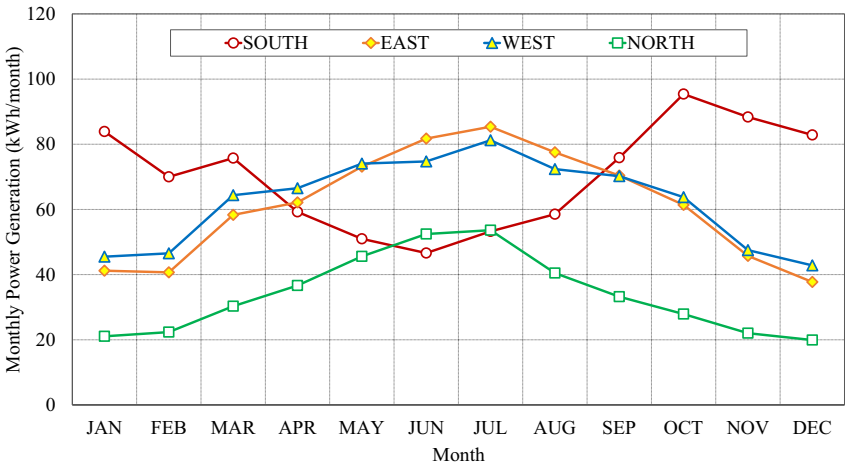

Fig. 3 (a)

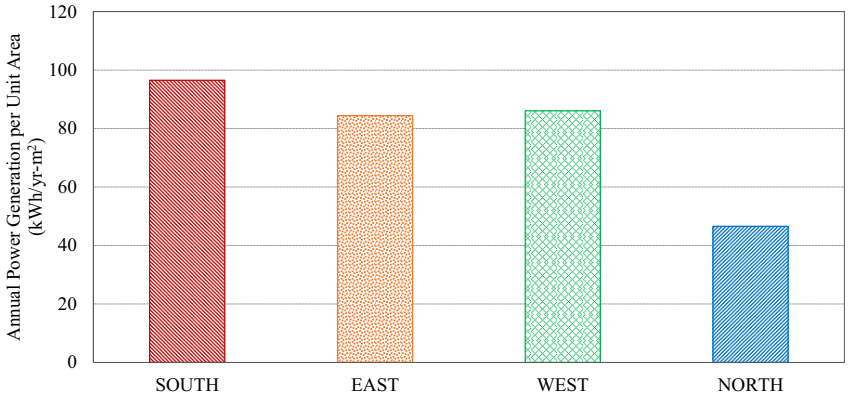

Fig. 3 (b)

Fig. 3: Electric power generation from BIPV II for different orientations: (a) monthly total; and (b) annual average power generation intensity

In general, the largest annual power generation was observed in the south-facing BIPV window whereas the smallest annual power generation was observed in the north-facing BIPV window. The east- and west-facing BIPV windows resulted in the similar amount of power generation. In addition, the east-, west-, and north-facing

BIPV windows generated more power during the summer period (May through August) than the winter period due to larger solar radiation and longer sunshine hours. On the other hand, the south-facing BIPV window generated less power during the summer period (especially in June) than the other periods due to the relation between the sun angle at a given time/location and a 90° exterior wall. That is, the projected area of the south-facing window during the summer period was relatively small to absorb solar radiation.

4.2. Building loads

The simulation results showed that the implementation of the BIPV window provided benefits in the annual building load reductions in comparison with the baseline case. This reductions came from the BIPV thermal performance that decreased shading coefficient in comparison with the base-case window (see Table 2). Fig. 4 presents the estimated distribution of the total annual building loads reduction from the implementation of the BIPV Type II windows in each of the orientations. The largest reductions occurred in the south-facing space; east- and west-facing spaces resulted in the similar annual reductions; and the north-facing space had the least reductions. This indicates that a south-facing space will be the most beneficial space in annual total building loads reduction from a BIPV window at a given location with a hot and humid climate.

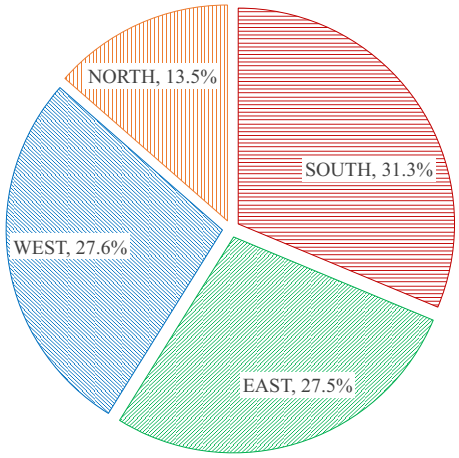

Fig. 4: Distribution of total annual building loads reductions for the implementation of BIPV type II windows according to the orientation

4.3. Cooling peak demands

The simulation results for the peak demands during the cooling season, including energy uses for cooling, lighting, others (i.e., miscellaneous equipment, heating, pumps, fan, and hot water), and for the generated BIPV power for the three BIPV types analyzed are presented below in Fig. 5.

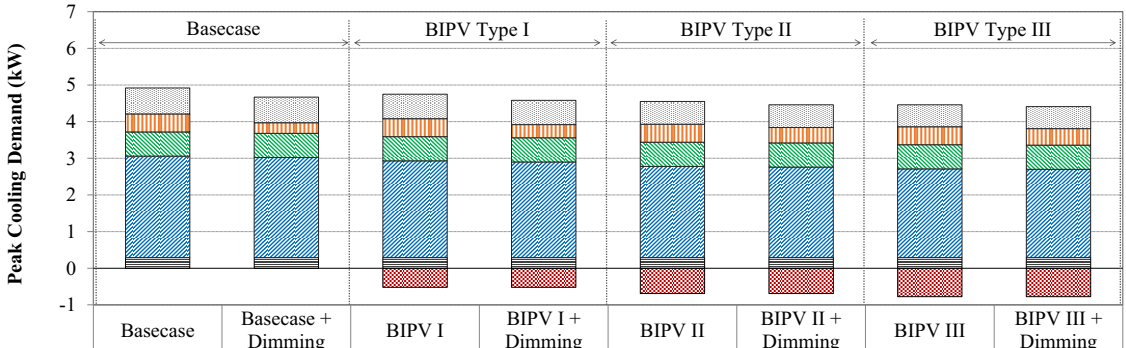

	Basecase	Basecase + Dimming	BIPV I	BIPV I + Dimming	BIPV II	BIPV II + Dimming	BIPV III	BIPV III + Dimming
Total	4.92	4.67	4.23	4.06	3.86	3.77	3.68	3.63
Pumps & Fan	0.71	0.70	0.67	0.66	0.62	0.62	0.60	0.60
Area Lights	0.49	0.29	0.49	0.36	0.49	0.42	0.49	0.45
Misc Equipmt	0.66	0.66	0.66	0.66	0.66	0.66	0.66	0.66
Space Heat	0.00	0.00	0.00	0.00	0.00	0.00	0.00	0.00
Space Cool	2.77	2.73	2.64	2.61	2.49	2.47	2.42	2.41
DHW	0.29	0.29	0.29	0.29	0.29	0.29	0.29	0.29
PV Power	0.00	0.00	-0.52	-0.52	-0.69	-0.69	-0.78	-0.78

Fig. 5: Comparison of peak demands during the cooling season

The BIPV type and daylight-dimming system reduced the peak demands in a range from 14.0% (0.69 kW) to

26.1% (1.29 kW), in comparison with the baseline case. When using a daylight-dimming system integrated with the BIPV window, the savings increased in both the cooling energy and the electrical lighting energy use. In general, the system's peak demands influences the determination of the system capacity, and thus the peak demands reductions indicate that there is a possibility for the cooling system to be downsized, which provides additional energy and cost savings due to lower compressor's power consumption.

4.4. Annual site energy use

As it has been presented above, the implementation of BIPV windows and daylight-dimming system influence the building energy performance: electricity power generation, decrease supplementary lighting, decrease building cooling loads, and decrease cooling peak demands. As a consequence, the BIPV window provided energy benefits in annual energy use of the building system. Fig. 6 presents the resultant annual energy use for the three analyzed window type, including cooling, heating, lighting, others (i.e., miscellaneous equipment, pumps, and hot water), and the BIPV power generation. In addition, Fig. 6 includes percent savings from the BIPV window in comparison with the code-compliant baseline which does not include a daylight-dimming system.

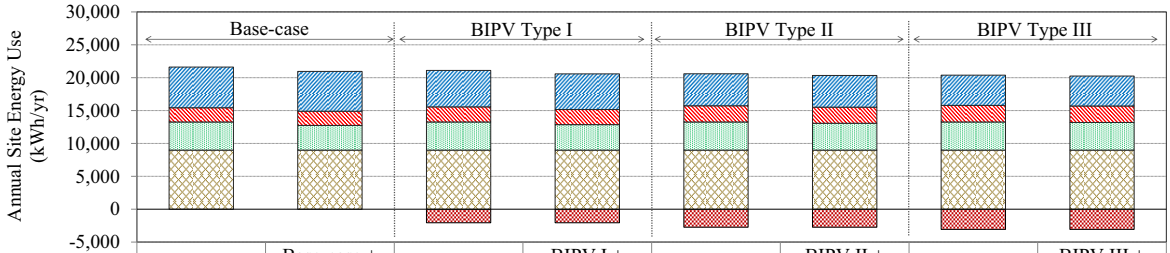

	Base-case	Base-case + Dimming	BIPV I	BIPV I + Dimming	BIPV II	BIPV II + Dimming	BIPV III	BIPV III + Dimming
Total	21,617	20,966	19,046	18,522	17,861	17,615	17,314	17,191
Cooling	6,186	6,060	5,541	5,425	4,862	4,820	4,585	4,550
Heating	2,155	2,157	2,288	2,290	2,454	2,455	2,521	2,522
Area Light	4,279	3,751	4,279	3,869	4,279	4,074	4,279	4,191
Others	8,997	8,997	8,997	8,997	8,997	8,997	8,997	8,997
BIPV Power	0	0	-2,059	-2,059	-2,731	-2,731	-3,069	-3,069

Fig. 6 (a)

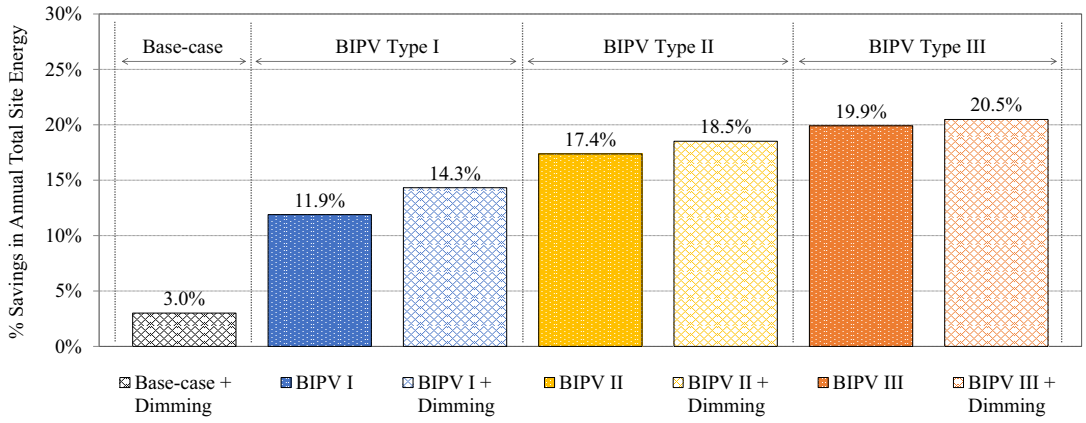

Fig. 6 (b)

Fig. 6: Comparison for annual site energy consumption: (a) annual energy use; and (b) percent savings against the base-case without a daylight-dimming system

The cooling energy use was significantly decreased with in a range from 10% (645 kWh/yr) for the BIPV type I to 26% (1,637 kWh/yr) for the BIPV type III. On the other hand, the heating energy use was increased from 6% (133 kWh/yr) for the BIPV type I to 17% (367 kWh/yr) for the BIPV type III. The increase/decrease amount of the cooling/heating energy use appeared to be caused by the BIPV window shading coefficient values (see Table 2); a low SHGC value led to a decrease in cooling energy use and an increase in heating energy use. In the simulations for a daylight-dimming system, the transparency value of the BIPV glazing appeared to influence on the electric lighting energy use; a higher transparency value resulted in bigger reduction in electric lighting energy use. Regarding the electric power generation, the higher electric power was generated from the BIPV type III because of the different BIPV's efficiency values (see Table 1).

In the calculation of the percent savings for the annual total site energy use, the generated electric power compensated the system's electricity consumption. The amount of the percent savings resulted from the BIPV window and a daylight-dimming system ranged from 11.9 to 20.5%. The BIPV type III resulted in the largest savings for the annual total site energy due to the significant cooling energy reduction and power generation. However, the daylight-dimming system using for the BIPV type III did not result in noticeable energy savings due to low transparency value. A cost analysis to evaluate economic benefits may be required to determine the optimal energy savings goals when using a daylight-dimming system for a BIPV window.

5. Summary and conclusions

To quantify the energy benefits of the BIPV window in hot and humid climates, a typical residential building was simulated in DOE-2.1e. A BIPV window module was developed for DOE 2.1e and implemented it into the 2009 IECC code-compliant residential building model. Based on the energy simulation results, potential energy benefits from utilization of the BIPV system were realized including: power generation, annual building loads, cooling peak demands, and annual total site energy use. Based on the analysis results completed in this study, the following conclusions can be made:

- The electric power generated from the BIPV window depends on its efficiency value, area, orientation, and incident solar radiation. The south-facing windows can produce the largest annual electricity, but the east- and west-facing windows present the highest potential to generate electricity during the summer period.
- Implementation of the BIPV window resulted in a reduction in the total annual building loads, ranged from 6 to 15%. In addition, the south-facing space was identified as the most beneficial space in reducing annual building loads. However, it should be noted that the BIPV power generation from the south-facing window was also reduced during the summer period when higher electricity power was consumed than the other periods. Therefore, the further study is required to optimize building loads reduction and BIPV power generation.
- The BIPV window and daylight-dimming system led to reductions in the peak cooling demands, from 14 to 26%. At the cooling peak day and time, the BIPV window significantly reduced the cooling energy use, and a daylight-dimming system resulted in additional savings in electrical lighting energy use. Therefore, the BIPV window has a potential to downsize the system due to the reduced peak demands; and it may result in additional energy savings due to lower compressor's power consumption.
- The BIPV windows provided electricity power generation, decreased electric lighting energy use, decreased annual building loads, and reduced he system's cooling peak demand. As a consequence, the percent savings in comparison with the base-case window were about 12 to 21%. This indicates that the BIPV window with the daylight-dimming system provide great energy benefits for a code-compliant residential building. However, a cost analysis to evaluate economic benefits may be required to determine the optimal energy savings goals when using a daylight-dimming system for a BIPV window.

References

bccResearch, 2011. Building-Integrated Photovoltaics (BIPV): Technologies and Global Markets. BCC Research. EGY072A, Wellesley, Massachusetts.

Chae, Y.T., Kim, J., Park, H., Shin, B., 2014. Building energy performance evaluation of building integrated photovoltaic (BIPV) window with semi-transparent solar cells. Applied Energy 129, 217-227.

Corrao, R., Morini, M., 2012. Integration of dye-sensitized solar cells with glassblock. Czasopismo Techniczne. Budownictwo 109 (2-B), 55-64.

Do, S.L., Haberl, J., 2015. Development procedure of an air-source heat pump base-case simulation model for a code-compliant residential building. Energy and Buildings 107, 11-25.

DOE2, 2015. DOE-2 Building Energy Use and Cost Analysis Tool: DOE-2.1e James J. Hirsch (JJH), DOE-2.com. Available from http://doe2.com/DOE2/index.html#doe21e

DOE, 2015a. Building Energy Codes Program, Texas. U.S. Department of Energy (DOE). Retrieved July 2, 2015, from https://www.energycodes.gov/adoption/states/texas

DOE, 2015b. Photovoltaics Research and Development. U.S. Department of Energy (DOE). Retrieved May 5, 2015, from http://energy.gov/eere/sunshot/photovoltaics-research-and-development

DOE, 2015c. Status of State Energy Code Adoption. U.S. Department of Energy (DOE). Retrieved July 2, 2015, from https://www.energycodes.gov/status-state-energy-code-adoption

Duffie, J.A., Beckman, W.A., 2013. Solar Engineering of Thermal Processes, fourth ed. John Wiley & Sons, Inc., Hoboken, New Jersey.

EIA, 2015. Texas State Energy Profile. U.S. Energy Information Administration (EIA). Retrieved May 5, 2015, from http://www.eia.gov/state/print.cfm?sid=TX

Episolar, 2015. Semi-Transparent Panels. Epicolar,Inc. Retrieved May 18, 2015, from http://www.episolar.us/#transparent

Haberl, J., Baltazar, J.C., Yazdani, B., Claridge, D., Do, S.L., Oh, S., 2014. Statewide Air Emissions Calculations from Wind and Other Renewables. Energy Systems Laboratory, Texas A&M Engineering Experiment Station. ESL-TR-14-07-01, College Station, Texas.

Haberl, J., Baltazar, J.C., Yazdani, B., Claridge, D., Oh, S., Mao, C., 2015. Statewide Air Emissions Calculations from Wind and Other Renewables. Energy Systems Laboratory, Texas A&M Engineering Experiment Station. ESL-TR-15-07-01, College Station, Texas.

ICC. 2009. 2009 International Energy Conservation Code (IECC). International Code Council (ICC), Inc., Falls Church, Virginia.

Kang, J.G., Kim, J.H., Kim, J.T., 2013. Performance evaluation of DSC windows for buildings. International Journal of Photoenergy 2013.

LBL, 1993. DOE-2 Supplement: Version 2.1E. Lawrence Berkeley Laboratory (LBL) and James J. Hirsch and Associates. LBL-34947, Berkeley, California.

LBNL, 2015. LBNL Windows & Daylighting Software: WINDOW Version 7.3. Lawrence Berkeley National Laboratory (LBNL). Available from http://windows.lbl.gov/software/window/window.html

Lee, J.W., Park, J., Jung, H.-J., 2014. A feasibility study on a building's window system based on dye-sensitized solar cells. Energy and Buildings 81, 38-47.

Li, D.H., Lam, T.N., Chan, W.W., Mak, A.H., 2009. Energy and cost analysis of semi-transparent photovoltaic in office buildings. Applied Energy 86 (5), 722-729.

Miyazaki, T., Akisawa, A., Kashiwagi, T., 2005. Energy savings of office buildings by the use of semi-transparent solar cells for windows. Renewable Energy 30 (3), 281-304.

NREL, 2015. The Open PV Project. National Renewable Energy Laboratory (NREL). Retrieved July 1, 2015, from https://openpv.nrel.gov/

SECO, 2015. Texas Building Energy Code, Single-Family Construction. State Energy Conservation Office (SECO). Retrieved July 2 2015, from http://seco.cpa.state.tx.us/tbec/singlefam.php

Servaites, J.D., Ratner, M.A., Marks, T.J., 2009. Practical efficiency limits in organic photovoltaic cells: Functional dependence of fill factor and external quantum efficiency. Applied Physics Letters 95 (16), 163302.

Sivanandan, A., 2009. BIPV Hotspots in the EU. Renewable Energy Focus. Retrieved May 4, 2015, from http://www.renewableenergyfocus.com/view/1708/bipv-hotspots-in-the-eu/

SNE, 2011. DSSC Technology Trend and Market Forecast (2008~2015). Solar & Energy Co., Ltd., Gyeonggi-do, South Korea.

Sze, S.M., Ng, K.K., 2006. Physics of Semiconductor Devices. John Wiley & Sons, Inc., Hoboken, New Jersey.

Yoon, S., Tak, S., Kim, J., Jun, Y., Kang, K., Park, J., 2011. Application of transparent dye-sensitized solar cells to building integrated photovoltaic systems. Building and Environment 46 (10), 1899-1904.

Conference Proceedings

Solar World Congress 2015

Daegu, Korea, 08 – 12 November 2015

Solar Constraints and Potential in Urban Residential Buildings

Chul Kim[1], Liliana Beltran[1]

[1] Texas A&M University, College Station (USA)

Abstract

Today, Asian cities have been full of high-rise and compact buildings with large population. In Seoul, Korean capital city where millions of people have lived, over 20 or 30 floors residential buildings are common sight. As a result, half of the Korean population is living in high-rise residential buildings like apartments. However, large residential buildings in cities have consumed huge energy provided from fossil fuels to support occupants' environmental convenience, and they are currently a major energy-consuming sector. To resolve this environmental and energy issues, solar systems are promising one of effective solutions to supplement energy demand for urban residential buildings. Therefore as fundamental approach this paper studies solar potential and constraints in high-rise residential buildings to understand unfavorable urban environment for solar energy based on diverse interferences from other urban factors. To maximize solar potential and to utilize effective renewable systems on the surface of buildings, this study analyses Korean typical multi-family housing buildings and also includes a case study to deal with an apartment complex to figure out the effective ways for solar energy. This result can be expected to be utilized for architects and engineers in their design process to plan low energy buildings.

Keywords: *Solar potential, High-rise buildings, Solar constraints, Building forms and arrangement*

1. Introduction

1.1. Backgrounds

Buildings, as a major energy consuming sector in the world, accounted for 21.2percent of total final energy consumption, consisting of 9.3percent and 13percent in commercial building and residential building respectively (Korean Energy Census, 2010). Building sector's share is still lower than transportation and industry sectors, but it will be expected to increase like other developed countries reported by IEA. They reported their residential buildings have averagely consumed about 27percent of total final energy consumption. In Korea, the Photovoltaic (PV) and Solar thermal (ST) market is consistently growing by government promotion projects since 2008, due to their green growth policy. Firstly, Korea Energy Management Corporation (KEMC), a public institution, has operated supply business projects for renewable energy systems such as PV and ST with financial packages. The budget are totally about 20 million won in 2015, and they have pursued green-village project that provides financial aid for owners to receive 35~50percent per total installation cost. However, unlike governmental support, major eight metropolitan cities in Korea just showed 8.3percent of renewable power production by region, and of that, the power portion by residential buildings is only 0.4percent in 2013 (Renewable Energy Dissemination of Statistics, 2013). Consequently, in Korea, to encourage solar system use is important strategy to improve energy efficiency of urban buildings. However, in the respect of building shape and arrangement, Korean high-rise residential buildings are unique and standardized unlike other countries' residential buildings. In a census on population and housing conducted Korean National Statistical Office (KNSO) in 2010, they also found that multi-family housing continuously has shown a growth from 53percent in 2005 to 59percent in 2010. Above all, over 75percent of total multi-family housing buildings is over ten stories buildings. Given this context, half of Korean today is closely connected to the life in high-rise residential buildings consuming lots of

Selection and/or peer review under responsibility of Scientific Committee
doi:10.18086/swc.2015.08.03 Available at http://proceedings.ises.org

energy to stay their urban life. Therefore, to make environmentally-friendly urban space, successful energy efficient strategies for urban residential buildings are required such as renewable systems.
Also, in today's global society, many countries are worrying energy matters that fossil fuels will definitely be depleted in near future even though fossil fuels are still necessary in all fields of industries and public livelihood. According to a new UN Department of Economic and Social Affairs (DESA) report in 2015, the world population will reach 9.6 billions people until 2050 (UN database, 2015) and International Energy Outlook 2013 by IEA reported that world energy consumption will increase 56percent from 2010 to 2040 by world economic growth and specially, electric power demand will grow by 80percent between 2012 and 2040 (IEO 2013). Hence, as mass energy consuming sectors, future buildings should be considered to increased energy consumption by growing economy. For that, it is required to achieve better design and energy efficiency in all kinds of manufacturing industries and in all kinds of buildings. As the result of this movement for energy saving, many world nations are planning to go into effect on mandatory building codes to design low and zero energy buildings and to renovate existing buildings into high performance buildings. Along many European countries' plan which will reach zero energy building (ZEB) between 2015 and 2030, Korean government has also driven the policy to phase in ZEB as mandatory policy from 2008 to 2025. This means that many multi-family housing, so called apartments in Korea, will have to consider renewable energy systems to satisfy mandatory zero-energy efficiency because only plan for passive design and efficient HVAC systems cannot guarantee ZEB performance on site. Therefore, in order to maximize building energy performance and to design better green buildings in urban area, urban solar constraints and potential should be properly understood and settled by designers and engineers. For this, this research studies urban solar potential based on high-rise residential buildings in Korea and, depending on the features of their typical forms and arrangement, the study can be generalized and utilized for whole country.

1.2. Objective of the study

The research goal is to study solar potential in urban areas and to focus on high-rise multi-family buildings which have been very dominating in Korean housing market. The study has three major purposes; At first, multi-family housing in Korea has shown standardized forms and arrangements. This is due to the fact that forms of multi-family housing have been affected by governmental institutes and contractors for decades and sometimes, their principles for building arrangement have been guided by District Unit Planning by regional governments. As a result, multi-family housing complex have shaped the urban context in Korean cities. While they are not particularly good in urban scape design, it can be useful to generalize and to establish dissemination strategy for renewable energy. On the second purpose of this study, in architectural viewpoint, solar potential on building envelope can be easily affected by building physical features such as mass projection and curved mass design. Besides, in large multi-family housing complex, solar potential may be strongly influenced by adjacent building structures. Last but not least, the development in very densely urban areas usually requires high energy efficiency and performance following their enhanced building energy codes and for that, renewable systems should be optimized and effectively planned in the buildings. Given this, this study will be meaningful in the importance for practical experts. Therefore, this study investigates Korean high-rise residential buildings focusing on their forms and arrangement, and diagnoses solar potential in single building level. And then, the study analyses solar potential through case study of urban residential complex. By means of the result of this research, architects, engineers and building owners can more understand solar potential and effectively design green buildings reflected urban solar strategies.

1.3. Research process

This study analyses solar potential on residential building envelope and roof where can be used for PV and ST. In single building and urban scale, this study looks at urban solar limitations and solutions. This research is composed of three-step procedure:

(a) The first step is to do literature review on solar potential. Solar potential is usually used to explain a term for solar applicability or solar radiation that is calculated by a ratio of area on the building envelope. This paper deals with some research and their result of solar potential studied by other authors.

(b) On the second step, the research is to study solar potential and constraints in single building types. For this, this study looks into main residential types in Korea and simulates their solar performance by doing simulation tools. With this analysis, solar limitations and solutions are drawn.

(c) At the last step, case study in the single building complex is carried out to estimate actual solar potential on the building surface. Then, analyzing high-rise multi-family complex is done because this can explain how building direction and arrangement in the complex can affect solar potential in urban context. As the final outcome, solar potential and constraints are analyzed to draw solutions.

2. Literature review

Housing market in Korea has greatly changed for last several decades in their types and forms. In 1975, detached house occupied over 92 percent of total housing by total ground area. However, multi-family housing [1] and row house[2] had explosively grown over 10 times from 6 percent to 63 percent in total residential stock (Housing Census, 2010). Actually, plenty of new cities had been constructed since 1980s with multi-family housing buildings and consequently, housing supply ratio recorded from 86 percent in 1995 to 118 percent in 2014 in housing census by KNSO. In 2013, over 71 percent of existing multi-family housing has over 15th stories, which means most of multi-family housing is high-rise buildings (Apartment Housing Statistics, 2013). Therefore this study regarding solar potential in Korean high-rise residential buildings can have powerful influence for many apartments to become better energy efficient.

There are many ways to optimize building solar potential in preceding research. Many studies have already showed possible approaches to improve solar access on the surface, but still have a distance to explain urban solar limitations in residential buildings. Because residential building types in Korea are different from other countries in their residential types, density and patterns. Also, research in Korea mainly focused on the right of solar access (Changho Choi, 2007, Dosung choi 2009). Building's major design parameters (i.e. building aspect ratio, azimuth, site coverage, density and arrangement) are generally considered to assess solar potential in urban area because these are largely able to affect solar potential on the envelope of buildings. According to a study by Dapeng Li et al (2015), the research reported solar potential in urban residential buildings that can be raised when building aspect ratio increases, and thus they studied increased site coverage. Also, this study revealed that photovoltaic(PV) and solar thermal(ST) yield decreased up to 50% and 26% respectively by mutual shade in high-density scenario. However, it explained solar systems to be able to satisfy yearly electrical and thermal demands of residential buildings. Min-Hee Lee et al (2009) conducted a feasibility study to review business value on solar systems and assessed solar potential depended on urban structure. For applicability to urban buildings, the research describes that roughness affects solar potential. Such result is especially remarkable in high-rise and high-density buildings. Similarly, while high-rise buildings has lower solar potential than low-rise buildings, it is possible that solar systems harvest stable solar energy since probable areas for solar system installation are generally converged to particular upper floors in special buildings. However, M. Karteris et al (2013) reported that PVs in the urban environment may not be efficient than suppositions. This is due to the fact that urban obstacles, such as density, heights and shafts, often significantly lower valid surface areas above 50% on the roofs. This research reviewed the actual solar potential as developing a model for roof-top surfaces through a statistical analysis by using existing multifamily buildings in a general Greek city, Thessaloniki. Like above studies, at present, availability and limitation on urban solar potential are still in progress. On account of specificity in location, design and analytic condition, more research to be generalized and exploited should be studied for more solar energy use in Korean urban areas.

[1] The definition of apartment is an over 5floors permanent building to include many households, and each household can independently live in their apartment. (KNSO, www.kostat.go.kr)

[2] Row house is a permitted building as a row house by law and its height is limited below 4 floors. Also, several households can live in row houses. (KNSO)

3. Single building analysis

3.1. Korean multi-family housing

In 2007, Ministry of Land, Transport and Maritime Affairs in Korea reported that residential buildings took up the largest portion in national cities and were occupying 68percent of all building stock. Among all cities, Seoul and Kyunggi-do have formed the largest metropolitan area where 43percent of Korean population has lived and the greatest number of residential buildings have been built. However, regardless locations, Korean multi-family apartment have typical patterns in their forms. Doosung Choi and Jinseok Do (2009)[1] surveyed 74 multi-family housing complex and 919 multi-family housing buildings built after 2007 to classify multi-family housing category. Consequently, it informed that flat-type and tower-type occupied 57percent and 43percent respectively among investigated building types. Building size depends on the number of units and it can be changed following building conditions. Classified single building types of multi-family housing are as below table.1. Types of multi-family housing have significance on analysis of solar potential because their building forms restrict surface areas that can get solar energy and be installed for renewable energy. Hence, as first step this research studied solar performance in single buildings.

Tab. 1: Dominative Multi-family Housing Types in Korea (Doosung Choi 2009)

Flat-type			Tower-type		
— type	Bending-type	L-type	L-type	Y-type	Single-wing type
68.1%	17.6%	14.3	30.9%	22.1%	21.5%

3.2. Solar potential analysis

The aims to solar potential in this study are to understand cause and effect of urban solar limitations in the scale of single building and urban complex. In general, the forms and envelope designs of multi-family housing are primary factors to affect solar potential on the building surface. Severe building shade can also reduce solar potential on the surface by adjacent buildings that usually causes shading through its high density or mass projection. Moreover, Korean residential building has an unique character that it relatively has broad surface area per volume to get more solar radiation due to general Korean resident's preference of sunshine. However, in the analysis of an independent building, there is no interference from adjacent urban environment and buildings. This being so, there is no solar influence caused by density or height that these factors can be possible in complex level. Therefore, assessment in building types focuses on the amount of solar radiation, orientation, seasonal changes and restrictions by building design.

Tab. 2: Multi-Family Residential Buildings for Single Building Analysis

	Flat-type			Tower-type		
	— type	Bending-type	L-type	L-type	Y-type	Single-wing type
Floor plan	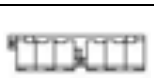	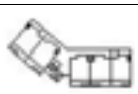			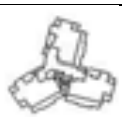	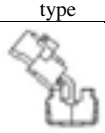
Units	6	5	4	3	3	4
Floor height (m)	2.8	2.8	2.8	2.8	2.8	2.8
Area (㎡)	571	404	827	569	523	694
Tilt (deg. E/W/S/N)*	90/90/0/0	90/50/0/0	90/90/0/0	90/90/0/0	76/120/166/76	90/141/0/51

* Horizon is 0 degree and counterclockwise rotation

For this, building height are decided to 16 stories that is one of standards to define Korean tower types, and also in single building analysis, building height don't affect building solar radiation and changes. This study simulated single buildings by utilizing IES-VE Apache and Sun-cast that can have ability to review solar radiation and building shade through their modules to estimate quantitative performance on the envelope.

[1] Doosung Choi (2009) defined a term of tower-type that ratio between long and short sides doesn't exceed 4:1 and by using one elevator and stairs, people can directly enter into their apartment units, and it is 16 and more stories with reference to Article 29.3.1 in Seoul Architecture Regulation. Also, Euntae Park (2007) gave tower-type a definition that ratio between long and short sides is under 4:1 on the authority of Article 86 for solar access right in the Building Code.

Building location is set on Seoul and Seoul weather data is extracted from ASHRAE design weather database v5.0, and the location is latitude 37.57N°, longitude 126.97E°, Altitude 86m and standard meridian 135.0E. Analysis duration is from January 1st to December 31th and their daylighting hours are based on monthly solar altitudes in Seoul calculated by VE-SunCast.

(1) Solar potential

In general, building forms in solar access, significantly affect solar gain and building shading to itself. Solar potential in each building type considered in aspect of annual average value, directional and seasonal effect to solar radiation. The longest, max and min solar gain sides on each direction side are reviewed of solar potential because diverse and tilted sides on the same direction show different solar potential due to different azimuth and projection by building designs. As a result of simulation analysis, solar radiation on the roof is the same as 105.2 W/㎡ hr because building roof has no shading by building itself. According to types, Flat-types basically have an advantage that long sides are commonly arranged to face south and can thus get more solar radiation in the amount of total solar potential. Hence, if Flat ㅡ type can face south, its most units can have an optimal direction for solar access. Values of simulation reported that annual solar radiation on long sides in typical floor by directions is that east, west, south and north are sequentially 65.2, 61.3, 81.8, 39.8 W/㎡ hr. Although Flat bending-type has partial refraction on the building mass, generally it can be exposed to originally arranged, because even though a bending side takes different azimuth, bending angle is less than 45 degree. Its each directional solar potential represents that east, west, south and north are 62.3, 49.6, 81.7, 39.3 W/㎡ hr in a row. Flat L-type has a form that its mass is perpendicular crossing which makes two continuing sides have completely dissimilar directions when they receive solar energy. At the same time, two perpendicular inner sides are relatively weak to gain solar energy due to be shaded by building mass itself. Its directional solar potential is 65.3, 62.0, 78.3, 39.9 W/㎡ hr in a row from east to west south and north. According to solar radiation data in passive design guideline (PCAP, 2012), average solar radiation* by directions in Seoul is that east, west, south and north on the vertical side are 65.9, 88.4, 96.5, 19.9 W/㎡ hr. Comparing solar potential to average solar radiation by building types in Seoul, there are some different ranges; on the east side, 94.5~99.0%, on the south side, 81.1~84.7%, on the west side, 56.1~70.2%, on the north side, 197.5~200.3%. Some values under average show that each type can have a weak-point on less solar potential sides. For example, Flat-bending is vulnerable to west and south sides.

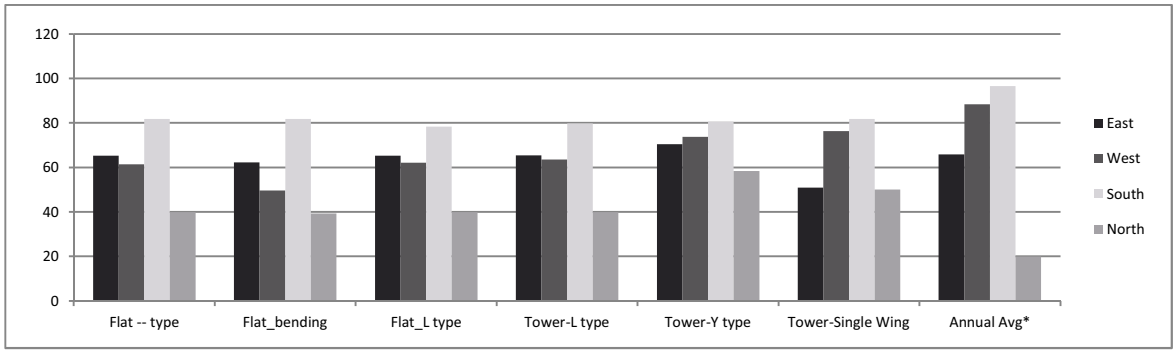

Fig. 1 Annual solar potential on the external walls (unit : W/㎡ hr)

Also, solar potential on long side by Tower L-type is that east, west, south and north are 64.5, 63.6, 79.8, 39.9 W/㎡ hr in a row, and solar potential in Tower Y-type is also 70.4, 73.7, 80.6 and 58.4 W/㎡ hr. Tower single-wing-type is 50.9, 76.4, 81.7 and 50.0 W/㎡ hr. On comparing these data to Seoul's average solar radiation, east side has 77.2~106.8% difference, west, south and north separately show 71.9~86.4%, 82.7~84.7% and 200.3~293.3% difference in solar radiation on the surface. One of causes is azimuth difference at each side on the building envelope and building itself shades its surfaces due to its roughness and projected mass, such as Tower single-wing type is delicate on east side. Actually, while optimal orientation in Seoul is east-south or south (135~210 degree), Tower types are comparatively exposed to unfavorable directions since their building forms preferentially decide their orientations before their building

arrangement. Consequently, even if all buildings face to the same direction on their placement, surface azimuth and area size on each side can be different owing to their types and forms have large effects on the amount of solar gain.

(2) Seasonal changes

On the other side, seasonal changes in Korea make considerable influence on solar potential by altering solar altitude, azimuth and daytime hours. Seoul's solar altitude is that spring and fall equinox are 52.4°, summer solstice is 75.9°, and winter solstice is 28.9° depended on Latitude 37° 34′. According to seasonal changes in Fig.2, east and north sides get the annual highest solar radiation on summer solstice and fall equinox. West pattern is similar with south in aspect that it takes large solar radiation on fall equinox. Besides, single building types and seasonal changes have a little correlation on their solar gain per the unit area even though they have azimuth difference on external surface. Hence, in respect of seasonal changes, influence on solar potential by single building types is insignificant.

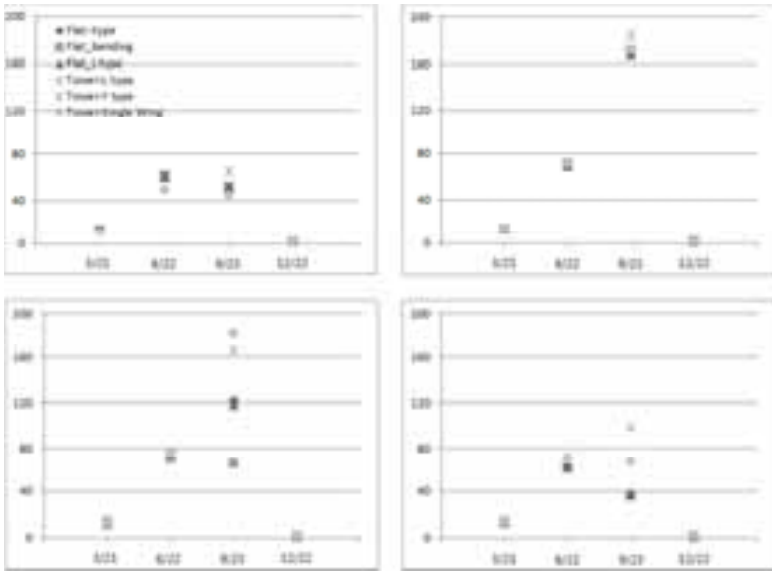

Fig. 2 Seasonal solar radiation on the external walls
(L-top: east, L-down: west, R-top: south, R-down: north, unit : W/m² hr)

Tab. 3: Building Mass Information

		Flat-type			Tower-type		
		— type	Bending-type	L-type	L-type	Y-type	Single-wing type
POP (%)		67	69	49	66	63	63
L/W *		4.12	1.87	1.47	0.95	1.10	0.91
Tilt (Max/ Min deg.)	E	90**	90/142	90/90	90/90	76/76	51/90
	W	90/90	142/50	90/90	90/90	120/120	141/90
	S	0/0	0/172	0/0	0/0	166/166	0/0
	N	0	142/0	0/0	0/0	76/165	51/0
Weak point	Sum-mer	 22 Jun 17:00	 22 Jun 16:00	 22 Jun 16:00	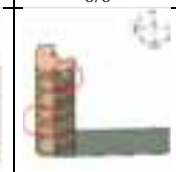 22 Jun 16:00	 22 Jun 10:00	 22 Jun 12:00
	Win -ter	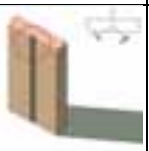 22 Dec 17:00	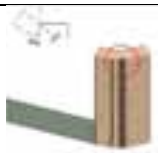 22 Dec 09:00	 22 Dec 11:00	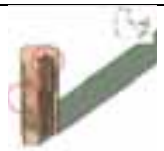 22 Dec 09:00	 22 Dec 12:00	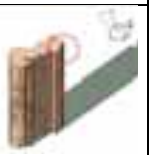 22 Dec 09:00

* Length/Width (L/W) ratio on a typical plan, ** Existing only one side on a particular direction

(3) Building constraints

So far, this study analysed directional and seasonal solar potential by single building types of multi-family housing. On the independent building level, solar limitations are as the following; 1) building itself shade, 2) solar potential changes on surface affected by seasonal changes on solar azimuth and altitude. On account of seasonal solar changes are natural, solar potential and limitations by building forms are studied in this part. Generally, building shape, which is able to alter building exposure to external environment, is reviewed in the design stage to reduce energy consumption and to increase energy efficiency. On the design planning, to examine building mass, some indicators such as Surface/Volume (S/V) ratio, Length/Width (L/W) ratio and POP ratio can be used. Therefore, to find limitations in the independent building level, building types are diagnosed through such indicators. Table 3 demonstrates POP and L/W in case building types. Applied POP equation is like this;

$$POP = 2\frac{\sqrt{\pi \times A_b}}{P_b} \times 100(\%) \qquad \text{(eq.1)}$$

In the equation from Passive Design Guideline (2012), A_b = building area, P_b = perimeter length. High POP building commonly has a benefit in building heat gain or loss, whereas low POP ratio building has a weak-point in building heat gain or loss. This is because low POP ratio indicates that the building has relatively lots of protruded parts on its envelope, and if its weak-point is not revised on building arrangement, self-shade can largely reduce solar potential. Among building types, Flat L-type has the lowest POP value and other buildings are almost alike. In the table.3, weak point of Flat L-type shows a probable problem in low POP ratio buildings. To improve solar potential, low POP ratio building should consider dented parts on the surface and have an optimal placement to avoid perpetual shade. L/W ratio is also normally optimized on 1.5:1 which can affect annual heating and cooling loads by changing heat gain area by solar radiation and shaded heat loss area. Flat-types have L/W ratio that is almost 1:5 or more. However, Tower-types take around 1:0 in L/W ratio, which means that they have a weak spot on the surface by their shapes. Given this, preferably, wider building surface on Tower types should be more exposed to optimal direction to have better solar potential and reduce building loads.

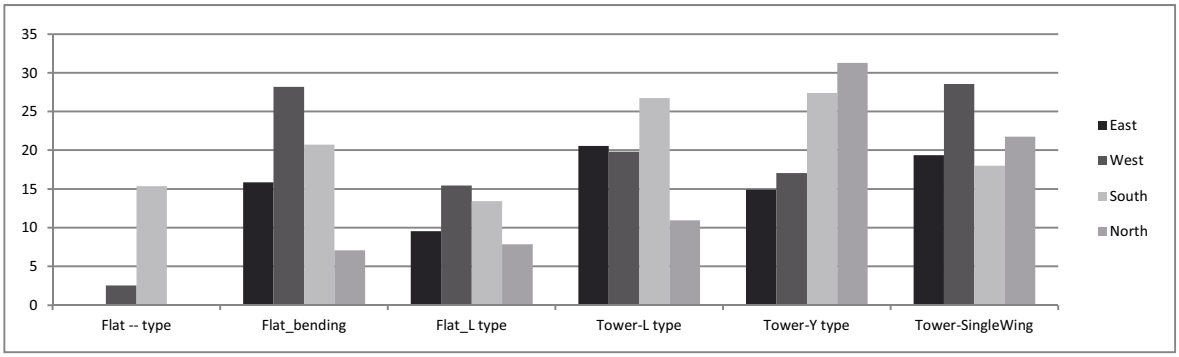

Fig. 3 Solar potential difference between max and min values on the same orientation (unit : W/㎡ hr)

Single buildings' self-shade presents another limitation. It makes solar potential difference and degradation on the same direction. Fig.3 reports how much self-shade by mass projection aggravates solar potential. Flat –type and Flat bending-type are almost even in their forms because it is merely 18 degree different on mass bending. On the contrary, in solar radiation on the same orientation, the bending makes large solar performance difference between the max and min values. Furthermore, Tower types reveal larger dynamic dispersion range than Flat types, which indicates Tower types in urban area are disadvantageous on solar potential and inevitable to have lower solar availability due to their structural problems. Accordingly, in order to solve these limitations in urban space, simplification on sun-exposed envelope and optimal arrangement to direction should be far outweighed.

4. Residential complex analysis

4.1. Arrangement of residential complex

Building arrangement methods have been developed following national building codes and the demands of social trends. Primary features of arrangement as follows: Since 1941, practice in fields of construction and design dominated by governmental institutes and construction contractors has generally used typical building drawings, which have affected current residential complex forms and urban context (Booseong Kang et al., 1999). After 1998, residential complex planning in Korea has a new trend that is remarkable changes of building forms. Some residential complex is consisted by only tower-type buildings, but most complexes of them have combination of flat-type and tower-type buildings. Also, the frequency of residential complex applied by diagonal line was increasing. The background of this is the result of chronological changes by preference of diversity, views and direction of urban scape planning. Moreover, wall area in flat-type-dominant residential complex is mainly larger than that in tower-type-dominant residential complex (Byeongho Lee et al., 2010). Also, all Korean residential buildings should meet governmental standard for solar access right in accordance with the provision of Article 53 in the National Building Code and Article 86 of the its Enforcement Ordinance. Thus every building that faces other buildings has to have 0.8 times distance between buildings based on due south (Yoonbok Seong et al., 2004). In this context, the solar limitation of case residential complex can have direct implication to improve solar potential in residential complex planning.

Tab. 4: Residential Complex (47BL) Information

Project : 47BL Dontan-2 District, Hwasung
Type : National sales and rental housing
Location : the whole region around Seoku-dong, Bansong-dong and Dongtan-myeon, Hwaseong-si, Gyeonggi-do located to 40km South from Seoul
Lot area (㎡) : 56,353
Floor area ratio (%) : 180 or less
Units : 930 households
Number of stories : 9F~23F
Building types : total 12 buildings (Flat – type, Flat-bending-type, Flat-L-type, Tower single-wing-type)

4.2. Solar performance

(1) Case information

This case study is to analyze solar performance of a residential complex in order to figure out the influence of building shade on the solar potential. The case complex is a design planning of a prize winner in 47 Block in Dongtan-2 District, Hwasung and it is currently under construction following this design. Above all, this project is a governmental project to distribute affordable houses to general people and the number of unit is around 930 households. Building size is diverse from 9 floors to 23 floors and east-southern located buildings are comparatively lower than west-northern located buildings due to satisfy a solar access code and get more sun shine that is preferred by many Koreans. IES-VE Apache and Sun-cast modules are used to analyze changes of solar potential and building shade on building surface. Weather data is Suwon, a neighboring city nearby Hwasung, of ASHRAE design weather database v5.0.

(2) Solar potential analysis

On the result of analysis, due to adjacent building's shades, gradation of solar potential is very different in vertical building surface. Solar potential on the surface in 20F is maximum value reflected by little influence of other buildings, and solar potential difference from 1F to 20F is the extent of building intervention that worsen urban solar potential and mainly become one of urban limitations for renewable use. In the table 5, the middle part located buildings in residential complex (702, 712) are Flat-bending-type (701) and Flat – type (712) that their forms are generally favorable performance to get solar energy than tower-types. However, in this complex, they are easily exposed by surrounding buildings which deteriorate solar potential on their different vertical stories, especially difference between 1F and 20F is obvious. For example, in 701 building, east side-solar potential shows about 3 times gap between 1F and 20F and if there is no interference

from other buildings, solar potential in each story by floor is the same as already confirmed in chapter 3. This means that in urban area, neighboring buildings can cause severe influence on solar potential and give rise to lower solar potential for use of renewable system.

On the east part in the complex, buildings (702, 710, 711) are Flat-bending-type (702, 710) and Flat-L-type (711) buildings. They represent that these buildings obtain almost same solar potential regardless their different stories and it signifies that the effect of adjacent buildings is small because the buildings are exposed to open space on the east side and there are only a few buildings along solar path. On the south side, buildings (708, 709) are Flat-L-type (708) and Tower single-wing-type (709). 708 building has a pattern that regardless of their floors, they show good efficiency due to open space in front of the buildings. Whereas east side of 709 building is influenced by 710 Buildings and its 1F solar potential is nearly one-third of 20F. On the west side are Flat-L-type (706, 707). Their solar potential gap by height is from 8.5 to 24.9 W/㎡ hr. Buildings located on the north are Flat – type (703) and Flat-L-type (704, 705). Their solar potential gap by height is from 0 to 25.1 W/㎡ hr. Also, comparing differences on the 1st floor, east, south, west and north side gap (max-min) are 48.8 W/㎡ hr, 26.2 W/㎡ hr, 52.1 W/㎡ hr and 14.2 W/㎡ hr respectively. East and west sides are relatively heavily affected by neighboring buildings. Therefore, in order to improve urban solar potential, the number of building in the middle part of complex should be relatively reduced or secure long distance from adjacent east and south buildings to make better solar potential.

Tab. 5 Solar Potential by Height and Direction (Unit: W/㎡ hr)

Bldg No.	EAST			SOUTH			WEST			NORTH			Note
	1F	10F	20F	1F	10F	20F	1F	10F	20F	1F	10F	20F	
701	28.4	72.1	78.7*	56.4	67.3	75.5*	56.4	67.3	75.5*	29.0	34.9	40.6*	*19F Value
702	74.8	75.0*	N/V	68.6	75.5*	N/V	24.8	34.7*	N/V	39.2*	40.8	N/V	*9F Value
703	68.9	69.9	N/V	61.7	74.4	N/V	34.0	37.9	N/V	35.9	36.1	N/V	
704	53.6	64.4	78.7	53.6	64.4	78.7	34.3	37.1	45.1	34.3	37.1	34.3	
705	52.0	58.6	73.9	63.0	62.2	76.2	63.0	69.2	76.2	26.9	45.9	32.0	
706	53.6	65.1	77.3	61.8	67.6	75.5	61.8	67.6	75.5	23.3	24.0	31.8	
707	53.1	66.6	78.1	62.6	68.8	75.7	62.6	68.8	75.7	26.9	33.9	46.3	
708	60.4	62.6	73.4	76.9	76.9	76.9	76.9	76.9	76.9	21.7	23.1	30.3	
709	27.2	69.6	79.6	78.9	74.9	74.2	69.6	69.9	76.9	25.4	31.0	50.1	
710	77.2	78.6	N/V	79.8	79.8	N/V	30.7	31.8	N/V	30.7	35.8	N/V	
711	75.7	77.2*	N/V	57.1	69.0*	N/V	57.1	69.0*	N/V	22.2	24.0*	N/V	*9F Value
712	39.3	43.6	78.7*	57.8	67.2	74.6*	57.8	67.2	74.6*	33.3	39.9	47.6*	*19F Value

(3) Urban solar limitations

Urban solar limitation in the complex is mainly building shades between adjacent buildings. Building interference significantly deteriorates solar potential on middle and lower floors (Tab.5). The approach to improve solar potential in arrangement level is two way; (1) building density planning, (2) distance and angle between adjacent buildings. Building density can be decided on the basis of principles of solar access. In this case study, residential building pattern, in density aspect, is that east and south-east located buildings are relatively lower than west and north-west located buildings. This is due to the fact that optimal direction for solar potential in Korea is south or south-east, and with optimal arrangement, lower front located buildings can have an advantage to reduce building interference to adjacent the back or the left other buildings. Therefore, building density planning based on optimal arrangement is one of better ways to settle urban solar limitation.

Fig. 4 Density and arrangement in a case high-residential complex

Another obstruction to solar potential is distance and angle between the front and the rear adjacent buildings. Below Fig.5 is an example of triangle interference. In general, residential complex is designed to have short distances between buildings to maximize using the floor area ratio. In Fig.5, the back building of the two front buildings is easily shaded by the front buildings, especially, in the middle and lower floors which is crucial one of urban limitations. Hence, to minimize building shaded area on the surface, suitable distance is secured from the front buildings or wider angle among two front located buildings is needed. Given this context, high-rise residential housing in Korea has particular points in parts of building forms and arrangement. Therefore, in order to maximize solar potential in urban area and to exploit it for renewable energy system, above-mentioned points should be considered in the design stages.

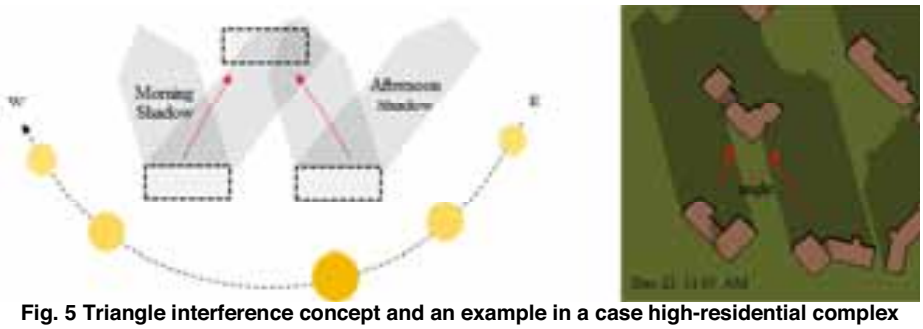

Fig. 5 Triangle interference concept and an example in a case high-residential complex

5. Conclusions

This study reviewed urban solar potential in high-rise residential buildings which are the most universal housing type in Korea. This study can be summarized as follows. In the single building level, surface azimuth and area size on each side can have large effect on the amount of solar gain. Also, building shapes can significantly affect solar potential because they can make self-shade on their surface which worsen vertical solar potential in urban areas. For instance, Flat-bending is weak to west and south side, and Tower single-wing type is feeble on east side when they face due south. Also, Tower types report larger dispersion range on the vertical solar potential than Flat types, which means Tower types in urban area are unfavorable on solar potential and inevitable to show lower solar availability because of such structural problems. On the other hand, high-rise residential building is disadvantageous for solar energy use. However, in urban environment, it is inevitable to avoid interference on solar potential between neighboring buildings due to high density. Therefore, high-rise residential building cannot help but consider effective mass design and arrangement to maximize solar potential and to use solar systems on upper floors or specific orientation. In triangle interference, in order to improve solar performance in lower and middle floors, proper distance is secured from the front buildings or larger angle among buildings is required. This study regarding building types and complex case can be valuable to understand urban solar potential in Korea. This result is expected to contribute, as a fundamental, for architect and engineers to create designs for low energy building.

6. References

Dapeng Li et al. (2015) Solar potential in urban residential buildings. Solar Energy 111, 225–235

M. Karteris et al. (2013) Urban solar potential in Greece: A statistical calculation model of suitable built roof areas for photovoltaic. Energy and Buildings 62, 459-468

Byeongho Lee et al. (2010) Comparative study of environmental sustainability in basic community planning for multiple stock housing based on lay-out types. Journal of Architectural Institute of Korea 26, 10. 271-282

Min-Hee Lee et al. (2009) An study on the application method of solar systems based on urban characteristics. Conference Journal of Architectural Institute of Korea 53. 693-696

Seonghwan Yoon and Seonyeong Jeong. (2009) Predictive Evaluation of Outdoor Thermal Environment in Summer of Apartment Housing According to Building Types and Site Planning Types, Journal of

Architectural Institute of Korea 25, 9. 321-328

Doosung Choi and Jinseok Do. (2009) A Study on the evaluation of the Residential Environment Efficiency by Arrangement of Multi-Family Residential Buildings - focused on the evaluation of daylight and view environment, Journal of Korea Institute of Ecological Architecture and Environment 9, 6. 57-64

Changho Choi et al. (2007) The possibility of PV application in Domestic Apartment and analysis of shade. Journal of Korean Institute of Architectural Sustainable Environment and Building Systems 1, 2. 1-7

Yoonbok Seong et al. (2004) A study on the variation of solar access right of apartment buildings according to site planning. Journal of Korea Institute of Ecological Architecture and Environment 4, 4. 35-45

Booseong Kang et al. (1999) A study on the spread of attitude to arrange standard housing buildings repeatedly at Korean housing estates. Journal of Architectural Institute of Korea 15, 9. 91-101

Passive design guideline (2012) Presidential Commission on Architecture Policy. available at www.greentogether.go.kr/fcs002004/actionFcs002004R01.do

Energy Census, Housing Census (2010), Apartment Housing Statistics(2013) Korea National Statistical Office. available at www.kostat.go.kr

Renewable energy dissemination of statistics (2013) Korea Energy Management Corporation. available at www.energy.or.kr

Conference Proceedings

Solar World Congress 2015
Daegu, Korea, 08 – 12 November 2015

ISES SWC2015

Design and layout optimisation of a pair of buildings regarding their solar potential

Marko Bizjak and Niko Lukač

University of Maribor, Faculty of Electrical Engineering and Computer Science, Smetanova ulica 17, SI-2000 Maribor, Slovenia

Abstract

Urban planners are often faced with the formulation of plans for multiple buildings, where they need to consider the available solar energy. Presented work tackles this problem using an evolution-based algorithm in combination with modelling of buildings within a real environment that was captured with laser-based LiDAR (Light Detection And Ranging) technology in order to optimise the design and layout of a pair of buildings regarding their solar potential. To solve the constrained optimisation problem the self-adaptive differential evolution (DE) is considered. The method was tested with a pair of rectangular buildings on a hilly LiDAR dataset, where the influence of shadowing between buildings and additional design parameters (the distance between buildings and orientation of the building pair) was analysed.

Keywords: *Solar potential, LiDAR, Buildings, Differential evolution*

**Corresponding author: Tel: +386 220-7436; E-mail address: m.bizjak@um.si*

1. Introduction

Solar energy has an important role for the development of sustainable urban areas. Buildings are accounted for 40% of total European energy consumption and a considerable amount of carbon emissions (Parliament, 2010). With appropriate utilisation of solar energy and effective solar building design we can significantly reduce carbon emissions and maximise passive solar heating as well as electricity production. Hence, the layout of buildings within urban areas needs to be planned with the available solar energy in mind. This can be difficult for urban planners, especially when designing layouts of buildings in a real environment, where the availability of solar energy can be affected by many factors, such as shadowing from surroundings (e.g. man-made objects, vegetation or terrain), local climate and terrain topography. Difficulty increases with the number of buildings planned to be build. Before we can optimise more buildings, it is imperative to know how to optimise a single building regarding its solar potential.

In the past few years, several approaches have been developed for the optimisation of a solar building (Bizjak et al., 2015; Hachem et al., 2011a; Ouarghi and Krarti, 2006). When another building is considered, further factors need to be considered, such as mutual shadowing and relative position. Various studies have focused on optimising the design of residential neighbourhoods regarding the availability of solar energy at the urban scale. Some (Hachem et al., 2013, 2012, 2011b; Kanters and Horvat, 2012) manually inspected parameter space using predefined values, whilst others (Kämpf and Robinson, 2009; Kämpf et al., 2010) used automatic approach. None of them considered actual environment from real locations or focused on the layout of a pair of buildings.

Hachem et al. (Hachem et al., 2011b) developed a methodology for the investigation of the influence of two-storey housing units design parameters and neighbourhood patterns on the received solar irradiance. They investigated straight and curved roads as site layouts. Later they (Hachem et al., 2012) investigated solar

doi:10.18086/swc.2015.08.04 Available at http://proceedings.ises.org

potential and energy demand for heating and cooling of housing units. Their work continued in 2013 (Hachem et al., 2013) where previously developed methodologies were used to perform a parametric study to develop a design methodology for solar residential neighbourhoods based on an evaluation system that uses weighted objectives method. Kanters and Horvat (Kanters and Horvat, 2012) studied the impact of geometry form of urban blocks regarding the solar potential. Kampf and Robinson (Kämpf and Robinson, 2009) proposed a novel evolutionary approach for optimising the placement of buildings regarding the availability of solar irradiation. However, buildings' design was not considered. Kampf et al. (Kämpf et al., 2010) developed a multi-objective optimisation algorithm to optimise geometric parameters of building design on a range of urban typologies.

In this work we present a novel optimisation of the design and layout of a pair of buildings within LiDAR data and investigate the influence of geometrical design parameters of a pair of buildings on the received solar irradiance. To our knowledge, this is the first method for the optimisation of a pair of buildings to consider environment of real locations. Real environment is provided by LiDAR (Light Detection And Ranging) data. LiDAR is an active remote sensing technology that scans surface topographies and is normally mounted on an aircraft. The result of such scanning is an unstructured point cloud. As manual inspection of parameter space is exhausting, an evolutionary approach is used to perform the optimisation based on the methodology used in (Bizjak et al., 2015). The proposed method is therefore performed in two stages. In the first stage, user provides the footprint of a building model, which is then used as a base model for both buildings modelled within LiDAR data. During the second stage the pair of buildings is optimised with a modified self-adaptive differential evolution (DE) (Brest et al., 2006). The optimisation criterion is the cumulative estimation of solar potential (Lukač et al., 2013) of both buildings. Next to the design parameters of a single building model we consider the following optimisation parameters: the distance between the pair of buildings and orientation of the pair.

The paper is structured into four sections. The next section describes the proposed method. The third section presents the results and the last section concludes this paper.

2. Design and layout optimization of a pair of buildings

The following subsections describe the proposed method in detail. Subsection 2.1 details the method for the optimisation of a solar building, which is the base for the proposed method. The next subsection describes the design and layout optimisation of a pair of buildings.

2.1. Basic method for the optimisation of a solar building

The basic method's input is a classified LiDAR (Light Detection And Ranging) point cloud (see Fig 1a) that is arranged into a regular 2.5D grid, where each cell is defined by the height and classification of the highest point in the cell (Bizjak et al., 2015). The empty cells are interpolated with inverse distance weighting (IDW) method (Shepard, 1968). Points are classified as either building, ground or vegetation. The utilisation of LiDAR data enables us the optimisation within a real environment, where the influence of the local climate, terrain topography and shadowing from buildings and terrain are considered. Buildings are then modelled on the 2.5D grid, where the following design parameters are considered: position, rotation, facades' height, roof's height and roof's slope, as shown in Figure 1b. Buildings' position is bounded by an area of interest, which is defined as a user selected polygonal area on the grid. When modelling is completed, the building is rasterised into the 2.5D grid (see Figure 1c), where the highest point of the roof over each covered cell is considered. The cells of the rasterised building represent the input to the method for solar potential estimation (Bizjak et al., 2015), which is the considered optimisation criterion. An evolutionary approach is considered for the optimisation of a building model regarding the received solar potential, based on methodology used in (Bizjak et al., 2015). Evolutionary algorithms are inspired by biological evolution (Brest et al., 2006). One of them is differential evolution (DE) which is a direct parallel search method developed by Price and Storn (Storn and Price, 1997) that operates with P n-dimensional vectors $x_{i,G}; i = 1, \dots, P$ as a population throughout the optimisation for each generation G. Each vector goes through mutation, crossover and selection operations in a single generation G. During the mutation and crossover new candidates are generated, while selection regulates which vector survives the current generation. The decision regarding which candidate is selected is

based on the estimation of solar potential which is described in the next section.

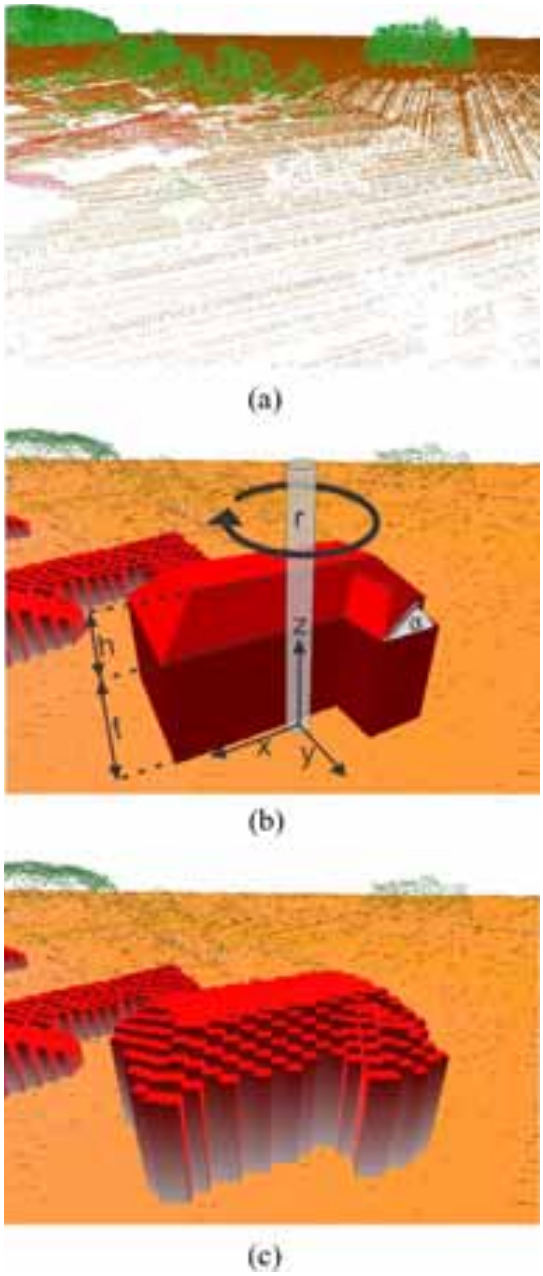

Figure 1: (a) Classified LiDAR point cloud; Building model on a 2.5D grid with the following building design parameters: r- rotation axis, f – facades' height, α – roof's slope and h – roof's height; (c) Cells of the rasterised building (Bizjak et al., 2015).

2.2. Building pair's solar potential maximisation

The optimisation method in (Bizjak et al., 2015) focuses only on the design of a single building, which is why this paper proposes a novel extension to the method's capabilities to assess the optimal design and layout of a pair of buildings. With an additional building, the influence of shadowing between buildings and the placement of a pair of buildings on a user defined area of interest can be estimated, in order to maximise the received solar irradiance. This is performed by introducing additional design parameters: the orientation γ of the pair of buildings and the distance d between the pair. The pair of identical buildings is parallel for any orientation angle. Two types of layouts of a building pair are considered. For the first layout type, the buildings lie on two parallel lines (see Figure 2a and equation 2) and for the other the buildings lie on the same line (see Figure 2b and equation 1). The lines for the layouts are defined as follows:

$$y = \tan(\gamma)\, x + \, y_P - \tan(\gamma)\, x_P \qquad \text{(eq. 1)}$$

$$y = \tan(\gamma)\, x + \; y_P - \tan(\gamma)\, x_P \pm \frac{\left(\frac{d+w}{2}\right)}{\cos\gamma} \qquad \text{(eq. 2)},$$

where $P(x_P, y_P)$ is the center point of the area of interest and w is the width of the building. Moreover, buildings can be mirrored over y-axis before rotated.

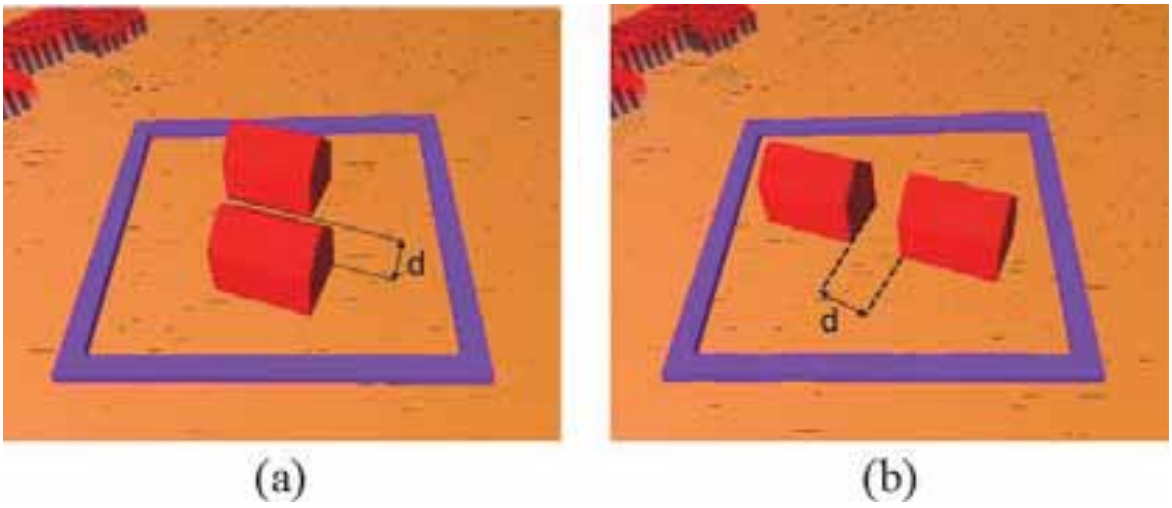

Figure 2: Two types of layout with orientation angle at 20°, where (a) buildings lie on two parallel lines and (b) buildings lie on the same line. The distance between buildings is defined by *d*.

The final model of the pair of buildings is rasterized into 2.5D grid by the rasterization of each individual building (see Figure 1c). The cells of both buildings are considered as input to the method for solar potential estimation (Lukač et al., 2013), that operates with the 2.5D grid that was generated with LiDAR data. Solar potential is roughly calculated as follows:

- Calculation of a normal vector for each building's cell.
- Time and location dependent terrestrial irradiance is calculated using cell's aspect and slope angles (Duffie and Beckman, 2006) together with long-term on-site diffuse and global solar irradiance measurements.
- The solar potential of a cell at a given time is defined as:

  $$I_c = \; I_{c_b}(1 - S_c) + I_{c_d} \left[\frac{\text{kWh}}{\text{m}^2}\right], \qquad \text{(eq. 3)}$$

  where I_{c_b} and I_{c_d} are the terrestrial direct and diffuse irradiances of a given cell, whilst $S_c \in [0,1]$ is the shadowing coefficient that affects the direct irradiance.
- I_c is considered between sunrise T_{sr} and sunset T_{ss} with the fixed time-step to estimate the daily solar insolation:

  $$J_c = \int_{T_{sr}}^{T_{ss}} I_c(t)dt \left[\frac{\text{kWh}}{\text{m}^2}\right]. \qquad \text{(eq. 4)}$$

- The solar potential is defined as an average daily insolation throughout the year (Lukač et al., 2013).
- The average amount of the daily solar energy the pair of buildings receives is the result of the fitness function. It is calculated as the sum of the solar potential of the pair's cells.

During the optimisation the initial population is not randomly generated over the parameter space only for the roof slope and the pair of building's orientation parameters. For these two parameters a simple heuristic is used, where the initial population is generated in Gaussian distribution with its peak at the expected value (Bizjak et al., 2015). Optimal roof slope is expected to be approximately at the location's latitude, whilst for the orientation most roof surfaces of the pair are assumed to be oriented towards equator. Figure 3 presents the workflow of the upgraded method.

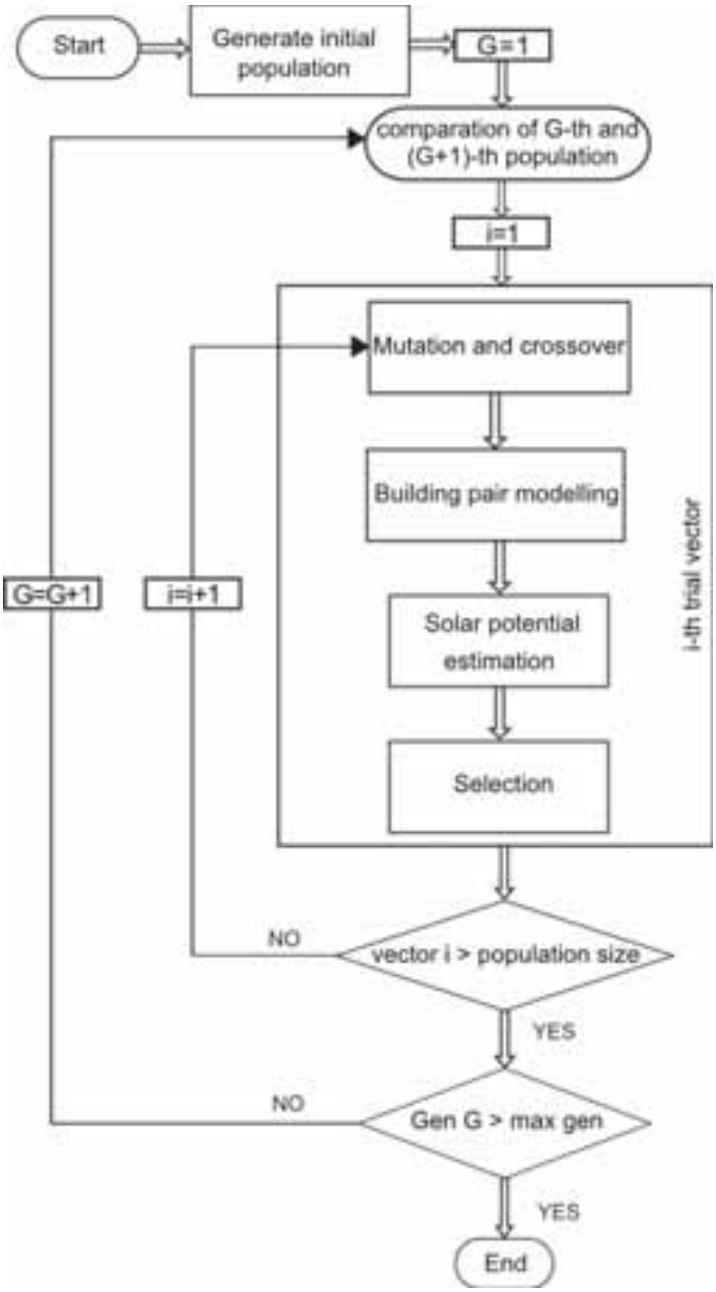

Figure 3: Workflow of the proposed method.

3. Results and discussion

The experiments were performed on two LiDAR datasets, one that represents a hilly landscape (located at 46° 37' 0.61" N, 15° 52' 37.59" E) and the other a flat landscape (46° 35' 59.43" N, 16° 13' 25.89" E) as can be seen in Figure 4. Testing was performed at a specified location on each dataset using a building in rectangular or L shape as a base for the optimisation of the pair. For the calculation of terrestrial irradiance of each pair of buildings candidate the average measurements from the closest meteorological station over the previous decade were used. The population size P for DE was set to 80 and the *DE/best/1/bin* strategy was considered, as proposed in (Bizjak et al., 2015).

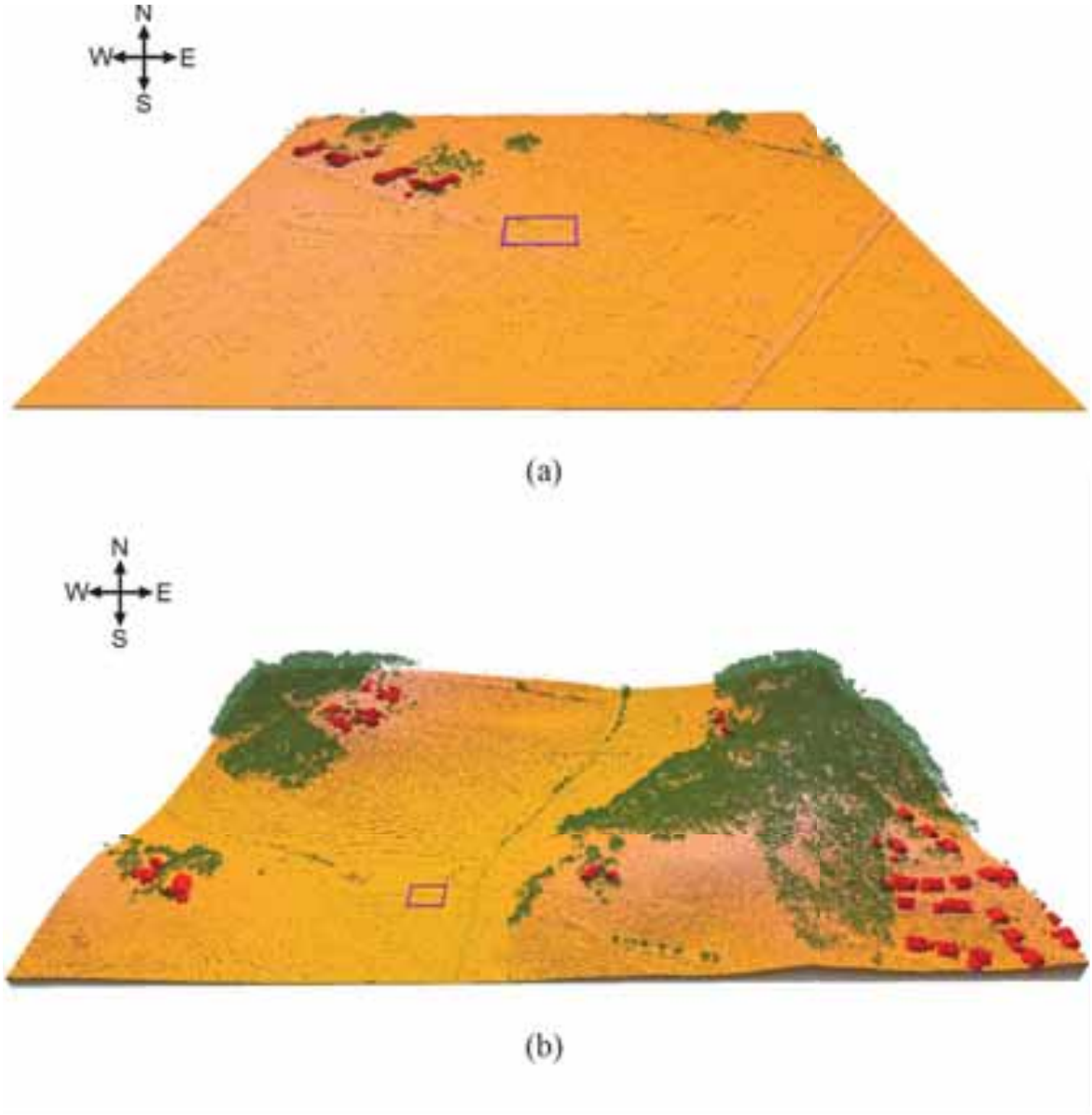

Figure 4: Flat (a) and hilly (b) LiDAR datasets with designated area of interest (purple rectangle).

The results of the optimisation for all combinations of layouts and datasets are presented in Figures 5 and 6. Figure 5 shows the optimised pairs of buildings on the flat LiDAR dataset. The buildings' roofs were sloped on average at 46° (±2°). Buildings' height varied for each pair, which is caused by the lack of shadowing from surroundings. The optimal orientation of both layouts for all pairs of buildings was on an east-west axis, where the most exposed roof surfaces were facing equator. The distance between the buildings was the maximum possible distance within the considered area for both layouts. This is a natural consequence of decreased shadowing between buildings as the distance increases.

Figure 6 presents the optimised pairs of buildings on the hilly LiDAR dataset. The buildings' roofs were sloped on average at 45° (±1°). The difference in slope is caused by different topography and geographic location of each dataset. Buildings' height was maximal, which is a consequence of shadowing from the hill. Higher building means lower shadowing and therefore better fitness. The optimal orientation of building pairs was on an east-west axis for all cases except for L-buildings on the same line (see figure 6c). The building pair was oriented 2° from the east-west axis. This occurred due to internal shadowing, which happens when a building's cell is shadowed by another cell from the building. The distance between buildings was maximum on this dataset as well.

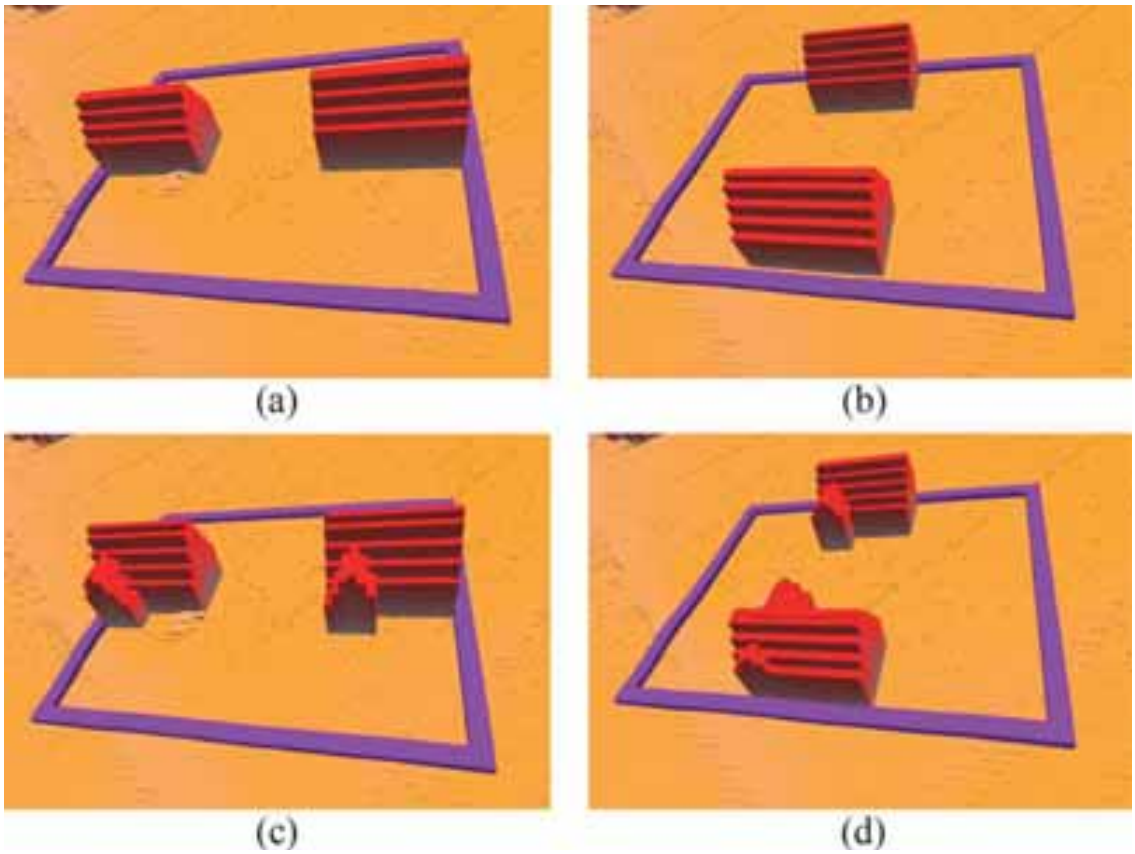

Figure 5: Results of the optimisation for buildings on the same line (a,c) and buildings on two parallel lines (b,d). Area of interest is located at a 2.5D grid generated from the flat LiDAR dataset (see Figure 4a).

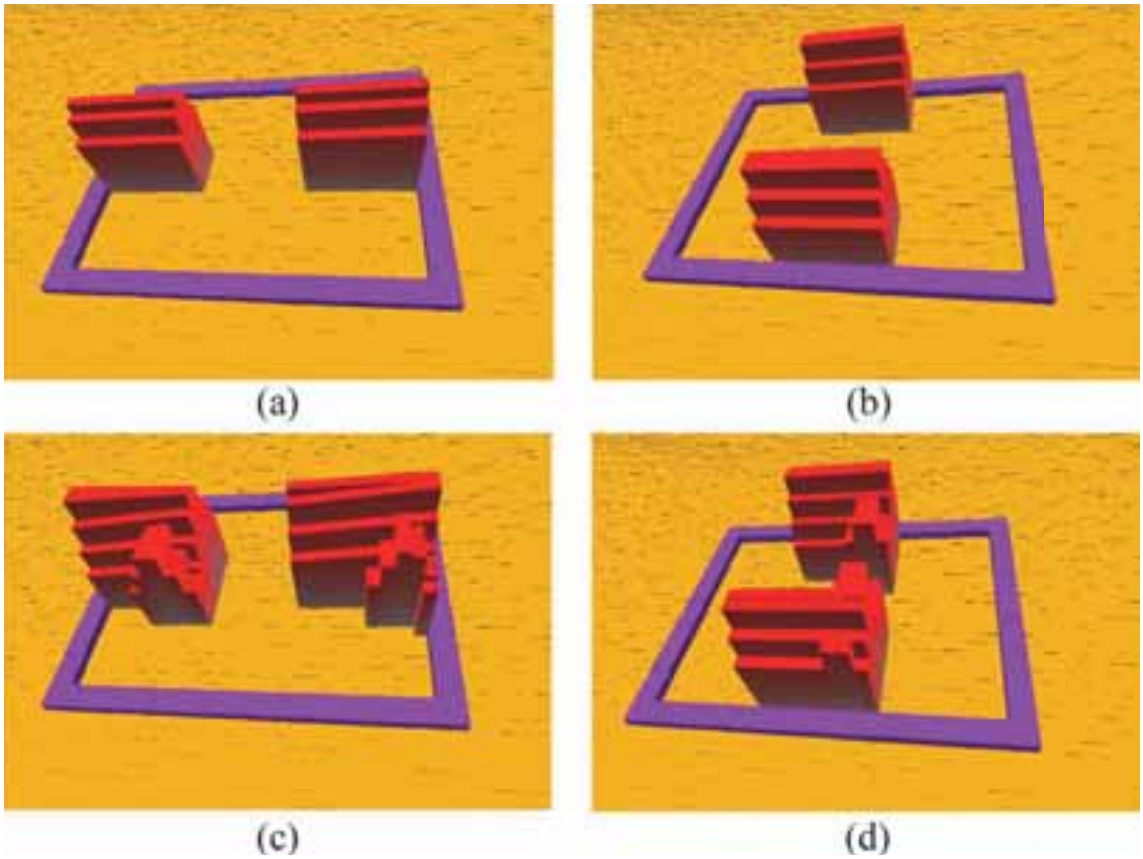

Figure 6: Results of the optimisation for buildings on the same line (a,c) and buildings on two parallel lines (b,d). Area of interest is located at a 2.5D grid generated from the hilly LiDAR dataset (see Figure 4b).

4. Conclusion

This paper presented a novel method for the design and layout optimisation of a pair of buildings regarding the received solar potential. The optimisation was achieved with a modified self-adaptive differential evolution. For each candidate, a pair of buildings was modelled and assessed regarding solar potential. The solar potential estimation considers shadowing from surrounding obstacles within real data and local climate. The results suggest, that the method successfully optimises a pair of buildings, where the distance between the buildings is maximal. To our knowledge, this is the first method that tackles the optimisation of two buildings within LiDAR data regarding solar potential.

Acknowledgements

This work was supported by Slovenian Research Agency under grants P2-0041, 1000-13-0552, and J2-6764. Thanks to the Slovenian Environment Agency for providing the pyranometer measurements.

References

Bizjak, M., Žalik, B., Lukač, N., 2015. Evolutionary-driven search for solar building models using LiDAR data. Energy Build. 92, 195–203. doi:http://dx.doi.org/10.1016/j.enbuild.2015.01.051

Brest, J., Greiner, S., Boskovič, B., Mernik, M., Žumer, V., 2006. Self-Adapting Control Parameters in Differential Evolution: A Comparative Study on Numerical Benchmark Problems. Evol. Comput. IEEE Trans. 10, 646–657. doi:10.1109/TEVC.2006.872133

Duffie, J.A., Beckman, W.A., 2006. Solar Engineering of Thermal Processes. Wiley-Interscience.

Hachem, C., Athienitis, A., Fazio, P., 2012. Evaluation of energy supply and demand in solar neighborhood. Energy Build. 49, 335–347. doi:10.1016/j.enbuild.2012.02.021

Hachem, C., Athienitis, A., Fazio, P., 2011a. Parametric investigation of geometric form effects on solar potential of housing units. Sol. Energy 85, 1864–1877. doi:10.1016/j.solener.2011.04.027

Hachem, C., Athienitis, A., Fazio, P., 2011b. Investigation of solar potential of housing units in different neighborhood designs. Energy Build. 43, 2262–2273. doi:10.1016/j.enbuild.2011.05.008

Hachem, C., Fazio, P., Athienitis, A., 2013. Solar optimized residential neighborhoods: Evaluation and design methodology. Sol. Energy 95, 42–64. doi:http://dx.doi.org/10.1016/j.solener.2013.06.002

Kämpf, J.H., Montavon, M., Bunyesc, J., Bolliger, R., Robinson, D., 2010. Optimisation of buildings' solar irradiation availability. Sol. Energy 84, 596–603. doi:10.1016/j.solener.2009.07.013

Kämpf, J.H., Robinson, D., 2009. A hybrid CMA-ES and HDE optimisation algorithm with application to solar energy potential. Appl. Soft Comput. 9, 738–745. doi:10.1016/j.asoc.2008.09.009

Kanters, J., Horvat, M., 2012. Solar Energy as a Design Parameter in Urban Planning. Energy Procedia 30, 1143–1152. doi:http://dx.doi.org/10.1016/j.egypro.2012.11.127

Lukač, N., Žlaus, D., Seme, S., Žalik, B., Štumberger, G., 2013. Rating of roofs surfaces regarding their solar potential and suitability for PV systems, based on LiDAR data. Appl. Energy 102, 803–812. doi:10.1016/j.apenergy.2012.08.042

Ouarghi, R., Krarti, M., 2006. Building Shape Optimization Using Neural Network and Genetic Algorithm Approach. ASHRAE Trans. 112, 484–491.

Parliament, E.U., 2010. Directive 2010/31/EU of the European Parliament and of the Council of 19 May 2010 on the energy performance of buildings. Off. J. Eur. Union.

Shepard, D., 1968. A Two-dimensional Interpolation Function for Irregularly-spaced Data, in: Proceedings of the 1968 23rd ACM National Conference, ACM '68. ACM, New York, USA, pp. 517–524. doi:10.1145/800186.810616

Storn, R., Price, K., 1997. Differential Evolution - A Simple and Efficient Heuristic for global Optimization over Continuous Spaces. J. Glob. Optim. 11, 341–359. doi:10.1023/A:1008202821328

Conference Proceedings

Solar World Congress 2015
Daegu, Korea, 08 – 12 November 2015

On Parameters Testing of an Innovative Mortar Made of Rice Husk to be Used for Housing Walls

Julio Barzola[1,3], Fausto Cabrera [1] and Mayken Espinoza[2,3]

[1] Universidad Laica VICENTE ROCAFUERTE, Guayaquil (Ecuador)

[2] Lund University, Lund (Sweden)

[3] Escuela Superior Politécnica del Litoral, Guayaquil (Ecuador)

Abstract

During the design and construction of house walls, certain factors such as building materials and external climatic conditions, which are essentials and influence in human comfort, are generally ignored. The rice husk is one of the most common organic wastes generated around the word, and in Ecuador this is not an exception. The aim of this work is to study the feasibility of using a mortar which contains rice husk crushed (RHC). To show this feasibility, experiments have been conducted with mortar samples of different proportions of water, cement, sand, and crushed rice husk. The variables tested in this work include several parameters such as: analysis of flow, compressive strength, curing time, and adhesivity. As part of this project, this particular mortar is used during the construction of the housing walls in prototype houses located in one city of the Ecuadorian coastline.

Keywords: *Mortar, fluidity, compressive strength, curing time, adhesivity*.

1. Introduction

The raising of the world population and consequently their food consumption, result in the increment of organic and inorganic wastes. The overabundance of residual wastes causes a hard impact over the environment, and therefore can produce irreversible environmental issues to solve for the future generations. There are different initiatives to reduce the environmental impacts caused by the population´s consumption. For example, the waste recycling process to reuse this material during the manufacture of other products can be mentioned. Previous studies (Mahvi et al., 2004) mention the rice husk as one of the most common organic wastes generated around the world. Nowadays, it is found in large quantities in husking machines of rice; which is often burned, and in some occasions is thrown into rivers and estuaries, causing pollution and obstruction (Ganesan et al., 2008).

Finding a suitable utility of the rice husk in building construction will help not only to decrease the amount of this waste in the ambient, but it also improves the physical and thermal characteristics of the materials involved in the wall fabrication (Barzola et al., 2015).

The purpose of this work is to reduce the pollution generated for the husk rice wasted, using this organic waste during the manufacturing process of the housing wall mortar. According to its use, mortars in civil constructions can be classified in different ways according to its binding and use (Simba, 2007). In the present work, an innovative mortar for building applications that requires lower strengths like masonry and plastering is taken into account. Based on the mentioned characteristic, the weight ratio of the components is considered. However, the economic aspects of this alternative mortar with RHC was not considered during this study. It has been suggested as the next phase of this research.

The mortar must meet with certain characteristics; one of them is not displaying segregation in both fresh and hardened states; at inner and outer walls of a building. For this purpose, all mortar must follow technical

Selection and/or peer review under responsibility of Scientific Committee
doi:10.18086/swc.2015.08.05 Available at http://proceedings.ises.org

processes and quality control in the laboratory, by reaching an optimal ratio among the constituent (Givi et al., 2010). The tests carried out over the mortars correspond to fluidity, compressive strength, curing time, and adhesion. Thus, the durability of mortar on the walls can be ensured, and it certainly will be complemented with the maintenance performed.

The rest of this paper is divided as follows: in Section 2, a detailed information about the materials and methods used to manufacture each sample is given. Section 3 is focused on the presentation of the results and discussions. Finally, the conclusions are given in Section 4.

2. Materials and methods

Along this section, information about the materials involved in the brick fabrication is given. The methodology followed and the composition for each sample mortar are presented.

2.1. Materials and mixture

Mortars are the result of a mixture of different materials, which in this work were added in different proportions. Among the materials used during the manufacture of the mortars are cement, rice husk crushed and other aggregates. Amount specification and characteristics about all of these materials are given in the following sub-sections.

2.1.1. Cement

The main constitutive element of the mortar is the cement. Ordinary Portland Cement (OPC) obtained from Holcim Cement Manufacturing Company of Ecuador conforming to ASTM-C1157 standard was used.

2.1.2. Rice husk crushed (RHC)

The rice husk was obtained from rice mill. Then, this waste was ground using mill for 30 minutes. Table 1 shows sieve analysis of the RHC conforming to ASTM-C33 standard.

Tab. 1: Sieve analysis of the RHC used in the samples

Sieve size	Cumulative Gram Retained	Cumulative % Retained	% Passing	ASTM – C33
3/8”				100
No. 4				95-100
No. 8	0.4	0.03	99.97	80-100
No. 16				50-85
No. 30	179.7	64.36	35.64	25-60
No. 50	119.6	73.94	26.06	10-30
No. 100	122.9	83.79	16.21	2-10
PAN	202.3	100	0	0

2.1.3. Aggregates

Graded river sand passing through 0.425 mm sieve with a fineness modulus of 2.01, and specific gravity of 2.58 was used as fine aggregate.

2.1.4. Mixture proportioning

A total of four series of mixtures were prepared in the laboratory trials. MSC0 series mixture which has traditional proportions of cement, sand and water were prepared as control specimens. MCA1, MCA2, MCA3 and MCA4 series mixture were prepared with different proportions of RHC and water.

Table 2 presents the amount and proportions used for the different samples. The amount of water is not affected because the container of the mixer is aluminum, and there is no absorption issue. (Mas i Barberà, 2006).

Tab. 2: Amount of the different elements in the sample mortars and water/cement ratio

Mortar	Cement (g)	Sand (g)	Rice Husk (g)	Water (g)	Water / cement
MCA1	233	700	23.3	200	0.86
MCA2	233	700	23.3	215	0.92
MCA3	233	700	46.6	220	0.94
MCA4	233	700	46.6	250	1.07

According to the information presented in Table 2, it is important to mention that each sample mortar has the same amount of cement and sand. The variable that has been subjected to change is the corresponding to the rice husk and water. The samples were prepared with two different amounts of rice husk, and four different quantities of water. The last column of Table 2 presents the ratio between the water and cement for each sample analyzed.

2.2. Preparation of test specimens

MCA1, MCA2, MCA3 and MCA4 series mixture were prepared by mixing the fine aggregate and powder materials (cement and RHC) in a laboratory mortar mixer. They were mixed in dry condition for 3 min followed by another 4 min after adding the water. The powder material in MSC0 series mixtures was only cement.

2.3. Mortar flow

Fluidity is the physical property of a material that shows the ability to flow. Considering that each sample is built from materials in different proportions, different values of fluidity are expected. Mortar flow is most sensitive to water content and air content. Once prepared, mortar samples were placed immediately at the flow table test in order to observe its workability. The test was done in accordance with the ASTM C 1437, the Standard Test Method for Flow of Hydraulic-Cement Mortar.

2.3. Compressive strength

Mortar strength is very important because it reflects the mortar's ability to carry intended loads. In our case, the adhesion force between the masonry and mortar in the wall. For all samples, cube specimens of size 50 X 50 X 50 mm were used for the compressive strength test of mortar. They were tested at the age of 7, 14 and 28 days. The test was done in accordance with the ASTM C 109, the Standard Test Method for Compressive Strength of Hydraulic-Cement Mortar.

2.4. Curing time

Another important property to analyze during the mortar fabrication is the hardening time, water retention and curing start. The mortar samples should be cured with the normal OPC hardening. The test was done in accordance with the ASTM C 191, the Standard Test Method for Time of Setting of Hydraulic-Cement by Vicat Needle.

2.5. Adherence

Adherence is a property that must maintain both fresh and hardened mortar. The test was done in accordance with the ASTM C 780, the Standard Test Method for Preconstruction and Construction Evaluation of Mortars for Plain and Reinforced Unit Masonry.

Additionally, sclerometer method is applied in housing prototypes built in order to test this mortar. This instrument measures compression strength in Q units, which can be converted in MPa units through of a curve supplied by the manufacturer. For each point to evaluate, ten measurements were made. Then, the median Q values are determined. These measurements are carried out in each both outer and inner walls, during the September 14, 2014; September 28, 2014 and May 23, 2015.

3. Analysis and discussion of results

3.1. Fluidity

Figure 1 shows the percentages of fluidity obtained during the measurements to the samples, i.e., MCA1, MCA2, MCA3 and MCA4, each one presenting different fluidity. The results are contrasted with a traditional pattern named MSC0, which does not contain crushed rice husk. Among the four samples of mortar with

crushed rice husk, results show that the MCA3 sample has better fluidity. This is as expected, because of the higher amount of water. This reduces the resistance to compression.

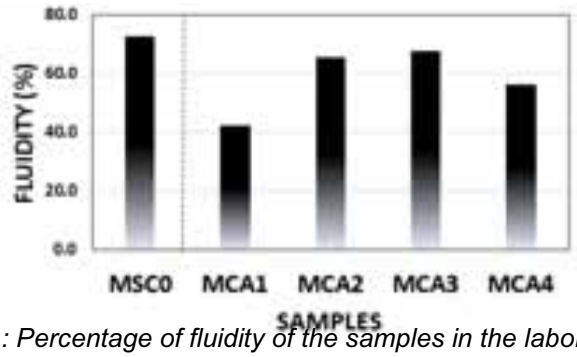

Fig. 1: Percentage of fluidity of the samples in the laboratory

3.2. Compressive strength

Figure 2 shows compression-resistance ratio. It is noticed that when W/C ratio increases, compressive strength decreases. Laboratory tests were performed on the day 7, 14 and 28. MCA1 shows a better performance in compressive strength, and therefore this sample was selected for being used in the construction of the walls in the prototypes.

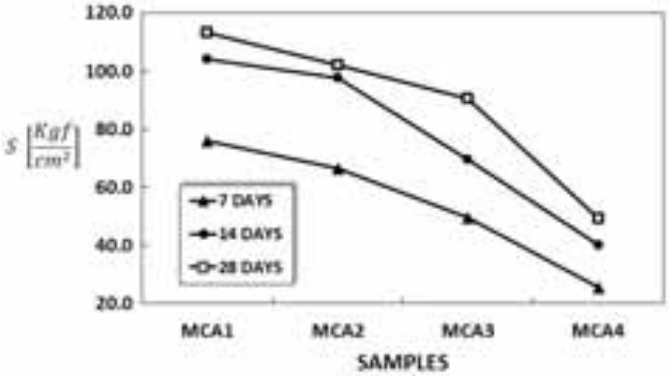

Fig. 2: Behavior of the compressive strength of the samples according ASTM C 109

Figure 3 presents a contrast between traditional mortar MSC0 and MCA1 selected. The traditional mortar always has a higher strength compared to mortar MCA1. In addition, on average MCA1 has a lower resistance compared to traditional mortar, since crushed rice husk also absorbs water; however, as discussed later, it has good adhesion.

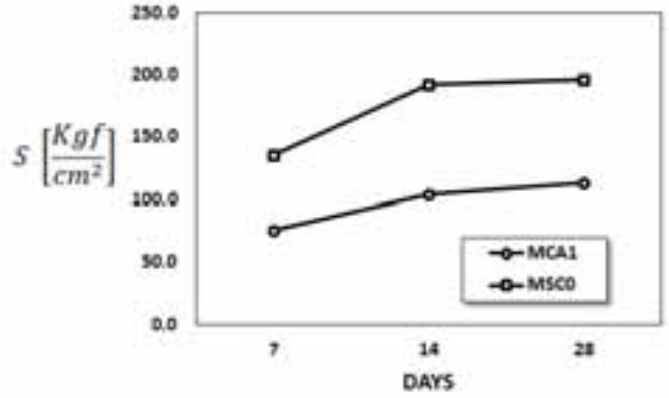

Fig. 3. Comparison of the Compressive Strength between the traditional mortar and mortar MCA1 selected.

3.3. Curing time

Figure 4 shows the Vicat needle experimental penetration behavior applied to the sample MCA1, the data were obtained every 15 minutes, according with the ASTM C 191, the Standard Test Method for Time of Setting of Hydraulic-Cement by Vicat Needle. The result presents a very good approximation between the experimental and the corrected (theoretical) curve. When 25 mm height is reached, the hardening of cement in the mortar is achieved, which corresponds to about 4 hours (243.3 minutes) of curing time. This was a reference value to consider for the curing stage of the mortars during their utilization in housing prototypes.

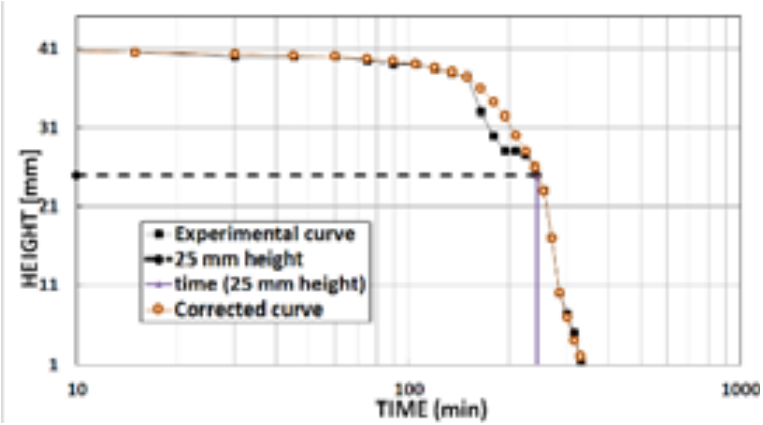

Fig. 4: Penetration curves Vicat needle applied to mortar MCA1

3.4. Adherence

Figure 5 depicts prototypes plastered with MSC0 and MCA1 mortars, the results showed good adhesion (Barzola et al., 2015). All the prototypes have the same dimensions (2.8 m by side) and characteristics. In order to improve the thermal isolation between the inner and outer ambient of the prototypes, windows and doors were treated. Special isolation treatment on the roof was applied.

Fig. 5: From left to right: Prototypes plastered A (MSC0), B (MCA1) and C (MCA1) in Atahualpa parishes.

Figures 6 - 8 show the sclerometer measurements which corroborated the resistance and adhesion of the mortars in each wall. For each point to evaluate ten measurements with the sclerometer were performed, and with these values the median was determined. This instrument measures compression strength in Q units, which can be converted in MPa units by using a curve supplied by the manufacturer. This process is carried out in each outer and inner wall of each module. The dates considered for analysis of the evolution of resistance were 14, 28 September 2014 and 23 May 2015.

Radar charts summarize the results of the medians of the data obtained from the external walls. These walls were labeled counter-clockwise, starting with the front wall, E1; right side, E2; posterior and left side are labeled as E3 and E4, respectively. Each colored line depicts the measurements of a particular date according to the legend box. It can be noted that the resistance at these test points has been increasing chronologically.

The results of applying sclerometer method evidences that the best compressive strength a short term is obtained with MSC0 mortar in Prototype A. However, the MCA1 mortar used to build the prototype C showed better median values compared with Prototype B. Note that Prototype C was built with brick block, unlike Prototype A and B with concrete block.

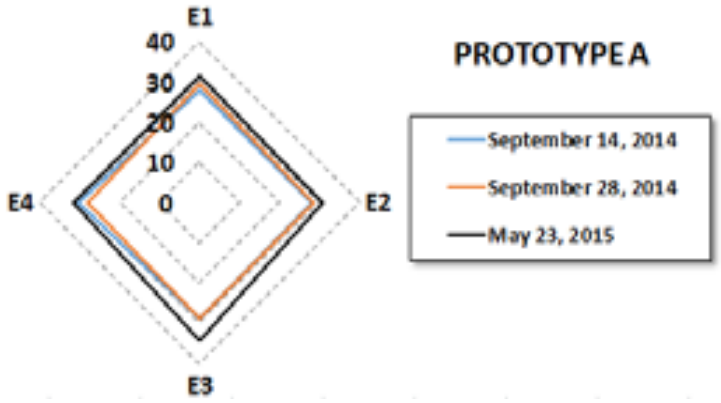

Fig. 6: Resistance performance at external walls prototype A

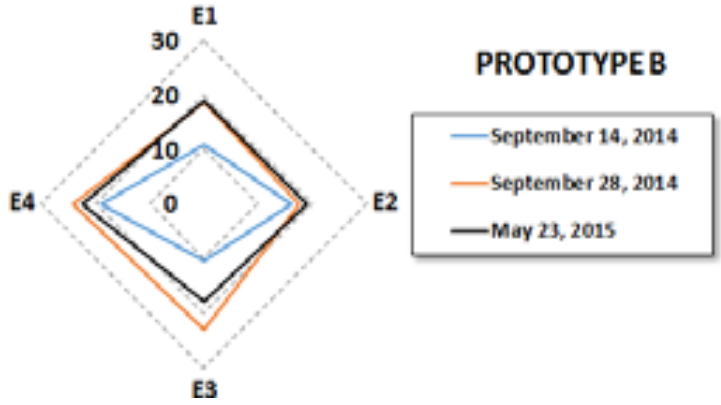

Fig. 7: Resistance performance at external walls prototype B

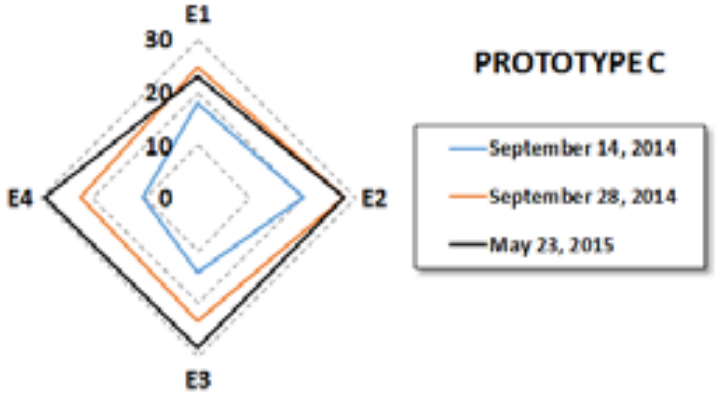

Fig. 8: Resistance performance at external walls prototype C

4. Conclusions

An innovative mortar, which contains RHC was tested. Although MCA1 mortar has lower compression strength compared to the traditional mortar, its feasibility for masonry and plastering due to both fluidity and adhesion performances is demonstrated.

In (Barzola et al., 2015), field test results of the MCA1 are shown. Two different geographical locations of the Ecuadorian coast were considered for this study, which have different weather conditions. The field test results show a thermal behavior similar to the expected if traditional mortar with OPC is used.

Finally, this study suggests that the mortar made of RHC represents a viable alternative to being used in wall constructions. At the same time using this type of mortar, the environmental impact of the overproduction of organic wastes is reduced.

5. References

Barzola, J., Cabrera, F., & Espinoza, M. (2015). Test Results of a Mortar Made of Crushed Rice Husk Used for Housing Walls. In proc. 13th LACCEI Annual International Conference (pp. 29–30). Santo Domingo, Dominican Republic.

Ganesan, K., Rajagopal, K., & Thangavel, K. (2008). Rice husk ash blended cement: Assessment of optimal level of replacement for strength and permeability properties of concrete. Construction and Building Materials, 22(8), 1675–1683.

Givi, A. N., Rashid, S. A., Aziz, F. N. A., & Salleh, M. A. M. (2010). Assessment of the effects of rice husk ash particle size on strength, water permeability and workability of binary blended concrete. Construction and Building Materials, 24(11), 2145–2150.

Mahvi, A.H., Maleki, A., Eslami, A., 2004. Potential of Rice Husk and Rice Husk Ash for Phenol Removal in Aqueous Systems. Am. J. Applied Sci. 1, 321-326

Mas i Barberà, X. (2006). Study and characterization of composite mortars for use in sealed interventions, replacements and retort of stone sculptural-ornamental elements (In Spanish). Universitat Politècnica de València. Spain. Retrieved from https://riunet.upv.es/bitstream/handle/10251/1941/tesisUPV2517.pdf

Simba, E. (2007). The waterproofing in new and existing buildings (In Spanish). Escuela Potècnica Nacional. Ecuador. Retrieved from http://bibdigital.epn.edu.ec/bitstream/15000/1982/1/CD-0562.pdf

Conference Proceedings

Solar World Congress 2015
Daegu, Korea, 08 – 12 November 2015

Estimating feasibility of regenerating PCM and Desiccant in room interior wall surfaces using pre-dried air through an external desiccant bed

Edson Manyumbu[1]

[1] Chinhoyi University of Technology, Chinhoyi, Zimbabwe

Abstract

Buildings account for a significant fraction of energy use. Reduction of energy use in buildings has been the subject of research for quite a while to date. Passive means for comfort provision is one way of energy use reduction in buildings. A passive humidity and temperature control requires regeneration of the participating building envelope materials at some point in order for the buffering to be possible when needed. The present work focuses on investigating the potential for regenerating interior building envelope materials of an office that have been enhanced with a desiccant (for moisture buffering) and a PCM (for temperature buffering). The simulation study reveals that with an appropriate design the regeneration of both PCM and desiccant is possible. In winter, the cooling of the PCM takes place at a faster rate because the outdoor air temperatures are highly subdued during the night. The significantly low temperatures, however, are not favorable for the silica gel regeneration but moisture content of as low as 0.04kg/kg is achieved at the fourth hour of regeneration while beyond this hour the moisture content starts to increase. Temperatures are on a decrease towards minimum as dawn approaches. In summer, it is possible to reach about 0.07kg/kg and at the same time being able to freeze PCM that to dispatch about 470W of cooling power for a 10-hour period.

Keywords: *Regeneration, Phase Change Material, Desiccant, Passive Humidity and Temperature Control*

1. Introduction

Buildings account for a significant percentage of national energy consumption and HVAC systems contribute a significant portion of the buildings' energy demand (Shilei et al., 2007). Research into passive cooling through the application of PCM has received a lot of attention (Shilei et al., 2007, Cabeza et al., 2007, Baetens et al., 2010, 2012, Karim et al., 2014). Key comfort parameters include humidity in addition to the commonly focused on parameter, temperature. While some interior finishes can offer some moisture buffering, it is usually not enough to render the expected comfort. Efforts towards the application of desiccants to interior building envelope materials as a means to enhance the moisture buffering capacity has been limited; one known investigation towards this end is that of Rudd (1994). Potential regeneration for interior surfaces laden with a desiccant at a constant temperature was investigated through spreadsheet simulation (Manyumbu and Martin, 2013). The investigation did not look into the regeneration of the PCM; the assumption was that there is a constant phase change temperature of the PCM always. In the current study, the investigation looks into the feasibility of regenerating both the desiccant as well as PCM.

2. Methods

2.1. The Regeneration Concept

The concept involves a solar channel that has a desiccant bed forming its absorber surface during day-time operation, fig. 1. At night the channel operate as an air dryer, fig. 2, drying ventilation air passing through into the room. While the air is dried in the process, it gets heated up since the process is exothermic (it

doi:10.18086/swc.2015.08.06 Available at http://proceedings.ises.org

release heat of adsorption). The slightly warmer dry air is then responsible for the regeneration of the interior wall surfaces that are laden with a PCM and a desiccant (silica gel).

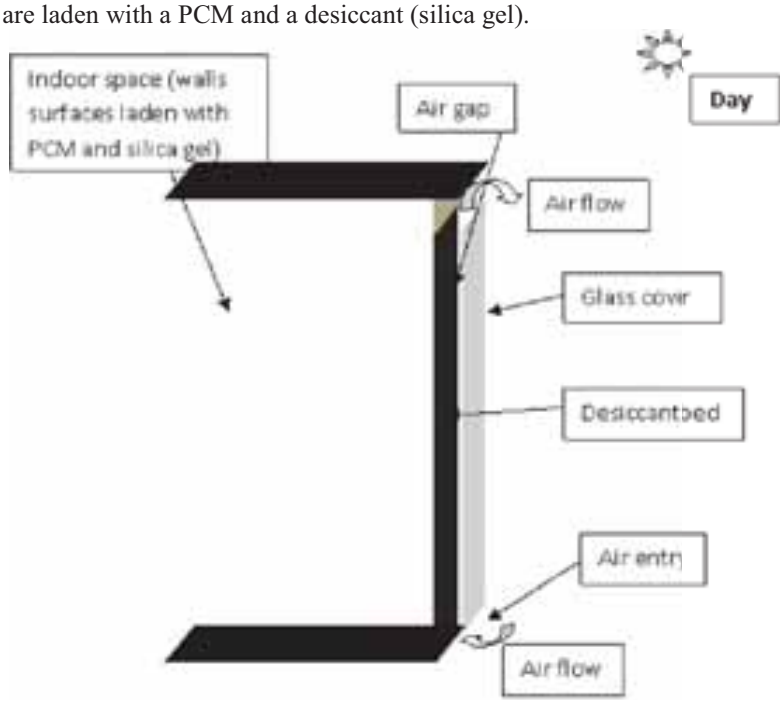

Fig. 1: Proposed Passive Regeneration Strategy for Exterior Desiccant

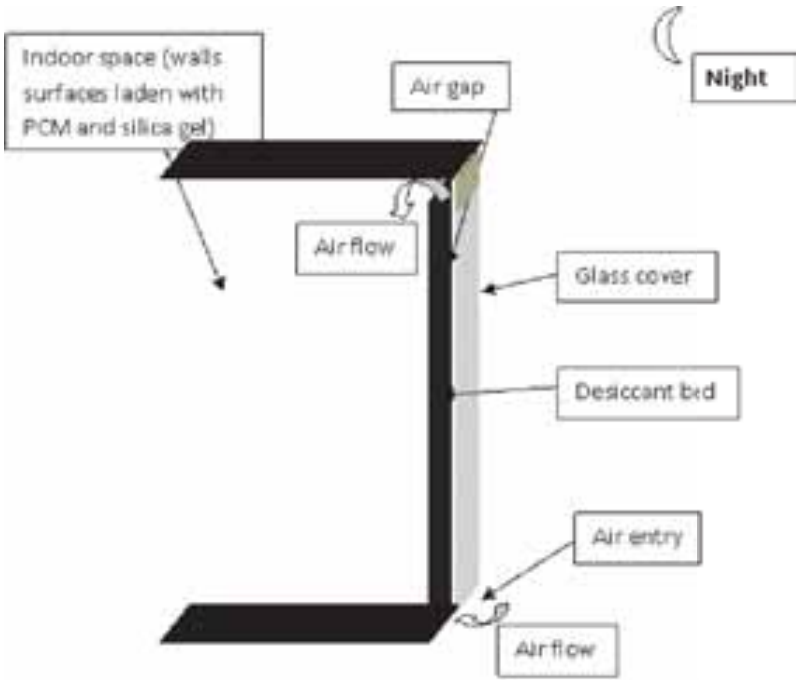

Fig. 2: Proposed Passive Regeneration Strategy for Interior Surfaces

2.2. Passive Ventilation _ Airflow

The air flow rate is based on the simulated results of Manyumbu et al. (2014). A PCM channel is expected to get charged during the day and then provide heating that then result in air flow in the channel at night time. According to Manyumbu et al (2014) the average velocity of air through the channel during charging and discharging is given by eq. 1.

$$u = \left(\frac{C_v g \beta L^2 b Nuk h_g}{24 \mu c_p} \right) \left(\frac{T_{pcm} - T_{in}}{Nuk / b + h_g} \right) \quad \text{(eq. 1)}$$

A ventilation flow rate of circa 1ach was obtained in the simulations and this is used as input in the current study.

2.3. Mathematical Formulations and Assumptions

Mathematical modeling and spreadsheet simulation are employed in this study. The mathematical modeling is based on the mass and energy principles while applying appropriate boundary and initial conditions. A Quasi-steady state and uniform assumptions are used in modeling the external silica bed processes. Parameters of importance are evaluated, these include exit air temperature and humidity. Energy balance equation for the external silica gel bed system during bed regeneration using solar energy including sorption heat can be generally represented by the following eq. 2.

$$T_f = T_a + \frac{\eta I A_c + Q_s}{2 \dot{m}_a c_p} \quad \text{(eq. 2)}$$

In eq.1, T_a is the environmental air temperature, η is the efficiency of converting solar radiation to useful thermal regenerating energy, I is the normal solar radiation received by the channel, c_p is specific heat capacity of air and Q_s is the sorption heat of silica gel. During the night, outdoor air temperature is dried as it passes through the channel whose absorber surface is the silica gel bed. Air conditions (temperature and humidity) are obtained based on the following eq. 3 and eq.4.

$$Q_{sorp,t-1} = m_a C_a \left(T_f - T_a \right) + m C_{sg} \left(T_{sg,t} - T_{sg,t-1} \right) \quad \text{(eq. 3)}$$

$$X_{ao} = \min \left(\left(X_{ai} + \frac{1 \times 10^{-4} m}{\dot{m}_a (1 + X)} \left(X - X_e \right) \right); 0.003732 e^{0.062T} \right) \quad \text{(eq. 4)}$$

Based on the obtained conditions of the bed and air, the humidity of the exit air is then obtained. The drying power of the silica gel bed depends on the initial dry state and this together with the ambient air conditions determines the extent to which the internal surfaces can be regenerated. Air leaving the bed is expected to be drier and warmer than the night outdoor air, but must still be cool enough to effect PCM regeneration. While elevated temperatures are favorable for the desiccant regeneration, PCM regeneration requires low temperatures. This conflict is somehow compensated by the heat of desorption since the process is endothermic.

2.4. External Bed Regeneration and Air Drying

Regeneration of the external silica gel bed is dependent on the condition of the bed, the conditions of the drying air and the amount of air that is responsible for the drying process. One limiting (or boundary) condition is the combination of the drying capacity of the air and the flow rate. If the air gets saturated it means it cannot absorb any more moisture. The amount of moisture removed from the silica gel bed is the function of moisture uptake by the drying air and its flow rate.

2.5. Internal Surface Regeneration

The condition of the air leaving the external silica gel bed determines the rate and extent of regeneration achievable. While it cannot be disputed that heating air improves its drying capacity, it must be noted that air humidity plays a significant role in the process. If air is saturated it does not matter at what temperature it is, it will not take up moisture. Low-temperature regeneration is possible if the regenerating air is pre-dried to low enough humidity levels. According to Ondier et al. (2010), it is clear that the relative humidity plays a significant role in the moisture exchange process. The temperature affects the rate of drying, but the relative humidity determines the extent of drying at the end of the process determined by the equilibrium moisture content. While saturated vapor pressure of moist air exponentially increase with temperature, Buck (1981), which trend is also followed by the reduction in moist air relative humidity, drying can sufficiently be achieved with relative humidity reduction in low temperature situations. Janssen (2011) concluded that the claim that thermal diffusion has a significant impact on vapor transport in porous media was flawed. According to Dalton's Law, moisture flux at a surface is given by;

$$\dot{m}_w = k\left(X_{sat} - X\right) \quad \text{(eq. 5)}$$

In eq.5 k is a constant that characterize the moisture exchange, X_{sat} is the saturation (equilibrium) moisture content while X is the moisture content, the difference of the two becomes the driving force. The surface vapor pressure is dependent on the moisture condition of the silica gel. X_{sat} and X are evaluated at the previous and current time steps respectively.

2.5.1. Silica Gel Regeneration

The relative humidity of the air leaving the external silica gel bed determines the rate and extent of silica gel regeneration achievable. The relative humidity is a function of both temperature and the specific humidity. The external silica gel bed dries the air and at the same time raises its temperature as the process is exothermic. The sorption heat generated during air drying will raise the temperature of the bed as well as that of the air being dried. Both drying and temperature increase lower the relative humidity, and this is desirable for the internal silica gel regeneration. However, it needs to be noted that the increase in temperature is not favorable for PCM regeneration. The specific humidity of air leaving the room is estimated based on eq. 6 below.

$$X_{ao} = \max\left(\left(X_{ai} + \frac{6\times10^{-5} m}{\dot{m}_a\left(1+X\right)}\left(X - X_e\right)\right); 0.0061X^{0.4329}e^{0.062T}\right) \quad \text{(eq. 6)}$$

In eq. 6 X_{ao} is the specific humidity of air leaving the room, X_{ai} is the specific humidity of air entering the room, X is the moisture content of silica gel, X_e is the equilibrium moisture content of silica gel, m mass of silica gel, $\dot{m}_a$ mass flow arte of air and is the temperaure of air in the room. Room air temperature is estimated using eq. 7 below assuming the relationship of a vertical surface and the air interaction with it convectionally (Paul and Alzwayi, 2010).

$$T_{room} = T_{PCM} + 0.38\left(T_{ai} - T_{PCM}\right) \quad \text{(eq. 7)}$$

In eq. 7, T_{room} is room air temperature, T_{PCM} is the PCM laden wall surface temperature and T_{ai} is the temperature of air entering the room from the external silica gel bed.

2.5.2. PCM Regeneration

PCM regeneration is a process of heat removal thereby freezing the PCM. The process, therefore, requires regenerating air that is at a lower temperature than the phase change temperature. The greater the temperature difference between the PCM and the regenerating air the improved the rate of regeneration and the regeneration extend that can then be achieved within the given regeneration period. The increase in air temperature during drying is therefore not desirable for PCM regeneration process. The night outdoor temperatures are highly subdued hence despite the increase of temperature because of the sorption heat during drying, the temperatures are still lower than the phase change temperature of around 26^{o}C. The heat transfer coefficient h at the wall surface is given by eq. 8 below. The heat transfer q is then denoted by the subsequent eq. 9.

$$h = 4.31\Delta T^{0.293} \quad \text{(eq. 8)}$$

$$q = 4.31\Delta T^{1.293} \quad \text{(eq. 9)}$$

PCM conduction has been ignored considering that the plaster/PCM mix will result in thermal bridges that are assumed to render the rate of conduction higher than the convective heat transfer rate. According to Amin et al (2009) for PCM of thickness less than 5mm, the heat flow resistance can be considered to be negligible. The heat transfer between the wall is, therefore, dependent on the difference between the wall and room air temperatures.

3. Results and Discussions

The simulations were carried out using a simple spreadsheet program based on the equations presented in the preceding sections. The results presented here are based on channel depth (air gap) of 0.02m, channel height

and width of 3m with 5kg of silica gel bed. While there are conflicting requirements in terms of conditions favorable for the regeneration of PCM and desiccant a compromise can be reached that result in desirable regeneration for both. The mass of silica gel in the external bed must be simulated in relation to other conditions such as the initial bed temperature and the desired temperature for the dried air meant for internal surfaces regeneration. The complexity of the processes involved requires a careful analysis in order to predict feasibility. The preliminary predicted regeneration conditions are; silica gel dryness of circa 0.07kg/kg and circa120 kg of PCM frozen if the phase change heat of fusion of 200kJ/kg is assumed. During summer the contribution of the desorption heat towards PCM regeneration is around 11% while in winter it is just 4% when the silica gel has reached the lowest best regeneration level.

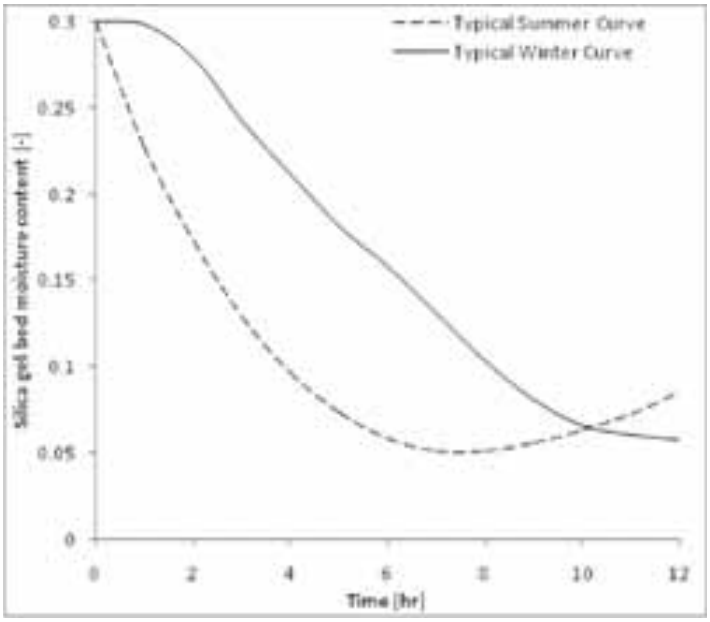

Fig. 3: The extent of external bed regeneration for a west-facing channel (January and June 1999 data)

From fig. 3, it is clear that it is possible to bring down the moisture content of silica gel bed within a solar channel from 0.3kg/kg to about 0.05kg/kg. It must be noted however that during summer, the regenerating process result in an increase of the moisture content of the bed beyond 8hours of regeneration. If the process is allowed to carry on up to 12hours the moisture content of the bed will approach 0.1kg/kg. In winter moisture content of around 0.05kg/kg is reached around the 12th hour of the regeneration process.

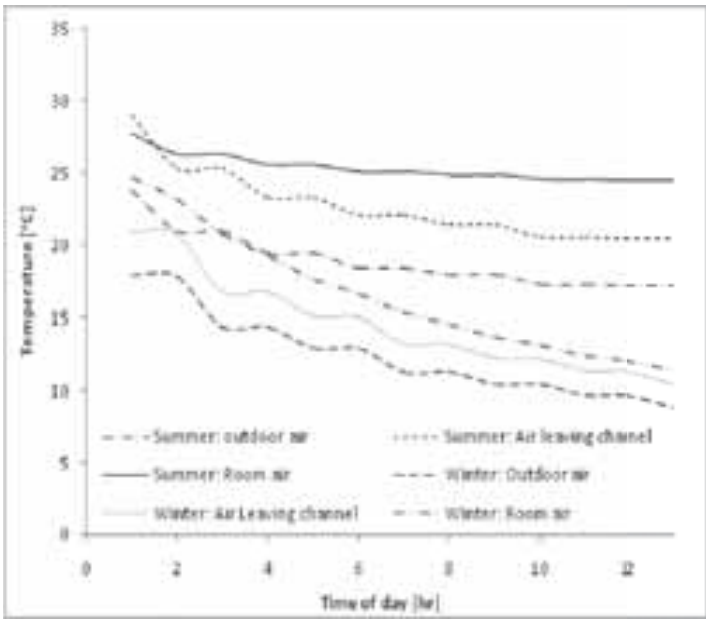

Fig. 4: Air conditions entering and leaving the external silica gel bed (based on January and June 1999 data)

Fig. 4 shows the outdoor temperatures, the simulated temperatures for air leaving the external silica gel bed as well as the room temperatures (estimated from a correlation between PCM surface temperature and natural convective air temperature of Paul and Alzwayi, 2010). The room air temperatures are generally quite low around due to very low outdoor temperatures. Low temperatures coupled with the fact that the drying effect of the external bed becomes less with time, continuing the regenerating process will instead result in an undesirable effect of increasing the moisture content of the interior surfaces. In summer, the effect is less due to generally higher temperatures. It is, therefore, important to have different regenerating time periods for the two seasons.

Fig. 5 below shows the simulated regeneration curves for both silica gel and PCM for the winter season. The moisture content of the silica gel of about 0.08kg/kg is possible. Beyond 6hours of the regeneration process, the moisture content approaches 0.1kg/kg (which is less effective during humidity buffering), hence it becomes advisable to stop the regeneration process since adequate PCM regeneration is already attained. For summer, the regeneration process must go all the stretch to get high PCM regeneration percentage, fig. 6.

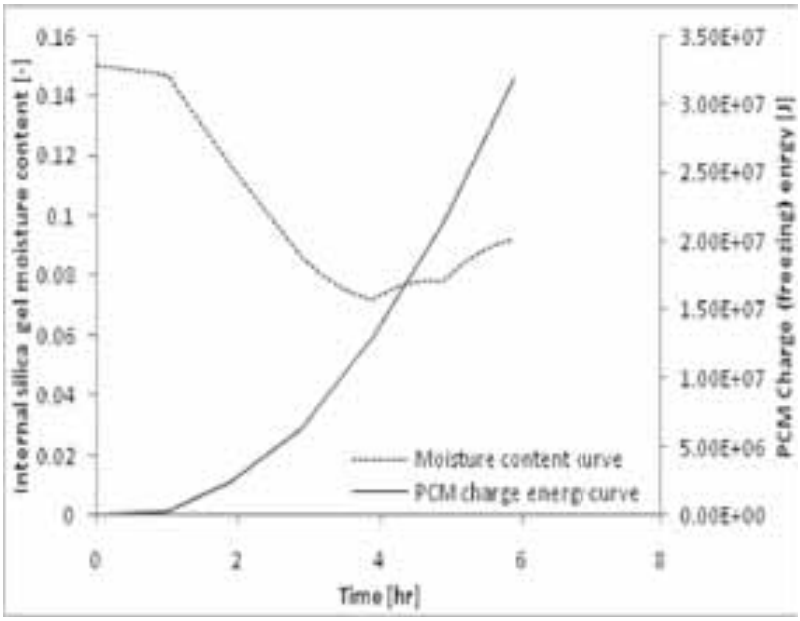

Fig. 5: The extent of internal surfaces regeneration (winter)

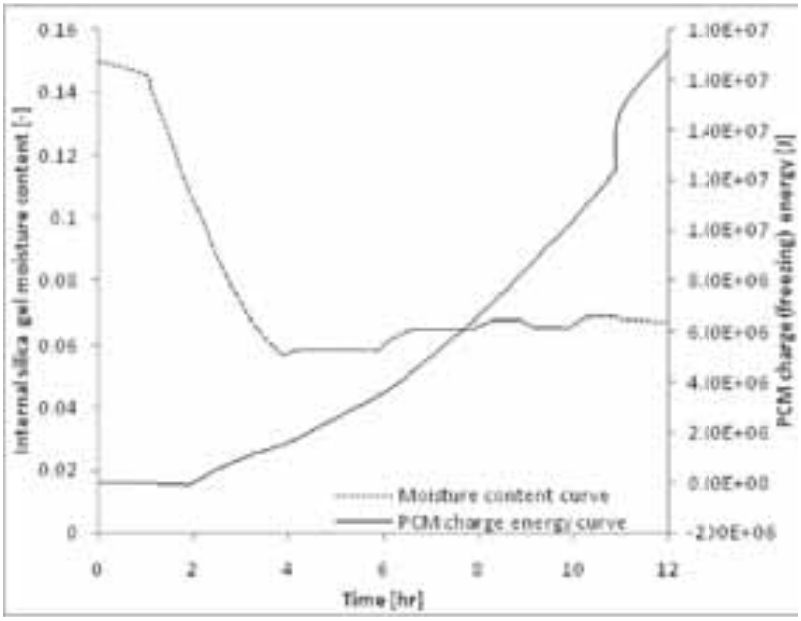

Fig. 6: Internal surface regeneration (summer)

An evaluation of the effectiveness of both the regenerated silica gel and PCM is shown in fig. 7 and fig. 8 below. Fig. 7 is indicating the effectiveness during winter with PCM phase change temperature being set at 27°C with varying mass of silica gel in the interior surfaces. PCM mass is assumed to be matching the available coolness from the regenerating air. A mass of 8kg of silica gel result in the highest performance of humidity buffering effectiveness (considering a 10% relative humidity change) of about 90%, and this correspond to a cooling effectiveness of 122%. This implies that there is possible over cooling of 22%.

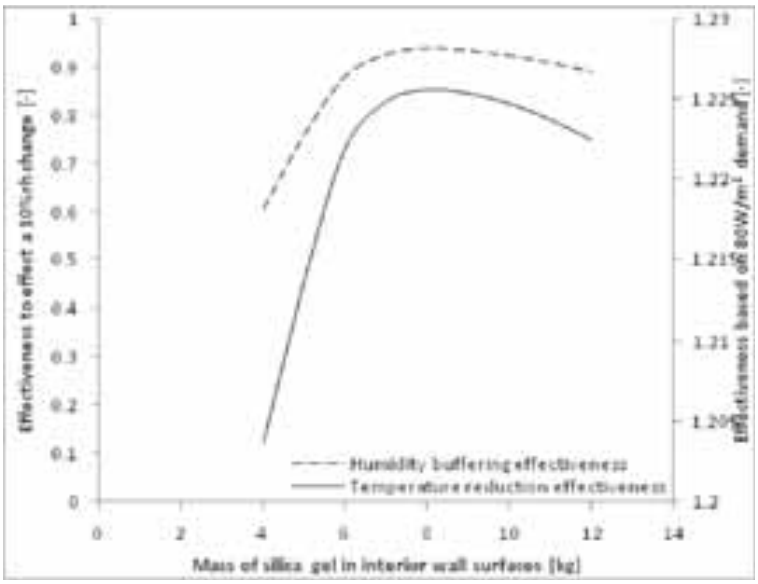

Fig. 7: Variation of the buffering effectiveness with varying silica gel mass within the interior walls for winter season (PCM phase change is set at 27°C), room volume is 27m³

Fig. 8 indicates the estimated humidity and temperature buffering effectiveness of the interior surfaces at varying masses of silica gel within the surfaces for the summer season. Evaluations were carried out at two PCM phase change temperatures of 27°C and 28°C. Improved buffering effectiveness is noted for both humidity and temperature, more so on the later. Elevated PCM phase change temperature results in increased temperature difference and hence improved regeneration. Similarly elevated temperatures have the effect of improving the drying effect of the room air and thus improved regeneration. It is clear that while silica gel regeneration is good, PCM regeneration is somewhat low because of the temperatures of the regenerating air which are fairly high.

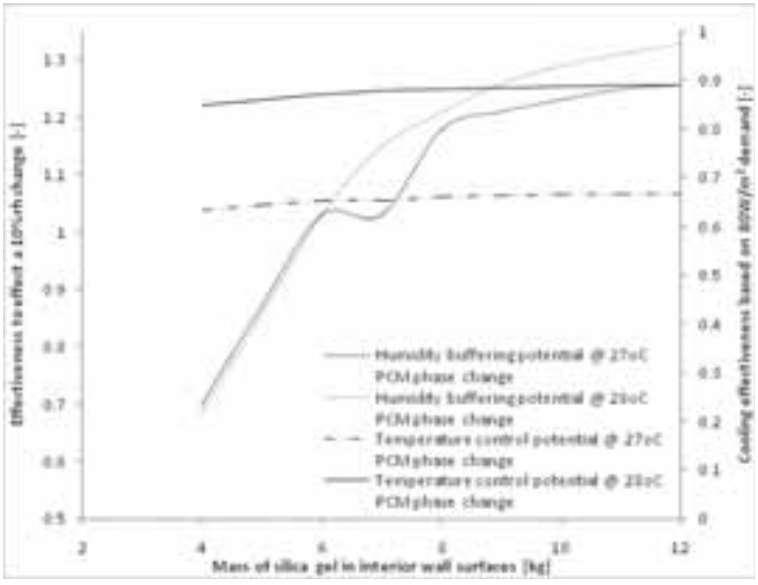

Fig. 8: Variation of the buffering effectiveness with varying silica gel mass within the interior walls for the summer season (PCM phase change is set at 27°C and 28°C), room volume is 27m³

4. Conclusions

The possibility for regenerating both the PCM and Silica Gel for temperature and moisture buffering in an office during daytime occupancy is demonstrated. Using simple mathematical transient models which were implemented in an excel spreadsheet the regeneration of both PCM and Silica Gel in interior wall surfaces could be predicted. Due to high parameter sensitivities and the rudimentary approach applied, it is imperative to conduct an experimental validation in order to firmly establish the feasibility. With further analyses and developments it is possible to have a feasible regeneration strategy that provides adequate humidity and temperature buffering passively for an office space for certain climates.

5. References

Shilei L., Guohui F., Neng Z., Li D., 2007. Experimental study and evaluation of latent heat storage in phase change materials wallboards. Energy and Buildings 39, 1088-1091

Cabeza L. F., Castellon C., Nogues M., Medrano M., Leppers R., Zubillaga O., 2007. Use of microencapsulated PCM in concrete walls for energy savings. Energy and Buildings 39, 113-119

Baetens R., Jelle B. P., Gustavsen A., 2010. Phase change materials for building applications: A state-of-the-art review. Energy and Buildings 42, 1361-1368

Karim L., Barbeon F., Gegout P., Bontemps A., Royon L., 2014. New phase-change materials components for thermal management of the light weight envelope of buildings. Energy and Buildings 68, 703-706

Rudd A. F., 1994. Development of a Moisture Storage Coatings for Enthalpy Storage Wallboard. ASHRAE Transactions: Research 100, 84-90

Manyumbu E., Martin V., 2013.Towards Passive Humidity Control for an Office Building, Modeling and Spreadsheet Simulation of a Desiccant Regeneration Strategy. Proceedings of the 2nd International Energy Storage Conference, Trinity, Ireland, pp. 171-175

Manyumbu E., Martin V., Torsten F., 2014. PCM-Solar Channel for Night Ventilation in a Passive Comfort Provision Strategy for an Office in Harare, Zimbabwe, Proceedings of the GRAND RENEWABLE ENERGY, Tokyo, Japan

Ondier G. O., Siebenmorgen T. J., Mauromoustakos A., 2010. Low-temperature, low-relative humidity drying of rough rice. Journal of Food Engineering 100 , 545–550,

Buck A. L., 1981. New Equations for Computing Vapor Pressure and Enhancement Factor, Journal of Applied Meteorology 20, 1527-1532

Janssen H., 2011. Thermal diffusion of water vapour in porous materials: Fact or fiction?, International Journal of Heat and Mass Transfer 54, 1548–1562

Alzwayi A. S., Paul M. C., 2010. An Analytical Investigation of the Physical Dimensions of Natural Convection Flow on a Vertical Heated Plate, Proceedings of the World Congress on Engineering Vol II, June 30 – July 2, 2010, London, UK

Amin N. A. M., Belusko M., Bruno F., 2009. Optimisation of A Phase Change Thermal Storage System, World Academy of Science, Engineering and Technology 3, 675–679

Conference Proceedings

Solar World Congress 2015

Daegu, Korea, 08 – 12 November 2015

CONCEPT 22/26, A HIGH PERFORMANCE OFFICE BUILDING WITHOUT ACTIVE HEATING, COOLING AND VENTILATION SYSTEMS

Lars P. Junghans[1]

[1] University of Michigan, Ann Arbor (USA)

Abstract

The introduced building concept goes beyond the conventional high performance building discussion by introducing an office building without any active systems for heating, cooling and ventilation. The building is accomplished in July 2013 and is located in the cold climate of Austria. The intelligent control of the building façade is the heart of the innovative building energy concept. It controls automated natural ventilation openings by using demand optimized automation strategies. Results of the first two years of building operation are demonstrating that the comfort level is acceptable in all seasons and that there are no complaints from beside the occupants. The exemplary realized building project demonstrates how innovative building automation technology can be used to reduce the total energy demand for building operation in a cold climate. Its technology can be used in other climate regions as an innovative hybrid ventilation concept.

Keywords: *Zero Net Energy Building, High Performance Building, Hybrid Ventilation, Solar Architecture*

1. Introduction

The introduced building concept goes beyond the conventional high performance building discussion by introducing an office building without any active systems for heating, cooling and ventilation. The building is accomplished in July 2013 and is located in the cold climate of Austria. The intelligent control of the building façade is the heart of the innovative building energy concept. It controls automated natural ventilation openings by using demand optimized automation strategies. Results of the first two years of building operation are demonstrating that the comfort level is acceptable in all seasons and that there are no complaints from beside the occupants. The exemplary realized building project demonstrates how innovative building automation technology can be used to reduce the total energy demand for building operation in a cold climate. Its technology can be used in other climate regions as an innovative hybrid ventilation concept.

Architects and engineers are in the agreement regarding the goal in net zero energy building design - to improve the building envelope so that the energy demand not met by passive systems could be covered by on-site energy harvesting systems (Torcellini,2006). Most researchers agree that this goals cannot be met in a building without active systems (Sartori,2012,Lu,2015).

Office buildings have relatively high internal heat gains from occupants, electrical appliances, artificial lighting and computer server stations. High internal heat gains result in generally higher room temperatures throughout the year. These higher room temperatures are helpful to reduce the heating energy demand in the winter but can increase the cooling energy demand in the summer. The right balance between heat gain and heat loss must be found to meet the thermal demands in all seasons.

The technical system of the “Concept 22/26” takes a different road then the conventional zero net energy building. An office building without any conventional active systems for heating, cooling and ventilation. The “Concept 2226” was realized in July 2013 and is located in the cold climate of Austria. The name Concept 2226 reflects the technical goal of operating a building in the highest thermal comfort levels at an internal temperature range between 22 and 26 C without any active systems. The thinking behind the Concept 22/26 system departs radically from conventional approaches.

doi:10.18086/swc.2015.08.07 Available at http://proceedings.ises.org

Two methods have been applied to achieve the goal of the Concept 22/26 building. First, the building envelope has been improved so that the internal heat release is able to cover the heating energy demand in the heating season. Then, an innovative building automation system has been developed to control the natural ventilation openings based on the internal carbon dioxide concentration, temperature levels, and occupant demands. The challenge is to ensure comfortable room conditions and indoor air quality without using conventional heating or cooling devices. The room temperature of a building is defined by the factors heat gains, heat loss and internal thermal heat storage effects. To reduce the energy demand for building operation, we must control these three factors in a way that the room temperatures are in or close to the thermal comfort field. In other words, the room temperatures must be relatively low in the summer time and relatively high in the wintertime.

The outline of this paper is as follows: First, the methodology of the technical concept are explained in section 2. Section 3 presents the results of the measurements and the occupant surveys. Section 4 presents the conclusions and implications.

Fig. 1: The realized office building Concept 2226 (Photo: E. Hueber)

2.1. Building Envelope

To meet the goal for the heating season, the "Concept 22/26" building is designred with a building envelope with an extremely low heat transfer and with a high thermal capacity. The huge time delay of the heat flow resulting from the 72 cm external wall construction helps to maintain comfortable conditions even in extreme cold time periods (Tay et al.,1974, Shaviv, 2001). The building has a triple glazing with a U-value of 0.6 W/m^2K and an SHGC value of 0.5. A blower door test was done after completion oft he building. The infiltration was measured to have an average air change rate of 0.08 1/h. The deep structured facade design with a huge dimension of the overhang and wingwall deals as a fixed shading device. No active shading devices is added to the building. The building has an uncovered concrete slab of 20 cm . It is used as an internal thermal mass.

Architects and engineers are in the agreement regarding the goal in net zero energy building design - to improve the building envelope so that the energy demand not met by passive systems could be covered by on-site energy harvesting systems (Torcellini,2006). Most researchers agree that this goals cannot be met in a building without active systems (Sartori,2012,Lu,2015).

2.2. Building Automation

The goal of the building automation design is to operate the natural ventilation openings in a way so that maximal comfort and indoor air quality can be achieved without the use of conventional HVAC units. A balance must be found to (1) ventilate the amount of fresh air that needs to be supplied to achieve indoor air quality requirements, and (2) conserved heat in the room in the heating season. A conflict arises in the transition period and the winter season when natural ventilation is used as the fresh air supply source and the external air temperature is below the minimal comfort indoor air temperature (Heisselberg and Tjelflaat, 2006). Fresh air supply is needed to insure an appropriate indoor air quality by removing internal pollutants like CO_2. However, natural ventilation in the heating season is a heat sink and the time period for natural ventilation should be as short as possible.

To avoid too cool temperatures even in extreme situations, a new building automation system controls natural ventilation openings individually for each room, depending on the user demand and the weather condition. It uses predictive control strategies to use renewable energy sources and sustainable grid energy in a more efficient way. To maximize the performance of the automated natural ventilation openings, a control logic was developed and tested in a simulation model. It uses an on-off controller with death band, DB, (also known as hysteresis controllers) to actuate natural ventilation openings, mechanical ventilation, and heating and cooling

devices. A night ventilation strategy is used to cool the internal thermal mass in the summer time (Haase and Amato, 2009).

The novel hybrid building automation uses automated window openers as the main part of the innovative building energy concept. It controls the natural ventilation openings based on the internal carbon dioxide concentration, temperature levels and the occupant demands to ensure comfortable room conditions in all seasons (El Mankibi and Michel, 2009). The hybrid control logic is extended by the control parameters of external humidity level and artificial lighting for the use in Building 22/26. It ensures that the internal thermal comfort limit for relative humidity will not be exceeded and considers the internal humidity emission of occupants. The control of the artificial lighting ensures that the illuminance value will meet the required threshold value of 500 Lux at occupied working spaces. It will also provide additional internal heat gains in extremely cold situations in the heating season. Figure 2 shows the flow plan of the building automation in a simplified form.

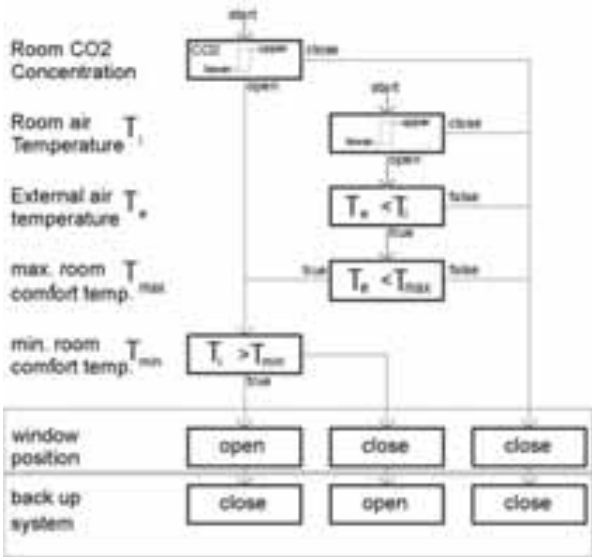

Fig. 2: Simplified illustration of the building automation

A simple predictive control strategy is integrated into the control strategy for the natural ventilation. The goal of the predictive control is to support the novel building automation system in operating the building in the winter or summer "mode". Predictive control is particularly important in the Concept 22/26 to avoid too cold temperatures caused by night ventilation. The operation mode is defined by the external temperature. The system predicts too cold temperatures when the external temperature undergoes a predefined treshold value for a given time period. It is the goal to use an advanced prdictive control logic in the future that involves single zone simulation tools.

The building control concept includes a back up operation to ensure comfortable room conditions in extreme cold weather situations. Additional internal gains are used for back up heating in time periods where extreme cold temperatures are expected in the morning hours. The artificial lighting is going to be used as additional heating to increase the surface temperature of the internal thermal mass. The back up system is controlled by the predictive control logic.

2.3. Measurement Device

Each room is equipped with an air temperature, humidity and a CO_2 concentration sensor. The sensors are located at the inside wall at a height of 1.1 m. The temperature, humidity and CO_2 concentration sensor is a GIRA SK01. The producer provides an accuracy of 0.3 K fort he temperature, 3 % fort he humidity and 50 ppm fort he CO_2 concentration. The room temperature, humidity and CO_2 concentration is measured for each room in the building since August 2013.

2.4. Occupant Survey

An occupant survey is done in March 2015 to validate the occupant satisfaction for the termal comfort and the internal air quality. The survey contains questions about the satisfaction in the winter and summer season in general . It also includes questions about the most extreme time periods in each season.
The questions are similar to the method introduced by Fanger (Fanger), where the occupant has 7 options to

evaluate the condition for much too warm, too warm, slightly warm, OK, slightly cold, too cold and much too cold. For the indoor air quality, the occupants have had five options: good, OK, acceptable, poor, very poor. Additional questions are asking for the gender, the typical type of clothing and the discomfort caused by air drag effects.

2. Results

3.1. Room Temperatures

Results for the first 1.5 years of operation are illustrating that the room temperatures are in the comfort level the winter season in all rooms of the building. The room air temperatures in the north oriented office space are 0.5 K below these of the south oriented office space. The internal surface temperatures are at an average of 22 C.

In the summer, the temperatures are in the comfort level in most of the time. There are a few hours with temperatures above the comfort standard in the west oriented office space. However, the temperatures are in the comfort field for 95% of the summer time.

Fig. 3 and Fig. 4 show the measured temperature in the west oriented office room at the most extreme weather periods in the winter (fig.3) and in the summer (fig.4). The west oriented open space office room has the highest challenge to be operated without mechanical systems because it does not have solar gains in the winter and does have extreme solar gains in the summer time. The room is occupied by maximal 8 people and each working space is equipped with a computer (180-230 W).

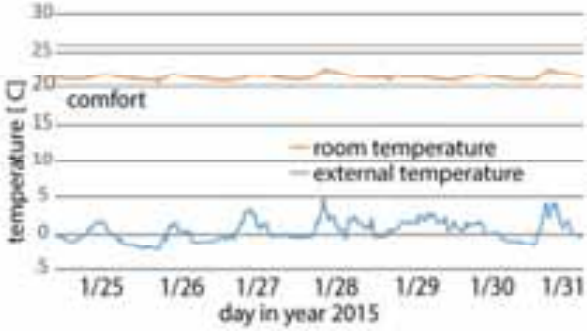

Fig. 3: External and room temperature for the west oriented office space in the coldest week in 2015

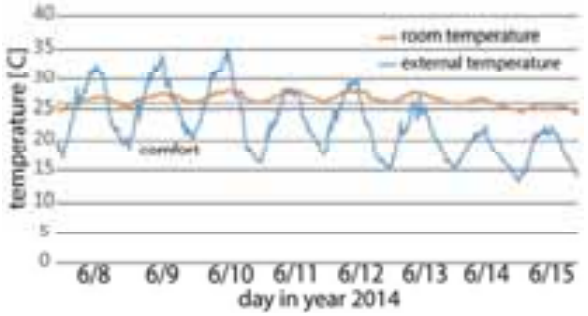

Fig. 4: External and room temperature for the west oriented office space in the warmest week in 2015

For the winter, the internal air temperature drops at time periods where the ventilation openings are open for fresh air supply. However, the temperature never goes below the comfort limit of 20 C.

The measured data for the hottest week in the summer time illustrates that the room temperature rise to as much as 3 K above the temperature goal of 26 C. It also illustrates that the night ventilation effect is not always sufficient to cool the internal thermal mass to an appropriate level (Haase et al.,2009). However, the time period with temperatures above the static comfort limit of 26 C is relatively short. The majority of occupants do accept higher temperatures when the external temperature is high (section 3.4).

3.2. CO_2 Concentration

Figure 5 shows the result of the CO_2 concentration for the west oriented office space. The measurement is done in the same time period in the winter like the temperature measurement in figure 3. It illustrates that the CO_2 concentration does not exceed the limit for the good indoor air quality of 1000 ppm. The automated natural ventilation opening is activated three to four times a day. A comparison between the room temperature (fig. 3) and the CO_2 concentration shows that the room temperature does not drop below the comfort limit at time periods where the ventilation opening are open.

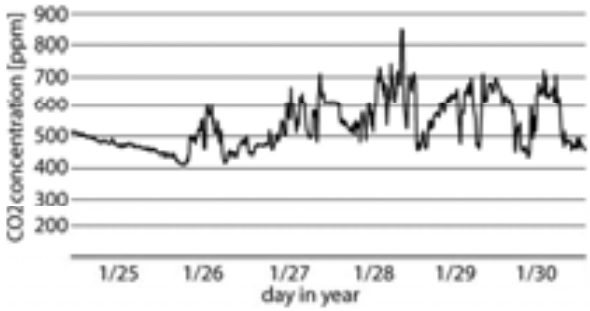

Fig. 5: CO_2 concentration in the west oriented office space in the coldest week in 2015

3.3. Relative Humidity

Figure 6 shows the internal relative humidity in the west oriented office space. The measurements show that the relative humidity is below 40%. It is above the recommended comfort limit of 30% and is therefore sufficient to meet the thermal comfort expectations (ISO norm). The constant relative humidity in the room is partly produced by the occupants. In the summer, the relative humidity is between 40 and 50%. It meets the comfort limit of 60%.

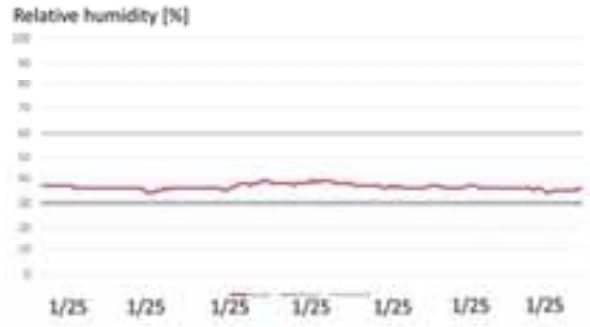

Fig. 6: Relative Humidity in the west oriented office space in the coldest week in 2015

3.4. Occupant Survey

Fig. 7 and fig. 8 shows the results of the occupant survey for the heating and the cooling season. It shows that the majority of the occupants are generally satisfied by the human comfort in both seasons.

Fig. 9 and Fig. 10 show the evaluation of the indoor air quality. The results are demonstrating that the occupants are satisfied with the indoor air quality in all seasons. None of the occupants evaluated the indoor air quality as to be only “acceptable”.

Fig. 11 shows the evaluation of the human comfort at the coldest period. It shows that the majority of the occupants are satisfied with the comfort in the extreme period. One female occupant describes the room temperature as to be too cold. However, there is a larger group of occupants evaluating it as to be slightly too warm.

Fig. 12 shows the comfort evaluation for the warmest time period. Like in the figures before, it illustrates that the majority of the occupants are satisfied with the thermal comfort in the warmest season. The diagram shows that there is a group of four occupants which are evaluating the thermal comfort as to be too warm. These four occupants are located in the west oriented office space.

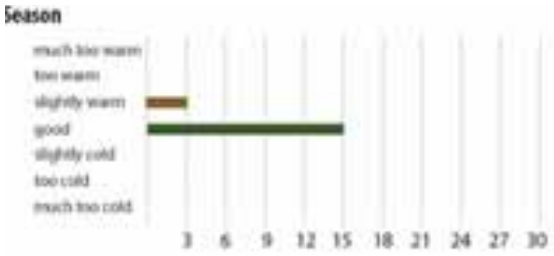

Fig. 7: Results of the occupant survey for the winter

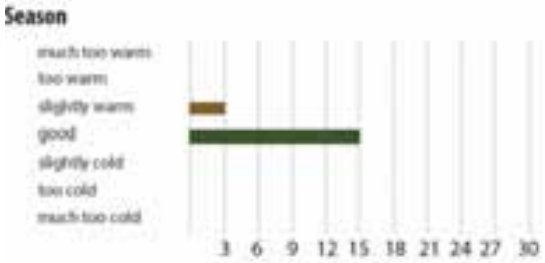

Fig. 8: Results of the occupant survey for the summer

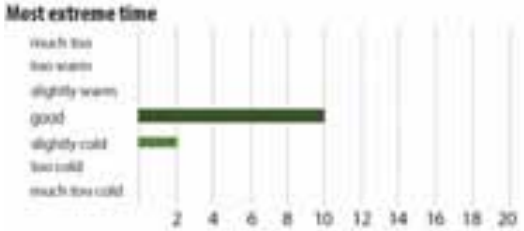

Fig. 9: Results of the occupant survey for the coldest time period in winter 2015

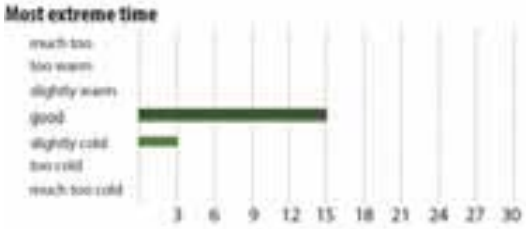

Fig. 10: Results of the occupant survey for the warmest time period in summer 2015

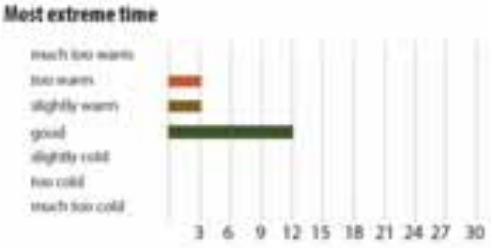

Fig. 11: Results of the occupant survey for the indoor air quality for the coldest time period in winter 2015

Fig. 12: Results of the occupant survey for the indoor air quality for the coldest time period in winter 2015

Notice: the occupants in the west oriented office space are mainly complaining about the temperatures with overheating in the time period from June 11 to June 13. The room temperatures in this time periods are above the comfort field even when the external temperature is relatively low. This illustrates that the adaptive comfort model introduced by Brager and DeDear (2008) is applicable in the controlled natural ventilation environment in this study.

None of the occupants have had any discomfort caused by the cold air drag effect at the ventilation openings or at the large windows. The occupants do not use additional local heating or cooling devices like resistance heaters to control the temperatures at the working space.

3.5. Indoor Air Quality

The Indoor air quality have been evaluated for the building at operation by a professional company. The concentration of the most critical components and pollutants have been measured. Also the VOC and germ concentration is measured. Their results are showing that the natural ventilation provides excellent indoor air quality conditions even in time periods where the ventilation openings are closed. Further tests will follow in the future. The results are showing that the pollution concentration is comparable like for a building with mechanical ventilation (Chou et al.2006).

3.6. Energy Demand

The total use energy demand for building operation including artificial lighting and electrical devices is measured for the Concept 22/26 for all time periods after completion of the project. The average specific use energy demand of the building is 38 kWh/m^2 year (measurement time period 9/1/2013 to 8/30/2014). The office space has a specific use energy demand of 42 kWh/m^2. The owner of the building operates the building with electricity that is produced with renewable energy sources (photovoltaic, hydropower). This type of primary energy source ensures that the building can be operated almost without greenhouse gas emission. The data shows that the use energy demand of the Concept 22/26 is 30% below comparable high performance buildings.

3.7. Improvements in Building Operation

Like every prototype, minor improvements needed to be done on the building control logic. (1) It was planned to operate only two ventilation openings per room to provide night ventilation. The operation logic have been changed to have 5 ventilation openings available for the night ventilation. (2) Some of the windows are now equipped with curtains to avoid radiation asymmetry in the summer time.

4. Conclusion

The measurement results for the Concept 22/26 building demonstrates that a building can be operated without conventional heating, cooling and ventilation systems in a cold climate when innovative building automation technology is paired with a well designed building envelope. It also illustrates that the demand controlled natural ventilation technology can significantly reduce the overall energy demand of an office building.

As indicated in the results section, measured room temperatures have been shown to be at least 21 C for all occupied hours in the year and in all rooms of the building. A small number of hours with overheating problems have been counted in the west oriented office space. However, the results demonstrate that the number of hours with overheating problems never exceed 3% of the total operation time of the building. Furthermore, the results of the occupant survey are illustrate that the higher temperatures are accepted when the external temperature is high.

In general, the automation concept of the Concept 22/26 is very effective in a building with hybrid ventilation to increase the number of hours where no mechanical heating or cooling is needed. The results are promising to be effective as a natural ventilation control in a hybrid ventilation system in even more challenging climate regions.

The results of the occupant survey illustrate that the controlled natural ventilation concept provides comfortable conditions for the majority of occupants in most of the operation time. It shows also that there is a minority of occupants, which are not satisfied in most extreme time periods with very cold or hot weather. Localized active solutions might be a good solution for these very short time periods.

On the basis of these results, we believe that the Concept 22/26 can be effectively applied into hybrid-ventilated office buildings suiltable for a wide range of climate regions.

5. References

Brager, G.,L. Baker, 2008, Occupant Satisfaction in Mixed-Mode Buildings, Proceedings, Air Conditioning and the Low Carbon Cooling Challenge, Windsor, UK, July.

Brandemuehl M.J., Braun J.E.,1999, Impact of demand controlled and economizer ventilation strategies on energy use in buildings, ASHRAE Transactions 1999, 105, 39-44

Chou P.C., Chiang C.M, Lee C.Y, Ho M.C., 2006, Influence of Ventilation Routes on Indoor Pollutant Elimination in a Working Environment, Indoor and Built Environment 15 473.
Emmerich S.J. ,2006, Simulated Performance of Natural and Hybrid Ventilation Systems in an Office Building, HVAC&R Research 12 (4) (2006) 975-1004

El Mankibi and Michel P.,2009, Hybrid ventilation control design and management" ASHRAE Transactions 2009

Haase M., Amato A.,2009, An investigation of the potential for natural ventilation and building orientation to achieve thermal comfort in warm humid climates, Solar Energy 83 (3) (2009) 389-399

Heisselberg, P. and Tjelflaat P.O.,1999, Design procedure for hybrid ventilation, Proceedings of HybVent Forum 1999, Australia

Lu Y.,Wang S., Shan K.,2015, Design optimization and optimal control of grid-connected and standalone nearly/net zero energy buildings, Applied Energy 155,463-477

Marszal A.J., Heiselberg P., Jensen R.L., Norgaard J.,2012, On-site or off-site enewable energy supply options? Life cycle analysis of a Net Zero Energy Building in Denmark, Renewable Energy, Volume 44, 154-165

Sartori I.,Napolitano A.,Voss K.,2012, Net zero energy buildings:A consistent definition framework, Energy and Buildings 48, 220-232

Shaviv E.,Yezioro A., Capeluto I.G.,2001, Thermal mass and night ventilation as passive cooling design strategy, Renevable Energy 24,445-452

Tay, A. 0., Stevenson, M. G. and de Vahl Davis, G. ,1974, Using the finite element method to determine temperature distributions in orthogonal machining. Proc. Inst. Mech. Eng. Lond. 1

Torcellini P., Pless S., Deru M.,2006, Zero Energy Buildings: A critical Look at the Definition; Conference paper NREL CP 550 39833

Appendix: **UNITS AND SYMBOLS IN SOLAR ENERGY**

In 1977, a committee of ISES developed a set of recommended nomenclature for papers appearing in *Solar Energy.* This is a condensed and revised version

Volume
Volumes are measured in m^3 or litres (1 litre = 10^{-3} m^3). Abbreviations should not be used for the litre.

Flow

Temperature
The S.I. unit is the degree Kelvin (K). However, it is also permissible to express temperatures in the degree Celsius (°C). Temperature differences are best expressed in Kelvin (K).
When compound units involving temperature are used, they should be expressed in terms of Kelvin, e.g. specific heat J kg^{-1} K^{-1}.

2. NOMENCLATURE AND SYMBOLS

Tables 1-5 list recommended symbols for physical quantities. Obviously, historical usage is of considerable importance in the choice of names and symbols and attempts have been made to reflect this fact in the tables. But conflicts do arise between lists that are derived from different disciplines. Generally, a firm recommendation has been made for each quantity, except for radiation where two options are given in Table 5.
In the recommendations for *material properties* (see Table 1), the emission, absorption, reflection, and transmission of radiation by materials have been described in terms of quantities with suffixes 'ance' rather than 'ivity', which is also sometimes used, depending on the discipline. It is recommended that the suffix 'ance' be used for the following four quantities:

$$\text{emittance} \varepsilon = \frac{E}{E_b}\left(or \frac{M_s}{M_{sb}} \right)$$

$$\text{absorptance } \alpha = \frac{\Phi}{\Phi_i}$$

$$\text{reflectance } \rho = \frac{\Phi}{\Phi_i}$$

$$\text{transmittance } \tau = \frac{\Phi}{\Phi_i}$$

where E and ϕ is the radiant flux density that is involved in the particular process. The double use of α for both absorptance and thermal diffusivity is usual, as is the double use of ρ for both reflectance and density. Neither double use should give much concern in practice.

Table 1: Recommended symbols for materials properties

Quantity	Symbol	Unit
Specific heat	c	J kg^{-1} K^{-1}
Thermal conductivity	k	W m^{-1} K^{-1}
Extinction coefficient[+]	K	m^{-1}
Index of refraction	n	
Absorptance	α	
Thermal diffusivity	α	m^2 s^{-1}
Specific heat ratio	γ	
Emittance	ε	
Reflectance	ρ	
Density	ρ	kg m^{-3}
Transmittance	τ	
Efficiency	η	
Wavelength	λ	m
Frequency	ν	s^{-1}
Stefan-Boltzmann constant	σ	W m^{-2} K^{-4}
Time	t, τ, Θ	s

[+] In meteorology, the *extinction coefficient* is the product of K and the path length and is thus dimensionless.

Quantity	Symbol	Range and sign convention
Altitude	α	0 to ± 90°
Surface tilt	β	0 to ± 90°; toward the equator is +ive
Azimuth (of surface)	γ	0 to 360°; clockwise from North is +ive
Declination	δ	0 to ± 23.45°
Incidence (on surface)	Θ, i	0 to + 90°
	Θ_z	0 to + 90°
	Φ	0 to ± 90°; North is +ive
	ω	-180° to +180°; solar noon is 0°, afternoon is +ive
eflection (from surface)	r	0 to + 90°

Table 3: Recommended symbols for miscellaneous quantities

Quantity	Symbol	Unit
Area	A	m^2
Heat transfer coefficient	h	W m^{-2} K^{-1}
System mass	m	kg
Air mass (or air mass factor)	M	
Mass flow rate	$\dot{m}$	kg s^{-1}
Heat	Q	J
Heat flow rate	$\dot{Q}$	W
Heat flux	q	W m^{-2}
Temperature	T	K
Overall heat transfer coefficient	U	W m^{-2} K^{-1}

Table 4: Recommended subscripts

Quantity	Symbol
Ambient	a
Black-body	b
Beam (direct)	b
Diffuse (scattered)	d
Horizontal	h
Incident	i
Normal	n
Outside atmosphere	o
Reflected	r
Solar	s
Solar constant	sc
Sunrise (sunset)	sr, (ss)
Total of global	t
Thermal	t, th
Useful	u
Spectral	λ

Table 5: Recommended symbols for radiation quantities

	Preferred name	Symbol	Unit
a)	Nonsolar radiation		
	Radiant energy	Q	J
	Radiant flux	Φ	W
	Radiant flux density	Φ	W m^{-2}
	Irradiance	E, H	W m^{-2}
	Radiosity or Radiant exitance	M, J	W m^{-2}
	Radiant emissive power (radiant self-exitance)	Ms, E	W m^{-2}
	Radiant intensity (radiance)	L	W m^{-2} sr^{-1}
	Irradiation or radiant exposure	H	J m^{-2}
b)	Solar radiation		
	Global irradiance or solar flux density	G	W m^{-2}
	Beam irradiance	G_b	W m^{-2}
	Diffuse irradiance	G_d	W m^{-2}
	Global irradiation	H	J m^{-2}
	Beam irradiation	H_b	J m^{-2}
	Diffuse irradiation	H_d	J m^{-2}
c)	Atmospheric radiation		
	Irradiation	$\Phi\downarrow$	W m^{-2}
	Radiosity	$\Phi\uparrow$	W m^{-2}
	Exchange	Φ_N	W m^{-2}

Retrofitting Electrically Heated Single-Family Houses to Net-Zero Energy

Ricardo Bernardo[1], Henrik Davidsson[1]

[1] Division of Energy and Building Design, Lund University, Lund (Sweden)

Abstract

Only in Sweden, single-family houses account for approximately 30% of energy use in all buildings and a large part uses only electricity for heating. The potential for improvements on energy efficiency in these houses is large. This study theoretically investigates retrofitting of electrically heated Swedish single-family houses by using an air-source heat pump for both space heating and domestic hot water. Combination with solar collectors and solar cells were also theoretically investigated. Since this solution is an add-on to the existing heating system the investment cost can be reduced compared with a new heat pump installation for domestic hot water. The total annual energy reduction for domestic hot water and space heating in a Swedish single-family house when using the combined heat pump and solar thermal collectors was estimated to be roughly 70%. The remaining electricity demand for electric appliances can be covered by approximately 10 kWp solar cells therefore reaching net-zero energy level.

Keywords: *retrofit, net-zero energy houses, solar thermal, heat pump, single-family houses.*

1. Introduction (SWC_Heading1)

In order to meet the current energy and climate targets for 2020 and 2050 in EU countries, the existing building stock needs to be addressed. A construction boom was experienced across Europe after the Second World War and there is now a need for renovation. Since such houses have high levels of energy consumption, this is a good opportunity to also perform an energy renovation. For example in Sweden, single-family houses account for about 30% of energy use in all buildings and a large part, around 500 000, uses only electricity for heating (Swedish Energy Agency, 2013). The potential for improvements on energy efficiency in these houses is large. A typical Swedish single-family house uses in average 12200 kWh/y for space heating, 4500 kWh/y for domestic hot water (DHW) and 5000 kWh for household electricity (Swedish Energy Agency, 2015). It is common to upgrade the space heating system, for example by installing an air-to-air heat pump. Commonly, this decreases the space heating demand to levels close to the energy used for domestic hot water, shown later in Fig. 3. However, simple and cost-effective renovation solutions for reducing the energy consumption for domestic hot water production are not wide spread today.

This study investigates theoretically the retrofitting of electrically heated Swedish single-family houses by using an air-source heat pump for both space heating and domestic hot water. The heat pump not only heats the indoor air but is also connected directly to the existing hot water heater (boiler). The investigation addresses the system configuration, comfort level, control strategies and energy savings. Combination with solar collectors and solar cells were also theoretically investigated. Since this solution is an add-on to the existing heating system no large changes are needed which has the potential to significantly reduce the investment cost in comparison with a new heat pump installation for domestic hot water.

At this stage the investigation excludes some of the practical challenges and assumes that existing air heat pumps reach desirable temperatures for domestic hot water. The focus is instead on evaluating whether a conventional air heat pump can alternate on providing heat for space heating and domestic hot water and still reach comfort on both. This is the ground for any further investigation. A short discussion on possible practical problems and future work is addressed under the discussion chapter.

doi:10.18086/swc.2015.08.08 Available at http://proceedings.ises.org

2. Method

A model was built in TRNSYS in order to theoretically assess the potential for energy savings and possible challenges of using an air-source heat pump for both space heating and domestic hot water in a Swedish single-family house. The goal is to model a hybrid heat pump that alternates between providing lower temperature heat to space heating and higher temperature heat for domestic hot water. This thought to achieve high system efficiency. A sketch of the system is shown below in Fig. 1.

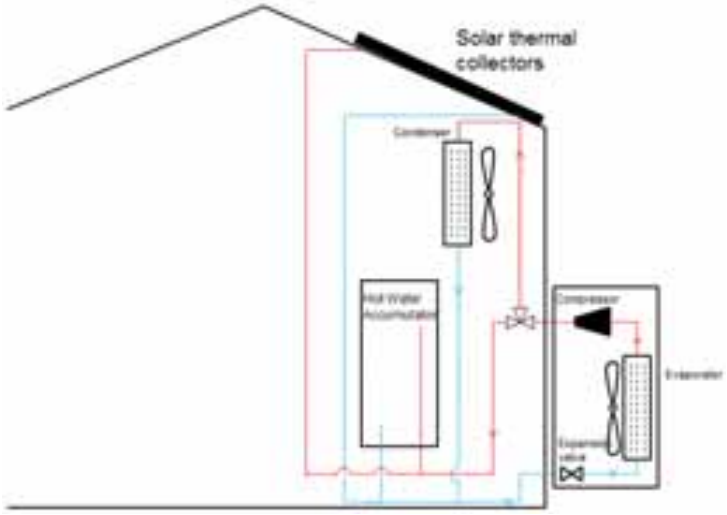

Fig. 1: Simplified sketch of the energy flow in the modelled system.

Since there is no standard TRNSYS model describing such a hybrid heat pump, the model was built by using two separate heat pump models: one air-to-air heat pump, Type922 Tess library (2015), and one air-to-water heat pump, Type941 Tess library (2015). For this purpose it was assumed that each of these heat pumps are common heat pumps in today's market and that they have conventional performance parameters such as described in the respective technical data sheets. In reality, a hybrid heat pump that delivers heat for both DHW and space heating at different temperatures may have different parameters and this is therefore a limitation of the investigation.

The operation of these two heat pumps was set in order to only allow one of them working at the time since the goal is to model one single heat pump. In this case, the air-to-water heat pump for DHW was prioritized. Hence, both the DHW storage and the house will work as heat "batteries" with only one heat source. These two heat "batteries" are charged alternately at different temperature levels and therefore at different efficiencies. In case there is deficit energy for space heating the existing direct electric heating was also modelled and is used as a backup heater. The heat pump starts at 20 °C and the direct electric heating at 18 °C. The solar collectors are used to preheat the incoming cold water to the air-to-water heat pump. When possible, during the summer period, the solar collectors alone will provide heat to DHW.

The model was used to estimate the comfort level, control strategies and energy performance. An overview of the modeled system in TRNSYS, the used components and the most relevant assumed parameters are illustrated in Fig. 2 and Tab. 1.

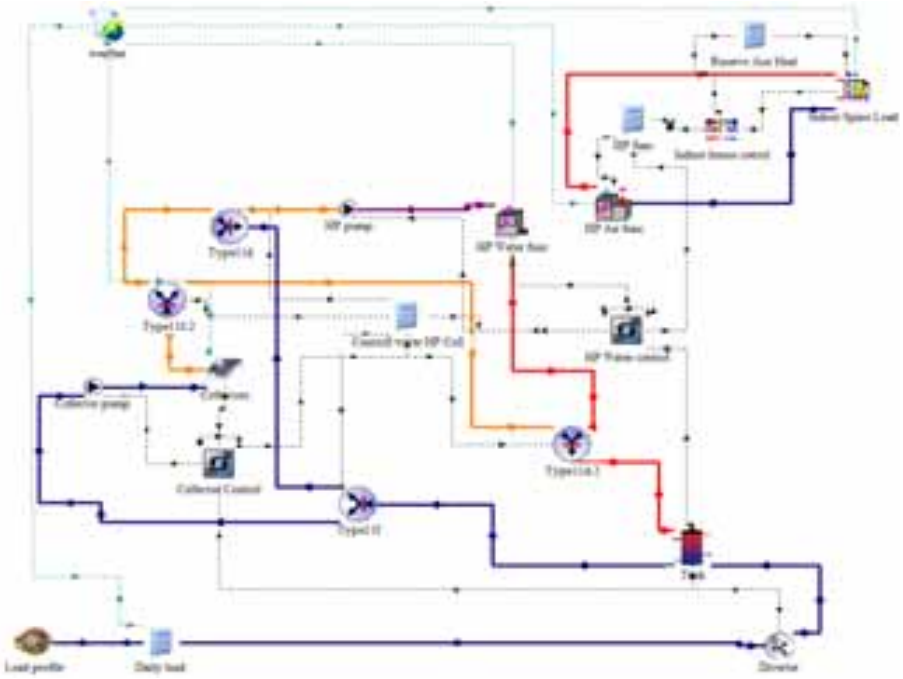

Fig. 2: Overview of the TRNSYS model.

Tab. 1: Parameters and TRNSYS types used in the simulation tool.

Type 12, house	The building has an average UA-value of 142 W/K. The internal gains were assumed to be approximately 900 W. Temperature setting 20 °C for the heat pump and 18 °C for the direct electric heating with a power of 7 kW.
Type 15, weather data	The weather data is data from Stockholm, Sweden.
Type922, air-to-air heat pump	The inputs are based in the heat pump model Thermia Aura (Thermia, 2015). This heat pump can work at two power levels: rated heating capacity 1,4-6 kW and rated heating power 0,3-1,7 kW.
Type941, air-to-water heat pump	The inputs are based in the heat pump model Nibe F2030 (NIBE, 2015) with a rated heating capacity 7 kW and rated heating power 1,8 kW
Type 1, flat-plate solar collectors	Collector area 6 m^2, zero-loss efficiency 0,8, efficiency slope 3,6 $W/m^2/K$, efficiency curvature 0,05 $W/m^2/K^2$ and first order incidence angle modifier 0,2.
Type 4, storage tank	Tank volume 0,3 m^3, 8 nodes, height of nodes 0,2m, U-value 1,15 $W/m^2/K$. No auxiliary heater is used, all the heat is provided by the air-to-water heat pump. The connections are fixed and placed at the top and bottom of the storage.

3. Results

The simulation results show that, in total, the heating energy (DHW plus space heating) was reduced from approximately 16760 kWh/y to 5170 kWh/y (69% decrease) without solar collectors and to 4790 kWh/y (71% decrease) with solar collectors (Tab. 2 and Fig. 3). The annual energy need for space heating was reduced from 12280 kWh/y to 4178 kWh/y. The heat pump in combination with solar collectors reduced the annual energy need for domestic hot water from 4480 kWh/y to 620 kWh/y.

Tab. 2: Energy use for DHW and space heating before and after the heat pump installation; with and without solar collectors.

	Before the heat pump installation (kWh/y)	After the heat pump installation without collectors (kWh/y)	After the heat pump installation with collectors (kWh/y)
Space heating	12280	4178	4178
DHW	4475	989	616
TOTAL	16755	5167	4794

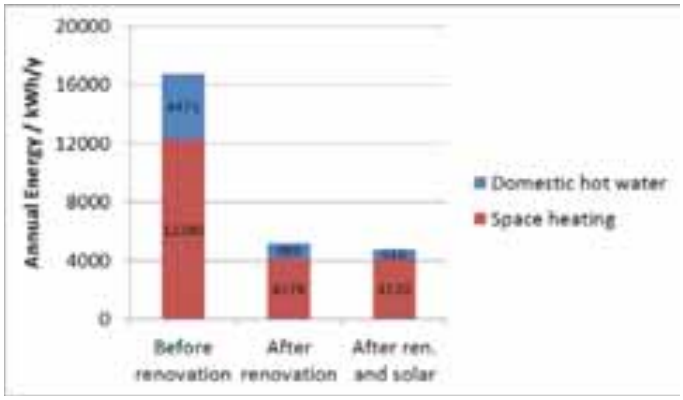

Fig. 3: Annual energy use before and after the heat pump installation, with and without solar collectors.

During the coldest winter months the heat pump was in fact not sufficient to provide all the required heat for space heating in order to keep the indoor temperature above 18 °C. To keep the indoor temperature above 18 °C during this period the existing direct electric heating system was used as an auxiliary heater. This situation corresponds to reality where standard air-to-air heat pumps also need support from a direct electric heater during the peak of the winter in Sweden. The comfort level reach for the indoor ambient and DHW is illustrated in Fig. 4.

Fig. 5 illustrates the energy load and production. In Tab. 3 the space heating energy is divided in two parts: the part covered by the heat pump (3667 kWh/y) and the remaining part covered by the existing direct electric heating system (511 kWh/y). If one excludes the direct electric heating and the use of solar collectors, the SCOP of the air-to-air heat pump is equal to 3,2 ($\frac{space\ heating\ load - direct\ electric\ heating}{heat\ pump\ energy\ for\ space\ heating - without\ direct\ electric\ heating} = \frac{12280-511}{4178-511}$). The SCOP of the air-to-water heat pump without solar collectors is equal to 4,5 ($\frac{DHW\ load}{heat\ pump\ energy\ for\ DHW}$).

It is roughly estimated that 10 kWp solar cells (67 m^2 solar photovoltaic modules at 15% efficiency) should be installed in order to cover the total annual electricity demand of roughly 5000 kWh/y for space heating and domestic hot water and additionally 5000 kWh that are estimated to be the average use of household electricity. Hence, net-zero energy level can be achieved.

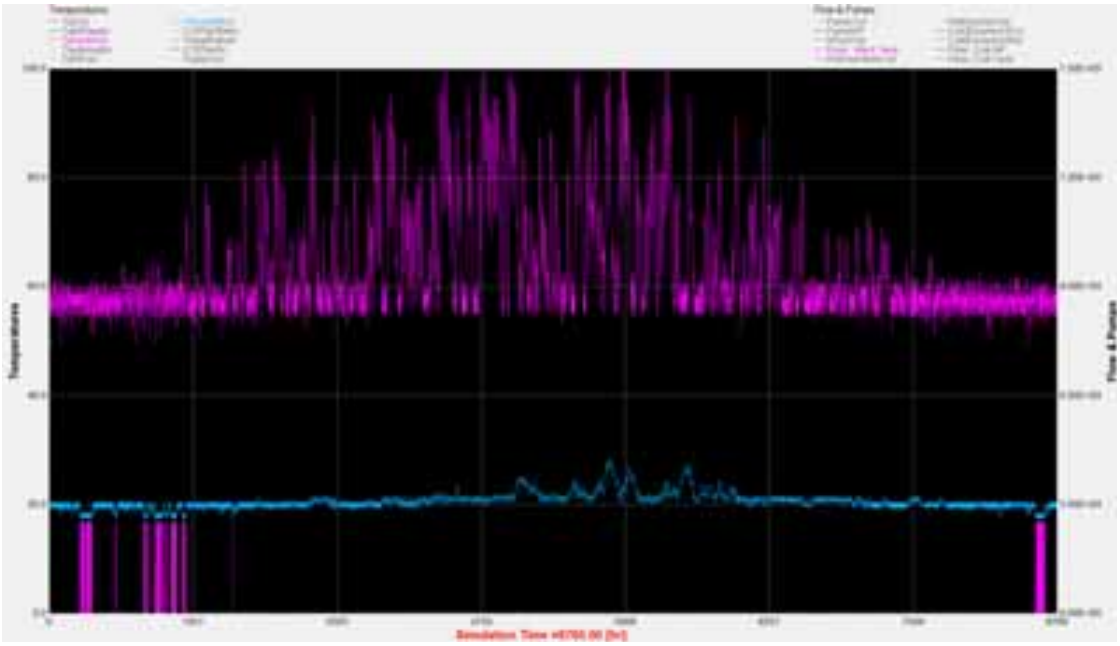

Fig. 4: Comfort analysis with heat pump and solar collectors: the upper curve shows the temperature at the top of the storage tank; the middle curve shows the indoor temperature of the house and the lower curve shows the use of the auxiliary direct electric heating system.

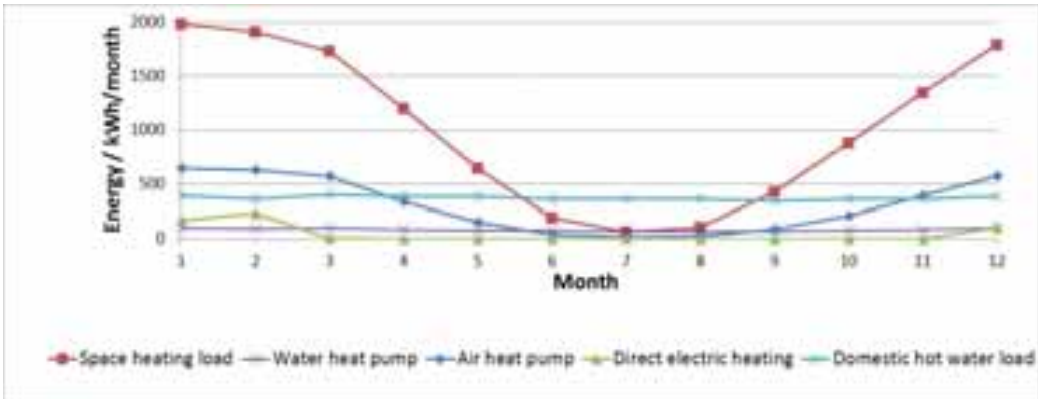

Fig. 5: Estimated monthly energy load and production.

Tab. 3: Space heating energy consumption divided in the part that is covered by the heat pump and the remaining covered by the existing direct electric heating system.

	Heat pump only used for space heating (kWh/y)	Heat pump also used for DHW (kWh/y)	Variation (kWh/y)	Relative variation (%)
Air heat pump	3740	3667	-73	-2
Direct electric heating	361	511	+150	+42
TOTAL space heating	4101	4178	+77	+2

4. Discussion

One practical challenge in retrofitting existing hot water storages is the fact that, in reality, these lack available connections to other heat sources such has heat pumps or solar collectors. This has been previously investigated and shown that the two available connections can be also used by for example solar collectors without a decrease in the system performance (Bernardo, 2013). This was kept outside of the scope of this

study.

The SCOP of the air-to-water heat pump is higher than expected and probably overestimated, especially when compared with the SCOP of the air-to-air heat pump that works at a lower temperature. The reason for this is the fact that the model did not include COP data for the desired temperature intervals and this was therefore extrapolated and probably overestimated. Improvements regarding this data are needed in future studies. This overestimation is thought to influence mostly the level of energy savings for DHW while the other results are thought not to change significantly.

The fact that the air-to-air heat pump is also used to provide energy for DHW showed almost no change on the annual energy spend for space heating. However, the contribution of the heat pump for space heating was decreased by 2% (73 kWh/y) which was compensated by a 42% increase (150 kWh/y) of the direct electric heating in the peak of the winter. This decrease in performance is largely compensated by energy savings on the DHW of approximately 3500 kWh/y.

The solar collector add-on does not provide a significant energy reduction since most of the energy is already saved by the heat pump. Since the SCOP of the air-to-water heat pump is 4,5, in order to save 1 kWh electricity to the heat pump the collectors need to produce in average 4,5 kWh of heat. Also, the existing hot water storage presents low levels of temperature stratification which also contributes significantly to the low output of the solar collectors.

Existing air-to-air heat pumps may not be able to reach the desired temperature for domestic hot water heating (approximately 55-60°C). This is a crucial limitation for the retrofitting and that needs further investigation. One possible solution is to install an extra small compressor as shown on the left hand-side in Fig. 6. Nonetheless, retrofitting can be complicated due to several factors such as complicated installation, different type of heat pump configurations in the market, problems with warrantee and insurances, low profitability, etc. Therefore, it might be more realistic to consider this concept for new heat pump installations instead. In that case a heat exchanger for the DHW can be installed as one of the multi-splits units as shown in the right-hand side in Fig. 6. The main competitive advantage of this new hybrid heat pump compared with a regular air-to-air heat pump is the large energy savings for DHW production. Depending on the eventual extra costs of using a stronger compressor that reaches 55-60°C, the extra investment may be compensated by such large energy savings. This needs further investigation that also includes costs.

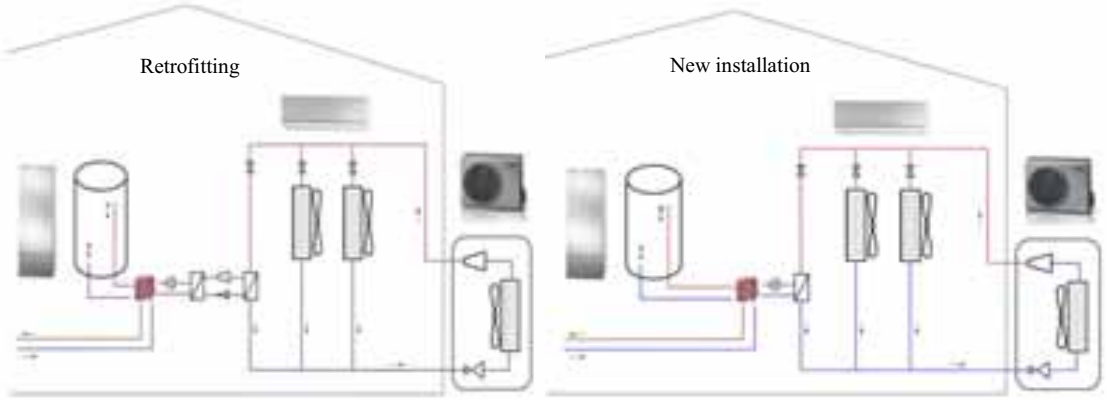

Fig. 6: Sketch of the hybrid heat pump for retrofitting (left-hand side) and new installations (right-hand side).

5. Conclusion

A model was built for assessing energy savings of retrofitting a common air-to-air heat pump for providing heat not only for space heating but also for domestic hot water (DHW). The heat pump was controlled in such a way to alternate the heat deliver between DHW and space heating at different temperatures and

therefore at different efficiencies. The DHW production was prioritized. Combining solar collectors into the system was also investigated.

The simulation results show that the total annual heating demand (DHW plus space heating) was reduced from 16755 kWh/y to 5167 kWh/y (69% decrease) without solar collectors and 4794 kWh/y (71% decrease) with 6 m^2 solar collectors. The annual energy need for space heating was reduced from 12280 kWh/y to 4180 kWh/y while the annual energy need for domestic hot water was reduced from 4480 kWh/y to 620 kWh/y. The remaining electricity demand for heating and electric appliances can be covered by approximately 10 kWp solar cells and therefore reaching net-zero energy level. The energy provided by 6 m^2 solar collectors was only 370 kWh/y which confirms that this is not profitable combination. This is explained by the combination with a high efficient heat pump and due to low levels of temperature stratification in the hot water storage.

The comfort analysis showed that in order to prevent the indoor temperature to fall below 18 °C in the peak of the Swedish winter the existing direct electric heating system had to use around 510 kWh/y. The rest was provided by the heat pump. The temperature in the hot water storage did not drop below 50 °C indicating a good comfort level.

Results indicate that this concept has potential for large energy savings but the implementation in retrofitting (and upgrading) existing air-to-air heat pumps can be significantly complicated and compromise therefore the cost-efficiency. It seems more realistic to apply the same concept at new installations where the heat pump can be chosen from the beginning to reach higher temperatures. Such extra cost needs to be compensated by the energy savings for domestic hot water production.

6. References

Bernardo, 2013. Retrofitting Conventional Electric Domestic Hot Water Heaters to Solar Water Heating Systems in Single-Family Houses-Model Validation and Optimization. Energies 6(2), 953-972, 2013.

NIBE, 2015. Available online at: http://www.nibe.se/Produkter/Luftvattenvarmepumpar/NIBE-F2030/. [Accessed May 2015].

Swedish Energy Agency, 2013. Energy statistics for one- and two-dwelling buildings, ES2014:05. Stockholm: Swedish Energy Agency.

Swedish Energy Agency, 2014. Available online at: http://www.energimyndigheten.se/Hushall/Din-uppvarmning/. [Accessed June 2015]

Tess Library, 2015. Thermal Energy System Specialists Component Library Package; Transient System Simulation Tool: Madison, WI, USA. Available online at: http://www.trnsys.com/tess-libraries. [Accessed 2012].

Termia, 2015. Available online at: http://www.thermia.se/docroot/dokumentbank/Thermia-Varmepumpar-Aura.pdf. [Accessed May 2015].

TRNSYS, 2015. TESS libraries available at http://www.trnsys.com/tess-libraries/ (last visited on April 2015).

Conference Proceedings

Solar World Congress 2015
Daegu, Korea, 08 – 12 November 2015

Design Proposal for Low Energy Buildings using Energy Simulation Program

Goopyo Hong[1], Hye Jin Kim[1] and Byungseon Sean Kim[1]

[1] Yonsei University, Seoul (Korea)

Abstract

The use of energy performance software will become a necessity in the early design stages to quantitatively verify the energy consumption of buildings. In this research, a simulation tool was used in designing a zero energy senior community center for an apartment complex. After comparing and evaluating case 1 (code) and case 2 (current design trend), each load element was analyzed to derive the low energy design for case 3. For case 3, the thermal performance of the insulation and windows as well as the lighting efficiency improved. In addition, photovoltaic solar power was considered as the renewable energy. For heating, the percentage of heat loss from opaque surfaces is 52%, while that from infiltration is 31% and that from window systems is 17%, demonstrating that the envelope has a significant effect on heat loss. For cooling, the percentage of heat gain due to window systems is 43%, while that due to lighting is 33%, that due to people is 17%, and that due to equipment is 7%, demonstrating that the internal and solar heat gain account for most of the energy loss, while the envelope has an insignificant effect. Photovoltaic solar panels were included as a source of renewable energy for the low energy design of case 3 to offset the heating and cooling energy consumption. It was found that using renewable energy would result in an energy surplus of 3,438kWh/year.

Keywords: *energy performance software, early design stage, zero energy design, renewable energy, PV*

1. Introduction

Buildings with improved energy consumption in Korea are being designed and constructed according to the Building Energy Conservation Design Standards (BECDS). The BECDS is categorized into sectors including construction, machinery, electricity, and renewable energy, and is applied to insulation, windows, high-efficiency mechanical and electric equipment, and renewable energy systems. Although the use of these materials is regarded as energy saving, it is difficult to quantify the amount of energy consumption. Thus, the standards are prescriptive requirements, not performance requirements. Also, the Korean government announced its goal to achieve the passive house standard by 2017 and zero energy standard by 2025. Likewise, Europe's target year for achieving zero energy houses is 2020 and that of the U.S. is 2025. In the future, building regulations will become more stringent in order to achieve low energy or zero energy buildings, and this will be a challenge for designers. As a result, architectural designers have focused on building geometry and envelope when designing low energy or zero energy buildings (Shady Attia et al., 2012).

In practice, a high level of expertise is required to apply passive and active techniques in the early design stages, since verifying energy performance is difficult, complex, and time consuming. The use of energy performance software will become a necessity in the early design stages of buildings in order to quantitatively verify energy consumption. In this research, EnergyPlus (Version 8.2) was used in designing a zero energy senior community center for an apartment complex. The energy consumption for designs adhering to the Korean government regulations and current design trends was verified. The purpose of this research is to analyze the technical elements used and determine the effects of energy demand. The findings

doi:10.18086/swc.2015.08.09 Available at http://proceedings.ises.org

could be considered and applied to future designs for low energy buildings.

2. Methods

Utilizing the senior community center as the subject building, EnergyPlus was used in this research to analyze and compare case 1 (code), which complied with the building code, and case 2 (design), which followed the current design trend. The elements affecting energy in case 1 were verified.

After evaluating and comparing case 1 and case 2, each load element was analyzed to derive the low energy design for case 3. Case 3 showed improved thermal performance of the insulation and windows. The only renewable energy source considered was solar power generation.

2.1 Case study

The subject building for this research is the senior community center within an apartment complex. Figure 1 shows the floor plan of the community center, with the living room, grandfather's room (Room 1), grandmother's room (Room 2), restrooms, kitchen, and storage rooms.

The heating system is floor heating via district heating. The cooling system consists of four air conditioners fitted to the ceilings in the living room, kitchen, and Rooms 1 and 2.

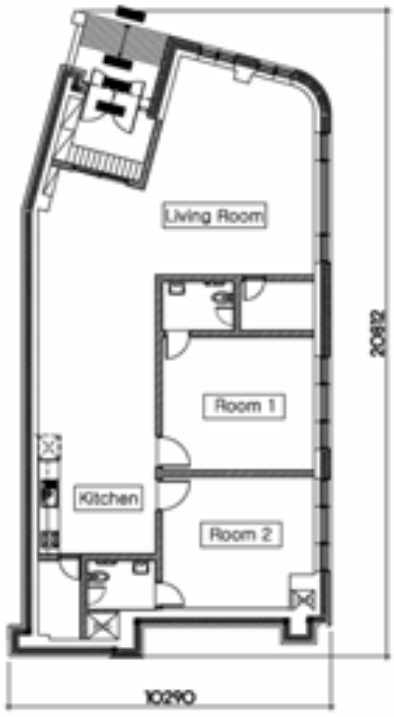

(a) Floor plan

(b) view of the senior community center

(c) seniors who are taking a rest in the living room

Fig. 1: Plan and photos of case study

2.2 Energy Simulation Program - EnergyPlus

Developed by the U.S. Department of Energy, EnergyPlus is a program that uses climatological data for load calculation and analysis of energy consumption characteristics. It combines the advantages of DOE-2 and BLAST and has several new functions. It is a simulation to have input and output text files. Users can set a

time-step to calculate the loads of a building. EnergyPlus then calculates the heating and cooling system and the requirements of the plant, and predicts the accurate space temperature and humidity as well as occupant comfort (Crawley et al. 2008).

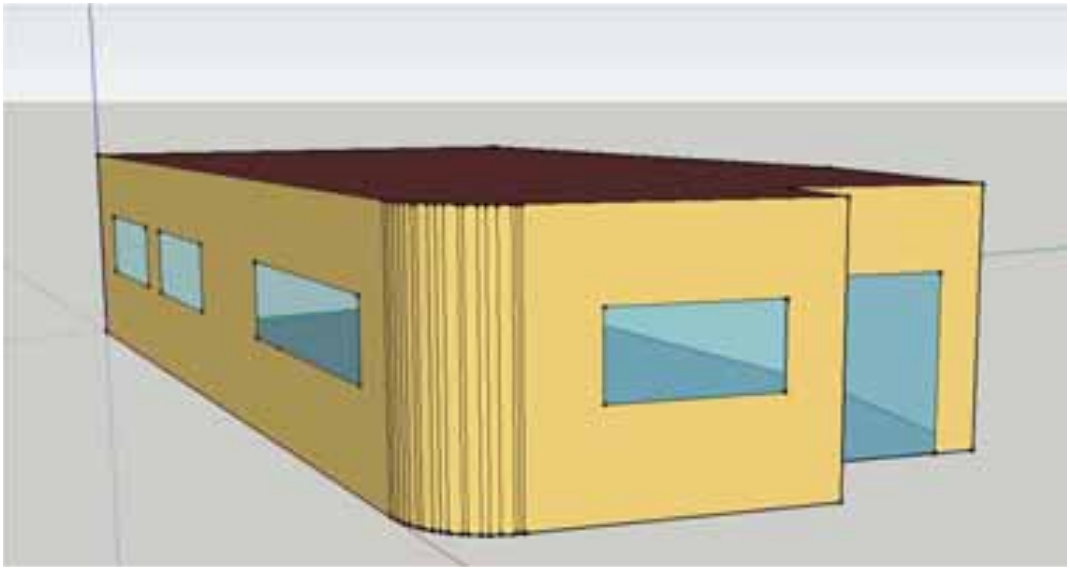

Fig. 2: Modelling using Sketchup

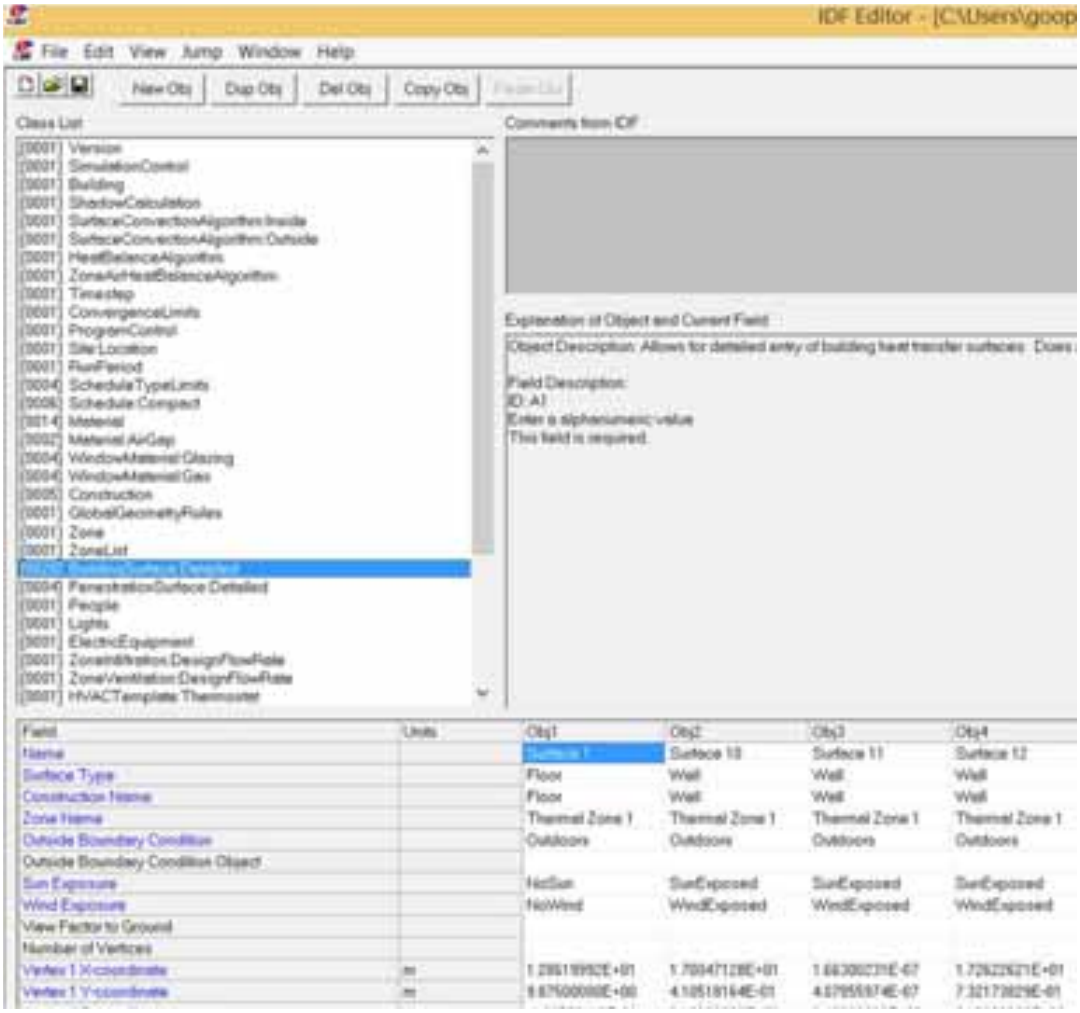

Fig. 3: Image of the EnergyPlus Input data

2.3 Model Conditions

Sketchup was used to model the subject building, as shown in Figure 2, and the model's data was entered into EnergyPlus. Figure 3 shows the values entered into the modeling wall of EnergyPlus. One zone was designated for the heating and cooling for the entire senior community center.

Table 1 shows the necessary elements for the building energy analysis of case 1 and case 2. The BECDS values from the middle region of Korea are shown in case 1. The data for case 2 reflect the values that are commonly used during construction. For the architectural sector, the thermal conductance of the roof, walls, floor, and window systems were calculated and entered. This was then repeated for the lighting, ventilation devices, and household appliances of the electrical sector. For the equipment sector, the district heating system installed was assumed to consist of an individual heating system, while the cooling system was assumed to consist of four air conditioners, each installed in the four main rooms. The number of occupants was 17, while the set point temperature for heating and cooling was set to 23℃ and 26℃, respectively. The amount of infiltration was presumed to be 0.1 h-1(ACH) and the ventilation was designed to be 0.5 h-1 (ACH).

Tab. 1: Condition of the case 1 & case 2

Contents		Case 1	Case 2
U-value (W/㎡ K)	Roof	0.29	0.23
	Wall	0.48	0.32
	Floor	0.34	0.29
	Window	2.70 (SHGC : 0.75)	1.76 (SHGC : 0.52)
	Door	3.70	3.26
Electric	Light	10W/㎡	
	Ventilation	0.5 ACH	
	Misc.	Equipment-television, refrigerator	
System	Boiler	Efficiency : 90%	
	System Air Condition	Capacity : 23kW	
Etc.	Occupants	17 people (0.1 person / ㎡)	
	Infiltration	0.1 ACH	

2.4 Schedule

A major factor in determining the energy consumption of a building is scheduling. It is important to set a reasonable schedule that considers occupant time, lighting, running time of household electric appliances, and the hours of operation of the building's systems for weekdays, weekends, and holidays. The time period set for this research was one year, starting on January 1st and ending on December 31st, with hours of occupation set from 7:00 AM to 9:00 PM. The contents of the schedule are shown in Table 2.

Tab. 2: Schedules

Content	Total / Week	Total/ Year
Occupancy	98 hours	5,096 hours
Appliances	98 hours	5,096 hours
Lighting	84 hours	4,368 hours
Ventilation	84 hours	4,368 hours

3. Results

3.1 Comparing case 1 and case 2

A simulation was used to verify the energy consumption for case 1 and case 2, with a focus on heating and cooling. Figure 4 shows the monthly heating and cooling energy consumption for case 1 and case 2.

The heating energy consumption of case 1 was 5,861kWh/year and that of case 2 was 4,722 kWh/year, which is 20% less than case 1. The use of improved materials that complied with the thermal conductance code for both insulation and windows system, led to approximately a 24% and 35% reduction in thermal performance, respectively. The cooling energy consumption of case 1 was 6,367 kWh and that of case 2 was 6,086 kWh, which is about 4% less than case 1. Therefore, enhancing the thermal performance of the insulation and window systems has a significant impact on heating energy consumption, but a minimal impact on cooling energy consumption.

According to the simulation results, case 2, which follows the current design trends in Korea, consumes 12% less heating and cooling energy than buildings that follow the BECDS (case1).

(a) Monthly Heating Energy **(b) Monthly Cooling Energy**

Fig. 4: Comparison of case 1 and case 2

3.2 Low Energy Design Elements

Figure 5 quantitatively shows the heating and cooling elements of case 1 according to load ratio. The heat loss through opaque surfaces was 52%, infiltration 31%, and window system 17%. This shows that the envelope has a significant effect on heat loss.

For cooling, heat gain due to window systems is 43%, lighting 33%, people 17%, and equipment (household electric appliances) 7%, which shows that the opaque surface has a minimal effect However, the window system, which is a major factor in solar heat gain, and other factors contributing to internal heat gain including people, lighting, and equipment, have a significant effect on the overall heat gain. It follows that the slight reduction of 4% in cooling energy consumption from case 1 to case 2 is due to the lack of change in the factors for internal heat gain.

The analysis shows that in order to reduce the heating load, the insulation for the walls, roof, and flooring must be improved. Infiltration is also a significant factor; insulation tape will thus be used during construction to reduce heat loss.

In order to reduce the cooling load, the solar heat gain through the window systems must be reduced by installing glazing with a low solar heat gain coefficient (SHGC). The internal heat gain factors such as people and equipment (household electric appliances) cannot be changed so it is more important to have highly efficient lighting.

Each factor for the load categories of case 1 was analyzed to reduce the energy consumption for the senior community center's design. The important objectives were to reduce the heating energy by enhancing the thermal conductance of the walls and window systems and to reduce the cooling energy by installing

windows with low SHGC glass and by installing LEDs.

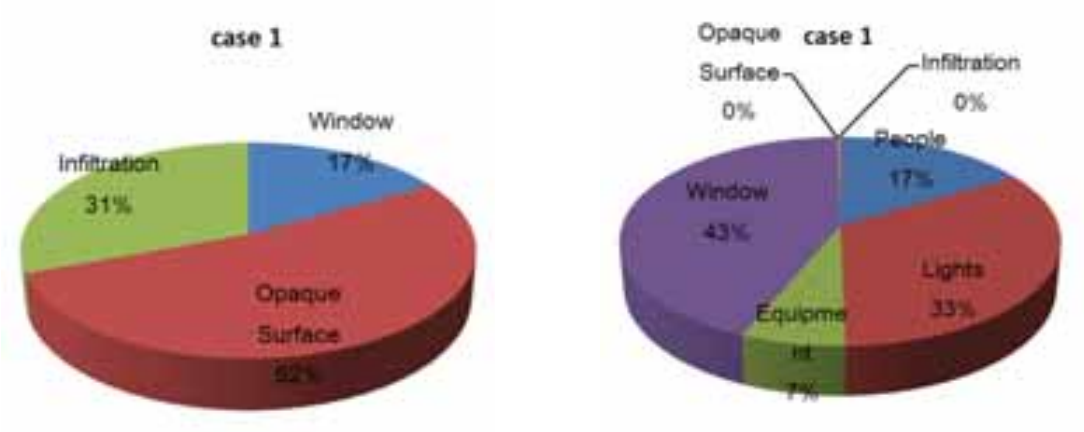

(a) Heat loss (b) Heat gain

Fig. 5: Analysis of the load elements

Table 3 shows the factors contributing to the low energy design for case 3. Compared to case 1, the thermal conductance for insulation decreased by 57%, while the thermal performance for window systems significantly improved by 60%, with a drastic decrease in the SHGC value and a 20% decrease in light density. In addition, solar panels were added to the plans for a zero energy design with renewable energy.

Tab 3. Condition of the case 1 & case 3

Contents		Case 1	Case 3
U-value (W/㎡ K)	Roof	0.29	0.17
	Wall	0.48	0.11
	Floor	0.34	0.16
	Window	2.70 (SHGC : 0.75)	1.03 (SHGC : 0.13)
	Door	3.70	2.1
Electric	Light	10W/㎡	8W/㎡
Renewable	PV system	-	8kW x 4hr/day

3.3 Energy Consumption-case 3

Figure 6 compares the heating and cooling energy consumption of case 1 and case 3. The heating energy consumption of case 3 was calculated to be 3,929kWh/year, which is 33% less than case 1, while the cooling energy consumption of case 3 was 4,313kWh/year, which is 31% less than case 1.

It was determined that the 33% reduction in heating energy consumption was due to the increase in the insulation of the wall and in the thermal conductance of the window systems. The cooling energy consumption was reduced by 31% by utilizing glass with an SHGC value of 0.134 for glazing, achieving a light density of 8w/㎡, and using LED lighting wherever possible.

To further reduce the energy consumption of case 3, the case 3 load ratios were analyzed, as shown in Figure 7. For heating, the infiltration was reduced and the insulation for the wall was improved. For cooling, the lighting density was reduced. However, since reducing light density can increase the heating load, it is necessary to calculate the lowest light density that does not fall below the recommended level of indoor illuminance.

(a) Heating Energy (b) Cooling Energy

Fig. 6: Comparison of case 1 and case 3

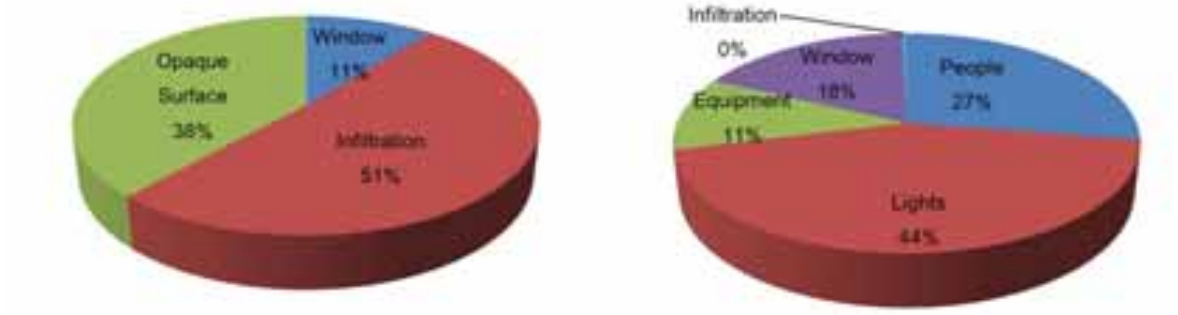

(a) Heat loss (b) Heat gain

Fig. 8: Analysis of the load elements in case 3

3.4 Photovoltaic using of renewable energy

Photovoltaic solar cells were included in case 3 to meet the need for renewable energy in a zero energy design. Figure 10 shows that the combined heating and cooling energy consumption is 8,242 kWh/year, while the solar panels produce 11,600 kWh/year. Therefore, by using renewable energy, the zero energy design is feasible and can result in a surplus of 3,438kWh/year.

(a) Photo of the installed PV system (b) monitor of PV generation in the senior center

Fig. 9: Analysis of the load elements in case 3

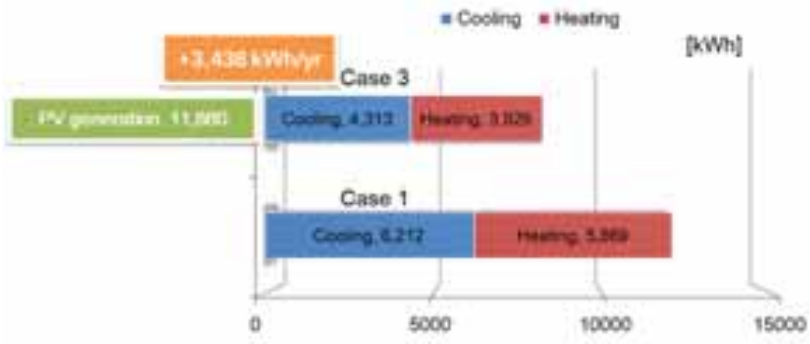

Fig. 10: Energy consumption and energy generation

4. Conclusions

An energy simulation was conducted to design a zero energy building accommodating a senior community center within apartment complexes in Korea. Case 1 was designed according to the Building Energy Conservation Design Standards (BECDS) and case 2 reflected the common designs of Korean construction companies. By analyzing the factors that affect heating and cooling in case 1, low energy design factors were derived to calculate the energy consumption for case 3, as shown below.

- Heating energy consumption was 5,861kWh/year for case 1, 4,722 kWh/year for case 2, and 3,929 kWh/year for case 3. Compared to case 1, case 2 and case 3 showed a 20% and 33% reduction, respectively.
- Cooling energy consumption was 6,367kWh/year for case 1, 6,086 kWh/year for case 2, and 4,313 kWh/year for case 3. Compared to case 1, case 2 and case 3 showed a 4% and 31% reduction, respectively.
- Analyzing the factors that affect heating and cooling for case 1 shows that 1) for heating, opaque surfaces are responsible for 52%, infiltration is responsible for 31%, and window systems are responsible for 17% of heat loss, which shows that the envelope has a significant effect on heat loss; 2) for cooling, window systems are responsible for 43% of the heat gain, lighting is responsible for 33%, people are responsible for 17%, and equipment is responsible for 7%, which shows that internal and solar heat gain account for most of the energy loss, while the envelope has an insignificant effect.
- Photovoltaic solar panels were included in the design as a source of renewable energy to offset the heating and cooling energy consumption of the low energy design of case 3. Using renewable energy would result in an energy surplus of 3,438kWh/year.

5. References

1. Shady Attia, Elisabeth Gratiaa, André De Herdea, Jan L.M. Hensenb, 2012, Simulation-based decision support tool for early stages of zero-energy building design, Energy and Buildings. 49, 2-15

2. Drury B. Crawley, Jon W. Handb, Michael Kummert, Brent T. Griffith, 2008, Contrasting the capabilities of building energy performance simulation programs, Building and Environment. 43, 661-673

3. Shady Attia, André De Herdea, 2011, Early Design Simulation Tools for Net Zero Energy Buildings: A comparison of ten tools, Building simulation 2011

4. Yiqun Pan, Zhizhong Huang, Gang Wu, 2007, Calibrated building energy simulation and its application in a high-rise commercial building in Shanghai, Energy and Buildings. 39, 651-657

5. Shady Attia, Mohamed Hamdy, William O'Brien, Salvatore Carlucci, 2013, Assessing gaps and needs for integrating building performance optimization tools in net zero energy buildings design, Energy and Buildings. 60, 110-124

6. ASHRAE Standard 90.1

7. Yimin zhu, 2006. Applying computer-based simulation to energy auditing : A case study. Energy and Buildings. 38, 421-428

Conference Proceedings
Solar World Congress 2015
Daegu, Korea, 08 – 12 November 2015

Heat Loss for a Run-Around Hybrid Ventilation System with Heat Recovery

Henrik Davidsson[1] and Ricardo Bernardo[1]

[1] Lund University, Lund (Sweden)

Abstract

The heat recovery system for ventilation is of major importance when low energy buildings are built. One alternative to the mechanical ventilation systems with heat recovery is to use a brine based run-around system that allows for heat recovery in for instance hybrid ventilated buildings. This type of heat recovery system has the potential to lower the need for electricity for the fans. Also, the installation has the potential to be simpler when pipes transporting the brine replace traditional air ducts. However, pipes needed to transport the brine will suffer from thermal losses. This will lower the efficiency of the heat recovery system. High losses could in practice make the system unusable. In order to estimate how much this affects the annual heat recovery a simulation tool was developed using TRNSYS. The result from the investigation shows that the losses for a system with 40 m pipes in total are approximately 300 kWh annually. This corresponds to approximately 9% of the energy savings from the ventilation heat recovery system. Insulating the pipes can reduce this heat loss by approximately 250 kWh annually.

Keywords: *Hybrid ventilation, Heat recovery,*

1. Introduction

One advantage with using hybrid ventilation is the reduced need for electricity consumed by the fans in a conventional mechanical ventilation heat recovery system. The importance for this becomes apparent when considering the following example: A typical single-family house in Sweden consumes approximately 4000 kWh to heat the incoming ventilation air. If a mechanical ventilation system with 75% heat recovery rate is used it means that 3000 kWh is saved on an annual basis. However, if we include the 456 kWh of electricity Swedish Energy Agency (2010) which corresponds to about 1370 kWh of primary energy (energy factor 3), the annual recovery rate is reduced to about 40%.

One alternative to this is to use natural or hybrid ventilation. However, hybrid ventilation systems normally lack the possibility to recover any of the energy that disappears with the outgoing ventilation air. This will lead to high energy consumption for heating and it could also result in a poor comfort in cold climates due to cold draught from the incoming ventilation air. One possibility could be to install hybrid ventilation systems with heat recovery. Recent development concerning heat exchangers with very low pressure drop has made these types of systems possible, Hviid and Svendsen (2011), and Davidsson et al. (2013a). These types of heat exchangers can be used in run-around heat recovery systems, Davidsson et al. (2013b). A typical run-around system equipped with a heat recovery system is shown in Fig. 1. The incoming air is heat exchanged in the water/air heat exchanger at the bottom of the building. The brine is then pumped to the top of the building where it is used to recover heat from the outgoing ventilation air. The heat is pumped to the bottom of the building and the circle is completed. The temperatures in the figure are used as an example to illustrate the heat recovery process.

However, in this type of system there will be losses from the indoor air to the brine. This means that heat will flow from the indoor air to the brine. In the end this means that the heat recovery rate for the system will be reduced. There are three effects that should be kept in mind regarding this heat loss:

doi:10.18086/swc.2015.08.10 Available at http://proceedings.ises.org

1. Heat will be lost from the room to the brine.

2. The increased brine temperature will reduce the heat transfer rate in the heat exchanger at the top of the house from the air to the brine.

3. The increased brine temperature will increase the heat transfer in the heat exchanger at the bottom of the house from the brine to the air.

This rather complex behavior makes it more difficult to estimate the heat loss effect from the system over a full year. Further complication arises when a full building is included in the energy system and therefore a dynamic simulation model is needed to quantify the above listed behavior.

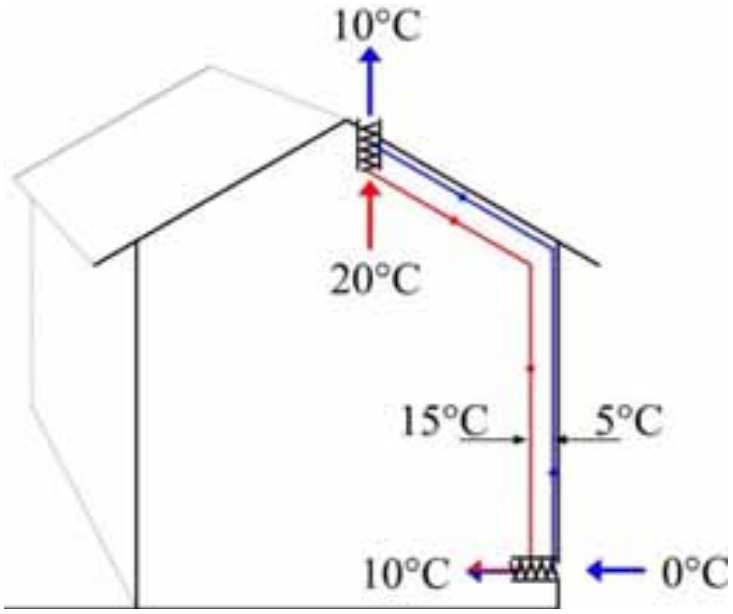

Fig. 1: Run-around heat recovery system suitable for hybrid ventilation.

2. Method

In order to investigate the consequences of heat losses in the pipes a TRNSYS simulation model was developed. The simulations do not include effects from dirt on the heat exchangers or air leakage. Nor does it include uneven consumption of electricity in the building or cooling during hours with overheating. The included TRNSYS components and the most important parameters are described in Table 1. The internal gains, window gains and thermal losses for the building are all included in the simulation in order to give a realistic surrounding for the ventilation system.

Tab. 1: Parameters and TRNSYS types used in the simulation tool.

Building, TRNSYS type 88	The building has an average U-value of 0.5 W/m²K. The thermal capacitance of the buildings was set to 40 MJ/K. This corresponds to approximately 100 m² concrete floor, 100 m² brick wall and it includes interior material and the roof.
Internal gains	Windows facing south (6.5 m² glazing area), west (6.5 m²), north (4 m²) and east (4 m²) with a g-value of 55% were installed in the building. This gives a glazing to floor area ratio of approximately 14 %, which is a typical value. The transmitted solar radiation was treated as internal gains of the building. The gain from people and electricity was set to 500 W continuously.
Weather data	The weather data is data from Malmoe in the south of Sweden. The weather data was obtained from Meteonorm (Meteonorm).

Ventilation: Heat exchangers, TRNSYS type 5b	The ventilation flow rate for all cases was set to 234 kg/h which is approximately equal to an air change rate of 0.5 changes per hour. This value was chosen in order to meet the requirements in the Swedish Building code BBR (2011). The brine in the ventilation circuit was assumed to be water. The temperature efficiency was set to 75%.
Pipes: type 31	The pipes for the run-around ventilation system were assumed to have an inner diameter of 12 mm and a total length of 20 meter for both flow directions, i.e. to the roof heat exchanger and to the bottom heat exchanger. The heat loss coefficient for the uninsulated and the insulated pipes are given in Table 2.

The heat resistance and thus the U-value of the pipes, uninsulated and insulated, where calculated using the program IsoDim from Isover (IsoDim). The values used in the different simulations can be seen in Table 2. The calculated values only includes the pipes. Connections and diverters are not included.

Tab. 2: Heat transfer rate for pipes with various insulation thickness.

Insulation thickness / mm	U-value / (W/m²K)
0	7.7
20	0.68
40	0.31
60	0.19
80	0.13
100	0.10

3. Result

This building was calculated to use 15000 kWh annually for space heating and heat for the ventilation. If the building is equipped with a heat recovery system, shown in Fig. 1, for the ventilation air the annual heating need is reduced to 11350 kWh per year. This assumes a temperature heat recovery efficiency of 75%. However, this simulation does not include any heat losses to the water piping system. If this is included the heating need is increased to 11660 kWh annually. This assumes a total piping length of 2·20 meters with heat loss rate for the water pipes assumed to be 7.7 W/(m²·K). The effects of insulating the pipes are shown in Fig. 2 and Fig 3. The first of the two figures shows the annual heating for buildings equipped with a run around ventilation system with heat recovery. The results show that not including any losses in the calculations for the ventilation system will result in an overestimate of its performance by approximately 300 kWh annually. However, insulating the pipes heavily will reduce this effect considerably resulting in only 50-100 kWh losses annually.

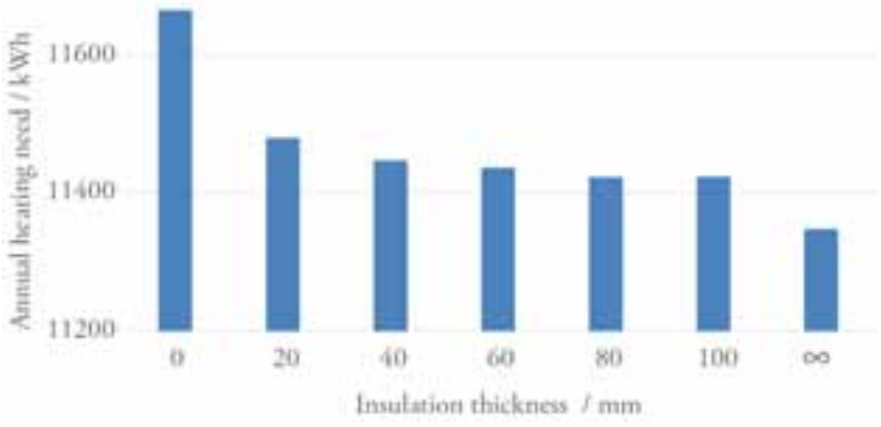

Fig. 2: The annual heating need for buildings with ventilation systems with different pipe insulation. Note the broken y-axis.

Fig 3 shows with red bars that the heat transfer in the Bottom HX increases as the losses are included. This happens since the air inside the building will heat the brine going to the Bottom HX. This is not beneficial for the total energy performance for the building since the heat comes from the building itself. At the same time the energy transferred in the roof HX will decrease. This is shown with blue bars. This happens since the brine is already heated and less energy can be transferred from the air to the brine. The phenomena can be described as a partly short circuited system. The losses in the pipes going from the bottom to the roof are indicated with black arrows and the losses for the pipes going roof to the bottom is indicated with grey arrows. The losses in the system matches the difference in energy transfer rate between the Bottom HX and the Roof HX. Note that both diagrams have broken y-axis.

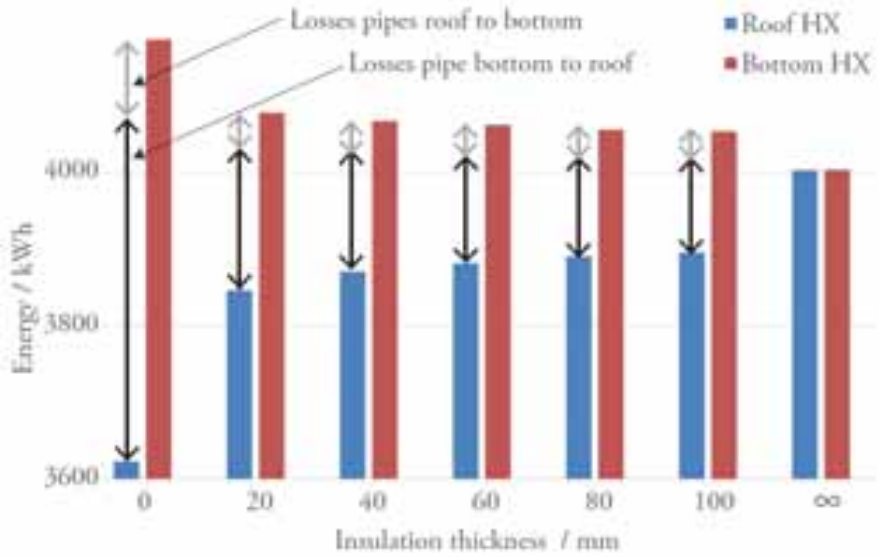

Fig. 3: Blue and red bars shows the heat transfer in the Roof HX (heat exchanger) and the Bottom HX. The black and the grey arrows indicate the thermal losses in the brine pipes. The black arrow is for the pipe going from the Bottom HX to the Roof HX and the grey arrow shows the losses related to the brine pipes going from the Roof HX to the Bottom HX. Note the broken y-axis.

Another consequence of the heat losses from the indoor air to the brine is that the heat exchanger at the bottom of the building will have slightly warmer incoming brine compared to a case with uninsulated pipes. The incoming air will therefore also be warmer. Simulations show that the incoming air is approximately 0.5°C higher for the case with uninsulated pipes compared to pipes without any heat losses.

4. Conclusion

Not insulating the pipes in a run-around heat recovery system will result in increased heating need. A typical one family house with a total of 40 m piping for the ventilation system will suffer from approximately 300 kWh higher energy need due to the pipe losses. However, insulating the pipes has the potential to lower the energy losses to approximately 50 kWh. It's also apparent that the losses from the pipe is heavily suppressed already by 20 to 40 mm insulation. Further insulation has limited impact.

Using uninsulated pipes will lead to a higher temperature for the incoming air due to heat losses from the indoor air to the brine. However, these losses only lead to a 0.5°C temperature rise for uninsulated pipes compared to pipes with no losses. This difference will not be significant for the performance of the ventilation system. A 1 kW_p PV module tilted in 40 ° placed in Lund in the south of Sweden produces approximately 1 000 kWh/year. That means that a 250 W_p module would produce approximately the same amount of electricity as the above discussed insulation saves for the ventilation system.

5. Discussion

Since the brine in the pipes can be considerably colder than the indoor temperature there is a large risk of having condensation on the pipes. This is not bad only for the energy performance. It can also cause humidity

related problems where the pipes are placed. If the pipes are insulated there will be less humidity from the indoor air that condense on the pipes.

One of the main advantages with a run around heat recovery system for retrofitting of ventilation systems in old building is the fact that the pipes needed for this system is in most cases easier to install than ducts are in a traditional balanced mechanical ventilation system. This is not discussed in this article even though it is well worth to mention.

The total savings of insulating the pipes in the ventilation system approximately corresponds to the annual electricity production from a 250 W_p PV module. However, it should be taken into account that the electricity from the PV panels could be used to run a heat pump therefore producing more that the needed 250 kWh.

6. Acknowledgement

Thanks to Håkan Gustafsson at ISOVER for guidance regarding the program IsoDim.

7. References

BBR (2011), Swedish Building Code, Boverkets Byggregler, ”BBR 19, 6 Hygien” http://www.boverket.se/globalassets/vagledningar/kunskapsbanken/bbr/bbr-22/bbr-avsnitt-6 (accessed 2015-09-29)

Davidsson, H., Bernardo, R., Hellström, B., 2013a “Theoretical and Experimental Investigation of a Heat Exchanger Suitable for a Hybrid Ventilation System”, Buildings 3, 18-38

Davidsson, H., Bernardo, R., Hellström, B., 2013b “Hybrid Ventilation with Innovative Heat Recovery—A System Analysis”, Buildings 3, 245-257

Hviid, C.H., Svendsen, S., 2011 “Analytical and experimental analysis of a low-pressure heat exchanger suitable for passive ventilation”, Energy and Buildings 43, 275-284

IsoDim, ISOVER, ISOVER IsoDim® version 3.07, http://www.isover.se/broschyrer+och+hj%C3%A4lpmedel/ber%C3%A4kningsprogram+teknisk+isolering (accessed 2015-09-29)

METEONORM. METEONORM 5.0 global meteorological database for solar energy and applied meteorology. Retrieved 2015-09-29, 2013, from http://www.meteotest.ch/en/

Swedish Energy Agency (2010), FTX-Aggregat Hus Med 130 m² Boyta—Jämförelse (in Swedish). Available online: http://www.energimyndigheten.se/Templates/Public/Pages/ProductGroupPageCompare.aspx?productGroupId=69&productCompareList=412,413,414,415,416,417,418,419&PageID=5552 (accessed on 2015-09-29)

Conference Proceedings

Solar World Congress 2015
Daegu, Korea, 08 – 12 November 2015

LIGHTING PERFROMANCE IN OFFICE BUILDINGS WITH BIPV FACADES: VISUAL AND NON-VISUAL EFFECTS

Xin Zhang[1] and Jiangtao Du[2]

[1] School of Architecture, Tsinghua University, Beijing (China)

[2] Department of Architecture and Civil Engineering, University of Bath, Bath (UK)

Abstract

BIPV facades (integrated with opaque or transparent PV panels) have been accepted as an innovative strategy to provide electricity, reduce peak electrical and cooling demands, improve daylighting utilization, and achieve energy efficiency in buildings. This study presents a preliminary simulation study of impact of BIPV façades on visual and non-visual effects of daylight in an office building. DAYSIM and EVALGLARE, two advanced packages, were used to evaluate daylighting and visual performances. In general lighting and visual conditions can be expressed by the calculated Daylight Autonomy (DA) across the working plane and Daylight Glare Probability (DGP) at vertical planes of specific positions. The non-visual effect of lighting was indicated by the vertical DA at the same vertical positions. It has been found that BIPV facade configurations obviously affect both visual and non-visual performances of daylight. A balance of proper daylighting conditions and visual comfort should be a critical issue in the process of an office façade design.

Keywords: *BIPV façades, Lighting, Visual Performance, Non-visual Effects, Office Buildings*

1. Introduction

Building Integrated Photovoltaics (BIPV) has been generally adopted as one important solution to directly utilize solar energy in buildings, especially for the systems installed at building facades (Farkas et al., 2013). With respect to studies during the last ten years, the BIPV facades (with opaque or transparent PV panels) can provide electricity, reduce peak electrical and cooling demands, improve daylighting utilization, and achieve energy efficiency in buildings (Quesada et al., 2012). A case study in two modern buildings showed that PV facade systems significantly benefit fossil energy savings and the reduction of CO2 emission in a hot and highly luminous climate (Alnaser et al., 2008). According to simulations in northern, central and southern Europe, urban factors (obstruction and orientation) would impact the energy performance of opaque PV façade and determine its optimal configurations composed of glazing and solid wall (Yun and Steemers, 2009). However, semi-transparent PV has actually received more attentions from designers and engineers for the modern façade systems. In Hong Kong such a transparent PV facade was investigated in an office building (Li et al., 2009), which has been proved to produce a clear decrease of electrical lighting and cooling energy consumption. Another study in a cold climate also expressed that semi-transparent PV façade has a large potential to improve overall energy efficiency than opaque façade due to its ability to utilize daylighting (Robinson and Athienitis, 2009). A German simulation enhanced the fact that lighting, heating and cooling loads in an office with semi-transparent PV glazing façade could be partially displaced through the electricity produced by the PV systems (Mende et al., 2011). In contrast to this study, a Brazil research found that a PV window works more efficiently in terms of artificial lighting and cooling loads under a tropical climate than the central European climate (Didone and Wagner, 2013). Recently, a more complicated façade design integrated with PV panels has occurred at the locations with warm climates. Two studies of PV facade in a sub-tropical climate presented that a ventilated double-skin structure could improve both PV performance and indoor thermal comfort in summer (Chow et al., 2009; Han et al., 2013). The

Selection and/or peer review under responsibility of Scientific Committee
doi:10.18086/swc.2015.08.11 Available at http://proceedings.ises.org

combination of shading devices and PV panels has been regarded as another interesting research topic. A movable shading device integrated with PV panels was proved as an efficient way to achieve the largest potential of energy savings for cooling and lighting use under central and southern European climates (Janak and Kainberger, 2009), while a similar result has been found in a study of fixed shading device at a Mediterranean location (Mandalaki et al., 2014).

Visual performance is also a crucial research focus of the PV façade in office buildings. An earlier investigation has preliminarily studied the visual amenity (glare, view, contrast and lighting model) and aesthetic quality of indoor spaces with various transparent PV windows at a Scandinavian location (Lien and Hestnes, 2000). The assessment of visual performance in this study was basically focused on qualitative aspects. Later, one study implemented under a similar climate has adopted quantitative methods including lighting measurements and subjective survey to evaluate lighting performance and visual comfort in a room with various transparent PV glazing facades (Markvart et al., 2012). It has been concluded that the integration of transparent thin-film PV in glazed facades could significantly influence occupants' perception of daylight in the room and the view to the outside. Based on a complicated simulation method, the impact of solar cell density of PV facade on indoor visual comfort was analyzed in an office building (Mende et al., 2011). The finding showed that the transparent solar cells in glazing façade might have a limited effect to keep a proper visual comfort and a supplement shading device might still be required.

Apart from the visual aspects, the non-visual effects of daylight (e.g. psychological and physiological issues) in an office have actually become a new research trend due to an increasing requirement for a healthy indoor working environment (Boyce et al., 2003). Even though daylight availability is generally accepted as a standard to justify a proper design, it is still necessary to implement more investigations in an office with various facades since there are still many unknown areas of human behavior related to daylighting (Aries et al., 2015).

Thus, it can be found that energy performance is only one of important issues in office buildings with PV facades. Directly and significantly influenced by the indoor lighting, occupants' health, well-being and work productivities in such a space could be more critical. This article therefore aims to study the visual and non-visual performances of daylight in an office building with various PV façade systems. A dynamic lighting and visual simulation was completed in an office at two locations of Beijing (China) and London (UK).

2. Methods

This section presents locations and climates, office and façade models, as well as simulation settings.

2.1 Locations and Climates

The simulation study was based on two locations with different climatic conditions: Beijing (39.9167° N, 116.3833° E) and London (51.5072° N, 0.1275° W). Beijing has a continent climate with cold winter and hot summer, while a typical temperate climate dominates at London. The annual sunshine hours for Beijing and London are 2707 and 1460 respectively (of a possible number 4383) (Database of World Climate & Temperature, 2015). Beijing has clearly 29% more sunny days than London.

2.2 Office and Façade Models

In this study a single office room has been chosen as a typical model (Fig.1), with a dimension of 5.4×3.6×2.85m (depth, width and height). The office room has one fully-glazed window facade, which the PV panels were integrated with. The window façade has a south-facing orientation. Five various façade configurations were studied as follows: bare window (no PV panels), façades with opaque PV panels (small and large areas), façade with semi-transparent PV panels (small and large areas). For the facades with bath types of PV panel, the large PV area means the ratio of glazing area to wall area is 30% (PV area: 70%), while the value for the small PV area is around 60% (PV area: 40%) (Fig.1). The surface reflectances of each room element are: 0.8 (ceiling), 0.6 (wall), 0.3 (floor) and 0.1 (glazing). The visual transmittance of façade glazing is 0.72 (clear float glass). The part of PV façade is made of the glass laminate thin film PV units with two outer layers (clear float glass, thickness 4mm, visual transmittance 0.9) and one middle layer (PV encapsulation panel, 0.8mm). The opaque PV encapsulation panel has a diffuse reflectance 0.1 whilst a

diffuse transmittance 0.3 was set for the semi-transparent PV encapsulation panel. An average diffuse transmittance of semi-transparent PV panel could be around 0.24.

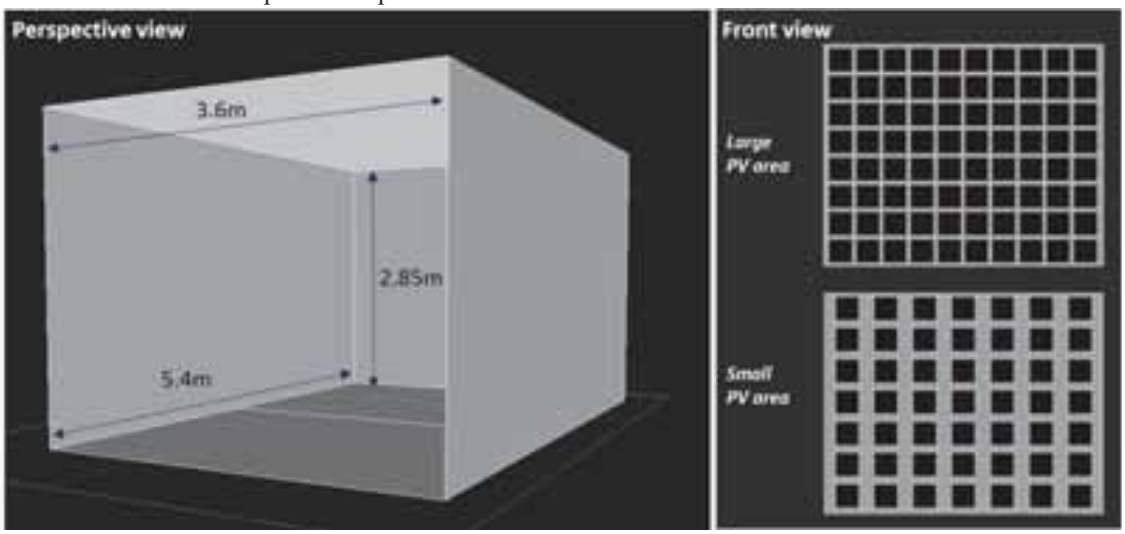

Fig. 1: Dimensions of office model (left: perspective) and configurations of two PV facades (right: front view).

2.3 Simulations

As for the basic daylight availability in this office, Daylight Autonomy (DA) and Daylight Factor (DF) across horizontal working plane (0.8m above floor) were calculated using a climate-based dynamic daylighting modelling tool DAYSIM (Reinhart and Herkel, 2000). A calculation grid with a 0.5m distance between two adjacent positions was used to get an average value of DA or DF. Also, eight positions were selected along the centre line of room from window to back wall, with a distance to window as follows: No.1-8 (0.51m, 1.18m, 1.86m, 2.53m, 3.21m, 3.88m, 4.56m and 5.23m). The design illuminance for DA assessment at the working plane is 500lux within a daily time period from 8am to 17pm.

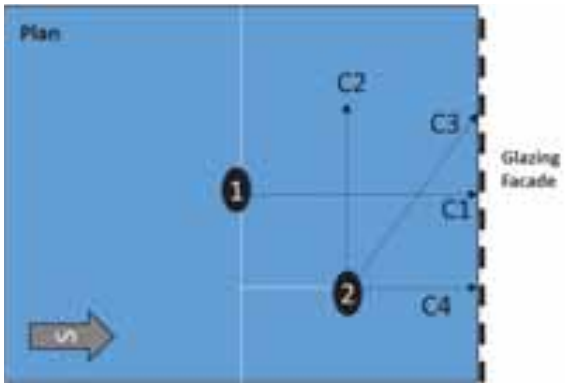

Fig. 2: Two positions and four view directions studied in this office (plan view).

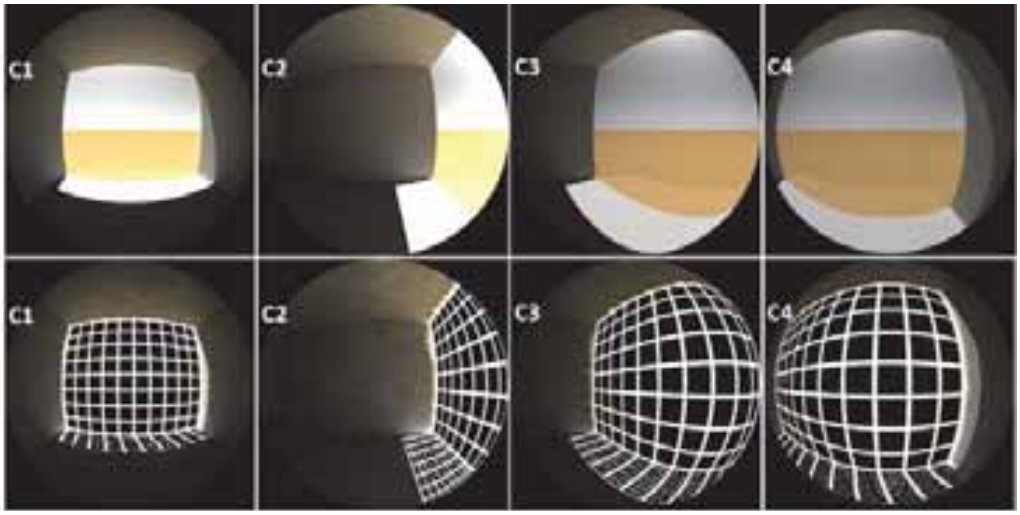

Fig. 3: Examples of rendering fish-eye images of four various views (up: glazing façade; bottom: PV façade).

In addition, two positions in the office were studied in terms of visual and non-visual lighting performances: No.1 & 2 (Fig.2). Position No.1 is exactly located at the room centre. Position No.2 is at the area near window, which could be regarded as a common place for a working station. The distances of position No.2 to window and side wall are 1.35m and 0.9m respectively. Four view directions were also defined at the two positions: C1 (at No.1, facing south), C2 (at No.2, facing east), C3 (at No.2, facing south east) and C4 (at No.2, facing south). C1 and C2 were the main views in this study. According to previous studies (Aries et al., 2015; Borisuit et al., 2014), the non-visual effect of daylight could be evaluated by the vertical illuminance received at the eyes of occupants. Thus, the daylighting availability at the two positions and along the four view directions has been assessed to indirectly indicate the effect. Similarly, two vertical DA values (illuminance threshold: 1000lux and 2000lux) were calculated at a height 1.2m (normal eye level of a sitting human being) using the DAYSIM for each view. In order to achieve a comprehensive visual performance of PV façade, a more complicated analysis was carried out in terms of Daylight Glare Probability (DGP) (Wienold and Christoffersen, 2006). Different from a conventional model Daylight Glare Index (DGI), DGP could be more suitable for assessing visual comfort in a real daylit space, especially for the window with a non-uniform surface luminance. Based on fish-eye images rendered by Radiance (Fig.3), DGP values were calculated at each view in a software package EVALGLARE (Wienold and Christoffersen, 2006). The glare metrics of DGP method are: DGP < 35%, imperceptible; 35% < DPP < 40%, perceptible; 40% <DGP < 45%, disturbing; DGP > 45%, intolerable. The dates for visual comfort evaluation were: spring equinox 20/03/2015; autumn equinox 23/09/2015; summer solstice 21/06/2015; winter solstice 22/12/2015. For each date, also, only three times 9am, 12pm and 15pm were analyzed.

Following a method to model PV glazing system (Didone and Wagner, 2013), BSDF (Bidirectional Scattering Distribution Function) of PV façades in this study was achieved according to various materials used for each layer. A software OPTICS (version 6.0) and International Glazing Database (version 29.0) from Lawrence Berkeley National Lab were the tools to produce Radiance material files used in all simulations.

3. Results and Discussions

This section includes a preliminary analysis of daylighting performance across the working plane, visual and non-visual performances in the office model with various PV façade systems. The five façade systems are named as: BW (bare window), LOP (large opaque PV facade), LTP (large semi-transparent PV facade), SOP (small opaque PV facade) and STP (small semi-transparent PV facade).

3.1. Daylight performance at the working plane

The daylighting level at the working plane is generally adopted to show a basic daylighting condition. Table 1 presents average DF and DA values at the working plane in various models. DF is a daylight metric to show a basic daylighting condition under CIE standard overcast sky condition.

Tab. 1: Average Daylight Factor and Daylight Autonomy in the office with various façade systems.

	BW	LOP	LTP	SOP	STP
DF (%)	9.49	2.2	4.06	5.26	6.32
DA (%): Beijing	86.96	43.64	64.34	72.87	78.04
DA (%): London	78.74	42.18	61.73	68.4	71.98

The façade with a large PV area normally gives rise to the minimum average DF, while the highest average value is found with the bare window. Taking the average DF of bare window as reference, the percentage DF differences of other façade systems are the following: -76.8% (LOP), -57.2% (LTP), -44.6% (SOP) and -

33.4% (STP). Interestingly, small opaque PV façade would still bring in more diffuse daylighting than the large semi-transparent PV facade. Based on the climate-based daylight modelling, nevertheless, DA is used to assess the daylighting availability taking into account locations and climates. Clearly, a higher average DA of Beijing can be found for each façade system than London, due to a better sky condition for daylight utilization. In response to the DF analysis, large opaque PV facades at both locations receive the lowest DA at the working plane, whilst small opaque PV facades would still lead to a relatively higher DA than large transparent PV facades. Reducing PV transmittance or increasing PV size would significantly lower the average DA in the office. Similarly, taking the DA of bare window as reference, the relative DA differences of PV facades are: LOP (Beijing: -49.82%; London: -46.43%), LTP (Beijing: -26%; London: -21.6%), SOP (Beijing: -16.2%; London: -13.13%) and STP (Beijing: -10.25%; London: -8.59%). Compared with London, Beijing sees a slightly [illegible] rally, a 43% decrease in PV size would reduce th [illegible] or 15% for transparent PV panels. However, a 0 [illegible] would lead to a reduction of relative DA differenc [illegible]

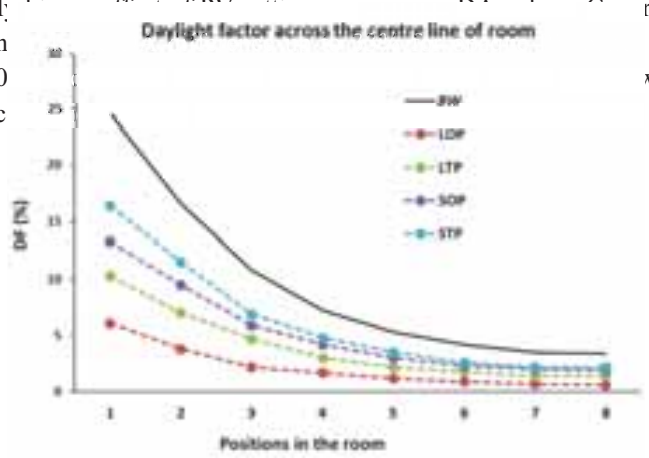

Fig. 4: Daylight Factors at the eight positions in the office with various façade systems.

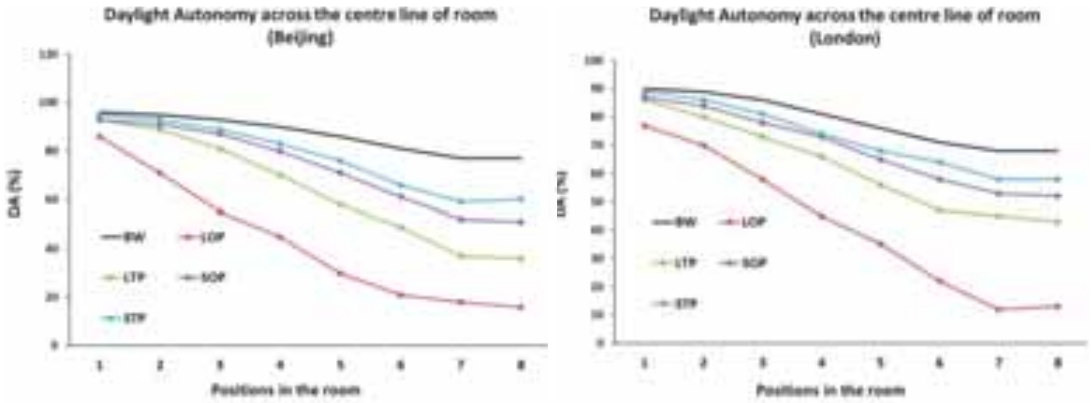

Fig. 5: Daylight Autonomy at the eight positions in the office with various façade systems (Beijing and London).

Fig 4 indicates variations of DF along centre line of the room with the five façade systems. An exponential decay of DF could be found for each façade system. With PV panels in the glazing facade, DF values have been clearly reduced along the room centre, especially for the area near window (distance to window < 2.7m). Normally, small PV size and transparent PV panel will give rise to a higher DF value than large PV and opaque panel from the window to back wall. The average DF values of the eight positions are: 9.49% (BW), 2.2% (LOP), 4.06% (LTP), 5.26% (SOP) and 6.32% (STP). In general, a 43% decrease in PV size would get an over doubled DF value for opaque panel and a 56% higher DF value for transparent panel, whilst a 0.24 increase in absolute transmittance value of PV panels would increase 100% and 20% DF value for large and small PV panels respectively. Similarly, variations of DA along the centre line of room have been displayed in Fig 5. Compared with other PV façade systems, large opaque PV façade has a much lower DA at both locations and only the perimeter area (No.1-3) has a DA >50%. Except for large opaque facade,

however, the first position No.1 (with a distance 0.51m to window) sees a similar DA value between bare window, while a DA divergence increases with the position moving towards back wall. For both Beijing and London, small PV facades could keep a DA > 50% at each centre position. Similar to average DA, the relative differences of DA between PV facades and bare window along centre line are smaller at London than Beijing.

Regards as the analysis above, a diffuse incident skylight under overcast sky could be heavily blocked by the large opaque PV panels. However, changing the size of semi-transparent PV panels would not bring in the difference as big as the opaque PV panels, due to a fact that the increased transmittance could significantly supplement one part of blocked diffuse daylight. For the DA analysis, nevertheless, the direct sunlight would be more difficult to block than the diffuse skylight by the application of PV panels in facades.

3.2. Visual performance of various facades

This section discusses the visual performance along four view directions in the office model with various façade systems at Beijing and London. The DGP was evaluated under a clear sky at the locations in order to investigate the worst visual condition with direct sunlight.

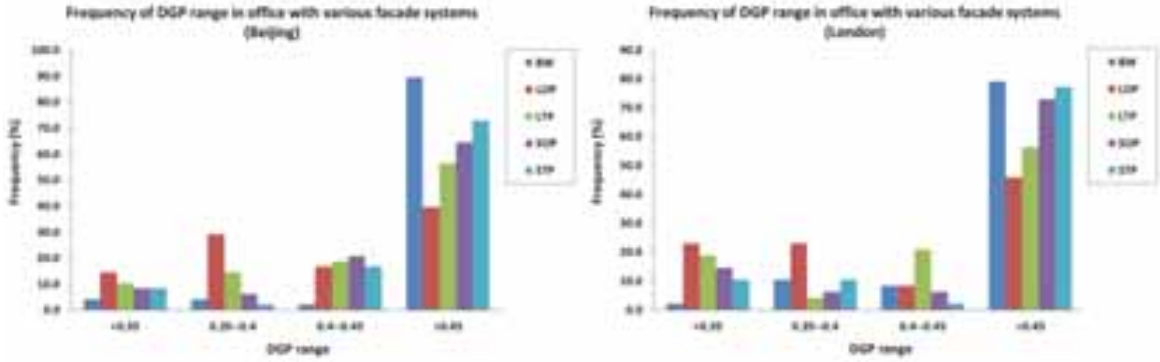

Fig. 6: Frequency distribution of four DGP ranges in the office with various façade systems

(Left: Beijing; Right – London).

First, a general visual performance has been discussed through a statistical analysis. Fig 6 shows the frequency distributions of four DGP ranges (see section 2.3) on four dates (20/03/2015; 21/06/2015; 23/09/2015; 22/12/2015) and three typical times (9am, 12pm and 15pm). The frequency was averagely analyzed with all four views (C1, C2, C3 and C4). Clearly, the biggest frequencies occur at DGP>0.45 (intolerable glare). DGP metrics show 0.4 is the threshold to justify visual comfort in a space (Wienold and Christoffersen, 2006). For the DGP>0.4 (visual discomfort), however, various façades have an occurrence frequency: Beijing – 91.7% (BW), 56.3% (LOP), 75% (LTP), 85.4% (SOP) and 89.6% (STP); London – 87.5% (BW), 54.2% (LOP), 77.1% (LTP), 78.4% (SOP) and 79.3% (STP). Accordingly, the potential to bring in a comfort visual environment in the office follows an order of lowest to highest as: BW>STP>SOP>LTP>LOP. In addition, the absolute differences of the frequency (DGP>0.4) between Beijing and London are: 4.17% (BW), 2.08% (LOP), -4.16% (LTP), 6.25% (SOP) and 10.41% (STP). Thus, Beijing office sees a relatively higher potential of visual discomfort than London office with bare window, large opaque PV and two small PV facades, whereas the large transparent PV façade would lead to a bit higher possibility to get visual discomfort in London office.

Second, as a main view facing outside, C1 has been specifically assessed with respect to visual comfort (DGP variations) in the model with five various façade systems (Fig 7 and 8) as below.

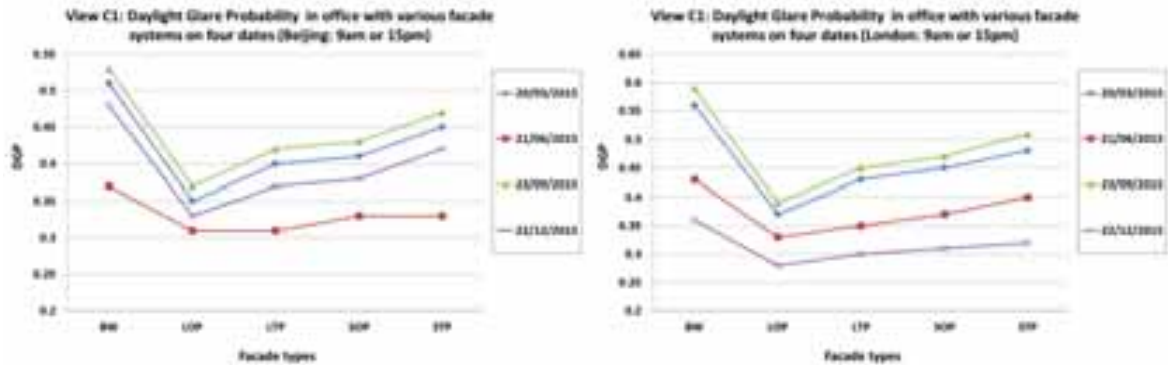

Fig. 7: Variations of Daylight Glare Probability in the office with various façade systems at 9am or 15pm (C1; Beijing: left; London: right).

Fig 7 displays varying DGP values of various facades in the morning (9am) or in the afternoon (15pm). Normally, a similar variation could be found on spring and autumn equinoxes: only large opaque PV façade could keep an acceptable visual environment; other façade systems would just bring in visual discomfort. Apparently, lower DGP values can be found on winter and summer solstices. All façade systems at Beijing office see a proper visual condition (DGP<0.4) on summer solstice, while a similar trend at London can be only found on winter solstice. Except for the bare window and small transparent PV façade at Beijing, other three facades have a DGP<0.4 on winter solstice. Interestingly, the summer solstice gives rise to an acceptable visual performance in the London office on the condition of using large opaque, large transparent and small opaque PV facades.

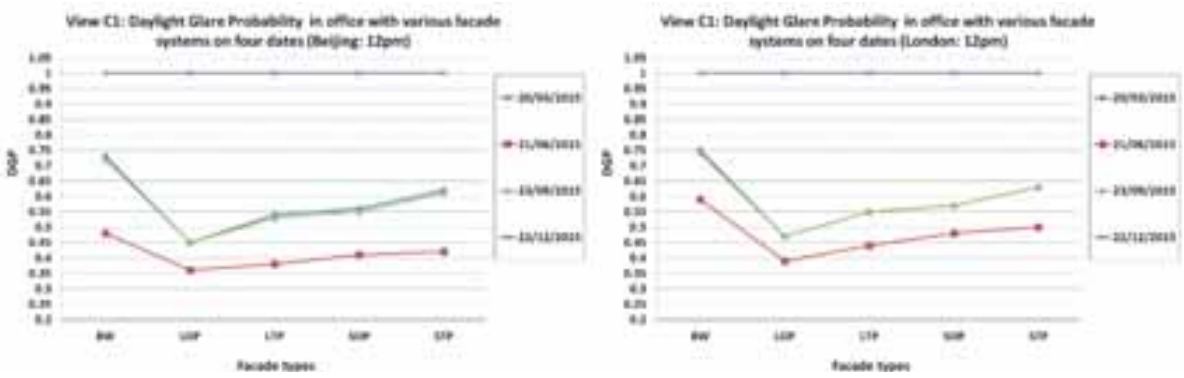

Fig. 8: Variations of Daylight Glare Probability in the office with various façade systems at 12pm (C1; Beijing: left; London: right).

The varying DGP values of various facades at noon (12pm) can be found in Fig 8. In general, it could be very hard to achieve a comfort visual environment in the office through the integration of PV panels in the glazing façade at Beijing and London. Even though the large opaque PV can block a lot of direct sunlight, DGP of LOP façade is still kept in a range of 0.35 — 0.4 (glare: perceptible). Beijing and London have a similar DGP varying trend: the highest value is found on winter solstice while summer solstice sees the lowest value; spring and autumn equinoxes have a middle value in between.

Third, view direction C2 (facing east) is commonly found in a typical office. The DGP assessment along this view is displayed in Fig 9, 10 and 11.

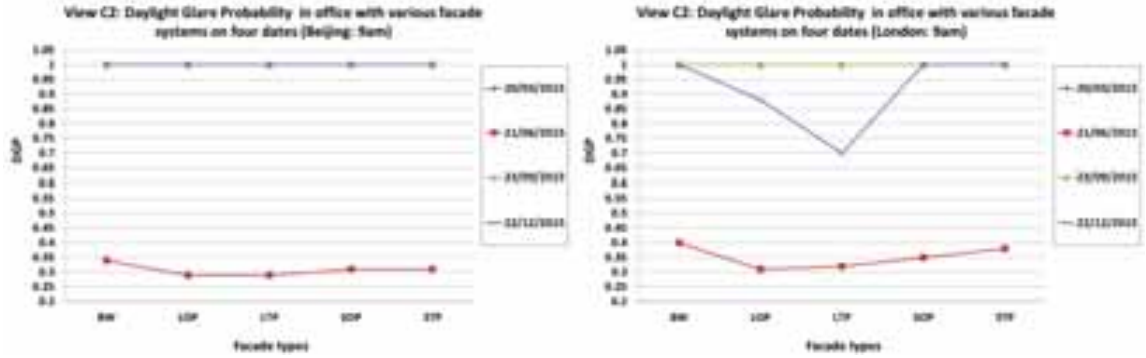

Fig. 9: Variations of Daylight Glare Probability in the office with various façade systems at 9am (C2; Beijing: left; London: right).

At time 9am in the morning (Fig 9), all façade systems could bring in a proper visual comfort (DGP<0.4) on summer solstice while a high possibility to be seriously disturbed by glare are found on other three dates. Two large PV facades would produce a good daylighting condition according to visual comfort

(DGP< 0.35; 'imperceptible' glare). For the time at noon (12pm), however, a more complicated DGP variation has been given regarding the Fig 10: the lowest DGP can be found on summer solstice at Beijing and on winter solstice at London, whereas both Beijing and London see the highest DGP on spring equinox. At Beijing, a proper visual condition (DGP<0.4) only occurs on summer solstice for PV facades. Also, the winter solstice and autumn equinox have a similar DGP performance. At London, large opaque façade can help achieve the lowest DGP and proper visual comfort (DGP≤0.4) on each date. With PV panels (both opaque and transparent), also, a very good visual environment is found on winter solstice (DGP≤0.35) at London office. Generally, London office has a relatively lower DGP value than Beijing office. In the afternoon (15pm, Fig 11), DGP variations of various façade systems are similar to those at noon (12pm, Fig 10). Spring equinox has the worst visual condition, whilst Beijing and London offices see the best visual comfort on summer solstice and winter solstice respectively. Besides, large opaque PV panel would bring in a proper visual comfort (DGP≤0.4) on all dates and at both locations. The use of PV panels (both opaque and transparent) could ensure the basic visual comfort (DGP<0.4) on winter and summer solstices at London office. However, a similar effect can be only found on summer solstice at Beijing. In terms of the analysis of three times 9am, 12pm and 15pm, an order of the potential to achieve visual comfort for all PV facades from highest to lowest is: LOP, LTP, SOP, and STP.

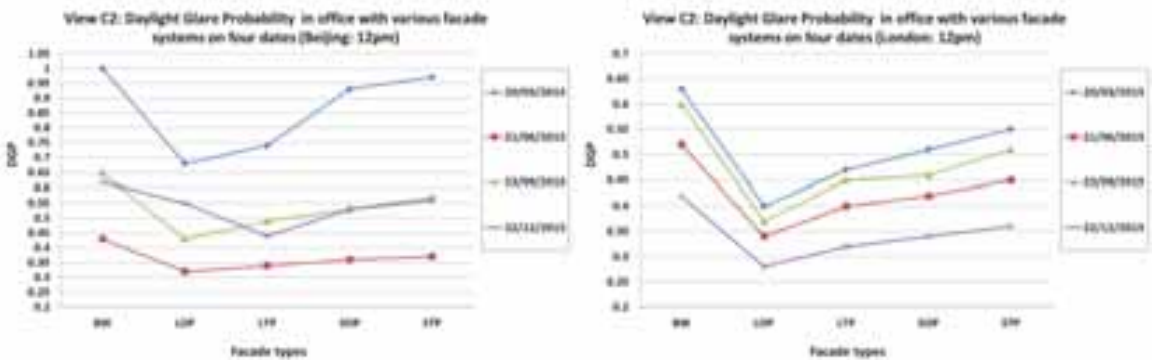

Fig. 10: Variations of Daylight Glare Probability in the office with various façade systems at 12pm (C2; Beijing: left; London: right).

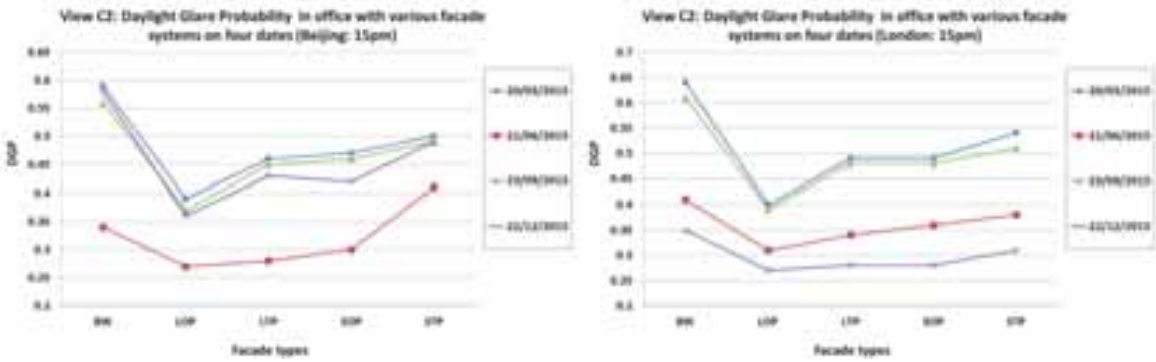

Fig. 11: Variations of Daylight Glare Probability in the office with various façade systems at 15pm (C2; Beijing: left; London: right).

From the analysis above, DGP variations could be explained by the combined effect of solar geometry and façade configurations. Compared with small PV panels, the large panels could block more direct sunlight that gives rise to a higher potential of visual discomfort. For the view facing south (C1), a higher solar altitude of summer solstice at noon results in a smaller daylighting level at the vertical surface of glazing façade, whereas the vertical daylighting level will go up with a lower solar altitude in winter. These could directly decide if a proper visual condition is achieved. When sunlight arrives from the side (9am or 15pm) on spring or autumn equinox, the lower solar altitude would lead to a higher daylighting level at the opposite side wall, which would make the wall brighter. Following this way, the view facing east (C2) will get a

similar visual performance at 9am and 12pm as the south-facing view at noon and in the afternoon respectively.

3.3 Non-visual performance of various facades

As mentioned in section 2.3, Daylight Autonomy (threshold: 1000lux and 2000lux) at four vertical positions was used to expressed the non-visual effects of daylighting with the occurrence of various façade systems. Tab 2&3 give the calculated DA values at the offices of Beijing and London. The larger is the DA, the higher is the possibility to active a positive non-visual effect of daylight.

Tab. 2: Daylight Autonomy at four vertical positions in an office with various façade systems (Beijing)

Daylight Autonomy (%) - Beijing						
Vertical Illuminance Threshold	**View**	**BW**	**LOP**	**LTP**	**SOP**	**STP**
1000lux	**C1**	91	45	75	81	82
	C2	89	36	65	76	79
	C3	94	64	84	88	89
	C4	94	72	86	90	90
2000lux	**C1**	77	17	44	53	61
	C2	71	12	35	45	54
	C3	87	26	60	71	77
	C4	89	38	65	75	80

Similar to the general daylighting performance at working plane, vertical DA values (1000lux and 2000lux) at the four positions of Beijing office in Table 2 follow a trend: LOP < LTP < SOP < STP < BW. Taking the bare window as reference, four PV facades have average percentage differences of vertical DA (threshold: 1000lux) as: -41% (LOP), -15.8% (LTP), -8.96% (SOP), -7.6% (STP) and vertical DA (threshold: 2000lux) as: -71.3% (LOP), -37% (LTP), -24.7% (SOP), -16.1% (STP). Increasing PV size would significantly reduce the vertical DA, especially for the large vertical illuminance 2000lux. For opaque PV panels, a 75% increase in PV size (from 40% to 70% wall area) would cause a fivefold percentage DA difference with 1000lux and a tripled percentage DA difference with 2000lux. However, transparent PV panels see a lower impact of the size change: a 75% increase in PV size will just get a doubled percentage DA difference for both thresholds. Normally, facing east (C2) receives the lowest vertical DA values with each façade system. With the small vertical illuminance 1000lux only the two positions (C1 and C2) with large opaque PV have a vertical DA < 50%, whereas more lower DA values can be found with the large vertical illuminance 2000lux: all positions (LOP), C1 & C2 (LTP), C2 (SOP).

Tab. 3: Daylight Autonomy at four vertical positions in an office with various façade systems (London)

Daylight Autonomy (%) - London						
Vertical Illuminance Threshold	**View**	**BW**	**LOP**	**LTP**	**SOP**	**STP**
1000lux	**C1**	80	48	67	71	75
	C2	76	40	58	65	69
	C3	85	58	73	78	80
	C4	86	65	77	80	83
	C1	68	21	47	53	60
	C2	62	9	36	48	52

2000lux	**C3**	76	36	56	64	68
	C4	78	43	61	68	72

Tab. 3 shows the vertical DA values in London office. A similar varying trend as Beijing office could be found here. The average percentage differences of vertical DA of PV facades to the bare window are as follows: for threshold 1000lux, -35.5% (LOP), -15.9% (LTP), -10.1% (SOP), -6.12% (STP); for threshold 2000lux, -61.6% (LOP), -29.6% (LTP), -18% (SOP), -11.3% (STP). With a 75% increase in PV size, the large opaque PV panel sees a 3.5 times percentage DA difference of small opaque panel, whereas the large transparent panel has a value slightly higher than the doubled percentage difference of small transparent panel. The large PV would give rise to a lower vertical DA (<50%), in particular for the vertical illuminance 2000lux or at the position facing east. Compared with Beijing office, it could be found that London office receives a smaller impact of PV panels on the vertical DA.

4. Conclusions

This simulation study was completed in an office with various PV façade systems, which focused on the impact of indoor daylighting on visual and non-visual performances of occupants. Several findings are given as follows:

(1) In modern office buildings, the energy efficiency could not be the only core issue considered by the BIPV façade designers and engineers. It would be necessary to implement a comprehensive daylight design in such buildings in terms of visual and non-visual effects.

(2) It could be possible to adopt a proper BIPV façade as a feasible design strategy in office buildings to achieve energy efficiency, a good general daylighting performance at the working plane, as well as an acceptable vertical daylighting level relating to non-visual performance at typical working stations.

(3) For a glazing façade with uniformly distributed PV units, size and transmittance of PV cells could be critical in terms of visual and non-visual daylighting design in office buildings. When considering opaque PV cells, it could be still possible to produce a relatively worse daylighting performance (visual and non-visual aspects), even with the occurrence of large glazing (e.g. 30% wall area).

(4) It would be difficult to keep a proper visual comfort at typical working times in office buildings with the vertical BIPV façade system. Extra shading devices (e.g. venetian blind, overhang, louvre, ect) would be strongly recommended in order to avoid glare and complete a normal office work in day time.

(5) For the vertical BIPV system integrated with building fenestrations, it could be possible to achieve a higher indoor daylighting performance at both horizontal and vertical planes, which are used to indicate a basic daylighting condition and a potential to active non-visual effect. However, a proper balance between horizontal and vertical daylight levels and visual comfort would be a big challenge.

Limitations: this study was based on a preliminary simulation with simple office and BIPV models. More complicated building spaces and façade systems will be studied in the next stage.

5. Acknowledge

This study received support from the National Natural Science Foundation of China through a research project (51478236): Lighting Models and Energy-efficient Design Strategies in Chinese Commercial Spaces.

6. References

Alnaser, N.W., Flanagan, R., Alnaser, W.E., 2008. Potential of making—Over to sustainable buildings in the Kingdom of Bahrain. Energy and Buildings. 40, 1304-1323.Quesada, G., Rousse, D., Dutil, Y., Badache, M., Halle‘, S., 2012. A comprehensive review of solar facades: Transparent and transluscent solar facades. Renewable and Sustainable Energy Reviews. 16, 2643-2651.

Aries, M.B.C, Aarts, M.P.J, Hoof, van.J, 2015. Daylight and health: A review of the evidence and consequences for the built environment. Light Research and Technology. 47, 6-27.

Borisuit, A., Linhart, F., Scartezzini, J-L., Munch, M., 2014. Effects of realistic office daylighting and electric lighting conditions on visual comfort, alertness and mood. Light Research and Technology. 0, 1-18.

Boyce, P., Hunte, C., Howlett, O., 2003. The benefits of daylight through windows. Report of Lighting Research Centre. USA. Available from: www.lrc.rpi.edu/programs/daylighting/pdf/DaylightBenefits. Final access: 9 Nov 2011.

Chow, T., Qiu, Z., Li, C. Performance evaluation of PV ventilated glazing. Proceedings of Building Simulation 2009. July 27-30, 2009. Glasgow, UK.

Didone, E.L. and Wagner, A., 2013. Semi-transparent PV windows: a study for office buildings in Brazil. Energy and Buildings. 67, 136-142.

Database of World Climate & Temperature. Available from: www.climatemps.com. Final access: 10 July 2015.

Farkas, K., Maturi, L., Scognamiglio, A., Frontini, F., Probst, M.C.M., Roecker, C., Lundgren, M., 2013. T.41.A.3/2 Designing Photovoltaic Systems for Architectural Integration: Criteria and guidelines for product and system developers. Report of IEA-SHC Task 41: Solar Energy and Architecture. Available from: http://task41.iea-shc.org/publications. Final access: 10 Sept 2015.

Han, J., Lu, L., Peng, J., Yang, H., 2013. Performance of ventilated double-sided PV façade compared with conventional clear glass façade. Energy and Buildings. 56, 204-209.

Janak, M. and Kainberger, R. Integrated building energy and lighting simulation in the framework of EU-light project. Proceedings of Building Simulation 2009. July 27-30, 2009. Glasgow, UK.

Lien, A. G. and Hestnes, A.G. Visual studies of transparent PV - elements. Proceedings of EUROSUN 2000. June 19-23, 2000. Copenhagen, Denmark.

Mandalaki, M., Tsoutsos, T., Papamanolis, N., 2014. Integrated PV in shading systems for Mediterranean countries: balance between energy production and visual comfort. Energy and Buildings. 77, 445-456.

Markvart, J., Iversen, A., Logadóttir, Ásta., Johnsen, K., 2012. Indoor light and visual comfort with solar cells in glass facades. Report: Sbi 2012:12, Danish Building Research Institute & Aalborg University. Available from: http://www.sbi.dk/indeklima/lys. Final access: 08 July 2014.

Mende, S., Frontini, F., Wienold, J. Comfort and building perfronance analysis of transparent building integrated silicon photovoltaics. Proceedings of Building Simulation 2011. November 14-16, 2011. Sydney, Australia.

Reinhart, C.F. and Herkel, S., 2000. The simulation of annual daylight illuminace distributions – a state-of-art comparison of six Radiance-based method. Energy and Buildings. 32,167–187.

Robinson, L. and Athienitis, A. Design Methodology for optimization of electrcity generation and daylight utilization for facade with semi-transparent photovoltaics. Proceedings of Building Simulation 2009. July 27-30, 2009. Glasgow, UK.

Yun, G.Y. and Steemers, Koen., 2009. Implications of urban settings for the design of photovoltaic and conventional facades. Solar Energy. 83, 69-80.

Wienold, J. and Christoffersen, J., 2006. Evaluation methods and development of a new glare prediction model for daylight environments with the use of CCD cameras. Energy and Buildings. 38: 743-757.

Demonstration of An Office Powered By Solar PV System

Bin-JuineHuang, Po-Chien Hsu, Y.H. Wang, J.H. Tsai, Leo Chen, Kang Li, KY Lee
Department of Mechanical Engineering, National Taiwan University, Taipei, Taiwan.

Abstract

The purpose of the present study is to demonstrate the concept of peak-suppression by energy saving and replacement of peak load by solar PV energy supply to replace nuclear power. An office with 150m^2 floor area and 14 employees was chosen as the demonstration site. The results show that retrofit for energy-saving reduces 65% energy and the solar PV system supplies 20%. The total energy reduction is 85%. The total investment of the solar PV system and the retrofit of energy-saving devices is around USD30,000. The net total energy saving in 20 years is USD 80,000, including M&O cost. The system has been run about one year. The measured average total power consumption of the office is reduced from 10.2 kW to 3.6 kW (after retrofit) in which solar PV supplies about half.

Keywords: solar PV energy, distributed solar system, solar energy office

1. Introduction

Grid power demand during peak load is caused mainly by energy consumption of air conditioning systems. Solar PV system is the best solution for peak-shaving. In addition, the utilization of solar PV power system should be for self-consumption, rather than feeding back to grid and causing transmission problem when solar PV is widely adopted. That is, solar PV distributed system will be one of the future major energy supplies in the world.

Since Taiwan is located in subtropical area, there is a peak load around 13:00 during summer around 34GW. From a long-term study, the power consumption of air conditoning contributes about 9 GW. Energy saving of air conditioning systems is thus most important.

Taiwan Government has set up a energy-efficiency classification for all air conditioners since 2010. Five categories are defined according to the energy efficiency ratio (EER) (W/W) and cooling capacity. See Table 1. However, EER of majority of air conditioners in the market or ever installed is below 3.5 (Category 3~5) . In 2010, 70% of air conditoners belongs to Category 5. Large potential of energy saving is feasible since the EER of the most advanced air conditioner in the market is higher than 5.6.

Table 1: Category of air conditioners

Type	Cooling capacity, kW	EER (W/W)				
Category		1	2	3	4	5
Integral-type	<2.2 2.2~4.0 4.0~7.1 7.1~10	>3.4	3.25~3.4	3.1~3.25	2.95~3.1	< 2.95
Split-type	<4.0	>4.17	3.93~4.17	3.69~3.93	3.45~3.69	<3.45
	4.0~7.1	>3.87	3.65~3.87	3.42~3.65	3.2~3.42	<3.20
	>7.1	>3.81	3.59~3.81	3.37~3.59	3.15~3.37	<3.15

Besides, lighting consumes about 10~15% energy in Taiwan. It is known that LED (light-emitting-diode) can save more than 50% lighting energy. Thus, lighting energy saving using LED is also feasible.
The cost of solar PV energy is reduced dramatically recently to bring the grid-parity age to come. Energy from solar PV is equal or cheaper than from the grid. High-efficiency air conditioning, LED lighting, and low-cost solar PV are all technically mature and available in the market for energy saving.

doi:10.18086/swc.2015.08.12 Available at http://proceedings.ises.org

The purpose of the present study is to demonstrate the concept of peak-suppression by energy saving first and then replacement of peak load by solar PV energy supply. This may be able to completely abandon nuclear power in Taiwan, as shown in Fig.1. An office in a 7-floor building located in Taipei with 150m^2 floor area and 14 employees was chosen as the demonstration site.

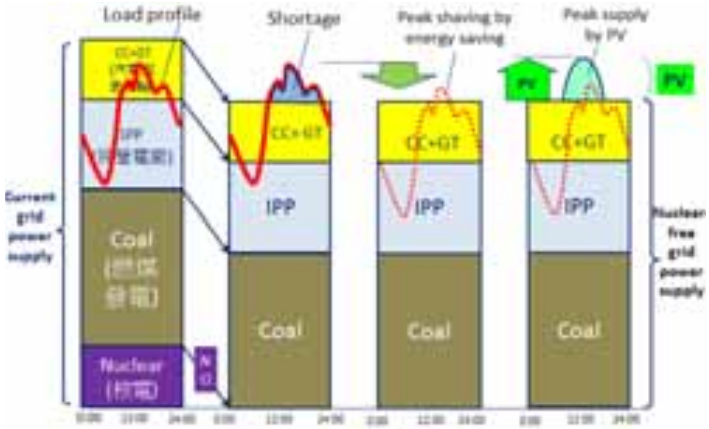

Fig. 1: The concept of nuclear power abandon by energy saving and using solar PV energy.

2. Retrofit of energy equipment and solar PV supply

2.1. Retrofit for energy saving

1. Energy consumption before energy-saving retrofit

The office of the Department of Mechanical Engineering, National Taiwan University, with 150m^2 floor area and occupied by 15 employees, was chosen as the demonstration site (D-1). The major energy consumption of the office comes from air conditoning, lighting, and PC. The power and daily energy consumption of air conditioners, lighting, and laptop PC was calculated and listed in Table 2. It is seen that the total power consumption for air conditioners, lighting, and PC reaches 10.16 kW and the daily total energy consumption reaches 81.3 kWh. 64% energy is consumed by air conditioners.

Table 2: Energy consumption before retrofit.

Daily consumption @8 h/day	Power input, kW	Daily energy, kWh/day
(1)Air conditioning		
Room 1: One split-type MW3299 BFR: cooling 7.3kW, COP 2.92	2.5	20
One window-type : cooling 5.8 kW, COP 2.9	2	16
Room 2: One window-type MW550BR: cooling 5.8kW, COP 2.9.	2	16
Energy consumption	6.5	52
(2)Lighting		
Room 1: Recessed fluorescent (47W)26 sets	1.222	9.8
Room 2: Recessed fluorescent (47W) 4 sets	0.188	1.5
Energy consumption	1.41	11.3
(3) PC		
Room 1: 13 laptop PC, 150W each	1.95	15.6
Room 2: 2 laptop PC, 150W each	0.3	2.4
Energy consumption	2.25	18
Total energy consumption (air conditioners, lighting, PC)	10.16	81.3

2. Energy-saving retrofit and energy consumption

To reduce energy consumption, four retrofitting was carried out: (1)air conditioning system is renewed with high-efficiency split-type air conditioner (Hitachi RAC-22NB) with COP 5.6; (2)lighting is retrofitted with LED luminaire with 100 Lm/W; (3)all lap-top computers are changed into notebook PC; (4)the window glass

is covered with low-E film to block IR part of solar radiation penetrating into the office. The above four retrofits results in 65% energy saving as shown in Table 3, at average power 3.6 kW (from 10.2 kW) and daily energy consumption 28.6 kWh/day (from 81.3 kWh/day).

Table 3: Energy consumption before retrofit.

Before energy-saving retrofit				After energy-saving retrofit			Energy saving
	Old equipment	Power input, kW	Daily energy, kWh/day	New equipment	Power input, kW	Daily energy, kWh/day	
(1)Air conditioner							
Room 1:	One split-type MW3299 BFR: cooling 7.3kW, COP 2.92	2.5	20	Five Hitachi split-type RAC 22NB: cooling 2.2kW, COP 5.6	2	16	20%
	One window-type : cooling 5.8 kW, COP 2.9	2	16				
Room 2:	One window-type MW550BR: cooling 5.8kW, COP 2.9	2	16	One Hitachi split-type RAC22NB: cooling 2.2kW, COP 5.6	0.4	3.2	80%
	Energy consumption	**6.5**	**52**		**4.4**	**19.2**	**63%**
(2)Lighting							
Room 1:	Recessed T8 fluorescent (47W)26 sets	1.222	9.8	Recessed T8 LED (30W): 20 sets	0.6	4.8	51%
Room 2:	Recessed T8 fluorescent (47W) 4 sets	0.188	1.5	Recessed T8 LED (30W): 4 sets	0.12	0.96	36%
Energy consumption		**1.41**	**11.3**		**0.72**	**5.76**	**49%**
(3)PC							
Room 1:	13 laptop PC, 150W each	1.95	15.6	13 NB, 30W each	0.39	3.12	80%
Room 2:	2 laptop PC, 150W each	0.3	2.4	2 NB, 30W each	0.06	0.48	80%
Energy consumption		**2.25**	**18**		**0.45**	**3.6**	**80%**
Total energy consumption (air conditioners, lighting, PC)		**10.16**	**81.3**		**3.57**	**28.6**	**65%**

Based on running time 8 h/day

2.2. Solar PV system design

A 6 kWp hybrid solar PV system is installed to replace another 20% energy. That is, 85% energy consumption is reduced in total.

The solar PV system is an isolated-type hybrid solar PV system (HyPV) which operates in Stand-alone PV Mode or Grid Mode, automatically. Fig.2 No solar PV energy is fed back to grid. When solar power generation and battery storage is sufficient, it operates in Stand-alone PV Mode and the load is powered completely by solar energy. When solar power generation and battery storage is not sufficient, it will switch to Grid Mode and the load is supplied completely by grid. The intelligent controller (MCU) performs optimal switching control between Stand-alone PV Mode and Grid Mode to reduce cycling of battery and ATS. The microprocessor-based MCU also carries out solar charging and system protection control, etc.

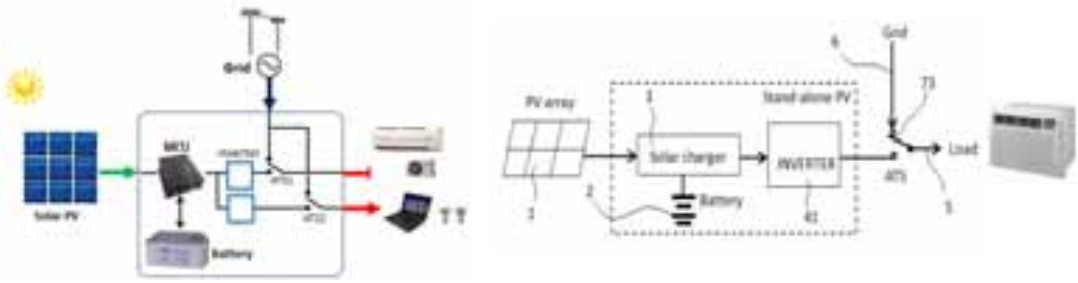

Fig. 2: Hybrid solar PV system (HyPV)

The HyPV utilizes nMPPO (near maximum-power-point operation) system design (Huang *et al*, 2006) to eliminate the conventional MPPT (maximum-power-point tracking control) but still keep optimal performance. This reduces MPPT energy loss and hardware cost and increases the reliability. The HyPV also utilizes direct PV charging control technique for battery to avoid energy loss and malfunction of conventional charger. This reduces cost and increases reliability. Fig.3 shows the installation of HyPV on roof-top for energy supply of the office.

Fig. 3: Hybrid solar PV system for office energy supply.

The design of 5.88 kWp solar PV system is shown in Table 4. To increase power generation, 1A-3P (one-axis 3-position) sun tracker is used to mount PV panels. The energy generation will be increased by 25% in Taipei (Huang *et al,* 2007). The solar PV system is divided into two 2.94 kWp subsystems. No.1 supplies 4 air conditioners (220VAC). No.2 supplies power to drive 2 air conditioners (220VAC) and LED lighting and PC's (110VAC) (Fig. 3). The installation is as shown in Fig. 4.

Table 4: PV system design.

Solar PV system:	
(1)energy generation capability, kWh/kWp-yr	900
(2)PV installed capacity, kWp	5.88
(3)system loss	10%
(4)power enhancement by 1A-3P	1.25
(5)average daily generation, kWh/day	16.31
(6)highest daily generation, kWh/day	24.47
(7)lowest daily generation, kWh/day	2.35
(8)max load, kWh/day	28.6
Battery storage:	
(1) Li-battery capacity, kWh	2.88
(2) running time at full load, hr	0.8
(3) running time for A/C, hr	1.2
(4) running time for lighting, hr	4.0

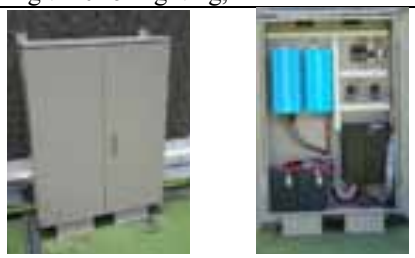

Fig 4: Chassis of HyPV for MCU, inverter and battery etc.

3. Test results

The installation of HyPV system including measuring system was completed in July 2014. The performance was monitored continuously from August, 2014. Fig. 5 shows the 5-month operation for No.1 unit which is used to supply 4 air conditioners. According to statistical data from the government monitoring network around Taiwan, the daily PV energy generation per unit PV installation is 2.47 kWh/kWp per day (900 kWh/kWp-yr). Fig. 6 shows that the 5-month performance of No.1 obtains 2.17 kWh/kWp per day in average which is 12% lower than the statistical data. This is due to low load energy consumption in fall season while air conditioner is not frequently used.

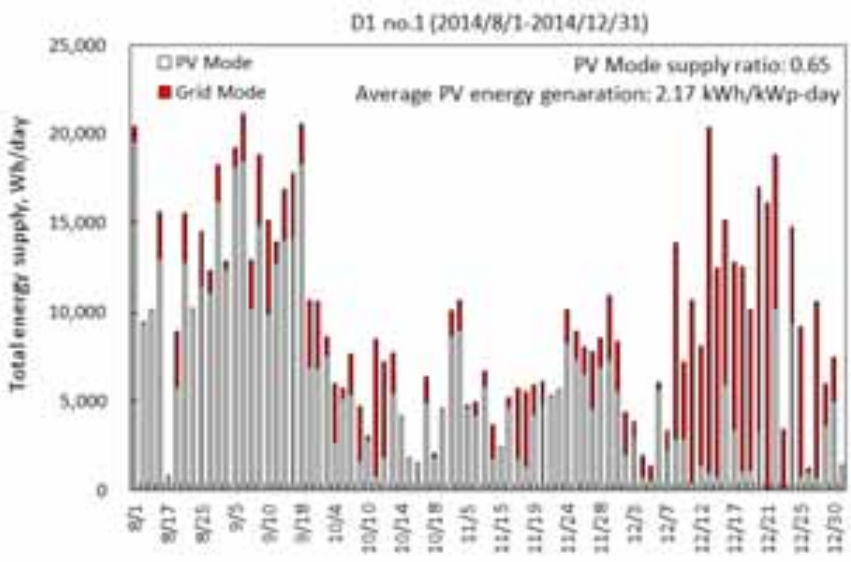

Fig 5: Long-term performance in No.1 unit.

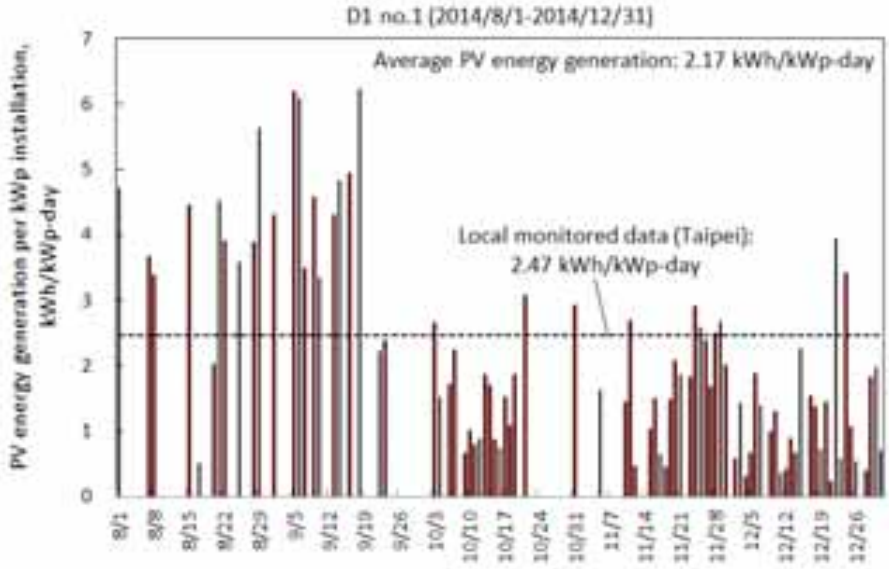

Fig 6: PV generation per kWp installed in No.1 unit.

The daily total energy supply (PV-Mode and Grid-Mode) of No.2 unit is shown in Fig 7. It reaches 2.67 kWh/kWp per day, 8.1% higher than the statistical result. This is due to the fact that the load energy of LED lighting and NB is supplied by No.2 unit which is not changed all year round.

Table 5 is the long-term results in PV energy generation and solar fraction. It shows that the PV energy generation per PV installed reaches 2.42 kWh/kWp per day (Fig.8), approaching the statistical result (2.47). This means that no PV energy generation loss for the whole D-1 system, even it is operated only in weekdays and at low load condition in fall season.

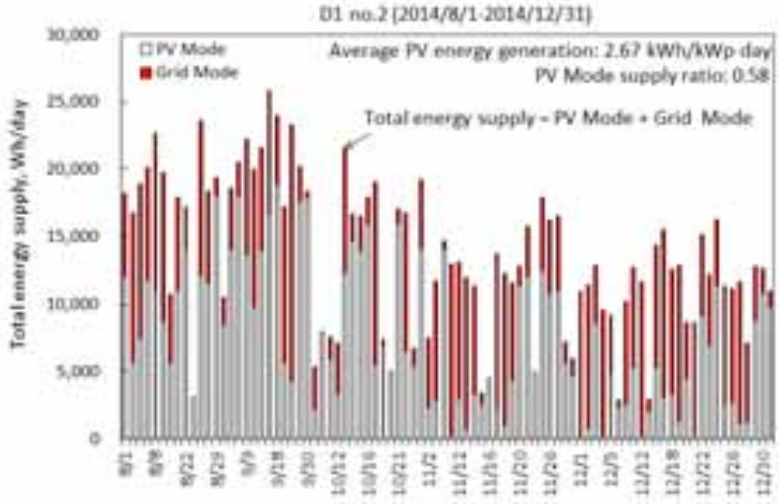

Fig 7: Long-term performance of No.2 unit.

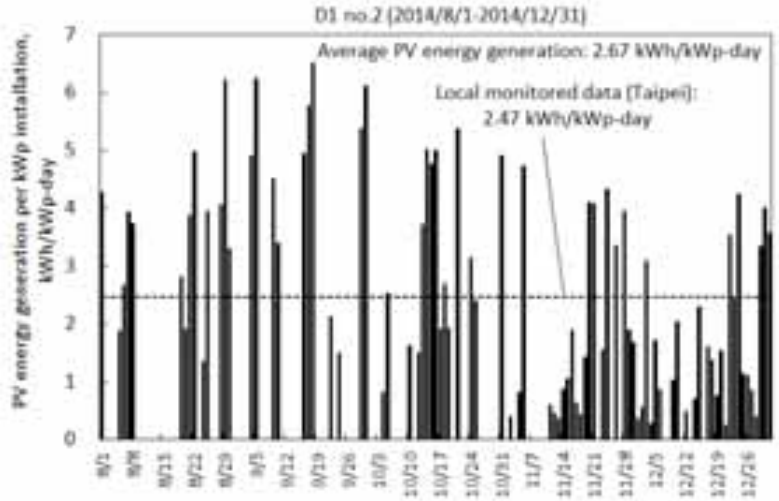

Fig 8: PV generation per kWp installed of No.2 unit.

Table 5: Performance of D-1 system in 2014.

D-1	No.1		No.2		No.1 PV generation loss, %	No.1+No.2	
	PV generation per kWp installation, kWh/kWp-day	Solar fraction	PV generation per kWp installation, kWh/kWp-day	Solar fraction		PV generation per kWp installation, kWh/kWp-day	Solar fraction
2014/8	3.71	0.88	3.5	0.61	-	3.61	0.745
2014/9	4.4	0.87	4.67	0.68	8.6	4.54	0.775
2014/10	1.59	0.75	3.7	0.7	52.7	2.65	0.725
2014/11	1.77	0.73	2.15	0.48	17.7	1.96	0.605
2014/12	1.21	0.29	1.95	0.4	33.3	1.58	0.345
Average	2.17	0.65	2.67	0.58	18.8	2.42	0.615

Fig 9 shows that the 7-month total energy supply (load) of D-1 in 2015 is lower than the estimation (28.6 kWh/day), except in summer. The PV-Mode supply ratio is 0.75. The load demand in March is quite low which increases the PV generation loss. However, the PV energy generation reaches 20.94 kWh/day in summer (June and July), 28% higher than average prediction. Fig.10.

The design of D-1 system is based on the concept of PV energy for self-consumption and small battery storage to reduce cost. The battery is used as a buffer to stabilize the instantaneous load only. The long-term test results for a year shows that the PV energy generation loss is low.

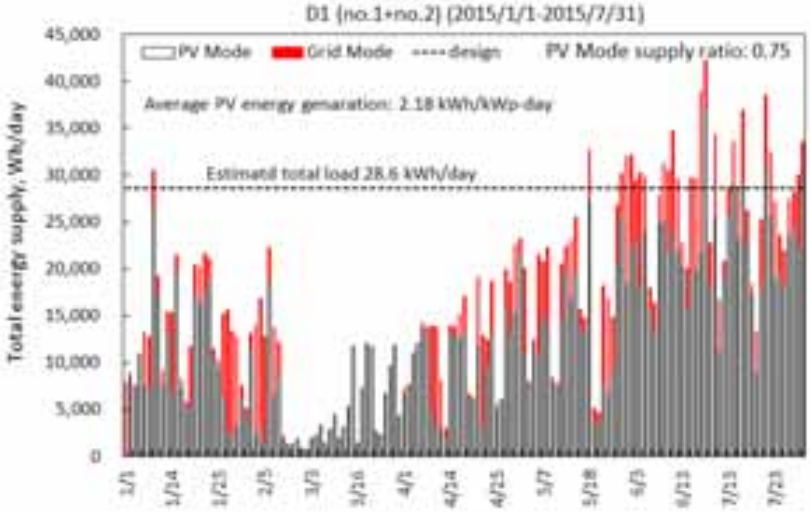

Fig 9: Total energy supply (load) of D-1 in 2015.

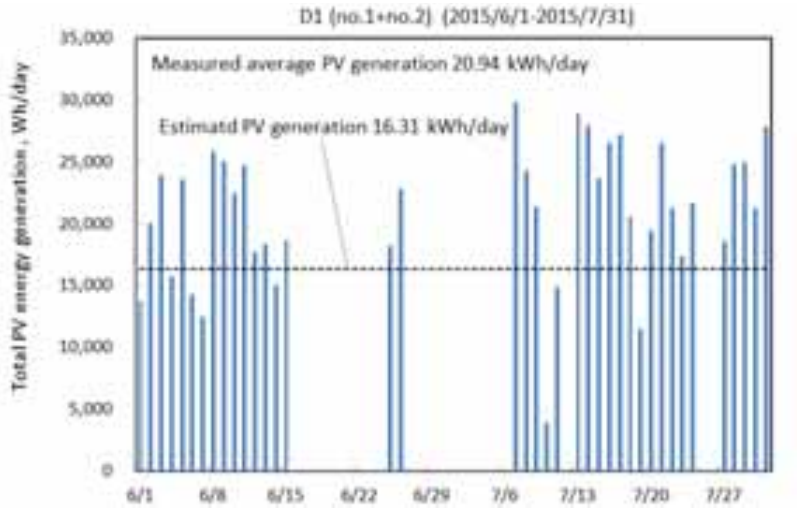

Fig 10: Overall performance of D-1 in 2015.

4. Economic Feasibility

The total investment of the solar PV system and the retrofit of air conditioning system, lighting devices, window insulation etc. is around USD30,000. The net total energy saving in 20 years is USD 80,000, including M&O cost. The system has been run about one year. The measured total power consumption of the office is reduced from 10.2 kW to 3.6 kW (after retrofit), about 65%. The solar PV system supplies about half of the rest of energy demand of the office. That is, 85% energy reduction in total.

The economic analysis (Table 5) shows that the total energy saving through retrofit and PV installation reaches 85% in Taipei (poor solar area) and 96% in Tainan (rich solar area). This indicates that the present demonstration system (D-1) can approach zero-energy office if installed in a solar rich area. The payback time is 8 yr in Taipei and 7.5 yr in Tainan.

5. Conclusions

The present study shows that, performing energy saving retrofit then utilizing solar PV energy to supply the remaining load demand in grid can solve the energy shortage problem, if nuclear power was abandoned in Taiwan. An office located in Taipei with 150m^2 floor area and 14 employees was chosen as the demonstration site (D-1). Four energy-saving retrofitting on air conditioning, lighting, PC, and anti-IR film on window glass results in 65% energy saving. A 6 kWp solar PV system is further installed to replace additional 20% energy. That is, 85% energy is saved in total. The solar PV system is an isolated-type hybrid solar PV system (HyPV) which operates under Stand-alone PV Mode or Grid Mode, automatically, by a

power controller. No solar PV energy is fed back to grid. The total investment for the solar PV system and the retrofit for energy saving is around USD30,000. The net total energy saving in 20 years is USD80,000, including M&O cost. System D-1 has been run more than one year. The solar PV system supplies about 60% final energy demand of the office.

If energy-saving in air conditioning and lighting can reach 60% as D-1 did in the whole country, the nuclear power (18%) can be abandomed by using solar PV installation to supply the remaining load demand with proper energy storage.

Table 5: Economic analysis.

Office hour: 8 h/d, 22 d/mon 1 USD = 32NT		Before retrofit		After retrofit (Taipei)			After retrofit (Tainan)		
		Load power (kW)	Daily load (kWh/day)	Load power (kW)	Daily load (kWh/day)	Reduction	Load power (kW)	Daily load (kWh/day)	Reduction
Total consumption (A/C, LED, NB)		10.16	81.3	3.57	28.6	65%	3.57	28.6	65%
Energy-saving (A)	Grid power (kWh/mon)	1,788		628		65%	628		65%
	Unit price (NT/kWh)	5.78		4.7			4.7		
	Monthly bill (NT/mon)	10,338		2,953		71%	2,953		71%
PV supply (B)	PV generation (kWh/mon)	-		359			560		
(A)+(B)	Grid power (kWh/mon)	1,788		269		85%	69		96%
	Unit price (NT/kWh)	5.78		3.27			3.27		
	Monthly bill (NT/mon)	10,338		881		91%	224		98%
	Monthly energy saving (kWh/mon)	-		1,519		85%	1,720		96%
	Monthly bill reduction (NT/mon)	-		9,457		91%	10,114		98%
	20-yr total saving (NT)			2,269,633			2,427,339		
	Initial investment (NT)			906,400			906,400		
	Yearly return on investment (%/yr)			7.52			8.39		
	Payback time (yr)			8.0			7.5		

6. Acknowledgement

This study was supported by National Energy Program II, MOST 103-3113-E-002-006 made by Ministry of Science and Technology, Taiwan.

7. References

Huang, B.J., Sun, F.S., Ho. R.W. 2006. Near-maximum-power-point-operation (nMPPO) design of photovoltaic power generation system. Solar Energy 80, 1003-1020.

Huang, B.J. and Sun, F.S. 2007. Feasibility study of 1-axis three-position tracking solar PV with low concentration ratio reflector. Energy Conversion and Management 48, 1273-1280.

PRELIMINARY FINDINGS FROM AN ANALYSIS OF LIGHTING ENERGY USE OF OFFICE BUILDING IN KOREA

Sung-Im Kim[1], Jin-Gyeong Kang[1], Hye-Sun Jin[1], Bo-Hye Choi[1], Jae-Han Lim[1], Seung-Yeong Song[1] and In-ho Yang[2]

[1] Ewha Womans University, Seoul (South Korea)

[2] Dongguk University, Seoul (South Korea)

Abstract

In Korea, energy consumption information for existing building is provided to primary energy consumption by fuel types (electric, gas, and district heating) from energy service utilities. To be more effective building energy management nationally, it should be to manage building energy consumption by end use. For this, it is the best approach to collect direct end-use metering data for all buildings but in practically very difficult because of expense and long time. Moreover, it is not appropriate only the application of the building energy simulation based on model to derive energy consumption by end use due to error with energy consumption of actual building.

Therefore LBNL has been developed algorithm to estimate energy end use since 1980, the results are EnergyIQ based on web service. The final goal of this research is to develop algorithm to estimate energy end use with real state of Korea, so by selecting the reference buildings to meet the statistical significance level, it is necessary to collect on-site metered data.

In this study, the end-use sub-metering of office building in Seoul is ongoing hourly into cooling, heating, ventilation, domestic hot water, lighting, office equipment, elevator, miscellaneous since 1 March 2015. Weather conditions are not a crucial factor for lighting energy consumption in existing office building. So based on this sub-metering data, first we carried out an analysis of lighting energy use profile to utilize basic data in lighting energy consumption estimation.

Keywords: *Office building, Lighting energy use, End-use sub-metering, Estimation of energy end-use consumption*

1. Introduction

The South Korean government is managing the monthly energy consumption of electricity, city gas (LNG), and district heating system used by its existing buildings through the integrated building energy management system. This information about energy consumption by source of energy may be useful for the management of the national energy supply and demand policy, but there is not enough detailed information about energy consumption to lead occupants to participate in effective and practical energy saving activities. Therefore, the energy consumption of buildings needs to be controlled depending on end-use energy. For example, the energy consumption of residential buildings should be divided according to end-use such as heating, cooling, hot water supply, lighting, ventilation, electric appliances, cooking, etc., while the energy use of office buildings should be segmented into heating, cooling, hot water supply, lighting, ventilation(air movement), electric appliances, vertical transportation(elevators/escalators), city water supply, etc.

Here, the approach methods to acquire energy consumption by end-use can be divided into building simulation, direct end-use metering, and end-use disaggregation. Building simulation is a very common method, but its shortcoming is the lack of reality, given that there is a significant difference between the building assumption conditions and the actual building characteristics. The direct end-use metering method requires high costs and cannot draw general conclusions due to a limited number of sample buildings for measurement. The end-use disaggregation method provides disaggregated data about energy consumption of end-use by adjusting the building simulation based on the measurement data and collected information of a sample building, and it is worthwhile to apply the method to domestic buildings. In order to apply the end-use disaggregation method, it requires developing a disaggregation algorithm fit to a domestic condition. According to H. Akbari (1995), in order to develop a disaggregation algorithm, it requires selecting sample buildings for measuring and collecting measurement data by end-use energy, paying on-site surveys to gather information about equipment inventories,

Selection and/or peer review under responsibility of Scientific Committee
doi:10.18086/swc.2015.08.13 Available at http://proceedings.ises.org

operation schedules, and the characteristics of buildings, and establishing a database of end-use energy after conducting an analysis of collected data, including regional climate characteristics. These databases are united through a statistical adjustment into a single database, based on which an end-use disaggregation algorithm will be developed.

We selected sample buildings for office building in Seoul and plans to install the measurement system to a total of 85 buildings to disaggregate end-use energy for a period of three years. The final purpose of this study is to develop disaggregation algorithm by identifying the characteristics of end-use through analysis of the above data for influential factors. This paper aimed to identify the characteristics of lighting energy use and to induce major influential factors through analysis of measurement data, which accounted for a relatively high-energy consumption ratio among non-HVAC energy in office buildings, and to use them as basic data in order to supplement and verify the end-use energy estimation equation.

2. Methodology

According to prEN 15193 (2006), the calculated method and the metered method are suggested as ways to determine the lighting energy use. The calculated method is once again classified into the comprehensive method and the quick method. The comprehensive method is to calculate an equation based on the actual building operation data (annual/monthly/hourly), and its shortcoming is that it cannot consider the energy consumption of some lighting control devices. In contrast, the quick method is to calculate an equation based on the standard data (annual), and although it can reduce the required time, it has its own limitation that it cannot consider the actual building conditions. The metered method is to measure energy consumption using electronic watt hour meters to the circuits in the low-voltage distribution panel, and provide the highest level of accuracy, but it is hard to be implemented due to cost and time.

Therefore, it is reasonable to develop an estimation equation of lighting energy use based on the monthly electricity bill data and the user input data. The basic input information to disaggregate lighting energy use from the total energy consumption through the estimation algorithm includes electricity bill information, building information, system information, operation information, and regional climate information (Fig. 1). To induce the required information, the influential factors in energy use need be taken into consideration by diving them into building factors, system factors, user factors, and weather factors. The building factors include the floor area (FLA), conditioned floor area (CFLA), number of floors (FLN), ceiling height (CLH), orientation (ORN), window-wall ratio (WWR), visible light transmittance (VLT), building age (BLAG), etc. The system factors include the type, power consumption and efficiency of lighting equipment(LTQ), lighting power density(LPD), interior illuminance(ILU), shading system(SHS), lighting control devices (manual, on-off, dimming, etc.)(LTCN). The user factors include operating time(OPHR), occupant density(OCD), behavioral patterns of occupants(OCS), and ownership(OWN), while the weather factors are the daylight factor(DAL), etc.(Fig. 2). The estimation equation of lighting energy based on these influential factors can be summarized as seen in Equation (1). This study will draw major influential factors through analysis of the measurement data of the sample buildings and will incrementally complement and verify the estimation equation.

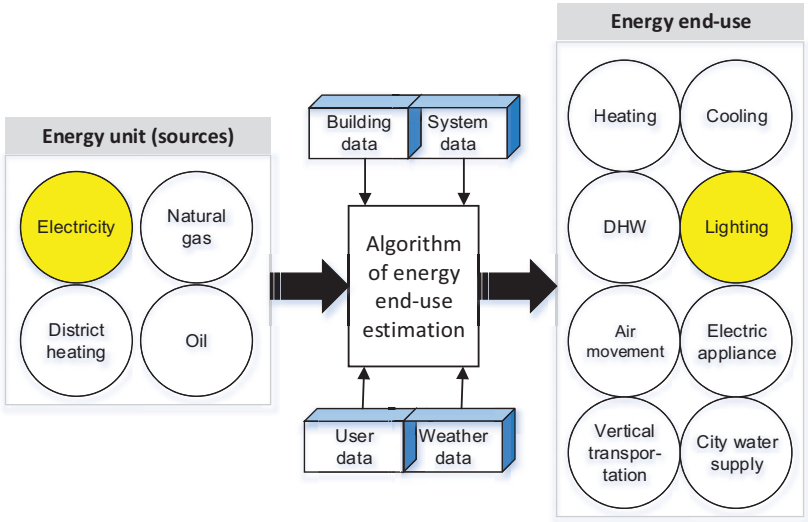

Fig. 1: diagram of the end-use energy disaggregation for office building

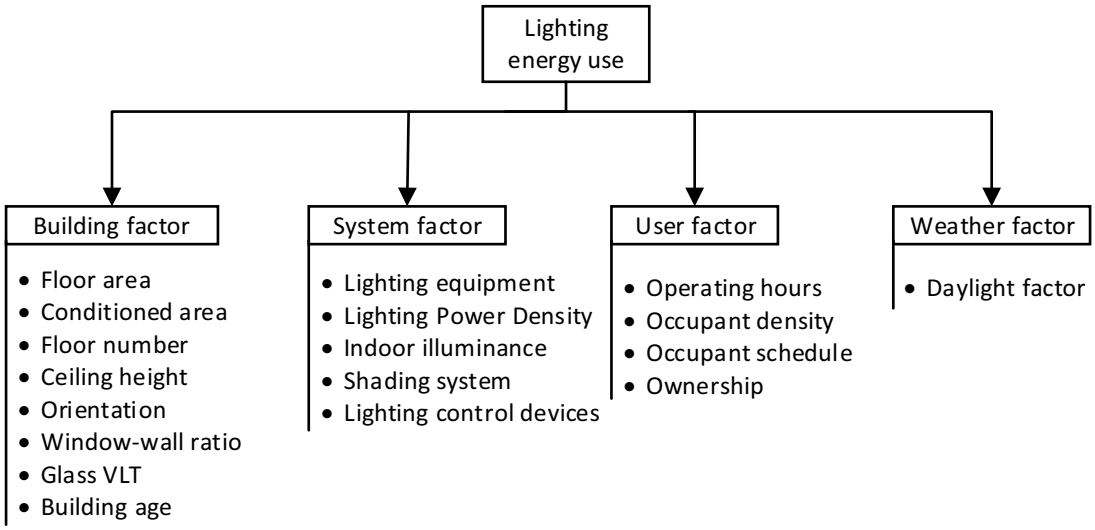

Fig. 2: Influential factors of building lighting energy use

$$E_{LT} = E_{LT0} + f_{LT}(BLD) + f_{LT}(SYS) + f_{LT}(USE) + f_{LT}(WEA) \quad \textbf{(eq. 1)}$$

$$f_{LT}(BLD) = \alpha_1 FLA + \alpha_2 CFLA + \alpha_3 FLN + \alpha_4 CLH + \alpha_5 ORN + \alpha_6 WWR + \alpha_7 VLT + \alpha_8 BLAG$$

$$f_{LT}(SYS) = \beta_1 LTG + \beta_2 LPD + \beta_3 ILU + \beta_4 SHS + \beta_5 LTCN$$

$$f_{LT}(USE) = \gamma_1 OPHR + \gamma_2 OCD + \gamma_3 OCS + \gamma_4 OWN$$

$$f_{LT}(WEA) = \delta_1 DAL$$

E_{LT}: **building lighting energy use**

E_{LT0}: **baseline lighting energy use**

$f_{LT}(BLD)$: **function of building factor**

$f_{LT}(SYS)$: **function of system factor**

$f_{LT}(USE)$: **function of user factor**

$f_{LT}(WEA)$: **function of weather factor**

$\alpha_n, \beta_n, \gamma_n, \delta_n$: **regression coefficients**

3. Case study

3.1 Description of the building

The target building for the measurement is summarized as seen in Tab. 1; it was located in the central district of Seoul(with a climate zone of the central region), and its construction was completed in 1990; it has total floor area of 1,265.1 ㎡ and has one underground floor and five ground floors. The use purpose, floor area, occupancy information, and lighting power density of each office floor can be seen in Tab. 2. The ceiling down-type fluorescent lights (FL) and electronic luminescence (EL) were used for office lighting, and the average indoor illuminance was 300lx; no lighting control systems were applied, while the indoor blinds were installed.

Tab. 1: Overview of case study building

Category	Contents
location	Seoul, Korea
building type	office & retail
building area(㎡)	198.5
gross floor area(㎡)	1,265.1
permitted/approved yr.	1989/ 1990
building size	B1F / 5F



whole view of the building **indoor view of 3rd office floor**

Tab. 2: Overview of each floor

FL.	B1F	1F	2F	3F	4F	5F
Usage type	Parking lot, Storage	Retail	Office	Office	Office	Conference room
Af(㎡)	305.2	196.7	198.4	198.4	198.4	167.9
Ac(㎡)	0	73.6	166.4	166.4	166.4	136.0
No. occupants	0	2	7	18	16	0
Business hrs.	-	10:00~20:00	09:00~18:00	09:00~18:00	09:00~18:00	-
LPD(W/㎡)	5.7	15.9	8.9	9.7	9.7	9.6
Lighting equip. (office)	• FL32W×2ea×27set (1,728W)	• EL20W×52set (1,040W) • FL32W×2ea×4set(256W) • total 1,168W	• EL20W×10set (200W) • FL32W×2ea×20set (1,280W) • total 1,480W	• EL20W×4set (80W) • FL32W×2ea×24set(1,536W) • total 1,616W	• EL20W×4set (80W) • FL32W×2ea×24set(1,536W) • total 1,616W	• EL20W×4set (80W) • FL32W×2ea× 18set(1,152W) • FL20W×2ea×2set (80W) • total 1,312W

The target office spaces for the measurement of lighting energy consumption were office spaces on the 2F-5F (Fig. 3) and the electronic watt hour meters mounted with the zigbee-type wireless transmission devices were installed to office lighting circuits in the distribution panel of each floor. The accumulated electricity consumption was measured by the hour starting from March 1, 2015 (Tab. 3) and the data measurement period for the analysis lasted until the end of July. After calculating the total electricity consumption of each floor, the

lighting energy use was computed, which can be summarized and seen in the following Equation (2).

Fig. 3: office floor plan for sub-metering lighting energy use (L: 2~4F, R: 5F)

Tab. 3: Overview of sub-metering system

analysis period	2015.03.01. 00:00 ~ 2015.07.31. 23:00	
sub-metering method	electronic watt hour meter on the lighting circuits in the low-voltage distribution panel per office floor (three-phase four-wire system, zigbee)	
		
electronic watt hour meter	**communication gateway**	**low-voltage distribution panel**

$$E_{LT} = \sum_{i=1}^{N} E_{LTi} \qquad \textbf{(eq. 2)}$$

i: number of office floor

3.2 Results and discussion

3.2.1 Hourly lighting energy use

The monthly average of lighting energy use during the weekdays by month was recorded as 79.7Wh/㎡ in March, 80.8Wh/㎡ in April, 73.8Wh/㎡ in May, 74.5Wh/㎡ in June, and 73.3Wh/㎡ in July, while that during the weekends by month were estimated at 6.8Wh/㎡ in March, 5.1Wh/㎡ in April, 6.7Wh/㎡ in May, 5.4Wh/㎡ in June, and 15.2Wh/㎡ in July.(Fig 4) The highest hourly average of lighting energy consumption by month was recorded at 4.7kWh at 17 pm on March 12, 5.1kWh at 17 pm on April 23, 5.3kWh at 16 pm on May 8, 4.5kWh at 12 pm on June 8, and 5.0kWh at 10 am on July 15, and the morning hours showed a higher

occurrence ratio of monthly average peaks of lighting energy consumption.

Fig. 4: average hourly lighting energy use

According to a study by Xin Zhou et al. (2015), the 24 hours of the weekdays can be divided into a total of 6 time zones: the morning communing hours, the morning working hours, the lunch hour, the afternoon working hours, the closing hours, and the night hours (Fig. 5), but the total period time can vary depending on time zones. The morning commuting hours (3 hrs.) ranging from 6 am to 9 am showed a sharp increase in lighting energy use, which remained at a constant level during the morning working hours (3 hrs.) spanning from 9 am to 12 pm. The lighting energy use during the lunch hour from 12 pm to 13 pm was reduced by 1.6-6.8% compared to the morning working hours. Although the light energy use during the afternoon working hours (4 hrs.) from 13 pm to 17 pm showed a relatively constant level but displayed a greater deviation compared to the morning working hours. The hourly lighting energy consumption declined over the lapse of the closing hours (4 hrs.) from 17 pm to 21 pm, which displayed a more steady incline than the morning working hours. The night hours zone from 21 pm to 6 am of the next day (9 hrs.) showed an almost flat incline, but displayed a much wider deviation depending on the presence and absence of overtime work. The weekends showed a similar deviation in lighting energy consumption like the night hours zone.

According to the monthly lighting energy consumption rate of each time zone, the afternoon working hours took up the highest percentage at 28.5%, followed by the morning working hours (21.5%), the closing hours (15.4%), the lunch hour (13.8%), the morning commuting hours (9.8%), and the night hours (7.6%), and the weekends & holidays (3.3%).(Fig. 6)

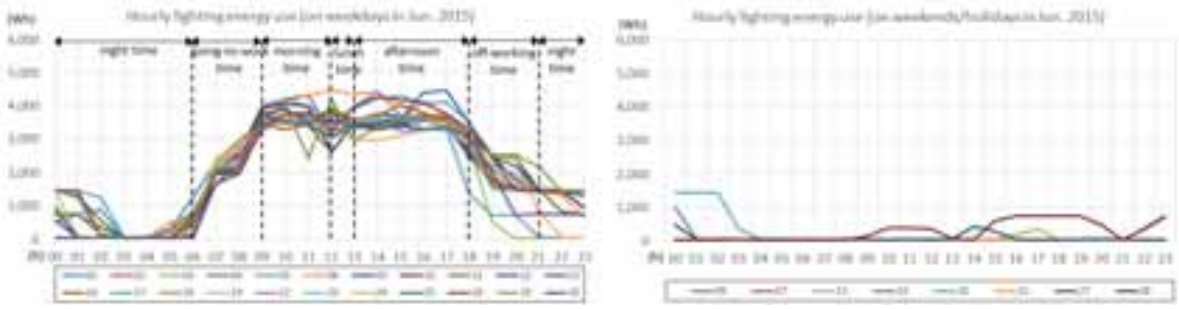

Fig. 5: hourly lighting energy use during 24 hours (L: weekday, R: weekend)

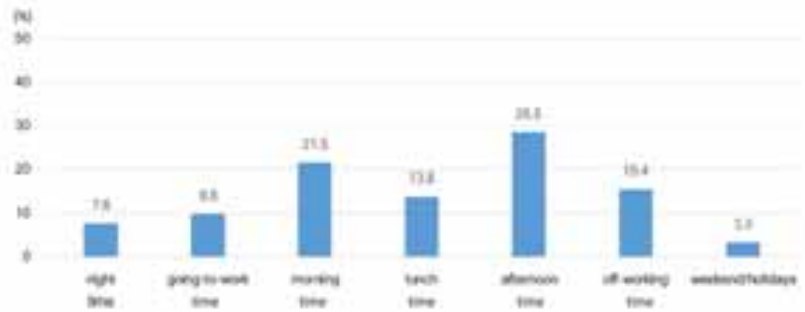

Fig. 6: The ratios of lighting consumption by time zone to lighting energy use per month

The hourly-based energy consumption of office lighting was recorded at 10Wh for the 3-5F offices, while that of the 2F office displayed a remarkably higher level of 20Wh. This was due to a high ratio of electronics lamps installed on the 2F office, almost 2 times that of the other office floors, as they were believed to consume more standby power than fluorescent lamps. (Tab. 4)

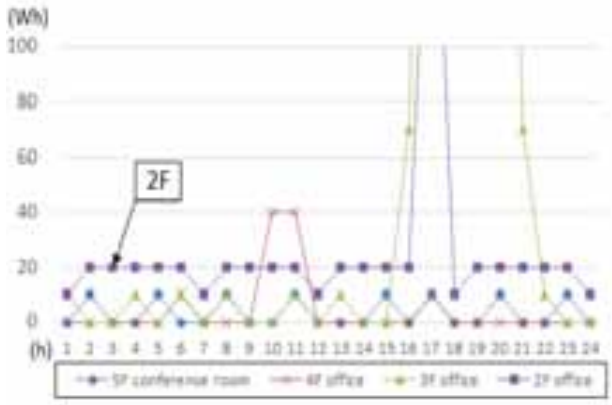

Fig. 7: base lighting energy use

Tab. 4: The ratios of electrics lamps power to total lamps power for office floor

Floor	2F office	3F office	4F office	5F conference room
EL power(W)	200	80	80	80
FL power(W)	1,280	1,536	1,536	1,232
total lamps power(W)	1,480	1,616	1,616	1,312
EL/total ratio(%)	13.5	5.0	5.0	6.1

EL: electrics lamps, FL: fluorescent lamps,

EL/total ratio: electrics lamps to total lamps power ratio

3.2.2 Daily lighting energy use

The ratios of the monthly average lighting energy consumption during the weekdays were recorded at 97.2% in March, 98.4% in April, 94.9% in May, 98.1% in June, and 95.1% in July, while those during the weekends 2.8% in March, 1.6% in April, 5.1% in May, 1.9% in June, and 4.9% in July. The average energy consumption ratio of the weekdays was estimated at 96.7%, while that of the weekends were at 3.3%.(Tab. 5)

Tab. 5: The ratios of monthly lighting energy use for weekday vs weekday/holiday

	Mar.2015	Apr. 2015	May 2015	Jun. 2015	Jul. 2015	avg.	SD
weekday(%)	97.2	98.4	94.9	98.1	95.1	96.7	1.7
weekend/holiday(%)	2.8	1.6	5.1	1.9	4.9	3.3	1.7

3.2.3 Monthly lighting energy use

The ratio of lighting energy use against the total energy consumption by month was recorded at 15.4% in March, 19.0% in April, 16.2% in May, 12.6% in June, and 10.1% in July. The monthly average lighting energy consumption was within 1,100~1,200kWh. The lighting energy consumption was relatively lower in May, as the working hours of the month were reduced by the increased number of holidays, which was 1.8 times more than the other months. As the air-conditioning operation started from June, the energy consumption surged, while the percentage of lighting energy use against the total energy consumption showed a declining tendency (Tab. 6).

Tab. 6: The ratios of energy use to whole building electricity consumption per month

	Mar.2015	Apr. 2015	May 2015	Jun. 2015	Jul. 2015
WHE(kWh)	7,632.3	6,367.7	5,498.2	8,749.0	11,281.5
LTE(kWh)	1,174.9	1,206.7	888.4	1,100.5	1,139.8

LTE/WHE ratio(%)	15.4	19.0	16.2	12.6	10.1
No. weekend/holiday	9	8	14	8	8
total operating hours (2F~5F)	1,505	1,788	1,290	1,544	1,586

WHE: whole building electricity consumption, LTE: lighting energy use

3.2.4 Correlation between lighting energy use and influential factors

As useful information was collected for the correlation analysis between lighting energy use of each office floor (2F~5F) of the case-study building and influential factors, the air-conditioned floor area was selected as a building factor, the lighting density and indoor illumination as system factors, and the number of occupants and use time as user factors can be seen in Tab. 7. According the results of the correlation analysis between the influential factors and light energy use, the correlation between the number of occupants and the use time revealed the highest coefficient of 0.95 in average, followed by the air-conditioned floor area, indoor illumination, and lighting density. The influential factors which belong to the user factors showed higher levels of correlation, but this was believed to be due to the design of the building to provide similar levels of lighting density to offices within the same building. Further studies need to be carried out in the future in order to conform the correlation between user factors and lighting energy use by comparing it with several different buildings.

Tab. 7: variable's values of correlation analysis

LTE(kWh)		2F Office	3F Office	4F Office	5F Conference room
Mar.2015		249.2	528.0	364.6	25.9
Apr. 2015		255.0	530.3	376.2	36.9
May 2015		207.8	394.9	261.3	18.9
Jun. 2015		255.3	528.7	298.0	13.5
Jul. 2015		252.5	557.9	308.8	15.0
FLA (㎡)		198.4	198.4	198.4	167.9
LPD (W/㎡)		8.9	9.7	9.7	9.6
ILU (lx)		269	309	289	286
OCD(person/㎡)		0.04	0.11	0.10	0.00
OPHR (avg. hrs.)	Mar.2015	424	441	335	192
	Apr. 2015	347	432	344	223
	May 2015	297	338	288	210
	Jun. 2015	333	495	321	196
	Jul. 2015	338	524	368	199

Tab. 8: Correlation coefficient of lighting energy use with influential factors

influential factor	BLD Factor	SYS factor		USE factor	
	CFLA	LPD	ILU	OCD	OPHR
Mar.2015	0.84	0.25	0.61	0.97	0.82
Apr. 2015	0.84	0.26	0.61	0.97	0.97
May 2015	0.86	0.17	0.57	0.95	0.97
Jun. 2015	0.86	0.17	0.57	0.95	0.97
Jul. 2015	0.80	0.20	0.63	0.92	1.00
avg.	0.84	0.21	0.60	0.95	0.95
ranking	3	5	4	1	1

4. Summary and Conclusions

In order to develop an estimation equation of lighting energy use of office building to be suitable to domestic situations, we analyzed the measurement data collected from the case-study building, identified the characteristics of lighting energy use, and drew major influential factors to be used as basic data to supplement and verify the estimation equation.

The major study results are as follows;

(1) For estimation of lighting energy use, this study examined the influential factors in energy consumption by classifying them into the building factors, system factors, user factors, and weather factors;

(2) The monthly average of lighting energy use of office building during the weekdays by month was recorded at 79.7Wh/㎡ in March, 80.8Wh/㎡ in April, 73.8Wh/㎡ in May, 74.5Wh/㎡ in June, and 73.3Wh/㎡ in July, while that during the weekends by month were estimated at 6.8Wh/㎡ in March, 5.1Wh/㎡ in April, 6.7Wh/㎡ in May, 5.4Wh/㎡ in June, and 15.2Wh/㎡ in July, and the morning hours showed a higher occurrence ratio of the monthly average peaks of lighting energy consumption;

(3) According to the monthly lighting energy consumption rate of each time zone, the afternoon working hours took up the highest percentage at 28.5%, followed by the morning working hours (21.5%), the closing hours (15.4%), the lunch hour (13.8%), the morning commuting hours (9.8%), and the night hours (7.6%), and the weekends & holidays (3.3%);

(4) This was due to a high ratio of electronic lamps installed on the 2F office, almost 2 times that of the other office floors, as they were believed to consume more standby power than fluorescent lamps;

(5) The ratios of the monthly average lighting energy consumption during the weekdays were recorded at 97.2% in March, 98.4% in April, 94.9% in May, 98.1% in June, and 95.1% in July, while those during the weekends 2.8% in March, 1.6% in April, 5.1% in May, 1.9% in June, and 4.9% in July. The average energy consumption ratio of the weekdays was estimated at 96.7%, while that of the weekends were at 3.3%;

(6) According the correlation between lighting energy consumption of each office floor within the case study target building and influential factors, the correlation with the number of occupants and use time showed the highest coefficients, followed by the conditioned floor area, indoor illumination, and lighting density.

Future studies need to conduct a comparative analysis by targeting numerous sample buildings in order to identi fy and confirm various possible correlations between lighting energy consumption and influential factors.

Acknowledgement

This research was supported by a grant(14AUDP-B079104-01) from Architecture & Urban Development Resea rch Program funded by Ministry of Land, Infrastructure and Transport of Korean government.

5. References

prEN 15193(2006): Energy performance of buildings-Energy requirements for lighting

KS A 3011; 1998(2003): Recommended levels illumination

Korea Energy Economics Institute, 2014. Energy Consumption Survey

http://www.eia.gov/ (accessed on 09.27.15)

H. AKBARI, 1995. Validation of an algorithm to disaggregate whole-building hourly electrical load into end us es. Energy 20(12), 1291-1301

Xin Zhou et al., 2015. Data analysis and stochastic modeling of lighting energy use in large office buildings in China. Energy and Buildings 86, 275-287

Yun et al., 2011. Effects of occupancy and lighting system use patterns on building energy consumption. Journa l of the Architectural Institute of Korea 27(5), 229-236

Conference Proceedings

Solar World Congress 2015
Daegu, Korea, 08 – 12 November 2015

TECHNO-ECONOMIC EVALUATION OF SOLAR WATER HEATING APPLICATIONS AT HOSPITALS IN SAUDI ARABIA

Hamad Almahmoud[1], Fahad A. Al-Sulaiman[2] and Hafiz Abd-ur-rehman[1]

[1] Mechanical Engineering Department, King Fahd University of Petroleum & Minerals (KFUPM), Dhahran, 31261, (Saudi Arabia)

[2] Center of Research Excellence in Renewable Energy (CoRERE), King Fahd University of Petroleum & Minerals (KFUPM), Dhahran, 31261, (Saudi Arabia)

Abstract

To contribute in reducing the electricity consumption rate and the harmful impacts of fossil fuels, a Solar Water Heating (SWH) technology is recommended to cover around 50% of hot water demand in hospitals in Saudi Arabia. The paper studies the techno-economic viability of two types of SWH collectors in five different cities of Saudi Arabia. Findings indicate that Najran and Tabuk are the most attractive places because they have the highest annual life cycle saving, the highest benefit to cost ratio, and the lowest payback period, while, in contrast, Jeddah is the lowest attractive city to use SWH. Moreover, the economic analysis shows the advantage of using glazed flat plate collector over evacuated tubes because it has shorter payback periods and higher annual life cycle savings.

Keywords: *Solar Water Heating, Evacuated tubes, glazed flat plate collector, Hospital, Saudi Arabia*

1. Introduction

The rapidly increasing demand of electricity and global warming are factors that have brought interests to find an environmental and efficient source of energy. Solar energy is the most abundant source of energy and it will be the future source of energy for countries that receive high amount of solar radiation such as Saudi Arabia. The conventional electric water heating technology is used in Saudi Arabia to meet the demand of the hot water. The process of water heating by electricity in a hospital with 200 beds consumes annually around 450 MWh and, therefore, employment of solar water heating (SWH) systems is recommended.

Oil is the main source of energy in Saudi Arabia, however, the enormous potential of solar energy has brought the government attention in 1980s and, therefore, different solar technologies were developed and tested [Huraib, 1996]. Saudi Arabia receives high intensities of solar radiation in most of its regions that makes it an attractive place for implementing solar energy systems. A study was conducted to assess the daily solar radiation for ten different cities in Saudi Arabia and it was reported that the daily solar radiation varied from 4.73 to 6.94 kWh per m^2 [Bahel, 1986]. Another study selected four different climatic zones in Saudi Arabia and found similar results [Zuhairy, 1995].

In the past decade, attention has been concentrated in optimizing energy consumption in large buildings such as hospitals. Around 5% of the energy consumed in hospitals is for water heating [Čongradac, 2012] with almost constant consumption of 9 GJ per bed throughout the year [Bujak, 2010]. Some studies have developed different technologies to enhance the use of renewable energy in hospitals, such as solar energy in combination with thermal aquifer energy storage [Paksoy, 2000], hybrid plant using solar thermal, photovoltaic, and phosphoric acid fuel cell systems [Bizzarri, 2006].

Solar water heating technology have been widely used for domestic applications. [Kablan, 2004] reported that a continuous rise of solar collector installations in the period 1970 to 1995 was observed in Jordan. Techno-economic evaluation for SWH system of glazed flat plate collectors in Oman was presented by [Gastli, 2011]In a different study, [Hafiz and Al-Sulaiman, 2014] reported the techno-economic evaluation for glazed and evacuated tube collectors for water heating of residential buildings for different cities in Saudi Arabia.

The demands for water heating in hospitals are huge and, therefore, there is a need to seek a cost effective solution based on solar thermal energy. This study evaluates the techno-economic feasibility of using two SWH systems for a hospital with 200 beds at different locations in Saudi Arabia. The findings will help decision makers and engineers to determine the technical and financial viability of potential renewable energy projects in hospitals in Saudi Arabia or other countries that have similar operating and weather conditions. A Solar Water Heating (SWH)

doi:10.18086/swc.2015.08.14 Available at http://proceedings.ises.org

technology is recommended to cover around 50% of hot water demand in hospitals in Saudi Arabia. This percentage is selected because the sun is available only on the daytime and it is a visible solution to use this percentage; otherwise, using a larger percentage means, a larger solar collector should be installed, which is not practical due to space limitation.

2. Metrological data and simulation

This study is performed to cover a large area of Saudi Arabia, which is situated between latitudes of 17.5°N and 31°N, and longitudes of 36.6°E and 50°E. The findings will also be useful to other locations that have similar weather conditions in other countries. In this study, five different cities were selected to cover different coordinates, which are Tabuk (north), Dhahran (east), Riyadh (center), Jeddah (west), and Najran (south). The metrological data of the five cities selected have been listed in Tab. 1 [NASA RETscreen, Renewable Resource Atlas].

Tab. 1: Climate data for the selected cities.

Location	Jeddah	Riyadh	Dhahran	Najran	Tabuk
Average daily solar radiation (kWh/m^2/d)	5.95	6.2	5.83	6.77	6.33
Air Temp (°C)	30.7	28.6	27.8	26.5	23.4
Earth Temp (°C)	29.8	29.2	28.1	26.7	24
Latitudes (ø)	21.7	24.9	26.3	17.6	28.4
Longitude	39.2	46.7	50.2	44.4	36.6
Elevation (m)	17	614	17	1212	768
Wind speed (m/s)	3.3	2.9	2	2.1	2.8
Relative humidity (%)	56.7	24.9	49.6	22.2	31.7

The metrological data for these cities, including air temperature, average daily solar radiation, atmospheric pressure, wind speed, and relative humidity were imported from NASA database. These data were further crosschecked with the experimentally recorded data by K.A.CARE [Renewable Resource Atlas, 2015] and the data for Tabuk city was corrected. Figure 1 illustrates the daily solar radiation data for a horizontal surface where Tabuk has the highest solar radiation during the summer months whereas, Najran has the highest radiation during the winter months. It also shows that, on average throughout the year, Najran has the highest solar radiation while Dhahran has the lowest solar radiation, which can also be noticed in Tab. 1.

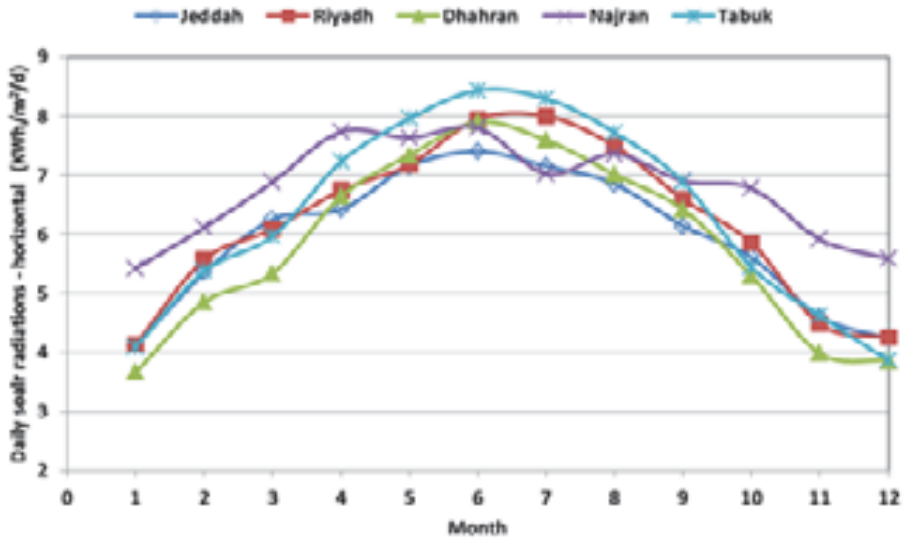

Fig. 1: Monthly variation of daily solar radiations on horizontal surface.

To get the best configuration for the collector, the study evaluated the SHW under two slopes. The first one is tilted at a slope equal to the latitude angle of the city selected, which represents the optimum value of the slope for a system to be used constantly throughout the year, while the other setting is for a horizontal surface. The findings have been shown in Fig. 2, which reveal the difference between the two settings.

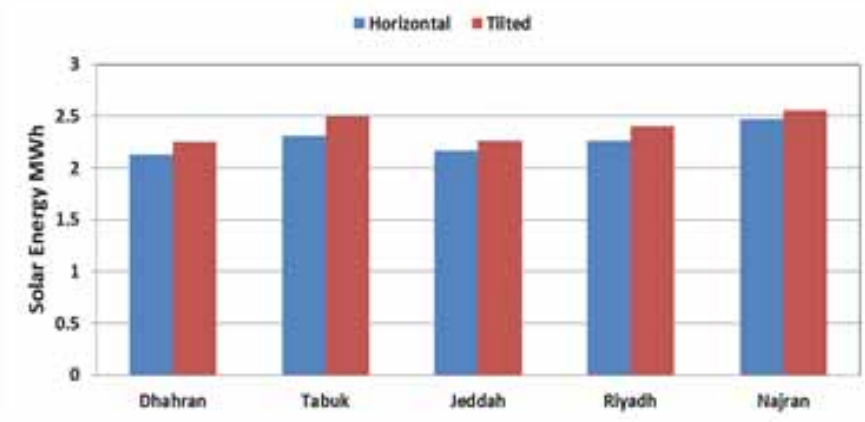

Fig. 2: Annual Solar Energy for horizontal and titled collectors.

There are three commonly used SWH technologies which are evacuated tube, glazed, and unglazed flat plate collectors. The temperature required for hot water in hospitals is between 50 and 60 °C and, therefore, only glazed flat plate collectors and evacuated tube collectors were selected to obtain the required temperature, meanwhile obtaining the required solar fraction with relatively a low aperture area [International Energy Agency, 2012]. Simulations were conducted for both technologies and the input data has been listed in Tab. 2 [Gastli, 2011, Abd-ur-Rehman and Al-Sulaiman, 2014]. Simulations were performed for evacuated tube collector to cover 50% solar fraction of the 200 beds hospital in Tabuk. Results indicate that the desired solar fraction can be achieved by using 21 collectors of evacuated tube type in Tabuk, which was used as a reference to analyze other four cities selected Similarly, simulations were performed for flat plate collectors under the same prevailing conditions and comparative analysis was conducted to obtain the optimum number of the collectors to be used for hospitals under different climatic conditions of Saudi Arabia. The technical and financial characteristics for both collector types have been listed in Tab. 3 [RETscreen].

Tab. 2: Input parameters for the evacuated tube collectors.

Parameter	Value
Number of beds	200
Occupancy rate (%)	80
Daily hot water usage estimate (L/day)	31,500
Hot water temperature (°C)	60
Operating days per week	7
Collector slope	Location latitude
Miscellaneous losses (%)	5
Storage capacity per square meter (L/m^2)	75
Conventional fuel type	Electricity
Seasonable efficacy (%)	90
Electricity rate ($/kWh)	0.03
Initial contingencies (labor, transportation etc.) (%)	5
Annual cost (O & M) (%)	5
GHG emission factor (tCO_2/MWh)	0.737
Fuel cost escalation rate (%)	2
Inflation rate (%)	2.5
Project life (years)	20

Tab. 3: Specifications for the evacuated and glazed collectors.

Solar Collector Type	Evacuated Tube	Glazed
Gross area per solar collector (m^2)	12.22	10.7
Aperture area per solar collector (m^2)	9.02	9.52
Fr (tau alpha) coefficient	0.53	0.63
Fr UL coefficient (W/m^2)/°C	1.42	3.88
Number of collectors	21	24
Capacity (kW)	132.5	160
Initial cost (US$)	77000	58500

3. Result and Discussion (results and discussion)

Evaluation and comparisons in terms of performance and economic viability have been conducted for both collector types. The solar fraction is defined as the percentage of the annual energy needs that the SWH system will cover. This value is set for Tabuk to be 50% for both flat plate and evacuated tube SWH systems. This means that the SWH system will cover half of the energy consumption and the rest of the energy requirements are met by a conventional heating system, which is electricity in our case. The findings, as shown in figure 3, demonstrate that the solar fraction varies from 49% to 55%, where Najran has the highest fraction and Dhahran has the lowest fraction. The variations of the solar fraction among the selected cities are relatively small which reflect the viability of using SWH in these cities.

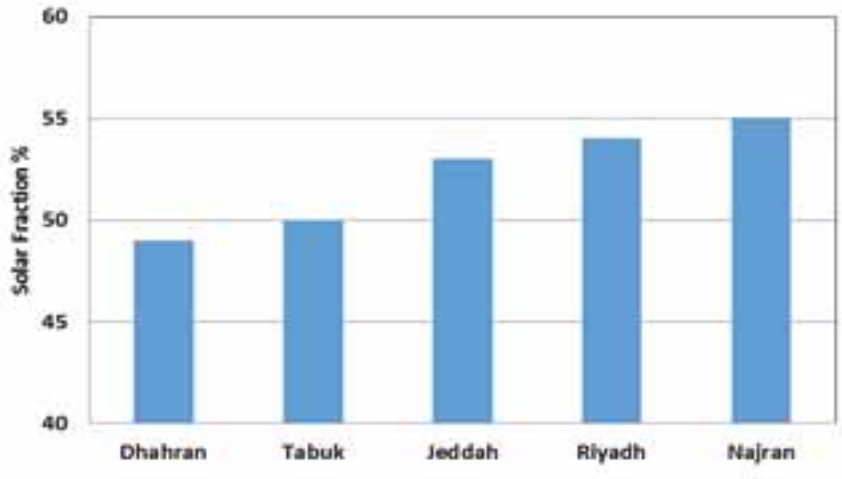

Fig. 3: Solar fraction of the annual energy needs covered by SWH.

The process of water heating to specific temperature by electricity consumes relatively a huge amount of energy, which is also function of input temperature to the system. Another evaluating term for a SHW technology is the electricity saving potential per year, which is the amount of energy that will be saved after using a solar heating system. It is directly proportional to the solar fraction, for example Tabuk has 50% solar fraction and it is expected to save 271 MWh annually, as shown in Fig. 3. Therefore, the conventional heating system will cover the rest of the total consumption, which is 271 MWh per year. Fig. 4 illustrates the annual electricity saving potential for each city on the left y-axis and the potential savings for whole project life on the right y-axis. The average electricity saving potential per year for all cities is 229 MWh and the average saving during the twenty years project life time is 4588 MWh.

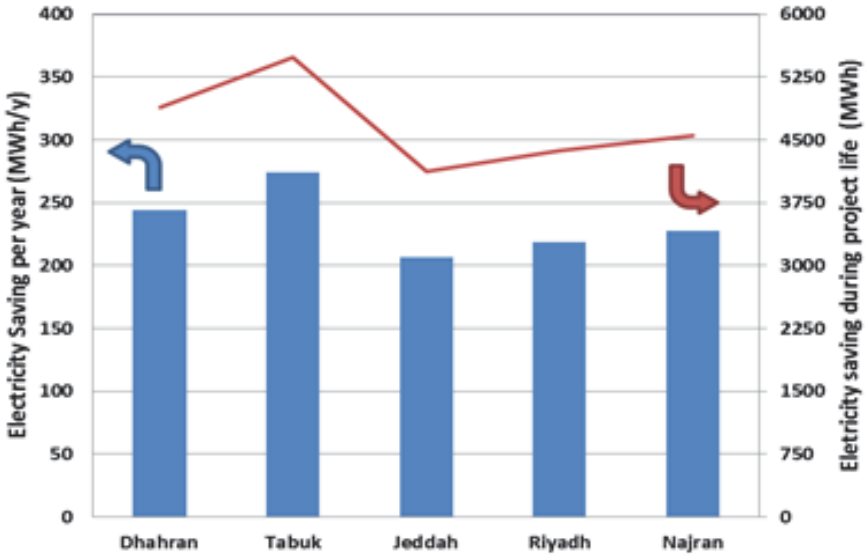

Fig. 4: Electricity saving potential.

The environmental advantages of using the SHW systems were also assessed. The study reports the amount of greenhouse gas (GHG) emissions that will be reduced after installing the environmentally friendly SWH system. Fig. 5 shows the annually expected GHG emissions reduction on the left y-axis while the total reduction of the emissions during the life-time of the project are shown on the right y-axis. It is shown that the highest amount of GHG emissions will be avoided in the cities of Tabuk and Najran, which reach 200 tons of annual CO_2 emissions. In addition, the cumulative reduction over the project life-time for these two cities is expected to be 4000 tons of CO_2 emissions.

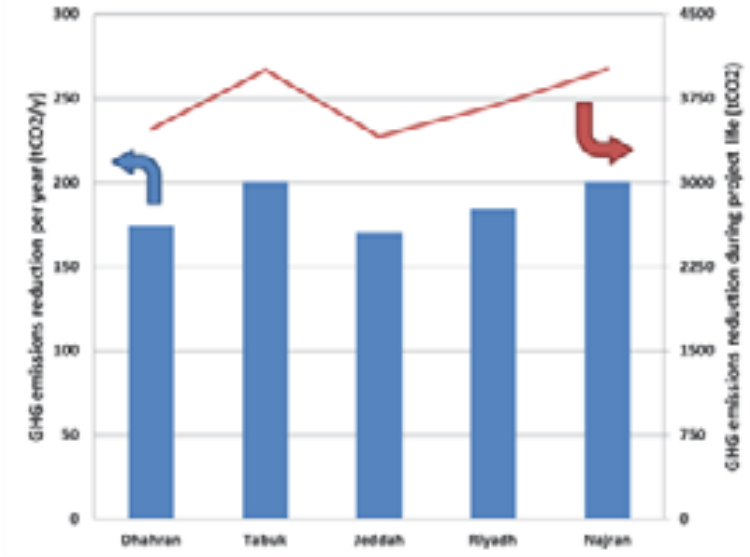

Fig. 5: GHG Emissions Reduction Potential.

After discussing the performance of the SWH technology, the economic viability of the system will be discussed next. It should be noticed the difference between the performance analysis where we have equivalent outputs for both evacuated and glazed collectors; the financial analysis will vary between the two technologies according to the initial cost and the annual saving of the project.

The payback period is the time for an investment to recoup its own initial cost from the savings it generates; the less time it takes the more desirable the project is. Fig. 6 presents the payback period of the project for both collector types. For the evacuated tube system, Najran and Tabuk have the shortest period of 8.9 years while the other cities have slightly longer periods, in which the maximum period takes place in Jeddah. Selecting flat plate collectors reveal better economic option because it recovers the initial cost faster for all the cities selected. The findings show that Najran and Tabuk, in terms of payback period, are the most attractive cities with flat plate

collectors at which they recover their initial cost in less than seven years.

Fig. 6: Payback Period.

Another economic evaluation parameter is the annual life cycle savings that would present the yearly cost saved and together with the solar fraction, a project can be evaluated economically. The annual savings for the evacuated tube system varies between $2054 and $3429 for Jeddah and Najran respectively, as shown in Fig. 7. The figure also shows the advantage of the flat plate type where its annual savings varies between $3389 and $5048 for Jeddah and Tabuk respectively.

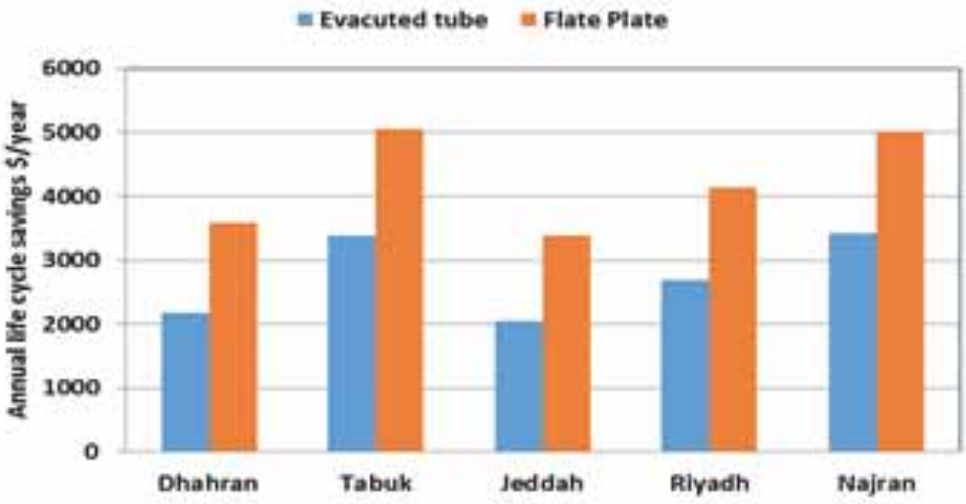

Fig. 7. Annual life cycle savings.

4. Conclusion

The study discussed the techno-economic feasibility of using SWH systems for five different cities in Saudi Arabia. The conclusions obtained from this study are:

- For the same number of collectors, the difference of solar fraction between the selected cities is relatively small which indicates viability of all regions in Saudi Arabia to adopt SWH technology.
- For all cities, the electricity saving potential is high and can reach up to 5400 MWh for project life time of 20 years. This also leads to high reduction in GHG emissions.
- For the same solar fraction in both evacuated tube and glazed SWH technologies, the economic analysis shows the advantage of using glazed flat plate collector because it has shorter payback periods and higher annual life cycle savings.
- Based on techno-economic evaluation, Najran and Tabuk are the most attractive places followed by Riyadh and Dhahran. Jeddah is the least attractive city among the five selected cities due to higher payback period and lower annual life cycle savings.

Acknowledgement

The authors acknowledge the support provided by Centre of Research Excellence in Renewable Energy (CoRERE), King Fahd University of Petroleum & Minerals (KFUPM), Dhahran, Saudi Arabia.

5. References

Abd-ur-Rehman, H. M., & Al-Sulaiman, F. (2014, March). Techno-economic evaluation of different types of solar collectors for water heating application in domestic sector of Saudi Arabia. In Renewable Energy Congress (IREC), 2014 5th International (pp. 1-6). IEEE.

Bahel, V., R. Srinivasan, and H. Bakhsh, 1986. Solar Radiation for Dhahran, Saudi Arabia. Energy 11(10), 985-989.

Bizzarri, G., Morini. G.L., 2006. New Technologies for an Effective Energy Retrofit of Hospitals. Applied Thermal Engineering 26(2), 161-169.

Bujak, J., 2010. Heat Consumption for Preparing Domestic Hot Water in Hospitals. Energy & Buildings 42(7), 1047-1055.

Čongradac, V., Prebiračević, B., Jorgovanović, N., & Stanišić, D, 2012. Assessing the energy consumption for heating and cooling in hospitals. *Energy and Buildings*, *48*, 146-154.

Duffie, J.A., and Beckman, W.A, 2013. Solar Engineering of Thermal Processes, 4th Edition John Wiley & Sons.

Gastli, A., and Charabi, Y. 2011. Solar Water Heating Initiative in Oman Energy Saving and Carbon Credits. Renewable and Sustainable Energy Reviews 15(4), 1851-1856.

Huraib, F. S., S. M. Hasnain, and S. H. Alawaji, 1996. Lessons Learned from Solar Energy Projects in Saudi Arabia. Renewable Energy 9(1), 1144-7.

Kablan, M. M, 2004. Techno-Economic Analysis of the Jordanian Solar Water Heating System." Energy 29(7), 1069-1079.

NASA satellite-derived global meteorology and surface solar energy climatology website for RETScreen parameter inputs. Retrieved from https://eosweb.larc.nasa.gov/sse/RETScreen/ [accessed 26.01.14].

Paksoy, H. O., Andersson, O., Abaci, S., Evliya, H., & Turgut, B 2000. Heating and Cooling of a Hospital using Solar Energy Coupled with Seasonal Thermal Energy Storage in an Aquifer. Renewable Energy 19(1), 117-122.

RETScreen. RETScreen® software online manual, solar water heating project model. RETScreen International Clean Energy Decision Support Centre. www.retscreen.net.

Renewable Resource Atlas, 2015. King Abdullah City for Atomic and Renewable Energy (K.A.CARE), Saudi Arabia, https://rratlas.kacare.gov.sa.

Technology Roadmap Solar Heating and Cooling. Paris: International Energy Agency, 2012. Print.

Zuhairy, Akram A., and A. A. M. Sayigh, 1995. Simulation and Modeling of Solar Radiation in Saudi Arabia. Renewable Energy 6(2), 107-118.

Analysis of the Thermal Behavior of Architectural Covers with Semi - Insulation and an Overlaid Green Layer System In Temperate Climates.

Juan Manuel Rodriguez[1] and Juan-Carlos Baltazar[2]

[1] Department of Architecture, University of Guanajuato, Guanajuato, Gto. Mexico.

[2] Department of Architecture, Texas A&M University, College Station, TX, United States of America

Abstract

This study evaluates experimentally the thermal behavior of architectural elements of insulate roofs, including semi-insulation material with overlaid green elements on vertical and horizontal planes, also known as green roofs, for temperate climates. The results of the study showed that the flux of heat transfer on the roof was reduced and provide a better controlled temperature in the interiors all the yearlong. Difference between the outside and inside temperature up to 4 Celsius degrees were observed frequently specially in the early and late hours of the days, which generate a steady comfort.

Keywords: *Building integrated green roof, Climatic Year Type, Thermal performance*

1. Introduction

Hot and humid climates demand significant electricity for cooling. In 2001, Texas implemented the Texas Emissions Reduction Plan (TERP) program that aims to diminish the pollution in the state by energy efficiency

The use of green architectural elements started to have presence in some types of buildings in Mexico, specifically the residential architecture is beginning to see some examples in general without a definite specific purpose, such as a fashion phenomenon in its alleged desire of being "sustainable", though these elements do not consider relevant aspects regarding the structural behavior of the decks, and less its thermal effects or behavior.

This study present a preliminary analysis of the recorded results from an example of this type of solution built it in order to identify the possible advantages and disadvantages that can be identified specifically in the overall thermal behavior in external conditions and interiors.

The Mexican housing type has been subordinated to the economic system, and consequently to prevailing economic conditions. In general, since beginning of the twenty century, it has widely avoid using insulating material and misuses the climate advantage of the region, being more marked in the country central region. This phenomenon primarily identified by change of more economic construction systems, but with fewer advantages in climate use. In earlier times, the constructive system comprised materials such as stone and adobe and more complete solutions based on those systems, which unfortunately with the pass of the time were disappearing. Because of the area climatic conditions, this phenomenon did not represent major problem, the differences between external and internal temperature have minimal variations as it will be shown in this study.

2. Methods

There are several concepts for defining the green roofs covers on buildings. Two categories are very well recognized, the ones called extensive, comprising covers where the plant substrate is not exceeding 0.1 m, also called by some "ecological cover", characterized by small plants and some grasses, and the intensive ones with distinguished thicknesses greater than 0.2 m., where it is possible to plant some type of trees. There is some ones in an intermediate case they have been called semi-intensive, employing features of both. The latter classification is the case analyzed in this study.

Another concept used to define this field of study is "Urban Naturalization", which includes the concept of "green roofs" employed by several research groups including the compilation by Spanish Society for the Promotion of Urban and Rural Naturalization (PRONATUR).

doi:10.18086/swc.2015.08.15 Available at http://proceedings.ises.org

The base of this study is the work done by Minke on reference to "Green roofs" research in Germany, a country to which he is regarded as one of the fastest developing and implementing these elements. Since 1974, Minke; has conducted research and development in the field of green buildings, affordable housing and especially in the field of earth constructions His works are not only in Europe but also in South America, Central America and India. Minke stated that in areas with cold climates, in winter the ground is frozen and kept for long periods at 0°C, even when the outside temperature is considerably lower. With a temperature of + 20°C inside and -20°C outside and soil temperature 0°C decreases the transmission heat loss of the roof (Minke 2004: 16).

According with the Minke´s hypothesis, in a climate with more solar radiation green roofs would have major advantages (Minke 2004: 17), however global climate conditions are contrasting, since in most places with solar radiation normally does not have conditions as those in cold areas and insulating characteristics therefore are not the same. Since in cold climates where water freezing functions as insulation, in temperate zones hardly water will freeze the rooftop. Therefore these benefits will not be capitalized.

The study arises from the following stages:

a) A green roof 6.5 m long and 3.1 m wide is implemented, with a slab based partly insulated panel "W" supported with metal light beams and with a concrete compression layer 0.7m thick, which together with the panel does not exceed 0.18 m.

b) On the cover a membrane is placed as insulation of the humidity of the vegetable substrate placed over the cover with a thickness of 0.12 m; in the peripheral region of the substrate a fraction of gravel is set and between the gravel and the “tezontle” substrate, in order to filter out excess water without eroding the vegetable substrate. In a secondary zone of the cover with an area of 2.2 m long and 1.82 m wide the depth of the plant substrate has a minimum thickness of 0.12 m to a maximum rate of 0.55 m.

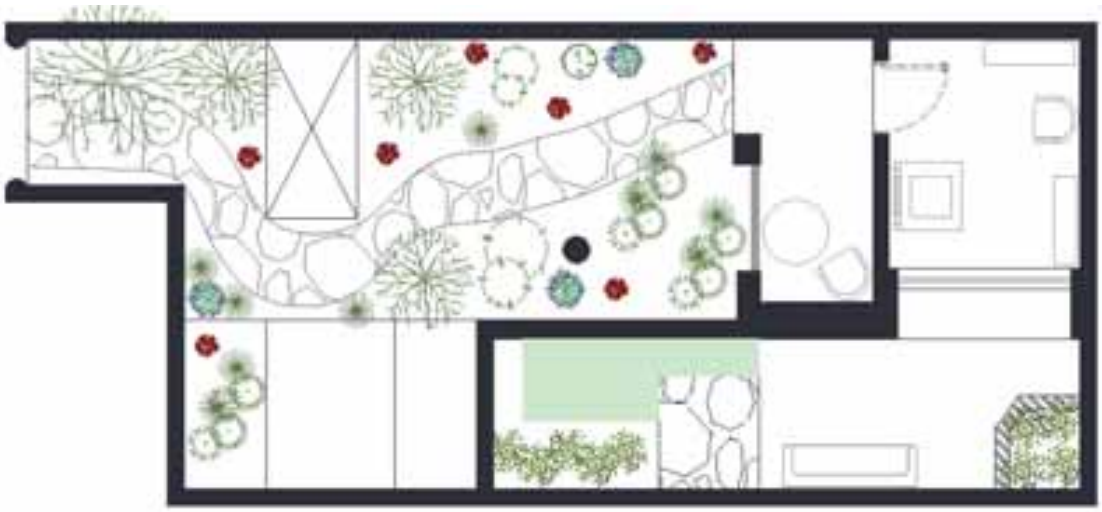

Fig 1: Plan view of the green roof.

The images below show some of the construction stages of the green roof:

Cover construction process

Cover basis completed

Implementation of vegetation cover

Integration of plant elements

Actual state of green roof

Fig. 2: Construction stages of the green roof

c) The plants used are native to the region, which has the characteristics of a semi-arid area. Specimens of mesquite (*Prosopis laevigata*), some specimens of huizache (*farnesiana Acacia, Acacia schaffneri*), a specimen of oak (*chihuahuensis Quercus*), a specimen of pine (*Pinus cembroides Zucc*.), a specimen of Garambullo (*Myrtillocactus geometrizans*), some specimens of Nopal (*Opuntia ficus-indica*), a couple sets of barrel cactus (*Echinocactus*), two specimens of rosemary (*Rosmarinus officinalis*), Evergreen (*Sedum praealtum*), Aranto (*Bryophyllum daigremontianum*) and wild grass.

d) For measuring some of the thermals performance a U30 HOBO weather station was installed where the outside and inside temperature is recorded, some case sensors are placed on the ground directly under the green roof cover, another in the upper part at 2.8 m and other at 1.65 meters high in the interior zone.

The Mexican normalization and certification organization for the construction, on reference to the decks in the

Mexican standard NMX-C-460-ONNCCE 2009 states that for Mexican thermal zones 1 and 2, the total thermal resistance of the enveloped must be at least 1.4 m^2K/W, and 2.1 m2K /W to achieve comfort and greater than 2.65 m^2K/W to save energy. Similarly, for 3A, 3B and 3C zones the values should be 1.4 m^2K/W, 2.30 m^2K/W to and 2.80 m^2K/W respectively. Regarding the indoor environment the NMX-AA-164-SCFI-2013 standard concerning sustainable building criteria and minimum requirements, it states that thermal comfort must be between reach between 18 and 25 °C.

With these benchmarks, the characteristics of the local microclimate are discussed from time records for a period longer than 50 years about 5 solar cycles, the comfort zone is determined by the model of Wakely which includes the definition of the scope comfort zone unlike other models, allowing you to adapt to different climatic zones, (Wakely,1979 in Tudela, 1982: 35-36), in this model the neutral temperature (*Tn*) it is called comfort center temperature *Tcc*, and is defined as follows: $Tcc = Tm/4 + 17.2$, where *Tm* is the annual average temperature. After the *Tcc* is determined, the temperature swing is identified from finding the range of the mean maximum and minimum extremes temperatures and from them the amplitude of the comfort zone.

The comfort zone, based on the period of the maximum and minimum temperature of 1959-2013 (for the city of Leon, Mexico), is determined to be 18.7 °C to 24.2 °C; next the Type Climatic Years are defined; for Maximum Activity (CYT-max) and for the Minimum Activity (CYT-min).

Figures 3 and 4 shows respectively the climatic years type for Maximum Activity (CYT-Max) and for Minimum Activity (CYT-Min) for the city of Leon, Mexico, for the period 1959-2013, comprising about 5 solar cycles.

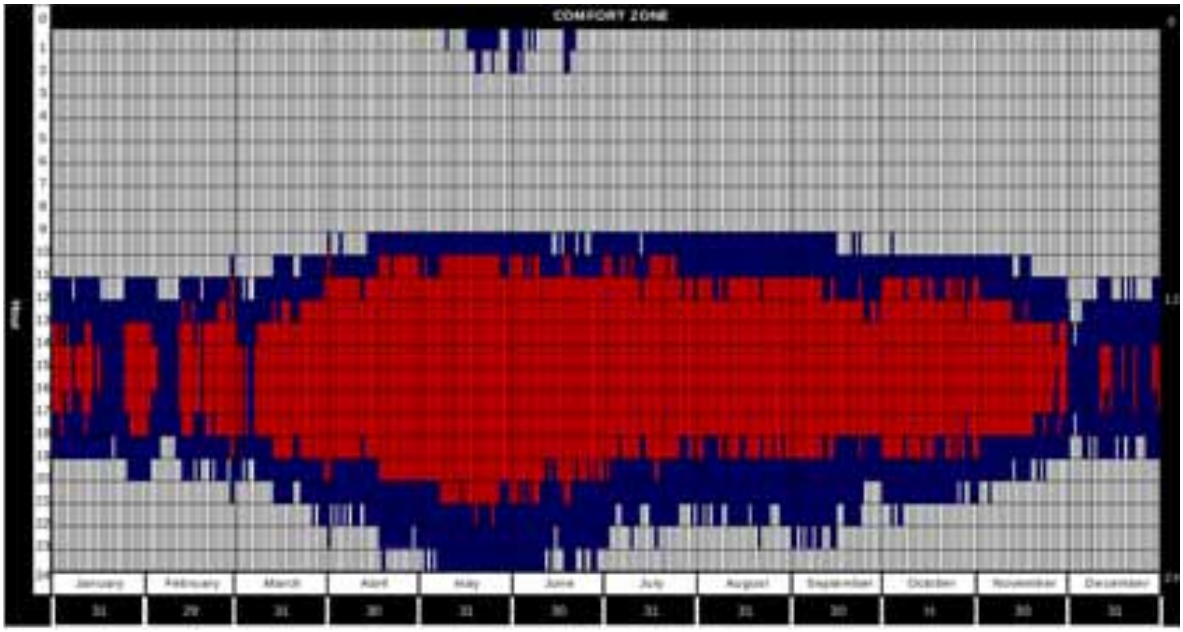

Fig. 3: Climatic Year Type for Maximum Activity (CYT-Max) for the Period 1959-2013. (Colors Represent Temperature Ranges: Greater Than 24.225 °C in Red, Between 18.725 and 24.225 °C in Blue, and Lower Than 18.725 in White)

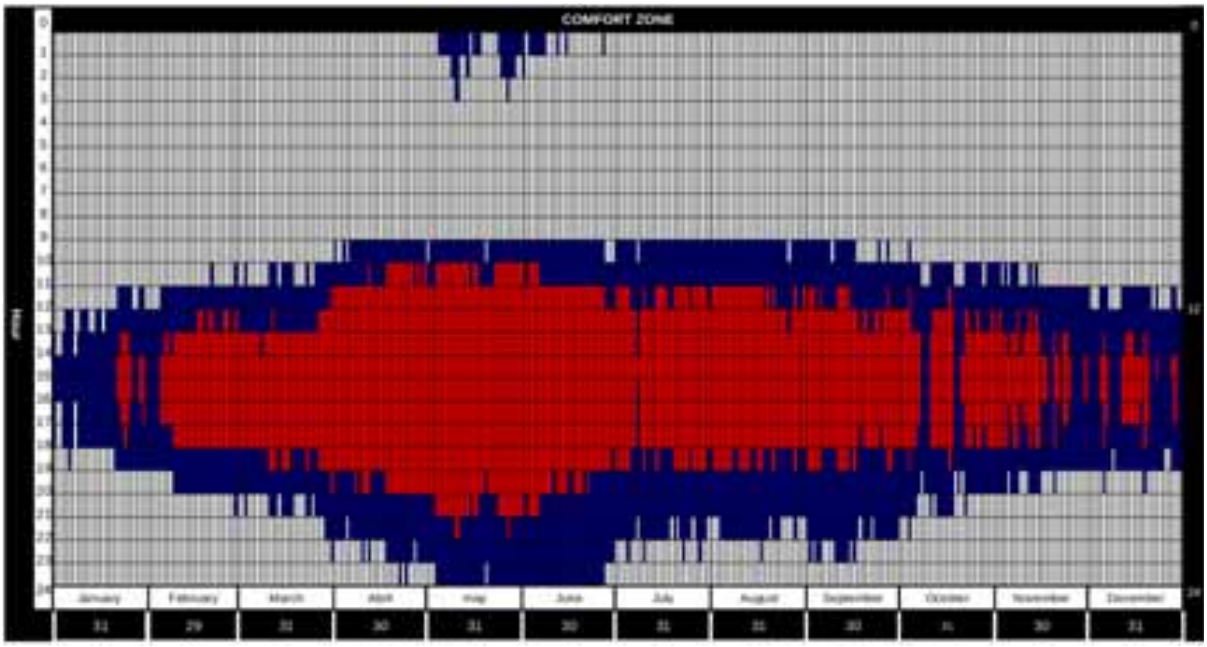

Fig. 4. Climatic Year Type for Minimum Activity (CYT-Min) for the Period 1959-2013. (Colors Represent Temperature Ranges: Greater Than 24.225 °C in Red, Between 18.725 and 24.225 °C in Blue, and Lower Than 18.725 in White)

3. Results

From the determination of the reference climate years types for major and minor solar activity considered from solar cycles of solar cycle number 19 to number 23, which covers the period of daily temperature of 1959-2013 and determining from this period CYT-MIN and CYT-MAX for the city of Leon Guanajuato. Based on these periods the behavior of the external temperature of the green roof cover is analyzed, and represented in a similar way to those of climate years as shown in the following figure.

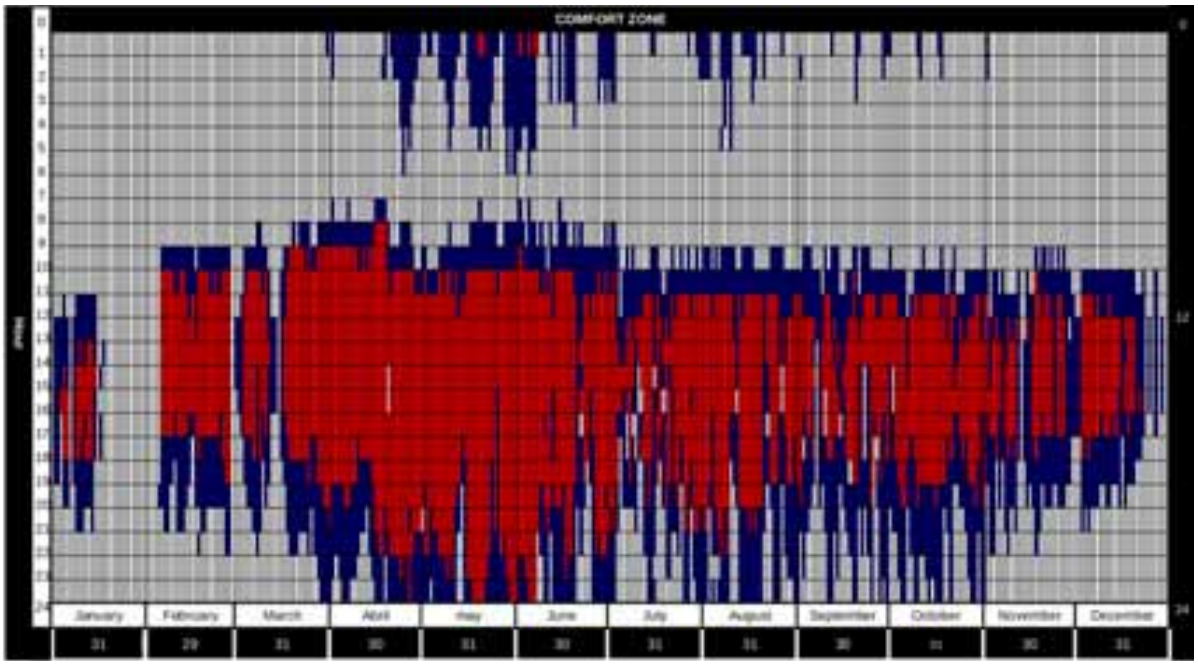

Fig. 5: Representation for the Comfort Zone with data for Outdoor Temperature over the Green Cover. (Colors Represent Temperature Ranges: Greater Than 24.225 °C in Red, Between 18.725 and 24.225 °C in Blue, and Lower Than 18.725 in White)

As for the results of the internal temperature in the two different positions of location sensors and 2.8 m and 1.65 m the results are presented in the figures below.

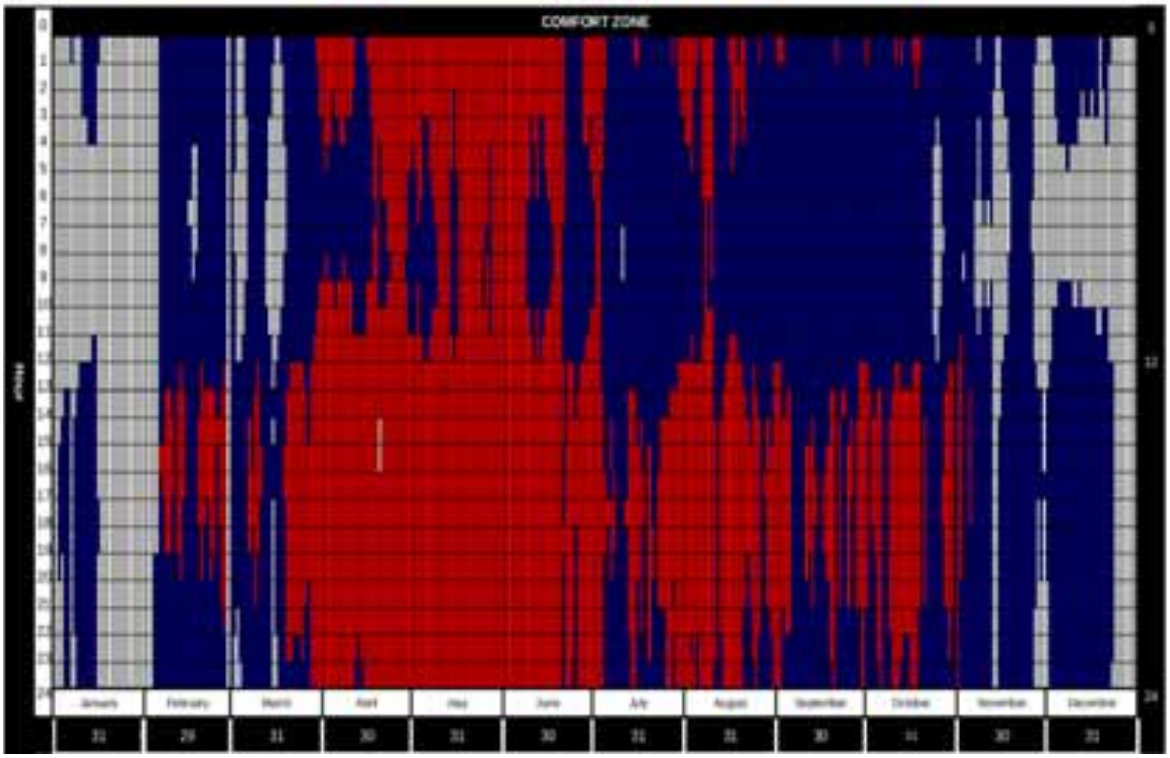

Fig. 6: Hourly Indoor Zone Temperature at 2.8 m Position. (Colors Represent Temperature Ranges: Greater Than 24.225 °C in Red, Between 18.725 and 24.225 °C in Blue, and Lower Than 18.725 in White)

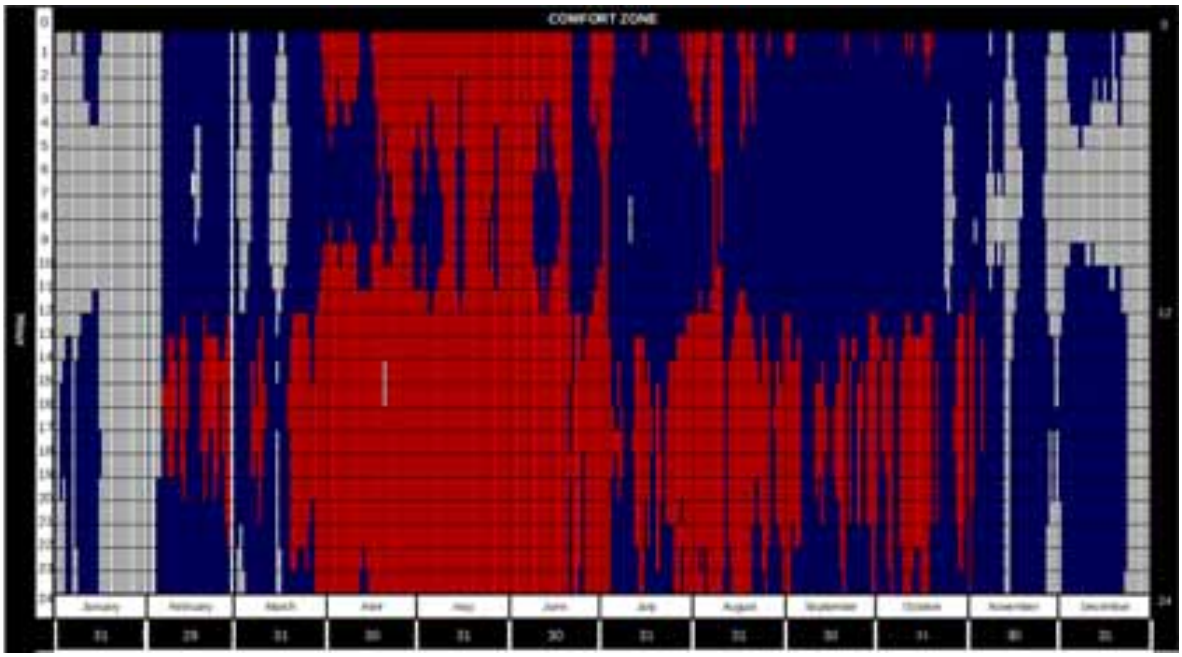

Fig. 7: Hourly Indoor Mid Zone Temperature at 1.65 m Position (Colors Represent Temperature Ranges: Greater Than 24.225 °C in Red, Between 18.725 and 24.225 °C in Blue, and Lower Than 18.725 in White)

In relation to the cover based on the Mexican standard NMX-C-460-ONNCCE-2009 and the method for estimating the thermal resistance of the envelope it was obtained a value of 2.16 m^2K/W, which is an equivalent to a global heat transfer coefficient of 0.464 W/ m^2K that when compared with those established by the standard for thermal zones the resulting value is in the range of comfort, Zones 1 and 2 are the zones defined for most of the areas comprising the center of the Mexico.

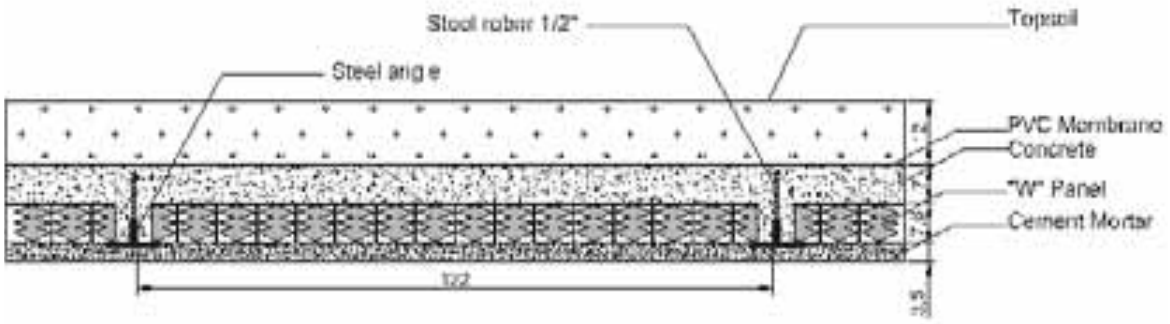

Fig. 8: Section of the deck structure

As for the overall analysis of the behavior of the temperature outside on the green cover and its correlation with the interior temperature shown in the graphs above; it can be seen that the overall difference is not significant, accounting for a difference between temperatures of approximately 2.6 °C and 2.5 °C, and presenting a difference between the exterior and interior extreme maximums within 5.2 °C and difference of 5.4 °C between high and medium internal sensors.

The analysis of historical temperature with reference to temperature measured on the green roof, it does not exceed 1.2 °C, yet if this historical temperature is analyzed with respect to the inner temperature the difference is even more significant of approximately 3.9 °C and a maximum temperature extreme of 6.8 °C.

Table 1: Daily behavior Historical Temperature for the period 1959-2013 and the outdoor temperature recorded over the green cover and indoor temperature for two different heights 2.8mts and 1.65 meters.

Higher Temperature Difference			Average Degree °C	Uncertainty relative	Standard deviation	%	Dispersion	Uncertainty random effects 90%	Uncertainty random effects 95%	Total Uncertainty 99.5%
Maximum	**5.17 °C**	Temperature Outdoor	20.6							
Minimum	2.7 °C	Temperature Indoor High 2.8 mts	23.3	-0.1	1.9	12.7	2.0	2.7	4.2	14.3
Maximum	**5.4 °C**	Temperature Outdoor	20.6							
Minimum	2.67 °C	Temperature Indoor Mid 1.65 mts	23.2	-0.1	1.9	12.6	2.0	2.7	4.2	14.2
Maximum	6.1 °C	Temperature Outdoor	20.6							
Minimum	1.13 °C	**Historical Temperature TCY-MAX**	19.4	0.1	0.8	5.4	1.3	1.8	2.8	9.4
Maximum	5.3 °C	Temperature Outdoor	20.6							
Minimum	1.17 °C	**Historical Temperature TCY-MIN**	19.4	0.1	0.8	5.7	1.3	1.8	2.8	9.4
Maximum	**6.83 °C**	Temperature Indoor High 2.8 mts	23.3							
Minimum	1.13 °C	**Historical Temperature TCY-MAX**	19.4	0.2	2.7	18.1	4.4	5.9	9.1	30.8
Maximum	**6.4 °C**	Temperature Indoor Mid 1.65mts.	23.2							
Minimum	3.8 °C	**Historical Temperature TCY-MAX**	19.4	0.2	2.7	18.0	4.3	5.8	8.9	30.3
Maximum	4.51 °C	Temperature Intdoor High 2.8 mts	23.3							
Minimum	1.7 °C	**Historical Temperature TCY-MIN**	19.4	0.2	2.7	18.3	4.4	5.9	9.1	31.0
Maximum	4.4 °C	Temperature Intdoor Mid 1.65 mts	23.2							
Minimum	1.6 °C	**Historical Temperature TCY-MIN**	19.4	0.2	2.7	18.2	4.4	5.8	9.0	30.5

4. Conclusions

Building systems in Europe and higher latitudes are different to tropical latitudes, as the ones covered in Mexico. In non-tropical latitudes the insulation is more stringent, while some tropical areas this is not critical; most of those regions is not considered at all.

The variations of the outside temperature to inside are not extreme so insulate buildings, and it is impractical and more costly to the general population. Mexican norms for housing construction begin to be more favorable especially in the minimum characteristics residences that could stress the need for climate protection conditions.

The overall average temperature decrease inside is not very high with reference to the outside temperature not exceeding globally 2.6 °C. Greater differences are found considering the historical temperature on climate year type for maximum activity, a difference of 3.9 °C.

The wall insulation process in the tropics is not rigorous, presenting significant infiltrations but they are not responsible of the changes on the outside temperature.

Solutions with green roofs called extensive, are intended to insulate the constructions of external weather conditions and care of the same is performed by the user; maintenance is secondary. Yet, the professional practice to implement green roofs are too expensive for widespread use, The thermal performance perhaps is not significant on temperate climates but there are other relevant aspects of their environmental use, that may have a greater impact and benefit for the environment, as the case of rainwater harvesting and soapy water recycling.

References

Britz, J., 2004, Naturacion Urbana, Cubiertas Ecologicas y Mejoramiento Ambiental, 2a. ed., Mundi-Prensa, España, 396 p.

Minke, G., 2004, Techos Verdes, Planificación, Ejecución, Consejos Prácticos, Fin de Siglo, Montevideo, Uruguay, 85p.

Mexican Standard Norm NMX-C-460_ONNCCE-2009, Organismo Nacional de Normalización y Certificación de la Construcción y Edificación.

Mexican Standard Norm NMX-AA-164-SCFI-2013: Edificación Sustentable: Criterios y Requerimientos Mínimos, Organismo Nacional de Normalización y Certificación de la Construcción y Edificación.

Tudela, F., (1982), Bioclima y Confort Térmico, CEPAL, México, 125 p.

Resource Assessment and Energy Meteorology

ISES International Solar Energy Society

Conference Proceedings

Solar World Congress 2015

Daegu, Korea, 08 – 12 November 2015

A Multilinear Model for Estimating the Monthly Global Solar Radiation in Qassim, Saudi Arabia

A. H. Maghrabi; M.H. Almalki

National Centre For Applied and Physics, King Abdulaziz City For Science and Technology, P.O. Box 6086 Riyadh 11442, Saudi Arabia

Abstract

Information on the global solar radiation is essential for many solar energy applications. Because of the cost of the measuring equipment, data on global radiation are not always available in most places, especially in developing countries. To overcome this difficulty, several attempts have been made to estimate solar radiation components from easy-to-measure atmospheric and/or geographical variables. In this study, monthly mean global solar radiation data for Qassim City, Saudi Arabia for the period from 1971 to 1998 were modelled using three meteorological variables: relative humidity, air temperature and atmospheric pressure. The predictability of the model was superior to the experimental data, showing a correlation coefficient (R) of 0.988. The mean percentage error (MPE) was less than 1%, the root mean square error (RMSE) was 0.02 and the mean bias error (MBE) was -1.1×10^{-4}. The performance model was validated using an independent data set for the period between 2003 and 2005. The statistical results were optimal and showed the ability of the model to predict the monthly global solar radiation for Qassim City for any period of time with less error. The predictability of some of the previously proposed models, which differed from each other in terms of the variables that they used and the number of variables contained, were tested to estimate monthly global solar radiation. The performances of these models were different in terms of predicting the experimental data.

Keywords: *Global radiation, Qassim, relative humidity, temperature, atmospheric pressure, Saudi Arabia*

1. Introduction

Solar radiation and its components are the most important and renewable energy source, affecting global climate and energy budget studies; hence the accessibility of solar radiation data is essential for the research community. Global radiation data are essentially required for different applications such as the architectural design of solar energy systems. Information on global solar radiation is not only needed at specific locations but by the worldwide community, Li and Lam (2000); Lu , et al. (1998); Zekai (2008); El-Sebaii et al. (2010)

The measurement of solar radiation requires equipment such as pyranometers, which need regular maintenance and calibration, Chineke (2008). For many developing countries such costly equipment is not usually available; hence elaboration of an alternative method using the available meteorological data to calculate and model the global radiation data is a common practice. Several empirical and semi-empirical models have been parameterized using available meteorological and geographical parameters to calculate solar radiation. These include sunshine hours, air temperature, latitude, and water vapor, El-Sebaii et al., (2010); Alvaro et al. (2013); Maghrabi (2009); Maghrabi et al. (2008); Antonio et al. (2015); Bulent, et al. (2015); Trabea and Shaltout (2000); Li, et al.(2013).

In this work, data on atmospheric pressure, relative humidity (RH) and air temperature have been used to

doi:10.18086/swc.2015.07.01 Available at http://proceedings.ises.org

model the monthly average daily global radiation for Qassim City, central Saudi Arabia.

2. Experimental Data and Validation Methods

Mean monthly global solar radiation data on a horizontal surface (H) were obtained from the Saudi Arabian Solar Radiation Atlas, published by the Saudi King Abdulaziz City for Science and Technology (KACST). The atlas has two versions. The first contains data collected by the Ministry of Agriculture and Water from 1971 to 1980 compiled by KACST; the second measurements of the global horizontal radiation between 1994 and 1996 obtained from KACST's solar radiation network, KACST (1999). Meteorological information for the two periods was obtained from the Presidency of Meteorology and the Environment (PME). Clear sky data were only considered in this study.The monthly averages of the extraterrestrial global radiation (Ho) were calculated for the given periods using the procedures (Duffie and Beckman 1991) as follows.

$$Ho = (1/\pi)IscE0(\cos\lambda \cos\delta \sin ws + (\pi/180)\sin\lambda \sin\delta ws) \quad \text{(eq. 1)}$$

Isc is the solar constant 1376 Wm^{-2} ,Eo is the correction factor of the Earth's orbi calculated by:

$$E0 = 1.00011 + 0.034221\cos\alpha + 0.00128\sin\alpha + 0.000719\cos(2\alpha) + 0.000077\sin(2\alpha) \quad \text{(eq. 2)}$$

α is the day angle, obtained from:

$$\alpha = 2\pi(nday - 1)/365 \quad \text{(eq. 3)}$$

δ is the solar declination (in degrees),

$$\delta = (180/\pi).(0.006918 - 0.399912\cos\alpha + 0.070257\sin\alpha - 0.006758\cos(2\alpha) + 0.000907\sin 2\alpha - 0.002697\cos 3\alpha + 0.00148\sin(3\alpha)) \quad \text{(eq. 4)}$$

and the hour angle of the Sun *ws* (in degrees) is calculated as:

$$ws = \cos{-1}\,[-\sin\lambda\sin\delta/(\cos\lambda\sin\delta)] \quad \text{(eq. 5)}$$

We first developed and tested the performance of the several models using regression methods. The calculation procedures began with simple correlation between the clearance index H/Ho (ratio of the measured global radiations to the average daily extraterrestrial radiation) and each meteorological parameter individually; then multiple regression analysis, using two and three parameters, was carried out. The best performing model was validated using an independent set of global radiation measurements for the period between 2003 and 2005. Finally, we selected several models, with different parameters, from the literature and tested their predictability against the measured global radiation.

The calculated H/Ho values were assessed in terms of mean percentage error (MPE), mean bias error (MBE), and root mean square error (RMSE), calculated as:

$$MPE = \frac{1}{N}\sum_{i=1}^{N}\left(\frac{V_{imeas} - V_{ical}}{H_{imeas}} \times 100\right) \quad \text{(eq. 6)}$$

$$MBE = \frac{1}{N}\sum_{i=1}^{N}(V_{imeas} - V_{ical}) \quad \text{(eq. 7)}$$

$$RMSE = \frac{1}{N}\sum_{i=1}^{N}\sqrt{(V_{imeas} - V_{ical})}^{2} \ , \quad \text{(eq. 8)}$$

where V_{imes} and V_{ical}, are the measured and calculated (H/Ho) values respectively, and N is the number of the measurements The significance of the proposed model was tested using t-statistics calculated according to Stone (1993), as:

$$t - stat = \sqrt{\frac{(n-1)MBE^2}{RMSE^2 - MBE^2}} \quad \text{(eq. 9)}$$

3. Results and Discussions

3.1 Model parameterisation

Table (1) presents the regression equations between the measured clear sky index and single, two, and three meteorological parameters. The statistical results of these equations are also given. It can be seen that the statistical parameters vary from one model to another. All the models presented an MPE below 2%, which can be considered an excellent performance. Additionally, all the models were significant according to their t-values, which were smaller than the critical value (3.106).

The three-variable models (eq. 16) presented the lowest RMSE and MBE and the highest correlation coefficient. The correlation coefficient of this equation was 0.98, and the MPE, RMSE and MBE were, respectively, 0.15%, 0.02, and -1.1×10^{-4}. The two-variable models showed improvements in their

correlation coefficients; their MBE, RMSE and MPE values were not as good as those of the one-variable models. Models with air pressure (as either single or second variable) gave a poorer performance than those use the air temperatures.

Table 1: Results of the regression analysis of the clearance index, H/Ho (ratio of the measured global radiations to the average daily extra-terrestrial radiation) and meteorological parameters.

Equation	R	MBE	RMSE	MPE	t
$\frac{H}{Ho} = 0.004T + 0.491$ (eq. 10)	0.85	0.0009	0.021	0.3340	0.183
$\frac{H}{Ho} = 0.0023RH + 0.6556$ (eq. 11)	0.86	-0.003	0.023	-0.38	0.455
$\frac{H}{Ho} = -0.0084P + 8.50$ (eq. 12)	0.88	-0.008	0.020	0.0349	0.078
$\frac{H}{Ho} = 0.649 - 0.0021RH + 0.00016T$ (eq. 13)	0.80	-0.002	0.024	-0.261	0.351
$\frac{H}{Ho} = 9.702 - 0.0021Rh + 0.00016T$ (eq.14)	0.91	0.0283	0.032	1.8556	5.93
$\frac{H}{Ho} = 7.463 - 0.0071P - 0.0003RH$(eq. 15)	0.91	0.001	0.018	0.345	0.491
$\frac{\mathrm{H}}{\mathrm{Ho}}$ =10.750-0.0068T-0.0105P-0.003RH (eq. 16)	0.98	-0.0001	0.0206	0.1555	0.033

Fig.1 shows the monthly variations of the measured and the calculated global solar radiation values obtained from (a) single and (b) two-variable models. It is obvious that the pressure-based model always overestimated the measured values. On the other hand, the RH-based and T-based models slightly overestimated the measured values in the months September, November and December and underestimated the measurements in the remaining months. Two-variable models showed the same behavior as the single T- and H-based models. All the models highly overestimated the global radiation measurements in April and May. This can be explained by the effect of the pre-monsoon dust events which are very frequent during these two months.

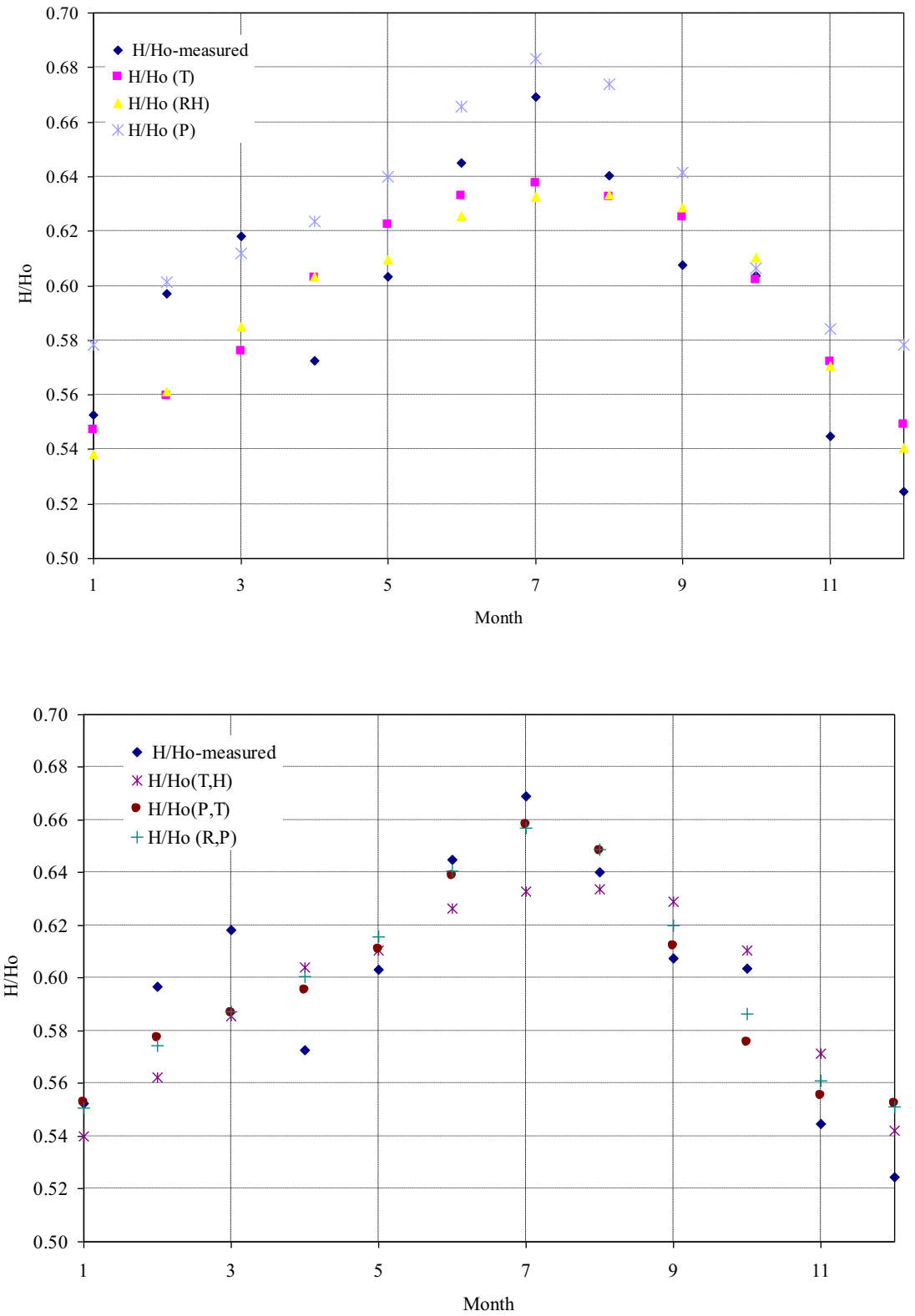

Fig 1. Monthly measured and predicted H/Ho from (a) single and (b) two-variable models.

Fig.2 displays the monthly measured and the calculated radiation from equation (16) (the model contains all three variables). Fig.3 is the scatter plot for the predicted and measured values. It is very evident that the three-variable model showed less deviation from the measured values and predicted with high accuracy. The data closely lie in the vicinity of the 1:1 line. The regression equation for the measured and predicted values has a slope of 0.98 (nearly equal to one) and an intercept of 0.01 (nearly equal to zero). This indicates a distinct relationship between the predicted and measured global radiation and rationalizes the excellent predictability of the model. Student's t-tests for this linear relationship at a significance level of $\alpha = 0.01$ were carried out and showed a t-value of 0.32, which is less than the critical value (3.106). This indicates the significance of the developed model in predicting the measured global solar radiation in Qassim.

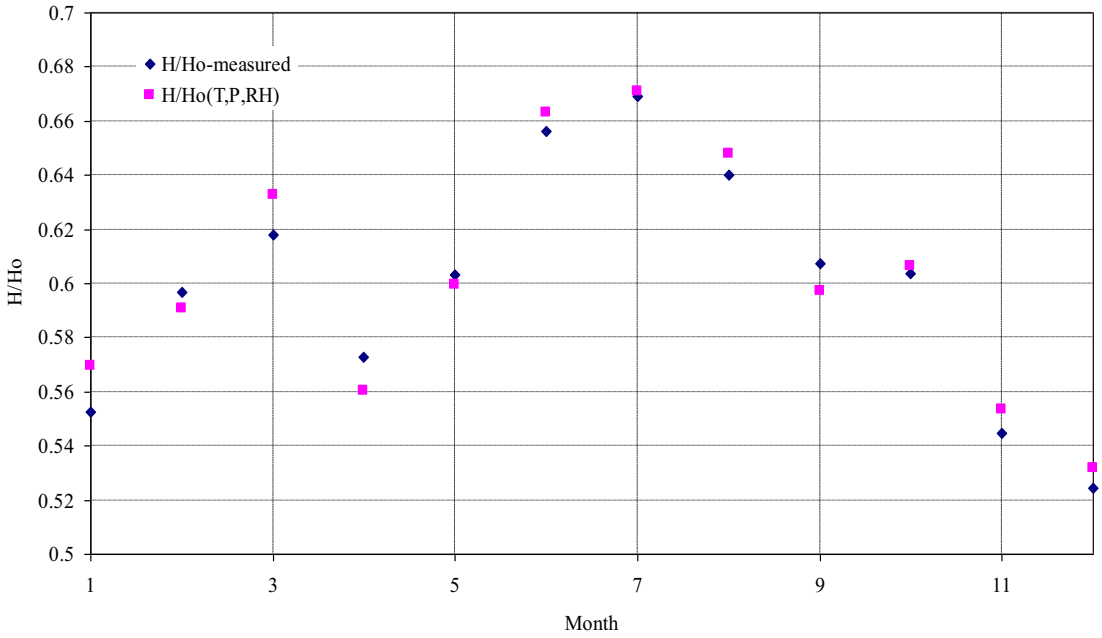

Fig.2. As in Fig.1, the measured data were compared with the predicted values calculated using equation (16).The dashed line is the 1:1 line and the straight line is the regression line.

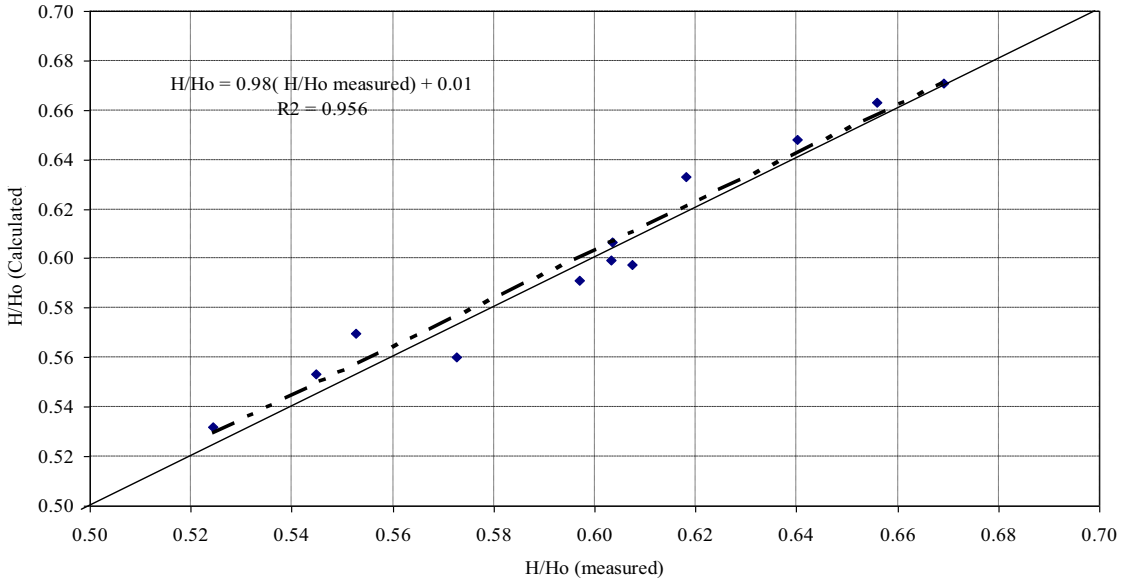

Fig.3. The measured H/Ho plotted against predicted values using equation (16). The straight line is the 1:1 line and te dashed line is the regression line between the two values.

3.2 Model Validation

The prediction of the proposed model (equation 16) for the global radiation in Qassim was tested using an independent data set. These data contain the mean monthly data on global solar radiation and the corresponding meteorological parameters for the period between 2003 and 2005. These data were obtained from the Saudi Presidency of Meteorology and the Environment.

Fig.4 indicates the monthly measured clearance index and the calculated values obtained from the model for the period between 2003 and 2005. The calculated H/Ho gives MPE =2.3 %, MBE -0.003, RMSE = 0.034, and t value =0.0921. These statistical results indicate an adequate performance of the model for this data set.

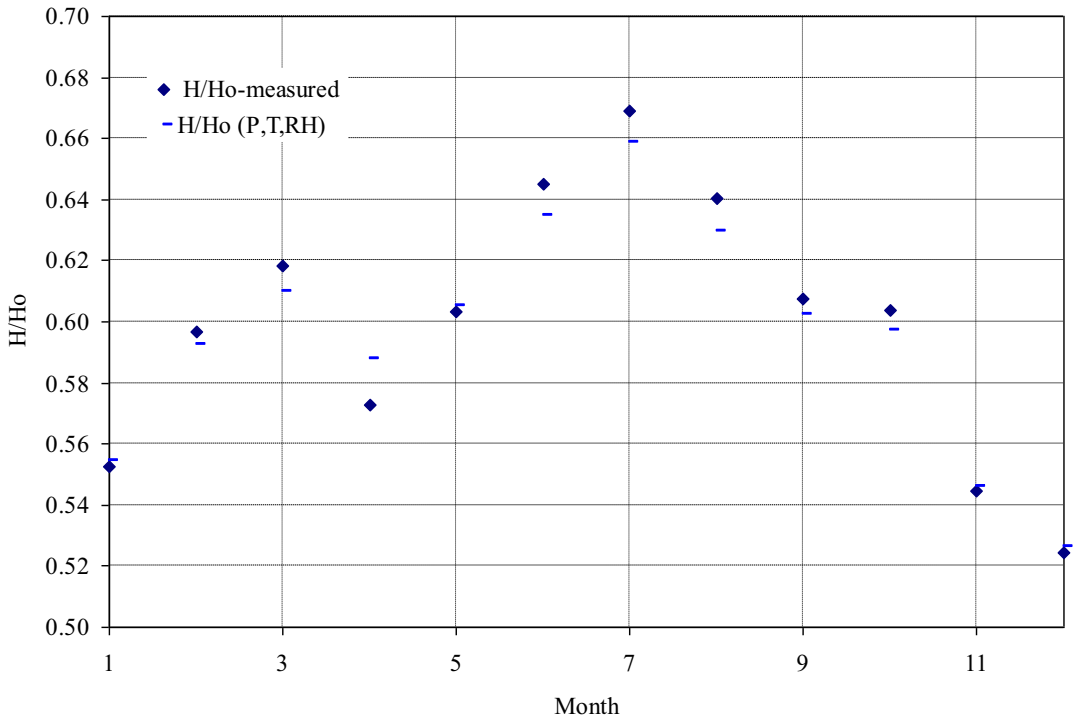

Fig.4. Monthly measured data for the period between 2003 and 2005 compared with their predicted values using the proposed model.

Fig.5 demonstrates the relationship between the measured and the predicted values of the clearance index for these data. The results show a close distribution of the data points around the 1:1 line, which verifies the ability of the model to predict global solar radiation in Qassim using independent measurements. The slope of the regression results for the measured and predicted values was 0.89 and the intercept was 0.052.

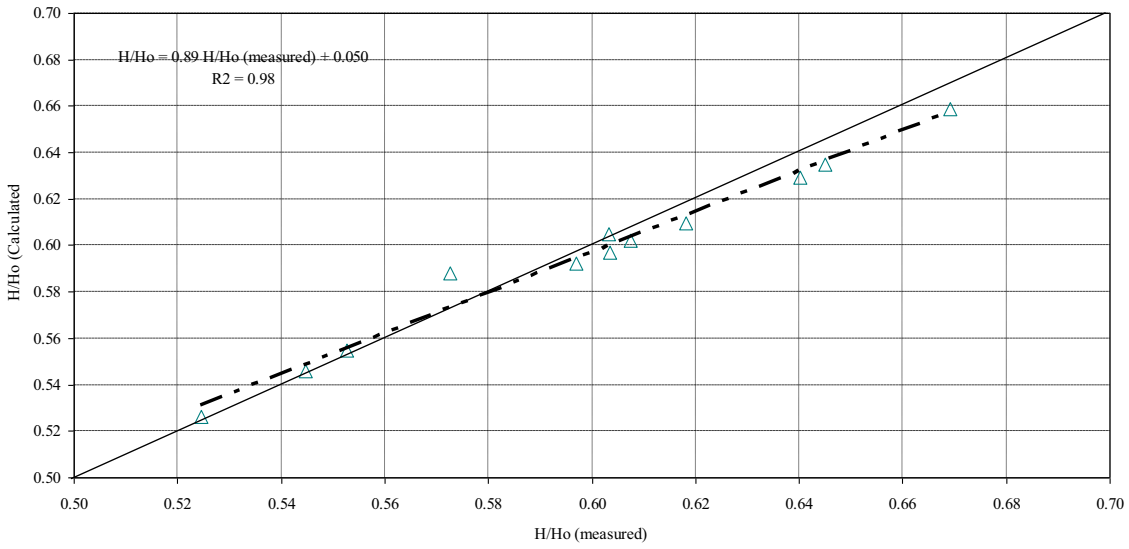

Fig. 5. As in Fig. 3, the figure plots the measured global solar radiation against the calculated values but for data between 2003 and 2005.

3.3 Comparisons with Other Models

Several models for predicting global radiation using meteorological parameters have been developed using data from different places around the world. In this study nine models were selected and their performances in predicting the measured global radiation data for Qassim for the period 1971 to 1996 were tested. Table (2) presents the functional form for the selected models and their statistical indicators. It can be seen that each model performed differently from the others. The RMSE values for all the models ranged between 0.27 and 0.069, MBE between 0.043 and 0.18. Apart from Bristow-Champbell model, all the models showed MPE values of less than 10%. Li et al.(2013) model was the best followed by the Adaramola (2012) model in predicting the measured data in Qassim. These two models contain three variables on them. Contrary, Bristow-Champbell (1984), Hargreaves et al. (1985), and Li et al. (2013) models showed the highest errors in estimating the measured data. According to the statistical tests all the models have poorer prediction in comparison with the proposed model in this study (equation 16) or even the single and multiple models.

Table 2: Functional of some of the selected models from the literature to calculate the measured H/Ho values for Qassim. The statistical results (MBE, RMSE, and MPE) for their predications are given.

	Form	MBE	RMSE	MPE(%)
Li et al (2013)	$\frac{H}{Ho}$ =0.064-1.1130T	0.132	0.231	5.43
Li et al (2013)	$\frac{H}{Ho}$ =1.025-0.879RH	0.143	0.272	8.620
Chen et al. (2004)	$\frac{H}{Ho} = 0.08 + 0.21(T_{max} - T_{\min})$	0.125	0.212	6.751
Adaramola (2012)	$\frac{H}{Ho}$ =1.419-1.1973(Tmin/Tmax)	0.161	0.201	5.820
Hargreaves etal 1985	$\frac{H}{Ho} = 0.153(T_{\max} - T_{\min})^{0.5} - 0.033$	0.146	0.261	9.351
Adaramola (2012)	$\frac{H}{Ho}$ =0.77-0.4656(RH/100) (Tmin/Tmax)	0.102	0.0749	4.793
Adaramola (2012)	$\frac{H}{Ho} = 0.845 - 0.464$(RH/100)	0.071	0.086	5.721
Bristow-Champbell (1984)	$\frac{H}{Ho} = 14.35[1 - \exp(-0.009(Tmx - T\min))^{0.549}$	0.183	0.136	10.457
Li et al (2013)	$\frac{H}{Ho}$ =-1.315+0.138(Tmax-Tmin)+0.8244RH	0.093	0.069	4.940

4. Conclusion

Solar radiation data are of great importance in many applications such as the design of solar energy systems and energy budget studies. In this study, monthly average daily global radiation on horizontal surface measurements between 1971 and 1998 were correlated with three meteorological parameters to develop an empirical model to estimate the global radiation for Qassim city, Saudi Arabia. These parameters are the air pressure, the mean air temperature and the relative humidity. The estimated radiation from the model presented excellent agreement with the measured data. The model has a correlation coefficient of 0.988, RMSE = 0.02, MBE = -1.1×10^{-4} and MPE less than 1 %. The model demonstrated an accurate estimation for the global radiation for Qassim using an independent data set for the period between 2003-2005. The performances of some models from the literature were conducted against the measured data for the period 1971-1998. The performances of these models were different in terms of predicting the experimental data

Acknowledgments

The authors thank the Saudi Presidency of Meteorology and Environment (PME) for kindly providing the surface climate data. The authors would also like to thank King Abdulaziz City for Science and Technology (KACST) for supporting this work.

5. References

Adaramola Muyiwa S. , 2012, Estimating global solar radiation using common meteorological data in Akure, Nigeria, Renewable Energy; 47:38-44.

Alvaro Lentz , David, K., Baltazarb, J., Haberla; 2014, Evaluation of Meteorological Base Models for Estimating Hourly Global Solar Radiation in Texas, Energy Procedia 57, 1189–1198, ISES 2013.

Antonio Dumas, A., Andrisani, Bonnici M., Graditi, G., Leanza, G., Madonia, M.,Trancossi, M., 2015, A new correlation between global solar energy radiation and daily temperature variations Solar Energy, 116, 117-124.

Bristow K., and Champbell G., 1984, On the relationship between incoming solar radiation and daily maximum and minimum temperature, Agric Forest Meteorol,31,159–66.

Bulent Yaniktepe, Yasin Alperen Genc, 2015, Establishing new model for predicting the global solar radiation on horizontal surface, International Journal of Hydrogen Energy, In Press.

Chen, R., Ersi, K., Yang, J., Lu, S., and Zhao, W., 2004, Validation of five global radiation models with

measured daily data in China, Energy Conversion and Management 45 (2004) 1759–1769

Chineke T C. Equations for estimating global solar radiation in data sparse regions. Renewable Energy 2008;33:827-31.

Duffie, J.A., Beckman, W.A., (1991), Solar engineering of thermal process, New York: Wiley.

El-Sebaii, A. A., Al-Hazmi, F. S., Al-Ghamdi, A. A., and Yaghmour, S. J. 2010. Global, direct and diffuse solar radiation on horizontal and tilted surfaces in Jeddah, Saudi Arabia. Appl. Energy 87:568–576.

Hargreaves GL, Hargreaves GH, Riley P, 1985 Irrigation water requirement for the Senegal River Basin. J Irrigat Drain Eng, ASCE;111:265–75.

Jin Z, Yezheng W, Gang Y. General formula for estimation of monthly average daily global solar radiation in China. Energy Convers Manage 2005;46:257–68.

King Abdulaziz City for Science and Technology, Saudi Arabian Solar Radiation Atlas, 1983 and 1998.

Li D and Lam J. 2000, Solar heat gain factors and the implications for building designs in subtropical regions. Energy Build.,32:47–55.

Li H. S. , W. B. Ma , X. B. Bu , Y. W. Lian & X. L. Wang ,2013, A Multiple Linear Regression Model for Estimating Global Solar Radiation in Guangzhou, China, Energy Sources, Part A: Recovery, Utilization, and Environmental Effects, 35:4, 321-327

Lu Z, Piedrahita RH, Neto CDS. 1998, Generation of daily and hourly solar radiation values for moeling water quality in aquaculture ponds. Trans ASAE;41:1853–9.

Maghrabi, A. H.Parameterization of a simple model to estimate monthly global solar radiation based on meteorological variables, and evaluation of existing solar radiation models for Tabouk, Saudi Arabia. Energy Cons. & Mang., 2009; 50,2754-2760.

Maghrabi, A.H. and Al-Mostafa Z. A. 2008, Correlation of global radiation with some meteorological parameters for Jeddah Saudi Arabia, Proc. 3rd solar energy society A-Pacific, Sydeny, Australia.

Stone, R.J. Improved statistical procedure for the evaluation of solar radiation estimation models. Sol. Energy, 1993, 51, 289–291.

Trabea AA, Shaltout MAM. Correlation of global solar radiation with meteorological parameters over Egypt. Renew Energy 2000;21:297–308.

Zekai, S., 2008. Solar energy Fundamentals and Modeling Techniques: Atmosphere, Environment Climate Change and Renewable Energy. Springer, Berlin (276 pp.).

Methodology to Stochastically Generate Synthetic 1-Minute Irradiance Time-Series Derived from Mean Hourly Weather Observational Data

Jamie M. Bright[1] , Peter G. Taylor[1,2,3] and Rolf Crook[1]

[1] Energy Research Institute, School of Chemical and Process Engineering, University of Leeds, Leeds (UK), LS2 9JT

[2] Sustainability Research Institute, University of Leeds, Leeds (UK)

[3] Centre for Integrated Energy Research, University of Leeds, Leeds (UK)

Abstract

Well geographically distributed high temporal resolution solar irradiance data is scarce, resulting in many studies using mean hourly irradiance time-series as an input. This research demonstrates that by taking readily available mean hourly meteorological observations of okta, wind speed, cloud height and atmospheric pressure; 1-minute resolution irradiance time-series that vary on a spatial dimension can be produced. The synthetic time-series temporally validates against observed 1-minute UK irradiance data with 99% K-S test confidence levels across 3 metrics of variability indices, ramp-rate occurrences and irradiance frequency. A new methodology is applied to existing research that produces two-dimensional cloud cover using a vector approach to add spatial correlation to irradiance time-series, as well as improvements to the clear-sky index calculations. The methodology is applied to a hypothetical configuration to demonstrate its capabilities.

Keywords: *irradiance generation, minute resolution, resource modelling, cloud edge enhancement.*

1. Introduction

Solar irradiance fluctuates on a 1-minute time scale or less (Sayeef et al., 2012) and is driven by the transport of atmospheric pollutants (Vindel and Polo, 2014), atmospheric losses, and cloud dynamics (Calinoiu, 2014). Large irradiance fluctuations can cause ramps in solar energy power generation outputs (Hummon et al., 2012), these power fluctuations can result in electrical problems and supply/demand issues such as over voltages in PV laden distribution grids (Widén et al., 2011). Furthermore, irradiance is dependent on geography, irradiance at locations across 1 km are affected by different optical losses as they can be obscured at different times. It is important, therefore, to utilise a solar irradiance data input that can capture these problematic fluctuations and spatial variations when theoretically considering power reliability and impacts on a high frequency time scale. Averaging solar irradiance data over different temporal frequencies results in loss of detail of the irradiance fluctuations. Figure 1 demonstrates how averaging irradiance data across different time-scales significantly underemphasises the actual incident irradiance fluctuations, as well as underestimating peak irradiance values.

Calibrated 1-min irradiance datasets are usually the output of isolated research projects and are often limited in duration, consistent measurement techniques, and geographic distribution. Sources of 1-min resolution irradiance data exist such as the World Radiation Monitoring Centre's Baseline Surface Radiation Network (BSRN), which will be used in a validation, however it is lacking in coarse geographical distribution. 1-hour resolution weather data, however, is widely collected and made available through national meteorological offices. This hourly data fails to capture the intermittent nature of solar irradiance (Sayeef et al., 2012); some solar irradiance models, therefore, use hourly datasets to artificially generate minutely irradiance time-series. Examples of such have been reviewed previously (Gueymard, 2012), with more notable methodologies using utilising a sun obscured type approach (Morf, 1998, 2011, 2013) and (Ehnberg and Bollen, 2005).

This paper presents a novel methodology that takes readily available mean hourly meteorological observation data of okta, wind speed, cloud height and atmospheric pressure; 1-minute resolution irradiance time-series that vary on a spatial dimension can be produced, which validate temporally against observed 1-minute UK irradiance data.

doi:10.18086/swc.2015.07.02 Available at http://proceedings.ises.org

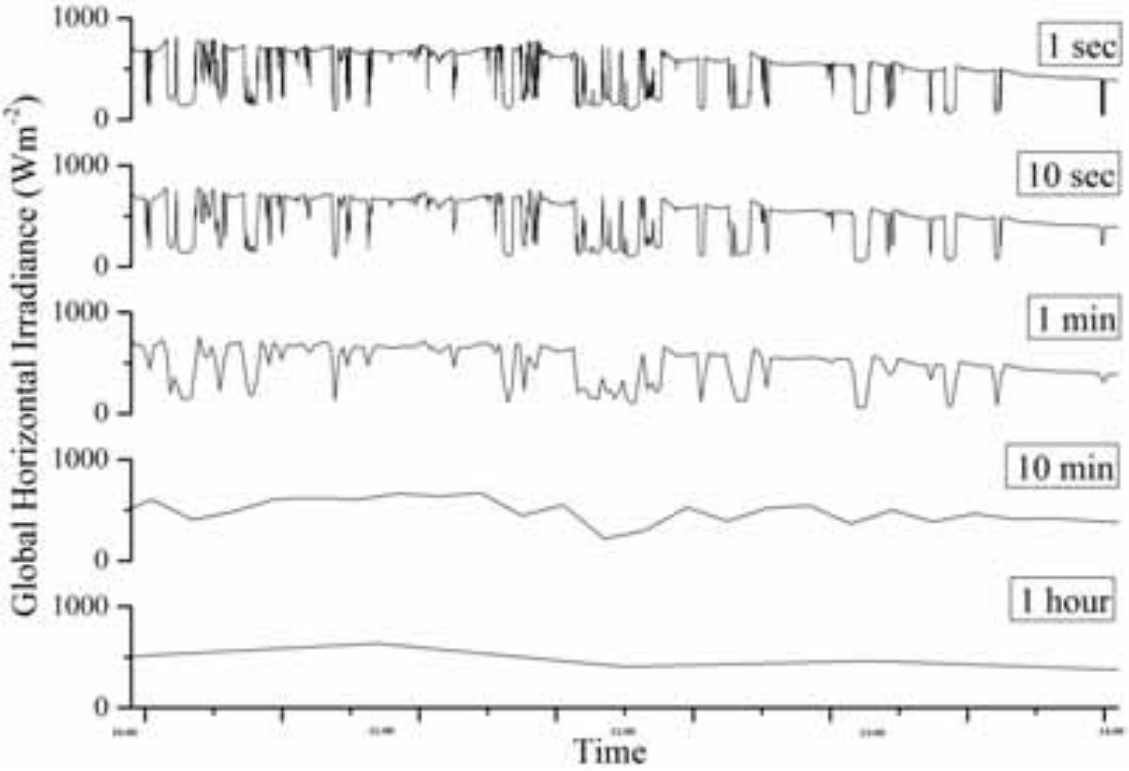

Fig. 1: Global horizontal incident irradiance in Leeds, UK on 25/06/2015 between the hours of 10:00 and 14:00. The data was logged using a horizontally-mounted silicon photodiode (BPW20) in short-circuit current mode with a linear current response converted to voltage with a transconductance amplifier, logged at 10 Hz using a 10-bit DAC. The data has been averaged across the timescales of, from top to bottom: 1 second, 10 seconds, 1 minute, 10 minutes and 1 hour.

2. Methodology

This work is an extension of the methodology by Bright et al. (2015) that demonstrated the success of taking mean hourly weather observation data to generate 1-min temporal resolution irradiance time-series. The original methodology has six distinct sections: cloud cover samples production, where descriptions of an hour of cloud are made; Markov chain production, produced through analysis of 12 years of mean hourly weather observation data to capture the patterns of transitions of each variable; the stochastic selection of variables, using probabilistic application of the variables guided by the Markov chains; calculation of global clear-sky irradiance, using standard irradiance modelling considering geography to determine the background irradiance; calculation of clear-sky index for each location, using statistics of optical losses derived as a function of the okta value; and finally calculation of incident irradiance upon an arbitrary plane, using methodologies from literature. For greater detail, the reader is referred to the work by Bright et al., (2015).

Significant developments have been made to the cloud cover samples production section and the calculation of clear-sky indices sections that allow for a spatial element to the previous temporal-only methodology. This section will discuss the production of cloud cover samples and their application in producing spatially correlating sun obscured time-series, and the updates to calculating the clear-sky indices and subsequent irradiance.

2.1 Cloud Cover Sample Production

Cloud cover samples are a description of an hour's cloud cover. The methodology is a sun-obscured type, which means that during periods when the sun is obscured, as indicated by the cloud cover sample, a clear-sky index value is applied to the global clear-sky irradiance. The clear-sky index is a fractional representation of the incident global horizontal irradiance from the available clear sky irradiance. Previously, the cloud cover samples were represented by a binary, single dimension vector describing each minute that

an arbitrary plane as obscured or unobscured, signified using 1s and 0s respectively. A new methodology is proposed that considers an area of sky with a randomly set number of clouds within it, as this will be moving across a static cluster with points of interest i.e. residential PV installations within a low voltage grid, each sample of cloud cover must represent the entire hour defined by the stochastic selection of the weather variables: cloud speed, u, and okta. The size of the area of sky is therefore a function of distance and time, 1.5km-by-u*3600, where 3600 is the number of seconds in an hour.

The cloud cover samples are lists of x and y coordinates for the centres of each cloud, and also includes their radii. The clouds are assumed to be circular with radii size adhering to the horizontal cloud length single power-law distribution (Wood and Field, 2011). The clouds' associated clear-sky indices are represented as optical thicknesses applied to all areas across the circle using a distribution that ranges from typical clear-sky indices lows of ~0.1, to highs of ~1.1, the implication of this is that across the circular cloud there will be sections above a clear-sky index of 1, indicating wispy or insignificant levels of cloud, whilst other areas indicate thicker sections, and therefore the clouds are not actually circular in application, instead the circle defines an area which cloud is allowed to form. In order to produce multiple samples, random numbers of clouds are selected, which are then given random x-y coordinates and radii drawn by the aforementioned distribution. The cloud cover fraction of each sample is analysed to determine the okta value, and is then sorted and stored appropriately in a larger matrix. Samples are then selected using an indexing based on the conditions stochastically selected through a Markovian process within the model simulation.

2.2 Clear-sky Fluctuations

Clear-sky indices fluctuate across different timescales. The cumulative probability distributions functions (CDF) for the frequency of occurrence of absolute step size changes for different time scales are shown in Lave et al. (2012). It is shown that 1-min and 1-hour data have very different statistics. To capture these fluctuations, the CDF profiles for the different time scales are applied to the clear-sky indices. Two vectors of fluctuations following the CDF profiles are drawn, one for clear periods, $\boldsymbol{F_0}$, the other for obscured periods, $\boldsymbol{F_1}$. For moments of obscured sky, the step changes are equally step downs as well as step ups.

To create $\boldsymbol{F_0}$ and $\boldsymbol{F_1}$, a step size change is selected following the appropriate cumulative distribution function, this increase is then linearly applied across the hour/10-min/minute, before being smoothed using a spline technique (using inbuilt Matlab functions (Matlab, 2012)) and can be represented for both as

$$\mathbf{F}_{(\mathbf{0}or\mathbf{1})}(t_0 : t_1) = \left(\mathbf{F}_{(\mathbf{0}or\mathbf{1}),t0} : T : 1 \pm s\right) \qquad \text{(eq. 1)}$$

$$s = \frac{\sum CDF_T < r}{100} \qquad \text{(eq. 2)}$$

where t_0 and t_1 are index references in minutes of current and future location within $\boldsymbol{F_{0or1}}$, T refers to the number of minutes within the operating frequency (when performing fluctuations on a 1-h period, T=60), $\boldsymbol{F_{t0}}$ refers to the fluctuation value at the previous index. The use of the colon, **:**, in the format $(t_0 : t_1)$ refers to the space within $\boldsymbol{F}$ between t_0 and t_1, and in the format $(x : n : y)$ refers to a linearly spaced vector starting at x and ending at y with n number of intervals. CDF_T refers to the appropriate cumulative probability distribution function, r is a random variate evenly distributed between 0 and 1, and finally s is the step size magnitude randomly extracted from the CDF.

2.3 Cloud Movement and Clear-sky Indices

Once the cloud cover samples are selected for each hour of the simulation, the samples are simulated to pass across the stationary targets within the spatial domain. To simulate the cloud direction, the locations are rotated in accordance with the cloud direction using rotational matrices as demonstrated in equation 3

$$\begin{bmatrix} x' \\ y' \end{bmatrix} = \begin{bmatrix} \cos\vartheta & -\sin\vartheta \\ \sin\vartheta & \cos\vartheta \end{bmatrix} \begin{bmatrix} x \\ y \end{bmatrix} \qquad \text{(eq. 3)}$$

where x and y denote the coordinates of the initial locations within the spatial domain, and x' and y' are the rotated coordinates by angle ϑ. The angle by which to rotate is determined using a normally distributed random walk, with standard deviation equal to 10, around a mean set to the previous cloud direction, this allows for gradual changes in direction. The cloud speed is determined stochastically (Bright et al., 2015) and so the cloud movements in relation to the locations of interest within the spatial domain are known.

The simulation works iteratively, progressing by one time-step at a time. Whilst the calculations are in a vectorised format, it is simplest to imagine a static rectangle with the locations of interest marked, being overlapped by a rectangle containing the clouds; at each moment it is determined whether or not a location is obscured by the cloud. For each iteration, the distance from the location of interest to the centre of each cloud within the sample is calculated. Firstly, let the length of the spatial domain be X_l and the length of the cloud sample be X_c, the coordinates of the location of interest and each cloud are (x_l', y_l') and (x_c, y_c) respectively. The distance from the location to the edge of the domain is

$$\partial x_l = X_l - x_l' \qquad \text{(eq. 4)}$$

while the distance from the cloud to the edge of the cloud environment is given by x_c. The overlap of domains is defined as the number of iterations, i, multiplied by the temporal resolution that the simulation is operating at, t. Therefore the distance in the x-direction from the location to the cloud, dx, is given by

$$\partial x = \partial x_l + x_c - it \qquad \text{(eq. 5)}$$

the distance along the y-axis from the location to the cloud is given by

$$\partial y = y_c - y_l' \qquad \text{(eq. 6)}$$

the horizontal distance from the location to the centre of the cloud is therefore calculated using Pythagoras' theorem as

$$d = \sqrt{\partial x^2 + \partial y^2} \qquad \text{(eq. 7)}$$

To produce a clear-sky indices vector for each location, the simulation enters an loop which cycles through each time step for the desired duration, and for each location. At each loop the locations are rotated according to the cloud movement direction as shown in equation 3, the x-y coordinates of each cloud sample are updated according to the cloud movement speed and time step before working through equations 4-7. At each loop it is determined if the location is covered by cloud. To do so, a logical *if* statement is applied, querying d against the radius of the cloud, r, such that

$$r > d \rightarrow B = 1 \text{ else } B = 0 \qquad \text{(eq. 8)}$$

where B is a Boolean matrix indicating the presence of cloud, and $\rightarrow$ denotes the use of a logical *if* statement. The iteration moves on until the end of the cloud sample. If a location moves beyond the sample

as it passes, the next sample is loaded and queried against using the same methodology.

B is used as a binary indicator for sun obscured. During periods of *B=1* when the cloud is present, a clear-sky index, k_c, is generated for each cloud present using distributions of clear-sky indices as a function of the okta number (Bright et al., 2015).

$$k_{ci} = f(okta) \quad \text{(eq. 9)}$$

The clear-sky index for overlapping clouds is found as the mean of the overlapping clear-sky indices

$$k_{ci}(\mathbf{B}=1) = \frac{1}{c}\sum_{n=1}^{c} k_{c,n} \quad \text{(eq. 10)}$$

Where subscript *i* is the current iteration, k_c***(B=1)*** are the clear-sky indices during moments of cloud, $k_{c,n}$ is the k_c value for the n^{th} term, and c is the total number of overlapping clouds index.

The clear sky indices vector, $\boldsymbol{k_c}$, for each property is calculated at each iteration, *i*. This iteration, *i,* must undergo a correction as a function of *x'* and *u* to account for spatial variability, where *u* is the cloud speed; $\boldsymbol{k_c}$ is therefore calculated as

$$i = i + \frac{x'}{u} \quad \text{(eq. 11)}$$

$$\mathbf{k}_{ci}(B=1) = kc_i \times \mathbf{F_1} \quad \text{(eq. 12)}$$

$$\mathbf{k}_{ci}(B=0) = kc_i \times \mathbf{F_0} \quad \text{(eq.13)}$$

Multiple irradiance time-series can now be drawn from any *x-y-z* location within a 1.5 km by 3600*u* km area, each with different arbitrary plane orientations and tilts, such as the different tilts and rotations of residential PV installations within a low voltage grid. Irradiance is calculated for each location using the methodology outlined in Bright et al. (2015), and the corresponding clear-sky indices, $\boldsymbol{k_c}$, are applied.

2.4 Cloud Edge Enhancement

Cloud edge enhancement, CEE, describes events whereby a point on the surface receives a larger amount of incident irradiance than is available in the clear-sky irradiance, the events are attributed to irradiance reflecting from the edge of cloud. The typical behavior of irradiance in the 60 sec leading up to, and after the largest 1 sec ramps is detailed by Lave et al. (2012). This behavior is applied to periods of transitions from clear to clouded moments.

The CEE behavior is normalised to 1 to form a correctional factor for both ramp up, CEE_{up}, and ramp down, CEE_{down} as a function of a magnitude, *M*. The magnitudes of the CEE ramps are determined through analysis of 1-min data from the BSRN against the corresponding mean hourly weather observational data from the same location. The frequency and magnitude of ramp events attributed to CEE correlate with the okta number, CEE events were defined as >25% of the clear-sky irradiance. CDF profiles of the magnitude for each okta were made allowing for random extraction following the appropriate distribution. The normalised

CEE correction factors are further corrected as a function of M, which is itself a function of okta, as detailed in equations 14-16

$$M = f(okta, CDF) \quad \text{(eq. 14)}$$

$$CEE_{up} = CEE_{up} \times (1 + M) \quad \text{(eq. 15)}$$

$$CEE_{down} = CEE_{down} \times (1 - M) \quad \text{(eq.16)}$$

The application of the CEE is performed using the Boolean matrix of cloud presence, B. Iterating through k_c and using a logical if statement that queries whether B undergoes a ramp on account of cloud cover, the appropriate M adjusted CEE correction factor, CEE_{up} or CEE_{down}, are applied to the time before and after the ramp as shown in equations 17 and 18

$$B_{i=1} = 0 \;\&\; B_i = 1 \rightarrow k_c(i-60 : i+60) = CEE_{down} \quad \text{(eq. 17)}$$

$$B_{i=1} = 1 \;\&\; B_i = 0 \rightarrow k_c(i-60 : i+60) = CEE_{up} \quad \text{(eq. 18)}$$

3. Application and Discussion

To illustrate how the output could be used, the model is applied to a hypothetical configuration for the location of Cambourne, UK. Cambourne is selected as there is a BADC 1-min resolution irradiance data set (BADC, 2013) which will allow a temporal validation; figure 2 depicts the configuration.

Table 1 shows the physical parameter inputs required for each of the locations within the simulation. The x and y coordinates are noted in reference to the centre of the spatial domain, C,1 defined as (750,750). The azimuth angles are defined as -180° to 180° East to West, with South being an angle of 0°.

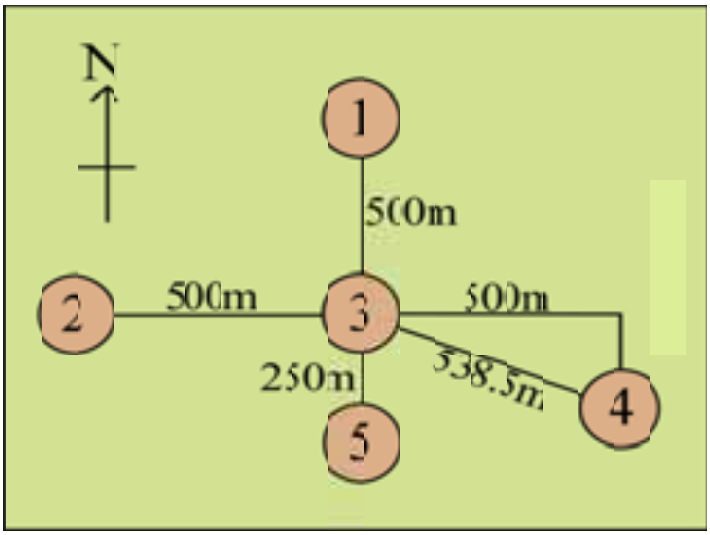

Fig. 2: A theoretical setup used to demonstrate the functionality of the model. The numbers indicate 5 different locations set in Cambourne, UK, of which spatio-temporally correlating irradiance time-series will be generated.

Tab. 1: Input physical parameters for the 5 locations as shown in figure 2. Note that the letter C denotes the centre of the spatial domain which represents *(750,750)*.

	1	2	3	4	5
x (m)	C	C - 500	C	C + 500	C
y (m)	C + 500	C	C	C - 200	C – 250
Azimuth *(°)*	0	0	0	0	0
Pitch *(°)*	0	0	0	0	0
Elevation *(m)*	87	87	87	87	87

The model is functional for all azimuth and tilts with reference to the input longitude and latitude, in this instance however the locations are assumed flat so that irradiance is reported in terms of global horizontal irradiance, the purpose of this is for comparison with the global horizontal observation irradiance data. The weather station in Cambourne, UK is at a longitude of -5.32656^{o} and latitude of 50.2178^{o}, with an elevation of 87 m above sea level.

The temporal resolution of 1 minute has a spatial granularity defined as the smallest distance between locations where a difference in irradiance can be observed. This is determined using the temporal resolution of *60 s* and the minimum and upper cloud speeds of *1* ms^{-1} and *~20* ms^{-1} to give a granularity of *60* to *~1200* $m.min^{-1}$. The average cloud speed is *10* ms^{-1} which gives typical granularity around *600* $m.min^{-1}$. The scenario depicted in figure 2 shows that the locations are separated by at least *250-1020* m and will therefore show appropriate differences. In order to observe spatially varying irradiance time-series for locations closer together, a decreased granularity would be required. This is achieved by increasing the temporal resolution e.g. from *60* s down towards *1* s.

Figure 3 displays a typical output from the model using inputs from table 1. The profile is typical of a clear day in mid-January for the location of Cambourne, UK. Typical patterns can be observed associated with the spatial correlation. Most notably around 700 minutes, there is a gradual ramp down in output at location 1 a few minutes before the other 4 locations undergo a similar ramp down, this is attributed to the wind speed and direction at the time, the clouds were travelling approximately north to south. At ~860 minutes, location 2 is the only location to undergo a large ramp down event.

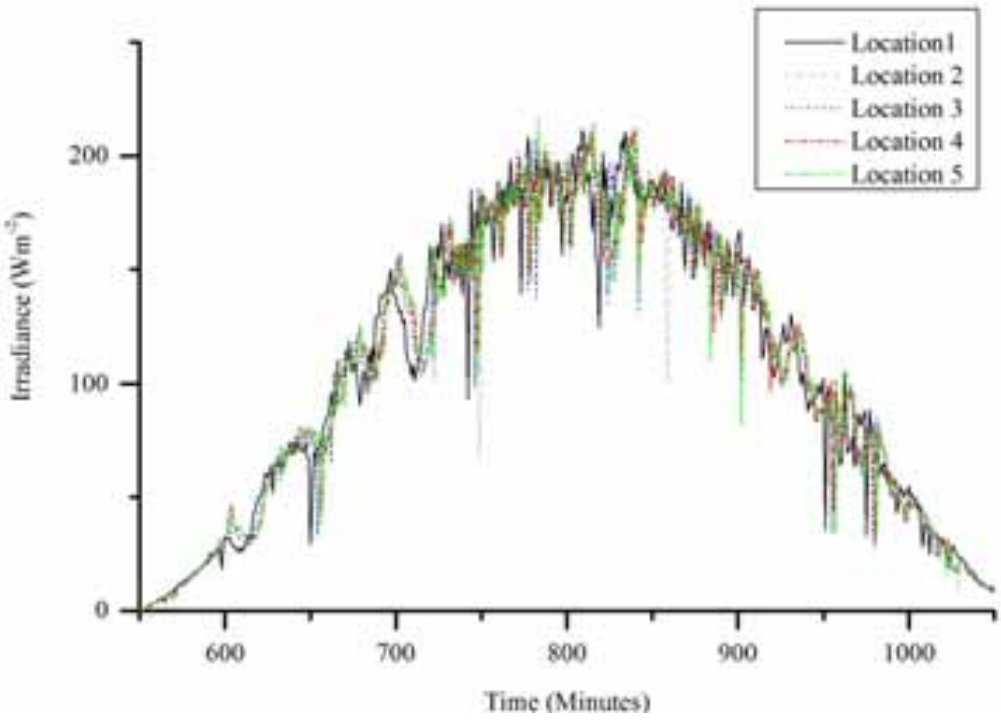

Fig. 3: Synthetic irradiance profiles across 5 locations on the 10th Jan using the described methodology for Cambourne, UK.

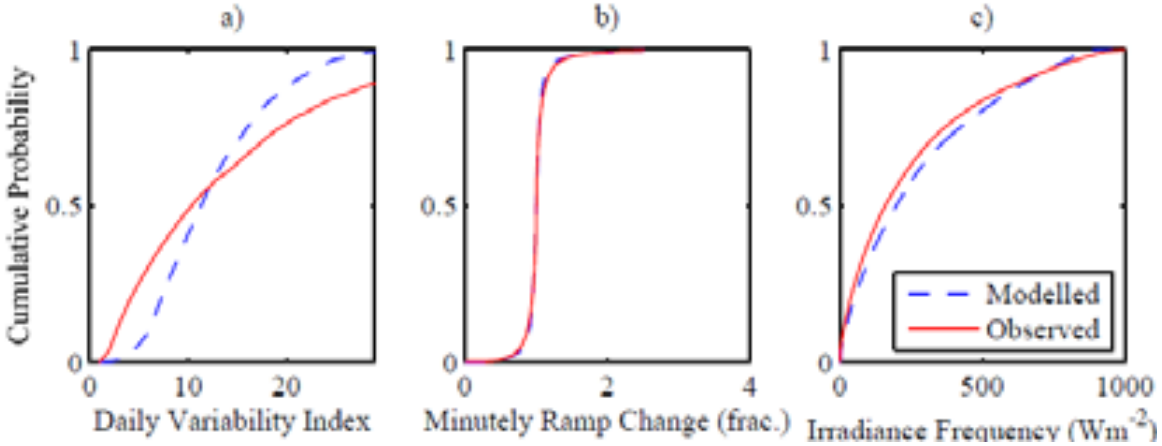

Fig. 4: Cumulative probability distribution plots of the (a) daily variability index, (b) the minutely irradiance ramp-up and ramp-down occurrences, and the (c) minutely global horizontal irradiance frequencies for both the modelled data and the measured data from Cambourne, UK.

4. Validation

Validation to date has focussed on a temporal basis only. All data processing was performed using the commercial software package Matlab r2012a (Matlab, 2012). Hourly weather observational data are taken from the BADC (BADC, 2013). As monitoring stations are occasionally taken off-line for repairs or upgrades for months at a time, 12 years of data are used to allow at least 10 years data for each variable that require a Markov chain to be created.

The simulation is run as detailed in the Application and Discussion section, and compared against the statistics obtained from the World Radiation Monitoring Centre – Baseline Surface Radiation Network (WRMC-BSRN, 2014) from BSRN station number 50, located in Cambourne, Cornwall, UK. Missing data points were ignored and deemed to not significantly impact the distributions for comparison.

Three metrics are used to validate the temporal nature of the model output, the variability index (Stein et al., 2012) cumulative probability function (CDF), the irradiance frequency CDF and the ramp rate CDF, denoted as VI, IF and RR respectively. The 2-sample Kolmogorov-Smirnov (K-S) test was carried out for each metric for each day of the year. When comparing the entire data sets against one another, the K-S validation technique is not appropriate due to the size. The subsets for comparison must be relatively small to gain any significant findings from the K-S test. For this reason the subset of each K-S test consisted of 7 of the same day's minutely data. For example, 7 modelled samples of the 1st January represent one subset, which is compared against a subset made from 7 samples of the same day from observational data.

The K-S test results are displayed in table 2 and comparative CDF profiles in figure 4. The RRs are captured well correlating with R^2=0.9998, and that 99.5% of days with the K-S test reject the null hypothesis that the modelled and observed minutely datasets are not from the same dataset with a confidence of 99%. The implications of this are that for each day of the year, only 0.5% of the days modelled did not produce statistically representative ramp rate data to a confidence of 99%. This means that for application of PV integration into the LV grid for example, the ramp rates seen in the synthetic irradiance time-series would be statistically accurate and allow for a good comprehensive study of how ramp rates impact upon the grid to a 1-min resolution. The daily VI CDF correlates with R^2=0.9777, and K-S at 95.9%. When comparing 1-min VI values for the whole datasets against one another in a frequency plot, the R^2 value is 0.9980 implying that throughout the year, the VI is captured, figure 4a however demonstrates that there is a more localised dependency with room for improvement. The daily VI value is the mean VI value recorded for that day. It can be seen that there is a slight overestimation of days with a VI between 7-15 and an underestimation of stable days between VI=0 to 7 and unstable days with VI >15, the implication of this is that the lower and higher daily variability extremes, where the variability is sustained over a lower time resolution, are slightly

Tab. 2: The percentage of days that reject the null hypothesis when performing the 2-sample Kolmogorov-Smirnov test on 7 of the same day of modelled and observational CDF profiles of 3 metrics.

K-S test significance Level	**90%**	**92.5%**	**95%**	**97.5%**	**99%**
Variability index	97.5%	97.5%	97.3%	96.4%	95.9%
Ramp rate occurrence	99.7%	99.7%	99.7%	99.7%	99.5%
Irradiance frequency	99.7%	99.7%	99.7%	99.7%	98.9%

less frequent than in reality. The VI is still captured at a satisfactory rate with K-S of 95.9% with only 4.1% of days accepting the null hypothesis that the observational and synthetic datasets are not the same, importantly of these 4.1% of days, there was no bias as to what time of the year these days occur, suggesting that there was no seasonal bias within the model. Potential reasoning is that within the observational data, a particular day for each of the 7 different years coincidentally had an overcast day each time, which when compared with a clear day generated by the model, would be dramatically unfavourably compared. The IF CDF correlates well with R^2=0.9980, and K-S at 98.9%. Figure 4c indicates a marginal overestimation in the lower range of irradiance magnitudes and a marginal underestimation in the extreme values of 900-1000 Wm^{-2}. The more extreme values within the models are functions of the clear-sky fluctuations and the cloud edge enhancements. It is possible that because the cloud edge enhancement correction described in section 2.4 only bands across 1-min before and after the CEE event, when in fact this 1-min is an average of all the events recorded within the study, it is entirely possible that a CEE event would span across 2 or more minutes depending on the speed of passing cloud, and so there is scope to make the correction a function of the cloud speed. Otherwise the validation is very strong and the magnitudes are captured well with only 1.1% of days accepting the null hypothesis with the K-S test.

5. Conclusion

This work has developed meaningful high temporal resolution irradiance time-series with a spatial correlation that temporally validates well. The irradiance time-series correlate spatially as a function of location, cloud speed and direction. The variability index, ramp rate occurrence and irradiance frequency metrics perform well using the 2-sample K-S test with a confidence level of 99%. The daily variability indices do tend towards midrange values, however the 1-minute variability index correlates excellently. The ramps present within the simulation have an excellent correlation to observation data with 99.5% of all days passing a 99% significance level K-S test.

Future work opportunities include further development of the temporal resolution as the nature of the methodology would allow it to be increased. This methodology would allow for theoretical high resolution simulations and studies of the impacts of solar variability and intermittency derived from readily available inputs of mean hourly weather observational data. The temporal methodology and Matlab script files are made freely available through download so that it can be adopted for any other application, and adapted to further the study (Bright et al., 2015).

6. Acknowledgments

This work was financially supported by the Engineering and Physical Sciences Research Council through the University of Leeds Centre for Doctoral Training in Low Carbon Technologies (Grant No.: EP/G036608/1).

7. References

BADC, 2013. British Atmospheric Data Centre – National Centre for Atmospheric Science – Natural Environmental Research Council. <http://badc.nerc.ac.uk> .

Bright, J. M., Smith, C. J., Taylor, P. G. and Crook, R., 2015. Stochastic generation of synthetic minutely irradiance time-series derived from mean hourly weather observation data. Sol. Energy **115**, 229–242.

Calinoiu, D-G., Stefu, N. Paulescu, M., Trif-Tordai, G., Mares, O., Paulescu, E., Boata, R., Pop N., and Pacurar A., 2014. Evaluation of errors made in solar irradiance estimation due to averaging the Angstrom turbidity coefficient. Atmos. Res. **150**, 69–78.

Ehnberg, J. and Bollen M., 2005. Simulation of global solar radiation based on cloud observations. Sol. Energy **78**, 157–162.

Gueymard, C. A., 2012. Clear-sky irradiance predictions for solar resource mapping and large-scale applications: Improved validation methodology and detailed performance analysis of 18 broadband radiative models. Sol. Energy **86**, 2145–2169.

Hummon, M., Ibanex, E., Brinkman G. and Lew D. 2012. Sub-hour solar data for power system modelling from static spatial variability analysis, Conference Proceedings in 2nd Annual Solar Integration Workshop, Lisbon. NREL/CP-6A20-56204.

Lave, M., Kleissl J., and Arias-Castro, E., 2012. High-frequency irradiance fluctuations and geographic smoothing. Sol. Energy **86**, 2190-2199.

Matlab 2012. Version 7.14.0.739 R2012a. The MathWorks Inc., Natick, Massachusetts.

Morf, H. 1998. The stochastic two-state solar irradiance model STSIM. Sol. Energy **62**, 101–112.

Morf, H. 2011. The stochastic two-state cloud cover model STSCCM. Sol. Energy **85**, 985–999.

Morf, H. 2013. A stochastic solar irradiance model adjusted on the Angstrom-Prescott regression. Sol. Energy **87**, 1–21.

Sayeef, S., Heslop, S., Carnforth, D., Moor, T., Percy, S., Ward, J. K., Berry, A., and Rowe, D. 2012. *Solar Intermittency: Australia's Clean Energy Challenge.* Tech. Rep., CSIRO.

Stein, J. S., Hansen C. W., and Reno, M. J., 2012. *The Variability Index: a new and novel metric for quantifying irradiance and PV output variability.* World Renewable Energy Forum, Denver, CO,.

Vindel, J. and Polo, J. 2014. Intermittency and variability of daily solar irradiation. Atmos. Res. **143**, 313–-327.

Widén, J., Carpman, N., Castellucci, V., Lingfors, D., Olauson, J., Remouit, F., Bergvist, M., Grabbe, M. and Waters, R. 2011. Variability assessment and forecasting of renewables: a review for solar, wind , wave and tidal resources. Renew. Sustain. Energy Rev. **44**, 356–375.

Wood, R. and Field. P. R.. 2011. The distribution of cloud horizontal sizes. J. Clim. 24. **24**, 4800–4816.

WRMC-BSRN, 2014, World Radiation Monitoring Center – Baseline Surface Radiation Network. PANGEA – Data Publisher for Earth and Environmental Science. <http://bsrn.awi.de/>.

Conference Proceedings

Solar World Congress 2015
Daegu, Korea, 08 – 12 November 2015

Intermittence forecasting of the solar resource in Corsica

Pierrick Haurant, Auline Rodler, Ghjuvan-Antone Faggianelli , Marc Muselli, Philippe Poggi

University of Corsica, UMR SPE CNRS 6134, F-20000 Ajaccio, France

Abstract

Island electrical small-scale grids are sensitive to variations in power production. In case of important integration of solar power in the energy mix, the solar resource intermittency becomes a high risk to the grid's stability. That is why a good knowledge of the variations is the first step to the massive optimized PV integration in the energy mix. This paper focuses on the forecasting of the solar resource variability. First, the solar resource variability characterization will be presented. It is based on a typological classification method that relies on variability scales which enable to distinguish the different dynamics. Afterwards, the predictability of variations is studied through forecasting models as a simple persistence, the k-Nearest Neighbors and Artificial Neural Networks (ANN). In this regard, time series of intervals classified according to their dynamics of variations have been generated and the forecasting performance, for different horizons and with different models were compared.

Keywords: Solar resource, variations, classification, forecasting, k-Nearest Neighbors, Artificial Neural Networks

1. Introduction

Island electrical grids are typical: they are small-scale and sensitive to variations in power production. In case of important integration of solar power in the energy production mix, the solar resource intermittency becomes a high risk to the grid's stability. This is the reason why, in France, it is considered that no more than 30% of the production power must be supplied by power plants using intermittent renewable energy sources. In Corsica Island, this threshold has already been reached in 2012, as a large amount of PV plants have been connected to the grid. This threshold is a constraint to the development of renewable energies on the island. Therefore, the aim would be to overpass this threshold without destabilizing the electrical grid.

A good understanding of the solar resource in Corsica, its variability, its territorial mitigation and forecasting are important challenges for the electrical grid's manager to overpass this threshold. The optimization of the territorial mitigation may present an opportunity to the development of renewable energies and their integration to a small electrical grid which is not connected to the mainland power grid. We can anticipate that the smoothing of the electrical photovoltaic power production by the compensation of the territorial mitigation will be insufficient to stabilize the grid. Finally, it seems essential to compensate the solar variability using other means of production or storage solutions.

The level of solar variation has to be forecasted so that the electrical grid manager can anticipate and can choose a control strategy concerning all the means of power production. In this context, the solar resource intermittence characterization in Corsica, the use of the territorial mitigation and the forecasting of variations are challenges to the grid's manager. For this, a new method of typological classification of variations has been developed and will be introduced.

2. Typological classification of the radiation

Indicators such as the clearness index k_t, the air-mass-corrected clearness index k'_t or the clear-sky index k_{Cls} give information on the sky's clearness or cloudiness. A segmentation of these indexes domains into two

doi:10.18086/swc.2015.07.03 Available at http://proceedings.ises.org

or three intervals are the result of a first classification. In the literature, we can find numerous segmentations of daily k_t values that have succeeded to different classifications (De Miguel et al., 2001; Li and Lam, 2001; Mefti et al., 2008; Notton et al., 2004; Rigollier et al., 2004). This first classification method has the advantage to be easy but has the disadvantage to be static: fluctuations of irradiations and the cloudy dynamic are smoothen by a daily mean and cannot be considered. Consequently, a changeable weather day can have the same daily clearness index as an invariably cloudy one. Other typological methods can consider the clouds dynamics by completing the discrimination indexes of the different types of radiation. Muselli et al. (2000) have used a set of discriminating parameters derived from k_t hourly and daily values in order to characterize three types of days (clear sky, overcast sky, cloudy sky), using classification method of Ward. Daily dynamic of the sunshine has been considered by a parameter entitled "Integral of the squared second derivative of hourly clearness index profile". Other typological methods consider cloudy dynamic : the mean clearness index segmentation is completed by the segmentation of mathematical quantities that quantify the signals roughness such as the fractal dimensions (Maafi and Harrouni, 2003) or using Dirichtlet decompositions (Soubdhan et al., 2009) or even the wavelet decompositions (Woyte et al., 2007).

All these new methods present the limit of discriminating by days, while in a single day we can have different weather dynamics. That is why these classifications unable an energy manager to anticipate the variability of the production: the knowledge of the category of a day to come does not allow knowing precisely the irradiation profile. It seems valuable to consider days as successions of irradiation profiles that can be subject to a classification.

3. Methodology: Variation scales

Irradiance dynamic regimes distinguish themselves by the variations form observed that can be characterized by two criteria: their duration and amplitude. The aim of this work is to set up a classification method of these regimes depending on these characteristics.

The variation scales dt are defined as the time interval for which relative variations of solar irradiance $G(t)$ are calculated. In this study, we are interested in the relative absolute variation $dG(t)$ between two successive moments separated by a time dt, neglecting existing variations in the interval $[t - dt\,;t]$ and following this relation:

$$dG(t) = \left|\frac{G(t)-G(t-dt)}{G(t-dt)}\right| \qquad \text{(eq. 1)}$$

3.1. Variations categories

Variation scales allow discriminating different variation dynamics. Indeed, variations which are too slow to be perceptible for a value of dt can be revealed for a superior value.

A typology can be built on scale variation following this procedure: considering a given variations scale, the issue will be to calculate and compare variations at a variability threshold noted S_{var}. Variations higher than this threshold will integrate the equivalent class that could be described as the class of the «perceptible variations at this scale ». Then, for example, two different variations scales dt_1 and dt_2 lead to three classifications, from the close to zero variations set to high variations one. It is convenient to choose the scales separated by larger orders of magnitudes, in order to discriminate completely different variation profiles.

3.2. Intervals delimitation

In a majority of cases, even in a very dynamic cloudy regime, variations are only punctually above the fixed threshold. Then, the classification conditions generate a large number of intervals of different classes following themselves. Two thresholds have been introduced in this optic. The first threshold called intra-interval threshold and noted S_{intra}, represents a maximal duration between two variations so that they can be grouped in the same interval. The other threshold is called inter-interval threshold and noted S_{inter}. It is comparable to a minimal duration of intervals.

The use of these two thresholds gives birth to a sequential procedure of interval determination following

three non-commutative steps:

1. The instability instants set t_{inst} are defined as a set of instants for which variations exceed the variability threshold S_{var};
2. All the instants between two variations separated by the inferior laps time of the intra-interval threshold S_{intra} are considered fluctuant : it is the grouping inter-interval step or homogenization step;
3. The intervals considered too short integrate adjacent intervals: it is the inter-interval grouping. If adjacent intervals to the studied one are of different classes, the inter-intervals grouping is done under a condition: if the interval is of maximal class, it will be concatenated to the adjacent one of nearest inferior class, else it will integrate automatically to the nearest interval of the superior class. These conditions are coherent with the electric network managers' point of view: it is convenient to outrank marginal events in order to consider in the worst case to limit the risks and to upgrade marginal events. However, in the first case where the over-classification is impossible, we consider that the oddness or the short variation duration takes over their intensity, the interval is downgraded.
4. The classification method and the variability interval definition and sunshine regimes need the determination of four specific parameters:
   - A variability threshold S_{var} above which we consider that there is instability; it has been fixed to 10 % in our study.
   - Scale variation values dt for the discrimination of the different sunshine regimes; it seems better to use different order of magnitudes in order to distinguish different dynamics. The magnitudes of a few seconds can find out strong and narrowed variations while those of a few minutes find strong variations and also slower and stronger ones. Thus, considering these observations, it seems appropriate to have two scales: $dt_1 = 1$ s and $dt_2 = 300$ s leading to a partition in three classes:
     - Class 0 (noted C_0): the variations of this class are perceptible neither for $dt = 1$ s, nor for $dt = 300$ s. There are no or very few variations ;
     - Class 1 (C_1): variations are perceptible only for $dt = 300$ s. These variations are slow and not very intense ;
     - Class 2 (C_2): variations are perceptible for $dt = 1$ s and $dt = 300$ s. They are narrowed and deep.
   - Intra- and inter- grouping interval thresholds (S_{intra} and S_{inter}), which we can evaluate the limits of the intervals. No objective criterion has been found for the thresholds determination. It is the reason why these thresholds are determined depending on the application we want to do with the intervals and the temporal resolution necessary to this application. The smaller the thresholds' values are, the smaller and more numerous will be the resulting intervals.

Figure 1 is an example of days separated into intervals ranked for $S_{var} = 0.1$; $dt_1 = 1$ s and $dt_2 = 300$ s and $S_{inter} = S_{intra} = 900$ s.

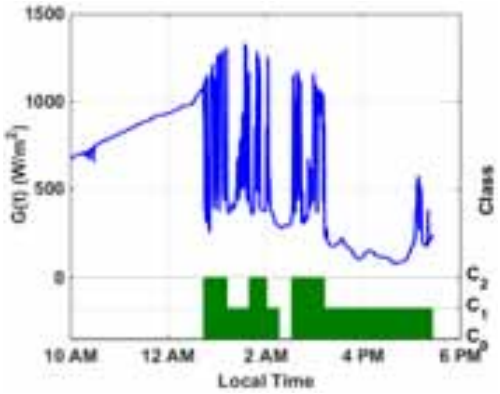

Figure 1 : An example of a daily irradiance curve and the variability classes associated

4. Forecasting of solar irradiance variation

In literature we can find a large amount of forecasting models to predict solar irradiance at different horizons (Kemmoku et al., 1999 ; Sözen et al., 2005 ; Mellit et al., 2005 ; Cao and Cao, 2006 ; Hocaoglu et al., 2008 ; Zervas et al., 2008 ; Chaabene et Ben Ammar, 2008 ; Paoli et al., 2010 ; Voyant et al., 2011 ; Marquez and Coimbra, 2011). These forecast concerns punctual irradiance values or the solar irradiance between two moments. For these two configurations no information is available on the short solar variations. Ideally, the aim would be to forecast for different small horizons in the range of the minute, on different lags at the same time. The shortest developed horizons until know are of 5 minutes on a single lag (Voyant, 2011). On the one hand, such a horizon does not seem sufficiently close to evaluate fast variations. On the other hand, a single lag does not allow to know a variation tendency (except if we refer us to past measures). Finally, this prediction does not leave the time to the grid manager to act on the system when a fluctuating regime is recognized. The ranks forecast seem interesting as it means that the variations of a future interval would be forecasted. The forecast methods which we have chosen are statistical based on:

- The k-Nearest Neighbor (k-NN): it is a technique following the philosophy that a succession of events of the same nature will lead always to a same consequence. Here k is the number of sequences. The principle of the k-NN consists to look for in a set of data identical events to the last observed. Then it is supposed that the future event will be the most often observed one after equivalent sequences observed in the historic.
- The Artificial Neural Network (ANN) is a learning algorithm inspired by biological neural networks. It represents a collection of neurons which are mathematical and computer representations of biological neurons. The mathematical representation is like an algebraic function which evaluates a weighted sum of the inputs matched to a bias, which is independent with the inputs.

Either the model has predicted the correct class or it has forecasted the wrong one, so that the performance of these models will be based on the percentage of times the class forecasted was the correct one. The models results will be compared to a primitive model, named the persistence. This model tends to reproduce the present event to the studied horizons.

4.1 Set of data

The classified irradiance data used in this study to test the different forecasting models were measured in 11 sites dispatched in Corsica Island (Fig. 2) during 2 years. The measurements are sampled at 1 s and synchronized. As a first step, the data collected in all sites have been concatenated in a same set in order to make a large sample as it is necessary for forecasting.

Figure 2 : Lucciana (42° 39' 49" ; 9° 25'28" ; 60) - 2 Oletta (42° 39' 36" ; 9° 19' 45" ; 52) - 3 Calvi (42° 33' 38" ; 8° 44' 48"; 31) - 4 Corte (42° 18' 04" ; 9° 09' 57" ; 381) - 5 Piana (41° 16' 03" ; 8° 41' 37" 12) - 6 Cargèse (42° 08' 40" ; 8° 35' 58" ; 30) ; 7 Ghisonaccia (42° 03' 54" ; 9° 22' 14" ; 65) - 8 Ajaccio (41° 55' 49" ; 8° 45' 23" ; 2) - 9 Sainte Lucie (41° 41' 59" ; 9° 20' 12" ; 66) - 10 Propriano (41° 39' 43" ; 8° 55' 02" 17) - 11 Bonifacio (41° 22' 17" ; 9° 12' 10" ; 46)

The variations classes have been determined according to the method previously introduced, using a variation threshold of 10 % and variations scales of 60 s and 300 s. The predictions realized in this study are based on time series defined as a sequence of observations for regular time steps. These observations are done based on identical acquisition methods and data processing. In our case, the observed days need to be

divided into constant time intervals for which we attribute fluctuation rank. Each measure has to be ranked using the method defined above. Then each time interval composed by ranked measures will get the mostly present fluctuation rank. The time series time step will be chosen based on the forecast demand in terms of temporal resolution and horizons.

80 % of the set of ranked intervals were used for the learning phase and 20 % were used for the assessments models performance.

4.2 Forecast with a persistence model

The persistence model is a simple model which considers that the event x_t at time t is repeated at time $t + h$, where h represents the horizon of the forecast:

$$\hat{x}_{t+h} = x_t \qquad \text{(eq. 2)}$$

This model has been implemented for ranked intervals of 15 min, 30 min and one hour. The model has been used to forecast horizons from 15min to maximum 6 hours. Figure 3 presents performance of the persistence model applied to these three types of intervals for the entire horizons predicted. First of all, we observe that whatever the size of the used ranked intervals, the predictions performance decrease when more lags are used. Above a number of lag the performance will not change much. For an interval of 15 min, we have a performance which changes from 83.3 % for lag 1, to 50.1 % for lag 6 to 33.3 % for lag 16. The performance does not change much and reach 32.9 % at lag 24. In the same way, the performance of the predictions for 30 min intervals changes from 72 % at lag 1 to 39.1 % for lag 6, decreasing then slightly. Finally, the correct forecast for a one hour interval will change between 66.9 % at lag 1 to 42.9 % at lag 6.

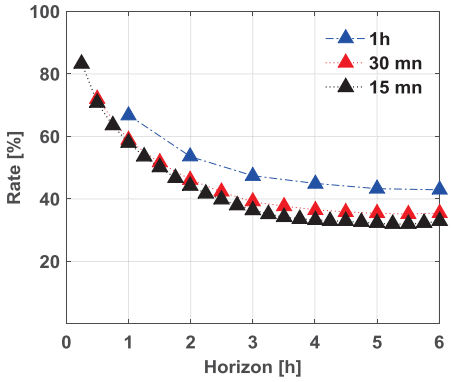

Figure 3 : Correct prediction rates obtained with a persistence as a function of horizons, using ranked intervals of 15 mn, 30 mn and 1 h.

For a same horizon we notice that longer (in terms of time) ranked intervals allow always better predictions for all the cases: for a horizon of 30 min the predictions with 30 min intervals (at lag 1) are better than with 15 min intervals (at lag 2). We have performance of 72 % for 30 min intervals and of 70.7 % for 15 min intervals. In the same way, one hour interval allow better predictions than with 30 and 15 min intervals, giving respectively 66.9 %, 58.8 % and 58 % of performance.

4.2. K-NN Forecast method

The k-NN method developed here is based on a historic of the successions of variation classes. The method consists in finding similar sequences of the k last past events in this historic. Then, the prediction at horizon h corresponds to the most frequently observed class that follows the sequences at lag h.

The optimization of the k-NN passes by the determination of the sequences size $k \in [1\,;8]$ and of the time series time step used as input. As the tests realized with the persistence model the intervals of 15 min, 30 min and one hour have been tested. The first results have shown that it is convenient to choose a k-NN model with k = 4:

- For a time step of 15 minutes (Fig. 4), the existence of forecast impossible for $k \in [5\,;8]$ puts into question their usability. Some sequences preceding the class to be predicted have not been found in the

historic so no class forecast has been possible. Taking k = 4 allowed all the predictions and give better results for h ∈ [1 ; 4]. It gave close results to the best results of the other horizons.

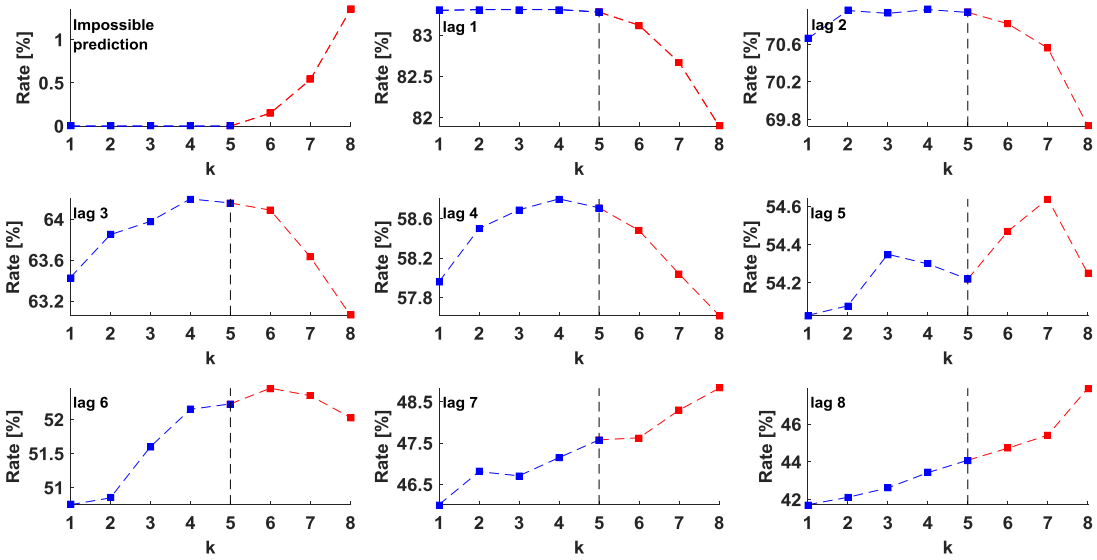

Figure 4 : Correct prediction rate as a function of the sequence size of the k-NN for different horizons, using 15 mn intervals

- For 30 minutes intervals (Fig. 5), the existence of impossible forecast for k ∈ [4 ; 8] show that these models are not reliable. The most performant model whatever the lag is 4-NN.

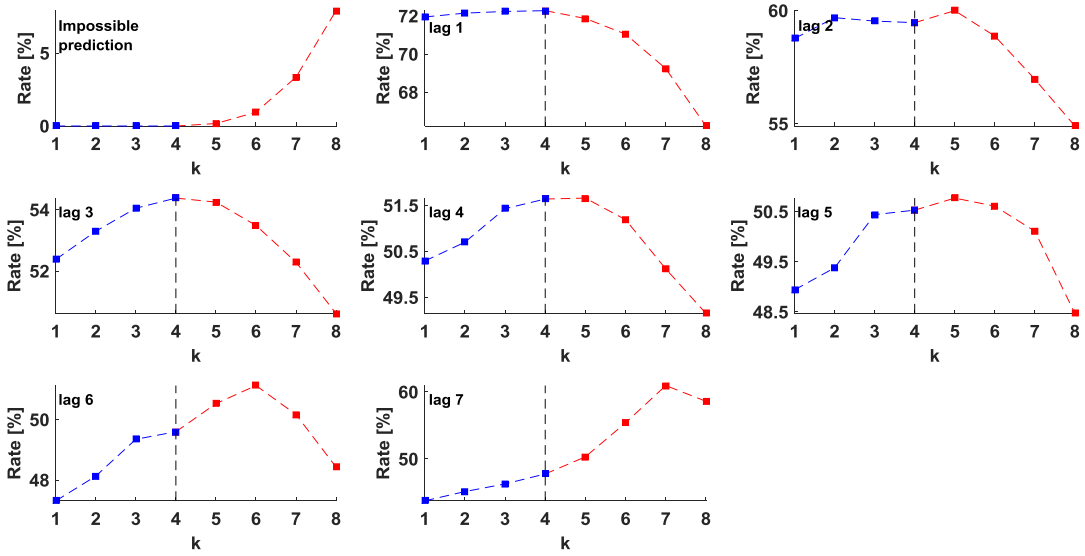

Figure 5 : Correct prediction rate as a function of the sequence size of the k-NN for different horizons, using 30 mn intervals

- Concerning the one hour interval (Fig. 6), impossible forecasts for k ∈ [5 ; 8] exist, so that we do not consider them. Then, the best forecasts are always reached with k = 3 or k = 4. We can notice that the performance of the 4-NN model are always higher than of the 3-NN for lags 1, 2 and 4 with small differences between 0.1-0.3 points. The 4-NN model has much better performance than model 3-NN for lags 3, 5 and 6 for differences between 0.5 and 7.2 points. In general, the 4-NN model presents the best results.

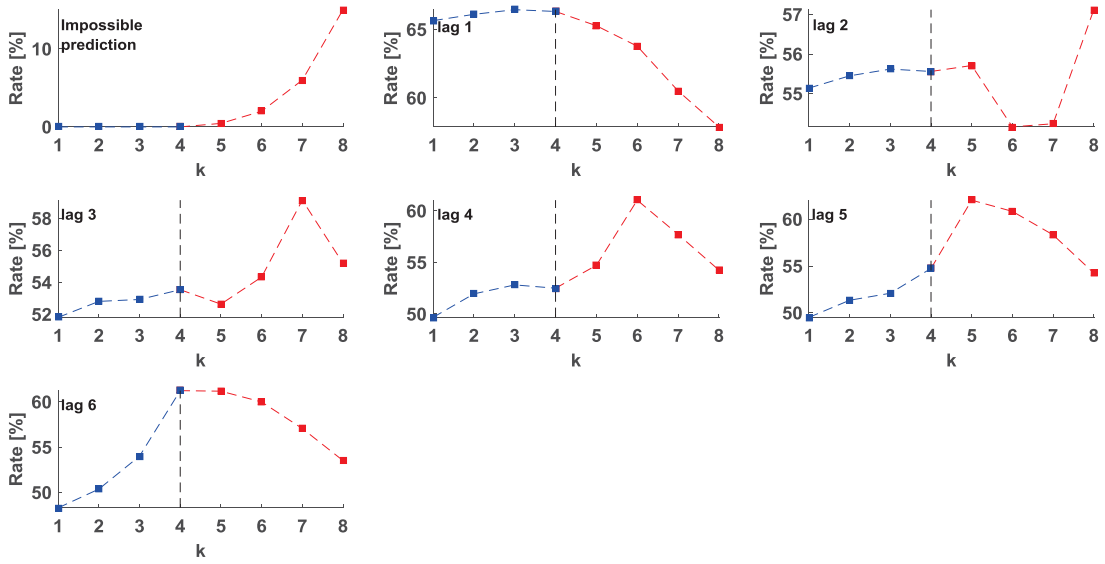

Figure 6: Correct prediction rate as a function of the sequence size of the k-NN for different horizons, using 1 h intervals

Finally, the performance of the 4-NN for the three ranked intervals studied are summed up on figure 7.

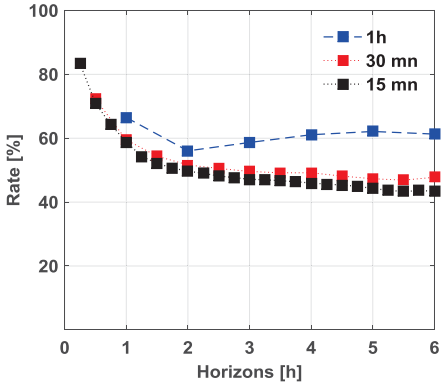

Figure 7 : Correct prediction rate obtained with a k-NN (k = 4) as a function of horizons, using ranked intervals of 15 mn, 30 mn and 1 h.

As the persistence, the longest ranked intervals give better results for distant horizons:

- The 15 minutes intervals allow 71.0 % of correct forecasts for 30 min horizons (at lag 2) while we have 72.3 % of good predictions, for the same horizon, with 30min intervals (à lag 1).
- The 15 minutes intervals give 58.8 % of correct predictions at one hour horizon (at lag 4), against 59.5 % with 30 minutes intervals (at lag 2) and 66.3 % with one hour intervals (at lag 1).

5. Artificial Neural Networks Forecast method

ANN have been applied to the time series representing the classes of variations. These classes are forecasted for different sizes of intervals and different horizons. In all the cases, only 6 lags have been forecasted in order to limit the complexity of the studied models.

The optimization of the ANN parameters is a major stake. Therefore, we have focused on the study of the number and the type of inputs as well as the number of hidden neurons N_c, conserving the rest of the ANN's structure (architecture, activation function, number of hidden layer, etc.). The optimization has been done by fixing one of these two parameters (i.e. the number and natures of the inputs or the number of hidden neurons) and varying the other one, following the method developed by Voyant et al. (2011). To start with, the inputs are defined and then the numbers of neurons of the unique layer hidden N_c are defined. The inputs have been optimized following two axes fixing $N_c = 1$:

1. The nature of the inputs, associating to the endogenous inputs exogenous inputs. The exogenous inputs used in this study are spatiotemporal indices: the measured instants of the events are detailed and are geographically located, since the historic is composed of measures done on 11 different sites on a period above one year and presenting discontinuities. Some successions of events can be linked to the site of measure and a temporality of the phenomenon can exist: some events successions are seasonal or daily. Three types of indexes have been studied independently each one from another :
   - A time index I_{tps} resuming the hour, the day, the month and the year of the event ;
   - A spatial index I_{geo} represented by the altitude of the measures site. This index is more representative than the geographic coordinates as the sites are very close to each other so that the coordinates would not be representative ;
   - A spatiotemporal index I_{Gcls} : the global radiation for clear sky daily conditions : Gcls, simulated by the ESRA model (Rigollier et al., 2000). The radiation depends on the position and the instant.
2. The number of inputs: we try to limit the number of inputs in order to reduce the complexity of the model. An iterative procedure has been set up to eliminate the unnecessary inputs. If we consider eight endogenous inputs and as many exogenous inputs a neural network is generated. The performance of the neural network is calculated and the weights between the inputs and the hidden units are examined. The input associated to the weakest weight is eliminated as it is considered unnecessary. This procedure is repeated until we have only one input. The model kept will be the one which maximizes the number of correct predictions.

We obtain from these optimizations different input choices according to the sizes of intervals. The model choice is difficult since their ranks are different from a lag to another: a model can be the best for prediction at a lag whereas it is the worst for predictions at another lag. A mean of the forecast on the six lags has been chosen to discriminate the different models. Only I_{tps} and I_{Gcls} indexes improve the ANN performance for 15 min classed intervals and lags higher than 1 (Fig. 8). The models using I_{tps} give the best results for lag 3 and 4 whereas I_{Gcls} increase the success rate for lag 2, lag 5 and lag 6, giving close results to the best ones for the other lags. These models need respectively 14 and 9 inputs. In this way, according to the Okham razor principle, it seems more interesting to keep the model with I_{Gcls} index for most cases. Only forecasts at lag 1 need endogenous data.

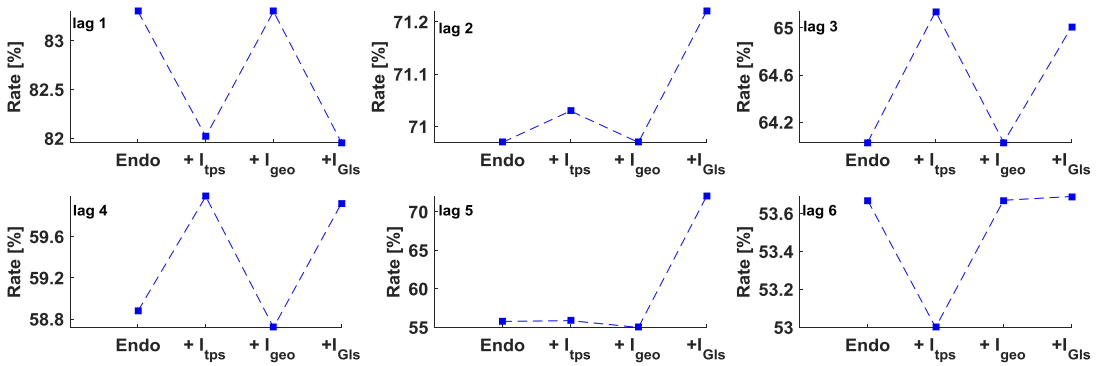

Figure 8: Correct prediction rate as a function of the type of ANN inputs for different horizons, using 15 mn intervals

For 30 minutes intervals, the indices tend to damage the models performance (Fig. 9). In this way the model using two endogenous inputs present the best performance for all the lags except for lag 3. This model will be put forward especially as it needs few inputs.

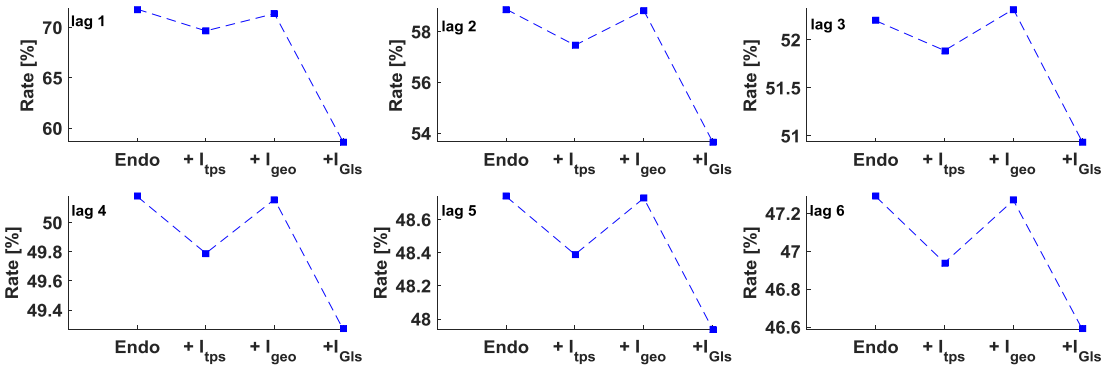

Figure 9: Correct prediction rate as a function of the type of ANN inputs for different horizons, using 30 mn intervals

Finally, concerning one hour intervals, the model using three endogenous inputs is the most promising. It allows better statistics for all the lags forecasted and needs few inputs.

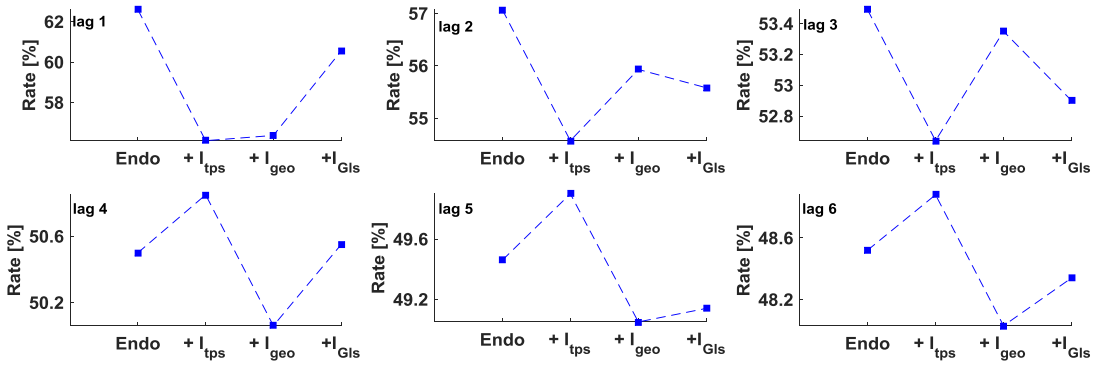

Figure 10: Correct prediction rate as a function of the type of ANN inputs for different horizons, using 1 h intervals

Concerning the number of hidden units in the unique layer, we must note that the number of parameters to evaluate for a ANN strongly increases with the number of hidden units: for a hidden layer with N_c neurons, N_e inputs and N_s outputs, the ANN will count $N_w = N_c(N_e + N_s)$ weights and N_c bias, a total $N_{tot} = N_c(N_e + N_s + 1)$ of parameters. It is important to limit at most N_c.

$N_c \in [1\,;8]$ have been tested for 15 min ranked intervals. We had slightly best performance for the three first lag with $N_c = 6$, $N_c = 7$ and $N_c = 5$ and the three following lags are a bit better forecasted with $N_c = 3$ and $N_c = 2$. But the small enhancements of the performance have to be relativized as the models are more complex so that $N_c = 1$ can be privileged since it is less complex and its performance are near the best more complex models.

For intervals of 30 minutes, 3 or 4 hidden neurons are needed to maximize the performance of the ANN at lag 1, lag 2 and lag 3 and that $N_c = 1$ shows the best results for predictions at lag 4, lag 5 and lag 6. $N_c = 1$ can be privileged: this model, which is the less complex, shows the best compromise between performance and complexity.

In the same way and for the same reasons, the ANN with $N_c = 1$ is preferred among $N_c \in [1\,;5]$ for one hour intervals.

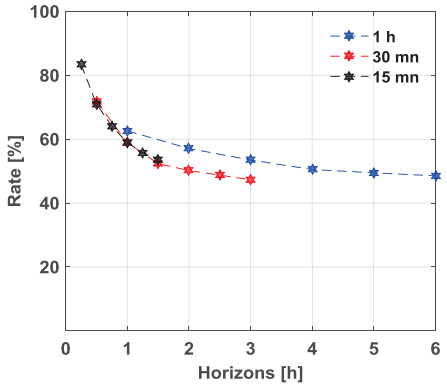

Figure 11 : Correct prediction rates obtained with an ANN as a function of horizons, using ranked intervals of 15 mn, 30 mn and 1 h.

6. Conclusions

The correct prediction rates for the studied horizons obtained with the optimized models are summed up in figure 12.

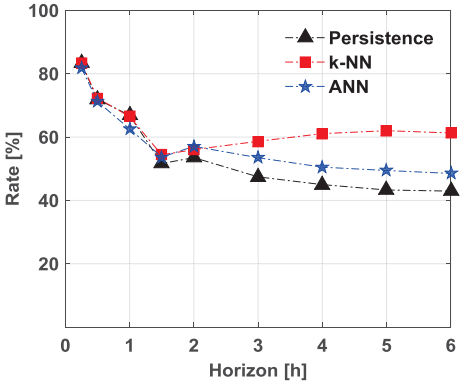

Figure 12: Correct prediction rate of the best model of each category as a function of horizons

We can see that whatever the model (persistence, k-NN or ANN), it is necessary to implement classified intervals of different durations as input to forecast variability classes at more or less far horizons:

1. for horizons above 1 hour, we can use classified intervals of 15 or 30 minutes. These inputs give close results whatever the model. However, it is interesting to input 15 minutes intervals for a best time resolution;

2. for horizons over 1 hour, it is necessary to input 1 hour intervals.

Besides, we can observe that for predictions at close horizon (between 15 minutes and 1 hour), the three studied models give quite similar results. For these horizons the persistence must be preferred to respect the Okham razor principle. For horizons between 1 hour and 2 hours, ANN gives best results and must be favored. Finally for horizons over 2 hours, the k-NN offers best performance and must be used. Thus an hybridation of these models should achieve better performance for prediction at all horizons.

In future works, Markow chains could be considered since it is possible to evaluate probability of transition from a class to another.

7. References

Cao, J., and Cao, S., 2006. Study of forecasting solar irradiance using neural networks with preprocessing sample data by wavelet analysis. Energy, 31(15), 3435–3445.

Chaabene, M., and Ben Ammar, M., 2008. Neuro-fuzzy dynamic model with Kalman filter to forecast irradiance and temperature for solar energy systems. Renewable Energy, 33(7), 1435–1443.

De Miguel, A., Bilbao, J., Aguiar, R., Kambezidis, H., and Negro, E., 2001. Di use solar irradiation model evaluation in the North Mediterranean Belt area. Solar Energy, 70(2), 143–153.

Hocaoglu, F. O., Gerek, m. N., and Kurban, M., 2008. Hourly solar radiation forecasting using optimal coefficient 2-D linear filters and feed-forward neural networks. Solar Energy, 82(8), 714–726.

Kemmoku, Y., Orita, S., Nakagawa, S., and Sakakibara, T., 1999. Daily insolation forecasting using a multi-stage neural network. Solar Energy, 66(3), 193–199.

Li, D., and Lam, J, 2001. An analysis of climatic parameters and sky condition classification. Building and Environment, 36(4), 435–445.

Maafi, A., and Harrouni, S., 2003. Preliminary results of the fractal classification of daily solar irradiances. Solar Energy, 75(1), 53–61.

Marquez, R., and Coimbra, C. F., 2011. Forecasting of global and direct solar irradiance using stochastic learning methods, ground experiments and the NWS database. Solar Energy, 85(5), 746–756.

Mefti, A., Adane, A., and Bouroubi, M., 2008. Satellite approach based on cloud cover classification: estimation of hourly global solar radiation from meteosat images. Energy Conversion and Management, 49(4), 652–659.

Mellit, A., Benghanem, M., Arab, A. H., and Guessoum, A., 2005. A simplified model for generating sequences of global solar radiation data for isolated sites : Using artificial neural network and a library of Markov transition matrices approach. Solar energy, 79(5), 469–482

Muselli, M., Poggi, P., Notton, G., and Louche, A., 2000. Classification of typical meteorological days from global irradiation records and comparison between two Mediterranean coastal sites in Corsica Island. Energy Conversion and Management, 41(10), 1043–1063.

Notton, G., Cristofari, C., Muselli, M., and Poggi, P., 2004. Calculation on an hourly basis of solar diffuse irradiations from global data for horizontal surfaces in Ajaccio. Energy Conversion and Management, 45(18-19), 2849–2866.

Paoli, C., Voyant, C., Muselli, M., et Nivet, M., 2010. Forecasting of preprocessed daily solar radiation time series using neural networks. Solar Energy, 84(12), 2146–2160.

Rigollier, C., Lefèvre, M., and Wald, L., 2004. The method Heliosat-2 for deriving shortwave solar radiation from satellite images. Solar Energy, 77(2), 159–169.

Soubdhan, T., Emilion, R., and Calif, R., 2009. Classification of daily solar radiation distributions using a mixture of Dirichlet distributions. Solar Energy, 83(7), 1056–1063.

Sözen, A., ArcaklIoglu, E., Özalp, M., and Caglar, N., 2005. Forecasting based on neural network approach of solar potential in Turkey. Renewable Energy, 30(7), 1075–1090.

Voyant, C., Muselli, M., Paoli, C., and Nivet, M, 2011. Optimization of an artificial neural network dedicated to the multivariate forecasting of daily global radiation. Energy, 36(1), 348–359.

Woyte, A., Belmans, R., and Nijs, J., 2007. Fluctuations in instantaneous clearness index: Analysis and statistics. Solar Energy, 81(2), 195–206.

Zervas, P., Sarimveis, H., Palyvos, J., and Markatos, N., 2008. Prediction of daily global solar irradiance on horizontal surfaces based on neural-network techniques. Renewable Energy, 33(8), 1796–1803.

Conference Proceedings

Solar World Congress 2015
Daegu, Korea, 08 – 12 November 2015

Enhancing satellite derived irradiance data for taking into account sub-pixel structures relevant for solar energy system analysis – current practice and future options

Hans Georg Beyer

Institute of Engineering. University of Agder, Grimstad (Norway)

Abstract

Satellite derived irradiance information currently approaches the status of a standard source for irradiance data used in solar energy system analysis. Due to intrinsic limitations in both spatial and temporal resolution, these data fail to give information of the full dynamics of the irradiance field in space and time. The analysis of systems comprising a sensibility to details of the temporal evolution of the irradiance field (i.e. systems comprising short-term storage elements) and of systems with sensibility to the spatial inhomogeneity of the irradiance field (i.e. large photovoltaic- or CSP-power plants) require knowledge of the "fine-structure of the irradiance field. Thus, methods for a respective enhancement of the satellite derived data are needed. This contribution presents various approaches discussed for setting up fine scale input data for the study of solar energy systems.

Keywords: fine scale irradiance data, irradiance field, temporal and spatial structure

1. Introduction

With the increasing availability of satellite derived irradiance information, this type of data set is more and more in use for the design and operation of solar energy systems, most notably PV- and CSP-systems. By this, the need for data measured on-site is reduced. However, due to basic limitations of the satellite-derived data, several requirements put by the intended application cannot be coped with this data type directly.

Grid integration studies and studies for systems involving either short-term storage devices (batteries) or show a sensibility to large power gradients, require data on the generated power - and thus on the irradiance - with a time resolution as short as one minute or even one seconds. With respect to spatial resolution, for a reliable modeling of both small and large solar installations, which can cover area from a few square meters up to square kilometers, respectively, information on the evolution of the area averages of the irradiance as well as on the inhomogeneity of this field is required. In this regard, the satellite-derived data are currently confined to a temporal sampling of - at best - a 10-15 min resolution. The spatial resolution is at best in the kilometer scale (depending on satellite type and data set), presenting spatially averaged information for the respective area, i.e. the pixel). Thus, in view of the requirements mentioned, the raw satellite information has to be enhanced in both space and time resolution by additional information to be fully applicable for all aspects of the system modeling.

2. Approaches

2.1 Enhancing the temporal resolution of irradiance information

The most direct approach concentrates on the temporal information, with the aim to paste synthesized high-resolution data into the low-resolution original sets. Pre-requisite is an appropriate model for temporal structure extracted from respective measurements. The models are mostly based on information directly

Selection and/or peer review under responsibility of Scientific Committee
doi:10.18086/swc.2015.07.04 Available at http://proceedings.ises.org

extracted from ground measured data. Basic work in this field was done by Skarveit and Olseth 92 by a detailed analysis of statistical properties of short term (here: down to 1 minute) values of the clears sky index. Models to describe the probability density function (PDF) and the autocorrelation characteristics of the sets are identified. Based on this, universally applicable tools to generate appropriate short term time series of global and diffuse irradiances with pre-described hourly averages have been developed, see e.g. Remund and Müller 2011. An alternative approach presented by Bright et al. 2015 is based on first describing the temporal evolution of the cloud cover given in octa and handling the distribution of clear sky index in dependence of the cloud cover. The temporal evolution of the cloud cover is modelled by a Markov approach (which could be extended to a spatial field). Fig. 1 gives examples for the resulting time series.

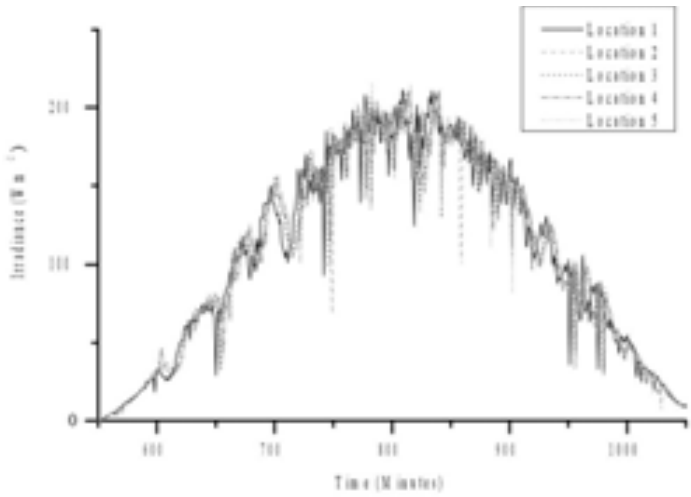

Fig. 1: Examples for daily time series of irradiances at different locations generated by the Bright et all 2015 model (taken from Bright et al. 2015). The mutual correlation of the series is up to now not tested.

Other more direct derivatives of the Olseth and Skartveit 1992 approach developed to cope with the direct normal irradiance as well are given by e.g. Beyer et al. 2010, Polo et al. 2011 and Fernández-Peruchena et al. 2015. Fig.2 gives examples for respective daily evolutions of the 1 min. global and direct normal irradiances.

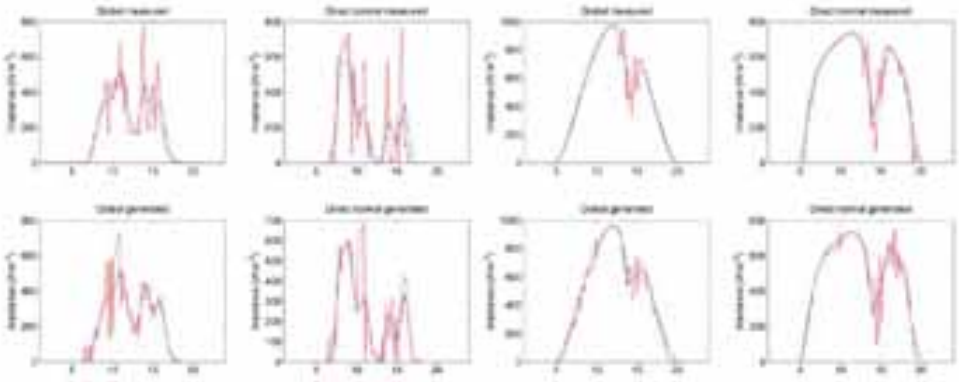

Fig. 2 Examples of daily evolution of global and direct normal irradiance with low (blue) and high (red) time resolution, Upper row presents measured data, data with high time resolution in lower row are synthetic (taken from Polo et al. 2009).

Validation of these schemes can be done by comparing simulations of the performance of solar energy systems for real and synthetic input data (see e.g. Beyer et al. 2010). When applying this approach to spatially distributed systems e.g. CSP-systems limitations are given by the fact, that it has to be assumed that the system is affected by a homogeneous irradiance field – which in general is not the case. This calls for additional information on the spatial statistics of the irradiance field.

2.1 Analysis of the spatial structure of the irradiance field based on fleets of point measurements

To gain the information on the time and space structure of the irradiance, dedicated measuring campaigns had been set up. Early examples as e.g. given by Beyer et al. 1993 and 1994 investigating the space/time structure of the irradiance field on scales of 100m and 1s respectively. More actual examples are e.g.

reported by Kuszamaul et al. 2010, Sengupta and Andreas 2010, Madhavan et al. 2015. Luger et al 2013 and Öchsner et al. report on a campaign analyzing both, the small scale structure of the irradiance field covering a MW scale PV system as measured by fleet of irradiance sensors and the reaction of the PV system. Based on the set of irradiance data, Luger et al. 2013 propose a method for the reconstruction of the field cased on the time series of the point measurements and (see figs. 3,4).

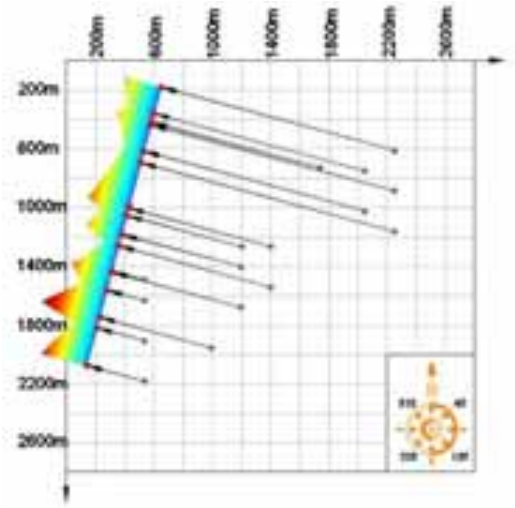

Fig. 3: Generating an irradiance field driven by measurements of a fleet of irradiance sensors. From the cross-correlation structure of the point data a cloud drift vector is derived. Assuming rigid clouds and an appropriate interpolation techniquwtime coherent irradiance bands can be constructed (taken from Luger et al. 2013).

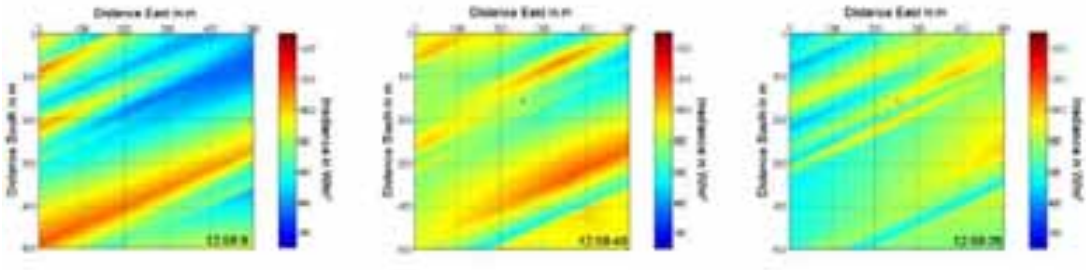

Fig. 4: Consecutive irradiance field situations generated by the method presented by Luger et al. 2013 (taken from Luger et al. 2013).

The procedure makes use of the assumption that the temporal evolution of a highly fluctuating irradiance the field is governed by the movement of shadow casting clouds, and is thus linked to the spatial structure of the cloud field and its displacement over time.

2.2 Analysis of the space/time structure of the irradiance field based on sky image analyses and models for the synthetizations of irradiance fields derived

As the structure of the irradiance field is governed by the evolution of the cloud field, the explicit analysis of cloud field geometry comes into the focus. With information on cloud field geometry and dynamics, the modulation of the irradiance by this field can be modelled with space and time resolution according to the resolution of the spatial cloud features.

As data source, ground based cameras proved useful. Fig.5 gives an example for raw and processed sky images presented by Nitche et al. 2014. The processing used here aimed at the separation of the pixels containing clouds. This cloud image offers the basis for an analysis of the clouds as two dimensions spatial structure.

As tool for the structural analysis, the description of the clouds as fractal object proved helpful. The fractal characterization of the cloud circumference was applied by e.g. Beyer et al. 1996. Based on the fractal dimension of the cloud circumference for a cumulous cloud field a scheme for the generation of a synthetic field with similar characteristics was set up. Fig. 6 shows a synthetic cloud shadow band. By assuming a

cloud drift speed, the shift over a (Generator-) area of interest can be modelled, resulting in a cloud modified irradiance time series at each point at the ground effected by the cloud field (see Fig. 7 for a single point series). It could be shown, that the resulting irradiance field can reflect statistical properties of the ground measured irradiance field (Beyer et al., Hammer and Stolzenburg 1993).

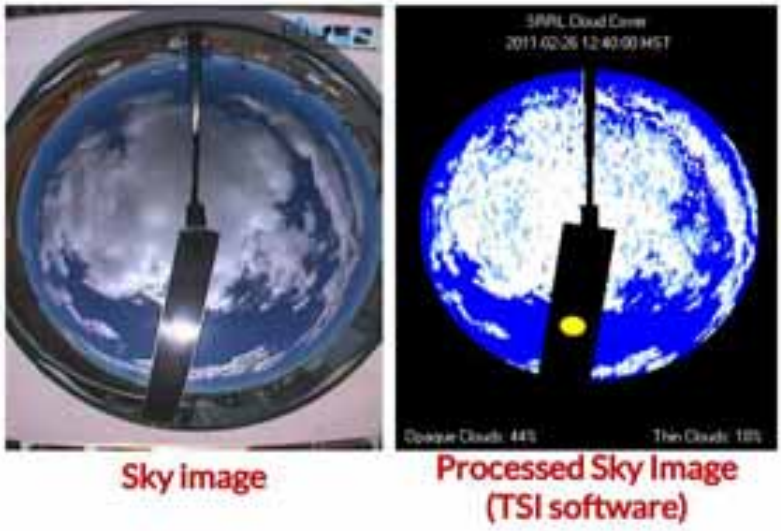

Fig. 5: Photographs taken by a sky imager. The image on the right is processed for cloud/clear sky separation. (taken from Nitsche et al. 2013).

Fig. 6: 2D Cloud band generated according to a fractal dimension of the cloud circumference (taken from Beyer et al. 1993).

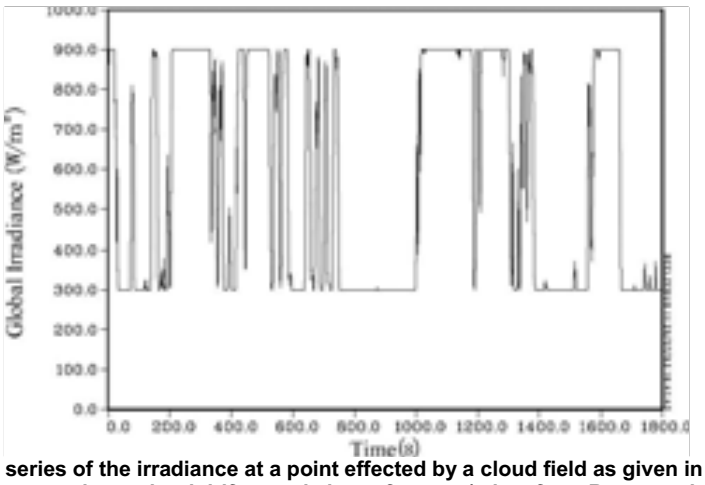

Figure 7: Time series of the irradiance at a point effected by a cloud field as given in Fig. 6. , drifted across assuming a cloud drift speed circumference (taken from Beyer et al. 1993).

This approach has been taken up by Cai 2014. An irradiance field modulated by a fractal cloud field generated similar to the abovementioned approach is shifted over a housing area area with high PV penetration of aprox 2*2 km^2 extension. Fig.8 gives an example for the cloud band and the resulting shadow pattern generated here. Fig.8 gives an example for the for the system reaction concerning the PV effected power at the substation and the voltage reaction of the grid.

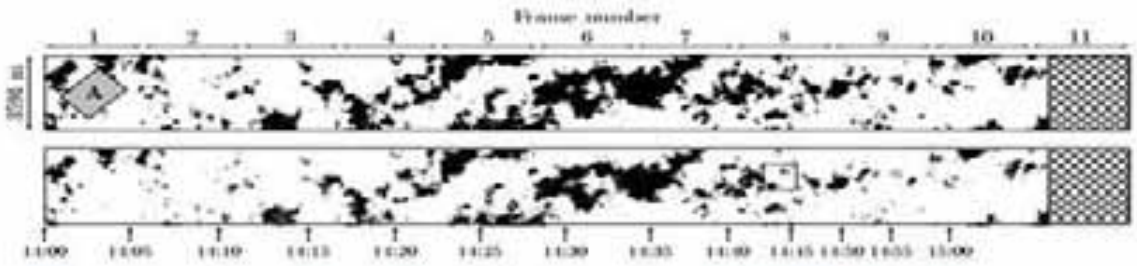

Fig. 8: A cloud band and resulting shadow pattern a given by Cai 2014. The time marks at the bottom are linked to the cloud drift speed assumed. The study area is marked by A (taken from Cai 2014).

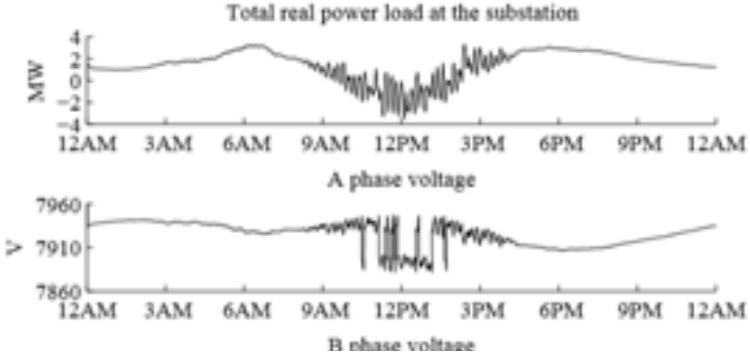

Fig. 9: Grid reaction to the passing cloud field. The upper graph the time pattern of the load of the substation effected by the PV generation, the lower graph gives the respective voltage response (the sharp transitions are caused by actions of transformer tap changes (taken from Cai 2014).

2.2 Other Methods for cloud field generation stemming

Another scheme for the generation of 2D cloud fields is based on information on cloud fraction, cloud and gap cords applying of cellular automata is suggested by Alexandow et al.2010. These automata give a procedure to populate a prescribed mesh with clouds according to the selected distribution properties and can be applied on various spatial scales. This procedure can be performed in steps of consecutive resolutions. Fig. 10 shows the result of such process.

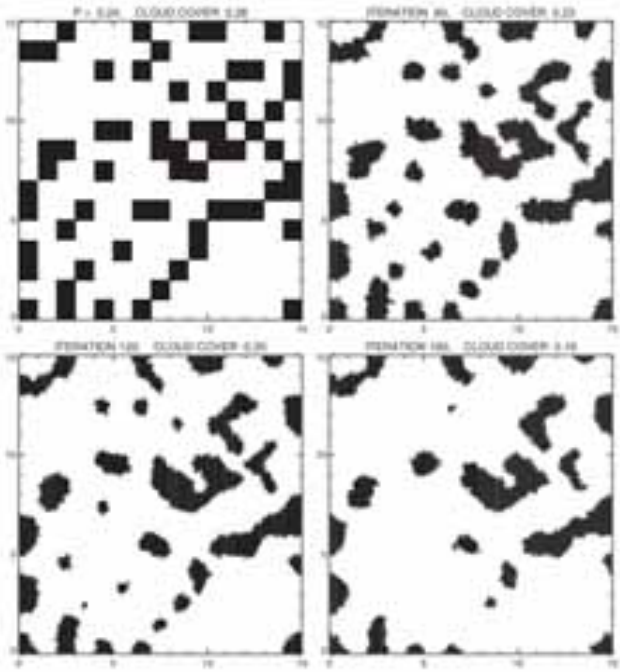

Fig. 10: The generation of a cloud field by a cellular automata scheme as given by Alexandrov et al. 2010. The resolution of the field increase with iteration (from top left to top right to bottom left to bottom right) (taken from Alexandrov et al. 2010

2.3 Methods for the synthetization of 3D cloud fields based on detailed distribution of cloud constituents

Based on detailed information of the structure of cloud fields, as e.g. liquid and ice water content derived from radar observations the 3D spatial structure of the respective fields can be extracted and be used for the generation of respective synthetic fields. Kew 2003 has set up a scheme for the generation of cirrus cloud fields. The model is based on 3D presentation of the spatial power spectral densities of the parameters inspected. The spectra form the basis of an inverse Fourier transform, which by randomly selected phases results in a stochastic filed. Fig. 10 shows an example for a 3D field of the ice water content covering 200km*200km with a resolution of 1km. This field generated according to desired large scale properties can form the basis for detatailed radiative transfer calculations giving a pattern of the irradiance at ground level.

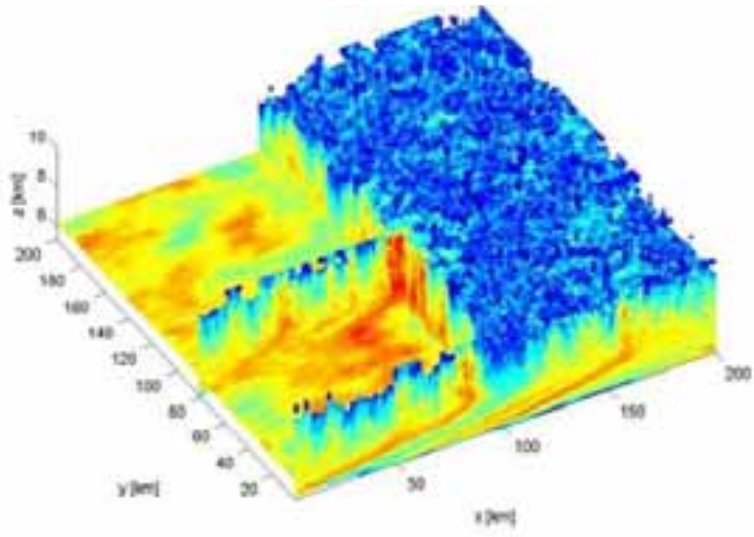

Fig. 10: Presentation of a synthetic 3D field of the ice water content (IWC). For demonstration a section is cut away (taken from Kew 2003).

2,4 A general procedure for the generation of cloud fields with arbitrary optimization goals

A more general scheme for construction of 3D clouds, that can handle various goal values for the statistical properties of the field is given by Venema 2005. It uses evolutionary algorithms to iteratively modified an initial field until is statistical properties approach the goal characteristics (e.g. power spectra). In fig.11 two examples for the outcome of this procedure are given, concerning a 2D field of cloud water content generated based on 1D measured power spectrum. The panel on the right shows the evolution of a cloud, constructed based on selected measured statistical cloud properties.

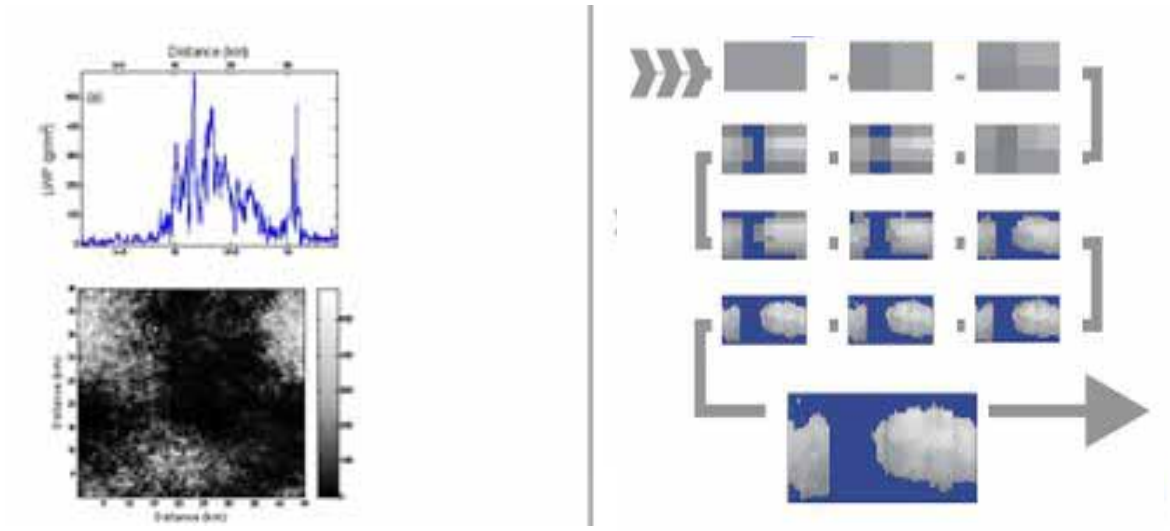

Fig. 11: Outcomes of a procedure of Venema 2005 to modify initial fields iteratively to present prescribed statistical characteristics. In the left panel a 2D field of cloud water content generated on the basis of a 1D spectrum is given. The right panel presents the evolution of a 3 D cloud structure by consecutive refining (starting upper lef) aimed to present selected measured statistical properties (taken from Venema 2005).

3 Conclusion

Over the years a variety of procedures had been developed to generate synthetic high-resolution (e.g. showing minutely resolution) irradiance time series that can be merged in sets with lower resolution (e.g. the seies derived from satellite information). For the generation of respective 2D fields, additional information on the spatial statistics have to be added. For this task most work is done be approaching the spatial structure of the irradiance field via the analysis of the spatial structure of the cloud field causing the statistical disturbance of the irradiance field. Various schemes for the generation of 2D cloud fields showing statistical properties close to the cloud characteristics derived from e.g. sky images. For application key parameters of the cloud field e.g. the average cloud cover ration must be extractable from the large scale information. New developments from basic meteorological research more directly tied to the modelling of the cloud physics offer new ways for an extension to the handling of 3D fields and the application of radiative transfer calculations to derive detailed spatial information of the irradiance field and, with information on spatial cloud dynamics (drift), detailed temporal information.

References

Alexandrov, M. D., A. Marshak, and A. S. Ackerman, 2010: Cellular statistical models of broken cloud fields. Part I: Theory, J. Atmos. Sci., 67, 2125–2151.

Beyer, H.G., M. Hübert, E. Ortjohann, J. Poplawska, J. Voß und P. Wieting: 1993, Grid interference of a locally high share of PV-energy - Effects of Short Term Fluctuations. Proc. of the ISES Solar World Congress 1993, Budapest, Hungary Vol. 3, 423-428

Beyer, H.G., M.Fauter, K.Schumann, H.Schenk, R.Meyer,R., Synthesis of DNI time series with sub-hourly time resolution 2010, Synthesis of DNI time series with sub-hourly time resolution, Proc. SolarPACES2010, Perpignan, France, 21-24.10

Bright, J., P. Taylor, R. Crook, Methodology to Stochastically Generate Spatially Relevant 1-Minute Resolution Irradiance Time Series from Mean Hourly Weather Data 2015, Bright, J., P. Taylor, R. Crook, 5th Solar Integration workshop, International Workshop on Integration of Solar Power into Power Systems, Brussels Belgium, 19.-20.10.

Cai, C. 2014, Fractal-based cloud shadow and irradiance model for power system analysis with high penetration of photovoltaics, Graduate Theses and Dissertations, Paper 13739.

Fernández-Peruchena, C.M., Blanco, M.J.,Bernado 2015, A., Increasing the Temporal Resolution of Direct

Normal Solar Irradiance Series in a Desert Location, Energy Procedia 69

Hammer and Stolzenburg 1993, Analyse kurzfristiger Fluktuationen der Solarstrahlung unter Berücksichtigung von Wolkenfeld Strukturen, Master thesis, University of Oldenburg, Germany

Kew, S., Development of a 3D fractal cirrus model and its use in investigating the impact of cirrus inhomogeneity on radiation, Master thesis, University of Reading, U.K.

Kuszamaul, S,, Ellis, A, Stein, J., Johnson, L. 2011, Lanai high-density irradiance sensor network for characterizing solar resource variability of MW-scale PV system, 35th Photovoltaic Speialists Conference Honululu, HI

Luger,S., Mock,J., Zehner, M.,, Lorenz, E.,, Kühnert.J., Weigl, T. Nagl,L., Rauscher,T., Becker, G., Betts,T., Gottschalg, R., 2013, 3D-SIM (3Dsolar Irradiance Modelling): The Optimization of an Irradiance Interpolation-Method and its Application for Central Europe, 28th EU PVSEC, Paris (France)

Madhavan, B.L., Kalisch, J., Macke, A. 2015, Shortwave surface radiation budget small-scale cloud network for observing small scale cloud inhomogeneity fields, Atmos, Meas. Tech. Discuss., 8, 2555-2589

Nitche, N., Trombe, P.-J., Cros, S., Schmutz,N., 2014, Using cloud fraction derived from all-sky camera to improve beam solar irradiance forecasting by time-series modelling, 14th EMS / 10th ECAC

Öchsner, P., Zehner, M., Lang, F., Rauscher, T., Weizenbeck. J., Weigl,T., Becker,G., Bettenwort, , G., Giesler, B., Betts, T. Gottschalg, R. 2013, Satial modelling of grid connected PV plants with 3d irradiance values, 28th EU PVSEC, Paris (France)

Polo, J, Zarzalejo, L.F., Marchante, R., Navarro, A.A. 2011, A simple approach to the synthetic generation of solar irradadiance time series with high temporal resolution, Solar Energy, 85

Remund, J and Müller,S.C. 2011 , Solar Radiation and Uncertainty Information of Meteonorm 7, proc. PVSEC 2011

Sengupta, M., Andreas,A., 2010, Oahu Solar Measurement Grid (1-Year Archive): 1-second Solar Irradiance: Oahu, Hawaii (Data); NREL Report Np. DA-5500-5606. http://dx.doi.org/1052451

Skartveit, O and Olseth, J.A., 199, The probability density and autocorrelation of short-term global and beam irradiance, Solar Energy, 48

Venema, V. 2003, An evolutionary search algorithm to gener-ate 3D cloud fields with measured cloud boundary statis-tics, report, http://www.meteo.uni-bonn.de/victor/articles/2003/ 2003 report cloud boundaries evol search.pdf

Conference Proceedings

Solar World Congress 2015
Daegu, Korea, 08 – 12 November 2015

Assessment of the quality of satellite derived irradiance data for Rwanda by comparison with data from a fleet of automated ground stations

Fabien Habyarimana[1], Hans Georg Beyer[2]

[1]Department of Physic, College of Science and Technology, University of Rwanda, BP3900, Kigali, Rwanda

[2]Institute of Engineering. University of Agder, Grimstad (Norway)

Abstract

Satellite data is a worldwide available data source, quality in regions with dense networks (eg. Europe, North America) well known as less data for comparison for central Africa.
Here, analysis of Satellite data source enhanced ground data now offered by Rwanda Environment Management authority (REMA) network.
REMA has installed around 22 Automatic Weather Stations (AWS) in Rwanda (surface area of Rwanda ~26000 km^2). Solar irradiance data are available since end 2013 with a time resolution of 5min. After passing through a quality check, a first analysis of this data base is done by the investigation of the applicability of standard models of both, their probability distribution and autocorrelation characteristics performed for temporal resolutions of 1day, 1h and 15min. As currently time synchronous ground and satellite derived data sets are missing these data are used here for but a first qualitative comparison to the Satellite derived data available
Keywords: Solar *irradiance, Satellite derived data, Automatic Weather station*

1. Introduction

To support planning concerning solar energy application in Rwanda, the quality of local solar resources is on important decisive. The spatial and temporal distribution of solar radiation resources are needed to be analyzed. Due to the limitation of available local measurement data of global solar irradiance in some regions of Rwanda, this problem is sort out by exploitation of the empirical model tools (Museruka and Mutabazi, 2007; Safari and Gasore, 2009) with daily means monthly results, and indirect measurement data sets from meteorological satellites (PVGIS, 2015) which covering 20 years with a temporal resolution of 15min. Currently, radiation data from several web services which offer irradiance information for Africa and Rwanda (PVGIS, 2015; GeoModel, 2013; NASA, 2015). However, each has its own limitation in space-time and accuracy level for the inspected region is no well-known. In this study, satellite derived irradiance from Photovoltaic Geographical Information System (PVGIS) has been used. PVGIS gives the hourly pattern of the average day of the month from the HelioClim-3 database with a temporal resolution of up to every15min and spatial (approx. 5 km) observations. Due to its excellent help and its integration of geographical database of solar radiation model, PVGIS has been exploited as interactive web for estimating the potential for solar energy in Rwanda and offers a long time series with daily monthly means of global horizontal irradiance values that cover the period 1985-2004. As complement, the daily global solar energy with 15-time resolution data supplied by GeoModel solar, Slovakia (GeoModel, 2013) is available from 2007 to 2012 for Kigali location and was also analyzed here. Currently, the new data set of solar irradiance at some particular location in wide variety of real operating environmental condition in Rwanda has been given by Rwanda Environment Management Authority (REMA), the global solar irradiance data with a high temporal resolution of 5min (Meteo Rwanda, 2014) in 17 districts of Rwanda where 22 automatic weather stations has been installed and operated since end of 2013. As the ground data measurement tool, these new automated weather station data has been analyzed for being a new source for technical assessment of solar energy potential in Rwanda and its

doi:10.18086/swc.2015.07.05 Available at http://proceedings.ises.org

quality is been investigated by a qualitative comparison with the existing satellite derived irradiance data model. Due to this problem we have propose to explore the similarity between the available global solar data from AWS and satellite derived irradiance data for Rwanda.

The objective of this paper is thus to give a first comparison of local irradiance provided by automated ground station data (AWS) versus satellite derived irradiance data for Rwanda

2. Solar radiation components at the ground level

The presented analysis of satellite derived data is based upon the global horizontal irradiance estimated at inclination of 15° degrees as tilted angle of inclination, fixed at azimuth 0^0(north) for both PVGIS and GeoModel**.** This global solar irradiance (G) received at ground level is taken as a sum of direct irradiance G_b, diffuse irradiance G_d and ground reflected irradiance G_r.
The ground measured data of global tilted radiation used, has been offered by the automatic weather station installed across the country and they are received from Meteo Rwanda. Due to the incoherent space and time resolution for these 3 sources data (PVGIS, GeoModel and AWS), the conversion for common resolution has been done, especially from 5 minutes (AWS data) to 15 minutes (Satellite derived data). In this study, the correlation for both set data (ground measurement and satellite derived data) was statistically tested by mean percentage error (MPE %), mean bias error (MBE) and root mean bias error (RMSE) as it is defined by Indira et al. (2012).

3. Data acquisition of global solar radiation in Rwanda

3.1 Satellite information

Global solar irradiance can be derived from weather satellites measurements. There are many sources of the global solar irradiance for Africa and including Rwanda such as NASA, NREL/SWERA, PVGIS/HelioClim and Solar GIS for free or by payment (PV magazine, 2014). The data sources here apply different versions of the Heliosat method (Hammer et al., 2003; PVGIS, 2015; GeoModel, 2013).

Figure 1 illustrates a map for annual irradiance sum over Rwanda, as given by PVGIS. This map refers to the average for the years 1994 to 2010.

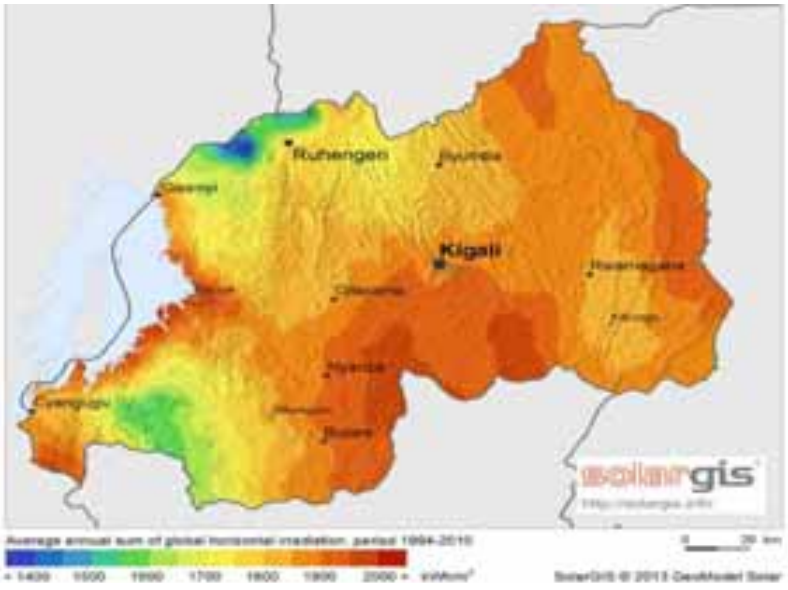

Fig.1: Average annual sum of global horizontal irradiation in Rwanda (GeoModel, 2013).

3.2 Surface observation

In 2013, Rwanda Environment Management Authority (REMA) has installed 22 automatic weather stations with 7 Automatic Weather Station for Hydro-meteorological (AWS-H) Observation located close to water bodies and 15 Automatic Weather Station (AWS-S) for synoptic observation installed on land (Meteo Rwanda, 2014). As an advantage, some of them are web-based and can be accessed online through Meteo Rwanda`s

authorization. Nowadays, in Rwanda, meteorological data are manually and automatically collected from weather countywide. The figure 2 represents some positioning of automatic weather station in Rwanda.

Fig. 2: Automatic weather station (AWS) in Rwanda (Meteo Rwanda, 2014).

The AWS offers local weather data (global solar irradiance) with 5 minutes of temporal resolution. These parameters are often needed for prediction of performance of solar system application. Additionally, each station for AWS is equipped the weather sensors, for monitoring data that can be used in assessment of current climate. The some AWS data bases are already containing the information monitored data from October 2013 until today, but some data are missing or incomplete for some AWS.

4. Checking the similarity of satellite derived datan and automated ground station data

4.1 Comparison of annual and monthly means

At country wide scale, due to the small extension of the country, here should be distinctive latitudinal gradient of global solar radiation on the territorial surface of Rwanda as represented on figure 1 from PVGIS. But as at local scale, terrain is the major factor characterizing the spatial distribution of global solar radiation. The trend of spatial distribution of solar irradiation is characterized by its continuous positive gradient from West to East region and from North to South region of Rwanda which is corresponding to the negative gradient of relief in Rwanda. The annual average of global solar radiation has been estimated for some locations from PVGIS and AWS; the results are represented on the figure 3.

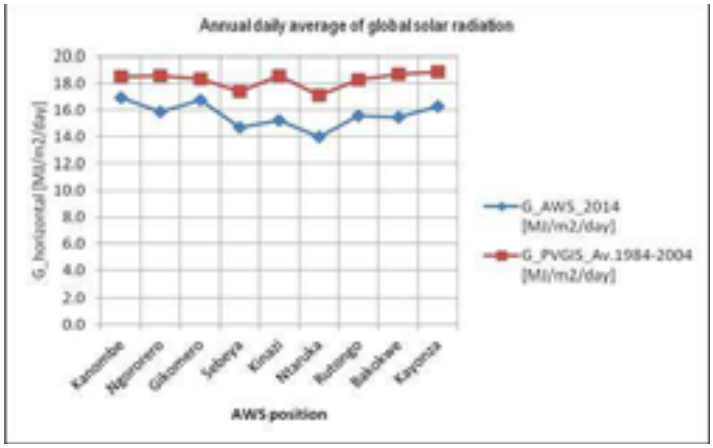

Fig.3: Annual daily average of global solar radiation from PVGIS (several years) and AWS (2014)

The annual average of the daily global solar radiation sum shows but small differences from station to station from both sets. It is remarkable that – by showing a similar station to station pattern – the satellite data give higher values throughout. This difference has to be traced back to be either a result from year to year variations or from an overestimation error in the satellite data. Table 1 gives the mean absolute MBE and percentage MPE deviation for various sites.

Table 1: Spatial variation of MPE, MBE and RMSE for data derived satellite (average 1984-2004) and automated ground station data 2014

Location	MBE[MJ/m2/day]	MPE[%]	RMSE [MJ/m2/day]
Kanombe	1.7	-10.2	2.8
Ngororero	2.6	-17.2	3.7
Gikomero	1.6	-9.9	2.7
Sebeya	2.7	-19.1	3.2
Kinazi	3.4	-23.8	4.4
Ntaruka	3.2	-23.8	3.9
Rutongo	2.7	-18.1	3.6
Bakokwe	3.2	-21.3	3.8
Kayonza	2.6	-15.9	3.2
Average	2.6	-17.7	3.5

Looking at the month-to month deviations of ground and satellite derived data (table 2, fig.4) it can be remarked, that the deviations are mostly pronounced in the May to August period. This may give an indication for a problem in the satellite derived data due to faulty assumptions on the monthly atmospheric turbidity.

Table 2: Monthly values of MPE, MBE and RMSE for satellite derived (multi year average) and automated ground station data (single year)

Month	MBE [MJ/m2/day]	MPE [%]	RMSE [MJ/m2/Day]
Jan	0.7	-4.9	0.3
Feb	3.0	-21.0	2.7
Mar	2.1	-14.4	1.7
Apr	2.6	-17.0	2.2
May	3.4	-23.7	3.4
Jun	5.3	-36.5	8.1
Jul	5.3	-32.4	8.1
Aug	5.9	-40.8	10.0
Sep	3.4	-22.0	3.4
Oct	0.0	-0.5	0.3
Nov	1.2	-8.4	0.5
Dec	-0.9	5.1	0.6

Looking at the analysis of results of table 2 shows that one only month of December the MPE is 5.1 (greater than 0), means that the data monitored from AWS is greater than data estimated from PVGIS. October presents a good agreement data for both set of data.

Analyzing the other satellite derived set, which allows for looking at year to year variations gives the same qualitative result of a positive Bias of the satellite data, being highest in the Mai to September period. The general overestimation for the satellite derived data again indicates a necessary adjustment of the assumptions of atmospheric turbidity used by the models.

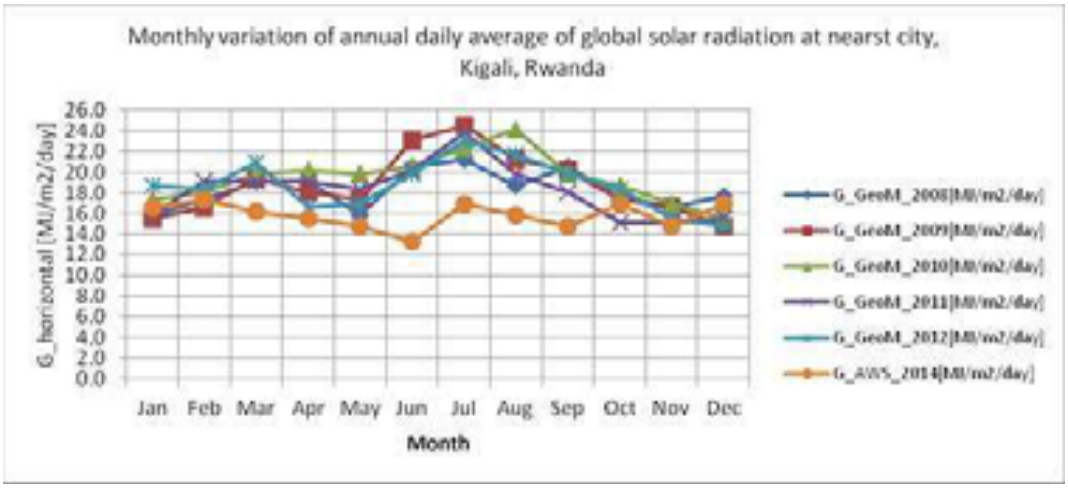

Fig. 4: Comparison of GeoModel and AWS global horizontal irradiance data on a monthly basis.

4.2. Comparison of cumulative distribution functions.

Based on 15 minutes of resolution available in the GeoModel and the ground station sets the similarity of the distribution functions of the 15min irradiances can be analyzed

The annual cumulative distributions for one site - Rutongo - is given in figure 11, shown here in the higher than presentation. The distributions refer to the 2014 ground data set and GeoModel sets for individual days.

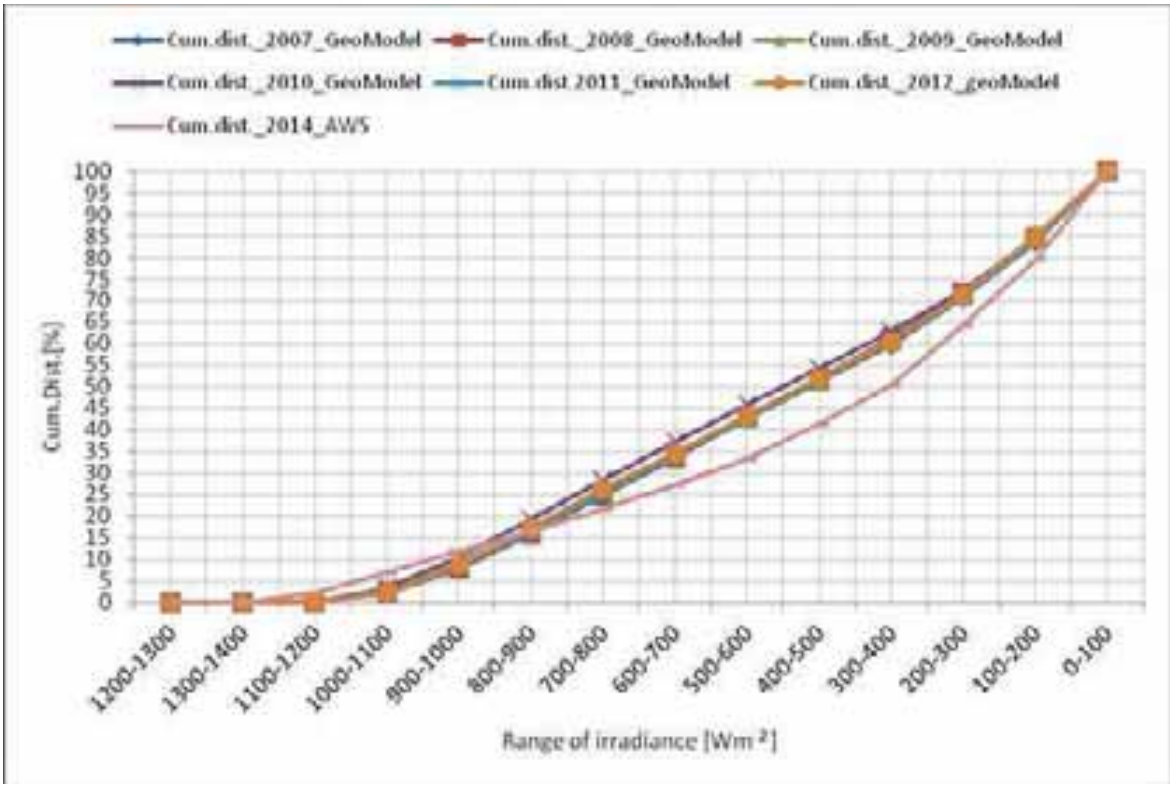

Fig.5: Cumulative distribution of global solar irradiance from multiple years GeoModel and 2014 AWS sets (shown here in the higher-than presentation.

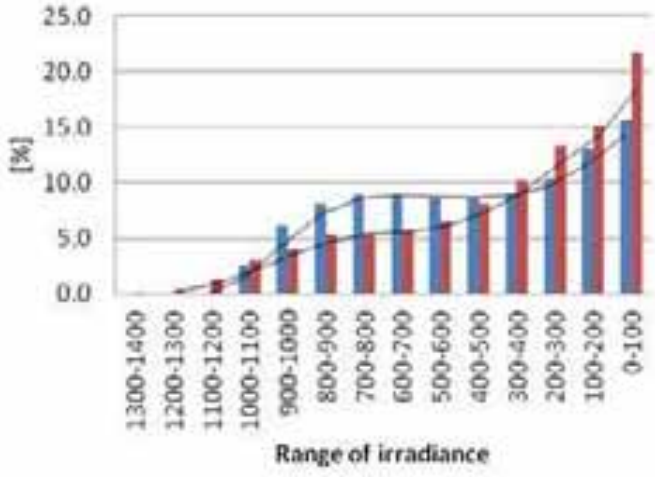

Fig.13: Histrgram of the 15min irradiances fo the 2014 ground data set (red) and the 2008-2014 satellite derived set (blue).

4.1 Conclusions on data similarity

Whereas the data confirm, that the basic spatial and temporal distribution of the ground measured irradiance can be reflected by the satellite derived sets, even from this problematic case of not time parallel data sets it has to be stated, that the quality of the satellite derived data needs improvement. From the error pattern it may be stated, that that a better representation of the atmospheric turbidity can lead to substantial improvements here.

5. Conclusions

In this paper a preliminary analysis of the quality of satellite derived irradiance data by using a set of newly installed ground stations in Rwanda is performed. Within the limitations enforced by the missing of time parallel data sets a need for the improvement of schemes for the derivation could be pointed out. However, this proves the value that should be given to this kind of in-situ measurements of the solar resource.

References

Hammer A., Heinemann D., Hoyer C., Kuhlemann R., Lorenz E., Müller R. and , Beyer H. G. ,2003. Solar energy assessment using remote sensing technologies, Remote Sensing of Environment, 86.

GeoModel , 2013. http://geomodelsolar.eu/home as of 15.05.2014

Indira Karakoti, Alekhya Datta and Singh S. K., 2012. Validating satellite-based solar radiation data with ground measurements, http://geospatialworld.net/Paper/Application/ArticleView.aspx?aid=30355#sthash.4Ic1ZCkf.dpuf

Meteo Rwanda, 2014. http://www.meteorwanda.gov.rw,

Museruka C. and Mutabazi A.,2007. Assessment of Global solar radiation over Rwanda, International Conference on Clean Electrical Power, 2007. ICCEP apos;07. Volume , Issue , 21-23 May 2007 Page(s): 670 – 676. DOI 10.1109/ ICCEP.2007.384312; Full paper: http://esp.ictp.it/personnel/associates/alphonse-mutabazi

NASA, 2013. http://power.larc.nasa.gov as of 05.02.2015

PVGIS, 2015. http://re.jrc.ec.europa.eu/pvgis/ as of 05.02.2015

PV magazine, *http://www.pv-magazine.com/archive/articles/beitrag/solar-resource-mapping-in-africa-_100009438/501/#ixzz3Wwdz6RvB]* as of 05.02.2015

Safari B. and Gasore J., 2009. Estimation of global solar radiation using empirical models. Asian Journal of Scientific Research 2.

Conference Proceedings

Solar World Congress 2015
Daegu, Korea, 08 – 12 November 2015

Optimal Weighting of Parameters for Constructing Typical Meteorological Year Datasets for Photovoltaic Power Stations Operated under Hot Dry Maritime Climates

Arttu Tuomiranta and Hosni Ghedira

Masdar Institute, Research Center for Renewable Energy Mapping and Assessment, Abu Dhabi, United Arab Emirates

Abstract

The objective of this study is to find an optimal set of the weights of different typical meteorological year (TMY) parameters for photovoltaic (PV) power plants operated under hot dry maritime climates. The TMY datasets are generated for a maximum period of six years, for which there are power output data available from a PV power station located in Abu Dhabi, United Arab Emirates and equipped with both polycrystalline silicon and cadmium telluride modules. After determining the typical yield year (TYY) i.e. the months with the plant yields closest to the long-term averages, the parameter weights that result in the closest month combination are found. In total, 19 TMY parameters are considered in the study. The TYY-based TMY parameter weighting approach proposed in this paper reduces the deviations of TMY-based yield estimates from the multiannual monthly averages as compared to the previously proposed TMY weighting sets. The resulting locally determined weight sets place approximately two third of the weight on irradiance variables and one third on parameters that are correlated with plant yield but not with irradiance. On an annual scale, no major benefit is derived from using the proposed TYY-based approach as compared to the previously proposed TMY weighting sets. In accordance with the objective, the weighting sets proposed in this study are expected to suit best the regions characterised by hot dry maritime climates such as the areas around the Persian Gulf and the Red Sea as well as the coastal regions of Egypt and Libya.

Keywords: *typical meteorological year, parameter weighting, photovoltaic power stations, hot dry maritime climate*

1. Introduction

Typical meteorological year (TMY) datasets are widely used to reduce the computation time and storage requirements when determining the optimal designs for photovoltaic (PV) power stations. In principle, the TMY datasets for PV plant projects should be constructed based on all the temporally variable parameters that have an impact on plant performance at the plant site. In addition, the parameters should be individually weighted based on their order of importance. As the relative differences in the importance of the parameters are highly location-specific, also the weights applied would ideally be adjusted based on the location.

Due to their abundant solar resource and proximity to major centres of electricity demand, the areas around the Persian Gulf and the Red Sea as well as the coastal regions of Egypt and Libya possess a large economic potential for PV power generation (Beták et al., 2012). These regions are characterised by a hot dry maritime climate and, therefore, significantly differ from the temperate climate regions that account for most of the world's installed PV capacity. The most important differences are related to operating cell temperatures, atmospheric aerosol loading, and humidity levels. Due to the high ambient air temperature levels typical of hot dry climates, the output power-weighted average operating cell temperature is exceptionally high. The highly variable aerosol loading of desert conditions contributes to the variation in dust deposition as well as the variability of the incident solar spectrum together with atmospheric water vapour. Consequently, the commonly used PV performance modelling methodology may not appropriately address the regional conditions. This is the case with the TMY construction methods as well.

doi:10.18086/swc.2015.07.06 Available at http://proceedings.ises.org

In order to adjust the weights of different TMY parameters to suit the hot dry maritime climate type, the present study aims to determine an optimal set of weights based on five to six years of data on the power output of a 10 MWp PV power station located in Abu Dhabi, United Arab Emirates and equipped with polycrystalline silicon (pc-Si) wafer-based and cadmium telluride (CdTe) thin-film modules mounted at a fixed, roughly polar-aligned tilt. In addition, the weights previously proposed by Marion and Urban (1995), Stoffel et al. (2010), Kalogirou (2003), and Cebecauer and Šúri (2015) are evaluated with the same data. Abu Dhabi has a typical hot dry maritime climate, therefore, supporting the generalisation of the results to other regions characterised by the same climate type.

2. Methodology

2.1 Plant Yield Data Processing

A TMY dataset constructed for a PV power station should be designed to represent conditions under which the yield of the station is equal to the long-term average yield. Normally, TMY datasets are constructed based on the time series of those individual months whose statistics are in the best accordance with the long-term monthly statistics. That is why in this study, the first step is to find the individual months, during which the considered PV power station generated the yield closest to the long-term monthly average yield.

The power station's central inverters have measured output power since May 2009. The inverter-specific measurements are summed up for power blocks equipped with each module type resulting in two time series. At the beginning of a PV plant's operating life, down-time periods are frequent because the plant's operation and maintenance (O&M) plan is still under development and defective components are being detected and replaced. Hence, the plant output data recorded during this initial phase are not considered in the analysis. The included data cover a six-year period from October 2009 until September 2015 for the pc-Si module time series and a five-year period from October 2010 until September 2015 for the CdTe module time series.

The raw output data are corrected for outage losses in order not to bias the long-term average calculation. The outage losses have been quantified by the plant's operator and given in the annual plant performance reports. As TMY construction is only dependent on the ambient conditions at the plant's site, not on the plant's age, the data are also corrected for time-dependent degradation. In accordance with Jordan et al.'s (2012) findings, the time-dependent degradation rates are assumed to be one per cent per year for both sections of the plant. Finally, the long-term monthly average yields are calculated based on the five (CdTe) or six (pc-Si) monthly values corresponding to each year of the available power output data. The set of the individual months, during which the considered PV power station generated the yield closest to the long-term monthly average yield, can be considered as the typical yield year (TYY).

2.2 Ambient Data Processing

The dataset of ambient parameters is generated for the same period and scale as the TYY dataset. The considered ambient parameters are measured in the close vicinity of the power station and comprise global horizontal irradiance (GHI), beam normal irradiance (BNI), diffuse horizontal irradiance (DHI), ambient air i.e. dry-bulb temperature (T), wind speed (WS), wind direction (WD), and relative humidity (RH). The original data consist of average values over intervals of five and ten minutes. Dew point temperature (T_{dp}) values are estimated based on T and RH measurements using the August-Roche-Magnus approximation (Alduchov and Eskridge, 1996). The final dataset of ambient parameters consists of time series of 19 monthly statistics specified in Tab. 1.

Tab. 1: Monthly statistics used in TMY dataset construction.

Statistic	GHI	BNI	DHI	T	WS	WD	RH	T_{dp}
average	✓	✓	✓	✓	✓	✓	✓	✓
maximum				✓	✓		✓	✓
minimum				✓	✓		✓	✓
range				✓	✓		✓	

According to the best practice, a TMY dataset should be based on 15 years or more of source data (Cebecauer and Šúri, 2015). In this case however, the objective is not to generate a dataset that is a good representative of long-term climatic conditions but rather a test bed for different parameter weights. In order to assess how well different weight combinations predict the actual plant performance, the time frame of the TMY dataset needs to be the same as that of the plant output data.

2.3 Evaluation of Parameter Weight Sets

The method proposed by Cebecauer and Šúri (2015) is used to construct TMY datasets in the present study. Drawing on the past work on TMY dataset construction, Cebecauer and Šúri base their method on the concatenation of continuous multivariate time series spanning those individual months that are found to provide the best agreement with long-term monthly statistics. The different TMY parameter weight sets proposed by other authors or developed here are integrated in Cebecauer and Šúri's methodology. The previously proposed weight sets under consideration are presented in Tab. 2.

Tab. 2: Previously proposed TMY parameter weight sets under consideration.

Variable	Statistic	TMY2	TMY3	Kalogirou	SGIS-PV	SGIS-CSP
GHI	**average**	12/24	5/20	8/32	0.75	0.23
BNI	**average**		5/20	8/32		0.7
DHI	**average**				0.2	0.03
T	**average**	2/24	2/20	2/32	0.05	0.04
	maximum	1/24	1/20	1/32		
	minimum	1/24	1/20	1/32		
	range			1/32		
WS	**average**	2/24	1/20	2/32		
	maximum	2/24	1/20	1/32		
	minimum			1/32		
	range			1/32		
WD	**average**			1/32		
RH	**average**			2/32		
	maximum			1/32		
	minimum			1/32		
	range			1/32		
T_{dp}	**average**	2/24	2/20			
	maximum	1/24	1/20			
	minimum	1/24	1/20			
	CDF	0.2	0.2	0.2	0.2	0.2

TMY2 (Marion and Urban, 1995), TMY3 (Stoffel et al., 2010), Kalogirou (2003), SGIS-PV (Cebecauer and Šúri, 2015), SGIS-CSP (Cebecauer and Šúri, 2015)

In order to determine the TMY months, Cebecauer and Šúri (2015) deploy two approaches used in parallel: comparison of single monthly statistics with their long-term counterparts and comparison of monthly empirical cumulative distribution functions (CDF) with their long-term counterparts. In this study, the most appropriate weights also for these two TMY determination approaches (11 possible combinations with

intervals of 0.1) are found based on the plant output data. When evaluating the previously proposed parameter weight sets however, the same TMY determination approach weights as used by Cebecauer and Šúri are adopted: 0.8 for single monthly statistics and 0.2 for monthly empirical CDFs.

3. Results and Discussion

The importance of correct weighting of TMY variables increases with the inter-annual variability of monthly plant yield levels. Fig. 1 presents this variability considering outage-corrected yield. It reaches its maximum in December with ranges of 17 and 21 per cent of the 5-year means with the pc-Si and CdTe modules, respectively. In the case of both module types, the months from May to October are characterised by a lower variability than the months from November to April. The variability of annual yield levels, in turn, is within a range of four per cent with the plant's pc-Si section and six per cent with the CdTe section.

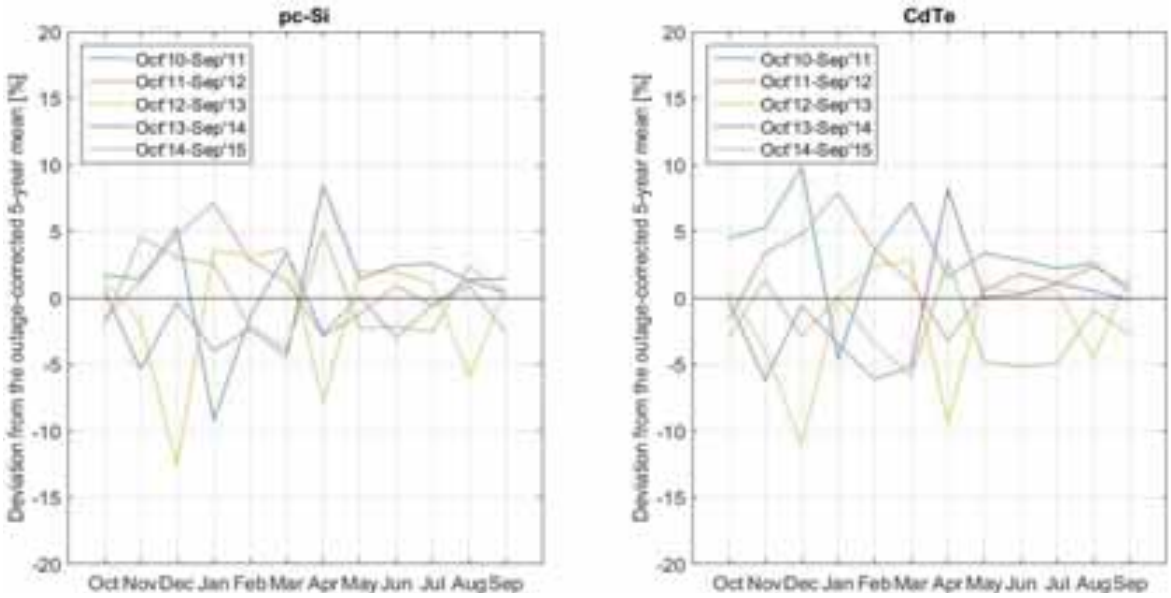

Fig. 1: Inter-annual variability of the outage-corrected monthly yields of the plant under consideration.

When determining the TYY months, outage-corrected plant yield data are further corrected for the assumed time-dependent degradation. The TYY months are found to be sensitive to the assumed rate of time-dependent degradation and therefore, a locally conducted degradation analysis is required to further improve the accuracy of the TYY month selection.

Fig. 2 compares the corrected TYY yields with the monthly mean yields. As can be seen from the figure, the monthly TYY yields are within a range from -2 to 2 per cent of the monthly means in all months apart from April and December in the case of the pc-Si modules and November in the case of CdTe modules. In both cases, the use of the TYY months results in the overestimation of the annual yield compared to the multiannual mean: by 0.9 per cent with the pc-Si modules and by 0.2 per cent with the CdTe modules.

The TMY dataset construction methods proposed by Marion and Urban (1995), Stoffel et al. (2010), and Kalogirou (2003) have not been designed for any specific solar energy technology. They consider a wide variety of different meteorological parameters and give half of the weight to irradiance variables. The two methods proposed by Cebecauer and Šúri (2015) for modelling the performance of PV and solar thermal power stations involve only three or four weighted TMY variables and place a 95 or 96 per cent weight on irradiance parameters, respectively.

After iterating through tens of thousands of different weighting sets for both sections of the power station, the sets resulting in TMY months with the greatest overlap with TYY are selected for further comparison. The respective weighting sets are presented in Tab. 3. With both module types, the combined weight of irradiance variables is 64 per cent. The remaining 36 per cent is placed on *T*'s monthly range in the case of the plant's pc-Si power blocks and on monthly average WS and minimum RH in the case of the CdTe

blocks. It is not clear why the use of these meteorological statistics resulted in the best agreement between the TMY and TYY months. The monthly average *T* was initially expected to exist in the optimal weighting sets together with irradiance parameters due to the significant impact of *T* on solar cell temperature. One reason for the somewhat surprising outcome may be the strong positive correlation between *T* and irradiance variables and the consequent positive correlation between *T* and plant yield. *T* range and average WS are also positively correlated with plant yield but exhibit low correlation with irradiance parameters. Thus, they may better capture the actual negative impact of *T* on plant yield. The TMY determination approach through CDFs is emphasised over individual statistics with a weight of 0.7 in both cases.

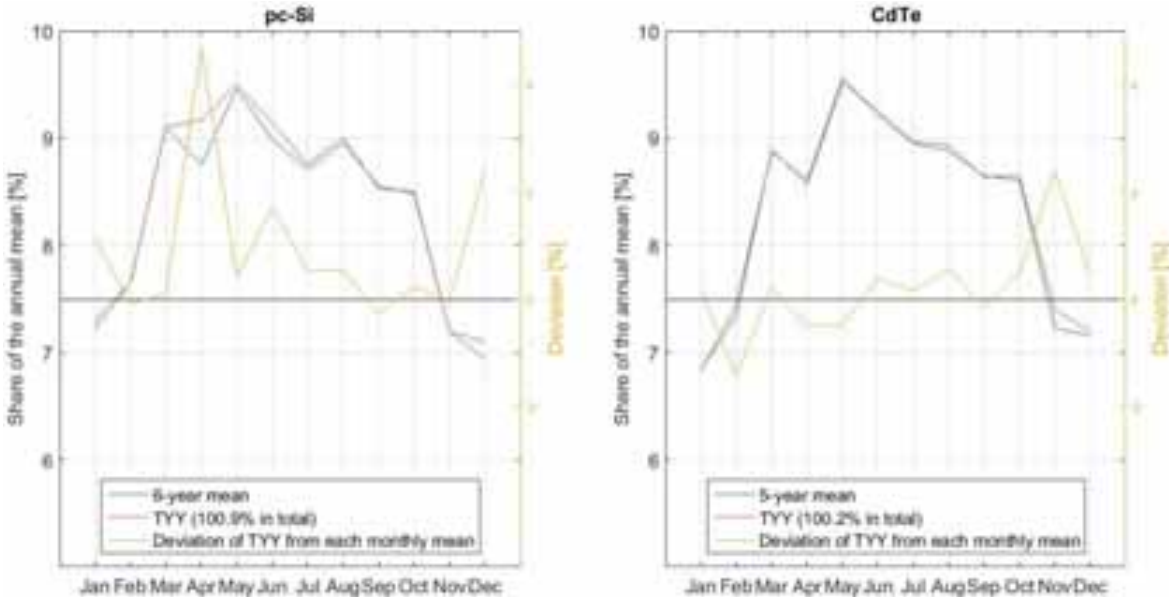

Fig. 2: Deviation of outage and time-dependent degradation-corrected TYY yields from monthly means.

Tab. 3: Weighting sets resulting in TMY months with the greatest overlap with TYY for both module types

Module type	GHI average	BNI average	DHI average	*T* range	WS average	RH minimum	CDF
pc-Si	0.11	0.23	0.30	0.36			0.7
CdTe	0.45	0.19			0.35	0.01	0.7

Fig. 3 compares the monthly yields estimated based on the different TMY weighting sets to the multiannual monthly mean yields. As can be seen from the figure, the monthly deviations are reduced in most cases when using the TYY-based weighting set (AD) as compared to the previously proposed sets. Fig. 4 shows the performance of the different sets in terms of root mean square error (RMSE) and bias. The improvement in RMSE is more significant with the CdTe section due to the better agreement of its TYY months with the multiannual monthly means. In both cases, RMSE is reduced, however. While RMSE measures the monthly average deviation, bias can be considered as the annually aggregated error. As implied by the bias bar graph of Fig. 4, the AD sets do not perform better than the previously proposed sets on an annual scale. In fact, the AD set for the pc-Si section results in the highest bias amongst all the sets. As this is due to the overestimating TYY yields, the bias can be reduced by using longer time series as the basis for TYY determination. The findings presented in Fig. 4 imply, however, that on an annual scale, the choice of the TMY parameter weighting set does not have a major impact on the estimated yield levels if the set is selected amongst the previously proposed sets.

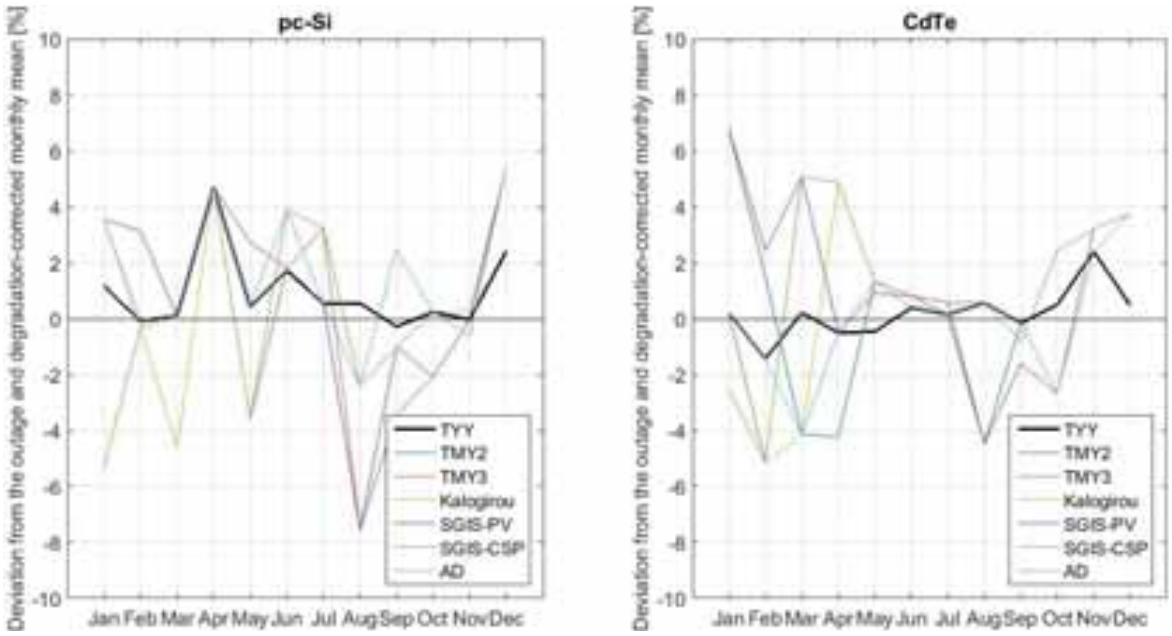

Fig. 3: Deviation of yield estimates based on different TMY variable weighting sets from the multiannual monthly mean yields (AD = weighting set optimised for the power station of interest)

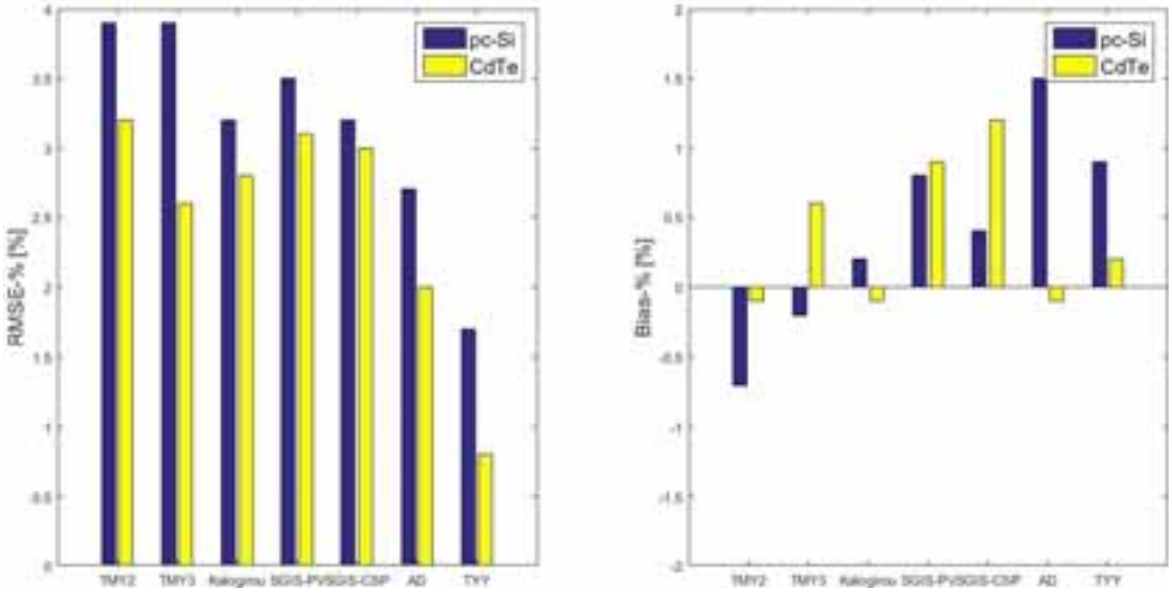

Fig. 4: Performance of different TMY variable weighting sets when compared to the multiannual monthly mean yields

4. Conclusion

In this study, weights of different TMY parameters are adjusted to suit PV plant performance assessment under the hot dry maritime climate type of Abu Dhabi. The results are expected to be generalizable to other regions characterised by the same climate type. The use of an appropriate weight set is the more important, the higher is the inter-annual variability of monthly yield levels. The variability is found to exhibit both seasonal dependence characterised by higher levels during winter months and technological dependence with higher levels for the CdTe module-equipped power blocks. In December, which is the month with the highest inter-annual yield variability, the difference in yield between the best and worst years can be more than 20 per cent of the multiannual mean yield.

The TYY-based TMY parameter weighting approach proposed in this paper reduces the deviations of TMY-based yield estimates from the multiannual monthly means as compared to the previously proposed TMY

weighting sets. The resulting locally determined weight sets place approximately two third of the weight on irradiance variables and one third on parameters that are correlated with plant yield but not with irradiance, *T* range and WS in specific. The performance of the proposed approach is highly dependent on the accuracy of TYY on a yearly scale and therefore, further improvement can be achieved by using longer yield time series and deploying locally identified rates of time-dependent degradation. On an annual scale, no major benefit is derived from using the TYY-based approach as compared to the previously proposed TMY weighting sets.

Acknowledgements

The authors want to thank Masdar Clean Energy for granting them access to the performance database of the PV power station operated in Abu Dhabi, Mr. Borja Aranaga and his team at Enviromena Power Systems for practical assistance with accessing the data, and Professor Peter Armstrong and Mr. Muhammad Tauha Ali at Masdar Institute for providing them with the dataset of ambient parameters and assistance with post-processing the data.

References

Alduchov, O.A., Eskridge, R.E., 1996. Improved Magnus Form Approximation of Saturation Vapor Pressure. J. Appl. Meteorol. 35, 601–609. doi:10.1175/1520-0450(1996)035<0601:IMFAOS>2.0.CO;2

Beták, J., Šúri, M., Cebecauer, T., Skoczek, A., 2012. Solar Resource and Photovoltaic Electricity Potential in EU-MENA Region, in: EU PVSEC Proceedings. Presented at the 27th European Photovoltaic Solar Energy Conference and Exhibition, Frankfurt am Main, Germany, pp. 4623–4626. doi:10.4229/27thEUPVSEC2012-6CV.3.51

Cebecauer, T., Šúri, M., 2015. Typical Meteorological Year Data: SolarGIS Approach. Energy Procedia, International Conference on Concentrating Solar Power and Chemical Energy Systems, SolarPACES 2014 69, 1958–1969. doi:10.1016/j.egypro.2015.03.195

Jordan, D.C., Wohlgemuth, J.H., Kurtz, S.R., 2012. Technology and Climate Trends in PV Module Degradation, in: Proceedings of the 27th European Photovoltaic Solar Energy Conference and Exhibition. Presented at the 27th European Photovoltaic Solar Energy Conference and Exhibition, Frankfurt am Main, Germany, pp. 3118–3124. doi:10.4229/27thEUPVSEC2012-4DO.5.1

Kalogirou, S.A., 2003. Generation of typical meteorological year (TMY-2) for Nicosia, Cyprus. Renew. Energy 28, 2317–2334. doi:10.1016/S0960-1481(03)00131-9

Marion, W., Urban, K., 1995. User's manual for TMY2s: Derived from the 1961-1990 National Solar Radiation Data Base (Technical Report No. NREL/SP-463-7668). National Renewable Energy Laboratory, U.S. Department of Energy, Golden, Colorado, USA.

Stoffel, T., Renné, D., Myers, D., Wilcox, S., Sengupta, M., George, R., Turchi, C., 2010. Concentrating Solar Power: Best Practices Handbook for the Collection and Use of Solar Resource Data (Technical Report No. NREL/TP-550-47465). National Renewable Energy Laboratory, U.S. Department of Energy, Golden, Colorado, USA.

QATAR DYNAMIC SOLAR ATLAS AND SOLAR RESOURCE ASSESSMENT

Yasir Mohieldeen, Luis Pomares, Daniel Perez-Astudillo, Dunia Bachour, Saiyed Wahadj

Qatar Environment and Energy Research Institute(QEERI), HBKU, Qatar Foundation, Doha, (Qatar).

Abstract:

Solar resource assessment is key preliminary to any successful solar energy production project. This study presents the solar resource assessment and mapping efforts that are currently being carried out at the Qatar Environment and Energy Research Institute (QEERI) in Qatar, to create a dynamic solar atlas for Qatar, showing solar irradiation, across the country, every 15 minutes. These data are essential for the successful harnessing and utilization of solar energy.

Rigorous analysis of solar irradiation components measured through ground monitoring stations combined with data derived from satellite imagery has made it possible to generate the dynamic atlas. The developed maps will help identify areas and locations with high solar energy generation potentials. Direct Normal Irradiance (DNI), Diffused Horizontal Irradiation (DHI) and Global Horizontal Irradiation (GHI) will be calculated from the satellite images and calibrated and validated with their corresponding ground measured values. The time series of these valuable maps will enable solar energy short-term forecasting and will contribute to the successful operation of solar energy production facilities in the country. The generated datasets will be available through a solar geo-portal on the World Wide Web.

Keywords: Solar atlas, solar irradiation, network optimization, METEOSAT MSG, solar monitoring stations, solar modeling, neural network, Heliosat, and solar forecasting.

1. Introduction:

The primary objective of this paper is to present the solar atlas development programme at Qatar Environment and Energy Research Institute (QEERI), a member of Qatar Foundation. The study will present the framework and the plan to achieve these goals. Achievements so far and the status of the solar atlas as it stands now (at the time of presenting this paper) are also included, along with the next/future steps.

The paper is structured as follows: First, a brief overview is given about Qatar and its electricity demand in the background section. Second, the need for the solar atlas and its importance to Qatar's solar energy plan is highlighted. The framework for the atlas development is described in section 2. Section 3 presents some concluding comments.

1.1 Background

The State of Qatar wants to generate 20% of its electricity requirement from solar power by 2020. This policy aims to meet the increasing electricity demand induced by increasing population and the associated urbanization with its energy-hungry life-style while adopting at the same time environmental-friendly renewable energy. Qatar's population has increased almost five times from 0.37 million to 1.74 million between 1986 and 2010, and six times between 1986 and 2014, as shown in Fig. 1.

doi:10.18086/swc.2015.07.07 Available at http://proceedings.ises.org

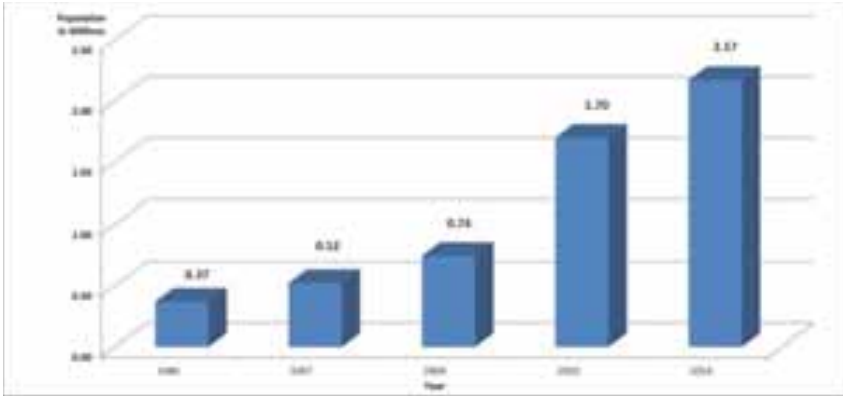

Fig. 1: Population growth in Qatar in millions

Source: (QSA, 2013; PC, 2006; TE, (2014)

The electricity and water company in Qatar KAHRAMAA has reported an increase in the maximum network load from 941 MW in 1988 to 3,990 MW in 2008 and reached 6255 MW in 2012 (KAHRAMAA, 2013). The number of customers increased from 132,429 in 1998 to 293,604 in 2013 (ibid, 2013)

This increase in demand is triggered also by changes in life-style, indicated by electricity per capita consumption figures. The per capita consumption grew from 12.963 KW in 1998 to 17.774 KW in 2007 (ibid, 2013).

To meet this increasing demand for electricity, and as a dry country with no hydro-power resources, Qatar has increased the number of gas-generated electricity plants in the 2000s from 3 to 8 plants. Electricity production over the last few years is shown in Fig. 2.

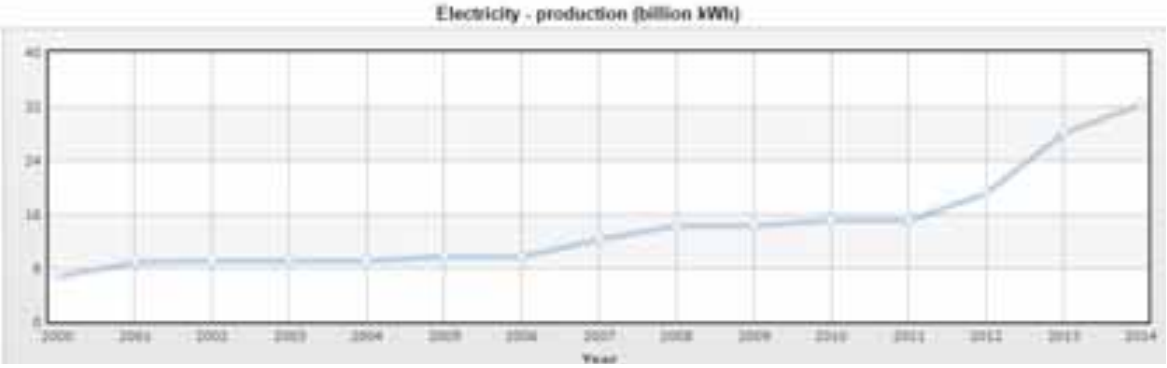

Fig. 2: Electricity Production in Qatar 2000-2014

Source: CIA World Factbook

Qatar is ranked as having the second-highest per capita ecological footprint among 150 countries, down from being the highest in 2012, according to the WWF's Living Planet Report (WWF, 2014). This report is published every two years. With these environmental concerns and the unstable oil prices in mind Qatar has decided to introduce clean renewable energy to produce electricity as opposed to non-renewable environmentally un-friendly natural gas.

Solar energy is arguably the most effective way to meet the increasing energy demand of Qatar and the region, for the following reasons: firstly, solar energy is renewable as opposed to the non-renewable gas and oil which are finite resources. Secondly, solar energy is clean and limits the emissions of Greenhouse Gases. Thirdly, using solar energy lengthens the life of oil and natural gas resources, and reserves them for future generations. .

A preliminary analysis of solar energy potentials carried out using historical data collected by Qatar Meteorological Department (QMD), reveals that there is a high potential of solar energy in Qatar. The ground-measured yearly average Global Horizontal Irradiation (GHI) for Qatar is 2113 kWh/m2/year (Bachour et al, 2013). GHI is suitable for the Photovoltaic (PV) method of converting solar energy into

direct current electricity.

Another analysis carried out by QEERI (Perez-Astudillo *et al*, 2013) using data from a ground solar station installed at QEERI, collecting Direct Normal Irradiance (DNI), Diffused Horizontal Irradiance (DHI) and GHI, confirms the solar energy potentials in Doha.

1.2 Why the Dynamic Solar Atlas

The Solar Atlas and solar mapping is key to successful implementation of any solar energy production program in Qatar. The Atlas helps identify areas and locations with high solar energy generation potentials. It helps in the identification of the optimum locations for solar panels. Qatar is a small country but the spatial variability in solar irradiation is variable because of the existence of micro-climates related to different land-covers and effects of the sea on inland climate. The atlas helps a wide range of professionals to better understand the spatial and temporal distribution of the solar irradiation in the country.

The dynamic atlas provides near-real time solar maps every 15 minutes of solar data including DNI, DHI and GHI. These datasets are accessible online through the World Wide Web. The atlas also provides now-casting and forecasting of solar irradiation data that can be used for solar energy production management.

The maps are produced through rigorous analysis of solar irradiation components measured through ground monitoring stations combined with data derived from satellite imagery. Solar information produced from satellite images are calibrated and validated with their corresponding ground measured values.

2. Method & Framework:

This section describes the plan adopted to develop the dynamic solar atlas. The steps that were undertaken and future plans are also highlighted. These steps could be summarized as: data collection; and modeling of solar irradiation.

2.1 Data collection

The collection of high quality solar irradiation data is a key to the development of the atlas of solar resources of Qatar. It is necessary to install two kinds of equipment: a METEOSAT satellite ground receiving station and a number of solar monitoring stations.

2.1.1 Satellite data:

Data from METEOSAT satellite EUMETSAT program has been used in the study. A METEOSAT Second Generation (MSG) ground receiving station has been procured and installed at the QEERI premises in Doha. The MSG is a geostationary meteorological satellite collects weather information all over the globe. The sensor onboard the satellite, known formally as the Spinning Enhanced Visible and Infrared Imager (SEVIRI), observes the full disk of the Earth with a repeat cycle of 15 minutes. It captures images in 12 spectral wavelength regions or channels. Many parameters related to solar irradiation are recorded by these channels. The Water vapour, Infra-Red (IR), and the visible channels of the satellite are the main channels that are utilized here for modeling and mapping solar irradiation. Atmospheric Motion Vectors (AMV) products are received every hour. AMVs show cloud speed and direction and are used for atmospheric and solar irradiation forecasting. Fig. 3 below shows the satellite ground receiving station installed at the QEERI premises.

(a) (b)

Fig. 3: The METEOSAT MSG ground receiving station installed at QEERI in Doha. (a) The 2 meter antenna on the roof-top at QEERI's premises. (b) The receiving and processing servers of the MSG data in the GIS lab.

The raw data captured by the antenna (Fig. 3a) are processed and modeled/converted to solar irradiation values by combining them with ground measurements recorded at the ground Solar Monitoring Stations (SMS). These ground measurements and SMS are discussed in the following section.

2.1.2 Ground measurements:

High quality ground solar irradiation components measurements in selected locations are needed to model, verify and calibrate the satellite data to produce accurate estimates of solar radiation for the whole country. To determine the locations and the number of stations needed in Qatar, existing solar data collected by the Qatar Meteorological Department (QMD) was obtained and analyzed. The QMD network consists of 12 stations, designed to measure meteorological data. Global Horizontal Irradiation is the only solar component that is measured by QMD network.

A collaboration agreement with QMD has enabled QEERI to use QMD's network to install solar equipment on selected stations.

To determine which stations in the QMD network to use for solar installation, a network optimization study was carried out on the network. The network optimization study also determines potential gaps in the network for solar measurements.

2.1.2.1 Solar Monitoring Stations (SMS) Network optimization:

Different techniques and methods have been developed by scientists and meteorologists to address the optimum site selection task (Singh et al, 2013; Mohajeri, 2010; Pardo-Igúzquiza, 1998).

The network was optimized first, by determining the maximum distance from a station that maintains acceptable relative variation in magnitude of solar irradiation. Second, by determining potential gaps in the network and cover them by new stations.

To determine the maximum distance with acceptable variability, the GHI data from the QMD network was analyzed. The QMD network of 12 stations is shown in Fig. 4 below.

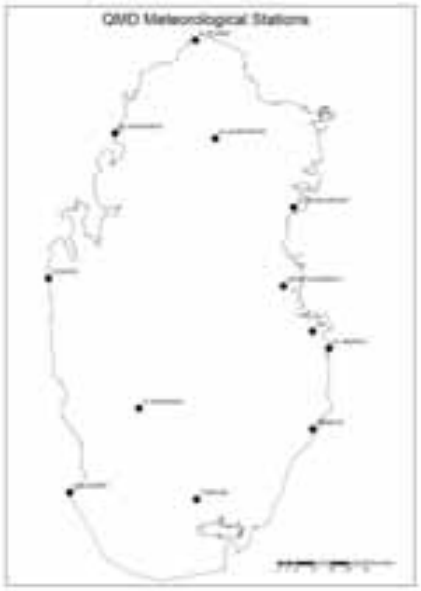

Fig. 4: Locations of the 12 solar monitoring stations operated by QMD.

GHI values were analyzed relative to the distances between the station sites. Daily and monthly GHI averages from QMD's stations were analyzed, along with corresponding GHI values derived from satellite images by Masdar Institute of Science and Technology (MIST)- the United Arab Emirates (MIST, 2015). Fig. 5 shows the relative variations, as a function of distance, of daily (red line) and monthly (blue) averages of GHI as measured at ground level by the 12 QMD stations. The (green) line is for monthly averages from satellite. The distances in the Figure are grouped in bins of 10 km, centered at 5, 15, 25 km intervals up to 160 km. For example the point at a distance of 65 km represents all pairs of stations with separation between 60 and 70 km. The relative variations of GHI are the averages for all pairs in each distance bin.

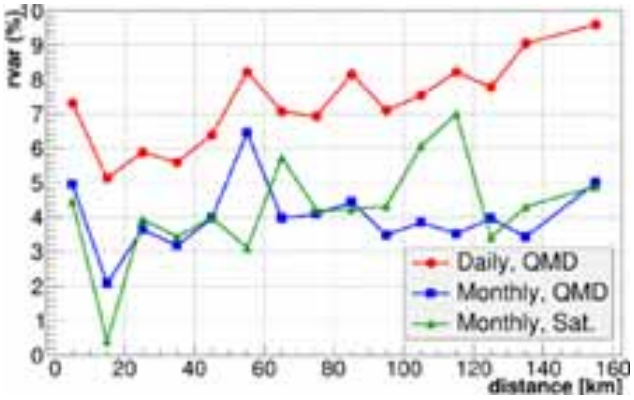

Fig. 5: Relative variations of GHI values as a function of distance between stations

Data Source: QMD, 2015

Fig. 5 shows that the selected stations less than 30km apart experienced 6% relative variation in their daily GHI measurements. Counter intuitively, a higher relative variation (7%) is found at the lesser distance of 5km, and this is attributed to stations being located in and around Doha City where various micro-climates are induced by variation in aerosol loads across the city. The authors consider 6% variation in daily GHI values of adjacent stations to be an acceptable variation.

In addition to the analysis of interstation solar radiation variability using QMD data, satellite imageries were also analyzed for network optimization. A 2010 average GHI image produced by Masdar Institute of Science and Technology derived from satellite data is analyzed using Moran's I index spatial statistics method.

The Moran's I index compares the differences between neighboring pixels and the mean to provide a measure of local homogeneity. The value range is between +1 and -1, where:

+1 = strong positive spatial autocorrelation, 0 = spatially uncorrelated, -1 = strong negative autocorrelation.

Results of the Moran's I index analysis are shown in Fig. 6.

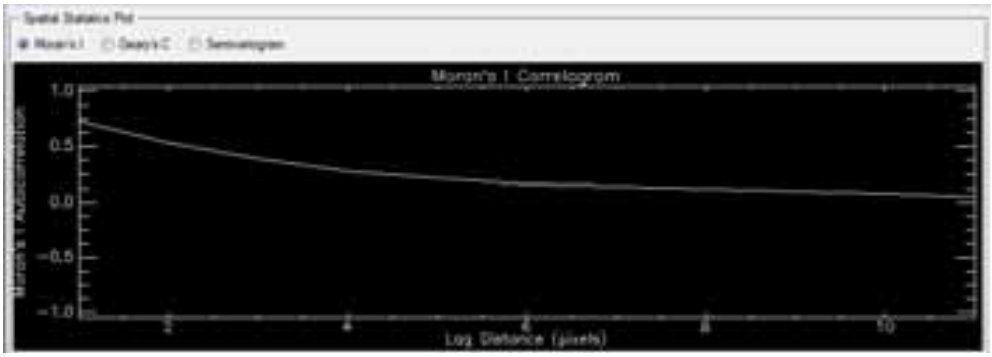

Fig. 6: Moran's I analysis on 2010 GHI pixel values.

Results of Moran's I analysis shows that the spatial correlation of the 2010 GHI values was strong within neighboring pixels. The index value did not start from the value of 1 as one would expect since neighboring pixel values should have exhibited high autocorrelation. This discrepancy was due to micro-climate and satellite model errors. The spatial autocorrelation decreases as the distance between the measurements increases, and is nearly lost (that is close to 0 Moran's index) when it reaches 8 pixels apart. Since the pixel size is 3 km, this distance is equivalent to 24 km. The analysis further confirms the results obtained from QMD data analysis. Generally, 30 km distance between ground stations is considered as appropriate for good spatial coverage (Perez et al., 1997).

The results above imply that GHI measurements taken at one location could be considered as representative of up to 25-30 km away from that location. That is to say, a solar station measurement could be considered representative of the local irradiation status within a 25km radius from that station. For the sake of accuracy and achieving an adequate research quality data a 20km radius is used here. Fig. 7 below shows a 20km radius buffer that is covered by individual station in the QMD network of SMS. The red circles represent gaps that need to be covered.

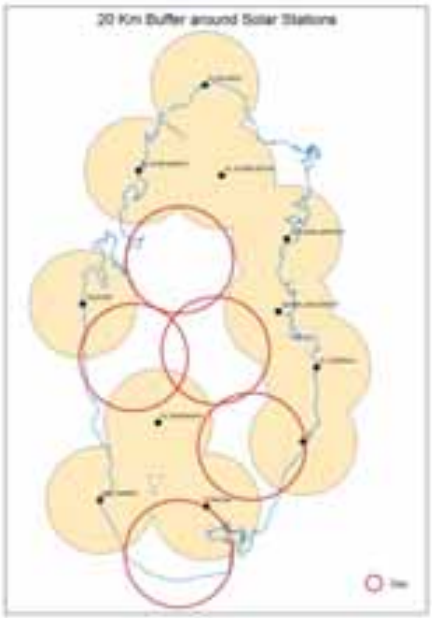

Fig. 7: Map of the coverage achieved with buffer zones of 20 km radius around QMD stations. The red circles show the locations of additional stations needed to cover the gaps.

Site visits were conducted to all existing and proposed stations for sites verification. Fig. 8 below shows a photo of one QMD stations during a site visit.

Fig. 8: Location of one of the QMD stations, south west of Doha.

2.1.2.2 Land see-breeze effect:

In order to ensure representative sampling of the solar irradiation, many factors that influence the spatial distribution of solar irradiation have to be taken into account in the site selection for stations. As Qatar is a peninsula, it was necessary to study the influence of the sea on Qatar solar resources. The two main sea phenomena that might have influence on solar radiation and are considered here are land-sea breeze phenomenon, and the mixed land-sea satellite pixel.

The influence of land-sea breeze on aerosols concentration and transportation in the atmosphere along coastal areas has been investigated by numerous studies (Tsai et al, 2011; Kolev et al, 1998). The land-sea breeze (Fig. 9) arises because of differential temperature between land and water surfaces. During the day winds develop over water near land due to differences in air pressure created by their different heat capacities, as solar radiation heats the land more quickly than the water, causing sea breeze (Fig. 9a). At night, water's high heat capacity prevents rapid loss in water temperature and therefore remains warmer than land causing the winds to reverse direction (from land to sea, causing land breeze (Fig. 9b).

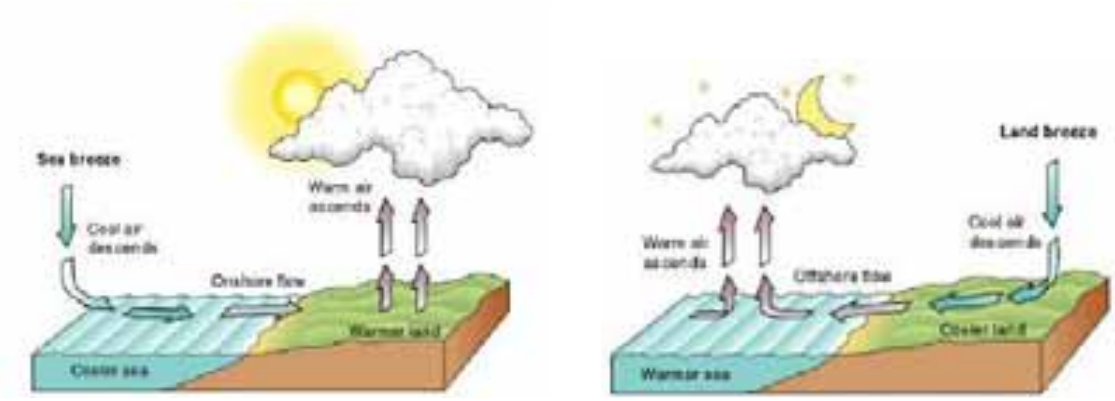

(a) Sea breeze **(b) Land breeze**

Fig. 9: Land-sea breeze phenomena.

These studies of land-sea breeze have shown that these phenomena lead to high concentration of aerosols in coastal areas and result in aerosol circulation (between land and water) along the coastal line This high concentration is due to the accumulation and the forward and backward movements of the aerosols between land and water, leading to aerosol entrapment around the coast. All pollution sent from land to the sea at night and early morning, returns back to the coast during the day. The high aerosol concentration leads to high diffusion of solar irradiation.

As for Qatar, the land-sea phenomena could be observed by the RAMS/ICLAMS model applied by the QMD for wind monitoring as shown in Fig. 10, on the 26th Sept 2015. Land breeze is shown in Fig. 10a (at 03:00

AM UTC time) early in the morning when the sea is warmer than the land, whereas see breeze is shown in Fig. 10b (at 11:00 AM UTC time) when the land started to heat up a clear reverse of wind direction took place from the Arabian Gulf into the eastern coast of Qatar.

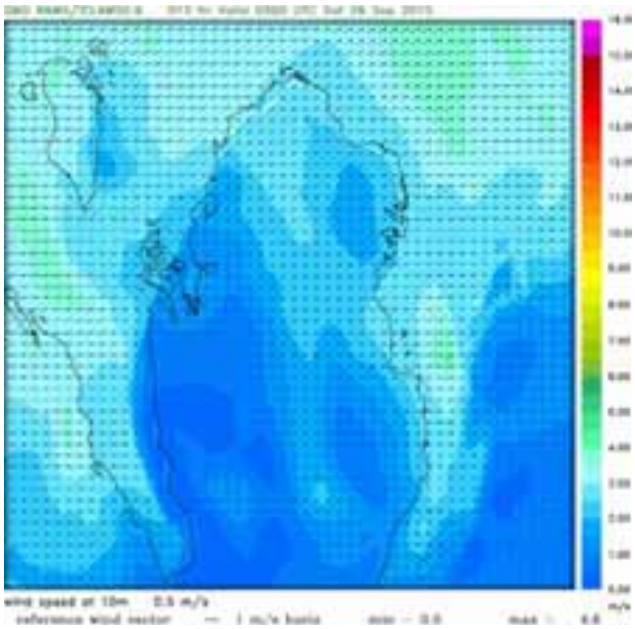

(a) Land breeze

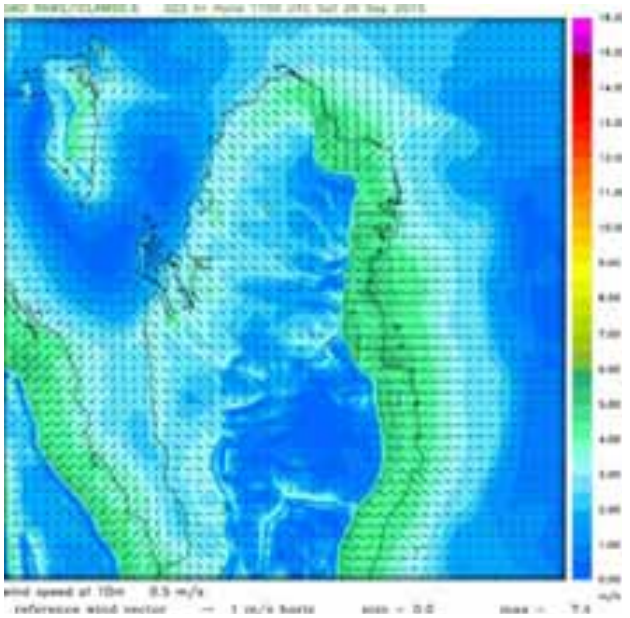

(b) Sea breeze

Fig. 10: A normal day Land-Sea Breeze sequence in Qatar, 26th Sep 2015.

Source: QMD, 2015

It should be noted that nine out of twelve of QMD stations are coastal stations, and located in areas most affected by the land-sea breeze phenomena and hence by aerosols. This means that the existing sampling structure/regime is biased and is not necessarily optimum for solar mapping.

To optimize the sampling of the solar monitoring stations network, more inland stations have been introduced by shifting some coastal stations to inland sites (Al Rwais, Qatar University, Doha Airport & Umsaid); and by introducing/proposing new inland station sites (Ghasham Farm, Jumailiah, Um Wishah, Suda-nithail, Camel Racing court). The final optimized SMS network is shown in Fig. 11 below.

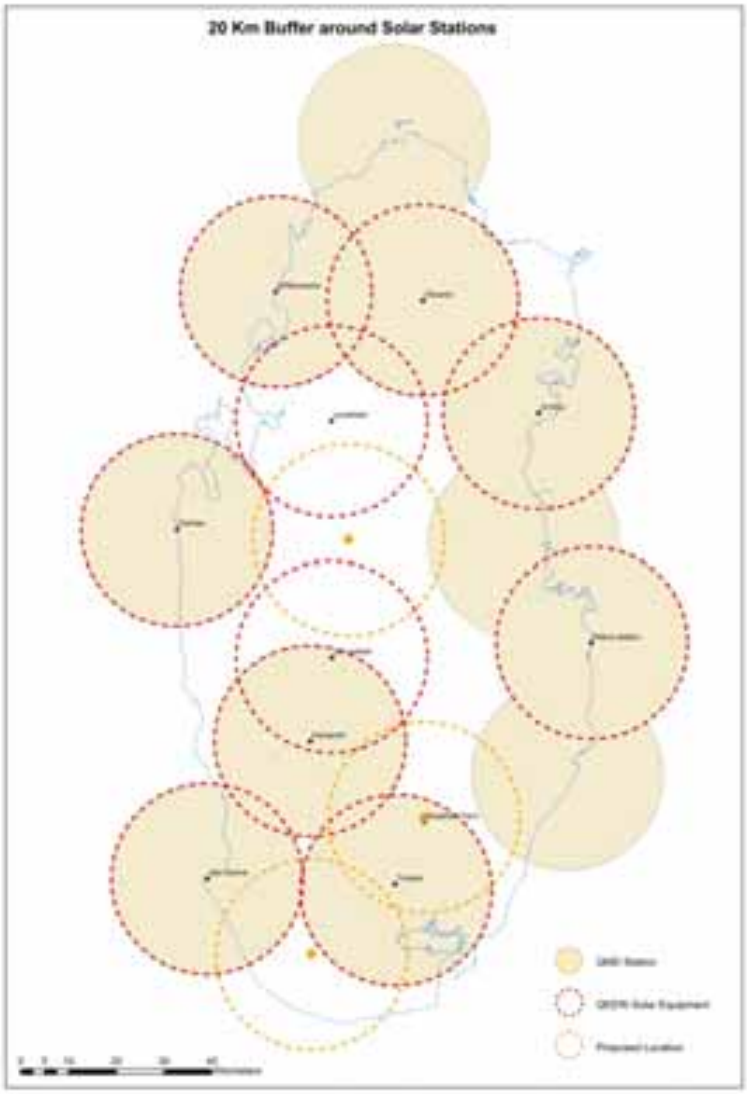

Fig. 11: Optimized Solar Monitoring Stations Network, with existing and proposed stations indicated.

Another reason for minimizing the number of coastal stations is to reduce the impact of the satellite "mixed-pixel" issue in the analysis when combining ground measurements with METEOSAT satellite images in the modeling. As the pixel size of these images is 3km, coastal station measurements might be analyzed with a pixel that partially covers land and water (mixed), and that could introduce in-accuracies to the model.

Based on the above optimized network, thirteen solar monitoring stations have been procured and are in the process of being installed in their respective sites. The next section discusses the processing of the data captured by the METEOSAT receiving station (Section 2.1.1) and the optimized SMS network (Section 2.1.2).

2.2. Data processing and solar modeling

This section describes how the satellite data collected by satellite ground receiving station and the ground measurements collected by the 13 monitoring stations are combined to create the atlas.

The SEVIRI satellite data are converted to solar irradiation estimates. Two methods are adopted to compare results. The first is to use existing empirical/physical models, in this case Heliosat model, and use local ground measurements data to adjust the model to Qatar climatic conditions.

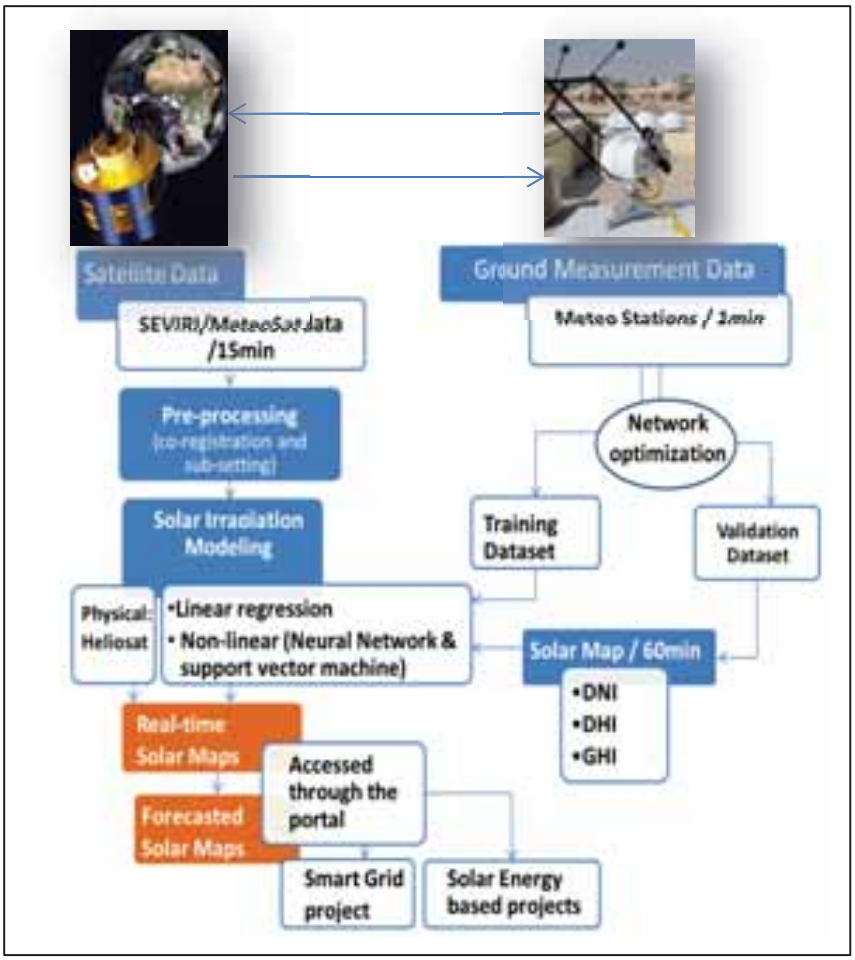

Fig. 12: The dynamic solar atlas framework

The main principle of the Heliosat method is the construction of a Cloud Index (CI) by comparing what is observed in the pixel by the sensor to what should be observed over that pixel if the sky were clear, which is related to the "clearness" of the atmosphere (Rigollier *et al*, 2002).

The CI is derived from the Meteosat 15 minutes satellite images. The CI is then used to calculate the atmospheric Clearness Index (Kc) values. First the Clear Sky solar radiation component is derived using Linke Turbidity values obtained from MACC II. Then the Kc is combined with CS solar radiation to produce all-sky solar radiation estimates from the satellite. The schematic diagram of this physical model is shown in Fig. 13 below.

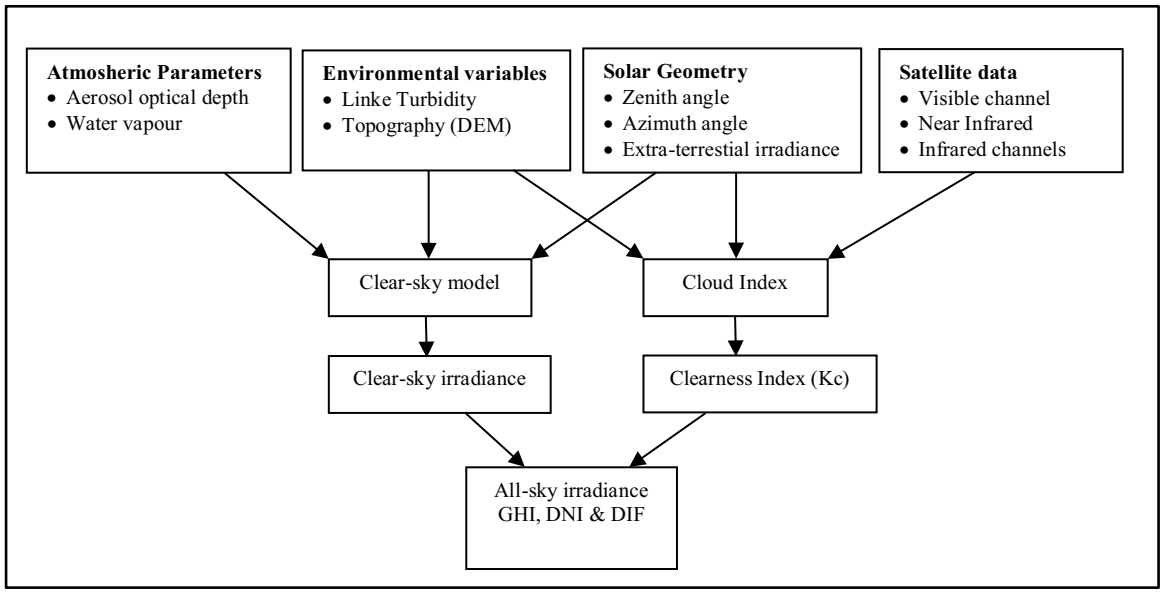

Fig. 13: Schematic diagram of the adopted Heliosat semi-physical all-sky solar radiation model

The satellite data used in the model and derived inputs to the model is listed in Table 1 below:

Model Input	Data source	Coverage period	Time step	Spatial Resolution
Cloud Index	Meteosat MSG Visible, NIR & IR channels	2005 to present	15 minutes	5 km
Atmospheric Optical Depth (AOD)	MACC II	2003 to present	Daily	125 km
Linke Turbidity	MACC II	2003 to present	Daily	125 km
Clearness Index	ESRA model	2005 to present	15 minutes	5 km
Water vapour	MACC II	2003 to present	Daily	125 km
Topography (DEM)	SRTM	Present	-	1km

Table 1: Input data to the satellite model

Ground measurements of daily GHI from nine QMD stations, with available measurements between2003-2013, were used to validate the satellite model results. The validation results and the uncertainty parameters of these daily GHI estimates are shown in Table 2 below. The mean relative RMSD for the stations was 11.5%. A relatively high coefficient of determination R^2 of 0.92 was depicted.

Station	MBD (Wh/m^2 day)	RMSD (Wh/m^2 day)	KSI	rMBD (%)	rRMSD (%)	KSI (%)	R^2
Dukhan	449.43	776.12	431.62	7.97	13.77	123.36	0.92
Turayna	63.96	601.34	17.88	1.09	10.21	5.11	0.92

AlShehaimiya	10.60	481.65	68.84	0.18	7.96	19.68	0.96
Ummsaid	235.28	708.94	336.36	4.12	12.41	96.13	0.91
Qatar University	204.33	595.18	269.30	3.50	10.20	76.97	0.94
AlKhor	95.75	697.08	195.80	1.62	11.80	55.96	0.91
AlKaranaah	238.81	690.89	283.94	4.06	11.75	81.15	0.91
AbuSamra	169.88	745.44	155.11	2.91	12.78	44.33	0.88
AlWakrah	126.68	727.61	132.80	2.17	12.48	37.96	0.89
Mean	**177.19**	**669.36**	**210.18**	**3.07**	**11.48**	**60.07**	**0.92**

Table 2: Validation results and the uncertainty parameters for the satellite-derived daily GHI

The resulted annual average GHI map for Qatar for the period 2003 to 2013, from the model, is shown in Fig. 14 below.

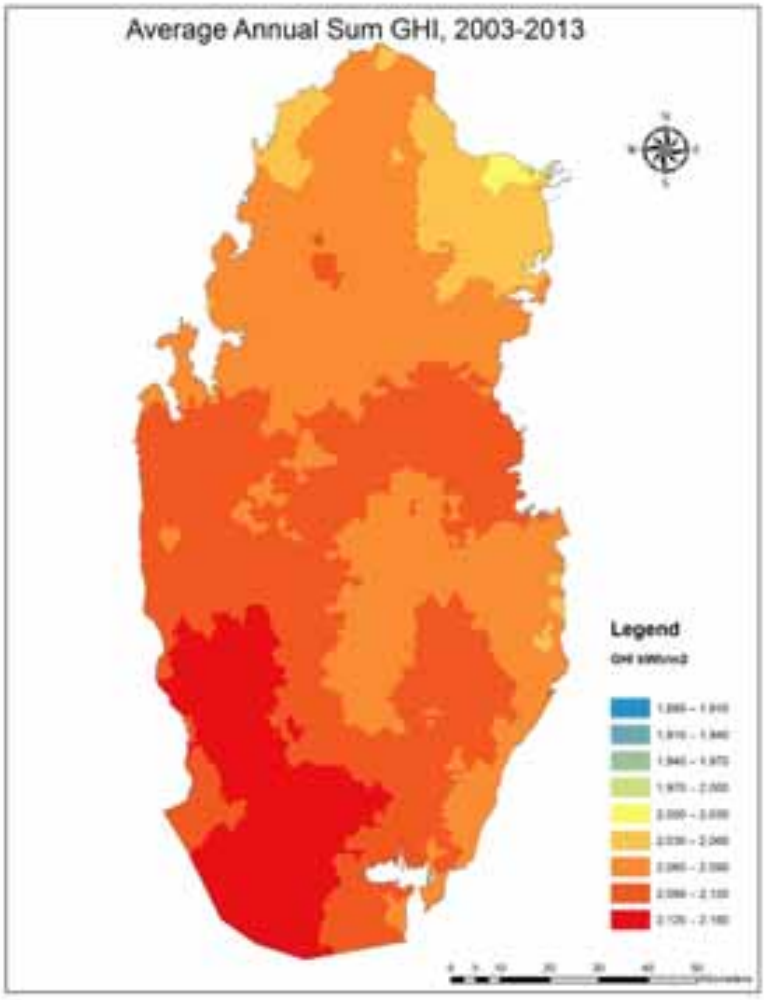

Fig. 14: Average Annual Sum GHI (kWh/m^2) for Qatar, 2003-2013

The second modeling method, that will be implemented, is a statistical model, regression analysis (linear,

and non-linear such as neural network). In this method the satellite data will be regressed with the ground measurement from the 13 monitoring stations to derive accurate estimates of solar irradiation from the satellite imageries. The data processing methods are shown in Fig. 12 above.

Output from the models and the data processing and analysis are near-real time (every 15 minutes) solar maps show the spatial distribution of the solar irradiation parameters in the country. These results are used for solar forecasting and now-casting of irradiation, as shown in Fig. 12 above. Statistical models and weather prediction models will be used for forecasting. The generated datasets would be used for instance for smart grid management and any other solar-energy based projects. These datasets are stored and organized in a data-portal and disseminated online through the World Wide Web. The data-portal is highlighted in the next section.

2.3 Results dissemination and data-portal:

The solar datasets produced by the modeling are organized by a data-portal. The portal is a database and an application that enable the dissemination and querying of geospatial data. The data-portal application is built on ESRI ArcGis Server, Java scripting, and python programing. A snapshot of the on-line Qatar solar atlas is shown in Fig. 13. Point, line and polygons geometries could be used to query the solar maps and to extract statistics and values from them.

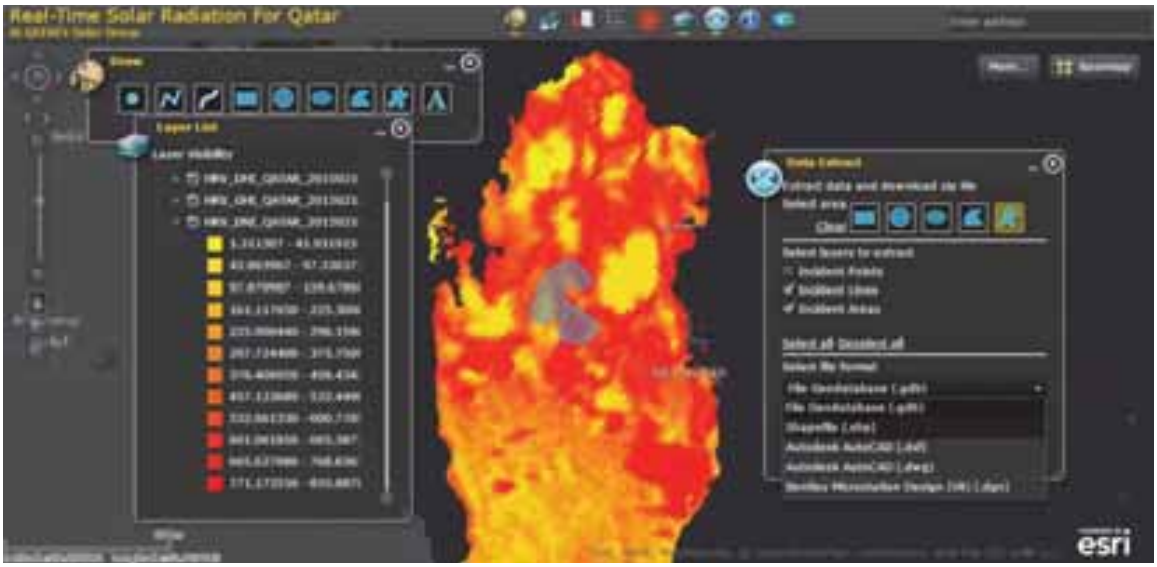

Fig. 13: A snapshot of the solar atlas geo-portal

3. Conclusion

The State of Qatar aims to generate 20% of its electricity requirement from solar power by 2020. This is to meet the increasing electricity demand caused by increasing population and to reduce the high ecological footprint resulted from dependency on oil and gas in generating electricity. Mapping the solar resources in Qatar and creating a solar atlas is key preliminary to the successful implementation of any solar energy project in the country.

This paper presented the solar resource assessment and mapping efforts that are currently being carried out at the Qatar Environment and Energy Research Institute (QEERI) in Qatar. A solar atlas for Qatar will be generated which will show solar irradiation, across the country, every 15 minutes. These data are essential for the effective harnessing and utilization of solar energy in the country.

Data collected by METEOSAT MSG satellite and by ground measurements have been combined and analyzed. The network of the ground measurement stations has been optimized in order to capture high quality data. The optimization was carried out based on rigorous analysis of daily GHI data collected by 12

QMD meteorological stations. The sea-breeze effect on solar energy, and the land-water mixed pixel issue were also taken into account in the optimization, by shifting some coastal stations to inland sites. The resulted average annual sum GHI map, derived from the Heliosat model, shows high potentials of solar energy generation using PV technologies. The time series of the 15 minutes GHI maps will also enable solar energy short-term forecasting and will contribute to the successful operation of solar energy production facilities in the country. The generated datasets will be made available and accessible through a solar geo-portal on the World Wide Web.

Acknowledgement:

The authors would like to thank Qatar Meteorological Department (QMD) for their collaboration and continuous support and for sharing their solar databases.

Bibliography:

Bachour D, Perez-Astudillo D, 2013. 'Ground-measurement GHI map for Qatar', Proceedings of SolarPACES 2013.

CIA World Factbook 2015.http://www.indexmundi.com/g/g.aspx?v=79&c=qa&l=en

ESRA model. http://www.oie.mines-paristech.fr/Valorisation/Outils/Clear-Sky-Library/

KAHRAMAA 2013. http://www.km.com.qa/AboutUs/Pages/ElectricitySector.aspx

Kolev, I., Parvanov, O. Kaprielov, B., Donev, E. &Ivanov, D. 1998. Lidar Observations of Sea-Breeze and Land-Breeze Aerosol Structure on the Black Sea. Journal of Applied Meteorology Volume 37, Issue 10, 1998.

MACC II model http://www.gmes-atmosphere.eu/services/aqac/global_verification/

MIST 2015. Masdar Institute for Science and Technology- accessed at: http://solaratlas.masdar.ac.ae

Mohajeri, N. & Amin G. 2010.Railway station site selection using analytical hierarchy process and data envelopment analysis.Computers & Industrial Engineering 01/2010; 59:107-114. DOI:10.1016/j.cie.2010.03.006.

PC 2006. The Planning Council – Qatar National Atlas 2006 – Doha, Qatar.

Perez, R., Seals, R., Zelenka, A. 1997. Comparing satellite remote sensing and ground network measurements for the production of site/time specific irradiance data. Solar Energy, 60, 89-96.

Pardo-Igu´zquiza, E. 1998. Optimal selection of number and location of rainfall gauges for areal rainfall

estimation using geostatistics and simulated annealing. Journal of Hydrology 210 1998.206–220.

Perez-Astudillo D, Bachour D, 2013. DNI, GHI and DHI ground measurements in Doha, Qatar. Proceedings of SolarPACES 2013.

QMD 2015. Qatar Meteorological Department, Qatar- Doha.

QSA 2013.Qatar Statistics Authority. "It's official: There are now more than 2 million people in Qatar" accessed at: http://dohanews.co/tag/qatar-statistics-authority/

Rigollier, C., Lefèvre, M., Cros, S. & Wald, L. 2002. HELIOSAT 2: An Improved Method For the Mapping of the Solar Radiation from METEOSAT Imagery. 2002 EUMETSAT Meteorological Satellite Conference, Sep 2002, Dublin, Ireland. EUMETSAT, Darmstadt, Ger-many, pp.585-592. <hal-00465571>

Singh, W. &Sengupta, J. 2013. An Efficient Algorithm for Optimizing Base Station Site Selection to Cover a Convex Square Region in Cell Planning.

TE 2014. Trading Economics available at: http://www.tradingeconomics.com/qatar/population

Tsai, H., Yuan C., Hung C., Lin C. 2011. Influence of sea-land breezes on the tempospatial distribution of atmospheric aerosols over coastal region. Journal of the Air & Waste Management Association.Volume 61, Issue 4, 2011.

WWF 2014. Living Planet report 2014. World Wildlife Fund.

Conference Proceedings

Solar World Congress 2015
Daegu, Korea, 08 – 12 November 2015

Improving the solar resource estimation in the United Arab Emirates using aerosol and irradiance measurements

Armel Oumbe[1], Helene Bru[1*], Chao Li[1], Philippe Blanc[2], Lucien Wald[2], Hosni Ghedira[3] and Dominique Goffe[4]

[1] Total New Energies, R&D Solar, 92069 Paris La Défense, France

[2] MINES ParisTech, PSL Research University, O.I.E. – Centre Observation, Impacts, Energy, CS 10207 – 06904 Sophia Antipolis cedex, France

[3] Masdar Institute, Research Center for Renewable Energy Mapping and Assessment, Abu Dhabi, PO Box 54224, United Arab Emirates

[4] Bertin Technologies, Energy Process Environment Department, 40220 Tarnos, France

* now at BHC Energy, 92100 Boulogne Billancourt, France

Abstract

A locally-adapted model to predict irradiance in the United Arab Emirates (UAE) has been developed. It is based on the McClear model and the HelioClim database, and it utilizes aerosol optical depth measurements from AERONET network, and high-precision measurements of irradiance collected at Madinat Zayed, UAE. The clear-sky part of the model consists of McClear model operated with ground-corrected Aerosol Optical Depth (AOD) as inputs. The all-sky part is made of HelioClim-3, recalculated with the AOD-corrected McClear as inputs, and then calibrated using irradiance measurements at one station. The locally-adapted model accurately estimates the global and direct irradiances. The estimated irradiances have been validated against measurements collected from 7 Rotating Shadowband Irradiometers distributed over the UAE. The obtained root mean square errors on the hourly means of irradiance are 4% for Global Horizontal Irradiance (GHI), 10% for Direct Normal Irradiance (DNI) in cloudless skies and 8% for GHI, 26% for DNI in cloudy skies.

Keywords: *solar resource, irradiance, aerosol optical depth, UAE*

1. Introduction

In many regions, the available solar resource data do not meet the requirements for solar plant simulation and feasibility studies. On the one hand, the satellite-based models that are used for long-term irradiance estimation are often not adapted to the potential sites of interest. Additionally, the measurements collected in ground-based stations are often not well processed and/or produced by not well maintained and calibrated stations. This is especially true for the regions where limited efforts have been made so far on the solar resource estimation, like in the Middle East. The research program Predisol aims to develop a locally-adapted tool to predict downwelling irradiances in desert environments in order to support present and future solar investments in the Middle East where the interest in solar power is rapidly increasing. The United Arab Emirates (UAE) have set a target to cover 7% of its electricity demand from renewable energy sources by 2020. As part of this effort, a 100 MW CSP plant, Shams-1, one of the largest plants of the World is operating in the middle of the UAE desert.

This paper presents the result of a joint effort between two research institutes and two private companies to improve the estimate of the solar resource in the Middle East region. State-of-the-art satellite-based models and irradiance measurement techniques have been used to improve the assessment of solar resource potential in the region. The high performance of McClear model (Lefèvre et al. 2014) in estimating the clear-sky

doi:10.18086/swc.2015.07.08 Available at http://proceedings.ises.org

irradiance in the UAE has already been demonstrated by Eissa et al. (2015). In this work, this performance has been enhanced thanks to a local adaptation with measurements of aerosol optical depth (AOD). The locally-adapted McClear is combined with the HelioClim-3 irradiance database (Blanc et al. 2011). The resulting model was then calibrated with high-precision measurements of irradiance collected from a ground station (AD1) located close to the Shams Power plant at Madinat Zayed, UAE.

2. Method

2.1. Background

- McClear model

McClear (Lefèvre et al. 2013) is a fully physical model that exploits the atmospheric properties provided by the EU-funded MACC (Monitoring Atmospheric Composition and Climate) project to estimate the surface downwelling solar irradiances in cloud-free conditions. McClear is based on the radiative transfer libRadtran (Mayer and Kylling, 2005) and uses a Look-Up-Table approach to enable routine calculations in real-time. The clearness indices –ratio between irradiance at the ground and irradiance at the top of the atmosphere– obtained by running libRadtran are stored in the abaci. The values that contain the abaci are called node points. Interpolation functions are used to interpolate between these node points. An optimization was made for the selection of the node points and interpolation functions in order to (1) minimize the number of node points to keep abaci as small as possible, (2) interpolate/extrapolate functions as fast as possible, and (3) obtain low differences with libRadtran outcomes: bias less than 3 Wm^{-2}, and 95% of the differences less than 20 Wm^{-2}.

The comparison between McClear irradiances and measurements from the Baseline Solar Radiation Network (BSRN) on various climates has shown that McClear offers similar or better performances (Lefèvre et al. 2013). In addition, Eissa et al. (2015) performed validations of the McClear model in the United Arab Emirates, and compared McClear's performances against the performance of two other models in the literature. They concluded that McClear was better in capturing the temporal variability of the DNI and similar performances were obtained for the GHI retrieval in this desert climate. They also observed an underestimation in estimating the DNI, which was explained by the overestimation of the AOD in the MACC data and the not accounting for the circumsolar radiation in McClear model.

- Helioclim-3 database

The HelioClim-3 (Blanc et al. 2011) surface solar radiation database is based on the irradiances retrieved from Meteosat Second Generation satellite images. This satellite-based method used to estimate the irradiances is named Heliosat-2. The principle of Heliosat-2 (Rigollier et al. 2004) is that the attenuation of the downwelling shortwave irradiance by the atmosphere over a pixel is determined by the magnitude of change between the reflectance that should be observed under a very clear sky and the currently observed one. The HelioClim-3 database covers Europe, Africa, the Mediterranean Basin, the Atlantic Ocean and part of the Indian Ocean with a spatial resolution of approximately 5 km and a temporal resolution up to 15 minutes and contains irradiance estimates from February 2004 onwards. The HelioClim databases are commercialized by Transvalor and are available, with other solar related web-services, at www.soda-is.com.

Qu et al. (2014) demonstrated the advantage of replacing the clear-sky model in HelioClim-3 with McClear. They obtained an improvement of HelioClim-3 in most cases, and with no degradation in the others.

2.2. Scheme

The all-sky irradiance is computed as a product between clear-sky (or cloud-free sky) irradiance and a clear-sky index (Oumbe et al., 2014). The following two ratios, Kc and Kcb, are called clear-sky indices (Beyer et al., 1996):

$$Kc = GHI / GHI_{clear\text{-}sky} \qquad \text{(eq. 1)}$$

$$Kcb = DNI / DNI_{clear\text{-}sky}$$

The estimation of irradiance under clear-sky condition is based on the McClear model. It has been observed

that the error on MACC AOD estimations leads to important deviations on the clear-sky irradiances in the region: up to 20% on DNI if the deviation is expressed as a root mean square deviation (Oumbe et al. 2013). The MACC AODs have been therefore calibrated using AOD measured by AERONET (Aerosol Robotic Network) stations in the UAE before being used as input for irradiance calculation in the region.

The clear-sky index, Kc_{HC3}, was extracted from HelioClim-3 database. The obtained all-sky irradiances are then locally adapted using the measurements collected at AD1. The probability density function of the difference Kc_{HC3} - Kc_{AD1} is estimated by a model which is then applied to all locations and periods to correct the Kc_{HC3}. Eventually, the $GHI_{estimated}$ and $DNI_{estimated}$ are derived (Figure 1).

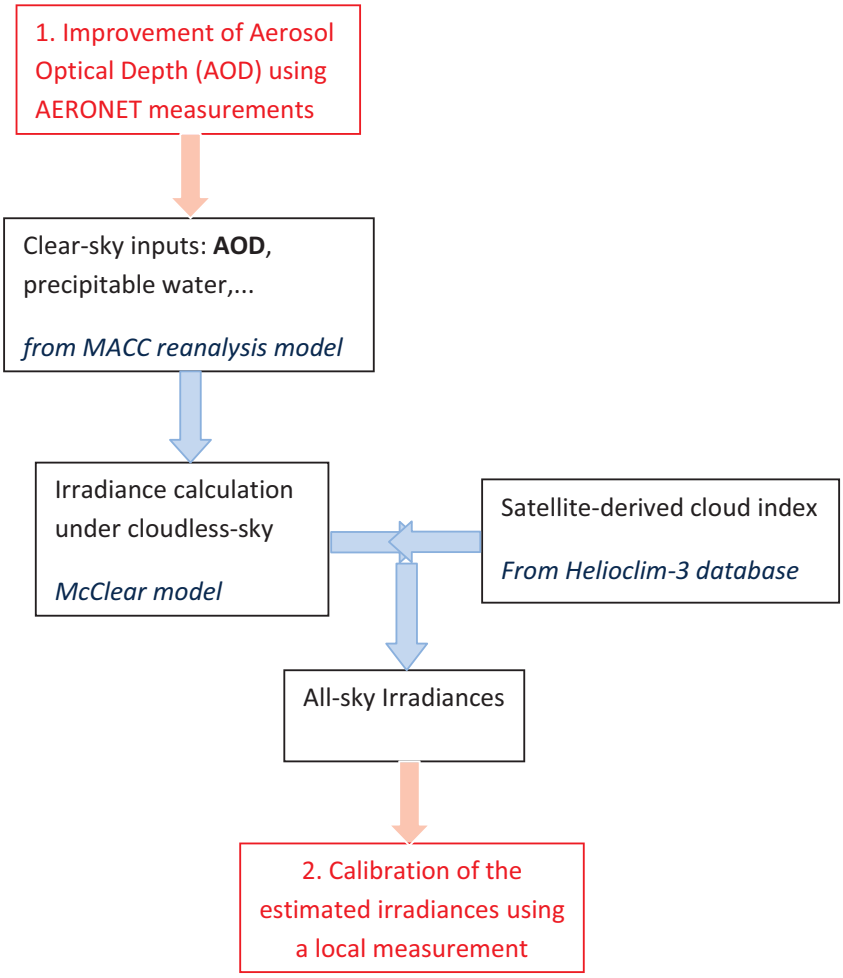

Fig. 1. Scheme of the Predisol model

The location map of the stations used in calibration and validation is shown in Figure 2.

2.3. AOD data and calibration

The AOD is a particularly critical input for irradiance estimation in desert region given its less-frequent cloud coverage and its dusty atmosphere. MACC re-analysis model provides partial and total AODs in reduced Gaussian Grid resolution: 1.125° in latitude, 1° to 20° in longitude from equator to pole (Benedetti et al., 2009). Every day at 0h, MACC predicts AODs at 0h, 3h, 6h, 9h, 12h, 15h, 18h and 21h (daily forecasting). Predicted quantities are total AOD at 550 nm, total AOD at 1240 nm, AOD of organic matter at 550 nm, AOD of black carbon at 550 nm, AOD of sea salt at 550 nm, AOD of dust at 550 nm and AOD of sulphate at 550 nm. The total AOD is the sum of all these individual AODs. The relative contribution of each aerosol species is used to determine the aerosol type, which is another input to McClear .

The NASA-operated AERONET program performs ground-based CIMEL CE-318 Sun photometer measurements, and converts them into estimates of aerosol optical properties. It provides a valuable validation data for satellite retrievals of aerosol optical properties. Datasets are available at

http://aeronet.gsfc.nasa.gov and contain AOD measurements at 16 different wavelengths as well as solar zenith angles, total water vapor column measurements and several inversion coefficients. Measurements at some AERONET stations correspond to a time-limited campaign performed over a short period of time. In 2004 the United Arab Emirates Aerosol Experiment took place contributing to a remarkable increase in AERONET data availability in the Middle East. Therefore, the bulk of measurements in the Middle East correspond to 2004. Only 5 of the 16 stations in the UAE have more than one year of measurements. The AOD at 550 nm ($AOD_{\lambda=550nm}$) is derived from AERONET AOD at 440 nm and AOD at 870 nm. AERONET level 2 - "cloud screened and quality assured" data were used in this study.

The comparison between MACC and AERONET AODs shows large deviations, partly due to the coarse spatial resolution of MACC. The MACC AOD product overestimates the AOD by 26% in the UAE. The relative root mean square deviation (RMSD) on the estimated AOD reaches 47%, but the correlation coefficient was around 0.8 showing that MACC reproduces the temporal variability of AOD in the region relatively well. No daily variation of deviation is observed, though significant monthly changes were observed in the deviation. The highest bias of 0.16 is reached in July, corresponding to the highest mean AOD where the lowest bias (0.04) was obtained in November. Overall, the accuracy of MACC decreases when the AOD increases. These deviations lead to significant error in the estimation of irradiances. Over all the AERONET stations, the deviation – by the means of root mean square error (RMSE) – between irradiances estimated (using the radiative transfer model libRadtran) with MACC aerosols and irradiances estimated with AERONET is 5% for GHI and 20% for DNI. The general overestimation of AOD leads to underestimation of GHI and DNI. The differences between measured and AERONET derived irradiances notably increases with the distance, due to the modification of aerosol loading. When the AERONET and pyranometric stations are 100 km away, the standard deviation reaches 7% for GHI and 18% for DNI. This gives important information about the spatial variability of AOD in the UAE desert, and shows the limitation of using aerosol properties that are measured (or estimated) on locations or grid cells that are more than 100 km away. (Oumbe et al. 2012).

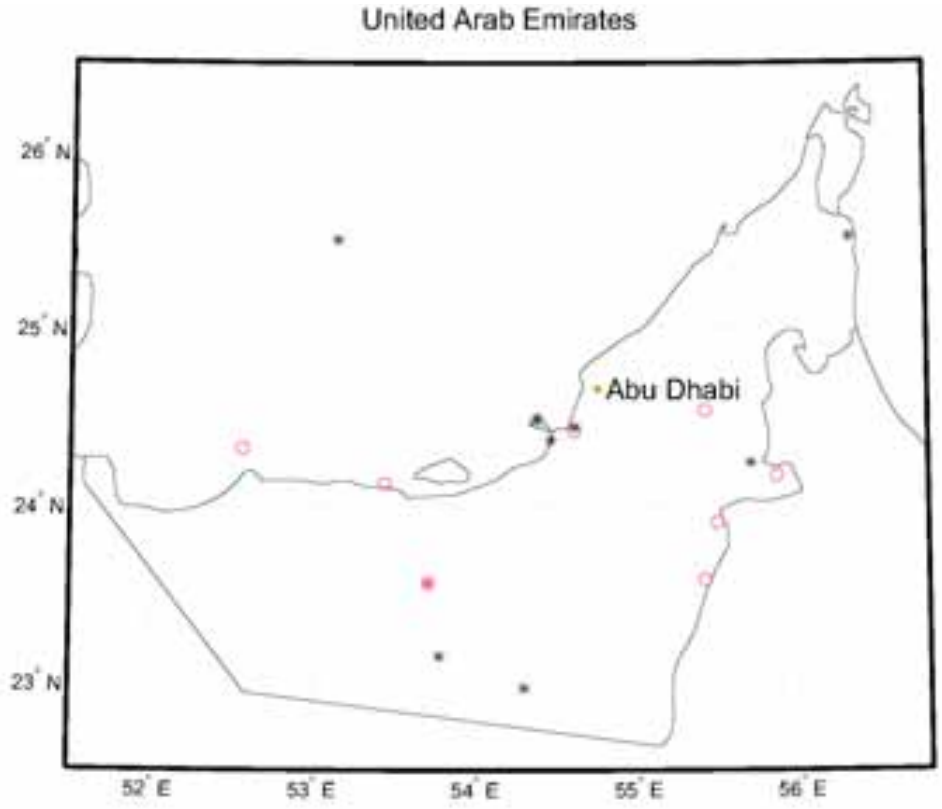

Fig. 2. Location of the Irradiance measuring stations (in red) and aerosol measuring stations (AERONET) (in black) in the UAE. The stars are stations used to calibrate the model (all AERONET and AD1) and the circles are stations used for model validation.

Since the spatial resolution of MACC aerosol database is greater than 100 km (1.125°), a local correction is necessary to properly reflect this actual spatial variability of the AOD. A correction function for MACC AOD was derived for each AERONET station. Then a global correction of MACC is AOD in the UAE was generated. This correction has improved the accuracy of AOD estimation at each AERONET station. The table 1 shows the performance of this correction: significant decrease of bias, noticeable decrease of RMSD, and no change in correlation coefficient.

	Original AOD	**Corrected AOD**
Bias	26% *(0.10)*	-2% *(-0.01)*
RMSE	47% *(0.17)*	36% *(0.13)*
Correlation coefficient	0.797	0.797

Table 1. Comparison between the original and the corrected MACC AOD and AERONET AOD. RMSE stands for root mean square error.

The Predisol clear-sky model was made of McClear operated with the MACC corrected AOD.

2.4. Irradiance measurement and calibration

The AD1 measuring station was specifically designed and commissioned for the Predisol project. It has been installed at Madinat Zayed near the Shams CSP plant. AD1 has provided high quality irradiance measurements with high temporal resolution. The station comprises the following instruments:

- a SOLYS 2 suntracker (Kipp & Zonen) supporting the radiative sensors and allowing for sun tracking and DHI (Diffuse Horizontal Irradiance) sensor shading,
- a CHP1 first class pyrheliometer (Kipp & Zonen) for measurement of the DNI component of irradiance. This sensor is equipped with a temperature probe in order to allow for temperature shift according to the sensor calibration curve,
- two secondary reference CMP11 Pyranometers (Kipp & Zonen), one being unshaded for GHI measurement, the other being shaded by a shadow ball for DHI measurement,
- a meteorological mast equipped with wind measurement (Vaisala WMT520), temperature and HR measurements (Vaisala HMP155), atmospheric barometer (Vaisala BARO-1),
- a data acquisition module (Vaisala QML201) with storage capacity and modem for data transmission, and a 24V autonomous power supply (2x90 W peak PV panels + 2x 12 V/130 Ah batteries).

Datasets are reported in a 1-min average (DNI, GHI, DHI) or a 10-min average (Temperature, Relative humidity, Atmospheric Pressure, Wind speed, Wind direction). Within the measurement period we noticed some meteorological events that could affect the quality of solar data:

- Morning condensation during fall/winter, characterized by droplets condensing on sensors.
- Sand storms during spring/summer, characterized by sudden drop of GHI and DNI, the latter falling to zero.
- Large temperature excursions in summer. During these periods, the outside temperature exceeds 47°C during at least one hour a day.

The quality of the data was monitored based on the three component test (Roesch et al., 2011):

$GHI / (DNI*\cos(SZA)+DHI) = 1.0\pm8\%$ for $GLOB1 > 50 Wm^{-2}$, $SZA < 75$ (eq. 2)

$GHI / (BNI*\cos(SZA)+DHI) = 1.0\pm15\%$ for $GLOB1 > 50 W^{-2}$, $75 < SZA < 93$

where SZA is the Sun Zenith Angle.

Routine maintenances (mainly cleaning and verification of alignment of the instruments) of the station were

found critical to maintain the quality of the measurements. Figure 3 illustrates the correlation between the number of maintenance operations in a month and the percentage of data passing the three component test over the period from April 2012 to December 2013. August 2012 clearly appears as a "bad month" with only 6 maintenance operations and a poor fraction of good data (65%). The poor result of October 2013 is due to the lack of DHI signal. Basically, in a desert region, at least one maintenance operation per day is needed for the high-precision station. TEMP1 is DNI*cos(SZA)+DHI.

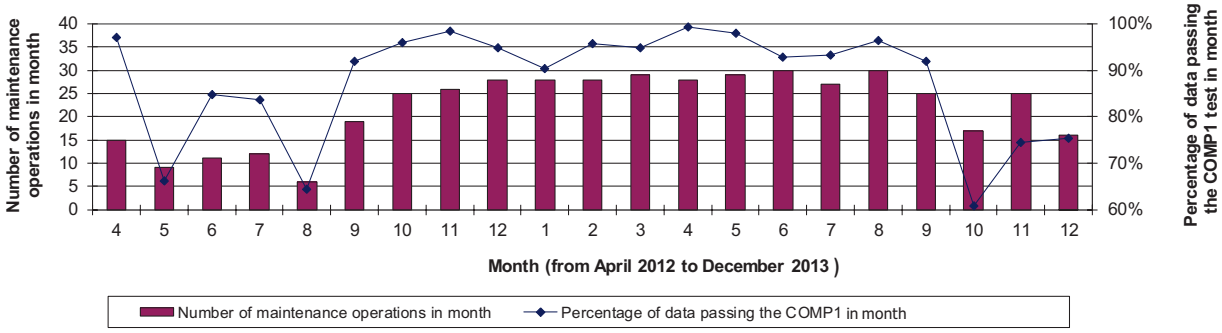

Fig. 3: Correlation between maintenance frequency and fraction of good solar data

The Predisol clear-sky model is proposed to replace the clear-sky model in the Middle East region of the HelioClim-3 database. This new database is calibrated with the quality-checked AD1 irradiance measurements. This calibration corrects systematic errors of the HelioClim-3 database in the region. E.g. we have noticed a clear under-estimation for the first hours in mornings, except in winter. After investigation, this almost systematic underestimation of GHI in the morning was found to be caused by the specular reflectance from the ground when the satellite observation direction is opposite to the sun direction, for high longitude. This under-estimation artifact due to high longitude implies a large global under-estimation of the non-calibrated GHI. The graphs presented in Figure 4 show the time series of the non-calibrated GHI and that of calibrated estimated GHI. With the calibration, the bias and RMSE drop respectively from 14% and 22% to 0% and 10%. The calibrated database is the Predisol irradiance database.

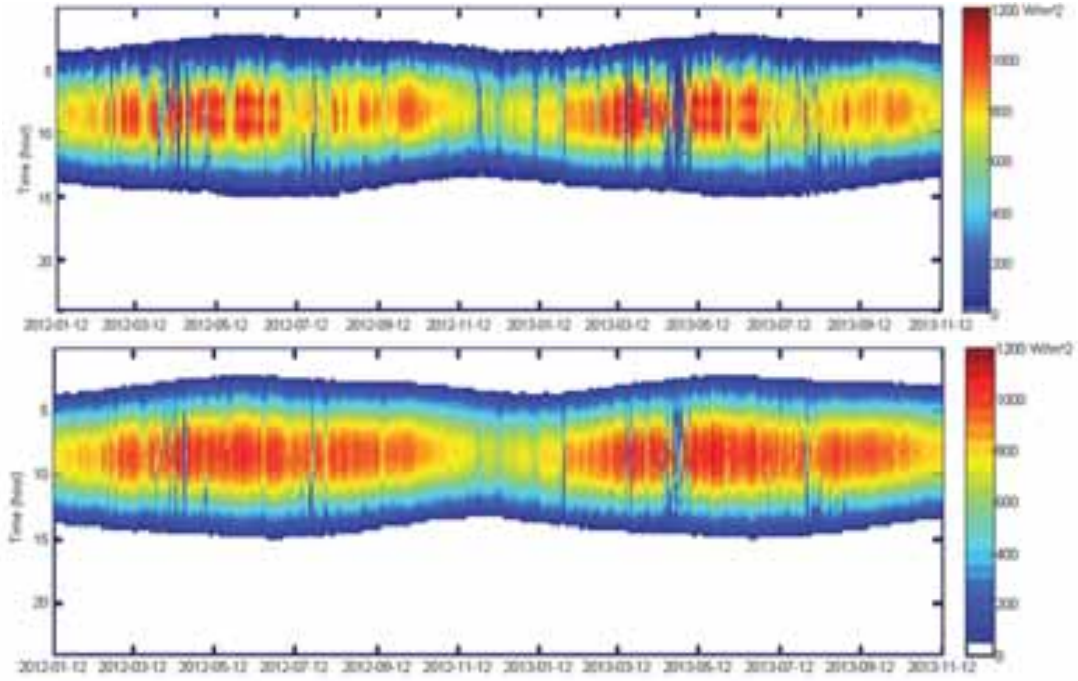

Figure 4: Timeseries of non-calibrated estimated GHI (at top) and of AD1 calibrated estimated GHI (at bottom) at AD1 station. Time is in UTC

A local transposition function has been then used to derive DNI from GHI.

3. Validation

The estimated irradiances have been validated against high-quality measurements taken by 7 Rotating Shadowband Irradiometers (RSI) managed by Masdar Company and maintained by CSP Services. The RSI is a silicon photodiode, the LI-COR LI-200 Pyranometer, integrated with a rotating shadowband. When the shadowband is stationary below the horizon of the photodiode, the GHI is measured. The DHI is measured when the shadowband masks the entire solar disc from the pyranometer. The DNI is then derived from the GHI and DHI measurements. The shadowband rotates once per minute. The irradiances are averaged and delivered in a 10-minute time step. The locations of the RSI stations used for validation are shown by the red circles in Figure 2.

The 10-min measurements of RSIs, and the 15-min estimates of Predisol were averaged hourly irradiances. Each hour corresponds to the end of integration period (h for]h-1, h]). The daily and monthly irradiation time-series were then computed. Deviations were computed by subtracting the measurements from the corresponding Predisol estimate. They were summarized by the bias, the standard deviation, the RMSE, and the Pearson correlation coefficient. Relative values are expressed with respect to the mean of the used measurements. See Table 2.

	HOURLY MEANS (26229 hours)				**DAILY MEANS (2331 days)**				**MONTHLY MEANS (68 months)**			
	Mean	*Bias*	*RMSE*	*CC*	*Mean*	*Bias*	*RMSE*	*CC*	*Mean*	*Bias*	*RMSE*	*CC*
DNI	**458 W/m^2**	**0%**	**26%**	**0.880**	**5051 Wh/m^2**	**0%**	**20%**	**0.797**	**154.1 kWh/m^2**	**-1%**	**10%**	**0.805**
GHI	**552 W/m^2**	**2%**	**8%**	**0.988**	**6107 Wh/m^2**	**2%**	**6%**	**0.966**	**188.7 kWh/m^2**	**2%**	**4%**	**0.990**

Table 2. Validation of global and direct irradiances. Measurements from all stations are combined. "Mean" is the mean of the measurements. CC stands for correlation coefficient. Bias and RMSE are expressed relative to "Mean".

Validation of the hourly means of irradiance show high coefficients of determination: 0.88 on DNI and 0.99 on GHI. The relative biases are close to zero: 0% on DNI and 2% on GHI and the relative root mean square error (RMSE) are low: 8% on GHI and 26% on DNI. Lower deviations are obtained on daily and monthly means of irradiance. There are still rooms for improvements on the DNI. These performances are better than those currently reported in the literature for the UAE (Eissa et al., 2012; Alobaidi et al., 2014; Gherboudj and Ghedira 2015).

The uncertainties of E-ANN (Eissa et al., 2013) for hourly irradiances in all-sky situations are similar for RMSE on DNI and higher for the bias on DNI and bias and RMSE on GHI. The relative bias and RMSE of E-ANN are respectively 6% and 26% for DNI and 3% and 12% for GHI. But the E-ANN validation is presented only on two stations. The ensemble artificial neural network (E-ANN) model, is a statistical model utilizing the Meteosat Second Generation images for irradiance prediction specifically over the region of the UAE. It requires a training beforehand. The E-ANN model was trained using reference data from three ground measurement stations for the full year of 2010 and validated over two independent stations for the full year of 2009.

The cloud-free situations represent 60 to 80% in the region. The performance of McClear and E-ANN models for cloud-free situations, taken from Eissa et al (2015), are compared to those of the new method – named Predisol (see Table 3). The enhancement of MACC AOD significantly reduces the bias on DNI estimation in cloud-free situations, leading Predisol to have less bias on DNI than McClear. The rest of performances of McClear and Predisol are close. McClear and Predisol perform better and E-ANN.

	Model	Bias	RMSE	CC
DNI (mean of measurements: 670 W/m²)	E-ANN	-9%	19%	0.607
	McClear	-4%	11%	0.837
	Predisol	**-0.6%**	**10%**	**0.894**
GHI (mean of measurements: 600 W/m²)	E-ANN	-6%	11%	0.947
	McClear	+2%	5%	0.982
	Predisol	**+3%**	**5%**	**0.995**

Table 3. Validations of cloud-free hourly DNI and GHI by ANN, McClear and Predisol

4. Conclusion

The calibration method exhibit very satisfactory results on GHI and DNI estimations over the UAE, even though it was based only on one year of irradiance measurement at one site. The obtained accuracy was better than those reported in the literature for the UAE. The generated irradiance database -resolutions: 3km and 15 minutes, period: 2004 to 2013- is therefore a reliable inputs data for feasibility studies and performance simulation of Solar Power Plant in the region. There is room for improvement of the DNI retrieval accuracy. It is expected that a higher resolution of AOD as inputs and /or a direct estimation of DNI, instead of transposition from GHI, would improve the model accuracy.

5. References

Alobaidi, M., Marpu, P., Ouarda,T., and Ghedira, H., 2014. Mapping of the Solar Irradiance in the UAE Using Advanced Artificial Neural Network Ensemble, Selected Topics in applied Earth Observations and Remote Sensing, Vol.7, Issue 8, pp.3668-3680.

Benedetti, A., Morcrette, J.-J., Boucher, O., Dethof, A., Engelen, R. J., Fisher, M., Flentje, H., Huneeus, N., Jones, L., Kaiser, J. W., Kinne, S., Mangold, A., Razinger, M., Simmons, A. J., and Suttie, M., 2009. Aerosol analysis and forecast in the European Centre for Medium-Range Weather Forecasts Integrated Forecast System: 2. Data assimilation. J. Geophys. Res. 114, D13205.

Beyer, H. G, Costanzo, C. and Heinemann, D., 1996. Modifications of the Heliosat procedure for irradiance estimates from satellite images. Sol. Energy, 56, 207–212.

Blanc, P., Gschwind, B., Lefèvre, M., and Wald L., 2011. The HelioClim Project: surface solar irradiance data for climate applications. Remote Sensing 3, 343–361.

Eissa,Y., Chiesa, M., and Ghedira, H., 2012. Assessment and recalibration of the Heliosat-2 method in global horizontal irradiance modeling over the desert environment of the UAE, Solar Energy, vol. 86, pp 1816-1825.

Eissa, Y., Marpu, P., Gherboudj, I., Ghedira, H., Ouarda, T., and Chiesa, M., 2013. Artificial neural network based model for retrieval of the direct normal, diffuse horizontal and global horizontal irradiances using SEVIRI images. Solar Energy, vol. 89, pp 1–16.

Eissa, Y., Munawwar, S., Oumbe, A., Blanc, P., Ghedira, H., Wald, L., Bru, H., and Goffe, D., 2015. Validating the downwelling solar irradiances estimated by the McClear model under cloud-free skies in the United Arab Emirates. Solar Energy 114, 17–31.

Gherboudj, I., and Ghedira, H., 2015. Assessment of solar energy potential over the United Arab Emirates using remote sensing and weather forecast data, Renewable and Sustainable Energy Reviews, In Press, doi:10.1016/j.rser.2015.03.099.

Lefèvre, M., Oumbe, A., Blanc, P., Espinar, B., Gschwind, B., Qu, Z,. Wald, L., Schroedter-Homscheidt, M., Hoyer-Klick, C., Arola, A., Benedetti, A., Kaiser, J. W., and Morcrette, J.-J., 2013. McClear: a new model estimating downwelling solar radiation at ground level in clearsky conditions. Atmos. Measur. Tech. 6, 2403–2418.

Oumbe, A., Qu, Z., Blanc, P., Lefèvre, M., Wald, L., and Cros, S., 2014. Decoupling the effects of clear atmosphere and clouds to simplify calculations of the broadband solar irradiance at ground level. Geoscientific Model Development, 7, 1661-1669.

Oumbe, A., Bru, H., Ghedira, H., Chiesa, M., Blanc, P., and Wald, L., 2012. Using AERONET to complement irradiance networks on the validation of satellite-based estimations, AGU Fall Meeting. http://adsabs.harvard.edu/abs/2012AGUFM.A11I0172O

Rigollier, C., Lefèvre, M., and Wald, L., 2004. The method Heliosat-2 for deriving shortwave solar radiation data from satellite images. Solar Energy, 77(2), 159-169

Roesch, A., Wild, M., Ohmura, A., Dutton, E. G., Long, C. N., and Zhang, T., 2011, Assessment of BSRN radiation records for the computation of monthly means. in: Atmos. Meas. Tech., 4, 339-354.

Qu, Z., Gschwind, B., Lefèvre M., and Wald, L., 2014. Improving HelioClim-3 estimates of surface solar irradiance using the McClear clear-sky model and recent advances in atmosphere composition. Atmos. Meas. Tech., 7, 3927–3933.

Conference Proceedings
Solar World Congress 2015
Daegu, Korea, 08 – 12 November 2015

ISES SWC2015 –THE STATE OF SOLAR ENERGY RESOURCE ASSESSMENT IN COSTA RICA

Natalia Alvarado[1], Rodrigo A. Escobar[2], John Boland[3], and Evelyn Quiros[4]

1 Universidad de Costa Rica, Costa Rica

2 Pontificia Universidad Católica de Chile, Santiago, Chile

3University of South Australia, Australia

4 Instituto Costarricense de Electricidad, Costa Rica.

Abstract

It is traditionally assumed in Costa Rica that given its geographical location there must be a large potential for electricity generation from solar energy. However, this potential has not been properly assessed with measurements of high quality up to modern standards, and therefore the country still lacks the information needed to either establish public policies to promote solar energy utilization or support the development of commercial projects. The current trend of increasing energy consumption in the country and the existing interest on increasing solar energy utilization require an updated analysis of the available solar resource in order to generate meaningful data that can be used by government and private parties.

Costa Rica has been measuring global horizontal irradiation for over 20 years in several stations distributed throughout the country, although in most cases the measurements have been conducted without quality control checks and postprocessing. This network of radiometric measurement stations was set out to identify regions with adequate levels of average daily sunlight in order to define regions in which solar energy systems could find engineering applications.

Currently the measurement network is operated for the ICE group (Costa Rican Institute of Electricity), and consists of Second Class Pyranometers CHP3 and First Class Normal Incidence Pyrheliometer CHP1, both from Kipp and Zonen brand. The information is stored as minute-averages and spans a period of four years. No locally developed and validated satellite estimation models have yet been reported, and instead the country relies on commercial data. There are no measurements of either diffuse or direct normal irradiance. A more complete climatological characterization of the solar resource is possible by using the measured data of global horizontal irradiance coupled with the existing diffuse fraction models such as (Boland, Lauret, & Ridley, 2010) and (Jing, Boland, & Ridley, 2012), which allow decomposing the Global horizontal into its direct and diffuse components. This represents a significant improvement in the amount and quality of solar information that is available for solar engineering applications in Costa Rica and can be published for public access.

key-words: solar data, irradiance, radiation, solar energy, resource assessment & climate, solar potential, Central America

1. Introduction

Costa Rica is located in the southern part of Central America, between the coordinates 8° 15’ – 11° 00’ North and 83° 30’ – 86° 00’ West. This area is located within the tropical belt of the Northern Hemisphere. To the

doi:10.18086/swc.2015.07.09 Available at http://proceedings.ises.org

north, the country borders with Nicaragua, and in the south with Panama. To the east and west the country is surrounded by the Caribbean Sea and the Pacific Ocean, respectively. The country has a rich geography that is associated with higher levels of precipitations, humidity and temperature. Costa Rica has a surface area of 51,100 km² and a population of approximately 4.3 million people.

More than 60 % of the population lives around the capital San José, which is located in the center of the country. This area is called the "Gran Área Metropolitana" (GAM) in Spanish also called Central Valley. The area is surrounded by mountains and it concentrates most of Costa Rica´s industry. The rest of the country consists mainly of natural reserves and agricultural land.

Energy Consumption

Costa Rica has a 98.6% electrification rate, which is the highest in Central America, and a per capita power consumption of about a 1,611 kWh/year. On average, a middle-income Costa Rican family's electric bill takes up 2% of its income—one of the lowest rates in the region, thanks to Costa Rica's higher per capita income and lower power prices owing to the large utilization of hydropower for electricity generation that reaches 91% of the total installed capacity, making it very dependent and vulnerable to weather variability. Today it is known that climate and climate variability (such as for example events like El Niño Southern Oscillation ENSO) can cause unusual atmospheric patterns in the country thus affecting the energy generation and increasing use the energy from fossil fuels.

Electricity demand presents a clear pattern with growing consumption during the morning and two daily peaks, one in the early afternoon and the second at dusk. The forecasted demand growth rate for the next few years is 4% annually. Solar energy is considered as an important potential source to meet the growing energy demand of Costa Rica.

As of now, there have been several different reports trying to characterize the solar resource in the country including the following documents: *Non-Conventional Energy Sources* (Electrowatt Engineering Services ltd, 1983), *Radiación solar global de Costa Rica* (Castro, 1987), *Mapas de radiación solar en Costa Rica* (Wright, 2002), *Map of solar resource of SolarGIS from satellite data* (Weigl, 2014), *Determinación del potencial de energía solar para generación eléctrica en Costa Rica*. (ICE, 2014).

Some of these reports were performed the ground data, but with low quality, because had a systematic errors. Due to this low quality of the data arises the need for modeling as a method of quality control and analysis of solar resource available in the country for its subsequent use as an energy source. In the Electrowatt document the information considered included 22 actinographs and 26 heliometers with data previous to 1982. The results indicated that the majority of the irradiation data was affected by systematic and random errors due to poor sensor operation and maintenence. Castro´s work (1987) reviewed all actinography and heliometer data available in the country and achieved similar conclusions, that the uncertainty levels on average of 10% with maximum of 25%. Wright´s work (2002) concluded that the density of measurement points was adequate although the data quality was low as it displays high uncertainty, short measurement periods, uncalibrated sensors, and substandard maintenance. Considering this, it is clear that a larger effort must be made to properly evaluate the available solar resource in Costa Rica.

2. Available Data

The data we choose to use with a model is data from three locations over same climate region, the north pacific region in Costa Rica (Liberia, Colorado and Nueva Colon). These data were collected as a response of campaign of measurement the national electricity company in Costa Rica.

Each station was equipped with a pyranometer (CMP3) and a pyrheliometer (CHP1) manufactured by Kipp and Zonen with Campbell-Stokes datalogger. The measurements include globaland direct normal irradiance values with sampling rate and minutal averaged storing rate. Every dataset has been reviewed using a quality control (QC) procedure based on the BSRN guidelines (McArthur, 2005).

Liberia and Colorado locations used have time series of measured irradiance since a 2009.In the following analysis only a full year of data (2014) is considered. Figure 1 present the location of the three stations considered here. These radiometric stations have similar geographical and climatological characteristics as the elevation and climate of the stations differ from 85 m to less 1000 m. These three stations are located in relative proximity as it was previously determined that the region has a large potential for solar energy utilization.

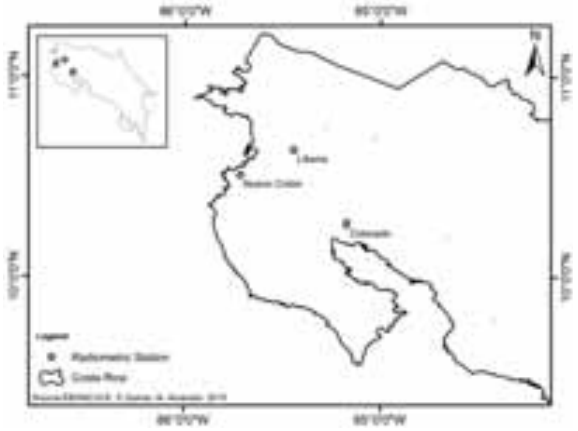

Station	Lat (deg.)	Lon (deg.)	Elev. (m)
Liberia	10.6	-85.4	990.7
Colorado	10.3	-85.2	999.2
Nuevo Colón	10.5	-85.7	85.0

Figure 1: Measurement stations location

3. The Boland-Ridley-Lauret (BRL) Model

However, for this paper, we have global and direct radiation is measured, for modelling solar energy applications, the amount of radiation on a surface is needed. Different models for estimating the diffuse fraction and correlating it to the clearness index, such as Orgill and Hollands, Erbs et al, Reindl et al (Duffie & Beckman, 1980). Also, Boland et al. (2010) presented a model based on predictors for finding the diffuse fraction from GHI data. The model utilizes the hourly clearness index, solar altitude, apparent solar time and a measure of persistence of global radiation level as predictors and allows estimating the diffuse fraction for measured datasets. The diffuse fraction is defined as the ratio between diffuse horizontal irradiation and global horizontal irradiation:

$$d = \frac{I_{diffuse}}{I_{global}} \tag{1}$$

According to Boland et al (2010), the diffuse fration can be also represented as:

$$d = \frac{1}{1 + e^{-5.38 + 6.63 k_t + 0.006 AST - 0.007 \alpha + 1.75 K_t + 1.31 \psi}} \tag{2}$$

Where k_t is hourly clearness index, AST the solar time, α the solar angle in degrees, K_t the daily clearness index, and ψ is the persistence.

4. Methodology

For this paper, it had been used at hourly data from 365 days of Liberia Station, 398 days of Colorado Station and 88 days of Nueva Colon Station.

The information obtained from the model (BRL), is compared with the diffuse fraction from the Orgill and

Hollands model (Duffie & Beckman, 1980) and the diffuse fraction obtained from DNI data. The diffuse fraction of the Orgill and Hollands model is:

$$d = \begin{cases} 1.0 - 2.49k_t & for\ k_t < 0.35 \\ 1.557 - 1.84k_t & for\ 0.35 \leq k_t \leq 0.75 \\ 0.177 & for\ k_t > 0.75 \end{cases} \quad (3)$$

For this work the minutal data was initially to convert to hourly data. With the calculated of k_t-hourly clearness index we applies an Orgill and Hollands model, the equation 3.

For the BRL model, equation 2, first step it to calculate the parameters is hourly clearness index, *AST* the solar time, the solar angle in degrees, K_t the daily clearness index, and ψ is the persistence detailed is in Boland et al. (2010)

Finally to determine the diffuse fraction from the minutes variables of GHI and DNI, it calculated the hourly averages, diffuse radiation is determined with the differential of the global radiation (GHI) and the horizontal component of direct radiation (DNI cos (θ_z)), the diffuse fraction was determined by applying the equation 1.

After include the information, we obtained the next figures 2 to figure 4.

5. Results

The diffuse fraction was obtained by a BRL model, have a right behavior curves expected by a data in the three locations. These patterns we associate with a good performance of this model in a north pacific Costa Rica region.

After a graphical comparison for the three points of data of the fit of the BRL model overlaid against Orgill and Holland model is shown in Figure 2 and Figure 4 where we can observe a very good fit to most of that data set of Liberia and Colorado. We observe seems to fit the data reasonably well but does not fit enough into the high clearness index region.

In a case of a Nuevo Colón, Figure 4 shows the fit between the two models where we see that both does not extend fit enough into the high clearness to low diffuse values, but this station has less quantity of data.

We need move onto formal error analysis, because we need to know if BRL model is performing better than other models.

Besides in a Figure 2 to 4, the result of used DNI fraction to calculate diffuse, but the result show very complex patterns, in the three points if possible that we have errors resulting from the operational problems, easily noticed by this type of plot. We recognized that any serious departure of data from the normally expected value is thus identified.

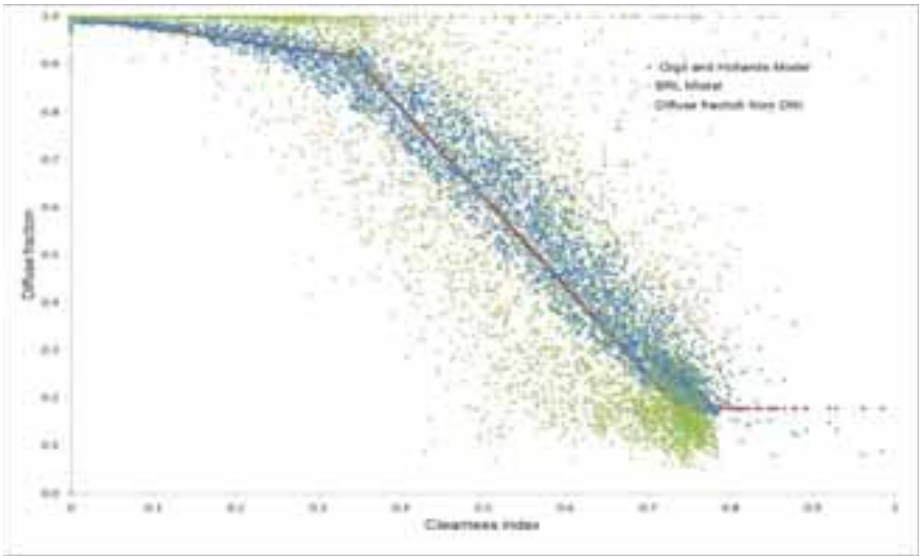

Figure 2. Liberia Data with BRL model, Orgill and Hollands model and Diffuse Fraction from DNI

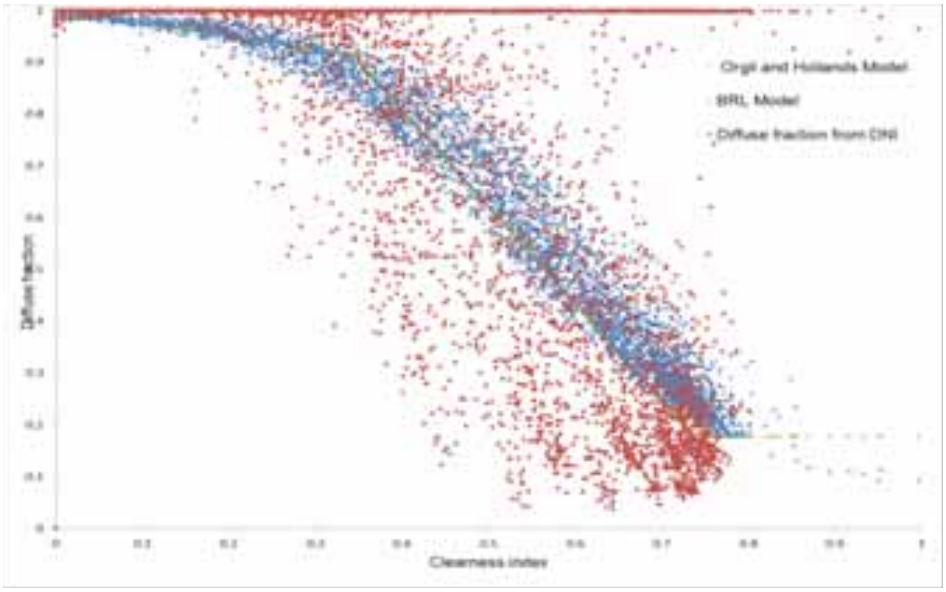

Figure 3. Colorado Data with BRL model, Orgill and Hollands model and Diffuse Fraction from DNI

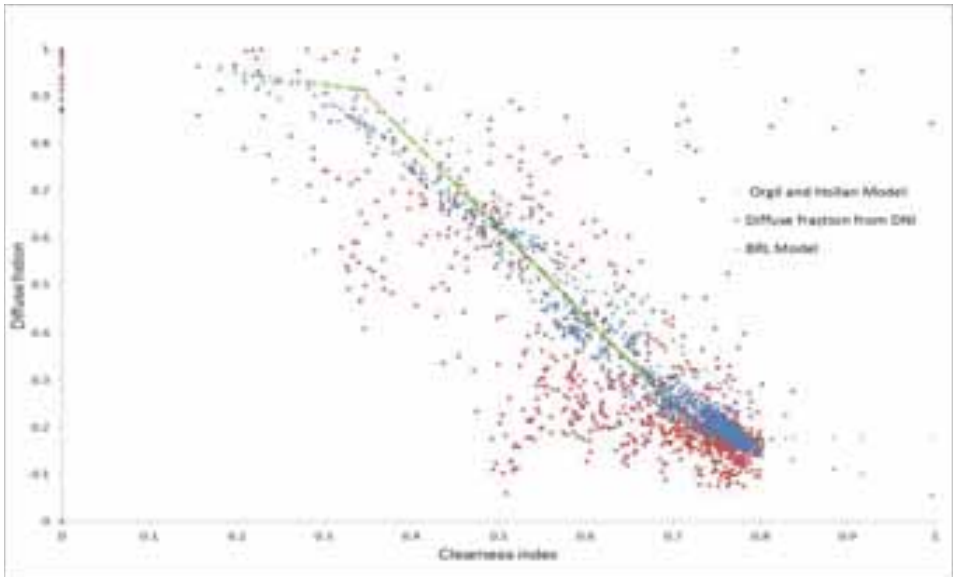

Figure 4. Nueva Colon Data with BRL model, Orgill and Hollands model and Diffuse Fraction from DNI

The points in the top right of the graphic can be caused for misalignment of the sensor CHP1, the data modeled with BRL and as obtained from measured data present conglomerate with low fraction of diffuse, so the DNI component is significant.

La información disponible actual es insuficiente, para su comparación con diferentes modelos. Adicionalmente, permitirá analizar la afectación de los patrones atmosféricos de la región ante el recurso solare. Costa rica debe generar bases de dato de calidad, que genere información requerida para su comparación con diferentes modelos

The available information is insufficient for comparison with various models applied. In addition, it did not allow analyzing the affectation of the weather patterns of the region on the solar resource.

6. Conclusions

The all figure we observe that BRL model and Orgill and Hollands models have the right behavior curves but the information from de DNI presents an involute acceptable some data out of it. Some reason of this because the measures have many errors.

We need move onto formal error analysis, because we need to know if BRL model is performing better than other models.

Costa Rica must generate reliable and high quality databases, with sufficient information for the use and verification of different solar models in order to determinate of the solar resource and its subsequent conversion to energy.

7. References:

Boland, J., Lauret, P., & Ridley, B. (2010). Modelling of diffuse solar fraction with multiple predictors. *Renewable Energy*(35), 478–483.

Castro, V. (1987). *Radiación Solar Global en Costa Rica.* San José, Costa Rica: Instituto Meteorologico Nacional.

Duffie, J., & Beckman, W. (1980). *Solar Engeneering of Thermal Processes.* Madison-Wisconsin: Wiley Interscience Publication.
Electrowatt Engineering Services ltd. (1983). *Non- Conventional Energy Sources.* San José: Instituto Costarricense de Electricidad.
ICE. (2014). *Determinación del potencial de energía solar para generación eléctrica en Costa Rica* . San José: ICE.
Jing, H., Boland, J., & Ridley, B. (2012). *Decomposing Global Solar Radiation into its Direct and Diffuse Components.* South Australia: School of Mathematics and Statistics, Barbara Hardy Institute, University of South Australia.
McArthur, L. J. (2005). *Operation Manual, Version 2.1.* Canada: BSRN.
Weigl, T. H. (2014). *Analysis of the Technical Potential and Profitability of Photovoltaic in Costa Rica*. Recuperado el 30 de 06 de 2015, de Acesolar: http://www.acesolar.org/ckfinder/userfiles/files/Master%20Thesis%20Toni%20Weigl%2C%20Solar%20Energy%20in%20Costa%20Rica.pdf
Wright, J. (2002). *Mapas de radiación solar en Costa Rica.* Heredia, Costa Rica: Universidad Nacional.

Conference Proceedings

Solar World Congress 2015
Daegu, Korea, 08 – 12 November 2015

SPANISH RENEWABLE ENERGY GENERATION SHORT-TERM FORECAST

Nicolas Perez-Mora[1,2], Victor Martinez-Moll[2] and Vincent Canals [2]

[1] SAMPOL Ingeniería y Obras, Palma of Majorca (Spain)

[2] University of Balearic Islands, Palma of Majorca (Spain)

Abstract

This work presents and compare four short-term forecasting methods for one day-ahead hourly values of Spanish solar and wind energy generation. From the four models analyzed, two are based on ARIMAX statistical methods and the other two are based on computational intelligence methods as Non-linear Autoregressive eXogenous Neural Networks (NARX). Both forecasting methodologies use the same numerical weather prediction data (NWP), consisting for solar energy, on solar irradiation and for wind power, on wind speed. The NWP data is combined in the model with the installed power of the different generation technologies in Spain. In addition to the NWP data, the models are fed with the aggregated solar and wind energy generation in hourly steps provided by the Spanish Transport System Operator (TSO).

The obtained results by the forecasting methods and by the different energy generation technologies are compared using different error metrics such as: MBE, RMSE, MAE, MAPE and MADPE.

Keywords: *Forecasting, Solar Irradiation, Solar Forecasting, Wind Forecasting, Energy Market, ARIMAX, Neural Networks, NARX, Time Series*

1. Introduction

A huge number of renewable energy power plants have been installed in the previous decade. This was due the subsidies promoting the construction of green power plants (Monteiro et al., 2013b) and the increase in the price of fossil fuels. These factors became a huge boost for the renewable energy generation, being the installation of renewables a profitable business (Monteiro et al., 2013a). Such expansion and the policies adopted by many countries to integrate renewables into the energy generation mix has brought a rearrangement of the energy market (Rubin and Babcock, 2013).

The integration of energy generated by green power plants into electric power system is priority, meaning that this power is fed into the system in preferential order within the energy mix. Although the volatility and variability of the renewable resource makes the integration in the grid difficult taking into account that the supply and load of electric power must be balanced at every instant.

In the Spanish Energy Market or Pool the total electricity power production is balanced in hour step with the demand. The electricity is traded in different markets: the main market "daily" (D) and the 6 regulation markets "intra-daily" (ID). In the daily market the producers release their bids at 12:00 for next day's hourly generation. The intra daily markets take place: at 17:00 for ID1, at 21:00 for ID2, at 01:00 for ID3, at 04:00 for ID4, at 08:00 for ID5, at 12:00 for ID6; the generators can release their bids covering each hour from a few hour after the auction time till the end of the auctioned day, as long as that bid modifies a previous bid placed in the daily market.

The energy mix is the result of the counter clockwise auctions where the demand and the cheapest combination of generation energies matches. The retribution for all the accepted generators in an hour will be the same and equal to the last and highest accepted bid in the auction. In order to always ensure the renewable energy

doi:10.18086/swc.2015.07.10 Available at http://proceedings.ises.org

acceptance into the generation mix the green energies place their bids at the legal minimum, 0€/MWh and its retribution would be calculated as the sum of the final auction price times the generated energy plus the generation subsidy stipulated by the government. Such situation brings variations on energy generation prices. Energy generators can increase their profit by matching their production with the high price hours (Perez-Mora et al., 2016). On the other hand, the grid operator may penalize the generator in case that the energy generation is different than the offered in the auction by charging the cost of the deviated energy.

A major drawback for technologies harvesting electricity out from volatile resources is the non-continuous availability of the resource. Solar energy depends critically on the variability of irradiance (Y. Gala et al., 2014), typically cloud cover cause rapid changes in the irradiance during the day (Chen et al., 2011) which brings along generation fluctuations. In the same way, wind energy generation depends on the wind direction, speed and its variations (Cassola and Burlando, 2012). This dependence on weather conditions may lead to wrong or inaccurate bids from the generators in the energy auction and therefore into a penalties from the grid operator. An accurate bid would therefore minimize the penalties. Wind and solar generators might pursue low penalties by relying on energy forecasts (Lange and Focken, 2006; Mahoney et al., 2012; Yang et al., 2012).

This paper presents two different approaches to forecasting for each technology. The first method is based on AutoRegressive Integrated Moving Average (ARIMA) supported with eXplanatory variable (ARIMAX) and other is based on Artificial Neural Networks (ANN), in particular, based on Nonlinear AutoRegressive models with eXogenous Neural Network (NARX). Both methods are proved to provide accurate energy resource forecasts, either through computational models as in ANN (Li and Shi, 2010; Qazi et al., 2015; Reikard, 2009) or using autoregressive models such as ARIMA (Erdem and Shi, 2011; Huang et al., 2012; Paulescu et al., 2013).

This paper is organized as follows: Next section provides an overview of the problem to approach. Section 3 describes the obtained data to use. In Section 4 the methodology used to approach the problem is explained. Section 5 presents the result obtained from the methodology and the conclusions from those is given in Section 6.

2. Problem description

The aim of this work is to propose a comparison between two sets of methods forecasting solar and wind power. Both of the methods are improved with a valid explanatory variable obtained from a Numerical Weather Prediction method (NWP). This comparison is carried out within a specific boundaries conditions such as Spanish Energy market abovementioned, in particular, the forecasts focus on the daily market being the forecast horizon from +12h to +36h in hourly step.

The importance on forecasting green energy generation lies in the variability along the time and markedly different generation potential between stations and different months of the year. In case of solar power it changes from a 540 MW minimum power peak in winter to a 5.6 GW maximum power peak in summer which implies the 12% of the total generation power injected into the grid. For wind power it varies from a minimum of 120 MW to a maximum of 16.9 GW reaching peaks of production which implies the 69.4% of the total injected power into the grid. Wind power does not necessarily follow the seasons per se, but it is possible to see an annual trend line. In 2014 wind power was the resource with the biggest share in the energy mix, 20.9%. The maximum injection power achieved by solar and wind into the grid reached a total of 19.4 GW.

It is important to bear in mind that the solar electricity generation in Spain includes two technologies: photovoltaic with an installed capacity of 4.16GW; and solar thermal power stations with an installed capacity of 2.3GW, additionally these power plants may have with a storage system.

Regarding wind power the main difficulty is the lack of information on wind farm layouts impeding the use of wind direction to estimate the power decrease due shadowing between wind turbines.

A common approach to the forecast problem over a wide region is to calculate individual forecast and sum the results up (Mellit and Pavan, 2010), and it is expectable that individual errors to partially cancel out when summing up the forecasts and thus, obtaining a more accurate prediction (Y. Gala et al., 2014). An aggregated forecast approach for a country like Spain it is an extremely complicated proceeding due the large amount of

installations, the variety of technologies and the lack of historical generation information from each generator. Thereby, the approach given in this paper is forecasting the aggregated power for the Spanish peninsular market for each technology. To do so, the forecast methods are supported with a valid explanatory variable which comprises a time series of hourly values.

The mentioned explanatory variables are obtained developing a NWP method. This method provides the cloudiness index and the wind speed for a certain location. In the case of wind power, the wind speed is presumed to be a sufficient and valid explanatory variable. In the other hand solar power, is related with irradiation on the collector surface, thus cloudiness index is inversely correlated with the solar generation. The cloudiness index is a useful information that helps modeling solar irradiation. A model has been developed based on the extraterrestrial radiation modified by the cloudiness index of each location. The obtained value is expected to have a high correlation to the actual irradiation of a given location (Biga and Rosa, 1980; Lorenz et al., 2009).

2.1. Forecasted Irradiation

In order to obtain the irradiation with the developed method it is required to calculate the extraterrestrial hourly radiation (G_0) for a given point (Duffie and Beckman, 2013).This calculation depends upon the location of the plant, the time of the year and the slope of the solar collectors. The radiation (G_0) is calculated according to (eq. 1):

$$G_0 = G_{SC}\left(1 + 0.033\, cos\frac{360n}{365}\right) cos\,\theta_z \qquad \text{(eq. 1)}$$

Where G_{SC} is a solar constant (1367 W/m^2), n is the day number of the year, θ_z is the zenith angle calculated in (eq. 2):

$$cos\,\theta_z = cos(\emptyset - \alpha)\, cos\,\delta\, cos\,\omega + sin(\emptyset - \alpha)\, sin\,\delta \qquad \text{(eq. 2)}$$

The latitude of the location is denoted by ∅, a is the slope of the collecting surface, δ is the declination or angular position of the sun calculated in (eq. 3) and ω is the hour angle or the angle of displacement of the sun calculated in (eq. 4).

$$\delta = 23.45\, sin\left(360\frac{284+n}{365}\right) \qquad \text{(eq. 3)}$$

$$\omega = (h_s - 12)\cdot 15 \qquad \text{(eq. 4)}$$

The solar time is denoted by h_s. The difference between the solar time and the standard time is calculated through the formula (eq. 5) and the result is given in minutes:

$$Solar\ time - standard\ time = 4(L_{st} - L_{loc}) + E + DLS \qquad \text{(eq. 5)}$$

Where L_{st} and L_{loc} are the longitudes for the standard meridian and the location, DLS references the possibility of having Day Light Savings and E is a value calculated through (eq. 6):

$$E = 229.2(0.000075 + 0.001868\cdot cos(B) - 0.032077\cdot sin(B) - 0.014615\, cos(2B) - 0.04089\cdot sin(2B)) \qquad \text{(eq. 6)}$$

And finally, B is calculated according (eq. 7):

$$B = (n-1)\frac{360}{365} \qquad \text{(eq. 7)}$$

The intensity of the solar resource that reaches the surface of the earth decreases with increasing values of cloudiness index or sky cover (Sharma et al., 2011). Taking this hypothesis as valid the method forecasts the irradiation (I_f) for a given location as dependent on the extraterrestrial hourly radiation (G_0) and the symmetrical of the forecasted cloudiness measured in 0 to 1 range (N_f). The values are calculated hourly according to (eq. 8):

$$I_f = G_0\cdot(1 - N_f) \qquad \text{(eq. 8)}$$

A similar model was presented by (Zhang et al., 2014), where global irradiance is obtained adding to the model the clouds transmissivity.

2.2. Forecasted wind speed

As mentioned before the wind speed and direction are directly related with the availability of a wind turbine to generate power. In the case of wind direction it could be useful to understand how the wind turbines shadow each other on a wind farm (Astariz et al., 2015; Sørensen et al., 2002), in order to improve the calculation of the explanatory variable. To do so, the wind farms turbine distribution is required, unfortunately this information is not easily accessible. Therefore the only contribution to the explanatory variable is the wind speed in the location. In (eq. 9) the power delivered by a wind turbine is given by (eq. 9):

$$P = \frac{1}{2} \cdot \rho \cdot A \cdot v^3 \qquad \text{(eq. 9)}$$

Where ρ is the air density, A is the area swept by the rotor and v is the wind speed through the blades.

2.3. Weighted explanatory variable

The value of the weighted explanatory variable used for Spain is calculated taking into account the forecasted time series, either irradiation or wind speed, in the measured places and the installed powers in those places. Spain irradiation (I_E) values are calculated according to (eq. 10):

$$I_E = \frac{1}{P_S} \sum_{n=1}^{50} I_{fn} \cdot P_{sn} \qquad \text{(eq. 10)}$$

Where I_{fn} is the forecasted irradiation on the n location, P_{sn} is the installed solar power for a given location, Ps is the total solar power accumulated in Spain and is calculated using (eq. 11).

$$P_S = \sum_{n=1}^{50} P_{sn} \qquad \text{(eq. 11)}$$

Spain wind speed (v_E) values are calculated according to (eq. 12):

$$v_E = \frac{1}{P_w} \sum_{n=1}^{50} v_{fn} \cdot P_{wn} \qquad \text{(eq. 12)}$$

Where v_{fn} is the forecasted wind speed on the n location, P_{wn} is the installed wind power for a given location, P_w is the total wind power accumulated in Spain and is calculated using (eq. 13).

$$P_w = \sum_{n=1}^{50} P_{wn} \qquad \text{(eq. 13)}$$

3. Data acquisition

The required data for both forecasting methods comprises two related time series, the aggregated energy generation and the explanatory variable. The historical data is obtained from the Spanish TSO, *Red Eléctrica de España* (REE). This solar generation data is available from 24/7/2013 and provides the time series of the national solar production in 10min step. In the other hand, wind generation is available from 1/1/2012 and provides the time series of national wind production in 10min step.

The installed power for solar and wind technologies is given by the Ministry of Industry. Detailed information of the installations, such as, location, technology, power and whether or not is connected to grid is provided. This information is processed and clustered according to the province division in Spain. In this way 50 aggregated installed powers are obtained. In the case of solar power, photovoltaic and solar thermal technologies are summed up in each region.

The NWP is based on an algorithm that analyses satellite images and predicts the climatic data (Zhang et al., 2014). The NWP data comprises three days ahead time span. The cloudiness and wind speed database starts

on 8/9/2014. In order to have a homogeneous database in the area of Spain, one station per province is used; those stations are located, mainly, in the province's main city, therefore 50 stations are selected for Spain. Stations are marked with black dots in Fig.1.

Fig. 1. Weather Stations Localizations

3.1. Possible source of errors

The variable grid used that takes as unit the provinces may lead into errors since the obtained NWP value is given for a point and it is used in the whole area regardless of either station or the power plant location. The asymmetry in the location of weather stations and the different shapes and sizes of the provinces avoid the possibility of spatial averaging of the NWP data used in (Lorenz et al., 2009) and only the aggregation of the weighted data in the whole country is carried out in this study.

The sum of photovoltaic and solar thermal power plants regardless of the different technologies comprising this categories may lead to errors while forecasting the final output.

The shadowing effect within wind farms due the location of the wind turbines in the land and the wind direction may bring power decreases in the local wind generation and thus affecting the aggregated generation.

For the extraterrestrial hourly radiation calculation a value of slope (α) is estimated, this value is fixed for all the solar power plants and during the year. The most common slope value for Spain is fixed at the average latitude value, 40º. The optimum yearly slope value for an installation could have been taken as the same as the latitude where it is located (Benghanem, 2011).

3.2. Time series correlation

The resulting acquired data gives two pairs of time series, one for solar forecasting and the other for wind forecasting. In order to study the rightness of the abovementioned suppositions two correlation studies have been carried out on the time series, Pearson correlation study and R^2 correlation study.

The results for solar, where irradiation and national solar generation are taken into consideration shows a good correlation (Fig.2a), with a Pearson factor of 0.90 and $R^2 = 0.816$.

The results for wind, where wind speed and national wind generation are taken into consideration shows a correlation (Fig.2b), with a Pearson factor of 0.79 and $R^2 = 0.63$. In the wind speed case the same study is made for wind speed to the power of three (cubic wind speed, v^3) since as seen in (eq. 9) it is related with wind

power. This study gives as Pearson factor a result of 0.73 and $R^2 = 0.54$; which is lower than the previous one and thus, simple wind speed is used to forecast.

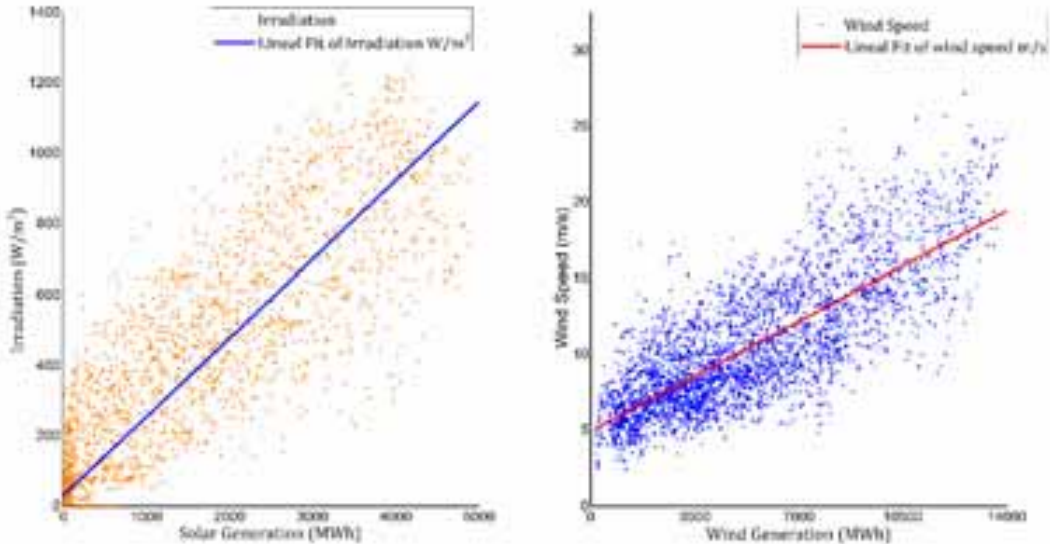

Fig. 2. Variables relation for (a) Solar Generation Vs Irradiation and (b) Wind Generation Vs Wind Speed.

4. Methodology

The relations between the explanatory variables and the generations are reasons to think that the likeness between the time series would be sufficient to calculate the aggregated energy generation (Fig. 3). Nevertheless the relation is not perfect, and in the case of wind is far to be close to 1, adding this to the variability and differences between the various installed power plants, technologies and performances precludes a reliable analytical model. Therefore a statistical forecasting method needs to be developed to obtain the aggregated power hourly generated in Spain.

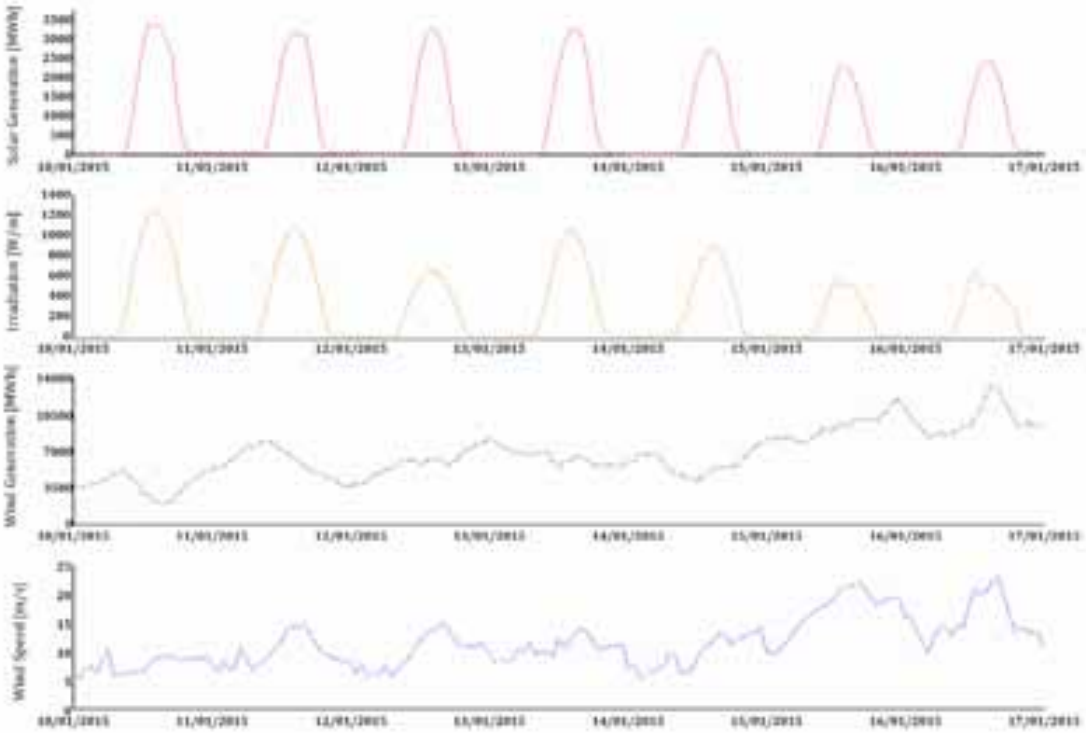

Fig. 3. Generation and proposed explanatory variables

This statistical model is fitted to time series data in order to forecast an extra time series to understand better and predict future values of the main time series. It is composed by an autoregressive model (p), moving average model (q) and differencing degree (D). Mathematically, it can be expressed as: ARIMA (p, D, q).

An approach to the forecast problem is given by the ARIMAX model. This model has been commonly used for forecasting renewable energy resources. Total irradiation is forecasted in (Dong et al., 2013; Reikard, 2009) and wind speed is forecasted in (Erdem and Shi, 2011; Liu et al., 2013).

The other proposed approach to the problem is using neural networks, these are found to outperform the regressions models when it comes to high resolutions (Reikard, 2009). Since the late 1990s ANN have been applied in energy forecasting using climatological variables as inputs to an ANN to predict generation values (Sulaiman et al., 2009). There are several ANN models that approach forecasting, in this work a NARX model is selected since they outperform other ANN models as MLP (Perez-Mora et al., 2015).

NARX model relates the current value of a time series to current and past values of the exogenous series influencing, therefore the series of interest (Da Silva Fonseca et al., 2012). This approach based on ANN which allow to find next values in a time series using past measurements of aggregated power and explanatory variable used as inputs to an autoregressive model with exogenous input (ARX) building therefore a NARX recurrent neural networks.

5. Results

Several combinations and configurations of ARIMAX and NARX models have been tried out to obtain the most accurate results. The configuration of each model is different for each energy source. Nevertheless the length of the time series is the same for both sources, starting on 8/9/14 and finishing on the forecasted days, 17/1/15. The days selected to forecast are a week in January which is the end of the available data set and has changes on weather conditions (cloud cover and wind speed) to evaluate the goodness of the obtained results. The parameters that achieve the best set of results are shown in this section.

For ARIMA forecasting the data is split in training set, 95%; and result comparison set, 5%. The length of the vector in the best performing configurations are shown in Tab. 1; where “MA”, stands for vector of non-seasonal moving average coefficients; “SMA”, stands for vector of seasonal moving average coefficients corresponding to an invertible polynomial; “AR”, stands for vector of non-seasonal autoregressive coefficients; “SAR”, stands for vector of seasonal autoregressive coefficients corresponding to a stable polynomial; and “D”, stands for integer indicating the degree of the non-seasonal differencing in the time series.

Tab. 1. ARIMA Configurations & Models

NN Method	MA	SMA	AR	SAR	D	Explanatory Variable
ARIMA Solar	3	0	5	0	0	Irradiation
ARIMA Wind	12	5	7	6	0	Wind speed

For NARX forecasting and in order to avoid over fitting, the data is split in training, 70%; validation, 15%; and result comparison and testing, 15%. The training method used in both cases is Levenberg-Marquardt back-propagation algorithm. The results obtained with the configurations are evaluated using the error measurements explain in this chapter. The best performing methods and neural network configurations are shown in Tab. 2; where “L”, stands for Linear; “ST”, stands for Sigmoid Tangent and “I” stands for Input layer.

Tab. 2. NARX Configurations & Models

NN Method	Number of layers	Neurons in each layer	Activation function	Explanatory Variable
NARX Solar	3	48-24-1	I-ST-L	Irradiation
NARX Wind	3	48-24-1	I-ST-L	Wind speed

The obtained results with the abovementioned methods are presented as an hourly time series of 168 values (equivalent to one week) in Fig. 4 and compared with the real generation.

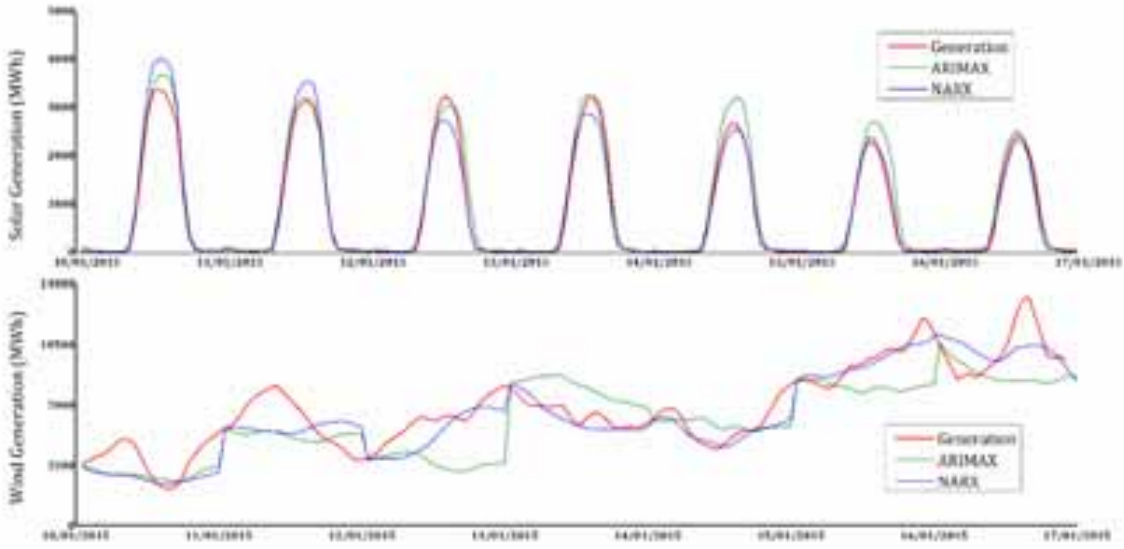

Fig. 4. Different forecast methods results comparison

In order to measure the accuracy of the predictions, the error between the forecasted values and real data is analyzed in this section. To validate the forecast methods in this work, the following calculations are used:

- Mean Bias Error (MBE), shows the deviation of the forecast divided by the installed power. This gives a perception of how the forecasted values are greater or lower than the real ones in percentage (eq. 14).
- Root Mean Square Error (RMSE), shows the deviation of the forecast divided by the installed power. With this error is possible to understand the deviation of the forecast in percentage (eq. 15).
- Mean Absolute Error (MAE), shows the absolute deviation of the forecast divided by the installed power. This gives a perception of the accuracy of the method in terms of percentage (eq. 16), this method is particularly useful for market deviations.
- Mean Absolute Percentage Error (MAPE), shows the same error divided by hourly generation; representing a percentage (eq. 17) (Tseng et al., 2002). This figure is useful to understand the accuracy of the forecast method. The percentage of error escalates when the value of generation is close to zero.
- Mean Daily Absolute Percentage Error (MADPE), the sum of the daily MAE is divided by the sum of the daily generation; thus represents a relative daily error (eq. 18). This figure is useful to understand the accuracy of the method in daily basis, solving MAPE's drawback when generation is close to zero.

$$MBE = \frac{100}{P_{ins}} \frac{1}{n} \sum_{t=1}^{n} S_{(t)} - F_{(t)} \qquad [\%] \qquad \text{(eq. 14)}$$

$$RMSE = \frac{100}{P_{ins}} \sqrt{\frac{1}{n} \sum_{t=1}^{n} \left(S_{(t)} - F_{(t)}\right)^2} \qquad [\%] \qquad \text{(eq. 15)}$$

$$MAE = \frac{100}{P_{ins}} \frac{1}{n} \sum_{t=1}^{n} \left| S_{(t)} - F_{(t)} \right| \quad [\%] \quad \text{(eq. 16)}$$

$$MAPE = \frac{100}{n} \sum_{t=1}^{n} \left| \frac{S_{(t)} - F_{(t)}}{S_{(t)}} \right| \quad [\%] \quad \text{(eq. 17)}$$

$$MADPE = \frac{100}{n} \sum_{d=1}^{n} \frac{\sum_{t=1}^{24} |S_{(t)} - F_{(t)}|}{\sum_{t=1}^{24} |S_{(t)}|} \quad [\%] \quad \text{(eq. 18)}$$

As presented before an ARIMA and NARX models for solar and wind energy generation for one day-ahead forecast have been developed. Both of the proposed models accepts as inputs either the hourly irradiation or the wind speed. The output are 24 hourly values of, either, the solar generation or the wind generation in Spain. After several simulations for the four proposed methods the best configuration found gives the results shown in Tab. 3 for the representative weeks evaluated (10/1/15 – 17/1/15).

Tab. 3: Results for ARIMA and NARX models forecasting solar and wind energy generation

	Error	10/1/15	11/1/15	12/1/15	13/1/15	14/1/15	15/1/15	16/1/15	Mean
ARIMAX SOLAR	MBE	1.8%	0.5%	0.8%	0.2%	2.8%	2.8%	0.2%	1.3%
	RMSE	2.8%	1.5%	3.4%	2.0%	4.5%	5.3%	1.7%	3.0%
	MAE	1.8%	1.0%	1.9%	1.2%	2.8%	2.9%	1.2%	1.8%
	MAPE	33.0%	32.9%	44.7%	20.5%	34.3%	51.6%	40.8%	36.8%
	MADPE	12.1%	7.3%	14.5%	8.9%	24.9%	32.7%	11.4%	**16.0%**
ARIMAX WIND	MBE	-3.9%	-3.7%	-10.3%	6.4%	-0.4%	-6.4%	-5.7%	-3.4%
	RMSE	5.4%	7.0%	11.9%	6.8%	4.9%	8.7%	9.4%	7.7%
	MAE	4.6%	6.0%	10.3%	6.4%	3.9%	6.9%	6.9%	6.4%
	MAPE	25.3%	21.9%	36.2%	23.4%	15.2%	15.4%	14.3%	21.7%
	MADPE	27.4%	22.5%	39.1%	22.9%	15.0%	16.7%	15.7%	**22.8%**
NARX SOLAR	MBE	2.6%	1.7%	-1.2%	-1.1%	-0.3%	0.8%	-1.0%	**0.2%**
	RMSE	4.8%	3.1%	3.2%	3.4%	1.4%	1.4%	2.1%	**2.8%**
	MAE	2.8%	2.1%	1.8%	2.1%	0.9%	0.9%	1.5%	**1.7%**
	MAPE	22.2%	32.5%	32.3%	36.9%	44.3%	43.7%	41.7%	36.3%
	MADPE	18.3%	14.6%	13.8%	15.1%	8.3%	10.5%	14.0%	**13.5%**
NARX WIND	MBE	-4.4%	-1.8%	-3.4%	-0.8%	-2.1%	-0.4%	-0.3%	-1.9%
	RMSE	5.9%	7.1%	4.6%	2.1%	3.5%	2.3%	6.1%	4.5%
	MAE	4.9%	6.2%	3.9%	1.7%	2.5%	1.8%	5.0%	3.7%
	MAPE	26.1%	24.2%	14.8%	5.9%	8.9%	4.2%	11.2%	13.6%
	MADPE	29.1%	23.4%	14.8%	6.0%	9.8%	4.3%	11.4%	**14.1%**

6. Conclusions

In this work an ARIMAX and NARX models for solar and wind energy generation forecasting have been developed. The model is developed to obtain hourly results for one day-ahead or main market, from +12 to +36h. Both of the proposed models accept as inputs the time series to forecast and explanatory time series to improve the accuracy of the results. In the case of solar power the explanatory variable used is the irradiation; for wind power the explanatory variable used is the wind speed.

Once the forecasts are compared with the error figures, the results point out that the proposed NARX method outperform ARIMAX for both generation forecasts. It also points out that solar forecasts are more accurate that wind forecasts.

Nevertheless, the solar generation results are very tight for ARIMAX and NARX methods. RMSE, MAE and MAPE values are practically the same and it only differs slightly for MADPE when NARX method (13.51%) outperforms ARIMAX method (15.98%). This indicator is the most reliable for generations which fall off to values close to 0MWh as the solar generation does during the night.

For wind generation the results are much clearer. NARX method outperforms ARIMAX in every single error figure. In terms of MAPE, the result for NARX is 13.62% and ARIMAX reaches 21.67%. MADPE values are similar to MAPE in this case.

The results of performance achieved with NARX method for solar and wind forecasts in terms of MADPE are very similar; 13.51% in solar and 14.12% in wind. On the other hand the results obtained with the ARIMAX method in terms of MADPE differ for solar and wind forecasts; while in solar forecast the result is similar to the achieved in NARX, 15.98%; the results in wind generation are much worse reaching 22.77%, which is the worst result obtained for any of the proposed forecasting methods.

MBE figure shows the trend of the error in forecasting, if it is either overestimated or it is a lower value of energy generation. When averaging this figure on weekly basis the absolute value tends to decrease since the errors cancel themselves.

7. Acknowledgements

This work is supported by the European Union under FP7 grant contract 'Solar Heat Integration Network' (SHINE) and the fellowship at Sampol Ingeniería y Obras S.A. (317085) in the framework of Marie-Curie initial research training network (ITN).

8. References

Astariz, S., Perez-Collazo, C., Abanades, J., Iglesias, G., 2015. Towards the optimal design of a co-located wind-wave farm. Energy 84, 15–24. doi:10.1016/j.energy.2015.01.114

Benghanem, M., 2011. Optimization of tilt angle for solar panel: Case study for Madinah, Saudi Arabia. Appl. Energy 88, 1427–1433. doi:10.1016/j.apenergy.2010.10.001

Biga, A.J., Rosa, R., 1980. Estimating solar irradiation sums from sunshine and cloudiness observations. Sol. Energy. doi:10.1016/0038-092X(80)90334-5

Cassola, F., Burlando, M., 2012. Wind speed and wind energy forecast through Kalman filtering of Numerical Weather Prediction model output. Appl. Energy 99, 154–166. doi:10.1016/j.apenergy.2012.03.054

Chen, C., Duan, S., Cai, T., Liu, B., 2011. Online 24-h solar power forecasting based on weather type classification using artificial neural network. Sol. Energy 85, 2856–2870. doi:10.1016/j.solener.2011.08.027

Da Silva Fonseca, J.G., Oozeki, T., Takashima, T., Koshimizu, G., Uchida, Y., Ogimoto, K., 2012. Use of support vector regression and numerically predicted cloudiness to forecast power output of a photovoltaic power plant in Kitakyushu, Japan. Prog. Photovoltaics Res. Appl. 20, 874–882. doi:10.1002/pip.1152

Dong, Z., Yang, D., Reindl, T., Walsh, W.M., 2013. Short-term solar irradiance forecasting using exponential smoothing state space model. Energy 55, 1104–1113. doi:10.1016/j.energy.2013.04.027

Duffie, J. a., Beckman, W. a., 2013. Solar Engineering of Thermal Processes: Fourth Edition, Solar Engineering of Thermal Processes: Fourth Edition. doi:10.1002/9781118671603

Erdem, E., Shi, J., 2011. ARMA based approaches for forecasting the tuple of wind speed and direction. Appl. Energy 88, 1405–1414. doi:10.1016/j.apenergy.2010.10.031

Huang, R., Huang, T., Gadh, R., Li, N., 2012. Solar generation prediction using the ARMA model in a laboratory-level micro-grid, in: 2012 IEEE 3rd International Conference on Smart Grid

Communications, SmartGridComm 2012. pp. 528–533. doi:10.1109/SmartGridComm.2012.6486039

Lange, M., Focken, U., 2006. Physical approach to short-term wind power prediction, Physical Approach to Short-Term Wind Power Prediction. Springer Berlin Heidelberg. doi:10.1007/3-540-31106-8

Li, G., Shi, J., 2010. On comparing three artificial neural networks for wind speed forecasting. Appl. Energy 87, 2313–2320. doi:10.1016/j.apenergy.2009.12.013

Liu, H., Shi, J., Qu, X., 2013. Empirical investigation on using wind speed volatility to estimate the operation probability and power output of wind turbines. Energy Convers. Manag. 67, 8–17. doi:10.1016/j.enconman.2012.10.016

Lorenz, E., Hurka, J., Heinemann, D., Beyer, H.G., 2009. Irradiance forecasting for the power prediction of grid-connected photovoltaic systems. IEEE J. Sel. Top. Appl. Earth Obs. Remote Sens. 2, 2–10. doi:10.1109/JSTARS.2009.2020300

Mahoney, W.P., Parks, K., Wiener, G., Liu, Y., Myers, W.L., Sun, J., Delle Monache, L., Hopson, T., Johnson, D., Haupt, S.E., 2012. A Wind Power Forecasting System to Optimize Grid Integration. IEEE Trans. Sustain. Energy. doi:10.1109/TSTE.2012.2201758

Mellit, A., Pavan, A.M., 2010. A 24-h forecast of solar irradiance using artificial neural network: Application for performance prediction of a grid-connected PV plant at Trieste, Italy. Sol. Energy 84, 807–821.

Monteiro, C., Fernandez-Jimenez, L.A., Ramirez-Rosado, I.J., Muñoz-Jimenez, A., Lara-Santillan, P.M., 2013a. Short-term forecasting models for photovoltaic plants: Analytical versus soft-computing techniques. Math. Probl. Eng. 2013. doi:10.1155/2013/767284

Monteiro, C., Santos, T., Fernandez-Jimenez, L.A., Ramirez-Rosado, I.J., Terreros-Olarte, M.S., 2013b. Short-term power forecasting model for photovoltaic plants based on historical similarity. Energies 6, 2624–2643. doi:10.3390/en6052624

Paulescu, M., Badescu, V., Brabec, M., 2013. Tools for PV (photovoltaic) plant operators: Nowcasting of passing clouds. Energy 54, 104–112. doi:10.1016/j.energy.2013.03.005

Perez-Mora, N., Canals, V., Martinez-Moll, V., 2015. Short-Term Spanish Aggregated Solar Energy Forecast. Springer-Verlag Berlin Heidelberg 2011, Palma de Mallorca, pp. 307–319. doi:10.1007/978-3-319-19222-2_26

Perez-Mora, N., Martinez-Moll, V., Canals, V., 2016. DHC load management using demand forecast. Energy Procedia 91, 557–566. doi:10.1016/j.egypro.2016.06.198

Qazi, A., Fayaz, H., Wadi, a., Raj, R.G., Rahim, N. a., 2015. The artificial neural network for solar radiation prediction and designing solar systems: a systematic literature review. J. Clean. Prod. 104, 1–12. doi:10.1016/j.jclepro.2015.04.041

Reikard, G., 2009. Predicting solar radiation at high resolutions: A comparison of time series forecasts. Sol. Energy 83, 342–349. doi:10.1016/j.solener.2008.08.007

Rubin, O.D., Babcock, B. a., 2013. The impact of expansion of wind power capacity and pricing methods on the efficiency of deregulated electricity markets. Energy 59, 676–688. doi:10.1016/j.energy.2013.07.020

Sharma, N., Sharma, P., Irwin, D., Shenoy, P., 2011. Predicting solar generation from weather forecasts using machine learning, in: 2011 IEEE International Conference on Smart Grid Communications, SmartGridComm 2011. pp. 528–533. doi:10.1109/SmartGridComm.2011.6102379

Sørensen, P., Hansen, A.D., Rosas, P.A.C., 2002. Wind models for simulation of power fluctuations from wind farms. J. Wind Eng. Ind. Aerodyn. 90, 1381–1402. doi:10.1016/S0167-6105(02)00260-X

Sulaiman, S.., Rahman, T.. A., Musirin, I., 2009. Partial Evolutionary ANN for Output Prediction of a Grid-Connected Photovoltaic System. Int. J. Comput. Electr. Eng. 1, 40–45. doi:10.7763/IJCEE.2009.V1.7

Tseng, F.-M., Yu, H.-C., Tzeng, G.-H., 2002. Combining neural network model with seasonal time series ARIMA model. Technol. Forecast. Soc. Change 69, 71–87. doi:10.1016/S0040-1625(00)00113-X

Y. Gala, A. Fernández, J. Dorronsoro, 2014. Machine Learning Prediction of Global Photovoltaic Energy in Spain, in: International Conference on Renewable Energies and Power Quality (ICREPQ'14). Springer Verlag, Cordoba (Spain).

Yang, D., Jirutitijaroen, P., Walsh, W.M., 2012. Hourly solar irradiance time series forecasting using cloud cover index. Sol. Energy 86, 3531–3543. doi:10.1016/j.solener.2012.07.029

Zhang, Y., Wistar, S., Piedra-Fernandez, J.A., Li, J., Steinberg, M.A., Wang, J.Z., 2014. Locating visual storm signatures from satellite images, in: 2014 IEEE International Conference on Big Data (Big Data). pp. 711–720. doi:10.1109/BigData.2014.7004295

Conference Proceedings
Solar World Congress 2015
Daegu, Korea, 08 – 12 November 2015

STATISTICAL MODELS TO PREDICT SOLAR RADIATION AT HIGH RESOLUTIONS

Philippe Lauret[1], Mathieu David[1], Pierre-Julien Trombe[2] and Faly Ramahatana-Andriamasomanana[1]

[1] PIMENT Laboratory/University of La Reunion, Saint-Denis (France)

[2] Technical University of Denmark, Lyngby (Denmark)

Abstract

In this work, we assess the performance of statistical models for intra-hour solar forecasting. More precisely, a linear recursive model and a nonlinear model are used for generating solar irradiance forecasts at temporal resolutions of a few minutes and over multiple horizons. Our approach is applied to forecasting solar irradiance at single sites using the sole historical ground observations of solar irradiance. The benchmarking of the forecasting methods is made at four sites that exhibit different sky conditions.

Keywords: *intra-hour solar forecasting, statistical models*

1. Introduction

The availability of accurate solar forecasts is of great importance for an efficient integration of large shares of solar energy into the electricity grid (Lorenz and Heinemann, 2012). To ensure reliable grid operation, utilities require accurate forecasts at different granularities and different forecasting time horizons (Kostylev and Pavloski, 2011). Depending on the forecast horizon, different input data and forecasting models are appropriate. Statistical models with on-site measured irradiance are adequate for the very short-term time scale ranging from 5 minutes up to 6 hours (Lorenz and Heinemann, 2012).

Today, solar forecasts are essentially produced on an hourly basis. However, there is a broad consensus among energy experts, electric utilities and regulatory authorities on the future need for intra-hour forecasts in order to accommodate the increasing share of photovoltaic power in power systems.

In this work, the focus is placed on lead times from 10 minutes to 3 hours ahead with a granularity of 10 minutes. Consequently, we assess the performance of two statistical models: a linear recursive model ARMA.rls (Ljung and Söderström, 1983) and a nonlinear model ν-SVM based on support vector machine (Smola and Schölkopf, 2004) for intra-hour solar forecasting. The benchmarking of the two methods is made at four sites that exhibit different sky conditions.

2. Data

Four sites are used to evaluate the performance of the forecasting methods. Three of these sites are island sites: Saint-Pierre and Le Tampon (Reunion island), Oahu-Hawaii (Wilcox and Andreas, 2010). The fourth one is located in Las Vegas (Andreas and Stoffel, 2006). The choice of the aforementioned sites aims at testing the different forecasting techniques for different sky conditions. Table 1 gives the details related to the four locations. The data (two years) used to build the models are Global Horizontal Irradiances (GHI) measured at the four stations. Contrary to the ARMA.rls method, the machine learning technique ν-SVM investigated in this work is a supervised learning method, which consists in learning input-output mappings from empirical data (the training dataset). Consequently, data have been divided into training and test datasets. The test dataset (one year) is used to evaluate the performance of the forecasting techniques. Table 1 gives also the mean GHI of the test year used to compute the relative error metrics (see section 5).

doi:10.18086/swc.2015.07.11 Available at http://proceedings.ises.org

Tab. 1: Locations under study

	Las Vegas (NV)	Oahu (HI)	Saint-Pierre (RUN)	Tampon (RUN)
Provider	NREL	NREL	PIMENT	PIMENT
Position	36.06N 115.08W	21.3N 158.1W	21.3S 55.5E	21.3S 55.5E
Elevation	615m	11m	75m	550m
Climate type	Desertic	Tropical	Tropical	Tropical
Period	2011 (Training) 2012 (Testing)	2010 (Training) 2011 (Testing)	2012 (Training) 2013 (Testing)	2012 (Training) 2013 (Testing)
Mean GHI testing period	544 $W.m^{-2}$	493 $W.m^{-2}$	538 $W.m^{-2}$	457 $W.m^{-2}$

3. Data processing

The Bird clear sky model (Bird and Huldstrom, 1981) is used to remove the daily and annual seasonalities in the global horizontal solar irradiance (GHI) time series then leading to the definition and use of the clear sky index:

$$k^* = G/G_{clsk} \qquad \text{(eq. 1)}$$

where G is the measured global irradiance and G_{clsk} is the output of the Bird clear sky model. With this methodology, the models designed in this work are dedicated to the stochastic part of the global radiation due to cloud cover, leaving the geometric and the deterministic part to be modeled by the clear sky model.

It is also a common practice to filter out the data in order to remove night hours. This choice is justified because during these periods there is obviously no significant solar radiation to generate electricity (i.e. low potential overnight). We chose to apply a filtering criterion based on the solar zenith angle (θ_Z): solar radiation data for which the solar zenith angle is greater than 80° have been removed. In addition, this filtering process allows to discard data with less precision as measurement uncertainties associated with pyranometers are typically much higher than ± 3.0% for SZA > 80°. Notice also that for the sunrise and sunset, the prediction is also very difficult (mainly in mountainous areas) owing to the geographical shield.

4. Forecasting methods

The performance of the linear ARMA.rls and nonlinear ν-SVM models are appraised against two reference models namely persistence and climatologic mean models.

4.1 Reference models

We propose to test our forecasting methods against reference models like persistence and climatology.

The persistence model is expressed as follows:

$$\widehat{k^*}(t+h) = k^*(t) \qquad \text{(eq. 2)}$$

This model assumes that the clear sky index for each forecasting time horizon h only depends on the previous value, which means that the sky conditions remain invariant between time t and time $t+h$.

We also propose the climatological mean model, which is independent of the forecast time horizon (Lorenz

and Heinemann, 2012). More precisely, this model performs a constant forecast of the clear sky index that corresponds to its mean historical value:

$$\widehat{k^*}(t+h) = mean\,(k^*(t))_{training\ period} \qquad \text{(eq. 3)}$$

4.2 ARMA.rls model

The Auto Regressive Moving Average (ARMA) model is a popular technique in the realm of solar forecasting. In particular, it has been extensively studied in renewable energy forecasting and, owing to its parsimony, it has turned out to be a very tough competitor to beat. Applications include, among others forecasting of wind power generation (Pinson, P., 2012), online power forecasting (Bacher et al., 2009) and wave energy flux (Pinson et al., 2012).

An ARMA(p,q) model with p AR terms and q MA terms is defined as follows:

$$\widehat{k^*}(t+h) = \theta_0 + \sum_{i=1}^{p} \theta_i k^*(t-i+1) + \varepsilon(t) + \sum_{j=1}^{q} \phi_j \epsilon(t—j) \qquad \text{(eq. 4)}$$

$\epsilon(t)$ is an independent and identically distributed random variable with a zero mean. The vector $\Theta = \left(\theta_0, \theta_1, \cdots, \theta_p, \Phi_{1,}, \cdots, \Phi_q\right)$ contains the set of parameters to be estimated. A classic setting based on a least-squares method and training data can be used to estimate the set of parameters (Chatfield, 2004).

However, in this work, to estimate the model's parameters, we chose a variation of the least squares method, namely the Recursive Least Square (RLS) method (see Ljung and Söderström, 1983 for details of implementation). This method offers the advantage of reducing the computational cost for estimating the model's parameters. In addition, the parameters are updated in real-time as new data become available (no training set is necessary here). This contrasts with more intensive estimation methods operating on a sliding window where the estimation process is being carried out at each time step. Hence, the RLS method is particularly well suited in an operational context where forecasts have to be timely delivered.

Regarding the structure of the ARMA model, the use of the classical ACF (Auto Correlation Function) and PACF (Partial Auto Correlation Function) techniques (Chatfield, 2004) led to the selection of the following orders $p = 6$ and $q = 2$.

4.3 ν-SVM model

The support vector machine (SVM) is part of the kernel based machine learning techniques used in classification tasks and regression problems (Smola and Schölkopf, 2004). The forecasted clear sky index for time horizon h is given by Eq. (5):

$$\hat{k}^*(t+h) = \sum_{i=1}^{n} \alpha_i\, k_{rbf}(\mathbf{x}_i, \mathbf{x}_*) + b \qquad \text{(eq. 5)}$$

k_{rbf} denotes the kernel radial basis function $k_{rbf}(x_p, x_q) = \exp\left[-\gamma\left|(x_p - x_q)\right|\right]$ with hyperparameter γ and b a bias parameter. SVM models are generally stated as a kernel-based method. Indeed, it can be shown that, given n training samples, the prediction for an input test vector $\mathbf{x}_*$ can be seen in terms of a linear combination of n kernel functions; each one centered on a training point $\mathbf{x}_i$. Notice that $\mathbf{x}_i$ and $\mathbf{x}_*$ are vectors that contain the p past values of the clear sky index. A variant of the SVM algorithm called ν-SVM allows controlling the amount of kernel functions used in the regression.

The parameter b (or bias parameter) is derived from the preceding equation and some specific conditions (see Smola and Schölkopf, 2004 for details). The coefficients α_i are related to the difference of two Lagrange multipliers, which are the solutions of a quadratic programming (QP) problem (Smola and Schölkopf, 2004).

Unlike artificial neural networks, which are confronted with the problem of local minima, here the problem is strictly convex and the QP problem has a unique solution. In addition, it must be stressed that not all the training patterns participate in the preceding relationship. Indeed, a convenient choice of a cost function i.e. Vapnik's ε-insensitive function (Smola and Schölkopf, 2004) in the QP problem enables to obtain a sparse solution. The latter means that only some of the coefficients α_i will be nonzero. The examples that come with non-vanishing coefficients are called Support Vectors.

The parameters related to the SVM optimization process are a parameter C that controls the trade-off between overfitting and generalization capability of the algorithm, a parameter ν that controls the amount of support vectors used in the regression and the parameter γ of the covariance function that controls the smoothness of the covariance function (Fonseca Junior et al., 2013). These parameters have been optimized through the use of a k-fold cross-validation procedure (Fonseca Junior et al., 2013). In the present study, regarding the implementation of the support vector regression, we used the LibSVM library (Chang et al., 2011).

5. Results

In the realm of the solar forecasting community, the commonly used error metrics are: the Root Mean Square Error (RMSE), Mean Absolute Error (MAE) and Mean Bias Error (MBE). Relative counterparts (rRMSE, rMBE and rMAE) are obtained by normalization with the mean GHI of the test period (see Table 1). The interested reader is referred to Lorenz and Heinemann (2012) for the definition of these error metrics.

In this work, a special focus is placed on the rRMSE. This error metric tends (unlike the rMAE) to be influenced by some extreme events or outliers. Nonetheless, most utility users find this metric suitable as large forecast error results in high financial losses (Lorenz and Heinemann, 2012).

Tables 2, 3 and 4 list respectively the rRMSE, rMBE and rMAE for each forecasting time horizon and for each location. As shown by these tables, one can a priori state that the performances of the different models depend heavily on the sky conditions experienced by each site. The persistence model is a good indicator of the type of climate experienced by a particular site. As seen, it seems that the Las Vegas location experiences high occurrences of clear sky situations while the insular sites (particularly Le Tampon and Oahu) exhibit more variable sky conditions.

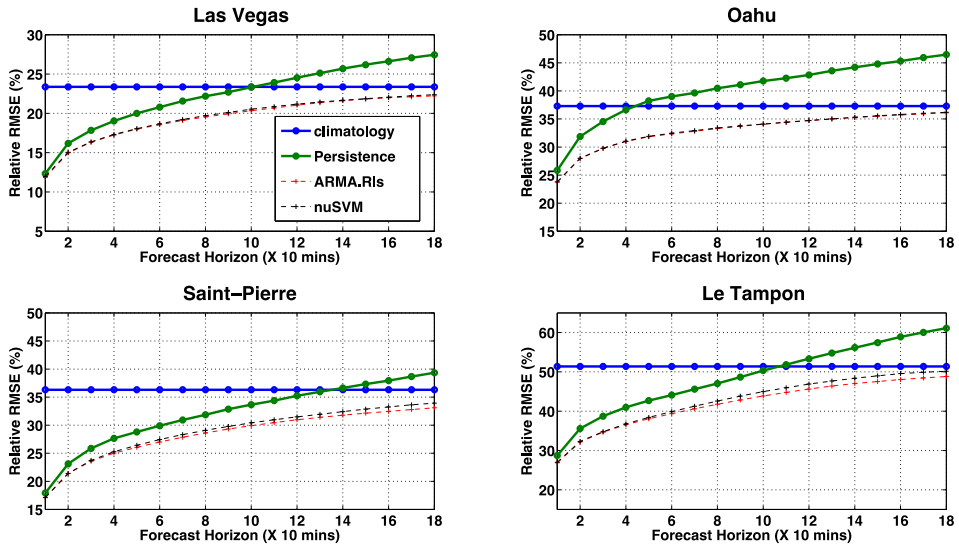

Fig. 1: Accuracy of intra-hour solar forecasting

Fig. 1 plots the rRMSE of the different methods for forecast horizon ranging from 10 minutes to 180 minutes. Fig.1 demonstrates the better performance of the SVM method (ν-SVM) and ARMA.rls model over the persistence model when the forecast horizon increases. As shown by Fig.1, the linear recursive model ARMA.rls performs equally well than the nonlinear SVM model. It even produces slightly better forecasts in the case of Saint-Pierre and Le Tampon. Further, the improvement is more pronounced as the forecast horizon increases. One may notice also that the performances of the linear and nonlinear models tend

towards that of the climatological mean. This behavior is consistent, as these methods tend to asymptotically model the mean of the data.

Overall, contrary to the ν-SVM model, it appears that the ARMA.rls method produces less biased forecasts (see Table 3). Regarding the rMAE metric, except for Las Vegas, the ARMA technique performs better than the SVM method.

Tab. 2: Relative RMSE in % for each location and for each forecast horizon. Pers, RLS and SVM correspond respectively for Persistence, ARMA.rls and ν-SVM models.

h+xx mins	Las Vegas (NV)			Oahu (HI)			Saint-Pierre (RUN)			Tampon (RUN)		
	Climatology		23.4	Climatology		37.3	Climatology		36.3	Climatology		51.3
	Pers	RLS	SVM	Pers	RLS	SVM	Pers	RLS	SVM	Pers	RLS	SVM
h+10	12.3	11.8	11.9	25.8	23.8	23.8	17.9	17.1	17.1	28.7	26.9	27.0
h+20	16.2	15.0	15.0	31.9	28.0	28.0	23.1	21.4	21.4	35.6	32.1	32.3
h+30	17.8	16.3	16.4	34.5	29.7	29.8	25.9	23.6	23.7	38.7	34.7	34.8
h+40	19.0	17.2	17.3	36.6	31.0	31.0	27.6	25.0	25.3	41.0	36.6	36.7
h+50	20.0	18.0	18.0	38.2	31.8	31.9	28.8	26.1	26.4	42.7	38.1	38.4
h+60	20.8	18.6	18.7	39.0	32.3	32.4	29.9	27.0	27.4	44.1	39.4	39.9
h+70	21.6	19.1	19.2	39.6	32.8	32.9	30.9	27.9	28.3	45.6	40.6	41.3
h+80	22.2	19.5	19.7	40.5	33.3	33.4	31.9	28.6	29.0	47.0	41.7	42.6
h+90	22.7	19.9	20.1	41.1	33.7	33.8	32.9	29.3	29.7	48.7	42.8	43.8
h+100	23.3	20.3	20.5	41.7	34.1	34.1	33.6	29.9	30.4	50.3	43.9	45.0
h+110	23.9	20.7	20.8	42.3	34.4	34.4	34.4	30.4	31.0	51.8	44.8	45.9
h+120	24.5	21.0	21.1	42.8	34.7	34.7	35.2	30.1	31.5	53.3	45.6	46.9
h+130	25.1	21.3	21.4	43.6	35.0	35.0	35.9	31.4	31.9	54.8	46.4	47.7
h+140	25.7	21.6	21.7	44.2	35.2	35.3	36.6	31.8	32.4	56.2	47.0	48.4
h+150	26.2	21.8	21.9	44.8	35.5	35.6	37.3	32.1	32.9	57.4	47.5	49.0
h+160	26.6	22.0	22.0	45.3	35.7	35.8	37.9	32.4	33.2	58.9	48.0	49.5
h+170	27.1	22.1	22.2	46.0	35.9	36.0	38.7	32.8	33.6	60.0	48.5	49.9
h+180	27.5	22.2	22.3	46.5	36.1	36.2	39.3	33.1	33.9	61.1	48.8	50.1

Tab. 3: Relative MBE in % for each location and for each forecast horizon

h+xx mins	Las Vegas (NV)			Oahu (HI)			Saint-Pierre (RUN)			Tampon (RUN)		
	Climatology		8.30	Climatology		3.95	Climatology		-4.25	Climatology		1.89
	Pers	RLS	SVM	Pers	RLS	SVM	Pers	RLS	SVM	Pers	RLS	SVM
h+10	0.15	0.15	0.45	0.15	0.47	0.59	0.08	-0.18	-0.65	0.42	0.45	-0.30
h+20	0.27	0.25	1.31	0.30	0.81	1.01	0.15	-0.30	-1.35	0.83	0.71	-0.74
h+30	0.37	0.34	1.79	0.47	1.03	1.23	0.18	-0.37	-2.25	1.24	0.94	-0.80
h+40	0.46	0.37	2.20	0.65	1.21	1.57	0.20	-0.46	-2.52	1.61	1.13	-0.80
h+50	0.56	0.40	2.70	0.82	1.35	1.75	0.20	-0.54	-2.72	1.97	1.29	-0.68
h+60	0.65	0.37	3.06	1.00	1.45	2.20	0.18	-0.64	-2.99	2.30	1.28	-0.37
h+70	0.73	0.36	3.39	1.19	1.52	2.34	0.14	-0.74	-3.26	2.62	1.32	-0.28
h+80	0.80	0.36	3.69	1.37	1.60	2.59	0.10	-0.84	-3.42	2.91	1.33	-0.20

h+90	0.88	0.36	3.93	1.54	1.66	2.56	0.03	-0.92	-3.68	3.18	1.34	0.01
h+100	0.95	0.36	4.11	1.70	1.71	2.55	-0.04	-0.99	-4.07	3.42	1.28	0.19
h+110	0.99	0.35	4.32	1.86	1.72	2.76	-0.14	-1.06	-4.26	3.62	1.21	0.42
h+120	1.04	0.33	4.55	2.00	1.72	2.96	-0.25	-1.15	-4.37	3.79	1.14	0.71
h+130	1.07	0.31	4.78	2.12	1.74	2.87	-0.37	-1.22	-4.50	3.93	1.05	0.95
h+140	1.10	0.29	5.01	2.23	1.76	3.00	-0.50	-1.30	-4.77	4.03	0.89	1.06
h+150	1.12	0.25	5.28	2.33	1.73	3.24	-0.65	-1.39	-4.95	4.10	0.66	1.23
h+160	1.14	0.22	5.48	2.42	1.71	3.39	-0.80	-1.50	-4.96	4.12	0.38	1.34
h+170	1.14	0.20	5.68	2.50	1.68	3.39	-0.96	-1.57	-5.00	4.11	0.17	1.40
h+180	1.13	0.22	5.79	2.56	1.70	3.54	-1.13	-1.71	-5.11	4.07	0.01	1.39

Tab. 4: Relative MAE in % for each location and for each forecast horizon

h+xx mins	Las Vegas (NV)			Oahu (HI)			Saint-Pierre (RUN)			Tampon (RUN)		
	Climatology		14.6	Climatology		29.2	Climatology		29.2	Climatology		42.2
	Pers	RLS	SVM	Pers	RLS	SVM	Pers	RLS	SVM	Pers	RLS	SVM
h+10	5.1	5.5	5.0	16.1	16.1	15.9	9.2	10.1	9.9	16.4	17.6	17.1
h+20	7.1	7.6	6.8	20.5	19.8	19.7	12.4	13.6	14.0	21.5	22.8	22.9
h+30	8.2	8.6	7.7	22.6	21.5	21.5	14.4	15.6	16.7	24.2	25.7	26.1
h+40	9.0	9.3	8.3	24.3	22.7	22.8	15.8	17.1	18.3	26.3	27.7	28.5
h+50	9.7	9.8	8.9	25.6	23.6	23.7	16.9	18.2	19.5	28.1	29.4	30.3
h+60	10.3	10.4	9.4	26.4	24.2	24.4	17.9	19.2	20.6	29.4	30.7	31.9
h+70	10.9	10.9	9.8	27.1	24.7	24.9	18.8	20.5	21.5	30.7	31.9	33.2
h+80	11.5	11.2	10.2	27.9	25.2	25.5	19.7	20.8	22.3	32.1	33.0	34.5
h+90	12.0	11.6	10.5	28.5	25.6	25.9	20.6	21.5	23.0	33.4	34.1	35.7
h+100	12.5	11.9	10.8	29.1	26.1	26.3	21.3	22.1	23.7	34.8	35.0	36.7
h+110	12.9	12.2	11.0	29.7	26.4	26.7	22.1	22.6	24.3	36.2	35.8	37.6
h+120	13.3	12.5	11.2	30.2	26.7	26.9	28.8	23.1	24.8	37.5	36.6	38.4
h+130	13.8	12.7	11.4	30.8	27.0	27.2	23.4	23.5	25.3	38.6	37.4	39.0
h+140	14.2	12.9	11.6	31.3	27.2	27.5	24.1	23.9	25.8	39.9	37.8	39.7
h+150	14.6	13.1	11.7	31.7	27.5	27.7	24.7	24.2	26.3	40.8	38.2	40.2
h+160	14.9	13.3	11.9	32.1	27.7	28.0	25.3	24.5	26.7	42.1	38.8	40.7
h+170	15.3	13.4	12.0	32.7	27.9	28.1	26.0	24.7	27.1	43.1	39.2	41.0
h+180	15.6	13.5	12.1	33.1	28.1	28.3	26.6	25.0	27.4	44.0	39.5	41.2

6. Conclusion

This work proposes a benchmarking of techniques for intra-hour solar forecasting. A machine learning technique such as support vector machine was evaluated against a recursive linear model and reference models like persistence and climatological mean. It was shown that a linear recursive technique like ARMA.rls performs equally well or slightly better than a non-linear method such as support vector machine.

As a conclusion, it appears that a simple technique like ARMA.rls could be a viable solution to predict solar radiation at high resolutions. In addition, the recursive estimation of the model's parameters makes the method very well suited to online forecasting.

7. References

Andreas, A., Stoffel, T., 2006. NREL Report No. DA-5500-56509. University of Nevada (UNLV): Las Vegas, Nevada (Data).

Bacher, P., Madsen, H., Nielsen, H.A, 2009. Online short-term solar power forecasting. Solar Energy. 83, 1772-1783.

Bird, R.E. , Hulstrom, R.L., 1981. Simplified the Clear Sky Model for Direct and Diffuse Insolation on Horizontal Surfaces, Technical Report No. SERI/TR-642-761, Golden, CO: Solar Energy Research Institute.

Chatfield, C., 2004. Time series analysis, an introduction, Chapman & Hall/CRC.

Chang, C.C, Lin, C.J, 2011. LIBSVM: A library for support vector machines, <http://www.csie.ntu.edu.tw/~cjlin/libsvm>.

Fonseca Junior, J. G. S., Ozeki, T., Ohtake, H. , Shimose, K., Takashima, T., Ogimoto, K., 2013. Analysis of Different Techniques to Set Support Vector Regression to Forecast Insolation in Tsukuba, Japan. Journal of International Council on Electrical Engineering, 3(2), 121-128.

Kostylev, V., Pavlovski, A., 2011. Solar power forecasting performance towards industry standards. In: Proceedings of the 1st International Workshop on the Integration of Solar Power into Power Systems, October 24, Aarhus, Denmark.

Ljung, L., Söderström, T., 1983. Theory and Practice of Recursive System Identification. Prentice-Hall International

Lorenz, E., Heinemann, D., 2012. Prediction of solar irradiance and photovoltaic power, in: Sayigh, A., (Ed.), Comprehensive Renewable Energy. Elsevier, Oxford, pp. 239-292.

Pinson, P., 2012. Very short term probabilistic forecasting of wind power with generalized logit–normal distributions, Journal of the Royal Statistical Society: Series C (Applied Statistics). 61, 555-576.

Pinson, P., Reikard, G., Bidlot, J.R., 2012. Probabilistic forecasting of the wave energy flux. Applied Energy, 93, 364-370.

Smola, A.J., Schölkopf, B., 2004. A tutorial on support vector regression. Statistics and Computing. 14, 199–222

Wilcox, S., Andreas, A., 2010. Solar Resource & Meteorological Assessment Project (SOLRMAP): Rotating Shadowband Radiometer (RSR), Kalaeloa Oahu, Hawaii (Data), NREL Report No. DA-5500-56497.

Conference Proceedings

Solar World Congress 2015
Daegu, Korea, 08 – 12 November 2015

VALIDATION OF GHI AND DNI PREDICTIONS FROM GFS AND MACC MODEL IN THE MIDDLE EAST

Luis Martin-Pomares[1], Jesus Polo[2], Daniel Perez-Astudillo[1] and Dunia A. Bachour[1]

[1] Qatar Environment and Energy Research Institute (QEERI), HBKU, Qatar Foundation, Doha, Qatar

[2] Energy Department, CIEMAT, Madrid, 28040, Spain

Abstract

Production of electricity from solar energy is gaining a tremendous significance. The integration of all solar energy power to the electricity grid challenges new horizons. Mainly, the prediction of short-term power generation to optimise its management, avoid situations of load reduction and anticipate supplying problems.

This paper presents a methodology to forecast hourly global horizontal solar irradiance (GHI) and direct normal irradiance (DNI) using global forecast system (GFS) model from NOAA and MACC model from ECMWF. Three clear sky models are tested to increase temporal resolution of GFS model from 3 hours to 1 hour. The forecasting horizon of the predictions is six days. The model has been validated using a ground radiometric station in Qatar with data from 2014 to 2015. The errors of the best model tested are 19% in terms of relative RMSD and -1.68% regarding relative bias for GHI. In the case of DNI, relative RMSD is 48.43%, and relative bias is -3.40%.

Keywords: *solar radiation forecasting, AOD forecasting, DNI prediction, Atmospheric aerosols*

1. Introduction

Solar energy is gaining an enormous significance due to the unsustainable current energetic model. In the case of solar power, technology to produce electricity, the integration of all these power to the electricity grid challenges new horizons. The most important are the estimation of short range power generation to optimise its management, avoid situations of load reduction and anticipate supplying problems (Pelland, Remund, Kleissl, Oozeki, & De Brabandere, 2013).

In this study, we present a methodology to forecast hourly global horizontal solar irradiance (GHI) and direct normal irradiance (DNI) using cloudiness from global forecast system (GFS) model from NOAA and AOD and water vapour predictions from MACC model from ECMWF. The forecasting horizon of the predictions is six days. The model has been validated using a ground radiometric station in Qatar with data from 2013 to 2015.

2. Experimental Solar Radiation Dataset

The radiometric data employed in this study for the validation is located in the Middle East. The instruments in the station are Kipp & Zonen high precision and measurements are available at the end of November 2012. The station is equipped with a Solys2 sun tracker with sun sensor kit for improved tracking accuracy and shading ball assembly for diffuse measurements. Mounted on the sun tracker are one CHP1 pyrheliometer for measuring DNI and two CMP11 pyranometers (one of them shaded) for GHI and DHI measurements; both pyranometers are fitted with CVF 3 ventilation units. Data from the monitoring station are collected as minute

doi:10.18086/swc.2015.07.12 Available at http://proceedings.ises.org

by minute averages in W/m^2. Maintenance and checks are conducted on a daily basis and consist of cleaning all sensors and tests on the tracking and alignment of the sensors and shadow ball as well as visual checks on the collected data (Bachour & Perez-Astudillo, 2014; Perez-Astudillo & Bachour, 2014). Two type of quality filters has been applied to the data. The first group of filters is based on physical limits of solar radiation. We have removed from the comparison values lower than zero and higher than extraterrestrial solar radiation. The second group of filters is more restrictive and is based on BSRN quality filters (Long & Dutton, 2002).

3. Methodology

The model developed uses 3-hourly solar radiation predictions from GFS model to obtain hourly values using a statistical downscaling model and a clear sky model.

The Global Forecast System (GFS) is a global numerical weather prediction model from NOAA. The GFS model covers the entire globe at a base horizontal resolution of 28 kilometres between grid points, which is used by the operational forecasters who predict weather out to 16 days in the future. In this work, we obtain hourly predictions for six days ahead.

The predictions of hourly GHI are calculated using directly the output variable DSWRF at a surface level from GFS model. The nearest grid output point of GFS model to each station is used as the basic predictions. Afterwards, 3-hourly values from GFS model are calculated as hourly values with the interpolation of k_c which is the quotient between measured global solar radiation and clear sky solar radiation. Clear sky solar radiation is calculated with three different models as they behave better than others depending on the climatic conditions of the sites. ESRA (Rigollier, Bauer, & Wald, 2000), SOLIS (Ineichen, 2008) and REST2 (Gueymard, 2008) clear sky models have been tested. Hourly atmospheric parameters of AOD at 550nm and water vapour column are obtained from MACC-II model (Monitoring Atmospheric Composition & Climate from ECMWF) for clear sky models. The spatial resolution of MACC-II model is 1.125ºx1.125º. MACC-II uses a comprehensive global monitoring and forecasting system that estimates the state of the atmosphere on a daily basis, combining information from models and observations, and it provides a daily 5-day forecast.

Once GHI hourly predictions are calculated, DNI hourly predictions are obtained using DirIndex model (Perez, P.Ineichen, E.Maxwell, R.Seals, & A.Zelenka, 1992).

An algorithm to detect clear sky days has been applied (Zarzalejo, Polo, Martín, Ramírez, & Espinar, 2009) to calculate to clear sky conditions. In such a case, the prediction for the next day for GHI and DNI components are made using the clear sky model. Fig 1. shows the schema of the methodology employed to obtain hourly predictions of GHI and DNI for six days ahead.

4. Results

The parameters to calculate the errors of the models are mean bias deviation (MBD), root mean squared deviation (RMSD) and its relative value as rMBD and rRMSD. The relative expressions are obtained using the following equations:

$$\mathrm{rMBD} = \frac{1}{N}\sum_{i=1}^{N}\left(\hat{x}_i - x_i\right) \qquad \text{(eq. 1)}$$

$$\mathrm{rRMSD} = \frac{\sqrt{\sum_{i=1}^{n}(x_i - \hat{x}_i)^2 / n}}{\overline{x}} \qquad \text{(eq. 2)}$$

where N is the population size, x is the observed value, $\overline{x}$ is the mean of observed values and $\hat{x}$ is the predicted value.

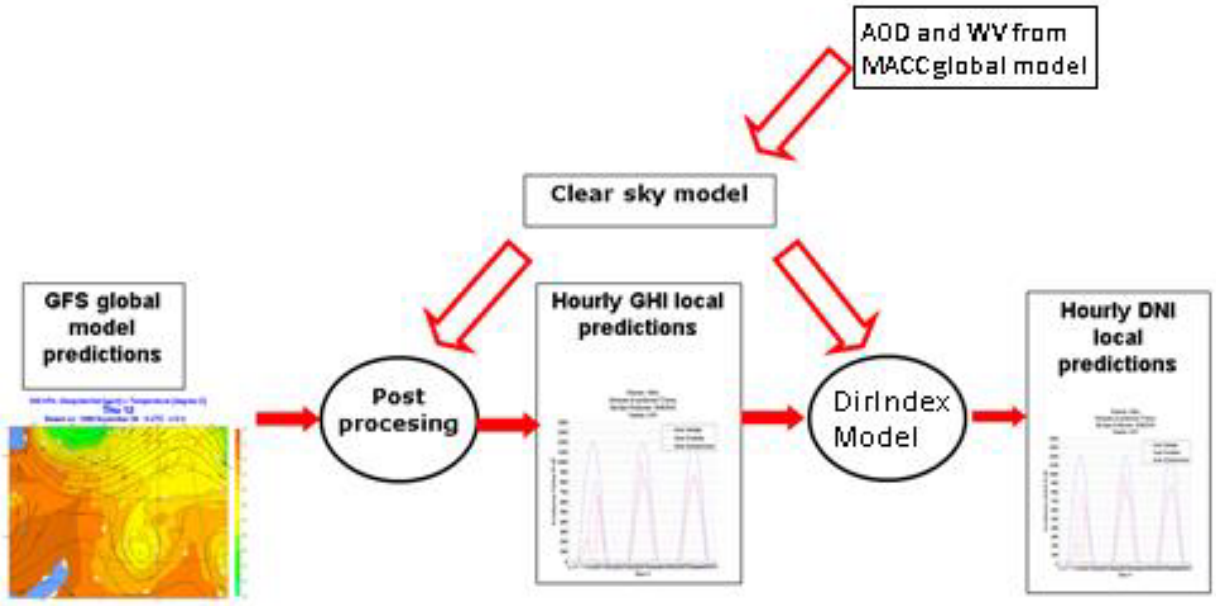

Fig. 1. Schema of the methodology used to obtain hourly predictions of GHI and DNI

Last parameters are often insufficient to establish a complete, coherent comparison for benchmarking. Due to this, additional measures for model quality based on the analysis of cumulative distribution function (CDF) are used. A comprehensive approach to analyse the deviations of measured and predicted data is applied. It is based on the Kolmogorov-Smirnov (KS) test and defines new parameters to quantify the similarity of the two CDFs. Although there are several statistical tests and ways of evaluating the goodness of a model, the KS test has the advantage of making no assumption about the data distribution and is thus a non-parametric, distribution-free test. The KS test determines if two datasets differ significantly. The test consists of comparing the distribution of a dataset to a reference distribution. It can be done by converting the list of data points to an unbiased estimator $S(x_i)$ of the CDF, $i = 1..N$, N is the population size. The KS statistic D is defined as the maximum value of the absolute difference between the two CDFs:

$$D = \max \left| S(\mathrm{x}_i) - \mathrm{R}\left(x_i\right) \right| \qquad \text{(eq. 3)}$$

where $R(x_i)$ is the CDF of the reference dataset. Thus, if the D statistic is lower than the threshold value VC, the null hypothesis that the two datasets come from the same distribution cannot be rejected. The critical value depends on N and is calculated for a 99% level of confidence as:

$$V_c = \frac{1.63}{\sqrt{N}}, \quad N \geq 35 \qquad \text{(eq. 4)}$$

This test detects smaller deviations in cumulative distributions than the $\chi 2$ test does. However, instead of using the original one, an extended KS test is used, in which the distances between the CDFs are calculated over the whole range of the variable x, i.e. the solar radiation. A discretization in $n = 1 \ldots m$ levels is applied here. In the following $m = 100$ intervals as a reasonable choice are used. Greater order of magnitude for$m$ is not recommended since it implies more computational cost for no improvement in the accuracy of the result. The interval distance p is thus defined as:

$$p = \frac{x_{\max} - x_{\min}}{m}, \quad m = 100 \qquad \text{(eq. 5)}$$

where x_{max} and x_{min} are the extreme values of the independent variable. Then, the distances between the CDFs are defined, for each interval, as:

$$D_n = \left| S\left(x_j\right) - R\left(x_j\right) \right|, \quad x_j \in \left[x_{\min} + \left(n-1\right) p, x_{\min} + np \right] \qquad \text{(eq. 6)}$$

The representation of the values D_n, along with the critical value, gives the complete testing behaviour of the CDF on the reference over the whole range. However, although application of the KS test contributes valuable information, it only materialises in the acceptance or rejection of the null hypothesis. In the next paragraphs, new parameters are proposed, which, based on the estimation of the distance between the two CDFs for the sets compared, define quantitative measures that can be used to rank models (Espinar et al., 2009).

The KSI parameter (Kolmogorov-Smirnov test Integral) is defined as the integral of the area between the CDFs for the two sets. The unit of this index is the same for the corresponding magnitude, the value of which depends on it. The KSI is defined as the integral:

$$KSI = \int_{x\min}^{x\max} D_n dx \qquad \text{(eq. 6)}$$

As D_n is a discrete variable and the number of integration intervals is identical in all cases, trapezoidal integration is possible over the whole range of the independent variable x. A percentage of KSI is obtained by normalising the critical area, $a_{critical}$:

$$KSI\% = \frac{\int_{x\min}^{x\max} D_n dx}{a_{critical}} * 100 \qquad \text{(eq. 6)}$$

where $a_{critical}$ is calculated as:

$$a_{critical} = V_c * (x_{max} - x_{min})$$

where V_c is the critical value for the level of confidence selected and (x_{max}, x_{min}) are the extreme values of the independent variable. Normalisation to the key area enables the comparison of different KSI values from various tests. The minimum value of the KSI Index is zero, in which case, it can be said that the CDFs of the two sets compared are the same.

Over, Over %, KSE and RIO parameters are also used to calculate the error of the models. More information about them can be found in (Espinar et al., 2009).

The assessment of the models proposed is performed with hourly ground radiometric data (GHI and DNI) for the period from 1st of January 2014 to 28th of February 2015. In the validation, only values for solar zenithal angle higher than 85 degrees are considered.

4.1 Results for ESRA clear sky model

In this section, the results for ESRA clear sky model is presented. The next graphics show the scatter plot for predicted and measured hourly GHI and DNI.

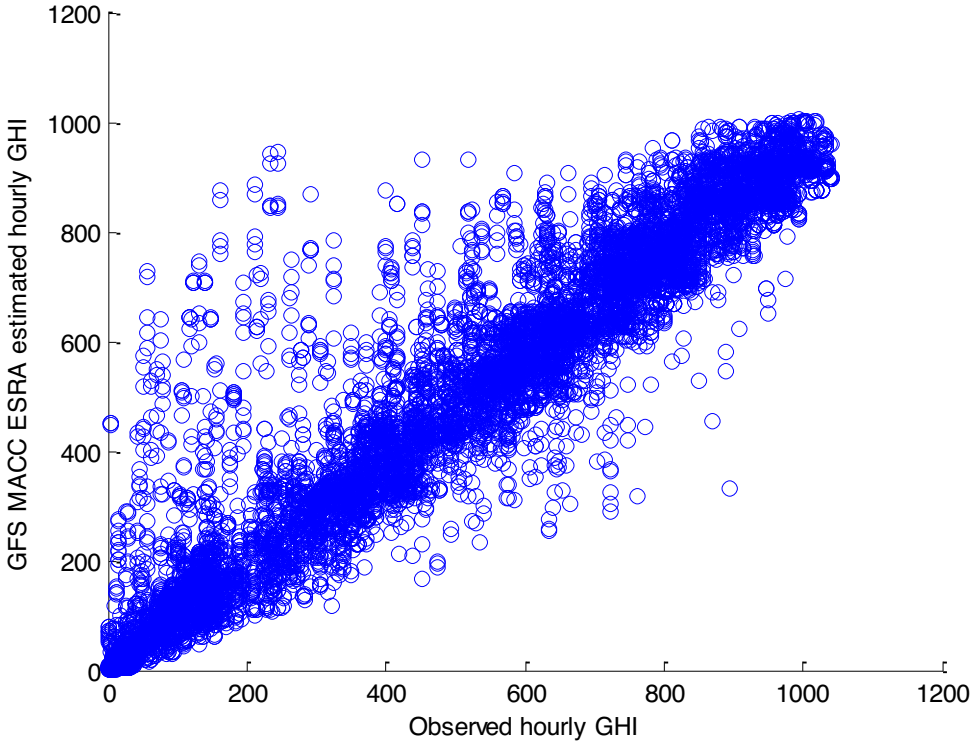

Fig. 2: Scattering plot of GFS ESRA clear sky model predictions and measurements of GHI for the next six days.

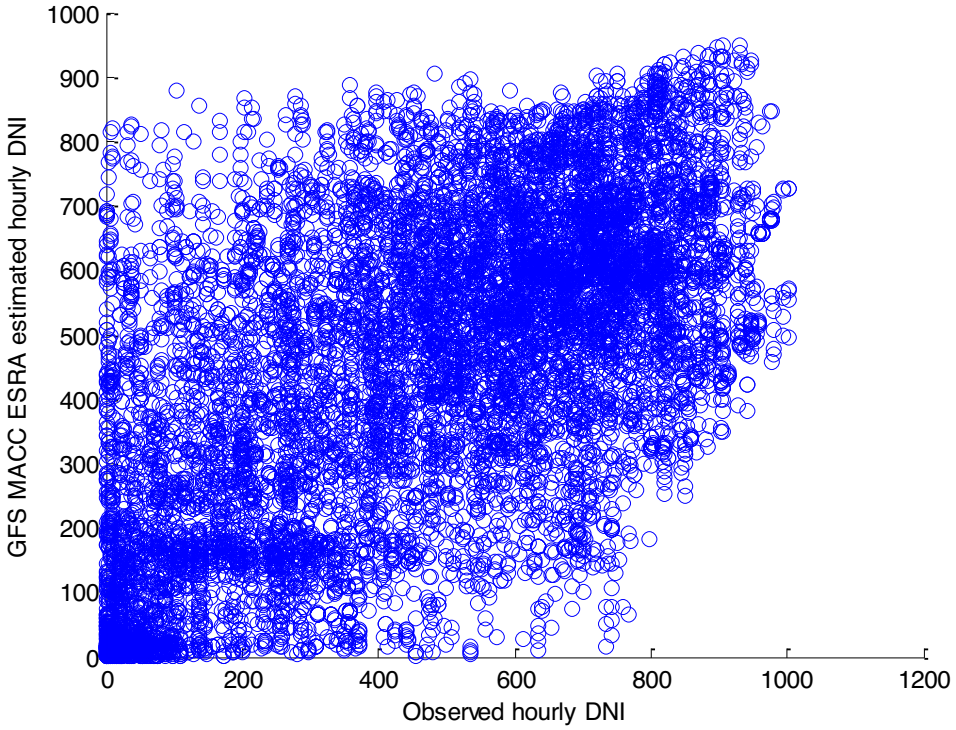

Fig. 3: Scattering plot of GFS ESRA clear sky model predictions and measurements of DNI for the next six days.

As can be seen in the last scatter plots, predictions of GHI are much better correlated than DNI predictions.

Next figures present forecasts (in blue colour) and measurements (in green colour) of hourly GHI and DNI and extraterrestrial solar irradiance (in red colour) in true solar time temporal reference for date 01/01/2014 for six days of prediction ahead as an example of the results of the model.

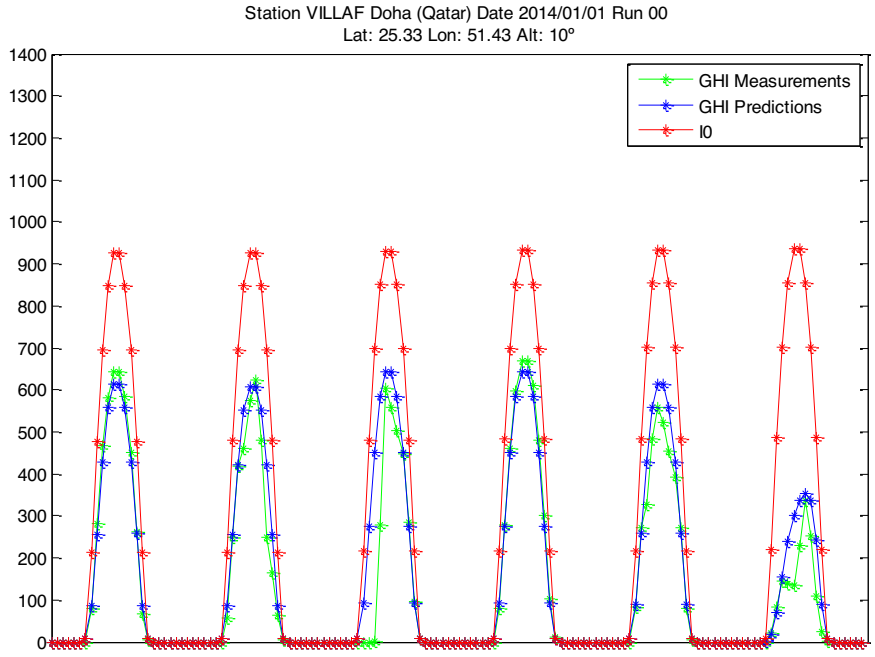

Fig. 4: GFS ESRA clear sky model predictions and measurements of hourly GHI for the next six days.

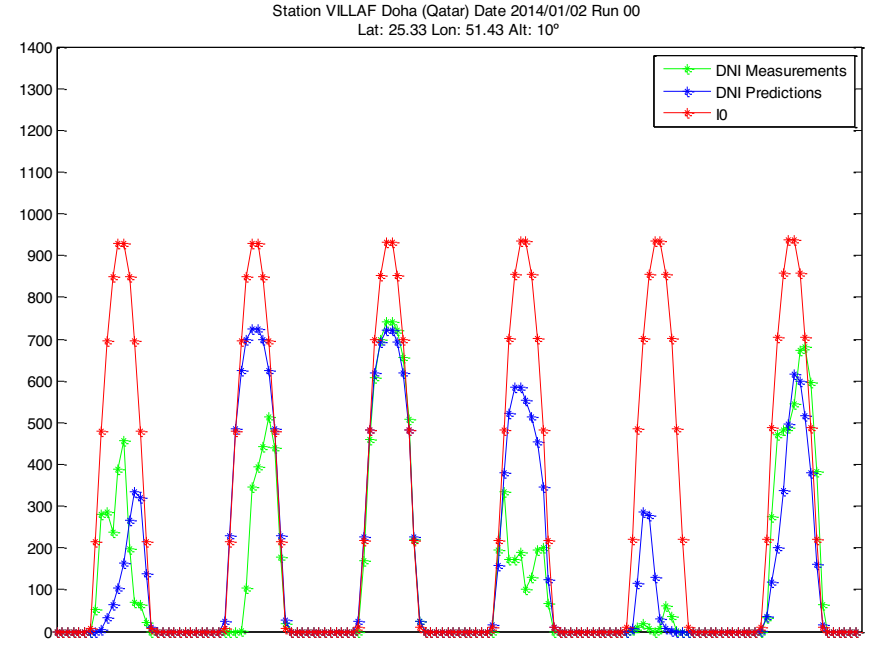

Fig. 5: GFS ESRA clear sky model predictions and measurements of hourly DNI for the next six days.

The next tables show MBD, RMSD, rMBD, rRMSD and R for GHI and DNI, for each day ahead of prediction from 1 to 6 and total errors of the models.

Tab. 1: Statistical errors of hourly GHI predictions validated with ground measurements. ERSA clear sky model

Day ahead	MBD (Wh/m2)	RMSD(Wh/m2)	rMBD (%)	rRMSD (%)	R
1	-11.39	87.54	-2.32	17.82	0.96
2	-8.36	94.34	-1.70	19.23	0.95
3	-8.61	94.88	-1.75	19.27	0.95
4	5.37	98.17	-1.08	19.80	0.95
5	-9.86	89.15	-1.98	17.87	0.96
6	-6.37	98.90	-1.28	19.91	0.95
TOTAL	**-8.32**	**93.93**	**-1.68**	**19.00**	**0.95**

Tab. 2: Statistical errors of hourly DNI predictions validated with ground measurements. ERSA clear sky model

Day ahead	MBD (Wh/m2)	RMSD(Wh/m2)	rMBD (%)	rRMSD (%)	R
1	-19.17	215.17	-4.17	46.78	0.67
2	-14.23	226.91	-3.10	49.41	0.62
3	-15.72	225.30	-3.42	48.96	0.63
4	-12.96	229.82	-2.78	49.33	0.61
5	-16.53	222.18	-3.56	47.77	0.63
6	-15.67	222.72	-3.39	48.25	0.64
TOTAL	**-15.71**	**223.73**	**-3.40**	**48.43**	**0.63**

GHI predictions are almost unbiased, and rRMSD is reasonably small. The value of rMBD decreases as the temporal horizon of prediction increases. On the contrary, the value of rRMSD increases as the horizon of prediction increases. The predictions are well correlated as the total mean value of R is 0.95.

DNI predictions have a small bias of around 3%. rRMSD is big in the case of DNI. The value of rMBD decreases as the temporal horizon of prediction increases. On the contrary, the value of rRMSD increases as the horizon of prediction increases. The predictions are relatively well correlated as the total mean value of R is 0.63.

Next, we present tables with MBD, RMSD, rMBD and rRMSD for GHI and DNI, for each hour ahead forecasted in true solar time (TST) within the first day of prediction.

In the case of GHI, rRMSD is lower in the central hours of the day and considerably high during sunrise and sunset. |The predictions are biased during the first hours of the day, most probably due to some walls near the station which hide the horizon when the sun is appearing in the sky. During the rest of the day, the model presents unbiased results with a considerable value in the last two hours of the day.

In the case of DNI, we have almost the same analysis. rRMSD is lower in the central hours of the day and considerably high during sunrise and sunset. |In this case, the predictions of DNI are not biased during the first

hours of the day because there is no wall between the pyrheliometer and the sun disk. During the rest of the day, the model presents unbiased results with a considerable value in the last two hours of the day.

Tab. 3: Statistical errors for each hour of the first day of prediction. Hourly GHI predictions validated with ground measurements. ERSA clear sky model

Hour ahead in TST	MBD (Wh/m2)	RMSD(Wh/m2)	rMBD (%)	rRMSD (%)
7	9.69	22.71	9.29	21.78
8	5.83	59.50	2.56	26.09
9	-7.46	77.55	-1.69	17.61
10	-5.20	104.58	-0.85	17.01
11	-8.01	112.95	-1.07	15.06
12	-18.97	116.95	-2.31	14.25
13	-23.85	113.39	-2.89	13.73
14	-20.70	106.64	-2.71	13.94
15	-15.88	98.49	-2.52	15.61
16	-15.41	80.41	-3.41	17.81
17	-24.90	61.58	-9.99	24.70
18	-9.17	27.92	-12.77	38.90

Tab. 4: Statistical errors of hourly DNI predictions validated with ground measurements. ERSA clear sky model

Hour ahead in TST	MBD (Wh/m2)	RMSD(Wh/m2)	rMBD (%)	rRMSD (%)
7	0.58	127.90	0.37	80.52
8	5.65	203.90	1.88	67.98
9	-21.56	231.66	-4.50	48.35
10	-13.18	239.33	-2.34	42.39
11	-9.16	231.93	-1.51	38.22
12	-12.71	226.03	-2.01	35.67
13	-16.73	232.43	-2.62	36.35
14	-18.56	233.91	-2.98	37.57
15	-15.83	232.01	-2.77	40.65
16	-26.62	232.13	-5.56	48.47
17	-67.71	222.38	-20.16	66.22
18	-34.74	129.01	-28.99	107.69

The next graphics show the Kolmogorov-Smirnov test (D_n) for hourly GHI and DNI. The black dotted line represents the critical limit, V_c, calculated for the number of values available.

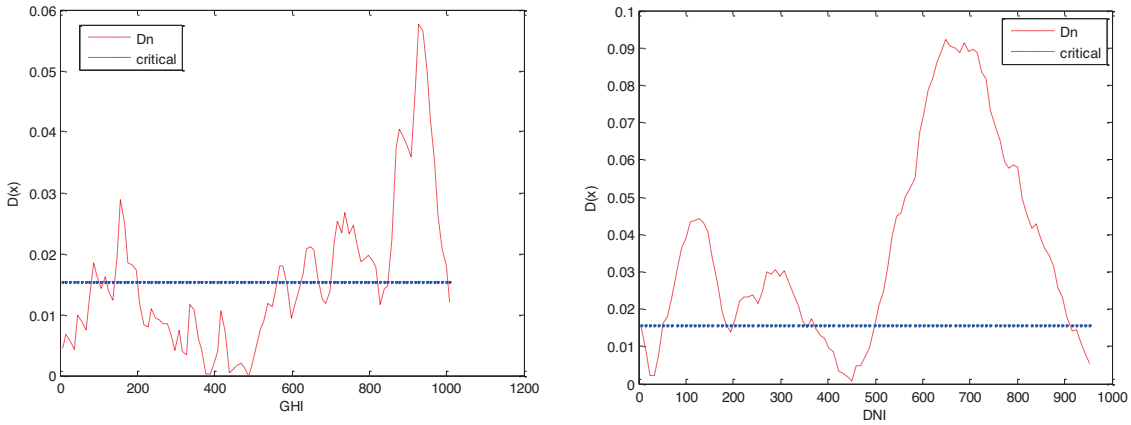

Fig. 6: Kolmogorov-Smirnov test for hourly GFS predictions and ground measurements of GHI and DNI (Wh/m^2) for Doha.

As we can see from the last graphics, there is a notorious difference in GHI predictions and measurements for high values. In the case of DNI, the difference is notorious for low and high values.

Next graphics show the distribution of hourly measurements (red line) and predictions (blue line) for GHI and DNI. The frequency of the range of values from 0 to 1000 Wh/m^2 for intervals of 100 Wh/m^2 is presented.

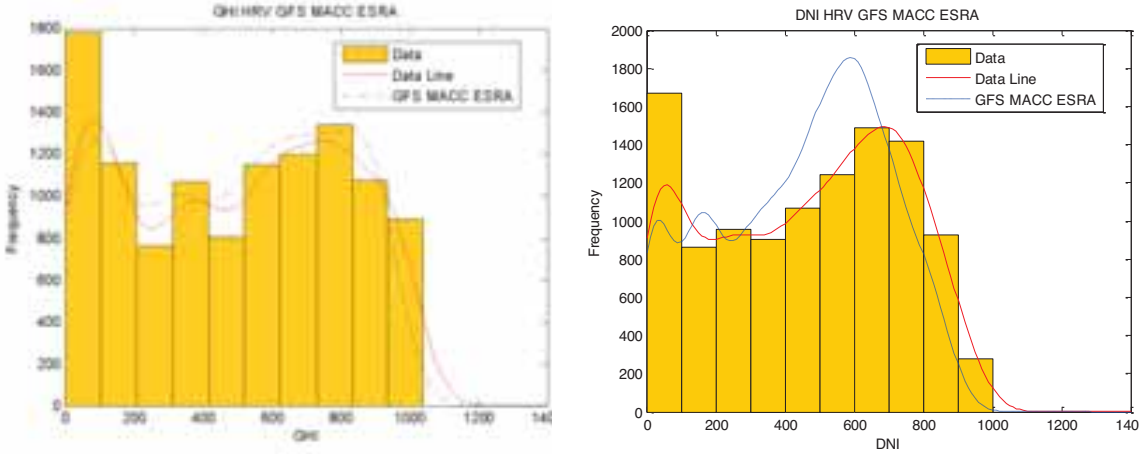

Fig. 7: Cumulative distribution function of hourly GHI and DNI predictions in DOHA.

Next graphics show the Cumulative Distribution Function of hourly GHI and DNI:

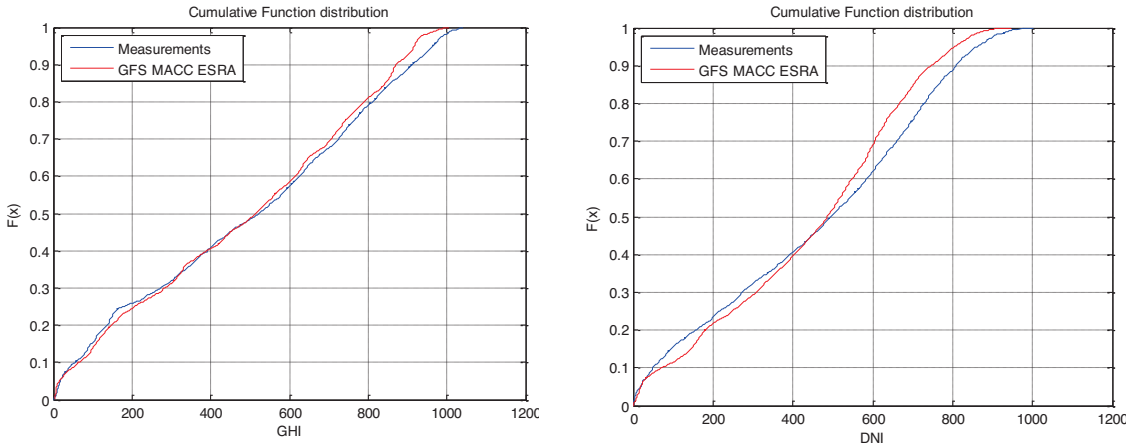

Fig. 8: Cumulative distribution function of hourly GHI and DNI GFS predictions and measurements in DOHA.

Finally, IKS, IKS %, Over, Over %, KSE and RIO for hourly GHI and DNI is presented:

Tab. 5: Errors for hourly GHI and DNI predictions in DOHA. ESRA clear sky model

Variable	IKS	IKS %	Over	Over %	KSE	RIO
GHI	15.98	102.95	4.77	30.73	133.69	76.34
DNI	34.68	232.24	21.48	143.86	376.10	212.26

As main conclusions for ESRA clear sky model, the results for GHI presents acceptable magnitude of the error regarding rRMSD. However, DNI is considerable high. One of the reasons could be that the model used to transform from GHI to DNI has been developed in the climatology of the USA and is not valid for the Gulf climate.

4.1 Results for SOLIS and REST2 clear sky models

In this section, we present the results for SOLIS and REST2 clear sky models. The next tables show MBD, RMSD, rMBD, rRMSD and R for GHI and DNI, for each day ahead of prediction from 1 to 6 and total errors of the models.

Tab. 6: Statistical errors of hourly GHI predictions validated with ground measurements. SOLIS clear sky model

Day ahead	MBD (Wh/m2)	RMSD(Wh/m2)	rMBD (%)	rRMSD (%)	R
1	-71.39	131.61	-16.62	30.64	0.92
2	-67.78	133.61	-15.70	30.95	0.91
3	-67.57	135.86	-15.56	31.27	0.91
4	-63.39	139.55	-14.52	31.97	0.89
5	-62.91	137.31	-14.51	31.67	0.90
6	-63.63	139.75	-14.56	31.97	0.90
TOTAL	**-66.10**	**136.32**	**-15.24**	**31.42**	**0.90**

Tab. 7: Statistical errors of hourly DNI predictions validated with ground measurements. SOLIS clear sky model

Day ahead	MBD (Wh/m2)	RMSD(Wh/m2)	rMBD (%)	rRMSD (%)	R
1	-62.43	243.11	-13.60	52.95	0.62
2	-51.26	249.78	-11.10	54.10	0.58
3	-49.12	246.56	-10.61	53.28	0.59
4	-37.23	250.16	-7.99	53.73	0.56
5	-42.23	242.86	-9.20	52.94	0.60
6	-42.47	249.98	-9.10	53.55	0.57
TOTAL	**-47.45**	**247.10**	**-10.26**	**53.43**	**0.59**

Tab. 8: Statistical errors of hourly GHI predictions validated with ground measurements. REST2 clear sky model

Day ahead	MBD (Wh/m2)	RMSD(Wh/m2)	rMBD (%)	rRMSD (%)	R
1	-17.82	91.73	-4.15	21.36	0.94
2	-12.31	91.10	-2.85	21.10	0.94
3	-12.22	97.02	-2.81	22.33	0.94
4	-4.09	97.69	-0.93	22.35	0.94
5	-3.98	105.38	-0.92	24.25	0.92
6	-2.71	106.47	-0.62	24.33	0.92
TOTAL	**-8.84**	**98.43**	**-2.04**	**22.67**	**0.93**

Tab. 9: Statistical errors of hourly DNI predictions validated with ground measurements. REST2 clear sky model

Day ahead	MBD (Wh/m2)	RMSD(Wh/m2)	rMBD (%)	rRMSD (%)	R
1	-71.92	240.23	-15.79	52.74	0.64
2	-61.99	247.43	-13.61	54.33	0.60
3	-61.74	242.45	-13.53	53.13	0.62
4	-47.69	245.26	-10.39	53.45	0.60
5	-52.53	239.70	-11.61	52.96	0.62
6	-52.22	246.62	-11.34	53.55	0.60
TOTAL	**-57.99**	**243.64**	**-12.70**	**53.36**	**0.61**

Conclusions for these clear sky models are similar as for ESRA model. Errors for SOLIS clear sky model are considerable high in term of rRMSD. The GFS-SOLIS models also present a substantial underestimation.

In the case of REST2 model, the errors regarding rRMSD are not so high for GHI. In the case of DNI, rRMSD is great and the value underestimated.

3.3 Data filtered with BSRN standards

In this section, we present the errors for ESRA clear sky model compared with ground measurements filtered with more restrictive BSRN quality filters. The next tables show MBD, RMSD, rMBD, rRMSD and R for GHI and DNI, for each day ahead of prediction from 1 to 6 and total errors of the models.

Tab. 10: Statistical errors of hourly GHI predictions validated with filtered ground measurements. ESRA clear sky model

Day ahead	MBD (Wh/m2)	RMSD(Wh/m2)	rMBD (%)	rRMSD (%)	R
1	-23.44	82.29	-3.62	12.71	0.94
2	-22.42	86.03	-3.46	13.27	0.94
3	-22.78	83.76	-3.51	12.91	0.94
4	-20.55	79.14	-3.15	12.15	0.95
5	-22.06	81.00	-3.39	12.43	0.94
6	-23.02	80.78	-3.52	12.37	0.94
TOTAL	**-22.37**	**82.19**	**-3.44**	**12.64**	**0.94**

Tab. 11: Statistical errors of hourly DNI predictions validated with ground measurements. ERSA clear sky model

Day ahead	MBD (Wh/m2)	RMSD(Wh/m2)	rMBD (%)	rRMSD (%)	R
1	-34.77	225.37	-6.08	39.44	0.41
2	-31.80	233.09	-5.57	40.82	0.36
3	-31.36	233.02	-5.49	40.76	0.37
4	-29.12	231.41	-5.05	40.13	0.34
5	-32.07	227.08	-5.59	39.60	0.37
6	-35.26	223.64	-6.15	39.00	0.40
TOTAL	**-32.39**	**228.95**	**-5.65**	**39.96**	**0.38**

The conclusions are similar as for ESRA model presented in section 4.1. There is a considerable decrease of the magnitude of rRMSD for GHI and DNI. It is because there are some reflections due to walls near to the station. This effect affects primarily to GHI. We have also detected a temporal deviation in the clock of around 2 to 5 minutes. When the deviation is corrected, rRMSD improves around 1% in the case of GHI.

5. Conclusion

The results show that the combination of the predictions of cloudiness from GFS and AOD and Water vapour from MACC and ESRA clear sky model provide good results for hourly GHI. In the case of DNI, the results are not so good. Bias can be removed using MOS, NN or correction with k_t and solar zenith angle matrix. We expect this model to have poor results regarding performance predicting variability of solar radiation due to coarse resolution of GFS model which is 3 hours. This last result has been presented recently in Task 46 of IEA. In the future, we are going to step up a mesoscale model customised for Qatar. The results in this paper will be used as a reference to improve prediction of solar radiation.

6. References

Bachour, D., & Perez-Astudillo, D. (2014). Ground measurements of Global Horizontal Irradiation in Doha, Qatar. *Renewable energy, 71*(0), 32-36. doi: http://dx.doi.org/10.1016/j.renene.2014.05.005

Espinar, B., Ramírez, L., Drews, A., Beyer, H. G., Zarzalejo, L. F., Polo, J., & Martín, L. (2009). Analysis of different comparison parameters applied to solar radiation data from satellite and German radiometric stations. *Solar Energy, 83*(1), 118-125. doi: doi: DOI: 10.1016/j.solener.2008.07.009

Gueymard, C. A. (2008). REST2: High-performance solar radiation model for cloudless-sky irradiance, illuminance, and photosynthetically active radiation ΓÇô Validation with a benchmark dataset. *Solar Energy, 82*(3), 272-285.

Ineichen, P. (2008). A broadband simplified version of the Solis clear sky model. *Solar Energy, 82*(8), 758-762.

Long, C. N., & Dutton, E. G. (2002). BSRN Global Network recommended QC tests, V2.0 BSRN Technical Report.

Pelland, S., Remund, J., Kleissl, J., Oozeki, T., & De Brabandere, K. (2013). Photovoltaic and Solar Forecasting: State of the Art.

Perez-Astudillo, D., & Bachour, D. (2014). DNI, GHI and DHI Ground Measurements in Doha, Qatar. *Energy Procedia, 49*(0), 2398-2404. doi: http://dx.doi.org/10.1016/j.egypro.2014.03.254

Perez, R., P.Ineichen, E.Maxwell, R.Seals, & A.Zelenka. (1992). Dynamic Global-to-Direct Irradiance Conversion Models. *ASHRAE Transactions-Research Series*, 354-369.

Rigollier, C., Bauer, O., & Wald, L. (2000). On the clear sky model of the ESRA -- European Solar Radiation Atlas -- on the heliosat method. *Solar Energy, 68*(1), 33-48.

Zarzalejo, L. F., Polo, J., Martín, L., Ramírez, L., & Espinar, B. (2009). A new statistical approach for deriving global solar radiation from satellite images. *Solar Energy, 83*(4), 480-484. doi: doi: DOI: 10.1016/j.solener.2008.09.006

Conference Proceedings

Solar World Congress 2015
Daegu, Korea, 08 – 12 November 2015

Algorithm for modelization and control of solar total radiation, using the derivative

Graciela M. Salum[1,2] and Rubén D. Piacentini[2,3]

[1]School of Physic Sciences and Nanotechnology, Yachay Tech, Urcuquí, Ecuador

[2]Instituto de Física Rosario (CONICET-Univ. Nacional de Rosario), Rosario, Argentina

[3]LESyC, IMAE, Univ. Nacional de Rosario, Rosario, Argentina

Abstract

Detailed knowledge of the solar resource is important for its possible applications in solar use, design of buildings and biological effects, among others. In this paper, we present an algorithm for the calculation of global solar irradiance based on a parametric model, which allows us to obtain global solar irradiance, at any geographical location and time of day. Also, we present a new algorithm using the derivative. Results were compared with measurements taken with a solar radiometer, supporting our arguments. We found percentage of discrepancy of 1.6% to 6.8% in days of May, 2007). Another very useful application of the algorithm is to determine the threshold levels of solar irradiance for Rosario and Concepción del Uruguay, Argentina. The algorithm produces an alert signal that is transmitted when an error happens. We present applications of the algorithm, which allow modifying the incorrect measurements in near real time, giving more confidence to the published data.

Keywords: *algorithm, model, solar radiation, data control*

Introduction

At the global level, there are few stations of measurement of solar radiation, and less still with the necessary maintenance. For example, Gaztelumendi (2003) reported that in 2002, 160 error warnings were registered in the Automatic Weather Stations (AWS) network of the Basque Country, Spain. These include 5% failure in communication, 5% failure of the booster station, 20% general failure of the station and 70% detected errors in the measurement of meteorological variables (of which there were 8% in the sun irradiation), i.e. the errors in the sun irradiation were 5.6% of the total error warnings. Thus, it is imperative to use the automatic control method for counting the data.

Data analysis makes it possible to identify factors that produce errors or systematic deviations. In the latter case, along with the hardware maintenance, it is necessary to take into account the location of the weather station (WMO, 1996).

The measurements recorder with instruments exposed to the elements are subject to a large number of possible failures/errors, which can be due to internal and external causes. Among the former the measurement of negative values may be mentioned: sensor or protective cover deterioration, peak voltage (Cede, 2004), time mismatch in the computer or acquisition system with respect to the real time. Some of the external causes for failures/errors are depositions of matter that obstruct the entry of radiation in the exterior dome, and the extreme winds that modify the tilt of the instruments.

The basic idea is to perform data control detecting the suspected values produced by an abnormal solar radiation distribution. If the data have an error then the program must send a signal about the failure to the support staff, and do the automatic correction.

The main issue, in relationship to the data provided by instruments exposed to the elements, is constant checking and verification. Consequently, the present work proposes the development of a methodology, supported by efficient algorithms, which would allow a constant systematic verification. This will significantly reduce the frequent data problems of external sensors.

doi:10.18086/swc.2015.07.13 Available at http://proceedings.ises.org

1.1 Analysis of data errors

An antecedent to this work, is the one realized by the Basque Service of Meteorology (BSM) which has more than 25 pyranometers (model CM11), complementing the measurements of atmospheric variables with its net of Automatic Weather Stations (AWSs) (Hernandez et al., 2003a, 2003b; Gaztelumendi et al., 2003). The AWSs of the BSM is a net located in about a 100 places of the Basque country in Spain and its validation procedure of values was based on a series of rules (Hernández et al., 2003a).
The validation rules are:
1- Data must be consistent with the technical specifications defined by the pyranometer.
2- Data must be consistent, i.e. they must satisfy the physics laws of the variable. Therefore

→ No solar irradiance during the night;

→ Daily evolution of solar irradiance under clear skies is characteristic, its graph being very similar to the Gaussian bell, symmetric with respect to the solar noon;

→ Solar irradiance values can exceed a certain percentage of the solar irradiance for clear sky conditions.

It is important to emphasize that the BSM considers the consistency of the solar irradiance essential for the meteorological variables (the graph must show the cloud progress; under clear sky conditions, the temperature develops in correlation with the solar radiation, although with a temporal delay).
3- Data must be coherent with the information of the nearest stations.
The most common data failures/errors are:

a- *Station failure*: when the station´s normal functioning has been interrupted (see Figure 1);

b- *Transmission failure*: communication problems;

c- *Storage failure*: the data disc or storage capacity is full;

d- Data failure: the station and the computer it connects to, communicate, but they are not synchronized (time and date) and the assigned data have incorrect time.

e- Zero positive shifts: when the sensor does not absorb the solar radiation (wavelengths in the spectral range of the instrument) it must indicate zero voltage. This error appears with positive values during the darkness periods, or during the day as well. There is a minimum threshold to be considered in the interpretation of the records. Some authors think that these values should be corrected to zero for night values and taken off for the diurnal values. Grossi Gallegos (2009) claims that the parasitic signal received (f.ex. artificial lighting, radio station or electric generator) in the sensor, or in the connecting cable, should be detected. In the case of a constant signal it is possible to correct the records only eliminating the false nocturnal values.

f- *Zero negative shifts:* this error is normally present when the internal dome has a different temperature to the cold connections of the sensor. For more data about this phenomenon, see the Kipp&Zonen web site (2007).

h- Sensor fail: since the sensor is outside, it could sometimes measure incorrectly during the day and due to other effects. The most common failures are moisture in the dome interior, lightning striking the sensor, problems in cabling and pyranometer break down.

i- Fault in calibration of the sensor: if the calibration factor is wrong, the signal is multiplied by a constant that does not belong to the sensor. These data will be higher or lower than they should be.

j- Wrong location of the sensor: the environment can produce shadows on the pyranometer (vegetation, buildings, its own station, etc.) (see Figure 1).

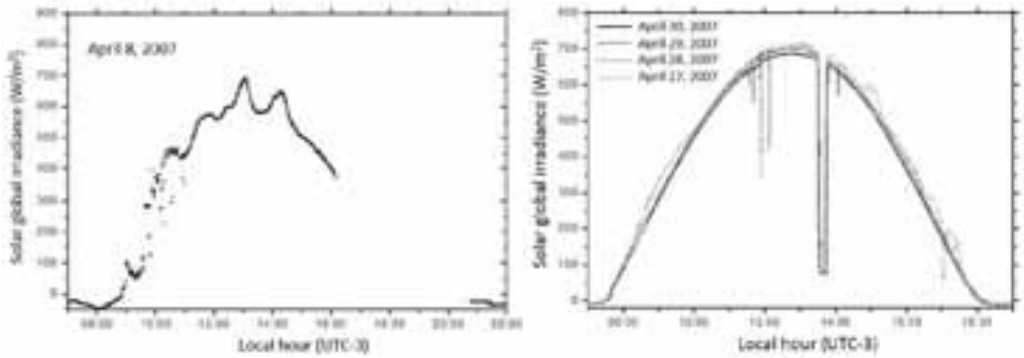

Fig.1. Solar data with failures in solar irradiance acquisition in Concepción del Uruguay, Argentina, in 2007. Left: Loss of data due to electrical failure in the station. Right: Wrong location of the sensor causing shadow from a water pipe.

k- Cosine error: the incident radiation on a horizontal plane has a value proportional to the cosine of incidence radiation at the zenith.
The errors listed above can occur randomly and simultaneously. According to Rudel (2003), the new stations, recording data simultaneously, do not generally verify their proper functioning.

1.2 Significant atmospheric events

Significant atmospheric events are exceptional manifestations of nature with significantly different values of the atmospheric variables from the average values. They usually are not caused by failures of the measuring system, and require more data and complementary equipment to evaluate the correct values. An example is the enhancement caused by the *edge effect* in the cloud, where the solar irradiance is similar or superior to the solar irradiance at top of the atmosphere (solar constant). This phenomenon was registered in Puna in the Atacama Desert and in the city of Recife (Brazil) by Piacentini et al. (2003 and 2010).
Furthermore, cloud effects, like the attenuation or increase of the radiation, are considered significant atmospheric events.
One of the rules when measuring solar radiation is that the value must be greater than the expected minimum under prevailing cloud cover (Hernández et al., 2003a). For the development of the present algorithm, the case of solar radiation values greater the extraterrestrial radiation has been taken into consideration. These values are not considered as errors as they could have been caused by some significant event like *cloud border effect* or *multiple scattering* in the cloud plane.

1.3 Solar radiation models

There are several models of total solar (or global) radiation: models based on meteorological data (Gul et al., 1998), cloud observations (Ehngerg and Bollen, 2005), isotropic sky models, with or without considering horizon brightening (Loutzenhiser, 2007), among others.
Usually, modelling of the radiative transfer is performed in different ways:
a) An integro-differential equation that describes the incidents of the direct and diffuse components at a given point, or
b) by using parametric semi-analytical models that are based on algebraic functions obtained by adjusting the solutions of the radiative transfer equations and mathematical formulae for these parameters.
Iqbal (1983) proposed three models (A, B and C), chosen for their simplicity and accuracy. For the present algorithm, we use the model C of Iqbal, based on studies by Bird and Hulstrom (1980) that developed a transmittance expression for the different attenuation processes in the atmosphere. The model needs three input parameters: water vapor column, broadband aerosol optical depth, and ozone and carbon dioxide column values.
When solar radiation enters the atmosphere, a portion of the incident energy is removed through scattering and absorption. Both considerably influence the spectrum, modifying the extraterrestrial spectral energy that passes through the atmosphere. The scattered radiation is called *diffuse radiation*. A portion of this scattered radiation goes back into space and a portion reaches the Earth's surface. The radiation that hits the Earth's surface in a straight line from the solar disk is called *direct radiation* (Iqbal, 1983).

1.4 Developed algorithm

The implemented algorithm has two important parts: A- the implementation of the C model; and B- the analysis of the dataset. The first part should determine the theoretical values of solar irradiation (at all times): global, direct and diffuse. In addition, it calculates the times of sunrise, noon and sunset. These values are obtained by implementing the C model for the entry parameters. The second part implies the reading of the text file and the searching of the real values (noontime, sunrise and sunset, and the values outside the range). Figure 2 describes the algorithm flow diagram.

1.4.1 Implementation of the C model

Input values must be read before the calculations. These values are:
A- The latitude, longitude and difference to the GMT. The algorithm calculates the sunrise, noon and sunset times.
B- The date, latitude, total ozone and carbon dioxide columns, precipitable water, atmospheric pressure, visibility, albedo and single scattering albedo. The algorithm calculates the solar irradiance values for each minute.

One advantage of this model is the possibility to count the total, direct and diffuse components, for posterior analysis.

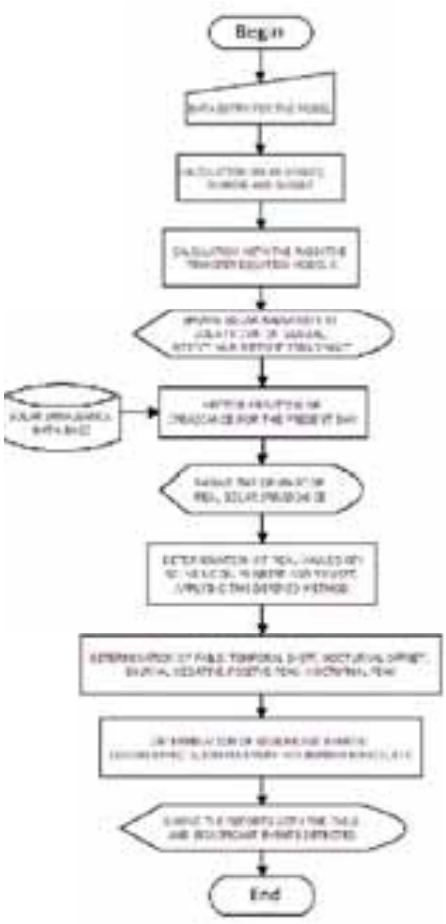

Fig. 2. Detection algorithm.

1.4.2 Search of real values

Once the data file has been copied as a vector, the present algorithm looks for the solar noon applying the derivative method.

The derivative method (proposed here) consistsin the calculation of the slope for the global solar irradiance, data by data, as follows:

$$slope\ (i) = \left[\frac{data(i) - data(i-1)}{\Delta t}\right] \qquad \text{(eq. 1)}$$

where Δt=1 minute. For this reason, the slope is just the difference between the current data and the previous data.

As can be seen in Figure 3, when midday occurs (maximum value of solar global irradiance, in red), the slope values pass from positive to negative (blue line).

Once noontime is found, the algorithm uses the theoretical data of the hours of sunshine for calculating the sunrise and sunset. From then on, the *derivative method* will be used for searching slopes steeper than the normal bell's slope.

In Figure 3, the global solar radiation data measured with the indicated pyranometer under clear skies (red line) and its slope (blue line) are drawn showing the signals, but not to scale. In Figure 4, the representation of some solar global irradiance data and the corresponding slope can be seen. There is a peak (see (i) in fig.4) of the solar global irradiance data and therefore a slope with positive data and negative in the case of (i +1), returning then to the value of the slope if there are no peaks.

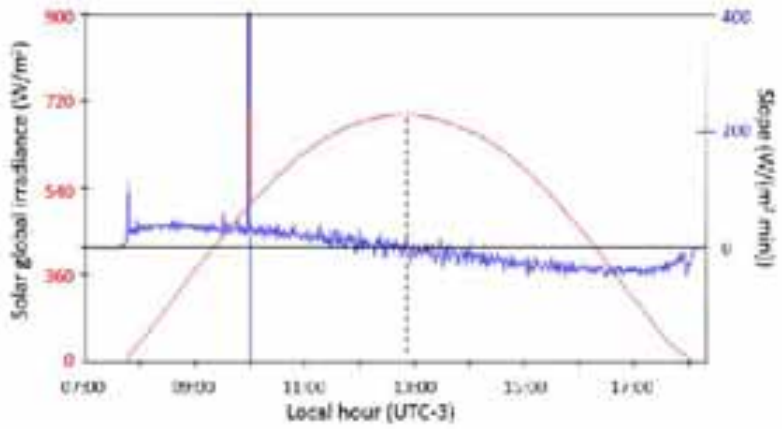

Fig. 3. Graph of example of solar global irradiance measured with a Kipp&Zonen pyranometer (red line) as a function of the local hour and superimposed the variation of the slope, data to data (blue line) (adapted from Salum et al., 2008).

The factor used to detect positive and negative peaks was found experimentally after working on several global solar radiation records. To find the peak this factor must be at least 1.3, i.e. the current data are 30% larger than the previous one.

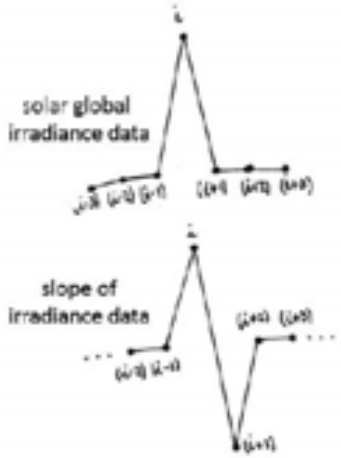

Fig. 4. Top: Scheme of positive peak in solar global irradiance. Bottom: Scheme of the slope (data to data) resulting from these values.

1.4.3 Detection of failures/errors

The software checks for failures/errors:

- *Systematic search for a nocturnal nonzero (or offset) value*

The algorithm searches nonzero values overnight, which is defined as the period from the end of twilight (about 45 minutes after sunset) until the beginning of the dawn (about 45 minutes before the sunrise). These values are averaged and shown in the report on the output screen.

- *Search for values that exceed the normal values*

This search consists in finding a threshold value above which the value is anomalous. The value chosen was 1528 W/m^2, which is one of the maximum values recorded and published internationally up to the present. This value was measured with a precision pyranometer at the peak of Tres Cruces, at 3900 m above sea level, in the high altitude intertropical desert of Puna de Atacama, in December 1997 (Piacentini et al., 2003).

- *Search for abnormal diurnal positive/negative peaks*

With the irradiance and slope data, the algorithm performs the scanning in compliance with the following rules:
a) The value of the current data must exceed the previous data value multiplied by a certain factor, and then returned to the previous value,
b) the current value of the slope is to be positive,
c) the posterior value of the slope must be negative, and
d) the phenomenon last less than three minutes (corresponding to three data) (see Figure 4).
If complying to these rules, the data is labeled a positive diurnal peak.
There are similar rules for negative peaks, but the slope is first negative and then positive.

- *Time shift*

The delta parameter (time shift) is calculated as the difference between the *actual solar noon time* and the *theoretical one*. The time shift is calculated and then the algorithm alerts this value. Furthermore, it automatically corrects the data and stores them in a data file (corrected solar radiation).

1.4.4 Combination of theoretical and real values

First, the algorithm applies the model C to the calculation of solar total irradiance, minute by minute. In figure 5, the graph of the real data (red line) and the model data (white line) is seen.

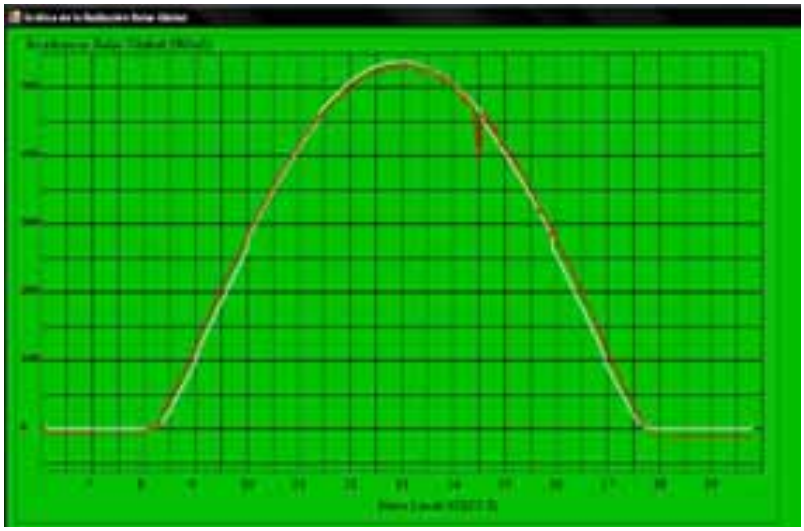

Fig. 5. Sample of the screen that shows the graph of the real data (red line) and the model data (white line).

3. Results

To implement the detection of daily features (solar noontime, the rising and setting of the Sun - dusk and dawn) and the positive and negative peaks of the acquired data, calculate the derivative, data by data, for the whole day

Figure 6 shows the first screen shot of the developed software for May 8, 2007. Here, the user enters the necessary parameters for the algorithm of the solar model for clear sky. Furthermore, it shows the solar radiation at noontime: total radiation is 629.99 W/m^2, the diffuse one is 239.21 W/m^2, and direct solar one is 580.64 W/m^2. The real value of the total solar irradiance at local noon is 640 W/m^2, resulting in a percentual difference (or percentage of discrepancy) for this day of 1.6%.

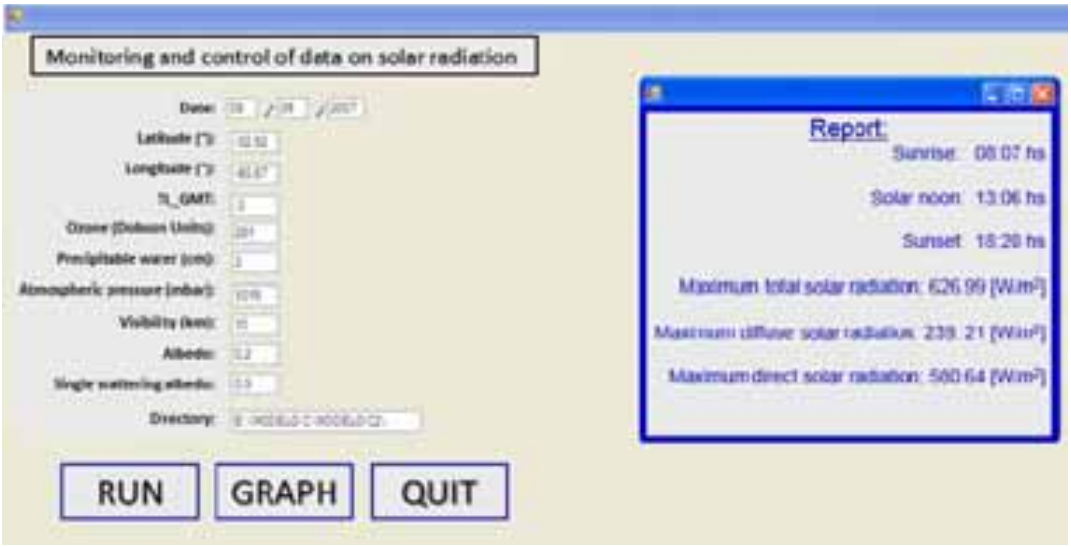

Fig. 6. Example of the initial screen and model results report for May 8, 2007.

On the left in Figure 7 below is the screenhot of the real data acquired (top) and the report of failures and significant events for May 8, 2007 (at the bottom). There was a peak at 10:00 am local hour, which was added to the real set of data (fictitious value of 900 W/m^2) in order to evaluate the algorithm. This peak turned out to be adequate. The data has a nocturnal offset (see fig.7) of -8.42 W/m^2. In addition, Figure 7 shows a time drift of 9.46 minutes.

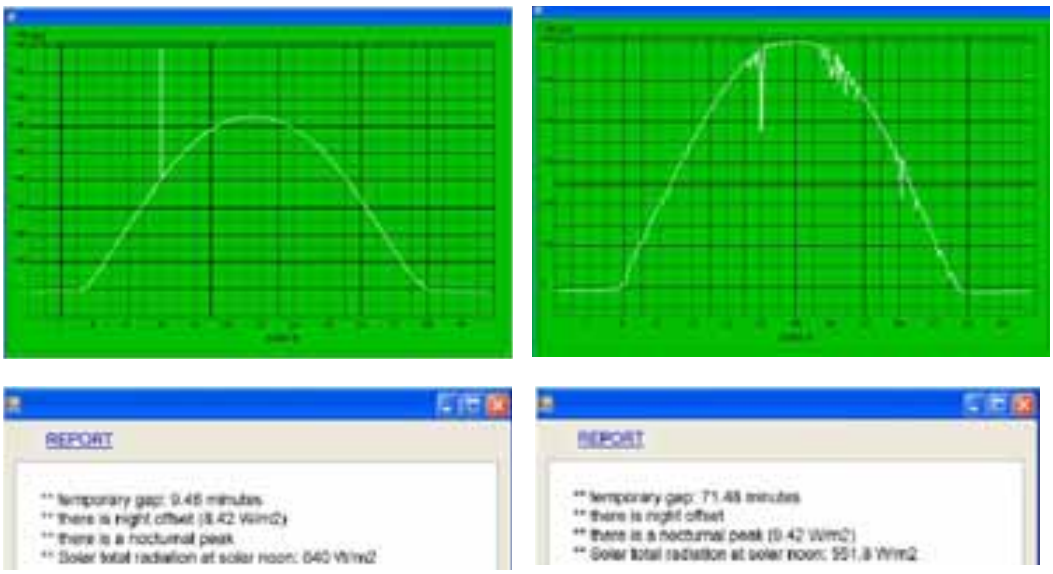

Fig. 7. Top: Graph of the real solar radiation data for: May 8, 2007 (left) and May 17, 2007 (right). Bottom: Reports corresponding to the days above.

For May 17, 2007, the software calculated the theoretical solar noon radiation at 592.13 W/m^2, diffuse radiation: 233.66 W/m^2, and direct radiation: 561.29 W/m^2. The real values of solar total irradiance at local noon was 551.8 W/m^2, resulting a porcentual difference of 6.8%. In Figure 7 Right, there are the graph screen of the real data acquired and the report of fails and significant events for this day. In the graph of data it was seen that and some of nocturnal offset. The report says that the nocturnal offset was of -9.41 W/m^2.

For May 18, 2007, the model solar noon values were 588.62 W/m^2, 233.08 W/m^2, and 559.27 W/m^2, for total,

diffuse and direct radiation respectively. The real values of solar total irradiance at local noon is 575.8 W/m^2, resulting a porcentual difference of 2.2%.

For May 19, 2007 the model solar noon values were 585.18 W/m^2, 232.51 W/m^2, and 557.29 W/m^2 for total, diffuse and direct radiation respectively. The real value of total solar irradiance at local noon was 551.8 W/m^2, resulting in a percentual difference of 5.7%. Figure 8 (left) is screenshot of the real data acquired and it shows the failures and significant events for this day. We can see a fictitious peak in the afternoon, which was added to the real set of data (of 9000 W/m^2). The search for the peak was successful. It shows a day without clouds and the nocturnal offset. The report says that the nocturnal offset was -8.70 W/m^2 and a time drift of 4.48 minutes.

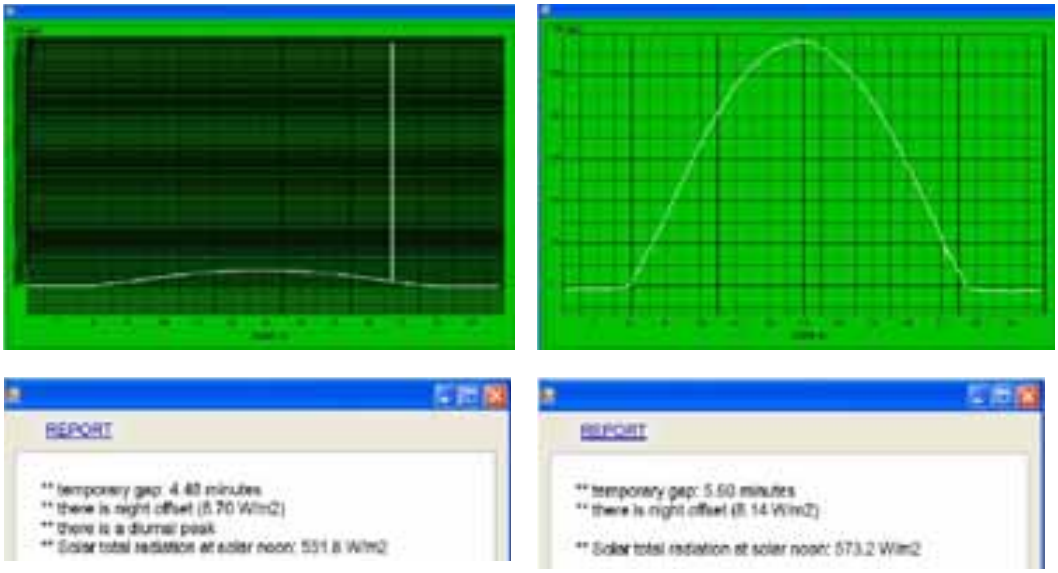

Fig. 8. Top: Graph of the real solar radiation data for May 19, 2007 (left) and May 25, 2007 (right). Bottom: Reports corresponding to the days above.

For May 25, 2007 the model solar noon values were 566.35 W/m^2, 229.33 W/m^2, and 546.19 W/m^2 for total, diffuse and direct radiation respectively. The real value of solar total irradiance at local noon is 573.2 W/m^2, resulting a porcentual difference of 1.2%. In the right of figure 8, there is a screenshot of the real data acquired and the failures and significant events for this day. The algorithm reports that the nocturnal offset was of -8.14 W/m^2 and a time drift of 5.60 minutes.

3. Conclusions and future perspectives

Data transmission, data storage, zero positive shifts, sensor failures, fault in calibration of sensor, wrong location of the sensor and cosine error are some of the failures that can be detected with the present algorithm. It proves that it is reliable for solar radiation data validation, resulting in a percentage of discrepancy values (percentual difference) of 1.6%, 6.8%, 2.2%, 5.7% and 1.2% for the total irradiance at local noon May 8, May 17, May 18, May 19 and May 25, 2007, respectively. For the days with peaks (diurnal and nocturnal), the detection was successful, as well as those for the time shift and the night offsets.

Some future perspectives are the extension of the algorithm (for solar radiation data) to other types of data that need a continuous monitoring of meteorological and air quality data.

6. Acknowledgements

The authors thank Elisabeth Griewank, professor of Yachay University for comments and help that greatly improved the manuscript.

6. References

Bird, R., Hulstrom, R.L., 1980. Direct insolation models. Trans. ASME J. Sol. Energy Eng., 103, 182-192

Bird, R., Hulstrom, R.L., 1981. A simplified clear sky model for direct and diffuse insolation on horizontal surfaces. SERI/TR-335-344 Solar Energy Research Institute, Golden, Colorado

Bird, R.E., Riordan, C., 1986. Simple solar spectral model for direct and diffuse irradiance on horizontal and tilted planes at the Earth´s surface for cloudless atmospheres, J. Clim. Appl. Meteor., 25, 87-97.

Cede A. Goddard Space Flight Center, NASA, comunicación privada, 2005.

Duffie, J., Beckman, W., 1980. Solar Energy Thermal Processes, John Wiley and sons, New York.

Ehngerg, J.S.G., Bollen, M.H.J., 2005. Simulation of global solar radiation based on cloud observations. Solar Energy, 78, 157-162

Gaztelumendi, S., Hernández, R., Otxoa de Alda, K., 2003.Some aspects on the operative use of the automatic Stations network of the basque country. Third International Conference on Experiences with AWSs, España

Geiger, M., Diabté, L., Ménard, L., and Wald, L., 2002. A web service for controlling the quality of measurements of global solar irradiation. Solar Energy, 73, 475-480.

Grossi Gallegos, H., 2009. Personal communication.

Gueymard, C.A., 2004. The Sun´s total and spectral irradiance for solar energy applications and solar radiation models, Solar Energy, 76, 423-453.

Gul, M.S., Muneer, T., Kambezidis, H.D., 1998. Models for obtaining solar radiation from other meteorological data. Solar Energy, 64, 99-108

Hernandez, R., Gaztelumendi, S., Otxoa de Alda, K., 2003a. Expertise of errors in radiometric networks. The case of the Basque Service of Meteorology. Third International Conference on Experiences with AWSs, España

Hernandez, R., Gaztelumendi, S., Otxoa de Alda, K., 2003b. Some aspects on the operative use of the automatic stations network of the Basque country, Hidrometeorological Monitoring and Forecast Office. Third International Conference on Experiences with AWSs, España

IPCC, 2007. Interguvernamental Pannel on Climate Change, The Scientific Basis Report 2007.

Iqbal, M., 1983. An introduction to Solar Radiation. Academic Press Inc., New York.

Ineichen, P., 2006. Comparison of eight clear sky broadband models against 16 independent data banks. Solar Energy, 80, 468–478

Kipp&Zonen web site – www.kippzonen.com or www.kippzonen.com/Download/52/CM-21-Pyranometer-Manual.pdf – manual version 1004, 2004. Last access June 2009.

Loutzenhiser, P.G., Manz, H., Felsmann, C., Strachan, P.A., Frank, T., Maxwell, G.M., 2007. Empirical validation of models to compute solar irradiance on inclined surfaces for building energy simulation. Solar Energy, 81, 254-267

Nunez, L.F., Neto, J., Carvalho, R., Carvalho, F., Prior, V., Henriques, D., 2003. Third International Conference on Experiences with AWSs, España

Piacentini, R.D. “Influencia del evento el niño 1997-1998 sobre las intensidades solares globales incidentes sobre Rosario, Argentina”. Avances en Energías Renovables y Medio Ambiente 2, 11.61, 1998.

Piacentini, R.D., Cede, A., Bárcena, H., 2003. Extreme solar global and UV irradiances due to cloud effect measured near the summer solstice at the high altitude desertic plateau Puna of Atacama, Journal of Atmospheric and Solar Terrestrial Physics, 65, 727-731.

Piacentini R.D., Salum G.M., Fraidenraich N. y Tiba C., 2010. Extreme total solar irradiance due to cloud enhancement at sea level of the ne Atlantic coast of Brazil, Renewable Energy, 36,409-412, Elsevier Editorial

Salum, G.M., Ipiña, A., Piacentini, R.D., 2008. Desarrollo de un algoritmo para la modelización de la radiación solar global y del control de datos. Mecánica Computacional, 26, 1774-1787.

WMO, 1996. Guide to Meteorological Instruments and Methods of Observations WMO 8, Geneva. http://www.wmo.int/pages/prog/www/IMOP/CIMO-Guide.html

Wolf, L.W., Zissis, G.J., 1985. The infrared handbook, Chapter 4: Atmospheric Scattering, Environmental Research Institute of Michigan.

Conference Proceedings

Solar World Congress 2015
Daegu, Korea, 08 – 12 November 2015

Photovoltaics in Swedish agriculture: Technical potential, grid integration and profitability

David Lingfors[1], Joakim Widén[1] Jesper Marklund[1], Magdalena Boork[2], David Larsson[3]

[1] Department of Engineering Sciences, Uppsala University, Uppsala (Sweden)

[2] SP Technical Research Institute of Sweden, Uppsala (Sweden)

[3] School of Business, Society and Engineering, Mälardalen University, Västerås (Sweden)

Abstract

This paper investigates the realizable potential for photovoltaic (PV) systems in Swedish agriculture. Marginal lands and available building areas for PV systems are quantified, and factors limiting the potential are analyzed. It is shown that the potential for PV in Swedish agriculture is high, but what is fully realizable is limited by the capacity of the rural power grid. A case study in the rural municipality of Herrljunga was conducted and scaled to national level. The study shows that the risk of surges in the medium voltage grid (10 kV) in rural areas are small in case where all roof surfaces with an annual solar irradiance of over 950 kWh/m^2 are used for solar power. The total electricity production from the Swedish agriculture, if all roof areas with this irradiance level were used, is estimated to 4 TWh annually. With solar power on all roof surfaces with an annual irradiance of at least 900 kWh per m^2 problems with voltage rise and overloads in the electricity grid might occur. The electrical grid capacities thus substantially limit how much solar power can be installed. Our results also show that the profitability limits the potential to 0.2 TWh on a national level, but that it could increase if more optimistic economic conditions are assumed.

Keywords: *PV potential, grid integration, agriculture, business models*

1. Introduction

Agriculture is a sector with a seemingly high potential for photovoltaic (PV) power generation. The abundance of land and different types of farm buildings provide several options for installing PV systems. At the same time, previous studies have shown that rural distribution grids are the grid types that are most sensitive to high PV power injections (Walla et al., 2012), which may limit the achievable generation capacity.

Previous studies of the potential solar power generation in Sweden has mainly been based on building statistics combined with assumptions about key parameters such as building dimensions. For example, Kjellsson (1999, 2000) estimated the building areas in agriculture that were available for solar power generation to 150 km^2. An important task for new studies in this field is to improve the estimates of the total potential by using more refined methods, and to determine the limiting factors in realizing this potential.

The aim of this paper is to quantify the realizable potential for PV power generation in Swedish agriculture, both on land and on buildings. Realizable potential is defined here to be the technical potential (PV capacity on available areas) reduced by constraints in the power grid and by what is economically profitable. The study combines analyses of GIS (geographic information system) data with power flow simulations of power grids. A case study is performed on the rural municipality of Herrljunga in western Sweden. These results are then combined with national statistics to estimate the realizable potential for the whole Swedish agricultural sector. Details on the findings in this paper can be found in the full project report (Norberg et al., 2015).

The paper is structured as follows. The methodology for determining the realizable potential is described in Section 2, the results are presented in Section 3, and a concluding discussion is included in Section 4.

Selection and/or peer review under responsibility of Scientific Committee
doi:10.18086/swc.2015.07.14 Available at http://proceedings.ises.org

2. Methodology

2.1. Available land and buildings

It is assumed that the lands primarily considered for PV installations are marginal lands, i.e. lands that are not profitable for agricultural use. The availability of marginal lands is determined from national statistics (Johnsson, 2008). However, all available land in the statistics cannot be used for PV, since the distance from the grid is too large, the land is shaded, difficult to build on or not accessible.

Available building roof areas are analyzed based on LiDAR (Light Detection And Ranging) data and property maps in ArcGIS (ESRI, 2015) for the municipality of Herrljunga, Sweden. Every building is linked to the low voltage (LV) grid connection node within the same property, determined from data provided by the local distribution grid operator (DSO), Herrljunga Elektriska AB. If there are no connections within the property the closest connection within a radius of 200 meters is linked to the building (see Fig. 1). The radius was set to 200 m based on the recommended cost for connection to the LV grid according to the Swedish Energy Market Inspectorate (Energimarknadsinspektionen, 2013a). This radius is of course not universally valid but depends on the profitability of each individual case.

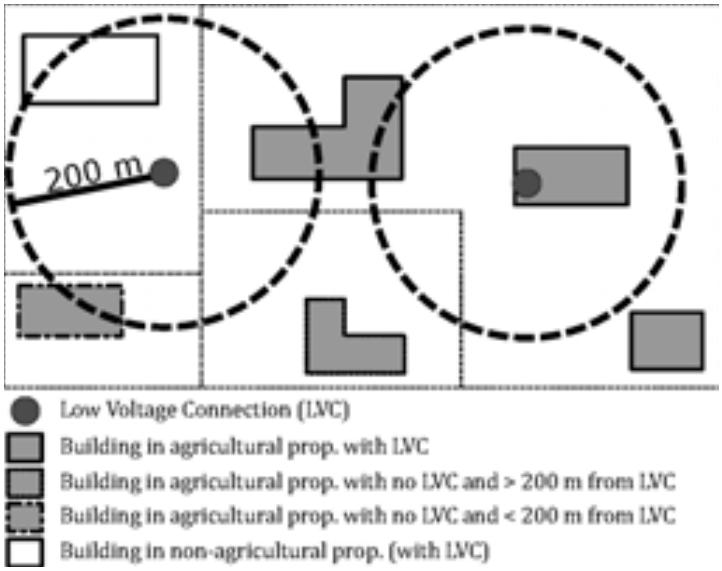

Fig. 1: Methodology for identifying agricultural buildings (grey) with potential for PV installation. Buildings within an agricultural property with a low voltage connection (LVC) or < 200 meter from any LVC are included in the analysis. In this example the south middle building will not be included.

2.2 Solar energy calculations

The solar resource potential on the building areas is quantified using the built-in tool *Solar Area Radiation* in ArcGIS, allowing both internal shading and shading from surrounding terrain, vegetation and buildings to be taken into account (Fu and Rich, 1999). Different thresholds for annual irradiance availability are studied (minimum level for installing PV), for instance 700 kWh/m^2/year meaning that only roof segments having at least 700 kWh/m^2/year are considered for PV installation. For generating data to the detailed grid simulations, PV systems on the available areas were simulated in the modeling environment Matlab using standard models for available solar irradiance and PV output power (Duffie et al., 1994). The following assumptions about losses were made:

(1) 15% of the available roof area was not considered due to obstacles such as chimneys etc. (Kjellsson, 1999).

(2) Shading from surrounding buildings, trees etc. was represented by a general removal of the beam component of the irradiance for solar angles ($\cos(\theta_i) < 0.2$).

(3) 15% efficiency of the PV cells assumed at standard test conditions. Overall PV system efficiency was assumed to be 85%.

(4) 19% of the total potential was excluded corresponding to the share of roofs not in sufficiently good condition for PV installation (Riksantikvarieämbetet, 2004).

2.3 Distribution grid simulations

Access to a very detailed database of grid data from the local DSO for both the medium voltage (MV) and low voltage (LV) grids in the studied area has made it possible to make detailed power flow simulations of the whole distribution grid. Hourly load data are available for all customers and also line-impedances of all connections in the grids. Only active load data were available, thus a constant load factor of 0.95 was assumed to derive the reactive load (Thomson and Infield, 2007). Balanced three-phase power flow for the whole grid was solved using Raphson-Newton's method implemented in Matlab. According to current Swedish regulations, short-term voltage fluctuations deviating 10% from nominal are allowed in the MV grid (Energimarknadsinspektionen, 2013b). To allow further voltage fluctuation in the LV grid, voltage fluctuations are limited to 5% in the MV grid. Furthermore, the maximal current allowed is specified for each line. The maximum PV penetration is thus limited by an overvoltage limit of 5% above nominal voltage or 1.05 p.u. and the specified load of current for each line.

2.4 Profitability limitations

The cost of PV systems has dropped considerably in the last decade. For Sweden the mean price was 13 SEK/W_p for systems larger than 20 kW_p (Lindahl, 2015). This should be compared to the avoided cost of electricity when self-consuming the PV electricity, which in our calculations is set to 0.45 SEK/kWh in the agricultural sector, which pay very low energy tax, whereas the corresponding figure for other businesses is 0.75 SEK/kWh. The excess share of the electricity generated is sold, with an expected price of 0.25 SEK/kWh, according to mean Nordpool spot prices, and additional incomes of 0.05 SEK/kWh from the grid owner and 0.18 SEK/kWh for electricity certificates. From 2015 it is also possible to get 0.60 SEK/kWh as a tax rebate, given annual net consumption, a fuse of $\leq$ 100 A, and a maximum of 30 MWh fed into the grid. Besides this it also possibly to be granted an investment subsidy of 30% for companies and 20% for others. The application rate is high and it has more been seen as a bonus, as the uncertainty of being granted the subsidy have been high. However, the Swedish government has in the last budget bill proposed significantly more funds the coming years (Brolund, 2015).

When estimating the profitability we therefore assume a maximal production of 60 MWh, of which 50% is fed into the grid. This gives a mean compensation for sold electricity of 0.38 SEK/kWh without tax rebate and 0.68 SEK/kWh including the tax rebate (see Tab. 1).

Tab. 1: Cases for the profitability assessment

	Investment [SEK/kW_p]	Discount rate	Self-consumption	Value of self-consumed electricity* [SEK/kWh]
Base case, agricultural	13 000	6%	50%	0.38
Base case, agricultural incl. tax rebate	13 000	6%	50%	0.68
Base case, other	13 000	6%	50%	0.40
Base case, other incl. tax rebate	13 000	6%	50%	0.70

*Also additional incomes from electricity certificates of about 0.15 SEK/kWh for 15 years.

It is however difficult to find profitability in the cases presented in Tab. 1. Therefore we examined some possible cases were profitability would increase. These are presented in Tab. 2. In the first case (1) a discussed investment subsidy within the agricultural program of Sweden is implemented. In (2) the compensation offered by some electricity suppliers for selling the electricity to the grid is higher than Nordpool spot prices, here assumed as 1.25 SEK/kWh. For how long this generous compensation will last is highly uncertain. In (3) we assume that the farmer has own capital to invest, and thereby lowering the discount rate. In (4) we assume the farmer to install the PV system, and thereby reduce the investment cost. Lastly in (5) we assume a large scale PV system (1 MW_p), for which own capital is used and all generated electricity is fed directly into the MV grid. We assume a distance of 500 meter from the PV field to the MV grid, which means a connection cost of 550 000 SEK (Svensk Energi, 2011).

Tab. 2: Cases for increasing profitability.

	Investment [SEK/kW_p]	Discount rate	Self-consumption	Value of self-consumed electricity* [SEK/kWh]
(1) Investment subsidy 40%, incl. tax rebate	7 800	6%	50%	0.68
(2) Higher sell rate, incl. tax rebate	13 000	6%	50%	1.18
(3) Own capital, incl. tax rebate	13 000	3%	50%	0.68
(4) Self-installed, incl. tax rebate	11 000	6%	50%	0.68
(5) Large-scale (1 MW_p), own capital, investment subsidy, 40%	6 000	3%	0%	0.30

*Also additional incomes from electricity certificates of about 0.15 SEK/kWh for 15 years.

2.5 Scaling to national level

It is difficult to make a fair scaling of the results in the case study in Herrljunga to national level. In Herrljunga there are 591 agricultural properties which can be compared to 350 000 nationally. A previous inventory of agricultural buildings in 10 different regions in Sweden showed that there were on average 6.5 buildings in each agricultural property (Riksantikvarieämbetet, 2004). This can be compared with 5.4 buildings per property in Herrljunga, which is at least in the same range as the previous study.

The solar resource availability varies significantly over Sweden. Therefore the available global annual solar resource was scaled for each county *c* compared to Herrljunga as;

$$G_c = \frac{\bar{G}_c}{\bar{G}_{hl}} G_{hl}, \qquad \text{(eq. 1)}$$

where $\bar{G}_c$ and $\bar{G}_{hl}$ are the mean annual global solar irradiance for 1979-2012 of county *c* and Herrljunga (*hl*) respectively and G_{hl} is the available solar resource on the roofs of Herrljunga derived from ArcGIS *Solar Area Radiation.* The hourly PV production $E_{c,h}$ depends on the incident solar angle $\theta_i^{c,h}$ as;

$$E_{c,h} = \begin{cases} G_{c,h}\eta & \text{if } \cos\left(\theta_i^{c,h}\right) > 0.2 \\ D_{c,h}\eta & \text{if } \cos\left(\theta_i^{c,h}\right) < 0.2 \end{cases}, \qquad \text{(eq. 2)}$$

where the G_h is the global irradiance and D_h is the diffuse irradiance at hour *h* and η is the fraction of the energy than can be extracted from the total incident solar irradiance and can be expressed as;

$$\eta = \eta_{PV}\eta_{sys}\eta_{obs}\eta_r, \qquad \text{(eq. 3)}$$

where $\eta_{PV} = 0.15$ is the module efficiency, $\eta_{sys} = 0.85$ is the PV system efficiency, $\eta_{obs} = 0.85$ is due to obstacles on the roof and $\eta_r = 0.81$ is due to available roofs of sufficiently good condition for PV installations (see section 2.2). The annual total power that can be extracted from the solar resource is thus;

$$E_c = \frac{N_c}{N_{hl}} \sum_{h=1}^{8760} E_{h,c}, \qquad \text{(eq. 4)}$$

where N_c and N_{hl} are the numbers of agricultural properties in county c and Herrljunga respectively.

3. Results

3.1. Potential PV generation capacity

The available marginal lands are found to be large (the Swedish average is in the order of 1 ha per agricultural property) and are therefore not considered to be limiting for the total PV capacity in the case study. Moreover, a total building roof area of 0.8 km^2 is available in the case study, corresponding to a total installed capacity of 120 MW. The results of allowing different irradiance thresholds for PV on these buildings in Herrljunga are shown in Fig. 2, indicating the total technical potential for PV (at 15% assumed efficiency).

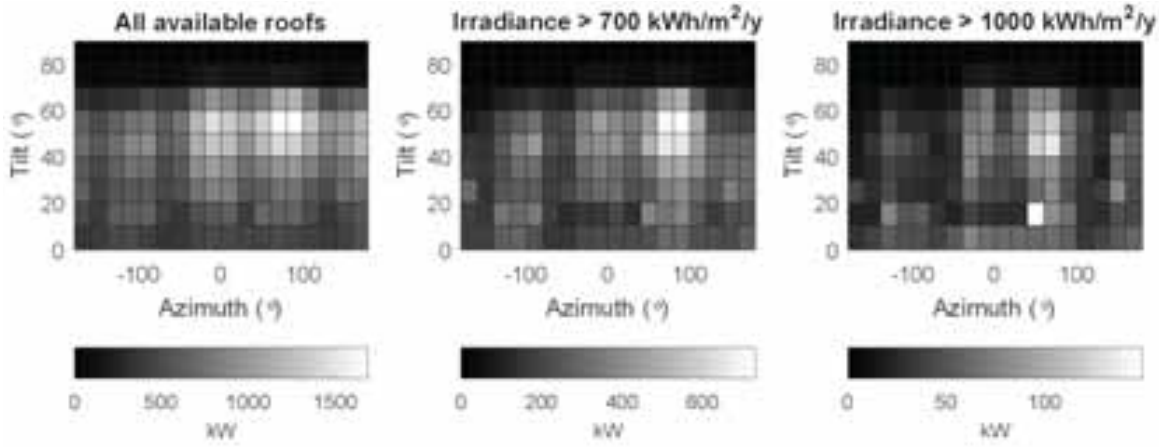

Fig. 2: Potential PV generation capacity on agricultural building roofs in the studied municipality, with three different requirements on annual irradiance. Note that the scale of the color bar differs between the subfigures.

The total potential as function of solar irradiance level is presented in Fig. 3. The total numbers of buildings having at least one roof segment of the solar irradiance level is included, as well as the total roof area and power production. In Tab. 3 key figures of an average agricultural property in Herrljunga are presented for three different solar irradiance levels. If scaling to national levels, following eq. 1-4, the total annual PV production would be 35.7, 13.5 and 2.5 TWh for the solar irradiance levels > 0, > 700 and > 1000 kWh/m^2 respectively.

Tab. 3: Key figures for an average agricultural property in the Herrljunga distribution grid for three different levels of annual solar irradiance; > 0 kWh/m^2 (all roofs), > 700 kWh/m^2, > 1000 kWh/m^2.

Key figures	All roofs	> 700 kWh/m^2	> 1000 kWh/m^2
Roof area (m^2)	1100	410	70
Solar irradiance (MWh/year)	940	360	62
PV capacity (kW)	170	62	10
PV power production (MWh/year)	128	48	8.3

3.2. Hosting capacity of rural distribution grids

In an early stage it was clear that the maximum accepted current in the lines would not be reached as Fig. 4 shows. The figure only displays line currents from the northern part of the grid but power flow simulations for the southern part gave similar results. Resulting histograms for MV grid voltages are shown in Fig. 5 together with the probability for voltage rise outside the allowed ±5% limits. All building areas with more than 950 kWh/m^2 annual irradiation (B) can be utilized without problems, but if building areas in the other categories (C and D) are used, there is a probability for overvoltage. However this risk is small, 0.13 % for C (> 900 kWh/m^2/year).

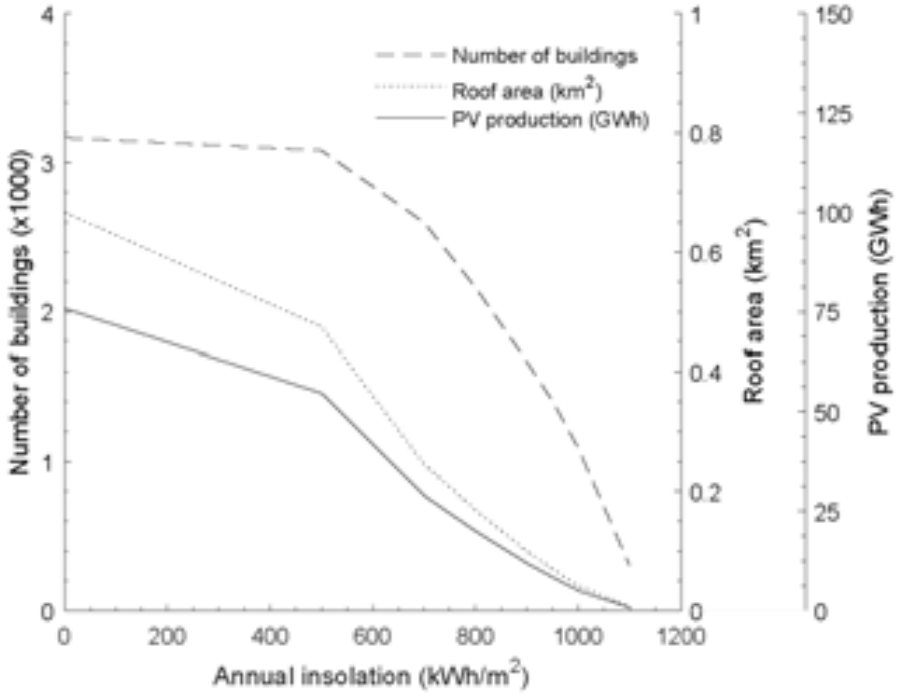

Fig. 3: Total potential for agricultural properties in Herrljunga.

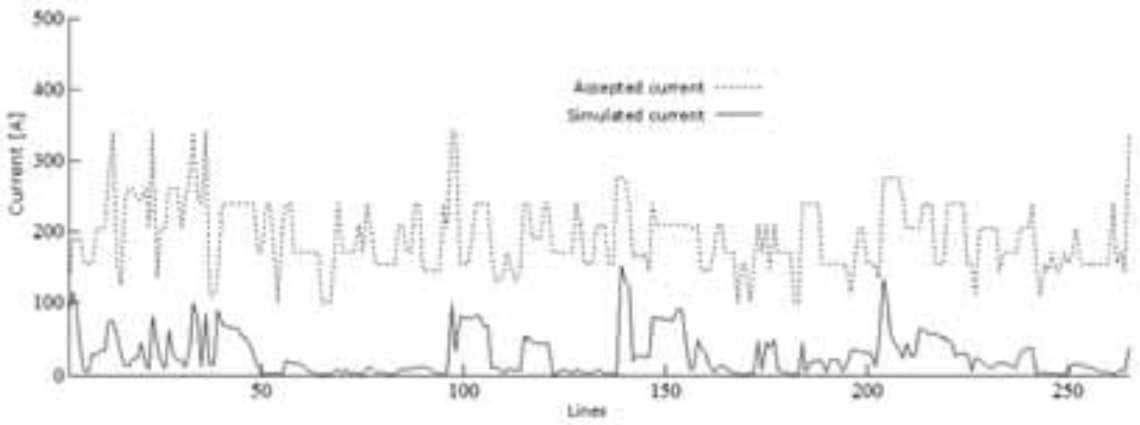

Fig. 4: Accepted current (dashed) and simulated current (solid) for each line in the northern part of the grid. In this figure the solar irradiance level was > 1000 kWh/m^2/year.

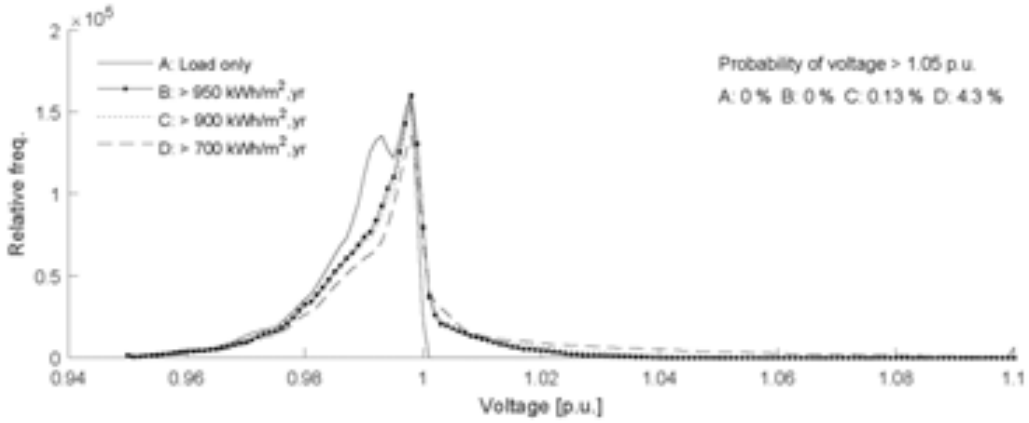

Fig. 5: Histogram of voltage in the medium voltage nodes for some different solar irradiance levels and for load only. All hours and nodes of the northern part of the grid are included. Also the probability for exceeding the overvoltage limit of 1.05 p.u. is presented in the upper right for the different cases.

3.3 Profitability of PV in agricultural sector

Following the assumptions in Section 2.4 it is not profitable to invest in PV without tax rebate. If tax rebate is included it is only profitable on the very best roofs, > 1 150 kWh/m^2/year. In Herrljunga there are almost no buildings with those conditions, scaled to national level only 0.2 TWh. In Tab. 4 an estimation of the annual yield and the scaled national potential is presented. As can be seen the national potential is low for profitable PV systems.

When it comes to the cases of improved profitability as presented in Tab. 2 there is a significant potential since locations with lower solar irradiance will become profitable (see Tab. 5). If own capital is used, giving a discount rate of 3% and a 40% subsidy on the investment is granted it is profitable to deploy large-scale PV fields of 1 MW$_p$, resulting in a total annual generation of 281 TWh, which is about twice as much as the Swedish electricity consumption. It should be noted that this is profitable from the farmers' perspective and only if the subsidies would be sufficient for all PV fields. Still, the potential will be limited by the overvoltage limit in the rural distribution grids of 4 TWh (see Section 3.2).

Tab. 4: Calculated income for a roof mounted PV system and the national potential at different solar irradiance levels.

Solar irradiance [kWh/m^2/year]	Annual yield on investment		National potential [TWh/year]	
	With tax rebate	Without tax rebate	Unlimited tax rebate	< 30 MWh tax rebate
700	0,0%	1,7%	14	11
800	0,0%	2,8%	10	8
900	0,0%	3,8%	7	5
1000	0,7%	4,7%	3	3
1100	1,4%	5,6%	0,5	0,5
1200	2,1%	6,4%	0	0

Tab. 5: Potential for cases with increased profitability

Case	Profitable solar irradiance level [kWh/m^2]	National potential [TWh/year]	
		Unlimited tax rebate	> 30 MWh tax rebate
Investment subsidy 40%	700	14	15
Higher sell rate	700	14	15
Own capital	850	9	8
Self-installed	1000	-	21
PV field, own capital, investment subsidy 40%	800	281*	

*All electricity from the PV field is assumed to be sold direct to the grid, with no tax rebate.

4. Concluding discussion

The results indicate that there is a considerable theoretical PV potential in the Swedish agricultural sector, but what is realizable is limited by the profitability, which at the current market situation is low, around 0.2 TWh on a national level. However, when including more or less optimistic scenarios, the profitability is no longer limiting; instead the hosting capacity of the rural distribution grid sets the limit to about 4 TWh/year. In this case the hosting capacity could be increased by different means, like curtailment, storage, grid enforcements or as previously shown for the same grid through smart allocation, where PV is only deployed at the strongest nodes (Lingfors et al., 2015).

The accuracy of the scaling to national level from the case study done for the distribution grid in Herrljunga is of course highly uncertain. Herrljunga only represents less than 2 ‰ of the agricultural sector of Sweden and it is not clear if Herrljunga is representative in terms of kind of farming or the condition of the grid. The difference in solar resource has been accounted for as described in Section 2.5, which means that no PV should be installed approximately from the 60th latitude northbound if the current level of solar irradiance of >1150 kWh/m^2/year were to be used.

5. References

Brolund, P., 2015. Budgetproposition 2015/16:1 [Swedish budget bill 2015/16: 1]. Sweden.

Duffie, J.A., Beckman, W.A., Worek, W.M., 1994. Solar Engineering of Thermal Processes, 2nd ed. J. Sol. Energy Eng. doi:10.1115/1.2930068

Energimarknadsinspektionen, 2013a. Metod för fastställande av skäliga anslutningsavgifter för uttag 16-25 A [Method for determening reasonable connection cost for 16-25 A fuses]. Sweden.

Energimarknadsinspektionen, 2013b. Energimarknadsinspektionens författningssamling [Statutes of the Swedish Energy Markets Inspectorate]. Sweden.

ESRI, 2015. ArcGIS Desktop [WWW Document]. URL http://desktop.arcgis.com/en/ (accessed 9.30.15).

Fu, P., Rich, P.M., 1999. Design and Implementation of the Solar Analyst: an ArcView Extension for Modeling Solar Radiation at Landscape Scales. 19th Annu. ESRI User Conf. 1–24.

Johnsson, B., 2008. Kartläggning av mark som tagits ur produktion [Survey of land taken out of production]. Jordbruksverket, Sweden.

Kjellsson, E., 1999. Potentialstudie för byggnadsintegrerade solceller i Sverige: rapport 1 : ytor på byggnader [Study of the potential for building integrated PV in Sweden: report 1: building surfaces]. Avdelningen för Byggnadsfysik, Lund.

Lindahl, J., 2015. National Survey Report of PV Power Applications in Sweden 2014.

Lingfors, D., Marklund, J., Widén, J., 2015. Maximizing PV hosting capacity by smart allocation of PV: A case study on a Swedish distribution grid, in: Proceedings of 44th ASES Annual Conference. State College, PA.

Norberg, I., Pettersson, O., Gustavsson, A., Kovacs, P., Boork, M., Ollas, P., Widén, J., Lingfors, D., Marklund, J., Larsson, D., Ingman, D., Jältorp, H., 2015. Solel i lantbruket - realiserbar potential och nya affärsmodeller [Solar electricity in agriculture - Realizable potential and new business models], Report 433, Agriculture & Industry. JTI – Swedish Institute of Agricultural and Environmental Engineering. Uppsala, Sweden.

Riksantikvarieämbetet, 2004. Lantbrukets byggnader 1993-2003 [Agricultural buildings 1993-2003]. Stockholm, Sweden.

Svensk Energi, 2011. Anslutning av större produktionsanläggningar till elnätet [Connection of larger power plants to the grid].

Thomson, M., Infield, D.G., 2007. Impact of widespread photovoltaics generation on distribution systems. Renew. Power Gener. IET 1, 10–16. doi:10.1049/iet-rpg

Walla, T., Widén, J., Johansson, J., Bergerland, C., 2012. Determining and increasing the hosting capacity for photovoltaics in Swedish distribution grids, in: 27th European Photovoltaic Solar Energy Conference and Exhibition. pp. 4414–4420. doi:10.4229/27thEUPVSEC2012-6DO.12.3

Conference Proceedings

Solar World Congress 2015
Daegu, Korea, 08 – 12 November 2015

Uncertainty evaluation of measurements with pyranometers and pyrheliometers

Jörgen Konings[1] and Aron Habte[2]

1 Hukseflux Thermal Sensors B.V., Delft (the Netherlands)

2 National Renewable Energy Laboratory, Golden, CO (U.S.)

Abstract

Evaluating photovoltaic (PV) cells, modules, arrays and systems performance of solar energy relies on accurate measurement of the available solar radiation resources. Solar radiation resources are measured using radiometers such as pyranometers (global horizontal irradiance) and pyrheliometers (direct normal irradiance).

The accuracy of solar radiation data measured by radiometers depends not only on the specification of the instrument but also on a) the calibration procedure, b) the measurement conditions and maintenance, and c) the environmental conditions. Therefore, statements about the overall measurement uncertainty can only be made on an individual basis, taking all relevant factors into account. This paper provides guidelines and recommended procedures for estimating the uncertainty in measurements by radiometers using the Guide to the Expression of Uncertainty (GUM) Method.

Special attention is paid to the concept of data availability and its link to uncertainty evaluation.

Keywords: *uncertainty evaluation, pyranometer, pyrheliometer, measurement, data availability*

1. Introduction

Within the American Society for Testing and Materials (ASTM) International Subcommittee G03.09 on Radiometry, a standard is developed that provides guidance and best practices for evaluating uncertainties when calibrating and performing outdoor measurements with pyranometers and pyrheliometers. The standard will describe a procedure that follows the guidelines in the Guide to the Expression of Uncertainty in Measurement, the GUM (JCGM 100, 2008). This method has been successfully applied to uncertainty evaluations of calibrations of and measurements with pyranometers and pyrheliometers (Habte et al., 2014; Reda et al., 2008; Reda, 2011).

The use of the GUM has become an accepted method to perform uncertainty evaluation, and for example the Baseline Surface Radiation Network (BSRN) recommends that all uncertainty calculations follow the procedure of the guide (McArthur, 2005). Within BSRN, a working group on uncertainty is established with the goal to calculate the uncertainty of BSRN data.

To illustrate the individual steps in the process of uncertainty evaluation, and to clarify the choices made, we present a worked example using real world data. We selected one day of pyranometer data from the National Renewable Energy Laboratory (NREL) Baseline Measurement System, located in Golden, CO, U.S; the 8th of June 2015 (Andreas and Stoffel, 1981). We assume that the pyranometer used to take these measurements is a secondary standard pyranometer with specifications that exactly match the requirements of its category. State of the art pyranometers have specifications that exceed the requirements of the ISO secondary standard category, and can reach lower uncertainties than presented here.

We go through both the formulation stage and the calculation stage in detail. We analyse the relative importance of the different uncertainty contributions, and make the link between uncertainty evaluation and the concept of data availability. Data availability is a new concept, which will be defined in chapter 4.

doi:10.18086/swc.2015.07.15 Available at http://proceedings.ises.org

2. Formulation stage: development of measurement model

We define the output quantity, or measurand, E as the one-minute average of global horizontal irradiance in W m^{-2}.

In the most basic pyranometer measurement model, the irradiance depends on two input quantities only:

- *V*, the pyranometer voltage output, measured in V
- *S*, the sensitivity of the pyranometer in V W^{-1} m^2

The measurement model is straightforward

$$E = \frac{V}{S} \qquad \text{(eq. 1)}$$

Other, more complicated, measurement models for pyranometers are in use that include corrections for systematic dependencies; i.e. temperature response, directional response, or response to net longwave radiation (zero off-set a). The process of uncertainty evaluation does not change, although the mathematics become more involved. For the scope of this paper, we limit ourselves to the basic measurement model.

With the measurement model established, the next step is to come up with factors that affect the uncertainty of the measurement. All factors are attributed to a specific quantity. The GUM only allows for uncertainty sources that apply to the input parameters. We present an approach where we also allow uncertainty sources to apply directly to the output parameter. The reasoning behind this is that certain pyranometer and pyrheliometer characteristics are stated explicitly in W m^{-2}, and are therefore best applied to the irradiance.

The GUM states that all knowledge of the (input) quantities is inferred from either repeated indication values (Type A evaluation of uncertainty) or scientific judgement (Type B evaluation of uncertainty). In high end meteorological networks such as the BSRN, it is considered best practice to take readings at a frequency of 1 Hz and store data as one-minute averages, together with the one-minute standard deviation, minimum and maximum value. However, irradiance is never constant; the 60 readings within a minute are not truly repeated observations. The variation within the minute can be caused by instrumental variation, but just as well by atmospheric variations on short timescales. Therefore, we argue that the standard deviation should not be taken into account when calculating the measurement uncertainty of a pyranometer or pyrheliometer measurement.

Without any Type A contributions present, all contributions are treated as Type B. For a Type B evaluation of uncertainty, often the only available information is that the quantity lies in a specified interval [*a*, *b*]. In these cases, the GUM recommends to use a rectangular or uniform probability distribution with limits *a* and *b*.

The judgement of which uncertainty sources to include or exclude has to be made on an individual basis for every application, and is fundamental to the process of uncertainty evaluation. We present a set of possible sources per uncertainty source, discuss the relevance, and assign specification limits.

3.1 Uncertainty contributions to the pyranometer voltage output

The voltage output of the pyranometer is measured with a device called a data logger: a voltmeter with the ability to store measurements. The manufacturer of the data logger normally specifies the measurement accuracy. In our scenario, we use a data logger with a specified accuracy of 10 µV, and treat this accuracy as a symmetric specification limit.

3.2 Uncertainty contributions to the sensitivity of the pyranometer

For the sensitivity S, we use the value as given by the manufacturer as 15.00 µV W^{-1} m^2 ± 0.15 µV W^{-1} m^2 where the number following the ± symbol is the expanded uncertainty with a coverage factor k = 2.

Calibration reference conditions are given as 20 °C instrument temperature, normal incidence solar radiation, horizontal mounting and an irradiance level of 500 W m^{-2}. This calibration is a single point calibration, which is different from the traditional meteorological calibration which results in an average sensitivity valid for a range of temperatures, angles of incidence and irradiance levels.

The term 'reference conditions' should be understood as the operating conditions under which the specified instrumental measurement uncertainty is the smallest possible (JCGM 200, 2012). In the theoretical case where all measurements would take place under these reference conditions, the calibration uncertainty as given by the manufacturer would suffice as the only contribution to the input quantity *S*. In practice, because all data points deviate from the reference conditions, the instrument characteristics have to be included in the uncertainty budget as well.

The most common set of characteristics is the list defined in ISO 9060 (ISO 9060, 1990) and most pyranometer and pyrheliometer manufacturers specify their instruments accordingly. These characteristics are defined both for pyranometers and pyrheliometers.

Of that list, the following apply to the input quantity sensitivity *S*.

- non-stability, the percentage change in sensitivity per year, relevant if the instrument has not been recalibrated recently. For our pyranometer, the secondary standard specification limit of 0.8 % per year applies. As the most recent calibration is about one year ago, we will use 0.8 % as a specification limit. ISO 9060 lists non-stability as a symmetric source, but we treat this uncertainty source as one-sided: the most common source of non-stability in thermal pyranometers is degradation of the black coating that absorbs the solar radiation. The coating can become less black over time, leading to a reduction in sensitivity. We use specification limits of [-0.8 %, 0 %].
- non-linearity, the change in sensitivity of the instrument for irradiance levels other than the reference condition (500 W m^{-2}) between 100 and 1000 W m^{-2}. We use the secondary standard specification limit of ± 0.5 % and apply it to the full measurement range.
- temperature response, the change in sensitivity of the instrument for temperatures other than the reference condition (20 °C). ISO 9060 states a limit of 2 % percentage deviation due to change in ambient temperature within an interval of 50 °C. In our scenario, the range of ambient temperatures is smaller than 50 °C, but we will use a specification limit of ± 1 % as a conservative estimate.
- tilt response, the change in sensitivity of the instrument for mounting orientations other than the reference condition (horizontal). In our example, we do not include the tilt response characteristic, because we are measuring global horizontal irradiance. When we measure tilted solar radiation with a pyranometer (for example in a plane-of-array setup) or direct solar radiation with a pyrheliometer, we do have to include tilt response in the uncertainty budget.

The ISO 9060 list of characteristics is not exhaustive; other effects can be considered as well. For our scenario, we will include an uncertainty contribution related to the level of maintenance. Pyranometer domes are subject to fouling. Fouling can be a continuous process, a slowly building layer of dust, or appear in bursts, for example due to sandstorms. The severity depends on the local conditions. For our scenario, clean air and daily cleaning, we estimate a maximum contribution of 0.5 %. This estimate is not based on any documented numbers, but is based on experience with and general knowledge of the behaviour of the instrument. In the GUM framework, this is allowed under the general header of 'scientific judgement'.

3.3 Uncertainty contributions to the global horizontal irradiance

We include three uncertainty sources that apply directly to the output quantity, the irradiance

- zero off-set a, the response to net thermal radiation. The pyranometer domes exchange radiation with the cold clear sky, cooling them down. This results in a negative offset in the irradiance. ISO 9060 specifies a limit of 7 W m^{-2} for 200 W m^{-2} thermal exchange. The thermal exchange, or net longwave radiation, varies with atmospheric conditions and altitude. 200 W m^{-2} is typical for very clear sky conditions at altitude, which fits nicely for our scenario. The offset is negative only, we use specification limits of [-7 W m^{-2}, 0 W m^{-2}]
- zero off-set b, the response to temperature gradients. As the ambient temperature increases and decreases, different parts of the instrument can be out of thermal equilibrium. ISO 9060 specifies a maximum value off-set of ± 2 W m^{-2} for a gradient of 5 °C per hour. We will use this value.
- directional response, the error caused by assuming the sensitivity to a normal incidence beam of irradiance is valid when measuring beams coming from any direction. ISO 9060 uses a specification limit of 10 W m^{-2} for a beam whose normal irradiance is 1000 W m^{-2}. In practice, this means that the relative specification limit is different with the position of the sun in the sky. With the sun in zenith (normal

incidence) the 10 W m^{-2} error on the normal incidence beam of 1000 W m^{-2} leads to a specification limit of 10 W m^{-2}/1000 W m^{-2} = 1 %. With the sun at 60 ° from zenith, the same normal incidence beam of 1000 W m^{-2} contributes cos(60 °)·1000 W m^{-2} = 500 W m^{-2}. The specification limit due to the 10 W m^{-2} error is then 10 W m^{-2}/500 W m^{-2} = 2 %.

In our example, we have a separate measurement of direct irradiance E_{direct} available, so we can apply the error to the direct component of the global horizontal irradiance only

$$a = \frac{10\ \text{W m}^{-2}}{E_{\text{direct}} \cos \Theta z} \qquad \text{(eq. 2)}$$

with Θ_z the zenith angle.

When no separate measurement of direct irradiance is available, a decent estimate of the specification limit of the directional response can be found by replacing E_{direct} in equation 2 by the global horizontal irradiance E itself.

The uncertainty sources are summarized in table 1.

Tab. 1: Summary of uncertainty contributions

Uncertainty source	Parameter	Specification limit *a*	Type	Distribution	Shape
data logger accuracy	*V*	10 µV	B	rectangular	symmetric
calibration uncertainty	*S*	1.5 %	B	normal (k = 2)	symmetric
non-stability	*S*	0.8 %	B	rectangular	one-sided (negative)
non-linearity	*S*	0.5 %	B	rectangular	symmetric
temperature response	*S*	1 %	B	rectangular	symmetric
maintenance	*S*	0.5 %	B	rectangular	symmetric
zero off-set a	*E*	7 W m^{-2}	B	rectangular	one-sided (negative)
zero off-set b	*E*	2 W m^{-2}	B	rectangular	symmetric
directional response	*E*	$\frac{10\ \text{W m}^{-2}}{E_{\text{direct}} \cos \Theta z}$	B	rectangular	symmetric

With the measurement mode developed and all quantities characterized, the measurand *E* is fully specified in terms of this information. The rest is applying the algorithms as laid out in the GUM, but involves no further judgement or decisions.

3. Calculation stage: propagation of distributions and summary of expanded uncertainty

The GUM uncertainty framework uses the values of the input quantities, their standard uncertainties and the sensitivity coefficients to form an estimate of the output quantity and the associated combined standard uncertainty.

The standard uncertainty of a quantity is the square root of the sum of the squares of all uncertainty sources that apply to that parameter

$$u(X) = \sum_j u_j \qquad \text{(eq. 3)}$$

where *j* sums over all uncertainty sources that apply to the input quantity *X*.

The introduction of one-sided uncertainty sources should lead to asymmetric uncertainty distribution of the measurement. Our current method is not yet suited to handle this. We choose to halve the one-sided

specification limits and treat them as symmetric. Future work should aim to improve on this, and allow asymmetric uncertainty distributions of the measurements.

We do not consider correlations between uncertainty sources in this method. Some uncertainty sources are clearly uncorrelated, such as data logger accuracy and non-stability, but others certainly have some level of correlation. Correlations, including correlations over time scales, are the subject of current research.

In table 2, the standard uncertainty of all quantities is calculated for the single data point at 11:45, with a pyranometer voltage output V of 15384 µV and a solar zenith angle Θ_z of 17.2°.

Tab. 2: Calculation of standard uncertainty of voltage output, sensitivity and irradiance for one data point

(Input) Quantity	Uncertainty source	u_i	Standard uncertainty
V = 15384 µV			
	data logger accuracy	10 µV	
			$u(V)$ = 10 µV
S = 15.00 µV W^{-1} m²			
	calibration uncertainty	0.08 µV W^{-1} m²	
	non-stability	0.03 µV W^{-1} m²	
	non-linearity	0.04 µV W^{-1} m²	
	temperature response	0.09 µV W^{-1} m²	
	maintenance	0.04 µV W^{-1} m²	
			$u(S)$ = 0.13 µV W^{-1} m²
E = 1025.6 W m^{-2}			
	zero off-set a	2.02 W m^{-2}	
	zero off-set b	1.15 W m^{-2}	
	directional response	5.92 W m^{-2}	
			$u(E)$ = 6.36 W m^{-2}

Note that the standard uncertainty of the irradiance u(E) is not the final result. The standard uncertainties in table 2 have to be combined to reach the so-called 'combined standard uncertainty' of the measurand $u_c(E)$. This is done using the law of propagation of uncertainty.

$$u_c(E) = \sqrt{c_V^2 u^2(V) + c_S^2 u^2(S) + c_E^2 u^2(E)} \quad \text{(eq. 4)}$$

where c_V, c_S, c_E are the 'sensitivity coefficients' of quantities V, S and E respectively.

The sensitivity coefficient of a quantity is the partial derivative of the output quantity with respect to that quantity. GUM defines this only for input quantities, but the definition can be extended to the output quantity to give a sensitivity coefficient equal to one (eq. 7). For our measurement model, the sensitivity coefficients are

$$c_V = \frac{\partial E}{\partial V} = \frac{1}{S} \quad \text{(eq. 5)}$$

$$c_S = \frac{\partial E}{\partial S} = -\frac{V}{S^2} \quad \text{(eq. 6)}$$

$$c_E = \frac{\partial E}{\partial E} = 1 \quad \text{(eq. 7)}$$

For the single data point we used as an example above, the combined standard uncertainty of the irradiance becomes

$$c_V = \frac{\partial E}{\partial V} = \frac{1}{S} = 0.07 \text{ µV}^{-1}\text{Wm}^{-2} \quad \text{(eq. 8)}$$

$$c_S = \frac{\partial E}{\partial S} = -\frac{V}{S^2} = -68.37\ \mu V^{-1} W^2 m^{-4} \quad \text{(eq. 9)}$$

$$c_E = 1 \quad \text{(eq. 10)}$$

$$u_c(E) = \sqrt{c_V^2 u^2(V) + c_S^2 u^2(S) + c_E^2 u^2(E)} = 11.2\ \mathrm{Wm^{-2}} \quad \text{(eq. 11)}$$

The combined standard uncertainty can be universally used to express the uncertainty of a measurement result, but it is preferable to define an interval about the measurement result that is expected to encompass a certain fraction of reasonable results for the measurand. This is achieved by multiplying the combined standard uncertainty with a coverage factor *k* to find the expanded uncertainty *U*. In practice, the coverage factor is chosen to reach a level of confidence of 95 %. The expanded uncertainty is then written with a subscript 95 to reflect this.

$$U_{95} = k u_c \quad \text{(eq. 12)}$$

This approach has the advantage of taking the abstract concept of uncertainty and applying a physical meaning. An irradiance reading of 1000 W m^{-2} with a symmetric expanded uncertainty U_{95} of 10 W m^{-2} can be understood to mean that if you would repeat that measurement 100 times, 95 times you would get a reading between 990 and 1010 W m^{-2}. This is a useful way of thinking when performing a risk analysis based on irradiance readings.

Choosing the right coverage factor is a complicated procedure, and is detailed in Annex G of the GUM (JCGM 100:2008). A simple approach is often adequate in measurement situations where the probability distribution is approximately normal and there is a significant number of effective degrees of freedom. When this is the case, one can use $k = 2$ to produce an interval having a level of confidence of 95 %, and $k = 3$ to produce an interval having a level of confidence of 99 %.

We introduced uncertainty sources with a rectangular probability distribution and although the effective degrees of freedom is significant (with a measurement rate of 1 Hz, we have 60 readings in the one-minute average), it is not infinite. However, we argue that using a coverage factor of 2 is a conservative and simple approach when analysing pyranometer of pyrheliometer measurements.

For the single data point, the final result is

$$U_{95}(E) = 2u_c(E) = 22.4\ \mathrm{Wm^{-2}} \quad \text{(eq. 13)}$$

The GUM recommends to report this measurement result as follows

"E = (1025.6 ± 22.4) W m^{-2}, where the number following the ± symbol is the numerical value of $U = ku_c$, with U determined from u_c = 11.2 W m^{-2} and k = 2 based on the normal distribution, and defines and interval estimated to have a level of confidence of 95 percent."

This result is valid for a single data point, but the analysis can be repeated for every data point. In this example, the only parameter that changes is the voltage output *V*, and therefore also the magnitude of the measurand *E*. When you perform this analysis over a full day, it can be seen that the expanded uncertainty varies over time.

In figure 1 the global horizontal irradiance is plotted with the expanded uncertainty drawn as error bars. As the irradiance increases, the absolute value of the expanded uncertainty increases as well, even as the relative value of the expanded uncertainty decreases.

Fig. 1: Measured global horizontal irradiance as a function of time, red bars give the expanded uncertainty values that correspond with a level of confidence of 95 %.

4.1 Analysis of relative importance per uncertainty source

It is possible to calculate the relative contribution of each uncertainty source to the expanded uncertainty. This way, it is possible to judge which uncertainty sources are dominant for this application. This information can be useful for purchasing decisions, product development and/or help to decide which systematic errors should be corrected for.

To calculate the relative contribution of an uncertainty source, first calculate the relative importance of all quantities as the ratio of the standard uncertainty of the quantity to the sum of the standard uncertainty of all quantities, weighed by their sensitivity coefficients.

For a quantity *X* this is

$$\frac{u(X)}{\sum_l c_l u(l)} \qquad \text{(eq. 14)}$$

where *l* sums over all quantities

The relative importance of one uncertainty source within a quantity is found directly from the ratio of the standard uncertainty to the sum of the standard uncertainties of all sources that apply to that specific quantity.

For an uncertainty source *i* this is

$$\frac{u_i}{\sum_m u_m} \qquad \text{(eq. 15)}$$

where *m* sums over all uncertainty sources that apply to the same quantity as *i*.

Multiply the two ratios to find the final contribution.

We work this out for three sources explicitly, and present the contributions of all sources in table 3, for the same single data point.

$$\frac{u_{\text{data logger accuracy}}}{\sum_{i=\text{data logger accuracy}} u_i} \cdot \frac{u(V)}{c_V u(V)+c_S u(S)+c_E u(E)} = 4.1\ \% \qquad \text{(eq. 16)}$$

$$\frac{u_{\text{non-linearity}}}{\sum_{i=\text{calibration uncertainty, non-stability, non-linearity, temperature response, maintenance}} u_i} \cdot \frac{u(S)}{c_V u(V)+c_S u(S)+c_E u(E)} = 8.7\ \% \qquad \text{(eq. 17)}$$

$$\frac{u_{\text{zero off-set b}}}{\sum_{i=\text{zero off-set a, zero off-set b, directional response}} u_i} \cdot \frac{u(E)}{c_V u(V)+c_S u(S)+c_E u(E)} = 5.0\ \% \qquad \text{(eq. 18)}$$

Tab.3: Calculation of relative contribution to the expanded uncertainty per uncertainty source for one data point

Input quantity	Uncertainty source	Relative importance per input parameter	Relative importance per uncertainty source
V = 15384 µV			
	data logger accuracy		4.1 %
		4.1 %	
S = 15.00 µV W^{-1} m^2			
	calibration uncertainty		15.0 %
	non-stability		6.9 %
	non-linearity		8.7 %
	temperature response		17.4 %
	maintenance		8.7 %
		56.7 %	
E = 1025.6 W m^{-2}			
	zero off-set a		8.7 %
	zero off-set b		5.0 %
	directional response		25.5 %
		39.2 %	

This procedure can be repeated for all data points. In figure 2, the expanded uncertainty is plotted as function of time, split per uncertainty source in a stacked area chart. Figure 2 a) gives the expanded uncertainty in W m^{-2}, figure 2 b) in percentage. For low irradiances, the uncertainty expressed in percentages becomes very high.

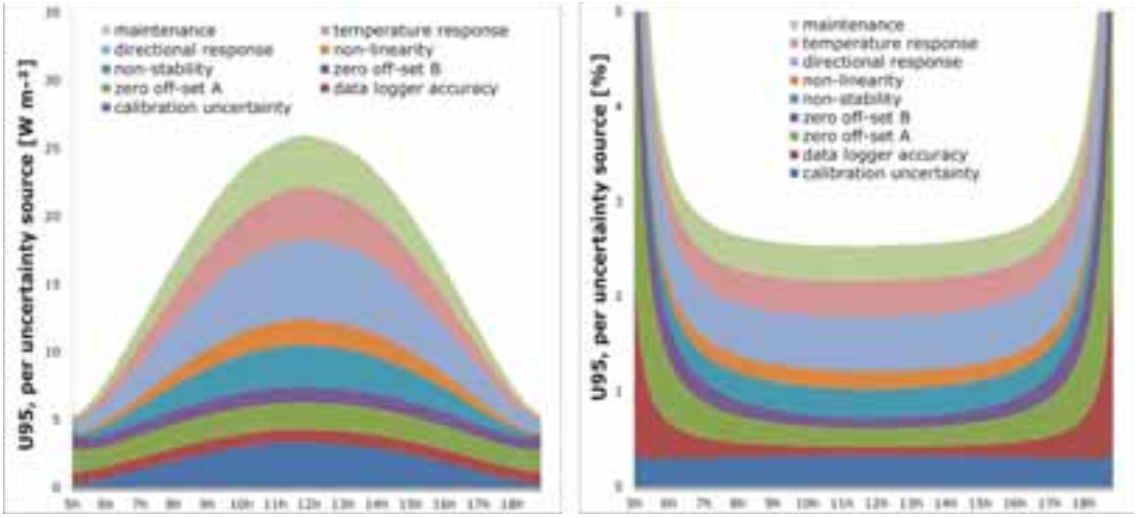

Fig. 2: Expanded uncertainty as function of time, split per uncertainty source.
The expanded uncertainty is expressed in a) absolute values in W m^{-2}, b) relative values in %.

In figure 3 we plot the relative contribution of each uncertainty source as a function of irradiance. Here it becomes clear that at low irradiance levels, the zero off-set a, dominates together with the zero off-set b and data logger accuracy. At higher irradiance levels, the directional response dominates, and the importance of the zero off-sets and data logger accuracy diminishes.

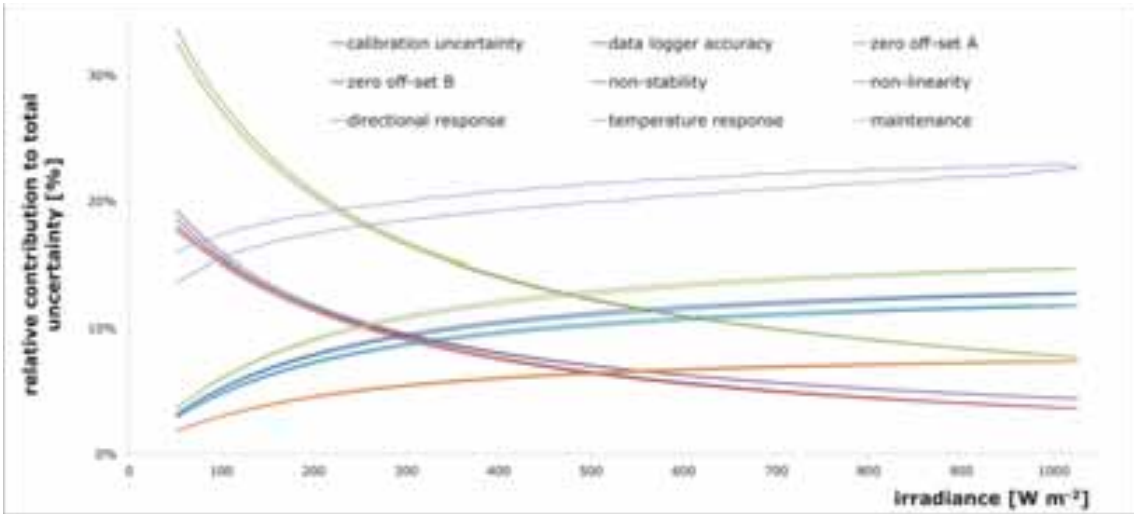

Fig. 3: Relative importance of each uncertainty source as a function of irradiance.

4. Data availability

The 'rated operating conditions' are defined as conditions that must be fulfilled during measurement in order that a measuring instrument performs as designed (JCGM 200:2012). For pyranometers and pyrheliometers, the condition that the optics (domes, windows) of the instrument are clean is a critical rated operating condition. Snowfall can obstruct the domes to no longer transmit solar radiation, leading to an underestimation. Rain droplets on a pyranometer can focus the incoming solar radiation, leading to an overestimation. Figure 4 gives visual examples of situations where the optics of the instrument are not clean.

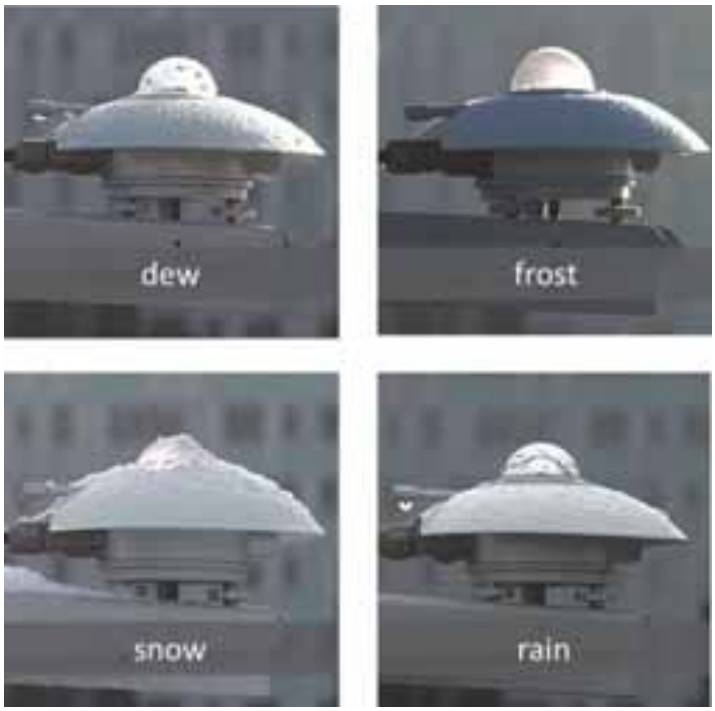

Fig. 4: Examples of pyranometers with domes that are not clean. These measurements cannot be assigned a meaningful measurement uncertainty.

In these situations, it is not possible to assign a meaningful measurement uncertainty to the instrument reading. Data points that fall outside the rated operating conditions should be flagged accordingly and considered as not available. This provides a definition of the concept of 'data availability': the percentage of data points over a certain time period that fall within the rated operating conditions of the instrument, and can be assigned a meaningful measurement uncertainty.

Data availability can be used as a requirement during site assessment, and can be useful for purchasing decisions or when determining the required level of maintenance during operation.

A trained user can recognize 'false' data point from a visual interpretation of the measurement data, but other methods are available that provide a more solid process of flagging data points. The BSRN uses a set of recommended Quality Control tests that compare measurement data with physically possible limits and extremely rare limits (Long 2012). A strong method is to combine separate measurements of global, diffuse and direct irradiance and compare the ratios between measured direct irradiance and the direct irradiance back-calculated from measurements of global and diffuse irradiance.

$$E_{\text{direct}} = E_{\text{global}} \cos \Theta z + E_{\text{diffuse}} \quad \text{(eq. 19)}$$

When measurements of direct radiation are not available, which is often the case in solar energy applications, it can be helpful to monitor the pyranometers, for example using webcam images. A study using webcam images in Delft, the Netherlands, over 26 days in the spring of 2015, found that without any measures to improve data availability, an average 80 minutes of data per day was lost due to early morning dew.

Ways to improve the data availability of pyranometers and pyrheliometers include the use of forced ventilation (using purpose built ventilation units) and direct heating of the instrument optics to keep the optics above dew point temperature and free of frost and snow. Both methods can be effective, and in the study above were able to increase data availability to 100 %. Figure 5 shows the visual difference between a heated and unheated pyranometer during frost.

Fig. 5: Visual difference between a heated (left) and unheated (right) pyranometer during frost. Data points measured with the left pyranometer can be assigned a meaningful uncertainty, data points measured with the right pyranometer have to flagged as not available.

Both methods can also induce off-sets on the thermal instruments. These off-sets will have to be included as an uncertainty source, and can become dominant for instruments that were not designed for use with ventilation or heating. Especially in environments with extreme conditions, the user will have to find a balance between data availability and measurement uncertainty.

Instruments that are specifically designed for use with ventilation or direct heating in mind will often include ventilation or heating off-sets in the data sheet.

For example, the left pyranometer in figure 5 uses a combination of a sapphire outer dome with 1.5 W internal heating and specifies a heating off-set of 0 to -1.5 W m^{-2} (Hukseflux 2015). This uncertainty source should be applied directly to the irradiance, with a specification limit of 1.5 W m^{-2} and be treated as a Type B uncertainty with a one-sided (negative) rectangular distribution.

5. Results and discussion

We presented a worked example of the uncertainty evaluation of one clear sky day of global horizontal irradiance measured with a pyranometer specified as a secondary standard pyranometer.

We used a method based on the GUM, according to the procedures and guidelines that are written into a standard that is in development within the ASTM International Subcommittee G03.09 on Radiometry. In the formulation stage, we developed the measurement model and defined the relevant sources of uncertainty. In

the calculation stage, we combined this information to find the expanded uncertainty of the measurement. As a separate analysis, we calculated the relative importance per uncertainty source.

We find an expanded uncertainty U95 of 2.2 % (k = 2) for a data point around solar noon, and we find the three dominant contributions to the measurement uncertainty; the directional response, the temperature response and the initial calibration uncertainty. For conditions with lower levels of irradiance, the zero off-sets and data logger accuracy become dominant.

Users have to adapt the analysis shown here to their own situation. In practice, this means they have to update the formulation stage with sources and specification limits for their own situation. The calculation stage does not change. Spreadsheets are available from the authors on request that can assist in this process.

The procedure presented is not capable of producing asymmetric confidence intervals, and does not incorporate correlations between different uncertainty sources, or correlations over time. Future work should improve on these matters.

We introduced the concept of data availability, and made a specific link of this concept with the process of uncertainty evaluation. Data availability can be a useful tool for site assessment, determining a maintenance schedule, purchasing decisions or product development.

6. References

Andreas, A., Stoffel, T., (1981). NREL Solar Radiation Research Laboratory (SRRL): Baseline Measurement System (BMS), Golden, Colorado (Data), NREL Report No. DA-5500-56488.

ISO 9060:1990(E) Solar energy - Specification and classification of instruments for measuring hemispherical solar and direct solar radiation.

JCGM 100:2008 Evaluation of measurement data – Guide to the expression of uncertainty in measurement (GUM).

JCGM 200:2012 International Vocabulary of Metrology – Basic and General Concepts and Associated Terms (VIM 3rd edition).

McArthur, L., 2005. World Climate Research Programme – Baseline Surface Radiation Network (BSRN) – Operations Manual Version 2.1.

Habte, A., Sengupta, M., Reda, I., Andreas, A., Konings, J., 2014. Calibration and Measurement Uncertainty Estimation of Radiometric Data: Preprint. 9 pp., NREL Report No. CP-5D00-62214.

Hukseflux, 2015, SR25_manual_v1508, User Manual SR25 Secondary standard pyranometer with sapphire outer dome, available from http://hukseflux.com/sites/default/files/product_manual/SR25_manual_v1508.pdf

Long, N., Dutton, E. G., 2012, BSRN Global Network recommended QC tests, V2.0, available from http://www.bsrn.awi.de/fileadmin/user_upload/redakteur/Publications/BSRN_recommended_QC_tests_V2.pdf

Reda, I.M., Myers, D.R., Stoffel, T.L., 2008. Uncertainty Estimate for the Outdoor Calibration of Solar Pyranometers: A Metrologist Perspective. NCSLI Measure, The Journal of Measurement Science, pp. 58-66.

Reda, I., 2011. Method to Calculate Uncertainty Estimate of Measuring Shortwave Solar Irradiance using Thermopile and Semiconductor Solar Radiometers. 20 pp., NREL Report No. TP-3B10-52194.

Conference Proceedings

Solar World Congress 2015
Daegu, Korea, 08 – 12 November 2015

ASSESSMENT OF DAILY ATMOSPHERIC TURBIDITY DATABASES USING AEROSOL OPTICAL DEPTH AND DIRECT NORMAL IRRADIANCE MEASUREMENTS

Luis Martin-Pomares[1], Jesus Polo[2], Daniel Perez-Astudillo[1] and Dunia A. Bachour[1]

[1] Qatar Environment and Energy Research Institute (QEERI), HBKU, Qatar Foundation, Doha, Qatar

[2] Energy Department, CIEMAT, Madrid, 28040, Spain

Abstract

This study presents the validation of atmospheric turbidity databases. It is divided into two parts. The first part shows the validation of three Aerosol Optical Depth (AOD) databases with worldwide coverage. AOD at 550nm estimates from MISR, MODIS-L3 satellites and MACC model and water vapour from NCEP are compared against measurements from 865 AERONET stations as ground-truth data for more than one year in each location.

The second part addresses the limitation that ground measurements of AOD are not always available. An alternative methodology is presented here to evaluate the AOD databases. It consists of comparing the daily Linke Turbidity Index (TL) obtained from the databases to the corresponding TL derived from DNI measurements.

All databases show a significant overestimation of AOD and errors in terms of rRMSD are between 85 and 118% in total for the AERONET stations validated.

Keywords: *Atmospheric aerosols, turbidity, solar radiation, AOD, TL*

1. Introduction

Aerosol Optical Depth (AOD) is the degree to which aerosols prevent the transmission of light by absorption or scattering of light and is defined as the integrated extinction coefficient over a vertical column of the unit cross-section (Albrecht, 1989).

AOD is a fundamental parameter for the modelling of solar radiation. It is mainly needed for clear sky models (Gueymard, 2008; Ineichen, 2008; Rigollier, Bauer, & Wald, 2000).The clear sky models are an essential component of many methods of solar radiation estimation from satellite images (Polo, Antonanzas-Torres, Vindel, & Ramirez, 2014; Rigollier & Wald, 1999). The measurements of AOD are scarce in the world due to the high cost of installing and running a station to measure this variable. Because of this scarcity, AOD estimated from satellite images or chemical transport models are widely used.

Another index to quantify turbidity is the Linke Turbidity (TL) index (Ineichen & Perez, 2002; Kasten, 1996; Linke, 1922) which establishes a relationship between the real and theoretical optical depth of the atmosphere and represents the degree of transparency of the atmosphere. It is an adequate approximation when quantifying the effects of absorption and dispersion of solar radiation when traversing the atmosphere. TL can be obtained directly from solar radiation ground measurements; however, due to the unavailability of ground data, it is derived from empirical adjustments (Kasten, 1980).

doi:10.18086/swc.2015.07.16 Available at http://proceedings.ises.org

Several validations of AOD databases in a regional scale have been presented previously (Antonanzas-Torres et al., 2014; Eissa et al., 2015; Ruiz-Arias, Dudhia, Gueymard, & Pozo-Vázquez, 2013; Zhong & Kleissl, 2015), but a global validation has not been done yet. In this study, we present first results of a comprehensive validation of three AOD databases (MODIS, MACC and MISR).

Besides, as in most of the locations, AOD measurements are not available, we present a methodology to estimate turbidity from solar radiation measurements. The turbidity of two sites obtained using Linke TL from Direct Normal Irradiance (DNI) ground measurements is presented to show the capabilities of this methodology.

2. Experimental Datasets

In this section, we present the experimental data used in this study.

2.1 Aeronet ground measurements

Field measurements from the NASA AERONET (AErosol RObotic NETwork) program are available all around the Globe. We have used in this study 865 stations from the AERONET network. The measurements were collected during different periods. For each AERONET station, the measurements of the CIMEL CE-318 Sun photometer were converted into aerosol optical properties and are available for public access (http://aeronet.gsfc.nasa.gov). The data sets include the aerosol optical depth (AOD) at eight different wavelengths, as well as the solar zenith angle and the total column content in water vapour (PW). The AERONET Level 2.0 products (cloud-screened and quality assured) are compared in Section 4 to the daily AOD at 550 nm from MODIS, MISR and MACC. Daily PW is compared with NCEP model.

2.2 Radiometric measurements

The radiometric data used in this study for the validation is located in China and South of Spain. DNI is measured with first class pyrheliometer. Global Horizontal Irradiance (GHI) and Diffuse Horizontal Irradiance (DHI) were also available from secondary standard pyranometers. Both stations have solar trackers and shading ball for DHI. Data is registered every 10 minutes in both stations, and hourly averages were calculated. BSRN quality checks (Long & Dutton, 2002) are applied to remove suspicious wrong data.

2.3 Aerosol and Atmospheric databases

The atmospheric and aerosol datasets, compared in this study, come from different sources. Daily values of AOD at 550nm from satellite and models are the following:

- MODIS-L3: daily values of AOD with a spatial resolution of 1ºx1º for the period from the year 2004 to the present.
- MACC (Monitoring Atmospheric Composition & Climate from ECMWF): daily values of AOD with a spatial resolution of 1.125ºx1.125º for the period from 2003 to the present.
- MISR (Multi-angle Imaging SpectroRadiometer): daily values of AOD with a spatial resolution of 0.5ºx0.5º for the period from 2001 to the present.

Daily PW from AERONET stations is validated with NCEP (National Centers for Environmental Prediction) for the temporal period coincident. The spatial resolution of NCEP data is 1ºx1º.

3. Methodology

The parameters to validate daily AOD at 550 nm and PW from different databases with AERNET stations are mean bias deviation (MBD), root mean squared deviation (RMSD) and its relative value as rMBD and rRMSD. The relative expressions are obtained using the following equations:

$$\mathrm{rMBD} = \frac{1}{N}\sum_{i=1}^{N}\left(\hat{x}_i - x_i\right) \qquad \text{(eq. 1)}$$

$$\mathrm{rRMSD} = \frac{\sqrt{\sum_{i=1}^{n}(x_i - \hat{x}_i)^2 / n}}{\bar{x}} \qquad \text{(eq. 2)}$$

where N is the population size, x is the observed value, $\bar{x}$ is the mean of observed values, and $\hat{x}$ is the predicted value.

The following parameters have also been calculated (Espinar et al., 2009). The correlation coefficient (R), Kolmogorov–Smirnov test Integral (KSI), and its relative magnitude (KSI (%)), the critical limit from the original Kolmogorov–Smirnov test (Over), and its relative (Over(%)), the evaluation parameter based on KSI and Over (KSE) and RIO, combination of the three most representative parameters: OVER (%), KSI (%), and RMSD (%).

3.1 Turbidity from DNI measurements

Besides, when AOD measurements are not available, we have used DNI measurements to validate the satellite and model estimates. We have extracted turbidity from DNI measurements after identifying clear sky conditions which can be done automatically or manually by visual inspection. We have used the last option. The values of TL are obtained using the inverse of a clear sky model for clear sky days at solar noon (Ineichen & Perez, 2002).

AOD at 550 nm from MODIS, MISR and MACC are converted to TL values using Ineichen correlation (Pierre, 2008) and daily PW from NCEP.

4. Results

In this section, we present the primary results.

4.1 Validation of Aerosol Optical Depth (AOD) from satellite and models

The next tables show the results for MBD, RMSD, rMBD, rRMSD, R, KSI, KSI (%), Over, Over(%), and RIO, (Espinar et al., 2009) for daily PW from NCEP model compared with AERONET measurements:

Tab. 1: Statistical errors of daily water vapour column from NCEP model compared with AERONET stations

MODEL	MBD	RMSD	rMBD (%)	rRMSD (%)	R
NCEP	0.17	0.65	16.87	42.66	0.72

Tab. 2: Errors for daily water vapour column from NCEP model compared with AERONET stations

MODEL	IKS	IKS %	Over	Over %	KSE	RIO
NCEP	0.27	94.03	0.11	47.25	141.28	91.89

As we can see from the results, NCEP database presents a considerable overestimation and rRMSD is considerably high.

The next tables show MBD, RMSD, rMBD, rRMSD, R, IKS, IKS(%), Over, Over(%), KSE and RIO for AOD at 550 nm for MODIS and MISR satellites and MACC model:

Tab. 3: Statistical errors of daily Aerosols Optical Depth (AOD) at 550 nm from MODIS and MISR satellite and MACC model compared with AERONET stations

SATELLITE/MODEL	MBD	RMSD	rMBD (%)	rRMSD (%)	R
MODIS	0.03	0.20	40.58	118.10	0.48
MISR	-0.02	0.17	6.66	85.60	0.29
MACC	0.02	0.18	32.07	101.86	0.33

Tab. 4: Errors for daily Aerosols Optical Depth (AOD) at 550 nm from MODIS and MISR satellite and MACC model compared with AERONET stations

SATELLITE MODEL	IKS	IKS %	Over	Over %	KSE	RIO
MODIS	0.06	56.77	0.02	25.25	82.02	99.46
MISR	0.05	96.66	0.02	46.69	143.35	114.52
MACC	0.06	87.38	0.02	46.28	133.66	117.75

All databases show overestimation which is considerably high in the case of MODIS and MACC. It has a direct effect on clear sky models output and solar radiation derived satellite from a satellite which will be underestimated in the case of using raw AOD values from these databases. MISR satellite presents better results globally in terms of rMBD and rRMSD, maybe due to its higher spatial resolution.

4.2 Validation of Aerosol Optical Depth (AOD)

The hourly values of DNI for a clear sky day selected manually for a location in Spain are shown in the next figures for several days. In the plots, measured clear sky DNI (blue), modelled clear-sky DNI (green), DNI estimated from satellite MODIS TL and DirIndex model (pink) and DNI estimated from satellite MODIS TL and Louche model (red). In the figure, we also show the values of daily TL estimated from MODIS satellite and calculated from measurements for all hourly values and two hours during the day at noon time (11:00 and 12:00 UTC). The values of TL are calculated from measurement at noon hours because there are some days which have clear sky conditions in most of the times of the day but not in all.

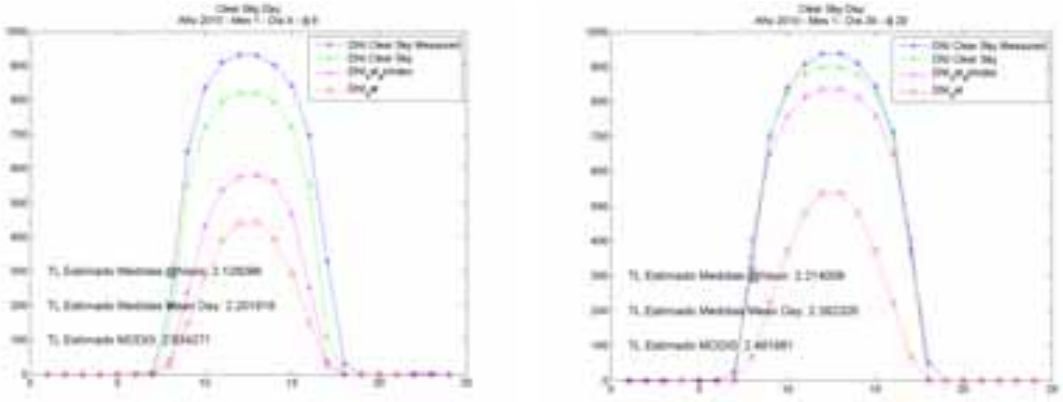

Fig. 1: TL estimated from MODIS and measurements of DNI for a clear sky day. 09/01/2010 and 29/01/2010 in Spain.

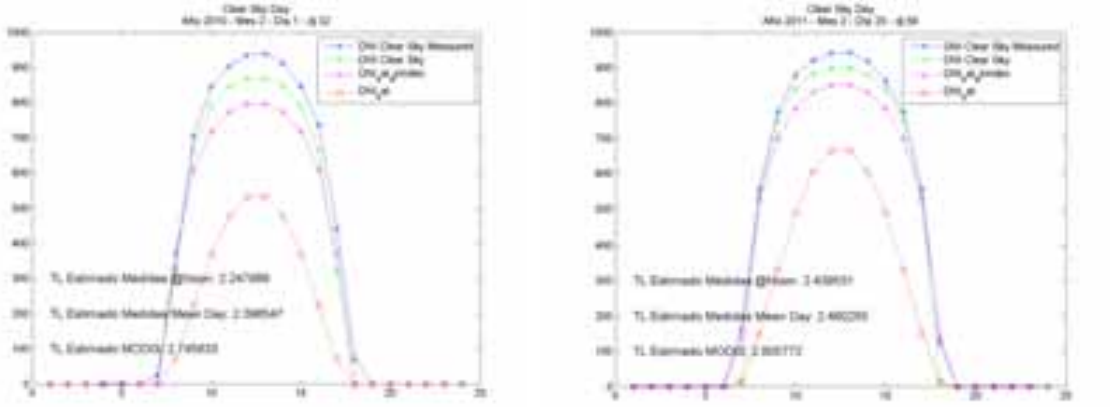

Fig. 2: TL estimated from MODIS and measurements of DNI for a clear sky day. 01/02/2010 and 25/02/2011 in Spain.

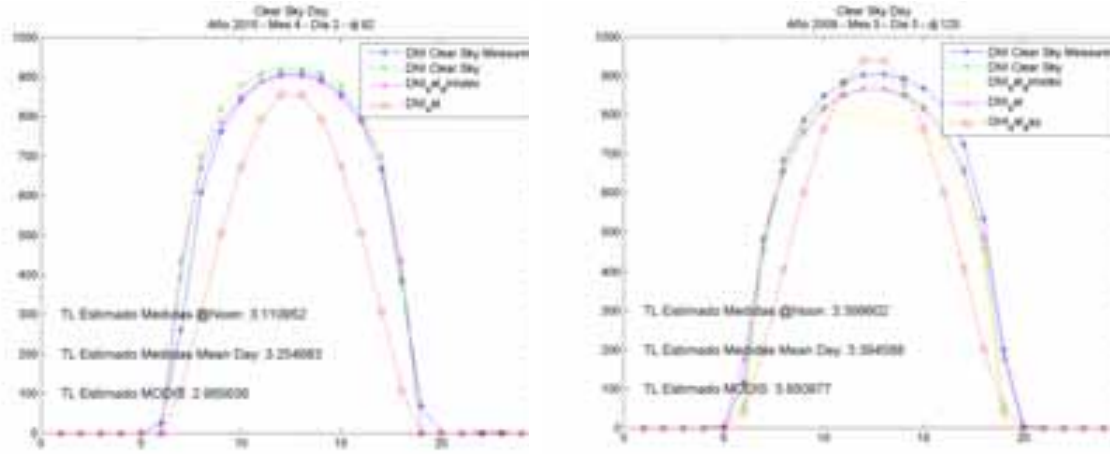

Fig. 3: TL estimated from MODIS and measurements of DNI for a clear sky day. 02/04/2010 and 05/05/2009 in Spain.

The next figures represent the same information as in the last ones but for cloudy conditions.

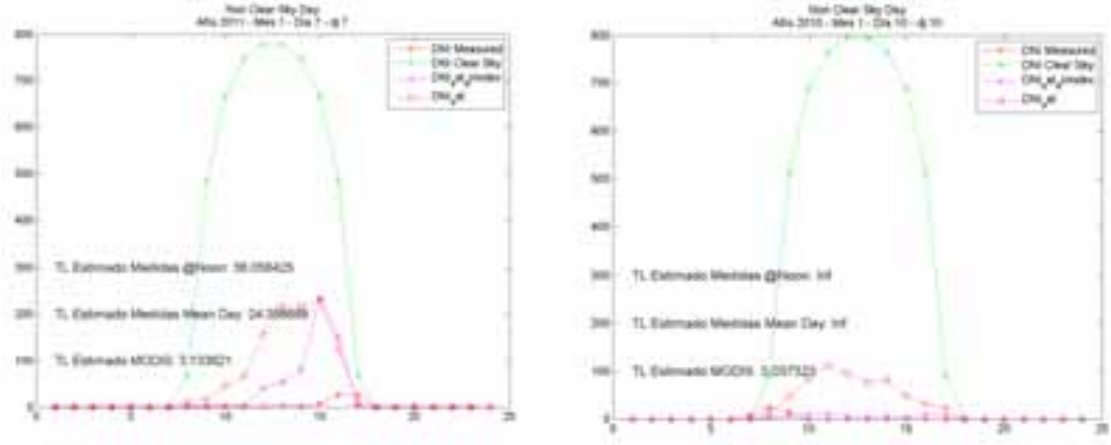

Fig. 4: TL estimated from MODIS and measurements of DNI for a cloudy sky day. 07/01/2011. 10/01/2010 in Spain.

With the values calculated from the daily selection, we have obtained daily time series of TL. The next figures show some examples of the relationship between daily Linke Turbidity (TL) estimated from MODIS satellite (red line) and estimated from measurements (blue line) with clear sky days for several months in the location in Spain. TL is obtained from several years of measurements:

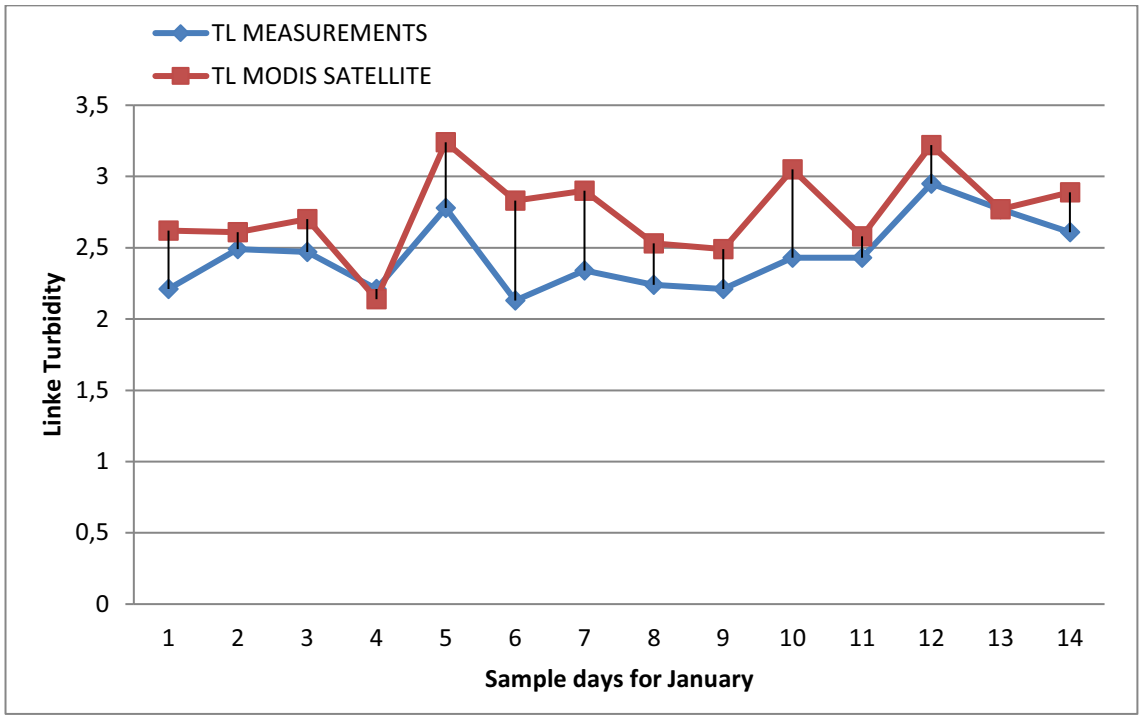

Fig. 5: Daily values of TL estimated from MODIS and measurements with clear sky days in January

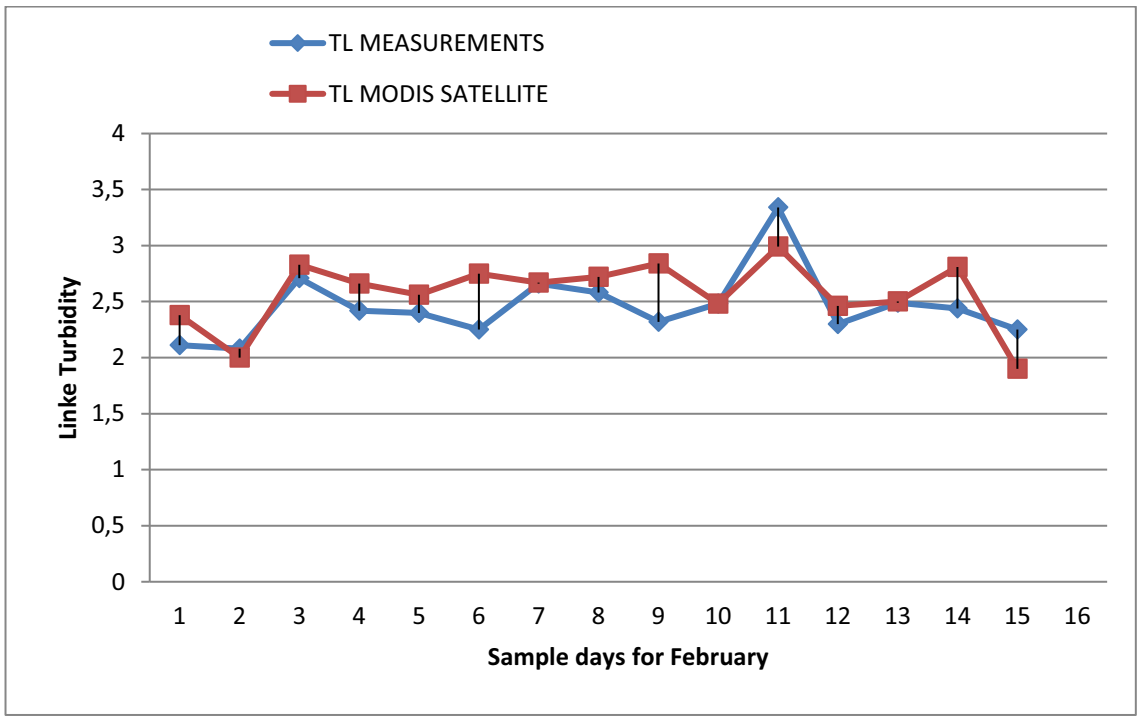

Fig. 6: Daily values of TL estimated from MODIS and measurements with clear sky days in February

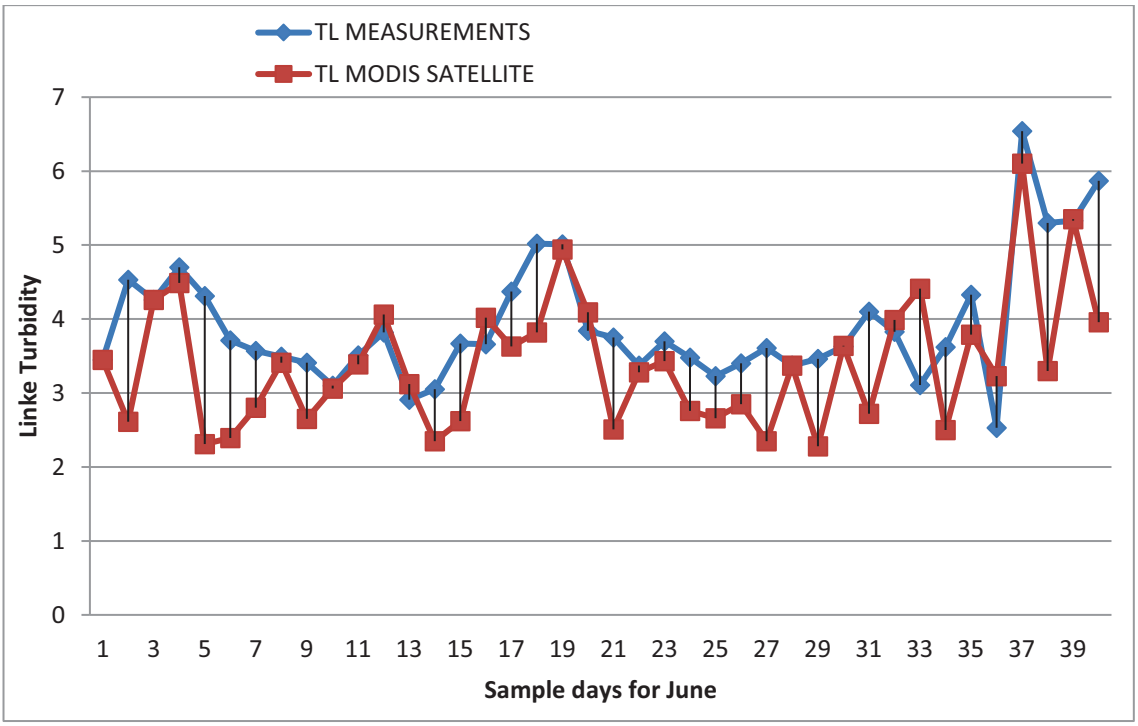

Fig. 7: Daily values of TL estimated from MODIS and measurements with clear sky days in June

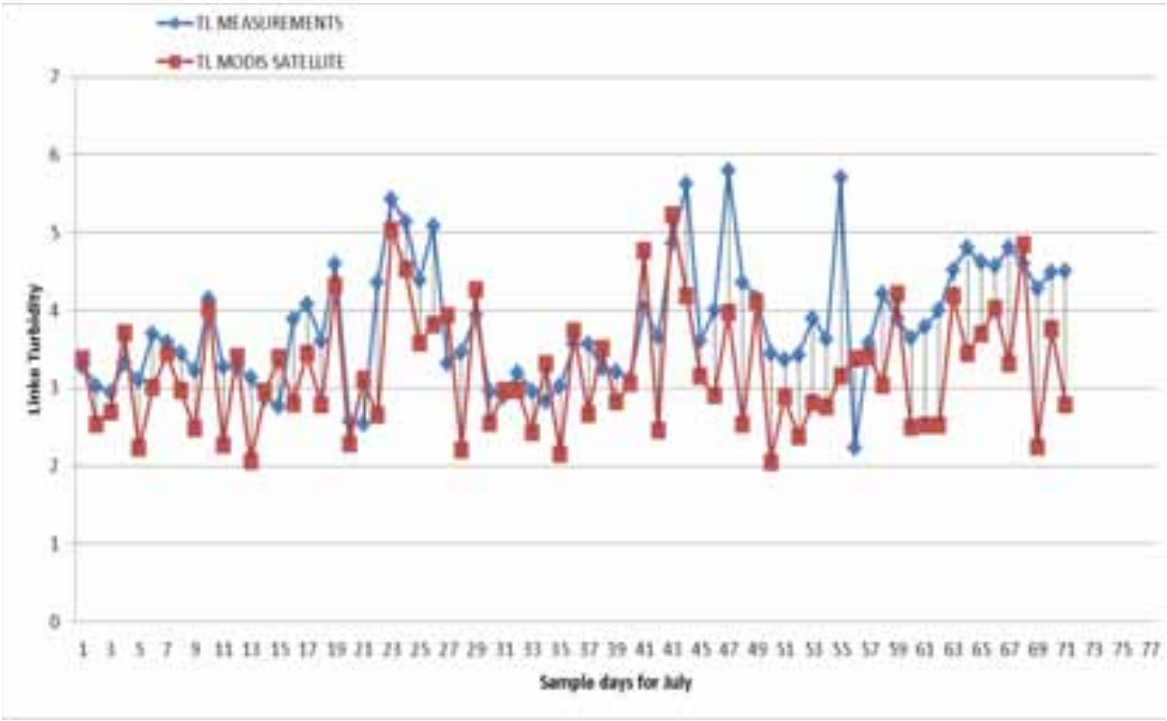

Fig. 8: Daily values of TL estimated from MODIS and measurements with clear sky days in July

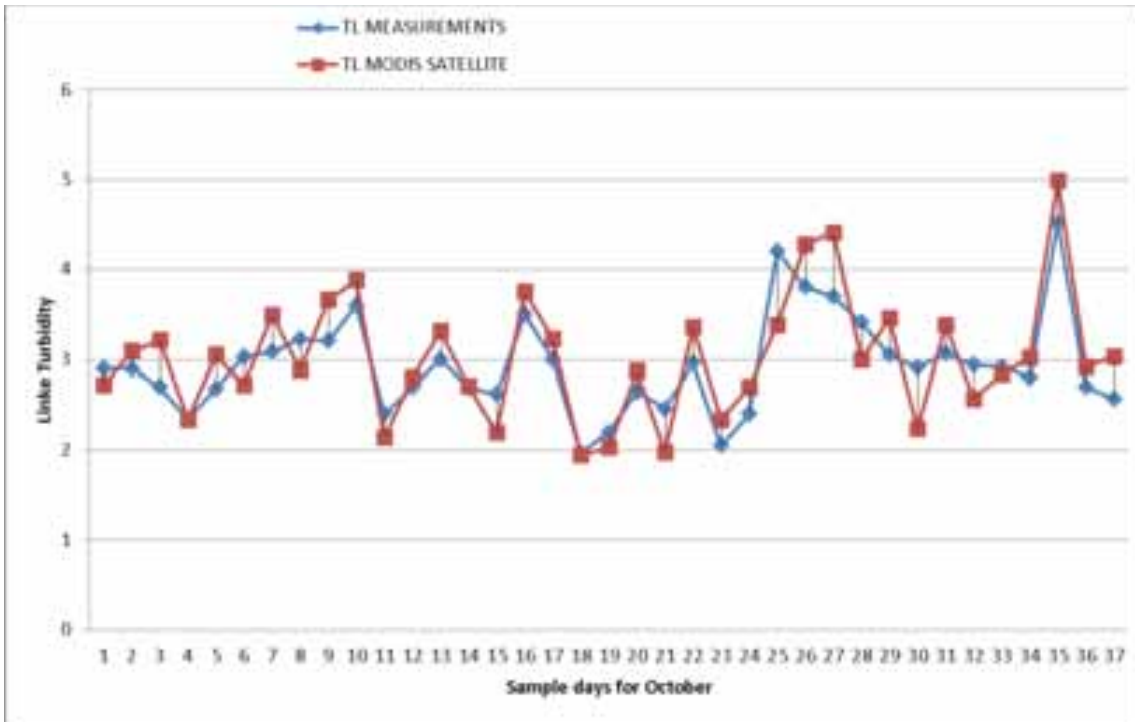

Fig. 9: Daily values of TL estimated from MODIS and measurements with clear sky days in October

As can be seen from last figures, MODIS database represents well turbidity for this location in Spain. The different observed between MODIS and TL derived from DNI measurement are due to deviations of clear sky models and raw spatial resolution of MODIS data.

Figure 10 presents the results of applying the same methodology to a location in south-west China at an altitude of 3000 meters. Monthly TL derived from DNI measurements (purple line) is compared with TL from MISR (red line), MACC (blue line) and Meteotest databases (red line). MODIS values have not been included in this graphic as the database only had values from June to September for this location. Most probably because MODIS have difficulties estimating AOD over high reflectivity land surfaces and in winter months, due to the altitude of the site, most likely this site is entirely covered by snow. It works better over the ocean/sea.

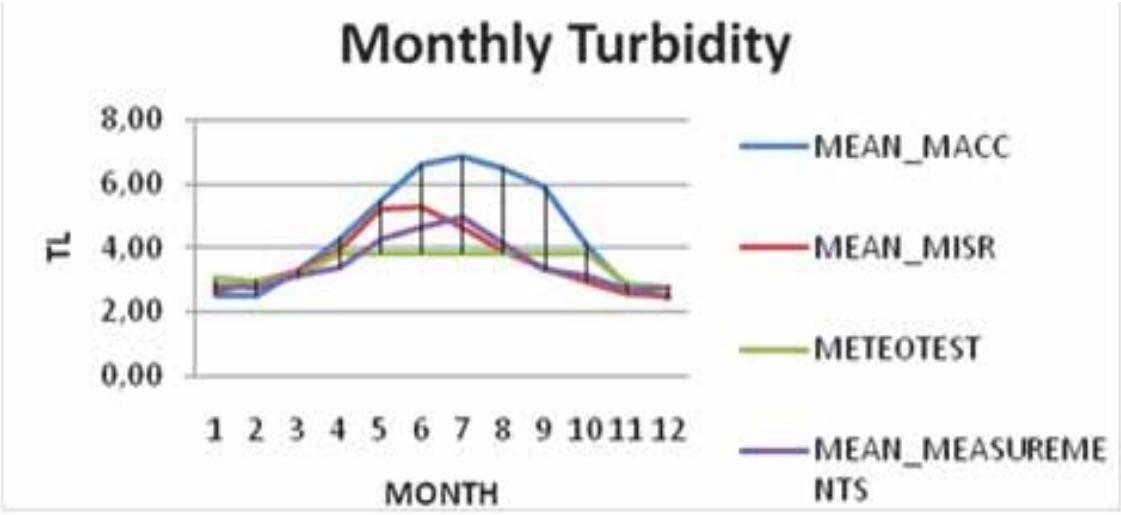

Fig. 10: Mean monthly Linke Turbidity values from DNI measurements, MACC, MISR and Meteotest database for a location in south-west of China

In this location, as can be seen in the last graphic, MACC presents a big overestimation. This resulted in obtaining yearly DNI estimations from satellite images around 30% less than ground measurements. MISR TL (AOD 550nm) estimations are the nearest to TL obtained from DNI measurements. Meteotest values don't follow the monthly dynamic of the turbidity.

The deviations between TL from databases (MODIS, MISR and MACC) and TL derived from DNI measurements can be corrected using different statistical methods (linear/non-linear). This process can be done to improve the calculations of clear sky models before the estimation/processing of solar radiation from satellite images

5. Conclusion

MODIS, MISR and MACC daily AOD at 550nm and daily PW from NCEP were compared against AERONET measurements for 865 locations. All databases show overestimation which is considerably high in the case of MODIS and MACC. This has a direct effect on clear sky models output and solar radiation derived satellite from a satellite which will be underestimated in case raw AOD values from these databases is used. MISR satellite presents better results globally in terms of rMBD and rRMSD, maybe due to its higher spatial resolution. Additionally, the difference in the quality between MISR and MODIS may also be induced by the different algorithms used to estimate the aerosols (not only the resolution). A methodology to estimate TL from DNI measurements was introduced. This can be used to correct turbidity in the databases before using it in models to derive solar radiation from satellite images.

In future works, we will create global uncertainty maps and a fusion daily AOD at 550nm and PW database combining AERONET data and corrected MODIS, MISR and MACC data using kriging techniques.

6. References

Albrecht, B. (1989). Aerosols cloud microphysics and fractional cloudiness. Science, 245, 1227–1230.

Antonanzas-Torres, F., Sanz-Garcia, A., Martínez-de-Pisón, F. J., Antonanzas, J., Perpiñán-Lamigueiro, O., & Polo, J. (2014). Towards downscaling of aerosol gridded dataset for improving solar resource assessment, an application to Spain. Renewable energy, 71(0), 534-544. doi: http://dx.doi.org/10.1016/j.renene.2014.06.010

Eissa, Y., Munawwar, S., Combe, A., Blanc, P., Ghedira, H., Wald, L., . . . Goffe, D. (2015). Validating surface downwelling solar irradiances estimated by the McClear model under cloud-free skies in the United Arab Emirates. Solar Energy, 114, 17-31. doi: http://dx.doi.org/10.1016/j.solener.2015.01.017

Espinar, B., Ramírez, L., Drews, A., Beyer, H. G., Zarzalejo, L. F., Polo, J., & Martín, L. (2009). Analysis of different comparison parameters applied to solar radiation data from satellite and German radiometric stations. Solar Energy, 83(1), 118-125. doi: doi: DOI: 10.1016/j.solener.2008.07.009

Gueymard, C. A. (2008). REST2: High-performance solar radiation model for cloudless-sky irradiance, illuminance, and photosynthetically active radiation Çô Validation with a benchmark dataset. Solar Energy, 82(3), 272-285.

Ineichen, P. (2008). A broadband simplified version of the Solis clear sky model. Solar Energy, 82(8), 758-762.

Ineichen, P., & Perez, R. (2002). A new air mass independent formulation for the Linke turbidity coefficient. Solar Energy, 73(3), 151-157. doi: doi: 10.1016/S0038-092X(02)00045-2

Kasten, F. (1980). A simple parameterization of the pyrheliometric formula for determining the Linke turbidity factor. Meteorologische Rundschau, 33(4), 124-127.

Kasten, F. (1996). The Linke turbidity factor based on improved values of the integral Rayleigh optical thickness. Solar Energy, 56(3), 239-244.

Linke, F. (1922). Transmissions-Koeffizient und Trübungsfaktor. Beitr.Phys.fr.Atmos., 10, 91-103.

Long, C. N., & Dutton, E. G. (2002). BSRN Global Network recommended QC tests, V2.0 BSRN Technical Report.

Pierre, I. (2008). Conversion function between the Linke turbidity and the atmospheric water vapour and aerosol content. Solar Energy, 82(11), 1095-1097. doi: doi: 10.1016/j.solener.2008.04.010

Polo, J., Antonanzas-Torres, F., Vindel, J. M., & Ramirez, L. (2014). The sensitivity of satellite-based methods for deriving solar radiation to a different choice of aerosol input and models. Renewable Energy, 68(0), 785-792. doi: http://dx.doi.org/10.1016/j.renene.2014.03.022

Rigollier, C., Bauer, O., & Wald, L. (2000). On the clear sky model of the ESRA -- European Solar Radiation Atlas -- with respect to the heliosat method. Solar Energy, 68(1), 33-48.

Rigollier, C., & Wald, L. (1999, 5/31/1999). Selecting a clear-sky model to accurately map solar radiation from satellite images.

Ruiz-Arias, J. A., Dudhia, J., Gueymard, C. A., & Pozo-Vázquez, D. (2013). Assessment of the Level-3 MODIS daily aerosol optical depth in the context of surface solar radiation and numerical weather modelling. Atmos. Chem. Phys., 13, 675-698.

Zhong, X., & Kleissl, J. (2015). Clear sky irradiances using REST2 and MODIS. Solar Energy, 116, 144-164. doi: http://dx.doi.org/10.1016/j.solener.2015.03.046

Conference Proceedings

Solar World Congress 2015
Daegu, Korea, 08 – 12 November 2015

Effect of Day-ahead Forecasts on Curtailment Planning of PV Power in Japan

Joao Gari da Silva Fonseca Junior[1], Yusuke Udagawa[1], Tetsuo Saito[1], Takashi Oozeki[2], Kazuhiko Ogimoto[1]

[1] The University of Tokyo, Institute of Industrial Science, Tokyo (Japan)

[2] National Institute of Advanced Industrial Science and Technology, Tsukuba (Japan)

Abstract

The objective of this study is to evaluate the effect that the accuracy of day-ahead forecasts of photovoltaic, PV, power generation has on forecast based curtailment of PV power. Two main regions of Japan were targeted, Kanto, which has a high potential for installations of roof-top PV systems; and Kyushu, which already has high levels of PV power penetration. To provide a qualitative measure of the importance of accurate PV forecasts with different levels of PV power generation, for each region, 2 penetration scenarios were assumed. One year of regional and day-ahead forecasts of PV power were done using numerical weather prediction data, support vector regression, and measured PV power generation data. The PV power generation data comes from to a set of 52 PV systems in Kyushu and to a set of 62 PV systems located in Kanto. The curtailment of PV power was planned one day ahead of time, using the PV power forecasts and a method based on residual loads. The results show that with current day-ahead forecasts it is possible to correctly predict the hours when curtailment will occur most of the time. For example, for Kyushu, curtailment was properly detected 83.1% of the time in a scenario of 8.64 GW of PV installed. For Kanto the values were between 73% and 80.5%. Regarding the effect of the forecast error, we found that it annualy represents near to 35% of the amount curtailed, indicating the importance of improvement of day-ahead forecasts in the curtaiment problem. Finally, the study shows that the relation between the months and hours of curtailment with the period of high forecast errors is crutial to the efficient use of the forecasts, and must be considered before using the forecasts to plan curtailment.

Keywords: *photovoltaic power generation, day-ahead regional forecasts, curtailment planning, support vector regression.*

1. Introduction

In Japan, since the enactment of a new feed-in tariff plan for renewable energy in June of 2012, the number of installations of photovoltaic, PV, power had a 4-fold increase, reaching 25 GW in February of 2015 (METI, 2015a). Such rapid growth is cause of concern, as Japan`s power systems are not prepared to deal with high levels of PV power penetration. In Kyushu region for example, the penetration of PV power has already reached particularly high levels, with 4.5 GW of installed capacity and other 4.1 GW authorized and waiting for grid connection as of December of 2014. Considering that the region has a minimum annual demand of power near to 7 GW, to keep the balance between demand and supply of power throughout the year became a difficult task for Kyushu's power utility. Problems derived from the inadequacy of current power systems to deal with high penetration of PV power are also affecting other regions in Japan, although at different levels.

Measures such as power market liberalization, increase of power transmission capacity between different power balacing areas, demand response systems, and power storage solution, can mitigate such problems.

Selection and/or peer review under responsibility of Scientific Committee
doi:10.18086/swc.2015.07.17 Available at http://proceedings.ises.org

Nevertheless, their implementation requires time and significant resources. Thus, while these measures are being considered and implemented, a short-term solution to deal with the current situation is necessary. In this regard, curtailment of PV power is seen a key measure to guarantee the stable operation of power systems without restricting the growth of PV systems installations.

Japanese power utilities will start to integrate renewable energy curtailment planning in their power systems and grid operation scheduling from 2016. The curtailment will be based on regional forecasts of PV power done at different forecast horizons, and with different levels of accuracy. As the forecast have variable accuracy throughout the year, it is crutial to know the impact that such variable accuracy will have on curtailment of PV power.

Although there is a variety of studies on methods to forecast power generation of renewable energy systems such as (Lorenz et al., 2012), (Diagne et al., 2012), (Paulescu et al., 2012), (Lauret et al., 2015), studies on their application to or of their impact on curtailment of PV power are scarce. On the other hand, available studies about curtailment, usually are focused on estimates of the total amount curtailed per country (Lew et al., 2013), local practices regarding curtailment (Rogers et al., 2010), or estimates of required curtailment given scenarios of renewable energy penetration (Garrigle et al., 2013), for example.

In this initial study we evaluate the impact of day-ahead regional forecasts of PV power generation on its curtailment plan. The study focus on two regions in Japan, the Kyushu region, which already has high levels of PV power penetration, and the Kanto region, which has the highest potential for roof-top PV installations in the country. For each region, data of 2010 was used; but the levels of PV power penetration were based on values of 2014. The forecasts of PV power were done one day ahead of time, in regional scale, and regarding current penetration of PV power in each prefecture within the regions. For each target day and PV power scenario, we compare curtailment based on regional PV power forecasts with the actual curtailment that would be necessary to avoid excess of PV power generation, and analyze the effects that the forecast errors will have on the curtailment plan.

2. Methods and Data

To plan curtailment for a day and region, first the corresponding regional PV power generation was forecasted. This section contains the description of the forecast method, curtailment method, data used and PV power penetration scenarios studied.

2.1. Forecast Method

To forecast regional PV power generation we used a method that employed support vector regression and numerical weather prediction, NWP, data. The support vector regression used was the ν support vector regression (Schölkopf et al., 1998), implemented on the LibSVM library (Chang et al., 2001). The NWP data included cloudiness, temperature and relative humidity; they came from the meso-scale model (5 km by 5 km of spatial resolution) of the Japan Meteorological Agency (Saito et al., 2006), released at 12h of the day preceding the target day. The forecasts were done hourly from 6h to 19h of each target day. This method was developed in previous studies, where further details are available (Fonseca et al., 2015).

The regional forecasts were calculated from sets of point forecasts for single PV systems installed in different locations within each region. Given the location of a single PV system, and for a given hour, the corresponding predictions of cloudiness, temperature and relative humidity, as well as the calculated extraterrestrial insolation are entered in a trained support vector regression algorithm, which then returns the corresponding amount of PV power generation. For each day of forecasts, we trained the algorithm before using it. The training used input data and PV power generation data of the 60 days preceding the target day. Thus, one forecast model was set for each day of forecasts. Once the point forecasts were done, the regional yield was calculated using a upscaling procedure described in Eq. 1 and Eq. 2.

$$|P_{pf}| = \frac{1}{P_{rt,pf}} \sum_{i=1}^{n} P_i \quad (1)$$

$$P_{reg} = P_{rt,reg} * \sum_{pf=1}^{m} |P_{pf}| * \alpha_{pf} \quad (2)$$

As Japan is geopolitically divided in prefectures, in Eq. 1 $|P_{pf}|$ is the normalized PV power generation per prefecture inside the target region. The PV power generation of each system i inside a prefecture is P_i (in kW), and $P_{rt,\mathrm{pf}}$ (in kW) is the total rated power of the PV systems inside the same prefecture. In Eq. 2, P_{ref} (in kW) is the regional yield, $P_{rt,pf}$ (in kW) is the regional installed capacity scenario, and α_{pf} is the ratio between the PV rated power in each prefecture by the total regional rated power.

2.2. Curtailment Method

To calculate the total amount of PV power to be curtailed in a target day we used a methodology based on the base and residual loads. The base load was regarded as the minimum amount of power demand that has to be supplied by power systems using conventional and non-renewable energy. This amount was assumed to be the minimal regional power demand value in a year. Any power demand higher than the base load is regarded as residual load. The residual load can be supplied by conventional power system or by PV power, if available. Nevertheless, PV power generation cannot exceed the residual load: if it does, curtailment happens. It should be noted that this method to identify when curtailment occurs does not consider wind power generation, optimized unit commitment planning, dispatch to other regions, or other ways to control excess of PV power. In spite of that, this method provide good reference values and it is a simplified version of the method suggested to power utilities by the Ministry of Economy Trade and Industry of Japan, when calculating acceptable levels of renewable energy penetration and estimating amounts of PV power to be curtailed (METI, 2015b), [13]. An example of forecast based curtailment plan and the required one, using this methodology, is in Fig. 1. The example shows the load curve for a few days of May of 2010, Kanto region, and a PV power penetration scenario of 14 GW.

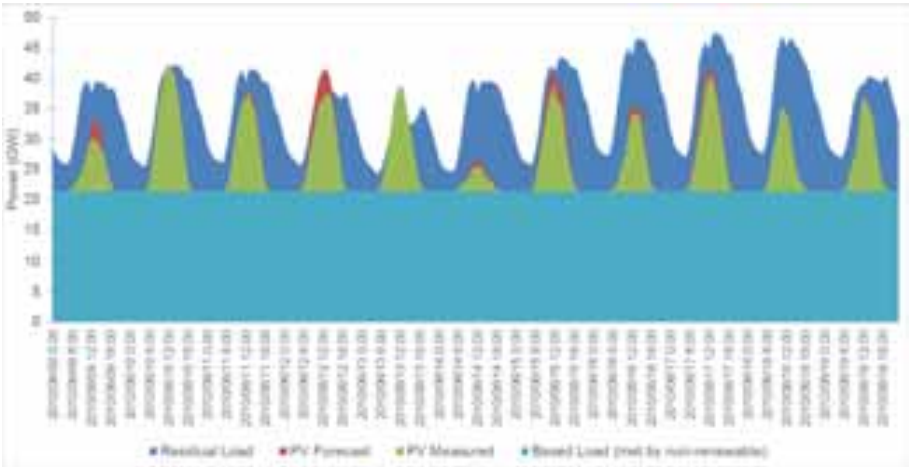

Fig. 1:Examples of planned versus required curtailment of PV power with the curtailment method used.

Following the proposed curtailment plan, on 2010/06/09, 2010/06/10, and 2010/06/17 in Fig. 1, there are forecast errors, but as the total PV power generated and forecasted are lower than the residual demand no curtailment is applied. On the other hand, on 2010/06/12, the forecast of PV power indicated that no curtailment would be required but in fact, as the PV power generated was higher than what was forecasted, curtailment was in reality required.

2.3. Target Regions' Data

To calculate the regional forecasts of power from single PV systems, data from systems installed in Kanto and Kyushu areas were used. The sets of PV systems and their power generation data are part of the Field Test Project sponsored by the New Energy and Industrial Technology Development Organization, NEDO. For Kanto region the set included 62 PV systems and for Kyushu, 52 PV systems. Both sets of PV systems are fairly dispersed within the regions so that they provide a good estimate of the regional yield normalized by the corresponding PV rated power. The sets included only PV systems for which there were complete power generation data of the period studied. In spite of that, due to the availability of power demand data, for Kyushu only 9 months of curtailment plan was done, from April 2010 to December 2010.

In addition to the PV power and power demand data for each region, current PV power penetration scenarios by region and prefecture were necessary to perform the analysis. Kyushu region is already facing a high penetration scenario, with 4.5 GW of PV power installed and another 4.1 waiting for grid connection as of December of 2014 (METI, 2015b). Therefore, for Kyushu both values were used in the scenarios studied. To calculate the equivalent penetration of PV power in 2010, both the PV power penetration values were divided by the peak demand of power in December of 2014. These ratios then were applied to the peak demand of power in Kyushu in December of 2010. To compare Kanto and Kyushu, the equivalent PV power penetration scenario for 2010 power demand in Kanto was calculated using the same logic. Thus PV power penetration ratios of Kyushu were applied to the power demand of Kanto in 2010. The PV rated power for both regions in 2 scenarios are presented in Tab. 1.

Tab. 1: PV rated power for Kanto and Kyushu and two penetration scenarios in 2010.

	Kanto Region	Kyushu Region
Scenario 1	14.93 GW	4.55 GW
Scenario 2	28.44 GW	8.64 GW

Finally, to calculate the regional PV power measured and forecasted in each scenario it is necessary information about the ratio between the PV rated power of each prefecture and the total regional rated power (α in Eq. 2). These ratios are also based on the real PV power installed in Kanto and Kyushu as of December of 2014. The same ratios were used for the scenarios of 2010; their values are in Tab. 2.

Tab. 2: Prefecture's PV rated power by the regional one (Kanto and Kyushu, December of 2014 [1]).

Kanto	Gumma	Tokyo	Chiba	Tochigi	Saitama	Ibaraki	Kanagawa
% of the regional value	0.1380	0.0782	0.1895	0.1467	0.1573	0.198	0.0923
Kyushu*	Saga	Oita	Miyasaki	Kumamoto	Fukuoka	Nagasaki	Kagoshima
	0.078	0.1253	0.1228	0.1482	0.2542	0.093	0.1785

*Okinawa although it is geopolitically part of Kyushu, it is out of the power balacing area of Kyushu power utility.

3. Error and Evaluation Parameters

The effect of the accuracy of the regional forecasts of PV power were evaluated in two ways: from the point of view of the error of the amount curtailed, and from the point of view of the detection error of the hours when curtailment should be applied. The performance of the forecasts and their impact on curtailment from the first point of view is evaluated using the annual mean bias error, MBE, and the mean absolute error, MAE. Both errors of the curtailment planning were calculated using the forecasts of PV power and the required curtailment. The MAE and MBE are calculated in GW as showed in Eq. 3 and Eq. 4.

$$MAE = \frac{1}{n}\sum_{i=1}^{n}\left|Cr_{pln} - Cr_{req}\right|_i \quad (3)$$

$$MBE = \frac{1}{n}\sum_{i=1}^{n} Cr_{pln} - Cr_{req\,i} \quad (3)$$

In Eq. 3 and Eq. 4 Cr_{pln} , for each target hour *i*, is the amount of curtailment of PV power planned, in GW, and Cr_{req} is the amount of curtailment that was actually required, in GW. Both errors were calculated with all the *n* hours of the target periods excluding night periods when forecasts were not made.

To analyze the impact of the forecasts' accuracy on curtailment plan from the point of view of required curtailment detection, a confusion matrix or contingency table as showed in Tab. 3 was used. From the confusion matrix several performance parameters can be inferred. However, in this study the main parameter used is the precision (also showed in Tab. 3) of the curtailment plan based on the forecasts: it shows in how many of all planned curtailment hours, curtailment was actually required. The precision in this case provides

information of how reliable the detection of required curtailment hours is when day-ahead regional forecasts of PV power are used. The calculation of the precision variable was done using data of all target period excluding night hours (the period outside the interval from 5 h to 19 h).

Tab. 3: Confusion matrix used to evaluate the PV power forecast based curtailment plan in Kyushu and Kanto.

		Required Curtailment		
		YES	NO	
Planned Curtailment	YES	A	B	Precision = A/(A+B)
	NO	C	D	

4. Results

As the analyses included 1 year of data of Kanto and 9 months of Kyushu, first, in subsection 4.1 we present the complete results for Kanto. In the subsection 4.2 the results for Kyushu are presented and compared with the results of the same period in Kanto.

4.1. Forecast based Curtailment for Kanto Area

For Kanto, with a minimum annual power demand of 21.4 GW, two PV power penetration scenarios were studied, 14.93 GW and 28.44 GW. For each penetration scenario day-ahead regional forecasts of PV power were made and used to decide when curtailment should be applied. Figures 2(A) and 2(B) contain the matrix confusion resulting from the comparison between forecast based and required curtailment for both scenarios.

(A) 14.93 of PV Power

Curtailment		Required: yes	Required: no	Precision
Forecast based	yes	58	17	77.3%
	no	13	5840	

(B) 28.44 of PV Power

B Curtailment		Required: yes	Required: no	Precision
Forecast based	yes	369	78	82.6%
	no	66	5840	

Fig. 2: Confusion matrix for the curtailment of PV power based on day-ahead regional forecasts for Kanto in two scenarios of PV power penetration 14.93 GW (A) and 28.44 GW (B) (values in hours).

The results in Fig. 2 show that in Kanto with a scenario of 14.93 GW of PV power, during one year, only 71 hours curtailment of PV are required. Of those hours the forecast based curtailment plan was able to detect 58 hours, and issued false alarms in 17 hours, yielding a precision of 77.3%. For a scenario of 28.44 GW, curtailment PV power becomes more common, being required on 435 hours. In spite of the increase of the hours in which PV must be curtailed, and therefore increasing the probability that the curtailment planning will include more forecast errors, the precision of curtailment plan based on forecasts of PV did not decrease. In fact, the precision was better reaching 82.6%.

This behavior is explained by the fact that in a scenario where PV power curtailment is seldom such as the one of 14.93 GW of PV rated power, throughout the year curtailment will happen mostly in peak hours of PV power generation (11h to 13h for example). These are also the hours where is more likely that large forecast error occur simply because of the magnitude of PV power generated. As high forecast errors imply in misdetection of required curtailment hours, occurrence of required curtailment exactly in the hours when large forecast errors can occur will result in a low detection of required curtailment. Once PV rated power is increased and curtailment becomes frequent in off-peak hours, the detection of required curtailment is improved because these hours will contain in average lower forecast errors. Increasing even further the PV rated power will cause not only the required curtailment related hours to increase but also the amount curtailed. In this situation, the detection of required curtailment with forecast based plan should decrease again, as even small forecast errors will become cause for misdetection of required curtailment.

The results in Fig. 3(A) and 3(B) show the performance of the forecast based curtailment regarding the error

in the amount curtailed. The errors were calculated using the required curtailment (based on a perfect forecast) as reference and, as in the case of Fig. 2, just for the hours within 5h and 19h.

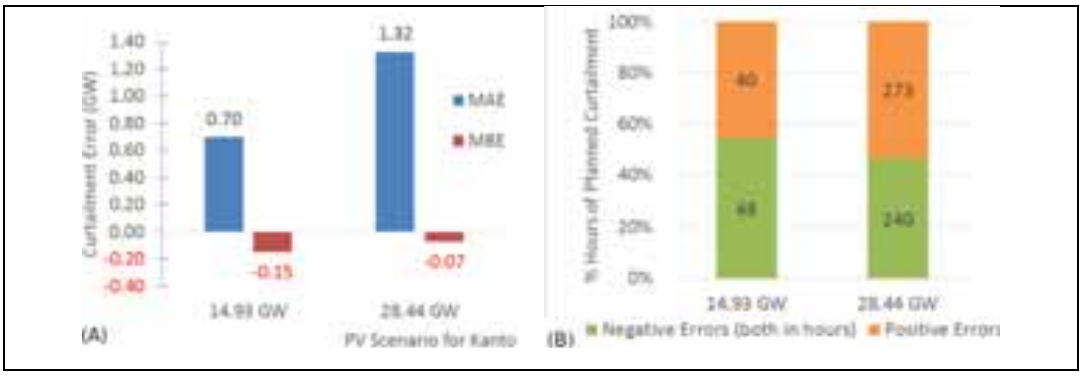

Fig. 3: Curtailment error with day-ahead regional forecasts for Kanto in two scenarios of PV power penetration (A), and frequency of curtailment errors according to their sign (B).

Both Fig. 3(A) and 3(B) show that increasing the number of hours when PV power is curtailed had a strong effect on the behavior of the error of the curtailment plan. When curtailment happens only in a few hours, it will happen mostly in peak hours. Forecast errors on these hours will be mainly related with underestimations of the real PV power generated. Thus, such errors will cause required curtailment not to be detected, or they will underestimate the amount of required curtailment. Once PV power penetration increases hours of required curtailment will be dispersed and both underestimations and overestimations of the real PV power generation will affect the curtailment plan. The general effect will be a balanced distribution of curtailment errors related with the accuracy of PV forecasts. This behavior is clear in the MBE of Fig. 3(A) and on the frequency of errors in Fig. 3(B).

Another issue that must be noted is regarding the importance of sign of the curtailment errors. If the error is positive more PV power was curtailed than necessary. The direct effect of this kind error is economic as PV systems owners may loose income of the selling of the amount curtailment in the case it is not compensated. Contrasting with that, if the curtailment error is negative, an insufficient amount of PV was curtailed. The result is excess of PV power on the grid, which may cause balancing and operation problems in the corresponding balancing area. Tab. 4 shows the mean positive and negative errors of the forecast based curtailment. In the same Tab. 4 the average amount of required curtailment in year is showed to provide a measure of the magnitude of the errors in relation to the amount usually curtailed.

Tab. 4:Mean positive and negative curtailment errors and average required curtailment (per hour of curtailment) in Kanto, 2010.

PV rated Power	Mean Positive Curtailment Error (GW)	Mean Negative Curtailment Error (GW)	Annual Average Curtailment Required (GW)
14.93 GW	0.604	-0.772	1.76
28.44 GW	1.17	-1.49	3.96

The results in Tab. 4, Fig. 2 and Fig. 3 show that for Kanto, 14.93 GW was a relatively low penetration scenario. Moreover, this scenario yielded more and higher negative curtailment errors than positive ones. Increasing the the PV rate power to 28.44 GW partially reversed such trend.

4.2. Forecast based Curtailment for Kyushu Area

For Kyushu area, the 2 PV power penetration scenarios were 4.55 GW and 8.64 GW. The first scenario is already realized and the second one should be reached in near future as another 4.1 GW are waiting for grid connection. Considering that Kyushu's minimum annual demand is 7.1 GW, both scenarios are of high penetration of PV power. In these cases, the required number of curtailment hours with the forecast based curtailment plan, for 9 months of data, was 207 hours and 644 hours. Both numbers are considerably higher than the corresponding values for Kanto region. The precision, calculated as showed in Tab 3, of the forecast

based curtailment plan compared with Kanto, and for the same period, is in Fig. 4.

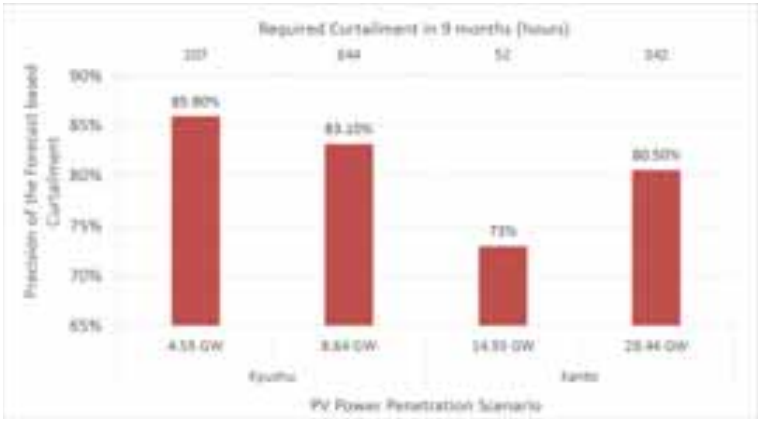

Fig. 4: Precision of required curtailment detection with a forecast based curtailment for Kyushu and Kanto in two PV power penetration scenarios.

Due to difference of power demand in both regions, Kyushu is clearly more sensitive to penetration of PV power than Kanto. In Fig. 4, the required curtailment hours in Kyushu for a PV rated power of 4.55 GW reached 207 hours. Doubling the PV rated power increased 3 times the required curtailment. For Kanto the situation was different, as even with 28.44 GW required curtailment hours were just slightly higher than half the number obtained with the highest PV power penetration scenario in Kyushu. This variation in the numbers of required curtailment hours affected signficantly the precision of the forecast based curtailment plan. This variation of the precision in detecting required curtailment hour is related with the PV forecast error magnitude and the period of the year when curtailment is required. To understand these relations, Fig. 5(A) and Fig. 5(B) show the normalized error of the PV power forecast throughout the year and the months and hours where curtailment was required.

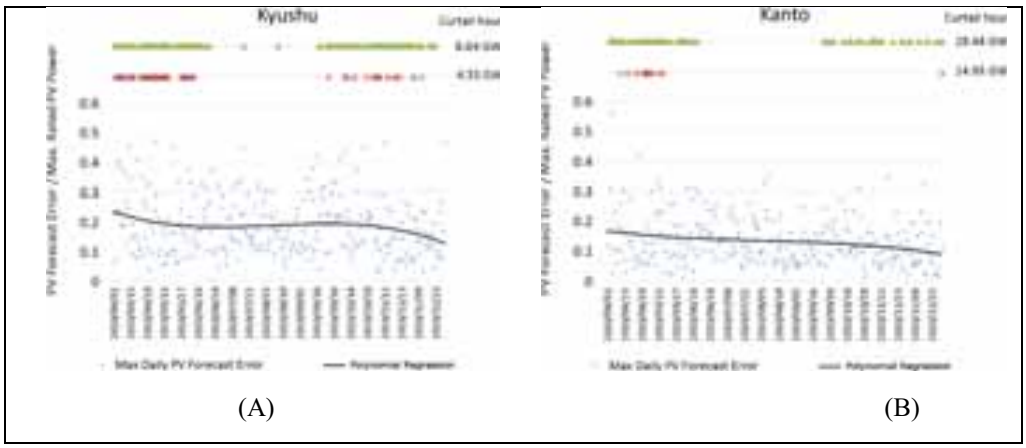

Fig. 5:Occurrence of required curtailment and maximum daily value of the PV forecast errors throughout the year for Kyushu (A) and Kanto (B).

Starting with Kyushu, the results show that even with 4.55 GW of PV power, curtailment is happening in most of the 9 months studied with the exception of the months of July to August, when it is summer in Japan and the power demand is high enough to use all PV power generation. Increasing further the PV rated power to 8.64 GW, causes further curtailment and some occurrences of it now in July and August. Looking at the behavior of forecast error of PV power, curtailment is happening in situations where the forecast error is high and when is low in an uniform fashion, regardless the scenario. Thus, the precision in detecting required curtailment presented low variation.

Focusing now in Kanto, with the lowest PV power scenario, curtailment is seldom and it is happening in April to May, where there is occurrence of high PV forecast errors. Increasing the requirement of curtailment to other months and hours, yield the use of forecasts with lower errors improving the precision of the forecast

based curtailment from 73% to 80% as showed in Fig. 4.

The results in Fig. 6 show the variation of the effect that the forecast error of PV power has on curtailment planned using these forecasts.

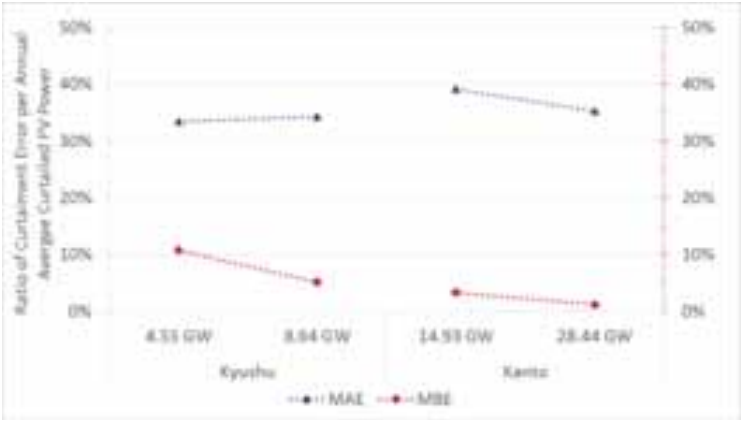

Fig. 6: Effect of the forecast error of day-ahead regional PV forecasts on curtailment planning according to the region and PV penetration scenario.

In this case a similar trend can be noted, increasing the amount of hour curtailed in Kanto caused the use of more forecasts with low errors. This yields lower errors on the execution of curtailment. For Kyushu, there was a slight increase of MAE, but the MBE was significantly reduced with the increase of PV power installed similarly to what happened in Kanto.

5. Conclusions

The objective of this study was to verify the impact that the accuracy of day-ahead regional forecasts of PV power has on a curtailment plan based on such forecasts. Two regions of Japan were analyzed, Kyushu where high penetration of PV power is already a reality, and Kanto, which has a high potential for roof-top installations of PV system. The impact of the accuracy of the forecasts was evaluated from the point of view of properly detecting the hours of required curtailment, and from the point of view of the error in the amount curtailed with a forecasts based curtailment plan.

The results showed that when required curtailment hours are few, the precision in detecting them was near to 70%. Increasing the number of hours of curtailment yielded the use of forecasts with a variety of errors, improving the precision parameter to near 80%. These results mean that in at least 70% of the time, a forecast based curtailment plan correctly determined the hours that curtailment is necessary. This means that, in the worst case, 30% of the curtailment hours will have to be located with intra-day forecasts or with improvements of day-ahead forecasts.

Regarding the effect of the forecast accuracy on the amount of PV power curtailed, the results show that annualy the curtailment error represented near to 35% of the average amount of PV power curtailed. The effect was strong as excessive curtailment yield financial losses to PV systems owners. However, considering the possibility of intra-day corrections on the curtailment plan, balacing area interconnections, storage solution and an optimized unit commitement plan, the effect of the forecast error can be significantly mitigated.

Finally, comparing both regions, it is clear that Kyushu, due to its low power demand, is already facing problems with high PV penetration. Even with 4.55 GW, curtailment was required in 207 hours of 9 months. In Kanto, the high demand of power (minimum annual value of 21 GW) yields a more confortable situation, as even with 14.93 GW of PV rated power only 70 hours in a year required curtailment. In spite of that, the required curtailment in this scenario happened exactly in months where high errors of PV forecasts occur, decreasing the forecasts usefulness. The obtention of these values provide important information about the efficacy of the forecast of PV power and about how they should be used. Moreover, they can be used to guide the use of forecasts and improvements of their accuracies. A limitation of this initial study is the use of base

load and residual demand related assumptions to characterize when cutailment happens. In following studies, these simplifications will be removed, and the analysis of the forecast error on curtailment of PV power will be further advanced by considering optimal unit commitement planning.

Acknowledgements

This work was supported by the New Energy and Industrial Development Organization, Japan, in the project Research and Development of PV Performance and Reliability Characterization Technologies.

References

[1] METI, なっとく！再生可能エネルギー　各種データの公開.. [Online in Japanese], Available: http://www.fit.go.jp/statistics/public_sp.html, [Accessed: 26-May-2015].

[2] Lorenz, E., Heinemann, D., and Kurz, C., 2012, Local and regional photovoltaic power prediction for large scale grid integration: Assessment of a new algorithm for snow detection, Progress in Photovoltaics Research and Applications, 20, 6, 760–769.

[3] Diagne, H. M., David, M., Lauret, P., and Boland, J., 2012, Solar Irradiation Forecasting: State-of-the-Art and Proposition for Future Developments for Small-Scale Insular Grids, in Proceedings of the World Renewable Energy Forum, Denver, USA.

[4] Paulescu, M., Paulescu, E., Gravila, P., and Badescu, V., 2012, Weather Modeling and Forecasting of PV Systems Operation, Springer.

[5] Lauret, P., Voyant, C., Soubdhan, T., David, M., and Poggi, P., 2015, A benchmarking of machine learning techniques for solar radiation forecasting in an insular context, Solar Energy, 112, 446–457.

[6] Lew, D., Bird, L., Milligan, M., Speer, B., Wang, X., Carlini, E. M., Estanqueiro, A., Flynn, D., Gomez-Lazaro, E., and Menemenlis, N., 2013. Wind and solar curtailment, in International Workshop on Large-Scale Integration of Wind Power Into Power Systems, 1–9.

[7] Rogers, J., Fink, S., and Porter, K., 2010, Examples of wind energy curtailment practices, NREL Subcontract Rep. NRELSR-550, 48737.

[8] Mc Garrigle, E. V., Deane, J. P., and Leahy, P. G., 2013, How much wind energy will be curtailed on the 2020 Irish power system?, Renew. Energy, 55, 544–553.

[9] Schölkopf, B., Bartlett, P., Smola, A., and Williamson, R., 1998, Support Vector Regression with Automatic Accuracy Control, Proc. ICANN98 Perspect. Neural Comput., pp. 111–116.

[10] Chang, C.-C., and Lin, C.-J., 2001, LIBSVM : a library for support vector machines.

[11] Saito, K., Fujita, T., Yamada, Y., Ishida, J., Kumagai, Y., Aranami, K., Ohmori, S., Nagasawa, R., Kumagai, S., Muroi, C., Kato, T., Eito, H., and Yamazaki, Y., 2006, The Operational JMA Nonhydrostatic Mesoscale Model, Monthly Weather Review, 134, 4, 1266–1298.

[12] Fonseca, Jr, J. G. S., Oozeki, T., Ohtake, H., Takashima, T., and Ogimoto, K., 2015, Regional forecasts of photovoltaic power generation according to different data availability scenarios: a study of four methods, Progress in Photovoltaics Research and Applications, 23, 10, 1203–1218.

[13] METI, 総合資源エネルギー調査会 省エネルギー・新エネルギー分科会 新エネルギー小委員会 系統ワーキンググループ（第 3 回） - 配布資料（METI/経済産業省）, [Online in Japanese], Available: http://www.meti.go.jp/committee/sougouenergy/shoene_shinene/shin_ene/keitou_wg/003_haifu.html, [Accessed: 28-Sep-2015].

Conference Proceedings

Solar World Congress 2015
Daegu, Korea, 08 – 12 November 2015

Estimation of greenhouse gas emission factors for natural gas in Bangladesh

H M Enamul Haque and Himangshu Ranjan Ghosh

Institute of Energy, Dhaka University, Dhaka-1000, Bangladesh

Abstract

Anthropogenic greenhouse gas emissions from fossil fuel burnings are strongly affected by fuel properties, operation procedure, emission control etc. Production of indigenous natural gas is around 23 billion metric tons/year from 120 wells of 19 fields in Bangladesh. At the production sites mole percent of methane in the natural gas varies from 93.50 to 98.00. Gas chromatography study on a sample from a natural gas based electric power station at Ashuganj shows that the fuel have lower heating value of 34.9389MJ/m^3, 96.60 mole percent CH_4, 0.54 mole percent N_2, 0.10 mole percent CO_2 and the rest other hydrocarbons. The average transmission and distribution losses of natural gas over the country is 1.77% and the estimated emission factors for main greenhouse gases are 55.52 gCO_2/MJ, 0.35 gCH_4/MJ and 0.17 gN_2O/MJ. Considering global warming potentials of Intergovernmental Panel on Climate Change 2007 report the equivalent CO2 emission factor for natural gas in Bangladesh is 115.04 gCO_2e/MJ.

Keywords: *Fossil Fuel, Greenhouse gases(GHG), GHG emission factors*

1. Introduction

Energy is a basic requirement for the existence and development of human life. The major percentage of the commercial demand of energy is generally supplied from the fossil fuels (coal, oil and natural gas). The demand for energy is growing at an alarming rate year after year.

Every year Greenhouse gases add to the carbon already present in atmosphere .The power sector is major source of carbon dioxide (CO_2) emission and accounts for about 36 % of the total CO2 emission in the world, 45 % in Asia and 40 % in Bangladesh. The power sector CO_2 emission has been increased at an average annual rate of 8.5 % from 1990 to 2004 in Asia as a whole (Shrestha et al. 2009). Because carbon dioxide is a good absorber of heat radiation coming from the Earth's surface, increased carbon dioxide acts like a blanket over the surface, keeping it warmer than it would otherwise be. With the increased temperature the amount of water vapour in the atmosphere also increases, providing more blanketing and causing it to be even warmer (Houghton, 2009). Due to heat trapping our earth is warming. Earth's average temperature has risen by 1.4°F over the past century, and is projected to rise another 2 to 11.5°F over the next hundred years (USEP online, 2015). The amount of CO_2 emission depends on carbon content of fossil fuel.

CO_2 emissions can be estimated fairly accurately based on the total amount of fuels combusted and the averaged carbon content of the fuels. However, emission factors for methane and nitrous oxide depend on the combustion technology and operating conditions and vary significantly, both between individual combustion installations and over time. Due to this variability, use of averaged emission factors for these gases, that must account for a large variability in technological conditions, will introduce relatively large uncertainties.

2. Methodology

The The IPCC Guidelines (2006) for estimating emissions from fossil fuel combustion estimate carbon emissions in terms of the species which are emitted. During the combustion process, most carbon is immediately emitted as CO_2. However, some carbon is released as carbon monoxide (CO), methane (CH_4) or

doi:10.18086/swc.2015.07.18 Available at http://proceedings.ises.org

non-methane volatile organic compounds (NMVOCs). Most of the carbon emitted as these non-CO_2 species eventually oxidizes to CO_2 in the atmosphere. The Reference Approach of IPCC 2006 can be used as an independent check of the sectoral approach and to produce a first-order estimate of national greenhouse gas emissions.

The Greenhouse Gas Emissions from stationary combustion can be found from the following equation 1

$$\text{Emission}_{GHG,fuel} = \text{Fuel Consumption}_{fuel} \times \text{Emission Factor}_{GHG,fuel} \quad \text{(equ. 1)}$$

Where:

$\text{Emissions}_{GHG,fuel}$ = emissions of a given GHG by type of fuel (kg GHG)

$\text{Fuel Consumption}_{fuel}$ = amount of fuel combusted (TJ)

To calculate the total emissions by gas from the source category, the emissions as calculated in Equation 1 are summed over all fuels:

$$\text{Emission}_{GHG,fuel} = \sum_{fuels} \text{Emissions}_{GHG,fuel} \quad \text{(equ. 2)}$$

The estimation of GHG emission factor from a fossil fuel burning is determined stepwise by estimating the consumption of fuels by fuel/product type, converting the fuel data to a common energy unit (TJ), selecting the carbon emission factors for each fuel/product type to estimate the total carbon content of the fuels, estimating the amount of carbon stores in products for long time, accounting for carbon not oxidized during combustion, converting emissions of carbon to full molecular weight of CO_2 and finally dividing the total estimated CO_2 by the total consumed fossil fuel.

3. Fuel sample collection and testing

Bangladesh produces gas from several different fields, and much of it is merged at the Ashuganj gas metering station (AGMS) before distribution via major trunk lines, some power plant customers, such as those of Jalalabad GasTransmission & Distribution System Ltd., receive gas from upstream of AGMS. Meanwhile,some gas fields feed their supply directly into the gas transmission grid downstream of AGMS. For this reason, the chemical composition, calorific value or other properties available from AGMS,would be more or less precisely for all natural gas combusted in Bangladesh.

On April 29, 2014,one sample of natural gas from Bakhrabad Gas Distribution Company Limited (BGDCL) at Ashuganj Power Station Company Limited (APSCL) has been analyzed at a gas cromotography system at Petroleum and MineralResources Engineering (PMRE) laboratory of the Bangladesh University of Engineering and Technology. The report showed that the sample had a Lower Heating Value (LHV) of 34.9389 MJ/m3Higher Heating Value (HHV) of 38.7536 MJ/m3(with a ideal gas density of 0.0442lb/ft3) as shown in Table 1.

Tab. 1: Chemical composition of Natural gas from BGDCL at APSCL

Gas	Composition	% Volume
Nitrogen	N_2	0.536
Carbon di-oxide	CO_2	0.090
Methane	CH_4	96.603
Ethane	C_2H_6	1.904
Propane	C_3H_8	0.378
i-Butane	C_4H_{10}	0.121
n-Butane	C_4H_{10}	0.085
i-Pentane	C_5H_{12}	0.053
n-Pentane	C_5H_{12}	0.037
Hexane	C_6H_{14}	0.095

Heptane	C_7H_{16}	0.072
Octane	C_8H_{18}	0.027
Nonane	C_9H_{20}	-
Decane	$C_{10}H_{22}$	-
Total		100.00

4. Estimation of GHG emission factor

Carbon dioxide (CO_2) emissions from natural gas combustion result from the release of carbon during combustion. The amount of carbon dioxide (CO_2) emissions are calculatedthrough the combustion Equation 3 of alkanes $C_nH_{(2n+2)}$.

$$C_nH_{(2n+2)} + \frac{3n+1}{2}(O_2 + 3.76\ N_2) \rightarrow n\ CO_2 + (n+1)\ H_2O + \frac{3n+1}{2}\ 3.76\ N_2 \qquad \text{(equ. 3)}$$

During combustion process, most carbon is emitted as CO_2immediately. CO_2emission factors for fossil fuel combustion will depend upon the carbon content of the fuel that is inherently chemical property and does not depend upon the combustion process or conditions. In case of perfect and complete combustion, nitrogen can be neglected as there is no NOx creation and no carbon monoxide as well. The GHG is computed in Table 2.

Tab. 2: GHG emission during combustion

Gas	Composition	Amount (g in one mole)	C content (in g)	H content (in g)	N content (in g)	O content (in g)	g CO_2	g N_2O
Nitrogen	N_2	0.090	-	-	0.090	-	-	0.141
Carbon di-oxide	CO_2	0.015	0.004	-	-	0.011	0.015	
Methane	CH_4	16.218	12.164	4.055	-	-	44.600	
Ethane	C_2H_6	0.320	0.256	0.064	-	-	0.938	
Propane	C_3H_8	0.063	0.052	0.012	-	-	0.190	
i-Butane	C_4H_{10}	0.020	0.017	0.004	-	-	0.062	
n-Butane	C_4H_{10}	0.014	0.012	0.002	-	-	0.043	
i-Pentane	C_5H_{12}	0.009	0.007	0.001	-	-	0.027	
n-Pentane	C_5H_{12}	0.006	0.005	0.001	-	-	0.019	
Hexane	C_6H_{14}	0.016	0.013	0.003	-	-	0.049	
Heptane	C_7H_{16}	0.012	0.010	0.009	-	-	0.037	
Octane	C_8H_{18}	0.005	0.004	0.001	-	-	0.014	
Nonane	C_9H_{20}	-	-	-	-	-	-	
Decane	$C_{10}H_{22}$	-	-	-	-	-	-	
		16.79	12.544	4.151	0.090	0.011	45.995	0.141

For each greenhouse gas, a Global Warming Potential (GWP) has been calculated to reflect how long it remains in the atmosphere, on average, and how strongly it absorbs energy. Gases with a higher GWP absorb more energy, per pound, than gases with a lower GWP, and thus contribute more to warming Earth. The global warming potentials of Intergovernmental Panel on Climate Change (IPCC, 2007) are given in Table 3.

Tab. 3: Global Warming Potentials

GHG	GWP
Carbon dioxide	1

Methene	25
Nitrous oxide	298

The average transmission and distribution losses of natural gas over the country is 1.77% (Tital, 2013-2014). Estimated volume of 1 mole Natural Gas is 0.024 m^3 and Heating value of Natural Gas (as per test report) is 0.919 MJ. The estimated emission factors for main greenhouse gases are 55.52 gCO_2/MJ, 0.35 gCH_4/MJ and 0.17 gN_2O/MJ. Considering global warming potentials of IPCC 2007 report the equivalent CO2 emission factor for natural gas in Bangladesh is 115.04 gCO_2e/MJ.

5. Conclusion

Greenhouse gas emission factors for natual gas in Bangladesh are 55.52 gCO_2/MJ, 0.35 gCH_4/MJ, 0.17 gN_2O/MJ and equivalent CO_2 emission factor is 115.04 gCO_2e/MJ.

6. References

Agency, United Stated Environmental Protection, 2015. http://www.epa.gov/climatechange/ghg emissions/index.html

Annual Report, 2013-2014, Titas Gas Transmission and Distribution Company Limited, Dhaka, Bangladesh

Houghton, Sir John, 2009. Global Warming, The Complete Briefing Third Edition, Cambridge university press

IPCC Guidelines for National Greenhouse Gas Inventories, 2006. http://www.ipcc-nggip.iges.or.jp/ public/2006gl/

IPCC Fourth Assessment Report: Climate Change, 2007. www.ipcc.ch/publications

Shrestha, R M, Anandarajah G and Liyanage M H, 2009. Factors affecting CO2 emission from the power sector of selected countries in Asia and the Pacific. Energy Policy, Vol. 37. Page 2375-2384

A NOVEL METHOD FOR CALIBRATION OF AEROSOL DATABASES WITH LIDAR-CEILOMETER MEASUREMENTS

D. Bachour, D. Perez-Astudillo, L. Martin-Pomares

Qatar Environment & Energy Research Institute, Qatar Foundation, HBKU, Doha, Qatar

Abstract

Satellite observations and chemical transport models used for the derivation of Aerosol Optical Depth (AOD) values have an extensive coverage worldwide and are widely used when ground-measured AOD is not available. However, satellite and modelled values present high uncertainties and cannot be always considered reliable especially at the level needed for solar radiation modelling. This work presents a methodology for calibrating existing AOD databases, which are commonly used as inputs to clear sky models for estimating clear-sky solar irradiances. This methodology makes use of ground-measured direct normal irradiance (*Hb*), integrated backscatter profiles of a lidar-ceilometer device, and *Hb* calculated from clear sky models with different AOD databases.

Keywords: *AOD, lidar, ceilometer, aerosol loads, DNI*

1. Introduction

In clear skies, aerosols are the main atmospheric component absorbing and scattering solar radiation. Their atmospheric extinction is generally described in terms of Aerosol Optical Depth (AOD), a useful parameter for the calculation of clear-sky solar irradiances. AOD can be directly measured by ground-based sun-photometers [Holben et al, 1998], or derived from satellite images such as MISR [Keller et al, 2007] and MODIS [Kosmopoulos et al, 2008] and from chemical transport models such as MACC [Cebecauer and Suri, 2010]. The direct measurements are the best option for determining AOD, but they have limited coverage. The indirect sources have wider coverage, but provide AOD data with lower temporal and spatial resolutions, and exhibit high uncertainties particularly in regions of high aerosol loads [Cebecauer et al, 2011; Gueymard, 2012].

Lidar-ceilometers measure atmospheric backscatter profiles as a function of time and height in the atmosphere. These profiles are normally used for the determination of the boundary layer height and cloud base height [Munkel, 2006]. However, they can also be used to extract aerosol information that can be used as an alternative to the AOD parameter in the modelling of solar radiation; indeed, a good correlation was found between lidar-ceilometer measurements and direct normal irradiance ground measurements in [Bachour and Perez-Astudillo, 2014].

2. Instrumentation and data used

The experimental data used here consist of clear days in the time interval 10 am to 1 pm, collected over a period of 12 months from December 2012 to November 2013. 214 clear days were selected for the analysis presented in this paper. The Vaisala ceilometer CL51 was used for the recording of the range-corrected atmospheric backscatter profiles. It uses a 910 nm pulsed diode laser. The reported backscattered signal has a vertical resolution of 10 m, with 15 km as maximum range. For more details about the CL51 instrument, the reader can refer to [Vaisala, 2015]. A CHP1 pyrheliometer [CHP1, 2015] mounted on a high precision Kipp and Zonen solar radiation monitoring station was used for the measurements of the direct normal irradiance as one-minute averages in W/m^2.

The clear-sky irradiation values used here were derived from the McClear and REST2 models. McClear estimates the solar radiation at ground level under clear sky conditions by using the abaci approach and interpolation functions. It uses mainly inputs from the MACC project. Aerosol information used by the McClear model consists of aerosol optical depth at 550 nm, Angström coefficient, and aerosol type from the MACC database. The model has been validated at several BSRN stations and gives good results [Lefèvre, 2013]. REST2 is a high-performance radiative model used to predict clear-sky broadband irradiances. It uses the Angström turbidity coefficient, the Angström wavelength exponent and aerosol single-scattering albedo as aerosol inputs to the model [Gueymard, 2008]. It is possible to use any AOD data with this model. For the irradiation data presented here, the aerosol information used with the REST2 model is extracted from the MISR and MACC databases.

doi:10.18086/swc.2015.07.19 Available at http://proceedings.ises.org

3. Methodology

The backscattered intensity profiles recorded by the CL51 during a clear day depend on the aerosol constituents of the atmosphere and provide information on their height as a function of time. Of interest for this analysis, are the atmospheric backscatter coefficients recorded as a two-dimensional dataset values, reported every 36 s, in 10-m steps up to 15 km height. From these measured backscatter coefficients, the hourly-averaged backscatter coefficients were obtained for each height step and summed thereafter up to 5 km height in the atmosphere. The 5 km height limit in the atmosphere was found to be representative of the dynamicity of the atmosphere in the studied location. The obtained integrated backscatter coefficient, named hereby the beta coefficient, is the starting point of the calibration method using lidar-ceilometer measurements as suggested here.

This high-resolution local aerosol information is used to validate indirectly the aerosol databases by measuring the performance of a clear-sky model through the hereby-called 'performance ratio':

$$Kp\_cs = Hb\_cs / Hb\_m, \qquad \text{(eq. 1)}$$

Where *Hb_m* is the ground-measured value of the hourly beam irradiance (also called DNI, direct normal irradiance) obtained from the quality-controlled 1-minute values of measured direct normal irradiance. The applied quality control checks follow the BSRN standards [Long and Dutton, 2002]. *Hb_cs* is the corresponding modelled clear-sky value, derived from a clear-sky model. This ratio measures the performance of the used clear-sky model. The calculated performance is then correlated to the corresponding measured integrated backscatter, the beta coefficient, and the resulting correlation is used in order to correct the DNI values derived from the clear-sky model. This way, aerosol information used as input to the clear-sky model is indirectly calibrated.

4. Results and discussion

Fig.1 shows the ratio of the DNI derived from the clear sky model McClear versus the ground-measured DNI, as a function of the integrated backscatter lidar-ceilometer signal. Fig.2 and Fig.3 show the performance ratio of the REST2 model using aerosol information from MISR and from MACC, respectively, as a function of the integrated backscatter lidar-ceilometer sigmal.

It can be seen that up to a certain value of the beta coefficient, the clear-sky models performs reasonably well; for higher values of the integrated backscatter coefficient, i.e., high aerosol loads, the performance of the clear-sky models degrades and leads to an overestimation of the direct normal irradiance, most likely related to an underestimation of aerosols in the used databases, as has been also shown by [Jiang et al, 2007] and [Polo and Estalayo, 2015].

The overestimation in DNI can be correlated with the integrated backscatter measurements derived from the lidar-ceilometer. The correlation will be used to calibrate the clear-sky models for high aerosol loads.

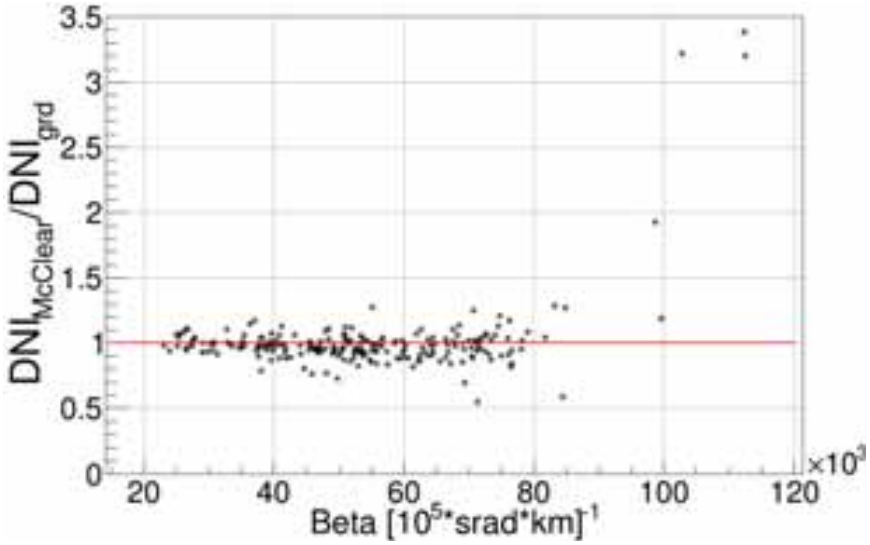

Fig. 1: Performance of the McClear model-derived beam irradiance vs. the integrated backscatter coefficient, at the hour from 11 am to 12 pm.

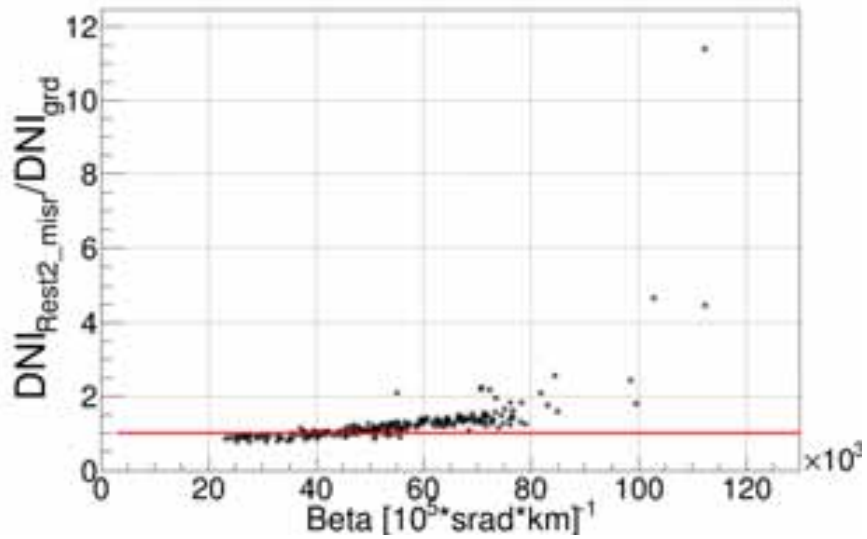

Fig. 2: Performance of the REST2 model-derived beam irradiance using aerosol from MISR vs. the integrated backscatter coefficient, at the hour from 11 am to 12 pm.

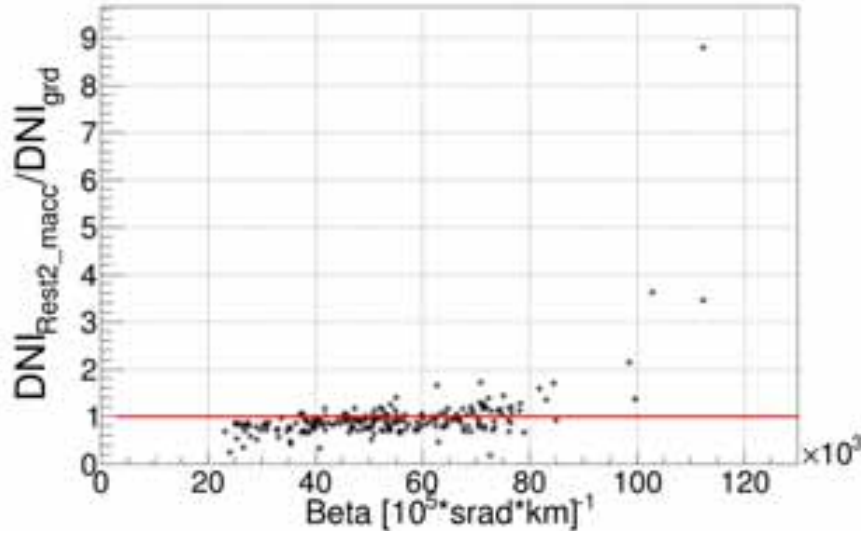

Fig. 3: Performance of the REST2 model-derived beam irradiance using aerosol from MACC vs. the integrated backscatter coefficient, at the hour from 11 am to 12 pm.

The decrease in performance at high beta values was quantified using an exponential function fitted to the ratios corresponding to beta values around 70000×10^5 $[srad.km]^{-1}$ and higher, where poor performance of the clear-sky models can be seen. The equation of the fit is the following:

$$Hb\_cs / Hb\_m = CF = \exp(slope * Beta + const), \quad \text{(eq. 2)}$$

Where Beta is the sum up to 5 km of the hourly-averaged backscatter lidar signals, *Hb_cs* is the hourly DNI derived from the clear-sky model, *Hb_m* is the hourly DNI derived from the ground measurements. *CF* stands for calibration function, and *slope* and *const* are parameters obtained from the applied fit.

The fitted function can then be used to correct the DNI values derived from the clear sky models for Beta values higher than the used Beta limit. The correction can be written as follows:

$$Hb\_cs,corr = Hb\_cs / CF, \quad \text{(eq. 3)}$$

where *Hb_cs,corr* is the corrected value of *Hb_cs*.

By using Eq.3 to calibrate the clear-sky model, the aerosol information used as input to the model is indirectly calibrated as a function of the lidar-ceilometer measurements.

Fig. 4 shows the performance of the corrected McClear model, after applying the function in Eq.3. The effectiveness of the calibration method as applied to the McClear model is noticeable on the data points corresponding to high beta values, i.e., high aerosol loads. The calibration of the REST2 model using MISR and MACC databases (not shown here) confirms the same.

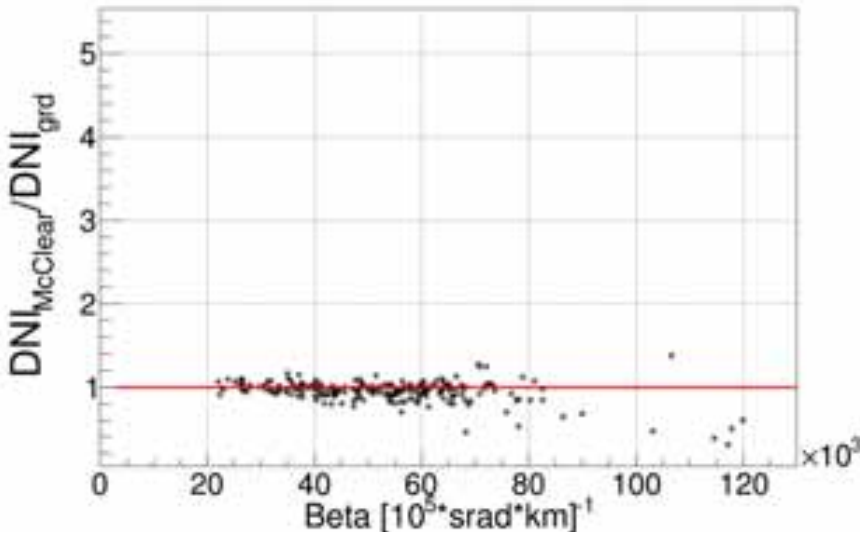

Fig. 4: Performance after calibration of the McClear model-derived beam irradiance vs. the integrated backscatter coefficient, at the hour from 11 am to 12 pm.

The effect of the suggested method on the calibration of the McClear model was evaluated using the relative mean bias error (MBE) and root-mean-square error (RMSE) of the performance ratios before and after calibration for different periods of time. The results for the hour 11 and 13 are listed in Table 1 and Table 2, respectively.

Tab. 1: Statistical indicators of the comparison of clear-sky model against clear-sky calibrated model using the beta coefficient, for the hour 10 to 11. rMBE and rRMSE are in %.

Model	rMBE	rRMSE
BEFORE CALIBRATION		
McClear	-1.05	24.16
REST2 with MISR	24.71	93.51
REST2 with MACC	-6.86	69.41
AFTER CALIBRATION		
McClear	-5.11	14.2
REST2 with MISR	8.36	25.16
REST2 with MACC	-14.64	29.67

Tab. 2: Statistical indicators of the comparison of clear-sky model against clear-sky calibrated model using the beta coefficient, for the hour 12 to 13. rMBE and rRMSE are in %.

Model	rMBE	rRMSE
BEFORE CALIBRATION		
McClear	1.96	29.22
REST2 with MISR	31.48	107.33
REST2 with MACC	-0.25	79.63
AFTER CALIBRATION		
McClear	-5.09	15.53
REST2 with MISR	5.5	23.98
REST2 with MACC	-13.18	27.37

Table 1 and Table 2 show that the calibrated dataset has lower rRMSE values for all the clear sky models as compared to the original clear-sky datasets. The rMBE value for the calibrated REST2 model with MISR database is also lower than the relative bias of the uncalibrated model, but higher for the calibrated clear-sky models using the MACC database. Since the calibration was only applied to the points with high beta values, the rMBE of the calibrated models shown in the tables are now dominated by the bias of the points with lower beta values; this discrepancy can be easily reduced and will provide smaller relative bias values when calibrating the DNI using all Beta values in the fit to obtain *CF*.

The noticeable decrease in the relative errors, when comparing the results before and after applying the suggested calibration method on the clear-sky models, shows the effectiveness of using the lidar ceilometer measurements as local aerosol information, which can be ultimately used as a reliable tool to correct the existing aerosol databases.

5. References

Bachour, D., Perez-Astudillo, D., 2014. Deriving solar direct normal irradiance using lidar-ceilometer. Solar Energy. 110, 316-324.

Cebecauer, T., Suri, M., 2010. Accuracy improvements of satellite-derived solar resource based on GEMS re-analysis aerosols. Proceedings of SolarPACES International Conference.

Cebecauer, T., Suri, M., Gueymard, C.A., 2011. Uncertainty sources in satellite-derived direct normal irradiance: how can prediction accuracy be improved globally?. Proceedings of SolarPACES International Conference.

Gueymard, C.A., 2008. REST2: High-performance solar radiation model for cloudless-sky irradiance, illuminance, and photosynthetically active radiation – Validation with a benchmark dataset. Solar Energy. 82(3), 272-285.

Gueymard, C.A., 2012. Temporal variability in direct and global irradiance at various time scales as affected by aerosols. Solar Energy 86, 3544–3553.

Holben, B.N., Eck, T.F., Slutsker, I., Tanre, D., Buis, J.P., Setzer, A., Vermote, E., Reagan, J.A., Kaufman, Y.J., Nakajima, T., Lavenu, F., Jankowiak, I., Smirnov, A., 1998. AERONET - A federated instrument network and data archive for aerosol characterization. Remote Sensing of Environment. 66(1):1-16.

Jiang, X., Liu, Y., Yu, B., Jiang, M., 2007. Comparison of MISR aerosol optical thickness with AERONET measurements in Beijing metropolitan area. Remote sensing of environment. 107 (1-2), 45-53.

Keller, J., Bojinski, S., Prevot, S.H., 2007. Simultaneous retrieval of aerosol and surface optical properties using data of the Multi-angle Imaging SpectroRadiometer (MISR). Remote Sensing of Environment. 107(1-2),120-137.

Kosmopoulos, P.G., Kaskaoutis, D.G., Nastos, P.T., Kambezidis, H.D., 2008. Seasonal variation of columnar aerosol optical properties over Athens, Greece, based on MODIS data. Remote Sensing of Environment.112(5), 2354-2366.

Lefèvre, M., Oumbe, A., Blanc, P., Espinar, B., Gschwind, B., Qu, Z., Wald, L.,Schroedter-Homscheidt, M., Hoyer-Klick, C., Arola, A., Benedetti, A., Kaiser, J.W.,Morcrette, J.J., 2013. McClear: a new model estimating downwelling solar radiation at ground level in clear-sky conditions. Atmospheric Measurement Techniques. 6, 2403-2418.

Long, C.N., Dutton. E.G., 2002. BSRN global network recommended QC tests, v2.0. BSRN Technical Report.

Munkel, C., 2006. Boundary layer and air quality monitoring with a commercial lidar ceilometer. Proc. SPIE 6367.

Polo., J, Estalayo., G, 2015. Impact of atmospheric aerosol loads on Concentrating Solar Power production in arid-desert sites. Solar Energy. 115, 621-631

CHP1, 2015. http://www.kippzonen.com/?downloadcategory/19192/Pyrheliometers.aspx. Last accessed September 2015.

Vaisala, 2015. http://www.vaisala.com/en/products/ceilometers/Pages/cl51.aspx. Last accessed September 2015.

Renewable Electricity Technologies: Photovoltaics

Conference Proceedings

Solar World Congress 2015
Daegu, Korea, 08 – 12 November 2015

Analysis of the Silicon Dioxide Passivation and Forming Gas Annealing in Silicon Solar Cells

Izete Zanesco and Adriano Moehlecke

Solar Energy Technology Nucleus (NT-Solar), Faculty of Physics,

Pontifical Catholic University of Rio Grande do Sul (PUCRS), Porto Alegre (Brazil)

Abstract

The passivation of silicon solar cells by the deposition of SiN_x anti-reflection coating is usual in the industry. However, materials such as SiO_2, TiO_2 and Al_2O_3 may be a cost-effective alternative and its analysis is mainly reported in silicon wafers. The goal of this paper is to present the development and analysis of silicon solar cells passivated with a thin layer of SiO_2 as well as the evaluation of the effectiveness of the annealing step in forming gas. The dry oxidation was performed before the TiO_2 anti-reflection coating deposition and the annealing in forming gas was performed in the same furnace. The temperature and time of the oxidation and the annealing step were experimentally optimized. The efficiency of 15.9 %was achieved. The highest average efficiency was found in the oxidation temperature range from 750 ºC to 800 ºC, during 7 minutes, caused by the increasing of open circuit voltage and fill factor. At short wavelengths, the internal quantum efficiency decreases slightly with the increasing of the oxidation temperature. The minority carrier diffusion length (L_D) of the solar cells processed with the oxidation temperature of 800 °C was around 1890 μm. The open circuit voltage shows a slight trend of increasing with the oxidation time. The annealing step in forming gas did not improve the average efficiency of the solar cells. Solar cells processed with oxidation and annealing presented higher internal quantum efficiency at short wavelengths than cells with only annealing.

Keywords: silicon solar cells, passivation, silicon oxide

1. Introduction

The industry of silicon solar cells is mainly based on conventional screen printing metallization and passivation of the phosphorus emitter with silicon nitride anti-reflection (AR) coating. The passivation reduces the recombination of minority charge carriers in the surface of the solar cells. The surface passivation with silicon nitride using plasma-enhanced chemical vapor deposition (PECVD) at low temperature (< 450 ºC) results in low surface recombination velocity on both p-type and n-type c-Si, as well as low absorption at short wavelengths (Aberle, 2001). Silicon nitride passivation for n^+ emitter provides positive interface charges, causing a field effect passivation (Rahman and Khan, 2012). Low surface recombination velocity of 1.6 cm/s on p-type c-Si with passivation by SiN_x deposited at 290 ºC was achieved (Wan et al., 2013).

The passivation with Al_2O_3 is also under investigation. The aluminum oxide has advantages over SiN_x when used to passivate the p^+ emitter, because Al_2O_3 presents a high density of fixed negative charges (Pawlik et al., 2014; Saynova et al., 2013). Surface recombination velocities below 2.9 cm/s and low interface state density were achieved with Al_2O_3 layers, performed by atomic layer deposition (ALD) (Werner et al., 2011). The surface recombination velocity of 90 cm/s was reported with Al_2O_3 as rear surface dielectric layer and this value was similar to that achieved with thermally grown SiO_2 (Schmidt et al., 2008). Duttagupta et al. (2013) reported that good passivation can be obtained with the AlO_x/SiN_x dielectric stack, deposited by PECVD and an AlO_x thickness of 5 nm is sufficient.

Thermally grown SiO_2 is the most effective c-Si surface passivation technique, but silicon dioxide has a low

doi:10.18086/swc.2015.05.01 Available at http://proceedings.ises.org

refractive index and, consequently, it is not good to form the anti-reflection coating. In this way, silicon dioxide is usually complemented by other dielectric layers. The interface defect density may be low after the growth of a thermal SiO_2 film on c-Si and a subsequent annealing in forming gas. The surface passivation behavior has also been investigated for SiO_2/SiN_x stack and the surface recombination velocity of 2.4 cm/s was found in n-type Cz silicon wafers passivated by SiO_2 thermally grown (Ye et al., 2010). Low dark current densities of <20 fA/cm^2 on textured n-type FZ silicon wafers were found. In this substrate, both surfaces were phosphorus doped and the sheet resistance was of 140Ω/□ (van Erven et al., 2008). In the frontal surface field solar cells with very low surface phosphorous concentrations, the passivation with a SiO_2/SiN_x stack demonstrated an increase in cell efficiency of around 0.5 % (absolute), compared to the standard PECVD-SiN_x passivation. For instance, n-type CZ-Si solar cell passivated by the SiO_2/SiN_x stack achieved the efficiency of 19.4% (Book et al., 2011). Another technique investigated was a stack of hydrogenated amorphous silicon and SiO_x deposited by PECVD and the surface recombination velocity of 120 cm/s on p-type FZ-Si substrate was achieved (Hofmann et al., 2008).

Titanium oxide may not provide efficient surface passivation, but it is used to form the AR coating, because presents low absorption in short wavelengths and has a high refractive index. This material is more suitable to passivate boron doped surfaces, but the technique used to deposit the layer influences the passivation. A layer of TiO_2 performed by atmospheric pressure chemical vapor deposition leads to a surface recombination velocity less than 30 cm/s, on a 200-Ω/□ boron emitter (Thomson and McIntosh, 2012). On the other hand, titanium oxide films performed by thermal atomic layer deposition provide the surface recombination velocity of 2.8 cm/s and 8.3 cm/s on n-type and p-type FZ-Si substrate, respectively (Liao et al., 2014).

As presented above, surface velocity recombination can be reduced by passivation using a dielectric film and by performing a surface electric field that repels the minority charge carriers. In this way, Bonilla and Wilshaw (2014) developed a technique using positively charged alkali ions (Na or K) embedded in a silicon oxide grown in a dry dichloroethylene (DCE) environment. Surface recombination velocities in the range of 6–15 cm/s were obtained in n-type FZ-Si.

Many studies were reported on the surface velocity recombination in Si-wafers, but the experimental analysis of the passivation on the performance of Si solar cells needs more investigation. Otherwise, the passivation with a thin layer of silicon dioxide, growth at temperature below 800 °C and combined with the TiO_2 AR coating, may be an alternative to the silicon solar cell industry. The goal of this paper is to present the development and analysis of the surface passivation with a thin layer of SiO_2, with and without annealing in forming gas, on the electrical parameters of silicon solar cells. The AR coating was formed with TiO_2 deposited by e-beam evaporation.

2. Solar cell processing and characterization

Solar cells were developed in p-type CZ-Si solar grade wafers with thickness of 200 μm and base resistivity from 1 Ω.cm to 20 Ω.cm. The process sequence to produce solar cells consists of the following steps: texture etching, RCA cleaning, phosphorus diffusion, phosphorus silicate glass (PSG) etching and RCA cleaning, dry oxidation and forming gas annealing, anti-reflection coating deposition, screen printing metallization on the frontal and rear face, firing of the metal pastes and laser edge isolation.

The n^+ layer was performed by phosphorus diffusion at 845 ºC using $POCl_3$ as source, resulting in the sheet resistance around 60 Ω/□. The thermal oxidation was carried out in a specific quartz tube furnace and the forming gas annealing was performed in the same furnace. The thickness of the TiO_2 anti-reflection coating, deposited by the e-beam technique, was of 60 nm. The depth of aluminum back surface field (Al-BSF) of around (5 ± 1) μm was estimated taking into account the peak temperature firing of 840 °C and the Al paste surface density of about 3.5 mg/cm^2 (Zanesco et al., 2014).

The temperature during thermal oxidation was ranged from 650 ºC to 900 °C and the short time of the oxidation was from 4 to 15 minutes, resulting in a thin layer of silicon dioxide of around 10 nm. The forming gas annealing temperature was ranged from 350 °C to 450°C and the processes were performed during 20 and 30 minutes.

Solar cells were characterized under standard conditions (100 mW/cm^2, AM1.5G and 25°C) in a solar simulator calibrated with a solar cell previously measured at CalLab - FhG-ISE (*Fraunhofer-Institut für Solare Energiesysteme*), Germany. The two-dimensional distribution of minority carrier lifetime and diffusion length was measured using the WT-2000PV device of Semilab, by μ-PCD (microwave induced photoconductivity decay) and LBIC (light beam induced current) technique, respectively. The minority carrier lifetime was measured after the thermal oxidation and with a SiO_2 layer in order to compare the passivation. The internal quantum efficiency was calculated starting from the measured external quantum efficiency and reflectance.

3. Results and analysis

3.1. Influence of the oxidation temperature

Tab. 1 presents the average values of the open circuit voltage (V_{oc}), short-circuit current density (J_{sc}), fill factor (FF) and efficiency (η) of the solar cells processed with different oxidation temperature (T_{oxi}), during 7 minutes. The highest average efficiency was found in solar cells processed with the oxidation temperature range from 750 ºC to 800 ºC. Comparing solar cells with and without passivation in Tab.1, we observe that the average efficiency increases from (14.3 ± 0.3)% to (15.6 ± 0.1)%, due to the SiO_2 passivation. The increasing of the efficiency of 1.3 % (absolute) is caused by the behavior of V_{oc} and FF. Moreover, Tab. 1 and Fig. 1-d show that the optimization of the SiO_2 passivation reduced also the standard deviation.

The electrical parameters of the best solar cells are reported in Tab. 2. The highest efficiency of 15.9 % was achieved in a solar cell processed at the oxidation temperature of 800 °C, due to mainly the increasing of the V_{oc} and FF, caused by the passivation.

Tab. 1: Average electrical characteristics of the silicon solar cells as a function of oxidation temperature (T_{oxi}).

T_{oxi} (°C)	Nº of Cells	V_{oc} (mV)	J_{sc} (mA/cm^2)	FF	η (%)
Without oxidation	18	586.9 ± 2.3	33.85 ± 0.06	0.719 ± 0.013	14.3 ± 0.3
650	18	592.3 ± 1.9	33.80 ± 0.11	0.754 ± 0.012	15.1 ± 0.3
750	18	593.4 ± 0.9	33.81 ± 0.07	0.785 ± 0.006	15.6 ± 0.1
800	18	593.9 ± 0.3	33.85 ± 0.08	0.770 ± 0.007	15.4 ± 0.2
850	17	592.2 ± 1.4	33.8 ± 0.4	0.73 ±0.04	14.6 ± 0.9
900	18	579 ± 6	33.83 ± 0.09	0.749 ± 0.019	14.7 ± 0.5

Tab. 2: Electrical characteristics of the silicon solar cells with higher efficiency as a function of oxidation temperature.

T_{oxi} (°C)	V_{oc} (mV)	J_{sc} (mA/cm^2)	FF	η (%)
Without oxidation	589.3	33.8	0.75	15.0
650	593.0	33.7	0.76	15.5
750	595.0	33.8	0.79	15.6
800	593.3	33.9	0.78	15.9
850	593.4	33.8	0.76	15.2
900	582.7	33.9	0.76	14.7

The Fig. 1 (a) and (b) show that higher values of open circuit voltage and fill factor were achieved at temperature oxidation of 800 °C and 750 °C, respectively. The V_{oc} increased about 7 mV when passivation step was implemented. The passivation affects also the fill factor. This parameter augments from 0.72 to 0.78 with the oxidation at temperature of 750 ºC – 800 ºC. The oxide growth at 900 °C reduces the V_{oc}, when compared to the results without oxidation. This temperature may cause a degradation of the substrate. Fig. 1 (c) indicates that the J_{sc} was not affected by the oxidation temperature and the SiO_2 passivation, because of the efficient aluminum back surface field (Al-BSF). Consequently, the higher efficiencies occur at the oxidation temperature of 750 °C and 800 °C, as Fig.1 (d) confirms.

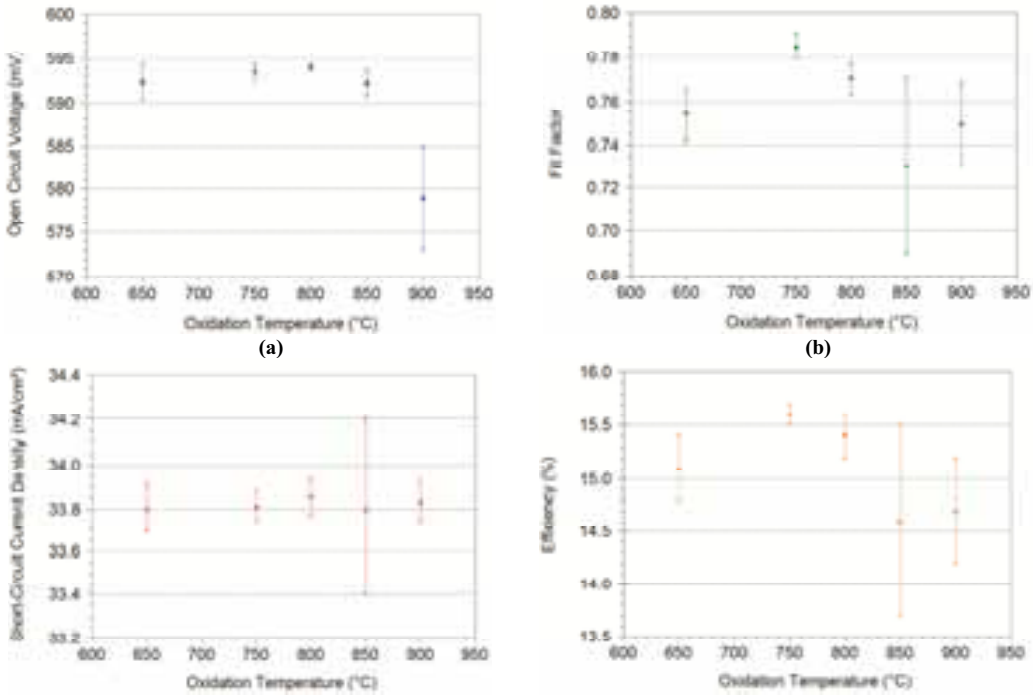

Fig. 1: (a) Open circuit voltage, (b) fill factor, (c) short-circuit current density and (d) efficiency of the solar cells as a function of temperature oxidation.

The Fig. 2 indicates that at short wavelengths, the internal quantum efficiency (IQE) decreases slightly with the increasing of the oxidation temperature because the SiO_2 passivation is less effective. With the increase of the oxidation temperature from 850 °C to 900 °C, the surface recombination velocity enhances of about two orders of magnitude, indicating that the SiO_2 passivation is worst.

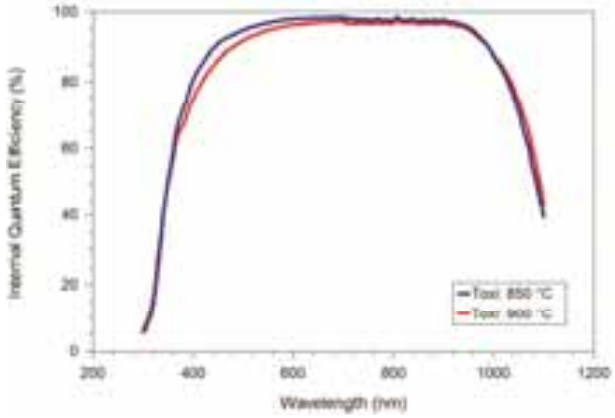

Fig. 2: Internal quantum efficiency of the silicon solar cells with the highest efficiency and processed at temperature oxidation of 850 °C and 900 ºC.

The effective minority carrier lifetime (τ_{eff}) was low for the oxidation temperatures evaluated and depends on the oxidation temperature, as Fig. 3 shows. The highest average values of 40 μs - 50 μs were found at temperature oxidation from 750 °C to 850 °C.

It's worth mentioning that the average initial minority carrier lifetime measured in 60 solar grade silicon wafers was of 39 μs and the final effective value takes into account the double pn junction formed by phosphorus diffusion, passivated with SiO_2 growth at different temperatures. Then, the process to fabricate the solar cells with the oxidation temperature range of 750 - 850 °C leads to the minority carrier lifetime slightly higher than the initial value. Fig. 3 shows also that low values of the minority carrier lifetime occur in the center of the wafers. For the range of oxidation temperature from 750 °C to 850 °C, the highest values of the lifetimes are of around 110 μs.

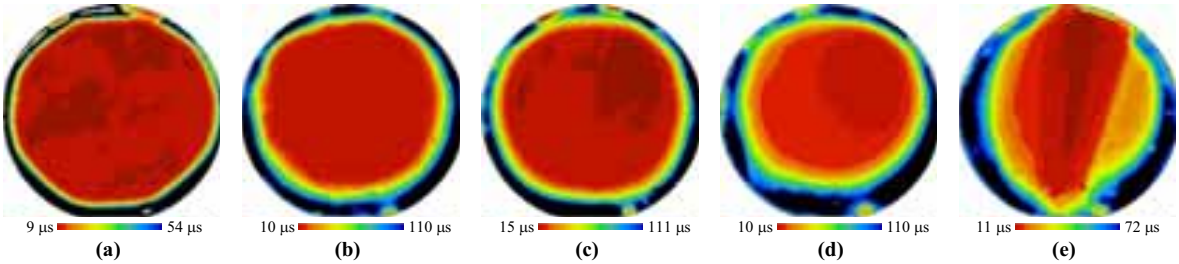

Fig. 3: The two-dimensional distribution of the minority carrier lifetimes measured by µ-PCD technique afterwards the oxidation during 7 minutes and temperature of (a) 650 ºC (τ_{eff} = 21 µs), (b) 750 ºC (τ_{eff} = 42 µs), (c) 800 °C (τ_{eff} = 43 µs) (d) 850 °C (τ_{eff} = 49 µs) and (e) 900 °C (τ_{eff} = 33 µs).

The Fig. 4 shows the comparison of the minority carrier diffusion length (L_D) of the solar cells processed with the oxidation temperature of 800 °C and 900 °C and without oxidation. The average L_D of the solar cells without oxidation step is around 1380 µm and this parameter enhances to 1890 µm, when the oxidation is performed at 800 °C. However, when the oxidation temperature is of 900 °C, the average minority carrier diffusion length decreased to 960 µm, indicating that the substrate was degraded during the oxidation process.

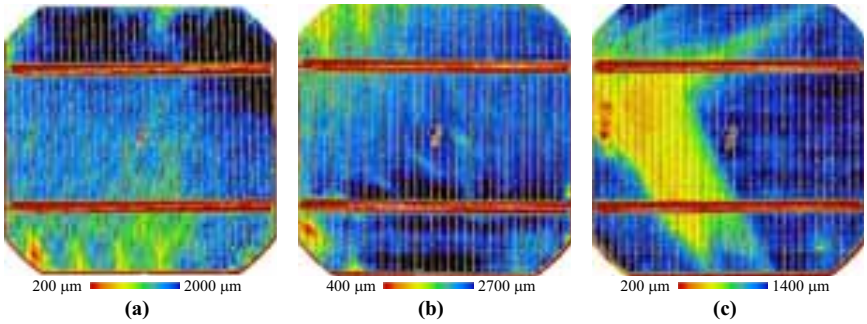

Fig. 4. The two-dimensional distribution of the minority carrier diffusion length of solar cells processed (a) without oxidation (L_D = 1380 µm) and (b) with oxidation temperature of 800 °C (L_D = 1890 µm) and (c) of 900 °C (L_D = 960 µm).

3.2. Influence of the oxidation time

The electrical characteristics of the solar cells processed by the oxidation time from 4 minutes to 15 minutes at the temperature of 800 ºC are presented in Tab.3. The highest average efficiency was found when cells were thermally oxidated during 7 minutes. The V_{oc} shows a slight trend of increasing with the oxidation time. Nevertheless, the J_{sc} decreases slightly when the oxidation time is increased, as Tab. 4 confirms. The Tab. 4 indicates that the highest efficiency of 15.9 % is obtained in solar cells processed at the oxidation temperature of 800 °C during 7 minutes.

Tab. 3: Average electrical characteristics of the silicon solar cells as a function of oxidation time (t_{oxi}).

t_{oxi} (min)	Nº of Cells	V_{oc} (mV)	J_{sc} (mA/cm^2)	FF	η (%)
4	17	593.2 ± 1.0	33.88 ± 0.11	0.751 ± 0.011	15.0 ± 0.3
7	18	593.9 ± 0.3	33.85 ± 0.08	0.767 ± 0.007	15.4 ± 0.2
15	15	594.1 ± 0.9	33.82 ± 0.10	0.753 ± 0.014	15.0 ± 0.3

Tab. 4: Electrical characteristics of the fabricated silicon solar cells with the highest efficiency as a function of oxidation time.

t_{oxi} (min)	V_{oc} (mV)	J_{sc} (mA/cm^2)	FF	η (%)
4	593.9	34.0	0.76	15.3
7	593.3	33.9	0.78	15.9
15	594.0	33.7	0.77	15.4

3.3 Analysis of the annealing step

Batches of solar cells were processed at temperature oxidation of 800 °C during 7 minutes and the annealing temperature and time were ranged. Starting from the results summarized in Tab.5, we observe that the annealing in forming gas at 400 °C did not improve the average efficiency of solar cells when compared to the results presented in Tab. 1. Moreover, the annealing temperature of 350 °C and 450 °C lead to lower efficiencies than that presented in Tab. 1 for the oxidation temperature of 800 °C, indicating that the annealing process at these temperatures did not improve the efficiency of the solar cells.

The open circuit voltage tends to increase with long annealing time. For annealing temperature of 400 °C and 450 °C, the V_{oc} increased about 2.5 – 3.0 mV, when the annealing time was increased from 20 minutes to 30 minutes. This result is confirmed in Tab. 6 that reports the electrical characteristics of the solar cells with the highest efficiency. For the best cells, the V_{oc} was improved up to 3 mV when the annealing time is augmented of 10 minutes.

With the annealing without the previous oxidation, an average efficiency of (15.3 ± 0.2) % was achieved, as shown in Tab. 5. This value is only 0.3 % (absolute) lower than the value obtained in devices with oxidation and annealing in forming gas and the reduction of the efficiency was caused by the decrease of V_{oc}, J_{sc} and FF.

Tab. 5: Average electrical characteristics of the solar cells processed with different parameters of forming gas annealing.

T_{An} (°C)	t_{An} (min)	Nº of Cells	V_{oc} (mV)	J_{sc} (mA/cm^2)	FF	η (%)
350	20	7	591.2 ± 1.3	33.84 ± 0.09	0.756 ± 0.017	15.0 ± 0.3
400	20*	6	590.7 ± 0.4*	33.73 ± 0.06*	0.774 ± 0.003*	15.3 ± 0.2*
	20	3	593.8 ± 0.8	33.88 ± 0.10	0.782 ± 0.007	15.6 ± 0.1
	30	2	596.7 ± 1.1	33.81 ± 0.11	0.800 ± 0.004	15.6 ± 0.1
450	20	5	591.5 ± 1.4	33.75 ± 0.10	0.766 ± 0.008	15.1 ± 0.3
	30	4	593.9 ± 0.5	33.78 ± 0.07	0.757 ± 0.022	15.1 ± 0.1

* with annealing and without previous oxidation.

Tab. 6. Electrical characteristics of the best silicon solar cells processed with different parameters of forming gas annealing.

T_{An} (°C)	t_{An} (min)	V_{OC} (mV)	J_{SC} (mA/cm^2)	FF	η (%)
350	20	591.1	33.7	0.77	15.4
400	20*	591.4*	33.7*	0.78*	15.4*
	20	594.1	33.8	0.79	15.6
	30	595.9	33.9	0.80	15.6
450	20	591.5	33.8	0.78	15.4
	30	594.4	33.9	0.77	15.4

* with annealing and without previous oxidation

The short-circuit current density is slightly affected by the annealing process, as Tab. 5 reports. The annealing temperature and time do not influence the J_{sc} and this conclusion is confirmed in Fig. 5 that compares the internal quantum efficiency of the best processed solar cells as a function of annealing temperature and time. Otherwise, the oxidation step improves the passivation, as shown in Fig 6. In this figure, the internal quantum efficiency of the solar cell processed at 400 °C during 20 minutes with oxidation and annealing steps is compared to the IQE of the cell processed with annealing and without oxidation. At short wavelengths, the IQE of cells with SiO_2 passivation is higher, indicating the effectiveness of the passivation. When the oxidation is implemented, the surface recombination velocity was reduced of about one order of magnitude.

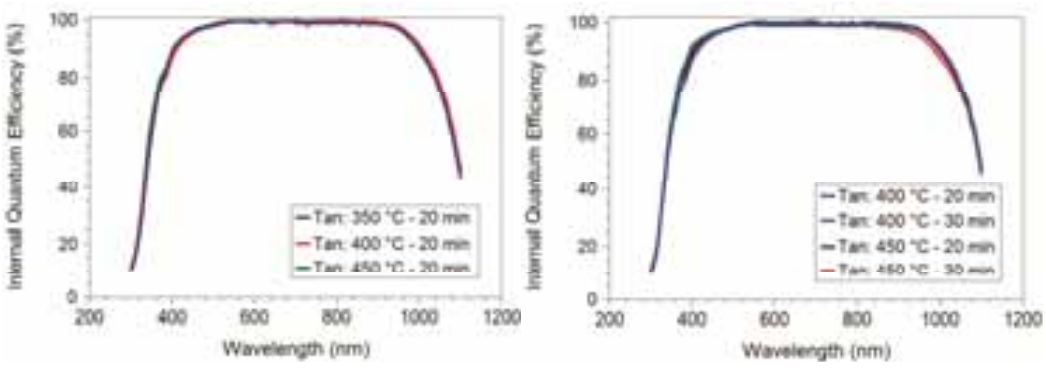

(a) (b)

Fig. 5: Internal quantum efficiency of the silicon solar cell with the highest efficiency as a function of (a) annealing temperature and processed during 20 minutes and (b) annealing time at the temperature of 400 °C and 450 °C.

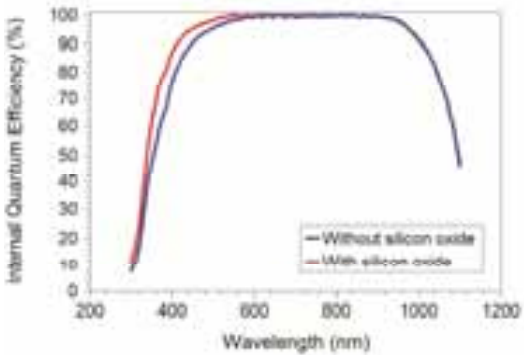

Fig. 6: Internal quantum efficiency of the silicon solar cell processed with and without oxidation step and annealing at the temperature of 400 °C during 20 minutes.

The Fig. 7 illustrates the two-dimensional distribution of the minority carrier lifetimes after the oxidation at the temperature of 800 °C during 7 minutes and annealing step during 20 minutes with different temperatures. In the sample without oxidation (see Fig. 8-a), but with annealing step, the average value of τ_{eff} was of 10 μs. This result confirms that oxidation at 800 °C improves the minority carrier lifetime, as Fig. 7 (c) shows. Values of the average effective minority carrier lifetime of around 80 μs – 95 μs were measured in samples processed at 400 °C and 450 °C. In this annealing temperature range, values of the τ_{eff} up to 125 μs were measured. Again, we can observe that the low values of the effective minority carrier lifetime occur in the center of the sample. Moreover, comparing Fig 3-c (τ_{eff} = 43 μs) to Fig. 7-c (τ_{eff} = 82 μs) and Fig. 7-d (τ_{eff} = 95 μs), we can notice that the average effective minority carrier lifetime may be increased if the annealing step is implemented.

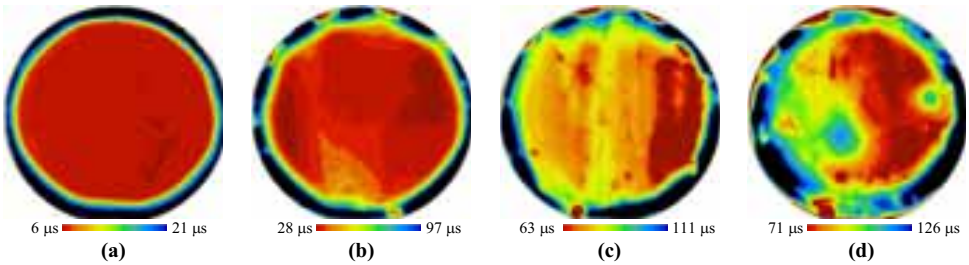

(a) (b) (c) (d)

Fig. 7: The two-dimensional distribution of the minority carrier lifetimes afterwards the oxidation at temperature of 800 °C during 7 minutes and annealing step during 20 minutes and temperature of (a) 400 °C (without oxidation) (τ_{eff} = 10 μs), (b) 350 °C (τ_{eff} = 48 μs), (c) 400 °C (τ_{eff} = 82 μs) and (d) 450 °C (τ_{eff} = 95 μs).

4. Conclusion

The passivation of silicon solar cells with a thin SiO_2 layer were experimentally optimized and analyzed. The

efficiency of 15.9 % was achieved in solar cells processed at the oxidation temperature of 800 ºC, during 7 minutes. The better average efficiencies were obtained in the oxidation temperature range from 750 °C to 800 °C, caused by the increasing of the open circuit voltage and fill factor. This result is related to the highest effective minority carrier lifetime, of 40 μs - 50 μs, measured in wafers processed in this oxidation temperature range. The short-circuit current was not affected by oxidation temperature, but the internal quantum efficiency decreases slightly with the increasing of the oxidation temperature. The minority carrier diffusion length of the solar cells processed with the oxidation temperature of 800 °C was around 1890 μm and decreased to 960 μm with the increasing of the oxidation temperature to 900 °C. The open circuit voltage shows a slight trend of increasing with the oxidation time, but the fill factor decreases. The annealing step in forming gas did not improve the average efficiency of solar cells and the open circuit voltage tends to grow with the increasing of the annealing time. The annealing temperature and time did not affect the short-circuit current density. The highest values of the average effective minority carrier lifetime of around 80 and 100 μs were measured in samples processed at annealing temperature of 400 °C and 450 °C, respectively. Solar cells processed with oxidation and annealing presented higher internal quantum efficiency at short wavelengths than cells with only annealing step.

Acknowledgments

This work was supported by the “Eletrosul Centrais Elétricas S. A.” (Eletrosul), under contract n° 88500014 and by the local utility “Companhia Estadual de Distribuição de Energia Elétrica”, under Contract n° CEEE-D9942400.

References

Aberle, A. G., 2001. Overview on SiN surface passivation of crystalline silicon solar cells. Solar Energy Materials & Solar Cells. 65, 239-248.

Bonilla, R. S., Wilshaw, P. R., 2014. A technique for field effect surface passivation for silicon solar cells. Applied Physics Letters. 104, 232903 1-5. DOI: 10.1063/1.4882161.

Book, F., Wiedenmann, T., Schubert, G., Plagwitz, H., Hahn, G., 2011. Influence of the front surface passivation quality on large area n-type silicon solar cells with Al-alloyed rear emitter. Energy Procedia. 8, 487-492. DOI:10.1016/j.egypro.2011.06.170.

Duttagupta, S., Lin, F., Shetty, K. D., Aberle, A. G., Hoex, Bram, 2013. Excellent boron emitter passivation for high-efficiency Si wafer solar cells using AlOx/SiNx dielectric stacks deposited in an industrial inline plasma reactor. Progress in Photovoltaics: Research and Applications. 21, 760-764. DOI: 10.1002/pip.1259.

Hofmann, M., Schmidt, C., Kohn, N., Rentsch, J., Glunz, S. W., Preu, R., 2008. Stack system of PECVD amorphous silicon and PECVD silicon oxide for silicon solar cell rear side passivation. Progress in Photovoltaics: Research and Applications. 16, 509-518. DOI: 10.1002/pip.835.

Liao, B., Hoex, B., Aberle, A. G., Chi, D., Bhatia, C. S., 2014. Excellent c-Si surface passivation by low-temperature atomic layer deposited titanium oxide. Applied Physics Letters. 104, 253903 1-4. DOI: 10.1063/1.4885096.

Pawlik, M., Vilcot, J. P., Halwax, M., Aureau, D., Etcheberry, A., Slaoui, A., Schutz-Kuchly, T., Cabal, R., 2014. Electrical and chemical studies on Al_2O_3 passivation activation process. Energy Procedia. 60, 85-89. DOI: 10.1016/j.egypro.2014.12.347.

Rahman, M. Z., Khan, S. I., 2012. Advances in surface passivation of c-Si solar cells. Mater Renew Sustain Energy. 1:1, 1-11. DOI 10.1007/s40243-012-0001-y.

Saynova, D. S., Janssen, G. J. M., Burgers, A. R., Mewe, A. A., Cianci, E., Seguini, G., Perego, M., 2013. Al_2O_3 passivation on c-Si surfaces for low temperature solar cell applications. Energy Procedia. 38, 872-880. DOI: 10.1016/j.egypro.2013.07.359.

Schmidt, J., Merkle, A., Brendel, R., Hoex, B., van de Sanden, M. C. M., Kessels, W. M. M., 2008. Surface passivation of high-efficiency silicon solar cells by atomic-layer-deposited Al_2O_3. Progress in Photovoltaics: Research and Applications. 16, 461-466. DOI: 10.1002/pip.823.

Thomson, A. F., McIntosh, K. R., 2012. Light-enhanced surface passivation of TiO_2-coated silicon. Progress in Photovoltaics: Research and Applications. 20, 343-349. DOI: 10.1002/pip.1132.

van Erven, A. J. M., Bosch, R. C. M., Bijker, M. D., 2008. Textured silicon surface passivation by high-rate expanding thermal plasma deposited SiN and thermal SiO_2/SiN stacks for crystalline silicon solar cells. Progress in Photovoltaics: Research and Applications. 16, 615-627. DOI: 10.1002/pip.841.

Wan, Y., McIntosh, K. R., Thomson, A. F., Cuevas, A., 2013. Low surface recombination velocity by low absorption silicon nitride on c-Si. IEEE Journal of Photovoltaics. 3, 554-559. DOI: 10.1109/JPHOTOV.2012.2215014.

Werner , F., Stals, W., Görtzen, R., Veith, B., Brendel, R., Schmidt, J., 2011. High-rate atomic layer deposition of Al_2O_3 for the surface passivation of Si solar cells. Energy Procedia. 8, 301-306. DOI:10.1016/j.egypro.2011.06.140.

Ye, L., Harder, N. P., Brendel, R., 2010. Effect of SiO_2 thicknesses in thermal-SiO_2/PECVD-SiN stacks on surface passivation of n-type Cz silicon substrates, 35th IEEE Photovoltaic Specialists Conference (PVSC), Honolulu, June 2010, pp 1207-1209. DOI: 10.1109/PVSC.2010.5614072.

Zanesco, I., Gonçalves, V. A., Moehlecke, A., 2014. Influence of the aluminum paste surface density on the electrical parameters of silicon solar cells. Energy Procedia. 57, 47-55. DOI:10.1016/j.egypro.2014.10.007.

Conference Proceedings

Solar World Congress 2015
Daegu, Korea, 08 – 12 November 2015

SELECTIVE BORON DIFFUSION WITHOUT MASKING LAYER USING BORIC ACID FOR SOLAR CELL EMITTER FORMATION

P. Ebrahimi, M. Kolahdouz*, M. Norouzi, E. Asl-Soleimani, F. Salehi

Faculty of Electrical and Computer Engineering, Thin Film Laboratory, University of Tehran, Tehran, Iran

Email: kolahdouz@ut.ac.ir

Abstract

In this article, we have used boric acid source to form the boron emitter in a selective way. And, the conditions of boron diffusion process were investigated. It was found that for 5% boric acid in DI water, the spinning of 3000 rpm for 15 sec and dry out process at 200°C are the most appropriate conditions.

Also, in this study, by using boric acid source, a selective doping method was developed. Therefore, it can be possible to have both light and heavy (under contacts) dopings on different areas of the wafer but without any extra masking layer (e.g. silicon dioxide) and undergoing only one drive-in process.

Keywords: *Boric acid, Emitter formation, Solar cell*

1. Introduction

Solar cells based on n-type c-Si wafers have raised growing interest since they feature clear advantages compared to the standard p-type Si; because of having lower sensitivity to metallic impurities and not degraded by the boron-oxygen pairs [1, 2].

Recently, there has been a remarkable increase in investigating spin-on or spray-on dopant (SOD) sources particularly in solar cell research and production. Low cost and neither toxic nor pyrophoric are advantages of these sources [3, 4]. Boron diffusion using BBr_3 is toxic and needs an additional etching step in order to diffuse either on one side of the sample or on specific areas. Since diffusion processes using Boron SOD films are common, we have used and developed a SOD process applying boric acid source to have boron emitter formation. By controlling the boric acid concentration in the solutions, temperature and the diffusion time, we have obtained a wide range of sheet resistances and doping profiles for solar cell applications. In this paper, the conditions of boron diffusion process, which includes the appropriate rotation (spinning speed) and temperature to drive out the excess solvents, were investigated. The output parameters such as carrier lifetime, sheet resistance and diffusion profile have also been measured. Finally, using this method, we were able to produce samples with selective diffusion areas without any extra masking layer, which can be used as the selective emitter for solar cell applications.

2. Experimental

doi:10.18086/swc.2015.05.02 Available at http://proceedings.ises.org

In order to achieve the desired properties of the boron emitter, n-type Cz <100>-oriented wafers of 1-3 Ωcm were used as the substrates. After standard Piranha cleaning, the solution of boric acid, known as H_3BO_3 (orthoboric acid), was spin-coated on the samples. Later, all samples were dried in the oven to remove the solvent. Subsequently, boron diffusion process was performed in a quartz tube furnace at different temperatures in the range of 950-1050 °C. The borosilicate glass (BSG) is removed in a HF solution after the furnace diffusion. Next, a thorough characterization of the process was performed using various techniques. The sheet resistance and the minority carrier lifetimes were measured respectively using four point probes and μ-PCD method. Electrochemical capacitance voltage profiler (ECVP) was applied to investigate the emitter surface doping concentration and the dopant profiles.

3. Result and Discussion

a. Boron Diffusion

The boric acid which exists in the crystalline phase was used as the solid source in this study. H_3BO_3 solutions with various concentrations can be prepared by dissolving different amounts of boric acid in DI water. The solubility in DI water at most at room temperature reaches up to 5wt% [1]. The formed anhydrous boric oxide (boron oxide) begins to soften at 325 °C [1]. The boron oxide then reacts with silicon to form SiO_2 and B, which then diffuses into the silicon by manipulating the temperature. After boric acid was dissolved in DI water, the samples were placed on a spinner and the SODs were drop-coated on the center of the sample. The required SOD solution (boric acid/DI water) for 1cm×1cm samples was 100 μl. In order to choose the appropriate layer deposition, we have first investigated various speeds and times. Then, the coated samples were baked at several different temperatures for 15 min to drive out the excess solvent (also called pre-deposition). Afterward, the samples were loaded in the diffusion furnace for 14 min consisting of N_2 gas as the ambient gas (drive-in step). Fig. 1 shows the optical microscope images of samples primarily dispersed by 5% boric acid solution after diffusion and BSG layer removal for different spinning speeds. It can be seen that 3000 rpm for 15 sec is appropriate for conformal coating. The process was also optimized for the appropriate temperature to drive out the excess solvents. It was examined at 50, 100, 150 and 200°C to check which gives the best uniformity of the final layer. It found that 200°C can result in the optimum layer (shown in Fig. 2).

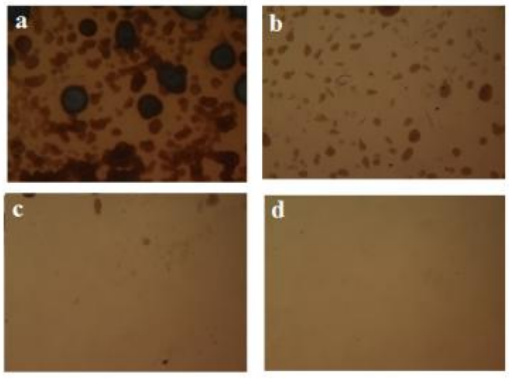

Fig. 1: Optical Microscopy image for different spin coat speed (a: 500 rpm, b: 1000 rpm, c: 2000 rpm, d: 3000 rpm) after drive-in step: 1050°C and 5% boric acid/DI water concentration.

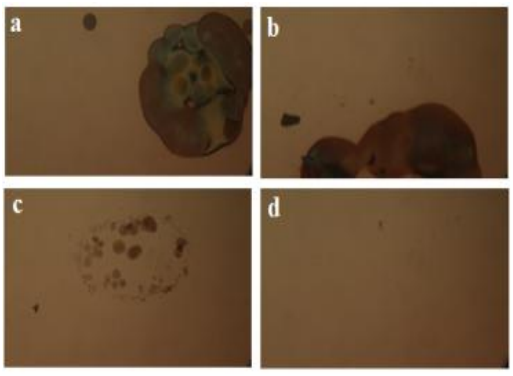

Fig. 2: Optical Microscopy image for different predep temprature (a: 50°C, b: 100°C, c: 150°C, d: 200 °C) after drive-in step: 1050°C and 5% boric acid/DI water concentration.

In addition, the effects of different concentrations of acid boric in DI water (1-5%) and different drive-in temperatures (950-1050°C) on the sheet resistance and the lifetime were studied and the results are shown in Table I & II. It can be seen that when the boric acid concentration or drive-in temperature increases, the sheet resistance decreases. On the other hand, the carrier lifetime unfortunately decreases as well. This results in an increase in the probability of contamination, and this is the reason. Fig. 3 shows the boron profile for different concentrations of boric acid solution, measured using ECVP. The surface concentration was assumed to the concentration at 10 nm deep inside the bulk and was found to be increasing in the range of 5.71-19.8×10^{19} cm^{-3} for different solutions used in the study. The junction depth was estimated to be in the range of 0.32-0.65 μm. The effects of different drive-in temperatures (950-1050°C) on the sheet resistance and the lifetime were also studied. The results are shown in Table II. According to this table, when the drive-in temperature increases, both sheet resistance and carrier lifetime will be decreased.

According to a previous report [5], two mechanisms of contamination and generation of dislocations due to a high B doping using this solid source are the reasons why the lifetime decreases. Fig. 4 shows the boron doping profiles at different temperatures, showing that we can have a good control on the depth of the profile (the both shallow and deep boron profiles) using boric acid as a diffusion source.

Table I: Sheet resistance and lifetime from different concentration of acid boric: pre-deposition time:15 min, drive-in time: 14 min, drive-in temp:1050°C.

Boric acid concentration (%)	Rsh (Ω/□)	τ (μs)
1	47.7	3.81
2	40.6	2.78
3	35.1	2.62
4	30.1	1.85
5	17.5	1.6

Table II: Sheet resistance and lifetime at different drive-in temperatures: pre-deposition time:15 min, drive-in time: 14 min, boric acid concentration:5%.

Temperature (°C)	Rsh (Ω/□)	τ (μs)
950	386.6	4.93
975	148.8	2.27
1000	58.8	2.01
1025	25.4	1.75
1050	17.5	1.6

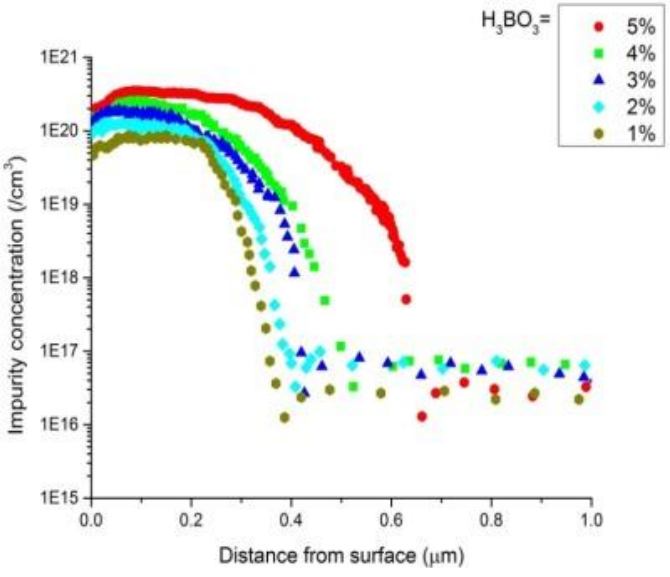

Fig. 3: Depth profile of boron in samples shown in Table I.

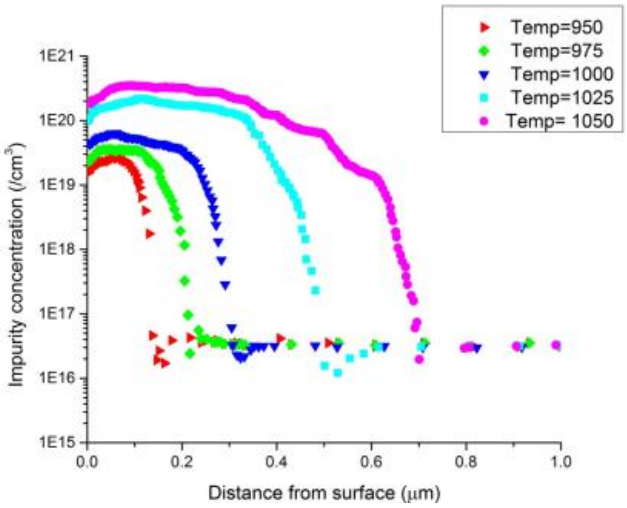

Fig. 4: Depth profile of boron in samples shown in Table II (Temp=°C).

b. Selective B Diffusion

The most interesting feature of this process compared to normal diffusion process is the ability to have a selective diffusion without having additional etching process. At first, photolithography was used to define windows in which the diffusion must be performed (shown Fig 5 b and c). After developing and post baking the resist, 200µl of 5% acid boric/DI water solution was applied on the patterned sample using spin-coating (see Fig. 5 d). Then, the sample was placed in an oven at 100°C for 15 min to drive out the solvent. Afterwards, the over-photoresist part of the boric acid was removed by lift off using acetone followed by DI water (Fig. 5 e). Finally, the sample was placed in the diffusion furnace in N_2 gas environment for 15 min at 1050°C.

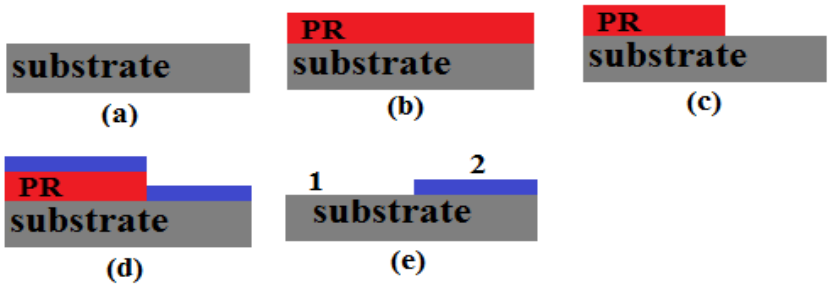

Fig. 5: Selective diffusion process with boric acid/DI water source. a) sample cleaning, b) photoresist spin coat, c) lithography, d) SOD & baking, e) photoresist (PR) lift off.

The ECVP measurements on these samples (shown in fig 6) show a remarkable difference in the surface concentration as a result of this selective process.

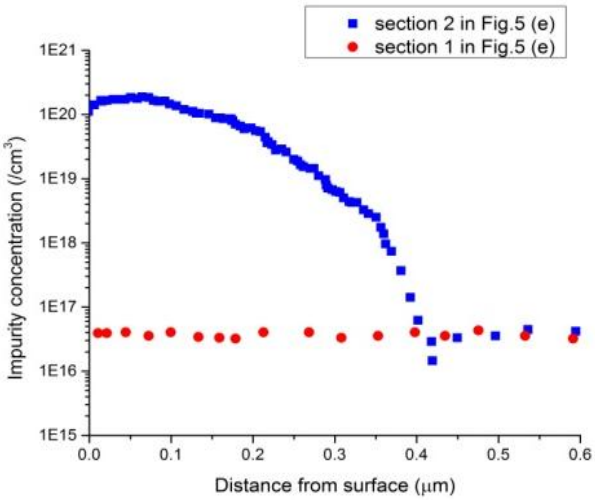

Fig.6: Depth profile of boron on a sample prepared as mentioned in Fig. 5. Section 1 and 2 are shown in Fig. e. Temperature: 1050°C, drive-in time 14 min.

In order to study the selective diffusion effect on the lifetime and sheet resistance, another experiment was designed. Therefore, after SODs were formed on the samples (100µl, 3000rpm and 15 sec), the coated samples were baked at different temps (50, 100, 150 and 200°C) to drive out the excess solvent. Next, samples were placed on the hotplate stirrer containing DI water in at 90°C for 3h so that the layer would be removed. Then, the samples dried and were loaded in diffusion furnace for 14 min with 4slm flow of N_2 gas.

The results of lifetime and sheet resistance are shown in Table III and Table IV respectively.

Table III: lifetime results at different pre-deposition temperatures: pre-deposition time:15 min, drive-in time: 14 min, boric acid concentration:5%.

Pre-dep Temp (°C)	τ (µs) : after 3h in the DI water	τ (µs): after drive-in diffusion
50	1.293	2.994
100	1.206	2.914
150	1.114	2.272
200	0.942	2.189

Table IV: sheet resistance results at different pre-deposition temperatures: pre-deposition time:15 min, drive-in time: 14 min, boric acid concentration:5%.

Pre-dep Temp(°C)	R_{sh} before process	R_{ah} after Dry	R_{sh} (Ω/□): after 3h in the DI water	R_{sh} (Ω/□): after drive-in diffusion
50	81.6	83	80	24.86
100	79.3	82.5	82	17.02
150	76.5	72.5	75.5	15.42
200	87.2	80.1	83.8	14.8

These tables clearly show that hot DI water can dissolve the solid layer formed on the samples and can be used as the potential etchant for this material. The ECVP measurements on the sample with and without etching with hot DI water are shown in Fig.7. This figure illustrates a remarkable difference in the surface concentration. In the other words, we have both light and heavy dopings in different areas of the wafer.

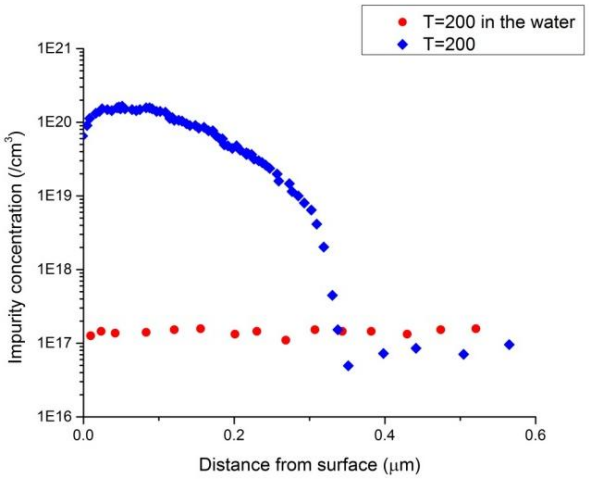

Fig.7: Depth profile of boron diffusion. Temprature:1050°C, drive-in time 14 min.

4. Conclusion

In this paper, we used boric acid source to formed boron emitter selectively on the n-type substrates. A thorough investigation of the effective parameters was performed to obtain the optimum conditions of boron diffusion process. It was found that spinning speed of 3000 rpm for 15 sec and 200°C drive-out bake result in a uniform dopant seed layer for the diffusion. The depth profile can be carefully controlled by monitoring the

boric acid solution concentration and the drive-in temperature. For selective cases, patterning can be done either by optical lithography and etching the unwanted parts using hot DI water or lift-off process. ECV measurements after selective process showed that the pre-deposition step (SOD) will not change the doping unless samples undergo a high temperature drive-in process.

5. References

[1] Kim, D. S., et al. 2007 "Silicon solar cells with boron back surface field formed by using boric acid" 22nd European Photovoltaic Solar Energy Conference

[2] Lee, Ji Youn, and Soo Hong Lee. 2004. "Boron back surface field using spin-on dopants by rapid thermal processing." JOURNAL-KOREAN PHYSICAL SOCIETY 44 1581-1586.

[3] Woods, William G. "An introduction to boron: history, sources, uses, and chemistry." Environmental health perspectives 102.Suppl 7 (1994): 5.

[4] Vick, G. L, and K. M. Whittle. "Solid solubility and diffusion coefficients of boron in silicon." Journal of the electrochemical society 116.8 (1969): 1142-1144.

[5] Das, Arnab. 2012."Development of high-efficiency boron diffused silicon solar cells."

Conference Proceedings

Solar World Congress 2015
Daegu, Korea, 08 – 12 November 2015

Spectral solar irradiance, atmospheric component and its relation with the production of photovoltaic current

Graciela M. Salum[1,2], Olga Vilela[3], Manoel Pedrosa[3,4], Javier Cruceño[2] and Rubén D. Piacentini[2,5]

[1]Scholl of Physic Sciences and Nanotechnology, Yachay Tech, Urcuquí, Ecuador

[2]Instituto de Física Rosario (CONICET-Univ. Nacional de Rosario), Rosario, Argentina

[3] Nuclear Energy Department, Federal University of Pernambuco, Recife - PE (Brazil)

[4] Instituto Federal de Educação, Ciência e Tecnologia de Pernambuco, Pesqueira, Brazil

[5]LESyC, IMAE, Univ. Nacional de Rosario, Rosario, Argentina

Abstract

We present results of spectral solar irradiance measured by a high quality doble-monocromator spectroradiometer in different seasons at the Astronomical Observatory of Rosario, Argentina. Since measures were done in the UV and visible ranges, we extended the measurements using the SMARTS model. Also, the model is applied to extend the analysis of spectral solar irradiance for Recife (Brazil) and Urcuquí (Ecuador). The maximum photovoltaic current for different solar cells (monolayer and multilayer) was derived using spectral irradiance associated to quantum efficiency of the PV cells. At 5th May 2013, the calculated photovoltaic currents were: 33.47 mA/cm^2 (mono-Si); 25.42 mA/cm^2 (poly-Si); 18.52 mA/cm^2 (CdTe); 12.28 mA/cm^2 (multilayer cell). The sensitivity of each cell technology to different atmospheric components (e.g., aerosols, water vapour, ozone) is also shown.

Keywords: *spectral, solar irradiance, photovoltaic cells, quantum efficiency*

1. Introduction

Solar spectral irradiance is one of the variables most difficult to be measured due to the requirement of high quality instruments (spectrorradiometers) with a periodic calibration and to the modification of the atmospheric components (gases and suspended particles, aerosols and clouds) that can vary rapidly. Even the Sun position changes more than1º in only some minutes. Consequently, special care needs to be taken in order to measure solar spectral irradiances in outdoor conditions. In the present work we present these measurements done in the Astronomical Observatory of Rosario, Argentina (32.95º S, 60.68ºW, 25 m asl) in different months of the year, with an OL756 portable UV-Vis spectroradiometer Optronics, a double monocromator, in the 280-400 nm and 400-750 nm (UV and visible) ranges.

We are mainly interested in the correlation of these spectral data with the photovoltaic (PV) current produced by (mono- and multi-) layer solar cells. Since usually these cells have quantum efficiencies that go up to the IR wavelength range, we used an extension of the data considering the SMARTS (Gueymard, 1995) algorithm. Currents (per unit area of the incident radiation) in the range of 10.02-38.3 mA/cm^2 can be obtained, depending on the maximum efficiency, the place and the spectral range of the considered cell. Theoretical analysis of the maximum limiting efficiencies has been obtained by Araújo and Martí (1994) with values of 40.8% for optimum single gap devices and of 86.8% for infinite number of gaps.

The significance of solar photovoltaic as a renewable energy source has been highlighted by Razykov et al. (2011) indicating that the PV market is growing at an annual rate of 35-40 %. Also the reduction to around 1 year in the time at which the solar cells equals the energy consumed for its production to the generated energy

doi:10.18086/swc.2015.05.03 Available at http://proceedings.ises.org

and the minimization of the environmental impact of a solar power plant has been discussed by Piacentini et al. (2013).

2. Results and discussions

2.1 Spectral solar irradiances

It was measured spectral solar irradiances at the Rosario Astronomical Observatory, Argentina, from 290 to 420 nm during clear sky days (with cloud coverage ≤ 25%) on horizontal plane, employing an Optronics OL756 spectroradiometer of the Institute of Physics Rosario (CONICET-National University of Rosario). This high quality instrument is a double monocromator (eliminating in this way the straylight effect that produces false signal at wavelength less than about 300 nm) with calibration lamp. In order to extend the wavelength range in the visible and infrared (IR) parts of the spectrum, we employed the SMARTS algorithm (Gueymard, 1995) for the model calculation of the solar spectral irradiance corresponding to the same day and hour of measurement.

The solar spectral global irradiance was modelled through SMARTS model using satellite data. The air temperature at 10 m, relative humidiy, total column precipitable water and surface albedo were obtained from the SSE/NASA, the ozone total column with OMI/NASA and AOD_{550m} (aerosol optical depth to 550 nm) with MODIS-Aqua Deep Blue.

The ozone and aerosol components were modified in order to have a very good match between model calculation and spectral measurements in the UV range. In order to adjust the model to measurement was used as a criterion "the area adjusted". This means, to find a small percentage difference between the areas of the irradiances. For May 03, 2013, the percentage difference was 0.12% and in the case of December 28, 2011 was 0.54%. In Fig. 1, it can seen the measurement superimposed to modelling.

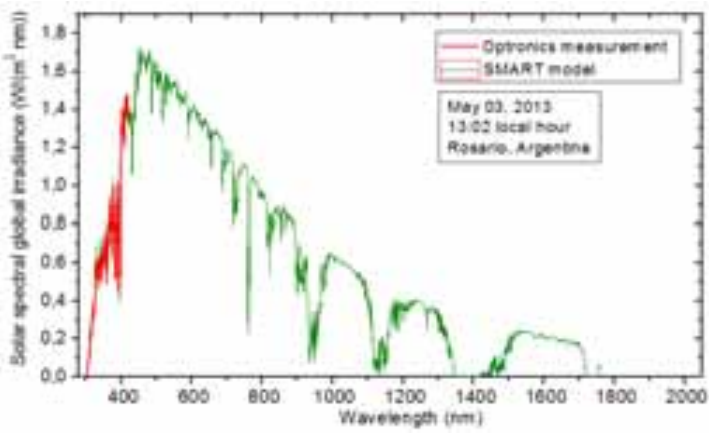

Figure 1: Solar spectral global irradiance incident on a horizontal surface for Rosario, Argentina, in May 03, 2013. The red line represents the Optronics measurement and the green line represents the SMART model result.

In Figure 2 (left), we display the solar spectral global irradiance for the days: December 28, 2011 at 13:03 local hour (=UT - 3); and May 05, 2013 at 13:02 local hour. The irradiances displayed in Figure 2 show the typical behavior of sun radiation in the UV-visible-IR ranges (see for example the reference spectrum of Gueymard, 1995), with strong absorption at certain particular wavelengths due to atmospheric gases.

In the Urcuqui case, since a lack of measurements, it was modelled the solar spectral global irradiance through SMARTS model using the same satellite data bases.

The selected days were: September 24 and July 21 because they are the days with the minimum (1.1°) and

maximum (80.6°) solar zenital angle respectively for the place, see Fig.2 (middle). The reason for the election site is based in the altitude of the Urcuquí, since this place is located at 2320 masl (meters above the sea level). Also, Urcuquí has a low aerosol optical depth (0.046 in September and 0.137 in July). The middle of Figure 2, we shows the solar spectral global irradiance calculated with the SMARTS for Urcuquí.

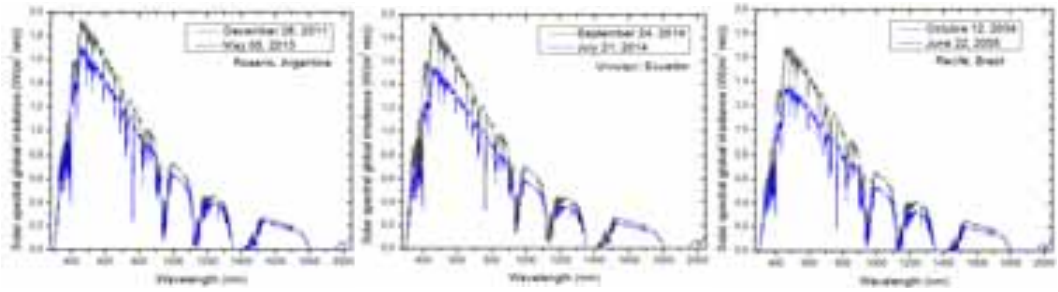

Figure 2: Solar spectral global irradiance incident on a horizontal surface for Rosario, Argentina (left), Urcuquí, Ecuador (middle) and Recife, Brazil (right). In the case of Rosario, the model was used to extrapolate the measurements and in the cases of Urcuqui and Recife all data was modeling.

Also, for Recife there is a lack of calibrated measurements, then it was modelled the solar spectral global irradiances for two day through SMARTS model using the same satellite data base. It was modeled the following days: June 22, 2005 and October 12, 2004 (see Fig.2, right).

2.2 Spectral quantum efficiency

The figure 3 shows the quantum efficiency for different types of solar cells. Quantum efficiency refers to the efficiency with which photons that reaches the cell is able to generate collectable carriers. It depends on the absorption characteristics of the solar cell. The upper limit wavelength for each type of cell is determined by the energy gap of the materials that composes the solar cell. Photons with energy lower than this limit is not absorbed.

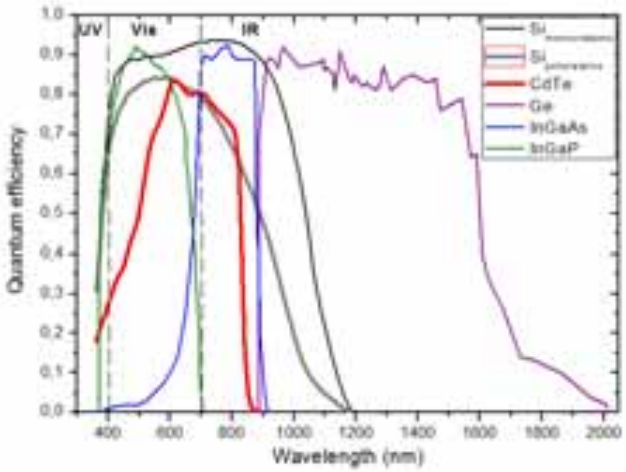

Figure 3: External quantum efficiency of different solar cells as function of wavelength.

The quantum efficiency of InGaAs, InGaP and Ge presented in Fig. 3 were obtained directly from the datasheet of a manufacturer of multijunction solar cells. The curves presented for the other materials (Fig. 3) were obtained using the relationship between quantum efficiency (QE) and spectral response (SR), presented by Field (1997) in equation (1).

$$QE = \frac{hc}{\lambda q} SR \qquad \text{(eq. 1)}$$

were q is the absolute value of electron charge, λ is the wavelenght, h is the Planck constant, and c the the speed of light in vacuum.

3. 2.3 Spectral and total surface density photovoltaic current

The photovoltaic current (per unit area) is produced in the solar cell by the interaction of solar photons with the material exposed to the Sun. This can be described mathematically through the following equations (2 to 4):

$$I_{FV,A} = \int_{\lambda_2}^{\lambda_1} \varphi . \varepsilon_\lambda . \Delta\lambda \quad \text{(eq. 2)}$$

$$\varphi = \frac{I(\lambda,t)}{E_f} . e^- \quad \text{(eq. 3)}$$

$$E_f = \frac{h.c}{\lambda} \quad \text{(eq. 4)}$$

being φ the maximum spectral surface density photovoltaic current, e^-= the electron charge, h = Planck´s constant, ε_λ the solar cell external quantum efficiency, $\Delta\lambda = \lambda_2 - \lambda_1$ the wavelength interval which is defined from the external quantum efficiency wavelength range of each solar cell, and E_f is a photon energy.

One of the purposes of studying the photogenerated current is the possibility to analyze the efficiency of the solar cell to capture solar radiation in different regions of South America. For example, Hau-Vei et al. (2014) presented a hybrid design of the GaAs combined with colloidal quantum dots, achieving a power conversion efficiency as high as 24.65% compared with traditional GaAs-based devices and current densities until approximately 23 mA/cm^2. Also, Mohammed et al (2013) presented a model for simulation of the enhancement of the photogenerated current por PN silicon photodetectors with impurities.

Figure 4 shows the maximum spectral surface density photovoltaic current, the particular quantum efficiency and the weighted value with external quantum efficiency for different solar cells for a typical clear sky day (May 5, 2012 in Rosario) around solar noon. We also indicate in the same figure the integral value of this weighted value ($\varphi.\varepsilon_\lambda$). The corresponding values of the surface density photovoltaic current are summarized in Table 1 showing that the maximum current corresponds to the mono-Si and the minimum one to InGaAs, in all cases.

Table 1: Integrated weighted surface density photovoltaic current (iFV,A) for different days of the year and for monolayer and polylayer solar cells. Also, the ratio between the maximum and minimum current values and the mean (with its standard deviation) values are included.

		$i_{FV,A}$ (mA/cm^2) for different solar cells							
Date (local hour = UT-3)	Place	InGaP	InGaAs	Ge	mono-Si	poly-Si	CdTe	Ratio max/min	Mean value (standard deviation)
28/12/2011 (13:02)	Rosario Argentina	17.09	13.97	18.68	38.30	29.04	21.15	2.13	23.7 (8.4)
05/05/2012 (13:02)	Rosario Argentina	14.82	12.28	17.86	33.47	25.42	18.52	2.73	21.9 (11.1)
24/09/2014 (13:00)	Urcuquí Ecuador	16.81	13.67	18.8	37.61	28.49	20.68	2.75	22.7 (8.8)
21/07/2014 (13:00)	Urcuquí Ecuador	13.68	11.33	15.70	30.96	23.96	17.01	2.73	18.8 (7.3)
22/06/2005 (11:30)	Recife Brazil	12.10	10.02	12.91	27.13	20.59	15.10	2.71	16.3 (6.4)
12/10/2005 (11:20)	Recife Brazil	15.03	12.48	16.54	33.87	25.67	18.75	2.71	20.4 (8.0)

Araújo and Martí (1994) obtained an optimum photogenerated current of 56.09 mA/cm^2 with their model, while Razykov et al. (2011) determined a short-circuit current density of 42.2 mA/cm2, with an efficiency of 24.7%. Steudel et al. (2012) presented a short-circuit current density of 17.94 mA/cm^2 in a CdTe solar cell for an air mass of 1.5. As it can be seen in Table 1, our calculations gave a range of 15.10 to 21.15 mA/cm^2 for the same type of solar cells with air mass between 1 and 1.54

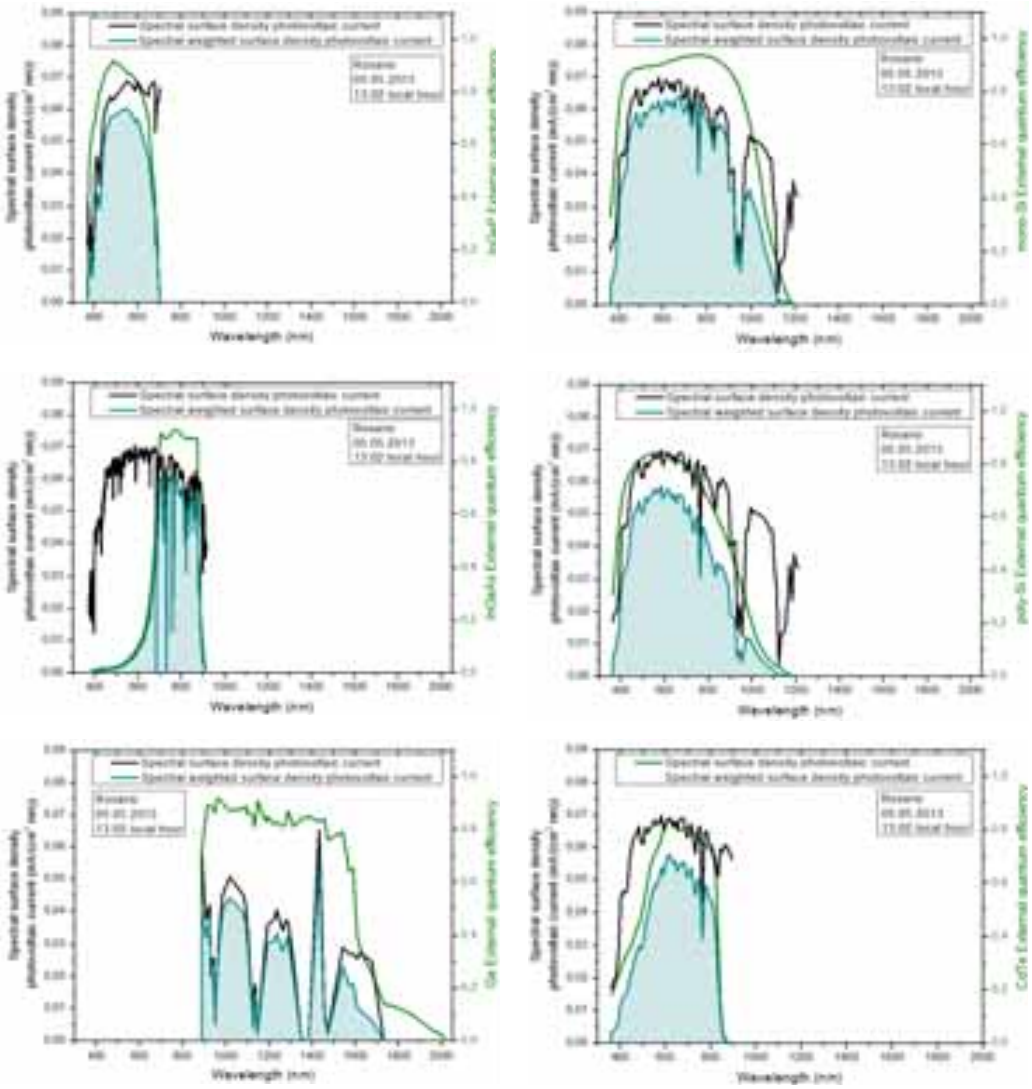

Figure 4: Spectral surface density photovoltaic current (black line) and weighted (cyan shading area) with external quantum efficiency (green line) for different solar cells determined for solar spectral irradiance measured the day May 5, 2013 at 13:02 local hour at the Astronomical Observatory of Rosario, Argentina. The integrated weighted surface density photovoltaic current is also given.

4. 2.4 Sensibility analysis

As a general criteria for the analysis of the influence of each atmospheric component on the surface density photovoltaic current, first it was analyzed if there is a significant wavelength superposition of the external quantum efficiencies and the atmospheric transmittance of given gases or aerosol. From Figure 5 and considering the criteria described before, it can be deduced qualitatively that the water vapor amount in the atmosphere influences meanly in the Ge solar cell. The total column ozone and the aerosols have more impact over the InGaP cells while they have less impact on Ge cells.

It was calculated the sensibility for three different parameters with the data of Rosario in December 28, 2011. The corresponding results of the sensitivity of the different atmospheric component variation on surface density photovoltaic current ($i_{FV,A}$) is given in Table 2. They confirm the initial hypothesis. To build the Table 2, each parameter (ozone, aerosol and water precipitation) were changed in ten percent and it was calculated the percentage change of the resulting surface density photovoltaic current.

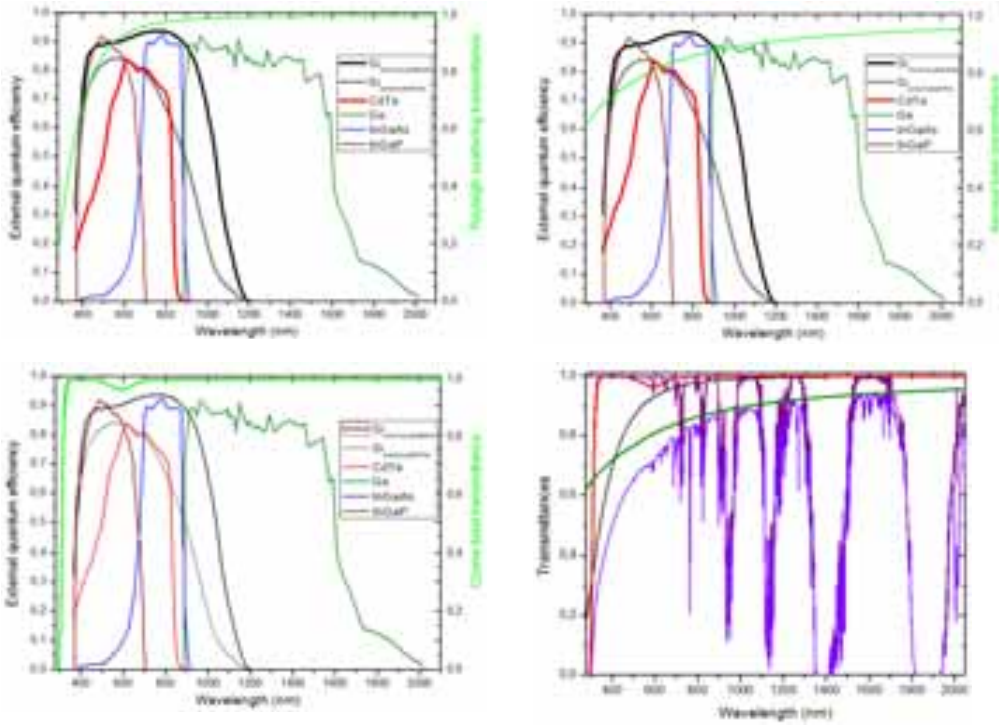

Figure 5: Transmittances and its relationship with the different external quantum efficiency of solar cells. Top left: Rayleigh scattering transmittance. Top Right: aerosol total transmittance. Bottom left: ozone total transmittance. Bottom right: All transmittance at December 28, 2011 in Rosario: ozone total (red line), Rayleigh scattering (black line), aerosol (green line), water vapor (purple line) and total (violet line) transmittances.

Table 2: Analysis of the sensitivity ($\Delta i_{FV,A}$ %) of atmospheric component variation on surface density photovoltaic current ($_{iFV,A}$) for Rosario in December 28, 2011. Top: with change of total column ozone. Middle: with change of AOD_{550nm}. Bottom: with change of precipitable water.

Parameters		$i_{FV,A}$ (mA/cm^2) for different solar cells					
		InGaP	InGaAs	Ge	mono-Si	poly-Si	CdTe
Total column ozone (DU)	265.5	17.09	13.97	18.68	38.30	29.04	21.15
	292.05	17.06	13.96	18.68	38.26	29.00	21.12
$\Delta i_{FV,A}$ %	10	0.176	0.071	0	0.104	0.138	0.142

Parameters		$i_{FV,A}$ (mA/cm^2) for different solar cells					
		InGaP	InGaAs	Ge	mono-Si	poly-Si	CdTe
AOD_{550nm}	0.2325	17.09	13.97	18.68	38.30	29.04	21.15
	0.25575	17.02	13.94	18.65	38.19	28.95	21.09
$\Delta i_{FV,A}$ %	10	0.410	0.215	0.161	0.287	0.310	0.284

Parameters	$i_{FV,A}$ (mA/cm^2) for different solar cells					
	InGaP	InGaAs	Ge	mono-Si	poly-Si	CdTe

Precipitable water (cm)	2.71	17.09	13.97	18.68	38.30	29.04	21.15
	2.98	17.09	13.97	18.68	38.30	29.04	21.15
$\Delta i_{FV,A}$ %	10	0	0	0	0	0	0

In the last case, a change of ten percentage in the precipitable water value did not produce a change in the surface density photovoltaic current.

5. 3. Conclusions and future perspectives

The main results and conclusions are:

-Spectral solar irradiance has been measured and modelled for Rosario (Argentina), Urcuquí (Ecuador) and Recife (Brazil), at different seasons permitting to have a wide wavelength range, in order to calculate photovoltaic current.

-Spectral and total surface density photovoltaic current shows a range between 10.02mA/cm^2 (for June 22, 2005, in Recife) and 38.3mA/cm^2 (for December 28, 2011, in Rosario).

-Sensibility analysis of atmospheric components of the total surface density photovoltaic current, shows that a change of ten percentage of the total column ozone and the same change in the AOD_{550nm} produces the largest decrease in the current solar cells of InGaP, in both cases, and smallest in the Ge solar cells. A change of ten percent in the precipitable water do not produce a change in a current of any solar cell.

6. Acnowkedgements

The authors like to acknowledge the following institutions: CONICET, Argentina, Yachay Tech University, CNPq - Brazil and persons Fernando Fernández and Joel Gornati.

7. References

Araújo, G.L., Martí, A., 1994. Absolute limiting efficiencies for photovoltaic energy conversion. Solar Energy Materials and Solar Cells. 33, 213-240.

Field, H., 1997. Solar cell spectral response measurement errors related to spectral bandwidth and chopped light waveform. 26th IEEE Photovoltaic Specialists Conference.Anaheim, California. 1997

Gueymard, C.A., 1995. SMARTS, A Simple Model of the Atmospheric Radiative Transfer of Sunshine: Algorithms and Performance Assessment. Technical Report No. FSEC-PF-270-95. Cocoa, FL: Florida Solar Energy Center.

Hau-Vei, H., Chien-Chung, L., Yu-Lin, T., Hsin-Chu, C., Kuo-Ju, C., Yun-Ling, Y., Wen-Yi, L., Hao-Chung, K., Peichen Y., 2014. Highly Efficient Hybrid GaAs Solar Cell Based on Colloidal-Quantum-Dot-Sensitization. Scientific Reports. 4 : 5734 | DOI: 10.1038/srep05734

Mohammed, W.F., Humoody, M.A., Al-Tikriti, M.N., 2013. Simulation of photogenerated current of PN silicon photodetector enhanced by impurity photovoltaic effect. Renewable and Sustainable Energy Reviews 26, 408–413

Piacentini, R.D., Schmidt J., Budini N., Vega M., Giandoménico E., Feldman S., Buitrago R., 2013. Photovoltaic materials and solar power plant optimization design in relation to its environmental impact. En el libro: Energy Book Series - Volume # 1: “Materials and processes for energy: communicating current research and technological developments”, 103-113.

Razykov, T.M., Ferekides, C.S., Morel, D., Stefanakos, E., Ullal, H.S., Upadhyaya, H.M., 2011. Solar photovoltaic electricity: Current status and future prospects. Solar Energy. 85 (8) 1580–1608

Steudel. F., Dyrba, M., Schweizer, S., 2012. Fluorescent borate glass enhances cadmium telluride solar cells. Proc SPIE, DOI: 10.1117/2.120126.004235

Express – analysis of Local Current Density Distribution Over the Area of PV Cells Using Thermovision Systems

Leonid D. Saginov

Russian Research Institute for Electrification of Agriculture, Moscow (Russia)

Abstract

The current density distribution over the area of photovoltaic cell is an important characteristic for at least two reasons. The first one - the homogeneity of the current density distribution characterizes the quality of solar cell production and second - the heterogeneity of the photocurrent distribution leads to local overheating of the solar cell and consequently decrease in its lifespan. The paper describes the methodology and experimental results of current density distribution research over the area of PV cell by thermovision-thermographic method. Silicon solar cells of different design where researched. Over the area of investigated samples, the spots of local Joule overheating are observed due to higher current density in these localities. The study of these spots by Laser Beam Induced Current (LBIC) method showed the presence of leakage current through p-n junction.

Keywords: *photovoltaic cell, thermal imaging system, infrared (IR) region of spectrum, forward- and back-biased diode, local leakage current, vertical multijunction solar cells, IR thermovision picture*

1. Introduction

The total peak power of photovoltaic (PV) stations is increasing annually by more than 20%. However, this power station lifespan remains twice less than those of atomic or thermal power station. The efficiency degradation of cells (and modules) is one of the main reasons of this. It is evident, that heterogeneity of the photocurrent distribution over the area of PV cell accelerates this degradation because of additional local overheating in spots with high current density.

Production of solar cells requires rapid and effective technology and function control of PV cells. Measurement of photovoltaic characteristics at the output of the production line is an integral feature of the functioning and technology. This measurement does not reflect the details of technology and in particular the important characteristics of the process uniformity for the plate area, which is important when increasing the area of the plates. The purpose of this paper is to identify the heterogeneity parameters of photoelectric conversion on the solar cell area by thermovision - thermographic method.

The method is based on the fact that any body with the temperature above absolute zero, in accordance with Planck's law, emits a continuous spectrum of electromagnetic waves. Infrared imager, sensing infrared region of the spectrum, forms the image. As the average temperature resolution of thermal imaging currently reaches 0.1 K (Weinreich, 2009), the presence of even small overheating will be shown in the infrared image.

2. Methodology of measurements

Si-monocrystal PV cell structure (and, accordingly, the built-in potential) was usual: on one side of p-type plate a diffused p-n junction was formed, on the other - a layer of p^+ for contacts. Photoelectric effect in PV cell is characterized by the current flow, arising from the absorption of solar radiation, through the PV cell built-in potential (if the load is connected to it). It is evident from PV cell equivalent model (Fig.1), PV cell heating is determined by R_{sh} ,R_{ser} resistances distribution over the area of the cell. Shunt resistance R_{sh} is connected in parallel with diode and characterizes the leakage currents of p-n junction, which should be minimal for high efficiency PV cell, i.e. resistance R_{sh} should be maximum. Series resistance R_{ser} is determined by metal - semiconductor contact resistance, n-layer distributed resistance and metallization routings resistance. It is important that all these parameters are distributed through plate area and completely depend

doi:10.18086/swc.2015.05.04 Available at http://proceedings.ises.org

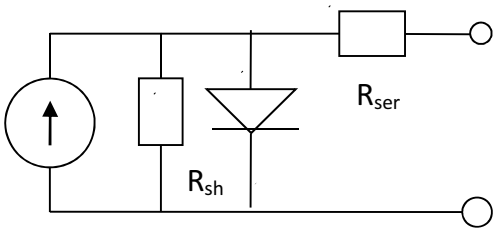

Fig.1: PV cell equivalent model

on the level and quality of photovoltaic production technology. Direct study of PV cell by thermovision system when illuminated by solar radiation or simulator is a complex task. The reason for this is the need to get rid of distracting reflections in infrared (IR) region of the spectrum that distort the IR image of the cell. In addition, silicon has high reflectance in IR region and hence low emissivity. Thus, it is necessary to ensure the flow of current through the PV cell in the absence of light illumination. This is achieved by applying voltage to the PV cell, provided that the contacts are ohmic. However, special measures should be taken to maximize the thermal contrast (Sviridov, 2002), including reflectionless arrangement. When the ratio R_{sh} / R_{ser} of order $10^2 – 10^3$ for usual PV cell and infinite generator resistance, the forward – biased (with respect to p-n junction) current will heat series resistance but reverse – biased will heat shunt resistance.

3. Research of ordinary PV cells

Si-monocrystal bifacial PV cell size (125x125) mm was selected for research. We used infrared NEC thermovision instrument TN5100 (HgCdTe time delay and integration detector, spectral range 8-12 mkm, minimum temperature sensitivity 0,05 K, field of view 20x30 °, working distance approximately 0,5 m).

Fig. 2-4 and Fig. 5-7 show IR thermovision pictures (TVP) of the mentioned above PV cell with current

Fig.2: TVP, *I*=0

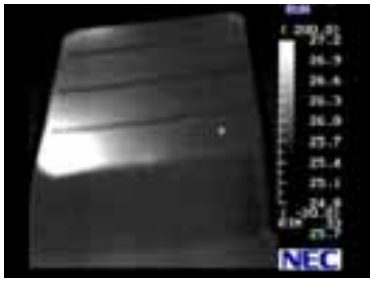

Fig.3: TVP, *I*= - 0,2A

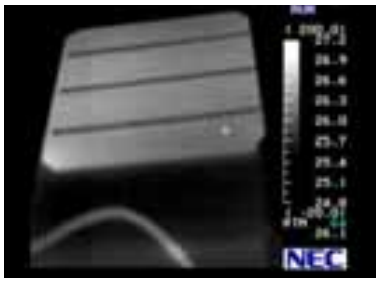

Fig.4: TVP, *I*= +1,4A

$I = 0$, forward (+) and reverse (-) directions with respect to the p-n junction. Fig. 2-4 show thermovision picture of p-n plate side. Comparison of IR pictures shows that the uniform temperature background when $I = 0$ (Fig.2) changes significantly at the current $I = - 0,2$ A (Fig.3). There are three different degrees of heating. The greatest overheating occurs in the left front corner of the plate, weaker heating in the left rear corner and the weakest - in the right rear corner. Local current density in Fig.3 is determined by the differential resistance of back-biased diode in this particular place. Obviously, the overheating of the place is due to the increase in leakage current through the R_{sh} in these areas. In this case, according to the degree of heating, the strongest current flows in the left front corner, smaller current in the left far corner and the weakest in the right rear corner of the cell image. In the case of forward biased photodiode (Fig.4, $I = +1,4$ A), the heating picture, determined by R_{ser} as mentioned above, is more uniform. Only left front spot picks out. It can be assumed that here the shunt resistance R_{sh} is comparable to series resistance R_{ser} , which is caused by shot on the end face of the p-n junction. In addition, in the Fig.4 three dark metallization routings are clearly visible, the emission of which is due to the metallization significantly lower than that of silicon.

The p^+ side TVP of the same cell (sample inverted to the right) is represented by Fig.5-7. The same three

Fig.5: TVP, *I*=0

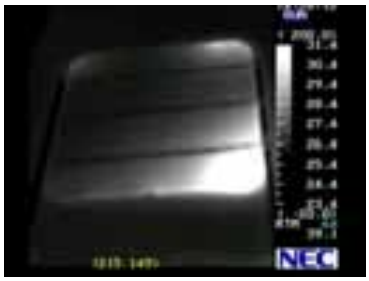

Fig.6: TVP, *I*= - 0,4A

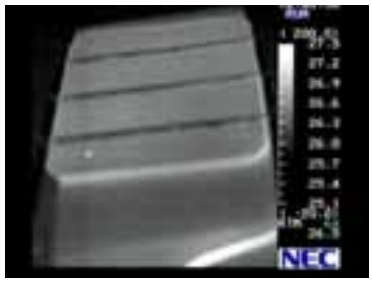

Fig.7: TVP, *I*= +1,8°

leakage areas through shunt resistance are observed with back bias (Fig.6), but to obtain the same temperature contrast picture, as in Figure 2, it is necessary to increase the current by two times (I = - 0,4 A). It confirms the fact that the source of the heating is on the lower (i.e. p-n) side of the cell. p^+ side of the cell, as would be expected, is heated uniformly with direct current (Fig.7), however, to get image contrast as in Fig. 4, the current must be increased (I = +1,8 A). In this case lower (p-n) side of the cell is warmer, as indicated by a significant reflection of the infrared light from the table in Fig.7. Note that the metallization routing on p^+ side is less clear than on p-n side (Fig.4); which may be caused by lower quality of contacts (e.g. non-ohmic) on the p^+ side of the cell.

These results confirm the use of thermovision system for PV cell technology analysis. Indeed, if in the technology process non-uniformity takes place in any area of Si-plate, heterogeneity arises (in p-n junction or tunneling in the metal-semiconductor contact due to, for example, pollution), the local current density at this point will change and it will lead to changes in temperature (Joule heat). Resulting local temperature inhomogeneities are fixed by thermovision system.

4. Comparative study of PV cell by thermovision system and LBIC

IR thermovision and LBIC methods are used for comparative study of 100 mm diameter cell with low efficiency of PV conversion (some less than 12%). Fig.8 shows TVP of this cell. The increase of temperature by 5 degrees corresponds to the transition from blue to raspberry color. The highest temperature is white color.

Fig.8: TVP 100mm cell

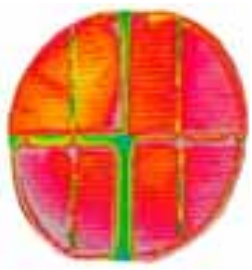

Fig.9: TVP catted cell

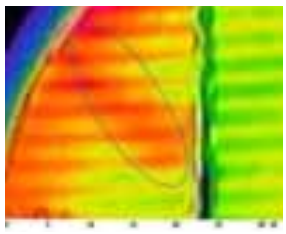

Fig. 10: TVP of upper left quarter

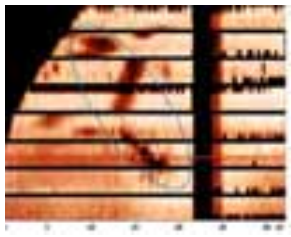

Fig.11: LBIC scan of upper left quarter

The characteristic features of the picture are: temperature increase is observed around the perimeter of the specimen, i.e. junction leakage currents increase from the center to the edges of the plate; there are local areas of high currents, for example, area 1; evident temperature non-uniformity of metallization routings.

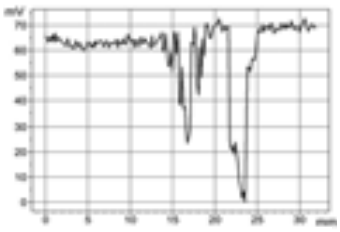

Fig.12: LBIC current along Fig. 9 red line

This PV cell was cut into four pieces for LBIC investigation. The corresponding TVPs are shown in Fig.9. The comparison of images in Fig.8 and Fig.9 shows that all the features of thermovision images remain. Upper left quarter of the cell with local inhomogeneity marked number 1 (Fig.9) was chosen for LBIC investigation using NT-MDT instrument «Spectrum». The field of scanning is ~ 20x35 mm. Fig.10 and Fig.11 show upper left quarter of cell and LBIC scan image of this area. In Fig.11 LBIC current reduction under laser illumination corresponds to the darkening of the picture. It is an evident coincidence of temperature increasing area (Fig.10) and low LBIC current (Fig.11), due to an increase in leakage current in

the last case. Fig.12 shows LBIC current along red line on Fig.11. There is correspondence to Fig.11: the right line (21-25mm) is in keeping with highway and left (15-20 mm) conforms to the darkening (leakage current increasing).

5. Thermovision pictures of Vertical Multijunction Solar Cell

TVP of silicon Vertical Multijunction Solar Cells (VMSC) were also researched in IR region 3-5 mkm. VMSC are made by connection (soldering) in series of ordinary PV cells with continuous metallization on p- and n-sides of the Si-plate and consequent cutting of the pile perpendicular to the p-n junction plane (Strebkov, 2010). When illuminated, the light front is perpendicular to the plane of p-n junction but is not parallel as for ordinary planar PV cell. The main advantage of VMSC (production by usual planar Si-processing) is high voltage with density more than 15 V/cm.

In our experiments we research VMSC with 25 microelements in series on facial side of the cell. Methodology of image getting is subtraction of the picture without bias out of the picture with forward or reverse bias. Fig.13 shows TVP of VMSC with reverse bias and Fig.14 - TVP of VMSC with forward bias. Comparison

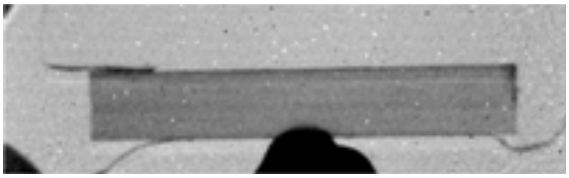

Fig.13: TVP of VMSC with reverse bias, V= - 30V, I= 10mA

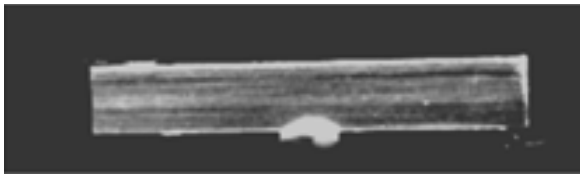

Fig.14: TVP of VMSC with forward bias, V= + 10V, I= 100mA

of these pictures leads to the conclusion about the inversion of temperature pattern. The reasons of this inversion require more detailed research. However, if we assume that the composition of the sample consists of microelements with different indices of ideality in the exponential diode characteristics, the ratio of the differential resistance will be inverted with forward and reverse bias. Accordingly, temperature pattern will also be inverted.

6. Conclusions

1. Thermovision-thermographic method is useful in inspection of PV cells quality and its production technology. Also, the functioning of solar power station in field conditions may be controlled to identify the faulty elements in the modules, substandard wiring and terminal connections, etc.

2. In the above procedure tests a lot of attention should be paid to the exclusion of side illumination, reflections, etc.

The author wishes to express his thanks for help with the measurements and design of this paper to V.N.Solaykov, R.Z. Khafizov and V.A. Bykov.

The work was done with financial support of the Ministry of Education and Science of the Russian Federation – the unique identifier of the applied scientific research is RFMEFI57514X0012.

7. References

Strebkov D.S., 2010. Matrix solar cells, GNU VIESH, Moscow.

Sviridov A.N., 2002. Thermal Contrasts Calculation in Thermovision Pictures. Prikladnaya Fizika. 2, 109-124.

Weinreich B., 2009. Thermal imagers. Photon International. 10, 150-183.

Development of Recycling Process of Photovoltaic Ribbon in Spent Solar Module using Water Vapor Generated by Waste Heat

Jin-Seok Lee[1], Bo-Yun Jang[1], Joon-Soo Kim[1], Young-Soo Ahn[1], Gi-Hwan Kang[2] and Jei-Pil Wang[*3]
[1]Advanced Materials and Devices Laboratory, Korea Institute of Energy Research, Daejeon 305-343, Korea
[2]Photovoltaic Laboratory, Korea Institute of Energy Research, Daejeon 305-343, Korea
[3]Department of Metallurgical Engineering, Pukyong National University, Busan 608-739, Korea
*Corresponding author, email: jpwang@pknu.ac.kr

New recycling process was attempted to recover copper substrate and to remove coating layer consisting of tin (Sn) and lead (Pb) of photovoltaic ribbon in spent solar module by means of oxidation using water vapor generated by waste heat. The oxidation behavior of the photovoltaic ribbon was studied under two different conditions of dry and moist atmosphere. The rate of oxidation was compared at 500°C in given conditions and the oxidized coating layer consisting of lead of 68.99wt% and tin of 31.21wt% was taken off from the substrate at room temperature. The chemical composition of copper ribbon after oxidation was analyzed using ICP-MS (Inductively Coupled Plasma Mass Spectrometry) and the purity of copper obtained was found to be about 99.5wt%. Further process using zone-melting furnace was consequently carried out fabricate high-purity copper and 4N grade of copper (≥ 99.99%) was finally obtained. The component of coating layer was safely stabilized as oxide forms of PbO and SnO.

Keywords: *Photovoltaic Ribbon, Oxidation, Water Vapor, Zone Melting, Copper*

1. Introduction

The increased energy consumption of recent industrial advancements has further increased the use of fossil energy, resulting in serious environmental problems and a growing concern over energy depletion. A great deal of research has been devoted to the development of new and renewable energy sources to solve these problems. In particular, the solar energy industry has prompted rapid growth of photovoltaic energy research.[1)] Unlike fossil fuels, photovoltaic cells are ecofriendly, powered by a renewable energy source, and have a lifetime of 15 years or more; as a result of these traits, their development is rapidly growing on the national and global scales.[2)]

With the growth of the solar energy industry, the volume of spent photovoltaic modules has continued to increase, with its cumulative volume estimated to reach about 130,000tons by the year of 2030. However, over 90% of the end-of-lifetime photovoltaic modules can be recycled, despite currently being buried in general landfills or completely neglected.[3)4)] For this reason, various studies have been carried out on the recovery and recycling of precious resources from spent photovoltaic modules, but in particular there have been very few attempts at recovering the copper in the photovoltaic modules.[5)]

Existing copper recovery methods involve oxidizing the copper ribbon electrode at high temperatures of 800°C or more in order to separate the oxidized coating layer from the base material. However, in this study a water oxidation method at a lower temperature of 500°C is used for oxidation, and a ball milling process is subsequently carried out in order to separate the oxidized coating layer from the base material. The recovered copper base is analyzed by ICP-MS (inductively coupled plasma mass spectrometry), and the oxidized coating layer is analyzed using XRF (X-ray fluorescence) and XRD (X-ray diffraction).

2. Methods and Materials

2.1 Experimental Setup

Figure 1 shows the experimental setup used in this study, which includes an electric furnace, a thermocouple and a heater, as well as a tube that connects a flask containing distilled water and the electric furnace for the injection of H_2O. To prevent the water vapor from condensing in the tube, the tube was wound with heating tape.

doi:10.18086/swc.2015.05.05 Available at http://proceedings.ises.org

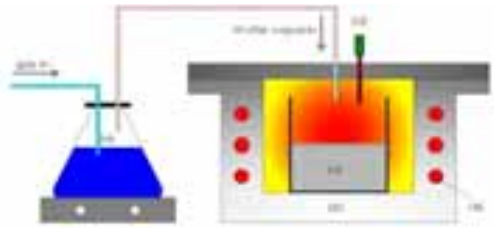

Fig. 1 Schematic of H_2O oxidation process (a: distilled water, b: furnace, c: photovoltaic ribbon, d: thermocouple, e: heater)

Figure 2 is an image of the ball milling equipment, which was used to oxidize the copper ribbon during the H_2O oxidation process and to separate the copper base from the oxidized coating layer, as well as an image of the milling balls used in the test.

Fig. 2 Ball milling equipment and used milling balls

Three 30mm diameter balls and 15 0.7mm diameter balls were used in the test.

Table 1. Chemical composition of photovoltaic ribbon analyzed by ICP-MS

Element	Weight, %
Cu	87.752
Pb	5.247
Sn	6.150
Nb	0.063
Ag	0.046

2.2 Test Materials

The chemical composition of the photovoltaic ribbon of KOSBON Co. used as the test material is given in Table 1. Based on the ICP-MS results, the ribbon contained 87.752% copper, 5.427% lead, 6.150% tin and trace amounts of niobium and silver.

3. Results

The spent photovoltaic module was heat treated under air condition at 500°C for 2h to recover the copper ribbon electrode from the module. The coating layer was then oxidized to separate and recover the copper base and the scale under the following reactions.

$2Cu + O_2(g) \rightarrow 2CuO$ (eq. 1)
$2Pb + O_2(g) \rightarrow 2PbO$ (eq. 2)
$2Sn + O_2(g) \rightarrow 2SnO$ (eq. 3)

Table 2 shows the thermodynamic properties for the oxidation reactions of copper, lead and tin, the main components of the copper ribbon electrode, as determined by HSC Chemistry[5.1].
Copper, lead and tin underwent forward reactions because their ΔG values were less than 0, as shown in the Table 2, confirming activated oxidation reactions.

Table. 2 Thermodynamic properties of oxidation reactions of copper, lead, and tin

$2Cu + O_2(g) = 2CuO$			
T	ΔH	ΔS	ΔG
C	Kcal	cal/K	Kcal
0	-74.504	-44.552	-62.335
100	-74.308	-43.955	-57.906
200	-73.987	-43.196	-53.548
300	-73.612	-42.479	-49.265
400	-73.211	-41.834	-45.05
500	-72.795	-41.258	-40.896

$2Pb + O_2(g) = 2PbO$			
T	ΔH	ΔS	ΔG
C	Kcal	cal/K	Kcal
0	-104.285	-47.342	-91.354
100	-104.056	-46.631	-86.655

200	-103.778	-45.974	-82.026
300	-103.483	-45.408	-77.457
400	-105.494	-48.774	-72.662
500	-105.154	-48.303	-67.808
2Sn + O_2(g) = 2SnO			
T	ΔH	ΔS	ΔG
C	Kcal	cal/K	Kcal
0	-134.256	-46.427	-121.574
100	-133.974	-45.544	-116.979
200	-133.732	-44.968	-112.455
300	-136.901	-51.263	-107.52
400	-136.543	-50.689	-102.422
500	-136.124	-50.11	-97.382

The chemical equations for the reactions of copper, lead and tin with oxygen and H_2O are shown below, and the thermodynamic properties of these reactions (as determined using HSC chemistry) are shown in Table 3.

$2Cu + 2O_2(g) + 4H_2O(g) \rightarrow 2Cu(OH)_2 + O_2(g) + 2H_2O(g)$ (eq. 4)

$2Pb + 2O_2(g) + 4H_2O(g) \rightarrow 2Pb(OH)_2 + O_2(g) + 2H_2O(g)$ (eq. 5)

$2Sn + 2O_2(g) + 4H_2O(g) \rightarrow 2Sn(OH)_2 + O_2(g) + 2H_2O(g)$ (eq. 6)

The copper, lead and tin that reacted with oxygen and H_2O also showed forward reactions because their ΔG values were less than 0, as shown in Table 3, confirming activated oxidation reactions. Based on these theoretical values, the oxidation test temperature was set to 500°C.

Table. 3 Thermodynamic properties of reactions of copper, lead, and tin with oxygen and H_2O

2Cu + $2O_2$(g) + $4H_2O$(g) = $2Cu(OH)_2$ + O_2(g) + $2H_2O$(g)			
T	ΔH	ΔS	ΔG
C	Kcal	cal/K	Kcal
0	-72.759	-47.729	-59.722
100	-77.249	-63.331	-53.617
200	-78.623	-66.593	-47.115
300	-80.327	-69.837	-40.3
400	-83.17	-74.398	-33.089
500	-86.065	-78.409	-25.443

2Pb + $2O_2$(g) + $4H_2O$(g) = $2Pb(OH)_2$ + O_2(g) + $2H_2O$(g)			
T	ΔH	ΔS	ΔG
C	Kcal	cal/K	Kcal
0	-129.511	-125.142	-95.329
100	-133.117	-136.384	-82.226
200	-136.83	-145.193	-68.132
300	-140.663	-152.538	-53.235
400	-146.934	-162.752	-37.378
500	-150.982	-168.357	-20.816
2Sn + $2O_2$(g) + $4H_2O$(g) = $2Sn(OH)_2$ + O_2(g) + $2H_2O$(g)			
T	ΔH	ΔS	ΔG
C	Kcal	cal/K	Kcal
0	-151.72	-86.529	-128.085
100	-155.35	-97.843	-118.84
200	-159.122	-106.791	-108.594
300	-166.418	-120.996	-97.069
400	-170.307	-127.25	-84.649
500	-174.258	-132.72	-71.645

First, to oxidize the coating layer through the use of water vapor, distilled water is placed in the flask connected to the furnace and boiled. In order to facilitate the injection of water vapor into the furnace, argon gas was injected into the flask at 100 cc/min After inserting the heat-treated copper ribbon into a furnace for 2h, the ribbon was heat treated at 500°C in order to facilitate the oxidation test. The original copper ribbon sample used in the test weighed 15g, and the H_2O oxidation tests were carried out at time intervals of 1, 3, 5 and 10 hrs. The oxidized copper was analyzed by SEM (scanning electron microscopy) to analyze the oxidized layer. Figure 3 shows images of the oxidized copper ribbons for each reaction time.

Afterwards, the copper base was recovered by ball milling at 90rpm for 1h and was analyzed by ICP-MS, and the oxidized coating layer was analyzed by XRF and XRD.

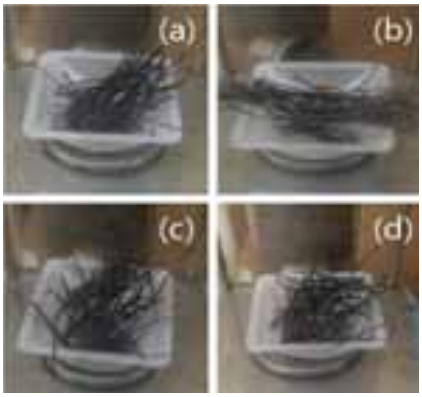

Fig. 3 H_2O oxidized photovoltaic ribbons(a: 1 h; b: 3 h, c: 5 h, d: 10 h)

4. Discussion

Rather than using the existing high temperature oxidation approach under atmospheric conditions at 800°C to recover copper from the copper ribbon electrode in the spent photovoltaic module, an H_2O oxidation approach was carried out at 500 °C for 1 h, 3h, 5h, and 10h. The weight of the oxidized copper ribbon increased by 0.32g after 1h H_2O oxidation, by 0.53g after 3h oxidation, by 0.98g after 5h oxidation, and by 1.20g after 10h oxidation. The amounts of distilled water consumed were 551.17g, 891.52g, 1673.24g, and 3172.48g, respectively. To compare the weight change between the air and H_2O oxidation tests under atmospheric conditions, an air oxidation test was carried out under atmospheric conditions, similar to the H_2O oxidation test, and the copper ribbon was heat treated for 1h, 3h, 5h, and 10h at 500 °C. The weight of the copper ribbon increased by 0.054g after 1h heat treatment, by 0.16g after 3h heat treatment, by 0.36g after 5h heat treatment, and by 0.38g after 10h heat treatment. Figure 4 shows the comparison of weight increases between the H_2O atmosphere oxidation and air atmosphere oxidation methods. As the graph shows, the weight increases from the H_2O method were much greater than those of the air atmosphere method, with the oxidized amount sharply increasing after 3h.

Figure 5 shows the SEM results of the coating layer of the H_2O oxidized copper ribbon. The left-most photo shows the coating layer of the copper ribbon before the oxidation test, where the lead and tin coating layers have thicknesses of 20μm and the thickness of the coating layer of the copper ribbon is 50μm after 1h H_2O oxidation, 160μm after 3h H_2O oxidation, 155 μm after 5h H_2O oxidation, and 146μm after 10h H_2O oxidation. These results confirm rapid oxidation after 1h of oxidation, which greatly increased the thickness of the oxidized coating layer. After 5h, the copper base and the oxidized coating layer were separated. The oxidized copper ribbon electrode was separated into the copper base and oxidized coating layer by ball milling.

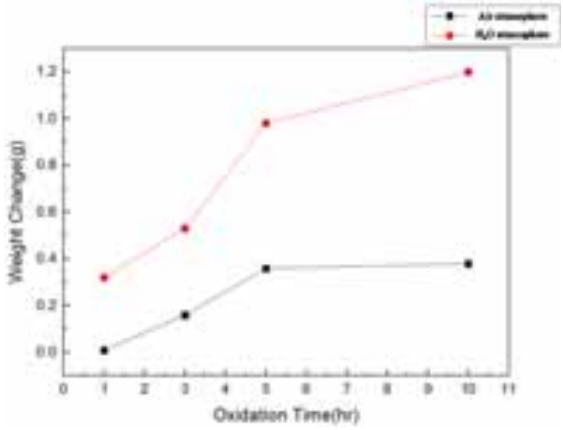

Fig. 4 Weight increases of air atmosphere and H_2O atmosphere oxidation conditions.

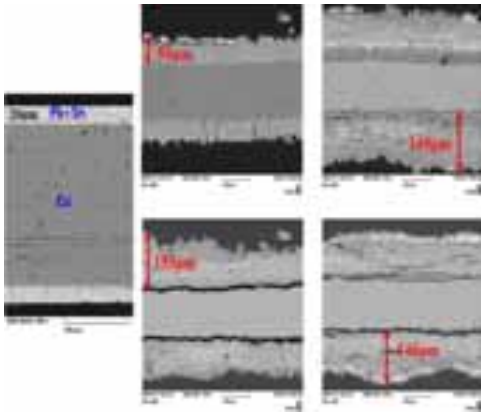

Fig. 5 Coated layer of oxidized photovoltaic ribbon sample analyzed by SEM

Table 4. Weight increase after H_2O oxidation and recovered oxide scale weight after ball milling process

Oxidation time, hr	Weight increase	Recovered oxide scale weight
1	0.32 g	0.35 g
3	0.53 g	1.53 g
5	0.98 g	5.94 g
10	1.20 g	6.54 g

Table 5. The recovered copper ribbon analyzed by ICP-MS

500 °C – 5 hours		800 °C - 30 mins	
Element	weight %	Element	weight %

Cu	98.106	Cu	99.554
Pb	0.992	Pb	0.027
Sn	0.716	Sn	0.297
Nb	0.065	Nb	0.071
Ag	0.003	Ag	0.009

Figure 6 shows the copper base and oxidized coating layer separated by ball milling, and Table 4 shows the weight increase after H_2O oxidation and the weight of the oxidized scale recovered by the ball milling process for each oxidation time. As shown in the table, 0.35g, 1.53g, 5.94g, 6.54g of

Fig. 6 The recovered copper ribbon and the oxide scale (a: 1 h; b: 3 h, c: 5 h, d: 10 h)

oxide scale were recovered at oxidation times of 1h, 3h, 5h, and 10h, respectively, and the amount of recovered oxide scale greatly increased after 5 h of oxidation time, indicating oxidation of most of the copper coating layer in the copper ribbon electrode at this point, allowing for good separation of the copper base and the copper coating layer. ICP-MS analysis of the recovered copper base showed that 98.106% pure copper could be obtained, and this result is compared to that of the 800 °C oxidized copper base in Table 5. The recovered oxide scale was analyzed by XRF and XRD and the results are shown in Table 6 and Fig. 7.

Table. 6 XRF data from the recovered oxide scale

500 °C – 5 h		**500 °C – 10 h**	
Element	Weight %	Element	Weight %
Cu	68.21	Cu	70.40
Sn	17.72	Sn	16.74
Pb	10.91	Pb	10.21
Cl	2.01	Cl	1.94
Zn	0.49	Zn	0.38
Si	0.47	Si	0.21
Al	0.16	Al	0.08

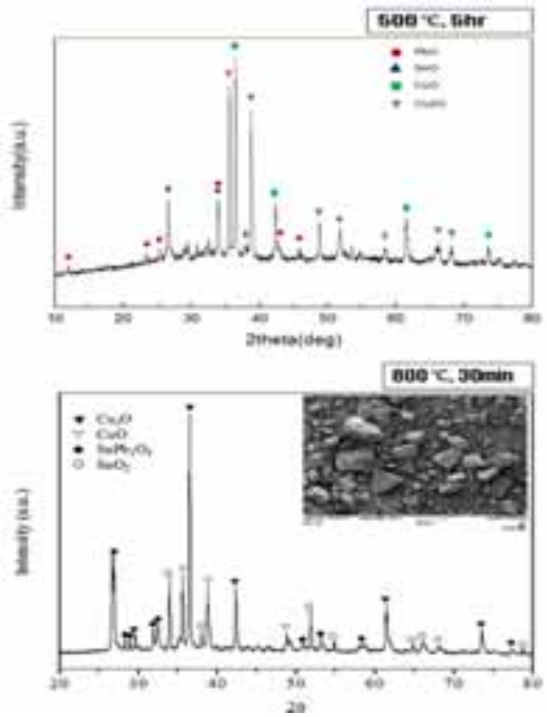

Fig. 7 The recovered oxide scale analyzed by XRD

5. Conclusions

Rather than using the existing high temperature oxidation method at 800°C in atmospheric conditions to oxidize copper ribbon electrodes for the separation of the base material from the oxide coating layer, this study used a H_2O oxidation method at 500°C, and the oxidized copper ribbon electrode was ball-milled to separate the base material from the oxide coating layer. The following results were obtained from the separation test:

(1) Based on the SEM results of the copper ribbon oxidized using the H_2O method at 500°C, the thickness of the coating layer of the copper ribbon was 50 μm after 1 h H_2O oxidation, 160 μm after 3h H_2O oxidation, 155μm after 5h H_2O oxidation, and 146 μm after 10h H_2O oxidation, with the oxidation proceeding more rapidly after 1h to greatly increase the thickness of the oxide coating layer, resulting in the separation of the copper base from the oxide coating layer after 5 h.

(2) Based on comparisons of the weight increase between H_2O oxidation and air atmosphere

oxidation at 500°C, the weight increase of the H_2O oxidized copper ribbon was about 3 times that of the copper ribbon oxidized by air atmosphere oxidation, confirming that more efficient oxidation is achieved with the water vapor method.

(3) After ball-milling to separate the copper base from the oxide coating layer, the weight of the recovered oxide scale was measured. 0.35g, 1.53 g, 5.94g and 6.5g of oxide scale could be recovered after oxidation times of 1h, 3h, 5h, and 10h, respectively.

(4) The ICP-MS analysis results of the recovered copper base after ball-milling showed that the purity of the recovered copper base was 98.106%, which was similar to that of the recovered copper base oxidized at 800°C.

(5) XRF and XRD analysis revealed that the recovered oxide scale contained 68.21% copper, 17.72% tin and 10.01% lead, all existing as oxides.

Acknowledgements

This work was supported by the Korea Institute of Energy Research (No. GP2012-0001-08).

Reference

1. Lee. J. S., Wang. J. P., Lee. W. J., Kim. Y. H., Jung. W. C., 2014. Study on fabrication of high purity copper from spent photovoltaic ribbon in solar module, Journal of Korean Inst. of resources recycling, pp. 33-37.
2. Max, M., Wolfgang, B., Martin, S., Andreas, M., Armin, R., 2013. Recycling paths of thin-film chalcogenide photovoltaic waster-Current feasible processes, Renewable Energy, 55, pp. 220-229.
3. Bruton, T.M., 1995. Production of high efficiency nomocrystalline silicon solar cell, Renewable Energy, 6, pp. 299-302.
4. Fthenakis, V.M., 2000. End-of-life management and recycling of PV modules, Energy Policy, 20, pp. 1051-1058.
5. Lee. J. S., Jang. B. Y, Kim. J. S., Ahn. Y. S., Kang. G. H., Wang. J. P., 2013. Recovery of copper from spent photovoltaic ribbon in solar module, Journal of Korean Inst. of resources recycling, Vol.22, No.5, pp. 50-55.

Conference Proceedings

Solar World Congress 2015
Daegu, Korea, 08 – 12 November 2015

THE ROLE OF STRUCTURAL AND CHEMICAL PROPERTIES IN *pm-Si:H* THIN FILMS TO DETERMINE THE OPTOELECTRONIC CHARACTERISTICS AND STABILITY BY SOAKING LIGHT FOR APPLICATIONS IN SOLAR CELL.

C. Álvarez-Macías *[1], E. Barrera Calva[1], F. González García[1], L. Gómez[2] and G. Santana[2].

[1]Universidad Autónoma Metropolitana-Iztapalapa, Área de Ingeniería en Recursos Energéticos. San Rafael Atlixco 186, Col. Vicentina, AP 55-534 C.P. 09340. . México, D.F.

[2]Instituto de Investigaciones en Materiales, Universidad Nacional Autónoma de México. A.P. 70-360, Coyoacán, C.P. 04510, México, D.F.

* Corresponding author: Carlos Álvarez Macías. Address: Unidad de Ciencias Básicas e Ingeniería, Departamento de Ingeniería de Procesos e Hidráulica, área de Ingeniería en Recursos Energéticos. Universidad Autónoma Metropolitana-Iztapalapa, San Rafael Atlixco 186, Col. Vicentina, AP 55-534. México, D.F. C.P. 09340. Tel: +52(55) 58 04 40 00 Ext (1236), Fax +52(55) 58 04 46 66.
e-mail: alvarez.krlos@gmail.com.

Abstract

We examine the role of structural and chemical properties of Hydrogenated polymorphous Silicon, *Pm-Si:H,* thin films on the optoelectronic characteristics and the level of stability under prolonged white light exposure at 100 mw/cm^2 (AM1.5 condition), for applications in solar cells. These thin films were grown by Plasma Enhance Chemical Vapor Deposition (PECVD) using diclhorolsilane (SiH_2Cl_2), instead of silane (SiH_4) as precursor gas, at different hydrogen dilutions (D_H). The nano-structural properties were confirmed by Raman measurements. The films compositions were determined by XPS measurements. From FTIR analysis we notice bonding configurations associated to photo-stability. Light soaking experiments during 250h show important behaviors on the electronic transport properties measurements to different levels of incorporated oxygen.

Keywords: Polymorphous Silicon, Solar Cell, Photoconductivity.

1. Introduction.

During the last decades extensive efforts have been made to overcome the light-induced degradation in amorphous silicon films. Currently huge interest has been drawn towards the use of nanocrystalline silicon as the intrinsic layer of a solar cell. At the same time, numerous works have been carried out to clarify the growth mechanism of amorphous, microcrystalline and polycrystalline silicon (a-Si:H, mc-Si:H and poly-Si) thin films [1]. Plasma-enhanced chemical vapor deposition (PECVD) using highly diluted silane (as precursor gas) in hydrogen mixtures allows the production of a wide range of silicon thin films with varying degrees of disorder [2]–[4]. The optimization of plasma conditions used for the growth of amorphous and microcrystalline silicon thin films has led to obtain different silicon crystalline phases (nanocrystals, microcrystals, etc.) embedded in an hydrogenated amorphous silicon, material called Hydrogenated polymorphous silicon (pm-Si:H) [4], [5]. Due to its specific nanostructure pm-Si:H is a suitable candidate for application in silicon-based thin film solar cells because, despite being heterogeneous, it exhibits improved electronic transport and stability properties after light-soaking compared to those of a-Si:H [4]. Normally, pm-Si films have been deposited by PECVD using highly diluted silane in hydrogen mixtures. However, the use of high hydrogen dilutions can contribute to an excessive incorporation of weak Si–H bonds into the pm-Si:H, obtaining in light-induced degradation of efficiency due to the so called Staebler–Wronski effect, resulting unsuitable for thin-film photovoltaic applications [6]. Alternative passivating atoms with higher mass and lower diffusion coefficient than hydrogen, such as chlorine, are being investigated. Consequently, Chlorinated silanes, i.e., SiH_2Cl_2, $SiHCl_3$ and $SiCl_4$ have been used aiming at the improvement of material properties [1]. The use of chlorine in PECVD processes

doi:10.18086/swc.2015.05.06 Available at http://proceedings.ises.org

has shows, i) increases crystallization process, ii) pos thermal annealing are no necessaries and iii) minor incorporation of weak Si-H bonds [4]. Recently, using dichlorosilane (SiH_2Cl_2) we have obtained different crystalline silicon formations (nc-Si to μc-Si) inside of the amorphous matrix, depending on the deposition conditions [3], [7], [8]. However, more extensive studies about the effects of chlorine chemistry in plasma systems are needed. In this work we had examined the role of structural and chemical properties of material to determine the optoelectronic characteristics of the material and, therefore, the level of stability under prolonged light exposure. We analyze the correlations between photoconductivity measurements and chemical composition, oxidation level, crystalline volume fractions, mean grain size and optical band gap.

2. Experimental.

Pm-Si thin films were grown in a conventional PECVD system with parallel plates of 150 cm^2 and 1.5 cm apart, activated by a RF signal of 13.56 MHz. Depositions were performed at pressures of 250 and 500 mTorr and hydrogen dilutions ratio, $R_H = H_2/(SiH_2Cl_2+H_2)$, of 83.3, 90.9, 93.8 and 95.2, keeping the other deposition parameters constant. Growth conditions are summarized in Table 1. Nano-structural analysis was performed using a Raman equipment model T64000 with Horiba Jobin-Yvon triple monochromator. The excitation source was an Ar+ Lexcel laser of 514.5 nm. All measurements were performed at room temperature in air. The samples were irradiated at a power of 20 mW in a spot size around 1 mm^2 to prevent laser-induced crystallization. The measuring range was between 400 and 600 cm^{-1}, the integration time of measurements was 1 min and the Raman signal was acquired by a cooled CCD detector. The atomic compositions were obtained by X- ray Photoelectron Spectroscopy (XPS) analysis in a VG Microtech Multilab ESCA 2000 system, equipped with a hemispherical-multichannel detector CLAM4-MDC, in which we determined the presence of Cl and O in the samples. Fourier transform infrared (FTIR) spectra of the films were recorded in absorbance mode using a Nicolet-210 FTIR spectrometer in the range 400–4000 cm^{-1} on thin-film samples deposited on polished crystalline silicon substrates. Optical properties were investigated by means of optical band gap, which was deduced from the absorption spectrum between 1 and 3.0 eV by a JASCO V630 spectrometer UV-VIS, using the Tauc Model, where the films thicknesses were obtained by typical profilometry. Variation of photoconductivity of all these films was investigated under a light intensity of 100mW/cm^2 for 250h of light soaking by measuring the current and voltage. The light soaking treatment was realized in homemade equipment under AM 1.5 spectrum and the temperature was controlled at 25ºC by heat dissipation.

3. Results and discussion.

3.1. STRUCTURAL PROPERTIES BY RAMAN.

Each spectrum obtained by Raman measurements was deconvoluted at the best fit corresponding to amorphous, nanocrystalline and microcrystalline phases [4], [9]. The peaks of the amorphous and microcrystalline phases are fixed at 480 cm^{-1} and 520 cm^{-1}, respectively [3], [10]–[12]. The third peak, associated to the nanocrystalline phase, is located at the best fit between 500 and 519 cm^{-1} [4], [12]. Each spectrum was deconvoluted following the next criteria: two Lorentzian curves, corresponding to nano and microcrystalline contributions, and a Gaussian curve corresponding to the amorphous phase [4]. We obtained the crystalline volume fraction, X_C, using relation 1 [4], [11], [13]. The area of the curves are designated as I_A, I_N, and I_C, for the peaks of amorphous, nanocrystalline and microcrystalline phases, respectively.

$$X_C = \frac{I_N + I_C}{I_N + I_C + I_A} \qquad \text{(eq.1)}$$

while the mean grain size, D_R, is calculated using relation 2 which is based on the quantum confinement model where $\Delta\nu$ is the frequency peak shift of the nanocrystalline phase with respect to 520 cm^{-1} [4], [11]. At the same table 1, values of both properties are also presented.

$$D_R = 2\pi\sqrt{2.24/\Delta\nu} \qquad \text{(eq.2)}$$

Table. 1 shows results of both X_C and D_R, as a function of dilution of hydrogen for both pressures. To detect the behavior of these parameters with better accuracy, the uncertainty of each data using standard deviation of three different deconvoluciones made to each spectrum was obtained.

Table 1. Growth conditions of *pm-Si:H* thin films deposited by PECVD, structural and optoelectronic Results as a function of dilution of hydrogen for both pressures.

RF Power = 150 W, flows: Ar = 50 sccm and SiH_2Cl_2 = 5 sccm. $T_{sustrato}$ = 200°C. Time of Growth 30 min			Structural Parameters		Effective Optical Band Gap	Photoconductivity % Degradation or improvement
Dilution D_H [%]	Thickness [nm]	Growth rate (nm/min)	X_C [%]	D_R [nm]	[eV]	$\left(\frac{\sigma_{p_1} - \sigma_{p_2}}{\sigma_{p_1}}\right)$
Pressure of 250 mTorr						
83.3	268	9.1	70 ± 18	2.7 ± 0.3	1.75 ± 0.09	**34%**
90.9	291	10.8	83 ± 14	2.4 ± 0.2	1.66 ± 0.09	**34%**
93.8	235	10.1	69 ± 7	3.2 ± 0.5	1.36 ± 0.03	**-15%**
95.2	284	11.8	94 ± 15	4.2 ± 0.4	1.18 ± 0.09	**-68%**
Pressure of 500 mTorr						
83.3	214	7.8	92 ± 12	2.8 ± 0.3	1.75 ± 0.04	**65%**
90.9	223	8.2	65 ± 16	3.1 ± 0.3	2.12 ± 0.03	**-92%**
93.8	245	9.4	95 ± 19	3.3 ± 0.2	1.15 ± 0.06	**-191%**
95.2	111	10.4	94 ± 16	3.4 ± 0.4	1.57 ± 0.05	**-16%**

Table 1 shows that for all samples the average of the nanocrystals size not greater than 5 nm in diameter, from which it follows that the optical properties of the films must be influenced by quantum confinement, which in turn will influenced by the density of these nanocrystals and their distribution within the matrix of amorphous silicon [8].

As seen from the table, for both pressures is observed that D_R tends to increase with hydrogen dilution. In the system SiH_2Cl_2 when SiH_xCl_y species (x + y <3) hit the surface of growth, both the hydrogen and chlorine are preferentially extracted as HCl. Exothermic reaction of atomic hydrogen with chlorine emit a considerable amount of energy sufficient to promote the local crystallization [3]. So by increasing the hydrogen dilution, more nanocrystals are formed in the films of pm-Si:H with increasing size. While the increased pressure the mean free path of the gas species decreases, decreasing the extraction of hydrogen and chlorine, and exothermic reactions thereby increasing the local crystallization of the material.

3.2. CHEMICAL PROPERTIES.

3.2.1. X-ray photoelectron spectroscopy, XPS.

Figure 1 shows the chemical composition profiles of all samples to different depths probed by sputtering the surface with argon ions for different erosion times in vacuum. The atomic percent corresponding to Cl, O and Si are reported, because hydrogen is not detectable by this technique.

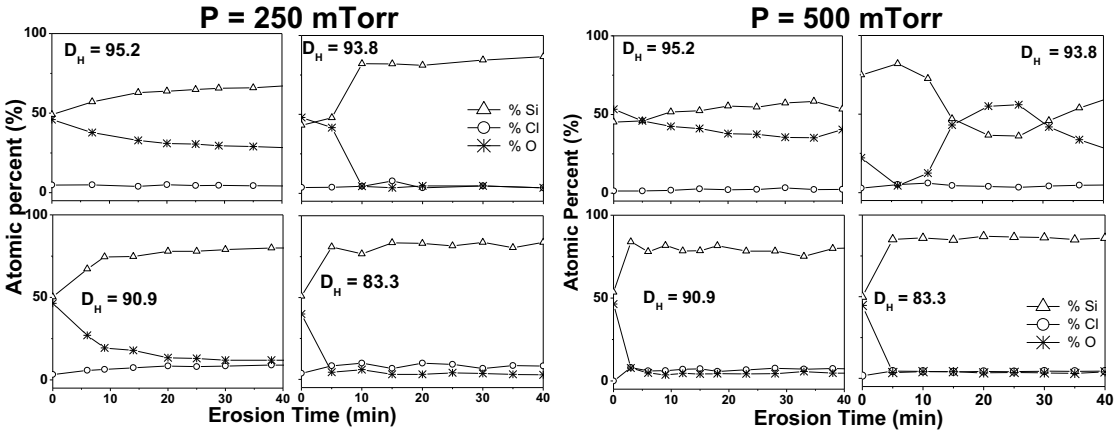

Fig. 1. Composition profiles of pm-Si:H thin films including atomic percents from Cl 2p, O 1s and Si 2p peaks for different argon ion erosion times.

Fig 1. Shows how the films are mainly composed by silicon (triangles). However, important concentrations of oxygen (asterisk) are detected in some samples. The amount of chlorine (circles) is always lower than 10%. It is possible to observe that in some cases Si and O concentrations changed with erosion time. In the film surface oxygen concentrations around 50% are detected in all samples. This value decreases to less than 15% with erosion time, except in some samples with elevated D_H where oxygen concentration remains above 25% for all erosion times. The appearance of O in some samples is the result of porous and less dense in the grain boundary regions, which facilitates absorption of oxygen on the surface of micro-voids, when the films are in ambient. Some studies have been noted that by introducing small amounts of oxygen introduced to the μc-network further decreased the optical absorption and conductivity [14]; these effects are discussed below.

These results suggest that the films deposited at D_H of 83.3 and 90.9 have qualitatively better measure of the density and compact structure compare to films deposited at D_H of 93.8 and 95.2, for both pressure. The high D_H values of our films can attributed to a more porous structure, possibly caused by the nucleation of nano-sized crystallites in the amorphous network.

3.2.2. Fourier transform infrared spectroscopy, FTIR.

Figure 2 shows the spectra of FTIR transmission curves in the wave number range 550–800 and 1900-2400 cm^{-1} for the most representative samples deposited at different D_H for pressures of 250 mTorr.

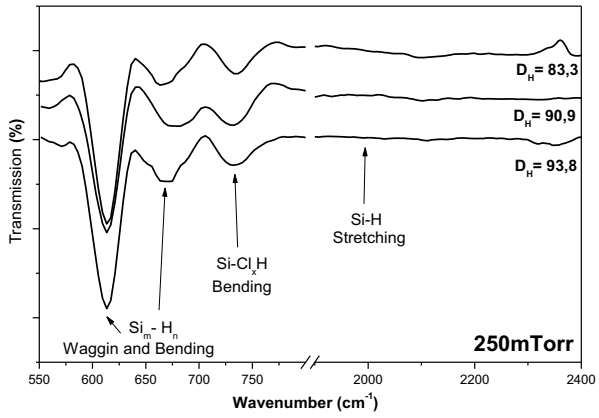

Fig 2. Infrared spectra of pm-Si:H films deposited at 250 mTorr showing the absorbance peaks, for three different hydrogen dilutions.

Fig. 2 exhibit that the Si-H stretching mode around 1900-2100 cm^{-1} cannot be distinguished in our samples.

This band is generally associated to silicon hydrides incorporated into the amorphous matrix which are related with weak hydrogen bonds that are prone to generate light induced degradation of the material [4], [11], [15]. Instead, the Si_mH_n wagging mode around 620-640 cm^{-1} and $SiCl_xH$ bending mode at 744–775 cm^{-1} is present in all cases [11] [16]. The Si_mH_n wagging mode has been correlated mainly with surface passivation of silicon nanocrystals in these type of pm-Si films [4], [10], [14]. Whereas $SiCl_xH$ bending mode is associated to the small amount of incorporated chlorine in the films (less than 10 at.%, agree with the XPS analysis) [16], [17]. Based in results of XPS the FTIR transmission spectra should show signature of the Si–O peak near 1000–1100 cm^{-1}, which also cant be distinguished.

From the perspective of application of these films as photovoltaic materials, having a high fraction crystalline in as grown films with low hydrides content in the amorphous matrix, is adequate for their utilization in silicon thin film solar cells.

3.3. OPTOELECTRONIC CHARACTERISTICS.

3.3.1. *Optical Band gap, E_g^{op} .*

Optical properties of our thin films were investigated from UV–VIS spectroscopy. Fig. 3 shows the variation of the effective optical band gap, E_g^{op} as a function of the structural properties through of D_R and X_C, for samples grown at 250 and 500 mTorr of pressure, respectively. The optical band gap energy E_g^{op} was obtained by the Tauc plot $(\alpha h\upsilon)^{1/2}$ vs. $(h\upsilon - E_g^{op})$ where α is the absorbance, ν is the frequency and h is the Planck constant. Tauc's plot is an effective method to determine the energy bandgap in amorphous thin film materials [18] [19].

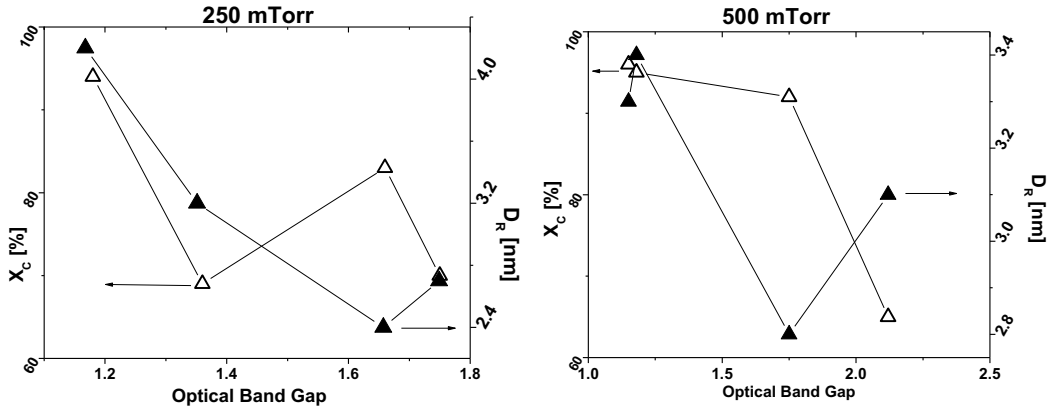

Fig. 3. crystalline volume fraction, X_C,(open triangle) and mean grain size, D_R,(solid triangle) as a function of Optical band Gap, E_g^{op}, to pressures of 250 and 500 mTorr.

We can see in fig. 3 is how E_g^{op} is modified by the structural parameters X_C and D_R and we found a tunable band gap in function of D_R. As seen from the figure, the E_g^{op} of films increases from 1.18 to 1.75 eV when D_R is decreased from 4.2 to 2.7 nm for samples grown at 250 mTorr, while for films 500mTorr it is difficult to comment this behavior due to the estimated values of D_R are almost a constant ($\Delta D_R <$ 1nm, see Table 1). However, it is too possible to note that E_g^{op} tends to decrease as X_C increase for both pressures. Accordingly, in the case of a mixed phase of crystalline and amorphous, i.e. nanocrystalline phase, the band gap should lie between amorphous and crystalline silicon. The typical value of the band gap of hydrogenated amorphous silicon (a-Si:H) is about 1.6 eV [19]. The higher band gap in pm-Si:H thin films in the present case may be due to the quantum size effect [8], [14], [19], [20]. So the behavior in E_g^{op} support the influence of quantum confinement as $E_g^{op} \approx E_g + \frac{\hbar^2 \pi^2}{2\mu D_R^{\,2}}$ where E_g^{op} is the bulk material gap and μ It is the reduced mass of electron-hole pair [8], [20]. Then E_g^{op} tends to decrease with the increase in D_R of embedded nanoclusters and randomly

distributed in the amorphous network of pm-Si:H thin films. One may argue that the increased band gap of the films is due to the presence of oxygen in these films. However the FTIR transmission of the films, taken immediately after the deposition, do not show the presence of Si–O bonds (near 1000–1100 cm^{-1}), though the feature appeared in some of the films when these are stored for a couple of week at room temperature.

3.3.1. *Photoconductivity, σ_p.*

Photoconductivity measurement of the samples, using white light illumination of 100mW/cm^2, during continuous light 250h were performed. We observe important behaviors in Photoconductivity for samples with high and low D_H and Pressure, as can be seen in fig 4. The results and D_R and X_C values obtained by Raman are mentioned in Fig. 4 and also in Tables 1.

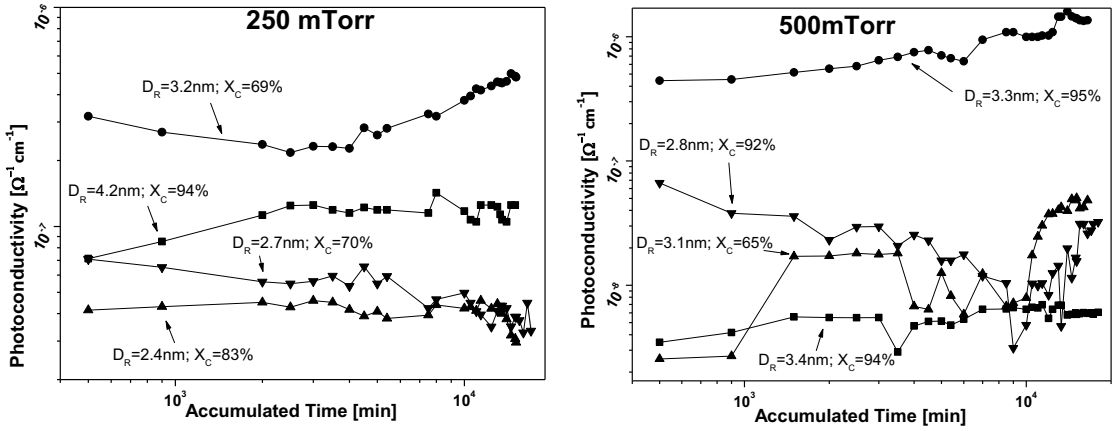

Fig. 4. Photoconductivity versus illumination time for pm-Si:H thin films

It is observed from Fig. 4 can not be distinguished stability in photoconductivity, instead we can see tendency to degrade over the time of light soaking in most films. We calculated different degradation rates of σ_p which are shown in Table 1 as $(\sigma_{pi} - \sigma_{pf})/\sigma_{pi}$, where σ_{pi} and σ_{pf} are inicial and final photoconductivity, respectively. If these values of degradation are negative then we call them improvement, so we could see improvement in the films whit high D_R and D_H for both pressures. This behavior could be due to improved pasivation process; sinse on the one hand, is closely related to the fact that the Si-O bond is stronger than the Si-Si bond and the Si-H bond. And the other, transport can be influenced by change in mobility due to the space charge between the crystalline and amorphous interfaces, by the incorporation of oxygen as a terminal bond.

4. Conclusion.

We have shown that optoelectronics characteristics of pm-Si:H thin films can be modulated by structural and chemical properties which depend of grown conditions is PECVD system using diclhorolsilane. The chlorine chemistry introduced by the silicon precursor favors the formation of nanocrystalline inclusions. Raman measurements confirm that our films are nanocrystalline, with crystal average size on the range 2–3.5 nm. We found by XPS measurements, films deposited with high D_H present a considerable amount of oxidation evidence. Since on the other hand, From Fourier transform infrared spectroscopy analysis we notice that weak silicon hydride (Si-H) bonds were not detected while bonding configurations associated to the silicon nanocrystal surface (Si_mH_n) were clearly observed. This result is largely related to possible photostability of our samples. By UV-Vis measurements we found a tunable band gap in function of D_R, with a behavior that support the influence of quantum confinement, while for the photoconductivity do not show stability in the samples, instead we obtained improvement of photoconductivity in the films whit high D_R and D_H for both pressures. Understanding structural and chemical properties of pm-Si:H thin films is key towards optimizing their electrical and optical properties for applications in solar cells.

5. Acknowledgements.

We acknowledge financial support for this work from CONACyT Mexico through postdoctoral scholarship CVU 165872. The authors are grateful to Dr. J.C. Alonso and Dr. A. Ortiz† for the use of laboratory facilities and Dr. A. Remolina for samples preparation.

6. References

[1] H. Shirai, "Role of chlorine in the nanocrystalline silicon film formation by rf plasma-enhanced chemical vapor deposition of chlorinated materials," *Thin Solid Films*, vol. 457, no. 1, pp. 90–96, Jun. 2004.

[2] R. Butté, S. Vignoli, M. Meaudre, R. Meaudre, O. Marty, L. Saviot, and P. Roca i Cabarrocas, "Structural, optical and electronic properties of hydrogenated polymorphous silicon films deposited at 150°C," *J. Non. Cryst. Solids*, vol. 266–269, pp. 263–268, May 2000.

[3] C. Álvarez-Macias, J. Santoyo-Salazar, B. Monroy, M. García-Sánchez, M. Picquart, A. Ponce, G. Contreras-Puente, and G. Santana, "Estructura y morfología de películas de pm-Si: H crecidas por PECVD variando la dilución de diclorosilano con hidrógeno y la presión de trabajo," *Rev. Mex. física*, vol. 57, no. 3, pp. 224–231, 2011.

[4] Álvarez-Macias, C., B.M. Monroy, L. Huertaa, M. Canseco-Martínez, M. Picquart, J. Santoyo-Salazar, M.F. García Sánchez, and G. Santana, "Chemical and structural properties of polymorphous silicon thin films grown from dichlorosilane," *Appl. Surf. Sci.*, vol. 285-B, pp. 431–439, 2013.

[5] A. F. M. U and P. R. Cabarrocas, "Shedding light on the growth of amorphous , polymorphous , protocrystalline and microcrystalline silicon thin films," *Thin Solid Films*, pp. 161–164, 2001.

[6] A. K. O. Odziej, "Staebler-Wronski effect in amorphous silicon and its alloys," *Sci. Technol.*, vol. 12, no. 1, pp. 21–32, 2004.

[7] C. Álvarez-Macías, B. M. Monroy, L. Huerta, M. Picquart, and M. F. García, "Influence of light-soaking treatment on the optoelectronics properties of silicon polymorphous thin films to be used in solar cells .," in *Photovoltaic Specialists Conference (PVSC), 2013 IEEE 39th*, 2013, vol. 39th, pp. 0526 – 0529.

[8] A. Remolina, B. M. Monroy, M. F. García-Sánchez, a Ponce, M. Bizarro, J. C. Alonso, a Ortiz, and G. Santana, "Polymorphous silicon thin films obtained by plasma-enhanced chemical vapor deposition using dichlorosilane as silicon precursor.," *Nanotechnology*, vol. 20, no. 24, p. 245604, Jun. 2009.

[9] A. Ali, "Mechanisms of the growth of nanocrystalline Si:H films deposited by PECVD," *J. Non. Cryst. Solids*, vol. 352, no. 28–29, pp. 3126–3133, Aug. 2006.

[10] S. Liu, X. Zeng, W. Peng, H. Xiao, W. Yao, X. Xie, C. Wang, and Z. Wang, "Improvement of amorphous silicon n-i-p solar cells by incorporating double-layer hydrogenated nanocrystalline silicon structure," *J. Non. Cryst. Solids*, vol. 357, no. 1, pp. 121–125, Jan. 2011.

[11] L. Zhang, J. H. Gao, J. Q. Xiao, L. S. Wen, J. Gong, and C. Sun, "Low-temperature (120°C) growth of nanocrystalline silicon films prepared by plasma enhanced chemical vapor deposition from SiCl4/H2 gases: Microstructure characterization," *Appl. Surf. Sci.*, vol. 258, no. 7, pp. 3221–3226, Jan. 2012.

[12] C. Tu, T. Chang, P. Liu, C. Yang, and L. Feng, "Performance enhancement of excimer laser crystallized poly-Si thin film transistors with fluorine implantation technology," *Thin Solid Films*, 2007.

[13] Y.-H. Chen, Y.-T. Liu, C.-F. Huang, J. C. Liu, and C. C. Lin, "Improved photovoltaic properties of amorphous silicon thin-film solar cells with an un-doped silicon oxide layer," *Mater. Sci. Semicond. Process.*, vol. 31, pp. 184–188, Mar. 2015.

[14] P. Gogoi, H. S. Jha, and P. Agarwal, "High band gap nanocrystallite embedded amorphous silicon prepared by hotwire chemical vapour deposition," *Thin Solid Films*, vol. 518, no. 23, pp. 6818–6828, Sep. 2010.

[15] B. Yan, L. Zhao, B. Zhao, J. Chen, G. Wang, H. Diao, Y. Mao, and W. Wang, "Hydrogenated amorphous silicon germanium alloy with enhanced photosensitivity prepared by plasma enhanced chemical vapor deposition at high temperature," *Vacuum*, vol. 89, pp. 43–46, 2013.

[16] T. Ito, K. Hashimoto, and H. Shirai, "Surface Chemistry of Si:H:Cl Film Formation by RF Plasma-Enhanced Chemical Vapor Deposition of SiH_2Cl_2 and $SiCl_4$," *Jpn. J. Appl. Phys.*, vol. 42, no. Part 2, No. 10A, pp. L1119–L1122, Oct. 2003.

[17] S. Jung, Y. Fujimura, T. Ito, and H. Shirai, "Chemistry of the chlorine-terminated surface for low-temperature growth of crystal silicon films by RF plasma-enhanced chemical vapor deposition," *Sol. Energy Mater.*, vol. 74, pp. 421–427, 2002.

[18] L. Guo, J. Ding, J. Yang, G. Cheng, Z. Ling, and N. Yuan, "Effects of high hydrogen dilution ratio on optical properties of hydrogenated nanocrystalline silicon thin films," *Appl. Surf. Sci.*, vol. 257, no. 23, pp. 9840–9845, Sep. 2011.

[19] V. S. Waman, M. M. Kamble, M. R. Pramod, S. P. Gore, a. M. Funde, R. R. Hawaldar, D. P. Amalnerkar, V. G. Sathe, S. W. Gosavi, and S. R. Jadkar, "Influence of the deposition parameters on the microstructure and opto-electrical properties of hydrogenated nanocrystalline silicon films by HW-CVD," *J. Non. Cryst. Solids*, vol. 357, no. 21, pp. 3616–3622, Nov. 2011.

[20] G. Santana, B. M. Monroy, a. Ortiz, L. Huerta, J. C. Alonso, J. Fandiño, J. Aguilar-Hernández, E. Hoyos, F. Cruz-Gandarilla, and G. Contreras-Puentes, "Influence of the surrounding host in obtaining tunable and strong visible photoluminescence from silicon nanoparticles," *Appl. Phys. Lett.*, vol. 88, no. 4, p. 041916, 2006.

Conference Proceedings

Solar World Congress 2015
Daegu, Korea, 08 – 12 November 2015

Study on amorphous Silicon single junction p-i-n PV cell

Al-Rajib Bhuiyan and Himangshu Ranjan Ghosh

Institute of Energy, University of Dhaka, Dhaka-1000, Bangladesh

Abstract

The performance of solar PV cells depends on its design, material properties and fabrication technology. In this study design and analysis on thin film single junction hydrogenated amorphous silicon (aSi:H) has showed that the efficiency of a single junction PV cell can be achieved upto 9.823% for with optimized window layer bandgap of 1.85eV. For this the current density is 13.827 mA/cm2, open circuit voltage is 0.987 volts and fill factor is 0.719. Moreover different interface recombination velocities are applied to investigate the impacts on short-circuit current density (Jsc), open-circuit voltage (Voc), fill factor (FF) and efficiency ( ). Higher recombination velocity of front and back contact give a detrimental impact on Jsc& . Jsc and drastically decline in the range where surface recombination speed are greater than 104 cm/s. it would be possible to yield efficiency more than 10% by reducing surface recombination speed from 107 cm/s to 104cm/s. The Quantum Efficiency (QE) curve has revealed that the cell has good spectral response in the wavelength range 0.4 µm – 0.65 µm which means that it would be a good candidate as a top cell of double junction/ micromorph solar cell configuration and as a middle cell in triple junction structure. The research has been carried out with AMPS-1D modelling and computer simulation program.

Keywords: *Thin film solar cell, Amorphous silicon solar cell*

1. Introduction

Amorphous silicon (aSi:H) technology was up to now the only thin film concept, that has entered into large scale production plants in turning out about 5MW/y. But already now aSi:H modules are sold at lower prices than wafer based crystalline silicon modules. However, compared to crystalline silicon the efficiency of commercially available aSi:H solar cell module suffer still from relative low efficiency. While in the research laboratory stabilized efficiencies over 13% have been demonstrated for small size cells. There is a gap between this record test cells and the translation into commercial modules. It is interesting to look into the various individual factors that cause efficiency losses for aSi:H technology between laboratory records cell and industrial production (Fonash, 2010).

The performance of solar photovoltaic cells depends on its design, material properties, and fabrication technology. Photovoltaic (PV) researchers present improved cells over the period of time, although the overall process is quite complex, expensive, and time consuming. Numerical simulation is the best approach for solar cell researchers, which help to find out an optimized structure with good fitted parameters. As a result fabrication complexity, costs, and time reduce significantly. The major objectives of numerical modeling and simulation in solar cell research are testing the validity of proposed physical structures, geometry on cell performance, and fitting of modeling output to experimental results. The numerical modeling has become indispensable tools for designing a high-efficiency solar cell. Numerical modeling is increasingly used to obtain insight into the details of the physical operation of thin-film solar cells. Over the years, several modeling tools specific to thin-film PV devices have been developed. A number of these tools have been reached in a mature status and are available to the PV community. In this study AMPS-1D simulation software (AMPS 1D 2015) has been used.

doi:10.18086/swc.2015.05.07 Available at http://proceedings.ises.org

2. Methodology

AMPS can simulate an extremely general semiconductor device structure. In the electrical part of the model, three coupled differential equations: the Poisson's equation and the two carrier continuity equation are solved simultaneously under non-equilibrium steady state conditions (i.e., under the effect of voltage or light bias, or both) by using the method of finite differences and Newton-Raphson technique, directly from the first principles (Belfar et al. 2011). The equations used are:

Poisson's Equation:

$$\frac{\partial^2 \psi(x)}{\partial^2 x} = \frac{\rho(x)}{\varepsilon} \qquad \text{(eq. 1)}$$

Hole Continuity equation:

$$G(x) - R(p(x), n(x)) - \frac{1}{q}\frac{\partial J_p(x)}{\partial x} = 0 \qquad \text{(eq. 2)}$$

Electron Continuity equation

$$G(x) - R(p(x), n(x)) + \frac{1}{q}\frac{\partial J_n(x)}{\partial x} = 0 \qquad \text{(eq. 3)}$$

Where $\rho(x)$ is the charge density

$$\rho(x) = q[p(x) - n(x) + p_T(x) - n_T(x) + N^+_{net}] \qquad \text{(eq. 4)}$$

And the electric field

$$E = \frac{\partial \psi(x)}{\partial x} \qquad \text{(eq. 5)}$$

where, ε is the dielectric constant,
E the electrostatic field, represents the position in energy of the local vacuum level,
x the position in the device,
p and n the valence-band hole density and the conduction band electron density, respectively,
q the electronic charge,
R the recombination rate,
p_T and n_T the trapped hole and electron population density, respectively,
N^+_{net} the net doping density, if any,
G the electron-hole pair generation rate,
$J_p$andJ_n the hole and electron current density respectively and
E_{FP} and E_F,, the hole and electron quasi Fermi levels.

In this study, the three state variables that completely define the state of a device have been taken to be the local vacuum level, ψ and the quasi-Fermi levels E_{FP} and E_{Fn}. Once these three dependent variables are known as a function of x, all other information about the system can be determined as functions of position. In thermodynamic equilibrium, the Fermi level is a constant as a function of position and hence the three Equation (1-3) essentially reduce to only one equation viz., the Poisson's equation. Therefore, the local vacuum level $\psi(x)$ is the only unknown to be solved for in thermodynamic equilibrium.

In the non-thermodynamic equilibrium steady-state, a system of three coupled non-linear second order differential equations in the tree unknown (ψ, E_{Fn}, E_{Fp}) are obtained, In order to solve these equations for state variables (ψ, E_{Fn}, E_{Fp}), we need six boundary conditions, two for each dependent variable. The first

two boundary conditions are modified versions of the ones used for solving Poisson's equation in thermodynamic equilibrium:

$$\psi(0) = 0 - \chi(L) - \varphi_{bL} + \varphi_{bO} - \chi(0) - V \qquad \text{(eq. 6)}$$

And

$$\psi(L) = 0 \qquad \text{(eq. 7)}$$

Where, L is length of the device,

$\chi(0), \chi(L)$ are the electron affinities at x = 0 and x = L, respectively and

V is the applied voltage.

The zero of $\psi = \psi(x)$ is generally chosen to be the position in energy of the vacuum level at the boundary point x = L. The boundary conditions for the Poisson's equations in thermodynamic equilibrium are Equation 6 with the applied voltage V term absent and Equation 7. The four other boundary conditions are obtained from imposing constraints on the currents at the boundaries at x = 0 and x =L. These constraints force the mathematics to acknowledge the fact that the currents must cross at x = 0 and x = L (the contact positions) by either thermo ionic emission or interface recombination. Expressed mathematically, we obtain the following:

$$J_n(0) = qS_{n0}[n(0)-n_0(0)] \qquad \text{(eq. 8)}$$
$$J_p(0) = qS_{p0}[p(0)-p_0(0)] \qquad \text{(eq. 9)}$$
$$J_n(L) = qS_{nL}[n(L)-n_0(L)] \qquad \text{(eq. 10)}$$
$$J_p(L) = qS_{pL}[p(L)-p_0(L)] \qquad \text{(eq. 11)}$$

Where, S_{n0}, S_{p0} are surface recombination velocities for electrons and holes respectively at the x = 0 interface and quantities

S_{nL}, S_{pL} are the corresponding velocities at the x = L interface.

The largest Value the can have is $\approx 10^7$ cm sec^{-1} dictated by thermionic emission. Here, n(0) (p(0)) are the electron (hole) density at x =0, n(L) (p(L)) are the same at x = L.

$N_0(0)$ ($p_0(0)$), $n_0(L)$ ($p_0(L)$) are the electron (hole) density in the thermodynamic equilibrium at x = 0 and x = L, respectively. With the help of the boundary conditioned stated above; the three Eq. 1 to 3 can be solved simultaneously for $\psi = \psi(x)$, $E_{fn} = E_{fp}$ (x) and $E_{Fp} = E_{Fp}(x)$. For this, the different terms in the equations are to be calculated first. The gape states and two Gaussian distribution functions to simulate the dangling bond states. The generation term in the continuity equations has been calculated using a semi empirical model (Leblanc et al., 1994) that has been integrated into the modelling programme. Both specular interference effects and diffused reflectance and transmittances due to interface roughness were taken into account.

3. Data and Result

Figure 1 gives the dark and light J-V characteristics of simulated aSi:H (p-i-n) single junction solar cell as calculated on the basis of model AMPS-1D. The calculated light J-V characteristics of the cell yield the following results:

Short circuit current density of Jsc= 13.827 mA/cm2,
Open circuit voltage Voc = 0.987 volt,
Fill-factorFF = 0.719,
Efficiency = 9.823 %.

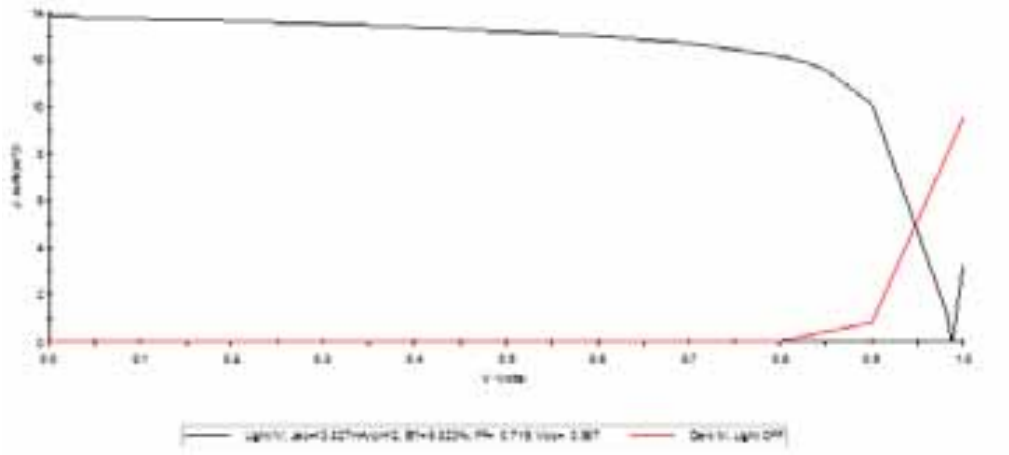

Fig. 1: Simulated J-V Characteristics curve of single junction (pin) aSi:H solar cell

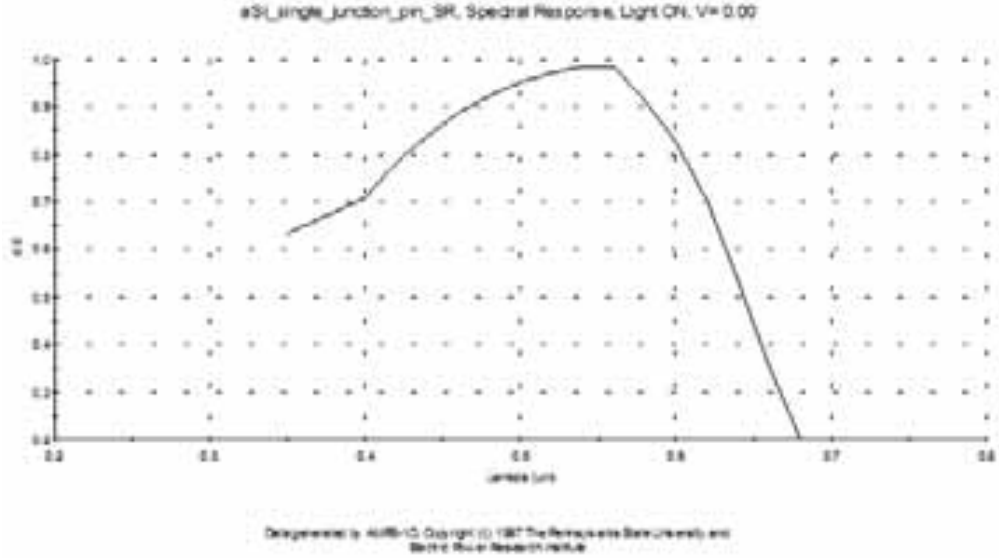

Fig. 2: Spectral response curve of single junction (pin) aSi:H solar cell

Figure 2 shows the quantum efficiency (QE) under AM1.5 illumination at 0 volts. From this SR curve it is clear that due to higher bandgap of aSi:H silicon, it has spectral response only below wavelength of 700nm. With respect to a band gap of 1.85 eV theband gap utilization is relatively low dueto the high levels of SRH recombination andthe relative broad valence and conduction-band tails.

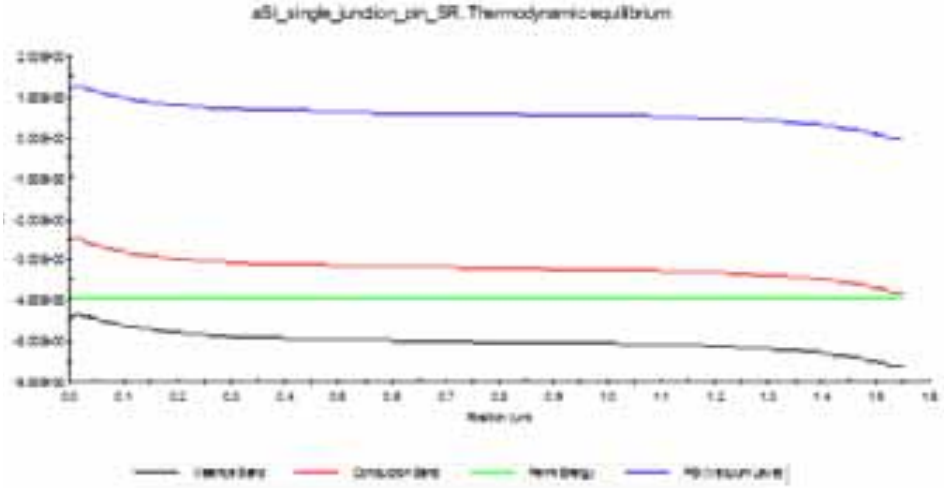

Fig. 3:Thermal equilibrium band diagram of aSi:H single junction solar cell

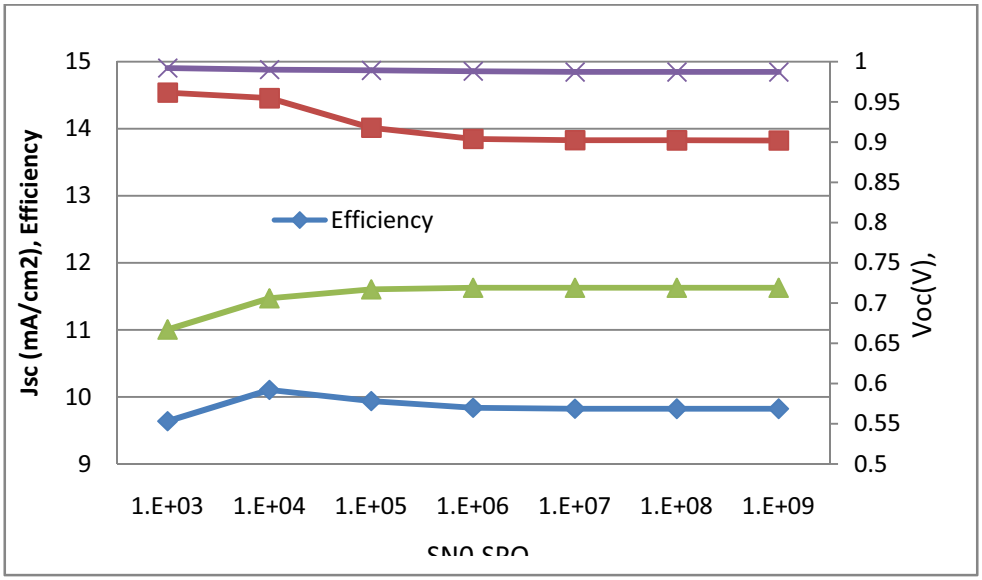

Fig. 4: Impacts on Voc, Jsc, FF& Eff come from the interface recombination speed

Interface recombination is one of the important recombination models. Different interface recombination velocities were applied to investigate the impacts on short-circuit current density (J_{sc}), open-circuit voltage (V_{oc}), fill factor (FF) and efficiency (Eff). The results are shown in Figure 5. In this simulation, the Rs mainly depends on thematerial properties, such as the interface recombination velocity, and whether the defects exist or not. Assume that the square of this solar cell is unity square centimeter. From Figure 4, it can be seen that Jsc and Eff drastically decline in the range where SNO and SPO are greater than 10^4 cm/s. The reason is that the increase in interface recombination velocity reduces the number of holes and electrons collected by the electrodes so that the short-circuit current reduces. Experimentally, the SNO, SPO, should be controlled into small value by optimizing the conditions of material growth in order to improve the conversion efficiency.

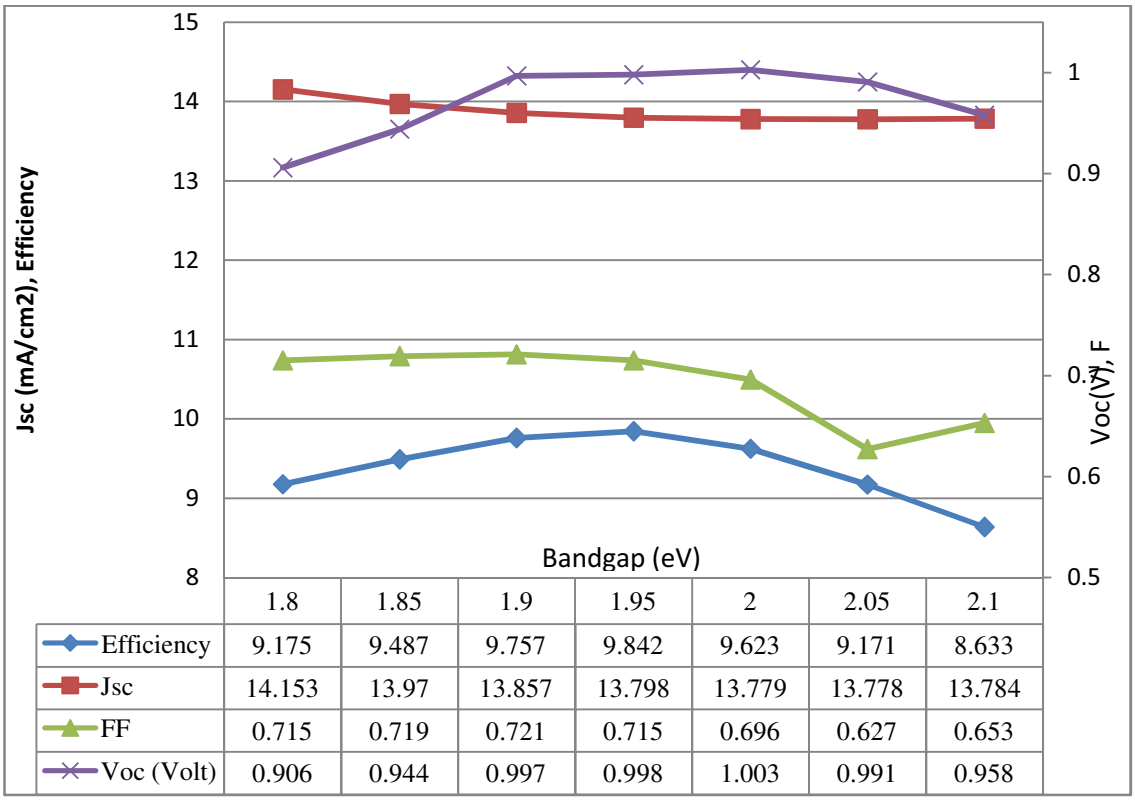

	1.8	1.85	1.9	1.95	2	2.05	2.1
Efficiency	9.175	9.487	9.757	9.842	9.623	9.171	8.633
Jsc	14.153	13.97	13.857	13.798	13.779	13.778	13.784
FF	0.715	0.719	0.721	0.715	0.696	0.627	0.653
Voc (Volt)	0.906	0.944	0.997	0.998	1.003	0.991	0.958

Fig. 5: Impacts on Voc, Jsc, FF& Eff come from the Window layer bandgap

Figure 5 gives the impacts on V_{oc}, J_{sc}, FF & Efficiency come from the window layer bandgap. From this figure it can be seen that the maximum efficiency of 9.82% has been achieved for window layer bandgap at 1.95 eV. Before and after the bandgap of 1.95 eV the efficiency decreases sharply due to decrease of photoconductivity and photosensitivity.

4. Conclusion

Win AMPS-1D simulation software, the best efficiency of this numerically designed single junction aSi:H solar cell is 9.823% with intrinsic layer thickness of 1200 nm and optimum window layer bandgap of 1.85eV. The obtained results show that the interface recombination speeds of front and back contact is crucial to short circuit current density and efficiency of aSi:H solar cell. Therefore one can increase the performance of aSi:H solar cell by minimizing the surface recombination speed of transparent conducting oxide. The Quantum Efficiency (QE) curve shows that the cell has good spectral response in the wavelength range 0.4 µm – 0.65 µm which means that it would be a good candidate as a top cell of double junction/ micromorph solar cell configuration and as a middle cell in triple junction structure.

5. References

Analysis of Microeletronic and Photonic Structures - AMPS-1D, 2015. *www.**amps**modeling.org/latest.html*

Belfar Abbas and Mostefaoui Rachida, 2011. Simulation of n_1-p_2 Microcrystalline Silicon Tunnel Junction with AMPS-1D in a-Si :H/µc-Si :H Tandem Solar Cells. *Journal of Applied Sciences, 11: 2932-2939.*

Fonash Stephen, 2010. Solar Cell Device Physics, 2nd Edition, Academic Press

Leblanc, F., J. Perrin and J. Schmitt, 1994. Numerical modeling of the optical properties of hydrogenated amorphous-silicon-based pin solar cells deposited on rough transparent conducting oxide substrates. J. Appl. Phys., 75: 1074-1087.

Conference Proceedings
Solar World Congress 2015
Daegu, Korea, 08 – 12 November 2015

CHALLENGES FOR THE DEVELOPMENT OF INKJET PRINTED $Cu_2(Zn,Sn)(S,Se)_4$ THIN FILM SOLAR CELL

Ahmed Ennaoui[1,4], Xianzhong Lin[2], Jaison Kavalakkatt[2], E. M. Vinod[1], Reiner Klenk[2], Martha Ch. Lux-Steiner[2,3]

[1]Qatar Environment and Energy Research Institute (QEERI), Hamad Bin Khalifa University, Qatar Foundation, P.O. Box 5825, Doha, Qatar
[2]Institute for Heterogeneous Material Systems, Helmholtz-Zentrum Berlin für Materialien und Energie,Hahn-Meitner-Platz 1, 14109 Berlin, Germany
[3]Free University of Berlin, Kaiserswerther Str. 16-18, 14195 Berlin, Germany
[4]College of Science and Engineering, Hamad Bin Khalifa University, Qatar Foundation, P.O. Box: 5825, Doha, Qatar

Abstract

Inkjet printing technique is a material-conserving technique, which can greatly reduce the production cost by reducing the wastage of materials during the deposition. Additionally, this method can be easily adapted to Roll-to-Roll processing for large-scale application. The most challenging issues that remain open for multi-component system such as $Cu_2ZnSn(S_xSe_{1-x})_4$ (CZTSSe) are: (1) Formulation of long-term stability raw material ink and (2) Optimization of electronic and electrical properties for high efficiency solar cell. We developed two different methods for ink formulation. The first one is based on preparation of nanoparticles such as ZnS, SnS and Cu_3SnS_4. The second method consists of metal salt precursors dissolved in organic solvents. We use metal salt solutions containing Cu, Sn, Zn and S precursors dissolved in dimethyl sulfoxide (DMSO) to prepare the ink. We used two deposition techniques (spin coating, inkjet printing) for the preparation of absorber layers. Both method lead to the production of kesterite films. However the metal salt based ink is well adapted to inkjet printing and the resulting solar cells with glass/Mo/CZTSSe/CdS/ZnO structure show total area (0.5 cm^2) efficiency of 6.4 %.

Keywords: *Inkjet printing, kesterite, thin film solar cell*

1. Introduction

Kesterite $Cu_2ZnSn(S,Se)_4$ (CZTSSe) has emerged as a promising candidate for solar energy conversion. The optical band gap of this material can be tuned between 1.0 eV and 1.5 eV by changing [S]/([S]+[Se]) ratio. Wang et al., have developed a solar cell with record efficiency of 12.6% obtained for CZTSSe absorbers from hydrazine-based solution [1]. However the fabrication process suffers from certain safety hazards due to the use of explosive and toxic hydrazine solvent. Previously, we have shown that CZTSSe thin film absorbers can be formed by annealing spin coated in-house formulated ZnS, SnS and Cu_3SnS_4 (CTS) nanoparticle (NP) inks [2-5]. Cao et al. have fabricated CZTSSe based solar cells with efficiency up to 8.5 % by using a similar binary and ternary chalcogenide nanoparticle as precursors to prepared CZTSSe absorber [6]. Another way is to use CZTS quaternary nanoparticles as precursors to fabricated CZTSSe thin films [7, 8]. This approach has led to an efficiency of 9.0 %. However, the nanoparticle (NP) synthesis process is time consuming and requires complicated steps. Moreover, long chain organic ligand is required to prevent the agglomeration of the nanoparticles during the synthesized process, which is difficult to be removed after thin film processing. Therefore, a ligand-exchange process to minimize the amount of carbon in the layers may be needed. Although the ligand exchange can reduce the carbon content in the layers, the resulting absorbers

doi:10.18086/swc.2015.05.08 Available at http://proceedings.ises.org

still containing large amount of carbon left near the back contact after the annealing step, which limit the performance of the solar cell device. A simple alternative approach developed by Ki et al., is based on Cu, Zn, and Sn precursors dissolved in DMSO leads to efficiency of 11.8% obtained by annealing the spin-coated Cu-Zn-Sn-DMSO solution [9, 10]. It has been reported that sodium has a positive influence on the morphology as well as electronic properties of CZTSSe absorbers, thereby enhancing the solar cell performance [11].

2. Experimental

2.1. Sample preparation

NP inks were prepared from ZnS, SnS and Cu_3SnS_4 (CTS) NP precursors in certain ratio mixed with oleylamine (solvent) and 1-dodecanethiol (capping agent) [5]. This mixture was heated to 130^{o}C with 10 ^{o}C/min and held at this temperature for 30 minutes. Thereafter, the mixture was further heated to higher temperature (200 °C-250°C) and stayed at this temperature for certain time to allow the growth of the NP. After cooling room temperature, the NP were precipitated by addition of excessive ethanol or acetone followed by centrifugation. The precipitated NP was dispersed in toluene or 1-hexanthiol to formulate the ink. Thin films were deposited by spin coating of using the NP inks. The residual solvents and organic surfactants surrounding the NP were removed by heating at 170 $^{\circ}$C and 350 $^{\circ}$C respectively for 2 minutes. It should be noted that a ligand exchange process is carried out with 0.04 M $(NH_4)_2S$ methanol solution for the sample cooled to RT from 170 °C. Thick films are obtained by repeating the spin coating and intermediate annealing at 350 °C. The processed CZTS NP film is further annealed at 580 °C for 25 minutes in Se atmosphere to form CZTSSe absorbers. The chemical composition of the absorber layer can be tuned by adjusting the ratio of NP precursors. It is also reported that the CZTSSe based SC performance is strongly dependent on the ratios of Cu/(Zn+Sn) and Zn/Sn [5]. The chemical reaction leading to the formation of CZTSSe can be represented as,

$$CTS+SnS+ZnS \xrightarrow{Se,\Delta} CZTSSe \text{ [5]}$$

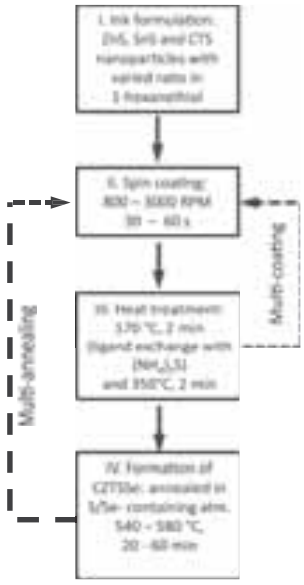

Figure 1: Preparation process of NP based CZTSSe absober layers[5]

Metal salt based CZTS ink were prepared by mixing Copper chloride, zinc acetate dihydrate, tin chloride dehydrate, thiourea and sodium fluoride in 12 mL DMSO with stirring overnight. The metal ratios of the ink precursor were Cu/(Zn+Sn) =0.73 and Zn/Sn = 1.02. NaF was directly introduced in the Cu-Zn-Sn-S ink with a concentration of 0.14 M. The resulting ink is well adapted for inkjet printing as revealed by the measurement of the contact angle. The best inkjet printing condition was found by adjusting the printing parameters (droplet volume less than 20 pl., printing speed set to 4.8 to 7.2 m/min). The resolutions in both

the X and Y directions for the printing were 400 dpi. With such conditions, the volume of ink needed for each printing on an 25.4 mm x 25.4 mm substrate is calculated to be less than 4 µL. Figure 2 shows the prepared ink and operating principle of inkjet printing. The as-deposited Cu-Zn-Sn-S precursor layers after printing were baked to remove the residual solvent on a pre-heated hot plate at 300 °C for 2 min. A second annealing in selenium containing atmosphere at 560 °C for 20 min allow the formation of well crystallized CZTSSe thin film absorbers.

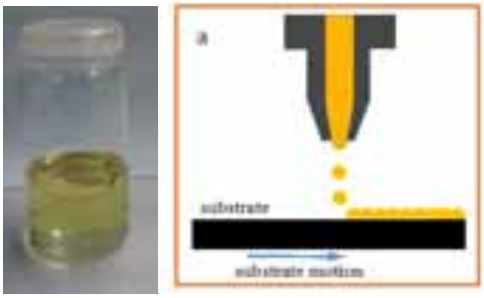

Figure 2: Formulated ink and operation principle of inkjet printing.

2.2 Fabrication of solar cells

Solar cells were fabricated by chemical bath deposition of a CdS buffer layer, and subsequently by sputtering of i-ZnO and aluminum doped ZnO window layers. A Ni/Al upper contact electrode was deposited by evaporation using a shadow mask. Finally solar cells with an area of 0.5 cm^2 were defined by mechanical scribing. The fabricated Solar cells with Mo/CZTSSe/CdS/i-ZnO/ZnO:Al/Ni:Al grids were studied for their photon conversion efficiency.

2.3. Characterization

X-ray diffraction (XRD) was used to verify the crystalline structure of NP and metal salt based CZTSSe absorber layers. Bruker D8-Advance X-Ray diffractometer was used with Cu K_α radiation in a step size of 0.02° and a step time of 5s. The contact angle was measured by using "contact angle system OCA" from data physics Instruments GmbH, Germany. The SEM image was recorded in a LEO 1530 GEMINI SEM of Zeiss at an acceleration voltage of 10 kV. Solar cell efficiency was calculated from J-V curves under 1.5 AM, 100 mW cm^{-2} illumination by using an in-house class A sun simulator.

3. Results and Discussion

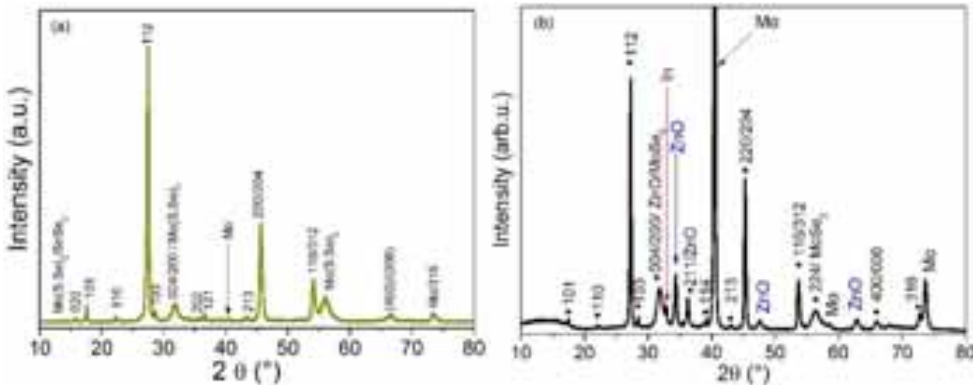

Figure 3: XRD patterns of (a) a NP based CZTSSe thin film and (b) metal salt based CZTSSe device.

XRD pattern in figure 3 (a) shows tetragonal structure for NP based CZTSSe sample. There are peaks from the Mo substrates as well. Peaks corresponding to $Mo(S,Se)_2$ are also observed. Usually Zn(S,Se) and CTS crystallographic peaks overlap with CZTSSe peaks, and it is difficult to identify the exact phase. It has been verified that there is no separate phase such as ZnS and CTS exist in CZTSSe using Raman spectroscopy (data is not shown here). Figure (3) (b) displays the XRD pattern of the metal salt based CZTSSe completed

device. Peaks assigned to CZTSSe are indexed as shown in the Figure. Since the measurement was performed on complete device, peaks related to window layer of ZnO and Mo substrate were also detected.

Figure 4 shows the contact angle of DMSO before (Figure 4a, 21.6°) and after adding Cu, Zn, and Sn metal salts (Figure 4b, 42.4°), which conform with the increase of the viscosity with increasing metal salts concentration. For the metal ratio used in this study (Cu/(Zn+Sn)=0.73 and Zn/Sn=1.02), the contact angle still below 90° suggesting the feasibility for the formation of a homogeneous film on Mo substrate by inkjet printing [12].

Figure 4: Contact angle of (a) DMSO and (b) formulated ink containing Cu-Zn-Sn-S precursor on Mo coated glass substrate.

Figure 5a shows the cross sectional scanning electron microscopy (SEM) image of NP based CZTSSe with a thickness of around 4.5 µm. It is a four layered structure with fine grain/large grain/fine grain/large grain arrangement on top of Mo layer. Device geometry is not shown here. The SEM image in Fig. 5b shows a complete metal salt route based CZTSSe device. Crack free compact CZTSSe is synthesized as shown in Fig.5b [12]. A layer of $MoSe_2$ is formed in-between the Mo layer and CZTSSe absorber layer due to the reaction between Mo and chalcogen Se (during selenisation). Generally, a thin $MoSe_2$ layer is helpful in adhesion and provides an Ohmic contact for the $Cu(In,Ga)Se_2$ (CIGS) solar cells [13]. These findings could be also applied to CZTSSe solar cells due to the similar properties between CZTS and CIGS. However, an excessively thick $MoSe_2$ layer may have adversely effect on the performance of CZTSSe solar cells because of the high resistance of lead to a high series resistance of $MoSe_2$ layer (in the range of 10^1 to 10^4 Ω.cm [14]).

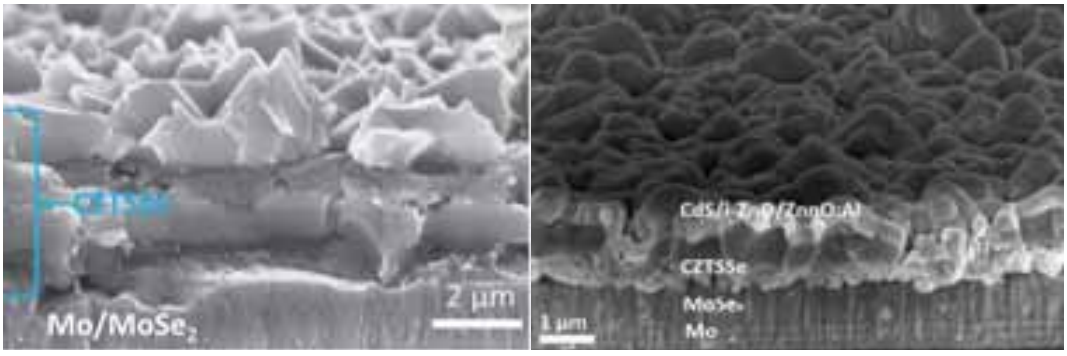

Figure 5: Cross-sectional scanning electron micrograph of NP based CZTSSe thin films (left) and the complete solar cell based on metal based CZTSSe (right).

The corresponding I-V characteristics measured in the dark and under AM 1.5 conditions are shown in Figure 6. The curves in blue show typical J-V curves of NP based CZTSSe solar cell under dark and illumination. Conversion efficiency of 3.0 % was achieved with an open circuit voltage (V_{OC}) of 306.5 mV, short circuit current density (J_{SC}) of 27.5 mA/cm^2, and fill factor (FF) of 35.0 %.

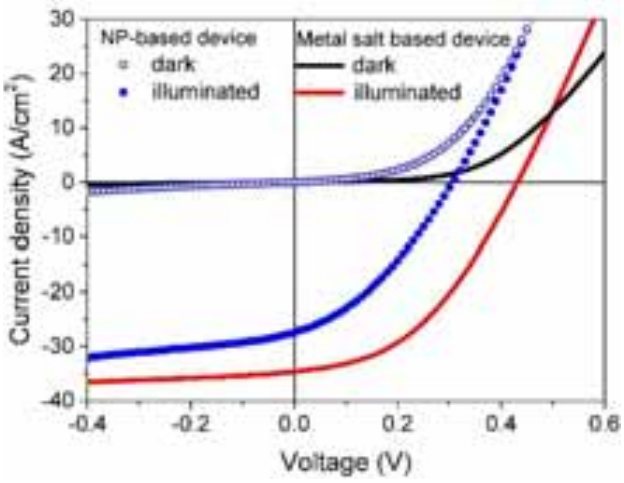

Figure 6: J-V characteristics in the dark and under illumination measured under AM 1.5 conditions for NP based CZTSSe device and metal salt based CZTSSe device. The area of the device is 0.5 cm^2.

Compared to spin coating method where most of the ink dropped on to spin coater substrates are spun away during rotation, inkjet printing method allows a uniform deposition with a negligible material waste due to the drop on demand properties. This reduces the material waste and cost of the solar cell. For example, in one of our studies, 20 µl ink is enough for the deposition of 1 µm thick absorber film in an inch^2 area [12]. Moreover, solar cells prepared with 0.5 cm^2 area in a glass/Mo/CZTSSe/CdS/ZnO structure demonstrated a power conversion efficiency of 6.4% (J-V curve in red in Figure 6). The V_{OC} was 431 mV, J_{SC} was 34.6 mAcm^{-2}, and fill factor FF was 42.8%. The series resistance, shunt resistance, and diode quality were found to be 5.7, 1230 Ω cm^2, and 2.3, respectively, by fitting the dark $J - V$ curve using one diode model.

The device performance is mainly limited by the low fill factor, which could be due to the high series resistance. Several factors may contribute to the high series resistance. One of the reason could be the thick $MoSe_2$ at the back contact. Another reason could be the fine grain layers near the back contact. We do not have a direct proof for that at the moment. Further studies are needed. The defect level studies on the CZTSSe thin films by photoluminescence (PL) and surface photovoltage spectroscopy (SPV) shows an increased $(Zn_{Cu})^+$, $[Zn_{Sn}+Cu_{Zn}]$ defect states and a dominating quasi donor-acceptor pair recombination in the recombination process [15]. We know the samples studied are Cu poor and Zn rich and the Cu and Zn disorder is already observed in the neutron diffraction studies as well [16]. This could also be a reason affecting the performance of the solar cell.

4. Conclusion and Outlook

Nanoparticle inks are affected by stability issues which is due to the agglomeration of NPs after certain time. To avoid this agglomeration long chain organic-ligand is used during the formation of ink. However, it is difficult to remove the long chain organic ligand which stabilizes the NPs completely from the thin films. A combination of ligand exchange and non-ligand exchange processes result a crack free CZTSSe absorber film. Selenisation lead to a layered structure with unwanted carbon in the grains. The carbon serves as a barrier for the growth of NP, however gives an efficiency around 1-3% [5]. we explored DMSO as solvent for the formulation of stable Cu-Zn-Sn-S precursor ink and by varying the concentration of Cu, Zn, and Sn metal salts, the viscosity can be controlled. The resulting ink is well adapted for inkjet printing as revealed by the measurement of the contact angle. Inkjet printing is more effective than the spin coating in terms of raw material utilization. Solar cells with glass/Mo/CZTSSe/CdS/ZnO structure with total area (0.5 cm^2) power conversion efficiency of 6.4% are demonstrated from thin film absorbers processed by inkjet printing technology of Cu-Zn-Sn-S precursor ink followed by selenisation. Inkjet printing allows the development of

Micro concentrator solar cell concept, which allows enhancing the efficiency of PV devices while reducing the material consumption. Furthermore, the adaptation and integration of micro-lenses for optimal concentration of light on micrometer size solar cell is a promising area of interest which can use micro-CPV with integrated optics without the need of tracking system.

5. References

1. W. Wang, M.T. Winkler, O. Gunawan, T. Gokmen, T.K. Todorov, Y. Zhu, D.B. Mitzi, Device Characteristics of CZTSSe Thin-Film Solar Cells with 12.6% Efficiency, Adv. Energy Mater., 4 (2014) 1301465.
2. X. Lin, A. Steigert, M.C. Lux-Steiner, A. Ennaoui, One-step solution-based synthesis and characterization of kuramite Cu3SnS4 nanocrystals, RSC Adv., 2 (2012) 9798.
3. X.Z. Lin, T. Dittrich, S. Fengler, M.C. Lux-Steiner, A. Ennaoui, Correlation between processing conditions of Cu2ZnSn(SxSe1−x)4 and modulated surface photovoltage, Appl. Phys. Lett., 102 (2013) 143903.
4. X. Lin, J. Kavalakkatt, K. Kornhuber, S. Levcenko, M.C. Lux-Steiner, A. Ennaoui, Structural and optical properties of Cu2ZnSnS4 thin film absorbers from ZnS and Cu3SnS4 nanoparticle precursors, Thin Solid Films, 535 (2013) 10-13.
5. X. Lin, J. Kavalakkatt, A. Ennaoui, M.C. Lux-Steiner, Cu2ZnSn(S, Se)4 thin film absorbers based on ZnS, SnS and Cu3SnS4 nanoparticle inks Enhanced solar cells performance by using a two-step annealing process, Sol. Energy Mater. Sol. Cells, 132 (2015) 221-229.
6. Y. Cao, M.S. Denny, Jr., J.V. Caspar, W.E. Farneth, Q. Guo, A.S. Ionkin, L.K. Johnson, M. Lu, I. Malajovich, D. Radu, H.D. Rosenfeld, K.R. Choudhury, W. Wu, High-efficiency solution-processed Cu2ZnSn(S,Se)4 thin-film solar cells prepared from binary and ternary nanoparticles, J. Am. Chem. Soc., 134 (2012) 15644-15647.
7. Q. Guo, G.M. Ford, W.-C. Yang, B.C. Walker, E.A. Stach, H.W. Hillhouse, R. Agrawal, Fabrication of 7.2% Efficient CZTSSe Solar Cells Using CZTS Nanocrystals, J. Am. Chem. Soc., 132 (2010) 17384-17386.
8. C.K. Miskin, W.-C. Yang, C.J. Hages, N.J. Carter, C.S. Joglekar, E.A. Stach, R. Agrawal, 9.0% efficient Cu2ZnSn(S,Se)4solar cells from selenized nanoparticle inks, Prog. Photovoltaics Res. Appl., (2014) 10.1002/pip.2472.
9. H. Xin, S.M. Vorpahl, A.D. Collord, I.L. Braly, A.R. Uhl, B.W. Krueger, D.S. Ginger, H.W. Hillhouse, Lithium-doping inverts the nanoscale electric field at the grain boundaries in Cu2ZnSn(S,Se)4 and increases photovoltaic efficiency, Physical chemistry chemical physics : PCCP, 17 (2015) 23859-23866.
10. W. Ki, H.W. Hillhouse, Earth-Abundant Element Photovoltaics Directly from Soluble Precursors with High Yield Using a Non-Toxic Solvent, Adv. Energy Mater., 1 (2011) 732-735.
11. C.M. Sutter-Fella, J.A. Stückelberger, H. Hagendorfer, F. La Mattina, L. Kranz, S. Nishiwaki, A.R. Uhl, Y.E. Romanyuk, A.N. Tiwari, Sodium Assisted Sintering of Chalcogenides and Its Application to Solution Processed Cu2ZnSn(S,Se)4Thin Film Solar Cells, Chem. Mater., 26 (2014) 1420-1425.
12. X. Lin, J. Kavalakkatt, M.C. Lux-Steiner, A. Ennaoui, Inkjet-Printed Cu2ZnSn(S, Se)4Solar Cells, Advanced Science, 2 (2015) n/a-n/a.
13. T Wada, N Kohara, S Nishiwaki, T. Negami, <Characterization of the Cu(In,Ga)Se2 Mo interface in CIGS solar cells.pdf>, Thin Solid Films, 387 (2001) 118-122.
14. J. Pouzet, J.C. Bernede, MoSe2 thin films synthesized by solid state reactions between Mo and Se thin films, Revue de Physique Appliquée, 25 (1990) 807-815.
15. X. Lin, A. Ennaoui, S. Levcenko, T. Dittrich, J. Kavalakkatt, S. Kretzschmar, T. Unold, M.C. Lux-Steiner, Defect study of Cu2ZnSn(SxSe1−x)4 thin film absorbers using photoluminescence and modulated surface photovoltage spectroscopy, Applied Physics Letters, 106 (2015) 013903.
16. S. Schorr, The crystal structure of kesterite type compounds: A neutron and X-ray diffraction study, Solar Energy Materials and Solar Cells, 95 (2011) 1482-1488.

Conference Proceedings

Solar World Congress 2015

Daegu, Korea, 08 – 12 November 2015

ISES SWC2015

A sensitivity analyses of a p-i-n perovskite solar cell with a fixed band gap

Kratzenberg M.G.[1], Rambo C.R.[1], Rüther R.[2], Beyer H.G.[3]

[1] Laboratório de Materiais Elétricos (LAMATE),
Universidade Federal de Santa Catarina (UFSC), Brazil

[2] Fotovoltaica UFSC – Grupo Grupo de Pesquisa Estratégica em Energia Solar, UFSC, Brazil

[3] Department of Engineering Sciences, University of Agder (UiA), Grimstad, Norway

Abstract

Solar cell developers should have the theoretical knowledge how to best manipulate the solar cell properties in order to improve in a most effective way the solar cell efficiency. Such knowledge can be obtained by the simulation of the solar cells efficiency. Here a validated analytical model is used in order to simulate the model efficiency of the hybrid p-i-n solar cell in a multidimensional property space. The analytical model is based on a self-consistent stationary quantum simulation of the charge carrier generation and is established on the drift diffusion and the Poisson equations. The model simplifies the numerical simulation of the carrier generation as a function of the penetration deepness of the solar radiation, where the total charge generation is obtained by integration of local generated charges over the whole absorber layer thickness. Recombination currents at the p and n transport layers are considered as a function of (i) the diffusion coefficients of the free charges, (ii) the excess and the moderation of charges at the front and the back of solar cell, (iii) the effective surface recombination velocities of these charges and the (v) the solar cells built-in voltage. By use of a sensitivity analysis, it is shown how the properties of an ideal perovskite cell should be manipulated in order to improve its efficiency.

Keywords: *Perovskite Solar Cell (PSC), Analytical PSC Model, Sensitivity Analysis.*

1. Introduction

Whereas photovoltaic power plants based on the widely used silicon solar cells are already economically viable without subsidies in several countries [1] in residential applications and on the industrial scale, climate change problems demand the usage of renewable energy sources in very large scale [2], which stresses large investments. In order to reduce this investment cost photovoltaic modules should be available at lower costs in the future. Such an demand may be accomplished with the hybrid perovskite solar cells, as it combines potentially a low manufacturing cost with very high efficiency values in a multiple junction cell structure [10]. As discussed in [10] a triple junction solar cell combined with a crystalline silicon cell would lead to a cell efficiency of up to 50 %, which will result to the efficiency of photovoltaic modules of approximately 40 %. The first commercially available hybrid photovoltaic modules are based on Dye Sensitized Solar Cells (DSSC) [3], and they are commercially available by the company Solaronix[1]. In 2010, the photovoltaic effect of the hybrid Perovskite material was unveiled [4], which lead at the state of the art to much higher solar cell efficiencies than the one obtained by dye sensitized solar cells. Remarkable in the research with the

[1] http://www.solaronix.com/solarcells/

doi:10.18086/swc.2015.05.09 Available at http://proceedings.ises.org

Perovskite solar cell is the unprecedented and strong tendency to high efficiency values within the short time frame of the research with this cell[1]. Due to its recent discovery it seams that the efficiency of these cells degrades over time. However a very promissing way in order to improve the stability of the perovskite solar cell efficiency over time is the encapsulation of the perovskite layer with a metal-oxide layer in order to protect it from the humidity of the air [11]. As shown by these authors such a protection result to an initial degradation of 10 % of the PCE, which stabilize after approximating 30 days. The use of standardized module encapsulation should further reduce the degradation of this solar cell, if used in a solar module.

At the state of the art the improvement of the efficiencies of the hybrid solar cells is mostly based on the exhaustive cell prototyping and measurements of the efficiency values of the cells manufactured in laboratories. However the potential benefits from mathematical modelling of the solar cell efficiency, as shown in [5, 6], should be more exploited in order to foster the velocity of their development. By having a mathematical model at hand, which expresses most accurately the solar cell efficiency as a function of its material properties and other engineering parameters, it can be analyzed theoretically which of the parameters or properties do lead to the most significant improvement of the solar cell efficiency. Therefore a multidimensional sensitivity analysis of the model variables of a perovskite p-i-n solar cell is here accomplished based on the analytical model elaborated in [5].

2. Tuneability of the properties of the perovskite cell

Whereas the organic component of the hybrid perovskite material provides the viability of its deposition in a solution, which permits the printing of the cell in a roll to roll process, the inorganic component of the perovskite solar cell forms an extended framework of strong covalent interactions, ionic interactions, or both of them, which permits the advanced engineering of the cell properties. As stated in [9], the optical and electronic properties of the perovskite material can be tuned to a great extend by replacing the halide ion, the metal ion or the organic cation. Furthermore the perovskite material has an excellent tuneability of its band gap by adjustment of the relation of its chemical composition [10], making it therefore fit for the optimization of its efficiency in single, double or multiple junction cells. The details highlight the remarkable tuneability of the perovskite cell properties, which show its high potential for further improvement of its efficiency in the near future.

3. Model description of the perovskite p-i-n solar cell

Using as reference the results obtained by a detailed numerical simulation, the authors Sun et al. [5] elaborated a simplified analytical model for four different types of perovskite solar cells considering a fixed band gap. For the present analyses only the p-i-n solar cell is analyzed in more detail based on its analytical model as this cell resulted in [5] to the highest measured and modelled efficiency values of 15.7 %. The p-i-n solar cell consists of a p-type and a n-type charge conduction layer, an absorber layer, also denominated as intrinsic i-type layer, a transparent front electrode layer and a reflecting the back contact layer. As it is considered that the excitons are principally generated within the charge neutral depletion zone, the enlargement of this zone by use of the undoped intrinsic layer, constituted by the perovskite material, does improve the probability of the generation of the free charges by means of the solar radiation. Whereas the majority carriers account for the generation of the free charges, the minority carrier's results to the recombination effect under explosion to light. The electron and the hole transport layers of n-type and p-type are considered as perfect conductors for the majority carriers and as imperfect blocking layers for the minority carriers. Whereas the p-layer conducts the majority holes to the cathode and blocks the minority flux of electrons to this electrode, the n-layer conducts the majority electrons to the anode and blocks the minority flux of holes to this second electrode.

[1] http://www.nrel.gov/ncpv/,

4. Initial parameter configuration based on measured results

Sun et al., 2015 [5] defined by use of the Optical Transfer Matrix method first the fundamental optical parameter of the analyzed cell, which are (i) the generation of free charges G_{max} = 1.4356 x 10^{23} $cm^{-2}s^{-1}$ (qG_{max} = 23 mA/cm²), and (ii) the average optical decay length λ_{ave} = 100 nm for the presented p-i-n solar cell. Wereas G_{max} gives the charge generation rate at the surface of the solar cell as function of the band gap λ_{ave} gives a measure of how the radiation intensity decays as it pentrates into the solar cell. Then, in order that the p-i-n model UI curves at AM1.5 irradiation $J_{light}(U)$ and in the dark $J_{dark}(U)$ fit to the measured UI curves, these obtained optical parameters and the measured ambient temperature T_a = 27.41 °C, were used in a regression using the algorithm 'lscurvefitt' of the Mablab™ program. This algorithm minimizes the sum of the least square deviations in-between the measured and the modeled UI curves and leads to the perovskite material properties considering a fixed solar cell thickness. Then, using the obtained model specification the cell efficiency for different absorber layer thicknesses was modeled in a unidimensional optimization process. The optimized cell was manufactured and its efficiency was validated with the optimized model efficiency. The authors obtained the following model properties: Diffusion coefficient of charges $D_n = D_p \approx$ 0.05 cm^2/s, front and back surface recombination velocities of charges s_f = 2 x 10^2 cm/s, s_b = 19.2 cm/s, number of charges participating at the recombination process Δn = 8.426 x 10^6 cm^{-3}, Δp = 1.3003 x 10^8 cm^{-3}, front and back surface recombination currents J_{f0} = 2.7 x 10^{-13} mA/cm^2, J_{b0} = 4.0 x 10^{-13} mA/cm^2, built-in voltage V_{bi} = 0.78 V, absorber layer thickness of t_0 = 450 nm, average optical decay length λ_{ave} = 100 nm. This optimization resulted to an cell efficiency of η = 15. 7% [5].

5. Results and discussion

As graphically shown in [5], the efficiency is a function of the recombination velocities of charges trough the front and the back transport layers s_f and s_b and the absorber layer thickness t_0. A reduction of s_f and s_b , and principally the front surface recombination velocity s_f , would improve the cell efficiency also by approximately 3 % (figure 4 in [5]). However, as given from the model equations the cell efficiency is sensible to more than those three variables. Therefore, in the present sensitivity analysis the efficiency is shown as a function of an increased number of model variables. The following material properties are considered as additional variables of which the efficiency is a function: (i) the average optical decay length (λ_{ave}) in context with the thickness of the intrinsic absorber layer (t_0), (ii) the diffusion coefficients of electrons and holes D_f and D_b, the built-in voltage V_{bi} .

Whereas the cell thickness seems to be the main factors in order to improve the cell efficiencies (see figure 3 is [5]), the melioration of the average optical decay length seems to be insignificant leading to an improvement of only 0.05…0.1 %, if a fixed optical decay length is considered. However, showing these two variables in a bi-dimensional space, while the other variables are are being fixed to the values in item 4, it can be seen that the efficiency can be considerably improved if it would be possible to reduce the optical decay length (Figure 1). As shown by the vertex line in this figure, the active layer thickness t_0 has to be adjusted as a function of the average optical decay length λ_{ave} in order to obtain the best efficiency values. In the best case this results to the augmentation of the efficiency from 15.7 % to around 17 % (Figure 1). Further improvement of the efficiency values can be obtained by manipulation of the diffusion coefficients and principally the diffusion coefficient of the holes D_p , which lead to an improvement of up to approximately 3 % of the efficiency (Figure 2). The variation of the built-in voltage resulted to an increase of the efficiency of approximately 1.8 % at V_{bi} of 1.4 eV. As to see from the Shockely-Quaisser efficiency curve the a band gap adjustment would improve the efficiency by less then 2 %.

Recommendations for the improvement of the efficiency of the p-i-n perovsktite cells

The perovskite material with the lowest average optical decay length λ_{ave} should be selected as this results to the conversion of the solar irradiance by use of smaller values of the cell thickness t_0 . The cell thickness t_0 should be adjusted as a function of the attained average optical decay length of the synthesized Perovskite absorber layer as shown by the blue vertex line in Figure 8, which shows the highest solar cell efficiency values within this function space. The perovskite material should be modified in order that the diffusion coefficients of the electrons and holes D_n and D_p are coming as high as possible. Especially high improvements can be obtained by the improvement of D_p , if D_n is at least higher than approximately 0.3 m²/s (Figure 2). The perovkite material and the organic conduction layer material should be selected in order to obtain the highest possible built-in voltage V_{bi} .

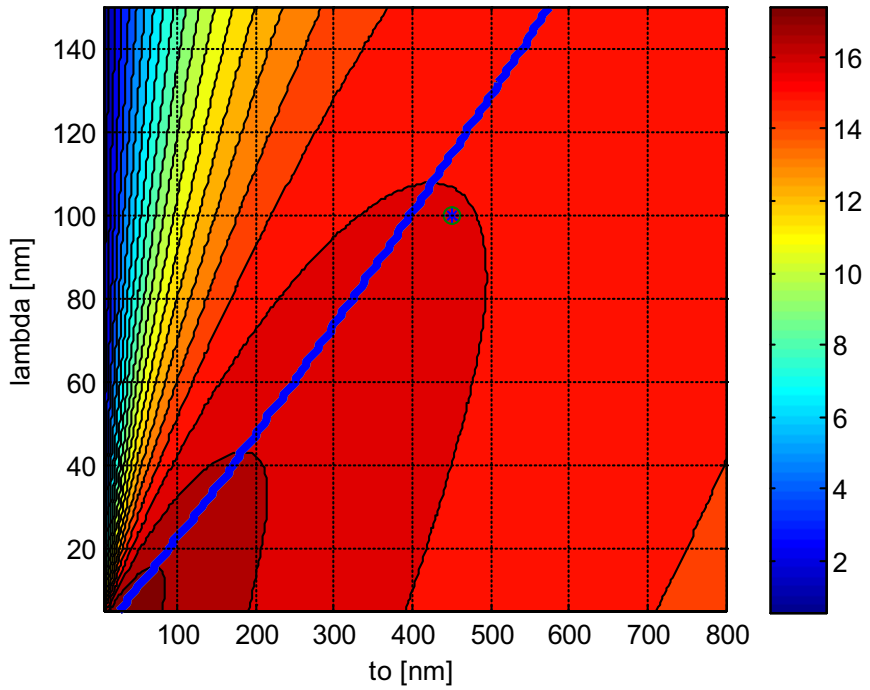

Figure 1: Modeled efficiency for a current generation of q x G_{max} = 23 mA / cm² as a function of the thickness of the absorber layer t_0 and the average optical decay length λ_{ave} with a vertex line of the maximal efficiency points (blue line) and the measured efficiency obtained in [5] (blue star surrounded by a circle).

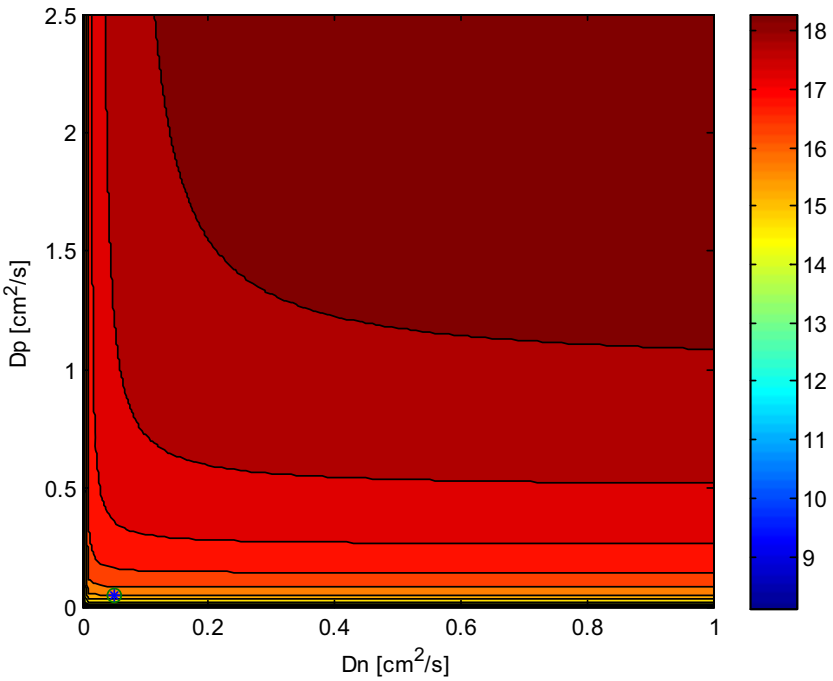

Figure 2: Cell efficiency for a current generation of q x Gmax = 23 mA / cm² as a function of the diffusion coefficient of holes D_p and diffusion coefficient of electrons D_n with maximum value of the efficiency of 18.8 % within the upper right part of the presented graphic and the measured efficiency in [5] (blue star surrounded by an circle).

6. Conclusions

In the present publication the perovskite cell efficiency is shown as a function of an extended variable space determined by the cell properties and manufacture parameters. The obtained results lead to a better understanding on how the efficiency of the p-i-n perovskite solar cell can be improved and results into recommendations to show how to modify these variables, in order to increase most successfully the solar cell efficiency. Whereas the melioration of each one of the single variables lead to a lower improvement of the efficiency the interplay or interdependence of the model variables in an nonlinear space lead to more substantial improvements, which are much higher than the improvements obtained by single variable variations.

References:

[1] Breyer C., Gerlach A., Global overview on grid-parity, Journal - Progress in Photovoltaics Research and Applications, pp. 1-16, John Wiley & Sons, 2012.

[2] Edenhofer O. et al., Renewable Energy Sources and Climate Change Mitigation - Special Report of the Intergovernmental Panel on Climate Change, Cambridge University Press, 2012

[3] B. O´Regan, M.G., A low-cost, high-efficiency solar cell based on dye-sensitized colloidal TiO2 films. Nature, 1991. 353: p. 737-739.

[4] Kojima, Akihiro; Teshima, Kenjiro; Shirai, Yasuo; Miyasaka, Tsutomu, Organometal Halide Perovskites as Visible-Light Sensitizers for Photovoltaic Cells. Journal of the American Chemical Society 131 (17): pp. 6050–6051, 2009

[5] X. Sun, R. Asadpour, W. Nie, A. D. Mohite and M. Ashraful Alam, 2015, A Physics-Based Analytical Model for Perovskite Solar Cells, IEEE Journal of Photovoltaics.

[6] J. M. Foster, H. J. Snaith, T. Leijtens, and G. Richardson, A model for the operation of perovskite based hybrid solar cells: formulation, analysis and comparison to experiment, Vol. 74, no. 6, pp. 1935–1966, 2014.

[7] M. A. Loi, J. C. Hummelen, Hybrid solar cells: Perovskites under the Sun, Nature Materials 12, pp. 1087–1089, 2013.

[8] L. H. Wong, Lydia Wong Research Group – Clean Energy Research Group – Applications, Perovskite Solar Cell, 2014, http://www.ntu.edu.sg/home/lydiawong/researchfoc4.html, Accessed on 21.09. 2015.

[9] R. Comin et al., Structural, optical, and electronic studies of wide-bandgap lead halide perovskites, Journal of Materials Chemistry, Royal Society of Chemistry, 2015.

[10] Emergence of Perovskite solar cells - Slide show presented by Professor M. Green, University of New South Wales - UNSW Australia, https://www.youtube.com/watch?v=ALHea8qW1jc, Accessed on 21.09. 2015.

[11] You et al., Improved air stability of perovskite solar cells via solution-processed metal oxide transport layers, Nature – Nanotechnology, pp. 1-8, October, 2015.

Substrate-type Hydrogenated Amorphous SiGe Thin Film Solar Cells with Ge-graded SiGe Layers on Opaque Substrates

Yoo Jeong Lee[1,2], Kwang Hoon Jung[1,2], Jung Wook Lim[1,2] and Sun Jin Yun[1,2*]

[1]Information & Communications Core Technology Research Laboratory, Electronics and Telecommunications Research Institute, Daejeon (Korea)

[2]Department of Advanced Device Engineering, University of Science and Technology, Daejeon (Korea)

Abstract

a-SiGe:H thin film solar cells with a light-abosrbing layer having differently graded Ge-compostion (C_{Ge})-profiles were fabricated to investigate the effect of C_{Ge}-profiling on the cell performance and light-induced degradation (LID). The C_{Ge}-profiles were linear normal profiling, nonlinear normal profilings, nonlinear reverse profiling, and nonlinear U-shape profiling. The cells with these C_{Ge}-profiles were compared to the cells with a constant $C_{Ge.}$ Among the samples, the cells with normal profilings showed better performances than the others. The efficiencies of the cells with linear and nonlinear normal profilings were 6.31 and 6.10%, respectively. Compared to the cells with constant-C_{Ge}, the efficiency of the cells with normal profiling was increased mainly due to the increase in the fill factor, which could be induced by the enhancement of internal field. The light-soaking experiment also showed that C_{Ge}-profilings can reduce LID. In this work, the use of a light-absorbing layer with graded C_{Ge}-profiling could improve the cell performance in terms of both efficiency and LID.

Keywords: *substrate-type solar cell, a-SiGe:H, Ge-composition profiling, light-induced degradation, internal field*

1. Introduction

Thin film photovoltaic devices based on hydrogenated amorphous silicon (a-Si:H) have been extensievley investigated in efforts to achieve high conversion efficiency and low-cost production. One of the most effective approaches used to achieve high efficiency is the fabrication of multi-junction (MJ) solar cells. The nip-type MJ cells on opaque and flexible substrates such as metal sheets or plastic films have also attracted much attention due to their promising applications including building- and device-integrated solar cells. Si-based MJ solar cells usually consist of a wide bandgap a-Si:H top cell (the optical bandgap energy, E_g = 1.7 –

Selection and/or peer review under responsibility of Scientific Committee
doi:10.18086/swc.2015.05.10 Available at http://proceedings.ises.org

1.8 eV) and narrow bandgap sub-cells. Hydrogenated microcrystalline Si (μc-Si:H) and hydrogenated amorphous silicon germanium (a-SiGe:H) are good candidates for the narrow bandgap materials because the E_g of μc-Si:H is approximately 1.1 eV (Kondo and Matsuda, 2001) and that of a-SiGe:H can be varied in the range of 1.1 – 1.8 eV by controlling the Ge-fraction (Xu et al., 1996). However, μc-Si:H film have a low deposition rate and low light absorption coefficient, which are drawbacks in view of productivity because the μc-Si:H films need to be thicker than 1.5 μm to sufficiently absorb incident sunlight (Vetterl et al., 2000; Guo et al., 1998). Therefore, a-SiGe:H films, which have high deposition rates and a high light absorption coefficient can be good alternatives for improving the productivity of MJ solar cells.

The E_g of an a-SiGe:H film can be lowered and the light absorbance in the long-wavelength region ~~is~~ can be increased by increasing the amount of the Ge-fraction. However, the defect density of a-SiGe:H films increases with Ge-content (Stutzmann et al., 1989; Beyer, 2010), and many defects at n-Si:H/i-SiGe:H and p-Si:H/i-SiGe:H interfaces are generated by band-gap discontinuities (Lundszien et al., 2002). Therefore, the incorporation of Ge adversely affects the collection of photo-generated carriers due to the decrease of drift length and the increase of recombination centers, and causes the deterioration of cell performance. Earlier studies investigating methods to reduce the bandgap discontinuity and defect density have focused on the insertion of buffer layers or Ge-composition grading at the p/i- and n/i-interface regions (Zimmer et al., 1998; Arya et al., 1989). We previously reported the effect of a-SiGe:H with linearly graded Ge-composition on solar cell performance in the relatively low Ge-composition ranging from 0 to 16% (Yun et al., 2012). The light-induced degradation (LID) effect has also been studied for a-SiGe:H thin film solar cells because LID is more severe in a-SiGe:H than a-Si:H thin film solar cells (Shima et al., 2005). The study on LID effect is very important because it is closely related to the long-term stability of the a-SiGe:H thin film solar cell module.

In the present work, the Ge-composition of a light-absorbing layer was graded throughout rather than the p/i- or n/i-interface regions, and the Ge-content was varied in the range of 0 - 33%. A Ge-content of 33% is significantly higher than the commonly used Ge-content in a-SiGe:H solar cells because the performance of cells having a Ge-content exceeding 20% has been reported to be deteriorated by defects (Jones et al., 1993). The purpose of the Ge-grading in this work is to utilize the advantage of a high Ge-content region for absorbing a wide solar spectrum and to reduce the disadvantage of defective Ge-rich region in the light-absorbing layer. The enhanced internal field which can improve the carrier collection would be caused by the Ge-composition grading throughout light-absorbing layer. We also explored the optimum Ge-grading profile to achieve high conversion efficiency of nip-type a-SiGe:H thin film solar cells, and the most effective Ge-profiling was suggested for obtaining high efficiency and long-term stability.

2. Experimental details

The nip-type a-SiGe:H single junction cells were fabricated in a single chamber plasma enhanced chemical vapor deposition (PECVD) system. The schematic structure of the a-SiGe:H solar cell is illustrated in Fig .1. Ga-doped ZnO (ZnO:Ga) layers deposited by an rf-magnetron sputtering technique were used as transparent electrodes. Ag films coated with 200 nm ZnO:Ga were used as back-reflectors. Intrinsic SiGe:H layers with a thickness of 200 nm were deposited on the n-Si:H layer at 200 ^{o}C using SiH_4 (100%), GeH_4 (1.5%, diluted in H_2) and H_2 (100%) as source gases. a-SiGe:H films with graded Ge-composition profiles were prepared by gradually varying GeH_4 flow rate from 0 to 100 sccm (normal profiling) or 100 to 0 sccm (reverse profiling). The 20 nm-thick n-Si:H and 25 nm-thick p-Si:H layers were deposited using PH_3 (1.5%, diluted in H_2) and B_2H_6 (0.5%, diluted in H_2) as doping gases. An Al grid was formed on the ZnO:Ga top electrode using an e-beam evaporation process. The cell area defined by the top electrode was 0.2 cm^2. The solar cells were characterized by solar simulator under AM 1.5G spectrum and 100 mW/cm^2 illumination intensity at room temperature. External quantum efficiency (EQE) measurement was also carried out to investigate the light-absorbing behavior of a-SiGe:H layers having different Ge-profiles. To estimate the LID, the a-SiGe:H thin film solar cells were light-soaked under 1sun at 25^{o}C for 140 h.

The Ge-composition (C_{Ge}) profiles of the a-SiGe:H films were analyzed using Auger electron spectroscopy (AES). UV-Vis spectroscopy was utilized to measure the absorbance of the a-SiGe:H films, and the E_g was determined by Tauc's plot utilizing the absorbance data.

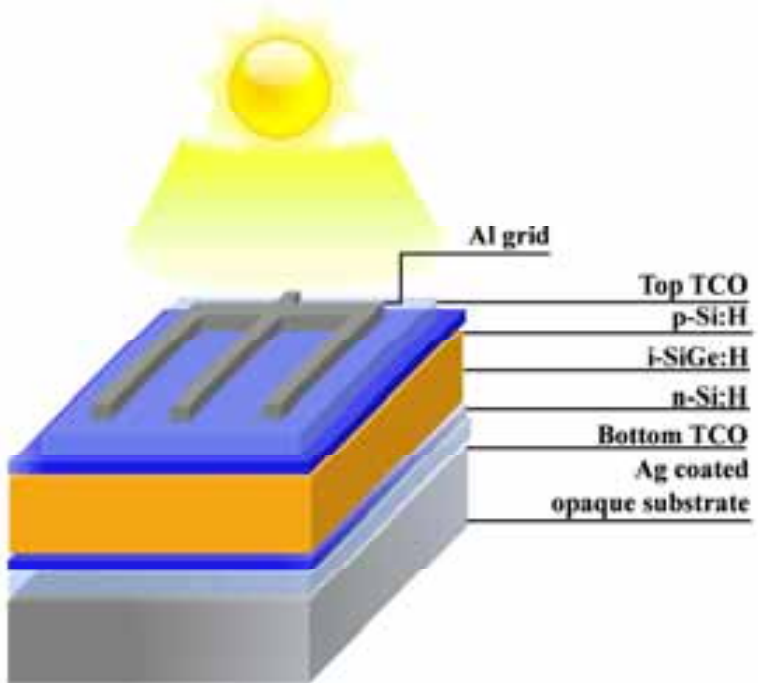

Fig. 1: Structure of the substrate-type a-SiGe:H thin film solar cells with Ge-composition profiled light-abosrbing layer.

3. Results and Discussions

First, thin film solar cells having a-SiGe:H light-absorbing layers with four different C_{Ge} profiles were fabricated to investigate the effect of Ge-profiling on cell performance. In this work, two different methods of C_{Ge}-grading were used; linear and nonlinear profilings. Cells with constant C_{Ge} in the a-SiGe:H light-absorbing layers were also fabricated to compare with the cells that had C_{Ge}-gradings.

The AES depth profiles of a-SiGe:H films with constant C_{Ge} and linear normal profiling are presented in Fig. 2(a), and those with nonlinear normal and reverse profilings are shown in Fig. 2(b). The thickness of the a-SiGe:H layer was 200 nm for all samples. The AES data in Fig. 2(a) shows that the C_{Ge} of the film deposited with GeH_4 100 sccm was approximately 33.0%, and that the Ge was uniformly distributed in the a-SiGe:H. Fig. 2(a) also shows that the C_{Ge} of the linear normal profiling sample changed linearly from approximately 33 to 0% and the average C_{Ge} in the film was 16.5%. The depth profiles of the nonlinear profilings are presented in Fig. 2(b). The C_{Ge} of the films with normal and reverse profiling decreased nonlinearly from approximately 33 to 0%, and increased from 0 to 33% in the depth direction, respectively. For the nonlinear C_{Ge}-profiled a-SiGe:H films, the average C_{Ge} was approximately 11.0% which is 5.5% smaller than that of the linear C_{Ge}-profiled film. To determine the bandgap energy (E_g) depending on the C_{Ge} of a-SiGe:H, the absorption coefficient of the films was obtained using UV-Vis spectroscopy. The E_g values of the films with C_{Ge} = 33, 16, and 0%, estimated by Tauc's plot, were 1.55, 1.66, and 1.75 eV, respectively, which were linearly decreased with respect to C_{Ge}. Then, the C_{Ge}-graded profiles correspond inversely to the E_g-graded profiles.

As briefly explained in the introduction section, the purpose of C_{Ge}-grading is to absorb a wide solar spectrum and to reduce the disadvantage of a Ge-rich region. However, to obtaining high efficiency, it is also very important that the C_{Ge}, i.e., E_g should be profiled to effectively collect carriers.

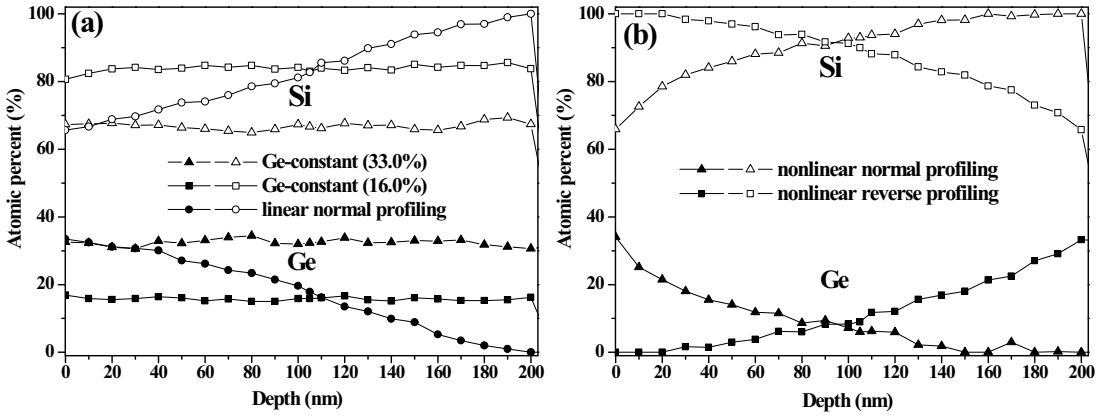

Fig. 2: AES depth profiles of a-SiGe:H films of (a) constant (33 and 16 %) and linearly graded C_{Ge} (33 - 0%) and (b) nonlinearly graded C_{Ge}-profiles (0-33 % or 33-0 %).

Figure 3 shows the schematic band-diagrams of thin film solar cells having a light-absorbing layer with E_g-profiles. As denoted by the arrows in the band-diagrams, the photo-generated holes and electrons are collected through p- and n-layers, respectively. The internal field in the light-absorbing layer with the E_g-profile could be enhanced either in view of hole or electron drift (Zambrano et al., 2004). The band-diagram of Fig. 3(a) shows that normal profiling can strengthen the internal field toward the p-layer and this allows holes to transport effectively from the n-side to the p-side in comparison to that of the E_g-constant light-absorbing layer denoted by the dotted line. On the other hand, the reverse profiling of Fig. 3(b) can enhance the internal field in the opposite direction to hole collection. With U-shape profiling, which is the complex structure of (a) and (b) as shown in Fig. 3(c), the additional internal field generates in the opposite direction to the carrier collections at both the p/i- and n/i-interface regions.

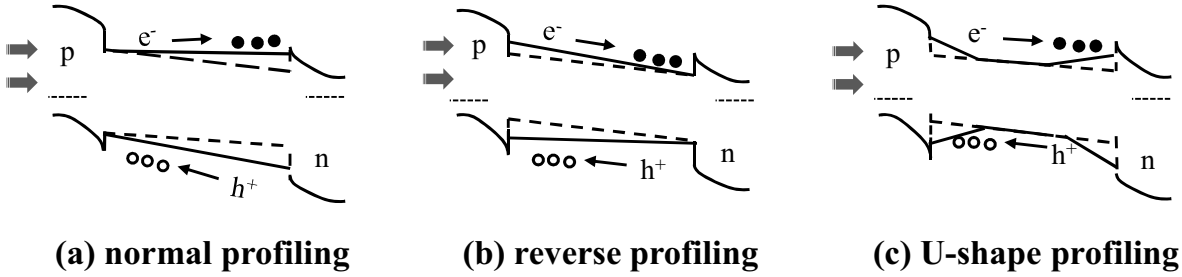

(a) normal profiling **(b) reverse profiling** **(c) U-shape profiling**

Fig. 3: Energy band-diagrams of the nip-type a-SiGe:H solar cells with (a) normal profiling, (b) reverse profiling, and (c) U-shape profiling; the dotted lines indicate the band-diagram of the cell with Ge-constant (33%).

For a-SiGe:H thin film solar cells, it has been reported that efficiency is limited by the collection of holes because the lifetime of holes is much shorter than electrons. Therefore, among the profilings shown in Fig. 3, the normal profiling is expected to be the most advantageous for the collection of holes in the nip-type a-SiGe:H solar cells fabricated in the present work.

To investigate which profiling is effective for obtaining high efficiency in practical a-SiGe:H thin film solar cells, single junction a-SiGe:H solar cells having different C_{Ge}-profiles were fabricated on opaque substrates. The cell performances are summarized in Table 1. The cell with linear normal profiling (Cell C) showed the highest conversion efficiency (η) of 6.30%. The η was approximately 20 and 29% higher than the cells with C_{Ge} = 33.0% (Cell A) and 16.0% (Cell B), respectively. The improvement of η was mainly attributed to the increase of fill factor (FF) which was induced by the improved shunt resistance. Normally, a strengthened internal field causes an increase in shunt resistance. It also has been generally known that the short-circuit current density (J_{SC}) of a-SiGe:H is considerably increased with increasing C_{Ge} (Agarwal et al., 2002). However, the Jsc of Cell C (15. 65 mA/cm^2) was a little higher than Cell A (15.43 mA/cm^2) although the average C_{Ge} of Cell C (16.5%) was much lower than that of Cell A (33.0%). In the case of Cell D with nonlinear normal profiling and an average C_{Ge} = 11.0%, the η was 6.10% and the J_{SC} was only 2.3% lower than that of Cell A.

The cells with reverse profiling (Cell E) and U-shape profiling (Cell F) showed an increased V_{OC} of 0.697V. The U-shape profiling consisted of 50 nm reverse profiling, 100 nm C_{Ge}-constant (C_{Ge} = 33.0%), and 50 nm normal profiling regions. The increased V_{OC} in both Cell E and Cell F could be explained that the wide bandgap region (C_{Ge} = 0%) of the a-SiGe:H layer was interfaced to the p-layer, as illustrated in Figs. 3(b) and (c). On the other hand, the J_{SC} of Cell E was significantly lower than that of Cell A. This might be because the C_{Ge} of Cell E was much smaller than that of Cell A and it was also difficult to collect holes due to the enhanced internal field in the opposite direction, as illustrated in Fig. 3(b). The generation of additional internal field in Cell E could be indirectly supported by the increase of shunt resistance compared to Cell A and Cell B with constant C_{Ge}, as shown in Table 1. In contrast to Cell C, Cell D, and Cell E with C_{Ge}-gradings, the shunt resistance of Cell F was rather decreased due to the additional internal field generated in the p/i- and n/i-interface regions in the opposite direction.

Table 1: Performance of the a-SiGe:H solar cell with different C_{Ge}-profiles

i-SiGeH layer (graded C_{Ge} from p- to n-side)		Cell ID	V_{OC} (V)	J_{SC} (mA/cm^2)	FF (%)	η (%)	R_{Sh} (Ω)	R_S (Ω)
Constant	C_{Ge} = 33.0%	A	0.669	15.43	50.8	5.24	1000	41
	C_{Ge} = 16.0%	B	0.703	13.83	50.2	4.89	1000	48
Linear normal profiling (from 33.0 to 0%) (average C_{Ge} = 16.5%)		C	0.679	15.65	59.3	6.31	2000	34
Nonlinear normal profiling (from 33.0 to 0%) (average C_{Ge} = 11.0%)		D	0.670	15.08	60.4	6.10	2100	31
Nonlinear reverse profiling (from 0 to 33.0 %) (average C_{Ge} = 11.0%)		E	0.697	10.43	58.9	4.28	1900	38
Nonlinear U-shape profiling (from 0% (p-side) to 33.0% (50 nm), constant 33.0% (100 nm) and 33.0 - 0% (n-side) (50 nm)) (average C_{Ge} = 22.0%)		F	0.697	13.15	42.3	3.87	890	57

The influence of C_{Ge}-grading on the the light-absorbing behavior was also examined by EQE measurement. Fig. 4 shows the EQE curves of the cells whose performances are listed in Table 1. The EQE curves of the cells with linear normal profiling (Cell C), nonlinear normal profiling (Cell D), and constant C_{Ge} (Cell A (33.0%) and Cell B (16.0%)) are presented in Fig. 4(a). The EQE values of Cell C and Cell D were larger than that of Cell A and Cell B in the wavelength region (500 – 730 nm) due to the enhancement of the internal field. In the long-wavelength region (730 – 850 nm), Cell C (16.5%) and Cell D (11.0%) showed smaller EQE values than Cell A (33.0%), but the EQE values of the Cell C and Cell D were significantly larger than that of Cell B (16.0%). The result clearly showed that the EQE values of Cell C (average C_{Ge} = 16.5%) and Cell D (average C_{Ge} = 11.0%) with graded C_{Ge}-profiles greatly increased compared to that with constant C_{Ge} (Cell B, C_{Ge} = 16.0%) especially in the long-wavelength region where the light-absorption is belived to depend

on the C_{Ge}, i.e. E_g. The EQE gain of Cell C and Cell D in the long-wavelength might be attributed to the presence of high C_{Ge} (> 16.0%) regions in the light-absorbing layer as well as the strenghtened internal field beneficially to hole collection.

In Fig. 4(b), the EQE curve of Cell D with the nonlinear normal C_{Ge}-profile is compared to the cells with different types of nonlinear profilings. In the case of the cell with reverse profiling (Cell E), which has the same average C_{Ge} as the Cell D, the EQE value was considerably smaller than Cell D in the wavelength region longer than 500 nm. It is thought to be owing to the internal field enhanced in the opposite direction to hole collection for the Cell E. The EQE value of the cell with U-shape profiling (Cell F) was also samller than that of Cell D in the wavelength region (500 - 730 nm). But, in the wavelength longer than 730 nm, the light-absorption of Cell F (average C_{Ge} = 22.0%) was larger than that of Cell D due to its much larger C_{Ge}.

The results shown in Fig. 4 and Table 1, clearly demonstrate that the normal profiling is the most advantageous for improving cell performance owing to the E_g-grading in the way beneficial to hole collection as well as the advantage to utilize a wide solar spectrum although the cell performance obtained using the single-chamber PECVD in this work was relatively low compared to reported performances of nip-type a-Si:H or a-SiGe:H thin film solar cells fabricated with multi-chamber systems (Cho et al., 2011; Li et al., 2006).

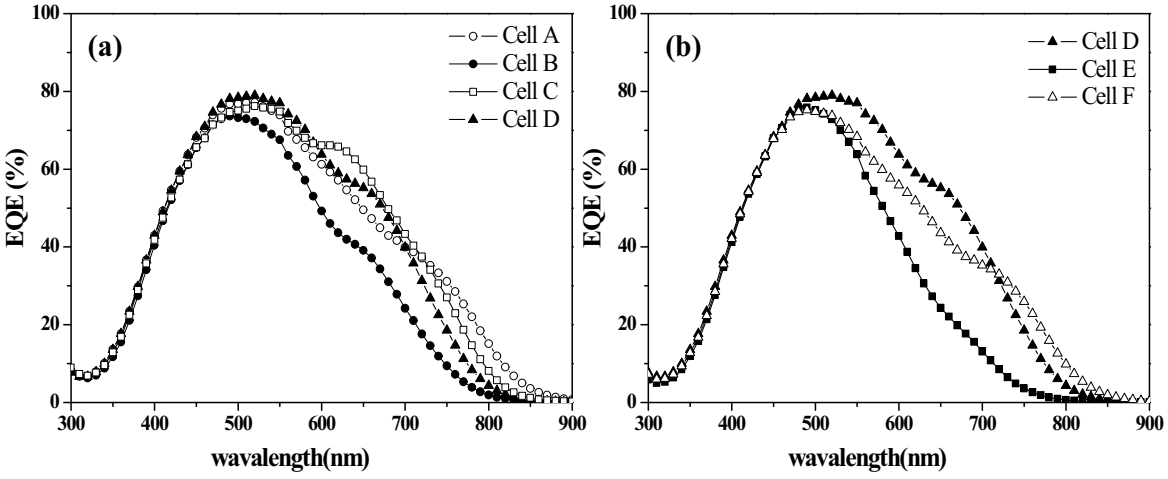

Fig. 4: EQE data of a-SiGe:H thin film solar cells listed in Table 1.

In order to consider the influence of C_{Ge}-grading on LID, the cells with C_{Ge}-constant (33.0%) (Cell A), linear normal profiling (Cell C), nonlinear normal profiling (Cell D), and nonlinear reverse profiling (Cell E) were light-soaked under 1sun at 25°C for 140 h. Fig. 5 shows the normalized FF and η as a function of light-soaking time. While there were not big differences between the cells in the V_{OC} and J_{SC} degradation behavior, the FF of Cell A was significantly decreased compared to the cells with C_{Ge}-graded profiling (Cell C, Cell D, and Cell E). Then, the η decrease of Cell A was approximately 40% while the η decrease of Cell C, Cell D, and

Cell E was approximately 25% by 140 h light-soaking. Especially, Cell C shows mostly the same LID behavior as Cell D and Cell E although the average C_{Ge} (16.5%) was considerably higher than the average C_{Ge} (11.0%) of Cell D and Cell E. The results obtained in this LID experiment clearly show that the C_{Ge}-grading in the light-absorbing layer of a-SiGe:H thin film solar cells is also advantageous for reducing LID, which has been considered to be a drawback of adding Ge in the light-absorbing layer.

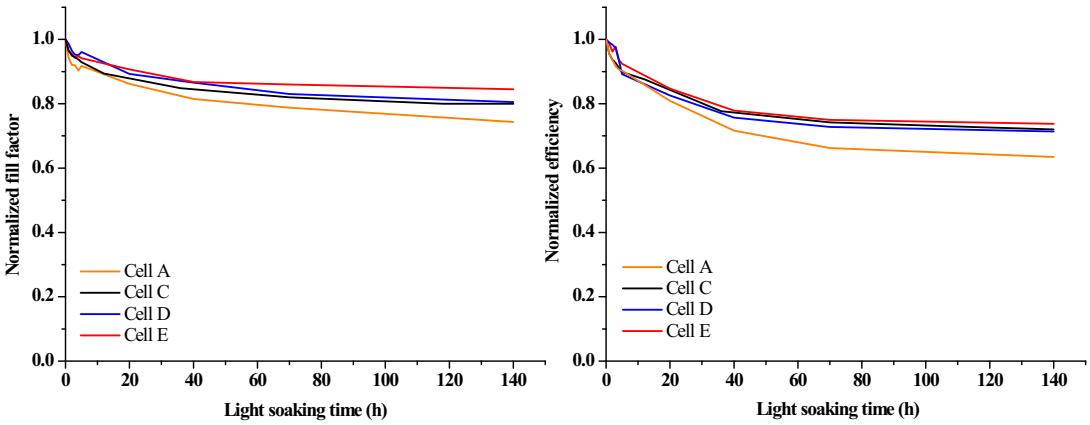

Fig. 5: Normalized FF and η of nip-type a-SiGe:H solar cells having graded C_{Ge}-profiles or constant C_{Ge} (33.0%) as a function of light-soaking time.

4. Conclusion

The influence of C_{Ge}-profiles on cell performance and LID was investigated for substrate-type a-SiGe:H thin film solar cells fabricated on opaque substrates. In this work, the cells with different C_{Ge}-profiles, such as linear normal, nonlinear normal, nonlinear reverse, and nonlinear U-shape profilings, were evaluated in comparison to that of constant C_{Ge}. The efficiency of cell with linear normal grading (average C_{Ge} = 16.5%) was 6.31% while the cells with constant C_{Ge} (16.0 and 33.0%) showed the efficiency of 4.89 and 5.24%, respectively. Among the C_{Ge}-profiles, normal profiling was found to be advantageous for enhancing light-absorption in the middle wavelength region because the E_g-grading was beneficial to hole collection. The LID experiment showed that the C_{Ge}-grading in the light-absorbing layer of a-SiGe:H thin film solar cells ~~is~~ was also advantageous for reducing LID. The use of C_{Ge}-profiling clearly shows that for nip-type a-SiGe:H solar cells, a light-absorbing layer with linear normal C_{Ge}-profiling is the most useful for obtaining high efficiency and long-term stability. The present work could suggest very useful C_{Ge}-profiling method for improving the performance of the a-SiGe:H single junction or a-Si:H/a-SiGe:H multi-junction solar cells.

5. Acknowledgement

This work was supported by the New and Renewable Energy of the Korea Institute of Energy Technology Evaluation and Planning (KETEP) grant funded by the Trade, Industry and Energy Ministry of Korea (Contract No: 20123010010150). One of the authors, S. J. Yun, was partially supported by the ETRI project (Account No: 15ZE1140).

6. References

Kondo, M., Matsuda, A., 2001. Low temperature growth of microcrystalline silicon and its application to solar cells, Thin Solid Films 383, 1-6

Xu, J., Miyazaki, S., Hirose, M., 1996. High-quality hydrogenated amorphous silicon-germanium alloys for narrow bandgap thin film solar cells, Journal of Non-Crystalline Solids 208, 277-281.

Vetterl, O., Finger, F., Carius, R., Hapke, P., Houben, L., Kluth, O., Lambertz, A., MuK ck, A., Rech, B., Wagner, H., 2000. Intrinsic microcrystalline silicon: A new material for photovoltaics, Solar Energy Materials & Solar Cells 62, 97-108.

Guo, L., Kondo, M., Fukawa, M., Saitoh, K., Matsuda, A., 1998. High Rate Deposition of microcrystalline silicon using conventional plasma-enhanced chemical vapor deposition, Japanese Journal of Applied Physics 37, 1116–1118.

Stutzmann, M., Street, R. A., Tsai, C.C., Boyce, J.B., Ready, R.E., 1989. Structural, optical, and spin properties of hydrogenated amorphous silicon-germanium alloys , Journal of applied physics 66(2), 569-592.

Beyer, W., 2010. Amorphous silicon-germanium and silicon-carbon alloys, in: Shah, A. (Eds.), Thin-film silicon solar cells. EPFL Press, pp. 76-87.

Lundszien, D., Finger, F., Wagner, H., 2002. A-Si:H buffer in a-SiGe:H solar cells, Solar Energy Materials & Solar Cells 74, 365–372.

Zimmer, J., Stiebig, H., Wagner, H., 1998. a- SiGe:H based solar cells with graded absorption layer, Journal of Applied Physics 84, 611-617.

Arya, R.R., Bennett, M.S., Rajan, K., Catalano, A., 1989. Role of interfaces on the performance and stability of amorphous silicon-germanium alloy p-i-n solar cells, Applied Physics Letters 55, 1894-1896.

Yun, S. J., Kim, J. K., Lim, J. W., 2012. Amorphous SiGe:H thin film solar cells woth light absorbing layers of graded bandgap profile, Electrochemical and Solid-State Letters 15(2), 9-12.

Shima, M., Isomura, M., Wakisaka, K., Murata, K., Tanaka, M., 2005. The influence of operation temperature on the output properties of amorphous silicon-related solar cells, Solar Energy Materials & Solar Cells 85, 167–175.

Jones, S. J., Chen, Y., Williamson, D. L., Zedlitz, R., Bauer, G., 1993. Microstructural transition and degraded opto-electronic properties in amorphous SiGe:H alloys, Applied Physics Letters 62, 3267-3269.

Zambrano, R.J., Rubinelli, F.A., Rath, J. K., Schropp, R.E.I., 2004. Computer-aided band gap engineering and experimental verification of amorphous silicon–germanium solar cells, Solar Energy Materials & Solar Cells 81, 73-86.

Agarwal, P., Povolny, H., Han, S., Deng, X., 2002. Study of a-SiGe:H films and n–i–p devices used in high efficiency triple junction solar cells, Journal of Non-Crystalline Solids 299–302, 1213–1218.

Cho, J. S., Baek, S., Lee, J. C., 2011. Surface texturing of sputtered ZnO:Al/Ag back reflectors for flexible silicon thin-film solar cells, Solar Energy Materials & Solar Cells 95, 1852-1858.

Li, H., Stolk, R. L., van der Werf, C. H. M., Franken, R. H., Rath, J. K., Schropp, R. E. I., 2006. Optimization of n–i–p protocrystalline SiGe:H thin film solar cells for application in thin film multijunction solar cells, Journal of Non-Crystalline Solids 352, 1941-1944.

Conference Proceedings

Solar World Congress 2015
Daegu, Korea, 08 – 12 November 2015

Simulation and Optimization of Single Silicon Nanowire Solar Cell with Radial Junctions

Ali Alimardani, Ebrahim Asl-Soleimani and Ali Afzali-Kusha

School of Electrical and Computer Engineering, University of Tehran, Tehran, Iran

Abstract

In recent years, both solar cell research and nanowire research have become popular topics in design and fabrication of semiconductor devices. The need for higher solar cell efficiencies at lower cost has been the main concern of scientists and engineers. Nanowire solar cell is one candidate for decreasing the cost of solar cell fabrication. The nanowire geometry has many advantages over planar bulk and thin-film solar cells in processes of photoconversion. They reduce the quantity and quality of material necessary to obtain the limits, which leads to lower cost. In addition, complex single-crystalline nanowires are able to be fabricated directly on low-cost substrates and electrodes. In this work, we simulate single vertical nanowire solar cell made from silicon with radial junction, in order to examine the influence of the different parameters of the cell structure on efficiency. Length and diameter of the cell, thicknesses of regions, dopant type and concentration are these parameters. The simulations enable one to find the optimized structure and predict the fabrication process.

Keywords: *: Nanowire solar cell, Core-shell nanowire, Radial junction, N-p structure, N-i-p structure.*

1. Introduction

Solar energy harvest has attracted much attention in the previous decades. The need for higher solar cell efficiencies at lower cost has become apparent, and at the same time synthetic control in nanoscience has improved such that high-performance electronic devices are becoming possible (Cao et al., 2010; Gunawan et al., 2008; Ford et al., 2009). In recent years, Nanowire solar cells have been investigated for improving optical absorption (Adachi et al., 2010; Li et al., 2009; Lin and Povinelli, 2011; Sivakov et al., 2009; Tsakalakos et al., 2007;) , collection efficiency (Garnett and Yang, 2010; Law et al., 2005) and some other potential benefits over traditional wafer-based or thin-film devices related to optical, electrical, and strain relaxation effects. Bottom up grown nanowires, usually by the vapor-liquid-solid (VLS) method, offer a simple and large area compatible method for synthesizing a dense array of silicon nanowires on low cost glass substrates (Adachi et al., 2013). Ordered arrays of vertical nanowires with radial junctions take advantage of all mentioned effects, although solar cells made using axial junctions or random arrays can still have some benefits over planar cells (Garnett et al., 2011). Nanowire photovoltaic devices have been fabricated using variety of materials including silicon, germanium, zinc oxide, zinc sulfide, cadmium telluride, cadmium selenide, copper oxide, titanium oxide, gallium nitride, indium gallium nitride, gallium arsenide, indium arsenide, and many polymer/nanowire combinations (Fan et al., 2009; Greene et al., 2007; Varghese et al., 2009; Wang et al., 2011; Wei et al., 2009; Yuhas et al., 2009; Williams et al., 2008)

In this paper, we simulate a radial junction silicon nanowire in order to investigate the effects of length and diameter, doping type and concentration and thickness of each region, on output parameters. At first step, we study the influence of length and diameter of the nanowire cell. Secondly, the thickness of each region in p-n junction and p-i-n are taken into consideration. The thicknesses of p-type, n-type and intrinsic layers have impacts on charge separation and consequently on photoconversion due to difference in electric field distribution. The type of dopants for core and shell of the cell and also the concentration of them affect the diffusion length and amount of the charge reach the contacts. All these effects can be compared by examining the short circuit current, open circuit voltage and efficiency of the simulated cell.

Selection and/or peer review under responsibility of Scientific Committee
doi:10.18086/swc.2015.05.11 Available at http://proceedings.ises.org

2. The Structure of Nanowire Solar Cell

A TCAD device simulator is exploited to analyze the influences of design parameters like doping concentrations and types, and thicknesses under AM1.5 solar spectrum. The structure of simulated cell is defined as a p-n or p-i-n radial junction with transparent contacts on top and bottom. Outside of the cell is coated and passivated by a silicon nitride layer. Fig 1. shows the defined structure for p-i-n junction cell.

Inner active layer and outer active layer can be either p-type or n-type silicon, with different doping concentrations and different thicknesses. The layer between them is an intrinsic layer which is eliminated in some cases to compare the effects of its existence and thickness with other cases. Numerical solutions are obtained by discretizing the cell structure in grid points whose spacing has to be short enough to follow microscopic variations of geometrical and electrical parameters. Once the geometries of the cell have been defined, material electrical properties, minority carriers recombination, doping concentrations, etc. are set to perform the simulations.

Fig. 1: The structure of nanowire solar cell

3. Simulation Results and Discussion

3.1. Effect of Nanowire Length

In first step, we simulate the nanowire structure for different lengths of the cell. By assuming constant diameter of 200nm and n-p junction with same thicknesses and doping concentration of $5\times10^{17}cm^{-3}$, the influence of cell length is taken into consideration. Open circuit voltage, short circuit current and the efficiency of the nanowire cell for different lengths are as in Table.1.

Table 1. Open circuit voltage, short circuit current and the efficiency of the nanowire cell for different lengths

Length (μm)	0.5	1	2	3	4
V_{OC} (V)	0.409	0.416	0.417	0.414	0.410
I_{SC} (pA)	2.44	3.64	5.02	5.88	6.50
Efficiency (%)	2.35	3.51	4.74	5.43	5.87

Increasing the length, results in more generation along the cell and due to improved collection efficiency of nanowires, short circuit current get higher values. Open circuit voltage is changed a little by changing the length, therefore maximum power of the cells almost occur in same voltages. In consequence, output power and the efficiency of the cell improve in longer cells.

3.2. Effect of Nanowire Diameter and Dopant Types

In order to study the impact of core and shell dopant types, we simulate the structure in four forms, and with different diameters to consider the thicknesses. N-type core, p-type shell and vice versa without intrinsic layer, and with intrinsic layer are these forms of structure. We assume that the layers in each case have the same thickness. For examining the influence of nanowire diameter on output parameters, the cell with four mentioned forms is simulated in different diameters. Fig.2 shows the efficiency of these four forms with different cell diameters.

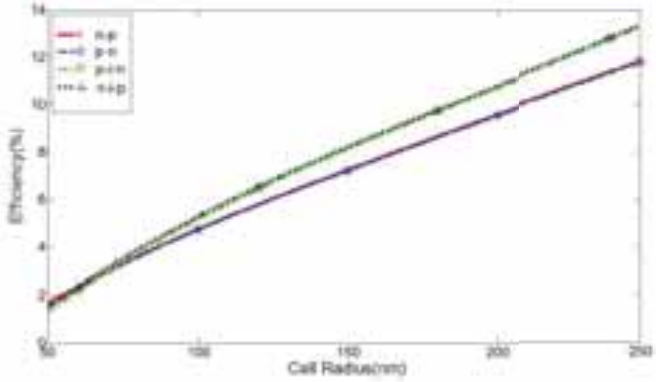

Fig. 2. The efficiency of different structure forms of nanowire solar cell with different lengths

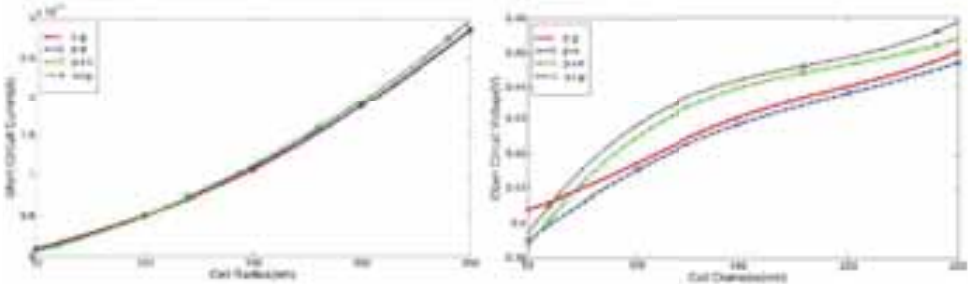

Fig. 3. (a) Short circuit current (b) Open circuit voltage, of different structure forms with different cell diameters.

It can be seen that in all cases, increasing the diameter improves the efficiency of the cell. These diameters are below the mean free path of the carriers, therefore almost all the generated carriers participate in the cell current. By increasing the area projected to solar light output power is increased due to higher level of photogenerated current and higher voltage. Fig.3.a and Fig.3.b show the short circuit current and open circuit voltage versus cell diameter.

It is shown that short circuit current changes almost proportionally to the area of the cells. But, longer diameter leads to higher open circuit and it will result in higher output power.

Another important phenomenon that should be taken into consideration is the difference between core and shell dopant type. Fig.2 shows that n-p junction (n-type core and p-type shell) has better efficiency than p-n junction cell. This improvement is not considerable and is due to difference in resistivity of the core and shell which also results in difference in open circuit voltage. This is also true for n-i-p in comparison with p-i-n structure.

Including an intrinsic layer in cell structure enhances the cell efficiency because electric field distributes in more positions across the nanowire and leads to higher voltages in constant diameters in comparison with structure with no intrinsic layer. Thus, open circuit voltage is also improves. Electric field distribution across the cell is shown in Fig.4.a and Fig.4.b for n-p and n-i-p structure.

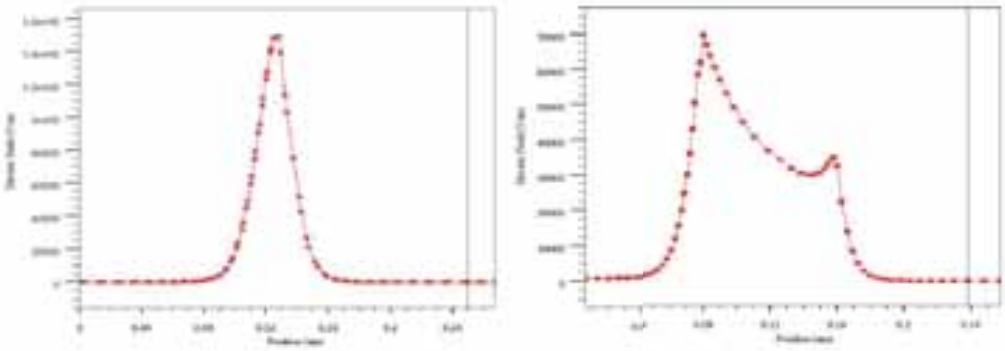

Fig. 4. Electric field along the radius of the cell, (a) p-n structure (b) p-i-n Structure

3.3. Effect of Active Layer Thicknesses

For next step, n-p and n-i-p junction cells are simulated with different active layer thicknesses. First, the n-p cell with radius of 100nm and then the n-i-p cell with radius of 120nm are studied. Fig.5.a and Fig.5.b show the efficiency of these structures respectively. In n-p cell the core radius is changed from 12.5nm to 87.5nm. In n-i-p cell, for three intrinsic thicknesses, the radius of the core is changed to investigate the efficiency.

It is depicted that by increasing the ratio of core thickness to cell thickness up to 0.6, the efficiency improves, but it reduces in higher ratios. This reduction is negligible in n-p structure. The thickness of intrinsic layer has different impacts on efficiency by changing the ratio. Thicker intrinsic layer raise the efficiency of the cell in middle ratios. But it causes reduction in efficiency in high and low ratios.

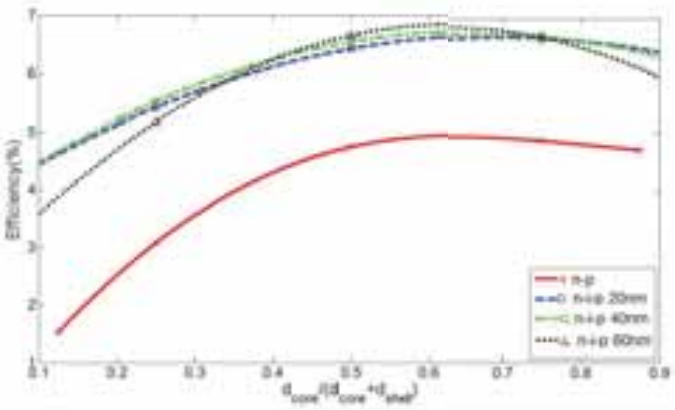

Fig. 5. The efficiency of n-p structure and n-i-p with different thicknesses of active layers

Fig.6.a shows the short circuit currents of both structures with variant core, shell and intrinsic layers' thicknesses and Fig.6.b shows their open circuit voltages.

It is seen that short circuit current increases when the ratio get higher values. The rate of this rise is higher in cell with thicker intrinsic layer. This is different for n-p structure in higher ratios. The intrinsic layer enhances the short circuit current in higher ratios. The open circuit voltage is determined by two parameters, the value of the electric field and the distance it distributes. In thinner intrinsic layer, in middle ratios, the value of electric field is higher and results in higher voltages. But while the ratio goes higher or lower, the distribution of electric field becomes the dominant parameter.

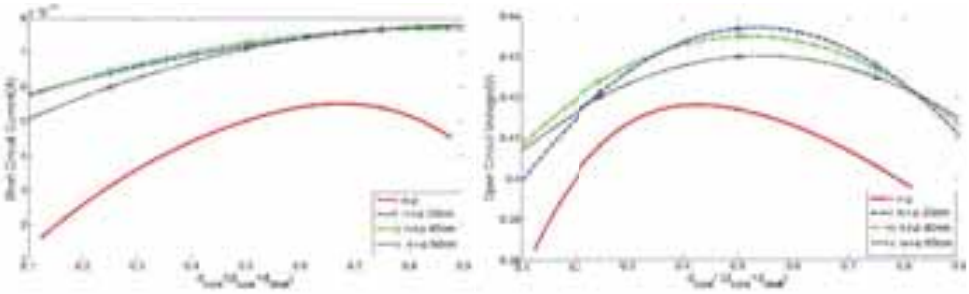

Fig. 6. (a) Short circuit current (b) Open circuit voltage of n-p structure and n-i-p with different thicknesses of active layers

3.4. Effect of Doping Concentration

Finally, the n-i-p structure with 40nm intrinsic layer, 20nm core and 60nm shell is simulated. The doping concentrations of both core and shell are changed in order to examine the efficiency, short circuit current and open circuit voltage. Fig.7 and Fig.8.a and Fig.8.b show these parameters.

It can be seen in Fig.7 that by increasing the doping concentration of both core and shell region, efficiency get higher values. The rate of increment reduces in higher concentrations. Short circuit current decreases because of more recombination in nanowire cell when doping concentration rises. But it enhances due to higher electric field especially near the junctions, thus different behaviors can be seen by changing the doping concentration in core and shell. Voltage changes by changing the electric field and in consequence it improves in higher levels of doping. By examining the Fig.8 it is confirmed that the efficiency in higher concentration of doping is higher because the voltage improves and the current does not change a lot. But in other concentration either current or voltage reduces considerably.

4. Conclusion

In this paper effective parameters of silicon nanowire solar cells' structure on efficiency are investigated by means of TCAD simulator. Length and diameter of the cell, thickness, type and doping concentration of p-type and n-type regions are studied. Longer and thicker cells have higher output powers and efficiencies.

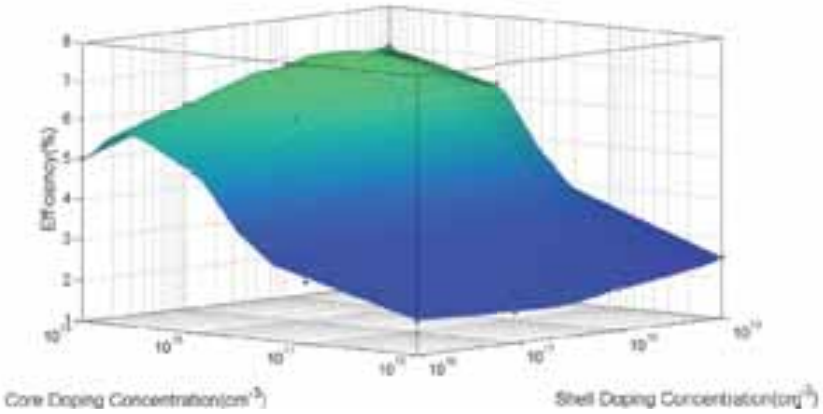

Fig. 7. The efficiency of the cell in different core and shell doping concentrations

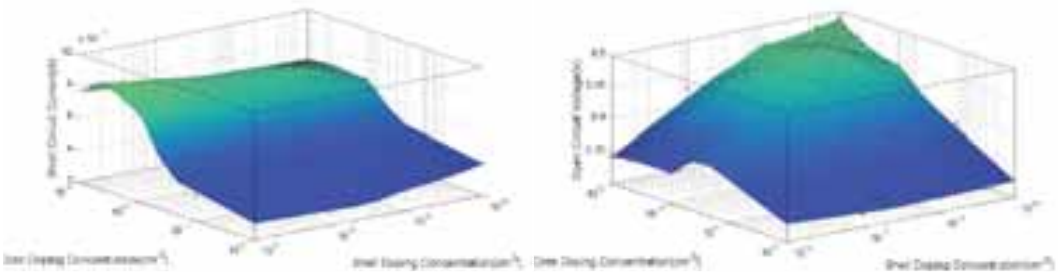

Fig. 8. (a) Short circuit current (b) Open circuit voltage of the cell with different core and shell doping concentrations

It is seen that n-p and n-i-p structures show better performance in comparison with p-n and p-i-n. Including an intrinsic layer in cell structure enhance the efficiency and in consequence, n-i-p structure shows the highest efficiency among the structures. For optimizing the thicknesses and doping concentrations different simulations are done. In different thicknesses the optimized structure is varied, it can be said that the efficiency of the cell with thicker intrinsic layer and core region got higher values. Increasing the doping concentration of the cell regions improve the efficiency. These analyzes will help one to optimize the structure of silicon nanowire solar cells before fabrication. By simulating all effects, generalizing and obtaining analytic relations from fitted curves, exact rules can be reached for predicting the optimized structures.

5. References

Adachi, M. M., Anantram, M. P., Karim, K. S., 2010. Optical Properties of Crystalline-Amorphous Core-Shell Silicon Nanowires. Nano Lett.10, 4093–4098.

Adachi, M. M., Anantram, M. P., Karim, K. S., 2013. Core-shell silicon nanowire solar cells. Sci. Rep.3, 1546 DOI:10.1038/srep01546.

Cao, L., Park, J., Fan, P., Clemens, B., Brongersma, M. L., 2010. Resonant germanium nanoantenna photodetectors. Nano Lett.10(4), 1229–33.

Fan, Z., Razavi, H., Do J., Moriwaki, A., Ergen, O., Chueh, Y., Leu, P. W., Ho, J. C., Takahashi, T., Reichertz, L. A., Neale, S., Yu, K., Wu, M., Ager, J. W., Javey, A., 2009. Three-dimensional nanopillar-array photovoltaics on low-cost and flexible substrates, Nature Mater.8(8), 648–53.

Ford, A.C., Ho, J.C., Chueh, Y., Tseng, Y., Fan, Z., Guo, J., Bokor J., Javey, A., 2009. Diameter-dependent electron mobility of InAs nanowires, Nano Lett.9(1), 360–65.

Garnett, E., Yang, P., 2010. Light trapping in silicon nanowire solar cells. Nano Lett.10(3), 1082–87.

Garnett, E. C., Brongersma, M. L., Cui, Y., McGehee, M. D., 2011. Nanowire Solar Cells. Annu. Rev. Mater. Res. 41, 269–95.

Greene, L., Law, M., Yuhas, B., Yang, P., 2007. ZnO-TiO2 core-shell nanorod/P3HT solar cells. J. Phys. Chem. C111(50), 18451–56.

Gunawan, O., Sekaric, L., Majumdar, A., Rooks, M., Appenzeller, J., Sleight, J. W., Guha, S., Haensch, W., 2008. Measurement of carrier mobility in silicon nanowires. Nano Lett.8(6), 1566–71.

Law, M., Greene, L. E., Johnson, J. C., Saykally, R., Yang, P., 2005. Nanowire dye-sensitized solar cells, Nat. Mater.4(6), 455–59.

Li, J., Yu, H. Y., Wong, S., Li, X., Zhang, G., Lo, P. G., Kwong, D., 2009. Design guidelines of periodic Si nanowire arrays for solar cell application, Appl. Phys. Lett95, 243113–1–3.

Lin, C., Povinelli, M. L., 2011. Optimal design of aperiodic, vertical silicon nanowire structures for photovoltaics. Opt. Express19(S5), A1148–A1154.

Sivakov, V., Andrä, G., Gawlik, A., Berger, A., Plentz, J., Falk, F., Christiansen, S. H., 2009. Silicon Nanowire-Based Solar Cells on Glass: Synthesis, Optical Properties, and Cell Parameters. Nano Lett.9, 1549–1554.

Tsakalakos, L., Balch, J., Fronheiser, J., Korevaar, B. A., Sulima, O., Rand, J, 2007. Silicon Nanowire Solar Cells. Appl. Phys. Lett.91, 233117–1–3.

Varghese, O. K., Paulose, M., Grimes, C. A., 2009. Long vertically aligned titania nanotubes on transparent conducting oxide for highly efficient solar cells. Nature Nanotechnol.4(9), 592–97.

Wang, K., Chen, J. J., Zeng, Z. M., Tarr, J., Zhou, W. L., Zhang, Y., Yan, Y. F., Jiang, C. S., Pern, J., Mascarenhas, A., 2010. Synthesis and photovoltaic effect of vertically aligned ZnO/ZnS core/shell nanowire arrays, Appl. Phys. Lett.96(12), 123105.

Wei, W., Bao, X., Soci, C., Ding, Y., Wang, Z., Wang, D., 2009. Direct heteroepitaxy of vertical InAs nanowires on Si substrates for broad band photovoltaics and photodetection. Nano Lett.9(8), 2926–34.

Williams, S. S., Hampton, M. J., Gowrishankar, V., Ding, I., Templeton, J. L., Samulski, E. T., DeSimone, J. M., McGehee, M. D., 2008. Nanostructured titania−polymer photovoltaic devices made using PFPE-based nanomolding techniques, Chem. Mater. 20(16), 5229–34.

Yuhas, B. D., Yang, P., 2009. Nanowire-based all-oxide solar cells, J. Am. Chem. Soc.131(10), 3756–61.

Conference Proceedings

Solar World Congress 2015
Daegu, Korea, 08 – 12 November 2015

Simulation of the Properties of Nano-Grooved Back Reflectors for Increasing the Efficiency of Solar Cells

Ali Alimardani, Ali Afzali-Kusha, Mahmoud Shahabadi and Ebrahim Asl-Soleimani

School of Electrical and Computer Engineering, University of Tehran, Tehran, Iran

Abstract

In recent years, both solar cell research and nanostructure research have become popular topics in design and fabrication of semiconductor devices. The need for higher solar cell efficiencies at lower cost has been the main concern of scientists and engineers. By improving synthetic control in nanoscience high-performance electronic devices are becoming possible. The reflectors that are high-conductivity metals used as back contact in solar cells. Nano-grooved back reflectors can increase the efficiency of solar cells by improving the light–matter interaction near the mirror surface. In this work, we simulate and investigate the electrical and optical properties of these reflectors and their effects on solar cell efficiency. For this purpose, the properties of the back reflector in different wavelengths are examined and output parameters of a GaAs cell with a back reflector optimized for visible wavelengths are considered to find the appropriate absorber thickness.

Keywords: Mirrors, Back reflectors, Nano-grooves, GaAs Solar cell

1. Introduction

Mirrors are key components in optical systems and currently used as back reflectors in a wide range of optoelectronic devices. These reflectors are usually metals with high-conductivity and used as back contact in solar cells. When the planar mirrors are used, the phase reversal that occurs when light is reflected from a metallic mirror produces a standing wave with reduced intensity near the reflective surface. This results in efficiency degradation in solar cells because the magnitude of the local electric field strength is suppressed near the mirror surface and leads to decreased light–matter interaction. This problem shows its importance particularly in thin film devices with sub wavelength active layers. In order to overcome this issue magnetic mirrors are exploit to cause an electric field with its highest value right at the surface of the mirrors (Schwanecke, 2007). Using these mirrors, the direction of magnetic field of an incident light wave is changed instead of the electric field, and as a result overall intensity in active layer will not be reduced. As back-reflectors they can control the reflection phase of the incident light waves and therefore manipulate the field distribution and optical resonances. The idea of incorporation of such mirrors to enhance the light absorption in sub wavelength devices is used in some recent works (Genevet, et al., 2012; Dotan, et al., 2013). Variety of metallic structures have been used for designing nanostructure surfaces (Fedotov et al., 2005; Kildishev, et al., 2012). In (Esfandyarpour, et al., 2014) a nanoscale groove array is patterned into a conventional metallic mirror to make magnetic mirrors. The phase and magnitude of the reflected wave can be controlled by choosing the dimensions of these nano-grooves.

In this work we simulate a GaAs solar cell with nano-grooved back reflector using FDTD method. The array of sub wavelength grooves in silver mirror filled with ZnO can be designed in a way that reflects the incident light with desired phases and magnitudes, therefore the light intensity can be manipulated in distances near the surface of the reflector. As a result one can optimize the absorber layer for defined back reflector structure. For this purpose, first we examine the properties of the back reflector in different wavelengths, especially in visible range, by changing the depth and width of the grooves. This helps to determine the dimensions of the grooves according to the wavelengths of solar radiation that generate more carriers. This is done by simulating the nano-grooved arrays with different dimensions in different wavelengths. Then, the electrical properties of optimized absorber which is determined by reflector design are studied in sunlight

doi:10.18086/swc.2015.05.12 Available at http://proceedings.ises.org

spectrum and compared with conventional cells with planar reflector.

2. Cell Structure and Simulation

A TCAD device simulator is exploited to analyze the influences of design parameters like groove depth and absorber thickness and examine the output parameters including absorption, optical field, voltage and current.

The cell is made of a back reflector, an absorber layer and transparent top contact. The back reflector is an array of sub wavelength grooves in silver mirror filled with ZnO that also can be serves as back contact. Absorber is an ultrathin GaAs layer that deposited on mirror surface.

Fig. 1b and Fig. 1c show the back reflector and compares the field distribution of it with planar back mirror (Fig. 1a). They show how the reflection of normally incident, 800 nm light from a conventional, silver mirror results in a standing wave with a suppressed electric field near its surface. A very similar field profile results when a reflector with a periodic groove array is illuminated with transverse electric (TE-polarized) light (Fig. 1c). The result changes when the grooved mirror is illuminated with transverse magnetic (TM-polarized) light (Fig. 1c). For this polarization the field profile shifts by a quarter wavelength and a standing wave with a maximum electric field near the surface of the mirror is produced.

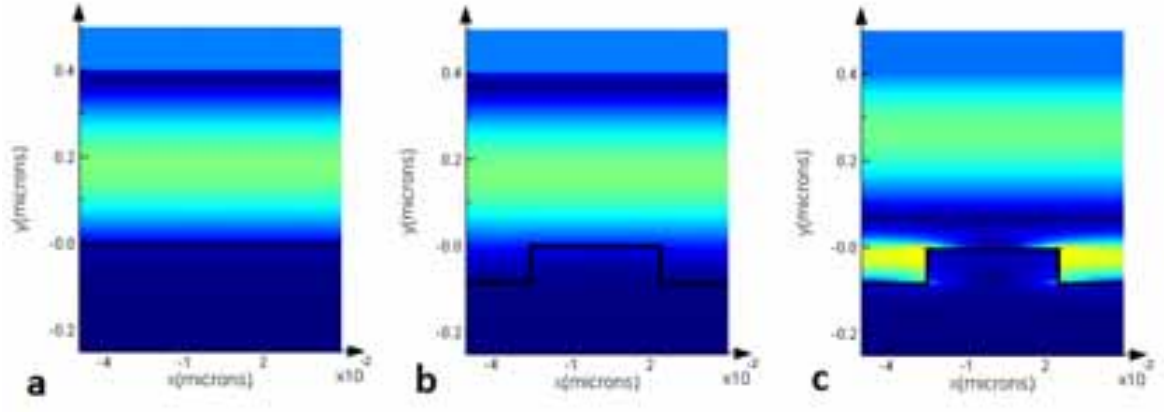

Fig. 1: Electric field distribution in a- Planar back reflector. b- Unit cell of nano-groove back reflector with TE polarization of incident light. c- Unit cell of nano-groove back reflector with TM polarization of incident light

3. Results and Discussion

In planar metallic mirrors, the reflection phase of incident light is related to the penetration and energy storage inside the metal which are fixed at each wavelength for a given metal. But in mirrors made by implementing periodic nano-grooves in silver back contact, by changing the dimensions of the grooves, different phases and magnitudes of reflected light wave in each wavelength can be reached. Fig. 2. shows $|E|^2$ which represents the light intensity, from the surface of mirror in Y-direction in three wavelengths of incident light with three groove depths and compare it with planar mirror.

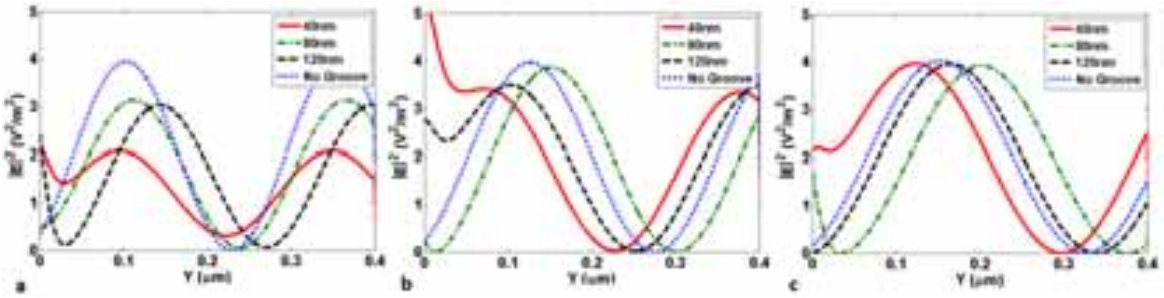

Fig2: $|E|^2$ distribution from the surface of mirror in Y-direction with incident wavelengths of a- 500nm, b- 600nm and c- 700nm with three groove depths and planar mirror.

It is seen that near the surface of planar mirror light intensity is about zero as it is predicted, but by implementing the nano-grooves and changing the reflection phase the light intensity has different value near the surface. The groove depths determine the intensity of light at the mirror surface and distances from that. In each wavelength, according to the light intensity profile which depends on groove depths, different absorber thicknesses may be optimal. In other words, if the thickness of absorber layer varies, the depth of the groove that causes the maximum absorption may differ. For example, for incident light of 500nm, if the absorber layer is about 30nm thick, groove depth of 40nm will make more absorption in cell than the other depths. But if the thickness of absorber layer is assumed to be about 120nm, the optimum groove depth will be 80nm.

In different wavelengths, also the influence of groove depth is different. For instance, it can be seen that the intensity of light wavelength of 600nm has higher value at the surface of the mirror with 80nm groove depth than 120nm. But this is opposite, in wavelength of 700nm. These figures show that absorber thickness, wavelength and groove depth are the key parameters for designing the solar cell with nano-groove back contact (by assuming fixed period of nano-grooves). Implementing the absorber layer changes the profile of electric field because of the reflection in interfaces of the layer and its absorption. Fig. 3. shows this profile for the cell with 100nm absorber thickness, incident light wavelength of 600nm and three groove depths.

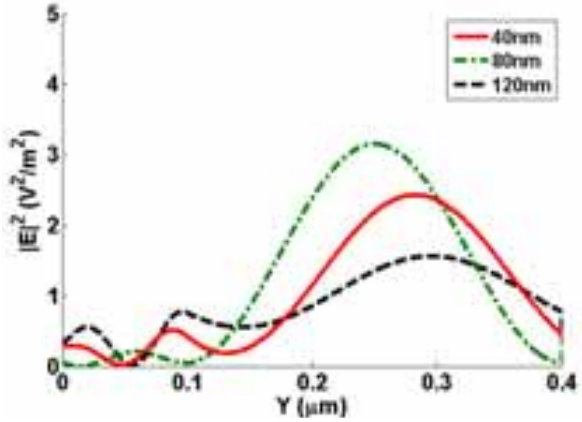

Fig. 3: $|E|^2$ distribution from the surface of the nano-grooved back reflector with existence of GaAs absorber layer and incident light of 600nm.

It is shown that light intensity has different profiles with changing the groove depth, thus, the thickness of the absorber layer which located on the surface of the mirror define the total absorption of the cell. For instance, if we assume that the absorber thickness is 100nm, it can be concluded that implementing 120nm groove depth in back reflector will result in more absorption than the other groove depths in this wavelength.

The electric field in absorber layer determines the absorption and in consequence, photogeneration in the cell. Fig. 4. shows the absorption of the cell in three wavelengths (500nm, 600nm and 700nm) with different groove depths and absorber thicknesses.

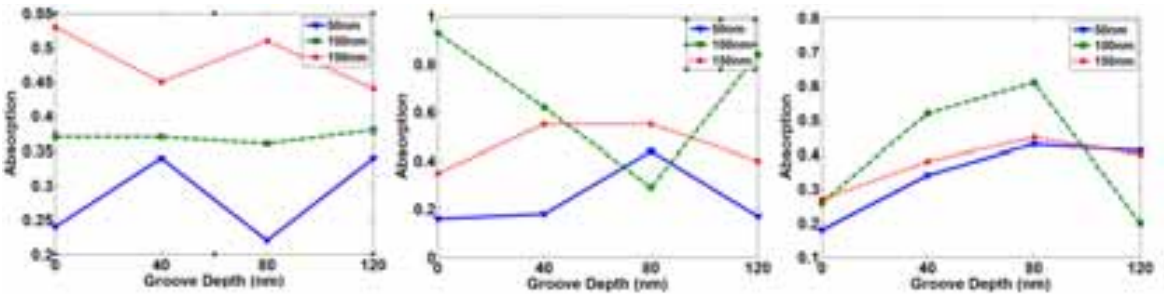

Fig. 4: Absorption of the cell with no groove and three groove depths, three absorber thicknesses and with incident wavelength of a- 500nm b- 600nm c- 700nm.

With incident wavelength of 500nm, increasing the absorber thickness results in more absorption, but groove depth has different effects in each thickness. The groove depth of 40nm in 50nm absorber thickness causes more absorption than the other but this is 80nm for thickness of 150nm. With two other wavelength of incident light wave, it is seen that absorber with 100nm thickness may have more absorption than 150nm thickness which is completely related to electric field distribution in this layer. Some groove depths in all wavelengths may cause less absorption in the cell than planar mirror. But total absorption in all wavelengths of solar radiation with consideration of absorber thickness will determine the absorbed power of the cell.

The absorption of the devices shows the available current they can produce in each wavelength. This analysis is necessary for all photodetectors, but is not enough for solar cells. In solar cells, the total absorption in all wavelengths of solar radiation should be considered. Thus, calculating the optimum thickness of absorber layer and groove depth is differ from single wavelength and the simulation results of light wavelengths in visible range that generate more carriers, can be a guideline to design better structures.

In solar cells, in addition to optical parameters including absorption and light intensity, electrical parameters should be taken into consideration. Therefore, semiconductors' equations also solved for the cell structure assuming a p-n junction in absorber area, and conventional output parameters of solar cells like short circuit current, open circuit voltage and efficiency are extracted. Fig. 5. Shows these parameters for three structures with different groove depths and compare them with a structure with conventional planar mirror.

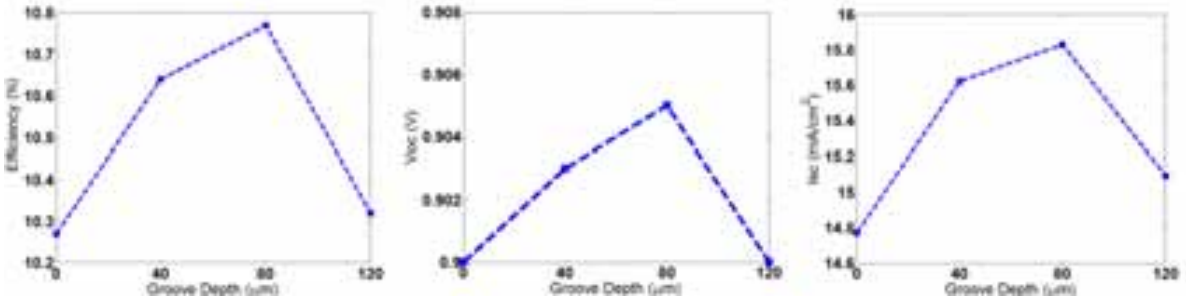

Fig. 5: a- Efficiency b- Voc and c- Isc for solar cell structure with no groove and three groove depths and absorber thickness of 100nm

It is depicted that patterning the nano-grooves in back reflector, can increase the photogenerated current and thus the efficiency of the solar cell. Open circuit voltage is changed slightly because it is strongly depends on the properties of absorber layer. Photogenerated current has logarithmic effect on this voltage. In different thicknesses of absorber layer, implementing the nano-grooves may result in different improvement and the optimum depth of groove may also change. In the simulated structure with absorber layer of 100nm, the optimum depth is 80nm.

4. Conclusion

In this work, the idea of patterning nano-grooves in back reflector of ultrathin solar cells is investigated. These grooves will make the reflector act similar to magnetic mirror which can increase the light intensity near the surface of the mirror. This improves the absorption and thus photogeneration in absorber layer and is considerable, especially in very thin solar cells. In order to examine the properties of these mirrors and finding the guidelines to design them for higher efficiency, the structure with different dimensions, incident wavelengths and in exposure of solar radiation is simulated and analyzed. Design of optimum structure depends on the constituent materials, absorber thickness and grooves' depth. Therefore, for a cell with given materials and absorber thickness, the groove thickness can be optimized by simulations. Engineering the shape and dimensions of these types of mirrors as reflectors in solar cells may lead to fabrication of new kind of ultrathin solar cells.

5. References

Dotan, H., Kfir, O., Sharlin, E., Blank, O., Gross, M., Dumchin, I., Ankonina, G., Rothschild, A., 2013, Resonant light trapping in ultrathin films for water splitting., *Nat. Mater.*, vol. 12, no. 2, pp. 158–64.

Esfandyarpour, M., Garnett, E. C., Cui, Y., McGehee, M. D., Brongersma, M. L., 2014, Metamaterial mirrors in optoelectronic devices., *Nat. Nanotechnol.*, vol. 9, no. 7, pp. 542–7.

Fedotov, V. A., Mladyonov, P. L., Prosvirnin, S. L. & Zheludev, N. I., 2005, Planar electromagnetic metamaterial with a fish scale structure.Phys. Rev. E72, 056613.

Genevet, P., Kats, M. A., Blanchard, R., Capasso, F., 2012, Nanometre optical coatings based on strong interference effects in highly absorbing media, *Nat. Mater.*, vol. 12, pp. 20–24.

Kildishev, A. V., Shalaev, V. M., Boltasseva, A., Emani, N. K. & Ni, X., 2012, Broadband light bending with plasmonic nanoantennas. Science335,427.

Schwanecke, A. S., 2007, Optical magnetic mirrors, *J. Opt. A Pure Appl. Opt.*, vol. 9, pp. L1–L2.

Conference Proceedings

Solar World Congress 2015
Daegu, Korea, 08 – 12 November 2015

THE DEVELOPMENT OF TUBULAR PLATINUM-EMITTER REACTOR FOR A SMALL-SCALE THERMOPHOTOVOLTAIC POWER SYSTEM

Yueh-Heng Li[1,2], Jing-Ru Hong[1]

[1] Department of Aeronautics and Astronautics, National Cheng Kung University, Tainan, 701, Taiwan, R.O.C.

[2] Research Center for Energy Technology and Strategy, National Cheng Kung University, Tainan, 701, Taiwan, R.O.C.

Abstract

This paper centers on the development of a micro-scale combustion-driven thermophotovoltaic (TPV) power generation system. The Micro-TPV system is a direct energy conversion device. It does not have any moving parts, and it converts the thermal power to electrical power directly. In this thesis, the first task is to design a combustor as an emitter for TPV power system. The characteristics of the combustor are to use catalyst tube with specific configuration and fuel/air mixture deployments to overcome the shortcomings of combustion instability and radical termination in a small-scale confined channel. Backward-facing step and perforated platinum tube are employed in a small-scale combustor to enhance flame stabilization and extend stable flammability. The stable operating range of the proposed tubular combustor is also verified.

Keywords: *thermophotovoltaic, platinum, emitter, combustion-driven.*

1. Introduction

Thermophotovoltaic (TPV) is a direct heat to electricity conversion approach, and the TPV conversion concept is straightforward. Thermal or infrared radiation is converted by a photovoltaic (PV) cell into electricity, and it is analogous to solar radiation converted by a PV cell into electricity. Compared to solar PV, TPV has two advantages. One is that TPV conversion is applicable to any high temperature heat source including the solar, combustion, nuclear and waste heat sources. Accordingly, using combustion to generate thermal radiation is considered as combustion-driven TPV system. The second benefit is that the efficiency can be enhanced by the control of the absorbed spectrum in the PV cell compared to solar PV. Nevertheless, combustion-driven TPV power generator is one of promising approaches to simultaneously harvest electric power and heat output. Because it does not involve any moving parts, its fabrication and assembly are relatively simple and easy. Research interest in combustion-driven TPV power generator has received intensive attention recently. Chou *et al.* (2014) designed a small-scale combustor with SiC porous medium and engaged in TPV system with the benefit of uniform thermal radiation. Li *et al.* (2010, 2011a, 2011b) attempted to convert flame radiation into electrical output via photovoltaic cells, to add iron pentacarbonyl into liquid hydrocarbon fuels for enhancing flame radiation and to coat metal oxide layer on a quartz tube for improving radiant efficiency. Li *et al.* (2009) and Yang *et al.* (2002) proposed a hydrogen-fueled micro-TPV combustor, and used backward facing step as flame stabilization mechanism. Besides, Yang *et al.* (2005) tested different emitting materials for enhancing radiant efficiency. Ferrari *et al.* (2014) outlined the current state-of-the-art of TPV system, and assessed the energy conversion of each component in TPV system.

Undoubtedly, the high surface-to-volume ratio of a small-scale combustor could lead to increasing heat loss to the surroundings and the possibility of radical termination on the wall. These effects may greatly reduce flame stability and fuel conversion efficiency in a small-scale combustor. In order to extend the stable

doi:10.18086/swc.2015.05.13 Available at http://proceedings.ises.org

operating range of a small-scale combustor, the utilization of quenching-resistant fuel, such as hydrogen (Zarvandi *et al.*, 2012), and catalytic materials (Li *et al.*, 2012), such as noble metals, in a small-scale TPV system has been considered as a promising manner to alleviate the above mentioned shortcomings. Since catalytic material is an important reaction enhancer for small-scale combustor, a novel concept is proposed here to use platinum, a noble metal, as the catalyst and the emitter for the small-scale TPV system. Besides, platinum is not only a catalytic material, but also a selective material (Yang *et al.*, 2005). The spectrum of illumination from platinum is prone to congregate in shorter wavelength region due to its larger emissivity in this region. Furthermore, it is much easier to manufacture a platinum emitter than the other selective emitters such as micro-machining tungsten and rare-earth oxide. For the quenching-resistant property, hydrogen is a promising fuel candidate for small-scale TPV power system due to its inherent large thermal diffusivity and high sticking coefficient to catalyst. Furthermore, hydrogen is a high-energy-density and quenching-resistant fuel. Therefore, hydrogen is a candidate for applying in micro-TPV power system. Platinum tubes are often used as a catalyst for hydrogen-fueled small-scale combustors [Volchko *et al.*, 2006]. However, the low volumetric energy density of hydrogen leads to the small-scale combustor that has to be operated at high fuel mass flow throughout. The high mass flowrate would further reduce the residence time for flame stability and complete combustion. Therefore, the flame-stabilizing mechanism is a pivotal consideration in small-scale combustor design.

In a small-scale channel, the mechanism of flame stabilization is strongly related to combustion efficiency and operational range. Akram and Kumar (2011) experimentally investigated combustion behaviors of methane-air mixture in meso-scale diverging channels, which showed an enhancement of flame blow-off limit compared to the plain channel. Wan *et al.,* (2015) implemented a wall cavity in a micro channel to extend the flame blow-off limit of H_2-air combustion. Li *et al.* (2012) applied the cavity flame holder to micro-channels with segmented catalyst on the inner walls. Nonetheless, non-uniform illumination of the emitter and reduced overall efficiency of TPV system are usually related to using improper flame stabilizers in a micro channel. Therefore, in the present study, a novel combustion chamber design is originated from the concept of our previous study with regard to segmented catalyst with cavity in a channel. In order to apply this concept to combustion-driven TPV system, a platinum tube with perforated-hole array is proposed and used as catalyst, emitter, and flame stabilizer to overcome the critical heat loss and to improve the flame instability. Concept, design, and demonstration of the small-scale tubular platinum combustor with perforated-hole array for future application in a small TPV power generation system are addressed and discussed in this paper.

2. Conception of the small-scale combustor

In our previous paper (Li *et al.*, 2012), applying segmented catalysts with cavities in a channel can integrate advantages of homogeneous and heterogeneous reactions, and enhance fuel conversion. The heterogeneous reaction in a prior catalyst segment produces chemical radicals and catalytically induced exothermicity, and homogeneous reaction can be subsequently ignited and anchored in the following cavity. The presence of cavities appreciably extends the stable operational range of the micro-reactor for a wide range of inlet flow velocities. To demonstrate and verify the above mentioned concept that is feasible in a small-scale TPV combustor, a preliminary numerical simulation is performed prior to experiments. A commercial code, CFD-ACE+, is modified to incorporate the detailed gas-phase and surface reaction mechanisms in CHEMKIN formats for the simulation. For simplicity, the small-scale combustor is modeled as a two-dimensional system. The platinum tube has two segments, 4.5 mm and 24.5 mm long, respectively, as shown in Fig. 1. The distance between segmented tubes is 1 mm. The dimension of segmented platinum tube is 5.3 mm in inner diameter and 6 mm in outer diameter, and the dimension of quartz tube is 8 mm in inner diameter and 10 mm in outer diameter. Accordingly, the area of cross section for inner tube and annular tube are approximate. The total length of the reaction channel is 30 mm long. The inner and outer equivalence ratios of the hydrogen-air mixtures are 0.3 and 0.6, respectively. The inlet temperature is 300 K. A uniform velocity profile is specified at the inlet and the flow velocity is fixed at 20 m/s for the platinum tube with and without segmentation. At the exit, pressure is specified with a constant ambient pressure of 101 kPa and an extrapolation scheme is used for species and temperature.

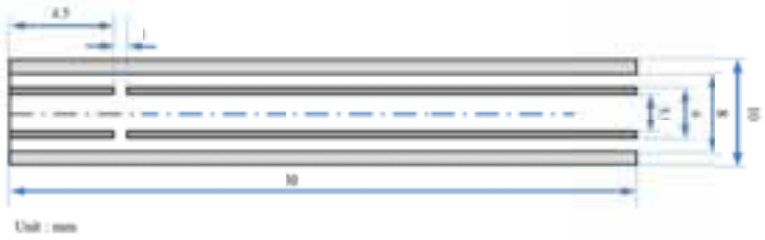

Fig. 1: Schematic diagram of segmented platinum tube for numerical simulation.

Chemical reaction mechanisms are used in the gas phase as well as on the catalyst surface. The homogeneous reaction mechanism of hydrogen-air combustion composes of 9 species and 19 reaction steps; these are adopted from the mechanism proposed by Miller and Bowman [1989]. The surface reaction mechanism is compiled primarily from that proposed by Deutschmann et al. [1996]. These reaction mechanisms have been used in previous studies and the comparisons with experimental results are satisfactory [Chen *et al.*, 2006].

Figure 2 compares the computed H_2 and OH mass fractions in both catalyst configurations. As to the conventional plain platinum tube, H_2 at the inner surface is initially reacted heterogeneously and provides catalytically induced exothermicity to assist hydrogen conversion at the outer surface, as seen in lower panel of Fig. 2. The overall fuel conversion rate of the conventional plain platinum tube is 83.8%. According to the computed OH mass fraction, the catalytically induced combustion is anchored on the outer catalyst surface. However, the anchoring position of gas-phase reaction is strongly related to the inlet condition in a conventional plain platinum tube. As to the segmented platinum tube, the distance for completion of hydrogen conversion is shorter than that in a conventional plain platinum tube. The overall fuel conversion rate of the segmented platinum tube is 95.2%. The gas-phase reaction is anchored on the gap between two tubes, as seen in the upper panel of Fig. 2. It appears that the gap between two tubes can enhance the flame stabilization by means of providing a low-velocity zone as well as collecting heat and chemical radicals from both sides. Consequently, the distribution of different equivalence ratios of fuel/air mixtures along both sides of catalyst surface can mutually assist heterogeneous and homogeneous reactions in a confined space, and hence prevent heat loss to the tube wall. The preliminary computation confirms that the proposed concept is applicable to a small-scale perforated-platinum combustor.

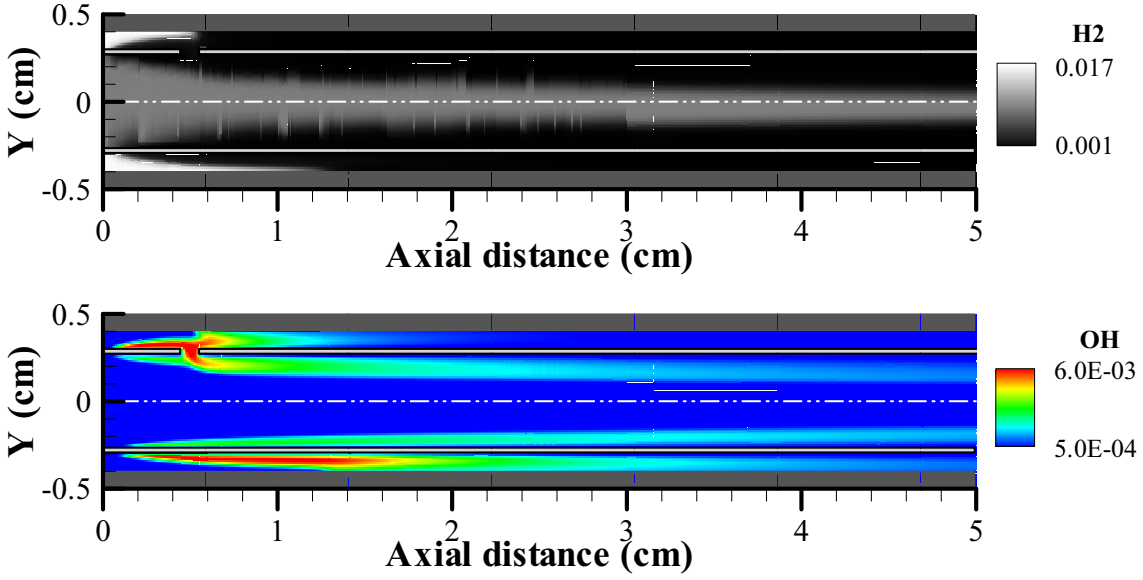

Fig. 2: Comparison of the computed contours of H_2 and OH mass fractions for the platinum tube with and without segmentation. The inner and outer equivalence ratios are 0.3 and 0.6, respectively, with the inlet velocity fixed at 20 m/sec.

3. Experimental apparatus

In order to realize the concept of segmented platinum tube in a confined channel, a small-scale platinum tube with perforated-hole array is designed in this study. The function of perforated-hole array is to simulate the gap between two platinum tubes. Figure 3 shows the schematic diagram of the proposed platinum combustion chamber with perforated-hole array and its corresponding pipes. The dimension of the platinum tube is 5.3 mm in ID, 6 mm in OD, and 30 mm in length with six perforated holes (1 mm in diameter) equidistantly placed around the tube at 5 mm away from the bottom of the platinum tube. The platinum tube is connected with a stainless steel tube with 1 mm in ID and 2 mm in OD. It makes a backward-facing step, which of length is 5mm, in the connection section. The platinum tube is confined in the quartz tube, which has a diameter of 8 mm in ID and 10 mm in OD. Hydrogen, utilized as fuel, and air are metered with electronic flowmeter (Brooks, 5850E) and calibrated in the range of 0-20 standard l/min. The pre-chamber filled with steel wool can provide a space to mix the fuel/air, as shown in the right hand-side of Fig. 3. Well premixed fuel/air mixtures with different equivalence ratios are separately delivered to the inner and outer tubes. The Reynolds number ranges from 377 to 1258 in the experiments. Therefore, the flow is assumed to be in laminar regime. In this study, two different platinum tubes, the conventional plain and perforated platinum tubes, are employed in the experiments to investigate the effects of fuel/air distribution and inlet flow velocity on the performance of the small-scale combustor. Figure 4 shows the experimental setup. A digital camera is used to record the combustion phenomenon in the combustor. For the irradiance measurement, the platinum combustor has to place inside the integrating sphere and the resulting radiant intensity is measured by the spectrum meter (Oceanoptic, USB2000+XR1), which has a uniform quantum efficiency ranging from ultraviolet (200 nm) to near-infrared (1050 nm) wavelength region. Various fuel/air mixtures are separately deployed and delivered to outside and inside of the tube, and the combustion phenomena of two platinum tubes are individually recorded via a digital camera. For monitoring temperature distribution and radiant intensity of two platinum tubes, an infrared thermal camera and a radiometer are used and recorded via a computer.

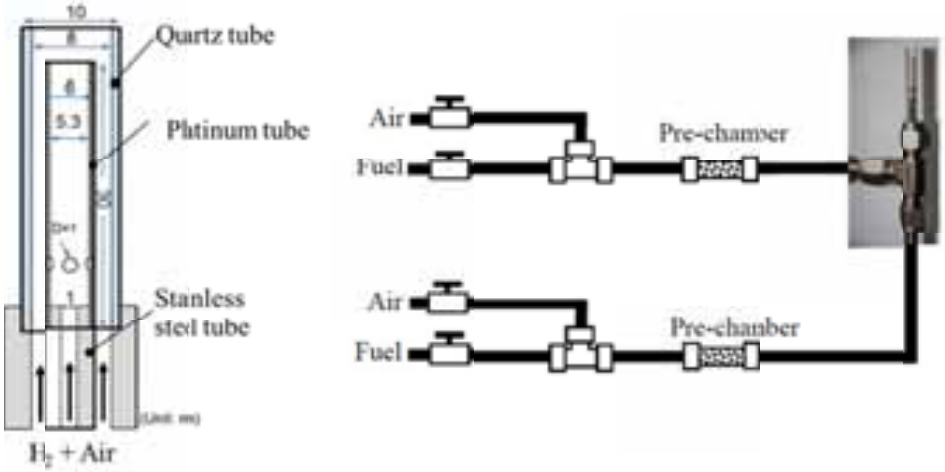

Figure 3: Schematic diagram of the platinum combustion chamber with perforated hole array and the corresponding pipes.

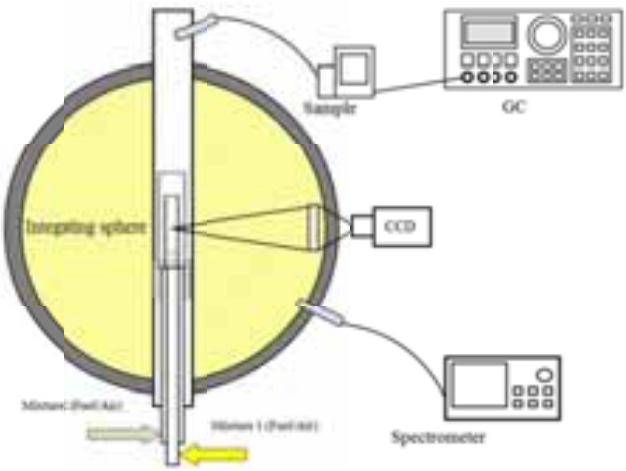

Figure 4: Schematic diagram of the experimental setup.

4. Results and discussion

Figure 5 shows the photograph of combustion phenomenon for two combustor cases under fixed fuel/air equivalence ratios and various inlet velocities (V = 5 and 10 m/s). The stream of ER = 0.6 mixtures is prone to induce both heterogeneous and homogenous reactions, while the ER = 0.3 stream induces only heterogeneous reaction. When ER_{in} = 0.3 and ER_{out} = 0.6, there is only heterogeneous reaction on the conventional plain platinum tubular combustor due to heat loss and the lack of flame stabilization mechanism, as shown in Fig. 5a. With the perforated-holes, the catalytically holding combustion can be seen on the tube (Fig. 5b). When the inlet velocity is increased to 10 m/s, the radiation from the two tubes becomes much brighter than the previous cases (Figs. 5a and 5b). This is due to that catalytically holding combustion can be induced and stabilized inside the combustion chamber under the flammable fuel/air condition. It is noted that there are bright illumination regions congregated in the downstream part of the conventional plain platinum tube under the condition of ER_{in} = 0.3 and ER_{out} = 0.6 (Fig. 5c). In principal, extensive hydrogen reaction on the outer surface of the catalyst can release large amount of catalytically induced exothermicity, which can sufficiently compensate the heat losses. Besides, when the inlet flow rate is further increased, the residual hydrogen can induce gas-phase reaction in the downstream of the platinum tubular combustor. As to the perforated platinum tubular combustor, it can be seen from Fig. 5d that flame is anchored on the perforated holes of the platinum tube. The presence of flame not only accelerates fuel conversion, but also heats up the platinum tube to become a bright emitter. Figure 6 displays the measured surface temperatures along the platinum tubes for the case of ER_{in} = 0.3, ER_{out} = 0.6 and V=10 m/s. The surface temperatures of the perforated-hole platinum tubular combustor are much higher than those of the conventional plain platinum tubular combustor. This is because that both heterogeneous and homogeneous reactions occur in the perforated platinum tubular combustor, but only heterogeneous reaction takes place in the plain platinum tubular combustor.

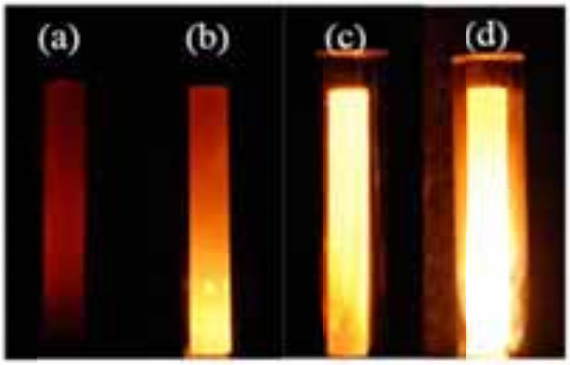

Figure 5. Photograph of combustion phenomenon for the cases: a conventional plain (a,c) and perforated platinum (b)(d) tubular combustor under the condition of ER_{in}=0.3 and ER_{out}=0.6 and various V=5 m/s (cases of a and b) and 10 m/s (cases of c and d). (The exposure time of photograph is fixed in 1/200 sec.)

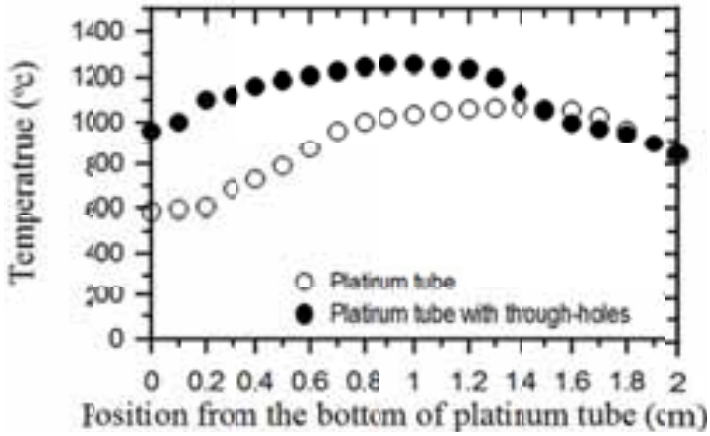

Figure 6. The measured surface temperatures along the plain and perforated platinum tubular combustors for the case of ER_{in} = 0.3, ER_{out} = 0.6 and V=10 m/s.

Figures 7 shows the operating range of the plain and the perforated platinum tubular combustors, respectively, with various fuel-air distributions under V = 10 m/s. Four distinct combustion phenomena, i.e., no illumination, heterogeneous reaction with dim red illumination, hetero- and homogeneous reaction with moderate illumination, and the combined hetero-/homo-geneous reaction with bright illumination, are identified by image observations and wall temperature measurements. For the plain platinum tubular combustor, conditions for bright incandescent illumination congregate in the higher inner and outer equivalence ratios (see Fig. 7a). The bright incandescent region is congregated in larger inner and outer equivalence ratios. The presence of backward-facing step in the conventional plain platinum tubular combustor primarily stabilizes the flame inside the tube, and heat loss from the tube can be reduced by means of heat release from catalytic induced exothermicity on the surface. Consequently, excessive fuel consumption in one side is necessary to sustain catalytically stabilized thermal combustion in the other side. Comparison of Figs. 7a and 7b indicates that the operating range with bright incandescent illumination for the perforated tubular combustor is much larger than that for the plain tubular combustor under the conditions of larger outer equivalence ratio. This is attributed to the presence of perforated holes for flame stabilization. The operating range of bright incandescent illumination for the perforated platinum tubular combustor is remarkably extended, especially for lower inner equivalence ratios. Regarding to the irradiance, the plain and perforated platinum tubular combustors are placed inside the integrating sphere connecting to spectrometer under the fixed equivalence ratios (ER_{in} = 0.3, ER_{out} = 0.6) and flow velocity (V=10 m/s). The measured irradiances are 18,052 W/m^2 for the conventional plain platinum tubular combustor and 19,858 W/m^2 for the perforated platinum tubular combustor.

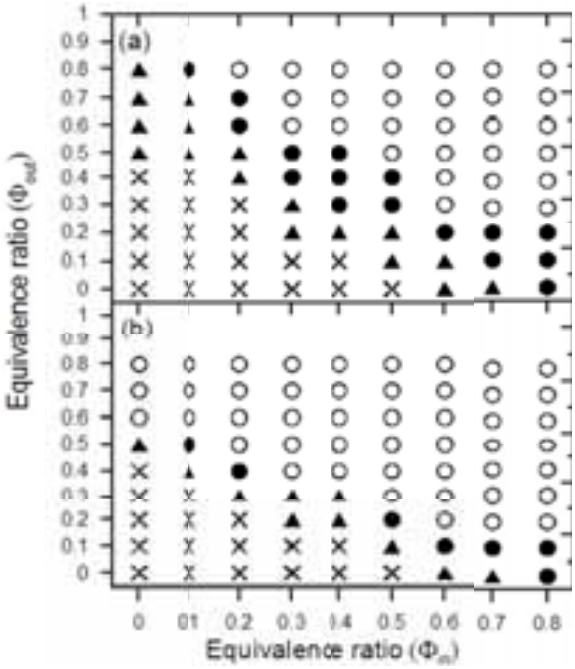

Figure 7. Operating range of a (a) plain and (b) perforated platinum tube under the condition of inlet flow velocity of 10 m/s. Symbols: (×) no illumination, (▲) heterogeneous reaction with dim red illumination, (●) combined hetero-/ homo-geneous reaction with illumination, and (○) hetero- and homogeneous reaction with bright illumination.

5. Conclusions

The result of a simplified simulation supports the concept of sustaining catalytic combustion on a platinum wall with a gap, and flames anchoring on the wall can contribute to efficiently heat up the wall temperature. For testifying the concept of our proposed micro-TPV combustor, an experimental study on the performance of the proposed perforated-platinum combustion chamber is made under various equivalence ratios and inlet velocities. Results demonstrate that the perforated-platinum tubular combustor can sustain the heterogeneous and homogeneous reactions, extend the operating range of the combustor, and enhance the incandescent illumination of the platinum tube. Besides, delivering fuel/air mixtures into two sides of platinum tube can reduce the heat loss from the chamber wall, and a perforated-hole can sustain flames anchoring on the wall in various flow velocities. These two novel approaches realize the application of simultaneously flame stability in a small-scale system and high illumination on the chamber wall. Therefore, the perforated-platinum

tubular combustor can serve as an effective emitter for the small-scale TPV power generation system as compared to the plain platinum tube. These facts suggest that future application of the proposed concept and design of the perforated-platinum combustor to a small-scale TPV power system is feasible.

6. References

Akram, M., Kumar, S., 2011. Experimental studies on dynamics of methane-air premixed flame in ,eso-scale diverging channels. Combust. Flame 158, 915-924.

Chen, C.P., Chao, Y.C., Wu, Y.C., Lee, J.C., Chen, G.B., 2006. Development of a catalytic hydrogen micro-propulsion system. Combust. Sci. Tech. 178, 2039-2060.

Chou, S.K., Yang, W.M., Li, Z.W., 2010. Porous media combustion for micro thermophotovoltaic system applications. Applied Energy 2010, 2862-2867.

Deutschmann, O., Schmidt, R., Behrendt, F., Warnatz, J., 1996. Numerical modeling of catalytic ignition. Proc. Combust. Inst. 26, 1747-1754.

Ferrari, C, Melino, F., Pinelli, M, Spina, P.R., 2014. Thermophovoltaic energy conversion: Analytical aspects, prototypes and experiences. Applied Energy 113, 1717-1730.

Li, Y.H., Wu, C.Y., Lien, Y.S., Chao, Y.C., 2010. Development of a High-Flame-Luminosity Thermophotovoltaic Power System. Chem. Eng. J. 162, 307-313.

Li, Y.H., Wu, C.Y., Li, H.Y., Chao, Y.C., 2011a. Concept and Combustion Characteristics of the High-luminescence flame for the Thermophotovoltaic Systems. Proc. Combust. Inst. 33, 3447-3454.

Li Y.H., Cheng, T.S., Lien, Y.S., Chao, Y.C., 2011b. Development of a Tubular-emitting Combustion-driven Thermophotovoltaic Power System. Proc. Combust. Inst. 33, 3439-3445.

Li Y.H., Chen, G.B., Wu, F.H., Cheng, T.S., Chao, Y.C., 2012. Effects of catalyst segmentation with cavities on combustion enchancement of blended fuels in a micro channel. Combust. Flame 159, 1644-1651.

Li, J., Chou, S.K., Huang, G., Yang, W.M., Li, Z.W., 2009. Study on premixed combustion in cylindrical micro combustors: Transient flame behavior and wall heat flux. Exp. Therm. Fluid Sci. 33, 764-773.

Miller, J.A., Bowman, C.T., 1989. Mechanism and modeling of nitrogen chemistry in combustion. Prog. Energy. Combust. Sci. 15, 287-338.

Volchko, S.J., Sung, C.J., Huang, Y., Schneider, S.J., 2006. Catalytic combustion of rich methane/oxygen mixtures for micropropulsion applications. J. Propul. Power 22, 684-693.

Wan, J., Fan, A., Lui, W., 2015. Flame-anchoring mechanism of a micro cavity-combustor for premixed H_2/air flame. Chemical Eng. J. 275, 17-26.

Yang, W., Chou, S., Shu, C., Li, Z., Xue, H., 2002. Combustion in micro-cylindrical combustors with and without a backward facing step. Appl. Therm. Eng. 22, 1777-1787.

Yang, W., Chou, S., Shu, C., Xue, H., Li, Z., 2005. Research on micro-thermophovoltaic power generators with different emitting materials. Institute of Physics Publishing 15, S239-S242.

Zarvandi, J., Tabejamaat, S., Baigmohammadi, M., 2012. Numerical study of the effects of heat transfer methods on CH_4/(CH_4+H_2)-Air premixed flames in a micro-stepped tube. Energy 44, 396-409.

Conference Proceedings

Solar World Congress 2015
Daegu, Korea, 08 – 12 November 2015

Electrical PV Array Reconfiguration Strategy against Partial Shading

Robert Alfie S. Peña[1,2], Erees Queen B. Macabebe[1] and Davide Del Col[2]

[1] Department of Electronics, Computer, and Communications Engineering, School of Science and Engineering, Ateneo de Manila University, Quezon City 1108, Philippines

[2] Dipartimento di Ingegeneria Industriale, Università degli Studi di Padova, Padova 35131, Italy

Abstract

Partial shading presents a huge problem for photovoltaic (PV) arrays because of mismatch losses. One way to maximize power output is to make the arrays dynamic. These dynamic PV arrays change configuration depending on shading pattern and strength. This work evaluates the electrical PV array reconfiguration (EAR) strategy in dynamic arrays that use total-cross tied topology through modeling and simulation. The approach searches for the optimum configuration which has the most equal row irradiance averages. A static 3×3 PV array model and a dynamic PV array model, which uses the EAR algorithm, were developed. The models were tested for binary- and random-irradiance shading. Results show that the EAR strategy suits some shading patterns and that the irradiance distribution affects improvement in power output. The simulations performed demonstrate both the limitations and benefits of using the EAR strategy in PV array reconfiguration.

Keywords: *electrical PV array reconfiguration, dynamic PV array, partial shading, simulation*

1. Introduction

Partial shading in photovoltaic (PV) arrays causes losses in power output. The different irradiance levels produce different current values. Thus, when modules exposed to different irradiance levels are connected in series, the total current is limited by the module with the lowest generated current. This mismatch in current can be reduced when other array topologies are used such as total cross-tied configuration (TCT). However, even with such change, different values for row currents still produce mismatch. Thus, dynamic PV arrays are introduced.

This paper explores dynamic reconfiguration in PV arrays with a view toward its use in smart PV systems that dynamically respond to partial shading. Companies like Trina Solar, SolarEdge, Enphase Energy, and Optistring already offer smart PV modules that mitigate mismatch due to nonuniform irradiance. These solutions are based on a hybrid power conversion architecture, where each PV module has either a power optimizer or a microinverter to obtain the maximum power from a partially shaded array (Burger et al., 2010; La Manna et al., 2014; MacAlpine et al., 2013). While these commercial, smart PV modules compete with dynamic PV arrays at the array level, these technologies can complement one another if reconfiguration is applied at the PV cell level to create a dynamically reconfigurable PV module. A power optimizer or a microinverter can then be attached to the module for coupling at the array level to reduce mismatch to a minimum.

The focus of this work is on a strategy for reconfiguration known as the electrical PV array reconfiguration strategy (EAR). The average improvement in power output is estimated and comparison of power output of static and dynamic arrays to determine power output improvement using the EAR strategy is accomplished through simulation using the popular one-diode PV model.

doi:10.18086/swc.2015.05.14 Available at http://proceedings.ises.org

2. Photovoltaic array model

2.1 One-diode PV cell model

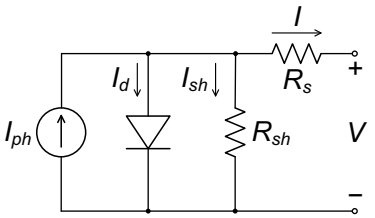

Fig. 1: Circuit representation of the one-diode PV model

One of the popular models that describes a PV cell is the one-diode model. The equivalent circuit of the model is shown in Fig. 1. It is composed of a current source representing the cell's photo-generated current I_{ph}, a single diode connected in parallel, a shunt resistance R_{sh} also connected in parallel and a series resistance R_s (Villalva et al., 2009). A two-diode model is more accurate, but accuracy is obtained at the expense of additional computation. Also, for crystalline silicon PV modules, the one-diode model is sufficient.

The equation describing the model is an expression for the current produced by the PV cell. Looking at the circuit in Fig. 1, the cell current I is just the algebraic sum of the currents of the upper node. Eq. 1 is called the characteristic or the I-V equation of the PV cell:

$$I = I_{ph} - I_{sat}\left(\exp\left(\frac{q(V+IR_s)}{n_d kT}\right)-1\right)-\frac{V+IR_s}{R_{sh}} \qquad \text{(Eq. 1)}$$

where I_{sat} is the diode's reverse saturation current, q is the elementary charge constant, n_d is the diode's ideality factor, k is the Boltzmann constant and T (K) is the absolute temperature of the cell p-n junction. The three terms correspond to the three currents that comprise the cell current: I_{ph}, I_d and I_{sh}. The second term is Shockley's equation for the diode current I_d, where the diode voltage $V_d = V + IR_s$. The third term represents leakage current due to junction defects as represented by the shunt resistance, I_{sh}, obtained by the application of Ohm's law.

2.2 Improved one-diode PV cell model

A serious problem that the classical one-diode model presents, at least for the purposes of this study, is its inadequacy in modeling what happens when a PV cell or module is reverse-biased. This happens when a module or an array is partially shaded. In a series-connected array, the PV module operating in the worst conditions dictates the performance of the whole array (La Manna et al., 2014). A PV cell or module breaks down when the reverse-bias voltage reaches the breakdown voltage (V_{br}) (Alonso-García et al., 2006). To resolve this, the model is modified to account for the avalanche breakdown phenomenon by describing the breakdown phenomenon in the expression for I_{sh} (Orozco-Gutierrez et al., 2014, 2013).

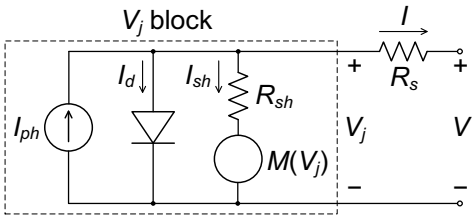

Fig. 2: Circuit representation of the modified one-diode PV model that considers behavior of PV cells in reverse bias

Fig. 2 shows the modified one-diode model equivalent circuit used in this study. Circuit components which are in parallel were lumped into a junction block. This junction block has V_j as its voltage which is equal to V_d. The component $M(V_j)$ represents the modification to the model which takes into account avalanche breakdown in PV cells or modules in reverse bias such that $I_{sh} = V_j M(V_j)/R_{sh}$ (Bishop, 1988). It considers the current through the shunt resistance as mainly the one affected by avalanche breakdown. While the primary

currents are the ones carrying the avalanche effects in other models for cells in reverse bias and parameters were sometimes meaningless or out of range as predicted by theory, the simplicity, wide use and the good fit with actual measurements of this model were instead considered here (Alonso-García and Ruíz, 2006). The modified cell model is:

$$I = I_{ph} - I_{sat}\left(\exp\left(\frac{qV_j}{n_d kT}\right) - 1\right) - \frac{V_j}{R_{sh}}\left(1 + \alpha\left(1 - \frac{V_j}{V_{br}}\right)^{-m}\right) \quad \text{(Eq. 2)}$$

where the additional variables included are α which is the fraction of ohmic current involved in avalanche breakdown exponent, V_{br} which is the junction breakdown voltage when a cell or module is reverse-biased and m which is the avalanche breakdown exponent (Bishop, 1988; Orozco-Gutierrez et al., 2014).

To complete the model, expressions for the other parameters must also be found. What has been described so far is the general characteristic *I-V* equation of a PV module. This equation depends on two parameters: I_{ph} and I_{sat}. Eqs. 3 and 4 are the formulas for I_{ph}:

$$I_{ph,STC} = \frac{R_s + R_{sh}}{R_{sh}} I_{sc,STC} \quad \text{(Eq. 3)}$$

$$I_{ph} = \left(I_{ph,STC} + K_I \Delta T\right)\frac{G}{G_{STC}} \quad \text{(Eq. 4)}$$

where I_{sc} (A) is the module's short-circuit current, K_I (A K^{-1}) is the temperature coefficient of the short-circuit current and G (W m^{-2}) is the irradiance that the module receives. The formulas for I_{sat}, on the other hand is Eq. 5 (Mäki and Valkealahti, 2012):

$$I_{sat} = \frac{I_{ph} - \dfrac{V_{oc,STC} + K_V \Delta T}{R_{sh}}}{\exp\left(\dfrac{V_{oc,STC} + K_V \Delta T}{n_d V_t}\right) - 1} \quad \text{(Eq. 5)}$$

where V_{oc} (V) is the module's open-circuit voltage and K_V (V K^{-1}) is the temperature coefficient of the open-circuit voltage (Villalva et al., 2009). The STC in the subscripts of some of the variables refers to the standard testing conditions which specify that junction temperature should be 25 °C, irradiance, 1,000 W m^{-2} and air mass AM 1.5 when measurements are made.

2.3 3×3 PV array with bypass diodes model

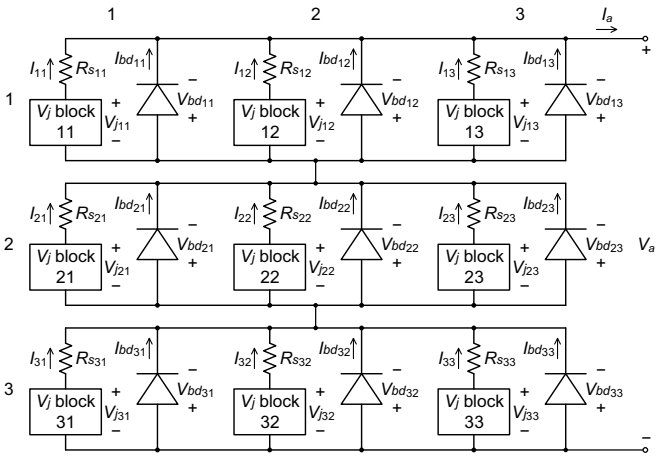

Fig. 3: Circuit representation of the PV array model

To demonstrate the construction of the PV array model, a 3×3 PV array is considered and is shown in Fig. 3. The modules are named according to their position in the array. For example, the module in the second row,

first column of the array is referred to as module 21. In general, for an $M\times N$ array, a module mn has $m \in \{1,2,3,\ldots,M\}$ as its row position and $n \in \{1,2,3,\ldots,N\}$ as its column position. The voltages, currents and resistances are numbered following the designation of the module e.g. V_{11}, V_{j11}, I_{11}, R_{s11} for module 11. Every module has a bypass diode attached to it in antiparallel position. The bypass diodes' voltages and currents also follow the designation of the module it is paired to e.g. V_{bd11}, I_{bd11} for module 11. The array circuit has 18 unique components consisting of nine modules and nine bypass diodes. Thus, the solution requires 18 voltage variables. These variables are stored in a vector called **x**. In general, for an $M\times N$ array, $\mathbf{x} = [V_{j11} V_{bd11} V_{j12} V_{bd12} \cdots V_{jMN}\ V_{bdMN}]^{\mathrm{T}}$, which contains MN variables.

To create the system of equations that describes the 3×3 PV array in Eq. 6, Kirchhoff's voltage and current laws (KVL and KCL) are applied to the circuit in Fig. 3. The 18 variables require that the system of equations consist of 18 equations. There are three rows in the array, so the system of equations can be split into three divisions, one division for each row, each division containing six equations. Each division has the same form, except for the last one. For the first division, the procedure is to first apply KVL to the five meshes in the array's first row. The convention chosen is such that meshes follow the clockwise direction. For the first mesh, $V_{j11} - I_{11}(V_{j11})R_{s11} + V_{bd11} = 0$. The same steps are done for the remaining four meshes. To obtain the last equation in the division, KCL is applied to the node connecting the array's first and second rows. The convention is chosen such that currents leaving the node are positive. The converse is true for currents entering the node. Thus, $\sum_{n=1}^{N}\left[I_{1n}\left(V_{j_{1n}}\right)+I_{bd_{1n}}\left(V_{bd_{1n}}\right)\right]-\sum_{n=1}^{N}\left[I_{2n}\left(V_{j_{2n}}\right)+I_{bd_{2n}}\left(V_{bd_{2n}}\right)\right]=0$. The same procedure was followed for the other divisions. However, the last equation of the third division differs because it is the application of KVL to the big mesh containing the array voltage V_a.

$$\mathbf{F}(\mathbf{x})=\begin{cases} V_{j_{11}}-I_{11}\left(V_{j_{11}}\right)R_{s_{11}}+V_{bd_{11}}=0 \\ -V_{bd_{11}}-V_{j_{12}}+I_{12}\left(V_{j_{12}}\right)R_{s_{12}}=0 \\ V_{j_{12}}-I_{12}\left(V_{j_{12}}\right)R_{s_{12}}+V_{bd_{12}}=0 \\ -V_{bd_{12}}-V_{j_{13}}+I_{13}\left(V_{j_{13}}\right)R_{s_{13}}=0 \\ V_{j_{13}}-I_{13}\left(V_{j_{13}}\right)R_{s_{13}}+V_{bd_{13}}=0 \\ \sum_{n=1}^{N}\left[I_{1n}\left(V_{j_{1n}}\right)+I_{bd_{1n}}\left(V_{bd_{1n}}\right)\right]-\sum_{n=1}^{N}\left[I_{2n}\left(V_{j_{2n}}\right)+I_{bd_{2n}}\left(V_{bd_{2n}}\right)\right]=0 \\ V_{j_{21}}-I_{21}\left(V_{j_{21}}\right)R_{s_{21}}+V_{bd_{21}}=0 \\ -V_{bd_{21}}-V_{j_{22}}+I_{22}\left(V_{j_{22}}\right)R_{s_{22}}=0 \\ V_{j_{22}}-I_{22}\left(V_{j_{22}}\right)R_{s_{22}}+V_{bd_{22}}=0 \\ -V_{bd_{22}}-V_{j_{23}}+I_{23}\left(V_{j_{23}}\right)R_{s_{23}}=0 \\ V_{j_{23}}-I_{23}\left(V_{j_{23}}\right)R_{s_{23}}+V_{bd_{23}}=0 \\ \sum_{n=1}^{N}\left[I_{2n}\left(V_{j_{2n}}\right)+I_{bd_{2n}}\left(V_{bd_{2n}}\right)\right]-\sum_{n=1}^{N}\left[I_{3n}\left(V_{j_{3n}}\right)+I_{bd_{3n}}\left(V_{bd_{3n}}\right)\right]=0 \\ V_{j_{31}}-I_{31}\left(V_{j_{31}}\right)R_{s_{31}}+V_{bd_{31}}=0 \\ -V_{bd_{31}}-V_{j_{32}}+I_{32}\left(V_{j_{32}}\right)R_{s_{32}}=0 \\ V_{j_{32}}-I_{32}\left(V_{j_{32}}\right)R_{s_{32}}+V_{bd_{32}}=0 \\ -V_{bd_{32}}-V_{j_{33}}+I_{33}\left(V_{j_{33}}\right)R_{s_{33}}=0 \\ V_{j_{33}}-I_{33}\left(V_{j_{33}}\right)R_{s_{33}}+V_{bd_{33}}=0 \\ -V_{bd_{13}}-V_{bd_{23}}-V_{bd_{33}}-V_a=0 \end{cases} \quad \text{(Eq. 6)}$$

Eq. 2, the characteristic *I-V* equation, was used to compute for values of $I_{mn}(V_{jmn})$ in the system of equations. On the other hand, the Shockley diode equation in Eq. 7 was used to compute for values of $I_{bd}(V_{bdmn})$ in the system of equations:

$$I = I_{sat,bd}\left(\exp\left(\frac{qV_{bd}}{n_{bd}kT}\right)-1\right) \quad \text{(Eq. 7)}$$

The mesh used to obtain the last equation in the system is especially chosen to create the Jacobian matrix **J**

of the vectorial function **F** with a diagonal containing nonzero elements. The Jacobian matrix is needed to use Newton's method for systems of nonlinear equations. In Newton's method, the equation $\mathbf{J}(\mathbf{x}_i)\Delta\mathbf{x} = -\mathbf{F}(\mathbf{x}_i)$ is solved for $\Delta\mathbf{x}$. Then, this vector is substituted in $\mathbf{x}_{i+1} = \mathbf{x}_i + \Delta\mathbf{x}$ for the new value **x**. There is an initial guess $\mathbf{x}_0$ that serves as the initial value of **x**. The two steps are repeated until convergence. In theory however, a convergent Newton's method is reached only after an infinite number of iterations. In practice, a tolerance that is small enough for one's purpose is set (Quarteroni and Saleri, 2006).

One important step in Newton's method is the choice of the initial approximation $\mathbf{x}_0$. The convergence of the method depends on it. The choice of $\mathbf{x}_0$ must be sufficiently close to the actual solution for Newton's method to converge (Quarteroni and Saleri, 2006). As stated earlier, V_a is swept from V_{oc} to zero. The actual value of the array's V_{oc} is unknown, so an approximate value for the modules' V_{oc}, solved using Eq. 8, is used (Orozco-Gutierrez et al., 2014):

$$V_{oc,init} = V_t n_d \ln\left(1 + \frac{I_{ph}}{I_{sat}}\right) \qquad \text{(Eq. 8)}$$

Assuming that the modules in the array have the same material properties and are under the same conditions, the array's V_{oc} is just a module's V_{oc} multiplied by the number of rows m. Another use of Eq. 8 is in populating the initial approximation $\mathbf{x}_0$. Because of the parallel connection, a module and the bypass diode connected to it always have the same voltage. So, $\mathbf{x}_0 = [V_{oc,init} V_{oc,init} \cdots V_{oc,init}]^T$.

2.4 3×3 PV array with bypass diodes program

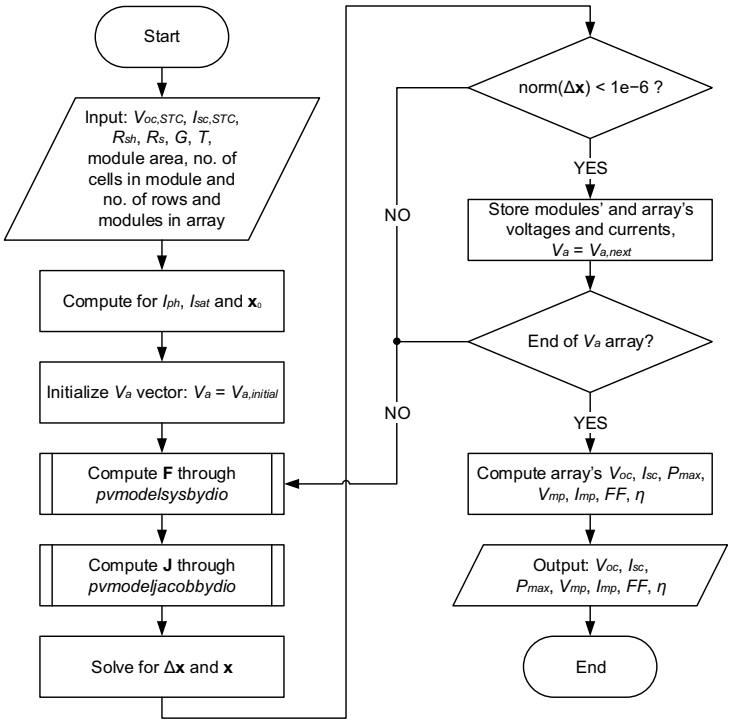

Fig. 4: Flowchart of the MATLAB function *pvmodelbydio*

The equations and the model described in the previous sections were programmed in MATLAB. They were incorporated into the function *pvmodelbydio*, shown in Fig. 4. The function takes G, the module's surface area and the number of rows and modules in the array as inputs or arguments. On the other hand, the outputs are the array's V_{oc}, I_{sc}, P_{max}, V_{mp}, I_{mp}, fill factor (FF) and efficiency (η) under given conditions. The conditions are dictated by the irradiance G that each module receives and the temperature of the module T. In the function, however, only G is an input. Module temperatures were set at 35, 45 and 55 °C. When the function is called, the program computes for I_{ph} and I_{sat} of all the modules in the array using Eqs. 4 and 5. $V_{oc,init}$ is also computed using Eq. 8 and is used to populate the initial approximation $\mathbf{x}_0$. Eq. 8 is also used to initialize the MATLAB vector for V_a from its approximate V_{oc} value to zero. Newton's method is applied

starting with the first element of the vector. It is repeated until a condition is reached that causes termination of Newton's method. In this case, termination is set when the norm of $\Delta\mathbf{x}$ reaches a tolerance of 1×10^{-6}. Thus, the system is solved for the first value of V_a. The steps are repeated for the next values of the array voltage. The whole process is akin to setting the array voltage at a specific level, and finding out the values of all the parameters of interest. To completely characterize the system then is to sweep the voltage from its open-circuit value down to zero and solving the resulting systems of equations.

3. Reconfiguration strategies and their simulation

Velasco-Quesada et al. proposed a scheme for the reconfiguration of PV arrays to minimize mismatch and therefore maximize power output (Velasco-Quesada et al., 2009). They called this the electrical array reconfiguration or EAR strategy. It is based on the principle of irradiance equalization that their group earlier explored (Velasco et al., 2005).

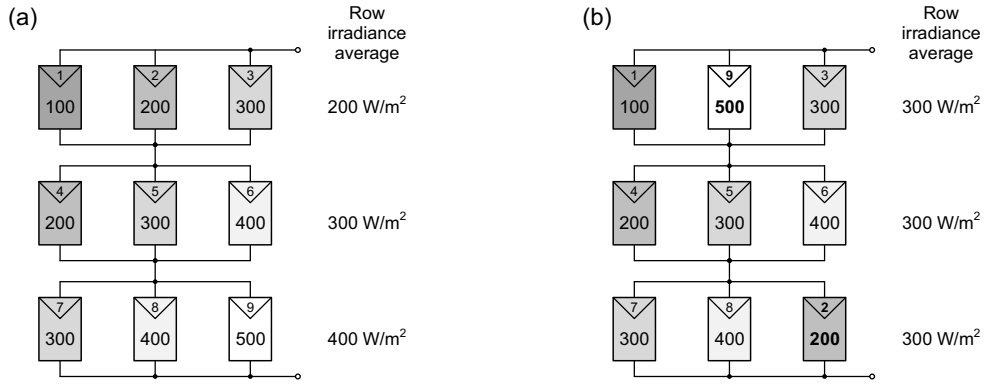

Fig. 5: Principle of irradiance equalization for dynamic PV arrays: (a) original configuration and (b) new configuration where modules 2 and 9 were interchanged

Irradiance equalization serves as a framework for the reconfiguration strategy for PV arrays in TCT configuration tested in this work. It works by configuring PV arrays in such a way that each row's average irradiance is as close as possible to the average irradiances of the other rows. The principle is illustrated with an idealized example in Fig. 5. Fig. 5(a) is the original configuration. In irradiance equalization, the configuration that minimizes the difference among the average row irradiances becomes the new configuration. Fig. 5(b) is such a configuration. The connections of modules 2 and 9 were interchanged resulting in equal average row irradiances.

Irradiance equalization works because it reduces the current mismatch among the rows which are connected in series. Even though the rows have different shading profiles, they will still produce currents which are close in value to one another because they have close average row irradiances. Previous studies show that cross-tied configurations such as TCT and bridge-link arrays do not only produce more power in the face of partially shadowed conditions but are also more reliable in terms of operational lifetimes as compared to serial-parallel (SP) arrays (Gautam and Kaushika, 2002; Kaushika and Gautam, 2003). The effect of a change in irradiance is mostly seen in the current produced by a PV module. The effect on voltage is minimal (Velasco-Quesada et al., 2009). This makes the parallel connection of modules possible with minimal effect on the current produced by a row. Mismatch still happens, but at the level of the series connection of rows. The array current is limited by the row that produces the lowest current. As already said for modules connected in series, the module in the worst operating conditions dictate the performance of the whole array. By employing irradiance equalization through array reconfiguration, current mismatch is reduced.

3.1 Electrical PV array reconfiguration strategy

As can be observed in the topology of TCT arrays, there are permutations which are equivalent in terms of power production. Cases of two interchanged parallel modules are redundant. Also redundant are interchanged rows in series. Computing for these irrelevant cases is just a waste of time. The EAR strategy discards these redundancies when considering the total number of configurations of interest (COIs) (Velasco-Quesada et al., 2009). For an $M\times N$ array, the number of configurations of interest is:

$$N_{coi} = \frac{(MN)!}{M!(N!)^m} \qquad \text{(Eq. 9)}$$

For a 3×3 array where $M = N = 3$, the total number of permutations possible is 9! = 362,880 while the number of COIs given by Eq. 9 is 280. Based on these numbers, it can be seen that considering only the COIs greatly reduces the number of configurations that the EAR algorithm has to consider.

The following are the steps that describe the algorithm to implement the EAR strategy:

1. The COIs are computed based on the size of the PV array.
2. The irradiance of each module in the array is estimated using the voltage and current values of individual modules.
3. For a COI, irradiance values of the modules in each row are averaged. Each row of the COI then has an associated average row irradiance. The same is done for the other COIs.
4. For a COI, an "irradiance equalization index" is computed for based on the average row irradiances. This index is just the difference between the maximum and minimum values among the average row irradiances. The same is done for the other COIs so each has an associated index. The COI with the lowest index becomes the target for the reconfiguration.
5. In case of COIs with equal indices, the tie is broken by computing for the number of module relocations needed to arrive there from the current configuration. The COI with the lowest number of relocations then becomes the target for the reconfiguration.

Table 1: Array sizes and number of configurations

Array size	Total number of configurations	Number of configurations of interest
3×3	362,880	280
4×4	2.09×10^{13}	2,627,625
5×5	1.55×10^{25}	5.19×10^{12}

A problem emerges when scaling is considered. Table 1 shows different array sizes and the corresponding total number of configurations and number of COIs. For a 3×3 array, only 280 COIs have to be considered and for square arrays larger than 3×3, implementation of the EAR strategy becomes harder because of the exponential jump in the number of COIs. This issue is fundamental in the EAR strategy as COIs are the framework for the scheme.

3.2 Simulation and performance tests of the strategies

The EAR algorithm was also implemented in MATLAB. Two models were constructed: a static array and a dynamic array using the EAR strategy. Also, two tests were conducted for the static and dynamic PV array models: binary- and random-irradiance shading. For the binary-irradiance test, 511 shading patterns containing all combinations of shaded modules were generated for each irradiance level. Random-irradiance shading, on the other hand, involved random irradiance values which follow uniform and normal distributions. 1,000 random shading patterns were prepared for both distributions. The simulations were run on desktop PCs with Intel Core i5-3450 (at 3.10 GHz) processors.

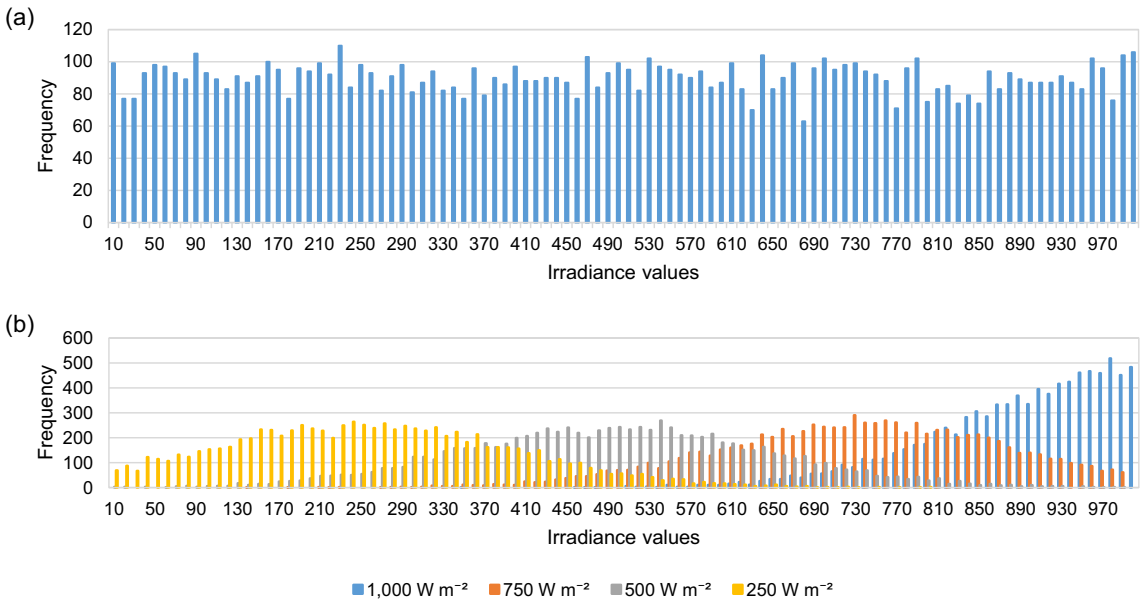

Fig. 6: Histogram of the random irradiance distributions: (a) uniform distribution and (b) normal distributions with different means and σ = 150 W m^{-2}

The histograms for the two random irradiance shading tests are shown in Fig. 6. The uniform distribution in Fig. 6(a) simulates a condition for a PV array where the change in irradiance of each PV module over time is drastic. The normal distribution, on the other hand, simulates a condition where the change in irradiance over time is more moderated or more concentrated within an irradiance range as seen in Fig. 6(b). In actual conditions, it could resemble different levels of cloudy conditions. The different levels are simulated as the means (μ) of the normal distribution: 1,000, 750, 500 and 250 W m^{-2}. A standard deviation (σ) of 150 W m^{-2} was chosen for the distributions. To give an idea of the range of irradiance values this σ brings, for a mean of 500 W m^{-2}, 95% of the values are within 2σ or within the range 200–800 W m^{-2}. 68% of the values are within a σ or within the range 350–650 W m^{-2}. Other values for the standard deviation could also be tested, but the results here are for σ = 150 W m^{-2}. The range of irradiance values was limited to 0–1,000 W m^{-2}.

Table 2: Parameters of the PV module and bypass diode used in the model

Parameter	Value	Parameter	Value
V_{oc}	21.7 V	R_s	1.4 Ω
I_{sc}	0.61 A	R_{sh}	2.31×10^4 Ω
V_{mp}	17.3 V	V_{br}	−15 V
I_{mp}	0.58 A	M	3
P_{max}	10 W	A	0.002
K_V	−0.0708 V K^{-1}	n_d	1.3
K_I	0.0034 A K^{-1}	n_{bd}	1.5
N_s	36	$I_{sat,bd}$	5.6×10^{-6} A

Table 2 gives the parameters used in the model for the PV module and bypass diode. The PV model used in this study is the GP010PA PV module by Alexan Commercial. K_V and K_I were obtained from outdoor experiments characterizing and measuring the performance of the modules. The values for the resistances R_s and R_{sh}, on the other hand, were obtained following the procedure for the modeling of PV modules (Villalva et al., 2009).

4. Results and discussion

The two tests were performed for both the static and dynamic PV arrays to compare their power outputs and ultimately to assess whether using the EAR strategy for dynamic arrays improves power output.

4.1 Binary-irradiance test results

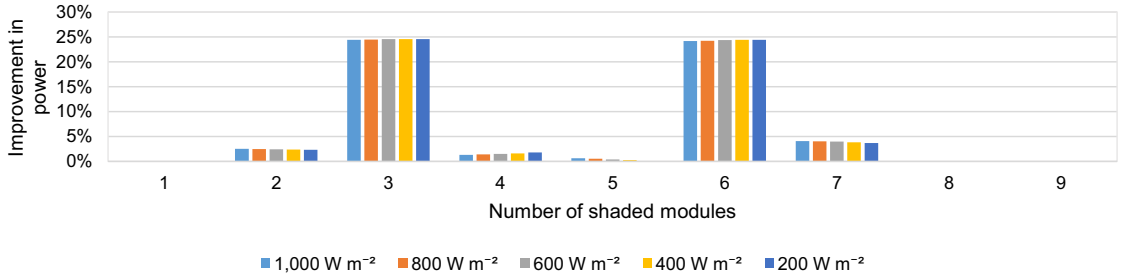

Fig. 7: Average percent improvement in power output of the 3×3 dynamic over the static PV array model in binary-irradiance shading at 35 °C; irradiance of shaded modules is 5% of unshaded level

Fig. 7 shows the results for the binary-irradiance shading test where each PV module in the array can either be shaded or unshaded. Both the static and EAR-based model were run 511 times for each irradiance and shading level. This is based on the total number of combinations possible for shaded and unshaded modules in the array. The unshaded irradiance level in a run can have a value of 1,000, 800, 600, 400 or 200 W m^{-2}, while the shaded irradiance level is 5% of the unshaded level. It can be seen that when a module is shaded and when only one module is unshaded (eight modules are shaded), using a dynamic array based on the EAR strategy does not improve power output. The principle on which the strategy is based, irradiance equalization, cannot optimize these cases. Otherwise, using dynamic arrays improved power output for other cases when the number of shaded modules is not one or eight.

Table 3: Percentage of shading patterns with decreased and increased power output due to the EAR strategy for 1,000 W m^{-2} unshaded irradiance level at 35 °C

No. of shaded modules	Total no. of shading patterns	Patterns with decreased power	Patterns with the same power	Patterns with increased power
1	9	0%	100%	0%
2	36	0%	75%	25%
3	84	0%	32.14%	67.86%
4	126	35.71%	21.43%	42.86%
5	126	47.62%	16.67%	35.71%
6	84	0%	32.14%	67.86%
7	36	0%	75%	25%
8	9	0%	100%	0%

From the results in Fig. 7, it can be observed that the EAR algorithm performs best when the number of shaded modules equals the number of columns in the array or is a multiple of it, as in the case when three and six modules are shaded. It was able to relocate the shaded modules into columns such that each row has the same number of shaded modules as the other rows. Average improvement in power when three modules are shaded (24.39%) in the case of 1,000 W m^{-2} is as much as nine times better than when two modules are shaded (2.53%).

The effect of using the EAR strategy in dynamic arrays on the number of patterns with decreased or increased power output is summarized in Table 3. Percent differences whose absolute value is less than 0.01 were taken to show no difference in power output between the static and dynamic arrays. The table also shows that the decrease in power is only seen when four or five modules are shaded. The case when five

modules are shaded serves as another illustrative example of the limitation of the EAR strategy. For instance, at an array temperature of 35 °C and unshaded irradiance level of 1,000 W m^{-2}, the dynamic array in 47.62% of the 126 shading patterns possible produced a decrease, instead of an increase, in power. This means that for these numbers, the EAR strategy is unable to optimize the power for some shading patterns.

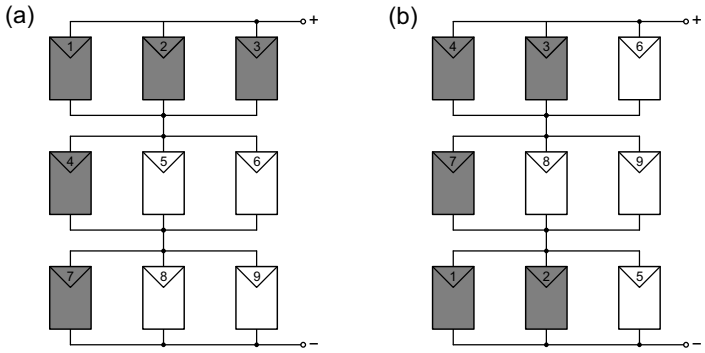

Fig. 8: Third case when five modules are shaded at 35 °C and unshaded irradiance level of 1,000 W m^{-2}: (a) original shading pattern and (b) shading pattern after reconfiguration using the EAR strategy

Fig. 8 shows a sample case of five shaded modules where the EAR strategy failed. The third shading pattern for five shaded modules at 35 °C and unshaded irradiance level of 1,000 W m^{-2} is shown in Fig. 8(a). This original configuration produced a power of 40.06 W. The resulting shading pattern after reconfiguration through the EAR strategy is shown in Fig. 8(b). It has a power of 35.29 W. Fig. 8 is a case of the reconfiguration strategy not being able to optimize a shading pattern. As the power outputs show, applying the EAR strategy reduced the power output instead of improving it. In Fig. 8(a), the whole of the first row is shaded. However, the bypass diodes connected to every panel served as an alternative path for the array current. In effect, the configuration actually has balanced currents. On the other hand, Fig. 8(b) has unbalanced row currents. The second row of this configuration has two unshaded modules, unlike the first and the third rows. The row currents are mismatched resulting in a lower power output as compared to the original configuration in Fig. 8(a).

4.2 Random uniformly distributed irradiance shading test results

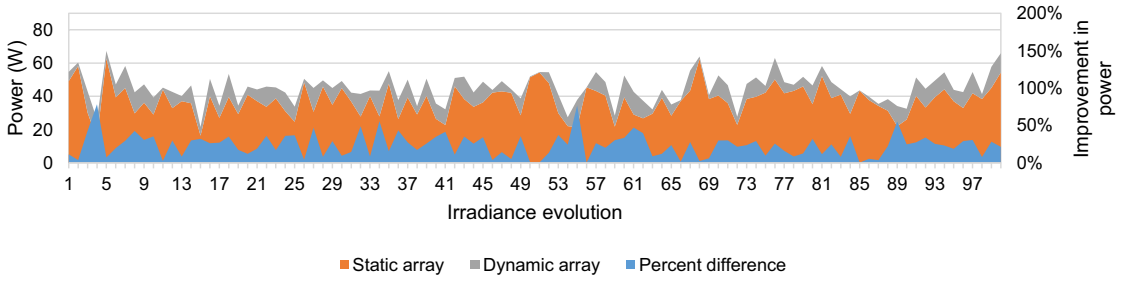

Fig. 9: Power output of 3×3 static and dynamic photovoltaic array models in random-irradiance shading (first 100 shading patterns) with uniformly distributed irradiance at 35 °C

For the first random-irradiance shading test, uniformly distributed shading patterns were generated. The simulation of the models was executed with each pattern as input. Fig. 9 shows the irradiance evolution and the output power for both static and dynamic arrays at 35 °C. The model was run 1,000 times for each distribution because there were 1,000 shading patterns generated for each distribution.

Table 4: Percent improvement in power of the dynamic arrays over the static array with uniformly distributed shading patterns

Improvement at 35 °C	Improvement at 45 °C	Improvement at 55 °C
21.12%	20.87%	20.61%

Table 4 shows the average improvement in power of the EAR-based dynamic over the static array when the irradiances in the shading pattern is uniformly distributed. With uniformly distributed shading patterns, improvements of above 20% can be expected. Percent improvement decreases with an increase in temperature, but the effect of temperature on the percent improvement is very minimal.

4.3 Random normally distributed irradiance shading test results

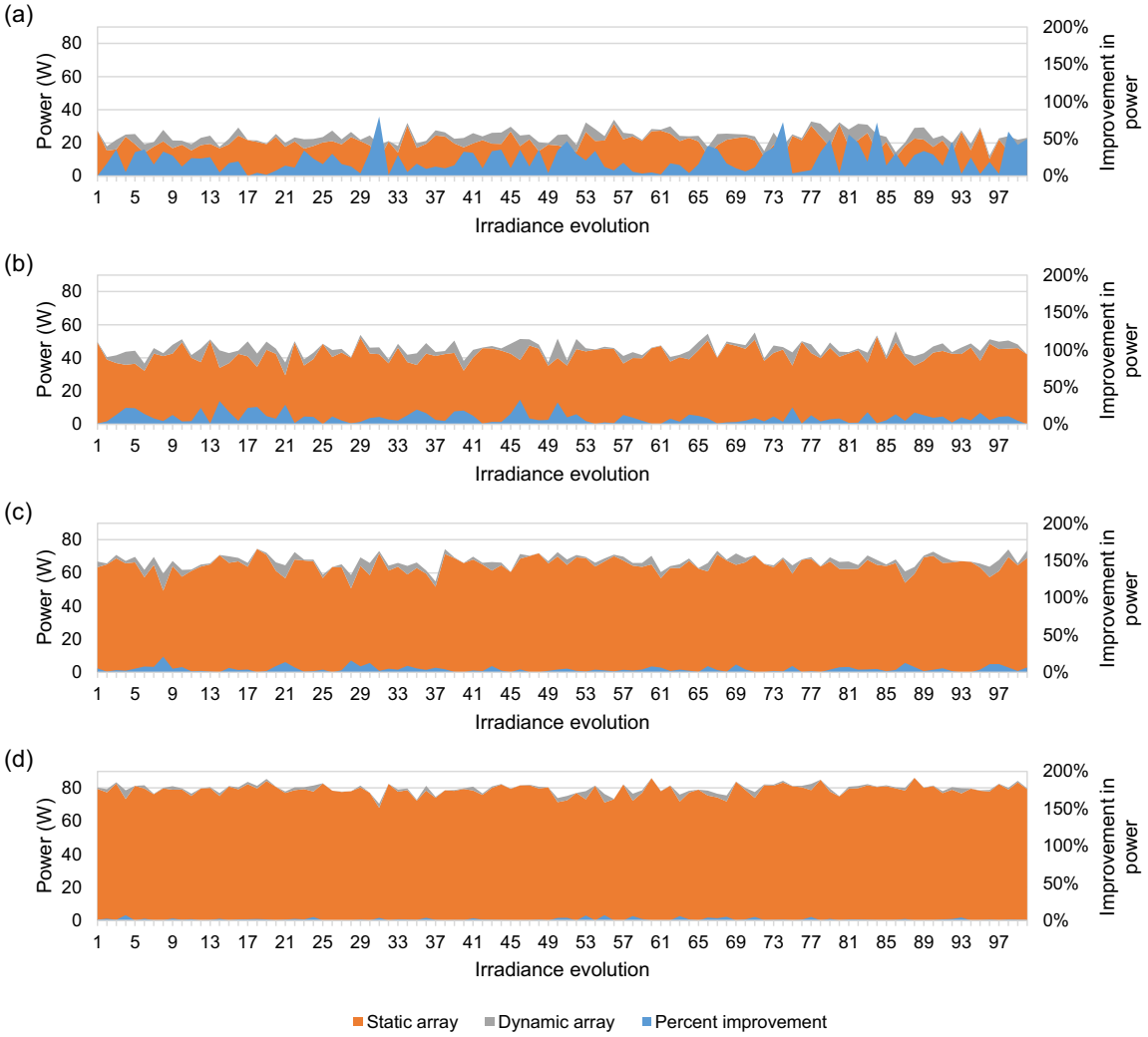

Fig. 10: Power output of 3×3 static and dynamic photovoltaic array models in random-irradiance shading (first 100 shading patterns) at 35 °C with normally distributed irradiance (σ = 150 W m^{-2}): (a) μ = 250 W m^{-2}, (b) μ = 500 W m^{-2}, (c) μ = 750 W m^{-2} and (d) μ = 1,000 W m^{-2}

Fig. 10 shows the results for the second random irradiance shading test with the distributions centered at different irradiances at 35 °C. The irradiance level at 1,000 W m^{-2} was taken as the maximum possible irradiance so the distribution centered at this value is only a half-normal distribution, as in Fig. 6. As seen in Figs. 10(a)–(d), the percent improvement of the dynamic over the static array is small for the irradiance distributions centered at 750 and 1,000 W m^{-2}. The percent improvement increases as the mean of the distribution decreases.

Table 5: Percent improvement in power of the dynamic arrays over the static array with normally distributed shading patterns

Irradiance distribution mean (W m^{-2})	Improvement at 35 °C	Improvement at 45 °C	Improvement at 55 °C
250	20.62%	20.35%	20.06%
500	9.63%	9.37%	9.09%
750	4.13%	3.96%	3.79%
1,000	1.52%	1.43%	1.35%

Table 5 summarizes the results of the random irradiance shading test. The values confirm that as the mean of the distribution increases, the percent improvement decreases. The values for the distribution centered at 250 W m^{-2} almost match those obtained for uniformly distributed irradiances. However, for the other distributions, percent improvement is much less than half that of the uniform distributions. It shows that as the irradiance distribution becomes more spread, the dynamic array becomes more effective in recovering power which is otherwise lost due to partial shading.

It must be noted however, that while the percent improvement is high for lower irradiances, actual deployment of a dynamically reconfigurable array will depend on the power requirements of the system versus the recoverable power, as estimated here. Table 5 also shows the effect of temperature on the percent improvement. As in the uniform distributions, percent improvement minimally increases as the temperature decreases.

5. Conclusion

This work demonstrates some of the limitations and benefits in using the EAR strategy in dynamic PV arrays through modeling and simulation. The binary-irradiance shading test showed that the algorithm works best for particular configurations. Specifically, irradiance equalization works best when the number of shaded modules equals the number of columns. On the other hand, the random-irradiance shading test revealed how the irradiance distribution affects power output improvement when a dynamic array is used. Dynamic reconfiguration is most effective when the distribution of irradiance each module receives is more uniformly spread. Thus, shading profiles must also be studied if dynamic reconfiguration is to be implemented. The two tests employed here can serve as platforms for evaluating dynamic reconfiguration strategies for PV systems. PV system designers benefit by considering these results that inform when and where to use the EAR strategy in dynamic PV arrays.

6. Acknowledgment

The authors thank the Engineering Research and Development for Technology program of the Philippine Department of Science and Technology (DOST-ERDT) for supporting this work and Erasmus Mundus Mobility with Asia-West 2013 (EMMA-West 2013) for providing R. A. S. Peña with a mobility grant that allowed completion of part of this work at Università degli Studi di Padova.

7. References

Alonso-García, M., Ruíz, J., Chenlo, F., 2006. Experimental study of mismatch and shading effects in the – characteristic of a photovoltaic module. Sol. Energy Mater. Sol. Cells 90, 329–340. doi:10.1016/j.solmat.2005.04.022

Alonso-García, M.C., Ruíz, J.M., 2006. Analysis and modelling the reverse characteristic of photovoltaic cells. Sol. Energy Mater. Sol. Cells 90, 1105–1120. doi:10.1016/j.solmat.2005.06.006

Bishop, J.W., 1988. Computer simulation of the effects of electrical mismatches in photovoltaic cell interconnection circuits. Sol. Cells 25, 73–89. doi:10.1016/0379-6787(88)90059-2

Burger, B., Goeldi, B., Rogalla, S., Schmidt, H., 2010. Module Integrated Electronics–An Overview, in: 25th European Photovoltaic Solar Energy Conference and Exhibition/5th World Conference on Photovoltaic Energy Conversion. Valencia, Spain, pp. 3700–3707. doi:10.4229/25thEUPVSEC2010-4EP.1.1

Gautam, N.K., Kaushika, N.D., 2002. Reliability evaluation of solar photovoltaic arrays. Sol. Energy 72, 129–141. doi:10.1016/S0038-092X(01)00085-8

Kaushika, N.D., Gautam, N.K., 2003. Energy Yield Simulations of Interconnected Solar PV Arrays. IEEE Trans. Energy Convers. 18, 127–134. doi:10.1109/TEC.2002.805204

La Manna, D., Li Vigni, V., Riva Sanseverino, E., Di Dio, V., Romano, P., 2014. Reconfigurable electrical interconnection strategies for photovoltaic arrays: A review. Renew. Sustain. Energy Rev. 33, 412–426. doi:10.1016/j.rser.2014.01.070

MacAlpine, S.M., Erickson, R.W., Brandemuehl, M.J., 2013. Characterization of Power Optimizer Potential to Increase Energy Capture in Photovoltaic Systems Operating Under Nonuniform Conditions. IEEE Trans. Power Electron. 28, 2936–2945. doi:10.1109/TPEL.2012.2226476

Mäki, A., Valkealahti, S., 2012. Power losses in long string and parallel-connected short strings of series-connected silicon-based photovoltaic modules due to partial shading conditions. IEEE Trans. Energy Convers. 27, 173–183. doi:10.1109/TEC.2011.2175928

Orozco-Gutierrez, M.L., Ramirez-Scarpetta, J.M., Spagnuolo, G., Ramos-Paja, C. a., 2014. A method for simulating large PV arrays that include reverse biased cells. Appl. Energy 123, 157–167. doi:10.1016/j.apenergy.2014.02.052

Orozco-Gutierrez, M.L., Ramirez-Scarpetta, J.M., Spagnuolo, G., Ramos-Paja, C.A., 2013. A technique for mismatched PV array simulation. Renew. Energy 55, 417–427. doi:10.1016/j.renene.2013.01.009

Quarteroni, A., Saleri, F., 2006. Scientific Computing with MATLAB and Octave, 2nd editio. ed, Texts in Computational Science and Engineering. Springer Berlin Heidelberg, Berlin, Heidelberg. doi:10.1007/3-540-32613-8

Velasco, G., Negroni, J.J., Guinjoan, F., Pique, R., 2005. Irradiance equalization method for output power optimization in plant oriented grid-connected PV generators, in: 2005 European Conference on Power Electronics and Applications. IEEE, p. 10 pp.–P.10. doi:10.1109/EPE.2005.219300

Velasco-Quesada, G., Guinjoan-Gispert, F., Piqué-López, R., Román-Lumbreras, M., Conesa-Roca, A., 2009. Electrical PV array reconfiguration strategy for energy extraction improvement in grid-connected PV systems. IEEE Trans. Ind. Electron. 56, 4319–4331. doi:10.1109/TIE.2009.2024664

Villalva, M.G., Gazoli, J.R., Filho, E.R., 2009. Comprehensive Approach to Modeling and Simulation of Photovoltaic Arrays. IEEE Trans. Power Electron. 24, 1198–1208. doi:10.1109/tpel.2009.2013862

Conference Proceedings

Solar World Congress 2015
Daegu, Korea, 08 – 12 November 2015

AN OUTDOOR PLATFORM FOR PV AGEING STUDIES: ELECTRICAL PARAMETERS EXTRACTION FROM IV CURVES

Ghjuvan Antone Faggianelli, Pierrick Haurant, Auline Rodler and Philippe Poggi

University of Corsica, UMR SPE CNRS 6134, Ajaccio (France)

Abstract

Accurate models for solar technologies are essential to evaluate the lifetime, ageing and degradation modes of these devices, depending on local climatic constraints. In this context, the DURASOL project aims to provide more sophisticated tools and methods for solar industries, based on studies in multi-site facilities with indoor and outdoor platforms under diverse and complementary climates. For solar cells and modules, simple diode modelling allows to determine several electrical parameters from IV curves: the series and shunt resistances, the photocurrent, the reverse saturation current of diode and the diode ideality factor. These parameters can be used for various applications such as analyze of performance losses, quality control and devices improvements. In this paper, we focus on their extraction through a Particle Swarm Optimization algorithm. Three approaches are compared, based on a direct optimization of the five electrical parameters and on the use of the short-circuit current I_{sc} and the open-circuit voltage V_{oc}. The tests realized on a synthetic IV curve show that the use of V_{oc} leads to a more robust and accurate model with both exact and noisy data.

Keywords: *Photovoltaic, Simple diode model, IV curve, Parameters extraction, Particle Swarm Optimization*

1. Introduction

The markets of solar technologies as photovoltaic (PV) are rapidly growing. However, long term performance and reliability remain major issues to provide warranties, develop insurance and subsidy programs, evaluate a long term investment risk or help the customer to choose between manufacturers. Therefore, methods for evaluating the lifetime, ageing and degradation modes of these technologies are necessary. Most of the time, simple assumptions of a constant and linear degradation rate performance per year are made for PV modules (Vázquez and Rey-Stolle, 2008). The impacts of non-linear and non-uniform degradations as well as their sources require further studies.

Environmental conditions and local climate have an important impact on PV energy efficiency and its evolution over time (Jordan et al., 2012; Jordan and Kurtz, 2013). Even well qualified modules can degrade more than expected when exposed to outdoor conditions (Sharma and Chandel, 2013). These degradations can be correlated to various stresses affecting solar modules lifetime such as temperature (heat, freezing, night-day cycles…), mechanical stresses (wind, snow load, hail…), atmosphere (salt mist, dust, sand, pollution…) and humidity (rain, dew, frost, fog…). Moreover, it must also be considered that each stress may show up some singular ageing effect as well as it can combine with other stresses. As an example, Mekhilef et al. (2012) focus on some environmental factors (dust, humidity and air velocity) and show that they should not be studied separately as their effects are linked up and each of them impacts the other two. Skoczek et al. (2009) also present the results of electrical performance measurements of hundreds crystalline silicon photovoltaic modules, following long-term continuous outdoor exposure. An important outcome is that visual inspection is generally not enough to track the module degradation and by no means answer the question of module lifetime. Advanced diagnostic tools are thus required to measure the degradations, quantify them and also explain the phenomena.

For PV technologies, some electrical parameters allow to analyze performance losses and lead to more

doi:10.18086/swc.2015.05.15 Available at http://proceedings.ises.org

accurate models and simulations. The extraction and interpretation of these parameters has a variety of important applications. They can, for example, be used for quality control during production or to provide insights into the operation of the devices, thereby leading to improvements in devices (Gottschalg et al., 1999). In this paper, we will focus on the series and shunt resistances R_s and R_{sh}, the photocurrent I_{ph}, the reverse saturation current of diode I_0 and the diode ideality factor n which can be obtained from IV curves through the monitoring of solar cells and modules. The variation of these parameters over time can be correlated to specific degradations (delamination, discoloration…) and thus allow to assess the ageing effects and the impact of environment. In their review of photovoltaic degradation rate methodologies, Phinikarides et al. (2014) present a list of possible sources of performance losses and their impact on some of these parameters. For example, the series resistance has a significant effect on both the fill factor and the conversion efficiency. The shunt resistance is crucial to photovoltaic system performance, especially at reduced irradiance levels (Priyanka et al., 2007). Inaccurate determination will provide a misleading interpretation on the impact of each parameter and lead either to an overestimation or underestimation of the degradation. The main difficulty of this type of study is thus to define measurement and extraction methods with a sufficient robustness and precision.

For this purpose, the DURASOL project aims to provide more sophisticated tools and methods for the PV, ST and CSP industries. This project, supported by the French National Research Agency as an "Invest for Future, EQUIPEX", relies on multi-site facilities with several indoor and outdoor platforms under various and complementary climates. It aims to compare analysis of indoor and outdoor ageing, determine accelerating ageing factors depending on climatic constraints and develop analysis methods for degradation mechanisms. On the medium term, it will provide deeper insight and understanding of degradation mechanisms allowing to design and manufacture new components with longer life-time and higher performances. As a first step, we focus on this paper on the extraction of electrical parameters through simple diode modelling.

2. IV curves processing

2.1. Measurement protocol

In order to get reliable information on a solar device, it is required to set up a robust measurement protocol. Depending on the method used for the calculation of electrical parameters, an important accuracy will be needed. As an example, curve fitting method needs to calculate the differential value dV/dI from the experimental data, which requires a very smooth IV curve (Zhang et al., 2011).

According to Gottschalg et al. (1999), there are three standard measurement strategies for measuring the IV characteristics of PV solar devices. One can apply the voltage in regularly distributed steps, control the current in regularly distributed steps or measure with a variable resistance load. Comparing the different measurement strategies clearly shows that it is better to measure devices with constant voltage steps. In the context of DURASOL project, we have opted for a measurement method based on the application of a voltage with a specific step. This is done with a test bench for PV characterisation through current-voltage measurements. This IV bench is connected to photovoltaic modules, on an outdoor platform which is being installed at the SPE Laboratory UMR CNRS, University of Corsica, France (Fig. 1). The site is located in a coastal zone (distance from the sea of less than 400 m) with a Mediterranean climate and exposed to salty sea spray. In addition to the current and voltage measurements, each module is also equipped with a temperature sensor (PT100) and the surrounding conditions (ambient temperature, solar radiations, wind speed and direction…) are measured on the platform. This facility allows to plot and back up the modules IV curves with a 5 minutes time step and at least 100 points per curve for a given temperature and irradiance. These parameters can be changed depending on the accuracy needed and the aim of the study. The only limitation here is to ensure that the computation time for each IV curve is not too high (of about 1s) in order to avoid variations of surrounding conditions during measurement.

Fig. 1: DURASOL platform at SPE Laboratory, University of Corsica

2.2. Single diode model

To study solar cells and modules, it is common to represent them with an electrical analogy. For electrical engineering applications, simple diode models are usually suitable (Askarzadeh and Rezazadeh, 2012; de Blas et al., 2002). This type of model allows extracting several electrical parameters: the series and shunt resistances R_s and R_{sh}, the photocurrent I_{ph}, the reverse saturation current of diode I_0 and the diode ideality factor n. These parameters influence the behavior of the IV characteristics and give information on solar device performance. Fig. 2 shows an equivalent circuit of a solar module based on a simple diode model.

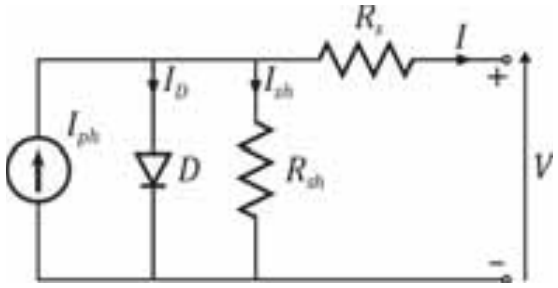

Fig. 2: Equivalent circuit of a solar module (simple diode model)

In this circuit, the current I can be simply expressed as:

$$I = I_{ph} - I_D - I_{sh} \quad \text{(eq. 1)}$$

With:

$$I_D = I_0 \left(e^{\frac{q(V+IR_s)}{nkT}} - 1 \right) \quad \text{(eq. 2)}$$

$$I_{sh} = \frac{V + IR_s}{R_{sh}} \quad \text{(eq. 3)}$$

Which leads to the transcendental equation:

$$I = I_{ph} - I_0 \left(e^{\frac{q(V+IR_s)}{nkT}} - 1 \right) - \frac{V + IR_s}{R_{sh}} \quad \text{(eq. 4)}$$

This equation is then resolved by an exact explicit method based on the Lambert W-function $W(z)$ (Jain, 2004):

$$I = \frac{R_{sh}(I_{ph} + I_0)}{(R_s + R_{sh})} - \frac{nkT}{qR_s} W(z) - \frac{V}{R_{sh}} \quad \text{(eq. 5)}$$

With:

$$z = \frac{qI_0}{nkT} \frac{R_s R_{sh}}{(R_s + R_{sh})} e^{\left(\frac{R_{sh}}{(R_s+R_{sh})} \frac{q[V+R_s(I_{ph}+I_0)]}{nkT}\right)} \quad \text{(eq. 6)}$$

The solution of this equation is obtained by the algorithm proposed by Fritsch et al. (1973). This method allows to express the current as a function of the voltage, the temperature and the five electrical parameters that we need to determine.

3. Parameters extraction methodology

From the experimental equipment presented in the previous section, it remains five unknown parameters that appear in (eq. 5). Their accuracy will depend on both the precision of the experimental data and the robustness of the method used for their determination. In addition to the measurement protocol, the main part of this work is thus to establish and validate a robust method for parameters extraction.

In the last decades, this problem has been treated frequently in literature with different methods which can be classified into three categories: analytic, iterative and evolutionary computational methods. Among these methods, we will focus in evolutionary algorithms which are the best suited with varying weather conditions (Tamrakar and Gupta, 2015). For this problem, we observe a large variety of algorithms such as Genetic (Jervase et al., 2001), Pattern Search (AlRashidi et al., 2011), Differential Evolution (Ishaque and Salam, 2011), Penalty-based Differential Evolution (Ishaque et al., 2012), Harmony Search (Askarzadeh and Rezazadeh, 2012), Simulated Annealing (El-Naggar et al., 2012) or Chaotic Asexual Reproduction Optimization (Yuan et al., 2014). In this paper, we propose the use of a Particle Swarm Optimization (PSO) algorithm which has been validated by several authors (Macabebe et al., 2011; Qin and Kimball, 2011; Sandrolini et al., 2010; Ye et al., 2009). According to Ye et al. (2009), this technique is accurate, fast, and easily applicable for the parameter extraction of solar cells from illuminated IV characteristics. Moreover, it does not particularly necessitate initial guesses as close as possible to the solutions, which is an important point as we can study a large amount of different PV solar devices. The interest of PSO algorithms for applications in power systems has also been demonstrated by Del Valle et al. (2008).

3.1. PSO configuration

The Particle Swarm Optimization is a metaheuristic which is trying to improve a candidate solution by successive iterations. It is inspired by social behaviour of living organisms such as bird flocking. The members of the population, the particles, are initially dispersed in the search area with random coordinates (position and velocity). At each iteration, the fitness of each particle is evaluated. The algorithm keeps in memory the best solution of each particle and the best solution obtained so far by any particle in the population. This information is then used to update the velocities and positions of all particles to improve the solution. Indeed, the choice of the PSO parameters will have a large impact on optimization performance (calculation time and accuracy). However, PSO algorithms use less parameters compared to other methods such as artificial neural networks and basic principles allow to define some of them more easily. Since 2006, the Standard Particle Swarm Optimization (SPSO) gathers these principles (Maurice Clerc, 2012; Zambrano-Bigiarini et al, 2013). Here, we use the following configuration for standard optimizations:

- Number of iterations: *variable;*
- Number of particles in swarm: 40;
- Cognitive acceleration coefficient: 2.8;
- Social acceleration coefficient: 1.3.

These parameters can always been modified depending on the problem and expectations. As an example, a compromise can be found between calculation time and accuracy by changing the number of iterations and particles.

3.2. Methods

According to the approach chosen in this paper, the most direct method would be to extract the five electrical parameters from (eq. 5) using a PSO algorithm. However, it is known that some of these parameters are interrelated or correlated to other parameters such as the short-circuit current I_{sc} or the open-circuit voltage V_{oc}. The advantage of these two variables is that they can also be obtained by measurements.

If we set the current to 0 in (eq. 4), the voltage takes the value of the open-circuit voltage V_{oc}:

$$I_{ph} - I_0\left(e^{\frac{qV_{oc}}{nkT}} - 1\right) - \frac{V_{oc}}{R_{sh}} = 0 \quad \text{(eq. 7)}$$

If we set the voltage to 0 in (eq. 4), the current takes the value of the short-circuit current I_{sc}:

$$I_{ph} - I_0\left(e^{\frac{qI_{sc}R_s}{nkT}} - 1\right) - \frac{I_{sc}R_s}{R_{sh}} = I_{sc} \quad \text{(eq. 8)}$$

From these two equations, it is possible, for example, to express n in terms of V_{oc} or I_{sc}:

$$n = \frac{qV_{oc}}{kT\ ln\left(\frac{-V_{oc}}{I_0R_{sh}} + \frac{I_{ph}}{I_0} + 1\right)} \quad \text{(eq. 9)}$$

$$n = \frac{qR_sI_{sc}}{kT\ ln\left(\frac{-I_{sc}R_s}{I_0R_{sh}} + \frac{I_{ph} - I_{sc}}{I_0} + 1\right)} \quad \text{(eq. 10)}$$

This approach allows to extract only four parameters with the PSO algorithm and to determine the fifth with (eq. 9) or (eq. 10). Moreover, it should increase the robustness of the optimization if we have reliable data for V_{oc} or I_{sc}.

4. Application

4.1. Comparison with a synthetic IV curve

In order to test the methods proposed in this paper, it is interesting to work with a synthetic IV curve. This approach presents many interests. First, this type of curve corresponds to perfect curve (without measurement noise) and allows to assess the maximum accuracy which can be reach by the model. As we know the exact value of all the parameters it is also possible to evaluate the accuracy of each of them and their impact on overall model performance.

Here, we use a set of parameters representative of a silicon solar cell (at $T = 306\ K$) and reported in several literatures (Ye et al., 2009):

- $I_{ph} = 0.7608\ A$;
- $I_0 = 3.223 \times 10^{-7}\ A$;
- $n = 1.4837$;
- $R_s = 0.0364\ \Omega$;
- $R_{sh} = 53.76\ \Omega$.

It is also required to determine V_{oc} and I_{sc}, which are used in this method. The exact value of I_{sc} can be directly calculated from (eq. 5) using the Lambert W-function. From this equation, it is also possible to extract the value of V_{oc} using a numerical solver such as *fsolve* function in MATLAB environment.

To determine the best approach, we compare the three possibilities presented in 3.2. The first consists in the application of a PSO algorithm to extract the five parameters from the IV curve. The other two are based on the same PSO algorithm but use V_{oc} and I_{sc} for the calculation of the diode ideality factor n with (eq. 9) or (eq. 10). In each case, we set the same initial values and boundaries:

- $I_{ph} = \max(I) \in [\max(I) ; 1.02 \max(I)]\ A$;
- $I_0 = 1 \times 10^{-6}\ A \in \left[1 \times 10^{-10} ; 1 \times 10^{-4}\right] A$;
- $n = 1.5 \in [1 ; 2]$ (not used when calculated with V_{oc} or I_{sc});
- $R_s = 1\ \Omega \in \left[1 \times 10^{-5} ;\ 1 \times 10^{2}\right] \Omega$;
- $R_{sh} = 1\ \Omega \in \left[1 \times 10^{-3} ;\ 1 \times 10^{5}\right] \Omega$.

The initial values are quite far from the researched parameters and the boundaries are large enough to match different types of solar cells.

To compare these methods, we run 10 simulations with 1000 iterations and 40 particles in each case. First, we focus on the error made on the current I by calculating the Mean Absolute Error (MAE) for each simulation. All the results are presented in Fig. 3 and show important variations between the three methods.

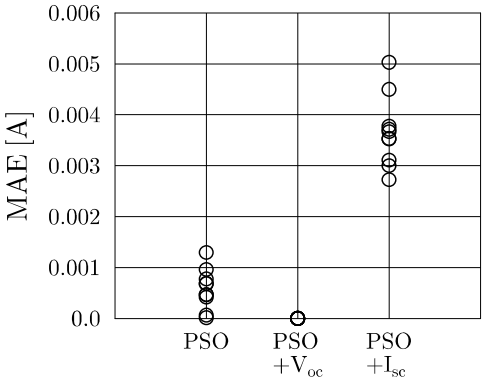

Fig. 3: Performance of the three methods on 10 simulations

The use of the PSO to extract the five parameters provides a MAE between 1.45×10^{-5} and $1.29 \times 10^{-3}\ A$. Even if these errors seem quite low, their differences show that the method is not particularly robust. Moreover, these errors still have an important impact on the electrical parameters, as seen in Fig. 4. As an example, the most impacted parameter, I_0, has a relative error varying between 1.80% and 244%. If we need a very high precision on parameters (relative error lower than 2% for each parameter), only one simulation in ten fulfilled this condition here. To ensure this precision each time, it will thus be necessary to run many simulations which will be time consuming if we apply this method on several solar modules with a low time step. It should also be noted that we did not observe any effect of error compensation between parameters. In each case, the lowest error on current is obtained when each parameter is the closest to its real value. We thus clearly observe that the optimization of this method to further reduce the error is not meaningless and will lead to a better extraction of parameters.

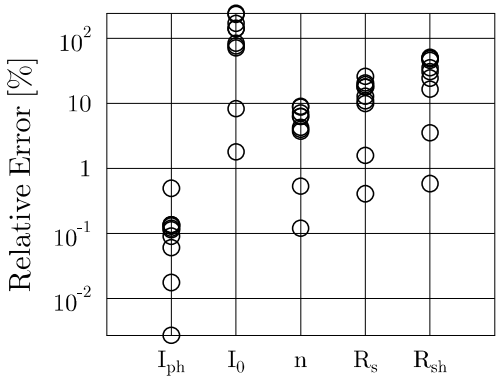

Fig. 4: Relative error of electrical parameters extracted by PSO on 10 simulations

As shown in Fig. 3, the addition of (eq. 9) with V_{oc} calculation significantly improves the performance of the optimization. We observe that all simulations tend to the exact solution, with a MAE of about $1.45 \times$

$10^{-17}\ A$, leading to a perfect extraction of all electrical parameters. This method is thus more robust and could be further improved by determining the best algorithm complexity (number of particles and iterations) while maintaining a high precision. The Fig. 5 also shows that much less iterations are necessary to reach a satisfying result. If we are looking for a MAE of about $10^{-5}\ A$, which corresponds to a near perfect extraction of parameters, we observe that 150 iterations are enough when we use the PSO combined with (eq. 9). If necessary, this result allows to bring an important decrease of calculation time.

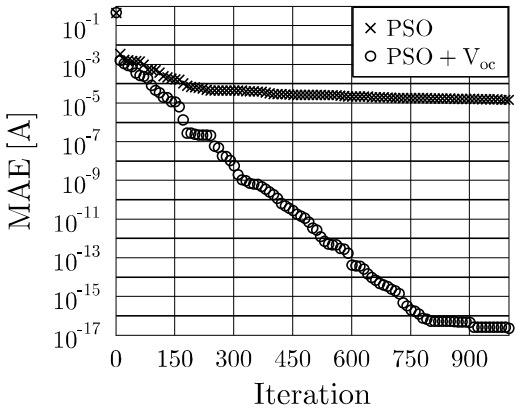

Fig. 5: Evolution of MAE depending on number of iterations

The third case, based on the addition of (eq. 10) with I_{sc} calculation, does not share the same results. Even if the approach is similar, the MAE is varying here between 2.72×10^{-3} and $5.03 \times 10^{-3}\ A$. This precision is thus not satisfying compared to the other methods and does not allow to obtain a reliable extraction of parameters. This difference comes from a stability problem due to the use of (eq. 10). In order to solve this equation, it is necessary to have a positive logarithm and thus:

$$\frac{-I_{sc}R_s}{I_0 R_{sh}} + \frac{I_{ph} - I_{sc}}{I_0} + 1 > 1 \qquad \text{(eq. 11)}$$

Which leads to:

$$\frac{1}{I_0}\left(I_{ph} - I_{sc}\left(1 + \frac{R_s}{R_{sh}}\right)\right) > 0 \qquad \text{(eq. 12)}$$

As I_{ph} is known to be very close to I_{sc}, this equation will often lead to a negative result and thus to an impossible solution during the optimization, decreasing its performance. To improve this method, it is possible to define more efficiently the boundaries and the initialization of the PSO algorithm. However, these conditions will change depending on the technologies studied and this lack of robustness is not suitable for this type of model. Here, the use of V_{oc} appears to be a more robust and reliable method.

4.2. Impact of uncertainties

In the application proposed in the previous section, we used a synthetic IV curve which has allowed to determine the exact value of all parameters. In a real case, even with high accuracy measurements, we have to deal with uncertainties. Here, we want to assess the impact of V_{oc} uncertainties on current and thus on electrical parameters extraction. As the ideality factor n is calculated from V_{oc}, the uncertainties on this parameter necessarily induce a loss of precision. In Fig. 6, we present this impact on the optimization (MAE on current I). In each case, 10 simulations have been run with a percentage error x such as $V_{oc,er} = V_{oc} \pm x(\%)V_{oc}$. We still observe the robustness of the method as all simulations tend to the same result for a given error x. However, it should be noted that a very high precision on V_{oc} is required to obtain reliable results. Indeed, this parameter appears to be very sensitive as we observe an almost linear relationship between the errors on V_{oc} and I.

The applicability of this method thus highly depends on both the precision of measurements and the precision desired for electrical parameters. For our application, we estimate that a MAE of about $10^{-4}\ A$ is more than enough to obtain a reliable extraction of electrical parameters. Here, it allows to extract all

parameters with the following relative errors: 5.03×10^{-3} % for I_{ph}, 6.65 % for I_0, 0.42 % for n, 1.58 % for R_s and 0.57 % for R_{sh}. However, it still requires an error of less than 0.1 % on V_{oc}, which may be difficult to achieve.

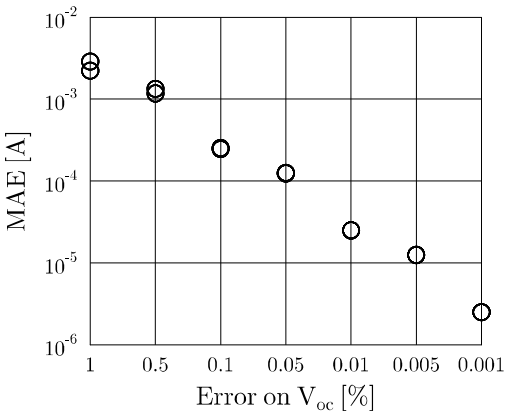

Fig. 6: MAE on current I depending on the error on V_{oc}

With higher error on this parameter, the standard method (direct optimization of all electrical parameters by PSO) could lead to a decrease of overall uncertainty. It is thus needed to compare also these two methods with more realistic IV curves, which may be subjected to measurement noise. For this purpose, it is possible to add a noise in current to assess its impact on parameters extraction. Here, we add a white Gaussian noise with a variance of 0.01, as presented in Fig. 7.

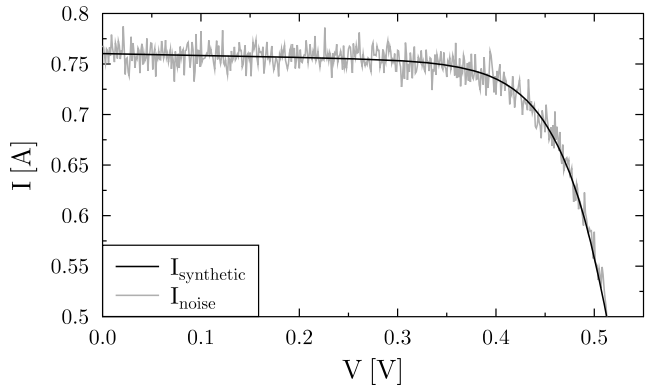

Fig. 7: Synthetic and noisy IV curves (zoom between 0.5 and 0.8 *A*)

In this case, it seems necessary to modify the boundaries of I_{ph}, as $\max(I)$ is no more an accurate value to rely on. We now use the following boundaries: $I_{ph} \in [0.95 \max(I) ; 1.05 \max(I)]$ A, which are broader than the previous ones. For the noisy IV curve, the two methods present an identical error on current I, with a minimal MAE of about 7.67×10^{-3} A on ten simulations. However, as in the previous cases, we still obtain a better robustness of the optimization by using the V_{oc}. Moreover, the electrical parameters are also more accurate with this method, as presented in Tab. 1. The only exception is observed for I_{ph} but the error remains low and the difference is not significant.

Even with noisy IV curves, the method proposed in this paper, based on the use of V_{oc}, still appears to be the best choice to extract the electrical parameters. These results could be probably improved with data processing such as filtering and smoothing which is a perspective of this work and will be assessed on real IV curves.

Tab. 1: Comparison of the two methods on a noisy IV curve

	Real values	PSO	PSO + V_{oc}	Relative Errors (%)	
				PSO	PSO + V_{oc}
I_{ph}	$0.7608\ A$	$0.7600\ A$	$0.7619\ A$	0.11	0.14
I_0	$3.223 \times 10^{-7}\ A$	$7.597 \times 10^{-7}\ A$	$2.464 \times 10^{-7}\ A$	135.71	23.54
n	1.4837	1.5737	1.4574	6.06	1.78
R_s	0.0364 Ω	0.0298 Ω	0.0372 Ω	18.13	2.07
R_{sh}	53.76 Ω	83.55 Ω	42.73 Ω	55.42	20.51

5. Conclusion

In this paper we proposed an alternative method to extract the electrical parameters from IV curves with a single diode model. The calculation of the diode ideality factor based on the open-circuit voltage allows to improve the parameters extraction with a Particle Swarm Optimization algorithm. In comparison with a direct optimization of all parameters, which is often used, this method provides much more accurate results. With a synthetic IV curve, it is possible to reach a MAE on current of about $10^{-17}\ A$, leading to a perfect extraction of parameters. This method is also more robust, as we reach similar precision for each simulation with less iterations. Even if a high accuracy on the open-circuit voltage is needed to obtain such results, we observed that it is still applicable for noisy IV curves which are more representative of real measurements.

In the framework of DURASOL project, this study will be applied on real IV curves from different solar PV devices. The next step of this work will thus focus on the real data processing (filtering and smoothing) and on their interpretation. The main contribution will concern the use of this valuable information in order to assess correlations between PV degradations and environmental conditions.

6. Nomenclature

Name	Symbol	Units
Temperature	T	K
Voltage	V	V
Open-circuit voltage	V_{oc}	V
Current	I	A
Short-circuit current	I_{sc}	A
Photocurrent	I_{ph}	A
Reverse saturation current of the diode	I_0	A
Diode ideality factor	n	-
Series resistance	R_s	Ω
Shunt resistance	R_{sh}	Ω
Boltzmann constant	k	$m^2.kg.s^{-2}.K^{-1}$
Elementary charge	q	C

7. Acknowledgements

This work concerning the DURASOL platform has been financed by the French National Research Agency through the French "Invest for Future, EQUIPEX".

8. References

AlRashidi, M.R., AlHajri, M.F., El-Naggar, K.M., Al-Othman, A.K., 2011. A new estimation approach for determining the I–V characteristics of solar cells. Solar Energy 85, 1543–1550. doi:10.1016/j.solener.2011.04.013

Askarzadeh, A., Rezazadeh, A., 2012. Parameter identification for solar cell models using harmony search-based algorithms. Solar Energy 86, 3241–3249. doi:10.1016/j.solener.2012.08.018

de Blas, M.A., Torres, J.L., Prieto, E., García, A., 2002. Selecting a suitable model for characterizing photovoltaic devices. Renewable Energy 25, 371–380. doi:10.1016/S0960-1481(01)00056-8

del Valle, Y., Venayagamoorthy, G.K., Mohagheghi, S., Hernandez, J.-C., Harley, R.G., 2008. Particle Swarm Optimization: Basic Concepts, Variants and Applications in Power Systems. IEEE Transactions on Evolutionary Computation 12, 171–195. doi:10.1109/TEVC.2007.896686

El-Naggar, K.M., AlRashidi, M.R., AlHajri, M.F., Al-Othman, A.K., 2012. Simulated Annealing algorithm for photovoltaic parameters identification. Solar Energy 86, 266–274. doi:10.1016/j.solener.2011.09.032

Fritsch, F.N., Shafer, R.E., Crowley, W.P., 1973. Solution of the transcendental equation we^w= x. Communications of the ACM 16, 123–124.

Gottschalg, R., Rommel, M., Infield, D.G., Kearney, M.J., 1999. The influence of the measurement environment on the accuracy of the extraction of the physical parameters of solar cells. Meas. Sci. Technol. 10, 796. doi:10.1088/0957-0233/10/9/306

Ishaque, K., Salam, Z., 2011. An improved modeling method to determine the model parameters of photovoltaic (PV) modules using differential evolution (DE). Solar Energy 85, 2349–2359. doi:10.1016/j.solener.2011.06.025

Ishaque, K., Salam, Z., Mekhilef, S., Shamsudin, A., 2012. Parameter extraction of solar photovoltaic modules using penalty-based differential evolution. Applied Energy 99, 297–308. doi:10.1016/j.apenergy.2012.05.017

Jain, A., 2004. Exact analytical solutions of the parameters of real solar cells using Lambert W-function. Solar Energy Materials and Solar Cells 81, 269–277. doi:10.1016/j.solmat.2003.11.018

Jervase, J.A., Bourdoucen, H., Al-Lawati, A., 2001. Solar cell parameter extraction using genetic algorithms. Meas. Sci. Technol. 12, 1922. doi:10.1088/0957-0233/12/11/322

Jordan, D.C., Kurtz, S.R., 2013. Photovoltaic degradation rates - an analytical review. Progress in photovoltaics: Research and Applications 21, 12–29.

Jordan, D.C., Wohlgemuth, J.H., Kurtz, S.R., 2012. Technology and climate trends in PV module degradation, in: Proceedings of the 27th European PV Solar Energy Conference. Frankfurt, Germany, pp. 118–124.

Macabebe, E.Q.B., Sheppard, C.J., van Dyk, E.E., 2011. Parameter extraction from I–V characteristics of PV devices. Solar Energy 85, 12–18. doi:10.1016/j.solener.2010.11.005

Maurice Clerc, 2012. Standard Particle Swarm Optimisation.

Mekhilef, S., Saidur, R., Kamalisarvestani, M., 2012. Effect of dust, humidity and air velocity on efficiency of photovoltaic cells. Renewable and Sustainable Energy Reviews 16, 2920–2925. doi:10.1016/j.rser.2012.02.012

Phinikarides, A., Kindyni, N., Makrides, G., Georghiou, G.E., 2014. Review of photovoltaic degradation rate methodologies. Renewable and Sustainable Energy Reviews 40, 143–152. doi:10.1016/j.rser.2014.07.155

Priyanka, Lal, M., Singh, S.N., 2007. A new method of determination of series and shunt resistances of silicon solar cells. Solar Energy Materials and Solar Cells 91, 137–142. doi:10.1016/j.solmat.2006.07.008

Qin, H., Kimball, J.W., 2011. Parameter determination of Photovoltaic Cells from field testing data using particle swarm optimization, in: 2011 IEEE Power and Energy Conference at Illinois (PECI). Presented at the 2011 IEEE Power and Energy Conference at Illinois (PECI), pp. 1–4. doi:10.1109/PECI.2011.5740496

Sandrolini, L., Artioli, M., Reggiani, U., 2010. Numerical method for the extraction of photovoltaic module double-diode model parameters through cluster analysis. Applied Energy 87, 442–451. doi:10.1016/j.apenergy.2009.07.022

Sharma, V., Chandel, S.S., 2013. Performance and degradation analysis for long term reliability of solar photovoltaic systems: A review. Renewable and Sustainable Energy Reviews 27, 753–767. doi:10.1016/j.rser.2013.07.046

Skoczek, A., Sample, T., Dunlop, E.D., 2009. The results of performance measurements of field-aged crystalline silicon photovoltaic modules. Progress in Photovoltaics: Research and Applications 17, 227–240. doi:10.1002/pip.874

Tamrakar, R., Gupta, A., 2015. A Review extraction of solar cell modelling parameters. IJIREEICE 55–60. doi:10.17148/IJIREEICE.2015.3111

Vázquez, M., Rey-Stolle, I., 2008. Photovoltaic module reliability model based on field degradation studies. Progress in Photovoltaics: Research and Applications 16, 419–433. doi:10.1002/pip.825

Ye, M., Wang, X., Xu, Y., 2009. Parameter extraction of solar cells using particle swarm optimization. Journal of Applied Physics 105, 94502. doi:10.1063/1.3122082

Yuan, X., He, Y., Liu, L., 2014. Parameter extraction of solar cell models using chaotic asexual reproduction optimization. Neural Comput & Applic 1–13. doi:10.1007/s00521-014-1795-6

Zambrano-Bigiarini, M., Clerc, M., Rojas, R., 2013. Standard particle swarm optimisation 2011 at cec-2013: A baseline for future pso improvements, in: Evolutionary Computation (CEC), 2013 IEEE Congress on. IEEE, pp. 2337–2344.

Zhang, C., Zhang, J., Hao, Y., Lin, Z., Zhu, C., 2011. A simple and efficient solar cell parameter extraction method from a single current-voltage curve. Journal of Applied Physics 110, 64504. doi:10.1063/1.3632971

Multi-objective genetic algorithm for the optimization of a PV system arrangement

Freitas, S.[1], Serra, F.[1], Brito, M.C.[1]

[1] Instituto Dom Luiz (IDL) - Faculdade de Ciências, Universidade de Lisboa (FCUL), Campo Grande, 1749-016 Lisboa, Portugal

Abstract

Urban landscapes feature complex topographies and many shadow casting elements, which can jeopardize the energy yield of building integrated photovoltaic (BIPV) systems. Phenomena like partial shading have a significant impact in the electric performance of PV modules, mostly when systems are deployed in conventional arrangements regardless of surrounding obstructions. The goal of this assessment is to test a multi-objective genetic algorithm (MOGA) in order to find one optimal string sizing and tiling, considering two different scenarios: a west facing building facade and a south facing rooftop, both located in Lisbon, Portugal. Relevant loss mechanisms are considered, such as hourly solar irradiance changes caused by shadow events, high incidence angles and module temperature. Optimization processes allow a reduction of around 24% and 23% in the cost of energy for the rooftop and the facade, respectively, when compared to a scenario that considers individual modules with micro-inverters.

Keywords: *Photovoltaic, partial shading, genetic algorithm, multi-objective optimization*

1. Introduction

Planning a PV system often relies on software-based approaches that employ averages of solar radiation and ambient temperature for the desired location. When non-obstructed areas are under consideration, such simplistic methodologies might be reliable as a means to estimate energy yields. However, when there is complex dynamic shadow casting (typical in urban environments), the incident solar radiation can vary dramatically throughout the day, requiring a more detailed system sizing procedure: as the connection between solar cells and modules is done in series (PV strings), partial shadow on one of the modules significantly impacts the production of the whole string.

Shadow patterns cast on surfaces make this a non-trivial problem for systems optimization. These problems cannot be fully represented and solved through well-defined mathematical expressions, since they deal with continuously changing and entangled variables. When a problem has neither a unique and obvious solution or the search space is overly large, or even if the problem has more than one objective, Genetic Algorithms (GA) (Goldberg, 1989) are numerical modelling procedures that can be used to reach one possible optimal solution. GA rely on the replication of the behavior of natural evolution of species in nature, and for that purpose populations of individuals are created, which are then subject to selection, recombination and mutation operators.

A different approach would be to avoid numerical optimization and invest in micro inverters as an alternative to conventional string based systems (Kurokawa et al., 1997). Micro inverters are immune to output power drop when a module is partially shaded thus avoid mismatch losses. Nevertheless, their installed power cost is higher and maintenance can be costly and hard to perform in urban environments, such as in vertical mounted systems.

The goal of the present assessment is to address two different surfaces to test a multi-objective GA aiming at maximizing the PV production of the system and minimizing system costs (wiring, module and inverter costs). The relevant losses to the system are considered together with solar radiation changes caused by shadow events. The solutions obtained are compared with micro inverter scenarios.

2. Methodology

In order to estimate the PV production of a system, solar radiation data is mandatory. However, while solar radiation long-term measurements in the horizontal plane are somewhat common, measurements on the tilted plane are rare, which demands the employment of a solar potential algorithm adapted to a 3D environment. The SOL model was used (Redweik et al.,2013) to calculate annual solar irradiance in a 3x6m^2 south facing rooftop

doi:10.18086/swc.2015.05.16 Available at http://proceedings.ises.org

and a 7x5m^2 west facing building façade (Fig. 1), obtained from a digital surface model (DSM) of the district of Campo Pequeno, in Lisbon, Portugal (38.74N, 9.15W), with 1m^2 resolution. A local typical meteorological year (TMY) data set allows hourly irradiation calculations for any point of the DSM, taking into account mutual shading between buildings and other urban elements.

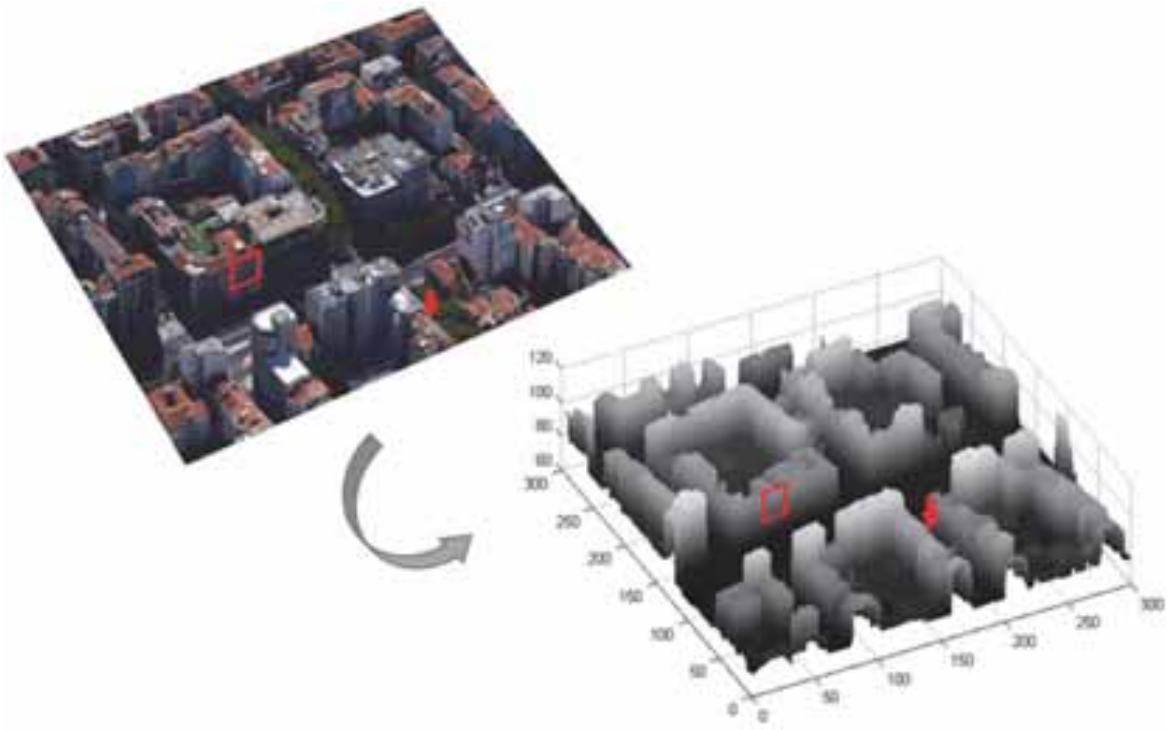

Figure 1 – Bird's eye perspective for the area under analysis and the respective digital surface model (DSM). The rooftop and façade case-studies are indicated in red.

The electricity production estimate considering relevant losses to the PV system typical 1m^2 PV module characteristics were considered and employed in the following equations (Marion, 2002):

$$T_{m,p,t} = T_{a,t} + \frac{T_{NOCT} - 20\ ^{o}C}{800\ W m^{-2}} G_{p,t} \quad \text{(eq. 1)}$$

where T_a is the ambient temperature in °C, NOCT is the Nominal Operating Cell Temperature, G is the Global irradiation on the tilted plane in Wh/m^2, the index *m* identifies one module, the index *p* identifies a position on the layout and *t* is the time index.

The effect of the temperature on the efficiency of each PV module can be estimated through (eq. 2) while the expected angular losses due to the angle of incidence in the panels is given by (eq. 3):

$$\eta_{m,p,t} = \eta_{ref}\left[1 + \Delta\eta(T_{m,p,t} - 25)\right] \quad \text{(eq. 2)}$$

$$AL_{\alpha,t} = \frac{\left(1 - e^{-\cos\alpha,t/a_r}\right)}{\left(1 - e^{-1/a_r}\right)} \quad \text{(eq. 3)}$$

where α is the irradiance angle of incidence and a_r the angular losses coefficient (Martin et al., 2001).

Then, as PV modules are connected in series in a string, by knowing the positions of the modules that belong to each string in the surface, the hourly expected energy yield in Wh of all PV strings can be estimated by:

$$E_{s,t} = min\left(G_{p,t}\eta_{m,p,t}AL_{\alpha,t}\right) n_{m,s} A \eta_{i,s} \quad \text{(eq. 4)}$$

where the index *s* identifies a PV string, the index *p* identifies the positions of the modules belonging to string *s*, $n_{m,s}$ is the total number of modules in string *s*, A = 1m^2 is the module area, and $\eta_{i,s}$ = 0.95 denotes an average

efficiency of the inverter *i* connected to string *s*. The *min*() function reflects the fact that the current in a string is determined by the lowest module current in that string.

The PV production function of a system layout with n_s strings can be defined by adding the hourly PV yield of all strings throughout the year:

$$E_{syst} = \sum_{s=1}^{n_s} \sum_{t=1}^{n_t} E_{s,t} \quad \text{(eq. 5)}$$

The total systems cost of a certain PV layout is assumed to cover three components: the cost of the modules plus the copper wiring required to connect the modules in series and the inverters needed to the conversion of the output current from DC into AC. Since the purpose of the optimization is the selection of the layout but not the full financial project evaluation of the project, no maintenance or operating costs nor discount rates were taken into account in the system costs function[1], which is defined by:

$$C_{syst} = C_m \sum_{s=1}^{n_s} n_{m,s} + \sum_{s=1}^{n_s} L_s C_s + \sum_{i=1}^{n_i} C_i \quad \text{(eq. 6)}$$

where L_s,and C_s are the length and wire costs for string *s*, respectively, and C_i is the cost of each of the chosen inverters for the PV system. A module price C_m= 150€/m^2 was considered. Thus, the first summation refers to the modules' costs, the second summation to the wiring costs and the third one to the inverters' costs.

The typical constraint of 3% for the maximum voltage drop allowed on a PV string was assumed. Regarding the inverters, in order to distribute the PV strings to a set of inverters, two main constraints must be calculated to prevent unfeasible solutions: $N_{m,i}$ the maximum number of modules connected in a string (eq. 7) and $N_{s,i}$ he maximum number of strings connected to a certain inverter *i* (eq. 8).

$$N_{m,i} \leq \frac{min\left(V_{s\_max}, V_{DC\ max,i}\right)}{V_{oc}[1 + \beta(-10 - 25)]} \quad \text{(eq. 7)}$$

$$N_{s,i} \leq \frac{I_{DC\ max,i}}{1.25 I_{sc}} \quad \text{(eq. 8)}$$

The relevant properties of 13 inverter models were considered (Table 1), including the maximum values allowed for the DC input current I_{DCmax}, the DC input voltage V_{DCmax},and the DC input power P_{DCmax}, as well as prices.

Table 1 – List of 12 inverter and 1 micro-inverter models.

Model	Pnom [kW]	Average price [€][2]	Vcc_max [V]	Icc_max [A]	Pcc_max [kW]
SMA micro	0.24	150	45	8.5	0.24
Fronius 1.5-1	1.5	893	420	13.3	1.5
Fronius 2.0-1	2	916	420	17.8	2
Fronius 2.5-1	2.5	938	420	16.6	2.5
Fronius 3.0-1	3	960	550	19.8	3
IG 20	1.8	832	500	14.3	2.70
IG 30	2.5	1220	500	19.0	3.60
IG 40	3.5	1568	500	29.4	5.5
Plus 60-V1	6	1474	600	27.5	6.32
Plus 70-V2	6.5	1579	600	30.0	6.88
Plus 80-V3	7	1678	600	32.0	7.36
Plus 100-V3	8	1693	600	37.1	8.43
Plus 120-V3	10	1885	600	46.2	10.59

[1] Thus assuming that the O&M costs are independent of the layout connection of the strings, which is an optimistic approach regarding the micro-inverter solution.

[2]Prices retrieved between December 2014 and August 2015 from (SMA, 2015), (CCL, 2014), (Energy Matters, 2014), (MG, 2014)

3. Results

The developed GA, fully described in Freitas et al., 2015, has achieved optimal solutions for the case-studies analysed in this paper with 23% and 24% lower costs of energy, and helped finding one possible solution to give the best trade-off between cost and energy yield.

Rooftop

The optimization process encompassed 50 individuals per generation, with 3% mutation rate, 10% elitism reinsertion rate and a maximum of 500 generations. The best individual in each generation has the lowest cost of energy (C_{syst}/E_{syst}) over a lifetime period of 25 years. In Fig. 2 the optimal layout for the partially obstructed rooftop under study shows 0.22€/kWh, with 5 clustered strings in the most sunlit areas and two places that have no modules (string number 0), while 0.29€/kWh corresponds to individual modules with micro-inverters.

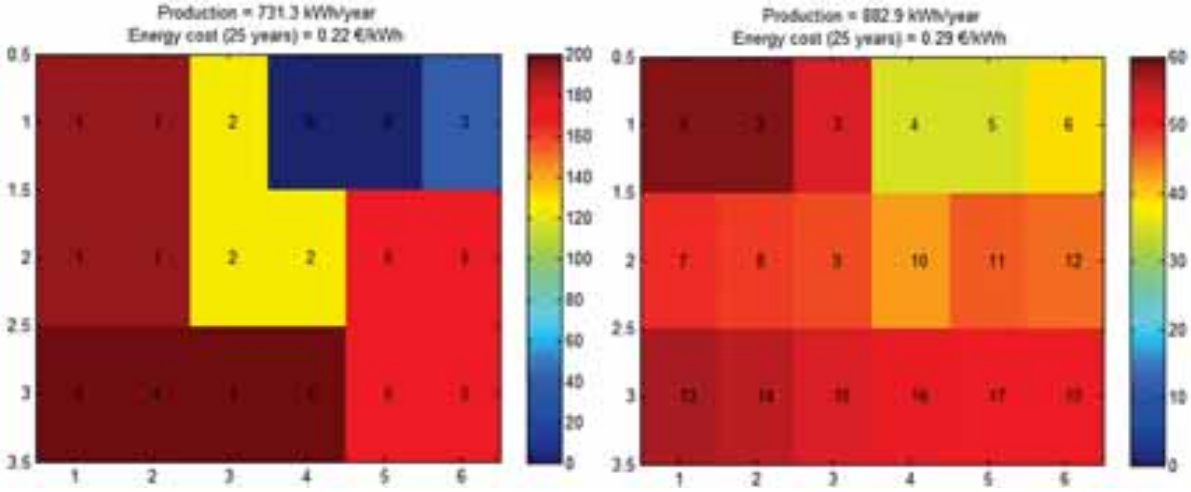

Figure 2 – On the plane perspective of the yearly total and per string PV production [kWh/year] of the optimized distribution of strings (left) and the micro-inverter scenario (right) for the rooftop case-study. Note the differences in the color scale values.

The overview of all individuals throughout the optimization process (Fig.3) reveals that 250 generations could have allowed for a decent optimal layout; however slight improvements were produced after. As all solutions are compared among each other based on their fitness, although some of the individuals with the best cost of energy are eliminated.

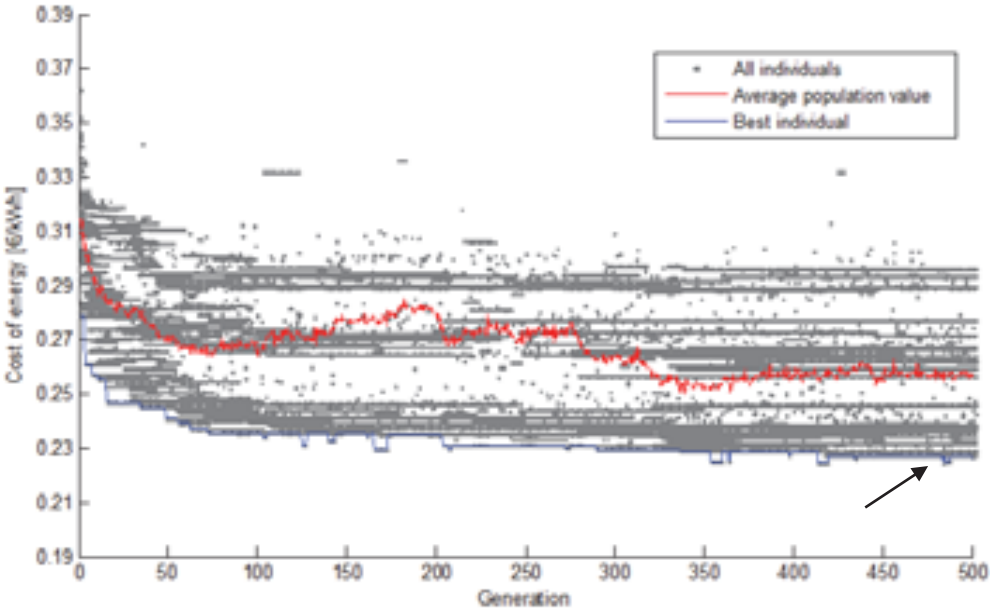

Figure 3 – Chart with the overview of the Cost of Energy in the course of the optimization process for the rooftop case-study.

All solutions in a generation can be organized in Pareto fronts (Fig. 4), i.e. groups of solutions which optimize both objectives (C_{syst} and E_{syst}) and that are compared among each other. The best fitted individuals belong to the highest Pareto front (red dots) and dominate all the other fronts. Looking specifically at the Pareto fronts

from the initial population and the last, the convergence of solutions throughout the generations is evident. Higher higher yielding solutions, at higher cost, are located in the right end of the front, while more affordable arrangements, but featuring lower electricity production, can be found in the left. The layout with micro-inverters is placed on the top right, achieving high yields but requiring very high investment, thus being far from the optimal solution (€/kWh).

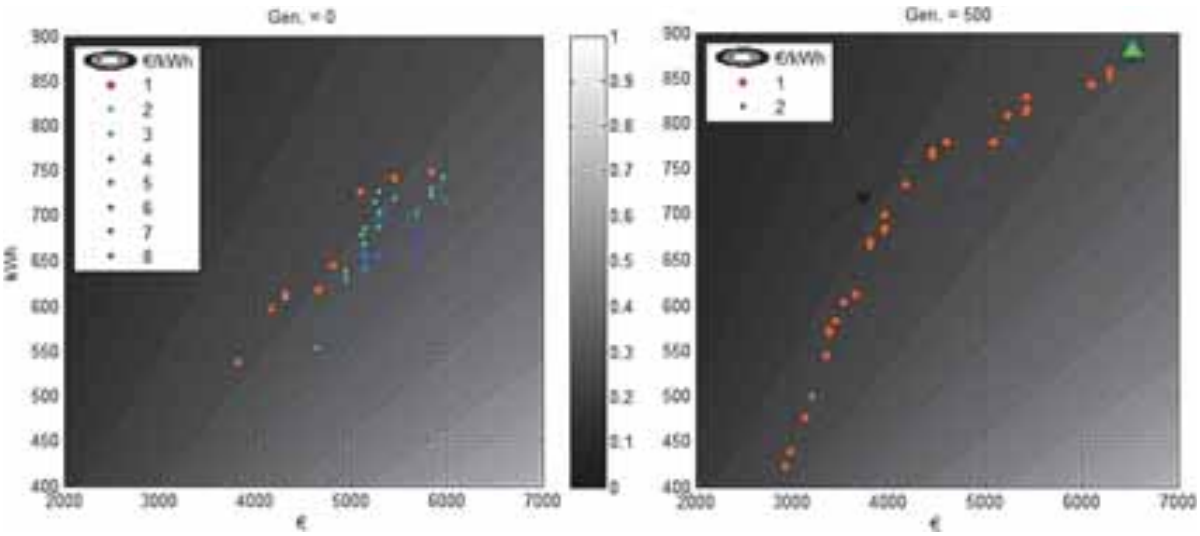

Figure 4 - Comparison between the Pareto fronts from the initial (left) and 500th (right) generations. The arrow points the individual with minimum €/kWh in 25 years of system lifetime (i.e. 0.22 €/kW h and 731 kW h/year) and the green triangle marks the location of the micro-inverter scenario.

Facade

The building facade case-study optimization followed the same procedure. In Figure 5 the optimal layout reveals that a west facing and also partially obstructed facade is able to match PV production of a rooftop in non-optimal conditions (0.30 vs 0.22 €/kWh). It is worth mentioning that this facade layout accounts for blanks that represent prohibited locations for modules, in this case due to windows or balconies.

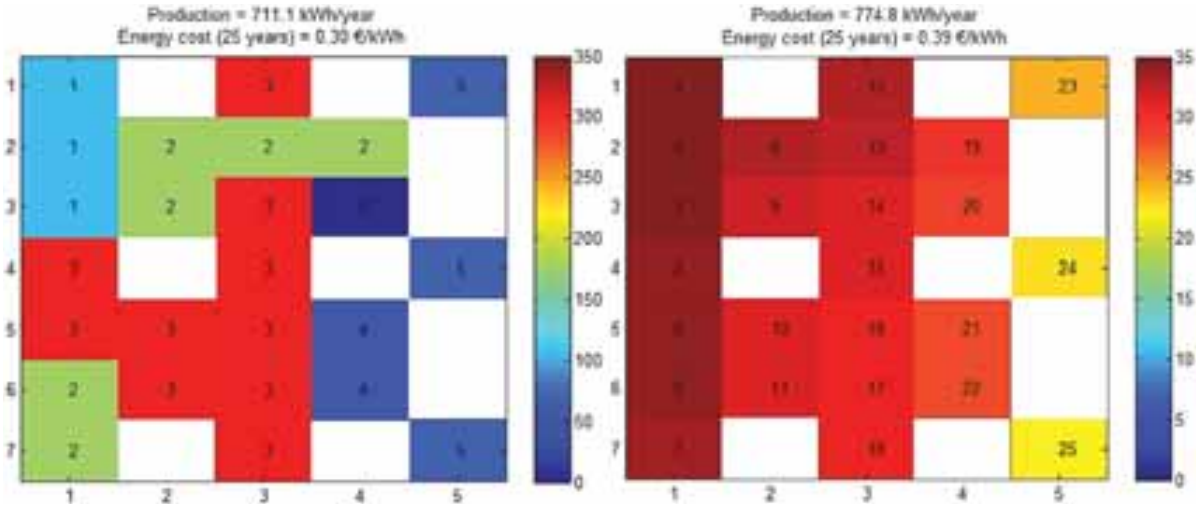

Figure 5 – On the plane perspective of the yearly total and per string PV production [kWh/year] of the optimized distribution of strings (left) and the micro-inverter scenario (right) for the facade case-study. Note the differences in the color scale values.

Again, optimization proves to be more cost-worthy than installing micro-inverters for all individual modules. The Pareto fronts of the initial population and 500th generation (Fig.6) also corroborate conclusions taken from the rooftop assessment.

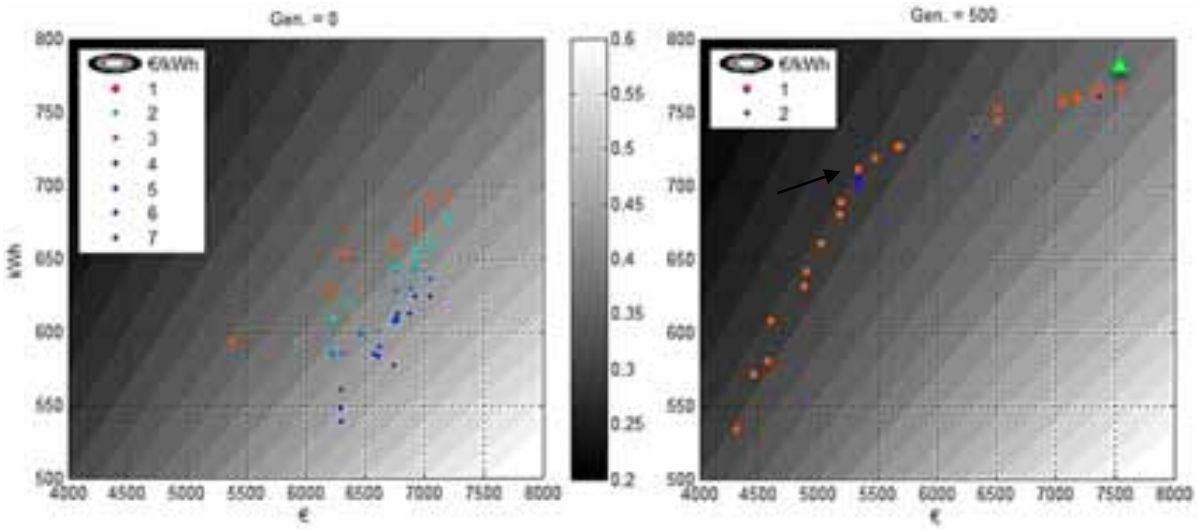

Figure 6 - Comparison between the Pareto fronts from the initial (left) and 500th (right) generations. The arrow points the individual with minimum €/kWh in 25 years of system lifetime (i.e. 0.30 €/kW h and 711 kW h/year) and the green triangle marks the location of the micro-inverter scenario.

4. Conclusions

A partially obstructed south facing rooftop and a west facing building facade were subject to a PV system sizing optimization using a multi-objective genetic algorithm (MOGA). This study aimed at the maximization of yearly energy yield, based on hourly solar radiation profiles obtained from a 3D urban-oriented solar potential model, and the minimization of wiring, modules and inverter costs, and the comparison with a micro-inverter scenario. Results show which PV string tiling strategies are more adequate in case the end-user has financial limitations or aims at the highest possible yield. By examining the arrangements with minimum cost of energy €/kWh, it is suggested that higher number of PV strings formed by individual modules using micro-inverters achieves the highest electricity yields, but the costs double those of the layouts with longer and clustered strings in the more sunlit areas. An improvement of 23% and 24% in the cost of energy is observed from the micro-inverter scenarios to the MOGA solutions.

5. References

Freitas, S., Serra, F., Brito, M.C., 2015. PV layout optimization: string tiling using a multi-objective genetic algorithm. Sol. Energy 118, 562 – 574

Goldberg, D.E., 1989. Genetic Algorithms in Search, Optimization, and Machine Learning. Addison Wesley

Kurokawa,K., Kamisako,K., Shimizu, T., 1997. Conceptual considerations on PV systems composed of AC modules. Sol. EnergyMater. Sol. Cells

Marion, B., 2002. A method for modeling the current–voltage curve of a PV module for outdoor conditions. Prog. Photovoltaics Res. Appl. 10, 205–214

Martin, N., Ruiz, J.M., 2001. Calculation of the PV modules angular losses under field conditions by means of an analytical model. Solar Energy Materials and Solar Cells 70, 25 – 38

Redweik, P., Catita, C., Brito, M., 2013. Solar energy potential on roofs and facades in an urban landscape. Sol. Energy 97, 332 – 341

SMA, Sunny Boy 240-US, Wholesale Solar. Retrieved August 2015 from:
http://www.wholesalesolar.com/products.folder/inverter-folder/SMA-Sunny-Boy-240-US.html

CCL Components, Fronius inverters. Retrieved December 2014 from:
http://www.cclcomponents.com/range.asp?ID=372

Energy Matters, Fronius IG. Retrieved December 2014 from:
http://store.energymatters.com.au/brand/fronius/products/inverters?show=48

MG Solar Shop, Fronius IG Plus. Retrieved December 2014 from: http://mg-solar-shop.com/fronius_ig_plus_150_v_3.html

6. Acknowledgments

Part of this work was supported by MIT Portugal Program for Sustainable Energy Systems and FCT grants SFRH/BD/52363/2013 and SFRH/BD/51377/2011, by Fundação Calouste Gulbenkian award and by project Suscity MITP-TB/C S/0026/2013.

Conference Proceedings

Solar World Congress 2015
Daegu, Korea, 08 – 12 November 2015

Bamiyan 1 MWp Solar Mini-Grid (Afghanistan)

Robert Foster[1], Tony Woods[2] and Ian Hoffbeck[3]

[1] Winrock International, Arlington, Virginia (USA)

[2] Sustainable Energy Systems International, Timaru (New Zealand)

[3] Future Solar Industries, Beirut (Lebanon)

Abstract

One of the world's largest solar mini-grids was installed for the community of Bamiyan in central Afghanistan in 2013. The 1 MWp photovoltaic/diesel hybrid mini-grid was installed by a partnership led by Sustainable Energy Services International (SESI) for the Government of New Zealand as part of international donor infrastructure development for the country. This paper details system design, operation, and lessons learned.

Keywords: *Mini-grids, photovoltaics, Afghanistan*

1.0 Introduction

Bamiyan formed part of the ancient Silk Road in central Afghanistan and lies 230 km northwest of Kabul at an altitude of >2,500 meters. The ancient history of Bamiyan is witness to the invasions of Genghis Khan in 1221, who massacred every person and living thing in Bamiyan at the still desolate "City of Screams." Marco Polo visited Bamiyan in1271 and wrote of its splendor and famed Buddha statues (sadly destroyed by the Taliban in 2001). Today the community is largely comprised of the Hazara ethnic group, and is a relatively peaceful haven designated as a UNESCO World Heritage Site (Rakotozonia, 2011). Bamiyan is also the gateway to Afghanistan's first national park at the beautiful Band-e Amir Lakes.

Due to its remote location and rugged terrain, Bamiyan has never been connected to the national electric grid, and only a modest diesel plant was used to supply power to the main bazaar area. Prior to the arrival of the solar mini-grid in Bamiyan in late 2013, some of the 20,000 villagers used small solar panels to provide some basic electric lights and communications for their homes. Some also used generators and rented out power to their nearby neighbors at an approximate cost of 300 Afs (~US$4.68) per bulb per month for four hours a day. This equates to around US$1.95 per kWh.. In the Mulah Ghulam neighborhood, the Afghan government through Ministry of Rural Rehabilitation and Development (MRRD) had also previously installed a diesel generator, but it did not operate for very long as with most diesel similar efforts in Afghanistan since diesel fuel was difficult to truck in and unaffordable for the residents. The absence of power metering for billing purposes also adds to the inability for isolated systems to achieve financial sustainability.

The New Zealand Ministry of Foreign Affairs (MoFA) approved development of a one MW solar-diesel hybrid mini-grid system, called the Bamiyan Renewable Energy Project (BREP) in 2012. The system was divided into three smaller systems in order to reach a larger customer base. An additional smaller system was initially planned for connection to the generator for the Bamiyan Bazaar. This plan was later modified for technical reasons. The equipment allocated for this smaller 40 kW system was reallocated for a system to power a portion of the community in the nearby Folaadi Valley.

Selection and/or peer review under responsibility of Scientific Committee
doi:10.18086/swc.2015.05.17 Available at http://proceedings.ises.org

The Bamiyan Renewable Energy Program (BREP) was contracted by the New Zealand Ministry of Foreign Affairs and Trade (MFAT) to provide power and built as a joint venture of Sustainable Energy Services International (SESI) and NetCon, both New Zealand registered companies. The BREP generation system provides high-quality, 230 V, 50 Hz electricity to about 1,800 households in several neighborhoods around the Bamyan City area. The installation began in August of 2012 with the system beginning operation in October, 2013. The total project cost was US$14.1 million, including all tranmission and distribution lines, capacity building and construction. After completion of construction, the system was given to Da Afghanistan Breshna Sherkat (DABS), the Afghan utility company who now wholly owns and operates the system. The BREP Project Developers included

- New Zealand Ministry of Foreign Affairs and Trade (MFAT)
- Sustainable Energy Services International: SESI (prime)
- DABS: Da Afghanistan Breshna Sherkat (national utility)
- NET Con (distribution)
- Stephenson & Turner Architects & Engineers
- Snowy Mountain Engineering Company: SMEC (review)

It should be noted that over the past four decades, several studies and falst starts have been made in Bamiyan to develop a small hydro-electric project. There exists sufficient hydro resource potential for developing a small ~750 to 1,000 kW hydro plant near Bamiyan in Topchi that could be implemented to help meet the growing energy needs of the community that will grow beyond the present solar mini-grid system. A complete feasibilty study and design for this proposed project was prepared by the USAID Afghanistan Clean Energy Program (ACEP) in 2010 by Winrock International (Winrock, 2010).

1.1 Initial Design Stages

The design of the system was definied and constrained by two factors. The first determination was the overall size of the community and the demand for energy. Secondly the budget available to meet the demand. The design of the system was undertaken by Sustainable Energy Services International. Primary considerations were:

- The average demand from each household, and time of day of consumption.
- The population size, and expectations of growth in population and power demand.
- Socioeconomic factors influencing system operation and management
- Environmental and human capacity factors impacting component selection

Average loads of 200 watts per household were allowed, and 1.5 kWh per household per day were estimated based on previous experience with rural electrification, and allowing some room for future growth in demand.

The system design expects either additional solar panels to be installed as the population and/or demand for power grows, or for the use of the diesel generator to increase to meet demand if additional investment in solar PV is not made.

The system is also designed to allow the solar PV and transmission/distribution network to be merged into the wider Afghan power network in future, with all components constructed to international standards.

Component selection was designed to allow for modular components for inverters that could survive the dust and heat of Afghanistan, and also be installed and maintained by semi-skilled staff. This led the designers to favour the AC bus architecture of SMA (Germany) equipment, coupled with the flooded lead acid technology of Crown Batteries (USA).

Key to the long term success of the project was for financial viability to be built into the project. Pre pay power meters were installed at each household, on the pole outside to reduce meter tampering and power theft. This has been successful. The tariff calculation was undertaken by DABS, and set at US$ 0.25 for domestic use and US$ 0.70 for commercial use. The contractor preferred a single flat tariff for all consumers

to avoid complication and more accurately reflect the cost of power for all consumers, but the split tariff was preferred by DABS.

To purchase power, consumers pay cash at the local bank into the DABS account, and then take the receipt to the DABS office who use an electronic dispensing unit to add power credits onto the consumer card. The consumer then takes the card back to their house and inserts the card into their meter to transfer the credit onto the meter. Consumers were required to purchase the prepay meter and consumer connection cable from DABS for the subsidised rate of US$30. DABS supplying the cable ensured that the correct cable quality was used. All household cables are buried, to reduce illegal temporary connections made to overhead lines.

2.0 Bamiyan Solar Mini-Grid Design and Components

The Bamiyan Renewable Energy Program (BREP) generation system provides 230 V, 50 Hz electricity to 2,400 households in several neighborhoods around the Bamyan City area. This 1,050 kW of power is divided between four generation sites: 400 kW at the Bamiyan New City site, 300 kW at the Hyderabad site, 300 kW at the Mullah-Gholam site and 50 kW at the Folaadi valley site. Each system has a main solar energy power plant and a backup diesel power plant. Each of the power generation sites is connected to a dedicated 20 kV transmission and 0.4 kV distribution system. These generation and distribution sites are not connected. The small site at Folaadi Valley connects directly to the distribution lines at 0.4 kV. A series of step down transformers reduces the voltages from the transmission lines and for supply into the distribution system. Each of the customer connections is 230 VAC and has a digital prepay electricity meter.

These provide energy to consumers 24 hours a day. For most of the year the solar energy system provides all of the power to the loads during the day while charging the batteries. During nighttime and times of poor solar insulation a diesel generator on site will automatically start and charge the batteries.

2.1 Power Generation

The solar modules provide the primary generation source, with the diesel as secondary source, and batteries for energy storage. Figure 1 below provides a visual representation of the generation system topography.

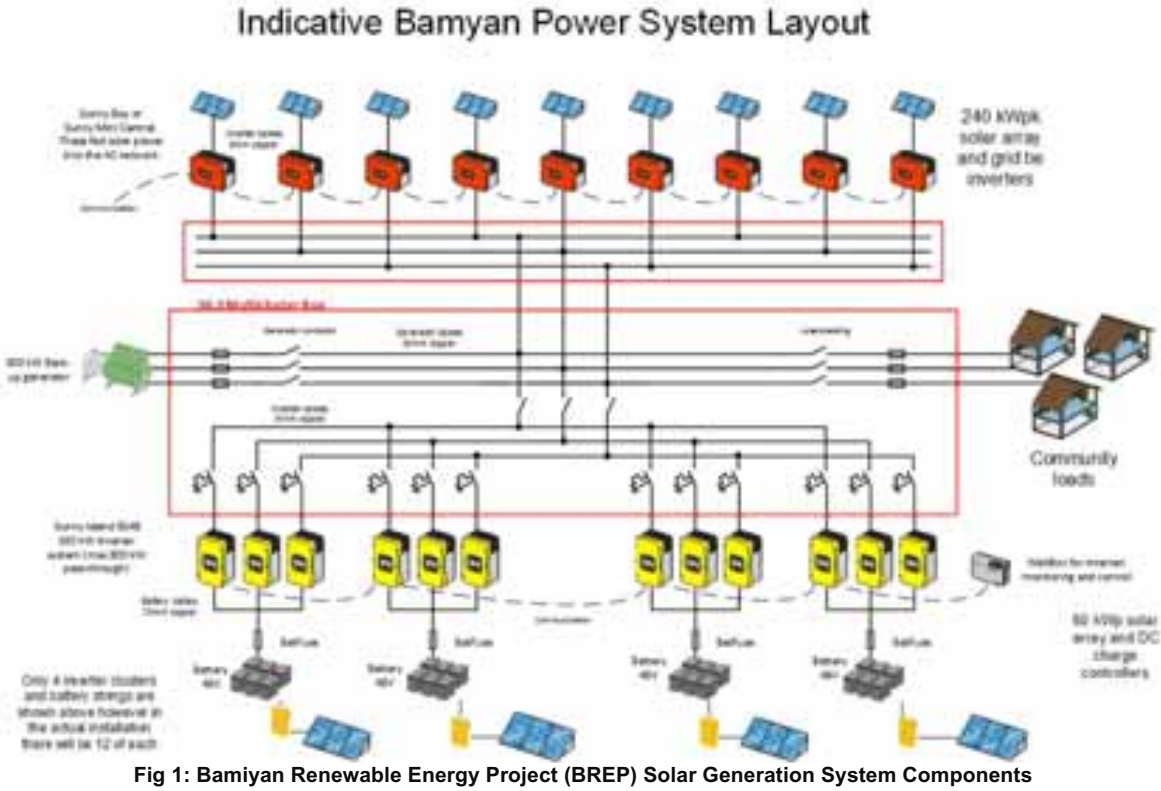

Fig 1: Bamiyan Renewable Energy Project (BREP) Solar Generation System Components

All components except for the solar modules, grid inverters, generator and transformer are contained within the powerhouse: an insulated, secured, weatherproof, and electrically grounded building on the grounds of the generation facility. All components are equipped with disconnects, allowing each component to be electrically isolated from any other component of the system. These disconnects variously include switches, fuses, relays and circuit breakers.

The primary power supply to the communities during daylight hours is directly from the solar arrays to the distribution network via the 3 phase AC inverters. Surplus power generation during the day is used to recharge the batteries, ready for use at night. The diesel generator is only used during bad weather or high demand periods.

2.2 Solar Modules and Inverters

Due to constraints of how much power can be sent to the batteries through the inverter/chargers, a small portion of the solar modules is directly connected to DC charge controller that uses the DC power to directly power the batteries. The battery inverters convert the DC power in the batteries to AC power that feeds to the grid. At the three large sites, the DC arrays consist of 288 modules; connected in arrays of 12 modules each to each charge controller. In total the system has 24 charge controllers, with two charge controllers each for the 12 battery banks. At Folaadi Valley, all 192 of the modules are connected to battery inverters. Each battery bank powers three battery inverters; with each of the three inverters providing one phase of power for the system. These 36 battery inverters all connect through the multicluster box that combines and controls power from the AC solar arrays, the diesel generator and also controls power fed back out to the grid.

The remaining solar modules are connected to the grid inverters. These are SMA three phase inverters installed at the site of the solar modules, and directly connected to the multicluster box. The site at Bamiyan New City has a slightly different configuration. It has 400kW of solar modules instead of the 300kW at Hyderabad and Mullah Gholam. This 100kW extra of solar modules is connected directly to the transformer. The Bamiyan New City generation site is connected to most of the high-power loads in Bamiyan City, including government buildings and large NGO offices. The design assumes that this portion of the city will experience higher day time loads from government offices and NGO's, thus the design is weighted towards higher day time power generation. The direct connection to the transformer bypasses the multicluster box and allows for the additional 100 kW of PV power to be supplied with minimal electrical losses.

The battery inverters are the "brains" of the power generation system. While all of the inverters are identical products, their software is configured differently to allow them to perform different functions. The 36 battery inverters are distributed into 12 clusters of three inverters each: one main cluster and 11 slave clusters. Each cluster has one master inverter and two slave inverters. The master inverter synchronizes the single-phase output of each inverter to create three-phase power output; controls the power draw from each of the two charge controllers for the cluster; and copies any changes in settings from itself to its two slave inverters. The main master inverter in the master cluster in turn controls these master inverters.

The master cluster has the same master-slave topography of the other clusters. However, it additionally controls the master inverter of each cluster. The main master inverter synchronizes the three-phase power output from each inverter; copies settings from itself to each of the main master inverters; and has the ability to start up or shut down the entire generation system. Not only does it control the master inverters, but it also controls some other elements of the system. These include the relays in the multicluster box for connecting and disconnecting the grid inverters, the battery inverters, the generator, and the transformer; a relay that remotely starts and stops the generator; and a relay that starts and stops the powerhouse ventilation fan.

Fig. 2: One of the Large BREP PV Arrays: 300 kWp at the Mullahghulam site

2.3 Diesel Generator

Each of the three large sites is equipped with a 275 kVA diesel generator made by FG Wilson. The diesel generator will automatically start when either the demand from the loads is more than the battery inverters and solar inverters combined can provide; or when the demand might cause the battery state of charge to drop to a low level. The generator is equipped with an external 3,000 liter fuel tank. The Folaadi valley site has a smaller 30 kW FG Wilson diesel generator. The main master inverter controls the autostart for the diesel generator at each site.

2.4 Battery Storage

The system uses flooded lead acid batteries manufactured by Crown (USA) for backup. Tab. 1 below gives the key parameters for the batteries used in the system.

Tab. 1. Battery Bank Parameters for the Bamiyan Solar Mini-Grid

Parameter	Value	Unit
Capacity	3750	Ah
Nominal Discharge Rate	20	hours
Nominal Operating Temperature	27	°C
Battery Voltage	8	V
Weight	860	kg
Cell voltage	2	V
Number of Cells	12	
Depth of Discharge	40	%
Cycle Life	3800-4000	Cycles
Batteries per Cluster	6	
Cluster Voltage	48	V
Batteries per Large Site	72	
Batteries at Folaadi Valley	12	
Total Batteries	228	

Each battery bank is charged and regulated by the two charge controllers in each cluster. As vented lead-acid batteries, the batteries must periodically have water added to the cells. To facilitate this process, each battery has a hose system connecting all of the cells. Each powerhouse is equipped with an automated battery watering system. This system consists of a water tank, a water deionizer and a battery-watering cart with a pump. This watering cart connects to the hose and automatically fills each cell to the appropriate level. The system is designed for a 40% depth of discharge. Under proper maintenance the battery bank should have a

lifetime of about 7 to 9 years of operation, or longer depending on how it is used and maintained. Figure 3 below shows the arrangement of the battery banks in the power house.

Fig. 3: Crown Battery Banks each at 48 V; 3,747 Ah at a C/20 Discharge Rate

2.5 Transmission and Distribution

The transmission and distribution system begins at the step up transformer at the generation site and ends at the customer connections. The three large systems produce 400V three-phase electricity at the generation site. A transformer at the generation site steps up the power from 400V to 20kV for transmission. At the interface between the transmission and distribution systems, another transformer steps down the 20kV three-phase electricity to 400V three-phase electricity. The network at Folaadi Valley has no 20kV portion due to the close proximity of the consumer loads, so no transformers are used.

Most of the loads in Bamiyan come from residential homes and hence are only single phase. Larger consumers, including government offices and businesses have a 3 phase supply and 3 phase meter. The distribution pole and lines used the original ACEP proposed distribution design for the Topchi hydro-power plant (Salinas, 2011). The transmission network was installed by NetCon, a New Zealand electrical lines company. The lines were built to New Zealand Standards and installed by professional NZ linesmen.

Each transmission and distribution network is equipped with a recloser that can automatically isolate the electrical lines from the generation source. In the case of faults on the line, the recloser will disconnect and reconnect the lines a few times to see if the fault opens. If the fault does not correct itself, the recloser will leave the lines disconnected until a technician can repair the problem.

Fig. 4: BREP electrical distribution system as installed by NetCon

Fig. 5: SMA Multi-cluster Hyderabad BREP Power House with Sunny Island Battery Charging Inverters

Fig. 6: SESI trained and utilized Afghan women technicians as part of the installation crew.

2.6 Interconnection Requirements

The generation system of the power planet produces 230 V electricity at 50 Hz. While this does match the power output of the rest of the Afghan grid, the system cannot connect with the rest of the Afghan electrical grid as currently configured. In order to connect, the Bamiyan system would have to synchronize to the grid signal. However, the battery inverters determine their own synchronization and are not able to synchronize to

an outside signal. If a utility operator would like to connect the Bamiyan system to an outside grid, the battery inverters and the batteries must be removed from the system. The grid inverters, however, can continue to be used after modifying the settings. This will allow the operator to reduce peak loads, but it will not allow them to store energy. As any outside system will likely have some manner of baseload power (e.g. hydro, gas) the system will not require the battery storage of the Bamiyan system. Ideally grid connection would occur before the lifetime of the batteries is completed. This will allow the solar modules to continue creating electricity without requiring the replacement of any energy storage equipment.

3.0 Community Development and System Operation

SESI maintained close contact with the community throughout the course of the project, soliciting their opinions and asking for support in construction and site monitoring. All of the local laborers were hired from communities nearby the power plant sites. In one community there was a problem with someone in the local community stealing grounding wires. The implementing partner worked with the local community to find the perpetrator and to prevent further theft in the future. Maintaining the support of the local community prevented members of the community from delaying the project or harassing the project staff.

The installation team encountered theft of system materials as a recurring problem. Specifically, some members of the local community would cut and steal the grounding cables used on the meter boxes in order to sell the copper for scrap. This problem persisted even when the issue was raised with the local leaders (shura). The project team was forced to delay livening the system in some communities for this reason. Operating the system is unsafe without proper grounding and so these communities had to wait until the theft stopped before they could be connected to the system. Most homes in Afghanistan on the national grid do not use grounding either and electrocution is a danger.

3.1 Metering and Tariffs

BREP uses a prepaid pay-as-you-go model for collecting revenue. This differs from the post-paid analog metered collection system common in the the rest of Afghanistan. Instead of the traditional analog electricity meter, each house is equipped with a digital meter that is charged by means of a charge card. The customer takes the card for their meter to the DABS office where they prepay for an amount of electricity. The DABS staff accepts their payment and adds value to their card by a dedicated charging machine housed in the office. The customer then takes this card back to the meter installed outside his or her home. They insert the card into the electrical meter, where the meter automatically subtracts the value from the card and adds it to it's own internal meter. The meter has a large backlit digital display that shows the current balance for the customer. When the balance reaches zero, the meter automatically disconnects the power.

Currently the electricity tariff is set at AFN 16 (USD $0.25) per kWh for residential customers and AFN 45 (USD $0.70) per kWh for government and business customers. However, the tariffs collected by DABS is not sufficient for the long term sustainable operation of the plant, which would require full depreciation of the batteries, solar PV and distribution lines to be deemed *fully sustainable*. This is actually much higher than the national tariff rate and represent as compromise. However, the cost of fuel alone for operating the plant on diesel backup is about 20 AFN (USD $0.30) per kWh. This means that any time the diesel generators are turned on, the plant is operating at a loss; even before taking into account costs other than diesel itself. The tariff should be high enough to pay for all of the fixed and variable operating costs of the plant as well as making extra money to replace equipment as it fails. The system currently covers all of its own operational and maintenance costs under the current tariff structure however as demands grow, and diesel consumption grows, the setting of the domestic tariff at a rate lower than recovery for diesel means that operating surpluses generated from running on solar PV will diminish over time.

There was some strong suggestions from development agencies to introduce load limiting systems in the supply to each household to *prevent households taking more than their fair share*. This was firmly rejected by SESI as it places a limit on growth, irresective of the willingness and ability to pay of consumers. Instead, our focus was on growing the system to meet demand and facilitate growth rather than the limiting of power and hence community development.

Gradually Bamiyan residents been signing up for the power system and willing to pay the interconnect fee. About 2,000 customers have signed up for BREP out of the 2,500 planned customers so far. Afghans often take a wait and see attitude to see if the system will work before signing up; they are also wary of the relatively high electric tariff as compared to their urban counterparts.

It is estimated that the system will be fully depreciated after 20 years, so the tariff would need to make, at least, 14 million dollars extra over the course of 20 years. As it stands, DABS are able to pay for variable costs of operation; including staff salaries, maintenance of equipment, tools and parts, but due to internal politics it heasitates to pay for fuel for the generators in winter. As of early 2015, DABS was requesting the government of New Zealand to still provide a diesel subsidy for the system operation and it has been shut down at times for lack of diesel fuel. Additionally, DABS must seek a capital injection or outside funding in order to replace equipment at the end of the equipment lifetime. This could be as early as 7 years from the date of installation in the case of the batteries. After parts start to fail, the entire system must be shut down until a new capital source is found.

3.2 System Operation and Maintenance

The largest capacity building need was educating the operator (DABS) about how to operate and maintain the plant. This including training DABS engineers and their participation in the installation of the system. In addition to the engineers, clerical and management staff was trained on how to properly manage an electrical system of this type, how to make customer connections, how to charge customer cards, and how to maintain an accurate accounting system. SESI-NetCon staff remained at the site to operate the system, allowing time to train DABS staff on the proper long-term maintenance of the system.

4.0 System Monitoring and Performance

Recognising the value of monitoring and evaluation to measuring long term project success or failure, Sustianable Energy Services International undertook on itself to perform detailed monitoring and evaluation activities with a professional social survey subcontractor to survey and record community attitudes and expectations on the project. These findings will be contrasted with a followup survey again to be undertaken by SESI and its subcontractor and a detailed report issued once 2 full years of operational data has been gathered.

Initial risks to public acceptance of the system related to the subsidy of other power networks elsewhere in Afghansitan, and the failure to use power meters on other smaller power networks in Bamyan prior to the BREP project. The lack of power metering and the reliance on the lightbuld basis of charging households for power menat that households were completely unaware of how much they actually paid for power. It was only with the introduction of power meters that they could compare their power costs with other cities, and then unfortunately they compared with subsidised power tariffs in cities like Kabul and Kandahar leading to incorrect perceptions that the people of Bamyan were being over-charged for power. This is despite the BREP solar installation reducing actual household power costs down from US$1.95 per kWh to US$0.25 per kWh. The willingness and ability to pay for power was clearly evident, and supported by the increasing demand for power measured over 2014/2015, however the public perception was based more on comparisons with other cities.

4.1 Online Monitoring

Each of the networks is monitored by a complete monitoring system that is web accesible via the local Bamyan cellphone network. The monitoring function allows online monitoring of error codes, power output, voltage and current, battery conditions and other core system parameters. This is extremely useful for troubleshooting and tuning the system to current needs, as well as additional support of DABS in the longer term. An example of the data gathered shown below in Fig. 1 below shows a typical operational period for the network in September 2015. The generator can be seen to have been required only once in this period, as shown by the green bars on the far left. The Total Multicluster Load Power (demand) can be seen shown by

the red line, and power output from the solar arrays by the blue line. The surplus power generated (kWh) is stored in the batteries and meets demand in the night hours.

Fig. 1: Example System Power Output and Load Demand

Expectations of power demand from the community have roughly met expectations, and power demand grew sharply in 2014 once the system was accepted by the community as being real and reliable. This is shown graphically in Fig. 2 below from monitoring from the installation at Hyderabad, one of the three large installations; which shows power demands from 2014 and 2015, and the average demand in bold.

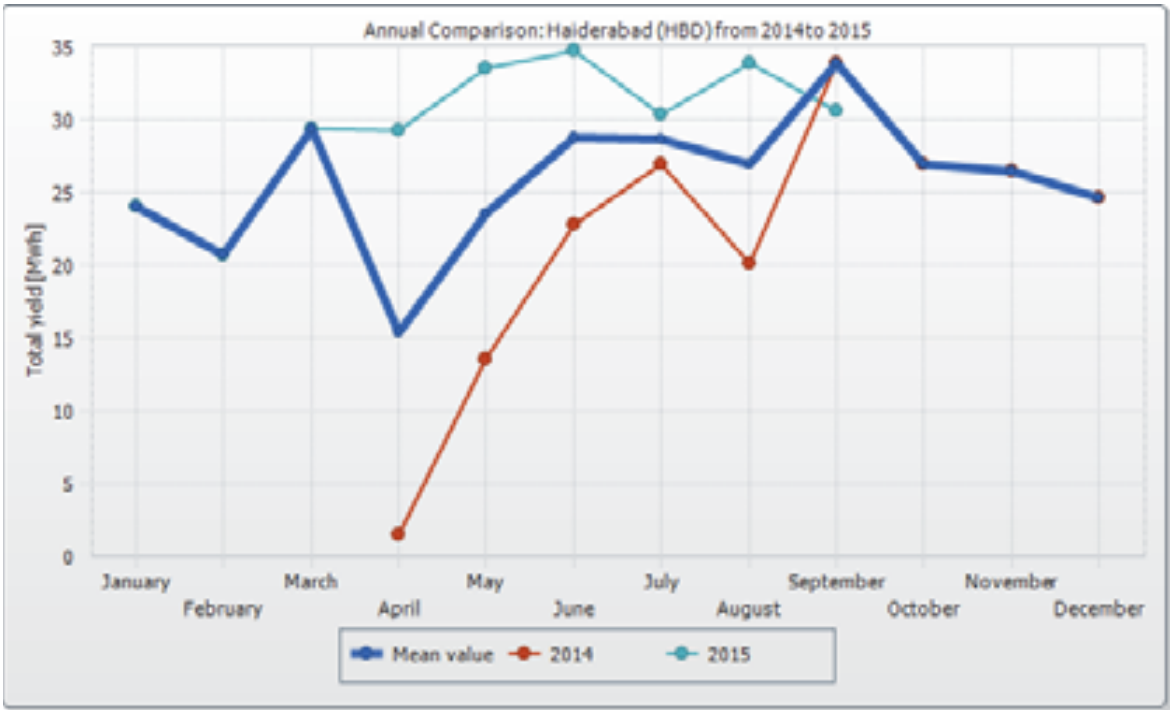

Fig. 2: Year to Year Energy Output Comparison at Hyderabad

5.0 Bamiyan Solar-Diesel 1 MW Mini-Grid LCOE Analysis

Markets currently serviced by diesel generators represent the largest potential market for many kinds of RE, especially solar energy which shares diesel's deployability across much of Afghanistan. To better understand the economics of solar-diesel mini-grids, an economic comparison between off-grid solar systems and diesel systems is considered for a real installed project in Afghanistan. This analysis compares the US $14 million (with T&D) 1 MW Bamiyan solar-diesel hybrid mini-grid energy system to an equivalent diesel only system. The diesel system considered is the same as the diesel backup generators powering the Bamiyan solar energy system, however they are operated more hours per day. The analysis assumes equal annual electricity sales for both systems.

5.1 Methodology and Assumptions

Two calculations are compared in this analysis. The first is the levelized cost of energy (LCOE) for both systems and the second is the net present value (NPV) for each system given an average sale price of the electricity generated. The LCOE calculation first considers the net present value of all costs associated with production of the system over its lifetime. This levelized cost is divided by the estimated energy production over the lifetime of the system, yielding the LCOE.

To assess the financial viability of the systems, a NPV calculation were performed. The profits for each year of the 20 year lifetime were calculated. Then all of these profits were discounted to present dollars, yielding the value of the system in today's dollars.

Electricity sold is considered instead of electricity generated because diesel generators often operate at only a proportion of their highest-efficiency loading. Because the solar system has battery backup, nearly all of the electricity produced can be sold. An exchange rate of 57 AFN per USD was used. A mid-range diesel price of 66 AFN per liter was used reflecting the Central Statistics Organization Q3 2014 data (however, current diesel prices in Bamiyan have recently come down to only 48 AFN per liter but can be expected to go back up in the future). DABS Bamyan currently offers a two-tiered tariff system: 16 AFN per kWh for residential consumers and 45 AFN per kWh for commercial consumers. This analysis assumes that 90% of the energy sold will be to residential customers, giving an average revenue of 17.9 AFN per kWh. Horizontal solar radiation was conservatively estimated at 5.0 kWh per square meter per day from a 2007 NREL estimates discussed in the solar resource section.

This analysis also assumes proper operation of the system. The battery depth of discharge is currently set at 40%, which the vendor (SESI) estimates will allow for a 12 year operational lifetime of the battery bank (depending on user operaiton and battery abuse, it could only be half of this lifetime). There will be some short-term incentive to set the depth of discharge lower (eg. 50%-80%). This will dramatically reduce the operational lifetime of the batteries and necessitate several replacements over the operational life of the system. A discount rate of 10% was assumed for the investments.

5.2 Life Cycle Cost of Energy (LCOE) Analysis

The table below shows key values determined by the analysis for both the solar and diesel systems. The LCOE of energy for the diesel only case was calculated at US$0.32 /kWh, while that for the solar diesel was calculated at US$0.46/kWh (about mid-range). The solar system may actually cost more depending on battery replacements. The LCOE for the solar system without batteries would be about half of this estimate.

Tab. 2. Bamiyan 1 MW Solar-Diesel Mini-Grid Analysis

Parameter	Diesel	Solar-Diesel
LCOE	$0.32	$0.46
NPV at Current Tariff	-$4,550,152.85	-$10,338,220.81
Average Tariff Needed for Profitability	AFN 48.4 (USD $0.61)	AFN 74.4 (USD $1.31)
NPV Sensitivity to Diesel Prices (Per dollar change)	$4.29 million	$0.26 million

Neither the solar-diesel nor the diesel only system is profitable at the 90% residential sales ratio. The solar system achieved a positive revenue flow, but was never able to make up for it's capital outlay if full cost recovery is desired. The diesel system never attained a positive cash flow. The solar system requires a somewhat higher tariff in order to reach profitability. It is likely that future projects similar to the Bamiyan project will be able to be completed with a lower capital outlay as PV prices continue to decline. The Bamiyan project was the first of it's kind in the region, and one of the top three largest solar-diesel mini-grids in the world. The solar system is much less susceptible to fluctuations in diesel prices. Because of the volatility of petroleum prices, this analysis assumed a constant price of diesel fuel as it is difficult to predict what the future costs will be. Such a scenario is unlikely and diesel prices will likely increase and decrease

over the 20-year analysis timeframe. The solar system will be much more able to maintain a long-term profitability in this respect. At current tariffs, DABS will have to subsidize future battery bank replacements for the DABS solar-diesel mini-grid if the wider national grid does not extend into Bamyan before the battery banks require replacement.

6.0 Key Success Factors

Three key factors contributing to the project's success are technical operation, safety, and long-term financial viability. Successful technical operation was completed after livening of the system, providing power to the customers, and demonstrating that the design goals of the system are met. Risks to the long-term successful operation of the system focus mainly on the technical capacity of DABS to operate the system and retain the trained staff needed to support it. This includes the need for DABS to invest in the system to cope with the inevitable growth in demand that can be expected with any commercial power supply network.

Success in safety will be partially determined by the proper operation and maintenance of the system. This could be jeopardized if the system is damaged, improperly maintained, or if public awareness and education about the system flags.

Future risks to the long term viability of the project in future include:

- Potential lack of access to qualified support staff, both commercially and inside DABS
- Potential lack of support from DABS Kabul to respond to needs of the local Bamyan DABS office
- Reduced consumer support if the system reliability is not maintained.
- Inability to perform scheduled maintenance and maintain an adequate depreciation account for future parts replacement and upgrade.
- Employee graft reducing financial viability of the system.
- Theft of system components.
- Over-subscription of electricity services inducing system failure.
- Encroachment of the ongoing conflict in Afghanistan to the area.

The long-term financial viability will determine if the system is operated adequately to arrive at the end of its useful design life. Proper financial management will play a key role in this success. This will include setting and maintaining proper electricity tariffs, preventing theft and fraud, as well as proper operation and maintenance to ensure correct system function long term.

7.0 References

Rakotozonia, Michael, 2011. Topchi Small Hyro Project: Archaeological Survey, report submitted to USAID Afghanistan Clean Energy Program, Kabul, Afghanistan.

Salinas, Oscar, 2011. Bamiyan Small Hydro Project: Distribution Report, NRECA, report submitted to USAID Afghanistan Clean Energy Program., Kabul, Afghanistan.

Winrock International, 2010. Topchi Small Hydropower Project (1000 kW): Detailed Feasibility and Engineering Report, submitted to USAID Afghanistan Clean Energy Program, Kabul, Afghanistan.

Conference Proceedings
Solar World Congress 2015
Daegu, Korea, 08 – 12 November 2015

Feasibility Study on Thermoelectric Conversion to Improve Photovoltaic Operation

Ma. Liwanag O. Montayre and Erees Queen B. Macabebe

Department of Electronics, Computer and Communications Engineering, School of Science and Engineering, Ateneo de Manila University, Quezon City 1108, Philippines

Abstract

Thermoelectrics (TE) is an emerging technology with a wide range of potential applications namely recapturing energy lost as wasted heat from burning fossil fuels as well as serving as a cooling agent. One viable application is to integrate thermoelectric devices with photovoltaic (PV) modules that suffer from performance issues because of heat. This study proposes a model where the TE device can help lower the temperature of the PV modules which will optimize its performance through an increase in generated output. The same device can also increase the total output power from the combined PV-TE system when the TE acts as a generator. The PV-TE system was simulated using Matlab software and results show that there is potential in using TE technology as coolant and generator improve the performance of the PV device. Experiments and actual deployment also reveal an improved output for the combined PV-TE system.

Keywords: *Thermoelectric cooling/generator, Photovoltaic module, conversion efficiency, PV-TE system, Seebeck coefficient, temperature difference*

1. Introduction

Fossil fuel energy has been constantly scrutinized for its negative impact on the environment. Not only does it harm the environment with its carbon emissions and depletion of natural resources that are running out fast, it is not as efficient as it seems. When power plants burn fossil fuel to produce electricity, only a fraction (roughly one-third) of it is converted to useful energy while the rest of it is lost as waste heat (Jones, 2012). Efforts have been made to recover this untapped source of energy and one of the best ways to achieve this is through thermoelectric technology.

Thermoelectrics (TE) uses a temperature gradient to generate electricity. This is made possible by two different semiconductor materials coupled together, arranged electrically in series and thermally in parallel (Rowe, 2006). When a temperature gradient is applied to it, current flows through the system resulting in a voltage difference. This phenomenon is called the Seebeck Effect. When voltage is applied instead, a temperature difference occurs which results in heating on one end and cooling on the other. This is called the Peltier Effect. A third phenomenon occurs called the Thomson Effect that plays a negligible role in the operation of practical thermoelectric modules (Tellurex, 2010).

Thermoelectrics is still a niche technology that is not widely used in the market due to the poor energy conversion efficiency of its devices. Given the right application however, its unique characteristics could prove beneficial. The most popular of these applications is cooling and refrigeration owing to its precise temperature control.

While thermoelectrics is not a well-known category in the field of renewable energy, photovoltaic (PV) technology is its most prominent. Unfortunately it is also susceptible to issues of conversion efficiency. Heating of the photovoltaic PV modules above standard conditions causes performance issues where the device suffers losses in performance efficiency due to high temperature due to high irradiance conditions which also lead to cell degradation (Najafi and Woodbury, 2012). Temperature affects the speed of electrons

doi:10.18086/swc.2015.05.18 Available at http://proceedings.ises.org

flowing through a circuit. The lower the temperature, the lower the resistance in the circuit, the better the performance (Teach Engineering, 2015). Increasing the temperature on the other hand will reduce the band gap of the semiconductors in the PV cells leading to more energy of the electrons which is not ideal in order to break the bond (PV Education, 2015). Cooling the solar cells allows them to function at a higher efficiency and produce more power. Increasing conversion efficiency of any alternative power generation system is crucial because conventional means of producing energy is cheaper.

A feasibility study on a photovoltaic-thermoelectric hybrid system was conducted by Van Sark where an idealized model was able to calculate the employment of present day thermoelectric materials that could lead to efficiency enhancements of up to 23% for roof integrated PV-TE modules. Instead of simple module cooling methods, the study proposed utilizing the thermal waste by attaching thermoelectric converters to the back of the PV modules resulting in a PV-TE hybrid module (Van Sark, 2011). A more comprehensive model of the combined system of the PVT-TEG was developed and simulated by Najafi and Woodbury (2013) where the TE Generator is also employed to convert the heat generated by photovoltaic or thermal collectors into electricity. The model illustrated a very detailed heat transfer process where the TE modules convert the temperature gradient to electricity and generate additional power from the excess heat which is an improvement to the overall performance of the system. Another approach by Park et al. (2013) focused on optimal hybridization between the PV and TE devices by using "full spectrum solar energy" by means of lossless coupling between the devices in hopes of reaching the ideal for efficient harnessing of solar energy. These studies have indicated that attaching a TE device to a PV device has improved the conversion efficiency and power output of the photovoltaic module.

The use of thermoelectric conversion as a strategy to mitigate the issue has been examined where a PV-TE hybrid utilizes thermal waste. Thermoelectric devices make ideal cooling agents because they are solid-state materials that are reliable, durable and compact, with zero maintenance, no noise and no mechanical parts (Teach Engineering, 2015). This paper proposes integrating TE devices, which actively use heat, to PV modules as its cooling mechanism. PV-TE systems have been explored in the past however the type of integration that is modeled in this study attempts to make use of the TE device's two functions albeit not in a simultaneous manner.

2. Designing theoretical models for feasibility testing

2.1. Visualized Model of Proposed PV-TE System

A layout of the design of the PV-TE model is shown in Fig.1 where a solar PV module was deployed. Data of the PV without any TE attachments was first collected and acted as the control. The data output was examined in contrast with PV data of the setup installed with TE devices.

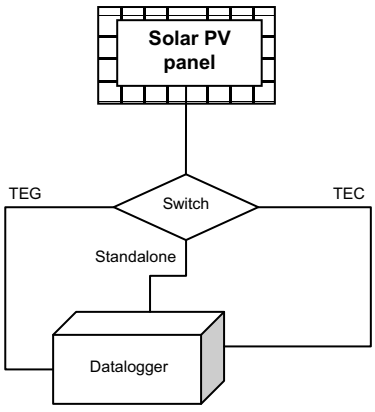

Fig. 1 Layout design of model to study the feasibility of the PV-TE System

The TE system alternated between energy harvesting mode and cooling mode as seen in Fig. 2. Data of the PV with TE attachments in generator or cooling mode were collected and compared with PV-only set of

data. Note that the TE device as a generator is an accepted form of cooling and has been an examined approach by many previous authors (Van Sark, 2011; Najafi and Woodbury, 2013; Park et al., 2013) as it absorbs heat from the PV modules so it can convert it to energy. This can be seen as a passive form of cooling, whereas when the TE device is in its actual cooling mode, this would be an active or forced form of cooling.

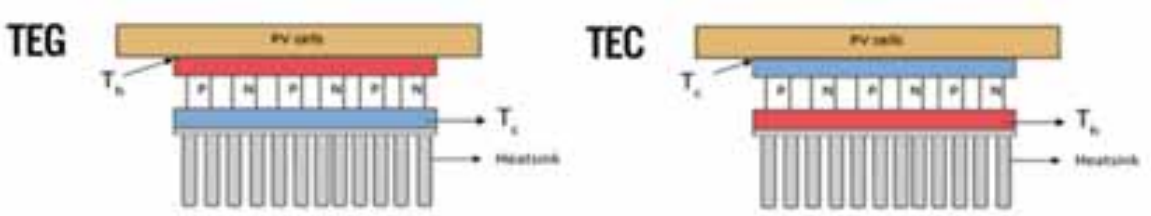

Fig. 2 Schematic of the PV-TE Section with (left diagram) in *generator* mode; and (right diagram) in *cooling* mode

As the TE system shifted from generator to coolant, the thermal equilibrium between the ambient air and PV was observed. The system remained a generator during parts of the day as it is judged to be more effective. It switched to a coolant during times it was seen more effective as such.

2.2. Mathematical Modeling

Typical TE module equations are described in existing literature (Diaconescu and Grigorescu, 2009) where the generator output voltage is given as follows:

$$V = S_M \Delta T = I\left(R_M R_L\right) \qquad \text{(Eq. 1)}$$

Where S_M is the device's Seebeck coefficient and $\Delta T = T_H - T_C$, I is the current through the load, R_M is the averaged module resistance and R_L is the load resistance. The current I through the load is given in Eq. (2) where N_S is the number of TE modules connected in series, and N_P is the number of TE modules connected in parallel.

$$I = \frac{N_S S_M \Delta T}{\left(\frac{N_S R_M}{N_P}\right) + R_L} \qquad \text{(Eq. 2)}$$

The general expression for generator output power P is typically given as the product of voltage V and current I but can also be calculated as seen in Eq. (3) derived from Eqs. (1-2) where N_T is the number of TE modules used and is calculated as $N_T = N_S \times N_P$.

$$P_{TE} = VI = R_L\left(\frac{S_M \Delta T}{R_M + R_L}\right)^2 = \left(\frac{N_T\left(S_M \Delta T\right)^2}{4R_M}\right) \qquad \text{(Eq. 3)}$$

The output power of the PV-TE system is the total of the power of the TE derived from Eq. (3) and output power of the PV derived from collected experimental data using the equation for power at the maximum point as given in Eq. (5) where E is the irradiance and A is the area of the PV module.

$$P_{PVTE} = P_{PV} + P_{TE} \qquad \text{(Eq. 4)}$$

$$P_{PV} = \frac{P_{\max}}{EA} \qquad \text{(Eq. 5)}$$

In thermoelectric cooling, precise temperature control is its strongest feature. The Peltier effect allows for a cold surface to cool to a temperature T_C and a hot surface to cool to a temperature T_H. This is made possible by the given equation described by Khattab et al. (2005):

$$V = S_M\left(T_H - T_C\right) + R_M I \qquad \text{(Eq. 6)}$$

3. Simulation and Hardware Design

3.1. Physical model and assumptions

The TE device used for the study is the commercially available TEC12706. The device is a single stage module that contains 127 pairs of thermoelectric p-type and n-type elements made of Bismuth Telluride with two terminals in dissimilar colors (black and red). This device has interchangeable polarity. The basic performance parameters of this TE device are listed in Table 1. (Ferrotec Corporation, 2014)

Table 1: Performance Parameters of the TEC12706

Parameter	Value
Dimensions	40mm x 40mm x 3.8mm
Maximum Operating Temperature, T_{max}	90 ~ 100 °C
Maximum Temperature Difference, ΔT_{max}	70 °C
Maximum Operating Voltage, V_{max}	15 V
Maximum Current, I_{max}	6 A
Maximum Cooling Power, Q_{max}	50 W
Resistance, R	1.98 Ω

Prior to performing simulations, the following assumptions are adopted to simplify the problem:

- The solar TEG is in steady-state.
- The configurations of the p-type and n-type elements are identical.
- The thermoelectric elements are connected electrically in series and thermally in parallel.
- The whole system is in a vacuum environment, so the heat loss due to heat convection is neglected. (Chen et al., 2013)
- The heat sink is not included in the computations, and the ambient temperature is assumed to be a constant specified by the weather report for that day.

The TE device is characterized by three parameters that are most vital in modeling its capabilities: namely, the module Seebeck coefficient, resistance and thermal conductivity. These properties can be approximated through manufacturer data. (Ferrotec Corporation, 2014)

Table 2: Performance Parameters of the GP005PA PV Module

Parameter	Value
Dimensions	190mm x 290mm x 15mm
Peak Power, P_{max}	5 W
Maximum Power Voltage, V_{mp}	18.29 V
Open Circuit Voltage, V_{oc}	22 V
Maximum Power Current, I_{mp}	0.273 A
Short Circuit Current, I_{sc}	0.3 A
Cell Efficiency	16.0 %

The PV device is a 5-Watt GP005PA acquired from local electronics retailer Alexan. It is a polycrystalline module with 36 cells connected in series in a 2x18 layout. The module has a voltage temperature coefficient of 0.32%. Table 2 presents the parameters of the solar PV module used in this study according to the device's datasheet.

3.2. Technical Feasibility Tests through Simulation

Simulation of the TE system's generator performance was accomplished through applying the mathematical

models in the matrix laboratory (MATLAB) software. The TE system was assumed to be installed to the backside of a PV module, where the latter acted as the former's heat source. Data gathered on PV performance—module temperature, irradiance, maximum power—together with corresponding meteorological data—average air temperature—available online (Weather Underground, 2014) as well as manufacturer data (Ferrotec Corporation, 2014) of the TE properties—module Seebeck coefficient, resistance, thermal conductivity—were utilized. Fig. 3 shows the general structure of how the software runs.

The same software technique was used to determine the total output power generated by a combined PV-TE system. This was compared with the output generated by a standalone PV system and analyzed.

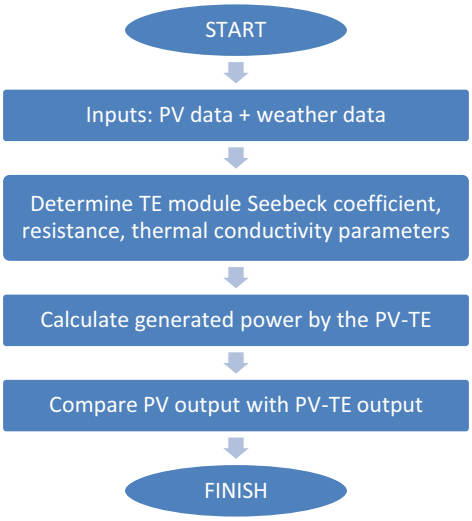

Fig. 3 Flow of the software program

Determining the thermal effect of the TE on the PV module was achieved through the relationship of the open circuit voltage (V_{OC}) of the PV with temperature. Among the attributes of the PV, the effect of temperature is most apparent to the V_{OC} (PV Education, 2015). A V_{OC} versus temperature profile of the GP005PA was used to model the thermal effects on the output of the PV:

$$V_{OC} = -0.0169T + 10.445 \qquad \text{(Eq. 7)}$$

Data results from the combined performances of the two simulations of TE as generator to PV and TE as coolant to PV were collected and evaluated against a PV-only model. Using Eq. (4) the study was able to determine the total output power of the system which is analyzed against the characteristics of a PV-only system.

3.3. Hardware Implementation

A simple hardware implementation was designed to test the proposed PV-TE system. A total of eight modules of the TEC12706 were fitted on the backside of the GP005PA and were connected in series. They were attached and distributed evenly to the backside of the PV module. Each TE device had heat sinks attached to the side not in contact with the PV. Thermal paste was used to ensure thermal contact between the components. Additional metal reinforcement was added to secure the components in place and to act as an extra heat sink to dissipate the heat. LM35 probes were inserted to log temperature data for analysis.

The PV-TE system was first deployed in a controlled environment indoors to determine the best parameters for use in outdoor conditions. A 500-Watt Tungsten Halogen lamp was chosen as a light source because its spectra matches closely to that of the sun. Experiments were carried out under a 110 W/m^2 rating for irradiance with a 2-hour duration. The current-voltage (I-V) curve tracer developed by Peña et al. (2013) was used in this study for the characterization of the PV modules.

Outdoor deployment was carried out on a rooftop with the devices propped on a metal stand. The duration for each collection of data took around 6-7 hours from morning until late afternoon. Data for all circuits were logged using Arduino software which were later processed in MATLAB and Microsoft Excel.

4. Results and Discussion

4.1. Device Characterization

The eight TEC12706 TE devices used in the study were characterized individually then in series by means of applying electrical current to them in increments. Fig. 4 shows the corresponding graph for the characterization of the TE devices in series. It shows the linearity of V versus ΔT curve. Thus, ΔT increases as voltage increases.

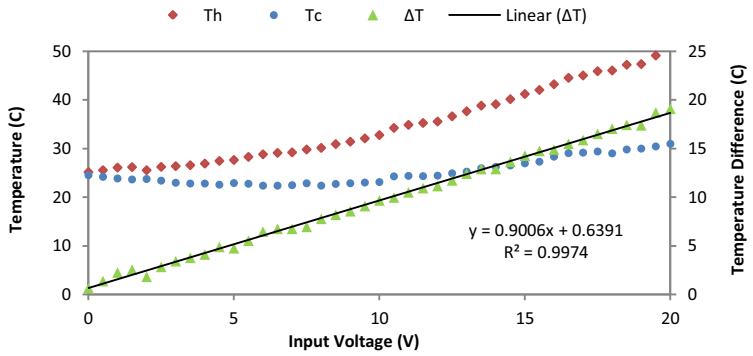

Fig. 4 Characterization of the TEC12706 in a series of 8 modules

The GP005PA PV device used in the study was characterized under outdoor conditions. The graphs in Fig. 5 exhibit the respective I-V and P-V curves with a solar irradiance of 919.8 W/m^2, temperature of 59.0 °C and a P_{max} of 5.802 W.

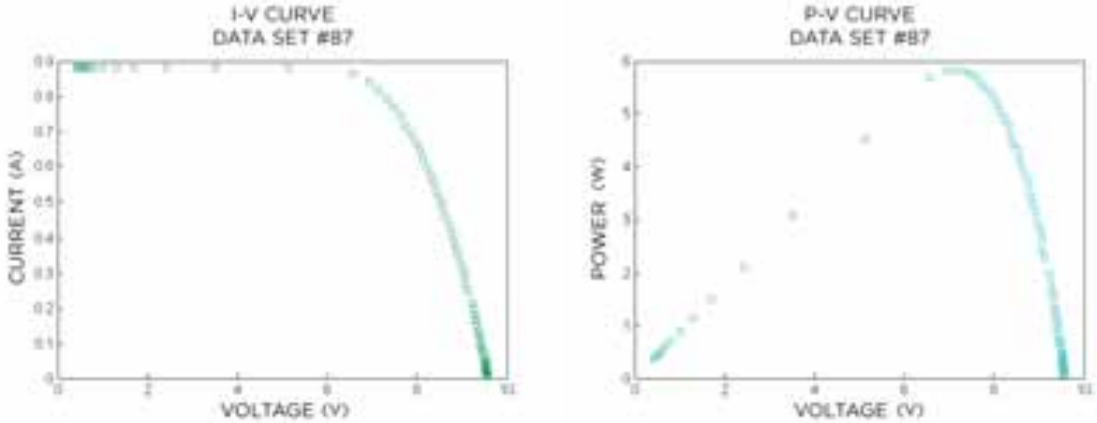

Fig. 5 I-V and P-V Curves of the GP005PA with the sun as the light source

4.2. Observations from Theoretical Modeling

One of the earlier TE models illustrated the attractive nature of the technology as a power generator in which a large output is possible given an equally large temperature gradient and with more modules used. For this model, the basis for maximum temperature is the highest estimated temperature for a solar PV module in conditions where irradiation is very high such as sometime around noon, which is 60 degrees Celsius. In ideal scenarios where the cooler side of the TE is dissipated well that it is at 0 °C, 60 °C in ΔT can be achieved. Fig. 6 shows the graphs of the TE output power versus temperature difference as a result of the simulation. In the figure, the maximum power (21 W) can be produced if 20 TE modules are placed at the backside of the solar PV module and ΔT = 60 °C. Even with ΔT = 30 °C, the TE can generate 5 W.

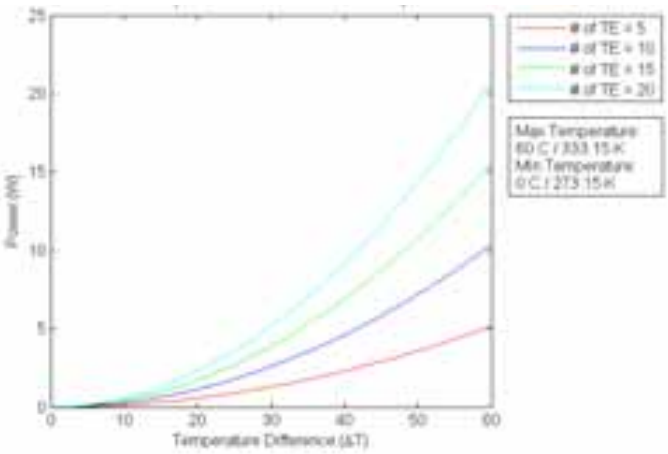

Fig. 6 Graph for TE output power versus temperature difference

The thermoelectric generation models used collected weather data (ie. irradiance, ambient air temperature) and PV data (ie. peak power, PV module temperature) from July 21, 2015, and TE attributes (ie. Seebeck coefficient, module resistance) to generate plots of TE and PV-TE system performances. Fig. 7 shows a comparison of the power output of the TE as a generator and the power output of the PV module, and the combined power output of the PV and TE. A comparison can be made of the power generated by the 5 W GP005PA PV device, an array of eight TEC12706 TE modules, and their combined output. It can be observed that solar irradiation and temperature have influence on the output power of the devices, while temperature levels appear proportional with the trend of the TE output. An average of 27.6% increase in PV output power was calculated when using the TE attachments compared to a PV-only setup.

The model to determine the thermal effect on the GP005PA PV device was designed using the parameters in Eqs. (6-7) and weather data from July 20, 2015. Variations in the temperature of solar PV modules greatly affect its open-circuit voltage V_{OC}. Thus, the V_{OC} parameter and its variations were investigated when the TE device was modeled as a coolant. Fig. 8 shows a comparison of the V_{OC} of the PV device with the TE device acting as a cooling mechanism, against the V_{OC} of the PV device alone. An average increase of 0.04% in the V_{OC} is noted.

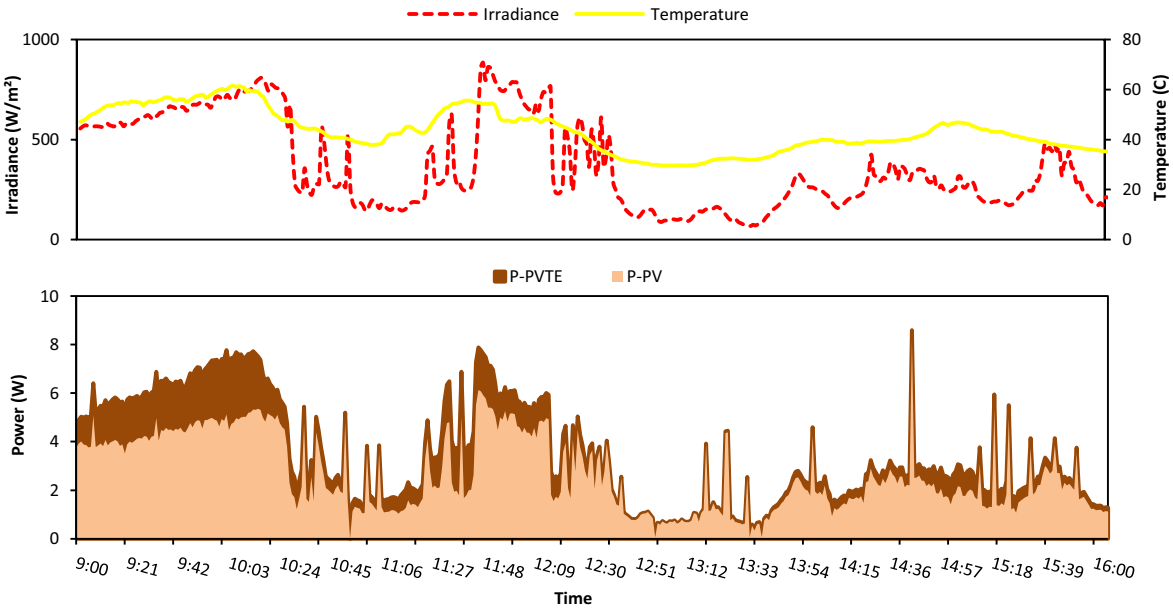

Fig. 7 Comparison of the theoretical power output of the 5W Polycrystalline PV device (*P*-PV), and its combined output power with the TEC12706 TE device (*P*-PVTE) as a *generator*

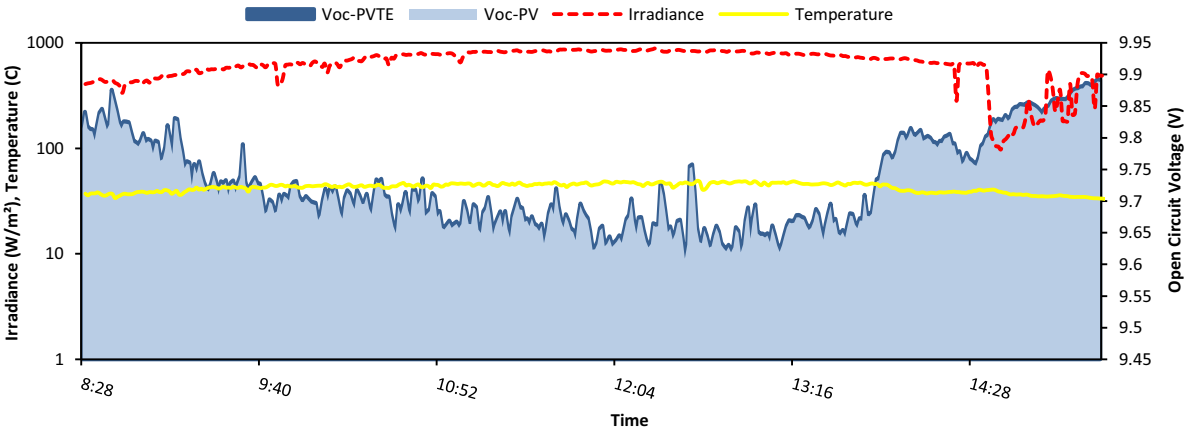

Fig. 8 **Comparison of the open circuit voltage output (V_{OC}-PV) of the 5W Polycrystalline PV device against the theoretical output V_{OC} of the PV with the TEC12706 TE device (V_{OC}-PVTE) as a *coolant***

4.3. TE as Generator

The results of the PV-TE prototype after it was deployed outdoors and observed for a number of days revealed a small but noticeable improvement compared to the standalone PV. Fig. 9 shows a comparison of the output power of the PV-TE system against the output power of the stand alone 5W PV module during outdoor deployment. An average increase of 1% in output power for the combined PV-TE was noted. Measurements were obtained on another day and an average increase of 1.9% in output power was observed. These however are not enough to match the projected increase in output power by the PV-TE model which theoretically indicated a 27.6% increase. It can be noted that similar to the model, the actual results showed that the trend of the output power followed irradiance levels, thus the current generated by the solar PV module dominated over the temperature variations and the effects on V_{OC}. The graph also revealed that the most noticeable improvement was in the morning when irradiance levels were observed to be high. This translates to high module temperature but lower ambient temperature, hence, greater ΔT.

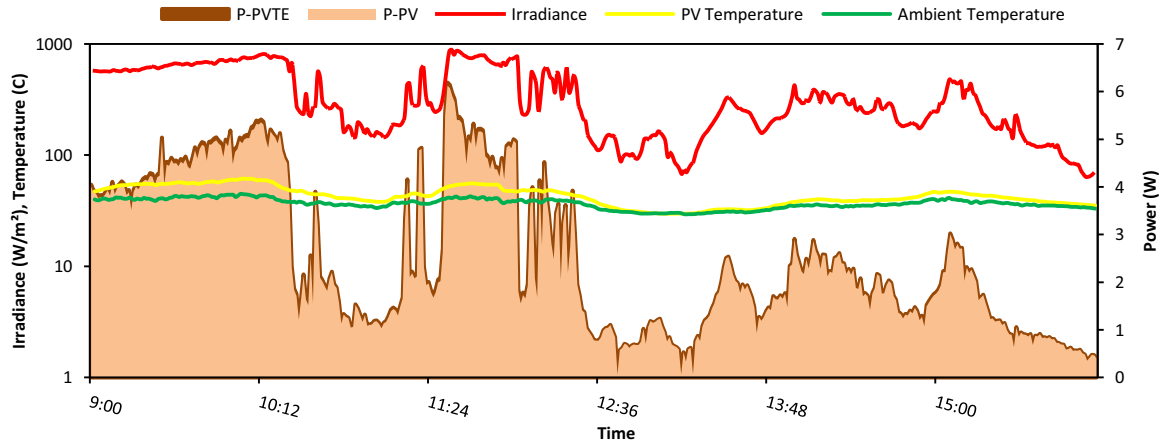

Fig. 9 **Comparison of the experimental output power of the PV-TE system (*P*-PVTE) with the TE as *generator* against the output power of the 5W PV alone (*P*-PV) after outdoor deployment**

4.4. TE as Coolant

Fig. 10 shows a general overview of the GP005PA PV device with TE attachments acting as a cooling mechanism to it. The 8V that was supplied to the TE array causing the cooling effect was determined in earlier lab tests where it showed the most promising results. It would seem that there is not much effect, in fact experimental results were less by an average of 3.7% from the simulated results. One noticeable observation is the ΔT indicative of cooling effectiveness when the difference is greater, which is apparent during the morning and late afternoon of the day. A zero to negative ΔT at midday around noon when PV temperature is hotter than the ambient, implies that the TE is not ideal as a coolant during this time.

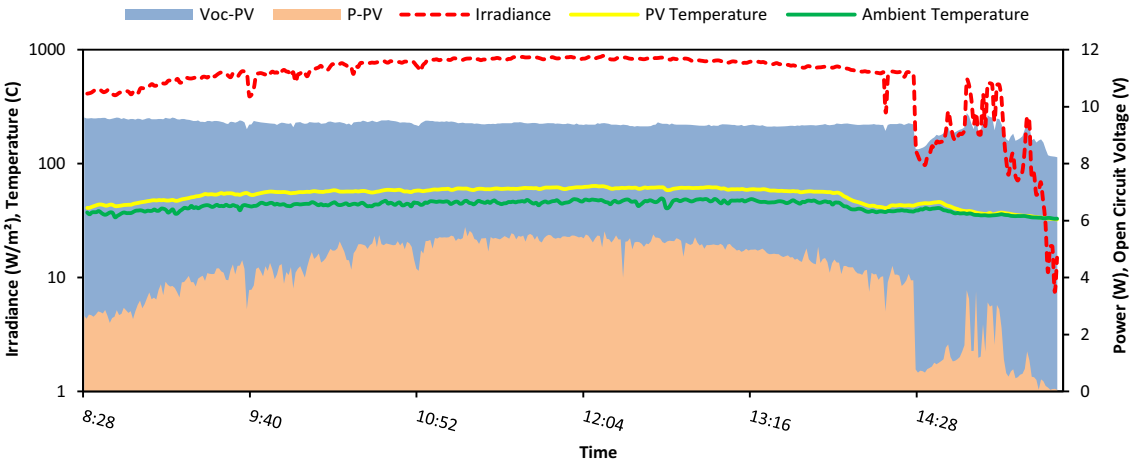

Fig. 10 Experimental effect of the TEC12706 TE devices as a *coolant* to the 5W PV device on its V_{OC} and P_{max} after outdoor deployment

The study also considered the relationship of irradiance to the performance parameters of the PV-TE and standalone PV systems by plotting irradiance versus output power for TE as generator (TEG) and irradiance versus V_{OC} for TE as coolant (TEC) from the data obtained in this study, which are shown in Fig. 11. Fig. 11a shows that the TEG has little effect on the power output though a small improvement in output power of the PV-TE system is observed. Fig. 11b shows that there is an improvement for PV performance with the TEC attachments. In general, at lower irradiance levels, the V_{OC} output of the PV-TE system is higher compared to a PV-only setup. This would indicate that at this range up to 600 W/m^2, it is when the TE cools the PV most effectively. This is supported by the Irradiance versus ΔT plot in Fig. 12 which shows that ΔT is negative (ie. hot side is cooler than the side emitting the cooling effect therefore ineffective) at high irradiance levels. Therefore, the TE devices are not recommended in cooling at high irradiance levels. On the average the difference is about 2% in V_{OC} in favour of the PV with TEC. Efficiency for this system taking into account the input needed by the TE calculated against the output of the PV is at 11.4%.

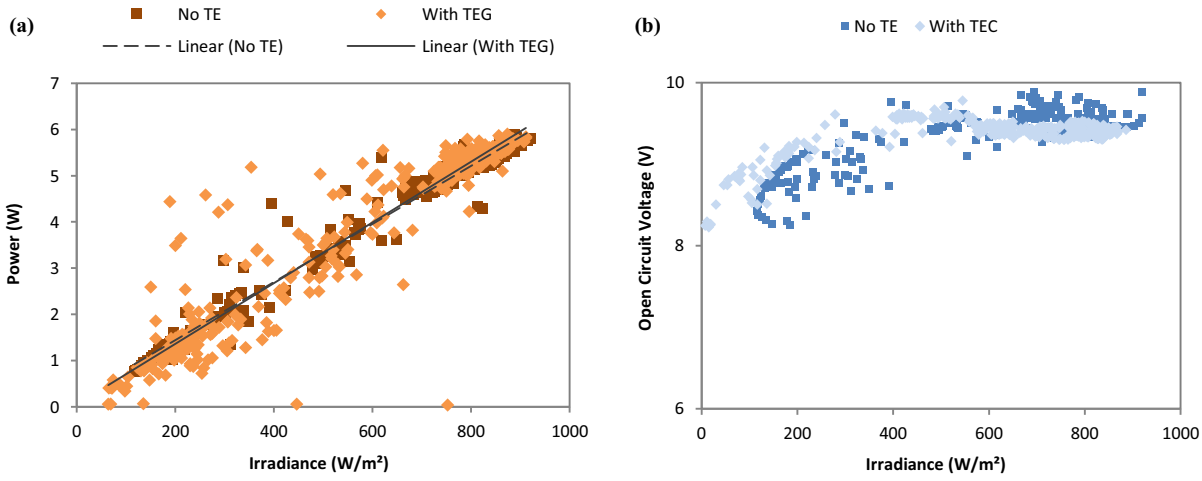

Fig. 11 Results of the performance parameters for PV-TE and PV-only measured against Irradiance: (a) output power for PV-TEG (as *generator*), and (b) open circuit voltage for PV-TEC (as *coolant*)

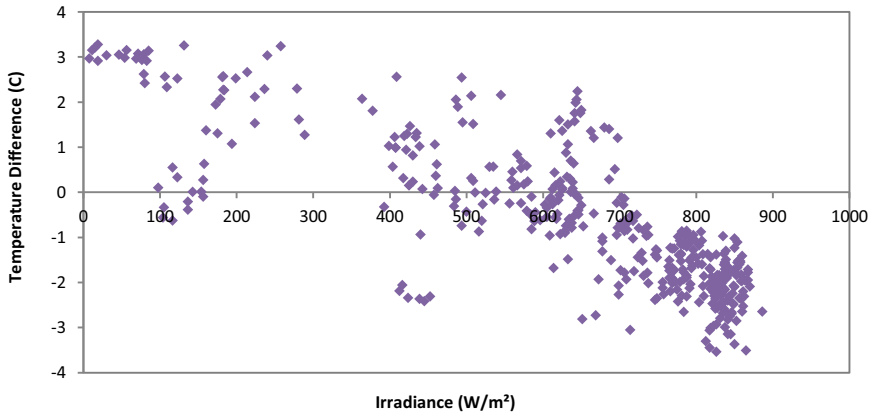

Fig. 12 Irradiance versus ΔT of the TEC in a PV-TE system

5. Conclusion

This study has shown that thermoelectric application has an effect on PV performance. In theory, the power generated by a PV-TE system with the TE in generator mode has a 27.6% improvement when compared to a standalone PV-only setup. Moreover, a 0.04% increase in the V_{OC} of the PV is also predicted when the TE acted as a cooling mechanism. After outdoor deployments were carried out to put the theory to the test, the increase in output power recorded for the PV-TE system with TEG was only about 1–1.9%. There was a noticeable improvement however on the TEC influence on the V_{OC} of the PV when it produced a 2% increase as compared to the standalone PV based on aggregated data. These results may be small but notable enough to indicate that the TE indeed does improve the power output of the solar PV module. Future research is strongly recommended with added features to the TE system such as better heat sink design and the utilization of boost converters that can potentially augment the effects of the TE on the PV module.

6. References

Chen, W.H., Wang, C.C., et al., 2013. "Modeling and simulation for the design of thermal-concentrated solar thermoelectric generator," Energy 64, 287-297.

Diaconescu, I., Grigorescu, L., 2009. "Thermoelectric Generator—An Alternative Electric Power Source," The Annals of 'Dunarea De Jos' University of Galati Gascicle XIV Mechanical Engineering, ISSN 1224-5615.

Ferrotec Corporation, 2014. "Thermal Reference Guide" [Online]. Available: http://www.ferrotec.com/technology/thermal/thermoelectric-reference-guide. [Accessed: 2015]

Jones, W., 2012. "Waste Heat to Electricity Breakthrough" [Online]. Available: http://spectrum.ieee.org/semiconductors/materials/waste-heat-to-electricity-breakthrough. [Accessed: 2015].

Khattab, N.M., El Shenawy, E.T., 2005. "Optimal operation of thermoelectric cooling driven by solar thermoelectric generator," Energy Conversion and Management 47, 407-426.

Krauter, S., 2004. "Increased electrical yield via water flow over the front of photovoltaic panels," Solar Energy Materials and Solar Cells, Vol. 82, Issues 1-2, 131-137.

Lee, S., Manalo, L.J., et al., 2012. "Sustainable Photovoltaic System with Cooling Optimization and Applications for Disaster Response," Undergraduate thesis, E.C.C.E. Dept., Ateneo de Manila Univ., Quezon City, Philippines.

Najafi, H, Woodbury, K.A., et al., 2012. "Evaluation Of Alternative Cooling Techniques For Photovoltaic Panels," M.S. thesis, Dept. of Mech. Eng., Univ. of Alabama, Tuscaloosa, Alabama.

Najafi, H., Woodbury, K.A., 2013. "Modeling and Analysis of a Combined Photovoltaic-Thermoelectric Power Generation System," Journal of Solar Energy Engineering 135, 031013-1—031013-8.

Park, K.T., Shin, S.M., et al., 2013. "Lossless Hybridization between Photovoltaic and Thermoelectric Devices," Nature.com Scientific Reports, Vol. 3, Issue 2123, 1-6.

Peña, R.A., Gamara, I.C., Pareja, K.A., 2013. "Current-Voltage Characterization and Thermal Imaging of Photovoltaic Modules," Undergraduate thesis, E.C.C.E. Dept., Ateneo de Manila Univ., Quezon City, Philippines.

PV Education, 2015. "Effect of Temperature" [Online]. Available: http://www.pveducation.org/pvcdrom/solar-cell-operation/effect-of-temperature. [Accessed: 2015]

Rowe, D.M., 2006. "Thermoelectrics handbook: macro to nano," CRC/Taylor & Francis, Boca Raton.

Teach Engineering, "Photovoltaic Efficiency: The Temperature Effect" [Online]. Available: https://www.teachengineering.org/collection/cub_/lessons/cub_pveff/attachments/cub_pveff_lesson02_fundamentalsarticle_v6_tedl_dwc.pdf. [Accessed: 2015].

Tellurex Corporation, 2010. "Introduction to Thermoelectrics" [Online]. Available: http:tellurex.com/pdf/introduction-to-thermoelectrics.pdf. [Accessed: 2015]Tritt, T., Subramanian M.A., 2006. "Thermoelectric Materials, Phenomena, and Applications: A Bird's Eye View," Materials Research Society Bulletin 31, 188-194.

Van Sark, W.G.J.H.M., 2011. "Feasibility of Photovoltaic-Thermoelectric Hybrid Modules," Applied Energy 88, 2785-2790.

Weather Underground, 2014. "Loyola Heights, Manila, Philippines Forecast" [Online]. Available: http://www.wunderground.com/weather-forecast/PH/Manila.html. [Accessed: 2015]

Designing an innovative secondary optics for parabolic trough

Daniela Fontani, Paola Sansoni, Franco. Francini, David Jafrancesco

CNR-INO National Institute of Optics,

Largo E. Fermi 6, Firenze (Italy)

Corresponding Author Email: daniela.fontani@ino.it

Abstract

A secondary optics for CPV parabolic troughs was developed to reduce the photovoltaic cells number. The proposed solution is a cylindrical Fresnel lens that transforms the focal line into a series of focal points. Its insertion inside the Concentrating PhotoVoltaic trough increases the solar concentration keeping unchanged the total collection efficiency of the system. The research includes optical design of the secondary collector and auxiliary analyses to control trough operation and to optimize trough collection efficiency.

Keywords: *secondary optics, optical design, trough, CPV, solar concentration*

1. Introduction

This paper describes a solution studied to reduce the number of photovoltaic cells in a linear parabolic trough (Bakos et al 2000, Kearney 2007, Kruger et al 2008, Prapas,et al 1987, Price et al 2002), which is used for the combined production of heat and electricity (Klapp et al 2007, Weiss and Rommel 2005). This solar trough combines photovoltaic and thermal systems: PV cells directly exploit the sunlight concentrated on them and their cooling system supplies thermal energy. Given that the linear concentrators act only in a direction that is normal to their length, consequently with a linear parabolic reflector the entire focal line must be covered by photovoltaic cells (Kearney 2007).

The secondary optical system examined in this study is interposed between the parabolic mirror and the linear row of photovoltaic cells. The sunlight collected by the parabolic reflector is intercepted by the secondary optics and concentrated, in portions, precisely in the direction where the concentrator may not work (along the longitudinal axis of the trough).

The working principle of the additional optical system appears evident placing a screen in the focal area: the secondary optics transforms the focal line into a series of focal points. Hence the proposed solution allows to reduce the number of PV cells while maintaining unchanged the total collection efficiency of the system because it simultaneously increases the concentration. In practice the production of electricity is not affected by the reduction of cells number, because it is balanced by an enhancement of solar concentration.

2. Positioning of the secondary optics in the solar trough

The starting point was an existing solar trough that combines photovoltaic and thermal systems (Bakos et al 2000, Klapp et al 2007, Kearney 2007 Kruger et al 2008, Prapas,et al 1987, Price et al 2002, Weiss and Rommel 2005). It concentrates the sunlight by means of a linear parabolic reflector over an articulated absorber. The focal image is a rectangle and it is focused on a row of squared photovoltaic cells. The cells are placed on a metallic tube of rectangular section, which acts as cooling system by means of a liquid flowing inside. The absorber is completed by an external protection tube in glass, enclosing cells and cooler. The photocells directly exploit the concentrated sunlight providing electricity, while the cooling system of the cells furnishes heat.

In this concentration geometry the secondary optical system must be located inside the first mirror (parabolic reflector) around and near the absorber, constituted by a glass tube enclosing a row of photovoltaic cells placed over a rectangular tube (cooler).

The parabolic reflector concentrates the solar rays in the direction transversal to the solar trough axis. Then the secondary optics intercepts these rays and it re-concentrates them also in direction of the trough axis. So the concentration is performed transversally by the trough; while it is performed transversally and longitudinally by the secondary lens. Hence the secondary optical system realises a concentration in the direction where the

doi:10.18086/swc.2015.05.19 Available at http://proceedings.ises.org

trough does not concentrate. In practice this secondary optics transforms the focal line into a series of focal points. This result can be easily visualized placing a screen in the focal area of the solar trough.

3. Design criteria for the secondary optics

The secondary concentrator (Giannuzzi et al 2010 Giannuzzi, et al 2011 , Giannuzzi, et al 2014, Jafrancesco et al 2010) was optically designed for an solar trough realized for the combined production of electricity and heat. It has a primary parabolic mirror that focuses the solar rays over a row of PV cells placed on a linear cooler. The aim is to decrease the number of required cells introducing a secondary optics that concentrates the light along the longitudinal direction of the trough.

The optical design of this secondary optics should be based on the characteristics of the existing solar trough and of the photovoltaic cells. The preliminary phase of the optical design is to simulate the optical system. Successively the solar trough parameters are analysed, to optimize the collection efficiency that maximised the obtainable energy. Finally the optical project of the secondary optics, in terms of geometrical parameters and optical characteristics (Winston et al 2005), is selected on the base of the analyses of the irradiance concentrated on the receiver (photovoltaic cells) (Güven and Bannerot 1986, Kandpal et al. 1985).

Auxiliary studies can assist in monitoring trough performance and in keeping high efficiency. Some examples of these additional analyses are summarised in Sect. 7: effects of collector deformation, axial defocusing, tracking errors and receiver alignment errors.

The proposed secondary optics is a lens, with cylindrical symmetry, which focuses in a point all the rays that arrive in a direction perpendicular to its surface, as shown in Fig. 1.

Considering that the rays coming from the parabolic reflector converge at the same point (the PV cell) is sufficient to design only a radial section of the lens that will be subsequently replicated on a cylindrical surface of radius R.

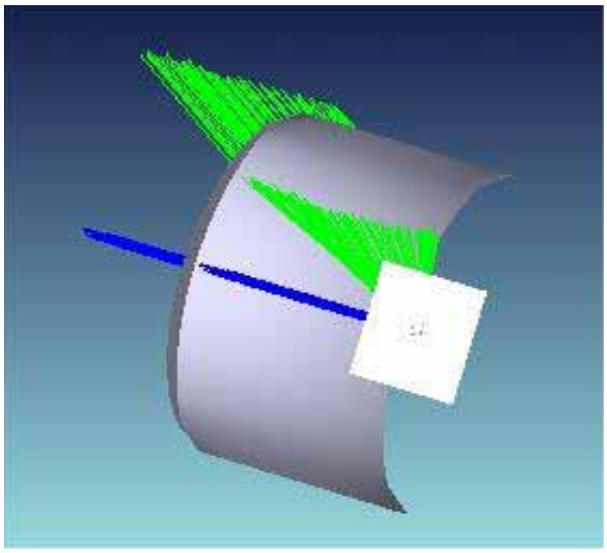

Fig. 1 - The secondary optics is a cylindrical Fresnel lens. It focuses in a point all the rays that arrive in a direction normal to its surface.

The criteria used to optically design the secondary cylindrical lens are summarised below.

1) The radius R of the cylinder depends on geometrical considerations linked to the size of the secondary optics and its position over the array of PV cells. There was a superior limit agreed with the optical manufacturers.

2) The transversal dimension Dt of the lens is determined by the f-number Fn = Dt / f, where f is the focal length of the lens, which must not be greater than R. Dt is chosen to have Fn <1, since it is known that the characteristics of an optical system are less critical for f-number less than 1.

3) Since the intention was to obtain a thin and weightless lens, it was established that his type had to be prismatic (Fresnel).

The result is a cylindrical Fresnel lens, whose profile is illustrated in Fig. 2. The figure shows the section of the lens, which contains 12 prisms that distribute the light on the PV cell. The total lens width L is composed of 12 prisms, each of which has width l, while the maximum height of the tooth is H. All the prisms in the central part have height equal to l, the width of each tooth.

The light intensity distribution on the PV cell obtained with the insertion of this secondary cylindrical Fresnel lens is presented and discussed in Section 5.

Fig. 2- The secondary optics is a cylindrical Fresnel lens with this profile.

4. Results of the optical design

The secondary optical system (Giannuzzi et al 2010, Giannuzzi, et al 2011, Giannuzzi, et al 2014, Jafrancesco et al 2010) was defined to be a cylindrical prismatic lens, of Fresnel type.

Figure 2 reports in detail the profile of the Fresnel lens with the characteristic angles αi of the individual prisms that define the optical design of the lens. The angle of prism surface inclination are symmetric, as the figure shows. From left to right of Fig. 2, the characteristic angles of the second face of each prism are: α1, α2, α3, α4, -α4, -α3, -α2, -α1, where a negative angle corresponds to a surface with the same inclination but in the opposite direction. The specific angles αi of each prism slope are calculated in the optical design simulation in order to optimise the light intensity distribution on the PV cell, balancing maximum obtainable power and maximum obtainable uniformity.

These data of the prismatic lens profile were used to generate the 3D cylindrical lens according to the criteria expressed in the previous section. This phase was executed using the Rhinoceros software, which allows to generate a three-dimensional file with IGES format. The screen output of the Rhinoceros software, reporting four different views of the secondary optics, is show in Fig. 3: the top-left image is a superior view, the top-right image is a perspective view, the bottom- left image is a frontal view, the bottom-right image is a lateral view from the right side.

As illustrated in Fig. 2, in the central part the upper surface of the prisms is almost flat: the angles α4 and -α4 approach zero.

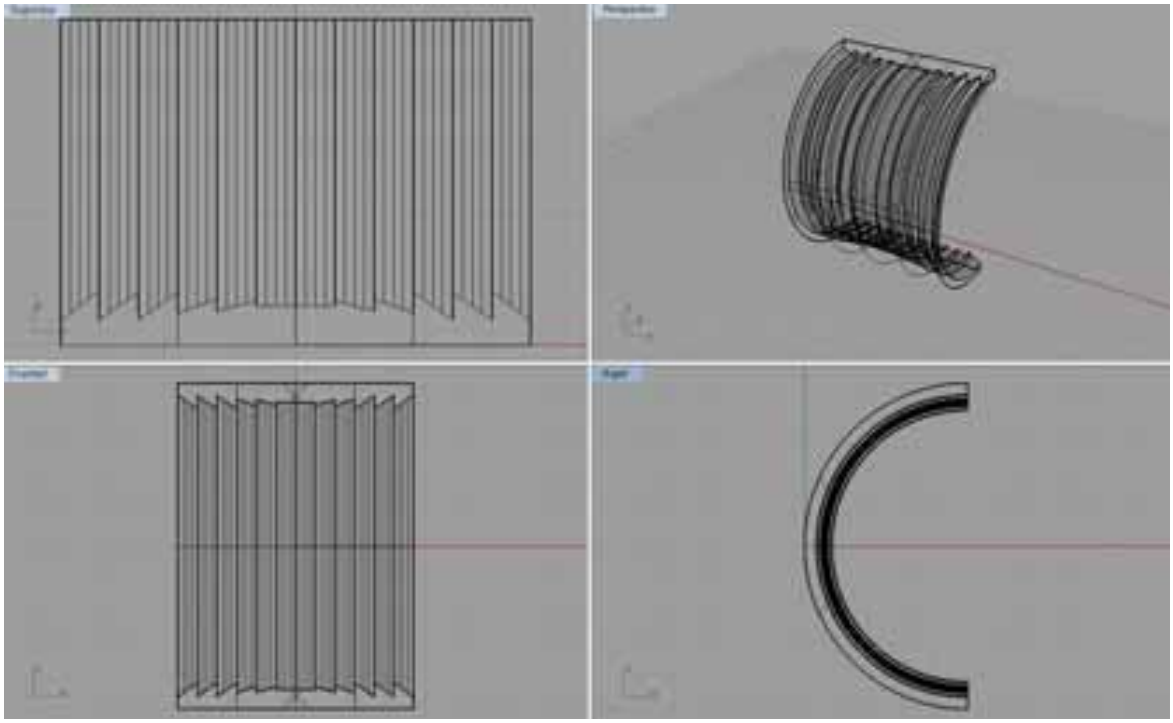

Fig. 3 - Rhinoceros drawings of the cylindrical Fresnel lens.

5. Behaviour of the prismatic lens in the parabolic trough

The prismatic lens is calculated for a photovoltaic cell of squared shape with dimensions 10mm x10mm, located at a distance d from the central flat face of the lens. The final cylindrical Fresnel lens has a diameter D, obtained from optical design simulations performed for a lens width L, with 12 prisms of size l.

The simulations were developed using a the specific ray-tracing software package Zemex-EE (by Radiant Zemax). One of their result, reported in Fig. 4, is the tri-dimensional rendering of the cylindrical Fresnel lens. The lens profile, corresponding to Fig. 2 is evidenced in orange in Fig. 4.

However the most significant result of the simulation is the irradiance light distribution over the photovoltaic cell, plotted in Fig. 5 in false colours. Figure 5 shows the irradiance distribution considering the prismatic lens inserted in the parabolic trough concentrator. The image frame is a square of 10mm x 10mm, which corresponds to the size of each PV cell.

The light focused by the secondary optics is quite uniformly distributed on the cell square. The great result is that the shape of the image is squared and it is illuminated almost with the same irradiance level. Only near the perimeter the irradiance has lower values. The uniformity of light distribution is a fundamental aspect when photovoltaic cells are employed, since they will work correctly only if they are uniformly illuminated. When the light is mostly focused on a portion of the PV cell, the cell converts light into electricity with a lower conversion factor. This loss of illumination uniformity can also affect (unbalancing the series of cells) the performance of the other PV cells.

The total collection efficiency is the product of the collection efficiency of the parabolic concentrator (95%) multiplied by the collection efficiency of the cylindrical Fresnel lens. Considering the entire solar spectrum was estimated a value of 75% for the total collection efficiency

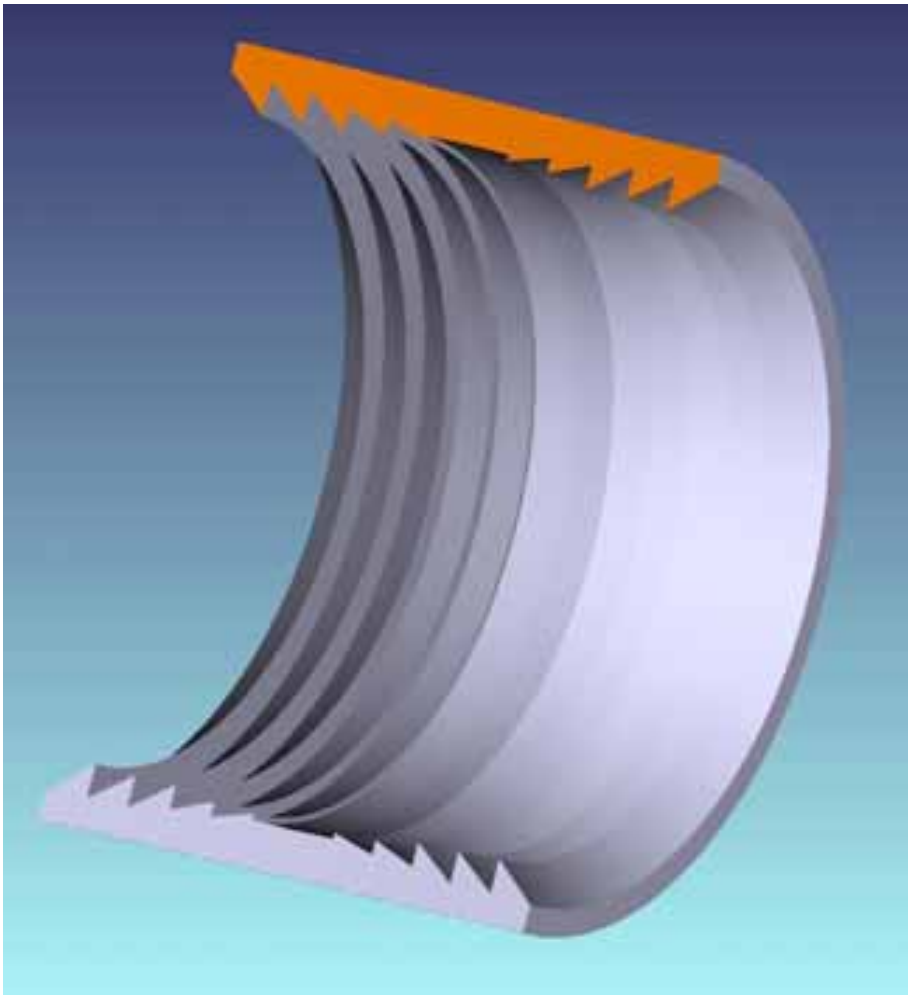

Fig. 4 – 3D rendering of the cylindrical Fresnel lens.

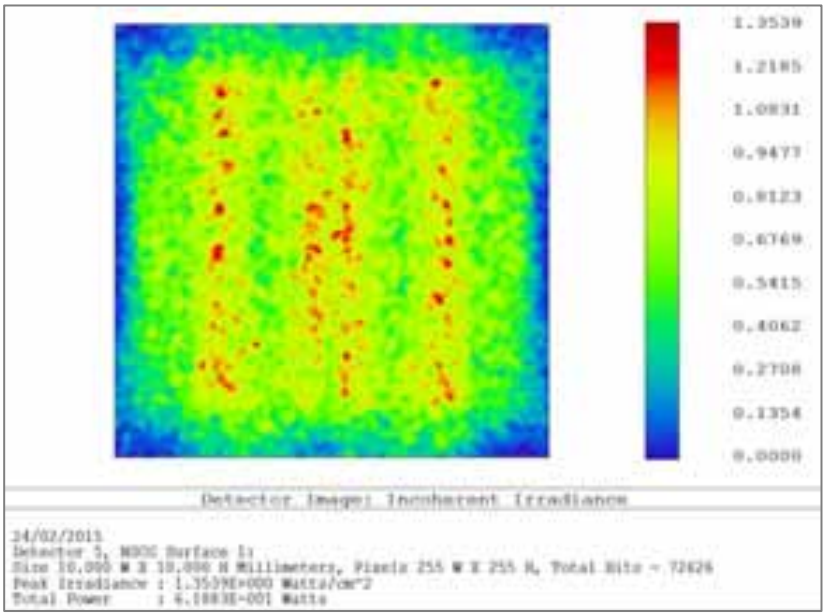

Fig. 5 – Image of the cylindrical Fresnel lens on the PV cell.

6. Simulations for the optical design

The optical design work (Güven and Bannerot 1986, Kandpal et al. 1985 , Sansoni et al. 2011, Winston et al

2005) consisted in simulating, analysing and optimising the optical configuration of the solar trough system. The optical simulations reproduced the system, whose main components are parabolic mirror (primary optics), cylindrical Fresnel lens (secondary optics) and photovoltaic cell (receiver). In particular the optical system was simulated in order to verify the optical behaviour in case of axial defocusing, tracking errors, alignment errors and deformations of the collector. For each of these cases were calculated:

• the collection efficiency of the system, that indicates how much of the power incident on the parabolic collector arrives at the receiver;

• the irradiance distribution on the receiver, that can give an idea of the uniformity of illumination of the receiver along a certain direction;

• the integrated power, that assesses the power collected by the receiver as a function of its width.

These analyses were exploited to define the optical parameters of the secondary optics; moreover they give fundamental information to optimise the solar trough performance. The results of the detailed studies are briefly discussed in Sect. 7.

The parabolic collector has a development of 1600 mm, a radius of curvature of 1600 mm and a focal length of 800 mm. The receiver, a PV cell of size 10mm x10 mm, is placed in the focal plane of the parabolic mirror. The Fresnel lens is placed at a distance d from the cell, on the side of the parabolic mirror.

For these simulations was considered only a small section of the parabola, of a width corresponding to that of the lens (L) and placed behind it. The reason is that it is this section that contributes to the collection efficiency; possible contributions from adjacent areas are compensated by the loss of light that impinges near the edges of the section.

The following list summarizes the parameters used in the simulations, subdivided for every principal optical component.

- Parabolic Concentrator: Parabolic Trough Concentrator (PTC) type; section width; curvature radius; total chord length; focal length; surface reflectance.

- Secondary Lens: cylindrical Fresnel lens type; dimensions; material; distance from the receiver; distance from parabolic mirror vertex.

- Screen: dimensions; distance from the receiver.

- Receiver 1 (for collection efficiency): dimensions; distance from parabolic mirror vertex.

- Receiver 2 (for irradiance profiles): dimensions; distance from parabolic mirror vertex.

- Source: plane with rectangular divergence; divergence angle; dimensions; distance from parabolic mirror vertex; power; wavelength (in these simulations the reference wavelength was 550nm).

- Number of rays (in these simulations 5 million rays were sufficient to have reproducible results).

The source projects on the parabolic reflector a homogeneous rectangular beam. The screen placed behind the receiver has the purpose of intercepting the rays emitted by the source in arrival on the receiver and on the secondary lens. In this way the obscuration effect of the tube is considered in the calculation of the collection efficiency of the whole optical system.

Receiver 1 and Receiver 2 are two detector planes of different size that are placed in the same position. They are used interchangeably for the calculation of collection efficiency (Receiver 1) and distribution of illumination irradiance (Receiver 2).

The z-axis is the optical axis, along which the propagation occurs rays; the x-axis is perpendicular to the drawing plane and is parallel to the longitudinal axis of the parabolic collector; the y-axis completes the right-handed triad. This reference system is used with all the objects (parabolic mirror, secondary lens and receiver).

The collection efficiency η of the whole optical system is defined as

$$\eta = \frac{P_{out}}{P_{in}} \qquad \text{(eq. 1)}$$

where Pout is the power that reaches the detector and Pin is the power that impinges on the section of the parabolic reflector.

7. Auxiliary investigations of trough performance

The study is completed with some analyses devoted to aspects essential for the correct functioning of the linear parabolic collector, assessing how to optimize the performance of the system (Diver and Moss 2007, Fontani et al. 2006, Fontani et al. 2011, Kandpal et al. 1985, Sansoni et al. 2011). These investigations examine in detail the consequences of axial defocusing of the receiver, deformations of the parabolic mirror, error in sun tracking, errors in aligning the optical components.

The axial defocusing (Sansoni et al. 2011) is an incorrect positioning of the receiver with respect to the focus of the parabola. It is studied by varying the distance of the receiver from the vertex of the parabola with displacement along the parabola's axis. The results are expressed using the trough collection efficiency η as a function of defocus, using the irradiance distribution on the receiver as a function of the distance from the centre varying the defocus and using the concentric integrals as a function of the cell width for various defocus values.

The collector deformations (Fontani et al. 2006) are the mechanical deformations of the primary parabolic mirror and they can be expressed by a variation of the conic constant K (K = 0 for perfect parabola). The results are expressed using the trough collection efficiency η as a function of K or as a function of the vertical displacement of the edge of the deformed collector.

The sun tracking errors (Fontani et al. 2011) occur when the sun's rays do not arrive perpendicularly to the entrance surface of the parabolic mirror because of an imperfect pointing. The effects of this tracking error are simulated by rotating the source around the x-axis and translating it in the y direction by an amount $A \cdot \tan\Phi$, where A is the source - parabola distance and Φ is the angle of rotation (tilt Φx); this is equivalent to the entire concentrator rotate about the longitudinal axis of the parabola. The results are expressed using the trough collection efficiency η as a function of tilt Φx, using the irradiance distribution on the receiver as a function of the distance from the centre for several tilt Φx values, using the concentric integrals as a function of the width of the cell varying the tilt Φx.

The errors of alignment (Diver, R.B., Moss, T.A, 2007) are the effects on the system performance due to any misalignment of the collector axis with respect to the North - South direction. In Parabolic Trough Collectors (PTC) without secondary lens the effect is a translation of the focal line along the linear receiver; in PTC with secondary lens the system collection efficiency may drop due to the small size of the PV cell. The situation is identical to the tracking errors but the source is rotated around the y-axis and translated along the x-axis. The results are expressed using the trough collection efficiency η as a function of tilt Φy.

The typical reference parameter for the system performance is the collection efficiency η of the whole solar trough (including primary parabolic mirror and secondary cylindrical Fresnel lens). The image focused by the secondary lens should concentrate the maximum power (maximise the trough collection efficiency η), but also uniformly illuminate the photovoltaic cell (maximise the receiver irradiance distribution, in Fig. 5).

8. Conclusion

The purpose was to develop a secondary optics for a solar CPV parabolic trough that increases the solar concentration and reduces the photovoltaic cells number keeping unchanged the total collection efficiency of the system. The solar trough is a Concentrating PhotoVoltaic system whose primary collector is a linear parabolic reflector. The proposed secondary concentrator is a cylindrical prismatic lens of Fresnel type. The primary parabolic mirror of the CPV trough concentrates the sunlight in a focal line, which is successively transformed by the cylindrical Fresnel lens into a series of focal points.

The research started with the optical design of the secondary component, selecting a configuration that optimizes collection efficiency of the whole system and uniformity of the PV cell illumination. The study proceeded with auxiliary analyses to optimize operative conditions and collection efficiency of the whole system. Finally specific simulations evaluated the possible future implementations.

The secondary optics was optically designed for an existing solar trough, already realized. This trough is used for the combined production of heat and electricity, with a parabolic mirror concentrating the sunlight over a line of photocells placed over a linear cooling system. The idea is to reduce the number of photovoltaic cells introducing a secondary optics to concentrate the light along the direction of the trough axis, where the trough does not concentrate.

The optical design of this secondary concentrator must take into account the characteristics of the existing trough and of the photovoltaic cells. The optical parameters of the secondary optics are principally determined by examining the irradiance distribution on the receiver. The study is completed by analyses and simulations of the effects due to collector deformation, axial defocusing, tracking errors and receiver alignment errors. The purpose of these auxiliary analyses is to maintain elevated performance of the solar trough in real working conditions.

9. References

Bakos, GC, Ioannidis, I, Tsagas, NF, Seftelis, I., 2000. Design, optimisation and conversion-efficiency determination of a line-focus parabolic-trough solar-collector (PTC). Applied Energy, 68 (1), 43-50.

Diver, R.B., Moss, T.A, 2007. Practical Field Alignment of Parabolic Trough Solar Concentrators. Journal of Solar Energy Engineering. May 2007, 129, 153-159.

Fontani, D., Sansoni, P., Francini, F., Jafrancesco, D., Mercatelli, L., Sani, E., 2011. Pointing sensors and sun tracking techniques. International Journal of Photoenergy 2011, 806518, 1-9.

Giannuzzi, A, Sansoni, P, Fontani, D, Francini, F, Jafrancesco, D, Mercatelli, L, Sani, E. 2010. Image optimization for a linear CPV system. Proceedings of EUROSUN Graz 28Sept-1Oct 2010.

Giannuzzi, A, Pierucci, G, Sansoni, P, Fontani, D, Francini, F, Jafrancesco, D, Mercatelli, L, Sani, E, 2011. Secondary optics design for mitigating tracking errors in a linear CPV system. 26th European Photovoltaic SOlar Energy Conference and Exibition.

Giannuzzi, A, Sansoni, P, Pierucci, G, Francini, F, Sani, E, Mercatelli, L, Jafrancesco, D, Fontani, D., 2014. Development of a secondary collector for an existing solar trough. WIT Transactions on Engineering Sciences, 88, 353-361.

Güven, HM, Bannerot, RB, 1986. Determination of error tolerances for the optical design of parabolic troughs for developing countries. Solar Energy, 36 (6), 535-550.

Jafrancesco, D., Cancro, C., Contento, G., Sani, E., Fontani, D., Mercatelli, L., Sansoni, P., Ferruzzi, D., Francini, F., 2010. Cheaper shapes for CPC preserving concentration efficiency. Proceedings of PVSEC Valencia 6-10 Sept 2010.

Kandpal, TC, Mathur, SS, Singhal, AK, 1985. Optical performance of a composite parabolic trough. Applied Energy, 19(3), 231-239.

Kearney, DW 2007. Parabolic Trough Collector Overview. Parabolic Trough Workshop 2007 at the National Renewable Energy Laboratory, Golden CO.

Klapp,, J, Cervantes-Cota, JL, Alcalá Chávez, JF, 2007. Towards a Cleaner Planet: Energy for the Future. Springer 2007.

Krüger, D, Pandian, Y, Hennecke, K, Schmitz, M. 2008. Parabolic trough collector testing in the frame of the REACt project. Desalination, 220 (1-3), 612-618.

Prapas, DE, Norton, B, Probert, SD. 1987. Optics of parabolic-trough, solar-energy collectors, possessing small concentration ratios. Solar Energy, 39 (6), 541-550.

Price, H, Lüpfert, E, Kearney, D, Zarza, E, Cohen, G, Gee, R, Mahoney, R. 2002. Advances in Parabolic Trough Solar Power Technology. J. Sol. Energy Eng.,124 (2), 109-125.

Sansoni, P., Fontani, D., Francini, F., Giannuzzi, A., Sani, E., Mercatelli, L., Jafrancesco, D., 2011. Optical collection efficiency and orientation of a solar trough medium-power plant installed in Italy. Renewable Energy 36, 2341-2347.

Weiss, W, Rommel, M, 2005.Solar Heat for Industrial Process: State of The Art – Medium Temperature Collectors. IEA-SHC Task 33/IV.

Winston, R, Miñano, JC, Benítez, P, Shatz, N, Bortz, JC, 2005. Nonimaging Optics. Elsevier Academic Press, Amsterdam.

Optical Sensors For Solar Pointing

Paola Sansoni, Daniela Fontani, Franco Francini and David Jafrancesco

CNR-INO National Institute of Optics,

Largo E. Fermi 6, Firenze (Italy)

Corresponding Author Email: paola.sansoni@ino.it

Abstract

A simple, efficient and low-cost sun tracking method is presented: it is based on optical pointers used as "sun finders" and on a double guiding system. A passive tracker provides the preliminary orientation, then an active system with the sun finder realizes fine positioning and adjustments. Two optical sensors for solar pointing are proposed discussing working principle and applications. The two-axis pointer is appropriate for solar concentrators coupled to optical fibers or tiny photovoltaic cells; while the one-axis sensor is suitable for linear tracking collectors. They can be adapted to every specific application and to every solar collection device. The sensors were optically characterized indoor, under controlled and reproducible conditions, and outdoor in real working situations.

Keywords: *sun finder, optical sensor, solar energy, optical test, sun concentrator.*

1. Introduction

A device based on the concentration of sunlight needs to track the sun in its movement in order to improve the system performance (Armstrong and Hurley, 2005; Lee et al., 2009; Mousazadeh et al., 2009). Solar systems based on light concentration require the use of an optical pointer because they can work only with direct sunlight. In Concentrating Photovoltaic (CPV) systems the primary optics is a Fresnel lens or a parabolic concentrator and a secondary optics can be added to improve pointing precision and plant collection efficiency (Altera Technical Staff, 2009; Chong and Wong, 2009). The required pointing precision is higher than the tenth of degree, which is not obtainable by passive trackers, based on the ephemerides of the year (Chen et al, 2006; Huang et al., 2009). The reasons are plant orientation problems, difficulties in keeping a high mechanical stability, wind action and high precision required by the concentrator type. Hence the solar plants employ an active tracker, based on a device that supplies to the moving system the information to correct the concentrators' orientation to maintain the alignment (Mohammad and Karim, 2012; Roth et al., 2004; Sadyrbayev et al., 2013). These devices utilized to provide the error signal to the control electronics, are commonly called "sun finders" (Bopp, 2014; Salawu and Oduyemi, 1986).

A tracking technique, based on optical sensors used as "sun finders", is discussed with a specific attention to practical realization and application of the solar pointers. The proposed strategy for sun tracking includes a double guiding system that uses two complementary procedures. The first one provides the preliminary orientation, then the second realizes the fine positioning and adjustments. The first tracking system is of passive type and it drives the motors to correctly orient the collector every day of the year. The second tracker is of active type and it employs an optical pointing system. The passive preliminary orientation is necessary to track the sun position when the solar light does not reach the pointer (in case of cloud passage or sun absence). In this way when the sun illuminates again the pointer, the active system can take the control of the collector orientation. The advantage of the double driving technique is to confer flexibility to the tracking system, which automatically follows every weather variation in all environmental conditions. The solar pointer is the optical device constituting the active guiding system of the tracking methodology. To improve the pointing precision, it is suggested the use a device including two sections, with different Field Of View apertures (FOV), corresponding to different accuracies.

This double guiding procedure to perform solar tracking is simple and effective; the realized pointers are reliable and inexpensive. The core of the active tracking system is the solar pointer. Two types of pointing sensors are presented, illustrating working principle, components, optical characterization and validation. The two-axis sensor, with pinhole, is suitable for solar concentrators coupled to optical fibers or tiny photovoltaic (PV) cells. The one-axis pointer, with slit, is appropriate for linear tracking collectors. These pointers can be adapted to every specific application and to every solar collection device. Installation and alignment become

doi:10.18086/swc.2015.05.20 Available at http://proceedings.ises.org

more and more crucial as the tracking precision increases. In practice, first the solar collectors should be properly placed on the ground, then the pointer must be accurately mounted and oriented. If the sensor is precisely aligned with the collector, the information coming from the sun finder is useful to compensate possible errors in the placement of the solar collectors. All sensors were tested in laboratory, in a controlled and reproducible environment, to provide an optical characterization of the devices. To complete the experimentation, the pointing sensors were tested outdoor, assessing their performance in operative conditions.

During the last 15 years these pointing sensors have been experimented (Fontani et al., 2011) and applied with success in different versions in several research projects concerning thermal solar concentrators (Sansoni et al. 2011), concentrating photovoltaics (Fontani et al., 2007a), hybrid solar collection systems (Ciamberlini et al., 2003), lighting (Ciamberlini et al., 2003; Fontani el al., 2007b; Sansoni et al., 2008). As essential component of devices for solar energy exploitation, the optical sun trackers have been used to perform outdoor optical tests, to experiment collector prototypes or to develop researches in the field of sun light collection. In the past decade the CNR-INO Solar Collectors Laboratory has collaborated with the major Italian actors, private and public, in the energetic research field.

2. Sun pointers for high concentration tracking

In the last decade Concentrating Photovoltaic (CPV) systems have improved their diffusion and the related electronics and optical components have experienced great technological and scientific developments. Photovoltaic cells of the last generation require concentrations that can exceed 700 suns. Consequently the associated optical systems must have a quite high value of posterior numerical aperture and a very tiny Field Of View (FOV). These requirements impose a very high angular precision to the systems for sun tracking. For tracking sensors that guide high concentration systems the typical required resolution is at least 0.1°.

Optical solar trackers have been developed and experimented by CNR-INO since 1997, implementing mechanics, electronics and software to realize prototypes (Ciamberlini et al., 2003; Fontani et al., 2011). The proposed two-axis pointer is basically a “pinhole camera” without lenses, whose scheme is reported in Fig. 1. It performs sun tracking on two perpendicular axes.

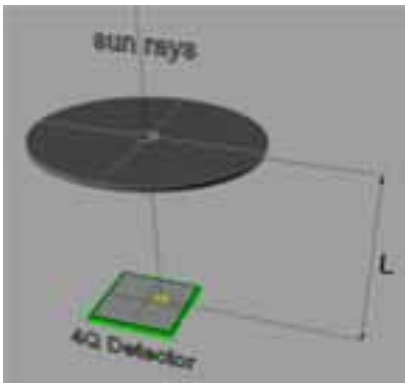

Fig. 1. A two-axis sun pointer, with pinhole.

A simplified version is represented by the one-axis pointing sensor, where the pinhole is replaced by a slit, as Fig. 2 shows. Pinhole or slit are coupled to a four quadrant photodetector. Two-axis sensors are suitable for fiber-coupled or CPV collectors. One-axis pointers are appropriate for solar troughs or linear lenses.

The working principle is illustrated in Fig. 1, which shows the main elements of the two-axis sensor: pinhole and four-quadrant detector (4Q-detector). The distance L, between pinhole and four-quadrant detector, determines the sensor Field Of View (FOV); L corresponds to the focal length of the collecting optics, hence the sun’s image moves on the photodetector with the same speed of the image on the PV cell. Sun’s image dimension and light intensity on the detector depend on the pinhole diameter d. The angular resolution of the sensor depends on detector dimensions, pinhole size and pinhole-detector distance. The lateral dimension s of the square photodetector is few millimeters.

The FOV aperture can be obtained as:

$$FOV = 2\,\mathrm{arctg}\frac{s}{2*L} \qquad \text{(eq. 1)}$$

For L = 50 mm and s = 5 mm, the total FOV aperture results 5.7°.

The one-axis pointer, in Fig. 2, is analogous to the two-axis sensor, but it mounts a slit over the photodetector. Consequently the four-quadrant detector can be substituted by a 2Q-detector.

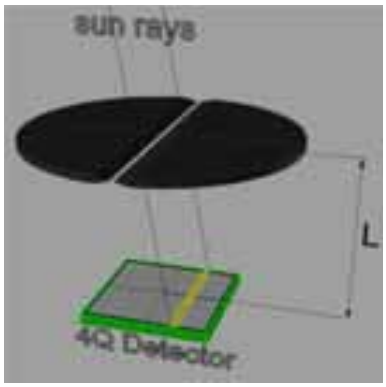

Fig. 2. A one-axis sun pointer, with slit.

3. Components and construction of the sensors

Detection configuration and light collection geometry were theoretically studied using ray tracing simulations, in particular referring to real solar plants involved in the CNR-INO research, briefly summarized in Section 1. Most of the detection geometries were obtained from ray tracing analyses of test prototypes or solar plants under development. The sensor realization evolved, customizing the pointer geometry and creating new detector typologies, on the basis of the experience in component production or driven by the extensive experimentation on the pointers.

Several versions of the described sun pointers were realized, optically characterized and practically applied on test installations and solar plants developed during 15 years of scientific experimental work (Ciamberlini et al., 2003; Fontani et al., 2007a, 2007b, 2011; Sansoni et al., 2008, 2011). Two-axis and one-axis sensors were implemented starting from the optical design, optimized in the study phase; and then suitable mechanics and electronics were developed. Two examples of two-axis pointer, with pinhole, are presented in Figures 3 and 4, showing the interior components.

Fig. 3. A two-axis sensor with narrow FOV and elevated precision.

Every sensor was previously tested in laboratory, in particular analyzing angular resolution and Field Of View aperture and then experimented in outdoor installations, testing functionality, performance and reliability. The optical characterization of the devices, performed indoor and outdoor, is summarized in Section 4, which also includes a validation by theoretical simulations; finally the assessment of the Field of View of the pointer is presented in Section 5.

Fig. 4. A two-axis sensor with large FOV.

The distance *L* can be adjusted, changing the FOV, to obtain the required precision. Figure 3 reports a version with elevated precision: *L* is 42 mm, so for detector side s = 5 mm the FOV is 7°. Figure 4 shows a two-axis sensor with *L* = 7 mm, whose FOV is 40° that corresponds to a lower precision with respect to the sun pointer in Fig. 3.

The dimensions of the four-quadrant detector was experimentally determined: typical values are 5 mm of squared detector side. The pinhole dimension depends on sensor and electronics and it was also experimentally defined. At the base of each well, forming the camera, there is a board mounting the four-quadrant detectors and their pre-amplifiers with gain adjustments.

As the sun pointer precision improves, the phases of sensor assembly and mounting on the solar collection plant become more critical: in particular it is essential to correctly and precisely place the detectors. Then the pointer must be mounted on the solar installation with the axis aligned to the collector axis. Sometimes the sensors are used in combination: for safety the solar pointer can contain two sections with different FOVs; the two sections are used in sequence, improving the precision, from the wide-angle section (low-precision section) to the narrow-angle section (high-precision section) (Sansoni et al., 2008).

The electronic system controlling the motor guide is of digital type. It employs an Input/Output DAQ device NI USB-6009 supplied by National Instrument. The I/O card is linked to a personal computer through a connection of USB type. The analogical inputs of the card are used to manage the photodetector with 2 or 4 quadrants of the solar pointer. The digital outputs are employed to guide the drivers of electric motors, which move the concentrators or the collectors' supports.

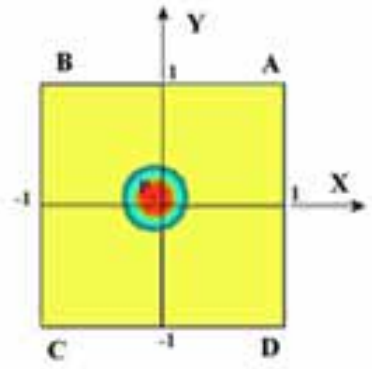

Fig. 5. Solar image on the four quadrant detector.

The position of the luminous spot is expressed by the coordinates of point $P(P_x;P_y)$, which is the barycenter of the solar image projected by the pinhole. P_x and P_y are the coordinates with respect to the reference axes of the detector surface (X;Y), indicated in Fig. 5. For the two-axis pointer they are:

$$P_X = \frac{(V_A + V_D) - (V_B + V_C)}{V_A + V_B + V_C + V_D} \qquad \text{(eq. 2)}$$

$$P_Y = \frac{(V_A + V_B) - (V_C + V_D)}{V_A + V_B + V_C + V_D} \qquad \text{(eq. 3)}$$

where V_A, V_B, V_C, V_D are the values (in Volts) of the output signals arriving from the four preamplifiers.

The elaboration procedure is analogous for the case of one-axis pointer, but considering only a single coordinate P_x .

4. Indoor and outdoor tests of the sensors

The sun pointers were optically characterized indoor and outdoor, preliminarily in laboratory with reproducible tests and successively with real measurements in direct exposure to the sun. This solar tracking methodology is based on an optical pointing system exploiting a two-axis sensor (or a one-axis sensor) as "sun finder". The two-axis sensor contains a photodetector coupled to a pinhole, while in the one-axis sensor it is coupled to a slit.

Suitable mechanics and electronics were realized for the prototypes of both pointers and to perform their optical characterization. The laboratory setup to test two-axis and one-axis sensors is illustrated in Fig. 6. A He-Ne laser beam is expanded to obtain a collimated beam. This light impinges on the pointer under test with different angles of incidence obtained by rotating the sensor. This experimentation has two purposes: the first is to test the angular sensitivity of the sun pointer; the second is to check the output voltage level. This latter must be sufficiently high with respect to the noise of the electronics; but at the same time the voltage level must guarantee a sufficient dynamic of the sensor.

Fig. 6. Optical system to tests the sun pointer in laboratory.

Afterward the sun tracking sensors were experimented with direct solar exposure, replicating the real installation in a solar plant. In these outdoor tests the optical tracking system was applied to different testing devices for sunlight collection: solar concentrators coupled to photovoltaic cells, optical fibers or linear metal pipes. To experiment the practical functionality and to measure the sensitivity of the solar pointers the technique described in Section 1 was simplified. Instead of employing the double guiding system the solar tracker used only a driving system of dynamic type based on the optical pointer.

Some exemplificative results of laboratory measurements and field experimentation on both sensors are presented in Figures 7-9. The plots report the position of the luminous spot on the detector versus angle of incidence of solar light: each measurement represents a characterization of the optical behavior of a sun pointer. Figures 7 and 8 compare the measurements performed in laboratory with the characterization obtained with direct exposure to the sun: Fig. 7 for two-axis pointer, with pinhole; Fig. 8 for one-axis pointer, with slit. Then Figure 9 reports the field measurements for both pointers: the comparison evidences a different slope of the curves that corresponds to a different sensitivity.

The two-axis sun pointer is the most precise one and it executes sun tracking in two directions achieving a very high sensitivity. It performs a sun tracking with an angular precision of 0.1° or higher. It is indicated for solar optical systems requiring high pointing precision, like collectors coupled to small PV cells or optical fibers, with dimensions (diameter/side) of few mm and sometimes inferior to 1 mm.

The one-axis sun pointer reaches the same precision of the two-axis pointer but only in one direction. Hence it can be applied to linear concentrators (like solar parabolic troughs or linear Fresnel lenses), in solar thermal plants or low concentration CPV systems.

The solar tracking system is effective and precise, mainly due to the simplicity of working principle and optical components. The sensors, which can be implemented with low costs, are reliable and adaptable to every solar plant. In case of sun shading or temporary sun absence, the control program provides a realignment of the collector in few seconds. The system is able to compensate possible errors in the positioning of the device, which should be correctly aligned to the Earth axis. The described optical pointers can track the sun's position with an angular precision of 0.1°, which is sufficient for the majority of solar plant.

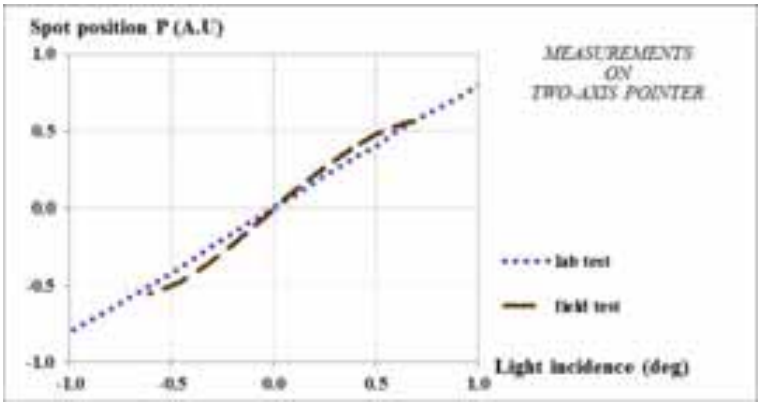

Fig. 7. Optical characterization of the sensor with pinhole.

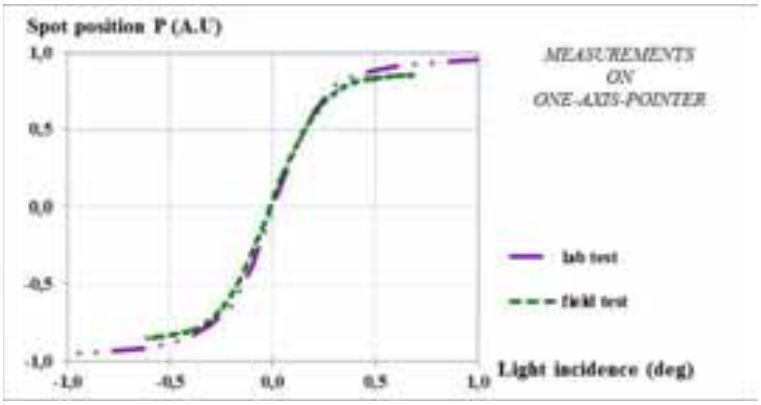

Fig. 8. Optical characterization of the sensor with slit.

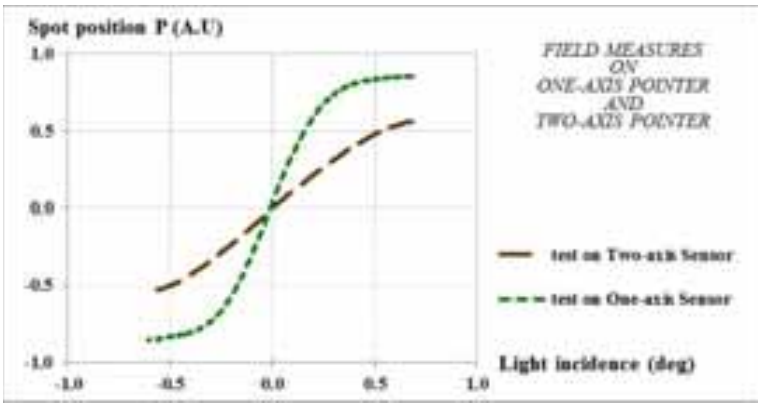

Fig. 9. Optical characterization of the sun pointers.

The validation of these experimental measurements was obtained by comparing the curves of Figures 7-9 with the theoretical data. For the curves in Fig. 7, the two-axis sun pointer was reproduced in a Zemax-EE optical simulation and the output signal was compared to the signal measured in indoor and outdoor tests. For the two-axis pointer, Figure 10 presents the comparison between the spot positions P obtained in the Zemax-EE simulation and corresponding values measured in the outdoor test. The position of the luminous spot projected on the detector is reported as a function of the incidence angle of the sunlight. The simulated curve is in fairly good agreement with the data measured in the field test.

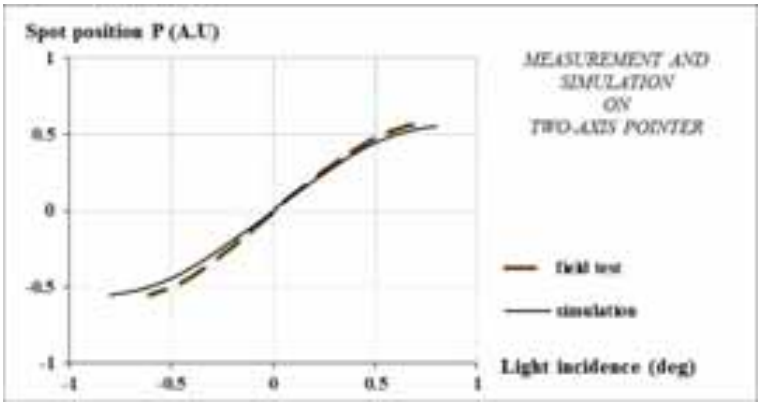

Fig. 10. Validation by ray tracing simulations for the two-axis pointer.

Each different realized sensor was examined indoor and experimented outdoor in order to assess detection characteristics and sun tracking precision. The optical characterization curves in Figures 7-9 were used to determine the zone of linear behavior of the pointers: this curve mathematically describes the working principle of each sensor and indicates its sensitivity. The validation in Fig. 10 confirms the accuracy of the experimental curves.

5. Measurement of the field of view of the sensors

Another fundamental parameter in the application of the pointers is the Field of View (FOV) aperture. The maximum sensitivity is obtained in the central part of the detector, while the total FOV aperture shows the extent of the range of operation of the sensor. The FOV aperture is obviously connected to the time in which the pointer is capable to re-track the sun in case of cloud passage or momentary absence of sunlight. The re-tracking time can be extended by using multiple sections with different FOV apertures or combining the active tracker with the passive tracker, based on the ephemerides of the year (discussed in Section 1).

Using the same set-up described in Fig. 6 it is possible to assess in laboratory the FOV of each sensor. The averaged data of these measurements are reported in Fig. 11: referring to Fig. 5, the plotted function is still the spot position P(Px;Py), given by Eq(2) and Eq(3). In practice this curve is the extension of the curves of Figures 7-9.

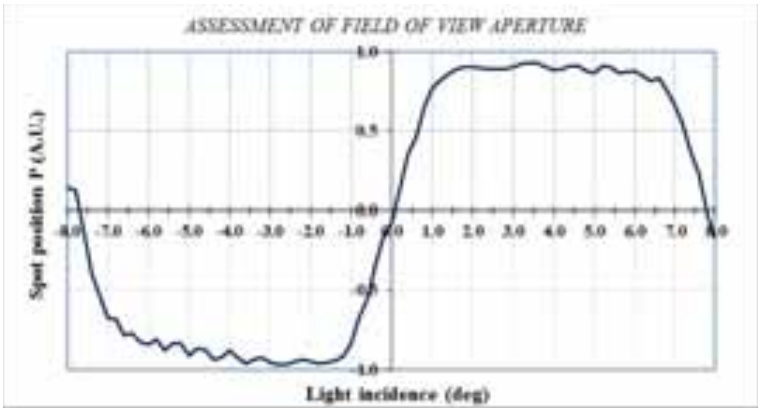

Fig. 11. Averaged measurements of the spot position P.

The spot position P remains approximately at the value of +1 (or -1) from the final angle of the linear zone to the edge of the detector. The measurement has been specifically carried from one detector border to the opposite one, even though usually the detector is mainly used in its central part. In the two lateral zones there is no more linearity between spot position P and angle of incidence, so the misalignment cannot be determined but it is however possible to try a re-alignment because the direction of the sun (in terms of up-down, left-right) is roughly known. Therefore it is useful to know the angular range within which the angular sensor still gives a valid signal in order to use it more completely. Figure 12 illustrates the two zones on the detector area: in the central zone (green in Fig. 12) P linearly depends on the incidence angle; while in the lateral zone (yellow in Fig. 12) P oscillates around +1 (or -1), and finally at the detector border the P value approaches 0.

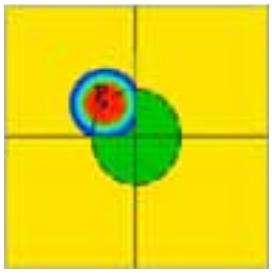

Fig. 12. Averaged measurements of the spot position P.

The determination of the FOV aperture is simply obtained from the complete plot of P values measured scanning the detector from one edge to the opposite one. In the example of Fig. 11, where the data are averaged on the measurements performed on a series of one-axis pointers, it is possible to use the sensor in a range between ± 7.5 degrees. Hence the total Field Of View aperture results 15 degrees. It is useful to remind that the FOV angle depends on the distance *L* between pinhole (or slit) and detector, which is chosen during the mounting of the device. Figures 3 and 4 show two pointers with different FOV: longer *L* gives narrower FOV and corresponds to higher angular precision (Fig. 3).

6. Conclusion

The proposed strategy for sun tracking includes a double guiding system that uses two complementary procedures: the first one provides a preliminary orientation, then the second realizes fine positioning and adjustments. The first tracking system is of passive type and it drives the motors to correctly orient the collector every day of the year. The second one is of active type and it employs an optical "sun finder". The double guiding system maintains the alignment in case of temporary sun absence or sun shading. The pointer perform an angular sensitivity higher than 0.1°, which is acceptable for many solar plants.

Two exemplificative optical pointing systems are proposed: the two-axis pointer that tracks on two perpendicular axes and the simplified one-axis pointer that tracks only in one direction. They can be adapted to every specific application and to every solar collection device. Installation and alignment become more and more crucial as the tracking precision increases. Solar installation placement, mounting and orientation of the sun pointer should be executed with particular attention to obtain an elevated tracking precision. If the sensor is precisely aligned with the collector, the information coming from the solar pointer is useful to compensate possible errors in the collector placement.

Sun pointing in one direction is required in linear collectors, solar trough collectors and linear Fresnel lenses. If the collector axis is parallel to the North-South direction, the tracking system must follow the sun in its daily excursion and the altitude of the sun over the horizon depends on Latitude and day of the year. If the collector axis is parallel to the East-West direction, the sun should not be tracked in its daily excursion. The proposed one-axis pointer can be applied to linear collectors for solar thermal plants or low concentration CPV systems.

Sun pointing in two directions is necessary to orient every concentrator with circular symmetry. In practice the tracking systems follows the sun position, which can be decomposed into two movements of single axis tracking. The combination of the two orientation adjustments gives the two-axis tracking. The proposed two-axis pointer performs solar tracking in two perpendicular directions with high sensitivity. It is indicated for solar optical systems requiring high pointing precision, like concentrators coupled to small PV cells or optical fibers.

In synthesis these optical pointing devices work as a pinhole camera without lenses. The working principle is simple, the device is adaptable and cheap, the pointer is effective and reliable.

7. References

Armstrong, S., Hurley, W.G., 2005. Investigating the Effectiveness of Maximum Power Point Tracking for a Solar System. IEEE Xplore, I, 204-209.

Chen, Y.T., Lim, B.H., Lim, C.S., 2006. General sun tracking formula for heliostats with arbitrarily oriented axes. Solar Energy Engineering 128, 245-250.

Chong, K.K., Wong, C.W.C., 2009. General formula for on-axis sun-tracking system and its application in improving tracking accuracy of solar collector. Solar Energy 83,3, 298-305.

Ciamberlini, C., Francini, F., Longobardi, G., Piattelli, M., Sansoni, P., 2003. Solar system for the exploitation of the whole collected energy. Optics and Laser in Engineering 39,2, 233-246.

Fontani, D., Francini, F., Sansoni, P., 2007a. Optical characterisation of solar collectors. Optics and Lasers in Engineering 45, 351-359.

Fontani, D., Francini, F., Jafrancesco, D., Longobardi, G., Sansoni, P., 2007b. Optical design and development of fibre coupled compact solar collectors. Lighting Research & Technology 39,1, 17-30.

Fontani, D., Sansoni, P., Francini, F., Jafrancesco, D., Mercatelli, L., Sani, E., 2011. Pointing sensors and sun tracking techniques. International Journal of Photoenergy 2011, 806518, 1-9.

Huang, Y.J., Wu, B.C., Chen, C.Y., Chang, C.H., Kuo, T.C., 2009. Solar Tracking Fuzzy Control System Design using FPGA. Proc. WCE 2009 Newswood Limited, I, 1-5.

Lee, C-Y., Chou, P-C., Chiang, C-M., Lin, C-F., 2009. Sun Tracking Systems: A Review. Sensors 9, 3875-3890.

Mohammad, N., Karim, T., 2012. Design and Implementation of Hybrid Automatic Solar-Tracking System. Journal of Solar Energy Engineering 135,1, 011013, 1-6.

Mousazadeh, H., Keyhani, A., Javadi, A., Mobli, H., Abrinia, K., Sharifi, A., 2009. A review of principle and sun-tracking methods for maximizing solar systems output. Renewable and Sustainable Energy Reviews 13, 1800-1818.

Roth, P., Georgiev, A., Boudinov, H., 2004. Design and construction of a system for sun-tracking. Renewable Energy 29, 393-402.

Sadyrbayev, Sh.A., Bekbayev, A.B., Orynbayev, S., Kaliyev, Zh.Zh., 2013. Design and Research of Dual-Axis Solar Tracking System in Condition of Town Almaty. Middle-East Journal of Scientific Research 17,12, 1747-1751.

Salawu, R.I., Oduyemi, T.A., 1986. An electronic sun pointer and solar tracking system. Solar & Wind Technology 3,3, 215-218.

Sansoni, P., Francini, F., Fontani, D., Mercatelli, L., Jafrancesco, D., 2008. Indoor illumination by solar light collectors. Lighting Research & Technology 40,4, 323-332.

Sansoni, P., Fontani, D., Francini, F., Giannuzzi, A., Sani, E., Mercatelli, L., Jafrancesco, D., 2011. Optical collection efficiency and orientation of a solar trough medium-power plant installed in Italy. Renewable Energy 36, 2341-2347.

8. Web References

Altera Technical Staff, 2009. Build an intelligent solar tracking system with FPGAs. FPGA Sources - EETimes India: www.eetindia.co.in/ART_8800561442_1800008_TA_30679a77.HTM (Feb. 2015).

Bopp, Matthias. A collection of solar finders designs. DD1US Astro Downloads, 2014: http://www.dd1us.de/Downloads/a%20collection%20of%20solar%20finder%20designs%200v5.pdf (Feb. 2015)

COMPARATIVE STUDY ON TWO PHOTOVOLTAIC AND THERMAL SOLAR MODULEDS WITH POINT-FOCUS FRESNEL CONCENTRATOR

Ning Xu, Jie Ji, Wei Sun and Wenzhu Huang

Department of Thermal Science and Energy Engineering, University of Science and Technology of China, #96 Jinzhai Road, Hefei City, Anhui Province, People's Republic of China

Abstract

In this paper, the electrical and thermal performances of both Fresnel concentrator photovoltaic/thermal (FCPV/T) modules with thermal collector and FCPV modules with passive cooling heat-sinks are investigated in experimental method. Both types of modules are equipped with triple-junction solar cells. Their geometric concentrating ratio is as high as 1090×. Comparative analysis has been conducted based on experimental data. The experimental results have been analyzed from the viewpoint of thermodynamics. From the first law point of view, it is found that the overall efficiency of the FCPV/T modules can exceed 80% but it drops significantly as the coolant water is heated up. Meanwhile, the electrical efficiency of the two types of modules can reach up to 28.9%. While from the second law point of view, a highest exergetic efficiency of 33.9% and 28.9% can be produced by the FCPV/T modules and the FCPV modules, respectively. Water temperature is found to play an insignificant role on the exergetic efficiency and irradiation influences dominantly. Besides, the electrical outputs of the two types of modules are almost equal at the same time even if notable operating temperature difference between their cells exists. Thermal profile of the CPV/T receiver has been simulated on the basis of a 3D heat transfer model developed in the thermal analysis software Comsol. The influence of beam irradiance and cell temperature on electrical efficiency is further studied. The results indicate that electrical performance of these modules is affected mainly by beam irradiance, and it is influenced little by cell operating temperature, which greatly differs from flat-plate PV/T modules.

Keywords: *PV/T, point-focus Fresnel, efficiency, exergy analysis, Comsol*

1. Introduction

A photovoltaic/thermal (PV/T) system is an integration of PV cells and solar thermal collectors which produces both electricity and heat simultaneously to increase its overall efficiency. The first investigation on PV/T system was presented by Martin Wolf (Wolf, 1976) in 1976. A large amount of experimental and theoretical studies on PV/T technology have been conducted during the decades (Amrizal, et al., 2013; Gang, et al., 2012; Tiwari, et al., 2009). Respect with the merit of a PV/T system lies in the reduction of demands on physical space and the equipment cost through the use of common frames and brackets as compared to the separated PV and solar thermal systems placed side by side, the cost of large area of photovoltaic cells is still higher than traditional power. Concentrator photovoltaic (CPV) system can reduce the area of solar cells by concentrating solar radiation onto small solar cells. If the cost of tracking assembly and concentrator is less than the cost of the saved solar cells, it could be an effective way to reduce the total cost of the system (Rabl, 1976). On the other hand, high efficient multi-junction solar cells are usually equipped in CPV systems to enhance the photovoltaic efficiency, which is rarely employed in systems without concentrator due to lack of economics. High efficient multi-junction solar cells have been developed and manufactured in both laboratories and factories. The efficiency of them is reported to be above 40% (Dimroth, et al., 2014; Green, et al., 2012; King, et al., 2012). On the CPV module level, photovoltaic efficiency over 35% have been reported (Ghosal, et al., 2014; Green, et al., 2015; Steiner, et al., 2015).

CPV systems can be generally classified as compound parabolic concentrator type (CPC) (Brogren, et al., 2001; Li, et al., 2014), parabolic trough type(Akbarzadeh and Wadowski, 1996; Coventry, 2005; Luque, et al., 1997), dish type (Chen, et al., 2014; Kribus, et al., 2006), linear Fresnel type (Liu, et al., 2014; Rosell, et al., 2005) and point-focus Fresnel type (Chengdong, et al., 2013; Wu, et al., 2012) according to the concentrator type. Among the CPV modules/systems, those with point-focus Fresnel lens recently have received more attention because of its advantages such as small volume, light-weight, mass production with low cost as well

doi:10.18086/swc.2015.05.21 Available at http://proceedings.ises.org

as effectively increasing the energy density. Xie et al. (Xie, et al., 2011) give a review on concentrated solar energy applications using Fresnel lenses in the last two decades, the highest photovoltaic conversion efficiency based on imaging Fresnel lens and non-imaging Fresnel lens is reported as over 30% and 31.5±1.7%, respectively. Amongst the existed point-focus Fresnel CPV systems, almost all the modules are passively cooled. Royne et al. (Royne, et al., 2005) believe that passive cooling could work well for single-cell geometries with flux level as high as 1000× suns, because there is large area available for heat sinking. However, for passively cooled CPV modules, the truth is that a large part of the already collected solar energy is dissipated as heat to the environment. Integrating the thermal collectors into a CPV module with point-focus Fresnel lens could be one of the potential solutions. Nevertheless, reports on point-focus Fresnel concentrator photovoltaic/thermal (FCPV/T) modules/systems are fragment. It is meaningful to investigate whether a FCPV/T system is better than a FCPV system whose cells are cooled passively, especially when they are close in manufacture cost.

In this study, an experimental rig containing two FCPV/T modules with thermal collector and two FCPV modules with passive cooling receivers were built. The modules are equipped with high-efficiency InGaP/GaAs/Ge triple-junction solar cells and the FCPV/T module was originally presented. The comparative investigation was conducted based on outdoor experimental data. The overall performance of these two types of modules were evaluated by energetic analysis and exergetic analysis. Thermal profile of the FCPV/T receiver was also analyzed with the employment of Comsol, a powerful thermal analysis software developed for various physics and engineering applications. The influence of beam irradiance and cell operating temperature on electrical efficiency is further studied on module level.

2. Description of the experimental setup

The photograph of the experimental setup is shown in Fig. 1. The experimental setup is built in Huainan (32.37 °N 116.59 °E), Anhui Province, China. It mainly consists of four parts, namely two FCPV/T modules and two FCPV modules, the two-axis tracking system, the water circulation system and the data acquisition system. The modules are equipped with high-efficiency InGaP/GaAs/Ge triple-junction solar cells whose photovoltaic efficiency is 31.4% (AM1.5D, 25 ^{o}C) under one sun. Two identical FCPV/T modules and two identical FCPV modules are mounted parallel in the same holder for comparison, as shown in Fig. 1. Each module consists of 15 receivers and 15 point-focus Fresnel lenses, mounting one for one in a 5×3 matrix. The area of each Fresnel lens is 330.2×330.2 mm^2, and the size of each solar cell is 10×10 mm^2, which means the geometric concentrating ratio of the modules is 1090×. For a single module, all the 15 solar cells are connected in series. The two FCPV/T modules are connected in series, so are the two FCPV modules. The electrical characteristics of the module are listed in Table 1, which is achieved by indoor testing under steady condition (DNI 900W/m^2, 20 ^{o}C, 4 m/s) and they are offered by the manufacturer. The two-axis tracking system maintains the modules tracking the sun automatically within a range of 0.3°.

Fig. 1: Photograph of the experimental rig

Tab. 1: Electrical characteristics of a module

Parameter	Variable	Value
Maximum power	P_{max}	402W±5%
Voltage@ P_{max}	V_{max}	38.3V
Current@ P_{max}	I_{max}	10.5A
Open circuit voltage	V_{OC}	45.2V
Short circuit current	I_{SC}	11.1A

The main difference between these two types of modules lies in their receivers. Both types of receiver consist of a solar cell and an aluminum heat-sink, as shown in Fig. 2. The solar cell is pasted at the center of front side of the heat-sink by thermal conductivity silica gel. The optical prism is pasted on the solar cell by optical silicone. A ceramic housing is arranged to surround the solar cell, which protects the solar cell against interference of unnecessary illumination. For the CPV/T receiver, an axial grooved tube is designed on the rear side of the heat-sink, through which water flows and takes heat away. The groove could increase the heat exchange area and it also enhances the convective heat transfer by disturbing the fluid. Therefore, the heat-sink of the CPV/T receiver serves as the thermal collector. Threads are made at both ends of the tube for pipe connection. As to the CPV receiver, large-area fins are employed to increase heat exchange area. Although the pipe connection increases the cost of FCPV/T module, the volume of its heat-sinks is smaller than the FCPV module's. Besides, there is no difference between the fabrication technologies for both types of receivers. As a consequence, the costs for the FCPV/T module and the FCPV module are almost the same.

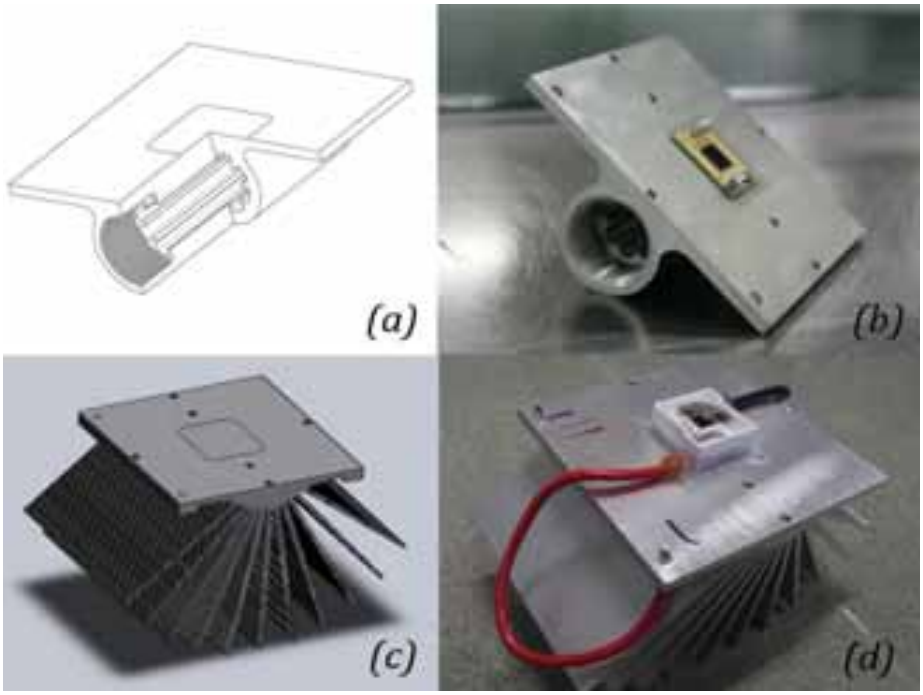

Fig. 2: Schematic and photograph of the FCPV/T and FCPV receiver

Fig. 3 shows the schematic of the water circulation in the FCPV/T system. Water is pumped from the bottom of the storage tank and flows through the tubes below the heat-sinks. Hot water flows back to the tank. The whole water circulation is a closed loop without secondary heat exchanger. Every 10 heat-sink tubes are connected in series by pipes. This arrangement divides the water circulation system into three branches and it also decreases the temperature difference on the water flow direction due to short flow distance, thus decreasing the impact on solar cells caused by water temperature gradient. At the inlet of each branch, a valve and a flow meter are installed to control and measure the water flow rate, respectively. Two pressure gauges are installed at the inlet and outlet of the main pipeline, respectively. All pipes and heat-sink tubes are insulated by insulation cotton with a thickness of 15mm. The volume of the tank in this system is 75L.

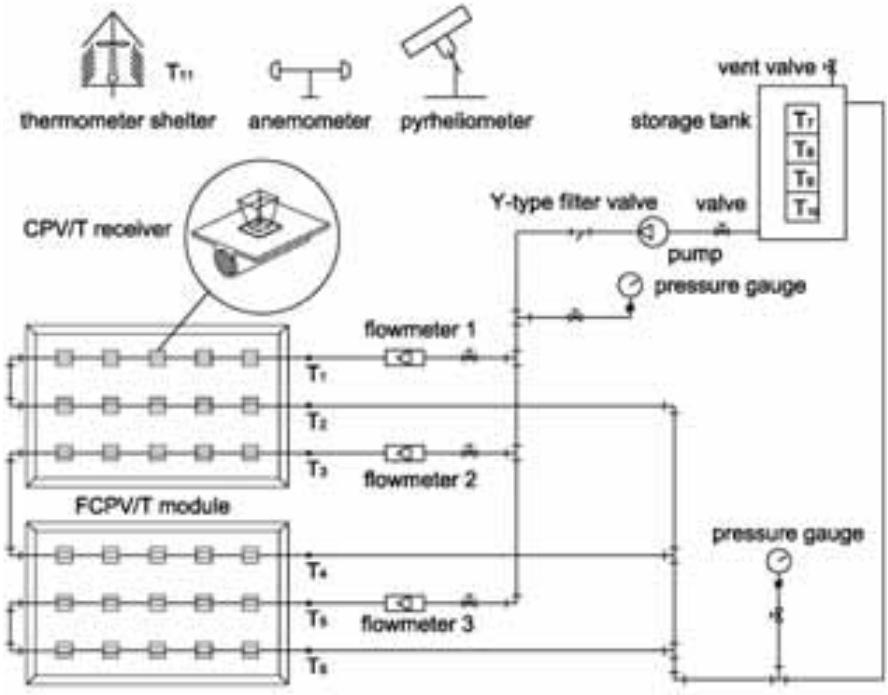

Fig. 3: Schematic of water circulation in FCPV/T system

The data acquisition system mainly consists of sensors and a data logger. The locations of sensors are also illustrated in Fig. 3. Inlet and outlet temperatures for each branch are measured by platinum resistances. The ambient temperature and the tank water temperatures are measured by T-type thermocouples. To eliminate the measurement error caused by temperature gradient in the tank, four equidistant temperature measuring points are arranged. The beam irradiance is measured by a pyrheliometer. Both temperature and beam irradiance are recorded by a data logger (Agilent 34970A) at an interval of 10s. Pressure and water flow rate are also recorded. A photovoltaic analyzer is used to measure and record the electrical output of the modules. The electrical data is recorded every 5 minutes. A thermal infrared imager is also employed to record the thermal profiles of the modules. Details of all the measurement instruments are listed in Table 2.

Tab. 2: Characteristics of sensors and measurement instruments

Device	Accuracy	Specification
Thermocouple	±0.2°C	T-type
Thermal resistance	±0.1°C	Pt 100
Pyrheliometer	2%	TBS 2-2
Data logger		Angilent 34970A
Flow meter	1%	Lmag_W800
Photovoltaic analyzer	1%	HT I-V400
Thermal infrared imager	±2°C	Fluke Ti400

3. Analysis methods

The overall performance of a PV/T system can be evaluated according to thermodynamics, economics, marketing and environmental implications, as demonstrated by Coventry and Lovegrove (Coventry and Lovegrove, 2003). Among the evaluation methods, the thermodynamic approach is popularly used in optimizing an engineering system that owe their thermodynamic imperfection to heat transfer, fluid flow and mass transfer irreversibility. Bosanac et al. (Bosanac, et al., 2003) believed that the economical and marketing approaches are affected by the political environment and are never universally valid. The thermodynamic approach based on energy and exergy analysis is more objective. Therefore, the analysis in this study is mainly from the viewpoint of thermodynamics.

3.1. First law efficiency of thermodynamics

From the first law of thermodynamics, the overall performance of a PV/T system can be evaluated by the energetic (first law) efficiency η_{PVT}. It is widely used in previous studies (Chow, et al., 2009; Ji, et al., 2007), which directly reflects the overall performance of a PV/T system. The first law efficiency is defined as follows:

$$\eta_{PVT} = \frac{E_t + E_{PV}}{A_F \int_{t_1}^{t_2} G_b dt} = \eta_t + \eta_{PV} \quad \text{(eq. 1)}$$

$$E_t = c_p m (T_2 - T_1) \quad \text{(eq. 2)}$$

$$E_{PV} = \int_{t_1}^{t_2} P_m dt \quad \text{(eq. 3)}$$

where E_t and E_{PV} are the thermal energy output and electrical output of a module, respectively. c_p is the specific heat of water, m is the mass of water in storage tank, and T_2 and T_1 represent the final and initial water temperature during the time period from t_1 to t_2, respectively. A_F is the area of Fresnel lens in a module and G_b is the beam irradiance measured by the pyrheliometer. η_t and η_{PV} are the thermal efficiency and the electrical efficiency of the module, respectively.

3.2. Second law efficiency of thermodynamics

Although the first law efficiency reveals the overall performance of a PV/T system intuitively, it ignores the difference between thermal energy output and electrical output produced by the modules in "quality", even if they are the same in "quantity" and measurable by the same physical unit. In fact, thermal energy cannot produce work until a temperature difference exists between a high temperature heat source and a low temperature heat-sink, while electrical energy can completely transform into work irrespective of the environment. In other words, the second law efficiency, namely the exergetic efficiency, offers a qualitative and standardized evaluation for the overall performance of a PV/T system. Exergy is simply the available energy obtained by subtracting the unavailable energy from the total energy, and is equivalent to the work transformable.

According to the work conducted by Fujisawa and Tani (Fujisawa and Tani, 1997), the second law efficiency of a PV/T system is expressed as eq. 4. This definition is on the basis of the assumption that the initial temperature of the fluid medium is equal to the ambient temperature.

$$\varepsilon_{PVT} = \varepsilon_t + \varepsilon_{PV} = (1 - \frac{T_a}{T_2})\eta_t + \eta_{PV} \quad \text{(eq. 4)}$$

where ε_t and ε_{PV} are the exergetic efficiency of solar cells and thermal collectors, respectively. T_a is the ambient temperature and T_2 is the final water temperature.

In eq. 4, the calculation of the exergy of solar radiation is not considered. Instead, the energy of radiation is taken as the exergy of radiation directly. Exergetic efficiency is the ratio of total exergy output to total exergy input (Hepbasli, 2008). Therefore, the exergetic efficiency can be defined as

$$\varepsilon_{PVT} = \frac{Ex_t + Ex_{PV}}{A_F \int_{t_1}^{t_2} \dot{E}x_{sun} dt} = \varepsilon_t + \varepsilon_{PV} \quad \text{(eq. 5)}$$

where Ex_t and Ex_{PV} are the thermal exergy output and electrical exergy output of a module, respectively. $\dot{E}x_{sun}$ is the exergy input of solar radiation. The exergy outputs are related to the energy outputs as follows:

$$Ex_t = (1 - \frac{T_a}{T_2})E_t \quad \text{(eq. 6)}$$

$$Ex_{PV} = E_{PV} \quad \text{(eq. 7)}$$

There are different methods to determine the exergy of radiation in evaluating the performance of PV/T system when using the exergy method. Among them, three most commonly used calculation methods are summarized by Chow, et al. , i.e.

$$\dot{E}x_{sun} = [1 + \frac{1}{3}(\frac{T_0}{T_{sun}})^4 - \frac{4T_0}{3T_{sun}}]G_b \quad \text{(eq. 8)}$$

$$\dot{E}x_{sun} = [1 - \frac{4T_0}{3T_{sun}}]G_b \quad \text{(eq. 9)}$$

$$\dot{E}x_{sun} = [1 - \frac{T_0}{T_{sun}}]G_b \quad \text{(eq. 10)}$$

where T_0 is the environment temperature and T_{sun} is the solar radiation temperature at 6000 K. Actually, the difference between results calculated by these three methods are less than 2%. In this study, eq. 10 was adopt.

3.3. Evaluation of thermal profile of the receiver

Cell operating temperature is believed to play a significant role in evaluation of performance of a PV/T system because it greatly influences the electrical output. However, it is difficult to measure cell temperature directly because of the lamination connection between solar cell and heat-sink. Fernandez et al. (Fernandez, et

al., 2014) proposed four methods to calculate the cell temperature of a high concentrator photovoltaic module, but they are either oversimplified (such as one-dimensional model) or required with adequate measurable data (such as ANN method). There is no doubt that a 3D thermal model can better describe the real thermal profile of the receivers. A number of thermal analysis software could be adopted to establish the 3D thermal model, and the core issues are providing the boundary conditions accurately. For the FCPV modules, their boundary conditions mainly include the beam irradiance, ambient temperature, and wind speed as well as wind direction. However, the wind direction is difficult to define because the modules always move. While for the FCPV/T modules, the boundary conditions primarily consist of beam irradiance, water temperature and ambient temperature. Fortunately, these parameters could be measured precisely. Therefore, the 3D thermal model of the CPV/T receiver could be solved in a more rational way by virtue of a thermal analysis software.

In this study, a powerful thermal analysis software Comsol is employed to simulate the thermal profile of the CPV/T receiver. Comsol is a finite element analysis, solver and simulation software for various physics and engineering applications, especially coupled phenomena or multiphysics. A 3D transient heat transfer model was developed as the simulation process described in Fig. 4. The 3D geometric model of the CPV/T receiver is firstly imported into the software, followed by mesh generation automatically. After defining the initial values and boundary conditions, the thermal profile of the receiver can be obtained by the solver. In this way, the thermal profile, especially cell temperature under a particular condition can be calculated. The cell temperature is treated as the average temperature of cell region on the CPV/T receiver.

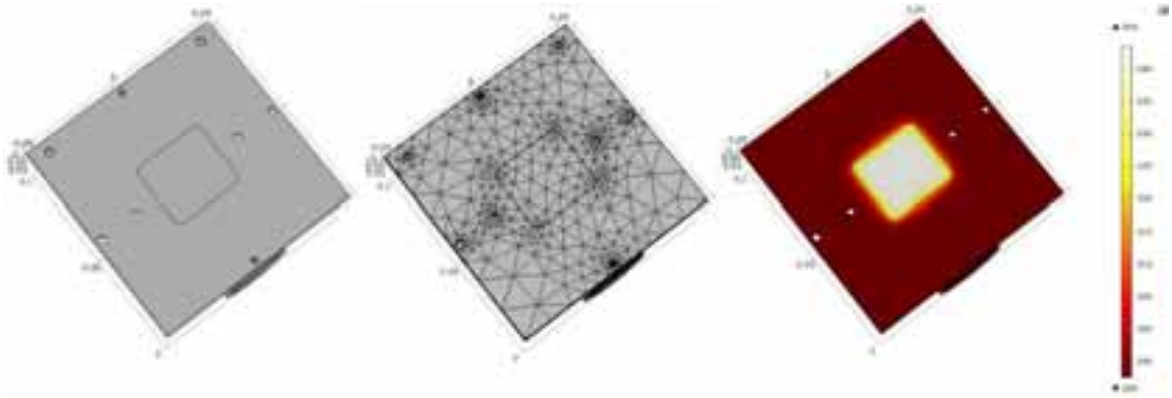

Fig. 4: Thermal analysis process by Comsol on a FCPV/T receiver

4. Results and discussion

A typical daily data in November 7th, 2014 is selected to show the results and followed by detailed discussions. Fig. 5 shows changes of measured weather data and temperature of water in storage tank from 10:00 am to 15:30 pm. As seen in Fig. 5, the ambient temperature changes in a small range between 15~17 °C, and the beam irradiance changes between 300~700W/m^2 with a steady stage from 11:00 am to 12:00 am. Water is heated from 25 °C to near 55 °C and water temperature drops a little after 14:30 pm. Wind speed in the daytime is always below 2m/s. Water flow rate of each branch is controlled at 0.33m^3/h which ensures water flows turbulently.

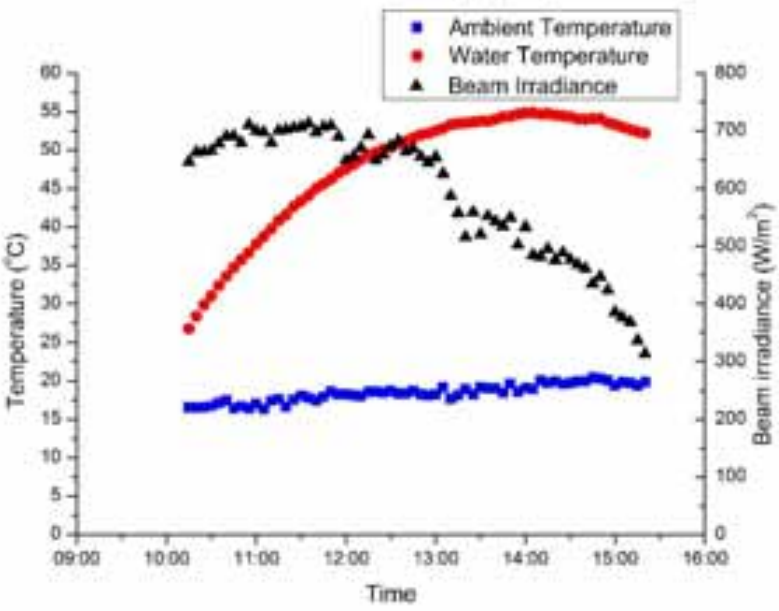

Fig. 5: Measured weather data and water temperature during experimental test

Electrical power yield of one FCPV/T module and one FCPV module are illustrated in Fig. 6. It is obvious that the higher beam irradiance is, the larger the power yield is. Power yield by both types of modules remain almost equal at the same time, regardless of how much irradiation they receive. Fig. 7 depicts the thermal profiles of the modules, which is captured by a thermal infrared imager. At the given moment, the temperature of CPV receiver is found to be higher than that of CPV/T receiver, as shown in Fig. 7. However, the corresponding power yields shows no difference. Considering the temperature difference between the two types of receivers, it can be deduced that cell operating temperature is not the dominant factor that influences the electrical performance of these modules. This feature is greatly different from flat-plate PV/T modules. Stated another way, the increase of water temperature would not lower the electrical efficiency of the FCPV/T modules significantly.

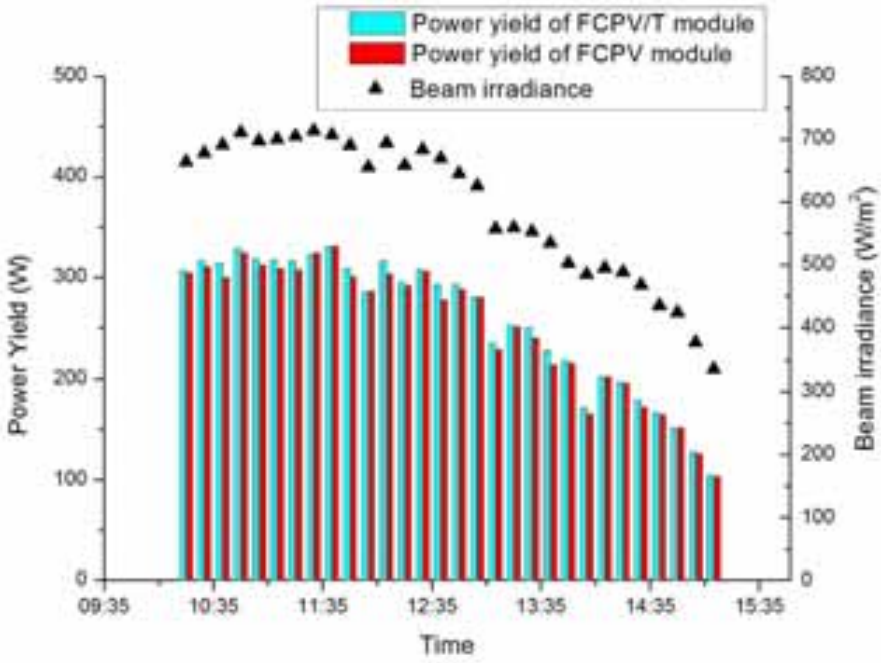

Fig. 6: Electrical power yield of FCPV/T module and FCPV module

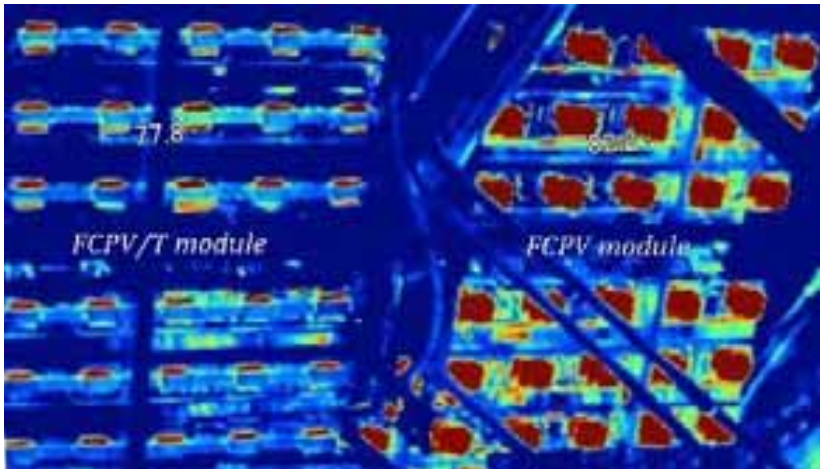

Fig. 7: Thermal profile of FCPV/T module and FCPV module

The variation of overall efficiency of the FCPV/T module and the FCPV module are shown in Fig. 8. From the viewpoint of the first law of thermodynamics, an overall efficiency of 80% can be obtained at the start of the experiment. It drops due to the decrease of thermal efficiency, which can be attributed to the descending irradiance and the decreasing temperature difference between cell temperature and water temperature. Besides, a highest electrical efficiency of 29.3% can be obtained and it changes with narrow fluctuation between 20.7% and 29.3%. On the other side, water temperature is found to play an insignificant role when the overall performance is viewed from the second law point. A highest exergetic efficiency of 33.9% and 28.9% can be produced by the FCPV/T module and the FCPV module, respectively. The exergetic efficiency is mainly affected by irradiance.

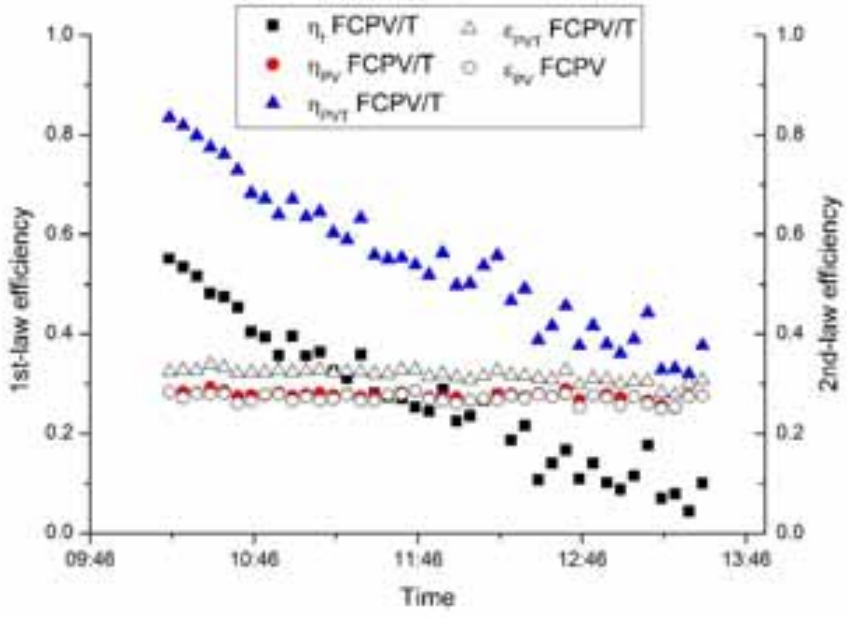

Fig. 8: Variation of overall efficiency of FCPV/T module and FCPV module

Fig. 9 depicts the variation of module electrical efficiency with beam irradiance and cell temperature. For better identification, the “beam irradiance-electrical efficiency” projection and the “cell temperature-electrical efficiency” projection are also marked in Fig. 9. Cell temperature is obtained by Comsol with the method proposed above, and the boundary conditions are based on experimental data. The calculation shows cell temperature changes between 60 °C and 90 °C, which is always lower than the design ceiling cell operating temperature of 100 °C. It can be seen that the electrical efficiency of the system is affected by cell temperature and beam irradiance together. Among the results, the highest electrical efficiency occurs under high irradiance

condition (where beam irradiance is near 700W/m^2) with a value of 29.3%. It decreases as the cell temperature increases within a narrow range. The electrical efficiency remains in a narrow range between 27% and 29% when beam irradiance is over 600W/m^2. However, the electrical efficiency drops steeply with the decrease of beam irradiance when beam irradiance is below 600W/m^2. This indicates beam irradiance has a dominated effect on module electrical efficiency, although cell temperature affects it as well.

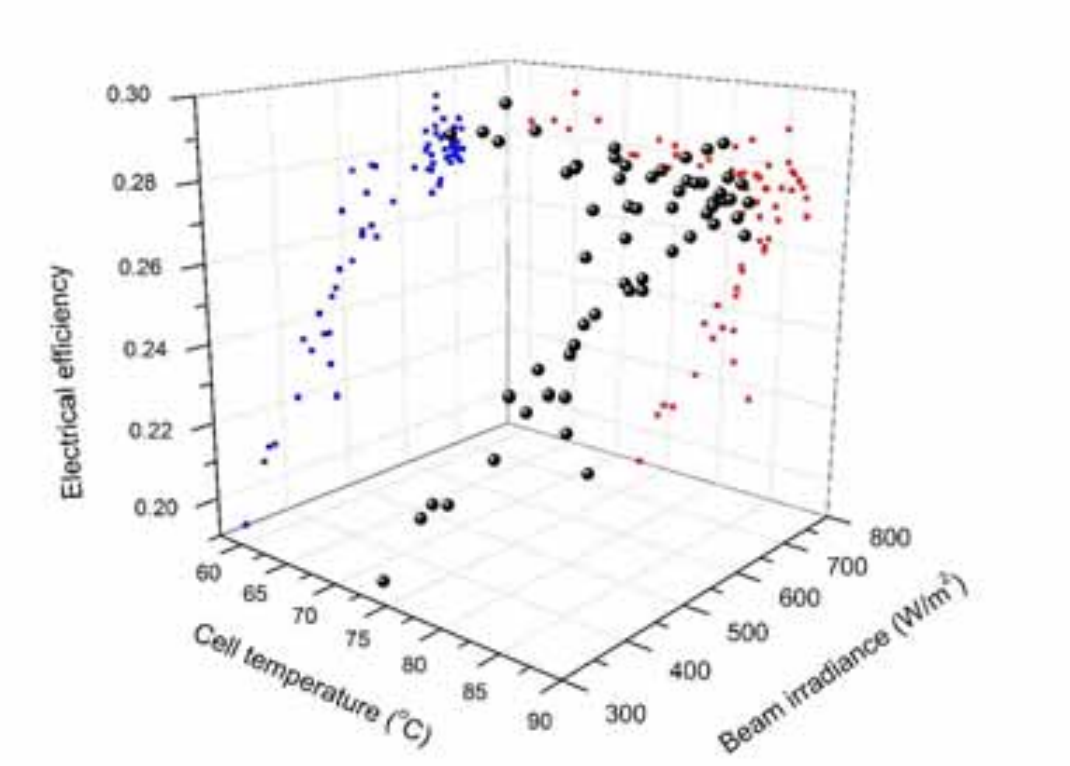

Fig. 9: Variation of electrical efficiency with irradiation and cell temperature

5. Conclusions

A comparative study on FCPV/T module with thermal collector and FCPV module with passive cooling heat-sinks were conducted. The overall performance of these two types of modules were evaluated by energetic analysis and exergetic analysis. The results show that the FCPV/T module can obtain an instantaneous electrical efficiency of 27% and a highest instantaneous thermal efficiency of 54%, which means its overall energetic efficiency can exceed 80%. From the second law point of view, a highest exergetic efficiency of 33.9% and 28.9% can be produced by the FCPV/T module and the FCPV module, respectively.

Electrical outputs of the two types of modules are found to be almost equal under the same environmental condition, even if distinct temperature difference between two kinds of module receivers exists. This indicates that cell temperature does not influence the electrical performance of the modules predominantly, which is greatly different from flat-plate PV/T modules.

Thermal profile of the CPV/T receiver has been simulated based on a 3D transient heat transfer model in Comsol. The boundary conditions of the model is acquired from experimental data. With the calculation, the influence of beam irradiance and cell temperature on electrical efficiency is further investigated. It can be concluded that beam irradiance has a dominated effect on the electrical efficiency of the modules, although cell temperature affects it as well. The electrical efficiency of the modules remains in a narrow range between 27% and 29% when beam irradiance is over 600W/m^2, but it drops steeply with the decrease of beam irradiance when beam irradiance is below 600W/m^2.

Acknowledgements

This work is supported by Grants from the National High Technology Research and Development Program

of China (863 Program) (No. 2013AA050403), the DongGuan Innovative Research Team Program (No. 2014607101008) and the Fundamental Research Funds for the Central Universities ((No. WK6030000008).

References

A. Akbarzadeh, T. Wadowski, Heat pipe-based cooling systems for photovoltaic cells under concentrated solar radiation, Applied Thermal Engineering, 16 (1996) 81-87.
N. Amrizal, D. Chemisana, J. Rosell, Hybrid photovoltaic–thermal solar collectors dynamic modeling, Applied Energy, 101 (2013) 797-807.
M. Bosanac, B. Sorensen, K. Ivan, H. Sorensen, N. Bruno, B. Jamal, Photovoltaic/thermal solar collectors and their potential in Denmark, Final Report, EFP Project, www. solenergi. dk/rapporter/pvtpotentialindenmark. pdf, (2003).
M. Brogren, P. Nostell, B. Karlsson, Optical efficiency of a PV–thermal hybrid CPC module for high latitudes, Solar Energy, 69 (2001) 173-185.
H. Chen, J. Ji, Y. Wang, W. Sun, G. Pei, Z. Yu, Thermal analysis of a high concentration photovoltaic/thermal system, Solar Energy, 107 (2014) 372-379.
K. Chengdong, X. Zilin, Y. Qiang, Outdoor performance of a low-concentrated photovoltaic-thermal hybrid system with crystalline silicon solar cells, Applied Energy, 112 (2013) 618-625.
T.T. Chow, G. Pei, K. Fong, Z. Lin, A. Chan, J. Ji, Energy and exergy analysis of photovoltaic–thermal collector with and without glass cover, Applied Energy, 86 (2009) 310-316.
J. Coventry, K. Lovegrove, Development of an approach to compare the 'value'of electrical and thermal output from a domestic PV/thermal system, Solar Energy, 75 (2003) 63-72.
J.S. Coventry, Performance of a concentrating photovoltaic/thermal solar collector, Solar Energy, 78 (2005) 211-222.
F. Dimroth, M. Grave, P. Beutel, U. Fiedeler, C. Karcher, T.N. Tibbits, E. Oliva, G. Siefer, M. Schachtner, A. Wekkeli, Wafer bonded four‐junction GaInP/GaAs//GaInAsP/GaInAs concentrator solar cells with 44.7% efficiency, Progress in Photovoltaics: Research and Applications, 22 (2014) 277-282.
E.F. Fernandez, F. Almonacid, P. Rodrigo, P. Perez-Higueras, Calculation of the cell temperature of a high concentrator photovoltaic (HCPV) module: a study and comparison of different methods, Sol. Energy Mater. Sol. Cells, 121 (2014) 144-151.
T. Fujisawa, T. Tani, Annual exergy evaluation on photovoltaic-thermal hybrid collector, Sol. Energy Mater. Sol. Cells, 47 (1997) 135-148.
P. Gang, F. Huide, J. Jie, C. Tin-tai, Z. Tao, Annual analysis of heat pipe PV/T systems for domestic hot water and electricity production, Energy Conversion and Management, 56 (2012) 8-21.
K. Ghosal, D. Lilly, J. Gabriel, M. Whitehead, S. Seel, B. Fisher, J. Wilson, S. Burroughs, Semprius field results and progress in system development, IEEE Journal of Photovoltaics, 4 (2014) 703-708.
M.A. Green, K. Emery, Y. Hishikawa, W. Warta, E.D. Dunlop, Solar cell efficiency tables (version 39), Progress in photovoltaics: research and applications, 20 (2012) 12-20.
M.A. Green, M.J. Keevers, I. Thomas, J.B. Lasich, K. Emery, R.R. King, 40% efficient sunlight to electricity conversion, Progress in Photovoltaics: Research and Applications, (2015) n/a-n/a.
A. Hepbasli, A key review on exergetic analysis and assessment of renewable energy resources for a sustainable future, Renewable and Sustainable Energy Reviews, 12 (2008) 593-661.
J. Ji, J.-P. Lu, T.-T. Chow, W. He, G. Pei, A sensitivity study of a hybrid photovoltaic/thermal water-heating system with natural circulation, Applied Energy, 84 (2007) 222-237.
R. King, D. Bhusari, D. Larrabee, X.Q. Liu, E. Rehder, K. Edmondson, H. Cotal, R. Jones, J. Ermer, C. Fetzer, Solar cell generations over 40% efficiency, Progress in Photovoltaics: Research and Applications, 20 (2012) 801-815.
A. Kribus, D. Kaftori, G. Mittelman, A. Hirshfeld, Y. Flitsanov, A. Dayan, A miniature concentrating photovoltaic and thermal system, Energy Conversion and Management, 47 (2006) 3582-3590.
G. Li, G. Pei, M. Yang, J. Ji, Y. Su, Optical evaluation of a novel static incorporated compound parabolic concentrator with photovoltaic/thermal system and preliminary experiment, Energy Conversion and Management, 85 (2014) 204-211.
Y. Liu, P. Hu, Q. Zhang, Z.S. Chen, Thermodynamic and optical analysis for a CPV/T hybrid system with beam splitter and fully tracked linear Fresnel reflector concentrator utilizing sloped panels, Solar Energy, 103 (2014) 191-199.
A. Luque, G. Sala, J. Arboiro, T. Bruton, D. Cunningham, N. Mason, Some results of the EUCLIDES photovoltaic concentrator prototype, Progress in Photovoltaics: Research and Applications, 5 (1997) 195-212.
A. Rabl, Comparison of solar concentrators, Solar Energy, 18 (1976) 93-111.
J.I. Rosell, X. Vallverdu, M.A. Lechon, M. Ibanez, Design and simulation of a low concentrating photovoltaic/thermal system, Energy Conversion and Management, 46 (2005) 3034-3046.

A. Royne, C.J. Dey, D.R. Mills, Cooling of photovoltaic cells under concentrated illumination: a critical review, Sol. Energy Mater. Sol. Cells, 86 (2005) 451-483.
M. Steiner, A. Bösch, A. Dilger, F. Dimroth, T. Dörsam, M. Muller, T. Hornung, G. Siefer, M. Wiesenfarth, A.W. Bett, FLATCON® CPV module with 36.7% efficiency equipped with four ‐ junction solar cells, Progress in Photovoltaics: Research and Applications, 23 (2015) 1323-1329.
A. Tiwari, S. Dubey, G. Sandhu, M. Sodha, S. Anwar, Exergy analysis of integrated photovoltaic thermal solar water heater under constant flow rate and constant collection temperature modes, Applied Energy, 86 (2009) 2592-2597.
M. Wolf, Performance analyses of combined heating and photovoltaic power systems for residences, Energy Conversion, 16 (1976) 79-90.
Y. Wu, P. Eames, T. Mallick, M. Sabry, Experimental characterisation of a Fresnel lens photovoltaic concentrating system, Solar Energy, 86 (2012) 430-440.
W. Xie, Y. Dai, R. Wang, K. Sumathy, Concentrated solar energy applications using Fresnel lenses: A review, Renewable and Sustainable Energy Reviews, 15 (2011) 2588-2606.

ISES International Solar Energy Society

Conference Proceedings

Solar World Congress 2015

Daegu, Korea, 08 – 12 November 2015

A New Tubular Photovoltaic Solar System with Low Sun Concentration

Claude Oiknine

Yuma SAS,Gargas, France

1. Summary

The Yuma project is to manufacture and commercialize a new photovoltaic (PV) energy solar system with leading partners. The tubular low sun concentration module, based on a disruptive design, provides a new optimized solution to produce green electricity in sandy or dusty environment. Originally developed and designed by a top-level research team, this system is protected by patents owned by the company.

The product successfully passed the prototype and preliminary performance tests. From early 2015, Yuma entered the industrialization and marketing phases with the ambition to be leader in the Sunbelt regions.

A short summary of photovoltaic market, based on outstanding analysis is given to show orders of magnitude of this market in the near future.

Keywords: *Photovoltaic, low sun concentration, one axis tracking, sun-belt market, grid parity, low LCOE*

2. The PV Market

2.1 Global PV market as of 2013

The global PV market progressed in 2013: after two years of approximately 30 GW of installations annually, the market reached 37 GW in 2013 and 40 GW in 2014. But the most important developments were the rapid development of PV in Asia, combined with a sharp drop of installations in Europe. As indicated in Global Market Outlook for photovoltaics, 2014-18:

"China became the top PV market in the world in 2013 and achieved the world's largest PV installation figure in one year with 11.8 GW connected to the grid, after Italy installed 9.3 GW in 2011 and Germany installed between 7.4 GW and 7.6 GW from 2010 to 2012. Japan scored 6.9 GW and took the second place in 2013, while the USA installed 4.8 GW."

2.2 Global PV market forecast by 2018

Previsions for the PV market in the near future are very encouraging: The same reference indicates:

"While European electricity demand is stagnating, this is not the case globally and PV growth will continue to be driven by local and global energy demand. The fastest PV growth is expected to continue in China and South-East Asia in general, with Latin America, the MENA countries and India following. The PV potential of the Sunbelt countries – where PV can already compete with diesel generators for peak power generation without financial support – could range from 60 to 250 GW by 2020, and from 260 to 1,100 GW in 2030. And with the faster than expected price decrease in PV technology that the industry experienced in recent years, even more countries will see PV as a competitive energy source before the end of this decade."

3. The Yuma Vision

3.1 The Yuma Vision

Yuma intends to provide a disruptive technology to unlock the Sunbelt PV potential

Selection and/or peer review under responsibility of Scientific Committee
doi:10.18086/swc.2015.05.22 Available at http://proceedings.ises.org

3.2 The untapped Sunbelt potential

According to Global Market Outlook for photovoltaics, 2014-18 and EPIA and "Unlocking the Sunbelt potential of photovoltaics, October 2010, EPIA:

"The 66 Sunbelt countries account for 5 billion inhabitants representing respectively 95% of the Sunbelt and 75% of the world's population. Their 6.800 TWh electricity consumption represents respectively 97% of the Sunbelt and 38% of the world's electricity consumption"".

In the Company vision the huge potential of these sun-rich countries is a key parameter to make possible the introduction of a PV system whose design has been thought for the specific conditions of this market.

3.3 Technology limitation of PV flat panels

Increasing module efficiency is a major strategy for reducing per-watt module price. Consistent improvements in PV cell efficiency have been realized for virtually every PV technology (Fig.7), and module efficiency has followed this trend, albeit with a time and performance lag; this trend is projected to continue.

As single-junction PV technologies approach the theoretical (Shockley-Queisser) efficiency limit for their respective semiconductor materials, the extent to which further cost reduction may be attributable to efficiency gains will be reduced, and more substantial cost reductions will need to be realized via other ways.

CPV technologies offer high efficiency performance. However, at the module scale, HCPV has to deal with major technological challenges as high temperature management in the module, high tracking precision to target small and costly multi-junction cells. At this stage HCPV developers haven't found the solution to solve these issues at a low cost.

3.4 The dust problem

Dust and sand storms are prominent issues for PV installations in many sun-belt countries. (See Fig 1)

First, dust is deposited on solar surfaces every day of the year, and because of the absence of rain, it is not naturally washed from the panel. For example, deposition rate on solar surfaces has been measured at approximately 12.5 g / cm^2/ month in Saudi Arabia. This deposition rate will induce an efficiency drop of 8 to 15 % per month. This dust requires frequent cleaning involving significant manpower and water; it impacts heavily the O&M cost of the PV array. During the life time of a solar field, about 0.5 $/W additional cost to the initial price of the panel has to be paid.

The "dust problem" points out that flat solar panels, originally developed in Western Countries , are not the best fit for these conditions.

Integration of a Levelized Cost of Electricity (LCOE) have to be taken into consideration by developer in a long term vision

PV LCOE in Sunbelt Countries is expected to range from 5 to 12 c€/kWh by 2020 and 4 to 8 c€/KWh by 2030. In North Chile and South Morocco PV solar fields reach already grid parity as indicated by A.T Kearney National Renewable Energy Laboratory, National Technology Laboratory, EPIA Set for 2020, World Bank

Fig.1: sand storm in UAE

3. Yuma Project: An Alternative solution

4.1 The Yuma technology

4.1.1 Yuma's cylindrical LCPV sun receiver

The photovoltaic module consists of glass tubes including in their inner upper part a thin Fresnel lens. The lens concentrates the sun energy ten times along the bottom of the tube where a narrow strip of silicon cells is located (See Fig 2). Each tube, including dry air at atmospheric pressure, is permanently sealed and thanks to a simple rolling system tracks the sun from East to West.

Cells are manufactured out of quite ordinary wafers used for flat panels, however the two electrical contacts are both in the back of the cell allowing automatization of the stringing. Therefore the cost of these cells is close to one sun ordinary cells.

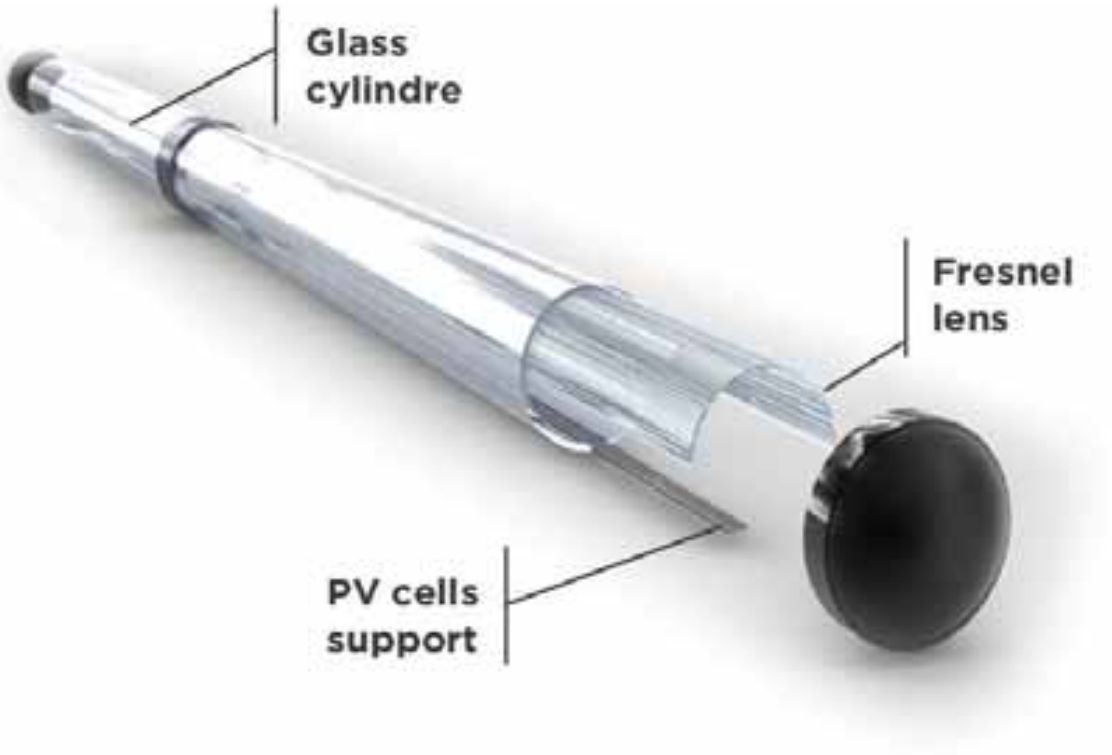

Fig.2: The Tenoga cylindrical LCPV module

Glass cylinder

A borosilicate glass tube with a 110 mm outside diameter and a 2000 mm length, both ends including a mechanical and electrical adaptor which allow a permanent closing of the tubes after assembly operations.
We chose standard tubes used for water heating in China where they are manufactured in huge quantity and at an affordable price. Borosilicate 3.3 was chosen for its good transparency and its proven resistance to UV and field conditions

Fresnel lens

A thin TPU film (around 100 µm thick) includes in one of its face a linear Fresnel Lens structure made of UV curing lacker; the TPU is slightly sticky on glass and the bond becomes very strong when heated. Moreover it has a good behavior when submitted to UV without yellowing.The Fresnel lens is located inside the glass tube on a 120° sector; its special design focused the solar irradiation linearly on a seven mm width-band, located on the low part of the tube.
The Fresnel Lens film was developed and manufactured by Film Optics specially for our application. The use of TPU allows a relative low cost and an easy integration in the glass tube. We chose Fresnel lens technology to avoid the use of big mirrors or sun concentrators.

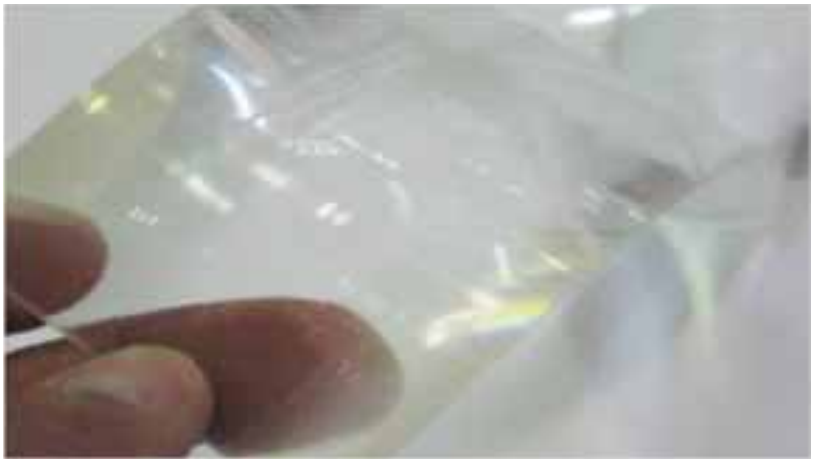

Fig. 3: Fresnel lens film

PV cells support

On a thin aluminum bar, located at the focal point of the Fresnel lens are connected in series forty MWT cSi photovoltaic cells with back contacts. This design allows to manufacture on the bar copper electrical contacts and to use an automatic process of pick and place to bond the cells on the bar. Bonding the cells must not introduce significant local electrical resistance; a special process using point soldering by laser was used.
Each tube will deliver around 25W.

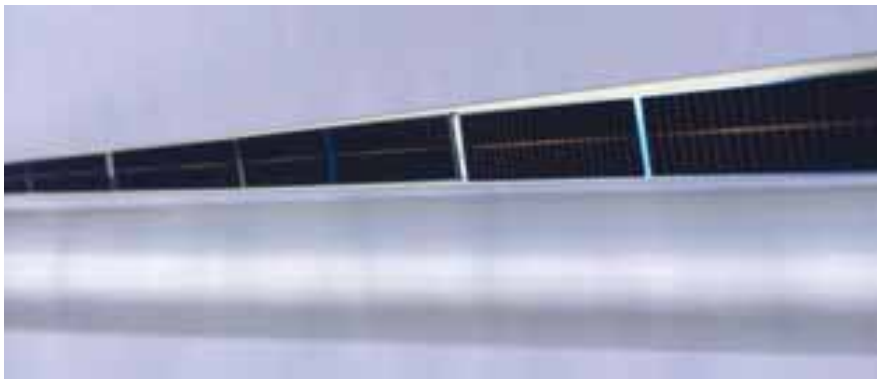

Fig. 4: PV cells support with back contact

Heat Sink

A Heat sink is made of a thin sheet of aluminum flattened by pre-stress against the inner wall of the tube; the bar with the solar cells is thermally bonded to the heat sink. The heat sink design is very important due to the large decrease of cells efficiency with temperature increase.

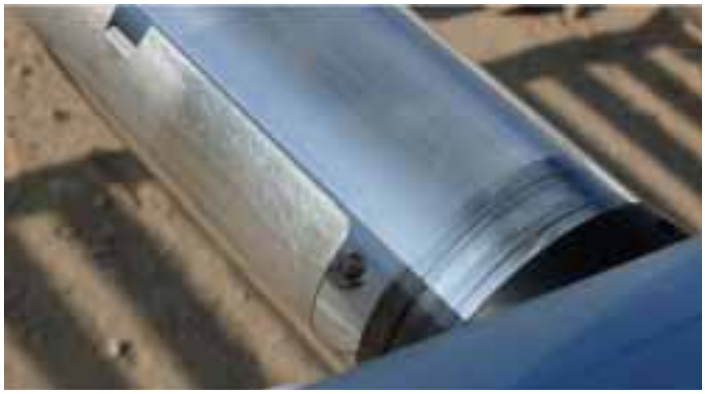

Fig 5: Heat sink

The thermal flux produced by the cells is quite small; therefore conduction through the heat sink and the glass tube occurs with a quite small loss of temperature. Radiation helps partly the cells to remain at a reasonable temperature. The area of the heat sink contributing to the cooling is about twice that existing on flat panel. Finally thermal flux is absorbed outside by natural or forced convection.
Laboratory simulations and site tests have confirmed that with a DNI of 1000 W/m^2 and with a wind speed of 0 km/hour, temperature elevation at the surface of the cells is no more than 30 °C above ambient temperature. With a 1 m/s wind this elevation will be 20 °C only.

So even with a sun concentration of ten, the design of the sun receiver and the efficiency of the heat sink avoid high temperature elevation of the cells.
Fig 23 shows a simulation of temperatures on the heat sink for a DNI of 1000 W/m^2 and without wind.

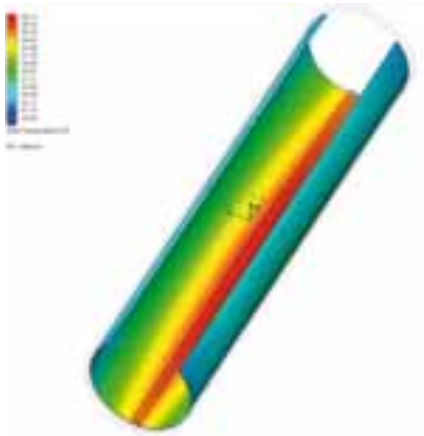

Fig. 6: Heat sink thermal simulation

4.1.2 Yuma's one axis tracking system

A one-axis tracking system enables each tube to rotate and to follow the sun in the East-West direction: hundreds of tubes can be rotated together driven by one small electrical motor.
The tracking system includes:

- A sun tracker with its control box
- A small electrical motor driving together a line of hundreds tubes
- A simple mechanism allowing the tube rotation without translation.

The whole mechanism with all electrical contacts is pre- installed in factory; it is protected against UV and dust inside Aluminum beams which are both support of the system and protection of components.

Fig. 7: Rolling mechanism stress tests

4.1.3 Ground installation

All cylindrical modules are mechanically and electrically «plug and play» connected to dedicated Aluminum beams. These beams include the electrical connections as well as the tube rotating mechanism and are ready to be installed on site.

The whole design enables a very easy and quick ground installation which *does not require any civil work.*

Moreover replacement of tube or of electrical motor does not require time nor special qualification.

Fig. 8: Pilot ground mounted installation

4.2 R&D

4.2.1 First Phase: Research

A first phase of R&D conducted in 2011-2013 focused on:

- Technical and economical feasibility studies
- Design of each component of the system including photovoltaic and mechanical items.
- Build pilot equipment and conduct laboratory tests and also tests in a desert environment in order to valid the system performances.

This first R&D phase has led Yuma to the installation of one prototype system tested in desert situation. This 500 W generator has strengthened the expected performance forecast of the future commercial product.

This first phase was supported by national institutions and private companies in particular Navallon Groupe.

Components developments:

Yuma uses basic components like standard borosilicate glass tubes and existing under-control technologies with a dedicated design for Yuma System, such as focusing optics developed by Film Optics in Great Britain and MWT cSi cells developed at Fraunhofer Institut in Germany.

Availability of components has always been a driver in the development of the Yuma technology.

4.2.2 Second Phase: Development

Supported by Institutional and financial partners as BPI (Banque Publique d'Investissement) , Midi Pyrenees Region in France and technological leaders as CEA, Fraunhofer lnstitut, Yuma has entered in a 2 years development phase leading to the construction of a 50 KW industrial pilot and the certification of the commercial product. (2016)

This phase includes additional components modification to fit industrial cost and time manufacture :

- *Lens:* Fresnel lens will use a 100 µm TPU substrate cheaper than PMMA and allowing a simple bonding process inside glass tube.
- *Cells:* Fraunhofer Institut tested successfully blue wafers produced by IrySolar in France. It will allow in the future production of MWT back contacts cells at competitive price
- *Electrical Connection:* Using technology Aluminum bars with copper electrical connections will enable to manufacture bars ready to include solar cells by a pick and place automatic bonding process.

5. Yuma system advantages:

Yuma PV solar system presents numerous advantages:

5.1 Price

The cost of a solar systems includes mainly the initial investment for the project, all hardware, ground preparation, financial cost, field installation, insurance, but also all the expenses during the life time of the array to allow a good installation efficiency (cleaning, new inverters).The energy produced during the life time of the PV generator depends on the sun irradiation and on the system efficiency. The LCOE which is the ratio of all costs divided by the total energy harvested in c$/kWh is a good integral indicator of the value of a solar field; today the lowest proposed LCOE is the key to win public tenders. Yuma, with a hardware cost around 0.5 $/W, a very low cost of installation and maintenance and a high level of irradiation, can reach LCOE less than 7c$/kWh.

5.2 Self cleaning

We showed that maintaining sun receivers clean is a main issue in order to maximalize the energy harvested. In our case the tubes are horizontal and separated by a small gap; therefore they collect much less dust and sand that flat surfaces. Moreover automatic dry cleaning, if necessary, is very easy and cheap.

5.3 Installation time

Is very small due to the facts that:

- There is no need of ground preparation and of concrete basis
- The forces due to wind are small and the system stays by its own weight
- Aluminum beams and supports come pre-integrated from factory
- Cylindrical sun receivers are put in place like Neon tubes

5.4 No danger of robbery

In several countries robbery of flat panels is quite usual because they can be used for TV; so the solar field has to be closed by fences and monitored by cameras. In our case it is very easy to rob a glass tube but there is no utility.

5.5 Flexibility

Future, more efficient, new cells can be incorporated in Yuma system very easily

5.6 Easy maintenance

Failure of a sun receiver or of an inverter will be automatically identified and replacement of the failed item is very quick and simple

6- Competition

Today more than 95% of solar fields are equipped with flat PV panels. Other technologies like thermal solar or PV with high sun concentration have not succeeded for the moment to gain a relevant part of the market:

the main reason is cost.
The idea to use PV with low concentration was tested some years ago [1], [2], [3] but without success; the main reason was the system design using big troughs leading to high cost.

7 Conclusions:

Yuma is building an industrial Pilot of 50 kW, based on a new tubular PV technology including low sun concentration and one axis tracking. This Pilot will be ready for real-life tests in desert conditions before the end of 2015. The maturity of this technology will allow us to market and manufacture Yuma systems before end 2016. . No other market solution provides comparable level of efficiency and competitiveness in sun-rich regions.

8- References

[1] Performance Results of a Low-Concentration Photovoltaic System Based on High Efficiency Back Contact Cells by Zachary S. Judkins, Keith W. Johnston, Charles Almy, Ryan J. Linderman, Brian Wares, Nicholas A. Barton, Matt Dawson, and Jack Peurach 2010 SunPower

[2] Low-Cost 20X Silicon-Cell-Based Linear Fresnel Lens
Concentrator Panel Mark O'Neill, A.J. McDanal, Don Spears, Clay Stevenson and David Gelbaum
Entech Solar, Inc., 13301 Park Vista Blvd., Suite 100, Fort Worth, Texas 76177 USA

[3] Technology:A Disruptive Low-Concentration PV Proposition From Cogenra by Herman K. Trabish November 21, 2013 by Herman K. Trabish
November 21, 2013

Conference Proceedings

Solar World Congress 2015
Daegu, Korea, 08 – 12 November 2015

Status and perspective of Concentrating Photovoltaic Systems: the results of the BioCPV project and opportunities for a sustainable energy supply to rural areas

Tapas K. Mallick[1], Leonardo Micheli[1], Sambhu Banerjee[2], Katie Shanks[1], S Lokeswaran[3], Hasan Baig[1], Fausto Calabria[1], Nabin Sarmah[4], Mark Walker[5], Marios Theristis[6], K S Reddy[3], Prakash Ghosh[7], Gavin Walker[8], Shibani Choudhury[2], Mohamed Pourkashanian[5], Tadgh O'Donovan[6], Joel Hamilton[8], Davide Poggio[5], Donald Giddings[8], Amit Hazara[2], S Balachandran[2], David Grant[8], William Nimmo[5], Lin Ma[5], Anil K Mathew[9], Ramansu Goswami[2], Amit Chakraborty[2], Debasree Dinha[2], Kunal Bandyopadhyay[2], Florencia Almonacid[10], Eduardo F. Fernandez[10].

[1]Environment and Sustainability institute, University of Exeter, Penryn TR10 9FE (UK)

[2]Department of Environmental Studies, Siksha-Bhavana, Visva-Bharati, Santiniketan 731235 (India)

[3]Heat Transfer and Thermal Power Laboratory, Department of Mechanical Engineering IIT Madras, Chennai 600036 (India)

[4]Department of Energy, Tezpur University, Tezpur, Assam, 784028 (India)

[5]Department of Mechanical Engineering, University of Sheffield, Sheffield, S10 2TN (UK)

[6]Institute of Mechanical, Process and Energy Engineering, School of Engineering and Physical Sciences, Heriot-Watt University, Edinburgh EH14 4AS (UK)

[7]Department of Energy Science and Engineering, IIT Bombay, Powai, Mumbai 400 076, (India)

[8]Faculty of Engineering, The University of Nottingham, Nottingham, NG7 2RD (UK)

[9]Centre for Biofuels, Biotechnology Division, CSIR-National Institute for Interdisciplinary Science and Technology, Thiruvananthapuram 695019 (India)

[10]IDEA Solar Energy Research Group, University of Jaen, Jaen 23071 (Spain)

Abstract

The present paper reports the results of the BioCPV project, a venture of six universities conceived to develop a novel integrated renewable energy system for an autonomous electrical power generation for rural electrification. Concentrating Photovoltaics (CPV) is coupled to an Anaerobic Digestion Biogas system through a smart control mechanism to maximize the efficiency and to supply electricity uninterruptedly. The excess electricity generated during the day time is used to generate hydrogen, stored using metal hydride technologies and released during evening hours as input of an electricity generator. The waste heat of the CPV is recovered and used to accelerate the biogas production. The outcomes of the research on concentrating photovoltaic technologies are resumed: two high-concentrating systems have been developed, different thermal and electrical models have been proposed and the results of innovative researches on optics, building-integration and cooling have been presented.

Keywords: *Concentrating photovoltaics, rural electrification, integrated renewable energy system*

1. Introduction

Global energy consumption is constantly increasing, driven by the emerging economies. In 2013, renewable

doi:10.18086/swc.2015.05.23 Available at http://proceedings.ises.org

energies contributed to the 5.3% of global power generation, and accounted for more than half of the yearly global power capacity installed (Renewable Energy Policy Network for the 21st Century, 2014). Despite the grid requirement for a balanced and continuous power supply, the electricity generated by renewable sources is generally fluctuating both on short-term (seconds to hours) and long-term scales (months to years) (Weitemeyer et al., 2014). Hybrid power plants with different renewable technologies have already been identified as efficient, cheap and sustainable options for rural electrification (Bajpai and Dash, 2012). In this light, the BioCPV project aims to contribute to the optimization of hybrid renewable power generation systems and to the electrification of a rural village in the eastern part of India. The system under development integrates concentrating photovoltaic (CPV), anaerobic digestion (AD) and hydrogen storage systems. The present paper reports the latest progresses made in terms of scientific achievements on the development of innovative concentrating photovoltaic systems.

2. Concept and system's configuration

The BioCPV system is installed in the village of Kaligunj – Pearon Pally, adjacent to Visva-Bharati, Santiniketan, West Bengal, India, and supplies renewable energy to 14 household, one school, one community building and 50 street lights. In the early stage of the project, a survey has been carried out to estimate the energy need of the village (Mallick et al., 2013). During summer the peak load was found to be 5.8kW, whereas during winter it dropped to 5.5kW. Therefore, the system configuration has been designed in order to meet the necessities of the villagers. Taking into account the load profile, the peak energy demands and the weather conditions of the locality, a 10kW high concentrating photovoltaic (HCPV) system has been designed. The energy produced by the HCPV is mainly used to supply electricity to the village, whereas, during the low-load times, part of it is used by an electrolyzer to produced hydrogen. The hydrogen is stored and used through a generator during the peak-consumption times. The same generator uses the biogas produced by an anaerobic digestion system: the food waste and the local biomass are used to generate the biogas. In order to maximize the performance of the system, the waste heat generated by the HCPV system is recovered and used to support the anaerobic digestion.

The HCPV is expected to supply the electrical energy needed: the energy surplus is stored by producing hydrogen and used during the low-irradiance hours. It consists of four HCPV units with two axis tracking: each unit is made of two primary concentrators and two receivers. The electrolyzer requires 1kW in input from the HCPV and is designed to work for 7 hours a day. It has an efficiency of 60 % and it is expected to produce about 3 liters of hydrogen per minute. The hydrogen is stored in a metal hydride system, which has an efficiency of 90-95 % and can release about 300 liters of hydrogen for 4 hours. The digester for the AD system has been dimensioned to produce daily an adequate amount of biogas. A maximum of 15kW of thermal energy can be recovered by the HCPV (K. S. Reddy et al., 2014) and used to support the anaerobic digestion.

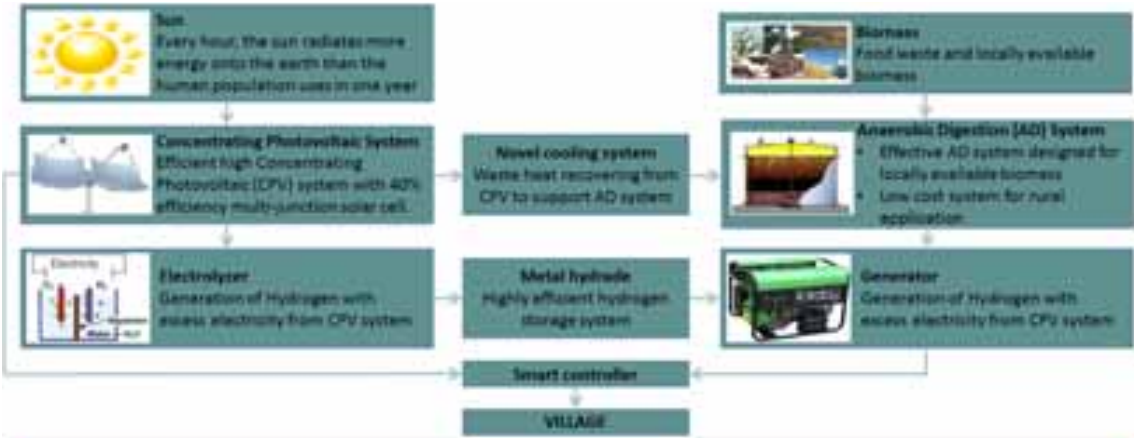

Fig. 1: Schematic of the BioCPV system.

The integrated renewable energy system designed for the BioCPV project has been demonstrated to be more beneficial than a single source system (Castellanos et al., 2015). A cost of $ 0.289 per kWh^{-1} was estimated

and is lower than that predicted for other technologies and scenarios ($ 0.335–1.332 per kWh^{-1}). According to the authors, the main reasons for this achievement are due to the synergy between the various production and storage elements at meeting the demanding load profile with a very high quality of supply.

2.1. Expected social and health benefits

The tribal communities residing in the villages of Kaligunj – Pearon Pally do not have access to the grid. These people are mostly dependent on leaf litters, forest wood, cow dung cakes for cooking and use kerosene lantern in the night time for education and other household activities, which is responsible for the indoor pollution as well. This lack of proper electrical/power facilities is deterrent for their development in terms of education, sanitation, health and entertainment. Electrification drive through renewable energy recourses like solar and biomass in the form of BioCPV system is conceived to face the problem of poverty, illiteracy, and lack of healthiness and also to ensure a clean and sustainable environment by reducing greenhouse gas emission thereby curbing indoor and outdoor pollution. Once implemented, the renewable energy harvesting system through AD/PV will generate employment opportunities among the tribals, make them self-sufficient and inculcate better competitiveness to take on the challenges of the rest of the world.

2.2. In-loco components installation

In the project site of Santiniketan, where the BioCPV system is being implemented, a control room has been built for housing different components of the system, such as the genset, the biogas engine or the inverter. Electrification works have been done for providing electricity to the designated households, school building, primary health center in the village. The Anaerobic Digester (Fig. 2) has been set up which will produce biogas (methane) with locally available aquatic weeds (such as water hyacinth and salvinia), kitchen waste, and cow dung as the source of inoculums. The biogas can be used for cooking purpose as well by the villagers and also used to generate electricity in the rainy season when the radiation is not enough to run the solar technologies at their highest capacity.

Fig. 2: Components of the AD system: gas chamber (a), main digester (b), predigester (c), chopper/grinder (d).

3. The concentrating photovoltaic systems

Concentrating Photovoltaic (CPV) systems make use of optical components which concentrate the incoming sunlight and focus it on solar cells. The concentrated light reaching the solar cell magnifies the production of energy several times. These optical components often referred to as concentrators, make use of reflective/ refractive principles of optics, individually or in combination for concentrating the sunlight.

3.1. 144-cell HCPV systems

A novel densely-packed HCPV system has been developed. The optics consists of a 125× primary and a 4× secondary optics that focus the sunlight onto a 144-cell receiver. The CPV system is equipped with two reflective geometries a square parabolic reflector as primary concentrator and 12 x 12 array of three-dimensional compound parabolic concentrators (CPCs) with optical homogenizer as secondary concentrator.

The geometrical concentration ratio for primary concentrator is 125× primary and secondary concentrator is 4×. The secondary concentrator integrated with CPV cell assembly and an active cooling system forms the complete CPV receiver. The incoming rays falling on the aperture of the parabolic dish will be reflected to CPCs. The CPCs will concentrate and redirects the rays towards the cell. The light rays which are parallel to the CPC's optical axis will not lose energy because it falls directly on the cell surface without any reflection, whereas the light rays entering the CPC within the acceptance angle will go multiple reflections in both CPC and homogenizer before reaching the cells. The homogenizer mounted on the exit aperture of the CPC will homogenize the flux distribution on the cell surface by multiple reflections. The irradiation distribution on one-fourth (6 x 6) of the 12x 12 CPV receiver is shown in Fig. 3 (S. Lokeswaran et al., 2015). The characteristics of the concentrators are resumed in Tab 1.

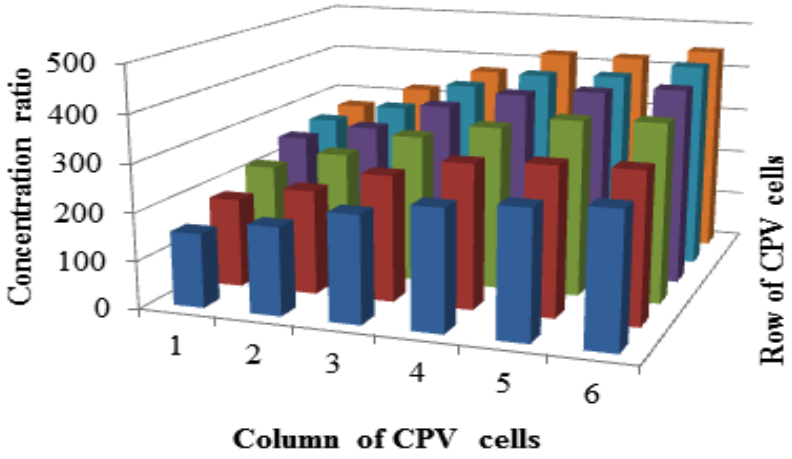

Fig. 3: Flux distribution for one-fourth of the array

Tab 1: Specifications of the concentrator optics.

Primary concentrator		Secondary concentrator	
Geometric concentration ratio	125×	Geometric concentration ratio	4×
Aperture area	3m×3m	Cell side aperture area	10mm 10mm
Rim angle	20°	Acceptance angle	30°
Focal lenght	3.37m	Length of CPC	25mm
f/d ratio	0.794	Length of the homogenizer	10mm

The design of the receiver has been conceived to lower the costs and reduce the electrical losses (Micheli et al., 2015e). The receiver is built on an insulated metal substrate (IMS) that gives mechanical support to the receiver, collects the electrical energy produced by the cell and facilitates the removal of the waste heat. It was already known that IMS had a similar resistance to fatigue to that of the direct bonded copper (DBC) boards (Mabille et al., 2013), dominantly used to produce the HCPV receivers. Within the BioCPV project, IMS have been demonstrated to have a thermal behavior similar to that of DBC and more advantageous in terms of fabricability and costs (Micheli, 2015).

Each board allocates 144 1cm^2-sized 3C40 cells, supplied by Azurspace. The geometry of all the components has been designed to fit the requirements of the standards and to grant acceptable thermal management and electrical performance to the assembly. The shape of the electrically conductive layer has been conceived to minimize the electrical resistance. One Schottky diode per cell has been employed in the receiver to avoid damages to shaded cells and to reduce the power losses in case of current mismatch among different series-connected cells. Aluminum wires have been bonded to interconnect the cells and the conductive layers: they have been sized to safely work even in presence of overcurrents.

Fig. 4: A prototype of the HCPV system developed for the BioCPV project.

The HCPV systems are required to work for 20+ years in outdoor conditions, with minimum degradation. For this reason, the developed receiver has been mechanically and electrically tested (Micheli, 2015). At 500x, each cell is expected to work at a maximum power point power of 14.7W, achieving, under 1000W/m^2 DNI, an efficiency of 29.4%. A full scale prototype of the HCPV system has been installed (Fig. 4) and is being tested on the roof of the Institute of Technology Madras, in Chennai (India).

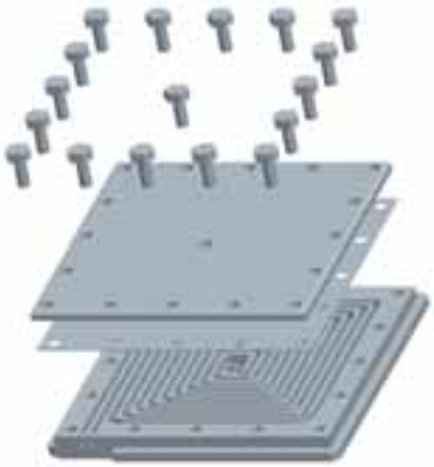

Fig. 5: Spiral Heat sink for CPV Cooling

The HCPV receiver is mounted on an active spiral mini channel heat sink, made of aluminum (S Lokeswaran et al., 2015). It consists of spiral flow mini channel heat sink with rectangular cross section channels where separate inflow and outflow paths with inlet and outlet ports were grooved as shown in Fig. 6 (K. Reddy et al., 2014). The base of the mini channel receives heat flux from the cells and the heat is transferred directly to the coolant by convection from the bottom surface and indirectly through the dividing wall. The large surface area of mini channel enables the coolant to take away large amounts of heat per unit time per unit area while maintaining a considerably low device temperature. Water is used as cooling fluid. The coolant enters the inlet port at ambient temperature and takes up the heat all the way through the flow path grooved in heat sink flowing clockwise towards the center. From the center the fluid flows anticlockwise towards outlet port through outflow channels located adjacent to the inflow channel. So, high heat fluxes can be dissipated at relatively low surface temperatures. The dimensions of the heat sink have been optimized to keep the HCPV module at a temperature of 80°C, with an overall pressure drop of 8.0 kPa. The solar radiation is concentrated on secondary reflector (CPC) which in turn concentrates onto the bottom surface of

the mini-channel spiral cooled receiver holding the 12 x 12 dense array of efficient triple junction PV cells.

3.2. Cassegrain Concentrator Photovoltaic System

Along with the large HCPV system, a cassegrain 500x HCPV module has been developed. The system consists of two reflective optics and a homogenizer, which concentrate the sunlight on a 1 cm^2-sized multijunction cell. The two-stage reflector configuration has been chosen to enhance the compactness of the module. The optics geometries (Tab 2) have been optimized to achieve an efficiency as high as 84.82% at normal incidence and limiting the losses in case of a ±1° tacking error (Shanks et al., 2014).

Tab 2: Specifications of the cassegrain concentrator optics.

Primary concentrator		Secondary concentrator		Homogeniser	
Geometric concentration ratio	125×	Geometric concentration ratio	3×	Geometric concentration ratio	9×
Aperture area	23cm×23cm	Aperture Area	5cm × 5cm	Aperture Area in	3cm × 3cm
Focal Length	27cm	Focal Length	7cm	Aperture Area out (Cell)	1cm 1 cm
Height of dish	2.8cm	Separation Distance from Primary	15.6cm	Length	7.5cm
Width of dish	23cm	Full system Height	20cm	f/d ratio	1.2

The surface roughness of the homogenizer can significantly affect the overall optical efficiency and to compensate for this inherent loss due to manufacturing processes, a new conjugate refractive reflective homogenizer (CRRH) was developed and proven capable of increasing the optical efficiency of the system by 6% (Shanks et al., 2015a). The new homogenizer was found to improve the optical efficiency by 3% at normal incidence (Fig. 6).

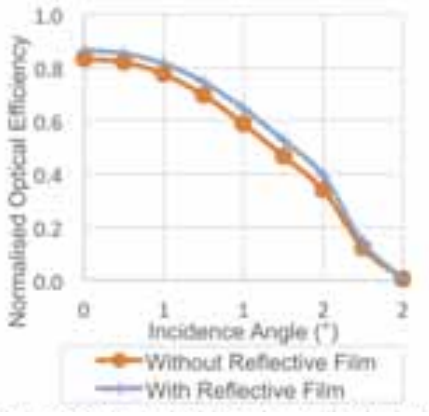

Fig. 6: Enhanced optical efficiency of the homogenizer due to the use of the reflective film (Shanks et al., 2015a).

The Cassegrain Concentrator Photovoltaic modules have been arranged in 3x3 arrays (Fig. 6) and are currently being outdoor tested in Spain and India.

Fig. 7: The 3x3 Cassegrain Concentrator Photovoltaic System a) top and b) side view.

3.3. Electrical and thermal modelling

Electrical and thermal modelling of HCPV is a fundamental research aim to optimize the design of the systems and the prediction of energy production. In this light, different studies on the electrical and thermal behavior of the HCPV systems have been presented and made available in literature (Almonacid et al., 2015; Fernández et al., 2015). A comparative studies demonstrated that the available models could predict the maximum power output of different HCPV systems with discrepancies lower than 5% (Soria-Moya et al., 2015). An integrated thermal-electrical model has been developed: it has been found that a 1cm^2-sized cell can be adequately cooled by an heat sink with a thermal resistance of 1.63 K/W or less (Theristis and Donovan, 2015).

3.4. Data logging and system integration

The data acquisition system produced for the BioCPV project differs from standard systems at it collects data from the off-grid system and stores them remotely, making them available through a real time interface (Calabria, 2015). Generally, the data recorded in a stand-alone system are stored in a “black box” that needs to be directly accessed in order for the data to be retrieved. On the other hand, biosciences data logging systems transmit the GPS coordinates to track the animal movements but the data is stored on the microprocessor directly and retrieved by following the GPS signal.

The system used in BioCPV has been programmed using LabVIEW, a software package developed by National Instruments (NI). The system, shown in Fig. 8, is composed of 5 independent units connected through a NI chassis. The NI controller is the cRIO-9024, a real time controller used for deterministic control, data logging and analysis. Three standard modules have been used for the acquisition of currents, voltages and temperatures. A communication module developed by the Science & Engineering Applications Datentechnik GmbH, based in Germany, has been configured to transfer the data through a M2M platform and has been connected to a GPS and a GSM positioning antennas

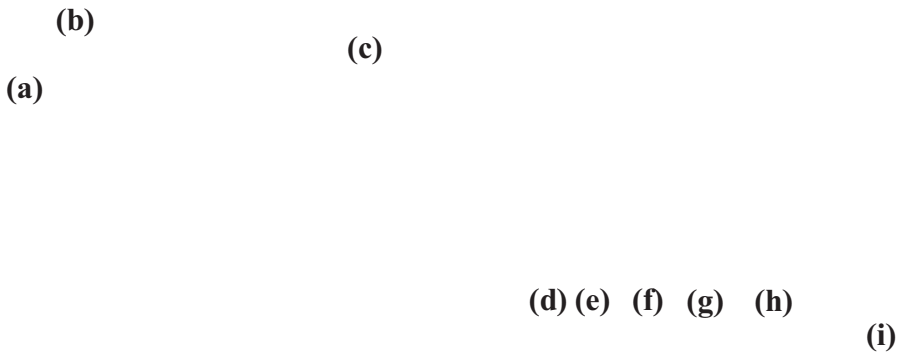

Fig. 8: The data logging system (Calabria, 2015): (a) GPS Antenna, (b) GSM Antenna, (c) NI 8-slot Chassis, (d)SEA 9721 3G Module, (e) Current Sensor (NI 9227), (f) Voltage Sensor (NI 9225), (g) Temperature Sensor (NI 9213), (h) CompactRIO 9024 microcontroller, (i) Power Supply

4. Scientific impacts on the future of HCPV

4.1. Future scenarios for HCPV optics

Shanks et al. (Shanks et al., 2015c) listed the main features of an ideal solar concentrating optical system which should be aimed for when designing a solar concentrator: 100% optical efficiency, uniform irradiance distribution, maximum acceptance angle, high optical tolerance, reliability and durability. Along with these characteristics, the optics should be cheap, easy to manufacture and to install as well as light in weight. In this light, the results of a multi-disciplinary work have been recently presented (Shanks et al., 2015b): the wings of white *Pieris* butterflies have been investigated to understand their applicability in HCPV. The white *Pieris* butterflies use their highly reflective white wings to increase their thorax (and hence flight muscles) temperature. To do this, they hold their wings in a v-shape, similar to a V-trough concentrator. It was found that, using the butterfly wings instead of a standard reflective film to concentrate the light on a 1cm multi-crystalline cell (Fig. 4), the electrical power output to weight ratio was enhanced by 17 times. Although the wings had a very high reflectance of >80%, this is not as high as reflective films available at present (>90%), however the wings have the advantage of being extremely lightweight. This lower weight and enhanced power to weight ratio would be a great benefit to CPV systems. HCPV systems in particular are often heavy and bulky due to the large optics used but developing a lighter reflective material could greatly expand their applications. In the research by Shanks et al., 2015b a single mono-layer of scale cells removed from the wings was able to perform as a high-reflective coating as well, enhancing its potential applicability in HPCV system as a new reflective coating or film material. The unique nanostructure of these wings is at present being investigated and replicated for a new reflective and lightweight material for CPV systems.

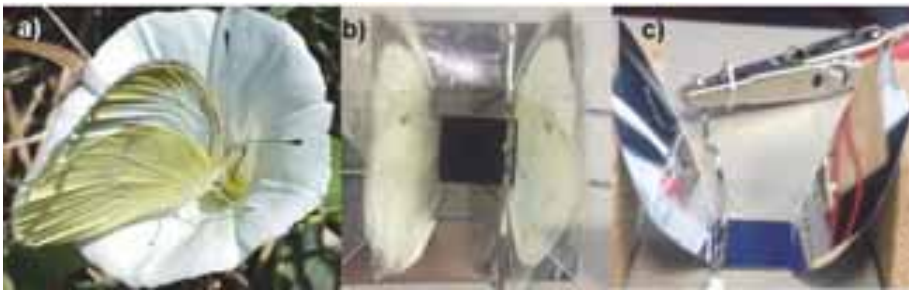

Fig. 9: (a) The cabbage white butterfly (photographed by Tina Pilipović, permission for use granted). (b) Top view of wings positioned in V shape with 1cm x 1cm solar cell at base of wings. (c) Side view of reflective film in shape of wings also positioned in V shape.

4.2. Building Integrated Concentrating Photovoltaics

The general principle of Building Integrated Photovoltaics (BIPV) is that PV modules are integrated into the building envelope, substituting standard glass and other cladding materials with glass/glass laminates encapsulating PV cells within. Incorporating the concentrating photovoltaics into any part of the building

architecture is referred to as Building Integrated Concentrating Photovoltaics (BICPV). These systems can be classified based on the type of concentrator used for achieving solar concentration. The systems may be classified primarily two type's (a) linear concentrators, (b) three-dimensional concentrators

An asymmetric design was applied to refractive based optics and a new generation of concentrator was developed for building integration. This system consisted of linear dielectric non-imaging concentrators with an asymmetric CPC and a geometric concentration ratio of 2.82. Three different systems were designed to have half acceptance angles of 0° and 55°, 0° and 66° and 0° and 77°. The optical analysis of these systems showed that the DiACPC-55 outperformed the other two designs. A prototype of the same was later reported (Sarmah et al., 2014). The indoor characterization of the system showed as maximum power ratio of 2.27 when compared to a similar non-concentrating counterpart. A detailed optical-thermal-electrical modelling procedure for such type of system was shown recently (Baig et al., 2013). Use of ray trace methods was made to carry out the optical analysis of the system. Based on the illumination profile found from the optical simulation, a coupled electrical and thermal simulation was carried out on the system. The impact of non-uniform illumination was also studied. A prototype was developed and tested for its electrical performance under 1000W/m^2. About 0.5% absolute drop in solar cell efficiency was observed due to non-uniformity at 5° incident angle.

The 3D concentrator principally concentrated the light from all the directions unlike the linear concentrators. One of the first designs proposed for building integration is the reflective 3D crossed compound parabolic concentrator (3DCCPC) for building integration (Mammo et al., 2012). The system consisted of an array of 3DCCPC placed over 1cm2 sized LGBC solar cells. The developed system was found to perform with optical efficiencies of 75 % experimentally for a 60° acceptance angle. An improved optical efficiency of 81% was achieved experimentally in the second prototype of the system. Based on the similar design a refractive based 3DCCPC was modeled and experimentally evaluated (Baig et al., 2014b). The refractive based system has higher acceptance angle as compared to the reflective type system. A detailed optical, electrical and thermal modelling of the system was carried out with experimental validation. A maximum power ratio of 2.67 and an acceptance angle of 80° were found when comparing the electrical output of the concentrator unit with the bare cell. The temperature was found to have a parasitic effect on the overall performance of the system bringing about 14.6% drop in the overall power production. A further enhancement to the above system was recently reported recently (Baig et al., 2014a), where light trapping was performed by applying a reflective film along the edges of the 3DCCPC concentrator. A maximum power ratio of 2.73 was observed at an incidence angle of 10°. The system optical efficiency improved, however this reduced the acceptance angle slightly. In another study, a 3D concentrator reported for the building integration is the Square Elliptical Hyperboloid (SEH) concentrator (Sellami and Mallick, 2013). Four different concentration ratios were investigated: 4×, 6×, 8× and 10×. Results showed that the 4× system gives higher optical efficiency compared to the other systems. A complete optical-electrical and thermal analysis of a 6×SEH based concentrator was studied under AM1.5G spectrum (Baig et al., 2015). A detailed analysis highlighting the illumination non-uniformity and its effect on the system performance has been presented (Baig et al., 2012).

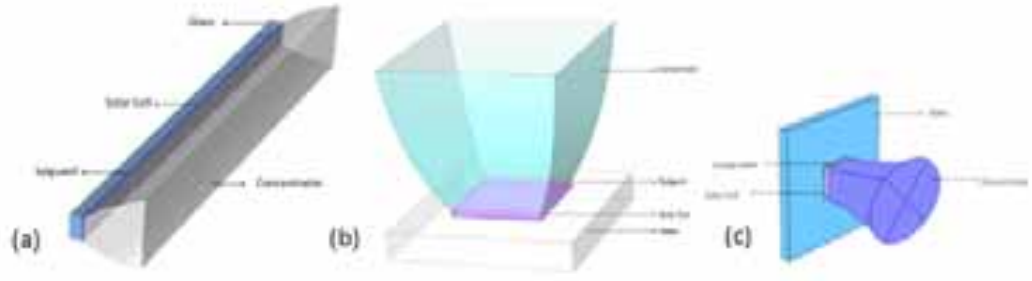

Fig. 10: (a) Linear Dielectric based concentrator (b) 3d CCPC concentrator (c) SHE concentrator

4.3. Passive micro-cooling for HCPV systems

Heat removal is a non-negligible concern in HCPV: any photovoltaic cell is negatively affected by the increase in temperature. The HCPV cells are therefore particularly sensitive to this issue because of the high

amount of heat produced. The heat sinks used in HCPV are generally made of Al and can contribute to more than 60% of the module's weight of the system (Timò, 2014). A reduction in the heat sink weight is beneficial for both the system's efficiency and the emissions' drop. In this light, micro- and nano-technologies offer new perspectives for HCPV cooling. Among the several solutions reviewed, the micro-fins under natural convective conditions have been found to be one of the most suitable for HCPV applications, due to their intrinsic simplicity and high potentials (Micheli et al., 2013). In order to find out the best geometry for HCPV applications, the thermal behaviour of micro-fins have been experimentally investigated. In this light, the correlations among the performance and the fin geometry have been determined (Micheli et al., 2015c). Moreover, the micro-fins have been found to have higher heat dissipation per unit of mass than convectional heat sinks or flat plates (Micheli et al., 2015d). For the first time, the applicability of micro-fins for an effective passive cooling of CPV has been proved: the reduction of temperature obtained by using micro-fins compared to a flat heat sink can lead to an enhancement in cell electrical efficiency up to 1% (Micheli et al., 2015f).

4.4. Ultra-High CPV

In recent years, the interest in for systems working at concentrations higher than 1000 suns, generally called Ultra-High concentrating Photovoltaic (UHCPV), is increased (Algora and Rey-Stolle, 2012), because of the potential in cost and material usage reduction as well as in efficiency enhancement (Vossier et al., 2012). Handling the large amount of heat produced by a cell under ultra-high concentration is one of the main challenges for the development of this solution. For this reason, the use of optimized least-material heat sinks has been investigated (Micheli et al., 2015a, 2015b): they were found able to passively cool a UHCPV systems, with a normalized cost ranging between 0.10 and 0.18\$/W_p for concentrations from 1000x to 8000x.

5. Conclusions

The BioCPV project addresses the rural electrification of an off-grid village in the west of India, by using an innovative renewable energy power system. Concentrating photovoltaic, anaerobic digestion and hydrogen technologies are integrated to produce continuous and reliable electricity. The present paper focuses on the latest outcomes of the researches conducted on concentrating photovoltaics. A large 2.5kW_p receiver and a cassegrain concentrator system have been designed and are currently being tested: the novel designs and the fabrication processes have been made available in literature to contribute to the development of more-efficient and reliable HCPV systems. Moreover, new thermal and electrical models have been presented. The BioCPV project team has investigated new scenarios that can in future benefit the development of HCPV. The butterfly wings can represent an innovative, light-weight solution for HCPV concentrators, whereas micro-fins can be used for the cooling of cells under natural convection.

Acknowledgments

The BioCPV project is jointly funded by EPSRC, UK (Ref No: EP/J000345/1) and DST, India (Ref No: DST/SEED/INDO- UK/002/2011). Authors acknowledge both the funding agencies for the support.

References

Algora, C., Rey-Stolle, I., 2012. The Interest and Potential of Ultra-High Concentration, in: Cristóbal López, A.B., Martí Vega, A., Luque López, A. (Eds.), Next Generation of Photovoltaics SE - 2, Springer Series in Optical Sciences. Springer Berlin Heidelberg, pp. 23–60. doi:10.1007/978-3-642-23369-2_2

Almonacid, F., Fernández, E.F., Mallick, T.K., Pérez-Higueras, P.J., 2015. High concentrator photovoltaic module simulation by neuronal networks using spectrally corrected direct normal irradiance and cell temperature. Energy 84, 336–343. doi:http://dx.doi.org/10.1016/j.energy.2015.02.105

Baig, H., Heasman, K.C., Mallick, T.K., 2012. Non-uniform illumination in concentrating solar cells. Renew. Sustain. Energy Rev. 16, 5890–5909. doi:10.1016/j.rser.2012.06.020

Baig, H., Sarmah, N., Chemisana, D., Rosell, J., Mallick, T.K., 2014a. Enhancing performance of a linear dielectric based concentrating photovoltaic system using a reflective film along the edge. Energy 73, 177–191. doi:10.1016/j.energy.2014.06.008

Baig, H., Sarmah, N., Heasman, K.C., Mallick, T.K., 2013. Numerical modelling and experimental validation of a low concentrating photovoltaic system. Sol. Energy Mater. Sol. Cells 113, 201–219.

Baig, H., Sellami, N., Chemisana, D., Rosell, J., Mallick, T.K., 2014b. Performance analysis of a dielectric based 3D building integrated concentrating photovoltaic system. Sol. Energy 103, 525–540.

Baig, H., Sellami, N., Mallick, T.K., 2015. Trapping light escaping from the edges of the optical element in a Concentrating Photovoltaic system. Energy Convers. Manag. 90, 238–246. doi:10.1016/j.enconman.2014.11.026

Bajpai, P., Dash, V., 2012. Hybrid renewable energy systems for power generation in stand-alone applications: A review. Renew. Sustain. Energy Rev. 16, 2926–2939. doi:10.1016/j.rser.2012.02.009

Calabria, F., 2015. Design of a 3G Enabled Data Acquisition System for BioCPV Off-grid Application. University of Exeter.

Castellanos, J.G., Walker, M., Poggio, D., Pourkashanian, M., Nimmo, W., 2015. Modelling an off-grid integrated renewable energy system for rural electrification in India using photovoltaics and anaerobic digestion. Renew. Energy 74, 390–398. doi:10.1016/j.renene.2014.08.055

Fernández, E.F., Almonacid, F., Mallick, T.K., Investigaci, C. De, 2015. Analytical Modelling of High Concentrator Photovoltaic Modules Based on Atmospheric Parameters. Int. J. Photoenergy 2015.

Lokeswaran, S., Mallick, T.K., Reddy, K., 2015. Optical analysis of secondary concentrator with homogenizer for dispersed 12 X 12 array CPV receiver, in: CPV-11.

Lokeswaran, S., Mallick, T.K., Reddy, K.S., 2015. Thermal Performance of a Solar Concentrating Photovoltaic Module with Spiral Mini Channel Heat Sink, in: International Conference on Polygeneration Technologies and Perspectives (ICP 2015). pp. 1–10.

Mabille, L., Mangeant, C., Baudrit, M., 2013. An innovative method for accelerated ageing study of CPV receivers: Thermal inhomogeneities mapping via electroluminescence. Conf. Rec. IEEE Photovolt. Spec. Conf. 3416–3420. doi:10.1109/PVSC.2013.6745182

Mallick, T., Sarmah, N., Banerjee, S., Micheli, L., Reddy, K.S., Ghosh, P., Walker, G., Choudhury, S., Pourkashanian, M., Hamilton, J., Giddings, D., Walker, M., Manickam, K., Hazara, A., Balachandran, S., Lokeswaran, S., Grant, D., Nimmo, W., Mathew, A., 2013. Design concept and configuration of a hybrid renewable energy system for rural electrification in India through BioCPV project, in: 4th International Conference on Advances in Energy Research (ICAER). Mumbai.

Mammo, E.D., Sellami, N., Mallick, T.K., 2012. Performance analysis of a reflective 3D crossed compound parabolic concentrating photovoltaic system for building façade integration. Prog. Photovoltaics Res. Appl. 20, n/a–n/a. doi:10.1002/pip.2211

Micheli, L., 2015. Enhancing Electrical and Heat Transfer Performance of High-Concentrating Photovoltaic Receivers. University of Exeter.

Micheli, L., Fernández, E.F., Almonacid, F., Reddy, K.S., Mallick, T.K., 2015a. Enhancing Ultra-High CPV Passive Cooling Using Least-Material Finned Heat Sinks, in: CPV-11.

Micheli, L., Fernández, E.F., Almonacid, F., Reddy, K.S., Mallick, T.K., 2015b. Optimization of the Least-Material Approach for Passive Ultra-High CPV Cooling, in: Photovoltaic Specialist Conference (PVSC), 2015 IEEE 42nd. IEEE, New Orleans, LA.

Micheli, L., Reddy, K.S., Mallick, T.K., 2015c. General correlations among geometry, orientation and thermal performance of natural convective micro-finned heat sinks. Int. J. Heat Mass Transf. 91, 711–724. doi:10.1016/j.ijheatmasstransfer.2015.08.015

Micheli, L., Reddy, K.S., Mallick, T.K., 2015d. Thermal Effectiveness and Mass Usage of Horizontal Micro-Fins under Natural Convection. Appl. Therm. Eng. (In Press).

Micheli, L., Sarmah, N., Luo, X., Reddy, K.S., Mallick, T.K., 2013. Opportunities and challenges in micro- and nano-technologies for concentrating photovoltaic cooling: A review. Renew. Sustain. Energy Rev. 20, 595–610. doi:10.1016/j.rser.2012.11.051

Micheli, L., Sarmah, N., Reddy, K.S., Luo, X., Mallick, T.K., 2015e. Design, Development, and Analysis of a Densely Packed 500x Concentrating Photovoltaic Cell Assembly on Insulated Metal Substrate. Int. J. Photoenergy 2015, 1–18. doi:10.1155/2015/341032

Micheli, L., Senthilarasu, S., Reddy, K.S., Mallick, T.K., 2015f. Applicability of silicon micro-finned heat sinks for 500× concentrating photovoltaics systems. J. Mater. Sci. 50, 5378–5388.

Reddy, K., Lokeswaran, S., Mallick, T.K., 2014. Performance Analysis of Spiral Flow Heat Recovery System for Cooling of CPV Module, in: CPV-10.

Reddy, K.S., Lokeswaran, S., Agarwal, P., Mallick, T.K., 2014. Numerical Investigation of Micro-channel based Active Module Cooling for Solar CPV System. Energy Procedia 54, 400–416.

Renewable Energy Policy Network for the 21st Century, 2014. Renewables 2014: Global status report.

Sarmah, N., Richards, B.S., Mallick, T.K., 2014. Design, development and indoor performance analysis of a low concentrating dielectric photovoltaic module. Sol. Energy 103, 390–401.

Sellami, N., Mallick, T.K., 2013. Optical characterisation and optimisation of a static Window Integrated Concentrating Photovoltaic system. Sol. Energy 91, 273–282. doi:10.1016/j.solener.2013.02.012

Shanks, K., Baig, H., Mallick, T.K., 2015a. The Conjugate Refractive-Reflective Homogeniser in a 500X Cassegrain Concentrator : Design and Limits Optical Surface Losses. In: PVSAT-11.

Shanks, K., Sarmah, N., Reddy, K.S., Mallick, T., 2014. The Design of a Parabolic Reflector System with High Tracking Tolerance for High Solar Concentration, in: CPV-10. Albuquerque.

Shanks, K., Senthilarasu, S., ffrench-Constant, R.H., Mallick, T.K., 2015b. White butterflies as solar photovoltaic concentrators. Sci. Rep. 5, 12267. doi:10.1038/srep12267

Shanks, K., Senthilarasu, S., Mallick, T.K., 2015c. High-Concentration Optics for Photovoltaic Applications, in: Pérez-Higueras, P., Fernández, E.F. (Eds.), High Concentrator Photovoltaics: Fundamentals, Engineering and Power Plants. Springer.

Soria-Moya, A., Almonacid Cruz, F., Fernandez, E.F., Rodrigo, P., Mallick, T.K., Perez-Higueras, P., 2015. Performance Analysis of Models for Calculating the Maximum Power of High Concentrator Photovoltaic Modules. IEEE J. Photovoltaics 5, 947–955. doi:10.1109/JPHOTOV.2015.2397605

Theristis, M., Donovan, T.S.O., 2015. Electrical-thermal analysis of III – V triple-junction solar cells under variable spectra and ambient temperatures. Sol. Energy 118, 533–546. doi:10.1016/j.solener.2015.06.003

Timò, G., 2014. Results of the APOLLON Project and Concentrating Photovoltaic Perspective. Milan (IT).

Vossier, A., Chemisana, D., Flamant, G., Dollet, A., 2012. Very high fluxes for concentrating photovoltaics: Considerations from simple experiments and modeling. Renew. Energy 38, 31–39.

Weitemeyer, S., Kleinhans, D., Vogt, T., Agert, C., 2014. Integration of Renewable Energy Sources in Future Power Systems: The Role of Storage. Renew. Energy 75, 12. doi:10.1016/j.renene.2014.09.028

Conference Proceedings

Solar World Congress 2015
Daegu, Korea, 08 – 12 November 2015

PHOTOVOLTAIC ENERGY PREDICTION ANALYSIS CONSIDERING TILT AND AZIMUTHAL ORIENTATION IN BRAZIL

Gabriel Mendonça de Paiva[1], Sérgio Pires Pimentel[1], Enes Gonçalves Marra[1] and Bernardo Pinheiro de Alvarenga[1]

[1] Federal University of Goias, Goiânia (Brazil)

Abstract

This article is about the analysis of photovoltaic (PV) potential generation in the city of Goiania, Goias, Brazil. The main objectives of this work are to predict reliably the energy production considering tilt and azimuthal orientation in this location and analyze the energy behavior and system performance along a simulation process. With the use of PVsyst, an example system of 2.5kWp of polycrystalline silicon had been considered for simulations of 1387 possible tilt-orientation sets in 5° scale. The annual energy production and the system Performance Ratio were obtained. As a conclusion, 180 of the total configurations were considered acceptable for payback time projects. The optimal energy generation set found differs from typical slope equal to location's latitude and orientation to north and was in 25° tilt and -5° azimuth, still leading to over 8 years payback time considering. As energy behavior, the system sensibility for azimuthal deviation is higher as higher is its plane tilt.

Keywords: Energy prediction, PV systems, PVsyst.

1. Introduction

One of the main advantages of Distributed Generation based on PV technology is the possibility of building integration, therefore the energy is generated close to the load (Macêdo, 2006). The integration of PV modules over building's roofs hides two important factors in which PV generation depend: tilt and azimuth angles. PV energy production depends in fact on many parameters such as PV array peak power, solar irradiation on module plane, module temperature, inverter efficiency and size, maximum power point tracking losses and other losses (Notton et al., 2010).

In order to make reliable energy prediction considering all main factors which influence PV generation, a simulation process with reliable data is required. It is well known that different irradiation data results in different predictions. When multi-year time series are used as reference for radiation data, deviations of 1% were found to Typical Meteorological Year (TMY) values and over 3% to synthetic data series (Cabecauer et al., 2011). Those deviations in total irradiance are different depending on plane tilt and location.

Also, different time resolution data may lead to different prediction and design as well. Using hourly average data, some important irradiation peaks and its respective inverter losses due to power limiting may not be noticed compared to one minute or 10 seconds resolutions (Burger and Ruther, 2006).

This study analyses the behavior of annual energy production and annual performance ratio of an example grid-connected PV system related to the variation of tilt and azimuth angles in the location of Goiania, Brazil. The reason of particular interest on these annual parameters is because Brazil currently has a policy which makes it possible for consumers only to reduce its electricity bills and not to sell energy, known as net metering. However, if the energy produced during a month exceeds the load demand it could be accounted in further periods up to three years later, in terms of revenues. In this case, those annual parameters could be applied for designing grid-connected (or stand-alone) PV systems. The radiation data related to this paper is compared with other available radiation data for this location.

doi:10.18086/swc.2015.05.24 Available at http://proceedings.ises.org

2. Simulation characteristics

A simulation model of a grid-connected PV System was created on PVsyst software. The chosen methodology of simulations on PVsyst can be described as a process of determination of the system output energy in periods of one hour along a year, based on the input parameters variation for each specific hour and mathematical models of the whole system.

The PV array is composed by series connection of 10 modules of 250Wp p-Si from YINGLI SOLAR (model YL-250P-29b). The solar inverter is a high frequency transformer (HFT) inverter from INGETEAM (model Ingecon Sun 2.5HF). Table 1 presents the main parameters for both module and inverter.

Tab. 1: Parameters of PV module and inverter of the simulated system.

PV Module	Solar Inverter
Yingli Solar YL250P-29b	Ingeteam Ingecon 2.5HF
P_{nom} = 250Wp	P_{nom} = 2500Wp (AC power)
I_{SC} = 8.831A	Min MPP Voltage = 130V
V_{OC} = 37.78V	Min Voltage for Pnom = 125V
I_{MP} = 8.263A	Max MPP Voltage = 450V
V_{MP} = 30.26V	Absolute Max PV Voltage = 550V
–	Power treshold = 20W

Other parameters defined on PVsyst were considered: 30m length of 2.5mm² cables in the DC side, resulting in 225.6mΩ of total cable resistance; standard PVsyst 1% MPPT loss; and 2.5% loss for voltage fixing. A fixed 5% loss due to soiling over the modules was also considered, independent of the module slope, although it tends to be higher in low inclination and lower in high inclination positions. This is because some estimations from some places result in average 5% soiling losses (Caron and Littman, 2013), even though measurements in the current location and for specific module inclination should be done for more realistic soiling evaluation. Losses of 0.5% were determined for system unavailability. The constant related to albedo irradiation estimation on tilted surface was defined as 0.2, a typical value used for urban areas.

The simulation process which estimate the PV annual energy generation had been done a synthetic hour data series based on monthly averaged values of irradiation data from NASA's satellite. The annual irradiation was compared to other available radiation data, like Project SWERA (Brazilian Atlas of Solar Energy SWERA), Meteonorm (available on PVsyst) and INMET (Institute of Meteorology of Brazil). Table 2 shows the equivalent irradiation on the horizontal plane over one year period from different radiation data.

Tab. 2: Annual Irradiation on the horizontal plane for different radiation databases.

Reference	I_{HOR} annual (kWh/m²)
Project SWERA(range)	1788 - 2044
NASA(average)	1927.5
Meteonorm(average)	1829.0
INMET(average)	1854.2
INMET(range)	1793 – 1926.1

The available data on PVsyst are average years from NASA (satellite) and Meteonorm (interpolation of solarimetric stations over the world). The data from INMET are measurements obtained from a solarimetric station with hourly measured values, installed in the city of Goiania, which leads to a range of annual incident irradiation on the horizontal plane from 1793 to 1926kWh/m², a variation of +3.8% or -3.3% from average value, considering a period of 12 consecutive years of measurements.

The available data from Project SWERA is a map of equivalent sun hours incident on the horizontal lpane of all regions of Brazil and it's obtained from interpolation of solarimetric stations over Brazil. The map of sun

hours lead to a range of annual incident irradiation on the horizontal plane from 1788 to 2044kWh/m² for the state of Goias, a variation of ±7% from the average value of 1916kWh/m².

The irradiation model used to determine irradiation in tilted planes was the Perez model (Duffie and Beckman, 2013), also available on PVsyst. The annual analysis is a result of hourly simulation of the complete system under synthetic hourly variation of climate data.

3. Simulation results

The system was simulated for all possible configurations in 5° scale of tilt and orientation variation, resulting in a map of 1387 possible sets of annual energy production and system Performance Ratio. During this process, the input parameters were fixed in the values determined in section 2.

Figure 1 shows the tilt angle or slope (β) and the surface azimuth angle (γ_s). As this case of study is related to a city of Brazil (South America), negative azimuth values mean that the module has rotated from north to east direction and positive values mean that it rotated to west direction.

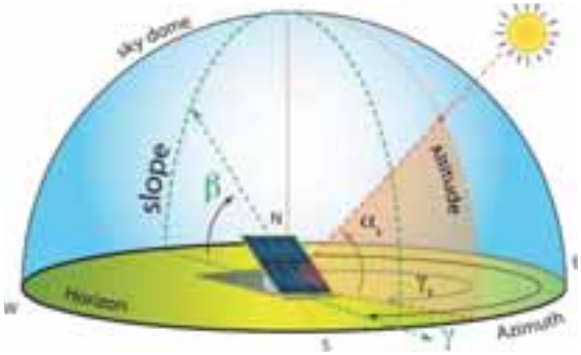

Fig. 1: Solar geometry defined for the energy prediction analysis.

The results analysis shows that the common sense (and traditional procedure) of tilting PV solar panels to a value equal to the location's latitude and 0° azimuth did not lead to optimal output. It was noticed that a maximum energy production for 5° scale of 3833kWh/year would occur when plane tilt = 25° and azimuth = -5° (or 5° to east direction). These conclusions were obtained mainly because of the albedo influence on total irradiation, which is calculated on PVsyst trough Equation 1. When the albedo constant ρ_g is omitted, the optimal generation gets closer to location's latitude (-16.7°).

$$I_{alb} = I\rho_g \left(\frac{1-cos\,\beta}{2}\right) \qquad \text{(eq. 1)}$$

In addition, 180 of the total possible configurations obtained less than 5% annual loss compared to the optimal set, meaning that there are many possible positions which lead to satisfactory energy production when only energy output or payback time are considered in the project.

Also from results analysis, it is possible to observe the system sensibility according to azimuth deviation considering fixed tilts. Figure 2 shows that the azimuth deviation of 180° in lowly tilted systems lead to low annual energy production losses, while in highly tilted systems, the annual loss increases.

Considering 15° of tilt inclination angle, the generation loss for 180° azimuthal deviation is around 15%, while in 90° tilt, the reduction from northbound is over 60%. Another interesting result concerning the azimuth deviation is that in highly tilted systems, the optimal energy generation was obtained in -55° azimuth, in east direction. The annual production was also higher in 55° azimuth than in 0°. This behavior was observed in module inclinations of 80° or higher for Goiania and this result could be verified to other locations.

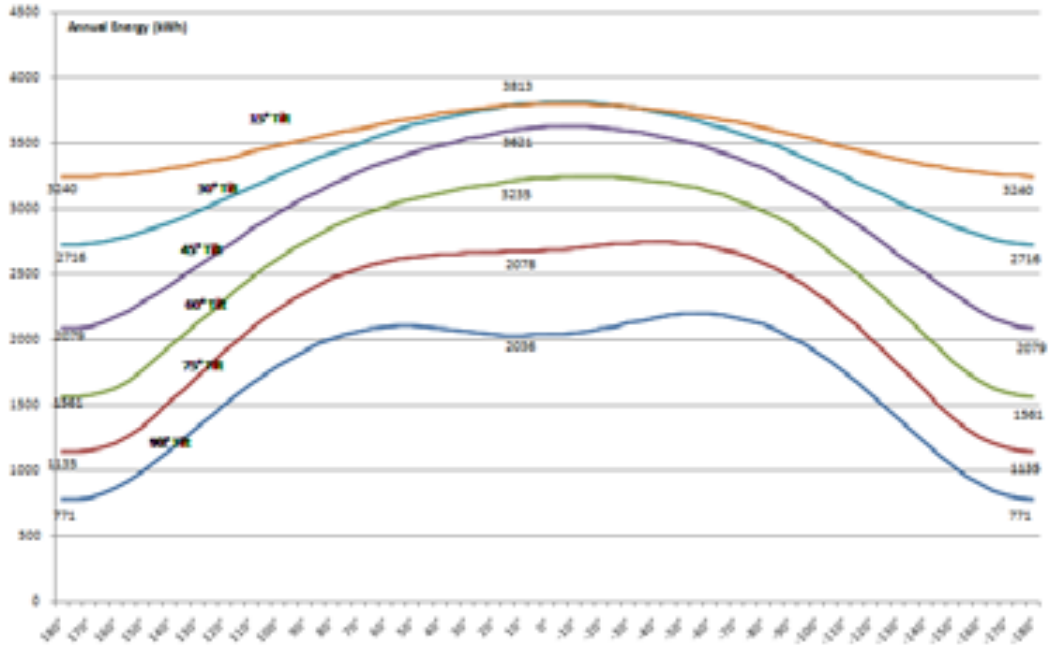

Fig. 2: Annual energy production in kWh/year as a function of azimuth for different tilt angles for the 2.5kWp system.

By now considering the Performance Ratio of the system observed during the simulations, it resulted in a range of values around 73 and 75% for most configurations and only reached lower values of 68% in extremely bad output configurations, when annual losses over 60% were obtained in respect to optimal. Figure 3 presents the PR behavior considering tilt and azimuth variations.

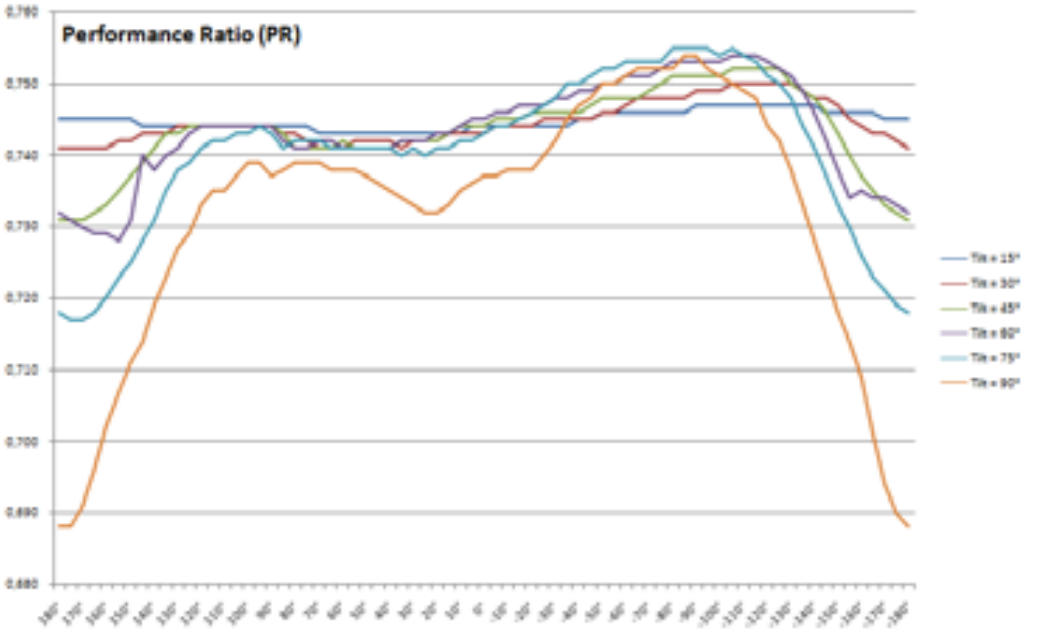

Figure 3: Annual Performance Ratio in % as a function of azimuth for different tilt angles for the 2.5kWp system.

Although the PR does not perform significant variations as function of module positioning, the factors that influence on it change significantly from optimal to minimal production configurations, like inverter efficiency losses, temperature losses in respect to Standard Test Conditions and incidence angle losses, due to light reflection. Inverter efficiency losses increase from 4% to 9%, losses from module temperature decrease from 11% to 4%, losses from incidence angle increase from 3% to 8% and from module efficiency due to low irradiance level increase from 0.5% to 7.5%.

4. Energy prediction analysis

If the irradiation incident in the module plane is compared to the global horizontal irradiation, the annual transposition factor could be obtained on PVsyst. Table 2 presents the transposition factors considering the use of Perez's model on PVsyst.

Tab. 2: Transposition Factors for different tilt and azimuth angles for Goiania obtained by Perez model on PVsyst.

Azimuth / Tilt	-90°	-75°	-60°	-45°	-30°	-15°	0°	15°	30°	45°	60°	75°	90°
90°	0.56	0.59	0.61	0.60	0.59	0.58	0.57	0.57	0.58	0.59	0.59	0.57	0.54
80°	0.64	0.68	0.70	0.71	0.70	0.70	0.69	0.69	0.69	0.69	0.68	0.66	0.62
70°	0.72	0.76	0.79	0.80	0.81	0.81	0.80	0.80	0.79	0.78	0.77	0.74	0.70
60°	0.79	0.84	0.87	0.89	0.90	0.90	0.90	0.90	0.88	0.87	0.84	0.81	0.77
50°	0.85	0.90	0.93	0.95	0.97	0.98	0.98	0.97	0.96	0.94	0.91	0.87	0.83
40°	0.91	0.95	0.98	1.01	1.02	1.03	1.03	1.03	1.01	0.99	0.96	0.93	0.89
30°	0.95	0.99	1.01	1.04	1.05	1.06	1.06	1.06	1.04	1.02	1.00	0.97	0.93
20°	0.98	1.01	1.03	1.05	1.06	1.07	1.07	1.06	1.05	1.04	1.02	1.00	0.97
10°	1.00	1.01	1.02	1.03	1.04	1.05	1.05	1.04	1.04	1.03	1.02	1.01	0.99
0°	1.00	1.00	1.00	1.00	1.00	1.00	1.00	1.00	1.00	1.00	1.00	1.00	1.00

Comparing the annual energy generation to the transposition factor values, it can be concluded that there is a strong linear dependence of energy generation on irradiation incident on module's planes.

The amount of energy output from a grid-connected PV system can be estimated from Equation 2 (Pinho and Galdino, 2014), when P_{PV} is the generator nominal power at STC, PR the performance ratio and sun hours are the equivalent hours of 1000W/m² irradiation per day obtained for the module plane in the specific location.

$$E(kWh) = P_{PV}(Wp).PR.\text{sun hours}.365 \qquad \text{(eq. 2)}$$

From Equation 2, it is possible to explain the linear dependence of energy output as function of incident irradiation on the module's plane, but it is also the result of the product of irradiation (in the form of equivalent sun hours) and the performance ratio.

Equation 2 also shows that the energy production by the PV system during a full year may vary in the range of incident irradiation on the horizontal plane from 1788 to 2044kWh/m². Then, as the energy output has a linear dependence on the irradiation and the PR will probably be near the same results of Figure 3.

5. Conclusions

It can be concluded that there are several tilt-orientation configurations that lead to satisfactory energy production in PV generation for this specific location in Brazil, since a number of180 (from 1387 possible) sets of tilt-azimuth configurations result in less than 5% annual energy losses in respect to optimal configuration.

Additionally, it was found that considering the solar irradiance available in Brazil, the optimal tilt-azimuth set was 25° module inclination and -5° azimuth which is not the typical inclination angle equal to local's latitude and orientation equal to 0° north. This example project would still lead to over 8 years payback time considering energy costs and policy in 2015.

Other conclusion is related to annual power production from PV System. Specific to fixed tilts, the annual production becomes more sensible to azimuthal deviation as higher is its inclination. The Performance Ratio of a system is almost invariable for tilt and azimuth deviation and only becomes significantly lower for extremely low production configurations (in this case, over 60% annual losses in respect to optimal), positions that are almost unviable for payback time projects.

Considering the location in Brazil related to this study, the energy generation of a PV system is linearly

dependent on the irradiation, which means that a variation of ±7% from the prediction in this paper may be classified as acceptable relative to real variations for different year periods.

6. Acknowledgments

Our special thanks to FAPEG (State of Goias Research Foundation) by their financial support on the publication of this study, to CAPES (Coordination for the Improvement of Higher Level Education Personnel, Brazil) for their financial support during the process of research, to the Federal University of Goias and the Electrical, Mechanical and Computation School (EMC) trough the Graduate Program in Electrical Engineering.

7. References

Macêdo, W. N., 2006. Análise do Fator de Dimensionamento do Inversor aplicado a Sistemas Fotovoltaicos Conectados à Rede. 201.

Notton, G., Lazarov, V., Stoyanov, L., 2010. Optimal sizing of a grid-connected PV system for various PV module technologies and inclinations, inverter efficiency characteristics and locations. 14.

Cabecauer, T., Skoczek, A., Suri, M., 2011. The effect of Solar Radiation data types on Calculation of tilted and suntracking solar radiation. 6.

Burger, B., Ruther, R., 2006. Inverter sizing of grid-connected photovoltaic systems in the light of local solar resource distribution characteristics and temperature. 14

Pereira, E. B., Martins, F. R., Abreu, S. L., Ruther, R., 2006. Brazilian Atlas of Solar Energy. 64.

Caron, J. R., Littman B., 2013. Direct monitoring of energy lost due to soiling on first solar modules in California.5.

Pinho, J. T., Galdino M. A., 2014. Manual de Engenharia para Sistemas Fotovoltaicos. 530.

Duffie, J. A., Beckman, W. A., 2013. Solar Engineering of Thermal Processes. 928.

The reference PV power plant-based method

Zoltán Kapros

Szent István University, Gödöllő, (Hungary)

Abstract

A new method has been developed by small scale power plants were built in a closely related place to estimate the power generation an any given time and give a short term forecast. This is called the reference power plant-based method. The essence of the method is a few references plants is under continuous monitoring, so an accurate estimation could prepare for the entire closely PV area in any time. It is possible, this method will able to forecasting. This could help while the balancing and the trading activity in the low voltage network. Thus, network integration of photovoltaic systems could be significantly facilitated.

Keywords: *Small scale photovoltaic*, *aggregator forecastind methode, clouds variability factor,*

1. Introduction

It is common that the photovoltaic power plants for predicting the clouds build solar radiation monitoring network (Bilionis et al., 2014). The application of similar solutions for the urban environment relatively could be more expansive and less accurate. In Hungary, the solar panels installed on rooftops rationally would be cover approximately 22.5% of the annual residential electricity consumption. For larger institutional buildings this number is nearly 8%. The technical potential is significant value, although the buildings are still typically not able to produce more power than consumed. In the event that available potential by 2020 is only 5% considered this, the expected target could be 555 GWh/year in the residential sector. This is approximately ten times bigger the total 2014 small scale PV production. In Hungary, the electricity network is basically centralized and not yet flexible enough to provide high VRE ratio will be available. The present study aims to provide a reference power plant based method to help the integration with the small-scale photovoltaic systems.

The PV GRID program showed the main network problems caused by the small scale photovoltaic systems and summarized the possible proposals for solutions. These solutions can be divided into five main groups from another own specific perspective:

- The surplus electricity production compared to consumer demand could be converted heat losses in the grid;
- Restricted effective photovoltaic electricity generation from the PV system (eg reactive power production, switch-off from the grid); avoid to actual overproduction ;
- Use some energy storage system with acceptation of the storage losses;
- In addition to making possible reversal of the current paths transformation losses with efficiency reduction by the larger power plants.

The important thing is the produced but also really consumed electricity production. The performance ratio (PR), for example, typically does not take into account as a negative quantity the produced, but not utilized energy. A system oriented new performance ratio value (PR_{net}) could be useful by the development and the optimization:

$$PR_{net} = \frac{(E_{pr} - E_{grl} + E_{grw} - E_{ow} - E_{st} - E_{bl})}{E_{us}} \qquad \text{(eq. 1)}$$

Where the PR_{net} is the system oriented performance ratio, E_{pr} is the net photovoltaic production [kW h^{-1}], E_{grl} is the transformation, distribution and other losses in the grid from the photovoltaic electricity production, E_{grw} is the total avoided grid losses due to the decentralized system near to the consumption. $E_{\tilde{o}w}$ is the PV

doi:10.18086/swc.2015.05.25 Available at http://proceedings.ises.org

power system losses (the system's own losses). E_{st} is the storage losses, if the battery option is available. E_{bl} is the blocked photovoltaic electricity production by the producer with automatic shutdown, reactive energy conversion, so on. E_{us} is the useful (really consumed part) energy.

So there is a need for indicators to characterize by complex way the photovoltaic systems and their grid integration quality. According to an IEA study (Müller, S. et al, 2014), the electricity price with a conventional fossil power plant portfolio could be expected between 86 and 94 USD/MWh. In the case when VRE (variable renewable energies) ratio could reach the 45% the electricity price would be higher (between 97 and 119 USD/MWh) with considering the additional network charges. In 2014 the EU supported "PV Parity" project modeled until 2030 to build 480 GW new photovoltaic power plants (PV Parity, 2013). According to the program the transmission grid cost can grow from the current costs from 0.5 euro / MWh to 2.8 euro / MWh up, but the distribution grid connected needs cause 9 EUR / MWh.

So by the integration ability one key component by the small scale photovoltaic systems is the reduction the variability and uncertainty with more accurate forecast. By these systems there is currently no cost-effective best practice method. In addition the forecasting tasks are complex challenges which are significantly differentiated:

- Planning, optimization, network assessment, ost - benefit analysis, evaluation of alternatives, verification by supports.
- 15 minutes schedule giving an electricity trader.
- Clarification of the planned schedule before the beginning of the relevant period.
- Clarification of the planned schedule within the relevant 15 miuntes long period.
- Forecast for a very short periods (balancing) forecast, for example only 1 minute ahead.

My PhD research in progress examines the possibilities by the last two points. Those solutions as the „Wavelet Variability Model" (Dyreson et al, 2014), which for multi-megawatt power plants are acceptable even for small scale sizes often not cost effective.

The reference PV power plant-based method is based on simple idea. In a given urban setting the individual systems will receive the similar environmental impacts (for example smog, air pollution, temperatures, or spectral distribution. In some cases it can be useful for making forecast.

2. Basic model description

By a monitoring the following two main tasks are given:

- Making analytical forecast for every minute performances.
- Improving the accuracy of these forecasts very shortly in advance.

The energy output of PV systems depends on more special effects, which hard and expensive to measure and evaluate in time, for example the solar radiation intensity, temperature or solar spectrum (Farkas, Seres, 2008). The reference value is the difference the expected performance which based on analytical analysis and actual measured power. In order that this error (difference) can be used as a reference value, several conditions must be met:

- to be a relative number, because a comparison of different systems output is the target;
- to characterize the various systems by a comparable manner with simple transparency.

The equivalent peak load hours are characterized by the energy-generating capacity in a given moment. It means if same amount of power will produced in one year, the equivalent peak load hours is equal the traditional peak load hours (Sharma, Tiwari 2012):

$$h_{ekv} = \frac{\zeta_{real}}{I_P} \qquad \text{(eq. 2)}$$

where I_p is the current value of the global radiation intensity [kW/m^2] and ξ_{real} is the total amount of solar energy production unit [kWh/m^2]. If the performance is expressed as an equivalent number of hours, the expected value can be written as follows:

$$h_{ekv,t}(t) = \frac{(G_{PV}(t) \times \eta(t) \times A)}{I_P} \qquad \text{(eq. 3)}$$

Where G_{pv} is the amount of daily global radiation in [kWh/day], η is the reference efficiency [%] and A is the useful photovoltaic solar surface [m^2]. The equivalent peak load hours shows a reachable capacity at a given moment with dimension of the hour or kWh/kW. If the system is functioning at a given time at a specific equivalent peak load hours, then in an imagined year with equal continuous output power, same value would result for the peak load hours for that year. This value represents an actual capacity of the PV power plant, which is clear, meaningful and comparable.

During the measurement, therefore in different periods of time it were determined the expected and the measured equivalent peak load hours. The series thus produced error factor is adapted to be forecast and made suitable systems to estimate the combined capacity in the closely related place (the formerly analytical forecast could be more precise). Determination of the relative error factor can be seen in the next table (Table 1.):

Tab. 1: Determination of the relative error factor

t_0	Δt	$h^*_{equ,t0}$ (expected equivalent peak load hours)	$h^m_{equ,t0}$ (measured equivalent peak load hours)	$H_{t0} = \lvert (h^*-h^m) \rvert / h^*$ (error factor)	$h^{**}_t = f(h^*_t, r_{t-k}, r_{t-k+1}, ..., r_{t-k+n})$ (short time prediction)
t_1	$t_1 - t_0$	$h^*_{equ,t1}$	$h^m_{equ,t1}$	h_{t1}	h^{**}_{t1}
t_2	$t_1 - t_0 = t_2 - t_1$	$h^*_{equ,t2}$	$h^m_{equ,t2}$	h_{t2}	h^{**}_{t2}
t_3	$t_1 - t_0 = t_3 - t_2$	$h^*_{equ,t3}$	$h^m_{equ,t03}$	h_{t3}	h^{**}_{t3}
...	...	...	...	...	...
t_n	$t_1 - t_0 = t_n - t_{n-1}$	$h^*_{equ,tn}$	$h^m_{equ,tn}$	h_{tn}	h^{**}_{t4}
...	...	...	...	...	
t_m	$t_1 - t_0 = t_m - t_{m-1}$	$h^*_{equ,tm}$	$h^m_{equ,tm}$	h_{tm}	h^{**}_{t5}

Based on the analytical model and real values $r_{(t-k)}$, ... $r_{(t-k+1),}$ $r_{(-1)}$, $r_{(0)}$ error factors are added. Based on $r_{(t-k)}$, $r_{(t-k+1)}$, ..., $r_{(t-k+n)}$ error factors, and the results of the traditional analytical model forecast for the expected equivalent peak load hours in t time it could be improve h^*_t for h^{**}_t. So there are two main steps, first of all $h^*_{equ,t}$ have to be counted, than after a monitoring it could be improve sort time in advance.

Therefore it is necessary to determine solar geometric data, the expected value of global radiation, and the characteristics of direct and diffuse radiation conditions. By the effective component of direct radiation it should be also considered the orientation of the solar panels. The ISES Pocket book gives the main equitation (Martin, 2005):

$$H_{\alpha,\beta} = RB_\alpha + D\cos^2(\frac{\beta}{2}) + (D+B)\rho\sin^2(\frac{\beta}{2}) \qquad \text{(eq. 4)}$$

With the R factor in the equitation 3 (solar panel tilt factor) at each moment it can be determined the perpendicular portion of the solar direct radiation reaching the surface depending on the inclination of the solar cell. The module temperature of the solar cell is important to estimate the cell efficiency. By the cell temperature estimation it was applied an approximate curve, which is considered as a typical for the relevant period (Figure 1.).

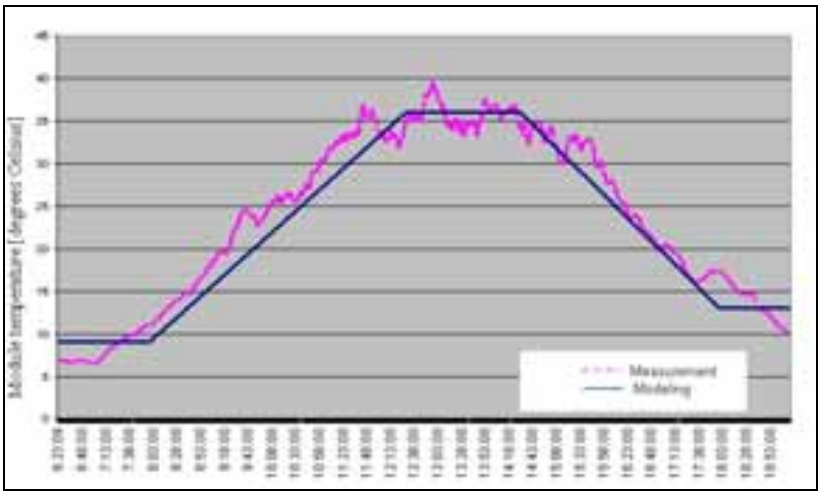

Fig. 1: Module temperature estimation

The other additional losses by determination of the electricity production were estimated according to the table. 2.

Tab. 2: The estimated electricity losses depending on the energy capacity of the effective part of the direct solar radiation

H [W m^{-1}]	Losses in DC system	Installation uncertain-ties	*Performance ratio of DC production*	Inverter losses	Other losses in AC system	Expected losses barring service function by Inverter	*Performance ratio*
>500	6%	2%	*92%*	5%	3%	0.5%	**84.46%**
240 – 499	9%	2%	*89%*	4%	3%	0.5%	**82.63%**
120 – 239	12%	2%	*86%*	6%	3%	0.5%	**77.43%**
< 119	15%	2%	*83%*	9%	3%	0.5%	**72.41%**

Thus, according to the above, I calculated totally 15.5 - 27.6% losses. Therefore in every minute it may be obtained to get the expected equivalent peak load hours:

$$h_{equ,AC}(t) = \frac{P_{AC}(t)[W]}{(P_p[kW]\times 1000)} \times 8760 \text{ , [h].} \qquad \text{(eq. 5)}$$

Where P_{DC} is the actual current PV performance to the grid and P_p is the nominal capacity of the PV system. From the differences between the observed (measured) and the expected equivalent peak load hours the error factors could be calculated according to the next equation:

$$H_{t-n} = \frac{(h^*_{t-n} - h^M{}_{t-n})}{h^*_{t-n}} \text{ , [\%].} \qquad \text{(eq. 6)}$$

It can be defined a specific series of error factors between t-n and t-m. From this the current characteristics of their changes (dH/dt) can be deduced:

$$\frac{dH}{dt} \approx \frac{\Delta H_{n-m}}{\Delta t_{n-m}} = \frac{(H_{t-n} - H_{t-n-1}) + (H_{t-n-1} - H_{t-n-2}) + ... + (H_{t-m+1} + H_{t-m})}{n-m} \text{ , [\% min}^{-1}\text{]}$$

(eq. 7)

where are true, that

$$t_{t-n} - t_{t-n-1} = t_{t-n-1} - t_{t-n-2} = ... = t_{t-m+1} - t_{t-m} \qquad \text{(eq. 8)}$$

Thus, the error factor prediction is described here:

$$H_t = H_{t-1} + (1+\frac{dH}{dt}) \approx H_{t-n} + (1+\frac{dH}{dt})^n \approx H_{t-n} \times (1+\frac{\Delta H_{n-m}}{\Delta t_{n-m}})^{0,4n}, [\%].$$

(eq. 9)

Under the average conditions the 0.4n exponent has formed to be approximately an optimal value during by measurements. View of the above the revised forecast comes according to next equation:

$$h_t^{**} = h_t^* + H_t \times h_t^* = h_t^* \times (1 + H_t), [\text{h}]. \qquad \text{(eq. 10)}$$

The parameters, which were used during the analysis and the measurements, are shown in Table 3.

Tab. 3: The main parameters of the tests

The duration of the predicted period	t_{t-n}-t_{t-n-1}	n	m
1 minutes	1 minutes	5 minutes	15 minutes

Therefore during the measurement and analysis the series of $h_{t,}^{**}$ was available in 5 minutes before time t. This gave the opportunity to give other forecast for the average performance in every full quarter-hour with 5 minutes before the end of the period. During the test the prediction for average performance (equivalent peak load hours) in 15 minutes periods based on 5 minutes measured data and 10 minutes predicted data with get from the presented method.. The method of determining is illustrated with nest equations.

$$h_{15\,\text{min}}^{m} = h_{t-14} + h_{t-13} + h_{t-12} + h_{t-11} + h_{t-10} \qquad \text{(eq. 11)}$$

$$h_{15\,\text{min}}^{\exp} = h_{t-9}^{**} + h_{t-8}^{**} + h_{t-7}^{**} + h_{t-6}^{**} + h_{t-5}^{**} + h_{t-4}^{**} + h_{t-3}^{**} + h_{t-2}^{**} + h_{t-1,}^{**} + h_t^{**} \qquad \text{(eq. 12)}$$

$$h_{t,15\,\text{min}}^{**} = \frac{h^{m}{}_{15\,\text{min}} + h^{\exp}{}_{15\,\text{min}}}{15} \qquad \text{(eq. 13)}$$

The significance of the error factor is stronger in these times when the radiation is more intensive, so the period between 10:00 – 16:00 were also separately analyzed.

3. The reference PV power plant model description

The reference PV power plant-method is based on the presented forecast which is extended to a whole photovoltaic plant area. Continuous monitoring system works only by the reference power plant and the basic data from others is known. There are two approaches are conceivable:

- forecast for balancing purpose;
- virtual smart grid group (aggregator) forecast for a 15 minute average performance.

So based on the analytical expected equivalent peak load hours ($h^*_{1,t}$) and these modified forecasts with the monitoring ($h^{**}_{1,t}$) for the reference power plant, as well as expectations for a second pv system ($h^*_{2,t}$) without monitoring the new modified values ($h^{**}_{2,t}$) also could it be estimated:

$$\frac{h_{1,t}^{**} - h_{1,t}^{*}}{h_{1,t}^{**}} \approx \frac{h_{2,t}^{**} - h_{2,t}^{*}}{h_{2,t}^{**}} = 1 - \frac{h_{2,t}^{*}}{h_{2,t}^{**}} \qquad \text{(eq. 14)}$$

Consequently $h^{**}_{2,t}$ could be counted with the next equation:

$$h_{2,t}^{**} \approx \frac{h_{2,t}^{*}}{1 - \frac{h_{1,t}^{**} - h_{1,t}^{*}}{h_{1,t}^{**}}} \qquad \text{(eq. 15)}$$

As noted above, in addition to the analysis of a reference power plant it also could be prepared the forecasts

for the 15 minute average performance ($h^{**}_{2,t,15m}$) by other nearby plants (which based on 5 minute measurement data from the reference system due to equation 13):

$$h^{**}_{2,t,15m} \approx \frac{h^{*}_{2,t,15m}}{1-\frac{h^{**}_{1,t,15m}-h^{*}_{1,t,15m}}{h^{**}_{1,t,15m}}} \qquad \text{(eq. 16)}$$

4. Data and methods

The research examined reference power plant owned by the Budapest District Heating Co. Ltd. (Főtáv Zrt.). The PV plant is located in the company' headquarter (Budapest, Kalotaszeg 31.) in the top of the 'D' building. The reference power plant was considered only one part of the whole (the one inverter part form the 8). With the same orientation and the same angle 19 panel units has a single inverter. The main data of the plant:

- Location: Latitude: 47.4584°, Longitude: 19.045°;
- PV module type: AS-60P 250 W ECO;
- Rated power of a panel: 250 W_p;
- The number of solar panels installed: 150;
- Position: +10.7 degrees (SSW) (as determined by measuring from map),
- Angle of inclination: 20 degrees
- Number of inverters: 8;
- The PV Power Plant nominal connection cpacity: 40 kW.

The main site of research is shown in Figures 2.

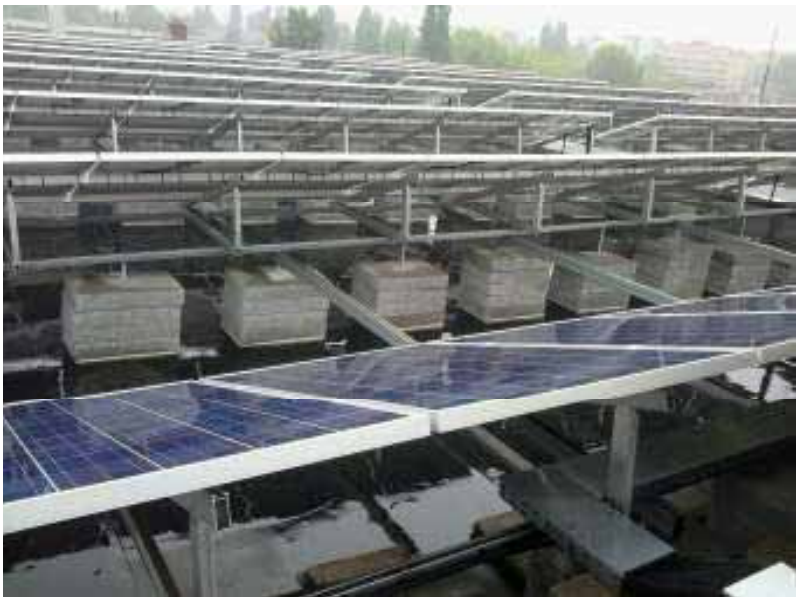

Fig. 2: The examined reference power plant

The eight independent inverters have enabled to forecast from one continuously measured inverter data to others, so the reference PV power plant model can be test in optimal situations (the systems are very close each others in the same position). This will be also tested another two system is located within a 10 km. The research analyzes data from seven different days which was randomly selected (Table 4. and Table 5.).

Tab. 4: The test days and characteristics

Number	Dates	The serial number of the day (d_n)	Sunrise (GT+1)	Sunset (GT+1)	Azimuth at sunrise (AZI_{SRT})	Azimuth at sunset (AZI_{SST})	Potential sunshine duration (N_0) [h]
1.	1 April 2014.	91	6:23:09	19:13:13	-97.58°	97.89°	12.84
2.	20 April 2014.	110	5:46:32	19:39:56	-108.07°	108.37°	13.89
3.	1 May 2014.	121	5:27:32	19:55:15	-113.55°	113.89°	14.16
4.	20 May 2014.	140	5:01:25	20:20:01	-121.36°	121.58°	15.31
5.	1 June 2014.	152	4:50:58	20:32:51	-124.80°	124.96°	15.69
6.	14 June 2014.	165	4:46:12	20:42:09	-126.86°	126.91°	15.93
7.	20. July 2014.	201	5:07:10	20:32:34	-122.58°	122.38°	15.42

Tab. 5: Characteristic of the analyzed days by the reference power plant

Dates	Throughout the day		Between 10:00 and 16: 00		Solar irradiation characteristics
	Average equivalent peak load hours	Maximum equivalent peak load hours	Average equivalent peak load hours	Maximum equivalent peak load hours	
	hour	hour	hour	hour	
1. 04. 2014.	3889	6766	5633	3427	sunny, slightly cloudy, stable light conditions
20. 04. 2014.	3047	9360	4245	1187	Cloudy volatile, rarely sunny
1. 05. 2014.	2604	8310	4609	1522	almost uniformly cloudy but periodically clear
20. 05. 2014.	4227	7679	6348	802	variably cloudy or clear sky, rapidly changing light conditions
1. 06. 2014.	2717	9528	4606	761	volatile cloudy typically, it is rarely sunny
14. 06. 2014.	4032	9089	5515	757	strong variably, cloudy or sunny wether
20. 07. 2014.	4252	7031	6261	1557	sunny, cloud drift infrequently, but otherwise stable

5. Validation results

To evaluate the reliability of the model it was introduced a special indicator that is able to characterize the variability of the particular days. This indicator is the variability factor, it signs with V. Determine of this value is deepen on the numbers of the bigger changes of the measured average AC power within one minute. The definition is shown with the equation 16 and 17 and is illustrated in the table 6 and 7. This indicator is unique in that the connected weight values larger when the sudden change is bigger.

So the variability factor for the all day:

$$V_{day} = 4a_1 + 3a_2 + 2a_3 + a_4 + 4b_1 + 3b_2 + 2b_3 + b_4 \qquad \text{(eq. 17)}$$

And for the period between 10:00 - 16:00:

$$V_{10-16} = 4a_{1'} + 3a_{2'} + 2a_{3'} + a_{4'} + 4b_{1'} + 3b_{2'} + 2b_{3'} + b_{4'} \qquad \text{(eq. 18)}$$

These factors in the investigated date are in the next: The confidence indicator correlates to the period considered as a unit specific value is shown in the table 8.

Tab. 6: Determination of variability factor for the measured days

Dates	Changes in average AC power within 1 minute								Variability factor V_{day} [unit/ day]
	Down				Up				
2014	Above 55%	Between 35%-55%	Between 15%-35%	Between 5%-15%	Above 55%	Between 35%-55%	Between 15%-35%	Between 5%-15%	
	a_1	a_2	a_3	a_4	b_1	b_2	b_3	b_4	Day
1.04.	0	1	2	55	0	0	9	51	131
20.04.	8	8	40	71	16	11	40	76	460
1.05.	2	6	21	68	5	4	19	65	271
20.05.	11	6	10	47	19	3	10	34	268
1.06.	3	7	34	108	12	9	38	106	466
14.06..	20	19	29	61	35	10	29	54	538
20.06..	2	0	7	26	3	0	6	23	95

Tab. 7: Determination of variability factor for the measured days between 10-16 hours

	Changes in average AC power within 1 minute								Variability factor V_{10-16} [unit/ 6 hours]
2014	Down				Up				
	Above 55%	Between 35%-55%	Between 15%-35%	Between 5%-15%	Above 55%	Between 35%-55%	Between 15%-35%	Between 5%-15%	
	a_1,	a_2,	a_3,	a_4,	b_1,	b_2,	b_3,	b_4,	10:00 –
01.04.	0	1	1	17	0	0	2	18	44
20.04.	5	3	15	21	9	4	17	24	186
01.05.	2	6	12	22	5	3	10	28	149
20.05.	7	4	2	5	12	1	2	8	112
01.05.	2	6	23	54	9	8	21	61	289
14.06.	19	18	13	28	32	6	9	22	370
20.07.	2	0	1	8	3	0	1	8	40

Tab. 8: Determination of the specific variability factors

	Variability factors	Length of the period	Specific variability factors
2014	V_{day} [unit/day]	Δt_{day} [hour]	$v_{nap} = V_{day} / \Delta t_{day}$, [unit/hour]
01.04.	131	12,84	10,20
20.04.	460	13,89	33,12
01.05.	271	14,46	18,75
20.05.	268	15,31	17,51
01.05.	466	15,69	29,71
14.06.	538	15,93	33,78
20.07.	95	15,42	6,16
	Variability factors	Length of the period	Specific variability factors
2014	V_{10-16} [unit/6 hours]	Δt_{10-16} [hour]	$v_{10-16} = V_{10-16} / \Delta t_{10-16}$ [unit/hour]
01.04.	44	6	7,33
20.04.	186	6	31,00
01.05.	149	6	24,83
20.05.	112	6	18,67
01.05.	289	6	48,17
14.06.	370	6	61,67
20.07.	40	6	6,67

The results of the forecast are demonstrated in Figure and 4 for a one day (2014.04.01). Figure 3 shows the relative error according to prediction with the equation 9, where the forecast is for a one minute equivalent peak load hour and it was made 5 minute earlier. Figure 4 shows the relative error according to prediction with the equation 12, where the forecast is for a 15 minutes average equivalent peak load hour and it was made also 5 minutes earlier, than the end of the period.

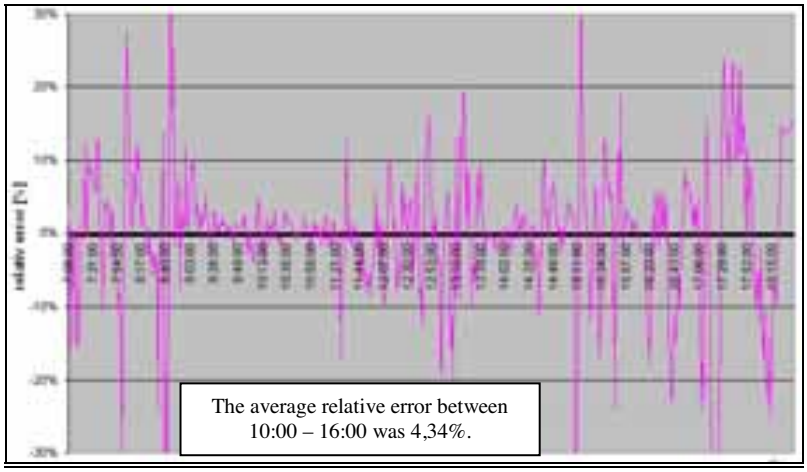

Fig. 3: Prediction with the equation 10 (AC relative error of the forecast, 01.04.2014)

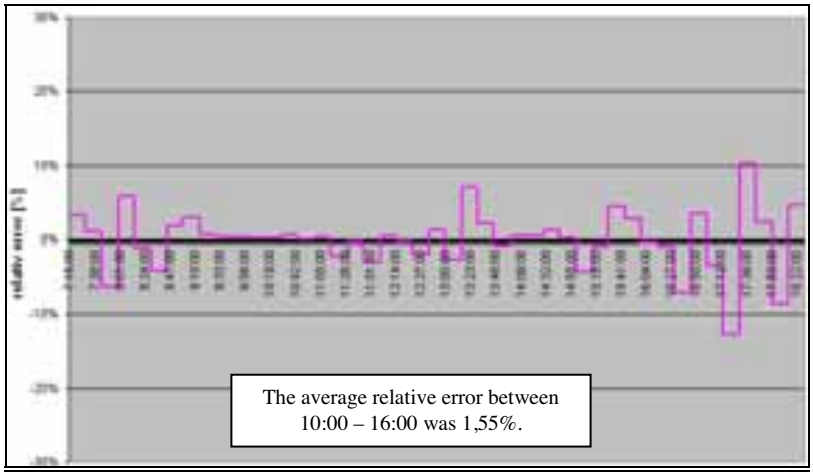

Fig. 4: Prediction with the equation 13 (AC relative error of the forecast, 01.04.2014)

Based on the differences between the monitoring forecasted values and the measurement data it was determined in both the absolute and relative errors for each minutes with the next equations..

$$\Delta h_t = \left| h_{ekv,t} - h_t^{**} \right| \text{, [hour]} \qquad \text{(eq. 19)}$$

$$h_h = 100 \times \frac{\Delta h_t}{h_{ekv,t}} \text{, [\%].} \qquad \text{(eq. 20)}$$

The results of the prediction for the reference power plant are shown in the table 9 and table 10.

Tab. 9: One-minute' forecast performance data between 10:00 and 16:00

	Absolute errors (equivalent peak load hour)				Relative errors				
	Average error	Above 200 hour	Between 100 and 200 hour	Under 100 hour	**Average error**	Above 15%	Between 10% and 15%	Between 5% and 10%	Under 5%
01. 04.	**235**	37,95%	20,22%	41,83%	**4,34%**	4,43%	5,26%	19,11%	71,19%
20. 04.	**885**	55,68%	13,85%	30,47%	**20,68%**	30,47%	13,02%	16,07%	40,44%
01. 05.	**693**	55,40%	24,38%	20,22%	**17,18%**	26,59%	12,47%	22,71%	38,23%
20. 05.	**798**	29,64%	17,73%	52,63%	**34,56%**	15,51%	0,55%	4,16%	79,78%
01. 05.	**1 203**	80,33%	9,97%	9,70%	**28,74%**	54,85%	12,19%	13,57%	19,39%
14. 06.	**1 880**	72,58%	13,02%	14,40%	**55,75%**	47,92%	5,54%	12,47%	34,07%
20. 07.	**175**	12,19%	16,90%	70,91%	**3,87%**	3,60%	1,39%	4,99%	90,03%

Tab. 10: Fifteen-minute' forecast performance data between 10:00 and 16:00
(5 minutes before the end of the period)

	Absolute errors (equivalent peak load hour)				Relative errors				
	Average error	Above 200 hour	Between 100 and 200 hour	Under 100 hour	**Average error**	Above 15%	Between 10% and 15%	Between 5% and 10%	Under 5%
01. 04.	**87**	12,50%	25,00%	62,50%	**1,55%**	0,00%	0,00%	4,17%	95,83%
20. 04.	**302**	37,50%	16,67%	45,83%	**6,63%**	12,50%	0,00%	29,17%	58,33%
01. 05.	**256**	37,50%	29,17%	33,33%	**5,92%**	12,50%	8,33%	25,00%	54,17%
20. 05.	**260**	29,17%	8,33%	62,50%	**4,36%**	8,33%	8,33%	4,17%	79,17%
01. 05.	**397**	58,33%	20,83%	20,83%	**9,29%**	20,83%	12,50%	20,83%	45,83%
14. 06.	**694**	75,00%	8,33%	16,67%	**13,09%**	37,50%	12,50%	16,67%	33,33%
20. 07.	**56**	8,33%	4,17%	87,50%	**0,93%**	0,00%	0,00%	8,33%	91,67%

The average relative error examining the relationship between Specific variability factors Student's t-test were performed. The square of the correlation coefficient by the fifteen-minute' forecast performance was 0.9854 between 10:00 – 16:00, so this mens a strong linear relationship. The confidence intervals for this tested case are summarized in Table 11.

Tab. 11: The forecast errors' critical values in the 95% confidence level
(5 minutes earlier prediction before the end of the 15 minutes period)

Specific variability factors [unit/hour]	Average relative error [%]
23.65	5 ± 1.46 = [3.54; 6.46]
47.85	10 ± 1.47 = [8.53; 11.47]
23.65 ± 7.04 = [16.61; 30.69]	5
47.85 ± 7.28 = [40.57; 55.13]	10

So, using the developed forecasting methodology for a 15-minute average performance in five minutes earlier to predict between 10 and 16 hour, when a specific variation factors are met 23.65 unit/h, with 95% confidence level true that the relative error of the forecast between 3.54% and 6.46% in Hungary. Furthermore, if the specific peak loads variation is less, than 40.57 unit/hour, it can be sure with a 95% confidence that the mean relative error of the forecast is less than 10%. If specific variability factors are less, than 16.61 unit/hour, the average relative error is better than 5%. The average value of the indicator during the tests was 28.3 unit/hour. This is very close to the 23.65, so it could be estimated an annual average of between 5-7% accuracy available between 10:00 -16:00.

Further analyzes are still in progress, but it is already clear that in some cases from the monitoring by only the inverter 1. No. a good prediction could be made for example with a relative error of 1.6% of the full power (inverter 8) performance between 10 and 16 hour.

6. Conclusions

The reference power plant-based method seems to be suitable for simultaneous modeling of the whole electricity energy production of more pv system in a low-voltage distribution grid with a smart grid, for short-term predictive modeling (balancing activity) and for prediction to keep the 15 minute schedule (trading activity).

The main research results so far:

- To establish a new factor (indicator);
- Anew analysis of the accuracy of forecast
- Analysis of other systems for the accuracy of forecast

7. References

Bilionis, I., Constantinescu, E. M., Anitescu, M., 2014. Data-driven model for solar irradiation based on satellite observations. Solar Energy 110, pp. 22-38.

Dyreson, A. R., Morgan, E. R., Monger, S. H., Acker T. L., 2014. Modeling solar irradiance smoothing for large PV power plants using a 45-sensor network and Wavelet Variability Model, Solar Energy 110, pp. 482-495.

Farkas, I., Seres, I., 2008. Operational experiences with small-scale grid-connected PV system, R&D in Mechanical Engineering Letters, Vol. 1, pp. 64-72.

Martin, C.L. and Goswami, D.Y., 2005. Solar energy pocket reference, International Solar Energy Society

Müller, S. /Ed/ (2014): The Power of transformation, OECD/IEA

PV Parity (2013): Cost and Benefits of PV Grid Integration, http://www.pvparity.eu/results/cost-and-benefits-of-pv-grid-integration/, downloaded: 2015.04.14.

Sharma, R., Tiwari, G.N., 2012. Technical performance evaluation of stand-alone photovoltaic array for outdoor field conditions of New Delhi, Applied Energy, 92. pp. 644-652.

Conference Proceedings

Solar World Congress 2015
Daegu, Korea, 08 – 12 November 2015

Geospatial Quantification of the Energy Economic Potential for Utility-Scale Photovoltaics: Case of the United Arab Emirates

Arttu Tuomiranta[1], Majd Jayyousi[1], Luis Calisto[1], Sgouris Sgouridis[2], S. Naseema Beegum[1], Mercedes Ibarra[1], Jacinto Estima[1] and Hosni Ghedira[1]

[1] Masdar Institute, Research Center for Renewable Energy Mapping and Assessment, Abu Dhabi, United Arab Emirates

[2] Masdar Institute, Department of Engineering Systems and Management, Abu Dhabi, United Arab Emirates

Abstract

An enhanced methodology for the assessment of energy economic potential for utility-scale photovoltaics is proposed in this paper. Independent methods are presented for the quantification of resource, technical, and economic potentials. The methodology is demonstrated through a case study focusing on the territory of the United Arab Emirates (UAE). The technical potential is computed by means of a locally validated PV plant performance model and the economic potential by estimating levelised cost of electricity (LCOE) based on detailed and spatially variable cost data. The results of the case study indicate a large potential for utility-scale photovoltaics in the UAE. At an electricity price of 0.07 USD per kWh, the economic potential is identified as approximately 10 EJ – 26-fold the country's electricity demand in 2013.

Keywords: solar photovoltaic, levelised cost of electricity, potential assessment

1. Introduction

Geospatial analysis based on geographic information systems (GIS) is a commonly used method for the site selection of solar photovoltaic (PV) power stations. The objective of such analysis is to identify the areas with the highest potential for PV power generation. The potential of a renewable energy source can be evaluated at three different levels: resource or theoretical potential (RP), technical potential (TP), and economic or energy economic potential (EP). Fig. 1 illustrates the potentials as three overlapping rectangles in two dimensions specified as surface area and unit-area-specific average energy content. RP assessment is a necessary first step when quantifying TP. TP, in turn, is the basis of EP assessment.

RP refers to the total amount of energy theoretically available in a renewable resource in the area of interest over a time period that is sufficiently long to cover most of the range of the resource's variability. Therefore, in the context of PV power generation, an appropriate definition of RP is the global normal irradiation (H_n) received in the area of interest during a typical meteorological year (TMY). There is a wide variety of scientifically validated models for geospatial solar resource assessment. Some of them are demonstrated by the International Renewable Energy Agency in their Global Atlas for Renewable Energy (International Renewable Energy Agency (IRENA), 2015). The maps visualising PV RP often show global horizontal irradiation (H) instead of H_n. Global horizontal irradiance (G) can be converted into global normal irradiance (G_n) by means of irradiance decomposition and transposition models. G and G_n are the first temporal derivatives of H and H_n, respectively.

TP is dependent on the energy conversion efficiency and land use-related limitations of the technology of interest. The power output of PV devices is reduced by loss mechanisms that are affected by ambient parameters. In accordance with RP, PV TP can be defined as the annual amount of electrical energy supplied by a group of PV power stations covering the entire technically suitable part of the area of interest. PV TP with and without territorial constraints has been evaluated by numerous authors for different parts of the

doi:10.18086/swc.2015.05.26 Available at http://proceedings.ises.org

Latin symbols

G	global horizontal irradiance [W/m²]
G_i	global irradiance incident on plane [W/m²]
$G_{b,n}$	beam normal irradiance [W/m²]
G_d	diffuse horizontal irradiance [W/m²]
G_{eff}	effective irradiance [W/m²]
G_n	global normal irradiance [W/m²]
$G_{toa,n}$	normal irradiance at TOA [W/m²]
H	global horizontal irradiation [J/m²]
H_n	global normal irradiation [J/m²]
I_{sc}	short circuit current of a solar cell [A]
N_c	number of solar cells per module
P_{stc}	module output power under STC [Wp]
T_a	ambient air temperature [K]
T_c	solar cell temperature [K]
v_w	wind speed [m/s]

Greek symbols

η_c	solar cell efficiency [%]
η_s	PV system efficiency [%]
θ	angle of incidence [rad]
θ_S	solar zenith angle [rad]
ϕ_S	solar azimuth angle [rad]

Subscripts

b	beam
c	solar cell
d	diffuse
eff	effective
i	incident
n	normal
S	the Sun
s	PV system
sc	short circuit
stc	standard test conditions
toa	top of the Earth's atmosphere
w	wind

Abbreviations

AC	alternating current
CdTe	cadmium telluride
CF	plant capacity factor
c-Si	crystalline silicon
DC	direct current
EP	economic potential
EPC	engineering, procurement and construction
GIS	geographic information system
LCOE	levelised cost of electricity
MBtu	million British thermal units
mc-Si	monocrystalline silicon
O&M	operation and maintenance
pc-Si	polycrystalline silicon
PV	solar photovoltaic
RP	resource potential
STC	standard test conditions
TMY	typical meteorological year
TOA	top of the Earth's atmosphere
TP	technical potential
UAE	United Arab Emirates
USD	United States Dollar

world (e.g. Beták et al., 2012; Domínguez Bravo et al., 2007; Lopez et al., 2012; Šúri et al., 2007). A widely used tool for the geospatial analysis of PV TP is PVGIS covering Europe, Africa, and Asia (European Commission, Joint Research Centre, Institute for Energy and Transport, 2014; Huld et al., 2005; Šúri et al., 2005).

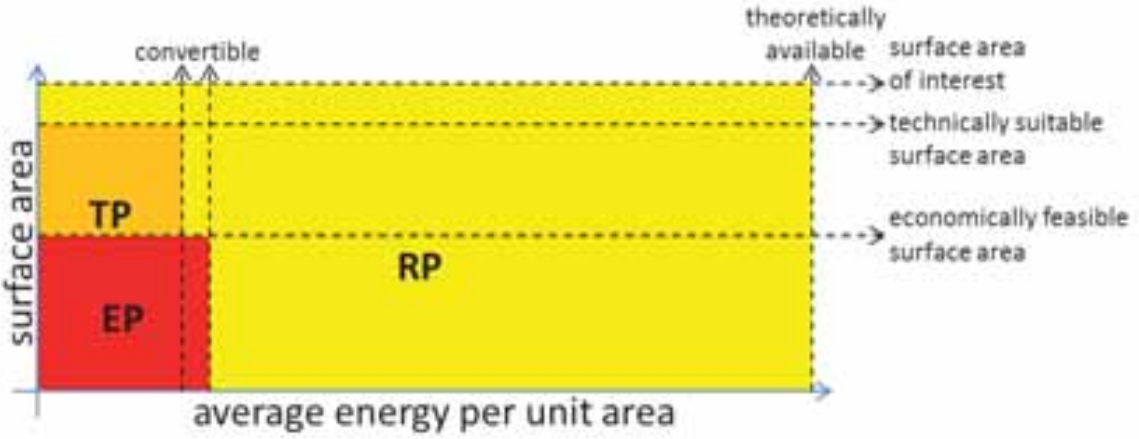

Fig. 1: The relation of renewable energy potentials to energy convertibility and site suitability

The economic viability of renewable energy-based power generation is primarily determined by its unit energy cost i.e. levelised cost of electricity (LCOE). Provided that consumers and policy makers do not have power source-specific preferences, there is no EP for a technology at a site where the competing technologies can generate electricity at a lower cost. Hence, in this paper, EP for a technology is defined as the amount of electrical energy that no other technology can supply at a lower cost in the area of interest. Due to the poor availability of component and infrastructure-related cost data, the quantification of EP is more difficult than that of TP. That is why when assessing PV EP, most authors have settled for fuzzy logic-based models which score sites based on their suitability for PV power generation rather than actually computing LCOE estimates. Suganthi et al. (2015) review studies applying fuzzy logic to PV EP assessment. While the LCOE-

based EP quantification is a common topic amongst the scholars of solar thermal technologies (starting from Broesamle et al., 2001), PV EP is found to be geospatially quantified based on LCOE estimates only in three published studies – by Sun et al. (2013) in Fujian, China and by Ossenbrink et al. (2013) and by Huld et al. (2014) by means of PVGIS in Europe.

In addition to the absolute level of PV EP, the focus of PV plant site zoning studies lies on the spatial variability of site suitability. Therefore, special attention should be paid to appropriately modelling the impact of spatially variable parameters, be they ambient variables or cost components. Sun et al. (2013) base their PV EP assessment on simplistic PV TP quantification assuming horizontally fixed PV array mounting and a performance ratio, which is constant in space. In other words, they assume the spatial variability of potential PV system output to be entirely dependent on the variability of H ignoring the impact of the other spatially variable ambient factors. Also, apart from the sites located near the Equator, PV arrays with fixed mount are usually tilted and therefore, irradiance incident on the plane of arrays (G_i) is the primary performance factor rather than G. By contrast, Ossenbrink et al. (2013) and Huld et al. (2014) consider G_i and vary PR in space addressing the nonlinear effects of T_a and G_i on module output power. Their performance ratio maps are based on a model proposed by Huld et al. (2011) for crystalline silicon wafer-based (c-Si) solar modules. Since Ossenbrink et al. (2013) and Huld et al. (2014) only analyse the LCOE of building-applied PV systems, it is justifiable to use a model that has been exclusively developed for c-Si modules as other module types are rarely used in such systems. As for the EP assessment of utility-scale photovoltaics however, it is important to also consider other module types. In addition to ambient parameters, some of the engineering, procurement and construction (EPC) as well as operation and maintenance (O&M)-related costs show spatial variation. The reviewed past PV EP assessment studies, however, assume all costs to be constant in space.

Previous work by Sun et al. (2013), Ossenbrink et al. (2013), and Huld et al. (2014) is enhanced by complementing PV EP quantification methodologies with more comprehensive PV performance modelling tools as well as more detailed and spatially variable cost data. This paper describes the modified methodology and presents the results of its application using five different PV plant configurations in the United Arab Emirates (UAE). Utility-scale photovoltaics in the UAE is an interesting subject for the case study due to the large potential indicated by previous studies (e.g. Beták et al., 2012; Mokri et al., 2013; Sgouridis et al., 2015) against the relatively modest installed capacity of 23 MWp (Abu Dhabi Future Energy Company PJSC, 2015; First Solar, Inc., 2015) and 340 MWp under development (Dubai Electricity & Water Authority, 2015; Middle East Solar Industry Association, 2015). In addition to proposing novel methods for PV EP assessment, this study aims to serve the various actors working on PV plant siting and zoning in the UAE by creating up-to-date high-resolution information about the spatial variability of PV EP in the country.

The proposed methodology is demonstrated at the hourly scale based on a database of irradiance and meteorological parameters for the year 2013. Spatial referencing is performed through an equal-area map projection with a resolution of 1000 metres. As each considered map pixel is assumed to be covered by the largest possible PV plant that can be fitted in the pixel, plant surface area does not show systematic spatial variability. However, due to the significance of latitude in optimal array inclination and row spacing, plant capacity does. Thus, capacity cannot be specified as a fixed PV plant configuration parameter.

The parameters of the five fixed plant configurations are specified in Tab. 1. The three commercially dominant PV materials are considered: monocrystalline silicon (mc-Si), polycrystalline silicon (pc-Si), and cadmium telluride (CdTe). The first three configurations are equipped with each of the three module types with fixed polar-aligned mounting. The two remaining configurations involve high-efficiency mc-Si wafer-based modules mounted on horizontal single axis or dual axis trackers. Inverters are sized based on an array-to-inverter loading ratio. The loading ratios given in Tab. 1 are approximate optimal loading ratios derived through plant design optimisation based on irradiance and meteorological observations made at a coastal (24.42 °N, 54.61 °E) and an inland site (23.90 °N, 55.50 °E) in the UAE over a three-year period from 2009 until 2011. The design optimisation is performed through maximising the simulated yield of each configuration in both locations by varying the loading ratio from 50 to 150 per cent at intervals of five per cent.

In the UAE, electricity is mostly generated by combined cycle power plants that use natural gas as the

primary fuel. Therefore, PV EP is calculated based on the price of natural gas under different market conditions. Drawing on the analysis of Sgouridis et al. (2015), resale prices at 6, 10, and 14 United States Dollars (USD) per million British thermal units (MBtu) are considered.

Tab. 1: PV power station configurations considered

Configuration identifier	Module type	Mounting method	Inclination	Array-to-inverter loading ratio
mc-Si-fm	mc-Si, N_c: 72, P_{stc}: 340 Wp	fixed mount	polar-aligned	115%
pc-Si-fm	pc-Si, N_c: 72, P_{stc}: 310 Wp	fixed mount	polar-aligned	115%
CdTe-fm	CdTe, N_c: 146, P_{stc}: 100 Wp	fixed mount	polar-aligned	110%
mc-Si-1t	mc-Si, N_c: 128, P_{stc}: 455 Wp	single axis tracking	horizontal	110%
mc-Si-2t	mc-Si, N_c: 128, P_{stc}: 455 Wp	tip-tilt dual axis tracking	-	105%

N_c: number of individual cells, P_{stc}: output power under standard test conditions (STC)

Sections 2-4 discuss each of the three levels of PV potential. All the three sections consist of two subsections. The first subsection describes the proposed methods while the second one specifies the case-specific inputs and shows the outcome of their application to utility-scale photovoltaics in the UAE. The case study follows the proposed methodology but due to limited data availability, simplifying assumptions are deployed.

2. Assessment of Resource Potential

2.1. Proposed Methodology

As explained in section 1, PV RP is defined as H_n in the territory of interest over a TMY. A TMY dataset is constructed instead of using the entire spatiotemporal database in order to reduce the computational requirements. Yearly average datasets are easier to generate but their usage is not recommended because they smoothen out natural variability and do not preserve persistence of temporal patterns and information related to the consistency and coevolution of different variables. This is problematic from the viewpoint of PV performance modelling as PV plant output is nonlinearly dependent on multiple ambient parameters. More information is preserved when using TMY dataset construction methods that are based on the concatenation of continuous multivariate time series spanning those individual months that are found to provide the best agreement with long-term monthly statistics (e.g. Cebecauer and Šúri, 2015; Kalogirou, 2003; Marion and Urban, 1995). How different variables are weighted when quantifying monthly representativeness depends on the application. Cebecauer and Šúri's (2015) proposal for the PV power generation-specific set of TMY variables is G, diffuse horizontal irradiance (G_d), and ambient air i.e. dry bulb temperature (T_a) with the respective weights of 0.75, 0.20, and 0.05. Thereby, T_a indirectly influences PV RP estimation. As for the source data, Cebecauer and Šúri (2015) recommend using time series of 15 years or more to establish a good representativeness of the long-term solar climate.

As H_n is an extensive physical property, an equal-area map projection (e.g. Mollweide projection or Lambert cylindrical equal-area projection) has to be applied to the TMY maps in order to avoid map pixel size-related bias in the pixel-specific H_n estimates. For example, when using the reference coordinate system of the Global Positioning System (WGS 84) with a spatial resolution of 0.02° and without an equal-area map projection, the pixel surface areas at 20 °N are approximately nine per cent greater than those at 30 °N.

H_n estimates are computed based on the equal-area projected TMY time series of maps of G, G_d, beam normal irradiance ($G_{b,n}$), solar zenith angle (θ_S), and solar azimuth angle (ϕ_S). In addition, a spatially constant time series of normal irradiance at the top of the Earth's atmosphere ($G_{toa,n}$) is required. An irradiance transposition model (e.g. Hay, 1979; Muneer, 1990; Perez et al., 1990; Reindl et al., 1990a) enables the conversion of these data into G_n maps. If not readily available, $G_{b,n}$ and G_d estimates can be derived from G

data by means of an irradiance separation i.e. decomposition model (e.g. Erbs et al., 1982; Perez et al., 1992; Reindl et al., 1990b). θ_S, ϕ_S, and $G_{toa,n}$, in turn, can be computed through a solar geometric algorithm (e.g. Blanc and Wald, 2012; Duffie and Beckman, 2006, pp. 12–16; Reda and Andreas, 2008). Finally, the resulting G_n maps are integrated over time into a single H_n map, which is further integrated over space to obtain a PV RP estimate for the territory of interest.

2.2. Resource Potential in the UAE

The spatiotemporal database of irradiance (G, $G_{b,n}$, and G_d) for the UAE is created by means of an artificial neural network-based model proposed by Eissa et al. (2013). The model uses satellite-based SEVIRI images as input data and has been developed based on ground observations from five monitoring stations in the UAE. The resulting irradiance maps cover the year 2013 with a temporal resolution of 15 minutes and a spatial resolution of 0.02° (in WGS 84). Minor discrepancies in the spatial resolutions of the source data are removed by resampling the anomalous maps through nearest-neighbour interpolation. Irradiance data gaps are filled by interpolating and extrapolating clear-sky indices calculated based on the McClear algorithm (Lefèvre et al., 2013). As the timeframe of the data used in this case study spans only one year, no TMY dataset is constructed. Hence, the results of the study cannot be generalised to other years.

The Mollweide equal-area projection is applied to the input data maps. When reprojecting the maps, their spatial resolution is converted from 0.02° to 1000 metres. As explained in section 2.1, solar position (θ_S, ϕ_S, and $G_{toa,n}$) has to be known in order to estimate G_n. The solar geometric parameters are computed by means of the Solar Geometry 2 (SG2) algorithm developed by Blanc and Wald (2012). The SG2 algorithm is selected because it is computationally efficient with an accuracy only slightly surpassed by Reda and Andreas's (2008) Sun Position Algorithm, which is commonly considered as the state of the art in terms of accuracy.

Transposition models, which convert G, $G_{b,n}$, G_d, and solar geometric data into G_i estimates, comprise transposition processes for $G_{b,n}$, diffuse sky irradiance, and ground-reflected irradiance. In the case of G_n, $G_{b,n}$ is not transposed as it is always normal to the receiving surface. Tuomiranta and Ghedira (2015) evaluate 18 sky diffuse and four ground-reflected irradiance transposition models under the conditions of the UAE. They find the best agreement with ground observations with the model proposed by Perez et al. (1990) for sky diffuse irradiance and the model proposed by Badescu (2002) for ground-reflected irradiance. Accordingly, the two models are used to generate the G_n maps in the present study.

Fig. 2 presents the findings of the PV RP assessment. The resulting H_n estimates translate into a PV RP of 872 EJ for the UAE. At the sites with the most abundant solar resource, H_n is estimated to be 17 per cent higher than at the least sunny sites, which are concentrated in the coastal areas.

3. Assessment of Technical Potential

3.1. Proposed Methodology

As discussed in section 1, PV TP is defined as the maximum amount of electrical energy that can be supplied from PV power stations to consumers in the territory of interest over a TMY. The geographic area considered in PV TP assessment is limited by technical suitability. In other words, any site whose utilisation is possible when cost-related criteria are not taken into consideration is assumed to have nonzero PV TP. The excluded sites include all areas that cannot be used for reasons other than economic, e.g. areas protected for their natural, cultural, or other public welfare-related value such as nature reserves, historical monuments, and areas under a restrictive urban planning code.

Prior to the actual plant performance simulation, PV plant system architecture needs to be determined for every site. Due to the definition of PV TP, the maximum surface area of each plant is the pixel area. Based on the desired loading ratio and row spacing requirements as well as the maximum number of modules in a string, the plant capacity and the other system configuration-related parameters are computed. In order to enable detailed PV EP assessment, it is recommended to calculate the numbers of at least those components, for which there are cost data available. The components, whose number is directly dependent on plant sizing, include solar modules, mounting structures, inverters, transformers, junction boxes, and cables.

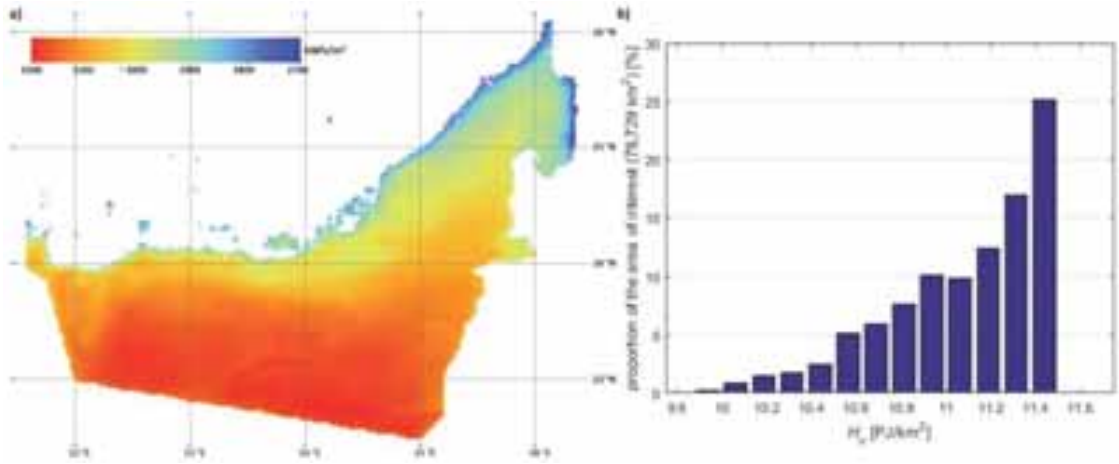

Fig. 2: PV RP in the UAE; a) map of H_n per m^2, b) histogram of H_n per km^2

The proportion of PV RP that can be converted into electricity depends on the ratio of G_i to G_n and PV system efficiency (η_s). While G_n stands for the theoretical maximum irradiance capable of being received by a solar module mounted on the Earth's surface, G_i refers to the irradiance actually incident on the module considering the mounting method and shading conditions. Geometric models (e.g. Duffie and Beckman, 2006, pp. 20–23; Marion and Dobos, 2013; Narvarte and Lorenzo, 2008) are used to compute the incidence angle of incoming irradiance (θ), which is input to a transposition model in order to obtain G_i in different plant configurations. Theoretically, a plant with dual axis tracking installed on a flat terrain with a very low ground coverage ratio can reach a unity G_i-G_n ratio.

By contrast, η_s cannot reach 100 per cent due to losses fundamentally associated with the operation of semiconductor-based solar cells: spectral mismatch and charge carrier recombination. In addition, utility-scale PV power conversion involves extrinsic optical losses, recombination via impurities, and parasitic losses. Each loss process is determined by both ambient and technological parameters. The ambient parameters of relevance include level, spectral distribution, and θ of incoming irradiance, T_a, sky temperature, wind speed (v_w), wind direction, and dust deposition. The technological parameters are subject to the selected module type and system architecture of each plant. Finally, the amount of electrical energy actually supplied to consumers is dependent on the losses of power transmission.

As illustrated in Fig. 3, the simulation of η_s is divided into three components: optical, thermal, and electrical modelling. Most of the models following this approach make use of the STC parameters that are commonly measured and available in module datasheets. Based on its STC parameters, a solar module's performance is known under a set of standard conditions to which the operating conditions can be compared.

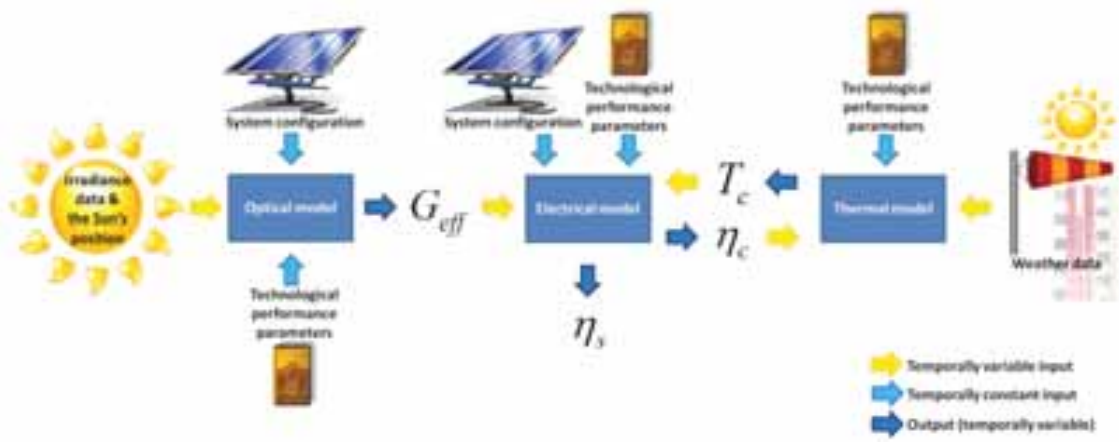

Fig. 3: Steps involved in modelling η_s

Under STC, a solar module receives irradiance that is normal to its surface and whose spectral distribution follows the standard spectrum at an air mass coefficient of 1.5 (G03 Committee, 2012). The purpose of an

optical model is to address the performance effects of the deviations of the spectrum and θ from STC. The additional attenuation due to dust deposition should be quantified. For this purpose, an optical model converts G_i and θ as well as dust deposition and spectral distribution-related data into effective irradiance (G_{eff}). G_{eff} is adapted from G_i such that a solar cell's short circuit current (I_{sc}) is always linearly dependent on it. In G_{eff}, the effects of changing spectrum, angular reflection losses, and dust deposition are isolated by normalising $G_{i,stc}$ (1000 W/m^2) by the ratio of I_{sc} to $I_{sc,stc}$. Thus, $G_{eff,stc}$ is equal to $G_{i,stc}$. I_{sc} is estimated by means of modifier equations for θ (e.g. Davis et al., 2002; Duffie and Beckman, 2006, p. 234; Souka and Safwat, 1966) and spectral distribution (e.g. Betts et al., 2004; King et al., 1998; Martín and Ruiz, 1999). The impact of dust deposition should be considered on its own (e.g. Kimber et al., 2006) as well as in association with θ and spectral modifiers (e.g. Martín and Ruiz, 2005).

The purpose of a thermal model is to simulate the temperature of a solar cell's photoactive layers (T_c), which is the primary effective variable involved in η_s modelling. The fundamental basis of the simulation of T_c is the heat transfer energy exchange of a solar cell's active components with the surrounding layers and ambient air. Therefore, T_c can be obtained through transient heat transfer modelling or by means of one of the numerous empirical and semi-empirical models and correlations (see e.g. Skoplaki and Palyvos, 2009a). The most significant ambient parameters are T_a, G_i, and v_w. Since the internal heating process within a solar cell depends on the efficiency at which the cell is converting radiation into electricity, most of the T_c modelling formulations also include cell efficiency (η_c) as an input variable.

The effective variables, G_{eff} and T_c, are converted into η_s by an electrical model with three components addressing power generation (e.g. De Soto et al., 2006; King et al., 2004; Mermoud and Lejeune, 2010; Sutterlueti et al., 2011), transmission, and conversion (e.g. Baumgartner et al., 2007; Driesse et al., 2008; King et al., 2007). A power generation model simulates all losses occurring inside solar cells. If T_c is simulated by means of a thermal model which is dependent on η_c, the thermal model and the electrical model for generation are coupled and, therefore, comprise a thermoelectrical model. The numerous empirical relationships (see e.g. Skoplaki and Palyvos, 2009b) between η_c and ambient and technological parameters are not recommended due to their weak generalizability across different locations and technologies. Nevertheless, the effects of time-dependent degradation (see e.g. Jordan et al., 2012) and performance mismatch between modules and arrays are generally considered through empirically determined, fixed loss percentages. Models for transmission and conversion address the losses occurring in conductors and power conditioning equipment, respectively. Power transmission losses are due to Joule heating and power conversion losses due to the conversion of direct current (DC) into alternating current (AC) in inverters and stepping up plant output voltage in transformers.

Furthermore, η_s is affected by a power station's auxiliary consumption. While inverter self-consumption during power conversion is considered by most inverter performance models, power losses due the consumption of trackers, air conditioning units, lighting, plant management equipment, and inverters' nocturnal standby operation have to be additionally quantified. The consumption levels of trackers and inverters are available in product datasheets. Air conditioning-related losses can be estimated by heat transfer modelling (e.g. International Organization for Standardization, 2008), which is also enabled by various software packages used for sizing air conditioning units.

The instantaneous PV plant output power can be computed as a product of G_i and η_s. As PV TP represents the amount of electricity supplied to consumers, the final step is the estimation of transmission losses for each site. Apart from the plants' own power consumption, all power demand is assumed to be concentrated on the urban areas excluded from the assessment. Transmission losses are computed for each site based on the weighted average distance to the nearest demand concentration areas using a reference high-voltage transmission line and increasing quadratically with plant output power. The transmitted power, when integrated over time and space, provides the PV TP of the territory of interest.

3.2. Technical Potential in the UAE

Area-wise, we exclude areas with conservation status as specified in the World Database on Protected Areas (International Union for Conservation of Nature and United Nations Environment Programme World Conservation Monitoring Centre, 2015) and urban status classified manually using open access geographical

information software. The excluded areas represent 21 and 2 per cent of the entire area of interest, respectively.

As explained above, PV TP assessment requires data on meteorological parameters in addition to irradiance – most importantly T_a and v_w. A locally calibrated global atmospheric model is used to retrieve the relevant data. Due to the optical and thermal models of choice, spectral data as well as data on sky temperature and wind direction are not needed.

Both the plant's system architecture and performance are simulated by means of a PV plant performance simulator (Tuomiranta, 2014). The simulator incorporates locally validated optical and thermal models and Sandia's electrical models for generation and conversion (King et al., 2007, 2004). The impact of soiling is addressed by a fixed loss percentage together with the dust deposition-dependent θ modifier model proposed by Martín and Ruiz (2005). This simplified approach is justified as PV arrays installed in the UAE can be assumed to be regularly cleaned. Therefore, dust deposition can be primarily considered as an O&M cost factor. Spectral correction is not applied due to the lack of models appropriately validated for desert climates characterised by severe aerosol loading. The thermal model found to provide the best agreement with local measurements is the one proposed by Schott (1985) (Tuomiranta et al., 2014). This semiempirical model predicts T_c based on T_a, G_{eff}, v_w, and η_c and is calibrated based on measurements made in Abu Dhabi (Tuomiranta et al., 2014).

As PV TP represents the maximum amount of electrical energy that can be supplied in a territory of interest, a single power station can be assumed to serve the entire territory rather than the areas in its proximity. Accordingly, transmission losses are estimated by means of an approximated power demand-weighted average distance to all urban areas where the country's entire demand for electricity is assumed to be concentrated. The electrical properties of transmission lines are based on the parameters published by Abu Dhabi Transmission & Despatch Company (2013).

The results of the PV TP assessment are illustrated in Fig. 4. Due to its comparatively high ground coverage ratio and average η_s, configuration mc-Si-fm provides the highest TP at all sites in the UAE. Therefore, the PV TP histogram presented in Fig. 4b is solely based on the transmitted yields of mc-Si-fm type of power stations. Out of the total PV TP of 51 EJ, 11 EJ (22 per cent) is represented by the protected areas and 94 PJ (2 per cent) by the urban areas. The maximum plant yield (mc-Si-fm, 23.22 °N, 52.60 °E, 681 TJ) is 183 per cent higher than the minimum yield (mc-Si-2t, 25.29 °N, 56.37 °E, 240 TJ).

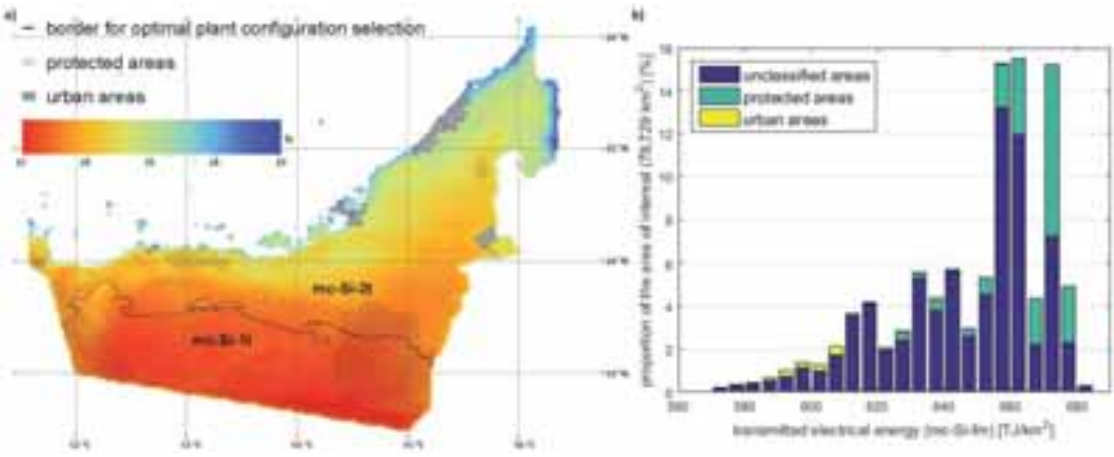

Fig. 4: PV TP in the UAE; a) map of CF and technically optimal plant configurations, b) histogram of transmitted electrical energy per km^2 separating the contributions of urban and protected areas

The map of Fig. 4a shows the spatial distribution of the highest simulated plant capacity factors (CF) considering transmitted electrical energy. Due to the high G_i-G_n ratio enabled by tracking, configurations mc-Si-1t and mc-Si-2t provide the highest CFs everywhere in the UAE. The G_i-weighted average T_c is lower in the case of configuration mc-Si-1t. Hence, configuration mc-Si-1t is the technically optimal choice for the southern part of the country, which experiences the highest G_i-weighted average T_a. The technically most appropriate site-configuration combination (mc-Si-1t, 23.69 °N, 53.23 °E, CF: 26.7%) provides 42 per cent

higher CF than the technically poorest combination (pc-Si-fm, 25.90 °N, 56.12 °E, CF: 18.9%). Amongst the fixed mount configurations, CdTe-fm power plants operate at the highest capacity factor (21% on average) at all sites.

4. Assessment of Energy Economic Potential

4.1. Proposed Methodology

PV EP assessment mainly involves the estimation of the level and spatial distribution of different cost components in order to appropriately capture the spatial dynamics of PV LCOE. In the present paper, PV LCOE refers to the cost of electricity supplied to consumers by a PV power station when considering the entire lifetime of the power project. LCOE is sensitive to numerous cost factors, some of which are difficult to be quantified accurately. Due to site-specific plant configuration and other spatial cost factors, most costs show spatial variability.

PV project-related cost data are often given in price per Wp of module capacity. When comparing different sites and technologies, this highly case-specific cost indicator can be regarded as excessively simplified. Therefore, Wp-based cost data are recommended to be converted into more appropriate cost component-tailored indicators, which enable the allocation of spatial cost factors more accurately to the components actually affected. Such a set of indicators is proposed in Tab. 2. In addition to cost categorisation, the table specifies the spatial factors influencing each of the cost components. These factors do not include plant configuration-related parameters (e.g. capacity, array area, cable volume), which are also varied spatially in the present analysis.

Accurate quantification of the cost factors specified in Tab. 2 requires access to data that are often non-existent or unavailable free of charge. However, through publicly accessible industry review studies and interviewing local industry experts, many of the factors can be approximated without costly data acquisition. Land values can be estimated by correlating point data from real estate market with relevant spatial data such as land use and population density. Earthworks cost can be estimated by multiplying publicly available cost estimates by cut and fill volumes calculated based on a digital elevation model. PV system design software can be used to convert Wp-based EPC costs to component unit-based costs. Estimates of the effects of land cover, wind load, and slope as well as project development, O&M, and road and grid connection costs for land and sea can be obtained from experts. A critical component of O&M is array cleaning if the area of interest is under severe dust loading. A three-dimensional chemistry transport model such as CHIMERE can be used to estimate the spatial variability of dust deposition. By means of published average soiling loss percentages, the dust deposition estimates can be correlated to the desired cleaning frequency.

4.2. Energy Economic Potential in the UAE

A detailed listing of the different cost data is presented in Appendix A. As shown in Fig. 5a, the spatial variability of LCOE is significantly higher than that of PV RP or TP. In fact, the LCOE levels in the country's mountainous areas are far higher than the maximum specified in the legend. The two most significant cost factors that can be identified based on Fig. 5a are cut and fill volume contributing to earthworks cost and soil consistency affecting the foundation EPC cost. The areas with LCOE levels higher than 0.10 USD per kWh are characterised by highly variable terrain elevation and consequently high earthworks costs. Most of the areas with LCOE levels ranging from 0.08 to 0.10 USD per kWh are either covered by loose sand causing inconsistency in the surface soil or located on islands with a poor access to supporting infrastructure. The minimum LCOE of 0.0657 USD per kWh is reached by configuration mc-Si-fm at the site coordinates of 24.00 °N and 52.50 °E.

The natural gas prices of 6, 10, and 14 USD per MBtu correspond to conventional power LCOE estimates of 0.06, 0.08, and 0.11 USD per kWh. As can be seen from the histogram of Fig. 5b, there is no PV EP anywhere in the UAE if natural gas price is 6 USD per MBtu. At the price of 10 USD per MBtu, 32 % (16 EJ) of the country's surface area provides conditions for economically feasible PV power generation. The proportion becomes as high as 96% (49 EJ) at the price of 14 USD per MBtu. Fig. 6 illustrates PV EP in the

UAE in case the LCOE of conventional power generation is 7 USD per kWh (natural gas at 8.1 USD per MBtu). The resulting entire PV EP is 11 EJ, out of which protected areas represent 10%.

Tab. 2: Proposed cost categorisation and the spatial cost factors under consideration

Cost category	Cost component	Cost unit	Spatial cost factors
Land	Land acquisition	USD/ha (plant area)	• land value
	Earthworks	USD/m^3	• cut and fill volume
EPC	Foundation	USD/m^2 (array area with fixed mount and single axis tracking) / USD/tracker (dual axis tracking)	• land cover • road distance to a cement factory/industrial area • slope
	Mounting structures	USD/m^2 (array area) / USD/tracker	• wind load • slope
	Solar modules	USD/Wp	
	Module cables	USD/module	• slope
	Solar cables / DC main cables	USD/m^3 (cable volume)	• slope
	Junction boxes	USD/junction box	• slope
	AC BOS	USD/MVA	• slope
	Civil works	USD/ha (plant area)	• slope
	Auxiliary systems	USD/Wp	• slope
Supporting infrastructure	Road connection	USD/km	• Euclidean distance to a road • slope
	Grid connection	USD/km	• Euclidean distance to a transmission line • land/marine connection • slope
	Substation	USD/substation	• slope
Intra-country transportation		USD/m^3/km	• road/Euclidean marine distance to a primary port
Project development		USD (% of total EPC)	
O&M	Arrays	USD/m^2/year (array area)	• dust deposition • slope
	Civil works	USD/ha/year (plant area)	• slope
	Power block	USD/power block/year	
	Plant management	USD/MWp/year	
	Utilities	USD/MWp/year	
	Road connection	USD/km/year	• Euclidean distance to a road • slope
	Grid connection	% of transmission line cost	

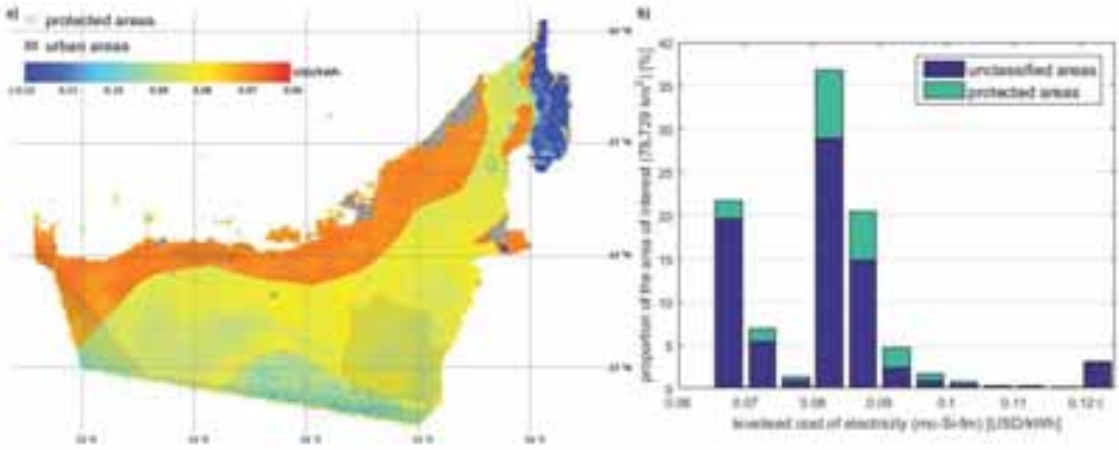

Fig. 5: PV LCOE in the UAE; a) map of minimum LCOE, b) histogram of the minimum LCOE estimates

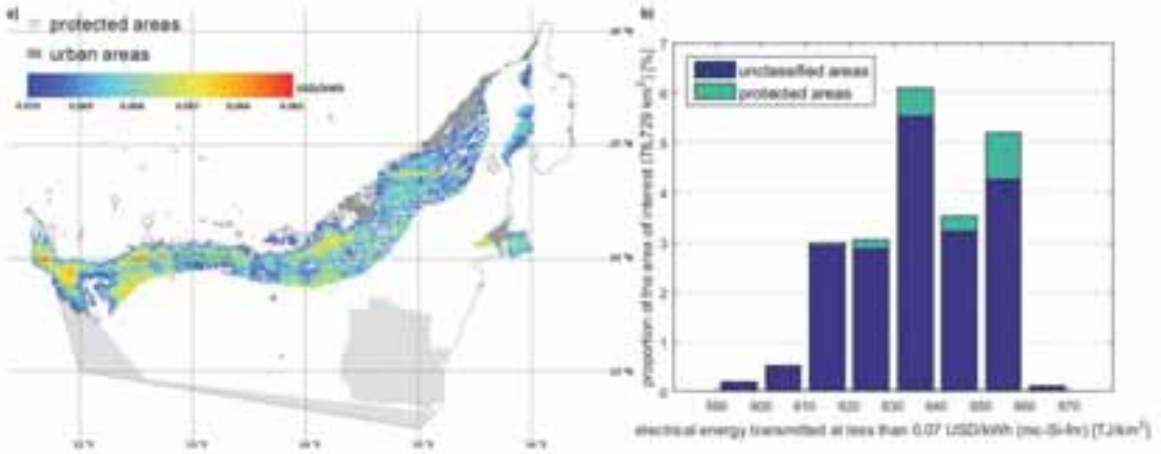

Fig. 6: PV EP in the UAE; a) map of LCOE in areas where PV competitive against natural gas at 8.1 USD/MBtu, b) histogram of transmitted electrical energy per km^2 from the highlighted area

In 2015, Dubai Electricity and Water Authority (DEWA) reached a financial close for a PV project of 200 MWp at a historically low price of 0.0598 USD per kWh (Dubai Electricity & Water Authority, 2015). This price is significantly less than the lowest LCOE level estimated in this study. It should be noted, however, that in this paper, PV potential is analysed from the governmental perspective. Thus, some cost components irrelevant for the companies bidding for DEWA's project need to be considered. These components are mainly related to land and supporting infrastructure. In addition, financial parameters such as debt-to-equity ratio have a great impact on LCOE but are highly company-specific. The presented analysis is based on financial parameter values typical of the industry.

5. Conclusion

This paper presents an enhanced methodology for the assessment of energy economic potential for utility-scale photovoltaics. It is shown that by only using publicly accessible literature and expert interviews, high-resolution information about the spatial variability of PV potential can be generated. The methodology can be further improved by using optical models that capture local spectral and dust deposition-related particularities and more refined cost parameters e.g. for foundation construction. Also, the power demand-driven cost factors should be taken into consideration when taking the high-level, systemic approach in future studies.

The presented case study confirms the UAE's tremendous PV potential indicated by previous studies by actually quantifying it for the entire country for the first time. Tab. 3 aggregates the findings and compares

them to the annual power demand in the UAE in 2013. As can be seen from the table, the PV EP is 26-fold the country's electricity demand when considering an electricity price of 0.07 USD/kWh. These findings together with the recent advances in further capacity building indicate a bright future for PV power generation in the UAE.

Tab. 3: Comparison of the different levels of PV potential to the UAE's annual electricity demand in 2013

Potential	Entire territory	% of annual electricity demand (0.4 EJ, 2013)	Unclassified territory	% of annual electricity demand (0.4 EJ, 2013)
PV RP	872 EJ	231,000%	670 EJ	177,000%
PV TP	51 EJ	13,500%	39 EJ	10,300%
PV EP (≤ 0.11 USD/kWh)	49 EJ	13,000%	37 EJ	9,900%
PV EP (≤ 0.08 USD/kWh)	16 EJ	4,200%	13 EJ	3,400%
PV EP (≤ 0.07 USD/kWh)	11 EJ	2,900%	10 EJ	2,600%

Acknowledgements

The authors want to acknowledge Afshin Afshari (Masdar Institute), Maryam Rashed Al Shehhi (Masdar Institute), Naira Chaouch (Masdar Institute), Yehia Eissa (Masdar Institute), Imen Gherboudj (Masdar Institute), Bilal Hassan (UAE Ministry of Energy), Karim Karam (Masdar Institute), Aram Kirakosyan (Masdar Institute), Francisco Luque (Masdar Clean Energy), Rita Sousa (Masdar Institute), Cristobal Verdu (Masdar Clean Energy), and Ahmad Yousef (UAE Ministry of Energy) for their valuable support during the course of the research project.

References

Abu Dhabi Future Energy Company PJSC, 2015. Masdar City Solar PV Plant [WWW Document]. URL http://www.masdar.ae/en/energy/detail/masdar-city-solar-pv-plant (accessed 9.10.15).

Abu Dhabi Transmission & Despatch Company, 2013. 2013 Seven Year Electricity Planning Statement (2014-2020) (Attachments). Abu Dhabi, United Arab Emirates.

Badescu, V., 2002. 3D isotropic approximation for solar diffuse irradiance on tilted surfaces. Renew. Energy 26, 221–233. doi:10.1016/S0960-1481(01)00123-9

Baumgartner, F.P., Schmidt, H., Burger, B., Bründlinger, R., Häberlin, H., Zehner, M., 2007. Status and relevance of the DC voltage dependency of the inverter efficiency, in: Proceedings. Presented at the 22nd European Photovoltaic Solar Energy Conference and Exhibition, Milan, Italy.

Beták, J., Šúri, M., Cebecauer, T., Skoczek, A., 2012. Solar Resource and Photovoltaic Electricity Potential in EU-MENA Region, in: EU PVSEC Proceedings. Presented at the 27th European Photovoltaic Solar Energy Conference and Exhibition, Frankfurt am Main, Germany, pp. 4623–4626. doi:10.4229/27thEUPVSEC2012-6CV.3.51

Betts, T.R., Gottschalg, R., Infield, D.G., 2004. Spectral Irradiance Correction for PV System Yield Calculations, in: EU PVSEC Proceedings. Presented at the 19th European Photovoltaic Solar Energy Conference, Paris, France, pp. 2533–2536.

Blanc, P., Wald, L., 2012. The SG2 algorithm for a fast and accurate computation of the position of the Sun for multi-decadal time period. Sol. Energy 86, 3072–3083. doi:10.1016/j.solener.2012.07.018

Broesamle, H., Mannstein, H., Schillings, C., Trieb, F., 2001. Assessment of solar electricity potentials in North Africa based on satellite data and a geographic information system. Sol. Energy 70, 1–12. doi:10.1016/S0038-092X(00)00126-2

Cebecauer, T., Šúri, M., 2015. Typical Meteorological Year Data: SolarGIS Approach. Energy Procedia, International Conference on Concentrating Solar Power and Chemical Energy Systems, SolarPACES 2014 69, 1958–1969. doi:10.1016/j.egypro.2015.03.195

Davis, M.W., Fanney, A.H., Dougherty, B.P., 2002. Evaluating building integrated photovoltaic performance models, in: Conference Record of the Twenty-Ninth IEEE Photovoltaic Specialists Conference, 2002. Presented at the Conference Record of the Twenty-Ninth IEEE Photovoltaic Specialists Conference, 2002, pp. 1642–1645. doi:10.1109/PVSC.2002.1190931

De Soto, W., Klein, S.A., Beckman, W.A., 2006. Improvement and validation of a model for photovoltaic array performance. Sol. Energy 80, 78–88. doi:10.1016/j.solener.2005.06.010

Domínguez Bravo, J., García Casals, X., Pinedo Pascua, I., 2007. GIS approach to the definition of capacity and generation ceilings of renewable energy technologies. Energy Policy 35, 4879–4892. doi:10.1016/j.enpol.2007.04.025

Driesse, A., Jain, P., Harrison, S., 2008. Beyond the curves: Modeling the electrical efficiency of photovoltaic inverters, in: 33rd IEEE Photovoltaic Specialists Conference, 2008. PVSC '08. Presented at the 33rd IEEE Photovoltaic Specialists Conference, 2008. PVSC '08, pp. 1–6. doi:10.1109/PVSC.2008.4922827

Dubai Electricity & Water Authority, 2015. DEWA announces Financial Close for 200MW IPP Phase II of the Mohammed bin Rashid Al Maktoum Solar Park [WWW Document]. URL https://e-services.dewa.gov.ae/newshist/details.aspx?id=02534610000000000000000002534610 (accessed 9.10.15).

Duffie, J.A., Beckman, W.A., 2006. Solar Engineering of Thermal Processes, 3rd ed. John Wiley & Sons, Hoboken, NJ, USA.

Eissa, Y., Marpu, P.R., Gherboudj, I., Ghedira, H., Ouarda, T.B.M.J., Chiesa, M., 2013. Artificial neural network based model for retrieval of the direct normal, diffuse horizontal and global horizontal irradiances using SEVIRI images. Sol. Energy 89, 1–16. doi:10.1016/j.solener.2012.12.008

Erbs, D.G., Klein, S.A., Duffie, J.A., 1982. Estimation of the diffuse radiation fraction for hourly, daily and monthly-average global radiation. Sol. Energy 28, 293–302. doi:10.1016/0038-092X(82)90302-4

European Commission, Joint Research Centre, Institute for Energy and Transport, 2014. Photovoltaic Geographical Information System (PVGIS) [WWW Document]. URL http://re.jrc.ec.europa.eu/pvgis/ (accessed 5.21.15).

First Solar, Inc., 2015. DEWA 13 Solar Plant [WWW Document]. URL http://www.firstsolar.com/en/About-Us/Projects/DEWA-13-Solar-Plant.aspx (accessed 9.10.15).

G03 Committee, 2012. Tables for Reference Solar Spectral Irradiances: Direct Normal and Hemispherical on 37 Tilted Surface. ASTM International.

Hay, J.E., 1979. Calculation of monthly mean solar radiation for horizontal and inclined surfaces. Sol. Energy 23, 301–307. doi:10.1016/0038-092X(79)90123-3

Huld, T.A., Friesen, G., Skoczek, A., Kenny, R.P., Sample, T., Field, M., Dunlop, E.D., 2011. A power-rating model for crystalline silicon PV modules. Sol. Energy Mater. Sol. Cells 95, 3359–3369. doi:10.1016/j.solmat.2011.07.026

Huld, T.A., Jäger Waldau, A., Ossenbrink, H.A., Szabó, S., Dunlop, E.D., Taylor, N., 2014. Cost Maps for Unsubsidised Photovoltaic Electricity (No. 91937), JRC Scientific and Policy Reports. European Commission, Joint Research Centre, Institute for Energy and Transport, Ispra, Italy.

Huld, T.A., Šúri, M., Dunlop, E.D., Albuisson, M., Wald, L., 2005. Integration of Helioclim-1 database into PV-GIS to estimate solar electricity potential in Africa, in: Proceedings. Presented at the 20th European Photovoltaic Solar Energy Conference, Barcelona, Spain.

International Organization for Standardization, 2008. Energy performance of buildings - Calculation of energy use for space heating and cooling (International standard No. ISO 13790:2008(E)). Geneva, Switzerland.

International Renewable Energy Agency (IRENA), 2015. Global Atlas for Renewable Energy [WWW Document]. URL http://irena.masdar.ac.ae/ (accessed 5.20.15).

International Union for Conservation of Nature, United Nations Environment Programme World Conservation Monitoring Centre, 2015. World Database on Protected Areas [WWW Document]. Prot. Planet. URL http://www.protectedplanet.net/ (accessed 10.30.15).

Jordan, D.C., Wohlgemuth, J.H., Kurtz, S.R., 2012. Technology and Climate Trends in PV Module Degradation, in: Proceedings of the 27th European Photovoltaic Solar Energy Conference and Exhibition. Presented at the 27th European Photovoltaic Solar Energy Conference and Exhibition, Frankfurt am Main, Germany, pp. 3118–3124. doi:10.4229/27thEUPVSEC2012-4DO.5.1

Kalogirou, S.A., 2003. Generation of typical meteorological year (TMY-2) for Nicosia, Cyprus. Renew. Energy 28, 2317–2334. doi:10.1016/S0960-1481(03)00131-9

Kimber, A., Mitchell, L., Nogradi, S., Wenger, H., 2006. The Effect of Soiling on Large Grid-Connected Photovoltaic Systems in California and the Southwest Region of the United States, in: Conference Record of the 2006 IEEE 4th World Conference on Photovoltaic Energy Conversion. Presented at the Conference Record of the 2006 IEEE 4th World Conference on Photovoltaic Energy Conversion, pp. 2391–2395. doi:10.1109/WCPEC.2006.279690

King, D.L., Boyson, W.E., Kratochvill, J.A., 2004. Photovoltaic Array Performance Model (Sandia report No. SAND2004-3535). Sandia National Laboratories, Albuquerque, NM, USA.

King, D.L., Gonzalez, S., Galbraith, G.M., Boyson, W.E., 2007. Performance Model for Grid-Connected Photovoltaic Inverters (No. SAND2007-5036). Sandia National Laboratories, Albuquerque, NM, USA.

King, D.L., Kratochvill, J.A., Boyson, W.E., 1998. Field Experience with a New Performance Characterization Procedure for Photovoltaic Arrays, in: Proceedings of the Second World Conference and Exhibition on Photovoltaic Solar Energy Conversion. Presented at the Second world conference and exhibition on photovoltaic solar energy conversion, Vienna, Austria.

Lefèvre, M., Oumbe, A., Blanc, P., Espinar, B., Gschwind, B., Qu, Z., Wald, L., Schroedter-Homscheidt, M., Hoyer-Klick, C., Arola, A., Benedetti, A., Kaiser, J.W., Morcrette, J.-J., 2013. McClear: a new model estimating downwelling solar radiation at ground level in clear-sky conditions. Atmos Meas Tech 6, 2403–2418. doi:10.5194/amt-6-2403-2013

Lopez, A., Roberts, B., Heimiller, D., Blair, N., Porro, G., 2012. U.S. Renewable Energy Technical Potentials: A GIS-Based Analysis (Technical Report No. NREL/TP-6A20-51946). National Renewable Energy Laboratory (NREL), Golden, Colorado, USA.

Marion, W.F., Dobos, A.P., 2013. Rotation Angle for the Optimum Tracking of One-Axis Trackers (Research Report No. TP-6A20-58891). National Renewable Energy Laboratory, Golden, CO, USA.

Marion, W., Urban, K., 1995. User's manual for TMY2s: Derived from the 1961-1990 National Solar Radiation Data Base (Technical Report No. NREL/SP-463-7668). National Renewable Energy Laboratory, U.S. Department of Energy, Golden, Colorado, USA.

Martín, N., Ruiz, J.M., 2005. Annual angular reflection losses in PV modules. Prog. Photovolt. Res. Appl. 13, 75–84. doi:10.1002/pip.585

Martín, N., Ruiz, J.M., 1999. A new method for the spectral characterisation of PV modules. Prog. Photovolt. Res. Appl. 7, 299–310. doi:10.1002/(SICI)1099-159X(199907/08)7:4<299::AID-PIP260>3.0.CO;2-0

Mermoud, A., Lejeune, T., 2010. Performance assessment of a simulation model for PV modules of any available technology, in: EU PVSEC Proceedings. Presented at the 25th European Photovoltaic Solar Energy Conference and Exhibition / 5th World Conference on Photovoltaic Energy Conversion, Valencia, Spain, pp. 4786–4791. doi:10.4229/25thEUPVSEC2010-4BV.1.114

Middle East Solar Industry Association, 2015. MENA Solar Outlook 2015.

Mokri, A., Aal Ali, M., Emziane, M., 2013. Solar energy in the United Arab Emirates: A review. Renew. Sustain. Energy Rev. 28, 340–375. doi:10.1016/j.rser.2013.07.038

Muneer, T., 1990. Solar radiation model for Europe. Build. Serv. Eng. Res. Technol. 11, 153–163. doi:10.1177/014362449001100405

Narvarte, L., Lorenzo, E., 2008. Tracking and ground cover ratio. Prog. Photovolt. Res. Appl. 16, 703–714. doi:10.1002/pip.847

Ossenbrink, H.A., Huld, T.A., Jäger Waldau, A., Taylor, N., 2013. Photovoltaic Electricity Cost Maps (No. 83366), JRC Scientific and Policy Reports. European Commission, Joint Research Centre, Institute for Energy and Transport, Ispra, Italy.

Perez, R.R., Ineichen, P., Seals, R.D., Maxwell, E.L., Zalenka, A., 1992. Dynamic global-to-direct irradiance conversion models. ASHRAE Trans. 98, 354–369.

Perez, R.R., Ineichen, P., Seals, R.D., Michalsky, J., Stewart, R., 1990. Modeling daylight availability and irradiance components from direct and global irradiance. Sol. Energy 44, 271–289. doi:10.1016/0038-092X(90)90055-H

Reda, I., Andreas, A., 2008. Solar Position Algorithm for Solar Radiation Applications (Technical Report No. NREL/TP-560-34302). National Renewable Energy Laboratory (NREL), Golden, CO, USA.

Reindl, D.T., Beckman, W.A., Duffie, J.A., 1990a. Evaluation of hourly tilted surface radiation models. Sol. Energy 45, 9–17. doi:10.1016/0038-092X(90)90061-G

Reindl, D.T., Beckman, W.A., Duffie, J.A., 1990b. Diffuse fraction correlations. Sol. Energy 45, 1–7. doi:10.1016/0038-092X(90)90060-P

Schott, T., 1985. Operation temperatures of PV modules, in: Proceedings of the Sixth E.C. Photovoltaic Solar Energy Conference. Presented at the E.C. photovoltaic solar energy conference, London, United Kingdom, pp. 392–396.

Sgouridis, S., Abdullah, A., Griffiths, S., Saygin, D., Wagner, N., Gielen, D., Reinisch, H., McQueen, D., 2015. RE-mapping the UAE's energy transition: An economy-wide assessment of renewable energy options and their policy implications. Renew. Sustain. Energy Rev. In press. doi:10.1016/j.rser.2015.05.039

Skoplaki, E., Palyvos, J.A., 2009a. Operating temperature of photovoltaic modules: A survey of pertinent correlations. Renew. Energy 34, 23–29. doi:10.1016/j.renene.2008.04.009

Skoplaki, E., Palyvos, J.A., 2009b. On the temperature dependence of photovoltaic module electrical performance: A review of efficiency/power correlations. Sol. Energy 83, 614–624. doi:10.1016/j.solener.2008.10.008

Souka, A.F., Safwat, H.H., 1966. Determination of the optimum orientations for the double-exposure, flat-plate collector and its reflectors. Sol. Energy 10, 170–174. doi:10.1016/0038-092X(66)90004-1

Suganthi, L., Iniyan, S., Samuel, A.A., 2015. Applications of fuzzy logic in renewable energy systems – A review. Renew. Sustain. Energy Rev. 48, 585–607. doi:10.1016/j.rser.2015.04.037

Sun, Y., Hof, A., Wang, R., Liu, J., Lin, Y., Yang, D., 2013. GIS-based approach for potential analysis of solar PV generation at the regional scale: A case study of Fujian Province. Energy Policy 58, 248–259. doi:10.1016/j.enpol.2013.03.002

Šúri, M., Huld, T.A., Dunlop, E.D., 2005. PV-GIS: a web-based solar radiation database for the calculation of PV potential in Europe. Int. J. Sustain. Energy 24, 55–67. doi:10.1080/14786450512331329556

Šúri, M., Huld, T.A., Dunlop, E.D., Ossenbrink, H.A., 2007. Potential of solar electricity generation in the European Union member states and candidate countries. Sol. Energy 81, 1295–1305. doi:10.1016/j.solener.2006.12.007

Sutterlueti, J., Ransome, S., Kravets, R., Schreier, L., 2011. Characterising PV Modules Under Outdoor Conditions: What's Most Important for Energy Yield, in: EU PVSEC Proceedings. Presented at the 26th European Photovoltaic Solar Energy Conference and Exhibition, Hamburg, Germany, pp. 3608–3614. doi:10.4229/26thEUPVSEC2011-4AV.2.41

Tuomiranta, A., 2014. Performance Modelling of Photovoltaic Power Stations for an Interactive Solar Energy Atlas of the Arabian Peninsula (Master's thesis). Aalto University, Espoo, Finland.

Tuomiranta, A., Ghedira, H., 2015. Evaluation of Decomposition and Transposition Models for Irradiance Data Conversion under Hot Desert Climates. Presented at the 3rd International Conference Energy & Meteorology (ICEM), Boulder, Colorado, USA.

Tuomiranta, A., Marpu, P., Munawwar, S., Ghedira, H., 2014. Validation of Thermal Models for Photovoltaic Cells under Hot Desert Climates. Energy Procedia, 2013 ISES Solar World Congress 57, 136–143. doi:10.1016/j.egypro.2014.10.017

Appendix A

Cost component	Reference value	Modelling approach	Reference
Land acquisition		Spatial interpolation of point data on land value	dubizzle.com, 2015. Land for Sale [WWW Document]. URL https://abudhabi.dubizzle.com/property-for-sale/land/ (accessed 9.10.15)
Earthworks	3.27 USD/m^3 (sand) 49 USD/ m^3 (rock)	Averaging publicly available cost data; a multiplier of 15 for moving rock from expert interviews; cut and fill volumes from a digital elevation model; not deployed with dual axis tracking systems	Ghantoot Group, 2015. Major Projects [WWW Document]. URL http://ghantootgroup.com/marine.html (accessed 1.10.15) Industry expert interviews
Foundation	6.36 USD/m^2 of arrays (ramming for fixed mount and single axis tracking with noncorrosive soil types) 9.54 USD/m^2 of arrays (ramming for fixed mount and single axis tracking with corrosive soil types) 462.65 USD/tracker (ramming for dual axis tracking with noncorrosive soil types) 800.75 USD/tracker (ramming for dual axis tracking with corrosive soil types) 19.08-39.76 USD/m^2 of arrays (concrete for fixed mount and single axis tracking) 1388-2892 USD/tracker (concrete for dual axis tracking)	Concrete foundation used with inconsistent terrains (loose sand); manual territorial classification; varying concrete foundation cost with a distance to an industrial area; linear slope dependence starting from a slope of 15% with dual axis tracking systems	Industry expert interviews United States Geological Survey, United States Department of the Interior Google Inc, 2015. Google Maps [WWW Document]. URL https://www.google.ae/maps (accessed 1.10.15)
Mounting structures	22.26 USD/m^2 of arrays (fixed mount with a maximum wind gust of 30 m/s and below) 26.72 USD/m^2 of arrays (fixed mount with a maximum wind gust of more than 30 m/s) 809.65 USD/tracker (single axis tracking with a maximum wind gust of 30 m/s and below) 971.58 USD/tracker (single axis tracking with a maximum wind gust of more than 30 m/s) 2344.42 USD/tracker (dual axis tracking with a maximum wind gust of 30 m/s and below) 2813.30 USD/tracker (dual axis tracking with a maximum wind gust of more than 30 m/s)	Linear slope dependence starting from a slope of 8.5° with dual axis tracking systems	Industry expert interviews
Solar modules	0.57 USD/Wp (mc-Si, 340 Wp) 0.50 USD/Wp (pc-Si, 310 Wp) 0.53 USD/Wp (CdTe, 100 Wp) 0.66 USD/Wp (mc-Si, 455 Wp)		pvXchange Trading GmbH, 2015. Price Index [WWW Document]. URL http://www.pvxchange.com/priceindex/default.aspx?langTag=en-GB (accessed 9.10.15) Industry expert interviews
Module cables	4.65 USD/module	Linear slope dependence (see mounting structures)	Industry expert interviews
Solar cables / DC main cables	27637.99 USD/m^3 of cables	Linear slope dependence (see mounting structures)	Industry expert interviews
Junction boxes	5981.27 USD/junction box	Linear slope dependence (see mounting structures)	Industry expert interviews
AC BOS	232,605 USD/MVA	Linear slope dependence (see mounting structures)	Industry expert interviews
Civil works	2.7 USD/m^2 of plant (consistent terrain)	Linear slope dependence (see mounting structures)	Industry expert interviews
Auxiliary systems	0.04 USD/Wp	Linear slope dependence (see mounting structures)	Industry expert interviews
Road connection	255,000 USD/km (gravel road)	Linear slope dependence (see mounting structures)	Archondo-Callao, R., 2000. Roads Works Costs per Km. World Bank Reports.
Grid connection	732,919 USD/km (HV transmission, land)	Linear slope dependence (see mounting structures);	Industry expert interviews

	7,273,552 $/km (HV transmission, marine)	plant-specific share: plant capacity/800 MWp	Winfield and Sterling. 2012. Electricity Transmission Costing Study. Parsons Brinckerhoff.
Substation	14,658,381 USD/substation	Linear slope dependence (see mounting structures)	Industry expert interviews
Intra-country transportation	0.06 USD/m^3/km (truck transportation) 0.03 USD/ m^3/km (barge transportation)	Island sites connected through barge transportation	Kariniemi, A. 2006. Puunkorjuu ja kaukokuljetus vuonna 2009. Metsätehon katsaus 19.
Project development	500,000 USD + 3% of the total EPC cost		Industry expert interviews
Array cleaning and maintenance	0.57 USD/m^2 of arrays/year (fixed mount, cleaning every four days) 0.62 USD/m^2 of arrays/year (single axis tracking, cleaning every four days) 0.74 USD/ m^2 of arrays/year (dual axis tracking, cleaning every four days)	Average dust deposition-dependent multiplier for array cleaning and maintenance cost; linear slope dependence (see mounting structures)	Industry expert interviews
Module and civil works maintenance	0.27 USD/m^2 of plant/year (fixed mount) 0.29 USD/m^2 of plant/year (single axis tracking) 0.35 USD/ m^2 of plant/year (dual axis tracking)	Linear slope dependence (see mounting structures)	Industry expert interviews
Power block maintenance	3349.51 USD/power block/year		Industry expert interviews
Plant management	4466.02 USD/MWp/year (fixed mount) 4846.62 USD/MWp/year (single axis tracking) 5739.82 USD/MWp/year (dual axis tracking)		Industry expert interviews
Utilities	2233.01 USD/MWp/year		Industry expert interviews
Road maintenance	4680 $/km/year	Linear slope dependence (see mounting structures)	Archondo-Callao, R., 2000. Roads Works Costs per Km. World Bank Reports.
Transmission line maintenance	3.7% of HV transmission line cost (land) 19.6% of HV transmission line cost (marine)		Winfield and Sterling. 2012. Electricity Transmission Costing Study. Parsons Brinckerhoff.
Interest rate	5%		
Rate of return	10%		
Debt-to-equity ratio	80:20		
Insurance cost	0.4% of capital cost		Speer, B., Mendelsohn, M., Cory, K., 2010. Insuring Solar Photovoltaics: Challenges and Possible Solutions (No. NREL/TP-6A2-46932).
Salvage value	10% of capital cost		Harder, E., Gibson, J.M., 2011. The costs and benefits of large-scale solar photovoltaic power production in Abu Dhabi, United Arab Emirates. Renew. Energy 36, 789–796.
Inverter replacement	50%	Occurring after 16 years of operation	Industry expert interviews
Tracker replacement	15%	Distributed over the entire lifetime	Industry expert interviews
Module replacement	6%	Distributed over the entire lifetime	Industry expert interviews
Module performance degradation	-0.7%/year (mc-Si-fm, mc-Si-1t, mc-Si-2t) -0.9%/year (pc-Si-fm) -0.6%/year (CdTe-fm)		Jordan, D. C., Wohlgemuth, J. H., Kurtz, S. R. 2012. Technology and Climate Trends in PV Module Degradation (No. NREL/CP-5200-56485)

Conference Proceedings

Solar World Congress 2015
Daegu, Korea, 08 – 12 November 2015

Qualitative analysis of thin-film CIGS and c-Si technologies in tropical environments

Wai Kean Yap[1], Mirza Humayun Baig[1], Edward Halawa[1] and Vishy Karri[1,2]

[1] Centre for Renewable Energy, Research Institute for the Environment and Livelihoods, Charles Darwin University, Darwin (Australia)

[2] Codesign Australia Pty. Ltd, Brisbane (Australia)

Abstract

The technological advancement in solar photovoltaic (PV) materials enabled system designers, engineers and end-users to select the best type of system for a given environment. This paper identifies and investigates the key environmental factors that affect the performance of two different PV technologies under the tropical climate; the thin-film copper indium gallium di-selenide (CIGS) and the conventional crystalline silicon (c-Si) systems. The annual Northern Australian climate consists of distinct wet and dry cycles and a cyclone-prone environment. The effects of real-world conditions on the panels were investigated experimentally. The measured performance of the PV systems showed a reduction of 19.6% and 9.2% for the maximum energy output and 34% and 22% reduction of the total daily energy production for the CIGS and c-Si systems respectively during the dry season period. The systems managed to regain their optimal efficiencies during the start of the wet season when the first rainfall occurred. This study highlighted the effects of soiling (dust accumulation), fauna droppings, shading and orientation on the PV system efficiencies in a tropical locale were presented. For the Northern Australian climate, CIGS and c-Si PV systems should be washed at least once during the dry season in order to maintain its original efficiencies. This paper concluded that real-world testing of PV technologies is crucial, and should complement the existing laboratory testing to accurately estimate the system's performance and behavior.

Keywords: *copper indium gallium di-selenide, crystalline silicon, environmental effects on PV, thin-film PV, CIGS, c-Si*

1. Introduction

The systems involved in the study presented in this paper are the thin-film copper indium gallium di-selenide (CIGS) and crystalline silicon (c-Si) panels. The thin-film systems are expected to perform well in slightly diffused light and their performance is not supposed to drop during hot days [1]. The following literature identifies the relevant studies on the thin-film CIGS and other conventional photovoltaic (PV) technologies in the tropical locale.

The most common effects studied on the performance of PV systems are the environmental effects. These effects are generally the effect of temperature, rainfall, humidity, cloud and wind speeds. Along with that, few external effects were also investigated, including the effect of shading, tilt angle and gradual degradation of the PV materials. However, what seems to be somehow ignored in the past studies is the effect of dust accumulation as it can be detrimental, specifically in the extended dry season locales in Northern Australia.

Dust particles can impinge on to the surface of a PV panel. The extent of dust accumulation mainly depends on wind, moisture, electrostatic charge, gravity and surface properties of the panels [2]. Jiang et al. carried out a controlled laboratory experiment to measure the effect of dust accumulation losses in different

doi:10.18086/swc.2015.05.27 Available at http://proceedings.ises.org

PV materials. The experimental results found that the PV output efficiency grew from 0% to 26% for dust deposition density increasing from 0 to 22g/m^2 [3]. However, the difference in reduction of efficiency due to cell types was not evident. On a different occasion, Kaldellis and Kapsali performed laboratory analysis and developed theoretical model to investigate the effect of dust in PV performance losses. However, they recommended performing real-life data analysis to map actual results [4]. Beattie et al. presented numerical and analytical models of dust accumulation that quantitatively coincide with a laboratory investigation of particle accumulation on a glass slide for PV in dry regions. Their study was laboratory based with controlled conditions and did not include real PV systems with environment data [5]. Also, Boyle et al. performed an experiment on dust accumulation on PV cover plates (not actual PV) and found 6% reduction in light transmission per g/m^2 of dust accumulation [6]. Study by Said and Walwil found 6% reduction after 5 weeks of exposure in Qatar [7].

The effect of soiling on PV panels in the Sahara region was investigated by Kalogirou et al. who suggested immediate washing after dust events [8]. Mohamed and Hasan observed gradual decrease of power from PV panels (type unknown) in Sahara environment of Libya due to the effect of dust accumulation. They suggested weekly washing during windy periods and at least a month for other months in order to maintain performance losses between 2 to 2.5% [9]. Piliougine et al., during an analysis of the dust losses in c-Si PV modules with different cover glasses in Malaga (Spain), found losses reached 15% in no rainfall period (> 2 months) and annually 6% losses due to dust accumulation [10]. Adinoyi and Saidfound 50% reduction in power of crystalline solar panels installed in Saudi Arabia which had not been cleaned for six months [11]. Various simulations and experiments to measure the effect of dust losses on PV systems were performed by Qasem et al. in the arid environment of Kuwait. They found that the worst angle for most non-uniform dust accumulation is 30^0 [2]. The PV materials experiencing the most losses due to dust shading are the wide band-gap materials. The materials could be categorized as c-Si, followed by Cadmium Telluride (CdTe) PV, whereas c-Si and CIGS PV systems were found to be less affected. The mean daily energy loss due to dust accumulation on the surface of PV was recorded 4.4% and could extend to 20% during no rainfall periods, as studied by Zorrilla-Casanova et al. [12]. This study was done in Spain with the author suggesting that the losses can vary depending on the location and angle of tilt at which the PV was installed. A study by Lorenzo et al. at their solar park dust investigation found detrimental aspects of homogenous dust accumulation which may also cause hot spot phenomenon, hence, a threat to the PV module lifetime [13].

Darwin, located in the Northern Territory (NT), has a unique climate with high monthly and annual solar radiation, distinct wet (humid and high rainfall) and dry (less humid and no rainfall) seasons, along with a highly cyclone-prone environment. This study, conducted at the Charles Darwin University's Outdoor Solar Facility as detailed in the following scripture, outlines actual quantified production loss figures over the dry and wet periods. In addition, this study also covers a unique tropical locale of Australia involving two often installed types of PV modules of different optical properties and attributes. A highly efficient inverter system was used to analyze the real production of the system.

2. System Description and Background

For experimental measurements, both systems were installed in the Casuarina Campus at the Charles Darwin University (CDU) (-12.37°S, 130.86°E). Fig. 1 shows the picture of the monitoring and evaluation solar

facility. The solar facility is an outdoor structure made of composite material, impregnated by thin-film CIGS PV material as roof sheeting, and fastened directly to the steel structure. The thin-film modules are bonded on the composite sheet away from the borders to avoid direct heat transfer from the steel structure. The modules are affixed using pressure sensitive adhesive to the Category 4 cyclone wind resistant glass reinforced composite backing of trapezoidal profile [14]. This 1.5kWp solar facility has local vegetation around and it is a home to numerous local birds and other fauna. Fig. 2 shows the c-Si PV system set up on one of the buildings adjacent to the CIGS setup. This 5.0kWp system was installed in the rooftop of the building, and similarly to the CIGS system, is grid-connected.

The two solar facilities were setup to monitor the influence and impact of environmental factors on the performance and production efficiency of both the systems. Incorporating the data from the Australian Bureau of Meteorology (BoM) weather station mounted at CDU, effects of real-world conditions on the panels such as dust, rainfall, fauna droppings, shading and orientation were investigated and discussed.

This study is in particular extremely interesting with the unique Northern Australian climate with high monthly and annual solar radiation, distinct annual wet (humid, high rainfall and cyclone-prone) and dry (less humid and virtually no rainfall). These two seasons highlight the natural effects of washing (due to rainfall) and soiling (dusts and fauna droppings build-up during the dry season) on the PV systems. The objective of this study is to complement the research of PV performance in the laboratory where the environmental parameters are often ignored in laboratory testings.

Fig. 1: The Outdoor Solar Facility for the 1.5 kWp CIGS system (ENER TSG200-GS2, Inverter: EnaSolar1.5KWGT-AUNZ) [14]

Fig. 2: The installed 5.0 kWp c-Si rooftop system (Auxin AXN-P6T275, Inverter: SunnyBoy SMA SB 5000TL-20)

3. Results and Discussions

3.1 PV power production

The power production for both the 1.5kWp CIGS and 5.0kWp c-Si systems were recorded, together with the rainfall data for the period from March 2014 to July 2015. The profile is shown in Fig. 3.

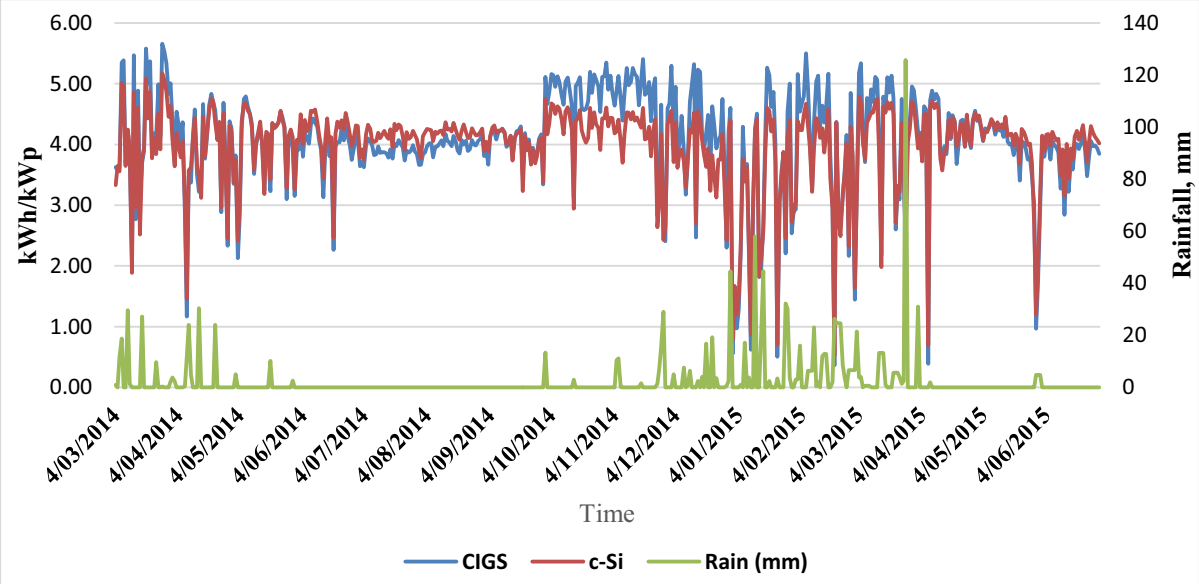

Fig. 3: Daily normalized power output and rainfall profile

From the plot, the power output for the two PV systems were fairly irregular during the annual wet season (March-May 2014 and November-April 2014/15). This was expected due to constant rainfalls, cloud cover and low radiation. During the dry season (June-October 2014 and March-June 2015), the power outputs were constant, which was expected due to clear skies and no rainfall.

The average power output recorded were higher during the wet season (although production was erratic), in the region of 5kWh/kWp for CIGS compared to 4kWh/kWp during the dry season. The c-Si system do not vary much, but similarly do have higher average compared to the dry season. Observing the period from March to June 2015 (start of the dry season), the average power outputs are slowly decreasing to the constant levels similar to the previous dry season (June-October 2014). This performance behaviour was expected. Overall the power output profiles were within the expected behaviour and both systems displayed similar qualitative relationship.

The power output increased significantly after the first recorded rainfall on the 30th of September 2014 for both systems. Taking a closer look at Fig. 3, the escalation in production after the first rainfall was observed to be much higher for the CIGS system as compared to c-Si system. There could be number of possible reasons for this increase in the power generation. One of the reasons is that the CIGS system has a rough surface material, which attracted more dust and accumulated a higher amount of dust particles compared to the much smoother surface of the c-Si system. Also, the efficiency of CIGS system does not drop in slightly diffuse light and on hot days compared to the c-Si system which are more sensitive to cloudy conditions and high temperatures [1].

The daily maximum energy output recorded for October showed a substantial increase of 19.6% and 9.2% (from the previous month, September) for the CIGS and c-Si systems respectively. This 'natural

washing' phenomena (due to rainfall) cleaned the surface of the panels, and thus contributes to this increase to the PV's original efficiency (as observed during the wet seasons). This phenomena is critical, especially for the Northern Australian climate, and highlighted to importance of washing during the dry seasons. These natural environmental effects are discussed in the next section.

3.2 Natural environmental effects - dust accumulation, fauna droppings and rainfall

Fig. 4 to 6 shows the amount of dust accumulation and fauna (birds and bats) droppings on the panel surface. This occurs mostly during the dry season, where no rainfalls were observed. The figures were obtained during the end of the dry season to highlight the dust and droppings accumulated over the period.

Fig. 4: c-Si panels, 26th August 2014

Fig. 5: CIGS panels, 22nd August 2014

Fig. 6: Fauna droppings on the panels - 1st August 2014

The increase in the power output, with increasing monthly solar exposure, is observed for the month of October. It is worth noting that the first rainfall recorded for this testing facility is on the 30th of September 2014. This natural washing of the panel surfaces by the rainfall had drastically improved the power output of

both the PV systems, as highlighted in the previous section. Fig. 7 shows the CIGS system after the first rainfall where the accumulated dust and soil are washed away.

Fig. 7: Naturally washed panels due to rainfall - 3rd October 2014

Fig. 8 shows the monthly normalized average and maximum production power for both of the PV systems and the maximum monthly solar irradiation. The maximum recorded power output for both systems are consistent with the Darwin climate; wet season (March-May 2014 and November-April 2014/15) and the dry season (June-October 2014 and March-June 2015). The maximum outputs recorded are lower for the dry seasons as compared to the wet seasons. The measured performance of the PV systems showed a reduction of 19.6% and 9.2% for the maximum energy output and 34% and 22% reduction of the total daily energy production for the CIGS and c-Si systems respectively for the dry season compared to the wet seasons. They are further discussed in the following sections

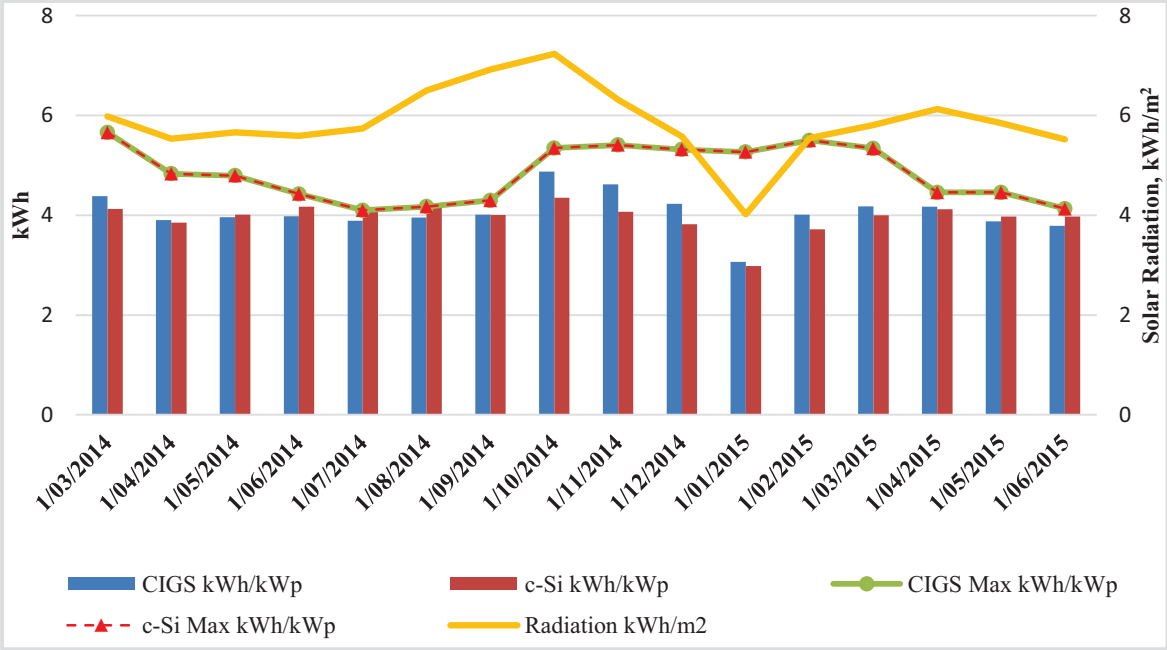

Fig. 8: Monthly normalized average and maximum kWh for CIGS and c-Si and maximum solar irradiation

3.2.1 Effects on the CIGS system

To further observe the role of rainfall on the system's performance efficiency, the maximum daily production was analysed against the rainfall and solar exposure data as shown in Fig. 8. For 2014, at the end of the wet

season (March-May), the maximum production power recorded was just over 7kWh/day. Entering to the dry season (May-October 2014), the maximum production power decreased steadily although the solar irradiation increases. The same profile (slowly reduced in efficiency) was observed in 2015 (April-June) during the start of the dry season.It was found that this level of production was not reached until it rained again on the 30th of September 2014. This rainfall washed away the accumulated dust from the surface of the panels. This observation further emphasized the critical effects of soiling and fauna dropppings on the surface of the CIGS panels.

The effect of soiling on the PV panels was investigated in the Sahara region by Kalogirou et al., where the authors suggested that panels to be cleaned after every dust event and once every 2 to 3 weeks during high dust seasons [8]. Mani and Pillai also suggested weekly cleaning during long dry spells [15]. The observations from this study concluded that CIGS systems installed in tropical Northern Australia should be washed at least once during the dry season to maintain its efficiency.

3.2.2 Effects on the c-Si system

The c-Si PV system was installed adjacent to the CIGS system within the same area, hence it experienced similar intensity and pattern of rainfall. Similarly to the CIGS, the increase in power production was observed after the first rainfall (30th of September 2014). The same hypothesis, may apply here that the rigorous natural washing (removing accumulated dust) of the solar panels by the rainfall is the reason for the increment in power generation. Furthermore, the weather conditions recorded from the closest weather stations (CDU and Darwin Airport) are very similar as well on both the days.

Similarly, in order to investigate the role of rainfall in system's performance efficiency, the maximum daily production was analysed against the rainfall and solar exposure data as shown in Fig. 8. For 2014, Darwin experienced its end of wet season rainfalls until May and the maximum power production recorded was about 23kWh/day. Analysing the data it is found that this level of production was not recorded until it rained on the 30th of September, removing the accumulated dust from the surface of the system. The same profile was observed in 2015 (April-June) during the start of the dry season. Similar to CIGS systems, it appears rational to suggest that c-Si PV systems installed in the tropical Darwin should also be washed at least once in between the dry season to maintain its original efficiency.

3.2.3 Performance comparison

The effect of dust accumulation in the case for c-Si system does not seem to affect the production performance to the same degree compared to the CIGS system. Physical observation of the two systems in this period shows that CIGS had attracted and accumulated more dust as compared to c-Si system.

In addition, the physique of the thin-film CIGS can be described as flexible, undulating with rough surface in contrast to a smoother surface of the conventional c-Si PV panels. Moreover, given the smooth surface of conventional panels would also have supported the removal of some dust through the regular moisture flow from the natural morning dew.

3.3 Effect of system orientation

As mentioned previously, both systems were installed in close proximity to each other (approximately 20m apart in the same area). However, the systems each has different orientations. The c-Si system was installed

on the east facing roof and the effect of this orientation can be seen in Fig. 9 (in the morning and late evening). The sudden drop in power generation after 3:30PM can be observed when the sun is located behind the building.

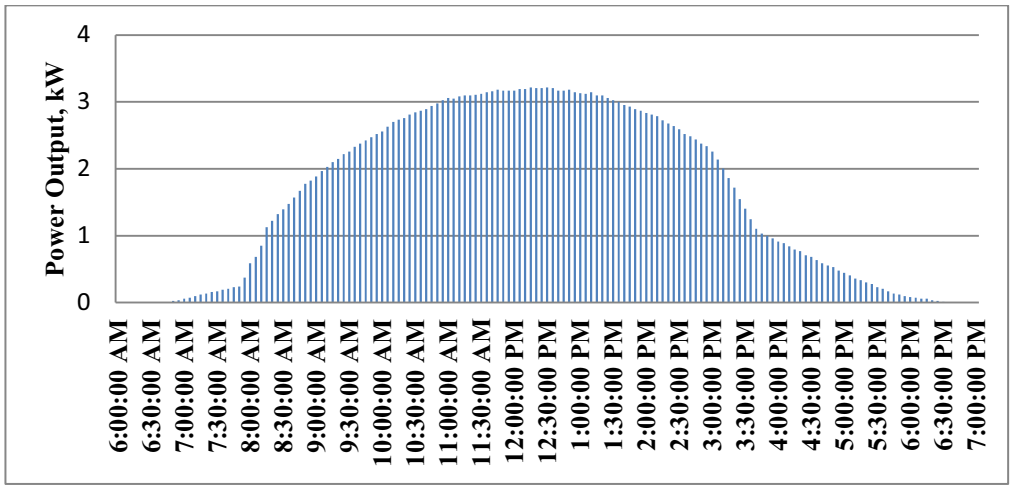

Fig. 9: Intraday power plot for the c-Si system on 17th September 2014

On the other hand, the CIGS system is installed facing north and the effect of this orientation can be seen in Fig. 10. The intraday power plot on the same day exhibits a smooth and uniform profile throughout the day, taking the maximum advantage of the sunshine hours, compared to the c-Si system. The CIGS system however, misses out on some sun time in the mornings and late afternoons. This was due to the fact that the experimental system is installed at a lower height over the ground and hence surrounded by tall trees around the area.

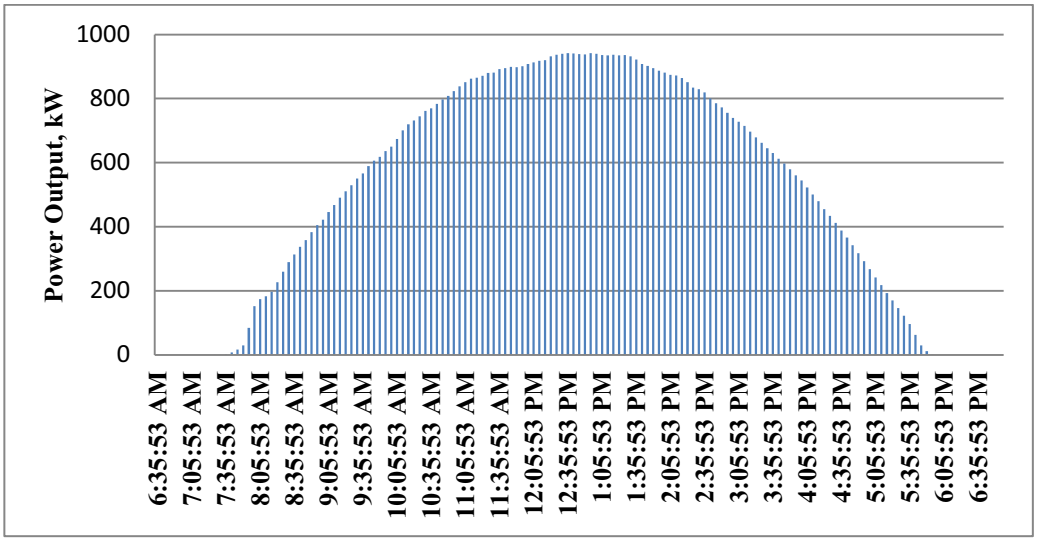

Fig. 10: Intraday power plot for the thin-film CIGS system on 17th September 2014

4. Summary and concluding remarks

This paper identifies and investigates the environmental factors that affect the performance of two different PV systems under the tropical climate; the thin-film CIGS and the traditional c-Si systems. For experimental measurements, both systems were installed in the Casuarina Campus at the CDU (-12.37°S, 130.86°E),

where the annual climate for Northern Territory, Australia consists of distinct wet and dry cycles and a cyclone-prone environment annually.

Utilizing the climate data obtained from the BoM, results showed the system performances under that the effect of dust, soiling and fauna droppings (on the respective panel surfaces), especially during the dry season, has significant affects on the power production of the systems. It was observed that during the dry season, such factors have the opportunity to collect on the respective panel surfaces.

The daily power output (Fig. 3) and the maximum monthly energy output (Fig. 8) recorded for both the CIGS and c-Si systems exhibited similar and expected behaviours; a constant decline in efficiency over the dry season, and the systems regain their original efficencies during the start of the wet season. When the first rainfall was recorded (end of September), the daily maximum energy output recorded for October showed a substantial increase of 19.6% and 9.2% for the CIGS and c-Si systems respectively. This 'natural washing' phenomena cleaned the surface of the panels, and thus contributes to this increase to the PV's original efficiency, and the effiencies were maintained over the season. In addition, the measured performance of the PV systems showed a 34% and 22% reduction of the total daily energy production for the CIGS and c-Si systems respectively for the dry season compared to the wet season. This was highlighted in Fig. 3 and 8, from October 2014 to March/April 2015. It was concluded that washing the panels once during the dry season is sufficient to maintain its orginal efficiencies.

The effect of shading and system orientation were also presented and discussed. Analysing the intraday power plot curve for both systems, it was concluded that the north-facing CIGS system exhibits a smoother profile compared to the east-facing c-Si system. However, the CIGS system was missing out on some amount of sun time during the early morning and in the late afternoon.

In conclusion, results showed a significant difference in the percentage increase in the power generation of the two different types of PV systems with same daily average solar exposure before and after the rainfall. There could be number of possible reasons for this difference of behaviour between the two systems. The two systems could have different response to diffuse sunlight/cloud cover, temperature and affinity for dust accumulation. Moreover, difference in the affinity for dust accumulation due to difference in surface material, smoothness, angle of tilt and height of system installed. Therefore, this finding makes a strong implication for further investigation of each system’s performance on an intra-day basis, also incorporating the necessary environmental factors of this tropical locale. This study highlighted that real-world testing of PV systems is crucial and important, and this should complement on the additional laboratory testings to accurately estimate the system performance and behaviour.

Acknowledgements

Special thanks to The Specialty Coatings (Aust.) Pty Ltd. for their contribution of the solar testing facility, especially to Dr. Dragos Petrescu for his expertise in developing this facility.

References

[1] Clean Energy Council, 2011. Consumer guide to buying household solar panels (photovoltaic panels). 28.

[2] Qasem, H., Betts, T.R., Mullejans, H., Albusairi, H., Gottschalg, R., 2014. Dust-induced shading on photovoltaic modules. Prog. Photovoltaics 22, 218-226.

[3] Jiang, H., Lu, L., Sun, K., 2011. Experimental investigation of the impact of airborne dust deposition on the performance of solar photovoltaic (PV) modules. Atmos. Environ. 45, 4299-4304.

[4] Kaldellis, J.K., Kapsali, M., 2011. Simulating the dust effect on the energy performance of photovoltaic generators based on experimental measurements. Energy 36, 5154-5161.

[5] Beattie, N.S., Moir, R.S., Chacko, C., Buffoni, G., Roberts, S.H., Pearsal, N.M., 2012. Understanding the effects of sand and dust accumulation on photovoltaic modules. Renew. Energy 48, 448-452.

[6] Boyle, L., Flinchpaugh, H., Hannigan, M., 2013. Impact of natural soiling on the transmission of PV cover plates. 39th IEEE Photovoltaic Spec. Conf. (PVSC), Tampa FL, United States, 6745150 3276-3278.

[7] Said, S.A.M., Walwil, H.M., 2014. Fundamental studies on dust fouling effects on PV module performance. Sol. Energy 107, 328-337.

[8] Kalogirou, S.A., Agathokleous, R., Panayiotou, G., 2013. On-site PV characterization and the effect of soiling on their performance. Energy 51, 439-446.

[9] Mohamed, A.O., Hasan, A., 2012. Effect of dust accumulation on performance of photovoltaic solar modules in Sahara environment. J. Basic Appl. Sci. Res. 2, 11030-11036.

[10] Piliougine Rocha, M., Carretero Rubio, J.E., Sidrach-de-Cordona, M., Montiel, D., Sanchez-Friera, P., 2008. Comparative analysis of the dust losses in photovoltaic modules with different cover glasses. 23rd Eur. Photovoltaic Sol. Energy Conf. Exhibit., Valencia, Spain, 2698-2700.

[11] Adinoyi, M.J., Said, S.A.M., 2013. Effect of dust accumulation on the power outputs of solar photovoltaic modules. Renew. Energy 60, 633-636.

[12] Zorrilla-Casanova, J., Piliougine, J., Carretero, J., Bernaola, P., Carpena, P., Mora-Lopez, L., Sidrach-de-Cordona, M., 2011. Analysis of dust losses in photovoltaic modules. World Renew. Energy Congr., Linkoping, Sweden, 2985-2992.

[13] Lorenzo, E., Moreton, R., Luque, I., 2014. Dust effects on PV array performance: in-field observations with non-uniform patterns. Prog. Photovoltaics 22, 666-670.

[14] Yap, W.K., Baig, M.H., Halawa, E., 2014. Performance monitoring and evaluation of a CIGS-roof integrated photovoltaic system under the unique tropical environment of Darwin, Northern Territory. Asia-Pacific Sol. Res. Conf., UNSW, Sydney, Australia.

[15] Mani, M., Pillai, R., 2010. Impact of dust on solar photovoltaic (PV) performance: Research status, challenges and recommendations. Renew. Sust. Energy Rev. 14, 3124-3131.

Conference Proceedings

Solar World Congress 2015
Daegu, Korea, 08 – 12 November 2015

Energetic and exergetic analysis of monocrystalline and polycrystalline photovoltaic modules

Suellen C.S. Costa, Janaína de O.C. Silva, Cristiana B. Maia, and Antonia Sonia A.C. Diniz

Pontifical Catholic University of Minas Gerais (PUCMinas)/Graduate Mechanical Engineering Program/Group of Energy Studies (GREEN-IPUC), Belo Horizonte (Brazil)

Abstract

In this paper, the concepts of energy and exergy are used to estimate and compare the performances of monocrystalline (m-Si) and polycrystalline (p-Si) silicon photovoltaics (PV) modules. The energetic efficiency is the ratio of the energy output of the module to the incident light energy (product of solar radiation and the area of incidence or area of the module). The exergetic efficiency is derived from the electrical parameters, the operating temperature of the modules, and the specific weather conditions. The electrical parameters of the modules were evaluated by adjusting module (nameplate) specifications to the climate variables obtained for the city of Belo Horizonte, Brazil. The m-Si module (190W) had energetic and exergetic efficiencies around 20% and 14%, respectively. In comparison, the p-Si module (210W) had an expected lower energetic efficiency of approximately 18% and exergetic efficiency about 13%. The modeling and analysis conditions are described in detail.

Keywords: *Photovoltaic modules, performance, energetic efficiency, exergetic efficiency.*

1. Introduction

Growing demand for electricity and the predicted depletion of fossil fuels are among the important factors to enhance research and financial incentives to facilitate use of renewable sources. According to Dincer et al. (2010), the decline in the supply of fossil energy in the world, associated with increased energy consumption and the continuing indications of global climate change, have driven research, innovation and market deployment for the realization of a global economy based on clean, renewable energy. Solar energy has to potential to provide a significant portion of the global energy demand—especially that associated with electrical power generation.

Renewable-electricity generation sources have capacity factors and availability factors less than optimum values (intermittent, dispatchable power). Semi-regular, periodic, and stochastic changes in resource availability affect the performance of systems using renewable energies throughout their livespans. One way to better address the impacts of changes or interuptions in resource availability is to use a *typical meteorological year* (TMY), which represents the behavior of weather variables generated from a data bank much longer than a year in duration. The TMY pattern is a set of experimental data that represents a typical year for a given location—and is used as baseline indicator for analysis and assessment giving annual averages that are consistent with the long-term averages for the location in question. The default year applies the knowledge of local weather procedures for evaluation, design, planning and operation of power plants from renewable sources. PV systems are among the energy conversion systems that have performances that are significantly influenced (controlled) through non-ideal conditions. The main factors contributing to the reduced PVmodule performance in operating conditions are the meteorological variables, mainly the ambient temperature and the solar radiation.

The performance of photovoltaic modules can be evaluated by processes applying the First and Second Laws of Thermodynamics, called energetic and exergetic analysis, respectively. According to Dincer (2002), the

doi:10.18086/swc.2015.05.28 Available at http://proceedings.ises.org

exergy analysis is a tool for assessing the ensemble of environmental impacts on the use of any energy source. The exergy analysis technique provides pathways toward the operation of more efficient and higher performance energy sources. This methodology can provide a valuable tool in reducing the real encountered losses of existing energy systems. Pandey et al. (2013) recommend application of exergy analysis when a comprehensive analysis is required. The *energy efficiency* of photovoltaic modules is the ratio of the generated energy to the solar radiation energy, not including the direct influence of some factors, such as thermal properties (Sarhaddi et al. (2010)). The *exergetic efficiency* considers climatic parameters, geometric factors, and operation of the modules (including thermal properties) and provides more realistic insights into the energy conversion process for photovoltaic modules. Joshi et al. (2009) point out that the energy of a photovoltaic system has two primary components: electrical and thermal energy. The electrical exergy can is equal to the actual electricity generated by the photovoltaic system, since it is completely available to be converted into work. The thermal energy available from solar cells is not used to generate useful work (i.e., is not used by these devices to generate electricity) in operating PV systems, becoming heat lost into the environment.

The performance of a photovoltaic module depends on variables such as ambient temperature, solar radiation, incident angle, dirt accumulation, and the type or technology of the photovoltaic cell utilized. The temperature has an important influence on the efficiency of the modules and therefore the entire PV array. Sahin et al. (2007) investigated the thermodynamic characteristics of photovoltaic cells based on their energy and exergy efficiency. Results indicated that energy efficiency ranged between 7 and 12% during operation under available sunlight, while the exergetic efficiency varied between 2 and 8%. According Xydis (2013), exergy losses are related to the temperature correction factor due to the increase in module temperature, representing 1.3% losses in system performance. Colombo et al. (2014) presented a general thermoeconomic analysis to assess the economic and environmental effects of energy integration system, taking into account the life cycle and the effect of inefficiencies due to off-design operation of systems. The method was applied to a case study from a photovoltaic power plant and a standard commercial power plant gas turbine (without cogeneration) deriving the final cost of a kWh. The evaluation of the economic cost was accomplished through termoeconômicas techniques, while exergy costs were assessed using both Extended Exergy Accounting (EEA) and the Thermo-Ecological Cost (TEC) methods. The results showed that a purely monetary evaluation can lead to contrasting results, and that the EEA and TEC cost indicators can generate different rankings among the alternatives studied.

Many studies on the performance evaluation using the First and Second Law of Thermodynamics have been applied in photovoltaic/thermal (PV/T), where a single system generates electricity and heat. Ceylan and Gürel (2015) experimentally evaluated a new PV/T system design for cooling of the PV modules and using the extracted heat to warm water. This PV/T system is a forced circulation system without pump. The exergy analysis of PV/T system has accounts for thermal exergy of the PV module and the solar collector, as well as variations of electric exergy. The authors derived that for the temperature of 45°C that the exergetic efficiency was 17%, while at 55°C, the exergetic efficiency was 21%.

Yazdanpanahiet et al. (2015) used combined analytical and experimental analysis to evaluate the exergetic efficiency of a PV/T system. The operating parameters were obtained through the experimental setup, which recorded the intensity of solar radiation, wind speed, ambient temperature, temperature of photovoltaic cells, the flow and fluid input temperature, and fluid output temperature, open circuit voltage and short-circuit, and the voltage and current at the maximum power point. The numerical simulation used a three-dimensional model under a constant thermal load and a 4-parameter current-voltage model. The model was modified to account for the exergetic efficiency and exergy losses in the PV/T system components. The results of this numerical simulation were compared with their experimental measurements. Additionally, a comparison between the modified exergetic efficiency used in the study and one from the literature showed that the modified exergetic efficiency obtained in this approach avoids the shortcomings of exergetic efficiency from the literature, since it derives the loss of exergy in the system PV/T directly.

The First and Second Law of Thermodynamics can be used to determine and compare the efficiencies of different PV module technologies from a fundamental analysis approach, but this method has not been widely used. This approach has mainly been incorporated to evaluate PV/T technologies. This paper aims to

analyze the performance of photovoltaic modules of monocrystalline silicon (m-Si) and polycrystalline silicon (p-Si), applying the concepts of the First and Second Law of Thermodynamics. The energetic and exergetic efficiencies have been evaluated, expanding reported mathematical models to assess the influence of meteorological variables for the city of Belo Horizonte, Brazil. This analysis has provided direct evaluation and comparison of the two, most widely used commercial silicon PV technologies.

2. Methodology

Photovoltaic modules are composed of several solar cells connected in series and/or parallel configurations to provide the required voltage and current (power) for the given application. Currently there are several types of cell technologies, both in research and commercial stages. The most most prevalent in the market (about 90%) use silicon, because of cost and availability factors. Bulk silicon cells can be crystalline silicon, monocrystalline and polycrystalline, and these are the most common commercial technologies. Thin films, such as those using amorphous Si, are also used, but have a far lower manufacturing base and a much lower performance capability. According to Green et al (2015), the monocrystalline silicon modules have demonstrated manufacturing line efficiencies to 22.9%, due to the high degree of crystalline quality, low defect and impurity levels, and innovative device design. The polycrystalline silicon modules have comercial efficiencies to about 19%, while the amorphous silicon thin film approaches can achieve efficiencies in the 10%-12% range.

In the studies of this paper, we analyze the performances of the two major Si PV module technologies (m-Si and p-Si), through modeling and simulation of *energy and exergy efficiencies*. In this analysis, the estimated time meteorological data using models of Duffie and Beckman (2006) and Lorenzo (1994) are incorporated into the models. The weather conditions were for the city of Belo Horizonte, Brazil, with 19.93° S latitude and longitude 43.93° S. The inclination of the PV modules was set at 20°, the ground reflectivity index for the urban area (ρ) at 18%, and average monthly atmospheric transparency indices ($\overline{K_T}$) (as indicated in Table 1) were incorporated with minimum and daily maximum temperature data and wind speed at this location, provided by *Solar and Wind Energy Resource Assessment* project (SWERA). Weather conditions for Belo Horizonte were validated with data provided by the National Institute of Meteorology (INMET) and with the TMY information obtained through SWERA.

Tab. 1: Average monthly atmospheric transparency index

Month	$\overline{K_T}$	Month	$\overline{K_T}$
Jan.	0.46	**July**	0.64
Feb.	0.45	**Aug.**	0.53
Mar.	0.64	**Sept.**	0.48
Apr.	0.53	**Oct.**	0.50
May.	0.55	**Nov.**	0.45
June	0.60	**Dec.**	0.41

Guimarães (1995)

The simulations were performed using the Engineering Equation Solver (EES) software. The energetic and exergetic efficiencies were estimated hourly for the year studied and included the variation of meteorological parameters and operating parameters of the PV modules. To estimate electrical and thermal parameters of the PV modules for different operating conditions, the reference condition was chosen as the nameplate values of the operating parameters. The PV modules used were (1) monocrystalline Si: module of the 190Wp nameplate power output and (2) polycrystalline Si: module of the 210Wp. Table 2 presents the complete nameplate electrical specifications for each of these PV module technologies.

Tab. 2: Electrical characteristics of the PV modules

	Monocrystalline Module	Polycrystalline Module
Power	190 Wp	210 Wp
Open circuit voltage ($V_{oc,ref}$)	21.68 V	33.05 V
Short circuit current ($I_{sc,ref}$)	11.80 A	8.23 A
Voltage at maximum power point ($V_{m,ref}$)	18.07 V	27.54 V
Current at maximum power point ($I_{m,ref}$)	10.52 A	7.64 A
Temperature coefficient for short-circuit current (α)	0.05%/°C	0.05%/°C
Temperature coefficient for open circuit voltage (β)	-0.38%/°C	-0.38%/°C
Nominal operating temperature of the photovoltaic (NOCT)	47 °C	47 °C
Temperature in standard operating conditions (STC)	25 °C	25 °C
Width module	1.580 m	1.480 m
Module Length	0.808 m	0.990 m

3. Mathematical Model

The PV generator consists of a set of modules whose performance may be influenced by weather conditions (e.g., intensity of solar radiation, the ambient temperature, and wind speed). Performance can be evaluated by applying the First and Second Law of Thermodynamics for the assessment of the respective energy and exergetic efficiencies. Energy efficiency for the theoretical case is given by (Pandy et al., 2013):

$$\eta_{\text{energy}} = \frac{V_{oc} * I_{sc}}{G_T * A} \quad \text{(eq. 1)}$$

where A is the area of the photovoltaic module; G_T; the solar radiation; V_{oc} is the open-circuit voltage and I_{sc} is the short-circuit current. The open-circuit voltage and short-circuit current can be obtained by the model proposed by Chouder et al. (2012):

$$V_{oc} = V_{oc,ref} - \beta(T_{c,ref} - T_c) + A_f \ln\left(\frac{G_T}{G_{ref}}\right) \quad \text{(eq. 2)}$$

$$I_{sc} = I_{sc,ref}\left(\frac{G_T}{G_{ref}}\right) + \alpha(T_c - T_{c,ref}) \quad \text{(eq. 3)}$$

where T_c is the module temperature. Variables with subscribed ref indicate the parameters in reference (or namplate) condition. The parameters of reference used in this modeling were taken from the datasheet provided by the manufacturer of the PV modules evaluated, considering the standard test conditions (STC). The solar irradiance was set at 1000 W/m². The β and α are the temperature coefficients for the open-circuit voltage and short-circuit current, respectively. A_f is the modified ideality factor of the diode, defined by (Chouder et al., 2012.):

$$A_f = \frac{n\sigma T_c}{q} \quad \text{(eq. 4)}$$

where n is the diode ideality factor (and in this study was set n = 1), σ, the Boltzmann constant, and q is the electronic charge.

The module temperature (T_c) is defined from the data set to the nominal operating condition of the module, as proposed by Pandey et al. (2013):

$$T_c = T_a + \left(\frac{NOCT - 20\,°C}{800\ W/m^2}\right) G_T \quad \text{(eq. 5)}$$

where NOCT is the nominal operating temperature of the module and T_a is the ambient temperature. The ambient temperature (T_a) was estimated of according with the model proposed by Lorenzo (1994), which

depends on the hour angle (ω) relating the displacement of the sun from noon and accounting for a displacement of 15 ° every hour, and the angle the sunset (ω_s), the completion of the sunlight period (Duffie and Beckman, 2006):

For $-\pi < \omega < \omega_s$, T_a is calculated by:

$$T_a = T_{aM}(i-1) - \frac{T_{aM}(i-1) - T_{am}(i)}{2}\left[1 + +cos\left(\left(\frac{\pi}{\left(\frac{\pi}{6} - \omega_s - 2\pi\right)}\,\omega\right) + \left(-\frac{\pi}{\left(\frac{\pi}{6} - \omega_s - 2\pi\right)}\,\omega_s\right)\right)\right] \quad \text{(eq. 6)}$$

In Eq. (6), T_{aM} and T_{am} are the maximum ambient temperature and minimum along a day, respectively, and i is the day of the year.

For $\omega_s < \omega < \frac{\pi}{6}$, T_a is calculated by:

$$T_a = T_{am}(i) + \frac{T_{aM}(i) - T_{am}(i)}{2} * \left[1 + \cos\left(\left(\frac{\pi}{\left(\omega_s - \frac{\pi}{6}\right)}\omega\right) + \left(-\frac{\frac{\pi}{\left(\omega_s - \frac{\pi}{6}\right)}\pi}{6}\right)\right)\right] \quad \text{(eq. 7)}$$

And for $\frac{\pi}{6} < \omega < \pi$, T_a is calculated by:

$$T_a = T_{aM}(i) - \frac{T_{aM}(i) - T_{am}(i+1)}{2}\left[1 + +cos\left(\left(\frac{\pi}{\left(2\pi + \omega_s - \frac{\pi}{6}\right)}\,\omega\right) + \left(-\left(\pi + \frac{\frac{\pi}{\left(2\pi + \omega_s - \frac{\pi}{6}\right)}\pi}{6}\right)\right)\right)\right] \quad \text{(eq. 8)}$$

To estimate the solar radiation on the inclined photovoltaic module(G_T), we used the isotropic sky model from Duffie and Beckman (2006) that considers the sum of direct components, the isotropic diffuse and diffuse solar radiation reflected by the ground:

$$G_T = G_b R_b + G_d \frac{(1+cos\,\beta_{in})}{2} + G\,\rho\,\frac{(1-cos\,\beta_{in})}{2} \quad \text{(eq. 9)}$$

In Eq. (9), G_b and G_d are the direct and diffuse solar radiation, respectively; G is the total incident solar radiation on a horizontal plane; R_b is the ratio between the total radiation incident on an inclined surface and a horizontal surface; ρ is the ground reflectivity, and β_{in} is the tilt angle of module.

The exergetic efficiency of photovoltaic modules is given by the ratio between output exergy and input exergy.

$$\varepsilon = \frac{\text{Output exergy}}{\text{Input exergy}} = \frac{\text{Ex}_{\text{elet}} - \text{Ex}_{\text{therm}}}{\text{Ex}_{\text{solar}}} \quad \text{(eq. 10)}$$

The input exergy is from the solar radiation:

$$\text{Ex}_{\text{solar}} = \left(1 - \frac{\text{T}_\text{a}}{\text{T}_{\text{sol}}}\right)\,\text{G}_\text{T} * \text{A} \quad \text{(eq. 11)}$$

The output exergy of the photovoltaic module is the difference between the electrical exergy and thermal exergy defined by Pandey et al. (2013):

$$\text{Ex}_{\text{elet}} = \text{V}_{\text{oc}}\text{I}_{\text{sc}} - (\text{V}_{\text{oc}}\text{I}_{\text{sc}} - \text{V}_\text{m}\text{I}_\text{m}) \quad \text{(eq. 12)}$$

$$\text{Ex}_{\text{term}} = \left(1 - \frac{\text{T}_\text{a}}{\text{T}_\text{c}}\right)\text{U} * \text{A}(\text{T}_\text{c} - \text{T}_\text{a}) \quad \text{(eq. 13)}$$

where V_m and I_m are the voltage and current at the maximum power point defined by (Chouder et al., 2012):

$$I_m = I_{m,ref}\left(\frac{G_T}{G_{ref}}\right) \quad \text{(eq. 14)}$$

$$V_m = V_{m,ref} - \beta\left(T_{c,ref} - T_c\right) \quad \text{(eq. 15)}$$

In Eq. (14) and (15), $I_{m,ref}$ and $V_{m,ref}$ are the voltage and current at the maximum power point for a reference condition. In Eq. (12), the variable U is the heat transfer coefficient:

$$U = 5.7 + 3.8 * v \quad \text{(eq. 16)}$$

where v is the wind speed. Thus, the exergetic efficiency is the ratio between the difference of electrical and thermal exergy by solar exergy. The thermal exergy is subtracted from the electric exergy, because the heat generated in the process of conversion of solar radiation into electrical energy is rejected, and is not used as a useful product:

$$\varepsilon = \frac{\text{output exergy}}{\text{input exergy}} = \frac{V_m I_m - \left(1 - \frac{T_a}{T_c}\right) U * A(T_c - T_a)}{\left(1 - \frac{T_a}{T_{sol}}\right) G_T * A} \quad \text{(eq. 17)}$$

4. Results

The monthly average estimated for the incident solar radiation on a horizontal surface were compared with experimental average monthly data for the years 2011-2013 for the city of Belo Horizonte/Brazil (provided by INMET as shown in Figure 1).

Fig. 1: Comparison of monthly averages of solar radiation to Belo Horizonte, Brazil

When comparing the values of the solar radiation estimated by the model with standard (TMY) year values, differences of up to 15% are possible. However, the overall performance and average annual are quite close. The standard (TMY) year is defined for a given location. There may occur substantial actual variations from one year to another, as seen in experimental curves obtained for the years 2011, 2012 and 2013 in Fig. 1.

The ambient temperature obtained by the model is shown in Figure 2, and it is compared with the standard year and with experimental data for the years 2011-2013. It is noted that experimental data varied significantly among the analyzed years. When comparing the data obtained by Lorenzo model (1994) and standard year, the data are very close, with maximum differences below 3%.

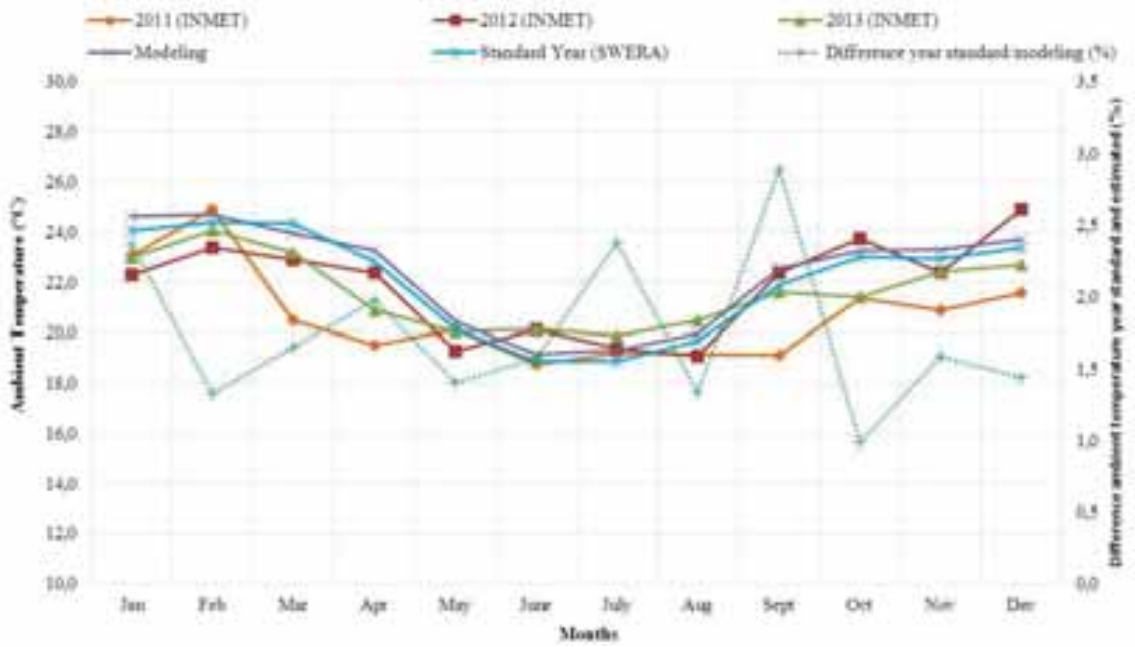

Fig. 2: Comparison of monthly averages of ambient temperature to Belo Horizonte, Brazil

Comparing the data obtained by this model with experimental data and data obtained by the TMY, it is concluded that the results are valid to estimate the performance of the solar radiation and ambient temperature for the city of Belo Horizonte, Brazil. Thus, these results were used as input data for estimating the radiation incident on the inclined photovoltaic modules (β_{in} =20°) and energy and exergy efficiency.

Figure 3 shows the monthly average values of ambient temperature and of solar radiation incident on the plane of the photovoltaic modules inclined (Belo Horizonte, Brazil).

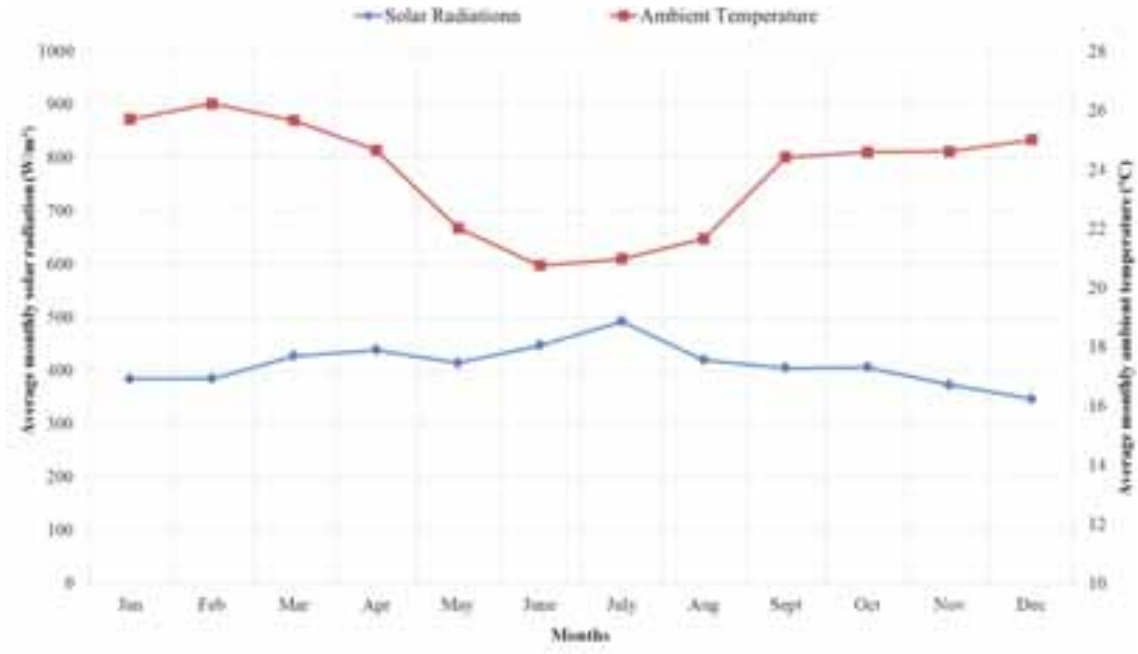

Fig. 3: Monthly average weather conditions for Belo Horizonte, Brazil

The months corresponding to winter in the southern hemisphere (June, July and August) have the lowest average monthly temperature indices—as expected. The months corresponding to summer in the southern hemisphere (December, January, February and March) have higher temperatures and lower values of solar radiation. This behavior can be attributed to both higher levels of atmospheric transparency that occurs in the

winter and the inclination of the modules fixed at 20°. Duffie and Bekman (2006) affirm that for maximize incident of solar radiation in winter, the solar equipment must have inclination equal to the local latitude module.

Figure 4 presents and compares the exergy efficiency of the photovoltaic modules m-Si (190Wp) and p-Si (210 Wp). The exergy due to solar radiation is the maximum work that can be used by the photovoltaic module. When comparing the values obtained for the m-Si and p-Si modules on a particular date, it is clear that the p-Si module presents higher values. The exergy due to solar radiation depends on the environmental parameters (ambient temperature, sun temperature and solar radiation) and the module area. As environmental parameters are the same for both modules, the higher values obtained by the p-Si (210Wp) can be attributed to its larger area. For this module, the temporal variation of exergy depends only on weather conditions. The value of solar exergy depends only of solar radiation and ambient temperature; while the rates of electrical and thermal exergy depend on solar radiation, ambient temperature and wind speed. As the month of July has the highest values of solar radiation, exergies were higher this month compared to the months of December or January.

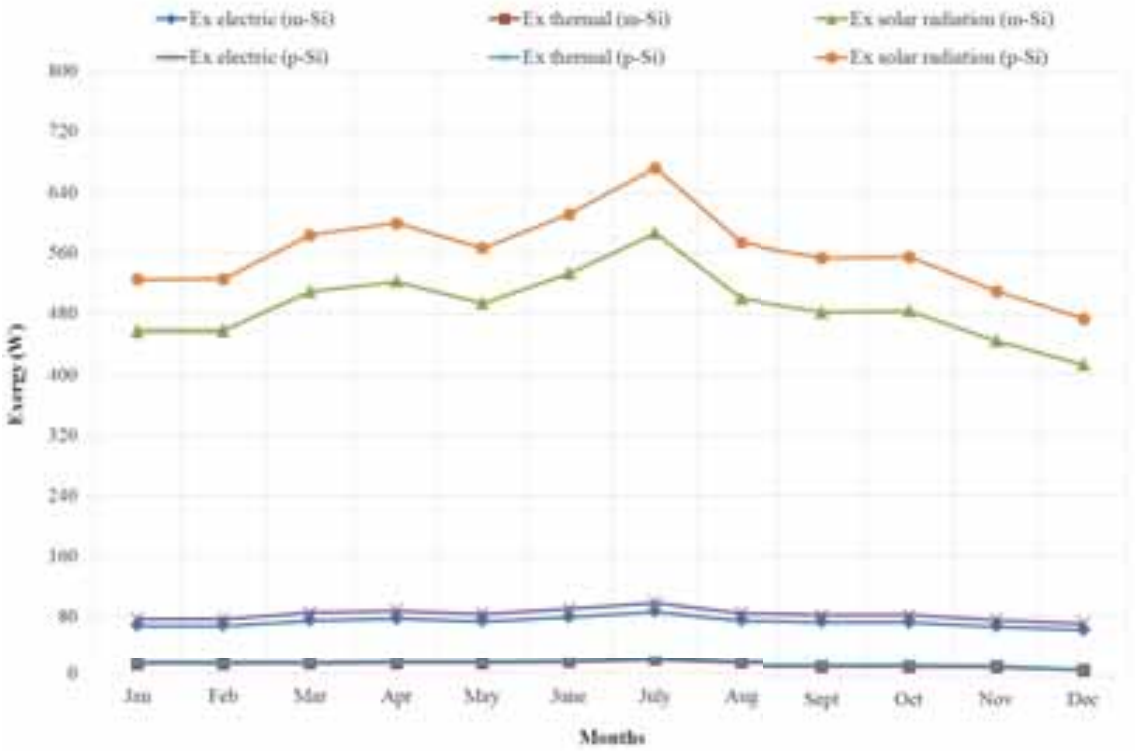

Fig. 4: Monthly averages of electrical and thermal exergias for m-Si and p-Si modules

The thermal exergy reduces the efficiency of the module. This loss can be reduced by minimizing two factors: the operating temperature of the cell and the heat transfer coefficient by convection. The electrical exergy depends on the electrical parameters of each cell and the particular technology. The electrical exergy of the PV modules can be maximized by reducing optical losses (e.g., using cells that absorb different portions oft he solar spectrum, and/or antireflection coatings to increase the photon absorption). Similarly, the value of solar exergy for the p-Si module (210Wp) were higher than m-Si module (190Wp), while the thermal exergy rates were approximately same for both technologies. In addition, the behavior throughout the year is similar for the three values of exergy, with highest values in July (Fig. 4).

The accumulation of dirt and dust are external environmental factors that can significantly affect the performance of photovoltaic modules. Piliougine et al (2013) evaluated the production of polycrystalline power modules with and without anti-soiling coatings. The authors report 12% loss in uncoated modules and 10% having the dust mitigting coating. According to the homogeneity of the distribution of the dust, these

losses can be even greater (e.g., shading can occur). Appels et al (2013) developed an experimental work on photovoltaic modules, and observed losses between 3-4% due to deposition of dirt, even with rain in the review period. The coating modules with non-stick (udst preventing) films contributes to the reduction of accumulation of dirt and minimize losses due to reflection.

Figure 5 shows the monthly average energy and exergy efficiencies for the m-Si module and p-Si module. The monthly average of the energy efficiencies of the m-Si module or the order of 20.0% and for the p-Si module this variation was 18.3%-18.6%. The results of the analysis of the exergetic efficiencies showed an average of 13.0% to 13.8% for the monocrystalline photovoltaic module, and between 12.5 and 13.3% for polycrystalline photovoltaic module (approximately).

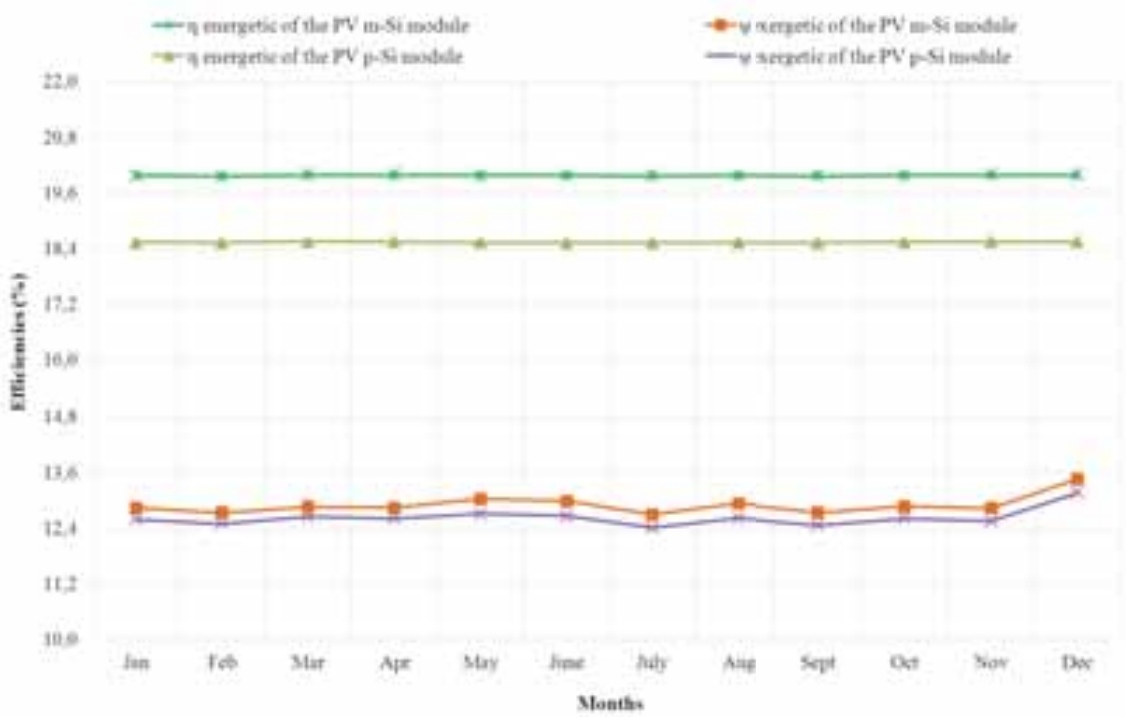

Fig. 5: Monthly averages of energetic and exergetic efficiencies for m-Si and p-Si modules

The polycrystalline module has higher measured power output compared with the monocrystalline module (Fig. 6). However, the area of p-Si module is larger, and has a lower energy efficiency values than the m-Si module. The behavior of the output power curves shown in Fig. 6, is a reflection of influence of the variation of the solar radiation on the output current of the modules These results show that although the input exergy and electrical exergy are higher in p-Si module compared to the m-Si, this is a consequence of the area and the nominal power (current and voltage) difference of the two types. Energy efficiencies and exergetic were higher for m-Si module. This is explained by inherent characteristics oft he m-Si technology that is characterized by less defective material and lower impurity levels than with the polycrystalline technologies. That is, a polycrystalline module would require greater area of the semiconductor for generate the equivalent power of a monocrystalline module because of its lower conversion capabilities.

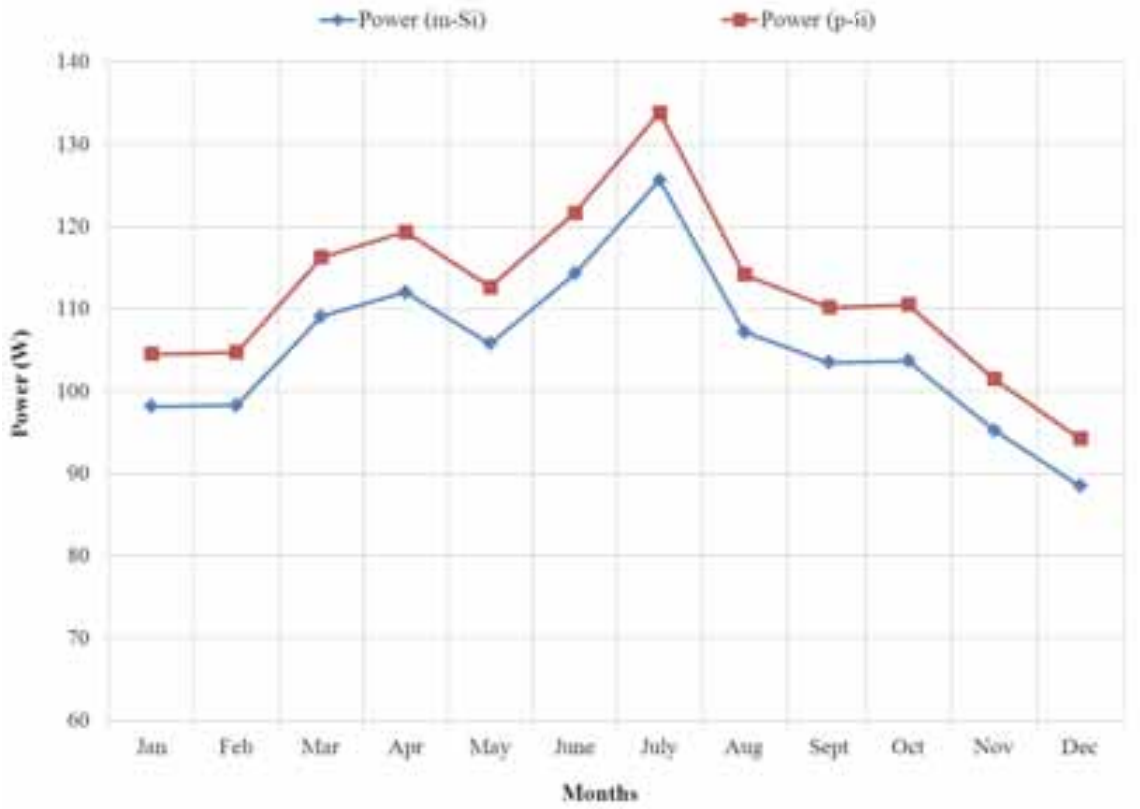

Fig. 6: Monthly average output power of the m-Si and p-Si modules

5. Conclusions

This study derives and uses a model incorporating TMY and PV module nameplate specifications to estimate and compare the energy and exergy efficiencies of photovoltaic of monocrystalline silicon and polycrystalline PV modules operating in the city of Belo Horizonte, Brazil. The module operating parameters were evaluated from mathematical models for solar radiation and temperature. The assessnent of efficiencies provides pathways to increase these values by reducing possible optical losses and the electrical conversion processes. The main losses related to photovoltaic technology are related to heat generation, which in this case is the heat rejected to the environment.

The m-Si module displayed higher values for average annual energy efficiency (19.9%) and exergy efficiency (13.3%). However, its exergy values were lower when compared to the p-Si module. These variations are explained by the energy and exergy differences in area between the module types and the inherent technology characteristics (i.e., the differences in crystalline quality and impurity levels).

Acknowledgments

The authors gratefully acknowledge the generous support of PUC Minas, FAPEMIG, CAPES and CNPq enabling us to perform this research. Also we thank L.L. Kazmerski, visiting research professor at PUC Minas, for his comments and suggestions for the analysis and presentation of this work.

6. References

1.Appels, R.; Lefevre, B.; Herteleer, B.; Goverde, H.; Beerten, A.; Paesen, R.; Medts, K.; Driesen, J.; Poortmans, J. Effect of soiling on photovoltaic modules. Solar Energy 2013; 96:283 – 291.

2. Ceylan, I.; Gürel, A.E. Exergetic Analysis of a New Design Photovoltaic and Thermal (PV/T) System. Published online 22 March 2015 in Wiley Online Library (wileyonlinelibrary.com). DOI 10.1002/ep.12108

3. Chouder, A., et al. Modeling and simulation of a grid connected PV system based on the evaluation of main PV module parameters. Simulation Modeling Practice and Theory 2012; 20:46 – 58.

4. Colombo, E.; Rocco, M.V.; Toro, C.; Sciubba, E. An exergy-based approach to the joint economic and environmental impact assessment of possible photovoltaic scenarios: A case study at a regional level in Italy. Ecological Modelling 2014

5. Dincer, I..The role of exergy in energy policy making. Energy Policy 2002;30:137–149.

6. Dincer, I., et al. Global Warming: Engineering Solutions, Springer New York Dordrecht Heidelberg, London, 2010.

7. Duffie, J.A.; Beckman, W.A. Solar engineering of thermal processes. 3 ed. New York: John Wiley & Sons, 2006.

8. Green, M. A., et al. Solar cell efficiency tables (Version 45). Progress Photovoltaic: Research and applications 2015; 23:1 – 9.

9. Guimarães, A.P.C. Estudo solarimétrico com base na definição de mês padrão e sequência de radiação diária. 1995. Universidade Federal de Minas Gerais - Graduate Course in Mechanical Engineering.

10.Joshi, A. S., Dincer, I., Reddy, B. V.. Performance analysis of photovoltaic systems: A review. Renewable and Sustainable Energy 2009;13:1884-1897.

11. Lorenzo, E. Electricidad Sola: Ingenieria de los sistemas fotovoltaicos. 1 ed. Espanha: Progensa, 1994

12. Pandey, A. K.; Tyagi, V. V.; Tyagi, S. K. Exergetic analysis and parametric study of multi-crystalline solar photovoltaic system at a typical climatic zone. Clean Techn Environ Policy 2013; 15:333 – 342.

13. Piliougine, M.; Cañete, C.; Moreno, R.; Carretero, J.; Hirose, J.; Ogawa, S.; Sidrach-De-Cardona, M. Comparative analysis of energy produced by photovoltaic modules with anti-soiling coated surface in arid climates. Applied Energy 2013, 112:626 – 634.

14. Sahin, A.D., Dincer, I., Rosen, M.A..Thermodynamic analysis of solar photovoltaic cell systems. Solar Energy Materials&Solar Cells 2007; 91:153-159.

15. Sarhaddi, F., et al. Exergetic performance assessment of a solar photovoltaic thermal (PV/T) air collector. Energy and Buildings 2009;42:2184–2199.

16. Xydis G. On the exergetic capacity factor of a wind - solar power generation system, Journal of Cleaner Production 2013, 47:437-445.

17. Yazdanpanahi, J.; Sarhaddi, F.; Adeli, M.M. Experimental investigation of exergy efficiency of a solar photovoltaic thermal (PVT) water collector based on exergy losses. Solar Energy 2015, 118: 197–208

Renewable Electricity Technologies: CSP, Biomass, Geothermal, Wind, Hydro, Ocean & Other

DYNAMIC SIMULATION AND EXPERIMENTAL RESEARCH OF OPEN AIR RECEIVER SYSTEM WITH CERAMIC FOAM ABSORBER

Qing Li[1], Fengwu Bai[1*], Zhifeng Wang[1], José Gonzalez Aguilar[2], Sijie Liu[3]

[1] The Key Laboratory of Solar Thermal Energy and Photovoltaic System, The Institute of Electrical Engineering Chinese Academy of Sciences, No.6 Beiertiao, Zhongguancun, Beijing100190, China,

[2] IMDEA ENERGY Institute, Avda. Ramón de la Sagra, 3 Parque Tecnológico de Móstoles E-28935 Móstoles, Madrid, Spain

[3] EDF - Asia Pacific Branch - China Division, R&D Center, Henderson Center Tower 2 Floor 12, 18 Jianguomennei Avenue, Beijing 100005, PRC

Abstract

This study investigated the heat transfer between air flow and ceramic foam absorber in open air receiver system using dynamics simulation based on Modelica language and Dymola solver. The experimental platforms of air receiver were built to validate the model, and the comparison between the experimental data and the simulation results showed this model was reliable to predict the dynamic performance of the air receiver system and to help optimize this system. The methodology of the model development and the implementation of the experiment are presented in this paper. Relied on the validated air receiver model, the sensitivity studies had been done to explore the influence of the absorber geometric parameters (thickness, mean cell size and porosity) on the volumetric ceramic foam air receiver performances. In addition, the optimization of the foam air receiver with the thermal efficiency as the objective function had been carried out based on the air receiver model and the optimization tool in Dymola.

Keywords: *Air receiver, ceramic foam, dynamic simulation, experimental validation, sensitivity studies, optimization*

1. Introduction

Due to its high concentration ratio and high efficiency, solar thermal power tower (STPT) technology has gained the worldwide attention, which is being vigorously promoted all around the world. The heat transfer fluid (HTF) used in the solar power tower system can be water, molten salt, thermal oils and air (Pavlovic et al., 2012; Romero et al., 2002). Compared with others, air as the working fluid has several advantages, such as no pollution to the environment, no phase transition, high operating temperature, no need for preheating. In the air STPT system, the air receiver plays the most significant role, which converts the concentrated solar radiation into the thermal energy of the air (Behar et al., 2013; Kribus et al., 1998). USA pioneered the first development of air receiver, which is the tube one. Since 1980s, volumetric air receivers started to be researched in Europe. The concentrated radiation flux can penetrate deeper into the volumetric air receiver due to its porosity and large extinction volume, which makes this type of air receiver more flexible than tube receiver (Avila-Marin, 2011). Refer to the material of the absorber in volumetric receiver, metal and ceramic are considered as the most appropriate materials for the high porous structure, especially silicon carbide ceramic, has large surface area, high-temperature capability, low density, and good mechanical strength, which is more suitable to be used in the high temperatures environment (Becker et al., 2006; Chavez and Chaza, 1991; Fend et al., 2004).

A lot of researches have been done numerically to study the silicon carbide ceramic foam using as the absorber in the air receiver. Some studiers focus on the macroscopic properties of the absorber based on certain simplifying assumptions. The influences brought by the air inlet velocity, the absorber porosity, the absorber thickness and mean cell size on the heat transfer performance of the receiver have been researched (Bai, 2010; Wu et al., 2011; Xu et al., 2011). Some other researchers proceed from the microscopic perspectives of the ceramic foam, and they chose to study the local heat transfer between the air flow and the solid of porous ceramic numerically (Wu et al., 2011; Wang and Pan, 2008). There are also some researchers look into the design of the ceramic foam air receiver, the optimum configuration have been found by

doi:10.18086/swc.2015.04.01 Available at http://proceedings.ises.org

comparing the thermal efficiencies and flow instabilities of volumetric absorbers with different configurations (Roldan et al., 2014).

Most researchers among them study the performances of the ceramic foam air receiver using the approaches of CFD simulation and experimental testing. Both of the two methods are time-consuming and not convenience to obtain the performance of the air receiver at all operating conditions. On the one hand, CFD simulation is commonly applied to evaluating the complex internal heat and mass transfer process, the geometry and meshing of the model should be pre-determined, which will bring the difficulty to change the parameters. On the other hand, the experimental testing is very costly to study the performance of the receiver with different designs. Therefore, dynamic modeling stands out to evaluate the sensitivity and do the optimization of the air receiver because of its convenience of changing every parameter. Up to now, some dynamic models were made to simulate the performance of the receiver in molten salt (Ferriere A, 1989) or water/steam (Xu et al., 2011; Yao et al., 2009; Yu et al., 2012) STPT. However, very few studies (Alvarez et al., 2009; Kribus et al., 2001) have focused on the dynamic simulations of the air receiver, which are indispensable for the sensitivity study and optimization on the STPT using air as HTF.

In this study, one-dimensional dynamic simulations are carried out for the ceramic foam air receiver by spatial discretization method. This modeling is based on the Modelica modeling language under Dymola software. Modelica is an object-oriented modeling language, which is freely available and has obtained high attention in recent years (Modelica Association, 2012). The ThermoSypro Library of EDF (developed by EDF and released under open source license) was used in the modeling, and the basic elements model of thermal Engineering are embodied in the ThermoSypro Library.

In order to validate the dynamic model of the air receiver, an experimental platform was set up. The receiver outlet air temperature from the experimental measurements and simulation results are compared, which shows good agreement between them.

Based on this validated air receiver model, the sensitivity studies have been done to explore the effects of the absorber geometric properties (thickness, mean cell size and porosity) on the volumetric air receiver performances. The temperature distributions for the absorber with different geometric properties are analyzed in this article. Moreover, built on the foundation of the optimization function in Dymola software, the optimal solution of geometric properties has been found with the thermal efficiency as the objective function.

2. Methodology

2.1. Physical model

Nomenclature

A	absorber surface area(m^2)	Re	Reynolds number
Cp	heat capacity (J kg^{-1} K^{-1})	T	temperatures (K)
d	mean cell diameter of the ceramic foam (m)	t	time (s)
DNI	direct normal irradiance (W m^{-2})	U	internal energy per unit volume (J m^{-3})
h	specific enthalpy(J kg^{-1})	u	superficial velocity (m s^{-1})
h_v	mean volumetric heat transfer coefficient (W m^{-3} K^{-1})	x	x-directional coordinate (m)
K_1	permeability coefficient (m^2)	y	y-directional coordinate (m)
K_2	inertial coefficient (m^{-1})	Greek symbols	
k	thermal conductivity (W m^{-1} K^{-1})	ε	porosity
L	thickness (m)	δ	Stephan Boltzmann constant (W m^{-2} K^{-4})
Nu_v	Nusselt number based on h_v	β	Rosseland mean extinction coefficient (m^{-}

			^{1})
P	pressure (Pa)	μ	dynamic viscosity (kg m^{-1} s^{-1})
q_{in}	radiation energy at inlet (W m^{-2})	ρ	density (kg m^{-3})
q_f	fluid mass flow per unit area (kg s^{-1} m^{-2})	Subscripts	
		f	fluid
q_{rad}	solid radiation force (W m^{-2})	s	solid
Q	inlet air superficial velocity (Nm^3/h)	in	inlet
$S(y)$	radiation source (W m^{-2})	out	outlet

The schematic of air receiver physical model is shown in Fig.1, where (a) is the configuration of the receiver including the insulation and ceramic foam absorber while (b) is the size and coordinate.

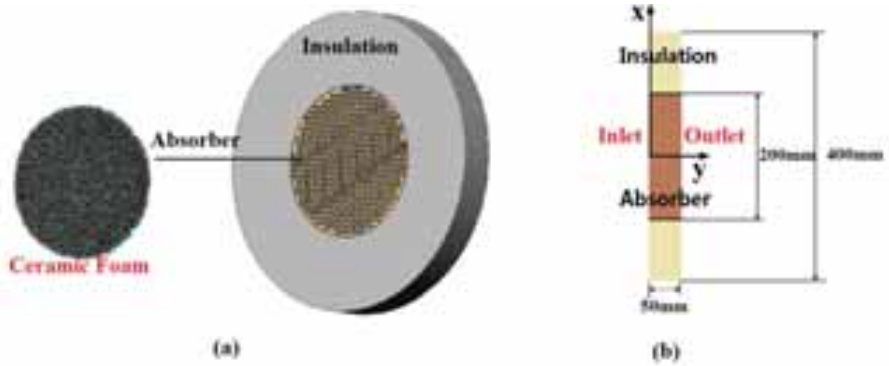

Fig. 1: Schematic of air receiver physical model: (a) configuration and (b) size and coordinates

Due to the difficulty of multidimensional simulation based on Modelica /Dymola, one dimension model was established by spatial discretization along the air flow direction (y-axis direction). The insulation was ignored in this model.

Air properties were defined as temperature dependent in this model, including the heat capacity, the density, the viscosity and the thermal conductivity because of the high working temperature of the receiver.

2.2. Numerical model

The following assumptions are made in order to simplify the problem. (1) The ceramic foam absorber is isotropic. (2) The air mass flow and the solar incident radiation flux are uniform on the surface of the absorber. (3) The heat insulation of the receiver is very well and the heat loss from the cylindrical out surface is ignored.

For spatial discretization, a number of sections are divided along the fluid flow direction. The energy conservation of section i is represented in Fig.2, including the conductive heat transfer inside air, the radiative and conductive heat transfer of the internal solid, the convective heat transfer between air and solid, and the penetrating solar energy source. Moreover, the convective and radiative heat losses at the air entrance surface are also embodied in the first section.

The energy conservation equations of solid and fluid are presented in eq. 1 and eq. 2, respectively.

For solid:

$$\frac{\partial\left[(1-\varepsilon)\cdot k_s\cdot\frac{\partial T_S}{\partial y}\right]}{\partial y}-\frac{\partial q_{rad}}{\partial y}-h_v\cdot(T_s-T_f)+\frac{\partial S(y)}{\partial y}=\rho_s\cdot(1-\varepsilon)\cdot Cp_s\cdot\frac{\partial T_S}{\partial t} \quad \text{(eq. 1)}$$

For fluid:

$$\frac{\partial\left(\varepsilon\cdot k_f\cdot\frac{\partial T_f}{\partial y}\right)}{\partial y}+h_v\cdot(T_s-T_f)-\frac{\partial(q_f\cdot h_f)}{\partial y}=\frac{\partial U_f}{\partial t}\cdot\varepsilon \quad \text{(eq. 2)}$$

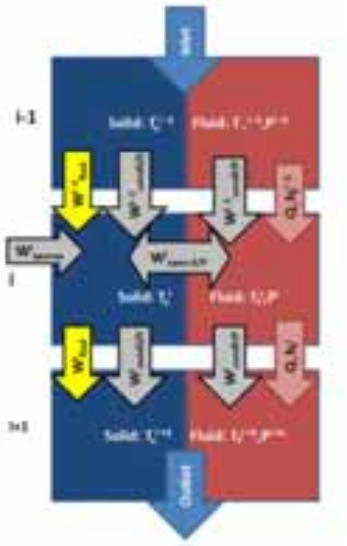

Fig. 2: Energy balance in absorber

In the equations, *S(y)* stands for the distribution of concentrated radiation flux inside the ceramic foam absorber as an exponential decay displayed in eq. 3 (Coquard et al., 2009). U_f represents the air internal energy expressed by eq. 4. q_{rad} means the radiation heat transfer in solid which plays a significant role as the absorber working at high temperature. According to the Rosseland radiation model, q_{rad} is determined using Eq. (5) (Cherif and Sifaoui, 2005; Zhao et al., 2004). β is the extinction coefficient of the ceramic foam, which can obtained by eq. 6 (Petrasch et al., 2007).

$$S(y) = q_{in} \cdot e^{-(\beta \cdot y)} \quad \text{(eq. 3)}$$

$$\frac{\partial U_f}{\partial t} = \left(\rho_f + h_f \cdot \frac{\partial \rho_f}{\partial h_f}\Big|_p\right) \cdot \frac{\partial h_f}{\partial t} + \left(h_f \cdot \frac{\partial \rho_f}{\partial P}\Big|_{h_f} - 1\right) \cdot \frac{\partial P}{\partial t} \quad \text{(eq. 4)}$$

$$q_{rad} = -\frac{16\delta \cdot T_s^3}{3\beta} \cdot \frac{\partial T_s}{\partial y} \quad \text{(eq. 5)}$$

$$\beta = \frac{0.56}{d} \quad \text{(eq. 6)}$$

The volumetric convective heat transfer coefficient between the air and the solid (h_v) is defined as a variation with the Nusselt number as eq. 7， which can be derived from eq. 8 and eq. 9 (Fu et al., 1998).

$$h_v = Nu_v \cdot \frac{k_f}{d^2} \quad \text{(eq. 7)}$$

$$Nu_v = \left(0.0426 + 1.236\frac{d}{L}\right) \cdot Re \quad \text{(eq. 8)}$$

($2 < Re < 836$)

$$Re = \frac{d \cdot u_f \cdot \rho_f}{\mu_f} \quad \text{(eq. 9)}$$

The expression of the pressure loss in the absorber is shown in eq. 10 – eq. 12 according to the classic Darcye-Forchheimer law (Moreira et al., 2004).

$$-\frac{\Delta P}{y} = \frac{\mu_f}{K_1} \cdot u_1 + 0.5K_2 \cdot \rho_f \cdot u_f^2 \quad \text{(eq. 10)}$$

$$K_1 = \frac{d^2}{150} \cdot \frac{\varepsilon^3}{(1-\varepsilon)^2} \quad \text{(eq. 11)}$$

$$K_2 = \frac{3.5}{d} \cdot \frac{1-\varepsilon}{\varepsilon^3} \quad \text{(eq. 12)}$$

Besides, the functions in ThermoSypro Library are used to obtain the variations of air's physical parameters, such as the heat capacity, the density, the viscosity and the thermal conductivity with corresponding air

temperatures and pressures.

3. Experimental validation

The experimental platform was set up in Badaling solar thermal power experimental base of China for validating the receiver model. The schematic diagram and one photograph of the experimental system are depicted in Fig. 3, and the system is compose of the solar furnace, air receiver, cooling device, draught fan and measuring devices. Air receiver of 200mm length is the key component of the system, which consists of the 50mm absorber, the 150mm cavity for air flow mixing, the insulation layer and the supporting component. The cooling device was used to cool the hot air to protect the draught fan and other devices, which was made up of a tank of honeycomb ceramic bulks.

Two thermocouples were installed on the central axis of the receiver 160 mm and 180 mm behind the front surface of the absorber to measure the receiver outlet air temperature. Since the input solar flux was not uniform, the air temperature distribution inside the absorber was not uniform in the radial direction. However, the air leaving the absorber was assumed to be thoroughly mixed 150 mm behind the front surface of the absorber which can be proved by that the temperatures of the two thermocouples differed by less than 5 K. Thus, the average temperature of these two thermocouples was used as the experimental receiver outlet air temperature.

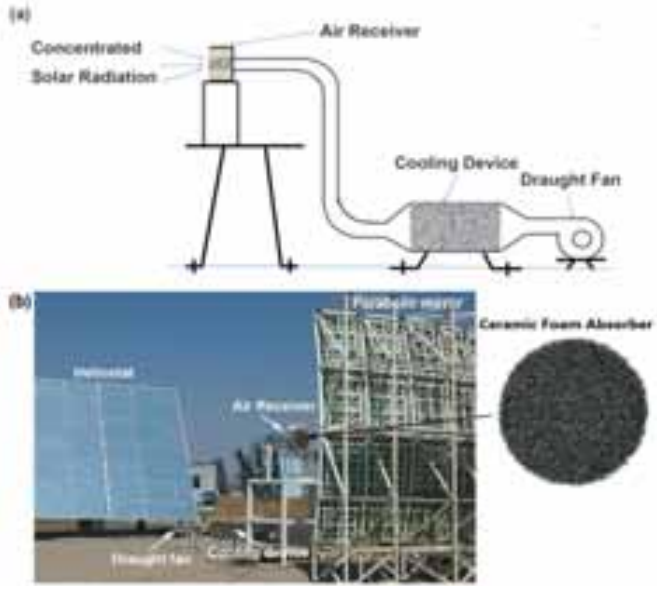

Fig. 3: Experiment system of air receiver: (a) schematic diagram and (b) system photograph

The solar radiation flux at the air receiver inlet surface is determined by the data tested through the "charge coupled device (CCD) camera + moving bar" indirect measurement, which is used as the inlet boundary condition in the dynamic simulation. The porosity, mean cell size, and thickness of the ceramic foam absorber are 0.65, 2.5 mm and 50mm, respectively. The air mass flow during the experiment was adjusted at 60Nm^3/h (the inlet air superficial velocity is 0.53m/s). The parameters of the absorber and the inlet air superficial velocity used in the dynamic simulation were set identical to the values in the experiment. The comparison between experimental measurements and simulation results of the air temperature at receiver outlet is shown in Fig. 4. The upper curve presents the DNI (direct normal irradiance) during the experiment time. DNI, solar radiation flux and air mass flow are the three inputs of the simulation model, which are achieved from the experiments. The receiver outlet air temperatures over time, obtained from experiment and simulation result, are depicted in the below diagram. We can see that the simulated outlet air temperature is in appreciable agreement with the experimental data, both of which show gentler variations than DNI. It can be concluded that the error between the two curves is less than 10%, mainly due to the limitations of the 1-D approach for the 3-D process, the discretization and round-off errors in the calculations, the uncertainties in the heat transfer coefficient model and radiation transfer functions and the measurement errors in the vortex

flow meter and the thermocouples. The vortex flow meter, model LUGBZ-40, had an accuracy of ±1.5% FS according to the manufacturer and the K type thermocouples used in the experiment had accuracies of ±2.5 K within the measurement range of 300-1000 K. Compared to experiments, using dynamic modeling approach can be more applicable for the investigation and optimization of the air receiver since it is more convenient to change the date of the receiver parameters such as the thickness, the mean cell size and the porosity.

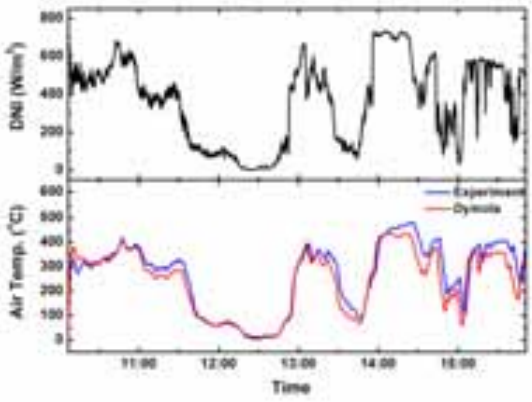

Fig. 4: Comparison between experimental measurements and simulation results of the outlet air temperature in air receiver system

4. Sensitivity studies

In order to research the influence of the structure of the absorber, we conducted a series of sensitivity study of the thickness, the mean cell size and the porosity of the ceramic foam absorber. The validated air receiver model described in this paper is the fundamental of these sensitivity studies. The inlet air superficial velocity is set as a constant value of 0.53m/s, and the inlet air temperature is 20°C. Also, we fix the concentrated solar radiation flux as 500 kW/m^2 in all the cases of this section. Under the same inlet air superficial velocity, inlet air temperature and incident energy flux, the thermal efficiencies for different cases can be reflected by the corresponding outlet air temperatures.

4.1. Effects of thickness

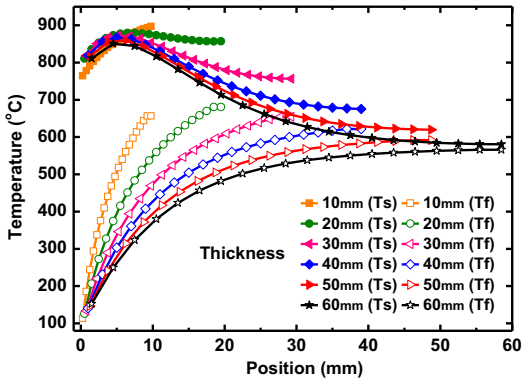

Fig. 5: The temperature distributions for different thicknesses

Fig. 5 shows the steady-state temperature distributions of the solid and fluid phase with different thickness but same porosity and mean cell size of the absorber (d = 3mm, ε = 0.5). As described in this figure, when the thickness is greater than 20mm, the fluid temperature decreases with the increasing of the thickness. Since the input power is fixed, the increase of the thickness will bring the decrease of the average volumetric heat power, which will reduce the fluid temperature. Another reason is that the volumetric convective heat transfer coefficient between the air and the solid will decrease with the increasing of the thickness, due to eq.

8, and it will decrease the heat exchange ability between air and solid. From the figure, we also can see the solid temperature at the outlet decreases with the increasing of the thickness. The reason is that the solid thermal resistance increases with the increasing of the thickness, which causes the large temperature drop of the solid. In addition, the temperature difference between the solid and air at the outlet decreases with the increasing of the thickness, that because the thicker the absorber is , the longer the heat exchange time and distance between fluid and solid are.

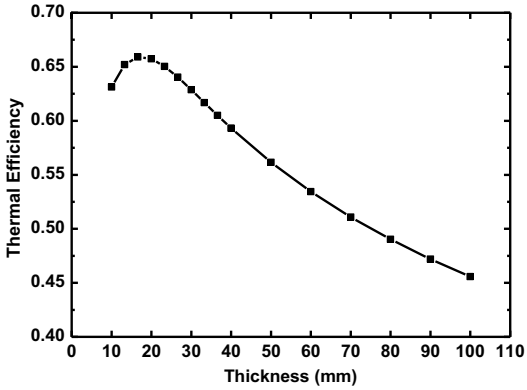

Fig. 6: The thermal efficiencies for different thicknesses on steady state

Fig. 6 is the thermal efficiencies at steady state with different absorber thicknesses but same porosity and mean cell size of the absorber (d = 3mm, ε= 0.5). It is can be seen in this figure, the thermal efficiency increases firstly and then decreases with the increasing of thickness, which comes highest when the thickness is 18mm. As mentioned before, the thermal efficiencies can be reflected by the outlet air temperatures under the same inlet air superficial velocity, inlet air temperature and incident energy flux, as eq.13. When the absorber thickness is rather small, the time of the air flow through the absorber will be very short, which caused the insufficiency of the heating and the reduction of the air outlet temperature. And also if the thickness is small enough, the solar radiation energy will penetrate out of the absorber, which will bring more heat loss. When the thickness is greater than 18mm, the fluid temperature will decrease with the increasing of the thickness. One reason is that the increasing of the thickness brings the reduction of the volumetric convective heat transfer coefficient between the air and the solid, as eq. 8, and the heat exchange ability between air and solid will drop. Another reason is that the solid temperature at the outlet decreases with the increasing of the thickness.

$$\eta = \frac{Q\cdot\left[\left(h_{f\,out}-\frac{P_{out}}{\rho_{f\,out}}\right)-\left(h_{f\,in}-\frac{P_{in}}{\rho_{f\,in}}\right)\right]}{q_{in}\cdot A} \qquad \text{(eq. 13)}$$

4.2. Effects of mean cell size

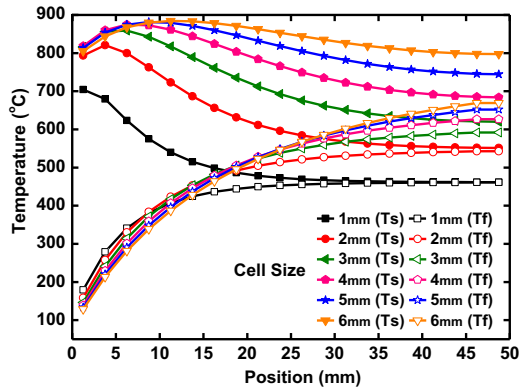

Fig. 7: The temperature distributions for different mean cell sizes

Fig. 7 shows the temperature distributions of the solid and fluid phase with same thickness and porosity of the absorber (L = 50mm, ε = 0.5) but different thickness at steady state. It can be seen in this figure that both the solid and fluid temperatures increase with the increasing of the mean cell size. According to eq. 6, the extinction coefficient of the absorber is inversely proportional to the mean cell size, means the bigger the mean cell size is, the small the extinction coefficient is, the more solar energy will penetrate into the absorber, which makes the increasing of the solid and fluid temperatures. From Fig. 7, we also can see the temperature difference between the solid and air at the outlet increases with the increasing of the mean cell size. The reason is that the volumetric convective heat transfer coefficient between the air and the solid decreases with the increasing of the mean cell size, as eq. 7.

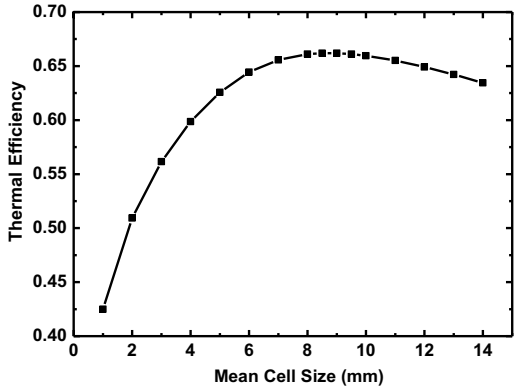

Fig. 8: The thermal efficiencies for different mean cell sizes on steady state

Fig. 8 is the thermal efficiencies at steady state with different mean cell sizes but same thickness and porosity of the absorber (L = 50mm, ε = 0.5). It is can be seen in this figure, the thermal efficiency increases first and then decreases with the increasing of mean cell size, which comes highest when the mean cell size is 8mm with the fixed inlet air superficial velocity, inlet air temperature, incident energy flux, absorber porosity, and absorber thickness. The reason is that when the mean cell size of the absorber is too big, the volumetric convective heat transfer coefficient between the air and the solid will be very small, and the heat exchanging capacity between air and solid will become weak, which will cause the decreasing of the air outlet temperature.

4.3. Effects of porosity

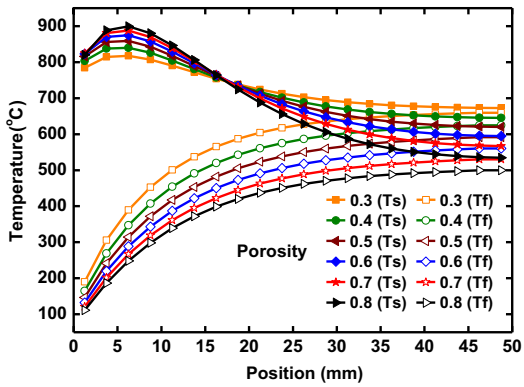

Fig. 9: The temperature distributions for different porosities

Fig. 9 shows the steady-state temperature distributions of the solid and fluid phase with different porosities but same thickness and mean cell size of the absorber (L = 50mm, d= 3mm). As we can see, the front solid temperatures of the absorbers with large porosities are higher than the temperatures of the absorbers with small porosities while the rear solid temperatures of the absorbers with large porosities are lower at the same position. The reason is that the solid of the absorber with large porosity is lighter, thus, the temperature of the

front solid is higher for absorbing the same incident energy. On the other side, the higher front temperature brings more heat loss on the surface of the receiver. It results in the reduction of the total energy penetrate into the receiver system, which makes the temperatures of the rear solid and the fluid relatively lower. The figure also shows that the solid temperature gradient of the absorber with large porosity is greater, which is owing to the larger solid thermal resistance. The larger the porosity is, the smaller the solid cross-sectional area is, and the larger the solid thermal resistance is. Furthermore, what we also can obtain from Fig. 9 is that the temperature difference between the solid and air at the outlet increases with the increasing of the porosity. The reason is that the lower air temperature makes the Reynolds number and the thermal conductivity decrease. According to eq. 7-eq. 9, the volumetric convective heat transfer coefficient between the air and the solid decreases with the lower air temperature, this makes the temperature difference between the solid and air at the outlet increases with the increase.

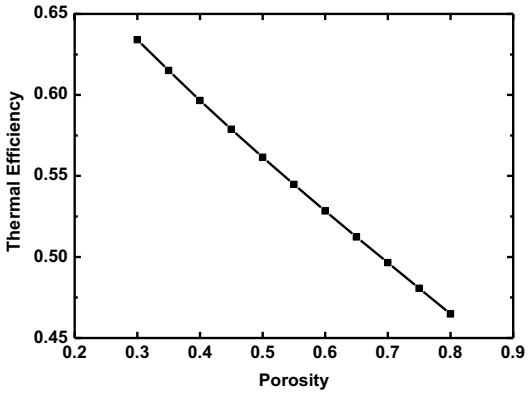

Fig. 10: The thermal efficiencies for different porosities on steady state

Fig. 10 is the thermal efficiencies at steady state with different porosities but same thickness and mean mean cell size of the absorber (L= 50mm, d= 3mm). It is can be seen in this figure, the thermal efficiency decreases with the increasing of the porosity. As explained before, larger porosity brings smaller solid cross-sectional area and larger thermal resistance in solid. And the larger thermal resistance causes greater temperature gradient in the solid, which results in the lower outlet solid and air temperatures. According to eq.13, the thermal efficiency also decreases with the increasing of the porosity as the outlet air temperature under the same inlet air superficial velocity, inlet air temperature and incident energy flux. Despite the smaller porosity can bring the greater the thermal efficiency, but considering the pressure drop and manufacture feasibility issues, the porosity should be kept in an appropriate range.

For the purpose of studying the influential factors of the heat transfer in the ceramic foam, the return air system is not considered in the model, which plays an important role in integrity and performance of open volumetric air receiver. Thus, the above-mentioned observations will be extended into the open volumetric air receiver integrated with the air return loop, based on the updated model in the future.

5. Optimization

The outlet air temperature and thermal efficiency at steady state are the most important indicators of air receiver performance, both of which are decided by the following five parameters: the solar radiation flux, the inlet air superficial velocity, the absorber thickness, the absorber mean cell size and the absorber porosity. In this section, we conduct the optimization of the air receiver system (without air return system) based on the air receiver model established in this article, and with the help of the optimization tool in Dymola software. Limited by the function of the Dymola software, we can only do the optimization on three parameters at most. Therefore, firstly we choose several different cases depend on the different solar radiation fluxes and inlet air superficial velocities. For each case, the optimal absorber geometric parameters (thickness, mean cell size and porosity) to achieve the maximum thermal efficiency are found, respectively. Table 1 shows the setting of the optimized parameters. Taking into account the feasibility of the manufacture, we define the ranges of these three parameters.

Tab. 1: Parameter setting of the optimization

Parameter	Minimum	Maximum	Unit
Thickness	10	100	mm
Mean cell size	1	6	mm
Porosity	0.3	0.8	1

Table 2 shows the optimization results under the same inlet air superficial velocity, as 0.53m/s, but with different solar radiation fluxes. As we can see, for various solar radiation fluxes, the optimized values of the absorber geometric parameters are the same. The highest outlet air temperature of the receiver increases with the increasing of the solar radiation flux, while the maximum thermal efficiency decreases with the increasing of the solar radiation flux.

Tab. 2: Optimization result with different solar radiation fluxes and fixed inlet air superficial velocity

Inlet air superficial velocity: 0.53m/s					
Solar radiation flux (kW/m^2)	400	450	500	550	600
Thickness (mm)	24.86	24.86	24.86	24.86	24.86
Mean cell size (mm)	4.09	4.09	4.09	4.09	4.09
Porosity	0.3	0.3	0.3	0.3	0.3
Pressure drop (Pa)	3753.70	3995.29	4222.97	4437.31	4639.05
Highest outlet air temperature (^{o}C)	618	674	727	775	821
Maximum thermal efficiency	0.737	0.722	0.707	0.692	0.677

Table 3 shows the optimization results under different inlet air superficial velocities, but with same solar radiation flux (500 kW/m^2). It can be seen from the table, for various inlet air superficial velocities, the optimized values of the absorber geometric parameters are almost the same. The highest outlet air temperature of the receiver decreases with the increasing of the inlet air superficial velocity, while the maximum thermal efficiency decreases with the increasing of the inlet air superficial velocity.

Tab. 3: Optimization result with different inlet air superficial velocities and fixed solar radiation flux

Solar radiation flux: 500 kW/m^2					
Inlet air superficial velocity (m/s)	0.35	0.44	0.53	0.62	0.71
Thickness (mm)	26.04	24.49	24.86	24.49	25.45
Mean cell size (mm)	4.06	4.11	4.09	4.11	4.07
Porosity	0.3	0.3	0.3	0.3	0.3
Pressure drop (Pa)	2514.22	3188.98	4222.97	5133.03	6558.83
Highest outlet air temperature (^{o}C)	870	772	727	628	564
Maximum thermal efficiency	0.608	0.681	0.707	0.751	0.771

Since the optimal geometric parameters for various solar radiation fluxes and inlet air superficial velocities are almost the same, we fixed the thickness, the mean cell size and porosity of the ceramic foam absorber as 25mm, 4.09 mm and 0.3, respectively; and we do the optimization of the solar radiation flux and inlet air superficial velocity to find the optimum condition to obtain the maximum thermal efficiency on the premise of the outlet air temperature is 800 ^{o}C. In consideration of the concentration ratio and the pressure loss, the ranges of the solar radiation flux and inlet air superficial velocity are limited as 0-2 m/s and 0-2000 kW/m^2. The result in Table 4 represents that when the solar radiation flux is 1825 kW/m^2 the inlet air superficial velocity is 1.75m/s, the maximum thermal efficiency of 0.769 can be achieved.

Tab. 4: Optimization result with fixed absorber geometric parameters and outlet air temperature

Thickness: 25mm, mean cell size:4.09mm, porosity:0.3, outlet air temperature: 800 ^{o}C			
Solar radiation flux (0-2000 kW/m2)	Inlet air superficial velocity (0-2 m/s)	Maximum thermal efficiency	Pressure drop (Pa)
1825 kW/m^2	1.75m/s	0.769	67885

The corresponding pressure drops are also depicted in the optimization result tables, which agree with the results in (Bai, 2010). The pressure drop in the ceramic foam is not the research emphasis of this paper.

6. Conclusions

In this article, the dynamic simulation model of ceramic foam open-loop air receiver, which is the most principal components in STPT using air as the HTF, was established using the object-oriented language Modelica based on Dymola simulation environment. The experiments of the air receiver had been carried out for the model validation, and the simulation results agree well with the experiment data. The sensitivity studies show that the absorber geometric properties (thickness, mean cell size and porosity) have distinct influences on the solid and fluid temperature distributions and the thermal efficiencies of the ceramic foam air receiver. The combination values of the absorber mean cell size, porosity, thickness, solar radiation flux and inlet air superficial velocity in certain ranges to achieve the highest thermal efficiency on the premise of the outlet air temperature is 800 ^{o}C were found by the optimization method using the receiver model.

In conclusion, this experiment validated model is reliable to predict the dynamic performance of the ceramic foam air receiver and can be used for receiver optimization in different STPT systems using this type of air receiver.

7. Acknowledgements

The present work was supported by National Natural Scientific Foundation of China (Grant No. 51376176).The research leading to these results has also received funding from the European Union Seventh Framework Program FP7/2007-2013 under grant agreement No.609837.

8. References

Alvarez, J.D., Guzman, J.L., Yebra, L.J., Berenguel, M., 2009. Hybrid modeling of central receiver solar power plants. Simul. Model Pract. Th. 17 (4), 664-679.

Avila-Marin, A.L., 2011. Volumetric receivers in Solar Thermal Power Plants with Central Receiver System technology: A review. Sol. Energy 85 (5), 891-910.

Bai, F.W., 2010. One dimensional thermal analysis of silicon carbide ceramic foam used for solar air receiver. Int. J. Therm. Sci. 49 (12), 2400-2404.

Becker, M., Fend, T., Hoffschmidt, B., Pitz-Paal, R., Reutter, O., Stamatov, V., Steven, M., Trimis, D., 2006. Theoretical and numerical investigation of flow stability in porous materials applied as volumetric solar receivers. Sol. Energy 80 (10), 1241-1248.

Behar, O., Khellaf, A., Mohammedi, K., 2013. A review of studies on central receiver solar thermal power plants. Renew. Sust. Energ. Rev. 23 12-39.

Chavez, J.M., Chaza, C., 1991. Testing of a Porous Ceramic Absorber for a Volumetric Air Receiver. Sol. Energ. Mater. 24 (1-4), 172-181.

Cherif, B., Sifaoui, M.S., 2005. Numerical study of heat transfer in an optically thich semi-transparent spherical porous medium. J Quant Spectrosc Ra 91(3), 363-372.

Coquard, R., Rochais, D., Baillis, D., 2009. Experimental investigations of the coupled conductive and radiative heat transfer in metallic/ceramic foams. Int. J. Heat Mass Tran. 52 (21-22), 4907-4918.

Fend, T., Hoffschmidt, B., Pitz-Paal, R., Reutter, O., Rietbrock, P., 2004. Porous materials as open volumetric solar receivers: Experimental determination of thermophysical and heat transfer properties. Energy 29 (5-6), 823-833.

Ferriere A, B.B., 1989. Development of an optical control strategy for the Themis solar plant: Part I - Themis transient model. Journal of Solar Energy Engineering 111 298 -303.

Fu, X., Viskanta, R., Gore, J.P., 1998. Measurement and correlation of volumetric heat transfer coefficients of cellular ceramics. Exp. Therm. Fluid Sci. 17 (4), 285-293.

Kribus, A., Doron, P., Rubin, R., Reuven, R., Taragan, E., Duchan, S., Karni, J., 2001. Performance of the directly-irradiated annular pressurized receiver (DIAPR) operating at 20 bar and 1,200 degrees C. J. Sol.

Energ-T. Asme. 123 (1), 10-17.

Kribus, A., Zaibel, R., Carey, D., Segal, A., Karni, J., 1998. A solar-driven combined cycle power plant. Sol. Energy 62 (2), 121-129.

Modelica Association, 2012. Modelica. a unified object-oriented language for physical systems modeling.

Moreira, E.A., Innocentini, M.D.M., Coury, J.R., 2004. Permeability of ceramic foams to compressible and incompressible flow. J. Eur. Ceram. Soc. 24 (10-11), 3209-3218.

Pavlovic, T.M., Radonjic, I.S., Milosavljevic, D.D., Pantic, L.S., 2012. A review of concentrating solar power plants in the world and their potential use in Serbia. Renew. Sust. Energ. Rev. 16 (6), 3891-3902.

Petrasch, J., Wyss, P., Steinfeld, A., 2007. Tomography-based Monte Carlo determination of radiative properties of reticulate porous ceramics. J. Quant. Spectrosc Ra. 105 (2), 180-197.

Roldan, M.I., Smirnova, O., Fend, T., Casas, J.L., Zarza, E., 2014. Thermal analysis and design of a volumetric solar absorber depending on the porosity. Renew. Energ. 62 116-128.

Romero, M., Buck, R., Pacheco, J.E., 2002. An update on solar central receiver systems, projects, and technologies. J. Sol. Energ-T. Asme. 124 (2), 98-108.

Wang, M., Pan, N., 2008. Modeling and prediction of the effective thermal conductivity of random open-cell porous foams. Int. J. Heat Mass Tran. 51 (5-6), 1325-1331.

Wu, Z.Y., Caliot, C., Flamant, G., Wang, Z.F., 2011. Coupled radiation and flow modeling in ceramic foam volumetric solar air receivers. Sol. Energy 85 (9), 2374-2385.

Wu, Z.Y., Caliot, C., Flamant, G., Wang, Z.F., 2011. Numerical simulation of convective heat transfer between air flow and ceramic foams to optimise volumetric solar air receiver performances. Int. J. Heat Mass Tran. 54 (7-8), 1527-1537.

Xu, C., Song, Z., Chen, L.D., Zhen, Y.A., 2011. Numerical investigation on porous media heat transfer in a solar tower receiver. Renew. Energ. 36 (3), 1138-1144.

Xu, E.S., Yu, Q.A., Wang, Z.F., Yang, C.Y., 2011. Modeling and simulation of 1 MW DAHAN solar thermal power tower plant. Renew. Energ. 36 (2), 848-857.

Yao, Z.H., Wang, Z.F., Lu, Z.W., Wei, X.D., 2009. Modeling and simulation of the pioneer 1 MW solar thermal central receiver system in China. Renew. Energ. 34 (11), 2437-2446.

Yu, Q., Wang, Z.F., Xu, E., 2012. Simulation and analysis of the central cavity receiver's performance of solar thermal power tower plant. Sol. Energy 86 (1), 164-174.

Zhao, C.Y., Lu, Y.J., Hodon, H.P., 2004. Thermal radiation in untralight metal foams with open cells. Int J Heat Mass Tran 47(14-16), 2927-2939.

Conference Proceedings
Solar World Congress 2015
Daegu, Korea, 08 – 12 November 2015

Zirconium carbide-nitride composite matrix based solar absorber structures on glass and aluminum substrates for solar thermal applications

[a]Belal Usmani, [b]Vivek Vijay, [c]Rahul Chhibber, [c]Laltu Chandra [a]Ambesh Dixit*

[a] Department of Physics, Indian Institute of Technology Jodhpur, Rajasthan, 342011, India
[b] Department of Mathematics, Indian Institute of Technology Jodhpur, Rajasthan, 342011, India
[c] Department of Mechanical Engineering, Indian Institute of Technology Jodhpur, Rajasthan, 342011, India

Abstract

Zirconium carbide-nitride absorber (ZrC-ZrN) and zirconium reflector tandem structures were prepared on glass and aluminum substrate, in conjunction with zirconium oxide (ZrO_x) anti-reflection coatings, using DC/RF magnetron sputtering system. The solar absorption properties of zirconium carbide-nitride absorber layers were optimized by controlling nitrogen flow during synthesis process for optimal solar thermal response. X-ray diffraction (XRD), scanning electron microscopy (SEM) and atomic force microscopy (AFM) measurements were carried out on fabricated absorber-reflector tandem structures to understand the structure-property correlation. We absorbed strong dependence of zirconium nitride fraction on solar thermal performance. We observed enhanced solar absorptance $\alpha \sim 0.86$ and thermal emittance $\varepsilon \sim 0.05$ at room temperature for structures fabricated with optimized synthesis parameters. The optimized structures are stable up to 150 °C in the air without any significant degradation in their solar performance.

Keyword: *Solar selective coatings, Sputtering, Structure, Optical property, Thermal stability*

1. Introduction

Solar thermal energy is getting attention due to its potential as compared to the other renewable energy resources. This can be used in various forms such as low temperature applications, e.g. solar water heating applications, intermediate and high temperature applications e.g. process heating (Mekhilef et al., 2011), power applications (Selvakumar and Barshilia, 2012). Such systems usually consist of several sub-systems such as collection/concentration of light, absorption/conversion of light into thermal energy and utilization to convert into electrical energy or for other application. The light to thermal energy conversion subsystem consists of special collection tubes, called as solar collectors (Kalogirou, 2004; Selvakumar and Barshilia, 2012). These collectors are coated with spectrally selective coatings, having a high absorptance in the wavelength range of 0.3- 2.5 μm and low emittance in wavelength range 2.5 to 25 μm in the mid to higher operating temperature ranges (Seraphin, 1997). The development of thermally stable solar selective coating is important for the maintenance free continuous operation of solar thermal systems/subsystems. There are continuous efforts to develop such material systems, which can withstand temperature, environmental conditions, and large thermal cycling for efficient photothermal conversion. Numerous solar selective coatings are developed using physical vapor deposition for mid-temperature (100 °C < T < 400 °C) applications. Some of them are commercialized successfully. For example, Zhang et al. developed SS-Al coatings using DC magnetron sputtering, with absorptance in the range of 0.93 - 0.96 and emittance of ~ 0.03 - 0.04 at room temperature. These are thermally stable upto 1h at 500 °C in vacuum (Zhang et al., 1998a, 1998b) and are used on evacuated glass tubes for solar hot water and steam applications. Lazarov's group

doi:10.18086/swc.2015.04.02 Available at http://proceedings.ises.org

developed TiN_xO_y oxynitride coatings with SiO_2 antireflection coatings on Cu and Al substrates with α=0.94 and ε=0.04 at 100 °C (Lazarov, 1993). S-Solar, Sweden, developed Ni-NiO metal-dielectric composite based absorber coating on Al substrates, with absorptance in the range 0.94-0.96 and thermal emittance of 0.13-0.15 at 100 °C for low temperature applications (Wackelgard and Hultmark, 1998). Electrodeposited black Chrome ($Cr-Cr_2O_3$) cermet coatings on Ni, Fe, Cu, stainless-steel substrate are developed and commercialized by by MTI in the United State and several other research and development groups (Bogaerts and Lampert, 1983; McDonald, 1975; Driver, 1981; Ignatiev et al., 1979; Smith et al., 1984; Sweet et al., 1984; Lampert, 1980; Holloway et al., 1980). H.C. Barshilia et al. developed $Cr_xO_y/Cr/Cr_2O_3$ transition metal oxide based multilayer absorber on Cu substrates for mid-temperature applications, exhibiting high absorptance (0.89-0.91) and low emittance at 82 °C (0.05-0.06) (Barshilia et al., 2008). N. Selvakumar et al and Vannoni et al have developed CrMoN/CrON tandem absorber on SS substrate with high absorptance (0.90 - 0.92) and low thermal emittance (0.13 - 0.15) for mid-temperature applications (Selvakumar et al., 2013, Vannoni et al., 2008). Yet such systems exhibit poor performance at elevated temperatures, especially thermal emittance at elevated temperatures, causing thermal loss in solar thermal systems. The oxidation of the metal content is the main reason for degradation of optical and thermal response in these cermet structures (Barshilia et al., 2008; Sebastian et al., 1997). Alike such oxide cermet structures, refractory metal carbo-nitride absorber systems may show significant improvement in their thermal stability in conjunction with their solar thermal performance. Considering the same, we investigated the solar thermal performance of zirconium carbide-nitride absorber- zirconium reflector tandem structures with zirconium oxide antireflection coating layer on glass and aluminum substrates.

2. Experimental details

The zirconium carbo-nitride absorber- zirconium reflector tandem structures were deposited on glass and aluminum substrate using DC/RF reactive magnetron sputtering. High purity (99.8%) zirconium (Zr) metal and (99.9%) ZrC targets were integrated with 4'' magnetron sputter gun for depositing Zr metal reflector, zirconium carbo-nitride absorber and zirconium oxide antireflecting coatings on glass and aluminum (Al) substrates. The glass substrates (25 x 76 x1 mm^3) were ultrasonically cleaned for 5 min in acetone and ethanol baths, respectively, without any mechanical polishing. Aluminum substrates were first mechanically polished with 2000 grade SiC abrasive paper to remove oxide layer and to reduce surface roughness, followed by ultrasonic cleaning in isopropyl alcohol and acetone for 10 minutes respectively. These cleaned substrates were used for fabricating the solar selective coating structures. The base pressure of deposition chamber was brought down ~ 6.0 x 10^{-6} mbar and sputtering processes were carried out at a constant working pressure ~ 2.0 x 10^{-2} mbar. The targets were pre-sputtered for ~15min before deposition of respective layers to clean any surface impurities such as oxide layers and process impurities. The detailed experimental process for deposition of individual layers is explained elsewhere (Usmani et al., 2015). Crystal phases and structure, microstructure and surface properties and elemental composition of the synthesized zirconium carbo-nitride absorber- zirconium reflector tandem structures in conjunction with zirconium oxide antireflection films were measured using X-ray diffraction (XRD), scanning electron microscope (SEM), atomic force microscope and X-ray energy dispersive system measurements. The reflectance spectra were measured in wavelength range (0.3 to 2.5 μm) by using Carry 5000 UV-Vis-NIR spectrophotometer in conjunction with standard Spectralon reference. The absorptance α was calculated using these measured reflectance spectra with respect to AM 1.5 solar spectrum. FTIR reflectance measurements were carried out in wavelength range (2.5 to 25 μm) and used to calculate the room temperature thermal emittance, ε. The thermal stability of these structures was studies by heating samples at ~ 150 °C for 2 hours at a constant heating rate ~ 5 °C/min, followed by free cooling to the room temperature. Thermal impact was investigated characterizing the structural/microstructural changes to understand the structure-property correlation on solar thermal performance on these zirconium carbo-nitride absorber-reflector structures.

3. Results and discussions

3.1 X-ray diffraction analysis

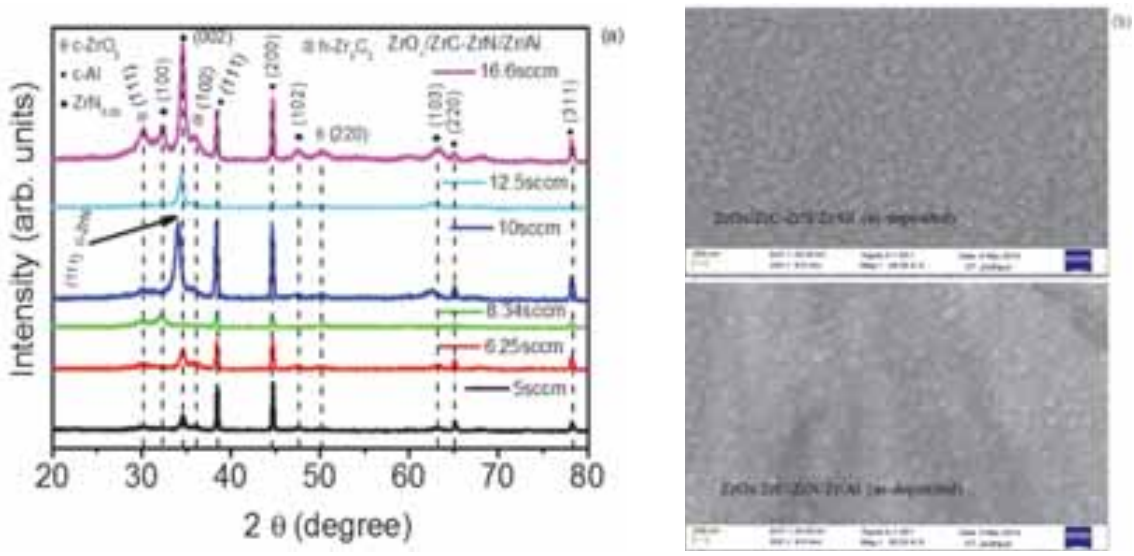

Fig. 1: (a) XRD spectra of ZrO_x/ZrC-ZrN/Zr absorber-reflector tandem selective coatings on aluminum substrate for different N_2 flow rates used for ZrC-ZrN absorber layer. **(b)** SEM images of ZrO_x/ZrC-ZrN/Zr absorber-reflector tandem structure deposited on aluminum and glass substrates.

The XRD pattern of ZrO_x/ZrC-ZrN/Zr absorber-reflector tandem selective coatings coated on Al substrate are shown in Fig. 1(a), with varying nitrogen flow rates used for synthesizing these structures. The diffraction peaks at 2θ = 38.42°, 44.74°, 65.07° and 78.22° correspond to (111), (200), (220) and (311) reflection plane from the aluminum substrate in all these XRD graphs. A strong peak at 2θ = 34.57° and weak peaks at 2θ = 32.39°, 47.57° and 63.18° correspond (002) and (100), (102), (103) diffraction planes for hexagonal zirconium nitride (h-$ZrN_{0.28}$) phase, respectively. Whereas, weak diffraction peak at 2θ = 36.09° correspond to (102) hexagonal zirconium carbide (h-Zr_3C_2) phase. The measured volume fraction of zirconium nitride is much larger than that of zirconium carbide suggesting a carbide system in nitride matrix. XRD results, for absorber-reflector tandem structure on glass substrates, are similar to that on aluminum substrates except Al substrate XRD pattern. XRD results on glass substrates, also substantiate larger zirconium nitride volume fraction in fabricated structures. Anti-reflecting ZrO_x layer exhibit mixed phase with dominating tetragonal zirconium oxide phase, as indexed in Fig. 1(a) (top panel). ZrO_x top layer scanning electron micrographs are shown in Fig. 1(b) for as deposited absorber-reflector tandem structures on glass and aluminum substrates. As deposited surfaces are smooth for both aluminum and glass substrates with micro granular structures ~ 100 nm, as shown in Fig. 1(b). In contrast to glass substrates, the surface structure of absorber-reflector tandem structures on Al substrates consists of substrate imprints and average surface roughness is ~ 10 ± 2 nm for both substrates.

3.2 Optical properties

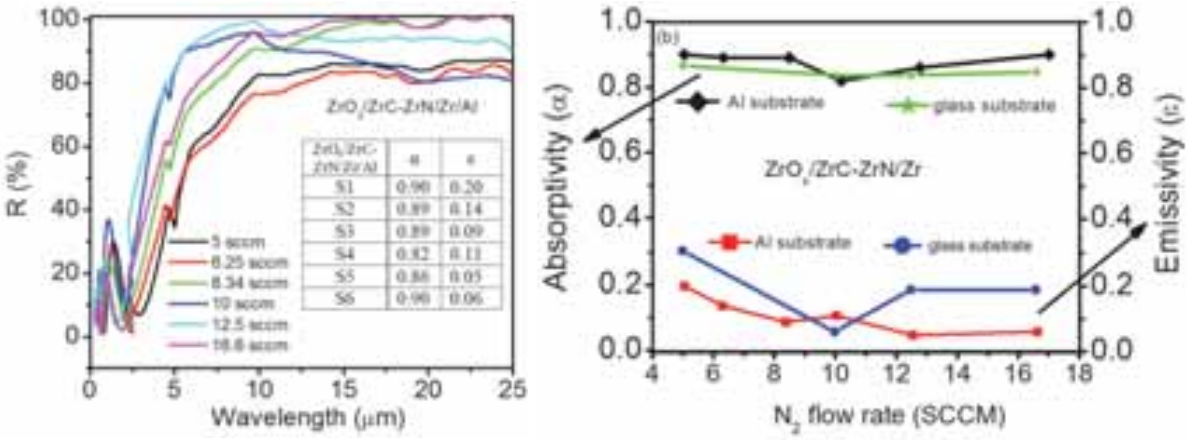

Fig. 2: (a) Reflectance spectra of absorber-reflector tandem selective coating deposited on aluminum substrate with varying nitrogen flow rate. **(b)** Calculated absorptance (α) and emittance (ε) values of absorber-reflector tandem structure selective coatings deposited on almunium and glass substrate.

The measured reflectance, as a function of wavelength, is plotted in Fig. 2(a) for ZrO_x/ZrC-ZrN/Zr absorber-reflector tandem structures on aluminum substrates in 0.2 – 25 μm range for different N_2 flow rates, used during synthesis. These reflectance measurments are used to calculate the absorptivity 'α' in ~ 0.3 – 2.5 μm range, and emissivity 'ε' in ~ 2.5 – 25 μm range, using Eq. (1) and (2);

$$\alpha = \frac{\int_{0.3}^{2.5} (1 - R(\lambda)) I_{sun}(\lambda) d\lambda}{\int_{0.3}^{2.5} I_{sun}(\lambda) d\lambda} \quad (1)$$

$$\varepsilon = \frac{\int_{2.5}^{25} (1 - R(\lambda)) E_b(\lambda) d\lambda}{\int_{2.5}^{25} E_b(\lambda) d\lambda} \quad (2)$$

Where $I_{sun}(\lambda)$ is ASTM G173-03 solar reference spectrum, AM1.5 and $E_b(\lambda)$ is the spectral radiance of a black body at temperature, T, and is given by Plank's law Eq. 3 (Duffie and Beckman, 1991) and R is the measured reflectance as a function wavelength. Here, Eq. 2 describes the emissivity against the total black-body radiation at given temperature T, which is defined as

$$E_b = \frac{C_1}{\lambda^5 [e^{C_2/\lambda T} - 1]} \quad (3)$$

Where $C_1 = 3.743 \times 10^{-16}$ W m^2 and $C_2 = 1.4387 \times 10^{-2}$ mK.

The measured values of α and ε are plotted in Fig. 2(b) as a function of different N_2 flow rates for both aluminum and glass substrates. The values of α and ε range from 0.86 – 0.90 and 0.05 – 0.14, respectively. The volumetric fraction of zirconium nitride strongly depends on the N_2 flow rates, and intermediate N_2 flow

rates produced optimal ZrN in ZrC-ZrN matrix structures. The absorber structure with maximum ZrN fraction showed optimal performance with absorptance ~ 0.86 and emittance ~ 0.05 for both substrates.

3.3 Thermal stability in air

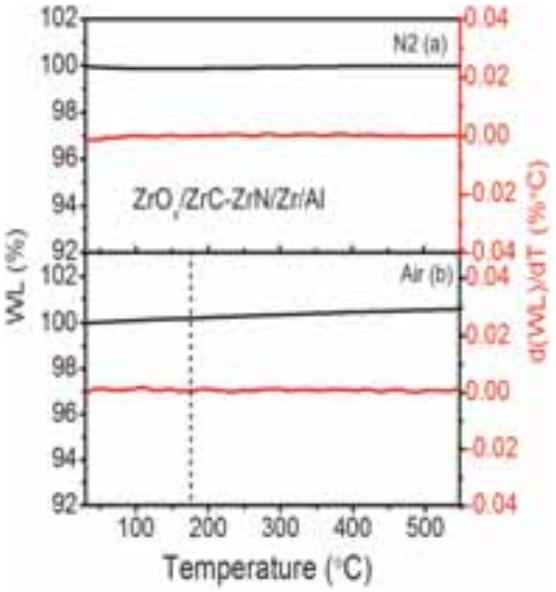

Fig. 3: Weight change percentage (WC %) versus temperature (°C) and differential of the weight change with temperature of ZrO_x/ZrC-ZrN/Zr absorber-reflector tandem selective structure deposited on aluminum substrate in (a) N_2 (b) air environment.

The ZrO_x/ZrC-ZrN/Zr absorber-reflector tandem selective structures were subjected to simultaneous thermal analysis (STA) measurements. The samples were heated upto 550 °C at a heating rate of 5 °C/min in nitrogen and air ambience. The measured weight change (WC) and differential weight change (d(WC)/dT) versus temperature are plotted in Fig. 3 for the best ZrO_x/ZrC-ZrN/Zr/Al sample with $\alpha \sim 0.86$ and $\varepsilon \sim 0.05$. These measurements did not exhibit any weight change under nitrogen ambience, whereas in air, weight gain started ~ 200 °C, as marked by dotted line in Fig. 3 (b). This weight gain was mainly due to oxidation of fabricated structures in air ambience, which was not observed in case of nitrogen ambience. These ZrO_x/ZrC-ZrN/Zr structures should be stable even at much higher temperatures, as Zr is the refractory material and ZrO_x top layer should avoid direct oxidation of underneath ZrC-ZrN absorber layer. Thus, another possibility for the observed weight change may be due to the oxidation of Al substrate itself. Such measurements were also carried out for ZrO_x/ZrC-ZrN/Zr structures on glass substrate and noticeable weight changes were not present at much higher temperatures, say 400 °C. Considering such degradation limit, ZrO_x/ZrC-ZrN/Zr structures with optimal solar performance $\alpha \sim 0.86$ and $\varepsilon \sim 0.05$ were subjected to the thermal cycling to 150 °C at 5 °C/min heating rate for 2 hours in air ambience to understand the thermal impact on solar performance. The X-ray diffraction patterns were recorded on these thermally treated samples and XRD graphs are plotted in Fig. 4 (a). The observed diffraction planes are in agreement with pristine samples with hexagonal zirconium nitride and zirconium carbide phases in conjunction with zirconium oxide mixed phases. These results suggest the robustness of ZrO_x/ZrC-ZrN/Zr absorber – reflector tandem structures against thermal impact. Surface microstructural degradations were investigated, for these ZrO_x/ZrC-ZrN/Zr heat treated structures, using SEM and AFM measurements and results are summarized in Fig. 4 (b) and (c). SEM micrographs, Fig. 4 (b), did not show any noticeable changes in surface morphology and are consistent with pristine samples, as shown in Fig. 2 (b). AFM measurements also substantiate the SEM results and the observed surface roughnesses are ~ 11.72 nm and ~ 17.85 nm for heat treated ZrO_x/ZrC-ZrN/Zr structures on aluminum and glass substrates. These roughness values are of the same order ~ 10.79 nm and ~ 17.20 nm for pristine ZrO_x/ZrC-ZrN/Zr structures on glass and aluminum substrates, respectively. These observations

suggest that ZrO_x/ZrC-ZrN/Zr structures are highly stable in the investigated temperature range and should have least impact on solar thermal properties.

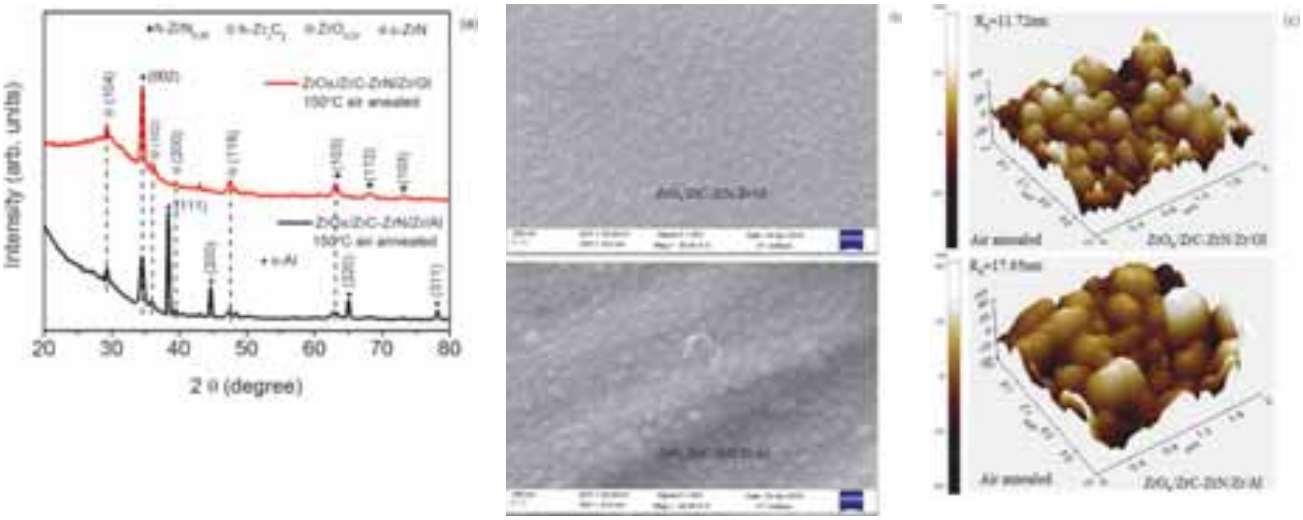

Fig. 4: (a) XRD graphs of air annealed ZrO_x/ZrC-ZrN/Zr absorber-reflector tandem selective structure deposited on glass and aluminum for 2h. **(b) & (c)** SEM and AFM images of air annealed ZrO_x/ZrC-ZrN/Zr absorber-reflector tandem selective structure deposited on glass and aluminum substrates for 2h.

The reflectance measurements were carried out for these ZrO_x/ZrC-ZrN/Zr heat treated samples in the entire 0.2 μm – 25 μm wavelength range and results are summarized in Fig. 5. The measured α and ε values are 0.82 and 0.09 as compared to 0.86 and 0.05 for pristine samples respectively. A small deviation in optical properties of these ZrO_x/ZrC-ZrN/Zr structures may be due to minor surface degradation, not noticeable in the present studies, suggesting insensitivity in the range of investigated temperature. This is in consistent with structural and microstructural measurements, where relatively no substantial changes were observed. These findings suggest that ZrO_x/ZrC-ZrN/Zr may be a good candidate for enhanced solar thermal performance and may exhibit long stability for low and medium temperature applications on glass and aluminum substrates.

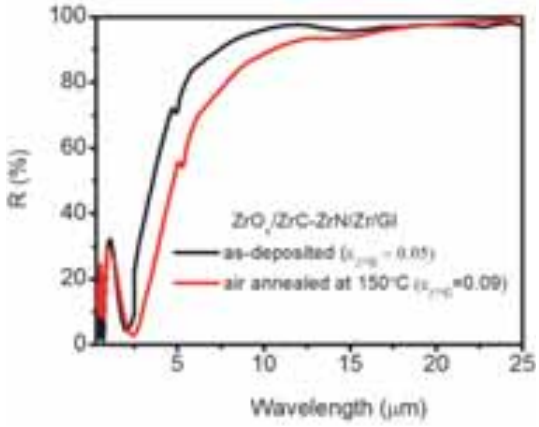

Fig. 5: Reflectance spectra of as-deposited and air annealed ZrO_x/ZrC-ZrN/Zr absorber-reflector tandem selective structure deposited on glass for 2h.

4. Conclusion

ZrO_x/ZrC-ZrN/Zr absorber-reflector tandem structures are optimized for both aluminum and glass substrates for optimal solar thermal performance by tailoring the zirconium nitride content in ZrC-ZrN absorbing layer. The intermediate nitrogen flow rate ~ 10 – 15 sccm has shown the best $\alpha \sim 0.86$ and $\varepsilon \sim 0.05$. The ZrO_x/ZrC-ZrN/Zr structures are stable in air upto ~ 150 °C without any noticeable degradation in their solar thermal performance as compared to pristine samples for both Al and glass substrates.

Acknowledgments

Authors acknowledge Ministry of New & Renewable Energy (MNRE), India through grant 15/40/2010-11/ST for financial support for the work

References

Bogaerts, W. F., and Lampert, C. M.**,** 1983. Materials for photothermal solar energy conversion, J. Mat. Sci. 18, 2847.

Barshilia, H.C., Selvakumar, N., Rajam, K.S., Biswas, A., 2008. Structure and optical properties of pulsed sputter deposited Cr_xO_y/Cr/Cr_2O_3 solar selective coatings, J. of Appl. Phys. 103, 023507(1)-023507(11).

Driver, P. M., 1981. An electrochemical approach to the characterization of black chrome selective surfaces, SEM 4**,** 1799.

Duffie, J.A., Beckman, W.A., 1991. Solar Engineering of Thermal Process, second ed. Wiley Interscience, New York.

Graf, W., Bruker, F., Kohl, M., Troscher, T., Wittwer, V., Herlitze, L., 1997. Development of large area sputtered solar absorber coatings, Journal of Non-Crystalline Solids 218, 380-387.

Holloway, P. H., Shanker, K., Pettit, R. B., and Sowell, R. R., 1980. Oxidation of electrodeposited black chrome selective solar absorber films, SAND-80-1045. Albuquerque, NM: Sandia National Laboratory.

Ignatiev, A., O'Neill, P., and Zajac, G., 1979. The surface microstructure -optical properties relationship in solar absorbers: black chrome, SEM **1,** 69.

Kalogirou, S. A., 2004. Solar Thermal Collectors and Applications, Progress in Energy and Combustion Science, 30, 231-295.

Kennedy, C., 2002. Review of Mid-To High-Temperature Solar Selective Absorber Materilas, NREL/CP-520-31267.

Koltun, M., Gukhman, G., Gavrilina, A., 1994. Stable selective coatings black nickel for solar collector surfaces, Sol. Energy Mater. Sol. Cells 33, 41-44.

Lazarov, M., Sizmann, R., Frei, U., 1993. Optimization of SiO2-TiN_xO_y-Cu interference absorbers, numerical and experimental results, SPIE 2017, 345-356.

Lampert, C. M., 1980, A chemical, structural, and optical characterization of a black chrome solar selective absorber, Ph.D. Thesis, Berkeley, CA: Lawrence Berkeley Laboratory.

McDonald, G. E., 1975. Spectral reflectance properties of black chrome for solar collector use, Sol. Energy, 17**,** 119.

Mekhilef, S., Saidur, R., Safari, A., 2011. A review on solar energy use in industries, Renewable and Sustainable Energy Reviews, 15, 1777-1790.

Selvakumar, N., Barshilia, H. C., 2012. Review of physical vapor deposition (PVD) spectrally selective coatings for mid- and high-temperature solar thermal applications, Sol. Energy Mater. Sol. Cells 98, 1-23.

Seraphin, B.O., 1997. Solar Energy Conversion: Solid State Physics Aspects: Topics in Applied Physics, Vol.31, Springer, Berlin.

Smith, G. B., McPhedran, R. C., and Derrick, G. H., 1985. Surface structure and the optical properties of black chrome, Appl. Phys. A, **36,** 193.

Sweet, J. N., Pettit, R. B., and Chamberlain, M. B., 1984. Optical modeling and aging characteristics of thermally stable black chrome, SEM, **10,** 251.

Sebastian, P.J., Quintana, J., Aliva, F., 1997. Retention of the high optical absorptance in thermally aged black chrome on variably sensitized Cu. Sol. Energy Mater. Sol. Cells 45, 65-74.

Selvakumar, N., Santhoshkumar, S., Basu, S., Biswas, A., Barshilia, H.C., 2013. Spectrally selective CrMoN/CrON tandem absorber for mid-temperature solar thermal applications, Sol. Energy Mater. Sol. Cells 106, 97-103.

Vannoni, C., Battisti, R., Drigo (Eds.), S., 2008. Potential for Solar Heat in Industrial Processes, IEA SHC Task 33 and Solar Paces-Task IV: Solar Heat for industrial Process.

Usmani, B., Vijay, V., Chibber, R., Dixit, A., 2015. Spectrally selective response of ZrO_x/ZrC-ZrN/Zr absorber-reflector tandem structures on stainless steel and copper substrates for high temperature solar thermal application, Sol. Energy, (Accepted)

Wackelgard, E., Hultmark, G., 1998. Industrially sputtered solar absorber surface, Sol. Energy mater. Sol. Cells 54, 165-170.

Zhang, Q.-C., 1998. Stainless-steel-AlN cermet selective surfaces deposited by direct current magnetron sputtering technology, Sol. Energy Mater. Sol. Cells 52, 95-106.

Zhang, Q.-C., Zhao, K., Zhang, B.-C., Wang, L.-F., Shen, Z.-L., Lu, D.-Q., Xie, D.-L., Zhou, Z.-J., Li, B.-F., 1998a. A cylindrical magnetron sputtering system for depositing metal-aluminium nitride cermet solar coatings onto batches of tubes, J. Vac. Sci. Technol. A 16, 628-632.

Zhang, Q.-C., Zhao, K., Zhang, B.-C., Wang, L.-F., Shen, Z.-L., Lu, D.-Q., Xie, D.-L., Zhou, Z.-J., Li, B.-F., 1998b. New cermet solar coatings for solar thermal electricity applications, Sol. Energy 64, 109-114

Conference Proceedings

Solar World Congress 2015
Daegu, Korea, 08 – 12 November 2015

Heat transfer in a porous absorber and in an insulated pipe for solar convective furnace system

Manish Sachdeva, Dheeraj Saini, Gajanand Saini and Laltu Chandra[1]

Indian Institute of Technology, Jodhpur (India)

[1]Correspondence: chandra@iitj.ac.in

Abstract

This paper deals with heat transfer analysis in sub-systems for a concept of solar convective furnace system. This system makes use of open volumetric air receiver for heat transfer to air, which is employed as working fluid. In this paper, experimental and numerical evaluation of transient heat transfer (a) in porous absorber and (b) in an insulated pipe is presented. This shows temperature development in absorber and the heating up of an insulated pipe with transport of hot air. Mathematical models to analyze one-dimensional heat transfer in porous absorber and insulated pipe are developed and solved using numerical techniques. The tool, thus developed, is validated using the corresponding experiments. Comparative analysis shows that the predicted and experimentally obtained transient temperature profiles are comparable for both these components. Variations of about 5-15% are observed between numerically and experimentally obtained values.

Keywords: *Absorber, insulated pipe, transient heat transfer, 1-D numerical analysis, experiment*

1. Introduction

In the concept of solar convective furnace the reflected radiation from a heliostat field is concentrated onto porous absorbers of an open volumetric air receiver (OVAR); see e.g. Hoffschmidt et al., 2003. The sucked atmospheric air through the pores of absorber extracts the generated heat from concentrated solar irradiance. The detailed design basis and evaluation of cylindrical absorber based OVAR is presented by Sharma et al, 2015a, 2015b. The obtained thermally mixed hot air at the OVAR outlet can be stored in thermal energy storage for various applications, like metal processing, see e.g. Patidar et al., 2015a, 2015b. The schematic of designed and installed solar air tower simulator (SATS) facility for evaluation of such a system is presented in Sharma et al. 2015a, 2015b. It is realized that the transfer of hot air through the piping system will result in its heating up-to the desired steady state. In other words, the piping system will attain thermal equilibrium with convected hot air for solar convective furnace system. Achieving this equilibrium state may take several hours, which is quite considerable. Besides, heat loss through insulation due to temperature difference between hot air and ambient starts with the operation of furnace system, Patidar et al., 2015a. This depends on pipe material and its thermal properties. Also, the increase in insulation temperature with time will enhance natural convective heat loss to ambient. It is to be emphasized that steady inlet temperature is desired process heat applications, like material processing. To reduce the required time for achieving steady-state, pre heating of sub-systems/components are required, see e.g., Vasiliev et al., 1987. In view of these observations following are presented in the paper:

a. Numerical and experimental evaluation of transient heat transfer in a porous absorber
b. Numerical and experimental evaluation of transient heat transfer from hot air to ambient in an insulated pipe.

Nomenclature

C_{pf}	*Specific Heat capacity of fluid (J/kgK)*	$\dot{Q}_{Nat.\ conv}$	*Rate of Natural Convective Heat transfer(W)*
C_{pins}	*Specific Heat capacity of insulation (J/kgK)*	$\dot{Q}_{stf}$	*Rate of Heat transfer from solid to fluid (W)*

doi:10.18086/swc.2015.04.03 Available at http://proceedings.ises.org

C_{ps}	Specific Heat capacity of pipe/absorber (J/kgK)	$\dot{Q}_{sti}$	Rate of heat transfer from solid to insulation (W)
D_a	Diameter of absorber(m)	r	radial coordinate of absorber/pipe
D_p	Diameter of each pore of absorber (m)	Ra	Rayleigh No.
$\dot{E}$	Electrical Power Input (W)	r_a	radius of absorber(m)
h_{ex}	Natural convective heat transfer coefficient(W/m^2K)	Re	Reynolds No.
h_f	heat transfer coefficient for internal heat transfer in fluid(W/m^2K)	r_p	radius of pore(m)
L	length of absorber (m)	r_{ins}	outer radius of insulation (m)
K_{ins}	Thermal conductivity of insulation(W/mK)	r_s	radius of solid pipe (m)
K_s	Thermal conductivity of pipe/absorber(W/mK)	t	time
n_p	no of pores	T	Temperature (K)
Nu_f	Nusselt number for fluid	T_a	Ambient Temperature (K)
Nu_{ex}	Nusselt number for natural convection	T_{inlet}	Temperature at inlet of absorber (K)
$\dot{m}_f$	mass flow rate(kg/s)	T_{ins}	Temperature of insulation (K)
Pr	Prandtl number	T_m	Mean Temperature of fluid (K)
$\dot{P}$	Power Transfer to pipe(W)	$T_{m,\,pipe\,inlet}$	Mean temperature of fluid at inlet of the pipe connecting the absorber
q''	heat flux on absorber radial surface (W/m^2)	$T_{m,\,pipe\,outlet}$	Mean temperature of fluid at the outlet of the pipe connecting the absorber
$\dot{Q}_{cond}$	Rate of Conductive Heat transfer (W)	T_{ra}	Temperature of air recirculating to the receiver(K)
$\dot{Q}_{fts}$	Rate of heat transfer from fluid to solid (W)	T_s	Temperature of pipe/absorber (K)
$\dot{Q}_{atp}$	Rate of heat loss to pipe from absorber during experiment (W)	z	z-coordinate (along pipe/absorber)

Greek Symbols

α_f	Thermal diffusivity of fluid (m^2/s)	ρ_{ins}	Density of insulation(kg/m^3)
α_{ins}	Thermal diffusivity of insulation (m^2/s)	ρ_s	Density of pipe/absorber (kg/m^3)
α_s	Thermal diffusivity of pipe/ absorber (m^2/s)	δ	Thickness of pipe (m)
$\emptyset$	porosity of absorber	Δl	Distance between any two thermocouples on insulation (m)

Abbreviations Used

OVAR	Open Volumetric air receiver	SATS	Solar Air tower Simulator
POA	Power on Aperture (W)	MFR	Mass flow rate (kg/s)

Subscripts Used

a	absorber/ambient	ins	insulation domain
avg	average	Inlet	Inlet of pipe/absorber
ex	external convection	p	Pores in absorber
f	fluid domain	s	solid domain
fd	fully developed length		

2. Transient heat transfer in porous absorber

As described, the developed concept of solar convective furnace concept is based on open volumetric air receiver (OVAR) (Fig. 1a), usually made of a ceramic or metal. The designed OVAR consists of cylindrical absorbers with circular porous and is made of brass (Fig. 1b). The thermal conductivity of brass is comparable to that of Silicon-carbide (SiC) in the considered temperature range. For more details refer to Sharma et al., 2015a, 2015b. Ambient air is heated to a high temperature as it flows through the circular pores. This unsteady process, eventually, leads to the desired steady state for given boundary conditions. Thus, to operate any process heat system based on such a receiver it is necessary to model the involved unsteady heat transfer process. For this purpose, both numerical and experimental evaluation of the designed circular pore based cylindrical absorber is presented in this section. The objective is to (a) develop an analysis tool and (b) understanding of the transient heat transfer process.

2.1 Mathematical model and numerical approach

For numerical analysis of a circular pore cylindrical absorber, the heat transfer process in porous absorber is mathematically modeled. The absorber is made of brass having thermal conductivity K_s~138W/mK. The involved modes are shown in Fig. 1c, which considers one-dimensional axial heat transfer in the pores with radial heat loss to ambient via insulation. During this process, air heats up to a higher temperature. This hot-air is utilized in a furnace and cooled to a temperature T_{ra}, which is higher than T_a. This relatively warm air is returned to OVAR through six injection ports that are marked G in Fig. 1a. The returned air gains heat from the absorber via external forced convection. A part of this air mixes with ambient and sucked through the pores of absorber. Thus, a fraction of the transferred heat to return air is reused. The return air system is not modeled in the presented analysis. This is obvious from the provided insulation around porous absorber as depicted in Fig. 1c. Further, the developed mathematical model assumes (a) uniform heat flux on the absorber surface exposed to electrical heating (b) volumetric heating owing to high thermal conductivity of brass (c) air as an ideal gas. Thus, the model simplifies the system into a one-dimensional heat transfer in solid, fluid and insulation domains. It should be emphasized that such a comprehensive tool will allow the first level analysis of new absorber designs.

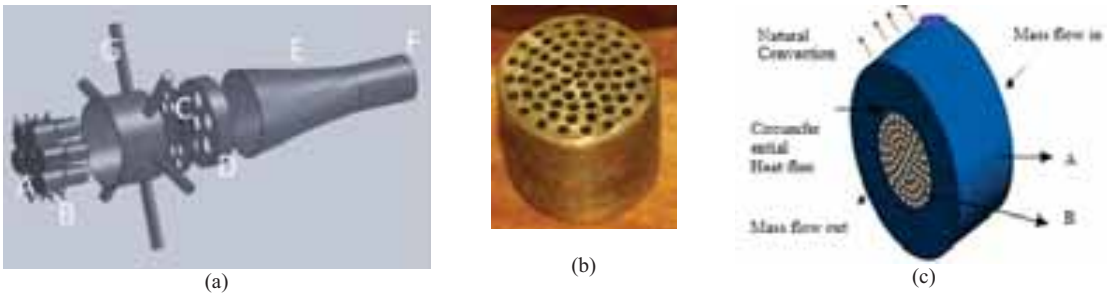

(a) (b) (c)

Fig. 1(a): Components of OVAR with A: Absorbers, B: Foot-piece, C: Anchor plate, D: mixer or perforated plate, E: Convergent nozzle, F: Outlet, G: Recirculating air injection ports, (b)Porous absorber of OVAR, (c) Porous absorber system model for numerical analysis with A:Insulation domain, B: Absorber(solid domain)

The model includes one-dimension conservation of energy equations in fluid, solid and insulation domains as in Eqn. 1-3. First-order explicit finite difference scheme is used for simultaneous l solution of the system of equations. Figure 2a and b depicts the control volume for fluid and solid domains. In the performed experiment Joule heating is applied to solid circumference of absorber that results in the desired volumetric heating. A small fraction of the input power conducted to the insulation and is finally lost to the ambient via natural convection (Fig 2d, e). The balance is transferred to ambient air via internal forced convection as shown Fig. 2b and c. The experimental parameters are presented in Table 1. The selected parameters are based on Sharma et al., 2015a and 2015b. The CFL condition (Anderson, 1995; Patankar, 1980) allows maximum time step of 0.13 ms for the considered final grid, which is obtained based on a grid dependence study. However, a smaller time step of 0.1 ms is selected for numerical heat transfer analysis. The length of absorber pore is 25.4 mm. The flow inside each pore is Laminar with Re ~ 102 and the corresponding Nusselt number for fully developed flow is 4.36 (Cengel, 2011; Incropera & DeWitt, 1996; White, 1998). However, the length of the absorber is of the order of its entry length, therefore, the Nusselt number for fully developed flow is modified using Eqn. 4, Subbarao, 2015.

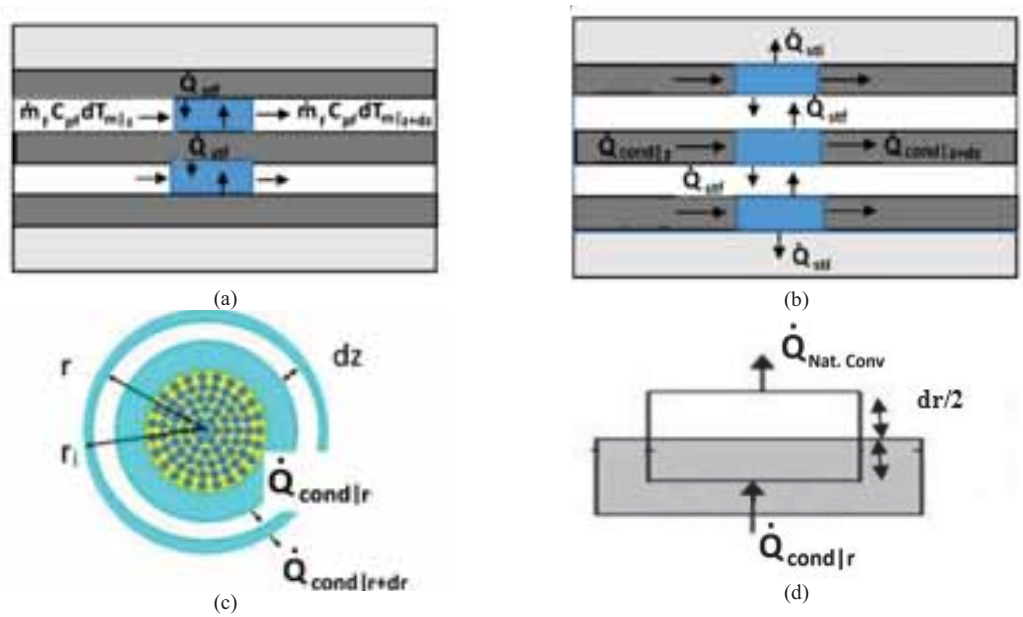

Figure 2: (a ,b)Control Volume for fluid and solid domain and (c, d) Control volume for insulation domain and its outer boundary condition

Solid:

$$\frac{\partial^2 T_s}{\partial z^2} - \frac{2h_f n_p r_p (T_s - T_m)}{K_s r_a^2 (1-\emptyset)} + \frac{2q''}{K_s r_a (1-\emptyset)} - \frac{2K_{ins}}{K_s r_a (1-\emptyset)} \frac{\partial T_{ins}}{\partial r}_{(r=r_a)} = \frac{1}{\alpha_s} \frac{\partial T_s}{\partial t} \quad \text{(eq. 1)}$$

Fluid:

$$\dot{m}_f \frac{\partial c_{pf} T_m}{\partial z} = 2\pi r_p n_p h_f (T_s - T_m) \quad \text{(eq. 2)}$$

Insulation:

$$\frac{\partial^2 T_{ins}}{\partial r^2} + \frac{1}{r} \frac{\partial T_{ins}}{\partial r} = \frac{1}{\alpha_{ins}} \frac{\partial T_{ins}}{\partial t} \quad \text{(eq. 3)}$$

The required heat transfer coefficient is estimated as follows:

$$Nu_f = 4.36 + \frac{0.086 (Re\ \mathrm{Pr} \frac{D}{L})^{133}}{1 + 0.1 Pr (Re \frac{D}{L})^{0.83}} \qquad 0.7 < \mathrm{Pr} < 7,\ \mathrm{Re} < 2300 \quad \text{(eq. 4)}$$

$$h_f = \frac{Nu_f k_f}{2r_p} \quad \text{(eq. 5)}$$

The initial and boundary conditions are as follows:

a. Initial condition: $T_{m.\ s.\ ins}(z = 0, t = 0) = 302.5K$
b. Inlet: $T_m(z = 0, t) = 305.7\mathrm{K}$, $\dot{m} = 0.00003\ kg/s$;
c. Insulated axial solid boundaries: $\frac{\partial T_s}{\partial z}\Big\}_{z=0.\ L\ and \forall t} = 0$
d. Solid-insulation interface: $T_s = T_{ins|r=r_s}$
e. External insulation surface: Natural convective heat loss is depicted as:

$$\frac{1}{r_{ins}} \frac{\partial T_{ins}}{\partial r}_{(r=r_{ins})} + \frac{h_{ex} (T_{ins(r=r_i)} - T_a)}{K_{ins} r_{ins}} = \frac{1}{2\alpha_{ins}} \frac{\partial T_{ins}}{\partial t}_{(r=r_{ins})} \quad \text{(eq. 6)}$$

Where h_{ex} is calculated using the following correlation for natural convection:

$$Nu_{ex} = \left[0.6 + \frac{0.387 Ra^{1/6}}{\left[1 + (0.559/Pr)^{4/9}\right]^{8/27}} \right]^2 \quad \text{(eq. 7)}$$

$$h_{ex} = \frac{Nu_{ex} K_f}{2r_{ins}} \quad \text{(eq. 8)}$$

2.2 Experimental set-up

Experiment is performed for validation of the developed transient tool for heat transfer in porous absorber. The schematic of experimental set-up is shown in Fig. 3a. Air is blown into a steel pipe with outer diameter (D) of 25.4 mm and length (L) of 24D. At the outlet of pipe an absorber is fitted, which is electrically heated by externally wrapped Nichrome wire, see Fig. 2a & b. The experimental absorber is made of brass with porosity ~52 percent (83 pores of diameter (D_p)=2mm), length (L_a) and diameter (D_a) of 25.4 mm. Pipe and absorber are insulated using ceramic wool for reducing heat loss to ambient as shown in Fig. 3a and 3b. The input power is controlled by varying voltage using an auto-transformer and mass-flow-rate of air is maintained using a flow control valve. Temperature is measured using the calibrated K-type thermocouples with uncertainty of about 1-2%. Data from thermocouples is recorded and stored in real-time using NI-WSN gateway data acquisition (DAQ) device. The temperatures were measured at various azimuthal and radial positions as depicted in Fig. 3c at the inlet and outlet of the absorber.

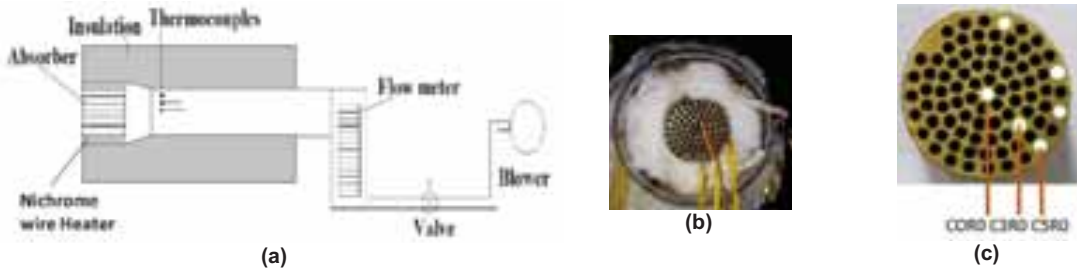

Figure 3: (a) Schematic of experiment set-up, (b): Front view of absorber with insulated , (c): Position of thermocouples on absorber

Table 1 shows the experimental parameters for the absorber. A part of the applied power to absorber is transferred to the connecting pipe via conduction. This heats up the air inside the pipe leading to an increase in temperature at the absorber inlet from 302.5 - 312K in 500 seconds. Thus, for validation of the developed numerical tool a time averaged inlet temperature of 305.7 K is used at the inlet. The net power input after subtracting the transfer to pipe as in Eqn. 9, is applied to absorber for this purpose. Thermocouples at various axial positions on the surface of insulation are mounted to estimate the rate of heat loss to ambient according to the second term on RHS of Eqn. 9. Also, thermocouples located on various radial positions at the pipe inlet and outlet are used to estimate mean air temperature at these positions, required for estimating the first term on RHS of Eqn. 9. An overall uncertainty of up-to 10% is attributed to (a) input power variation (b) temperature and mass flow rate measurements (c) manual operation and variable ambient conditions. Further, the numerical tool is designed to solve the equations with constant as well as variable fluid properties. For variable property the best fit curves are considered (Ekanayke, 2015; Boutelop, 2015). The properties of insulation and absorber materials are considered as constants. These are defined as average values in temperature range of 300-600K to cover the expected experimental conditions.

Tab. 1: Experimental and computational parameters for absorber

Parameter	Value	Parameter	Value
Mass Flow Rate	0.0003 *kg/s*	Power transfer to pipe ($\dot{P}$)	1.25 W
Reynolds Number	102	Net power input ($\dot{E}$- $\dot{P}$)	19.65 W
Current	1.95 ±0.05A	T_{inlet}	302.5 – 312 K
Resistance	5.5 ±0.1 Ω	$T_{inlet,\ time\ averaged}$	305.7 K
Electrical Power Input ($\dot{E}$)	20.9 W	Equivalent Radiative Heat Flux	20 kW/m2
Effective POA/MFR	65.5 kW/kg/s	Equivalent concentration (suns)	80 Suns
$K_{s,avg.}$	138.7W/mK	$Cp_{s,\ avg}$	0.413 kJ/kgK
$\alpha_{f,\ avg}$	19.9 m^2/s	$Cp_{f,\ avg}$	1.009 kJ/kgK

$$\dot{Q}_{atp} = \dot{m}_f c_{pf,}\left(T_{m,pipe\ outlet} - T_{m,pipe\ inlet}\right) + \Sigma h_{ex} 2\pi r_{ins} \Delta l (T_{ins} - T_a) \quad \text{(eq. 9)}$$

2.3 Results

Figure 4a shows the transient variation of temperature in pores located at different radial positions as shown in Fig. 3c. It is observed that the temperature development is practically comparable at all these three locations with a variation of about ±1˚C. This confirms the assumption that heat is uniformly distributed throughout the solid and that the bulk fluid temperature is, practically, comparable. This situation will be different including air return system in which radial variation of fluid temperature is expected as shown in Sharma et al., 2015a, 2015b. Thus the code will be extended in the near future including this effect as well. A

comparison between the numerically analyzed bulk-mean and measured air temperature with respect to time is shown in Fig. 4b. The maximum difference of ~ 10% is observed between these values. For simulation both constant and temperature dependent air properties are used. Thus, it can be safely stated that such a tool will be extremely useful for predicting unsteady heat transfer process in absorber for process heat application.

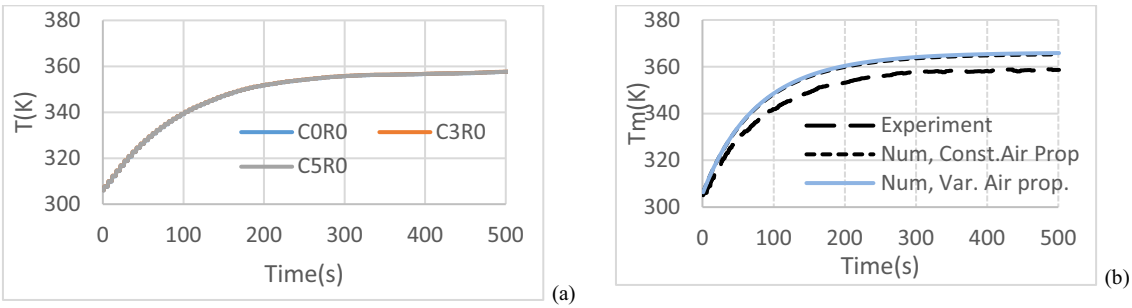

Figure 4 : (a)Variation in temperature between different absorber pores as observed in the experiment (b): Comparison between 1-D and measured bulk-mean air temperature with time

3. Heat transfer in an insulated pipe

As described, hot air is transported in an insulated pipe to thermal energy storage for its use in, for example, solar convective furnace to achieve steady state. Attaining the desired steady state will be influenced by (a) heating up of the piping network and (b) heat loss to ambient via insulation from hot air. Thus, understanding and development of a transient analysis tool will support the operation of such a system. For this purpose, a one-dimensional heat transfer model is developed and validated with the performed experiment under the same conditions.

3.1 Numerical approach

For the development of one-dimensional tool, the insulated piping system with air-flow is represented using three domains, namely, fluid (air), solid (pipe) and insulation. The control volumes for each domain are shown in Fig. 5a, b and d. The derived energy equations in each domain are solved, simultaneously, using a numerical scheme. The hot fluid entering the pipe loses heat to the solid (pipe material) and finally to ambient via insulation with external natural convection. Further, the solid domain loses heat to the ambient via natural convection at its axial boundary ($z=0,\ L$), the control volume of which is shown in Fig. 5c. For fluid domain, instantaneous mass-weighted average temperature equation is derived ignoring storage as heat is convected. For the solid domain, the conduction in the radial direction is neglected considering small pipe thickness in comparison to the pipe length. For insulation domain, heat transfer in radial direction is considered on account of a lower thermal resistance at its radial boundary in comparison to axial boundary as a result of higher surface area for convective losses.

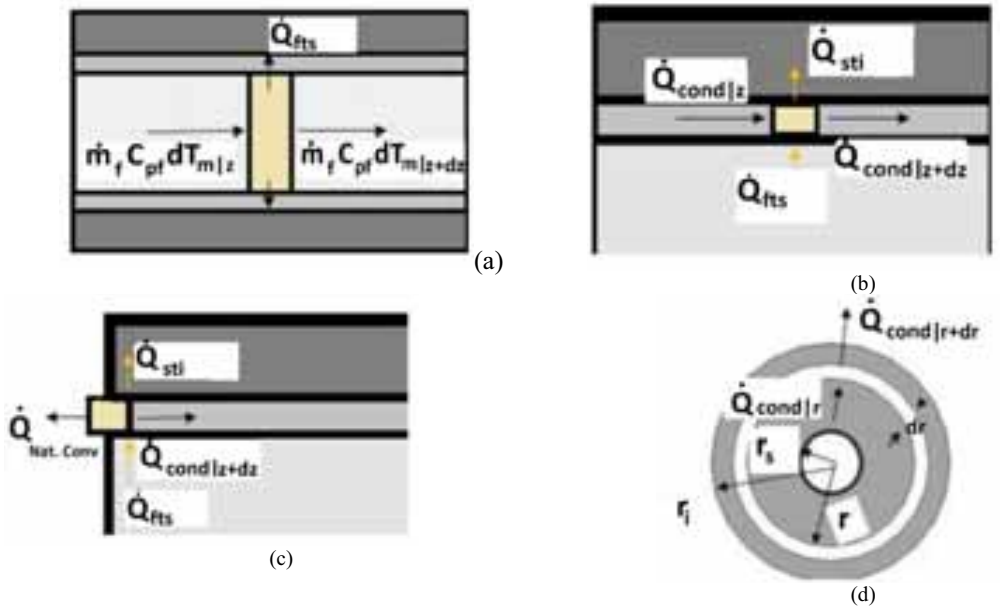

Figure 5 (a, b, d): Control volume of fluid, solid and insulation domain, (c): Control Volume for boundary conditions(z=0,L) for solid domain

Energy equations in solid (pipe), fluid and insulation domains are given by Eqn. 10, 11 and 12, respectively. The partial differential equations are solved with first-order accuracy. Explicit forward-difference-scheme with uniformly spaced grid points in fluid and solid pipe domain is employed for discretization. Corresponding CFL conditions (Patankar, 1980; Anderson, 1995) are satisfied in each domain for the considered mesh sizes and time steps. Average values of material properties, like thermal conductivity, density, viscosity, etc. in the temperature range was considered and assumed to be constant. This is acceptable for the performed experiment with limited temperature range. However, the tool will be generalized with variable fluid properties at the next step, once validated.

Solid (Pipe) Domain:

$$\frac{\partial^2 T_s}{\partial z^2} + \frac{h_f(T_m - T_s)}{K_s \delta} + \frac{K_{ins}}{K_s \delta} \frac{\partial T_{ins}}{\partial r}_{(r=r_s+\delta)} = \frac{1}{\alpha_s} \frac{\partial T_s}{\partial t} \quad \text{(eq. 10)}$$

Fluid Domain (instantaneous):

$$\frac{\partial T_m}{\partial z} = -\left(\frac{2\pi r_s h_f}{\dot{m}_f c_{pf}}\right)(T_m - T_s) \quad \text{(eq. 11)}$$

Insulation:

$$\frac{\partial^2 T_{ins}}{\partial r^2} + \frac{1}{r}\frac{\partial T_{ins}}{\partial r} = \frac{1}{\alpha_{ins}} \frac{\partial T_{ins}}{\partial t} \quad \text{(eq. 12)}$$

The boundary and initial conditions are as follows:

a. The inlet temp of fluid : $T_m(z = 0, t) = 400\text{K}$
b. Initially the solid pipe and insulation domain are at ambient temperature:
   $\therefore T_s(z, t = 0) = T_{amb} = T_{ins}(r, z, t = 0)$
c. Natural convection boundary condition at axial boundaries for solid domain i.e. z=0 and z=l represented by equation 10.

$$\frac{\partial}{dz}\left|(-1)^n (K_s 2\pi r\delta)\frac{\partial T_s}{dz}\right|_{z=0,L} + h_f 2\pi r(T_m - T_s) + K_{ins} 2\pi r \frac{\partial T_{ins}}{dr}_{(r=r_s+\delta)} + h_{ex} 2\pi r\delta(T_s - T_a) = 2\pi r(\delta)\rho_s C_{ps}\frac{\partial T_s}{dt} \quad \text{(eq. 13)}$$

Here, n= 1 if z=0 & n= 2 if z= L and h_{ex} is estimated using the following Nu correlation

d. Natural convection boundary condition at radial boundary of the insulation domain while axial boundaries are assumed to be insulated similar to absorber as shown in Eqn. 6

Dittus-Boelter correlation (Cengel, 2011) for internal air-flow is used for estimation of heat transfer coefficient in fully developed region as in Eqn. 14. This is modified in the entry length region using Eqn. 15. Natural convection based heat loss coefficient to ambient from the exposed solid and insulation surfaces is estimated through Rayleigh number using Eqn. 17. Equations 16 and 18 represent the heat transfer coefficient relationship with corresponding Nusselt no and characteristic length for internal and external flow respectively.

$$Nu_{f,fd} = 0.027 * Re^{0.8} Pr^{\frac{1}{3}} \quad \text{(eq. 14)}$$

$$\frac{Nu_f}{Nu_{f,fd}} = \left(\frac{x}{2r_s}\right)^{-0.0054} \quad \text{(eq. 15)}$$

$$h_f = \frac{Nu_f k_f}{2r_s} \quad \text{(eq. 16)}$$

$$Nu_{ex} = \left[0.6 + \frac{0.387 Ra^{1/6}}{\left[1 + \left(^{0.559}/_{Pr}\right)^{4/9}\right]^{8/27}}\right]^2 \quad \text{(eq. 17)}$$

$$h_{ex} = \frac{Nu_{ex} k_f}{2\delta} \quad \text{(eq. 18)}$$

3.2 Experimental set-up

The designed and installed experimental set-up and its schematic are shown in Fig. 6a & 6b. In this experiment, to achieve a constant high temperature at the pipe inlet (*z=0)*, a heating element is designed. Heating element is a separate steel-pipe of 25.4 mm diameter in which three porous bodies (absorbers) are fitted at different axial locations. Their purpose is to allow effective heat transfer to air as well as thermal mixing. A Nichrome wire of 0.25 mm diameter is wrapped on external pipe surface for additional Joule heating. Needless to say, the porous bodies will introduce extra pressure drop, which is not of primary concern for the present purpose. Thus, in experiments, at the outlet of heating element air stream at uniform temperature is obtained. It requires sometime to achieve the steady value in the heating element. Therefore, it is bypassed through a valve into atmosphere. Once the steady air temperature is reached the inlet valve of main pipe is opened and atmospheric bypass valve is closed. In this way at the main pipe inlet of 53.6 mm diameter a constant temperature boundary condition is maintained throughout the experiment. Calibrated thermocouples are mounted inside and on the surface of 0.7 m long insulated main pipe at several axial and radial positions, see Fig. 6c. Temperature of pipe and insulation is also recorded using NI DAQ device. Table 2 presents the input parameters for the experiment conducted for code validation. For a fixed mass flow rate inlet, hot wire anemometer was used to measure the velocity at a reference temperature of 30 ˚C. Radius of Insulation greater than the critical radius of insulation (~53.6 mm) was chosen for validation (Incropera, 1996; White, 1998; Holman, 1997). An uncertainty of ~5-10% is attributed to fluctuations in ambient temperature, power and error in measuring the temperature via thermocouples.

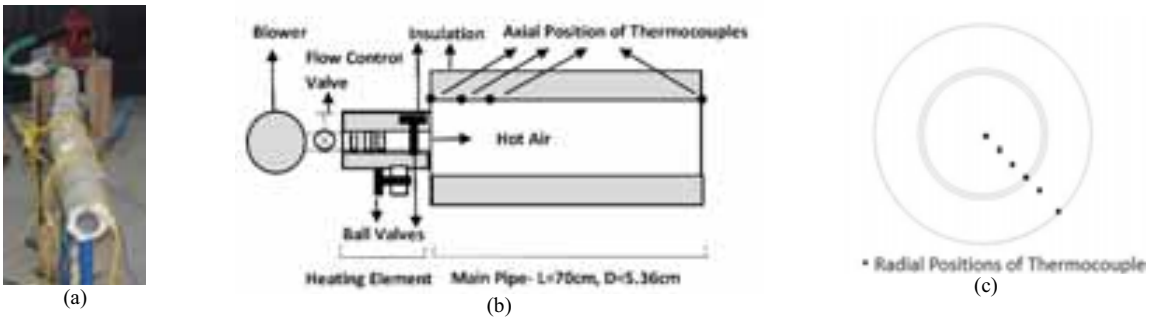

(a) (b) (c)

Figure 6: (a, b) Experimental set-up and its schematic; (c) Position of Thermocouples

Tab. 2: Experiment Input Parameters for pipe

Parameter	Value
Avg. Mass Flow Rate	0.005 kg/s
Velocity	2.2 ±0.1m/s at 304K
Current for electrically heating the absorbers	3.15 ±0.05A
Resistance	62.5 ±0.1 ohm
Reynolds Number	4707
$T_{m \text{ at } z=0}$	400± 2 K
$T_{s \text{ at } z=0=t}$	314± 1 K

3.3 Results

Constant air temperature boundary condition at the main-pipe inlet ($T_{m \text{ at } z=0}$ = 400 K) with mass flow rate of ~0.005 kg/s is imposed on in both experiment and numerical analysis. A comparison between unsteady heat transfer experiment and 1-D numerical analyzed data for hot-air flow in the insulated pipe is shown in Fig. 7a, b and c. These are for bulk or mean temperature of air, solid (pipe) at the outlet and for insulation at the inlet and outlet over time. Generally, higher air temperatures are estimated numerically in comparison to experiment. The temperature differences of solid at the pipe inlet and outlet in Fig. 7b indicate a better correlation for heat loss is required within the thermal entry length. However, the general trend of temperature development is captured adequately. Figure 7c depicts that the code under-predicts the losses to the ambient as a result of under-prediction of insulation temperature. This is consistent with the over-predicted temperatures of solid and fluid at the outlet. The maximum differences between numerically and experimentally obtained values are ~5-15%. Therefore, it is expected that this tool will be helpful in analyzing and predicting unsteady heat transfer in a piping network for furnace system. (Patidar et al, 201b).

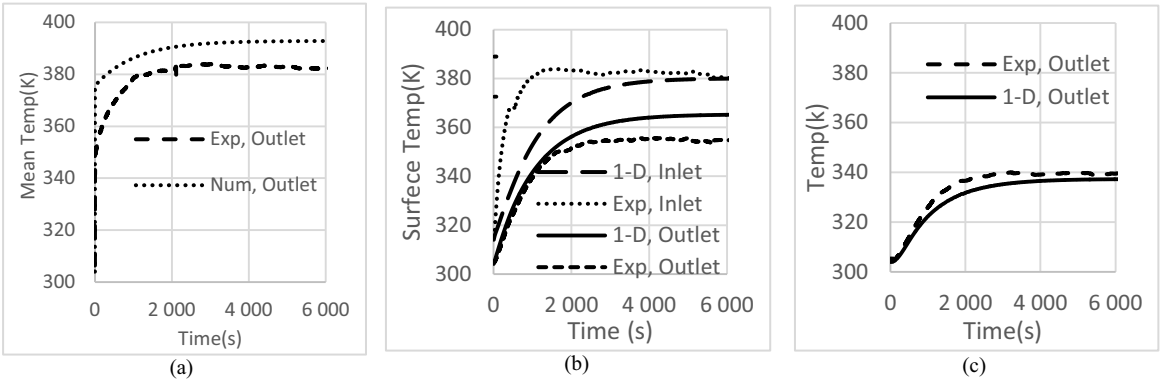

Fig7: Comparison between 1-D analysis and experiment for fluid (a), solid pipe (b) and insulation (c) domains.

4. Conclusion

The paper deals with the development of validated mathematical models for unsteady heat transfer analysis in a porous absorber and of an insulated pipe. These are sub-systems for a solar convective furnace. The developed tool has its application in designing receiver and piping network of a solar convective furnace system. For developing this system level tool one-dimensional modeling approach of the considered sub-systems/components, like, porous absorber and insulated pipe is considered. For solving these equations a first-order accurate explicit numerical scheme is utilized. Experiments are performed for validation of the adopted model and numerical method. The comparison between experiment and numerically analyzed data, namely, air, solid and insulation temperatures reveal a variation of about 5-15%. This is expected as the modeling is limited to one-dimension and utilizes simplified experimental correlations. However, even with these known limitations, it can be safely stated that such a tool will be extremely valuable in predicting performance of the desired solar convective furnace system.

5. References

Anderson Jr., J. D., 1995. Computational fluid dynamics: the basics with applications, McGraw Hill Inc.

Bouteloup P., 2015 September 1, http://bouteloup.pierre.free.fr/lica/phythe/don/air/air_nu_plot.pdf

Cengel Y.A., 2011. Heat and Mass Transfer, Fourth Edition, McGraw Hill Inc.

Hoffschmidt B., Téllez F. M., Valverde A., Fernández J., Fernández V., 2003. Performance evaluation of the 200-kWth HiTREC-II open volumetric air receiver. Journal of Solar Energy Engineering, 125, pp. 87–94.

Holman J.P., 1997. Heat Transfer, eighth ed., McGraw-Hill Publishers, New York, pp. 38–39.

Ekanayke P. 2015 September 1. ninova.itu.edu.tr/tr/dersler/ucak-uzay-fakultesi/965/uck.../ekkaynaklar

Incropera F.P., DeWitt D.P., 1996. Introduction to heat transfer, third ed., John Wiley Publ., New York, pp. 93–99.

Material Properties, 2015 September 1, http://www.engineeringtoolbox.com

Patankar S.V., 1980. Numerical Heat Transfer and Fluid Flow, McGraw Hill Book Company

Patidar D., Tiwari S, Sharma P, Chandra L, Shekhar R, 2015a. Open volumetric air receiver based solar convective aluminum heat treatment furnace system, Energy Proc. 69, pp. 506-517.

Patidar D., Tiwari S., Sharma P., Pardeshi R., Chandra L., Shekhar R., 2015b. Solar convective furnace for metals processing, JOM, pp. 9 pages, DOI: 10.1007/s11837-015-1633-z.

Sharma P., Sarma R., Chandra L., Shekhar R., Ghoshdastidar P. S., 2015a. Solar tower based aluminum heat treatment system: Part I. Design and evaluation of an open volumetric air receiver, Solar Energy, 211, pp. 135-150.

Sharma P., Sarma R., Chandra L., Shekhar R., Ghoshdastidar P. S., 2015b. On the design and evaluation of open volumetric air receiver for process heat applications, Solar Energy, doi:10.1016/j.solener.2015.05.027.

Subbarao P.M., 2015 September 1,http://web.iitd.ac.in/~pmvs/courses/mel242/mel242-27.ppt

Vasiliev L.L, Kiselev V. G, Matveev Yu N., Molodkin F.F., 1987 Heat Pipe Heat Exchangers, Nauka Technica, Minsk, (in Russian).

White F M, 1998.Fluid Mechanics, Fourth Edition, WCB McGraw-Hill

Conference Proceedings

Solar World Congress 2015
Daegu, Korea, 08 – 12 November 2015

Experimental Set-up for Investigation of Air-Flow and Dust Deposition in Heliostat Field: Design and Evaluation

Nibodh Boddupalli, Navneet Kumar Yadav and Laltu Chandra[1]

Indian Institute of Technology Jodhpur, Jodhpur (India)

[1]Correspondence author: chandra@iitj.ac.in

Abstract

In this paper, design and evaluation of an experimental setup for analyzing air-flow and to understand dust deposition on heliostats in a field-layout is presented. For this purpose, a heliostat field is designed and air-flow is investigated for the selected staggered arrangement of heliostats. The evaluation clearly revealed the presence of flow separation and wake behind an inclined heliostat models. Such complex flow field will affect dust deposition on heliostat and may even induce vibration. Hence, experimentation would be necessary to investigate the flow field in these regions. The developed experimental set-up based on detailed flow analysis will be useful for understanding the dust deposition and wake induced vibration of heliostats in field layout.

Keywords: *Experimental Set-up Design, Dust Deposition, Heliostat Field, LDV, CFD, RANS & LES*

1. Introduction

Depleting conventional sources of non-renewable energy has been one of the key reasons for research into alternate sources of energy like solar energy. There are different methods to harness solar energy. One of them is concentrated solar thermal power (CSP) which uses reflectors to focus solar radiation onto a receiver that transfers the received heat to a heat transfer fluid. One of the CSP technologies is heliostat based central power tower. The heliostats collectively focus incident sunlight onto a central receiver. On account of high concentration, temperature of the order of 1000 °C is achievable. This heat can be employed for process heat and power generation. Desert regions, like, Rajasthan receive high solar irradiation (~ 6-7 kW.hr/m^2/day) and are well suited for such a technology. However, dust poses a serious challenge in operating such a system (Gupta, 1986). High wind speed in such regions initiates saltation process (Singh et al., 2015). The lifted dust particles are carried by wind. When this wind blows over a field of heliostats, the particles get deposited on heliostats. The dust deposition reduces the reflectivity of heliostats (Niknia et al., 2012). This reduction lowers the overall heat recovery and, therefore, efficiency of the CSP plant. Therefore, if a parameter describing such a loss could be considered while designing the field itself, it would enable operating a plant under the desired condition.

With the importance of this aspect in mind, Yadav et al. (2014) investigated dust deposition on single and multiple aligned heliostat models in a wind tunnel at a Reynolds number of 60,000. The k-ε based Reynolds Averaged Navier-Stokes (RANS) approach was used for simulation. Further, flow measurement was performed around a heliostat using laser Doppler velocimetry technique. It was observed that the calculated time-averaged flow features are captured upstream and not reproduced downstream of the heliostat model with flow separation for an inclination angle of 25° with respect to horizontal surface. It was also observed that the wake region further downstream is adequately captured. Further, this investigation revealed that non-uniform or even localized dust deposition on heliostat is possible under certain condition. Localized deposition can be mitigated by cleaning effect, if predicted appropriately with a numerical tool. This investigation indicated the need for an improved modelling for analyzing air-flow around heliostats in a field layout, especially, in the flow separation region. However, it was insufficient for evaluating dust deposition on heliostats in a staggered arrangement, which is commonly employed (Falcone, 1986; Lipps and Vant-Hull, 1978; Vittitoe and Biggs, 1981). Considering these limitations, the presented paper aims at designing an experimental setup to understand the air-flow around heliostats in a field-type layout. For this purpose a step-wise strategy is adopted. The first step is a field design to simulate flow pattern around 1:10 scale-down heliostat models placed in staggered manner. For this purpose, geometric similarity of heliostat and field arrangement is adopted. In second step, different numbers of model heliostats, like, 3, 5, and 7 are organized in staggered fashion for a particular height of tower

doi:10.18086/swc.2015.04.04 Available at http://proceedings.ises.org

and latitude of location, which is Jodhpur based on the maximum elevation angle. In next step, detailed flow analysis is carried out using RANS approach to design an experimental set-up, which is capable of simulating a free-flow condition. Finally, Large Eddy Simulation (LES) is performed to understand, especially, the near-wake region behind a heliostat, which is not captured appropriately with RANS model. These steps are presented in the subsequent sections.

2. Field Design

As the starting point, a heliostat field is designed for Jodhpur (altitude ~ 26°) with 1m x 1m reflecting plate and 10m central tower height using Matlab code based on the mirror density criterion by Siala and Elayeb (2001) (see Fig. 1). This field design is intended for an indigenously developed open volumetric air receiver based 100kWth equivalent solar convective furnace system (Singh et al., 2015). In the Fig.1, heliostats are represented by circles. The diameter of the circles is equal to the diagonal of the heliostat. The designed field is extended up-to 30m in radius and span of 90°. The field consists of heliostats arranged in essential and staggered rows based on a no-blocking condition referred to by Siala and Elayeb (2001). The rows of heliostats are distributed radially into groups as shown in Fig. 1. These differ in their azimuthal and radial spacing. Rows of one group have equal azimuthal angular spacing between adjacent heliostats. It is to be noted that air-flow pattern depends on the positions, angular orientation and elevation of heliostats. The elevation and azimuthal angles are calculated (Xiudong et al., 2007) that vary with time and day. This yielded a maximum value of 65° throughout the year for 22nd of December. The designed field with the maximum elevation angle of 65° is scaled down geometrically for 1:10th size of the considered heliostats. The distances between heliostats are provided in Table 2. For flow similarity, the Reynolds number is to be maintained between actual and scaled-down heliostat models. The Re of the flow on the actual heliostat on a typical day in Jodhpur with an average of 7 m/s is ~ 421,000. To maintain Re with model-heliostat, the free stream air velocity ~ 70 m/s is required. Therefore, in future, attempts will be made to perform experiments with water at reduced velocity. The presented experimental set-up is designed for a free-stream air velocity up-to 20 m/s, which corresponds to Re ~ 132,000.

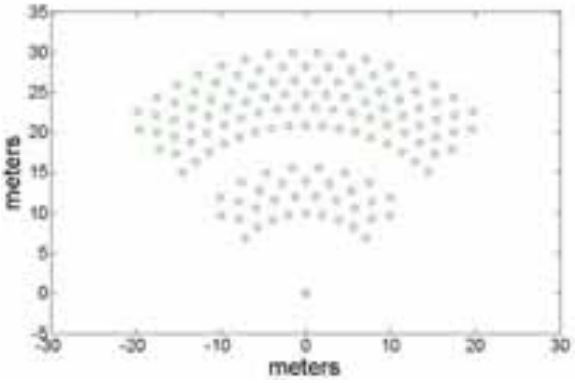

Fig. 1: Designed heliostat field

Tab. 1: Field specifications

Size of Heliostat	1 x 1 m2
Number of Heliostats	139
Tower Height	10 m
Maximum radius	30 m

Tab. 2: Scaled down distances

Between adjacent heliostats (cm)	Between rows of heliostats (cm)
20	Minimum - 17.3
	Maximum - 22.1

3. Computational Fluid Dynamics (CFD) analysis

Yadav et al. (2014) observed higher dust deposition on heliostats encountering the free stream air compared to those in the wake of preceding heliostats. The relative positioning of aligned heliostats also affected dust deposition on the aft heliostats. Following design considerations are made for experimental set-up:

a. Height and width should allow free-stream flow development from heliostat surfaces

b. The length is sufficient to allow far-wake development, indicated by a uniform velocity.

Computational Fluid Dynamics is employed to numerically solve equations of fluid flow around heliostats. The two CFD methodologies are used considering time-averaged and unsteady flow features:

3.1. Reynolds Averaged Navier-Stokes (RANS) approach

For RANS simulation, based on previous investigations, the standard two-equation k-ε model proposed by Launder and Spalding (1972) is used. This is a semi-empirical model in which turbulence kinetic energy k and

its dissipation rate ε are analyzed using their transport equations. These additional equations are solved simultaneously with governing equations of mean velocity and pressure (Kuzmin and Mierka, 2006; Furbo, 2010) for incompressible flow:

$$\nabla \bullet \overline{u} = 0 \tag{1}$$

$$\frac{\partial \overline{u}}{\partial t} + \overline{u} \bullet \nabla \overline{u} = -\nabla \overline{p} + \nabla \bullet \left(\left(\nu + \nu_T \right) \left[\nabla \overline{u} + \nabla \overline{u}^T \right] \right) \tag{2}$$

Where, ν and ν_T are molecular and turbulent eddy kinematic viscosity, respectively. The statistical eddy viscosity models the effect of unresolved velocity fluctuations in mixing. In the standard k-ε model, it is calculated by $\nu_T = C_\mu k^2 / \varepsilon$. The transport equations of k and ε in space are as follows:

$$\frac{\partial k}{\partial t} + \overline{u}_j \frac{\partial k}{\partial x_j} = \frac{\partial}{\partial x_j} \left[\left(\nu + \frac{\nu_T}{\sigma_k} \right) \frac{\partial k}{\partial x_j} \right] + \nu_T \left(\frac{\partial \overline{u}_i}{\partial x_j} + \frac{\partial \overline{u}_j}{\partial x_i} \right) \frac{\partial \overline{u}_i}{\partial x_j} - \varepsilon \tag{3}$$

$$\frac{\partial \varepsilon}{\partial t} + \overline{u}_j \frac{\partial \varepsilon}{\partial x_j} = \frac{\partial}{\partial x_j} \left(\frac{\nu_T}{\sigma_\varepsilon} \frac{\partial \varepsilon}{\partial x_j} \right) + C_{e1} \frac{\varepsilon}{k} \nu_T \left(\frac{\partial \overline{u}_i}{\partial x_j} + \frac{\partial \overline{u}_j}{\partial x_i} \right) \frac{\partial \overline{u}_i}{\partial x_j} - C_{e2} \frac{\varepsilon^2}{k} \tag{4}$$

Where, σ_k is the turbulent Prandtl number for kinetic energy. The turbulent length scale (L_0) could be obtained from k and ε as $\varepsilon = k^{3/2} / L_0$. The standard values of the model constants of the above equations are: $C_\mu = 0.09$, $C_{\varepsilon 1} = 0.09$, $C_{\varepsilon 2} = 0.09$, $\sigma_k = 1.0$, $\sigma_\varepsilon = 1.3$

3.1.1. Geometry

The employed 3-D models representing a part of the designed heliostat field using scale-down heliostat models are presented in Fig. 2a, b and c. The required minimum numbers of heliostat for staggered configuration is 3. Here, there is no heliostat with more than one adjacent heliostat in the same row (Fig. 2a). To investigate the interaction of wake from nearby heliostats, a representative field with 5 and 7 heliostats is considered (Fig. 2b, c). These layouts correspond to an elevation angle of 25°. In Fig. 2 distance between adjacent heliostats is 20 cm and the distance between two rows is 22.1 cm as in Table 2 (Yadav et al., 2014).

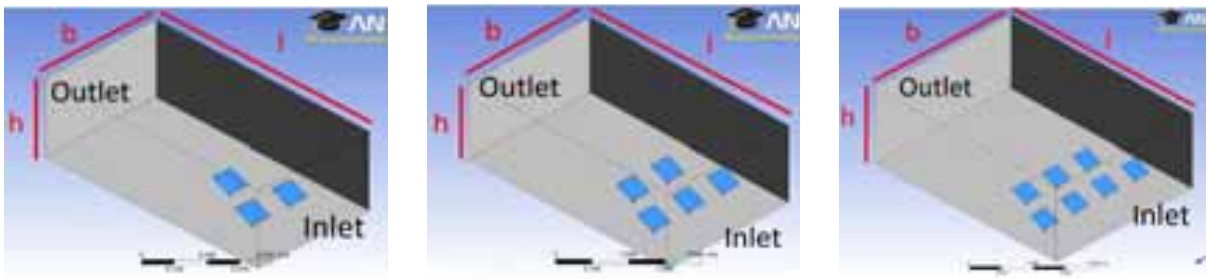

(a) (b) (c)

Fig. 2: Dimensions l x b x h =: a) 120 cm x 60 cm x 40 cm; b) 120 cm x 70 cm x 40 cm; c) 120 cm x 90 cm x 45 cm.

3.1.2. Mesh

The flow domain is discretized by dividing into smaller control volumes called mesh elements. Polyhedral mesh elements are considered. A mesh with smaller element size is said to be a finer mesh. Figure 3 shows the employed polyhedral mesh element at the middle plane of domain. CFD simulations are performed for an average mesh resolution of 1, 2, 3 & 4 mm (Table 3) on all the geometries.

Tab. 3: (a) Edge size and (b) Inflation resolution

Edge sizing (mm)
1
2
3
4

S.no	Boundary Layer	
	Over heliostat mirror	Over enclosure wall
1	0.1 mm, 1.2 growth, 7 layers	0.2 mm, 1.2 growth, 10 layers
2	0.1 mm, 1.2 growth, 7 layers	0.3 mm, 1.2 growth, 7 layers
3	0.2 mm, 1.2 growth, 4 layers	0.3 mm, 1.2 growth, 7 layers


(a)


(b)

Fig.3. a) Polyhedral mesh at the middle plane of study domain; b) Fine volume cell near heliostat geometry and inflation over wall and heliostat plate.

3.1.3. CFD set-up and Mesh dependency

The standard k-Ɛ turbulence model, elaborated earlier, using the pressure-velocity coupled SIMPLE algorithm as available in ANSYS-FLUENT 13.0 was employed for CFD analysis. The validation of adopted set-up is presented by Yadav et al. (2014) and Singh et al. (2015). Thus, no separate validation is provided in this paper. In these simulations, the considered maximum uniform axial-inlet velocity is 20 m/s with 3% turbulence intensity. For the gradient calculations, least-square scheme is employed. The first-order upwind scheme is employed for calculating momentum, kinetic energy (k) and its dissipation ($\mathcal{E}$) equations with a convergence criterion of 10^{-5}. The generated meshes for grid dependence investigation are given in Table 4.

Tab. 4: Mesh resolution

S. No.	Geometry	Mesh resolution	Avg. Y+	Mesh elements
1	3 heliostats	4 mm	3.5	1.34 million
2	5 heliostats	4 mm	5.7	2.00 million
3	7 heliostats	4 mm	5.8	3.93 million

3.2. Large Eddy Simulation (LES) approach

In large eddy simulations, the sub-grid scales are filtered out and larger scales are resolved by the adopted filter or grid resolution and analyzed. The dimensionless implicit grid-filtered Navier-Stokes equations for an incompressible fluid are given as follows:

$$\frac{\partial \overline{u}_i}{\partial x_i} = 0 \tag{5}$$

$$\frac{\partial \overline{u}_i}{\partial t} + \frac{\partial}{\partial x_j}\left(\overline{u}_i \overline{u}_j\right) = -\frac{\partial \overline{p}}{\partial x_i} - \frac{\partial \tau_{ij}}{\partial x_j} + \frac{1}{\mathrm{Re}}\frac{\partial^2 \overline{u}_i}{\partial x_j x_j} \tag{6}$$

Where, $\overline{u}_i$ is the velocity component of the resolved scales, p is the pressure and Re is the Reynolds number. The turbulence stresses, τ_{ij} represent the effects of small scales on resolved structures and proportional to the mean velocity gradients, the large-scale strain rate tensor S_{ij}:

$$\tau_{ij}^a = \tau_{ij} - \frac{\delta_{ij}}{3}\tau_{kk} = -2\mu_T \overline{S}_{ij} \tag{7}$$

Where, τ_{ij}^a is the anisotropic part of the sub-grid scale Reynolds stresses τ_{ij} and δ_{ij} is Kronecker delta. The trace of the stress tensor is usually added to the filtered pressure p. The expression for eddy viscosity μ_T determined by Smagorinsky model (Smagorinsky, 1963) is as follows:

$$\mu_T = \rho\left(C_S \Delta\right)^2 \left|\overline{S}\right| \tag{8}$$

Where, Δ is the filter width which is proportional to the grid size, ρ is the density, C_S is the Smagorinsky constant, $\left|\overline{S}\right| = \left(2\overline{S}_{ij}\overline{S}_{ij}\right)^{1/2}$ is the magnitude of large-scale strain rate tensor. Further, Germano et al. (1991) proposed a dynamics sub-grid stress model which calculates C_S as a function of space and time by using two filters, test and grid filters. In dynamics model, Lilly (1992) proposed a least squares method to calculate C_S.

3.2.1. Geometry

Due to the computationally expensive nature of LES, this simulation is conducted over a smaller geometry with only one heliostat model as shown in Fig. 4 with corresponding dimensions in Table 5. This setup is experimentally analyzed in Yadav et al. (2014). This is utilized in this paper for validation of LES approach.

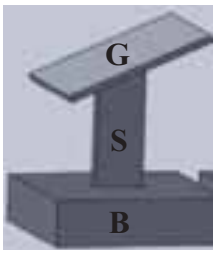

Fig. 4: Single heliostat

Tab. 5: Dimension of heliostat used in LES analysis

Component	Dimension (mm)
Glass Mirror (G)	60 x 60 x 3
Stand (S)	18 x 6 x 50
Base (B)	68 x 74 x 20

3.2.2. Mesh and CFD set-up

For the current study, sub-grid stress model is employed to simulate flow around a single heliostat with dimensions (see Table 5) as in Yadav et al. (2014). Uniform axial velocity as 16 m/s is applied at inlet with no perturbation as in the performed experiment. At walls, no slip boundary condition is used. SIMPLE algorithm is used with pressure-velocity coupling. Least-squares cell based scheme is used for gradient calculations. For continuity and momentum equations, bounded central differencing is used. The Y-plus at the heliostat plate ~ 2 (see Fig. 5b) as suggested by Davidson (2009). The total number of cells in the domain is around 1.0 Million. Fig. 5a shows the polyhedral mesh at the middle plane of the domain.

Fig. 5: (a) Polyhedral mesh at the middle plane of the domain; (b) Y-plus at the heliostat plate is ~ 2.

4. Results

4.1. RANS

Figure 6a shows various lines, namely, horizontal, longitudinal and vertical along which RANS analyzed axial-velocity is reported in Fig. 6b, c, and d. One of the representative heliostats is identified by symbol 'a'. Fig. 6b clearly depicts deceleration of axial velocity towards heliostat for the cases with 3, 5 and 7 heliostats. In these simulations the elevation angle is 25°. The arrow (→) indicates flow direction from left to right. It can be inferred that the axial-velocity, finally, develops to the maximum value, as expected, in far wake. This confirms that the considered length allows development of wake, as envisaged. The plotted time-averaged axial-velocity along the lines designated as "horizontal" and "vertical" enable tracking velocity changes. Figures 6c and 6d show that the calculated axial-velocity develops to free stream value of ~ 20 m/s near the wall along vertical and horizontal lines. Further, to evaluate whether the height of experimental set-up will allow using heliostat with the maximum elevation angle of 65°, additional calculations are performed. This is shown in Fig. 6d. This clearly indicates that the flow develops to free-stream condition over heliostat and eventually remains the same until viscous wall effect is encountered. Therefore, it can be safely stated that the considered length, breadth and height of 1700 mm x 1000 mm x 500 mm will be sufficient. However, a larger experimental domain of 2000 mm x 1200 mm x 600 mm is considered with ~ 20% safety margin. This is currently under fabrication and experimental results will be reported in near future.

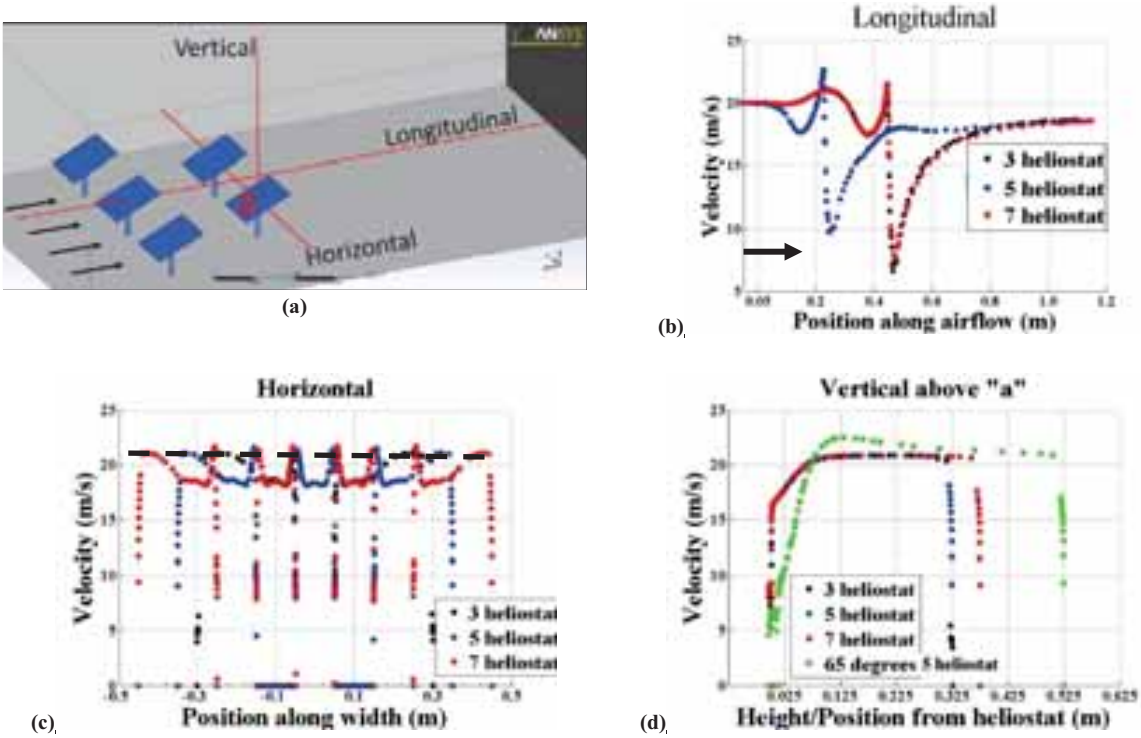

Fig. 6: (a) Geometry showing lines along which velocity is plotted. (b) Longitudinal line axial to the direction of flow, (c) Horizontal line through rear row of heliostats, (d) Vertical line above heliostat labeled "a" (including result for 65° elevation)

Velocity contours and streamlines are given in Fig. 7 for visual representation of the flow field. The velocity contour and streamlines in Fig. 7a and b clearly indicates the strongly affected region behind a heliostat. This results in formation of vortex, as expected, behind the heliostat. Figures 7c and d show the streamlines on a horizontal plane passing through the centers with 3 and 5 heliostats, respectively. Practically, no difference is observed as the wake develops eventually to free stream as depicted in Fig. 6b. However, the existence of heliostat in wake affected region may lead to its induced vibration resulting in a higher spillage loss or even distorted focus on receiver.

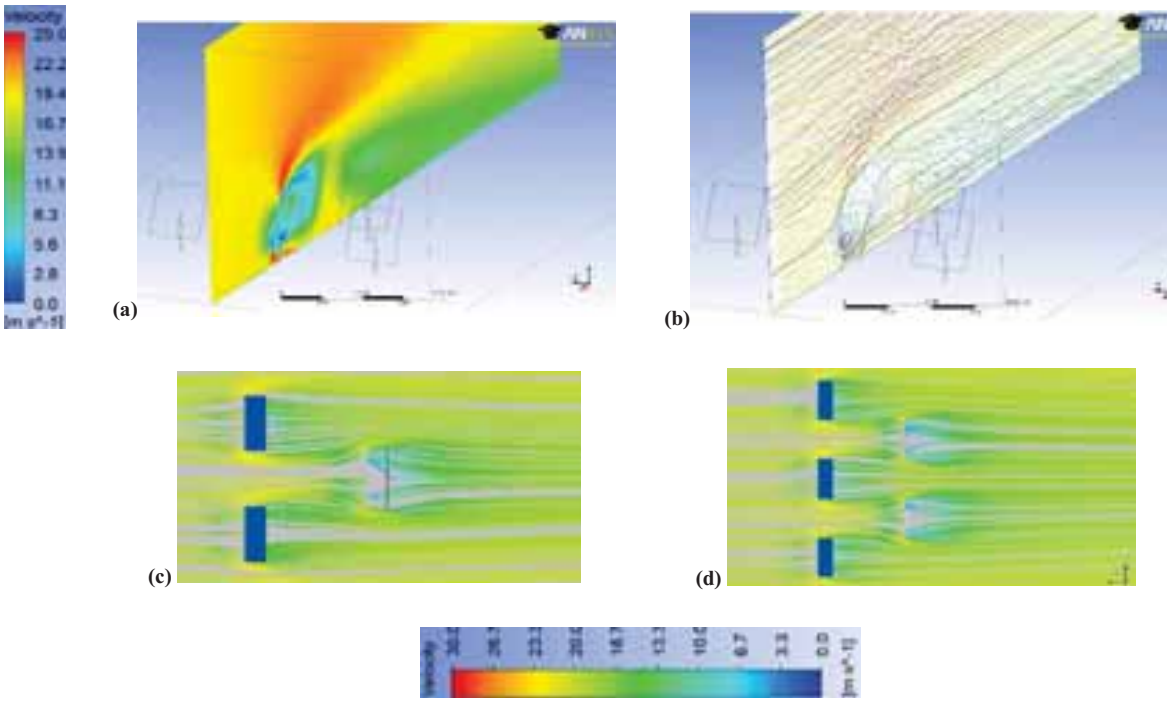

Fig. 7: (a) Velocity contour (b) Streamlines and vectors in vertical plane through a heliostat, (c) Streamlines at horizontal mid-plane through 3 heliostats and (d) through 5 heliostats

4.2. LES

It should be emphasized that RANS showed clear limitations in predicting near-wake region of heliostat. This region is characterized by high RMS values as observed in experiments. The previous studies (Breuer et al., 2003; Rodi, 1993) of flow past an inclined plate revealed that the separated flow shows complicated and highly unpredictable behavior. Obviously, the standard k-$\mathcal{E}$ model was not suitable. In order to capture the dynamic behavior of flow behind the heliostat model, LES analysis is performed using zero-equation sub-grid scale model as proposed by Germano et al. (1991). The LES analyzed instantaneous iso-surface of coherent structures for a given vorticity is shown in Fig. 8a behind the model heliostat. This is colored with velocity. These flow structures are expected to cause induced vibration and also affect the dust deposition on the subsequent heliostats. Thus, a parameter based on wake-based factor is required for field design. Fig. 8b shows the comparison between LES analyzed and measured axial-velocity using Laser Doppler Velocimetry (LDV). The velocities are plotted at seven locations, from 5 mm to 30 mm with 5 mm gap and at 200 mm from the trailing edge of the heliostat plate along the axial axis of plate, marked as 1 to 6 & 7 on horizontal axis respectively. Further, LES analyzed and experimentally estimated RMS values of axial-velocity are plotted at similar locations in Fig. 8c. It could be observed that the LES analyzed values are within ± 10% of the experimentally measured values. Thus, it can be safely stated that the performed LES provided useful details about mean and fluctuating flow quantities. However, further improvement using one-equation model is expected.

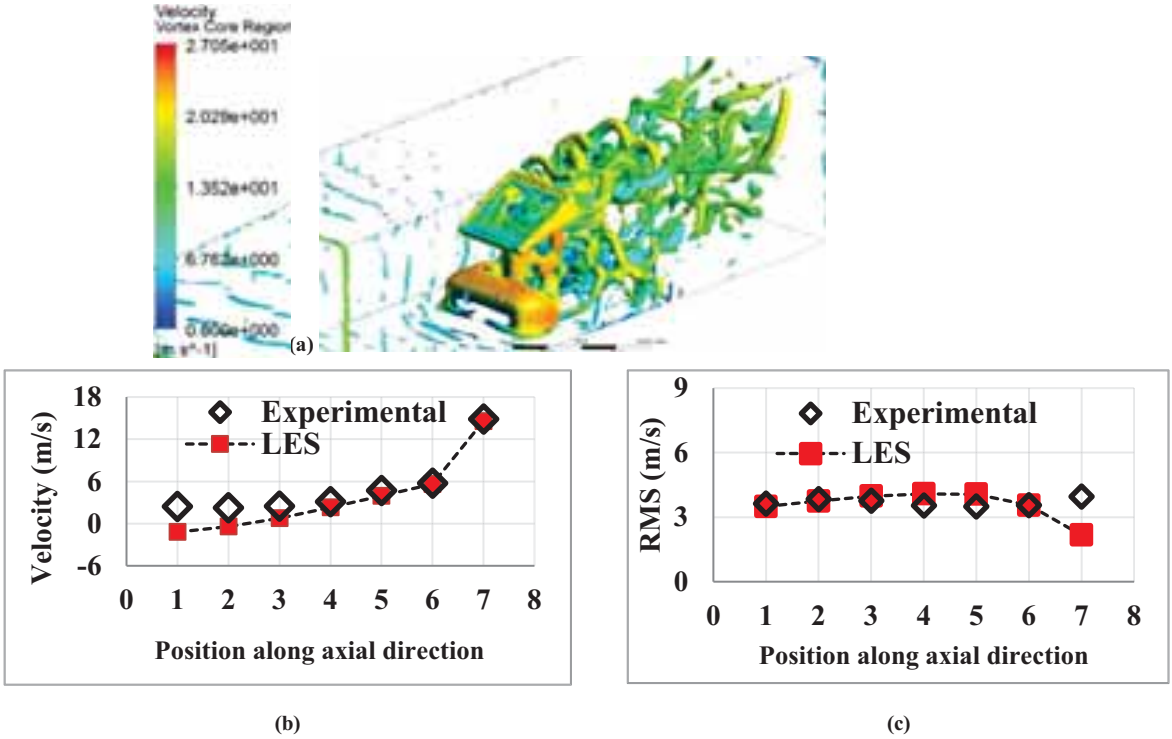

Fig. 8: (a) Coherent flow structures correspond to 620 Hz; (b) Time-averaged Mean Velocity and, (c) RMS velocity along an axial line behind the heliostat at 5, 10, 15, 20, 25, 30 & 200 mm from trailing edge represented by numbers 1 to 6 & 7, respectively.

5. Conclusion

This paper presents the design and evaluation of an experimental set-up for analysis of fluid flow and dust deposition on heliostats in a field layout. For this purpose, a basic field using scale-down heliostat models is designed using available literature. Afterwards, using the validated RANS CFD approach a detailed air-flow analysis around heliostats is performed. This reveals that even with an extreme inclination angle of 65°, an experimental domain of 2000 mm x 1200 mm x 600 mm will allow wake and flow development to free-stream values. Further, detailed LES analysis showed the presence of coherent structures behind a heliostat, which is expected to induce vibration if a heliostat is exposed. Therefore, it is concluded that correction parameters Considering the stability and safety of the operation based on wake-related and dust-deposition factors will be

required for a more realistic evaluation of field- design and performance. The designed experimental set-up is currently under fabrication and experimental results will be reported in future.

6. Acknowledgements

The authors acknowledge the received infrastructure and financial support from IIT Jodhpur and Ministry of New and Renewable Energy (MNRE) funded project vide sanction letter no. 15/40/2010-11/ST. The authors extend their thanks to Vikash Goenka for his assistance during the draft of this manuscript.

7. References

Breuer, M., Jovičić, N., Mazaev, K., 2003. Comparison of DES, RANS and LES for the separated flow around a flat plate at high inclination. Int. J. Numerical Methods Fluids 41, 357-388.

Davidson, L., 2009. Large Eddy Simulation: how to evaluate resolution. Int. J. Heat Fluid Flow 30, 1016-1025.

Falcone, P.K., 1986. A handbook for solar central receiver design. Sandia National Laboratories.

Furbo, E., 2010. Evaluation of RANS turbulence models for flow problems with significant impact of boundary layers. UPTEC F10061; Master thesis.

Germano, M., Piomelli, U., Moin, P., Cabot, W.H., 1991. A dynamic subgrid-scale eddy viscosity model, Phys. Fluids A3, 1760-1765.

Gupta J.P., 1986. Moisture and thermal regimes of the desert soils of Rajasthan, India, and their management for higher plant production. Hydrol. Sci., J. 31, 347-359.

Kuzmin, D., Mierka, O., Turek, S., 2007. On the implementation of the k−ε turbulence model in incompressible flow solvers based on a finite element discretization. Conference Int. J. of Computing Sci. and Mathematics. 1, 193-206.

Launder, B.E., Spalding, D.B., 1972. Mathematical Models of Turbulence, Academic Press, London.

Lilly, D.K., 1992. A proposed modification of the Germano subgrid-scale closure method, Phys. Fluids A4, 633-635.

Lipps, F.W., Vant-Hull, L.L., 1978. A cell-wise method for the optimization of large central receiver systems. 20, 505–516.

Niknia, I., Yaghoubi, M., and Hessami, R., 2012. A novel experimental method to find dust deposition effect on the performance of parabolic trough solar collectors. Int. J. Env. Studies, 69 (2), 233-252.

Rodi, W., 1993. On the simulation of turbulent flow past bluff bodies, J. Wind Eng. Ind. Aerodynamics 46 & 47, 3-19.

Siala, F.M.F., Elayeb, M.E., 2001. Mathematical formulation of a graphical method for a no-blocking heliostat field layout, Renewable Energy, 23(1), 77–92.

Singh, G., Saini, D., Yadav, N., Sharma, R., Chandra L., Shekhar, R., 2015. Dust deposition mechanism and cleaning strategy for open volumetric air receiver based solar tower sub-systems. Energy Procedia 69, 2081 – 2089.

Smagorinsky, J., 1963. General circulation experiments with the primitive equations, Monthly Weather Review, 91(3), 99-164.

Vittitoe, C., Biggs, F., 1981. A user's guide to helios: a computer program for modeling the optical behavior of reflecting solar concentrators, part I. Introduction and code input. Sandia National Laboratories.

Xiudong, W., Zhenwu, L., Zi, L., Hongxin, Z., Zhengguo, N., 2007. Optimization Procedure for Design of Heliostat Field Layout of a 1MWe Solar Tower Thermal Power Plant. Proc. of SPIE 6841 684119, 1–10

Yadav, N.K., Pala, D., Chandra, L., 2014. On the understanding and analyses of dust deposition on heliostat. Energy Procedia 57, 3004 – 3013.

Conference Proceedings

Solar World Congress 2015
Daegu, Korea, 08 – 12 November 2015

Comparison-based Study on A Novel Point and Line Coupling-focus Solar Tower System Employing Linear Fresnel Heliostats

Yanjun Dai, Xian Li

Institute of Refrigeration and Cryogenic Engineering, Shanghai (China)

Abstract

The design and analysis of a beam-down solar tower system represents an extremely complex problem due to its performance dependent on various interrelated factors. A novel heliostat with linear Fresnel reflecting technology is employed in the beam-down solar tower and investigated theoretically in this paper, being its superior wind-resistance performance compared with convectional heliostat. In order to investigate the concentrating principle of linear Fresnel heliostat, a comparison-based study of these parameters and efficiencies is implemented herein. The effects of the hyperboloid eccentricity on both the sun-shape and the geometry of the heliostat are analyzed. The effect of the aberration in optics for the linear Fresnel heliostat on the image at the focal plane has been investigated.

Keywords: *Point and line coupling-focus solar tower, beam-down, linear Fresnel heliostat, optical analysis*

1. Introduction

It is well known that the energy and environmental crisis has been promoting the development of solar thermal technologies, where concentrating solar tower technology has been proven to be a fairly efficient way of converting solar energy into thermal energy or electricity (Kalogirou, 2004). As for the traditional concentrating solar tower, solar energy from a large array of heliostats is focused onto a tower that captures the heat by a receiver, and then converts that heat to electricity using a steam generator and a steam turbine. However, it can be pretty expensive in terms of building a low heat-loss tower and pumping heat transfer fluid (HTF) such as molten salt up to the tower top which usually mounted at hundred meters high to the ground. In order to overcome these shortcomings, beam-down solar tower (BST) has been proposed and developed, where a second set of beam-down concentrator (BC) directs the solar radiation back down to a central receiver (CR) placed on the ground, instead of having the heat-capturing system up at a high tower. On account of aforementioned merits BST technology is considered as one of the promising ways to harvest solar energy and is worth continuing research.

A variety of studies on optical performance of various BST systems are in the literature. The concept of BST was proposed for the first time by Rabl (1976) and then developed at the Weizmann Institute in Israel (Segal and Epstein, 1997). Segal and Epstein (1999, 2000, 2003) described the optics of the BST system, where two types of secondary reflectors, hyperboloid and elliptical were investigated for a comparative study. However, a single solar ray per heliostat was considered, and shading and blocking effects have been neglected. Detailed optical analysis of BST systems with the hyperboloid concentrators and the compound parabolic concentrator (CPC) have been performed (Leonardi, 2012; Wei et al., 2013), but solar flux distribution on the absorber surface of the CR have not been involved.

In this paper, a BST system employing strong wind-resistance linear Fresnel concentrating technology which is named as point-line-coupling-focus (PLCF) system, is introduced and investigated theoretically. Based on the MCRT, the optical analysis model of PLCF system is developed considering the incident angle, solar position, optical errors, and sun-tracking angles. Comparison-based study on the optical performance between PLCF and convectional systems is implemented.

doi:10.18086/swc.2015.04.05 Available at http://proceedings.ises.org

2. PLCF system description

A schematic of concentrating concept of BST including a linear Fresnel heliostat and a beam-down concentrator (BC) is shown in Fig. 1. A hyperboloid reflector is used as the BC. The incident rays hit on the surfaces of Linear Fresnel heliostat facets. The heliostat tracks sun and reflects incident rays to the BC, and then these rays are concentrated downwards to the final focal point at the focal plane. The concentrating process of this BST is mainly composed of focusing effects of heliostat and BC. The detailed parameters of linear Fresnel heliostat has been introduced by Li et al. (2015). As shown in Fig. 1, l_m and H_h are the length and the height of the linear Fresnel heliostat, respectively. D is the distance between the heliostat and the cavity receiver. H and H_{max} are the height of point A and the maximum height of the hyperboloid reflector, respectively. F_1 and F_2 are the upper focus (target point) and lower focus (focal point), respectively. r_{max} is the maximum radius of the hyperboloid reflector.

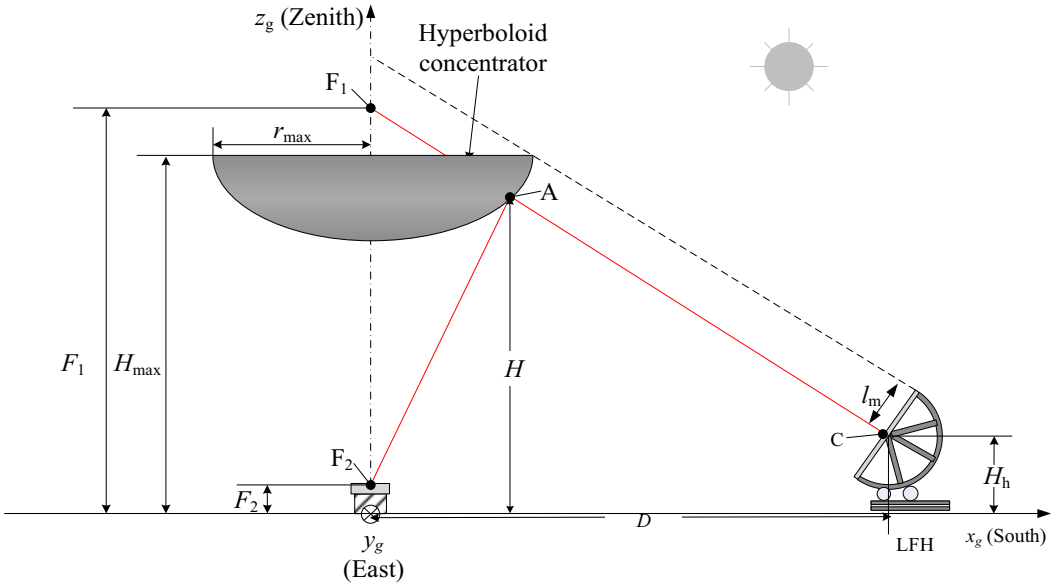

Fig. 1: Schematic diagram of geometric parameters of the PLCF system with the hyperboloid concentrator

3. Optical analysis models

3.1. Sunshape

Because sun rays are not strictly parallel, the sun rays hitting on the surface of the sub-mirror are modelled as a conic bundle where the rays of the bundle are weighted with a non-uniform energy distribution. Based on the concept of sun-shape profile, the intensity distribution I of solar disk proposed by Johnston (1998) can be calculated as

$$I = I_o \frac{1+\beta\sqrt{1-\frac{\vartheta}{\vartheta_s}}}{\pi\vartheta_s^2\left(1+\frac{2\beta}{3}\right)} \qquad \text{(eq. 1)}$$

where ϑ denotes the angle of a surface element on the solar sphere, I_o is the intensity in the center of the solar disk, β is the limb darkening parameter.

3.2. Normal vector of optical surface

The normal vector ($\mathbf{N_F}$) of the optical surface where rays currently hit is expressed by a unified differential formula (Cui et al., 2012) derived from surface equations f of the investigated geometric surface:

$$\mathbf{N_F} = \begin{bmatrix} f_x \\ f_y \\ f_z \end{bmatrix} = \begin{bmatrix} \dfrac{\partial f(x_g, y_g, z_g)}{\partial x_g} \\ \dfrac{\partial f(x_g, y_g, z_g)}{\partial y_g} \\ \dfrac{\partial f(x_g, y_g, z_g)}{\partial z_g} \end{bmatrix} \quad \text{(eq. 2)}$$

3.3. Optical surface errors

It is generally assumed that all surface errors follow a Gaussian distribution (Rabl, 1985) characterized by the standard deviation. The variances of each individual error distribution can be summed to one total equivalent variance, σerr, which describes the composite effect of all errors, namely the specularity error, the slope error, the shape error, the alignment error, and the tracking error. The simple Rayleigh method of surface error (Cooper and Steinfeld, 2011) for generating surface error is given as

$$\theta_{err} = \sigma_{err}\sqrt{-2\ln U} \quad \text{(eq. 3)}$$

$$\phi_{err} = 2\pi U \quad \text{(eq. 4)}$$

$$\mathbf{M}' = \cos\theta_{err}\mathbf{M} + \sin\theta_{err}\left(\sin\phi_{err}\mathbf{u}_x + \cos\phi_{err}\mathbf{u}_y\right) \quad \text{(eq. 5)}$$

where ζ_{err} and ϕ_{err} are defined as the azimuthal angular and circumferential components of the surface error, respectively. U is the random number with uniform distribution in the interval of 0 and 1. M′ is deviant reflected vector with surface error. $\mathbf{u_x}$ and $\mathbf{u_y}$ are unit vectors in the Cartesian x-component and y-component directions, respectively.

3.4. Concentration ratio

The concentration ratio is defined as

$$C = \frac{A_h}{A_{sp}} \quad \text{(eq. 6)}$$

where A_h and A_{sp} represent the total aperture area of heliostat field and the spot area at the lower focal plane.

3.5. Optical efficiency

Optical performance index Optical efficiency of the BCST system is related to significant factors involving cosine efficiency ε_{cos}, shading and blocking efficiency ε_{sb}, interception efficiency ε_{it}, and the atmospheric attenuation efficiency ε_{aa}. Instantaneous optical efficiency with respect to above efficiencies, proposed by Schmitz et al. (2006), is expressed as

$$\eta_o = \eta_{cos}\eta_{sb}\eta_{it}\eta_{aa}\rho_h\rho_{BC} \quad \text{(eq. 7)}$$

where ρ_h and ρ_{BC} indicate the reflectance of LHF and BC, respectively.

4. Results and discussion

4.1. The effect of the structure of hyperboloid reflector

As shown in Fig. 2, the optical surface of hyperboloid reflector is mainly affected by the eccentricity e and the upper and lower focuses. Considering F_1 = 75m and F_2 = 5m, the effect of e on the hyperboloid structure is analyzed. Fig. 2(a) shows the relationship between e and the maximum radius r_{max}. As shown in Fig. 2(a), the r_{max} increases with the increase of the eccentricity e which shows an increasing trend. When $e > 50$, the increase of r_{max} is limited and trends to be stable. In addition, the distance D increases with the increase of r_{max}. Fig. 2(b) reveals the effect of e on the hyperboloid surface. As can be seen, under the identical conditions, the size of the hyperboloid surface increases with the increasing e. When e trends to infinity, hyperbolic mirror transfers to be the plane mirror.

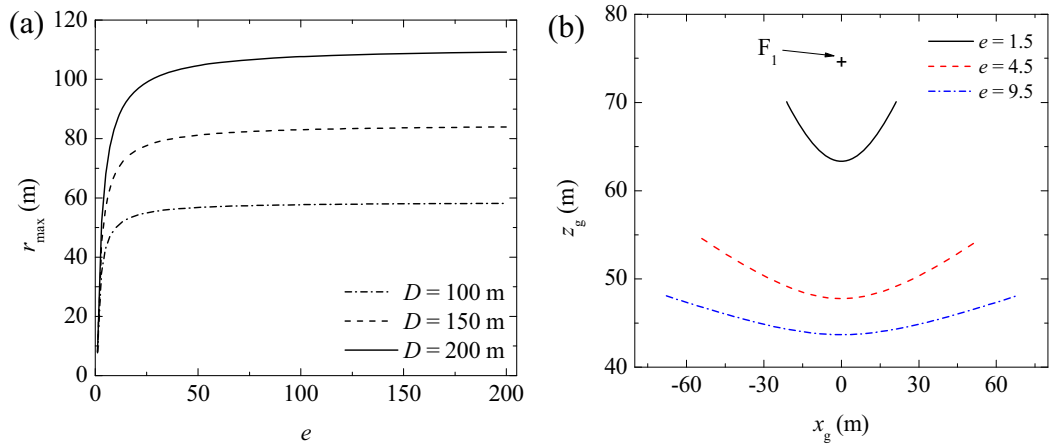

Fig. 2: The effects of D and e of geometric parameters on the shape of the hyperboloid reflector: (a) the maximum radiu r_{max} as a function of *e*; (b) the effect of parameter *e*

In this case, the magnification M is the ratio of the image size of the upper focal plane to the image size of lower focal plane. Based on the optical analysis of MCRT method, considering sun angle effects, the single ray reflected from point C is used to reveal characteristics of the spot on the lower focal plane. Fig. 3 shows the effects of D and e on the spot characteristics of a single ray reflected from the geometric center of heliostat. Fig. 3(a) shows the effect of the parameters of e and D on the spot sizes of the upper and lower focal planes. With the increase of e, the spot size of lower focal plane decreases. When e trends to infinity, the spot size of the focal plane trends to be the same. Fig. 3(b) is the relationship between e and M which increases sharply with the increase of e from 1 to 4.5, and the amplification factor decreases sharply. Therefore, the increase of D in a certain extent can weaken the negative effect caused by the magnification of the hyperboloid mirror, and can improve the concentration ratio. The comparison-based results show that the MCRT optical analysis model developed in this paper has the reasonable accuracy.

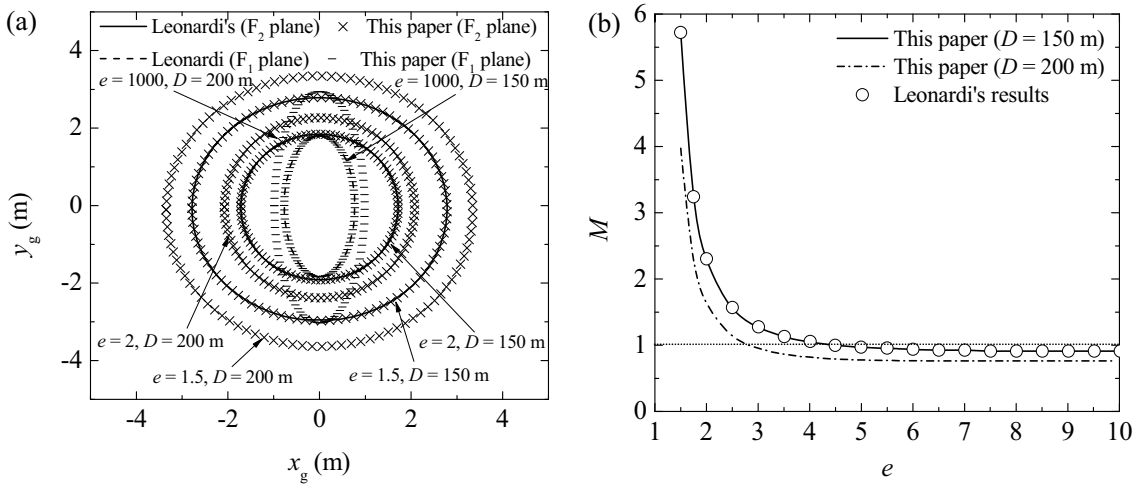

Fig. 3: The effects of *D* and *e* on the spot characteristics of a single ray reflected from the geometric center of heliostat: (a) the effect on the spot size; (b) the effect on the magnification *M*

4.2. The effect of structure parameters of linear Fresnel heliostat

The effect of heliostat structure parameters on optical properties is analyzed under the conditions of H_h=5m, F_1 = 75 m, F_2 = 5 m, r_{max} = 44.1 m, γ = 0°, α = 90°, D = 150 m, e = 3. With the diameter of 10 m of the circular heliostat (as shown in Fig. 4), the linear Fresnel heliostat is divided into five mirrors.

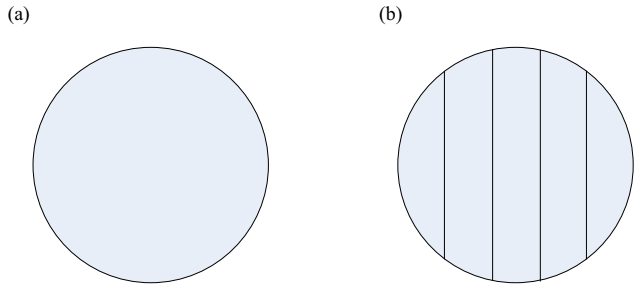

Fig. 4: Schematic diagram of heliostats: (a) convectional circle-plate heliostat (CH); (b) circle linear Fresnel heliostat (diameter of 10m)

Fig. 5 shows comparison results of the spot sizes of LFH and CH at the upper and lower focal planes. As shown in Fig. 5, the LFH has the smaller spot sizes compared to CH.

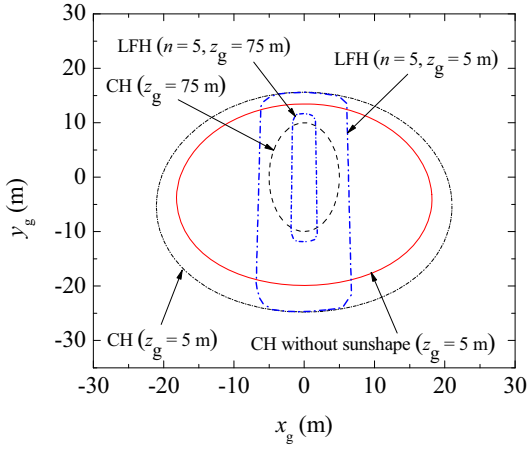

Fig. 5: Comparison results of the spot sizes of LFH and CH at the upper and lower focal planes

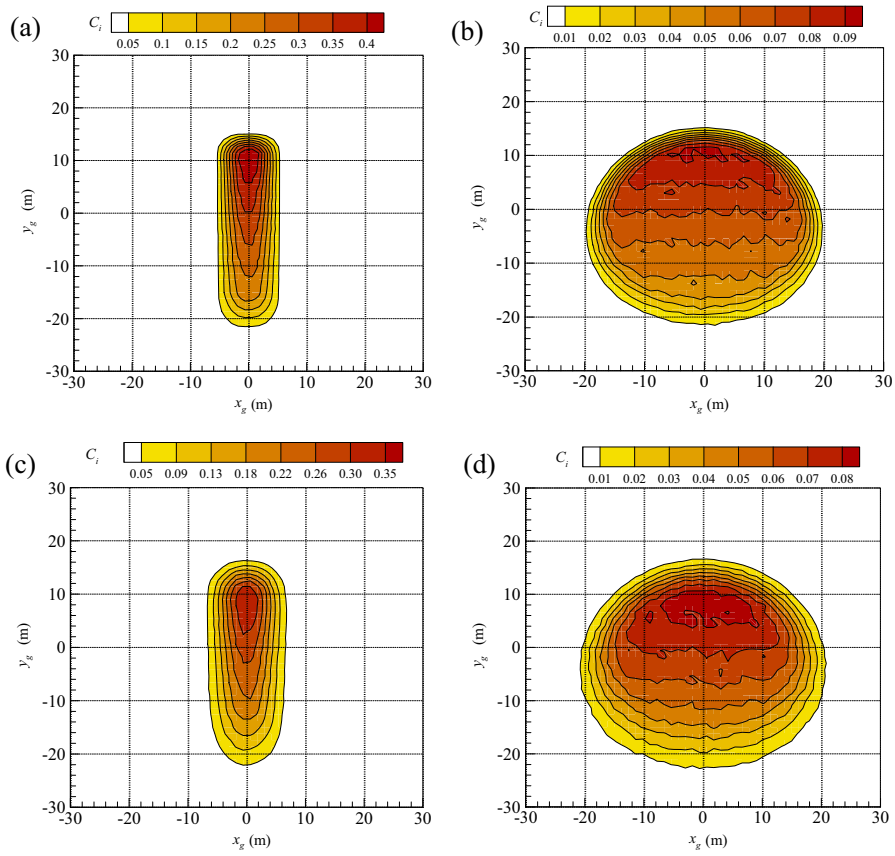

Fig. 6: Comparison results of the local concentration ratio of the spot for LFH and CH: (a) LFH without optical error; (b) CH without optical error; (c) LFH with optical error; (d) CH with optical error (σ_{err} = 3.5 mrad)

Concentrating ratio C is an important index to evaluate the solar concentrating characteristics. Fig. 6 shows comparison results of the local concentration ratio of the spot for LFH and CH. The effect of optical errors has been considered herein. Analysis shows that the linear Fresnel heliostat has obvious advantages in concentrating ratio. Comparative analysis of optical error of focal spot local concentration ratio can be found and certain extent increase of the focal spot size causes the decrease in concentrating ratio. However, the differences in local concentration ratio distribution between two heliostats are extremely limited.

4.3. The effect of structure parameters of heliostat mirror

The shape of the heliostat mirror has an important effect on the focusing performance. Here, the spot sizes of various length-width ratios are investigated with D = 150 m and e = 3. Fig. 7 reveals the effect of length-width ratio on the characteristic of the spot at the lower focal plane. The diameter of CPC is 20 m. Fig. 7(a), 7(b), and 7(c) represent the length-width ratios of 1:1, 5:1, and 2:1, respectively. As can be seen, when the length-width ratio is 1:1, the LFH has the highest optical efficiency of 73.1%.

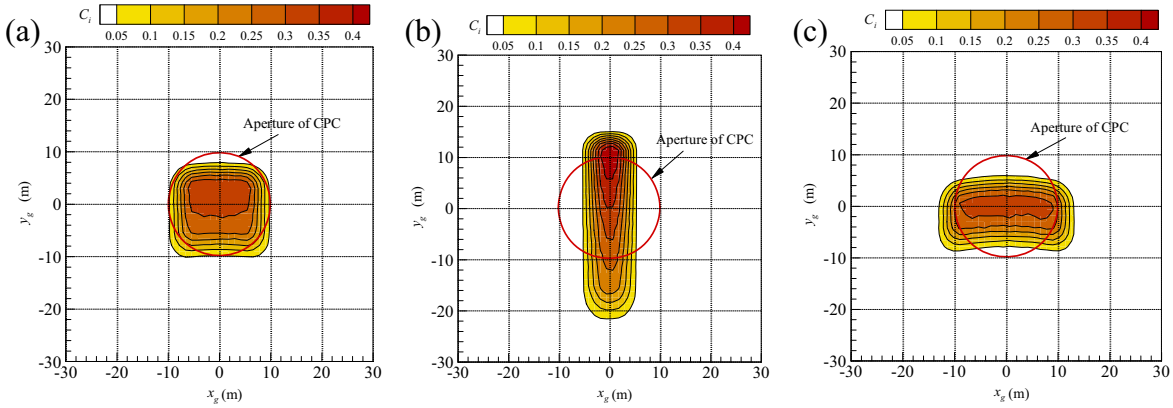

Fig. 7: The effect of length-width ratio on the characteristic of the spot at the lower focal plane: (a) length-width ratio of 1:1 with spillage loss of 26.9%; (b) length-width ratio of 5:1 with spillage loss of 41%; (c) length-width ratio of 2:1 with spillage loss of 31.2%

4.4. Comparison-based analysis of optical efficiency

The comparison-based analysis of optical efficiency is implemented considering the shape of heliostat shown in Fig. 8. Fig. 9 shows the effect of the solar position and design parameters on the cosine efficiency as well as the shading and blocking efficiency. The aperture area of heliostat is 100 m^2 facing south with the coordinates (-150, 0, 5). The parameters of hyperboloid reflector is e = 3, F_2 = 5 m. The aperture radius of CPC is 11 m.

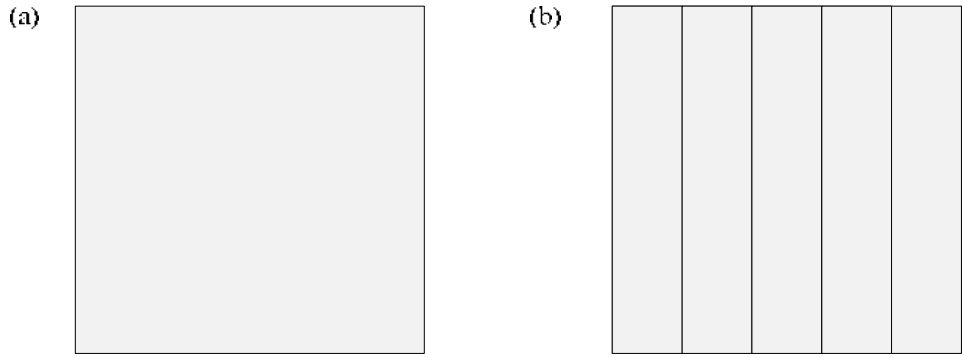

Fig. 8: Schematic diagram of heliostats: (a) convectional rectangle-plate heliostat; (b) rectangle linear Fresnel heliostat

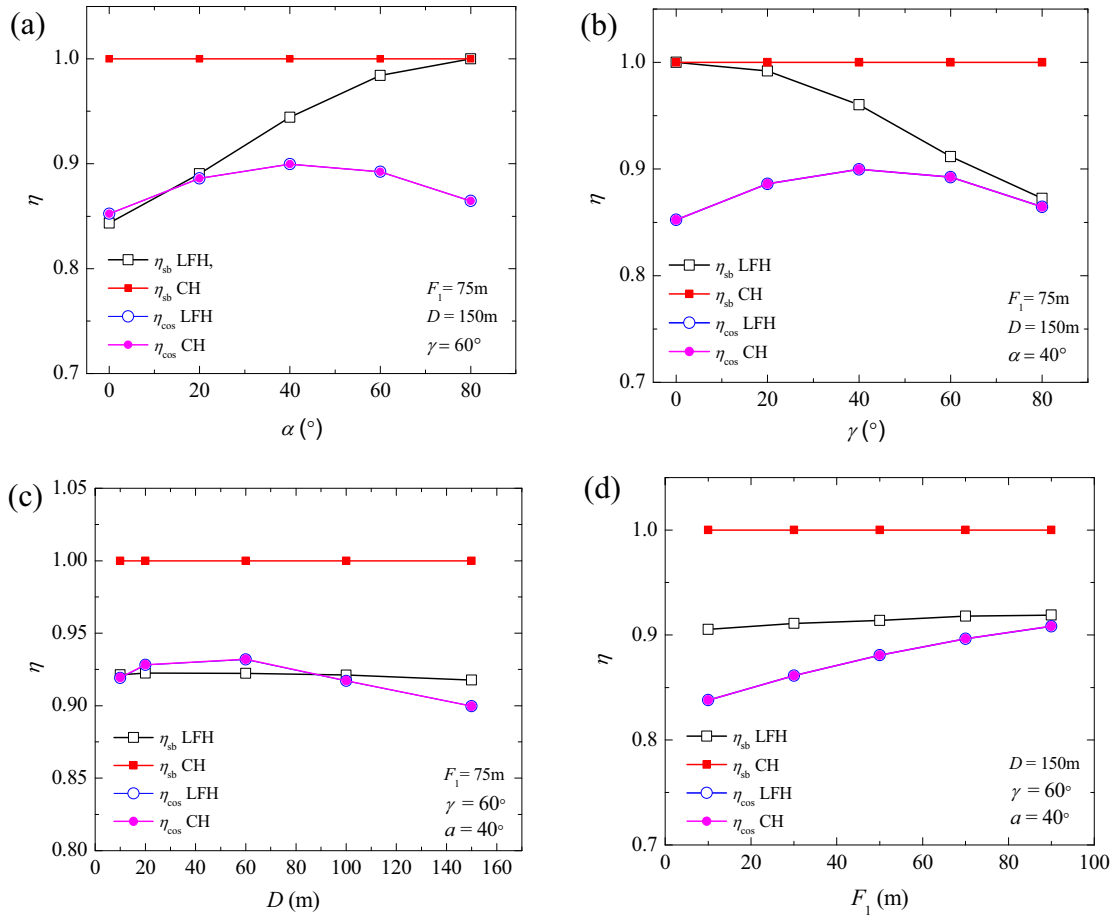

Fig. 9: The effect of the solar position and design parameters on the cosine efficiency as well as the shading and blocking efficiency: (a) the effect of solar altitude; (b) the effect of solar azumith; (c) the effect of the distance D; (d) the effect of the upper focus F1

As shown in Fig. 9, LFH and CH have the identical cosine efficiency which is not affected by the parameters of solar position and D. In addition, the LFH has a greater impact than CH with respect to the effects of solar position (solar angles) on shading and blocking efficiency. As shown in Fig. 9(c) and 9(d), the parameters of D and F_1 have limited impact on the shading and blocking efficiency. The effect of the shape of mirror (shown in Fig. 10) on the optical efficiency is studied herein.

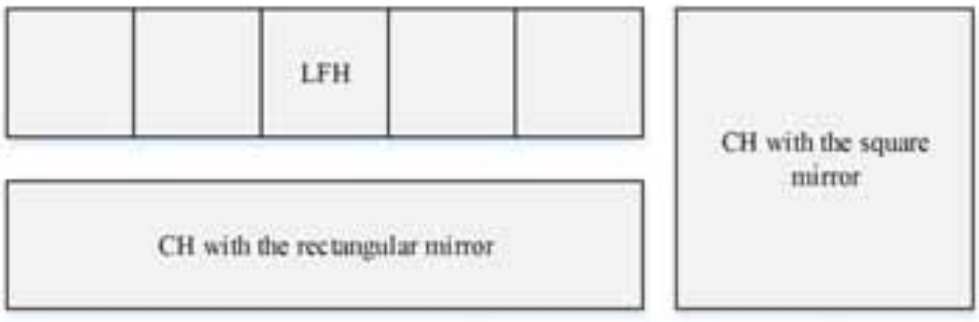

Fig. 10: The structures of LFH and CH with the identical area

Under the conditions of the aperture radius of 4.9 m, the solar altitude of 82°, the aperture area of the heliostat of 100 m^2 facing south, the coordinates (-150, 0, 5). The parameters of hyperboloid reflector (e = 3, F_1 = 75 m, F_2 = 5 m), the detailed comparison results are listed in Table 1. As can be seen, the shading and blocking efficiency of LFH is slightly lower than that of CH, however, the interception efficiency of LFH is obviously superior than that of CH. Thus, the optical efficiency of LFH is approximately 3.4 times the optical efficiency of a CH. In addition, the length-width ratio of 1:1 has the optimal optical efficiency.

Tab. 1: Comparison results of the optical efficiency of LFH and CH solar thermal system under various solar azimuth

Solar azimuth	LFH				Rectangular mirror				Square mirror			
	η_{cos}	η_{sb}	η_{it}	η_{o}	η_{cos}	η_{sb}	η_{it}	η_{o}	η_{cos}	η_{sb}	η_{it}	η_{o}
0°	0.879	1	0.968	0.620	0.879	1	0.202	0.130	0.879	1	0.281	0.180
20°	0.877	1	0.970	0.620	0.877	1	0.210	0.130	0.877	1	0.290	0.185
40°	0.870	1	0.972	0.616	0.871	1	0.217	0.133	0.871	1	0.295	0.187
60°	0.861	1	0.973	0.611	0.861	1	0.221	0.139	0.861	1	0.31	0.195
80°	0.849	0.998	0.973	0.601	0.849	1	0.230	0.142	0.849	1	0.32	0.198

5. Conclusions

A novel heliostat with linear Fresnel reflecting technology is employed in the beam-down solar tower and investigated theoretically in this paper, being its superior wind-resistance performance compared with convectional heliostat. The comparison-based study on the convectional heliostat and linear Fresnel heliostat is implemented. Following conclusions can be drawn:

(1) Analysis results shows that the linear Fresnel heliostat has obvious advantages in concentrating ratio and spot size.

(2) The shape of the heliostat mirror has an important effect on the focusing performance. The optimal length-width ratio is 1:1 in order to achieve the highest optical efficiency.

(3) Under the same conditions, the optical efficiency of LFH is approximately 3.4 times the optical efficiency of a CH.

6. Acknowledgements

This work was supported by National Natural Science Foundation Project of China under the Contract No. 51276112.

7. References

Cooper, T., Steinfeld, A., 2011. Derivation of the angular dispersion error distribution of mirror surfaces for Monte Carlo ray-tracing applications. Journal of Solar Energy Engineering, 133(4), 044501–044504.

Cui, F.Q., He, Y.L., Cheng, Z.D., Li, D., Tao, Y.B., 2012. Numerical simulations of the solar transmission process for a pressurized volumetric receiver. Energy 46(1), 618–628.

Johnston, G., 1998. Focal region measurements of the 20 m2 tiled dish at the Australian national university. Sol. Energy 63(2), 117–124.

Leonardi, E., 2012. Detailed analysis of the solar power collected in a beam-down central receiver system. Sol. Energy 86, 734–745.

Li, X., Dai, Y.J., Wang, R.Z., 2015. Performance investigation on solar thermal conversion of a conical cavity receiver employing a beam-down solar tower concentrator. Sol. Energy 114, 134 – 151.

Rabl, A., 1976. Tower reflector for solar power plants. Sol. Energy 18, 269–271.

Rabl, A., 1985. Active solar collectors and their applications. New York: Oxford University Press.

Segal, A., Epstein, M., 1997. Modelling of solar receiver for cracking of liquid petroleum gas. J. Sol. Energy Eng. 119, 48–51.

Segal, A., Epstein, M., 1999. Comparative performances of 'tower-top' and 'tower reflector' central solar receivers. Sol. Energy 65, 207–226.

Segal, A., Epstein, M., 2000. The optics of the solar tower reflector. Sol. Energy 69, 229–241.

Segal, A., Epstein, M., 2003. Optimized working temperatures of a solar central receiver. Sol. Energy 75, 503–510.

Schmitz, M., Schwarzbozl, P., Buck, R., Pitz-Paal, R., 2006. Assessment of the potential improvement due to multiple apertures in central receiver systems with secondary concentrators. Sol. Energy 80(1), 111–20.

Wei, X.D., Lu, Z.W., Yu, W.X., Xu, W.B., 2013. Ray tracing and simulation for the beam-down solar concentrator. Renewable Energy 50, 161–167.

Conference Proceedings

Solar World Congress 2015

Daegu, Korea, 08 – 12 November 2015

3D Shape Measurement of Solar Concentrator Based on Orthogonal Fringe Reflection Method

Huibin Zhu[1], Zhifeng Wang[1], Jianhan Zhang[1] and Qiang Yu[1]

[1] Key Laboratory of Solar Thermal Energy and Photovoltaic System, Institute of Electrical Engineering, Chinese Academy of Sciences, Beijing 100190, China

Abstract

Fringe reflection technique is an effective tool to measure the solar concentrator surface slopes, and then reconstruct the surface shape from gradient. However, most of the fringe reflection systems are based on four-step phase shifting method, which need eight figures at least. In order to increase the measurement speed, a new orthogonal fringe reflection method is proposed to measure the shape of solar concentrator, which requires only two fringe images to complete the 3D shape measurement of solar concentrator. The performance of this 3D shape measurement system is demonstrated with experiments.

Keywords: *Shape measurement; Orthogonal fringe reflection; Solar concentrator*

1.Introduction

In a concentrating solar plant, the solar field consisting of a large number of collectors, which collects and concentrates the solar energy onto the receiver, is the major cost component of a plant. To obtain a homogeneous flux distribution on the receiver, the collectors shape must be highly precise to low the energy losses. The ideal shape and optical efficiency of the collector maximizes the energy input of the receiver and has a high impact on the plant performance. Therefore, it is very important to test and evaluate the quality of the surfaces for guaranteeing the optical performance. However, due to technical restraints in the manufacturing and installing process, deviations from the optimum collector shape leading to energy losses on the receiver cannot be completely avoided. On the other hand, it is necessary to measure and adjust the optical quality of the collectors in the manufacturing process. To test and qualify the collectors, a measurement tool for measuring the surface profile with adequate precision should be needed.

Many different techniques for shape measurement of solar collectors have been proposed by a variety of researchers in the past decades. In 1978, Sandia National Laboratories presented a measurement system based on a laser ray trace tester for solar parabolic trough collectors[1]. This system scanned the surface with a laser beam, detected the reflected beam on a target and obtains the normal of the collector surface. This system is sufficiently accurate, but the setup is time consuming and the implementation to large surfaces might be difficult. This limitation is overcame by photogrammetry which measure 3D shapes by calculating the coordinates of the collector surface based on a series of photographies of collector taken from different positions[2]. This method is also time consuming and not suitable for large surfaces since the measured surface has to be equipped with a large number of target points. Recently, Ulmer et al. developed a new

doi:10.18086/swc.2015.04.06 Available at http://proceedings.ises.org

method for measuring the slope error of heliostat based on deflectometry[3-6,22]. Later, we use the similar approach combined with temporal phase unwrapped technique and novel easy calibration method to measure the heliostat facet[7,21]. And there are some other methods to measure the shape of solar collector, which are shown in [8-16]. Most of the fringe reflection systems are based on four-step phase shifting method, which need eight figures at least. In order to increase the measurement speed, a new orthogonal fringe reflection method is proposed to measure the shape of solar concentrator, which requires only two fringe images to complete the 3D shape measurement of solar collector, and is very fast compared with the four-step phase shifting method.

On the other hand, one of the major challenges in fringe-reflection measurement is to realize the shape reconstruction efficiently. In several cases it is sufficient to know the local gradient; however, it is also important to obtain the height information of the solar collector as well. If the shape is known, it is easy to align the collector according to the measured shape results. To obtain the shape of the solar collector, a numerical shape reconstruction method is needed. Essentially there are two different approaches for integration: local and global integration techniques [17,18]. Local method: it integrates along predetermined paths. The advantage of this method is that it is simple and fast. However, the locality of calculation causes a high dependency from data accuracy, and the propagation of height increments along paths also means propagation of errors. Global method: it tries to minimize a designed cost function. The advantage of this method is that there is no propagation of error. But the implementation has certain difficulties and somehow is not easily convergent. So, the desired surface reconstruction method should have the properties of both local and global integration methods; it needs to preserve local details without propagating the error along a certain path. In order to handle this problem, we choose a generalized Hermite interpolation approach employing radial basis functions (RBFs) for the shape reconstruction from the gradient data. This method has the advantage that it can be applied to scattered data. It allows us to integrate data sets with holes, irregular sampling grids, or irregularly shaped boundaries [19]. Finally, the performance of this 3D shape measurement system is demonstrated with experiments.

2.Principle of fringe reflection method

The optical properties of solar collector such as reflectivity do not allow us to apply the direct structured light illumination principle, because the projected structured light is reflected along the mirror direction and no light reaches the CCD sensors. However, it is possible to capture the reflective structured light and obtain the surface information of solar collector based on the fringe reflection technique. The main idea of this reflection technique is that: a fringe pattern generated by the computer can be projected onto a target screen, and the distorted fringe pattern from the solar collector is captured by the CCD camera, which is reflected by the surface under test. The distortion of the fringe pattern depends on the local slope variations and the height of the surface. By establishing the mathematical models, which combine the phase difference between the corresponding point on the reference surface and the measured object, the surface height and slope, the shape of the measured solar collector surface can be determined based on approximation employing radial basis functions discussed below. The schematic diagram of this measurement principle is shown in Figure 1.

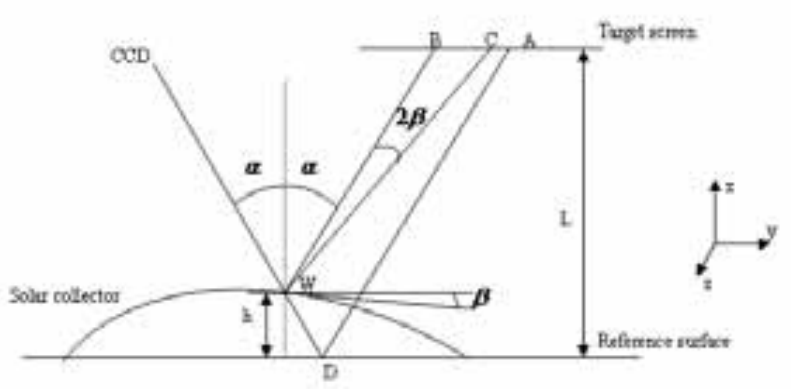

Figure 1: The schematic diagram of fringe reflection technique.

Figure 1 shows the optical configuration of the measured system. A fringe pattern generated by computer from a DLP projector is reflected off the solar collector and captured by CCD camera. The camera sees point A on the target screen with fringe pattern through the reference surface point D. Because of the solar collector surface with height value h and tilted at an angle β in the y direction, the collector surface point W reflects point C on the target screen. It is easy to obtain that the distance difference between the reflected point A and surface point C is related to the surface height and slope in both x and y direction. In this paper, the phase-shift profilmetry can be used to determine this difference. Based on the geometrical configurations in Figure 1, the relationship between the phase difference $\Delta\varphi(x,y)$, the slope $\tan\theta$ and the height h of the collector surface can be established as [24]:

$$\begin{aligned}\theta_x(x,y) &= \frac{\Delta\varphi_x(x,y)p_x}{2\pi(L-h)} \\ \theta_y(x,y) &= \frac{\Delta\varphi_y(x,y)p_y}{2\pi\sec(\alpha)^2(L-h)+\Delta\varphi_y(x,y)p_y\tan(\alpha)}\end{aligned} \tag{1}$$

where (x,y) is the pixel coordinate, $\theta_x(x,y)$ and $\theta_y(x,y)$ are the angles of the measured surface in the x and y directions, respectively, L is the height of the target screen to the reference surface, α is the angle of the camera, $\Delta\varphi_x(x,y)$ and $\Delta\varphi_y(x,y)$ are the phase difference, p_x and p_y are the period of the fringes projected onto the screen in the x and y directions, respectively, h is the height from surface point W to the reference surface. The pattern phase distribution of each observed point can be evaluated by the phase retrieved method.

3.Orthogonal fringe reflection method

Although the phase-shifting method which need eight figures at least is an effective tool to measure the solar concentrator surface slopes, reasonable faster way to obtain both horizontal and vertical phase maps from a single fringe image. In this section, a new orthogonal fringe reflection method is proposed to measure the shape of solar concentrator, which is designed as a two-directional fringe pattern shown in Fig. (2) and requires only two fringe images to complete the 3D shape measurement of solar concentrator. The orthogonal fringe pattern can be expressed as

$$I(x,y) = 255\left[0.5 + 0.25\cos\left(2\pi\frac{x}{p_x}\right) + 0.25\sin\left(2\pi\frac{y}{p_y}\right)\right] \tag{2}$$

where p_x and p_y are fringe periods in the horizontal and vertical directions. The fringe phase values in both x and y directions can be calculated by the two-dimensional windowed fourier ridges method.

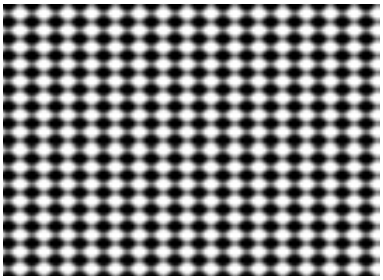

Figure 2: Orthogonal fringe

4.System calibration

The system calibration is very important in the shape measurement, because several different devices and objects are involved in the measurement system, such as CCD camera, projector, target screen, solar collector. Firstly, the CCD camera can be calibrated precisely by Tsai algorithm to provide the intrinsic and extrinsic parameters by using the checkerboard pattern. The system information about pixel size in both x and y directions, rotation angles and translational components for the transform between the measurement screen and the camera coordinate can be obtained. The next calibration algorithm is the reference plane calibration. This requires the measurement of the flat reference surface with respect to the camera position and involves the measurement of the phase distribution of the flat reflective surface across the measurement scene. This reference phase distribution is required in order to obtain the correct phase shift information from the measurement object. A novel virtual reference plane based on Zernike polynomials fitting method is presented. In the measurement system, the phase difference between the reference surface and collector surface should be determined. Because the solar collector is large, it is not easy to directly obtain the reference surface phase as size as the measured object. In order to solve this problem, the Zernike polynomials fitting method can be used to obtain the reference phase distribution: a small flat surface acts as reference plane, based on the phase distribution of the flat surface in both horizontal and vertical directions and Zernike polynomials fitting method, the phase distribution of virtual reference plane in the field of view during the whole measurement operation can be fitted. Once the calibration is finished, the system is ready for measurement.

5.Shape reconstruction

From Equation (1), it is easy to find out that not only the slopes but also the height of the collector surface has an influence on the position of the observed point on the screen. In order to obtain the height of object, we should reconstruct the collector shape from gradient data, which is very important to absolutely measure and evaluate the optical character of solar collector. To reconstruct the shape, one has to use the numerical integration method. But, most existing methods have different drawbacks: they either suffer from error propagation, or they introduce global errors due to unknown boundary conditions. The desired shape reconstruction method should have both local and global integration methods, which means that it should preserve the local details without propagating the error along a certain path. In this paper, the interpolation approach is used to reconstruct the shape from gradient data[19]. The gradient data is given as

pairs $(p_x(X_i), p_y(X_i))$, where $p_x(X_i)$ and $p_y(X_i)$ are the measured slopes of the collector at X_i in x and y directions, respectively ($1 \le i \le N$). Define the interpolate to be

$$z(X) = \sum_{i=1}^{N} \alpha_i \phi_x(X - X_i) + \sum_{i=1}^{N} \beta_i \phi_y(X - X_i) \tag{3}$$

where α_i and β_i are coefficients and ϕ is a radial basis function. ϕ_x and ϕ_y denote the analytic derivative of ϕ with respect to x and y , respectively. To obtain the coefficients in Equation (3), the analytic derivatives of the interpolate ϕ with the measured gradient data are matched as:

$$z_x(X_i) = p_x(X_i);\ z_y(X_i) = p_y(X_i); \tag{4}$$

The coefficients can be determined by solving the following linear equations:

$$\begin{pmatrix} \phi_{xx}(X_j - X_i) & \phi_{xy}(X_j - X_i) \\ \phi_{xy}(X_j - X_i) & \phi_{yy}(X_j - X_i) \end{pmatrix} \begin{pmatrix} \alpha_i \\ \beta_i \end{pmatrix} = \begin{pmatrix} p_x(X_i) \\ p_y(X_i) \end{pmatrix} \tag{5}$$

Based on the resulting coefficients α_i and β_i , the collector surface can be reconstructed by using the interpolate in Equation (3). The radial basis function ϕ can be chosen to be the Wendland's function[20] :

$$\phi(r) = \frac{1}{3}(1-r)_+^6(35r^2 + 18r + 3), r = \sqrt{x^2 + y^2} \tag{6}$$

This has two reasons for choosing the function. Firstly, Wendland's function allows one to choose their continuity according to the smoothness of the given data. This function is in $C^4(R_+)$ and leads to an interpolant, which is three times continuously differentiable and guarantees the integrability condition. Secondly, the compact support of the function allows one to adjust the support size in such a way that the solution of Eq. (5) is stable in the presence of noise [19]. To achieve this, one has to choose an appropriate scaling factor ρ . In [23], the authors showed that with an increasing support radius the interpolation error (i.e., the deviation from the measured slope data) increase, while the evaluation error (the deviation of the reconstructed shape) decreases. A larger support radius leads to more stable reconstruction in the presence of noise.

In the measurement, the amount of data is rather large. To solve such large data, the following method is presented: firstly, the data sets are split into a set of overlapping patches. On each patch, the data is interpolated and the calculated up to a constant of integration. Secondly, the least-squares fitting scheme is used to obtain the reconstructed surface on the entire field.

In Equation (1), both parameters L and α are unknown, an iterative strategy is applied to obtain the shape of measured collector surface:

1) Calculate the phase difference $\Delta\varphi_x$;
2) Let the height $z^0 = 0$, calculate the gradient $\tan\theta$ from Equation (1);
3) Reconstruct the height z^m of each patches from the gradient data, then obtain the entire field shape based on fitting scheme;
4) Calculate the difference between the adjacent iterative results $\Delta = z^m - z^{m-1}$;

5) If Δ is bigger than the iterative termination condition, calculate the gradient data from Equation (1) again. Then, return step 3); Otherwise, go to step 6);
6) Iterative terminate, recover the shape of collector.

In order to demonstrate the ability of proposed method, a simulation is conducted. The simulated function is defined by

$$z = 3(1-x)^2 \, \mathrm{e}^{(-x^2-(1+y)^2)} - 10\left(\frac{x}{5} - x^3 - y^5\right) \mathrm{e}^{(-x^2-y^2)} - \frac{1}{3}\mathrm{e}^{(-(1+x)^2-y^2)} \tag{7}$$

where the in-plane dimension x and y are both limited within a range from -3 to 3 mm with a sampling of 200×200 points. The true height is shown in Figure 3. The radial basis function integration method is used to integrate the shape within 13×13 subsets with a subset size of 20×20 and 25% overlap between neighboring subsets. Figure 4 (a) depicts the reconstructed shape on overlapping patches. Figure 4(b) and (c) show the reconstructed shape and the reconstructed height error. The deviation of height errors (RMS) is only less than 6×10^{-4} mm.

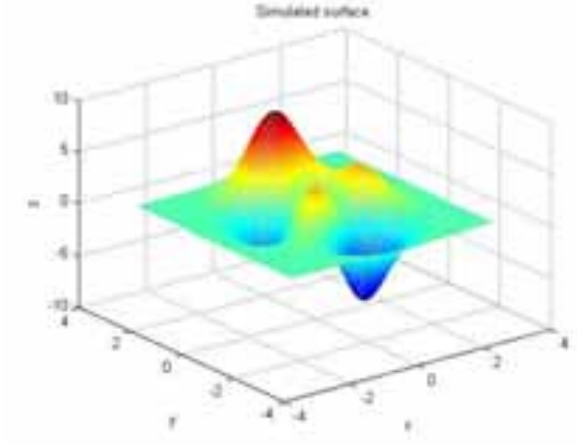

Figure 3: Simulated surface.

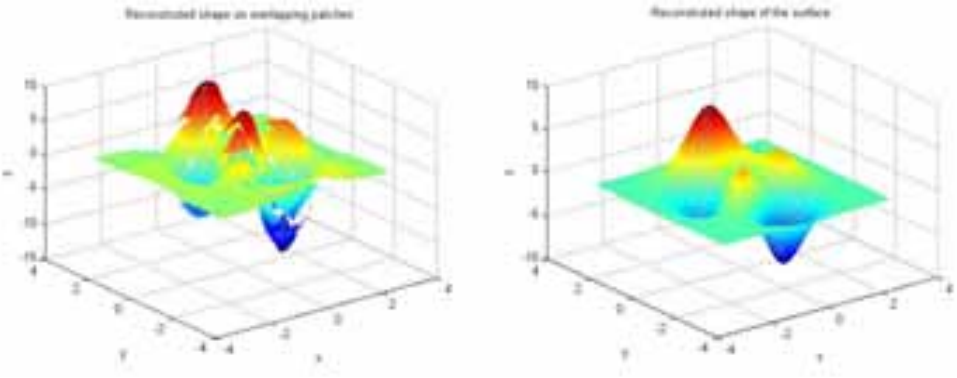

(a) (b)

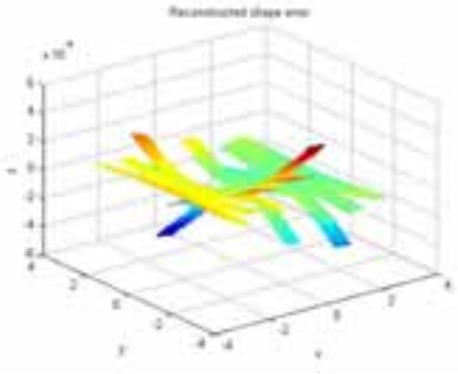

(c)

Figure 4: (a) Reconstructed shape on the overlapping patches; (b) Reconstructed shape of surface; (c) Reconstructed shape error.

6.Experiment

An experimental investigation of the feasibility of the proposed method is carried out as well. A RP3 inner mirror is measured with the fringe reflection technique. Figure 5(a) shows the two-dimensional pattern on the screen, which is projected on the target screen, the distorted patterns are captured by CCD camera (shown in Fig.5(b)). Figure 6 (a) - (d) show the slope distribution and slope error in both x and y directions, respectively, in which the local discontinuous areas are due to the phase unwrapped algorithm of the two-dimensional pattern. The slope errors (RMS, deviation from the ideal slope of shape) are: 2.6129mrad (x-direction), 0.1460mrad (y-direction). The proposed reconstructed method is then utilized to integrate the gradient data to reconstruct the shape of collector, which is shown in Figure 7 (a). In Fig. 7(b), it is the reconstruction error, (deviation from the ideal shape) which shows that this reconstruction method is efficient even in the presence of the phase-unwrapped errors of Fig 6(a)-(d).

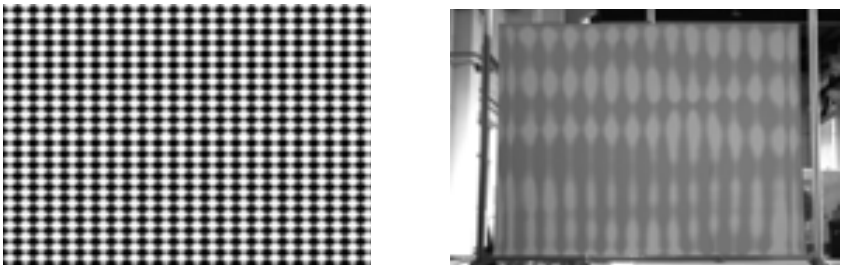

(a) (b)

Figure 5: (a) The two-dimensional pattern on screen; (b) The distorted pattern.

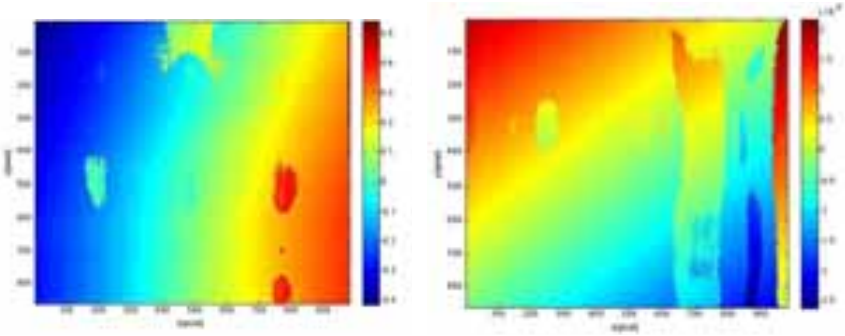

(a) (b)

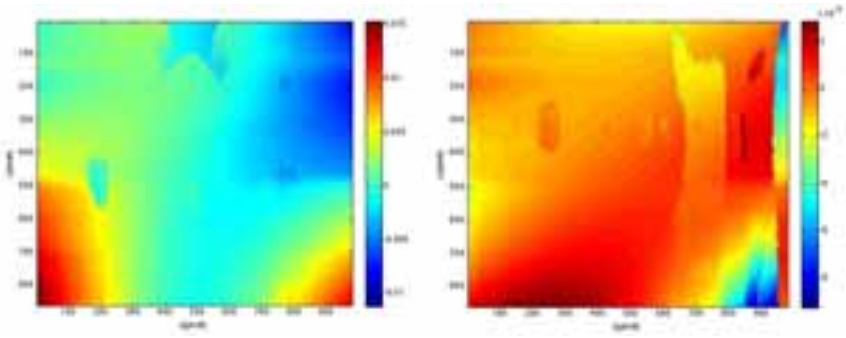

(c) (d)

Figure 6: (a) Slope distribution in the x-direction; (b) Slope distribution in the y-direction; (c) Slope error distribution in the x-direction; (d) Slope error distribution in the y-direction;

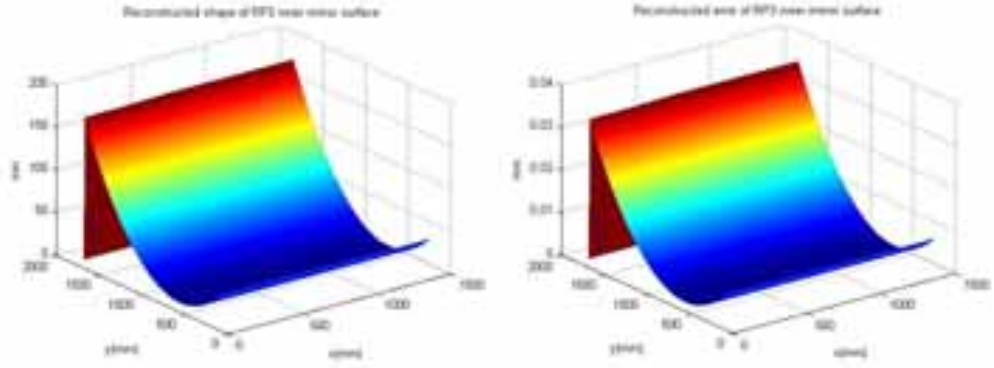

(a) (b)

Figure 7: (a) Reconstructed shape of RP3 inner mirror surface; (b) Reconstructed error.

7.Conclusion

In this paper, a solar collector surface measuring system based on orthogonal fringe reflection technique was built. The orthogonal fringe was projected onto a target screen and the deformed pattern modulated by the measured collector was captured by CCD camera. By establishing the mathematical relationship between phase difference and the gradient values of collector surface, the slope results were obtained. A shape reconstruction method based on approximation employing radial basis functions was proposed. Compared with the classical four-step phase shifting method, the proposed technique required only two fringe images to achieve 3D shape measurement of solar concentrator. The experiment measurement results demonstrated that not only were fine details preserved, but also the global shape was reconstructed as well, and even higher global accuracy. Furthermore, this measurement system made it possible to measure a large class of solar collectors.

Acknowledgements

The authors acknowledge the financial support from Supported by The National Natural Science Foundation of China (Grant No.61505211 and 51306171), The National Key Technology R&D Program (2012BAA05B02) .

References

1. Hansche B. Laser Ray Trace Tester for parabolic trough solar collectors. NDT Technology Division

9352, Sandia Laboratories, New Mexico, 1978, ISBN 87664-407-8.

2. Xiao J, Wei XD, Lu ZW, Yu WX, Wu HS. A review of available methods for surface shape measurement of solar concentrator in solar thermal power applications. Renewable and Sustainable Energy Reviews. 2012; 16:2539-2544.
3. Ulmer S, Marzr T, Prahl C, Reinalter W, Belhomme B. Automated High Resolution measurement of heliostat slope errors. Proceedings of the SolarPACES Conference. Berlin, Germany. 2009.
4. Marz T, Praul C, Ulmer S, Wilbert S, Weber C. Validation of two optical measurement methods for the qualification of the shape accuracy of mirror panels for concentrating solar systems. Journal of Solar Energy Engineering. 2011; 133:031022 1-7.
5. Ulmer S, Heinz B, Pottler K, Lupfert E. Slope error measurements of parabolic troughs using the reflected image of the absorber tube. Proceedings of the SolarPACES Conference. 2006.
6. Ulmer S, Marz T, Prahl C, Reinalter W, Belhomme B. Automated high resolution measurement of heliostat slope errors. Solar Energy. 2011; 85(4):681-7.
7. Zhu HB, Wang ZF, Wang HR. Novel method for shape measurement system of heliostat mirrors based on fringe reflection and its calibration. Proceedings of the SolarPACES Conference. Morocco. 2012.
8. Pottler K, Röger M, Lüpfert E, Schiel W. Automatic non-contact quality inspection system for industrial parabolic trough assembly. Journal of Solar Energy Engineering. 2008; 130(1):011008-5.
9. Pottler K, Lupfert E, Johnston G, Shortis MR. Photogrammetry: a powerful tool for geometric analysis of solar concentrators and their components. Journal of Solar Energy Engineering 2008; 127:94-101.
10. Roger M, Prahl C, Ulmer S. Fast determination of heliostat shape and orientation by edge detection and photogrammetry. Proceedings of the SolarPACES Conference. Las Vegas, NV USA, 2008.
11. Lehmann AG. Rapid heliostat surface measurement using reconstruction from camera images, Proceedings of the SolarPACES Conference. Granada, Spain, 2011.
12. Montecchi M, Benedetti A, Cara G. Fast 3D optical-profilometer for shape-accuracy control of parabolic-trough facets. Proceedings of the SolarPACES Conference. Granada, Spain, 2011.
13. Jones SA, Gruetzner JK, Houser RM, Edgar RM, Wendelin TJ. VSHOT Measurement Uncertainty and Experimental Sensitivity Study. Proceedings of the 32nd Annual Intersociety Energy Conversion Engineering Conference, Vol. 3, pp. 1877-1882.
14. Andraka C, Sadlon S, Myer B, Trapeznikov K, Liebner C. Rapid reflective facet characterization using fringe reflection techniques. Proceedings of the Energy Sustainability 2009, San Francisco, California, USA.
15. Diver RB, Moss T. Practical field alignment of parabolic trough solar concentrators. Journal of Solar Energy Engineering. 2009; 129:153-159.
16. Francini F, Fontani D, Sansoni P, Mercatelli L, Jafrancesco D, Sani E. Evaluation of Surface Slope Irregularity in Linear Parabolic Solar Collectors. International Journal of Photoenergy. 2012; pp 921780 1-6.
17. Wei T, Klette R. Height from gradient using surface curvature and area constraints. Third Indian Conference on Computer Vision, Graphics and Image Processing, 2002, pp. 204-210.
18. Wu Z, Li L. A line-integration based on method for depth recovery from surface normals. Computer Graphics and Image Process, 1988: 43, 53-66.
19. Ettl S, Kaminski J, Hausler G. Generalized hermite interpolation with radial basis functions considering only gradient data. Curve and Surface Fitting: Avignon 2006, Nashboro Press, 141-149.
20. Wendland H. Piecewise polynomial positive definite and compactly supported radial basis functions of minimal degree. Advances in Comp. Math, 1995: 4, 389-396.

21. Zhu H.B., Wang Z.F., Shape measurement and reconstruction of solar concentrator based on two-dimensional phase shift method, Energy Procedia, 69, 1921-1927, 2015.

22. Nitzan Goldberg, Amichai Zisken, Heliostat surface estimation by image processing, Proceedings of the SolarPACES Conference. Beijing, China, 2014.

23. S. Lowitzsch, J. Kaminski, M. C. Knauer, and G. Häusler, "Vision and modeling of specular surfaces," in Vision, Modeling, and Visualization 2005, G. Greiner, J. Hornegger, H. Niemann, and M. Stamminger, eds. (Akademische VerlagsgesellschaftAka GmbH, 2005), pp. 479–486.

24. Yang S.L., Chen Y.F., The Vector analysis and the application of fringe reflection method. National Cheng Kung University, Master thesis, 2007.

Conference Proceedings

Solar World Congress 2015
Daegu, Korea, 08 – 12 November 2015

Heat conductivity performance of SiC and Si_3N_4 as volumetric receiver under concentrated irradiation

M. Nakakura[1], M. Ohtake[1], T. Yoshida[1], K. Matsubara[2], T. Kodama[1], K. Yoshida[3]

[1] Faculty of Engineering, Niigata University, Ikarashi 2-nocho 8050, Nishi-ku, Niigata 950-2181, Japan

[2] Faculty of Engineering, Niigata University: Professor, Doctor of Engineering, Ikarashi 2-nocho 8050, Nishi-ku, Niigata 950-2181, Japan

[3] Institute of Applied Energy: Counselor, Doctor of Engineering, 1-14-2, Nishi-Shimbashi 1-Chome, Tokyo 105-0003, Japan

Abstract

Recently, researchers of Niigata University and the Institute of Applied Energy (IAE) developed an air receiver-evaluation system equipped with 30kW_{th} point-concentration simulator to support solar-thermal usage in middle to high temperature. 147mm×147mm×100mm monolithic silicon carbide (SiC) honeycomb block used as volumetric receiver sample, and some experimental results were gathered from demonstration tests. Also, its three-dimensional simulation method was developed on FLUENT 14.5, in parallel. This simulation, based on dual-cell approach, considers that thermal non-equilibrium between solid and fluid domains in porous region defined as volumetric receiver material. And, its calculation regions include the upper and lower air domains in the porous region; therefore, this method is able to analyze the influence of inlet/outlet air flow. Under the same condition with tests, power on aperture (POA) and air-mass flow rate (AMF), some numerical results indicated similar results. This paper describes an example compared simulation and computational result. Also, a comparison between receiver outlet air temperature and solid/fluid max temperature caused by receiver material (SiC and Si_3N_4: silicon nitride) is presented.

Keywords: *CSP, Volumetric receiver, Receiver evaluation, Three-dimensional simulation, Receiver material*

1. Introduction

At present, solar thermal assessment have been carried out by many institutes and researchers, for renewable and clean solar thermal usage attract attention as an alternative energy to fossil fuels (Tsoutsos et al., 2003; Reif and Alhalabi, 2015). In Europe and United States, parabolic-trough solar plants are in operation to produce electricity to grid through the commercial operating. But its ability of electricity production is not enough for energy demand grown larger every year. On the other hands, tower type Concentrated Solar Power (CSP) plant is possible to achieve higher temperature than traditional solar plant because of its high concentrating ratio; therefore, there is a possibility of making a high efficiency generation (Ávila-Marín, 2011). A tower CSP plant combined with traditional Combined Cycle (CC), also called Solar-driven Combined Cycle (SCC), for practical solar-thermal utilization is expected to solve the energy problem people face today (Poživil et al., 2014). In order to realize the SCC technology, there are some studies of volumetric receiver using porosity material (mesh, foam, or honeycomb etc.) and its material (metal or ceramics etc.) (Fend et al., 2004; Ávila-Marín et al., 2014; Sallaberry et al., 2015). But, these research are still on fundamental stage and a lot of information (e. g. receiver geometry, material and thermal property etc.) are necessary to design high-temperature and -durability receiver.

In 2013, researchers of Niigata University and IAE developed an air receiver-evaluation system used a world-class 30kW_{th} beam-down point concentration sun simulator and its three-dimensional simulation method for

doi:10.18086/swc.2015.04.07 Available at http://proceedings.ises.org

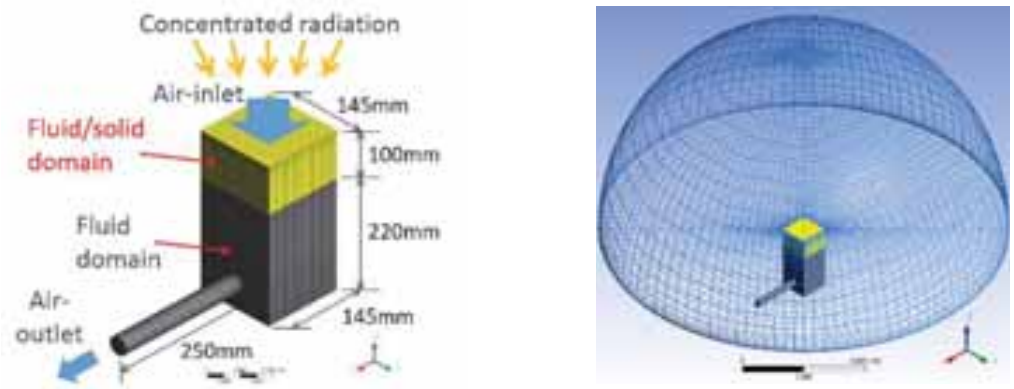

(a) The mesh of volumetric receiver (b) The calculation domain

Fig. 1 The three-dimensional simulation model.

research and development of solar-thermal receivers in middle to high temperature range (Nakakura et al., 2015). This evaluation system is possible to test by a beam-down point concentration, independent of unstable natural environment. Also, its simulation based on the dual-cell approach considers that thermal non-equilibrium between fluid and solid domain. Its numerical model includes upper/lower fluid domain on receiver; accordingly the influence of inlet-/outlet-air on receiver is able to analyze in detail. In this paper, the receivers of SiC and Si_3N_4 are simulated to reveal their suitability as volumetric receiver material.

2. Calculation model and boundary conditions

The computational model of the volumetric receiver flow and heat transfer was developed on ANSYS FLUENT 14.5. Figure 1 shows the mesh model of volumetric receiver and its calculation domain. Receiver material domain defines that porous medium have a solid domain within fluid one, and its size is similar to experimental sample 145mm×145mm×100mm. In this simulation, this porous domain is assumed to be a honeycomb geometry adapting the drag coefficient of rectangular to air flow direction. This three-dimensional simulation based on the dual-cell approach considers that the thermal non-equilibrium between the solid and fluid domain of the porous. Also heat flux distribution performed linear interpolation is adapted to the porous-surface as a boundary condition. This flux distribution was measured using Niigata University's $30kW_{th}$ sun simulator through the scanning of a gardon gage (Nakakura et al., 2015). The outlet plane is used to definite air-mass flow rate (AMF), and the boundary of each plane is insulated. This calculation domain include upper and lower domain of the porous as a feature, hence this method is able to analyze the influence of inlet-/outlet-air flow effected to the porous medium.

The continuity and momentum equations are expressed as:

$$\nabla \cdot (\gamma \rho \vec{v}) = 0 \; ; \qquad \text{(eq. 1)}$$

$$\nabla \cdot (\gamma \rho \vec{v} \vec{v}) = \; -\gamma \nabla \rho + \nabla \cdot \mu \gamma (\nabla \vec{v} + \nabla \vec{v}^T) + \gamma \vec{B}_f - \left(\frac{\gamma^2 \mu}{K} \vec{v} + \frac{\gamma^3 C_2}{2} \rho |\vec{v}| \vec{v} \right). \qquad \text{(eq. 2)}$$

This momentum equation is added by the pressure loss term arising from the viscosity and inertia in the porous domain. In this equation, γ represents porosity, B_f is body force, 1/K is viscous loss coefficient, and C_2 is inertial loss coefficient. This model assumes incompressible ideal gas, and considers the temperature dependency of density, viscosity and specific heat. Also SST k-ω model is used as turbulence equation; it follows,

$$\frac{\partial}{\partial x_i}(\rho k u_i) = \frac{\partial}{\partial x_j}\left(\Gamma_k \frac{\partial k}{\partial x_j} \right) + G_k - Y_k \; , \qquad \text{(eq. 3)}$$

$$\frac{\partial}{\partial x_i}(\rho \omega u_i) = \frac{\partial}{\partial x_j}\left(\Gamma_\omega \frac{\partial \omega}{\partial x_j} \right) + G_\omega - Y_\omega + D_\omega \; . \qquad \text{(eq. 4)}$$

In this instance, Γ is effective diffusivity, Y is dissipation due to turbulence, G is generation term, and D_ω is cross-diffusion term. The subscript k represents turbulence kinetic energy, and ω represents specific

Tab. 1: The calculation parameters.

Elements	Porosity γ	Material	Density ρ_s (kg m^{-3})	Thermal conductivity k_s ($Wm^{-1}K^{-1}$)	Specific heat C_{ps} ($J\ kg^{-1}\ K^{-1}$)	
179202	0.538	SiC	3200	90	1000	
		Si3N4	3300	27	650	
Specific surface A_{fs} (m^{-1})	Heat transfer coefficient at radiated surface h_{fs} ($W\ m^{-2}\ K^{-1}$)	Ambient air temperature T_{amb} (K)	Viscos loss coefficient 1/K[X, Y, Z]	Inertial loss coefficient C_2[X, Y, Z]	Apparent absorptivity α_{app}	Apparent emissivity ε_{app}
2105	114.2	300	0, 0, 0	100, 100, 0.432	0.70, 0.83	0.70, 0.83

dissipation rate. Energy equations based on the dual-cell approach can be written as:

$$\frac{\partial}{\partial t}\left(\gamma\rho_f E_f\right) + \nabla\cdot\left(\vec{v}\left(\rho_f E_f + p\right)\right) = \nabla\cdot\left(\gamma k_f \nabla T_f - \left(\sum_i h_i J_i\right) + \left(\bar{\bar{\tau}}\cdot\vec{v}\right)\right) + h_{fs}A_{fs}\left(T_s - T_f\right) \quad \text{(eq. 5)}$$

$$\frac{\partial}{\partial t}\left((1-\gamma)\rho_s E_s\right) = \nabla\cdot\left((1-\gamma)k_s\nabla T_s\right) + h_{fs}A_{fs}\left(T_f - T_s\right). \quad \text{(eq. 6)}$$

The dual-cell approach solves each energy equation for fluid/solid domains, under thermal non-equilibrium assumption; so it takes into consideration of the interaction of heat transfer, in porous domain. Each energy equation of solid/fluid domain is added non-equilibrium source. In these energy equations, E refers to total energy, k is thermal conductivity, and h_{fs} is heat transfer coefficient at radiated surface, A_{fs} is specific surface. The subscript f represents fluid domain, s represents solid domain. Also, surface-radiation is treated as a boundary condition without using radiation models, described as:

$$Q_{total} = \alpha_{app}Q_{solar} + Q_{rad} \quad \text{(eq. 7)}$$

$$Q_{rad} = \sigma\varepsilon_{app}\left({T_{amb}}^4 - {T_{surf}}^4\right) \quad \text{(eq. 8)}$$

In this equation, Q_{solar} refers to heat flux distribution adapted to porous surface, α_{app} and ε_{app} are apparent absorptivity and emissivity due to receiver geometry, σ is Stefan-Boltzmann constant, T_{amb} is ambient air temperature, and T_{surf} is porous surface temperature. Table 1 summarizes numerical parameters used in this simulation.

3. Simulation results and analysis

3.1. Results of three-dimensional simulation

Figure 2 indicates that a comparison between experimental results and simulation ones. The y-axis shows ΔT or efficiency, and the x-axis is POA/AMF. The ΔT is calculated from difference between the outlet air temperature and the ambient air temperature. Also, the efficiency represents the ratio of thermal absorption on an exhaust bulk air temperature to power-on-aperture (POA). Firstly, through some calculations under the same condition with the test, the numerical analysis is able to obtain the similar results with experimental ones in both of ΔT and efficiency. Hence, this simulation method indicates the accuracy of simulation as volumetric receiver evaluation. The difference of ΔT in the high-temperature range is estimated by temperature-independence on the porous media. Also, in the experimental tests, efficiency is calculated from heat-absorption of coolant water and exhaust air to POA; therefore, the value calculated from experimental results is lower than simulation results because there is a heat-conduction loss from air to water.

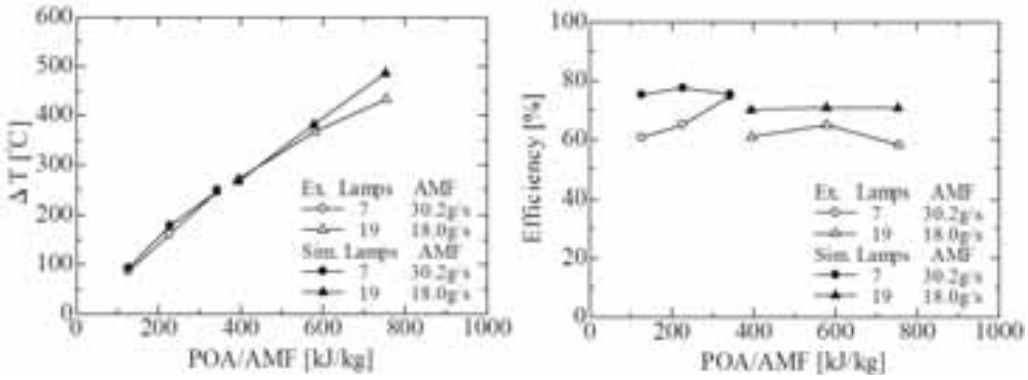

(a) Delta T (b) Efficiency

Fig. 2 Comparison between experimental results and simulation ones.

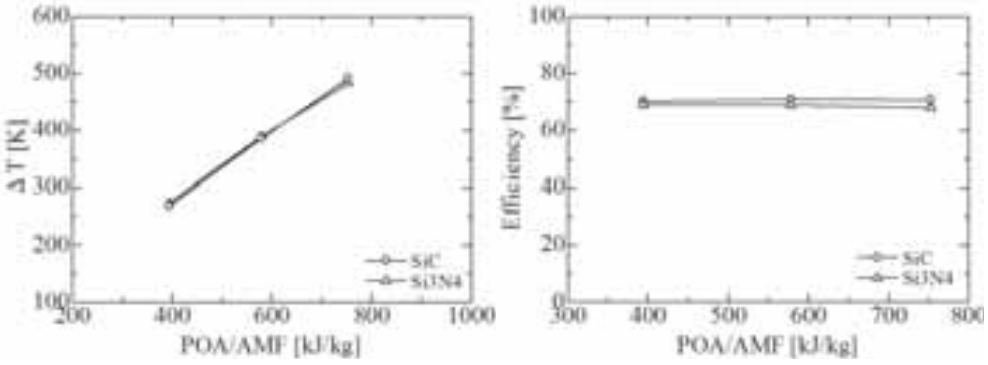

(a) Delta T (b) Efficiency

Fig. 3 Comparison between SiC and Si_3N_4.

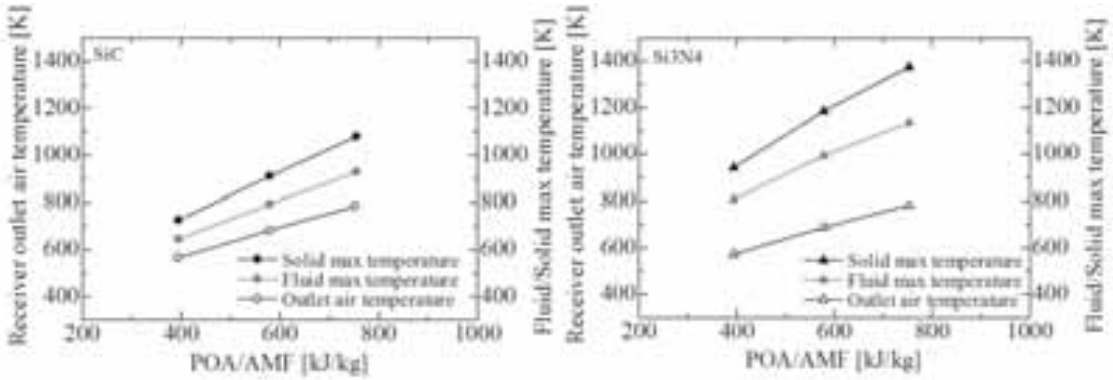

(a) SiC (b) Si_3N_4

Fig. 4 Outlet air temperature and solid/fluid maximum temperature.

Figure 3 designates results of ΔT and efficiency from some calculation fed the physical property of SiC or Si_3N_4. There are no significant difference both of ΔT and efficiency on the values. Approximately, ΔT is 500K, and efficiency is 70% both of cases.

Figure 4 shows a comparison of the outlet air-temperature and the solid/fluid maximum temperature in SiC or Si_3N_4. The outlet air-temperature, as shown in Fig. 3, don't reveal a difference between SiC and Si_3N_4. However, there are large gap on the solid and fluid maximum temperature. In relation to the solid maximum temperature, Si_3N_4 derives 1375K, and SiC shows 1061K. The difference in temperature between the solid max- and outlet air-temperature is 592K and 270K, in each case. Also, on the fluid maximum temperature, Si_3N_4 is 1134K, and SiC is 932K. The difference in temperature between the fluid max- and outlet air-temperature shows 351K and 141K, in each case. This cause of the differences between Si_3N_4 and SiC will be

discussed in detail, below.

3.2. Analysis of contours

SiC and Si_3N_4 as a volumetric receiver material will be discussed from some counters of results acquired in subsection 3.1. All of the following figures are obtained from a state of POA/AMF=800kJ/kg.

Figure 5 indicates that fluid-temperature distribution on Z-X cross-section of the calculation model. The ambient air is heated on porous domain, and exhausted through the outlet pipe at approximately 800K. In the case of Si_3N_4, high temperature air reach down to more deep position than SiC. Also, the highest temperature appears into the slightly downward spot, not on the irradiated surface in both cases. These results are guessed from influence of inlet air-flow.

Similarly, figure 6 shows solid-temperature distribution on Z-X cross-section of the simulation model. There is the radial heat conductivity from irradiated centre in both cases. In the deep position of Si_3N_4, solid-temperature is higher than SiC, likewise the fluid-temperature. Also, slightly, solid-temperature at end of the porous media is lower; therefore large temperature distribution is able to be confirmed than SiC.

Figure 7 represents temperature distribution of porous surface. The thermal conductivity and specific heat of Si_3N_4 are lower than SiC. Hence, it is easy to increase temperature of irradiated point, but it is hard to expand the heat around the porous media.

Figure 8 shows a streamline of SiC. About a streamline, there was no noticeable difference between SiC and Si_3N_4. This simulation is possible to verify the behaviour of air-flow on the volumetric receiver from the upper and lower calculation domain. The ambient air is inhaled into the porous from extensive area, and accelerated at the outlet pipe.

By these counters, the solid maximum temperature of Si_3N_4 is approximately 300K higher, and, according to the low conductivity, temperature distribution is tend to be larger than SiC; therefore, only in the point of heat transfer performance, SiC is speculated the advantage as volumetric receiver material than Si_3N_4.

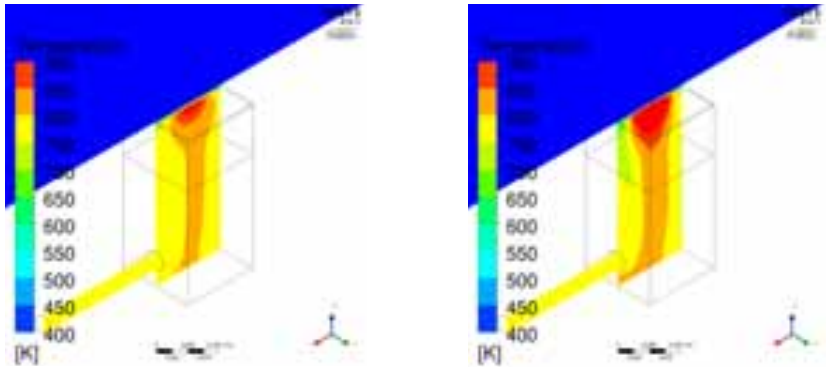

(a) SiC **(b) Si_3N_4**

Fig. 5 Fluid temperature distribution on Z-X cross-section.

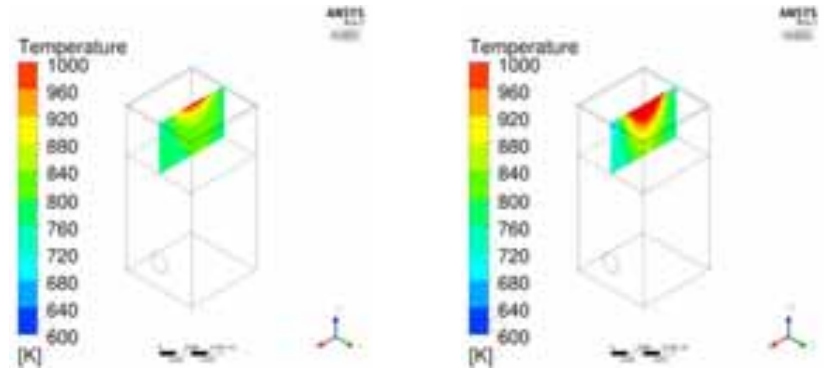

(a) SiC **(b) Si_3N_4**

Fig. 6 Solid temperature distribution on Z-X cross-section.

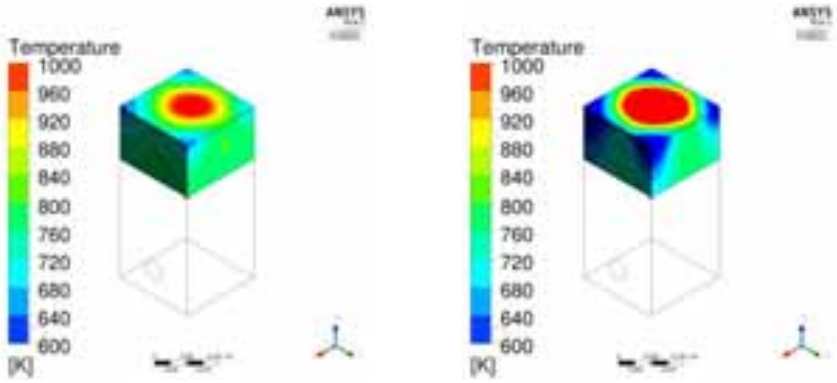

(a) SiC (b) Si_3N_4

Fig. 7 Temperature distribution of porous surface.

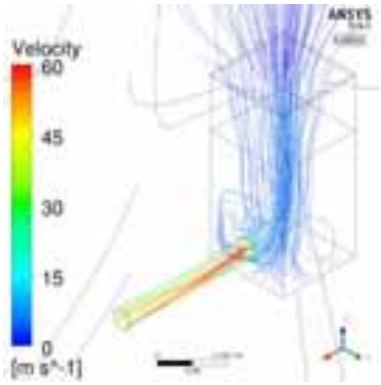

Fig. 8 Streamline.

4. Conclusion

(1) Niigata University and the Institute of Applied Energy developed a volumetric receiver evaluation system using world-class 30kW_{th} point-concentration sun simulator and its three-dimensional simulation method.
(2) The accuracy as a simulation method was confirmed by the comparison between experimental- and numerical-results; therefore this method is able to be used in data acquisition related to the volumetric receiver or new design one.
(3) Under the same condition of POA and AMF, there was not much of a difference in the outlet air-temperature between SiC and Si_3N_4. Nevertheless, on the porous media, SiC possessed a small temperature distribution comparatively, hence the advantage of SiC as volumetric receiver was verified in the point of heat transfer ability.

5. References

Avila-Marin, A.L., 2011. Volumetric receivers in Solar Thermal Power Plants with Central Receiver System technology: A review. Sol. Energy 85, 891-910.
Avila-Marin, A.L., Alvarez-Lara, M., Fernandez-Reche, J., 2014. Experimental results of gradual porosity wire mesh absorber for volumetric receivers. Energy Procedia 49, 275-283.
Fend, T., Pitz-Paal, R., Reutter, O., Bauer, J., Hoffschmidt, B., 2004. Two novel high-porosity materials as volumetric receivers for concentrated solar radiation. Sol. Energy Mater. Sol. Cells 84, 291-304.
Nakakura, M., Ohtake, M., Matsubara, K., Yoshida, K., Cho, H.S., Kodama, T., Gokon, N., 2015. Development of a receiver evaluation system using 30 kWth point concentration solar simulator. Energy Procedia 69, 497-505.
Poživil, P., Aga, V., Zagorskiy, A., Steinfeld, A., 2014. A pressureized air receiver for solar-driven gas turbines. Energy Procedia 49, 498-503.

Reif, J.H., Alhalabi, W., 2015. Solar-thermal powered desalination: Its significant challenges and potential. Renew. Sustain. Energy Rev. 48, 152-165.
Sallaberry, F., García de Jalón, A., Zaversky, F., Vázquez, A.J., López-Delgado, A., Tamayo, A., Mazo, M.A., 2015. Towards standard testing materials for high temperature solar receivers. Energy Procedia 69, 532-542.
Tsoutsos, T., Gekas, V., Marketaki, K., 2003. Technical and economical evaluation of solar thermal power generation. Renew. Energ. 28, 873-886.

Conference Proceedings

Solar World Congress 2015
Daegu, Korea, 08 – 12 November 2015

NUMERICAL INVESTIGATION OF SOLAR PARABOLIC TROUGH RECEIVER UNDER NON UNIFORM SOLAR FLUX DISTRIBUTION

C. Ananthsornaraj [1] and K. S. Reddy[2]

[1] Research Scholar, Heat Transfer and Thermal Power Laboratory, Department of Mechanical Engineering, Indian Institute of Technology Madras, Chennai-600036, INDIA

[2] Professor, Heat Transfer and Thermal Power Laboratory, Department of Mechanical Engineering, Indian Institute of Technology Madras, Chennai-600036, INDIA

Abstract

Three dimensional numerical modeling of parabolic trough receiver is performed to study the non uniform flux distribution on the outer surface of the receiver by coupling Monte Carlo Ray-Tracing Method (MCRT) with the Finite Volume Method (FVM) and calculated non uniform flux distribution is considered as a thermal boundary condition. The numerical model is solved by considering RNG k–ε turbulent model. In this paper, different Heat Transfer Fluids (HTF) with respect to the various operating parameters such as mass flow rate, Direct Normal Irradiation (DNI), inlet temperature and ambient conditions are considered. The temperature profile of both absorber and glass envelope follows the non-uniform solar heat flux distribution curve. Three dimensional temperature distribution of the absorber tube is calculated numerically for different inlet temperature and velocity of HTF. The maximum solar heat flux attained by the PTC receiver is 9753.3 W/m^2, 19506 W/m^2, 29260 W/m^2, and 39013 W/m^2 when the DNI are 200 W/m^2, 400 W/m^2, 600 W/m^2, and 800 W/m^2 respectively.

Keywords: *Solar Energy; Parabolic Trough Collector; Non uniform flux distribution; Computational Fluid Dynamics*

1. Introduction

Parabolic Trough Collector (PTC) system is having considerable attention among the other solar concentrators because it needs only single axis tracking and moderate receiver operating temperature. The receiver is the key element of the PTC system where solar radiation is absorbed and converted into thermal energy (Kalogirou, 2004). The receiver is placed on the focal line and it heats the Heat Transfer Fluid (HTF) which flows through it. The incident solar radiation which falls on the collector eventually gets concentrated on the receiver surface which gets converted into thermal energy. The heat transfer process of receiver can be summarized as: the incident solar radiation on the absorber, the convection heat transfer between the HTF and the absorber, the conduction and radiation heat transfer through the absorber wall and the glass tube, and the heat transfer from the glass tube to the ambient (Mahoney, 2002). Non uniform flux developed on the outer surface of receiver due to the concentration of solar energy results in thermal stress and circumferential temperature difference on the absorber wall are the prime reason for the failure of PTC receiver tube. The temperature increase depends on the geometrical concentration ratio and optical properties of the collector as well as fluid flow in the absorber tube. Accurate studies are needed to find three dimensional temperature distributions of the absorber tube and its thermal expansion and deformation for any safe and efficient operation. Deformation of the absorber tube takes place due to a non-uniform thermal expansion (Iverson et al., 2011). Due to this deformation of PTC receiver, it will go out of focal point and causes different problems such as decreasing the life time of collector, breakage of cover glass tube and also it drops optical efficiency of the collector. Edenburn et al., (1976) predicted the efficiency of a PTC by using an analytical heat transfer model for evacuated and non-evacuated cases. The results showed good agreement with

doi:10.18086/swc.2015.04.08 Available at http://proceedings.ises.org

measured data obtained from SNL collector test facility (Pope et al., 1973). Ratzel et al., (1979) carried out both analytical and numerical study of the heat conduction and convective losses in an annular receiver for different geometries. Three techniques were proposed to reduce the conduction heat loss: evacuation, over sizing the annular receiver while keeping the Rayleigh number below 1000 over the range of operation and use of gases with low thermal conductivity. Clark (1982) analyzed the effects of design and manufacturing parameters that influenced the thermal and economical performance of parabolic trough receivers

Recently, Cheng et al., (2012) reported a three-dimensional simulation of a parabolic trough solar collector with non-uniform solar flux conditions by incorporating the FVM and the MCRT method, in which the effects of the properties of different HTFs to the whole temperature distributions in the receiver, the thermal loss and the collector efficiency were numerically studied Moreover, the effects of the DNI, Reynolds number and emissivity of the inner tube wall on the outlet temperature, average temperature of absorber outer wall, thermal radiation loss and efficiency, and the concentrating characteristics of the parabolic trough solar collectors PTC (He et al., 2011) were discussed. Because of the non-uniform distributions of the solar energy flux, there exist CTD of the absorber and the cover, which has a crucial influence on the circumferential stress and the deformation of the receiver tubes. Numerous studies have been carried out to investigate the temperature distributions and thermal stress fields of tubes and receivers with various material conditions. A numerical analysis had been conducted by Chen et al., (2004) to study the effect of using porous material for the receiver on temperature distributions. Experiments were conducted by Fend et al., (2004) to research the temperature distributions on the volumetric receivers used two novel porous materials. Numerical simulations are used to investigate the detailed temperature distribution, and its corresponding structural deformation of the stainless steel tube of PTR. The simulations are performed by combining a MCRT code and Finite Volume Method. The non-uniform concentrated solar heat flux on the steel pipe was obtained through the MCRT method (He et al., 2011). The fluid–solid coupled heat transfer was solved with the finite volume method. The concentrated solar heat flux was used as a boundary condition of the fluid–solid coupled heat transfer modeling. In the annular vacuum gap, the conduction was ignored, and the infrared radiation heat transfer was treated as a gray enclosure and modeled with S2S radiation model. In the CFD simulations, the studied PTR (Fig. 1) was assumed to be structurally rigid, and its surfaces have wavelength independent properties. The HTF (heat transfer fluid) had temperature dependent properties. Güven et al., (1986) established an optical model which used a ray-tracing technique to evaluate the optical performance and determined the optical errors by means of a statistical analysis. Valladares et al., (2009) proposed a numerical simulation of the optical, thermal and fluid dynamic behavior of a single-pass solar PTC and extended the study by replacing the absorber with counter-flow concentric circular heat exchangers (double-pass). Kumar et al., (2009) investigated heat transfer enhancement of solar receivers with porous insertions by numerical simulation and found that significant heat transfer improvement (64.3%) was obtained. Stuetzle et al., (2002) proposed a 2D unsteady state analysis of solar collector absorber to calculate the collector field outlet temperature: the model was solved by discretizing the partial differential equations obtained by the energy balance.

2. Description & Specification of PTC System

The parabolic solar collector tube consists of cylinder. The inner tube is a metallic tube and the outer tube is a glass tube. Fig. 1 shows the physical geometry and cross section of PTC, which is made by bending a sheet of reflective material into a parabolic shape surface. A receiver tube is placed along the focal line of the parabolic reflective collector. The receiver tube usually includes an inner absorber tube and a glass cover. The glass cover is used for reducing heat loss; as well as the annular space between the inner tube and the glass cover is vacuumed, which helps to decrease the convection heat loss. Fig.1, should include the following processes: convection heat transfer between the HTF and the absorber; solar irradiation absorption in the absorber; conduction heat transfer through the absorber wall; heat transfer from the absorber to the glass tube; solar irradiation absorption in the glass tube; conduction heat transfer through the glass tube; heat transfer from the glass tube to the atmosphere, etc. Particularly, both the convection and the radiation heat transfer occur between the outer absorber surface and the inner glass tube surface. The convection heat transfer mechanism depends on the annulus pressure (KJC Operating Company, 1993). It may either be

molecular conduction or free convection. The heat transfer from the glass tube to the atmosphere is also caused by convection and radiation, where the convection is either forced or natural, depending on whether there is wind around the glass tube.

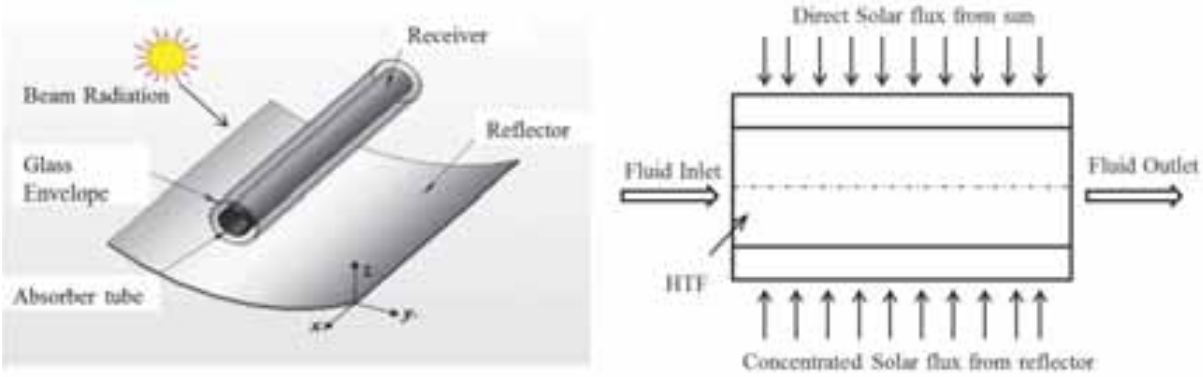

(a) (b)

Fig. 1: Physical model (a) Schematic of PTC (b) Cross section view

The radiation heat transfer occurs due to the temperature difference between the outer absorber surface and the inner glass tube surface, so does the glass tube and sky.

3. Numerical modeling and analysis

The simulations consist of Monte-Carlo ray tracing, CFD modeling. Firstly, Monte-Carlo ray tracing was used to calculate the concentrated solar radiation heat flux distribution on the stainless steel tube (absorber tube) of PTR. This flux distribution is treated as a boundary condition of the CFD analysis. Secondly, CFD was used to model the flow and heat transfer (including convection, conduction and radiation heat transfer) in the PTC receiver.

3.1 Governing Equation

The geometrical model of PTC receiver is shown in Fig.1. The heat transfer process in PTC can be summarized as: the incident solar radiation on the absorber, convection heat transfer between HTF and absorber, conduction and radiation heat transfer through the absorber wall and the glass tube, and heat transfer from the glass tube to the ambient.

As the test conditions shown in Table 1, the fluid flow is in turbulent and in steady state conditions. So the governing equations is given by (Cheng et al., 2010)

$$\partial / \partial x_i(\rho u_i) = 0 \qquad \text{(eq. 1)}$$

$$\rho C_p u_i \frac{\partial T}{\partial x_i} = (k + k_i)\frac{\partial}{\partial x_i}\left(\frac{\partial T}{\partial x_i}\right) \qquad \text{(eq. 2)}$$

$$\frac{\partial T}{\partial x_j}\left(\rho u_i u_j\right) = -\frac{\partial P}{\partial x_i} + \frac{\partial}{\partial x_j}\left[(\mu + \mu_i)\left(\frac{\partial u_i}{\partial x_j} + \frac{\partial u_j}{\partial x_i}\right) - \frac{2}{3}(\mu + \mu_i)\frac{\partial u_i}{\partial x_i}\delta_{ij} - \frac{2}{3}\rho k\delta_{ij}\right] + F \qquad \text{(eq. 3)}$$

3.2 Boundary conditions

The boundary conditions used in this study are:

(1) For the fluid domain, the inlet boundary conditions are defined as the mass flow rate and inlet temperature of HTF. Similarly the outlet boundary condition is fully developed flow condition. Adiabatic boundary condition is applied at both the ends of the receiver walls (Thermal insulation at the absorber end).

Inlet: $m = m_{in}$, $T = T_{inlet}$ $kin = 0.005\rho u_x^2$, $\varepsilon_{in} = C\mu\, \rho_f\, k_{in}^2 / \mu_t$

Where $C\mu = 0.09$, $\mu_t = 100$

Outlet: Fully developed flow condition

(2) Periodic boundary conditions are used for the absorber tube's inlet and outlet. The inner absorber tube walls are considered no-slip and no-penetration .The outer wall of the absorber tube receives a non uniform heat flux. The lower half receives almost concentrated solar radiation while the upper half receives direct solar radiation

(3) The inner surface of absorber tube and the heat transfer fluid were defined as coupled fluid–solid interfaces in which the energy is conserved.

(4) The outer surface of absorber tube and inner surface of glass envelope are formulated by the surface-to-surface radiation

(5) The outer surface of the glass envelope was defined with a mixed boundary with convection and radiation.

(a) Convection boundary condition: (i) if the convection was assumed to be natural (no wind around the PTC receiver) the correlation to estimate heat transfer coefficient .

$$h = {Nu_{D,g}\lambda}\Big/{D_{g,o}} = {\left(\left(0.48\, Ra_{D,go}^{\,0.25}\right)\lambda\right)}\Big/{D_{g,o}} \qquad \text{(eq. 4)}$$

(ii) if the convection was assumed to be forced (presence of wind around the PTC receiver) the experimental correlation to calculate the heat transfer coefficient (Mullick and Nanda, 1989)

$$h = 4V_w^{\,0.58} D_{g,o}^{\,-0.42} \qquad \text{(eq. 5)}$$

(b) Radiative boundary condition**:** The Stefan– Boltzmann law is used to calculate the net radiation transfer by assuming that the glass cover is a small convex gray object in a large blackbody cavity (sky, approximated 8℃ below the ambient temperature). i.e. surface to ambient condition

(6) For the inlet and outlet of the receiver's annulus space, symmetry boundary condition is used such that the normal gradients of all flow variables are zero.

3.3 Computational domain and Properties of HTF:

The computational domain includes the absorber tube domain (solid), the liquid oil domain (fluid) . The material for the solid domain is stainless steel and the thermal conductivity is fixed at 54 W /m.K. Syltherm 800 liquid oil was used as the working fluid. And the properties of working fluid, such as: isobaric specific heat capacity (cp), thermal conductivity (l), density (r) and dynamic viscosity (m) should be selected to simulate the heat transfer process in absorber tube by FLUENT. The properties of HTF are considered to be temperature dependent (He et al., 2011).

3.4 Grid independent study

To guarantee that the computed results were accurate and reliable, a grid independence study was conducted. Simulations with three grids (50,000, 60,000, 70,000, 80,000 elements) were performed. Four different grids are chosen to calculate the temperature difference between the inlet and outlet of PTC receiver for the same boundary conditions. There are less than 2% differences temperature increment between grid 3

and grid 4. The authors concluded that 80,000 elements are enough for this study, and grid 4 with 80,000 elements was used all over this study. It is a traditional grid independence test method for the fluid and heat transfer problem. It should be noted that the minimum grid density is limited by the systematic error.

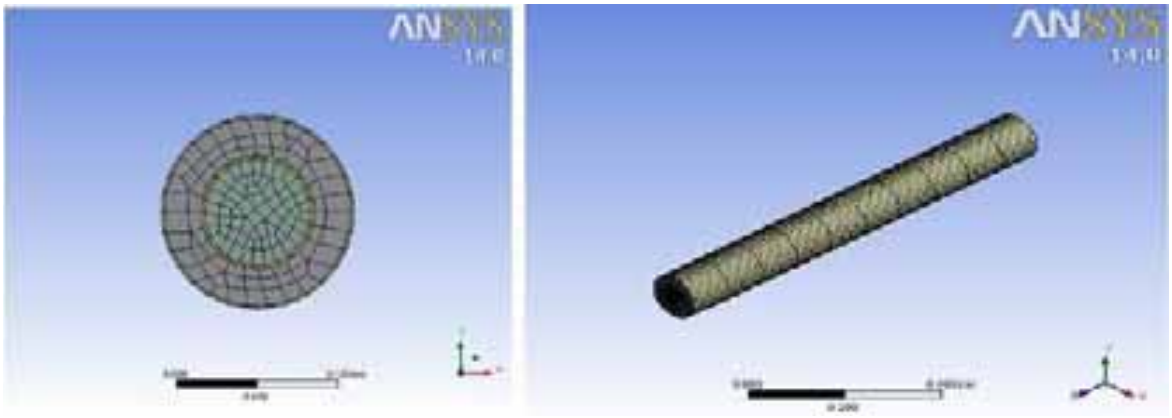

Fig. 2: Grid generated view of fluid region, absorber and glass envelope

4. Numerical modeling and Analysis

A three dimensional mesh was generated and used in this study, see Fig. 6. Dense grids were generated near the bellows where large temperature gradient exists. This three dimensional conjugate heat transfer problem was solved using the CFD software Ansys 14. The standard k–e model (high Reynolds number) was used along with conventional wall functions in this study. The SIMPLE algorithm was used to couple the pressure and the velocities with the second order upwind method used for the advection terms in the momentum equations and for the energy equation. User defined functions (UDF) were used to define the concentrated solar radiation flux on the selective coating and the circumferential distributed source term of the glass envelop. The used discretizations of all the solved equations were second order. The convergence criterion was set to 10^{-4} for continuity and momentum equations and 10^{-7} for energy equation. Radiative heat loss from the receiver pipe solely depends on the emissivity of the pipe, temperature of the pipe and the temperature of the surrounding objects. Hence the receiver pipe and the glass envelope were assumed to be gray and diffuse, and were simulated by surface-to-surface (S2S) radiation model. The glass envelope is assumed to be opaque to the radiation within the infrared energy spectrum.

.4.1 Monte Carlo Ray Tracing (MCRT) Method

The flowchart of the Monte Carlo Ray-Trace method for the photon energy concentrating and collecting process of the whole PTC system is shown. The reflection Ray vector Rs is expressed according to the Fresnel law. Once the photon packet is initialized, the photon is moved, traced in the PTC system, and judged if it hits a boundary (surface) of one of the subsystems or components (such as the glass tube, the reflector and the absorber) on the way of the photon propagated where it may be reflected, absorbed or transmitted. The photon is repeatedly moved until it either escapes from or is absorbed by the system. If the photon hits a boundary when propagating, the corresponding judgment of reflecting, absorbing or transmitting event is adopted by the Monte Carlo method. If the photon escapes from the system, the corresponding parameter of recording the escaped photons is updated. If the photon is absorbed, the position of the absorption and the absorbed energy weight are recorded. This process is repeated until the desired numbers of photons have been propagated. Then the code validations are made and the non-uniform solar energy flux distribution is calculated.

4.2 Combine MCRT Method with FVM

The solar energy flux distribution on the outer wall of the inner absorber tube calculated by in-house developed Monte Carlo Ray- Trace (MCRT) code, then this flux is treated as the heat flux boundary for the simulation model in the FLUENT software with a self developed subroutine program. The self-developed

subroutine program forms a data file of the solar energy flux distribution that can be read by the FLUENT software as a boundary condition, while treating the solar absorption as a surface phenomenon.

5. Validation of Proposed Numerical Model

To further validate the reliability of the presented model, numerical simulations are simulated at the same operating conditions as Sandia test (Dudley.et al., 1994). The calculated heat flux by coupled MCRT and FVM method is validated with the existing model .The present model shows the 15% deviation with the existing developed model. Similarly the simulated circumferential temperature distribution of absorber also validated with existing model.

5.1 Validation of MCRT Code:

To validate the MCRT code, the calculation is performed on the same conventional PTSC as described .(He et al., 2011).using the MCRT method. Figure 10 shows the comparison between the circumferential local concentration ratio (LCR) distribution calculated by the MCRT method in this paper and by the semi infinite integration formulation .From that can be obviously seen that the two LCR distributions have a good agreement, which proves the MCRT code applied in the present study is accurate and reliable. Fig.2 presents the heat flux on the parabolic trough receiver surface. Numerical results show that the predicted results agree well with Wu et al., (2014), which also proves that the MCRT method used in the present study are feasible and the numerical results are reliable.

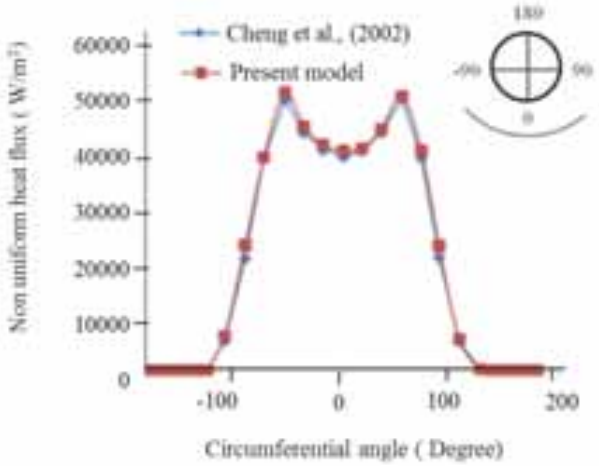

Fig. 4: Non uniform heat flux distribution around the receiver

5.2 Validation of Coupled FVM - MCRT Heat transfer Process:

To validate the simulation method for the coupled heat transfer process within the PTR, the simulation method is performed on the experimental model presented in Dudley et al (1994).

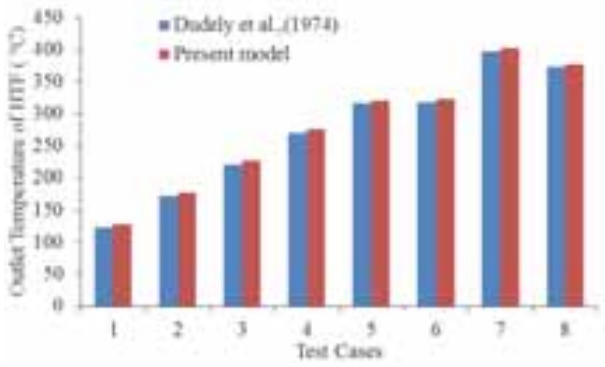

Fig. 5: Validation of receiver outlet temperature with Dudley et al., (1974)

The simulation results and the experimental data under the same conditions. The model results are validated using the data provided by the Sandia National Laboratory .It is indicated that the simulation results agree well with the experiment data, validating the accuracy of the simulation method for the coupled heat transfer process. Tests were also performed with vacuum and with air at ambient pressure in the annulus, and without the glass envelope. The measured data considering the vacuum in the annulus is given in Table 2 and the corresponding validation results are demonstrated in Figure 5. Most of the experiments were done using Syltherm 800 as the HTF, and its thermal properties .The results obtained were overall close to the measured data, with a difference of 4 to 8 ºC.

6. Results and Discussion

The developed simulated model is used to simulate the Non uniform heat flux distribution of receiver. The temperature distribution of the receiver along the length of the absorber tube as well as around the circumferential direction of the PTC receiver. The outlet temperature of HTF is calculated for the given type and mass flow rate of HTF. The simulations are carried out with vacuum condition, around 10^{-4} Torr pressure in annulus region. Due to this the convective heat losses from the absorber to the envelope are negligible, and most of the solar energy absorbed by the coating surface is transferred to the HTF. The temperature distributions of the solar receiver are crucial for the collection of the heat, which will further affect the efficiency of the collector. It is found that the inlet velocity and temperature of the HTF and the DNI will bring an important impact on the temperature distribution of the receiver, which will be numerically investigated in this section. The density, specific heat capacity, viscosity and conductivity of the fluid and the physical properties on the tube material properties are dependent on the temperature distribution of the HTF and it is also estimated from the equations. In the calculation, the velocity in the receiver tube is a parabolic form in fully developed flows. However, it should be pointed out that in real cases the distribution of the inlet velocity of the HTF in tubes presents a parabolic form. In order to simulate a real environment, applying real inlet velocity distribution is important for the improvement of the simulation results, and this issue should be further investigated in the future.

6.1 Non uniform Solar Heat Flux distribution on the outer surface of absorber

An optical model is also developed to calculate the non uniform solar flux distribution around the receiver by using MCRT method. The solar flux density distributions on the outer surface of absorber tube are illustrated in Figures 6 (a) and (b), respectively. The concentrated solar energy is mainly distributed on the bottom surface of the absorber tube.

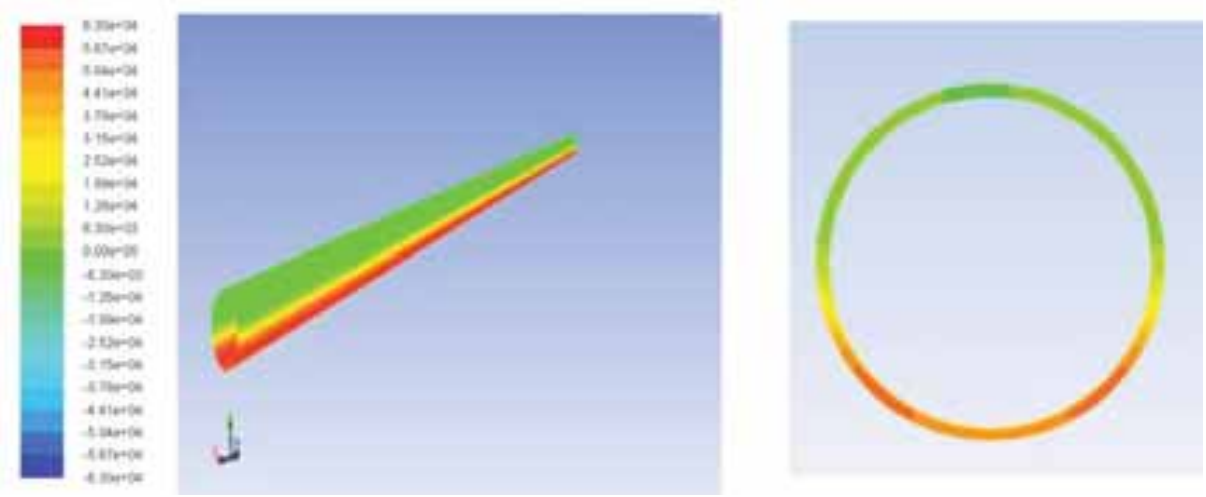

(a) (b)

Fig. 6: Non uniform flux distribution of the receiver for DNI =1000 W/m^2 (a) Axial length (b) Cross section view

The asymmetry in the two sides of the peak heat flux on the absorber is due to the presence of simulated tracking error. Because of this non uniform concentrated solar flux distribution, temperature distribution of PTC receiver in circumferential direction also non uniform. The heat flux distribution on the outer surface of absorber tube for the DNI of 800 W/m^2 and 1000 W/m^2 is shown in Figs. 6. The asymmetric distribution of heat flux in circle direction is obviously, but the heat flux distribution in axial direction (x) is uniform, as shown in Fig. 6. In order to further confirm the accuracy of the proposed MCRT code for calculating the solar energy flux distribution of the whole PTC system, numerical simulation is carried out at the same collector solar flux at about 48766 W/m^2 at the bottom portion of the absorber tube while the lowest solar flux is 1000 W/m^2 at the top portion of the absorber tube. The maximum solar heat flux attained by the PTC receiver is 9753.3 W/m^2, 19506 W/m^2, 29260 W/m^2, and 39013 W/m^2 when the DNI are 200 W/m^2, 400 W/m^2, 600 W/m^2, and 800 W/m^2 respectively.

6.2 Temperature Distribution of PTC Receiver:

Temperature distribution of PTC receiver plays the important role to determine the thermal efficiency and heat loss of PTC. The temperature contours at the absorber outlet with different inlet temperature of HTF for the DNI = 1000 W/m^2 and Inlet velocity = 1 m/s are shown in the Figure.7. The inlet temperature of HTF is high, the outlet temperature of absorber increased significantly.

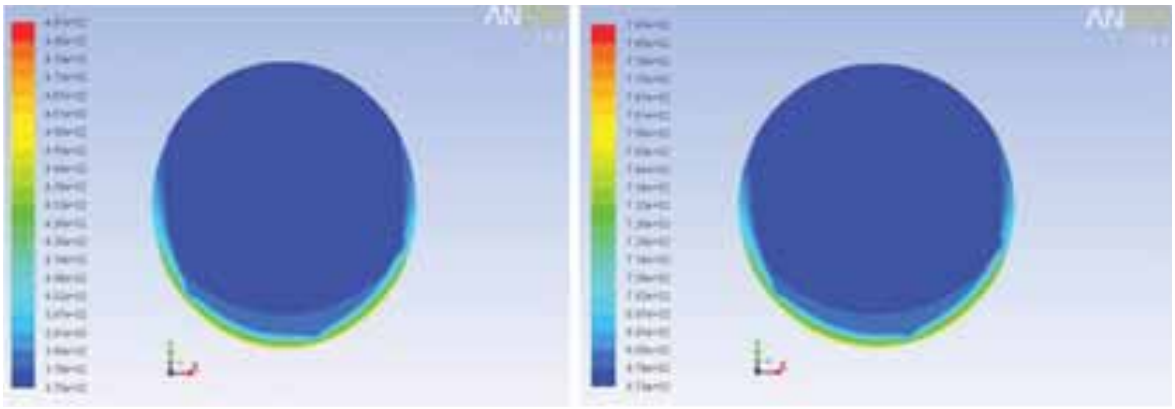

(a) (b)

Fig.7 : Temperature contours at the absorber outlet for DNI = 1000 W/m^2, V = 1 m/s for different inlet temperature (a) 100°C (b) 400°C

The non uniform radiation distribution also causes a non uniform temperature distribution. The shape of that distribution. Figure .8 shows the circumferential temperature distribution for the outer absorber surface and

the outer glass surface as function of circumferential angle around the receiver when the inlet temperature of HTF is 100˚C & 400˚C and also the DNI is 1000 W/m^2. The temperature distributions are generally smoother than the incident radiation distributions. The difference between absorber tube and HTF temperatures is significant. This is primarily due to the low heat transfer coefficient which is caused by the lower mass flow rates of HTF.

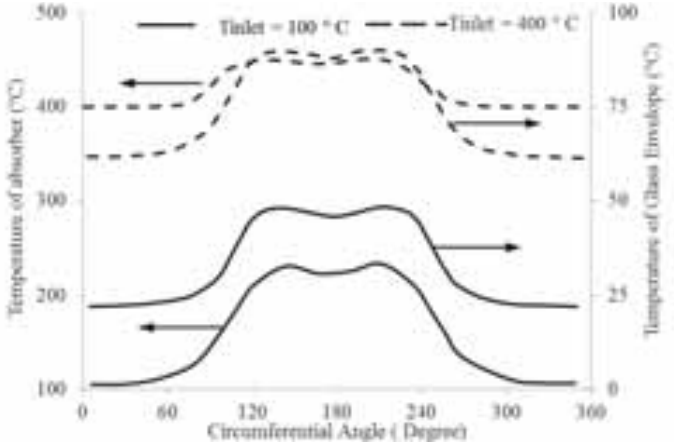

Fig. 8: Circumferential temperature distribution of absorber tube and glass envelope for Tinlet = 100˚C & Tinlet = 400˚C

For this reason, there is also a significant temperature difference between the bottom portion of the absorber surface exposed to the concentrated solar radiation and the top portion of the absorber surface which receives the direct normal irradiation from the sun. For the Tinlet = 100˚C & Tinlet = 400˚C , the difference between maximum and minimum absorber temperature is 131˚C and 55℃ respectively The convective heat transfer coefficient of HTF is increased by increasing the temperature of HTF, due to this temperature difference between the bottom and top of absorber surface and temperature difference between the HTF and absorber tube is also decreased. Similarly from the Figure , For the Tinlet = 100˚C & Tinlet = 400˚C , the difference between maximum and minimum glass envelope is 23˚C and 29 ˚C respectively. The temperature profile of both absorber and glass envelope follows the non-uniform solar heat flux distribution which indicates that the conduction in both tubes is relatively small. The temperature of the outer surface of the absorber is higher than that of the inner surface since the outer surface is the heating surface, and the maximum temperature difference is very small.

The temperature of the absorber is symmetric and increases by moving along the HCE far away from the inlet. The temperature distribution is estimated for the different inlet velocity of HTF .Fig. 9 shows the distribution of the temperature difference on the cross sectional planes of the absorber tube along the flow direction of HTF and length of the PTC receiver. The temperature difference was calculated through the difference between the maximum temperature and minimum temperature on the PTC receiver. At the entrance part of receiver, effect of temperature difference is maximum.

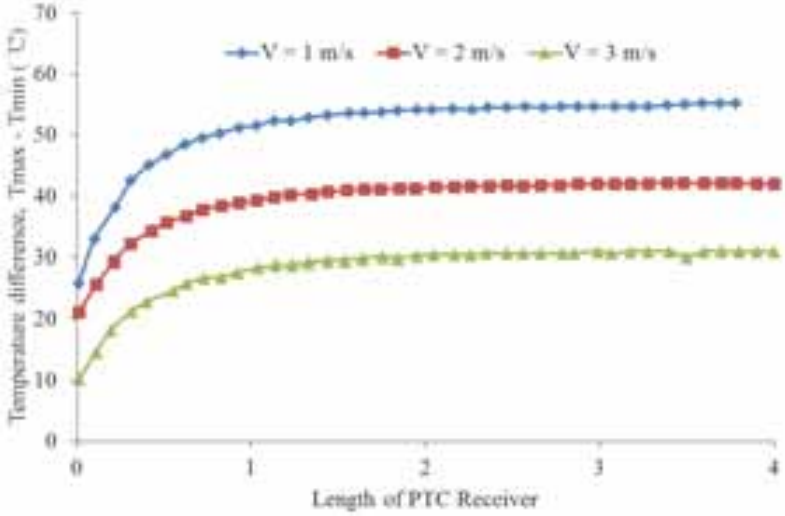

Fig. 9: Temperature distribution along the length of the PTC receiver for different inlet velocity

When the length of the receiver is within 1m, temperature difference of PTC receiver increases exponentially. Similarly when the length of receiver is greater than 1m (after the entrance region), the temperature difference almost approach constant path. This temperature difference is plotted for various HTF velocities from 1m/s to 3 m/s. However, the temperature difference decreases from 55.5˚C to 31˚C when the HTF velocity changes from 1 to 3 m/s. Therefore, the temperature differences are mainly dependent on the HTF velocity. The lower HTF velocity will cause higher temperature differences on sectional planes of the absorber tube, and this maximum temperature difference is the main cause of the breakage of PTC receiver

7. Conclusion

In this paper, three-dimensional numerical simulation of coupled heat transfer characteristics in the receiver tube is performed by combining the MCRT method and the FVM using Fluent software. Three typical testing conditions are chosen from the experiment to validate the physical model and simulation code. Numerical results show that the predicted results agree well with the experimental data, the average relative error is within 3%. The heat flux distribution on the outer surface of absorber tube was heterogeneous in circumferential direction but uniform in axial direction. Then, the coupled method was used to simulate the LS-2 Solar Collector for method verification. And the outlet temperatures of four cases were counted out and compared with Dudley et al.'s report data. The application of MC in combination with FV allowed for the incorporation of non-uniform temperature and heat transfer distributions and the identification of critical peak temperatures and heat fluxes. The temperature distributions of the absorber and the glass envelope surface are similar with the distributions of the solar energy flux. The HTF temperature difference of the cross-section decreases with the increase of the inlet velocity of the HTF, increases with the rising DNI, and almost remains the same with the increase of the inlet temperature of the HTF. Similarly when the length of receiver is greater than 1m (after the entrance region), the temperature difference almost approach constant path. This temperature difference is plotted for various HTF velocities from 1m/s to 3 m/s. However, the temperature difference decreases from 55.5˚C to 31˚C when the HTF velocity changes from 1 to 3 m/s. Therefore, the temperature differences are mainly dependent on the HTF velocity. The lower HTF velocity will cause higher temperature differences on sectional planes of the absorber tube, and this maximum temperature difference is the main cause of the breakage of PTC receiver.

Acknowledgement

The financial support provided by CSIR (Council of Scientific and Industrial Research), Government of India through the technology development project is acknowledged.

Nomenclature

C, μ	k-ε model constants
DNI	Direct Normal Irradiance (W/m^2)
g	acceleration due to gravity (m/s2)
h	heat transfer coefficient (W/m2K)
Nu	Nusselt number
P	pressure (Pa)
Ra	Rayleigh number
Re	Reynolds number
T	Temperature (K)
u,v	velocity component

Greek Symbols

λ	thermal conductivity (W/mK)
k_{in}	turbulent kinetic energy at the inlet
ρ	density (kg/m^3)
μ	dynamic viscosity (Pa.s)
μ_t	turbulent viscosity (Pa.s)
ν	kinematic viscosity (Pa.s)

Subscripts

a	absorber
f	heat transfer fluid
g	glass envelope
in	inlet
max	maximum
min	minimum
o	outlet

8. References

Chen, W., Liu, W., 2004. Numerical analysis of heat transfer in a composite wall solar collector system with a porous absorber. Appl Energy, 78, 137–49

Cheng, Z.D., He, Y. L., Cui, F.Q., Xu, R.J., Tao, Y.B., 2012. Numerical simulation of a parabolic trough solar collector with non-uniform solar flux conditions by coupling FVM and MCRT method, Sol. Energy 86, 1770–1784.

Cheng, Z.D., He, Y.L., Xiao, J., Tao, Y.B., Xu, R.J., 2010. Three-dimensional numerical study of heat transfer characteristics in the receiver tube of parabolic trough solar collector, Int. Commun. Heat Mass Transfer 37 (7), 782–787.

Clark, J., 1982. An analysis of the technical and economic performance of a parabolic trough concentrator for solar industrial process heat application. Int J Heat Mass Trans. 25(9), 427–438.

Dudley, V.E., Kolb, G.E., Mahoney, A.R., Mancini, T.R., Matthews, C.W., Sloan, M., Kearney, D., 1994. Test results: SEGS LS-2 solar collector, Report of Sandia National Laboratories, SANDIA-94-1884

Edenburn, M.W., 1976, Performance analysis of a cylindrical parabolic focusing collector and comparison with experimental results. Sol Energy 18(5), 437-444.

Fend, T., Paal, R.P., Reutter, O., Bauer, J., Hoffschmidt, B., 2004. Two novel high-porosity materials as volumetric receivers for concentrated solar radiation. Sol Energy Mater Sol Cells. 84, 291–304

Forristall R., 2003. Heat transfer analysis and modeling of a parabolic trough solar receiver implemented in engineering equation solver. National Renewable Energy Laboratory.

Güven H, Bannerot R., 1986. Derivation of universal error parameters for comprehensive optical analysis of parabolic troughs. Journal of Solar Energy Engineering, 108, 275–81.

He, Y.L., Xiao, J. Cheng, Z.D., Tao, Y.B., 2011. A MCRT and FVM coupled simulation method for energy conversion process in parabolic trough solar collector, Renewable Energy 36 (3), 976–985.

Iverson, BD., Flueckiger, SM., Ehrhart, BD., 2011. Through heat collection element deformation and solar intercept impact. SolarPACES Conference, Spain.

Kalogirou.SA., 2004. Solar thermal collectors and applications. Progress in Energy and Combustion Science 30, 231-295

KJC Operating Company, 1993. Final Report on HCE Heat Transfer Analysis Code. SANDIA Contract No. AB-0227. Albuquerque, NM: Sandia National Laboratories

Kumar, K. R., Reddy, K. S., 2009. Thermal analysis of solar parabolic trough with porous disc receiver. Appl Energy, 86, 1804–1812

Mahoney, R., 2002. Advances in parabolic trough solar power technology. J. Solar Energy Eng. 124, 109–

125

O'García-Valladares, Velázquez, V., 2009.Numerical simulation of parabolic trough solar collector: improvement using counter flow concentric circular heat exchangers. International Journal of Heat and Mass Transfer, 52(3), 597–609.

Padilla, R., Demirkaya, G., Goswami, Y. D., Stefanakos, E., Rahman, M., 2011. Heat transfer analysis of parabolic trough solar receiver. Applied Energy, 88(12), 5097– 5110

Pope R, Schimmel W., 1973. An analysis of linear focused collectors for solar power. In: Eighth Intersociety Energy Conversion Engineering Conference. Philadelphia, PA. 353–359.

Ratzel, A., Hickox, C., Gartling, D., 1979. Techniques for reducing thermal conduction and natural convection heat losses in annular receiver geometries. J Heat Trans, 101(1), 108–113.

Stuetzle. T., 2002. Automatic control of the 30 MWe SEGS IV Parabolic trough plant. Master's thesis, University of Wisconsin-Madison.

Conference Proceedings

Solar World Congress 2015
Daegu, Korea, 08 – 12 November 2015

Refractive based solar tracker with fixed concentration spot

Héctor Garcia[1], Carlos Ramirez[1] and Noel Leon[1]

[1] Tecnológico de Monterrey, Campus Monterrey, Monterrey (México)

Abstract

Solar energy has become one of the most promising renewable energies being the most widespread used nowadays. In order to achieve an optimum performance, both photovoltaic and solar thermal applications require the use of some kind of solar tracking technique. A solar tracking concentrator (STC) has to adapt to the changes in the sun's position throughout the day and even more so, throughout the year.

The present paper attempts to describe in detail the design of a state-of-the-art STC in which the concentration spot is fixed. The tracking system is based on refracting the sunlight onto a constant direction, contrary to existing solutions which reflects it. Having a constant direction of radiations makes possible to implement a stationary Fresnel lens to concentrate the solar power for any application desired. The system is designed and validated using mathematical models and simulation software to prove the feasibility of the concept.

Keywords: *Solar tracking system, solar concentration, solar energy, refraction*

1. Introduction

Most research efforts on solar energy have focused on photovoltaic (PV) cells development, however, commercial PV cells have only achieved an efficiency of 15% to 20% so far (Green et al. 2009), while high concentration photovoltaic (HCPV) have efficiency slightly above 40% (Pérez-Higueras et al. 2011).

Another research line explores the use of solar thermal energy (STE), in which case two main issues must be overcome. Firstly, solar radiation must be concentrated for high temperature applications; this is due the low density nature of such energy. Secondly, for most solar concentrators, solar rays must fall perpendicular to the concentrator at all times. Therefore, a solar tracking concentrator (STC) must be used. These requirements also apply for HCPV.

This work was carried on to explore the feasibility of a STC using a semi-passive solar tracking device consisting in two arrays of prisms and a Fresnel lens. A peculiarity of the system is the fixed position of the Fresnel lens therefore, if the prism array can indeed track effectively the sun's path there will be a constant position concentration spot that can be used either in HCPV or CSP applications.

Achieving this constant spot is non-trivial and could represent an important breakthrough since having a non-constant spot means that the receiver which captures the energy must move along with the tracker, elevating in many cases the cost of implementation.

2. Design of the STC

2.1 Concept Layout

The presented STC is an optic system that concentrates solar radiation with minimal movement. It has two layers of PMMA triangular prisms one placed above the other that redirect the received solar rays in a constant vertical direction toward a fixed Fresnel lens. Prism within a layer are identical one another. The first array of prisms rotate all of its components to the same angle, its rotation axis is parallel to the y-axis. In a similar manner, the second set of prisms rotate synchronously but having a rotation axis parallel to the x-axis. Both layers are located directly above a Fresnel lens as seen in Fig. 1.

doi:10.18086/swc.2015.04.09 Available at http://proceedings.ises.org

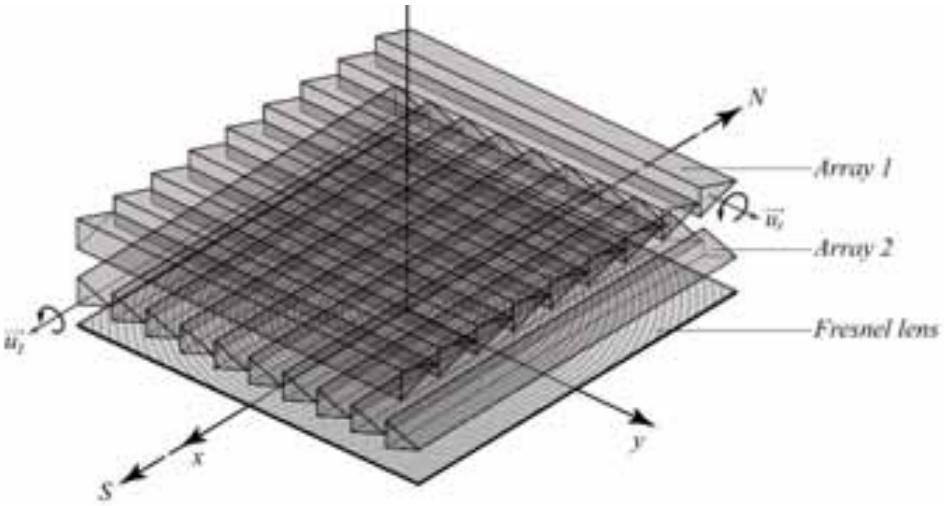

Fig. 1: STC system concept with fixed Fresnel lens

Figure 2 shows the lateral views of the proposed concept. This configuration allows to have the Fresnel lens in a fixed horizontal position; which significantly reduces the wind loads and more importantly it offers the virtue of having a stationary concentration spot, unlike many other STC which have a robust mechanical tracker that has to support all the moving components.

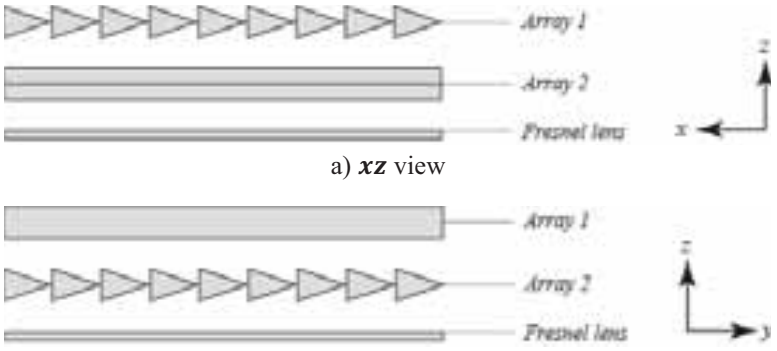

a) $\boldsymbol{xz}$ view

b) $\boldsymbol{yz}$ view

Fig. 2: STC system concept - XZ and YZ view

2.2 Prism

The initial concept employs triangular prisms, with the peculiarity that the polyhedron has an isosceles triangle as base, whose equal side's measure l and form an angle of ε. Prism's depth or height is h, as shown in Fig. 3. In any given prism the rotation axis goes through the body's center of mass, since prism are uniform longitudinally this coincides with the triangular gravicenter of the base. Consequently, the resultant torque due to gravity vanishes (Hibbeler, 2006).

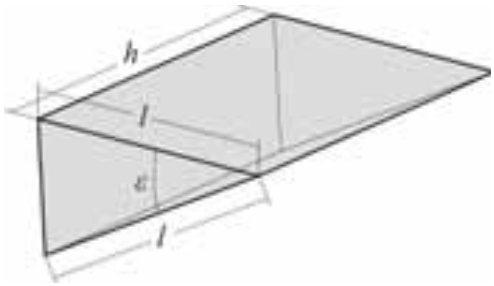

Fig. 3: Prism's dimensions

Since the rotation is the same within an array only one actuator for the mechanical movement is needed. The

mechanism can be idealize as a four-bar linkage similar to a window shutter but instead of blocking the sun's light, they redirect those solar rays by the refraction throughout the PMMA prisms.

There are two sets of prisms, upper and lower layer are identified by sub index 1 and 2 respectively. The prisms' inner angle are ε_1 and ε_2, as shown in Fig. 4. These values are not necessarily the same, although within each array all PMMA elements must be identical to one another.

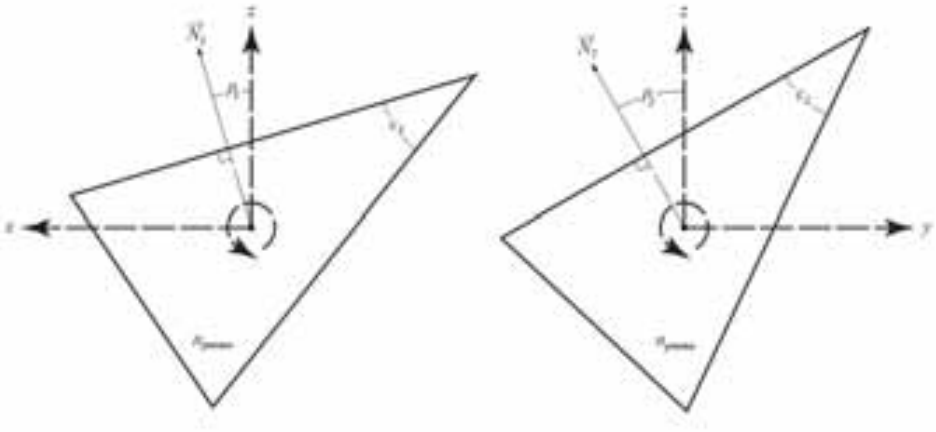

a) Upper layer b) Lower layer

Fig. 4: Prism's parameters

The geometry and refractive index are the key parameters of the prism. The design assumes that all prisms within the array are identical in both key parameters, thus the angle of rotation is shared, allowing the array to be driven by a single actuator. Additionally, this concept contemplates both upper and lower arrays to be made of the same material, however such consideration is not necessary.

Figure 4a shows the upper layer geometry, rotation axis is parallel to system's y-axis and a rotation by an angle of ρ_1; likewise Fig. 4b illustrates lower layer prism geometry with rotation axis parallel to system's x-axis and prism rotation by an angle ρ_2. For both cases the default position and reference point for the measurement of the rotation angle is referenced to the z-axis and the normal vector to the face of the prism.

2.3 Light Trajectory

Figure 5a illustrates required trajectory of the solar rays to successfully reach the receiver. For illustrative purpose only one prism of each layer is shown. The circular mark indicates where the beam changes medium. Emphasizing that the rays B and D are within the respective prisms. The upper layer is the first part of the system responsible for starting the solar tracking. Prisms rotate an adequate angle ρ_1 as shown in Fig. 5b to obtain the following trajectory:

A. Solar rays from the sun: These beams change direction throughout the day, they reach the 1st array of prisms and refract according to Snell's law.

B. Solar rays within the prisms of the 1st array: Inside the prism rays travel until reaching the opposite prism's side, where they exit by refracting when they change mediums.

C. Solar rays exiting the 1st array, toward 2nd array: These beams have the peculiarity of lacking a x component; this is accomplished by selecting ρ_1 accordingly. The path is presented in a XZ view, however exiting solar ray C not necessarily has a downward vertical direction, and has a non-zero y component as seen in Fig. 5c.

The following layer is located immediately below and it constitutes the second stage of the solar tracking system. Similarly prisms rotate an adequate angle ρ_2 as shown in Fig. 5c to obtain the following trajectory:

C. Solar rays from the 1st array: Coming from the upper layer, with the peculiarity of zero x component as described before. In other words ray is contained in plane YZ.

D. Solar rays within the prisms of the 2nd array: Inside the prism rays travel until reaching the opposite

prism's side, where they exit by refracting when they change mediums. Rays are also contained in plane YZ.

E. Solar rays exiting the 2nd array, toward Fresnel lens: These beams have the peculiarity of lacking both a x and y components; this is accomplished by selecting ρ_2 accordingly. Contrary to rays exiting from the first array, these beams do have a downward vertical direction.

The joint work of both arrays complete the tracking system, afterwards the solar rays must be concentrated into a fixed spot, and this is achieved by the next part of the system.

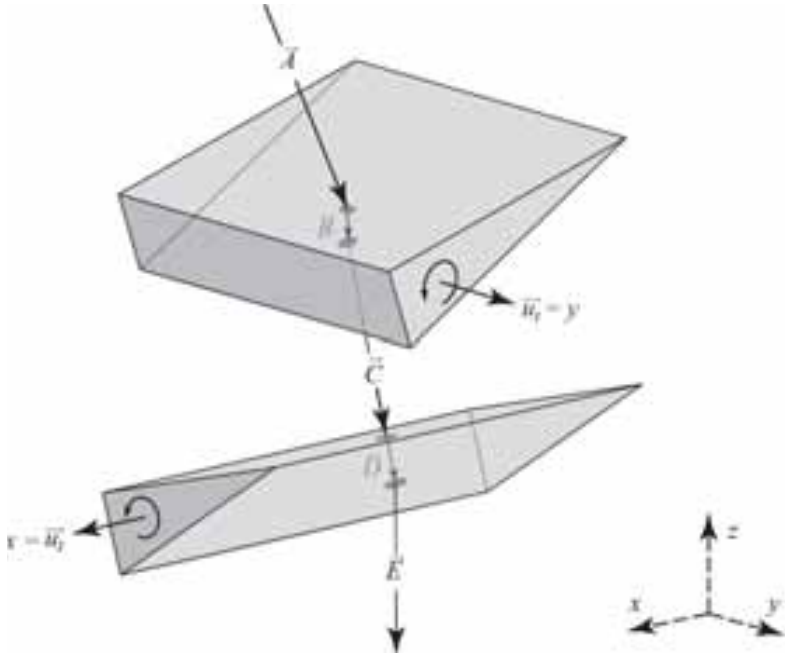

a) Isometric view

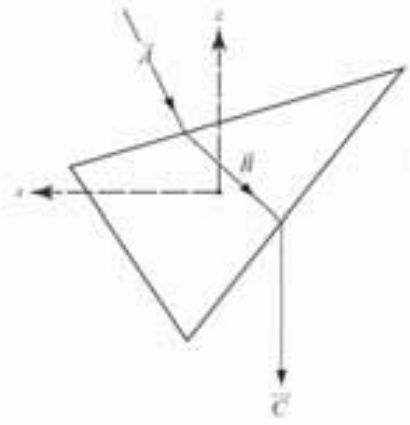

b) Upper layer: XZ view

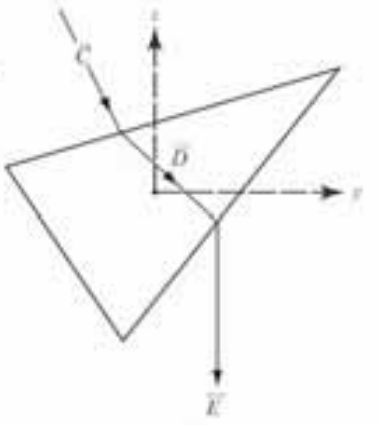

c) Lower layer: YZ view

Fig. 5: Ray's path through upper and lower layer.

2.4 Fresnel lens

The Fresnel lens is a type of compact lens that is able to concentrate solar energy in a reduced area; it is essentially a chain of prisms, in which each one represent the slope of a lens surface (Barone, 2005). The function of this optical device in the proposed system proposed is to receive the rays refracted by the two arrays of prisms and concentrate them in a fixed receiver. Since the solar rays reach the concentrator in a constant direction after going through both layers of prism, the lens can remain stationary.

3. Mathematical model

3.1 Dispersion by a prism

Many authors address the issue of the path of light through a prism, with one important consideration: it is assumed that the edge of the prism in which the two faces meet, with an angle ε, is perpendicular to the plane which contains the incident, transmitted, and emergent rays. (Born et al. 1999)

A ray entering a prism, as shown in Fig. 6, will emerge having been deflected from its original direction by an angle δ_{dev} known as the angular deviation. In terms of the SPSTC, this property is used to achieve the tracking as will be explain in detail later.

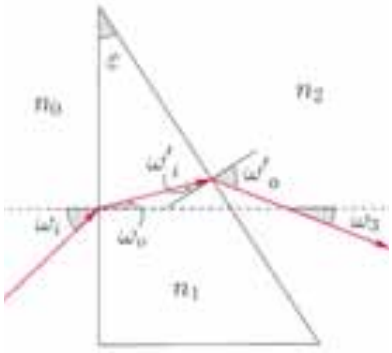

Fig. 6: Passage of a ray through a prism

Equations (1) and (2) are results of Snell's law, where n is the refractive index of the medium in question:

$$\omega_o = \sin^{-1}\left(\frac{n_0}{n_1}\sin\theta_0\right) \quad \text{(eq. 1)}$$

$$\omega'_o = \sin^{-1}\left(\frac{n_1}{n_2}\sin\omega'_i\right) \quad \text{(eq. 2)}$$

Additionally to Eqs. (3) and (4) are obtained by summation of angles, using the fact that the dashed line is perpendicular to the entrance face of the prism.

$$\omega'_i = \varepsilon - \omega_0 \quad \text{(eq. 3)}$$

$$\omega_3 = \omega'_0 - \varepsilon \quad \text{(eq. 4)}$$

For a prism in air as in the proposed concept, $n_0 = n_2 \simeq 1$. Defining $n_1 = n_{pmma}$, the deviation angle δ_{dev} is given by

$$\delta_{dev} = \omega_i + \omega_3 \quad \text{(eq. 5)}$$

Substituting Eqs. (1) to (4) into (5) yields:

$$\delta_{dev} = \omega_i + \sin^{-1}\left(n_{pmma}\sin\left[\varepsilon - \sin^{-1}\left(\frac{1}{n_{pmma}}\sin\omega_i\right)\right]\right) - \varepsilon \quad \text{(eq. 6)}$$

Abelman [2008] proposed a simplification of Eq. (6) if the incident angle ω_i and prism apex angle ε are both small, $\sin\theta \approx \theta$ and $\sin^{-1} x \approx x$, an important remark is that angles are expressed in radians. This allows the nonlinear equation in the deviation angle δ_{dev} to be approximated by:

$$\delta_{dev} \approx \omega_i + \left(n\left[\varepsilon - \left(\frac{1}{n}\omega_i\right)\right]\right) - \varepsilon \quad \text{(eq. 7)}$$

$$= \omega_i + n\,\varepsilon - \omega_i - \varepsilon \quad \text{(eq. 8)}$$

$$= (n - 1)\varepsilon \quad \text{(eq. 9)}$$

Furthermore the refractive index depends on wavelength λ, therefore for a thin prism the deviation angle varies with wavelength according to:

$$\delta_{dev}(\lambda) \approx [\,n(\lambda) - 1\,]\,\varepsilon \quad \text{(eq. 10)}$$

Considering to Eq. (6), it's evident that the deviation suffered by a monochromatic beam throughout a given prism is a function only of the incident angle at the first face, since apex angle ε and refractive index are fixed. Figure (7) shows a plot of the deviation angle for $n = 1.48$, for a variety of apex angles.

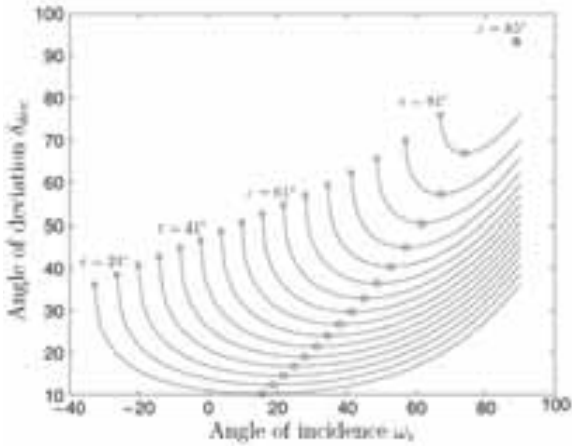

Fig. 7: Deviation δ_{dev} response to incident angle ω_i for several prism's apex angle ε (Abelman, 2008)

Figure 7 shows maximum and minimum deviation, for several values of ε, as squares and circles respectively. An important observation is how if the apex angle is increased the response plot tends to move up and to the right. Ultimately meaning a smaller range of admissible incident angles. For even larger apex angles, all rays that go inside the prism suffer a total internal reflection. On the contrary case if apex angle decreases too much, then Eq. (9) is a valid approximation and since refractive index is consider constant, then deviation depends solely on apex angle, which is also constant once implemented.

It should be notice that in the STC proposed the initial assumption described at the start of this section is not met for the first stage of the tracking system (upper layer). Since the plane which contains the incident, transmitted, and emergent rays is not always perpendicular to the prism edge; however, the repercussion apex angle has on deviation is a good starting point to understand how it affects the tracking system for redirecting sunlight. Furthermore another approach must be done to overcome the 3-dimensional ray.

3.2 Snell law in a 3-dimentional environment.

The physical phenomenon involved in this system, in both prisms arrays and Fresnel lens, is known as light refraction that obeys Snell's law. Nevertheless, the conventional form can only be applied when working in the same plane; however, the nature of solar rays' movement throughout the day and prism normal to the incident face produces non-constant working planes. Therefore, vector analysis must be performed to find an extrapolation of Snell's law for a 3-dimensional environment.

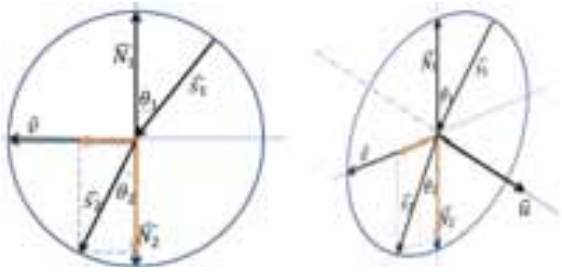

Fig.8: (a) Snell's law in a plane; (b) Snell's law in space

Equation (10) defines the output direction based on the orthogonal vectors that define the plane seen in Fig. 8a. An extrapolation of Snell's Law is shown in Eq. (11) in function of vectors $\hat{s}_1$ and $\widehat{N}_1$ only, which are the incident ray, and the normal vector to the surface, respectively. (Garcia et al, 2014)

$$\hat{s}_2 = (\sin\theta_2)\,\hat{v} + (\cos\theta_2)\widehat{N}_2 \qquad \text{(eq. 10)}$$

$$\hat{s}_2 = \frac{n_1}{n_2}\widehat{N} \times \left(-\widehat{N} \times \hat{s}_1\right) - \widehat{N}\sqrt{1 - \left(\frac{n_1}{n_2}\right)^2 \left(\widehat{N} \times \hat{s}_1\right) \cdot \left(\widehat{N} \times \hat{s}_1\right)} \qquad \text{(eq. 11)}$$

Equation (11) offers an analytical vectorial approach for light refraction; therefore, it is necessary to express incoming rays as unit vectors that represent the beam's direction, and the normal vector to the surface where rays incident.

3.3 Solar ray's directional vector

Figure 9 shows the direction of incoming solar rays. Setting the coordinate system as shown, where South and East coincide with x and y-axis respectively. Based Duffie and Beckman (1991) solar altitude α and azimuth γ may be obtained given a solar latitude, therefore the directional vector may be calculated.

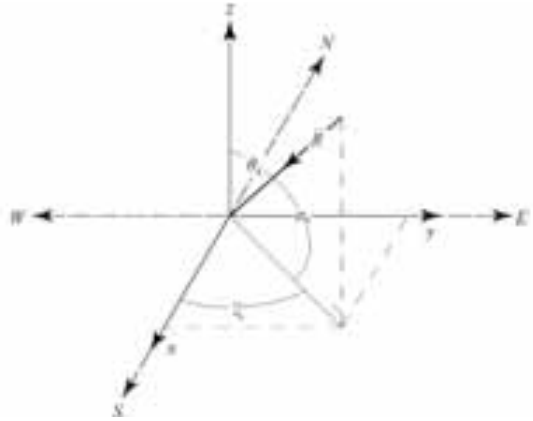

Fig. 9: solar ray in vector form

$$\vec{R}_{\gamma_s,\alpha_s} = -\cos(\alpha_s)\cos(\gamma_s)\,\hat{x} - \cos(\alpha_s)\sin(\gamma_s)\,\hat{y} - \sin(\alpha_s)\,\hat{z} \qquad \text{(eq. 12)}$$

Given any point of the year directional vector $\vec{R}_{\gamma_s,\alpha_s}$ is obtained. These beam will strike onto a prism, for which the normal vector to the plane must be calculated. This can be achieve rather easily doing a 2-dimensional analysis depending solely on the apex angle ε and the rotation ρ given to the prism

4. Solar Tracking

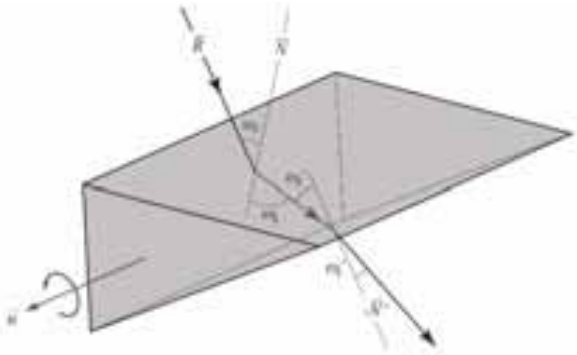

Fig. 10: Passage of a ray through a prism

Matlab implementation of mathematical model is based on Eqs. (11) and (12), functions are programed in order to know the path of light for any given parameters. One key element in the code is an analogy to the deviation formula, which for a given input ray's direction, incident normal vector is calculated and using Eq. (12) the direction inside the prism is obtained. Later internal normal vector in output face is computed to obtain the output direction of the path described by light beams as shown in Fig. 10

Tab. 1: Solar angles at given time at latitude $\varphi = 25°39'15''N$

Day of the year	120th
Solar time	10:30am
Solar azimuth angle (γ_s)	66.6257
Solar altitude angle (α_s)	66.2054

Tab. 2: Solar angles at given time at latitude $\varphi = 25°39'15''N$

Azimuth	Altitude	Incident solar ray		
γ_s	α_s	A_x	A_y	A_z
66.6257°	66.2054°	−0.160066	0.370348	−0.915

Given the solar angles, the directional components of solar rays are calculated, with the help of Matlab, the behavior of a ray through the prism for all possible rotations is obtained. The first stage of the STC is to control and eliminate if possible the component C_x, as stated earlier. It's important to realize that not all rotations generate an output ray, this happens when internally all light is reflected instead of being refracted, or if solar rays reach the prism at the non-active side of the triangle.

Figure 11a shows the behavior of x component for different apex angles ε_1 through all possible prism rotations ρ_1 (for a particular solar azimuth and altitude angles stated in Table 1).

It can be seen in Fig. 11 how if apex angle ε_1 increases the system will not be able to eliminate the desired component C_x; meanwhile when it does, there may be two rotations values: ρ_1 and ρ_1' that accomplish the desired output. Figure 11b shows a closer look to appreciate the points where response intersects horizontal line corresponding to $C_x = 0$.

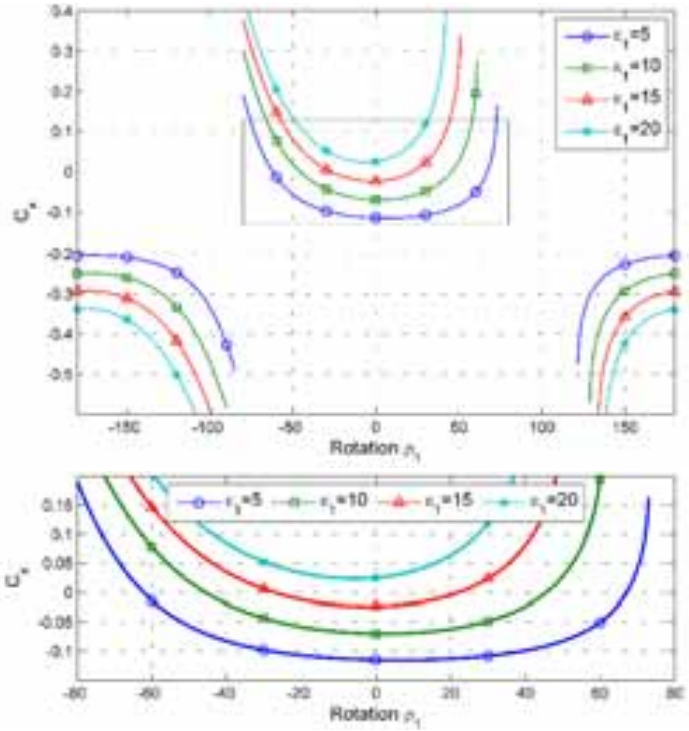

Fig. 11: a) Output response C_x for prism rotating ρ_1 for distinct values of ε_1, b) zoom view

Figure 12a shows the best rotation available for a wide range of apex angles that accomplish the minimum component $|C_x|$, meanwhile Fig. 12c shows component C_x achieve, for instance, in this particular case how apex angles higher than 17° can't achieve the desire output.

It can be proved that when rotation ρ_1 exist such that $C_x = 0$ then Eqs (13) to (15) stand true, meaning the output ray's direction is constant despite being multiple values of rotation ρ and independent to the prism apex angle ε.

$$C_x = 0 \qquad \text{(eq. 13)}$$

$$C_y = A_y \qquad \text{(eq. 14)}$$

$$C_z = \sqrt{1 - C_y^2} \qquad \text{(eq. 15)}$$

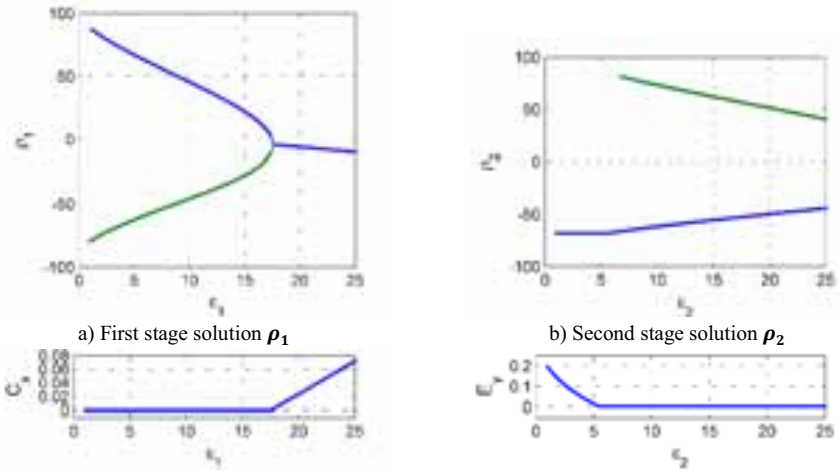

a) First stage solution $\boldsymbol{\rho_1}$ b) Second stage solution $\boldsymbol{\rho_2}$

c) First stage $\boldsymbol{C_x}$ output d) Second stage $\boldsymbol{E_y}$ output

Fig. 12: Best solution found for distinct values of apex angle $\boldsymbol{\varepsilon}$

Therefore despite the system's parameters for the 1st stage the rays will reach the 2nd stage in a given direction $\vec{C}$, from where the same analysis is perform to obtaining the best rotation available and the permissible apex angle to achieve the desire task.

5. Proof of concept

Additionally to the mathematical model a computer simulation using ray trace software and an idealized scale model consisting of two individual prism was constructed to corroborate the behavior of rays through the prisms. For instance the fact that given an input direction there exist different rotations that provide the same output can be seen in Fig. 13.

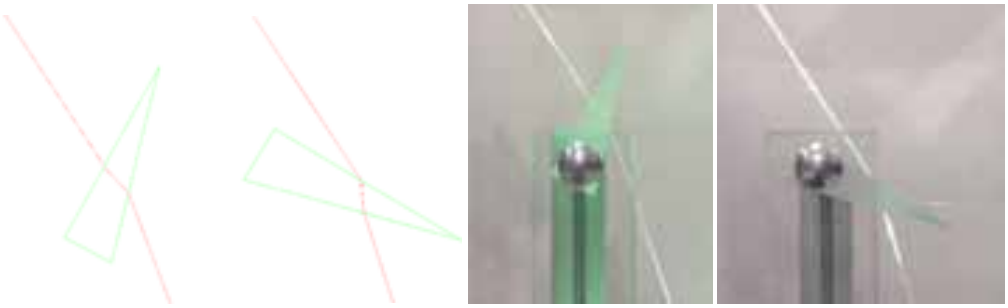

a) TracePro simulation b) Experimental model

Fig. 13: Two different rotation angles $\boldsymbol{\rho}$ with same output

An important remark is the Fresnel lens beneath the tracking system is not included in the model. Since initial design contemplates a conventional Fresnel lens to deal with the concentration part, the only requirement is that rays reach the lens perpendicularly to the surface.

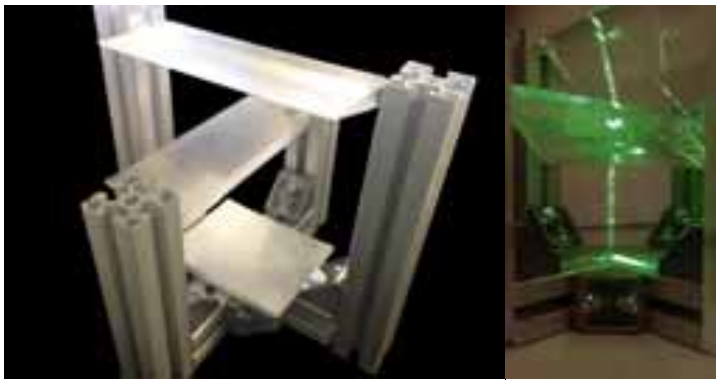

Fig. 14: Scale prototype as proof of concept

The present analysis was done for a particular time, however a deeper analysis is needed to see the system performance throughout the year, the fact that it works for an arbitrary moment does not assure the correct functionality for every day at all hours

6. System performance throughout the year

As stated before the behavior of solar angles throughout the year can be calculated as shown in Fig. 15, however we must acknowledge that the system may not be able to cover all possible solar values, therefore the system's target is set from 9 to 15hrs.

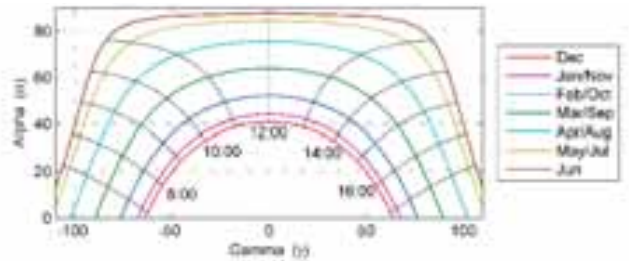

Fig. 15: Solar angles throughout the year, at latitude $\varphi = 25°39'15''N$

To view the tracker performance for a given pair of apex angles ε_1 and ε_2 the system is simulated via matlab to evaluate every possible pairwise values (γ, α) within the desired time window to apply the tracking algorithm and obtain the best output found. The primary interest is the angle θ formed between the theoretical direction $\vec{E}_s$ and the outcome ray $\vec{E}_r$ generated by the algorithm is closest to cero.

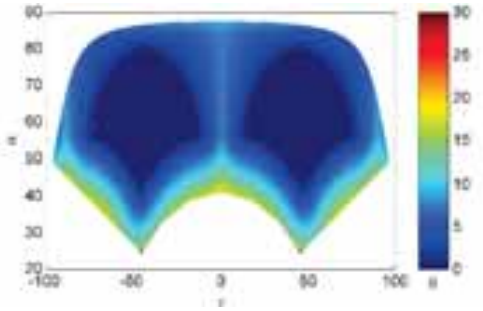

Fig. 16: Output ray variation θ from desire output with $\varepsilon_1 = 15.85$, $\varepsilon_2 = 15.28$

Notice there is a good tracking in two main areas shown in blue zones, however there is a gap at the center region $(\gamma = 0)$, additionally angles close to lower limit do not have a satisfactory response in the green zone.

6.1 Backtracking rays

Snell's refraction equation stands for both directions. Therefore one may think of refraction as a bijective function. Since the reversibility holds at each refracting surface, it holds also for even the most complicated light paths. In particular for the path define while going through an acrylic prism, as shown in Fig. 17a. Furthermore this same principle applies to the complete trajectory described by incoming solar rays and tracking system output rays as represented in Fig. 17b.

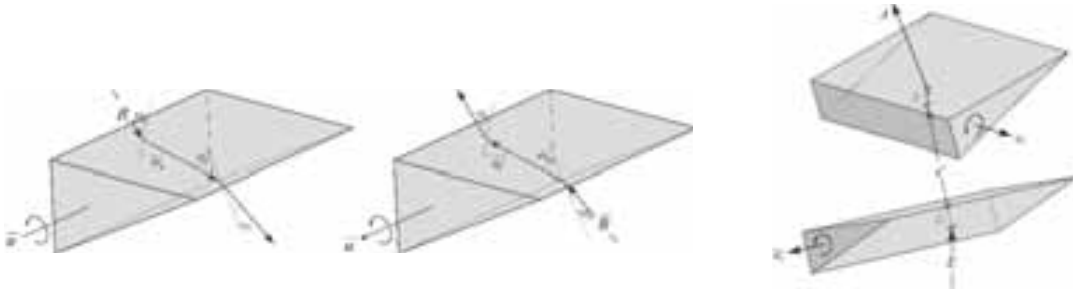

a) Throughout a single prism b) Through tracking system

Figure 17: Ray path in reverse direction

Therefore given a set of parameters ε_1 and ε_2 instead of doing the algorithm for every possible point (see fig. 15) a simpler approach arises which consists in calculating all possible reverse paths backtracking ray $\vec{E}$. This is simply obtained for every combination of rotation angles (ρ_1, ρ_2); graphing them to obtain a scatter plot that represents the system's admittance rays for which we can redirect accurately with $\theta = 0$, as shown in Fig 18.

Figure 18 shows just some simulations that were done, since plots are symmetrical only one side is computed. In the iterations the variations in ε shift the zone accordingly. Additionally the behavior of the system to ε also appears to have a direct correlation, as lower values tend to be close to upper limit and vice versa.

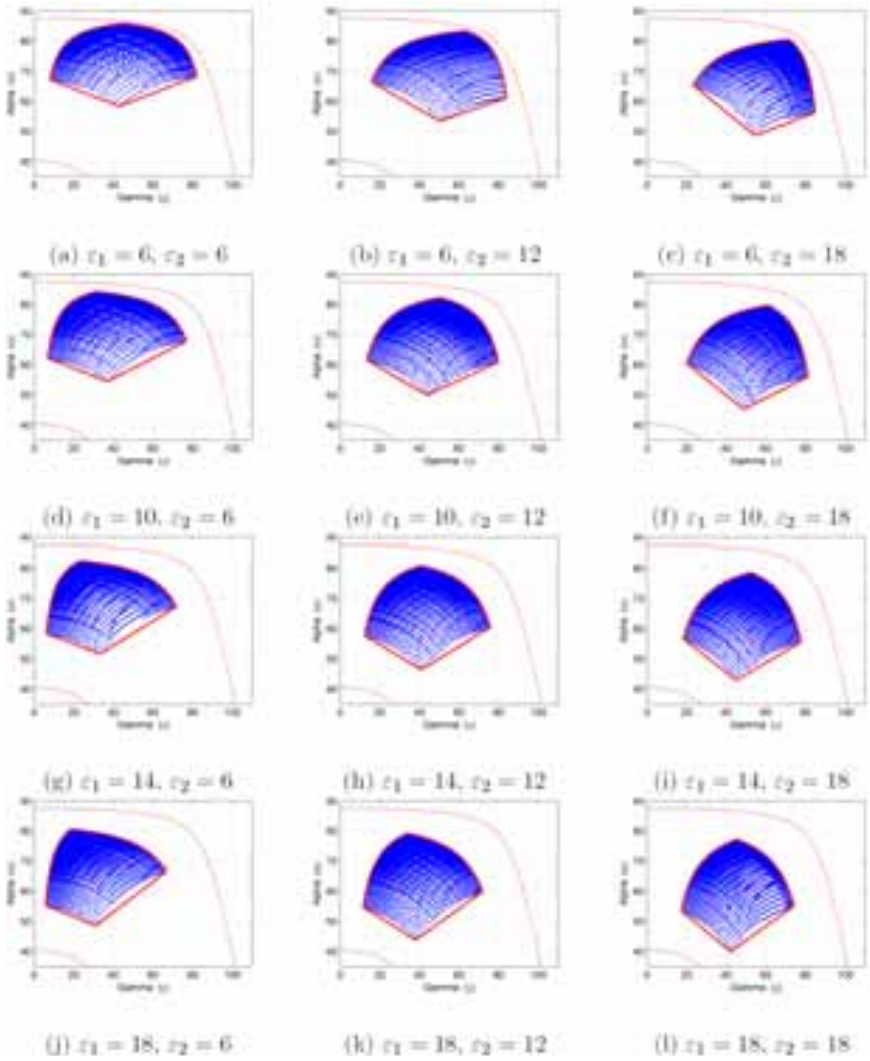

Fig. 19: Matlab simulation for different set of apex angles

7. Concluding remarks

A tracking algorithm was also implemented on Matlab to determine the required rotations values for a given time. The only design parameters for the present concept are the apex angles of the prisms in each layer, since the system relies on refraction of light there are physical constrains (Leutz and Susuki 2001): the critical angle plays an important role on the ability to correctly redirect light to the desire direction. For instance the second layer of prism al paths are in the same plane, since rays theoretically have $C_x = 0$, therefore analysis shown in Fig. 7 is valid, and deviation angle plays a direct role in the ability to redirect rays accordingly. Unfortunately this means that for times around noon ($\gamma = 0$) the gap previously mention in Fig. 16 will always be present, since at that time the prism needs to give a null deviation, but from Eq. (9) that may only be achieve having a low apex angle sin refractive index is constant. From Fig. 7 we know that a low value of ε restrain of ability

to redirect rays, since the maxium deviation is restricted therefore a small apex angle helps the center gap but impairs zones where γ is close to the limit.

A STC is feasible using solely PMMA prism that rotate accordantly to the suns position, but with range of operation limitants. The selected values must be such that the time of operation of the system is maximized.

A three-dimensional mathematical model was developed to describe the path of a collimated light beam through a translucid solid medium. This vectorial approach was successfully implemented in Matlab being able to characterize the ray's path along the system, additionally a real life scale prototype and the TracePro computer simulation were used to validate the model.

The tracking is achieved by separating the dual axis movement and implementing two independent rotational movements that work hand by hand to refract efficiently solar rays. Doing so offers a simpler approach in tracking the Sun which ultimately would result in cheaper but reliable solution for most of the possible Sun's positions.

The current implementation has a fixed Fresnel lens which reduces greatly the mechanical effort of the system, since the tracking is performed by the rotating prisms arrays, which have the virtue of being lightweight individual prisms instead of a robust big heliostat, with the already mentioned trade-off.

A tracking mathematical algorithm was program in Matlab to obtain the best rotations for a given set of parameters $(\varepsilon_1, \varepsilon_2)$ throughout the year, however a deeper analysis must be done to understand the efficiency of the system.

The article presents a functional design and model capable of tracking the sun fairly well; nonetheless, there is still a vast area of opportunity for the improvement and optimization of the proposed STC. Additionally the presented work focuses on the light path toward a fixed objective, however light attenuation effects caused by the prism material must be furthermore studied to understand the real amount of energy the system can harvest from the sun.

8. Acknowledgement

The authors would like to thank the Institute of Renewable Energy (IER-UNAM) and the Mexican Center for Innovation in Solar Energy (CeMIE-Sol) for funding the present project through the Strategic Project #05: "Development of solar thermal storage units"; otherwise its development would have not been possible.

9. References

Abelman, S. and H. Abelman, Approximations of nonlinear phenomena arising in angular deviations of light rays that emerge from prisms. Computers & Mathematics with Applications, 55(3): p. 408-422. (2008)

Barone S, Directed Fresnel lenses. 2005, US Patent 2005/0041307A1.

Born, M., et al., Principles of Optics: Electromagnetic Theory of Propagation, Interference and Diffraction of Light, Cambridge University Press, 1999

Duffie J. and Beckman W.: Solar engineering of thermal processes. Wiley, 1991.

Garcia H, Leon N, Ramirez C, Rotating Prism Array for Solar Tracking. Energy Procedia. Volume 57, Pages 265–274, 2014

Green M., Emery K., Hishikawa Y., Warta W.: Progress in Photovoltaics: Research and Applications Solar. Cell Efficiency Tables. Volume 17, Issue 5, pages 320–326, 2009.

Hibbeler, R.C., Mecánica de materiales, Pearson Educación, 2006

Leutz R. and Suzuki A.: Non-imaging Fresnel Lenses: Design and Performance of Solar Concentrators. Springer, 2001.

Pérez-Higueras, P., E. Muñoz, et al.: High Concentrator PhotoVoltaics efficiencies: Present status and forecast. Renewable and Sustainable Energy Reviews 15: 1810-1815, 2011.

Conference Proceedings

Solar World Congress 2015
Daegu, Korea, 08 – 12 November 2015

Development of a Solarized Rotary Kiln for High-Temperature Chemical Processes

Lucia Arribas[1], Veselin Miroslavov[1], Selvan Bellan[1], Manuel Romero[1], Jose Gonzalez-Aguilar[1]

[1]Unit of High Temperature Processes, IMDEA Energy Institute, E-28935, Mostoles (Spain)

Abstract

This work presents the design, characterization and commissioning of a directly-irradiated solar rotary reactor, which can be used for multiple applications such as chemical reactions (solar chemistry), thermochemical process or studies about mechanical strength and attrition of different materials, focusing on thermochemical reactions of manganese oxide. The main features of the reactor and test bed are as follows: samples are directly irradiated by concentrated radiation provided by a 7kWe high-flux solar simulator (HFSS) and a rotating cavity that promotes good mass and heat transfer, as well as high surface area for the reactions. Optical simulations and CFD analysis show that 1 kW of incident power and 1700 K can be achieved at the reaction zone, which is located at the secondary focus of the high-flux solar simulator. Manganese oxide cylindrical pellets (85% Mn_3O_4, 15% Mn_2O_3, mean particle size 3.5 mm) are used to perform the thermochemical reactions. X-Ray Diffraction is used to analyze the pellets composition before and after the test. A full conversion of the initial 15% of Mn_2O_3 is achieved.

Keywords: *solar reactors, solar simulator, rotary kiln, manganese oxide*

1. Introduction

Enhance the renewable energy contribution to the global energy mix is necessary in order to reduce global warming. Generally, however, the main disadvantage of some renewable resources such as solar or wind is their lack of dispatchability, since their production depends on transient weather conditions. For the generated renewable energy to be used when it is needed, it should be either stored or transformed into another type of fuel.

Short-to-long term thermal storage can be achieved using concentrated solar energy with the addition of thermal storage, thermochemical storage or by producing solar fuels such as hydrogen; which makes possible to implement high-flexible dispatching strategies. Recent studies focus on thermochemical storage and solar fuels (Romero and Steinfeld, 2012). Both processes are based on the use of concentrated solar radiation, which requires adequate optical concentration systems and optimized solar reactors that are capable to withstand high temperatures, where thermal losses are minimized, and which favor mass and heat transfer (Alonso and Romero, 2015).

Solar reactors are classified into directly and indirectly heated reactors, depending on whether particles are directly irradiated or not. Particle reactors can be in turn classified into stacked, fluidized or suspended, and entrained bed configurations. This paper will focus on a rotary kiln that functions as a stacked bed and a brewed oven.

Advantages of a rotary kiln are that they produce relatively low radiation heat losses and uniformly high temperatures, and that the reactive material can be directly irradiated, which leads to intensive heat and mass transfer (Tescari et al., 2013). However, they present technical disadvantages associated with the presence of moving parts, such as the complexity of achieving a balanced rotation, sealing the structure and measuring temperatures inside the rotating tube.

A number of rotary solar reactors have been already employed in research. The Roca reactor (Haueter et al.,

doi:10.18086/swc.2015.04.10 Available at http://proceedings.ises.org

1999), commissioned at the Paul Scherrer Institute (PSI), is a solar rotary reactor of 10 kW designed to produce the thermal reduction of zinc oxide (ZnO) into zinc (Zn) and oxygen (O_2). The Zirrus reactor (Müller et al., 2006), also designed at the PSI to reduce zinc oxide, consisted of a rotating cavity where centripetal acceleration forced the reactant ZnO to cover the cavity wall. Unlike Roca, where the ZnO was both the reactant and the insulating material, these two functions were decoupled in the Zirrus. Thus, the Zirrus reactor was composed of an inner cavity wall impermeable to gas diffusion, but capable of functioning at the decomposition temperature of ZnO in a corrosive environment containing ZnO, gaseous Zn and O_2.

A rotary reactor that produced lime by calcination of calcite was tested in the solar furnace of PSI (Meier et al., 2004). This 10-kW reactor was basically a rotary kiln of 600 mm length and 350 mm diameter, operated horizontally and in a continuous mode. The raw material was stored in a hopper that is placed on top of the rear part of the reactor. The rotation speed was between 2-7 rpm.

A rotary reactor by the German Aerospace Center (DLR) for solar thermochemical energy storage (Neises et al., 2012) was used to perform the reduction of cobalt (II, III) oxide to cobalt (II) oxide and O_2. The total flow used was between 4-8 l/min and a maximum rotational speed of 6 rpm was achieved.

Recently, a rotary reactor for thermochemical energy storage with copper oxide was tested in the solar furnace HoSIER at UNAM, Mexico (Alonso et al., 2015). The reactor body, including the stainless steel housing and an insulation layer of porous alumina, was stationary. Only the reaction chamber rotated around a central axis, connected to an engine at the back of the reactor. The reaction chamber was a rotary cylinder made out of alumina, with an inner diameter of 57.5 mm, an outer diameter of 67 mm and a length of 74 mm. Typical operating conditions were a volumetric flow rate of 10 l/min and rotational speed of 4 rpm.

2. Reactor design and experimental setup

The objective of the reactor design is to get a versatile device that can be used in different processes without many changes. Examples of applications are chemical reactions (solar thermochemistry), thermochemical processes or studies about mechanical strength and/or attrition of different materials. Specifically, this work presents the reduction of manganese oxide (Mn_3O_4). The reactor is presented in Fig. 1 and is composed of the following elements:

A reacting cavity which consists of a fixed conical aperture with a large enough aperture for the incoming radiation (an upper diameter of 11 cm, a lower diameter of 38 mm and a height of 80 mm), and a rotary tube of alumina (with an outer diameter of 45 mm, an inner diameter of 35 mm, and a length of 500 mm). The axial rotation of the tube produces homogeneous temperature, and high mass and heat transfer in the reaction zone. To minimize heat losses, ceramics bricks are used as insulation.

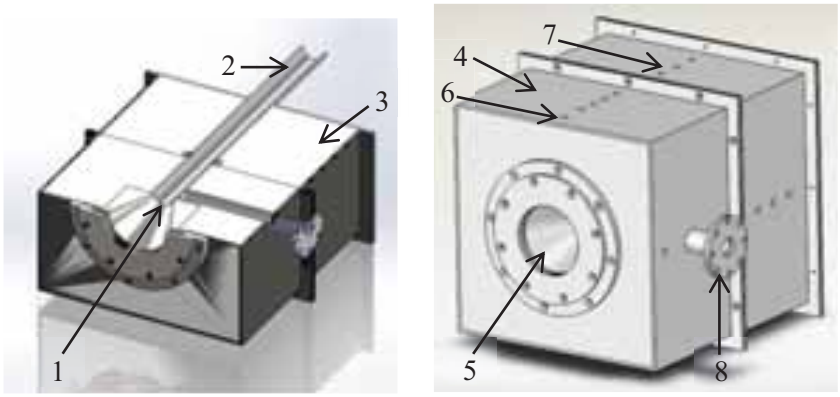

Fig. 1: Scheme of rotary kiln. (1) Cavity; (2) rotary tube of alumina; (3) ceramics bricks; (4) stainless steel housing; (5) quartz glass window; (6) gas inlet; (7) thermocouples places; (8) window for pyrometer

As working in a controlled atmosphere is desirable, air tightness is necessary. To achieve it, the reactor has an external housing of stainless steel, where measuring instrumentation is also located, and a quartz window of high transmittance that allows particles to be directly irradiated and seals the cavity. This window should be clean during experiments, thus the gas feeding is performed by four gas inlets located at the lateral wall of the reactor. The external dimensions of the reactor are 40x35x35 cm^3. 28 K-type thermocouples are installed at different axial and radial distances, and two inside the tube. A window has been included in one of the lateral walls of the facility in order to measure temperatures with a pyrometer. An electric motor rotating at 1390 rpm is employed to move the tube at approximately 92 rpm (9.63 rad/s) through a 1/15 reducer.

Two photographs of the rotary kiln are showed in Fig. 2, where it is possible see the final setup. The axis of rotation is fixed by two treads, one at back cover of the housing and another at gas outlet, behind the gear. Instruments devices installed are the following: a relative pressure transducer at gas inlet; a pressure drop transducer between inlet and outlet; a flowmeter; 30 K-type thermocouples; a pyrometer. All of them connected with data acquisitions cards in order to monitor the course of the experiments by a LabView software. Gas outlet is carried to the gas conditioner and later to the gas analyzer (Siemens Ultramat 23).

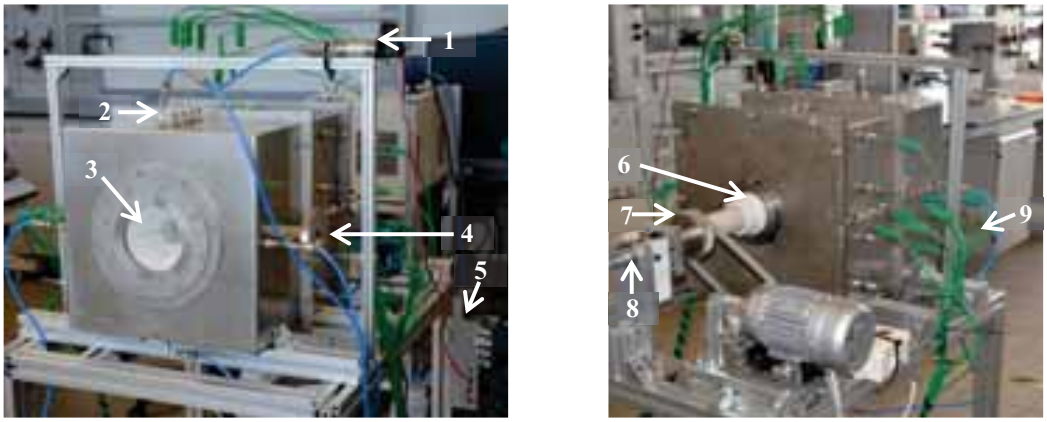

Fig. 2: Front view (left) and back view (right) of rotary kiln. (1) Pressure transducer; (2) gas inlet; (3) window; (4) window for pyrometer; (5) data acquisition card; (6) tread; (7) gear; (8) gas outlet; (9) thermocouples

To avoid particles reaching the conical part, the reactor is tilted 4º with respect to the horizontal and a ceramic ring is placed in the tube inlet. As particles can also move towards the outlet, another ceramic ring was placed at the end of the reaction zone (4 cm behind the inlet), but which did not restrict the gas flow. However, it was observed after the firsts commissioning experiments that some powder still reached the conical part, so the front ceramic ring was replaced by one with a smaller aperture (as shown in Fig. 3).

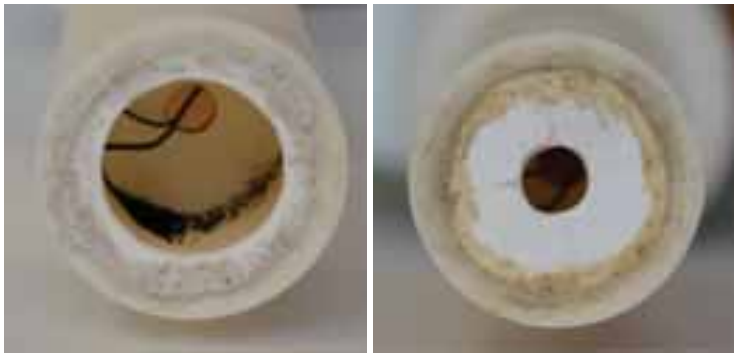

Fig. 3: Ceramics rings. Front ring was changed after first experiments in order to avoid sample losses

3. Numerical Analysis

In order to characterize the reactor, an optical analysis was conducted using the Monte Carlo Ray-tracing software TracePro 7.2, and the flow was numerically simulated by means of COMSOL Multiphysics 4.4.

The optical analysis aimed at determining the optimal position of the reactor with respect to the high flux solar simulator (HFSS) that maximizes sample temperatures and calculating the radiation distribution in the different parts of the reactor.

The optical system contains the main optical components of the high flux solar simulator, a 7kWe Xenon arc lamp and an ellipsoidal reflector. The lamp arc is located at the first focus of the reflector, and radiation is concentrated at the second focus. The optical model included a light source that accurately describes the arc shape and was obtained from CCD images of real arc discharge (showed in Fig. 4).

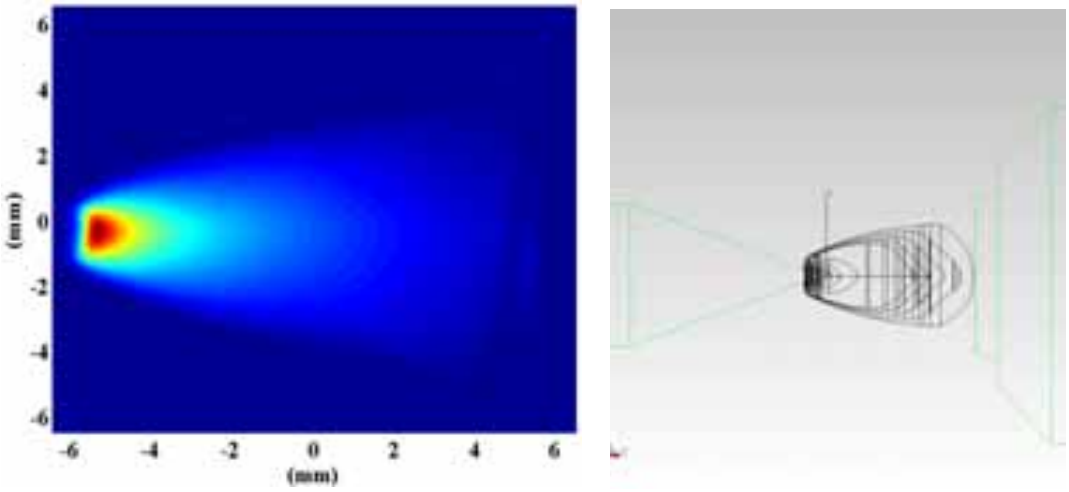

Fig. 4: Discharge arc, CCD image (left) and TracePro model (right)

The definition of the reflector scattering properties was based on the Bidirectional Scattering Distribution Function (BSDF), which consists of measuring the light scattering from a surface in difference directions. For this model, the Elliptical Gaussian BSDF was used.

The number of rays determines simulation times and the resolutions of maps. In order to obtain enough resolution in the simulated maps in reasonable time scales, 139,000 rays were fixed (1000 rays per surface). The total power of the light source was set to 1 kW and results were then scaled according to experimental measurements conducted at the focus.

A square surface (80 mm side length) was located at the focus and rays were traced. The total power in the surface is 443.21 W in the simulations, whereas 1397 W were measured experimentally (Fig. 5), therefore scale factor is 3.15.

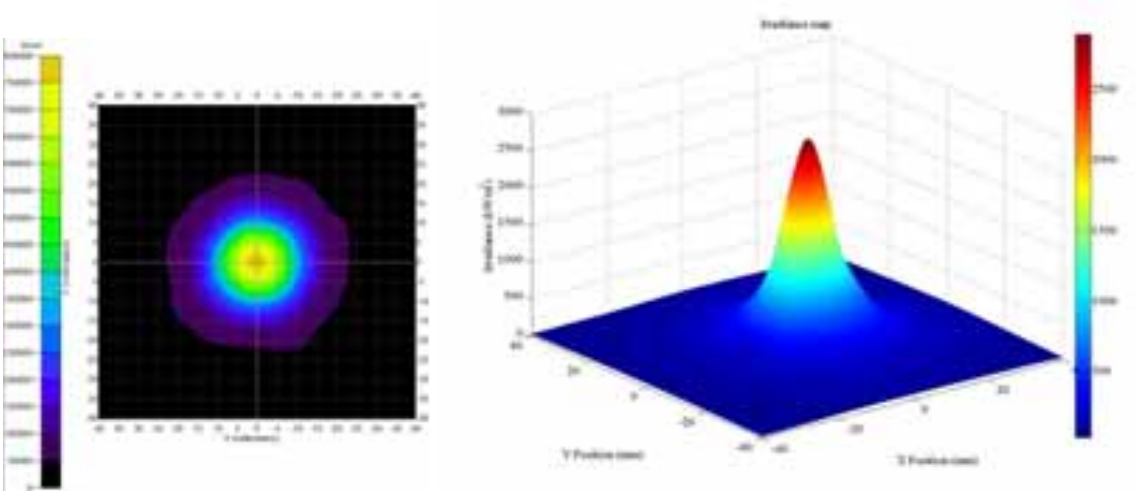

Fig. 5: Radiation measurement at the second focal point, ray tracing (left) and experimentally (right)

The cavity of the reactor (conical part and rotary tube) was implemented by means of gray-body Lambertian surfaces with a 30% absorptance. A schematic of geometry simulated can be seen in Fig. 6. The reactor is inclined 4 degrees with respect to the horizontal. The distance between the secondary focus (target plane) and the central point of the reactor cavity inlet is referred to as *d*. Four cases with different values of *d* were numerically simulated: 5 cm (outside tube), 0 cm (at the tube inlet), and 1 cm and 3 cm inside tube.

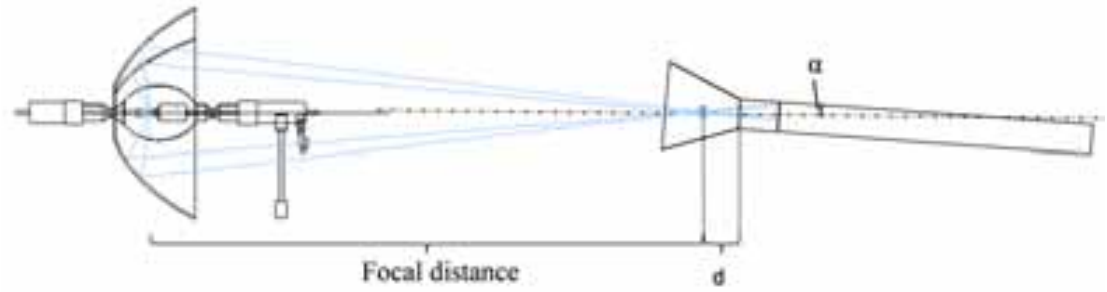

Fig. 6: Scheme of solar simulator and the cavity of the reactor

Results showed that the optimal positions of the reactor with respect to the solar simulator were either when *d* was equal to 0 cm or 1 cm, since the total power at reaction zone was higher than when *d* was equal to 5 cm outside tube and 3 cm inside tube. Table 1 shows the results from simulation with $d = 0$ cm. The total power is around 1 kW at the reaction zone (the first 4 centimeters of the tube), and the stagnation temperature, calculated from Stefan-Boltzmann law with emissivity equal to 1 (ideal radiator), is almost 1750 K.

Irradiance maps of the different parts of the reactor are shown in Figs. 7 and 8 (the latter covering the reaction zone). It can be seen that, from the reactor inlet to the ceramic ring, the maximum power is achieved just in front of the ceramic piece where the sample will be located. Case 2 refers to optical analysis results for ceramic ring with smaller aperture (Fig. 3) performed after experimental tests.

Tab. 1: Total Power at different parts of the reactor obtained by ray tracing, once weighed by real power of the source (2 kW)

Zone	Total Power (W)	Total Power (W) case 2
Cone	1243.59	1745.11
Ring	105.79	819.52
Reaction lower	525.34	101.26
Reaction upper	641.46	114.44
Reaction total	1166.81	215.70

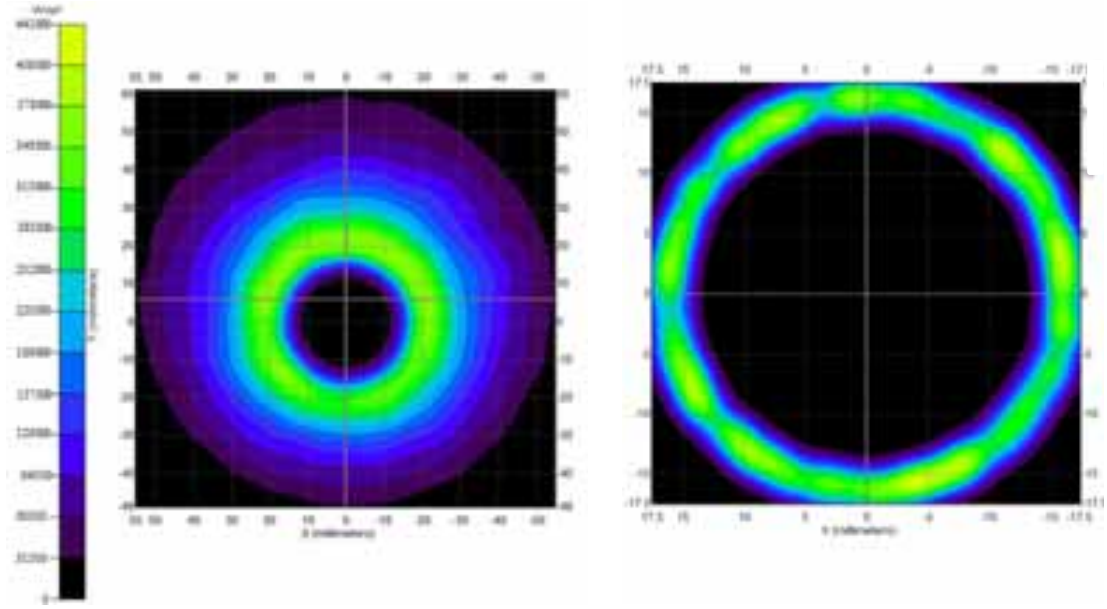

Fig. 7: Irradiance maps: cone (left) and front ring (right)

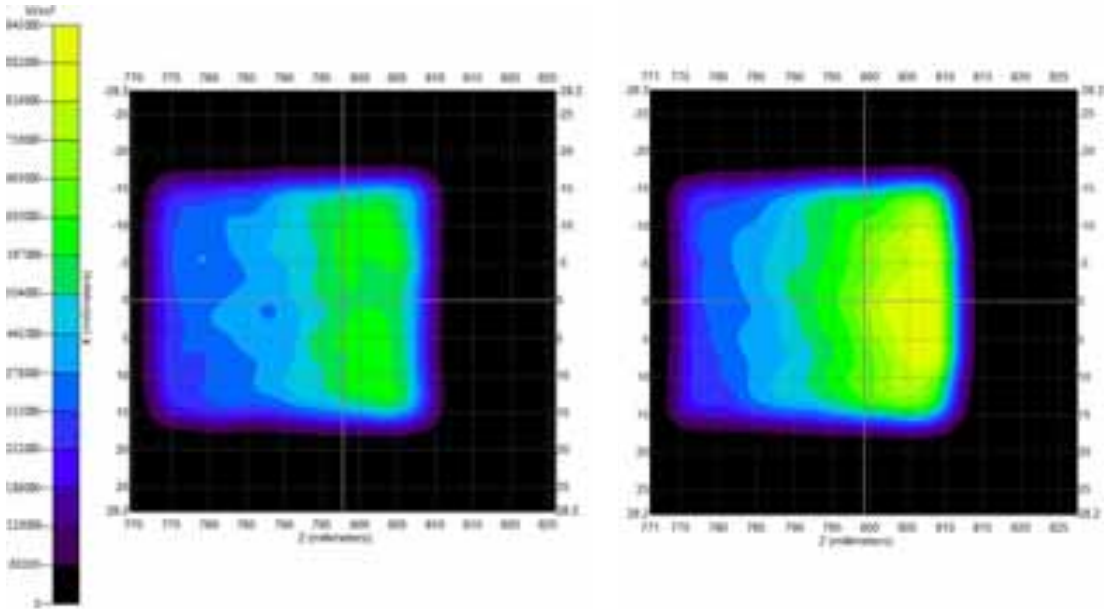

Fig. 8: Irradiance maps: lower half (left) and upper half (right)

The preliminary CFD analysis was conducted to study and assess the flow field and temperature distributions in the reactor. The reactor model was three-dimensional in order to take into account the four flow inlets, which are situated at fixed locations around the circumference. Simulations were thus conducted in one quarter of the geometry (including a flow inlet) in order to reduce the required computational times. Periodic boundary conditions were employed for the flow at the interfaces.

An unstructured mesh was built (with cell growth controlled by the flow physics), with around 65,000 elements. A conjugate heat transfer model was employed.

Boundary conditions of inlet velocity (varying between 1-20 m/s, in the parametric study), outlet pressure (atmospheric) and radiative flux were established. Irradiance variables in both the conical section and the reaction zone were fixed from the ray tracing results and taken as constant values in the simulation. Convective heat transfer between the reactor housing and ambient (at 300 K), and radiative heat transfer between the front window and ambient were simulated.

Figure 9 shows the velocity field in the cavity. As expected, maximum velocities are achieved in the center of the tube. Gas velocity increases along the conical section due to the reduction in the flow cross-sectional area. This enhances the mixing of the gas and avoid reactants deposits on the window.

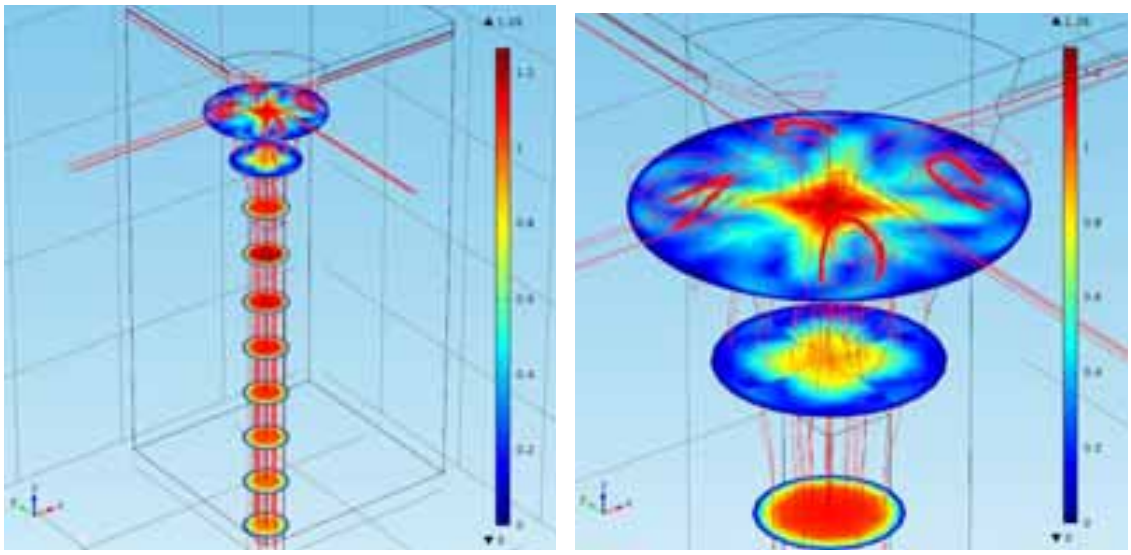

Fig. 9: Velocity field and streamlines at the cavity (left) and cone (right) for gas inlet velocity of 3 m/s (total flow 33 cl/s)

Temperature results are presented in Fig. 10. Maximum temperatures of around 1700 K are achieved in the reaction zone, in agreement with the optical calculations. The housing remains at 300 K, which demonstrates the correct sizing of the insulation. Simulations at higher velocities yield similar fields, with slightly lower temperatures (increasing velocity from 3 to 20 m/s gives a reduction in temperatures of around 50 K), since gas has room temperature at the inlets and cools the reactor more to higher flow (more gas, more convective heat transfer).

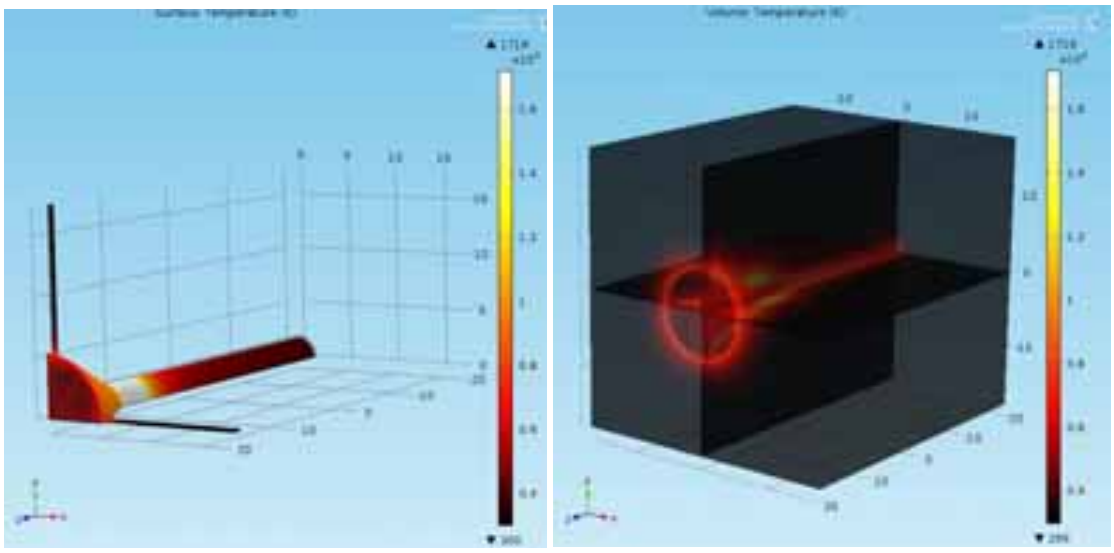

Fig. 10: Temperature distribution of the rotary kiln at a gas inlet velocity of 3 m/s (total flow 33 cl/s)

The evolution of temperature with time in different parts of the reactor is shown in Fig. 11. Temperature increases rapidly in the first minute (high slope), but the rate of change subsequently decreases. Temperatures are practically constant after 20 minutes, except at insulation, which has a much larger thermal inertia.

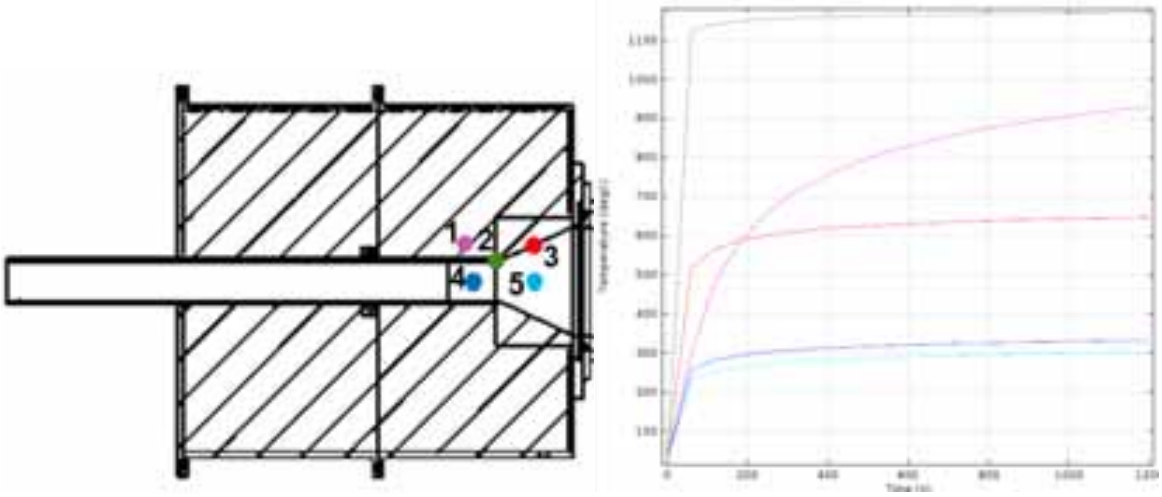

Fig. 11: Scheme of points studied (left) and temperature evolution versus time at those points of the reactor at initial velocities of gas of 3 m/s (total flow 33 cl/s) (right). Points: 1 (pink), 2 (green), 3 (red), 4 (blue), 5 (cyan)

Achieving homogenous temperatures rapidly means that is not necessary introduce rotation in the model with complete geometry of the reactor, since it is possible consider a constant radiation at surface of the tube. When a reactive material is located at the reaction zone, movement helps to get homogenous temperature at the sample and favoring heat and mass transfer with the gas.

Temperatures obtained from CFD results at the reaction zone are similar to the corresponding in experimentation. However, it is necessary improving CFD model in order to approximate it to reality at gas heating.

4. Experimental Results

The objective of the experimental part is the commissioning of the set up. Before the chemical reaction application, the reactor should be experimentally characterized. Firstly, response function of the reactor is determining monitoring evolution of the oxygen concentration at reactor outlet after fast changes in gas composition at reactor inlet. Secondly, an inert sample (silicon carbide) is used to perform thermal characterization in order to know the reactor behavior at high temperature with different irradiance, such as the changes in the reactor materials and maximum temperatures achieve at the different parts of the reactor. Finally, thermochemical reaction of manganese oxide is carried out.

In order to determine the response function, air is fed through the inlets until steady state conditions are established in the working section. It is considered that the steady state is reached when the oxygen concentration becomes stable (it does not change more than 2% in 3 minutes). At this point, the air feed is changed from air to nitrogen and the transient measurements of the oxygen concentration are analyzed (shown in Fig. 12). First, 66 seconds are necessary for the first nitrogen atoms to reach the location where gas is analyzed. Afterwards, the decrease in oxygen concentration approximately follows a negative exponential function, $\exp(-t/t_m)$, with a time constant of $t_m = 51$ seconds (the time constant has been taken as the time at which 63.21% of the total decrease has occurred).

Thermal characterization was conducted with the HFSS. An alumina screen was placed in front of the reactor as thermal shield to protect the external housing from the intense radiation (as shown in Fig. 13).

An inert silicon carbide sample was used in the first series of experiments to conduct the thermal characterization of the reactor. Different levels of radiation attenuation were employed in the facility, implemented by means of partially transparent radiation screens with various open area fractions.

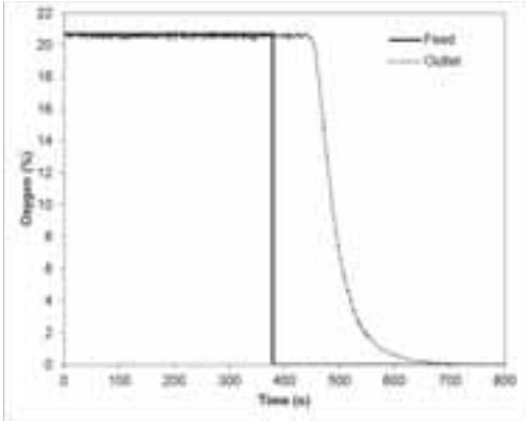

Fig. 12: Oxygen evolution when air is changed to nitrogen

Two tests are performed. A test with attenuation levels of 59%, 50% and 32%, and another test with attenuation levels of 32% and 0%. HFSS is turned off to change the screen attenuation and then it is turned on. Figure 14 shows the temporal evolution of temperatures in cavity, measured in both tests. Temperatures plotted in the figure include those measured at the conical section, the gas reaction zone (measured with two thermocouples), and outer tube wall temperature at the reaction zone. A list of the maximum operating temperatures achieved in the facility is given in Table 2. One of the thermocouples in the reaction zone was damaged during the test with lowest attenuation and data is not shown for it after that time (the maximum operating temperatures of K-type thermocouples is typically 1200 ºC).

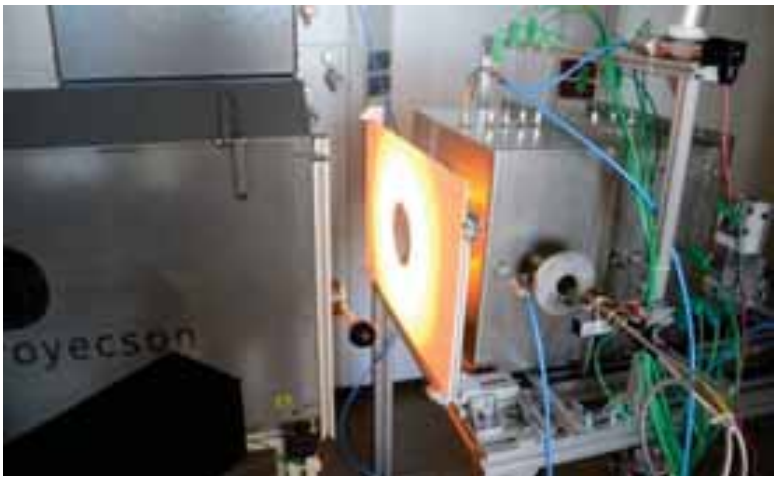

Fig. 13: Setup rotary kiln in front of high flux solar simulator

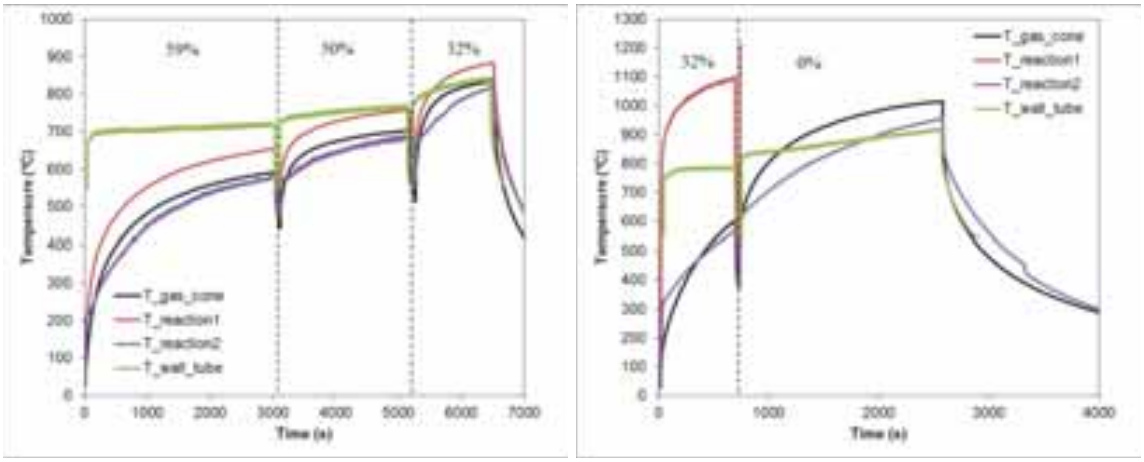

Fig. 14: Temperatures traces: attenuation levels of 59%, 50% and 32% (left); attenuation levels of 32% and 0% (right)

Tab. 2: Maximum temperature achieved in operation for different attenuations (the thermocouple was damaged during te test at 0% attenuation)

Attenuation	T max (ºC)
59%	655
50%	760
32%	1085
0%	>1200

Once the thermal characterization is done, experiments with thermochemical reactions were conducted. Manganese oxide cylindrical pellets (a mixture composed of 85% Mn_3O_4 and 15% Mn_2O_3, mean particle size 3.5 mm) were introduced in the reaction zone of the cavity. Redox reactions are the following:

Oxidation: $4\ Mn_3O_4 + O_2 \rightarrow 6\ Mn_2O_3$ (around 700 ºC)

Reduction: $6\ Mn_2O_3 \rightarrow 4\ Mn_3O_4 + O_2$ (around 950 ºC)

Air was fed while heating the working section in order to produce the complete oxidation of Mn_3O_4. The air supply was changed to nitrogen when temperatures of the reaction zone are higher than 700 ºC (temperature of the oxidation) in order to produce the reduction of Mn_2O_3. Results are showed in Fig. 15, where the full test is represented and reduction area is amplified. When oxygen concentration reaches steady state conditions at temperatures above 700 ºC, the air is changed to pure nitrogen. In this part of the experiment, an increase in the oxygen concentration is observed because of the reduction reaction. In order to study the variation in oxygen concentrations, this is compared to the variation that occurs at ambient temperatures (i.e., without reaction) when air is changed to pure nitrogen. The difference between both curves is due to the oxygen that is released during the reduction reaction.

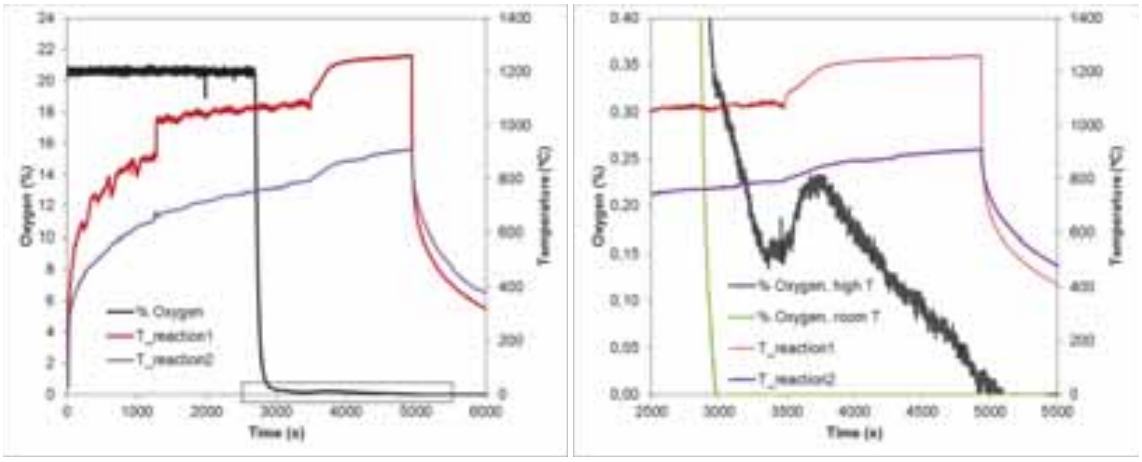

Fig. 15: Temperatures and oxygen concentration evolution, attenuation level of 32%. Full test (left), zoom on reduction reaction (right)

After the experiment, particles were removed from the reactor and analyzed (photographs of them before and after the experiment are shown in Fig. 16). It can be seen that after the tests, particles are brown in color (as opposed to black, initially) and partially worn down at the edges. Figure 17 presents histograms of particle sizes fed and discharged. It is clearly observable that sizes decrease during the test, between 0.2 and 0.4 mm, approximately. X-Ray Diffraction (Fig. 18) confirms that these particles are 100% Mn_3O_4; hence, a full conversion of the initial 15% of Mn_2O_3 is achieved.

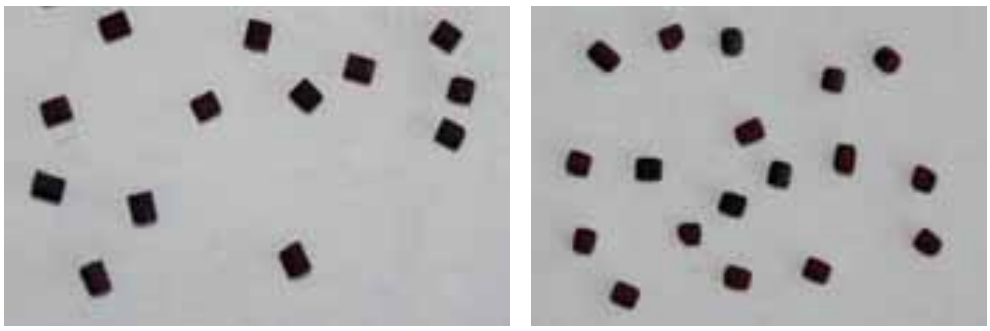

Fig. 16: Particles fed (left), particles discharged (right)

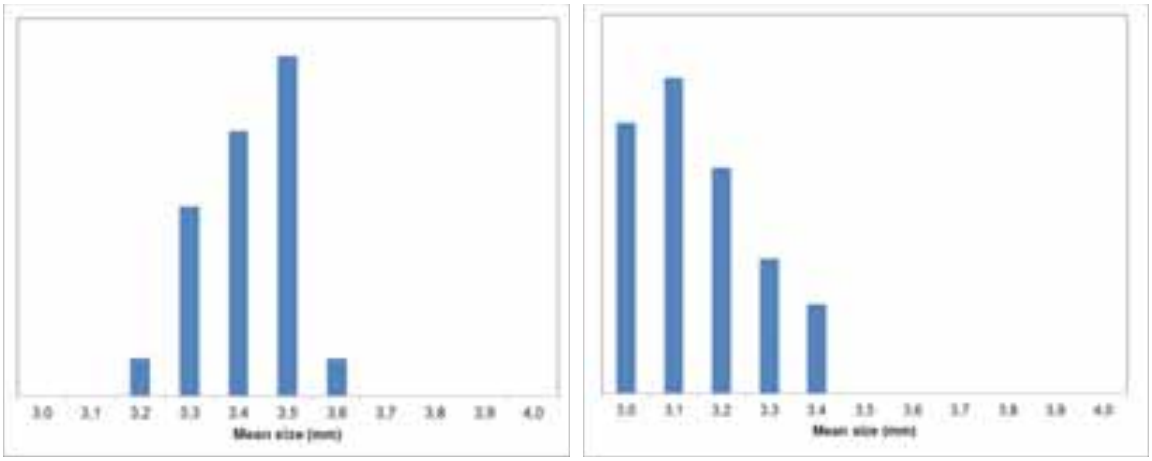

Fig. 17: Mean particle size distributions of particles fed (left) and particles discharged (right)

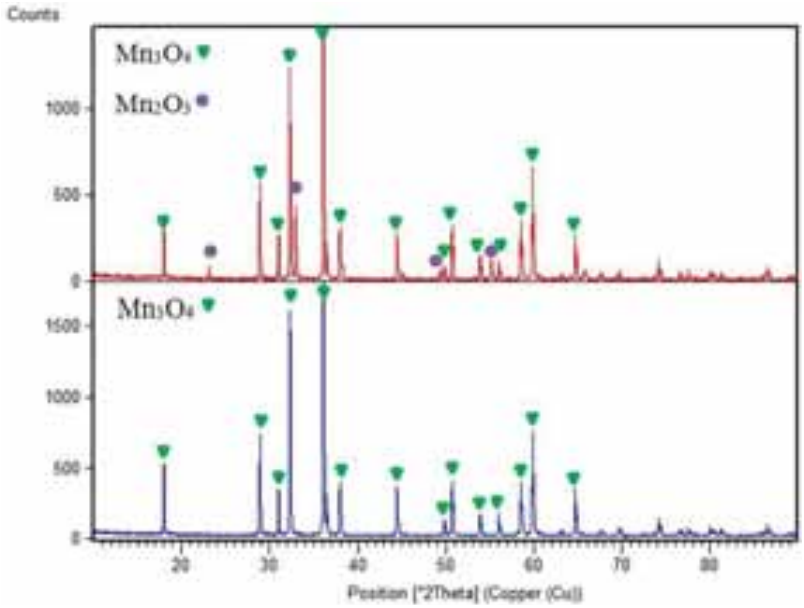

Fig. 18: X-Ray Diffraction results: particles fed (top), particles discharged (bottom)

5. Conclusions

A rotary kiln for experiments in a HFSS have been design, built, simulated and commissioned. The design allows reacting particles to be directly irradiated at high flux and high temperature conditions.

Optical analysis by Monte Carlo ray tracing was conducted to select the optimal position of the reactor relative to the HFSS in order to achieve a total power at the reaction zone of around 1 kW.

A preliminary CFD model was developed for the empty reactor and without rotation. Results indicated that

the maximum temperature was achieved at the reaction zone (1700 K).

Commissioning experiments in the 7kW$_e$ HFSS demonstrated that is possible to reach high temperatures at the reaction zone (1500 K). Thermochemical reaction experiments with manganese oxides (85% Mn_3O_4 y 15% Mn_2O_3) were performed, with air being fed during the heating of the kiln, and nitrogen when temperatures reached 700 ºC. The production of oxygen was measured at high temperatures from the reduction chemical reaction. Discharged material was 100% reduced (Mn_3O_4).

6. References

Alonso, E., Perez-Rabago, C., Licurgo, J., Fuentealba, E., Estrada, C.A., 2015. First experimental studies of solar redox reactions of copper oxides for thermochemical energy storage. Solar Energy. 115, 297-305.

Alonso, E., Romero, M., 2015. Review of experimental investigation on directly irradiated particles solar reactors. Renewable and Sustainable Energy Reviews. 41, 53-67.

COMSOL Multiphysics Version 4.4, COMSOL AB, Stockholm, Sweden, 2013. www.comsol.com

Haueter, P., Moeller, S., Palumbo, R., Steinfeld, A., 1999. The production of zinc by thermal dissociation of zinc oxide- Solar chemical reactor design. Solar Energy. 67, 161-167.

LabView Version 2013, National Instruments Corporation, Austin, USA, 2013. www.ni.com/labview

Meier, A., Bonaldi, E., Cella, G., Lipinski, W., Wuillemin, D., 2004. Design and experimental investigation of a horizontal rotary reactor for the solar thermal production of lime. Energy. 29, 811-821.

Müller, R., Haeberling, P., Palumbo, R., 2006. Further advances toward the development of a direct heating solar thermal chemical reactor for the thermal dissociation of ZnO(s). Solar Energy. 80, 500-511.

Neises, M., Tescari, S., Oliveira, L., Roeb, M., Sattler, C., Wong, B., 2012. Solar-heated rotary kiln for thermochemical energy storage. Solar Energy. 86, 3040-3048.

Romero, M., Steinfeld, A., 2012. Concentrating solar thermal power and thermochemical fuels. Energy & Environmental Science. 5, 9137–9674.

Tescari, S., Neises, M., Oliveira, L., Roeb, M., Sattler, C., Neveu, P., 2013. Thermal model for the optimization of a solar rotary kiln to be used as high temperature thermochemical reactor. Solar Energy. 95, 279-289.

TracePro Version 7.2, Lambda Research Corporation, Littleton, USA, 2012. www.lambdares.com

Acknowledgements

The research leading to these results has been conducted under the grant Plan Nacional ENE2011-29293 funded by the Spanish Ministry of Science and Innovation, which the authors gratefully acknowledge. The collaboration and funding of the regional government of the Community of Madrid and the European Social Fund, through the funding of the project ALCCONES (Storage and Conversion of Concentrating Solar Thermal Energy, S2013/MAE-2985), and the European Union, through the Seventh Framework Research Programme STAGE-STE (Scientific and Technological Alliance for Guaranteeing the European Excellence in Concentrating Solar Thermal Electricity, ENERGY.2013.10.1.10), are also particularly appreciated.

Conference Proceedings
Solar World Congress 2015
Daegu, Korea, 08 – 12 November 2015

DESIGN AND FABRICATION OF HIGHLY ENVIRONMENTAL STABLE Cr-Fe-Ni oxides/ ZrO_2-SiO_2 COMPOSITE OXIDE BASED TANDEM ABSORBER FOR SOLAR THERMAL POWER GENERATION APPLICATIONS

T. Vijayaraghavan, M. Shiva Prasad, S. Sakthivel* and S.V. Joshi

Centre for Solar Energy Materials, International Advanced Research Centre for Powder Metallurgy, and New materials, Balapur PO, Hyderabad-500 005, India.

Abstract

A new Cr-Fe-Ni oxides/ZrO_2-SiO_2 composite oxide based tandem absorber is designed and developed for high performance ORC based solar thermal applications. The Cr-Fe-Ni composite oxide based absorber layer is designed to have nanoporous structure and covered with an antireflective protective layer. The tandem absorber layer was developed by a combination of chemical and sol-gel methods. By varying process parameters like duration, temperature and withdrawal speed, different combinations of Cr-Fe-Ni oxides/ ZrO_2-SiO_2 composite absorber layers with varying refractive indices were developed on a suitable SS substrate. The optimized thickness of absorber layer along with the antireflective layer exhibited high absorptance (α= > 0.94) and low thermal emittance (ε = 0.11– 0.14 at 300 °C). More specifically, this novel tandem coating has excellent optical properties along with high corrosion resistance (withstands > 400 h in salt spray test). It has good thermal stability in an open air atmosphere and is well suited for low and medium temperature solar thermal applications.

Keywords: *Tandem absorber layer, Cr-Fe-Ni composite oxide, ZrO_2-SiO_2, antireflective layer*

Introduction

Solar collectors play an important role in areas such as hot water heating systems of buildings and steam generation for various industrial applications and power production. They convert sunlight to thermal energy which is then converted to electrical energy (Agnihotri and Gupta, 1981; Duffie and Beckman, 1991; Gordon, 2001; Kennedy, 2002; Kalogirou, 2004). Conventionally, most of the selective absorber coatings preferred for concentrated solar collector application are developed by the expensive PVD route particularly magnetron sputtering (Adsten et al.,(2000); Barshilia et al., (2008); Graf et al., (1997); Juang et al., (2010); Koželj et al., (2009); Nunes et al., (2003); Selvakumar and Barshilia, 2012; Teixeira et al., (2001, 2002); Wäckelgård et al., (2001); Yin et al., (2009); Zhang, 1998). Currently the entire concentrated solar thermal power (CSP) program is working to reduce the cost of solar thermal power technology. One of the approaches is to operate the CSP system using cost effective solar collectors in open air atmosphere conditions instead of using expensive evacuated solar collectors. To accomplish this, efficient selective collectors are needed that have high optical properties and high stability to corrosion, in addition to enhanced thermal properties. For efficient photo thermal conversion, solar collectors must have high solar absorptance (α) in an active solar region (300-2500 nm) and a low thermal emittance (ε) in the IR radiation wavelength range (3-25 μm) at an optimal operational temperature. However, most of the current coatings do not have stability against corrosion and air and this is the main problem faced while operating the collectors in an open atmosphere (Barshilia et al., (2008); Koželj et al., (2009); Selvakumar and Barshilia, 2012; Tulchinsky et al., (2014)). Moreover, the coatings need to be stable in air in case the vacuum is breached.

doi:10.18086/swc.2015.04.11 Available at http://proceedings.ises.org

Solar selective coatings can have high optical properties, stability against air at operational temperature, long environmental stability, high scratch and abrasion resistance, and high mechanical integrity. Coatings prepared by an economic process (e.g. electrochemical deposition technique (Lee, 2007; Moise et al., (2001); Newby, 1999; Zeng et al., (2009)), thermal oxidation (Aries, 1986, 1987, 1991; Boydag, 1986; Douglass and Pettit, 1981), chemical oxidation (Sharma et al., (1988); Uma et al., (1987)), sol-gel process (Bostrom et al., (2008); Kozelj et al., (2009); Katumba et al., (2008)) etc on easily available substrates (e.g. stainless steel) with a combination of above mentioned properties would be a great choice for power generation by a concentrated solar power (CSP) system. Nowadays, solar absorptance of most common high-quality commercial absorbers is about 95 % and the thermal emittance is < 10 %. The techniques that have been attempted so far for the cost efficient solar absorber coatings such as electrochemical deposition, thermal oxidation, chemical and sol-gel process have faced many challenges to produce coatings with high optical efficiency, high environmental and thermal stability.

Very few studies have reported high optical efficiency with temperature and corrosion stabilities for solar absorber coatings made by sol-gel process. For example, such a coating was prepared from polysiloxane as a binder and Co_3O_4 as a spinel pigment on 304 stainless steel by spin-coating (Andrea Ambrosini et al., (2010)). Spectrally selective absorber coatings were prepared by spin- coating of nickel nanoparticles embedded in alumina and coated with an antireflective layer made of silica, alumina, or silica–titania mixture (Bostrom et al., (2005)); Orelet al., (2003)) reported doping of $CuCoMnO_x$ by Ti in a polysiloxane resin. The films were used in order to increase the weather resistance and showed absorptance of 0.86 – 0.91 and emittance below 0.036. Tulchinsky et al., (2014) reported the thermal chemical reaction between a titania sol–gel precursor with the copper manganese spinel to form a new material, $Cu_{0.44}$ $Ti_{0.44}$ $Mn_{0.84}Fe_{0.28}O_3$, having a bixbyite structure. Although solar absorptance of the films was reported around 97.4 %, no data was provided for the emittance of the film. Chao-Ching Chang reported poly(urethane)-based solar absorber coatings containing copper chloride and nanogold composite synthesised by solution-chemical technique. The solar absorptance and thermal emittance of this coating were shown to be only around 0.846 and 0.09, respectively (Chao-Ching Chang et al., (2013)). Copper–cobalt oxide thin films deposited on aluminium substrates via a facile sol–gel dip-coating method showed solar absorptance of 3.4 %. (Amun Amri et al., (2013)). A higher value of solar absorptance and better stability is needed for the films to be suitable for concentrated solar thermal power application.

Martin Joly et al., (2013) produced multilayered chrome-free black selective surfaces for solar thermal energy conversion by a low-cost sol–gel dip-coating method. The optical properties of solar absorptance and thermal emissivity at 100 °C of the Cu–Co–Mn–Si–O based nano crystalline thin films were shown around 0.95 and 0.12. The coatings were stable up to a maximum of 360 °C in air which surpasses that of the conventional robust black chrome coatings existing in the market. But there was no report on the weather stability of the novel multilayer absorber coating.

For concentrated solar thermal power plant (CSP) application, coatings are required in a large area and development of solar receiver tubes with all the properties like high solar absorptance, low thermal emissivity, high weather and thermal stabilities by an economic way is the main objective in order to reduce the cost of solar electricity production. In view of the above, herein, we report a novel Cr-Fe-Ni oxides/ ZrO_2-SiO_2 nanocomposite oxide based tandem absorber system developed by a combination of chemical oxidation and sol-gel process for high performance ORC based solar thermal applications having excellent optical properties along with high corrosion resistance and good thermal stability in an open air atmosphere and their optical and structural characterisations.

2. Experimental

2.1. Sample preparation

The thin nanoporous structure composite oxides of absorbing layers were developed on smooth highly specular reflecting mirror of stainless steel substrates. The base absorber films were developed by controlled chemical oxidation process on a special variety of stainless steel tube (SS-316) having the composition of C: 0.08, Mn: 2, P: 0.045, S: 0.030, Si: 0.75, Cr: 16-18 and Ni: 10-14**;** and Fe: 69-73 wt % respectively, using a precise temperature controllable chemical bath reactor and an optimum parameters like molar ratio of acid mixture, temperature, and duration. 1M sodium dichromate salt dispersed in a mixture of sulphuric acid and water (3:5) was used for the development of nanoporous base absorber layer. The detailed preparation procedure of the absorber layer has been described elsewhere (Sakthivel et al., (2013)). In a preliminary step of the process, the SS tube sample is cleaned with a mild detergent solution and rinsed with tap water followed by deionised water and finally wiped with a soft cotton cloth using an organic solvent, preferably

isopropyl alcohol (IPA), to make it free of any external impurities adhering to the surface. The cleaned substrate is then dried either by an air drier or by keeping it at 100 ^{0}C for 5-10 min in an air–oven. The dimensions of SS tube used for this study were 500 mm x 500 mm x 1.25 mm (L x W x Thickness).

2.2. Development of nanoporous composite absorber layer on SS 316 tubes

The cleaned substrates are immersed into an acid bath for chemical oxidation in a temperature range of 80-90 °C for 20-30 min. During the chemical oxidation process, the metal atoms on the surface of substrates are partially oxidized by the acid mixture to obtain a type of nanoporous composite oxide layer. After chemical oxidation, the SS tubes turned to grey in colour with a glassy appearance. The absorber layer developed SS tube was then washed thoroughly with tap and distilled water and finally wiped with a soft cotton cloth using with an organic solvent, preferably isopropyl alcohol (IPA). The cleaned absorber layer developed substrate was then dried by an air drier for 2-5 min.

2.3. Development of optical enhancing layer on absorber layer coated SS 316 tubes

After drying, the optical enhancing protective layer comprising ZrO_2–SiO_2 composite, was deposited by dip coating process using a composite sol obtained by mixing zirconium propoxide and 3-glycidoxy propyltrimethoxysilane (GPTS) compound in a mixture of isopropyl alcohol (IPA, Alfa Aesar) and Isopropoxyethanol (IPE, Alfa Aesar) to obtain a stable suspension. The composition of the coating suspension for this layer was in the ratio of Zr (n-Pro): IPA: IPE: GPTS = 6.94:78.52:12.94:1.60 (wt %). ZrO_2-SiO_2 composite coating sol was coated on the absorber coated steel substrates using dip-coating technique. No binder/additive was used for the coating. Increase in withdrawal speed resulted in increase of coating thickness and in turn the packing density. To obtain highly optical enhancing thin films, the coating speed and curing temperature were altered from 2 mm sec^{-1} to 5 mm $^{-1}$sec and 100-300 °C respectively. It was noted that the film showed a high optical enhancing (antireflection) property (> 8 % solar absorptance from 300-2500 nm) even at low possible curing temperature, 100 °C. Hence it is suitable for making cost effective tandem absorber layer for solar thermal application.

2.4. Characterization methods

Optical and structural properties of the absorber layers were measured after the coating layer development. The diffuse reflection spectral measurements in the UV/ Vis /near-IR region were carried out by a Cary 5000 spectrophotometer equipped with a standard integrating sphere (110 mm dia) at room temperature in the spectral interval of 0.3 – 2.5 μm with a scanning speed of 1200 nm min^{-1}. Normal emittance measurements in the infrared wavelength region were carried out by a Bruker vertex 70 FTIR (Fourier Transform Infrared) spectrophotometer equipped with a standard integrating sphere using an evaporated gold mirror as a reference plate. All the measurements were done in the spectral interval of 2.5 – 25 μm with a scanning velocity of 2.5 KHz.

The normal absorptance (α) and emittance (ε) values were calculated using standard equations as described in literature (Bostrom et al., (2003)). The solar absorptance, α_{sol} of the sample was calculated as a weighted fraction between absorbed radiation and incoming solar radiation using an AM 1.5 spectrum. The direct normal solar irradiance, I, is defined according to the ISO standard 9845-1 (1992) where an air mass of 1.5 is used (Bostrom et al., (2003)).

The thermal emissivity (thermal loss) of coatings corresponding to a particular temperature (ε_t) was calculated as described in literature (Sakthivel and Srinivasa rao, 2015). However, values of thermal emittance of black body at each temperature were used instead of using a theoretical black body distribution as is generally used in literature (Bostrom et al., (2003); Lundh et al., (2010)). FTIR spectrometer equipped with the standard accessories of black body furnace and a high pressure cell (sample compartment) supplied by Bruker optic GmbH was used for the measurement of thermal radiation emittance. For thermal emissivity calculation, initially the thermal radiation emittance spectra (2.5-25 μm) of both black body and selective absorber layer coated sample were measured one after another by heating black body furnace and coated sample in the sample compartment at temperature range starting from 100 to 300 °C. Finally, the thermal emissivity was calculated by using this formula, ε_t= sample emittance radiation /Black body emittance radiation generated at the same temperature from 2.5-25 μm.

X-ray diffraction pattern was recorded by using Bruker AX D8 XRD equipment having CuK_α X-ray source. The scan was taken in the range 0-100° with an increase of 0.01°at duration of 2s step^{-1}. Surface morphology of absorber layers was studied by field emission scanning electron microscopy, FESEM (Hitachi model S4300SE/N) operated at 20 kV. Energy dispersive spectroscopy (EDS) was carried out for all the films during SEM study.

Coating thickness and refractive index of the composite layers were measured using a spectroscopic ellipsometer (Model: M-2000V, J. A. Woollam Co. Inc.) in the wavelength range of 350–1000 nm. Water contact angle was measured by a drop shape analyser DSA 100 (Kruss GmbH, Germany) to verify the surface roughness (hydrophobicity/hydrophilicity) of the absorber layer. The chemical composition and oxidation state of the composite layers were analysed by X-ray photoelectron spectrometer (Omicron-ESCA+) equipped with Al Kα anode and Raman spectrophotometer (Model: HR 800, Horiba Jobin-Yvon, France).

3. Results and discussion

3. 1. Design of Cr-Fe-Ni nanocomposite oxide / ZrO_2-SiO_2 tandem absorber

The schematic diagram of Cr-Fe-Ni nanocomposite oxide / ZrO_2-SiO_2 tandem absorber is shown in Fig. 1. An absorber–reflector tandem absorber concept was used to develop the absorber on SS substrates, where in the Cr-Fe-Ni nanocomposite oxide layer and smooth SS surface (surface roughness around <1 micron) act as absorber layer and infrared reflector, respectively. It is well known that the optical properties of transition metal based coatings can be tailored by controlling the stoichiometry, which affects the density of free electrons in the d band (Seraphin, 1979). Based on this concept, the first absorber layer Cr-Fe-Ni composite oxide was designed to have higher amount of Cr oxide content (called as HfMoN(H)) than the Fe and Ni oxides in order to achieve high selective property with suitable refractive index which matches with second layer (optical enhancing layer (antireflective layer)) for further optical enhancement.

The tandem design used for the fabrication of highly environmentally stable absorber system is illustrated in Fig. 1. Cr-Fe-Ni nanocomposite oxide layer with nanoporous structure (11-14 nm pore size) was prepared by controlled chemical oxidation process using optimum process parameters like a process temperature, 80-90 ^{0}C, process duration, 20-30 min and an optimum concentration of acid mixture, 1M sodium dichromate salt dispersed in a mixture of sulphuric acid and water (3:5), respectively. Followed by the deposition of absorber layer by the above described controlled chemical oxidation, the optical enhancing layer (antireflective layer) with weather resistant property is deposited by the dip coating process using a composite sol of ZrO_2-SiO_2 prepared by a sol-gel method.

Figure 1. Schematic diagram of the Cr-Fe-Ni oxides / ZrO_2-SiO_2 composite oxide layer deposited on stainless steel tube

3.2 .FE-SEM

The FE-SEM representative images of Cr-Fe-Ni nanocomposite oxide absorber layer developed on SS-316 mirror (smooth surface) are shown in Fig. 2. It can be observed in this figure that the surface morphology of Cr-Fe-Ni composite oxide absorber layer on SS-316 polished surface (Fig. 2a) comprises a nanoporous morphological structure of 13–17 nm in diameter, because of the controlled chemical oxidation of metal atoms on the surface of SS plate. Particularly, Cr, Fe and Ni were the predominant metal atoms involved in the oxidation process. The surface morphology of ZrO_2-SiO_2 (Fig. 2b) deposited on the absorber layer in the tandem system uniformly covered all the nanopores. Furthermore, the layer deposited on the absorber layer for the optical enhancement and protection from weather and corrosion was very uniform and without cracks and pinholes.

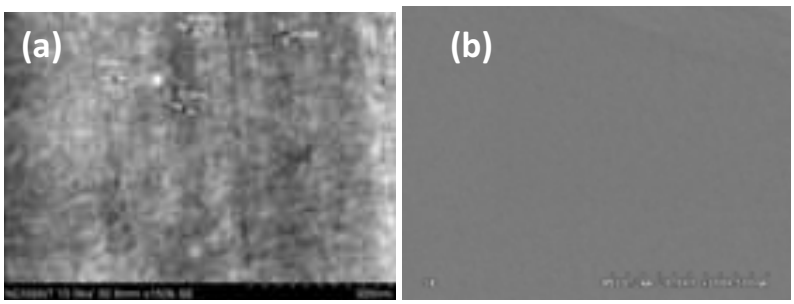

Figure 2. FE-SEM surface morphology of (a) Cr-Mn-Fe composite absorber layer with nanoporous structure (Pore size around 13-17nm); (b) Tandem absorber layer of Cr-Fe-Ni oxides / ZrO_2-SiO_2 composite oxide layer generated on SS tube

3.3. X-Ray Diffraction (XRD) results

The results of the incident angle XRD studies for the absorber layer comprised of Cr-Fe-Ni composite oxide layer developed using optimized conditions are shown in Fig. 2 and are compared with the diffraction peaks of bare SS-316 sample. The peaks observed in the bare substrate indicate an austenitic type of steel (Fig. 3 FCC peaks labelled "a"). It is surprisingly noted that the XRD patterns of chemically oxidized samples are quiet similar to the bare substrate. The reason could be that a high content of iron (69-73 %) in the substrate which dominated during analysis as compared to other components like chromium, manganese, nickel which are presented in lower concentration. Moreover, the atomic number of chromium, nickel, and copper are very close to metallic iron. From XRD analysis it is quite difficult to distinguish if the element is in low concentration or the layer thickness in nano range.

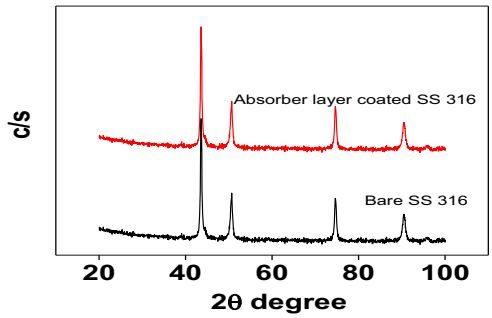

Figure 3. XRD patterns of both bare and absorber layer developed on SS-316 polished plate

3.4. X-Ray photoelectron spectroscopy (XPS) results

The coating compositions of the base absorber layer and the oxidation states of each element were clearly confirmed by XPS. Fig. 4 (a-d) shows the high resolution core level X-ray photoelectron spectra (XPS) for an absorber layer developed on SS 316 polished surface. The Cr 2p spectrum (Fig. 3(a)) consists of 2 peaks centered at 576.73 and586.35, which originate from Cr $2p^{3/2}$ and Cr $2p^{1/2}$ electrons in Cr_2O_3 (Hsin-Yen Cheng et al., (2013); Teixeira et al., (2002); Wu et al., (2013)). The Fe 2p spectrum (Fig. 3(b)) exhibited four peaks centered at 707.14, 709.29eV, 726.40 and 730.03 which correspond to Fe $2p^{3/2}$ and Fe $2p^{1/2}$ of FeO and Fe_2O_3 (Srinivasa Rao and S.Sakthivel, (2015); Tulchinsky et al., (2014)). The Ni 2p spectrum (Fig. 3(b)) exhibited 2 peaks centered at 853.05 and 870.39 eV, which correspond to Ni $2p^{2/3}$ and Ni $2p^{1/2}$ of NiO (Ewa Wackelgard et al., (1998)). The 1s spectrum of oxygen (Fig. 3(d)) of the absorber coating (Cr-Fe-Ni oxide layer) revealed the presence of two peaks centered at 530.42 and 531.25 eV, which correspond to oxides Fe, Ni and Cr. From this result, it is clear that the nature of composite absorber layers formed by the controlled chemical oxidation method may depend upon the process conditions. According to XPS analysis, the surface composition of the absorber layers in atomic percentage was in the ratio of 17.97: 6.28: 2.22: 73.53 (Cr: Fe: Ni: O).

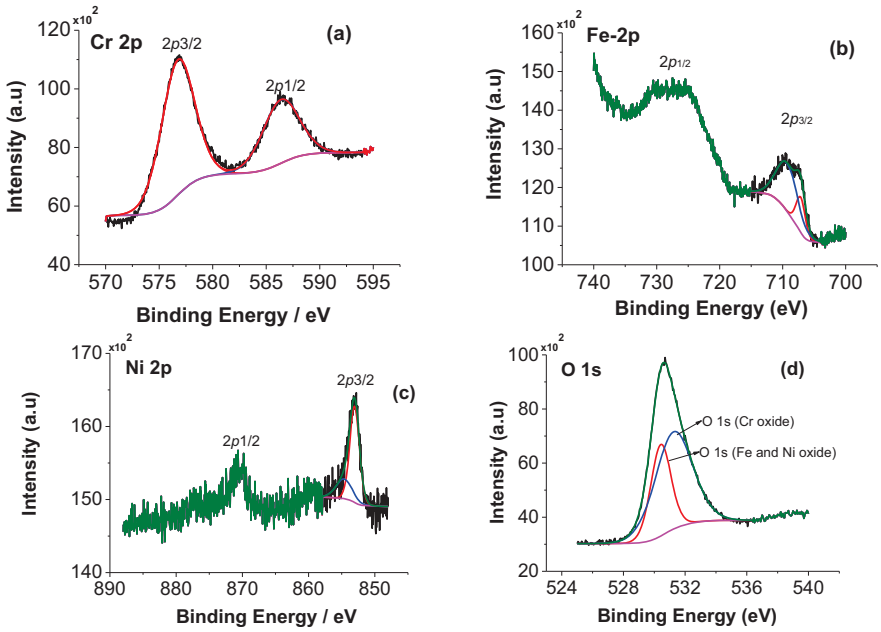

Figure 4. X-ray photon electron spectra of absorber layer developed on SS 316 polished surface

3.5. Solar absorptance of single and tandem absorber systems:

Fig. 5 and Table. 1 summarize the reflectance spectra measurement at room temperature for the absorptance characteristics of the corresponding nanocomposite selective absorber layer with nanoporous morphological structure prepared with the optimum conditions of process temperature, duration, and using with an optimum concentration of acid mixture: 85 °C, 20 min and 1M sodium dichromate salt dispersed in a mixture of sulphuric acid and water (3:5), respectively. The reflectance spectrum of Cr-Fe-Ni nanocomposite oxide layer with nanoporous morphological structure shows a little higher reflectance in the solar range corresponding to a low solar absorptance of 86.1 %. However, the absorber layer further coated with the optical enhancing layer (antireflective layer) using a composite sol of ZrO_2-SiO_2 by sol-gel dip coating process. The optical enhancing layer deposited with an optical withdrawal speed of 3 mm sec^{-1} followed by curing at 300 °C for 2 h exhibits high solar absorptance, 94.3 %.

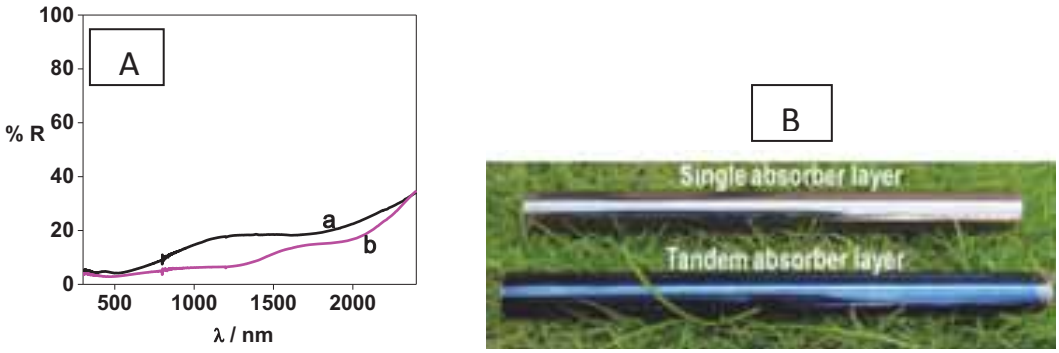

Figure 5A. Comparison of reflectance spectra of Cr-Fe-Ni nanocomposite oxide (a) and Cr-Fe-Ni oxides /ZrO_2-SiO_2 Tandem absorber layers (b), 5B. Image of 0.5 m long single and Tandem absorber layers coated SS 316 tubes.

3.6. Thermal emissivity characterization:

Thermal emissivity characterisation of the both single absorber layer (Cr-Fe-Ni nanocomposite oxide layer) and two layer tandem absorber layer (Cr-Fe-Ni nanocomposite oxide layer/ ZrO_2-SiO_2 sol-gel layer) exhibits high solar absorptance developed on the polished surface of SS 316 and was carried out by FT-IR spectrophotometer using special accessories like a black body furnace and high temperature sample cell unit. The thermal emittance of both black body furnace and samples were measured at different temperatures starting from 100 °C to 300 °C with an interval of 50 °C. Finally, the thermal emissivity of the coatings was

calculated from the measured thermal emittance data of sample and black body furnace using the standard equation as described in the literatures (Carlsson et al. (2000), Öhl et al. (2004), Price et al. (2004)).

Typical thermal emissivity spectra were derived for single and tandem absorber layers from their emittance and black body emittance spectra were recorded at different temperatures from 100-300 °C and represented in Fig. 6 and Table. 2. The thermal emissivity of heat radiations from both types of layers on SS substrates are increased with increasing of temperature. Compared to the single absorber layer coated sample, a little lower value of emissivity is noted for the tandem absorber sample due to covering of nanopores in the absorber layer by the AR layer. Further, it is clearly noted that the tandem absorber layer shows low thermal emissivity value of 0.067-0.144 at 300 °C. However, the single nanocomposite absorber layer having nanoporous morphological structure shows a high thermal emissivity range of 0.106-0.172 measured from 100 °C to 300 °C. The reason for observing a high thermal emissivity could be the presence of pores in the absorber layer.

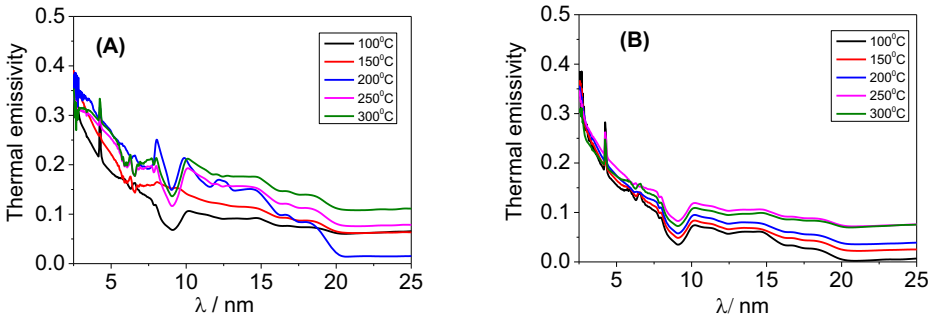

Figure 6. (A) Thermal emissivity spectra of single absorber layer (Cr-Fe-Ni nanocomposite oxide layer) and (B) Two layer tandem absorber layer (Cr-Fe-Ni nanocomposite oxide layer/ ZrO_2-SiO_2 sol-gel layer) developed on SS-316 polished surface measured at different temperatures.

Table 1. Thermal emissivity data of single absorber layer (Cr-Fe-Ni nanocomposite oxide layer) and two layer tandem absorber layer (Cr-Fe-Ni nanocomposite oxide layer/ ZrO_2-SiO_2 sol-gel layer) measured at different temperatures.

Temperature (^{0}C)	ε (2.5-25μm)	
	Single	Tandem
100	0.106	0.067
150	0.127	0.079
200	0.138	0.090
250	0.150	0.116
300	0.172	0.144

3.7. Optical thickness and refractive index results of nanocomposite oxide absorber and optical enhancing layers

The thickness and refractive index of Cr-Fe-Ni nanocomposite absorber and ZrO_2-SiO_2 based optical enhancing layer (antireflective along with corrosion protection) developed by the optimum conditions were estimated by ellipsometer are represented in Table. 2. The experimental data has been fitted with theoretically simulated spectra using a suitable mathematical model for optical constants of the materials. From the fitting, the thicknesses of the layers and the optical constants of the materials have been determined similar as our earlier work (Sakthivel and Srinivasa rao, 2015). The deposited absorber layer (Cr-Fe-Ni nanocomposite oxides) and optical enhancing layer (ZrO_2-SiO_2) layers were modelled using the Cauchy dispersion model for generating the refractive indices and extinction coefficients spectra. The thickness and refractive index values of the absorber layer are around 140 ± 5nm and 1.88 ± 0.01and optical enhancing layer 70 ± 5nm and 1.70 ± 0.01, respectively. High optical properties of high solar absorptance, >94 ±0.1% and low emittance,

<0.15±0.01 were observed only for the optimum thickness of the absorber and optical enhancing layer. The absorber layers generated at the thickness of < or > 140 ± 5 nm with optical enhancing layer (ZrO_2-SiO_2) at the thickness of 70 ± 5 nm the optical properties of either absorptance or emittance were not observed in a satisfactory level. Moreover, the thickness of the absorber layer was found to increase from 140 ± 5nm to 300 nm with increase in the net deposited oxide content on the substrate due to increase of process duration from 20 to 30 min. The refractive index value was also found to increase from 1.88 to 2.41 due to increase of oxide content.

Table 2. Summarises the optical property, thickness and refractive index data of composite oxide and Tandem absorber layers

Sample	α	$\varepsilon_{300\,^0C}$	Thickness (nm)	Refractive index
Cr-Fe-Mn composite absorber layer	86.28	0.172	140	1.88
Cr-Fe-Mn /ZrO_2 -SiO_2 Tandem absorber layer	94.30	0.144	140/70	1.88/1.7

3.8. Corrosion stability of nanocomposite oxide absorber layer and Tandem absorber system

To understand the corrosion and thermal resistance behaviour of both single and tandem absorber system, the coatings were subjected to a salt pray test for proving the corrosion and weather stability in a salt pray chamber following the *ASTM method (ASTM 13117)* using 5 % NaCl solution and generating vapours at a temperature of 35 °C /min. After every cycle test (24 hours) the coating was inspected for the change in properties of solar absorptance and thermal emissivity at a maximum temperature, 300 °C by UV-Vis-NIR and FT-IR spectrophotometer with thermal emissivity accessories of high pressure cell and black body furnace. According to the salt spray experiments, the tandem absorber layer was found to have no changes in its absorptance and emittance properties even after 20 days salt spray test. However, the sample deposited with the nanocomposite layer only could withstand the salt spray test for a maximum of 10 days.

Table. 3: Changes of solar absorptance and thermal emittance measured at 300^{0}C of single and Tandem absorber system developed on SS-316 polished surface.

Duration (day)	Abs (α)		$\varepsilon_{300\,^0C}$	
	Single	Tandem	Single	Tandem
	86.21	94.41	0.172	0.146
1	86.13	94.29	0.173	0.143
2	86.91	94.37	0.172	0.146
5	86.03	94.22	0.175	0.141
10	86.13	94.30	0.176	0.144
15	84.16	94.35	0.220	0.143
20	81.57	94.19	0.231	0.145

3.9. Thermal stability

An important requirement for absorber coatings is long-term thermal stability, ideally in air. Thermal stability is sometimes based on thermal properties of the individual materials or the processing temperature parameters. Since thermal instabilities and degradation of the solar absorber layers are major parameters of interest for long-term stability of the selective solar absorbers, the stability of the single and tandem absorber layer developed on the polished surface (SS 316) was tested under a thermal cycle test (maximum up to 300 °C) suitable for medium ORC based solar collectors usually operating at the temperature range from 200 °C-250 °C. To determine the durability and thermal stability of the coatings a precise temperature controllable furnace (Nabertherm model L 5/12/P330**)** in an open air environment and was utilized for this

study. It has digital PID-temperature control and temperature programme with 40 segments to allow the operator to run the furnace with a specific heating rate, soaking and cooling hours. To evaluate the thermal stability, the samples were annealed in air at 300 °C and for a maximum of 100 cycles. Each cycle comprised of 2h heating to attain 300 °C, 2h soaking duration, and 5-6h cooling to reach the ambient temperature. The dependence of optical properties of the coatings on the thermal treatment was investigated. The solar absorptance and thermal emittance at 300 ^{0}C were measured using a UV–Vis–IR and FT-IR-Spectrophotometer and the detailed measurement procedures have been reported elsewhere [Sakthivel et al]. According to the experiments, both the single and tandem absorber layer was found to have no remarkable changes in their absorptance and emittance properties even after 100 cycles. However, after 350 °C the coatings started to degrade, >10 % of absorptance changes were observed even after 10 cycles and no changes in thermal emissivity property.

Table 4. The effect of annealing at 300 ^{0}C in air, on the solar absorptance and thermal emittance measured at 300 ^{0}C single and Tandem absorber system developed on SS-316 polished surface.

Cycle	α_{sol}		$\varepsilon_{300^\circ C}$	
	Single	Tandem	Single	Tandem
0	86.29	94.32	0.170	0.143
10	86.32	94.56	0.172	0.144
20	86.41	94.18	0.171	0.145
30	86.24	94.53	0.169	0.141
40	86.46	94.48	0.172	0.144
50	86.42	94.41	0.173	0.145
60	86.35	94.49	0.175	0.144
70	86.26	94.43	0.173	0.145
80	86.31	94.22	0.171	0.146
90	86.25	94.37	0.173	0.142
100	86.23	94.35	0.174	0.146

4. Conclusion

A novel tandem layer design of Cr-Fe-Ni oxides/ZrO_2-SiO_2 composite oxide selective absorber layer developed on an austenitic stainless steel (SS-321) substrate has proved to show have excellent optical properties (α_{sol}:94.3 %; $\varepsilon_{300\,^\circ C}$; 0.144) along with high corrosion resistance (>400 h withstand in salt spray test) and good thermal stability in an open air atmosphere. This novel design will thus allow an increase in the operating temperature in the solar field up to 300 ^{o}C, leading to improved performance and reduced cost of ORC based solar thermal power generation.

Acknowledgements

The authors are grateful to Dr. G. Sundararajan, Director of ARCI for his great support for this research. They also wish to thank Mr. A. Srinivasa Rao, Mr. V. Premkumar and Dr. H. Neha for their help during deposition experiments and characterizations.

References

Agnihotri, O.P., and Gupta, B. K., 1981. Solar Selective Surfaces. 1st ed. Wiley-Interscience Publication, New York.

Amun Amri, XiaoFei Duan, Chun-Yang Yin, Zhong-Tao Jiang, M. Mahbubur Rahman, Solar absorptance of copper–cobalt oxide thin film coatings with nano-size, grain-like morphology: Optimization and synchrotron radiation XPS studies, Applied Surface Science 275 (2013) 127– 135.

A. Srinivasa Rao and S. Sakthivel, A highly thermally stable Mn-Cu-Fe composite oxide based solar selective absorber layer with low thermal loss at high temperature, Alloys and compounds. 644 (2015) 906-9151.

B. O. Seraphin, Solar energy conversion: solid state physics aspects, Topics in Applied Physics, vol. 31, Springer, Berlin, 1979, 24–35.

B. Carlsson, K. Möller, M. Köhl, U. Frei, S. Brunold, Qualification test procedure for solar absorber surface durability, Sol. Energy Mater. Sol. Cells 61 (2000) 255–275.

C. S. Uma, L.K. Malhotra, K.L. Chopra, Spectrally selective surfaces on stainless steel produced by chemical conversion, Thin solid films 147 (1987) 243-249.

Chao-Ching Chang, Ching-Li Huang, Cheng-Liang Chang, Poly(urethane)-based solar absorber coatings containing nano gold, Solar Energy 91 (2013) 350–357.

D.L. Douglass, R.B. Pettit, The selective solar absorptance of in situ-grown oxide films on metals, Solar Energy Materials 4 (1981) 383-402.

Duffie, J. A., Beckman, W.A., 1991. Solar Engineering of Thermal Processes. Wiley-Interscience, New York.

D. Tulchinsky , V. Uvarovb, I. Popov , D. Mandler, S. Magdassi, A novel non-selective coating material for solar thermal potential application formed by reaction between sol–gel titania and copper manganese spinel, Solar Energy Materials and Solar Cells 120 (2014) 23 – 29.

D. Tulchinsky, V. Uvarov, I. Popov , D. Mandler, S. Magdassi, A novel non-selective coating material for solar thermal potential application formed by reaction between sol–gel titania and copper manganese spinel, Solar Energy Materials & Solar Cells 120 (2014) 23–29.

Ewa Wackelgard*, Characterization of black nickel solar absorber coatings electro plated in a nickel chlorine aqueous solution, Solar Energy Materials & Solar Cells 56 (1998) 35-44.

E. Wäckelgård, G. A. Niklasson, C. G. Granqvist, Selectively solar-absorbing coatings, in: J.Gordon (Ed.), Solarenergy – The State of the Art, Firsted., James & James, London,2001,pp.109–144.(ISE Spositionpapers).

F.S. Boydag, The optical properties of some steel surfaces with different surface preparations for high temperature use, Solar Energy Materials 13 (1986) 185-195.

Gordon, J., 2001. Solar Energy, the State of the Art. James & James, London.

G. Katumba, G. Makiwa, T.R. baisitese, L. Olumekor, A. Forbes, E. Wackelgard, Solar selective absorber functionality of carbon nanoparticles embedded in SiO_2, ZnO, NiO matrices, Phys. Stat. Sol. (c) 5 (2008), 549-551.

H. Price, C. Gummo, M.J. Hale, R. Fimbres, R. Mahoney, R. Cipriani, Developments in high-temperature parabolic trough receiver technology, in:International Solar Energy Conference, Portland, OR, United States, 11–14 July.2004, article no. 65178, 2004, pp. 659–667.

H.C. Barshilia, N. Selvakumar, K.S. Rajam, A. Biswas, Structure and optical properties of pulsed sputter deposited $Cr_xO_y/Cr/Cr_2O_3$ solar selective coatings, Journal of Applied Physics 103 (2008) 1-11.

H. C. Barshilia, N. Selvakumar, K.S. Rajam, A. Biswas, Optical properties and thermal stability of TiAlN/AlON tandem absorber prepared by reactive DC/RF magnetron sputtering, Solar Energy Materials and Solar Cells 92 (2008) 1425–1433.

Hsin-Yen Cheng, Jau-Wern Chiou, Jyh-Ming Ting, Yonhua Tzeng, Reactively co-sputter deposited a-C: H/Cr thin films: Material characteristics and optical properties, Thin Solid Films 529 (2013) 164–168.

J. A. Duffie, W.A. Beckman, Solar Engineering of Thermal Processes. Wiley-Inter science, New York, 1991.

J. Vince, A.S. Vuk, U.O. Krasovec, B. Orel, M. Kohl, M.Heck, Solar absorber coatings based on CoCuMnOx spinels prepared via the sol–gel process: structural and optical properties, Solar Energy Materials and Solar Cells 79 (2003) 313–330.

K. R. Newby, Functional chromium plating, Metal Finishing 97 (1999) 223–247.

Kennedy, C.E., 2002. Review of Mid- to High-Temperature Solar Selective Absorber Materials. NREL Tech Report, NREL/TP-520-31267.

K.D. Lee, Preparation and characterization of black chrome solar selective coatings, Journal of the Korean Physical Society 51(2007) 135–144.

L. Aries, P. Fort, J.A. Flores, J.P. Traverse, Analysis of the conversion coating on Ferric stainless steel of selective absorbers, Solar Energy Materials 14 (1986) 143-159.

L. Aries, D. Fraysse, J.P. Traverse, R. Calsou, Growth of selective coating on stainless steel, Thin Solid films 151 (1987) 413-428.

L. Aries, M. El Bakkouri, J.Roy, J.P. Traverse, Thermal oxidation study of thin magnetite-based coating from iron-chromium alloys, Thin solid films 197 (1991) 143-155.

L. Wu, J. Gao, Z. Liu, L. Liang, F. Xia, H. Cao, Thermal aging characteristics of CrN_xO_y solar selective absorber coating for flat plate solar thermal collector applications, Solar Energy Materials & Solar Cells 114 (2013) 186–191.

M. Adsten, R. Joerger, K. Järrendahl, E. Wäckelgård, Optical characterization of industrially sputtered nickel-nickel oxide solar selective surface, Solar Energy 68 (2000) 325-328.

M.K. Öhl, M. Heck, S. Brunold, U. Frei, B. Carlsson, K.M. Öller, Advanced procedure for the assessment of the life time of solar absorber coatings, Sol. Energy Mater. Sol. Cells 84 (2004) 275–289.

M. Koželj, A.Š. Vuk, I. Jerman, B. Orel, Corrosion protection of Sunselect, a spectrally selective solar absorber coating, by(3-mercaptopropyl)trimethoxysilane, SolarEnergyMaterials and SolarCells 93 (2009)1733–1742.

M. Lundh, T. Blom, E. Wackelgard, Antireflection treatment of Thickness Sensitive Spectrally Selective (TSSS) paints for thermal solar absorbers, Solar Energy 84 (2010) 124–129.

Martin Joly, Yannik Antonetti, Martin Python, Marina Gonzalez, Thomas Gascou, Jean-Louis Scartezzini, Andreas Schuler, Novel black selective coating for tubular solar absorbers based on a sol–gel method, Solar Energy 94 (2013) 233–239.

Nunes, V.Teixeira, M. L. Prates, N. P. Barradas, A. D. Sequeira, Graded selective coatings based on chromium and titanium oxynitride, Thin Solid Films 442 (2003)173–178.

N. Selvakumar, H.C. Barshilia, Review of physical vapour deposited (PVD) spectrally selective coatings for mid to high-temperature solar thermal applications, Solar Energy Materials and Solar Cells 98 (2012) 1-23.

Q. C. Zhang, Stainless-Steel-AlN cermet selective surface deposited by direct current magnetron sputtering technology, Solar Energy Materials and Solar Cells 52 (1998) 95–106.

R. Juang, Y. Yeh, B. Chang, W. Chen, T. Chung, Preparation of solar selective absorbing coatings by magnetron sputtering from a single stainless steel target, Thin Solid Films 518 (2010) 5501–5504.

S. Sakthivel, V. Premkumar and A. Srinivas Rao “An improved solar selective absorber coating with excellent optical absorptance, low thermal emissivity and excellent corrosion resistance property and a process of producing the same” Indian patent Application no. 1129/DEL/2013.

S.A. Kalogirou, Solar thermal collectors and applications, Progress in Energy and Combustion Science 30 (2004) 231–295.

The method for the emissivity measurement of the heater using FTIR is prescribed in Japanese Industrial Standards JIS R 1801.

T. Bostrom, E. Wackelgard, G. Westin, Solution-chemical derived nickel–alumina coatings for thermal solar absorbers, Solar Energy 74 (2003) 497–503.

T. K. Bostrom, E. Wackelgard, G. Westin, Durability tests of solution-chemically derived spectrally selective absorbers, Solar Energy Materials and Solar Cells 89 (2005) 197–207.

T. Bostrom, J. Jensen, S. Valizadeh, G. Westin, E. Wackelgard, ERDA of Ni-Al2O3/SiO2 solar thermal selective absorber, Solar Energy materials and solar cells 92 (2008) 1177-1182.

T. N. L. Andrea Ambrosini, Chad L. Staiger, Aaron C. Hall, Marlene, Bencomo, Ellen B. Stechel, Improved High Temperature Solar Absorbers for use in Concentrating Solar Power Central Receiver Applications, Sandia National Laboratories, Albuquerque, New Mexico 87185 and Livermore, California 94550, 2010.

V. C. Sharma, A. Sharma, P. Ilenikhena, Chemical oxidation and spectral selectivity of Austenitic stainless steel AISI 321 (For use in solar-Energy Application), Energy 13 (1988) 749-754.

V. Moise, R. Cloots, A. Rulmont, Study of the electrochemical synthesis of selective black coatings absorbing solar energy, International Journal of Inorganic Materials 3 (2001) 1323–1329.

V. Teixeira, E. Sousa, M. F. Costa, C. Nunes, L. Rosa, M. J. Carvalho, M. Collares- Pereira, E. Roman, J. Gago, Spectrally selective composite coatings of Cr–Cr_2O_3 and Mo–Al_2O_3 for solar energy applications, Thin Solid Films 392 (2001) 320–326.

V. Teixeira*, E. Sousa, M.F. Costaa, C. Nunes, L. Rosa, M.J. Carvalhob, M. Collares-Pereira, E. Roman, J. Gago, Chromium-based thin sputtered composite coatings for solar thermal collectors, Vacuum 64 (2002) 299–305.

W. Graf, F. Brucker, M. Köhl, T. Tröscher, V. Wittwer, L. Herlitze, Development of large area sputtered solarabsorber coatings, Journal of Non-Crystalline Solids 218 (1997) 380–387.

Y. Yin, Y. Pan, L.X. Hang, D.R. McKenzie, M.M.M. Bilek, Direct current reactive sputtering Cr–Cr_2O_3 cermet solar selective surfaces for solar hot water applications, Thin Solid Films 517 (2009) 1601-1606.

Z. Zeng, A.Liang, J.Zhang., A review of recent patents on trivalent chromium plating, Recent Patents on Materials Science2 (2009) 50–57.

Conference Proceedings

Solar World Congress 2015
Daegu, Korea, 08 – 12 November 2015

Heliostat Tailored to Brazil

Andreas Pfahl[1], Pedro Henrique Silva Bezerra[2], Erwin Hölle[3], Phillip Liedke[1], Érico Tadao Teramoto[2], Johannes Hertel[1], Marcelo Lampkowski[2], Celso Eduardo Lins de Oliveira[4].

[1]German Aerospace Center, DLR, Institute of Solar Research, Stuttgart, (Germany)
[2]Faculdade de Ciências Agronômicas, UNESP, Botucatu, (Brazil)
[3]SOLTEC, Rosenfeld, (Germany)
[4]Faculdade de Zootecnia e Engenharia dos Alimentos, USP, Pirassununga, (Brazil).

Abstract

For Brazil, it is important to realize a high national production share because of high import fees and to obtain cost reduction related to implementation of the CSP technology. The rim drive concept offers an alternative for expensive heliostat drive solutions with slew and linear drives from abroad. Sandwich facets (which are usually foreseen for rim drive heliostats) are not available from Brazilian manufacturers and are replaced by a steel frame work structure with mounted 4 mm glass mirrors. The mirrors were bent along one axis. A two-axis curvature, while being optically more precise, would result in excessive stress of the mirrors when short focal lengths (present case: 30 m) have to be attained. For an 8 m² heliostat, the mirror panel was divided into six stripes. The stripes have to be canted to reach a sufficiently small focal spot. A prototype heliostat was designed and built. High stiffness and sufficient durability of the mirror facets against wind loads was reached. For the considered heliostat area of 8 m², the proposed framework design could be further simplified, but for 16m² heliostats (or bigger) it seems to be adequate. A heliostat with high local production share can be accomplished using the rim drive concept. High stiffness can be reached also without sandwich facet mirrors by using a framework mirror support structure with one rim as part of it. Short focal lengths can be achieved by dividing the mirror into several stripes bent in one single axis. The components described increases the feasibility of be manufactured in Brazil and makes possible to avoid increments in CSP plant costs related to import fees.

Keywords: S*olar tower plant; heliostat; mirror facet; local content; FEM; wind loads*

1. Introduction

Due to the great demand for renewable energy sources for electricity and heat generation, different technologies have been made available with increasingly affordable and competitive market costs. Concentrated Solar Power (CSP) technology uses direct solar radiation concentrated to generate heat onto a small area for producing electricity. The main concentrator types of CSP plants are the cylindrical-parabolic troughs concentrators, linear Fresnel concentrators, parabolic dish concentrators (also known as dish/engine systems) and heliostat fields, redirecting sunlight to a stationary receiver (power tower). The first type uses mirrors in the form of parabolic troughs. The absorber positioned at the focal line of the collector is usually a metal tube coated with a layer of selective paint and encased by a second glass tube which should be evacuated to avoid losses by convection. The second type, based on Fresnel technology, uses rotatable linear reflectors to concentrate the radiation on a fixed linear tube absorber. The third type consists of parabolic dishes which are reflectors of paraboloid shape usually with a Stirling engine and a generator located at each focal point. Finally, in the fourth type of technology, up to thousands of mirrors are used to concentrate sunlight on a fixed central receiver (Corgozinho et al., 2014). CSP technologies represent a good alternative to conventional sources for heat and electricity production in Brazil (EPE, 2012). Brazil is a country with high solar resource in significant areas of

Selection and/or peer review under responsibility of Scientific Committee
doi:10.18086/swc.2015.04.12 Available at http://proceedings.ises.org

the country. On the other hand, with the presence of a strong industrial and agro-industrial sector entails a high demand of electricity, which is predominantly generated by hydroelectric plants. Increasingly often, due to lack of water, these plants cannot cover the demand during the dry season. The overall goal of the CEISA (Heliothermic Energy Studies (CSP): Educational Consortium for the Integration and Sustainability in the Agro-industry) project was to foster the international cooperation in the area of CSP generation. The project serves as a foundation for the research in the field of sustainable energy generation using the CSP technology and its applications within the agricultural sector in Brazil, where a process heat with a temperature of over 300 °C is needed. Within this project, a heliostat for Brazilian applications was developed with specifications according to the SMILE (Solar-hybrid Microturbine Systems for Cogeneration in Agroindustrial Electricity and Heat Production) project. SMILE is a national R&D project that aim to build two 100 kWel solar/biofuel hybrid thermal power tower plants in Brazil for generate electricity and co-generation of heat by integration with two agro-industrial applications (a dairy factory and a slaughterhouse in Caiçara do Rio do Vento, RN, and in Pirassununga, SP, respectively). The project is being financed by BNDES and industrial partners, coordinated by GREEN/USP (Research Group on Recycling, Energy Efficiency and Numerical Simulation/University of São Paulo), and implemented in partnership with DLR (German Aerospace Center) and Solar Institute Jülich – FH Aachen University of Applied Sciences. Due to the astigmatism effect and the relatively small power range smaller heliostats are expected to result in a better overall efficiency of the system. A small panel size of 8 m² (3.21 m x 2.5 m) was determined as optimal size, from both technical and transportation point of view. The HFLCAL software was used to determine the optimum number and positioning of the heliostats for the two plants. Based on these results, an optimum focal length of 30 m was calculated. Because of very high import tax rates, the use of domestic components and materials presents significant economic advantages. An already existing Brazilian heliostat design (Fig. 1) was considered too expensive, due to its reliance on imported drives, as well as the insufficient stiffness of its mechanical components. The aim of the present work is to find a design which allows for a high local production content and which has a sufficiently rigid structure.

Fig. 1: Drives of a first heliostat design with comparably expensive drives from abroad and too flexible mirror support structure (mirror not complete).

2. Approaches for high local content

2.1 Rim drives

From a broad variety of heliostat concepts (Coventry and Pye, 2014) (Pfahl, 2014) the rim drive concept (Pfahl et al., 2013) was individuated because of its avoidance of excessively expensive high precision drives, which would require to be imported. An illustration of a heliostat with horizontal primary axis and rim drives is given by Fig. 2. The 1st (red) rim can be supported by a guidance bar with rolls to increase stiffness. The 2nd rim (blue)

is fixed to the mirror panel. The drive for the primary axis is mounted at the pylon, the drive for the secondary axis on the first rim. The gears may be realized by chains with bevel wheels (which have low backlash when pre-tensioned) or by winch wheels (which eliminate backlash). Both rims are locked during stow to relieve the drives and cables or chains under storm conditions.

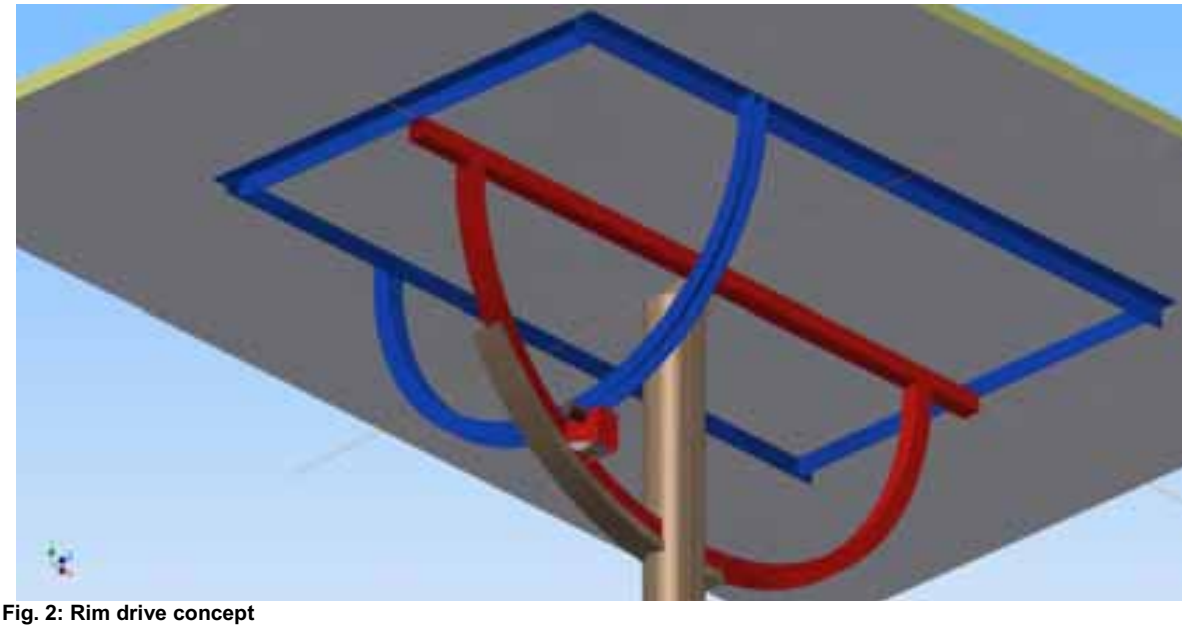

Fig. 2: Rim drive concept

The main advantages of the rim drive concept are: 1) small loads on the drives, 2) the backlash of the drives can be relatively high because of the long lever arm (distance between drives and centre of rotation) realized by the rims, which enables the usage of low cost drives (Fig. 3), 3) reduced loads on bearings, mirror panel, upper part of pylon and stow-position-locking devices during stow. On the other hand additional parts (rims, guidance bar for first rim, and stow-position-locking devices) are required. However, local manufacture of those is possible.

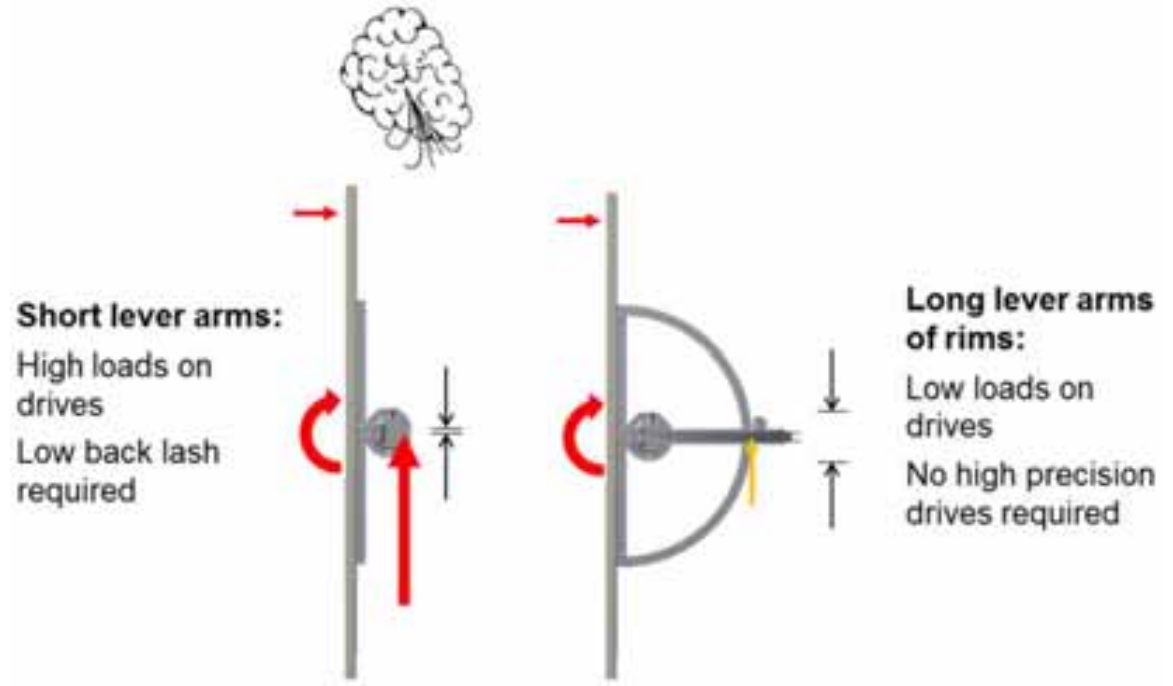

Fig. 3: Reduced requirements on drives due to longer lever arms realized by rims.

2.2 Framework mirror support structure

The first rim drive heliostat was built with sandwich panel (Fig. 4) (Pfahl et al., 2015). However, sandwich panels are not available in Brazil yet and thus their use would result in high transport cost and import taxes.

Fig. 4: First rim drive heliostat with sandwich mirror panel

Therefore, a framework mirror-support-structure with 4mm mirrors was chosen as an alternative for the sandwich facets. At this design the 2nd rim is integrated in the frame work (Fig. 5).

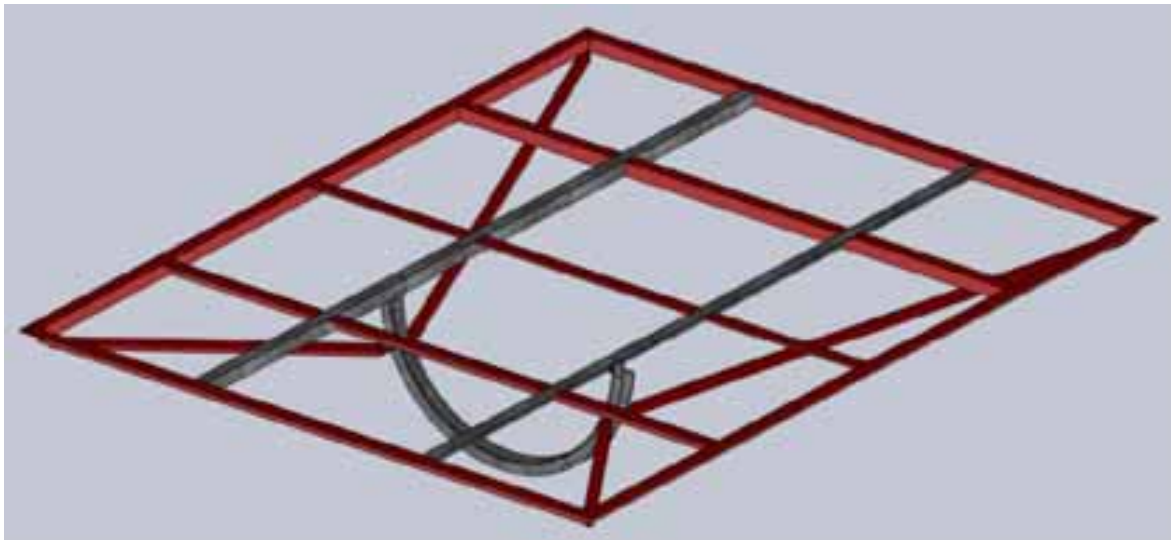

Fig. 5: Framework design of mirror support structure

2.3 One-dimensionally bent mirror stripes

For the solar power plants of the SMILE project, a relatively short focal length of only 30 m is required, resulting in a comparably small curvature radius of 60 m for the mirrors. To avoid excessive mechanical stress, the mirrors are bent only in one dimension. To achieve the required small focal spot of the reflected rays on the receiver the mirror is divided into six stripes of 2.5 m x 0.54 m x 4 mm. These mirror facets are canted to each other to achieve a step-wise approximation of a parabolic shape.

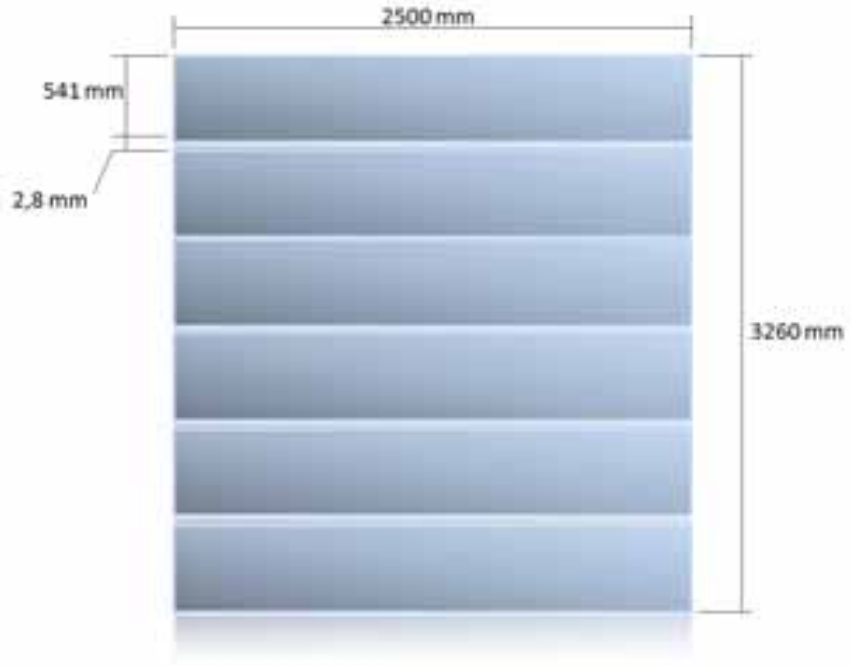

Fig. 6: Dividing of mirror surface into six stripes of only one dimensional bending.

Because of the small width of only 0.54 m thermal expansion is not critical in that direction. Hence, thermal expansion has to be accounted for only in the direction of the facet's length. This simplifies the connections of the mirrors with the steel frame which are realized by simple metal sheets bent to form "L" profiles. The metal sheet is flexible and allows for the compensation of thermal expansion differences between the steel frame and the mirror facets (Fig. 7). The "L"-shaped metal sheet can be adapted to the mirror curvature by choosing the angle α and by rotating it around the axis of the upper mounting screw. The defined geometry requires low amount of steel and simple handling during installation and further, it is an alternative with the ability to move even after installed on frame. The mirror stripes were switched on the metal sheet by double-faced scotch tape manufactured by 3M company, resistant to wind force and weather.

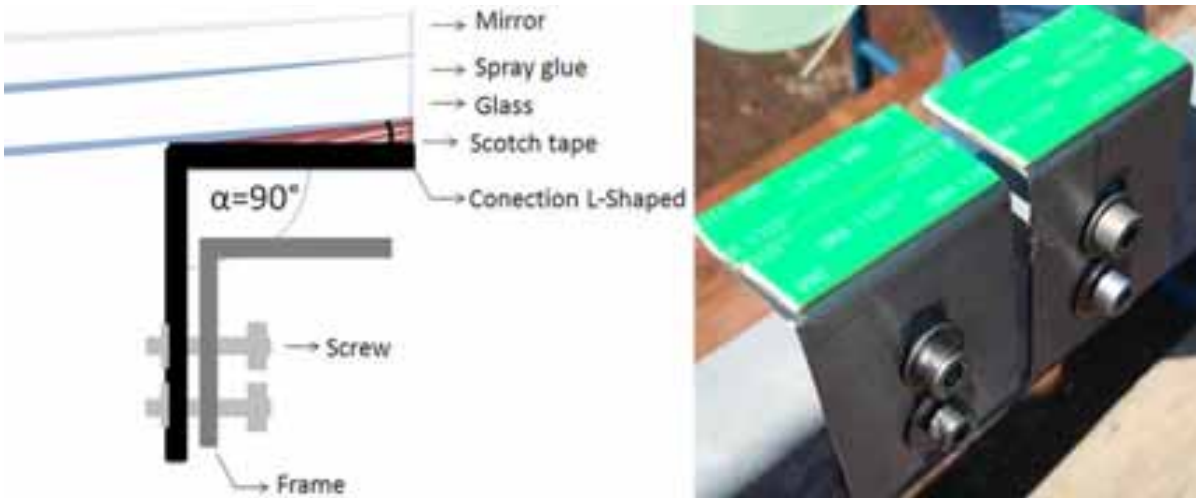

Fig. 7: "L"-shaped metal sheets as flexible connection between steel frame and mirror stripes.

3. Dimensioning

By FEM-analyses (Finite Elements Method), stress and deformation of the metal structure was computed. Maximum wind loads were determined according to (Pfahl et al., 2011b). The shape of the pressure distribution was known from full scale measurements (Pfahl et al., 2014). The maximum stress of 60 MPa is far below the acceptable value of structural steel (Fig. 8).

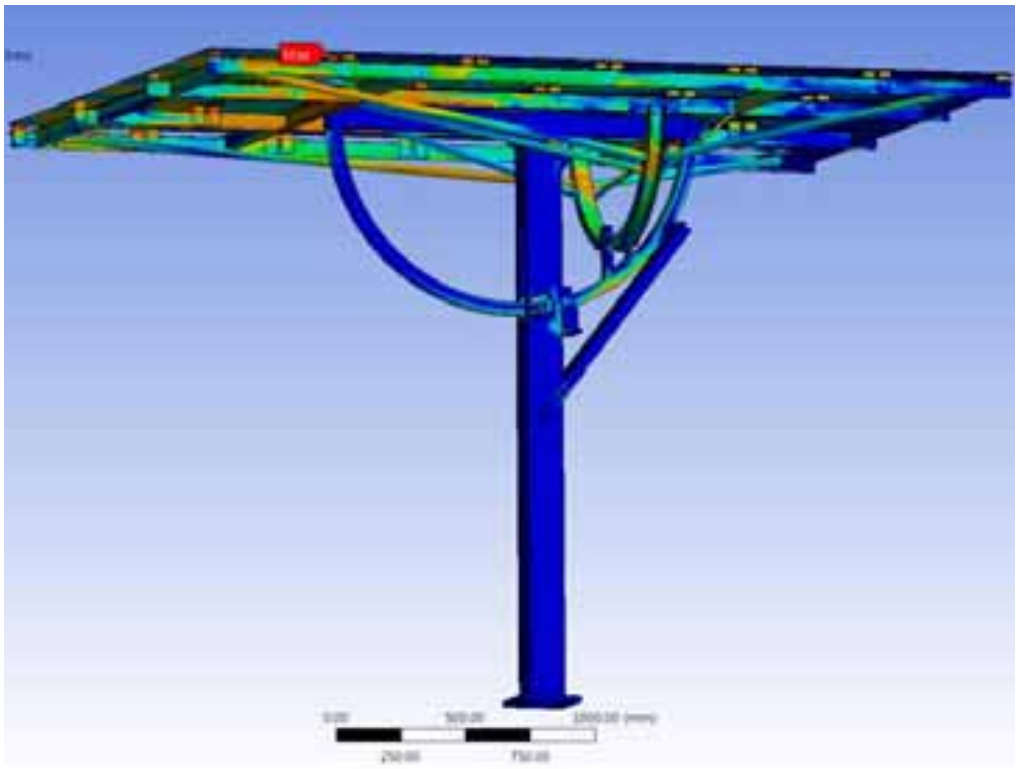

Fig. 8: FEM simulation of stress of the heliostat structure at storm conditions.

The stress of the mirror facets was calculated separately. It was concluded that four connecting points would lead to excessive stress (Fig. 9) (Von Reeken et al., 2011). Therefore, the amount of connecting elements per facet was increased to twelve.

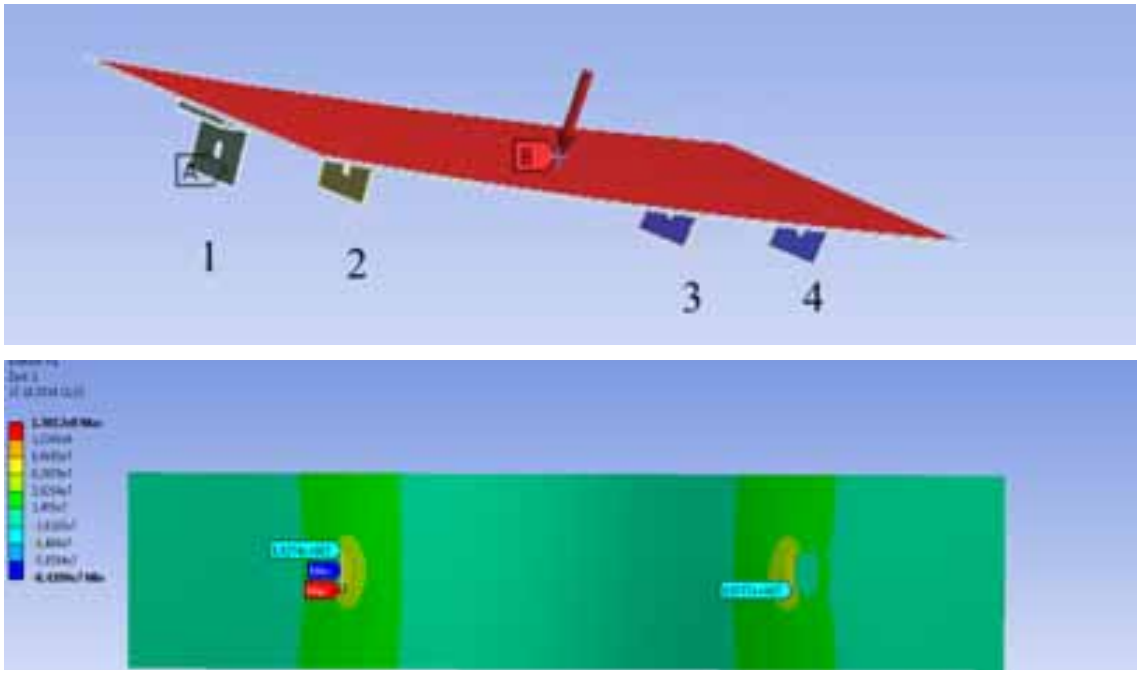

Fig. 9: FEM calculations of stress of mirror panel.

4. Improvements of prototype

4.1 Stiffness

A rim drive heliostat prototype with frame work mirror support structure of 8 m² was realized (Fig. 10). The mirror support structure was observed to be excessively flexible regarding bending about its diagonals, leading to deformation of the 2nd rim.

Fig. 10: First frame work mirror support structure with too high flexibility regarding bending about its diagonals.

Therefore, additional bars were included to avoid this deformation. Additionally, diagonal bars across the whole panel were added (Fig. 11). By these measures a sufficient stiffness was reached.

Fig. 11: Frame work mirror support structure with diagonal bars across the panel and bars for fixing of the 2nd rim for high stiffness.

Furthermore, for upright panel positioning, excessive flexibility of the vertical axis, entailing deformations of the 1st rim were observed. Therefore, the "U"-profile of the 1st rim was closed (Fig. 12) to mitigate this issue and improving the overall stiffness of the system.

Fig. 12: "U"-profile of 1st rim (left); closed profile of 1st rim (right) for increased stiffness.

4.2 Mirror support

The results of the FEM calculation of the mirror facets were validated by mechanical tests. The mirrors are connected to four bars of the steel frame. It was investigated whether only one connection per bar (and four connections per facet) would lead to excessive stress, as predicted by the FEM computations. For this, a glass stripe of 2.5m x 0.54m x 4mm was connected to the steel frame by twelve "L"-shaped metal sheets. The maximum hinge moment in stow position was determined according to Pfahl et al., (2011a). For the stow position, the peak hinge moment results from instantaneously increased pressure on the wind facing edge of the mirror panel. The pressure increase is caused by eddies hitting the mirror panel at the edge (Pfahl et al., 2011b). This was simulated by loading the glass stripe mounted at the edge of the panel by sand. The weight which would lead to the peak hinge moment was calculated. Indeed, the glass broke before the calculated required maximum weight was reached (Fig. 13). Hence, only four central mirror mounting devices would not be sufficient to withstand the expected storm wind loads.

Fig. 13: Breakage of 4mm glass stripe before reaching of maximum expected load.

In a successive step, the amount of mirror connections was doubled. Each glass stripe was connected to the four bars with two "L"-shaped metal sheets for each bar located at the edges of the glass stripe. With the eight mirror connections the glass stripe could be loaded with the full amount of sand simulating the maximum wind load (Fig. 14).

Fig. 14: Glass stripe of 4mm thickness loaded with sand simulating the maximum expected wind loads.

The established methodology for assembling the mirror facets was the best sequence found from the viewpoint of practicality reduced risk of damage. First, the "L"-shaped metal sheets were positioned coplanar to the metal frame (Fig. 15). The stripe composed by glass and mirrors showed sufficient stiffness to withstand the tension on the external connectors, while being flexible enough to provide the height of curvature.

Fig. 15: Assembling of the stripes using L-shaped metal sheet.

5. Conclusions

A heliostat with high local production share can be accomplished using the rim drive concept. High stiffness can be achieved also without sandwich facet mirrors by using a framework mirror support structure with one rim as part of it. Short focal lengths can be reached by dividing the mirror into several stripes bent in one single axis. For 8 m² heliostats the framework structure appears to be extensive. For bigger heliostats (16m² or 32m²) an accordant framework structure could be used and seems to be adequate. For 8 m² heliostats the framework structure should be simplified by using closed profiles for the basic frame which would allow to reduce the amount of bars of the framework. The components described increases the feasibility of be manufactured in Brazil and makes possible to avoid increments in CSP plant costs related to import fees.

Acknowledgements

The authors thank DAAD, CAPES and GIZ-Brazil for their financial and consultant support of the iNoPa-CEISA project.

References

Corgozinho, I. M., Martins Neto, J. H., Corgozinho, A. A., Modelo de simulação de uma planta solar-elétrica utilizando o software Trnsys. V Congresso Brasileiro de Energia Solar. Recife, 31.04.2014.

Coventry, J.; Pye, J. Heliostat cost reduction – where to now? Solar PACES 2013, Energy Procedia 49, 2014, p. 60-70.

EPE. Análise da inserção da geração solar na matriz elétrica brasileira. Nota técnica. Ministério de Minas e Energia. Rio de Janeiro, mai. 2012. Available at <http://pt.scribd.com/doc/213250230/NT-EnergiaSolar-2012>. Date of access: 29.05.2014.

Pfahl, A., Buselmeier, M., Zaschke, M., 2011a. Determination of Wind Loads on Heliostats. Proc. SolarPACES 2011 conference, Granada.

Pfahl, A., Buselmeier, M., Zaschke, M, 2011b. Wind Loads on Heliostats and Photovoltaic Trackers of Various Aspect Ratios. Solar Energy 85, 2185-2201.

Pfahl, A.; Randt, M.; Holze, C.; Unterschuetz, S., 2013. Autonomous light-weight heliostat with rim drives. Solar Energy 92, p. 230-240, 2013.

Pfahl, A., Brucks, A., Holze, C., 2014. Wind Load Reduction for Light-Weight Heliostats, Energy Procedia 49, 193-200.

Pfahl, A., Randt, M., Meier, F., Zaschke, M., Geurts, C.P.W., Buselmeier, M., 2015. A Holistic Approach for low Cost Heliostat Fields. Energy Procedia.

Von Reeken, F., Gabeler, L., Schiel, W., 2011. Determination of Probability of Breakage of Parabolic Trough Reflector Panels. Proc. SolarPACES 2011 conference, Granada.

PERFORMANCE COMPARISON OF TWO TYPES OF TECHNOLOGIES ASSOCIATED WITH A POSITIVE ENERGY BUILDING: A REVERSIBLE HEAT PUMP/ORC UNIT AND A HEAT PUMP COUPLED WITH PV PANELS

Olivier Dumont[1], Carolina Carmo[2], François Randaxhe[1], Sylvain Quoilin[1] and Vincent Lemort[1]

[1] Aerospace and Mechanical Engineering Department, Faculty of Applied Sciences, University of Liege (Belgium)

[2] Department of Energy Technology, Aalborg University, Aalborg (Denmark)

Abstract

To achieve the 20-20-20 targets in 2020 and the European objectives in the longer term, it is imperative to drastically reduce greenhouse gas emissions from the residential building sector. In this context, the development of Positive Energy Buildings (PEB) is promising. This work compares the annual performance of two competing systems. First, a conventional solution, consisting of a passive house coupled with a water to water heat pump and photovoltaic panels (HP/PV). On the other hand, a passive house with a solar thermal roof combined with a reversible heat pump unit / organic Rankine cycle (HP/ORC). Both systems are designed for a maximum net electrical output of 5.29 kW. Dynamic simulations are performed using the Dymola software. The net annual electrical production (considering electricity consumed to fulfil the thermal load of the building) is 667 kWh for the reversible HP/ORC system and 3835 kWh for the HP/PV system in the basic Danish study case. Following that, a study of influence with different climates is performed and some guidelines are deduced to select optimum study cases where the HP/ORC system could become more competitive than the HP/PV classical solution.

Keywords: *Reversible heat pump/organic Rankine cycle unit, Photovoltaics panels, Positive Energy Building, annual simulation, economic analysis.*

1. Introduction

Positive Energy Buildings have been increasingly investigated recently. Moreover, from 2019, all new buildings will have to produce from renewable energy has much as they consume on an annual basis (European parliament, 2010). The objective of this paper is to assess an innovative technology to obtain a positive energy building and compare it with a conventional HP/PV solution. The innovative technology solution consists in coupling a reversible heat pump/organic Rankine cycle unit (HP/ORC) with a passive building, a solar roof and a horizontal ground heat exchanger (Quoilin et al, 2015). This system is flexible because of the reversibility of the heat pump (HP) which can also run in organic Rankine cycle mode (ORC) to generate electricity (Fig. 2). There are, in fact, three possible modes of operation. First, the heat pump mode can cover the thermal demand of the house (includes domestic hot water - DHW - and floor heating - FH) when weather conditions are unfavourable, for example in winter. But, when the sunlight is sufficient, the heat produced by the solar roof is directly used to charge the storage to supply DHW and FH (direct heating mode - DH). Finally, when the storage is fully charged, the excess heat produced by the solar roof generates electricity through the ORC cycle. The HP/ORC reversible system has been studied for the first time in 2011 (Schimpf et al, 2011). This study showed the economic benefits in the particular case of a house with geothermal borehole and a solar collector of modest size (12 m^2). Thereafter, the passive house concept coupled with a solar roof large (138.8 m^2) and coupled with a horizontal ground heat exchanger (300 m long) was patented by the company Innogie (Innogie, 2013). Following this, an optimal design (Quoilin et al, 2015), followed by an experimental campaign (Dumont et al, 2015) have demonstrated the feasibility of the system. The nominal power generation ORC mode is equal to 5.29 kW with an efficiency of 7%, while the HP mode presents a thermal power condenser of 13 kW with a nominal coefficient of performance (COP) of 4.2.

doi:10.18086/swc.2015.04.13 Available at http://proceedings.ises.org

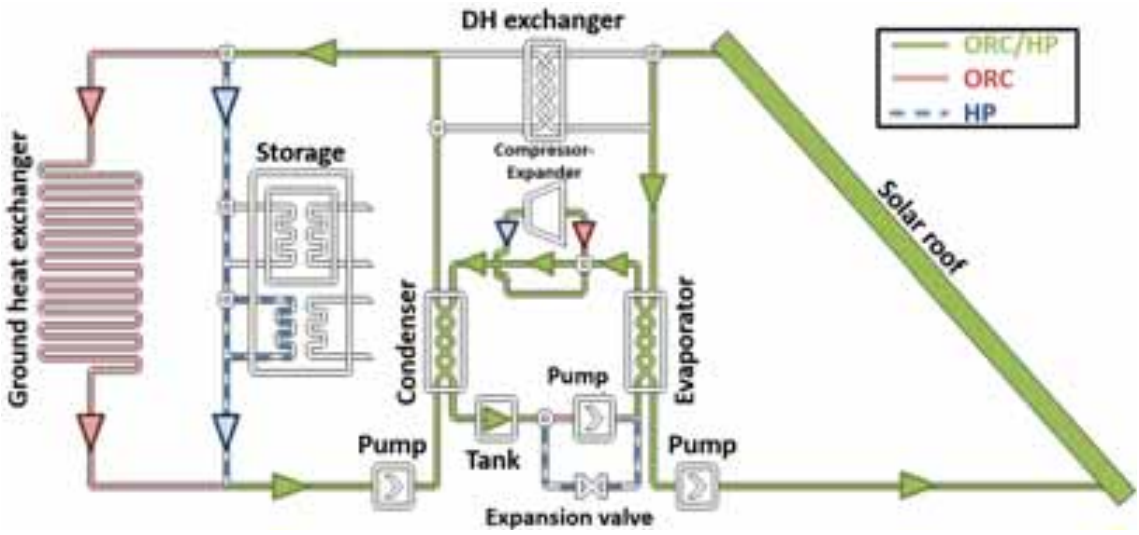

Fig. 1: Scheme of the global system showing the three operating modes (organic Rankine Cycle (ORC), heat pump (HP) and direct heating (DH))

2. Description of the model

The model is simulated with Dymola/modelica software coupled with Thermocycle (Quoilin et al, 2014) libraries and CoolProp (CoolProp, 2015). The global model with the passive house, the reversible HP/ORC unit, the solar roof, the horizontal ground heat exchanger and the thermal heat storage has been extensively described in a former paper (Dumont et al, 2014). This section briefly summarizes each sub-model.

2.1 Sub-models

- The reversible HP/ORC unit is modelled trough validated semi-empirical models based on experimentation (Dumont et al, 2015).
- The storage model (Heat Storage Water Heater) comes from the Thermocycle library (Quoilin et al, 2014).
- The solar roof is modelled with Klein's equation (Klein, 1975).
- The house model consider 5 zones based on the real Danish house. Solar gains, air infiltration, occupancy behaviour in terms of internal gain and domestic hot water consumption are taken into account.

More details are provided for each sub-model of the reversible HP/ORC system coupled with the passive house in (Dumont et al, 2014).

The performance of this system is compared with a mature system to get a Positive Energy Building (PEB), a water to water heat pump coupled with PV panels (HP/PV). The PV panels are modelled based on a detailed model (De Soto et al, 2006). The area of the PV panels is determined in a way to get the same peak electrical production in summer nominal conditions (5290 W for 44 m^2). The heat pump, the building model, the occupant behaviour are all fixed in the same way as for the reversible HP/ORC unit.

2.2 Global model

The inputs of the global model are the meteorological data (in terms of outdoor temperature and direct normal radiation) and occupant behaviour in terms of electrical consumption, internal gains and domestic hot water consumption. The control strategy to select the operating mode is based on the following idea: Insuring the thermal comfort inside the building while maximizing the net electrical production.

3. Results

Results from typical days of the year with mode changes are detailed in a former paper (Dumont et al, 2014). This section aims at evaluating the annual performance of the system.

3.1. *Performance criterions*

- Gross electrical production [kWh]: annual electrical production of the ORC (or of the PV panels in the case of the HP/PV).
- Net electrical production [kWh]: annual electrical production of the ORC (or of the PV panels in the case of the HP/PV) minus the heat pump consumption and the non-HVAC consumption.
- Running benefits [€], evaluated following Danish electricity market (Eq. 1). C_r is the retail price of electricity on the grid [€/kWh], $C_{r,HP}$ is the retail price for heat pump systems [€/kWh] and C_{bb} is the buy-back tarif of electricity to the grid [€/kWh]. C_x is equal to C_{bb} if electrical production is higher than the electrical consumption (non-HVAC) and equal to C_r in the opposite case. kW_{ORC} is the ORC electrical power [kW], $kW_{cons,l-a}$ is the electrical consumption (non-HVAC) et kW_{HP} is the heat pump power consumption. Tariffs are provided from real data (Energinet, 2015).

$$B = \int_0^t \left(C_x\,(kW_{ORC} - kW_{cons,l-a}) - C_{r,HP}.kW_{HP}\right).dt \qquad \text{(eq. 1)}$$

- Self-production rate (γ_S), which is the fraction of the gross production consumed directly in the building (eq. 2).

$$\gamma_S = \frac{\sum \min\,(W_{cons.},W_{prod})}{\sum W_{prod}} \qquad \text{(eq. 2)}$$

- Self-consumption rate (γ_d), which is the fraction of building electrical consumption produced by the gross electrical production (eq. 3).

$$\gamma_D = \frac{\sum \min\,(W_{cons.},W_{prod})}{\sum W_{cons.}} \qquad \text{(eq. 3)}$$

3.2. Basic case

The annual performance comparison is performed between the HP/ORC system and the HP/PV system in the case of the real house located in Denmark (500 litres storage and 1491 kWh of lightning and appliances electrical consumption) in Tab. 1. First, the heat pump electrical consumption is 45% higher in the case of the HP/PV because this system does not benefit from the thermal heat furnished by the direct heating mode (1394 kWh). Also, the gross electrical production is lower in the case of the HP/ORC system. This is explained by the rather constant efficiency of the PV panels while the ORC efficiency (and solar roof efficiency) are very largely affected by part load conditions (low solar irradiation, low outdoor temperature).

Tab. 1: Comparison of the annual performance between the reversible heat pump/organic Rankine cycle unit (HP/ORC) and the PV panels coupled with the heat pump (PV/HP)

System	HP/ORC	HP/PV
Non HVAC electrical consumption [kWh]	1491	
Heat pump consumption [kWh]	812	1185
Gross electrical production [kWh]	2970	6511
Net electrical production [kWh]	667	3835
Thermal load (domestic hot water & floor heating) [kWh]	4403	
Thermal energy provided by direct heating [kWh]	1394	0
Running benefits [€]	-78	494
Self-production rate [-]	8.9	9.1
Self-consumption rate [-]	9.2	39

Following this, it is logical that the net electrical production and the running benefits are higher in the case of the HP/PV system. Furthermore, the self-consumption and self-production rates are significantly lower in the case of the HP/ORC system. Fig. 2 allows to understand this. The peak electricity demand between 6 p.m. and 7 p.m. is covered by the PV panels while the ORC stop working a little bit before 6 p.m.

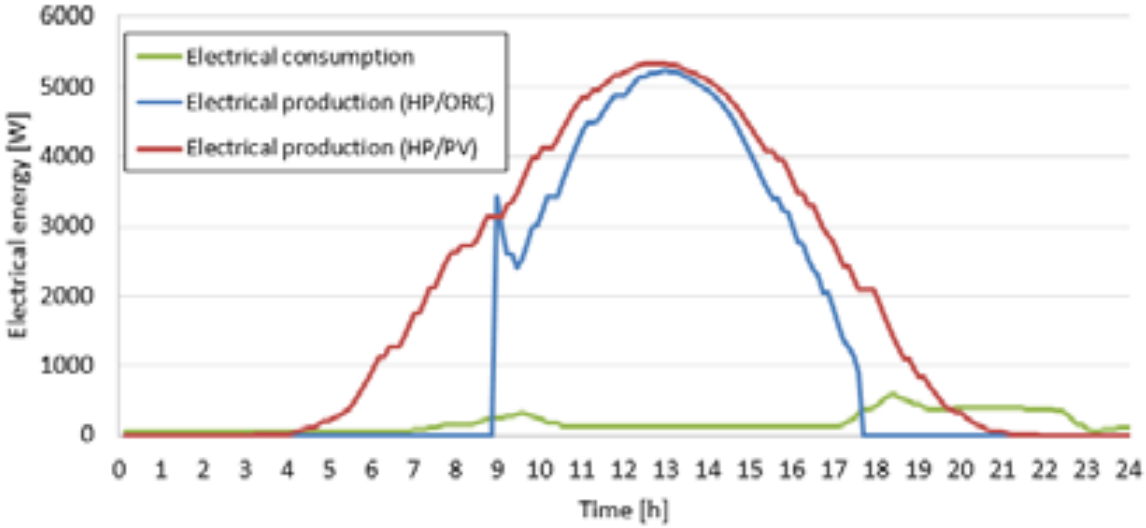

Fig. 2: Hourly electrical production and consumption for a typical summer day

3.3 Influence of the climate

The basic case has shown higher performances for the HP/PV system. It is also interesting to study the influence of the climate regarding the evolution of the performance of both systems. Fig. 3 presents the gross electrical production and the heat pump electrical consumption for 5 typical climate in Europe (from north to south). First, the same conclusion as stated in section 3.2 can be deduced: the heat pump consumption is significantly lower with the HP/ORC system thanks to the direct heating mode. In southernmost locations, the heat pump is not even necessary anymore to fulfil the heat requirements of the buildings for this system. This means that in location close to Roma and Palermo, the use of a reversible heat pump/organic Rankine cycle does not make any sense. Also, the ORC gross production increase more than the PV panels production because the ORC system works more and more often closer to nominal conditions in southernmost locations. The direct heating heat (not shown in Fig. 3) presents a maximum in Torino. This is explained by the fact that if the weather is too cold, the roof is not warm enough to heat the storage but if the weather is too warm, the thermal load is lower.

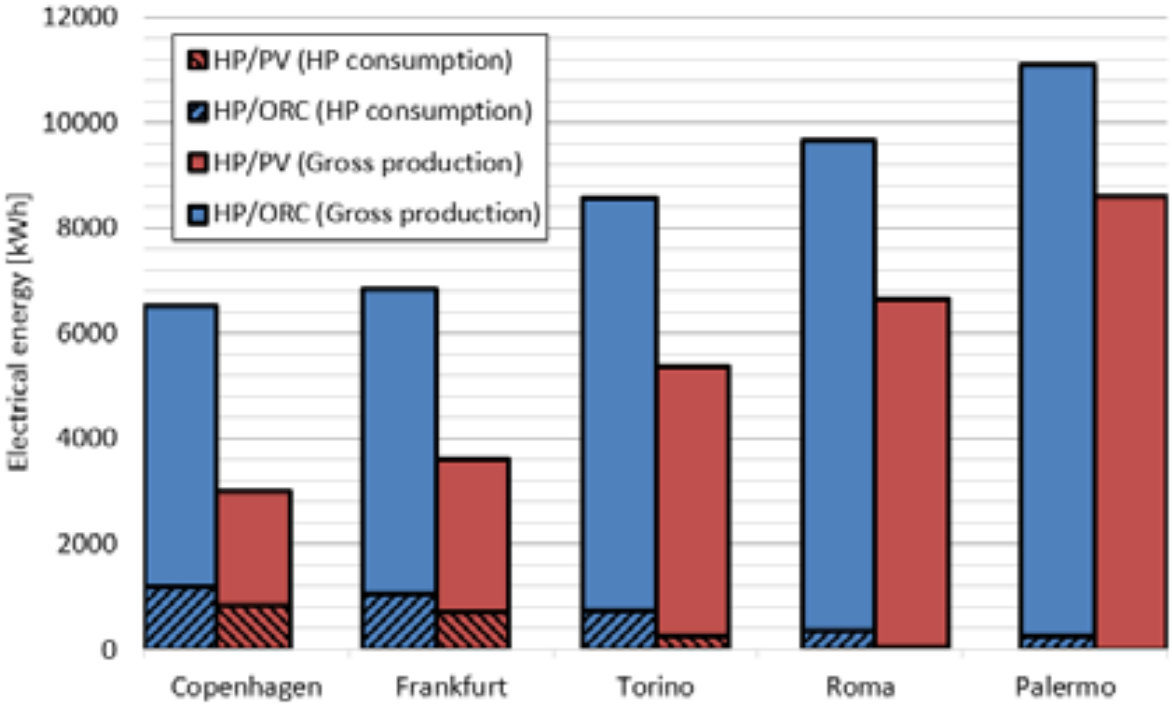

Fig. 3: Comparison of the gross electrical production and the heat pump electrical consumption for both systems (HP/ORC and HP/PV) for 5 typical climates in Europe.

3.3 Analysis of results

Results in the basic case and with five different location have shown that the HP/PV system present better overall performance in terms of net electrical production, running benefits and matching of electricity demand and consumption.

The HP/ORC system presents two advantages. On the one hand, the investment costs are rather low since the cost are very close to a classical heat pump (addition of a pump and a four way valve for the reversibility in ORC mode). On the other hand, the electrical consumption is lower for the HP/ORC system thanks to the heat provided by the roof (Direct Heating). This is a non-negligible advantage of the system since it can reduce electricity consumption during peak of electricity.

This study shows that the HP/ORC system is more efficient in location close to Torino thanks to the direct heating mode. The direct heating mode does not reduce ORC running hour because it works at much lower roof temperatures. Therefore, cases where thermal load are higher could be very interesting and make the HP/ORC system more competitive than the HP/PV system. Some examples with high thermal load could be large buildings, buildings with poor insulation, building with high domestic hot water needs (sports hall, swimming pool…

4. Conclusion

This paper compares two systems that allow getting a Positive Energy Building: a reversible HP/ORC unit and a HP/PV system. A dynamic model is developed and exploited to analyse annual performance. It has been shown that in the basic study case (Denmark), the HP/PV system is more profitable. Following this, a study of influence with five different typical European climates has shown that mid-Europe is an optimal location for the HP/ORC system. But, still, the HP/PV system performs better.

This lead to study more influence parameters. Since the direct heating mode is a significant advantage of the HP/ORC system, this could be exploited in cases where thermal load of the building is higher. This will be studied in future works.

5. Nomenclature

B	Running benefits [€]
DH	Direct Heating
DHW	Domestic hot water
γs	Self-production rate [-]
γd	Self-consumption rate [-]
FH	Floor-heating
HP	Heat Pump
ORC	Organic Rankine Cycle
PV	Photovoltaics panels
HP/ORC	Reversible HP/ORC system
HP/PV	PV panels coupled with a HP

6. References

Coolprop library, 2015. http://www.coolprop.org, consulted the 5th of January 2015.

De Soto, W., Klein, S. A., Beckman, A., 2006. Improvement and validation of a model for photovoltaic array performance, Solar Energy, 80, 78-88.

Dumont, O., Carmo, C., Randaxhe, F., Quoilin, S., Lemort, V., 2014. Simulation of a passive house coupled with a heat pump/organic Rankine cycle reversible unit, 9th International Conference on System Simulation in Buildings.

Dumont, O., Quoilin, S., Lemort, V., 2015. Experimental investigation of a reversible heat pump / organic Rankine cycle unit designed to be coupled with a passive house to get a Net Zero Energy Building, International Journal of Refrigeration, doi:10.1016/j.ijrefrig.2015.03.008.

Energi-net, http://energinet.dk/DA/El/Solceller/Har-du-solceller/Sider/Pristillaeg.aspx, consulted the 5th of january 2015.

European parliament, 2010. Directive 2010/31/EU of the European parliament and of the council of 19 May 2010 on the energy performance of buildings, http://eur-lex.europa.eu/LexUriServ/LexUriServ.do?uri=OJ:L:2010:153:0013:0035:EN:PDF

Innogie ApS, 2013. Thermal solar absorber system generating heat and electricity, United States Patent Application Publication, US 2013/025778 A.

Klein, S. A., 1975. Calculation of flat-plate loss coefficient, Solar Energy, 17.

Quoilin, S., Dumont, O., Harley, K., Lemort, V., 2015. Design, modeling and performance optimization of a reversible Heat Pump / Organic Rankine Cycle prototype. ASME Journal of Engineering for Gas Turbines and Power, doi:10.1115/1.4031004

Quoilin, S., Desideri, A., Wronski, J., Bell, I., Lemort, V., 2014. ThermoCycle: A Modelica library for the simulation of thermodynamic systems, 10th International Modelica Conference, Modelica Association., 10.3384/ECP14096683, Lund.

Schimpf, S., Uitz, K., Span, R., 2011. Simulation of a solar assisted combined heat pump-organic Rankine cycle system, World renewable Energy Congress

Conference Proceedings

Solar World Congress 2015
Daegu, Korea, 08 – 12 November 2015

Dynamic modeling and control strategies analysis of a novel small CSP biomass plant for cogeneration applications in building

Adriano Desideri[1], Simone Amicabile[2] , Fabrizio Alberti[2] , Silvio Vitali-Nari[3], Sylvain Quoilin[1], Luigi Crema[2], Vincent Lemort[1]

[1] University of Liège, Campus du Sart Tilman - Bat: B49 - P33 4000 Liège, Belgium

[2] ARES Unit, Fondazione Bruno Kessler, 38123 Povo, Trento (Italy)

[3] ACCIONA, Sevilla, Andalucia, Spain

Abstract

A concentrated solar power (CSP) biomass combined heat and power (CHP) system based on organic Rankine cycle (ORC) technology developed in the framework of the EU founded BRICKER project is presented. The CHP system coupled with heat recovery ventilation technology and novel insulation material has the aim of reducing the energy consumption of existing building by up to 50%. A simplified approach to implement a dynamic model of the CHP system is proposed. The model is firstly used to investigate the performances of the CHP system control logic under extreme working condition. Secondly, the effectiveness in ensuring safe working conditions and in maximizing the sun power usage of two different solar field control approaches is investigated simulating the developed model over a reference day.

Keywords: *Hybrid CSP, organic Rankine cycle system, Dynamic modeling*

1. Introduction

Over the past 30 years the electric industry has been characterized by a transition from a vertical production structure towards a horizontal one based on the deployment of intermittent renewable resources (Hinkley et al., 2011). Among renewable energy technologies, concentrated solar power (CSP) systems have been increasingly considered worldwide as a key technology for meeting the renewable energy demand (Resnick Institute, 2012) (Mediavilla et al., 2013). Due to the high capital cost, the total CSP installed capacity is still low, with only 3.6 GW_{el} installed at the end of 2013 (IEA, 2014) . Research activities, with a focus on cost reduction, have been commissioned by leading research institute in Europe and in the US (Pitz-Paal et al., 2007) (Hinkley et al., 2011), and significant reductions are expected especially for the thermal storage (TES) and the heat transfer fluid (HTF) components by the end of this decade. Another approach to achieve competitiveness in the current market consists in hybridization with fossil fuels (Peterseim et al., 2013). Hybridizing these plants has not only the benefit of reducing the cost but it also enables the CSP unit to be dispatchable when the solar source is low. Several plants worldwide have demonstrated the advantages of this solution (Agency, 2014). In recent years, the hybridization of CSP technology with biomass has gained attention and its potential has been investigated by several authors (Peterseim et al., 2014a) (Soria et al., 2015). The concept has been successfully demonstrated since the end of 2012 by the 22 MW_{el} Termosolar Borges plant in Catalonia, Spain (NREL, 2013). This solution allows to move CSP technology towards agricultural area, rich in biomass and waste material, enabling locations with lower levels of direct normal irradiance (DNI) compared to DNI required by CSP standalone systems (Peterseim et al., 2014b). A technical economic assessment of a combined heat and power (CHP) system, using organic Rankine cycle (ORC) technology integrated with a hybrid CSP-biomass heat source, has been recently investigated (Sterrer et al., 2014). The study compares, by means of a transient analysis, the economic profitability of a hybrid CSP system for three different locations in central Europe, concluding that the retrofit of biomass plants with

doi:10.18086/swc.2015.04.14 Available at http://proceedings.ises.org

CSP technology is a promising approach, to improve the economic performances. In this context the EU founded BRICKER project aims to develop a scalable, replicable, high energy efficient, zero emissions and cost effective CSP-Biomass trigeneration system, based on ORC technology, to refurbish existing public-owned non-residential buildings. The CHP unit together with lightweight facades, and phase change material insulation technology, is expected to reduce the building energy consumption by at least 50%. Three systems are being developed in Spain, Belgium and Turkey to demonstrate the concept feasibility. In this contribution, a dynamic model of the CSP-biomass CHP system under development in Cáceres, Spain is presented. The transient model, developed in the Modelica language (Mattson et al., 1997), is simulated under extreme conditions to investigate the capability of the control logic in ensuring safe working operation. During the last years dynamic modeling has been increasingly recognized as a powerful tool to analyze the performance of CSP power system under transient conditions. Casati et al. (2012) developed a dynamic model of a novel ORC power block for a CSP system with a direct thermal storage, in order to investigate the controllability aspect under extreme critical conditions. The performance of a micro CSP-ORC system, over four reference days, has been analyzed by means of a detailed dynamic model by (Ireland et al., 2014). More recently Dickes et al. (2015) investigated model reduction methods for dynamic modeling of the solar field and the thermal storage of a micro CSP power unit, in order to increase the computational effectiveness of the models. In the presented work, a simplified modeling approach of the CSP-Biomass-ORC system is proposed. The proposed modeling approach allows for a robust and efficient model still capable of predicting the main time constants characterizing the overall system. The simulation results are analyzed and discussed and guidelines for the future work are drawn.

2. System description

The EU founded BRICKER project aims at demonstrating that retrofitting existing buildings with passive and active cutting edge technologies can lead to enormous energy savings. The project comprises the installation of a novel CHP unit based on renewable energy sources to meet the thermal and electrical building demand, coupled with heat recovery ventilation system, lightweight facades and innovative insulation material to decrease the building energy consumption. In this work the control logic of the CHP system is presented and its effectiveness is investigated by means of dynamic modeling. The complete layout of the CHP system under development in Cáceres, Spain is reported in Figure 1. The system is composed by two main loops. In the first loop the thermal energy collected by the parabolic trough collectors (SF) and produced by biomass combustion in the boiler (BMB) is transferred by a heat transfer fluid (HTF) to the ORC power block for electricity production and to the second loop via a heat exchanger (HXI). The synthetic thermal oil, TherminolSP, is selected as heat transfer fluid as it is widely used for CSP applications thanks to its low operating pressure, high thermal stability (up to 335°C) and good heat transfer characteristics (Alberti et al., 2012). Starting from the bottom left of Figure 1 it is possible to recognize the solar field, where the HTF is pre-heated from (a) to (b) before entering the biomass system (d), reaching the maximum temperature at the outlet of the boiler (e). The fluid is then pumped through HXI from (f) to (g) and through the ORC power block which are connected in parallel. At the outlet of the ORC unit, the fluid mixes with the stream coming from HXI (h).

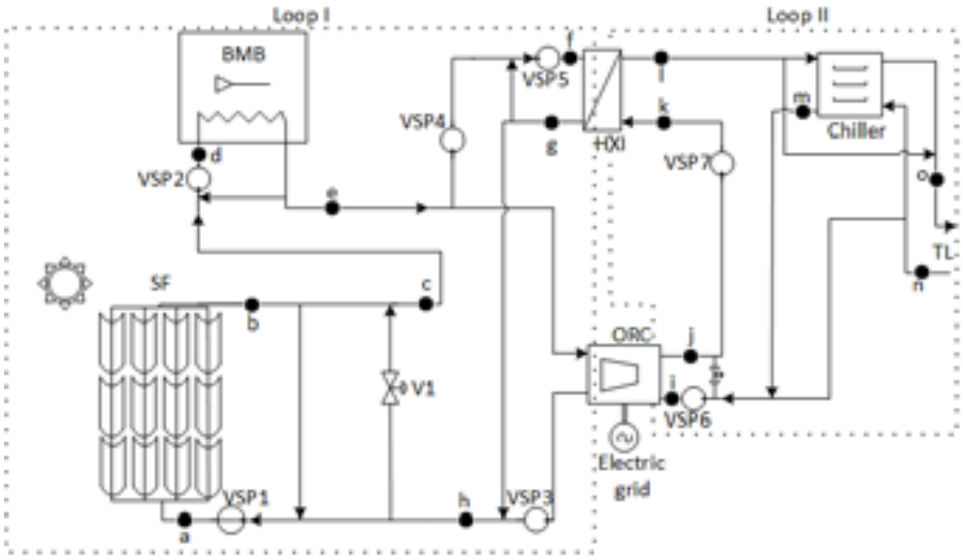

Fig. 1 Schematic flow diagram of the bricker CHP system.

Loop II comprises the adsorption chiller, the ORC condenser cooling side, the secondary side of HXI and the connection to the thermal load of the building. Looking at the right part of Figure 1 the heat transfer fluid is first pre-heated in the ORC condenser from (i) to (j), and then it is pumped through HXI from (k) to (l) where it reaches the maximum temperature of loop II. The fluid is then directed to the Chiller or to the building depending on the thermal demand. A description of the different components is reported in the list below.

- Parabolic trough collectors with evacuated tubular absorber are selected being the most reliable and proven technology in the CSP field (Cabello et al., 2011). In particular the selected collectors are characterized by a maximum temperature of 250°C that perfectly fits the nominal working temperature of the system. A total of 12 collectors are connected in 4 parallel loop of 3 collector each. The solar field dimension results from a compromise between the available area on the demo building roof and on the seasonal thermal demand. The solar field works as a pre-heater for the biomass boiler, reducing the amount of biomass burnt during the day. Each solar collector is characterized by a net collecting surface of 54 m^2.

- The biomass boiler covers a fundamental role in the system as it provides together with the solar field the thermal power required by the ORC unit and by HX1. If there is a sudden demand of extra power, a larger amount of biomass is burnt to keep the outlet temperature close to the set point value.

- The thermal energy from the biomass and the solar field is converted into electrical energy by the ORC power block. The ORC unit converts thermal energy into electrical energy based on the same principle of the steam Rankine cycle. The major difference with a traditional Rankine cycle is related to the employed working fluid which is an organic compound. The thermodynamic characteristics of the working fluid make the ORC technology a viable and interesting solution for low temperature power generation compared to a steam Rankine cycle. ORC systems have been proven to be a reliable mature and efficient technology over the years (Angelino et al., 1984) and their application to renewable energy sources for small scale power generation (5-200 kW_{el}) is gaining popularity at a commercial level (Quoilin et al., 2013). The unit installed in the system can be operated in generation or cogeneration mode with an electrical power ranging between 100 and 70 kW_{el} respectively. The electrical power can be sent to the building or the national grid. In cogeneration mode the thermal energy dissipated at the condenser is used by the cooling water for meeting the building thermal demand.

- A heat exchanger is used for thermal energy transfer between loop I and loop II. The brazed plate type is selected as it offers very good heat transfer performance in single phase with an extreme

compact design (Palm and Claesson, 2006). In order to satisfy the cooling demand during the summer season an adsorption chiller machine is included in Loop II. The selected chiller is of the silica gel-water type. This machine can be fed with a thermal input ranging between 60 – 90°C (Wang and Vineyard, 2011).

3. Control Strategy

3.1 Technical boundaries and operational logic

In this section a description of the control logic implemented on the presented system is described and discussed. The technical boundaries of the different components are listed hereunder:

- Solar field: a minimum mass flow rate must be guaranteed in the parabolic through collectors to avoid high film temperature that could deteriorate the thermal oil. An autonomous warning control is provided by the manufacturer. When the outlet temperature of the solar field reaches a certain value, electrical motors are activated defocusing the collectors in order to decrease the temperature. A partial or total defocusing can be selected by the user.
- Biomass boiler: the boiler works in a range between 150 and 500 kW_{el} with the former value representing the shutdown condition. The temperature gradient comprises between 5 K and 30 K. The system operates at a constant mass flow of 9.5 kg/s and is equipped with a recirculation circuit and an internal control which regulates the amount of biomass burnt to keep the temperature at the outlet at a user-defined set point. Power modulation is characterized by time constant between 30 seconds up to 2 minutes. This is mainly related to the kinetics limit of the combustion chemical process and to the air inflow adjustment. A limit of 1 daily start/stop is recommended by the manufacturer but it is preferably to maintain the biomass boiler at a minimum range in order to keep high efficiency, low pollutions and reduced maintenance. The boiler start-up is a slow process that can take up to 50 minute.
- ORC unit: it requires at the evaporator a constant thermal oil mass flow rate of 2.5 kg/s and it is capable of handling heat source temperature deviation in the order of 20 K from the nominal value of 245°C.
- Adsorption chiller: it can handle temperature inlet variation in the order of plus minus 5 K from its nominal value. Proper control of HXI are required in order to respect these boundary limits.

Given the above mentioned technical boundaries, a correct operation of the system depends on finding the right balance between the solar field and the biomass boiler working condition. In particular, high controllability of the solar field is required in order to guarantee safe biomass boiler operation avoiding biomass shut-down. In order to achieve this goal the solar field is equipped with a recirculation and a by-pass stream as shown in Figure 1. A constant mass flow rate equal to the nominal value required by the ORC evaporator of 2.5 kg/s is ensured to the solar field by running pump VSP1 at a fixed speed, avoiding high film temperature issues. A highly responsive control logic is developed by installing a PI controller (PI1) on the by-pass valve V1 to regulate the biomass inlet temperature T_d and by exploiting the solar field internal defocusing mechanism. In nominal condition the mass flow at the outlet of the ORC unit is pre-heated in the solar field and the by-pass valve V1 is closed. If the DNI overcome its nominal value the solar field outlet temperature T_b increases and so does the biomass boiler inlet temperature T_d. The by-pass valve is opened by the PI controller to mitigate the temperature increase at biomass inlet T_d. As VSP1 runs at constant speed, mass flow rate equal to the one flowing through V1 is recirculated from SF outlet to the inlet, further increasing the solar field outlet temperature T_b. A chain mechanism is activated pushing T_b towards the defocusing set-point value. When T_b overpasses the set-point, automatic defocusing occurs, reducing the thermal power delivered by the collector fields and avoiding biomass shut down. On the other hand, sudden decrease of sun power are handled by the biomass internal control (PI2) which increases the biomass fed to the combustion chamber maintaining T_e at its nominal value. In case the heat rejected from the ORC's condenser is not sufficient to satisfy the thermal demand of the building, extra power has to be delivered to the water loop of the system via HXI. The heat exchange rate of HXI is controlled by a recirculation system

with pump VSP4 and VSP5. The latter is kept constant at a fixed speed. As the adsorption chiller works at a constant inlet temperature, $T_{l,}$ to guarantee high COP values, an increase in thermal demand corresponds to an increase in mass flow through HXI. A PI (PI3) controlling the rotational speed of VSP4 is implemented to maintain the temperature, T_l, close to its set-point. In table 1 the controlled and control variables of the three PI characterizing the plant logic are summarized.

Tab 1. : Table summarazing the controlled and control variables of the three PI contrellers of the implemented control logic.

Controller	Controlled variables	Control variables
PI1	Valve V1 aperture	T_d
PI2	Amount of biomass burnt	T_e
PI3	Pump VSP4 rotational speed	T_l

4. Dynamic Modeling

The proposed control strategy presented in section 3 is investigated under transient conditions by means of a dynamic model of the plant. The model is developed using the Modelica object-oriented modeling language (Elmqvist and Mattsson, 1997), and are based on the ThermoCycle library (Quoilin et al., 2014). The thermal oil flowing through loop I of the plant is always in liquid state and it is assumed to behave as an incompressible fluid. It is modeled following the table based approach proposed by the Modelica standard library. Temperature, T, is selected as the fluid model state variable. Density, ρ, and specific heat capacity, c_p, are computed fitting constant n-order polynomials on user-defined table data. Specific enthalpy, h, specific entropy, s, and the other thermodynamic properties are calculated from the integrals and derivatives of the derived polynomials, $\rho(T)$ – $c_p(T)$. As the presented dynamic models can be used for both compressible and incompressible fluids, pressure, p, and specific enthalpy, h, are selected as state variables. The Modelica table based media model uses an internal solver to retrieve the temperature value in order to compute the other thermodynamic properties. In Figure 2 the developed dynamic model of the oil loop (loop I) of the system is shown. This work focuses on investigating the effectiveness of the control logic in the oil loop which is considered the most critical aspect of the system. Perfect ideal control is assumed in the water loop (loop II). The building thermal demand (TL) is modeled by means of a source of mass flow fed to the HXI secondary side. In the following sub-sections, the dynamic models of the system components are briefly described.

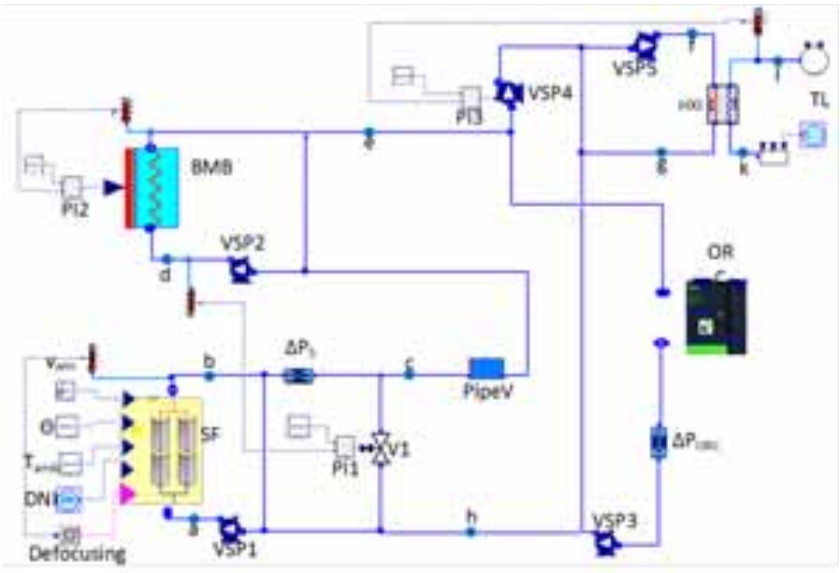

Fig. 2 Modelica model of the system from the Modelica/Dymola graphical user interface (GUI).

4.1 Solar field

Assuming homogeneous pressure drop and equal ambient input data, the solar field can be modeled as a single row of 3 collectors in series with a forth (1/4) of the total mass flow flowing through it. The parabolic through collector model of the *ThermoCycle* library is used. Given the large ratio between the diameter and the length of the parabolic through unit, the modeling approach is based on a finite volume one-dimensional discretization along the collector axial axis. The model is composed by two subcomponents. The *Flow1Dim* component models the fluid flow through the heat collector element (HCE) accounting for energy and mass accumulation. The thermal inertia in the HCE is accounted by a the *MetalWall* model. The radial energy balance between the HCE and the ambient is modeled with a semi-empirical correlation derived from typical values of solar collectors of comparable size. This approach allows reducing the number of equations increasing the computational time, while still modeling the main time constant characterizing the solar field dynamics.

4.2 Biomass boiler

No information where provided by the manufacturer on the biomass burning process. As a consequence a simplified approach is adopted to simulate the boiler. The biomass burning process is modeled as a zero-dimensional model where the power from the biomass combustion is imposed by the user, defining a value between 0, shut-down, and 1, maximum power. A first order model allows to account for the combustion dynamic with a fixed time constant. The oil side and the tube metal walls are modeled with a discretized one-dimensional approach. The oil flow through the boiler is modeled with a *Flow1Dim* component, accounting for energy accumulation, while the thermal energy capacity of the metal walls is modeled using the *MetalWall* component. The thermal inertia of the boiler is tuned in order to reproduce typical values that are found on boiler of the same size (500 kW_{el}). The dynamic is check by simulating the warm up of the boiler, and verifying that the period of time required to reach the desired set point in temperature is close to realistic values (1 to 2 hours).

4.3 Oil-Water heat exchanger

The oil-water heat exchanger is modeled using the *Hx1DInc* model of the ThermoCycle library. It models a counter-current plate heat exchanger based on the connection of three discretized one-dimensional subcomponents. Two *Flow1Dim* components accounting for mass and energy accumulation of the fluids flowing on the two sides of the exchanger, and one *MetalWall* component accounting for energy accumulation in the metal plates. The model are discretized based on the finite volume approach with an upwind scheme. No pressure losses are considered in the two *Flow1Dim* models. Equation 1 is used to model the convective fluid-wall heat transfer coefficient to account for mass flow variation:

$$U = U_{nom} \left(\frac{\dot{m}}{\dot{m}_{nom}}\right)^{n} \qquad \text{(eq. 1)}$$

where the exponent n varies depending on the flow regime between 0.65 and 0.8.

4.4 ORC power unit

In a small capacity ORC unit, the dynamic is mainly defined by energy and mass transfer phenomena characterizing the heat exchanger components, as the expansion and compression processes are characterized by very small time constants. A semi-empirical curve is derived based on experimental data to predict the electrical output power as a function of the heat source temperature at the evaporator inlet and the heat sink temperature at condenser inlet. In order to account for the dynamics characterizing the evaporation process a model equivalent to the one used for the oil-water heat exchanger is selected.

4.5 Piping

In order to account for the volume of the piping system between the solar field and the biomass boiler, the *PipeV* component is used. The model is a lumped one dimensional model accounting for mass accumulation in liquid phase in a defined constant volume. A constant pressure is imposed by the model, allowing for a robust resolution of the system of equation of the overall plant model.

4.6 Pump, pressure drop, bypass valve and PID

The *Pump* model from the ThermoCycle library is used to simulate the pump units installed on the system. It is a lumped fictitious model simulating the compression of a fluid in a turbo or volumetric machine, where given the flow fraction or the pump frequency, a constant volumetric and isentropic efficiency, the mass flow and the consumed power are computed. No dynamics are considered as the time constant characterizing the compression processes are very small compared to the ones regulating heat transfer phenomena. Pressure drop through the solar field and the ORC evaporator heat exchanger are modeled with the lumped ΔP model of the *ThermoCycle* library. The model computes a punctual pressure drop assuming fluid incompressibility and no thermal energy losses to the ambient. A linear and quadratic pressure drop terms are used to compute the total pressure drop. The homotopy function (Casella et al., 2011) is used during initialization to set the pressure drop to zero, facilitating the convergence of the solver. Finally the expansion of the fluid through the by-pass valve of the solar field system is modeled with the *Valve* model from the *ThermoCycle* library. The model is a lamped model where no dynamic and thermal energy losses to the ambient are considered. Finally the PID described in section 3 are implemented in Modelica using the *PID* model of the *ThermoCycle* library.

5. Results and discussion

The dynamic model of the complete system described in section 4 and controlled according to the control logic described in section 3 is simulated under transient conditions. The main goal of this study is to investigate if the whole system can be safely and efficiently operated with the proposed automated control logic. From the safety point of view, the main concern is related to the biomass boiler, the ORC system and the adsorption chiller, which need to be operated respecting the technical boundaries described in section 3. From the efficiency point of view, maximum exploitation of the solar resources should be ensured in order to minimize the biomass combustion rate. At the same time keeping the oil temperature at the ORC evaporator inlet (T_e) and the water temperature to the adsorption machine (T_l) close to their nominal values, allows for on-design working conditions maximizing the overall system efficiency. The dynamic model of the whole plant is simulated under a transient condition representative of an extreme reference situation characterized by a periodically sharp drop of the solar input due to the passage of a series of clouds (Casati et al., 2012). The thermal load at the oil-water heat exchanger is assumed constant over the simulation time imposing a constant mass flow rate on the secondary side of the HXI component. The results are shown in Figure 3.

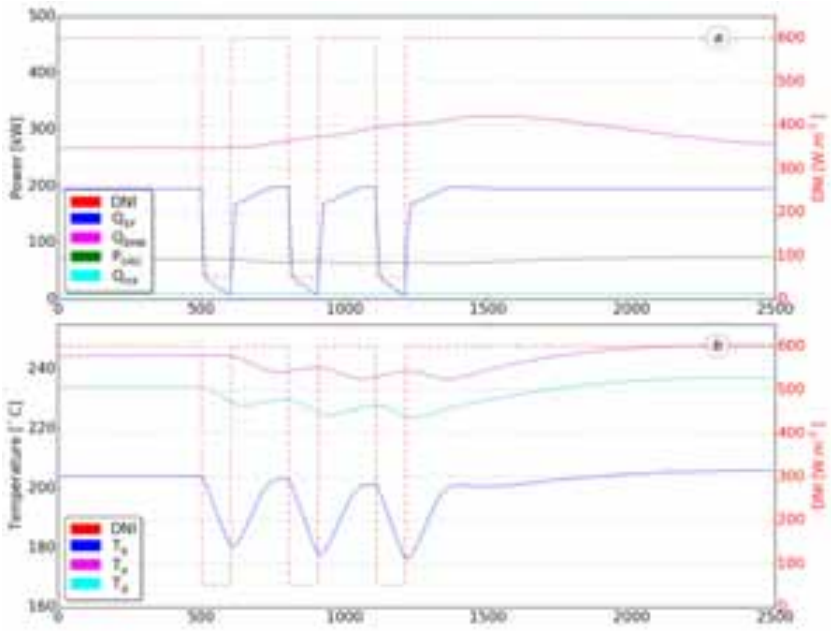

Fig. 3: Dynamic simulation results of the whole plant model as shown in Figure 2. The red dotted represents the DNI: it drops by 100% of its nominal value in 2 s, remain constant for 200 s then returns to its nominal value in 2 s. the interval between two subsequent drop is 200 s. (a) Thermal power delivered by the solar field, the biomass, the ORC evaporator and the HX oil/water evaporator (b) Temperature values in key points of the system.

The solar input drop is modeled by applying a signal with three subsequent ramps to the DNI input of the solar field model. The DNI drops by 90% of its nominal value, perturbing the initial steady state condition. From the results, it appears that the time constants characterizing the biomass system are large enough to cause an overlapping effect of the disturbances. The variation of the controlled biomass thermal power, Q_{BMB}, is shown in Figure 3a. Despite the sharp drop of the power absorbed in the solar field, Q_{SF}, the ORC electrical power, P_{orc}, is maintained close to its nominal value with a maximum deviation of 10%. The temperatures variation are reported in Figure 3b. The significant oscillations of the temperature at solar field outlet, T_b, are dumped by the biomass boiler recirculation system and the temperature at the boiler inlet, T_d, results characterized by much lower variations maintaining the biomass boiler temperature gradient between 9 and 15 K. The results show that through a mild regulation of the biomass boiler the system is able to run the ORC unit close to its nominal working condition despite the sharp drop of sun power. The effectiveness of the biomass system in decoupling the solar field from the ORC unit is assessed. In order to investigate and compare the performance of partial and total defocusing control logic implemented on the solar field, the dynamic model is simulated during a reference summer day in Caceres, Spain. The high value of the DNI is expected to trigger the defocusing mechanism. Two different simulations are run, one considering a constant negligible building thermal demand and one considering a variable thermal load based on available empirical data. In Figure 4 the simulation results for a partial (PD) and a total (TD) solar field defocusing are compared when a constant low building thermal demand is assumed. The simulation starts at 5:00 am and last for 17 hours. During the night the DNI is zero and the biomass is running close to its maximum power to provide the thermal energy required by the ORC power block. When the sun rises, at around 6:00 am, the thermal power provided by the solar field, Q_{SF}, starts increasing and the biomass power, Q_{BMB}, is consequently decreased by the control as the thermal power demand stays constant as shown in Figure 4a. Looking at Figure 4b, the increase of T_b causes the temperature at biomass inlet, T_d, to rise. As a consequence PI1 starts opening V1 to bypass the solar field and keep T_d close to its nominal point. The mass flow through the solar field by-pass valve and the solar field recirculation circuit increases proportionally as shown in Figure 4c. This mechanism boosts T_b towards its upper limit value, pushing the solar field into the defocusing mode and avoiding the shut-down of the biomass boiler. As the defocusing mode is activated, the system behavior changes significantly depending on the adopted defocusing approach. In the PD case, solid lines, one forth of the solar field is defocused. The partial decrease in the solar collector effective surface allows for a smooth decrease of the solar field outlet temperature, T_b, bringing the system in a second steady working condition. In the TD case, dashed lines, the total defocusing of the solar collector causes a sharp decrease of the evaporator outlet temperature down to its minimum value which consequently triggers the solar field to exit the defocusing mode. As the DNI is roughly constant during the simulated reference day, the focusing-defocusing control runs continuously. A continuous control of the biomass system to overcome the sharp changes of the solar field thermal power is deemed necessary. As a consequence the overall system is characterized by an oscillatory trend. When the sun starts to set between 17:00 and 18:00, T_b reaches its lowest value that triggers the solar field to exit the defocusing mode. The drop of solar energy at the end of the day is compensated by the biomass power which is increased to meet the required thermal power demand.

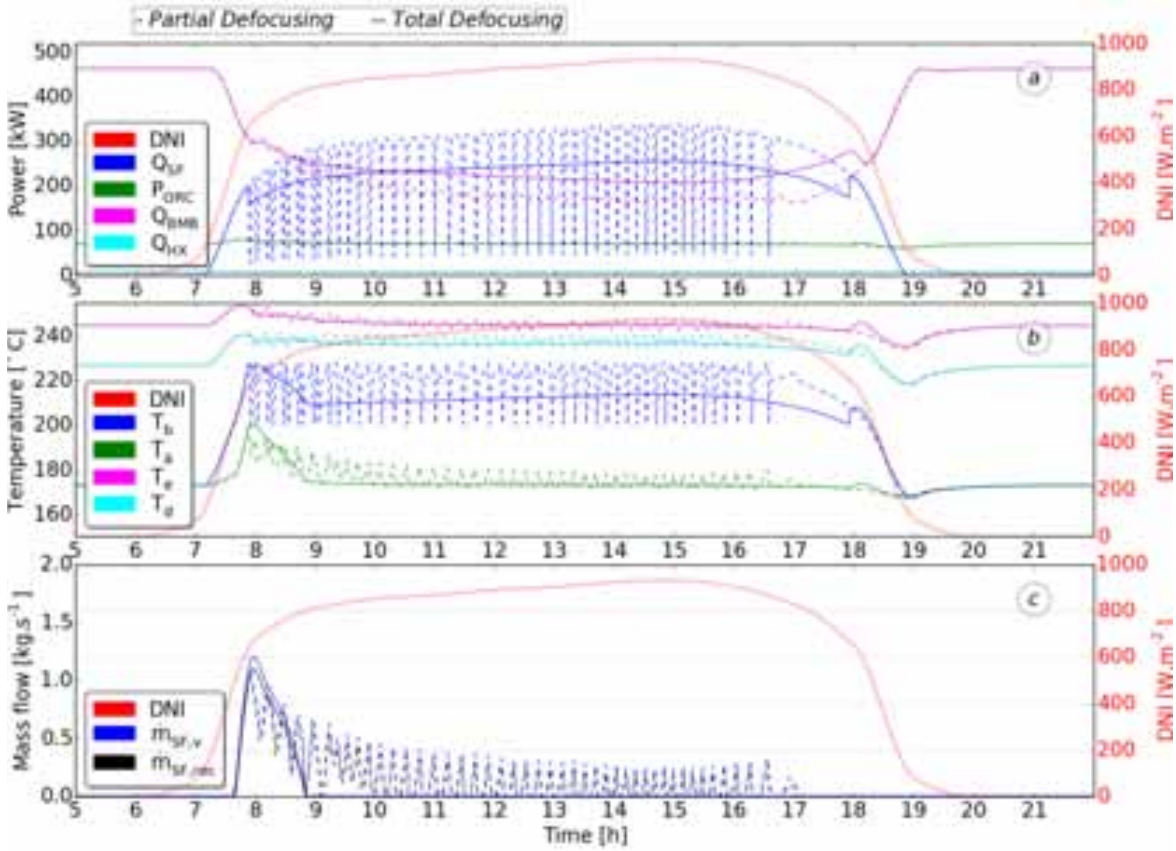

Fig. 4 Dynamic simulation results of the whole plant model during a reference summer day in Cáceres, Spain. The dashed line represents the results for a solar field control strategy based on a total defocusing, the solid line for a partial defocusing. (a) Thermal power delivered by the solar field, the biomass, the ORC evaporator and the HX oil/water evaporator (b) Temperature values in key points of the system (c) Mass flows of the solar field bypass and recirculation system.

Overall both defocusing methods are able to maintain the system in safe working conditions during the simulated reference day. The temperature gradient at the biomass boiler is kept between 18 and 8 K. The ORC power block is run continuously with a maximum power deviation of 12.6% and 14% in the PD and the TD case respectively. At the cost of a continuous regulation of the solar field inclination, the TD approach allows a reduction of the total thermal energy delivered by the biomass boiler of 8% with respect to the PD mode consuming a smaller amount of biomass. Defining the solar fraction, $E_{SF,r}$ as:

$$E_{SF,r} = \frac{E_{SF}}{E_{BM}} = \frac{\int \dot{Q}_{SF} dt}{\int \dot{Q}_{BM} dt} \qquad \text{(eq. 2)}$$

where E_{SF} is the total energy delivered by the solar field and E_{BM} is the total energy delivered by the biomass over a period of 17h from 5:00 to 22:00. The TD approach results in a solar fraction of 59% while the PD in a solar fraction of 47%. The simulation results for the same reference day considering a variable thermal load demand are reported in Figure 5. As in the previous simulation, the DNI increase triggers the defocusing mechanism around 8:00 am. The PD approach brings the system to a steady condition while the TD approach causes an oscillatory behavior in the system. As shown in Figure 5a, around 9:00 am the building thermal demand start increasing and more power is required by HX1, Q_{HX}. As more thermal energy is required, the solar field inlet temperature T_a decreases and so does T_b reaching its lowest value which causes the solar field to exit its defocusing mode around 9:30 am. From this time on the TD and PD approaches lead to the same results. As the thermal demand keeps increasing during the day, the biomass boiler power is regulated to meet the thermal needs. From a safety point of view the control logic is able to maintain the biomass boiler temperature gradient between the required limit with a minimum of 9 K and a maximum of 20 K. The ORC power block inlet temperature experience the biggest drop around 19:00 and 21:00 when the sun goes

down and the biomass is brought close to its maximum value to provide the requested thermal power. The ORC evaporator inlet temperature smoothly decrease reaching a minimum value of 233°C which corresponds to an electrical power drop of 17% with respect to the nominal power. Overall the TD case allows a reduction of the biomass boiler of only 0.5% with respect to the PD case as the two approaches leads to the same plant trend for most of the time. As a consequence a solar fraction of 53% and 54% is found for the PD and the TD case respectively.

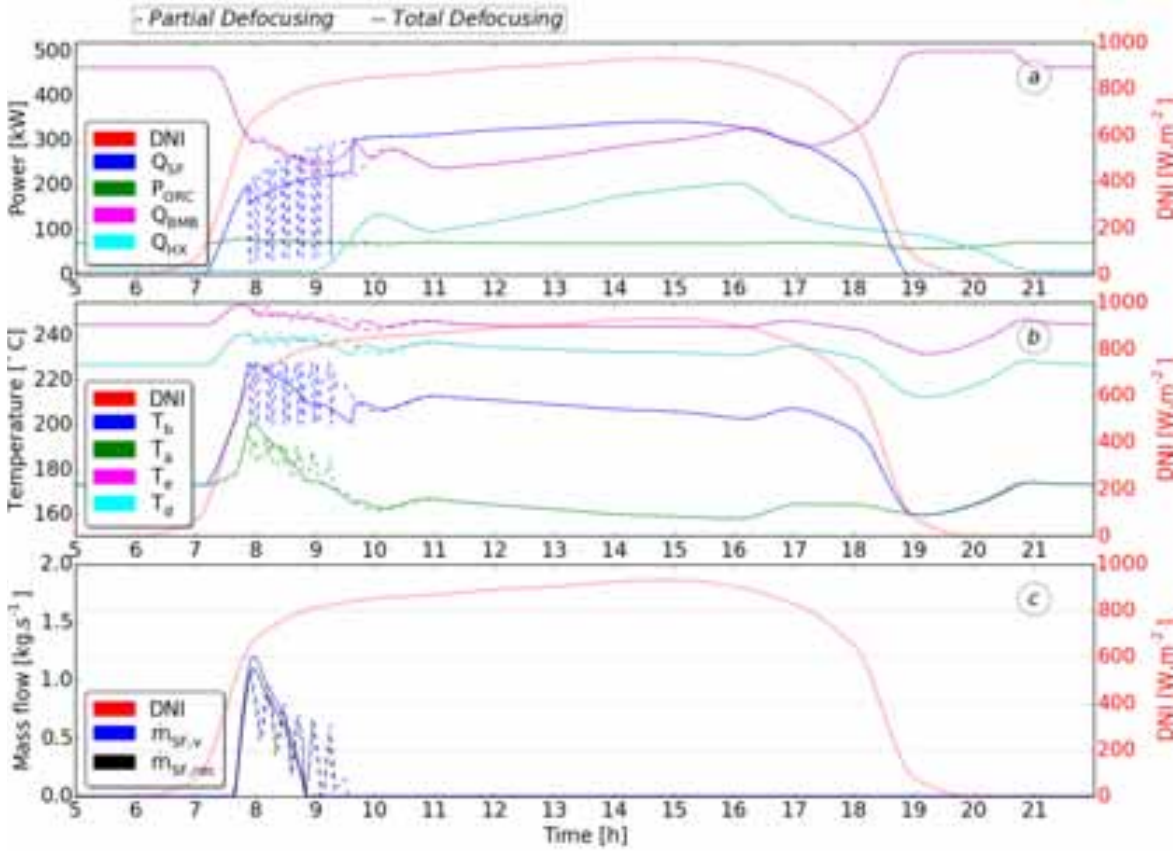

Fig. 5 Dynamic simulation results of the whole plant model during a reference summer day in Cáceres, Spain with variable thermal power load. The dashed line represents thre results for a solar field control strategy based on a total defocusing (TD) , the solid line for a partial defocusing (PD). (a) Thermal power delivered by the solar field, the biomass, the ORC evaporator and the HX oil/water evaporator (b) Temperature values in key points of the system (c) Mass flows of the solar field bypass and recirculation system.

6. Conclusions and future work

In this work the CSP-biomass CHP system based on ORC technology developed in the framework of the EU founded BRICKER project is presented. The system has the goal of meeting the building energy demand with the employment of only renewable energy sources. A detailed description of the different system component is reported. Given the technical boundaries of the different component, a control logic is developed to maintain safe operating condition during different working conditions. In order to test the implemented control logic a dynamic model of the whole system is developed. The dynamic model is based on the Modelica programming language and the components models are developed based on the *ThermoCycle* library adopting a simple modeling approach. The reaction to the passage of sub- sequent clouds, causing the solar input to drop to 90% of its nominal value, is simulated to test the control capability to ensure safe condition. The effectiveness of the biomass boiler to decouple the solar field to the HXI and ORC units is assessed. The system is able to withstand fast variation of the sun power as demonstrated by the results of the first simulation reported in Figure 3. Variation in solar field outlet temperature of 30 K results in variation at the evaporator ORC inlet temperature of 8 K causing a decrease in electrical power of 8% with respect to its nominal power. Furthermore, two solar field defocusing approach are investigated in two

different conditions, one with constant thermal power and one with variable thermal power. In both situations the two approaches allows to operate the system within the safety limits imposed by the ORC unit and the biomass boiler. The effectiveness of the two approaches in exploiting the sun power is assessed in terms of the solar fraction. The TD approach allows to increase the solar fraction of up to 12 percentage point compared to the PD case at the cost of continuously running the electric motor of the solar field. In the next phase of the project, the developed dynamic model will be integrated with the model of the adsorption chiller and of the reference building to investigate in detail the control strategy that allows to maximize the solar fraction while maintaining safe working conditions.

7. Acknowledgement

The result presented in this paper is part of the BRICKER project (www.bricker-project.com). This project has received funding from the European Union's Seventh Framework Programme for research, technological development and demonstration under grant agreement No 609071. The information reflects only the author's view and the Commission is not responsible for any use that may be made of the information it contains.

References

IEA, 2014. Technology Roadmap Solar Thermal Electricity - 2014 edition.

Alberti, F., Crema, L., Bozzoli, A., 2012. Heat Transfer Analysis for a Small-Size Direct-Flow Coaxial Concentrating Collector. J. Sol. Energy Eng. 134, 041009. doi:10.1115/1.4007297

Angelino, G., Gaia, M., Macchi, E., 1984. Review of Italian Activity in the Field of Organic Rankine Cycles. VDI Berichte.

Cabello, J.M., Cejudo, J.M., Luque, M., Ruiz, F., Deb, K., Tewari, R., 2011. Optimization of the size of a solar thermal electricity plant by means of genetic algorithms. Renew. Energy 36, 3146–3153. doi:10.1016/j.renene.2011.03.018

Casati, E., Desideri, A., Casella, F., Colonna, P., 2012. Preliminary Assessment of a Novel Small CSP Plant Based on Linear Collectors , ORC and Direct Thermal Storage. SolarPaces Conf.

Casella, F., Sielemann, M., Savoldelli, L., 2011. Steady-state initialization of object-oriented thermo-fluid models by homotopy methods. 8th Model. Conf. 86–96.

Dickes, R., Desideri, A., Lemort, V., Quoilin, S., 2015. Model reduction for simulating the dynamic behavior of parabolic troughs and a thermocline energy storage in a micro-solar power unit.

Elmqvist, H., Mattsson, S.E., 1997. Modelica — the Next Generation Modeling Language an International Design Effort. Proc. 1st World Congr. Syst. Simul. 1–5. doi:10.1.1.16.3600

Hinkley, J., Curtin, B., Hayward, J., \Wonhas, A., Boyd, R., Grima, C., Tadros, A., Hall, R., Naicker, K., Mikhail, A., 2011. Concentrating solar power – drivers and opportunities for cost-competitive electricity 1–32.

Ireland, M., Orsoz, M., Desideri, A., Quoilin, S., DesuBrisson, J.G., 2014. Dynamic modeling and control system definition for a micro-CSP plant coupled with thermal storage unit, in: Proceedings of ASME Turbo Expo 2014: Turbine Technical Conference and Exposition.

Mattson, S.E., Elmqvist, H., Broenink, J.F., 1997. Modelica: An international effort to design the next generation modelling language. J. A 38, 16–19.

Mediavilla, M., de Castro, C., Capellán, I., Javier Miguel, L., Arto, I., Frechoso, F., 2013. The transition towards renewable energies: Physical limits and temporal conditions. Energy Policy 52, 297–311. doi:10.1016/j.enpol.2012.09.033

Palm, B., Claesson, J., 2006. Plate Heat Exchangers: Calculation Methods for Singleand Two-Phase Flow. Heat Transf. Eng. 27, 88–98. doi:10.1080/01457630500523949

Peterseim, J.H., Hellwig, U., Tadros, A., White, S., 2014a. Hybridisation optimization of concentrating solar thermal and biomass power generation facilities. Sol. Energy 99, 203–214. doi:10.1016/j.solener.2013.10.041

Peterseim, J.H., Tadros, A., Hellwig, U., White, S., 2014b. Increasing the efficiency of parabolic trough plants using thermal oil through external superheating with biomass. Energy Convers. Manag. 77, 784–793. doi:10.1016/j.enconman.2013.10.022

Peterseim, J.H., White, S., Tadros, A., Hellwig, U., 2013. Concentrated solar power hybrid plants, which technologies are best suited for hybridisation? Renew. Energy 57, 520–532. doi:10.1016/j.renene.2013.02.014

Pitz-Paal, R., Dersch, J., Milow, B., Téllez, F., Ferriere, A., Langnickel, U., Steinfeld, A., Karni, J., Zarza, E., Popel, O., 2007. Development Steps for Parabolic Trough Solar Power Technologies With Maximum Impact on Cost Reduction. J. Sol. Energy Eng. 129, 371. doi:10.1115/1.2769697

Quoilin, S., Broek, M. Van Den, Declaye, S., Dewallef, P., Lemort, V., 2013. Techno-economic survey of organic rankine cycle (ORC) systems. Renew. Sustain. Energy Rev. 22, 168–186. doi:10.1016/j.rser.2013.01.028

Quoilin, S., Desideri, A., Wronski, J., Bell, I., Lemort, V., 2014. ThermoCycle: A Modelica library for the simulation of thermodynamic systems 683–692. doi:10.3384/ecp14096683

Resnick Institute, 2012. Grid 2020 Towards a Policy of Renewable and Distributed Energy Resources.

Soria, R., Portugal-Pereira, J., Szklo, A., Milani, R., Schaeffer, R., 2015. Hybrid concentrated solar power (CSP)–biomass plants in a semiarid region: A strategy for CSP deployment in Brazil. Energy Policy 86, 57–72. doi:10.1016/j.enpol.2015.06.028

Sterrer, R., Schidler, S., Schwandt, O., Franz, P., Hammerschmid, A., 2014. Theoretical Analysis of the Combination of CSP with a Biomass CHP-plant Using ORC-technology in Central Europe. Energy Procedia 49, 1218–1227. doi:10.1016/j.egypro.2014.03.131

Wang, B.K., Vineyard, E. a, 2011. Adsorption Refrigeration. Ashrae.

Conference Proceedings

Solar World Congress 2015
Daegu, Korea, 08 – 12 November 2015

Impact of model reduction on the dynamic simulation of a micro-scale concentrated solar power system integrated with a thermal storage

Rémi Dickes*, Noé Weber, Vincent Lemort and Sylvain Quoilin

Energy Systems Research Unit
Aerospace and Mechanical Engineering Department, Faculty of Applied Sciences
University of Liège (Belgium)
*corresponding author: rdickes@ulg.ac.be

Abstract

Because of the intermittent nature of solar irradiances, micro-scale solar thermal power systems almost never operate in nominal operating conditions. They are characterized by strong transients and require robust, fast and accurate dynamic simulation tools to permit a proper evaluation of their performance. Model reduction, i.e. the simplification of detailed models, is an attractive method to improve the computational efficiency while simulating such systems. In this context, a μCSP plant featuring a solar field of parabolic troughs, a thermocline storage and a 5kWe power unit is investigated. Both the solar field and the thermocline storage are modeled with complex and simplified methods. The whole power plant is simulated under identical operating condition and deviations between the simulation results are analyzed. Benefits and limitations of the current modeling approach are assessed. Improvements for the modeling of the thermocline storage are identified, implemented and validated. The Modelica language is used as simulation tool and the models developed in this work are integrated in the open-source ThermoCycle library.

Keywords: *thermocline storage, concentrated solar power, model reduction, dynamic modeling*

1. Introduction

Energy security issues and global warming due to the extensive use of fossil fuels are nowadays almost universally recognized (IEA, 2015). Together with other growing technologies, concentrated solar power (CSP) is increasingly developed to help extend the share of renewable energy in the world's power generation (IEA, 2014). A major advantage of CSP over other technologies is the ability to couple the solar thermal power plant with a simple and cost-effective thermal energy storage (TES). Surplus of thermal power collected by the solar field during sunny periods can be easily stored to be latter used in low radiation conditions, hence improving the plant's capacity factor, its flexibility and reducing the cost of electricity. Besides well-known large-scale applications (Lovegrove and Stein, 2012), concentrated solar power can also be used in micro-systems (μCSP) for supplying useful heat and electricity to a local demand, e.g. in remote off-grid areas (Orosz, 2012). Given the intermittent nature of solar irradiances and the local energy demand, μCSP systems often work far from their nominal design conditions and are submitted to strong transients. Powerful dynamic modeling tools are therefore required to simulate the effective performance of μCSP systems in real operating conditions and to optimize the control strategy. However, high computational speed, robustness and accuracy must be achieved by the dynamic models to permit a direct application of these tools in optimization problems. An interesting method to reach such goals is to use simplified models for simulating each component of the power plant. This method is referred to as *model reduction* and is the subject of this contribution.

doi:10.18086/swc.2015.04.15 Available at http://proceedings.ises.org

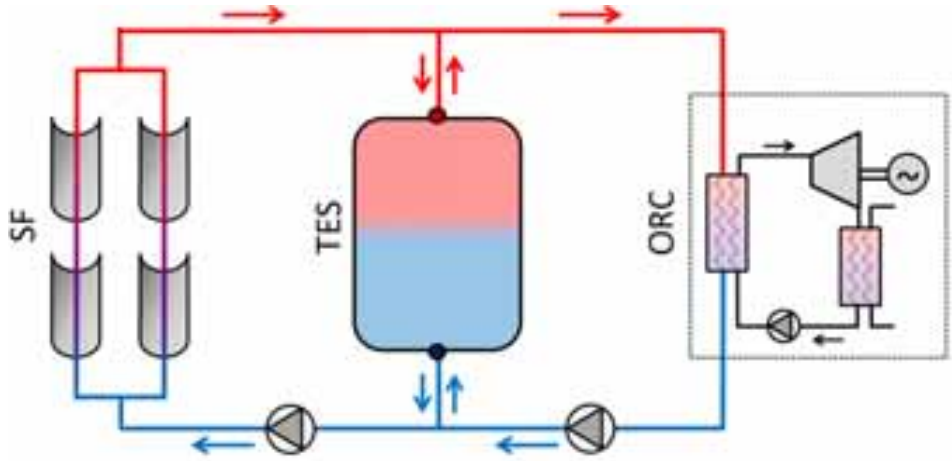

Fig. 1: Schematic layout of the µCSP plant considered in this work (red lines: hot HTF – blue line: cold HTF).

The CSP system considered here is depicted in Figure 1. The power plant features a solar field (SF) of parabolic trough collectors (130 m²), a 5kWe non-recuperative organic Rankine cycle (ORC) and a thermocline storage (15m³). Therminol 66 is used as heat transfer fluid (HTF) and two circulating pumps control its flow rate through the solar field, the TES and the ORC. For the sack of conciseness, neither the control strategy nor technical data of the power plant are described in this manuscript. Detailed information regarding these aspects is available in a previous article also dedicated to this research project (Dickes et al., 2014).

In a previous work (Dickes et al., 2015a), the authors proposed two innovative approaches for modeling both the solar field and the thermocline storage. These methods aimed to simplify the simulation of these components by making the models less complex. In order to assess the loss of accuracy caused by the simplified approaches, results of simulation in identical operating conditions were compared with predictions given by deterministic (i.e. detailed) models. However, this comparison was only performed for each component individually. In this contribution, it is proposed to further evaluate the validity of model reduction by simulating the whole µCSP plant with both detailed and simplified methods. Only the solar collectors and the thermal energy storage are studied in details. Model reduction of the organic Rankine cycle is beyond the scope of this report. Results of simulation under identical operating conditions are compared and analyzed to assess the limits and benefits of the current approach. Improvements required for the modeling of the thermal storage are identified, developed and validated.

The Modelica language (Elmqvist and Mattsson, 1997) is used as simulation platform and thermo-physical properties of the fluids are computed with the free-access CoolProp library (Bell et al., 2014). Furthermore, all the models developed in the frame of this project are included in the open-source ThermoCycle library (Quoilin et al., 2013) dedicated to the modeling of thermal systems and under development at the University of Liège. Results presented in this paper are mostly derived from a MSc thesis performed by Noé Weber at the University of Liège. Additional information unpublished in this paper can be found in the original manuscript (Weber, 2015).

2. Model reduction and global simulation

In this section, a short description of the models already developed for the thermal storage and the solar field is first given. Additional information about the models development and the results of the individual comparison can be found in the authors' preceding publication (Dickes et al., 2015a). The whole power plant is then simulated by coupling together the solar field and the thermocline storage. Results from detailed and simplified models in identical weather conditions are then discussed and analyzed. For the sake of clarity, the different models developed in the following sections, with their main characteristics, are summarized in the Appendix (see Table 2).

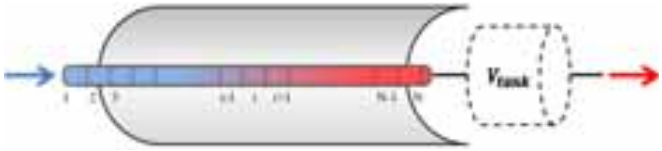

Fig. 2: one-dimensional discretization of a PTC (with a fictive tank connected to the outlet for the simplified model)

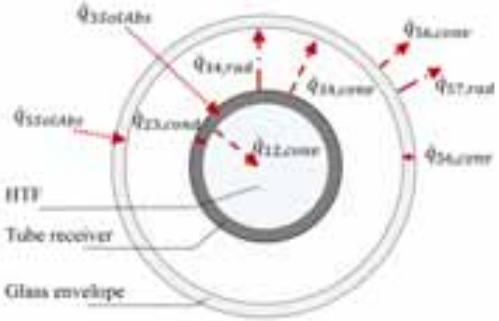

Fig. 3: Radial heat balance taking place in a parabolic trough collector

2.1. Solar thermal collectors – description of the simplified and the detailed models

Parabolic trough collectors (PTCs) are linear concentrating systems made of long, parabolic-shaped mirrors and an absorber tube placed along the focal axis of the parabola. In order to evaluate the temperature profile of the heat transfer fluid circulating along the receiver tube, a common approach is to discretize the tube along its axial axis in a number of cells of constant volume in which the energy balance is evaluated (see Figure 2). In order to determine the net heat power absorbed by the fluid in each cell, two options are proposed as described here below.

- Detailed method (referred to as *model PTC$_A$*): as depicted in Figure 3, the net heat power absorbed by the HTF can be evaluated by solving the radial heat balance between the surrounding environment, the glass envelop, the absorber tube and the fluid (Forristall, 2003). To account for the dynamic behavior of the collectors in transient operating conditions, thermal capacitances of the different components are considered. The number of cells used for the discretization is a key parameters that must be selected correctly. It must be high enough to limit the effects of numerical diffusion (Peterson, 1992) while ensuring low computational times.
- Simplified method (referred to as *model PTC$_B$*): an alternative approach to calculate the net heat power absorbed by the HTF is to use a calibrated correlation computing the effective heat losses of the PTC in function of the operating conditions (Dickes et al., 2015b). By using such correlation, the steady-state temperature profile along the collectors can be easily derived. The dynamic response of the parabolic troughs is accounted by connecting a fictitious fluid reservoir in series with the solar field outlet, as shown in Figure 2. The reservoir acts as a dynamic damper and smooth out the temperature changes simulated by steady-state model at the solar field outlet.

Results from the individual comparison demonstrate good agreements between the two modeling methods in most working conditions. Significant deviations are observed for fast transient conditions (i.e. with time constants lower than the residence time of the fluid within the collectors). Indeed, the single reservoir used as thermal inertia does not properly simulate the progression of the temperature gradients within the collector tubes. However, these fast effects are localized and remain negligible in long-term simulations.

2.2. Thermocline storage – description of the simplified and detailed models

The storage system used in the μCSP plant is a single-tank stratified storage, also called *thermocline* storage. It is entirely filled with heat transfer fluid and, by taking advantage of the vertical stratification due to the density gradient, both cold and hot zones are stored in a single reservoir. Like for the solar collectors, two modeling methods are used to characterize the thermocline storage.

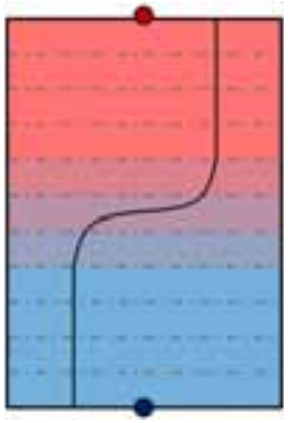

Fig. 4: one-dimensional finite-volume method for modeling a thermocline storage

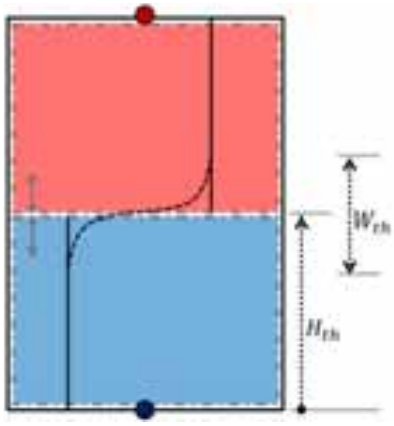

Fig. 5: two-zone moving-boundary method for modeling a thermocline storage

- Detailed method (referred to as *model TES_A*): in a physically-based approach, a thermocline system can be modeled with a one-dimensional finite-volume method. The reservoir is assumed cylindrical and discretized along its vertical axis in a finite number of isothermal cells of constant volume (as illustrated in Figure 4). In each cell, both mass and energy balances are evaluated while accounting for heat losses to the environment, mass exchange and conductive heat transfer between adjacent cells. Because of the low velocity of the fluid within the tank, a high discretization must be performed to limit the effect of numerical diffusion, resulting in long computational time. In this paper, a 200-cell discretization is chosen for the detailed model TES_A.
- Simplified method (referred to as *model TES_B*): a simpler approach to simulate a thermocline storage is to consider a two-zone moving-boundary model. The tank is divided into two isothermal zones, a hot and a cold one, of variable volume. Mass and energy balance only need to be calculated twice, once for each zone, which drastically increases simulation speed. If the tank is fully charged (resp. discharged), then only the hotter zone (resp. the colder zone) subsists in the tank. The temperature transition profile between the two zones is modelled as half a period of a cosine symmetrically centered on the boundary between the two zones, as depicted in Figure 5. In a first time, the thickness of the thermocline region (W_{th} in Figure 5) is assumed constant, whatever the operating conditions.

Results from the individual comparison demonstrate good agreements between the two modeling methods if a proper calibration of the thermocline thickness is performed. Furthermore, the simplified method demonstrate a drastic decrease in the simulation time (up to 99%) when compared to the deterministic model.

2.3 Power plant simulation

In order to further evaluate the validity of the simplified models, the whole power plant is simulated during two complete days by connecting together the model PTC_A (resp. PTC_B) to the model TES_A (resp. TES_B). The same control strategy is applied for the circulating pumps and identical weather conditions are used as inputs. The first day has a quasi-perfect solar irradiance shape and it is used as reference to calibrate the thermocline thickness W_{th} of the simplified model TES_B. As depicted in Figures 6 and 7, really good agreements are found between the simplified and the detailed simulations. Regarding to the solar field, both the outlet temperature and the mass flow rate are reproduced with high precision during shinny periods. It can also be seen that deviations in the outlet temperature prediction arise only in strong off-design conditions. However, these periods correspond to zero-flow conditions in the solar field which do not influence the rest of the power plant. The thermal storage is also well represented with the simplified model TES_B. As depicted in Figure 7, both the thermocline position (H_{th} in Figure 5) and the discharge temperature at the top port of the storage are correctly simulated along the day. Although promising, these results are biased since the thermocline thickness W_{th} of the model TES_B has been calibrated a posteriori to fit properly the predictions of the complex model.

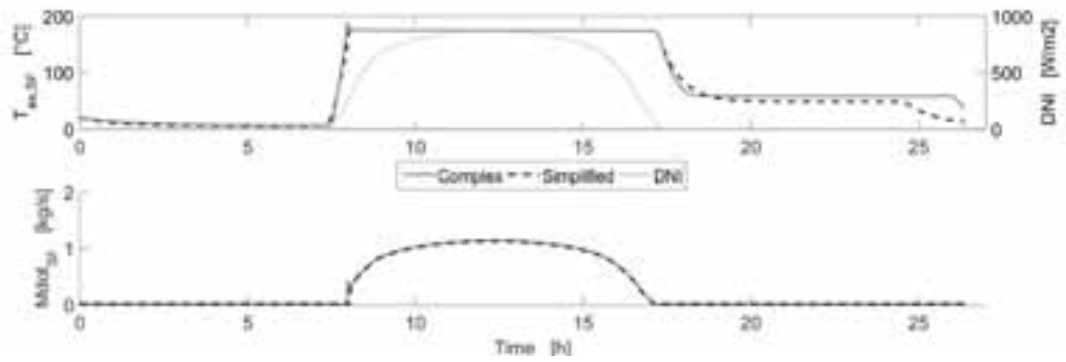

Fig. 6: Day 1 – Outlet temperature (top fig.) and mass flow rate (bottom fig.) modeled in the solar field

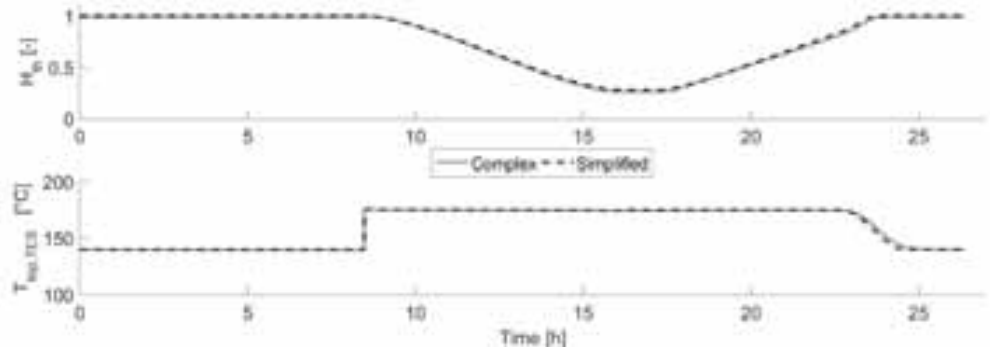

Fig. 7: Day 1 – Thermocline position in the tank (top fig.) and discharge temperature at the top port of the TES (bottom fig.)

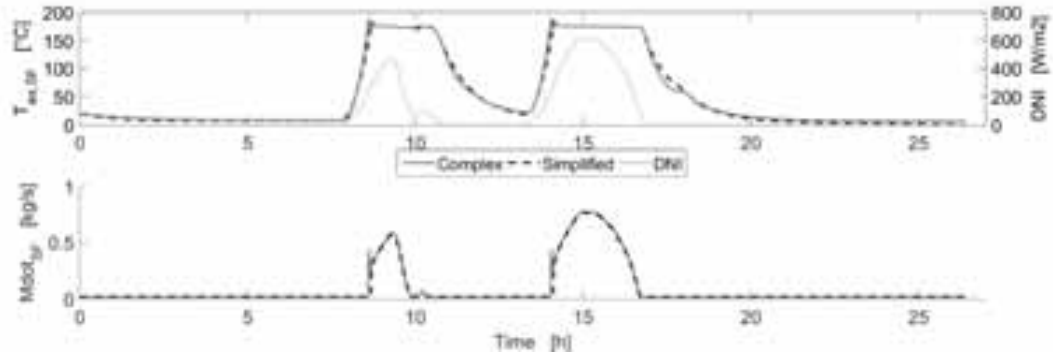

Fig. 8: Day 2 – Outlet temperature (top fig.) and mass flow rate (bottom fig.) modeled in the solar field

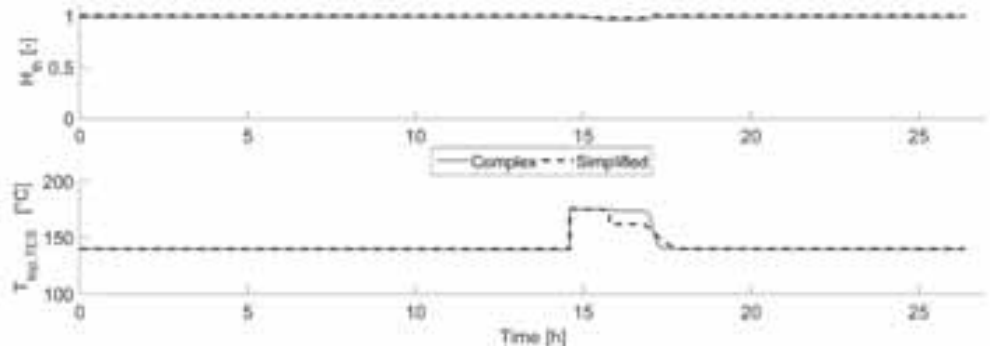

Fig. 9: Day 2 – Thermocline position in the tank (top fig.) and discharge temperature at the top port of the TES (bottom fig.)

The power plant is simulated during a second day characterized by poorer solar conditions and the thermocline thickness is kept unchanged. As shown in Figure 8, parabolic troughs are once again simulated correctly and good agreements are observed for both the mass flow and the outlet temperature of the solar field. Concerning the thermal energy storage, results are less enthusiastic. The assumption of a constant thermocline thickness leads to significant mispredictions of the discharge temperature at the top port of the tank, as illustrated in Figure 9. Indeed, the simplified model considers the thermocline as a fixed transition profile moving together with two sub-volumes. If a flow reversal happens before the storage is charged enough to have the "hypothetical" thermocline zone entirely comprised inside the tank, a nonphysical discontinuity of the temperature is simulated at the top port of the storage. Same errors also occur in the case of partial discharge of the TES. For more information about this numerical problem, a detailed description of the phenomena is provided in Weber's thesis (Weber, 2015). This observation poses the problem that, with the present simplified method, the thermocline thickness must be fitted a posteriori, when the results of the complex model are already available. A convenient method to thwart the issue is to determine the dynamic evolution of the thermocline thickness in the storage throughout the day, as a function of real-time parameters, so that the model could be used with no need of retrofitting. The next section is devoted to the development of such model.

3. Model improvements of the thermocline storage and global simulation

It this section, the methodology used to develop an improved model of the thermal energy storage is presented. This new model is then validated by simulating the complete power plant over the same two days as in section 2.3.

3.1 Thermocline storage – modelling improvement

As explained previously, the thermocline thickness within a stratified tank does not remain constant and making such an assumption leads to significant mispredicitons. In order to derive a law that represents the dynamic evolution of the thermocline thickness, the dynamics taking place inside the tank are simulated with the detailed model TES_A in various conditions. Evolutions of the thermocline thickness with different mass flow rates in both charging and discharging modes, but also in standby conditions, are calculated and analyzed. Results demonstrate that the evolution of the thermocline thickness is mainly function of the time and the fluid mass flow rate. As depicted in Figure 10 (in the case of charging processes), the thermocline thickness W_{th} can be interpolated by an equation of the form

$$W_{th} = K_{th} \,.\sqrt{t} \qquad \text{(eq. 1)}$$

where t is the time since the beginning of the charge and K_{th} is a parameter depending of the mass flow rate $\dot{m}$, i.e.

$$K_{th} = a \,.\sqrt{\dot{m}} + b \qquad \text{(eq. 2)}$$

as illustrated in Figure 11. Coefficients a and b in equation 2 are calibrated for both charging and discharging processes and their values are provided in the Appendix. Regarding standby periods, it is found that the thermocline thickness increases linearly with respect to the time i.e.

$$W_{th} = c_{sb} \,.\, t \qquad \text{(eq. 3)}$$

where c_{sb} is another constant parameter given in the Appendix. By implementing these correlations in the two-zone moving-boundary model, an improved approach for simulating the thermocline storage (referred to as *model* TES_C) is finally obtained.

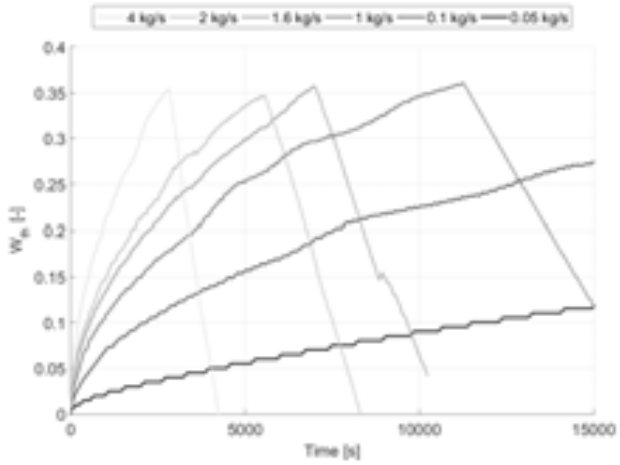

Fig. 10: Evolution of the thermocline thickness as a function of time with various mass flow rates

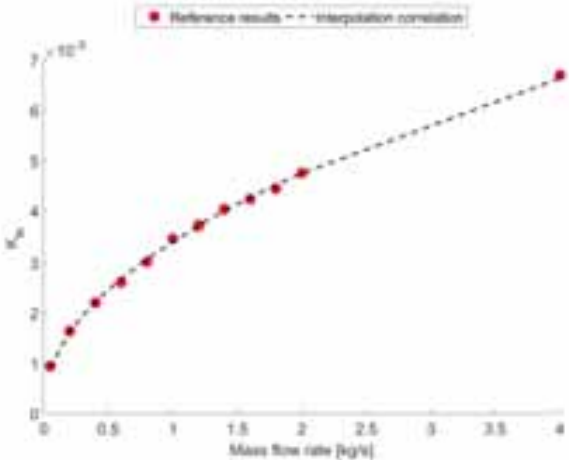

Fig. 11: Evolution of the parameter K_{th} as a function of the mass flow rate

3.2 Power plant simulation

In order to validate the new model TES_C presented here above, the whole power plant is simulated during the same two days as in section 2.3, and results obtained by the combination of models PTC_B-TES_C are compared to the reference/detailed model PTC_A-TES_A. Since the simplified method for modeling of solar field has demonstrated to be reliable, only results relative to the thermal storage are depicted in Figure 12 and 13; these figures corresponding to the first and the second day respectively. It can be seen that, for both days, the two-zone moving-boundary approach permits once again to predict correctly the position of the thermocline inside the tank (i.e. H_{th} in Figure 5). Furthermore, the correlations used to compute dynamically the thermocline thickness permit to replicate much better the behavior of the storage. Without any pre-calibration, the evaluation of the thickness W_{th} is properly predicted for both days and mispredictions of the discharge temperature are drastically decreased compared to results of the initial model TES_B. Simulations performed for two other days can be found in Weber's thesis (Weber, 2015) and identical observations are drawn. In conclusion, the new model TES_C of the thermocline coupled to the simplified model PTC_B of the solar collectors permit to replicate correctly predictions of the complex models.

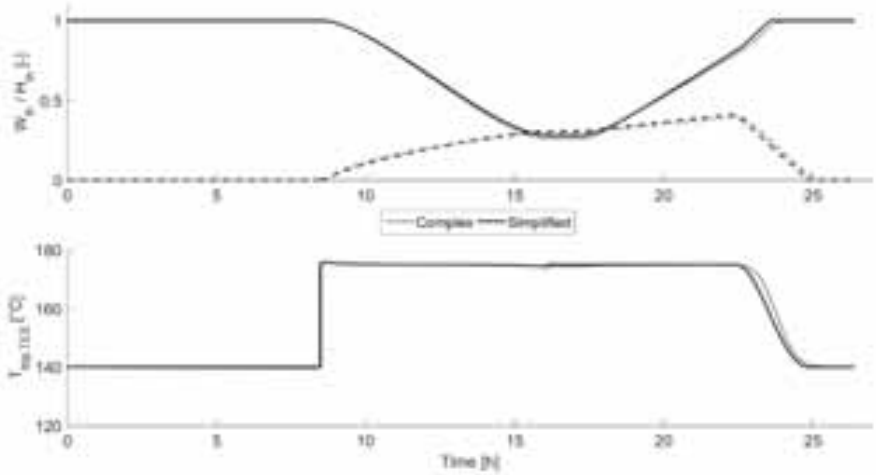

Fig. 12: Day 1 –Position H_{th} and thickness W_{th} of the thermocline inside the tank (top) and discharge temperature at the top port of the TES (bottom)

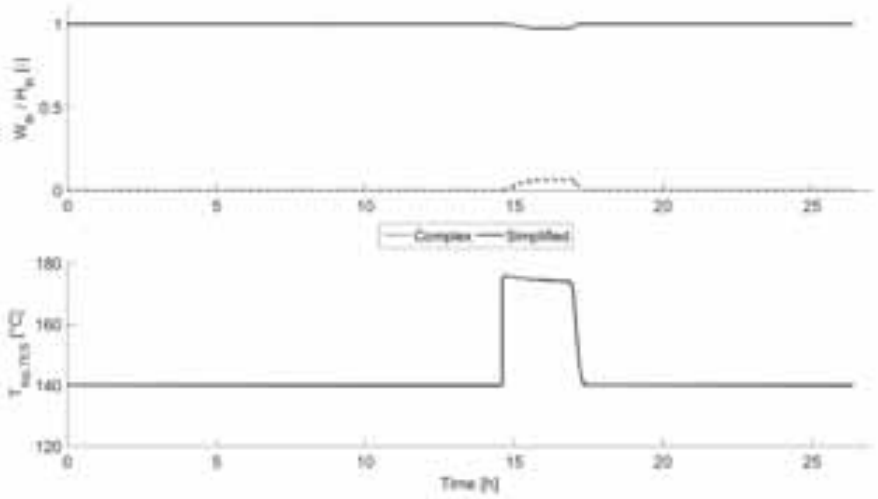

Fig. 13: Day 2 –Position H_{th} and thickness W_{th} of the thermocline inside the tank (top) and discharge temperature at the top port of the TES (bottom)

4. Simulation speed, number of variables and accuracy

In the previous sections, it is shown that simplified modeling methods can be used instead of complex ones to simulate a small-scale solar thermal power plant. The main motivation of this approach is to improve numerically the simulations by increasing the computational speed. In order to highlight such an improvement, both the number of variables and the simulation times required by the three models investigated in this paper are summarized in Table 1. All the simulations were run on Dymola© 2015 with an Acer Aspire V5, CPU Intel Core i5 2.7 Ghz, 8GB RAM.

A first observation is the sharp decrease in the number of variables between the two simplified models and the reference case (up to 90% for the complete power plant). As explained previously, the detailed model of the storage (TES_A) needs to solve the energy and the mass balances in the 200 discretized cells, whereas both simplified methods (TES_B and TES_C) only consider two sub-tanks of variable volume. The additional correlations implemented in the model TES_C increase slightly the number of variables but these remains largely fewer than for the detailed model TES_A. Regarding the solar field, the deterministic calculation of the radial heat balance in each cell requires almost 3000 variables whereas the simplified method reduces this number to 600. Besides the number of variables, it can be seen that simplified models are between 75 and 215 times faster than the detailed one. The tremendous gain in computational speed is extremely valuable when performing long-term simulations, or when using directly these dynamic modeling tools in iterative problems like optimizations.

Tab. 1 – Number of variables and simulation times for each model of the complete power plant (with the relative reduction compared to the reference case given in parenthesis)

	Detailed model (PTC_A - TES_A)	**Simplified model (PTC_B - TES_B)**	**Improved model (PTC_B - TES_C)**
No. of variables (TES)	4607	77 *(- 98%)*	442 *(- 90%)*
No. of variables (µCSP)	7602	735 *(- 90%)*	1100 *(- 85%)*
Simulation time (Day 1)	5680 sec	75 sec *(- 98%)*	66 sec *(- 99%)*
Simulation time (Day 2)	9960 sec	46 sec *(- 99%)*	43 sec *(- 99%)*

5. Conclusion and future work

Because of the intermittent nature of solar irradiances, μCSP systems almost never operate in nominal working conditions. They are characterized by strong transients and require powerful dynamic simulation tools to permit a proper evaluation of their performance. Model reduction, i.e. the simplification of detailed model, is an attractive method to improve the computational efficiency when simulating such systems. In this context, a μCSP plant consisting of a thermocline storage, a solar field of parabolic trough collectors and a 5kWe ORC is considered. Both complex and simplified models are developed for the solar field and the thermal energy storage.

In a previous work, an individual comparison applied to each component demonstrated the great potential of simplified methods to replicate predictions of the detailed models. In this contribution, it is proposed to further evaluate the validity of model reduction by simulating the whole μCSP plant under identical operating conditions by connecting together these detailed and simplified models. Results demonstrate good agreements for the solar collectors. However, the initial assumption of a constant thermocline thickness in the thermal storage leads to significant errors. Therefore, empirical correlations are identified and implemented in the model to simulate the dynamic evolution of the thermocline thickness within the tank as a function of real-time parameters. This new model of the storage is integrated in the μCSP plant and much better results are demonstrated. Regarding numerical aspects, the number of variables is drastically decreased by using the simplified models, e.g. 85% less when considering the complete power plant. Besides increasing the robustness, the reduced number of variables permits the simplified models to achieve much faster computational speed for a same simulation (up to 99% less time).

In conclusion, model reduction has demonstrated to be a convenient and powerful tool to permit a direct application of dynamic modeling in iterative problems (e.g. control optimization) or for long-term simulations. Really good agreements are found between simulation results of the simplified and the detailed models, but there is still room for improvements. As an example, future works include to change the shape of the transition profile implemented in the two-zone moving-boundary model of the TES. Indeed, better accordance with the complex model could be achieved by using a LCDF function (Bayón and Rojas, 2014).

Appendix

Tab. 1 – Characteristics of the different models investigated for the solar field and the thermal storage

Solar field		**Thermocline TES**		
model PTC_A	**model PTC_B**	**model TES_A**	**model TES_B**	**model TES_C**
Detailed	*Simplified*	*Detailed*	*Simplified*	*Simplified bis*
(solves the radial heat balance and accounts for the thermal inertia of the different component in balance in each cell)	(uses a semi-empirical correlation to calculate the steady-state temperature profile and a single fictive reservoir at the solar field outlet)	(tank discretized in 200 cells of constant volume and evaluation of both the mass and the energy balance in each cell)	(two-zone moving-boundary model of the storage with a constant thermocline thickness in any operating conditions)	(two-zone moving-boundary model of the storage with a dynamic calculation of the thermocline thickness in function of the operating conditions)

Tab. 3 – Coefficients of the correlations used to calculate the thermocline thickness

Name	Value
a_{ch}	*3.23 e-3*
b_{ch}	*1.86 e-4*
a_{disch}	*2.97 e-3*
b_{disch}	*9.98 e-4*
c_{sb}	*6.74* e-7

Nomenclature

Acronyms

CSP	Concentrated Solar Power
DNI	Direct Normal Irradiance
HTF	Heat Transfer Fluid
ORC	Organic Rankine Cycle
PTC	Parabolic Trough Collector
SF	Solar Field
TES	Thermal Energy Storage

Subscripts

A	model A
B	model B
C	model C
ch	charging
disch	discharging
ex	exhaust
sb	standby
th	thermocline
top	top port of the storage

Symbols

a	Coefficient of interpolation, -
b	Coefficient of interpolation, -
c	Coefficient of interpolation, -
H	Normalized height, -
K	Coefficient of interpolation, -
Mdot, $\dot{m}$	Mass flow rate, kg/s
T	Temperature, °C
t	Time, sec
V	Volume, m³
W	Normalized thickness, -

References

Bayón, R., Rojas, E., 2014. Analytical function describing the behaviour of a thermocline storage tank: A requirement for annual simulations of solar thermal power plants. Int. J. Heat Mass Transf. 68, 641–648.

Bell, I.H., Wronski, J., Quoilin, S., Lemort, V., 2014. Pure and pseudo-pure fluid thermophysical property evaluation and the open-source thermophysical property library coolprop. Ind. Eng. Chem. Res. 53, 2498–2508.

Dickes, R., Desideri, A., Bell, I., Quoilin, S., Lemort, V., 2014. Dynamic modeling and control strategy analysis of a micro-scale CSP plant coupled with a thermocline system for power generation, in: Proceedings of Eurosun ISES 2014. Aix-les-Bains (France).

Dickes, R., Desideri, A., Lemort, V., Quoilin, S., 2015a. Model reduction for simulating the dynamic behavior of parabolic troughs and a thermocline energy storage in a micro-solar power unit, in: Proceedings of ECOS 2015. Pau (France).

Dickes, R., Lemort, V., Quoilin, S., 2015b. Semi-empirical correlation to model heat losses along solar parabolic trough collectors, in: Proceedings of ECOS 2015. Pau (France).

Elmqvist, H., Mattsson, S.E., 1997. Modelica — the Next Generation Modeling Language an International Design Effort, in: Proceedings of the 1st World Congress on System Simulation. Singapore.

Forristall, R., 2003. Heat Transfer Analysis and Modeling of a Parabolic Trough Solar Receiver Implemented in Engineering Equation Solver, Contract. Golden, CO.

IEA, 2015. International Energy Agency - Report on Energy Security [WWW Document]. URL http://www.iea.org/topics/energysecurity/

IEA, 2014. International Energy Agency -Technology Roadmap: Solar Thermal Electricity [WWW Document]. URL http://www.iea.org/

Lovegrove, K., Stein, W., 2012. Concentrating solar power technology - Principle, developments and application, Woodhead Publishing Series in Energy. Woodhead Publishing.

Orosz, M.S., 2012. Thermosolar and photovoltaic hybridization for small scale distributed generation: application for powpower rural health. Massachusetts Institue of Technology.

Peterson, P.F., 1992. A method for predicting and minimizing numerical diffusion. Numer. Heat Transf. Part B Fundam. An Int. J. Comput. Methodol. 21, 343–366.

Quoilin, S., Desideri, A., Bell, I., Wronski, J., Lemort, V., 2013. Robust and computionally efficient dynamic simulation of ORC systems: the Thermocycle modelica library, in: Proceedings of the AMSE-ORC Conference 2013. Rotterdam (NL).

Weber, N., 2015. Dynamic model reduction of a thermocline storage integrated in a micro-scale solar power plant. University of Liège.

Conference Proceedings

Solar World Congress 2015
Daegu, Korea, 08 – 12 November 2015

Performance Analysis of Solar Tower Power Plants Driven Supercritical Carbon Dioxide Recompression Cycles for Six Different Locations in Saudi Arabia

Fahad A. Al-Sulaiman [1], Maimoon Atif[2] and Hafiz Abd-ur-rahman[2]

[1] Center of Research Excellence in Renewable Energy, Research Institute, King Fahd University of Petroleum & Minerals, Dhahran, 31261, (Saudi Arabia)

[2] Mechanical Engineering Department, King Fahd University of Petroleum & Minerals, Dhahran, 31261, (Saudi Arabia)

Abstract

In this study, thermodynamic analysis of supercritical carbon dioxide (sCO_2) recompression Brayton cycles integrated with solar thermal tower systems was carried out. First part of the model deals with generating a surround heliostat field layout. This heliostat field is then optimized for optical performance on annual basis using an evolutionary algorithm called the differential evolution. The other part of the model deals with modeling a recompression Brayton cycle, which uses the heat collected at the central receiver through the heliostat field. The developed mathematical model was implemented for six different locations (cities) in Saudi Arabia for comparative analysis. The selected cities were Tabouk (North), Madinah (West), Dhahran (East), Riyadh (Central), Bishah (South), and Najran (South). In addition, an auxiliary heat exchanger was also added before the expansion turbine to keep the turbine inlet temperature constant and, thus, to keep the net power output uniform. The target net power output was set to be 40 MW. The findings reveal that the highest annual average heat collected was for Madinah, 938,400 kWh/day, and the second highest was for Tabouk, 933,100 kWh/day. Consequently, the least amount of annual average fuel hybridization required was 5.82% for Madinah and 6.34% for Tabouk during daytime hours.

Keywords: *Solar tower power plant, supercritical CO_2, recompression Brayton cycle, hybrid solar power plant, heliostat optimization, Saudi Arabia*

1. Introduction

Solar tower or central receiver system comprises of a field of mirrors on the ground, which directs the solar radiation to a receiver mounted at the top of on a central tower. The receiver converts the solar radiation into heat and drives a thermodynamic cycle, which is usually a Brayton or a Rankine cycle, to generate power. Each individual mirror in the field is called a heliostat and it is equipped with a two-axes tracking system. As compared to parabolic troughs, solar towers can achieve higher temperature as more sunlight can be concentrated on a single receiver and the loss of heat can be minimized. Moreover, solar towers provide an opportunity to increase the capacity factor by using a thermal storage system and to maximize the power generated by allowing flexible generation strategy along with higher efficiency levels. With these advantages, A solar tower can be a tough competitor to parabolic trough in the future market with gained operating experience and reduced cost (IRENA, 2012).

In a study conducted by (Noone et al., 2012), a biomimetic pattern was proposed for the heliostat field layout. The model was based on the discretization of the heliostat surface for the calculation of the optical performance parameters, specifically the shading and blocking factor and the intercept factor. In their approach, a heliostat surface was divided into cells, however, this approach can be time consuming. (Besarati and Yogi Goswami, 2014) performed an optimization of the same biomimetic heliostat field pattern. In their study, a method was proposed to identify the potential shadowing and blocking heliostats for the calculation of the shading and

Selection and/or peer review under responsibility of Scientific Committee
doi:10.18086/swc.2015.04.16 Available at http://proceedings.ises.org

blocking factor. Using their approach, a case study was carried out for the design of 50 MWth solar tower plant for Dagget, California.

A code called HFLCAL (Schmitz et al., 2006) was developed by the German Aerospace Center to optimize a heliostat field on annual basis. The code calculates the intercept by describing an analytical function, which computes the reflected image of each heliostat as a circular normal distribution. Their analysis was carried out for two latitude locations, i.e. 20° N and 40° N.

In a different study conducted by (Pitz-Paal et al., 2011), annual optimization of a heliostat field for solar to chemical energy conversion efficiency was performed for solar fuels production. The optimization was carried out by coupling genetic algorithm and the Nelder-Mead algorithm. It was concluded that the chemical process selected has a high impact on the basic design parameters and the performance. Furthermore, their study was carried out for a latitude location of 36.12°.

(Collado and Guallar, 2012) developed a code named Campo which takes into account thousands of heliostat co-ordinates for the optimization process. The code was validated in a different study (Collado and Guallar, 2013) using the literature data collected from Gemasolar (a solar tower power plant). In their study, more than desired number of heliostats was generated. Then optimization of the generated heliostat field was carried out by applying radial increments in the heliostat rows manually. And finally, the heliostats which had lower annual optical performance were eliminated to acquire the desired number of heliostats. Their study was carried out for Seville, Spain (latitude 37.46° N)

The Chinese Academy of Science developed a code for the heliostat field layout optimization called HFLD (Wei et al., 2010a, 2010b). In their code, the optimization was based on the receiver geometrical aperture and an efficiency factor. However, the intercept factor was calculated using the Monte Carlo ray tracing method. As a result, the accuracy will depend upon the number of rays traced and, consequently, this will result in a high computation time. Using this code, a new layout was also proposed for the PS10 power plant. Furthermore, this study was conducted for a latitude location of 40.4° N.

In a study by (Yao et al., 2009), a power plant was modeled using TRNSYS and integrated with HFLD (Wei et al., 2010a, 2010b) developed by the Chinese Academy of Science for the demonstration of 1 MW central receiver plant in Dahan, China. The basic flow calculation in the solar central receiver system and their integration to a plant were described. On the other hand, (Le Moullec, 2013) performed a techno-economic study on a coal fired power plant with a supercritical CO_2 Brayton cycle and a post combustion CO_2 capture mechanism. It was observed that the reduction of cost avoided CO_2 was 45% and the reduction in the levelized cost of electricity (LCOE) was 15%, without storage and transport, when compared to a reference supercritical coal fired power plant equipped with a standard carbon capture process.

The effect of a transient solar heat input on a supercritical CO_2 split expansion Brayton cycle was studied by (Iverson et al., 2013). They studied the performance of the turbomachinery in response to a fluctuating solar heat source. It was observed that the thermal mass in the system effectively enables the Brayton cycle to continue to run for short periods until the thermal input can recover.

It can be observed from the literature review that no study has been conducted when integrating a sCO2 recompression Brayton cycle with a solar thermal tower system accounting for the actual optical losses of the heliostat field. Furthermore, no study considers DE optimization technique for the optimization of the heliostat field on annual basis. In this article, a heliostat field was first generated for six selected locations (cities) in Saudi Arabia; and then these generated heliostat fields were optimized on annual basis while calculating all the necessary optical performance parameters of all the heliostats at every step of the optimization. The selection of the locations takes into consideration different potential geographical locations of the proposed solar power system. The locations selected for the analysis were Tabouk (North), Madinah (West), Dhahran (East), Riyadh (Central), Bishah (South) and Najran (South). Then, after calculating the heat collected through the solar thermal system for the selected cities, comparative performance analysis was carried out for the aforementioned cities. The results of the current research will be a valuable reference for both researchers and engineers in the solar thermal power field.

2. Mathematical modeling

A mathematical model was developed to achieve the objectives of the present study. The first part of the mathematical model deals with generating a preliminary heliostat field in a radial staggered configuration. The generated heliostat field is then tested for its optical performance, and there are five parameters which constitute the optical performance of the heliostat field layout namely the shadowing and blocking factor, the intercept factor, the atmospheric attenuation factor, the cosine factor, and the actual mirror reflectivity. The generated heliostat field is then optimized on annual basis using an evolutionary algorithm called the differential evolution (HFLODE: Heliostat Field Layout Optimization using Differential Evolution). Finally, a recompression Brayton cycle using sCO_2 as a working fluid was integrated with the solar thermal tower system with a net power output of 40 MW. Comparative performance analysis was carried out for six different locations nin Saudi Arabia while taking into account the direct normal incident irradiation for all of these locations.

2.1 Generating a heliostat field

The characteristic diameter is the distance between the center of the adjacent heliostats and it is defined by

$$DM = DH + dsep + x_1 \quad \text{(eq. 1)}$$

where DM is the characteristic diameter, DH is the heliostat diagonal and $dsep$ is any additional security distance between the heliostats. Here, x_1 is one of the optimizing parameters. By varying the value of this paramter, we can control the azimuthal spacing between the adjacent heliostats.

The minimum radial distance between the heliostat rows is equal to the height of an equilateral triangle and it is defined as

$$\Delta R_i = x_{2,i} DM \cos 30° \quad \text{(eq. 2)}$$

where $x_{2,i}$ is the second optimizing parameter and i denotes the zone of the heliostats. Using the parameter $x_{2,i}$ the radial spacing between the rows of the heliostats can be controlled and in turn the optical performance of the heliostats.

2.2 Solar positioning model

In order to calculate the instantaneous optical efficiency of the heliostat field, it is necessary to include a solar positioning model which can be defined as (Duffie and Beckman, 2013)

$$\delta = \frac{23.45\pi}{180} \sin\left(2\pi \frac{284 + n_d}{365}\right) \quad \text{(eq. 3)}$$

$$\omega_{sunrise} = \cos^{-1}(\tan\phi \tan\delta) - \pi = -\omega_{sunset} \quad \text{(eq. 4)}$$

$$\alpha_s = \sin^{-1}(\cos\phi \cos\delta \cos\omega_s + \sin\phi \sin\delta) \quad \text{(eq. 5)}$$

$$\gamma_s = \mathrm{sgn}(\omega_s) \left| \cos^{-1} \frac{\sin\alpha_s \sin\phi - \sin\delta}{\cos\alpha_s \cos\phi} \right| \quad \text{(eq. 6)}$$

where δ is the solar declination angle, ω_s is the hour angle, n_d is the day of the year, ϕ is the latitude angle, α_s is the solar altitude, and γ_s is solar azimuth angle. Note that all angles are in radians.

2.3 Optical efficiency of the heliostat field

The total optical efficiency as defined by (Collado and Guallar, 2012) is

$$\eta_{opt}(x,y,t) = \rho \cos\omega(x,y,t) f_{at}(x,y) f_{sb}(x,y,t) f_{itc}(x,y,t) \quad \text{(eq. 7)}$$

where ρ is the reflectance of the heliostats, $\cos\omega$ is the incidence cosine between the incident sun ray and the normal to the heliostat surface, f_{sb} is the shadowing and blocking factor, f_{itc} is the intercept factor accounting for the fraction of the reflected rays intercepted by the receiver, and f_{at} is the atmospheric attenuation efficiency. Furthermore, x, y, and t represent the co-ordinates and time, respectively. The detail modeling of these five parameters was demonstrated in our previous study (Atif and Al-Sulaiman, 2015).

Tab. 1: Basic design and operating parameters used for the heliostat field and the central receiver (Collado and Guallar, 2013; Collado, 2008; Ho and Iverson, 2014)

Tower optical height, *THT*	130 m
Heliostat height , *LH*	9.75m
Heliostat width, *LW*	12.3m
Extra security distance, *dsep*	3m
Receiver diameter (cylindrical), *DR*	9.44
Receiver size, *LR*	9.44
Fraction of mirror area of heliostat	0.9642
Total number of heliostats	2646
Mirror reflectance × cleanliness, ρ	0.88 × 0.95
Standard deviation of sunshape errors,	2.51 mrad
Standard deviation of tracking errors,	0.63 mrad
Standard deviation of beam quality errors	1.88 mrad
Emittance of the receiver surface, ε	0.85
Absorptance of the receiver surface, α_R	0.95

2.4 Optimization of the heliostat field

The differential evolution is a population based optimization technique, which is characterized by its simplicity, robustness, few control variables, and fast convergence (Abido and Al-Ali, 2009). Because the DE technique is an evolutionary algorithm, it is suited for non-linear and non-differentiable optimization problems as well.

The strategy applied in this technique is to use the difference between randomly selected vectors to generate a new solution. For each solution in the original population, a trial solution is generated by performing the process of mutation, recombination, and selection operations. The old and new solutions are compared and the best solutions emerge in the next generation.

Furthermore, the DE in most instances as compared to the annealed Nelder and Mead approach, adaptive simulating annealing and the breeder genetic algorithm outperformed all of the aforementioned optimization techniques in terms of the required number of function evaluations necessary to locate a global optimum of the test functions (Storn and Price, 1997). Therefore, the DE was selected in this study.

The following equation is used for calculating the monthly averaged annual optical efficiency of the heliostat field:

$$\eta_{maa} = \frac{\sum_{j=1}^{12} \int_{t=sunrise}^{t=sunset} \eta_{opt} dt}{\sum_{j=1}^{12} \int_{t=sunrise}^{t=sunset} dt} \qquad \text{(eq. 8)}$$

where η_{maa} is monthly averaged annual heliostat field efficiency, the subscript *maa* denotes monthly annual averaged, and *j* denotes the average day of each month from January to December for the whole year as given in (Duffie and Beckman, 2013; Klein, 1977). This equation was used as the objective function for optimization.

2.5 Central receiver

The radiation heat losses, the convection heat losses and the optical losses were considered for the modeling of the central receiver as discussed next. The modeling of the central receiver was performed in EES. The equation for the radiation heat losses was given by (Sheu and Mitsos, 2013) as

$$Q_{rad} = F_{view} A_R \varepsilon \sigma T_R^4 \qquad \text{(eq. 9)}$$

where F_{view} is the radiation shape factor, A_R is the radiative area of the central receiver, ε is emissivity of the receiver, σ is the Stefan Boltzmann constant, and T_R is the receiver temperature.

The equation for convective heat losses from the central receiver is given as

$$Q_{conv} = A_R h_{conv} (T_R - T_{amb}) \qquad \text{(eq. 10)}$$

where h_{conv} is calculated by Bejan correlation for vertical chamber with natural convection and is defined as (Segal and Epstein, 1999)

$$h_{conv} = 0.557 \times 10^{-6} \left(\frac{T_R - T_{amb}}{H_t}\right)^{0.25} [\text{kW/ m}^2 - \text{K}] \qquad \text{(eq. 11)}$$

where H_t is the total height of the solar tower and T_{amb} is the ambient temperature.

where

$$Q_u = Q_{net} = \alpha_R Q_{in} - (Q_{rad} + Q_{conv}) \qquad \text{(eq. 12)}$$

$$Q_{in} = \eta_{opt} Q_{solar} \qquad \text{(eq. 13)}$$

$$Q_{solar} = I A_h \qquad \text{(eq. 14)}$$

Here, α_R is the absorptance of the receiver, I is the direct normal incident radiation, A_h is the total area of the heliostats, Q_u (or Q_{net}) is the net useful energy gained at the receiver, Q_{solar} is the total incident energy on the heliostat field, and Q_{in} is the net energy gained at the receiver.

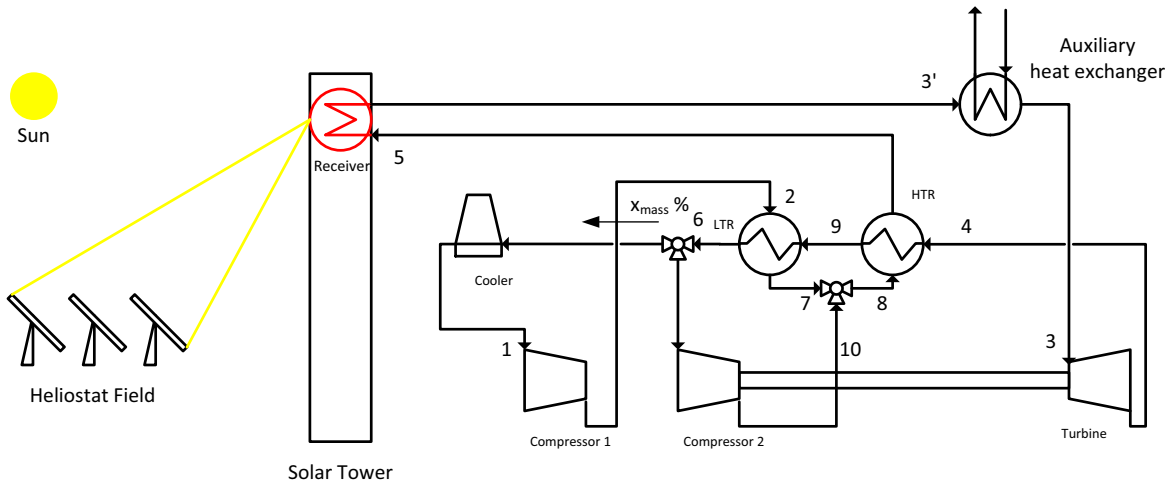

Fig. 1: Recompression closed loop supercritical carbon dioxide Brayton cycle with auxiliary heater

2.6 Closed loop sCO_2 recompression Brayton cycle

In a previous study by the authors (Al-Sulaiman and Atif, 2015), it was demonstrated that the recompression Brayton cycle demonstrated the highest thermal efficiency as compared to other Brayton cycles. Therefore, this cycle was selected for this study. In the recompression Brayton cycle (Figure 1), the flow is split into two streams after the low temperature regenerator and before passing through the cooler. These two streams are the one that flows to the main compressor through the cooler and the other one flows to the recompression compressor. Consequently, the system rejects less heat and the compressor work is reduced, which in turn causes the thermal efficiency to improve. The analysis of the Brayton cycle was also performed in EES and this code was integrated with the central receiver. The modeling of this cycle is presented as follows.

The power input of the first compressor is defined as

$$W_c = x_{mass}\dot{m}(h_2 - h_1) \quad \text{(eq. 15)}$$

where x_{mass} is the fraction of the mass flow rate through the first compressor, $\dot{m}$ is the mass flow rate of sCO_2, and h is the specific enthalpy.

The power input of the second compressor is defined as

$$W_{c2} = (1 - x_{mass})\dot{m}(h_{10} - h_6) \quad \text{(eq. 16)}$$

The useful energy gained at the receiver is defined as

$$Q_u = \dot{m}(h_3' - h_5) \quad \text{(eq. 17)}$$

The heat added by the auxiliary heater is defined as

$$Q_{aux} = \dot{m}(h_3 - h_3') \quad \text{(eq. 18)}$$

The turbine power can be defined as

$$W_T = \dot{m}(h_3 - h_4) \quad \text{(eq. 19)}$$

Tab. 3: Basic design and operating parameters used for the sCO_2 recompression Brayton cycle

Temperature at the inlet of compressor (first compressor)	31.25° C
Turbine inlet temperature T_3 (*TIT*)	570° C
Pressure at the inlet of the compressor (first compressor)	7.4 MPa
Pressure ratio	2.7
Mass flow rate $\dot{m}$	469.2 kg/s
High temperature regenerator effectiveness (Chacartegui et al., 2011)	0.85
Low temperature regenerator effectiveness	0.7
Isentropic efficiencies of the compressors (Chacartegui et al., 2011)	0.8
Isentropic efficiency of the turbine (Chacartegui et al., 2011)	0.9
Thermal efficiency of the cycle η_{th}	0.4517
Net power output by the cycle	40079 kW ≈ 40 MW

Applying the energy balance on the high temperature regenerator to obtain

$$h_4 - h_9 = h_5 - h_8 \quad \text{(eq. 20)}$$

Applying the energy balance on the low temperature regenerator to obtain

$$x_{mass}(h_7 - h_2) = h_9 - h_6 \quad \text{(eq. 21)}$$

The energy rejected at the cooler is defined as

$$Q_{out} = x_{mass}\dot{m}(h_6 - h_1) \quad \text{(eq. 22)}$$

The net power output of the cycle is defined as

$$W_{net} = W_T - W_C - W_{C2} \quad \text{(eq. 23)}$$

The thermal efficiency of the cycle is given by

$$\eta_{th} = \frac{W_{net}}{Q_u + Q_{aux}} \quad \text{(eq. 24)}$$

The fraction of fuel hybridization required to keep a constant power output is given by

$$f_{hybrid} = \frac{Q_{aux}}{Q_{solar} + Q_{aux}} \quad \text{(eq. 25)}$$

The input solar share is defined as

$$X_{solar} = \frac{Q_{solar}}{Q_{solar} + Q_{aux}} \quad \text{(eq. 26)}$$

3, Results and discussion

In this study, a complete thermodynamic analysis of the solar thermal tower system integrated with a closed loop sCO_2 recompression Brayton cycle was performed. This analysis was carried out for six different locations in Saudi Arabia taking into account each of the locations' direct normal irradiation. The target net power output was 40 MW and the analysis was carried out in accordance with this net power output. This net power output was made uniform and for this purpose an auxiliary heat source was added. This plant would be operational with the input solar energy and auxiliary heat source for daylight hours; nonetheless, for nighttime operation the plant would operate on auxiliary heat source. Detailed analysis of the input solar share and the auxiliary heat provided has also been performed. Table 1 lists the design parameters of the heliostat and the central receiver which were used in this study whereas the operating conditions of the recompression sCO_2 Brayton cycle are listed in Table 2. Finally, in Table 3 the details of the cities including the latitude and longitude with the annual heat collected at the central receiver is provided.

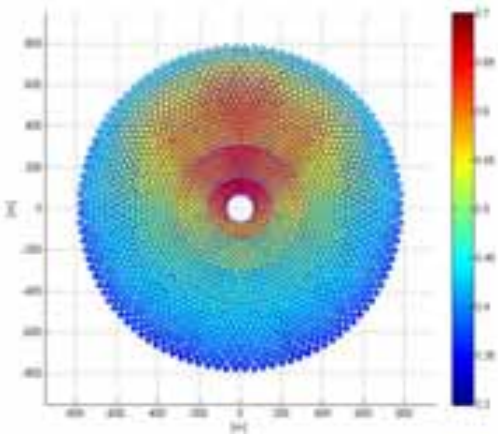

Fig. 2a Contours of the optical efficiency of the optimized heliostat field on annual basis for Tabouk, Saudi Arabia

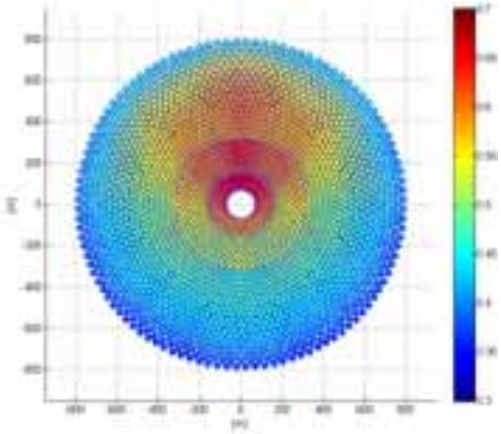

Fig. 2b: Contours of the optical efficiency of the optimized heliostat field on annual basis for Madinah, Saudi Arabia

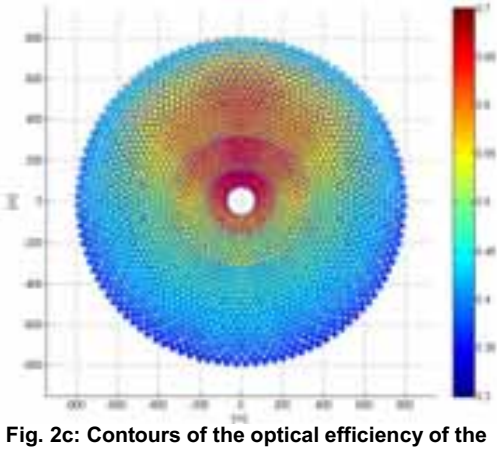

Fig. 2c: Contours of the optical efficiency of the optimized heliostat field on annual basis for Dhahran, Saudi Arabia

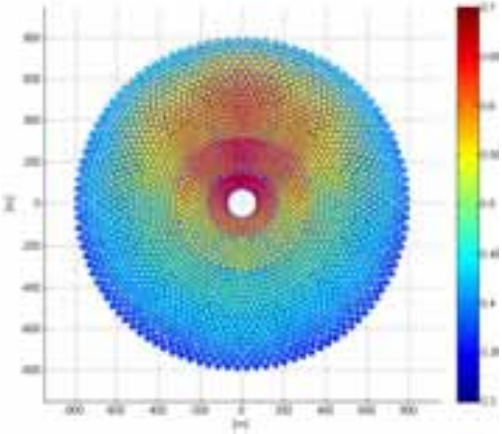

Fig. 2d: Contours of the optical efficiency of the optimized heliostat field on annual basis for Riyadh, Saudi Arabia

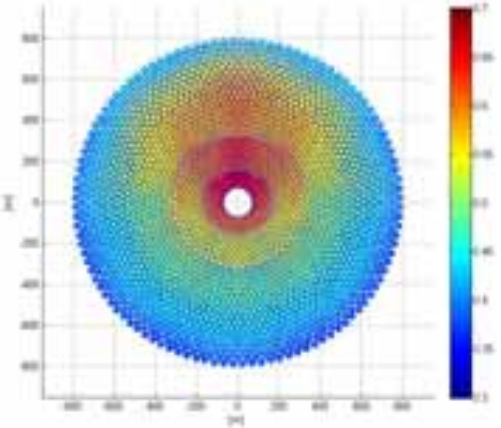

Fig. 2e: Contours of the optical efficiency of the optimized heliostat field on annual basis for Bishah, Saudi Arabia

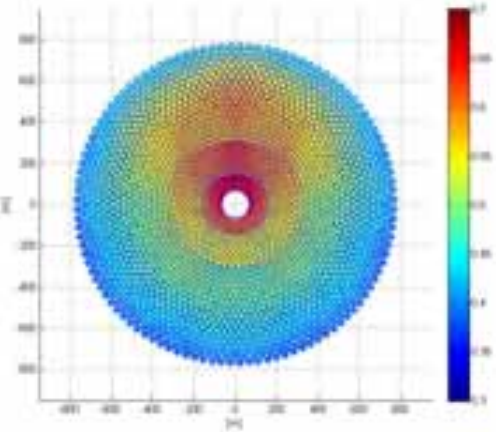

Fig. 2f: Contours of the optical efficiency of the optimized heliostat field on annual basis for Najran, Saudi Arabia

The solar resource data for each of the locations aforementioned was taken from a renewable energy resource website sponsored by NASA ("Surface meterology and Solar energy," n.d.). The data available on this website is averaged over a period of 22 years from 1983 until 2005. The averaged values over a month of direct normal irradiation are available there. A preliminary generated heliostat field was optimized on monthly averaged annual basis. Therefore, Equation 8 was used for the annual optimization for all the locations considered in this study. This code calculates all the necessary optical performance parameters of all the heliostats at every step of the optimization until the best layout of the generated heliostat field is found. The optimized heliostat fields for all of selected locations have been depicted in Figures 2a-2f.

As the data available on the aforementioned website was available on monthly basis, the average efficiencies of each month for all the locations were calculated after the heliostat fields were annually optimized. These efficiencies were used as an input to the EES code for the analysis of the receiver and recompression Brayton cycle. In this study; optical, convection heat, and radiation heat losses were taken into account, whereas the conduction heat losses were neglected from the receiver.

Figures 3a – 3f depicts bar graphs for the average heat collected for each month, for Tabouk, Madinah, Dhahran, Riyadh, Bishah, and Najran, respectively. Moreover, it can be observed that Madinah has the highest annual average heat collected in kWh/day (Table 3), whereas Tabouk has the second highest and Dhahran has the lowest. For Tabouk, Madinah, Dhahran, and Riyadh; the highest heat collected is in the month of June, whereas for Bishah and Najran it is not the case. Furthermore, it will be more preferable to install a plant where there are fewer fluctuations in the solar irradiation, such as Madinah (Figure 3b) and Bishah (Figure 3e). Such operating conditions will results in more stable operations. Therefore, the lifetime of the plant increases and its cost decreases.

A closed loop sCO_2 recompression Brayton cycle was integrated with the central receiver where the net heat collected was used as an input to the Brayton cycle. The modeling of the Brayton cycle was performed in such a way that heat gained at the receiver was used as an input value to the cycle rather than the turbine inlet temperature. Consequently, the temperature T_3' will not remain constant and will depend upon the irradiation of a particular location. Thus, the power output will not be uniform. To address this, an auxiliary heat exchanger was added before the turbine so that if the net heat gained at the receiver is low, extra heat will be added to keep the turbine inlet temperature constant and hence to keep the power output uniform. For this study, the turbine inlet temperature was fixed at 570° C and the net power output was fixed at 40MW. Figure 4 illustrate the percent hybridization required for all the cities during daylight hours. In other words, these bar graphs also show indirectly the amount of auxiliary heat required to keep a uniform power output in the daytime. From the figure, it can be observed that Madinah requires least amount of external fuel hybridization, i.e. only 5.82%, whereas Tabouk requires second least 6.34% and Najran requires third least i.e. 7.62%. During nighttime, the auxiliary boiler is working.

Tab. 3: Performance comparison of different locations of Saudi Arabia

City	Longitude	Latitude	Average annual heat collected at the central receiver (kWh/day)
Tabouk	36.5° E	28.5° N	933103
Madinah	39.5° E	24.5° N	938388
Dhahran	50.5° E	26.5° N	827420
Riyadh	46.5° E	24.5° N	855262
Bishah	42.5° E	20.5° N	882216
Najran	44.5° E	17.5° N	893359

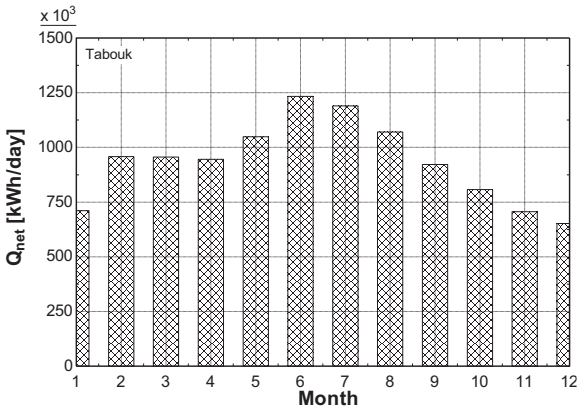

Fig. 3a: Average heat collected at the central receiver for Tabouk, Saudi Arabia

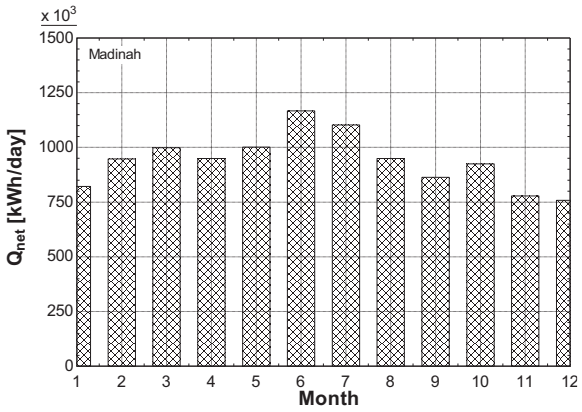

Fig. 3b: Average heat collected at the central receiver for Madinah, Saudi Arabia

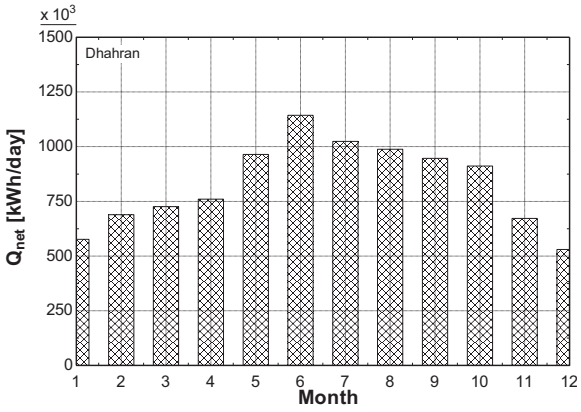

Fig. 3c: Average heat collected at the central receiver for Dhahran, Saudi Arabia.

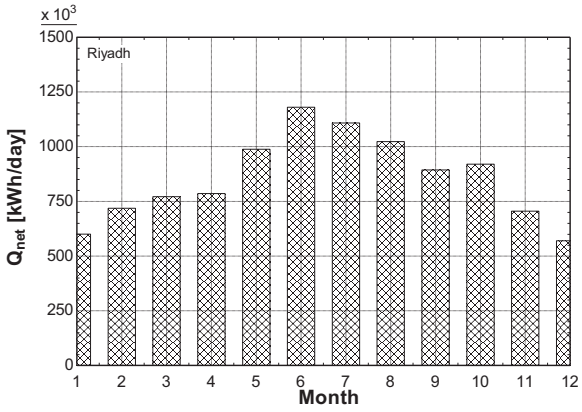

Fig. 3d: Average heat collected at the central receiver for Riyadh, Saudi Arabia.

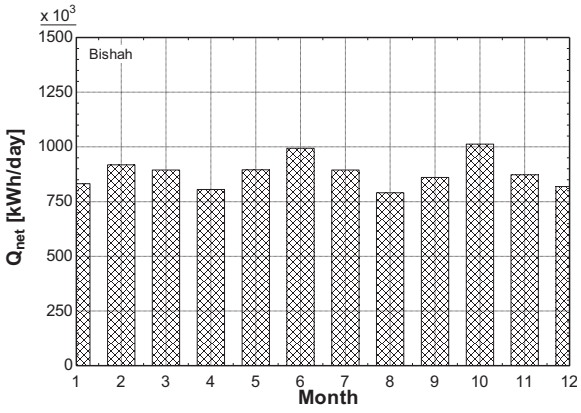

Fig. 3e: Average heat collected at the central receiver for Bishah, Saudi Arabia.

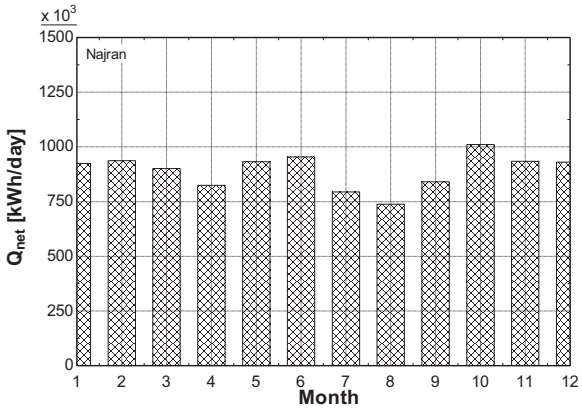

Fig. 3f: Average heat collected at the central receiver for Najran, Saudi Arabia.

4. Conclusions

A complete thermodynamic analysis of a solar thermal tower system when integrated with a sCO_2 recompression Brayton cycle was performed for six different locations in Saudi Arabia considering the local solar irradiation intensity for each location. The selected locations for the analysis were Tabouk (North), Madinah (West), Dhahran (East), Riyadh (Central), Bishah (South), and Najran (South). Heliostat fields were first generated and tested for their optical performance for these locations. The optical efficiencies of the generated heliostat fields were then optimized on annual basis considering all the optical performance parameters at every step of the optimization. A closed loop sCO_2 recompression Brayton cycle was then integrated with the central receiver where the heat is captured, which is reflected from the heliostat field. Furthermore, to keep the net power output uniform, an auxiliary heat exchanger was added before the expansion turbine. The findings indicated that the highest annual average heat collected was for Madinah (938,400 kWh/day) and the second highest was for Tabouk, (933,100 kWh/day). Similarly, the least amount of annual average fuel hybridization required was 5.82% for Madinah, and 6.34% for Tabouk during daytime.

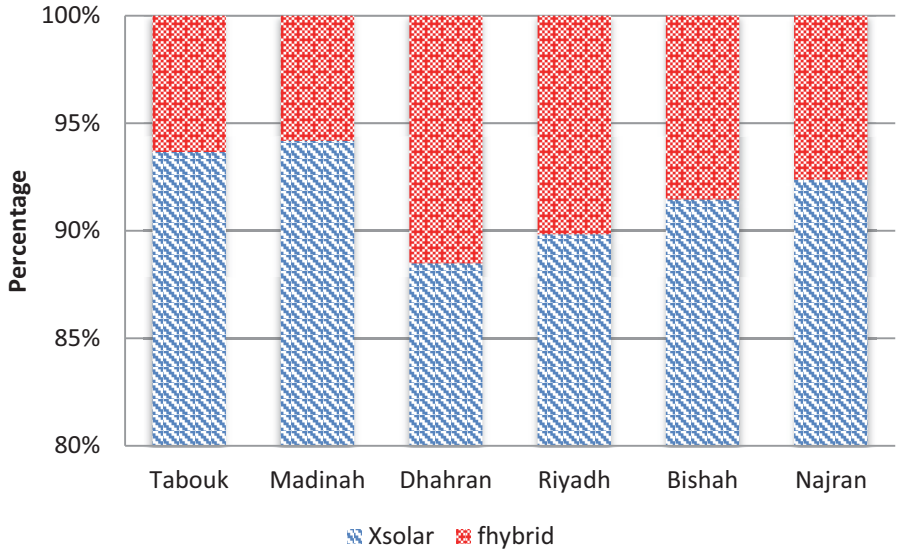

Fig. 4: Percentage of annual hybridization required for all of the locations considered.

Acknowledgement

The authors acknowledge the support of King Fahd University of Petroleum & Minerals (KFUPM), Dhahran, Saudi Arabia, for this work through project # SB121010.

References

Abido, M.A., Al-Ali, N.A., 2009. Multi-objective differential evolution for optimal power flow, in: 2009 International Conference on Power Engineering, Energy and Electrical Drives. IEEE, pp. 101–106. doi:10.1109/POWERENG.2009.4915212

Al-Sulaiman, F.A., Atif, M., 2015. Performance comparison of different supercritical carbon dioxide Brayton cycles integrated with a solar power tower. Energy 82, 61–71. doi:10.1016/j.energy.2014.12.070

Atif, M., Al-Sulaiman, F.A., 2015. Development of a mathematical model for optimizing a heliostat field layout using differential evolution method. Int. J. Energy Res. 39, 1241–1255. doi:10.1002/er.3325

Besarati, S.M., Yogi Goswami, D., 2014. A computationally efficient method for the design of the heliostat field for solar power tower plant. Renew. Energy 69, 226–232. doi:10.1016/j.renene.2014.03.043

Chacartegui, R., Muñoz de Escalona, J.M., Sánchez, D., Monje, B., Sánchez, T., 2011. Alternative cycles based on carbon dioxide for central receiver solar power plants. Appl. Therm. Eng. 31, 872–879. doi:10.1016/j.applthermaleng.2010.11.008

Collado, F.J., 2008. Quick evaluation of the annual heliostat field efficiency. Sol. Energy 82, 379–384. doi:10.1016/j.solener.2007.10.007

Collado, F.J., Guallar, J., 2013. A review of optimized design layouts for solar power tower plants with campo code. Renew. Sustain. Energy Rev. 20, 142–154. doi:10.1016/j.rser.2012.11.076

Collado, F.J., Guallar, J., 2012. Campo: Generation of regular heliostat fields. Renew. Energy 46, 49–59. doi:10.1016/j.renene.2012.03.011

Duffie, J.A., Beckman, W.A., 2013. Solar Engineering of Thermal Processes, Fourth Edi. ed. John Wiley & Sons, Inc., Hoboken, NJ, USA. doi:10.1002/9781118671603

Ho, C.K., Iverson, B.D., 2014. Review of high-temperature central receiver designs for concentrating solar power. Renew. Sustain. Energy Rev. 29, 835–846. doi:10.1016/j.rser.2013.08.099

IRENA, 2012. Renewable Power Generation Costs in 2012 : An Overview. Abu Dhabi, United Arab Emirates.

Iverson, B.D., Conboy, T.M., Pasch, J.J., Kruizenga, A.M., 2013. Supercritical CO2 Brayton cycles for solar-thermal energy. Appl. Energy 111, 957–970. doi:10.1016/j.apenergy.2013.06.020

Klein, S.A., 1977. Calculation of monthly average insolation on tilted surfaces. Sol. Energy 19, 325–329. doi:10.1016/0038-092X(77)90001-9

Le Moullec, Y., 2013. Conceptual study of a high efficiency coal-fired power plant with CO2 capture using a supercritical CO2 Brayton cycle. Energy 49, 32–46. doi:10.1016/j.energy.2012.10.022

Noone, C.J., Torrilhon, M., Mitsos, A., 2012. Heliostat field optimization: A new computationally efficient model and biomimetic layout. Sol. Energy 86, 792–803. doi:10.1016/j.solener.2011.12.007

Pitz-Paal, R., Botero, N.B., Steinfeld, A., 2011. Heliostat field layout optimization for high-temperature solar thermochemical processing. Sol. Energy 85, 334–343. doi:10.1016/j.solener.2010.11.018

Schmitz, M., Schwarzbözl, P., Buck, R., Pitz-Paal, R., 2006. Assessment of the potential improvement due to multiple apertures in central receiver systems with secondary concentrators. Sol. Energy 80, 111–120. doi:10.1016/j.solener.2005.02.012

Segal, A., Epstein, M., 1999. Comparative performances of `tower-top' and `tower-reflector' central solar receviers. Sol. Energy 65, 207–226. doi:10.1016/S0038-092X(98)00138-8

Sheu, E.J., Mitsos, A., 2013. Optimization of a hybrid solar-fossil fuel plant: Solar steam reforming of methane in a combined cycle. Energy 51, 193–202. doi:10.1016/j.energy.2013.01.027

Storn, R., Price, K., 1997. Differential Evolution – A Simple and Efficient Heuristic for global Optimization over Continuous Spaces. J. Glob. Optim. 11, 341–359. doi:10.1023/A:1008202821328

Surface meterology and Solar energy [WWW Document], n.d. URL https://eosweb.larc.nasa.gov/cgi-bin/sse/sse.cgi?skip@larc.nasa.gov

Wei, X., Lu, Z., Wang, Z., Yu, W., Zhang, H., Yao, Z., 2010a. A new method for the design of the heliostat field layout for solar tower power plant. Renew. Energy 35, 1970–1975. doi:10.1016/j.renene.2010.01.026

Wei, X., Lu, Z., Yu, W., Wang, Z., 2010b. A new code for the design and analysis of the heliostat field layout for power tower system. Sol. Energy 84, 685–690. doi:10.1016/j.solener.2010.01.020

Yao, Z., Wang, Z., Lu, Z., Wei, X., 2009. Modeling and simulation of the pioneer 1MW solar thermal central receiver system in China. Renew. Energy 34, 2437–2446. doi:10.1016/j.renene.2009.02.022

Conference Proceedings

Solar World Congress 2015
Daegu, Korea, 08 – 12 November 2015

The dynamic performance of different configurations of Solar Aided Power Generation (SAPG)

Jiyun Qin, Eric Hu, Graham J. Nathan

School of Mechanical Engineering, the University of Adelaide, Adelaide (Australia)

Abstract

Solar Aided Power Generation (SAPG) is defined as solar heat used to displace extraction steam to preheat the regenerative Rankine cycle (RRC) power plant's feedwater. In an SAPG plant, heat exchangers (termed as solar preheaters, SP) facilitate the heat exchange between solar heat and feedwater. Depending on the locations of the SPs in the power plant, an SAPG plant can have different configurations. In order to respond to solar variations, SAPG plants can be controlled using different approaches. The performance of SAPG plants with different configurations and controlled using a different approach has been compared by using real solar radiation data from Adelaide, Australia. Solar radiation data from two consecutive periods of five days during summer and winter were used for simulation. The results show that the performances of the SAPG plant with different configurations and approaches to control are different, and there is an optimum configuration and approach to control for the SAPG plant.

Keywords: *Solar Aided Power Generation, Plant configurations, Series configuration, Parallel configuration, Dynamic performance.*

1. Introduction

A Solar Aided Power Generation (SAPG) plant is a variant of the regenerative Rankine cycle (RRC) power plant. In an RRC power plant, steam is extracted from the steam turbine to preheat the feedwater in a feedwater heater (FWH). In an SAPG plant, solar thermal energy carried by the heat transfer fluid (HTF) is used to displace the heat of the extraction steam by preheating the feedwater. The displaced extraction steam can be expanded further to produce power. Compared with solar-only power plants, an SAPG plant has advantages of lower cost and higher solar to power efficiency (Hu et al., 2010).

In an SAPG plant, a heat exchanger (called a solar preheater, SP) is used to facilitate the heat exchange between the solar thermal energy and heat of the feedwater. The heat exchanger can be arranged in parallel or series with the FWHs. Most of previous studies about the SAPG plant are based on the configurations that the SP is in parallel with the FWHs of power plants (Yan et al., 2010; Yang et al., 2011; Peng et al., 2013, 2014a, 2014b; Hou et al., 2015). In contrast, some recent studies about the SAPG plant are based on the configuration that the SP is in series with the FWHs (Hou et al., 2013; Wu et al., 2015). Based on the steady state simulation, Yan et al. (2010) and Yang et al. (2011) found that more solar input leads to higher technical performance. Peng et al. (2013, 2014a, 2014b) assessed an SAPG plant by using daily solar radiation data from different seasons. It was found that the efficiency of the solar field is influenced by the variations in solar radiation. Hou et al. (2013, 2015) and Wu et al. (2015) evaluated SAPG plant performance by using annual solar radiation data. Hou et al. (2013) assessed an SAPG plant without any solar storage system while Wu et al. (2015) assessed an SAPG plant with a solar storage system. It is found that the performance of the SAPG plant is influenced by the solar radiation. However, these previous studies about the SAPG plant are based on the single configuration. The comparison between different configurations is

Selection and/or peer review under responsibility of Scientific Committee
doi:10.18086/swc.2015.04.17 Available at http://proceedings.ises.org

lack of study.

In order to respond to solar variability, the extraction steam of an SAPG plant can be controlled with different approaches. Hou et al. (2013, 2015) and Wu et al. (2015) evaluated the SAPG plant based on an assumption that feedwater outlet temperature of FWHs keeps unchanged. This means that all the extraction steam should be adjusted in response to solar resources. However, the SAPG plant can also be controlled with varying feedwater outlet temperature of FWHs. This means that the extraction steam can be adjusted in pre-set order to respond to solar resource variability. This may help to improve the performances of the SAPG plant.

Hou et al. (2013) evaluated SAPG performance by using real solar radiation data. The result showed that the performance of an SAPG plant is influenced by the solar radiation. However, the SAPG plant in the papers of Hou (2013) and Peng (2013, 2014a, 2014b) are based on the parallel configuration. It is necessary to compare the dynamic performance of four configurations controlled using different approaches under variations of solar radiation.

2. Concept description

Depending on the locations of Solar Preheaters, an SAPG plant can have four different configurations, termed as Parallel 1 (P1), Parallel 2 (P2), Series 1 (S1) and Series 2 (S2) configurations. Figures 1 to 4 shows the schematic diagram of P1, P2, S1 and S2 configurations, respectively. As shown in Fig. 1 and 2, in the P1 the P2 configurations the SP is parallel with the FWHs of the power plant. In the P1 configuration, each FWH has one parallel SP, while in the P2 configuration, all the high pressure FWHs or low pressure FWHs have one parallel SP. As shown in Fig. 3 and Fig. 4, in the S1 and the S2 configurations the SP is in series with the FWHs of the power plant. In the S1 configuration, the SP is located in series between FWH3 and DEA (deaerator) to displace the extraction steam before the extraction point at DEA (points A, B and C in Fig. 3), or is located in series between FWH8 and the condenser to displace the extraction steam after the extraction point at DEA (points D to H in Fig. 3). In the S2 configuration, the SP is located in series between the boiler and FWH1 to displace the extraction steam before the extraction point at DEA (points A, B and C in Fig. 4), or is located in series between DEA and FWH5 to displace the extraction steam after the extraction point at DEA (points D to H in Fig. 4). In the S1 configuration, the extraction steam is displaced from lower pressure extraction points to higher pressure extraction points; while in the S2 configuration, the extraction steam is displaced from higher pressure extraction points to lower pressure extraction points.

In order to respond to solar variability, the SAPG plant can be controlled with two typical approaches: (1) at a constant feedwater temperature exiting FWH (CT); or (2) at a varying feedwater temperature exiting FWH (VT). The CT approach means that the outlet temperature at each FWH is maintained as constant by adjusting the extraction steam flow rates at all designated displaced extraction points (i.e. points A to C or E to H in Figs. 1 to 4). The VT approach means that the extraction steam flow rate at the designated displaced extraction points (i.e. points A to C or E to H in Figs. 1 to 4) is displaced in pre-set order to respond to solar resource variability. In the VT approach, the two most typical pre-set orders are: (1) the extraction steam is displaced in order from higher pressure extraction point to lower pressure extraction point, which is termed as the HL-VT approach; or (2) the extraction steam is displaced in order from the lower pressure extraction point to the higher pressure extraction point, which is termed as the LH-VT approach. Different configurations can be controlled with different approaches in response to solar variability. Table 1 summarises the configurations and their possible control approaches.

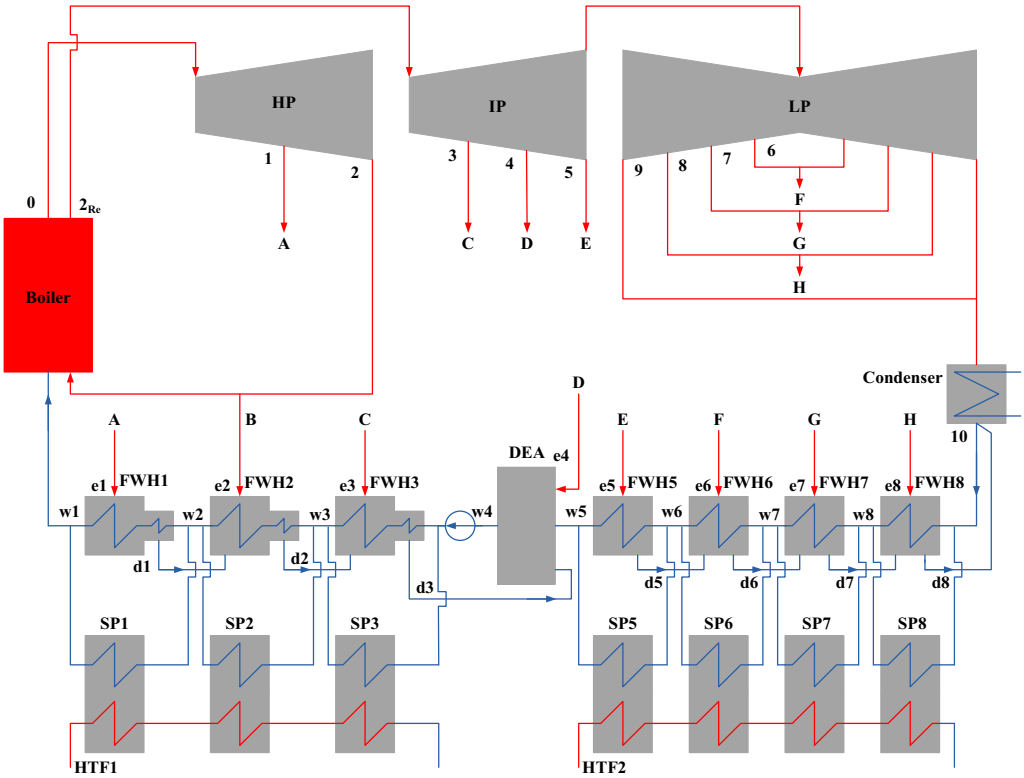

Fig. 1: Schematic diagram of a Parallel 1 (P1) SAPG plant, HTF 1 is used to displace the extraction steam at points A to C and HTF2 is used to displace the extraction steam at points E to H.

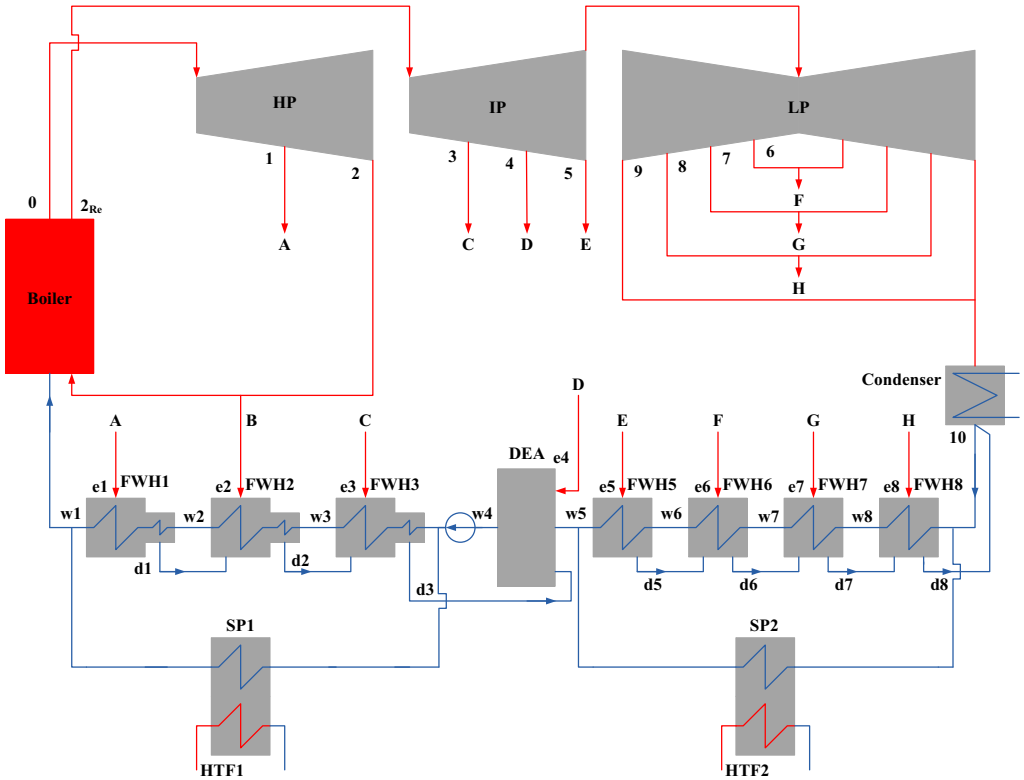

Fig. 2: Schematic diagram of a Parallel 2 (P2) SAPG plant, HTF 1 is used to displace the extraction steam at points A to C and HTF2 is used to displace the extraction steam at points E to H.

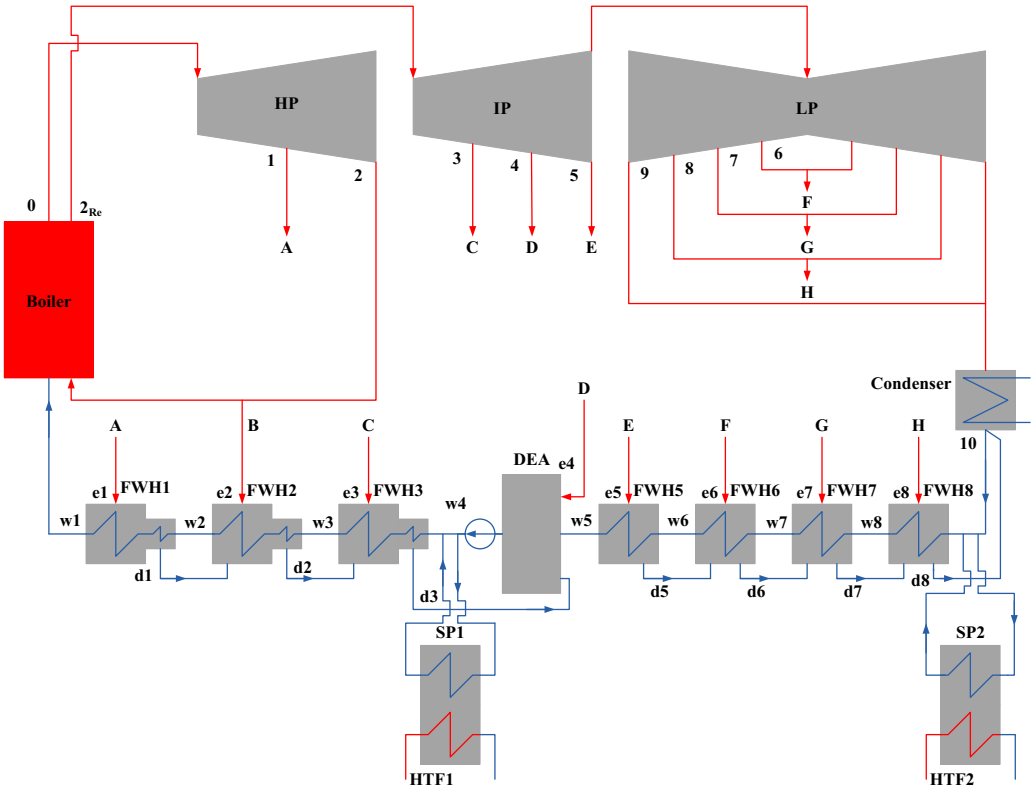

Fig. 3: Schematic diagram of a Series 1 (S1) SAPG plant, HTF 1 is used to displace the extraction steam at points A to C and HTF2 is used to displace the extraction steam at points E to H.

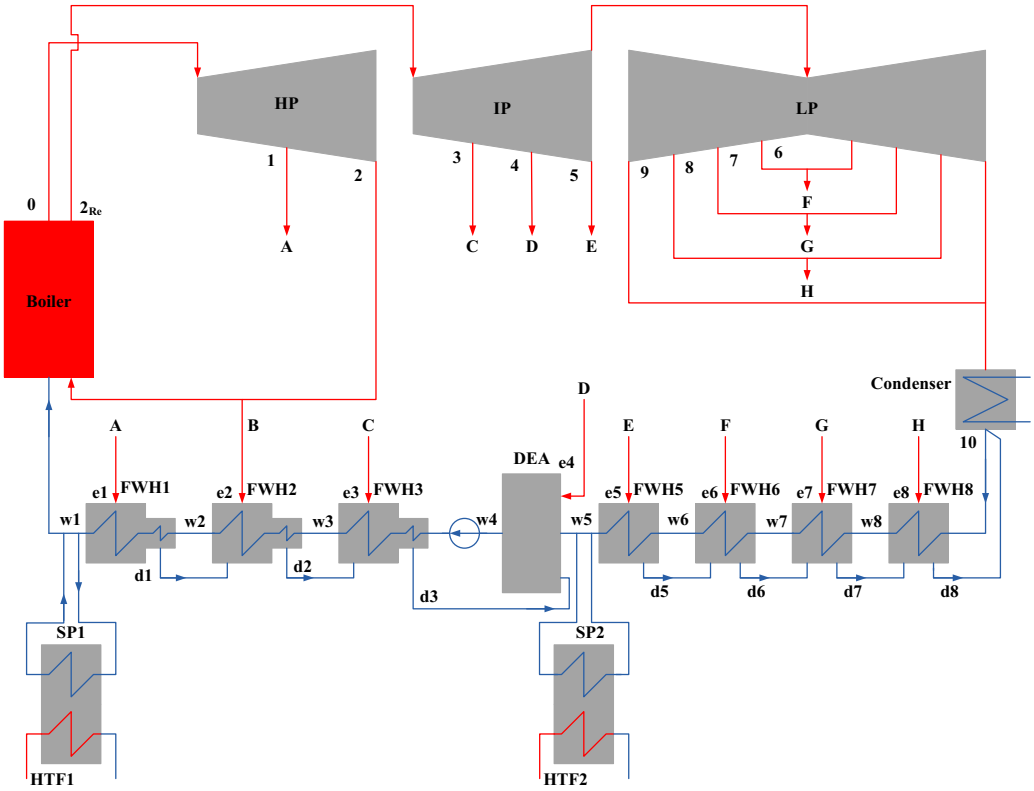

Fig. 4: Schematic diagram of a Series 2 (S2) SAPG plant, HTF 1 is used to displace the extraction steam at points A to C and HTF2 is used to displace the extraction steam at points E to H.

Table 1: Four configurations and their possible control approaches

Configuration	Locations of SPs	Control approach
Parallel 1 (P1)	Parallel with FWH	CT
Parallel 2 (P2)	Parallel with FWH	CT
		HL-VT
		LH-VT
Series 1 (S1)	Series with FWH	CT
Series 2 (S2)	Series with FWH	CT
		HL-VT

3. Methodology

3.1. Pseudo-dynamic model

In order to evaluate the performance of an SAPG plant under variable solar radiation, a pseudo-dynamic model has been developed. The pseudo-dynamic simulation models of four configurations are based on steady state simulation. The steady state simulation model is developed by using the matrix method of an SAPG plant (Hou et al., 2013). The pseudo-dynamic models simulate the technical performance of an SAPG plant at a series of time intervals. At each time interval, the SAPG plant is assumed to be operated at a steady state. A stable mass flow rate of HTF at a constant temperature in each time interval is input into the model.

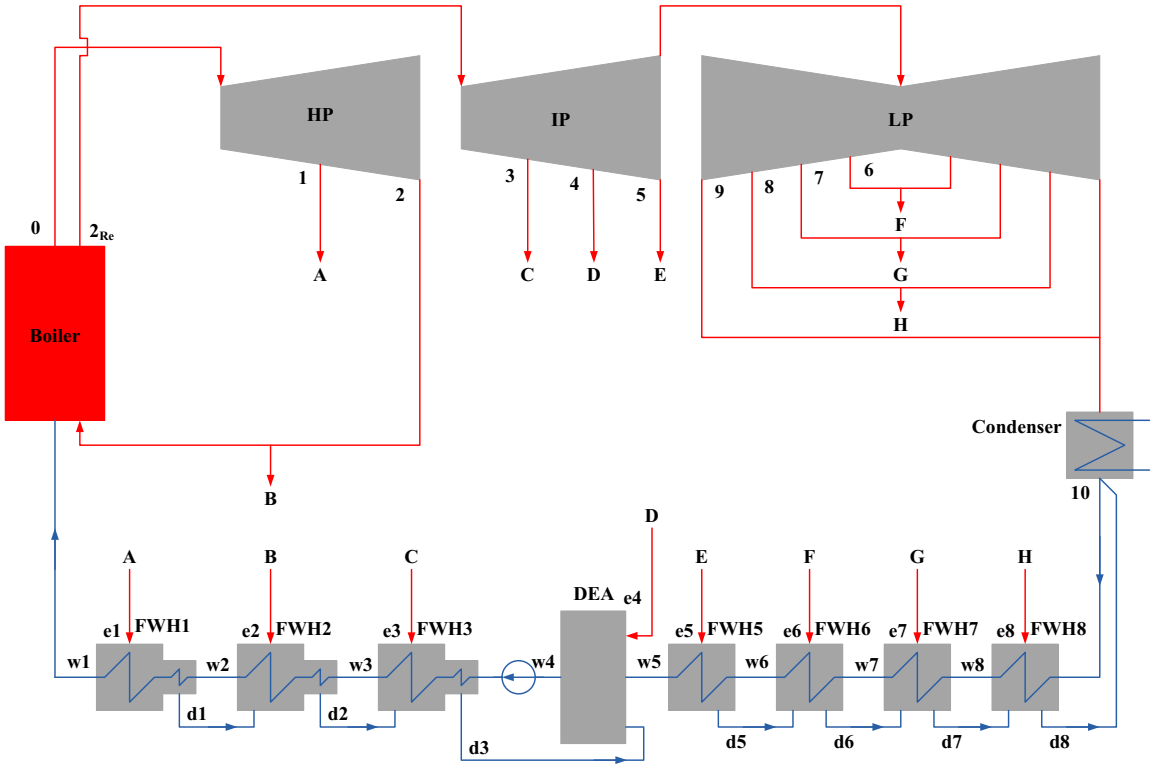

Fig. 5: Schematic diagram of a reference power plant used to demonstrate the matrix method; the power plant has seven closed FWHs and one deaerator (DEA).

Figure 5 shows a reference power plant used to demonstrate the matrix method. As shown, the reference power plant has seven closed FWHs and one deaerator which is an open FWH. In the matrix method, the

simulation is based on the heat and mass balance calculation of the FWH system. The heat and balance equation of the FWH system is given as,

$$\begin{pmatrix} q_1 & \cdots & \cdots & \cdots & \cdots & \cdots & \cdots & 0 \\ r_2 & q_2 & \ddots & \ddots & \ddots & \ddots & \ddots & \vdots \\ r_3 & r_3 & q_3 & \ddots & \ddots & \ddots & \ddots & \vdots \\ r_4 & r_4 & r_4 & q_4 & \ddots & \ddots & \ddots & \vdots \\ \tau_5 & \tau_5 & \tau_5 & \tau_5 & q_5 & \ddots & \ddots & \vdots \\ \tau_6 & \tau_6 & \tau_6 & \tau_6 & \tau_6 & q_6 & \ddots & \vdots \\ \tau_7 & \tau_7 & \tau_7 & \tau_7 & \tau_7 & \tau_7 & q_7 & \vdots \\ \tau_8 & \tau_8 & \tau_8 & \tau_8 & \tau_8 & \tau_8 & \tau_8 & q_8 \end{pmatrix} \cdot \begin{pmatrix} y_A \\ y_B \\ y_C \\ y_D \\ y_E \\ y_F \\ y_G \\ y_H \end{pmatrix} + \begin{pmatrix} \dot{Q}_{Solar,1}/\dot{m}_0 \\ \dot{Q}_{Solar,2}/\dot{m}_0 \\ \dot{Q}_{Solar,3}/\dot{m}_0 \\ 0 \\ \dot{Q}_{Solar,5}/\dot{m}_0 \\ \dot{Q}_{Solar,6}/\dot{m}_0 \\ \dot{Q}_{Solar,7}/\dot{m}_0 \\ \dot{Q}_{Solar,8}/\dot{m}_0 \end{pmatrix} = \begin{pmatrix} \tau_1 \\ \tau_2 \\ \tau_3 \\ \tau_4 \\ \tau_5 \\ \tau_6 \\ \tau_7 \\ \tau_8 \end{pmatrix} \quad \text{(eq.1)}$$

where q_i (kJ/kg) is the specific enthalpy decrease of extraction steam in the ith FWH; τ_i (kJ/kg) is the specific enthalpy increase of the feedwater in the ith FWH; and r_i (kJ/kg) is the specific enthalpy decrease of the drained steam from the (i-1)th FWH in the ith FWH. For the Closed FWHs (FWH 1 to 3 and 5 to 8 in Fig. 5) and the Open FWH (DEA in Fig. 5), the q_i, τ_i and r_i are described as follows:

Closed FWH: $q_i = h_{ei} - h_{di}; \tau_i = h_{fi} - h_{fi+1}; r_i = h_{di-1} - h_{di}$

Open FWH: $q_i = h_{e4} - h_{w5}; \tau_i = h_{w4} - h_{w5}; r_i = h_{d3} - h_{w5}$.

In Eq.1, $y_i (i = A\ to\ H)$ equals the $\dot{m}_i/\dot{m}_0$, and $\dot{m}_i$ (kg/s) is the mass flow rate of extraction steam at each extraction point, $\dot{m}_0$ (kg/s) is the mass flow rate of steam through the boiler (point 0 in Fig. 5).

In order to evaluate the performance of the four configurations of an SAPG plant, the solar power output, and solar power output per solar collector area are calculated.

- Solar power output (W_{Solar}, MW):

$$W_{Solar} = W_{Total} - W_{Ref}, \quad \text{(eq. 2)}$$

where W_{Total} (MW) is the total power output of the power plant after solar input (power boosting purpose), and W_{Ref} (MW) is the output of the power plant without solar input.

- Solar power output per solar collector area (kWh/m^2):

$$x_{Solar} = \frac{W_{Solar}\Delta t}{1000.\mathrm{A}_{Solar}}, \quad \text{(eq. 3)}$$

where W_{Solar} (MW) is the solar power output, A_{Solar} (m^2) is the solar collector area.

3.2. Solar resource

In the present paper, historical solar radiation data from 2010 for Adelaide (34ºS, 138ºC) were selected for the evaluation. The historical data were taken from the Australia Government Bureau of Meteorology (BOM, 2014). The solar radiation data for two consecutive five typical days in summer and winter were used for the simulation. Figure 6 and 7 show the hourly solar radiation of consecutive five typical days in summer and winter, respectively.

3.3. Case study

The power plant shown in Fig. 5 is used as case study for comparison. It is a 300MW sub-critical power plant and the solar heat is used to displace the extraction steam at points A to C. In order to displace the extraction steam, it is assumed there is a 10 ºC temperature difference between the feedwater temperature and HTF temperature, so the temperature of HTF from the solar field is at 280 ºC. The solar heat is assumed to be collected by the LS-2 parabolic trough solar collector. The area of each set of LS-2 solar collector is

235.5 m2 (Length 47.1 m, Width 5 m). It is assumed that 200, 300, 400 and 500 sets of LS-2 solar collectors are used to collect solar heat for feedwater preheating purposes. The simulation of the LS-2 solar field is based on the previous work of Zhou et al. (2015).

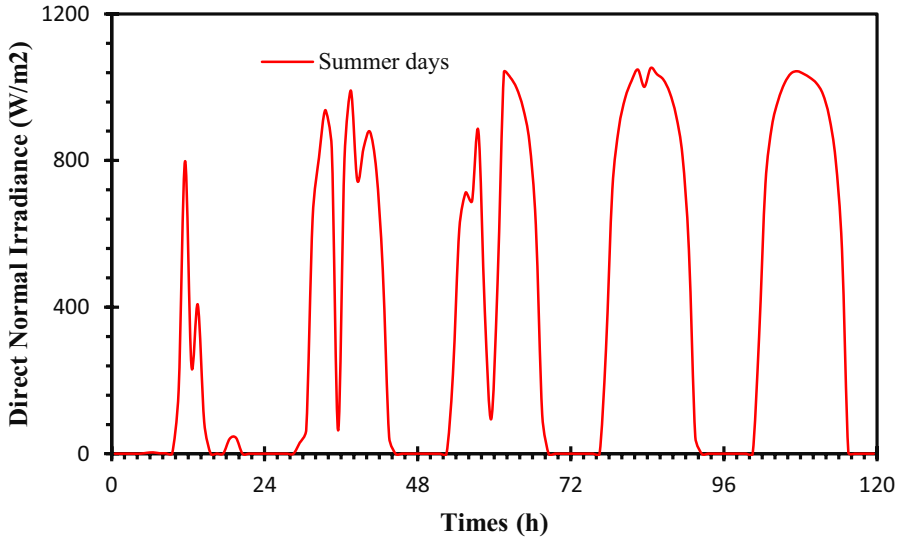

Fig. 6: Hourly Direct Normal Irradiance (W/m^2, DNI) on five consecutive typical days in summer for Adelaide.

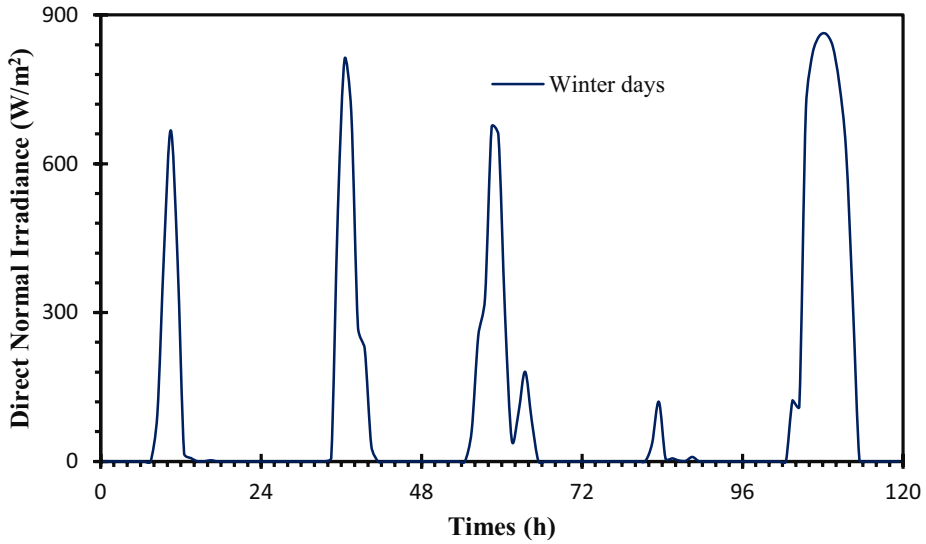

Fig. 7: Hourly Direct Normal Irradiance (W/m^2, DNI) on five consecutive typical days in winter for Adelaide.

4. Results

Figures 8 and 9 present the hourly solar power ouptut of SAPG plants with different configurations and controlled with different approaches on five consecutive typical days in summer and winter using 500 sets of parabolic trough solar collectors to produce the HTF. As shown in these figures, the P1 configuration and the P2 configuration both controlled in the CT approach have the same hourly solar power output. These two secnarios are the most common SAPG plants of previous works. It is also shown that the P1 configuration controlled in the LH-VT approach and the S1 configuration controlled in the CT approach also have the

same hourly solar power output. The results of Figures 8 to 9 also show that the P2 configuration controlled in the HL-VT approach has the highest hourly solar power output on the days both in summer and winter, and the P1 configuration controlled in the LH-VT approach and the S1 configuration controlled in the CT approach have the lowest hourly solar power output.

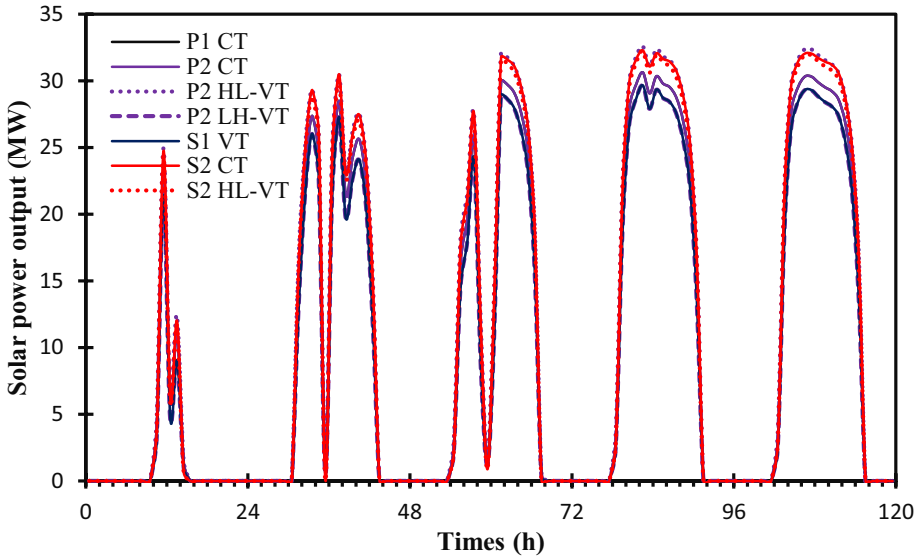

Fig. 8: Hourly solar power output of different configurations controlled with different approaches on five consecutive typical days in summer using 500 sets of parabolic trough solar collectors to produce HTF. P1 and P2 configurations both controlled in the CT approach is the most common SAPG plants of previous works.

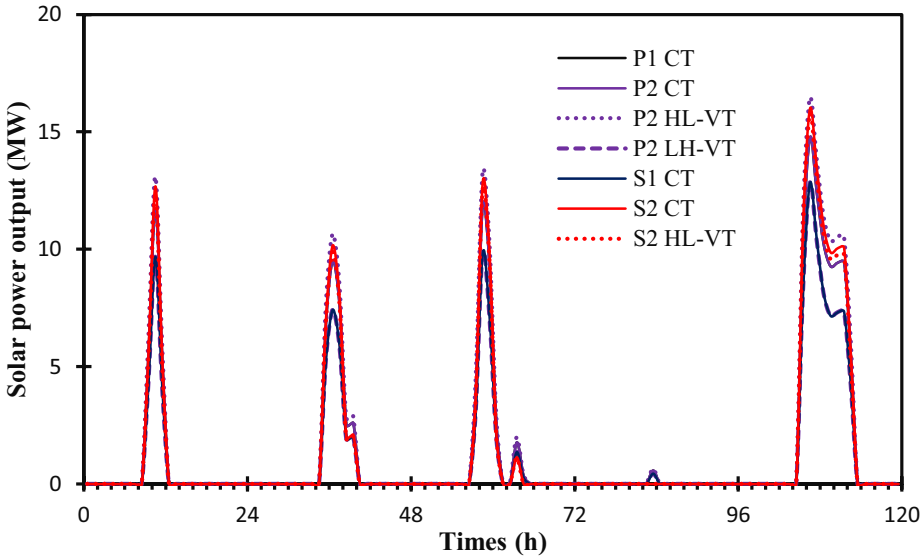

Fig. 9: Hourly solar power output of different configurations controlled with different approaches on five consecutive typical days in winter, using 500 sets of parabolic trough solar collectors to produce HTF. P1 and P2 configurations both controlled in the CT approach is the most common SAPG plants of previous works.

From Fig.8 to 9, it is also shown that the S2 configuration controlled in the CT and HL-VT approach have second and third best hourly solar power ouput. However, in the S2 configuration, the HTF temperature exiting the SP changes with variations in solar radiation. In other configurations, the HTF temperatures exiting the SPs remain constant at 180 ^{o}C, which is lower than in the S2 configuration. This means that the heat loss in the solar collectors of the S2 configuration is higher than the other configurations. Namely, the solar filed efficiency of the S2 configuration is lower than other configurations. Figure 10 and Figure 11

show the HTF temperature exiting the SP on five consecutive days in the summer and winter, respectively. It is shown that the S2 configuration controlled in the VT-HL appraoch have higher HTF temperature exiting SP than the S2 configuration controlled in the CT appraoch. This means that the heat loss in the solar collector of the S2 configuration controlled in the VT-HL appraoch is higher than the S2 configuration controlled in the CT appraoch.

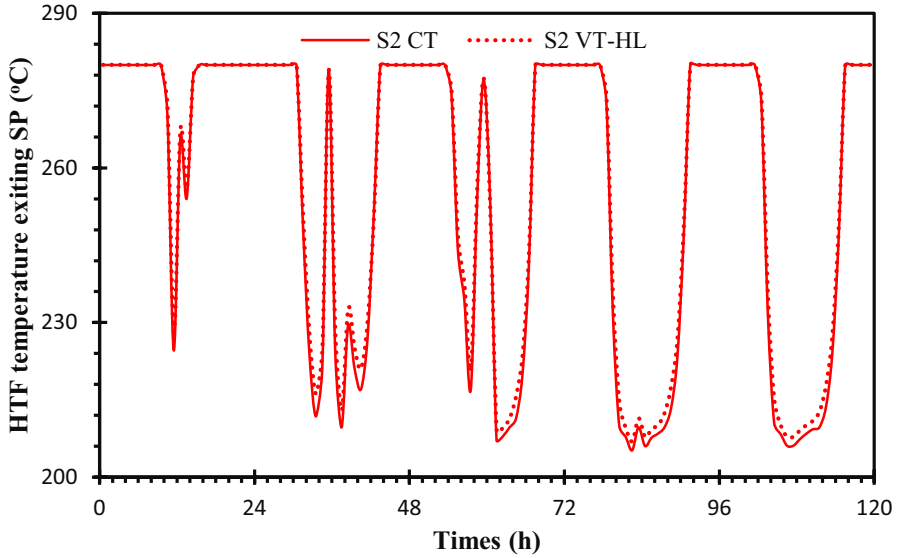

Fig. 10: HTF temperature exiting SP (ºC) for S2 configuration controlled in CT and HL-VT approach on five consecutive typical days in summer, using 500 sets of parabolic trough solar collectors to produce HTF.

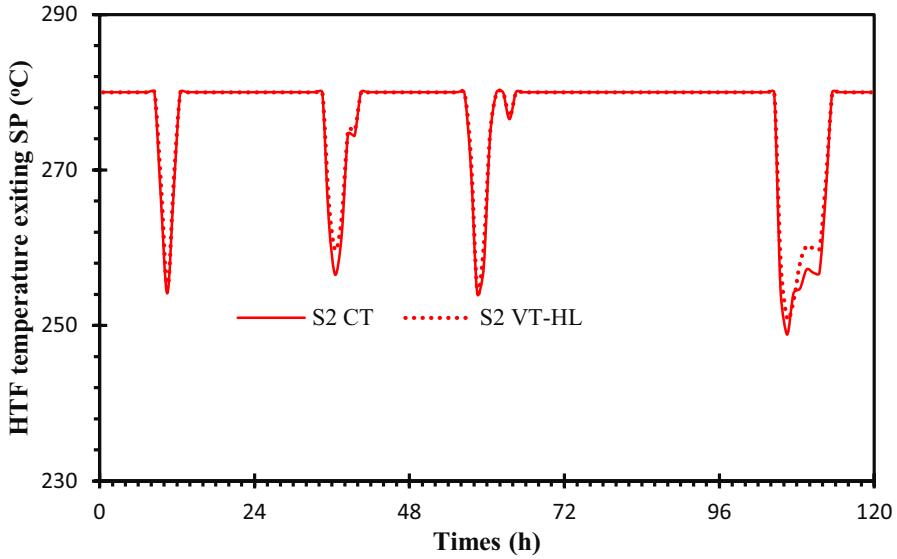

Fig. 11: HTF temperature exiting SP (ºC) for S2 configuration controlled in CT and HL-VT approach on five consecutive typical days in winter, using 500 sets of parabolic trough solar collectors to produce HTF.

Figures 12 to 13 present the daily solar power output per solar collector area (x_{Solar}) for the SAPG plant with different configurations on five consecutive typical days in summer and winter, respectively. It is shown in Figures 12 and 13 that the P2 configuration controlled in the HL-VT approach have the maximum x_{Solar} in both summer and winter days. This is caused by the highest hourly solar power output. From Figures 12 and 13, the results indicate that for the S1 consifugration controlled in the CT appraoch and P1 configuration controlled in the LH-VT approach, the x_{Solar} increases with the incremental solar collector area. The reason is thought to be cuased by the larger solar collector area means more solar thermal energy used for

displacement purpose, which means more high quality (higher pressure extraction steam) extraction steam is dispalced. In contrast, for the other cases, the x_{Solar} decreases with the incremental solar collector area.

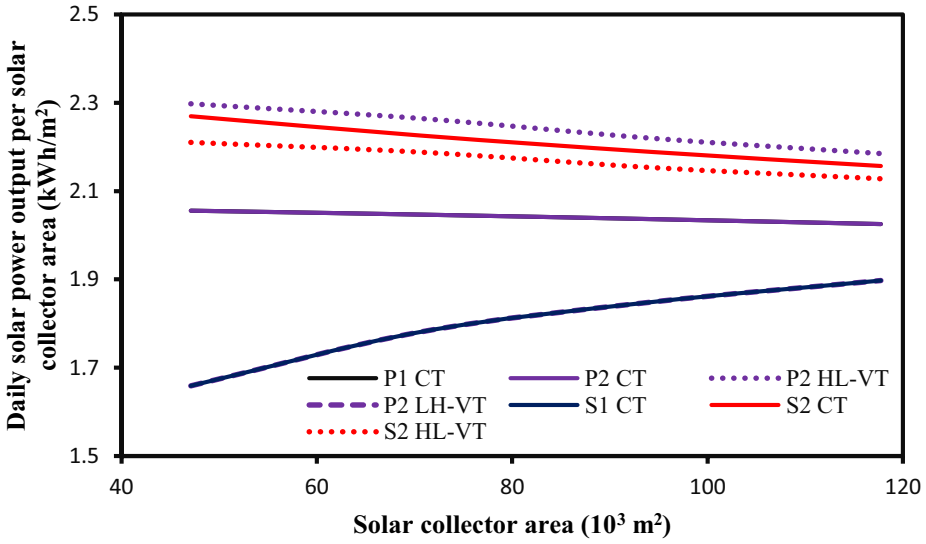

Fig. 12: Daily solar power output per solar collector area (x_{Solar}, kWh/m²) on five consecutive days in summer.

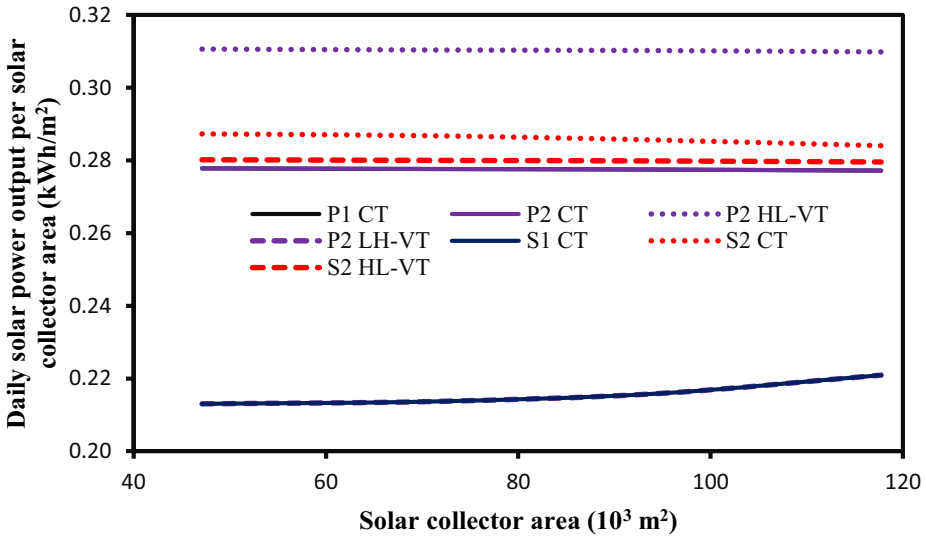

Fig. 13: Daily solar power output per solar collector area (x_{Solar}, kWh/m²) on five consecutive days in summer.

Tab. 4: Ratio of power output on five consecutive days in summer to that in winter

No. of collector sets	P1CT	P2CT	P2HL-VT	P2LH-VT	S1CT	S2CT	S2VT-HL
200	7.40	7.40	7.40	7.79	7.79	7.90	7.89
300	7.37	7.37	7.30	8.34	8.34	7.76	7.82
400	7.34	7.34	7.16	8.57	8.57	7.66	7.70
500	7.31	7.31	7.05	8.59	8.59	7.59	7.61

Table 4 presents the ratio of power output on five consecutive days in summer to that in winter ($W_{Solar}\Delta t_{Summer}/W_{Solar}\Delta t_{Winter}$). The higher $W_{Solar}\Delta t_{Summer}/W_{Solar}\Delta t_{Winter}$ means the higher impact of variations in solar radiation on SAPG's performance. It is shown that the P2 configuration controlled in the HL-VT appraoch has the lowest $W_{Solar}\Delta t_{Summer}/W_{Solar}\Delta t_{Winter}$. This means that variatios in solar radiation have the lowest impact on the performacne of P2 configuration controlled in the HL-VT approach. It is also shown that for the P2 configuration controlled in the LH-VT approach and S1 configuration, $W_{Solar}\Delta t_{Summer}/W_{Solar}\Delta t_{Winter}$ increases with the incremental solar collector area. In contrast, for other cases, $W_{Solar}\Delta t_{Summer}/W_{Solar}\Delta t_{Winter}$ decreases with the incremental solar collector area. This means that for the P2 configuration controlled in the LH-VT approach and S1 configuration, the impact of variatios in solar radiation on the SAPG's performance increases with the incremental solar collector area, while for other cases, the impact of variations in solar radiation decreases with the incremental solar collector area.

5. Conclusions

Pseudo-dynamic simulation models of four possible configurations of the SAPG plant, together with three alternative control strategies for the power boosting operation mode have been developed. The dynamic performances of different SAPG plants have been analysed using hourly solar radiation data in 5 consecutive summer and winter days in a location (Adelaide, Australia), respectively. The total solar power output of the SAPG plant and the daily solar power output per unit solar collector area ($\boldsymbol{x_{Solar}}$) were used as criteria to analyze the dynamic performance of SAPG plants with different configurations and control approaches. The results show that:

- the P2 configuration controlled in the HL-VT approach has the highest hourly solar power output, while the P2 configuration controlled in the LH-VT approach and the S1 configuration controlled in the CT approach have the lowest hourly solar power output in both winter and summer;
- For the S2 configuration, the HTF temperature exiting the SP is higher than other configurations. This indicates that the heat loss in the solar collectors of the S2 configuration is higher than the other configurations;
- The P2 configuration controlled in the HL-VT approach has the highest $\boldsymbol{x_{Solar}}$ in both summer and winter days;
- The variations in solar radiation have the lowest impact on the performance of P2 configuration controlled in the HL-VT approach while have the highest impact on the P1 configuration controlled in the LH-VT approach and the S1 configuration controlled in the CT approach;
- The P2 configuration controlled in the HL-VT approach is the best among the seven configurations and control approaches combinations in the selected location (Adelaide, Australia).

6. References

Australian Government Bureau of Meteorology (BOM), 2014. One minute solar data. http://reg.bom.gov.au/climate/reg/oneminsolar/.

Hu, E., Yang, Y.P., Nishimura, A., Yilmaz, F., Kouzani, A., 2010. Solar thermal aided power generation. Applied Energy. 87, 2881-2885.

Hou, H.J., Yu, Z.Y, Yang, Y.P., Chen, S., Luo, N., Wu, J.J., 2013. Performance evaluation of solar aided feedwater heating of coal-fired power generation (SAFHCPG) system under different operating conditions. 112, 710-718.

Hou, H.J., Wu, J.J., Yang, Y.P., Hu, E., Chen, S., 2015. Performance of a solar aided power plant in fuel saving mode. Applied Energy. http://dx.doi.org/10.1016/j.apenergy.2015.01.092.

Peng, S., Hong, H., Jin, H.G., Zhang, Z.N., 2013. A new rotatable-axis tracking solar parabolic-trough collector for solar-hybrid coal-fired power plants. Solar Energy. 98, 492-502.

Peng, S., Hong, H., Wang, Y.J., Wang, Z.G., Jin, H.G., 2014. Off-design thermodynamic performances on typical days of a 330 MW solar aided coal-fired power plant in China. Applied Energy. 130, 500-509.

Peng, S., Wang, Z.G., Hong, H., Xu, X., Jin, H.G., 2014. Exergy evaluation of a typical 330 MW solar-hybrid coal-fired power plant in China. Energy Conversion and Management. 85, 848-855.

Wu, J.J., Hou, H.J., Yang, Y.P., Hu, E., 2015. Annual performance of a solar aided coal-fired power generation system (SACPG) with various solar field areas and thermal energy storage capacity. Applied Energy. 157, 123-133.

Yan, Q., Yang, Y.P., Nishimura, A., Kouzani, A., Hu, E., 2010. Multi-point and Multi-level Solar Integration into a Conventional Coal-Fired Power Plant. Energy & Fuels. 24, 3733-3738.

Yang, Y.P., Yan, Q., Zhai, R.R., Kouzani, A., Hu, E., 2011. An efficient way to use medium-or-low temperature solar heat for power generation-integration into conventional power plant. Applied Thermal Engineering. 31, 157-162.

Zhou, L.Y., Li, Y.Y., Hu, E., Qin, J.Y., Yang, Y.P., 2015, Comparison in net solar efficiency between the use of concentrating and non-concentrating solar collectors in solar aided power generation systems. Applied Thermal Engineering. 75, 685-691.

Conference Proceedings

Solar World Congress 2015
Daegu, Korea, 08 – 12 November 2015

Concentrating or non-concentrating solar collectors for Solar Aided Power Generation?

Jiyun Qin, Eric Hu and Shengcao Yuan

School of Mechanical Engineering, the University of Adelaide, Adelaide (Australia)

Abstract

A hypothesis has been put forward that using non-concentrating solar collectors in a Solar Aided Power Generation (SAPG) plant might be a more efficient and economical option than using concentrating solar collectors. Few previous works on this topic have been carried out due to the perception that concentrating collectors produce higher temperature (solar) heat, thus higher solar thermal to power efficiency of the SAPG plant. However, other factors related to concentrating collectors, such as collecting only direct solar radiation, taking up more land area to install them, and higher capital and operation costs, have been overlooked. In this paper, a detailed comparison study between using concentrating or non-concentrating solar collectors in an SAPG plant have been undertaken. The results show that using non-concentrating solar collectors in an SAPG plant is superior in some cases.

Keywords: *Solar Aided Power Generation, Net solar efficiency, Concentrating solar collectors, non-concentrating solar collectors.*

1. Introduction

Due to the high capital costs of stand-alone solar power plants, integrating the solar thermal energy into a conventional fossil fired power plant attracts great interest nowadays. Solar Aided Power Generation (SAPG) is a method of integrating solar thermal energy carried by heat transfer fluid (HTF) into a conventional fossil fired power plant. In an SAPG plant, the HTF could be used to displace the extraction steam by preheating the feedwater to boiler at various temperature (and pressure) levels (Hu et al., 2010). The saved/displaced extraction steam by solar heat can expand further to generate power.

Generally, both concentrating solar collectors and non-concentrating solar collectors can be used in an SAPG plant. Since concentrating solar collectors can produce HTF at higher temperatures (200°C - 450°C), and non-concentrating solar collectors can produce HTF at lower temperatures (50°C - 200°C), concentrating solar collectors and non-concentrating solar collectors can be used to displace the extraction steam at different temperature levels. Yan et al. (2010) and Yang et al. (2011) found that displacing the extraction steam at higher temperature levels can produce more power output. Therefore, the previous works of Hou et al. (2013, 2015), Wu et al. (2015) and Peng (2013, 2014a, 2014b) evaluated the SAPG plant using concentrating solar collectors to displace the extraction steam at high temperature levels. However, the advantages of non-concentrating solar collectors could not be ignored. Concentrating solar collectors can only collect direct solar radiation (I_N). Nevertheless, non-concentrating solar collectors can absorb both direct solar radiation and diffuse solar radiation (I_D). Therefore, on a given piece of land, non-concentrating solar collectors may collect more solar heat than concentrating solar collectors. Zhou et al. (2015) compared using concentrating solar collectors and non-concentrating solar collectors in an SAPG plant by using the concept of Net Solar Efficiency. The net solar efficiency of an SAPG plant is defined as the power output from solar thermal energy in the SAPG plant divided by the total solar energy radiation falling on the land of the solar field. It was found that using non-

doi:10.18086/swc.2015.04.18 Available at http://proceedings.ises.org

concentrating solar collectors has advantages above using concentrating solar collectors from the net solar thermal point view. However, previous work of Zhou et al. (2015) has not considered the differences of capital and installation costs between concentrating and non-concentrating solar collectors. An economic comparison of using concentrating and non-concentrating solar collectors in an SAPG plant is needed.

2. Methodology

On a given piece of land, solar collectors with different layouts lead to different thermal outputs of the solar field. In this study, a solar field model has been developed that can calculate the solar annual useful heat output (from concentrating and non-concentrating fields) at different temperature levels under local weather conditions (for a given location). In the model, the annual output is the sum of annual hourly yields of the field and the layout of the solar fields including the shading factor between rows of the collectors has been considered. The outputs of the solar field model are fed into an SAPG plant simulation model developed in-house to calculate the solar power generation. In the study, a parabolic trough (PT) solar collector is used as the representative of concentrating solar collectors and the evacuated tube (ET) solar collector is used as the representative of non-concentrating solar collectors.

2.1. Parabolic trough solar collectors

The useful thermal energy produced by the PT solar collectors ($\dot{Q}_{useful,PT}$, kW) is calculated as:

$$\dot{Q}_{useful,PT} = \dot{Q}_{absorb,PT} - \dot{Q}_{loss,PT} \quad \text{(eq. 1)}$$

where $\dot{Q}_{absorb,PT}$ (W) is the solar energy absorbed by PT solar collectors and $\dot{Q}_{loss,PT}$ (W) is the heat loss of the solar field.

In Eq.1, the $\dot{Q}_{absorb,PT}$ is given as:

$$\dot{Q}_{absorb,PT} = \eta_{op,PT} I_N \cos\theta_{i,PT} K_{\theta,PT} \eta_{Row\ shading,PT} \eta_{end,loss} F_e A_{PT} \quad \text{(eq. 2)}$$

where $\eta_{op,PT}$ is the optical efficiency of the solar collector, I_N (W/m^2) is the Direct Normal Irradiance (DNI), $\theta_{i,PT}$ is the local solar radiation incidence angle, $K_{\theta,PT}$ is the incidence angle modifier of the solar collector, $\eta_{Row\ shading,PT}$ is the row shading of the solar collector, and $\eta_{end,loss}$ is the aperture area of the solar field. In Eq.2, each factor is calculated from previous work of Zhou et al. (2015).

The heat loss of the solar field in Eq. 1 can be divided into two parts. One is the heat loss of heat pipes $\dot{Q}_{loss,pipe,PT}$ (W) and the other is the heat loss of the PT solar collectors $\dot{Q}_{loss,collector,PT}$ (W). The heat loss is dependent on the solar collectors. In this study, LS-2 PT solar collectors are used as a case study. The $\dot{Q}_{loss,collector,PT}$ and $\dot{Q}_{loss,pipe,PT}$ of an LS-2 solar collector are given as:

$$\dot{Q}_{loss,collector,PT} = b_1 K_{\theta,PT} \dot{Q}_{absorb,PT} + (b_2 + b_3 \Delta T)\Delta T A_{PT}, \text{ (Dudley et al., 1994)} \quad \text{(eq. 3)}$$

where b_1 is 0.00007276, b_2 is 0.00496 (W/m^{2}K), b_3 is 0.00691 (W/m^{2}K^2) and ΔT is the temperature difference between the mean loop temperature of the solar collector and the ambient temperature.

$$\dot{Q}_{loss,pipe,PT} = (0.01693\Delta T - 0.0001683\Delta T^2 + 6.78 \times 10^{-7}\Delta T^3) A_{PT}. \text{ (Patnode, 2006)} \quad \text{(eq. 4)}$$

2.2. Evacuated tube solar collectors

The useful thermal energy produced by ET solar collectors is the product of the thermal efficiency of the ET solar collector and the solar radiation absorbed by the ET solar collector, which is given as:

$$\dot{Q}_{useful,ET} = \eta_{ET}\dot{Q}_{absorb,ET}, \quad \text{(eq. 5)}$$

where $\dot{Q}_{absorb,ET}$ (W) is the solar energy collected by the ET collectors and η_{ET} is the thermal efficiency of the ET solar collector.

Based on the experimental data, Budihardjo and Morrison (2009) found that the thermal efficiency of the ET solar collectors can be given as:

$$\eta_{ET} = 0.536 - 0.824\frac{\Delta T}{I_G} - 0.0069\frac{\Delta T^2}{I_G}, \quad \text{(eq. 6)}$$

where ΔT is the temperature difference between mean loop temperature and ambient temperature, and I_G (W/m2) is the global solar radiation.

In Eq. 5, the $\dot{Q}_{absorb,ET}$ is given as (Du et al., 2013):

$$\dot{Q}_{absorb,ET} = I_G\eta_{Row\ shading,ET}A_{ET}, \quad \text{(eq. 7)}$$

where $\eta_{Row\ shading,ET}$ is the row shading factor of the parallel row and A_{ET} is the area of the ET solar collectors.

For the ET solar collectors, global solar radiation falling on the collectors can be given as (Duffie et al., 2006),

$$I_G = I_D\frac{(1+\cos\beta)}{2} + I_N\cos\theta_{i,ET}, \quad \text{(eq. 8)}$$

where β is the tilt angle (the angle between the collector plane surface and the horizontal), $\theta_{i,ET}$ is the local solar radiation incidence angle, and I_D (W/m^2) and I_N (W/m^2) are solar diffuse radiation and direct radiation, respectively.

In Eq.8, the incidence angle of the ET solar collectors is given as (Duffie et al., 2006):

$$\cos\theta_{i,ET} = (\cos L\cos\beta + \sin L\sin\beta\cos A_{ZS})\cos\delta\cos\omega + \cos\delta\sin\omega\sin\beta\sin A_{ZS} + \sin\delta\,(\sin L\cos\beta - \cos L\sin\beta\cos A_{ZS}), \quad \text{(eq. 9)}$$

where Azs is Azimuth angle, L is the Latitude, ω is hour angle and σ is the solar declination angle.

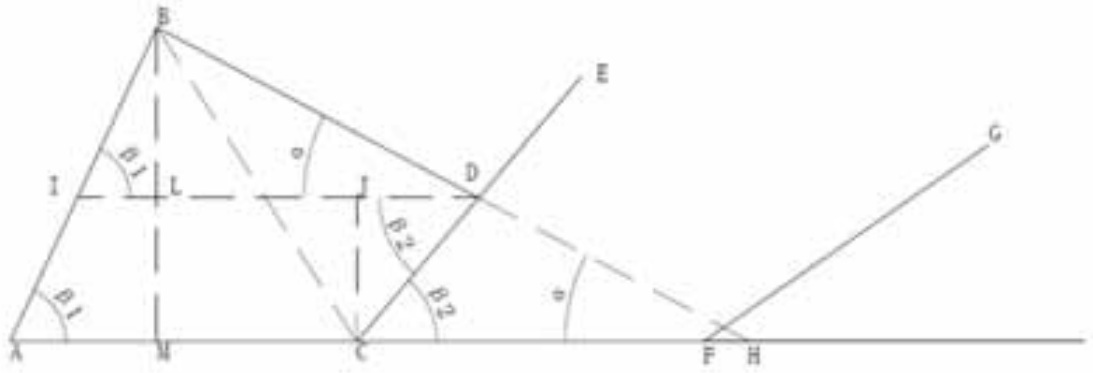

Fig. 1: Two dimensional drawing of the three rows' ET solar collectors.

In Eq.7, the row shading factor should be considered if ET solar collectors are installed in rows. Figure 1 presents a row shading analysis for three rows of ET collectors. For the first row of ET solar collectors, there

is no shading on the collectors. As a result, the shading factor for the first row of ET collectors can be ignored. For the second row of ET solar collectors, the shading factor can be given as:

$$\eta_{Row\ shading,ET,2} = 1 - \frac{CD}{CE}. \quad \text{(eq. 10)}$$

The CD can be given as:

$$CD = \frac{CJ}{\sin\beta_2} = \frac{ML}{\sin\beta_2} = \frac{BM-BL}{\sin\beta_2}. \quad \text{(eq. 11)}$$

In Eq.11,

$$BM = l\sin\beta_1. \quad \text{(eq. 12)}$$

$$BL = BD\sin\alpha. \quad \text{(eq. 13)}$$

where the length of the collector is l (m) and the altitude angle is α.

By using the trigonometric functions, Eq. 10 can be given as:

$$\eta_{Row\ shading,ET,2} = 1 - \frac{l\sin\beta_1 - \frac{\sqrt{l^2+d^2-2ld\cos\beta_1}.\sin\left(180^o - \cos^{-1}\frac{(\sqrt{l^2+d^2-2ld\cos\beta_1})^2+d^2-l^2}{2d\sqrt{l^2+d^2-2ld\cos\beta_1}} - \beta_2\right)}{\sin(\beta_2+\alpha)}\sin\alpha}{\frac{\sin\beta_2}{l}} \quad \text{(eq. 14)}$$

where the distance between two rows is d (m)

In the second row, for the N[th] row of ET solar collectors the shading factor can be given as:

$$\eta_{Row\ shading,ET,N} = 1 - \frac{l\sin\beta_{N-1} - \frac{\sqrt{l^2+d^2-2ld\cos\beta_{N-1}}.\sin\left(180^o - \cos^{-1}\frac{(\sqrt{l^2+d^2-2ld\cos\beta_{N-1}})^2+d^2-l^2}{2d\sqrt{l^2+d^2-2ld\cos\beta_{N-1}}} - \beta_N\right)}{\sin(\beta_N+\alpha)}\sin\alpha}{\frac{\sin\beta_N}{l}}$$

. (eq. 15)

As shown in Eq.14 and 15, the different tilt angle (β) of each row of ET solar collectors have different shading factors. By adjusting the tilt angel (β) of each row in Eq. 15, a minimum shading factor can be calculated. Then, by using the minimum shading factor of each row, the $\dot{Q}_{absorb,ET}$ is calculated by using the Eq. 7.

2.2. Net solar efficiency

On a given piece of land, solar collectors with different layouts lead to different thermal outputs of the solar field. Integration of different amounts of solar thermal energy with different temperature levels into an SAPG plant can also produce different power outputs. The net solar efficiency of an SAPG plant is defined as the power output produced by the solar energy divided by the total solar radiation falling on the given piece of land, which is given as (Zhou et al., 2015):

$$\eta_{Net} = \frac{W_{Solar}}{\dot{Q}_{Total,land}}. \quad \text{(eq. 16)}$$

where W_{Solar} (W) is the power output from the solar thermal energy in the SAPG plant and $\dot{Q}_{Total,land}$ (W) is the total solar radiation falling on the given piece of land.

3. Case study

In the present paper, both the ET and PT solar collectors were installed at three cities Quito (Ecuador, 0°N, 78°W), Reykjavik (Iceland, 64°N, 22°W) and Adelaide (Australia, 34°S, 138°E), respectively. On the given piece of land with same area, the solar thermal energy produced by the ET solar collectors are used to displace extraction steam with lower temperature levels (extraction steam to low pressure feedwater heater) and solar thermal energy produced by the PT solar collectors are used to displace extraction steam with higher temperature levels (extraction steam to high pressure feedwater heater), as shown in Fig.2 and Fig. 3.

In this study, it is assumed that the land area of 1,000 m^2 (length of 40 m, width of 25 m) is used to install the ET and PT solar collectors, respectively. For the ET solar collectors, the distance between each row of solar collectors is 8 m. For the PT solar collectors, the distance between each row of solar collectors is 10 m. Therefore, there are 8 rows ET solar collectors and 3 rows PT solar collectors installed in the land area. It is assumed that the size of each set of the ET solar collector is 10m×25m and the size of each set of the PT solar collector is 5m×40m (the width of the LS-2 PT solar collector is 5m). Therefore, on the given 1,000m^2 land, the area of the ET solar collector is 1,250 m^2 for the ET solar collector and 600m^2 for the PT solar collector. The parameters of ET and PT solar collectors on the given land are shown in Table 1.

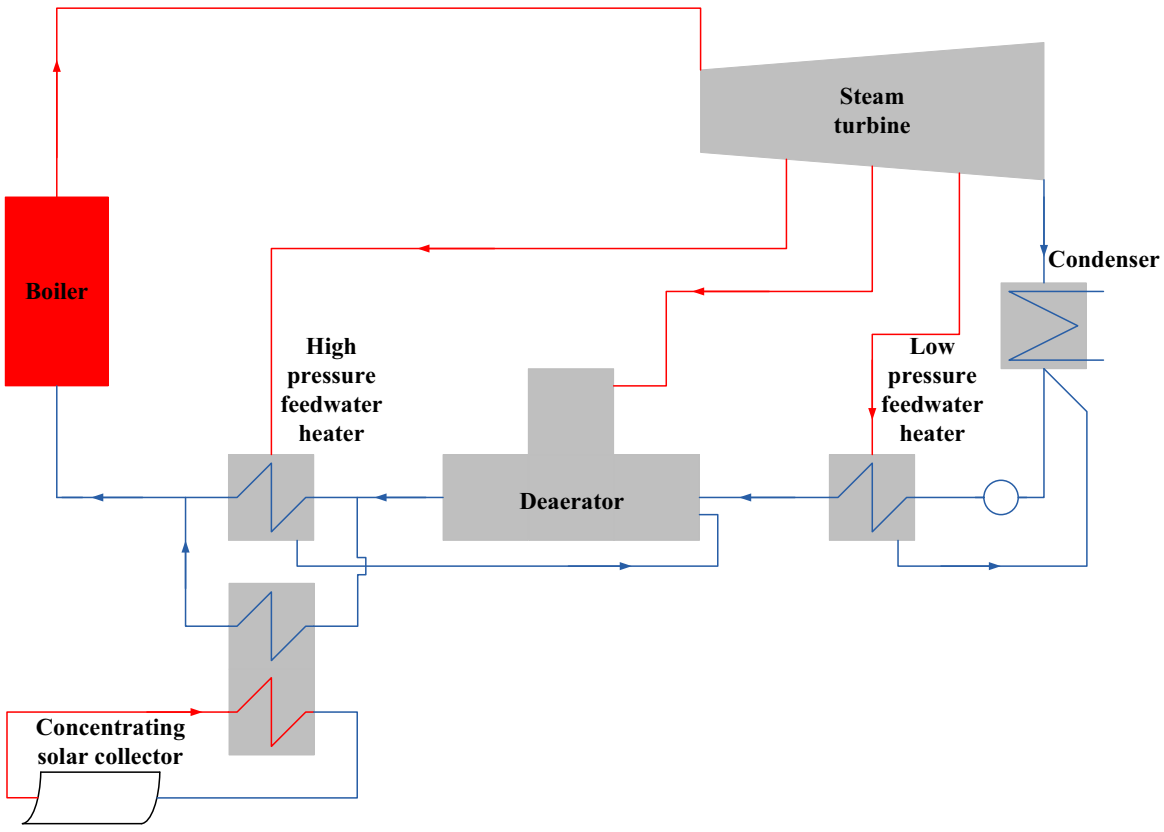

Fig. 2: Case studies of the concentrating solar collector (i.e. PT solar collector) integrated into an SAPG plant to displace the extraction steam to high pressure feedwater heater.

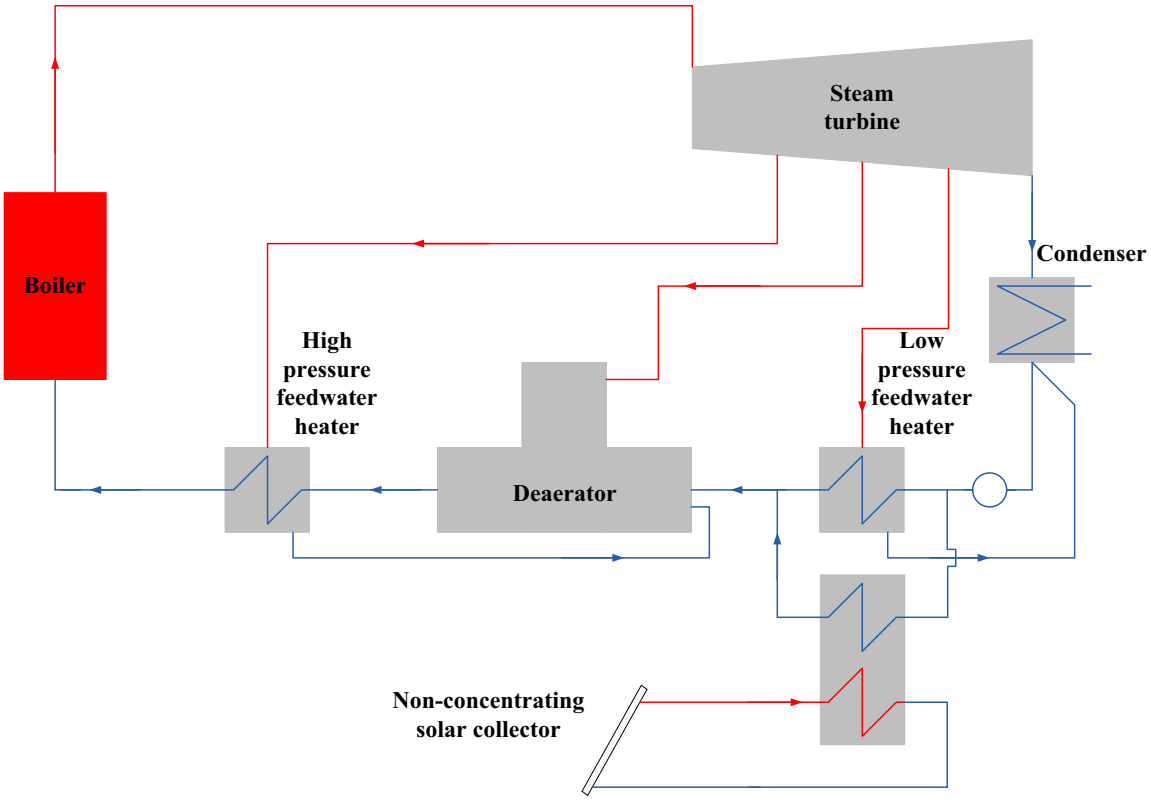

Fig. 2: Case studies of the non-concentrating solar collector (i.e. ET solar collector) integrated into an SAPG plant to displace the extraction steam to low pressure feedwater heater.

Tab. 1: Parameters of ET and PT solar collectors

Solar collector	Model	Total area (m^2)	Cost (AU$/$m^2$)
ET	VHP 30	1,250	255
PT	LS-2	600	651

It is also assumed that the solar thermal energy is integrated into 300 MW and 600 MW subcritical power plants based on the simulation results of Yan et al. (2011). Yan et al. (2011) pointed that the solar thermal to power efficiencies of displacement of high pressure extraction steam (Fig. 1) and low pressure extaction steam (Fig. 2) are 36% and 23% for a 300MW power plant and 41% and 24% for a 600 MW power plant. After the calculation of the useful thermal energy produced by the solar collectors, the solar power output can be calcualted by using the solar thermal to power efficiencies of the SAPG plant.

4. Results

Tab. 2: Annual useful thermal energy produced by evacuated tube (ET) and parabolic trough (PT) solar collectors

	Quito (Ecuador, 0°N, 78°W)	Adelaide (Australia, 34°S, 138°E)	Reykjavik (Iceland, 64°N, 22°W)
$Q_{Total,land}$ (MJ)	9,976,994	8,257,336	4,787,782
$Q_{useful,ET}$ (MJ)	4,963,798	4,012,944	2,530,093
$Q_{useful,PT}$ (MJ)	2,678,270	1,924,509	671,999

Table 2 presents the annual useful thermal energy produced by ET and PT solar collectors. $Q_{useful,ET}$ and

$Q_{useful,PT}$ are then can be integrated into the power plant for power generation purpose. The solar radiation is calculated based on the Bird Clean Sky Model (Bird et al., 1981).It was found that Quito has the highest annual solar radiation in three locations, and Reykjavik has the lowest annual solar radiation in three locations. It is also shown that annual useful thermal energy produced by the ET solar collectors is higher than that produced by the PT solar collectors in three locations. The reason is thought caused by the higher total solar collector area (Table 1) in the given land.

Tab. 3: Annual solar radiation in different locations calculated by the Bird Clean Sky Model

	Quito (Ecuador, 0°N, 78°W)	Adelaide (Australia, 34°S, 138°E)	Reykjavik (Iceland, 64°N, 22°W)
Annual DNI (kWh/m^2)	3451.4	3235.8	2520.2
Annual direct radiation (kWh/m^2)	2369.1	1921.7	1055.2
Annual diffuse radiation (kWh/m^2)	402.6	372.0	277.5

The results of Table 2 also show that for the ET solar collectors, the annual useful thermal energy produced in Quito is 1.24 times higher than in Adelaide and 1.96 times higher than in Reykjavik. However, for the PT solar collectors, the annual useful thermal energy produced in Quito is 1.39 times higher than in Adelaide and 3.98 times higher than in Reykjavik, which is higher than the ET solar collectors. The reason for this is thought to be that ET solar collectors can absorb both direct solar radiation and diffuse solar radiation, while PT solar collectors can only absorb direct solar radiation. The proportion of diffuse solar radiation in global solar radiation in Reykjavik and Adelaide are higher than Quito, which is shown in Table 3. Another reason is that the working area of ET solar collectors is higher than PT solar collectors on a given piece of land.

Tab. 4: Net solar efficiencies of evacuated tube (ET) and parabolic trough (PT) solar collectors

		Quito (Ecuador, 0°N, 78°W)	Adelaide (Australia, 34°S, 138°E)	Reykjavik (Iceland, 64°N, 22°W)
300MW	$\eta_{Net,ET}$	11.4%	11.2%	12.2%
	$\eta_{Net,PT}$	9.7%	8.4%	5.1%
600MW	$\eta_{Net,ET}$	11.9%	11.7%	12.7%
	$\eta_{Net,PT}$	11.0%	9.6%	5.8%

Table 4 shows the net solar efficiencies of ET and PT solar collectors in three locations. It is shown that the ET solar collector has higher net solar efficiencies than the PT solar collector. The reason for this is thought to be that on a given piece of land, the number of ET solar collectors can be arranged more than PT solar collectors. This means that the collector area of the ET solar collectors is higher than that of the PT solar collectors. It is also shown that the net solar efficiency of ET solar collector is highest in Reykjavik and the net solar efficiency of PT solar collector is highest in Quito. The reason is thought to be that Reykjavik is furthest from the equator in three locations and have highest proportion of diffuse radiation and Quito is closest to the equator in three locations and have highest proportion of direct radiation.

Tables 5 and 6 present the annual electricity production and cost of electricity (COE) of ET and PT solar collectors used in SAPG plants with 300MW and 600MW subcritical power plants, respectively. In present paper, the calculation of the COE only includes the cost of the solar collectors. The capital cost of the solar collectors is calculated by using the collector's cost in Table 1. From Tables 5 and 6, for both types of solar collectors, the COE increases with increasing the latitude of installed locations. When ET and PT solar collectors are installed on the same land area, the COE of ET solar collectors is lower than the COE of PT solar collectors, especially in places with higher latitude. Moreover, the advantage of ET solar collectors in cost is more obvious when the latitude is increasing. In other words, if the installed location of the solar collectors is further from the equator, the COE of ET solar collectors is cheaper than the COE of PT solar collectors. The reason for this is thought to be that when the latitude is increasing, the proportion of direct solar radiation is decreasing and the proportion of diffuse solar radiation is increasing.

Tab. 5: Annual electricity production ($Q_{electricity}$) and cost of electricity (COE) of evacuated tube (ET) and parabolic trough (PT) solar collectors used in an SAPG plant with a 300 MW subcritical power plant

	Quito (Ecuador, 0°N, 78°W)	Adelaide (Australia, 34°S, 138°E)	Reykjavik (Iceland, 64°N, 22°W)
$Q_{electricity,ET}$ (kWh)	317,312	256,383	161,645
COE_{ET} (AUD/kWh)	0.05	0.08	0.10
$Q_{electricity,PT}$ (kWh)	267,827	192,450	67,200
COE_{PT} (AUD/kWh)	0.09	0.25	0.34

Tab. 6: Annual electricity production ($Q_{electricity}$) and cost of electricity (COE) of evacuated tube (ET) and parabolic trough (PT) solar collectors used in an SAPG plant with a 600 MW subcritical power plant

	Quito (Ecuador, 0°N, 78°W)	Adelaide (Australia, 34°S, 138°E)	Reykjavik (Iceland, 64°N, 22°W)
$Q_{electricity,ET}$ (kWh)	330,920	267,530	168,673
COE_{ET} (AUD/kWh)	0.05	0.08	0.10
$Q_{electricity,PT}$ (kWh)	305,025	219,180	76,533
COE_{PT} (AUD/kWh)	0.08	0.22	0.30

5. Conclusions

The net solar efficiencies and cost-performance of using concentrating (e.g. Parabolic trough) and non-concentrating (e.g. Evacuated tube) solar collectors into an SAPG plant have been compared by using the solar radiation data in three cities Quito (Ecuador, 0°N, 78°W), Reykjavik (Iceland, 64°N, 22°W) and Adelaide (Australia, 34°S, 138°E), respectively. It is found that,

- Although the thermal efficiency of parabolic trough (PT) solar collectors is higher than the thermal efficiency of evacuated tube (ET) solar collectors, the net solar efficiency of ET solar collectors is higher than the net solar efficiency of PT solar collectors.
- The net solar efficiency of ET solar collectors in Reykjavik is hightest, and the net solar efficiency of PT solar collectors in Quito is hightest.
- The cost of electricity (COE) of using ET solar collectors is lower than the COE of using PT solar collectors.

In conclusion, on a given land with the same area, non-concentrating solar collectors (e.g. ET solar collectors) are superior to concentrating solar collectors (e.g. PT solar collectors) in both technical and economical terms.

6. References

Bird, R. E., and R. L. Hulstrom, 1981, Simplified Clear Sky Model for Direct and Diffuse Insolation on Horizontal Surfaces, Technical Report No. SERI/TR-642-761, Solar Energy Research Institute.

Budihardjo, I., Morrison, G., 2009. Performance of water-in-glass evacuated tube solar water heaters, Solar Energy. 83, 49-56.

Dudley, V.E., Kolb, G.J., Mahoney, A.R., Mancini, T.R., 1994. Test result: SEGS LS-2 solar collector, National Laboratories.

Duffie, J. A., Beckman, W.A., 2006. Solar Engineering of Thermal Processes, Forth ed. Wiley, New Jersey.

Du, B., Hu, E., Kolhe, M., 2013. An experimental platform for heat pipe solar collector testing, Renewable and Sustainable Energy Reviews, 17, 199-125.

Hu, E., Yang, Y.P., Nishimura, A., Yilmaz, F., Kouzani, A., 2010. Solar thermal aided power generation. Applied Energy. 87, 2881-2885.

Hou, H.J., Yu, Z.Y, Yang, Y.P., Chen, S., Luo, N., Wu, J.J., 2013. Performance evaluation of solar aided feedwater heating of coal-fired power generation (SAFHCPG) system under different operating conditions. 112, 710-718.

Hou, H.J., Wu, J.J., Yang, Y.P., Hu, E., Chen, S., 2015. Performance of a solar aided power plant in fuel saving mode. Applied Energy.

Patnode, A. M., 2006. Simulation and performance Evaluation of Parabolic trough solar power plant. University of Wisconsin-Madison.

Peng, S., Hong, H., Jin, H.G., Zhang, Z.N., 2013. A new rotatable-axis tracking solar parabolic-trough collector for solar-hybrid coal-fired power plants. Solar Energy. 98, 492-502.

Peng, S., Hong, H., Wang, Y.J., Wang, Z.G., Jin, H.G., 2014. Off-design thermodynamic performances on typical days of a 330 MW solar aided coal-fired power plant in China. Applied Energy. 130, 500-509.

Peng, S., Wang, Z.G., Hong, H., Xu, X., Jin, H.G., 2014. Exergy evaluation of a typical 330 MW solar-hybrid coal-fired power plant in China. Energy Conversion and Management. 85, 848-855.

Wu, J.J., Hou, H.J., Yang, Y.P., Hu, E., 2015. Annual performance of a solar aided coal-fired power generation system (SACPG) with various solar field areas and thermal energy storage capacity. Applied Energy. 157, 123-133.

Yan, Q., Yang, Y.P., Nishimura, A., Kouzani, A., Hu, E., 2010. Multi-point and Multi-level Solar Integration into a Conventional Coal-Fired Power Plant. Energy & Fuels. 24, 3733-3738.

Yan, Q., Hu, E., Yang, Y.P., Zhai, R.R, 2011. Evaluation of solar aided thermal power generation with various power plants. Int. J. Energy. 35, 909-922.

Yang, Y.P., Yan, Q., Zhai, R.R., Kouzani, A., Hu, E., 2011. An efficient way to use medium-or-low temperature solar heat for power generation-integration into conventional power plant. Applied Thermal

Engineering. 31, 157-162.

Zhou, L.Y., Li, Y.Y., Hu, E., Qin, J.Y., Yang, Y.P., 2015, Comparison in net solar efficiency between the use of concentrating and non-concentrating solar collectors in solar aided power generation systems. Applied Thermal Engineering. 75, 685-691.

Development of a mathematical analysis model for solar updraft tower plant (SUTP) system

Young Jae Choi[1], Yong Jin Kim[1], Sub Lee Song [2] and Yoon Won Park [1]

[1] Department of Nuclear and Quantum Engineering, Korea Advanced Institute of Sceince and Technology 291 Daehak-ro, Yuseong-gu, Daejeon, Republic of Korea

[2] Sustainable Energy and Environment Convergence Education Team, Handong Global University, 558, Handong-ro, Heunghae-eup, Buk-gu, Pohang, Gyeongbuk, Republic of Korea

Abstract

In a solar updraft tower plant (SUTP) system, heated air by solar heat under the transparent collector rises up through the updraft tower. When wind passes by, the turbine generator under the tower produces electricity. New mathematical analysis model was developed with considerations about realistic physical pressure drops through the whole SUTP system. The new analysis model was validated by the experimental data of prototype plant in Manzanares, Spain. The new model was well corresponded with the experimental data.

Keywords: *Solar chimney, Manzanares prototype, SUTP*

1. Introduction

The use of fossil fuel caused significant climate changes like global warming. This situation makes the melt of glacier, sea water level rise. To solve these problems, renewable energy sources are emphasized these days like wind energy and solar energy. The solar updraft tower plant (SUTP) is considered as a promising alternatives among various renewable energy sources. Solar updraft tower system is an electricity generating system using updraft air flow generated by solar energy. The SUTP is composed of three components such as solar collector, updraft tower and power generators. The schematic diagram of SUTP is shown in Fig. 1. In the SUTP system, heated air under the transparent collector induces updraft air flow to the tower due to density difference between inside and outside of the chimney. Air turbine is located at bottom of solar tower to generate electricity using this highly accelerated air. In this system, air under transparent collector is heated up and density difference of air induces updraft air flow in tower located at center of collector. When heated air flow by solar collector rise up through the solar chimney, the turbine generator produce the electricity in the bottom of chimney. The SUTP would be effective in the area of the large amount of solar energy and wide geographical areas for sufficient air flow like the desert regions. Compared to conventional solar power generation, this system has several advantages, such as very simple structure and low maintenance cost.

The first solar chimney design was developed by J. Schlaich, and a pilot plant prototype was built in Manzanares, Spain, in 1981. The 50-kW prototype operated and produced electricity for 8 years, showing the feasibility of a solar chimney power plant. An experimental evaluation of the protytype and

doi:10.18086/swc.2015.04.19 Available at http://proceedings.ises.org

the preliminary test results of the prototype plant were reported by Haff et al. [1, 2]. These authors presented the basic principles of solar chimney power plants, such as the construction cost and large-scale plants. Bernardes et al. [3] developed an analytical and numerical model for a solar chimney power plant, and heat transfer under the collector was investigated using thermal ananlysis. A water storage system was established under the collector. Additionally, simulation calculations were compared with experimental results from the pilot plant in Manzanares. Pretorius et al. [4, 5] evaluated a numerical model for the performance of a large-scale solar chimney power plant. A computer simulation program was used to solve the governing equation and heat transfer equation. A comprehensive analysis of the solar chimney was conducted under various situations. A preliminary study examining the influence of several factors was conducted using a mathematical model. Two comprehensive studies from the Pretorious and Bernardes papers on heat transfer in the collector were summarized by Bernardes et al. [6]. Their paper compared the comprehensive governing equation for the collector and chimney. Additionally, the assumptions pertaining to the governing equations were compared with respect to continuity, momentum and the energy equation. The convective heat transfer schemes in the collector were compared under several situations. Zhou et al. [7] conducted a comprehensive review of solar chimney power plants, providing information on the description, physical process, experimental and theoretical study status, among others. Koonsrisuk et al. [8] developed a mathematical model of a solar chimney power plant and validated the result with an actual physical plant. They predicted the performance of a large-scale commercial solar chimney and found the optimum design for high power output. Guo et al. [9] predicted the annual performance of an SCPP in Sinkiang, China. The effect of the collector and chimney radii on the power output was estimated, and the potential annual power requirement of SCPPs in the Hami region was presented.

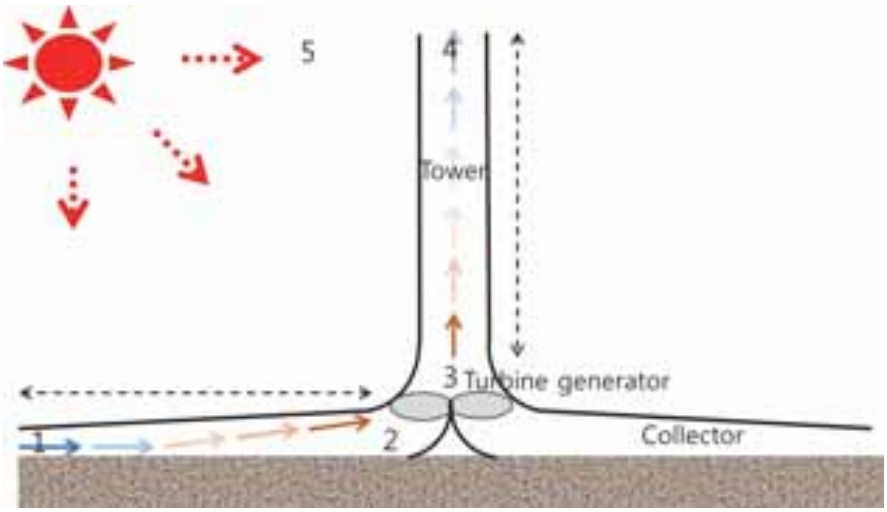

Fig. 1: Schematic diagram of SUTP

In this study, new mathematical analysis model was developed with considerations about realistic physical pressure drops through the whole SUTP system. The new analysis model was validated by the experimental data of prototype plant in Manzanares, Spain. Temperature rise of air through collector was calculated considering heat transfer of collector system, including absorption, reflection, and radiation. Pressure drop and mass flow rate was calculated through iteration process using MATLAB. The final output power can be predicted from pressure, density, temperate and pressure drop at each

point. All the essential parameters, such as temperature, pressure, density, and output power, were compared with the results of Manzanares pilot plant and were found to be in a good agreement.

2. Mathematical model development

2.1 Assumption

The new model is based on several assumptions: ideal gas law, steady state, radially one-dimensional flow under collector, the adiabatic tower wall. From these assumptions, the thermal analysis in the collector was conducted. The solar irradiation was the only heat source. The absorbed heat into the collector roof and the ground was assumed to transfer the heat into the air flow by convection heat transfer. The radiative heat emissions from the collector roof and the ground were also considered. The solar tower scale was selected to dimension of the pilot plant in Manzanares, Spain to validate the measured data with our developed mathematical model. But the roof height of collector was inclined to the tower center. Thus, inlet collector height is 1.2 m and height is increased linearly, so outlet collector height is 2.5 m.

Tab. 1: Dimensions of solar updraft tower plant

Tower height	194.6 m
Tower radius	5.08 m
Collector radius	122 m
Collector inlet height	1.2 m
Collector outlet height	2.5 m

In calculation of turbine pressure drop, the ratio of the pressure drop across the turbine to the total driving pressure was assumed to 2/3. Many researcher have assumed the optimum values of pressure ratio is 2/3. In this study, the pressure ratio across the turbine was optimized using our developed mathematical model.

2.2 Thermal analysis in the collector

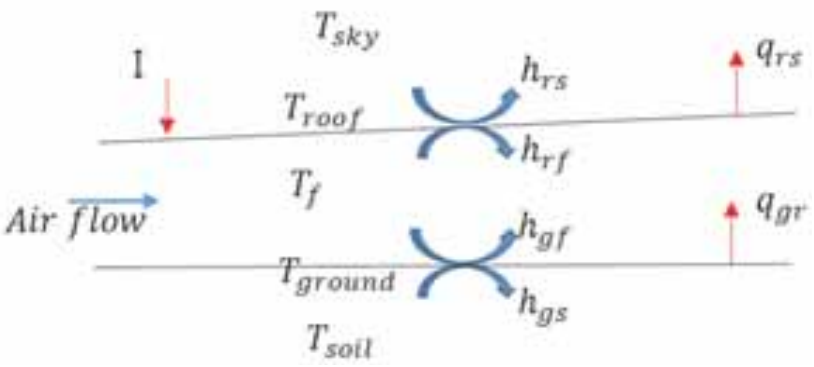

Fig. 2: Thermal analysis in the collector

The schematic diagram of heat transfer circuit in the collector is shown in Fig. 2. $\mathrm{h}_{rs}, \mathrm{h}_{rf}, \mathrm{h}_{gf}$ and h_{gs} is convective heat transfer coefficient and $\mathrm{q}_{rs}, \mathrm{q}_{gr}$ is radiative heat flux from roof to sky and from ground to roof. The solar irradiation heated the collector roof and ground, then the heated roof and ground transfer the heat the air flow in the collector. The heat transfer equation is following:

Roof: $\mathrm{I}\alpha_r + q_{gr} = h_{rs}(T_r - T_s) + h_{rf}(T_r - T_f) + q_{rs}$ (eq. 1)

Air: $h_{rf}(T_r - T_f) + h_{gf}(T_g - T_f) = \frac{\dot{m}C_p}{2\pi r}\frac{dT_f}{dr}$ (eq. 2)

Ground: $I\tau_r\alpha_g = h_{gf}(T_g - T_f) + h_{gs}(T_g - T_{soil}) + q_{gr}$ (eq. 3)

Left side of equation is incoming heat from the surrounding and right side of equation is output to surrounding. Equation (1),(2),(3) is thermal heat transfer equilibrium equation in roof, air and ground. I is the total solar irradiation on collector, τ_r is transmittance of roof and α_r and α_g are the absorption coefficient of the roof and ground. Temperature of sky is calculated by the ambient temperature. The temperature of soil was assumed constant at all area. The equation of radiative heat flux and heat transfer coefficient is following:

$q_{gr} = \frac{1}{\frac{1}{\varepsilon_g}+\frac{1}{\varepsilon_r}-1}\sigma(T_g^4 - T_r^4)$ (eq. 4)

$q_{rs} = \varepsilon_r\sigma(T_r^4 - T_{sky}^4)$ (eq. 5)

$h_{rs} = 3.87 + 0.0022\left(\frac{v_w\rho c_p}{\mathrm{Pr}^{\frac{2}{3}}}\right),\ (v_w: ambient\ air\ velocity)$ (eq. 6)

$h_{rf} = h_{gf} = 3.87 + 0.0022\left(\frac{v\rho c_p}{\mathrm{Pr}^{\frac{2}{3}}}\right),\ (v: collector\ air\ velocity)$ (eq. 7)

$h_{gs} = 2\sqrt{\frac{k\rho c_p}{\pi t}}$ (eq. 8)

When the collector roof temperature exceeds the ambient temperature and collector inside situation, equation (6) and (7) can be used. Equation (8) is ground heat transfer coefficient and t is second of time.

2.3 Pressure drop

The driving force for air flow in the SUTP system was designated by considering the density difference between inlet and outlet of the tower. It is described as (eq. 9). The pressure drops due to friction losses through the overall SUTP system would disturb the flow. Along the flow path of the SUTP system, friction losses and form losses on the tower were considered. The ratio of turbine pressure drop to total driving force was assumed to be 0.66. It is an optimized value for high power performance of turbine. Mass flow rate of the system was calculated by computing the iterative in-house MATLAB code.

Driving force=$\Delta P_{tot}=\int_0^{H_c}(\rho_{out}-\rho_{in})gdz$ (eq.9)

$\Delta P_{tur}=\Delta P_{tot}-\Delta P_{drop}$ (eq.10)

$\Delta P_{drop}=\Delta P_{tur.in}+\Delta P_{f,chim}+\Delta P_{k,out}$(eq.11)

$\Delta P_{tur.in}=K*\frac{\rho}{2}*V_2^2$: Turbine inlet form pressure drop

$\Delta P_{f,chim}=f*\frac{H}{D}*\frac{\rho}{2}*V^2$: Chimney frictional pressure drop

$\Delta P_{k,4}=K_{out}*\frac{\rho_4}{2}*V_4^2$: Chimney outlet form pressure drop

The pressure drop of turbine makes the wheel rotate, generating the electricity. It is the difference between the driving force and pressure drop over chimney as (eq.10). The pressure drop of system is the sum of the pressure drop over a form loss at turbine inlet, friction loss at chimney wall and chimney outlet form loss as (eq. 11). The ultimate goal of the draught equation is to determine the pressure drop across the turbine. Using this pressure drop, the power generated by the turbine may be calculated.

2.4 Power output

The flow of air through the tower of the solar tower power plant drives a turbine at the base of the tower. The turbine drives a generator which generates electricity. The power output of the system was calculated by the (eq. 12). η_{tg} is turbine efficiency and V_{avg} is volumetric flow rate of air. For the maximum of power on system, the pressure ratio across the turbine play an important role in calculating the performance. Many researcher have assumed the optimum values of pressure ratio is 2/3. In this study, the pressure ratio across the turbine was optimized using our developed mathematical model.

$P_{out}=\eta_{tg}\Delta P_{tur}V_{avg}=\eta_{tg}\Delta P_{tur}v_{tur}A_c$ (eq.12)

2.5 Calculation algorithm

The overall power performance of solar updraft tower plant was calculated following an algorithm using MATLAB. The procedure of calculation is following figure 3. The pressure, temperature and density in region of 2, 3 and 4 were obtained using the thermal analysis and several equation. Then, the mass flow rate of system was assumed to some values. The air velocity of each region can be calculated using mass conservation equation. Air flow pressure drop of system can be calculated at several regions. The form pressure drop at chimney inlet, friction pressure loss at chimney wall and outlet form pressure loss at chimney outlet were obtained, then the velocity can be calculated using the pressure drop conservation equation. Mass flow rate was recalculated from obtained velocity. Then, the calculation cycle was recurred until the small difference between the previous value and current value. After the iteration process, the power output of system can be calculated.

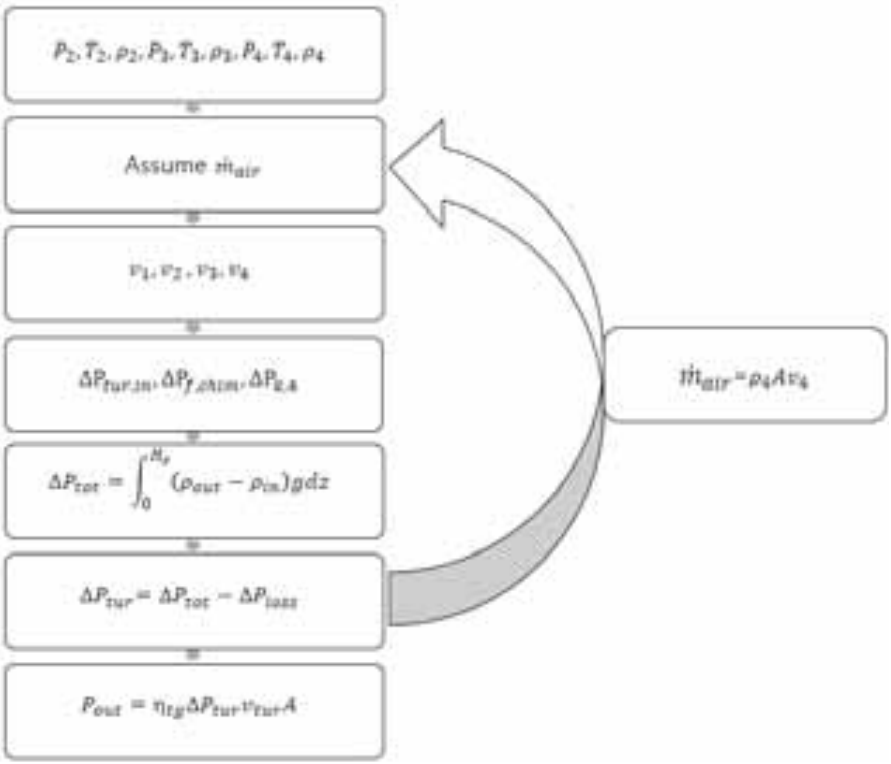

Fig. 3: Calculation algorithm of SUTP

3. Results and Discussion

3.1 Validation of developed model with manzanares experimental data

To validate the new mathematical model, information of the ambient temperature and solar irradiation data on 2nd of September in 1982 from the Haff's paper were utilized for the initial condition. The calculated result of the power output, pressure drop, velocity and temperature change in the collector were compared with the real data. In fig. 4, solar irradiation at Manzanares region was measured and the profile was obtained at all day long. Ambient temperature at Manzanares region was also figured in fig. 5.

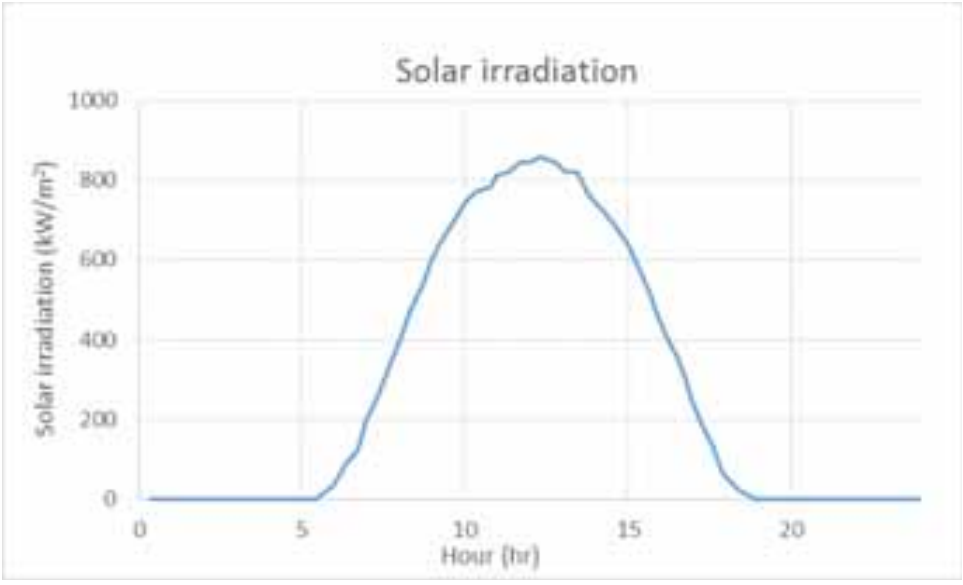

Fig. 4: Measured solar irradiation at Manzanares on 2 September 1982

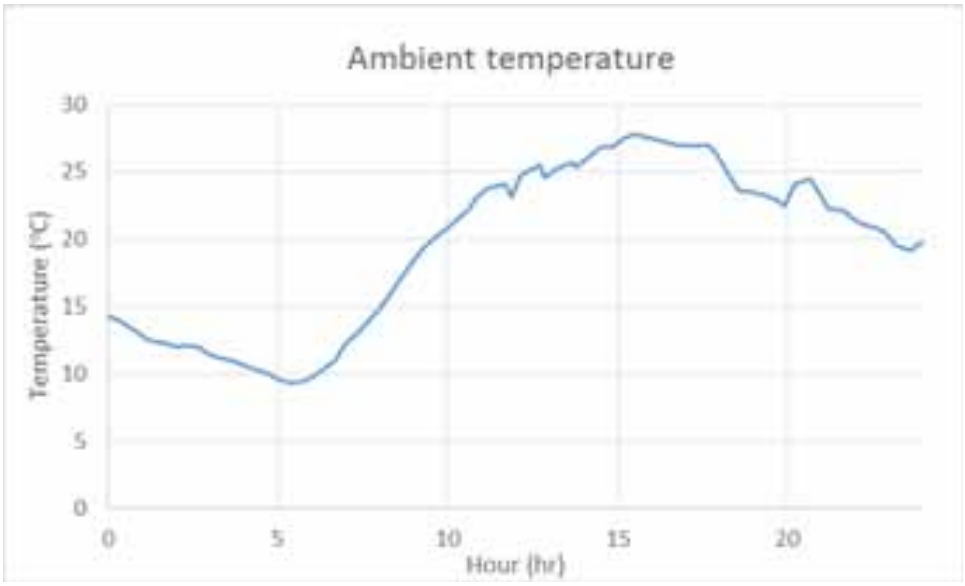

Fig. 5: Measured ambient temperature at Manzanares on 2 September 1982

In calculation of SUTP performance, ambient temperature and solar irradiation was used as initial conditions. Using this values, the calculated output power was compared with measured values at fig. 6. Overall trend of power is similar, but the calculated power is slightly higher at early morning. The maximum power is about 34 kWe at the 12 pm. The power at night is zero because there is no solar irradiation. At fig.7, temperature rise in collector was compared with measured data. The trend is similar, but the temperature rise until 8 am is quite different. But the temperature rise at daytime is similar from about 15 ^{o}C to 20 ^{o}C. At fig. 8, air velocity at chimney was compared with the measured data. Measured velocity profile is quite fluctuating, so it is difficult to compare each other. But, overall trend of velocity is similar, and the calculated velocity data is underestimated than measured one. At fig. 9 and 10, the calculated pressure difference at total system and turbine system were compared with measured one. The trends are also similar each other.

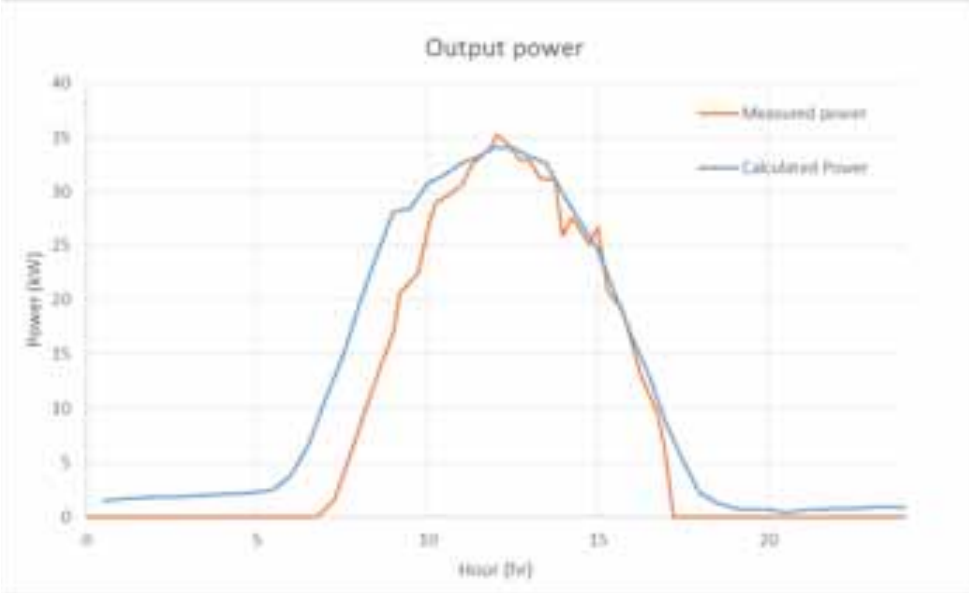

Fig. 6: Comparison of calculated power with measured power

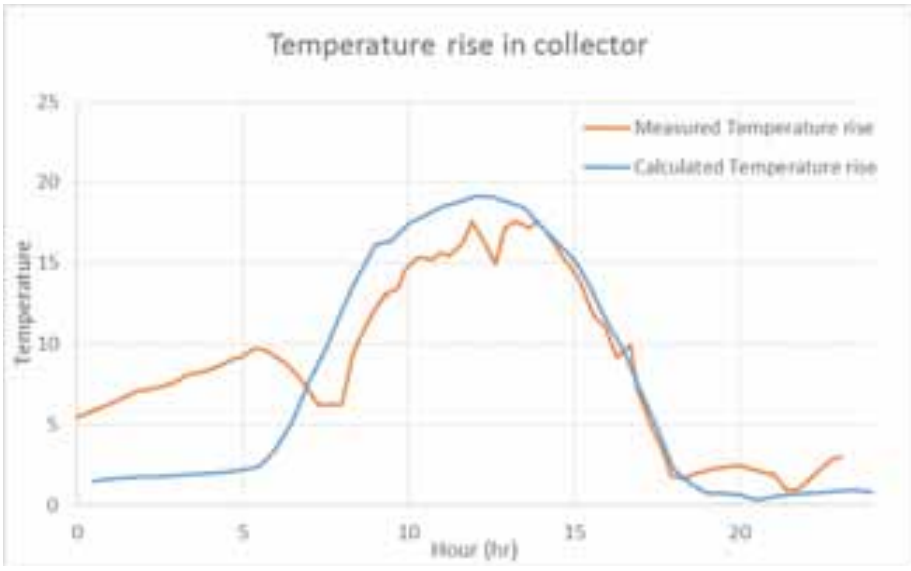

Fig. 7: Comparison of calculated temperature rise with measured temperature rise at collector

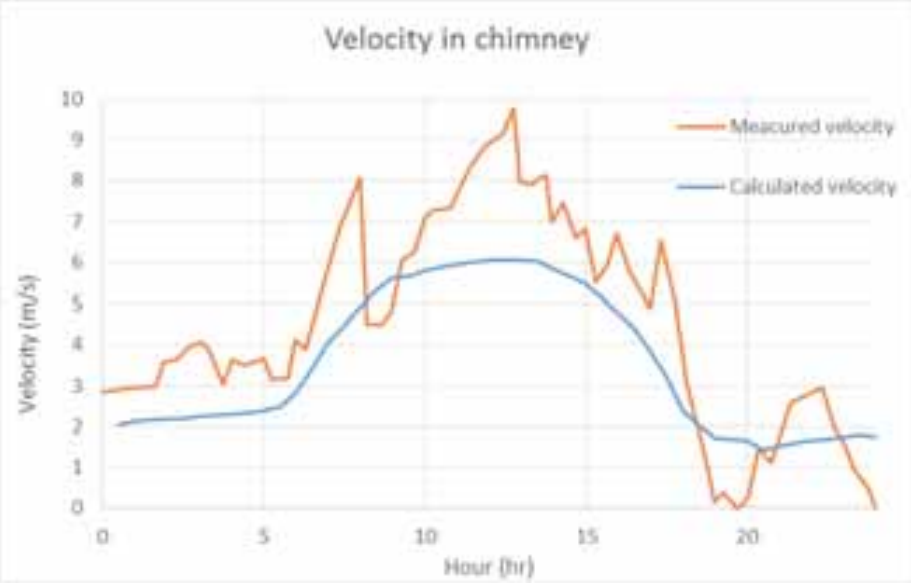

Fig. 8: Comparison of calculated velocity with measured velocity at chimney

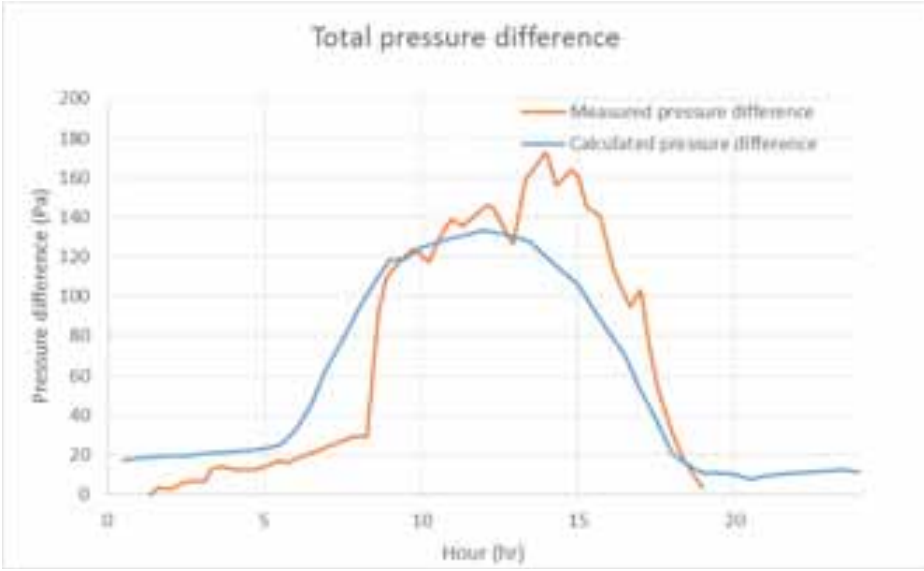

Fig. 9: Comparison of calculated total pressure difference with measured total pressure difference

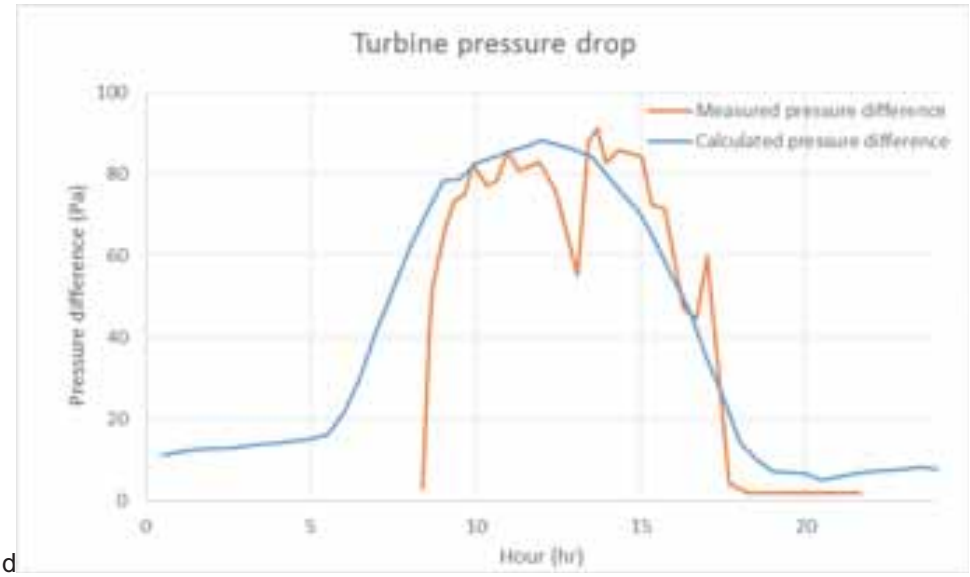

d

Fig. 10: Comparison of calculated turbine pressure difference with measured turbine pressure difference

3.2 Large scaled SUTP

Idea of solar updraft tower plant was suggested for the high electricity production at the dry area where the solar energy is abundant and water storage is deficient. For the high electricity production, scale of solar chimney should be expanded to obtain the high power. Many research evaluate performance of large scaled solar chimney. In this paper, the large scaled tower was assumed to operate ordinarily at same condition of Manzanares initial value like ambient and solar irradiation. At that conditions, the size of solar tower was changed like following table. 2. Slope of collector is linearly tilted from inlet to outlet of roof. Other basic values are same with values of the manzanares calculation. From the figure 11 to 15, the result of the large scale tower plant was obtained. The maximum power is about 130 MWe at 12 pm. The temperature rise in the collector is maximum 35 ^{o}C at 12 pm. The air flow velocity at chimney is highest value of 20 m/s at day time. The maximum pressure difference profile followed also similar trend. From the large scaled analysis, we could estimate the performance of system at the specific tower dimension.

Tab. 2: Dimensions of large scaled solar updraft tower plant

Tower height	1,000 m
Tower radius	100 m
Collector radius	3,000 m
Collector inlet height	5 m
Collector outlet height	10 m

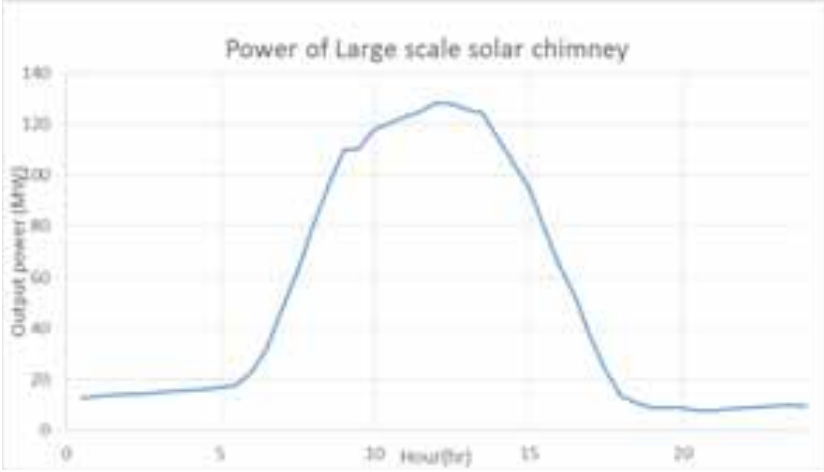

Fig. 11: Calculated output power of large scaled SUTP

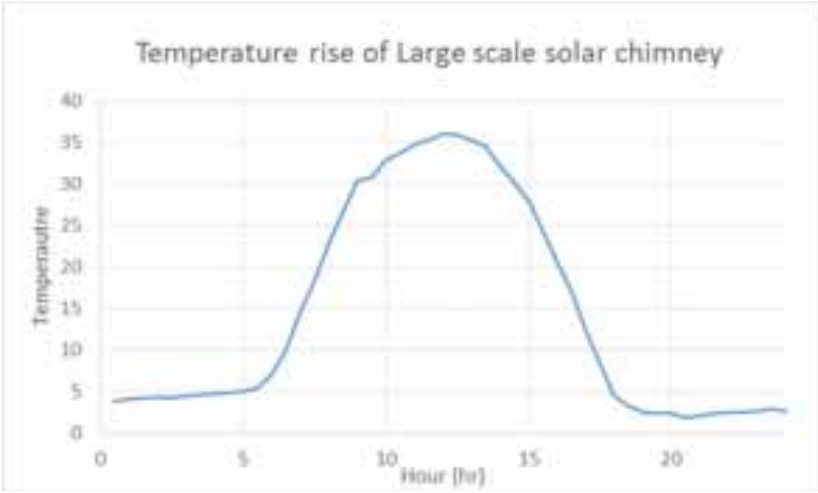

Fig. 12: Calculated temperature rise of large scaled SUTP

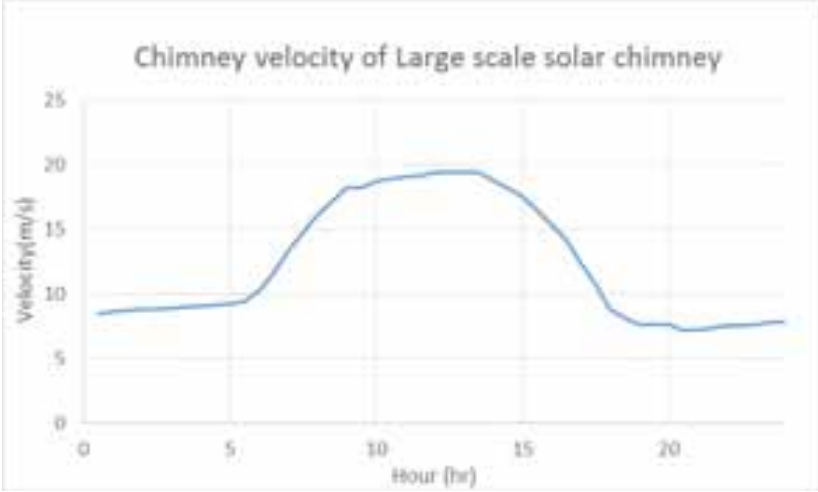

Fig. 13: Calculated chimney velocity of large scaled SUTP

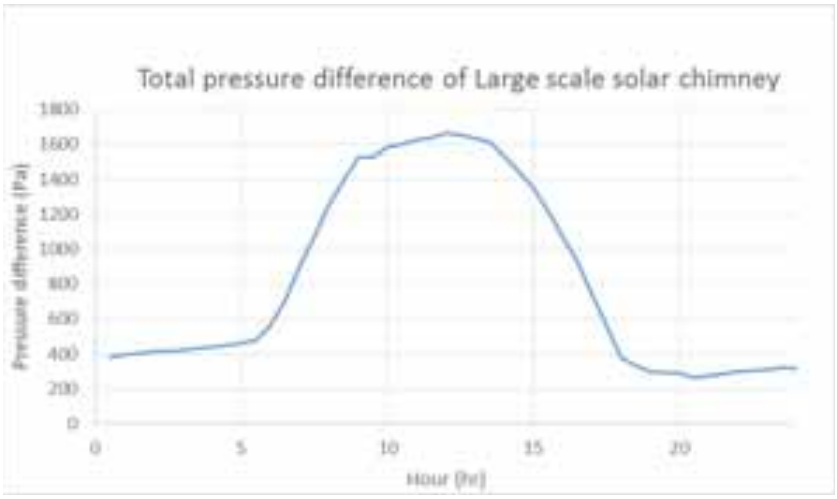

Fig. 14: Calculated total pressure difference of large scaled SUTP

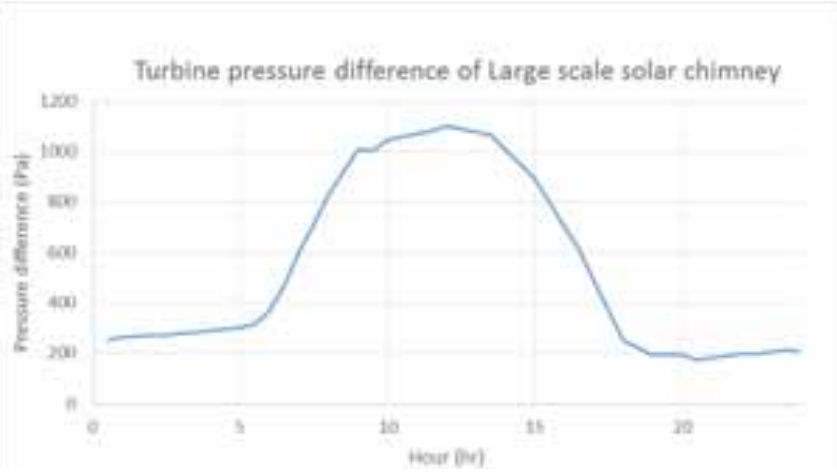

Fig. 15: Calculated turbine pressure difference of large scaled SUTP

4. Conclusions

A new mathematical analysis model was developed to evaluate the performance of SUTP system. The prediction of new model was compared with experimental data. The new model was validated with measured data, and the trends of overall data was considerably well-estimated. By using this mathematical method, large scaled SUTP system was also evaluated. The output power scale was about 100MWe. But there are many defect on our model development, so more comprehensive study for improving the model should be conducted.

5. Reference

[1] Haaf W, Friedrich K, Mayr G, Schlaich J. Solar chimneys Part I: principle and construction of the pilot plant in Manzanares. Int J Sustain Energy 1983;2(1):3–20.
[2] Haaf W. Solar chimneys Part II: preliminary test results from the Manzanares pilot plant. Int J Sol Energy 1984;2(2):141–61.
[3] Bernardes MAd, Voß A, Weinrebe G. Thermal and technical analyses of solar chimneys. Sol Energy 2003;75(6):511–24.

[4] Pretorius, J. P., 2004, “Solar Tower Power Plant Performance Characteristics,” M.Sc.Eng. thesis, University of Stellenbosch, Stellenbosch, South Africa.

[5] Pretorius, J. P. and Kroger D. G., “Critical evaluation of solar chimney power plant performance,” Solar Energy, vol. 80, no. 5, pp. 535–544, 2006.

[6] Bernardes, M.A.d.S., Von Backstro¨m, T.W., Kro¨ ger, D.G., 2009. Analysis of some available heat transfer coefficients applicable to solar chimney power plant collectors. Solar Energy 83, 264–275.

[7] Zhou XP, Wang F, Ochieng RM. A review of solar chimney power technology. Renew Sustain Energy Rev 2010;14(8):2315–38.

[8] A. Koonsrisuk, T. Chitsomboon, Mathematical modeling of solar chimney power plants, Energy, 51 (2013), pp. 314–322

[9]P. Guo, J. Li, Y. Wang, Annual performance analysis of the solar chimney power plant in Sinkiang, China, Energy Convers Manage, 87 (2014), pp. 392–399

Conference Proceedings

Solar World Congress 2015
Daegu, Korea, 08 – 12 November 2015

Solar thermal energy performance model for an interactive solar energy atlas for the Arabian Peninsula

Mercedes Ibarra[1], Miguel Frasquet[1], Abdulaziz Al Rished[2], Arttu Tuomiranta[1], Sami Gasim[2] and Hosni Ghedira[1]

[1] Masdar Institute of Science and Technology, Research Center for Renewable Energy Mapping and Assessment (ReCREMA), P.O. Box 54224, Abu Dhabi, United Arab Emirates

[2] King Abdullah City for Atomic & Renewable Energy (KACARE), P.O. Box 2022, Riyadh 11451, Saudi Arabia

Abstract

The authors present the integration of a solar thermal energy performance model in an already existing solar atlas infrastructure. With this tool, the user will be able to select the design parameters of a solar power plant and the key performance indicators will be delivered. In particular, this paper presents the two performance models proposed to assess the performance of utility-scale solar thermal power plants. The results of these models have been used for the evaluation of the potential of solar energy in the Arabian Peninsula.

Keywords: *solar thermal energy (STE), simulation, parabolic trough collector (PTC), central receiver systems (CRS).*

1. Introduction

Until now, countries like Saudi Arabia and UAE have based their energy consumption on its great resources of oil and gas. However, the Middle East is a region with high solar energy potential. The use of solar energy to produce electricity instead of burning fossil fuels would have several advantages, like avoiding consuming a well valued resource, and reducing the dependence of a finite resource.

To impulse the development of solar energy projects, KACARE proposed the development of a solar atlas, where the solar irradiance potential would be offered to the general public. The website is online and operational (KACARE, 2015). Moreover, a joint project between ReCREMA and KACARE aims to include a solar technology assessment layer into the atlas, where the performance of several solar technologies will be available. The technologies included in the solar simulator will be photovoltaic solar energy (PV) and solar thermal energy technologies, like parabolic trough collectors (PTC) and central receiver systems (CRS).

In this paper, the models used in the solar simulator for the solar thermal technologies are presented and compared. The spatial aspects of the simulation are analyzed to improve the speed and performance of the simulator. As an example of the capabilities of the model, two plants are designed and their annual performance is calculated.

2. General overview of the solar atlas operation

There are three kinds of inputs for the solar technology assessment atlas: the user defines the major characteristics of the plant (i.e. design net output power, solar multiple and hours of storage), the pixels on the map states the location-related information and the fixed inputs are logic design assumptions specified in the model to simplify it and avoid long computation times, benchmarked with industrial standards.

Once the inputs are defined, the model performs two calculations for each pixel of the map. First, the layout of the plant is determined. Then, the tool estimates the annual performance of the plant.

doi:10.18086/swc.2015.04.20 Available at http://proceedings.ises.org

3. Performance models

3.1. CRS Model

During the first step of the design point evaluation, a detailed power block model is used to calculate the required power at the steam generator. This power block model simulates a 50-100 MWe state of the art steam Rankine cycle. Bigger sizes would imply a significant drop of the optical efficiency due to the extreme atmospheric attenuation in the Arabian Peninsula.

Therefore, sizes bigger than 100 MWe are assumed as multiples of the power block model. The partial load behavior is also modeled assuming sliding pressure control, and performance maps are created to be implemented in the annual performance calculations. Knowing the power absorbed at the steam generator and the solar multiple (defined by the user), the power absorbed by the receiver can be estimated. Using this value and the information provided by each pixel (design direct normal irradiance and latitude), the height of the tower and the size of the receiver are optimized through pre-calculated DELSOL3 optimizations. The optimization has been done with the economic parameters incorporated, although the user will not be able to change the values. In this optimization, the pre-calculated data is limited to 105 possibilities for each variable and the rest of the possible combinations are interpolated from the data.

The layout of the solar field cannot be obtained by interpolation and therefore, it should be calculated for each case. For that purpose, a complete optical model in MATLAB has been developed. This optic model discretizes the field using a cell pattern similar to DELSOL3 approach, and takes into account the optical behavior of each cell. The shadowing and blocking (S&B) engine uses an intelligent neighbor selector and the classic approach of surface projection. Fig. 1 shows the validation results of the S&B engine proposed, against a ray-tracing code and its evolution along the year.

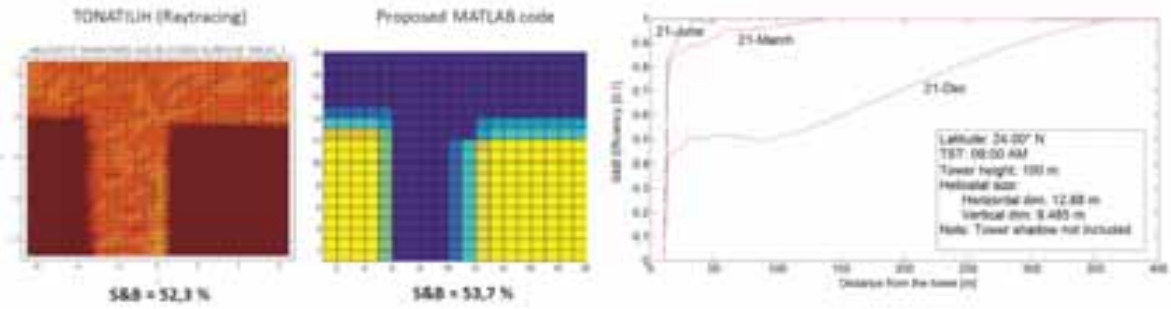

Fig. 1: S&B validation of the proposed code in MATLAB using Tonatiuh Raytracing

The evaluation of the flux at the receiver necessary to determine the spillage, is numerically calculated using a circular Gaussian approach similar to the one used in HFLCAL. The computer program HFLCAL was developed by Michael Kiera at the German company Interatom during the project GAST (GAS-cooled Solar Tower) in the early 1980's (Kiera, 1989). Once the optical efficiencies are calculated, the optical model re-arranges the cells and calculates the optimum field layout.

The size of the receiver is interpolated from the pre-calculated DELSOL3 optimization data and introduced into a thermodynamic receiver model. The receiver model calculates the thermal efficiency of the receiver as well as other outputs needed for the overall model e.g. molten salts mass flow rate, salts-pump consumption. The partial load behavior is also calculated and represented in a set of performance maps which will be used in the annual performance model.

The Fig. 2 shows an example of the solar field created by the model. The rather circular geometry agrees with the DELSOL3 optimizations and reflects the fact that in areas with a significant atmospheric attenuation, as the case of the Arabian Peninsula, circular fields are preferred against North/South fields. This field creation takes into account energy performance and economic parameters. If only the energy performance were taken into account, the resulted solar field will have very high tower with big receivers

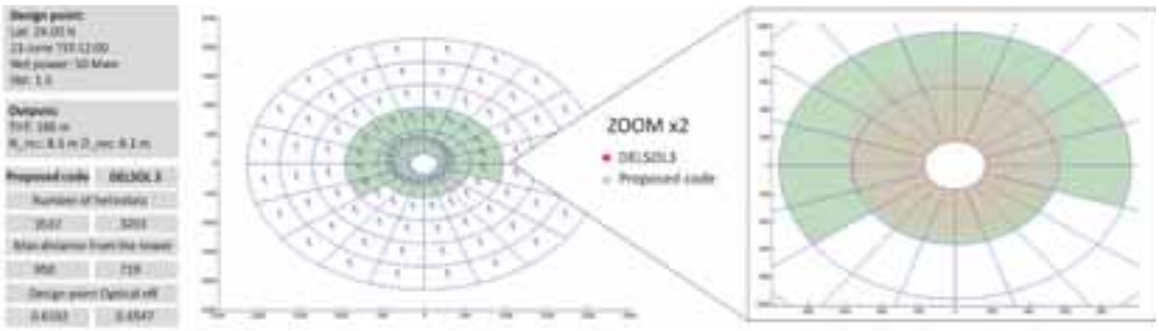

Fig. 2: Solar field layout created by the proposed model

3.2. PTC Model

The PTC plant design, which is defined by the spatial organization of the collectors, is easier to determine. The PTC collectors are arranged in loops of collectors in series. Ideally, every loop receives the same irradiance and heats a fraction of the thermal oil by the same temperature difference. Hence, the aperture area of a PTC solar field depends on the desired power, the available incident power (Q_{sun}) and the performance of one loop to transform this incident power in thermal energy.

Therefore, the calculation of the efficiency of one loop in design conditions is needed to design the power plant. To do so, first the amount of energy available for the loop and then the optical and thermal losses of the collector are calculated. Once the plant design is determined, the annual performance of the plant can be simulated. For every time step, the simulator uses the meteorological database associated to the pixel to follow the same step than for the design.

First, the available incident power (Q_{sun}) is defined by the following expression:

$$Q_{sun} = \mathrm{G_b} \cdot \cos\theta_i \cdot A_{apert} \qquad \text{(eq. 1)}$$

where G_b is the direct irradiance, θ_i is the incidence angle and A_{apert} is the aperture area of the solar field.

Then, the absorbed energy by the collector tube is calculated following the guidelines proposed by the GuiSMo project Eck et al. (2014) that recommends including accurate optical efficiency information of the collector, the incidence angle modifier (IAM), the end losses and the shading effects.

The optical efficiency is calculated by eq.2. It is assumed that the solar field is periodically cleaned and that the value of F_d (cleanliness factor) changes randomly among certain values that follow a normally distributed function, and so do the reflectivity of the mirrors, the transmissivity of the tube cover and the absorptivity of the tube. This method was proposed by Zaversky et al. (2012) and the values used are based on the SEGS experimental data.

$$\eta_{opt,0^\circ} = r_{0^\circ} \cdot \gamma_{0^\circ} \cdot \tau_{0^\circ} \cdot \alpha_{0^\circ} \cdot F_{d,0^\circ} \qquad \text{(eq. 2)}$$

where r_0 is the reflectivity of the parabolic mirrors, γ_0 is the geometric intercept factor of the collector, τ_0 is the transmissivity of the receiver's glass cover and α_0 is the absorbance of the selective coating on the metallic pipe, all at θ=0º.

The IAM is determined by:

$$\mathrm{K}(\theta) = 1 - \mathrm{a_0} \cdot \theta - \mathrm{a_1} \cdot \theta^2 + \mathrm{a_2} \cdot \theta^3 + \mathrm{a_3} \cdot \theta^4 \qquad \text{(eq. 3)}$$

where θ is the incidence angle and the coefficients used are a_0=2.2307·10^{-4}, a_1=1.1·10^{-4}, a_2=3.18596·10^{-6} and a_3=-4.85509·10^{-8}.

The end losses (f_{end}) and the shading effects ($f_{rowShadow}$) are calculated following the equations, from Eck et al. (2014):

$$f_{end} = 1 - f_m \cdot \tan\theta / l_{col} \qquad \text{(eq. 4)}$$

$$f_{rowShadow} = \max\left[0, \min\left[1, \frac{d_{row}}{w_{col}} \frac{\sin\alpha_s}{\cos\theta}\right]\right] \quad \text{(eq. 5)}$$

where l_{col} and w_{col} is the length and width of the collector, d_{row} is the distance between rows, f_m is the focal length of the parabola and α_s is the solar altitude.

The energy absorbed by the tube is defined as:

$$Q_{abs} = Q_{sun} \cdot IAM \cdot \eta_{\text{opt},0^\circ} \cdot f_{end} \cdot f_{shadow} \quad \text{(eq. 6)}$$

The receiver thermal losses are calculated following the regression lines obtained by Burkholder et al. (2008) for the Schott PRT70:

$$H_L = b_0 + b_1 \cdot (T_{HTF} - T_{amb}) + b_2 \cdot {T_{HTF}}^2 + b_3 \cdot {T_{HTF}}^3 + b_4 \cdot G_b \cdot \cos\theta \cdot {T_{HTF}}^2 + \\ + \sqrt{V_w} \cdot (b_5 + b_6 \cdot (T_{HTF} - T_{amb})) \quad \text{(eq. 7)}$$

where T_{HTF} is the temperature of the fluid, T_{amb} is the ambient temperature, V_w is the wind speed and the coefficients are shown in Tab. 1.

Tab. 1: Values of the coefficients for the heat losses calculations (Burkholder, 2008).

b_0	4.05
b_1	0.247
b_2	-0.00146
b_3	5.65E-6
b_4	7.62E-8
b_5	-1.70
b_6	0.0125

The thermal losses of the piping are calculated following the method proposed by Patnode (2006):

$$H_{L,Pip} = c_0 \cdot (T_{HTF} - T_{amb}) + c_2 \cdot (T_{HTF} - T_{amb})^2 + c_3 \cdot (T_{HTF} - T_{amb})^3 \quad \text{(eq. 8)}$$

where c_0=1.693·10^{-2}, c_1=1.683·10^{-4}, c_3=6.78·10^{-7}.

Once the amount of thermal energy provided by the solar field is calculated, the control algorithm determines the amount of energy sent to the power block and thermal storage.

For the determination of the efficiency and power production of the power block the model uses the equation proposed by Llorente et al. (2011).

$$\eta_{PB} = a_1 + a_2 \cdot \exp\left(-P_{in} / a_3\right) \quad \text{(eq. 9)}$$

where the P_{in} is the power delivered to the power block after the heat exchanger (η_{HEX}=0.95), a_1 = 0.397, a_2 = -0.243 and a_3 = 28.23 MWt

The model is compared with the performance of a solar plant located in similar desert conditions: the 100 MW Shams 1 solar plant, operated by Shams Power Company, owned by Masdar, Total and Abengoa, located in Madinat Zayed (UAE). The solar field has 627,840 m^2 of parabolic trough, divided in four section. The particularity of the design of this plant was the addition of a gas booster before the turbine, to increase the steam temperature the feeds it, which allows an increase of the efficiency of the turbine.

The data used, provided by Shams Power Company, has allowed the comparison of the power output from the solar field (before going to the power block) for the same conditions (DNI and ambient temperature) and compared with the actual values obtained in the field. Due to the particular configuration of the power block, the power production could not be included in the comparison. The scatter density plot of the measured

($P_{SF,meas}$) and predicted solar field power ($P_{SF,mod}$) is shown in Fig. 3, where the correspondence of the model values with the measured is good with a slight overestimation of the production in the model for lower values.

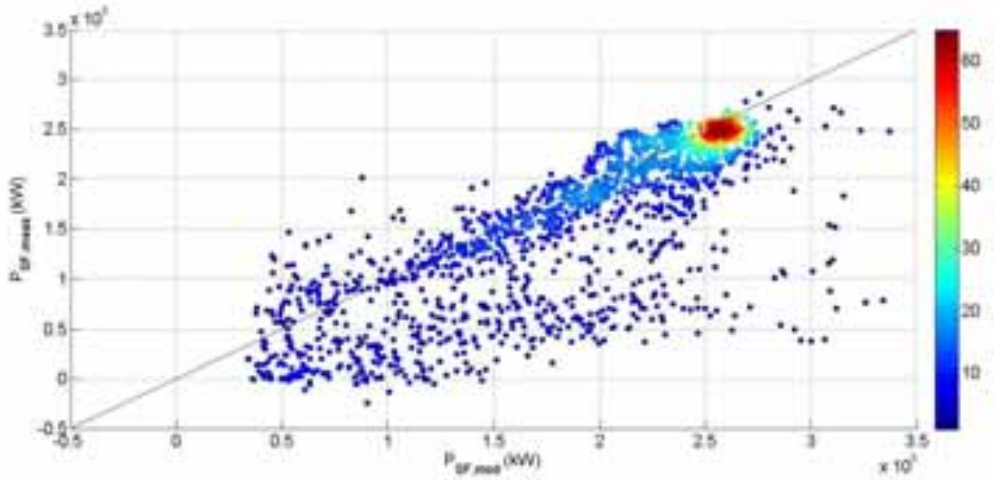

Fig. 3: Scatter density plot for power measured and power predicted by the model

4. Preliminary results

4.1. Geographic influence on the design of power plants

In this work, the presented models have been used to analyze the effect of the geography distribution of the input variables (G_b, solar angles) on the final design of the plants.

In Fig. 4 a map of the distributions of the direct solar irradiance G_b in 2013 of Saudi Arabia is shown. The country is located between the parallels 35 and 15 in the northern hemisphere, which means almost 15° of amplitude. This great extension affects the distribution of the DNI, with an increasing gradient that goes from north to south. However, the greater values are found at the west of the country, by the coast.

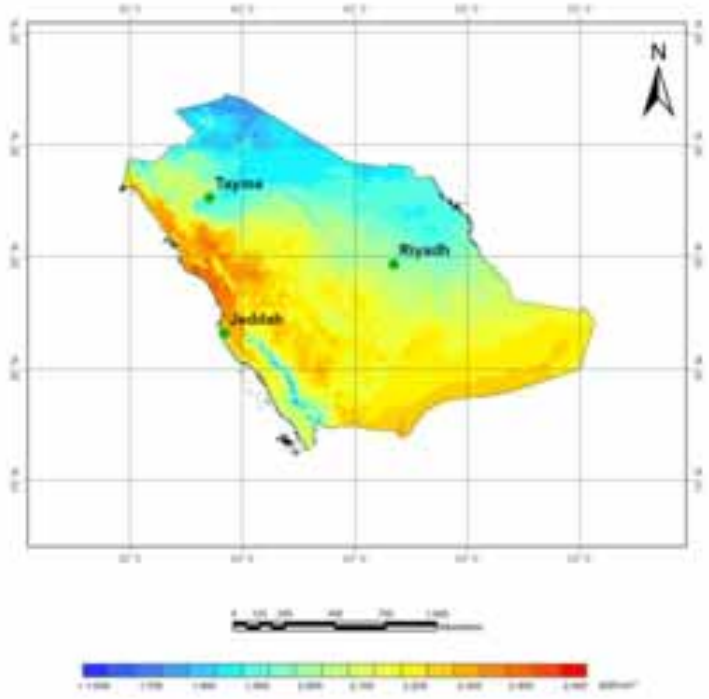

Fig. 4: Beam irradiance on Saudi Arabia on 2013

In Fig. 5 and 6 the effect of the design beam irradiance and the latitude on the design of the plants is shown. The latitude affects the position of the sun in relation to the the collectors or heliostats and it therefore has an impact on the incidence angle value. The southern the location, higher the sun will reach in the sky and smaller the incidence angle will be. As a consequence of this, the smaller the latitude (south), the smaller the area required to reach the desired power in the design conditions. Regarding the height of the tower, it gets taller when going south because the solar angles allow circle shaped heliostat field. This means that the heliostats are closer and the tower is higher.

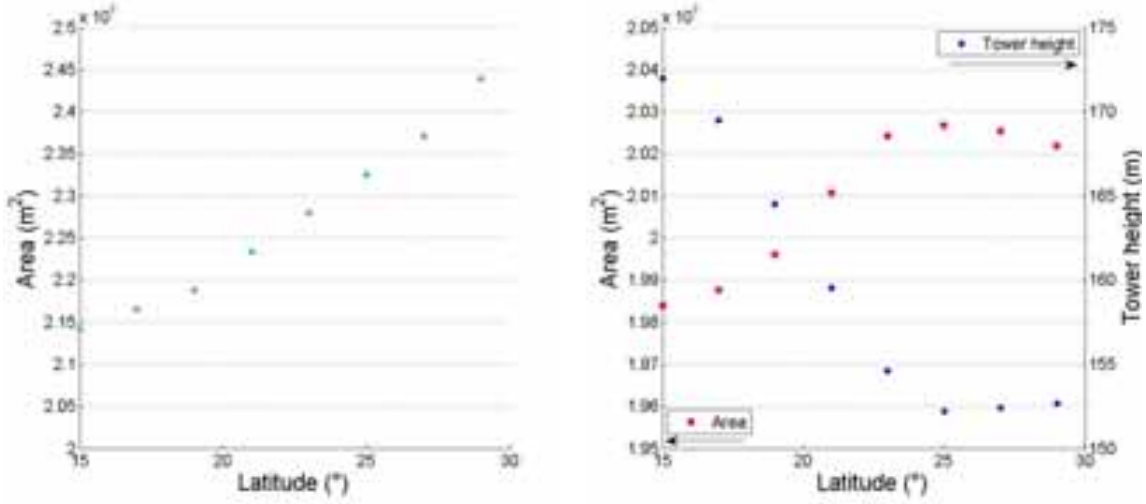

(a) (b)

Fig. 5: Effect of the latitude on the design of the plant (a) PTC and (CRS)

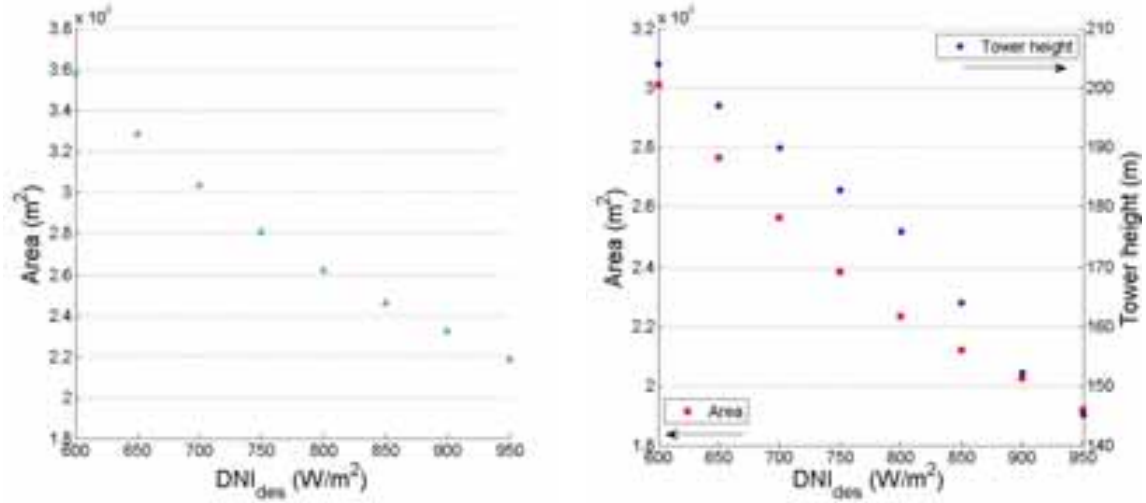

(a) (b)

Fig. 6: Effect of the design beam irradiance on the design of the plant (a) PTC and (CRS)

Regarding the effect of the DNI (Fig) has on the design, the greater the DNI, smaller area will be needed to cover the desired power on the design conditions. Hence, the higher the DNI, the smaller the plant will be. Again, this means that as we go south in the country, the required area will be smaller.

As the DNI values and solar angles are no constant along the year, the choice of the design point (DNI and solar angles) will affect the performance of the plant. If a winter design date is chosen, the plant will be overdimensioned and most of the time the plants will be producing more energy that what they were designed for, having to dump most of this energy by defocusing. If a summer design date is chosen, the plant may be underdimensioned, producing under the desired power for most of the year.

4.2. Case study: design of a plant in Riyadh

The models presented in the previous section have been used to design two plants in Riyadh, which has a latitude of 24.53° and a beam irradiance on design of 843.9 W/m^2. The results of this exercise are shown in Tab.1.

Tab. 1: Comparison of the designed plants for Riyadh

Design point	Design CRS	Design PTC
Latitude: 24.53N	Tower Height: 186 m	Collectors per loop: 4
Longitude: 46.44E	Dimension receiver: 8.1 x 6.1 m^2	Number of loops: 151
21-June solar noon	Number heliostats: 3537	Total number SCA: 604
Design net power: 50MWe	Max distance of the tower: 950 m	Aperture area: 3.44 ·10^5 m^2
SM:1.5	Optical efficiency: 0.6102	

Fig. 7 and 8 show the summary of the simulation for the two solar fields of Tab. 1: each square represents the hourly average power delivered by the solar field of every month. The DNI resource is the same for both technologies, the months with less resource being March, April and May.

However, the production of the CRS solar field is more constant through the year than PTC solar field one. The reason of for this difference divergence discrepancy is the different in incidence angle between the two technologies. In winter, when the sun is lower, the PTC optical efficiency decreases more significantly due to single-axis tracking.

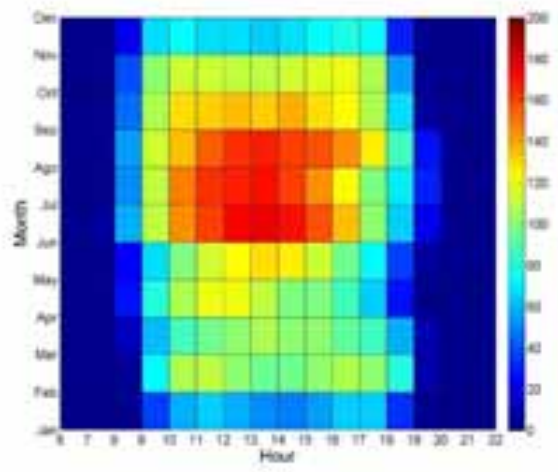

Fig. 7: Average power delivered to the power block by the parabolic trough collector solar field for every hour of every month

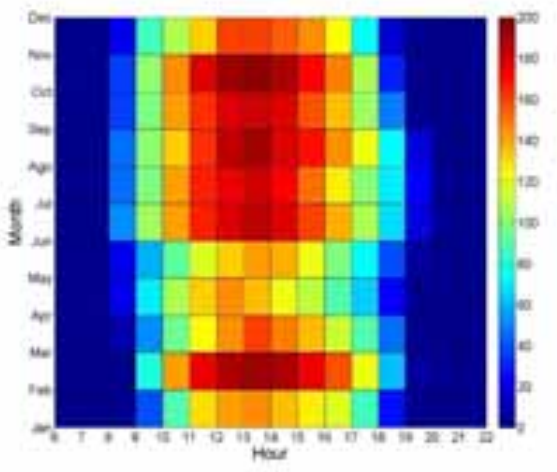

Fig. 8: Average power delivered to the power block by the central receiver system (heliostats and receiver) for every hour of every month

5. Conclusions

This paper presents the model used in a solar technology atlas for Saudi Arabia. The models for two technologies are presented: PTC and CRS. Both models are validated, either with real operational data or from widely accepted industry codes. In this work, a special focus has been given to the design step of the calculations.

Therefore, the presented models have been used to analyze the effect of the geography distribution of the input variables on the final design of the plants. The southern the location, both the beam irradiance and the solar angles values allow the reduction of the area of the solar field to reach the same power. Moreover, due to the

solar angles in low latitudes, in the case of the CRS the tower gets higher and the heliostat field design will be more compact.

As a final step, two plants have been designed in Riyadh and their annual performance has been calculated. A more stable thermal energy is delivered to the power block in the case of CRS, being the PTC more variable seasonably.

6. References

Burkholder, F., Kutscher, C., 2008a. Heat-Loss Testing of Schott's 2008 PTR70 Parabolic Trough Receiver. NREL TP-550-42394, pp. 1–54.

Eck, M., T. Hirsch, J.F. Feldho, D. Kretschmann, J. Dersch, A. Gavilan Morales, L. Gonzalez-Martinez, C. Bachelier, W. Platzer, K.-J. Ri_elmann, and M. Wagner. Guidelines for csp yield analysis. optical losses of line focusing systems; definitions, sensitivity analysis and modeling approaches. Energy Procedia, 49(0):1318 - 1327, 2014. Proceedings of the SolarPACES 2013 International Conference.

K.A.CARE, Renewable Resource Atlas. http://rratlas.kacare.gov.sa. Accessed on 26/Oct/2015.

Kiera, M.: Heliostat Field: computer codes, requirements, comparison of methods. In: Becker, M., Böhmer, M. (Eds.): GAST – The Gas-Cooled Solar Tower Technology Program. Proceedings of the Final Presentation. Springer Verlag, Berlin 1989.

Llorente García I, Álvarez JL, Blanco D. Performance model for parabolic trough solar thermal power plants with thermal storage: Comparison to operating plant data. Solar Energy 2011;85:2443-60.

Patnode A. Simulation and Performance Evaluation of Parabolic Trough Solar Power Plants. Master Thesis. University of Wisconsin-Madison. 2006.

Zaversky F, García-Barberena J, Sánchez M, Astrain D. Probabilistic modeling of a parabolic trough collector power plant – An uncertainty and sensitivity analysis. Solar Energy 2012;86:2128-39.

Conference Proceedings

Solar World Congress 2015
Daegu, Korea, 08 – 12 November 2015

Exergoeconomic Assessment of a Solar Polygeneration Plant

Roberto Leiva-Illanes [1,2], Rodrigo Escobar [2], Jose Cardemil [3]
[1] Departamento de Mecánica, Sede Viña del Mar. Universidad Técnica Federico Santa María,
Av. Federico Santa María 6090, Viña del Mar, Chile.
[2]Departamento de Ingeniería Mecánica y Metalúrgica, Pontificia Universidad Católica de Chile,
Vicuña Mackenna 4860, Macul, Santiago, Chile.
[3]Facultad de Ingeniería. Universidad Diego Portales,
Av. Ejército 441, Santiago, Chile.
e-mail: roberto.leiva@usm.cl , rleivaillanes@puc.cl

Abstract

This paper shows the results of an exergoeconomic assessment of a solar polygeneration plant. Solar polygeneration plant consists of a concentrated solar power (CSP) type parabolic trough, a multi-effect desalination MED module, a refrigeration absorption module, and process heat module, in order to produce electricity, desalinated water, cooling and process heat respectively.

A solar polygeneration plant is justified due to the high demand for the products produced, where a CSP plant produces high residual heat (waste heat) that is possible to leverage through polygeneration.

The methodology allows coupling thermodynamic equations and economic relations in order to solve complex systems. Polygeneration plant was evaluated to be installed in Crucero, in northern Chile where the direct normal irradiance reaches values of 3,389 kW h/m^2/year.

The results indicate that the polygeneration plant has an energy efficiency of 62.8%, an exergy efficiency of 24.5%, products cost rate of 10,713.2 USD / h and a net present value (NPV) of 4.3 MUSD.

Keywords: *CSP, MED, CHP, cooling, polygeneration, exergoecononomic, thermoeconomic.*

1. Introduction

Concentrated solar power (CSP) produces electricity, but it can also be coupled with other technologies in a polygeneration scheme to produce other products, such as desalination water, industrial cooling and process heat (Serra et al., 2009), especially where those products are in short supply and when there is high solar irradiation. The combined production of products by polygeneration scheme permits to increase the thermodynamic efficiency of the consumed resources. Polygeneration can transform waste heat into useful heat to drive other processes. Exergoeconomic analysis combines both economic and thermodynamic analysis (1st and 2nd law of thermodynamics) by applying the concept of cost that is an economic property, and the concept of exergy that is a thermodynamic property. The main objectives of exergoeconomic analysis are: to identify the location, magnitude and sources of exergy destruction and losses in an energy system; to calculate the cost associated with these losses; to assess the production costs of each product in the energy conversion system, which has more than one output; to facilitate feasibility and optimization studies for energy system; to assist in decision-making procedures concerning plant operation and maintenance; and to compare technical alternatives (Tsatsaronis, 1993).

Concentrated solar power (CSP) technologies can be parabolic trough collector (PTC), central receiver (CR), linear fresnel (LF) or dish-Stirling (DS). CSP-PTC has proven to be the most mature and lowest cost solar thermal technology (IRENA, 2012). Multi-effect distillation (MED), multi-stage flash (MSF) and reverse osmosis (RO) represent the most reliable, commercially proven and efficient methods to provide fresh water by desalination, and can be coupled with the CSP plant (Palenzuela et al, 2011; Cipollina et al, 2009). Absorption and vapor compression are the most important technologies to produce industrial cooling (Infante

Selection and/or peer review under responsibility of Scientific Committee
doi:10.18086/swc.2015.04.21 Available at http://proceedings.ises.org

and Kim, 2013; Hassan et al, 2012). Solar absorption systems utilize the thermal energy from solar collector to separate a refrigerant from the refrigerant/absorbent mixture. Solar absorption systems have been published in some studies (Sarbu and Sebarchievici, 2013; Ullah et al., 2013). Industrial process heat is used in different industrial processes. The thermal energy demand is below 300 °C (Fernández-García et al., 2010).

Finally, exergoeconomic analysis of polygeneration systems with fossil fuel as main energy source has been published in some studies. A few studies have been made on exergoeconomic analysis of polygeneration systems with CSP plant but there is not study on exergoeconomic analysis with the current scheme polygeneration.

This work shows the results by using a model to simulate a polygeneration plant, which consists of a CSP-PTC, a MED desalination plant, a single effect LiBr/H2O absorption refrigeration plant, and a process heat plant for the production of four products: electricity, desalination water, industrial cooling and process heat.

2. Work description

2.1. Objectives and methodology

The objective of the present study is to evaluate exergoecomically a solar polygeneration plant producing power, desalinated water, industrial cooling and process heat. Figure 1 shows the polygeneration plant studied.

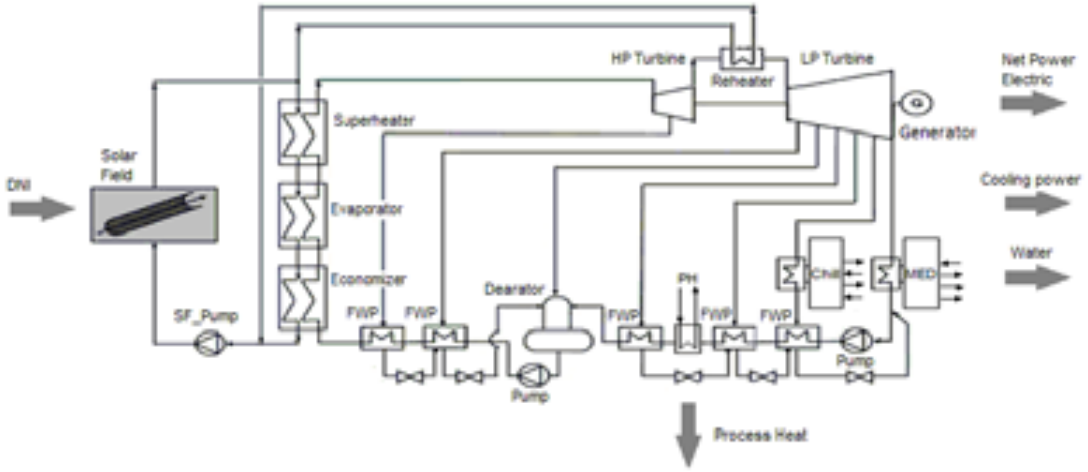

Fig. 1: Configuring solar polygeneration plant.

The methodology followed is presented in Figure 2. First, from preliminary design and modeling of CSP-PTC plant, multi-effect distillation (MED), absorption refrigeration plant, and a heat exchanger, different coupling points are evaluated to select the most appropriate in technical terms. After that, aggregation level is selected allowing the delimitation of the boundaries analysis (Figure 3). Then, a physical structure and productive structure is obtained and the fuels and products are determined. Subsequently, different models are defined: thermodynamic model (1st and 2nd law of thermodynamics), economic model (determination of investment costs, operation and maintenance), exergoeconomic model (Bejan et al, 1996) (determination exergetic unit cost USD/kWh, fuel cost rate, product cost rate, destruction cost rate, total cost rate USD/h, and exergoeconomic factors) and financial model. Finally, the system is solved.

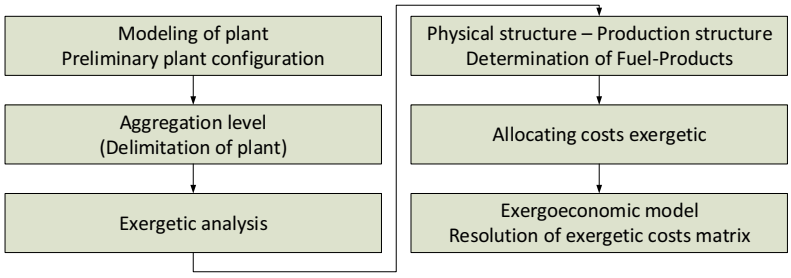

Fig. 2: Methodology.

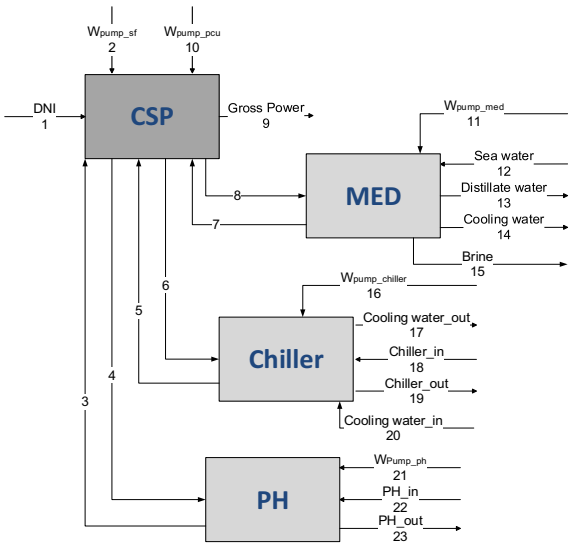

Fig. 3: Aggregation level for exergoeconomic assessment in polygeneration plant.

IPSEpro was used for the modeling and simulations of the system. This software allows to elaborate the flowsheet of a process using the components available in libraries or created by user. It then solves the flowsheet using Newton-Raphson method, linearizing the non-linear equations at starting value. Matlab and EES (equation engineering solver) were used to obtain characteristic parameters in each plant and to exergoeconomics assessment.

The polygeneration plant was evaluated to be installed in northern Chile, Crucero, latitude -22.14°, longitude -69.3°, DNI 3,389 kWh/m^2/year (Escobar et al, 2015).

2.2. Design problem.

Preliminary design and model plants were done separately and subsequently coupled so as to operate in a scheme polygeneration. The CSP-PTC plant is configured with a solar collector field with Skal-et, thermal fluid Dowtherm A and a power block of 55 MW of gross capacity. The power conversion unit consists of a regenerative Rankine cycle with reheat and five extractions. The CSP plant was modeled without thermal energy storage and without backup system. The desalination plant was modeled with 12 effects parallel-cross feed MED plant with 11 feed preheaters. The refrigeration plant was configured with a single-effect LiBr-H_2O absorption chiller with 5 MW of power cooling. As a final point, a heat exchanger was configured for the production of process heat, with 7 MW power heating.

Each plant was validated separately. There is no information about plants operating under this polygeneration scheme. The CSP-PTC plant was validated from Blanco et al. (2011), the MED plant was validated from Zak et al. (2012), and the refrigeration plant was validated from Herold et al. (1996).

2.2.1. Coupling of technologies.

Several coupling points were evaluated between CSP plant and other plants. The most appropriate point of coupling was selected (Figure 1) according to the technical constraints imposed by each system.

MED plant was coupled with CSP plant condenser. In the chosen configuration it was not possible to regulate the amount of water produced. Given that MED plant must operate within a temperature range of 64 to 74 °C (Al-Karaghouli et al, 2013), it was necessary to increase LP turbine backup pressure from 0.06 bar to 0.37 bar (see Table 1). Therefore, electric power was reduced to increase this pressure.

The solar field aperture area must increase to maintain electrical power, but it will increase investment cost and LEC. Polygeneration plant should increase solar field aperture area from 294.534 m^2 to 356,063.7 m^2 equivalent to increase aperture area in 20.9 %.

Desorber of the absorption refrigeration plant required operating temperature within 80 to 110°C (Srikhirin et al, 2001). Absorption refrigeration plant is coupled to the LP turbine 5th extraction where temperature is 108.3°C (see table 1).

Main parameters of polygeneration plant are presented in Table 1.

Tab.1: Polygeneration plant design.

Solar field	Value Unit
Irradiance at design day, SM=1.4	1010.0 W/m^2
Solar Field inlet/outlet temperature	293.0 °C / 393.0 °C
Collector efficiency	0.68
Aperture area	356,063.70 m^2
Power conversion unit	Value Unit
Gross power production	55.55 MW
HP turbine inlet pressure/temperature	103.57 bar / 373 °C
HP turbine extraction pressure/temperature	30.6 bar / 234.9 ºC
LP turbine 1st extraction pressure/temperature	12.77 bar / 341.6 ºC
LP turbine 2nd extraction pressure/temperature	6.18 bar / 259.6 ºC
LP turbine 3rd extraction pressure/temperature	5.99 bar / 256.2 ºC
LP turbine 4th extraction pressure/temperature	2.63 bar / 175.9 ºC
LP turbine 5th extraction pressure/temperature	1.17 bar / 108.3 ºC
LP turbine back pressure/temperature	0.37 bar / 73.9 ºC
HP turbine / LP turbine isentropic efficiency	85.2% / 85.0%
Generator and Motor mechanical and electrical efficiency	98.0 %
Pumps isentropic efficiency	70.0 %
Multi Effect Desalination	Value Unit
Feed seawater intake temperature	25.0 °C
Feed seawater intake salinity	0.042 kg/kg
Feed seawater after down condenser temperature	35.0 °C
Maximum salinity in each effect	0.072 kg/kg
Top Brine Temperature (TBT)	65.0 °C
GOR	9.07
Fresh water production	37,341 m^3/day
Concentration factor	1.71
Single stage absorption chiller	Value Unit
Cooling power	5.0 MW
Chilled water inlet / outlet temperature	10.0 °C / 6 °C
Cooling water inlet temperature (absorber)	25.0 °C
Cooling water outlet temperature (condenser)	35.0 °C
Inlet temperature desorber	108.5 °C
COP	0.70
Process Heat	Value Unit
Heating power	7.0 MW
Hex inlet / outlet temperature	63.0 °C / 90.0 °C

2.2.2. Decision variables.

Decision variables used are: LP turbine back pressure, LP turbine 5th extraction pressure, isentropic efficiency of turbine and of pump. LP turbine back pressure varies between 0.28 to 0.40 bar, it influences the inlet temperature to the first effect of the multi-effect desalination module. LP turbine 5th extraction pressure varies between 1.00 to 1.30 bar, it influences the desorber inlet temperature of the cooling system. Isentropic efficiency varies between 80% to 90% in turbine and between 65% to 75% in pump.

2.2.3. Exergoeconomic and economic parameters.

Exergetic analysis considered reference temperature 25°C, reference atmospheric pressure 1.013 bar, and reference mass fraction LiBr 0.5542 kg/kg.

Investment cost MUSD (CAPEX) and operating and maintenance cost MUSD/year (OPEX) considered are: 241.13 and 4.0580 in CSP (IRENA, 2012; NREL, 2013), 22.85 and 1.2587 in MED plant (Li et al., 2013; Verdier et al., 2011; Trieb eta al., 2009; Trieb et al., 2008; IEA-ETSAP and IRENA, 2012), 3.15 and 0.0069 in Refrigeration plant (Mokhtara et al., 2010; Lazzarin, 2013; Misra et al., 2003, Infante and Kim, 2013.), and finally 0.197 and 0.0004 in process heat plant (Turton, 2012). It has been considered a horizon of 25 years and a discount rate of 10%.

For financial evaluation, sales prices of each product were considered: electric energy 0.12 USD/kWh (CNE, 2015), electric power: 9.5 USD/kW/month (CNE, 2015), desalinated water: 3.5 USD/m^3 (Wood Mackenzi, 2014), cooling: 0.1 USD/kWh (CDEC-SING, 2014; Demir et al, 2008), process heat: 0.08 USD/kWh (CDEC-SING, 2014; Kecebas et al, 2013). Chile has an imposition rate on the utility of 21% (SII, 2015). A constant depreciation over the plant lifetime is chosen here.

In the model, variations of kinetic energy, potential energy, and pressure drops in the lines were disregarded.

2.3. Models developed.

The exergoeconomic assessment involves applying a thermodynamic model where are made mass balances (eq. 1), energy balances (eq. 2) and exergy balances (eq. 3). For determining the exergy specified (eq. 4) the potential and kinetic exergy were disregarded. It is calculated the different kind rates of exergy, such as, exergy work rates (eq. 5), exergy process heat rates (eq. 6), exergy physical rates (eq. 7), exergy chemical rates (eq. 8), and exergy rates from sun (eq. 9). Thereby thermodynamic properties and rates of exergy in each stream are determined.

$$\sum(\dot{m}_{in} - \dot{m}_{out}) = 0 \quad \text{(eq. 1)}$$

$$\sum(\dot{m}_{in} h_{in}) - \sum(\dot{m}_{out} h_{out}) - \dot{W} + \dot{Q} = 0 \quad \text{(eq. 2)}$$

$$\sum(\dot{Q}\left(1 - \frac{T_0}{T}\right)) - \dot{W} + \sum(\dot{m}_{in} e_{in}) - \sum(\dot{m}_{out} e_{out}) - \dot{E}_D = 0 \quad \text{(eq. 3)}$$

$$e = e_{ph} + e_{ch} + e_p + e_k \quad \text{(eq. 4)}$$

$$\dot{E}_{work} = \dot{W} \quad \text{(eq. 5)}$$

$$\dot{E}_{heat} = \left(1 - \frac{T_0}{T}\right)\dot{Q} \quad \text{(eq. 6)}$$

$$\dot{E}_{ph} = \dot{m} e_{ph} = \dot{m}((h - h_0) - T_0(s - s_0)) \quad \text{(eq. 7)}$$

$$\dot{E}_{ch} = \dot{m} e_{ch} = \dot{m}\left(-\Delta G + \left(\sum_p n e_{ch} - \sum_R n e_{ch}\right)\right) \quad \text{(eq. 8)}$$

$$\dot{E}_{sun} = A \cdot DNI \cdot (1 + \frac{1}{3}\left(\frac{T_0}{T_{sun}}\right)^4 - \frac{4}{3}\left(\frac{T_0}{T_{sun}}\right)) \quad \text{(eq. 9)}$$

Additionally, It is calculated the energy efficiency in power plant (eq. 10), coefficient of performance (COP) in Single stage absorption chiller (eq. 11), energy efficiency in process heat (eq. 12), energy efficiency in MED (eq. 13), utilization factor of polygeneration plant (eq. 14), gained output ratio (GOR) in MED (eq. 15), exergy efficiency (eq. 16), and solar multiple (SM) (eq. 17).

$$\eta_{CSP} = \frac{\dot{W}_{net}}{\dot{Q}_{in}} \quad \text{(eq. 10)}$$

$$\eta_{PH} = \frac{\dot{Q}_{out}}{\dot{Q}_{in} + \dot{W}_{pump}} \quad \text{(eq. 11)}$$

$$COP_{abs} = \frac{\dot{Q}_{chiller}}{\dot{Q}_{desorb} + \dot{W}_{pumps}} \quad \text{(eq. 12)}$$

$$\eta_{MED} = \frac{\dot{m}_{distillate} h_{distillate}}{\dot{Q}_{in\_med} + \dot{W}_{pumps}} \quad \text{(eq. 13)}$$

$$\eta_{polygeneration} = \frac{\dot{W}_{net} + \dot{m}_{distillate} h_{distillate} + \dot{Q}_{chiller} + \dot{Q}_{out}}{\dot{Q}_{in}} \quad \text{(eq. 14)}$$

$$GOR = \frac{\dot{m}_{distillate}}{\dot{m}_{steam\ 1st\ effect}} \quad \text{(eq. 15)}$$

$$\varepsilon = \frac{\dot{E}_{out}}{\dot{E}_{in}} = 1 - \frac{\dot{E}_D}{\dot{E}_{in}} \quad \text{(eq. 16)}$$

$$SM = \frac{\dot{Q}_{th,solar\ field}}{Q_{th,power\ block}{}_{design\ point}} \quad \text{(eq. 17)}$$

The economic model is then applied. This is quantifying the capital investment cost rates (eq. 18), the operating and maintenance cost rates (eq. 19), and the total cost rates (eq. 20).

$$\dot{Z}_k^{CI} = \frac{CC_L}{\tau}\frac{PEC_k}{\sum_k PEC_k} \quad \text{(eq. 18)}$$

$$\dot{Z}_k^{OM} = \frac{OMC_L}{\tau}\frac{PEC_k}{\sum_k PEC_k} \quad \text{(eq. 19)}$$

$$\dot{Z} = \dot{Z}_k^{CI} + \dot{Z}_k^{OM} \quad \text{(eq. 20)}$$

Later it is developed the exergoeconomic model. By exergy balance costs (eq. 21) it is obtained exergy cost unitary c_j and exergy cost rate $\dot{C}_j$ (eq. 22) for each stream.

$$\sum_{j=1}^{n}(c_j\dot{E}_j)_{k,in} + \dot{Z}_k^{CI} + \dot{Z}_k^{OM} = \sum_{j=1}^{m}(c_j\dot{E}_j)_{k,out} \quad \text{(eq. 21)}$$

$$\dot{C}_j = c_j\dot{E}_j = c_j(\dot{m}_j e_j) \quad \text{(eq. 22)}$$

With these results it is calculated the exergy destruction cost rate (eq. 23), exergy destruction ratio (eq. 24), relative cost difference (eq. 25), and exergoeconomic factor (eq. 26).

$$\dot{C}_{D,k} = c_{F,k}\dot{E}_{D,k} \quad \text{(eq. 23)}$$

$$y_{D,k} = \frac{\dot{E}_{D,k}}{\dot{E}_{F,tot}} \quad \text{(eq. 24)}$$

$$r_k = \frac{c_{P,k} - c_{F,k}}{c_{F,k}} = \frac{c_{F,k}\left(\dot{E}_{D,k} + \dot{E}_{L,k}\right) + \left(\dot{Z}_k^{CI} + \dot{Z}_k^{OM}\right)}{c_{F,k}\dot{E}_{P,k}} \quad \text{(eq. 25)}$$

$$f_k = \frac{\dot{Z}_k}{\dot{Z}_k + c_{F,k}\left(\dot{E}_{D,k} + \dot{E}_{L,k}\right)} \quad \text{(eq. 26)}$$

For evaluating economic, it is calculated the levelized cost (eq. 27) of energy (LEC), of water (LWC), of cooling (LCC), and process heat (LHC). crf is the capital recovery factor (eq. 28).

$$LC = \sum_{j=0}^{n}\frac{capex_j crf + opex_j + Cf_j}{(1+i)^j}/(Annual\ Production_j) \quad \text{(eq. 27)}$$

$$crf = \frac{i(1+i)^n}{(1+i)^n - 1} \quad \text{(eq. 28)}$$

Finally, it is calculated the net present value (NPV) (eq. 29) and internal rate of return (IRR) (eq. 30).

$$NPV = \sum_{j=0}^{n}\frac{Cash\_in_j - Cash\_out_j}{(1+i)^j} \quad \text{(eq. 29)}$$

$$0 = \sum_{j=0}^{n}\frac{Cash\_in_j - Cash\_out_j}{(1+IRR)^j} \quad \text{(eq. 30)}$$

3. Results and discussion.

3.1. Monthly production, production in clear day and production in partial day.

Polygeneration plant receives 968.6 GWh/year from the sun, of which 666.03 GWh/year are transferred to the power conversion unit. Consequently, gross electric energy produced is 186.9 GWh/year, net electrical energy is 179.5 GWh/year, water produced is 5.32 Mm^3/year, power cooling is 16.9 GWh/year and power

heating is 23.7 GWh/year. Average monthly net electrical energy is 14.9 GWh/month, water is 0.44 Mm^3/month, power cooling is 1.41 GWh/month, and power heating is 1.97 GWh/month (Figure 4).

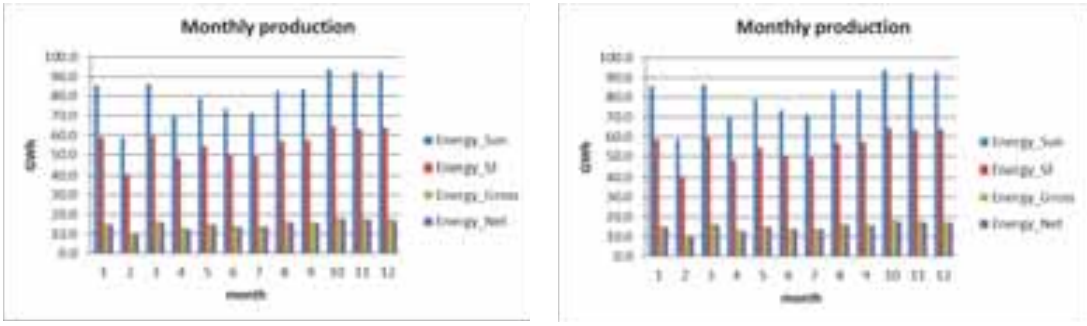

Fig. 4: Monthly production of: a- energy sun, energy solar field (SF), energy_gross (electricity), energy_net (electricity). b- energy_net (electricity), energy_ cooling, energy process heat (ph) and water volume.

In Figure 5 the monthly exergy destruction is presented. Average monthly exergy destruction is 50.7 GWh/month for polygeneration plant, 47.1 GWh/month in CSP plant, 3.2 GWh/month in MED plant, 0.3 GWh/month in cooling plan, and 0.1 GWh/month in heating plant.

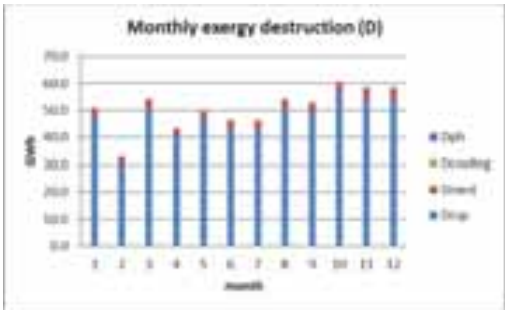

Fig. 5: Monthly exergy destruction in CSP plant, MED plant, Cooling plant and Process Heat plant (ph).

Production was analyzed on a clear day on December 21 (Figure 6a) and on a partial day on June 19 (Figure 6b). Some collectors in the solar field must be out of focus (partial defocusing) on clear day from 10:00 to 18:00 to maintain maximum production of plant design. Thermal energy storage could return this extra energy to power conversion unit.

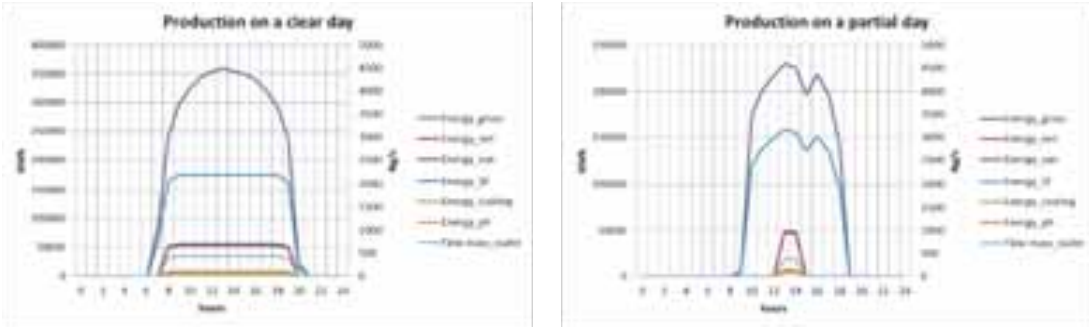

Fig. 6: Production on a: a- clear day, b- partial day.

In a partial day, such as in Figure 6b, energy collected by the solar collectors is insufficient to operate at full load and it must operate at partial loads. Consequently, polygeneration plant produces less energy. A backup system could improve polygeneration plant production.

3.2. Exergoeconomic assessment results.

In relation to the exergoeconomic assessment: exergy destruction cost rate plus total cost rates (capital investment plus operating and maintenance) are 9332.0, 1156.3, 123.9 and 32.8 USD/hour for CSP plant, MED plant, cooling plant and heating plant respectively. Relative cost differences are 99.0%, 99.0%, 92.8% and 46.5%. Exergoeconomic factors are 97.6%, 97.0%, 84.9% and 43.2 10% for CSP plant, MED plant, cooling plant and heating plant respectively. According to these indicators, it is recommended to optimize

CSP plant. This requires reducing total cost rates (capital investment plus operating and maintenance) in demerit of equipment efficiency. Effects of cooling plant and heating plant are marginal, although the location of these plants affects performance of CSP plant.

Operating on a clear day or partial day has a direct impact on exergetic unit cost and product cost rate, as shown in Figure 7.

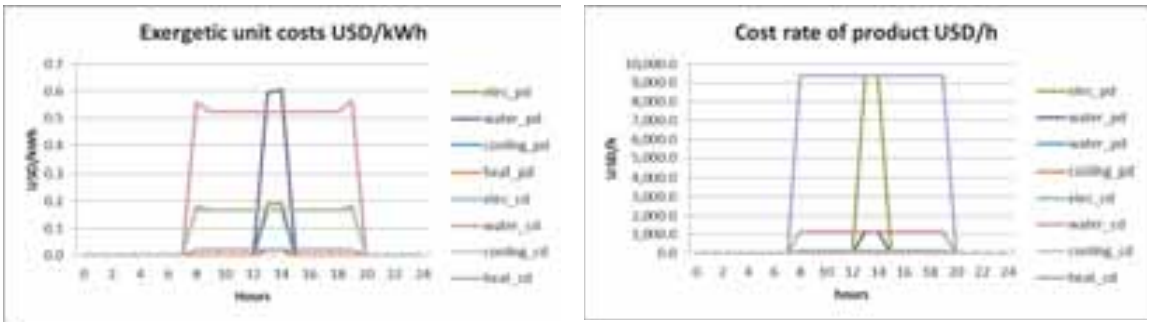

Fig.7: a- Exergetic unit costs USD/kWh. b- Total product cost rate of USD/h. (pd: partial day, cd: clear day)

3.3. Solar multiple results.

Minimum total cost rate of products (electricity + water + cooling + heat process) and minimum total levelized cost (LEC + LWC + LCC + LHC) is reached at solar multiple of 1.3 (see Figures 8 and 9). Minimum total product cost rate is 10713.3 USD/h, the minimum LEC is 0.168 USD/kWh and the minimum LWC is 0.734 USD/m^3 for annual production.

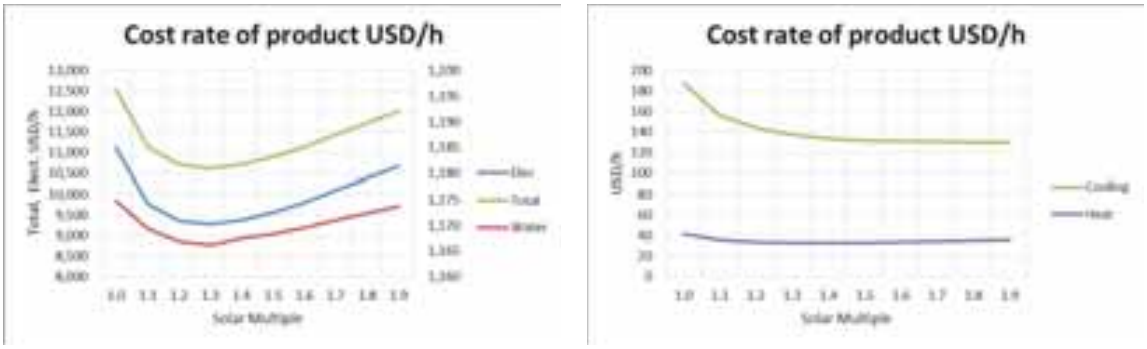

Fig.8: Product cost rate of: a- Total, electricity and water. b- Cooling and heat process.

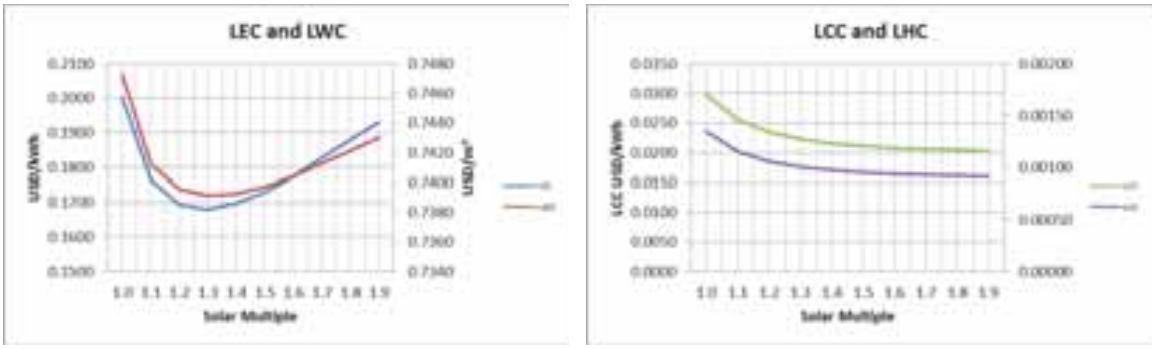

Fig. 9: a- Levelized energy cost (LEC) USD/kWh and Levelized water cost (LWC) USD/m3. b- Levelized cooling cost (LCC), Levelized heating cost (LCH) USD/kWh.

The production of each of the products is raised by increasing the solar multiple, see Figure 10, but also increases investment costs, operation and maintenance costs. Thus, the criterion for selecting the optimal size of the plant in CSP plant is where the minimum LEC is reached (Montes et al., 2009). In the case of polygeneration plant the criterion for selecting the optimal size of the plant is where the minimum total product cost rate is reached that matches with minimum LEC, minimum LWC and minimum total levelized cost.

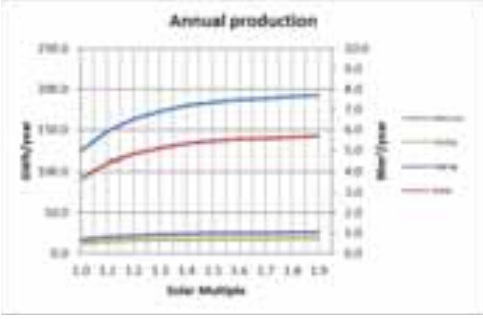

Fig.10: Polygeneration plant production.

3.4. Decision variables.

The results are presented in Figures 11 and 12. Minimum product cost rate is produced at a pressure of 0.28 bar but the maximum NPV occurs at 0.4 bar by varying LP turbine backup pressure. On the other hand, minimum cost rate of product is produced at the same pressure of maximum NPV by varying LP turbine 5th extraction pressure.

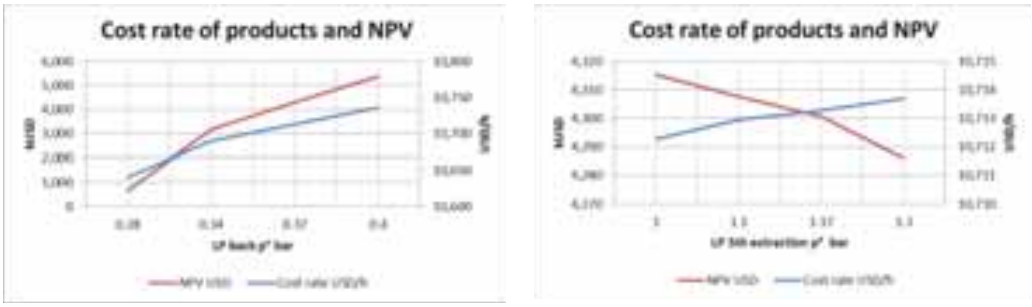

Fig.11: Effects of: a- LP turbine backup pressure, b- LP turbine 5th extraction pressure.

Fig.12: Effects of Isentropic efficiency in: a- turbine, b- pump.

3.5. Energy efficiency.

In Figure 13 Sankey diagram of polygeneration plant is presented. Utilization factor of polygeneration plant is 62.78%. The efficiencies are: 68.8% in solar field, 30.6% in the power conversion unit, 20.9% in CSP plant, 89.9% in MED plant, 99.98% in heating plant and a COP of 0.7 in cooling plant.

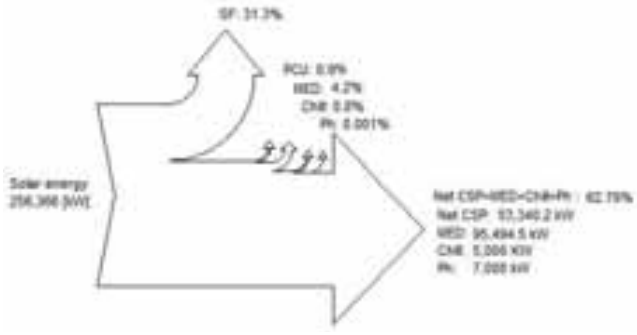

Fig. 13: Sankey diagram of polygeneration plant.

3.6. Exergetic efficiency and exergy destruction.

In Figure 14 Grassmann diagram of polygeneration plant is presented. The exergetic efficiencies are: 24.5% in polygeneration plant, 57.1% in solar field, 52.7% in power conversion unit, 24.7% in MED plant, 66.9% in heating plant, and 33.9% in cooling plant.

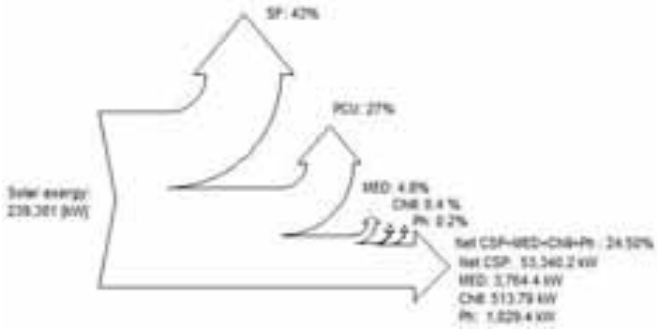

Fig. 14: Grassmann diagram of polygeneration plant.

In Figure 15 exergetic efficiency and exergy destruction in each subsystem are presented and evaluated. Exergy destruction are the following: 43.0% in solar field, 27.0% in power conversion unit, 77.6% in CSP plant, 4.8% in MED plant, 0.4% in cooling plant, 0.2% in heating plant, and 75.4% in polygeneration plant. Figure 14 shows that the effect on the destruction of exergy in cooling plant and heating plant is marginal.

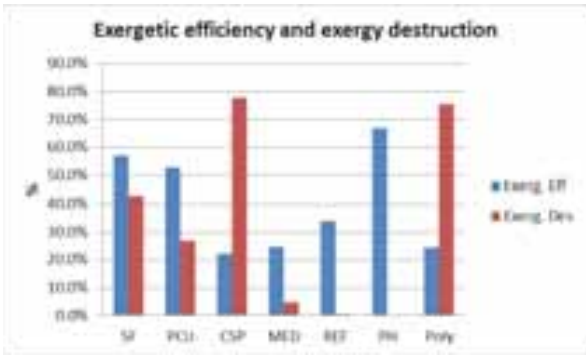

Fig.15: Exergetic efficiency and exergy destruction in polygeneration plant.

In Figure 16 exergetic efficiency is presented in each component of CSP plant. The main components where exergy destruction occurs are: solar collectors (43.0%), evaporator (11.4%), reheater (4.8%), economizer (3.8%), superheater (2.2%), LP turbine (1.8%), generator (1.0%), HP turbine (0.9%) and CFWP3 preheater (0.4%).

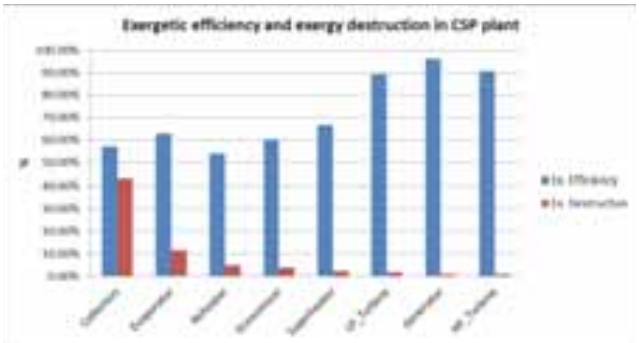

Fig. 16: Exergetic efficiency and exergy destruction in main components of CSP plant.

In Figure 17 exergetic efficiency in main components of MED plant is presented. The main components where exergy destruction occurs are: Effect 1 (1.11%), condenser (0.75%), and second to twelfth effects (from 0.24% to 0.16%).

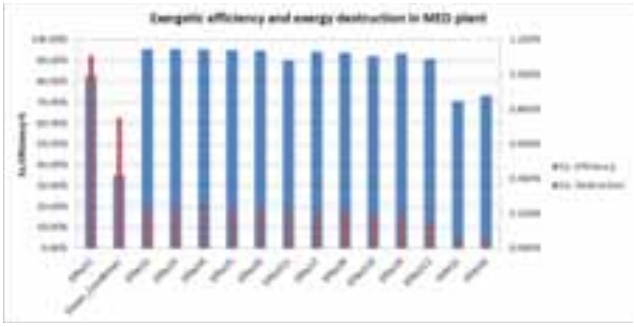

Fig. 17: Exergetic efficiency and exergy destruction in main components of MED plant.

In Figure 18a exergetic efficiency in main components of cooling plant is presented. Main components where exergy destruction occurs are: absorber (0.44%), desorber (0.06%), condenser (0.05%), and evaporator (0.05%).

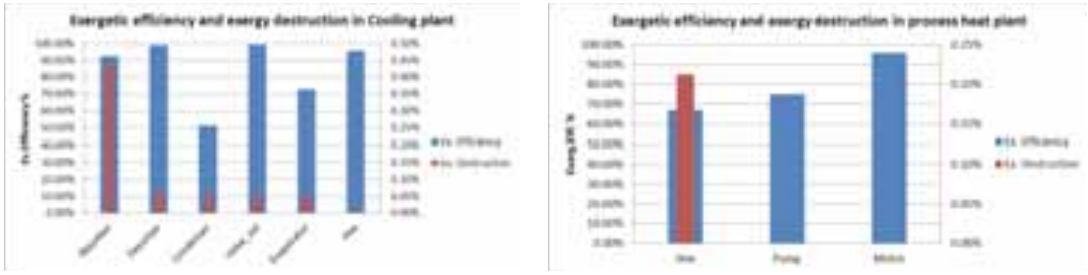

Fig. 18: Exergetic efficiency and exergy destruction of a- cooling plant. b- process heat plant

Finally, in Figure 18b exergetic efficiency in process heat plant is presented. The component where most exergy destruction occurs is the heat exchanger (0.21%).

4. Conclusions

The achievements of this work are the design and simulation of a solar polygeneration plant for the production of electricity, desalinated water, industrial cooling and process heat, using a CSP-PTC plant, a MED plant, a simple effect absorption cooling plant, and a heat exchanger for process heat, simulated hourly, and performing an exergoeconomic analysis.

In terms of energy efficiency, a polygeneration plant that operates individual plants has more efficiency. Polygeneration plant has a utilization factor of 62.7% (20.8% CSP, 89.9% MED, 0.701 refrigeration and 99.9% process heat) meanwhile CSP plant has an efficiency energy of 20.9%.

In terms of exergy efficiency and exergy destruction, polygeneration plant exergetic efficiency is 24.5%. In CSP plant the highest exergy destruction is produced in solar field and power conversion unit. The second highest is produced in MED plant. Destruction of exergy in cooling plant and heating plant is marginal. The main components where exergy destruction occurs in CSP plant are solar collectors (43.0%), evaporator (11.4%), reheater (4.8%), economizer (3.8%), and superheater (2.2%).

A production on clear day generates surplus energy, which can be stored in thermal energy storage. Thermal energy storage could return this extra energy to power conversion unit and raise the plant availability.

According to the exergoeconomic assessment, it is recommended to optimize CSP plant since CSP plant has the biggest total cost rate. This requires reducing total cost rates (capital investment plus operating and maintenance) in demerit of equipment efficiency.

Regarding solar multiple, the minimum LEC and LWC occurs with a solar multiple of 1.3. LEC varies from 0.17 to 0.20 USD/kWh, LWC ranges from 0.739-0.747 USD/m^3, LCC varies from 0.02 to 0.03 USD/kWh, and LHC varies from 0.001 to 0.0013 USD/kWh. The criterion for selecting the optimal size of the plant is where the minimum total cost (product cost rate) is reached.

When it comes to varying the decision variables, the main results in polygeneration plant are a product cost rate of 10,713.2 USD/h and NPV of 4.3 MUSD. LP turbine backup pressure, LP turbine 5th extraction pressure, temperature effects condenser outlet in MED plant, and temperature effects condenser in cooling plant are evaluated. Minimum product cost rate is produced at a pressure of 0.28 bar but the maximum NPV occurs at 0.4 bar by varying LP turbine backup pressure.

As future actions the study should incorporate a thermal energy storage (TES) and backup, as well as, apply optimization tools.

Acknowledgments

This research work was funded by CONICYT-PCHA/Doctorado_Nacional/año2013-folio21130634 and Fondecyt 1130621.

References

1. Al-Karaghouli, A., and Kazmerski, L., Energy consumption and water production cost of conventional and renewable-energy-powered desalination processes. Renewable and Sustainable Energy Reviews, 24, 2013.
2. Bejan, A., Moran, M., and Tsatsaronis, G., Thermal Design and Optimization. John Wiley & Sons, 1996.
3. Blanco-Marigorta, M., Sanchez-Henríquez, M., and Peña-Quintana, J., "Exergetic comparison of two different cooling technologies for the power cycle of a thermal power plant," Energy, vol. 36, no. 4, pp. 1966–1972, Apr. 2011.
4. Centros de Despacho Económico de Carga del Sistema Interconectado del Norte Grande (CDEC-SING), www.cdec-sing.cl.
5. Cipollina, A., Micale, G., and Rizzuti, L., Seawater Desalination: Conventional and Renewable Energy Processes. Springer Science & Business Media, 2009, p. 320.
6. Comisión Nacional de Energía, CNE, Estadistica de precios, 2015. http://www.cne.cl/estadisticas/electricidad/
7. Demir, D., Mobedi, M., and Ülkü, S. A review on adsorption heat pump: Problems and solutions.Renewable and Sustainable Energy Reviews, 12(9):2381 – 2403, 2008.
8. Escobar, R., Cortés, C., Pino, A., Salgado, M., Bueno, E., Ramos, F., Boland, J., Cardemil, J. Estimating the potential for solar energy utilization in Chile by satellite-derived data and ground station measurements, Solar Energy, Volume 121, November 2015, Pages 139-151.
9. Fernández-García, A., Zarza, E., Valenzuela, L., and Pérez, M. Parabolic-trough solar collectors and their applications. Renewable and Sustainable Energy Reviews, 14(7):1695– 1721, 2010.
10. Hassan, H., and Mohamad, A., "A review on solar cold production through absorption technology," Renew. Sustain. Energy Rev., vol. 16, no. 7, pp. 5331–5348, Sep. 2012.
11. IEA-ETSAP and IRENA. Water Desalination Using Renewable Energy. Technology Brief. Technical report, 2012.
12. Infante, C., Kim, D., Techno-economic review of solar cooling technologies based on location-specific data, International Journal of Refrigeration, Volume 39, March 2014, Pages 23-37
13. IRENA, International renewable energy agency, Renewable energy technologies: cost analysis series. Concentrating Solar Power. 2012.
14. Kecebas,A., Ali Alkan, M., Yabanova,I. and Yumurtaci, M. Energetic and economic evaluations of geothermal district heating systems by using ANN. Energy Policy, 56(0):558 – 567, 2013.
15. Keith E. Herold, Reinhard Radermacher, and Sanford A. Klein. Absorption Chillers and Heat Pumps. CRC Press, 1996.
16. Lazzarin, R. Solar cooling: PV or thermal? a thermodynamic and economical analysis. International Journal of Refrigeration, 2013.
17. Li, C., Yogi Goswami, and Elias Stefanakos. Solar assisted seawater desalination: A review.Renewable and Sustainable Energy Reviews, (19):136–163, 2013.
18. Misra, R., P.K. Sahoo, S. Sahoo, and A. Gupta. Thermoeconomic optimization of a single e!ect water/libr vapour absorption refrigeration system. International Journal of Refrigeration, 26:158–169, 2003.
19. Mokhtara, M., Muhammad Tauha Alia, Simon Bräunigerb, Afshin Afsharib, Sgouris Sgouridisa, Peter Armstronga, and Matteo Chiesa. Systematic comprehensive technoeconomic assessment of solar cooling technologies using location-specific climate data. 87 (12):3766–3778, 2010.

20. National Renewable Energy Laboratory (NREL). System advisor model (SAM) case study: Andasol-1,2013.https://sam.nrel.gov/sites/sam.nrel.gov/files/content/case_studies/sam_case_csp_physical_trough_andasol-1_2013-1-15.pdf
21. Palenzuela, P., Zaragoza, G., Alarcón-Padilla, D., Guillén, E., Ibarra, M., and Blanco, J. Assessment of different configurations for combined parabolic-trough (pt) solar power and desalination plants in arid regions. Energy, 36(8):4950 – 4958, 2011.
22. Sarbu, I., Sebarchievici, C., Review of solar refrigeration and cooling systems, Energy and Buildings, Volume 67, December 2013, Pages 286-297, ISSN 0378-7788, http://dx.doi.org/10.1016/j.enbuild.2013.08.022.
23. Serra, L., Lozano, M., Ramos, J., Ensinas, A., and Nebra, S., "Polygeneration and efficient use of natural resources," Energy, vol. 34, no. 5, pp. 575–586, May 2009.
24. Servicios de Impuestos Internos, SII, 2015. www.sii.cl
25. Srikhirin, P., Aphornratana, S., and Chungpaibulpatana, S. A review of absorption refrigeration technologies. Renewable and sustainable energy reviews, 5(4):343– 372, 2001.
26. Trieb F, Müller-Steinhagen H, Kern J, Scharfe J, Kabariti M, Al Taher A. Technologies for large scale seawater desalination using concentrated solar radiation. Desalination 2009.
27. Trieb F, Müller-Steinhagen H. Concentrating solar power for seawater desalination in the Middle East and North Africa. Desalination 2008.
28. Tsatsaronis, G. 1993. Thermoeconomic analysis and optimization of energy systems. Progress in energy and combustion science 19, 227-257.
29. Turton, R. Analysis, Synthesis and Design of chemical processes. Prentice Hall, NJ, 2012.
30. Ullah, K.R., Saidur, R., Ping, H.W., Akikur, R.K., Shuvo, N.H., A review of solar thermal refrigeration and cooling methods, Renewable and Sustainable Energy Reviews, Volume 24, August 2013, Pages 499-513, ISSN 1364-0321, http://dx.doi.org/10.1016/j.rser.2013.03.024.
31. Verdier, F. MENA Regional Water Outlook. Part II. Desalination Using Renewable Energy. Technical report, Fichtner, 2011.
32. Wood Mackenzie, CRU Group, Mining Council, 2014, made available through Consejo Minera at www.consejominero.cl
33. Zak, G., Thermal desalination: Structural optimization and integration in clean power and water. Master's thesis, Massachusetts Institute of Technology, 2012.

Nomenclature

A : aperture area, m^2
a_i: coefficients for collector efficiency, -
Cash_in: Cash inflows, USD/year
Cash_out: Cash outflows, USD/year
capex : capital expenditure, USD
cf : fuel cost, USD/year
$\dot{C}$: cost rate associated with exergy transfer or exergy cost rate , USD/h
$\dot{C}_j$: exergy cost rate, USD/h
$\dot{C}_{D,k}$: exergy destruction cost rate, USD/h
$\dot{C}_{L,k}$: exergy loss cost rate, USD/h
$\dot{C}_{F,k}$: exergy fuel cost rate, USD/h
$\dot{C}_{P,k}$: exergy product cost rate, USD/h
c_j : cost per unit of exergy or exergetic unit cost, USD/kWh
$c_{F,k}$: cost per unit of exergy fuel, USD/kWh
$c_{P,k}$: cost per unit of exergy product, USD/kWh
cfr: capital recovery factor, %
COP: Coefficient of performance, -
D: exergy destruction, kWh
DNI: direct normal irradiance, W/m^2
e : exergy specified, kJ/kg
e_{ch} : chemical exergy specified, kJ/kg
e_k : kinetic exergy specified, kJ/kg
e_p : potential exergy specified, kJ/kg
e_{ph} : physical exergy specified, kJ/kg
$\dot{E}$: time rate of exergy or exergy rate, kJ/s
$\dot{E}_{heat}$: time rate of exergy heat process, kJ/s
$\dot{E}_{ch}$: time rate of exergy chemical, kJ/s
$\dot{E}_{sun}$: time rate of exergy from sun, kJ/s
$\dot{E}_{ph}$: time rate of exergy physical, kJ/s
$\dot{E}_{work}$: time rate of exergy work, kJ/s
$\dot{E}_D$: time rate of exergy destruction rate, kJ/s
$\dot{E}_{D,k}$: time rate of exergy destruction rate of element k, kJ/s
$\dot{E}_{L,k}$: time rate of exergy loss rate, kJ/s
$\dot{E}_{F,k}$: time rate of exergy fuel rate, kJ/s
$\dot{E}_{P,k}$: time rate of exergy product rate, kJ/s
i: discount rate, %
E_{anual} : annual electricity, kWh/year
E_{th_an} : annual heat, kWh/year
f_k : exergoeconomic factor, %
G: Gibbs function, kJ
G_b: direct normal irradiance, W/m^2
GHI: global horizontal irradiance, W/m^2
GOR: gained output ratio, -
h : enthalpy, kJ/kg
IRR: internal rate of return, %
LC: levelized cost, USD/kWh o USD/m^3
LCC : levelized cooling cost, USD/kWh
LEC : levelized energy cost, USD/kWh

LHC : levelized heat cost, USD/kWh
LWC : levelized water cost, USD/m^3
$\dot{m}$: flow rate, kg/s
n: number of moles (eq. 8), kmol
n: number of time periods, years
NPV: net present value, USD
opex : operational expenditure or operation and maintenance cost, USD/year
$\dot{Q}_{th,power\ block}$: thermal power demanded by the power block, W
$\dot{Q}_{th,solar\ field}$: thermal power produced in the solar field, W
$\dot{Q}$: heat rate, kJ/s
r_k : relative cost difference, %
SM : solar multiple, -
T : temperature, °C
T_0 : ambient temperature, °C
TBT: top brine temperature, °C
$\dot{W}$: work rate, kJ/s
$y_{D,k}$: exergy destruction ratio
$\dot{Z}_k^{CI}$: capital investment cost rates, USD/h
$\dot{Z}_k^{OM}$: operating and maintenance cost rates, USD/h
$\dot{Z}$: total cost rates, USD/h

Greek symbols

ε : exergetic efficiency
η : efficienccy
τ : average annual time of plant operation at nominal capacity

Abbreviations

CFWP: condensate feed water preheater
Chill: chiller
CHP: combined heat and power
CDEC: centro de despacho económico de carga
CNE: comisión nacional de energía
CR: central receiver
CSP: concentrated solar power
DS: dish Stirling
EES: Engineering equation solver
FWP: feed water preheater
G: generator
HEX: Heat exchanger
HP: high pressure
LF: linear fresnel
$LiBr/H_2O$: Lithium bromide / water
LP : low pressure
MED: multi-effect desalination
MSF: multi stage flash
OCR: organic rankine cycle
P: Products
PCU: Power unit convertion
PH: process heat
PHH: Preheater
PTC: parabolic trough collector
R: reactants
RO: reverse osmosis
SF: solar field
SGFWP: steam generator feed water preheater
SII: servicio de impuestos internos
SING: Sistema interconectado del norte grande

Hybrid Solar Tower Pilot Plants for Co-Generation of Heat and Power for Brazilian Agro-Industry

Gilles Maag[1], Kimberly Tolentino de Oliveira[1], and Celso Eduardo Lins de Oliveira[1]

[1] University of São Paulo, Faculty of Zootechny and Food Engineering, Pirassununga, SP (Brazil).

Abstract

A currently undergoing project of two 100 kW_{el} central tower receiver concentrating solar power pilot plants for co-generation of heat and electricity for agro-industrial consumers is being presented. A strong agro-industrial sector and high solar resource make Brazil an ideal candidate for such a system. Grid-independent energy availability is ensured by hybrid firing of the plants' micro-turbines with bio-diesel. A steady-state-based model using DNI (Direct Normal Irradiance) values calculated from measured GHI (Global Horizontal Irradiance), using the DISC model, is applied to predict the yearly production of electricity of one of the plants and its degree of coverage of the associated slaughterhouse's requirements. An optical efficiency matrix of the heliostat field was obtained through ray-tracing simulations using the dedicated software tool Tonatiuh. Calculated yearly solar electricity production is 137 MWh, 76.5% of which can be used by the slaughterhouse, covering 48.5% of its consumption, the remainder being covered by bio-diesel. 23.5% of the produced solar electricity can be supplied to the grid. The yearly solar-to-electricity efficiency of the plant is 11.3%.

Keywords: c*o-generation, concentrated solar power, distributed generation, hybrid, solar tower, agro-industry, pilot plant.*

1. Introduction

CSP (Concentrating Solar Power) technology has been deemed a promising route for heat and power supply of agro-industrial processes in regions benefiting from high solar resource (> 2,000 $kWh \cdot m^{-2} \cdot y^{-1}$) as is the case for wide areas of Brazil, especially the North-East and Center regions. In regions of poor grid reliability and high electricity prices, CSP can be advantageous compared to other new renewable sources such as photovoltaics and wind power, by ensuring grid-independent energy availability thanks to thermal energy storage and hybridization with biofuels, and the possibility of co-generation of process heat. Previous studies considering implementation of solar energy applications in industry or agro-industry were able to individuate a significant potential for energy, process heat and cooling supply (Fuller, 2011; Mekhilef et al., 2011; Quijera et al., 2011a, 2011b; Tora et al., 2010).

To promote the use of CSP and demonstrating the functioning of the technology, the construction of two pilot-scale central tower receiver co-generation plants and their integration with agro-industrial facilities is currently undergoing in Pirassununga, São Paulo (case #1) and Caiçara do Rio do Vento, Rio Grande do Norte (case #2). Both plants use solar/bio-diesel hybrid-powered Brayton cycles, with 390 and 250 kW_{th} cavity receivers, respectively, operating with air at 1,173 K and 4.5 bar, powering 100 kW_{el} micro-turbines, as have been successfully operated and tested in past (Amsbeck et al., 2010). The solar field consists of 75 (case #1) and 47 (case #2) heliostats, each having a paraboloid-shaped, rectangular reflective surface of 8 m^2 area. A focal length of 30 m was chosen, close to the average distance to the receiver aperture (whose diameter is 0.9 m), situated at 25 m height. A design of the solar field and a process schematic are shown in Fig. 1.

Selection and/or peer review under responsibility of Scientific Committee
doi:10.18086/swc.2015.04.22 Available at http://proceedings.ises.org

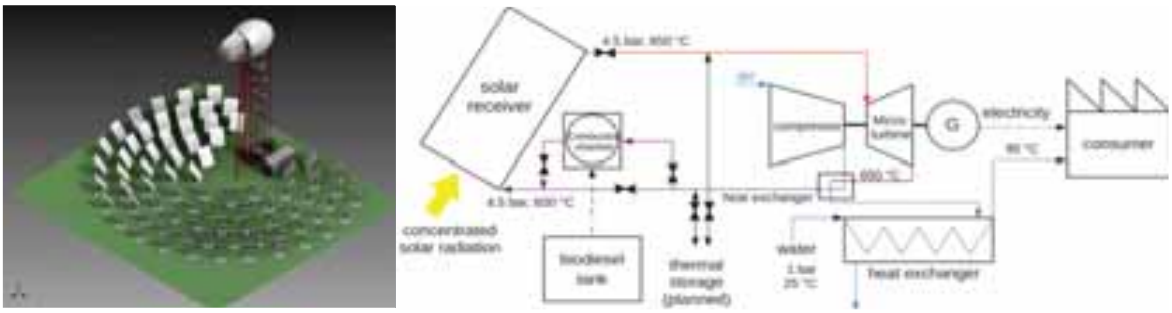

Fig. 1: Design of heliostat field for plant #1 (left), and process schematic of the two 100 kW_{el} hybrid solar tower plants (right).

Co-generation and tri-generation applications for microturbines (Buck and Friedmann, 2007; Ho et al., 2004; Kaikko and Backman, 2007), as well as solar turbine systems of various sizes and degrees of hybridization (Barigozzi et al., 2012; Le Roux et al., 2011; Schwarzbözl et al., 2006) have been proposed. The pilot plants are planned to provide energy and process heat supply to a school slaughterhouse (case #1) and a dairy factory (case #2). In this work, the performance of plant #1, in terms of electricity supply, is predicted using a numerical model based on 10 min steady-state intervals using DNI obtained from measured GHI data at the installation location.

2. Methodology

2.1. Solar resource

At the considered location (21°57' S, 47°26' W), only measured GHI data is available, in 10-min intervals, over a measurement period of 6 years. DNI values were estimated using the DISC model (Maxwell, 1987; Ineichen et al., 1992). From the individual data points, a probability distribution function f(DNI,m,h) is obtained for each discrete month m and hour h interval. Using a Monte Carlo numerical approach, the DNI at any time t is statistically determined using the following relationship:

$$\Re = \frac{\int_0^{\mathrm{DNI}(t)} F(\mathrm{DNI})|_{m,h}\, d\mathrm{DNI}}{\int_0^{\mathrm{DNI}_{\max}} F(\mathrm{DNI})|_{m,h}\, d\mathrm{DNI}} = \frac{\int_0^{\mathrm{DNI}(t)} F(\mathrm{DNI})|_{m,h}\, d\mathrm{DNI}}{1}, \quad \text{(eq. 1)}$$

with $F(\mathrm{DNI})|_{m,h}$ being the cumulative distribution function and$\Re$a random number [0;1[. The underlying assumption is that DNI values are statistically independent from those at previous times. This assumption, while differing from realistic conditions, is possible since steady-state conditions of the solar plant are assumed in each discretization interval (see Section 2.5.).

2.2. Solar resource

The radiative solar power incident on the heliostat field is then:

$$\dot{Q}_{\mathrm{field}}(t) = \mathrm{DNI}(t) A_{\mathrm{field}}, \quad \text{(eq. 2)}$$

with the reflective field area A_{field} = 602 m^2 and the radiative power entering the receiver cavity is:

$$\dot{Q}_{\mathrm{receiver,in}}(t) = \dot{Q}_{\mathrm{field}} \eta_{\mathrm{field}}\big(\alpha(t), \gamma(t)\big), \quad \text{(eq. 3)}$$

with $\alpha(t)$ and $\gamma(t)$ being the elevation and azimuth angle of the solar vector at time t, computed using the PSA Algorithm (Blanco-Muriel et al., 2001). A field efficiency matrix for 6 intervals $\Delta\alpha$ and 12 intervals $\Delta\gamma$ was computed using a collision-based Monte Carlo model of the heliostat field and the receiver aperture with the software Tonatiuh (Blanco et al., 2005). Linear interpolation was then used to determine $\eta_{\mathrm{field}}(\alpha,\gamma)$.

Net power absorbed by the receiver is:

$$\dot{Q}_{\mathrm{receiver,net}}(t) = \dot{Q}_{\mathrm{receiver,in}} - \dot{Q}_{\mathrm{reradiation}} - \dot{Q}_{\mathrm{conduction}}, \quad \text{(eq. 4)}$$

with

$$\dot{Q}_{\mathrm{reradiation}}(t) = \varepsilon \sigma T^4, \quad \text{(eq. 5)}$$

where T is the receiver temperature. Assuming the receiver efficiency

$$\eta_{\text{receiver}}(t) = \frac{\dot{Q}_{\text{receiver,net}}(t)}{\dot{Q}_{\text{receiver,in}}(t)}, \quad \text{(eq. 6)}$$

to be 90% at nominal operation point (21st December, solar noon, DNI = 1,000 W m^{-2}, denoted by subscript "N") allows to calculate $\dot{Q}_{\text{receiver,net,N}}$ at the same point using Eq. 6. If constant receiver temperature T = 1,173 K, and ambient temperature T_∞ = 298 K are assumed, $\dot{Q}_{\text{conduction}}$ and $\dot{Q}_{\text{reradiation}}$ are constant and can be determined using Eqs. 4 and 5 at nominal operation point. $\dot{Q}_{\text{receiver,net}}(t)$ can then be calculated at every time by Eq. 4. If the combined losses are higher than $\dot{Q}_{\text{receiver,in}}(t)$, receiver operation is stopped. Similarly, an upper threshold of $\dot{Q}_{\text{receiver,in,max}} = 1.05\dot{Q}_{\text{receiver,in,N}}$ is defined.

2.3. Consumer requirements

Based on their 2013 production and typical electricity consumption values per amount of produced meat, the consumer's yearly electricity consumption $W_{\text{consumer,}}$ is estimated to be 215 MWh$_{\text{el}}$. Assuming 30% of this value being for refrigeration (operated 24 hours-a-day) and 70% for plant operation during working hours (9 hours-a-day, 8am – 5pm), the following consumer power consumption is determined:

$$P_{\text{consumer}}(t) = \begin{Bmatrix} 54.4\ \text{kW}_{\text{el}}, \text{8am - 5pm} \\ 6.8\ \text{kW}_{\text{el}}, \text{5pm - 8am} \end{Bmatrix}. \quad \text{(eq. 7)}$$

2.4. Power block

No thermal losses are assumed between receiver and microturbine. The microturbine is assumed to have a constant thermal efficiency etaturbine = 0.28. Electrical power produced from solar source is then:

$$P_{\text{solar}}(t) = \dot{Q}_{\text{receiver,net}}\eta_{\text{turbine}}. \quad \text{(eq. 8)}$$

If the solar resource is insufficient to cover the consumer's requirement, the remainder is delivered by biofuel:

$$P_{\text{biofuel}}(t) = \begin{Bmatrix} P_{\text{consumer}}(t) - P_{\text{solar}}(t), \text{for: } P_{\text{consumer}}(t) \geq P_{\text{solar}}(t) \\ 0\ \text{kW}_{\text{el}}, \text{for: } P_{\text{consumer}}(t) < P_{\text{solar}}(t) \end{Bmatrix}. \quad \text{(eq. 9)}$$

On the other hand, if the solar resource exceeds the consumer's needs, and the legislative framework allows for it, solar electricity can be supplied to the grid:

$$P_{\text{grid}}(t) = \begin{Bmatrix} P_{\text{solar}}(t) - P_{\text{consumer}}(t), \text{for: } P_{\text{solar}}(t) \geq P_{\text{consumer}}(t) \\ 0\ \text{kW}_{\text{el}}, \text{for: } P_{\text{solar}}(t) < P_{\text{consumer}}(t) \end{Bmatrix}. \quad \text{(eq. 10)}$$

The field efficiency, reactor efficiency, and total plant efficiency are obtained as follows:

$$\eta_{\text{field}}(t) = \frac{\dot{Q}_{\text{receiver,in}}(t)}{\dot{Q}_{\text{field}}(t)}, \eta_{\text{receiver}}(t) = \frac{\dot{Q}_{\text{receiver,net}}(t)}{\dot{Q}_{\text{receiver,in}}(t)}, \eta_{\text{plant}}(t) = \frac{P_{\text{solar}}(t)}{\dot{Q}_{\text{field}}(t)}. \quad \text{(eq. 11)}$$

The solar fraction of total produced electrical energy, the solar fraction of the slaughterhouse's consumption, and the fraction of solar electricity delivered to the grid are defined as:

$$\varphi_{\text{solar}}(t) = \frac{W_{\text{solar}}(t)}{W_{\text{biofuel}}(t)+W_{\text{solar}}(t)}\ ,\ \varphi_{\text{consumer,solar}}(t) = \frac{W_{\text{solar}}(t)-W_{\text{grid}}(t)}{W_{\text{consumer}}(t)}\ ,\ \varphi_{\text{solar,grid}}(t) = \frac{W_{\text{grid}}(t)}{W_{\text{solar}}(t)}. \quad \text{(eq. 12)}$$

2.5. Yearly/monthly performance and discretization

Heat energy consumed Q or generated electrical work W over a given time lapse $t_0 \leq t \leq t_f$ – here: one month or one year - is obtained by integration. A numerical solution is obtained by discretization in time intervals Δt = 600 s, over which time-dependent variables are assumed to be constant.

$$\{Q, W\} = \int_{t_0}^{t_f}\{\dot{Q}(t), P(t)\}dt \approx \sum_{i=1}^{(t_f-t_0)/\Delta t}\{\dot{Q}_i, P_i\}\,\Delta t. \quad \text{(eq. 13)}$$

Finally, the capacity factors of the solar plant and of the power block are:

$$c_{\text{solar}} = \frac{W_{\text{solar}}}{P_{\text{solar,N}}(t_f-t_0)}\ ,\ c_{\text{power block}} = \frac{W_{\text{solar}}+W_{\text{biofuel}}}{(P_{\text{solar,N}}+P_{\text{biofuel,N}})(t_f-t_0)}. \quad \text{(eq. 14)}$$

3. Results

Figure 2 shows the electrical power generation from solar source and the consumer's consumptions for three different selected examples of day: (a) on 21st December, with DNI(t) > $DNI_{85\%}$, (b) on 21st March, with DNI(t) varying over the entire statistical distribution, and (c) on 21st June, with DNI(t) < $DNI_{30\%}$. In is shown that for days with very good solar resource, the entire daytime consumption of the slaughterhouse can be supplied by solar energy.

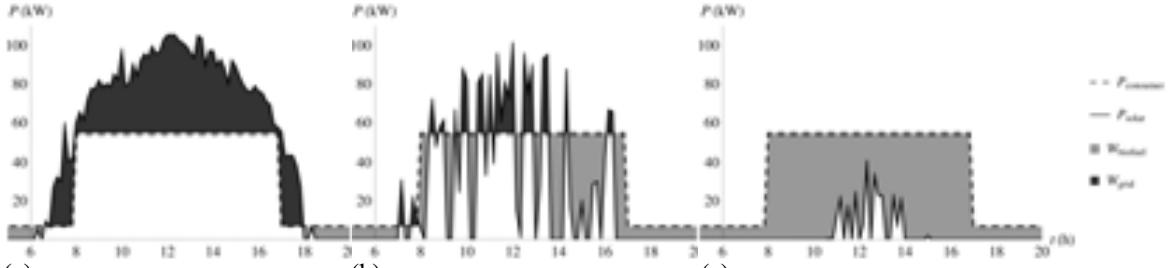

Fig. 2: Electricity generation from solar source and consumption by the slaughterhouse for: (a) Dec. 21st, DNI(t) > $DNI_{85\%}$; (b) Mar. 21st; (c) Jun. 21st, DNI(t) < $DNI_{30\%}$.

However, for less sunny days, such as case (b) or (c), significant amounts of biofuel are needed to supply the required electricity. Especially in case (b), the addition of TES (Thermal Energy Storage) could significantly decrease this amount.

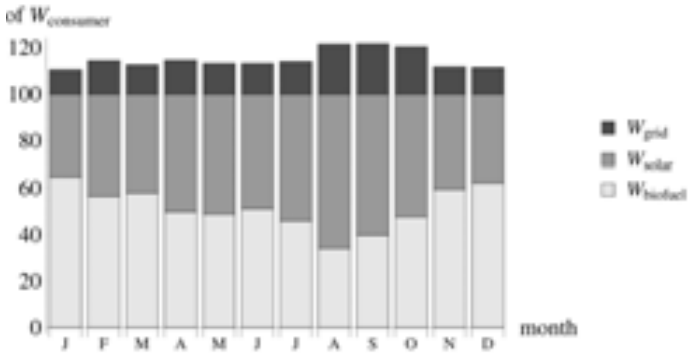

Fig. 3: Monthly source and utilization distribution of generated electricity in % of $W_{consumer}$.

This solar fraction is shown in Fig. 3 for each month, which shows the totally generated electrical energy per source and destination, as a percentage of total consumption by the slaughterhouse. The solar fraction of the slaughterhouse varies between 35.2% in January and 65.9% in August, with a yearly value of 48.5%. These relatively high solar fractions are favored by the hourly distribution of the consumer's consumption, which is significantly higher during daytime. The solar fraction of total electricity generated lies between January's 41.4% and August's 71.9%. The yearly average is 55.2%. These values are higher, since a yearly average of 23.5% of solar energy is supplied to the grid, since it exceeds the consumption. The addition of a TES system would allow to reduce the biofuel consumption, currently at 44,360 l y^{-1}, if bio-diesel (LHV = 32.3 MJ l^{-1}) were to be employed. The present analysis does not assume biofuel-generated electricity to be supplied to the grid. Depending on the biofuel type/cost and electricity market prices, this may however be the case.

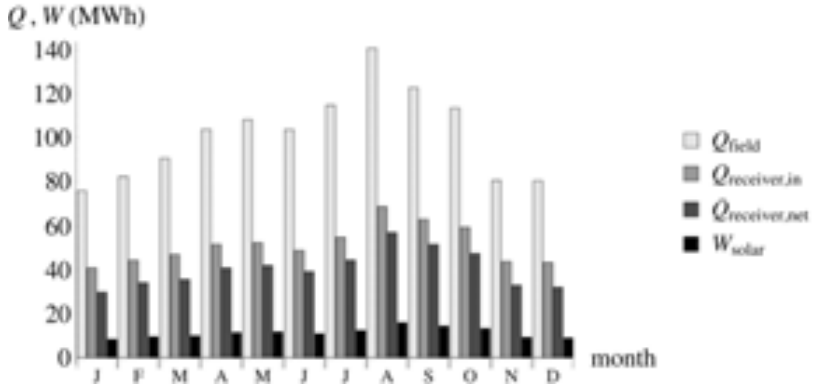

Fig. 4: Monthly energetic performance of solar plant.

Figure 4 shows the performance of the solar plant in terms of field, receiver, and power block energy losses. The solar-to-electrical energy efficiency of the plant is slightly varying seasonally (10.7% - 11.8%) due to differences in field efficiency. The yearly value is 11.3%. While this value is relatively low, also due to the small size and pilot nature of this plant, the total efficiency of the plant can be significantly improved by co-generation of power and heat, which will be done for this plant, but an analysis of which is out of the scope of this work. From both Fig. 3 and 4 it is observable that, due to the tropical location of the plant, the influence of astronomical factors (length of day, sun elevation) on plant performance is superseded by that of seasonal atmospheric phenomena (such as dry/wet period), resulting in poor summer performance, compared to late winter/early spring.

Tab. 1: Summary of nominal (on Dec. 21, solar noon, DNI_N = 1,000 W m^{-2}) and yearly plant parameters.

Nominal parameters			Yearly parameters		
$\dot{Q}_{field,N}$	kW	602.0	Q_{field}	MWh	1,216.5
$\dot{Q}_{receiver,in,N}$	kW	397.0	$Q_{receiver,in}$	MWh	621.0
$\dot{Q}_{receiver,net,N}$	kW	357.2	$Q_{receiver,net}$	MWh	489.9
$P_{solar,N}$	kW_{el}	100.0	W_{solar}	MWh_{el}	137.2
$P_{biofuel,N}$	kW_{el}	0.0	$W_{biofuel}$	MWh_{el}	111.3
$P_{grid,N}$	kW_{el}	45.6	W_{grid}	MWh_{el}	32.3
$\dot{V}_{biofuel}$	l/h	0.0	$V_{biofuel}$	l	44,360*
$\eta_{field,N}$		0.659	η_{field}		0.510
$\eta_{receiver,N}$		0.900	$\eta_{receiver}$		0.789
$\eta_{turbine,N}$		0.280	$\eta_{turbine}$		0.280
$\eta_{plant,N}$		0.166	η_{plant}		0.28
$\varphi_{solar,N}$		1.000	φ_{solar}		0.552
$\varphi_{consumer,solar,N}$		1.000	$\varphi_{consumer,solar}$		0.485
$\varphi_{solar,grid,N}$		0.456	$\varphi_{solar,grid}$		0.235
			c_{solar}		0.157
			$c_{power\ block}$		0.284
*if bio-diesel (LHV = 32.3 MJ l-1) is used.					

A summary of the nominal and principal yearly parameters of the plant can be found in Tab. 1.

4. Conclusions

A steady-state-based numerical model for the prediction of a solar/biofuel hybrid central tower receiver power plant was formulated and used to simulate the performance of a 100 kW_{el} pilot plant to be built in Pirassununga, São Paulo, Brazil, to deliver electricity and heat to a slaughterhouse. The results show a yearly generation potential of 137.1 MWh_{el} from solar energy. A yearly average of 76.5% of the produced solar electricity can be used by the slaughterhouse, covering 48.5% of its consumption. The remainder is covered by bio-diesel (44,360 l y^{-1}). The remaining 23.5% of the produced solar energy can be sold to the grid. Alternatively, TES would allow to postpone the generation of this energy fraction, allowing for a reduction in bio-fuel consumption. The energy balance of the solar plant shows a total plant efficiency of 11.3%. An influence of dry/wet season on the plant performance is observed, as opposed to the typical summer/winter effect generally observed at higher-latitude locations.

Acknowledgements

The authors thank Lars Amsbeck and Andres Pfahl (DLR) for the dimensioning and design of the heliostat field and Maicon D. Bastos for the slaughterhouse consumption data. The image of the planned solar plant is courtesy of Rafael Gonsales Neto (Solinova, Ltda.). The SMILE (Solar-hybrid Micro-turbine Systems for Co-generation in Agro-industrial Electricity and Heat Production) project is funded by BNDES (under the FUNTEC financing line), Elektro (Eletricidade e Serviços) S/A, and Solinova, Ltda.

Nomenclature

A	area, m^2
c	capacity factor
F	cumulative probability distribution function
f	probability distribution function
h	discrete hour interval
m	discrete month interval
P	Electric power, W
Q	Thermal energy, kWh
$\dot{Q}$	Thermal power, W
T	Temperature, K
t	time, s
W	Electric energy/work, kWh
Greek letters	
α	Elevation angle of solar vector, °
γ	Azimuth angle of solar vector, °
ε	Surface emissivity
η	Energy conversion efficiency
σ	Stefan-Boltzmann constant, 5.6703 10^{-8} W m^{-2} K^{-4}
φ	fraction
Other symbols	
$\Re$	pseudo-random number [0;1[
Subscripts	
0	initial
x%	x^{th} percentile

el	electric
f	final
field	heliostat field
N	nominal
receiver,in	incident on receiver aperture
receiver,net	Net absorbed by receiver
Abbreviations	
DNI	direct normal irradiance, W m^{-2}
GHI	global horizontal irradiance, W m^{-2}
LHV	lower heating value, MJ kg^{-1}
TES	thermal energy storage

References

Amsbeck, L., et al. 2010. Test of a solar-hybrid microturbine system and evaluation of storage deployment, in: Proceedings of SolarPACES 2010 Conference, Perpignan, France, September 21-24, 2010.

Barigozzi, G., et al., 2012. Thermal performance prediction of a solar hybrid gas turbine. Sol. Energ. 86, 2116-2127.

Blanco, M., et al., 2005. The Tonatiuh Software Development Project: An Open Source Approach to the Simulation of Solar Concentrating Systems. In: Proceedings of the ASME 2005 International Mechanical Engineering Congress and Exposition, Orlando, FL, USA, November 5-11, 2005.

Blanco-Muriel, M., et al., 2001. Computing the solar vector. Sol. Energ. 70, 431-441.

Buck, R., Friedmann, S., 2007. Solar-Assisted Small Solar Tower Trigeneration Systems, J Sol. Energ. Eng. 129, 349-354.

Fuller, R.J., 2011. Solar industrial process heating in Australia - Past and current status. Renewable Energ. 36, 216-221.

Ho, J.C., Chua, K.J., and Chou S.K., 2004. Performance study of a microturbine system for cogeneration application. Renewable Energ. 29, 1121-1133.

Ineichen, P., et al., 1992. Dynamic global-to-direct irradiance conversion models. ASHRAE Transactions 98, 354-369

Kaikko, J., Backman, J., 2007. Technical and economic performance analysis for a microturbine in combined heat and power generation. Energy 32, 378-387.

Le Roux, W.G., Bello-Ochende, T., Meyer J.P., 2011. Operating conditions of an open and direct solar thermal Brayton cycle with optimized cavity receiver and recuperator. Energy 36, 6027-6036.

Maxwell, E.L., 1987. A Quasi-Physical Model for Converting Hourly Global Horizontal to Direct Normal Insolation. SERI Technical Report SERI/TR-215-3087.

Mekhilef, S., et al., 2011. A review on solar energy use in industries. Renewable Sustainable Energ. Review 15, 1777-1790.

Quijera, J.A., et al., (2011) Integration of a Solar Thermal System in a Dairy Process. Renewable Energ. 36, 1843-1853.

Quijera, J.A., et al., (2011) Usage of solar energy in industrial process. Chem. Eng. Transactions 25, 875-880.

Schwarzbözl, P., et al. (2006) Solar gas turbine systems: Design, cost, and perspectives. Solar Energ. 80, 1231-1240.

Tora, E.A., El-Halwa, M.M. (2010), Integration of Solar Energy into Absorption Refrigerators and Industrial Processes. Chem. Eng. Technol. 9, 1495-1505.

Conference Proceedings

Solar World Congress 2015
Daegu, Korea, 08 – 12 November 2015

Solar Thermal Reduction of Metal Oxides as a Promising Way of Converting CSP into Clean Electricity on demand

I. Vishnevetsky*

Weizmann Institute of Science, Rehovot (Israel)

Abstract

Available main results of full endothermic reduction of different metal oxides with promising for solar thermochemical redox cycles for hydrogen production and electricity generation on demand are compared. New experimental results of preliminary non solar and solar tests related to an influence of such process parameters as the partial pressure of product gases, the rate of heating and cooling, temperature of metal vapours deposit sites on the morphology and purity of reduced metals, apparent kinetic parameters, undesired by-products formation and intensity of reoxidation are discussed. It is shown that pure reduced metals with strong metal-oxygen bond strength as aluminum and magnesium can be obtain in vacuum with fast preheating rate 150-200 degree per minute with temperatures and CO partial pressure at deposit sites no higher than 460-600°C and 0.07-0.1 mbar. Morphology of such reduced metals also strongly depends on deposit temperatures and can vary from conglomerates composed of submicron and nanocrystallines (50-60°C at water cooling deposit site), metallic flakes with spherical or flat micron and submicron particles (200°C about) to metallic plates (400-600°C). The main positive and negative results of different oxides reduction are described and promising ways of future desirable investigations are proposed.

Keywords: *metal oxides, reduction, solar thermal, clean electricity, CSP, accumulation of solar energy*

1. Introduction

The main challenge of solar energy industrial application is not stable DNI that strongly depends on time of day and year and whether conditions. So processes, which allow using on demand metals reduced periodically during sunny weather, are promising. Such metals accumulate significant amount of solar energy during the endothermic reduction step followed by the exothermic oxidation step of thermochemical redox cycle when this energy can be directly converted into electricity using the metal-air fuel cells or transferred to hydrogen fuel in the hydrolysis reaction. The main problems of hydrogen energetics are storage and transportation of hydrogen fuel. Here reduced metals can be transported to a place of electricity production on demand where hydrogen will be produced close to a fuel cell on a vehicle board or near other autonomous sources of heat and power.

Last 15-20 years R&D of solar redox cycles for hydrogen and electricity production attracts a considerable interest that reflects in a significant amount of publications Reviews of such investigations were presented by Fletcher (2001), Steinfeld and Palumbo (2001), Kodama (2003), Steinfeld (2005), Roeb M. et al. (2012) and Muhich C. et al. (2015). Features of solar thermochemical redox cycles for hydrogen production from water as a function of reactants' main characteristics were described by Vishnevetsky et al. (2011). Reduction step can be oriented to full or partial reduction especially for metals with higher valence. Partial reduction or splitting usually produces suboxides in a solid phase and need lower temperatures but demonstrates lower hydrogen productivity per unit mass of solid and usually suitable for continuous hydrogen production in a solar plant cyclically with reduction step (Hydrosol project; Konstandopoulos and Agrofiotis, 2006; Scheffe and Steinfeld, 2014), It does not solve the problems related to hydrogen storage and transportation especially at a solar plant area with concentrated optics. So only full reduction, that provides higher productiveness of redox cycle for hydrogen production and electricity on demand will be considerate here.

Before solar reactor design not solar tests help to realize preliminary investigation of forward, backward reactions and morphology of reduced metals at more stable than solar conditions. Not solar setups based on conventional electrical devices must be designed to simulate different heating and cooling facilities typical for solar reactors. Three possible options of preliminary not solar reactors were described by Vishnevetsky et al. (2005, 2010, 2011b).

First one provides one side heating usually typical for solar reactor. Thermal energy here spreads in the radial direction from the SiC tube, heated by an electric current till 400 A. Such reactor was used for forward reaction investigation when the main products are vapour of a reduced metal, CO and small amount of CO_2. Reaction progress leads to layerwise volatilization of reaction mixture described by Osinga et al.(2004) as shrinking packed bed.

doi:10.18086/swc.2015.04.23 Available at http://proceedings.ises.org

The second one imitates a solar tubular reactor (see Fig, 3d below) where a cylindrical electrical furnace simulates 2D-CPC. This reactor is used for reduction of metals with boiling point higher then reaction temperature when product appears in liquid phase and does not leave the reaction zone. Morphology of the reduced metal depends on the solidification conditions and will be discussed below.

The third one, presented in the experimental section (Fig.6), provides fast heating that especially important for reaction with complicated chemistry in order to avoid by-product formation during preheating. Wide range of temperature distribution on metal vapour deposit sites in IH reactor (Vishnevetsky et al., 2013) allows investigating not only forward but also backward reaction as function of temperature at deposit sites.

Solar thermal chemical reactors for full metal oxides reduction through thermal decomposition or carbothermic reduction are available today not only at laboratory but also at a pilot scale. They can be operated at atmospheric pressure and in vacuum condition. The progress achieved during last 15 years is widely presented in the literature.

Laboratory and pilot scales of a ‘‘rotating-cavity’’ solar reactors for the thermal dissociation of ZnO were developed in PSI and ETH, Switzerland. Continuously injected ZnO powder is distributed on the rotating inner cylindrical wall, accumulates solar flux and protects cavity wall from overheating. Such reactors can provide forward reaction temperature till 2300 K. The first 10 kW version was presented by Haueter et al. (1999) and the modernized version by Schunk et al. (2008). Dynamic modelling and 100 kW pilot scale demonstration were described by Villasmil et al. (2014a, 2014b) and by Meier, (www.stage-ste.eu). Smaller 1kW solar reactor with a rotating cavity, continuously injected ZnO particles and hemispherical glass window was developed in Processes, Materials, and Solar Energy Laboratory (PROMES-CNRS), France and described by Abanades et al. (2007).

One of the main technological challenges of window solar reactors is reliable protection of quartz window from reduced metal vapour deposition. One of such way to protect flat windows is creating vortex-type stable flow with significant flow rate of carrier gas which is induced toward the aperture, similar to a tornado flow configuration proposed by Kogan and Kogan (2002). Other way to protect window is two cavity reactor developed in PSI and ETH, Switzerland. 5 kW laboratory scale reactor was described in details by Wieckert et al. (2004) and Osinga et al. (2004a, 2004b). 300 kW pilot scale was presented by Wieckert et al. (2007). Its possible industrial futures proposed by Epstein et al. (2008). The main principle of two cavity reactor is heating of reaction mixture not by direct CSP but by secondary radiation from the solar absorber placed in the upper cavity which prevents the penetration of metal vapours to the quartz window from the lower cavity where reaction can be proceed at 1500 K. Such reactors can be used for batch tests and for continues feed operation. Testing of international SOLZINC 300 kW pilot scale batch reactor with packed bad mixture of ZnO with beech charcoal was tested in Solar Research Facility Unit of WIS, Israel, using beam down optic and biggest CPC in the Wold.

Presented ways of window protections do not solve this problem completely especially during a long continuous operation of a reactor. The other way is non-windowed solar reactors developed in WIS, Israel. Such reactors can be tubular (Adinberg and Epstein, 2004) or with ceramic crucible (Vishnevetsky et al., 2006). Here SiC ceramic parts (tubes or crucibles) are sealed and irradiated with indirect or direct CSP. Advanced SiC ceramics as Hexoloy SA, for example, must possess superior strength characteristics and high working temperature to withstand the high temperature gradient from the colder flange for safe sealing to the hot reaction zone. Such 30 kW laboratory scale reactors were tested in the WIS Solar Tower using parabolic mirror and CPC as second and third concentrators after heliostats.

Light elements with strong metal oxygen bond strength need very high temperature for carboreduction of their oxides at atmospheric pressure. As it is well known according Le Chatelier’s principle vacuum conditions can reduce significantly temperatures of such reactions but need additional energy consumption for pumping. Different energy and temperature estimations as function of pressure were presented by Vishnevetsky and Epstein (2015). This 10 kW vacuum solar reactor was developed and tested in WIS, Israel, and presented below in Fig.7. Stoichiometric reaction mixture (a few tens of grams) of oxides with beach charcoal was compressed to pellets 1 cm diameter using 10wt.% of sugar as a binder. The main test results obtained during magnesia, alumina and boria solar carboreduction in vacuum are presented by Vishnevetsky et al. (2012, 2013, 2014, 2015). According preliminary investigation a sharp temperature drop from the hot reaction zone to the deposit site is necessary in order to avoid the recombination during metal vapor deposotion. So design of this vacuum reactor with spherical quartz window was accompanied by numerical simulation of temperatures and stress distribution (Vishnevetsky et al., 2012, Ben-Zvi, 2013), that was confirmed by good resistance of the quartz window during tests and measuring temperature values which changed from 1900 K in the reaction zone till 320 K about at water cooling deposit site. This reactor was modified later by adding the second option as uncooled deposit area to study vapour deposition at higher temperature for getting liquid reduced metal.

Miniature (1g reactant) solar vacuum reactor was also developed and tested in CNRS-PROMES, France (Abanades et al., 2008 and Chambon et al., 2010).

New available solar and not solar test results are presented below. It includes effecting of such process parameters as the partial pressure of product gases, the rate of heating and cooling, temperature of metal vapours deposit sites on the

morphology of reduced metals, on apparent kinetic parameters, undesired by-products formation and intensity of reoxidation. The main challenges and possible ways to avoid these problems also will be discussed.

2. Thermodynamics

The main equations of thermochemical redox cycle for full oxides reduction are thermal carboreduction (Eq.1a) or thermolysis (Eq.1b) followed by hydrolysis (Eq.2) or oxidation in metal-air fuel cells (Eq.3) of fully reduced metals:

$$Me_xO_y + yC = xMe + yCO \quad \text{(eq.1a)}$$

$$Me_xO_y = xMe + \left(\frac{y}{2}\right)O_2 \quad \text{(eq.1b)}$$

$$xMe + yH_2O = Me_xO_y + yH_2 \quad \text{(eq.2)}$$

$$xMe + 0.5yO_2 = Me_xO_y \quad \text{(eq.3)}$$

Partial reduction of oxides can be realized for metals with higher valence at lower temperatures, but it is not considered here as hydrolysis/oxidation of suboxides have lower productiveness.

As it is well known the reaction summarized in Eq.1a is not solid-solid reaction (Berman amd Epstein, 1999; Byung-Su Kim et all., 2006) but gas-solid reaction (Me_xO_y+yCO=xMe+yCO_2) with intermediate gas product CO_2. Depending on the reaction temperature, CO_2 is fully or partially transformed to CO through the Boudouard reaction (C+CO_2=2CO). For carboreduction processing at atmospheric pressure Boudouard reaction usually is responsible for the reaction rate. Full conversion of CO_2 to CO occurs at 1100 -1200°C or lower temperatures when reduced metal has a catalytic effect as tin, e.g. (Epstein et al., 2010). In vacuum condition temperature of full conversion in Boudouard reaction is 600-700°C and CO_2 is usually fully transforms to CO at higher temperatures suitable for carboreduction of alumina and magnesia as an example. During carboreduction of light elements with complicated chemistry a series of more solid-gas reactions with intermediate suboxides and oxicarbides formation takes place.

All thermodynamic estimations were made using A. Roine HSC Chemistry Computer Code. According data presented in Fig.1 temperature of full conversion strongly increases with metal-oxygen bond strength as atom mass decreases and according Le Châtelier's principle can be reduced under vacuum conditions. In the other hand the lighter metals are more productive for hydrogen production per unit mass of a reduced metal. Also must be taken into account that despite the fact that thermolysis is free of CO, its reduction temperature is significantly higher than carboreduction temperature, and can be implement only at lower pressure of product gases that could be realized or at atmospheric pressure using significant amount of carrier gas, or at vacuum conditions. Figs.2b and 2c indicate that reaction temperature of ZnO carboreduction at atmospheric pressure is lower than ZnO thermolysis temperature at 1 mbar. Also it is usually impossible to prevent fully the reoxidation of reduced metals by pure oxygen. For today conversion achieved during ZnO thermal dissociation is 40% about (see section 4.1), whereas conversion of ZnO carbothermal reduction is 85-95% according XRD quantitative analysis (Wieckert et al. 2007; Vishnevetsky and Epstein, 2007). On the other hand, if carbon in Eq.1a was produced from bio source as charcoal, for example, its using can be considered as positive from economic and ecological point of view because product CO is an additional fuel and resulting CO2 will absorbed by plants, which will be used later for new charcoal production.

Besides advantages regarding high hydrolysis productivity of lighter elements with high metal-oxygen bond strength (Vishnevetsky et al. 2008, 2011a; Rosenband and Gany, 2010) their disadvantage is higher reduction temperature at atmospheric pressure that need vacuum conditions (compare ZnO and MgO carboreduction in Fig.2c, d) but also by-products formation during preheating of reactant mixture on the base of elements with higher valence, as shown in Fig.2e, f. Here it is possible to compare thermodynamics of carbothermic reduction of oxide with simple (ZnO, MgO) and complicated (Al2O3, B2O3) chemistry.

Another feature of carboreduction or splitting of oxides is output of CO or O_2 gases which usually contact with reduced deposited metals at the exit of the reactor that provokes reoxidation in backward reaction especially with oxygen. Possible way to avoid this future is the presence in the reaction zone of some amount of easily oxidizable element whose oxide is not gaseous but solid. Examples of equilibrium diagram for such reaction for Zn reduction, as an example, are presented in Fig.3

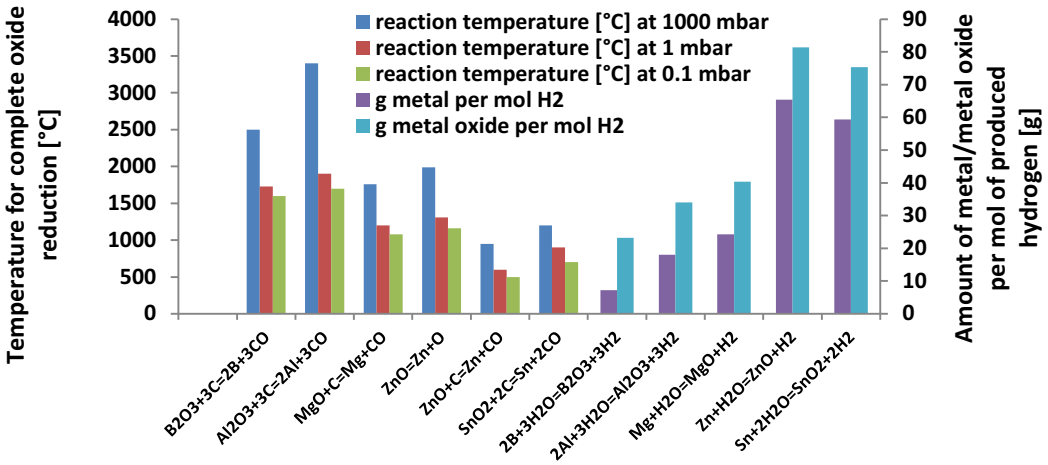

Fig.1: Thermodynamic estimation (Antti Roine HSC Chemistry Computer Code) of temperature for complete oxide reduction and productiveness of hydrolysis reaction

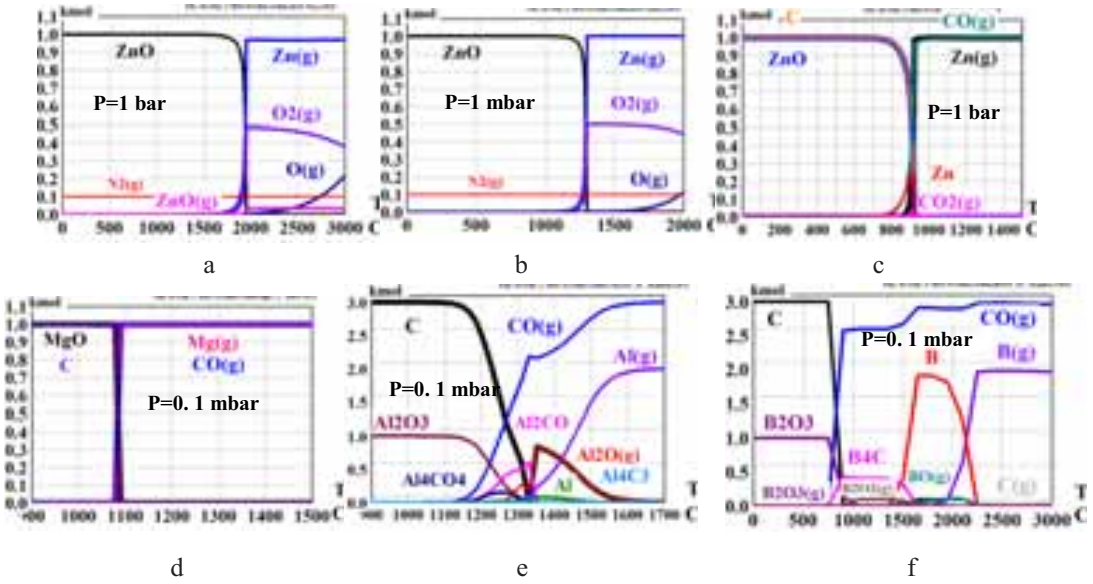

Fig.2: Equilibrium diagrams of (a) ZnO splitting at atmospheric pressure and (b) in vacuum; carboreduction of (c) ZnO at atmospheric pressure and (d) magnesia, (e) alumina, (f) boria in vacuum

As it is possible to conclude addition to the ZnO powder some amount of easily oxidizable element can significantly decrease reoxidation of reduced zinc. Of course, Molybdenum is not the best candidate for this but a small amount of light easily oxidizable element as boron, for example, can solve the problem catching the oxygen in the hot reaction zone made of a high temperature ceramic in a solar reactor. Equilibrium diagrams in Fig.3 (c, d) demonstrates that only 8.8 weight % of boron not only prevents Zn reoxidation but also significantly decreases temperature of zinc vapour production even at atmospheric pressure (compare Fig.3 c, d with thermal splitting in Fig.2 a, b). Bororeduction thermodynamically occurs at all temperatures and boron, unlike Mo, presents in the equilibrium diagram in oxidized form together with pure zinc also at low temperatures. In this case separation of reduced zinc from boron oxide can be realized during vaporization of Zn at temperatures higher than 900-1000°C at atmospheric pressure when boron oxide still liquid. If reaction proceeds at higher temperatures when Zn is in gas form, liquid B_2O_3 rests in a hot reaction zone. This process is free of CO_2 and could provide pure zinc solving the problem of Zn recombination because of instead gas product O_2 or CO there is liquid B_2O_3 which does not leave the hot reaction zone together with Zn. So following experiments of ZnO decomposition with small addition of pure boron powder could be very promising. Here it must be marked that such process is more suitable for recovering zinc oxidized in zinc-air fuel cells whereas for hydrogen production pure boron could be used itself. Boron oxide produced here can be used in different industries such as metallurgical, atomic energy, electronic and others or reduced to boron using solar energy.

Thermodynamic analysis indicates that bororeduction of magnesium oxide has no advantage over its carboreduction because of by-products as magnesium borides formation and a presence of boron oxides and suboxides in gaseous phase.

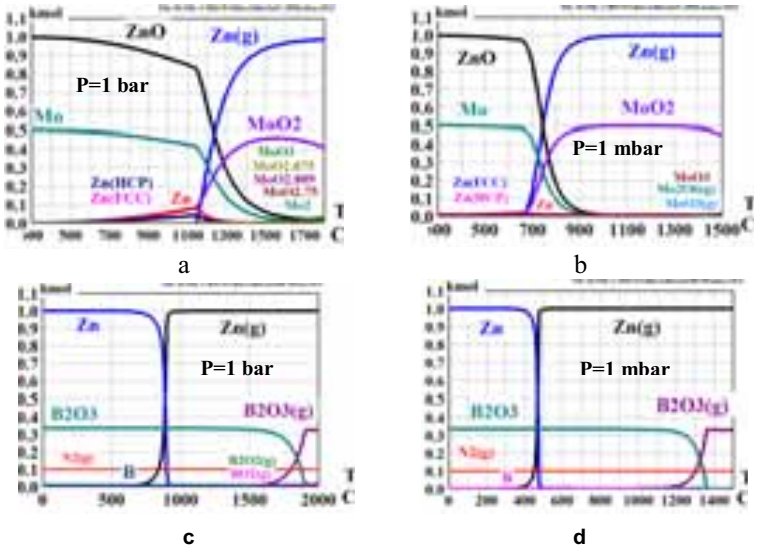

Fig. 3: Equilibrium diagrams of 1 mole ZnO decomposition at the presence of 0.5 mole of molybdenum: (a,b) and (c,d) 0.667 mole of boron at (a,c) atmospheric pressure; (b,d) in vacuum.

3. Experimental results and discussion

3.1. Morphology of carbo reduced metals depending on conditions of their vapors condensation or liquid product solidification

As it is possible to conclude from available results, metal hydrolysis can be realized using fine powder (Vishnevetsky et al. 2007, 2008, 2009, 2011a and Epstein et al, 2010) or liquid metal (Berman and Epstein, 2000). 10 μm conglomerates composed of micron and submicron particles have higher productivity compare with powder with larger particles or bubbling of liquid metal with water vapor.

Reduction of metals with boiling point higher than reaction temperatures provides product in a liquid phase which does not leave the reaction zone. Morphology of the reduced metal depends on the conditions of solidification (Vishnevetsky et al., 2010) and can present big conglomerates (Fig.4 a) or micron and submicron particles solidificated on the inert supports as 10 μm alumina particles, for example (Fig.4 b, c). Conversion of reduced tin was about 90%.

When reaction temperature is higher than boiling point of reduced metals in reaction conditions their morphology depends on quenching procedure. Quencher/cooler on the base of Cyclone with cold purge gas was used in SOLZINC pilot plant (Wieckert et al., 2007). It allows providing zinc powder with conglomerates till 10-20 μm composed of micron and submicron particles (Fig.5 a, b) and purity 85-95% as was mentioned above.

Morphology of metals deposited on surfaces of cold zone installed after hot reaction area (Figs.6, 7) strongly depends on temperature of a deposit site and on CO partial pressure at the deposit area. Deposits on water cooled surfaces usually represent powder with flakes deposited on sites with temperatures 50°C about or thin metallic films located on outer layers of a deposit or in a transition area from the hot to cold zone.

Fast cooling of Al vapors leads to formation of conglomerates composed of nanocrystallines, typical for flakes (Fig. 8 a, b) or composed of submicron spherical particles of Al (Fig. 8 c, d, e). Vacuum reactor (Fig. 7a) with water cooling deposit tube at 50-60°C was modified by adding the second option as uncooled deposit area to study vapour deposition at higher temperature for getting liquid reduced metal (Fig. 7b). Depending on insulation thickness and weather conditions temperature of the stainless steel tube can change from 340°C till 680°C. The best results with Al weight percent 97% according EDS were available in tests with hotter deposit site at temperature no higher than 460°C. Photo of metal plates (bright side contacting with the steel tube) collected from the lower cup and SEM image of outer matte side are presented in Fig. 8 f, g.

Maximal total weight conversion of reduced Al was 90% at avg./max. CO partial pressure 0.04/0.07 mbar and avg./max. reaction temperature 1525/1600°C. Increasing CO partial pressure till 0.2/0.4 mbar leads to conversion decreasing till 35-45%.

SEM images of magnesium deposited at sites with different temperatures are presented in Fig.9. Here also fast cooling of the magnesium vapor on the water cooled tube leads to formation of big conglomerates (Fig,9 a, b) composed by submicron crystals with 100% Mg contents (Fig.9 c). Deposit on transition area from hot to water cooled zone with temperature 200°C about composed by metallic flakes also arranged to spherical forms (Fig.9d). SEM image of inner layer with 100wt.% Mg contents deposited on place 6 in IH reactor (Fig.6b) with temperature 600°C about is presented in Fig.9e and the outer layer of the deposit from the same place with 70wt.% of Mg and 30% of MgO in Fig.9 f. Total conversion of Mg reduced in the solar vacuum reactor at avg./max P_{CO}=0.03/0.07 mbar and avg./max $t_{reaction}$=1535/1575°C was 90-95% related to reacted magnesia and 60-65% related to loaded magnesia because of significant amount of non-reacted sintered conglomerates (Fig. 10).

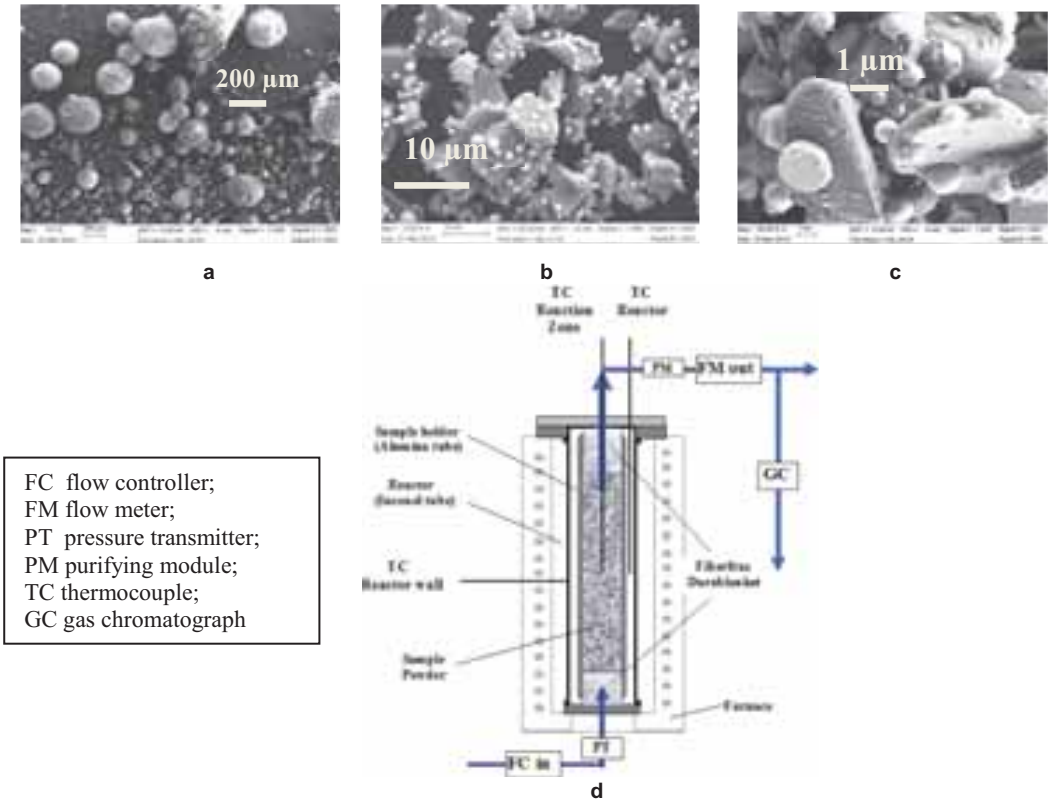

Fig. 4: Morphology of carbo reduced Sn: (a) stoichiometric ratio without inert support and (b, c) with 10 µm alumina powder as inert support loaded with reaction mixture into (d) tubular batch reactor

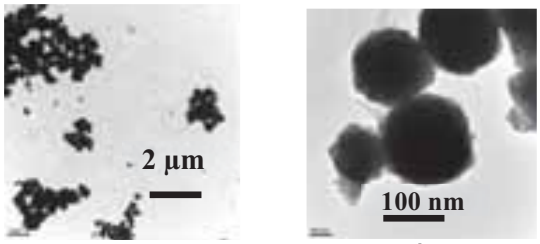

Fig.5: Morphology of SOLZINC powder (TEM images at different magnifications).

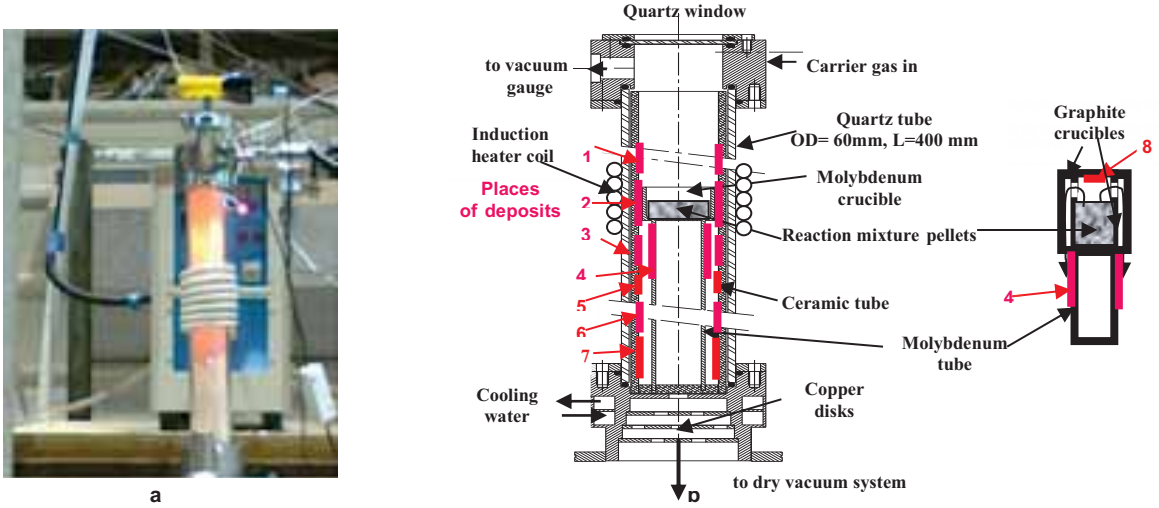

Fig.6: IH vacuum reactor: (a) photo of the Induction Heating (IH) vacuum reactor during operation; (b) principle schemes of non-solar IH setup (temperature in reaction crucibles 1400-1800°C and on deposit sites from 200°C to 1500°C)

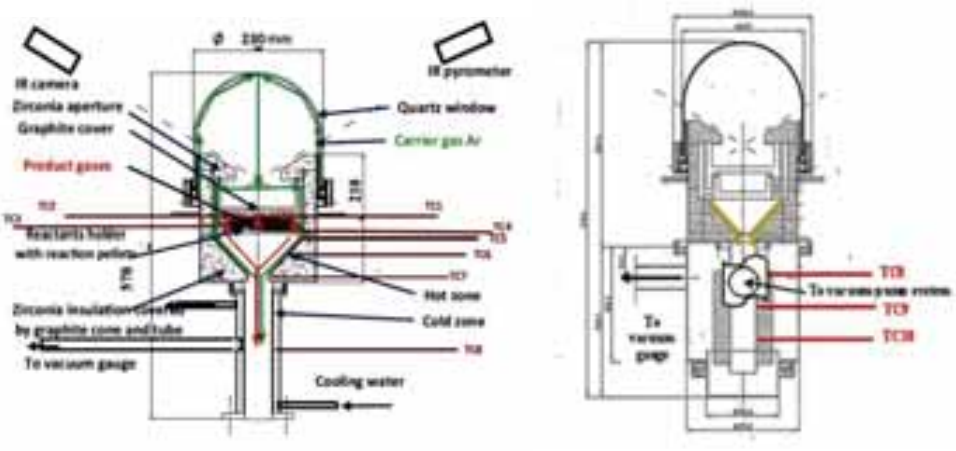

a b

Fig.7: Vacuum 10 kW solar reactors: schematic cross section of the solar reactor with (a) water cooling deposit site and (b) hotter deposit site

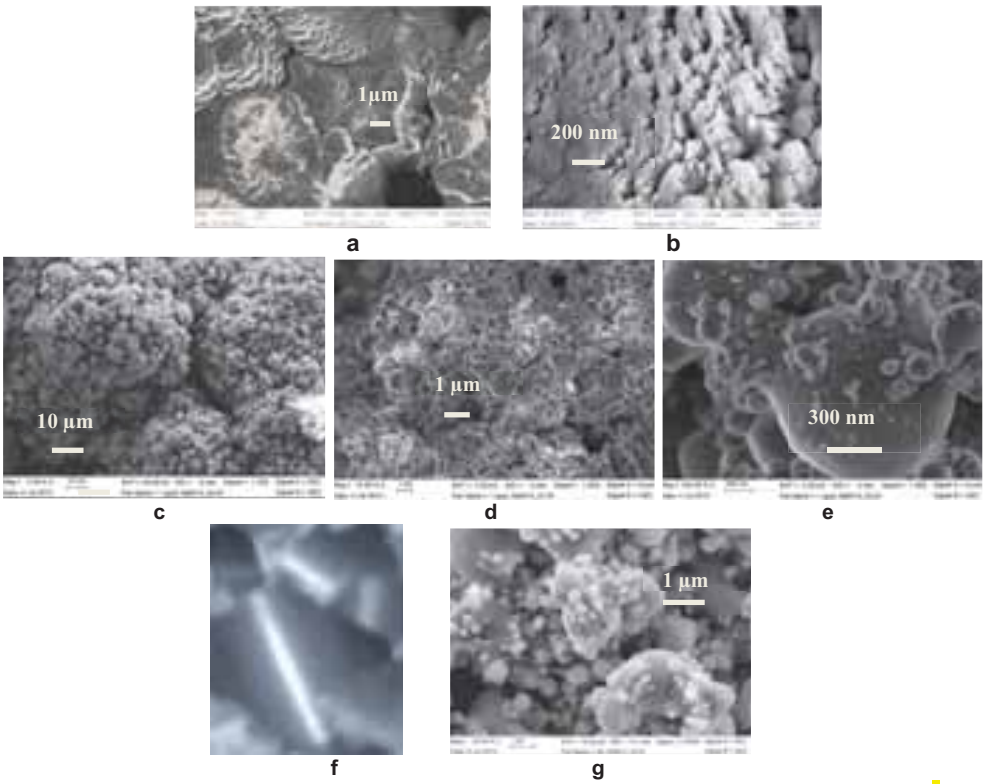

a b c d e f g

Fig. 8: (a, b, c, d, e) SEM images of pure Al deposits in the water cooled site (50-60°C) of the solar reactor: (a,b) Al flake ($P_{CO\ avg./max.}$=0.04/0.07 mbar); (c, d, e) thin Al film ($P_{CO\ avg./max.}$=0.064/0.18 mbar), ; (f) photo of bright side metal plates contacting with the not cooled stainless steel tube at temperature no higher 460◦C and (g) SEM image of its matte side with 95wt.% Al ($P_{CO\ avg./max.}$=0.05/0.125 mbar)

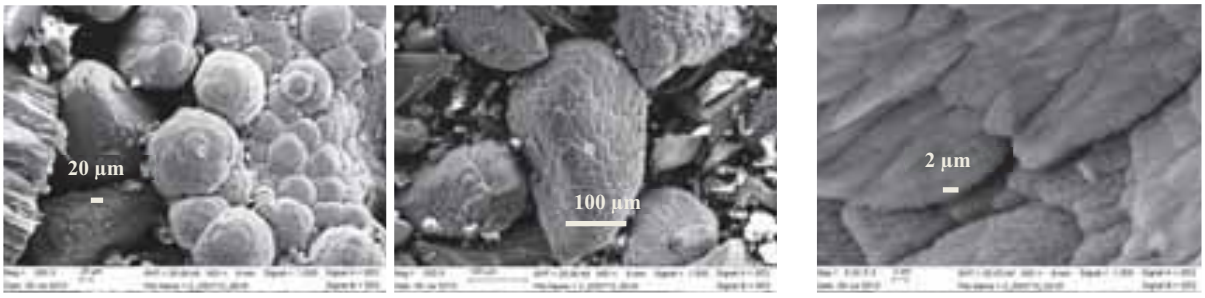

a b c

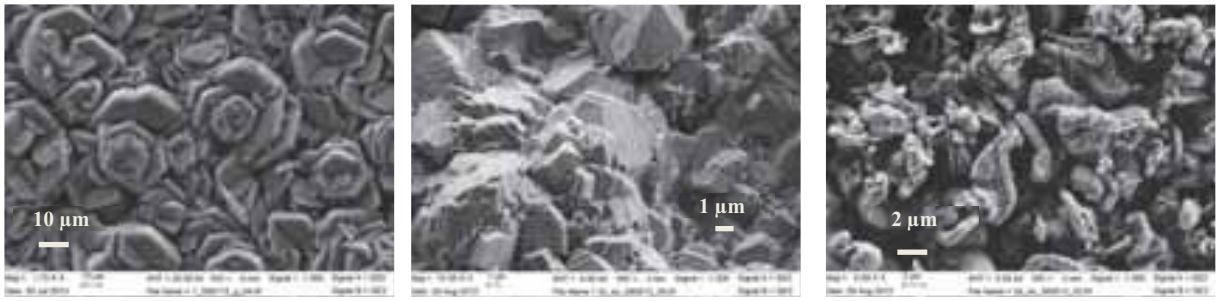

Fig.9: (a, b, c,) SEM images of pure Mg flakes deposited in the water cooled zone of solar reactor ($P_{CO\ avg./max.}$=0.03/0.07 mbar); (d) magnesium film deposited on transition area of solar reactor with temperature 200°C ($P_{CO\ avg./max.}$=0.019/0.055 mbar); (e) inner layer of the deposit with 100 wt.% Mg at low part of zirconia tube in IH reactor with temperature about 600°C ($P_{CO\ avg./max.}$=0.13/0.35 mbar); (f) outer layer of the deposit from the same place with 70 wt.% Mg and 30 wt.% MgO ($P_{CO\ avg./max.}$=0.24/0.5 mbar)

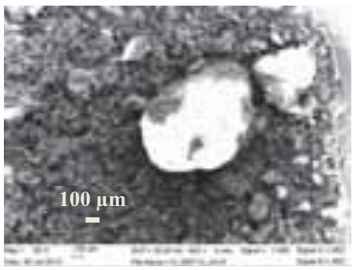

Fig.10: Non-reacted residual after magnesia carboreduction

3.2. Apparent activation energy as a function of CO partial pressure.

Unlike true activation energy of the reacting molecules apparent activation energy does not have such physical meaning and can depend on many parameters of a specific setup, including the partial pressure of participating gases that can be found in the literature (Ruiz and Delmon, 1992, as an example).

According LeChatelie principle CO partial pressure is a main parameter responsible for a rate of carboreduction reaction at given temperature. As it was mentioned above in Thermodynamics section such reactions realized as gas solid reactions where CO_2 is the main intermediate gas product that is usually fully transforms to CO at high temperatures suitable for carboreduction of alumina and magnesia.

When one of the main reaction product is gas, the rate of reaction can be estimated through its initial flow rate (Vishnevetsky and Epstein, 2009) related to amount of suitable elements in loaded reactants. Reaction rate of alumina and magnesia carboreduction was estimated as initial conversion rate through the CO release. The main measured parameters that must be taken into account are CO flow rate, reaction temperature and CO partial pressure (Fig.11). As it is possible to see, CO release in vacuum conditions presents in two peaks: CO in first peak is related to carbon and oxygen in sugar as a binder and in charcoal impurities and CO in second peak is a product of the reaction under consideration. First peak usually accompanied by small amount of H_2, CH_4 and CO_2 (Vishnevetsky et al., 2014). When carboreduction is carried out at atmospheric pressure at lower temperatures (ZnO and SnO_2 as an example) significant amount of CO_2 presents also in the main peak (Wieckert et al., 2007; Epstein et al., 2010) that also must be taken into account for initial conversion rate estimation. Starting of the second peak developing in vacuum condition is presented in Fig.11c, where τ_0 is time of the second peak onset and other τ_i (i=0,1, 2…) is times when CO flow rate develops. Conversion during any initial time period related to loaded moles of oxides can be calculated through release of CO and CO_2 (if any) using Eq.4 and initial conversion rate according Eq. 5 where initial amount of released oxygen atoms is divided to total amount of oxygen atoms in loaded oxide. Taking into account the short time difference between τ_i and τ_{i+1} related temperature and pressure can be simply averaged between τ_i and τ_{i+1}.

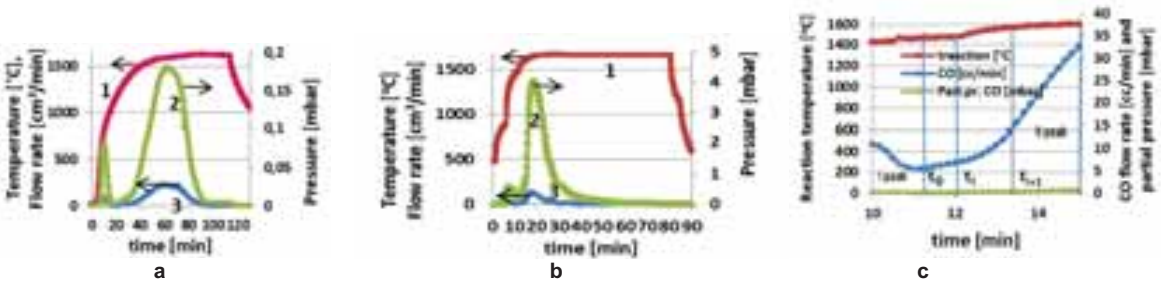

Fig.11: Main reaction parameters 1- Reaction temperature, 2 – CO partial pressure, 3 CO flow rate (alumina case): (a) batch solar reactor with slow preheating; (b) IH reactor with fast preheating; (c) second peak starting

$$Conversion = \frac{\text{mols CO} + 2*\text{mols}CO_2}{y*\text{loaded mols } Me_x O_y} \quad \text{(eq.4)}$$

$$\frac{dConv._{initial}}{d\tau} = \frac{\int_{\tau_i}^{\tau_{i+1}} \left(F_{CO}(\tau) + 2*F_{CO_2}(\tau)\right) d\tau}{22.4*10^3*y*\text{loaded mols}Me_xO_y*(\tau_{i+1} - \tau_i)} \quad \text{(eq.5)}$$

Examples of Arrhenius plots for different averaged CO partial pressure are presented in Fig.12a. As it is possible to conclude higher pressure leads to higher apparent activation energy and higher pre-exponential factor which is proportional to the total number of reactants collisions. The last one confirms once again that oxide reduction with carbon has solid gas character (oxide with CO which is generated in Boudouard reaction of product CO_2 with loaded C). Apparent activation energy of alumina and magnesia carboreduction as function of CO partial pressure is presented in Fig.12b. It is possible to conclude that E_a sharply decreases at pressure less than 0.1 mbar and smoothly increases with higher pressure.

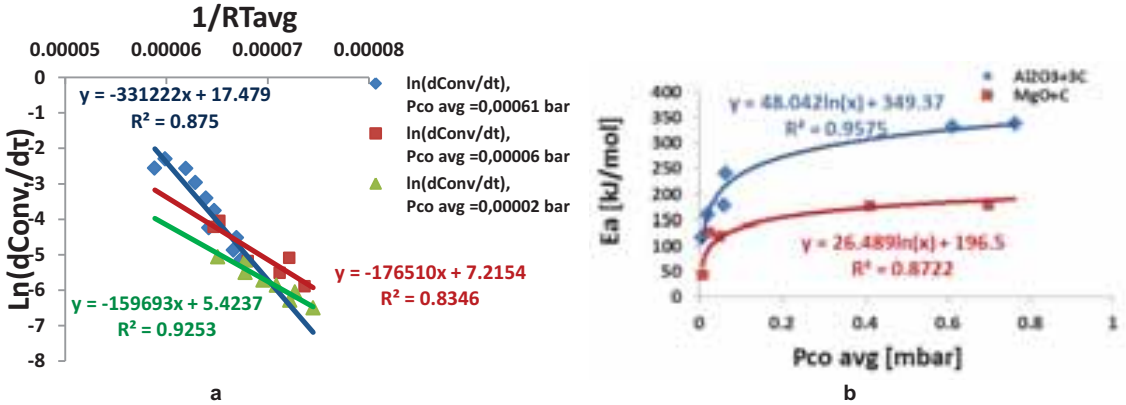

Fig.12: (a) Examples of Arrhenius plots for different averaged CO partial pressure (alumina case) and (b) apparent activation energy as function of averaged CO partial pressure (alumina and magnesia case)

4. Current challenges of metal oxides thermal reduction and possible ways to overcome them

4.1 Recombination of Zn produced by thermal dissociation

As it is mentioned in Thermodynamics section, one of the main challenges of thermal splitting is recombination of reduced metals in backward reaction. The results achieved using laboratory rotating cavity reactor (Schunk et al., 2008) was Zn content in filtered particles at the range from 18.7 to 41.7 mole% of pure Zn and tests results of pilot scale reactor (Villasmil et al., 2014b) also provide only12–49% depending on the flow rate of Ar injected to a quench area. CNRS-PROMES reactor (Abanades et al., 2007) provide 70% Zn yield but using small cavity with ID=20 mm, whereas no pure zinc was produced when cavity ID was 30 mm.

ZnO thermal dissociation also was tested in the vacuum solar reactor with water cooling deposit site presented in Fig.7a by replacing all graphite parts to the same size parts made of a high density zirconia without cover that allows reaching 1800°C in reaction zone with loaded 15-20g ZnO pellets. Total maximal pressure was about 1 mbar and O_2 partial pressure is about 0.1 mbar. Full Zn conversion was no higher than 46% whereas according XRD quantitative analysis in some samples Zn wt.% reached 58-73%.

It was also demonstrated by Chambon at al.(2010) that in CNRS-PROMES vacuum reactor where 1g sample pellet was placed close to the refrigerator (on the distance of 4 cm only) it was possible to increase the mole fraction of reduced zinc from 10% to 75% decreasing total pressure from 20 kPa to 5 kPa.

After ZnO thermal dissociation tests in IH vacuum setup (Fig.6) with molybdenum crucible it was possible to get from deposit place 7 (with not very low temperature, about 300°C) bluish deposit with 96-100 wt. % Zn content that was about 75% of all Zn in loaded ZnO (FIg.13). Tests were run with 10g ZnO pellets at temperatures 1400-1500°C and partial pressure of oxygen was negligible, less than 0.004 mbar.

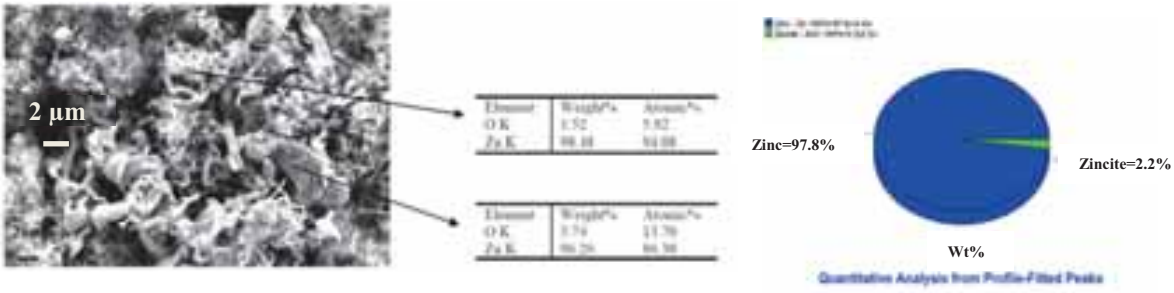

Fig.13: (a) SEM image with EDS analysis and (b) XRD quantitative analysis of the bluish deposit at the low part of zirconia tube with 97.8 wt.% of Zn

At the same time the surfaces of molybdenum crucible and support tube were covered by MoO_2 with small addition of $Zn_2Mo_3O_8$. Zn recombination was not happened because of Mo cached the most of oxygen already in hot zone that is confirmed by thermodynamics (Fig. 3a, b) where instead gases Zn and O_2 (Fig.2a, b) only Zn(g) and MoO_2 are presented as reaction products.

4.2 By-product formation and possible oxide sintering at slow heating rate in batch reactors

Thermochemical batch reactor is the most convenient and safe for using concentrated solar energy especially in vacuum conditions. But the main challenge of batch reactor is relatively slow heating rate of the reactant loaded into a cold reactor. As it is possible to conclude from data in Fig.14a (details are presented by Vishnevetsky and Epstein (2015)), slower heating rate leads to reaction starting at lower temperature that provokes by-product formation in processes with complicated chemistry (Fig.2 e, f). As a result the reaction occurs at lower average temperature. Reaction time is longer (Fig.14b) that also could provoke possible reactant sintering and a significant amount of unreacted residual (Fig.10).

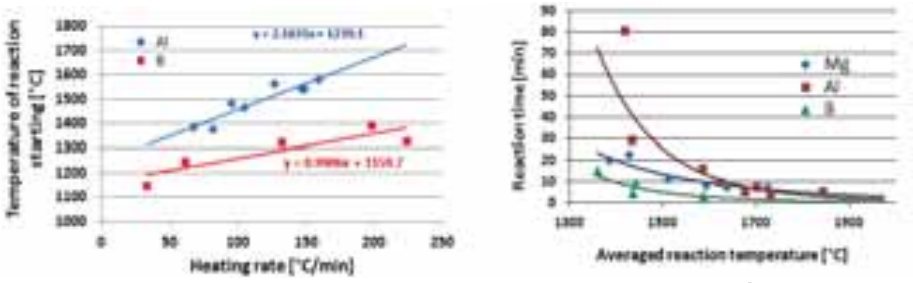

a b

Fig.14: (a) Temperature of reaction starting as function of the preheating rate and (b) reaction time at half the height of the CO peak as a function of the averaged reaction temperature.

Possible way to circumvent these problems is using a feeder reactor when reaction pellets doses by a vibrating vacuum feeder to a preheated vacuum reactor (Fig.15 a). Preheating and consumption times of reaction pellet dosed to the preheated reactor were estimated by Ben-Zvi (2015).The main results are presented in Fig.15b, c.

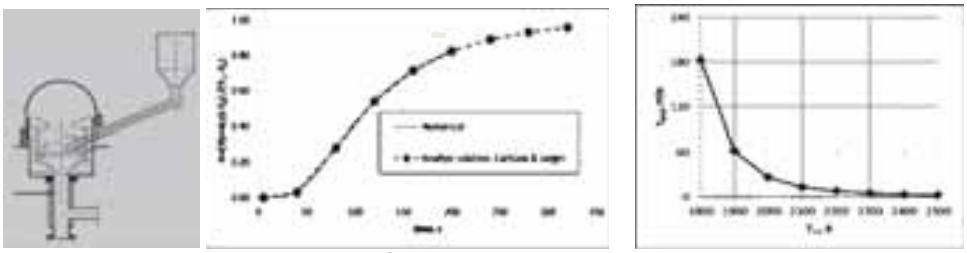

a b c

Fig. 15: (a) Solar reactor with vibrating vacuum feeder; (b) preheating and (c) consumption time of reactant pellets as function of reaction temperature (alumina case, P_{COavg}=8.17E-4 bar Ea ~337 kJ/mol)

According numerical and analytical estimation for alumina case, as an example, (Ben-Zvi, 2015) preheating time (Fig.15b) of 10 mm diameter spherical pellets is 5-6 min in the reactor with a feeder (1D transient conduction with initial pellet temperature T_0 =300K and prescribed outer temperature, T∞.) whereas in the batch reactor it is need one hour to reach the desirable temperature in the reaction zone (Fig.11a). In contrast to the preheating rate, pellets consumption time in a feeder reactor (Fig.15c) depends on temperature in the reaction zone and can be comparable with the pellets consumption time in a batch reactor (1-1.5 hours at 1600°C).

5. Conclusions

- Solar and non-solar setups developed during last 10-15 years for investigation of full reduction of metal oxides promising for solar thermochemical redox cycles for hydrogen production on demand are briefly described.
- Morphologies of reduced metals with different metal oxygen bond strength and boiling points were presented for various quenching conditions.
- Analyses of the purity of reduced metals with strong metal-oxygen bond strength as aluminum and magnesium show that metals with 95-100% purity and total conversion of reacted oxides at the level of 90-95% is possible when avg./max. CO partial pressure and temperature at the cold deposit area no higher than 0.07/0.2 mbar and 460°C in the case of aluminum and 0.1/0.35 mbar and 600°C in the case of magnesium. Rising of temperature and/or pressure results in recombination of reduced metals.
- Morphology of deposited aluminum and magnesium also strongly depends on deposit temperatures and can vary from conglomerates composed of submicron and nanocrystallines (50-60°C at water cooling deposit site), metallic flakes with spherical or flat micron and submicron particles (200°C about) to metallic plates (400-600°C).

- Apparent activation energy of alumina and magnesia carboreduction was estimated through an initial conversion rate as function of CO partial pressure. It was shown that this energy sharply decreases at pressure less than 0.1 mbar and smoothly increases with higher pressure.
- It was shown that significant recombination by oxygen of thermal dissociated Zn can be prevented by presence of an easily oxidizable element. Deposits with 98-99% pure zinc were available after tests with Mo crucible as sample holder in the IH reactor. It was demonstrated thermodynamically that small amount of boron could serve as the best easily oxidizable agent. Further confirmation in future experiments is required.
- It was experimentally confirmed that slow preheating rate in the batch vacuum reactor leads to decreasing temperature of reaction starting and averaged reaction temperature, resulting in undesirable by-product formation in forward reactions with complicated chemistry and possible sintering of oxides during longer preheating and reaction time. The possible way to prevent such disadvantage is using the reactor with a vacuum feeder. Preheating and consumption time of reactant pellets dosed to the hot reactor are estimated by a numerical simulation.
- Desirable following investigation of bororeduction of oxides with relatively heavy metal atoms and R&D of a vacuum reactor with vibrating vacuum feeder are proposed.

Acknowledgements

Invaluable assistance of my colleges from Solar Research Facilities Unit and Chemical Research Support, as well as the EC/FP7/ENEXAL project for financing is gratefully acknowledged.

References

Abanades, S, Patrice Charvin, P., Flamant, G., 2007. Design and simulation of a solar chemical reactor for the thermal reduction of metal oxides: Case study of zinc oxide dissociation, Chemical Engineering Science 62, 6323 – 6333.

Abanades, S., Charvin, P.,Lemort,F.,Flamant,G.,2008. Novel two-step SnO_2/SnO water-splitting cycle for solar thermochemical production of hydrogen. International JournalofHydrogenEnergy33(21),6021–6030.

Adinberg R., Epstein M., 2004. Experimental study of solar reactors for carboreduction of zinc oxide, Energy 29 , 757–769.

Ben-Zvi, R., 2013. Numerical simulation and experimental validation of a solar metal oxide reduction system under vacuum. Sol. Energy 98, 81–189.

Ben-Zvi, R., 2015. Transient one-dimensional reactive pellet simulation, Sol. Energy 115, 10–15.

Berman, A., and Epstein, M., 1999. The kinetic model for carboreduction of zinc oxide J. Phys. IV France 9, Pr3-320

Berman, A., and Epstein, M., 2000. The kinetics of hydrogen in the oxidation of liquid zinc with water vapor, Int. J. Hydrogen Energy, 25, pp. 957–967.

Byung-Su Kim, Jae-Min Yoo, Jin-Tae Park and Jae-Chun Lee, 2006. A kinetic study of the carbothermic reduction of zinc oxide with various additives. Materials Transactions, Vol. 47, No. 9, 2421 - 2426

Chambon, M., Abanades, S., Flamant, G., 2010. Solar thermal reduction of ZnO and SnO_2: Characterization of the recombination reaction with O_2, Chemical Engineering Science 65, 3671–3680.

Epstein, M., Olalde, G., Santén, S., Steinfeld, A., Wieckert, C., 2008. Towards the industrial solar carbothermal production of Zinc, J. Sol. Energy Eng., 130, 014505-1-4.

Epstein, M., Vishnevetsky, I., Berman A., 2010. The SnO2/Sn carbothermic cycle for splitting water and production of hydrogen, ASME Journal of Solar Energy Engineering 132, 031007–1–7.

Fletcher, E.A., 2001. Solarthermal processing: a review. J. Solar Energy Eng. 123, 63–74.

Frommherz, U., Osinga,T., Steinfeld, A., Wieckert, C., 2002. Experimental investigation of the solar carbothermic reduction of ZnO using two cavity solar reactor. http://www.pre.ethz.ch/publications/0_pdf/sci_rep/solzinc_Annex2002b.pdf

Haueter, P., Moeller, S., Palumbo, R., and Steinfeld, A., 1999. The production of zinc by thermal dissociation of zinc oxide – solar chemical reactor design, Solar Energy 67, 161–167. Hydrosol project, http://160.40.15.244/hydrosol/index.html

Kodama, T., 2003. High-temperature solar chemistry for converting solar heat to chemical fuels. Progress in Energy and Combustion Science 29, 567–597.

Kogan, A., and Kogan, M., 2002. The Tornado Flow Configuration—An effective method for screening of a solar reactor window, ASME J. Sol. Energy Eng., 124(3), pp. 206–214.

Konstandopoulos, A.G., Agrofiotis, C., 2006. Hydrosol : Advanced monolithic reactors for hydrogen generation from solar water splitting. Revue des Energies Renouvelables. 9, 121 – 126.

Meier A., STAGE-STE Presentation of Paul Scherrer Institute (PSI) Solar Technology Laboratory, www.stage-ste.eu

Muhich Christopher L., Ehrhart Brian D., Al-Shankiti Ibraheam, Ward Barbara J., Musgrave Charles B., Weimer Alan W., 2015. A review and perspective of efficient hydrogen generation via solar thermal water splitting. WIREs Energy Environ. doi: 10.1002/wene.174 (in press).

Osinga, T., Frommherz, U., Steinfeld, A., Wieckert, C., 2004a, Experimental investigation of the solar carbothermic reduction of ZnO using a two-cavity solar reactor, J. Sol. Energy Eng 126, 633-637.

Osinga,T., Olalde, G and Steinfeld, A., 2004b. Solar carbothermal reduction of ZnO: shrinking packed-bed reactor modeling and experimental validation. Ind. Eng. Chem. Res. 43, 7981-7988.

Roeb M., Neises M., Monnerie N., Call F., Simon H., Sattler C., Schmücker M. and Pitz-Paal R., 2012. Materials-related aspects of thermochemical water and carbon dioxide splitting: A Review. Materials, 5, 2015-2054.

Rosenband, V., Gany A., 2010. Application of activated aluminum powder for generation of hydrogen from water, International Journal of Hydrogen Energy, 35 , 10898-10904.

Ruis P. and Delmon B. (Eds), 1992. New developments in selective oxidation by heterogeneous catalysis. Studies in surface science and catalysis, 72, 123-132.

Scheffe J.R. and Steinfeld A., 2014. Oxygen exchange materials for solar thermochemical splitting of H_2O and CO_2: a review, Materials Today , 17(7), 341-348.

Schunk, L. O., Haeberling, P., Wepf, S., Wuillemin, D., Meier, A., Steinfeld, A., 2008. A receiver-reactor for the solar thermal dissociation of zinc oxide, J. Sol. Energy Eng., 130, 021009-1-6.

Steinfeld, A., Palumbo, R., 2001. Solar thermochemical process technology. In: Meyers, R.A. (Ed.), Encyclopedia of Physical Science and Technology, 15. Academic Press, pp. 237–256.

Steinfeld, A., 2005. Solar thermochemical production of hydrogen—a review. Solar Energy 78, 603–615.

Villasmil, W, Meier, A. Steinfeld, A., 2014a. Dynamic modeling of a solar reactor for zinc oxide thermal dissociation and experimental validation using IR thermography, J. Sol. Energy Eng. 136, 010901-1-11.

Villasmil, W., Brkic, M., Wuillemin, D., Meier, A., Steinfeld, A., 2014b. Pilot scale demonstration of a 100- kWth solar thermochemical plant for the thermal dissociation of ZnO, J. Sol.Energy Eng.136, 011016-1-11.

Vishnevetsky, I., Epstein, M., Rubin R., 2005. Simulation of thermal and chemical processes in annular layer of ZnO–C mixtures. J. Solar Energy Eng. 127, 401-412.

Vishnevetsky, I., Epstein, M., Ben-Zvi, R., and Rubin, R., 2006. Feasibility study on nonwindowed solar reactor: ZnO carboreduction as an example, Sol. Energy, 80(10), pp. 1363–1375.

Vishnevetsky, I., Epstein, M., 2007, Production of hydrogen from solar zinc in steam atmosphere, International Journal of Hydrogen Energy, 32, pp. 2791–2802

Vishnevetsky, I., Epstein, M., Abu-Hamed, T., Karni, J., 2008. Boron hydrolysis at moderate temperatures: first step to solar fuel cycle for transportation, J. Sol. Energy Eng. 130, 014506 1-5.

Vishnevetsky, I., Epstein, M., 2009, Tin as a possible candidate for solar thermochemical redox process for hydrogen production, ASME Journal of Solar Energy Engineering 131, 021007–1-8

Vishnevetsky, I., Epstein, M., Feldman Y., 2010. Preventing conglomeration of reduced fine powder in solar thermochemical redox cycles based on metals with low melting and high boiling points, Proceedings of the Mechanical Engineering Congress & Exposition, November 12-18, Vancouver, British Columbia, Canada, paper IMECE2010-38097.

Vishnevetsky, I., Berman, A., Epstein, M., 2011a. Features of solar thermochemical redox cycles for hydrogen production from water as a function of reactants' main characteristics, International Journal of Hydrogen Energy 36, Issue 4, 2817–2830.

Vishnevetsky, I., Epstein, M., 2011b. Metal oxides reduction in vacuum: setup development and first experimental results. Proceeding of 17 International Symposium Solar PACES; September 20–23, Granada, Spain, paper 23698.

Vishnevetsky, I., Ben-Zvi, R., Epstein, M., 2012. Solar metal oxide reduction under vacuum, experimental investigation of the alumina case, Proceeding of 18 International Symposium Solar PACES; September 11–14, Marrakesh , Morocco

Vishnevetsky, I., Ben-Zvi, R., Epstein, M., Barak, S., Rubin, R., 2013. Solar carboreduction of alumina under vacuum, JOM. J. Min. Met. Mater. Soc. (TMS) 65, 1721–1732.

Vishnevetsky, I., Epstein, M., Rubin, R., 2014. Solar carboreduction of alumina under vacuum, Energy Procedia 49, 2059–2069 (Proceedings of the SolarPACES 2013 International Conference)

Vishnevetsky, I., Epstein, M., 2015. Solar carbothermic reduction of alumina, magnesia and boria under vacuum, Solar Energy 111, 236-251.

Wieckert, C., Palumbo, R, Frommherz, U., 2004, A two-cavity reactor for solar chemical processes: heat transfer model and application to carbothermic reduction of ZnO, Energy 29, 771–787 (SolarPACES 2002).

Wieckert, C., Frommherz, U., Kräupl, S., Guillot, E., Olalde, G., Epstein, M.,. Santén, S., Osinga, T., Steinfeld, A., 2007. A 300 kW solar chemical pilot plant for the carbothermic production of zinc, J. Sol. Energy Eng. 129(2), pp. 190-196.

COLD TESTINGS OF A WINDOWED FLUIDIZED BED REACTOR USING QUARTZ SAND FOR SOLAR GASIFICATION OF COKE

N. Gokon[1,*], T. Tanabe[2], H. S. Cho[1], T. Hatamachi[2], T. Kodama[3]

[1] Center for Transdisciplinary Research, Niigata University, 8050 Ikarashi 2-nocho, Nishi-ku, Niigata 950-2181, Japan

[2] Graduate School of Science and Technology, Niigata University, 8050 Ikarashi 2-nocho, Nishi-ku, Niigata 950-2181, Japan

[3] Department of Chemistry & Chemical Engineering, Faculty of Engineering, Niigata University, 8050 Ikarashi 2-nocho, Nishi-ku, Niigata 950-2181, Japan

Abstract

A windowed fluidized bed reactor prototype was studied and developed for solar thermochemical gasification of coal cokes with steam and CO_2. The windowed fluidized bed reactor is assumed to be combined with a newly developed beam-down optics. Recently, quartz sand was employed as a chemically-inert bed material for the fluidized bed and worked as a thermal transfer/storage medium inside the reactor for coke gasification under direct light irradiation. In order to design a laboratory-scale prototype windowed fluidized-bed containing of quartz sand and coke particles, the reactor model of fluidized bed was made from a transparent acrylic resin to allow us to observe a fluidizing particle through the sidewall of the reactor body; a branching tube is equipped with the sidewall of the reactor to continuously supply coal-coke particles from a screw feeder. In the present study, in order to evaluate fluidization performance of coal-cokes, the pressure loss between the inlet and outlet gases was examined, and descending coal-coke particles on the sidewall of the reactor was observed in the reactor model. The moving velocity and distance of descending particles from the top to bottom of fluidized bed were measured by the visual observation of the tracer particles on outside wall of reactor model.

Keywords: *Solar thermochemical gasification, Coal-cokes, Fluidized bed reactor, Cold testing*

1. Introduction

Coal gasification using CO_2 or steam as an oxidant is a highly endothermic process at high-temperature, and is used to produce solar-hybrid syngas (solar-fuel) composed of a mixture of hydrogen and carbon monoxide. Solar gasification is a promising key technology for thermochemical conversion, which can produce clean gaseous fuels from solid carbonous material by using high-temperature solar heat [1-6]. The greatest advantage of solar-driven gasification is the storage of a significant fraction of solar energy as the chemical energy of the synthesized fuel molecules, and the fuels can reduce the net CO_2 emissions to the environment and conserve fossil fuels.

$$CH_n(coal) + H_2O(l) = CO + (1+n/2)H_2 \qquad \Delta H_{298K} = 175\ kJ/mol \qquad (1)$$

$$CH_n(coal) + CO_2 = 2CO + n/2H_2 \qquad \Delta H_{298K} = 172 kJ/mol \qquad (2)$$

The calorific value of coal or carbon feed can theoretically be upgraded by about 45% when the process heat required to drive the reactions (1) and (2) is provided by concentrated solar radiation. Syngas derived from solar energy can be thermochemically converted to hydrogen via water–gas shift reaction; to liquid hydrocarbon fuels such as diesel, kerosene, and gasoline via Fischer–Tropsch synthesis; or directly used as a combustion fuel for power generation.

The present authors in Niigata University study a windowed reactor prototype using fluidized bed of coal cokes particles, and have proposed to combine the windowed solar chemical reactor, such as a solar gasifier, with a newly developed solar reflective tower or beam-down optics [7-10]. Recently, quartz sand was employed as a chemically-inert bed material for the fluidized bed and as a thermal transfer/storage medium inside the reactor for coke gasification under direct light irradiation. In order to design a laboratory-scale $30kW_{th}$ prototype windowed fluidized-bed containing of quartz sand and coke particles, the reactor model of fluidized bed was made from a transparent acrylic resin to allow us to observe a fluidizing particle through the sidewall of the reactor body; a branching tube was equipped with the sidewall of the reactor to continuously supply coal-coke particles from a screw feeder [11].

doi:10.18086/swc.2015.04.24 Available at http://proceedings.ises.org

In the present study, in order to evaluate fluidization performances of coal-cokes, the pressure loss between the inlet and outlet gases was examined, and descending coal-coke particles on the sidewall of the reactor was observed in the reactor model. The moving velocity and distance of descending particles from the top to bottom of fluidized bed were measured by the visual observation of the particles on outside wall of reactor model.

2. Experimental procedure

2.1. Preparation of quartz sand as a bed material

Quartz sand was purchased from Japan Pure Chemical Co., Ltd. The quartz sand was sieved using mesh screens into four particle size ranges: 100–200 μm, 200–300 μm, 300–500 μm, and 500–700 μm; the quartz sand of 300–500 μm size was used as the chemically inert bed material for investigation. Real and bulk densities of quartz sand at 25 °C are 2.6 g cm^{-3} and 1.3 g cm^{-3}, respectively. The loading amount of quartz sand was 2000 g. The layer height/layer diameter ratio (L/D ratio) was 1.17.

2.2. Fluidized-bed reactor cold model (FBCM)

Fig. 1 shows schematic view of a fluidized bed reactor cold model (FBCM) with a transparent quartz window at its top. The reactor model of laboratory-scale prototype windowed fluidized-bed containing of quartz sand and coke particles was fabricated. The FBCM was made from a transparent acrylic resin to allow us to observe a fluidizing particle through the sidewall of the reactor body; a branching tube was equipped with the sidewall of the reactor in order to continuously supply coal-coke particles from a screw feeder. In the present study, an orifice type distributor was newly designed in order to enhance an internal circulation of fluidizing particle; a number of pores were densely arranged in a center of the distributor, while pores were sparsely located in a circumference of the distributor [11].

Fig. 2 shows photographs of the FBCM. A windowed fluidized-bed reactor can prevent direct contact, ensuring an interspacing gap between the coal-coke particles and window. It assumed that concentrated solar radiation passes downward through the window and directly heats the FBCM of fluidizing particles. A draft tube is located at the center of the fluidized particle bed inside the reactor, and is possible to remove itself in order to evaluate the impact on internal circulation of quartz sand. For the internally-circulating fluidized bed (ICFB) with draft tube, inlet gas (air in this study) is allowed to flow into the draft tube and annulus region between the internal tube and reactor wall. In this reactor design, it is expected that the fluidizing particles are always transported upward in the draft tube and move downward in the annulus region. This forced circulation pattern will enable solar energy to be transferred from the top to the bottom of the fluidized particle bed; the bed temperature remains high and homogeneous, thus preventing localized overheating of some areas within the bed. Therefore, by directly heating the bed, the solar gasification will occur in the fluidized bed inside the reactor.

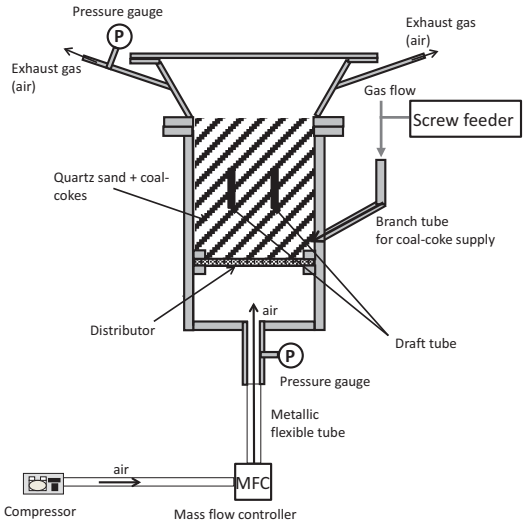

Figure 1 Experimental set-up for fluidization performances of mixture of the coal-coke and quartz sand using the reactor model of fluidized bed reactor.

Figure 2 Photograph of experimental system using fluifdized bed reactor conbined with screw feeder for coal-coke supply.

2.3. Fluidization performance testing using the designed reactor model of fluidized bed reactor

Fluidization performances of mixture of the coal-coke and quartz sand using the reactor model of fluidized bed reactor were examined in this study. The quartz sand of 300-500 μm size was selected and used for testing in the series of experiment. 40 g of coke particles were mixed with 2000 g of quartz sand, and the mixture was loaded in the fluidized bed region of the reactor tube. The static bed heights were 140 mm before fluidization. The air flow into the bottom of reactor was controlled by mass-flow controller; the gas stream was passed through the distributor; the internally circulating fluidized bed was formed inside the reactor resulting in the fluidization of mixture of coal-coke and quartz sand. The air could be flowed at volumetric gas velocities of 0-100 N $dm^3 \cdot min^{-1}$ (superficial gas velocities of 0-0.147 $m \cdot s^{-1}$) to examine the fluidization performances of mixture of the coal-coke and quartz sand. The gas pressures at gas inlet and outlet were measured by using pressure gauge, respectively. In addition, the descending cokes and sand particles on the sidewall of the reactor were observed in the reactor model. The moving velocity and distance of descending particles from the top to bottom of fluidized bed were measured by the visual observation of the particles on outside wall of reactor model. From the fluidization performances, the impacts of internal circulation of mixture of coal-coke particle and quartz sand on the fluidization state in the fluidized bed reactor are evaluated.

3. Results and Discussion

A windowed reactor model of fluidized bed reactor designed for solar coke gasification using quartz sand as a bed material was used in the series of experiments. The reactor model was used for the fluidization performance testing of mixture of coal-coke and quartz sand in this study. Figure 3 shows relationship between pressure loss of fluidized bed and gas velocity in the reactor model of fluidized bed reactor with/without draft tube. Figure 3 (a) is the results for use of internally circulating fluidized bed with draft tube, while Figure 3 (b) exhibits the results for use of fluidized bed without draft tube. As seen in Figure 3 (a), the values for U_{mf} and pressure loss for the fluidized bed reactor with the draft tube (U_{mf} = 0.071 m s^{-1}, and pressure loss of 1.67 kPa) were almost the same with those for that without draft tube (U_{mf} = 0.077 m s^{-1}, and pressure loss of 1.63 kPa) (Fig. 3 (b)). This result means that draft tube in the reactor did not impact on the gas velocity and pressure required for making fluidization. Namely, the draft tube did not facilitate a formation of fluidized bed at boundary region between fixed bed and fluidized bed. However, in a higher gas velocity region than the value for U_{mf}, a pressure loss for the fluidized bed with draft tube slightly decreased with increasing gas velocity; a pressure loss for that without draft tube is almost constant although increasing gas velocity. This result for lowering pressure loss indicates that the orifice type distributor enhances an internal circulation of mixture of coal-coke and quartz sand; in addition, the presence of draft tube embedded in the fluidized bed forms a coordinate internal circulation of bed particles in the reactor. This tendency appeared similarly at the previous results of the batch-type fluidization testing for use in a mixture of coal-coke and quartz sand without screw feeder [11]. This result for decreasing pressure loss indicates that a draft tube have a potential to enhances a fluidization of mixture of coal-coke and quartz sand in a reactor. The effectiveness of draft tube appears prominently in higher gas velocity than the U_{mf} value (U_{mf} = 0.071 $m \cdot s^{-1}$).

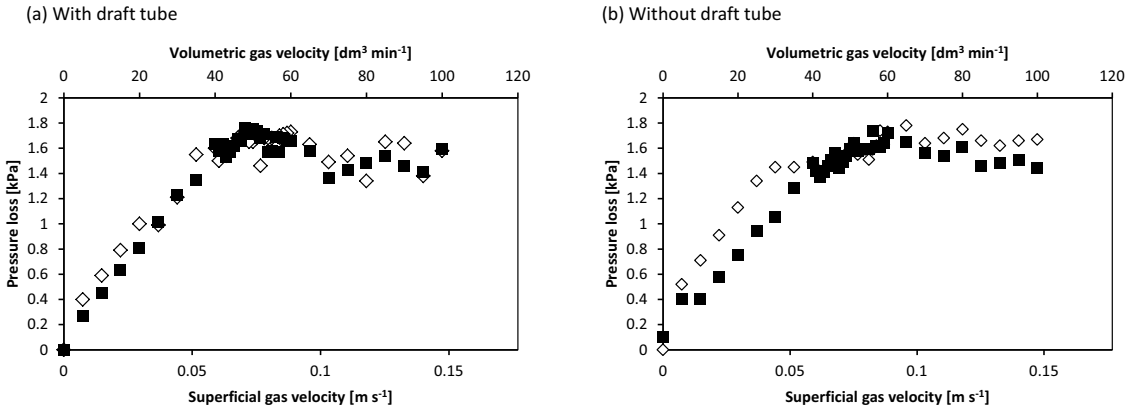

Figure 3 Relationship between pressure loss of fluidized bed and superficial gas velocity in the designed reactor model of fluidized bed (a) with or (b) without draft tube. A mixture of quartz sand and coal coke particles are used as a fluidization medium in the reactor model. The open plot is the results for increasing gas velocity, and the closed plot is the result for decreasing gas velocity in the figures.

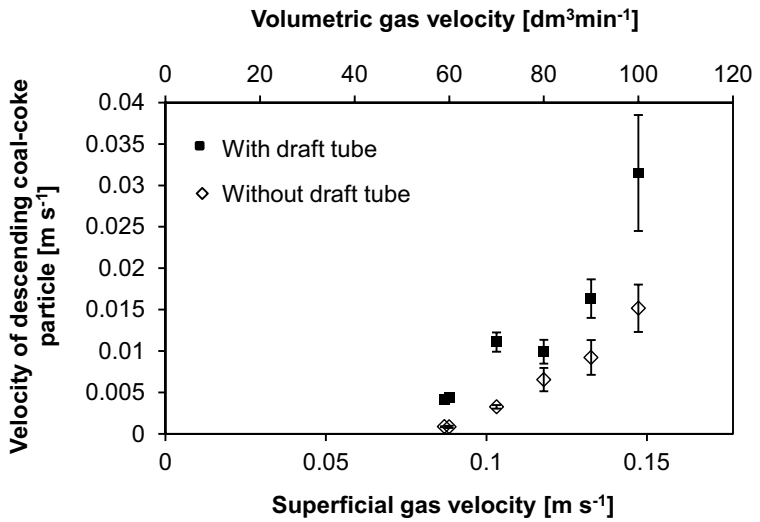

Figure 4 Relationship between descending coal-coke particle of fluidized bed and superficial gas velocity in the designed reactor model of fluidized bed reactor with/without draft tube. The descending particles were observed at a position of 35 mm below height from the bed surface.

A velocity of descending particle are measured at different bed height, the results are shown in Figure 4-6. The result observed at a position of 35 mm below height from the bed surface appears in Figure 4. The mixture of quartz sand and coal coke particles was fluidized in the reactor model, and coal-coke was observed as a descending particle. The open plot is the result for without draft tube, and the closed plot is the result for with draft tube in the figures. A velocity of descending particle increases with increasing gas velocity for fluidized bed reactor with and without draft tube. The velocity of coal-cokes at the bed layer (0.25H, H = bed height) is 1.5-5.1 times higher in the fluidized bed with draft tube than that without draft tube in a wide range of superficial gas velocity U = 0.088-0.147 m·s^{-1}. This means that the use of draft tube dominantly enhances the mobility of coal-cokes at higher gas velocities than U_{mf}. The tendency for increasing velocity of descending coal-coke particle was obviously observed in comparison to the only use of quartz sand [11]. These results shown in Figure 4 mean that coal-coke is descended at a fast velocity on the outer wall of the reactor tube in the fluidized bed in comparison to the quartz sand; the use of draft tube enhances the velocity of descending coal-coke in a mixture bed of coal-coke and quartz sand at a wide gas velocity range.

The results for velocity of descending particle at further deep depth of the fluidized bed are shown in Figure 5. The velocity of descending coal-coke particle was measured at a position of 55 mm below height from the bed surface. The velocity of coal-cokes is 1.9-7.5 times higher in the fluidized bed with draft tube than that without draft tube in a wide range of superficial gas velocity U = 0.088-0.147 m·s^{-1}. The result indicates that the velocity of descending coal-coke was decreased with the deep layer (0.4H) of the fluidized bed with and without draft tube, but coal-coke in the fluidized bed with draft tube could be moving down relatively faster than that without draft tube as the bed layer was increasing depth. On the other hand, the velocity of descending quartz sand was also decreased with the deep layer, but the velocity of quartz sand in the fluidized bed with draft tube was 2 times higher than that without draft tube in a range of U = 0.088-0.147 m·s^{-1}[11]. This means that coal-coke particle can be subject to influence by using draft tube.

Figure 6 show the results for the velocity of descending coal-coke particle at the middle layer (0.46H, H = bed height) of the fluidized bed. The velocity of descending particle was measured at the position of 65 mm below height from the bed surface. The velocity of coal-cokes is 2.4-7.5 times higher in the fluidized bed with draft tube than that without draft tube in a wide range of superficial gas velocity U = 0.088-0.147 m·s^{-1}. As seen in Figure 4-6, a difference of velocity of coal-coke particle between fluidized bed with and without draft tube remains at high gas velocity although the bed layer is deeper. The results for velocity of descending coal-coke particle means that an internally-circulating fluidized bed with draft tube enhances velocity of descending coal-coke particle at bed layer for the surface to middle depth (0.46H) in the velocity range of U = 0.088-0.147 m·s^{-1}.

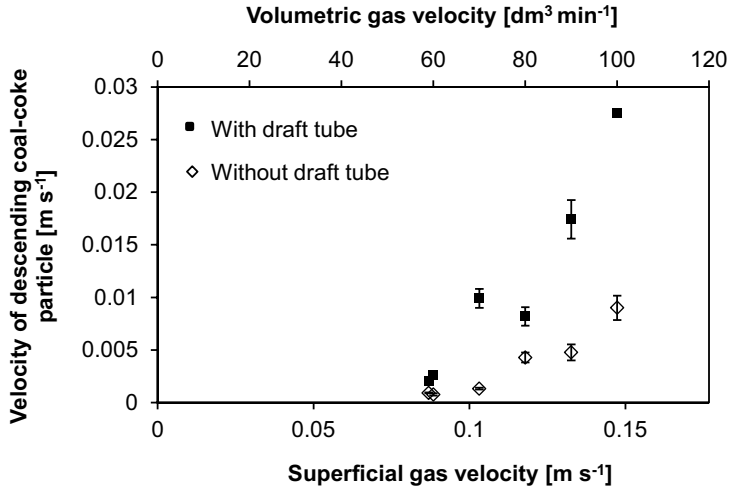

Figure 5 Relationship between descending coal-coke particle of fluidized bed and superficial gas velocity in the designed reactor model of fluidized bed reactor with/without draft tube. The descending particles were observed at a position of 55 mm below height from the bed surface.

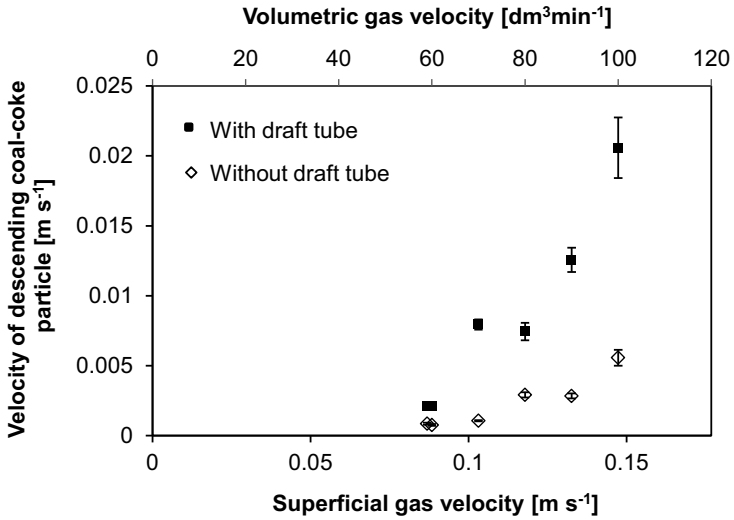

Figure 6 Relationship between descending coal-coke particle of fluidized bed and superficial gas velocity in the designed reactor model of fluidized bed reactor with/without draft tube. The descending particles were observed at a position of 65 mm below height from the bed surface.

Table 1 Moving distance of descending coal-coke particles in the fluidized bed reactor with/without draft tube on the sidewall of reactor.

Volumetric gas velocity [dm³ min⁻¹]	Superficial gas velocity [m s⁻¹]	With draft tube			Without draft tube		
		Branch tube [dm³ min⁻¹]		*Moving distance of descending particles [mm]	Branch tube [dm³ min⁻¹]		*Moving distance of descending particles [mm]
		Volumetric gas velocity [dm³ min⁻¹]	Superficial gas velocity [m s⁻¹]		Volumetric gas velocity [dm³ min⁻¹]	Superficial gas velocity [m s⁻¹]	
59	0.087	2.9	0.0043	80(±4)	3.4	0.0050	70(±6)
60	0.088	2.2	0.0032	78(±5)	3.0	0.0044	72(±5)
70	0.10	2.5	0.0037	82(±3)	2.0	0.0029	75(±3)
80	0.12	1.9	0.0028	85(±3)	2.1	0.0031	78(±4)
90	0.13	1.6	0.0024	91(±4)	1.7	0.0025	80(±2)
100	0.15	1.6	0.0024	95(±5)	1.6	0.0024	88(±2)

* Moving distance : moving distance from fluidized surface to bottom

A moving depth of descending coal-coke particle on the sidewall of the reactor is observed in a range of U = 0.088-0.147 m·s^{-1}.The results are listed in Table 1. The moving depth of descending particle was measured from the surface of fluidized bed to the disappearance height (the particle is moving towards the center of fluidized bed) on the sidewall of reactor. The branch tube is used to feed coal-coke particle into the fluidized bed of quartz sand by gas passing, and the volumetric and superficial gas velocities for the branch tube are listed in Table 1. In the case of the fluidized bed with draft tube, coal-coke particle is moved down to 80 mm depth (0.57H) at U = 0.087 m·s^{-1}. The moving distance increases with increasing gas velocity. The muximum distance of 95 mm (0.68H) at U = 0.15 m·s^{-1} is almost corresponded to a lower surface of draft tube. The results indicate that draft tube has a functional role in conveying a descending particle at deeper layer along the sidewall of the reactor. On the other hand, in the case of the fluidized bed without draft tube, the moving distances are 70 mm (0.5H) and 88 mm (0.63H) at U = 0.087 and 0.15 m·s^{-1}, respectively. The moving distance increases with increasing with gas velocity, however, the moving distance in the fluidized bed with draft tube is superior to that without draft tube in a range of U = 0.087-0.15 m·s^{-1}. The results for the moving distance indicates that an internally-circulating fluidized bed with draft tube have a potential to move a fluidizing particle downward on sidewall of the reactor as well as upwards moving in the center region of the fluidized bed. Furthermore, as seen in Table 1, it is striking that the gas velocities passed through the branch tube are relatively lower for the internal-circulation with draft tube than the conventional fluidized bed without draft tube. The results for gas velocities in the branch tube means that coal-coke particles feeded through the branch tube can be easily to enter into an internally-circulating fluidized bed of quartz sand with draft tube in comparison to a fluidized bed without draft tube. One of the reasons will be due to high mobility (moving distance at deeper layer and moving velocity along the sidewall) of coal-coke particles in an internally-circulating fluidized bed with draft tube.

In the next step, based on the results in this study, a laboratory-scale prototype windowed fluidized-bed of quartz sand and coke particles feeded by screw-feeder will be fabricated and tested for coal-coke gasification under continuous supply of coal-coke conditions by concentrated Xe-beam or solar radiation.

4. Summary

A laboratory-scale prototype windowed fluidized-bed containing of quartz sand and coke particles was designed and, the reactor model of fluidized bed was made from a transparent acrylic resin to allow us to observe a fluidizing particle through the sidewall of the reactor body; a branching tube was equipped with the sidewall of the reactor to continuously supply coal-coke particles from a screw feeder. The fluidization performances of coal-cokes, the pressure loss between the inlet and outlet gases was examined, and descending coal-coke particles on the sidewall of the reactor was observed in the reactor model.

This result for decreasing pressure loss indicates that a draft tube have a potential to enhances a fluidization of mixture of coal-coke and quartz sand in a reactor. The effectiveness of draft tube appeared prominently in higher gas velocity than the U_{mf} value (U_{mf} = 0.071 m·s^{-1}). As seen in Figure 4-6, a difference of velocity of coal-coke particle between fluidized bed with and without draft tube remained at high gas velocity although the bed layer was deeper. The results for velocity of descending coal-coke particle means that an internally-circulating fluidized bed with draft tube enhances velocity of descending coal-coke particle at bed layer for the surface to middle depth (0.46H) in the velocity range of U = 0.088-0.147 m·s^{-1}. The results for the moving distance indicates that an internally-circulating fluidized bed with draft tube have a potential to move a fluidizing particle downward on sidewall of the reactor as well as upwards moving in the center region of the fluidized bed. Furthermore, as seen in Table 1, it is striking that the gas velocities passed through the branch tube are relatively lower for the internal-circulation with draft tube than the conventional fluidized bed without draft tube. The results for gas velocities in the branch tube means that coal-coke particles feeded through the branch tube can be easily to enter into an internally-circulating fluidized bed of quartz sand with draft tube in comparison to a fluidized bed without draft tube. If the behaviour of coal-coke particles is done at high-temperature, gasification performances of gasification rate will be expected under the continuous supply of coal-coke particles feeded through the branch tube.

5. References

1. D. W. Gregg, R. W. Taylor, J. H. Campbell, J. R. Taylor, A. Cotton, Solar Energy 25, 353–364 (1980).

2. R. Taylor, R. Berjoan, J. Coutures, Solar Energy 30 [6], 513–525 (1983).

3. A. Z'Graggen, P. Haueter, G. Maag, A. Vidal, M. Romero, A. Steinfeld, International Journal of Hydrogen Energy 32, 992−996 (2007).

4. A. Z'Graggen, P. Haueter, G. Maag, M. Romero, A. Steinfeld, International Journal of Hydrogen Energy 33, 679−684 (2008).

5. A. Z'Graggen, A. Steinfeld, International Journal of Hydrogen Energy 33, 5484–5492 (2008).

6. P. von Zedtwitz, A. Steinfeld, Industrial & Engineering Chemistry Research 44, 3852–3861 (2005).

7. T. Kodama, N. Gokon, S. Enomoto, S. Itoh, T. Hatamachi, ASME Journal of Solar Energy Engineering132[4], 041004-1-6 (2010).

8. N. Gokon, R. Ono, T. Hatamachi, L. Liuyun, H.-J. Kim, T. Kodama, International Journal of Hydrogen Energy 37[17], 12128-12137 (2012).

9. N. Gokon, T. Izawa, T. Abe, T. Kodama, International Journal of Hydrogen Energy 39, 11082-11093 (2014).

10. N. Gokon, T. Izawa, T. Kodama, Energy 79, 264-272 (2015).

11. N. Gokon, T. Tanabe, T. Shimizu, T. Kodama, Cold Test with a Benchtop Set-up for Fluidized Bed Reactor Using Quartz Sand to Simulate Gasification of Coal Cokes by Concentrated Solar Radiation, SolarPACES 2015, Cape Town, South Africa, 2015.

Conference Proceedings

Solar World Congress 2015
Daegu, Korea, 08 – 12 November 2015

REDOX AND FLUIDIZATION PERFORMANCES OF Co_3O_4/CoO FOR SOLAR THERMOCHEMICAL ENERGY STORAGE

N. Gokon[1,*], S. Yokota[2], H.S. Cho[1], T. Hatamachi[3], T. Kodama[3]

[1] Center for Transdisciplinary Research, Niigata University, 8050 Ikarashi 2-nocho, Nishi-ku, Niigata 950-2181, Japan

[2] Graduate School of Science and Technology, Niigata University, 8050 Ikarashi 2-nocho, Nishi-ku, Niigata 950-2181, Japan

[3] Department of Chemistry & Chemical Engineering, Faculty of Engineering, Niigata University, 8050 Ikarashi 2-nocho, Nishi-ku, Niigata 950-2181, Japan

Abstract

Thermochemical energy storage using redox pair of Co_3O_4/CoO powders was studied for thermal energy storage (TES) using concentrated solar radiation as the energy source. Reversible chemical reactions (reduction – oxidation redox cycles) of oxides under air atmosphere are used to storage significant thermal energy via the enthalpies of the chemical reactions at high-temperature. A promising concept for solar TES is proposed using fluidized bed with Co_3O_4/CoO redox pair. In the present study, the effects of particles size of Co_3O_4/CoO powders on thermochemical storage performances are investigated in order to explore the potential of the material for fluidized-particle bed reactor. The Co_3O_4 powders with particle sizes of 100-200, 200-300, 300-500 and 500-700 μm were used to test redox performances by thermo-gravimetric analysis. A flowability (fluidization state) of Co_3O_4 powders in a fluidized bed reactor for thermochemical energy storage is also examined in this study. A basic relationship between pressure drop of inlet gas and gas flow rate was experimentally examined using bed materials with different particle sizes by a small-scale quartz reactor at ambient pressure and temperature.

Keywords: *Solar thermochemical storage, redox material, Co_3O_4/CoO, Fluidized bed reactor*

1. Introduction

Concentrated solar radiation has some specific properties such as high density, heterogeneous distribution of thermal flux, and frequent thermal transients due to the fluctuating insolation resulting from cloud passage. Thus, concentrated solar power (CSP) system requires to effectively storage the high temperature heat in order to realize long-term operation of the system such as around-the clock operation. Also, solar chemical reactor for solar hydrogen production can convert the high-temperature solar heat into chemical fuels via endothermic thermochemical process, for example, two-step water-splitting cycle, methane reforming and gasification of carbonous materials.

Thermal energy can be stored as sensible, latent or thermochemical heat. Thermochemical heat storage (TCS) presents higher energy densities than sensible or latent heat, and it can be used at higher temperature ranges. The thermochemical heat storage consists of charge, storage and discharge steps. The high-temperature heat provided by concentrated solar radiation is used to proceed with an endothermic reaction of reversible chemical reaction during the charge step. Thus, the high-temperature heat can be chemically stored as reaction products. Finally, the reaction products are used in order to recover the high-temperature heat through an exothermic reaction of reversible chemical reaction during the discharge step. Redox pair operating at temperature range of 600-1000ºC, much higher than the operational limit of 600ºC for current state-of-the-art molten nitrate salt heat transfer fluid, is eligible for next–generation CSP plants (Agrafiotis et

doi:10.18086/swc.2015.04.25 Available at http://proceedings.ises.org

al., 2014a, Carrillo et al., 2014), while redox pair at temperature range of 800-1000ºC works for solar methane reforming and gasification of carbonous materials to produce hydrogen and synthetic gas.

The choice of the redox pair for TCS are important with regard to thermodynamics, energy storage capacity, material costs, reaction kinetics, toxicity and cyclic behavior (Worner et al., 2012). A redox cycle through a hercynite cycle ($FeAl_2O_4$) was studied for TCS by the University of Colorado (Ehrhart et al., 2014). A redox pair of CuO/Cu_2O was recently tested for TCS (Alonso et al., 2015). Wong evaluated various metal oxides as a TCS medium by thermodynamic calculation and experimental analysis (Wong, 2011). Among those which were suitable for TCS, a redox pair of Co_3O_4/CoO showed beat re-oxidation kinetics. Recently, Co_3O_4/CoO redox pair has been studied for some TCS performances from the viewpoints of thermodynamic analysis, material testing and reactor/heat exchanger developments (Schrader et al., 2015, Neises et al., 2012, Tescari et al, 2014, Carrillo et al., 2014, Pagkoura et al., 2014, Agrafiotis et al., 2014a and Agrafiotis et al., 2015b).

Co_3O_4/CoO redox pair store and release energy through the following redox reaction:

$$Co_3O_4 \rightarrow 3CoO + 1/2O_2 \qquad \Delta H = 196.5 \text{ kJ/mol-reactant at } 950\ ^{o}C \qquad (1)$$

Co_3O_4 presents a high potential for TCS and fits the operation temperature for CSP plants (Wong, 2011) and solar chemical reactor. A promising concept for CSP plants provided with a volumetric air central receiver using Co_3O_4/CoO redox pair is proposed and studied (Agrafiotis et al., 2014a).

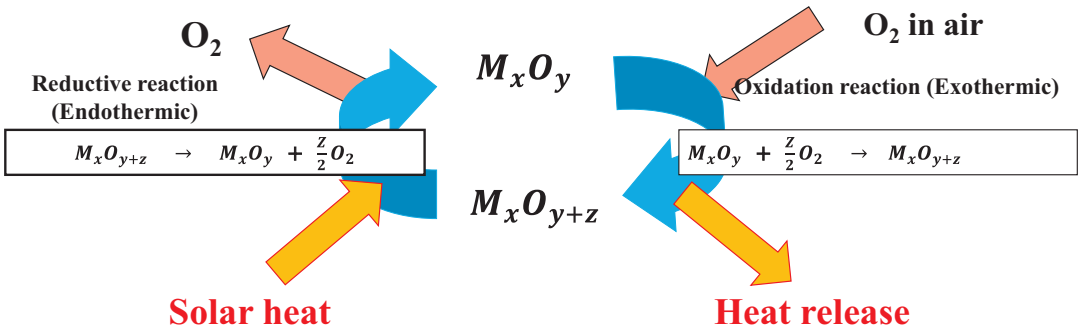

Figure 1. Schematic diagram of thermochemical energy storage by M_xO_{y+z}/M_xO_y redox pair.

The present authors in Niigata University have been developing windowed receivers/reactors prototype using fluidized bed of reacting (coal cokes, and metal oxides) or chemically-inert (quartz sand) particles, and have proposed to combine the windowed solar chemical reactor/receiver with a newly developed solar reflective tower or beam-down optics. In the present study, the effects of particles size of Co_3O_4/CoO powders on TCS performances are investigated in order to explore the potential of the material for fluidized-particle bed reactor. A flowability (fluidization state) of Co_3O_4 powders in a cold testing of fluidized bed reactor is also examined in this study.

2. Experimental procedure

2.1. Preparation of Co_3O_4 powders for fluidization testing and thermochemical storage testing

Co_3O_4 powders were purchased from Japan Pure Chemical Co., Ltd in Japan. The Co_3O_4 powders were divided into four particle size ranges: 30–100 μm, 100–300 μm, 300–500 μm, and 500–700 μm. The Co_3O_4 powders of all particle sizes were prepared for investigation of fluidization state in a cold testing of fluidized bed reactor and thermochemical storage testing by using thermogravimetry reactor (Thermo plus EVO 2/TG-DTA series manufactured by Rigaku Co. ltd.) and a differential scanning calorimeter (DSC). The Co_3O_4 powder of 30–100 μm and 500–700 μm size were used as the redox material for investigation on redox performances.

2.2. Fluidization testing of Co_3O_4 powders by a small-scale quartz reactor of fluidized bed

A basic relationship between pressure loss of inlet gas and outlet gas was experimentally examined using Co_3O_4 powders with different particle sizes by a small-scale quartz reactor at ambient temperature in order to examine a flowability (fluidization state) of Co_3O_4 powders in a fluidized bed reactor for thermochemical storage processes. Fig. 2 shows an experimental setup for flowability test of fluidizing particles by using a small-scale quartz reactor. The diameter of the quartz reactor tube was 25 mm with a thickness of 2 mm, and a length of 48 mm. A porous quartz frit (the hole diameter is 40 μm) was used as the distributor for the small-scale quartz reactor.

Each size of Co_3O_4 powders (21-28 gram) was tested as the fluidized bed of chemical storage material. The Co_3O_4 powder was put into the quartz reactor. The bed height of Co_3O_4 powder inside the reactor is 25 mm for all the particle size. Air was flowed upwards from the bottom of the reactor through the distributor to create the fluidization of Co_3O_4 powder under various air flow rates. A pressure difference for the inlet and outlet gas was measured under various gas flow rates by manometer. The relationship between pressure loss of fluidization gas and flow rate was experimentally examined using each size of Co_3O_4 powder.

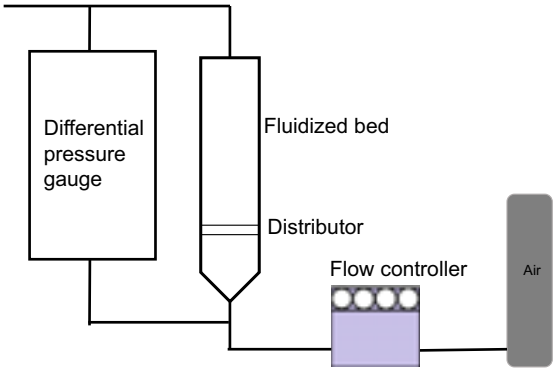

Figure 2. Flowability test of CeO_2 particles ranged in variety size by a small-scale quartz reactor.

2.3. Thermochemical storage testing by thermogravimetry reactor and DSC measurement

Approximately 100 mg of Co_3O_4 powder was packed into a platinum cup (5 mm in diameter and 5 mm deep), and mounted on the balance in a ceramic reaction chamber. Fig. 3 shows experimental set-up for thermogravimetry reactor used for endothermic thermal reduction (TR) step of Co_3O_4 powder and exothermic air oxidation (AO) step of CoO powder. The Co_3O_4 powder mounted in the thermogravimetry reactor were first heated to 1373K with different heating rates of 10 K/min and 30 K/min using an electric furnace, while passing air (purity 99.9%) through the reactor at a flow rate of 0.2 $dm^3 \bullet min^{-1}$(nor) controlled by mass flow controller (KOFLOC RK1700), in order to perform the TR step for heat charging. The temperature of the Co_3O_4 powder was controlled using an R-type thermocouple in contact with the platinum cup. The powder was heated at a constant temperature of 1373 K for 30 min. The weight change of the powder by O_2 release during AO step for heat discharging was measured against time in order to monitor a degree of reaction fraction of AO step.

A reaction conversion α for O_2 release and uptake during the TR and AO step was defined as follows:

$$\alpha = \frac{m - m_i}{m_f - m_i} \quad (2)$$

where m and m_i are weight of sample at time t and initial weight, respectively; m_f is final weight when an ideal reaction proceeds. In thermogravimetry, the reaction fraction α was calculated by the measured weight change of sample.

Subsequently, the powder subjected to the TR step was cooled to 1073 K in air stream at a flow rate of 0.2 $dm^3 \bullet min^{-1}$(nor) to perform the subsequent AO step in an electric furnace of thermogravimetry reactor, and the AO step was continued for 30 min. The temperature of the sample was too controlled using a R-type thermocouple in contact with the platinum cup. The weight change of the powder by O_2 uptake during AO

step was measured against time in order to monitor a degree of reaction fraction of AO step.

The TR and AO steps were alternately repeated three times.

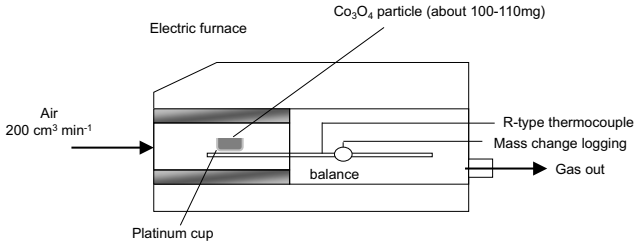

Figure 3. Schematic of the thermogravimetry reactor for thermochemical energy storage using Co_3O_4/CoO redox pair.

The chemical energy storage capacity at the redox temperature and sensible heat capacity arising from the Co_3O_4 and CoO powders were measured for the Co_3O_4/CoO redox pair using a differential scanning calorimeter (DSC). Also, the redox temperature of Co_3O_4/CoO redox pair was estimated from a measurement of endothermic and exothermic peaks by DSC. The specific heat C_p values of the Co_3O_4/CoO redox pair before and after the cyclic reaction were also measured to estimate the dependence of the sensible heat on the temperature using the DSC. The programmed heating and cooling rates for the DSC measurements were as follows: 1) a heating rate of 10 K/min between room temperature and 1000 °C, 2) 30 min at 1000 °C, 3) a cooling rate of 10 K /min down to 800 °C, and 4) 30 min at 800 °C. The heating/cooling cycle in the DSC was repeated three times in air stream.

3. Results and Discussion

3.1. Fluidization testing of Co_3O_4 powders by a small-scale quartz reactor of fluidized bed

Fig. 4 shows results for fluidization testing using a fluidized bed reactor. The Co_3O_4 powder with different particle sizes between 50 and 700 μm diameter was used and tested as a bed material for the fluidized bed reactor. For the particle size of 50-100 μm, a pressure loss initially increased with superficial gas velocity of inlet gas, and reached the small peak of 690 Pa at a velocity of 0.068 m·sec^{-1}. Subsequently, the pressure loss plateaued and then increased to about 1460 Pa. This behavior of pressure loss for the superficial gas velocity indicates that the velocity of 0.068 m·sec^{-1} corresponds to start a fluidization of Co_3O_4 powder; a minimum superficial gas velocity (U_{mf}) = 0.068 m·sec^{-1} for the particle size 50-100μm. Similarly, for the particle size of 100-300 μm, a peak value for pressure loss was reduced to about 510 Pa in comparison to that for the particle size 50-100 μm, while the value of U_{mf} slightly decreased to 0.054 m·sec^{-1}. In addition, the plateau region where the value for pressure loss is stable for increasing superficial gas velocity of inlet gas, was apparently expanded when the particle size was used.

According to the results in this figure, the fluidization state can be categorized into three regions: fixed layer, bubble fluidization and turbulent fluidization regions. Firstly, a pressure loss increases with increasing a superficial gas velocity. This region was called to fix bed layer, and U_{mf} was corresponded to the following value for the peak of the pressure loss. It was observed that hereafter, a particle started fluidizing. By further increasing a superficial gas velocity, the pressure loss plateaued. In this region, a particle bed made a bubbling fluidization. Beyond the bubbling fluidization, the pressure loss increased again, a particle bed formed a turbulent fluidization. The fluidization state aimed in this study is a lower superficial gas velocity and a mild fluidization of a particle bed in the reactor. Thus, a bubble fluidization was targeted in this study. Based on the experiments of fluidization testing of Co_3O_4 powder, the powder with a smaller size which enables it to make a bubbling fluidization under a lower passing air are favorable for the fluidized bed reactor operating a thermochemical energy storage.

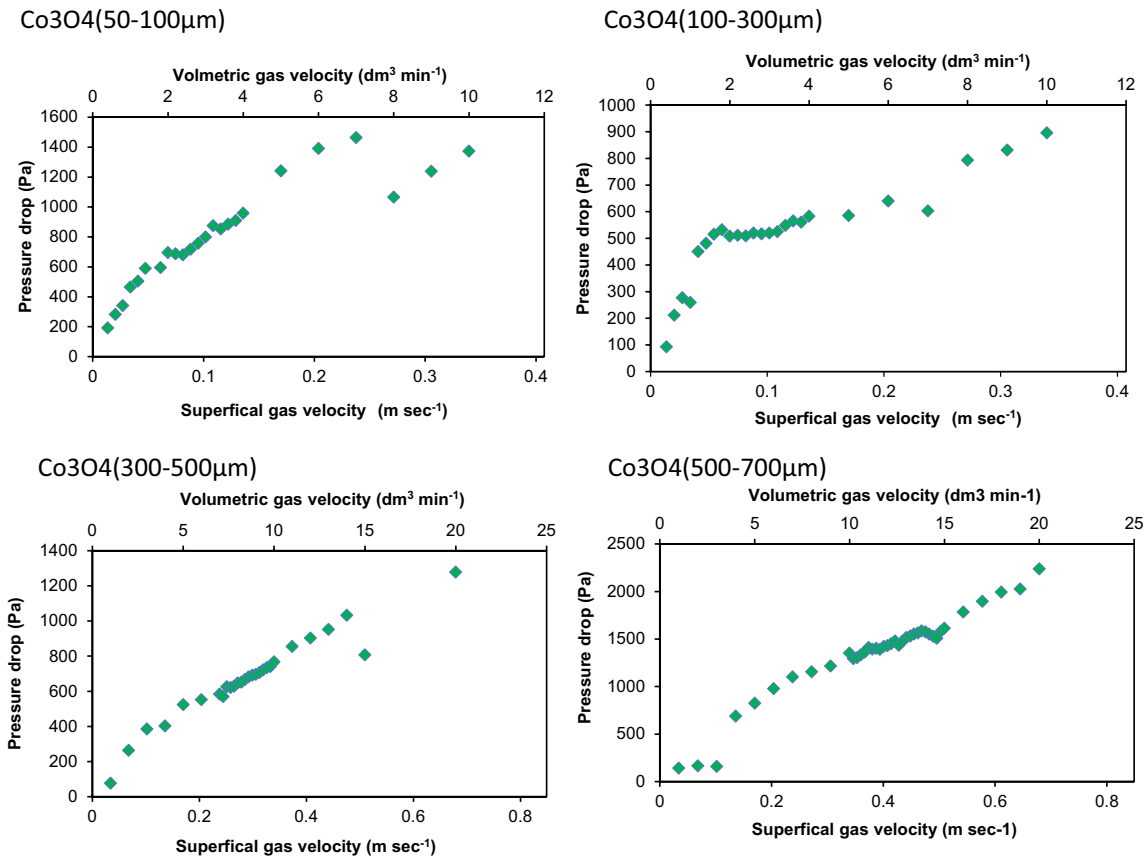

Figure 4. Pressure drop of fluidized bed using various Co_3O_4 powder size

3.2. Thermochemical storage testing by thermogravimetry and DSC measurements

Fig. 5 shows redox reactivity and cyclic performances of Co_3O_4 powder with different particle sizes by thermogravimetry analysis. The heating–cooling operation was performed by a trapezoid mode in order to drive each step as much as possible at temperature of 1100°C and 800°C. For the particle size of 30-100 μm, the weight of sample rapidly decreased with increasing temperature of the sample and reached almost stoichiometric weight change of the sample (Co_3O_4 = 3CoO + 1/2O_2) during TR step. The conversion α of HC step was 99.7, 99.4 and 99.5% for 1st, 2nd and 3rd cycles, respectively. Subsequently, when temperature of the sample decreased in the AO step, the sample returned back to almost initial weight (3CoO + 1/2O_2 = Co_3O_4). The conversion α of AO step was 99.1, 99.2 and 98.6% for 1st, 2nd and 3rd cycles, respectively. Similarly, the weight change of sample for the particle size of 500-700 μm presented superior reactivity and cyclic stability as well as that for particle size of 30-100 μm. Thus, the redox reactivity and cyclic reactivity was independent of the particle size of Co_3O_4 powder.

Fig. 6 shows reaction rate of the Co_3O_4/CoO redox during TR and AO steps for Co_3O_4 powder with the particle size of (a) 30-100 μm and (b) 500-700 μm. The heating–cooling operation was performed by a trapezoid mode. The reaction rate in each step was expressed by a time-derivative of reaction conversion $\frac{d\alpha}{dt}$ for O_2 release and uptake during the TR and AO step. For the particle size of 30-100 μm, the temperature that TR step starts was about 910°C at all cycles. The peak rate in the TR step was $\frac{d\alpha}{dt}$ = about 0.3 at temperature of 945°C. The profiles of reaction rate were reproducibly observed in the TR step at all cycles. On the other hand, for the particle size of 500-700 μm, the temperature that TR step starts was about 920°C at all cycles. The peak rate in the TR step was almost the same ($\frac{d\alpha}{dt}$ = about 0.3) at temperature of 945°C. This means that TR step can start with lower (10°C) temperature as a particle size of Co_3O_4 powder is smaller, but the peak rate in TR step is independent of the particle size. In the case of AO step, the

temperature that AO step starts was almost the same (800°C) with the particle size of 30-100 μm and 500-700 μm, thus was independent of particle size. The reaction rate at a maximum in AO step was 840-850°C, and lower than that for TR step. The results indicate that oxidation reaction of CoO is rate-determining step for thermochemical storage using Co_3O_4/CoO redox pair.

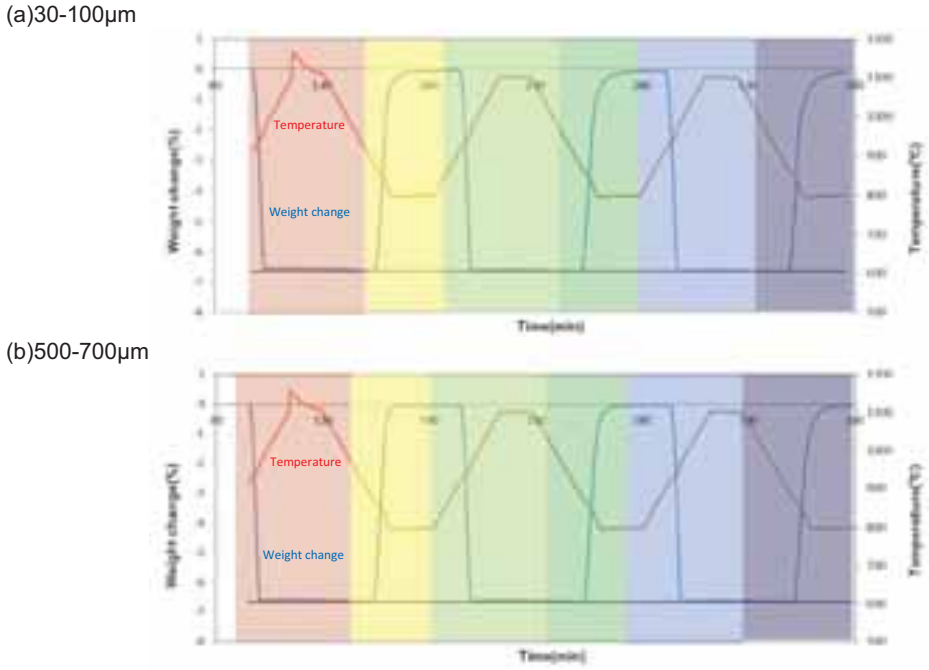

Figure 5. Redox reactivity and cyclic reactivity of Co_3O_4 powder with the particle sizes of (a) 30-100 μm and (b) 500-700 μm. Red and blue lines are temperature and weight change of the sample, respectively. The heating–cooling operation was performed by a trapezoid mode.

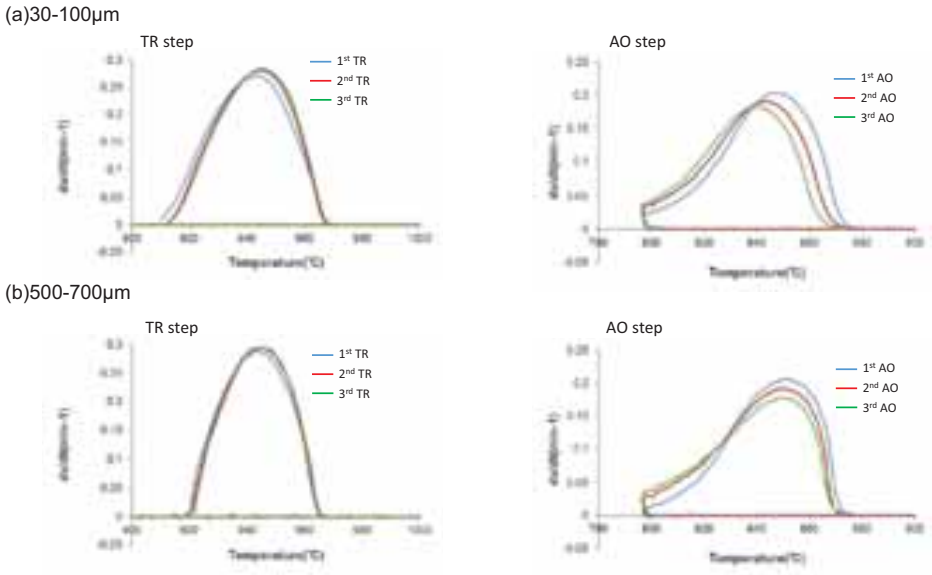

Figure 6. Reaction rate of the Co_3O_4/CoO redox during TR and AO steps for Co_3O_4 powder with the particle size of (a) 30-100 and (b) 500-700 μm. The heating–cooling operation was performed by a trapezoid mode.

Fig. 7 shows comparison for weight change of powder sample with the particle sizes of 30-100 μm and 500-700 μm during TR and AO steps. In the experiments, the samples were subjected to each step without keeping constant temperature of 1100°C for TR step and 800°C for AO step. Namely, the heating–cooling operation was performed by a rectangle mode in order to simulate a heat charging/discharging of Co_3O_4/CoO redox by using a fluidized bed reactor under a concentrated solar radiation. The thermal reduction of Co_3O_4 into CoO proceeded completely for both particle sizes. However, the air oxidation of CoO into Co_3O_4 was

apparently slower for the particle size of 30-100 μm than for that of 500-700 μm in the temperature range of 700-850°C. In order to compare the oxidation rate of CoO during AO step under the heating (charging)-cooling (discharging) operation, the reaction rate of the Co_3O_4/CoO redox during TR and AO steps was plotted against reaction temperature. The plot of reaction rate is shown in Fig. 8. The profiles of reaction rate were reproducibly observed in the TR and AO steps at all cycles. As seen in Fig. 8(a), the temperatures that TR step starts were 915°C for the particle size of 30-100 μm and 920°C for 500-700 μm. Also, the temperatures that TR step terminates were about 965°C for both particle sizes. Further, a peak rate in the TR step was $\frac{d\alpha}{dt}$ = about 0.3 at temperature of 945°C. The temperatures and peak rate for the TR step were almost the same with the results by the different operation mode. However, as seen in Fig. 8(b), for the AO step, the temperatures that AO step starts were 890°C for the particle size of 30-100 μm and 880 °C for 500-700 μm. Also, the temperatures that AO step terminates were 780°C for the particle size of 30-100 μm and 790°C for 500-700 μm. The results for reaction temperatures mean that a temperature region for the AO step expands further high- and low-temperature as a particle size of Co_3O_4 is smaller. The peak rare in the AO step was greater for the particle size of 500-700 μm than that for 30-100 μm. The peak rate in the AO step was $\frac{d\alpha}{dt}$ = about 0.20 at temperature of 865°C for the particle size of 30-100 μm, while that was $\frac{d\alpha}{dt}$ = about 0.22 at temperature of 855°C for 500-700 μm. The temperatures and peak rate for the AO step were different by the operation modes.

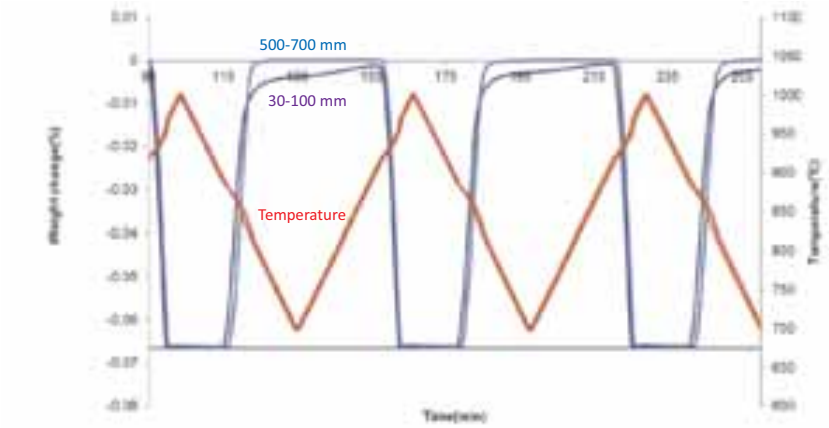

Figure 7. Redox reactivity and cyclic reactivity of Co_3O_4 powder with the particle sizes of 30-100 and 500-700 μm. Red and blue lines are temperature variation and weight change of the sample, respectively. The heating–cooling operation was performed by a rectangle mode.

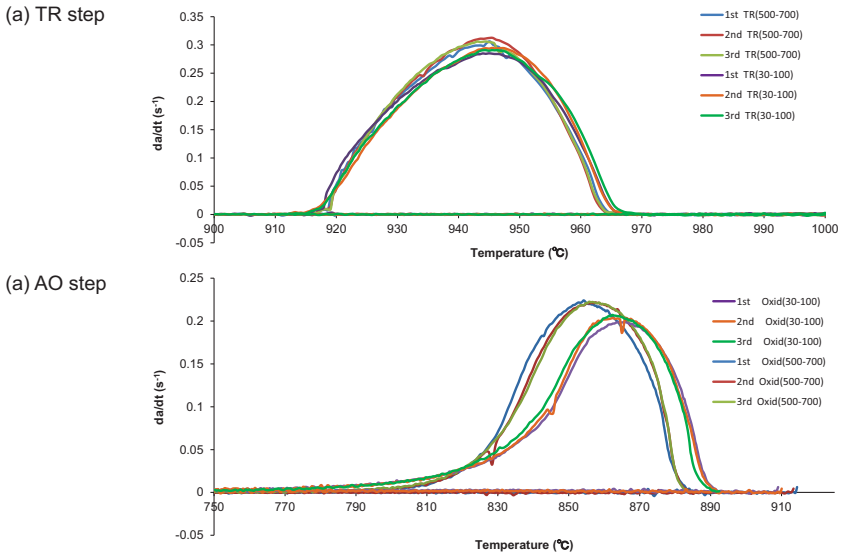

Figure 8. Reaction rate of the Co_3O_4/CoO redox during TR and AO steps for Co_3O_4 powder with the particle size of 30-100 and 500-700 μm at (a) TR and (b) AO steps. The heating–cooling operation was performed by rectangle mode.

Fig. 9 shows the DSC results for the thermal storage capacities of the Co_3O_4/CoO redox material with particle size of (a) 30-100 and (b) 500-700 μm in the charging and discharging modes. The amounts of thermochemical heat storage during the charging and discharging modes were measured at the peak area. For the results of the 30-100μm, as seen in Fig. 9(a), there was a major endothermic peak at temperatures of 949–951°C during the TR step, while a major exothermic peak was observed at temperatures of 853–866°C during the AO step in the 3 cycles. The endothermic and exothermic peak corresponded to the Co_3O_4/CoO redox reaction. The enthalpy changes, ΔH, (Co_3O_4 = 3CoO + 1/2O_2 for an endothermic TR step; 3CoO + 1/2O_2 = Co_3O_4 for an exothermic AO step) were estimated from an integration of the peak area. In addition, the reaction conversions, α, for each step were calculated from the theoretical enthalpy changes, $\Delta H_{theoretical}$. The values of $\Delta H_{theoretical}$ were calculated by thermodynamic software of Factsage. The values of ΔH and α were listed in Table 1. The values of ΔH and α for the 1st TR step were slightly less than those for the 2nd and 3rd TR steps, but each step could almost stoichiometrically charge and discharge. Thus, the values of ΔH and α indicate that the Co_3O_4/CoO redox reaction ideally proceeded in viewpoint of quantitative thermal charging/discharging. For the results of the 500-700 μm, as seen in Fig. 9(b), there was a major endothermic peak at temperatures of 950–954°C during the TR step, while a major exothermic peak was observed at temperatures of 854–862°C during the AO step in the 3 cycles. The endothermic and exothermic peak corresponded to the Co_3O_4/CoO redox reaction was observed at almost same temperature, respectively. The values of ΔH and α for the particle size were listed in Table 2. The results for ΔH and α indicate that the particle size did not impact on the values of ΔH and α in quantitative viewpoint (Fig. 5 and 7), but effect on a kinetic viewpoint (Fig. 6 and Fig 8(b)).

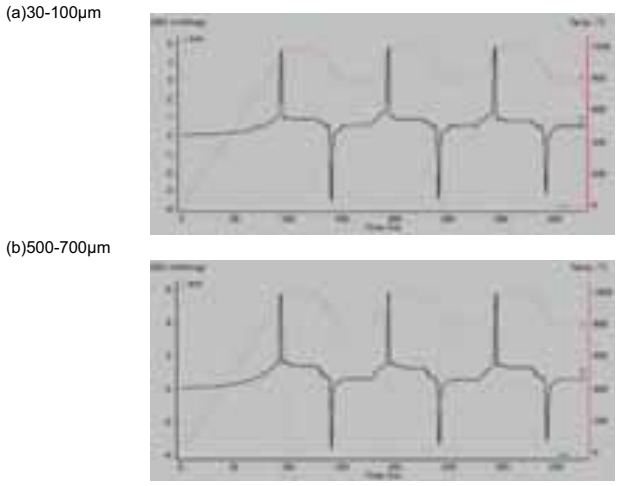

Figure 9. DSC analysis of Co_3O_4/CoO redox material with particle size of (a) 30-100 and (b) 500-700 μm. The heating–cooling operation was performed by a trapezoid mode.

In addition to the thermochemical heat storage based on the value of ΔH, the specific heat values C_p, depending on the temperature in the range of 800–1000°C, were experimentally measured for the Co_3O_4/CoO redox material, and the sensible heat was experimentally estimated to evaluate the thermal storage performances. As a reference, the values of the heat storage capacities for a molten carbonate salt (Na_2CO_3) were calculated using the thermodynamic equilibrium software FactSage ver 6.4. Fig. 10 shows the heat storage capacities per unit weight for the redox pair with the particle size of 30-100 and 500-700 μm. The values for the heat storage capacities were plotted as a standard based on a temperature of 800°C. As shown in Fig. 10, the discontinuous increments are equivalent to the amounts of thermochemical heat due to the Co_3O_4/CoO redox reaction at reaction temperatures of 930-975°C. A sensible heat from the oxidized solid phase of Co_3O_4 enhanced the heat storage capacities in the temperatures of 800-930°C. Beyond the reaction temperature over 975°C, sensible heat from the reduced solid phase of CoO contributed to the increase in the heat storage capacity. The heat storage capacity for the redox pair with the particle size of 30-100 μm was almost the same storage level in comparison to that with the particle size of 500-700 μm. Also, the heat storage capacities for the Na_2CO_3 molten salt discontinuously increase due to latent heat of solid-

liquid phase transition at a temperature of 858°C, and has a heat storage capacity of > 500 kg/kJ at temperatures in the range of 858-930°C, which is higher than that for the redox pair. However, the thermochemical heat strongly contributes to enhancing the thermal storage capacities of the redox pair. The thermal storage capacity for the redox pair is two times higher than that of the molten salt at 1000°C. These results indicate that the thermochemical heat storage for the redox pair is available to use in solar thermochemical processes and CSP, as well as that of the carbonate molten salts. From the viewpoint of the temperature range, using the redox pair for thermal storage may be appropriate for the solar tower/beam down receiver system using fluidized particle bed using high-temperature air as a heat transfer fluid.

Table 1 Enthalpy change and reaction conversion in each step for Co_3O_4/CoO redox material with the particles size of 30-100μm.

	1st TR	1st AO	2nd TR	2nd AO	3rd TR	3rd AO
Enthalpy change, Δ*H*	756.1 J/g	-830.5 J/g	812.2 J/g	-829.2 J/g	814.3 J/g	-829.2 J/g
Reaction conversion, α	92.7 %	99.2 %	99.9 %	99.7 %	99.8 %	99.7 %

Table 2 Enthalpy change and reaction conversion in each step for Co_3O_4/CoO redox material with the particles size of 500-700μm.

	1st TR	1st AO	2nd TR	2nd AO	3rd TR	3rd AO
Enthalpy change, Δ*H*	755.6 J/g	-824.4 J/g	812.0 J/g	-822.1 J/g	811.8 J/g	-805.8 J/g
Reaction conversion, α	92.6 %	99.2 %	99.5 %	98.9 %	99.5 %	96.9 %

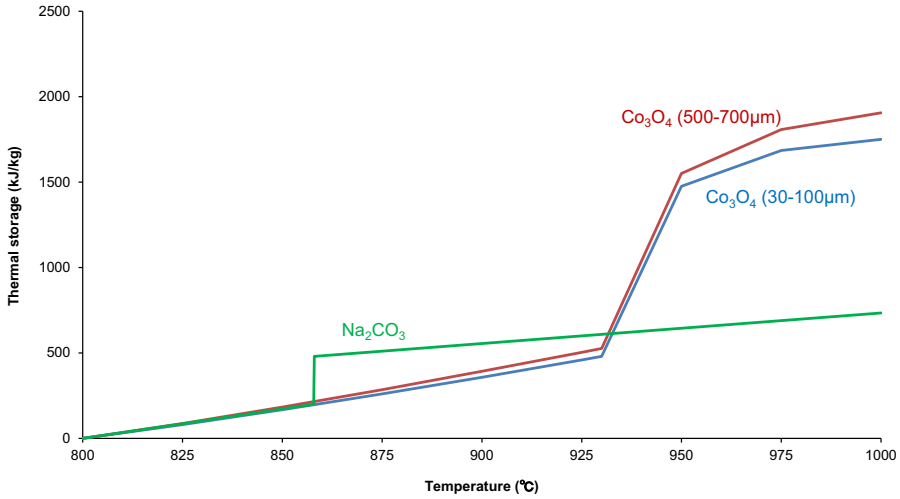

Figure 10. Heat storage capacities per unit weight (kg) for Co_3O_4/CoO redox material. The heat storage capacity at temperature of 800 ºC as a standard is set to zero.

4. Summary

The present authors in Niigata University have been developing windowed receivers/reactors prototype using fluidized bed of reacting (coal cokes, and metal oxides) or chemically-inert (quartz sand) particles, and have proposed to combine the windowed solar chemical reactor/receiver with a newly developed solar reflective tower or beam-down optics. In the present study, the effects of particles size of Co_3O_4/CoO powders on TCS performances were investigated in order to explore the potential of the material for fluidized-particle bed reactor. A flowability (fluidization state) of Co_3O_4 powders in a cold testing of fluidized bed reactor was also examined in this study.

For the fluidization testing of Co_3O_4 powders by a small-scale quartz reactor of fluidized bed, the fluidization state aimed in this study was a lower superficial gas velocity and a mild fluidization of a particle bed in the

reactor. Thus, a bubble fluidization was targeted in this study. Based on the experiments of fluidization testing of Co_3O_4 powder, the powder with a smaller size which enabled it to make a bubbling fluidization under a lower passing air were favorable for the fluidized bed reactor operating a thermochemical energy storage. From the viewpoint of stability of fluidization, the particle size of 100-300 μm showed the minimum pressure loss at the value of U_{mf} among the all particle size tested.

For the thermochemical storage testing by thermogravimetry and DSC measurements, the heating–cooling operation was performed at 1100-800°C by a trapezoid and rectangle modes in order to evaluate a heat charging/discharging performances of Co_3O_4/CoO redox with different particle size. TR step could start with lower (10°C) temperature as a particle size of Co_3O_4 powder was smaller, but the peak rate in TR step was independent of the particle size. Oxidation reaction of CoO was rate-determining step for thermochemical storage using Co_3O_4/CoO redox pair. In DSC measurement, the endothermic and exothermic peak corresponded to the Co_3O_4/CoO redox reaction was observed at almost same temperature, respectively. The results for ΔH and α indicate that the particle size did not impact on the values of ΔH and α in quantitative viewpoint (Fig. 5 and 7), but effect on a kinetic viewpoint (Fig. 6 and Fig 8(b)).

5. References

Agrafiotis, C., Roeb, M., Schmu¨cker, M., Sattler, C., 2014. Exploitation of thermochemical cycles based on solid oxide redox systems for thermochemical storage of solar heat. Part 1: Testing of cobalt oxide-based powders. Solar Energy 102, 189-211.

Agrafiotis, C., Roeb, M., Schmu¨cker, M., Sattler, C., 2015. Exploitation of thermochemical cycles based on solid oxide redox systems for thermochemical storage of solar heat. Part 2: Redox oxide-coated porous ceramic structures as integrated thermochemical reactors/heat exchangers. Solar Energy 114, 440-458.

Alonso, E., Pe´rez-Ra´bago, C., Licurgo, J., Fuentealba, E., Estrada, C. A., 2015. First experimental studies of solar redox reactions of copper oxides for thermochemical energy storage. Solar Energy 115, 297-305.

Carrillo, A. J., Moya, J., Bayón, A., Jana, P., O'Shea, V. A. P., Romero, M., Gonzalez-Aguilar, J., Serrano, D. P., Pizarro, P., Coronado, J. M., 2014. Thermochemical energy storage at high temperature via redox cycles of Mn and Co oxides: Pure oxides versus mixed ones. Solar Energy Materials & Solar Cells 123, 47-57.

Ehrhart, B., Coker, E., Siegel, N., Weimer, A., 2014. Thermochemical cycle of a mixed metal oxide for augmentation of thermal energy storage in solid particles. Energy Procedia 49, 762-771.

Neises, M., Tescari, S., de Oliveira, L., Roeb, M., Sattler, C., Wong, B., 2012. Solar-heated rotary kiln for thermochemical energy storage. Solar Energy 86, 3040–3048.

Pagkoura, C., Karagiannakis, G., Zygogianni, A., Lorentzou, S., Kostoglou, M., Konstandopoulos, A. G., Rattenburry, M., Woodhead, J. W., 2014. Cobalt oxide based structured bodies as redox thermochemical heat storage medium for future CSP plants. Solar Energy 108, 146-163.

Schrader, A. J., Muroyama, A. P., Loutzenhiser, P. G., 2015. Solar electricity via an Air Brayton cycle with an integrated two-step thermochemical cycle for heat storage based on Co_3O_4/CoO redox reactions: Thermodynamic analysis. Solar Energy 118, 485-495.

Tescari, S., Agrafiotis, C., Breuer, S., de Oliveira, L., Neises-von Puttkamer, M., Roeb, M., Sattler, C., 2014. Thermochemical solar energy storage via redox oxides: materials and reactor/heat exchanger concepts. Energy Procedia 49, 1034-1043.

Wörner, A., Binyami, S., Giger, F., Soupart, J.-B., Gonzalez-Aguilar, J., Steinfeld, A., Trettin, R., 2012. The TCS Power Project Thermochemical Energy Storage for Concentrated Solar Power Plants, SolarPACES, Marrakech, Morocco, 2012.

Wong, B., 2011. Thermochemical Heat Storage for Concentrated Solar Power, Final Report for the US Department of Energy, San Diego, CA, USA.

Visible active silver sensitized mixed phase ZnO photocatalyst

S. K. Samdarshi[a1*] and B. M. Rajbongshi[b]

[a]Centre for Energy Engineering and Centre for Excellence in Green and Efficient Energy Technology, Central University of Jharkhand, Ranchi 835205, Jharkhand, India
[b]Department of Energy, Tezpur University, Tezpur-784028, Assam (India)
[*]drsksamdarshi@rediffmail.com

The present work reports synthesis of highly photoactive silver-sensitized mixed phase ZnO nanoparticles. The structural, optical and chemical characterizations of the prepared materials were done using XRD, TEM, UV–DRS, PL and EPR. The photoactivity of the nanoparticles was assessed through photocatalytic degradation kinetics of methylene blue. The rate constant of the photocatalytic degradation of methylene blue using silver sensitized mixed phase ZnO was found to be 3.7 and 1.2 times higher than monophasic (wurtzite) ZnO without and with silver sensitization, respectively, under visible light. The increase in the activity is mainly attributed the synergy of the interacting phases at the homojunction and the surface plasmon resonance due to the metallic silver.

Keywords: Photocatalyst, surface plasmon resonanace, mixed phase

1. Introduction

Two of the most investigated semiconductor photocatalysts-TiO_2 and ZnO, have some inherent constraints in achieving high photocatalytic activity due to their large band gap, which restricts the photo-absorption only to the UV region of solar spectrum and low separation probability of photo-generated charge carriers leading to high recombination. To overcome these constraints different techniques such as doping [Vazquez et al. 2015, Kumar et al. 2015], formation of nanocomposite [Wenga et al. 2014], sensitization [Pawar and Sunyong, 2014] and mixed phase transformation [Nair et al.2011] had been implemented for such semiconductor photocatalysts. Recently, it has been reported that these problems can also be alleviated by plasmonic/ semiconductor photocatalyst [Chiu et al. 2015 and Rajbongshi et al. 2014a]. Surface plasmon resonance of metal at UV and visible region can extend photo activity in higher wavelength also. Further, noble metal Ag acts as electron scavenger which enhances the life time of energetic charge carriers by reducing their recombination probability. Also many researchers have reported that mixed phase TiO_2 shows photocatalytic activity under visible light. Recently Rajbongshi et al. reported that like TiO_2, mixed phase (wurtzite and zincblende) of ZnO also shows higher photocatalytic activity under visible light [Rajbongshi and Samdarshi, 2014b]. But the main challenge of synthesis of mixed phase ZnO is in ensuring the suitable synthesis conditions in addition to an appropriate matching substarte for the formation of metastable zincblende phase of ZnO [Ashrafi,2007]. The challenge of synthesis of metastable zincblende (ZB) phase with wurtzite (WZ) subdomian has been recently solved by a single-step and simple synthesis procedure using dopant as a substrate. But none of the dopants used were known to show plasmonic resonance under visible light. This encouraged the present work to study the photocatalytic activity of the mixed phase ZnO with Ag sensitization to take the advantage of surface plasmon resonance; and wurtzite and zincblende homojunction. The basic investigation suggest that Ag can act as a sensitizer and a substrate for the formation of mixed phase ZnO as reported earlier[Rajbongshi and Samdarshi, 2014b]. Some studies on the role of Ag in formation of mixed phase have been reported earlier in the case of ZnS [Synnott,2013; Tsuji,2006].

[1] Corresponding Author, E-mail: drsksamdarshi@rediffmail.com; Mobile: +91 9435490522

doi:10.18086/swc.2015.04.26 Available at http://proceedings.ises.org

In this present study Ag sensitized mixed phase ZnO photocatalyst was synthesized by sol-gel co-precipitation method. The photocatalytic activity was studied under visible light for methylene blue degradation for the synthesized photocatalyst.

2. Material and Methods

2.1. Material synthesis

The chemicals used for synthesis of Ag doped ZnO were zinc acetate dihydrate $(CH3COO)_2$ Zn. $2H_2O$, silver nitrate, sodium hydroxide pellets (NaOH) and ethanol. Sol-gel co-precipitation method was used as reported earlier [Rajbonghi and Samdarshi 2014b] to synthesize the sample. The calcinations temperatures were 400 and 425^{o}C for Ag-senistized single phase (AZ(M)) and Ag-sensitized mixed phase ZnO (AZ(S)), respectively. For comparison single phase ZnO(without Ag sensitization)was also synthesized and calcined at a temperature of 400^{o}C.

2.2. Characterization

Structural and morphological analysis was done by XRD (Rigaku Miniflex, Japan) and TEM (model JEM-100CX II (JEOL Japan). The spectral response of the material was evaluated using a UV–DRS spectrophotometer (Shimadzu UV-2200, Japan) with diffuse reflectance attachment. The photoluminescence spectrum was recorded using a photoluminescence spectrometer (LS55, Perkin Elmer, USA) for studying the trap states. Further study on oxygen vacancy and defects on the material was done using ESR spectrometer (JEOL, Model: JES-FA200).

2.3. Photocatalytic activity test

The photocatalytic activity of the synthesized nano-material was studied using probe pollutant - methylene blue (MB) with visible irradiance at the reactor surface of 14.5 W/m^2 at 28^{o}C. The adsorption-desorption equilibrium was ensured by keeping the catalyst loaded MB in dark for one hour. The change in the concentration of the sample was recorded by correlating it with the absorbance of the sample, measured using UV-Vis spectrophotometer (Shimadzu 1700, Japan) at the wavelength of 650 nm for MB.

3. Result and discussions

XRD spectra of pristine ZnO and Ag doped ZnO are shown in Fig.1a,b. Pristine ZnO is monophasic wurtzite(Fig.1a). Among the Ag-sensitized samples, AZ(M) shows the mixed phase of wurtzite (JCPDF: 891397) and zincblende (JCPDF: 652880) phases of ZnO while AZ(S) is single phase of wurtzite (Fig.1b). The diffraction peak (111) at $\theta = 38^o$ is identified for metallic Ag which matches with the JCPDS file No: 893722. Another extra peak can be identified for AgO in Ag doped ZnO sample. The particle size that has been calculated using Scherrer formula [Zachariah et al.,2008] is given in Table 1. From the Table it can be seen that mixed phase sample AZ(M) posses higher particle size for zincblende ([111] plane) phase.

Table 1: Particle size and band gap of the synthesized sample

Sample	Particle size (nm)		Band gap (eV)
	WZ	ZB	
ZnO	14.2	-	3.12
AZ(M)	13.3	18.6	2.93
AZ(S)	12	-	3.03

Fig.1c shows the TEM image of the sample AZ (M) wherein the presence Ag of about 20nm in size is clearly visible. The particle size from TEM analysis accords well with XRD results. The formation of wurtzite (WZ) and zincblende (ZB) polymorph of ZnO with an additional phase for metallic silver is shown in Fig.1d. The d-spacing for wurtzite and zincblende is found to be 0.25 and 0.23nm, respectively, and that of Ag to be 0.21nm. So AZ (M) is a combination of homo- and heterojunction of wurtzite-zincblende ZnO and ZnO-Ag, respectively.

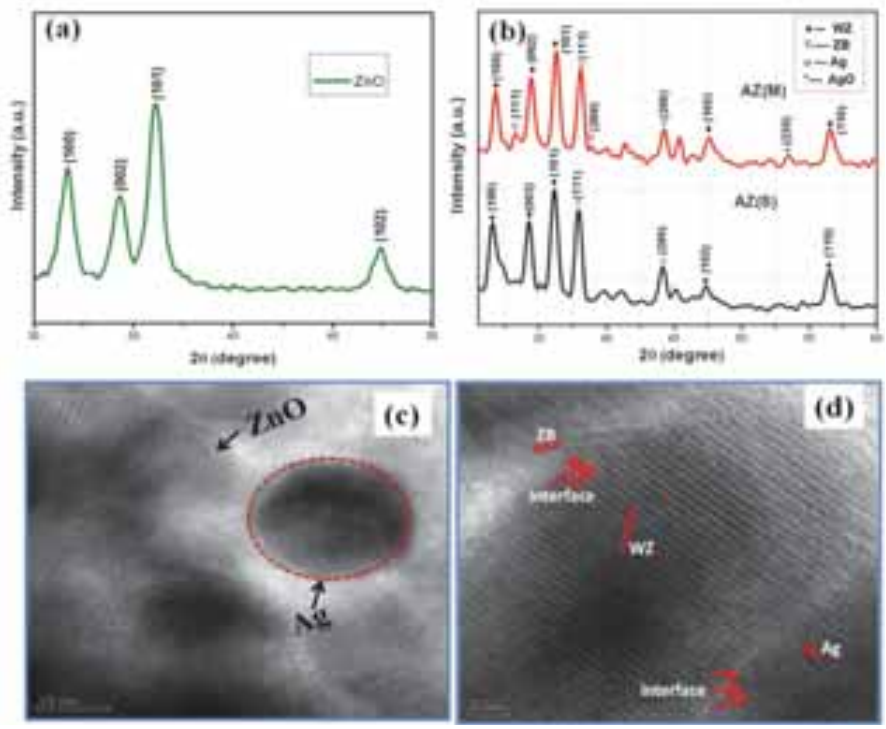

Fig.1: XRD spectrum of (a) Pristine ZnO (b) AZ(M), AZ(S); (c) and (d)TEM micrograph of AZ(M)

UV-DRS spectrum of pristine and Ag-ZnO sample is shown in Fig. 2a. All the Ag-sensitized samples show red-shift compared to the pristine ZnO. The band gap of the materials calculated using Tauc's equation [Xu, H., and Zhang, L., 2009.] is found to be 3.03 and 2.93 eV for AZ(S) and AZ(M), respectively while that of the pristine ZnO it is 3.12 eV (Table 1). In UV-DRS spectrum it can be observed that samples AZ(S) and AZ(M) show absorption peak near at 410 and 550nm, respectively. It has been reported that Ag shows a typical absorption peak in the range 400-550 nm due the surface plasmon resonance [Ansari et al., 2013; Logar et al., 2010]. So the peaks at 410 and 550nm are ascribable to the surface plasmon resonance of metallic silver. The emission centered at 370nm is due to the near band edge emission for ZnO. The PL spectra measured at excitation wavelength 325nm are shown in Fig.2b. The visible emission intensity of Ag doped ZnO sample was lower than the pristine ZnO ascribing the quenching of fluorescence due to the Ag, which increases the electron hole pair life time. The quenching of PL intensity (Fig.2b) is higher in AZ(M) which may due to synergistic effect of WZ-ZB homojunction and also Ag-ZnO heterojunction. PL spectra also reveal the increase of oxygen vacancies after Ag doping in ZnO.

Oxygen vacancy and the local environment of Ag are also investigated through EPR analysis (Fig.2c). Both pristine ZnO and AZ(S) show the EPR signal with g value 1.9 but AZ(M) shows a shift with g value at 1.8. These signals are ascribed to impurities or defects due to oxygen vacancies and broadening of the signal

for AZ(M) sample indicates increase in the oxygen vacancy. The g value 2.1 is assigned to zinc vacancy in the sample. The EPR signal at g value 2.35 in the sample AZ(M) is assigned to the Ag^{+} which indicates the presence of high amount of AgO in the sample [Deng et al.,2008]

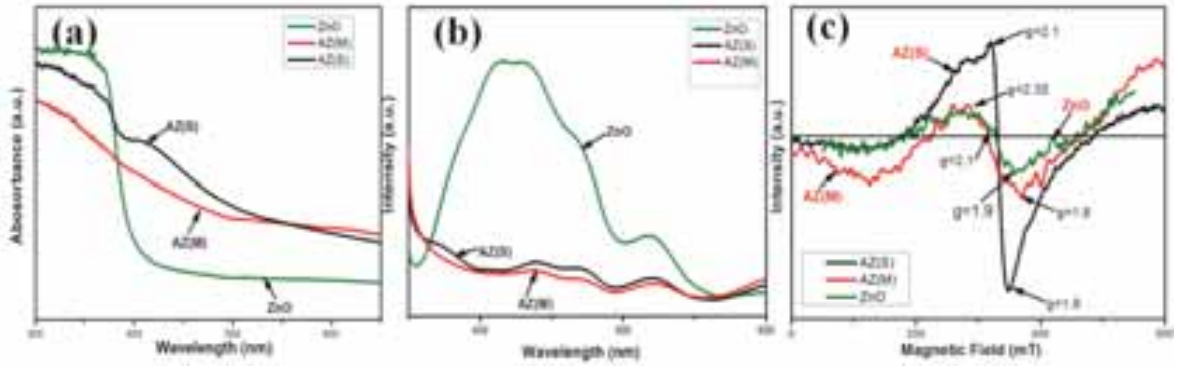

Fig. 2: (a) UV-DRS (b) PL and (c) EPR spectrum of the samples.

3.1. Photocatalytic activity test

To evaluate the photocatalytic activities of Ag-ZnO photocatalyst the degradation of methylene blue (MB) was investigated under visible light. Fig.3a shows the degradation kinetics of MB over Ag-sensitized ZnO samples. It is evident from the Fig.3 that the Ag-sensitized ZnO samples show excellent visible light activity compared to the pristine ZnO for methylene blue degradation. The degradation rate constant was calculated using $\ln(C/C_o)$ vs. time curve (Fig.3b) and it is found to be 0.007 and 0.006 min^{-1} for AZ(M) and AZ(S), respectively. But pristine ZnO shows a rate constant of 0.002 min^{-1}. So, AZ(M) shows 3.7 and 1.2 times higher photocatalytic activity under visible light compared to monophasic sensitized and unsensitized ZnO. The higher photocatalytic activity of AZ(M) compared to pristine ZnO and AZ(S) indicates the synergistic effect of mixed phase homojunction which increases the charge carrier migration and separation; and Ag nanoparticles anchored surface plasmon effect on ZnO nanoparticles. SPR of Ag enhances the photocatalytic activity by increasing electron concentration in ZnO. Besides these, increase in the life time of the photogenerated charge carrier also reduces due to the reduction in probability of the recombination of the charges which again helps in the enhancement of photocatalytic activity.

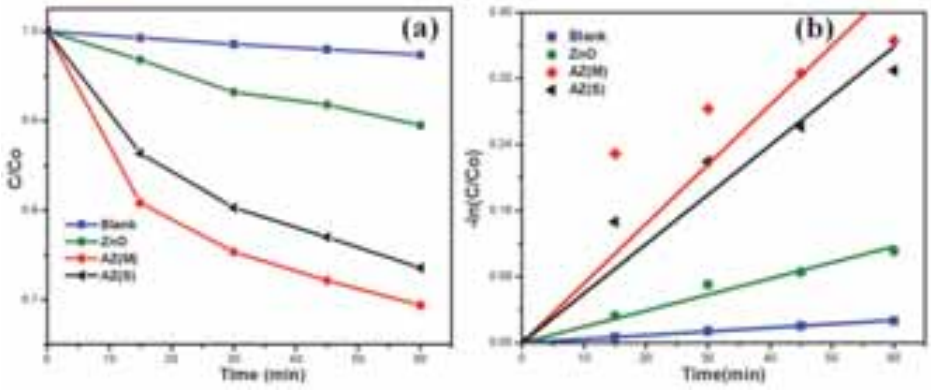

Fig. 3: (a) photocatalytic degradation of MB, (b) $\ln(C/C_o)$ vs. time curve for determination of rate constant

4. Conclusion

In conclusion, we have demonstrated synthesis of Ag-doped ZnO having mixed phase(wurtzite and zincblende) ZnO with an advantage of surface plasmon resonance of noble metal Ag. Surface plasmon resonance helps in extending the absorption spectrum of the photocatalyst in the visible region. Homo-junction interface of wurtzite-zincblende of ZnO helps in the separation and migration of the charge carrier to the surface. Photocatalytic activity study concludes that the mixed phase Ag-sensitized ZnO shows higher photocatalytic activity compared to pristine and single phase ZnO with and without sensitization due to the presence of homojunction of wurtzite-zincblende ZnO and heterojunction of Ag-ZnO on multiple aspects of the photocatalytic activity.

References

1. Ansari, S. A., khan, M. M., Ansari, M. O., Lee, J., Cho, M. H., 2013. Biogenic synthesis, photocatalytic and photoelectrochemical performance of Ag-ZnO nanocomposite, J.Phys.Chem.C 117, 27023-27030.
2. Chiu, H.M., Yang, T.H., Hsueh, Y. C., Perng, T.P., Wu, J.M., 2015. Fabrication and characterization of well-dispersed plasmonic Pt nanoparticles on Ga-doped ZnO nanopagodas array with enhanced photocatalytic activity, Applied Catalysis B: Environmental, 163, 156–166.
3. Deng, R., Zou, Y., Tang, H., 2008. Correlation between electrical, optical properties and Ag^{2+} centers of ZnO:Ag thin films, Physica B 403, 2004–2007.
4. Kumar, R., Umar, A. , Kumar, G., Akhtar M.S., Wang, Y., Kim S.H. 2015. Ce-doped ZnO nanoparticles for efficient photocatalytic degradation of direct red-23 dye, Ceramics International. 41, 7773–7782.
5. Logar, M., Jancar, B., Sturm, S., Suvorov, D., 2010. Weak polion multilayer ssisted in situ synthesis as a route toward a plasmonic Ag/TiO_2 photocatalyst, Langmuir, 26, 12215-12224.
6. Nair, R.G., Paul, S., Samdarshi, S.K. 2011. High UV/visible light activity of mixed phase titania: A generic mechanism, Solar Energy Materials & Solar Cells. 95, 1901–1907.
7. Pawar, R.C., Lee, C. S., 2014. Single-step sensitization of reduced graphene oxide sheets and CdS nanoparticles on ZnO nanorods as visible-light photocatalysts, Applied Catalysis B: Environmental, 144, 57–65.
8. Rajbongshi, B. M., Ramchiary, A., Jha, B. M., Samdarshi, S. K., 2014. Synthesis and characterization of plasmonic visible active Ag/ZnO photocatalyst, J Mater Sci: Mater Electron. 25, 2969–2973.
9. Rajbongshi, B. M., Samdarshi, S.K., 2014. Cobalt-doped zincblende–wurtzite mixed-phase ZnO photocatalyst nanoparticles with high activity in visible spectrum, Applied Catalysis B: Environmental 144, 435– 441.
10. Ashrafi, A. B.M.A., Jagadish, C. 2007, Review of zincblende ZnO: stability of metastable ZnO phase, J. Appl. Phys.102, 071101.
11. Sotelo-Vazquez, C., Noor, N., Kafizas, A. , Quesada-Cabrera, R., , Scanlon, D. O., Taylor , A., Durrant, J.R., Parkin, I. P.,2015. Multifunctional P-doped TiO_2 films: A new approach to self-cleaning, transparent conducting oxide materials, Chem. Mater.27, 3234–3242.
12. Synnott, D. W., Seery, M. K., Hinder, S. J., Colreavy, J., Pillai, S. C., 2013. Novel microwave assisted synthesis of ZnS nanomaterials, Nanotechnology 24, 045704
13. Tsuji, I., Kato, H., Kudo, A., 2006. Photocatalytic hydrogen evolution on ZnS-$CuInS_2$-$AgInS_2$ solid solution photocatalysts with wide visible light absorption bands, Chem. Mater. 18, 1969-1975.
14. Wenga, B., Liua, S., Zhanga, N., Tangb, Z.R., Xu, Y.J. 2014. A simple yet efficient visible-light-driven CdS nanowires-carbon nanotube 1D–1D nanocomposite photocatalyst, Journal of Catalysis. 309, 146–155.
15. Zachariah, A., Baiju, K.V., Shukla, S., Deepa, K.S., James, J., Warrier, K.G.K., 2008. Synergistic effect in photocatalysis as observed for mixed-Phase nanocrystal-line titania processed via sol gel solvent mixing and calcination, J. Phys. Chem. C 112, 11345–11356.
16. Xu, H., Zhang, L., 2009. Controllable one-pot synthesis and enhanced photocatalytic activity of mixed-phase TiO2nanocrystals with tunable brookite/rutile ratios, J. Phys. Chem. C 113 , 1785–1790.

Conference Proceedings

Solar World Congress 2015
Daegu, Korea, 08 – 12 November 2015

Thiolate Capped Noble Metal Particles as Novel Sensitizers for Solar Cells

Ziyu Cheng, Wenguang Fan and Michael K.H. Leung

Ability R&D Energy Research Centre, School of Energy and Environment, City University of Hong Kong, Hong Kong, China

Abstract

MPA (3-Mercaptopropionic acid) capped noble metal particles (Ag, Au) are studied in this project as sensitizers for solar cells. TiO_2 nanotube arrays were fabricated via etching anodization method. The MPA capped noble metal sensitizer was deposited onto the surface of the TNAs using in-situ hydrothermal method. Different initial molar ratios of Ag and Au were investigated. The specimens were characterized using FE-SEM, HRTEM, XRD, XPS and UV-vis spectroscopy. Photoelectrochemical measurements, including *J-V* curves, stability test and electron lifetime assessment, were conducted to examine the performance of the sensitized TiO_2 materials. It is found that the Ag (0) @ Ag (+) – MPA nanocluster showed the best performance in light energy conversion. Better stability was also achieved compared to previous works.

Keywords: *Nano-photocatalyst, visible-light activation, nano metal clusters, solar cell sensitization.*

1. Introduction

Metal-cluster-sensitized solar cell uses silver glutathione (Au-GSH) nanoclusters deposited on the mesoporous TiO_2 film as the photoanode (Kamat et al. 2014). The light-electricity conversion efficiency reached about 2.3% under AM 1.5 illumination. The mechanism of the excitation of the Au-GSH nanoclusters was characterized and reported in the literature (Linic et al. 2011). The excitation behavior of the Au-GSH nanoclusters is size-dependent and similar to that of dye molecules rather than plasmonic particles. The small nanoclusters composed of metal atoms behave as big molecules.

Recently, investigators studied the use of hybrid nanomaterials as sensitizers in liquid-junction solar cells illustrated in Fig. 1 (Chen et al. 2013, Fan et al. 2014). When there are incident photons with energy exceeding the semiconductor's bandgap energy, the electrons of the semiconductor can absorb the photon energy and be excited to the conduction band, leaving positively charged holes in the valence band. The excited free electrons will migrate through the circuit under the built-in potential difference. The holes capture electrons from the electrolyte so some species are oxidized. Meanwhile, when the free electrons reached the cathode, they reduce the oxidized species in the electrolyte. The chemical state of the electrolyte remains unchanged and the net effect of the cell is converting the photon energy to electricity. On the other hand, the excited free electrons may simply recombine with the holes without producing any useful electricity.

In liquid-junction solar cell, the hybrid nanomaterial consists of noble metal particles and organic compound. The metal-organic hybrid nanomaterials can absorb long-wavelength photons and inject charge carriers to the electrode, which is same as the roles played by traditional dye and quantum dots. The hybrid materials have shown some very intriguing and promising features and good chance to a step-forward in the field. The main objective of this research is to develop noble metal (silver and gold) based hybrid nanomaterials for enhancing solar photovoltaic performance.

Selection and/or peer review under responsibility of Scientific Committee
doi:10.18086/swc.2015.04.27 Available at http://proceedings.ises.org

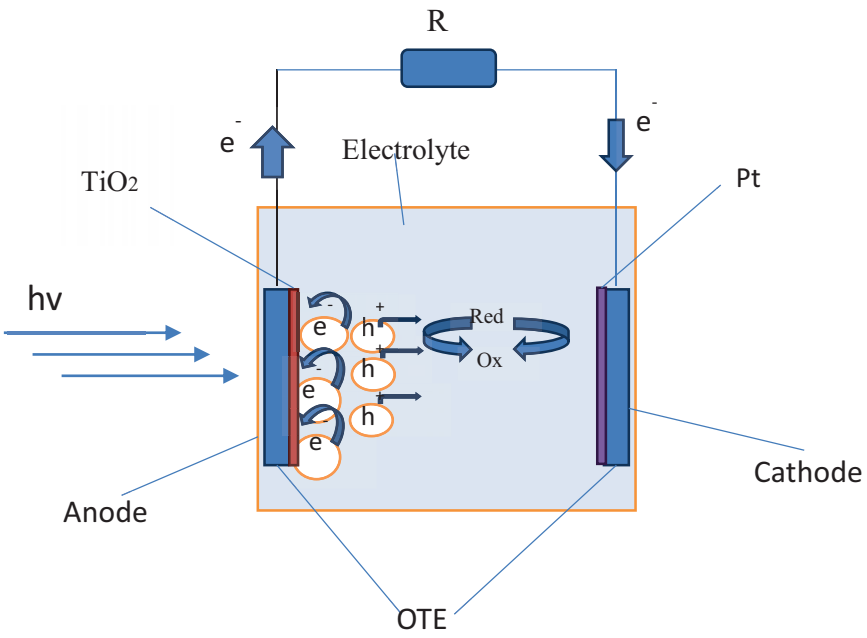

Fig. 1: Mechanism of liquid-junction solar cell

2. Experimental

2.1. Sample fabrication

Etching anodization method is a commonly employed fabrication approach of self-ordered titanium nanotube arrays (TNAs) and has been a relatively mature means. Although the first nanotubes did not show very neat morphology, it demonstrated the effect of F^- ions on fabricating TNAs. A series of studies explored the impacts of pH value, the water content, the organic electrolyte system (such as ethylene glycol), constant voltage, duration and so on. Under the existence of anodic voltage and conductive electrolyte, the metallic titanium is firstly oxidized to TiO_2 and the H^+ in the electrolyte is reduced to H_2. If there was no etching ions (e.g. F^-) in the electrolyte, the reactions lead to formation of a compact oxide layer on the surface of Ti. Addition of F^- ions leads to formation of $[TiF_6]^{2-}$. The $[TiF_6]^{2-}$ species is water soluble, therefore reaction (eq. 1) represents an etching process of the as-formed TiO_2. During the anodization process, the F^- ions are driven to the anode under the electrical field, penetrate the as-formed amorphous TiO_2, and undergo reaction (eq. 1). If all the parameters are within a certain range, the combination of above mentioned processes lead to the formation of independent tube array (Roy et al. 2011). After anodization, a post-annealing treatment converts the amorphous TiO_2 into crystalline structures. The crystal phase can be determined by the annealing temperature.

$$TiO_2 + 4H^+ + 6F^- \rightarrow [TiF_6]^{2-} + 2H_2O \qquad \text{(eq. 1)}$$

The deposition of noble metal (Ag) onto the TiO_2 nanotube arrays occurs in dark condition. Silver nitrate (Strem, 99.9%) aqueous solution was mixed with 3-Mercaptopropionic acid in a glass vial. Then, 1 M NaOH (Sigma Aldrich, 97%) was added drop by drop into the vial till the mixture returned to clear and then the pH value was adjusted to 9.0. deionized (DI) water was added into the solution till the solution reached 15 mL. One piece of TNAs foil was placed into the vial with the TNA facet facing down. A dose of 5 mL ethylene glycol (Sigma Aldrich, 99%) was added into the vial. The solution was then purged with N_2 gas for 20 minutes. The vial was placed in a Teflon vessel with 25 ml DI water. The Teflon vessel was fixed and sealed into a stainless steel autoclave. The whole system was then heated in a 120 ^oC oven for 4 hours. The autoclave was then taken out of the oven and cooled down to room temperature. The sample was washed with DI water, and dried in nitrogen steam. We fabricated samples of different Ag:Au molar ratios: 3:1, 1:1 and 1:3 as shown in Fig. 2.

Au-GSH nanoclusters was deposited onto titanium dioxide fluorine-doped tin oxide (TiO_2-FTO) glass electrodes. The deposition followed a modified in-situ hydrothermal approach. Basically, 0.06g of gold (III) chloride trihydrate (Aldrich, ≥99% trace metal basis) and 0.07g of L-glutathione reduced, was mixed in 75 ml of DI water in a round bottom flask. TiO_2-FTO-glass electrodes were immersed into the solution and the solution was purged with N_2 gas. Then the flask was heated and refluxed at 70 ℃ for 24 hours. During the entire experiment, the solution kept being bubbled with N_2 gas.

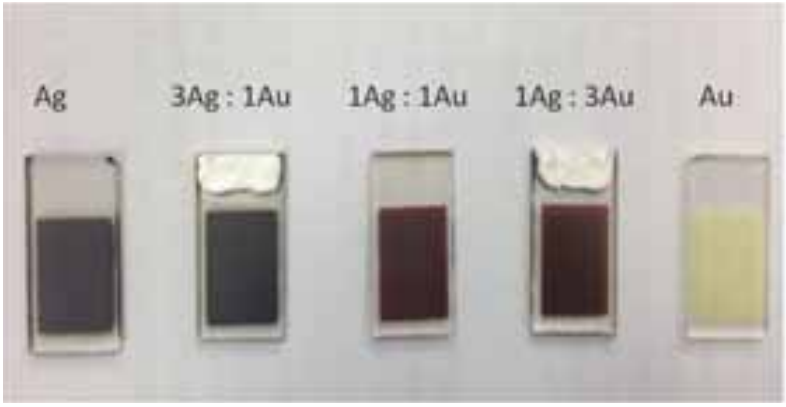

Fig. 2: TiO_2-nanoparticle-FTO samples

2.2. Material characterization

The light absorption ability of the sensitizers was examined using UV-Vis spectroscopy, where a small aliquot was taken from the remaining liquid after the in-situ hydrothermal deposition. Characterization of the morphology was carried out using field-emission scanning electron microscopy (FE-SEM) with acceleration voltage of 5.0 kV, and high-resolution transmission electron microscope (HRTEM) at 200 keV. For FE-SEM, the sample was cut into small pieces and attached to an aluminum plate with conductive silicon tapes and then subjected to observation. For HR-TEM, the sample was scratched off from the foil and dispersed onto a copper mesh with the help of ethanol. Elemental composition of the samples was analyzed using energy dispersive X-ray spectroscopy (EDX) equipped on the FE-SEM. The crystalline structure of the samples was scanned using X-ray diffraction (XRD), with Cu Kα radiation, from 2θ of 20° to 80° with steps of 0.02°. The surface energy state and chemical composition was analyzed with X-ray photoelectron spectroscopy (XPS) with Al Kα as the excitation source.

2.3. Photoelectrochemical performance

The photoelectrochemical (PEC) measurements were conducted using the three-electrode cell setup. The sample was assigned as the working electrode. The other two electrodes, the counter electrode and reference electrode, was a platinum plate and a saturated calomel electrode (SCE), respectively. A 2-cm diameter quartz window is located in one wall of the cell and its distance from the working electrode was kept at 2 mm to minimize the light absorption by the electrolyte in the spacing. A redox electrolyte was filled into the cell which was prepared through mixing 0.5M sulfur powders and 0.5 M sodium sulfide solution. The experiment was carried out under exposure to artificial sunlight obtained mounting a neutral density metallic filter and an AM 1.5G filter on a 300-W Xe lamp (Newport). The incident power density at the working electrode was adjusted to approximately 100 mW/cm^2 and was kept the same for every measurements. A potentiostat instrument (Solartron) was used to conduct the measurements and collect the data.

3. Results and discussion

3.1. Material properties

In the SEM and TEM images (Figs. 3 and 4) of samples fabricated show the deposition of nanoparticles onto the TiO_2 nanostructures. The EDX measurements (Table 1) indicate that the nanoparticles are Ag and Au.

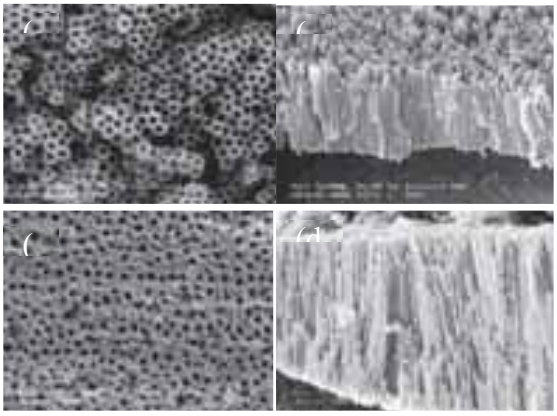

Fig. 3: SEM images of TNAs

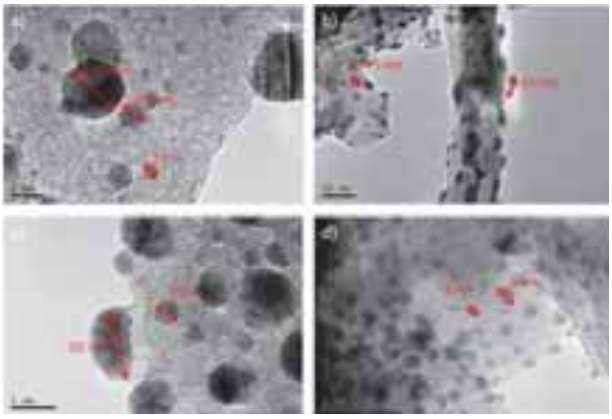

Fig. 4: TEM of TNAs with Ag and Au deposition

Table 1: Atom percentage from EDX analyses

Element	Sample 1 Ag	Sample 2 3Ag:1Au	Sample 3 1Ag:1Au	Sample 4 1Ag:3Au	Sample 5 Au
O	59.06	51.41	52.18	57.98	61.57
Ti	31.73	29.58	28.19	31.02	31.5
S	1.21	3.86	3.73	1.86	0.48
Ag	2.39	4.45	3.1	0.9	0
C	5.6	7.1	8.59	6.43	5.6
Au	0	1.31	1.13	1.81	0.85

3.2. PEC performance

Figure 5 shows the UV-Vis absorption of the five samples. The Au modification yields better visible-light absorption. The *J-V* curves of the samples are shown in Fig. 6. Ag-MPA sensitized TNAs exhibits the best performance. The short-circuit current density is 1.5 mA/cm^2, which is 38 times greater than that of bare TNAs electrode (0.04 A/cm^2).). On the other hand, the Au Sample 5 is not satisfactory. The sample sensitized by Au-MPA nanoclusters did not show much increase in performance compared to bare TNA. The overall trend shows that Ag-based sensitizers exhibit higher photo-activity than the Au-based counterpart.

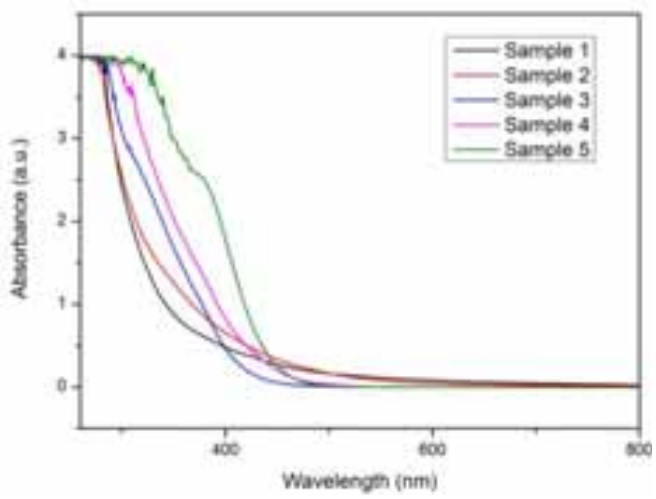

Fig 5: Ultraviolet-Visible spectral absorption

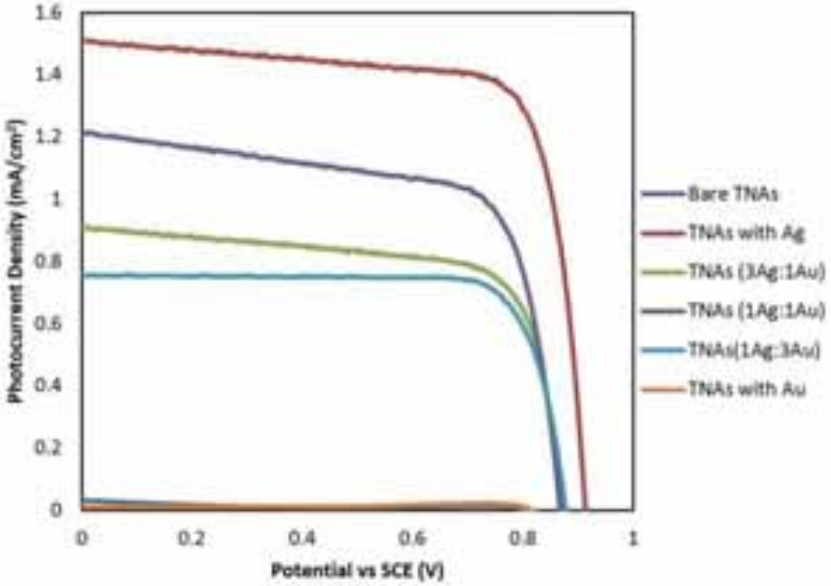

Fig. 6. PEC performance of samples fabricated

\

4. Conclusion

TiO_2 nanotube arrays fabricated by anodization have uniform morphology with pore diameter of ~100 nm and tube length of ~6 μm. After annealing, the TNAs are transformed into Anatase phase with a trace amount of Rutile. MPA capped Ag nanoparticles are deposited onto the surface of TNAs through the in situ-hydrothermal method. The nanoparticle diameter is 6~7 nm. The nanoparticles are classified as nano-clusters. The deposition of the Ag-MPA nanoclusters onto TNA can boost the PEC performance for significant increase in solar conversion efficiency.

5. Acknowledgment

The authors would like to acknowledge the financial support by GRF Project 9042044.

6. References

Chen, Y.-S., Choi, H. & Kamat, P. V., 2013. Metal-cluster-sensitized solar cells. A new class of thiolated gold sensitizers delivering efficiency greater than 2%. Journal of the American Chemical Society 135, 8822-8825.

Fan, W., Jewell, S., She, Y. & Leung, M. K. H., 2014. In situ deposition of Ag-Ag_2S hybrid nanoparticles onto TiO_2 nanotube arrays towards fabrication of photoelectrodes with high visible light photoelectrochemical properties. Physical Chemistry Chemical Physics 16, 676-680.

Kamat, P. V., 2014. Emergence of new materials for light-energy conversion: Perovskites, metal clusters, and 2-D hybrids. Journal of Physical Chemistry Letters 5, 4167-4168.

Linic, S., Christopher, P. and Ingram, D. B., 2011. Plasmonic-metal nanostructures for efficient conversion of solar to chemical energy. Nature Materials 10, 911-921.

Roy, P., Berger, S. and Schmuki, P., 2011. TiO_2 Nanotubes: Synthesis and Applications. Angewandte Chemie-International Edition 50, 2904-2939.

Conference Proceedings

Solar World Congress 2015
Daegu, Korea, 08 – 12 November 2015

SYNTHESIS OF PHOTOCATALYTIC ACTIVE TITANIUM DIOXIDE NANOTUBES AND THE EFFECT OF CALCINATION

Kioko Stella[1], Mghendi Mwamburi[1] and Lars Österlund[2]

[1] Department of Physics, School of Science University of Eldoret, P.O Box 1125, Eldoret, 30100, Kenya

[2] Department of Engineering Sciences, The Ångström Laboratory, Uppsala University, P.O. Box 534, 75121 Uppsala, Sweden

Abstract

Photocatalytic active, well-ordered TiO_2 nanotubes (TNTs) were synthesized using electrochemical anodization of a Ti substrate. A third generation electrolyte comprising mixture of ethylene glycol and ammonium fluoride in water was used to grow the TNTs at 60 V and 2 h deposition time. The effect of post-annealing on the physical properties and the photocatalytic activity of the TNT samples at two different temperatures, 300°C and 400°C was investigated. Further, the effect of pre-annealing of Ti substrate foil before growth of TNTs between 250°C and 650°C was investigated. Calcining at 300°C and 400°C for 1 h transformed the TNTs from amorphous to anatase phase. SEM images reveal dense and self-organization of TNTS for Ti foils annealed at 350°C and 440°C. The photodegradation rate of MB was twice as high for samples annealed at 400°C compared to those annealed at 300°C. The length of the TNT reached a maximum of 8.85 μm on Ti foils pre-annealed to 440°C for 1 h, after which a drastic reduction to 4.87 μm and 4.24 μm was observed on Ti foils pre-annealed to 525°C and 625°C respectively. The wall thickness systematically decreased as 32 nm, 31 nm, 29 nm, 21 nm, and 20 nm, respectively, when TNTs were grown on Ti foils heated at 250°C, 350°C, 440°C, 525°C, and 625°C.

Keywords: *Anodic, Titanium dioxide, Nanotubes, Photocatalytic*

1. Introduction

Titanium dioxide nanotubes (TNTs) prepared by electrochemical anodization have a high surface to volume ratio with size dependent physicochemical properties (Rani, 2010). TNTs with controlled dimensions have shown promising properties in many applications such as dye sensitized solar cells, photocatalysis, gas sensing, biomedical and antimicrobial applications (Rani, 2010). Titanium dioxide (TiO_2) photocatalysts were first used for remediation of environmental pollutants in 1977, when Frank and Bard reported the reduction of CN^- in water (Frank and Bard, 1977), leading to a dramatic increase in research in this area (Fujishima, 1999). Other binary semiconductors that have been studied as photocatalysts include ZnO, WO_3, Fe_2O_3, CdS and ZnS but hitherto TiO_2 stands out as superior for most practical applications. TiO_2 photocatalysis works at room temperature with supply of low intensity UVA light (< 390 nm); practically of the order 1 mW/cm^2 or higher. Photo-generated electrons in the conduction band of TiO_2 are reducing enough to produce superoxide from dioxygen (Fujishima et al., 2000), and the holes in the valance band are sufficiently low (with respect to the vacuum level) for oxidation reactions. Moreover, TiO_2 is resistant towards photo-corrosion, it is chemically stable in aqueous solutions, and it is non-toxic (Hsien et al., 2000). However, the large band gap of TiO_2 limits its application for efficient solar energy utilization. The most commonly used crystalline structures of TiO_2 are anatase and rutile with energy band gaps of about 3.2 eV and 3.0 eV, respectively. This means that only about 4% of the entire solar spectrum can be utilized by TiO_2. Anatase TiO_2 films are reported to have higher conversion efficiency, photocurrent and electron diffusion length than rutile films of same thickness (Park et al., 2000; Tanaka et al., 1991). Preparation and post-treatment methods can further enhance the photocatalytic activity. For example TiO_2 nanotubes and

doi:10.18086/swc.2015.04.28 Available at http://proceedings.ises.org

nanowires are reported to have high photocatalytic activity because of a large surface area to volume ratio and efficient collection of charge carriers at their interfaces. The photocatalytic efficiency of TiO_2 films has been improved by pre-heat treatment, post-heat treatment and doping. For films made by electrochemical anodization, spray pyrolysis, hydrothermal, dip coating, impurities arising from chemical solutions used during deposition can be removed by heat treatment. TNTs made by anodic oxidation are generally amorphous with high recombination centers limiting their photocatalytic activity (Li et al., 2012; Ghicov et al., 2006), although ways to promote crystallization have been reported by (Grimes et al., 2009). TNTs can however readily be crystallized upon calcination. Anatase TiO_2 has previously be been prepared by calcining amorphous TNTs between 300^{o}C and 400°C (Regonini et al., 2010). Annealing amorphous TiO_2 nanotubes at temperatures between 450 °C and 750 °C was shown to yield mixtures of anatase and rutile phases (Li et al., 2012). The effect of substrate annealing on the TNT structure has also been studied and shown to influence the growth mode (Weizhen et al.2011; Zheng et al., 2015).

In this study, electrochemical anodization of Ti foils has been performed to fabricate TNTs using a so called third generation electrolyte with the purpose of investigating the effect post-annealing on the TNT structure and photocatalytic activity. Further, the effect of pre-annealing the Ti substrate foil on the TNT physical properties is also investigated.

2. Experimental

2.1. Preparation and electrodeposition of TNTs on non-annealed Ti foils

Ti foils with dimension 15mm×15mm×0.25 mm were used as anode materials (purity 99.7%, Sigma Aldrich) in a two electrode setup. A Pt foil with size 25mm×25mm×0.25 mm was used as counter electrode (purity 99.9%, Sigma Aldrich). Prior to use the electrode foils were cleaned by sonication in ethanol for 5 minutes, and then rinsed in distilled water and dried in a stream of nitrogen gas. Anodization was performed using a constant DC voltage of 60 V. All chemicals used in this work were purchased from VWR chemicals Sweden with stated purity 99.9 % or better. Electrolyte solutions with the following compositions were used to prepare TNTs on non-annealed Ti foils: (i) 95 vol% ethylene glycol, 5 vol% water, and 0.37 g ammonium fluoride (NH_4F) corresponding to 0.1 M, and (ii) 47.5 vol% ethylene glycol, 2.5 vol% water and 0.37g NH_4F corresponding to 0.2 M. Anodization was done for 2 h. The as prepared TNT samples were rinsed in distilled water and dried in a stream of nitrogen. The as prepared TNTs were subsequently annealed in air for 1 h. The morphology of as prepared samples was characterized by scanning electron microscopy (SEM; Zeiss 1550, Jena, Germany) employing 1 to 10 kV acceleration voltages with an in-lens secondary electron detector. The TNT length was measured by profilometry (DektakXT, Bruker, Germany). The crystallinity and phase composition was measured using X-ray diffraction (XRD) with 2θ between 20 and 80° using a Philips D5000 diffractometer employing averaged Cu $K_{\alpha 1}$ (λ = 1.5418 Å) radiation. The photocatalytic activity of the samples was measured using a homebuilt photocatalytic reactor, which continuously can measure the methylene blue (MB) concentration in the reactor as a function of UV illumination by recording the calibrated transmittance of the 670 nm absorption band due to MB in the well-stirred solution with a diode laser (Bozhidar, 2011). A concentration of 1 ppm MB in 100 mL water was used in the experiments.

2.2 Preparation and electrodeposition of TNTs on pre-annealed Ti foils

Prior to anodization the Ti foils were heated in an oven at varying temperatures between 250°C to 625°C in steps of about 100^{o}C in a stream of nitrogen for 1 h. After annealing, the Ti substrates were cleaned by sonication in ethanol for 5 minutes, rinsed in distilled water, and finally dried in a stream of nitrogen gas. The anodization electrolyte comprised of 93 vol% ethylene glycol, 7 vol% water and 0.15 M NH_4F. Anodisation was done in 100 mL Teflon beaker using electrode separation distance of 3 cm at 55VDC for 2 hours. Samples were prepared using an optimized electrolyte preparation procedure where ammonium fluoride was first mixed with water and magnetically stirred. The solution was then added to ethylene glycol and magnetically stirred. The TNTs were then calcined at 400^{o}C to obtain anatase crystalline structure after which characterization of the samples was done.

3. Results and discussion

3.1 Post-annealed TNTs on non-annealed Ti foils

Figure 1 shows SEM images of two samples, TNT07 and TNT08 measured at different magnification, but grown under the same electro-deposition conditions as described section in 2.1. Both TNT sample have tube diameters 120 nm and 10 nm wall thickness, and the TNTs are arranged in hexagonal structure.

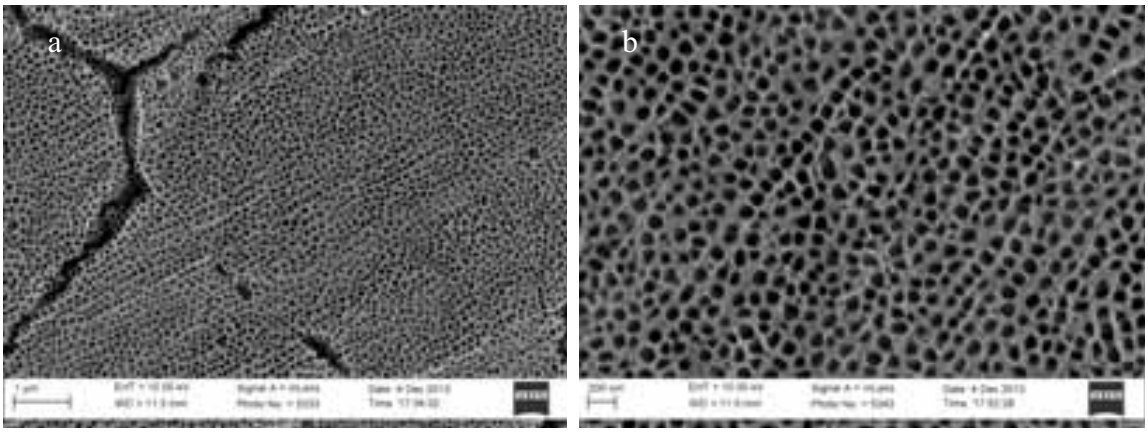

Fig. 1: SEM images for sample TNT 07 and TNT 08 with different magnifications prepared by anodisation for 2hours in 0.2 M NH_4F, 95% Ethylene glycol and 5% H_2O

The as-prepared TNTs were amorphous but on calcining samples TNT07 and TNT08 at 400°C and 300°C, respectively, for 1 h, the TNTs crystallized as shown Fig. 2 XRD diffractograms. It is seen that both samples exhibit predominately the anatase phase, with minor reflections form rutile crystals. The XRD diffractogram in Fig. 2 show that the intensity ratio of the <004> to the <001> reflection is higher for the sample annealed at 400°C than the sample annealed at 300°C. Rutile <111> and <211> reflection peaks are also observed which are more intense in the sample annealed at 400°C.

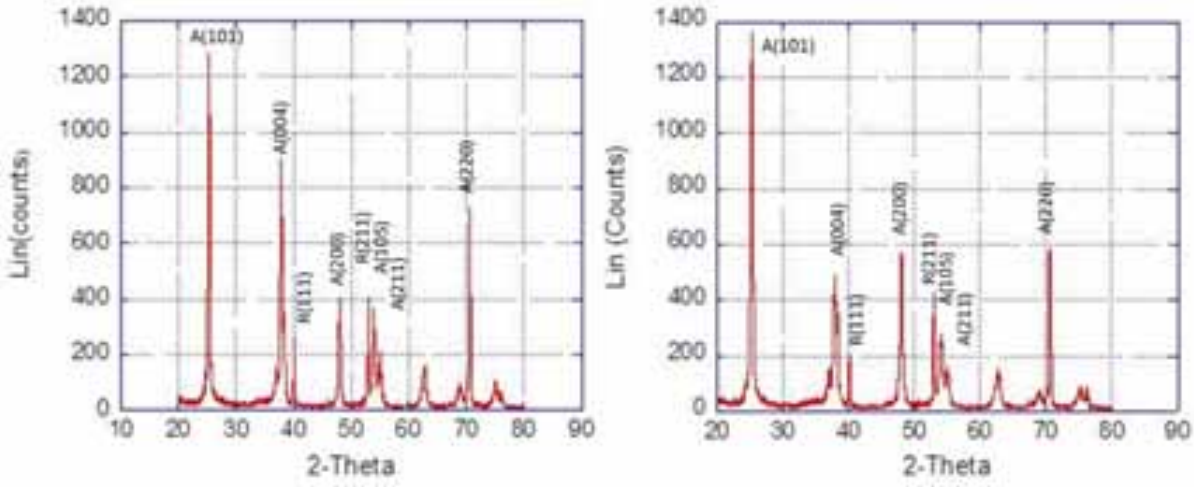

Fig. 2: XRD diffractograms of samples (a) TNT07 calcined at 400°C and (b) TNT08 calcined at 300°C.

Scherrer analysis of the <101> reflection peak was used to obtain a rough estimate of the crystallite size, *d*, viz.

$$d = \frac{0.94\lambda}{\beta cos\theta}$$

where 2θ = 25.27° and 2θ = 25.25° for the sample annealed at 400 °C and 300 °C, respectively, β is the FWHM corrected for the instrumental line broadening, yielding d = 37 nm and 32 nm, respectively, indicating a crystallite growth with increasing annealing temperature, as expected.

The photocatalytic properties of the samples, where measured in 1 ppm MB solutions. The calibrated MB concentration, as measured by the 670 nm laser intensity integrated in the reactor, is shown in figure 3a, and shows a linear decrease of transmittance in the solution as a function of increasing MB concentration, thus validating the performance of our experimental setup. The photocatalytic degradation rate of sample TNT08 post-annealed at 300°C (Fig. 1b) is k_{dec} = 0.0019 min^{-1}, while that of TNT07 post-annealed at 400°C (Fig. 1a) is k_{dec} = 0.0035 min^{-1}. We attribute this to a higher degree of crystallinity after post-annealing at 400°C, and possibly due to the increased rutile content which has been reported to enhance the photocatalytic activity due to synergetic bandgap matching of rutile and anatase particles that are in physical contact to each other (Su et al., 2011)

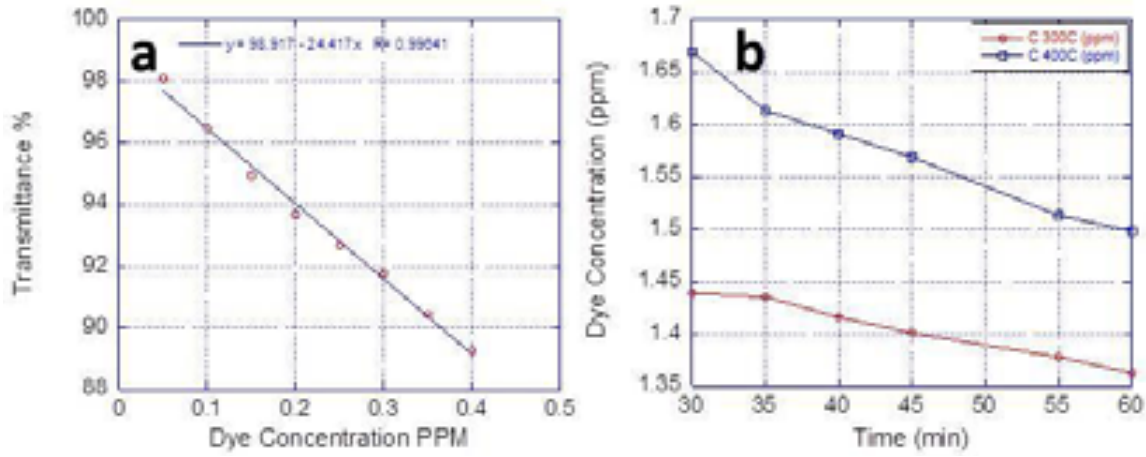

Fig: 3 (a) MB calibration curve for photocatalytic measurements (b) Methylene blue degradation for samples TNT 07 and TNT 08 calcined at 400°C and 300°C. The illumination time in (b) started at time = 30 min.

3.2 TNT on pre-annealed Ti foils

SEM images of a pristine non-annealed Ti foil and annealed Ti foil are shown in Fig. 4. It is seen that the micro-structure and surface morphology are changed upon annealing. Heating of Ti foils brings about rearrangement, crystal growth, as well as surface oxidation of the Ti foil that can facilitate TNT nucleation by providing new reactive sites. The pristine Ti metal foils are polycrystalline in nature and characterized by randomly distributed grain boundaries which act as defect sites for TNT nucleation (Grimes and Mor, 2009). Thus the defect sites act as templates for TNT growth. Substrate heating influences the crystal structure and mechanical behavior of the Ti foils which influences the TNT nucleation and growth. Annealing smoothens the Ti foil which and improves the order and arrangement of TNTs, as we now discuss.

SEM images of TNTs grown on annealed Ti foils pre-annealed between 250°C and 625°C are shown in figure 5 (a-e). SEM images taken from the bottom side of the TNTs are shown in figure 5f. For the non-annealed TNT bottoms, the TNTs have clear grain boundaries. The distribution and size of TNTs is irregular. Some are pentagonal, others are hexagonal, some are small others are large. This irregular distribution and size effects are inherent in the Ti foil and come about during processing of the Ti foils and are transferred to TNTs during the growth process in electrochemical anodization. Pre-heating treatment rearranges the atoms

within the Ti foil through diffusion and smoothen the surface. The inset in figure 5f shows TNTs grown on annealed Ti foils. Here the bottom parts of the TNTs are more densely packed and almost cylindrical

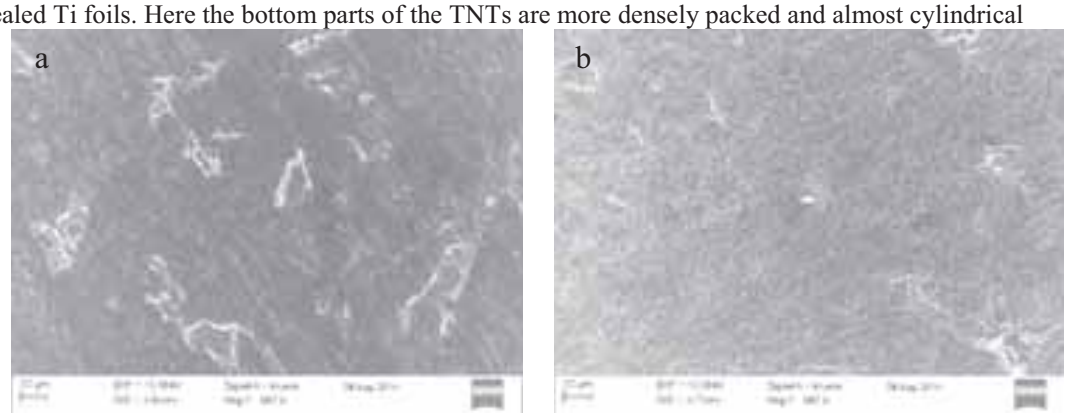

Fig. 4: SEM Images of (a) non annealed Ti foil, and (b) annealed Ti foil.

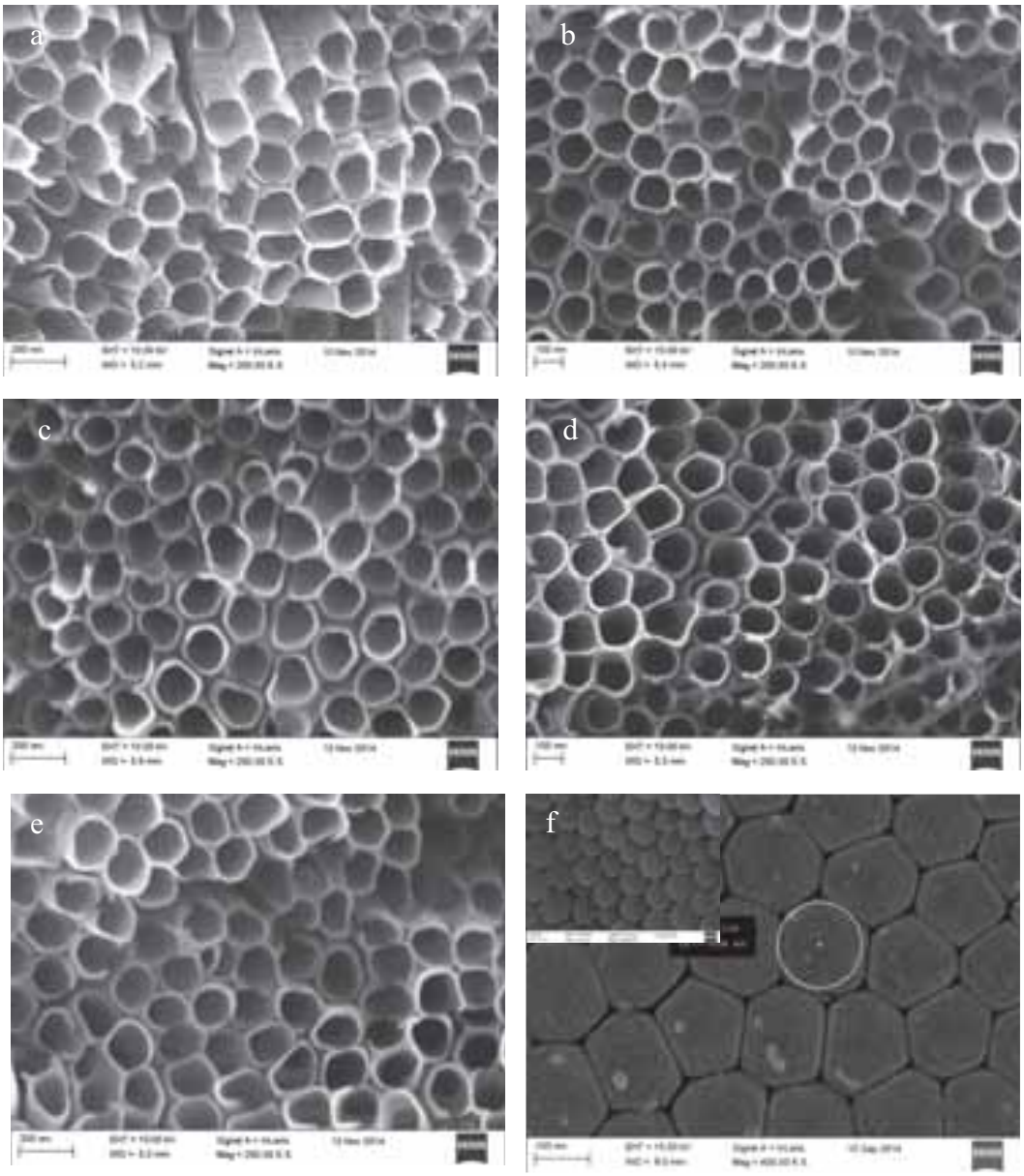

Fig. 5: SEM top-down images of TNTs grown on pre-annealed Ti foils at (a) 250°C (b) 350°C (c) 450°C, (d) 525°C (e) 625°C, and (f) SEM images from scraped off TNT bases grown on non-annealed, and in the inset, annealed Ti foils.

Annealing helps to reduce residual stresses developed during the process of fabricating the Ti foils (Zheng et al., 2015). Heat treatment changes the structure, mechanical properties of the Ti foils improving the structural and mechanical properties of the annealed of the Ti foil which affect the growth of TNTs during the process of anodization as reported by Xialong et al. (Xialong et al, 2010). In the latter study it was noticed a change in microstructure in Ti foil through the formation of V- like structures with ultrathin walls as a result of rearrangement of atoms within the Ti foil. Annealing causes atoms to migrate in a crystal lattice reducing defects and dislocations in the material which in turn changes hardness and ductility of material. While by preheating Ti foil we induce superior properties, it should be noted that from the findings of Zheng and colleagues (Zheng et al., 2015), Ti foil has been shown to exhibit different stages when heated in a so called microforming process. Temperatures below 300^{o}C brought about elastic and work hardening stages. At 450^{o}C the material exhibited elastic, work hardening and softening periods. Fracture strain set in at 450^{o}C and increased thereafter because of the occurrence of the softening behavior with deformation setting in when the temperature was increased (Zheng et al., 2015). With increasing annealing temperature stress on Ti foil is reduced and when the foil is used to grow TNTs, the initiation of TNT growth is affected. A compromise has to be attained where pre-annealing gives desirable TNT growth, structure and high-order with good characteristics.

Figure 6a shows the influence of physical properties of TNTS of Ti foils pre-heated at 250^{o}C, 350^{o}C, 440^{o}C, 525^{o}C, and 625^{o}C. Nanotube inner diameter significantly drops by 18 nm from 158 nm to 140 nm when Ti foils are heated to 350^{o}C. At higher annealing temperatures the inner diameter of the TNTs exhibits only a slight decrease of inner diameter. A similar trend is noticeable for the outer diameters of the TNTs. These results show that most of rearrangement of the crystal atoms within the Ti foil that act as nucleation sites for TNT takes place when the Ti foil is heated between 250^{o}C and 350^{o}C. Packing of the TNTs continues at higher annealing temperatures. This difference in packing of TNTs is seen in the SEM images in figure 5, and the dramatic change of TNT packing above 250^{o}C is clearly evident.

The wall thickness for Ti foils pre-heated at 250^{o}C, 350^{o}C, 440^{o}C, 525^{o}C, and 625^{o}C reduces as 32 nm, 31 nm, 29 nm, 21 nm, and 20 nm, respectively. In fluoride containing electrolytes, wall thickness is a function of electrolyte concentration, water content and anodizing voltage. At high fluoride contents, thin walls are produced because of effects of chemical etching. As seen in figure 6b only short nanotubes were grown on Ti foils annealed at 525 ^{o}C and 625 ^{o}C. This means with all other anodizing parameters kept constant in growing all the TNTs, the effect of etching of tube walls is most pronounced for the short nanotubes. Short TNTs means disorder, since the metal\oxide base interface is etched away in the fluoride containing electrolyte leaving spacing between growing TNTs. Longer TNTs protect the electrolyte from reaching the metal\oxide base interface. This explains why we have drastic reduction in wall thickness from 29 nm to 21 nm in TNTs grown on Ti foil heated at 440 ^{o}C and 525 ^{o}C, respectively, together with the use of already deformed electrode with reduced stress. As seen in figure 6b the TNT length drastically reduces by almost twice from about 8850 nm to 4870 nm.

When Ti foils were heated from 250°C to 625°C, the TNT length first increased as 7490 nm, 7970 nm, 8850 nm, for the pre-heat treatment at 250^{o}C, 350^{o}C and 440^{o}C, respectively, after which the length was observed to decrease at higher temperatures beyond 450^{o}C (Fig. 6b). At 525°C and 625^{o}C, the TNT length decreased as 4870 nm and 4240 nm, respectively. Several factors have been reported to influence the growth of TNT, among them being pH of electrolyte, diffusion, temperature of solution and stress induced effects. In ethylene glycol containing electrolytes, high ammonium fluoride content means high pH. This increases the rate of chemical dissolution hindering TNT growth. High temperatures of electrolyte in ethylene glycol containing electrolytes means reduced viscosity of the bulk ethylene glycol solution leading to fast migration of the fluoride ion which diffuses at twice the rate of oxygen ion thereby affecting growth of TNT. This explains why viscous electrolytes such as glycerol and ethylene glycol have been known to produce well-ordered and long nanotubes because the rate of diffusion of F^{-} is reduced enabling growth (Paulose et al., 2007). Aqueous electrolytes only produce TNTs only a few um long because of chemical dissolution\oxidation (Beranek et al. 2003). Stress builds up during oxidation of Ti foil in electrochemical anodization and is present in the growing nanotubes (Macak; 2008). Heating Ti foils at temperatures between 250-450^{o}C reduces stress on Ti foil (Zheng et al., 2015). In this work, the proposition is that the remaining

stress on Ti foil after annealing at this temperature coupled with stress induced effects during anodization can influence the oxidation\dissolution behavior in the anodization set up initiating growth, self-organization and cause an increase in nanotube growth length as shown in figure 6b for TNTs grown on Ti foil pre-annealed at 250°C, 350°C and 440°C. The reduction in nanotube length in figure 6b, when Ti foils are heated at 525 °C and 625 °C, can be explained by the fact that at temperatures above 450°C stress on Ti foil is minimal, fracture and deformation has set it on the Ti foil (Zeng et al., 2015. The formation of tube bottom (TiO_2) layer at the metal\oxide interface is permanently exposed to compressive stress (Macak; 2008). A reduction in nanotube length as shown in figure 6b means that the fluoride containing electrolyte easily penetrated to the lower part of the nanotube bottom base eroding the nanotube bottoms, and at the same time hinder oxidation\dissolution behavior at the metal\oxide layer. Eventually this leads to reduced growth. We conclude that a mechanically deformed Ti foil, when used as anode electrode in the electrochemical anodization, will perform poorer than a normal working anode which has not undergone deformation. Since the formation of TNTs takes place at the anode and it is the working electrode, care should be taken not to anneal Ti foils above 440°C.

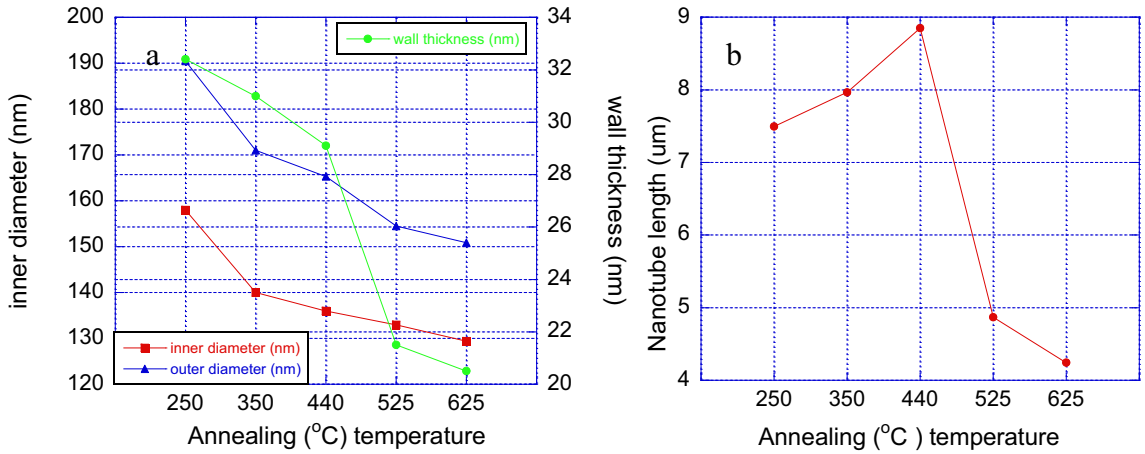

Fig. 6: (a) A graph of physical parameter (inner, outer and wall)dimension (b) Nanotube length of TNTs anodised on preheat treated Ti foils at different temperature in 93% ethylene glycol, 7% vol water and 0.15 M NH_4F for 2 hours in 55VDC

4. Conclusions

The effect of Ti annealing temperature on already grown amorphous titanium dioxide nanotubes has been explored. Heat treatment on the as-prepared amorphous TNTs at 300°C and 400°C gives predominantly TNTs with anatase phase, with minor reflections form rutile crystals. The grain sizes as deduced from Scherrer analysis of XRD diffractograms yield d = 37 nm and 32 nm for the TNT07 and TNT08 samples, respectively, demonstrating larger grain sizes with increasing calcination temperature of the amorphous TNTs, and a tendency for alignment along the <004> direction. The rate of photodegradation of methylene blue is higher for the sample annealed at 400°C than that annealed at 300°C which is attributed to increasing crystallinity, and possibly higher percentage of inter-mixed rutile phase. The effect of Ti foil annealing before growth of TNTs is further explored and found to influence nanotube growth, the nanotube structure, and optical properties of the nanotubes. Ti foils annealed between 250°C and 625°C gave an increase in nanotube length up to 440°C, beyond which there was a great reduction in nanotube length from about 8850 nm at 440°C to 4870 nm for Ti foil heated at 525 °C. Nanotubes wall thickness reduced systematically up to about 29 nm at 440°C after which the wall thickness reduced to 21 nm for nanotubes grown on Ti foil heated at 525°C. The outer diameter reduces from 165 nm at 440°C to 154 nm at 525°C. There is structural rearrangement of nanotube structure with better and closer hexagonal packing of the TNTs achieved at 440°C, but beyond this temperature, disorder sets in due to shortening of TNTs which are due to effects of chemical etching as a result of exposure to electrolytes. In this work we propose titanium foils for growing TNTs using electrochemical anodization in ethylene glycol and ammonium fluoride electrolytes should be heated in an atmosphere of nitrogen for one hour at 440°C. The as prepared amorphous nanotubes should

further be calcined at 400^{o}C to get pure anatase for photocatalytic applications since it is the best phase for photocatalytic applications.

5 Acknowledgement

The authors wish to acknowledge the International Science Program (ISP), Uppsala University, Sweden together with the Department of Engineering Sciences, Solid state Division; Uppsala University, Sweden for all Material and financial support in this work. University of Eldoret, Kenya is also acknowledged for enabling this work to be done at Uppsala University Sweden.

References

Bozhidar, I. S., Nina, V. K., Gianluca, L. C., 2011. Novel integrated reactor for evaluation of activity of supported photocatalytic thin films: Case of methylene blue degradation of TiO_2 and nickel modified TiO_2 under UV and visible light Colloids and surfaces, A: Physicochem. Eng. Aspects 382: 219-225.

Frank, S. N., Bard, A. J., 1977. Heterogeneous Photocatalytic Oxidation of Cyanide Ion in Aqueous Solutions at TiO_2 Powder, Journal of the American Chemical Society 99: 303–330.

Fujishima, A., Hashimoto, K. Watanabe, T. (1999). TiO_2 photocatalysis: fundamentals and applications, Tokyo Bkc.

Fujishima, A., Rao, T. N., Tryk, D. A., 2000. Titanium Dioxide Photocatalysis. Journal of Photochemistry and Photobiology C Photochemistry Reviews 1: 1-21.

Ghicov, A., Tsuchiya, H., Macak, J..M., Schmuki, P., 2006. Annealing effects on the photoresponse of TiO_2 nanotubes. Physica Status Solid A Applied Research, 203 (4): 28-R30Grimes C. A. Mor G. K., (2009). TiO_2 Nanotube Arrays Synthesis, Properties, and Applications Springer Science Business Media, LLC.

Hsien, Y. H., Wang,, K. H., Ko, R. C., and Cang, C. Y., 2000. Photocatalytic degradation of wastewater from manufactured fiber by titanium dioxide suspensions in aqueous solution: a feasibility study. Water Sci. Tech.42: 95–99.

Li, D., Shiwei, L., Li, S., Huang, X., Cao, X., Li, J., 2012. Effects of geometric and crystal structures on the photoelectrical properties of highly ordered TiO_2 nanotube arrays. J. Mater. Res. 27, 1029–1036.

Park, J.H., Kim, S., Bard, A.J., 2006 . Novel Carbon-Doped TiO_2 Nanotube Arrays.

Rani, S., Roy S. C., Paulose, M., Varghese O. K., Mor, G. K.., Kim, S., Yoriya, S., LaTempa, T. J., Grimes, C. A., 2010. Synthesis and applications of electrochemically self-assembled titania nanotube arrays. Phys. Chem. Chem. Phys. 12, 2780.

Regonini D., Jaroenworaluck A., Stevens R., Bowen C. R. 2010. Effect of heat treatment on the properties and structure of TiO2 nanotubes: phase composition and chemical composition. Surf. Interface Anal. 42: 139–144.

Sarmad 2010. Annealing Effect on the growth nanostructured TiO_2 thin films by pulsed laser deposition (PLD). Journal of Eng. & Tech, No: 3291. 921-929.

Shiqi, L., Zhang, G., Guo, D., Yu, L., Zhang, W., 2009. Anodization Fabrication of Highly Ordered TiO_2 Nanotubes. J. Phys. Chem., 113, 12759–12765..

Tanaka, K.., Capule , M. F. V, Hisanaga , T., 1999. Effect of crystallinity of TiO_2 on its photocatalytic action. Chemical Physics Letters. 187 : 73-76.

Weizhen, H., Park, S., Shin, D., Yoon, S., 2011. Effect of Annealing Ti Foil on The Structural Properties of Anodic TiO_2 Nanotube Arrays. Journal of the Korean Physical Society, Vol. 58, No. 3, 575_579.

Zheng, Q., Shimizu, T., Ming, Y., 2015. Ti foil annealing at different temperatures on properties of thin pure titanium foils Manufacturing Rev. 2015, 2, 3.

Conference Proceedings

Solar World Congress 2015
Daegu, Korea, 08 – 12 November 2015

Growth and Optimization Processes Towards Self-organized and Highly Ordered Titanium Dioxide Nanotubes for Photocatalytic Applications

Kioko Stella[1], Mghendi Mwamburi[1] and Lars Österlund[2]

[1] University of Eldoret, Department of Physics, School of Science. P.O. Box 1125, Eldoret, 30100, Kenya.

[2] Uppsala University, Department of Engineering Sciences, The Ångström Laboratory, Uppsala University, P.O. Box 534, SE-751 21 Uppsala, Sweden.

Abstract

Highly- ordered and self-organized titanium dioxide nanotubes (TNT) for photocatalytic activity were fabricated by anodization method, and characterized using scanning electron microscopy, X-ray diffraction, UV-Vis spectrophotometry, and profilometry. Anodization electrolyte preparation and growth conditions were studied towards the growth of ordered TNTs by systematically varying electrolyte composition and mixing procedures. TNTs were grown by anodizing pure titanium foils in a third generation electrolyte consisting of 0.2 M ammonium fluoride and water. For optimization purposes, the samples were anodized at a constant DC voltage of 60 V for two hours while varying the electrolyte composition by employing different ways of mixing the electrolyte so as to achieve a homogeneous solution. The concentration of fluoride was varied between 0.005 M to 0.3 M, while the water content was varied between 3 and 50 vol %. Introducing a two-step anodization procedure, improved TNT structures were achieved. The as-prepared TNTs between 87 nm and 170 nm; and wall thickness between 20 nm to 40 nm depending on anodizing conditions were amorphous, and were found to transform into highly crystalline anatase structure upon calcination at 400^{o}C. The physical dimensions of the TNTs varied with length between about 7.2 nm to 46 nm; inner diameter. The TNTs were shown to be active for methylene blue photo-degradation, and that reaction rate was shown to be more than twice as high on the two-step anodized TNTs.

Keywords: *Anodization, TiO_2, nanotubes, photocatalysis.*

1. Introduction

Titanium dioxide nanotubes (TNT) have attracted considerable interest due to its wide applicability in a variety of fields such as gas sensing, photocatalytic pollutant degradation, dye sensitized solar cells, self-cleaning surfaces, antibacterial coatings and biomedical application (see Rani, 2010, and references therein). Various ways to prepare TNTs have been reviewed by Macak et al, (2007) and Rani et al (Rani, 2010). Anodic oxidation of Ti foils has been shown to yield high quality TNTs (Mizukoshi et al., 2013), by judicious control of parameters such as electrolyte concentration, applied voltage, pH and temperature. Several different types of electrolytes have been reported over the years to grow ordered TNTs. This includes the so-called first, second, third and fourth generation of electrolytes (Raja, 2010). The nature of electrolyte (aqueous or non- aqueous) plays a key role, and has been found to influence the TNT growth. In viscous organic electrolytes TNTs with smooth walls are obtained at low water concentrations (Macak et al, 2007). In such electrolytes high order is achieved because of reduced rate of dissolution. High water content favors transition to sponge like structures rather than nanotubular structure (Kiyoung et al., 2013). Aqueous electrolytes give rise to high chemical dissolution rates causing dissolution of the oxide, thus resulting in short TNTs of just a few micrometers. Nanotube dimensions have been tailored by controlling the concentration of electrolyte (Paulose et al., 2007), voltage (Regonin et al., 2013), water content (Macak et al., 2005), anodizing time (Choi et al., 2006; Crawford et al., 2007), and temperature (Prida et al., 2007;

Selection and/or peer review under responsibility of Scientific Committee
doi:10.18086/swc.2015.04.29 Available at http://proceedings.ises.org

Varghese et al., 2005). In fluoride containing electrolytes the structure of TNT depends on the amount of the fluoride content. Increasing the fluoride content increases the pH, which in turn affects the oxidation/dissolution behavior due to fast etching of the Ti substrate. Low concentrations are required to obtain uniform nanotubular structures since they minimize oxide dissolution into the electrolyte.

In this work, TNTs were grown using electrochemical anodization employing a so called "third generation" electrolyte containing ammonium fluoride, ethylene glycol and water, and optimum processes parameters were established. A second anodization step was adopted and shown to result in TNTs with improved physical properties. Finally, the photocatalytic activity of the TNT s towards photo-degradation of methylene blue in water solution was demonstrated.

2. Experimental

2.1 Titanium dioxide nanotube preparation

2.1.1 Materials

Ti foil with dimensions 8 mm × 8 mm × 0.25 mm was employed as anode material (purity 99.7%, Sigma Aldrich). Prior to use the Ti foils were cleaned by sonication in ethanol for 5 min, and then rinsed in distilled water and dried in a stream of nitrogen gas. A Pt counter electrode with size 25 mm × 25 mm × 0.25 mm (Sigma Aldrich, purity > 99.7%) was used. The electrolyte mixing procedure was varied to see the effect on the TNT morphology and order of nanotubes. A mixture of ethylene glycol (Ethane-1, 2-diol, $C_2H_6O_2$, Sigma Aldrich, purity > 99.8%), ammonium fluoride (NH_4F, Sigma Aldrich, purity >99.99%), and distilled water was used for the reaction. The relative amounts of the chemicals were varied, as described below. All anodisation experiments were done with a two-electrode system a constant voltage of 60 V using 100mL Teflon reaction cell. The electrode separation was fixed at 30 mm.

2.1.2 Electrolyte mixing conditions

NH_4F is a white solid which is immiscible in ethylene glycol but very soluble in water. Proper mixing of the electrolyte solution is crucial to obtain homogenous mixtures with proper NH_4F concentration. Here three sets of mixing procedures were adopted, which differed in how NH_4F was mixed with ethylene glycol: (A) All chemicals were simultaneously mixed in a teflon reaction beaker with a magnetic stirrer for 30 min. (B) NH_4F was first dissolved in H_2O and vigorously hand shaken. The solution was then added to ethylene glycol to yield the desired composition, while constantly stirred with a magnetic stirrer. The solution was then ultrasonicated for 3 minutes. (C) NH_4F was first disolved in water and mixed with magnetic stirring. The solution was then transferred to the teflon reaction beaker containing ethylene glycol and magnetically stirred. In all three cases, the as prepared samples were cleaned by immersing them in deionized water for 3 min and dried in a stream of nitrogen gas. Anodization was done for 2 h.

2.1.3 Water concentration

TNT were grown using 3 vol%, 5 vol%, 7 vol%, 10 vol%, 15 vol%, 20 vol%, 30 vol% to 50 vol% in all set of experiments to investigate the effect of water content on TNT growth. The concentration of NH_4F was kept constant at 0.1 M. Anodization was done for 3 h using method (C) of electrolyte preparation.

2.1.4 Fluoride concentration

The NH_4F concentration was varied between 0.05 M to 0.3 M while keeping the ethylene glycol (95 vol%) and H_2O concentration (5 vol%) fixed. Anodization was done for 2 hours.

2.1.5 Two-step anodization

A two-step anodization was employed using an electrolyte consisting of 0.1 M NH_4F in 95 vol% ethylene glycol and 5 vol% H_2O. The electrolyte mixing procedures in (A), (B) and (C) were employed to study their effect on TNT Growth. In the first step of anodization, TNTs were grown in 0.1M NH_4F, 95 vol % Ethylene glycol and 5 vol % H_2O for 4 hours in 60V DC after which they were removed by ultra sonicating the samples in ethanol for 5 minutes , and rinsed in deionized water. The samples were finally dried in a stream of nitrogen prior to a second 1.5 h anodizing step at 60 V using the same electrode separation distance was

30 mm.

2.2 Characterization

The TNT were characterized by scanning electron microscopy (SEM) using a Zeiss microscope (Zeiss 1550, Jena, Germany). An acceleration voltage of 10 keV and an in-lens secondary electron detector were employed. X-ray diffraction (XRD) was performed with a Philips D5000 diffractometer employing averaged Cu $K_{\square}$ (λ = 1.541056 Å radiation. A profilometer (DektakXT, Bruker, Germany) was used to measure the thickness of the opal and inverse opal films. Reflectance measurements were performed in UV/Vis/NIR transmittance spectra taken in the 300–1000 nm range with a Perkin-Elmer Lambda 900 spectrophotometer. Photocatalytic measurements were performed in a reactor described in detail elsewhere (Stefanov, 2011) consisting of a continuously stirred reaction cell with a 670 nm laser to measure the absorbance of methylene blue (MB) in situ during UV illumination. A standard 4 W BLB tube lamp (4W F4T5/BLB, OSRAM, Germany) operated at λ = 365 nm) was used as a light source. The lamp intensity was measured with a calibrated thermopile detector (Ophir, North Andover, MA, USA) and was measured to be 2.44 mW cm^{-2} at the UV tube wall. The intensity distributions at the position of the film in the reactor was estimated to be 0.38 mW cm^{-2}. A concentration of 1 ppm methylene blue in 100 mL deionized water was employed in all experiments. The absorbance of MB at 670 nm was continuously monitored during UV illumination. The absorbance of the water solution without methylene blue was used as a reference for the absorbance measurements.

3. Results and discussion

3.1. Electrolyte preparation

Figure 1 shows top-view SEM images of TNTs obtained from a one-step anodization process employing different electrolyte mixing conditions. Figures 1a shows an image of TNTs grown using an electrolyte prepared by method A in Section 2.1.2, using 0.2 M NH_4F, 95 vol% ethylene glycol and 5 vol% H_2O, whereby all chemicals were simply mixed in the Teflon reaction beaker and mixed with a magnetic stirrer. Deposition of un-reacted NH_4F is visible as particles and non-porous layers on top of the TNTs. Figure 1b shows a SEM image of TNTs grown from electrolyte prepared by dissolving NH_4F in water, and shaking till it was fully dissolved in the water (method B). Adding NH_4F solution to the ethylene glycol results in less amounts of unreacted NH_4F which is visible as non-porous layer on top of the TNTs. Small amounts of NH_4F are however deposited on top of TNT layer, meaning that it was not fully mixed. In Figure 1c shows a SEM image from TNTs grown from uniformly mixed electrolyte where NH_4F was added in water and carefully mixed with a magnetic stirrer to ensure that all the fluoride ions fully dissolved (methods C). Only after complete pre-mixing, the NH_4F solution was added to bulk ethylene glycol solution under stirring to obtain a homogeneous solution. This procedure produced densely packed and well-ordered TNTs with 120 nm diameter, 20 nm wall thickness and length of about 23 μm. The as prepared TNTs were immersed in distilled water for 3 minutes and dried in a stream of oxygen, followed by ultrasonication in isopropyl alcohol to remove top non- porous yielding well organized nanotubes.

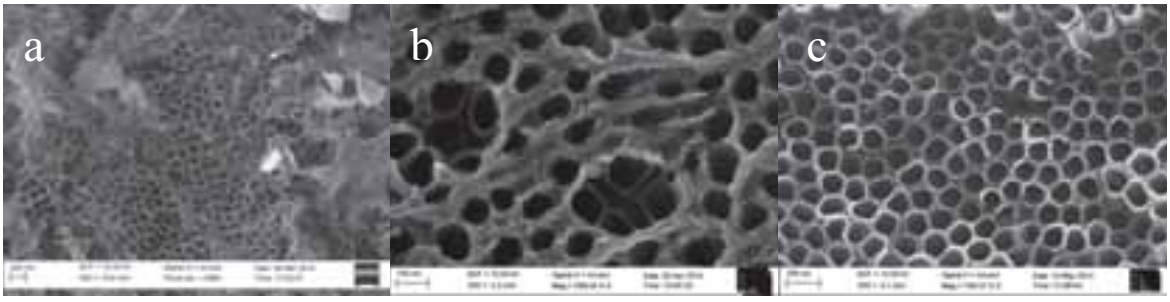

Fig. 1 Dependence of mixing condition: TNT prepared from anodization of Ti foil in a freshly prepared electrolyte consisting of 95% ethylene glycol, 5% H_2O and 0.2 M NH_4F at 60 V for 2 hours, according to mixing procedures (a) method A, (b) method B, and (c) method C (see Section 2.1.2).

Figure 2 shows SEM images from a batch of TNTs grown with different water concentrations between 3

vol% and 50 vol% at a fixed concentration of 0.1 M NH_4F. Compact and smooth nanotubes are grown at low water contents because of reduced chemical dissolution rates on the oxide layer. At high water content

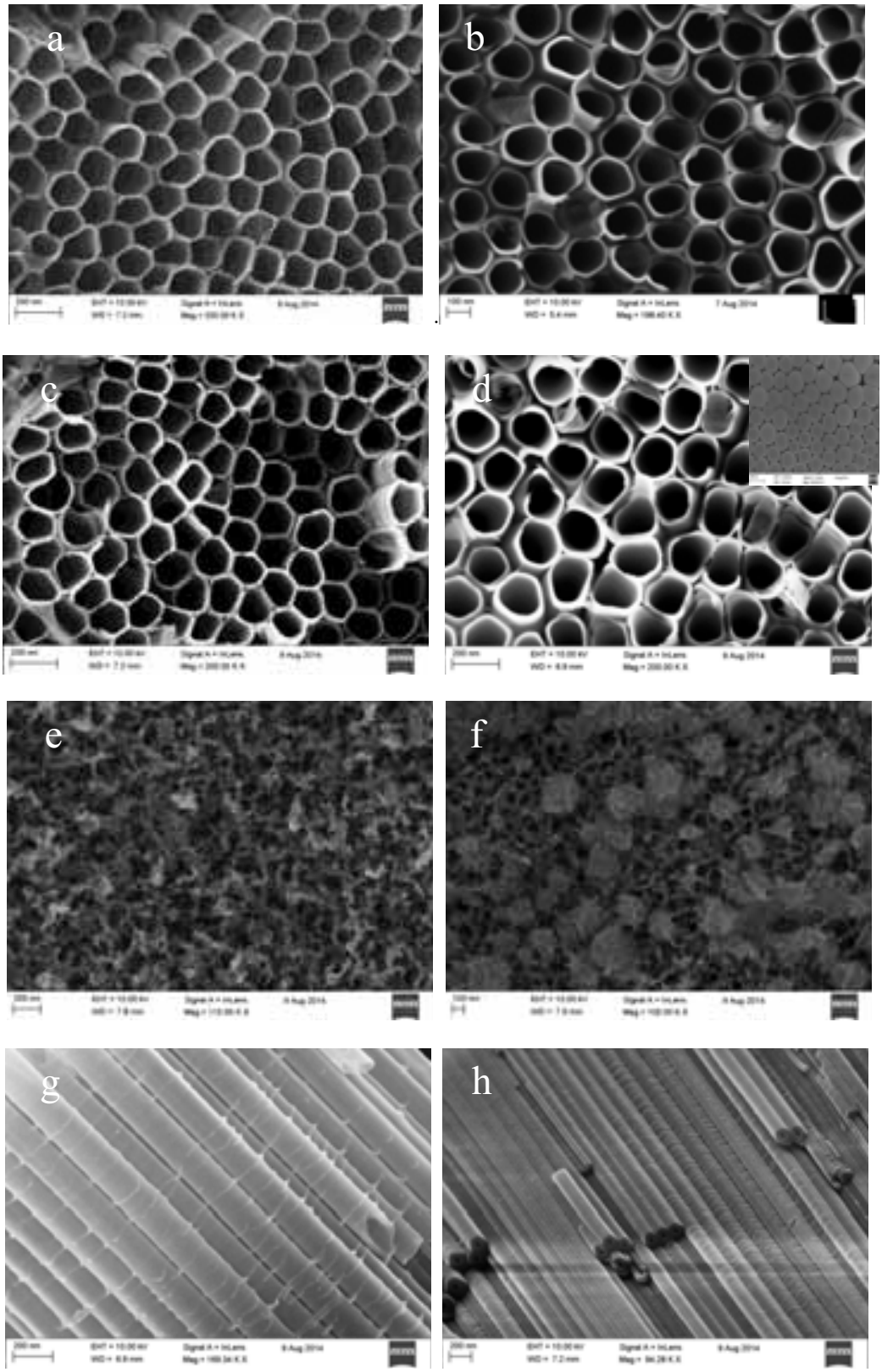

Fig. 2 SEM images showing TNTs prepared from an electrolyte in 0.1 M NH4F with varying H2O concentrations: (a) 3 vol%, (b) 10 vol%, (c) 7 vol% (d) 10 vol % (e) 15 vol% (f) 50 vol%. (g) and (h) show cross sections showing 10 % H2O and 3% H2O respectively. The anodization was carried out at 60 V for 3 hours.

(>10%), ripples are formed as seen in the cross-section image in Fig. 2g. due to etching of the nanotube walls by the F^- ions. The minimum water content for growth of well-ordered structure has been reported to be 0.18 vol% employing 20 V anodizing potential (Raja et al. 2007). When the water content is less than 1 vol%, the formation of long nanotubes (> 300 nm) is impossible no matter the applied voltage (Yin et al., 2010). In our case, well-ordered TNTs were grown at low water contents between 3% H_2O and 7 % H_2O. At higher concentration exceeding 10 vol % less ordered sponge-like structures were formed (Fig 2e and f). At high concentrations the viscocity of electrolytes is decreased leading to an increasing dissolution rate and disordered growth.

The water concentration affects the crystallinity of the nanotubes. Figure 3a shows XRD diffractogram from samples made with different water concentrations, which were post-annealed at 400°C in an oven for 1 h. All TNTs exhibit anatase stucture but the anatase peaks diminish with increasing water concentrations at 10%. The most developed crystalline TNTs are obtained at < 10 vol% H_2O.

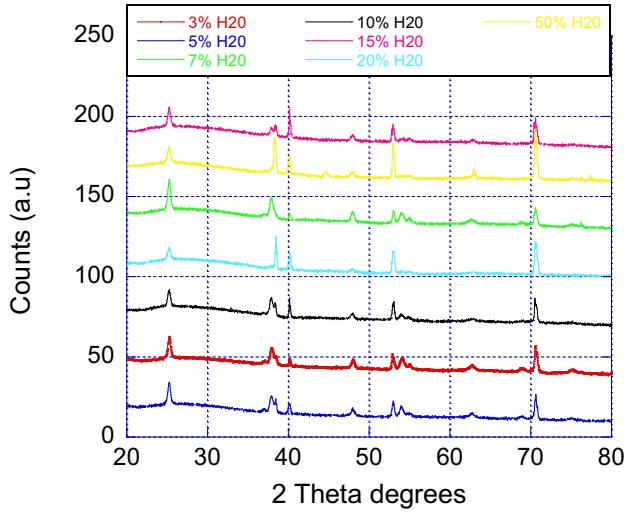

Fig. 3 XRD diffractograms of TNTs prepared with varying water concentrations in 0.1 M NH4F anodized at 60 V for 3 hours.

3.3 Fluoride concentration

Figure 4 shows top-view SEM images of TNTs obtained from a one-step anodization process with varying NH_4F concentration between 0.05 M and 0.3 M.

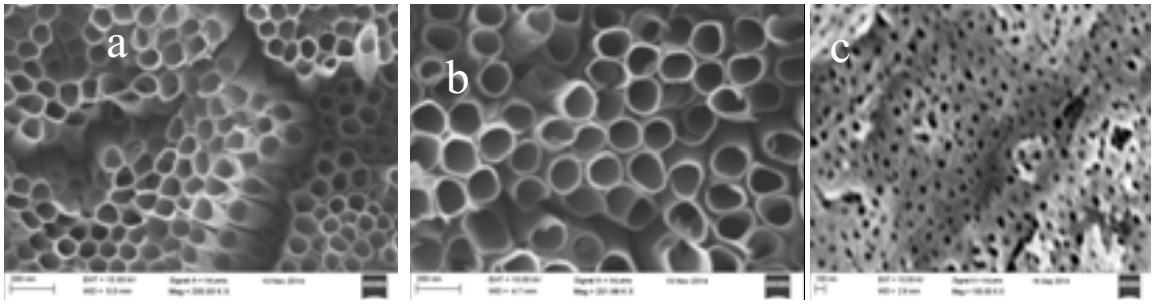

Fig. 4 Selected SEM images of TNTs obtained with varying NH_4F: (a) 0.3M, (b) 0.1M (c) 0.05M, respectively, in 95 vol% ethylene glycol and 5 vol% H_2O. (d) XRD diffractograms at varying NH_4F concentrations of 0.05M, 0.1M, 0.15M, 0.2M and 0.5M. Anodization was done at 60 V for 2 h using electrolyte preapartion method C.

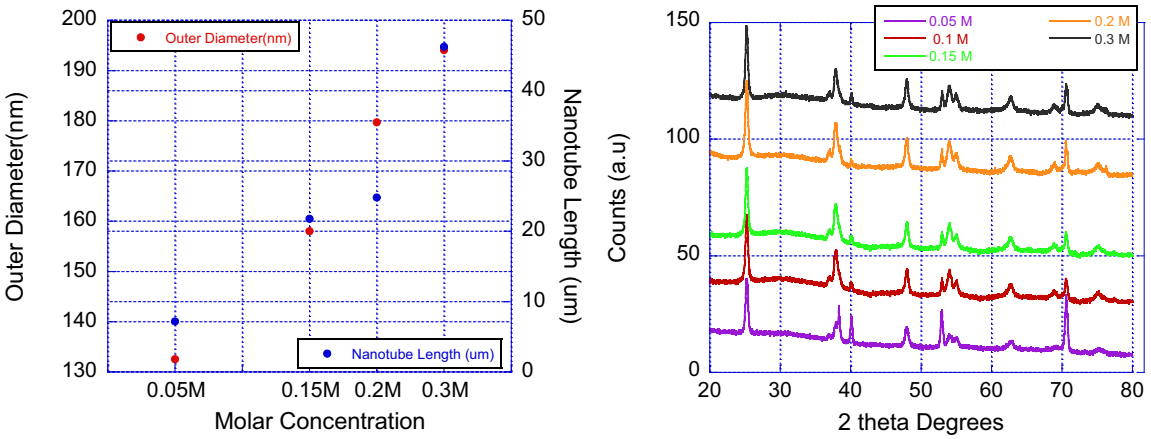

Fig. 5 Outer diameter and length of TNTs verses NH_4F molar concentration prepared by anodization at 60 V for 2 h in an electrolyte containing 95 vol% ethylene glycol and 5 vol% H_2O at varying molar concentrations using method C of electrolyte preparation.

The F^- ions act as powerful oxidants of the Ti plate leading to formation of TiO_2. The fluoride ions react to form Ti fluoride complexes as shown in reaction 3 from which TNTs are formed according to reaction 4 (Macak et al., 2007), viz.

$$4\ H_2O + 4\ e^- \rightarrow 2\ H_2 + 4\ OH^- \quad \text{(eq. 1)}$$

$$Ti \rightarrow Ti^{4+} + 4e^- \quad \text{(eq. 2)}$$

$$Ti^{4+} + 6F^- \rightarrow [TiF_6]^{2-} \quad \text{(eq. 3)}$$

$$[TiF_6]^{2-} + 2H_2O \rightarrow TiO_2 + 6F^- + 4H^+ \quad \text{(eq. 4)}$$

$$TiO_2 + 6F^- + 4H^+ \rightarrow [TiF_6]^{2-} + 2H_2O \quad \text{(eq. 5)}$$

Increasing the fluoride content in the electrolyte increases the rate of nanotube formation. For example the length of the nanotubes as measured by profilometry is increased as 7.2 µm, 22.6 µm, 24.8 µm and 46.2 µm for concentrations 0.05 M, 0.1 M, 0.2 M and 0.3 M, respectively. By increasing the amount of F^- ions, the rate of chemical etching on the nanotubes also increases causing thinner walls, as evident from fig.ure 4 (a) and (b). Fig. 4d shows XRD diffractograms for TNTs prepared at different NH4F concentrations between 0.05M and 0.3M. A well-developed anatase phase structure is obtained in all cases. The distribution of the reflections was however observed to change as a function of F^- concentration, with the <101> orientation slightly increasing with F^- concentration, which correlates with the decreasing wall thickness and suggests that (101) planes develop perpendicular to the growth direction. At 0.3 M the intensity of the <101> reflection is reduced. This may be explained due to the effect of increased etching rates on the surfaces of the TNTs. From these results, it appears that a NH_4F concentration around of 0.2 M in the 95 vol% ethylene glycol and 5 vol% water electrolyte yields optimum growth conditions for long, well-ordered TNTs.

3.4 Second step anodization

In Figure . 6 a-d SEM images of TNTs formed after the two-step anodization procedure described in Section 2.1.5. It is evident that the TNT array is more ordered and uniform than those formed in the corresponding one step anodization (Figure 1).

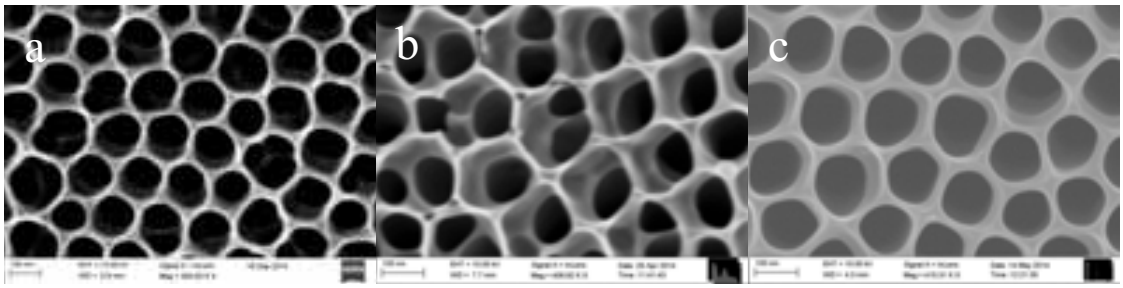

Fig. 6 SEM images of TNTs formed after two-step anodization procedure, employing (a) method A, (b) method B, and (c) method C, respectively, in the second anodization step. The electrolye compositon was 0.1 M NH_4F in 95 vol% ethylene glycol and 5 vol% H_2O.

Superior order and structure are obtained when the electrolyte is thoroughly mixed (method C), thus enhancing reaction between the participating species in anodization reactions. The crystallinity is poor as seen in XRD in Fig 7 (a) because TNTS were grown from un-optimized electrolyte conditions procedure (A) with impurities of unreacted species in electrolyte being trapped as nanotubes grow thus introducing defects and affecting crystallinity. Image (b) is from procedure (B). In the two-step anodization procedure, TNT grow from a pre-textured surface from the first anodization step, and this has been reported to cause fast initiation of pore nucleation and ordering (Zhao et al. 2007). The TNTs are seen to be arranged in a hexagonal super lattice.

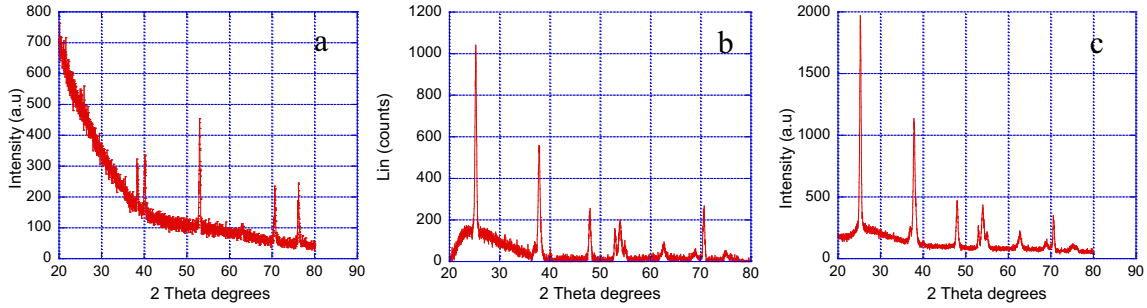

Fig. 7 XRD diffractograms TNTs formed after two-step anodixation obtained after different electrolyte mixing protocols to prepare the first anodization step. (a) Prepared according to method (A), (b) method (B), and (c) method (C) respectively.

It is evident that well-developed crystalline anatase TNT were obtained for samples which were prepared according to methods B and C in the first anodization step.

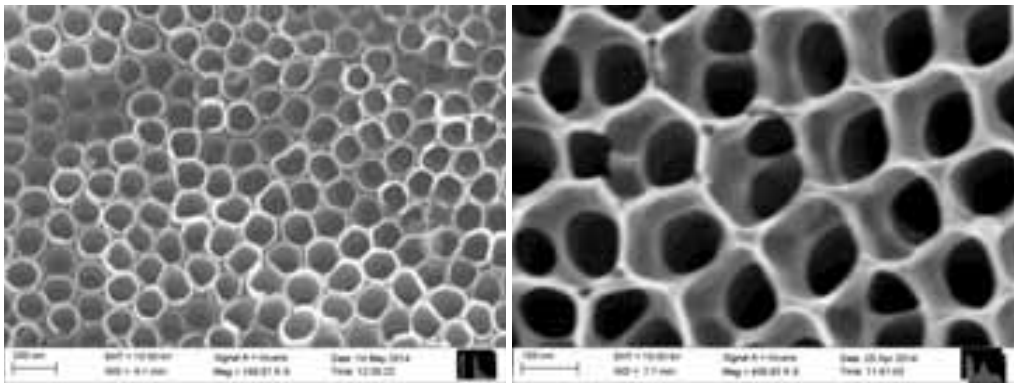

Fig. 8 SEM images of nanotubes anodized using different electrolyte mixing conditions. (a) Sample R21 from Optimized process in first step anodisation method (C) (b) SEM images of sample 14 after second step anodization using method (A).

When the optimized electrolyte preparation procedure (C) is applied to prepare electrolyte for growing TNTs in a second step anodization, a more crystalline well developed anatase phase is obtained (Figure) 7 c. The particle size of ammonium fluoride is reduced in every step of magnetic stirring exposing large area for the electrolyte to oxidize of the Ti plate during anodization. This leads to faster formation of the complex

$[TiF_6]^{2-}$ from which TiO_2 is formed. It also ensures that the concentration of ammonium fluoride participating in the reaction is as expected since all the fluoride particles take place in the chemical reaction due to reduced size. The crystallinity of the sample is dependent on the electrolyte preparation procedures. The presence of unreacted particles in the formation of any material in our case TiO_2 film will be an impurity and introduce defect sites on TiO_2 film reducing crystallinity.

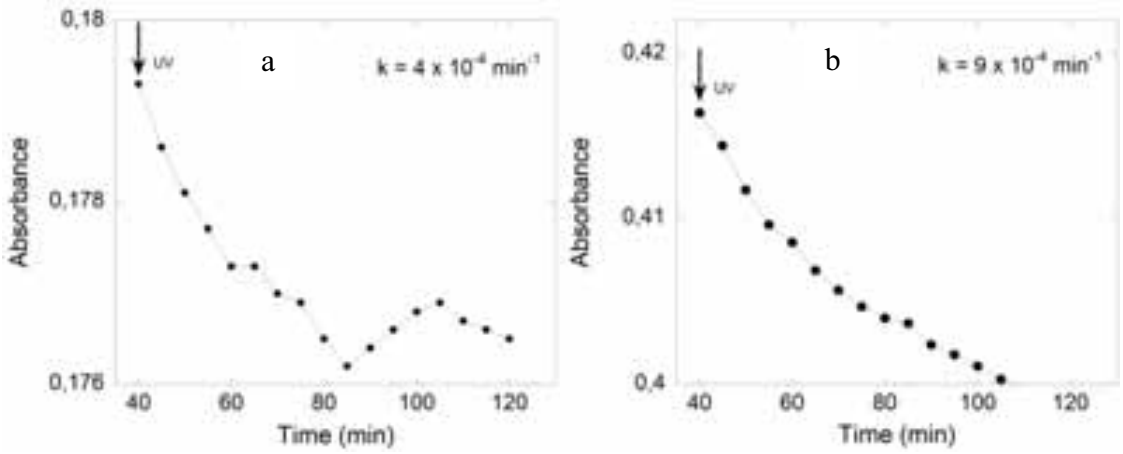

Fig .9: Photocatalytic degradation of methylene blue (1 ppm) in deionized water by TiO_2 nanotube samples (a) prepared according to the 1-step method C, and (b) two-step method A, respectively. Illuminations was done with a 370 nm BLB lamp with lamp power of about 0.4 m W cm^{-2} at the position of the sample surface. The pseudo-first order rate constants are shown as insets in the figures.

Figure 8 a shows top-view SEM images of Sample R 21 of TNTs obtained from optimized one-step anodization process described in section 3.1, while Figure 8 b show SEM image from a two-step anodization process. A well-ordered uniform nanotublar structure is obtained after the second step of anodisation. We attribute the improved nanotube properties to template assisted nucleation on top of the nanotube structures formed after the first anodization step. During a one-step anodization on a Ti foil, nucleation and nanotube growth takes place at random sites. By introducing a template through a first anodization step, a pre-defined pattern for nanotube nucleation is made. Nanotubes grow on already ordered imprints and retain the order as they grow. The intermittent cleaning and electrolyte exchange removes impurities and improves the quality of subsequent nanotube growth.

Finally, the photocatalytic activity of the porous TNT structures was determined by measuring the decomposition of MB. The photocatalytic degradation rates for one sample from the 1-step and one from the 2-step anodization procedure were measured and determined to be k = 4×10^{-4} min^{-1} and k = 9×10^{-4} min^{-1}, respectively, from a pseudo-first order kinetic analysis (Figure. 9). The rate constant for the (non-optimized electrolyte) TNTs from second step anodisation was found to be more than twice as large compared to the one from the 1-step anodization procedures, confirming the microscopy results that the 2-step process yields higher quality TNTs.

4. Conclusion

The preparation procedures of highly ordered and self-organized titanium dioxide nanotubes for photocatalytic application have been presented. Optimized growth conditions including electrolyte preparation, water content, ammonium fluoride concentration and second step anodization have been explored. Water content and ammonium fluoride concentrations are known to influence the order and self-organization through high chemical dissolution and fast etching rates. Here we show that although NH_4F is an essential component in the formation of TiO_2 by oxidation of Ti plate and formation of $[TiF_6]^{2-}$ complex. Increasing ammonium fluoride beyond 0.2 M in this work causes thinning of nanotube walls, and introduces disorder in the nanotube structure. Increasing the water content increases the rate of chemical dissolution causing ripples on the nanotubes. Beyond 10 vol% a sponge-like structure is obtained. An optimized

electrolyte preparation procedure where NH_4F is first dissolved in water followed by magnetic stirring to fully dissolve the NH_4F particles and subsequent transferring the NH_4F solution in ethylene glycol ensures that all participating species in the electrolyte are intimately mixed forming a homogeneous solution. Magnetic stirring in both stages of electrolyte mixing reduces the particle size; which is an important parameter in determining how fast the reaction will proceed. Furthermore, ensuring all particles are intimately mixed improves the crystallinity by reducing impurities and defects on the TiO_2 nanotube structure as nanotubes grow. A second step of anodization improves the order and self-organization of the nanotubes, and hence the photocatalytic activity. Growing nanotubes employing a second step anodization and using the optimized electrolyte preparation procedure is expected to further enhance the photocatalytic activity. We propose that the two-step anodization method, followed by use of optimized electrolyte procedure, a water content of 3 vol% and ammonium fluoride of between 0.1 M and 0.2 M can be used to fabricate well-ordered TiO_2nanotubes which are photocatalytic active.

5. Acknowledgement

The authors wish to acknowledge the International Science Program (ISP), Uppsala University, Sweden together with the Department of Engineering Sciences, Solid state Division; Uppsala University, Sweden for financial support and supervision of this work. University of Eldoret is also acknowledged for enabling this work to be done at Uppsala University Sweden.

6. References

Backman, U., Auvinen, A., Jokiniemi, J. K. 2005. Deposition of nanostructured titania films by particle-assisted MOCVD, Surf. Coat. Technol. 192, 81-87.

Bai, J., Zhou, B. X., Li, L. H., Liu, Y. B., Zheng, Q., Shao, J. H., Zhu, X. Y., Cai, W. M. M. 1995. J. Photochem. Photobiol., A 89, 177.

Berger, S., Kunze, J., Schmuki, P., Valota, A. T, LeClere, D. J., Skeldon, P., George, E. T., 2010. Influence of Water Content on the Growth of Anodic TiO_2 Nanotubes in Fluoride-Containing Ethylene Glycol Electrolytes. J. Electrochem. Soc., 157, C18-C23.

Curtis, T. P., Walker, G., Dowling, B. M., Christensen, P. A. 2002. Fate of Cryptosporidium oocysts in an immobilised titanium dioxide reactor with electric field enhancement. Water Res. 36, 2410–2413.

Dumitriu, D., Bally, A. R., Balli, C., Hones, F. P., Schmid P. E., Sanjines R., Levy, Parvulescu V. I., 2000, Photocatalytic degradation of phenol by TiO_2 thin films prepared by sputtering. Appl. Catal. B, 25, 83-92.

Kiyoung, L., Mazare, A., Schmuki, P., 2014. One-Dimensional Titanium Dioxide Nanomaterials: Nanotubes. Chem. Rev. 2014, 114, 9385–9454.

Macak, J. M., Albu, S. P., Schmuki, P., 2007. Towards ideal hexagonal self-ordering of TiO_2 nanotube. Phys. Stat. Sol. (RRL) 1, 181-183.

Macak, J. M., Tushiya, H., Ghicov, A., Yasuda, K., Hahn, R., Bauer, S., Schmuki, P., 2007. Current Opinion in Soild state and Materials Science 11, 3-18.

Macak, J. M., Sirotna, K., and Schmuki, P., 2005. Self-organized porous titanium oxide prepared in Na_2SO_4/NaF electrolytes. Electrochimica Acta. 50, 3679-3684.

Masuda, H., Satoh, M., 1996. Fabrication of gold nano dot array using anodic porous alumina as an evaporation mask. Jpn. J. Appl. Phys., 35, L126.

Mor, G. K., Varghese O. K., Paulose, M., Shankar, K.., Grimes, C. A., 2006. A review on highly ordered vertically oriented TiO_2 nanotube arrays: Fabrication, material properties, and solar energy applications. Sol. Energy Mater. Sol.Cells. 90, 2011-2075.

Negishi, N., Iyoda, T., Hashimoto, K., Fujishima, A., 1995. Preparation of transparent TiO_2 thin film

photocatalyst and its photocatalytic activity. Chem. Lett. 24, 841-842.

Palouse ,M., Prakasam, H. E., Varghese, O. K.. L., Popat, P. K. C., Mor, G. K., Desai ,T. A., Grimes, C.A. 2007. TiO_2 Nanotube Arrays of 1000 μm in Length by Anodization of Titanium Foil: Phenol Red Diffusion. J. Physical Chemistry C, 111, 14992-14997.

Parida, K. M., Martha, S., Das, D., Biswal, P., 2010 . Facile fabrication of hierarchical N-doped GaZn mixed oxides for water splitting reactions. Journal of Materials Chemistry 20, 7144–7149

Raja, K. S., Misra, M., Paramguru, K., 2005. Formation of self-ordered Nano tubular structure of anodic oxide layer on titanium. Electrochem. Acta 51 154-165.

Rani, S., Roy, S. C., Paulose, M., Varghese, O. K.., Mor, G. K.., Kim, S., Yoriya, S., LaTempa, T. J., Grimes, C. A., 2010. Synthesis and applications of electrochemically self-assembled titania nanotube arrays. Phys. Chem. Chem. Phys. 12, 2780-2800.

Regonini, D., Bowen, C. R., Jaroenworaluck, A., Stevens, R., 2013. A review growth mechanism, structure and crystallinity of anodised TiO2 nanotubes. Mater Sci. Eng. 74, 377-406.

Stefanov, B. I., Kaneva, Puma, V. G. L., Dushkin, C. D., 2011. Novel integrated reactor for evaluation of activity of supported photocatalytic thin films: case of methylene blue degradation on TiO_2 and nickel modified TiO_2 under UV and visible light, Colloids and Surfaces A. 382, 1-3.

Varghese, O. K., Paulose, M., Shankar, K. Mor, G.K.,Grimes, C. A., 2005. Water photolysis properties of micron-length highly-ordered titania nanotube-arrays. J. Nanosci. Nanotechnol. 7, 1158-65.

Yin, H., Liu, H., Shen, W. Z. 2010**.** The large diameter and fast growth of self-organized TiO_2 nanotube arrays achieved via electrochemical anodization. Nanotechnology, 21, 035601.

Yoshiteru M., Naoya M. 2010. Photocatalytic Activities and Crystal Structures of Titanium Dioxide by Anodization: Their Dependence upon Current Density. Mater. Trans. 51, 1443-1448.

Zhao, J., Wang, X., Sun, T., Li, L. 2007. Crystal phase transition and properties of titanium oxide nanotube arrays prepared by anodization. Journal of Alloys and Compounds 434-435, 792-795.

Conference Proceedings

Solar World Congress 2015
Daegu, Korea, 08 – 12 November 2015

Thermodynamic Evaluation and Optimization of a Solar-Geothermal Hybrid System in Northern Chile

José Miguel Cardemil[1], Felipe Cortés[1,2], Andrés Díaz[1], Rodrigo Escobar[3]

[1] Universidad Diego Portales, Ejército 441, Santiago, Chile

[2] Fraunhofer Chile Research, Center for Solar Energy Technologies (CSET). Vicuña Mackenna 4860, Macul, Santiago, Chile

[3] Pontificia Universidad Católica de Chile, Vicuña Mackenna 4860, Macul, Santiago, Chile

Abstract

Chile is developing a national strategy to reduce the external dependence on energy supply sources, for which renewable resources must provide 20% of the electricity generation by 2025. As the northern part of the country exhibits a large arid desert area that has the highest radiation levels in the world and a considerable amount of active geothermal areas, proposing the hybridization of both renewable resources together is deemed advantageous considering the benefits that each resource presents and allows exploring potential synergies between both. A thermodynamic model is developed using the Engineering Equation Solver (EES) software in order to evaluate the performance of a single-flash power plant assisted by a parabolic trough collector system for four different geothermal reservoir conditions. The benefits of delivering the solar thermal energy to the superheating or evaporating processes are analyzed, in order to achieve the maximum 2nd law efficiency for the generation of additional power, or to reduce the geothermal fluid flow consumption. The results in the single-flash hybrid system show that the superheating process generates 0.23 kW of additional power per kW of thermal energy, while enhancing the brine evaporation produces only an additional 0.16 kW of power per kW of solar thermal energy. Hence, the single-flash hybrid power plant is able to produce at least 20% of additional power output and increase at least 3% the exergetic efficiency. This hybrid flash system presents a promising alternative towards the generation of additional power output and extending the lifetime of a geothermal well.

Keywords: *Solar Energy, Geothermal Energy, Hybrid scheme, Thermodynamic analysis*

1. Introduction

Chile is a relatively small country located along the west coast of the southern half of South America, which is endowed with a wide range of natural resources and through the production, addition of value and exportation of such resources it has emerged as a successful economy. However, the country has evinced over the last years several energy issues due to its high dependence on fossil fuels such as crude oil and natural gas, of which more than 90% are imported (CNE, 2013). Currently, the country's primary energy consumption is dominated by fossil fuels, which accounts for 66% of the energy consumed, while renewable energy sources comprising hydroelectricity, wood-based biomass and incipient solar and wind farms, are responsible for the remaining 34% mostly due to the large contribution of hydropower sources (CNE, 2013). This scenario indicates that Chile is a net energy importer and establishes a complex situation due to the difficulties in fulfilling the energy demand growth associated to additional economic and social development. Responding to this situation, the Chilean government has proposed a national strategy based on decreasing the external dependence of the energy supply focusing on promoting the so-called "*Non-Conventional Renewable Energy sources*" (NCRE), defined as small-scale hydro (under 20 MW), biomass, wind, solar, geothermal and tidal energy sources. Large-scale hydropower is considered a renewable source although its already large contribution to the Chile energy mix and its techno-economical maturity does not merit further government

Selection and/or peer review under responsibility of Scientific Committee
doi:10.18086/swc.2015.04.30 Available at http://proceedings.ises.org

support for additional development. The government has defined that the existing NCRE quota should grow up to 20% of electricity injected to the interconnected systems by 2025. Currently, NCRE accounts for 9% of the total installed capacity (2,242 MW), whereas 40% corresponds to wind, 23% solar PV, 19% biomass, 16% small scale hydro and 2% biogas (CIFES, 2015). In addition, the government has recently proposed the "*Agenda Energía 2050*", which establishes a schedule to reach the aforementioned goal, along with measures to promote their development (Ministerio de Energía, 2014).

Chile presents a long and narrow territory that extends for 4,330 km, with a wide range of climates due to its vast extension. There is a huge potential for renewable energy, especially at the northern region, which exhibits the most arid desert in the world along with a low presence of clouds and high altitude over the sea level resulting in exceptionally clear skies with low aerosol contents. Recent investigations indicate the existence of a significant solar energy potential in the northern regions, where the annual average of daily global horizontal irradiation (GHI) reaches levels higher than 7.5 kWh/m^2, and whereas the daily average of direct normal irradiation (DNI) present values higher than 9 kWh/m^2 (Escobar et al, 2014, 2015). Furthermore, the Chilean territory is also located in the "*Pacific ring of fire*" accounting over 15% of the world's active volcanoes and more than 300 active geothermal areas through the country, with an estimated resource potential of 16,000 MWe (Hogson, 2013). There are currently more than 20 geothermal areas under exploration in Chile, where the geothermal reservoirs present temperatures over 150ºC and are located no deeper than 3,000 meters (Lahsen et al., 2010). According to this, the northern region of the country accounts for at least six already explored geothermal areas and more than 25 other sites with potential for geothermal generation. The present study proposes to assess the use of these two renewable resources combined in a hybrid scheme, configuring a power plant capable of take advantage of the benefits that each source presents. Solar energy is available during day hours according to the specific climate conditions in a given site; while geothermal energy does not present variations by season. Although, the installation of such systems requires a longer period for deployment than the time needed for solar systems. Considering the high potential of both sources in the northern region of Chile, the present study focuses on the optimization of hybrid schemes that enable the possibility of exploiting these two sources together efficiently.

Hybrid solar-geothermal schemes have been proposed in several previous studies that focused on different technologies for exploiting the geothermal resources, such as single-flash (Mir, 2011), double-flash (Lentz and Almarza, 2006, Mir et al., 2011) and binary plants (Greenhut et al., 2010, Astolfi et al., 2011, Zhou et al., 2013, Zhou, 2014, Ruzzenenti et al., 2014) which were commonly combined with parabolic trough system. Lentz and Almarza (2006) proposed a hybrid system to increase the steam quality by integrating a solar field to a geothermal flash plant located at Cerro Prieto, Mexico. This work also analyzed two different alignments for the solar collectors, N-S and E-W. Later, the authors also evaluated the increase on steam production associated with the liquid-steam mixture by increasing the enthalpy of the geothermal resource. One of the issues presented was the corrosion caused by the geothermal fluid, which limited the performance of the hybrid system. Considering this aspect, Greenhut et al. (2010) assessed the performance of a system by including a heat exchanger between the solar and geothermal fluid, in order to compare the thermodynamic and economic performance of a binary and single-flash system on a steady-state condition. Astolfi et al. (2011) presented a solar concentration plant and a binary geothermal plant based on an organic Rankine cycle (ORC). The study was based on hourly simulations, where the solar resource of two different sites in Italy and the United States were compared by means of the levelized cost of energy associated with the operation of these plants. The research evidenced the attractiveness of incorporating solar energy to low-enthalpy geothermal systems. Later, Mir et al. (2011) developed an evaluation of solar-geothermal systems in order to estimate the effect of increasing the fluid temperature and enhancing the steam generation process, thus achieving higher power production at the geothermal system by adding a solar field of parabolic trough collectors. This allowed quantifying a reduction of geothermal resource consumption up to 10%, considering the same power output than a stand-alone geothermal plant. Recently, Zhou et al. (2013) proposed a binary geothermal system with solar boosting to investigate the effects on the hybrid system performance of parameters such as ambient temperature, solar irradiance, geographical location and resource quality. The power output and the economic performance adjusting parameters were analyzed and compared with stand-alone solar and geothermal plants, showing an outstanding potential on these aspects. They also focused on the synergies of the hybrid system to determine the potential for improvement on efficiency and cost reduction. Another recent study evaluated a

hypothetical ORC plant employing different working fluids. The effect of the fluid used within the power block on the life cycle assessment and exergy utilization from the geothermal resource was estimated and established that the sustainability of the resource relates to the surface of the heat exchanger and the operating conditions of the solar field (Ruzzenenti, 2014).

The aforementioned studies show a growing interest in the efficiency and utilization of the hybrid solar-geothermal systems. However, there are several issues that have not yet been addressed, which are crucial to determine the real potential towards the hybridization of both resources. Most of the studies analyzed the potential for increasing the power output, determining the economic benefits and comparing between all the configurations proposed, taking advantage of the solar energy system for configuring a thermal booster to the geothermal power plant, thus achieving higher thermal efficiencies, energy production and a significant reduction in the cost of electricity. The results agree that there is an improvement opportunity as the hybrid schemes can reduce the high costs associated with the exploitation of renewable energy resources. Nevertheless, there are still some aspects yet to be investigated in order to quantify the real potential from these hybrid systems and benefits on operating the subsystems combined. In this context, the exergetic or 2nd law efficiency of the combined system can be maximized by a proper optimization of the size and the configuration of the hybrid scheme.

Here it is proposed to study the single-flash geothermal technology, with the objective to develop a thermodynamic model of a solar-geothermal hybrid system that can optimize its operation under several resource conditions, maximizing the 2nd law efficiency of using both energy sources with the intent to determine the most effective way to utilize the solar energy captured by the parabolic trough collectors and address the potential benefits such as the reduction on the geothermal fluid extraction rate. To this end, an hourly simulation of a full year of the hybrid solar-geothermal power plant operation was developed in order to evaluate the system performance at one location in the northern region of Chile.

2. System description

Geothermal plants are commonly classified by its capacity: small (under 5 MW), medium (over 5 and under 30 MW) and large scale (over 30 MW) (Bertani, 2010). The small scale plants consider binary and back pressure systems, whereas medium are often associated to flash plants, and finally large scale plants usually refer to dry steam units. In this study, the focus is on medium scale flash geothermal power plants whose hybridization has already been proposed (Lentz and Almarza, 2006a, 2006b, Greenhut, 2010, and Mir, 2011). Regarding the solar technologies, solar thermal energy at medium and high temperature can be supplied by concentration systems of which the parabolic trough collectors are most appropriate for combined use in a geothermal facility due to its modularity and flexibility of installation and operation (Peterseim, 2014).

The single-flash system is one of the most common schemes for geothermal power plants in the world, accounting for 41% of the installed capacity and energy produced (Bertani, 2010). This system is considered the simplest way to convert the geothermal energy into electricity when a steam-liquid mixture composes the geothermal fluid. Fig. 1 corresponds to a single-flash hybrid system integrated to parabolic trough collectors array. The proposed hybrid scheme aims to allow the evaluation of the solar resource impact for superheating and evaporating the geothermal brine. The solar superheating is used to superheat the steam obtained from the separation process in the geothermal flash plant while the solar evaporator is used to increase the evaporation rate.

3. Thermodynamic model

The simulation model for the solar-geothermal hybrid systems proposed was developed using the Engineering Solver Software (Klein, 2015), which is widely used by the scientific community dealing with thermodynamic-related simulations. It allows for the solution of algebraic equations governing the cycles and easily communicates with a thermodynamic properties database based on REFPROP-NIST (Lemmon, 2002).

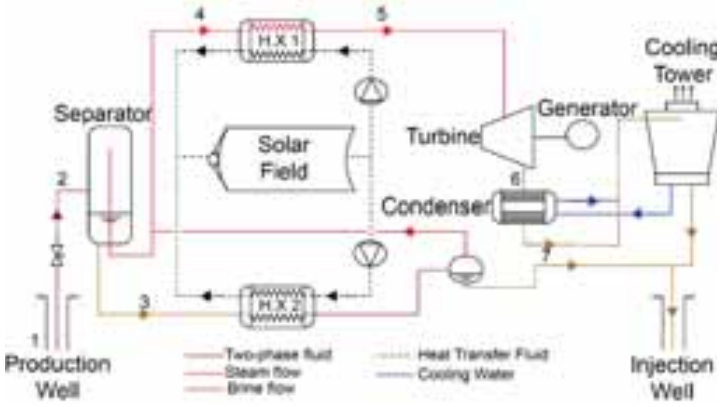

Fig. 1: Single-flash hybrid power plant scheme

The energy analysis is based on the 1st law of thermodynamics, neglecting kinetic and potential energy variations:

$$\dot{Q} - \dot{W} = \sum \dot{m}_{out} h_{out} - \sum \dot{m}_{in} h_{in} \quad \text{(eq. 1)}$$

where $\dot{Q}$ denotes the heat transfer rate, $\dot{W}$ the work transfer from the system, $\dot{m}$ the mass flow rate, h are the specific enthalpies and the subscripts in and out denote the inlet or outlet of the system, respectively.

The exergetic analysis is based on the 2nd law of thermodynamics, using the following exergy balance expression:

$$\dot{X}_{heat} - \dot{W} = \sum \dot{X}_{out} - \sum \dot{X}_{in} + \dot{X}_D \quad \text{(eq. 2)}$$

where $\dot{X}_{heat}$ is the exergy transfer by heat, $\dot{X}_{out}$ the exergy outlet, $\dot{X}_{in}$ the exergy inlet and $\dot{X}_D$ the exergy destruction.

The exergy transfer by heat ($\dot{X}_{heat}$) can be obtained using the following expression:

$$\dot{X}_{heat} = \left(1 - \frac{T_0}{T}\right) \dot{Q} \quad \text{(eq. 3)}$$

where T_0 is the environmental temperature, and T the temperature of the heat source.

The exergy flow in each component is expressed as follows:

$$\dot{X}_i = \dot{m}_\iota [(h_i - h_0) - T_0 (s_i - s_0)] \quad \text{(eq. 4)}$$

where $\dot{m}_\iota$, h_i and h_0 represents the flow rate, specific enthalpy at the state i and environmental state, respectively; s_i and s_0 the specific entropy at the same states. Hence, in order to evaluate the performance of the hybrid system, the 2nd law efficiency is used according to the following expression:

$$\eta_{II} = \frac{\dot{W}}{\dot{X}_{geo} + \dot{X}_{HTF}} \quad \text{(eq. 5)}$$

where $\dot{W}$ indicates the net power delivered by the hybrid system, $\dot{X}_{HTF}$ and $\dot{X}_{geo}$ are the exergies delivered by the heat transfer fluid from the solar field and geothermal field, respectively. The solar exergy is considered as the provided by the heat transfer fluid (HTF) and expressed as follows:

$$\dot{X}_{HTF} = \dot{m}_{HTF} \left[(h_{HTF,out} - h_{HTF,in}) - T_0 \left(s_{HTF,out} - s_{HTF,in} \right) \right] \quad \text{(eq. 6)}$$

where state HTF, out and HTF, in corresponds to the solar field outlet and inlet, respectively.

On the other hand, the exergy from the geothermal resource is defined as (Kanoglu, 2012):

$$\dot{X}_{geo} = \dot{m}_{geo} [(h_1 - h_0) - T_0 (s_1 - s_0)] \quad \text{(eq. 7)}$$

where the state 1 represents the geothermal reservoir. The exergy of the geothermal resource only considers the reservoir conditions, since the brine generated at the separation process is considered an exergy loss, according to the established technical literature (Agung, 2014, Jalilinasrabady 2012).

3.1 Geothermal resource

For the purpose of this study, four geothermal reservoir characteristics were examined: two considering compressed liquid (cases 1 and 3) and two considering saturated water-steam mixture (cases 2 and 4), as shown in Table 1 (Ocampo, 1998, Anderson, 2014). Therefore, the brine production on the geothermal field is assumed to follow the choked well flow proposed in DiPippo (2008), where the relation between the total mass flow of geothermal fluid is function of the wellhead pressure, as expressed by the following equation:

$$\dot{m}_{geo} = 99.663 - 2.6287P_2 + 0.5802{P_2}^2 - 0.04212{P_2}^3 \quad \text{(eq. 8)}$$

where $\dot{m}_{geo}$ is the mass flow rate extracted from the well and P_2 is the pressure at which the separator operates. The flashing process in the well between the states 1 and 2 is considered as isenthalpic, neglecting any change in the kinetic or potential energy according to previous studies (DiPippo 2008 and 2013). Other operating conditions for the system considered herein are summarized in Table 2.

Tab. 1: Geothermal reservoir characteristics

Resource	Temperature	Enthalpy	Pressure	References
Case 1	240 ºC	1038 kJ/kg	100 bar	(Ocampo, 1998)
Case 2	235 ºC	1351 kJ/kg	31 bar	(Anderson et al., 2014)
Case 3	210 ºC	900 kJ/kg	35 bar	(Anderson et al., 2014)
Case 4	205 ºC	1146 kJ/kg	17 bar	(Anderson et al., 2014)

Tab. 2: Hybrid solar-geothermal reference conditions

Parameters	Value
Ambient temperature	15 ºC
Ambient pressure	0.8 bar
Heat exchanger effectiveness	70%
Solar irradiance	1000 W/m^2
Maximum solar HTF temperature	391 ºC
Condensing temperature	50 ºC

3.2 Solar field model

For the purpose of this study, the solar field is considered as an arrangement of parabolic trough collectors using Therminol VP-1 as heat transfer fluid. The performance of the system is determined by using the model developed by Duffie & Beckman (2006), later adapted by Wendel (2010). The amount of solar thermal energy output rate ($\dot{Q}_{solar}$) is calculated by accounting the relation between the collector performance and the loss factors related to the utilization of direct normal irradiation ($\dot{G}_{b,T}$), as follows:

$$\dot{Q}_{solar} = A\left[f_{shadow} f_{corner} \dot{G}_{b,T}(a_1 + a_2\Delta T) f_{dirt} IAM - b_1\Delta T - b_2\Delta T^2\right] \quad \text{(eq. 9)}$$

where the parameters included in this equation are: A the solar field collection area, ΔT the temperature difference between the average temperature of the HTF and ambient temperature, IAM the incident angle modifier, f_{shadow} the losses factor due to shadowing, and f_{corner} the loss factor due to the collectors corner. Finally, the optical coefficients a_1 and a_2, the thermal coefficients b_1 and b_2; and the dirtiness coefficient f_{dirt} in (eq. 9), are given by the collector properties according to the manufacturer data (Hublitz and Spinnler, 2003, Lüpfert et al., 2001). The EuroTrough collector is used for a variety of application such as industrial process heat and electricity generation, and it was selected for the solar-geothermal hybrid system because of the low specific investment cost.

3.3 Turbine model

Geothermal turbines generally operate at wet steam conditions and therefore its isentropic efficiency is affected by the amount of moisture present in the steam during the expansion process. As the moisture increases, the turbine reduces its efficiency. This effect can be quantified by using Baumann's rule (DiPippo, 2008), which proposes that a 1% average extra moisture causes roughly a 1% drop in the turbine efficiency.

Hence, the isentropic efficiency is defined as:

$$\eta_T = \eta_{TD}\left(\frac{x_{in}+x_{out}}{2}\right) \quad \text{(eq. 10)}$$

where η_{TD} represents the turbine efficiency at dry steam conditions, x_{in} is the inlet dryness fraction and x_{out} the outlet dryness fraction.

The variation in the inlet turbine temperature is given by the solar resource availability and the pressure drop at the inlet nozzle of the turbine, which limits the mass flow admitted by the device. Chaibakhsh (2008) developed a relationship between the mass flow, temperature and pressure drop over the steam turbine as follows:

$$\dot{m}_{in} = \frac{K}{\sqrt{T_{in}}}\sqrt{P_{in}^2 - P_{out}^2} \quad \text{(eq. 12)}$$

where $\dot{m}_{in}$ represents the inlet mass flow rate, K the mass flow coefficient, T_{in} the inlet temperature, P_{in} the inlet pressure and P_{out} the outlet pressure.

The heat exchanger considered in this work to deliver the solar thermal energy towards the steam was modeled using the effectiveness-NTU method (Nellis and Klein, 2009).

4. Results and discussion

4.1 Stand-alone power plant results

The optimization methodology for the single-flash plant and each geothermal reservoir was developed by varying the separation pressure in order to achieve the highest power output possible. The separation pressure optimizes the amount of geothermal fluid through the system and the steam generation at the separator. The maximum amount of power output possible as a function of the separation pressure is shown in Fig. 2. The amount of power output generated by each reservoir is highly related to the thermodynamic state of the geothermal fluid, where the two cases with higher power production correspond to those with higher enthalpy. Case 1 presents higher resource temperature, yet it is not enough to generate a similar power production as in cases 2 and 4.

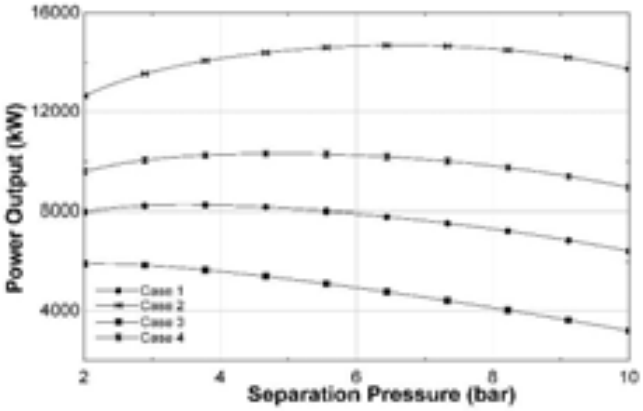

Fig. 2: Power output of the reservoir as function of separation pressure

4.2 Single-flash hybrid power plant

4.2.1 Additional power generation

The solar thermal energy in the single-flash hybrid scheme is added in two heat exchangers (HX) as shown in Fig. 1. The first HX is used for superheating the steam, while the second HX generates additional steam in the separator system. The additional power produced by both devices, when there is solar thermal energy available, was evaluated considering the reservoir case 2 as shown in Fig. 3. The HX 1 generates a higher amount of additional energy per kW of solar power delivered. For every kW of thermal energy the superheating process generates 0.23 kW of additional power output. Delivering the solar thermal power to the superheating process increases the steam quality at the turbine discharge, which improves the turbine efficiency. On the other hand, the HX 2 generates only 0.16 kW of additional power per kW of solar thermal power. Nevertheless, it has to be considered that the first HX can only superheat the steam flow until it reaches 320 ºC due to the HX effectiveness limitation.

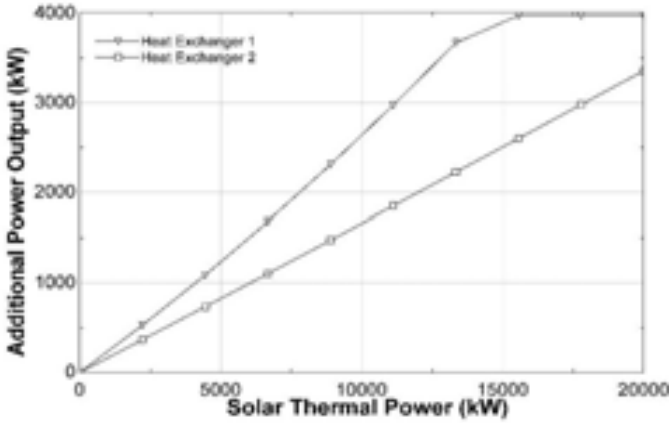

Fig. 3: Additional power output as function of solar thermal power

This situation is observed in Fig. 4, where the superheated steam temperature and additional steam generation as function of the solar thermal power is shown. Each additional kW of solar thermal power causes an increase of 0.012 ºC in the steam temperature and/or generates 0.00035 kg/s of additional steam. The optimization of the integration of both energy resources is developed by varying the separation pressure and solar thermal power in order to achieve the maximum 2nd law efficiency.

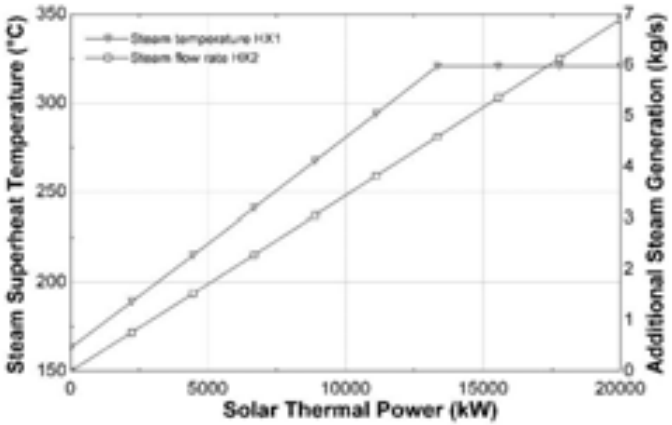

Fig. 4: Superheated steam temperature and additional steam generation as function of solar thermal power

The exergetic efficiency increases whenever solar thermal energy is supply to the superheating process. In contrast, using the solar energy to generate additional steam produces a lower rate of power, which is reflected in a reduction of the 2nd law efficiency. Fig. 5 shows the effect of the solar thermal power addition in the 2nd law efficiency for the four cases. The exergetic efficiency increases on the four cases proposed until it reaches a maximum and then it decreases. As the solar power is added, the amount required for each case is defined by the flow rate and temperature of the steam. The geothermal reservoirs with high enthalpy allow the separator to produce a higher amount of steam and at a higher pressure. This causes the hybrid single-flash plant to require a higher amount of thermal power as the enthalpy of the resource increases to achieve the maximum 2nd law efficiency. The maximum exergetic efficiency for the hybrid system proposed is achieved once the superheat steam reaches a temperature of approximately 320 ºC. Increasing the solar field aperture area to deliver additional thermal power to the HX 2 decreases the power production as shown in Fig. 3. This effect causes the reduction of the exergetic efficiency. The results of the geothermal only and single-flash hybrid power plants are shown in Table 3. The optimization routine indicates that the hybrid scheme increase slightly the separation pressure to achieve the maximum 2nd law efficiency. This benefits the system because a higher separation pressure reduces the flow rate and increases the steam temperature, which requires a lower amount of thermal power to achieve the maximum 2nd law efficiency. In the four cases analyzed for the single-flash power plant, the efficiency and power output increase as long as thermal power is delivered towards the superheating process. The power output for the single-flash hybrid presents at least 20% of additional power output and the 2nd law efficiency increase by more than 2.9%, for each reservoir case.

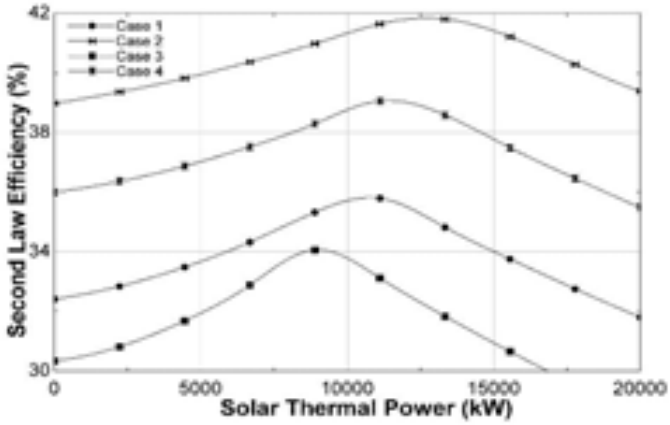

Fig. 5: 2nd law efficiency of the reservoir as function of solar thermal power

4.2.1 Geothermal flow rate reduction

The single-flash hybrid power plant can be used for a second purpose, which is reducing the geothermal fluid consumption thus allowing an extended geothermal well lifetime. This is carried out considering the power output of a single-flash only power plant fixed. Thereby, whenever there is solar energy available, the hybrid system is able to reduce the geothermal flow and compensates with the superheating of the steam or enhancing the steam generation until it reaches the fixed power output. The geothermal flow rate reduction is achieved by increasing the separation from the choked well flow considered in (eq. 8). The superheating process was used for this case due to the higher power production rate as it is integrated with the solar thermal energy. The effect of adding solar thermal power to the geothermal flow rate is studied for the proposed cases, as shown in Fig. 6. The higher enthalpy resources present a higher pressure, which enhances the reduction of the geothermal fluid given the geothermal well choked-flow conditions. The amount of geothermal flow reduction is directly related to the separation pressure and amount of steam that can be superheated. Cases 2 and 4 present higher steam rates, which is reflected in a considerable reduction of the geothermal fluid flow. This reduction achieves a stable point when the steam reaches it maximum superheat temperature given by the steam characteristics at the inlet of the HX.

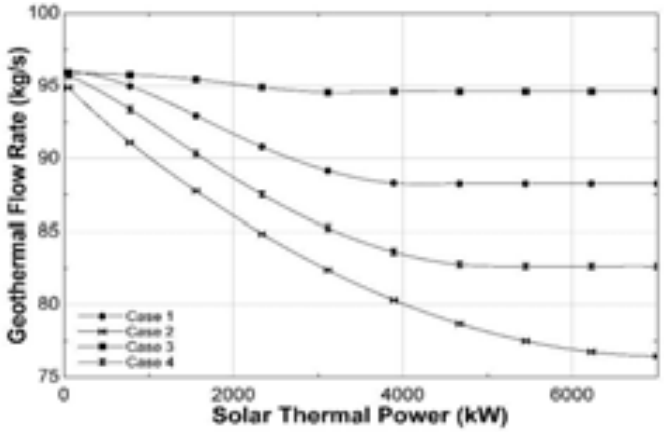

Fig. 6: Geothermal flow rate as function of the solar thermal power.

The high enthalpy resources present an increase of the 2nd law efficiency as long as the geothermal flow rate is reduced, as shown in Fig. 7. Cases 2 and 4 present a considerably increase in the 2nd law efficiency caused by the pressure and steam through the system. Once the superheat process reaches the maximum capacity the efficiency starts decreasing. Case 1 presents a geothermal flow reduction, which is still unable to produce a considerable increase in the 2nd law efficiency. As mentioned, the pressure at which each separator operates according to each reservoir conditions contributes to the reduction in the geothermal fluid flow. Case 3 presents no improvement in the 2nd law efficiency due to the low pressure at which the separator operates, which is determine by the lower enthalpy from the reservoir.

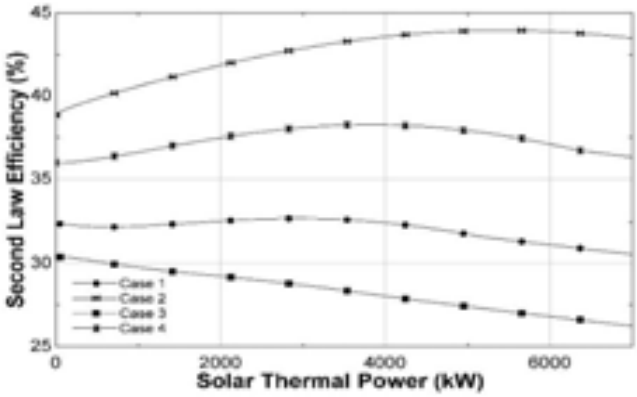

Fig. 7: 2nd law efficiency as function of solar thermal power for reducing the geothermal flow rate

The optimum results from the single-flash hybrid for geothermal flow reduction purpose are shown in Table 3. Case 3 does not present any difference because the integration presents a decrease in the 2nd law efficiency. As on the other cases, it can be seen how the geothermal flow is reduced while the 2nd law efficiency is increased. The geothermal flow rate can be reduced up to 16% depending on the reservoir conditions.

Tab. 3: Single-flash hybrid power plant results

	Single-flash power plant				Additional power generation				Geothermal flow rate reduction			
Parameters	Case 1	Case 2	Case 3	Case 4	Case 1	Case 2	Case 3	Case 4	Case 1	Case 2	Case 3	Case 4
Separation temperature (ºC)	138.8	163	123.7	150.6	139.3	167.6	129.2	158.5	179.7	188.7	123.7	185
Separation pressure (bar)	3.49	6.67	2.22	4.82	3.54	7.47	2.63	5.95	9.95	12.19	2.22	11.22
Power output (kW)	8237	14689	5915	10308	10818	18434	7900	13050	8237	14689	5915	10308
Steam flow rate (kg/s)	20.24	30.49	16.71	23.18	20.15	29.6	15.75	21.86	-	-	-	-
Geothermal flow rate (kg/s)	95.77	95.44	96.22	95.76	-	-	-	-	89.44	77.53	96.18	83.71
2nd law efficiency (%)	32.41	38.83	30.33	35.99	35.84	41.78	33.95	38.88	32.71	43.95	30.33	38.27
Solar collection area (m^2)	-	-	-	-	15000	19600	12200	15000	4300	7900	-	5500

5. Transient simulation of hybrid power plant

The transient simulations consider hourly meteorological data from a selected location in Chile, Crucero, which displays excellent solar resource while being relatively close to existing geothermal prospection sites (Escobar et al, 2015). This region is well known for the large number of clear days throughout the year, while a few cloudy periods are present during February due to the "altiplanic winter" effects and in proper wintertime, in this case during the months of June to August. Total direct normal irradiance (DNI) in Crucero amounts to over 3500 kWh/m^2-year, possibly the highest in the world. The geothermal flow presents a high thermal inertia because of minimum variation of the reservoir conditions throughout the year. There is no thermal energy storage considered partly due to the higher additional costs involved and partially since the power dispatchability (understood as power production able to supply expected electricity grid demand as requested with minimum variability) is achieved by the combination of the solar-geothermal hybrid system able to produce baseload conditions. The analysis presented in the previous sections evaluated the optimum conditions for the operation of the hybrid systems, in which the 2nd law efficiency is maximized. Case 2 was selected to evaluate the performance of the single-flash hybrid system under the design conditions considering the common variation of the solar resource along a year. The transient simulations for the single-flash hybrid system are developed with the objective to maximize the power output or minimize the geothermal flow consumption throughout the year by integrating the hourly simulation results.

5.1 Additional power generation

The performance of the hybrid single-flash for two representative days with clear and cloudy skies are shown in Fig. 8, for which as a reference the hybrid scheme generates 14.68 MW when there is no DNI available.

During a clear day, there are hours with DNI higher than the rating conditions, causing the system to reach its maximum capacity of 18.43 MW. The alternative of using HX 2 for periods with high DNI does not compensate the investment costs, due to the low additional power generated. As in the northern region of Chile there are only a small number of cloudy days, the hybrid scheme is still able to generate during low levels of DNI. For example, as observed in Fig. 8, at a DNI of 400 W/m^2 the hybrid scheme can produce 6.7% of additional power output.

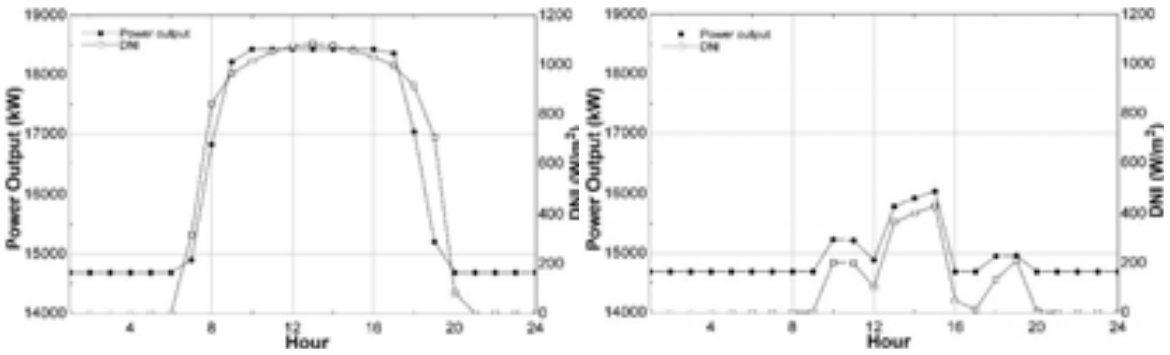

Fig. 8: Single-flash hybrid power plant daily performance

The results from the hourly simulations during a full year are shown in Fig. 9. The dark blue zones represent the base power production of the single-flash geothermal-only power plant, which corresponds to 14.68 MW, while the color code corresponds to the extra power derived by integrating the solar collector arrangement. As mentioned, the altiplanic winter effects during February reduce the production to the levels of the geothermal-only power plant. During spring, the higher average of power output is produced, reaching 17.53 MW when solar energy is available, while autumn presents a lower performance with an average power production of 16.71 MW. The performance of the hybrid single-flash system during the year presents an average power output 7% higher than the single-flash geothermal-only plant. Higher radiation values during summertime do not translate directly into additional power generation as the solar field is dimensioned with a design DNI of 1000 W/m^2, where higher DNI values only result in collector defocusing.

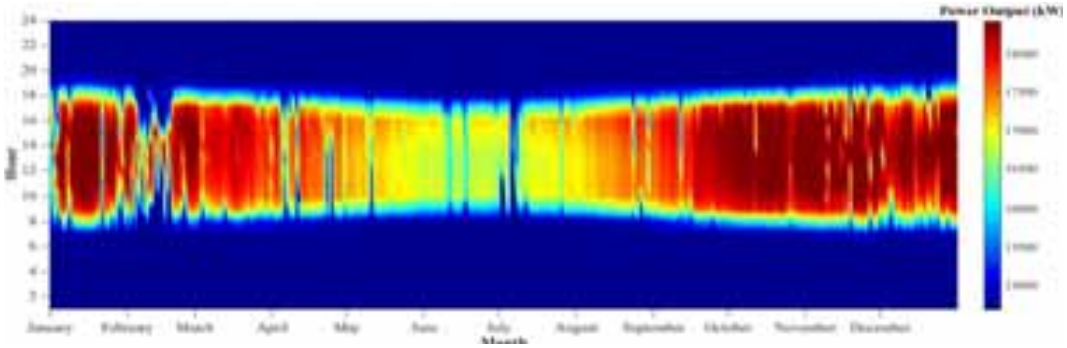

Fig. 9: Single-flash hybrid power plant year performance

5.2 Geothermal flow rate reduction

The hybrid single-flash power plant performance is able to reduce the geothermal fluid flow consumption during the year as shown in Fig. 10. The geothermal-only power plant operates with a geothermal flow rate of 95.43 kg/s, which is represented with the red layer. The lower amount of geothermal fluid flow that the hybrid system can achieve by integrating the solar thermal power is 76.84 kg/s considering the same base power output of 14.68 MW. The best performance in terms of geothermal fluid flow reduction is achieved during the spring with an average of 80.5 kg/s, while the worst operational results are observed during autumn where the solar system reduces the flow rate to only 82.9 kg/s. The average geothermal fluid flow is reduced during the year to 89.19 kg/s. Similar to what was presented in section 5.1, higher radiation values during summertime do not translate directly into additional geothermal fluid flow reductions, as the solar field is dimensioned with a design DNI of 1000 W/m^2, where higher DNI values only result in collector defocusing.

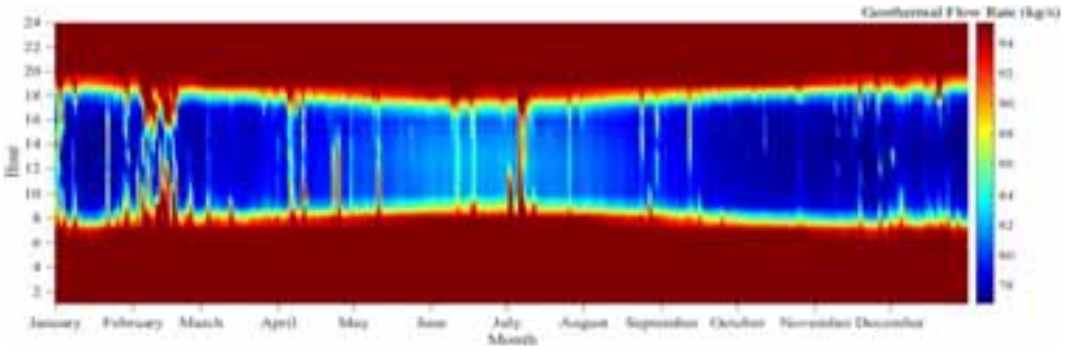

Fig. 10: Single-flash hybrid power plant year performance

6. Conclusions

An evaluation for a solar-geothermal hybrid power plant was developed in order to estimate their performance over a year. The optimization of the thermal power provided by the solar field showed that the superheating and evaporating process are able to increase the power generation, with the superheating process presenting higher rates (0.23 kW) of additional power output per kW of thermal power integrated to the single-flash hybrid plants. Delivering solar thermal energy in order to increase the steam temperature increases the 2nd law efficiency and allows the turbine to operate in a region of increased efficiency. Considering the hybridization of these two renewable resources, utilization of high-enthalpy geothermal resources shows greater promise given that the higher steam flow rates allow a better performance for the superheating process resulting in additional power generation and higher exergetic efficiencies. The solar field aperture area that maximizes the 2nd law efficiency of the flashing hybrid power plant is directly related to the steam flow conditions. The geothermal resources with higher enthalpy presented a larger reduction on the geothermal flow rate consumption due to the separation pressure at which they operate. Considering the reduction rate of the geothermal fluid produced by the solar energy, a 20-year useful life of a production well can be extended in at least 1 ½ years generating approximately 4.5 GWh of additional power output during. The benefits from the hybridization of these renewable sources are evident in terms of the power production increase during peak hours and the useful life extension for the production well. Furthermore, the hybrid scheme is a simple design considering the implementation of components that are common in a stand-alone geothermal power plants and concentrated solar power plants. For the Chilean energy market, the solar-geothermal power system presents an interesting yet still undeveloped alternative that can help fulfill the renewable energy utilization targets. These hybrid systems constitute an additional opportunity to diversify the energy resources utilization, with environmentally friendly base load energy using the large renewable potentials existing in the country.

7. Acknowledgements

The authors gratefully acknowledge financial support from project Fondecyt 1130621 of the Chilean CONICYT.

8. References

Agung Pambudi, N., Itoi, R., Jalilinasrabady, S., Jaelani, K., 2014. Exergy analysis and optimization of Dieing single-flash geothermal power plant. Energy Conversion and Management. 78, 405-411.

Anderson, E., North, J., Hopcroft, P., Laird, J., Wardhana, A., 2014. Geothermal Science & Data Solutions, GSDS WellSim, New Zealand. htpp://gsds.co.nz.

Astolfi, M., Xodo, L., Romano, M. C., Macchi, E., 2011. Technical and economical analysis of a solar–geothermal hybrid plant based on an Organic Rankine Cycle. Geothermics. 40, 58-68.

Bertani, R., 2010. Geothermal Power Generation in the World 2005 – 2010 Update Report. 41.

Chaibakhsh, A., Ghaffari, A., 2008. Steam turbine model. Simulation Modelling and Practice Theory. 16, 1145-1162.

CIFES, 2015.Centro Nacional para la Innovación y Fomento de las Energías Sustentables. www.cifes.gob.cl.

CNE, 2013. Balance Nacional de Energía 2012. Elaborado por la División de Prospectiva y Política Energética

del Ministerio de Energía. Santiago, Chile. www.minenergia.cl.

DiPippo, R., 2008. Geothermal Power Plants: Principles, Applications, Case Studies and Environmental. 2nd ed. BH.

DiPippo, R., 2013. Geothermal double-flash plant interstage reheating: An updated and expanded thermal and exergetic analysis and optimization. Geothermics. 48, 121-131.

Duffie, J.A., Beckman, W., 2006. Solar Engineering of Thermal Processes. 3erd ed. John Wiley & Sons.

Escobar, R., Pino, A., Cortés, C., Bueno, E., Ramos, F., & Cardemil, J. M., 2014. Solar energy resource assessment in Chile : Satellite estimation and ground station measurements. Renewable Energy. 71, 324-332.

Escobar, R., Cortés, C., Pino, A., Salgado, M., Bueno, E., Ramos, F., Boland, J., Cardemil, J.M., 2015. Estimating the potential for solar energy utilization in Chile by satellite-derived data and ground station measurements. Solar Energy.

Greenhut, A. D., Tester, J. W., Dipippo, R., Field, R., Love, C., Nichols, K., Batini, F., Price, B., Gigliucci, G., Fastelli, I., 2010. Solar-Geothermal Hybrid Cycle Analysis for Low Enthalpy Solar and Geothermal Resources. Proceedings World geothermal Congress, Bali, Indonesia. 25-29.

Hodgson, F., January/February 2013. "Focus on Chile". Geothermal Resources Council.

Hublitz, A., Spinnler, M., 2003. Technical Comparison of Different Solar-Assisted Heat Supply Systems for a Multi-effect seawater distillation unit. ISES Solar World Congress. 14–19.

Jalilinasrabady, S., Itoi, R., Valdimarsson, P., Saevarsdottir, G., Fujii, H., 2012. Flash-cycle optimization of Sabalan geothermal power plant employing exergy concept. 43, 75-82.

Kanoglu, M., Cengel, Y., Dincer, I., 2012. Efficiency Evaluation of Energy Systems. Springer.

Klein, S.A., Alvarado F.L., 2015. Engineering Equation Solver. V9.812-3D. http://www.fchart.com/.

Lahsen A., Muñoz N., and Parada M.A., 2010. Geothermal Development in Chile, Proceedings World Geothermal Congress, Bali, Indonesia, 25-29.

Lemmon, E.W., Mclinden, M.O., Huber M.L., 2002. Reference Fluid Thermodynamic and Transport Properties (Refprop).

Lentz, Á., Almarza, R., 2006a. Parabolic troughs to increase the geothermal wells flow enthalpy. Solar Energy. 80, 1290-1295.

Lentz, Á., Almarza, R., 2006b. Solar–geothermal hybrid system. Applied Thermal Engineering. 26, 1537-1544.

Lüpfert, E., Geyer, M., Zentrum, D., Schiel, W., 2001. Eurotrough Design Issues and Prototype Testing At Psa. Power. 1–5.

Ministerio de Energía, 2014. Agenda de Energía. Gobierno de Chile.

Mir, I., Escobar, R., Vergara, J., Bertrand, J. 2011. Performance Analysis of Hybrid Solar-Geothermal Power Plant in Northern Chile. World Renewable Energy Congress. 1281-1288.

Nellis, G.F., Klein S.A., 2009. Heat Transfer. Cambridge

Ocampo, J., Pelayo, A., De León, J., Goyal, K., Box, T., 1998. Reservoir characteristic obtained from steam decline trends in the Cerro Prieto Geothermal Field. 23rd Workshop on Geothermal Reservoir Engineering.

Peterseim, J.H., White, S., Tadros, A., Hellwig, U., 2014. Concentrating solar power hybrid plants – Enabling cost effective synergies. Renewable Energy. 67, 178-185.

Ruzzenenti, F., Bravi, M., Tempesti, D., Salvatici, E., Manfrida, G., Basosi, R., 2014. Evaluation of the environmental sustainability of a micro CHP system fueled by low-temperature geothermal and solar energy. Energy Conversion and Management. 78, 611–616.

Wendel, M., 2010. Metodologia para simulação transiente de uma pequena central heliotérmica. MSc Thesis. Universidade Federal de Santa Catarina.

Zhou, C., 2014. Hybridisation of solar and geothermal energy in both subcritical and supercritical Organic Rankine Cycles. Energy Conversion and Management. 81, 72-82.

Zhou, C., Doroodchi, E., Moghtaderi, B., 2013. An in-depth assessment of hybrid solar–geothermal power generation. Energy Conversion and Management. 74, 88-101.

Conference Proceedings

Solar World Congress 2015
Daegu, Korea, 08 – 12 November 2015

Renewable Electricity Production Effect on the Energy Balance of Latvia

Peteris Shipkovs[1], Galina Kashkarova[1], Kristina Lebedeva[1], Janis Shipkovs[1], Lana Migla[1]

[1] Institute of Physical Energetics, Riga (Latvia)

Abstract

The paper presents current situation in the Latvian Energy sector, the place and the role of renewable energy resources in the Energy and Electricity production. The dynamics of the energy consumption and production is described along with evaluation of the environmental, legislative, and economic aspects of renewable energy use.

Keywords: *Renewable Energy Resources, Renewable Electricity, Energy Consumption, Energy Balance*

1. Introduction

The climate changes, pollutions, and energy insecurity are among the greatest problems of our time. According to the EU directives, the Energy sector is one of the areas in which the EU Member States have been sharing competence. The time span from 2014 to 2020 is a transitional phase for the EU's Energy policy, when the relevant objectives set for 2020 are to be achieved, with future objectives elaborated.

In particular, by 2020 the EU has to achieve the following climate and energy policy objectives set by the European Council of March 2007:

- to reduce greenhouse gas (GHG) emissions by 20% relative to the 1990 level;

- to increase the share of renewable energy resources (RES) in the energy consumption by 20%;

- to improve the energy efficiency by 20%.

In compliance with the EU legal acts on the climate and energy, the Latvian objective by 2020 is to ensure 40% of RES share in the final energy consumption.

Latvia has already made substantial improvements in the energy balance owing to the diversion from the use of fossil fuels (especially fuel oil or solid fuel) to that of wood biomass. In the time span from 1990 to 2013, the use of fossil fuels rapidly decreased – of liquid fuels by 59.7%, of solid fuels by 82.3%, and of natural gas by 49.6%, while the total wood biomass, biogas and biofuel use increased by 105%. According to the EuroStat, Latvia is currently holding the second place among the EU 28 Member States as to the RES share in the final energy consumption, and in 2013 reached 37.10% of the total gross final consumption.

2. Strategy and Policy Targets on Renewable Energy Use

The key directions of the efficient, well-balanced, market-oriented energy policy of Latvia set forth in the informative report "Long-Term Energy Strategy 2030 – Competitive Energy for Society" (Energy Strategy 2030, approved by the Cabinet of Ministers at the meeting of 28 May 2013) are aimed at the

doi:10.18086/swc.2015.04.31 Available at http://proceedings.ises.org

development of the state economy's competitiveness, promoting welfare of the society.

The main task of Energy Strategy 2030 is to ensure a positive impact of the energy sector on the national economy of Latvia, at the same time striving to achieve secure and sustainable energy supply, i.e.:

– secure energy supply – a stable energy supply and developed infrastructure provided for energy consumers;

– sustainable energy supply – reduced dependence on the imported energy resources; implementation of new and efficient technologies for the RES use and of the measures for improvement of energy efficiency.

The Energy Strategy 2030 envisages a 50% decrease in the energy import from non-EU suppliers, with a half of the total final energy consumption in the state ensured by RES, which is to be achieved by increasing the RES share in the heat, electricity and transport sectors.

Currently, in order to increase the energy production from domestic energy resources, to decrease the use of fossil fuels as well as to reduce the GHG emissions, different renewable energy sources (RES) are used for energy production. As shown in Table 1, the RES (the **bold text**) use has a stabile tendency for growth in general and, in particular, for electricity production.

Table 1: Dynamics of Primary Energy Resource Consumption (PJ).

	2010	2011	2012	2013	2014
Natural gas	61.3	54	50.8	50.3	45.4
Oil products	64.6	59.5	58.4	59.3	59.7
Coal and coke	4.5	4.6	3.8	3	2.5
Electricity (imported)	14.3	14.4	17.8	18	19.2
Hydro energy	**12.7**	**10.4**	**13.3**	**10.5**	**7.2**
Fuel wood	**45.6**	**46.9**	**52.5**	**53.1**	**55.9**
Wind energy	**0.18**	**0.26**	**0.4**	**0.43**	**0.5**
Biogas	**0.56**	**0.92**	**2.2**	**2.7**	**3.1**
Others	0.07	0,08	0.07	0.14	0.13
Total	203.81	191.06	199.27	197.47	193.63

The National strategy as well as plans and programs have been developed in view of reducing the negative environmental impacts of the energy sector, promoting the use of Renewable Energy Sources.

The RES segment in the electricity production comprise hydropower plants, wind power plants, biogas power plants and biomass power plants, as well as cogeneration stations utilizing RES (Table 1, Table 2).

Table 2 illustrates the share of RES in the total energy consumption and its share in the electricity production (Shipkovs *et al*., 2014).

Table 2: Share of RES.

	2000	2010	2013	2014
Share of RES in the total energy consumption, %	29.5	35	37.1	34.0
Share of RES in the electricity production, %	47.7	49.3	56.9	42.6

The main RES types in our country are the fuel wood and hydro resources, which in 2014 accounted for 34% of the total consumption of energy resources.

Over the last ten years (2004-2014) the total consumption of RES has increased by 12%.

Fuel wood is the most commonly used RES in Latvia, and its share in the total energy consumption in the time from 2010 to 2014 increased from 23.4% to 30.2%. In 2014, the share of fuel wood in RES consumption was 82.1%, which is 3.4 PJ or 4% more than in 2013 (Fig. 1).

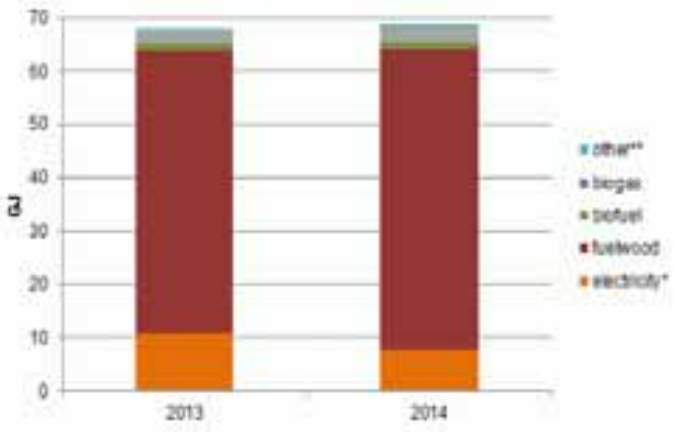

Fig. 1: Consumption of renewable energy resources in 2013 and 2014, GJ.

In 2014 the total consumption of fuel wood grew by 6% as compared with 2013 (see Fig. 1); consumption changes are also seen in the breakdown by sectors. The share of fuel wood increased both in households and in transformation sector for heat and electricity production. The main fuel wood consumers are households, which mostly use firewood (85%). In 2010, the share of consumed fuel wood in households was 42.9%, in 2013 – 45.4%, and in 2014 – 46.3%. The fuel wood consumption by sectors is shown in Fig. 2.

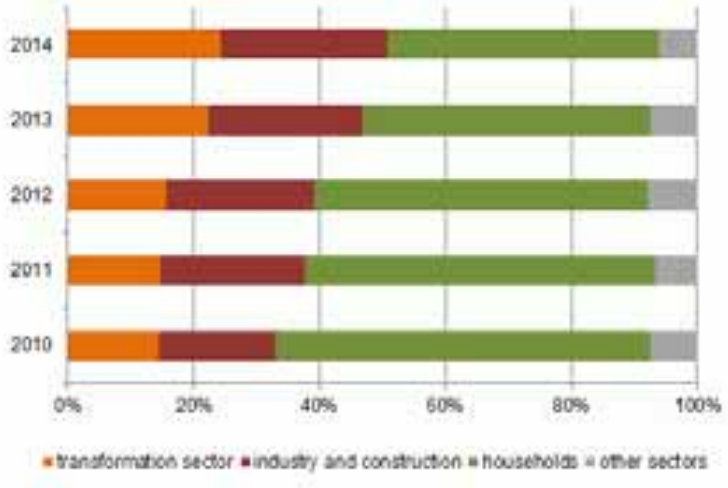

Fig. 2: Fuel wood consumption in Latvia, %.

Over the time span 2010-2014 the share of fuel wood in transformation sector increased by 9.8%, in 2014 reaching 24.3% of the total consumption in Latvia. In the transformation sector mainly wood chips are used (86.5%). The greatest growth in consumption of fuel wood in the transformation sector was recorded in 2014, when the share of wood chips grew by 25.1% as compared with 2013. This was due to the new CHP plants which started their operation in 2014, and to the annually increasing RES share along with reduced share of natural gas. Since 2007, the installed electrical capacity of RES CHP plants by 2014 had increased 12 times, reaching 121 MW; the electricity production increased 16 times, reaching 669 GWh, which accounts for 22% of the total electricity produced in CHP plants.

Directive 2009/28/EC of the European Parliament and of the Council on the promotion of the use of energy from renewable sources stipulates that the share of energy from RES by 2020 must account for at least 40% of the final energy consumption. In 2008, this share in Latvia was 29.81%, in 2010 – 35%, in 2013 – 37.1%, and also in 2014 this percentage slightly rose, reaching 34 %. Each Member State is obliged to ensure that by 2020 the share of electricity produced from RES (biofuel, biogas) and consumed in transport is at least 10% of the final consumption of energy in transport (in 2013 Latvia reached 3.08%).

In Latvia, current legislation foresees promotion of purchasing the energy produced from RES, namely, the electricity produced by the cogeneration plants using local energy sources.

The next planned steps in order to promote further use of RES in Latvia are as follows:

- Participation in the EU Emission trading.
- Introduction of energy tax (CO_2 tax).
- Setting the overall RES target in the primary energy supply, with sectoral and type breakdown.
- Implementation of pilot projects.
- Organization of public awareness campaigns about RES.

3. Electricity Market

The electric energy makes the basis for economic development of every country, and the global demand for this energy is constantly growing. As of now, the use of fossil or nuclear sources for energy production becomes problematic for many reasons. The only real environment-friendly way of producing electric power is the use of renewables, which are considered as the main energy source in the future.

In Latvia, the shortage of local energy creates dependence on electricity importers (see Table 3 for the electricity supply dynamics). Therefore, to reduce this dependence, it is necessary constantly to increase power generation capacity, which in turn contributes to an increase in hazardous emissions and greenhouse effects reinforcement.

Table 3: Electricity Supply in Latvia (GWh).

	2000	2005	2009	2010	2011	2012	2013	2014
Total electricity supply	5922	7053	7223	7500	7340	7859	7564	7457
Gross electricity generation including:	4136	4905	5569	6627	6094	6167	6209	5140
from renewable energy resources:	2824	3414	3555	3635	3078	4109	3534	2803
large HPPs*	2794	3263	3391	3445	2823	3627	2852	1925
small HPPs	25	62	66	75	64	80	60	68
biomass power plants	–	6	4	9	13	65	215	319
biogas power plants	–	36	44	57	107	223	287	350
wind power plants	5	47	50	49	71	114	120	141
from fossil energy resources:	1312	1492	2014	2992	3017	2059	2675	2337
large CHPs**	1163	1278	1476	2402	2425	1409	1957	1648
other CHPs	149	214	538	590	592	650	718	689
Net electricity imports	1786	2148	1654	873	1245	1691	1355	2317

* Daugava cascade – Riga HPP, Kegums HPP, and Plavinas HPP
** Riga CHP-1 and Riga CHP-2, source: JSC "Latvenergo"

One of the ways to reduce the electricity imports might become additional sources of energy, especially clean ones. Increase in the electricity production from different renewable sources is shown in Table 4.

The electricity market in Latvia has been open since 1 January 2015. Pursuant to the amendments to the Electricity Market Law of 18 September 2014, households have an opportunity to freely choose the provider and agree on the electricity price based on an agreement just like legal entities. The amendments to the Electricity Market Law of 18 September 2014 further envisage special tariffs for the protected consumers.

Along with complete opening of the electricity market as of 1 January 2015, a support instrument for protected consumers was introduced.

Table 4: Increase in the electricity production from different RES.

Energy sources	Installed capacity, MW		Electricity production, GWh		Electricity production increase from 1995 to 2013
	1995	2013	1995	2013	
Wind	1	67	0	120	× 120
Hydro (big)	1504	1560	2934	2912	× 0.99
Hydro (small)	3	29	3	60	× 20
Solar batteries (PV)	0	0,1	0	0,056	× 0.056
Biomass (total)	0	55	0	215	× 215
Biogas	0	53	0	287	× 287
TOTAL			2937	3534,056	× 1.21
Electricity consumption			5193	4 387	
RES-e part			56.50%	80.56%	× 1.43

Table 5 presents the dynamics of installed electric capacity of power plants and combined heat and power (CHP) plants which use renewable energy sources for electricity production.

Table 5: Installed electric capacity of power and CHP plants using RES (MW).

	1990	1995	2000	2010	2011	2012	2013	2014
Hydropower plants	1 487	1 507	1 513	1 576	1 576	1 576	1 589	1590
Wind power plants	-	1	2	30	36	59	67	69
Biomass power plants and CHP plants	-	-	-	5	5	23	55	63
Biogas CHP plants	-	-	-	11	25	43	53	58
Total	1 487	1 508	1 515	1 22	1 642	1 701	1 764	1780

Over the last years the capacity of hydropower plants did not change much; in turn, the electric capacity of other power and CHP plants grew significantly. For instance, capacity of wind power plants in 2014, as compared with 2013, rose by 3%, and compared with 2012 – by almost 17%. The electric capacity of biogas CHP plants in 2014 grew by 9.4% as compared with 2013, while this indicator for biomass power plants and CHP plants was 14.5% greater in 2014 than in 2013, and 174% greater as compared with 2012. One of the factors promoting RES development is the State support, which allows selling electricity within the mandatory procurement framework.

In 2014, the energy production from RES promoted the mandatory procurement of electricity and investment support from the EU Cohesion Fund, the Climate Change Financial Instrument, and the European Agricultural Fund for Rural Development. Renewable energy is closely linked to the country's energy independence, environmental protection and climate change, as well as to its impact on the competitiveness of the economy. Now it is vitally important to increase the independence of Latvian energy sector. For this purpose serves the use of RES which increases a positive impact on reducing the energy dependence on imported energy and the share of RES in final energy consumption.

As shown in Fig. 3, the greatest share (over 70%) of electricity from RES is produced by hydropower plants. In 2014, hydropower plants with the capacity >10 MW (Plavinas Hydropower Plant, Riga Hydropower Plant and Kegums Hydropower Plant) produced 1 925 GWh of electricity, or 68.7% of the total electricity produced from RES.

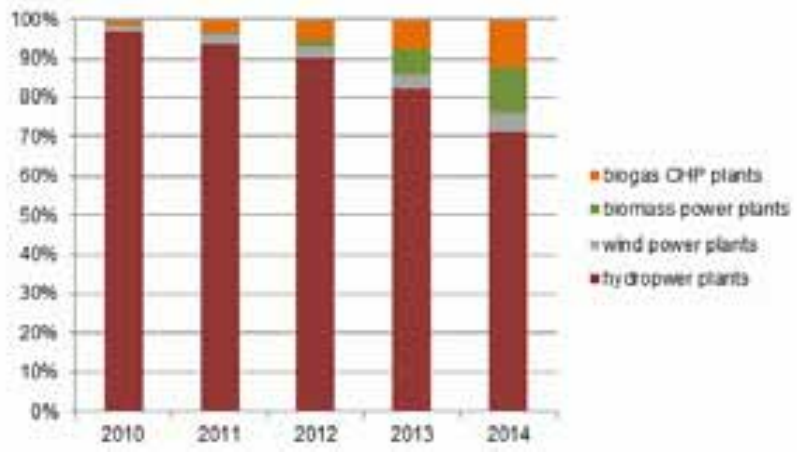

Fig. 3: Electricity produced from renewable energy resources, %.

Important contribution to the total renewable energy balance is being made by three large hydro stations: Kegums Hydroelectric Power Plant (HPP) – 264.1 MW, Plavinas HPP – 884 MW, Riga HPP – 402 MW. To increase the installed capacity of hydropower, reconstruction of the hydro generation units is underway (see Table 6).

Table 6: Planned reconstruction of Hydro Power Plants.

	Year	Number of turbines	Increase of utilization rate	Increase in generation
Plavinas HPP	2014-2016	2	5% ... 9%	+18 GWh
Kegums HPP	2014- 2017	3	5% ... 6%	+22 GWh
Riga HPP	2017- 2021	6	3.5%... 5%	+25 GWh

Small hydropower plants had played a special role at the beginning of Latvian electrification and local electricity grid development. This was worth expanding, so at the end of 1926 there were installed 26 HPPs with the total capacity of turbines 1.5 MW and of power generators 1.26 MW. The Latvian hydro resource potential was first analyzed in 1931. Small hydropower development continued until the beginning of 70-ies. At that time, construction of large power plants and transmission lines was developed. With time, the operation of small HPPs became unprofitable, and from 1963 to 1977 they were decommissioned. In turn, from 1992 to 2012 there were put into service 143 small HPPs, 91% of which were restored or reconstructed and only 9% rebuilt (Shipkovs *et al*. (2013)).

The theoretical potential of Latvian small and medium-sized rivers as energy sources is calculated to be ~ 900 million kWh. Technically achievable potential of hydro energy resources (taking into account mining and processing facilities and technological transformation capabilities) is 150-300 million kWh per year. Currently, only 20-40 % of the real small river resource potential is utilized. This potential can be increased by improving the existing HPP technologies and power generation efficiency.

With a greater than 40% share of cogeneration in the total gross electricity production, Latvia is among the top three member states in the EU, as all thermal electricity is produced by CHP plants (Shipkovs *et al*., 01.2013). The total installed CHP capacity more than doubled from 2006 and reached 1.252 MWe in 2013, with the number of CHP plants increased from 43 to 166 and the electricity generation increased by 60% reaching 3.2 TWh in 2013. The combined cycle turbine operating on natural gas is a prevailing technology at four largest public district heating CHP plants, with ~ 85% share in the total CHP capacity and > 60% – in the CHP electricity and heat generation in 2013. Gas engines are most often used at smaller CHP units (<20 MW) where among the 162 existing CHP plants there are only 46 autoproducers CHP plants. The CHP generation is concentrated in a small number of major CHP units, which is the main reason for rather big fluctuations in the CHP electricity and heat generation (see Fig. 4).

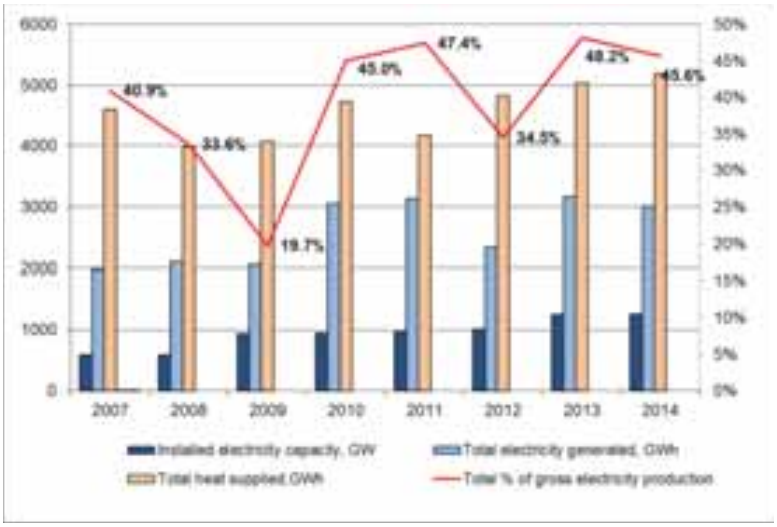

Fig.4: CPH installed capacity and generation.

With a greater than 78.9 % share, the natural gas is the major fuel used at CHP plants, followed by wood biomass and biogas (see Fig. 5) whose share is ever growing.

In 2014, CHP plants supplied almost 60% of the total produced heat to widespread district heating systems, covering ~ 70% of the households' heat demand and approx. 22% of the total heat demand in Latvia.

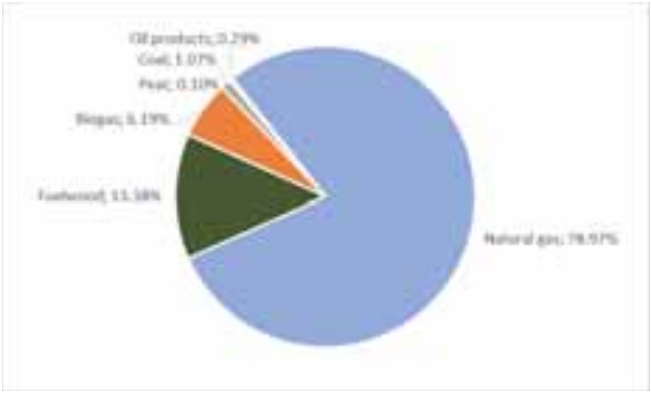

Fig.5: Structure of fuel consumption by CHP plants (2014).

Until the beginning of the year 2009, biogas was produced by "Riga Water Ltd." at its water purification plant (capacity of 2 MWe), with the resulting electricity spent for their production needs at Riga landfill "Getlini Eco" (installed capacity of 5 MWe), LAU Study and Research Farm "Vecauce" (total capacity 270 kWe, and two plants at Liepaja landfills (total capacity of 1 MWe) In 2009, Latvian entrepreneurs (58 in number) received a quota for biogas production with a total installed capacity of ~ 54 MWe. In the same year, one unit of the North landfill Daiba was put into operation with a capacity of 170 kWe, and a number of biogas plants (the total installed capacity of 10-12 MWe) was launched. In March, 2010, the "MC" Ltd. biogas plant was put into operation. In 2014, already 54 biogas plants were operating, of which: at domestic landfills – 7, operating with domestic waste water – 1, with food production residues or waste water – 2, in agricultural sector – 44 (the total installed capacity 58 MW, with 350 GWh of electricity produced).

The estimates obtained for the biogas potential are shown as related to agricultural and industrial branches (Fig. 6); also, the technically achievable potential of biogas that could be obtained from household waste was estimated to be 0.3 TWh.

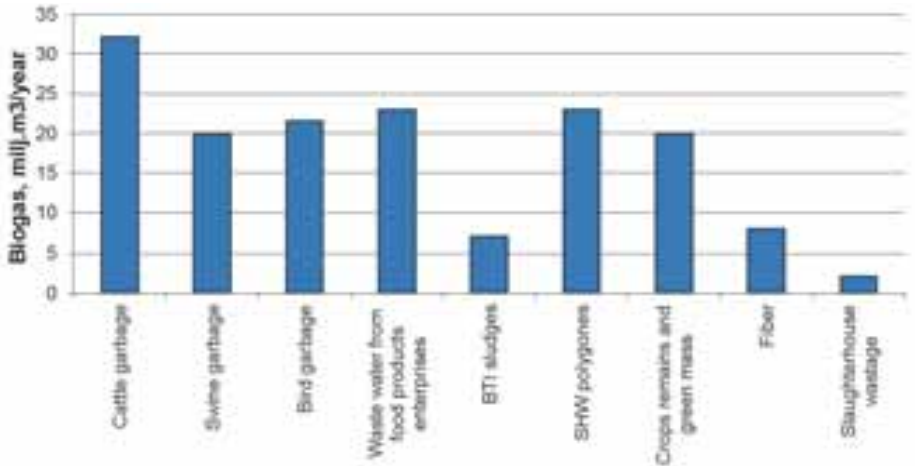

Fig.6: Biogas production potential.

As concerns wind energy, Latvia possesses a very good potential for its development along the Baltic Sea coastline, especially owing to a high voltage transmission line running there (see Fig. 7). Accordingly, the wind power plants are installed mostly in the seaside area, with totally produced electricity of 140 GWh.

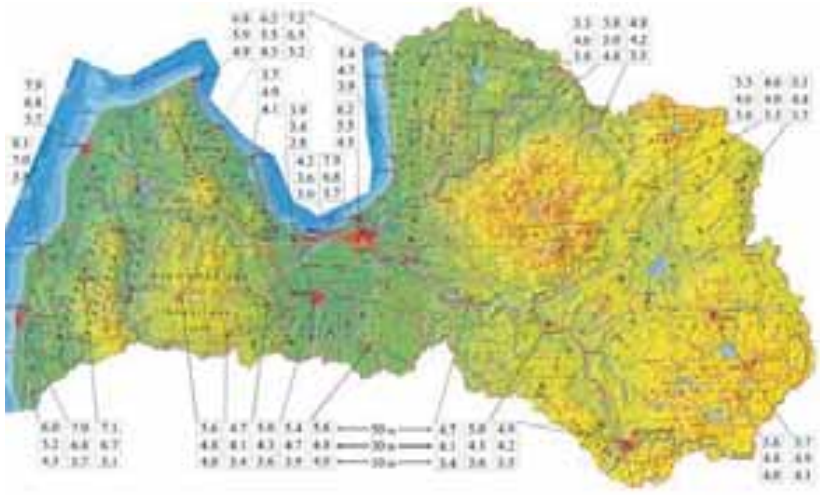

Fig.7: Wind map (on 10 m, 30 m, and 50 m heights).

Wind power output rose quickly, from 2 MW in 2000 to 69 MW in 2014; in particular, when the wind power farm "Pope" had been built in 2012, the country's installed wind power capacity was doubled (up to 68 MW). So far Latvia uses only 5 % of its wind power potential. The wind map in Fig. 7 made up for the whole country shows that wind farms could be constructed along practically all its coastlines. The related branch should continue the development at a steady pace, given the fact that the renewable energy action plan envisages increasing the wind turbine fleet's capacity to 416 MW by 2020 (180 MW offshore included).

Latvia is firmly embarked on the electricity supply source diversification process, which will enable our country to gradually wean itself off the electricity imports and even eliminate the impact of hydropower's up-and-down performance on the renewable energy share of its electricity mix.

Concerning the use of solar energy for electricity generation in Latvia, it is insignificant up to now; still, in 2013 solar energy (PV solar panels) came in sight, with the produced electricity of 0.2 TJ.

4. Conclusions

In Latvia, the potential for RES use development in high in terms of all factors: technical, social, and the market.

Firewood and wood waste will remain the most important source of bio-energy in the future. However, contribution of bio-energy is closely associated with possibility of using it not directly as fuel for electricity and heat generation but also for production of fuel for transport, with reducing the costs of RES use technologies.

Today, many problems in the RES use area exist – e.g. high costs of equipment, low interest among the policy makers, and, as a result, deficiency of national support; still, despite these problems, there are also opportunities for development, namely: liberalization of energy supply, focussing on the decentralized energy production, higher prices for fossil fuels, etc.

The progress in developing the energy production technologies using renewable energy resources has been made in many countries; however, there is a need to make the results widely known, to transfer and exchange technologies and practices. Recent development of different technologies for this purpose opens new possibilities for RES use also in small countries such as Latvia.

Availability of the economic instruments for promotion of RES in the electricity market and for heat generation would help Latvia in its search for the opportunities to encourage RES application through Kyoto mechanisms and building up the required legal and administrative framework. The combination of the mentioned measures should create necessary operating conditions for new RES power plants (especially for large-scale wind farms) and conversion of the existing power stations on biomass to cogeneration plants. In Latvia, economic stimuli have been established for construction and operation of small HPPs, WPPs and CHP plants. In particular, power plants using RES for electricity production have priority access to the transmission and distribution systems in Latvia.

In Latvia, renewable electricity generation is stimulated through a complex support system based on a feed-in tariff, which also includes elements of a quota system and tenders. The existing state support mechanisms for energy production from renewable energy resources are being assessed and revised by The Ministry of Economics. Stringent supervision of subsidized electricity producers, and stricter controls with limited timeframe for the implementation of RES projects have been introduced. In January 2014, a new tax for subsidized electricity producers was introduced, which should be paid by the companies receiving financial support for power generation from RES or from combined heat and power plants. Although the access of renewable energy plants to the grid is subject to the general legislation on energy, the electricity from renewable sources is not given priority. Also, devices for heat production from RES are not given priority connection, and there is no special legislation promoting the connection of RES heating devices to the heat transmission network at the national level.

Scanning of current energy strategies shows that Latvia has its energy strategy and plans while generally no specific strategies regarding solar power. Another major effort is to identify and analyze the supportive structures that exist for those who intend to invest in the solar power and to investigate it.

The structure of the modern energy supply systems in combination with renewable energy resources is promoted by new progressive technologies that increase the efficiency of renewable energy utilization and pledges support for a wider RES use.

The review of all renewable energy resources which could be more or less used for electricity production shows that Latvia has real possibilities for achieving its targets for the future. Latvia has already a 20-year experience of creating a viable energy policy to provide the State with stable energy supply and promote effective and rational energy utilization. Progressing in the relevant technologies and developing the State laws will lead to creation of a stable energy sector that in turn will promote rational and effective RES use.

Acknowledgements

This work has been supported by the State Research Program "LATENERGI".

5. References

Shipkovs P., Bezrukov V., Pugachev V., Bezrukov Vl., Silutins V.. 2013. Research of the wind energy resources distribution in the Baltic region. Renewable Energy an International Journal No 49, Elsevier, 119-123.

Shipkovs P., Kashkarova G., Lebedeva K., Migla L.. (01.2013.). Development of Biomass Utilization in Latvia. Journal of Energy and Power Engineering, USA. Volume 7, Number 1, 01.2013. ISSN1934-8975. 96-101.

Shipkovs P., Kashkarova G., Lebedeva K., Migla L., Snegirjovs A., Shipkovs J.. (2014.). Potential and Analysis of Grid Integrated Renewables in Latvia. Elsevier's Energy Procedia, Volume 57, 2014. 735-744.

Solar Heating and Cooling: Fundamentals & Applications

Conference Proceedings

Solar World Congress 2015
Daegu, Korea, 08 – 12 November 2015

Numerical model for pressure drop and flow distribution in a solar collector with horizontal U-connected pipes

Federico Bava[1] and Simon Furbo[1]

[1] DTU Civil Engineering, Technical University of Denmark, Brovej, Building 118, 2800 Kgs. Lyngby (Denmark)

Abstract

The development of a numerical model for calculating the pressure drop and flow distribution across a solar collector in isothermal conditions is described in this paper. More specifically, the considered collector layout is that of a harp collector with U-type configuration. The different hydraulic resistances causes unbalance of flow distribution in the absorber pipes, so this aspect had to be considered in order to correctly evaluate the pressure drop. The model was written in Matlab and makes use of pressure drop correlations found in literature for both friction losses and local losses. The model was compared in terms of overall pressure drop against measurements which were performed on an Arcon Sunmark HT 35/10 collector. Different flow rates, temperatures and fluid types were tested during this validation process. In case of pressure drops larger than 1 kPa, the relative error between model and measurements was no larger than 7%, while the absolute average value no larger than 3%. For smaller pressure drops the relative difference was usually larger, but still within the accuracy of the differential pressure sensor. Concerning the flow distribution, it was found that the flow regime was the main parameter affecting the results. Turbulent regime resulted in a much more uniform flow distribution across the absorber pipes compared to laminar regime.

Keywords: *solar collector, pressure drop, flow distribution, friction losses, propylene glycol, heat transfer fluid, temperature, flow rate.*

1. Introduction

The pressure drop over a solar collector is a parameter which must be known and taken into account, when connecting collectors in a solar collector field both in series and parallel. In fact, the pressure drop influences the flow distribution throughout the field, affecting its overall efficiency and energy output, and determines the requirements of the pumps which need to be installed to supply the field in the most efficient way.

The standard norm ISO 9806 does not provide strict guidelines on how to measure the pressure drop characteristic curve, as it states that "the fluid used in the collector for the test shall be water or a mixture water/glycol (60/40), or a mixture recommended by the manufacturer. The temperature of the fluid shall be (20±2) °C" (ISO 9806). Additionally, the conditions during the test may differ significantly from the actual operating conditions of the collector, both in terms of fluid type and temperature. For this reason, it could be useful to have a model able to derive the pressure drop of a collector for different temperatures and fluids, starting from a single test carried out in a specific operating condition.

The most common layout used when manufacturing large flat plate collectors is harp U-type layout, where a number of parallel pipes connecting two manifolds, which have inlet and outlet on the same side. Almost all solar collector field. On the other hand, the parallel pipe design has the disadvantage that perfectly uniform flow distribution cannot be achieved. The flow distribution in flat plate collectors with parallel pipes has been the topic of many investigations, as it may strongly affect the collector efficiency. In fact, several studies show that the efficiency diminishes for decreased uniformity of flow distribution, as a consequence of non-uniform outlet temperatures for the different collector pipes (Chiou, 1982). Wang and Wu (1990) proposed a discrete numerical model to predict the flow distribution in solar collector arrays with vertical

doi:10.18086/swc.2015.10.01 Available at http://proceedings.ises.org

pipes in U-type configuration, taking into account buoyancy force. The flow rate in the riser tubes decreases monotonically with the inlet manifold distance. The same trend was found by Jones and Lior (1994), who considered a single collector with vertical pipes and neglected buoyancy. Weitbrecht et al. (2002) carried out both an experimental and analytical study on the flow distribution in a Z-type collector, investigating the influence that the inset of a pipe into the manifold has on the pressure drop across the tee junction. However, only laminar flow and one specific tee geometry are considered.

Fan et al. (2007) studied the flow and temperature distribution in a large solar collector with 16 U-connected horizontal tubes. A numerical model, based on CFD calculations and taking into account buoyancy, and experimental measurements are compared. The results show that the flow distribution is dominated by friction (and hence buoyancy can be neglected), if the velocity in the collector pipes is high compared to the temperature rise across the collector. In large solar collector fields in Denmark each row usually consists of a number of collectors between 10 and 25 (Windeleff and Nielsen, 2014), so the temperature rise in each collector is relatively small, while the flow rate is relatively high. Consequently, it can be considered that buoyancy plays a minor role in the flow distribution in this kind of installations.

The aim of the study presented in this paper was to develop a numerical model for calculating the pressure drop over a U-type collector. Benchmark of the model was a solar collector for large collector fields, so the flow across the collector could be considered controlled by friction only and the model was developed accordingly.

2. Material and method

2.1. Solar collector design

The developed model was based on the design of U-type large scale collectors. These collectors usually have a number of horizontal pipes welded to absorber strips and connecting two vertical manifolds located along the sides of the collector with their outlet at the top corners of the external frame (Figure 1).

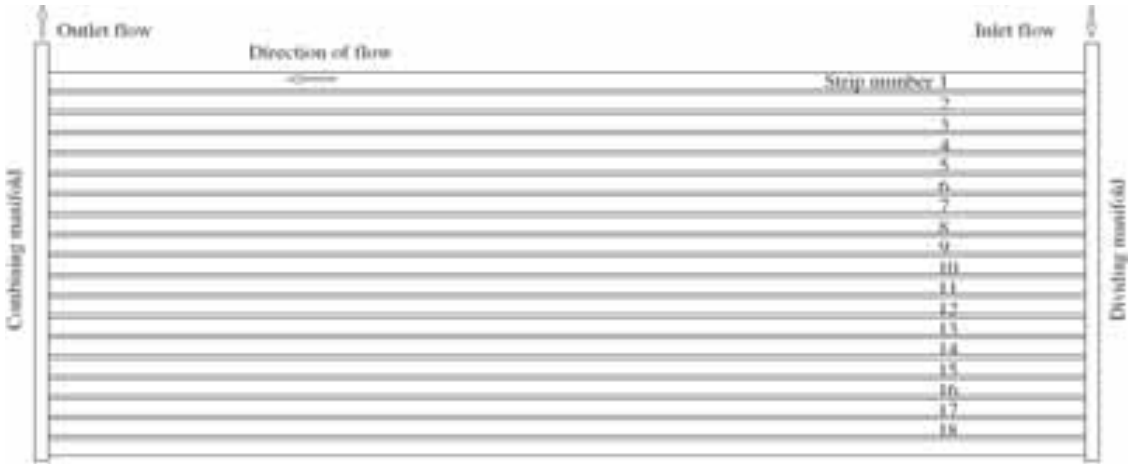

Figure 1: Sketch of a U-type absorber with horizontal pipes.

The choice of this design for the model was motivated by the fact that this is the most frequently adopted design when manufacturing large collectors for solar heating field applications. In fact, these collectors are easy to assemble and quick to connect to one another when they are installed side by side in a field.

The developed numerical model was validated in terms of pressure drop against measurements carried out on a collector of this type, more specifically an Arcon Sunmark HT-SA 35/10 collector, having an aperture area of 12.60 m^2. The collector piping was made of copper and had circular cross section. The 18 horizontal pipes were 5.80 m long, had an inner diameter of 9.1 mm and an intermediate spacing of 122 mm. The manifolds had an inner diameter of 32.9 mm.

Though, as long as the general collector design is preserved, the model can be easily modified to treat also collectors having for example a different number of horizontal pipes, various manifold and pipe diameters.

2.2. Pressure drop correlations

In a solar collector, as well as any other hydraulic circuit, the total pressure drop is given by the sum of two types of pressure losses: friction (or major) losses and local (or minor) losses. Friction losses occur in pipe flow because of viscous effects generated by the pipe surface. Local losses are due to variations of the velocity vector. Valves, bends, tees and abrupt changes in a pipe cross-sectional area are examples of components causing local pressure losses.

The friction loss along a straight pipe of constant cross section is a function of the flow velocity, pipe length, pipe diameter and a friction factor which strongly depends on whether the fluid flow is turbulent or laminar. This pressure loss is calculated by the Darcy-Weisbach equation:

$$\Delta p = \lambda \frac{l}{D_h} \frac{\rho w^2}{2} \qquad \text{(eq.1)}$$

where Δp is the pressure drop [Pa],

λ is the Darcy friction factor [-],

l is the pipe length [m],

D_h is the pipe hydraulic diameter, which equals the inner diameter for a full flow circular pipe [m],

ρ is the fluid density [kg m^{-3}],

w is the mean fluid velocity [m s^{-1}].

As mentioned above, the friction factor depends on the type of flow regime and, if this is turbulent, on the roughness of the pipe as well. The parameter indicating whether a flow is laminar or turbulent is the Reynolds number, defined as

$$Re = \frac{w \rho D_h}{\mu} \qquad \text{(eq.2)}$$

where Re is the Reynolds number [-],

μ is the fluid dynamic viscosity [Pa s].

Density and viscosity are properties characteristic of each fluid and are strongly dependent on the temperature. Water and propylene glycol/water mixtures are the most common fluids used in solar thermal applications. Water thermophysical properties are well known and are easily found in literature. For the density, (eq.3) was used, while the dynamic viscosity was evaluated through (eq.4).

$$\rho = 1000.6 - 0.0128\ T^{1.76} \qquad \text{(eq.3) (Furbo, 2015)}$$

$$\log_{10} \mu = \log_{10} (1.002 \cdot 10^{-3}) + (20 - T)/(T + 96) \cdot [1.2378 - 1.303 \cdot 10^{-3}\ (20 - T) + 3.06 \cdot 10^{-6}\ (20 - T)^2 + 2.55 \cdot 10^{-8}\ (20 - T)^3] \qquad \text{(eq.4) (Kestin, 1978)}$$

Given the large variability of the properties of propylene glycol/water mixtures found in literature and in product datasheets, these were experimentally investigated at the Department of Chemical Engineering of the Technical University of Denmark, making use of an Anton Paar DMA 4100 densimeter and an Anton Paar AMV 200 viscometer. Three samples with glycol concentration of 40%, 45% and 50% were tested at temperatures between 20 °C to 80 °C with an intermediate step of 10 °C. The experimental data points were then interpolated with the polynomial expressions (eq.5) and (eq.6).

$$\rho = 1013 - 0.2682\ T + 0.7225\ x - 1.94 \cdot 10^{-3}\ T^2 - 4.964 \cdot 10^{-3}\ x\ T \qquad \text{(eq.5)}$$

$$\mu = (-2.881 - 6.721 \cdot 10^{-3}\ T + 0.2839\ x + 1.959 \cdot 10^{-3}\ T^2 + -7.036 \cdot 10^{-3}\ x\ T - 1.883 \cdot 10^{-5}\ T^3 + 4.862 \cdot 10^{-5}\ x\ T^2) \cdot 10^{-3} \qquad \text{(eq.6)}$$

where T is the fluid temperature [°C],

x is the mass concentration of propylene glycol in the mixture [%].

Laminar flow regime is characterized by low values of Reynolds number, while turbulent flow occurs for higher values. In literature it is often stated that, for fully developed flow in a circular pipe, laminar flow occurs for Re<2300, and turbulent flow for Re>4000 (Holman, 2002). The flow regime between laminar and turbulent is referred to as transitional regime. In reality, the exact value at which change in flow regime occurs is extremely difficult to determine and depends on whether small disturbances are present. In the developed model, flow was assumed laminar for Re<2300, and turbulent for Re>3100, as a result of a series of tests carried out to evaluate transition in flow regime in the HT collector pipes.

In case of laminar flow, Darcy friction factor was calculated through Hagen-Poiseuille law:

$$\lambda = \frac{64}{Re} \qquad \text{(eq.7)}$$

For turbulent flow in smooth pipes, Blasius correlation (eq.8) was used, as the collector manifolds and pipes were made of commercial copper tubes, characterized by very small absolute roughness (Binder, 1973).

$$\lambda = \frac{0.3164}{Re^{0.25}} \qquad \text{(eq.8)}$$

Although not used in the present study, other friction factor correlations were implemented in the model, such as those proposed by Colebrook (1939) and Haaland (1983) for turbulent flow in pipes of known roughness, and by Joseph and Yang (2010) for any flow regime in smooth pipes.

Following the example of Jones and Lior (1994), the friction factor in the transition region (2300<Re<3100) was calculated by linear interpolation between the value obtained from (eq.7) for Re=2300 and that obtained from (eq.8) for Re=3100.

Regarding local losses, in the solar collector under investigation the only discontinuities were represented by the tees connecting the horizontal pipes to the manifolds. The correlations used to model the pressure losses in tees were mainly obtained by Idelchik (1994). Though, Idelchik's correlations refer to tees with sharp edges and without any inset, while the collectors under investigation presented 2-3 mm inset of the horizontal pipes into the manifold. As even short insets have been proven to be able to affect the pressure drop across tees (Ohnewein et al., 2015), Idelchik's correlations were corrected based on the results from Ohnewein et al. (2015).

2.3. Numerical model

Using the pressure drop correlations described in the previous section, a numerical model was developed in Matlab in order to compute the flow distribution and the resulting pressure drop across the collector. The input data to the model are design characteristics of the collector hydraulics and operating conditions of the heat transfer fluid (type of fluid, volume flow rate and temperature). The fluid temperature, which is assumed to be constant throughout the collector, is used to determine density and viscosity of the fluid.

Given an initial flow rate as input, the model assumes that this flow is uniformly distributed in all horizontal pipes and the resulting pressure drop for each of the possible fluid paths is calculated. Because a uniformly distributed flow is assumed, the pressure drop increases from one strip to the next (see strip numbering in Figure 1), as the fluid path becomes longer due to additional manifold segments. In reality, the pressure drop has to be the same, irrespective of the path the fluid follows, resulting in an adjustment of the flow rate in each strip.

2.4. Experimental setup for pressure drop measurements

To validate the model, the pressure drop across a large solar collector was measured in different operating conditions and compared to the value given by the model. The collector used for this purpose was a HT-SA 35/10 manufactured by the Danish company Arcon-Sunmark (see Section 2.1).

A differential pressure sensor TA-SCOPE from the company TA Hydronics, was used to measure the pressure drop across the collector. The instrument has a nominal accuracy which is given by the higher value between 0.1 kPa and 1% of the measured value.

The flow rate supplied to the collector was measured by a Kamstrup MP115 electromagnetic flow meter. Its accuracy is stated to be within ±0.5%. Additionally, the instrument was tested with different fluids,

temperatures and flow rates at the end of the pressure drop tests and its nameplate calibration factor was confirmed.

Transparent plastic pipes were connected to the inlet and outlet of the collector at one end and to the pressure sensor at the other end, as shown in

Figure 2. The transparent pipes made it easier to verify that no air was present in the circuit, which otherwise would alter both flow rate and differential pressure measurements.

Figure 2: Solar collector HT-SA 35/10 used for the validation and plastic pipes arrangement for pressure drop measurement.

Pressure drop measurements were carried out for different flow rates (between 0.08 and 0.72 liters s-1, corresponding to 0.3 and 2.6 m3 h-1) and at two temperature levels (approximately 25 °C and 70 °C), both using pure water and a 50% propylene glycol/water mixture as heat transfer fluid. The tests were performed in cloudy sky conditions, so that the temperature rise across the collector was negligible and the assumption of isothermal flow introduced in the model was fulfilled.

3. Results

3.*1. Validation of the model*

The comparison between measured and calculated pressure drops as function of the flow rate is shown in Figure 3 and Figure 4 for water and 50% propylene glycol/water mixture. Given the configuration of the hydraulic circuit, it was possible to test volume flow rates up to 2.6 m^3 h^{-1}, corresponding to pressure drops

of approximately 9-10 kPa. The lower boundary of the tested flow rate was determined by the error of the differential pressure sensor, which became increasingly predominant when measuring pressure drops lower than 1 kPa.

Note that the data points referred to as "25 °C" were actually characterized by mean fluid temperatures between 19 °C and 33 °C while those at "70 °C" between 67 °C and 77 °C.

In both diagrams, the typical quadratic relation between pressure drop and flow rate can be observed, as the different groups of points are approximately aligned along parabolic trajectories. Additionally, the influence of the fluid temperature on the pressure drop across the collector can be noted by comparing the different series of points within the same diagram. As expected, a fluid flow at lower temperature caused a higher pressure drop, provided that equal flow rates are compared.

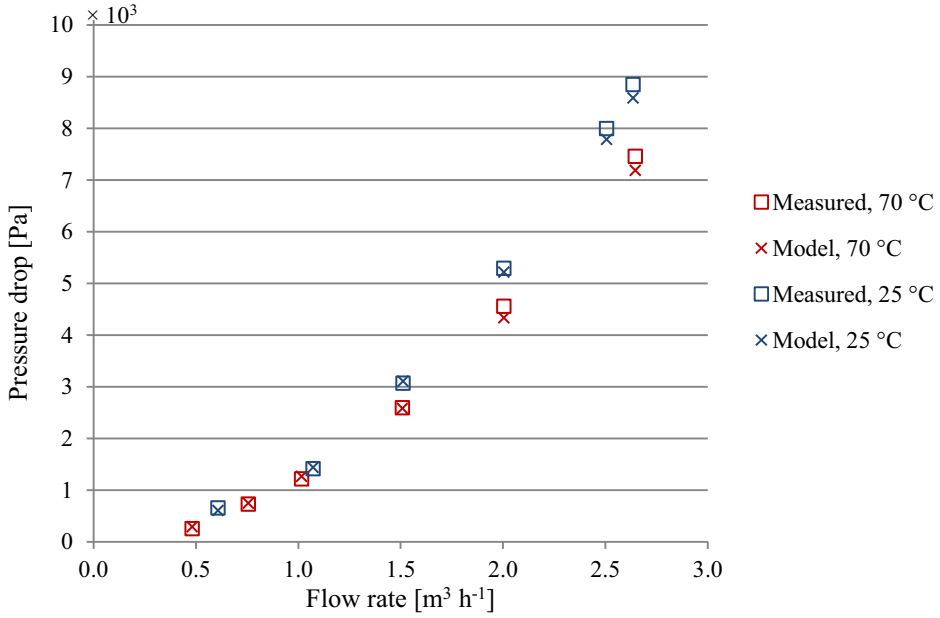

Figure 3: Comparison between measured and calculated pressure drops for water.

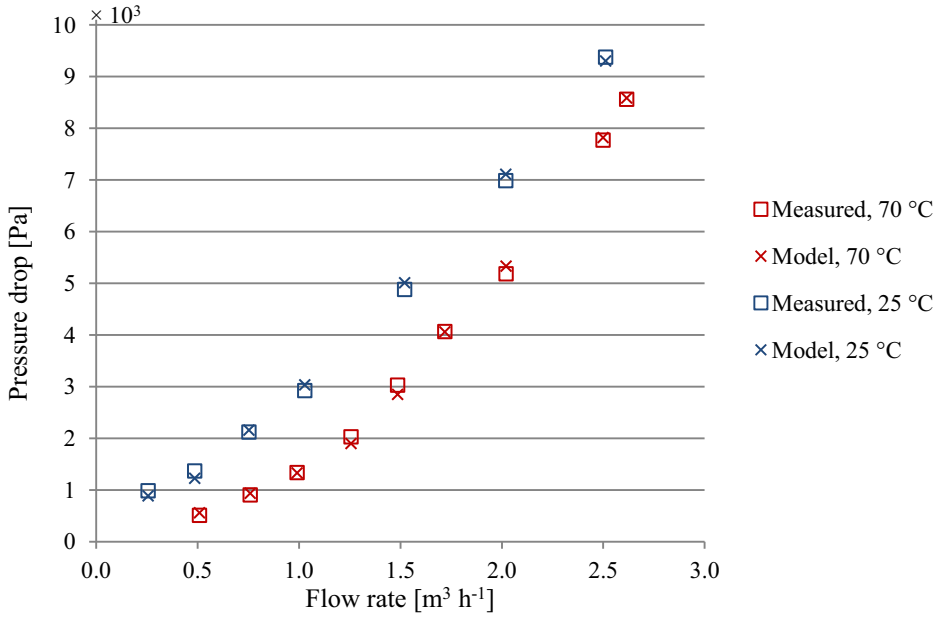

Figure 4: Comparison between measured and calculated pressure drops for 50% propylene glycol/water mixture.

3.2. Flow distribution

Using the developed model, it was possible to calculate the flow distribution inside the HT 35/10 collector at different flow rates and fluid types. The case with water at 20 °C was investigated. Water flow across the horizontal pipes of the collector was either laminar or turbulent at a temperature of 20 °C depending on the flow rate.

The flow distribution is shown Figure 5, where the flow distribution is expressed in terms of the parameter χ, defined by (eq.9) as:

$$\chi_i = \frac{V_i}{\sum_{i=1}^{18} V_i} \qquad \text{(eq.9)}$$

where χ_i is the fraction of the total collector flow rate flowing in the i-th horizontal pipe [-],

V_i is the volume flow rate in the i-th horizontal pipe [m^3 h^{-1}].

In case of a perfectly uniform flow distribution, the parameter χ would have a constant value of 5.56%, regardless of the horizontal pipe number.

The flow distributions shown in Figure 5 are decreasing, from the top to the bottom of the collector, with the only difference being the slope of the profiles.

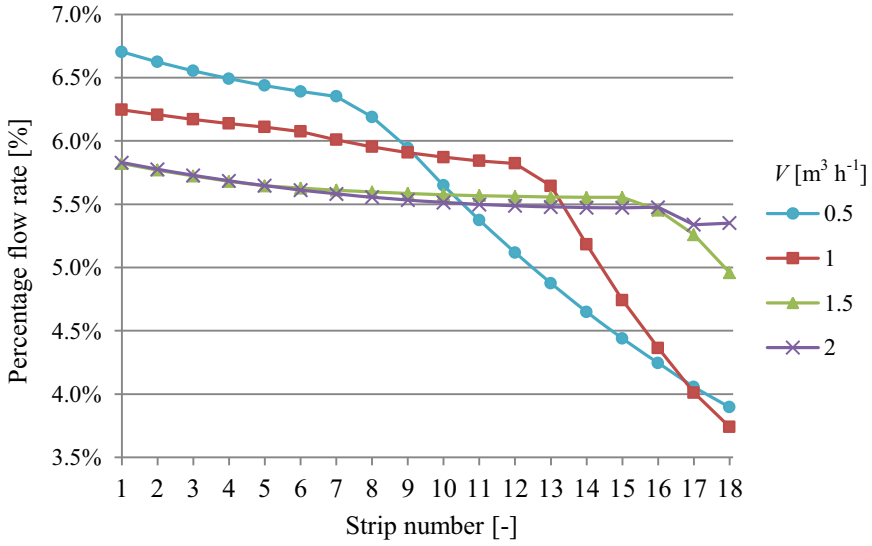

Figure 5: Flow distribution inside the collector at different flow rates for water at 20 °C.

As can be seen in Figure 5, in case of flow rates of 0.5 and 1 m^3 h^{-1}, laminar regime took place and a much less uniform distribution occurred. In these conditions χ varied between 3.7% and 6.7%. For higher flow rates the flow regime became turbulent and the flow distribution became more uniform and similar to that of water at 70 °C.

Although the pressure drop across the horizontal pipes played the most significant role in all cases, its importance for the different paths was quite different, depending on the flow regime. In case of turbulent regime in all horizontal pipes, the pressure drop along these represented 85%-89% of the total collector pressure drop for the top pipe, and 75%-77% for the bottom pipe. The remaining part was caused by forward and return manifolds as well as tee junctions. In case of laminar regime, the pressure drop in the horizontal pipe was 86%-92% of the total for the top pipe, and 48%-54% for the bottom pipe.

4. Discussion

The pressure drop values given by the model matched the measured values with a reasonable accuracy. If pressure drops higher than 1 kPa were considered, the average absolute value of the relative differences between model and measurements was lower than 3% for both tested fluids. All relative differences were within ±7%, with the only exception of a single point which had a 10% deviation.

For pressure drops lower than 1 kPa, the relative differences were slightly higher. In general, the lower pressure drop measured, the higher deviation was found: the highest deviation (15%) was found for a pressure drop of 0.2 kPa. Nevertheless, as the absolute difference between model and measurement in this case was equal to 0.04 kPa, this was well within the accuracy of the differential pressure sensor (0.1 kPa). Beside the accuracy of the instruments, other sources of error might be the assumptions made by the model, such as linear interpolation between laminar and turbulent conditions in case of transitional regime and fully developed flow throughout the pipes.

As expected, given the same temperature and flow rate, the pressure drop for the glycol/water mixture was larger than that of water, due to the much higher viscosity.

Additionally, the pressure drop for both fluids was higher at lower temperatures, due to the increased viscosity. Nevertheless, this effect was much more relevant for the 50% glycol/water mixture than for water. This was due to two main factors. Firstly, the kinematic viscosity of water decreases by a factor of 2.7 when the temperatures increases from 20 °C to 80 °C, while that of a 50% glycol/water mixture decreases by a factor of 5 for the same temperature variation. Secondly and more importantly, the higher viscosity characterizing the glycol/water mixture caused the Reynolds number in the horizontal pipes to be lower than 2300, meaning laminar flow regime. Even at the highest tested flow rate of 2.5 m^3 h^{-1}, the glycol/water mixture at 25 °C was still characterized by a completely laminar regime (Re<1500), entailing much higher friction factors compared to those at the higher temperatures.

Despite its secondary importance, also the higher density contributed in increasing the pressure drop at lower temperatures, and again the effect was more important for the glycol/water mixture, as its density varies by 3.8% in the range 20 °C-75 °C, compared to 2.3% for water.

Concerning the flow distribution, the results given by the model showed a decrease in flow rate from the top to the bottom pipes. This was the obvious consequence of the fact that only friction was considered as driving force for the flow distribution, so that the longer the hydraulic path, the higher the resistance.

A large difference appeared to exist when comparing flow distributions obtained for different flow regimes. Because of the weak dependence of the friction factor on the Reynolds number in the turbulent regime, the friction factor can been considered approximately constant in all horizontal pipes. Due to the geometry of the collector, the flow regime in most part of the manifold was turbulent, when it was turbulent in the horizontal pipes. This entailed that the pressure losses both in manifold segments and tees were relatively small compared to that occurring across the horizontal pipes, and it could be compensated by a slight unbalance in the collector flow distribution. As the pressure drop coefficients for tees in laminar regime are much higher than in turbulent regime and the laminar friction factor behaves similarly, the flow rate in the last tubes needed to diminish abruptly in order to cause the same pressure drop as the previous hydraulic paths.

When using water at 20 °C, the higher viscosity caused the flow regime inside the horizontal pipes to change from completely laminar to completely turbulent, depending on the flow rate (Figure 5). At 0.5 m^3 h^{-1}, the flow regime in all the horizontal pipes was laminar, while that in the manifold was initially turbulent and then, as more fluid was diverted to the horizontal pipes, laminar. The precise tee junction after which the change in flow regime occurred can be identified looking at the change in slope in the curves in Figure 5: a milder slope corresponds to turbulent flow in the manifold, while a steeper slope to laminar flow. The main reason for this behavior was that the local loss coefficients for tees in laminar regime are more sensitive to flow conditions than in turbulent regime, so they varied more significantly from one pipe to the next. As the hydraulic resistance between two consecutive pipes differed more significantly, this needed to be compensated by a larger difference in flow rates. A secondary reason is the linear dependence of the friction pressure drop on the flow rate in laminar conditions, which, compared to the quadratic dependence in turbulent conditions, required a larger variation in flow rate to compensate the varying pressure drop across the horizontal pipes.

Increasing the flow rate, the distribution became more uniform, as a longer part of the manifolds experienced turbulent conditions and the regime inside the horizontal pipes became transitional (V=1 m^3 h^{-1}) and then turbulent (V≥1.5 m^3 h^{-1}).

When using the presented model to evaluate the flow distribution in a solar collector, a user should keep in mind the assumptions and simplifications which were introduced, such as linear interpolation between laminar and turbulent friction factor for the transition region, fully developed flow along the horizontal pipes and manifold segments, and reliability of literature correlations when applied to the treated cases. The model was validated only in terms of overall pressure drop across the collector, and not in terms of flow distribution.

5. Conclusions

A model for estimating the pressure drop across a solar collector with U-type configuration in isothermal conditions was developed in Matlab. The model was validated against pressure drop measurements carried out on a HT-SA 35/10 collector in different conditions of flow rate, fluid type and temperature.

For pressure drops higher than 1 kPa, all relative differences between model and measurements were within ±7%, apart from one point. On average, the relative difference between model and measurements was within ±3%. For lower pressure drops the relative difference increased up to a maximum value of 15%, but always within the accuracy of the differential pressure sensor (0.1 kPa).

As expected, flow rate and viscosity were the main factors influencing the pressure drop, so different fluids having similar values for these two parameters gave almost identical pressure drops. This suggests a pressure drop curve for a glycol/water mixture at relatively high temperature can be evaluated using water at sufficiently low temperature, provided that in these conditions the two fluids have similar viscosity and density.

Regarding the flow distribution, it was found that this was mainly affected by the flow regime in the manifolds. Turbulent regime throughout the manifolds entailed a much more uniform flow distribution than laminar flow. This was mainly due to the strong dependence of the local losses for the tee junctions in laminar conditions, which caused relatively large difference in pressure drop even at small flow rate variation, as that occurring between two consecutive tees. If the presented model is used to evaluate the flow distribution in a solar collector, the introduced assumptions and simplifications must be taken carefully into account.

6. Acknowledgment

The first author is thankful to the Marie-Curie Actions - Initial Training Network research programme of the European Union which supported him through the SolNet-SHINE project. The authors are also grateful to the company Arcon-Sunmark A/S for having made available the HT-SA collector used during the study.

7. References

Binder, R.C., 1973. Fluid Mechanics, fifth ed. Prentice Hall.

Chiou, J.P., 1982. The effect of non-uniform fluid flow distribution on the thermal performance of solar collector. Solar Energy 29(6), 487-502.

Colebrook, C.F., 1939. Turbulent flow in pipes, with particular reference to the transition region between smooth and rough pipe laws. Journal of the Institution of Civil Engineers 11, 133-156.

ISO Standard 9806, 2014. Solar energy – Solar thermal collectors – Test methods.

Fan, J., Shah, L.J., Furbo, S., 2007. Flow distribution in a solar collector panel with horizontally inclined absorber strips. Solar Energy 81(12), 1501-1511.

Furbo, S., 2015. Using water for heat storage in thermal energy storage (tes) systems, in: Cabeza, L.C. (Ed.), Advances in Thermal Energy Storage Systems. Woodhead Publishing Series in Energy, pp. 31-47.

Haaland, S.E., 1983. Simple and Explicit Formulas for the Friction Factor in Turbulent Flow. Journal of Fluids Engineering (ASME) 105(1): 89-90.

Holman, J.P., 2002. Heat transfer, ninth ed. McGraw-Hill, New York.

Idelchik, I.E., 1994. Handbook of hydraulic resistance, third ed. CRC press.

Jones, G.F., Lior, N., 1994. Flow distribution in manifolded solar collectors with negligible buoyancy effects. Solar Energy 52(3), 289-300.

Joseph, D.D., Yang B.H., 2010. Friction factor correlations for laminar, transition and turbulent flow in smooth pipes. Physica D 239, 1318-1328.

Kestin, J., Sokolov, M., Wakeham, W.A., 1978. Viscosity of liquid water in the range -8 °C to 150 °C. Journal of Physical and Chemical Reference Data 7, 941-948.

Kovacs, P., Persson, M., Wahlgren, P., Jensen, S., 2012. Quality assurance in solar thermal heating and cooling technology - Pressure drop over a solar flat plate collector using various heat transfer fluids. Deliverable D2.2 – R2.13 of Project IEE/08/593/SI2.529236 supported by Intelligent Energy Europe. [Available online at http://www.estif.org/, accessed on 18/09/2015]

Ohnewein, P., Hausner, R., Preiß, D., 2015. Hydraulikdesign von parallelen Kollektormodulen in solarthermischen Großanlagen. Neue Energien 2020 – ParaSol project (preliminary version, from personal comunication with Ohnewein P.).

Wang, X.A., Wu, L.G., 1990. Analysis and performance of flat plate solar collector arrays. Solar Energy 45(2), 71-78.

Weitbrecht, V., Lehmann, D., Richter, A., 2002. Flow distribution in solar collectors with laminar flow conditions. Solar Energy 73(6), 433-441.

Windeleff, J., Nielsen, J.E., 2014. Solar District Heating in Denmark. Danish Energy Agency and PlanEnergi.

Performance of Wall-Mounted Non-Tracking Solar Thermal Collector with a Parabolic Mirror for Concentration

Ryo Kashiide[1], Atsushi Akisawa[1], Koji Enoki[2]

[1] Tokyo University of Agriculture and Technology, 2-24-16, Nakacho, Koganei, Tokyo 184-8588, Japan

[2] The University of Electro-Communications, 1-5-1, Chofugaoka, Chofu, Tokyo 182-8585, Japan

Abstract

This study examined the performance of a solar collector with a linear parabolic mirror mounted vertically on walls. In order to simplify the system, it does not have sun tracking function and focuses on hot water supply only during winter which dominates annual hot water demand. The objectives are to design optimal shape of the parabolic concentrator by simulations and to demonstrate the heat recovery by experiments. The inclined angle and the focal length of the paraboloid are the design parameters. Since the parabolic mirror does not truck the sun, there should be the optimal setting of the design parameters which maximize the thermal energy collection during winter season. The simulation results indicated that the inclined angle of 25 ° and the focal length of 95 mm would be optimal, based on which the proposed collector was made and tested outdoors. The experimental results showed that the temperature of the hot water actually gained 45.8 degC in February, 2015.

Keywords: *Solar Water Heater, Parabolic mirror, Solar concentration,*

1. Introduction

In energy use of residential sector in Japan, the share of hot water demand is about 30%. Therefore, solar water heaters are considered effective to save fuel consumption for hot water supply. While solar water heaters are set on the roof conventionally, vertically–installed type solar collectors are also available in the market recently, especially for apartment houses. They are placed on the fence of veranda. One drawback of vertical setting is that solar collecting performance is not high enough so that the temperature of hot water is relatively low. Therefore, this study proposes a vertical solar collector with a parabolic mirror to concentrate solar light to get higher temperature.

CPC (compound parabolic concentrator) is a well-known technique for solar collectors with concentration, which consists of two parabolic mirrors. Although CPC is capable to collect sun light within a certain range of incident angle without sun tracking, the structure is complicated. In contrast, the device proposed by this study simply consists of one parabolic mirror without sun tracking. The merits of the proposed device are the following. It can be mounted on building walls which are not used for solar collectors in Japan. The area of solar absorber is much smaller than flat type collectors, which leads to cost reduction because the absorbers are expensive component due to anti-reflective coating.

There are two design parameters for the parabolic mirror, that is, inclined angle and focal length. Tamata(1) investigated the effect of the inclined angle on the performance of the parabolic mirror when the

doi:10.18086/swc.2015.10.02 Available at http://proceedings.ises.org

focal length of the parabolic mirror was assumed constant. In this study, the focal length is also considered in addition to the inclined angle. Since the parabolic mirror does not truck the sun, there should be the optimal setting of the design parameters which maximize the thermal energy collection.

The objectives of this study are to find optimal design of the parabolic concentrator by ray-tracing simulations and to demonstrate the heat recovery by experiments. It should be noted that the performance of heat recovery in winter season is discussed in the study because hot water demand is much larger in winter than that in summer in Japan.

2. Solar thermal collector with a parabolic mirror

Figure 1 shows the cross-sectional view of the thermal collector. The thermal collector is assumed to be installed on vertical walls. It consists of a linear parabolic mirror for concentration and an absorber at the bottom. The focus of the parabolic mirror is designed to be located on the top surface of the absorber. In this study, the collector is assumed to be 100 mm wide as shown in Fig.1. The angle noted as φ is the inclined angle of the parabolic shape. P represents the focal length, and H indicates the aperture width of the collector. The absorber is divided into five segments to investigate the position that sun light is reflected by the mirror.

Sun light coming to the parabolic mirror is reflected to the focus when the angle φ is equal to the sun elevation. In the other cases, the reflected sun light is distributed on the absorber. The local energy flux changes time to time due to the sun movement.

Figure 2 shows the shape of paraboloid corresponding to various combinations of φ and P. The larger φ and P become, the longer the paraboloidal shape expands. It indicates that the aperture width H strongly depends on φ and P. Because the amount of sun light captured by the absorber is determined by the aperture size of H. It is necessary to find the optimal combination of φ and P in order to maximize the heat recovery.

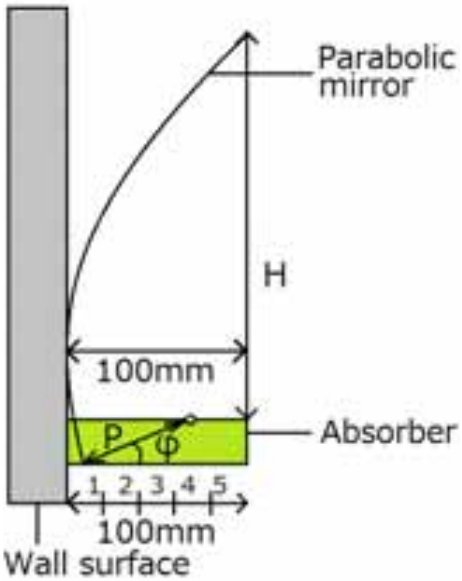

Fig.1 Cross-section of the proposed solar collector

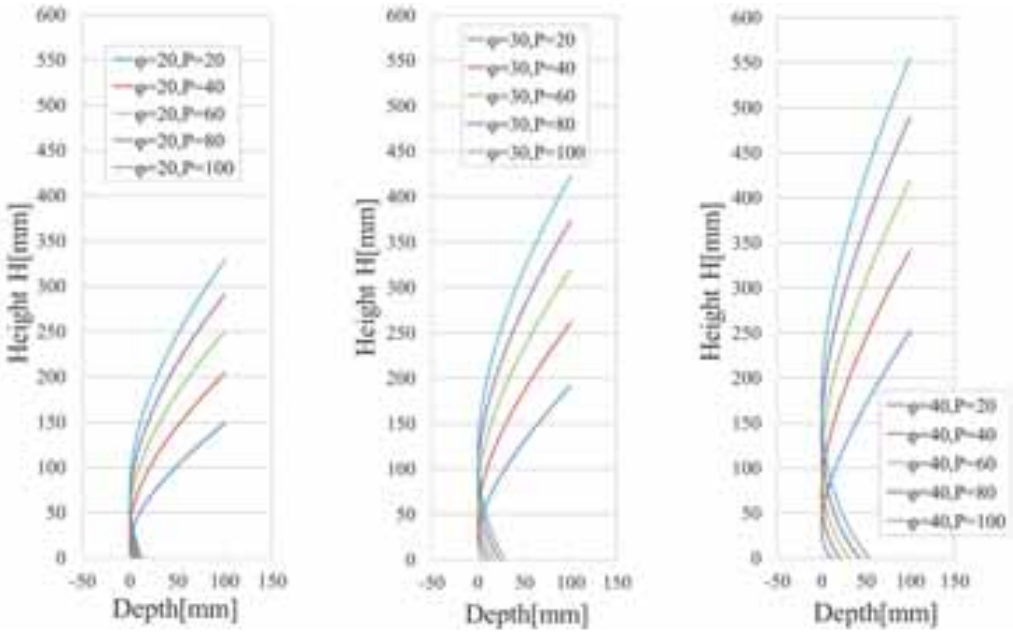

Fig2. Parabolic shape change by design parameter

3. Optimal design of the parabolic mirror

3.1 Simulation method and assumptions

This study investigates the influence of P change when φ is 15~40 degree. The ray tracing tool named Trace Pro was employed to calculate the sun light directly captured by the absorber and indirectly reflected by the mirror.

Simulation period is from November to February and location is Tokyo. Both Light reflectance rate of a parabolic mirror and heat absorption rate of the absorber are assumed 100 % to observe the maximal performance. The solar collecting device faces to the south and solar constant is 1067 W/m^2.

3.2 Thermal energy collection in winter season

Figure 3 shows the results for various combinations of P and φ. The graph indicates that there is a peak over P for a given φ. The reason why collected thermal energy increase is that H is extending as P is increasing. Larger H collects more sun light to the absorber. On the other hand, in the case where P becomes too large, thermal energy collection decreases because parabolic mirror cannot reflect sun light to the absorber enough when the sun elevation is low. Figure 4 shows example of the light collecting behavior when P is 30 mm or 90 mm and the sun elevation is 20 degree. Sun light is reflected to the absorber when P is 30 mm. In contrast, sun light is reflected out of the absorber when P is 90 mm.

Figure 3 also indicates that optimal P that obtains the peak of thermal energy collection becomes small when φ becomes large. The peaks of every φ settings seem to make a concave curve which has a peak at 95 mm of the focal length when φ is 25 degree. The peak is understood as the global maximum of the heat recovery by the proposed way.

According to this analysis, the optimal design is obtained with the parameters of φ=25 degree and P=95

mm. The aperture width H =321mm. The position of the focal length on the absorber is 86 mm from the wall surface. Therefore, sun light is reflected to the inside of the focal length on the absorber when the sun elevation is larger than 25 degree. Sun light is reflected to the outside of the focal length on the absorber or outside of the device when the sun elevation is lower than 25 degrees.

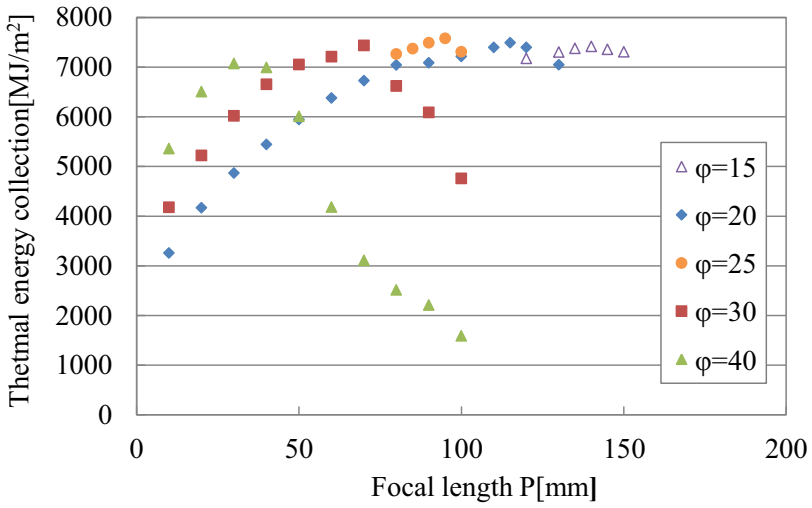

Fig.3 Thermal energy collection

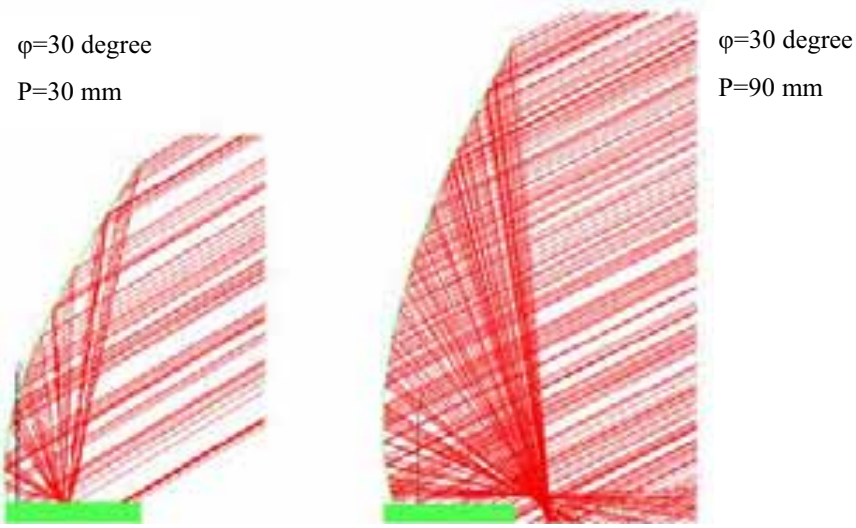

Fig.4 Light collecting behavior

(The φ is larger than the sun elevation)

4. Energy density distribution on the absorber

Figure 5 shows the energy recovery of the entire absorber in each month in the optimal design case with φ=25 degree and P=95 mm. The monthly performance is almost same approximately. It should be noted that the distribution of sun light changes because the reflection by the parabolic mirror depends on the sun elevation. The local heat recovery performance is evaluated in this section in order to understand the profile of the solar concentration on the absorber. The absorber is divided into five segments as shown Figure 1 to

investigate which part collects solar energy well. In this optimal design case, the focus is located in the part 5 of the absorber. Figure 6 shows the light collecting behavior when the sun elevation is 20, 25, 30, and 40 degree. It can be seen from the Figure that sun light is reflected to the part 5 or outside of the absorber when the sun elevation is lower than 25 degree while sun light is reflected to the part 4 and 5 when the sun elevation is higher than 25 degree. As the sun elevation becomes larger, the reflected rays shift inward on the absorber so that the part 1, 2, and 3 get heated when the sun elevation is considerably higher than 25 degree. Figure 7 indicates local heat recovery by the segments. The highest performance is observed at the part 5 in December. It is because the maximum sun elevation is 31 degree in December. The contribution of the part 5 is significantly large compared with that of the other parts. In November and January, the performance of the part 4 and 5 dominates the heat recovery. In contrast, the part 3 takes the maximum position in February where the performance of the part 5 is much reduced. In sum, the part 4 and 5 are recognized as important parts to recover solar thermal energy while the part 3 works well in February. It is also suggested that the contribution of the part 1 is insignificant.

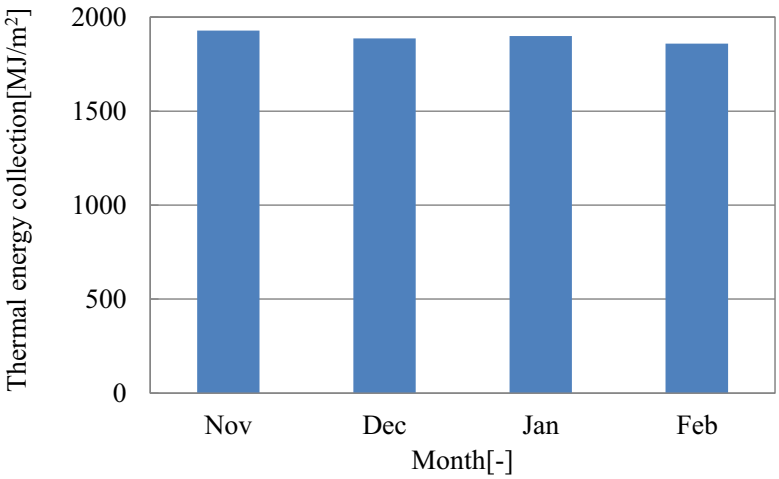

Fig.5 Thermal energy collection in each month

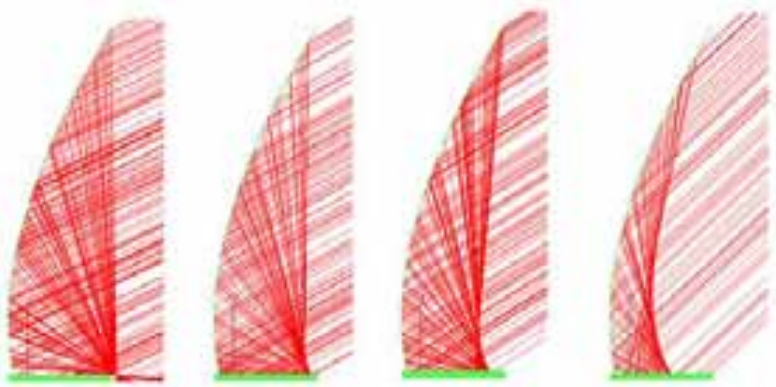

Fig.6 Light collecting behavior (φ=25°, P=95mm)

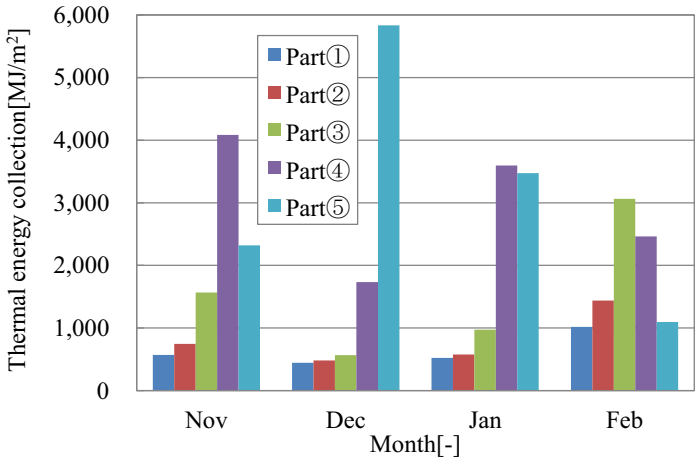

Fig.7 Thermal energy collection of each part

5. Monthly performance compared with conventional solar collectors

To demonstrate the usefulness of the proposed device, comparison of monthly performance was conducted among three collectors. One is the device proposed in this study, another is a flat plate collector of vertical type, and the other is a conventional flat plate collector inclined at 30 degree. The index is the average energy density on the absorber because higher temperature is beneficial for domestic hot water production. Figure 8 shows the results of monthly thermal energy density of above 3 collectors. It is seen that the proposed device and the vertical type flat collector have similar profile throughout a year while the conventional flat type collector holds almost stable energy density in any month. The proposed device collects solar energy significantly higher than the others, more than twice from October until March in terms of the density. On the other hand, the performance of the proposed device is less than the conventional collector from May until July. Heating load for hot water increases in winter, but reduces in summer. Because the pattern is in accordance with the profile of energy density of the proposed device, the proposed device is advantageous to produce hot water required in each month.

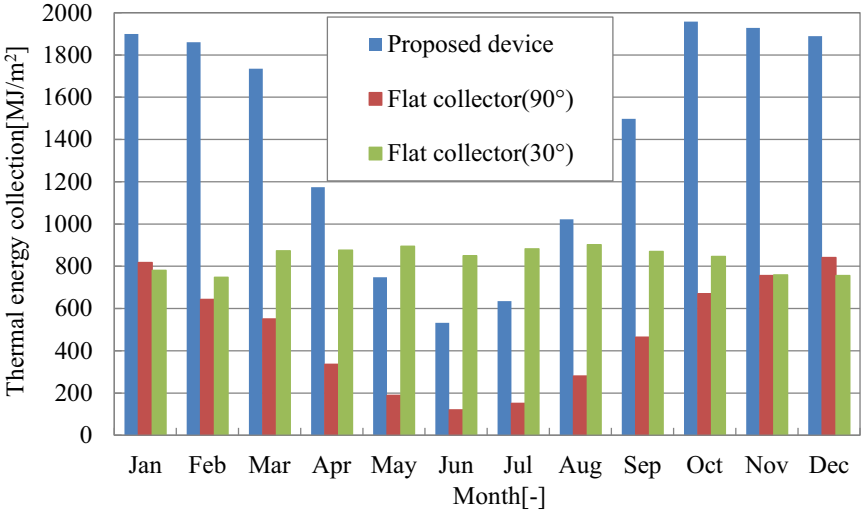

Fig.8 Monthly thermal energy collection

6. Heat collection experiments

6.1 Experimental setup and conditions

The experimental device was made based on the optimal design, which photo is shown in Figure 9. Five copper pipes with chrome plating were used as the absorber. The pipes were not thermally insulated just for preliminary experiments. The water in the tank was circulates through the device by a pump. Figure 10 illustrates the water flow in the absorber. In addition, Figure 10 shows temperature measurement points and corresponding thermocouple number. Thermocouple numbers from 1 to 6 were for water temperature measurement and numbers from 7 to 11 were for surface temperature measurement of the copper pipes.

The device was set up to face south at Tokyo University of Agriculture and Technology Koganei Campus in Tokyo. Measurement days were 29th January and 2nd February. Measurement time was from 9:00 to 16:00 in order to avoid the shade. The maximum temperature was 8.0 degC and the minimum temperature was 3.9 degC during the experiment on 29th January. On the other hand, the maximum temperature was 9.4 degC and the minimum temperature was 5.4 degC during the experiment on 2nd February. Thermocouples ware calibrated to have the accuracy of water temperature measurement to be ± 0.5 degC and the accuracy of surface temperature measurement of copper pipes to be ± 1.0 degC. Measurement interval of temperature was 10 s. The amount of water was 2 litters and the flow rate was controlled to be 0.2 l/s.

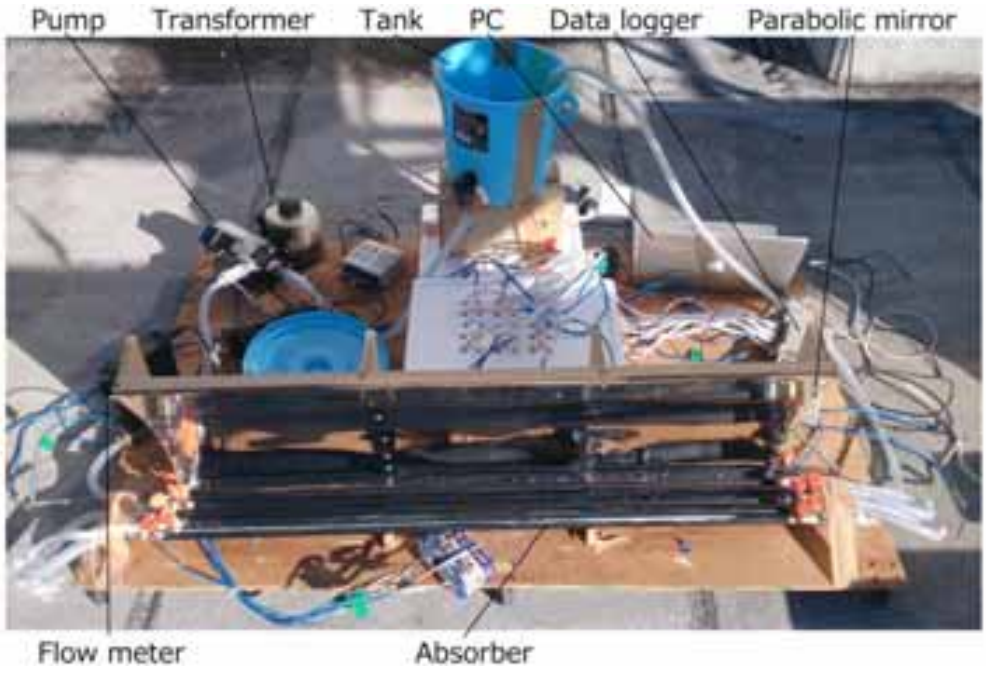

Fig.9 Experimental setup

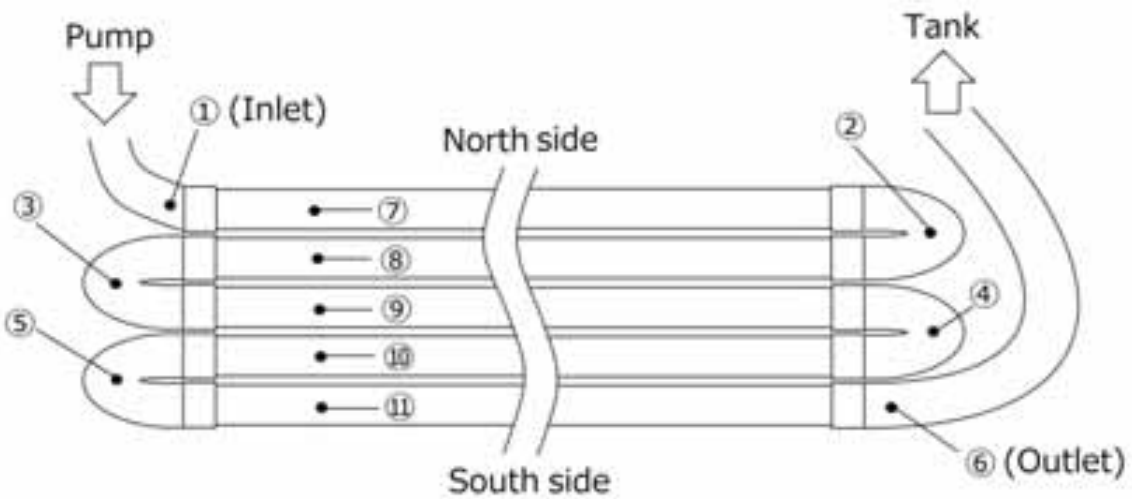

Fig.10 Schematic of the absorber

6.2 Water temperature behavior with / without parabolic mirror

Figure 11 shows the measurement results of the water temperature behavior with the parabolic mirror on 2nd February, which also shows the direct irradiance. The measurements of thermocouples from 2 to 4 were similar to that of number 1 and the measurement number 5 was similar to that of number 6. Therefore, the results of number 2, 3, 4, and 5 were not shown in Figure 11. As the graph shows the water temperature continued to rise over time, and rose up to 45.9 degC at around 12:00. Temperature difference of 5 degC was obtained from the inlet (Thermocouple number 1) to the outlet (Thermocouple number 6). Direct irradiance was 0 kW/m^2 after 15:30 due to the shade of other building. Therefore, the temperature of number 6 is lower than number 1 due to heat dissipation because the pipes have no insulation.

Figure 12 shows the results of the water temperature behavior without the parabolic mirror on 29th January. Although the water temperature rose to 30.9 degC at around 13:00, temperature difference between inlet and outlet of the absorber was very small. The water temperature was falling because the weather became cloudy after 13:30.

The experimental results with / without mirror clearly reveal that the concentration by the parabolic mirror is certainly effective to boost the temperature of hot water. It should be noted that the temperature could be higher than the experiment if the absorber is well insulated.

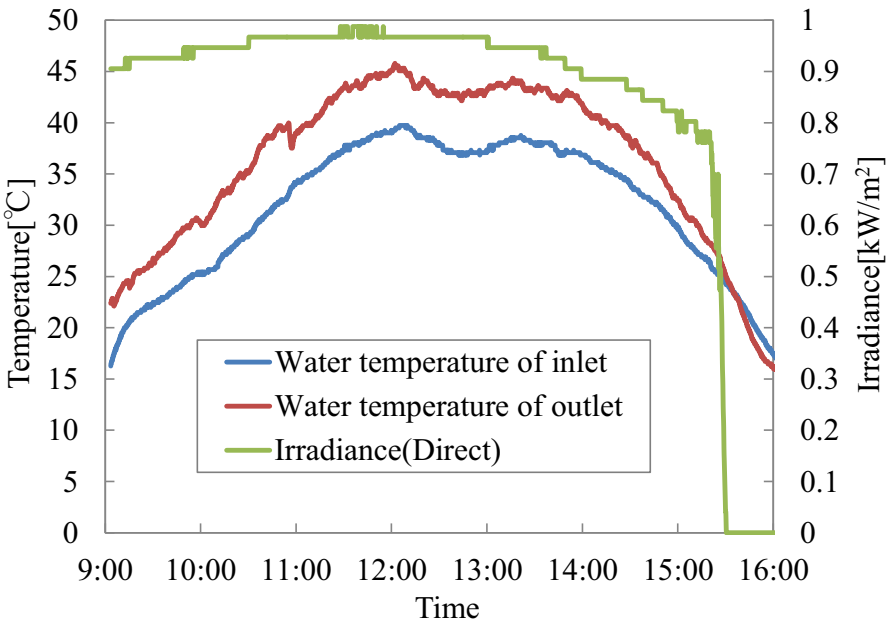

Fig.11 Behaviors of water temperature and irradiance

(With concentration)

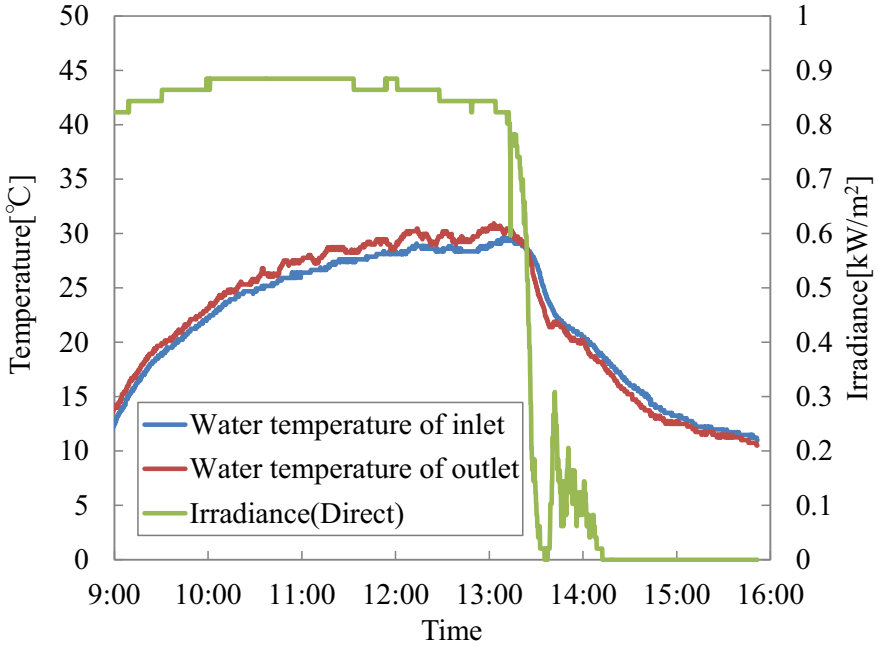

Fig.12 Behaviors of water temperature and irradiance

(Without concentration)

7. Conclusion

This study proposed a solar collector with concentration by a parabolic mirror which is assumed to be mounted on vertical walls. To be simplified, the mirror shape is just a parabola and no sun tracking is equipped. The optimal design of the parabolic mirror was derived from sensitivity analysis to maximize solar heat recovery in winter, which is achieved with the parameter settings of φ=25 degree and P=95 mm.

The simulation results suggest that the attained energy density by the proposed debice is more than twice as much as that of conventional inclined flat plate collectors in winter. It will be advantageous to get high temperature hot water.

The performance of the proposed device was also examined by experiments in winter. Even though they were considered preliminary, the concentration by the parabolic mirror was confirmed effective to produce higher temperature than that without mirror by 15 degC.

References

[1] Asahi Tamata, Atsushi Akisawa, Yuki Ueda and Koji Enoki, DESIGN OF WALL MOUNTED SOLAR COLLECTOR WITH A PARABOLIC MIRROR, Grand Renewable Energy 2014

[2] Hua Qin, Chengxin Lei, Hanfa Liu, Yong Wang, Wenfeng Yuan, Optical design of an aspherical cylinder-type reflecting solar concentrator, Energy, vol.57, pp.751-758, 2013

[3] Soteris A. Kalogirou, Solar thermal collectors and applications, Progress in Energy and Combustion Science, vol.30, pp.231-295, 2004

[4] M. Antonelli, A. Baccioli, M. Francesconi, U. Desideri, L. Martorano, Electrical production of a small size Concentrated Solar Power plant with compound parabolic collectors, Renewable Energy, vol.83, pp.1110-1118, 2015

[5] K. Devanarayanan, K. Kalidasa Murugavel, Integrated collector storage solar water heater with compound parabolic concentrator – development and progress, Renewable and Sustainable Energy Reviews, vol.39, pp.51-64, 2014

Conference Proceedings

Solar World Congress 2015
Daegu, Korea, 08 – 12 November 2015

Experimental Validation of a Compound Parabolic Concentrator Mathematical Model

García-Valladares O.[2], Santos-González I.[1], Gómez V.H.[2], Ortega N[2].

[1]Posgrado en Ingeniería (Energía), Universidad Nacional Autónoma de México, Privada Xochicalco s/n, Temixco, Morelos 62580, México. irsag@ier.unam.mx

[2]Instituto de Energías Renovables, Universidad Nacional Autónoma de México, Privada Xochicalco s/n, Temixco, Morelos 62580, México. ogv@ier.unam.mx

Abstract

In this work the numerical simulation and experimental validation of a Compound Parabolic Concentrator (CPC) are presented. The numerical model solve the governing equations of continuity, momentum and energy inside the CPC receiver tube, together with the energy equation in the receiver tube wall and the thermal analysis in the solar concentrator. The model can predict the increment of temperature between the inlet and outlet section of the CPC, the thermal efficiency and the pressure drop through the CPC together with the flow variables (mass flow rate, temperature and pressure) in each control volume in which the CPC is divided.

A prototype of a CPC has been designed and built using a cylindrical receiver with a real concentration rate of 1.8, acceptance angle of 30°, and aperture area of 0.17 m^2.

The protocol ANSI-ASHRAE 93-1986 standard was used with appropriate instrumentation for measuring the different variables in the CPC. For this prototype experimental tests were performed using water as working fluid for a wide range of inlet water temperatures and mass flow rates.

Statistical analysis was carried out in order to compare variations between the experimental results and numerical results. According to the results, the numerical model provides good tendencies for the design and optimization of CPCs.

key-words*: solar energy, CPC, numerical model, characterization curves, statistical analysis*.

Nomenclature

A_a	Receiver tube heat transfer area, [m^2]
A_c	Cover heat transfer area, [m^2]
A_r	Reflector heat transfer area [m^2]
A_t	Fluid flow cross section area [m^2]
D_{in}	Internal diameter [m]
e	Specific energy ($h+v^2/2+gz \sin\theta$) [J/kg]
f	Friction factor [dimensionless]
g	Gravitational constant [9.81 m/s^2]
h	Enthalpy [J/kg]
h	Heat transfer coefficient [$W/(m^2K)$]
I	Solar irradiance [W/m^2]
K	Thermal conductivity [W/mK]
m	Mass [kg]
$\dot{m}$	Mass flow rate [kg/s]
P	Pressure [Pa]
p	Perimeter [m]
q	Heat flow per unit area [W/m^2]

doi:10.18086/swc.2015.10.03 Available at http://proceedings.ises.org

q_u	Heat flux per receiver unit area from fluid to wall [W/m^2]
r	Radius of the receiver tube [m]
T	Temperature [°C]
$\vec{V}$	Velocity in the axial direction [m/s]
v	velocity [m/s]
x	Axial coordinate

Greek letters

β	Inclination angle of receiver tube [degree]
γ	Length of tangent [m]
ε	Emittance [dimensionless]
θ	Angle of incidence on collector [degrees]
θc	Half-acceptance angle [degrees]
ρ	Density [kg/m^3]
σ	Stefan-Boltzman constant (5.6697x10^{-8}W/m^{2}K^4)
τ_w	Wall shear stress (N/m^2)
Δt	Temporal discretization step [s]
ΔT	Temperature difference [°C]
Δx	Spatial discretization step [m]
Φ	Two-phase frictional multiplier [dimensionless]

Subscripts

a	Receiver tube
amb	Ambient
c	Cover
conv	Convective
f	Fluid
g	Gas
in	Inlet
j	Number of control volume
l	Liquid
r	Reflector
rad	Radiative
sky	Sky
tp	Two-phase

Superscripts

-	Arithmetical average over a control volume
~	Integral average over a control volume
$[X]_{j-1}^{j}$	Difference between the variable X at the outlet section and the inlet section.

1. Introduction

The alternative to reduce dependence on fossil fuels and the amount of CO2 emitted into the atmosphere is the use of renewable energies. Water is generally heated by commercial fuels (LP gas, natural gas, electricity) in urban areas to be used for space heating, domestic or industrial processes. The majority of commercial fuels are directly or indirectly produced by fossil fuels which have limited reserves and contribute greatly to the global warming. The integration of renewable energy systems will utilize clean and sustainable energy to reduce the dependence of fossil fuels and provide long term energy savings.

Solar energy collectors transform solar radiation into heat and then transfer this heat to a fluid. The compound parabolic concentrator (CPC) is a versatile solar collector due to the amount of applications and geometries that can be used. The CPC is a good choice for applications in direct evaporation or water heating near its boiling point, because these stationary collectors have a good quality rate between cost and performance at medium temperature levels [1]. The CPC could be used in a great variety of solar applications for low and medium temperature ranges; the most important is the heat production for industrial processes, such as sterilization, pasteurization, drying, distillation, adsorption and absorption cooling, etc.

CPCs consist basically of three elements: receiver, cover and reflector. In order to achieve good CPC performance, a numerical model is a useful tool in order to design it. In this work a numerical model of the CPC was carried out; then a CPC was designed and built selecting carefully the geometry and material of each component. Appropiate instrumentation was selected and used in order to compare the experimental data of the CPC under different working conditions with the model results in order to validate it.

2. CPC Design

The design of the reflector portion of a CPC tubular receiver (Figure 1) is determined by the diameter of the receiver and the desired concentration factor. The reflector geometry is given in two separate parts:

An involute section $|\theta| < \theta_c + \pi/2$ and a segment of a parabola $|\theta| > \theta_c + \pi/2$

$\gamma(\theta) = r\theta \quad \text{for} \quad |\theta| \leq \theta_c + \frac{\pi}{2}$ (Involute)

$\gamma(\theta) = \left[r \frac{\theta + \theta_c + \frac{\pi}{2} - \cos(\theta - \theta_c)}{1 + \sin(\theta - \theta_c)} \right] \quad \text{for} \quad \theta_c + \frac{\pi}{2} \leq |\theta| \leq \frac{3\pi}{2} - \theta_c$

The curve is generated by increasing θ in radians, calculating the length γ and the X,Y coordinates.

$$x = r \sin\theta - \gamma \cos\theta$$
$$y = -r \cos\theta - \gamma \sin\theta$$

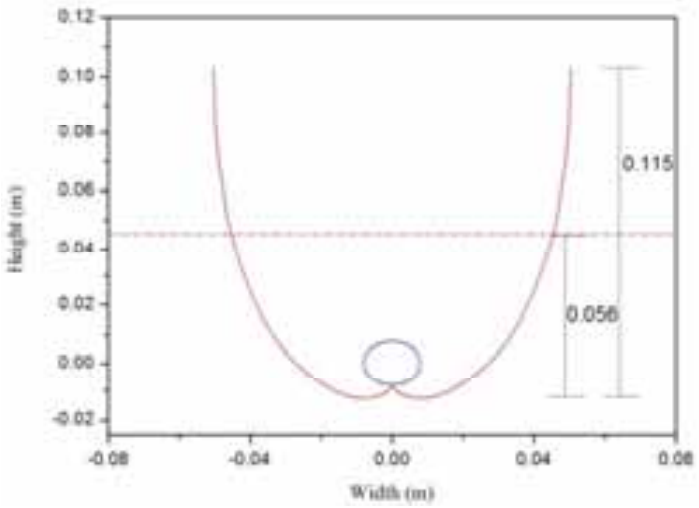

Figure 1. A CPC tubular receiver design.

In practical applications the upper part of the reflector are less efficient to reflect solar rays to the receiver. For this reason, it is truncated and the cost of reflective material is reduced. Table 1 shows the percentage of material saved when truncation is applied.

Table 1. Truncated and non-truncated final designs.

	Non-truncated (m)	Height truncated (m)	% Reduction
Height	0.115	0.056	51
Aperture	0.100	0.090	10
Reflector perimeter	0.281	0.163	42.1

3. Numerical model

The CPC was designed using a one-dimensional numerical model that solves the governing equations of continuity, momentum and energy. The fluid flow inside the receiver tube, the heat conduction in the receiver tube wall, and the heat transfer in the solar concentrator were solved in a segregated manner. For

more detailed of the numerical model see N. Ortega, et. al. [2] .

Figure 2 shows a control volume in CPC and the energy balances in each component (receiver tube, cover and reflector, Fig 2a) together with a control volume for the fluid flow (Fig 2b)

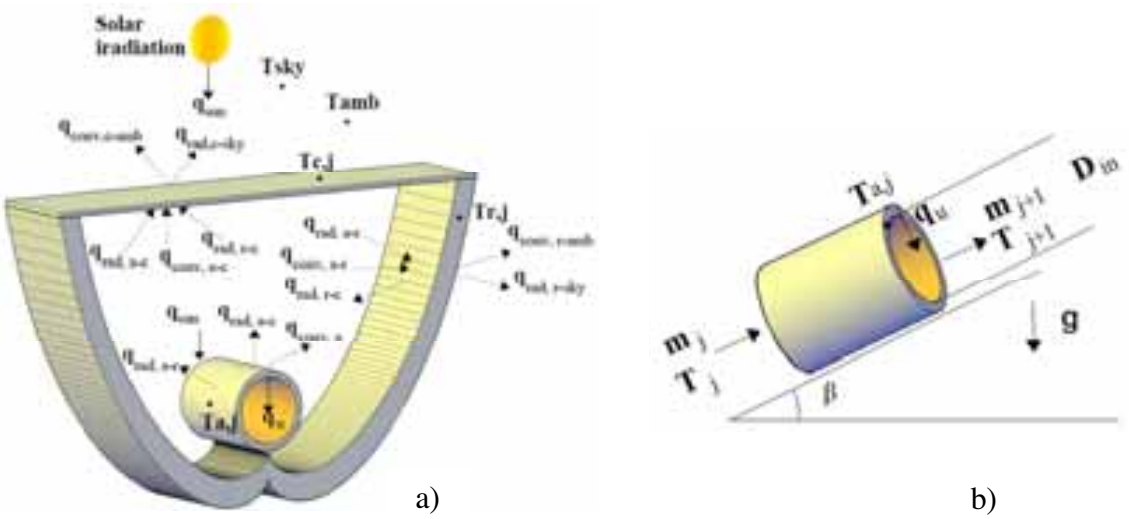

Figure 2. A CPC control volume. a) energy balance in each component; b) the fluid flow control volume.

For the fluid flow inside the receiver tube (see Fig 2b), the following governing equations have been integrated using a control volume analysis and a step by step method in the flow direction.

Continuity:

$$[\dot{m}]_{j-1}^{j} + \frac{\partial m}{\partial t} = 0 \tag{1}$$

The mass flow rate is obtained from the discretized continuity equation: $\dot{m}_j = \dot{m}_{j-1} - \frac{A_t \Delta x}{\Delta t}\left(\bar{\rho}_{tp} - \bar{\rho}_{tp}^{o}\right)$ (2)

Momentum:

$$\left[\dot{m}_g V_g + \dot{m}_l V_l\right]_{j-1}^{j} + \Delta x \frac{\partial \tilde{m}}{\partial t} = -[P]_{j-1}^{j} A_t - \tilde{\tau}_w p_{Ar.j} \Delta x - mgsin\beta \tag{3}$$

The discretized momentum equation is solved for the outlet pressure:

$$P_j = P_{j-1} - \frac{\Delta x}{A_t}\left\{\pi D_{in} \Phi \frac{\bar{f}}{4} \frac{\bar{m}^2}{2\rho_{tp} A_t^2} + \left[\frac{\dot{m}}{\Delta x}\left(x_g \vec{V}_g + \left(1 + x_g\right)\vec{V}_l\right)\right]_{j-1}^{j} + \frac{\bar{m} - \bar{m}^o}{\Delta t} + \rho_{tp} A_t g sin\beta\right\} \tag{4}$$

Energy:

$$\left[m_l e_l + m_g e_g\right]_{j-1}^{j} + \frac{\partial(\bar{m}_l \bar{e}_l + \bar{m}_g \bar{e}_g)}{\partial t} - A_t \Delta x \frac{\partial \tilde{P}}{\partial t} = \tilde{q}_u p \Delta x \tag{5}$$

From the energy equation and the continuity equation, the following is obtained for the outlet enthalpy:

$$\mathrm{h}_j = \frac{\left(2\pi D_{in} \Delta x\right) q_u - a\dot{m}_j + b\dot{m}_{j-1} + cA_t \Delta x / \Delta t}{\dot{m}_j + \dot{m}_{j-1} + \bar{\rho}_{tp}^{o} A_t \Delta x / \Delta t} \tag{6}$$

Where:

$$q_u = \mathrm{h_f}\left(T_{a,j} - (\bar{T}_j + \bar{T}_{j+1})/2\right) \tag{7}$$

$$a = \left[x_g \vec{V}_g + \left(1 - x_g\right)\vec{V}_l\right]_j^2 + gsin\beta\Delta x - h_{j-1} \tag{8}$$

$$b = \left[x_g \vec{V}_g + \left(1 - x_g\right)\vec{V}_l\right]_j^2 + gsin\beta\Delta x + h_{j-1} \tag{9}$$

$$c = 2\left(\overline{P}_{j-1} - \overline{P}^{o}_{j-1}\right) - \overline{\rho}^{o}_{tp}\left(\mathrm{h}_{j-1} - 2\overline{\mathrm{h}}^{o}_{j-1}\right) - \left(\overline{\rho}\overline{V}^{2}_{j-1} - \overline{\rho}^{o}\overline{V}^{o\,2}_{j-1}\right) \tag{10}$$

The discretized equations are coupled using a fully implicit step by step method in the flow direction. From the known values at the inlet section and the wall boundary conditions, the variable values at the outlet of each CV are iteratively obtained from the discretized governing equations. Outlet values are the inlet values for the next CV. The procedure is carried out until the end of the receiver tube is reached.

The heat conduction in the receiver tube wall has been written assuming one-dimensional transient temperature distribution. A characteristics CV is shown in Figure 3, where P represents the central node, E and W indicate its neighbors. The CV faces are indicated by e, w, n, and s. Integrating the energy equation over this CV, the following equation was obtained.

$$\left((\tilde{\mathrm{q}}_{\mathrm{sun}} - \tilde{q}_{rad,a-c} - \tilde{q}_{rad,a-r} - \tilde{q}_{conv,a})\mathrm{P_n} - \tilde{\mathrm{q}}_{\mathrm{u}}\mathrm{P_s}\right)\Delta\mathrm{x} + (\tilde{\mathrm{q}}_{\mathrm{w}} - \tilde{\mathrm{q}}_{\mathrm{e}})\mathrm{A}_t = \mathrm{m}\frac{\partial\tilde{\mathrm{h}}}{\partial\mathrm{t}} \tag{11}$$

here $\tilde{\mathrm{q}}_{\mathrm{u}}$ was evaluated using the convective heat transfer coefficient and temperature in the fluid flow and receiver wall temperature in each CV, and the conductive heat fluxes are evaluated from the Fourier law: $\tilde{\mathrm{q}}_{\mathrm{e}} = \mathrm{k}_{\mathrm{e}}(\partial\mathrm{T}/\,\partial\mathrm{x})_{\mathrm{e}}$ and $\tilde{\mathrm{q}}_{\mathrm{w}} = \mathrm{k}_{\mathrm{w}}(\partial\mathrm{T}/\,\partial\mathrm{x})_{\mathrm{w}}$

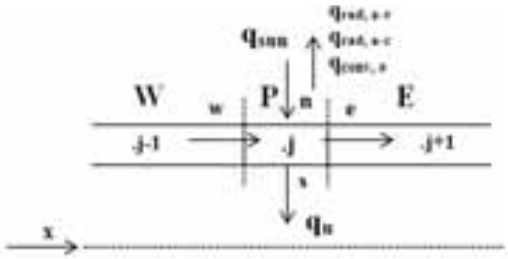

Figure 3. CV for the receiver tube wall.

The useful energy gain (q_u) is equal to the cover incident solar energy reduced by optical losses in the concentrator, the thermal losses in the cover, the reflector, and the receiver tube.

In order to calculate the receiver tube, cover and reflector temperatures in each CV; it is necessary to solve iteratively the following equations of energy balance of each component:

Receiver: $q_{sun,a} - q_{rad,a-c} - q_{rad,a-r} - q_{conv,a-c} - q_{conv,a-r} - q_u = 0$ (12)

Cover: $q_{abs,c} + q_{rad,a-c} + q_{conv,a-c} + q_{rad,r-c} - q_{conv,c-env} - q_{rad,c-sky} = 0$ (13)

Reflector: $q_{abs,r} + q_{rad,a-r} + q_{conv,a-r} - q_{rad,r-c} - q_{conv,r-env} - q_{rad,r-sky} = 0$ (14)

With equation (12, 13 and 14), the following equations are obtained:

$$T_r = \frac{(h_{rad,a-r}+h_{conv,a-r})T_a + h_{conv,r-amb}T_{amb} + h_{rad,r-sky}T_{sky} + (h_{conv,r-c}-h_{ra,r-c})T_c}{h_{rad,a-r}+h_{conv,a-r}+h_{conv,r-amb}+h_{rad,r-sky}+h_{conv,r-c}-h_{ra,r-c}} \tag{15}$$

$$T_c = \frac{(h_{rad,a-c}+h_{conv,a-c})T_a + h_{rad,c-sky}T_{sky} + h_{conv,c-amb}T_{amb} + (h_{conv,r-c}-h_{ra,r-c})T_r}{h_{rad,a-c}+h_{conv,a-r}+h_{rad,c-sky}+h_{conv,c-amb}+h_{conv,r-c}-h_{ra,r-c}} \tag{16}$$

$$T_a = \frac{(h_{rad,a-c}+h_{conv,a-c})T_c + (h_{conv,a-r}+h_{ra,a-r})T_r + q_{sun,a} - q_u}{h_{rad,a-c}+h_{conv,a-c}+h_{conv,a-r}} \tag{17}$$

The convective heat transfer coefficient between the receiver tube and the reflector and between the receiver tube and cover were expressed by [3]:

$$h_{conv,a-r} = 3.25 + 0.0085\frac{(Ta-Tr)}{2D_{out}} \quad (18)$$

$$h_{conv,a-c} = 3.25 + 0.0085\frac{(Ta-Tc)}{2D_{out}} \quad (19)$$

$$h_{rad,r-c} = \frac{\sigma(T_c^2+T_r^2)(T_c+T_r)}{(1-\varepsilon_c)/\varepsilon_c+((1-\varepsilon_r)/\varepsilon_r)(A_c/A_r)}\frac{A_r}{A_a} \quad (20)$$

$$h_{rad,c-sky} = \varepsilon_c\sigma(T_c^2 + T_{sky}^2)(T_c + T_{sky})\frac{A_c}{A_a} \quad (21)$$

$$h_{rad,r-sky} = \varepsilon_r\sigma(T_r^2 + T_{sky}^2)(T_r + T_{sky})\frac{A_r}{A_a} \quad (22)$$

$$h_{rad,a-c} = \frac{\sigma(T_a^2+T_c^2)(T_a+T_c)}{(1/\varepsilon_c)+(A_c/A_a)((1/\varepsilon_a)-1)} \quad (23)$$

$$h_{rad,a-r} = \frac{\sigma(T_a^2+T_r^2)(T_a+T_r)}{(1-\varepsilon_r)/\varepsilon_r+((1-\varepsilon_a)/\varepsilon_a)(A_r/A_a)} \quad (24)$$

The convective heat transfer coefficients between the cover and the ambient and between the reflector and the ambient are expressed by Duffie and Beckman [4]:

$$h_{conv,c-amb} = (5.7 + 3.8v)\frac{A_c}{A_a} \quad (25)$$

$$h_{conv,r-amb} = (5.7 + 3.8v)\frac{A_r}{A_a} \quad (26)$$

The numerical model can predict the increment of temperature between the inlet and outlet of the collector, the efficiency, the energy gain by the transport fluid and the pressure drop of the CPC together with the flow variables (mass flow rate, temperature and pressure) in each control volume in which the CPC is divided. The numerical model can be used with fluid mixtures and with or without phase change in the fluid flow.

4. Experimental setup

Figure 4 shows the CPC designed and built. The real concentration is 1.8, acceptance angle is 30° and aperture area of 0.17 m^2. Table 2 shows the characteristics of geometry and materials used in the construction of this CPC.

Figure 4: CPC designed and built.

Table 2: Geometrical characteristics and materials used for the CPC

Parameter	Characteristics
Cover	
Low-iron tempered glass	transmittance=0.91
Thickness (mm)	4
Reflector	
Anodized aluminum	reflectance=0.90
Thickness (mm)	0.35
Receiver	
Copper	½" nominal diameter
Internal/ external Diameter (mm)	14.5/15.9
Selective surface	absorptance=0.90
CPC	
Acceptance angle (°)	30
Maximum concentration	2.00
Real concentration ratio	1.80
Width (m)	0.090
Height (m)	0.057
Length (m)	1.95

An experimental setup was constructed (Figure 5). Proper instrumentation to control and register the different variables of the system together with a program to save the experimental data was developed. The following variables are register every 3 second in experimental tests: temperatures, global solar irradiance at the collector plane and mass flow rate. The instrumentation used and their uncertainties for the evaluation of CPC are shown in Table 3.

Figure 5. Experimental unit.

Table 3: Instrumentation

	Instrument	Operating range	Uncertainties
Temperature meter	Thermistor	-40 a 150°C	±0.1°C
	K-type thermocouple	-20 a 750°C	±1.1°C
Mass flow meter	Coriolis	0 a 20 kg/min	±0.1%
Radiation meter	Pyranometer-class II	285 a 2800 nm	±1%

5. Experimental tests

The tests were carried out in the Solar Platform of the Instituto de Energías Renovables of the Universidad Nacional Autónoma de México, located at Temixco, Morelos, México, at 18°50.36' N and at 99°14.07' W, with an altitude of 1219 m above sea level. In Temixco, the yearly average ambient temperature and solar irradiance on the horizontal plane are 23.1 °C and 20.05 MJ/m^2 day, respectively.

The collector is mounted on the support structure and the collector angle is set according to the day of the year of the test. CPC mass flow rate and inlet temperature were maintained constant with the recirculation loop, pump, and electrical heaters installed in the storage tank for cold water. The water coming from the CPC was stored in the hot water storage tank. The water in the hot water storage tank was returned with the recirculation pump to the cold water storage tank to fix a new temperature and mass flow rate to repeat the process.

The experimental tests were performed using water as working fluid at solar noon. The mass flow rate, inlet and outlet temperature at the collector, the ambient temperature and the irradiance at the collector plane were registered every 3 seconds.

6. Results

Figure 6 shows the thermal efficiency against the temperature difference between fluid inlet temperature and ambient temperature in relation with the solar irradiance at the CPC plane. The experimental and numerical results with a mass flow rate of 0.7 kg/min and 1.0 kg/min are shown. The errors bars in figures represent the uncertainty obtained in the experimental measurement.

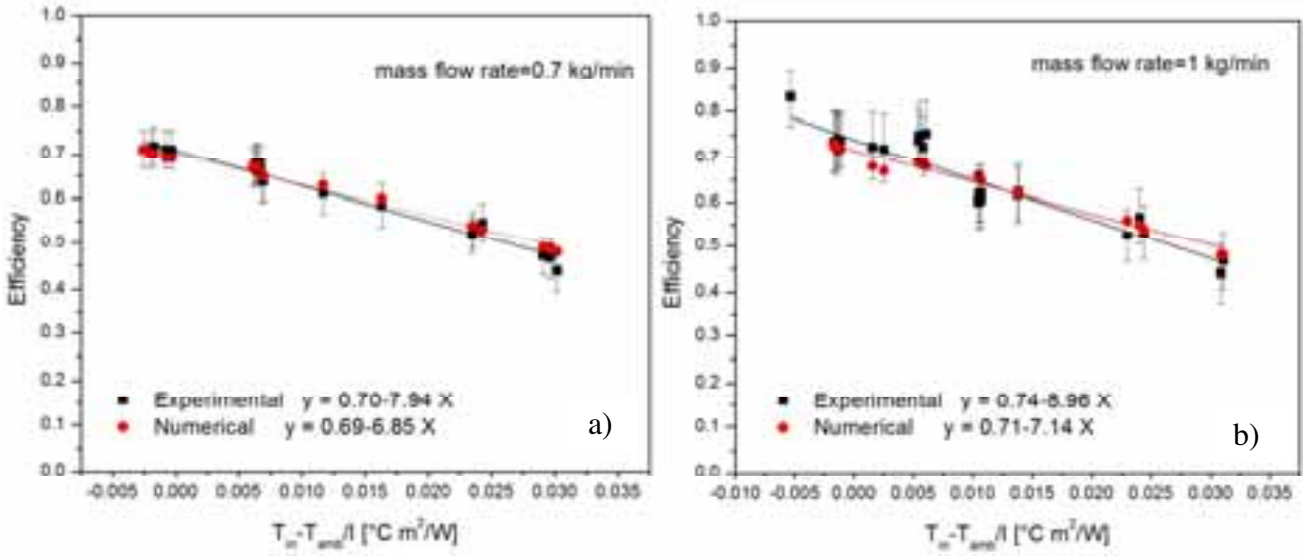

Figure 6. Numerical and experimental thermal efficiency results with a mass flow rate of: a) 0.7 kg/min and b) 1.0 kg/min.

The error and standard deviation between the experimental data and numerical results are shown in Table 4.

Table 4. Comparison between experimental and numerical results for the thermal efficiency.

Mass flow rate (kg/min)	Efficiency	
	Error (%)	Standard deviation (%)
0.7	±2.5	±1.9
1.0	±4.5	±3.2

Figure 7 shows the comparison of the increment of temperature through the CPC between the numerical results and experimental data for two different mass flow rate.

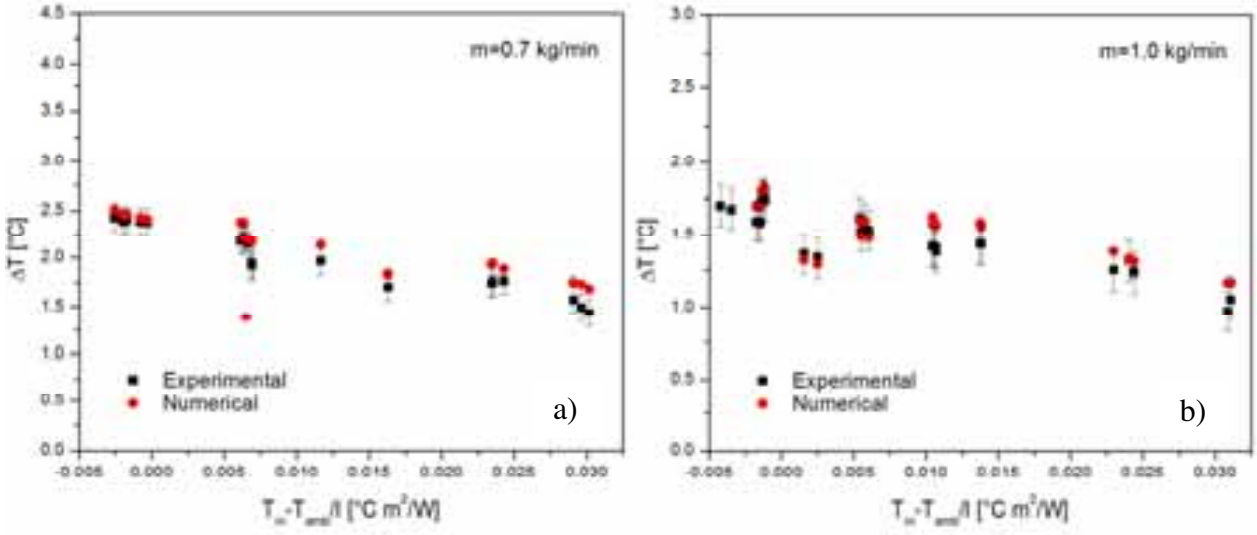

Figure 7. Comparison of the increment of temperature through the CPC between the experimental and numerical results for a mass flow rate of: a) 0.7 kg/min and b)1.0 kg/min.

The error and standard deviation between the experimental data and numerical results are shown in Table 5

Table 5. Comparison between experimental and numerical results for the increment of temperature.

Mass flow rate (kg/min)	ΔT	
	Absolute error (°C)	Standard deviation (°C)
0.7	±0.10	±0.06
1.0	±0.17	±0.17

7. CONCLUSIONS

The numerical model developed is based on the applications of governing equations and used empirical correlations. The numerical algorithm solves in a segregated manner the subroutines: heat conduction in the receiver tube wall, fluid flow inside the receiver tube and the useful energy gain in the solar concentrator.

A prototype of CPC with a real concentration of 1.8 and aperture area of 0.17 m^2 was designed and built. The experimental and numerical results were compared in order to validate the model.

Numerical model has proven to be reliable and was validated with experimental data of the CPC. The results have been satisfactory. The comparison between the experimental and numerical results shows that the numerical model provides good results and tendencies.

REFERENCES

[1] Collares-Pereira M. CPC type collectors and their potential for solar energy cooling applications. Proceedings of the Second Munich Discussion Meeting on Solar Assisted Cooling with Sorption Systems, Munchen, 1995, paper No. 5.
[2] Ortega N, García-Valladares O, Best R, Gómez VH. Two phase flow modelling of a solar concentrator applied as ammonia vapour generation in an absorption refrigerator. Renewable Energy 2008; 33:2064-2076
[3]Hsieh, C.K. Thermal analysis of CPC collectors, Solar Energy 1981; 27:19-29.
[4]Duffie, J.A., Beckman, W.A. Solar engineering of thermal processes, 2nd Ed. New York: Wiley Interscience, 1991; 174–354.

ACKNOWLEDGEMENTS

This work was partially supported by the following projects: PAPIIT project IT100812-3, FORDECYT project 190603, SENER-CONACyT project 117914 and CEMIE-Sol project 12.

Conference Proceedings

Solar World Congress 2015
Daegu, Korea, 08 – 12 November 2015

STUDY OF A THERMAL–PHOTOVOLTAIC SOLAR HYBRID SYSTEM

Haruhiko MIYANABE [1], and Keizo YOKOYAMA [1]

1 Kogakuin University, Japan

Abstract

The solar hybrid panel used in this research includes, besides a PV part, a heat acquisition part consisting of flat heat pipes and heat collection pipe on the back of the solar PV module. The system is capable of simultaneously converting solar energy into both electricity and heat. It has the potential to improve total solar energy conversion efficiency while reducing generation losses caused by rising temperature of the solar PV module. This study aims to achieve practical use of this solar hybrid panel. The report describes basic characteristic of the heat pipe used for the heat-collecting module. The energy balance of the system was simulated and compared against measurement data. Sensitivity analysis was also performed. As a result, the heat pipe was found to function normally when the angle of tilt is at least 10 degrees.

Keywords: *Photovoltaic, Solar thermal, Hybrid, Experiment, Simulation*

1. Introduction

Photovoltaics have become popular throughout the world. Their conversion efficiency is about 10–15%. The current efficiency is not very high. Utilization of solar heat, on the other hand, has a conversion efficiency of 40–50%. However applications of solar heat are limited. Therefore, various studies are being conducted to extend utilization technology (E. Yandri, 2011).

A thermal-solar hybrid system has characteristics of both photovoltaic power generation and solar heat collection. This report provides an overview of demonstration experiments on such a system, and the system's performance characteristics.

2. Composition of the thermal-solar hybrid panel

The solar hybrid panel used in this research includes, besides a PV part, a heat acquisition part consisting of flat heat pipes and heat collection pipe on the back of the solar PV module. The system is capable of simultaneously converting solar energy into both electricity and heat (see Fig. 1 and Fig. 2). It has the potential to improve total solar energy conversion efficiency while reducing generation losses caused by rising temperature of the solar PV module. Fig. 3 shows the installed condition and Fig. 4 shows a schematic diagram of the system.

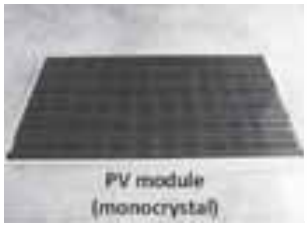

Fig. 1: Solar hybrid panel

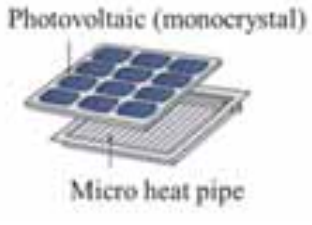

Fig. 2: Constitution of the Solar hybrid panel

Fig. 3: Appearance of solar hybrid system

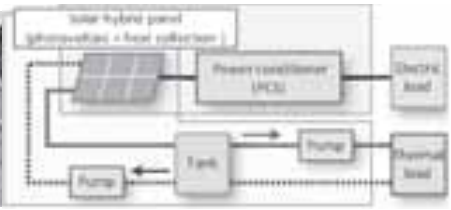

Fig. 4: Schematic of solar hybrid system

doi:10.18086/swc.2015.10.04 Available at http://proceedings.ises.org

3. Overview of research

Although the aim of this research is to achieve practical use to the solar hybrid panel, this report develops an understanding of the basic characteristics of the heat pipe used in the heat-collecting module. A simple simulation of the energy balance was conducted. Sensitivity analysis was also performed while varying a number of parameters.

4. Overview of micro flat heat pipe

Table 1 provides an overview of the heat-collecting module used in the solar hybrid panel. Fig. 3 shows a schematic diagram of heat transfer in the micro flat heat pipe.

The heat pipe has a capillary structure and has a working fluid sealed inside. The principle of heat transfer is as follows: When the heat pipe is heated, working fluid is vaporized, and it moves upward from the bottom of the heat pipe. At the top of the heat pipe, it is condensed by cooling, and when it becomes a liquid it returns again to the bottom of the pipe due to the capillary phenomenon. In this way, heat transfer is carried out continuously.

Table 1: Overview of heat pipe

Outer dimensions (height x width x thickness) [mm]	765×60×3
Material	Pure aluminum (extruded)
Working fluid	Acetone
Thermal conductivity [W/cm^2]	37.35
Isothermality	Less than 1 [K/m]
Max. heat flow density [W/cm^2]	100 to 200
Working temperature range [ºC]	-50 to 170
Internal withstand pressure [MPa]	5.07 or higher
External withstand pressure [MPa]	3.92

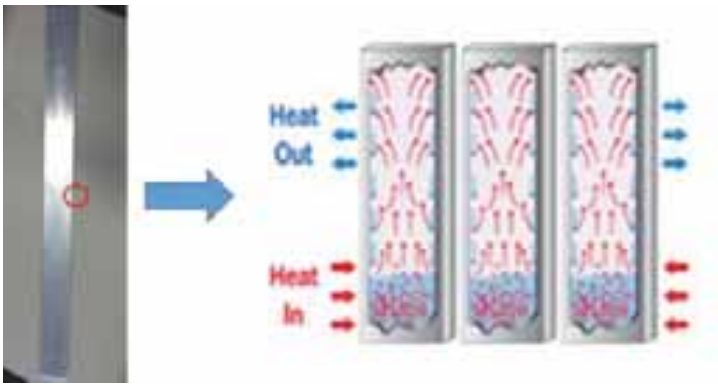

Fig. 5: Schematic diagram of heat transfer of heat pipe

5. Heat pipe characteristic test

Experiments were conducted to determine how heat transport conditions of the heat pipe changed due to angle of tilt, heat input, presence or lack of insulation on the back side, and differences in length.

5.1 Overview of experiment

The experiment used a mask-formed flat heating element to evenly heat the entire pipe. In a product, the added heat is collected by water at one end of the heat pipe, but in this experiment the heat is radiated to the outside via the air. Figure 3 is a schematic diagram of the solar hybrid panel, and the experimental equipment was built to simulate this, as shown in Fig. 4. Insulation (1 and 2) on the heating element side was used to reduce heat loss from the flat heating element.

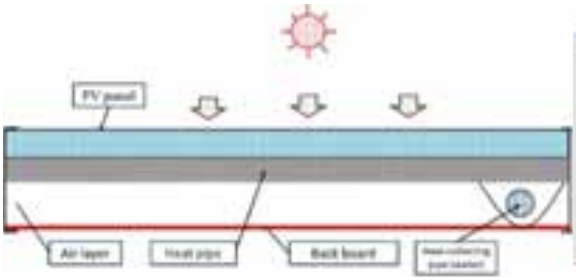

Fig. 6: Schematic diagram of solar hybrid panel

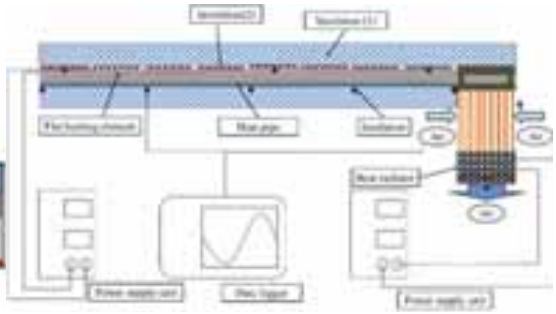

Fig. 7: Diagram of experiment

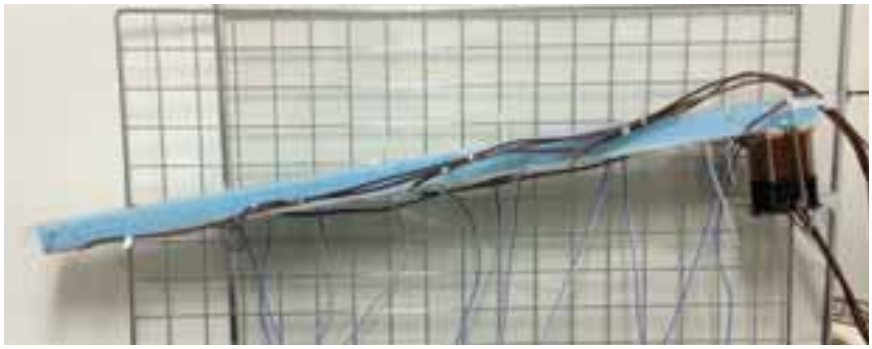

Fig. 8: Experiment equipment

5.2 Experiment cases

There were five experiment parameters: angle of tilt, heat input, presence or lack of insulation on the back side, heat radiation air flow, and differences in length. The experiment was carried out for 64 cases by combining the parameters from Table 2. Measurement points are indicated in Table 3 and Fig. 9.

Table 2: Experiment parameters

Parameter	Number of levels	Levels
Angle	6	0°,5°,10°,20°,45°,90°
Heat input*	5	217 W/m^2 (10 W) 435 W/m^2 (20 W) 651W/m^2 (30 W) 871 W/m^2 (40 W) 1085 W/m^2 (50 W) 1302W/m^2 (60 W)
Radiator air flow	3	Standard (0.033749 m^3/s) 50% 25%
Insulation	2	With insulation, without insulation
Heat pipe length	2	Type-M (60 mm × 765 mm), Type-L(60 mm × 955 mm)

*Corresponds to intensity of solar radiation passing through PV panel.

Table 3: Measurement points

Measurement points	Nounber oh points
Panel back side temperature	CH1, CH3, CH5, CH7, CH9
Flat heating element	CH15,CH17,CH19
Outside air temperature	CH11
Outlet temperature	CH19

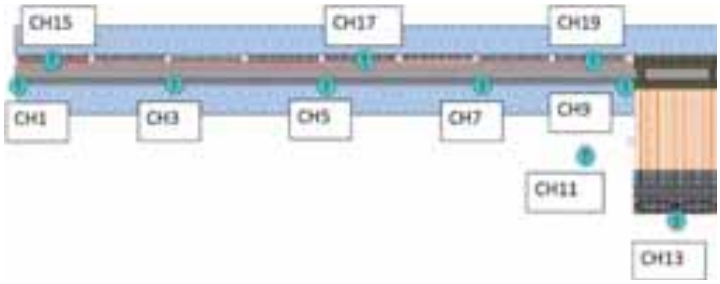

Fig. 9: Measurement points

5.3 Test results

(1) Angle of tilt and heat input (Fig. 10)

As the angle of tilt of the heat pipe increases, the average back side temperature decreases, and the heat pipe functions normally. With low heat input of 10 W or 20 W, the back side average temperature decreases by 5 degrees or more. When heat input is 30 W or higher, the back side average temperature decreases with an angle of inclination of 10 degrees or more and there is also equalization of the temperature distribution. Therefore, it can be said that heat transport of the heat pipe functions properly if the angle of inclination is10 degrees or more.

(2) Heat radiation air flow (Fig. 11)

When heat radiation decreases, average temperature of the heat pipe back side rises. This is because a larger amount of heat is radiated when the air flow of the radiator is high. If heat input is high, the difference in temperature due to the difference in heat radiation increases. In the case with heat radiation air flow of 50% and heat input of 60 W, the back side average temperature rose by approximately 3ºC. The heat radiation performance is not affected very much with low heat input of around 10 W.

(3) Effects of insulation (Fig. 12)

In the case with insulation, back side average temperature is about 1°C higher than with no insulation. This is because, when there is no insulation, heat is radiated from the surface of the uninsulated heat pipe.

(4) Comparison of heat pipe length (Fig. 13)

A comparison was performed based on differences in length. When heat radiation air flow is low, the temperature of a long heat pipe rises somewhat, but otherwise there is hardly any difference.

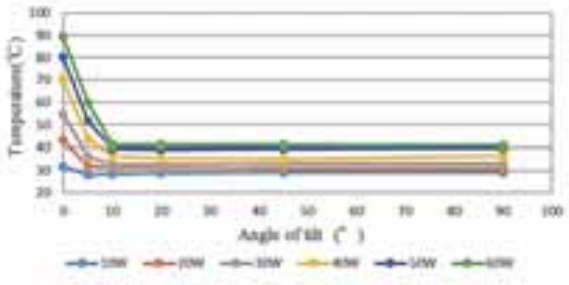

Fig. 10: Relationship of angle of tilt and heat input different

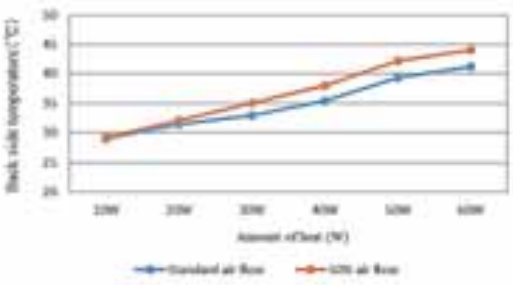

Fig. 11: Comparison of back side temperatures with radiation air flow rates

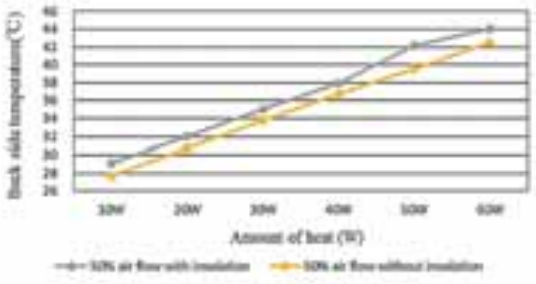

Fig. 12: Comparison of back side temperatures with difference in insulation

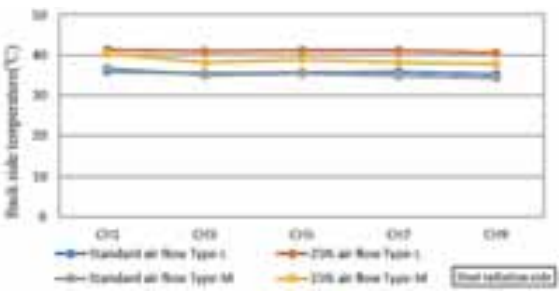

Fig. 13: Results of length comparison corresponding to 40W to 40W

6. Energy balance of the panel

A simulation model was created based on the schematic diagram (Fig. 14) of solar hybrid panel. The model was implemented in spreadsheet software using the heat balance equations given in Table 4. Table 6 shows the spreadsheet.

In the simulation, the heat-collecting pipe efficiency was defined by comprehensively taking into account factors such as the type of mounting of the heat-collection part and the water temperature. The PV panel was assumed to be integrated with glass (reflection and absorption only; thermal conductivity the same as glass), and surface reflectance was assumed to be 5%. The temperature difference at both sides of the heat pipe was assumed to be 1ºC. Thermal conductivity of the back side of the panel was assumed to be due to convection only and radiation was ignored because the surface is facing the rooftop. Thermal resistance of the acrylic panel on the back side was included in the thermal resistance of the air layer.

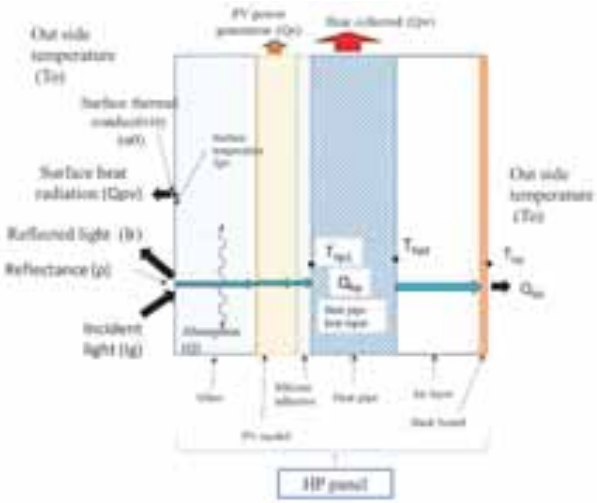

Fig. 14 Energy balance schematic diagram

Table 4: Heat balance calculation equations

Amount of reflection	W/m^2	Ir	=	(Ist+Isky)*ρ	(eq. 1)
Amount of heat absorption	W/m^2	Ia	=	(1-ρ)*Is	(eq. 2)
PV panel surface temperature	ºC	Tpv	=	(Qw+Qbp)*R+Thp1	(eq. 3)
Amount of heat radiation at PV surface	W/m^2	Qpv	=	(Tpv-To)*αo	(eq. 4)
PV power generation	W/m^2	Qe	=	Is*η	(eq. 5)
Thermal resistance	km2/W	R	=	Tpv/λpv+Tsi/λsi	(eq. 6)
HP surface temperature	ºC	Thp1	=	Thp2+1.0	(eq. 7)
HP heat input	W/m^2	Qhp	=	Is-Ir-Qpv-Qe	(eq. 8)
Amount of heat collected	W/m^2	Qw	=	Qhp*ηh	(eq. 9)
Heat collection efficiency	%	ηh	=	Qw/Is	(eq.10)
Heat balance	W/m^2	Sh	=	Is-Ir-Qpv-Qw-Qbp-Qe	(eq. 11)
Precision	%	ε	=	Qw/Qwe	(eq. 12)
Surface heat transfer coefficient	W/m^{2}K	αo	=	αor+αoc	(eq. 13)
Radiation	W/m^{2}K	αor	=	ε0*4*σ*Tm^3	(eq. 14)
				ε0 assumes that radiation rate is 0.9	
				Tm=Tmp+273.16	Tmp= Surface temperature of panel (assumed to be 40 ºC)
Convection	W/m^{2}K	αoc	=	5.0+3.4v (v≤5m/s)	(eq. 15)
			=	6.14v^0.78(v>5m/s)	(eq. 16)

Table5: Symbols

Quantity	Symbol	Unit
Outside air temperature	*To*	ºC
PV panel surface temperature	*Tpv*	ºC
Heat pipe surface temperature	*Thp1*	ºC
HP back side temperature	*Thp2*	ºC
Back side temperature	*Tbp*	ºC
Intensity of solar radiation on tilted surface	*Is*	W/m^2
Amount of reflection	*Ir*	W/m^2
Amount of heat absorption	*Ia*	W/m^2
Surface heat transfer coefficient	*αo*	W/m^2K
Convection heat transfer coefficient	*αoc*	W/m^2K
Radiation heat transfer coefficient	*αor*	W/m^2K
Thermal conductivity	*αbp*	W/m^2K
Thermal conductivity	*R*	Km^2/W
Back side heat transfer coefficient	*Rair*	Km^2/W
Amount of heat radiation at PV surface	*Qpv*	W/m^2
PV power generation	*Qe*	W/m^2
Heat pipe heat input	*Qhp*	W/m^2
Amount of heat collected	*Qw*	W/m^2
Amount of heat radiated at back side	*Qbp*	W/m^2
Measured amount of heat collected	*Qwm*	W/m^2
Heat balance	*Sh*	W/m^2
PV power generation efficiency	η	%
Heat pipe heat transfer efficiency	ηhp	%
Heat collection efficiency	ηh	%
Precision	ε	%
Reflectance	ρ	
Glass thickness	*tpv*	m
Silicone adhesive thickness	*tsi*	m
Wind speed	*v*	m/s

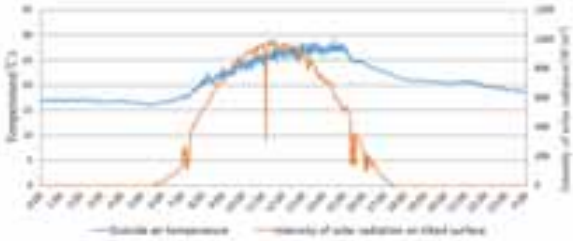

Fig. 15: Outdoor air temperature and intensity of solar radiation on tilted surface (calculation)

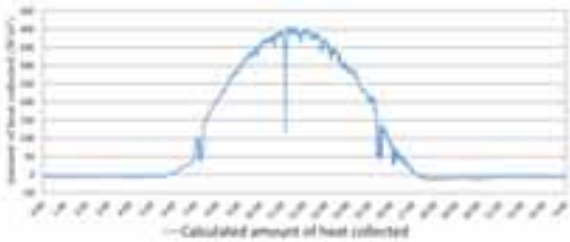

Fig. 16: Amount of heat collection

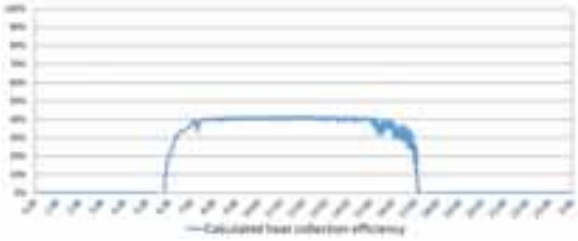

Fig. 17: Heat collection efficiency (calculation)

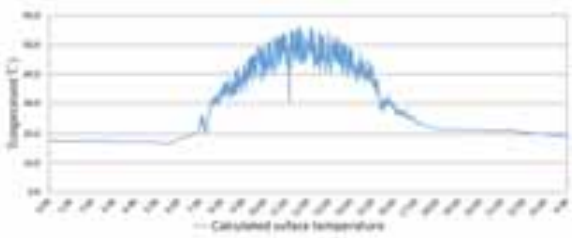

Fig. 18: Heat pipe back side temperature (calculation)

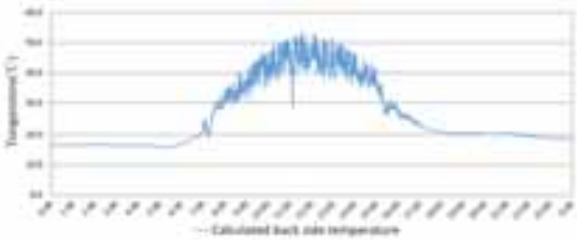

Fig. 19: Heat pipe surface temperature (calculation)

6.2 Energy balance sensitivity analysis

Variation in the amount of heat collected was analyzed while varying the wind speed and silicone grease conductivity in the heat balance spreadsheet for the solar hybrid panel (Table 6). Fig. 20 and 21 graph the amount of heat collected when the wind speed and silicone grease conductivity are varied. The following points are evident in the results.

Table 6: Heat balance spreadsheet for solar hybrid panel

Month	Day	Hour	Outside air temperature	Wind speed	Intensity of solar radiation on tilted surface	Reflectance	Amount of reflection	Amount of heat absorption	PV panel surface temperature	Surface heat transfer coefficient	Amount of heat radiation at PV surface	PV power generation efficiency	PV power generation	Glass thickness	Thermal conductivity
			To	v	Is	ρ	I r	Ia	Tpv	αo	Qpv	η	Qe	tpv	λpv
			ºC	m/s	W/m2	-	W/m2	W/m2	ºC	W/m2K	W/m2	%	W/m2	m	W/mK
9	22	11:30	25.3	0.7	972.8	0.05	48.6	924.2	48.1	13.65	311	0.12	116.7	0.002	0.78

Silicone grease thickness	Thermal conductivity	Thermal resistance	Heat pipe surface temperature	Heat pipe heat input	Heat pipe heat transfer efficiency	Amount of heat collected	HP surface temperature	Thermal resistance of air layer	Back side temperature	Back side heat transfer coefficient	Amount of heat radiated at back side	Heat collection efficiency
tsi	λsi	R	Thp1	Qhp	η	Qw	Thp2	Rair	Tbp	αbp	Q b p	ηh
m	W/mK	Km2/W	ºC	W/m2	%	W/m2	ºC	Km2/W	ºC	W/m2K	W/m2	%
0.001	0.8	0.004	46.2	496.4	0.805	399.6	45.2	0.07	38.4	7.38	96.8	41%

(1) Sensitivity analysis of thermal conductivity of the silicone adhesive.

Heat conduction performance of the silicone adhesive was evaluated. Thermal conductivity of the currently used silicon adhesive is 0.8 W/mK. If the silicon adhesive is changed to one with higher or lower thermal conductivity, there is almost no change in the amount of heat collected at and above 0.2 W/mK. This calculation is carried out assuming that thickness of the silicon adhesive is 1 mm, and therefore in the actual equipment the thickness is will be less, and the effect is likely to be even smaller.

(2) Sensitivity analysis of the wind speed

The amount of heat collected was compared when wind speed is varied. With a high wind speed, the convection heat efficiency increases, and thus the amount of heat collected decreases. It is evident that the size of this decrease is about 2%/(m/s).

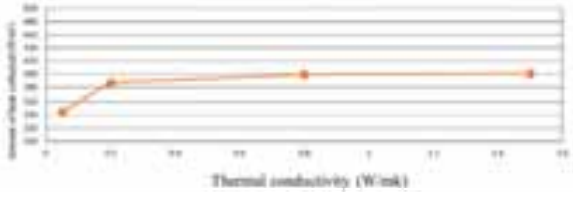

Fig. 20: Silicone adhesive conductivity sensitivity

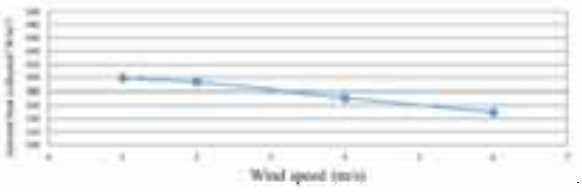

Fig. 21: Wind speed sensitivity

7. Conclusion

Basic experiments were carried out to develop an understanding of the characteristics of the heat pipe used in this solar hybrid panel. Also, a simulation model was created, and sensitivity was analyzed. The following findings were obtained as a result.

(1) Heat pipe properties

- Length of the heat pipe has little effect, and if the angle of tilt is at least 10 degrees, the system operates normally regardless of the intensity of solar radiation.

- If the heat radiation air flow rate is decreased, then temperature decreases when heat pipe temperature increases.

- When there is insulation, temperature of the heat pipe rises, and when there is no insulation, temperature of the heat pipe falls due to radiation of heat from the uninsulated surface.

(2) Energy balance simulation

- In sensitivity analysis of the energy balance, it was found that thermal conductivity of silicone adhesive does not have an effect on the amount of heat collected.

- In sensitivity analysis of wind speed, it was found that the amount of heat collected decreases as wind speed increases.

In the future, we plan to further evaluate performance of the solar hybrid system by measuring the amount of heat collected and the amount of power generated in the actual system.

8. References

Erkata Yandri, Naoto Hagino, Haruhiko Imada, Kazutaka Itako, Hiro Yoshida, Effect of internal heating on thermal performance of hybrid photovoltaic & thermal (PV/T) collector, 2011, SWC2011.

Conference Proceedings

Solar World Congress 2015
Daegu, Korea, 08 – 12 November 2015

WIND PRESSURE DISTRIBUTION ON THROUGH CONCENTRATOR

Qiong Zou[1], Zhengnong Li[1], Honghua Wu[1], RaoKuang[2], Yi Hui[1]

[1] College of Civil Engineering, Hunan University, Changsha, Hunan Province, China

[2] Laboratory of Energy Thermal Conversion and Control of Ministry of Education, School of Energy and Environment, Southeast University, Nanjing, China

Abstract

Aiming to get a precise understanding of wind pressure distribution on trough concentrator surface, wind tunnel experiments on trough concentrator model were carried out in HD-3 atmospheric boundary layer wind tunnel at Hunan University in this study. The length scale of the trough concentrator was 1:15, and 324 measuring taps were arranged symmetrically on both sides, with 162 taps on each. The distribution contours of mean wind pressure coefficient and fluctuating wind pressure coefficients on mirror surface under typical working conditions were obtained. The variation of mean wind pressure coefficient of some taps with yaw angles and pitch angles were provided. Extreme wind pressure was calculated by Hermite moment-based method, and the extreme wind distribution was also presented in this article.

Keywords: *Trough Concentrator, Wind Tunnel Experiments, Wind Pressure Distribution, Hermite moment-based method,*

1. Introduction

From the beginning of the 70's of the last century, a lot of various experimental solar thermal power stations were invested in developed countries. Solar thermal power is a widely discussed research topic in engineering field, and trough solar power generation (shown in Fig.1) is an internationally dominating technique with a good commercialization prospect. Since solar thermal power stations are usually located in the open, flat areas, wind load has to be properly estimated. By studying wind pressure distribution on mirror surface of heliostat and parabolic dish collectors through boundary layer wind tunnel experiment, Peterka and Derickson put forward the algorithm of wind load design on heliostat and parabolic dish collectors. Hosoya and Peterka have conducted a series of wind tunnel tests. Their tests presented the peak load and the distribution of local pressure across the face of the solar collector.The research of wind load on heliostat surface with different Reynolds numbers was done by Pfahl. Naeenia and Yaghoubi studied trough solar concentrator by conducting numerical simulation and wind tunnel experiments, and different wind loads on mirror surface with different pitch angles. Gong introduced an algorithm for wind-induced response calculation. He also studied the wind load characteristics on mirror surface as well as the characteristics of wind field around a trough concentrator through on-site measurement.

doi:10.18086/swc.2015.10.05 Available at http://proceedings.ises.org

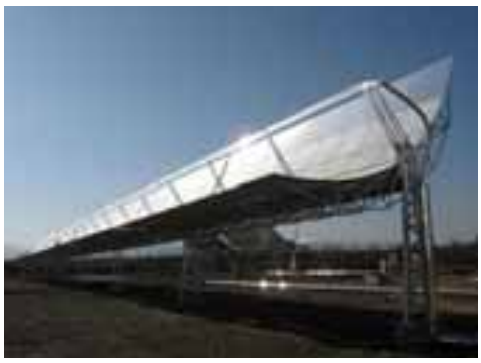

Fig. 1: Trough concentrator (The picture is from National solar thermal Union)

The trough concentrator surface is in an arch shape, thus it can be known that the wind pressure distribution on it is complex. However, there are quite a few researches have been done for the wind pressure distribution on such structures in China. And the wind resistance design of trough concentrator in China is thus in accordance with the existing specifications or technical standard of other countries. However, due to different geographical features and climate condition, the requirements on the strength and rigidity of the concentrator group cannot be met while designed in accordance with such codes. Although there have been some advances for trough collectors in wind tunnel testing and in field measurement, there are still some limiting aspects of the measurement. Compared with previous wind tunnel test, in this paper, in order to obtain more accurate experimental data, the number of wind pressure measuring taps has been increased to 324. In addition, this paper presented the distribution of mean and fluctuating wind pressure on mirror surface. Aiming to get a precise understanding of wind load distribution on trough concentrator surface, wind tunnel experiments on trough concentrator model were carried out in HD-3 atmospheric boundary layer wind tunnel at Hunan University in this study.

2. General information of the experiment

2.1. Experimental apparatus

The experiment was carried out in HD-3 atmospheric boundary layer wind tunnel in Wind Tunnel Laboratory of Hunan University. The wind tunnel was a straight type boundary-layer wind tunnel with low speed. The cross section of the experiment area had a width of 3 meters and a height of 2.5 meters, while the wind speed in the experimental segment was continuously tunable in the range of 0.5~20m·s-1. Cobra probe system could be applied to measure the mean wind speed, turbulence intensity and fluctuating wind power spectrum of flow fields. The pressure measuring apparatus was a DTCnet System made by PSI Corporation. The DTCnet System has 8 modules, and each module has 64 channels, the measuring range is 0.36PSI, with accuracy± 0.05%.

2.2. Experimental model

The trough concentrator prototype consisted of mirror surface, a supporting girder, left and right fin plates, a heat collecting pipe bracket, a transmission system and pillars on both sides. The horizontal projection of mirror surface was 12.2×6.75m, as shown in Fig.2. The mirror surface consisted of 96 small mirrors with a gap of 0.02~0.05m between them. The length scale of the trough concentrator was 1:15 (Fig.3). In order to measure the wind pressure on front and back mirror surface simultaneously in the pressure measuring experiment on mirror surface, 324 measuring taps were arranged symmetrically on both sides, with 162 taps on each. The measuring taps on front surface were arranged in a sequence from A~T, while the measuring taps on back side were arranged in the sequence of AX~TX corresponding to the taps on front surface, as shown in Fig.4. Since the length scale was small, the gaps between small mirrors in the prototype were ignored in experimental the model, the mirror surface in the experimental modal only consisted of two parts.

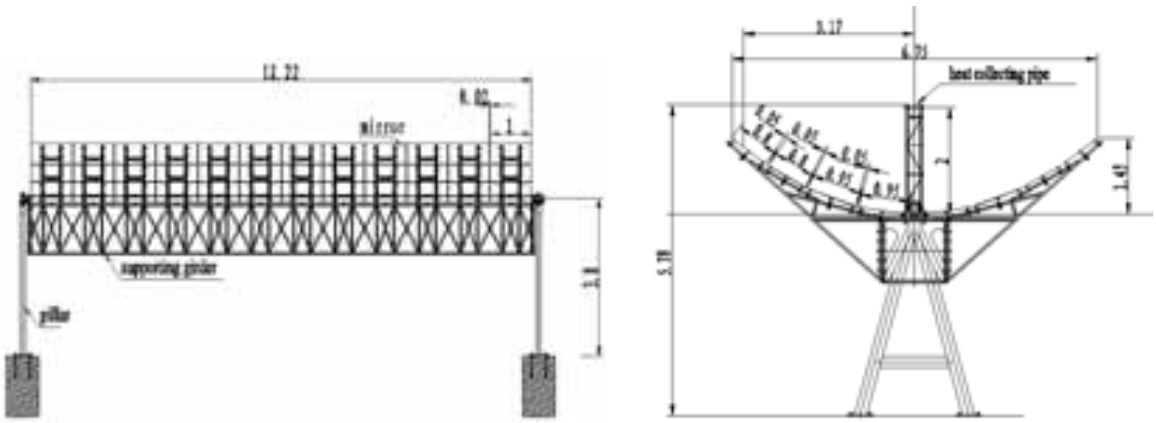

Fig.2: Structure of a trough concentrator

Fig.3: Model of a trough concentrator (1:15)

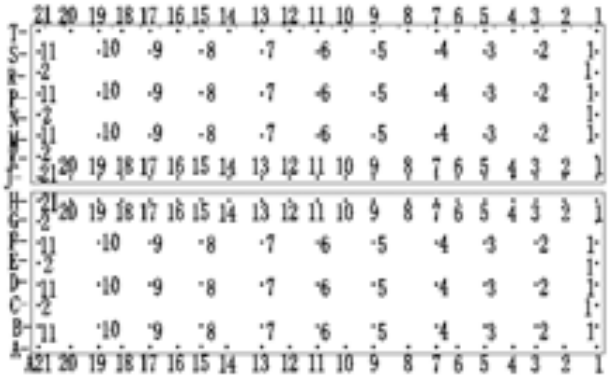

Fig.4: Layout of pressure measuring taps

2.3. Experimental conditions

In the wind tunnel experiment, the horizontal angle of concentrator θ increases from 0° to 180° in increments of 5 clockwise. The vertical elevation angle β of mirror surface increases from 0° to 90° in increments of 10 clock wise, totally 10 different angles. Consequently, 37*10=370 operating conditions are included. The sketch map of the angle of mirror is shown in Fig.5. Because the trough concentrator is a symmetric structure along X axis and Y axis, when the pitch angle is greater than 90°, for example, the pitch angle is 150°, and the yaw angle is 0°(150-000), the wind load of the trough solar collector of 150-000 condition is analogous to that of 30-180 condition. Therefore, we only measured the wind loads for the pitch angle in the range of 0°~90° in wind tunnel test. (Operating condition is expressed in the form of "pitch angle of mirror surface -yaw angle", for instance, 30-000 indicates an operating condition with pitch angle of 30 ^{o} and yaw angle of 0 ^{o}).

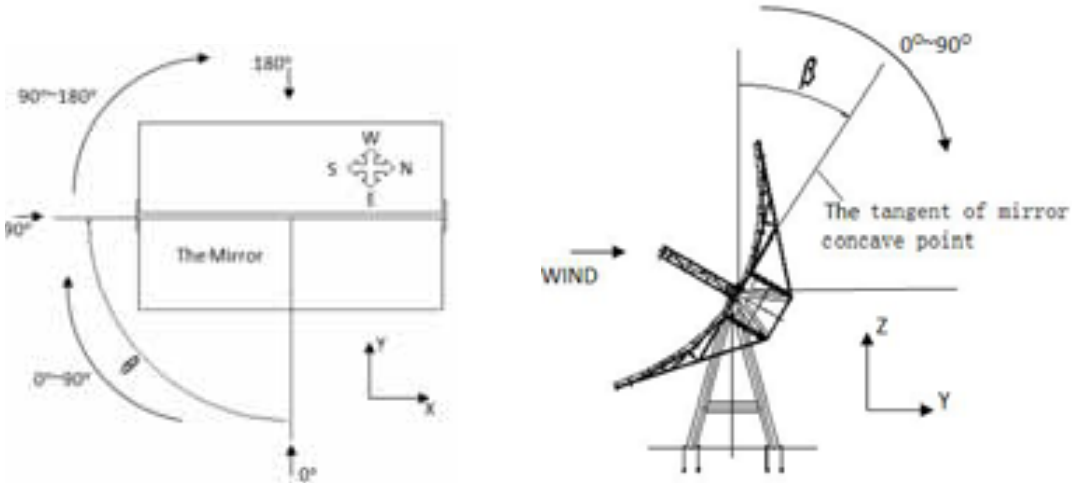

Fig.5: Horizontal wind angle of concentrator in wind tunnel

2.4. Wind field simulation

The comprehensive comparison for the near-ground wind field of wind load codes between China and Europe and America were made, including the mean velocity profile and turbulence intensity profile, fluctuating wind spectrum, etc. The mean velocity profiles of Chinese and Euro codes have a faster increase than other countries, but the mean velocity profile has little difference in the codes of different countries. Compared with other countries, the turbulence intensities in Chinese code are relatively small. For example, with terrain category B (such as the building sparse open country, suburb, forests) and at the height of 10m, the turbulence intensity value of Chinese code is 0.12, the minimum value of the other countries is 0.19, and the maximum value is 0.26.

Based on the terrain roughness characteristics of the site where the trough concentrator is located, the spire-roughness technique was used to simulate the atmospheric boundary layer wind field in wind tunnel according to international experiment method and current Chinese Code on terrain category B. Wind velocity profile is expressed by Equation (1):

$$V_z = V_b \left(\frac{Z}{Z_b} \right)^{\alpha} \qquad \text{(eq. 1)}$$

Where Z_b is the standard reference height; V_b is the mean wind speed at the standard reference height; Z is the height above ground; V_z is the wind speed at the height Z; α is the surface roughness index. The experiment in this study is to simulated terrain category B, so the value α was set to be 0.15 accordingly.

The turbulence intensity profile is calculated according to Equation (2) and (3):

$$I_z(z) = I_{10} \bar{I}_z(z) \qquad \text{(eq. 2)}$$

$$\bar{I}_z(z) = \left(\frac{Z}{10} \right)^{-d} \qquad \text{(eq. 3)}$$

where the turbulence intensity at the height of Z is $I_z(z)$; I_{10} is the nominal turbulence intensity at the height of 10m; the surface roughness index is set as 0.14; Z is the height above ground; d is 0.15. The wind velocity profile and turbulence intensity profile are shown in Fig. 6. The power spectrum of longitudinal fluctuating wind speed is compared with power spectrum by ESDU in Fig. 7.

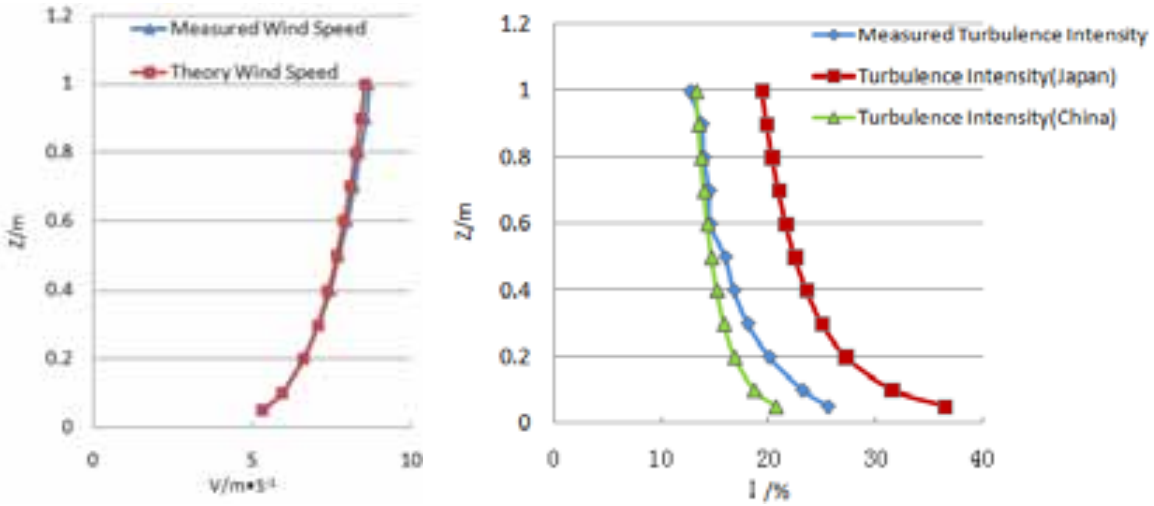

Fig. 6: Mean wind speed profile and the turbulence intensity profile

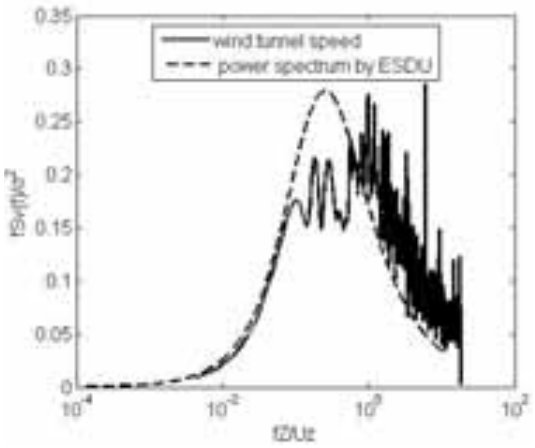

Fig. 7: Wind speed power spectrum of along wind fluctuating wind

3. Processing of experiment data

The measuring taps were arranged symmetrically at the same location on the front side and back side of mirror surface in wind tunnel experiment, respectively. Equation (4) is the calculation equation of net wind pressure coefficient for each measuring position on mirror surface:

$$C_{Pi}(t)=\frac{P_i^f(t)-P_i^b(t)}{\frac{1}{2}\rho V_H{}^2} \qquad \text{(eq. 4)}$$

where $C_{Pi}(t)$ is wind pressure coefficient; i is the serial number of measuring tap; $P_i^f(t)$ and $P_i^b(t)$ are the wind pressures of measuring taps on front side and backside (the leeward side when pitch angle and yaw angle are 0°). With a sampling frequency of 312.5 Hz, 10000 P_i data were recorded for each measuring taps. ρ is the air density in experiment; V_H is the wind speed of the reference tap, and the height of the reference velocity is 0.67m which corresponds to a prototype height of 10m, which is in accordance with Chinese code[10]. By analyzing $C_{Pi}(t)$, the mean wind pressure coefficient, fluctuating wind pressure coefficient could be calculated according to Equation (5) ~(6).

$$C_{Pi,mean}=\frac{1}{N}\sum_{i=1}^{N}C_{Pi}(t) \qquad \text{(eq. 5)}$$

$$C_{Pi,rms}=\sqrt{\frac{1}{N-1}\sum_{i=1}^{N}\left(C_{Pi}(t)-C_{Pi,mean}\right)^2} \qquad \text{(eq. 6)}$$

where $C_{Pi,mean}$ is the mean wind pressure coefficient of the measuring tap i; $C_{Pi,rms}$ is the fluctuating wind pressure coefficient of the measuring tap i; $C_{pi}(t)$ is the time history value of the wind pressure coefficient of a certain measuring tap; i =1, 2, ..., N , N is the number of samples.

4. Distribution of wind pressure

4.1. Distribution of mean wind pressure

The contour map of mean wind pressure coefficient on mirror surface in typical operating condition is shown in Fig. 8.

As shown in Fig. 8, when yaw angle and pitch angle are 0°, the wind pressure coefficients on mirror surface are all positive values. The maximum value is located in the region a little above the middle part of mirror surface. As pitch angle increases, the position of the maximum wind pressure moves toward the edge of mirror surface in the windward. The maximum wind pressure appears at the edge as well as near the concave tap of the mirror surface because of its arch shape when pitch angle reaches 60°. This is different from the wind pressure distribution on heliostat surface. Wind pressure coefficient on the lower part of mirror surface becomes negative when pitch angle reaches 90°. When yaw angle increases to 45°, wind pressure coefficient starts to decrease from the edge of mirror in the windward to the leeward along with the increase of pitch angle. When yaw angle is 90°, pitch angle variation has little influence on wind pressure coefficient distribution because wind direction is parallel with mirror surface. Furthermore, the wind pressure coefficient on the whole mirror surface is small, varying from 0.04 to 0.67. When yaw angle is 135°, wind pressure coefficients on mirror surface are generally negative because the back side of mirror surface is windward, and maximum value appears at the edge of mirror surface in the windward, and the wind pressure distribution pattern is similar to that when yaw angle is 45°. When yaw angle is 180°, wind pressure coefficients are all negative, and the maximum value appears at the central part of mirror surface, the wind pressure distribution pattern is similar to that when the yaw angle is 0°.

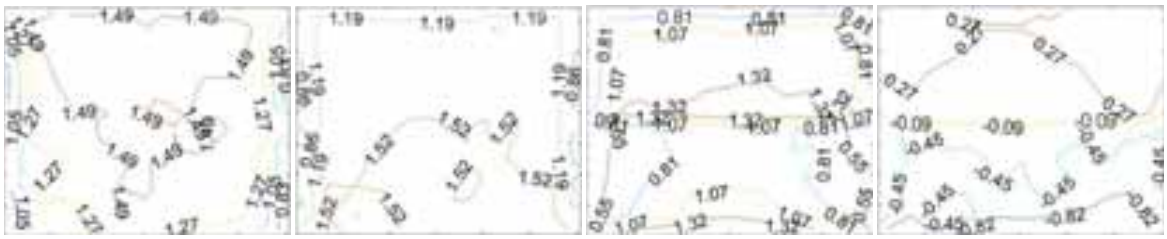

(a) Condition 00-000 (b) Condition 30-000 (c) Condition 60-000 (d) Condition 90-000

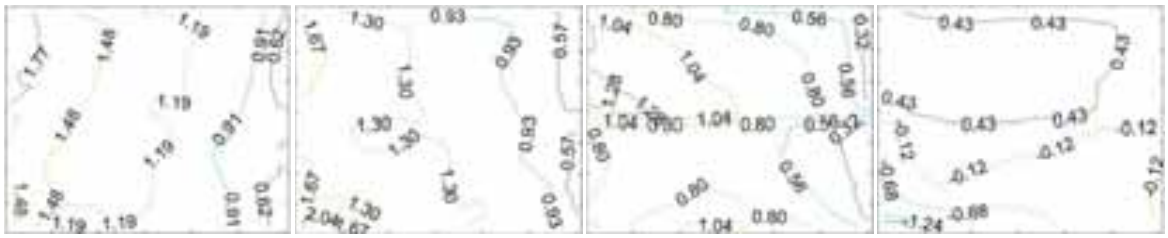

(e) Condition 00-045 (f) Condition 30-045 (g) Condition 60-045 (h) Condition 90-045

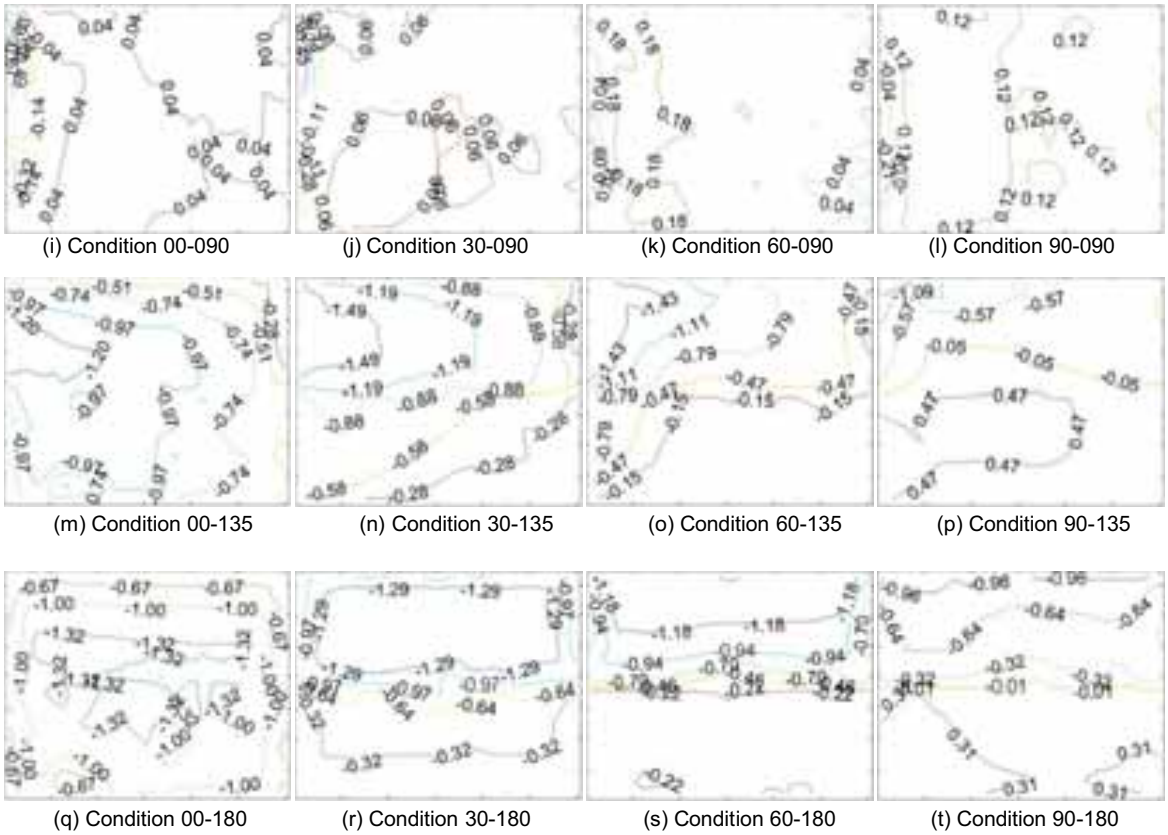

(i) Condition 00-090 (j) Condition 30-090 (k) Condition 60-090 (l) Condition 90-090

(m) Condition 00-135 (n) Condition 30-135 (o) Condition 60-135 (p) Condition 90-135

(q) Condition 00-180 (r) Condition 30-180 (s) Condition 60-180 (t) Condition 90-180

Fig. 8: Contour map of mean wind pressure coefficient at the measuring taps on concentrator surface

4.2. Distribution of fluctuating wind pressure

The contour of fluctuating wind pressure coefficient on mirror surface under typical operating condition is shown in Fig. 9. When yaw angle is 0^o, the maximum fluctuating wind pressure coefficient moves toward the edge of mirror surface in the windward as pitch angle increases. This is because cylindrical vortex forms at the edge of mirror surface when air flow reattaches to mirror surface as soon as it is separated by the thin mirror in the windward. Consequently, the maximum fluctuating wind pressure coefficient appears at the edge of mirror surface. When pitch angle increases to 90^o, besides the maximum fluctuating wind pressure at the edge of mirror surface, another two maximum wind pressure coefficients appear symmetrically in the central part of mirror surface in leeward. This is resulted from two symmetrical vortices formed in the leeward after the separation of air flow separated at the edge of mirror surface. When yaw angle increases to 45^o, fluctuating wind pressure distribution shows a similar pattern despite pitch angle changes. It decreases from the edge of mirror surface in windward to leeward. When yaw angle is 90^o, fluctuating wind pressure distribution changes in a gradient pattern because strong air flow separation happens at the edge of mirror surface. When yaw angle is 135^o, the fluctuating wind pressure distribution at different pitch angle is similar to the distribution of mean wind pressure. When yaw angle is 180^o, the fluctuating wind pressure distributions at pitch angle of 0^o, 30^o and 60^o are similar to the distribution of mean wind pressure. In general, fluctuating wind pressure distribution on mirror surface is similar to the distribution pattern of mean wind pressure.

(a) Condition 00-000 (b) Condition 30-000 (c) Condition 60-000 (d) Condition 90-000

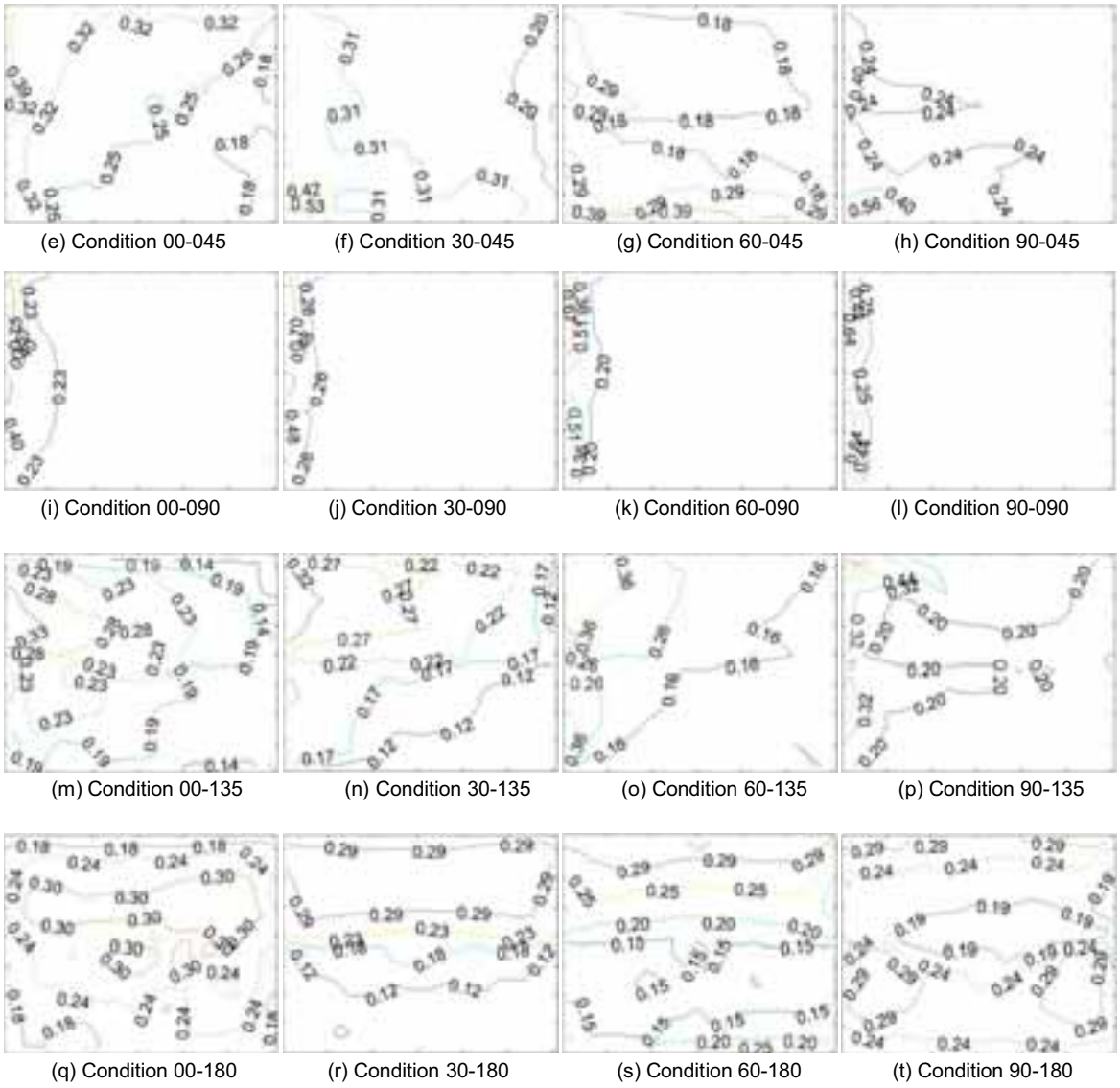

(e) Condition 00-045 (f) Condition 30-045 (g) Condition 60-045 (h) Condition 90-045

(i) Condition 00-090 (j) Condition 30-090 (k) Condition 60-090 (l) Condition 90-090

(m) Condition 00-135 (n) Condition 30-135 (o) Condition 60-135 (p) Condition 90-135

(q) Condition 00-180 (r) Condition 30-180 (s) Condition 60-180 (t) Condition 90-180

Fig. 9: Contour map of fluctuating wind pressure coefficient distribution on concentrator surface

5. Variation of mean wind pressure coefficient with the yaw angles on mirror surface

The variation of mean wind pressure coefficient of some measuring tap on mirror surface with yaw angles are shown in Figure 10. A11, A20 and D6 are measuring taps located near the edge, corner and central part of the same mirror surface (marked as surface A), respectively. The mean wind pressure variation curve of these taps shows the same trend under four pitch angles. When yaw angle is 90^o, the mean wind pressure coefficient value changes from positive to negative or vice versa. This is a favorable condition for wind resistance because the wind pressure coefficient value is relatively low. At the pitch angle of 90^o, the wind pressure coefficient values of measuring taps A11 and D6 are smaller than that at other three pitch angles. However, a large negative wind pressure coefficient, roughly 2.76, appears at measuring tap A20 at pitch angle of 90^o and at yaw angle of 35^o. This is quite different from that of heliostat and deserves attention in the process of wind resistant design. T11, T20 and P6 are measuring taps located on the same mirror surface (marked as surface B), and the mean wind pressure coefficient variation curves of these taps are consistent despite the change of pitch angle. With the exception of the measuring tap T20 located at the corner, the solar collector has fortunate condition when the yaw angle and pitch angle are both 90^o.

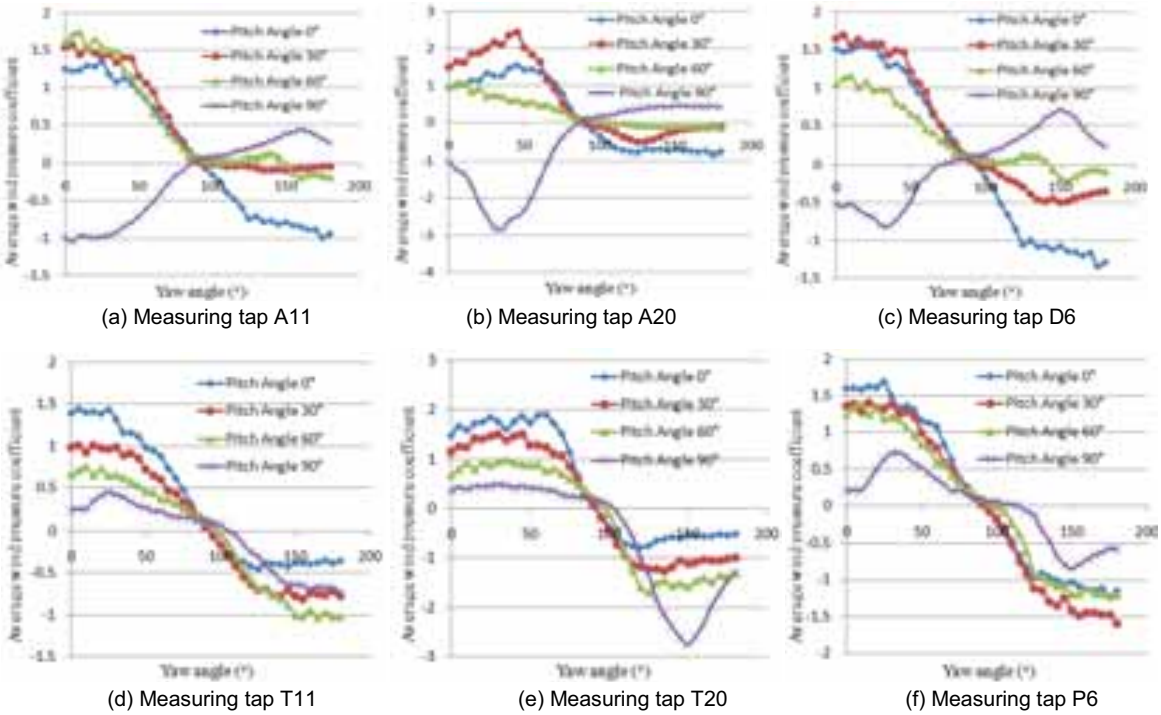

(a) Measuring tap A11 (b) Measuring tap A20 (c) Measuring tap D6

(d) Measuring tap T11 (e) Measuring tap T20 (f) Measuring tap P6

Fig. 10: Mean wind pressure coefficient variation curves at typical measuring taps

6. Extreme wind pressure

Zou Q and Li Z have proved that when pitch angle of mirror surface is large, the wind pressure distribution on mirror surface shows non-Gaussian characteristics. When we calculate the extreme wind pressure coefficients of the non-Gaussian regions on mirror surface by Peak-Factor, the Peak-Factor method is defective for calculating extreme pressure coefficients. Because the peak factor method is based on the assumption that the wind pressure distribution is Gauss distribution. Therefore, in this article we use Hermite moment-based method to calculate the extreme wind pressure coefficients.

Kwon and Kareem (2009) revisit the non-Gaussian peak factor for univariate stationary non-Gaussian processes and clarify the expression of the Hermite moment-based non-Guassian peak factor as (Kareem and Zhao,1994; Kwon and Kareem, 2009):

$$\overline{x}_{ng} = \partial\left\{\left(\beta+\frac{\gamma}{\beta}\right)+h_3\left(\beta^2+2\gamma-1+\frac{1.98}{\beta^2}\right)+h_4\left[\beta^3+3\beta\left(\gamma-1\right)+\frac{3}{\beta}\left(\frac{\pi^2}{6}-\gamma+\gamma^2\right)+\frac{5.44}{\beta^3}\right]\right\} \quad \text{(eq. 7)}$$

where γ is Euler's constant (≈ 0.5772); $\beta=\sqrt{2\ln(v_0T)}$; v_0 is the mean zero upcrossing rate of a standardized non-Guassian process $x(t)$, which is obtaind from a general non-Guassian process $X(t)$ as $x(t)=\left[X(t)-\mu_X\right]/\sigma_X$; μ_X is mean value of $X(t)$; σ_X is the standard deviation of $X(t)$; T is time duration; ∂, h_3, h_4 are parameters of moment -based Hermite modle, which gives a transformation from a standard Guassian process $y(t)$ to the standardized ono-Guassian process $x(t)$ as :

$$x(t)=\partial\left\{y+h_3\left(y^2-1\right)+h_4\left(y^3-3y\right)\right\} \quad \text{(eq. 8)}$$

where the parameters h_3, h_4 control the shape of the distribution, ∂ is the scaling factor.

$$\partial=\left(1+2h_3^2+6h_4^2\right)^{-\frac{1}{2}},\quad h_4=\frac{\sqrt{1+1.5(\gamma_4-3)}-1}{18}.\quad h_3=\frac{\gamma_3}{4+2\sqrt{1+1.5(\gamma_4-3)}} \quad \text{(eq. 9)}$$

where γ_3 is skewness of a process $x(t)$; γ_4 is kurtosis of a process $x(t)$.

Extreme wind pressure distribution could be derived from equation (7)~(9). Because article length is limited, the maximum and minimum wind pressure coefficient distribution maps on mirror surface under some operating condition are shown in Fig. 11 and Fig. 12, respectively. As shown in the contour, the maximum and minimum values move to the edge of mirror surface with the increase of yaw angle and pitch angle; High pressures are typically concentrated around the edges of the collector because of flow separation or vortex formation from the corner where the most wind damage, such as breakage of the mirror is expected to occur.

(a) Condition 00-000 (b) Condition 30-045 (c) Condition 60-045 (d) Condition 90-050

Fig. 11: The maximum wind pressure coefficient on concentrator surface under typical and the most unfavorable operating conditions

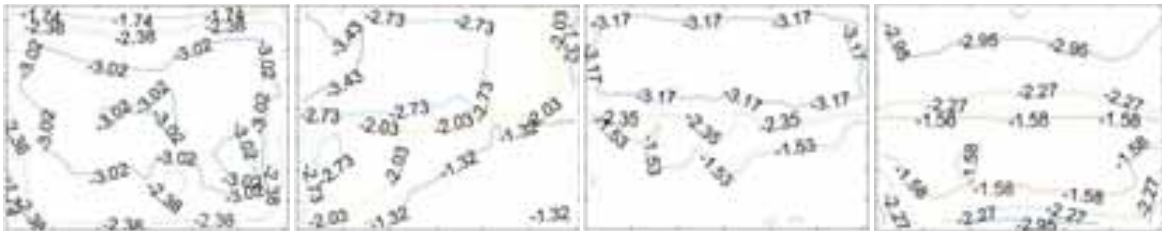

(a) Condition 00-180 (b) Condition 30-135 (c) Condition 30-180 (d) Condition 60-180

Fig. 12: The minimum wind pressure coefficient on concentrator surface under typical and the most unfavorable operating condition

7. Conclusion

- As the pitch angle and the yaw angle increase, wind pressure distribution on mirror surface changes obviously, and the maximum wind pressure coefficient moves toward the edge of mirror surface close to wind.
- High pressures are typically concentrated around the edges of the collector, and the breakage of the reflector panels at the edge is expected to occur. Therefore, the mirror panels should be improved in stiffness of the edge parts to resist wind-induced vibration.
- Peak factor method is not suitable for the calculation of the extreme wind pressure of trough condenser. Because the wind pressure distribution on mirror surface shows non-Gaussian characteristics. In this article , we use Hermite moment-based method to calculate the extreme wind pressure coefficients.
- The wind pressure distribution pattern on mirror surface and wind pressure coefficient value derived from the analysis in the article can be used as reference for the optimization design of concentrator group and the research on mirror surface deformation control.
- Some limiting aspects of the measurement are figured out. Firstly, pitch angle of solar collector could vary from 0^o~360^o. In this study, pitch angles measured are in the range of 0^o~90^o, and these information about wind loads at these pitch angles will be studied in the future. Secondly, this study is research the isolated collector. Actually, in practical engineering solar collectors are work in groups, thus the interference effects of neighboring collector need to be studied in the future.
- All conclusions drawn in the article can be applied to trough concentrator with plane size and height

similar to that of the concentrator in the article. For concentrators whose height and size are quite different from that of the prototype in the article, the wind pressure distribution may deviate from the findings in this article and more research needs to be carried out.

8. Acknowledgments

The work described in this paper was supported by National Natural Science Foundation of China (No:51278190，51178180,51308524).

9. References

Cook, N.J., Mayne, J.R., 1980. A refined working approach to the assessment of wind loads for equivalent static design. J. Journal of Wind Engineering and Industrial Aerodynamics, 6(1): 125-137.

Cook, N.J., Mayne, J.R., 1979. A novel working approach to the assessment of wind loads for equivalent static design. J. Journal of Wind Engineering and Industrial Aerodynamics, 4(2): 149-164.

Gong, B., et al., 2013. Fluctuating wind pressure characteristics of heliostats. J. Renewable Energy, 50: 307-316.

Gong, B., et al., 2012. Field measurements of boundary layer wind characteristics and wind loads of a parabolic trough solar collector. J. Solar Energy, 86, 1880-1898.

Gong, B., et al., 2012. Wind-induced dynamic response of Heliostat. J. Renewable Energy, 38(1): 206-213.

GB50009-2012, 2012. Load Code for the Design of Building Structures, Beijing: China Architecture and Building Press.

Hosoya, N., et al., 2008. Wind tunnel tests of parabolic trough solar collectors. J. National Renewable Energy Laboratory Subcontract Report NREL/SR-550-32282.

Hong, X.J., Gu, M., 2004. The equivalent static pressure and response along-wind. J. Journal of Building Structures, 34(7):39-43.

Kwon D, Kareem A, 2009. Peak factor foe non-Gaussian processes revisited. In Proceeding of the 7th Asia-Pacific Conference on Wind Engineering , Taipei.

Kasperski, M., 2003. Specification of the design wind load based on wind tunnel experiments. J. Journal of Wind Engineering and Industrial Aerodynamics, 91(4): 527-541.

Kumar, K.S., Stathopoulos, T., 2000. Wind loads on low building roofs: a stochastic perspective. J. Journal of structural engineering, 126(8): 944-956.

Kareem A, Zhao J, 1991. Analysis of non-Gaussian surge response of tension leg platforms under wind loads. J. Journal of Off-shore Mechanics and Arctic Engineering, 116:137-144.

Naeeni, N., Yaghoubi, M., 2007. Analysis of wind flow around a parabolic collector (2) heat transfer from receiver tube. J. Renewable Energy, 32(8), 1259-1272.

Pfahl, A., Uhlemann, H., 2011. Wind load on heliostats and photovoltaic trackers at various Reynolds numbers. J. Journal of Wind Engineering and Industrial Aerodynamics. 99(9), 964-968.

Peterka, J.A., Derickson, R.G, 1992. Wind load design methods for ground-based heliostats and parabolic dish collectors. R. Sandia National Labs., Albuquerque, NM (United States).

Peterka, J.A., et al., 1990. Wind loads and local pressure distributions on parabolic dish solar collectors. R. Solar Energy Research Inst., Golden, CO (USA); Colorado State Univ., Fort Collins, CO (USA).

Zou Q, Li Z, Wu H, et al., 2015. Wind pressure distribution on trough concentrator and fluctuating wind pressure characteristics. J. Solar Energy, 120: 464-478.

ISES International Solar Energy Society

Conference Proceedings

Solar World Congress 2015

Daegu, Korea, 08 – 12 November 2015

GEOMETRICAL PARAMETRIC ANALYSIS TO FIND OPTIMUM CONFIGURATION OF A SOLAR CONCENTRATOR WORKBENCH USING LINEAR FRESNEL TECHNOLOGY

Alexandre Bittencourt[1], Victor C. Pigozzo F.[1], Júlio César Passos[1], Gabriel Mendes Cascaes[1], André Burigo[1]

[1]Universidade Federal de Santa Catarina, Florianópolis (Brasil)

Abstract

In this study, a numerical model was developed in order to obtain the optical efficiency of a solar collector with a linear Fresnel concentrator. This model was build based on the ray-tracing and Monte Carlo methods. The goal was to use this model to obtain the parameters required to build a linear Fresnel workbench in our laboratory. With this model it was possible to obtain the optimum configuration of a linear Fresnel workbench taking into account physical and financial constraints.

Keywords: *Renewable Energy, Solar Energy, Numerical Model, Linear Fresnel, Concentrated Solar Power*

1. Introduction

Linear Fresnel solar concentration technology is associated with lower costs and greater simplicity of manufacture when compared to other solar concentration technologies available in the market (Muñoz-Antón et al, 2014). However, this technology is relatively new and more studies on this subject need to be carried out. In this regard, the implementation of a linear Fresnel solar collector workbench on the roof of one of our facilities is being investigated in our laboratory. In order to obtain the most promising configuration for this workbench, in terms of fulfilling our objectives, taking into account the physical and technical constraints of the laboratory, a series of algorithms was developed to evaluate the influence of the geometric parameters on the performance. In these algorithms parameters such as the number of mirrors, mirror spacing, mirror curvature, height of the absorber element and the aperture area of the absorber element are varied. With the model developed the geometric efficiency of the collector was evaluated with the position of the sun varying during the day. This model was validated using the software SolTrace, developed by the National Renewable Energy Laboratory (NREL, 2015). The linear Fresnel workbench will be used to study direct steam generation (DSG) and the associated technical thermal issues. The profile of the distribution of the solar radiation flux on the absorber element was determined since this parameter is of great importance regarding DSG technologies.

2. Linear Fresnel Solar Concentrators

The linear Fresnel collector is a type of concentrated solar power (CSP) technology. There are four main types of CSP technologies in the market: the solar tower and the parabolic dish (which involve punctual concentration), and the linear Fresnel and the parabolic trough (which involve linear concentration). Each technology has its particular characteristics, with advantages and disadvantages. Currently, the use of linear Fresnel technology for direct steam generation seems to be favored (Muñoz-Anton et al., 2014). In 2012 there were 29 CSP plants installed around the world and 31 plants under construction (Pavlovic et al., 2012). In most of these the parabolic trough concentration technology is used. Despite the increasing number of plants being installed, the viability of this technology still relies heavily on government incentives and an increase in production levels, which would result in a cost reduction (Wagner, 2008).

The linear Fresnel collector is composed of several elements. One of these is the absorber assembly, which is composed of an absorber element and often a cavity in which the absorber element is mounted. The absorber element usually consists of a single metal tube or a bundle of tubes with a spectrally selective coating to absorb

doi:10.18086/swc.2015.10.06 Available at http://proceedings.ises.org

as much of the concentrated radiation as possible and minimize the emission in the infrared spectrum (Duffie and Beckman, 2006). These tubes are generally made of stainless steel and the working thermal fluid flows inside. The cavity serves to promote the greenhouse effect and thus reduce thermal losses. It can work with a secondary reflector (Zhu et al., 2013).

Next to the ground are the rows of mirrors that reflect radiation to the absorber assembly. These may be flat or have a slight concavity to improve the concentration rate (Abbas et al., 2013). The rows of mirrors are generally orientated in a north-south axis, and they follow the sun's movement during the day, from east to west. The influence of the mirror curvature on the profile of the concentrated radiation was studied in this paper.

3. Geometric Model Using Monte Carlo Ray-Tracing

In order to evaluate the Fresnel configuration a routine was implemented in Matlab. In this routine the Monte Carlo Ray-Tracing (MCRT) method was used, in which the trajectory and energetic weight of each ray are defined using probabilistic functions. The MCRT method is a powerful tool for analyzing the optical characteristics of solar concentrators (Cheng et al., 2014).

The interactions of each ray with the collector elements have been analyzed, and the optical proprieties of these elements, such as reflection, absorption and transmission, can be taken into account (Delatorre et al, 2014). The optical efficiency of the collector is obtained when these parameter are included in the simulation (Zhu, 2013).

However, since this paper focuses on the analysis of the geometric efficiency, parameters such as the mirror reflectivity, the glazing transmissivity and the selective coating of the absorber element are not considered in the primary analysis. This simplification does not represent the real absorber, but it provides the distribution of the radiation concentration in the aperture plane, which will be useful later for thermal evaluations (Facão and Oliveira, 2011). To determine the geometric efficiency of the collector, aimed at obtaining the best configuration for the workbench, this approximation provides good results with great simplicity.

Another simplification is made by considering the absorber assemble as a flat surface which represents its aperture area. The objective is to obtain the concentrated radiation profile in this aperture area and the total concentrated radiation.

This model is equipped to analyze both plane and curved mirrors and its validation was carried out applying two different approaches. First, a plane mirror model was obtained and validated using the software SolTrace of the NREL (National Renewable Energy Laboratory). SolTrace is a highly rated software program designed for this purpose and it has been validated in several experimental studies (SolTrace, 2015), (Wendelin, 2003), (Wendelin et al. 2013), (Maliage and Roos, 2012). However, SolTrace is not an optimization tool and it is not suitable for analyzing several conditions in a row.

Later a model of an existing collector, the FRESDEMO, was developed and the concentrated radiation profile in the absorber was compared with that obtained by Abbas et al. (2013). In this case, the mirrors were slightly curved.

Figure 1 shows several of the dimensions of the collector: the width of the receiver (Wr), the width of each mirror (Wm), the width of the collector (Wcol), the receiver height (hr), the spacing between adjacent mirror lines (Sm), the number of mirror lines (n) and the mirror curvature (Cm).

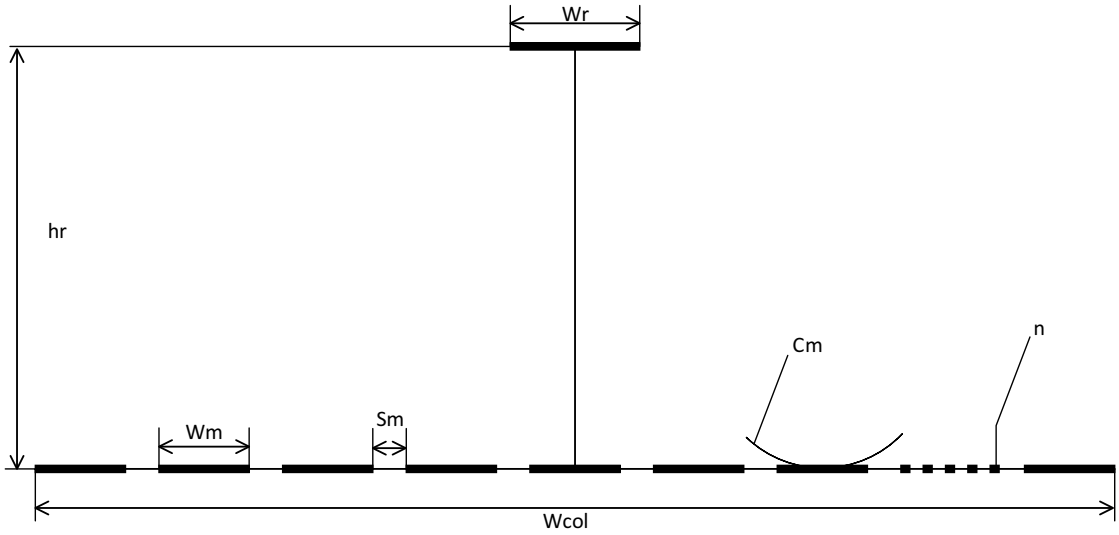

Figure 1: Dimensions of the collector.

4. Results

Since the experimental Fresnel collector is to be installed on the roof of one of the LEPTEN laboratory facilities, spatial and financial constraints must be taken into account. The first constraints are the total width and length of the collector. The area were the Fresnel will be installed is 6m wide and 12m long and thus it is limited to a width of 5m (W_{col} = 5m) to allow easy access for installation and maintenance. The length of the collector was similarly limited to 12m. Considering the collector width limit the other variables can be changed in order to analyze the geometric efficiency.

The geometric efficiency is defined as the ratio between the amount of rays (or energy) that impinge on the width of the receiver aperture and the rays reaching the entire collector width, as shown in equation 1, where η_g stands for the geometric efficiency while n_{r_abs} and n_{r_coll} are the number of rays produced by the MCRT that hit the absorber and the collector aperture, respectively. A useful relation to characterize the Fresnel collector is the filling factor defined in equation 2. This is the relation between the mirror field area and the total area of the collector.

$$\eta_g = n_{r\_abs}/n_{r\_coll} \quad \text{(eq. 1)}$$

$$ff = W_m * n/W_{col} \quad \text{(eq. 2)}$$

The first simulations showed that some of the variables can be kept constant without significantly influencing the final geometric efficiency. This initial analysis is of qualitative rather than quantitative importance. The influence of the spacing between mirrors on the efficiency was the first factor analyzed. In this analysis the mirror width and height were fixed at 300mm and 3500mm, respectively, and the receiver width was defined as 10% greater than the width of the mirrors. The number of mirror rows varied between 10 and 16, and the spacing between mirror lines varied from zero to the maximum allowed respecting the collector width. As shown in Figure 2, for most of the numbers of mirror rows analyzed the maximum efficiency was reached with the largest mirror spacing possible. The only case where the maximum efficiency was not observed at the maximum spacing was 10 rows of mirrors. This is because greater spacing between the mirrors reduced the losses due to shading and blocking, but a limit was reached when significant shadowing and blocking were no longer present. On the other hand, greater mirror spacing means that the mirrors at the extremities will be even farther from the absorber assembly, increasing the loss due to its increased inclination.

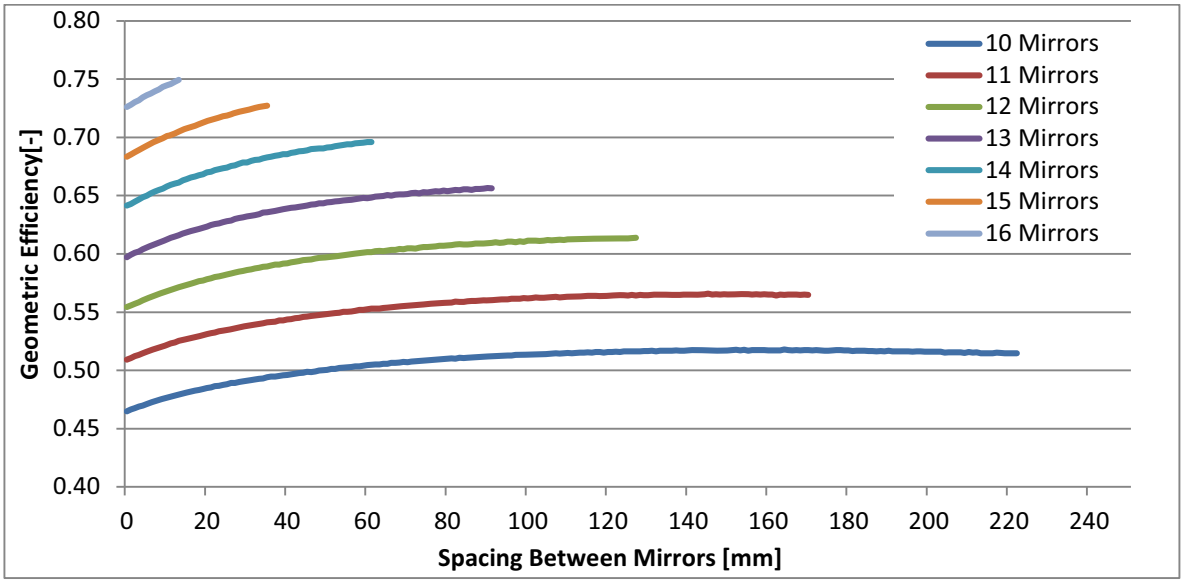

Figure 2: Influence of the number of mirror lines and the spacing on the geometric efficiency.

Therefore, it can be concluded that for all of the cases to be analyzed the maximum spacing between mirror lines will give the best results.

The next step was to determine the influence of the receiver width to mirror width ratio on the efficiency and the results are shown in Figure 3. The efficiency increases with the receiver width as the receiver can intercept more rays reflected from the mirrors. However, the larger the receiver is the larger the shadow it produces on the mirror field will be. For this reason, there comes a point where the efficiency begins to decrease with an increase in the area of the receiver aperture. The curve reaches a maximum at approximately$W_r = 1.1 * W_m$. In this analysis the receiver height is fixed at 3.5m and the spacing between mirrors is set as larger as possible. The same analysis was carried out for different mirror widths and for all cases the same result was achieved. Thus, the relation $W_r = 1.1 * W_m$ was maintained constant in all other analyses. All of these studies were carried out considering plane mirrors. Later, it is shown that for curved mirrors this ratio is far lower, and the receiver width is smaller than the mirror width.

The influence of the receiver height on the geometric efficiency was analyzed by fixing the mirror width at 300mm and using the largest possible spacing between rows. It was observed that on increasing the receiver height the efficiency also increased. It was also concluded that the receiver height has a very weak relation with the other variables.

The analysis is bi-dimensional, which means that the geometrical efficiency obtained is in fact a transversal geometric efficiency. In a three dimensional case, taking into account the collector length, there is another type of loss called end losses. A real-scale Fresnel collector must be sufficiently long to ensure that these end losses are minimal. Because the collector analyzed is short (length = 12m) these losses are large when the sun is low in the sky, for instance, during winter. For flat mirrors, for receiver heights larger than 3500mm the increase in the efficiency is minimal.

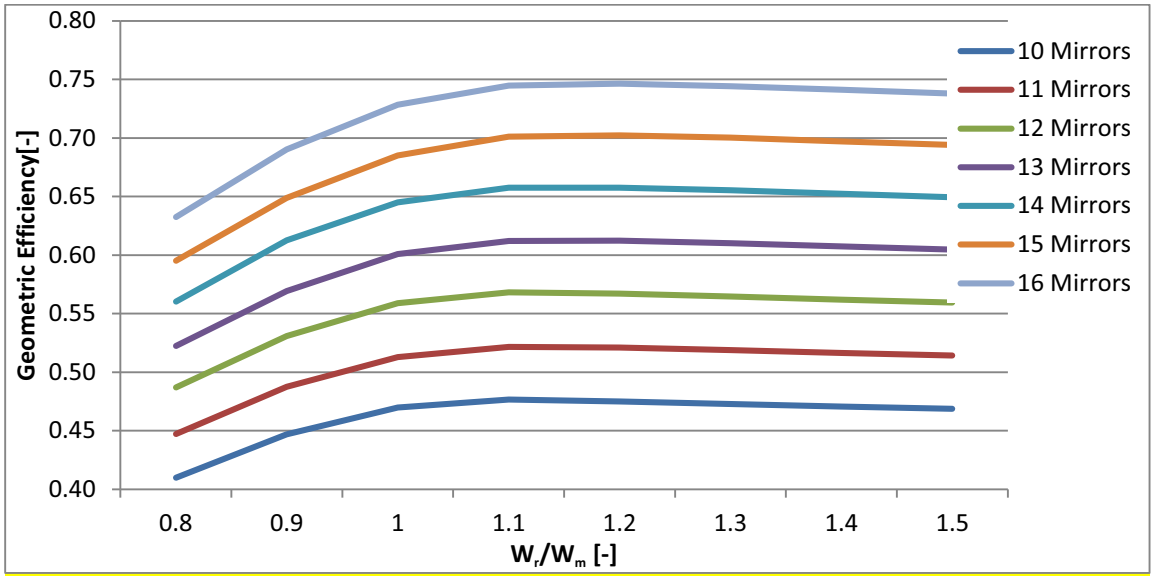

Figure 3: Relation between receiver width and mirror width.

This increase in the efficiency with the receiver height is even more difficult to observe for curved mirrors, as shown in Figure 4. This figure is for the specific case of a collector with 10-mirror rows, each mirror with a length of 450mm each, curved, with an average focus of 1.1 times the absorber height, and using the maximum spacing between mirrors. Other cases were studied and presented similar results.

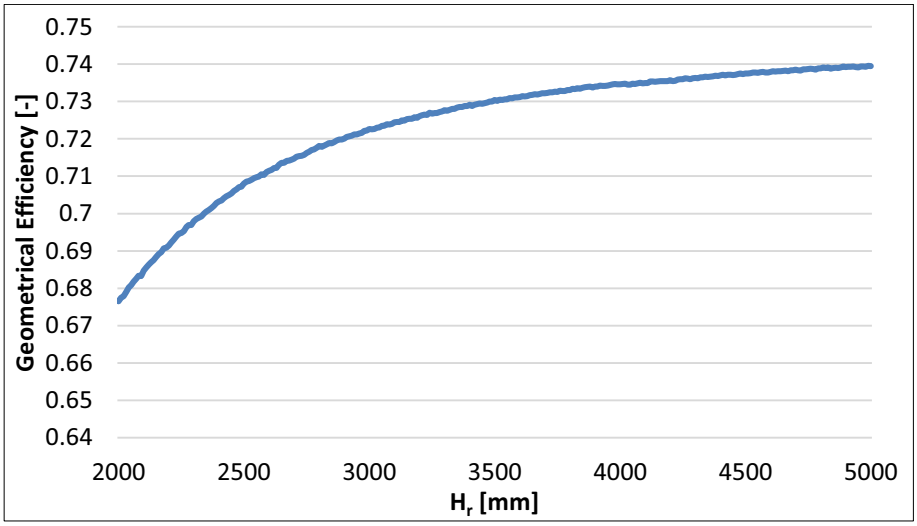

Figure 4: Influence of the receiver height on the geometric efficiency.

The relation between the number of mirror rows and different mirror sizes in the form of a filling factor was analyzed. Figure 5 shows the results for plane mirrors and $W_r = 1.1 * W_m$ using the largest possible spacing and a receiver height of 3500mm. The same analysis was performed for curved mirrors for different focus distances; however, by analyzing these results the conclusions were the same as in the case of flat mirrors.

The filling factor defines a relation between the number of mirror lines and the mirror width, as defined in equation 2. Thus, obtaining the curves for different numbers of mirror lines, varying the filling factor is sufficient to characterize the collector geometry.

As expected, the larger the filling factor the better the efficiency will be and the same is true for a greater number of lines. However, despite the higher efficiency, these cases are not always practical or economically feasible since a greater number of lines requires more components like tracking devices, axes, mirrors and control devices.

Another important observation in relation to Figure 5 is that for low filling factors the efficiency rises considerably with the filling factor, and for filling factors close to unity the increase in the efficiency is not as great. This analysis shows that one can operate with filling factors between 0.9 and 0.95 with an efficiency only 3% lower than the maximum efficiency. This allows some flexibility to deal with costs and building issues associated with the project.

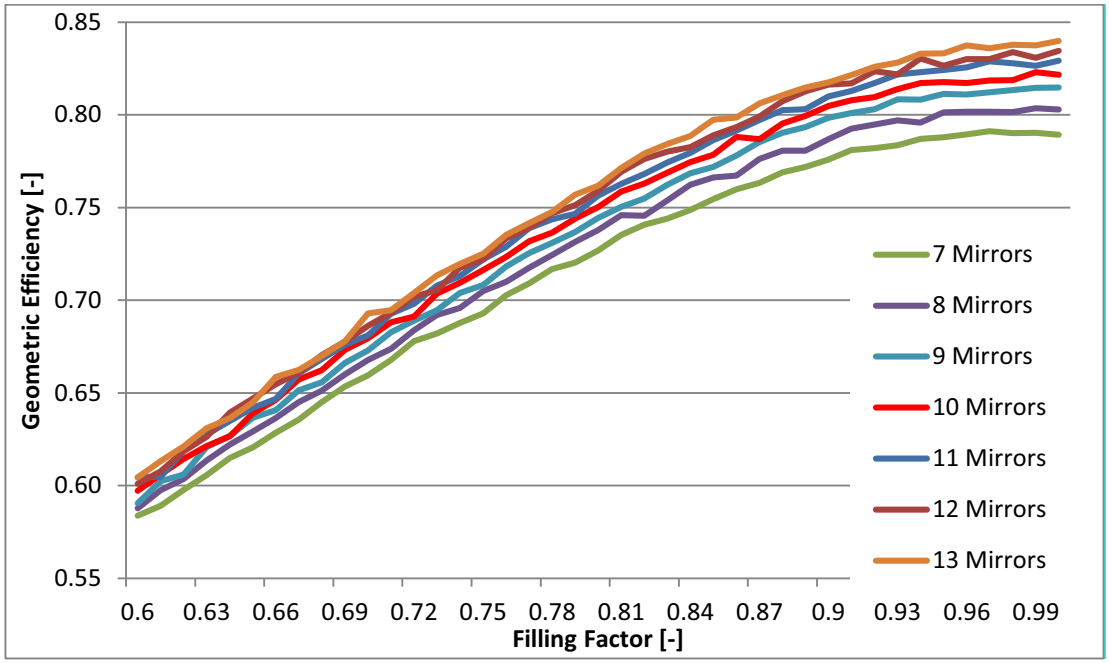

Figure 5: Influence of filling factor and number of mirror lines on efficiency.

The influence of the mirror curvature on the concentrated radiation which is focused on the absorber aperture was analyzed. The distribution of the concentrated radiation over the absorber aperture throughout the day, for different focal lengths, is shown in the Figures 6, 7 and 8. The focal length reported herein is the mean distance between the mirrors and the middle of the absorber aperture area. These figures relate to a collector with 10 mirror rows of 450mm, the absorber height is 3000mm and the maximum spacing between mirrors is applied. Three focal lengths were analyzed: 1.0, 1.1 and 1.2 times the receiver height.

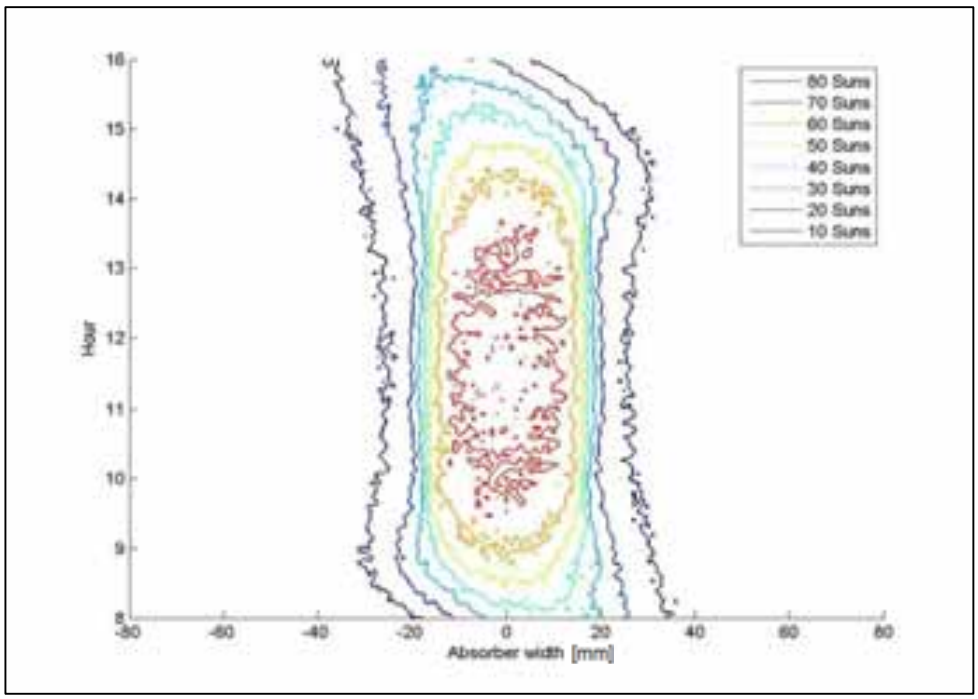

Figure 6: Profile of the concentrated radiation for a focal length 1.0 times the receiver height.

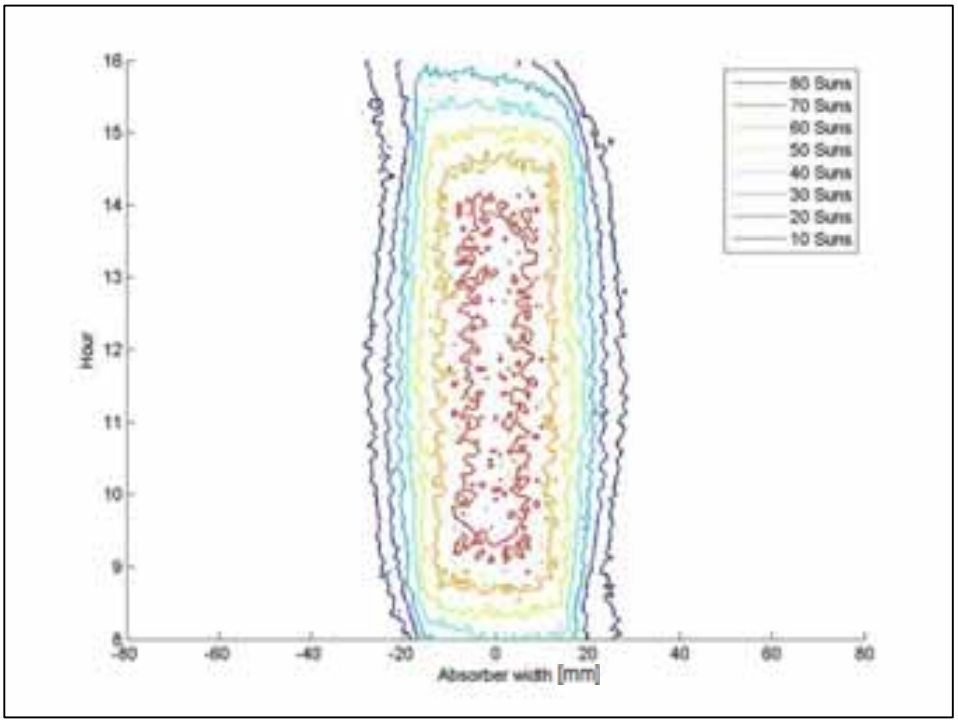

Figure 7: Profile of the concentrated radiation for focal length 1.1 times the receiver height.

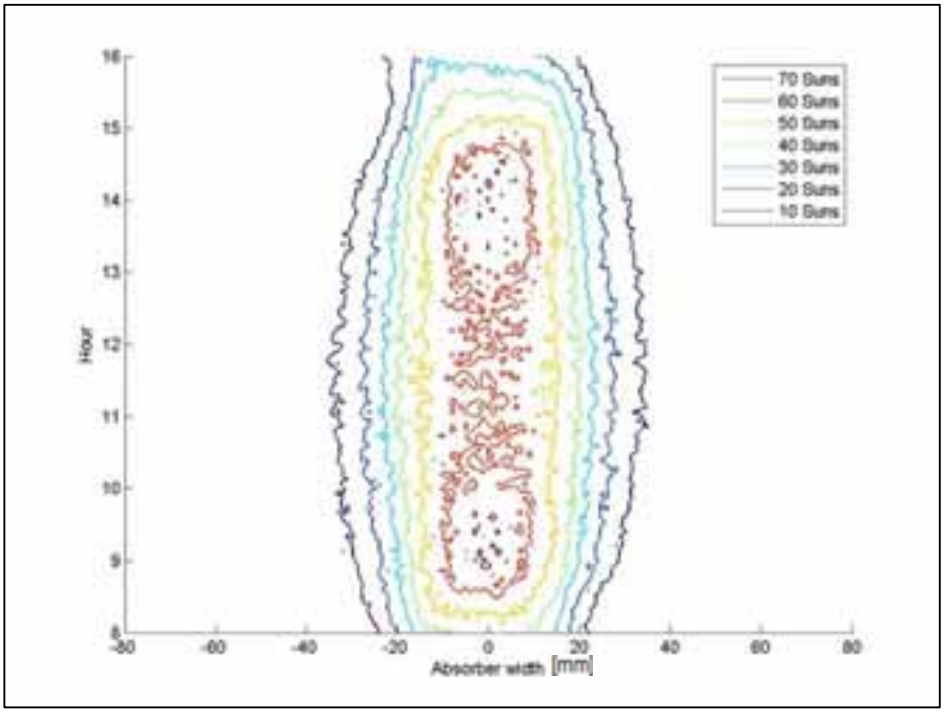

Figure 8: Profile of the concentrated radiation for focal length 1.2 times the receiver height.

It can be seen that for a focal length 1.0 times the receiver height the profile for the concentrated radiation on the absorber aperture area is more homogeneous during the day. This is of interest, since the collector operation will be steadier during the main solar hours of the day. These concentrated radiation profiles favor the use of a set of tubes in the absorber assembly, because this configuration provides good operational flexibility. Muñoz-Anton et al. 2014 demonstrated that in this configuration, for a set of four tubes in a DSG operation, one can set the flow to pass first through the outermost tubes to allow preheating and then through the inner tubes for the phase change. Other numbers of tubes and flow configurations can be used in order to obtain better use of the concentrated profile. The higher the number of tubes for the same flow the lower the diameters can be and, therefore, the heat exchange coefficient will be improved. However, lower diameters also lead to higher pressure losses (Abas et al., 2013).

Focal lengths of shorter than 1.0 and greater than 1.2 times the receiver height were also studied, but they

produced a much more disperse profile than those shown in Figures 6, 7 and 8.

5. Model Validation

This model was validated using the SolTrace software, available from the National Renewable Energy Laboratories. The reliability of SolTrace has been validated via several experimental studies. However, this software does not allow the plant parameters to be changed automatically according to the time of day, making it difficult to generate an optimization routine.

To validate the model, several Fresnel configurations were simulated under the same radiation conditions using both software programs. The results obtained with the model developed in this study were very close to those provided by SolTrace.

A commercial collector FRESDEMO was then modeled, considering curved mirrors, and the results compared with data available in the literature.

Initially, a collector configuration was implemented in SolTrace and compared with the Matlab results for an entire day, as shown in Figure 9. The validation was carried out in both the transversal and longitudinal directions. The longitudinal direction represents the end losses.

For all cases the collector was oriented along the north-south axis and it tracked the sun in the east-west direction during the day. The maximum difference in the values for the concentrated radiation heat flux obtained using the model developed in this study and SolTrace was 1.1%. Considering the end losses (the longitudinal case) this maximum difference was 18.5%. This large difference is observed for high incidence angles which will almost never occur in real applications.

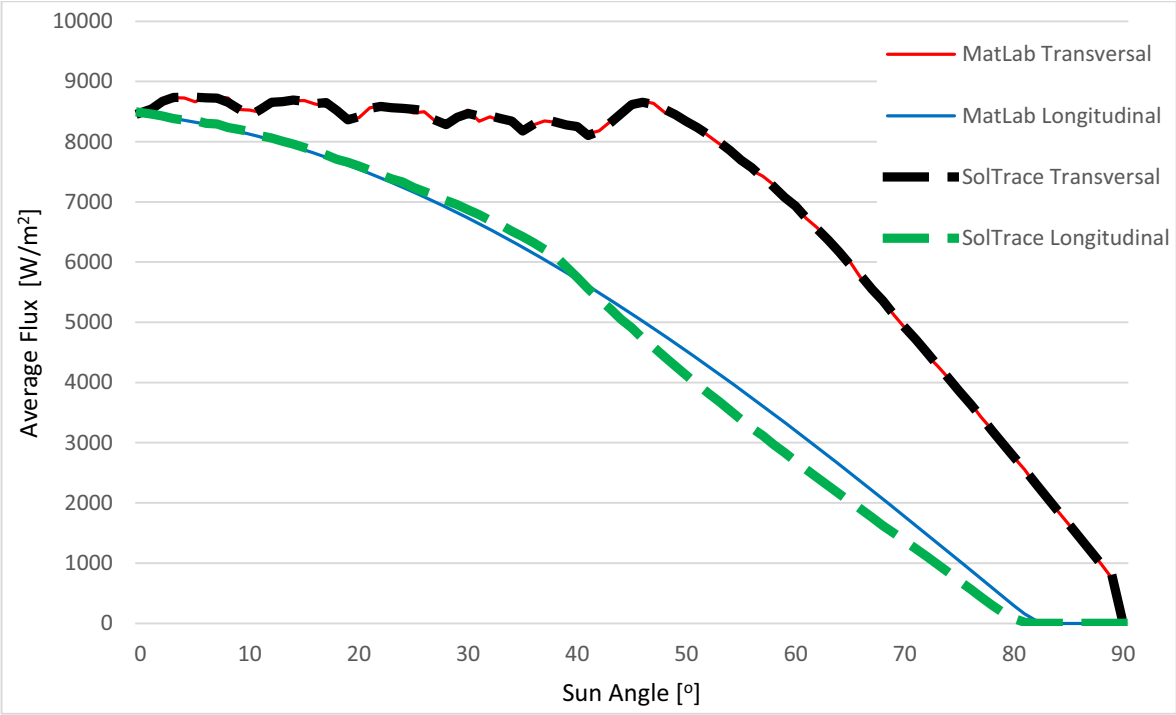

Figure 9: Comparison between the model and SolTrace results.

Figures 10 and 11 show a comparison between the results for the concentrated radiation in the absorber aperture plane for the FRESDEMO collector obtained by Abbas et al. (2013) and with the model presented herein. The focal length used by Abbas et al. (2013) was not reported and thus the focal length used in the model was 1.1 times the mean distance between the mirrors and the absorber. Our model showed good agreement with the radiation profile presented by Abbas et al. (2013). This simulation was carried out using the collector parameters reported by Abbas et al. (2013).

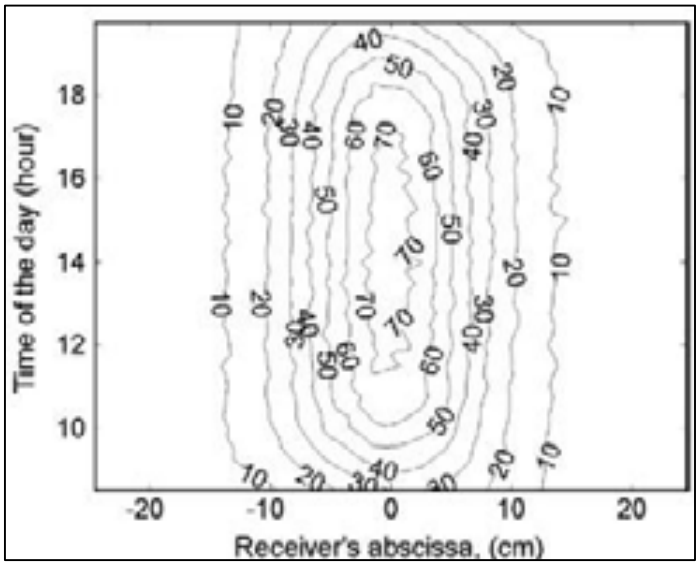

Figure 10: FRESDEMO concentrated radiation profile for the receiver (source Abbas et al., 2013).

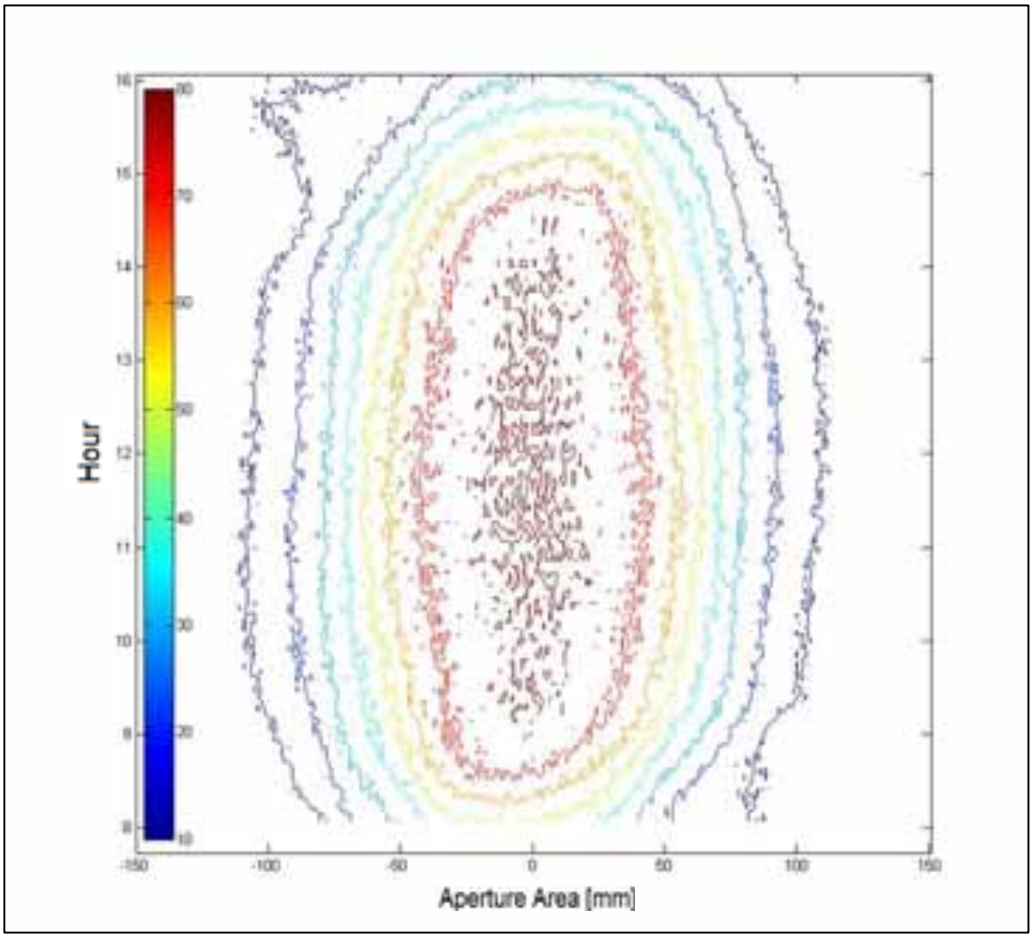

Figure 11: Concentrated radiation profile for the receiver obtained with our model.

6. Conclusions

The model described herein showed good agreement with SolTrace. With this new model it was possible to simulate several aspects of the collector geometry, to make comparisons and to achieve the best configuration for the proposed application. To simplify the work, sensitivity analysis was initially carried out and it was found that some variables do not have a strong relation with others. These variables were then maintained fixed in the subsequent optimization analysis.

An important conclusion is that the mirror row spacing should be the maximum allowed respecting the total

collector width, in order to achieve the best geometric efficiency. The receiver height was also analyzed and 3.5m was selected as an appropriate value in terms of efficiency and operational aspects. For this receiver height and using flat mirrors the best value for the receiver width to mirror width ratio was 1.1.

Considering the constraints identified using the model developed it was possible to evaluate the influence of the geometric configuration of the Fresnel on its efficiency. This study allowed the final configuration of the workbench to be installed in the laboratory to be defined, that is, 10 rows of mirrors with a width of 450mm, with the absorbing assemble placed at a height of 3m. The absorber assembly adopted is the trapezoidal cavity, using a set of four parallel absorber tubes. The trapezoidal cavity was selected due to its technical and constructive advantages and the multitube absorber provides some flexibility in relation to the operational strategies.

The total width of the four tubes is 140mm. The reflective mirrors have a slight curvature which allows the absorber element width to be smaller than that of the mirrors. This bending increases the rate of concentration in the central area of the absorber element, as shown in Figures 6, 7 and 8.

7. References

Abbas, R., Muñoz-Antón, J., Valdés, M., Martínez-Val, J.M., 2013. High concentration linear Fresnel reflectors. Energy Conversion and Management. 72, 60-68.

Cheng, Z.D., He, Y.L., Cui, F.Q., Du, B.C., Zheng, Z.J., Xu, Y., 2014. “Comparative and sensitive analysis for parabolic trough solar collectors with a detailed Monte Carlo ray-tracing optical model”. In Applied Energy 115, 559–572

Delatorre, J., Baud, G., Bézian, J.J., Blanco, S., Calior, C., Cornet, J.F., Coustet, C., Dauchet, J., El Hafi, M., Eymet, V., Fournier, R., Gautrais, J., Gourmel, O., Joseph, D., Meilhac, N., Pajor, A., Paulin, M., Perez, P., Piaud, B., Roger, M., Rolland, J., Veynandt, F., Weitz, S., 2014. Monte Carlo advances and concentrated solar applications. Solar Energy 103, 653 – 681.

Duffie, J. A., Beckman, W. A., 2006. Solar Engineering of Thermal Processes. John Wiley & Sons, Inc. 3rd ed.

Facão, G., Oliveira, A. C., 2011. Numerical simulation of a trapezoidal cavity receiver for a linear Fresnel solar collector concentrator. Renewable Energy 36, 90-96.

Flores Larsen, S., Altamirano, M., Hernández, A., 2012. Heat loss of a trapezoidal cavity absorber for a linear Fresnel reflecting solar concentrator. Renewable Energy. 39, 198-206.

Maliage, M., Roos, T. H., 2012. The flux distribution from a 1.25m2 target aligned heliostat: comparison of ray tracing and experimental results. South African Solar Energy Conference SASEC.

Muñoz-Antón, J., Abbas, R., Martínez-Val, J., Montes, M., 2014. Going further with Frenel receiver: new desing window for direct steam generation. Energy Procedia 49, 184 – 192.

NREL. National Renewable Energy Laboratory. Information on the United States government agency NREL. Avaliable in: < http://www.nrel.gov>. Acessed on 11 March 2015.

Pavlović, T. M., Radonjić, I. S., Milosavljević, D. D., Pantić, L. S., 2012. A review of concentrating solar power plants in the world and their potential use in Serbia. Renewable and Sustainable Energy Reviews 16, 3891-3902.

SOLTRACE. SolTrace Optical Modeling Software. http://www.nrel.gov/csp/soltrace/download.html. Accessed on 20 August 2015.

Wagner M. J., 2008. Simulation and Predictive Performance Modeling of Utility-Scale Central Receiver System Power Plants. University of Wisconsin-Madison.

Wendelin, T., 2003. SolTRACE: A New Optical Modeling Tool for Concentrating Solar Optics. Proceedings of the ISEC 2003: International Solar Energy Conference, 15-18 March 2003, Kohala Coast, Hawaii. New York: American Society of Mechanical Engineers, pp. 253-260; NREL Report No. CP-550-32866.

Wendelin, T., Dobos, A., Lewandowski, A., 2013. SolTrace: A ray-tracing code for complex solar optical systems. Technical Report. NREL/TP-5500-59163.

Zhu, G., 2013. Development of an analytical optical method for linear Fresnel collectors. Solar Energy 94, 240-252.

Zhu, G., Wendelin, T., Wagner, M. J., Kuntscher, C., 2013. History, current state, and future of linear Fresnel concentrating solar collectors. Solar Energy.

Conference Proceedings

Solar World Congress 2015
Daegu, Korea, 08 – 12 November 2015

STRUCTURAL AND OPTICAL PROPERTIES OF SEVERAL IRON-MANGANESE OXIDES TO PREPARE THIN FILMS AS SOLAR SELECTIVE ABSORBERS

Elisa Sánchez[1], Enrique Barrera[1], Federico González[1], Ricardo Rosas[1], Eduardo Ríos[2]
[1] Universidad Autónoma Metropolitana, Distrito Federal, México
[2] Universidad Autónoma Chapingo

Abstract

In this work, the behavior of the mixture to form manganese iron oxides used as pigments for application in solar absorbers is investigated. Polished aluminum as substrate was covered with mixed Fe:Mn oxide by the impregnation method. After drying the thin films, the samples were submitted to different heat treatment temperatures. Chemical structure and optical properties were respectively evaluated using XRD and UV-Vis-IR spectrophotometry technique. The evolution of different structural phases during the addition of manganese ions process is discussed with Rietveld refinement of the X-ray diffraction. The results indicated a phase mixture of the two oxides for concentrations x = 0.87, 0.5 and a solid solution x = 0.93, 0.35, however the best selectivity values were obtained in the sample x = 0.35, indicating the addition of manganese is crucial for the pigment applied to solar applications substrate.The thin film profilometry let us to evaluate thin film thickness and the surface roughness. Finally, the effects of mixed oxides chemical composition on the solar selectivity (α / ε), will be discussed.

Keyword; *Selective coatings, hematite, absorptance*, *emittance, Rietveld method.*

1. Introduction

Domestic water heating systems with solar energy technologies, are still at the date, a subject of study because the conversion of thermal solar energy in these systems depends largely on the materials used as absorbers, specially in their optical properties[Kenenndy 2002]. Selective surfaces of high solar absorptance (α) and low thermal emittance (ε) are used as the solar absorber [Duffie, 199, Zhang 2000]. The selectivity values (α/ε) depend on the precursors, the deposition method and also of the substrate used.
The most significant methods are chemical electrodeposition [Reza et al, 2015], sputtering [Barshilia, 2008], vacuum evaporation, spray pirolysis [Avila et al, 2004], sol gel [Tulchinsky et al, 2014, Vince et al 2003], painting technique [Orel, 2005] and electroplating[Driver 1977] have commercial application for large-scale production. Today, the problem of the available selective surfaces is that they are not only rather expensive but also appropriate for large scale production. The solution lies in the selective properties paints applied with a method easy and inexpensive: painting method.

The types of paint can be categorized as Thickness Insensitive Spectrally Selective (TISS) or Thickness Sensitive Spectrally Selective (TSSS) [Orel, 2005, 2007]. It is possible to obtain a high solar absorptance (> 0.95) but the thermal emittance should be about 0.5 for TISS paints [Orel et al., 2007]. Several studies have shown that using paints based on metal oxides [Geng, 2012] as $FeMnCuO_x$ transition can achieve acceptable selectivity values. The solar selective coating is one of the most important components of the solar collectors. Their optical properties must influence favorable both the efficient absorption of sunlight and low heat energy losses through the solar collector [1]. Some preparation methods for these coatings are spray pyrolysis, [2] and by the impregnation of FeCuMnOx and Fe_3O_4 pigments [3], [4]. In this work, it is

Selection and/or peer review under responsibility of Scientific Committee
doi:10.18086/swc.2015.10.07 Available at http://proceedings.ises.org

investigated the behavior of the mixture to form manganese iron oxides used as pigments for application in solar absorbers. Polished aluminum as substrate was covered with several mixed ratios Fe:Mn oxide by the impregnation method. After drying the thin films, the samples were submitted to different heat treatment temperatures. Chemical structure and optical properties, using XRD and UV-Vis-IR spectrophotometry technique, were respectively evaluated. The thin film profilometry let us to evaluate thin film thickness and the surface roughness. Finally, the effects of mixed oxides chemical composition on the solar selectivity (α / ε), is discussed.

The hematite (α-Fe_2O_3) [Hosseini, 2008] and α-Mn_2O_3 in bixbite phase were used as red and black pigments since ancient times. Now they are used in various industrial applications for paints, enamels and plastics thanks to its low price, low toxicity and high thermal and chemical stability. In phase α-Mn_2O_3 the Mn 3+ ions are coordinated octhaedrically, while ions O are 4 Mn ions, so close. The $(Fe1\text{-}xMnx)_2O_3$ [Saha, 2002] system is interesting because the extreme phases crystallize in different space groups. The phase with x = 0 (Fe_2O_3) does in the rhombohedra system with space group R-3c (Fig 1a) while the phase with x = 1 (Mn_2O_3) crystallizes in the cubic system (Fig 1b), with space group Ia3. The crystal structure of the pigment has an influence on its optical properties. The objective of this work is to study the optical characterization of selective surfaces containing different amounts of Fe-Mn ions for use as pigments for solar absorbers. The crystal structure of the pigment has been studied by XRD [Rietveld, 1969, Lutterotti, 1992], the optical surface characterization was performed by uV-VIS-infrared spectrometry and the details of the surface morphology were conducted with profilometry.

Theoretically solar absorptance is defined as the fraction between absorbed radiation and solar radiation. It was calculated according to equation 1. where λ is wavelength, R(λ) reflectance and Is (λ) normal irradiance.

$$\alpha_s = \frac{\int_{0.3}^{2.5} I_s(\lambda)\big(1 - R(\lambda)\big)d\lambda}{\int_{2.5}^{20} I_s(\lambda)d\lambda} \qquad (eq\ 1)$$

The thermal emittance is a ratio between a radiation emitted by the surface and the radiation that a black body at the same temperature emmit , which is presented as:

$$\varepsilon_s = \frac{\int_{2.5}^{25} E(\lambda,T)\big(1 - R(\lambda)\big)d\lambda}{\int_{2.5}^{25} E(\lambda,T)d\lambda} \qquad (eq\ 2)$$

Where E (λ, T) is the spectrum of the radiation of a black body at temperature T.
The objective of this work is to obtain the chemical, surface and optical characterization of solar selective thin films containing different quantities of Fe-Mn ions, used as pigments, for solar absorbers applied with a method type painting.

2. Experimental

2.1 Preparation of $(Fe_xMn_{1-x})_2O_3$

Mixed Fe:Mn and single oxide powder by the co-precipitation method were prepared, under the following procedure: Iron (III) chloride hexahydrate ($FeCl_3$ $6H_2O$) and manganese (II) chloride ($MnCl_2$ $4H_2O$) were mixed while maintaining a molar ratio 2: 1. This mixture was added to a 1M solution of NH_4OH, where a chemical precipitate occurred, that after washed with distilled water, let's to obtain our powder to prepare the solar selective thin film on Al substrate. Other compositions of mixed oxides prepared were in the proportions: Fe: Mn (2.2: 0.8, 2.8: 0.2)

2.2 Paint coatings

The Aluminum substrate were immersed in the different suspension containing various Fe:Mn, molar ratios. The thin film were submitted at different thermal treatments: 100, 150, 200 and 300° C, in order to observe

the thermal stability of the films.

2.3 Instrumental

The phase identification of the synthesized powders was performed using a Bruker-D8 Advance X-ray diffractometer with Cu Kα radiation (1.5406 A°) in a Bragg Brentano geometry and a one-dimensional position-sensitive silicon strip detector (Bruker, Lynxeye) operating in the 0-D mode. The 2θ step size used in the registered data is equal to 0.02^0. The patterns have been analyzed by the Rietveld method of the Fullprof program [Rodriguez, 2001]. The Rietveld method consists of simulating a diffraction pattern and refining a proposed structural model until a satisfactory match is found between the experimental and simulated patterns, the method is a full-profile approach that was initially introduced for the refinement of crystal- structure parameters but has been expanded for application in quantitative phase-analysis. The simulated XRD pattern is calculated from a large number of parameters, including crystal-structure parameters of each component phase, a scale factor for each constituent phase to adjust the relative intensities of the reflections, parameters describing the peak profile and the background, and other parameters in the simulation.
Reflectance spectral of the spectrally selective paint coatings were measured in the wavelength interval 0.3-20 μm. A Varian UV/ Vis/NIR spectrophotometer equipped with an integrating sphere was used to record reflectance spectra in the wavelength interval 0.3-2.5 mm. The infrared wavelength interval, 2.5-20 mm, was covered with an Infrared spectra are recorded on a Thermo Scientific Nicolet IS50 FTIR equipped with a gold-coated integrating sphere

With the total spectral reflectance, measured into two wavelength range is it easy build a reflectance spectra both in the uV.Vi and NIR in a Medium IR Those measurements can be used to determine the optical properties of the solar selective thin films.
The average thickness and surface morphology of the coatings were measured by means of a profilometer Bruker DektakXT.

3. **Results and discussion**

3.1 XRD patterns and Rietveld Method

Results are shown in Fig. 1 and reflection lines at 2θ = 24.18°, 33.20°, 35.67°, 40.91°, 49.5°, 54.11°, 62.49° and 64.05° indicate pure Fe_2O_3 structure, relative to (0 1 2 1), (1 0 40), (1 1 0), (1 1 3), (0 2 4), (1 1 6), (2 1 4) and (3 0 0) planes,. The diffraction lines at 2θ = 23.27°, 33.14°, 38.45° assigned to (2 1 1), (2 2 2), (4 0 0) planes correspond to the pure oxide Mn_2O_3, indicate the diffraction pattern of a solid solution. The absence of Manganese oxide in the samples x=0.93 in the diffraction pattern indicate that Mn^{3+} cations are introduced in the Fe_2O_3 lattice structure and confirms the formation of a solid solution, as identified by the displacement of the diffraction line. The sample x=0.87 to x=0.5 present phase segregation.
Rietveld Refinement graphs (experimental data and difference theoretical data) of the materials after the heat treatments are presented in Fig. 2. The parameters such as refined cell parameters, atomic positions and percentage of phases present in the mixtures are presented in Table 1.

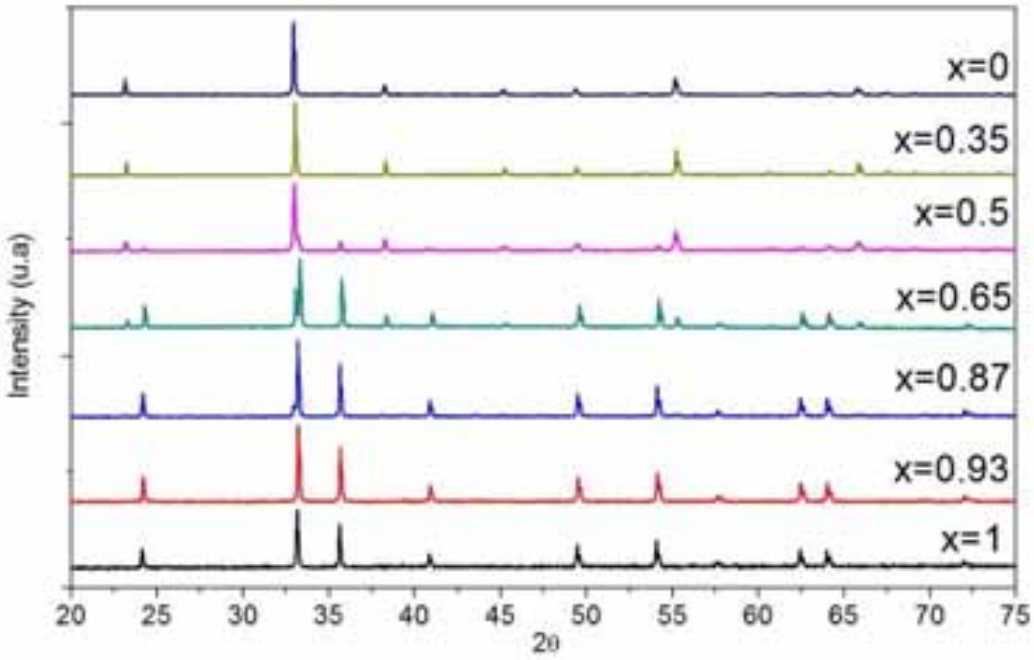

Fig. 1 XRD patterns of oxides prepared at different molar concentration at 800 °C.

The structural parameters of each sample were evaluated by the XRD study. A Corundum and a bixbyite structural phase for Fe_2O_3 and Mn_2O_3 pure compound was obtained respectively. Also both phases in the samples with mixtures of ions, are observed. A Rietveld Refinement graph (experimental data and theoretical data difference) of a representative material after heat treatments is presented in Fig. 2. The parameters such as refined cell parameters, atomic positions and percentage of phases present in the mixtures, are summarized in Table 1.

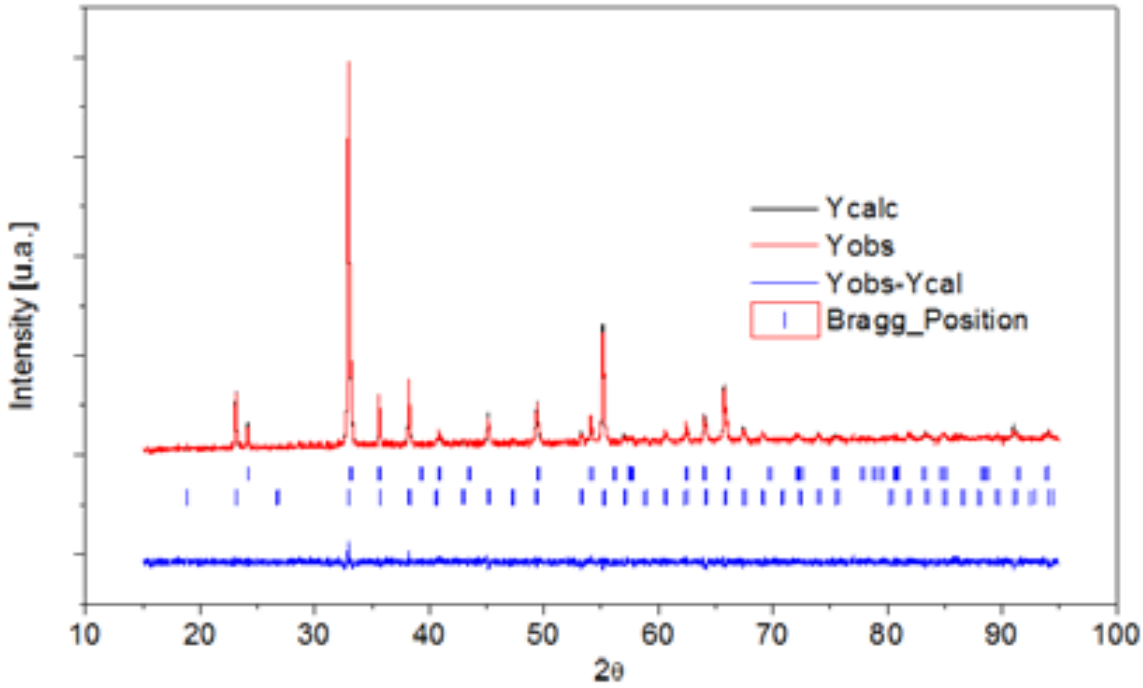

Fig. 2 XRD patterns of oxides prepared at different molar concentration at 800 °C.

Table 1: Result of the Rietveld refinement for the several pigments prepared.

Experimental Composition	%wt Phase	Space group	Lattice parameters (°A)			
			a=b=c	a=b	c	$\chi 2$
0	(100) Mn_2O_3	Ia-3	9.4173	-	-	1.36
0.35	(100) Mn_2O_3	Ia-3	9.4174	-	-	1.39
0.5	(58.9)Mn_2O_3	Ia-3	9.414	-	-	1.38
	(41.1) 2.70	R-3c	-	5.037	13.737	
0.87	(97.30) Fe_2O_3	Ia-3	9.414	-	-	1.39
	(2.70)Mn_2O_3	R-3c		5.036	13.738	
0.93	(100) Fe_2O_3	R-3c	--	5.036	13.738	1.36
1	(100) Fe_2O_3	R-3c	--	5.037	13.734	1.38

Quality refinement setting for the samples studied has a satisfactory value. No traces of hydroxyl groups into the structures are observed. The concentration of the two phases for the Fe: Mn samples, 1: 1, 2.2: 0.8, 2: 1, were obtained. Different concentrations result in a change in the percentages of each phase present in the solution, i.e., a greater amount of Mn in the solution, increased the cubic phase (Mn_2O_3), these results are summarized in Table 1.

3.2 Spectral selectivity

Considering the reflectance spectra of some representative samples, figure 3, using the two equations, 1 and 2, it was easy evaluate the solar absorptance and thermal emittance of the films, respectively, with the procedure described by Duffie and Beckman, in the regions of UV / Vis / NIR wavelength, see table 2. Also in this table it is represented some other properties of the prepared thin films, like the thin film thickness and surface roughness.

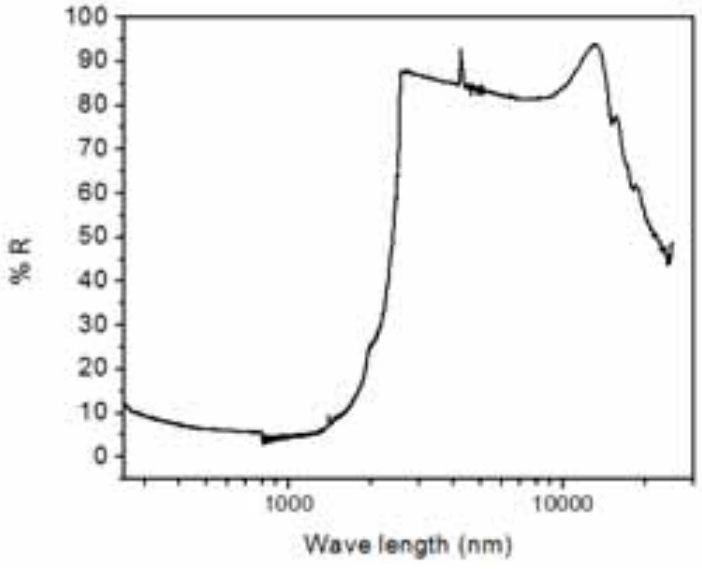

Fig. 3 Direct-hemispherical reflectance of a representative sample $(Fe_xMn_{x-1})_2\ O_3$; x=0.35 at 800°C

3.3 Perfilometry

In addition, 3D roughness parameters based on the value of Ra, were obtained in this work; where Ra is defined as the roughness average. Table 2 includes the results in this parameter and Fig. 4 shows 3D surface images employed to obtain this parameter for the thin films onto Al substrate. The strong increase in roughness with paint technique is clear

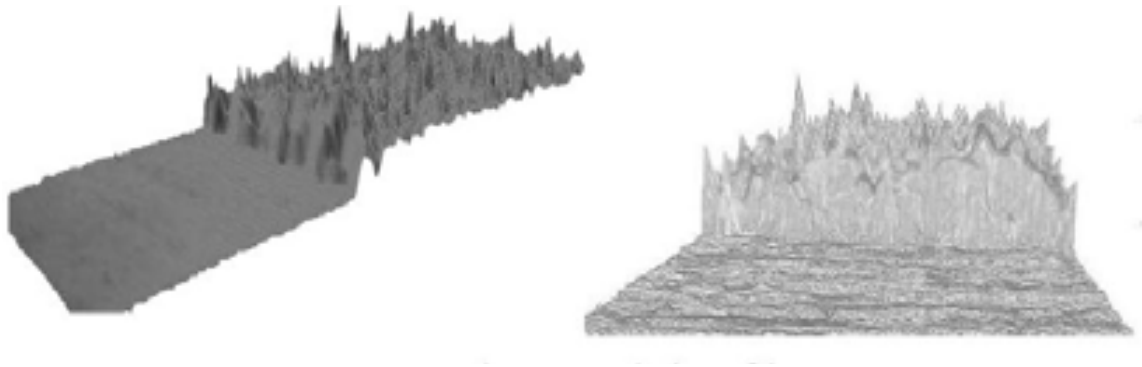

Fig. 3. Surface morphology representation 3D of representative *(*$(Fe_xMn_{1-x})_2O_3$ thin films on Al substrate.

Table 2 The optical properties, surface roughness and thin film thickness as a function of the chemical composition of the thin films.

Sample x=	Property			
	Optical		Morphology	
	absortance	emittance	Surface Roughness(µm)	Film thickness(µm)
0	0.918	0.31	0.55	15
0.35	0.931	0.29	0.45	20
0.5	0.899	0.38	0.41	18
0.87	0.894	0.30	0.5	16
0.93	0.897	0.38	0.6	14
1	0.695	0.49	0.75	18

4. Conclusions

Solar selective thin films of iron oxides and mixed oxides of Fe:Mn were prepared and characterized by several chemical and spectrophotometric technique like XRD (Rietvelt method), surface profilometry and UV-Vis-NIR. This way, it was possible to evaluate the photothermal optical properties of several thin film coatings. The mixed oxides prepared, show better optical properties for the photothermal conversion of solar energy, having a great thermal stability, that could be used for solar colector working even at mid temperature. At the date we are optimizing the main experimental parameters in order to optimize the optical properties of the solar films.

5. References

Avila G., E. Barrera C, L. Huerta, Cobalt oxide films for solar selective surfaces, obtained by spray pyrolysis, Solar Energy Materials & Solar Cells 82 (2004) 269–278.

Chemlal S., A. Larbot, M. Persin, J. Sarrazin, M. Sghyar, M. Rafiq, Cobalt spinel CoAl2O4 via sol–gel process: elaboration and surface properties, Materials Research Bulletin, 35 (2000), pp. 2515–2523.

Dipika Saha, A Das Sharma, A Sen, H.S Maiti, Preparation of bixbyite phase (MnxFe1−x)2O3 for NTC thermistor applications, Materials Letters, Volume 55, Issue 6, September 2002, Pages 403-406.
Dudita, M., Isac, L., & Duta, A. (2012). Influence of solvents on properties of solar selective coatings obtained by spray pyrolysis. Bulletin of Materials Science, 35, 997–1002
Duffie JA, Beckman WA (1991) Solar Engineering of Thermal Processes, 2nd Edn. Wiley, New York
Geng Q.F., X. Zhao, X.H. Gao, G. Liu Sol–gel combustion-derived CoCuMnOx spinels as pigment for spectrally selective paints ,Journal of American Ceramic Society, 94 (2011), pp. 827–832.
Geng Q.F., X. Zhao, X.H. Gao, S.R. Yang, G. Liu Low-temperature combustion synthesis of CuCr2O4 spinel powder for spectrally selective paints Journal of Sol–Gel Science and Technology, 61 (2012), pp. 281–288.
Geng Qingfen, Xin Zhao, Xianghu Gao, Hongchao Yu, Shengrong Yang, Gang Liu, Optimization design of CuCrxMn2−xO4-based paint coatings used for solar selective applications, Solar Energy Materials and Solar Cells, Volume 105, October 2012, Pages 293-301, ISSN 0927-0248.
Hosseini-Zor i M., F. Bondioli, T. Manfredini, E. Taheri-Nassaj, Effect of synthesis parameters on a hematite–silica red pigment obtained using a coprecipitation route, Dyes and Pigments, Volume 77, Issue 1, 2008, Pages 53-58.
Japelj, B., Sûrca Vuk, A.,Vilčnik, A., Orel, B., Slemenik Perše, L., & Jerman, I. (2008). Preparation of a TiMEMO nanocomposite by the sol–gel method and its application in coloured thickness insensitive spectrally selective (TISS) coatings. Solar Energy Materials and Solar Cells, 92, 1149–1161.
Kennedy CE (2002) Review of mid- to high-temperature solar selective absorber materials. NREL/TP-520-31267, National Renewable Energy Laboratory, Golden, CO
Kennedy CE, Price H (2005) Progress in development of high-temperature solar-selective coatings. In: Proceedings of ISEC, Orlando, Florida, USA
Lutterotti L, P Scardi, P Maistrelli, J. Appl. Crystallogr., 25 (1992), p. 459.
N Etherden et al. A theoretical feasibility study of pigments for thickness-sensitive spectrally selective paints 2004 J. Phys. D: Appl. Phys. 37 1115.
N Etherden, T Tesfamichael1, G A Niklasson and E W¨ackelgård, A theoretical feasibility study of pigments for thickness-sensitive spectrally selective paints, J. Phys. D: Appl. Phys. 37 (2004) 1115–1122.
Orel Zorica Crnjak , Marta Klanjsek Gunde, Spectrally selective paint coatings: Preparation and characterization, Solar Energy Materials & Solar Cells 68 (2001) 337-353.
Orel, B., Spreizer, H., Slemenik Perše, L., Fir, M., Sûrca Vuk, A., & Merlini, D. (2007). Silicone-based thickness insensitive spectrally selective (TISS) paints as selective paint coatings for coloured solar absorbers (part I). Solar Energy Materials and Solar Cells, 91, 93–107.
Orel, B., Spreizer, H., Sûrca Vuk, A., Fir, M., Merlini, D., & Vodlan, M. (2007). Selective paint coatings for coloured solar absorbers: Polyurethane thickness insensitive spectrally selective (TISS) paints (part II). Solar Energy Materials and Solar Cells, 91, 108–119.
Orel, Z., Klanjšek Gunde, M., & Hutchins, M. G. (2005) Spectrally selective solar absorbers in different non-black colours. Solar Energy Materials and Solar Cells, 85, 41–50.
Q.C. Zhang Recent progress in high-temperature solar selective coatings, Sol. Energy Mater. Sol. Cells, 62 (2000), pp. 63–74
Reza Elyasi, Seyed Mostafa Nowee, Hamed Azizi Namaghi, Navid Ramezanian, Preparation and characterization of absorbing tubes with spectrally selective coatings using economical methods for low- to mid-temperature solar thermal collectors, Solar Energy Materials and Solar Cells, Volume 141, October 2015, Pages 57-70, ISSN 0927-0248.
Rietvelt, H. M., A Profile Refinement Method for Nuclear and Magnetic Structures, J. Appl. Cryst. (1969).
Rodriguez-Carvajal J., Commission Powder Diff. Int. Union Cryst., Newsletter, 26 (2001), pp. 12–19
Wijewardane, D.Y. Goswami, A review on surface control of thermal radiation by paints and coatings for new, Renewable and Sustainable Energy Reviews 16 (2012) 1863– 1873.
Yang G.Q., B. Han, Z.T. Sun, L.M. Yan, X.Y. Wang, Preparation and characterization of brown nanometer pigment with spinel structure , Dyes and Pigments, 55 (2002), pp. 9–16.

6. **Acknowledgments**

The authors would like to thank CONACyT, México for supporting this research (CB-2011-01-166032; CB-2010-01-154962)

Conference Proceedings

Solar World Congress 2015

Daegu, Korea, 08 – 12 November 2015

Comparison study on domestic photovoltaic/thermal, photovoltaic and solar thermal systems based on validated TRNSYS model

Jinfeng Chen[1], Yanjun Dai[1] and Ruzhu Wang[1]

[1]Institute of Refrigeration and Cryogenics, Shanghai Jiao Tong University

Engineering Research Centre of Solar Power and Refrigeration, MOE

Shanghai, 200240 China

Abstract

In this investigation, a revised photovoltaic/thermal collector model based on TRNSYS TESS type 560 was developed to do the year-round performance prediction of both glazed and unglazed PV/T system. Simultaneously, a photovoltaic/thermal collector with the designed parameters was fabricated and tested to validate the model. Results showed that the simulation has a good agreement with experiment results. The mean error of both thermal and electrical efficiency is less than 15%. Furthermore, four domestic systems, including glazed and unglazed photovoltaic/thermal, photovoltaic and solar thermal systems, were built in TRNSYS. Annual performance of the four systems was obtained and analyzed. Compared with PV，glazed PV/T can supply extra 3850.4 MJ heat, but the power generation decreases by 24.1%. The glazed PV/T SDHW system shows a similar trend of SF and auxiliary heat with the flat plate SDHW system. The variation of SF is between 19.2% and 80.5% with an annual average value of 45.9%. The unglazed PV/T system can supply 339.5 kWh electricity and offer 806.3 MJ heat for preheating, which result in a low SF of 12.9%. Based on the view of comprehensive utilization of solar energy, the glazed PV/T system seems to be a more promising solution in SDHW system.

Keywords: *photovoltaic/thermal collector; TRNSYS simulation; performance comparison*

1. Introduction

Solar photovoltaic (PV) modules are now widely used for power generation to lead a sustainable and low-carbon economy. However, the temperature of PV modules is increased by the absorbed solar radiation that is not converted into electricity, causing a decrease in conversion efficiency. Increasing the temperature of the PV module by 1 °C will lead to a decrease of the solar electrical efficiency of crystalline and amorphous silicon cells by 0.5% and 0.25%, respectively(Skoplaki and Palyvos 2009). Thus, a variety of researches have been done to decrease the temperature of PV panels in order to increase their conversion efficiency. The very first attempt to explore the possibility of using the heat generated on PV panels as usable thermal energy was conducted in the late 70s(Kern Jr and Russell 1978), while the experimental studies utilizing proprietary devices showed up in the mid 90s(Bhargava, Garg et al. 1991, Garg, Agarwal et al. 1994, Bergene and Løvvik 1995).

Although the idea of combining the PV panel and solar thermal collector has shown a lot of advantages, the development and research on commercial PV/T system is slow. The early experimental studies involving PV/T systems were performed by modifying a commercial PV panel with a heat exchanger installed at the back of it(Huang, Lin et al. 2001). During the past few years there have been significant technological advancements concerning all types of PV/T collectors (Daghigh, Ruslan et al. 2011, Ibrahim, Othman et al. 2011, Tyagi, Kaushik et al. 2012) and some commercial products start to show up in the market. At present, four types of PV/T collectors that focus on working media: air(Joshi and Tiwari 2007, Kumar and Rosen

Selection and/or peer review under responsibility of Scientific Committee
doi:10.18086/swc.2015.10.08 Available at http://proceedings.ises.org

2011), water(Dubey and Tiwari 2008, Chow, Pei et al. 2009), refrigerant(Chow, Pei et al. 2010) (Omojaro and Breitkopf 2013)and heat pipe(Wu, Zhang et al. 2011), are available.

With the low price of PV modules and the high government subsidies, many families in China now choose to install household photovoltaic systems. Meanwhile, most of them have already installed the solar thermal collector systems for domestic hot water (DHW) supply. As the demand for electricity and thermal energy shows up in the same time, in this way, the PV/T system seems to be the most promising renewable energy solution without extending the installation area.

In this paper, A system model is built in TRNSYS and the year-round performance comparison of PV/T (glazed and unglazed), solar thermal and PV system is conducted. The performance characteristics of the four different systems are analyzed to supply the basis for selection of different domestic solar systems.

2. PV/T component model and validation

2.1. Unglazed PV/T component

Type 560 in TRNSYS Electrical Library (TESS) is intended to model an unglazed solar collector which has the dual purpose of creating power from embedded photovoltaic (PV) cells and providing heat to a fluid stream passing through tubes bonded to an absorber plate located beneath the PV cells. It relies on linear factors relating the efficiency of the PV cells to the cell temperature and also the incident solar radiation. The cells are assumed to be operating at their maximum power point condition. Fig.1 shows the heat transfer model of this type and the thermal model of this collector is based on algorithms presented in Chapter 6 of the classic “Solar Engineering of Thermal Processes” textbook by Duffie and Beckman(Duffie and Beckman 1980).

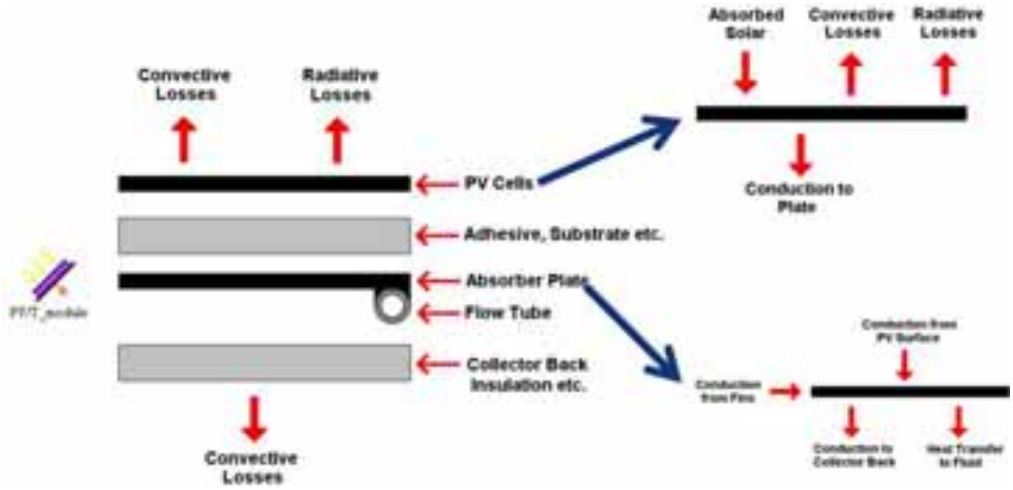

Fig. 1: Heat transfer model of unglazed PV/T component

2.2. Glazed PV/T component

In order to model a glazed PV/T module, a single glaze cover model is appended to the existing model of type 560. The glaze cover heat transfer and solar transmission model is based on the Chapter 6 of the classic “Solar Engineering of Thermal Processes” textbook by Duffie and Beckman(Duffie and Beckman 1980). The new model is complied in Fortran and name type 560b in order to call it from TRNSYS.

2.3. Component validation

In order to validate the two PV/T components in TRNSYS, two PV/T solar collectors were fabricated and tested. The main parameters of the two components are listed in Tab. 1. The experiment system schematic diagram is shown in Fig.2 and the experiment system picture is displayed in Fig.3. The temperatures of the system are measured by a group of PT1000 sensors (A class, error: 0.1 ºC). The water flow rate is measured by an integrating flow meter with an accuracy of ±5% （of reading）. The ambient condition is monitored by a micro weather station (Davis 6152c) and Kipp & Zone CM22 pyranometer , and the accuracies of the

radiation and temperature are ±5%（of reading） and ±0.5 °C, respectively. The power generation of the PV module is monitored by a DC voltage and current sensor with a accuracy of ±5%（of reading）. All the data is captured and handled by a Graphtec GL800 acquision system.

Tab. 1: Main parameters of PV/T components

Collector area (m^2)	2
Nominal efficiency of PV panel (%)	15
Tube spacing(m)	0.125
Tube diameter(m)	0.01
Absorber thickness	0.0003
Glass cover transmittance	0.9
Number of glass cover	0/1
Glass cover spacing (m)	0.03
Temperature coefficient of PV cell efficiency(1/°C)	-0.005
Radiation coefficient of PV cell efficiency($h.m^2/kJ$)	0.000025
Storage tank volume (m^3)	0.15

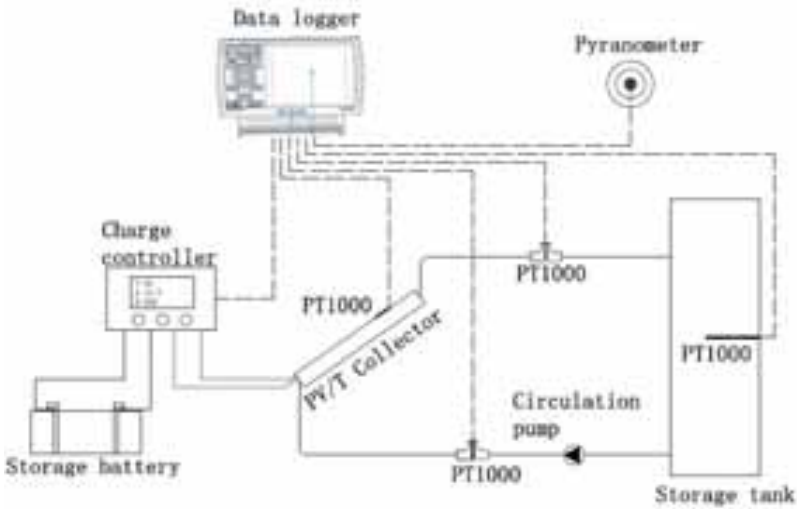

Fig. 2: Schematic diagram of experiment system

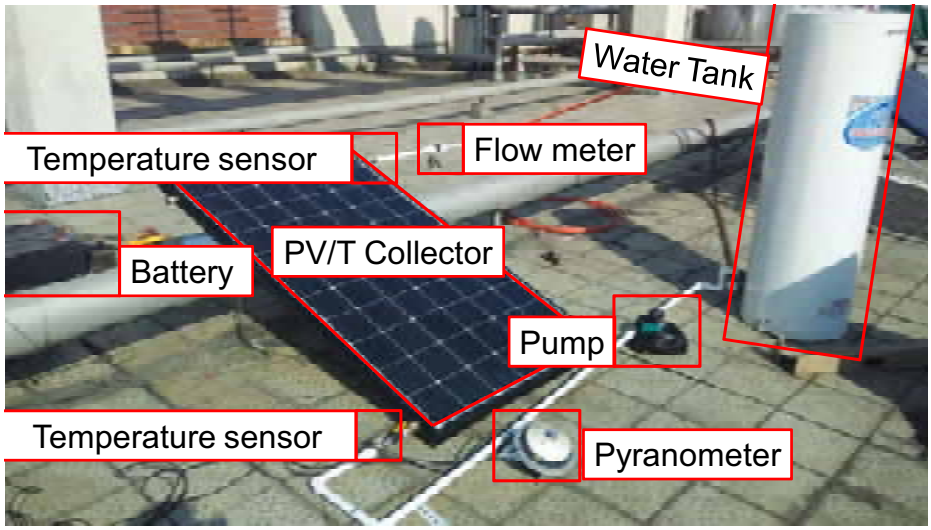

Fig. 3: Picture of experiment system

The experiment was done on June 13th and the ambient conditions including solar radiation intensity and ambient temperature are shown in Fig. 4. The average solar radiation intensity on the titled surface and ambient temperature during the test are 767 W/m^2 and 22.1 ^{o}C, respectively. The initial water temperature in the tank is 20 ^{o}C.

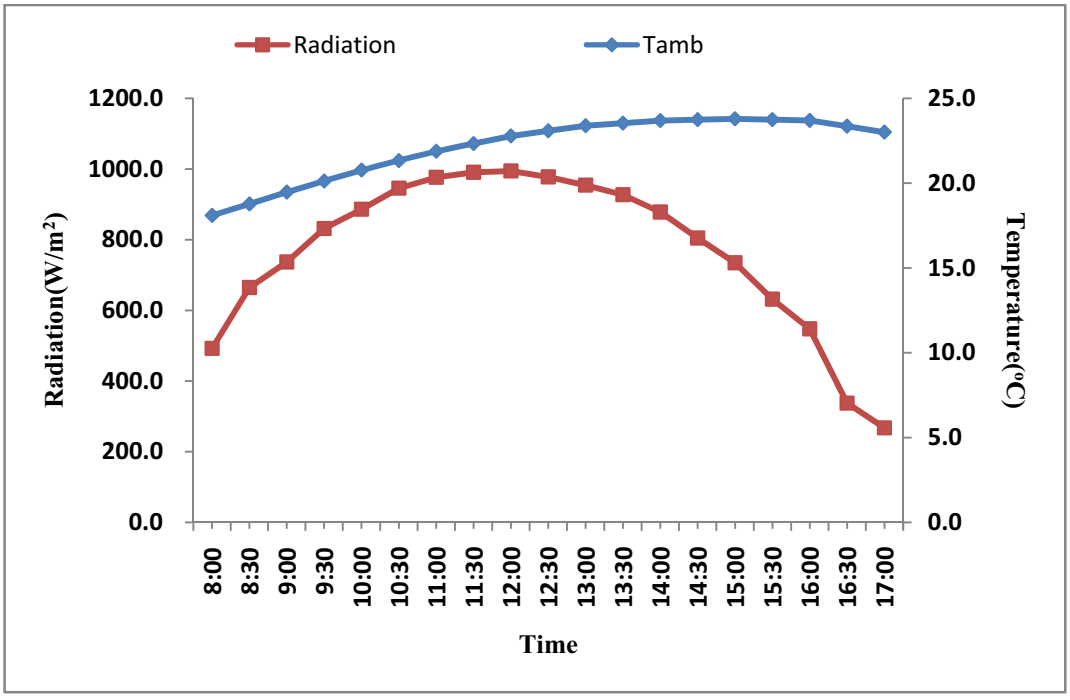

Fig. 4: Ambient condition of experiment

The comparison of electrical efficiency of both systems is shown in Fig. 5. The simulated result shows nearly the same trend with the experiment value. The maximum relative error (RE) of the electrical efficiency is about 8.5% due to the loss of efficiency in MPPT controller.

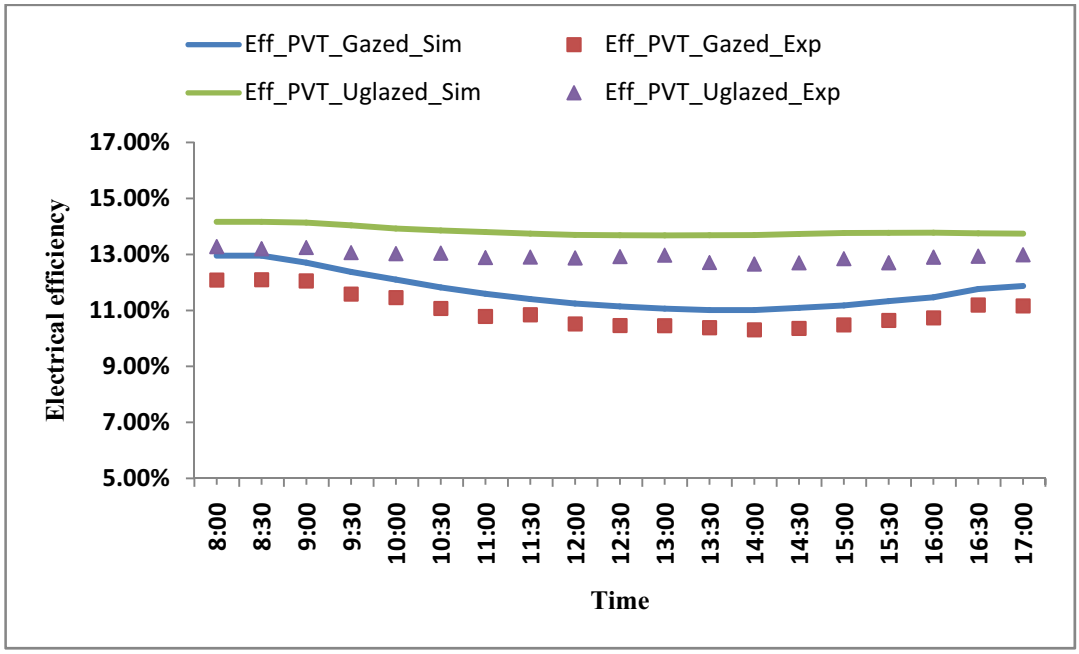

Fig. 5: Comparison of Electrical efficiency between experiment and simulation

Fig. 6 shows the tank temperature between experiment and simulation. The tank temperature started at 20 ^{o}C and rised to 50.1 ^{o}C and 30.3 ^{o}C for the glazed PV/T and unglazed PV/T system respectively. The simulated tank temperature is nearly consistent with the experimental value with a maximum RE of about 12.9 %. The tank loss coefficient is set as a constant in the simulation model but in the experiment, it is influenced by the ambient conditions, such as the wind speed. Furthermore, the loss of pipes and pump is neglected in the simulation model.

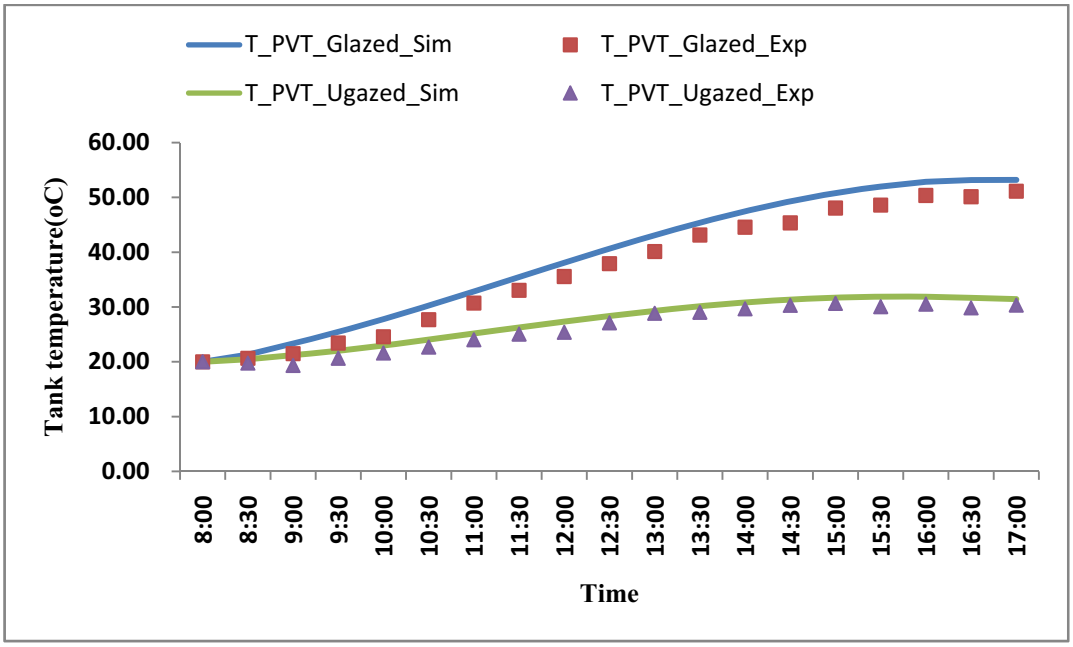

Fig. 6: Comparison of tank temperature between experiment and simulation

3. TRNSYS model description

3.1. System description

In order to make a comparison of the PV/T system performance with the traditional flat plate solar collector

on solar domestic hot water (SDHW) system, three system models with different solar collectors are built in TRNSYS. The schematic diagram of SDHW system is shown in Fig. 7. A diverter and a mixer is set to maintain the hot water supply temperature as 45 °C. An auxiliary heater is applied to provide auxiliary heat when the outlet temperature is lower than 45 °C . The DHW demand displayed in Fig. 8 is a real test schedule of a Shanghai family of 3 people. The peak of DHW load appears in the morning, noon and evening. Furthermore, a traditional PV panel is studied to analyze the difference of electrical performance between PV/T and PV. The main type numbers and parameters of the components in the model are listed in Tab. 2.

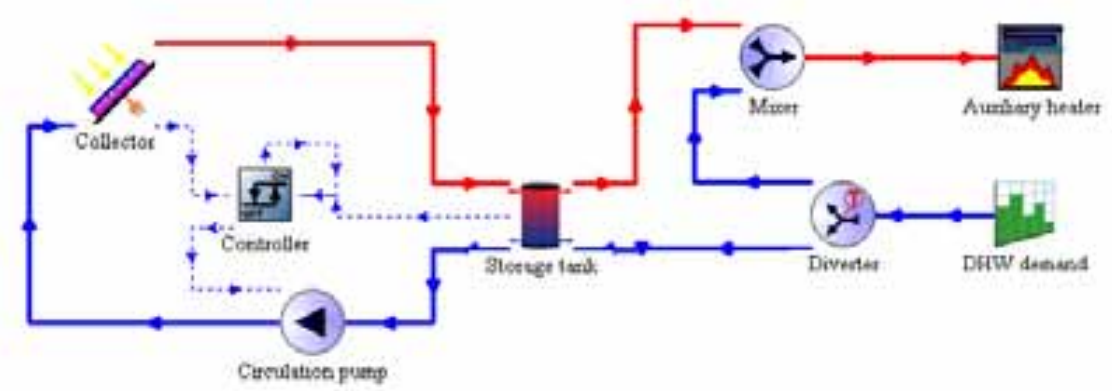

Fig. 7: Schematic diagram of SDHW system

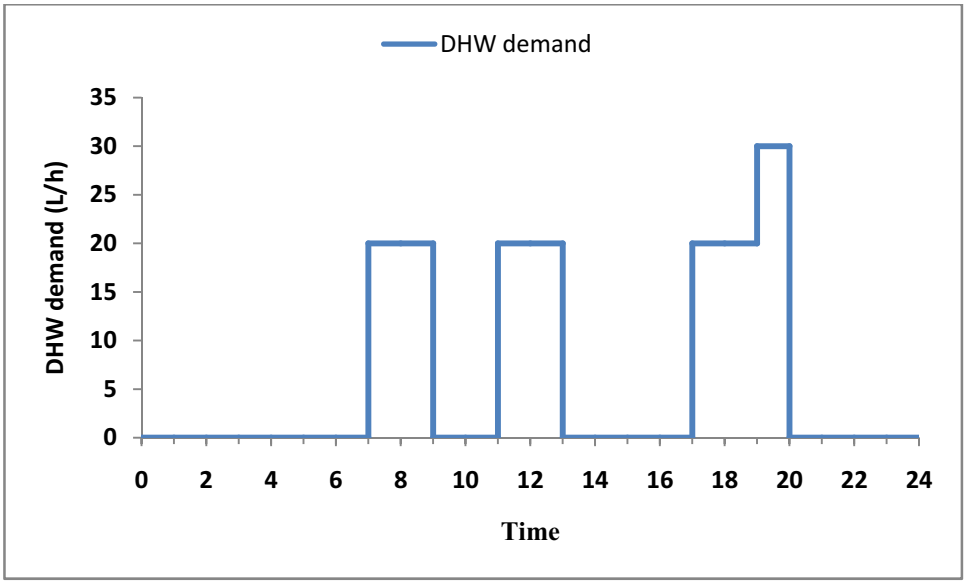

Fig. 8: Schedule of DHW demand

Tab. 2: Main type numbers and parameters of the components

Component name	TRNSYS type number	Main parameters
PV/T (glazed/unglazed)	Type 560b/560	area: $2m^2$ rated electrical power: 300W inclination angle: 30^o
Flat plate solar collector	Type 1	area: $2m^2$ efficiency curve: $\eta = 0.749 - 5.6 * (T_{in} - T_{amb})/G$ inclination angle: 30^o
PV panel	Type 562	rated electrical power: 300W inclination angle: 30^o
Tank	Type 4e	volume: 150L
Circulation pump	Type 3d	rated power: 45 W rated flow rate: 140kg/h
Controller	Type 2b	temperature difference: 8(on)/4(off)
DHW demand	Type 14h	shown in Fig.8
Diverter	Type 11b	
Mixer	Type 11d	
Auxiliary heater	Type 700	

A CN-Shanghai-583670. tm2 (Typical Meteorological Year Version 2) format weather data file is read as the boundary conditions of the simulation model. The replenishment water temperature of the storage tank is set as the mains water temperature, which changes with the ambient conditions seasonally.

3.2 Performance index

For purpose of evaluating the performance of the four different systems, the following performance index is calculated based on the simulated results:

(1) Average thermal efficiency

$$\eta_{th} = \frac{Q_{tank}}{\int A * G_{solar}} \qquad \text{(eq. 1)}$$

(2) Average electrical efficiency

$$\eta_{ele} = \frac{E_{PV}}{\int A * G_{solar}} \qquad \text{(eq. 2)}$$

(3)Solar fraction

$$SF = \frac{Q_{total} - Q_{aux}}{Q_{total}} \qquad \text{(eq. 3)}$$

4. Results and discussion

4.1 Electrical performance

The annual electrical performance of PV/T and PV system is displayed in Fig. 9. Compared with pure PV system, the unglazed PV/T system shows a slight enhancement on the electricity generation and electrical efficiency. The annual electricity output of the unglazed PV/T and PV system are 339.5 kWh and 335.2 kWh, respectively. However, the glazed PV/T system shows a significant decrease in electricity generation due to the high temperature of the PV panel. The annual electricity output of the glazed PV/T is 254.6 kWh, which is 80.6 kWh lower than the PV system. The average electrical efficiency of unglazed PV/T, glazed PV/T and PV system are 12.5%, 9.4% and 12.3%.

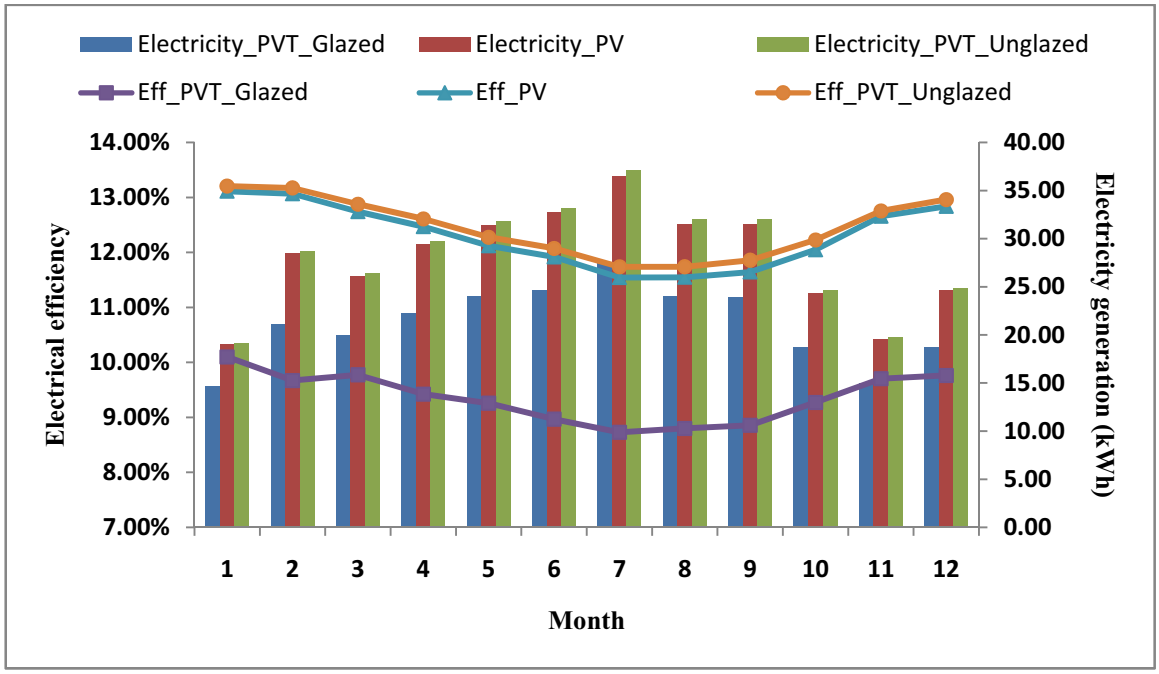

Fig. 9: Annual electrical performance of PV/T and PV system

4.2 Thermal performance

The annual thermal performance of PV/T and flat plate solar collector system is shown in Fig. 10. Because the emissivity of PV surface in the glazed PV/T is much higher than the absorber in flat plate solar collector, the heat collected by glazed PV/T system is 24.2% lower than the flat plate solar collector. The average thermal efficiency of glazed PV/T and flat plate solar collector are 29.3% and 40.0%, respectively. Nevertheless, the heat loss coefficient of unglazed PV/T system is dramatically higher than glazed PV/T system due to lack of glass cover. The PV panel in unglazed PV/T system is exposed to the ambient, so both convection and radiation heat transfer coefficient is significantly higher than the glazed system. As a consequence, the unglazed PV/T system can only supply 806.3 MJ heat for preheating of the SDHW system.

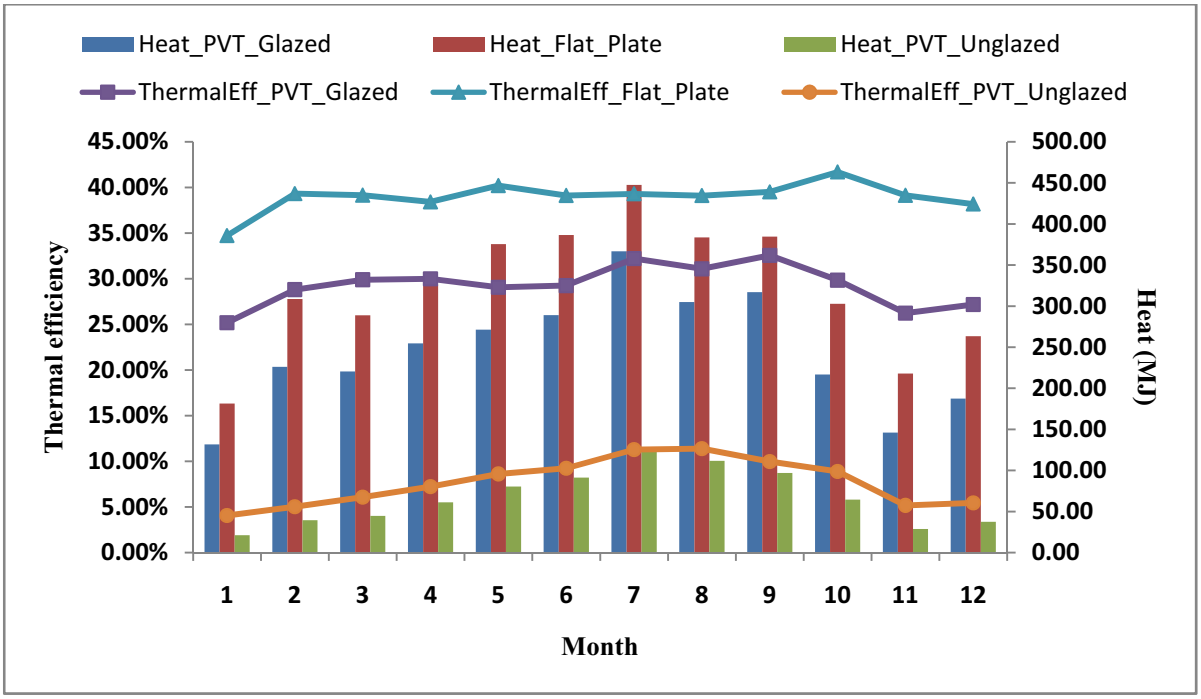

Fig. 10: Annual Thermal performance of PV/T and flat plate solar collector system

4.3 Solar fraction and auxiliary heat

Fig.11 shows the solar fraction as well as the auxiliary heat of PV/T and flat plate SDHW system. For the flat plate SDHW system, the solar fraction (SF) ranges from 26.4% to 95.9% and the annual average solar fraction reaches 60.1%. The required auxiliary heat is about 2907.5 MJ. The glazed PV/T SDHW system shows a similar trend of SF and auxiliary heat with the flat plate SDHW system. The variation of SF is between 19.2% and 80.5% with an annual average value of 45.9%. According to the analysis above, the heat collected in the unglazed PV/T SDHW system can only serve as a preheating, which result in a low average SF of 12.9%.

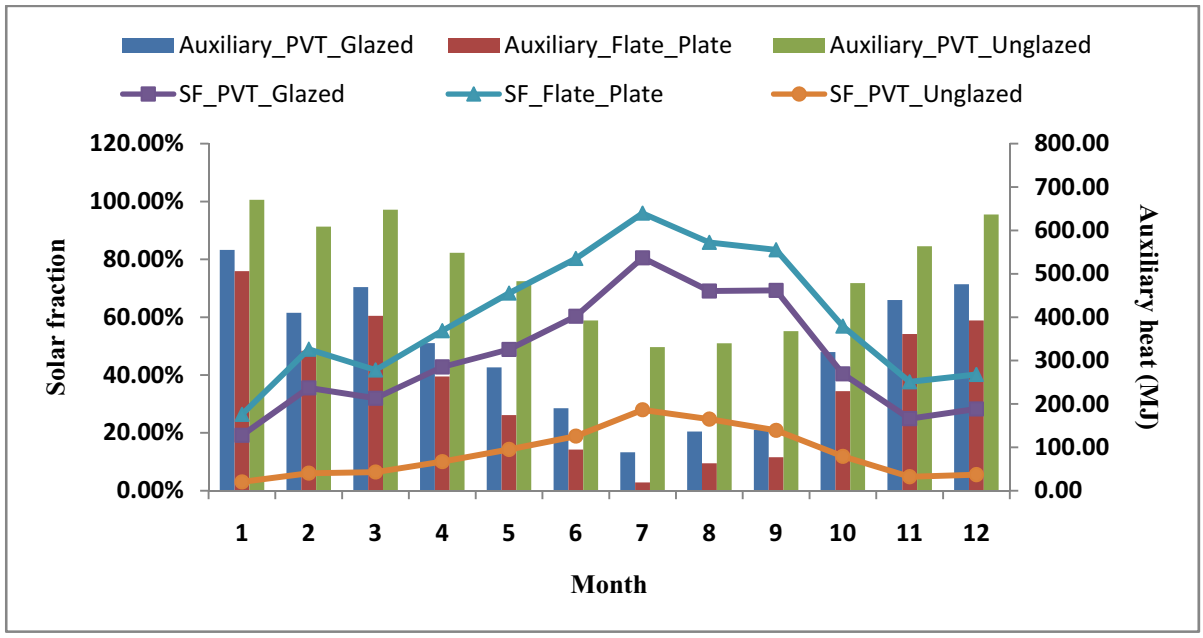

Fig. 11: Solar fraction and auxiliary heat of PV/T and flat plate solar collector system

5. Conclusion

In this investigation, a revised photovoltaic/thermal collector model based on TRNSYS TESS type 560 was developed and validated to do the year-round performance prediction. Three SDHW system as well as a PV models are built in TRNSYS to analyze the electrical and thermal performance of PV/T components applied in SDHW system. The following conclusion can be drawn from the investigation:

(1) According to the validation, the revised model based on TRNSYS TESS type 560 is accurate enough to do the performance prediction of PV/T SDHW system.

(2) Compared with pure PV system, the unglazed PV/T system shows a slight enhancement on the electricity generation and electrical efficiency. The glazed PV/T system shows a significant decrease in electricity generation due to the high temperature of the PV panel. The average electrical efficiency of unglazed PV/T, glazed PV/T and PV system are 12.5%, 9.4% and 12.3%.

(3) The heat collected by glazed PV/T system is 24.2% lower than the flat plate solar collector because of the high emissivity. The average thermal efficiency of glazed PV/T and flat plate solar collector are 29.3% and 40.0%, respectively. As a consequence of high heat loss coefficient, the unglazed PV/T system can only supply 806.3 MJ heat for preheating of the SDHW system.

(4) For the flat plate SDHW system, the annual average solar fraction reaches 60.1%, resulting in an auxiliary heat of 2907.5 MJ. The glazed PV/T SDHW system shows a similar trend of SF and auxiliary heat with the flat plate SDHW system. The variation of SF is between 19.2% and 80.5% with an annual average value of 45.9%. The SF of unglazed PV/T SDHW system is 12.9%.

(5) Based on the view of comprehensive utilization of solar energy, the glazed PV/T system seems to be a more promising solution in SDHW system.

Acknowledgement: This study is supported by the National Science Foundation (No.51476099)

6. References

Bergene, T. and O. M. Løvvik (1995). "Model calculations on a flat-plate solar heat collector with integrated solar cells." Solar energy **55**(6): 453-462.
Bhargava, A. K., H. Garg and R. K. Agarwal (1991). "Study of a hybrid solar system—solar air heater combined with solar cells." Energy Conversion and Management **31**(5): 471-479.
Chow, T. T., G. Pei, K. F. Fong, Z. Lin, A. L. S. Chan and M. He (2010). "Modeling and application of direct-expansion solar-assisted heat pump for water heating in subtropical Hong Kong." Applied Energy **87**(2): 643-649.
Chow, T. T., G. Pei, K. F. Fong, Z. Lin, A. L. S. Chan and J. Ji (2009). "Energy and exergy analysis of photovoltaic-thermal collector with and without glass cover." Applied Energy **86**(3): 310-316.
Daghigh, R., M. H. Ruslan and K. Sopian (2011). "Advances in liquid based photovoltaic/thermal (PV/T) collectors." Renewable & Sustainable Energy Reviews **15**(8): 4156-4170.
Dubey, S. and G. N. Tiwari (2008). "Thermal modeling of a combined system of photovoltaic thermal (PV/T) solar water heater." Solar Energy **82**(7): 602-612.
Duffie, J. A. and W. A. Beckman (1980). Solar engineering of thermal processes, Wiley New York etc.
Garg, H., R. Agarwal and J. Joshi (1994). "Experimental study on a hybrid photovoltaic-thermal solar water heater and its performance predictions." Energy Conversion and Management **35**(7): 621-633.
Huang, B. J., T. H. Lin, W. C. Hung and F. S. Sun (2001). "Performance evaluation of solar photovoltaic/thermal systems." Solar Energy **70**(5): 443-448.
Ibrahim, A., M. Y. Othman, M. H. Ruslan, S. Mat and K. Sopian (2011). "Recent advances in flat plate photovoltaic/thermal (PV/T) solar collectors." Renewable & Sustainable Energy Reviews **15**(1): 352-365.
Joshi, A. S. and A. Tiwari (2007). "Energy and exergy efficiencies of a hybrid photovoltaic-thermal (PV/T) air collector." Renewable Energy **32**(13): 2223-2241.
Kern Jr, E. and M. Russell (1978). Combined photovoltaic and thermal hybrid collector systems, Massachusetts Inst. of Tech., Lexington (USA). Lincoln Lab.
Kumar, R. and M. A. Rosen (2011). "A critical review of photovoltaic-thermal solar collectors for air heating." Applied Energy **88**(11): 3603-3614.
Omojaro, P. and C. Breitkopf (2013). "Direct expansion solar assisted heat pumps: A review of applications and recent research." Renewable & Sustainable Energy Reviews **22**: 33-45.
Skoplaki, E. and J. A. Palyvos (2009). "On the temperature dependence of photovoltaic module electrical performance: A review of efficiency/power correlations." Solar Energy **83**(5): 614-624.
Tyagi, V. V., S. C. Kaushik and S. K. Tyagi (2012). "Advancement in solar photovoltaic/thermal (PV/T) hybrid collector technology." Renewable & Sustainable Energy Reviews **16**(3): 1383-1398.
Wu, S. Y., Q. L. Zhang, L. Xiao and F. H. Guo (2011). "A heat pipe photovoltaic/thermal (PV/T) hybrid system and its performance evaluation." Energy And Buildings **43**(12): 3558-3567.

Conference Proceedings

Solar World Congress 2015
Daegu, Korea, 08 – 12 November 2015

Solar cookers with latent heat storage for intensive cooking application

Asfafaw H. Tesfay [1], Mulu B. Kahsay [1] and Ole J. Nydal [2]

[1] School of Mechanical and Industrial Engineering, Ethiopian Institute of Technology-Mekelle, Mekelle University P.O.box 231, Mekelle, Ethiopia

[2] Department of Energy and Process Engineering, Norwegian University of Science and Technology, 7491 Trondheim, Norway

Abstract

Many developing countries use biomass as their primary energy supply. Unwise utilization of biomass affects the environment, health and safety of women and children in particular. In addition, it causes indoor air pollution, which is a reason to the deaths of millions. This paper demonstrates solar cooker with an integrated PCM thermal storage and heat transportation loop suitable for high temperature applications. The system is designed to particularly suite *Injera* baking application. *Injera*, a yeast-risen flat bread type is the most common staple food type served three to four times a day in Ethiopia. A similar food type is also eaten in, Eritrea, Somalia, Sudan and Yemen. The system storage has a capacity of about 250ºC and retains the heat for about two days. The storage is coupled polar mounted concentrator with fixed receiver and steam heat transfer fluid. The steam circulates naturally between the evaporator and condenser in a closed loop. The study has demonstrated indirect charging, simultaneous charging-discharging and discharging of the stored heat. The frying pan is a custom-made aluminum plate casted by embedding a 10mm coiled stainless steel steam pipe as heating element. The pan is 500mm in diameter and 30mm thick, and the fins are 20mm in diameter and 140mm long. The fins are immersed into a 20kg PCM, which is coupled to a 1.8m diameter parabolic dish collector. The solar fryer demonstrates Injera baking for average family size on top of a heat storage charged by a solar energy. This baked Injera able to cover three to four days food consumption of the family.

Keywords: *solar energy, solar cooker, solar Injera baking, parabolic dish cooker,*

1. Introduction

1.1. Background on solar cooker and thermal storage

Many developing countries use biomass as primary energy supply for their household's energy consumption. This energy in return affects the environment, health and the livelihood development of the people. In these countries women and children are often in charge of fetching firewood and cooking, in which they spent most of their valuable energy and time traveling long distance in search of this fuel. In addition, they are also the most affected from indoor air pollution from this energy and traditional cookstoves.

On the other hand, the progress of solar cookers technology is very slow in spite of their benefits. One reason for this can be lack of integration between social and technology researches. Secondly, the outreaches of these cookers often do not consider the active participation of end users. Moreover, many studies of solar cooker focus on direct cooking and with low temperature heat storage for low temperature applications.

Many developing countries, which are dependent on biomass, have huge potentials of solar energy that can potentially substitute the role of biomass. However, solar energy technologies have rarely introduced in these places. Moreover, solar thermal technologies in general have not reached a robust stage of mass production and distribution. Although some countries have introduced solar box cookers, their success has been limited due to technological and social factors in which none of the cookers enabled night cooking and indoor use. Such technical limitations also affect users' norm of cooking, which may cause a social ban on the adoption

doi:10.18086/swc.2015.10.09 Available at http://proceedings.ises.org

of new technology.

To improve acceptance of solar cookers and assure their widespread use, a continuous improvement in technical development, social awareness and thermal storage is required. Thermal energy storage helps to store the surplus energy during the day and keep it for late evening use. In addition, it helps to supply nearly uniform heat during the process of cooking. Some solar cooker design features allow charging and discharging simultaneously. For example, A. Lecuona et al.'s solar cooker could cook family lunch while charging the storage simultaneously [1]. The stored heat of this cooker allows dinner cooking and breakfast heating for the following day. Such design features help to expand the acceptance of solar cooking. Another solar cooker design, which used heat pipes, flat-plate collector and integrated indoor phase change material (PCM) storage, was able to cook food at noon, evening and keep the food warm at night and the following morning [2]. The solar fryer in this paper will solve these barriers and enable users to perform any time indoor cooking practice. The use of PCM storage for cooking is increasing and diversifying with time. For example, H.M.S. Hussein et al. [2] have tested a PCM storage coupled to flat plate collectors for indoor cooking and heating of food during the evening. In addition, A. Lecuona et al.'s [1] portable solar cooker with PCM storage enables day and nighttime cooking.The purpose of this paper is therefore to design an indirect solar cooker with latent heat storage, which is dedicated for baking the Ethiopian food called Injera.

Injera is yeast-risen flat bread with slightly spongy texture. It is the most common food type, which is served three to four times a day. Similar food type is also eaten in, Eritrea (Injera), Somalia (Canjeero), Sudan and Yemen (Lahoh) [3]. Injera is used to bake on a clay stove called "Mitad". The baking process demands a significant amount of energy, which mainly comes from biomass as most of the populations live without access to electricity. The biomass based Injera kitchen is full of smoke and soot that affects the health of millions. The solar stove designed in this study has tried to give a solution for this acute problem.

2. Materials and Methodology

2.1. Heat storage

The heat storage in this paper is designed to accommodate 20 kg of solar salt (nitrate salt mixture of 40% KNO_3 and 60% $NaKO_3$), which is sufficient to supply heat for an average household size. This PCM is selected based on the baking temperature requirement of Injera. The storage configuration contains a baking plate with embedded stainless steel steam pipe and down going aluminum fins. These fins are design to transport optimal conduction heat to the PCM. This design halts any direct contact of the steam and the PCM. More over the storage has a 10% vacant space to avoid any pressure development and volume variation during phase transition of the PCM. The schematic of the whole system is given in Fig.1. The thermosyphon loop is designed to simplify the heat transfer mechanisms over long distances.

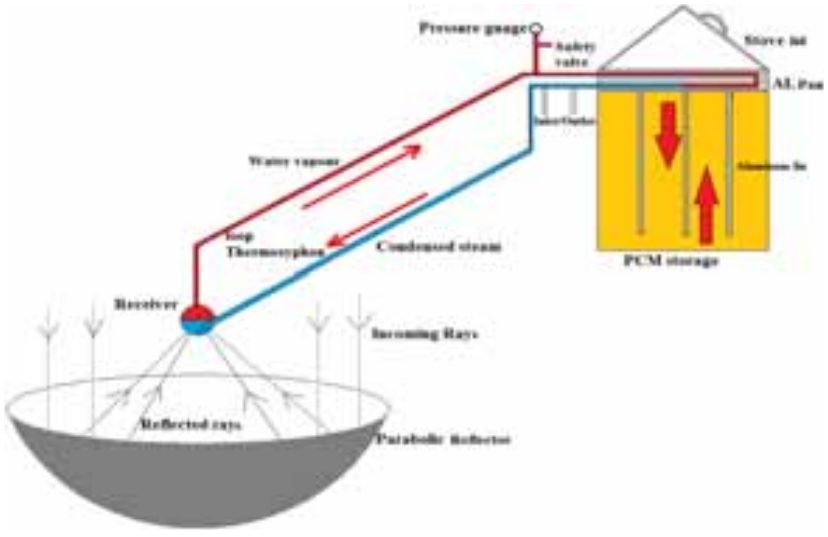

Fig.1: Schematic of the developed system

The frying pan has an embedded stainless steel (SS) steam pipe, which is the heating element of the system and it resembles a heating element of modern electric stoves. The system was coupled to 1.8m parabolic dish collector filmed with alando solar reflector. This system was tested at Mekelle, Ethiopia (13°28'48.30"N latitude). The concentrator design used polar mounted reflectors with fixed receiver philosophy. The list of sensors and equipments used during the experiment this research is given in Table 1.

Table 1: system components

Label	Description	Label	Description
A	Pressure relief valve	F	Inlet, out let and directional control valves
B	Pressure gauge	G	Parabolic dish reflector
C	Tracking sensor	H	Data logger
D	DC motor	I	K-Type Thermocouples
E	Solar PV source	J	Receiver

2.2. Parabolic dish concentrator design

In solar power generation, the use of pressurized steam is a common practice. However, its use for small-scale application such as cooking is rare. In fact there exists some large-scale steam solar cookers; however, they use low-pressure steam. For example, Scheffler steam rice cooker uses steam in the range of 3bar. On the other hand, high-pressure steam solar cookers are not commonly used due to their technical and safety concerns while generating the steam.

a) Collector design

The fixed receiver of this concentrator was used to generate steam and in return this steam was used to charge the heat storage. Parabolic dishes can be manufactured from optimized petal shaped sheets with due attention on precision design and manufacturing as studied by Lifang and Steven [4]. The other and easier way to get parabolic dish for solar concentration purpose is to customize existing satellite dishes by filming them with appropriate reflector materials. The parabolic dish used in this paper is a six petal satellite dishes. The dish is filmed with a self-adhesive aluminum reflector, Miro high reflective 95 and thicknesses of 0.5mm.

b) Receiver design

The receiver used in this research is developed by welding of two cylindrical cups of black steel. The cups have 100mm diameter, 5mm thickness and 40mm height. Figure 2 shows the actual pictures of the receiver during experiment. Random temperature measurements in the illuminated area of the receiver lie between 300 to 1150°C. However, larger part of the receiver is exposed to radiation loss.

Figure 2 Receiver of a parabolic dish collector

c) Thermal performance

The thermal efficiency of the system is given by the ratio of the useful energy stored to the energy incident at the concentrator's aperture. The storage energy is the sum of the energy stored in the PCM and in the aluminum fins. Hence, the thermal efficiency of the system is computed by:

$$\eta_{th} = \frac{c_{Al} m_{Al} (T_f - T_i) + m \int_{T_i}^{T_f} c_p dT}{A_a I_B} \quad (1)$$

Where cp is the effective heat capacity of the PCM

Both normal and diffuse radiation enters the aperture area of any solar collectors. However, in concentrating collectors only the direct radiation can be focused on the receiver.

The thermal analysis of the system was performed only for its solid phase sensible heat-storing ability as it was not fully charged. The systems reached 187°C as maximum temperature of the storage during the experiments of this paper. Therefore, the thermal performance for this test was found 23%. The performance of the systems was affected by non-smooth manual tracking, dust on the reflector and some damages on the collector as shown in Fig. 3, which affect its focusing. In addition, this system was exposed to higher wind speed, which resulted in higher convective heat loss from its receiver and the system as whole.

d) Tracking mechanism

The system used a gear mechanism auto tracker to track the sun in the east-west direction. The tracker has 50kg carrying capacity and use 9V DC motor driver. The motor gets its power from a 10W PV source. The gear ratio of the motor is 1:600 and its shaft runs at 9 rpm. This speed is further reduced in to a 1:10 gear ratio to transfer the required torque to track the collector. This speed of the motor allows the mechanism to catch up the position of the sun in case the sun comes out of longer time stay in clouds. A light diode and a shading device control the motor. The reflector starts to track the sun automatically until the sensor becomes perpendicular to the sun radiation. Tracking happens when the sun shines and if there is no sun, there is no tracking.

e) Insulation

Aerogel and Rockwool insulations were used to insulate the storage and the steam pipelines respectively. The insulations maximum working temperature is about 650°C and the maximum working temperature of the system was set to 250°C (by adjusting the pressure relief valve) and the design thickness of the insulation is 25mm for the heat storage and 50mm for the steam pipeline. The insulations thermal conductivity is 0.03W/Km and 0.07 W/Km respectively and they have the same surface emissivity of 0.05.

f) Pipe lines

The steam pipeline is 10mm in diameter and 1mm thickness. This pipe is used as a pipeline of the thermosyphon loop and as a heating element for the frying pan. The pipe has 100bar design pressure and is used for 40bar working pressure. The pipeline used Swagelok connectors and valves. A pressure gage is used to measure the pressure of the steam and regulated with the help of a safety valve that reliefs the pressure when it passed the pre-set value (40bar). The pipeline was used to flash before the beginning of every experiment to avoid air inclusion.

3. Results and discussion

The storage integrated solar fryer developed in this research is shown in Fig. 3 and 7. The polar mounted concept eases the demand of tracking mechanism in the secondary axis. The fixed receiver was found suitable for steam generation. The steam circulates between the evaporator (receiver) and frying pan (condenser) in a closed loop naturally. The steam carries the heat from the receiver and drops it on the frying pan (casted aluminum plate). The fins attached to this plate in return carries this heat to the PCM by conduction. The unit was tested for simultaneous charging-discharging, discharging of a fully charged storage and discharging of

partially charged storage (cloudy day). The solar radiation used when analyzing the system thermal efficiency is shown in Fig. 3(b).

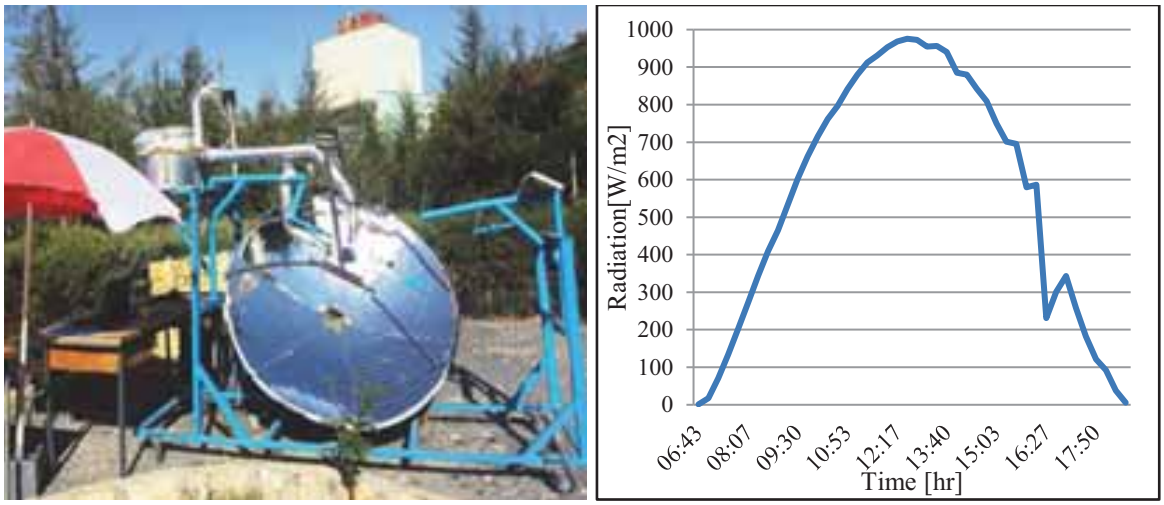

Figure 3: 1.8m parabolic dish collector with PCM storage (Mekelle Unit) Figure 1: Global solar radiation of Mekelle on 27-02-2014, when the stove reach 187°C

The storage charging process has simulated using COMSOL multiphysics 4.3. In this simulation a 20kg of solar salt with circularly rolled plate fins instead of many cylindrical fins. The 2D and 3D simulation results show the 20kg solar salt storage is fully charged in about seven hours, when a 250°C continuously circulating steam is used to charge. The simulation considers a constant loss of 15°C from the storage. The fins assumption has reduced the overall charging time of the storage. The simulation has shown the charging of the PCM found between two fins is very quick; however, the PCM adjacent to the storage wall and bottom changes its phase very slowly. This simulation result suggests to half the dimension of the gap between the fin and the storage wall (side and bottom). Therefore, the PCM thickness between the fin and the wall should be 20mm. Moreover, it was found rolled plate fins charge the PCM faster than rod fins. In addition to the PCM charging development, the simulation has also run to show the thermal resistance effect of the SS pipe wall on the frying pan as shown in Fig. 4(b).

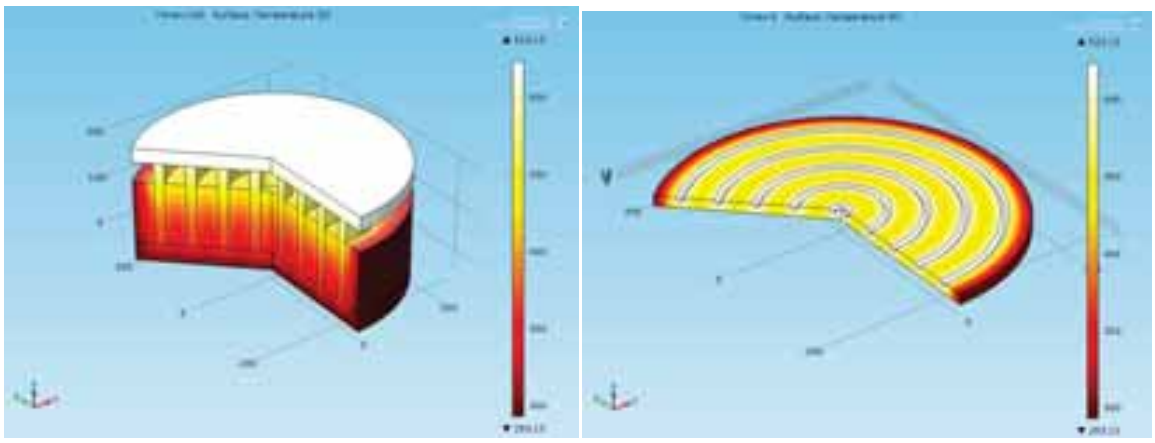

Figure 4: COMSOL simulation of a) PCM charging and heat transfer between SS and aluminum wall, b) frying pan with embedded SS steam pipe

3.1. Simultaneous charging-discharging

In this system, when the collector starts focusing the radiation on the receiver, the regulated water inside the receiver starts boiling and a vapor at low temperature starts circulating in the closed loop of the thermosyphon loop. In the first day of the test, the stagnation temperature of the system was not reached the melting point of the PCM. Though, the storage was tried to be charged in successive days using the advantage of the PCM's heat retention ability this did not help to charge the storage fully, this was probably mainly due to the huge

heat losses from the receiver.

The test was then preceded to a simultaneous charging-discharging during the peak hours of solar radiation. When simultaneous charging-discharging test was started, the circulating steam and temperature was 160°C and 150°C respectively. During this test the intended application, Injera and bread baking, was perfect regardless of literature values. When baking was started, the circulating steam and the storage have experienced a sudden drop of temperature. However, the temperature has slowly recouped during the baking period. Figure 5 shows the baking and charging behavior of the system during simultaneous charging-discharging.

In the first cycles, the progress of the storage temperature was very slow, because it took extended time to took the food from the frying plate. And this was accompanied by large losses from the baking surface. However, when this time was reduced by improving the baking surface interaction baking surface as shown in the last two cycles of Fig 5, the baking speed and storage temperatures have improved.

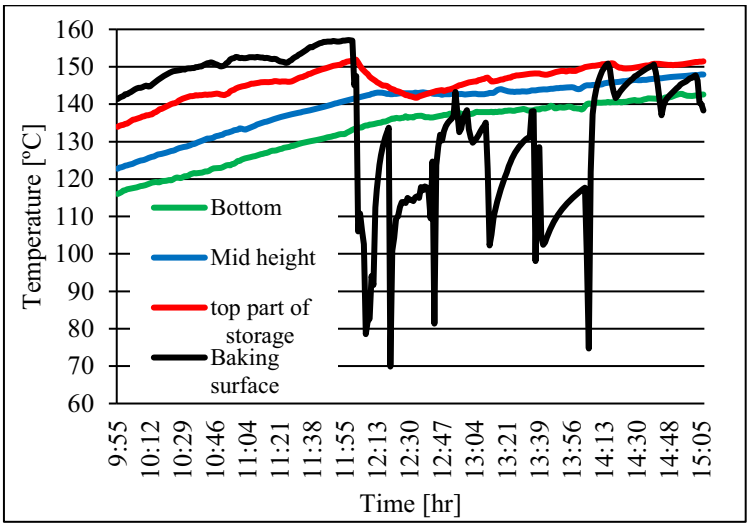

Figure 5: PCM charging and baking practice simultaneously from the sun

In the beginning of Injera baking on this stove, the surface texture of the frying pan was rough and it stacked the Injeras. Taking out the baked Injera from the surface of the frying pan was a big challenge. In addition, the quality of the Injera was not attractive. To avoid the sticking impact of the aluminum-baking surface, a borosilicate glass has been placed on top of it, but the Injera quality remained unattractive. However, the frying pan was suitable for bread baking. Simultaneous changing-discharging process helps to utilize more energy during the day. However, the storage charging process took more time as the inlet heat splits in to charging and baking.

a. Discharging of a fully charged PCM storage

In this study, an artificial resistor heating element was coiled around the receiver in order to melt the salt fully. The heating element has been delivering a uniform and regulated heat. The heating element was set to a maximum temperature of 450°C, at which it was delivering an average power of about 700W to the receiver. This power was equivalent to the solar power supply obtained from a 1.2m parabolic dish concentrator with 80% optical efficiency and $800 w/m^2$ average beam radiation. The storage took about eight hours of phase change duration.

The stored heat was tested to bake Injera and bread needs of average household size, i.e. 19 Injeras and six breads. The stored heat was run for about four hours of intensive baking and the remaining heat was left to discharge naturally while it was still capable of performing another cooking. The Injera baking speed of this test was faster compared to ordinary electric and biomass stove baking speed. In the baking process, the Injera consumes the phase transition heat. And the bread baking process consumes sensible heat of the solid PCM. The nearly uniform temperature drop with short baking cycle during Injera baking cycles shows the role of the heat buffer/storage to perform isothermal practice. The sticking problem of the baking surface has been improved with continuous heating and polishing with oil. Consequently, the baking process and the quality of

the Injera's were improved.

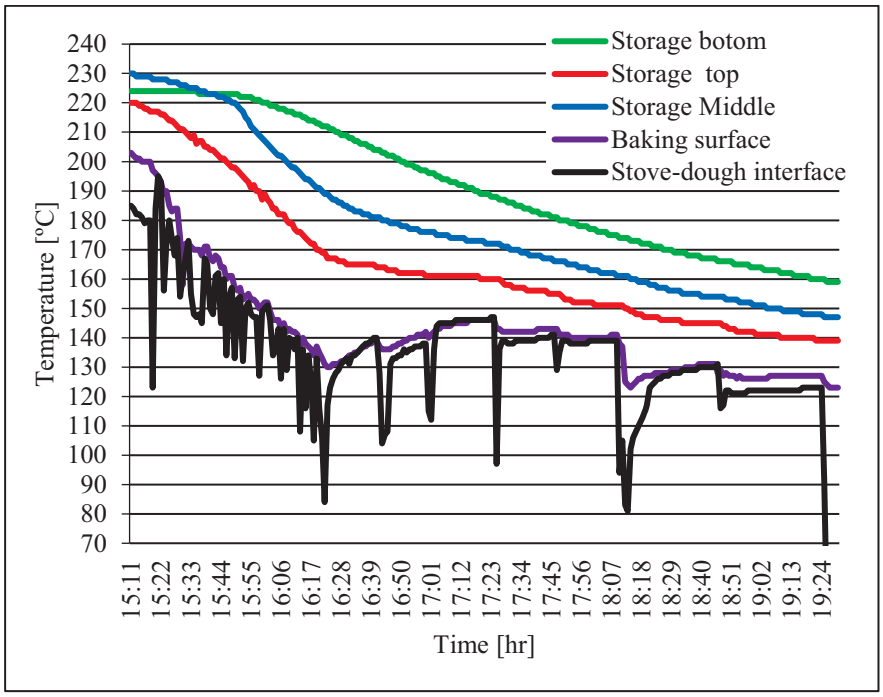

Figure.6: PCM discharging through backing

b. Discharging of partially charged storage

The third practical test for this system is to prove if it works for cloudy seasons; when the available radiation is not capable to melt the salt. Successive Injera baking tests were performed from a partially charged storage. The baking tests show smooth baking process with very good Injera quality, which is the same as the quality of Injera baked on customary Injera stove as shown in Fig. 7. This system has smooth baking surface texture similar to the ordinary stove and it used oil seeds to polish it. Unlike oil, oil seeds have the ability to give smooth baking surfaces by filling its irregularities.

Figure 7: Injera baking process and the final Injera quality

This system has been giving demonstration of solar Injera baking to local media, Mekelle University communities, and external guests. The demonstration has impressed many students, internal and invited

professors from six universities, media and to the university community at large. In addition to the routine solar Injera baking on test demonstration, one planed demonstration was arranged. The aim of this demonstration was to create awareness how solar energy was able to bake Injera and cook the different common Ethiopian dishes. The university community has appreciated the innovation of the research's role in mitigating climatic and health problems caused from extensive use of biomass fuel during Injera baking and cooking processes. Figure 17 shows the Injera baking process, which includes polishing, pouring, and taking off and the final Injera.

The Injera baking cycles plotted in Fig. 8 shows the Injera baking process was taking on average three minutes per cycle. This graph indicates another important point, i.e. during Injera baking; it is not the surface temperature that matters most but also the heat transfer. In many of the experiments, the baking surface temperature was unbelievably abled to bake Injera as low as at 60 and 80ºC. For instance, nearly all of the Injera baking cycles shown in Fig. 18 are below 110°C. This result is very attractive compared to literature values (180-220°C), which can possibility revolutionized the stove technology.

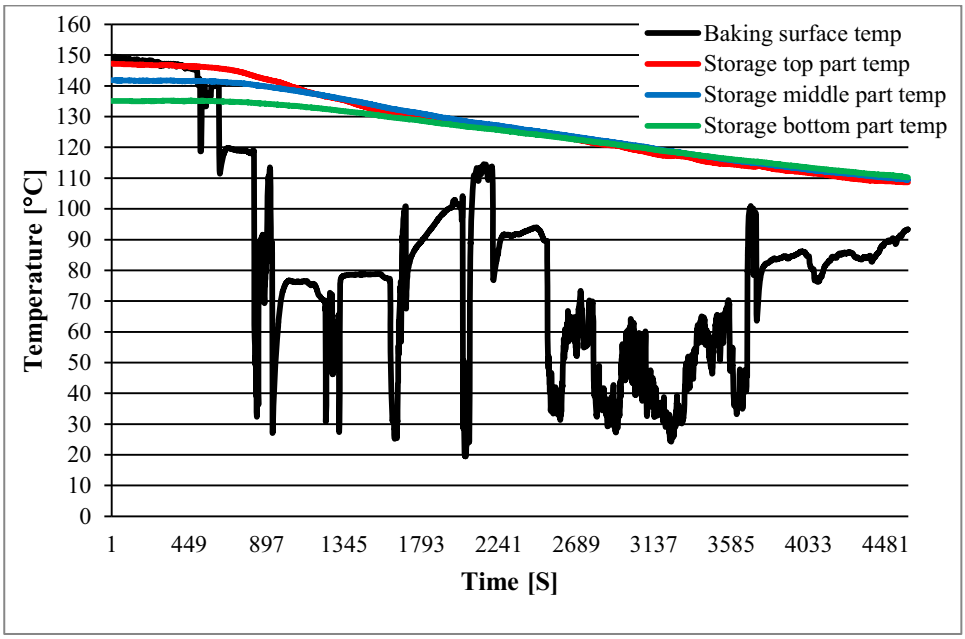

Figure 8: Injera baking from a partially charged PCM storage

Figure 9: serving solar prepared meal

Conclusion

A concept for Injera baking (Ethiopian bread) on top of a heat storage charged from a solar concentrator has been developed and demonstrated. Heat transfer by a thermosyphon principle, with water as the working fluid at about 40-bar pressure. Vapor is generated at the heat absorber in the focus point of the parabolic concentrator and condenses in coiled tube, which is casted into an aluminum baking plate. The baking plate has heat-conducting rods extending into a latent heat storage ("solar salt", Nitrate mixture). The following conclusions can be noted: Injera can be baked on an aluminum surface, provided the surface is sufficiently smooth and otherwise prepared similarly as for the traditional clay based pan during the frying process. Injera can be baked at lower temperatures (110-150°C) than previously assumed (180-220°C), as long as sufficient heat transfer can be maintained during the baking process. The required temperature will then depend on the material of the baking plate. A boiling/condensing natural circulation loop (thermosyphon) is feasible with water as the heat transfer fluid. As the water volume is small, the high pressure is manageable but requires high quality pipe and valve components. A boil-off startup procedure is operationally easy. The system can be optimized with respect to losses in the heat transfer loop, in particular at the absorber. The absorber is a spherical boiler in a fixed position, with the solar illuminated area moving from one side to the other during the daily sun tracking.

4. References

[1] Antonio Lecuona et al., Solar cooker of the portable parabolic type incorporating heat storage based on PCM, Applied Energy, vol. 111; pp: 1136–1146, 2013

[2] H.M.S. Hussein et al., Experimental investigation of novel indirect solar cooker with indoor PCM thermal storage and cooking unit, Energy Conversion and Management 49 (2008) 2237–2246.

[3] http://en.wikipedia.org/wiki/Injera, [last retrieved on 10.09.2014]

[4] Lifang Li and Steven Dubowsky, A new design approach for solar concentrating parabolic dish based on optimized flexible petals, Mechanism and Machine Theory, vol. 46; pp: 1536–1548, 2011.

[5] Abduljalil A. Al-Abidi et al., Experimental study of melting and solidification of PCM in a triplextube heat exchanger with fins, Energy and Buildings, Vol. 68; pp: 33–41, 2014.

[6] Taha K. Aldoss and Muhammad M. Rahman, Comparison between the single-PCM and multi-PCM thermal energy storage design, Energy Conversion and Management, vol. 83; pp: 79–87, 2014.

[7] Robynne E. Murray and Dominic Groulx, Experimental study of the phase change and energy characteristics inside a cylindrical latent heat energy storage system: Part 1consecutive charging and discharging, Renewable Energy, vol. 62; pp: 571-581, 2014.

[8] Liang Zhang et al., An indoor experimental investigation of the thermal performance of a TPLT-based natural circulation steam generator as applied to PTC systems, Applied Thermal Engineering, vol. 62; pp: 330-340, 2014.

[9] Foong Chee Who, Jørgen Løvseth, and Ole Jørgen Nydal, "Heat Capacity Measurements of NaNO3 – KNO3 Binary System", submitted paper to International journal of Thermophysics, 2011.

[10] R T Dobson and J C Ruppersberg, flow and heat transfer in a closed loop thermosyphon: part I-theoretical simulation, Journal of Energy in South Africa, Vol. 18; pp: 32-80, 2007.

Conference Proceedings
Solar World Congress 2015
Daegu, Korea, 08 – 12 November 2015

Night Radiative Cooling With Unglazed PVT-Water Collectors: Experimental Results and Estimation of Cooling Potential

Jose I. Bilbao[1] and Alistair B. Sproul[1]

[1] University of New South Wales, Sydney (Australia)

Abstract

A PVT-Water collector was built and tested 24 hours per day during a period of six months in Sydney, Australia. The results provided enough experimental data to accurately build and tune a PVT model of the system in TRNSYS. The experimental setup included a pyrgeometer used for the calculation of the radiation losses to the sky. This article presents the experimental results obtained during the night radiative cooling periods and results from simulations carried out with the tuned TRNSYS model for the estimation of the sky cooling potential for this application. The results show that the unglazed PVT water system can achieve good levels of night cooling (around 750 Wh/m^2 of cooling per night during summer months) with radiation losses accounting for circa of 60% of the total cooling achieved and convection losses for 40%. Simulations show that similar night radiative cooling levels are obtained for other climates with minimum of 400 Wh/m^2 per night in Singapore to around 900 Wh/m^2 in Tucson, Arizona.

Keywords: *Sky Cooling, Night Radiative Cooling, PVT-Water*

1. Introduction

The use of night radiative cooling has been explored (Robinson and Sharp, 2012) and tested (Hamza et al., 1995) in several systems and applications, particularly in the cooling of buildings using PVT systems (Fiorentini et al., 2015; Yong et al., 2015). However, most of the examples found in the literature are carried out without accurate measurements of the sky temperature (except for Eicker and Dalibard, 2011), so estimations of the effective sky temperature are used instead. Unglazed PVT systems, either using air or water as the working fluid, are particularly well suited to provide radiative cooling due to the non-selective nature of the absorber (solar cells). However, limited information can be found in the literature regarding the portion of cooling provided by convection losses and by radiation losses. In the case of PVT air systems, the total cooling obtained can sometimes be mixed with the effects of ventilating a building using cooler ambient air, also known as night purging. On the other hand, in PVT water systems the portion of cooling done by convection and radiation losses of the absorber can be calculated directly.

This study uses high resolution experimental data (one minute) to tune and validate a TRNSYS model that has shown to produce very good levels of accuracy (Bilbao and Sproul, 2012), which in turn is used to simulate the potential of radiative cooling in different climates. The aim of the study is to provide a first comparison between experimental and simulation results and a detailed analysis of the night radiative cooling potential of unglazed PVT-water modules using a validated model. The measured data and simulations show promising results for night radiative cooling. However, further work is required and more and better sky temperature measurements are required across the world to properly assess radiative cooling.

2. Method

An experimental setup was built at the University of New South Wales (UNSW), Sydney, Australia. The setup involved a PVT water system, a weather station and a 24/7 data logging system. The weather station included a pyranometer for measuring solar irradiance and a pyrgeometer for the calculation of the sky

doi:10.18086/swc.2015.10.10 Available at http://proceedings.ises.org

temperature, both installed on the plane of the PVT system (34° tilt and 7° azimuth). The experimental data was used to tune and validate a steady state PVT model developed in TRNSYS by the authors (Bilbao and Sproul, 2012), called Type850. The model is capable of taking into account the sky temperature for the accurate calculation of radiative thermal losses to the sky.

The validated model was then used to estimate the night radiative cooling potential on different climates for rooftop PVT installations in TRNSYS. A detailed description of the experimental setup and the validation process is presented below.

2.1 Experimental Setup and Data Quality

The experimental setup uses a closed circuit water system connecting the PVT water module with a 100 liters storage tank. A frameless Siemens PV module (SM110) was used to build the PVT-water module using a fully wetted collector. The system is completed by a pump which maintains the water circulating between the PVT module and the tank 24 hours a day, unless a stagnation experiments is being carried out. This setup provides a natural way of 'resetting' the system each day, by releasing to the environment the thermal energy stored in the tank during the day, via night radiative cooling using the PVT module.

Table 1 shows all the sensor and logging equipment used for the experiment. Uncertainty calculations for the measurements and a more detailed description of the experimental setup can be found in Bilbao and Sproul (2015).

Table 1 – Measurement Equipment used in the Testing Rig

Type and Model	Measurement
Thermocouple 1	Inlet temperature (°C)
Thermocouple 2	Outlet temperature (°C)
Thermocouple 3	Lower end of PVT module, between PV module and collector (°C)
Thermocouple 4	Top end of PVT module, between PV module and collector (°C)
UCC Flow Meter DFC9000	Flow rate (pulses)
Hukseflux Pyranometer SR12	Global irradiance at module plane (W/m^2)
Hukseflux Pyrgeometer IR02	Far infrared radiation at module plane (W/m^2)
Vaisala Weather Transmitter WXT520	Ambient Temp (°C), Wind Speed (m/s), Relative Humidity (%), measured two meters above PVT module
dataTaker DT505	Log PVT data (currents, voltages, temperatures, and flow rate)
dataTaker DT80	Log weather data

Much care was taken in designing and building the experimental setup in order to collect as much data as possible. However, there were small problems during the six months the system was collecting data, from sensors, to the PVT module, to the pump, that impeded the logging of good quality data during the whole period. Thus, only days with a full data set were used for this publication, as shown in Table 2, which are equivalent to four months of full data.

Table 2 - Number of days with good quality experimental data

Data	Jan 12	Feb 12	Mar 12	Apr 12	May 12	Jun 12	Total days
PVT – PV	30	29	23	3	22	30	137
Irradiance	31	29	31	22	26	30	169
Sky Temp	13	29	31	19	24	30	146
Total days	**13**	**29**	**23**	**3**	**22**	**30**	**120**

A summary of the weather data (POA solar irradiance, daily average dry bulb temperature, and daily average sky temperature) obtained during the months of the experiment is shown in Fig. .

Fig. 1: Summary of Weather Data

2.2 Tuning of the model and experimental validation

The tuning and validation method consisted in an iterative process using theoretical values as a starting point for each parameter in the model. Selected parameters of the model were varied on each iteration and the residuals against the experimental results calculated. The electric parameters were fitted first (efficiency and temperature coefficient of the PV cell) followed by thermal parameters (heat loss coefficients and total heat transfer coefficient between the absorber and the fluid, $U_{pv\text{-}f}$).

The theoretical values used for the parameters provided acceptable results in thermal and electrical outputs with mean bias errors (MBE) below 2%. Hence, only few parameters were fine-tuned resulting in a MBE of -0.4% and a coefficient of variation for the root mean square error (CVRMSE) of 9.8% for the electrical output, while for the thermal output the best result obtained was an MBE of 0.1% and a CVRMSE of 16.3%. However, for this study the thermal output and thermal losses of the PVT system are most relevant for evaluating the night radiative potential. A linear regression (see Figure 1) for the thermal losses shows good agreement between the experimental data and the model with an R^2 of 0.96 for hourly data, which confirms the good performance of the model.

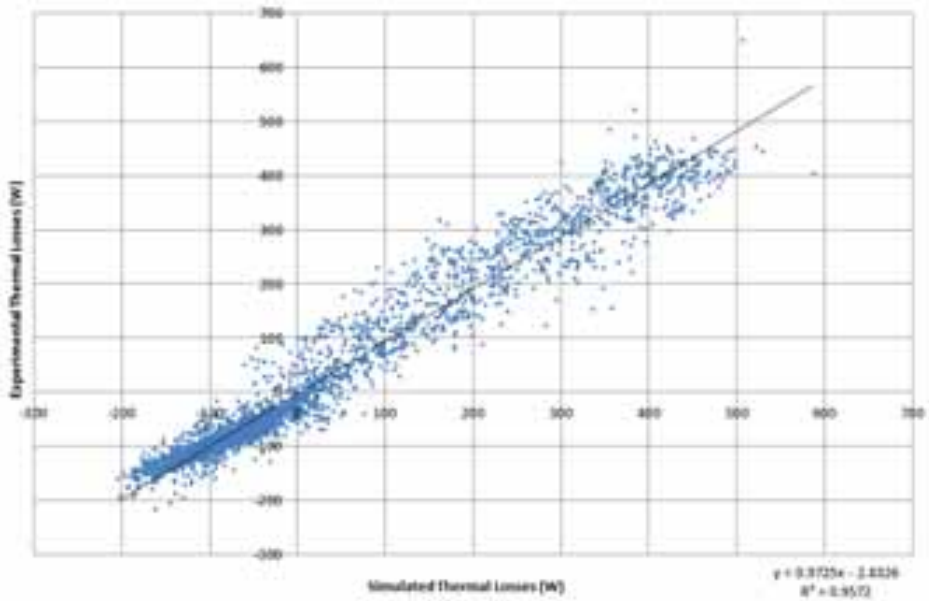

Fig. 2: Comparison of Simulated Thermal Losses (TRNSYS Model) and Experimental Thermal Losses

2.3 Annual Simulations for Different Climates

Simulations were carried out using TRNSYS 16. The tuned model Type 850 was selected for the PVT-water module (of 1 m^2) in conjunction with standard TRNSYS types for pump (Type3b), pipes (Type709), weather engine (Type15), and water tank (Type4c). The water tank was used as a thermal mass reservoir in order to imitate the scenario of providing night radiative cooling to a building. The tank starts ends the day warm and then is progressively cooled during the night by the PVT system. This resembles the experimental setup described above and provides a more realistic simulation than assuming a constant inlet temperature for the PVT system.

Other important assumptions are described below:

- Meteonorm TMY2 weather files were used for all locations.

- PVT modules on all locations were assumed to be installed flat on a 10 degrees tilt roof facing south or north, depending on the hemisphere. Given the high levels of insulation at the back of the PVT modules this could be considered equivalent to a BIPVT roof installation.

- Potential effects of the surroundings were not taken into account. However, the effects of potential heat islands (within the urban landscape) are minimized by choosing a rooftop installation with 10 degrees tilt which ensures a good sky view factor.

- A constant flow rate of 0.02 kg/s.m^2 was used.

- The cities of Singapore, Tucson (Arizona), Sydney (Australia), and Hamburg (Germany) were selected for this study given their diverse climate classifications (Af, BSh, Cfa, and Dfb respectively).

3. Results and Discussion

The analysis of the experimental data showed that, on average, the PVT-water system can provide, on average, circa of 750 Wh/m^2 of cooling per day on Sydney climate during summer months (Jan-Mar). The cooling potential increases, as expected, during autumn and winter months to 1,000 Wh/m^2, as shown in Figure 3. However, building cooling is usually not required during these months, at least on the Sydney climate, except for very specific building loads like data centers.

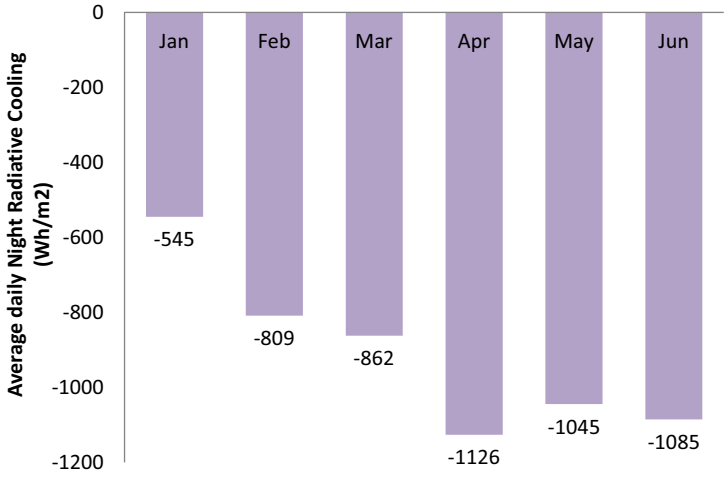

Fig. 3: Average Daily Night Radiative Cooling by a PVT-water module in Sydney from measured data

The results on show good potential for using PVT water systems for night cooling in Sydney climate. However, in order to design systems and really assess the cooling potential it is important to understand how this cooling is achieved, i.e., the portion of radiative and convective heat losses at night as part of the total cooling. The model developed in TRNSYS (Type850) was hence used to calculate the heat losses of the PVT-water module (top radiation, top convection, and back and edges) during night time using the same weather data obtained from the experiment. The results (Figure 4) show that radiation losses (Q_{rad}) account on average for 57% of the total heat losses, while convective losses (Q_{conv}) from the top surface of the

module are responsible for the 40% of the heat loss and the back and edge losses (Q_{be}) for only the 3%. Figure 4b also shows that the radiative cooling portion is slightly larger during winter months (mostly due to the increase of clear nights in Sydney when compared to summer) but is still relevant during summer. This ratio however is not fixed and depends greatly on the inlet water temperature and wind speed. For example, the closer the inlet water temperature is to ambient, the less important will be the convective heat loss to ambient and the more relevant will be the portion of radiative heat losses. This effect can be clearly observed in the simulation results for a clear summer night shown in Figure 5. In the simulation (from 8pm to 5am) the sky radiative cooling increases during the night as the sky temperature drops (effectively increasing the gap with the ambient temperature) while the convective losses drop as the temperature of the inlet water becomes closer to ambient temperatures.

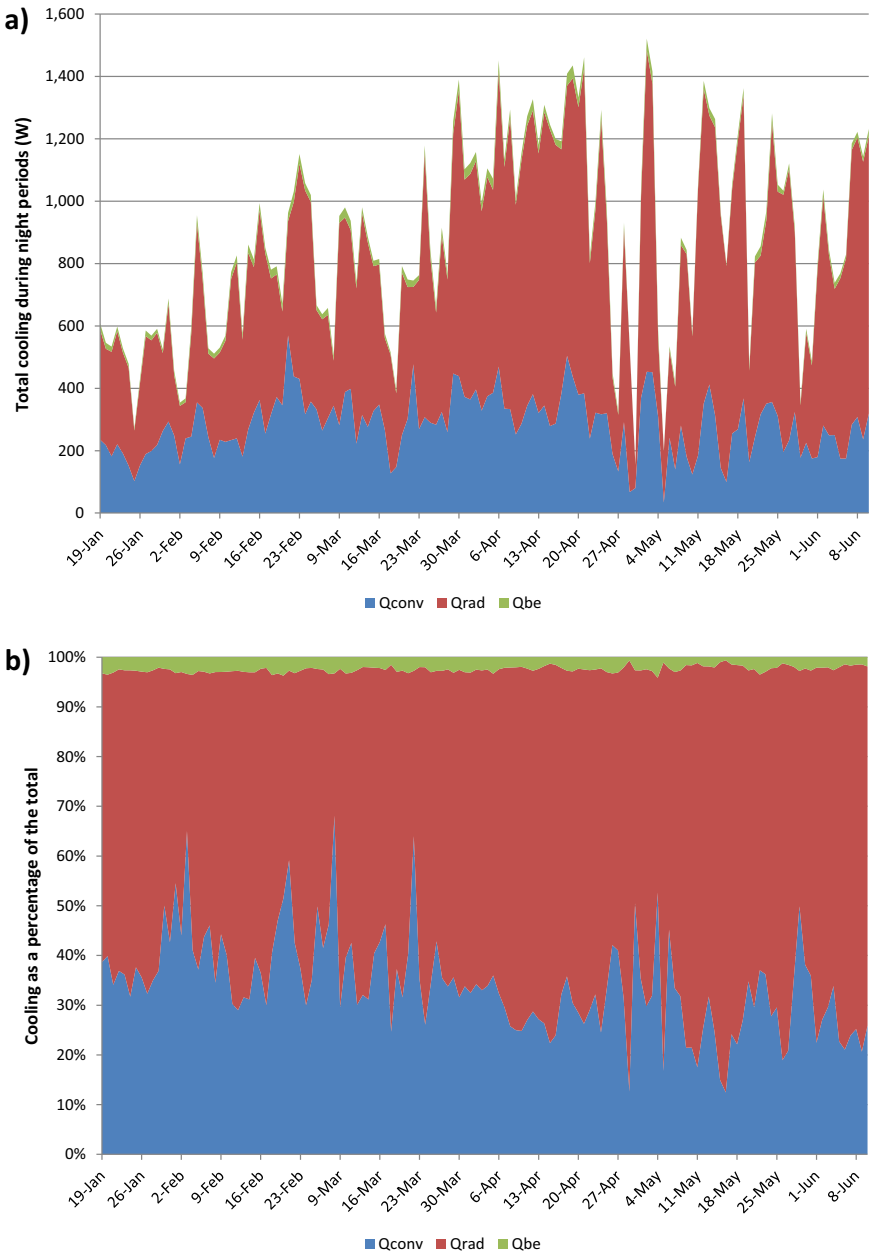

Fig. 4: Estimated daily heat losses or 'cooling' (top convection, top radiation, and back and edge) for the experimental PVT water system during night periods, in a) Wh and b) as a percentage of the total

These results have important ramifications and present interesting options for unglazed PVT modules, as they could be used for combined cooling/heating cycles, providing electricity, space heating during day winter months and cooling during clear summer nights, effectively a trigeneration system. An efficient hydraulic design for the PVT system is of paramount importance, as the benefits of providing space cooling/heating and the potential efficiency gains by cooling the PV cells can be outweighed by an inefficient water and air moving system (Farshchimonfared et al., 2015).

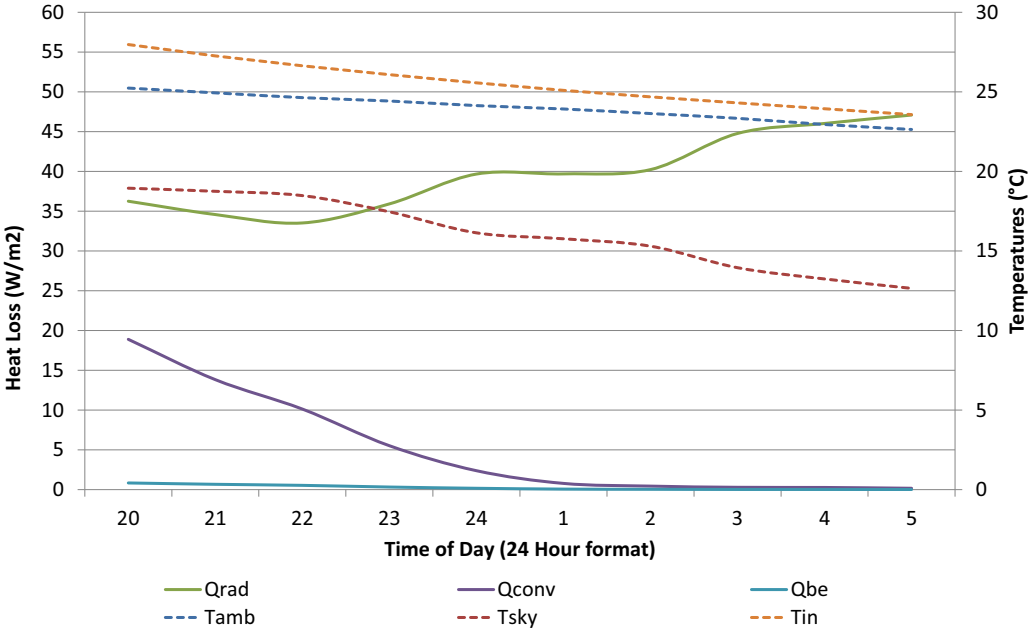

Fig. 5: Convective and radiative losses during a night

Of course, the cooling (and heating) capacity will depend on the weather conditions of the specific site and the type of installation along with tilt, orientation, and surroundings. This type of night radiative cooling might not be suitable for tropical zones, with high humidity and overcast days, but it might prove successful for temperate climates. Therefore, a set of simulations were carried out for four different climates (cities of Singapore, Tucson, Sydney, and Hamburg) in order to assess the potential of night radiative cooling under different conditions. A summary of the results for the year-long simulations are presented in Figure 6.

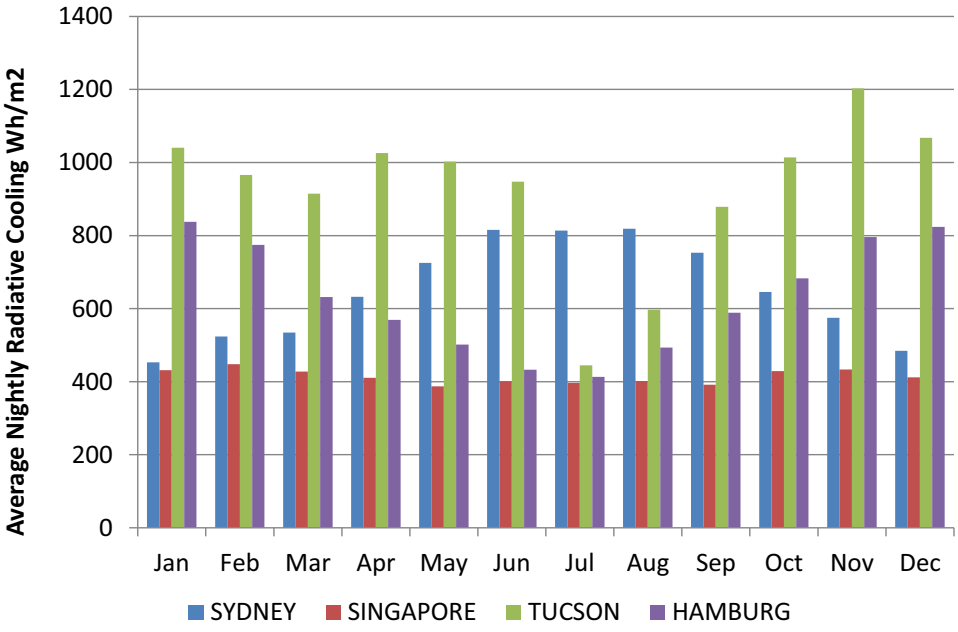

Fig. 6: Average PVT nightly radiative cooling during the year for different locations

As expected, the climate of Singapore produced limited night cooling potential around the year, with the average hovering around 400 Wh/m^2 per night. The drier climate of Tucson provided more than double of the cooling capacity with an average of 925 Wh/m^2 per night during the year. The night radiative cooling potential in Tucson is relatively constant during the year except for the months of July and August corresponding to the monsoon season in Arizona. On the other hand, Sydney offers similar night radiative cooling as Singapore during the (Sydney) summer months, with an increase cooling potential in winter (notice that Figure 3 shows measured data for Sydney and Figure 6 shows simulated data for Sydney with TMY2 data files, hence the discrepancy in values). A similar result is obtained for Hamburg, but with the corresponding seasons for the north hemisphere, with around 450 Wh/m^2 of cooling per night during summer and more cooling potential during winter (when the additional cooling potential is probably not needed). However, autumn and spring seasons (when present) seem to offer the best balance between night radiative cooling potential and cooling need.

Despite the difference in climates the model showed that on average it is always possible to obtain some level of night radiative cooling (see Figure 7). When compared to the output of convective cooling during night time, the results from the model and TMY2 weather files show a predominance of the radiative heat loss portion of at least 80% of the total. This differs from the measured results from the test rig built at UNSW in Sydney where the convective portion was closer to 40%. Given the fact that Type850 model shown good agreement to the measured data when using the logged weather data for the site, the difference can only be attributed to the weather file and difference in location. Furthermore, when running a simulation for Sydney with TMY2 data and the PVT module tilted at 30 degrees instead of 10 degrees, the model does show an increase in convective cooling and reduction in radiative cooling (Figure 7).

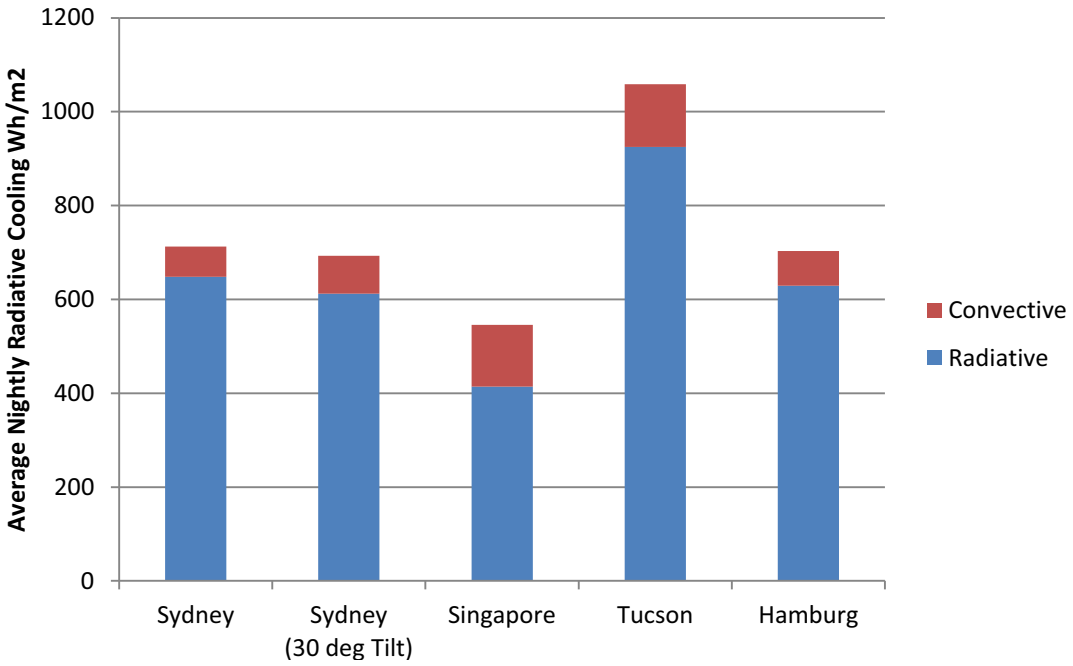

Fig. 7: Average PVT nightly radiative and convective cooling for different locations

If night radiative cooling is a better option than night purge or normal air conditioning for providing space cooling to buildings will depend on many factors including HVAC design and climate, as mentioned above. However, night radiative cooling using PVT water systems (using unglazed PVT modules) could be used as a complement for those technologies.

Further work and a more extensive analysis are required in order to explore and optimize the use of PVT water systems as a real trigeneration option. Moreover, with research already underway to assess the solar potential of all surfaces in the built environment (Redweik et al., 2013) it could be possible to use a similar approach to assess the night radiative cooling potential by including a sky view factor analysis.

4. Conclusions

PVT systems can offer important levels of night radiative cooling, which depends on the climate. From Singapore to Tucson (Arizona), the results of the simulations showed radiative cooling potential of the unglazed PVT system from 400 Wh/m^2 to 900 Wh/m^2 per night and that it is possible to provide cooling through the whole year, which might be beneficial for some applications like data centers. An additional 10% to 20% cooling can be obtained from convective cooling, although the portion of radiative and convective cooling depends on many variables including weather and system design and operation. More importantly, results seem to indicate that night radiative cooling is a real possibility for complementing night purge and other low energy cooling options. Consequently, it makes sense to use unglazed PVT systems already integrated into buildings as tri-generation systems, in order to use the full potential of the technology.

5. References

Bilbao, J. I., Sproul, A. B., 2012. Analysis of Flat Plate Photovoltaic-Thermal (PVT) Models. World Renewable Energy Forum (WREF 2012), Denver.

Bilbao, J. I., Sproul, A. B., 2015. Detailed PVT-water model for transient analysis using RC networks. Solar Energy, 115, 680–693.

Eicker, U., Dalibard, A. 2011. Photovoltaic–thermal collectors for night radiative cooling of buildings. Solar Energy, 85, 1322–1335.

Fiorentini, M., Cooper, P., Ma, Z., 2015. Development and optimization of an innovative HVAC system with integrated PVT and PCM thermal storage for a net-zero energy retrofitted house. Energy and Buildings, 94, 21–32.

Hamza, A., Ali, H., Taha, I.M.S., Ismail, I.M. , 1995. Cooling of water flowing through a night sky radiator. Solar Energy, 55, Pages 235–253.

Farshchimonfared, M., Bilbao, J. I., Sproul, A. B., 2015. Channel depth, air mass flow rate and air distribution duct diameter optimization of photovoltaic thermal (PV/T) air collectors linked to residential buildings. Renewable Energy, 76, 27–35.

Robinson, B.S., Sharp, M.K., 2012. Space Cooling Potentials for Ambient Sources with Thermal Energy Storage. World Renewable Energy Forum (WREF 2012), Denver.

Redweik, P., Catita, C., Brito, M., 2013. Solar energy potential on roofs and facades in an urban landscape. Solar Energy, 97, 332–341.

Svensson, M. K., 2004. Sky view factor analysis – implications for urban air temperature differences. Meteorological Applications, 11, 201–211.

Yong, C., Yiping, W., Li, A., 2015. Performance analysis on a building-integrated solar heating and cooling panel. Renewable Energy, 74, 627–632

Conference Proceedings

Solar World Congress 2015
Daegu, Korea, 08 – 12 November 2015

Performance Analysis of Concave Cavity Surface Receiver for a Non – imaging Solar Concentrator

K. S. Reddy and T. Srihari Vikram

Heat Transfer and Thermal Power Laboratory, Department of Mechanical Engineering,

Indian Institute of Technology Madras, Chennai – 600 036, INDIA

Abstract

In the present study, a numerical investigation of concave surface cavity receiver of non-imaging solar concentrator is carried out considering various operating and geometrical parameters such as mass flow rate of the fluid, solar radiation and receiver configuration. The fluid outlet temperature, pressure drop across the coil for different receiver configurations are studied along with the heat loss estimation of concave cavity surface receiver for non-imaging concentrating collector. The convective and radiative heat loss from the receiver surface is calculated based on 3-D numerical simulations. For helical receiver, the temperature rise is found to be 30°C (0.5kg/min) and 17°C (1kg/min) respectively; whereas for helical-spiral receiver, the temperature rise is found to be 27°C (0.5 kg/min) and 15°C (1 kg/min). The pressure drop across the coil ranges between 1kPa to 14kPa for different mass flow rate and solar radiation for two configurations of the receiver. The present model can be used for estimating the heat transfer and fluid flow characteristics of helical receiver for EHC.

Keywords: Solar energy, Non-imaging collectors, concave cavity surface receiver, Process heat

1. Introduction

The use of conventional fuels such as oil for process heat applications is slowly finding their way to the renewable energy means. One of the most promising renewable energy sources is solar thermal which can be widely used for variety of applications ranging from process heating to power generation. IRENA (2015) briefs that solar thermal can fulfill the process heat demands irrespective of its geographic location. It discusses the technical highlights, process and technology status detailing about the various options for process heat applications. It also presents a brief insight of various process heat systems installed all around the world. Lauterbach et al., (2010) reports that industrial sector is one of the most promising application for solar process heat application. Solar thermal heat is used for the following broad categories of industrial applications such as “heating of fluid streams”, “heating of baths/vessels” and “drying” and studied the feasibility of solar collectors for the industrial applications (Lauterbach et al., 2011). The development of new collectors provides scope for its use in industrial process heat applications. The emergence of new medium temperature collectors provides opportunities for the use of solar thermal energy because they can supply higher temperature demands and can co-exist with the installed high temperature heat networks (Martinez et al, 2012).

Non-imaging optics involves the design of optical components for solar concentrating systems. For given concentration ratio, non-imaging optics provides wide acceptance angles for solar applications. A non-tracking, non-imaging solar concentrator with low heat loss has been proposed and its optical and thermal performance has been investigated by Ustaoglu et al., (2015). It was found that the absorber temperature is uniform and with a concentration ratio of 2.51, the concentrator, even at an absorber temperature of 373 K, operates with an average efficiency of 47.8%, although the absorber is assumed to have a gray surface. The concentrator’s thermal efficiency has been compared with that of other solar collectors, and found to be higher than that of conventional solar collectors. Kaiyan et al., (2011) presented a novel multiple curved

doi:10.18086/swc.2015.10.11 Available at http://proceedings.ises.org

surfaces compound concentrator. It consists of a parabolic and a flat contour. It consists of focus at the backside which is extremely useful and convenient for some applications. The comparison with traditional paraboloid and CPC has been carried out. Garcia-Botella et al., (2006) presented an analysis of elliptical concentrators studying on concentration ratio and analysed for some applications such as concentrators and illuminators. A new 3-D asymmetric concentrator (hyperbolic concentrator) is studied based on different theories. Based on ray tracing analysis, it has been shown that 3-D concentrator in the shape of hyperbola intercepts maximum incident rays can be used for non-tracking solar application (Garcia-Botella et al., 2009).

Ali et al. (2010) compared the optical performance of 2-D and 3-D elliptical hyperbolic concentrator (EHC) and found that the optical efficiency of 2D and 3D system are 63% and 78% respectively. Ali et al., (2011) presented optical performance of 3D static circular and elliptical hyperboloids. Four different configurations of hyperboloids are studied based on the ray tracing techniques and flux distribution at the receiver aperture has been presented. The parametric studies have been carried out and the optical efficiency of the systems have been compared and have been compared and evaluated. It has been found that elliptical hyperboloid performs better than other three configurations. A detailed parametric study on the elliptical hyperbolic concentrator has been performed by Ali et al., (2013). The overall performance of the concentrator was assessed based on the acceptance angle, effective concentration ratio and optical efficiency. Optimization of the concentrator profile and geometry has also carried out to improve the overall performance and flux distribution at receiver aperture for different geometric parameters have also been presented. The optical efficiency of the system has been estimated to be 27% with concentration ratio of 20x and wide range of incidence angles (±30°).

Helical coil receiver was proposed for solar desalination applications using elliptical hyperboloid concentrators (Reddy et al., 2014). 2-D ray tracing has been carried out to study the optical performance of the proposed system and a parametric study has been carried out for fluid flow and heat transfer in helical coil and the system has been optimized for higher performance. The experimental performance investigation of EHC for process heat applications has been carried out by Ali et al., (2014). The maximum stagnation temperature and outlet fluid temperature was found to be 150°C and 90°C at flow rate of 0.5 kg/min. Ray tracing analysis has been carried out to estimate the flux at receiver plane and compared with that of the IR images. Experiments have been carried out for two different flow rates and the outlet temperature of the fluid has been determined.

In the present study, a numerical investigation of concave cavity surface receiver with helical and spiral coils used in elliptical hyperbolic concentrator (EHC) is carried out considering various operating and geometrical parameters such as mass flow rate, solar radiation, receiver configuration etc. and the outlet temperature of the fluid and the pressure drop across the receiver coil has been estimated. The heat loss analysis from the concave cavity surface receiver has also been carried out to study the performance of the concave cavity surface receiver by varying the incident solar radiation and emissivity of the surface.

2. Modelling of Helical – Spiral coil for Elliptical Hyperbolic Concentrator

2.1 Elliptical Hyperbolic Concentrator

Elliptical Hyperbolic Concentrator (EHC) consists of a hyperbolic concentrator with elliptical aperture both at top and bottom and a receiver placed at the bottom to collect the incident solar energy and convert to useful thermal energy. The receiver consists of helical coil which is wound in a elliptical shape to capture the incident concentrated solar radiation. The schematic of side view of the elliptical hyperbolic concentrator system is shown in Fig.1. The working fluid flows through the bottom of the receiver and gets heated due to

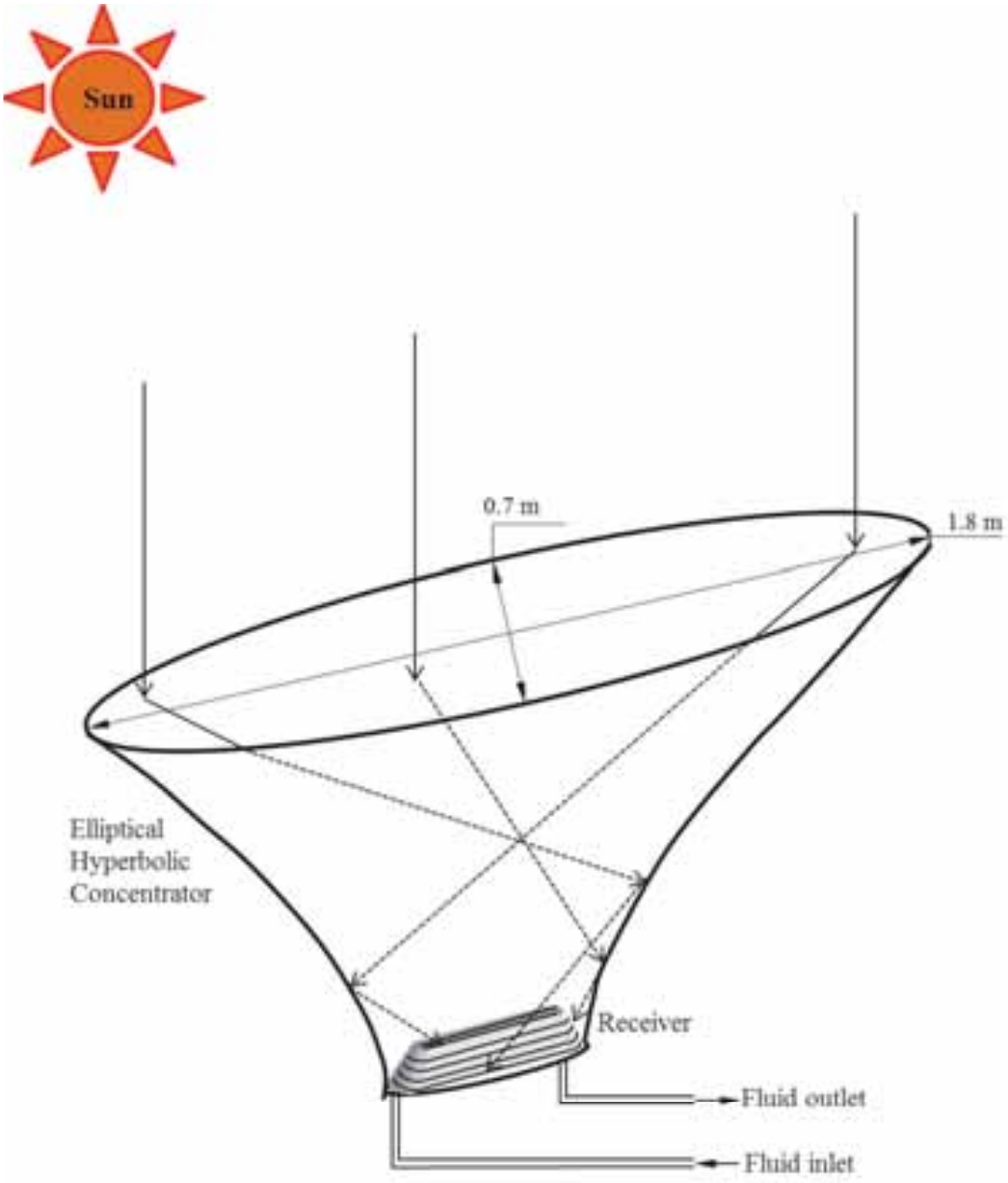

Fig. 1: Elliptical Hyperbolic Concentrator system (side view)

the incident solar energy and leaves at the top. EHC is a non-imaging concentrating collector having wide acceptance angle and does not require tracking.

2.2 Modelling of Helical-Spiral Coil

The helical receiver is a concave cavity surface receiver consisting of copper tube (Diameter: 6mm, No. of helical turns: 7; spiral turns: 5) wound in the elliptical shape (Fig. 2) is placed in the bottom aperture of EHC. The receiver coil is wound over a trapezoidal metal plate to hold in proper position. The trapezoidal metal plate forms a concave cavity. The working fluid (water) enters the receiver coil at the bottom and leaves at the top. The front view and bottom view of the concave cavity surface is shown in Fig. 2 and the helical coil receiver with and without spiral coil is shown in Fig. 3

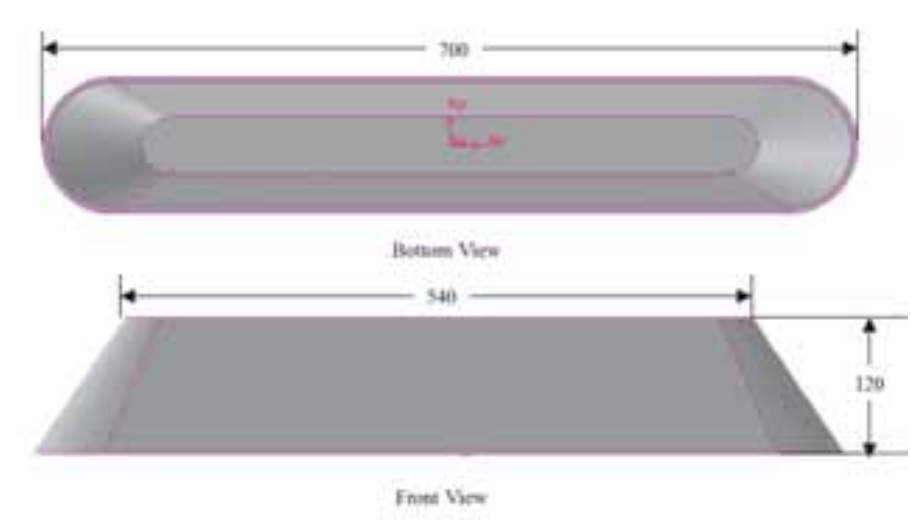

Fig. 2: Concave cavity surface receiver

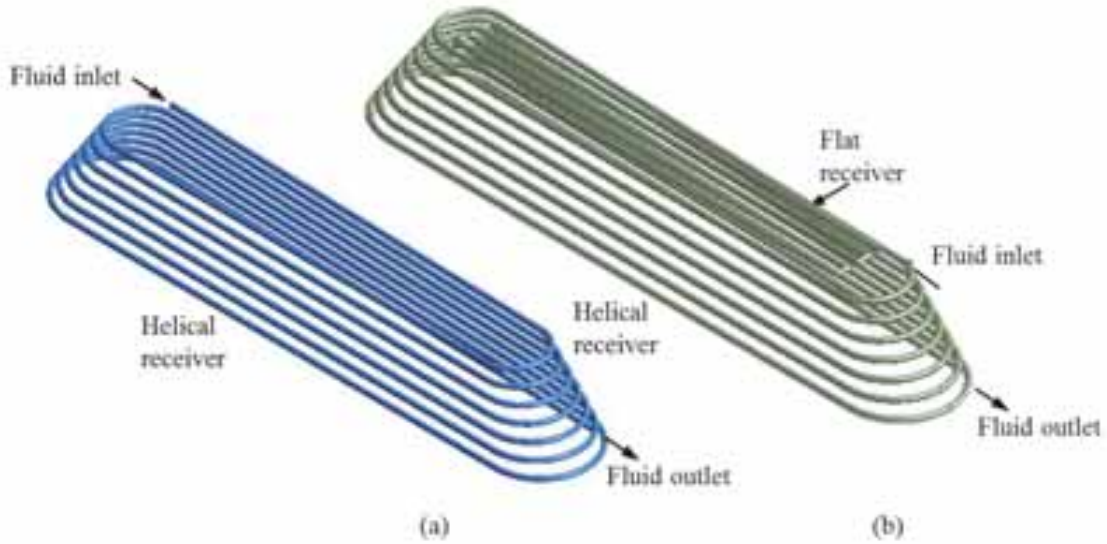

Fig. 3: Helical coil receiver (a) without spiral (b) with spiral

The geometry of the concave cavity surface receiver has been modelled using modelling software, GAMBIT 2.4.6. The helical coil receiver has been modelled using ANSYS Workbench V14.5.

2.3 Mathematical model

The flow and heat transfer simulations are carried out by solving the system of governing equations simultaneously:

Continuity equation is given by:

$$\nabla \cdot \vec{V} = 0 \qquad \text{(eq.1)}$$

Momentum equation is given by:

$$\vec{V} \cdot \nabla(\rho \vec{V}) = -\nabla p + \mu . \nabla^2 \vec{V} + \rho \vec{g} + \vec{F}_c \qquad \text{(eq.2)}$$

Energy equation is given by:

$$\vec{V} \cdot \nabla(\rho C_p T) = k \nabla^2 T \qquad \text{(eq. 3)}$$

The laminar, steady state and 3-D governing equations are solved in ANSYS FLUENT V14.5 using an implicit solver. Along with the above-mentioned conditions, surface-to-surface radiation model is also incorporated to account for the radiation exchange between the surfaces of the concave cavity surface receiver.

2.4 Boundary Conditions

The concentrated solar radiation falls on the concave cavity surface receiver placed at the bottom aperture of EHC. Hence the outer surface of the trapezoidal cavity is subjected to heat flux and the bottom surface of the cavity surface is insulated to minimize the heat loss from the receiver. To account for the effect of atmosphere, a spherical domain is considered which is 5 m in radius. This model has been used to estimate the heat losses from the receiver. Similarly to account for fluid flow and heat transfer analysis, the receiver coil is subjected to various boundary conditions. As the receiver coil is wound around the trapezoidal (concave cavity) surface, the concentrated solar flux is applied on the outer walls of the receiver coil. The mass flow rate is specified at the inlet of the receiver at the bottom and the pressure outlet is set at the outlet of the receiver at the top. The computational domain and boundary conditions of the concave cavity surface receiver and receiver coil are shown in Fig. 4.

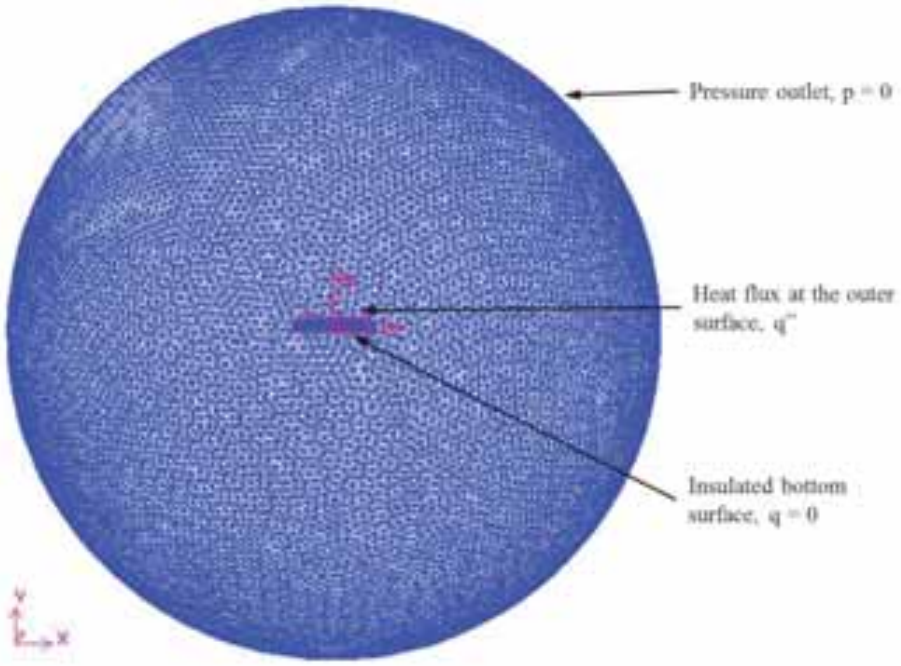

(a)

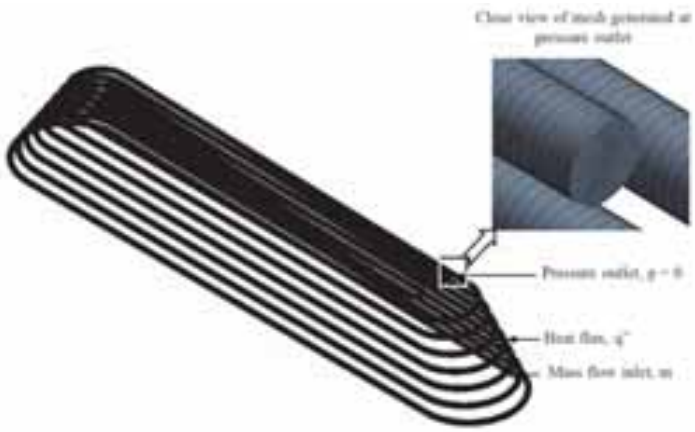

(b)

Fig. 4 : Computational domain and boundary conditions (a) Concave cavity surface receiver (b) Helical – Spiral receiver coil

2.5 Numerical Procedure

The computational domain of the concave cavity surface is created using GAMBIT 2.4.6. The atmosphere surrounding the concave cavity surface receiver is modelled such that the cavity receiver is placed inside large spherical domain. The size of the external domain is increased until it had an insignificant effect on the working fluid and heat flows from the receiver. In the present analysis, external domain is considered as 5 m diameter based on the numerical simulations. The fine mesh is considered for the receiver and coarse mesh is considered for outer atmosphere/domain. The computational domain of concave cavity surface considered in the present study is shown in Fig. 4. For pressure velocity coupling, SIMPLE algorithm has been used, with body force weighted algorithm for discretization of pressure with first order upwinding scheme for the discretization of equations. For the fluid flow simulations, A convergence criterion of 10^{-3} was imposed on the residuals of the continuity equation, momentum equation. A convergence criterion of 10^{-6} is considered for energy equation. The present numerical procedure for heat loss from concave cavity surface receiver is validated with Reddy and Kumar model (2009) and found to vary within acceptable limits. The present numerical procedure is validated with two different models (i) conical tube bundle and (ii) spiral coil. The fluid flow and heat transfer characteristics of conical tube bundle has been studied by Ke et al, 2011. The heat transfer and heat transfer coefficient obtained by Ke et al (2011) for the inlet flow velocity of 0.1 m/s has been compared with the present numerical procedure and the results are tabulated (Table 1) and shows good agreement. The heat transfer and flow characteristics of spiral coil carried out by Naphon (2011) is compared at flow rate of 0.05 kg/s. Table 1 shows the comparison of experimental and numerical results for heat transfer rate and outlet temperature of the spiral coil.

Tab. 1: Validation of numerical procedure

Parameter	Ke et al, 2011	Present numerical procedure	Naphon, 2011	Present numerical procedure
Heat transfer coefficient (W/m^2K)	150	152.46	-	-
Heat transfer (W)	307.45	310.35	2785.25	3031.72
Outlet fluid temperature (°C)	-	-	34.65	35

3. Performance analysis of concave cavity surface receiver

3.1 Heat loss analysisfrom concave cavity surface receiver

The 3-D numerical simulations have been carried out to estimate the heat losses from the concave cavity surface receiver. The effect of the parameters like DNI and emissivity of the receiver are varied to study the heat losses from the concave cavity receiver.

The heat losses from the receiver are estimated based on the following equations:

$$Q_{total} = h_{total} A_s (T_w - T_a) \quad \text{(eq.4)}$$

$$Q_{rad} = h_{rad} A_s (T_w - T_a) \quad \text{(eq.5)}$$

$$Q_{conv} = Q_{total} - Q_{rad} \quad \text{(eq.6)}$$

3.1.1 Effect of solar radiation

The effect of solar radiation on the heat loss from the concave cavity receiver is studied by varying the incident solar flux on the surface of the concave cavity surface receiver. Fig. 5 shows the temperature contours of the concave cavity surface receiver for solar radiation of $250 W/m^2$ at theoretical maximum heat flux of 10150 W/m^2. The maximum surface temperature at the receiver is about 470 K. Fig. 6 shows the temperature contours of the concave cavity surface receiver for solar radiation of 1000 W/m^2 at maximum heat flux of $40607 W/m^2$ incident on the receiver. The maximum surface temperature on the receiver is about 933K.

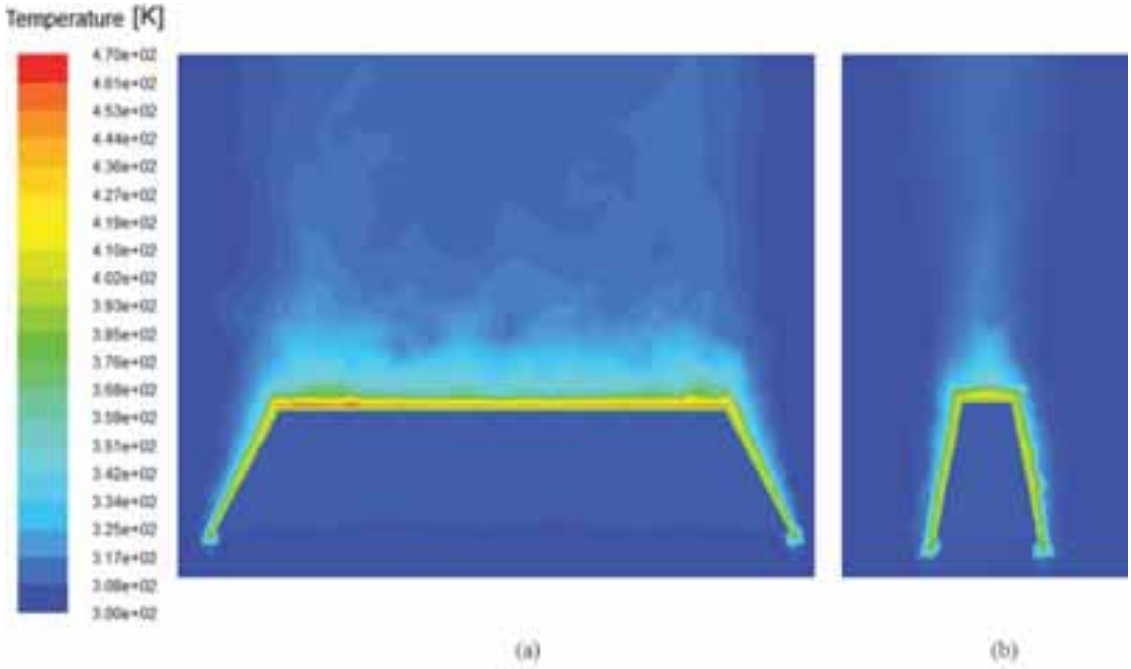

Fig. 5: Temperature contours of concave cavity surface receiver at different planes for DNI = 250W/m^2 (a) Z = 0 (b) X = 0

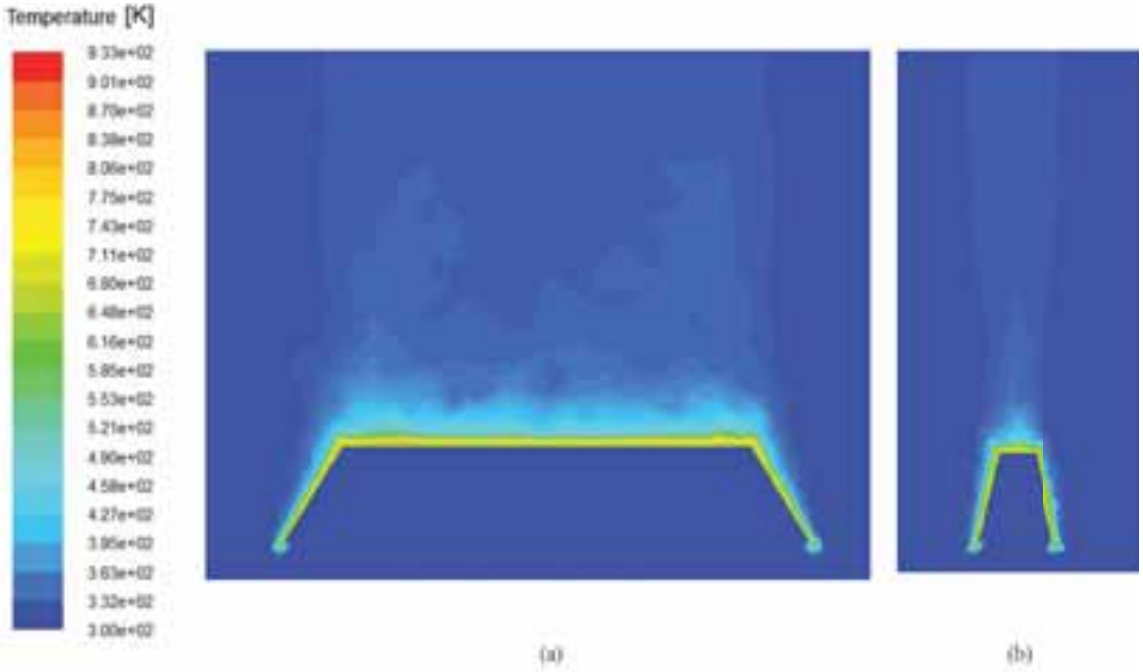

Fig. 6: Temperature contours of concave cavity surface receiver at different planes for DNI = 1000W/m^2 (a) Z = 0 (b) X = 0

3.1.2 Effect of emissivity of receiver surface

The emissivity of the receiver surface is varied to study the effect on heat loss from the receiver surface. The emissivity of the receiver surface is set to 1 as it is coated with black matt paint. The temperature contours for receiver at an emissivity of 1 for average heat flux value is shown in Fig. 7

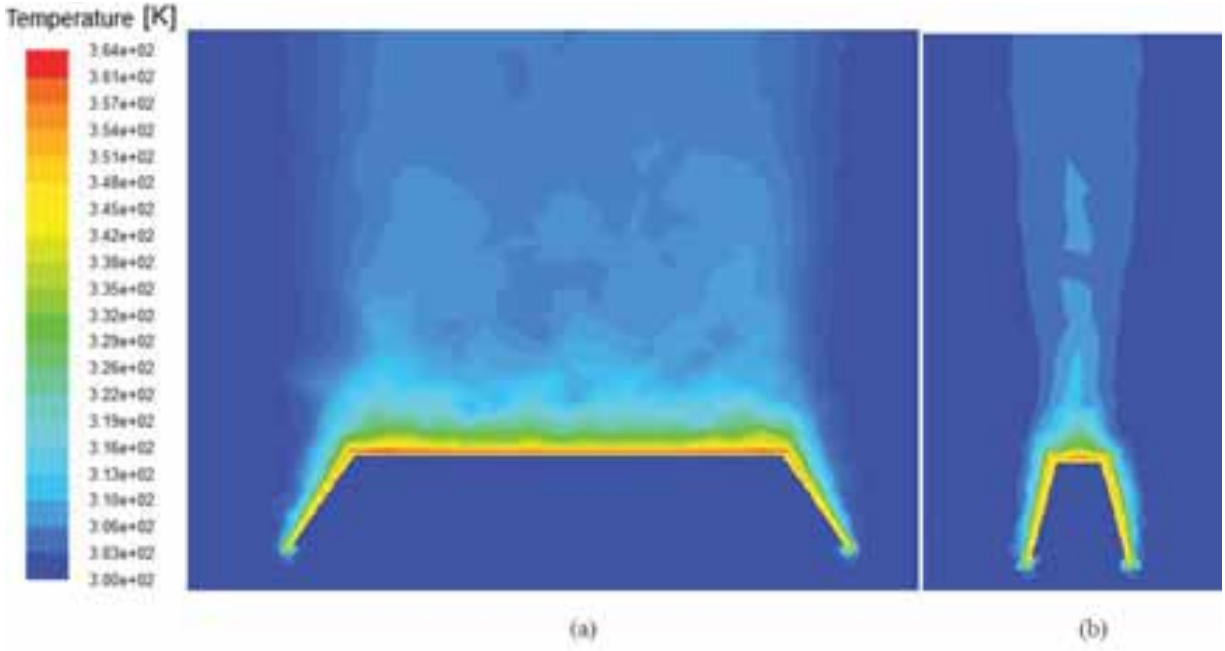

Fig. 7: Temperature contours of receiver (ε =1) at different planes for DNI = 1000W/m^2 (a) Z = 0 (b) X = 0

The comparison of heat losses and the maximum temperature in the receiver surface is calculated and tabulated in Table 2. The values correspond to the average heat flux incident on the receiver surface.

Tab. 2: Comparison of parameters for different DNI and emissivity

Parameter	DNI = 250 W/m^2		DNI = 1000 W/m^2	
	ε = 0	ε = 1	ε = 0	ε = 1
Maximum Temperature (°C)	70	44	123	112
Convective Heat loss (W)	28	28	111	111
Radiative Heat loss (W)	-	17	-	65
Surface temperature of receiver (°C)	47	44	113	91

3.2 Fluid flow and heat transfer analysis of helical-spiral coil receiver

The fluid flow and heat transfer analysis have been carried out to estimate the outlet temperature of the fluid and the pressure drop across the coil. The two types of coil configuration are studied to study the performance of the system.

3.2.1 Effect of solar radiation

The incident solar radiation on the receiver surface is varied to study the effect on the receiver performance. The solar radiation values of 250 W/m^2 and 1000 W/m^2 are considered in the present study. The outlet temperatures are calculated for two different configurations are estimated. For helical receiver, the temperature rise of 57°C (0.5kg/min) and 38°C (1kg/min) is observed for 1000W/m^2. At solar radiation of 500 W/m^2, the temperature rise is found to be 30°C (0.5kg/min) and 17°C (1kg/min) respectively. The effect of solar radiation incident on the receiver is studied and found that there is temperature difference of 27°C for twice increase in solar radiation.

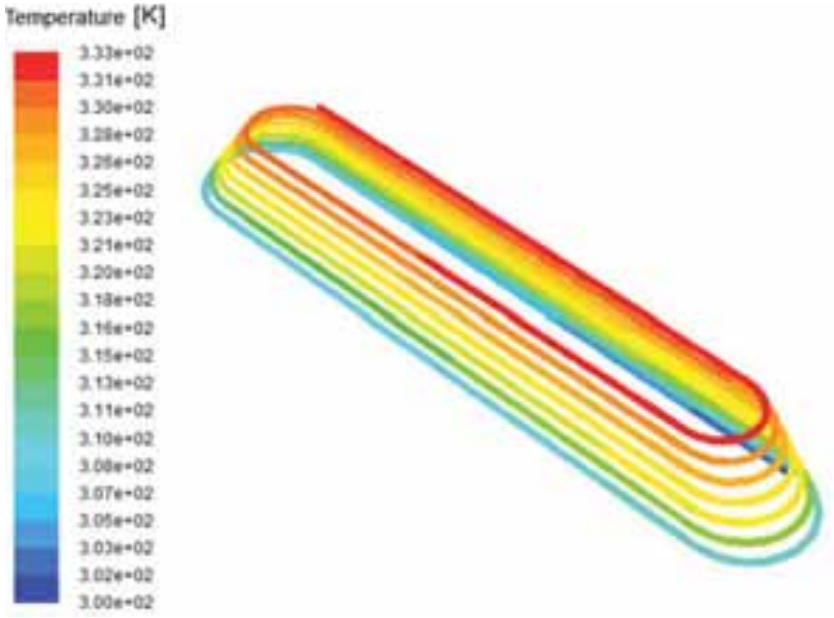

Fig. 8: Temperature contours of helical receiver for DNI of 500W/m^2

3.2.2 Effect of flow rate

The effect of flow rate on the receiver performance has been carried out. The flow rate values of 0.5 and 1 kg/min have been considered for the present analysis. Based on the flow rate, it is observed that at solar radiation of 250W/m^2, the temperature rise was found to be about 27°C and a pressure drop of 13023 Pa for 0.5 kg/min and temperature rise of 17°C and pressure drop of 14062 Pa was observed for 1 kg/min. For twice the mass flow rate, the variation of average fluid temperature is about 20°C for helical receiver.

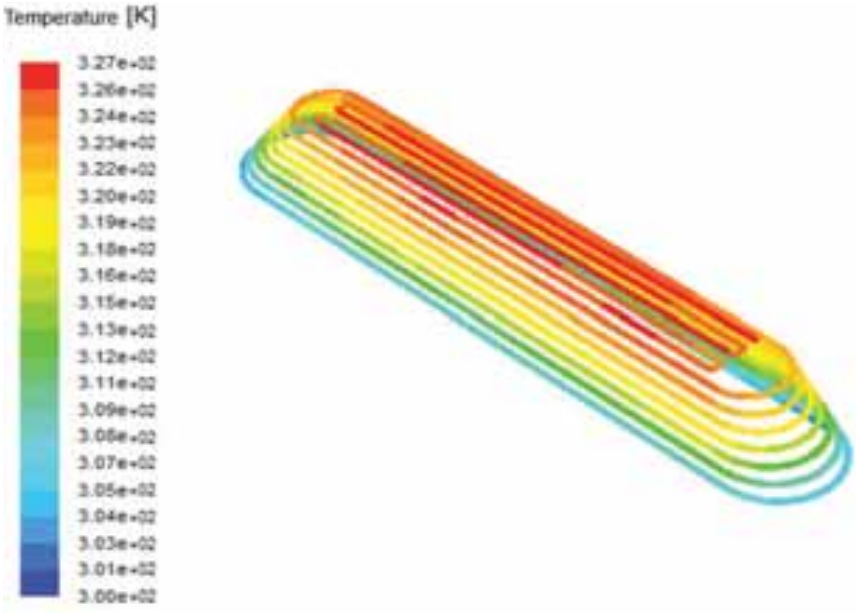

(a)

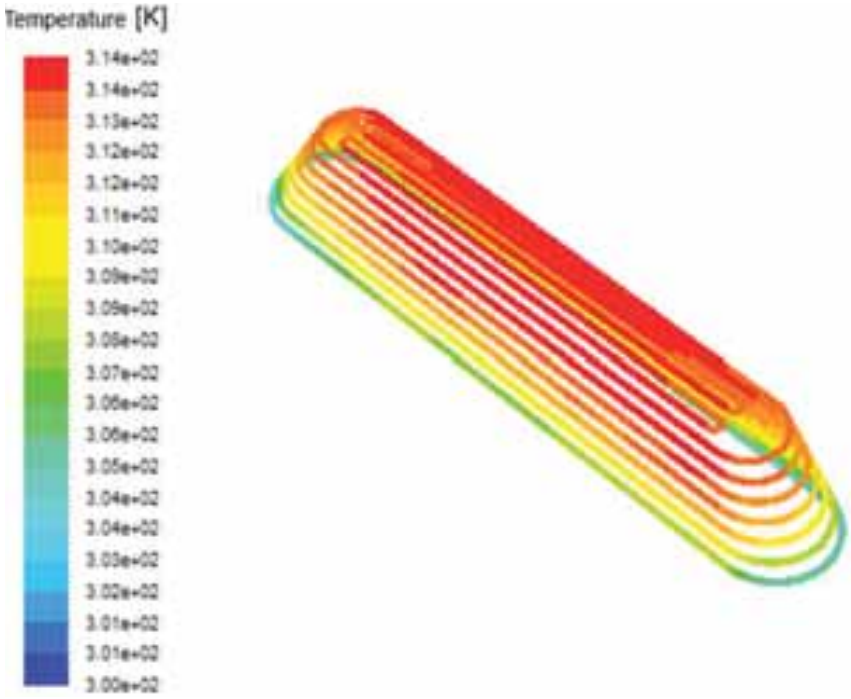

(b)

Fig. 8: Temperature contours of helical - spiral receiver surface for different flow rates and DNI = 250W/m^2

(a) 0.5 kg/min (b) 1 kg/min

The variation of the temperature of the fluid along the coil length for the helical receiver is shown in Fig. 7. It is observed that, for the flow rate of 0.5 kg/min, the outlet fluid temperature is 87°C and for 1 kg/min, it is about 65°C.

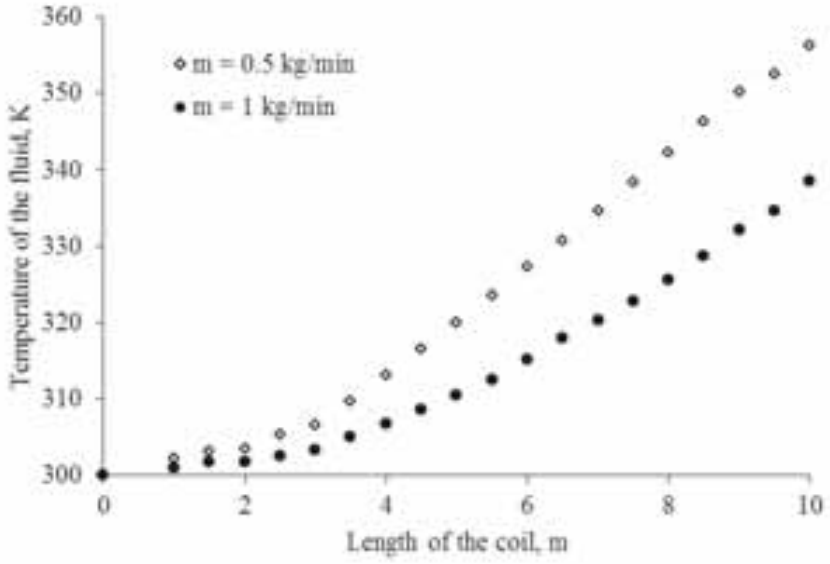

Fig. 9: Variation of average fluid temperature along coil for helical receiver

3.3 Performance investigation of helical-spiral coil receiver

The performance investigation of the helical-spiral receiver is carried out considering the useful heat transfer to the fluid and the heat loss from receiver comprising of the conductive, convective and radiative heat losses from the system. The heat collection efficiency of the receiver is given by (Reddy at al., 2014):

$$\text{Heat collection efficiency} = \frac{\text{Energy absorbed by the fluid}}{\text{Energy incident on the receiver}} \qquad \text{(eq. 7)}$$

Based on the analysis, it is found that receiver heat collection efficiency is about 84%.

4. Conclusion

In the present study, 3-D numerical investigations have been performed to study the heat loss from the concave cavity receiver surface and the fluid outlet temperature and the pressure drop across the helical coil. The heat loss analysis from the concave cavity surface receiver has been carried out by varying the incident solar radiation and emissivity of the surface. The study has been carried out for different parameters such as different solar insolation values, emissivity of the receiver surface and flow rates. Based on the analysis, For helical receiver, the temperature rise is found to be 30°C (0.5kg/min) and 17°C (1kg/min) respectively; whereas for helical-spiral receiver, the temperature rise is found to be 27°C (0.5 kg/min) and 15°C (1 kg/min). The pressure drop for helical receiver varies between 1kPa to 8kPa and 3kPa to 14 kPa for helical-spiral receiver. The present 3-D model can be used to study the performance of the helical coil receiver for elliptical hyperbolic concentrator.

Nomenclature:

C_p	Specific heat capacity (J/kgK)
$\vec{F}_c$	Centrifugal force (N)
g	Acceleration due to gravity (m/s^2)
k	Thermal conductivity (W/mK)
m	Mass flow rate (kg/min)
p	Pressure (Pa)
q''	Heat flux (W/m^2)
Q	Heat losses from the receiver (W)
T	Temperature (°C or K)
$\vec{V}$	Velocity vectors

Greek symbols

ε	Emissivity
ρ	Density (kg/m^3)

Subscripts

a	ambient
conv	convective
rad	radiative
total	total

5. References

Ali, I.M.S., Kew, P.A., O'Donovan, T.S., Reddy, K.S., Malick, T.K., 2010. Optical performance evaluation of a 2-D and 3-D novel hyperboloid solar concentrator, In: World Renewable Energy Congress XI, Abu Dhabi, 1738–1743

Ali, I.M.S., O'Donovan, T.S., Reddy, K.S., Mallick, T.K., 2010, Optical performance of circular and elliptical 3-D static solar concentrators. National Solar Conference, American Solar Energy Society, Arizona, USA.

Ali, I.M.S., O'Donovan, T.S., Reddy, K.S., Mallick, T.K., 2013. An optical analysis of a static 3D concentrator, Solar Energy, 88, 57–70.

Ali, I.M.S., Vikram, T.S., O'Donovan, T.S., Reddy, K.S., Mallick, T.K., 2014. Design and experimental analysis of a static 3-D elliptical hyperboloid concentrator for process heat applications, Solar Energy, 102, 257–266.

Eames, P. C., Norton, B., 1993. Detailed parametric analyses of heat transfer in CPC solar energy collectors, Solar Energy, 50 (4), 321-338

Garcia-Botella, A., Balbuena, F., Alvarez, A., Vazquez, D., Bernabeu, E., 2009. Ideal 3D asymmetric concentrator, Solar Energy, 83, 113–117.

Garcia-Botella, A., Fernandez-Balbuena, A., A., Bernabeu, E., 2006. Elliptical concentrators, Applied Optics, 45 (29), 7622–7627

IEA-ETSAP and IRENA Technology Brief E21, 2015. Solar Heat for Industrial Processes – A Technology Brief.
Kaiyan, H., Hongfei, Z., Tao, T., 2011. A novel multiple curved surfaces compound concentrator, Solar Energy, 85, 523–529
Lauterbach, C., Schmitt, B., Jordan, U., Vajen, K., 2010. Potential for Solar Process Heat in Germany - Suitable Industrial Sectors and Processes. Proc. EuroSun. Graz.
Lauterbach, C., Javid R., S., Schmitt, B., and Vajen, K., 2011. Feasibility Assessment of Solar Process Heat Applications, Solar World Congress, Kassel.
Martínez, V., Pujol, R., Moià, M., 2012. Assessment of medium temperature collectors for process heat, Energy Procedia, 30, 745 – 754.
Reddy, K.S., Mallick, T.K., Vikram, T.S., Sharon, H., Design and optimisation of elliptical hyperboloid concnetrator with helical receiver, Solar Energy, 108, 515-524
Ustaoglu, A., Okajima, J., Zhang, X.-R., Maruyama, S. 2015. Performance evaluation of a nonimaging solar concentrator in terms of optical and thermal characteristics. Environ. Prog. Sustainable Energy. doi: 10.1002/ep.12236

INTRODUCTION AND ANALYSIS OF A HYBRID SOLAR THERMAL POWER AND COOLING COGENERATION SYSTEM WITH LINEAR FRESNEL SOLAR COLLECTOR

Jinghui Song[1], Jishuai Ma[2] and Yanjun Dai[2]

[1] Electric Power Research Institute of Guangdong Power Grid Co., Ltd., Guangzhou (China)

[2] Institute of Refrigeration and Cryogenics, Shanghai Jiao Tong University, Shanghai (China)

Abstract

Based on the linear Fresnel concentration technology, a hybrid solar thermal power and cooling cogeneration system has been developed aiming for the solar thermal utilization in hot climate regions. The thermal from the solar Fresnel collectors can be used for air condition with high efficiency solar absorption cooling, and can also be used for power generation with Organic Rankine's cycle (ORC) cycle. It mainly consists of linear Fresnel solar collector, molten salt thermal storage tank, steam drum, ORC power generation equipment and absorption chiller. And this paper introduces the running modes under different kinds of solar radiation conditions. The system will turn on the heat storage mode when the incident solar rays are strong, and will switch to the heat release mode under poor insolation. Actually, we can choose to run the hybrid system in the mode of cooling or electricity generation in response to our needs. The Fresnel solar collector acts a crucial role in different running mode. Therefore, simulations on the mirror field and the absorber of the collector are operated respectively. On the basis of the results, we make the optimal operation strategies for the hybrid system. According to the analysis above, we can draw the conclusions. The hybrid solar thermal power and cooling cogeneration system is designed with several running modes, which guarantees the system runs stably and reliably.

Keywords: *solar thermal utilization, solar Fresnel collector, ORC cycle, absorption cooling, power generation*

1. Introduction

Solar energy is certainly the most considerable renewable and clean energy with the reserves of fossil energy decreasing, while the consumption increasing. Solar thermal utilization is quite an important way to use the generous energy from the sun. However, the traditional solar utilization manners in low temperature level area cannot meet the demand of industrial production. Various concentration technologies are needed to gather solar energy of high quality. The linear Fresnel solar collector with cavity receiver is an economical manner in middle temperature level area, compared with the trough solar collector which is relatively more mature. It concentrates sunlight with a series of discrete mirrors to heat the working fluid flowing through the cavity receiver up to about 300℃. The collected energy can be used to various processes, such as cooling, electricity generation, industrial heating and seawater desalinization.

Absorption refrigeration circulates with water or ammonia as the refrigerant are harmless to the environment and the ozone layer; And the cycle is driven by heat energy, which includes, in addition to the use of boiler's steam, fuel's combustion heat, waste heat, exhaust heat, solar energy and other low grade heat. The working medium mostly used in the absorption chiller is lithium bromide solution which performs well in operation.

doi:10.18086/swc.2015.10.12 Available at http://proceedings.ises.org

The entire device, except the pumps and valves, mainly consists of the heat exchangers, so that the machine works smoothly and noiselessly. Meanwhile, the refrigerator is running in a vacuum condition, and the structure is simple, safe, reliable and easy to install. The downside is that the solution of lithium bromide in the atmosphere has a very corrosive harm to metals, thus resulting in a higher requirement for the pipes of the equipment, and additional larger cooling load. 1.n lift cycle for Li-Br absorption chiller is an improved cycle based on single effect cycle and two stage cycle. In the cycle, the flow process of Li-Br solution is improved, making one part of the fluid circulate in the way of single effect cycle and the other part in the way of two stage cycle.

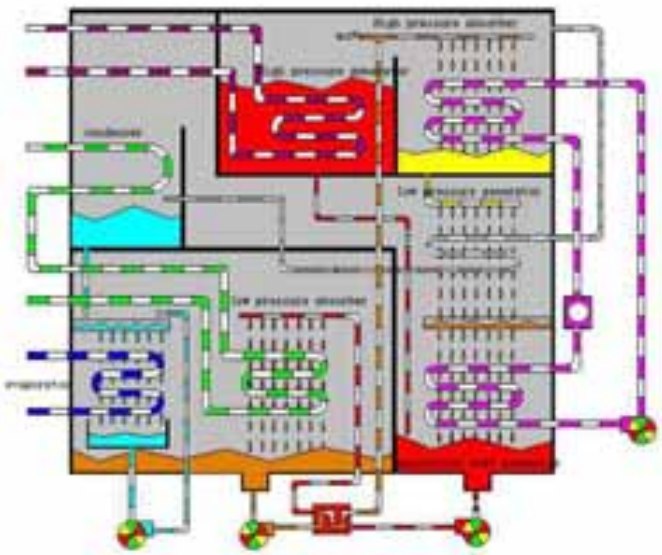

Fig. 1 Flow diagram of the 1.n lift cycle

The organic Rankine's cycle (ORC) is similar to the ordinary Rankine's cycle except that it uses the organic fluid not water as the working medium whose boiling temperature is low and the vapor pressure is high. The ORC may utilize the heat resource of low grade in power generation. The working medium absorbs heat from the heat resource and vaporizes quickly which is to drive the turbine.

In the solar thermal power generation field, heat storage is quite important to ensure the whole system operate continuously and effectively. The material storing the heat is more likely to be the phase change material (PCM) and nitrate is the common choice. Most nitrate's melting point is about 300℃ and the outstanding advantage of the salt is the low price, and low corrosivity and stable physical performance below 500 ℃. The disadvantage is that the heat of solution is small (only 20-30 kcal / kg), and the thermal conductivity is low[only 0.7 kcal / (m • h • ℃)], so that it would be overheated partially. However, compared with other molten salts, nitrates are still in the ascendant.

Solar salt is a kind of composite of nitrates which is the best choice in solar thermal molten salt power generation. Because it has the highest upper limit temperature (600 ℃), so it can keep the steam turbine operating at peak efficiency. In addition, it is one of the cheapest nitrate molten salt. But the Solar salt's freezing point is too high (220 ℃), comparing with the synthetic oil whose freezing point is only about 10 ℃ (Therminol VP-1,13 ℃). Therefore, some protective measures aiming at the high freezing point need to be taken to increase the strength of pipes, valves and other facilities, which would increase the operational and management costs. Given this, ternary molten salt Hitec (142 ℃), Hitec XL (120 ℃) are compounded, the freezing points of which are reduced a lot, and the upper limit temperature is decreased little. Thus, the synthetic molten salt has a broad application prospects in solar thermal power generation.

2. Hybrid system

2.1 Components

This solar thermal system is to achieve the functions including cooling, power generation, heat storage, domestic hot water preparation and many other features. Four linear Fresnel solar collectors in series are applied in the system, the absorber of which has a half cylinder trough cavity. The refrigerator is 1.n lift Li-Br absorption chiller, with a cooling capacity of 50kW. Organic Rankine's cycle power generator is used and the organic working fluid is R11, and generating power is 5kW. The refrigerator and power generator are designed and positioned in parallel and sharing one cooling tower, not working at the same time due to the limited collector area. The thermal storage use the hitec molten salt as the medium, storing heat according to the phase change latent heat. In addition, the system incorporates a drum for generating stable and high quality steam, equipped with an electric heater as an auxiliary heat source. Furthermore, a plate heat exchangers is assembled to produce domestic hot water through heat exchange with the steam drum.

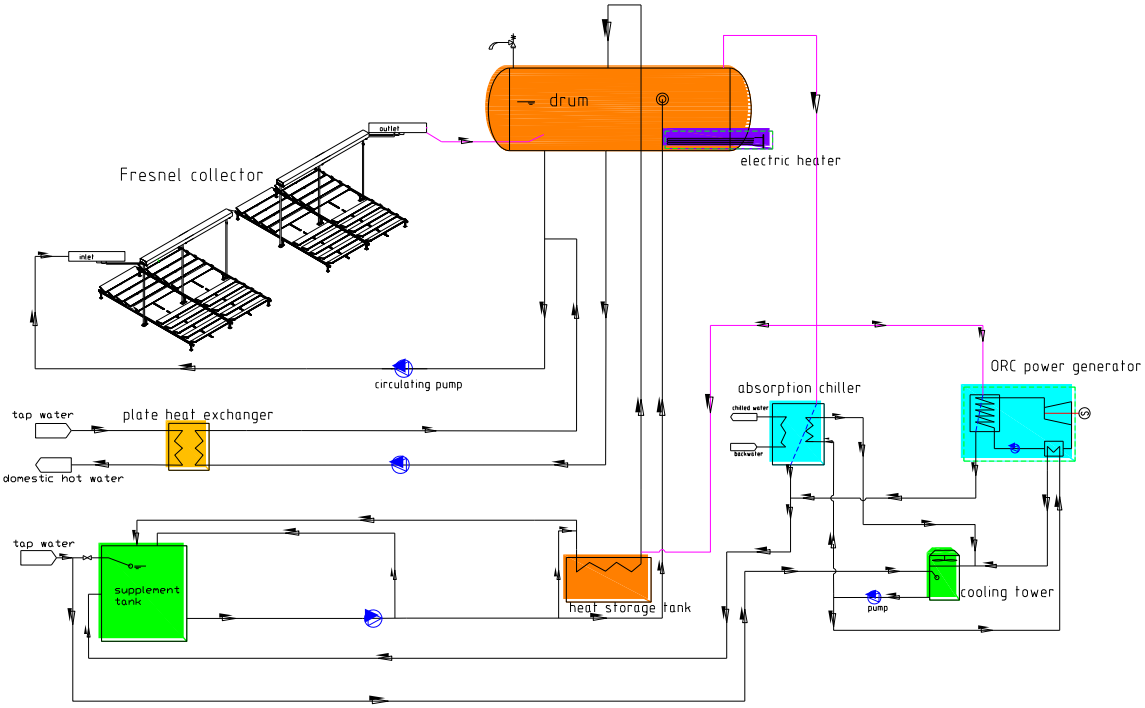

Fig. 2 schematic diagram of the hybrid system

2.2 System process

This system is a direct steam generation system (DSG), and the cycle working fluid is water. In the absorber of the collector, the water is heated to steam or mixture of water and vapor and flows into the drum where the vapor and the water are separated. The liquid water returns to the absorber through the drop tube. Meanwhile, the steam, heated by the electrical heater if necessary, runs out of the drum directly and entrances the terminal equipment, the refrigerator or the power generator. After driving the terminal equipment, the steam becomes liquid water and flows into the supplement tank. A circulating pump is there to deliver the water from the tank to the drum, where the steam and the water mix together to generate the steam that meets the demand. When the collector can't provide sufficient heat to produce steam, the electrical heater is enabled for additional heating.

When the solar radiation is intense, the steam generated in the drum is of high quality and surplus to drive the terminals. The heat that is spare from the steam would be stored in the heat storage tank. The water coming out of the tank returns to the supplement tank, mixing with the backwater from the terminals, and

returns to the drum. When the solar radiation is weak, the heat storage tank, probably in combination with the collectors, could heat the water into steam for driving the terminals. If the terminals and the heat storage tank are not in use, the high temperature steam or water is switched into the plate heat exchanger to produce domestic hot water.

2.3 Running modes

The system is endowed with great flexibility to achieve variable functions and is able to runs in several operation modes which are switched through controlling the valves. Table 1 is a scan of all running modes.

Table 1 Seven running modes of the hybrid system

[1]	C-T	Collector mode	Collectors provide the complete production needs of steam.
[2]	C⊕E-T	Auxiliary heating mode	Collectors, joint with electric heater, provide heat for the steam generation
[3]	C-T // S	Heat storage mode 1	The steam provides heat for the terminal and heat storage tank in parallel.
[4]	C-S	Heat storage mode 2	The steam provides heat only for the heat storage tank.
[5]	C⊕S-T	Exothermal mode 1	Collectors and the heat storage tank in series provide heat for steam generation.
[6]	S-T	Exothermal mode 2	Only the heat storage tank provides heat for steam generation.
[7]	C-D	DHW mode	The steam heated by the collectors is used to produce domestic hot water.

Note: The symbol ⊕ means the two equipment are in series while // in parallel.

3. Simulation

In the hybrid system, the solar collector plays a pivotal role in operation modes. And the performance of it has an essential effect on the refrigerator and power generator. Therefore, it is necessary to figure out the characteristics of the linear Fresnel collector. Simulation software TracePro and Fluent are used to establish the optical model and the heat transfer model of the collector respectively.

3.1 Optical simulation

First, according to the design parameters of the reflective mirrors and the cavity absorber, as well as the mirrors' slant angles in different incident angle of light, establish the mirror field and absorber model in TracePro's workspace (see Figure 3 (a)), and define the surface properties and light source. Then ray tracing simulation is carried on(see Figure 3 (b)) and the radiation energy distribution on the glass cover and the inner wall of the cavity is obtained.

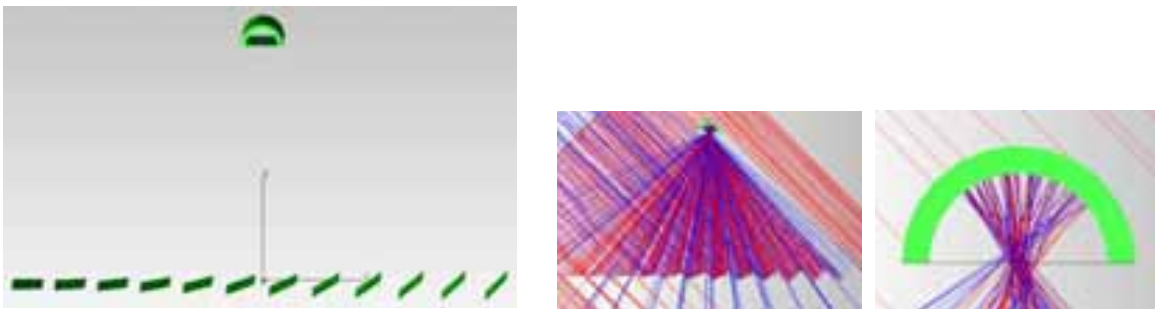

(a) (b)

Fig. 3 Geometry model of the collector and the ray tracing（$\alpha = 45°$）

The lights reflected by the mirror field converge onto the absorber, forming a facula of high energy density along the glass cover. Part of the lights reflected by the glass cover, most lights transmit through and disperse on the semi-circular inner wall of the absorber uniformly.

3.1.1 Energy flux density distribution

In the middle of the cavity absorber, take a cross section perpendicular to the longitudinal direction of the cavity, and the energy flux density distribution in polar coordinates is presented in Figure 4 and Figure 5(a). The incident angles are 45°and 90° respectively.

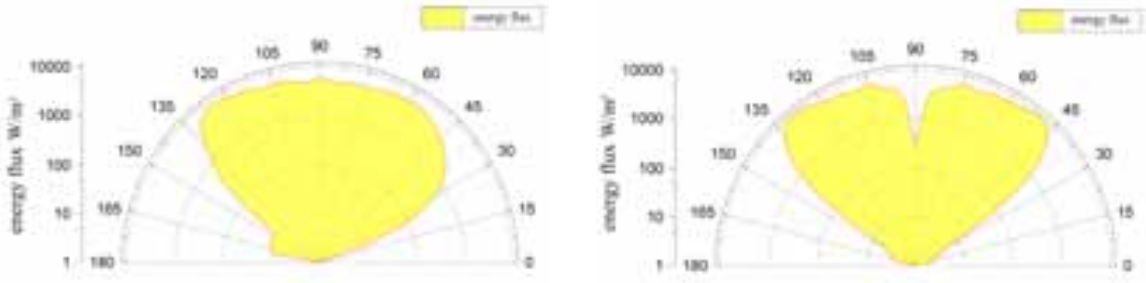

(a) $\alpha = 45°$ (b) $\alpha = 90°$

Fig. 4 Polar diagrams of the energy flux density on the inwall of the cavity

From Fig. 4 and Fig. 5(a) the characteristics of the energy flux density distribution on the cavity wall appear as follows: (a) with the rise of the incident angle, the energy density increases on the whole; (b) when the incident angle is 90° , there is a low ebb in the distribution of the energy flux density at the radius angle; The cause is the shadow the absorber project on the mirror field; (c) no matter how much the incident angle is, the energy falling on the cavity concentrate within the radius angle range of 30°-150°. Thus, the absorber's heat pipes should be arranged within the angular range.

3.1.2 Width of the facula

The width of the facula on the glass cover tells the concentration performance of the collector. Figure 5(b) shows the incident energy flux on the glass cover. As is seen, the width, the energy flux on the edge of which is 300W/m^2, decreases with the incident angle rising from 0° to 90°. According to the width of the facula, the geometric concentration ratio of the collector can be calculated (Table 2).

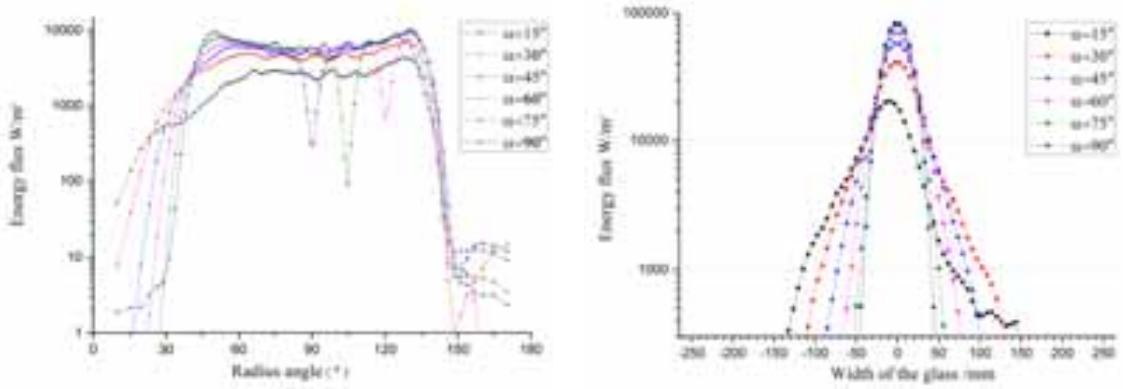

(a) on the inner wall of the cavity (b) on the glass cover

Fig. 5 Rectangular diagrams of the energy flux density on the absorber

Table 2 The facula width of the glass cover and the geometric concentrating ratio

Incident inclination angle	15°	30°	45°	60°	75°	90°
Facula's width/mm	285	240	190	145	110	95
concentration ratio	21.1	25.0	31.6	41.4	54.5	63.2

3.2 Heat transfer simulation

On the basis of the optical simulation's results, the appropriate distribution of the tubes in the cavity of the absorber is determined (see Fig. 6). There are five tubes that distributed within 30° ~150° where the heat flux energy is high and uniform. The boundary condition on the inner wall of the cavity is the energy flux distribution that is calculated in the optical simulation. Figure 7 shows the temperature contour on the cross section of the absorber. The aluminum fins between adjacent tubes transfer heat from the concentrated radiation to the tubes, however, is not able to deliver heat fleetly for the medium on both side of them perform weak in heat conduction.

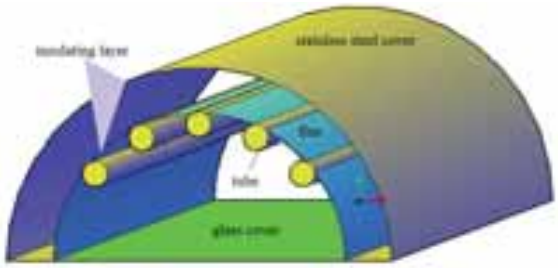

Fig.6 structure of the absorber

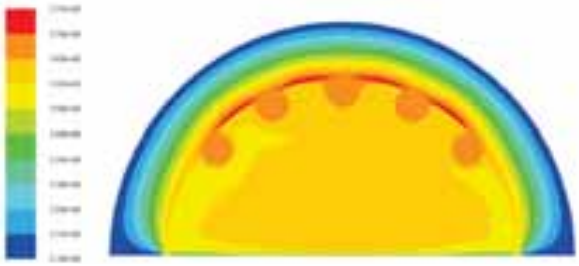

Fig.7 temperature contour of the absorber

The air's temperature is high and near to the water flowing through the tube, therefore the heat loss occurring on the glass cover is mainly in form of convection and radiation. Fig.8 shows the thermal efficiency and the heat loss ratio of the radiation of the absorber. The efficiency decreases with the rise of temperature of the water entering the tubes, and is about 54% when the water is 100℃. The pressure in the tube is high enough to ensure the water wouldn't vaporize. The radiation heat loss of the absorber maintains a steady level, about 1/3, which will rises slowly when the water's temperature is higher than 80℃. The convection heat transfer through the glass cover still dominates the whole heat loss of the absorber.

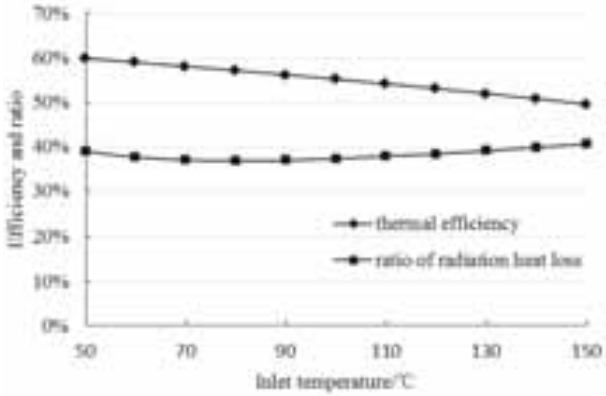

Fig.8 thermal efficiency and the heat loss ratio of the radiation of the absorber

The steam used in the terminals is about 120℃ where the efficiency of the collector is about 50%, so the heat collecting capacity of the collector is at least 2 times the steam heat consumption of the refrigerator and power generator. Considering the extra factors the simulation ignores, the practical efficiency is definitely lower than 50%, the mirrors' area of the collector is a key to guarantee the system performs well.

4. Conclusion

According to the introduction and simulation of the components and system, we could draw the conclusion as follows. The hybrid solar thermal power and cooling cogeneration system is designed with several running modes, which guarantees the system runs stably and reliably. In good weather condition, the system can meet the demand of cooling or electricity continuously. In poor condition, the storage unit works and can supply

supplementary heat for at least one hour. The Fresnel collector performs well in light concentration. The light incident into the cavity is focused on the angular range 30°~150°, and the facula formed on the glass cover is 9.5mm at minimum. As to the heat transfer property, the temperature of the tubes and fins in the cavity distributes even and uniform. The thermal efficiency of the collector is about 55% when the inlet temperature of water is 100℃ more or less. When matching the collector with the refrigerator or power generator, the heat collecting capacity should be considered carefully. The flexibility and reliability are reflected mostly by using the heat storage tank.

5. References

[1] Jianming Liu, 2012. Technology of solar thermal power generation[M]. Beijing: House of Chemical Industry.

[2] Anica Trp et al, 2006. Numerical analysis of the thermal behavior of a shell-and-tube heat storage unit using phase change materials [J].Applied Thermal Engineering. 26, 1830–1839.

[3] Hamid Ait Adine et al, 2006. Analysis of the influence of operating conditions and geometric parameters on heat transfer in water-paraffin shell-and-tube latent thermal energy storage unit [J]. Applied Thermal Engineering.26, 1830–1839.

[4] Xian L et al, 2010. Numerical heat transfer analysis of the packed bed latent heat storage system based on an effective packed bed model. Energy, 35, 2022-32.

[5] Pablo Dolado et al, 2011. Characterization of melting and solidification in a real scale PCM-air heat exchanger: Numerical model and experimental validation [J]. Energy Conversion and Management. 52, 1890–1907

Thermodynamic analysis of a solar flat plate water heater using extended surface absorber tube

K.Balaji [a], S.Iniyan[a*] and A.Idrish khan [a]
[a] Dept. of Mechanical Engineering, Anna University, Chennai 600 025, India
mr.kbalaj@gmail.com, iniyan777@hotmail.com*, idrish92@gmail.com.

Abstract

This paper studies the effect of an absorber tube with and without an extended surface of a solar flat plate water heater. The investigation of this system is carried out using with data acquisition system. Here, a tube and rod are used as an extended surface inside an absorber tube. The extended surfaces are frictionally engaged with the inner side of the tube wall, and it is kept in the axial flow direction of the fluid flow path. The various performance factors such as friction factor and non-dimensional numbers are analyzed. The results show that the outlet temperature of the extended surface absorber tube collector is 8 °C higher when compared to the plain tube collector. Also, it was found that the rod extended surface gives a higher outlet temperature when compared to the tube extended surface. While there was low friction loss, no impact on the pressure drop was found using extended surface inside the absorbing tube.

.

Keywords: Solar flat plate water heater, extended surface absorber tube, non-dimensional number

1. Introduction

Solar flat plate water heating system plays a dynamic role in using solar energy. Active and passive techniques are used for enhancing the heat transfer rate in this system. Nowadays researchers are trying to modify the system and heat transfer fluid (passive), both of which play a vital role in enhancing the efficiency of the collector. The passive technique involves using helical, spiral and curved shaped tubes, twisted tape, micro and longitudinal fins apart from nanofluids. The performances of the systems are analyzed based on the flow type, non-dimensional number, thermal performance, the effect of friction and so on.

[1] This review paper highlights the work done using helical, spiral and curved shaped tubes for both single-phase and two-phase fluids. As much as single-phase heat transfer studies have been reported for the above-mentioned passive types; two-phase heat transfer characteristics have rarely been reported. Most of the work has been done for flow characteristics and pressure drop. [2-7] Different types of twisted tape inside an absorber tube have been worked for achieving better heat transfer rate. Several performance factors like friction factor, pressure drop and heat transfer have been analyzed experimentally and computationally. The effect of natural and forced circulation of heat transfer fluid has been reported using single-phase flow. Here, there are two types of twisted tapes used inside an absorber tube with different configurations namely - trailing edge and helical, which are subjected to comparison. In the helical twisted tape, for various twist angles of **3 to 7**, the heat transfer and the pressure drop were found to be increased.

The Nusselt number correlation was analyzed for the trailing edge twisted tape (comprising of full-length twist, twist with rod and spacer fitted at the trailing edge for lengths of 100, 200 and 300mm for twist angles of **3 – 5**). It was reported that the spacer fitted was better than all other configurations. The author also developed a new correlations for various twisted absorber tubes. The trail edge twisted tape was found to give better results than that of the helical twisted tape. Compared to the plain tube, the overall thermal efficiency enhancement lied from 38.7% to 53.3% at an increased pressure drop of 8.9%. [8, 9] The twisted tape attached with a wire nail and V-cut and their performance factors were evaluated and reported. While the heat transfer in these configurations was higher than the normal twisted tape, both these configurations have not been compared amongst themselves. In the above research works, the performance factors have been analyzed, and it has been reported that there was an enhancement of heat transfer while using twisted tapes. The ratio of pitch to diameter is an important parameter for twisted tapes, and it decreases with increasing pressure drop and heat transfer rate.

doi:10.18086/swc.2015.10.13 Available at http://proceedings.ises.org

[10] The simulation on the circular tube edge fold twisted tape was done, from which the thermal and hydraulic behavior were studied. The increase in the heat transfer in this case was accounted because of the tangential velocity and asymmetrical velocity profile. [11, 12] Thermal performance and friction factor have been analyzed using nanofluids with different twisted tapes and micro fins. Micro finned tube with double twisted tapes gave much higher heat transfer rate than all other types using nanofluids. This paper does not focus on the effect of pressure drop. [13] The experimental investigation on air gap for solar water heater using honeycomb structure with different bottom arrangement has been done. The results indicated that a 3mm gap from the bottom for a single honeycomb unit gave optimum results. Heat removal factor and collector efficiency factors were defined using uncertainty analysis and were compared with experimental data. [14] Theoretical analysis was performed to study the entropy generation and pressure drop for the solar collector with passive technique. The heat transfer fluid was used with metal oxides of nanoparticle at various volume fractions. The exergy destruction has been analyzed based on entropy generation for CuO nanoparticle. The entropy generation is less for CuO than that of other nanoparticle metal oxides. [15] Circular tube with longitudinal fins has been analyzed experimentally. It has been reported, that higher pressure drop occurs in staggered arrangement compared to continuous fin. [16, 17] The efficiency of the collector was theoretically and experimentally reported for sheet and tube solar water heater using rectangular duct and fin. The above analysis states that there is an enhancement of heat transfer when using staggered arrangement on absorber tube for various profiles. The objective of the present work is to design the solar water heater with low heat transfer resistance between the absorbent and absorber tube in order to increase the convective heat transfer coefficient without affecting the flow of an absorbent.

2. Experimental setup and data acquisition

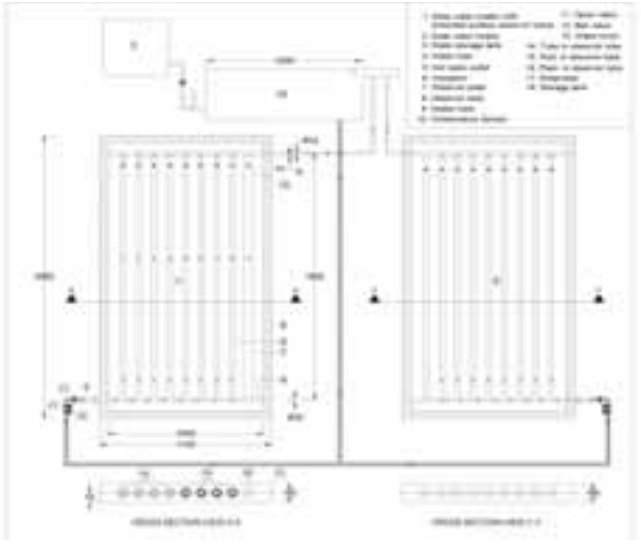

Fig: 1 Top view of solar water heater with and without modification

The study was carried out at the Institute for Energy Studies, Anna University, Chennai. The solar water heater collector was designed for 2 m^2 as per the dimensions are shown in Table.1.

a. Fig.1 shows two water heaters - one with (1) and one without modification (2). Open loop system was used.
b. Both flat plate solar collectors were placed in outdoor condition and oriented towards South with a tilt angle of 13º according to the topographical conditions.
c. The level of the tank was checked every 15 min. The system accelerated the driving force till there was no density difference in the absorbing fluid. The absorber plate absorbed the radiation emitted from the sun, which was transferred through the glass cover.
d. The insulations were provided for minimizing heat loss from the system to the surrounding. The selection of diameter for the extended surface rod and tubes were based on circumference and contact surface.

e. The experiment started at 9.00 am and readings was taken from 10.00 am. Before recording the data, primary work steps were taken like cleaning the glass, removing of residual water from the collectors, and inspecting the collector. The storage tank was filled with clean water every morning at 8.30 am and completely drained in the evening at 5.00 pm.

f. The setup ran from March 28th to May 9th and the following data were recorded at every 5-minute intervals. Measurements were taken multiple times and averaged to reduce experimental error. Solar radiation, ambient temperature, riser tube inlet and outlet temperatures were recorded continuously and averaged for every 30 min interval. On the final day, it was wound that there were a clear peak and deviation in radiation because of which that day was chosen for this study.

g. Thermocouple T – type was used for measuring the temperature with an error of 0.4% to its base value. The thermocouple was placed at each end of the riser tube at a 5mm distance of separation. The intensity of radiation was measured with the help of a pyranometer with an error of ±5% to its base value.

Table.1 Collector parameters

Collector Parameter	**Standards**
Type	Flat plate, 2 m^2, black paint, Single glass, tilt angle 13º.
Heat absorbent fluid	Water
Absorber plate area	1.62 m^2
Sun temperature	4350 K
Optical efficiency of the glass	0.82
Glass thickness	4 mm
Diameter of absorber tube	I.D = 13.8 mm, thickness of 1 mm
Lower and upper header	I.D = 22.3 mm, thickness of 1.5 mm
Insulation width	70 mm
Number of riser tube	9
Connecting pipe	I.D = 25.4 mm
Bottom insulation	Glass wool
Sidewall insulation	Thickness of 5 mm, wood
Absorber plate	Thickness of 4 mm, copper
Tube in tube	O.D = 2.5 mm, t = 0.5 mm, N= 8, L = 1500 mm, Copper
Rod in tube	D = 2.5 mm, N = 8, L = 1500 mm, Copper

3. Data reduction

Thermodynamic and Hydraulic analysis

Assumptions:

- At all the points in the system, the properties of the absorbent remain constant.
- All the processes are in steady state.
- Potential and kinetic energies are neglected.
- There is no soot formation and chemical reaction taking place inside the system.
- There is no mass loss in the absorbent fluid inside the system.

3.1. Energy and Mass balance

$$\sum \dot{E}_{in} = \sum \dot{E}_{out} \quad \text{(eq.1)}$$

$$\sum \dot{m}_{in} = \sum \dot{m}_{out} \quad \text{(eq.2)}$$

Energy balance equation can be expressed as

$$\dot{Q} + \sum \dot{m}_{in}\, \dot{h}_{in} = \dot{W} + \sum \dot{m}_{out}\, \dot{h}_{out} \quad \text{(eq.3)}$$

Whereas, $\dot{Q}_s$ is Available solar energy, expressed by the following equation [7]

$$\dot{Q}_s = I\ A_c \quad \text{(eq.4)}$$

Heat absorbed by the water (absorbing fluid) is

$$Q_{ab} = m\, C_p\, (T_{out} - T_{in}) \quad \text{(eq.5)}$$

3.2. Pressure Drop Analysis

$$\Delta P = f\, \frac{\rho V^2}{2}\, \frac{\Delta l}{d} \quad \text{(eq.6)}$$

$f = \frac{64}{Re}$ For laminar flow

$f = \frac{0.079}{(Re)^{\frac{1}{4}}}$ For turbulent flow

$$V = \frac{\dot{m}}{\rho \frac{\pi}{4} (D_H)^2}$$

Here K is loss coefficient, and D_H is hydraulic diameter

3.3 *Non-Dimensional number*

Nusselt number

$$Nu = \frac{h_i\, D}{K} \quad \text{(eq.7)}$$

$$\frac{1}{U_0 A_0} = \frac{1}{h_i A_i} + \frac{\ln \frac{D_0}{D}}{2\pi\, L\, K_w}$$

Prandtl number

$$Pr = \frac{C_p\, \mu}{K} \quad \text{(eq.8)}$$

Reynolds number

$$Re = \frac{D_i\, \rho\, V}{\mu} \quad \text{(eq.9)}$$

4. Result and discussion

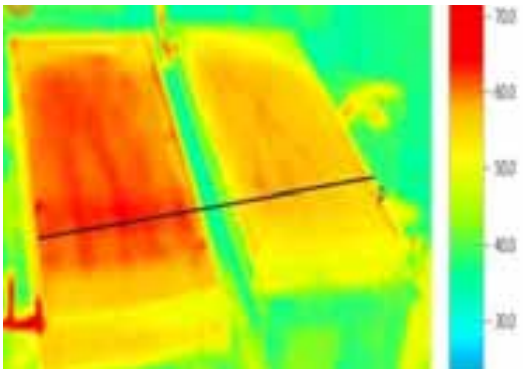

Fig: 2 (a) Thermal image

Fig.2 (b) Profile view

Fig.2 a and b shows that the temperature of the collector 1 is higher than that of collector 2. In Fig. 2 (b) Profile view, the cross section clearly shows that the peak temperature difference achieved by 8 °C. Testo 875-2 instrument was used for the thermal image. Fig. 2 (a) taken at a reflection temperature of 20 °C. The temperature range was given at the right side of the Fig. 2 (a). The average temperature of the collector 1 and 2 is 62 °C and 54 °C respectively. There is a gap between collector 1 and 2 and it impact on profile view curve. In the profile view, the gap is shown as slag in temperature. The cross section line is drawn at 0.675m from the bottom of the collector. The increase in temperature is due to increase in contact surface area with the axial flow to the water, and the extended surface reduces the thermal and viscous boundary layer. Only at maximum radiation, the maximum temperature difference is achieved. There is no temperature difference between rod and tube extended surface during acceleration and deceleration of radiation. The friction factor is increased for extended surface due to increase in the contact surface with the water. The rod extended surface has higher efficiency than the tube and plain tube configuration in all operating condition because of the thermal mass of the extended surface and friction factor.

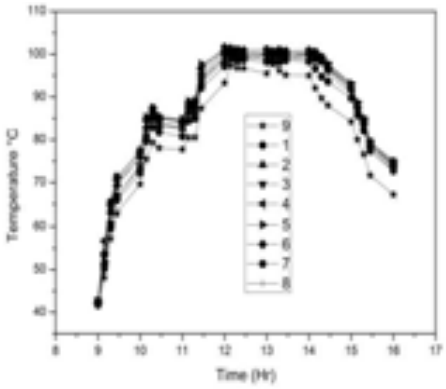

Fig.3: Time Vs Tubes outlet temperature

The arrangement of tubes shown in fig. 1. In Fig.3 first four tubes contain tube extended surface and are compared with a plain tube. Whenever the retardation takes place in radiation, there is a major peak in temperature differences has been achieved. In a constant peak radiation, there are no changes in outlet temperature of the tube. The heat absorbing fluid absorbed the heat, and it changed the phase so the maximum heat capacity achieved by the heat absorbing fluid in a peak radiation. While compared with plain tube there is an average difference in temperature around 8 °C achieved. The result shows that 4^{th} tube gives much better heat transfer compared with other tube because of its focus point. The extended surface increases the wetted surface area which in turn increases the heat extraction from the tube wall to the fluid.

Radiation which fell on earth surface on 9/5/14 is shown in fig 4. There is an unsteady radiation for up to 11.45 am and thereafter gradual retardation took place. Maximum peak achieved at the time of 11.45 am. The collector performance was analyzed for this day because of its unsteady radiation. This graph showed the average temperature of each tube outlet and compared with each other. The tube and rod in extended tube surface show clear performance ranges for different radiations. There was no major deviation in outlet temperature. Whenever the mass flow rate is higher, it affects 1 to 2 °C in each tube. Rod in the tube will result in better performance compared to the tube in tube extended surface. The intensity of solar radiation decreases from 01.00 pm. Hence the heat input to the collector is decreasing. The temperature difference between inlet and outlet decreases gradually which decreases the driving the force. Hence it reduces the instantaneous efficiency of the collector. The instantaneous efficiency is poor in morning and evening may be due to the higher reflection of solar radiation by the glazing which reduces the heat transfer.

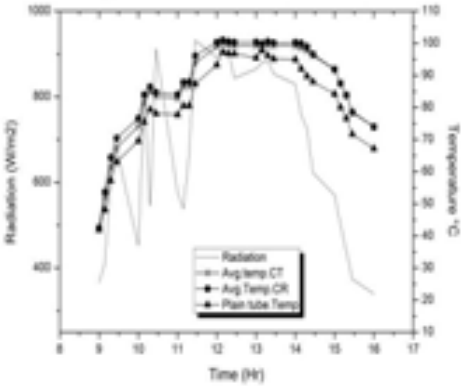

Fig.4 Time Vs Temperature difference with and without extended surface

Fig.5 shows the analysis of the outlet temperatures of both the collector. Collector 1 gives maximum output temperature in a peak radiation. During acceleration and retardation, there are no temperature changes in outlet because of the velocity of the heat absorbing fluid. In a thermosyphon process, the heat absorbing fluid leaves the system only when density difference is high. The velocity of the absorbing fluid is the determining factor for the outlet temperature of the collector. The temperature difference between inlet and outlet temperature is high. The extended surface increases the contact surface area which in turn increases the heat removal from the tube wall to the fluid. Hence there is a gradual increase in the Reynolds number for extended surface which in turn increases the instantaneous efficiency of the collector.

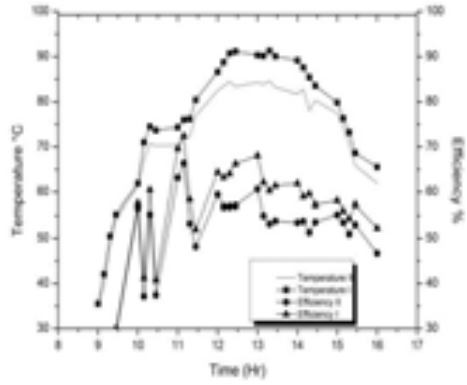

Fig.5: Time Vs Efficiency, Outlet temperature

Fig.6 explain that extended surface at leading edges will enhance the inertia forces of the heat absorbing fluid, so it reduces the viscous boundary layer. The extended surface absorber tube of the rod has maximum velocity than the tube in tube extended surface and plain tube. A thin boundary layer forms nearer to the wall surfaces, and it is stationary with respect to the surface. The thickness of the layer will be reduced when enhancing the velocity of the absorbing fluid till the free stream velocity is reached. There is no boundary layer at free stream velocity.

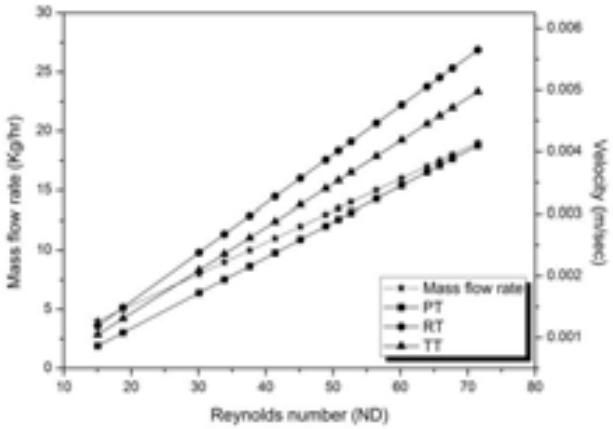

Fig.6: Effect of Reynolds number at different mass flow rate.

Fig.7 gives a clear picture about the relationship between Nusselts number and Reynolds number. When mass flow rate increases, inertia force also increased and reduced the thickness of the viscous boundary layer. It enhances the heat transfer coefficient. The Nusselts number rises with increasing Reynolds number if the mass flow rate is increased. The extended surfaces are frictionally contact with the inner side of the tube wall, and it extends the contact surface of the water flowing through it, so it reduces the plate temperature. The heat removal rate from the absorber plate of the extended surface collector is higher than that of the plain tube collector, and it has the minimum plate temperature. The rate of heat transfer from the absorber tube to water is high for the extended surfaces. The rod extended surface collector has very less absorber plate temperature than the plain tube and tube extended surface collector at same intensity of radiation due to the mass of the rod extended surface. A stably stratified layer of light and warm water is sustained near the top of the extended surface which absorbs the heat. The warmer water near the bottom of the absorber tube induces the convective motion, and it increases the velocity. A thin boundary layer forms near the wall, and it is stationary with respect to the surface. Buoyance force removes the energy from the fluid, higher than shear force. The turbulence is damped against the buoyancy force, and the heat transfer is entirely due to laminar flow in flat plate collector. Free convection increases with increase in the Nusselt number, and it is dominating the performance of the collector. Free convection is stronger when the Reynolds number is low. Due to increase in contact surface, the extended surface has higher Nusselt number.

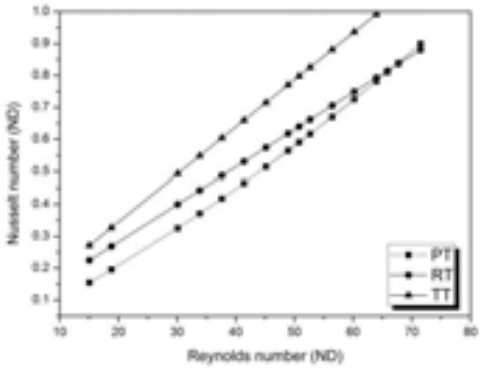

Fig. 7: Effect of Reynolds number on heat transfer

Fig. 8 shows the variation of friction factor with respective to the Reynolds number. Darcy friction factor is derived with the help of velocity of the flowing fluid inside the tube. Darcy friction only for tubes inside the collector. The viscous boundary layer is hampering the absorbing fluid velocity, and it will reduce Reynolds number. The pressure drop is measured for entire collector using head losses, and it is used for measuring the fanning friction factor. The extended surfaces have very less enhancement in friction factor compared to other types of heat transfer enhancement devices like twisted tape and grooved tube. Because of this extended surfaces are frictionally engaged with the inner wall, and it is fixed with the axial flow direction of the water. These heat transfer enhancement devices are highly suitable for the passive technique. As it is evident from the figure, the higher pressure drop is obtained for higher Reynolds number, and it decreases with a decrease in the flow rate.

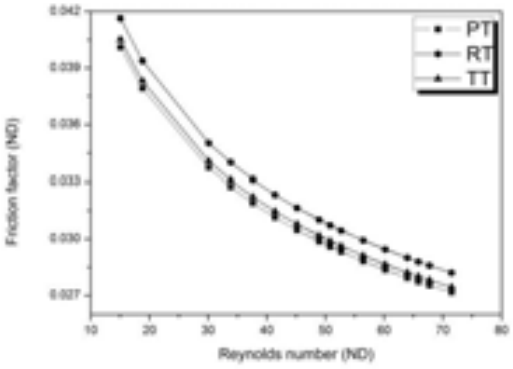

Fig.8: Effect of Reynolds number on viscous of the absorbing fluid

Fig.9 clearly shows the deviation of theoretical outlet temperature with experimental. Maximum deviation between the experimental and theoretical data was 10%. The theoretical outlet temperature of the collector does not consider the thermal loss inside the collector, so the value is higher than experimental.

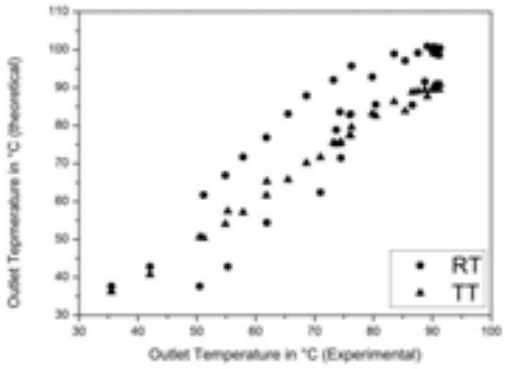

Fig.9: Comparison of experimental and theoretical outlet temperature data of the collector

5. Conclusion.

The experimental study of solar water heater with extended surface absorber tube was performed, and the Rod extended surface provides higher heat transfer rate compared to Tube extended surface because of the mass flux of the extended surface. Extended surface reduces the thermal and viscous boundary layer, so it increases the convective heat transfer rate. The velocity is increased by means of increasing the shear production, and the extended surfaces have been found to be effective in augmenting the heat transfer. The efficiency of the modified collector is increased by 22%. Extended surface also increases the non-dimensional numbers and friction factor.

Nomenclature

A_c	Collector area, m^2
C_p	Specific heat, $Jkg^{-1}K^{-1}$
D_h	Hydraulic diameter, m
f	Friction factor, Non dimension
I	Intensity of radiation, Wm^{-2}
k	Thermal conductivity, $W\ m^{-1}K^{-1}$
k_i	Thermal conductivity of insulation material $W\ m^{-1}K^{-1}$
k_w	Thermal conductivity of the tube wall, $W\ m^{-1}K^{-1}$
L	Length of the tube, m
m	mass flow rate, kgs^{-1}
N	Number of tubes, Nondimension
Nu	Nusselt number, Nondimension
Pr	Prandtl number, Nondimension
Re	Reynolds number, Nondimension
Q_{ab}	Heat absorbed, W
T_{Out}	Outlet temperature of the collector, K
T_{in}	Inlet temperature of the collector, K
T_a	Atmospheric temperature, K
V	Velocity, ms^{-1}

Greek Symbol

ρ	Density, kgm^{-3}
μ	Dynamic viscosity, Nsm^{-2}
μ_w	Dynamic viscosity of tube wall, Nsm^{-2}
η	Efficiency, %

Suffix

PT	Plain tube
RT	Rod as extended surface
TT	Tube as extended surface

Reference

[1] Naphon P, Wongwises S. A review of flow and heat transfer characteristics in curved tubes. Renewable and Sustainable Energy Reviews. 2006;10:463-90.
[2] Jaisankar S, Radhakrishnan TK, Sheeba KN. Experimental studies on heat transfer and friction factor characteristics of thermosyphon solar water heater system fitted with spacer at the trailing edge of twisted tapes. Applied Thermal Engineering. 2009;29:1224-31.
[3] Jaisankar S, Radhakrishnan TK, Sheeba KN. Studies on heat transfer and friction factor characteristics of thermosyphon solar water heating system with helical twisted tapes. Energy. 2009;34:1054-64.
[4] Jaisankar S, Radhakrishnan TK, Sheeba KN. Experimental studies on heat transfer and friction factor characteristics of forced circulation solar water heater system fitted with helical twisted tapes. Solar Energy. 2009;83:1943-52.
[5] Jaisankar S, Radhakrishnan TK, Sheeba KN. Experimental studies on heat transfer and thermal performance characteristics of thermosyphon solar water heating system with helical and Left–Right twisted tapes. Energy Conversion and Management. 2011;52:2048-55.
[6] Jaisankar S, Radhakrishnan TK, Sheeba KN, Suresh S. Experimental investigation of heat transfer and friction factor characteristics of thermosyphon solar water heater system fitted with spacer at the trailing edge of Left–Right twisted tapes. Energy Conversion and Management. 2009;50:2638-49.
[7] Ananth J, Jaisankar S. Investigation on heat transfer and friction factor characteristics of thermosiphon solar water heating system with left-right twist regularly spaced with rod and spacer. Energy. 2014;65:357-63.
[8] Murugesan P, Mayilsamy K, Suresh S. Heat Transfer and Friction Factor Studies in a Circular Tube Fitted with Twisted Tape Consisting of Wire-nails. Chinese Journal of Chemical Engineering. 2010;18:1038-42.
[9] Murugesan P, Mayilsamy K, Suresh S, Srinivasan PSS. Heat transfer and pressure drop characteristics in a circular tube fitted with and without V-cut twisted tape insert. International Communications in Heat and Mass Transfer. 2011;38:329-34.
[10] Cui Y-z, Tian M-c. Three-dimensional numerical simulation of thermal-hydraulic performance of a circular tube with edgefold-twisted-tape inserts. Journal of Hydrodynamics, Ser B. 2010;22:662-70.
[11] Eiamsa-ard S, Wongcharee K. Single-phase heat transfer of CuO/water nanofluids in micro-fin tube equipped with dual twisted-tapes. International Communications in Heat and Mass Transfer. 2012;39:1453-9.
[12] Eiamsa-Ard S, Wongcharee K. Heat transfer characteristics in micro-fin tube equipped with double twisted tapes: Effect of twisted tape and micro-fin tube arrangements. Journal of Hydrodynamics, Ser B. 2013;25:205-14.
[13] Abdullah AH, Abou-Ziyan HZ, Ghoneim AA. Thermal performance of flat plate solar collector using various arrangements of compound honeycomb. Energy Conversion and Management. 2003;44:3093-112.
[14] Alim MA, Abdin Z, Saidur R, Hepbasli A, Khairul MA, Rahim NA. Analyses of entropy generation and pressure drop for a conventional flat plate solar collector using different types of metal oxide nanofluids. Energy and Buildings. 2013;66:289-96.
[15] El-Sayed SA, El-Sayed SA, Abdel-Hamid ME, Sadoun MM. Experimental study of turbulent flow inside a circular tube with longitudinal interrupted fins in the streamwise direction. Experimental Thermal and Fluid Science. 1997;15:1-15.
[16] Ho C-D, Chen T-C, Tsai C-J. Experimental and theoretical studies of recyclic flat-plate solar water heaters equipped with rectangle conduits. Renewable Energy. 2010;35:2279-87.
[17] Ho CD, Chen TC. Collector efficiency improvement of recyclic double-pass sheet-and-tube solar water heaters with internal fins attached. Renewable Energy. 2008;33:655-64.

Conference Proceedings

Solar World Congress 2015
Daegu, Korea, 08 – 12 November 2015

ISES SWC2015

Evaluation of the Impact of Stagnation Temperatures in Different Prototypes of Low Concentration PVT Solar Panels

João Gomes[1], Sílvio Bastos[2], Mafalda Henriques[2], Linkesh Diwan[1], Olle Olsson[1]

[1] University of Gävle, Sweden

[2] Instituto Politécnico de Castelo Branco, Portugal

Abstract

Photovoltaic thermal (PVT) solar panels produce both thermal and electric power from the some area. This paper concerns a PVT design where the series connected strings of cells are laminated using silicone to an aluminium receiver where the heat transfer fluid flows.

An evaluation of the impact of reaching high temperatures in the cell structural integrity and performance is presented. Eight small test receivers were made in which the following properties were varied: Size of the PV cells, type of silicone used to encapsulate the PV cells, existence of a strain relief between the cells, size of the gap between cells and type of cell soldering (line or point soldering).

These test receivers were placed in an oven for one hour, under eight different monitored temperatures. The temperature of the last round was set at 220°C which well exceeds the highest temperature the panel design can reach. Before and after each round in the oven, the following tests were conducted to the receivers: Electroluminescence (EL) test, IV-curve, diode function, and visual inspection.

The test results showed that the receivers made with the transparent silicone and strain relief between cells experienced less micro-cracks and lower degradation in maximum power. No prototype test receiver lost more than 30% of its initial power, despite the large cell breakage shown in some receivers. Prototype receivers with transparent (softer) silicone showed much far less cracks and power decrease when compared to red (harder) silicone receivers. As expected, larger cells are more prone to develop micro-cracks after exposure to thermal stress. Additionally, existing micro-cracks tend to grow in size into larger micro-cracks relatively fast with thermal stress. The EL imaging taken during our experiment leads us to observe that it seems far easier for existing cracks to expand than for new cracks to appear.

Keywords: *Stagnation Temperature, Electroluminescence test, IV-Curve, Concentration, PVT*

1. Introduction

Photovoltaic thermal (PVT) solar panels produce both thermal and electric power from the same area. Combining solar thermal and photovoltaic can be a way to increase the efficiency of the silicone cells by reducing the working temperature through active cooling (Giovinazzo et al. 2014).

Concentration allows a cost reduction by decreasing the receiver size in the panel. As per Giovinazzo et al. (2014), the biggest advantage of this type of collector design is to decrease material cost by reducing the amount of expensive components utilized (solar cell, receiver and/or selective surface).

Combining concentration with PVT (C-PVT) can also prove to be advantageous. However, concentrating does not bring only advantages. For non-concentrating collectors PVT, one disadvantage is

doi:10.18086/swc.2015.10.14 Available at http://proceedings.ises.org

the longitudinal shading caused by the frame or the absence of reflector on some solar incidence angles. This can have a very large impact on the electrical performance, if measures such as placing extra diodes are not taken (Gomes et al, 2013).

Stagnation temperature is reached when the heat losses of the panel are equal to the energy received from the sun. Another particularly important disadvantage of concentration is the increase of the stagnation temperature which can cause damage to the materials of the collector, in particular to the solar cells. This issue will be covered in detail in this paper.

A C-PVT collector was designed to produce 240W (electricity) and 1250W (thermal). An installation with 8 prototype C-PVT collectors has been made in a warm country and was found to produce only 1200 W (el). After one day, during which the stagnation temperature was reached, the production was found to have degraded significantly to 200W (el).

The most critical part in the manufacture of the PVT collector is the receiver, including all processes from the soldering of the cells to the choice of the materials (Khatri et al. 2011). Problems with the manufacturing process of the prototypes, in particular with the cell soldering, account for the difference between expected 1920W (el) and the initially obtained electrical output of 1200W. Such issues can easily be eliminated by process automation with an automatic tabbing stringer machine.

However, a more important issue that was discovered in this prototype C-PVT installation was the post-stagnation electrical power reduction to 200W. A number of hypotheses on the possible reasons for this decrease have been identified and a set of tests were designed to with the goal of gathering data to evaluate each hypothesis.

The Electroluminescence test (EL) is a powerful tool used to control the quality of the PV cell strings. Using this technique it is possible to identify defects that are not visible to the naked eye such as micro-cracks and black (or "dead") areas. These two defects are the principal cause of power losses in the cell strings, a fact which can be confirmed in the IV-Curve test (Chaturvedi et al. 2012).

2. Description of the collector and its components

Fig. 1 shows a schematic of the collector viewed from the top while fig. 2 shows a picture of the actual collector. The total size of the collector is 2.31 x 0.955 m. The length of the thermal receiver is 2.290 m and the height is 0.158 m (Bernardo et al. 2011).

The efficiency for direct (or "beam") light η_{direct} of the collector 70%, while the efficiency for diffuse light $\eta_{diffuse}$ is 50,8% (Gomes et al. 2014). Furthermore, the linear loss coefficient a_1 is 4,484 W/(m^{2}K) and the secondary loss coefficient a_2 is 0,0034 W/(m^{2}K).

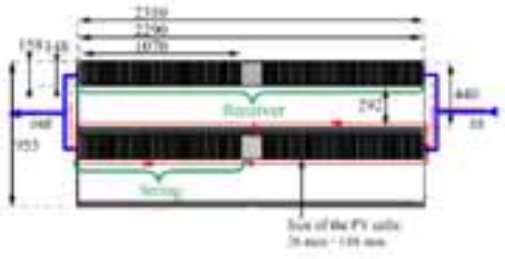

Fig. 1 - Top view of the PVT hybrid collector. The water connections are in blue and the electrical connections in red (Gomes et al. 2014)

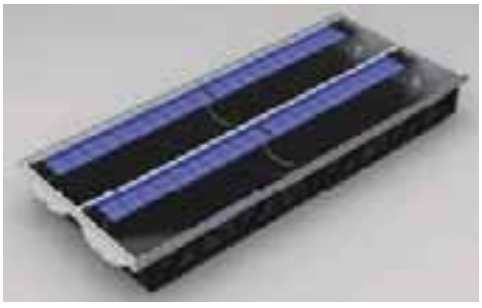

Fig. 2 - Solarus PVT hybrid collector

Reflector: The reflector geometry of the studied collector was initially developed by Vattenfall and the design is called Maximum Reflector Concentration (MaReCo) which belongs to a family of stationary reflectors patented by the Swedish company Solarus Sweden Sunpower AB. The reflector is composed of

a compound parabolic and circular reflective material used to concentrate the solar radiation which is made of anodized aluminum with a total solar reflectance ρ_{total} of 95%.

Receiver: The receiver is made of a 2.29m alumunium extrusion with a maximum expansion of 8 milimeters. The cells and silicone are laminated on both sides of the receiver.

Cell encapsulation: Cell encapsulation is done with two layers of silicone. The bottom layer: between the receiver aluminium core and the cells. The top layer: between the cells and the air.

In the prototypes created for the tests, two types of silicone gels are used: A highly transparent and electrically insulating silicone is used in the top layer but it could also be used in the bottom layer. A reddish brown silicon that is equally electrically insulating but has better thermal conductivity can only be used in the bottom layer since it is not transparent and if used on the top layer would block the sunlight from reaching the cells. The red silicone is considerably stiffer than the transparent silicone and thus transmits more stress to the cells when the receiver experiences thermal expansion.

Silicone Solar Cell: There are several cell string designs but the standard consists of 2 strings of 38 PV cells connected in parallel for each receiver side. Both the front side and the back side of the receiver consist of two PV strings each. The measured prototypes have two different cell sizes: a) 28mm*148mm or b) 52mm*148mm. This way, total number of PV cells per collector can be 152 or 304 cells, depending on the prototype design.

Glass: The module contains a glazed protection which is made of low iron glass with a solar weighted transmittance τ_{glas} of 95% (Gomes et al. 2014).

3. Description of the stagnation temperature issue

Eight C-PVT collectors and six concentrating thermal (T) collectors were installed in a warm country as show in figure 3. The eight C-PVT collectors were connected to eight micro-inverters. Four thermal loops were connected to a central tank. Three loops contained two PVT and two T while one loop had only two PVT collectors.

Fig. 3 -Test installation at latitude 30^0

The water outlet was not connected in the first day which was a very sunny and warm summer day. This implies that the collector has reached stagnation temperature which is around 175 ^{o}C.

One hour after installation, the combined output of the eight PVT was measured and found to be only 1200 W (el) instead of the expected 1920W (el). It should also be noted that the eight PVT collectors may also have been exposed to sunlight without cooling, prior to the installation. In the morning of the following day, the electrical production of the installation was again measured and it had been greatly reduced to only 200W.

The first measured electrical output of 1200W is well below the theoretical value expected of 1920W. This decrease is clearly a manufacturing problem which the company that produced the prototypes is aware that it is caused by the manual hand soldering process and that the company will solve this matter with the purchase of an automatic tabbing stringer machine during Q3 of 2015.

However, a more important issue that was discovered in this prototype C-PVT installation was the electrical power reduction to 200W that the installation showed in the second day, after prolonged stagnation. Four hypotheses on the possible reasons for this large decrease have been identified and are described below:

- The diodes broke down due to the high temperature
- The thermal expansion of the copper cell ribbon has damaged the cells
- The thermal expansion of the aluminium receiver has damaged the cells
- Unsoldering of the copper ribbon from the cells caused by the stagnation

The thermal part of the C-PVT installation was not affected in any way by stagnation. No leaks were found as well as no reduction in thermal power output. In fact, a slight thermal output increase has been reported since the solar cells are not converting the solar irradiation into electricity.

The thermal part of the C-PVT installation was not affected in any way by stagnation. No leaks were found nor any reduction in thermal power output. In fact, a slight thermal output increase has been reported, and is understandable as the solar cells are no longer capturing a portion of the energy and converting it to electricity.

4. Method

The prototype receivers:

In order to discover the cause of the electrical performance reduction, eight prototype small receivers were manufactured at the company that made the prototypes C-PVT in the installation: Solarus Sunpower Sweden AB. Table 1 details the characteristics of each small receiver:

Table 1 - Characteristics of the eight small receivers

Receiver	Cell size	Cells number	Cell Gap	Soldering	Silicone layers	Tabbing Strip
Receiver 1	1/6	7	No	Line soldering	Red-Transparent	Straight
Receiver 2	1/6	6	No	Line soldering	Transparent-Transparent	Straight
Receiver 3	1/6	6	Yes	Line soldering	Red-Transparent	Strain relief
Receiver 4	1/6	6	Yes	Line soldering	Transparent-Transparent	Strain relief
Receiver 5	1/6	6	Yes	Two points soldering	Transparent-Transparent	Strain relief
Receiver 6	1/6	7	No	One point soldering	Transparent-Transparent	Straight
Receiver 7	1/3	4	Yes	Line soldering	Transparent-Transparent	Strain relief
Receiver 8	1/3	4	No	One point soldering	Transparent-Transparent	Straight

The 8 receivers were identical with the exception of 6 parameters that were varied: Cell size, cell gap, cell number, soldering type, type of silicon used, existence of the strain relief. Four parameters are further explained below:

- Two cell sizes were used: 1/3 (52*148mm) and 1/6 (28*148mm)
- The cell gap is the space between the cells. *"No"* means the small standard gap while *"Yes"* means a longer gap (approximately triple of the standard gap)
- The strain relief is simply a bump in a long copper busbar that is designed to cope with the thermal expansion and prevent cell damage.
- The strain relief is simply an exaggerated "s" shape bent in the tabbing strip between each cell, designed to absorb thermally-induced mechanical stress without passing it on to the cells.
- The silicone is applied in two layers. A bottom layer placed on the aluminium receiver before the

cells. And a top layer placed after the bottom layer has totally solidified and at the same time as the solar cells. Two types of silicone were used. A soft transparent silicone with a high transparence and high dielectric resistance and a harder red silicone with no transparence, similar dielectric properties and a lower heat resistance.

Test method:

The test consists in placing the receiver 8 times inside an oven for one hour each time with a gradual increase of the oven temperature. In the first round the receiver temperature will be raised from 0°C to 60°C and in the next rounds 80°C, 100°C, 130°C, 150°C, 180°C, 200°C, 220°C.

It is important to point out that the collectors stagnation temperature is 175°C. Nevertheless, the tests at 200°C and 220°C give interesting results in order to determine a safety margin.

After each thermal cycle, the following parameters are recorded:

- Electroluminescence (EL) Test: IR photograph of the cells on the receiver was made using a Digital Rebel XTi Black Canon Camera without an IR filter. The system features an image size of (3,888 x 2,592) in RAW format with 10 megapixels. The test was done in a completely dark chamber. Cells were in forward bias with a current close to 4A. This test allowed the team to spot microcracks which are not visible to the naked eye.
- IV Curve test in a solar simulator: Pmax, Imax, Vmp, Isc, Voc, FF
- Diode Function test
- Visual Inspection: note the condition of the cells, any discoloration, etc.

An important note is that the cells in the prototype receivers are soldered manually which means that some micro-cracks arise from prototype production issues that will not occur in automatic cell soldering production. For this and other reasons, a baseline scenario was also tested recording all the above shown parameters. Additionally, the cells in the prototype installation displayed in figure 3 are also manually soldered.

5. Results and Discussion

The first small receiver to be tested had very similar characteristics to the collectors of the installation shown in figure 3.

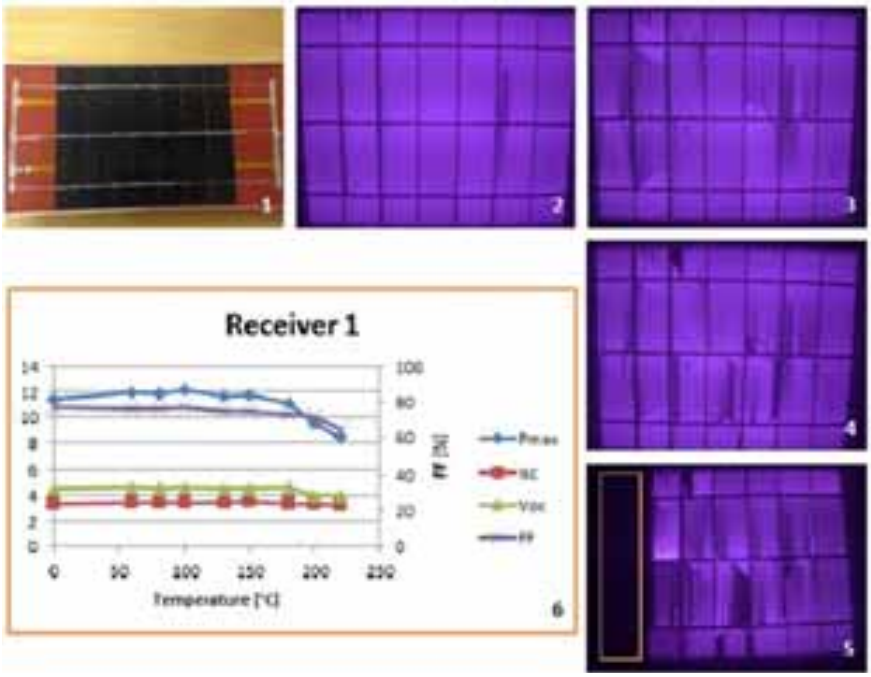

Fig. 4 – 1) Receiver 1; 2) Baseline; 3) Round 5 (150°C); 4) Round 6 (180°C); 5) Round 8 (220°C); 6) Parameters of the IV curve at different temperatures (Isc shown in the left Y axis).

As expected, after round 3 (exposure to 150°C), the EL test showed that the string has dark areas and a large number of micro-cracks which lead to a power decreases shown in figure 4 below. Raising the temperature in following heating rounds has significantly increased the amount of dark areas and micro-cracks. In the last round one cell became completely black caused by a short circuit between the top and bottom of the cell. The reason for the short circuit has not been determined but a likely explanation is that the solder on the top ribbon melted (or simply got contact) through a crack and reached the bottom ribbon.

The only difference between the first receiver and the second is the bottom silicone layer. In receiver 2, transparent silicone was used on both layers. From the 5 rounds of EL tests shown in figure 5, it is possible to see a large increase in microcracks after round 4 (180°C). Despite this, the IV curve basic parameters remain more or less constant throughout the 8 rounds with only a minor power decrease.

The number of micro-cracks in receiver 1 is higher than in receiver 2 for all temperatures, despite the baseline test (image 2) showing similar numbers.

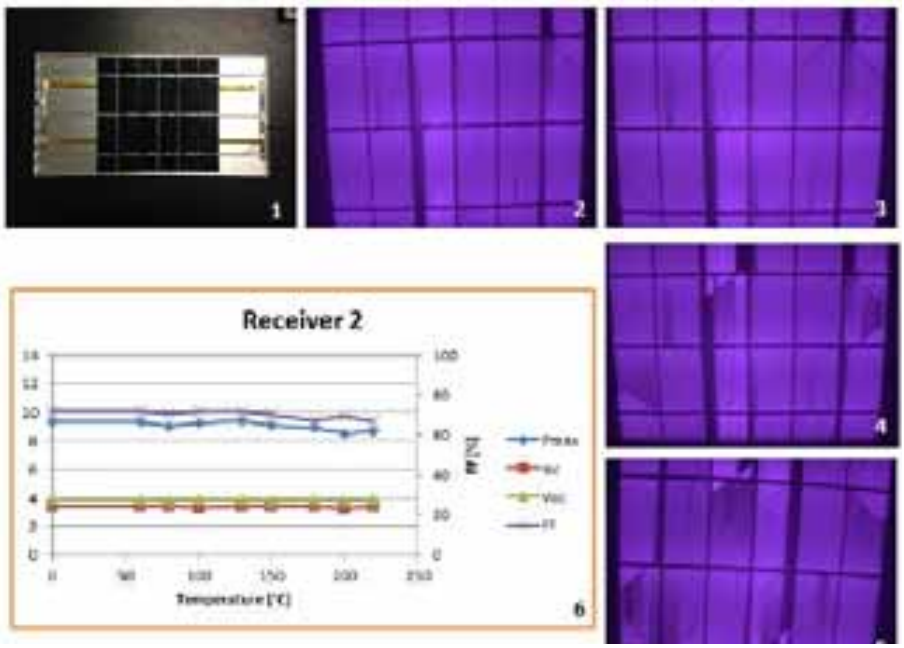

Fig. 5 – 1) Receiver 1; 2) Baseline; 3) Round 5 (150°C); 4) Round 6 (180°C); 5) Round 8 (220°C); 6) Parameters of the IV curve at different temperatures (Only Isc on the left axis).

The main goal of building receiver 3 and 4 was to test the impact of reducing the stress on the cell caused by the thermal expansion of the ribbon. This way, a strain relief bend was inserted before and after each cell. In order to isolate the impact of the different types of silicones two receivers were made: One with red silicone (receiver 3) and another with transparent silicone (receiver 4). The results from receiver 3 can be seen in Fig. 6 and from receiver 4 in Fig. 7.

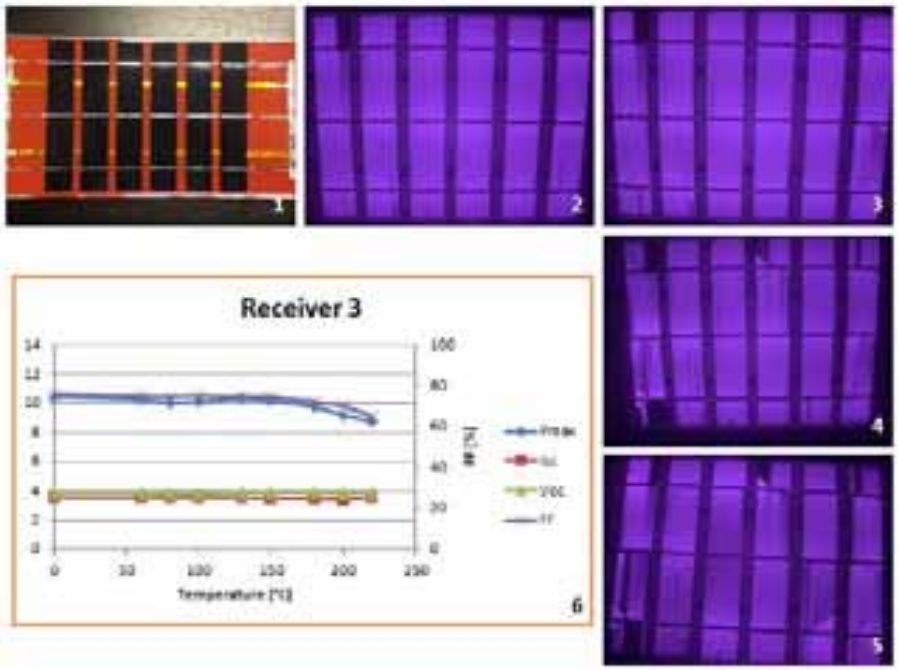

Fig. 6 – 1) Receiver 1; 2) Baseline; 3) Round 5 (150°C); 4) Round 6 (180°C); 5) Round 8 (220°C); 6) Parameters of the IV curve at different temperatures (Isc shown in the left Y axis).

The EL tests in Figure 6 show that in a receiver with red silicone, even with the strain relief between the cells, a large number of micro-cracks appear when exposed to higher temperature (180°C). Compared with receiver 1, receiver 3 exhibits a smaller power drop, albeit still displaying a significant power drop in the last 2 rounds.

In Fig. 7, the cells of receiver 4 have no significant damage along the 8 rounds, representing an improvement from the results obtained with receiver 2. However, receiver 4 showed one black cell in the last round likely caused by the same reason as in the receiver 1. The same black cell that appeared at round 7 (200°C) is also responsible for the sharp 15% drop. Excluding that effect, the power remains considerably constant.

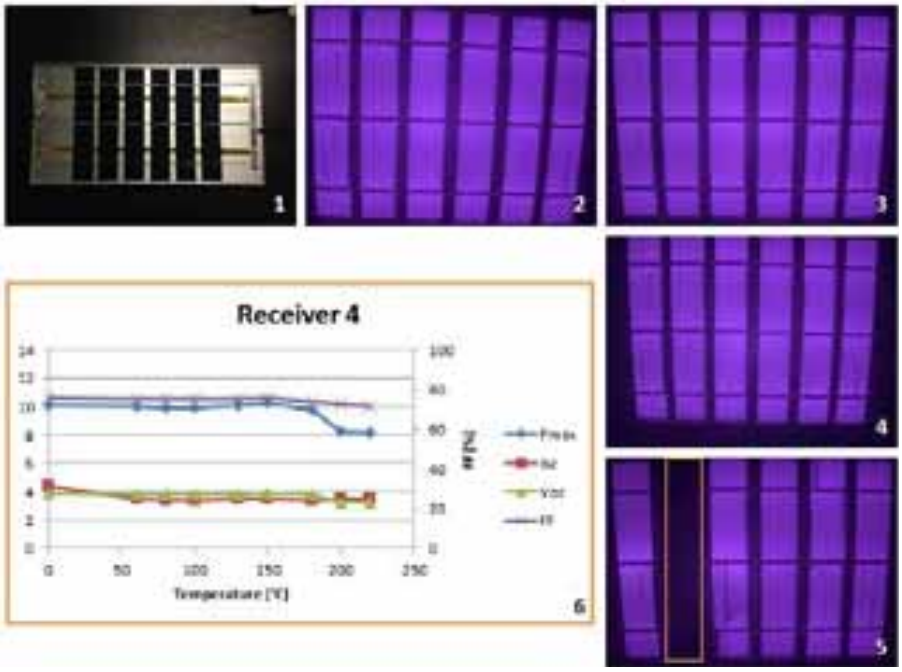

Fig. 7 – 1) Receiver 1; 2) Baseline; 3) Round 5 (150°C); 4) Round 6 (180°C); 5) Round 8 (220°C); 6) Parameters of the IV curve at different temperatures (Isc shown in the left Y axis).

Since our research group did not have, at the time of these tests, access to an expensive automatic cell soldering machine, it was also important that the group investigated the impact of different manual soldering techniques. This was accomplished with receivers 5 and 6 that have been made with point soldering instead of continuous soldering, like all previous receivers. Receiver 5 was done with two point soldering and strain relief, while receiver 6 had no strain relief and only one point soldering.

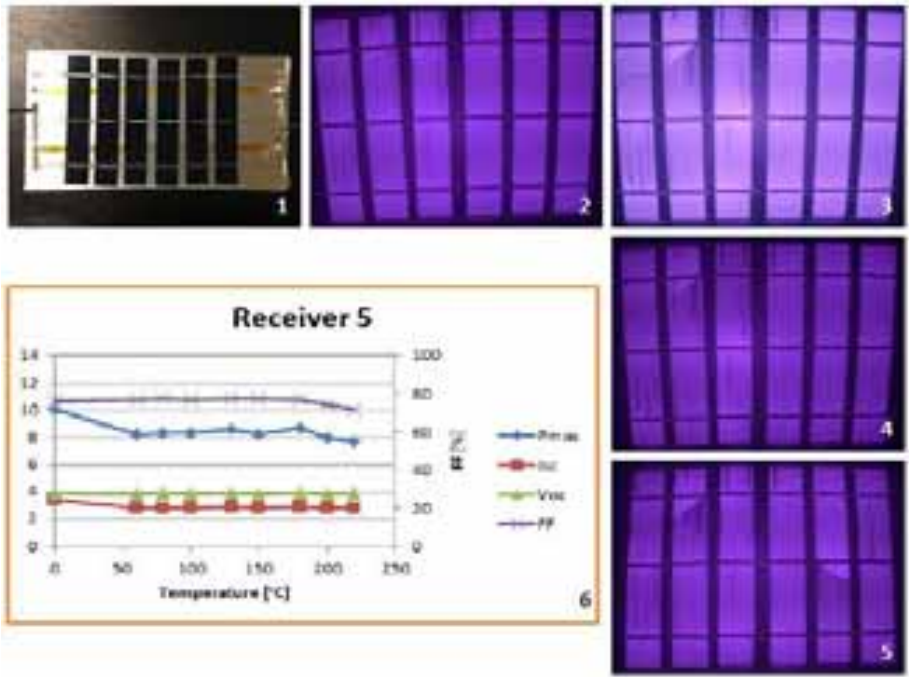

Fig. 8 – 1) Receiver 1; 2) Baseline; 3) Round 5 (150°C); 4) Round 6 (180°C); 5) Round 8 (220°C); 6) Parameters of the IV curve at different temperatures (Isc shown in the left Y axis).

In the graph of figure 8, it is visible that the Pmax of receiver 5 has one initial decrease at 50°C . This is due to the two broken cells shown in image three and it is likely to have been cause by our cell handling. If this effect is excluded, the Pmax remains relatively stable. It is interesting to note that only at 220°C one extra microcrack appears. The one point point soldering has much smaller electrical contact between the busbar and the cell than the line soldering but this shows no consequences in our measurements.

In figure 9, the Pmax of receiver 6 also remains fairly stable until one the cell becomes dark at 200°C (round 7) which seems to indicate that there are no large differences between one and two point soldering as well as with the existence of strain relief. One microcrack appears at 180°C and another appears 220°C.

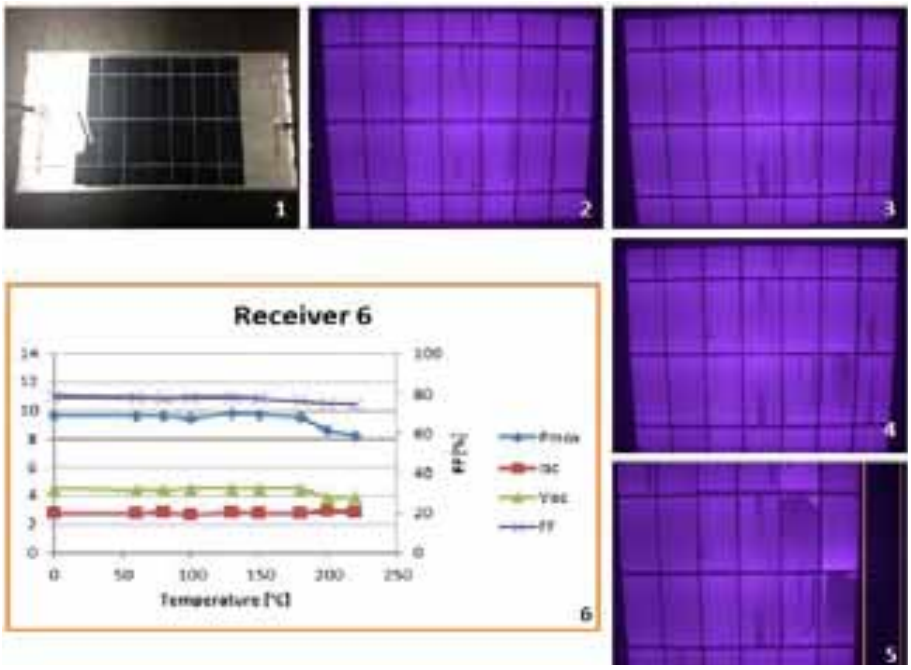

Fig. 9 - 1) Receiver 1; 2) Baseline; 3) Round 5 (150°C); 4) Round 6 (180°C); 5) Round 8 (220°C); 6) Parameters of the IV curve at different temperatures (Isc shown in the left Y axis).

Receivers 7 and 8 were made to evaluate the impact of temperature in larger cells (148mm*52mm). Receiver 7 was made with a much larger gap than usual between the cells, with line soldering and with strain relief between all cells while receiver 8 was made without strain relief, with point soldering and with a standard gap between cells.

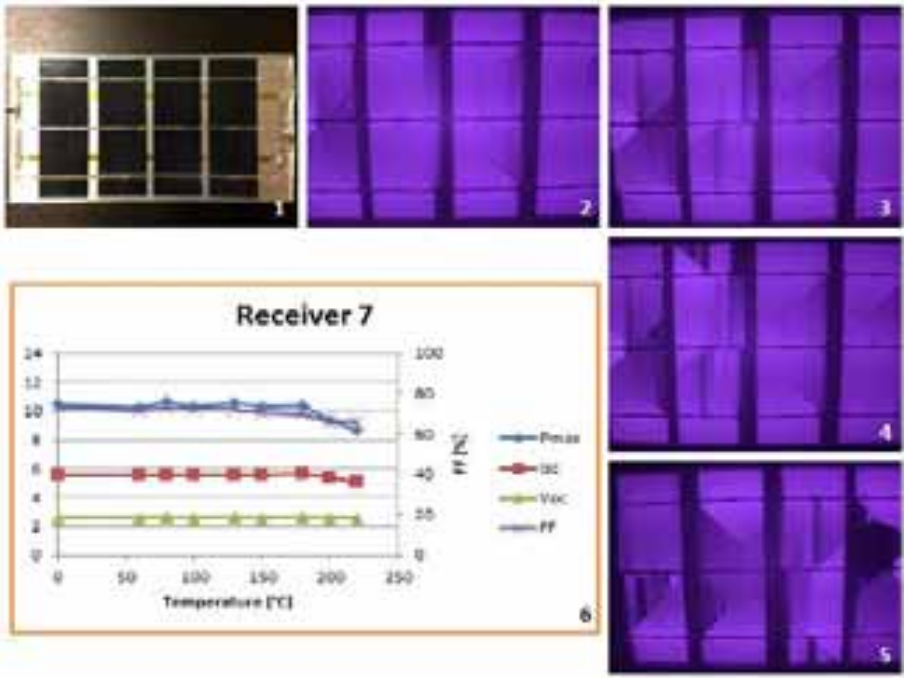

Fig. 10 - 1) Receiver 1; 2) Baseline; 3) Round 5 (150°C); 4) Round 6 (180°C); 5) Round 8 (220°C); 6) Parameters of the IV curve at different temperatures (Isc shown in the left Y axis)

Despite having more precautions against stagnation, receiver 7 shows more cell breakage then receiver 8 at any temperature. This seems to point that on large cells the effect of having large gaps with strain relief is less important than the type of soldering.

Strangely, the decrease in power is more pronounced in receiver 8 than in receiver 7. However, it must

be noted that receiver 2 starts off from a much worst baseline scenario since it shows some microcracks from start. From all the testing accomplished, it also seems safe to state that existing microcracks expand at fast rate than new microcracks are created.

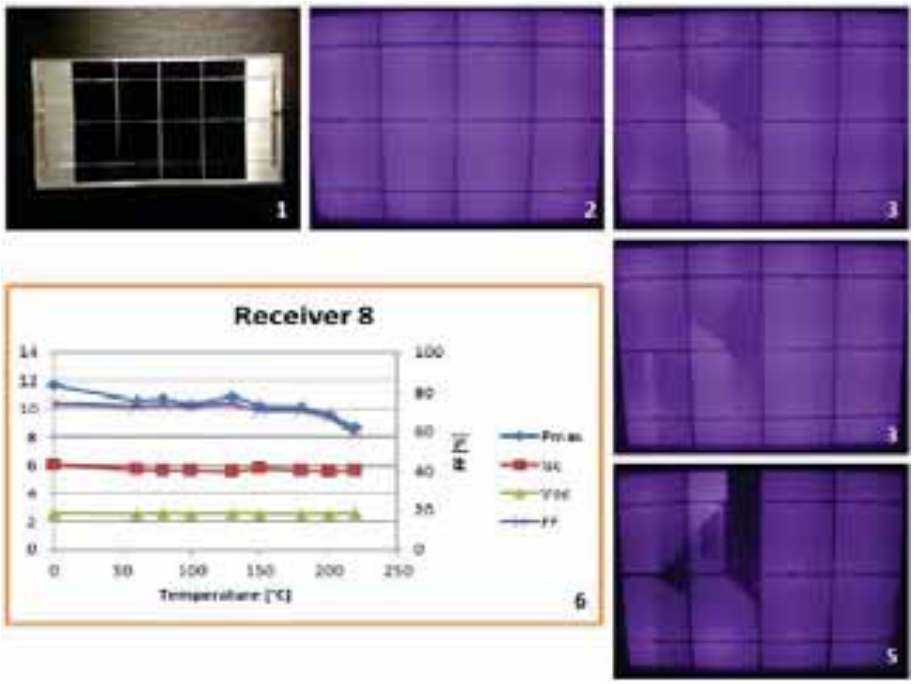

Fig. 11 - 1) Receiver 8; 2) Baseline; 3) Round 5 (150°C); 4) Round 6 (180°C); 5) Round 8 (220°C); 6) Parameters of the IV curve at different temperatures (Isc shown in the left Y axis)

Figure 12 and 13 compare the decrease in Pmax of the different receivers at different temperatures rounds. Receiver 2 shows the most steady Pmax across all temperatures Receiver 5 is also fairly stable is one excludes the handling problem on round 1. Receiver 1 shows an increase of power that is difficult to explain and is assumed to have been a human error. Overall, receivers with red silicone have the highest power decrease, if external factors are excluded. The existence of gaps seems to reduce the number of microcracks. No prototype test receiver losses more than 30% of its initial power, despite the large cell breakage shown in some receivers by the EL testing.

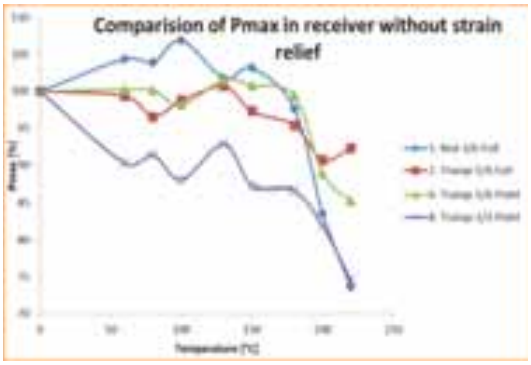

Fig. 13 - Comparison of Pmax decrease in receivers without strain relief

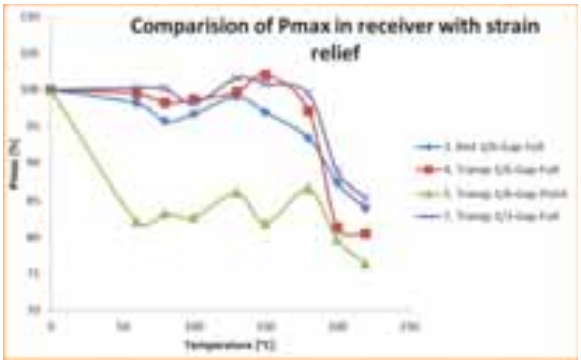

Fig. 12 - Comparison of Pmax decrease in receivers with strain relief

6. Conclusion

Eight different receivers have been built and were successfully tested to assess the impact of temperature variations in performance and cell structural integrity.

Two types of black areas in the cells were identified from the tests. They are namely irregularly shaped areas which are due to micro-cracks and regular rectangular areas which are due to broken finger contacts on the front of the cell. It was also noted that the majority of the micro-cracks were initiated at the soldering points, which is understood to be because of the different expansion coefficients.

From the previous figures, it is clear that receivers built with transparent silicone show far less cracks and power degradation after being exposed to the stagnation temperatures. This is understood to be due to two main reasons: 1) the transparent silicone is less rigid than the red silicone and thus further absorbs the mechanical stress of thermal expansion in the aluminium receiver; 2) the red silicone due to its lower viscosity is normally made in a thinner layer which further penalizes its ability to absorb mechanical stress.

No prototype test receiver lost more than 30% of its initial power, despite the large cell breakage shown in some receivers. After 8 rounds of testing, it was possible to conclude that the diodes were working perfectly at all temperatures, although the diode specifications stated a maximum junction temperature of only 200°C.

Larger cells are more prone to develop micro-cracks due to thermally induced stresses. From the tests that have been made, point soldering seems to lead to a reduction in the number of micro-cracks and black areas, especially in receivers with larger cells (148*52mm instead of 148*26mm). However, the impact of micro-cracks in the Pmax of receivers with point soldering is also larger because the smaller contact area between the ribbon and the cell.

From the electroluminescence images, the receiver presenting the lowest amount of micro cracks after round 8 (at 220°C) is receiver 5. This receiver has point soldering and strain relief between each cell. Receiver 4 and receiver 6 also exhibit low amounts of micro-cracks but both have a full black cell, possibly due to a contact between the top and bottom ribbon through the cell. Receiver 2 shows the most steady Pmax across all temperatures. Receiver 5 is also fairly stable if one excludes the handling problem on round 1.

Existing micro-cracks tend to grow in size into larger micro-cracks relatively fast. The EL imaging taken during our experiment leads us to conclude that it is far easier for existing cracks to expand than for new cracks to appear.

A limitation of this work was the absence of a fully automatic tabbing machine. Since this is expensive equipment, our team had to use manual soldering. However, by setting a baseline scenario for comparison, this limitation was addressed.

It is important to point out that the thickness of the bottom silicone layer is of the upmost importance in reducing the transference of thermally induced stress to the cells. The impact of the variations in the thickness of silicone in the thermal stress suffered by the cells has not evaluated in this paper and should be address in a future study.

7. References

[1] C. Giovinazzo, L. Bonfiglio, J. Gomes, B. Karlsson, 2014, “Ray Tracing Modelling of an Asymmetric Concentrating PVT”, Aix-les-Bains (France).

[2] R. Khatri, S. Agarwal, I. Saha, S. Singh, B. Kumar, 2011, “Study on long term reliability of photo-voltaic modules and analysis of power degradation using accelerated aging tests and electroluminescence technique”, Freiburg (Germany).

[3] P. Chaturvedi, B. Hoex, T. Walsh, 2012, "Broken metal fingers in silicon wafer solar cells and PV modules", Singapore.

[4] R. Bernardo, H. Davidsson, N. Gentile, J. Gomes, C. Gruffman, L. Chea, C. Mumba, B. Karlsson, 2012, "Measurements of the Electrical Incidence Angle Modifiers of an Asymmetrical Photovoltaic/Thermal Compound Parabolic Concentrating-Collector".

[5] J. Gomes, J. Junge, B. Karlsson, 2014, "Defining an annual energy output ratio between PV and solar thermal", Aix-les-Bains (France).

[6] J. Gomes, L. Diwan, R. Bernardo, B. Karlsson, 2013, "Minimizing the Impact of Shading in a Stationary Asymmetric Concentrating PVT Collector", ISES, Mexico.

Conference Proceedings

Solar World Congress 2015
Daegu, Korea, 08 – 12 November 2015

Experimental evaluation of the influence of infiltration on the efficiency of solar flat plate collectors

Elisiane S. A. Paiva[1], Antonia Sonia A. C. Diniz[1], Lucas P. P. Faria[1], Thiago A. Silvério[1], Rafael O. Barreto[1] and Cristiana B. Maia[1]

Pontifical Catholic University of Minas Gerais (PUCMinas)/Department of Mechanical Engineering, Belo Horizonte (Brazil)

Abstract

PBE (Brazilian Labeling Program) is a national program in Brazil that aims to establish standard criteria to compare the energetic efficiency and quality of several devices, such as refrigerators, vehicles, and flat plate solar collectors. The vast majority of solar collectors tested by PBE fail in the topic of infiltration of water condensation. Arguably, the presence of water inside the collector decreases its efficiency, since part of the solar radiation is lost to heat the infiltrated water. However, the determination of the heat losses due to infiltration has not yet been proven in actual flat plate solar collectors, since it has not yet been properly measured. The aim of this study was to evaluate the influence of water infiltration in the efficiency of flat plate solar collectors, evaluating devices from three classes of energetic efficiency: A, B, and C. For the samples evaluated, it was observed that the influence of the amount of water infiltrated on the efficiency is not significant. Therefore, this criterion should not be used to promote the rejection of the collector.

Keywords: *Efficiency, Solar collector, Infiltration*.

1. Introduction

A significant part of the energy consumption in residential segment is attributed to water heating (Prado and Gonçalves, 1998). According to Ghisi et al. (2007), it is estimated that refrigerators, freezer, air conditioners and electric showers account for nearly 60% to 70% of the Brazilian´s residential energy consumption. Also, except for the northeast of Brazil (the hottest region of the country), 81-92% of the Brazilian population use electric showers. Since electric showers consist of an electric-resistance water heater, they require very high electrical power (Oliveira and Rebelatoo, 2015). Flat plate solar collectors use the incident solar radiation to heat the water. Since Brazil has high levels of solar radiation and the solar collectors are able to operate with direct and diffuse components of solar radiation, these devices can successfully replacing electric showers. The basic parameter to consider in an analysis of a solar collector is its thermal efficiency, which depends on the collector parameters and thermal losses.

The efficiency of a solar collector depends upon how much a working fluid carries away the heat from the collector. Techniques are used to enhance the performance of solar collectors, mainly divided in increasing the heat transfer coefficient between the absorber plate/tube and the working fluid, using special type of coatings on the absorber (i.e, solar selective coatings), and increasing the thermal conductivity of the working fluid using nanoparticles (Suman, Khan and Pathak, 2015). Nanofluids are a mixture of liquid (base fluid) and nano sized particles (1-100 nm) suspended (Ferrouillat et al., 2013) that can be used instead of conventional heat transfer fluids (Al-Shamani et al., 2014).

Different countries have different standards to characterize and evaluate the efficiency of solar collectors. The most important standard for collector testing in Europe establishes a steady-state method and allows the application of a quasi-dynamic method performed outdoors. Osório and Carvalho evaluated and compared

doi:10.18086/swc.2015.10.15 Available at http://proceedings.ises.org

both the steady-state and the quasi-dynamic methods, showing similar results. The advantage of the quasi-dynamic tests was in terms of the time required to perform the analysis. Cruz-Peragon et al. (2012) proposed a 2D finite difference method to validate a characterization of a solar collector. Steady and transient states were analyzed under different operating conditions and results depicted the robustness of the method.

Sözen, Menlik and Ünvar (2008) developed a new formula based on artificial neural network to determine the efficiency of flat-plate solar collectors, for different conditions of ambient temperature, date, time, solar radiation, declination and azimuth angles.

In Brazil, there is a national program to evaluate and classify the solar collectors based on their energetic efficiency, named PBE – Programa Brasileiro de Etiquetagem (Brazilian Labeling Program). The efficiency is evaluated through a series of standard tests performed in laboratories, taking account several parameters, such as hydrostatic pressure, sealing, and water infiltration. According to the results, the collectors receive a grade from A to E, depending on the specific monthly energy production - PEME, according to the values shown in Table 1. One of the tests performed is the thermal shock, in which the device is exposed to water, and the maximum amount of infiltrated water is 5 g/m^2 of area. If the amount of infiltrated water exceeds this value, the solar collector is rejected.

It is well known that the infiltrated water reduces the efficiency of a solar collector, but the influence of the amount of water on the thermal efficiency has not been properly measured. The objective of this paper is to evaluate the thermal efficiency of solar collectors subjected to different levels of water infiltration. The tests were performed in devices evaluated as A, B, and C according to PBE Brazilian Program.

Tab. 1: Classification of the solar collector according to the energy production

Grade	Range of PEME (kWh/month-m^2)
A	PEME > 77
B	71 < PEME < 77
C	61 < PEME < 71
D	51 < PEME < 61
E	41< PEME < 51

2. Experimental setup

Experimental tests for the determination of the thermal efficiency of flat-plate solar collectors were performed in a closed location, using a Solar Simulator. This device consists of a eight special lamp system, with total power of 40kW, and the radiation spectrum similar to the sun. The artificial sky is composed of two tempered glass plates; between them, cool air flows, in order to simulate the radiation heat losses between the solar collector, sky and the wind generator system (Fig. 1).

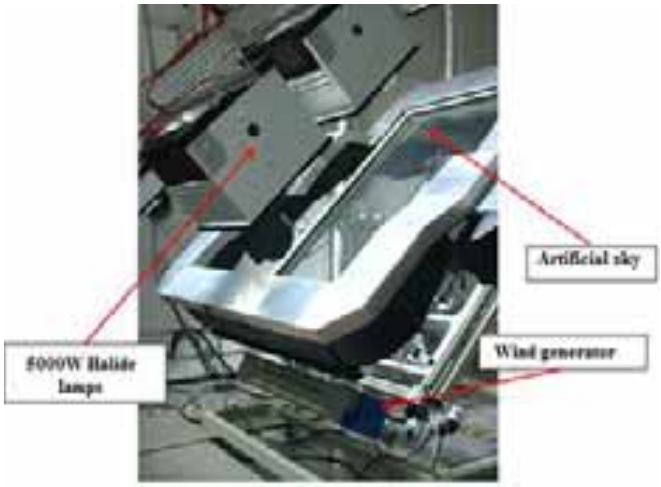

Figure 1 – Solar simulator, front view

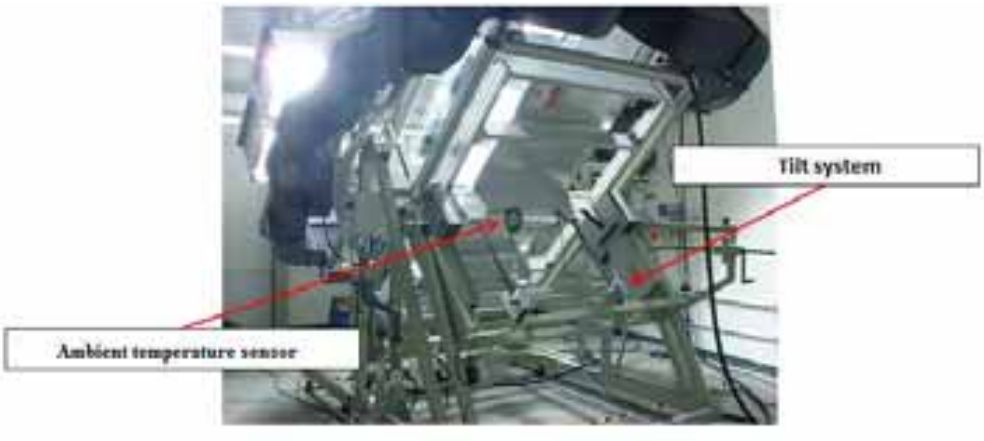

Figure 2 – Solar simulator, rear view

Figure 3 – Solar simulator and pyranometer

The tests followed Brazilian Standards NBR 15747-1 and NBR 15747-2. NBR 15747-1 specifies the reliability and durability requirements, safety and thermal performance of solar collectors for heating liquids. NBR 15747-2 specifies test methods for validating the durability requirements, reliability, safety and thermal performance of solar collectors for heating liquids presented in the previous standard.

In order to determine the efficiency, measurements of incident radiation on the solar collector plane, inlet and outlet water temperatures, volume flow rate and ambient temperature were performed, with the sensors indicated in Figures 2 and 3. A Precision Spectral Pyranometer (PSP) is used to determine the solar radiation, as indicated in Fig. 3. Platine resistance thermometer (PT100) are used to determine the inlet and outlet water temperatures and the ambient temperature (Fig. 2). The volume flow rate is measured with a volume flow meter. The wind velocity is controlled to be within the range specified by the Standards.

Based on the Quality Technical Regulations for Solar Water Heating Systems and Equipment, elaborated by the Brazilian National Institute of Metrology, Quality and Technology (INMETRO), the proof of non-compliance of the solar collector due to the infiltration and condensation must be performed through the thermal shock and rain penetration tests. The amount of infiltrated water is measured by the comparison of the

weight of the solar collector before and after the exposure of the device to water for a pre-determined time interval. In order to be approved on the certification test of water penetration, the maximum acceptable amount of infiltrated water is 5 g/m^2. The ambient temperature inside the Solar Simulator was kept between 15°C and 30°C.

A, B and C collectors were tested, in order to evaluate how the class influenced the results.

Water was inserted into the collectors, in pre-established quantities, using a syringe. The range of leakage was determined from the maximum allowed quantity of 5g/m². The standard states that the solar collectors when subjected to rain penetration test must present a maximum infiltration of 5 g / m². The infiltrated water withdraw collector heat to warm itself, which could reduce its efficiency. It is not defined in the standard reason for the threshold value of 5 g / m² have been adopted. For each collector, four tests were performed, in quantities equal to 10 g/m^2, 20 g/m^2, and 30 g/m^2, named, respectively, Test 1, Test 2, Test 3 and Test 4. The dimensions and quantities of infiltrated water are presented in Table 2.

Tab. 2: Dimensions and amount of infiltrated water

Collector	Area (m^2)	Amount of water (g)			
		Test 1	Test 2	Test 3	Test 4
A	1.7068	0	17	34	51
B	1.0060	0	10.06	20.1	30.2
C	1.0171	0	10.17	20.35	30.5

3. Analysis

The collector efficiency is defined as the ratio of the useful gain over some specified time period to the incident solar energy over the same time period (Duffie and Beckman, 2006)

$$\eta = \frac{\int Q_u dt}{A_c \times \int G dt} \quad \text{(eq.1)}$$

In eq. 1, G is the instantaneous solar radiation on the collector plane (W/m^2), A_c is the collector area (m^2) and Q_u is the useful energy gain.

The solar radiation is measured on the collector plane, as indicated in Fig. 3. The collector area is determined by the product of the width and length. The useful energy gain is determined by a energy balance between the outlet and inlet fluid.

$$Q_u = \dot{m}(h_o - h_i) \quad \text{(eq.2)}$$

Where $\dot{m}$ represents the mass flow rate of the water inside the collector, h represents the specific enthalpy and the subscripts *o* and *i* refer to the outlet and inlet. The enthalpy change is determined by:

$$h_o - h_i = c_p(T_o - T_i) \quad \text{(eq.3)}$$

The mass flow rate and the outlet and inlet temperatures are measured during the tests.

4. Results and discussion

In order to evaluate the influence of the infiltrated water in several kinds of solar collectors, type A, B, and C collectors were chosen. Table 3 shows the PEME and the uncertainties of the collectors, based on the tests performed without infiltration of water. It is important to mention that the PEME did not considerably change with the infiltrated water, with maximum variation of 4.3%, relative to type A collector.

Tab. 3: PEME and uncertainties collectors us without water infiltration tests

Collector	PEME (kWh/month-m^2)	Uncertainty (kWh/month-m^2)
A	84.87	0.32
B	83.90	0.34
C	75.66	0.37

The classification follows the range of values specified in Table 1.

Solar collector efficiency is expressed in the form of either a linear or a quadratic equation (Duffie and Beckman, 2006). The equations can be used to estimate the energy performance of a solar heating system. Based on the measurements the efficiency expressions were found for the collectors, for the tests performed. The expressions are given in Table 4. The average efficiency is defined as the efficiency for an abscissa of 0.02, which corresponds to the average value for a bath. The uncertainty is shown in the last column.

Tab. 4: Efficiencies of the solar collectors

	Expression	Efficiency with 0.02	Uncertainty
Collector A – Test 1	$\eta = 70.22 - 466.32\left(\frac{T_m - T_a}{G}\right)$	60.89%	0.32%
Collector A – Test 2	$\eta = 70.81 - 496.84\left(\frac{T_m - T_a}{G}\right)$	60.87%	0.33%
Collector A – Test 3	$\eta = 71.19 - 618.26\left(\frac{T_m - T_a}{G}\right)$	58.83%	0.41%
Collector A – Test 4	$\eta = 70.93 - 526.00\left(\frac{T_m - T_a}{G}\right)$	60.41%	0.37%
Collector B – Test 1	$\eta = 63.68 - 452.72\left(\frac{T_m - T_a}{G}\right)$	54.62%	0.34%
Collector B – Test 2	$\eta = 66.05 - 556.52\left(\frac{T_m - T_a}{G}\right)$	54.92%	0.38%
Collector B – Test 3	$\eta = 66.30 - 587.38\left(\frac{T_m - T_a}{G}\right)$	54.55%	0.40%
Collector B – Test 4	$\eta = 66.48 - 582.33\left(\frac{T_m - T_a}{G}\right)$	54.84%	0.41%
Collector C – Test 1	$\eta = 62.16 - 541.53\left(\frac{T_m - T_a}{G}\right)$	51.33%	0.37%
Collector C – Test 2	$\eta = 62.53 - 494.04\left(\frac{T_m - T_a}{G}\right)$	52.65%	0.34%
Collector C – Test 3	$\eta = 62.48 - 511.62\left(\frac{T_m - T_a}{G}\right)$	52.25%	0.36%
Collector C – Test 4	$\eta = 62.58 - 578.14\left(\frac{T_m - T_a}{G}\right)$	51.02%	0.41%

Figures 4 to 6 show the efficiency curves for collectors A, B, and C, respectively.

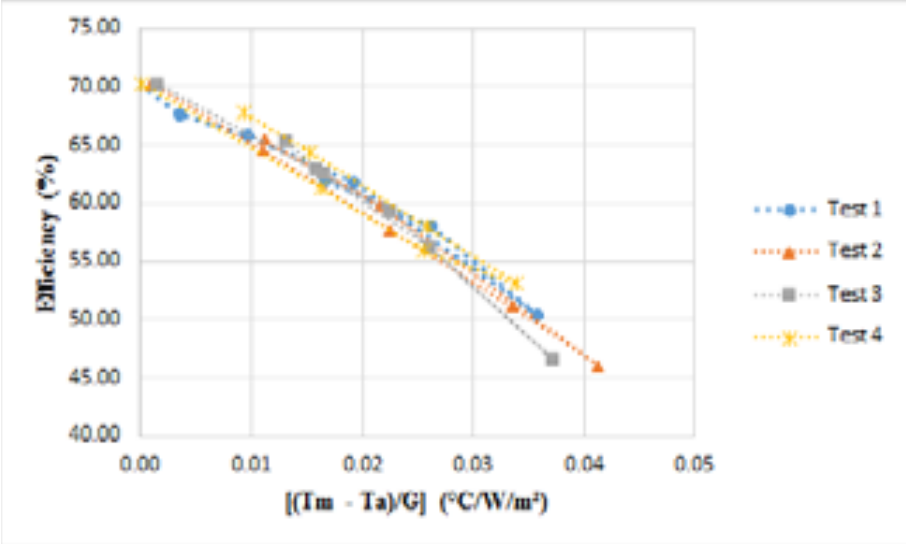

Figure 4 – Experimental collector efficiency for type A collector

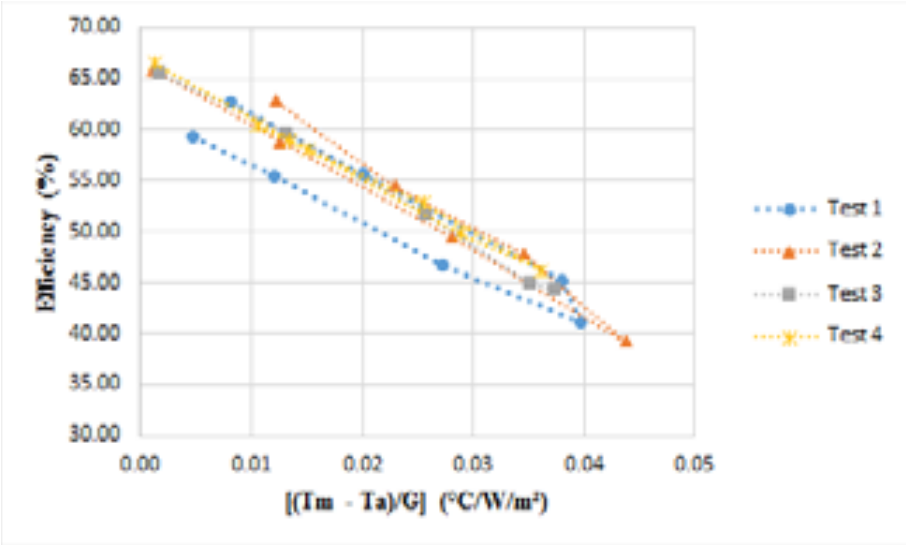

Figure 5 – Experimental collector efficiency for type B collector

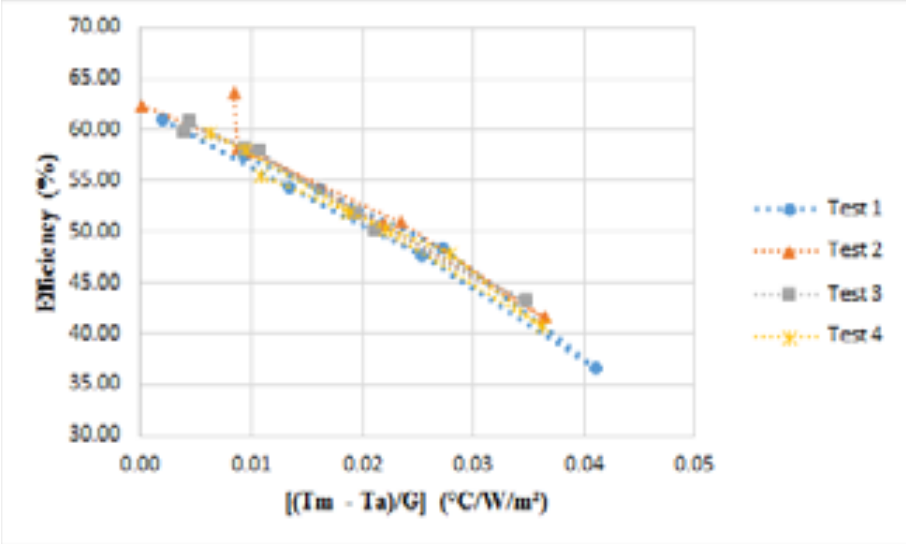

Figure 6 – Experimental collector efficiency for type C collector

It can be seen that the infiltration of water did not provide significant variations on the collector efficiency. The maximum variations of the average efficiency were 2.06%, 0.37% and 1.63%, for collectors A, B, and C, respectively. It is worth noting that, for type B collector, the efficiencies were within the uncertainty range, meaning that, for this collector, the water did not cause any effect on the average efficiency. It was not possible to determine a relationship between the amount of infiltrated water and the efficiency.

The Brazilian Standard specifies that, when the amount of infiltrated water in a solar collector exceeds 5 g/m^2 of area in the thermal shock test, it is rejected. The analysis performed showed that it was not possible to determine a decrease of the efficiency when values of 10, 20 and 30 g/m^2 of water are infiltrated. Therefore, the amount of 5 g/m^2 should not be considered to reject the new solar collector.

5. Conclusions

In this paper, it was evaluated the influence of water infiltration in a solar collector. There is not relationship between the infiltration and the classification of the collector A, B or C. Solar collectors of different specific monthly energy production were chosen to the analysis. The efficiency curve was obtained for the collectors without water and, subsequently, 10, 20 and 30 g/m^2 of water were infiltrated in the collector and the test was repeated.

The analysis showed that no significant variations of the efficiency or specific monthly energy production were observed with the infiltrated water for any type of collector, and that it could not be identified a relationship between the amount of water and the efficiency. Therefore, it can be concluded that the acceptable limits of the Brazilian Standard are too strict and should be rectified. The Standard is now in a revision process, in which the new limit is 30 g/m^2 to a higher period of sun exposure. Nevertheless, the analysis showed that, even this value is too strict.

Acknowledgments

The authors are thankful to PUC Minas, FAPEMIG and CNPq.

5. References

Al-Shamani, A.N.; Yazdi, M.H.; Alghoul, M.A.; Abed, A.M.; Ruslan, M.H.; Mat, S.; Sopian, K., 2014. Nanofluids for improved efficiency in cooling solar collectors – A review. Renewable and Sustainable Energy Reviews, v. 38, p. 348-367.

Cruz-Peragon, F; Palomar, J.M.; Casanova, P.J.; Dorado, M.P.; Manzano-Agugliaro, F., 2012. Characterization of solar flat plate collectors. Renewable and Sustainable Energy Reviews, v. 16, p. 1709-1720.

Duffie, J.A., Beckman, W.A., 2006.Solar engineering of thermal processes, third ed. John Wiley and Sons,Nova York.

Ferrouillat, S.; Bontemps, A.; Poncelet, O.; Soriano, O. Gruss, J.A., 2013. Influence of nanoparticle shape fator on convective heat transfer and energetic performance of water-based SiO_2 and ZnO-naofluids. Applied Thermal Engineering, v. 51, p. 839-851

Ghisi, E.; Gosch, S.; Lamberts, R., 2007. Electricity end-uses in the residential sector of Brazil. Energy Policy, v. 35, p. 4107–4120

Oliveira, M.H.F.; Rebelatto, D.A.N., 2015. The evaluation of electric energy consumption in the Brazilian residential sector: A technological improvement proposal in order to increase its efficiency. Renewable and Sustainable Energy Reviews, v. 49, p. 836-844.

Osório, T.; Carvalho, M.J., 2014. Testing of solar thermal collectors under transient conditions. Solar Energy, v. 104. P. 71-81.

Prado, R.T.A.; Gonçalves, O.M.. 1998. Water heating through electric shower and energy demand. Energy and Buildings, v. 25, n. 1, p; 77-82.

Sözen, A.; Menlik, T.; Ünvar, S., 2008. Determination of efficiency of flat-plate solar collectors using neural network approach. Expert Systems with Applications, v. 35, n. 4, p. 1533-1539.

Suman, S.; Khan, M.K.; Pathak, M., 2015. Performance enhancement of solar collectors—A review. Renewable and Sustainable Energy Reviews, v. 49, p. 192-210.

Conference Proceedings

Solar World Congress 2015
Daegu, Korea, 08 – 12 November 2015

A STUDY ON RELATIONSHIP BETWEEN THE ENERGY BALANCING AND THE REAL EXPERIMENT IN A HYBRID SOLAR HEATING SYSTEM

H.W. Choi[1], C.H. Son[2], J.I. Yoon[2] and K.H. Choi[2]

[1] Graduate school of Refrigeration and Air-Conditioning, Pukyong National University, Busan(Republic of Korea)

[2] Dept. of Refrigeration and Air-Conditioning, Pukyong National University, Busan(Republic of Korea)

Abstract

Research of the hybrid solar collector that can heat air and liquid simultaneously has been conducted for enhancement of the usage of solar energy. Thermal efficiency of this solar collector was investigated ranging from various operating conditions. This efficiency of the collector, however, was hard to generalize because of many factors that effect on the efficiency more than the traditional solar collector. Thus, in this study, the efficiency of hybrid collector was expressed by the energy balance and the efficiency of the collector was also investigated according to operating and external conditions. As a result, efficiency of the air side was increased with the increment of the inlet liquid temperature when the other conditions were constant different with traditional solar air heater. In case of liquid heating performance, efficiency was decreased with increment of inlet liquid temperature and decrement of solar radiation same as the traditional solar collector for hot water. Total thermal efficiency expressed as the ratio of the useful energy gain of heating mediums(air and liquid) to the incident of solar radiation was decreased with increment of inlet heating temperature and decrement of solar radiation similar with the traditional solar collector. Those tendencies are similar with the results of previous study, thus it can be regarded that the efficiency expressed from the energy balance as in appropriate. Furthermore, from these results it is expected to generalize the evaluation method of the hybrid solar collector and contributing for practical use if additional experiment with more various conditions are conducted.

Keywords: *Solar thermal system, Hybrid solar collector, Air-conditioning, Hot-water supply, Energy saving*

1. Introduction

In the use of solar energy, flat plate solar collector usually has been used for making hot water or heated air. In case of solar water heater, many research was conducted for enhancing the thermal efficiency(S. Sadhishkumar and T. Balusamy, 2014) and these heated water can be used for hot-water supply system in building, heat source for regenerating of liquid desiccant in liquid desiccant dehumidifier system(K. Gommed and G. Grossman, 2007; Mahmut et al, 2015) and so on. In case of solar air heater, it can be used in many field like drying application(M.A. Karim and M.N.A. Hawlader, 2004), air conditioning system(Ali Al-Alili et al., 2004; Zhi Yu et al., 2014) and so on.

But, different with this, study about hybrid solar collector heater that can make both hot water and heated air have been conducted(K.H. Choi et al., 2014; H.W. Choi et al., 2014; H.W. Choi et al., 2015). This collector can be applied for air conditioning system as well as hot water supply system. So, the usage of hybrid solar collector per unit area is being a more than traditional flat plate solar collector. But, efficiency of hybrid solar collector was hard to generalize because of the many factors that effect on the efficiency.

Thus, in this study, the efficiency of hybrid collector was expressed by the energy balance. And the efficiency of the collector was also investigated according to operating and external conditions by using the heat removal factor and the heat loss coefficient calculated from measured values when the air and liquid were heated simultaneously in flat plate solar collector. Furthermore, this paper put the purpose on the confirming of performance of hybrid solar collector when it was heating both air and.

doi:10.18086/swc.2015.10.16 Available at http://proceedings.ises.org

2. Experimental apparatus and method

Hybrid solar collector was made by installing air channel beneath the absorb plate of flat plate solar collector for hot water, so it can make hot water and heated air. Actual feature of hybrid solar collector is shown in Fig. 1. Fins were installed in air chnnel for enhancing the heat transfer rate from absorber to flow air. It has a $2m^2$ absorbing area and installed 33° angle from horizontal and azimuth 171° in Busan, South Korea. Fig. 2 shows the schematics of hybrid solar collector system.

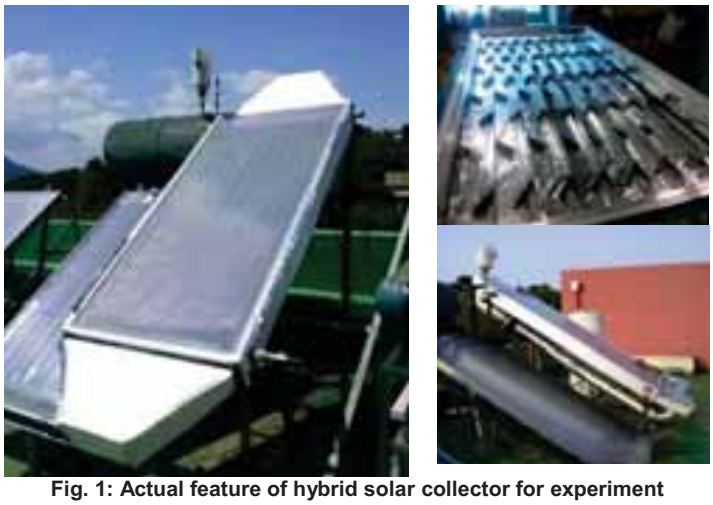

Fig. 1: Actual feature of hybrid solar collector for experiment

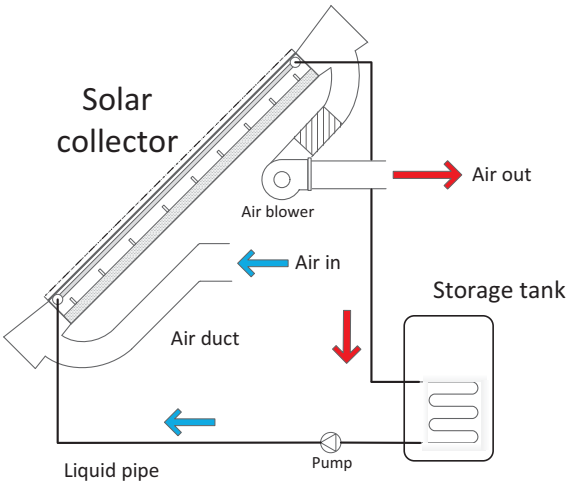

Fig. 2: Schematics of hybrid solar air-water heater system

Experiment was conducted at clear day. Air mass flow rate was changed from 0.02 kg/s to 0.10 kg/s on constant liquid mass flow rate 4 l/min and both air and liquid was heated simultaneously. Outdoor air was used directly as inlet air and T-type thermocouple was installed at lower side, center, upper side, left side and right side of absorbing plate for measuring mean temperature of absorber plate. Temperatures of inlet and outlet air were also measured by T-type thermocouple and liquid temperatures at inlet and outlet were measured by PT-100.

3. Data analysis

In this study, thermal efficiency of collector was defined using energy balance when the air and liquid were heated simultaneously. Useful thermal energy is defined as the heat gain of heating mediums and it also can be expressed by energy input and output as

$$\dot{Q}_u = \dot{Q}_{air} + \dot{Q}_L = \dot{Q}_i - \dot{Q}_o \qquad \text{(eq. 1)}$$

At this time, Q_i and Q_o can be written as equation (2), (3)

$$\dot{Q}_i = G\tau\alpha A_c \quad \text{(eq.2)}$$

$$\dot{Q}_o = U_{L,t}A_c(T_c - T_a) \quad \text{(eq.3)}$$

So, equation (1) can be rewritten as equation (4).

$$\dot{Q}_{air} + \dot{Q}_L = \dot{Q}_i - \dot{Q}_o = G\tau\alpha A_c - U_{L,t}A_c(T_c - T_a) \quad \text{(eq.4)}$$

Overall heat loss coefficient of collector can be written as equation (5) from equation (4).

$$U_{L,t} = \frac{G\tau\alpha A_c - (\dot{Q}_{air} + \dot{Q}_L)}{A_c(T_c - T_a)} = \frac{G\tau\alpha - (q_{air} + q_L)}{T_c - T_a} \quad \text{(eq.5)}$$

Heat gain of liquid can be written as equation (6) from "Hottel-Whillier-Bliss equation"(Duffie and Beckman, 1991).

$$\dot{Q}_L = \dot{m}_L C_{p,L}\left(T_{o,L} - T_{i,L}\right) = F_{R,L}A_c[G\tau\alpha - U_{L,L}\left(T_{i,L} - T_a\right)] \quad \text{(eq.6)}$$

At equation (6), $U_{L,L}$ is defined as heat loss coefficient of liquid side and the heat gain of air is condidered as heat loss of liquid side. This value can be assumed as constant value on the constant air and liquid mass flow rate and temperature difference between inlet air and outdoor air. it can be written as equation (8) from equation (7) if outoor air used as inlet air.

$$\dot{Q}_L = G\tau\alpha A_c - U_{L,L}A_c(T_c - T_a) \quad \text{(eq.7)}$$

$$U_{L,L} = \frac{G\tau\alpha A_c - \dot{Q}_L}{A_c(T_c - T_a)} = \frac{G\tau\alpha - q_L}{T_c - T_a} = f(\dot{m}_{air}) \quad \text{(eq.8)}$$

$U_{L,L}$ is changed by inlet air temperature, air and liquid mass flow rate. But in this experiment, $U_{L,L}$ is considered as a function of air mass flow rate as shown in equation (8) because only outdoor air used for inlet air directly and experiment was conducted on constant liquid mass flow rate. Heat gain of air side can be written as equation (9)

$$\dot{Q}_{air} = \dot{m}_{air}C_{p,air}\left(T_{o,air} - T_{i,air}\right) = \dot{Q}_i - \dot{Q}_o - \dot{Q}_L \quad \text{(eq.9)}$$

Heat gain of air side can be rewritten as equation (10) by substituting the equation (2), (3), and (6) to equation (9).

$$\dot{Q}_{air} = \dot{Q}_i - \dot{Q}_L - \dot{Q}_o = G\tau\alpha A_c - F_{R,L}A_c\left[G\tau\alpha - U_{L,L}\left(T_{i,L} - T_a\right)\right] - U_{L,t}A_c(T_c - T_a) \quad \text{(eq.10)}$$

The maximum heat gain of air side can be obtained when the whole collector surface is at the inlet air temperature. Then, heat removal factor of air side that represent the ratio of heat gain to maximum heat gain can be written as equation (11).

$$F_{R,air} = \frac{\dot{m}_{air} C_{p,air}(T_{o,air} - T_{i,air})}{G\tau\alpha A_c - F_{R,L} A_c [G\tau\alpha - U_{L,L}(T_{i,L} - T_a)] - U_{L,t} A_c (T_{i,air} - T_a)} \quad \text{(eq.11)}$$

So, heat gain of air side can be rewritten as equation (12).

$$\dot{Q}_{air} = F_{R,air} A_c \{G\tau\alpha - F_{R,L}[G\tau\alpha - U_{L,L}(T_{i,L} - T_a)] - U_{L,t}(T_{i,air} - T_a)\} \quad \text{(eq.12)}$$

The thermal efficiency of a collector is defined as ratio of the useful thermal energy to the total incident solar radiation. So, thermal efficiency of liquid side is expressed as equation (13) from equation (6).

$$O_L = \frac{\dot{Q}_L}{G A_c} = \frac{F_{R,L} A_c [G\tau\alpha - U_{L,L}(T_{i,L} - T_a)]}{G A_c} = F_{R,L}\tau\alpha - F_{R,L} U_{L,L} \frac{(T_{i,L} - T_a)}{G} \quad \text{(eq.13)}$$

Thermal efficiency of air side can be written as equation (14) from equation (12).

$$O_{air} = \frac{\dot{Q}_{air}}{G A_c} = \frac{F_{R,air} A_c \{G\tau\alpha - F_{R,L}[G\tau\alpha - U_{L,L}(T_{i,L} - T_a)] - U_{L,t}(T_{i,air} - T_a)\}}{G A_c} \quad \text{(eq.14)}$$

It can be rewritten as equation (15).

$$O_{air} = F_{R,air} \left\{ \tau\alpha (1 - F_{R,L}) + \frac{[F_{R,L} U_{L,L}(T_{i,L} - T_a) - U_{L,t}(T_{i,air} - T_a)]}{G} \right\} \quad \text{(eq.15)}$$

In the equation (15), relation of inlet heating medium temperature, ambient temperature, solar radiation and thermal efficiency of air side is derived. In this equation, η_{air} will be increased if inlet liquid temperature is increased or solar radiation is decreased If the inlet liquid temeprature is larger than ambient temperature. And if inelt air and ambient temperature is same, η_{air} will be change with $(T_{i,L} - T_a)/G$ to linear on the constant air and liquid mass flow rate. Total thermal efficiency of collector can be written as the sum of the thermal efficiency of air and liquid side. It can be expressed as follows:

$$O_t = \frac{\dot{Q}_L + \dot{Q}_{air}}{G A_c} = O_L + O_{air} = A - B\left(\frac{T_{i,L} - T_a}{G}\right) - C\left(\frac{T_{i,air} - T_a}{G}\right) \quad \text{(eq.16)}$$

Where,

$A = (F_{R,air} + F_{R,L} - F_{R,air} F_{R,L})\tau\alpha$

$B = F_{R,L}(1 - F_{R,air}) U_{L,L}$

$C = F_{R,air} U_{L,t}$

Therefore, total thermal efficiency of collector is written as heat removal factor and heat loss coefficient of two heating medium with operating conditions. Then if the heat removal factor and heat loss coefficient of each heating mediums can be obtained from experiment, total thermal efficiency or thermal efficiency of each heating medium is expected to predict. And also, A, B and C can be assumed as constant value on the constant temperature difference between inlet air and outdoor air, air and liquid mass flow rate.

4. Results and discussion

In this experiment, temperatures of two heating mediums and collector was measured with change of air mass flow rate on the constant liquid mass flow rate at noon that was shown similar solar radiation. Fig. 3 shows the measured temperatures of air, liquid and absorbing plate with air mass flow rate.

Outlet air temperature was decreased with increment of air mass flow rate and also temperature difference between inlet and outlet liquid was decreased with increment of air mass flow rate. It was considered as a result of the increment of heat transfer from liquid pipe to flow air with incremnet of air mass flow rate.

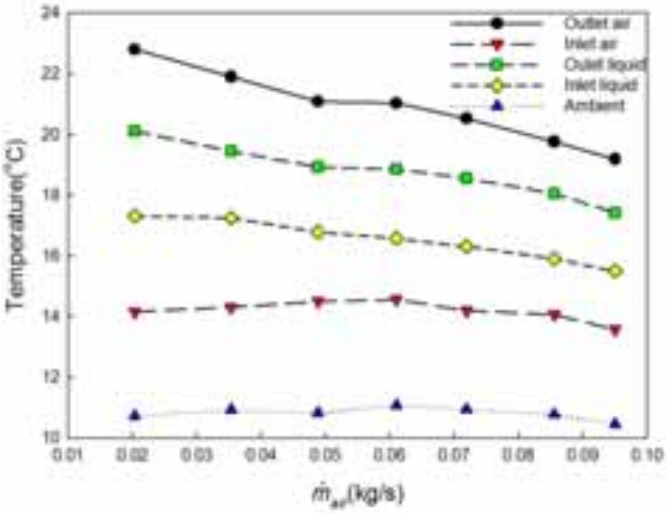

Fig. 3: Temperature profile when the air and liquid were heated simultaneously

Heat gain of each heating medium with solar intensity was shown in Fig. 4. Heat gain of liquid was higher than air on the low air mass flow rate. But it was decreased and the heat gain of air was increased with increment of air mass flow rate due to the increment of heat transfer from liquid pipe to flow air. Total heat gain in hybrid solar collector was increased with increment of air mass flow rate and it means extra heat gain was occured in addition to heat transfer from liquid to air with increment of air mass flow rate. it considered as a result of the heat transfer enhancement from absorbing plate to flow air with increment of air mass flow rate as well as from liquid pipe.

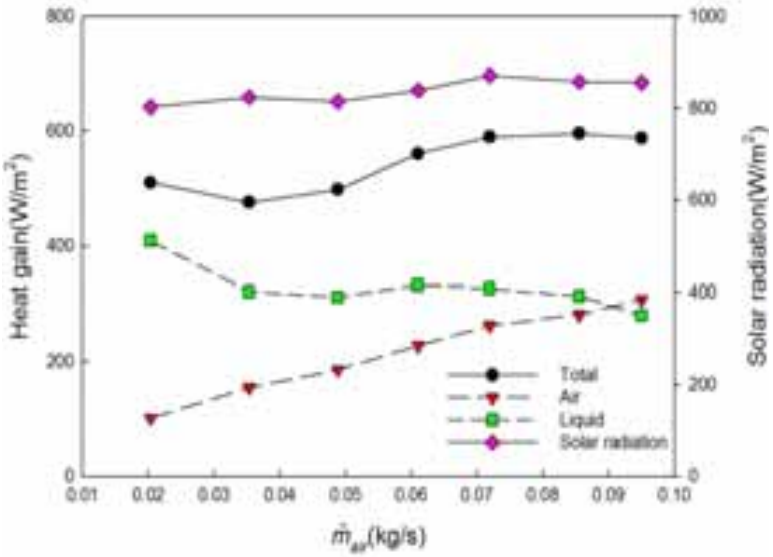

Fig. 4: Useful energy of collector and solar radiation

Heat loss coefficient of collector calculated from equation (5), (8) using measured value was shown in Fig. 5. Heat loss coefficient of liquid side was increased with increment of air mass flow rate. This result signifies that the heat transfer from liquid pipe to flow air was enhanced with increment of air mass flow rate. Whereas, total heat loss coefficient of collector was slightly decreased with increment of air mass flow rate because of the increment of heat transfer from liquid pipe and absorbing plate to flow air as previously stated.

Fig. 6 shows heat removal factors of air and liquid side. Heat removal factor of air side was increased with increment of air mass flow rate. As previously shown, this tendency is considered as a result of heat transfer increment from absorbing plate and liquid pipe to flow air with increment of air mass flow rate and by this, heat removal factor of liquid side was decreased with increment of air mass flow rate.

At this time, heat removal factor and heat loss coefficient can be expressed as a function of air mass flow rate from the experiment result as shown in Fig. 5, 6. In other words, heat removal factor and heat loss coefficient of

collector at specific air mass flow rate can be predicted when the outdoor air was used as inlet air on constan liquid mass flow rate. Therefore, total thermal efficiency of hybrid solar collector can be expressed as a function of air mass flow rate, inlet temperature of liquid, ambient temperature and solar radiation.

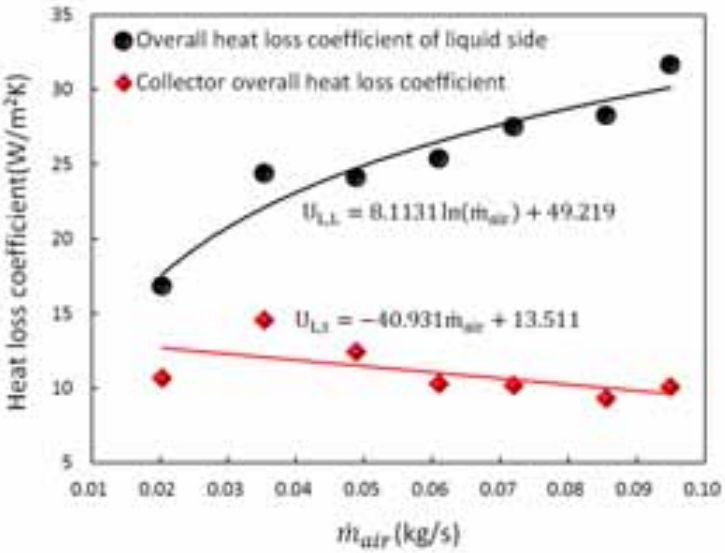

Fig. 5: Overall heat loss coefficient of collector and liquid side

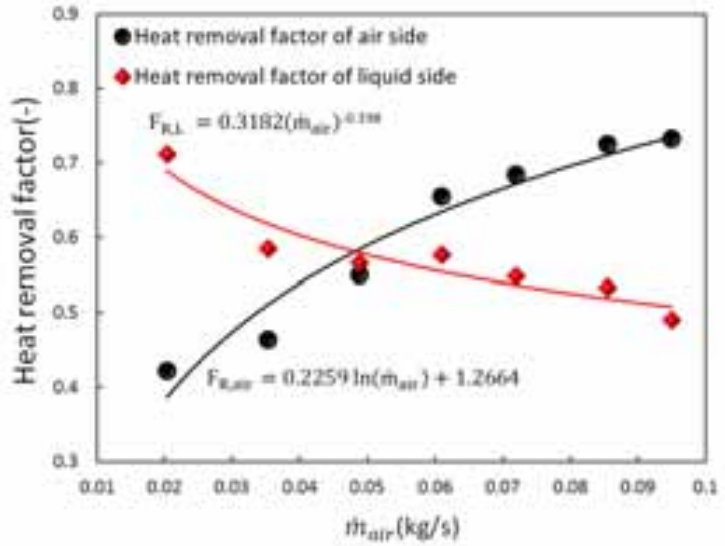

Fig. 6: Heat removal factor of air and liquid side

Namely, thermal efficiency can be predicted with respect to each operation and external condition using heat removal factor and heat loss coefficient obtained from experiment. Fig. 7 shows the thermal efficiency of air and liquid side with $(T_{i,L} - T_a)/\mathrm{G}$. using equation (13), (15). The efficiency of air was changed to linear because the temperature difference between inlet air and ambient was as small as ignored. These tendency was included in equation (15). The higher slope angle of air efficiency curve means that the higher efficiency increase of air side when the inlet liquid temperature was increased when the other conditions are same and it was increased with increment of air mass flow rate.

In case of the thermal efficiency of liquid, it was shown the maximum thermal efficiency about 0.6 while the air was also heated and it was decreased with increment of inlet air temperature, air mass flow rate and decrement of solar radiation. It is similar with tranditional flat plate solar collector for hot water but, decline of efficiency was higher than traditional flat-plate solar collector for hot water because heat gain of flow air was also considered as a heat loss of liquid.

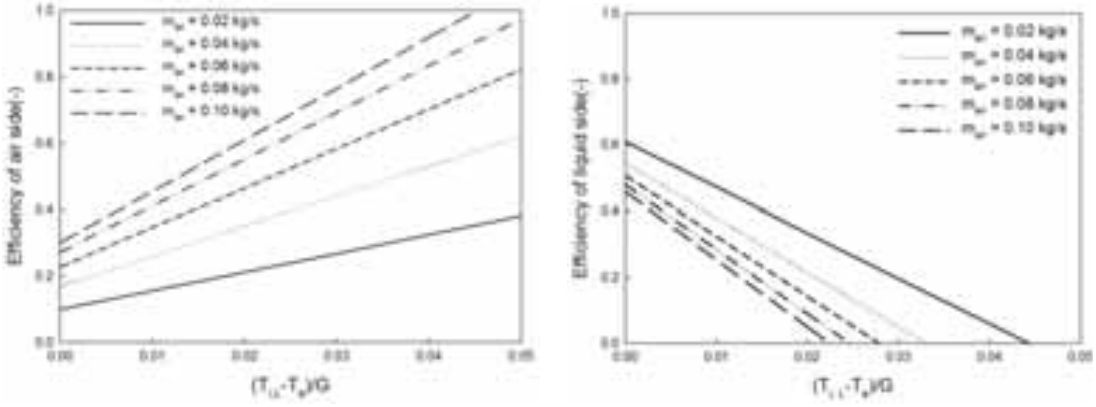

Fig. 7: Prediction of the thermal efficiency of hybrid solar collector; (a) air side (b) liquid side

Fig. 8 shows total thermal efficiency of hybrid solar collector including heat gain of air and liquid. Total thermal efficiency was increased with increment of air mass flow rate, solar radiation and decrement of temperature different between inlet liquid and ambient. Maximum total thermal efficiency of collector expressed as A in equation (16) was shown from 0.710 to 0.759 with air mass flow rate. And also, heat loss coefficient of liquid side expressed as B in equation (16) shown from 4.974 to 8.151 and it is decreased with increment of air mass flow rate.

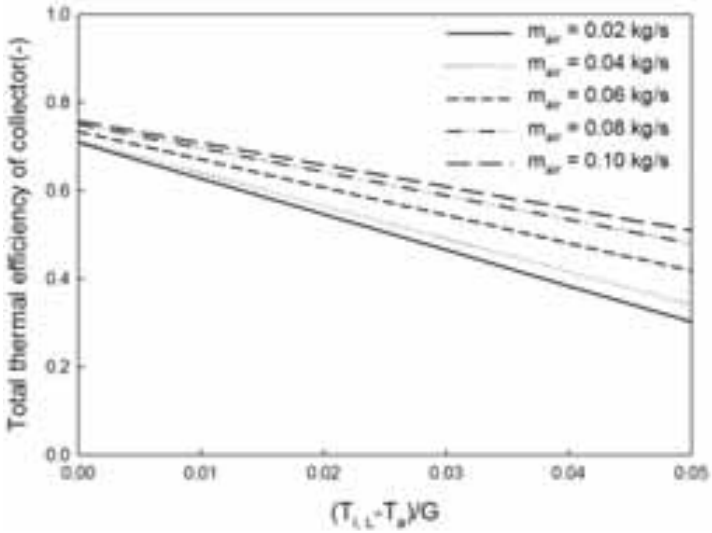

Fig. 8: Prediction of total thermal efficiency of collector

5. Conclusions

This study conducted a performance evaluation when the air and liquid were heated simultaneously in flat plate solar collector and the efficiency of hybrid solar collector influced by many factors was confirmed using the equation expressed by energy balance.

As a result, efficiency of the air side was increased with the increment of the inlet liquid temperature when the other conditions were constant and the efficiency of liquid side was decreased with increment of inlet liquid temperature and decrement of solar radiation. Total thermal efficiency of collector was decreased with increment of inlet air and liquid temperature and decrement of solar radiation similar with the traditional solar collector. From these results, the tendency of efficiency change confirmed using expressed equationit considered as an appropriate and it is expected to generalize the evaluation method of the flat plat solar collector that heating air and liquid simultaneously if additional experiment with more various conditions are conducted.

6. References

S. Sadhishkumar, T. Balusamy. Performance improvement in solar water heating systems—A review. Renewable and Sustainable Energy Reviews 2014; 37:191-198

K. Gommed, G. Grossman. Experimental investigation of a liquid desiccant system for solar cooling and dehumidification. Solar Energy 2007; 81(1):131-138

Mahmut Sami Buker, Saffa B. Riffat. Recent development in solar assisted liquid desiccant evaporative cooling technology-A review. Energy and buildings 2015; 96(1): 95-108

M.A. Karim, M.N.A. Hawlader. Development of solar air collectors for drying applications. Energy Conversion and Management 2004; 45(3):329-344.

Ali Al-Alili, Yunho Hwang, Reinhard Radermacher. Review of solar thermal air conditioning technologies. International Journal of Refrigeration 2014; 39:4-22.

Zhi Yu, Jie Ji, Wu Wang, Guiqiang Li, Jingyong Cai, Haifei Chen, Experiment and prediction of hybrid solar air heating system applied on a solar demonstration building. Energy and Buildings 2014; 78:59-65

Choi K. H, Yoon. J. I, Son. C. H, Choi. H. W and Kim. B. A, Experimental Study for Thermal Performance of Hybrid Air-Water Heater Using Solar Energy during Heating Medium Working Simultaneously, Journal of the Korean Solar Energy Society, Vol. 34, No. 3, pp. 115-121, 2014

Choi. H. W, Yoon. J. I, Son. C. H and Choi. K. H, Performance Estimation of Hybrid Solar Air-Water Heater on Single Working of Heating Medium, Journal of the Korean Solar Energy Society, Vol.34, No.6, pp. 49-56, 2014.

Choi H.W, Fatkhur R, Yoon J.I, Son C.H, Choi K.H, A Study on Thermal Storage Performance and Characteristics of Daily Operation of a Hybrid Solar Air-Water Heater, Journal of the Korean Solar Energy Society, Vol.35, No.3, pp. 73-79, 2015.

MEGlobal, Ethylene Glycol Product Guide, http://www.meglobal.biz/media/product_guides/MEGlobal_MEG .pdf, Accessed 7, Sep, 2015

Duffie JA, Beckman WA. Solar engineering of thermal processes, New york: JOHN WILEY & SONS, INC; 1991.

Ebru Kavak Akpinar, Fatih Koçyiğit. Experimental investigation of thermal performance of solar air heater having different obstacles on absorber plates. International Communications in Heat and Mass Transfer 2010; 37(4):416-421.

A.P. Omojaro, L.B.Y. Aldabbagh. Experimental performance of single and double pass solar air heater with fins and steel wire mesh as absorber. Applied Energy 2010; 87(12):3759-3765

Conference Proceedings

Solar World Congress 2015
Daegu, Korea, 08 – 12 November 2015

Solar and heat pump systems, analysis of several cases in Russia

Andreu Moià-Pol[1], Víctor Martínez-Moll[1], Julian David Hertel[1] ,Rashid Nazmitdinov[2,1], Pavel Gladyshev[3]

[1]University of Balearic Islands, Physics department, P. Mallorca (Spain)

[2] BLTP, Joint Institute for Nuclear Research, 141980 Dubna, (Russian Federation)

[3] Dubna University, Dubna, Moscow Region (Russian Federation)

Abstract

Russia has a few renewable energy facilities in the buildings. In the buildings, the main source of the energy is provided by Russian fossil fuel resources. Based on the EU experience, Russia has started own research activity in the field of renewable energies in order to reduce the energy consumption. The combination of solar thermal with heat pump systems (SHP) is one of the promising systems that can provide the renewable energy in extreme weather conditions. Solar heating with a heat pump system for buildings has been designed to achieve different values of the fraction of a primary energy saving using the Flat Plate Collectors (FPC) for Solar Thermal (ST) and other supply energies like solar photovoltaic (PV) or wind technology, and having the higher efficiency of the system with net zero energy in thermal production.

Keywords: *Solar Thermal, Heat Pump, Photovoltaic, geothermal, combisystems*

1. Introduction

The combination of solar-thermal collectors and heat pumps provides interesting possibilities for innovative and energy efficient heating systems, with a high fraction of solar energy. Despite its high cost, these systems are gaining more and more importance due to the rising cost of the limited fossil resources. The Task 44 concluded in 2012 that it is possible: i) make up 87% of renewable energy share combining solar thermal and photovoltaic energy supply; ii) or to reach about 90% of renewable energies with geothermal resources.

This study analyzes one configuration of solar systems with a new water-to-water heat pump, in different cities of the Russian Federation, meant to cover all space heating and domestic hot water demand with renewable energy, solar and wind according to the weather conditions. PV has been a very interesting way to produce electricity and thermal energy if we combine this with heat pumps(vapor compression cycle). The final price for households in Russia varies from night tariff 3 c€/kWh to day tariff 9,6 c€/kWh in 2014 (without taxes), and the PV cost between 5 to 10 c€/kWh according to the Russian average radiation and supposing 20 years of duration. PV has not arrived to grid parity in Russia like in other northern countries of the EU. Counting that a modern compression machine has a 3-5 Coefficient of Performances (COP), and according to the Directive 2010/31/EU it's considered like another kind of renewable energy, the actual cost of thermal production with heat pumps is 1-4 c€/kWh depending on the working temperatures, refrigerant and quality of the machine (ASHRAE).

The resulting thermal energy costs obtained for FPC for DHW, simplified cost are from 3 to 7 c€/kWh depending on the collector type and the working temperature in Russia and solar radiation, in Russia ranges from 700-1500 kWh/m^2. The cost of the natural gas in Russia (it's one of the largest producers in the World) it's between 1,2-1,4 c€/kWh, very low compared with the ST and even with the Heat Pump. For the areas where there is gas pipe the solar thermal is only competitive for DHW not for heating, in this case it is not competitive yet, so we have to add the environment cost or the increasing of the gas prices. The fossil fuels are growing more than 0% annually, and the gas for households has grown more than 16% the last years (Gazprom), it's quite sure they won't reduce the price in the future.

doi:10.18086/swc.2015.10.17 Available at http://proceedings.ises.org

Tab. 1: Results of one year simulation different Russian cities for domestic hot water

Location	Latitude	Solar Radiation	FPC. Working temperature 45ºC-75ºC		SHP. Working temperature 0ºC-75ºC	
			Solar Efficiency	Solar Fraction	Solar Efficiency	Solar Fraction
Vladivostok	43º	1.320	72%	21%	71%	83%
Irkutsk	52º	1.126	63%	28%	65%	80%
Samara	53º	1.119	64%	30%	65%	77%
Moscow	55º	973	63%	32%	66%	73%
Ekaterinburg	56º	1.059	52%	23%	66%	76%
Krasnoyarsk	56º	1.045	55%	16%	64%	75%
Dubna	57º	1140	59%	26%	66%	69%
Saint-Petersburg	59º	894	47%	30%	67%	69%
Yakutsk	62º	1.086	44%	28%	58%	61%
Average		**1.085**	**58%**	**26%**	**65%**	**74%**

Recently, reductions in electric PV costs and mature technology of air-to-water and water-to-water heat pump have provided a new model: solar-electric assisted heat pump. This system comes with fewer drawbacks than solar thermal energy, a smaller price tag for residential applications. Nevertheless, the best system will be a combination of both. The development of modern net zero-energy buildings (NZEB) became possible not only through the progress made in new renewable energy and construction technologies and techniques, but it has also been significantly improved by the combination of all the techniques and advanced combisystems.

The Geothermal heat pump systems have only just begun to penetrate the Russian market in the opposite of countries with similar weather conditions (Sweden, Denmark, Germany,..). Until now there the conventional sources where most known. The maximum values of COP are 4.24 in the southern regions of Russia, and the minimum values of, correspondingly, 2.73 in the north.(Vassiliev and Gornov 2010). For this system they need a vertical borehole at least 40 meters deep and horizontal of 400 m. of length, and not always there are the correct conditions, space or environment to do it, with a big initial investment. From previous studies it has been studied that geothermal can have a similar efficiency like the combisystem with solar thermal and heat pumps.

2. Description of the system

The auxiliary energy is coming from a heat pump (water-to-water system with inverter control) usually used for geothermal systems that can work with electricity from the grid or the PV system. A high efficiency heat pump in the range of 5 to 20 kW has been used to cover the energy needs of households with low energy demand occupied all the year.

Simulating the whole year system we reach different solar fractions depending on the efficiency of the system, the working temperature of the storage system, and the different COP of the heat pump. This system can operate with outside temperatures from -20ºC to 20ºC, with a high solar fraction and with a high efficiency of the solar collector. The storage operating temperature has to change during the year according to the external temperature and the solar radiation, in order to obtain a higher efficiency from the collector, and to work with the maximum efficiency of the heat pump. Only in summer or spring the solar energy can be used directly for thermal production. The FPC works in serial with the heat pump during the cold days and parallel during hot days, usually it will be in the spring and summer. Finally we will use the cooling of the evaporator to increase the PV efficiency. This system can have a very high performance coefficient and adapt its efficiency for whichever conditions. It is ideal for both cold and mild climates.

The typical configuration of the solar thermal systems is with a fixed working temperature, near to 60ºC. But in the task 44 a lot of cases have been studied with a heat pump working temperature lower than 60ºC, due to the fact that this high efficiency system can supply the rest of the energy with electricity. Most of the geothermal heat pumps are working with a maximum temperature of 20ºC in the evaporator, and they can arrive to 60ºC in the condensator to cover all the thermal energy demand. The southern countries we could use unglazed collectors and air-water systems(Moià-Pol et Alt 2012) but in the northern countries, where there are some months with a lot of hours below 0ºC, we need to work at temperatures below 25ºC (Moià-Pol

et Alt 2014) and work with high efficient FPC, specially designed for extreme conditions. There are some manufactures that providea good quality water-to-water heat pump, with high efficiency, working with an inverter compressor. The studied one has a maximum heating power of 13 kW and a nominal COP of 3,56 for heating temperatures of 35ºC-45ºC, and evaporating from -5ºC to 10ºC, with a refrigerant R-410A.

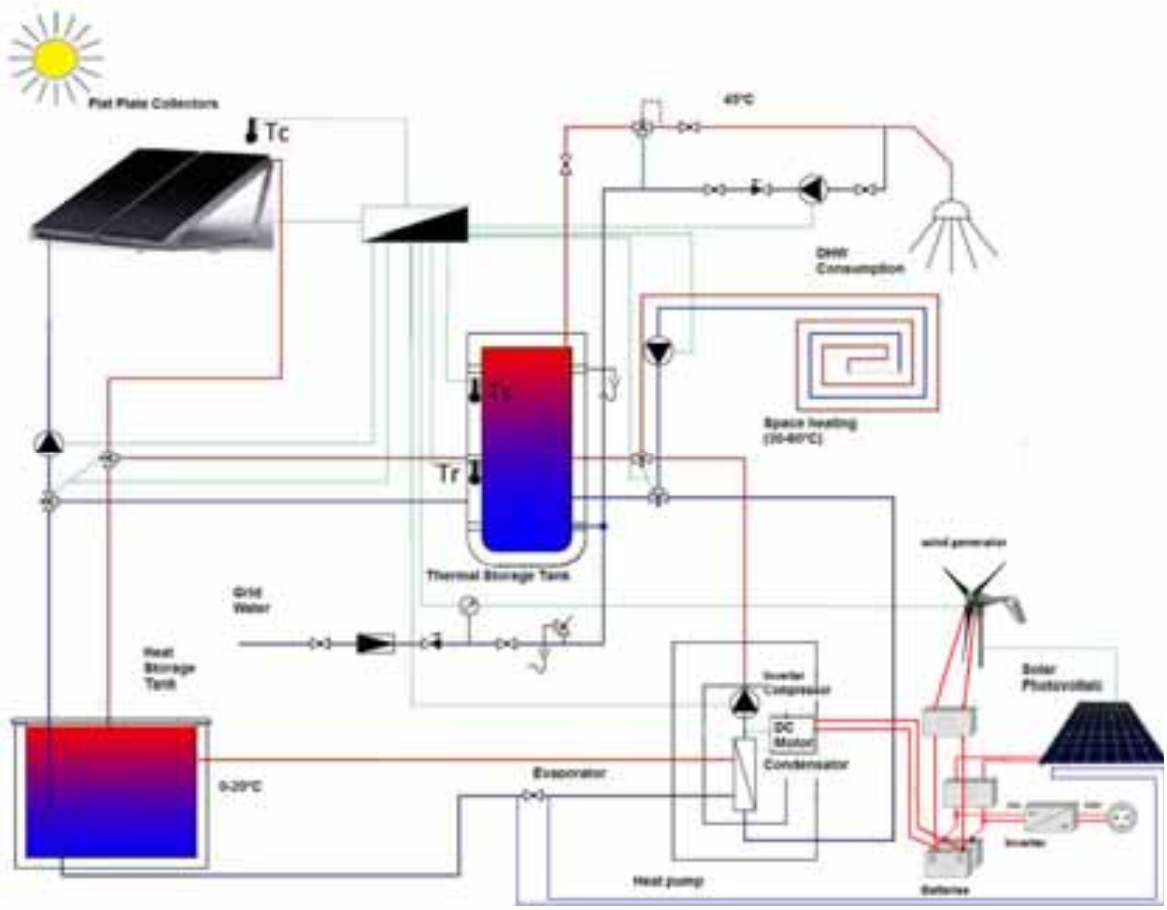

Fig. 1: Figure of the Solar Thermal and PV Heat Pump system for DHW and Space Heating

The Photovoltaic system has been a standard one, the panels with polycrystalline silicon 260Wp, and the inverter with an nominal efficiency of 95,5%, with a 95% of cleanliness and 2% of losses in the cables.

3. Simulation and Results

We have studied different houses within the Moscow region, and developed a simulation program from the conclusions and detailed analysis from other studies (c) using the typical meteorological year (TMY). In this second study, we have considered the PV for self-consumption, with small electrical storage with batteries; because the net metering contract with the electrical company doesn't exist yet in Russia nor in most of the EU countries.

ST Collector Efficiency $\eta = 0{,}807 - 3{,}075(T_m-T_a)/G - 0{,}022((T_m-T_a)/G)^2$ (eq. 1)(e)

Unitary Energy Consumption Heat Pump $kWe = 1{,}20122-0{,}0400633Ta+0{,}0010877Ta^2$ (eq. 2)(d)

PV Efficiency $\eta = Ta - 0{,}036G$ (eq. 3)

For the considered model mentioned above, the solar thermal energy has priority in front of other renewable energy sources, and reduces the overheating in the solar panels.

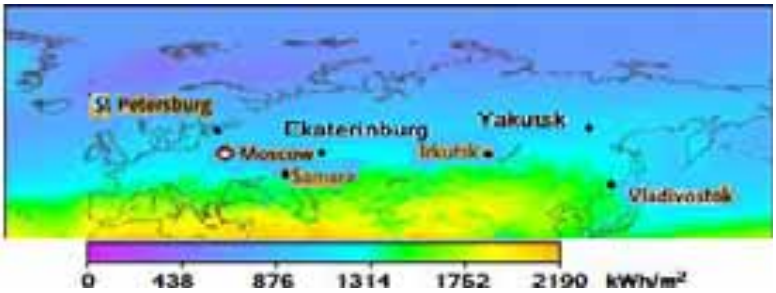

Fig. 2: Annual Solar Radiation per sqm in Russia. Source; Mattihas Loster 2006

Eight locations have been studied consisting of a constant hot water demand for 4 people during all the year. The typical residence considered is a cottage of 160 m² heating space for the eastern regions and a house with 80 m^2 heating space for the western regions, for the new emerging upper middle class. The studied houses have two floors, according to that the residence has been modeled into two zones: a conditioned zone representing a 50% of the total floor area during the day and another conditioned zone during the night. It has been supposed that it's a good quality house, according to sustainability criteria (insulation, orientation,..), when we are using renewable energies we need a low demand to make the system cheaper, with an efficient ventilation system. It has been considered the Russian law 2003 for the insulation (according to building regulations and rules 23-02-2003).

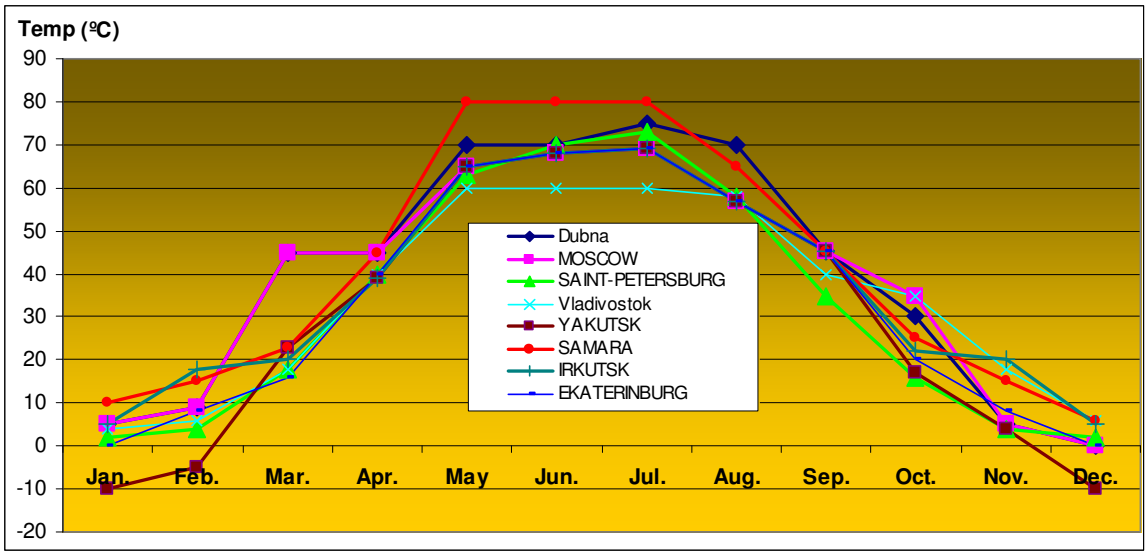

Fig. 3: Figure of the averaged solar monthly working temperature (ºC) for Russian Cities during a typical year

In the northern locations the annual maximum solar energy with the medium temperature of the solar collector between 25 and 30ºC (Moià-Pol et Alt 2014). In figure 3 we can see the considered working temperatures, in order to have a minimum efficiency of the 60% for each month, except for Yakutsk where we have -40ºC during December and January, and in this case we have taken the minimum temperature that can work the heat pump, -10ºC with an efficiency of the FPC of a 40%. For temperatures lower than 25ºC the efficiency of the FPC is higher but the energy requirements are lower and, therefore there are many hours with excess energy for a given storage volume. Each location has a different surface, according to the annual thermal necessities as to achieve a similar solar fraction. When the outside temperatures are rising the thermal energy demand is decreasing and during several months there is enough energy to cover the thermal energy demand so it's not necessary to work at the maximum efficiency point. We can work at higher temperatures to avoid overheating and stagnation problems. The system can only be solar thermal between 40 to 70ºC.

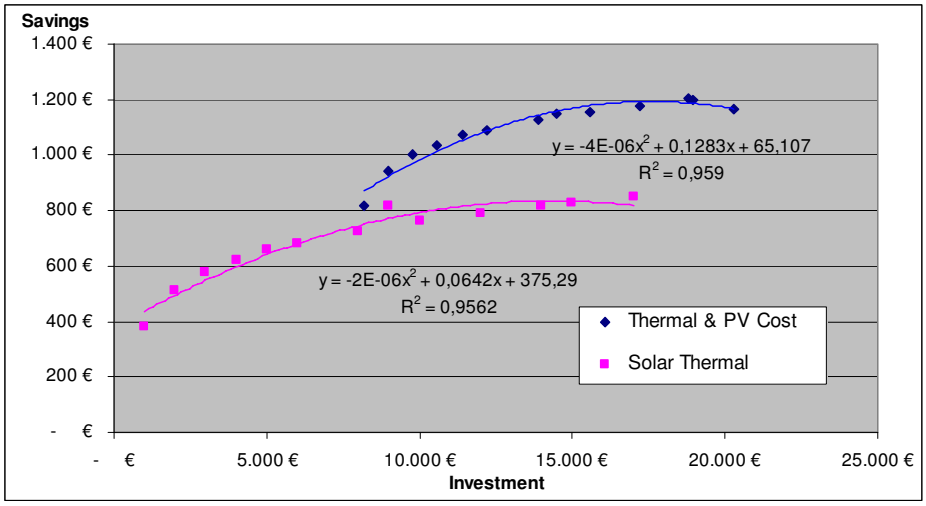

Fig. 4: Figure of the savings vs. investment with PV and ST for Moscow Region.

In order to avoid having a low averaged efficiency we should look for the optimal point of solar panels to accomplish the maximum solar energy gains without overheating. The medium temperature will be usually in winter lower than 20 ºC and in spring and autumn lower than 50ºC, in summer the FPC are working with more than 60 ºC in all the locations. When the medium temperature of the collectors would be higher than 45ºC we will make a direct heat transfer to the DHW or heating system, in parallel with the heat pump. The system according to have a high solar thermal fraction will have high temperatures at summer, with some overheating and stagnation problems.

According to the energy cost-efficiency of the PV and the FPC, we have studied different scenarios to find the optimal point of the system, without taking into account the heat pump and the storage of the buffer tank. The lower prices of the PV could imply to use 100% of this technology instead of using solar thermal, but with a detailed analysis of all the system, according to the COP, and thermal demand every month we can see the optimal point is between 12 and 30 m^2 in Moscow's region, depending on the electric tariffs, thermal demand and climate conditions.

a. Resume of the results.

Comparing all the locations, we could arrive to a similar efficiency for the solar thermal panels, with high renewable thermal fraction (heat pump + solar thermal), combined with PV, this can be a solution for supplying the 100% of the thermal energy demand.

Increasing the PV system we could cover the rest of the energy demand of the household, but this isn't the aim of this study. Combining with wind power, we can optimize the system in some locations with extreme conditions. The heat pump manufactures have made a big effort the last years in order to arrive to high efficiency systems, and the market of geothermal systems has increased. The heat pump with solar panels working in low temperatures could open a big market in locations with low radiation; even if they have cheap energy prices, like Russia.

Tab. 2: Results of one year simulation in four locations for DHW and Heating demand for a house of 160 m^2.

Location	Thermal Demand(kWh)	Solar Energy kWh/m^2	Electric Energy kWhe	ST m^2	Solar Thermal Fraction	Average FPC Efficiency	Power of the PV (Wp)
VLADIVOSTOK (L43)	13900	86,9	4614	13	83%	71%	3,3
MOSCOW (L55)	14690	91,8	5185	20	65%	64%	5,2
DUBNA (L57)	11875	148,4	3406	18	68%	64%	3,0
SAINT-PETERSBURG(L59)	11548	72,2	4100	24	69%	67%	4,9

We can see at the table that the size of the system depends on the solar radiation and the weather conditions. At continental climates with latitudes lower 55º, it gives us systems bigger than the conclusions of the Task

44, with 12 m^2 and storage of minimum of 1 m^3, in our case it's 13-18 m^2 with an storage minimum of 1,25 m^3.

Tab. 3: Results of one year simulation in five locations for DHW and Heating demand for a house of 80 m^2.

Location	Thermal Demand(kW)	Solar Energy kWh/m^2	Electric Energy kWhe	ST m^2	Solar Thermal Fraction	Average FPC Efficiency	Power of the PV (Wp)
IRKUTSK (L52)	8706	108,8	2579	17	78%	65%	2,6
SAMARA (L53)	10017	125,2	3221	18	74%	65%	2,9
MOSCOW(L55)	6449	40,3	1600	14	73%	66%	2,1
EKATERINBURG(L56)	10170	127,1	4562	18	73%	66%	4,3
KRASNOYARSK (L56)	10164	127,1	3090	15	75%	64%	3,0
YAKUTSK (L62)	23587	294,8	5863	24	60%	55%	5,5

At Boreal or Polar Climates or latitudes higher than 55º, the initial dimension of the system is very big, we will need a big investment for houses of 160 m^2, at this latitudes for smaller houses we can compare with the results of the Task 44. Other systems could be studied with seasonal storage, with water or chemical storage, and other technologies like wind turbines or hybrid geothermal heat pumps. Other scenarios with cooling demand will have to be studied in order to improve the system, and increase the PV system. Absorption machines with new refrigerants could be developed in order to be able to have solar cooling systems with competitive prices, but at this moment it's cheaper to use compression machines.

Actually in the market there are good geothermal heat pumps, and combisystems with air-to-water systems, but not yet a combination of all of them. This study only wants to make a first approach of these systems in Russia, it will be needed to analyze more in detail for each location, developing new algorithms to study the seasonal storage and make a test laboratory of this new system in a Russian research Institute. The results will change every year according to the prices of the devices and the energy cost.

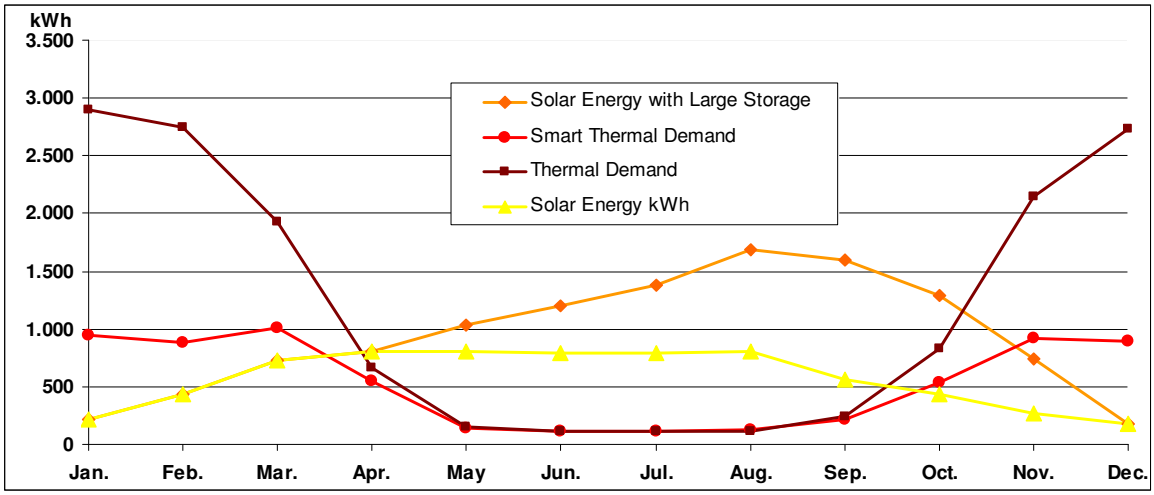

Fig. 5: Figure annual Thermal Demand and Solar Thermal production in Moscow Region

From figure 5, we see a normal thermal demand, an intelligent demand, with control temperatures and with timetable. We can see also with a solar thermal fraction of the 73% there are 5 months with overheating, that we can have stagnation problems. There are some parameters to be optimized for arrive to a high ST fraction, like the available volume in order to have a big buffer tank and arrive to have a seasonal storage, or share the solar thermal energy the months that we don't use to district heating systems, very common in the Russian cities.

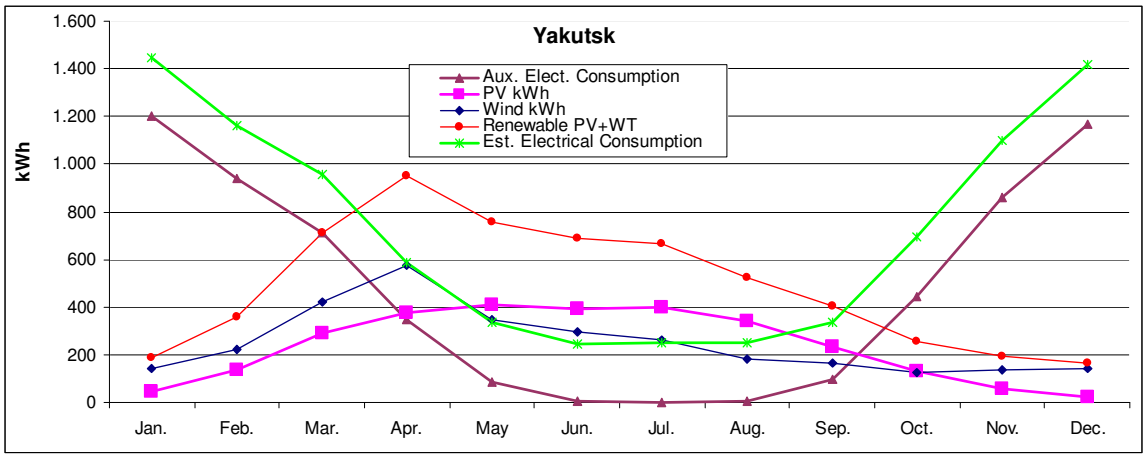

Fig. 5: Figure annual Electric production vs. demand, using PV and Wind Turbine in Yakutsk

In some cities with low solar radiation in winter, where they have some months with an average speed of wind up to 3 m/s. We have studied Yakutsk, Ikurtsk and Ekaterinburg where the wind energy has been simulated that could provide a wind turbine, working with 10% of the equivalent time. This could reduce the surface of the PV system and make more constant the renewable fraction every month, but actually the price of the wind power energy it's more expensive than the PV systems, when we have less than 20% of the equivalent hours working, and we have to add other problems, like noise and structure cost. The PV and the wind market for households also have to be analyzed for the government authorities, in order to allow net metering to avoid usage of batteries in this system, as we get closer to grid parity in Russia every year.

When we are working to NZEB we will need a big surface for the solar thermal and photovoltaic panels that some constructions, due to urban models, don't have at hand. In these study no one of the cases the surface of these systems it's more than the house surface. These parameters have to be included in future studies, in order to have the best solution for each case, when we have vertical constructions. Actually some of these systems have already been studied in the Task 53 - New Generation Solar Cooling and Heating Systems (PV or Solar Thermally Driven Systems).

Tab. 4: Comparing cost of the system vs. Geothermal in Moscow Region

	Estimated cost		**Estimated cost**
Heat Pump	6.000 €	Heat Pump	6.000 €
Solar Thermal + Pipes	8.500 €	Borehole	12.000 €
Thermal Storage Tanks	5.000 €	Pipes	7.400 €
PV System	3.600 €	PV System	6.000 €
Total	**23.100€**		**31.400 €**

There are some heat pump manufacturers that sell hybrid systems, geothermal and air for heating applications, in order to reduce the initial cost of the borehole and piping system. This could also be analyzed in future studies, adding solar thermal fraction, and finding the optimal point. In table 3 we can see that the estimated cost of the proposed system can be 30% cheaper than a conventional geothermal with close loop, but in the second case we can have excess of electricity production. Both systems, if they are designed during the construction project, could be cheaper and have fewer cost, the piping and thermal storage tank could be at the basement of the building with small over cost.

The savings of these systems are about 100% of the thermal energy demand. That means pay-back between 10-20 years, depending on the energy cost. If we compare this with other systems, like hydrogen fuel-cells, there are two times more expensive (40.000 €-60.000 €) and they need electricity for work, with efficiency lower than 50%.

Another advantage of these systems is that they can provide also cooling for the house during the summer, and saving investments of another system.

This system will be installed in Palma and in Dubna, to have real testing results, improve the simulation program, algorithms and find new technologies, materials and systems to have the optimal system for the cold countries will be able to have the same possibilities to arrive to Net Zero Energy Buildings.

4. Conclusions

FPC and PV with heat pump systems are a good solution for family households in Russia, both technologies are necessary in order to arrive to the future scenarios of zero emissions and net-zero energy building, and cover all the thermal demand. The combination FPC and PV in one planar construction is possible. Using in this case a semi-transparent PV not only reduces the overall cost of FPC and PV, but ensure the optimal ratio of generated heat and electrical energy. In the future, as a semi-transparent PV can be used hybrid organic-inorganic solar cells. Net Zero thermal Energy Building are in Europe a technical and economic reality, with the expected future increase of the fossil fuel price and the reduction of the alternative technology costs. This new combisystems opens new options to cover all the energy demand of the houses with an optimized mix, which benefits from the synergies of the different technologies.

Other combinations, like geothermal with solar thermal or seasonal storage could be analyzed in future studies, according to the results of the real test.

ACKNOWLEDGEMENTS. The authors acknowledge the financial support from Russian Foundation for Basic Research, grant No. 14-43-03544 and Programa Pont “La Caixa” per a grups de recerca de la UIB.

5. References

1999 ASHRAE Handbook. HVAC Application. Chapter 31. Energy Resources, American Society of Heating, Refrigeration, and Air-Conditioning Engineers, Inc.

Andreu Moià Pol, Víctor Martínez Moll, Ramon Pujol Nadal and Rashid Nazmitdinov. Proceedings of the Eurosun 2014, .

Andreu Moià Pol, Víctor Martínez Moll, Miquel Alomar Barceló, Ramon Pujol Nadal. Solar and heat pump systems. An analysis of several combinations in Mediterranean areas. Proceedings of the Eurosun 2012, Rijeka, Croatia.

Daikin, catalogue 2014.

Gazprom. Investor Strategy Day 2012

GREENIUS. Task 33. Jürgen Dersch, Volker Quaschning 2003. www.greenius.net

Grigoriy Vassiliev, Victor Gornov. Geothermal Heat Pump Systems Efficiency in Russia. Proceedings World Geothermal Congress 2010. Bali, Indonesia, 25-29 April 2010

http://www.iea-shc.org/task44 & http://task53.iea-shc.org/

http://www.globalpropertyguide.com

Jean-Christophe Hadorn, A new IEA SHC Task 44 & HPP Annex And analysis of several

combinations for a low energy house. Proceedings of the EuroSun 2010, Graz, Austria.

TISUN. Catalogue 2014.

Conference Proceedings

Solar World Congress 2015
Daegu, Korea, 08 – 12 November 2015

THE LIFE CYCLE COST OF STANDALONE SOLAR AIR-WATER HEAT PUMPS FOR AUSTRALIAN HOMES

Gazinga Abdullah[1], Wasim Saman[2], Martin Belusko[3], David Whaley[4]

School of Engineering, University of South Australia, 5095, Mawson Lakes, Australia

Abstract:

To combat increasing electricity prices due to the high operating costs of conventional reverse cycle air-air-heat pumps (RC-AA-HP), they can be powered by standalone PV systems as a radical demand side energy management solution. However, the heavy power consumption of their compressors necessitates very large and expensive standalone photovoltaic (PV) systems. Alternatively, reversible air-water heat pumps (RC-AW-HP) are integrated with thermal storage units, hence with downsized capacity RC-AW-HP but large thermal storage, the building thermal load can be handled equally. The resultant benefits of standalone PV powered RC-AW-HP, is the potential to need smaller, hence, less costly battery storage. One issue associated with using a standalone PV system is the excess power generated. However, the excess power can be utilized to power domestic heat pump water heater (D-HP-WH) which has a different load profile. Previous researches have not focused on such a system configuration, this study focuses on the techno-economic feasibility of a highly optimized component configuration for such a system to meet the entire all-year round space conditioning and domestic hot water demands of a typical Australian house in three vastly different Australian climatic conditions. The entire system is modelled and simulated in TRNSYS and coupled with GenOpt to carry out the optimization. The lifecycle cost assessment on the most optimized component configuration for 0.2% annual hours loss of load probability in generated electricity, reveal that the twenty years life cycle cost is AU$ 76,917 in Brisbane, AU$ 88,539 in Adelaide and AU$ 120,454 in Melbourne. These life cycle costs are higher than case of conventional RC-AA-HP and D-HP-WH run by grid electricity, consequently, powering RC-AW-HPs with standalone PV system is currently not cost competitive with powering them with grid electricity.

Keywords: *solar air-conditioning systems, heat pumps, photovoltaic, standalone*

1. Introduction

An increase in the market-penetration of RC-AA-HP is the main cause behind the rise not only in total usage of, but also in peak electricity demand. In Australia, peak air-conditioning (AC) demand occurs for short periods of time, i.e. only around 40 hours every year (Productivity commission, 2013). However, the entire electricity infrastructure should have sufficient capacity to handle any peak demand. Handling growing residential AC peak electricity demands requires ongoing upgrades in electricity infrastructure (Johnston, 2006). This has resulted in a rapid increase in electricity prices in several countries. In the case of Australia, prices have increased rapidly since 2007 (Carbon and Energy Market, 2012), and almost 50% of the rise was attributed to recouped investments in network infrastructure upgrades. To reduce such ongoing costly investment, a residential demand side energy management solution is necessary. Residential grid-connected photovoltaic (PV) systems lack potential for reducing peak air conditioning demands due to a time mismatch between midday peak PV generated power and residential evening air-conditioning peak demands. Utilizing standalone PV systems to power AC may offer radical demand side solutions. However, a large capacity battery is needed to buffer sufficient energy required to support the operation of large capacity of RC-AA-HP compressors during non-sunshine hours. As per current market status, battery banks, despite dramatic cost reduction are still prohibitively expensive, standalone PV to power RC-AA-HP is deemed economically unfeasible (Dan, et al. 2013; Gupta, 2011). Alternatively, RC-AW-HP is integrated with thermal storage, which allow meeting building peak demand with a downsized compressor capacity (Ehyaei et al., 2010; International Energy Agency and Energy Technology Systems Analysis Programme, 2013; Rismanchi et al., 2013). Trade-offs between the capacity of the PV array size, the battery bank, the heat pump and the thermal storage volume facilitate configurations that reduce the system life cycle cost. A drawback of standalone PV systems is what to do with excess power (Walid et al., 2011), practically, with the poor load factor of residential AC in Australia. But, that excess power can be utilised to operate doemstic heat pump water

doi:10.18086/swc.2015.10.18 Available at http://proceedings.ises.org

heater (D-HP-WH). A resultant benefit is that little oversizing is required, but the system still meets the entire 12 month thermal demand of the building. Previous studies have mostly focused on solar assisted AC, i.e.; less attention has been given to the economics of standalone AC, particularly in such configurations for combined space conditioning and domestic water heating. This study focus on optimizing the size of such system component configuration, with the aim of minimizing the system life cycle cost. The system will be sized for the thermal demands of typical Australian houses in, three vastly differnt Australian climate zones.

2. Building and system specifications

Since space conditioning, domestic hot water demand, and availability of solar radiation are all influenced by the climatic conditions of the site, the size and cost of the system will be site dependent. Thus, the system will be sized for the three different Australian climatic conditions selected: Brisbane, Adelaide, and Melbourne. To make research findings applicable to typical Australian homes, the space conditioning demand for a typical, detached, two story single family houses with 180 m^2 conditioned area was determined (Wong, 2013). In regard to the thermal fabric of the house, it was constructed of brick-veneer and insulated to meet the minimum Australian mandatory building thermal energy efficiency requirement of 6 stars energy rating criteria. According to that rating, the minimum annual thermal energy required to maintain the house thermally comfortable should not exceeds 43 MJ/m^2 in Brisbane, 96 in Adelaide, and 114 in Melbourne (Nation Wide house energy rating scheme, 2012). The domestic hot water demand is taken from the demand pattern provided in Australian standard AS/NZS 4234:2008 for evaluating energy consumption of hot water systems (Australian/New Zealand Standard, 2008).

The standalone heat pump is constructed from a PV and thermal subsystem, see figure (1). The PV subsystem, which includes the PV panels, lithium ion battery bank, and the DC-AC inverter, provides all the power required to run the thermal subsystem. The PV is monocrystalline with a conversion efficiency of 16%; the battery is lithium ion allowing a discharge depth limited to 80% of its available capacity. The inverter is sized according to the peak-power required by the load. The charge controller logic is set to prioritizing meeting the demand, then charging the battery. The PV panel is oriented due north and tilted with angle equal to the local latitude.

The thermal subsystem includes two sub-subsystems. One sub-subsystem is a RC-AW-HP which maintains the temperature of the water inside a stratified water storage tank below 10^oC in summer and above 45^oC in winter. The RC-AW-HP has nominal coefficient of performance of 3.2 in cooling mode and 4 in heating mode. But the performance at part load condition adjusted by with the normalized performance data for one of market available RC-AW-HP brand using its online published technical data. Two pumps are used to circulate the water; one in the heat pump-thermal storage loop activated with RC-AW-HP, one in the thermal storage-air handler unit loop activated with the air handler unit fan whenever there is a space conditioning demanded. A variable speed fan is used to control the flow of air supplied to the house through a ducted system set to control and maintain zones at setting temperatures suggested by (Nationwide house energy rating scheme, 2012). The maximum flow of the supplied air is limited to 8 air-changes per hour, and the parasitic power of the fan and pumps is scaled with the RC-AW-HP capacity. The thermal storage unit is assumed to be sensible stratified water tank that heats/cools the air when water circulates through the air-handler unit. The tank is simulated with 20 nodes, and the insulation level around the storage tank set to R2.7 (0.37 $W/m^2.k$) (AIRAH, 2013). The storage function changes from chilled buffer storage in summer to hot buffer storage in winter and the inlet and outlet ports location was optimized concurrently with the season.

The other sub-subsystem is a heat pump water heater, used to maintain the temperature of the water inside an insulated tank at 60^oC to prepare sanitary hot water sufficient for four persons in a house. The heat pump performance data is normalised from the manufacturer's published catalogue data for four heat pump capacities.

Figure (1) shows the components and configuration of the system

3. Methodology

3.1 Evaluation criteria

Technical criteria was used to correctly size the system component to adequately meet the three building thermal loads; space heating in winter, space cooling in summer, and water heating all year around. For standalone systems, matching energy demand and available energy capacity should be viewed not only in terms of the daily or yearly energy required but also in terms of demand time. Hence, the annual hour's loss of load probability is used for sizing both the thermal and the electrical subsystems. The criteria are based on the number of hours throughout the year when the demand exceeded the system's available capacity. The current system is sized for the following annual hours loss of load probability targets: the RC-AW-HP is sized for 5% of the space thermal conditioning demand, the D-HP-WH for no more than 1% of the domestic hot water demand, and standalone photovoltaic subsystem for 0.2% of the electricity demand of both heat pumps.
The optimization was performed using component sizes as design variables, life cycle cost as objective and standalone as constraints. For speed and accuracy, Hybrid algorithm is chosen for finding the optimal component size.
The economic criterion used is a life cycle cost for twenty years. All cash flow related to the system is discounted back using real discount rates. The life of components is adjusted to the study period by replacing or reselling at salvage value equal to the remaining life of the component.

3.2 TRNSYS project model:

TRNSYS 17 (TRaNsient SYstem Simulation Program) (Klein, 2012) is used to build a complete project model that represents the standalone solar PV subsystem, RC-AW-HP, and D-HP-WH in separated subproject models. Project components include those from the TRNSYS standard library, TESS (Thermal Energy System Specialists) library and three more components developed by the researcher. The project model is coupled with GenOpt optimization (Wetter, 2011) developed at Lawrence Berkeley National Laboratory for minimization of a cost function.

3.3 Economic parameters

Table (1) below lists parameters that feed into the economic model, all of which are gathered by the researchers from online retail price lists and suppliers based mainly in Australia.

Table (1) details related to price of components that feed to the economic model (C refer to component specific capaicty).

Component	Initial cost	Installation	Cost reduction	Maintenance	Life years
Photovoltaic panel (kW)	1900/C (C in kW)	1200/kW	0	0.03% of purchase cost	25
Battery bank (kWh)	1100/C (C in kWh)	6% of purchase cost	50% by 2035	0	10
Inverter, charger, and maximum power point tracker	(508.9*C+ 885.76)+925 (C in kW)	0	0	0	10
Reverse cycle air-water heat pump	581.6+447.6*C (C in kW)	$AU 2500	16% by 2035	5% of purchase cost	15
Heat pump water heater	5.3538*C+ 819.9 (C in m^3)	$AU 500	16% by 2035	5% of purchase cost	15
Pump	269+239.6 *C (C in kg/s)	$AU100 per pump	0	0	15
Storage tank	680*C + 720 (C in m^3)	$AU100	0	0	15
Air-handler unit	35.95*C+680.69 (C in kW)	0	0	0	20

The financial parameters used in the economic model are a 2.2% inflation rate and a 7% nominal discount rate. Also, the Australian government subsidies installing PV and D-HP-WH under a Small-scale Renewable Energy Scheme, offering a rebate called the small scale renewable energy technology certificate (STC)

(Clean Energy Regulator). With this rebate, householders can receive a discount based on the number of STCs that the system is eligible for. Market prices for STCs fluctuate, but currently stand at around AU$ 35 per STC. The number of STCs that a system may attract depends on its size and the geographical location where it is to be installed. For PV systems, each 1 kW is eligible for a cash- back equal to AU$ 622 in Brisbane, and AU$ 725 in both Adelaide and Melbourne. For the D-HP-WH, the number of STCs depends on both the manufacturer and size of the tank. But D-HP-WH which can displace highest energy should be eligible for AU$ 1484 (i.e. 42.2 STC) in both Adelaide and Brisbane, and AU$ 1621 (i.e. 46.3 STC) in Melbourne. These rebates are deduced from the life cycle cost after the optimization.

4. Results and discussion:

6.1 Technical optimization:

System optimization was carried out to reduce the system life cycle cost by varying components sizes but maintaining the above mentioned targeted reliability in annual hours loss of load probability constraints. To guarantee the accuracy of optimal results, each optimization was repeated six times with a different preliminary component size estimated for each of the above stated climate zones. Each optimized configuration was obtained after more than 500 year rounds simulations with 7.5 minute time step. Table (2) lists the components size yields from an optimization which configured the most minimized life cycle cost system. The discrepancy between different component sizes appropriate for each climate is strongly linked with the amount of highest thermal load, the amount of highest heat pumps electrical energy demand, the season when these demands occur, and at what time of day, and how long it continued. For the current research targeted reliability, if the system's available capacity fits the building yearly load profile and the climatic pattern of the site, then it should be practically applicable when it is sized to operate as a standalone system.

Table (2) shows the optimal size of each RC-AW-HP, for each climate zone. In Brisbane, despite the minor space conditioning demand for sensible cooling and heating, compared to Adelaide, a relatively very large thermal storage, i.e. 7.4 m^3, and a large capacity RC-AW-HP, i.e. 3 kW, was needed compared to that anticipated. For Brisbane, this is due to the need to remove the high humidity which dictates maintaining a larger quantity of water chilled at and below 10^oC. Apparently, during the night, less electrical energy is consumed by the RC-AW-HP when using large chilled water storage; instead, the second pump operates more in circulating the vast ready chilled water. This expains why a smaller battery (20 kWh) is needed in Brisbane, compared to those required in both Adelaide and Melbourne. In Brisbane, concurrency of summer high solar intensity with a high cooling load enables the PV system to amply generate the required power to run the heat pumps and recharge the battery.

Table (2) optimized size of components forming the minimized life cycle cost of the standalone system.

	Battery (kWh)	RC-AW_HP (kW)	Photovolatic (kW_p)	Thermal storage (m^3)	D_HP_WH (m^3)
Brsibane	20	3	9	7.4	0.27
Adelaide	28	2	9	7.8	0.34
Melbourne	44.5	5	12	3	0.34

Contrary to Brisbane, in Melbourne the peak space conditioning demand occurs in winter, and lasts for several successive days, the significant part of it occurring at night. When compared to Adelaide, relatively larger capacity RC-AW-HP, i.e. 5 kW, was needed to charge heat in a smaller volume thermal storage, i.e. 3 m^3. Obviously, maintaining a smaller volume of heated water and using a more powerful RC-AW-HP demands less electrical energy than in the case of using downsized RC-AW-HP and a large volume hot storage. Also, when compared to Adelaide and Brisbane, the capacity of the PV panel is larger, i.e. 12 kW_p, since it generates less electrical energy under days with overcast skies. Inevitably, a considerably larger battery bank capacity, i.e. 44.5 kWh, was also required to avoid power interruption during the day and guarantee continuous night operation.

Table (2) shows that for Adelaide, the optimized configuration requires smaller RC-AW-HP, i.e. 2kW, and large thermal storage, i.e. 8 m^3, than the other two climates. This is due to a high peak sensible cooling demand and significant heating load. On account of the noticeable variation between electrical and thermal storage sizes in hot and cold climates; it can be concluded that using large chilled water storages for space cooling in summer considerably reduces the required battery capacity for the same annual loss of load

probability. Unlikely, using hot storage for space heating not have that considerable potential to reduce the minimum required battery capacity.
The capacity of the configured PV panel, i.e. 9-12 kW_p, may look a little large for residential buildings, but the system configuration is standalone with a superior degree of reliability, less than 5 hours per year the electricity demand is not met. Should more annual hour's electrical loss of load portability be tolerated, the size and cost of the electrical parts of the system will reduce substantially, but then the system need to be assisted by mains-grid electricity.
In terms of sizing the D-HP-WH, the size that was found to be suitable for Brisbane was a 270 litre tank and heating rate of 75 litres per hour, while those suitable for Adelaide and Melbourne were 340 litre tanks and heating rates of 75 litres per hour. The power that was needed to operate the heat pump was added to the power required to run the RC-AW-HP during the optimization. The daily D-HP-WH power pattern is similar throughout the year, but higher in winter than in summer. Adding the D-HP-WH power profile caused the PV subsystem to be a slightly oversized, but significant amount of the PV dumped power was usefully utilized by the D-HP-WH.
It is important to emphasize that these configurations do not represent those with the best fit technical configuration for the building load, nor for the selected climate zones. They represent configurations that with a given component cost and target constraints, lead to obtaining the component configurations that have minimized life cycle cost systems. Should the system to be sized for other climates, by loading the applicable load profile, or other cost or constraints targets, the project model can be used to determine the optimized standalone system's components configuration.

6.2 Economic evaluation:

The twenty years life cycle cost of the most optimized component size configuration presented in table (2) was found to be AU$ 83,907 in Brisbane, AU$ 96,814 in Adelaide and AU$ 130,782 in Melbourne. Depending on the size of the PV panel and the climate, when government rebates in the form of STCs are added to both the PV panel and the D-HP-WH, the life cycle cost reduces in Brisbane to AU$ 76,917 , in Adelaide to AU$ 88,539 and in Melbourne to AU$ 120,454. If the system life cycle cost break down to the life cycle cost of main forming components then it becomes obvious which component costs dictate the cost of the system.
Figure (2) shows in each of the three climate zones, the greatest cost is associated with the battery, followed by the PV panels, followed by the thermal storage unit. If the percentage of investment attributed to the battery and the thermal storage are cross-correlated and compared for the three climate zones, it becomes evident that, when the percentage cost of thermal storage is higher, the percentage cost attributed to the battery is less. Since the price of the cubic meter of thermal storage is less than the price of each kWh battery capacity it replaces, with larger thermal storage the life cycle cost of the system must in all probability decrease correspondingly. To be more specific, in space cooling dominated climates, large chilled water storage can reduce the minimum capacity of a battery required for settling standalone solar PV powered RC-AW-HP.

Figure (2) the life cycle cost break down to main forming components in the three climates

6.3 Competitiveness with conventional system:

To investigate how such standalone PV powered RC-AW-HP and D-HP-WH is cost competitive in comparsion with powering them by grid electricity, the life cycle cost of the PV subsystem is compared with the twenty years running cost of the conventional RC-AA-HP and D-HP-WH if electricity is purchase from the grid. The comparison is shown in figure (3). Clearly, the investment required in the reliable standalone PV system is enormously higher than purchasing the power from the grid for running the conventional systems in the three climate zones. Hence, the economic potential of space conditioning houses with RC-

AW-HP off-grid is weak in comparsion with current component costs and electricity charges. Unless in case of remote dwellings where costly investment in constructing new or extending electricity network infrastructure is needed to sustain powering conventional AC. Adding these infrastructure costs to the running cost can influenec individual householders to select the presented standalone PV powered heat pumps instead of paying for infrastucture network extensions.

Figure (3) comparing the twenty years running cost and standalone PV subsystem life cycle cost in the three climates

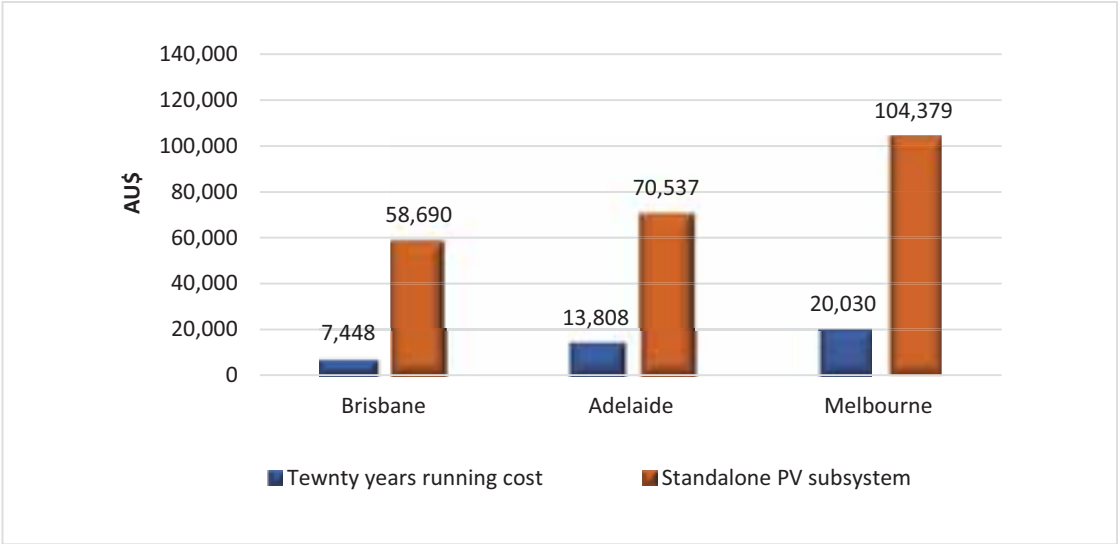

5. Conclusion:

In this study, a TRNSYS 17 project model is used to optimize the configuration of components forming the standalone PV subsystem powering RC-AW-HP and D-HP-WH for the thermal demand of typical Australian house in three vastly different Australian climatic zones. The life cycle cost of most optimized configuration of these systems with rebate was found to be AU$ 76,917 in Brisbane, AU$ 88,539 in Adelaide and in Melbourne AU$ 120,454. It has been found that chilled water storage can contribute to reducing the capacity of the battery, consequently, the overall standalone system cost. Whether investment in such a system is cost competitive with purchasing electricity from the grid to power conventional RC-AA-HP and D-HP-WH in residences; the life cycle cost of the standalone PV subsystem is compared with a 20 year discounted electricity cost needed to power conventional RC-AA-HP and D-HP-WH. The results demonstrate that purchasing electricity from the grid to run these conventional options costs much less than investing in a standalone PV subsystem. Indeed, unless the tariff increase considerably, or, the cost of batteries decrease significantly, or the householder is faced with heavy investment in electricity infrastructure charges, it is currently uneconomic to invest in a standalone PV driven air to water heat pump systems.

6. Acknowledgment:

The first author would like to thank the Higher Committee for Education Development (HCED) in Iraq for sponsoring her PhD study at University of South Australia.

7. References:

AIRAH, 2013. AIRAH Handbook. Australian Institute of Refrigeration, Air-conditioning and Heating. 5th edition. Melbourne, Australia.

Australian/New Zealand Standard 4234:2008, 2008. Heater water heating systems- Calculation of energy consumption.

Carbon and Energy Market, 2012. Electricity Prices in Australia: An International Comparison. A report to the Energy Users Association of Australia.

Dan, W., Lu, A., Priyan, M. and Tuan, N., 2013. Financial analysis of solar cooling systems in Australia, Australian Solar Cooling 2013 Conference. Sydney, Australia.

Department of Industry, 2013. Your Home: Technical Manual. 5th ed. Commonwealth of Australia.
Ehyaei, M. ; Mozafari, A. ; Ahmadi, A. ; Esmaili, P. ; Shayesteh, M. ; Sarkhosh, M. ; Dincer , 2010.

Potential use of cold thermal energy storage systems for better efficiency and cost effectiveness. J. Energy and buildings, 42 ,2296-2303.

Gupta, Y., 2011. Research and Development of a Small-Scale Adsorption Cooling System. Arizona State University.

International Energy Agency and Energy Technology Systems Analysis Programme, 2013. Heat pumps Technology Brief.

Johnston, W., 2006. *Solar air conditioning: Opportunities and obstacles Australia*. ISS Institute.
Klein, S. A., 2012. TRNSYS 17 Transient System Simulation Program user manual. University of Wisconsin-Madison.

Nationwide House Energy Rating Scheme, 2012. NatHERS Software Accreditation Protocol.
Otanicar, T., R. Taylor, and P. Phelan, 2012. Prospects for solar cooling - An economic and environmental assessment. J. Solar Energy, 86 (5), 1287-1299.

Productivity Commission, 2013. *Electricity Network Regulatory Frameworks*. Canberra.

Rismanchi, B; Saidur, R. ; Masjuki, H. ; and Mahlia, T. , 2013. Modeling and simulation to determine the potential energy savings by implementing cold thermal energy storage system in office buildings. J. Energy conversion and Management, 75, 152-161.

Tony W. and Lucy C., 2014 . Fair pricing for power. Grattan Institute.

Walid, A. ; Kazerani, M. and Salama, M., 2011. Fluctuations Generated From Large Grid-Connected Photovoltaic Systems. IEEE Transaction on Energy conversion, 26 (1), 318-326.

Wetter, M., 2011. "GenOpt Generic Optimization program User Manual, Version 3.2.0", December.

Wong, J.P., 2013. Development of representative dwelling designs for technical and policy purposes, Prepared for Energy Efficiency Division, Department of Resources, Energy and Tourism. Ian Swain.

http://www.cleanenergyregulator.gov.au/

Conference Proceedings

Solar World Congress 2015
Daegu, Korea, 08 – 12 November 2015

THE EXPERIMENT OF A NEW TYPE OF BUILDING INTEGRATED SOLAR RADIANT HEATING SYSTEM

Yu Yingying[1], Niu Baolian[1] and Shi Liangyan[1]

[1] School of Energy and Mechanical Engineering, Nanjing Normal University, Nanjing (China)

Abstract

A heat pipe radiant heating system is discussed, combined with the building and solar energy by heat pipe. The system is composed with solar collector, heat pipe and radiant heating terminal. The heat pipe delivered the heat of solar absorbed by itself from outdoors to indoor and then heating the room by radiant. This paper adopts a combination of experimental and simulation to test and analysis the system. The results showed that the indoor average temperature can reach above 16℃ during the daytime in winter, and the temperature distribution is uniform. The system is an energy-saving and practical building integrated solar radiant heating system.

Keywords: *solar building, radiant heating, gravity heat pipe, zero-energy consumption*

1. Introduction

In the hot summer and cold winter areas without central heating in China, most buildings use small separated heating equipment such as air conditioning, heaters and electric blankets. However, low operating efficiency and high energy consumption can lead to energy waste and environmental pollution when widely-ranging. Thus, it is essential to find an energy-efficient and comfortable way of heating.

Solar energy is clean and efficient and non-polluting, and the solar thermal technology in buildings has been have a certain development in many countries.

Susheela and Sharp (2001) designed and tested a heat pipe system that could be installed on existing homes without demolishing the wall of the building. The absorber portion was mounted on the outside of a south-facing wall, with water contained in tanks as the thermal mass on the inside of the wall. Experiments were performed outdoors, and system efficiencies (defined as the ratio of power delivered to the room over incident insolation) reached as high as 60% during sunny days. Computer simulations were also performed to model the performance of the unit.

Primarily based on design improvements recommended by Susheela and Sharp, Albanese et al. (2012) tested a bench-scale experimental model. Experimental variations included fluid fill levels, addition of insulation on the adiabatic section of the heat pipe, and fins on the outside of the condenser section. Filling the heat pipe to 120% of the volume of the evaporator section and insulating the adiabatic section achieved a system efficiency of 85%. Addition of fins on the condenser of the heat pipe did not significantly enhance overall performance. The heat pipe system provided substantial gains in performance relative to conventional direct and indirect gain passive solar systems and, thus, presents a promising alternative for reducing building energy use.

To better understand system performance in realistic weather conditions, in particular, the relatively cloudy and cool conditions, Robinson et al. (2013) designed, built and installed a full-scale prototype of the heat pipe system in a classroom on the University of Louisville campus in Louisville, KY. During the spring heating season of 2010 (January–April), maximum daily peak thermal efficiency was 83.7% and average daily peak thermal efficiency was 61.4%. The maximum hourly average room gain achieved during the season was 163 W/m^2. On days with good solar insolation, the thermal storage was heated to temperatures

doi:10.18086/swc.2015.10.19 Available at http://proceedings.ises.org

sufficient to provide significant energy to the classroom – even during the coldest days of the season. During the longest period (4 days) of low insolation during the season, average hourly heat delivery to the room from storage remained positive, and was never less than 16.6 W/m^2.

Operation temperature of solar heating systems makes the use of a radiant floor to transfer heat into the conditioned spaces suitable. Compared with thermal storage wall, temperature radiant floor heating system has more advantages in terms of indoor thermal comfort. In recent years, the application of heat pipe in solar radiant heating becomes more and more.

Manillez et al. (2005) studied and tested the solar floor radiant heating system that 15.36m^2 collector to meet the heating and hot water load of 172m^2 room. The solar fraction recorded this day was of 0.468, that is, solar energy supplied 46.8% of the combined heating and hot water loads, one of the highest solar fractions of the season.

Zhang Yufeng et al. (2006) studied the performance of a carbon-steel/water thermosyphon and applied it to low-temperature under-floor heating system. Experimental investigation has been done to find out the effect of inclination angle (-4°~90°), evaporative length (30~180mm), temperature (40~60 ℃), flow rate (0.1~0.3m^3/h) and flow direction (forward flow, counter flow) of hot water on thermosyphon performance. The evaporator section of the carbon-steel tube is heated by hot water while its condenser section is cooled by air. Experimental results indicate that the thermosyphon performance with counter flow is much better than that with forward flow. The heat transfer rate and surface temperature of condenser section increase with the rise of hot water temperature and flow rate. With increasing inclination angle and evaporative length, heat transfer rate and surface temperature increase at first, and then start to decline after attaining their maxima. This thermosyphon works well in all experimental conditions, and it yields the highest thermal performance with the evaporative length of 120mm, inclination angle of 38°, flow rate of 0.3m^3/h, temperature of 60℃, and counter flow of heating water.

The existing experimental studies about heat pipe radiant heating systems with water, the heat transfer loss is inevitable between the water and heat pipe. Besides, the pump needs energy consumption. The building integrated solar radiant heating system can reduce the irreversible loss and improve energy efficiency. The system absorbs solar thermal by heat pipe and heating the room directly by radiant without any power consumption when the solar radiation is enough. This paper will analyse the indoor temperature distribution of the system, and the influence of evaporative length and quantity of working fluid on the performance of heat pipe to further explore the method of improving the syetem efficiency and indoor thermal comfort.

2. Experimental study

2.1. System introduction

The building integrated solar radiant heating system is composed of an outdoor heat collector, an indoor heat release module and heat pipes as Fig. 1 shows. The system uses heat pipes as heat transfer component. The evaporator section is placed in the solar collector. While the temperature rose, the working fluid inside the evaporator section absorbs the heat and evaporates to gas and run into the condenser section. When the gas enters into the condenser of heat pipe, it will sent heat into the indoor air and then turn into liquid, finally it will return back to the evaporator of the heat pipe. Then the new cycle will carry on and solar energy will be transferred into the room. In order to prevent heat transfer from indoor to outside, we use the gravity heat pipe with a thermal diode effect.

Compared with the traditional solar hot water floor radiant heating system, the heat pipe radiant heating system directly transmitted the solar thermal energy for indoor radiant heating without the middle transfer medium, which will reduce the irreversible loss of heat transfer between water and working fluid and improve the utilization rate of solar energy. The system is suitable for office buildings, kindergartens and secondary school classrooms and other daytime office spaces, and it can provide the basis for residential heating temperature, reduce fuel consumption.

The gravity heat pipe used in the system is 3.12m in total length, and the evaporator section is about 1.8m

with 8mm outer diameter, the condenser section is 1.2m with 12mm outer diameter, the insulation section is 120mm with 12mm outer diameter. The working fluid of the gravity heat pipe is R600a and the tube of heat pipe is made of cooper with 1mm thickness of pipe wall. The collector part is basically the same as the ordinary plate type solar collector, that mainly consisted by the collector body, heat insulation material, heat absorbing layer and the transparent glass cover. The heat absorbing layer is the core design of the system, which is borne by the evaporator section of heat pipe with fins. The surface of fins is planted with a blue film, and it wrap up the heat pipe in 360° to absorb the maximum possible radiation and to raise the working fluid temperature. Between the heat pipe and the frame, 60mm thickness insulation cotton is used to keep the heat, and on the top of the collector, the organic transparent glass is used to transfer solar sunshine.

2.2. Test method

The experimental testing system is composed of two parts:

(1) Tests of heat transfer performance of single heat pipe

The experimental test system is shown as Fig.1. a HukseflUxLP02 short wave radiation sensor is used to measure insolation values with and the sensitivity of 12.13μV/(w•m^{-2}). Fluke hot wire anemometer is used to measure the wind speed with the sensitivity of 0.01m/s, twenty J-type thermocouples were placed in the evaporator and condenser respectively, to assess temperature difference between of them at the same time. Another one J-type thermocouples was placed outside to measure ambient air temperature. All data was collected using Agilent 34972 a.

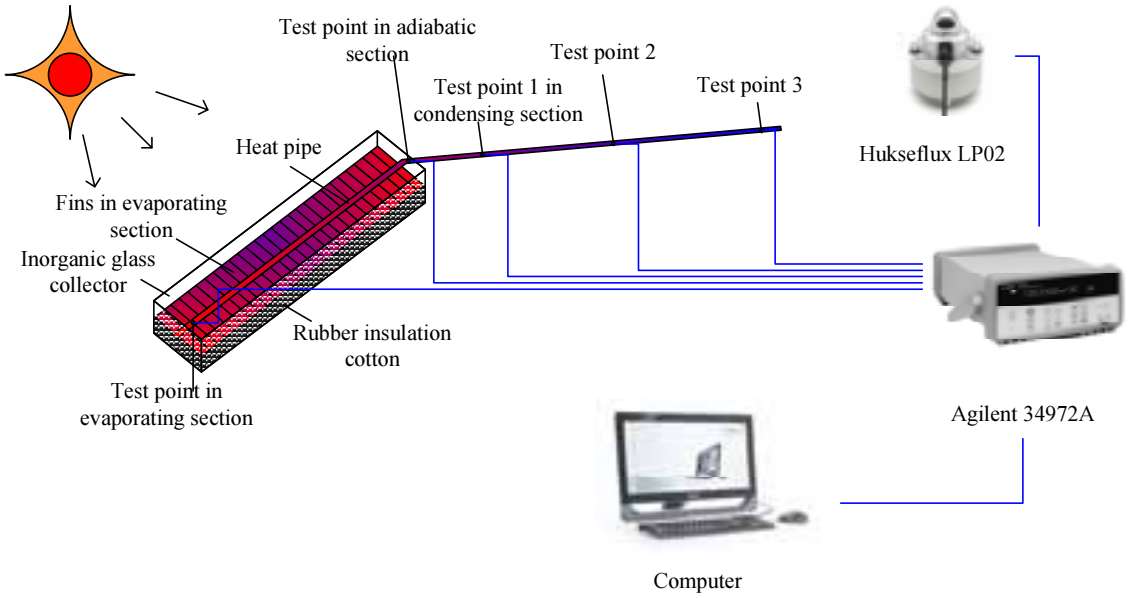

(2) Tests of building integrated solar radiant heating system

The installation of gravity heat pipe of the system is shown as Fig.2. The GHPRHS prototype was fabricated, which used a plate solar collector as evaporator. The collector was consisted of nine copper tubes (10mm diameter) wrapped with fins soldered on the rubber insulation cotton (40mm thick). The dimension of the fins was 138mm×180mm×1mm. The total length of the each heat pipe was 3 m. and the diameter of the condenser was 12mm. The total surface area of the collector was 2.2 m^2. The fin surface was a selective black coating surface. The 2m×1.4m glazing consisted of 3.18 mm thick glass with an anti-reflective coating. At the indoor section, the copper pipe was fixed on the groove of the insulating material with the distance of 200mm between of them, which was covered with aluminum sheet with high thermal conductivity. In addition, 40mm thick insulation layer was put on the floor to avoid the heat loss from the floor. Above these heat pipes, laminate flooring was put on in order to simulate the real floor. The whole indoor surface area was 2.4m^2. All the condenser of the heat pipes were mounted at 5° from the horizontal.

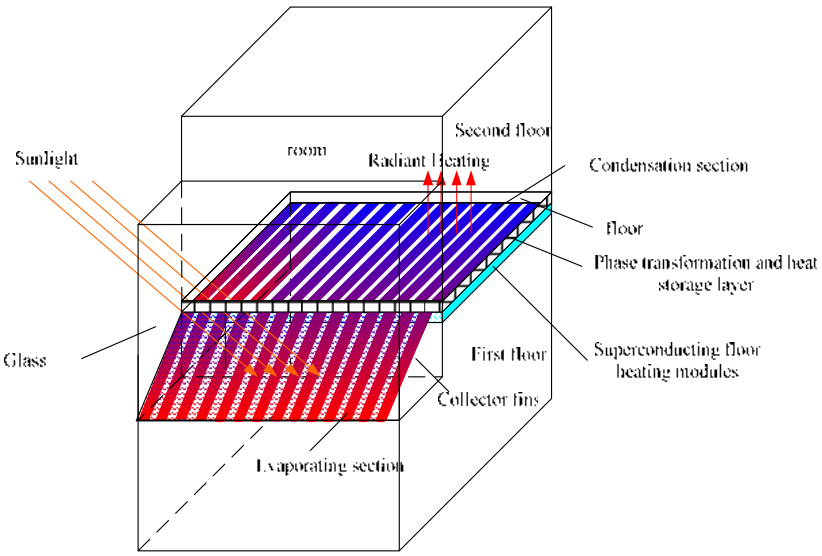

Fig. 2: The installation of the building integrated solar radiant heating system

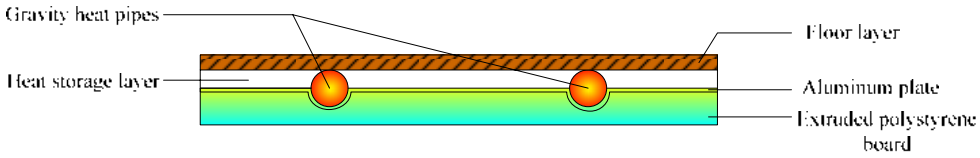

Fig. 3: The structure of indoor radiant heating model

3. Results and discussion

3.1. Theoretical model

Traditional evaluation method of heat pipe heat transfer performance is to compare the equivalent heat conduction coefficient, its mathematical expression is:

$$\lambda_{eff} = \frac{4L^2}{{d_0}^2} \cdot \left[\frac{1}{\left(\frac{\ln(d_0/d_i)}{2e}\right)+\frac{\lambda}{\alpha_e d_f e}+\frac{\lambda}{\alpha_c d_f c}+\frac{\ln(d_0/d_i)}{2c}}\right] \cdot \lambda \qquad \text{(eq. 1)}$$

The equivalent heat conduction coefficient is directly evaluated, and the parameters are easy to be measured. However, it still has shortcomings. By the formula, the longer the heat pipe is and the smaller the diameter is, the equivalent heat condunction coefficient will be high even if the heat transfer coefficient of the evaporating and condensating section are not high, especially for heat pipe with long length. This is exactly the deficiency of the equivalent heat conduction coefficient. The equivalent convection heat transfer coefficient is introduced to the model by Yu Tao(2008) and establish the formula as follow:

$$\alpha_{eff} = \frac{2\lambda Q(L_c+L_e)}{2\pi\lambda d_i(T_e-T_c)L_c L_e - Q d_i(L_c+L_e)\ln(d_0/d_i)} \qquad \text{(eq. 2)}$$

Here, α_{eff} is a weighted average of the boiling heat transfer coefficient and the condensation heat transfer coefficient, which is a comprehensive reflection of boiling and condensation heat transfer processes in the heat pipe. Besides, the right parameters of eq.2 can be obtained by measurement. Therefore, it is objective to evaluate the heat transfer performance, especially the gravity heat pipe by the equivalent convection heat transfer coefficient.

3.2. Heat transfer analysis of heat pipe with different charging ratio

Fluid charging rate is an important parameter to study the heat transfer performance of gravity heat pipe. When charging rate is too low, heat pipe will appear dry phenomenon; and when it is too high, heat pipe will appear boiling limit. The existing researches showed that the appropriate charging rate for heat pipe is between 30%~ 80%. Therefore, this experimental study on the filling rate in this range to observe the variation of heat transfer performance with the charging rate of two phase flow heat pipe, and provide a theoretical and experimental basis for the heat pipe radiant heating system.

A series of daily outdoor tests have been performed, the amount of working fluid was varied in the range of 30g-80g corresponding to a ratio of fill charge volume to inner volume of the evaporator zone range of 30%-80%. The variation are given in Fig.5 including temperature in the condensing section, temperature difference of evaporating and condensing section and the equivalent convection heat transfer coefficient, the variation of temperature difference of evaporating and condensing section, the variation of the equivalent convection heat transfer coefficient with time in the same solar irradiance. It can be seen in Fig. (a) that the higher the charging ratio, the higher the temperature of condensing section after the start-up process. It's because the condensate film is the main factor to affect the heat resistance in condensing section in the same solar irradiance. The steam quantity follows the same trend as the charging ratio increasing, more steam generated in the evaporating section, the more steam be condensed in the condensing section, which will increase the thickness of condensate film and heat transfer thermal resistance. In addition, higher charging ratio made the steam flow faster and the friction between the steam and liquid film increasing, which will also increase the thickness of condensate film and is unfavourable to the heat transfer in the condensing section. While the condensation heat transfer coefficient decreases, the amount of steam generated by the evaporation section increases, leading to the rise of tube wall temperature of condensing section.

Fig.(b) shows that the temperature difference between the evaporating and condensing section are all increased first and then decreased and tend to be stable with different charging ratio. This is because the heat pipe needs time to start-up, and the evaporating temperature rise sharply in start-up time while the condensing temperature rise gradually after the steam reached a certain value in evaporating section. Higher charging ratio needs more time to start-up. Therefore, the time of temperature difference tends to be stable is shortest when the fluid amount is 30g in Fig.(b). It also can be seen from Fig.(b) that the temperature difference between the evaporating and condensing section is bigger with more charging ratio. This is because high charging ratio will lead more steam generated in the evaporating section and the condensing liquid in the condensing section increased, and the temperature of condensing liquid is always lower than that of the boiling liquid in evaporating liquid pool, which will reduce the temperature of tube wall of condensing section.

Fig.(c) shows that the equivalent heat transfer coefficient decreased with the increase of charging ratio. This is because when the charging ratio is low, the liquid level of liquid pool in the evaporating section is low and the heat transfer resistance is small which is beneficial to the liquid boiling in the liquid pool and the heat transfer coefficient of evaporating section is relatively large. However, when the charging ratio is higher, the liquid level of liquid pool increased and the heat transfer thermal resistance is larger, which decrease the velocity of bubble movement in the evaporating section and reduce the boiling heat transfer in the liquid pool, so that the heat transfer coefficient of evaporating section is reduced. Besides, the condensation heat transfer coefficient is also decreased with the increase of liquid charging ratio, and the equivalent convective heat transfer coefficient is the comprehensive reflection of the evaporating and condensing section, so the equivalent convection heat transfer coefficient decreased with the increase of liquid charging ratio.

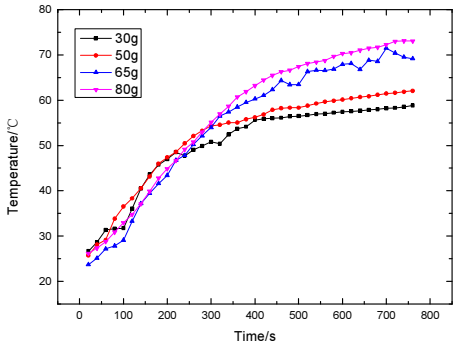

(a)Variation of temperature in the condensing section

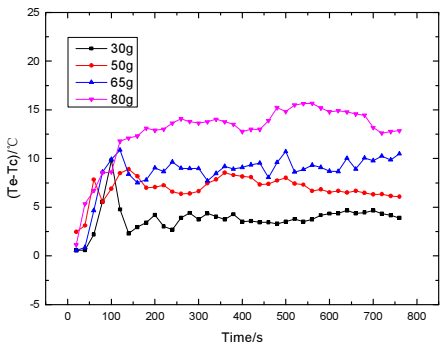

(b) Variation of temperature difference of evaporating and condensing section

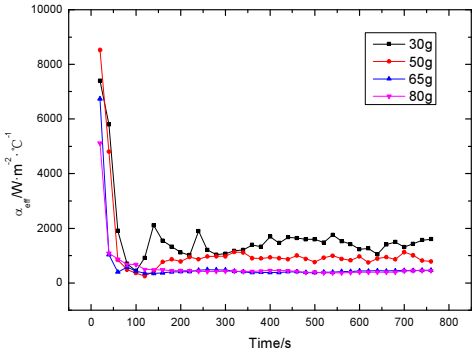

(c) Variation of the equivalent convection heat transfer coefficient with time

Fig.5 The curve of heat transfer performance of heat pipe with different charging ratio

Table 1 is the calculated data of heat pipe heat transfer performance in different charging ratio. According to the data, the higher the charging ratio is, the smaller the heat transfer coefficient of condensing section, which is consistent with the analysis in Figure 5. However, the higher the working quality of the evaporation section, the more quantity of condensing heat release and the higher the solar thermal utilization rate of the heat pipe. This is because the temperature of tube wall of condensing section increases with the increase of working fluid, which lead to the temperature difference between the tube wall and the steam inside larger. Compared with the heat transfer coefficient, the temperature difference has a greater impact on the condensing heat release. Therefore, the higher charging ratio can lead to more quantity of condensing heat release, as a result, the solar thermal utilization rate of heat pipe can be higher with the high charging ratio.

Although the higher charging ratio brings the more heat energy from the condensing section, and will probably lead to the overheating of the condensing section. It can be seen from Fig.2 that the temperature of tube wall of condensing section can be up to 70℃ when the charging ratio is 60% and 80%. However, the tube wall temperature of indoor heating pipe should not be higher than 60℃ according to relevant regulations (2008). Indoor heating temperature is too high to get human thermal comfort with the local overheating. Comprehensively considering the heat pipe condensing temperature and heat release, the best liquid charging ratio is about 45%~50% in the system, with highest pipe wall temperature about 60℃ and the heat quantity about 70W highest pipe wall temperature is about 60℃ and the heat quantity is about 70W.

Tab. 1: Table of heat transfer performance in different charging ratio

Quantity of working fluid	Filling radio	t_v/℃	t_w/℃	h_c/W·(m^{-2}K^{-1})	Q′	η
30g	30%	59.5	57.2	565.53	58.8	0.341
50g	45%	63.1	59.7	426.78	66.8	0.402
65g	60%	72.3	66.1	325.24	98.7	0.473
80g	75%	78.1	69.2	259.08	178.1	0.823

3.3. Heat transfer and indoor thermal environment analysis of the radiant heating system

The experimental data were collected continuously under the condition of sunny days in winter in Nanjing.

Figure 6 shows the variation of indoor and outdoor parameters with time. It can be seen from the figure that the variation trends of the evaporating and condensing temperature are consistent, which increase and decrease with the solar irradiance. When the solar irradiance is about 100W/m^2, the heat pipes began to start-up and the evaporating and condensing temperature gradually increased, and it reached a maximum at 12:00 and then decrease. After about 16:00, the condensing and the indoor temperature tend to be equal and the heating collect is ineffective. In winter, the effective heating time is about 6 hours from 10:00 to 16:00. During 11:30 to 12:30, the solar irradiation has high intensity, and the temperature of condensing section is so high that leading the indoor temperature above 35℃. This is due to the non-thermal storage wall and

without heat storage material in the experimental room, and the heat storage material will be added to reduce the indoor temperature and maintain the human comfortable temperature.

Comparing the indoor air temperature and outdoor air temperature variation curves in figure 6, the outdoor air temperature is in range of 3.5~9.2℃ with the average temperature 6.9℃, while the indoor average temperature is 22.5℃, the average temperature difference can reach about 15℃. The results show that the indoor air temperature is greatly improved under the building integrated solar radiant heating system.

Figure 7 shows the curve of indoor temperature during the effective heating time, the two curves are respectively gained by the average value at the height of 1.0m and 1.7m in the room. The results show that the temperature difference is relatively small, which is very small with the variation range from 0.01℃ to 0.77℃. Therefore, the air temperature distribution in the room is relatively uniform and no obvious temperature stratification appears. Compared with the system proposed by Ji Jie(2011), the floor radiant heating system has a more uniform temperature field distribution and the indoor thermal comfort is higher.

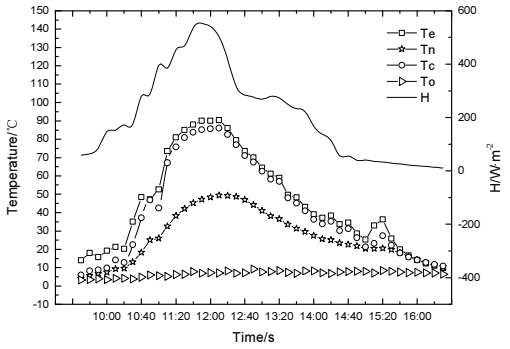

Fig.6 Variation of parameters versus time of indoor and outdoor

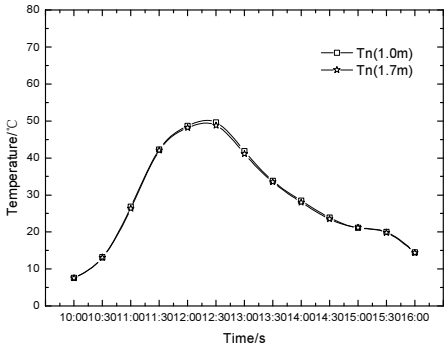

Fig.7 Variation of temperatures of air in the room versus time

From the analysis above, it shows that the system can run normally in sunny days and is an economic, environmentally friendly, and effective passive solar heating system. The indoor temperature can reach up to 20℃ in 30 minutes under the irradiance of 400W/m^2, while the outside temperature is around 5~6℃. Therefore, in the regions with abundant light supply, even if the outdoor temperature is very low, the system is still able to meet the needs of winter indoor heating with good heat-preservation wall.

Nomenclature

α_{eff}	equivalent convection heat transfer coefficient	d_0	outer diameter of heat pipe
λ	heat transfer coefficient of pipe shell	d_i	internal diameter of heat pipe
Q	heat flux of heat pipe	t_v	steam temperature in heat pipe
L_c	length of condensing section	t_w	tube wall temperature of heat pipe
L_e	length of evaporating section	h_c	heat transfer coefficient
T_e	temperature of evaporating section	Q'	heat release of condensing section
T_c	temperature of condensing section	η	solar thermal utilization

4. Conclusion

This work focuses on the testing of the performance of gravity assisted heat pipe and the radiant heating system, and gets the following conclusions:

(1) Charging ratio has a great impact on the performance of gravity heat pipe. The equivalent heat transfer coefficient decreased with the increase of charging ratio, while the quantity of heat release rose with charging ratio. Comprehensively considering the heat pipe condensing temperature and heat release, the best liquid charging ratio is about 45%~50% in the system, with highest pipe wall temperature about 60℃ and the

heat quantity about 70W highest pipe wall temperature is about 60℃ and the heat quantity is about 70W.

(2) The system is currently only used for indoor heating in winter, and in order to prevent the overheating in summer, installing globe valve on every heat pipe. Latter, the separated heat pipe will be taken to paralleling connect with hot water system in the heating system, which can produce hot water in summer when the heating system stop by the switch of the control valve. In non-heating period, the valve between the heat pipe radiant heating system and the collector will be closed, and the valve between hot water system and the collector will be open. It can also realize the energy saving in summer, using solar collector to heat the water and provide the hot water for life.

5. Acknowledgements

This research has been supported by National Natural Science Foundation of China (Grant No. 51208265) and the Natural Science Foundation of the Jiangsu Higher Education Institutions of China (Grant No. 12KJB56006).

6. References

Akbarzadeh A, Charters W W S, Lesslie D A, 1982. Thermocirculation characteristics of a Trombe wall passive test cell.J. Solar Energy. 28(6): 461-468.

Zalewski L, Chantant M, Lassue S, et al, 1997. Experimental thermal study of a solar wall of composite type. J. Energy and Building. 25(1): 7-18.

Susheela, N., Sharp, M.K., 2001. A heat pipe augmented passive solar system for heating of buildings. J. Energy Eng. 127 (1), 18–36.

Evaluation standard for green building. GB/T 50375-2006.

Roger W. Haines, C. Lewis Wilson. 2008. HVAC System Design Handbook. M.

Wang Xin, Zhang Yinping, Xiao Wei, et al, 2009. Reviw on thermal performance of phase change energy storage building envelope. J. Chinese Science Bulletin. 54(6): 920-928.

Luca B, Roberto D, Marco S, 1998. Energy analysis of a passive solar system. J. Revue Generale de Thermique. 37(5): 411-416.

Martinez P J, Velazquez A, et al, 2005. Performance analysis of a solar energy driven heating system. J. Energy and Buildings. 37: 1028-1034.

Zhang yufeng, Xie hui, Li deying, Niu baolian, 2006. Experimental investigation on heat transfer performance of carbon-steel/water thermosyphon. J. Journal of Tianjin University. 39(2): 223-228.

Gan wenhui, 2010. The reseatch character of floor radiation heating based on heat pipe technology. Taiyuan University of Technology.

Ji Jie, Luo Chenglong, Sun Wei, et al, 2011. Experimental study on a dual-functional solar collector integrated with building. J. Acta Energiae Solaris Sinica. 32(2): 149-153.

Albanese, M.V., Robinson, B.S., Brehob, E.G., Sharp, M.K., 2012. Simulated and experimental performance of a heat pipe assisted solar wall. Solar Energy 86, 1552–1562.

Brian S. Robinson, M. Keith Sharp, .2013. Heating season performance of a full-scale heat pipe assisted solar wall. J. Solar Energy. Volume 87, 76-83.

Luo Chengjie, Ji Jie, Xiong Jihai, et al, 2014. Characteristics of a building-integrated dual-function solar collector in passive space heating. J. Acta Energiae Solaris Sinica. 35(11): 2159-2164.

Zhao jianhui, Tan feipeng, Zhang yapping, 2014. Characteristic analysis of gas-liquid separated type heat pipe applied to radiant floor heating system. J. Building Energy Efficiency. (3): 1-3.

Guobing Zhou, Jing He, 2015. Thermal performance of a radiant floor heating system with different heat storage materials and heating pipes. J. Applied Energy. 138: 648-660.

Conference Proceedings

Solar World Congress 2015
Daegu, Korea, 08 – 12 November 2015

WATER QUALITY ON SOLAR WATER HEATERS IN REMOTE ISLANDS

Kai-Chun Fan[1], Keh-Chin Chang[1] and Kung-Ming Chung[1]

[1] Energy Research Center, National Cheng Kung University, Tainan, Taiwan

Abstract

The use of solar water heaters (SWHs) in Taiwan's remote islands has encountered scaling and corrosion problems attributed to sources of water. In this study, the Langelier Saturation Index (LSI), Ryznar Stability Index (RSI), Puckorius Scaling Index (PSI) and Larson-Skold Corrosive Index (LSCI) were employed to assess scaling and corrosion caused by tap-water and groundwater used for SWHs in Penghu, Kinmen, and Lienchiang Counties. The LSI, RSI and PSI results show a slight scaling tendency in Penghu County, but there is a corrosion tendency in Kinmen and Lienchiang Counties. Nevertheless, all LSCI values show a serious corrosion tendency. In addition, chloride ion (Cl^-) concentration levels are all higher than 35 mg/L, resulting in corrosion found in absorbing plates of SWHs using 304 stainless steel. Therefore, more corrosion-resistant metals are required for SWHs.

Keywords: *solar water heater; remote islands; water quality; scaling; corrosion*

1. Introduction

Solar thermal energy is widely used in many countries (Weiss et al., 2014). SWHs are mainly composed of four parts: solar collector, water storage tank, piping, and control systems. The absorbing plate is generally made of copper, aluminum, stainless steel or flexible polymer. Packing material between inside and outside barrels for a stainless-steel water storage tank is for thermal insulation. In Taiwan, the climatic conditions are predominantly sunny. The solar radiation ranges from 1,200 to 1,700 kWh/m^2/year. To disseminate SWHs, the Bureau of Energy, Ministry of Economic Affairs (BEMOEA, 1986–1991 and 2000–present) and some regional governments have established subsidy programs (Chang et al. 2013). The Energy Research Center at National Cheng Kung University (ER/NCKU) has been authorized by the BEMOEA to organize an operation unit for the second subsidy program since 2000. The accumulated area of solar collectors installed in 2012 reached 2.25 million m^2 (Lin et al. 2013). Note that the Low Carbon Island Project, including Penghu, Kinmen and Lienchiang Counties, was also launched in 2012 and promotion of SWHs was part of the project.

Service period of SWHs is of great concern for end users. In 2013, telephone interviews were conducted by the ER/NCKU for 6,482 SWHs installed in 2000, in which 3,379 end users (52.1%) were reached. The survey showed that there were 95.3% systems in operation, indicating the service period of SWHs more than 12 years at least. Further, malfunction of SWHs has been reported from time to time. In the period of 2000-2012, 942 cases were documented by the ER/NCKU, in which 555 of them (58.9%) were associated with leakage (corrosion or pitting) in absorbing plates, gate valves, storage tanks or pipe joints, resulting a reduction in service period (1-5 years).

In Taiwan, water resources are rich. Tap-water is the principal domestic water supply and the water quality is stable. In contrast, the principal domestic water sources in remote islands are tap-water from desalination and re-treatment groundwater. To assess water quality on SWHs in remote islands, this study sampled tap-water and groundwater from households with SWHs. Analyses of water quality were conducted, including pH, total alkalinity, total hardness, chloride, and sulfate. The water quality assessment methods including LSI, RSI, PSI and LSCI, were employed to estimate the tendency of scaling and corrosion (Langelier 1936;

doi:10.18086/swc.2015.10.20 Available at http://proceedings.ises.org

Ryznar 1944; Larson and Skold 1958; Carrier 1965; Puckorius 1983; Degremont 1991; Seneviratne 2007; Prisyazhniuk 2007; Gacem et al 2012). The values of LSI, RSI, and PSI are primarily used to estimate the scaling potential of calcium carbonate ($CaCO_3$) in water. It is also known that LSI is the oldest and most commonly used. However, Seneviratne (2007) thought LSI does not estimate the corrosivity of water because corrosion may still occur due to dissolved oxygen and solids, such as chlorides or sulfates which increase the conductivity of water and corrosion rates. Nevertheless, the LSCI proposed by Larson and Skold (1958) can be employed to estimate the corrosiveness of water on low-carbon steel and steel samples. In this study, the water quality survey aimed to address the corrosion problem on the service life of SWHs.

2. SWHs in remote islands

As shown in Fig. 1, Penghu County (119°19' to 119°43' E, 23°12' to 23°47' N) with 37,151 households lies approximately on the Tropic of Cancer. There are five townships (Husi, Baisha, Siyu, Wang-An and Cimei township) and one city (Magong city). Kinmen County (118°24' E, 24°27' N) with 36,558 households, made up of 12 jurisdictional islands, is located in the subtropical oceanic climate zone. There are six townships (Jincheng, Jingsha, Jinhu, Jinning, Lieyu and Wuqiu). Lienchiang County (119°51' to 120°31' E, 25°55' to 26°44' N) with 2,423 households, which also lies within the subtropical oceanic climate zone, is the smallest county in Taiwan. There are four townships (Nangan, Beigan, Jyuguang and Dongyin). Juguang Township includes two major islands: Dongju Island and Xiju Island.

As previously mentioned, scaling and corrosion are of great concerns for SWHs in remote islands. As shown in Fig. 2a, there is pipe blockage caused by scaling (calcium carbonate analyzed by X-ray diffraction). Figure 2b shows pitting near the weld on a storage tank, made of 304 stainless steel. The maximum diameter of pitting hole was larger than 1 mm. Figure 2c shows absorption tube and pipe welding (304 stainless steel) leaks due to corrosion and subsequent scaling. It is considered that the pitting problem was caused by poor welding, high chloride concentration in the water, and high temperature accelerated corrosion.

Fig. 1: Remote islands location map.

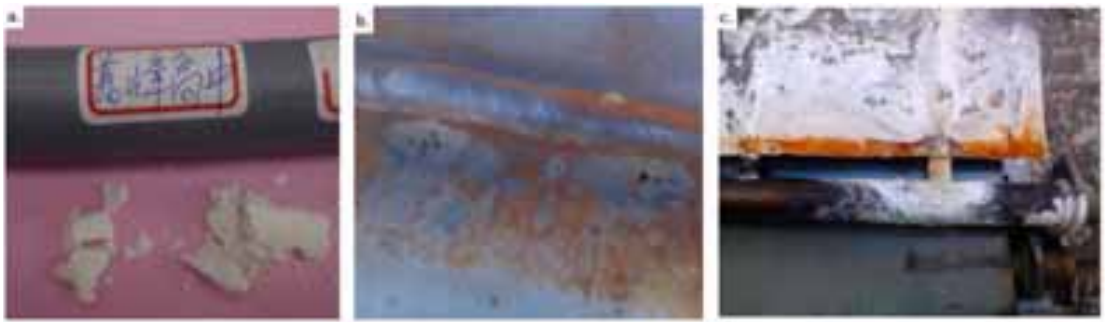

Fig. 2: (a) scaling of the connecting pipe; (b) pitting near the weld on storage tank; and (c) corrosion and scaling on solar collector plate.

In Taiwan, most tubes of collector plate and water storage tanks are made of 304 stainless steel, which is an alloy with higher levels of chromium (Cr) and nickel (Ni). It is known that the corrosion resistance of stainless steel is due to a sufficient amount of chromium to form a thin layer of a passivation film (chromium oxide). When the passive film is damaged by corrosion, uniform or localized corrosion will occur on the surface. According to the study by Parrott and Pitts (2011), when welding stainless steel, the high temperatures in the slow cooling process make the chromium and carbon form chromium carbide near the weld, causing the chromium to deplete. This makes the chromium passivation film easily damaged by corrosion, forming a significant local corrosion. Kopeliovich (2012) showed that electrochemical corrosion (oxidation-reduction reaction) by the chloride ions breaks down the passivation film on a stainless steel surface, and then causing pitting. Thus, presence of chloride ions (Cl^-) accelerates the corrosion rate. Figure 3 shows the concentration limits of 304 and 316 stainless steel at pH = 7 by chloride ions (Huang and Huang 2006). As the temperature reaches 80 ˚C, pitting occurred in 304 stainless steel, when the chloride ion concentration is higher than 35 mg/L. For 316 stainless steel, pitting occurred when the chloride ion concentration is higher than 130 mg/L.

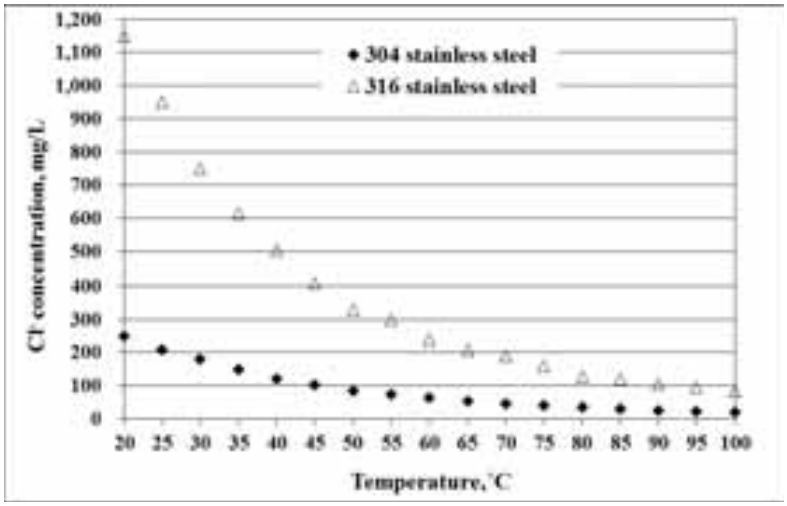

Fig. 3: Concentration limits of stainless steel corroded by chloride ions. (Huang and Huang, 2006).

3. Water quality Index-Assessment Methods

Water quality data for tap-water and groundwater were obtained from households with SWHs installed in 2013 and 2014. LSI, RSI, PSI, and LSCI were employed to assess scaling and corrosion in SWHs. The water qualities were analyzed by the Sustainable Environment Research Center/NCKU. In the remote islands, the temperature of SWHs can reach 70~80 ˚C in summer. Therefore, the designed water temperature was at 80 ˚C in this study.

3.1. LSI Assessment Method

Langelier (1936) first proposed a procedure for calculating the degree of saturation of water with respect to calcium carbonate, known as Langelier Saturation Index (LSI). Prisyazhniuk (2007) pointed out that LSI makes it possible to estimate the ability of water to corrode steel, or the tendency of water to form scaling.

Interpretation of LSI was given by Carrier Air Conditioning Company (U.S.), as shown in Table 1 (Carrier 1965). In the "Handbook of Drinking Water Quality" (DeZuane, 1997), LSI is given as follow.

$$LSI = pH - pH_S \quad (1)$$

where pH is measured in a solution of hydrogen ion activity; pH_S is a saturated sodium carbonate solution of hydrogen ion activity, as shown in Equation 2.

$$pH_S = (9.3+A+B)-(C+D) \quad (2)$$

where:

$A = (\log_{10}(TDS) -1)/10$; TDS: total dissolved solids, mg/L

$B = -13.12 \log_{10} (T + 273) + 34.55$; T : temperature, ˚C.

$C = \log_{10}$ (Hardness) - 0.4; Hardness, mg/L

$D = \log_{10}$ (Alkalinity); Alkalinity concentration, mg/L

Tab. 1: Interpretation of LSI (Carrier 1965)

LSI Value	Indication
2.0	Scale forming but non corrosive
0.5	Slightly scale forming and corrosive
0.0	Balanced but pitting corrosion possible
-0.5	Slightly corrosive but non-scale forming
-2.0	Serious corrosion

3.2. RSI Assessment Method

Ryznar Stability Index (RSI) was proposed by Ryznar (1944). The index is based on the calcium carbonate saturation index in water and can estimate the ability of scaling or corrosion, where $RSI = 2pH_S - pH$. Further, Table 2 shows the interpretation of RSI (Carrier 1965).

Tab. 2: Interpretation of RSI (Carrier 1965)

RSI Value	Indication
4.0 – 5.0	Heavy scale
5.0 – 6.0	Light scale
6.0 – 7.0	Little scale or corrosion
7.0 – 7.5	Corrosion significant
7.5 – 9.0	Heavy corrosion
> 9.0	Corrosion intolerable

3.3 *PSI Assessment Method*

The Puckorius Scaling Index (PSI) was proposed by Puckorius (1983). PSI is a modification of RSI with similar interpretations as shown in Table 2. When estimating the scaling and corrosion tendency of the solution, PSI addressed the buffering capacity in water and the maximum quantity of precipitate that can form when bringing water to equilibrium (Puckorius 1983). Therefore, the equilibrium pH (pH_{eq}) is adopted rather than pH, in which $PSI = 2pH_S - pH_{eq}$, where $pH_{eq} = 1.465 \times \log_{10}(\text{Alkalinity}) + 4.54$. The scaling was more serious with a smaller value of PSI, while a tendency of corrosion is observed for PSI > 6.0. It is also noted that the pH value for PSI is calculated according to the balanced hydrogen-ion activity in a solution, rather than measuring the pH with relevant apparatus. Therefore, the resulting PSI value is considered to be more accurate, comparing to both LSI and RSI values.

3.4 LSCI Assessment Method

The Larson–Skold Index (LSCI) describes the corrosivity of water toward mild steel (Larson and Skold 1958). The index is based on an evaluation of in-situ corrosion of mild steel lines transporting Great Lakes water. The index is the ratio of equivalents parts per million (ppm) of sulfate (SO_4^{2-}) and chloride (Cl^-) to the ppm of alkalinity in the form of bicarbonate plus carbonate ($HCO_3^- + CO_3^{2-}$), as given in Equation 3.

$$LSCI = \frac{C_{Cl^-} + C_{SO_4^{2-}}}{C_{HCO_3^-} + C_{CO_3^{2-}}} \quad (3)$$

where C was the concentration of mg/L (ppm); SO_4^{2-} was sulfate; Cl^- was chloride; HCO_3^- was bicarbonate; and CO_3^{2-} was carbonate.

LSCI does not considered temperature or pH buffering capacity as factors affecting corrosion behavior. However, previous studies indicated that stainless steel, copper, and aluminum can demonstrate pitting corrosion in environments that contain chlorine ions (Gallegos et al. 2005; Liang and Zhang 2006; Ghali 2010; Parrott and Pitts 2011; Kopeliovich 2012). Further, LSCI was interpreted as follows (Prisyazhniuk 2007):

LSCI < 0.8 — chlorides and sulfates did not influence the natural formation of the protective film;
0.8 < LSCI < 1.2 — chlorides and sulfates would hinder the formation of a protective film. A higher, as compared with normal, rate of steel corrosion was observed;
LSCI > 1.2 — as the value of the index grew, an increasingly higher rate of localized corrosion was observed.

4. Results and Discussion

Seneviratne (2007) demonstrated that scale formation and corrosion become more significant, as the temperature of a system increases. In this study, a hypothetical temperature of 80 °C was employed to estimate the indicators for assessing scaling and corrosion. Corrosion of metal components in SWHs is expected to be more significant when LSI value is less than zero, RSI value is greater than 7.0, PSI value is greater than 6.0, and LSCI value is greater than 0.8.

4.1 *Penghu County*

The results for SWHs using tap-water in Penghu County are shown in Table 3. Based on the analyses, the values of LSI, RSI and PSI showed a slight scaling tendency when SWHs using tap-water have, except for Siyu Township with a slight corrosion tendency due to a lower pH value. In addition, The LSCI is the ratio of ppm (mg/L) of SO_4^{2-} and Cl^- to the ppm of alkalinity. For the tap-water from desalination or groundwater re-treatment, it contains higher salts. The values of LSCI values for SWHs using tap-water are greater than 1.2, indicating a serious corrosion problem. Thus, although the values of LSI, RSI and PSI showed tap-water show a slight scaling tendency, a higher value Cl^- will result in corrosion of the passivation film on stainless steel surface. For SWHs using groundwater, the results are shown in Table 4. The values of LSI, RSI and PSI values show a serious scaling tendency for SWHs using groundwater, while the values of LSCI indicate a serious corrosion problem.

Also as shown in Tables 3 and 4, the levels of Cl^- concentration are greater than 127.3 and 203.0 mg/L for tap-water and groundwater, respectively. According to the study by Huang and Huang (2006), when the water temperature of SWHs reaches 80 ˚C and the Cl^- concentration level was higher than 35 mg/L, pitting would occur for SWHs using 304 stainless steel. Thus, the use of tap-water or groundwater for SWHs in Penghu County encounters a high risk of corrosion. Thus, 316 stainless steel or another corrosion-resistant material is required for extension of service period of SWHs.

Tab. 3: Assessment of scaling and corrosion tendency of tap-water quality in Penghu County

Tap-water	Magong	Husi	Baisha	Siyu	Wang-an	Cimei
Alkalinity, mg/L	87.9 ± 49.3	69.6 ± 40.0	257.2 ± 71.5	81.0 ± 5.3	110.0 ± 53.7	116.0 ± 5.7
pH	7.8 ± 0.5	7.7 ± 0.3	8.0 ± 0.3	7.2 ± 0.1	7.7 ± 0.1	7.8 ± 0.3
Cl^-, mg/L	177.3 ± 38.5	176.1 ± 24.3	223.4 ± 62.4	127.3 ± 7.5	253.5 ± 79.9	281.5 ± 13.4
SO_4^{2-}, mg/L	48.9 ± 23.5	49.5 ± 24.9	41.9 ± 15.9	11.7 ± 4.7	70.5 ± 15.1	38.5 ± 3.0
TDS, mg/L	494.3 ± 99.7	473.6 ± 112.6	774.8 ± 62.7	338.0 ± 3.5	672.0 ± 524.6	788.5 ± 31.8
Hardness, mg/L	111.0 ± 61.0	91.1 ± 55.7	126.5 ± 34.2	55.6 ± 63.6	172.5 ± 79.9	255.0 ± 0.0
HCO_3^-, mg/L	86.9 ± 48.7	69.1 ± 39.6	254.8 ± 71.4	80.9 ± 5.3	109.4 ± 53.3	115.2 ± 6.1

CO_3^{2-}, mg/L	0.9 ± 1.0	0.4 ± 0.5	2.4 ± 1.7	0.1 ± 0.0	0.6 ± 0.4	0.8 ± 0.4
LSI	0.7 ± 0.8	0.3 ± 0.5	1.4 ± 0.3	-0.3 ± 0.5	1.0 ± 0.5	1.3 ± 0.3
RSI	6.5 ± 1.2	7.0 ± 0.9	5.1 ± 0.4	7.8 ± 0.9	5.8 ± 0.9	5.3 ± 0.3
PSI	7.0 ± 1.5	7.5 ± 1.3	5.0 ± 0.7	7.7 ± 0.9	6.1 ± 1.2	5.5 ± 0.1
LSCI	3.7 ± 2.6	4.1 ± 2.0	1.2 ± 0.8	1.7 ± 0.1	3.2 ± 1.0	2.8 ± 0.0

Tab. 4: Assessment of scaling and corrosion tendency of groundwater quality in Penghu County

Groundwater	Magong	Husi	Baisha	Siyu	Wang-an*	Cimei
Alkalinity, mg/L	153.0 ± 40.0	177.3 ± 128.7	286.0 ± 107.0	138.5 ± 78.5	144.0	287.5 ± 13.4
pH	8.4 ± 0.3	7.5 ± 0.4	8.0 ± 0.3	7.7 ± 0.3	7.4	7.9 ± 0.0
Cl^-, mg/L	306.8 ± 151.8	203.0 ± 89.9	254.7 ± 67.0	214.0 ± 116.0	893.0	236.5 ± 46.0
SO_4^{2-}, mg/L	37.3 ± 16.8	35.1 ± 7.6	66.5 ± 15.8	114.9 ±138.7	7.7	124.5 ± 33.2
TDS, mg/L	764.8 ± 309.4	562.8 ± 146.5	842.7 ± 206.5	616.0 ± 390.3	2050.0	1018.0 ± 53.7
Hardness, mg/L	127.6 ± 77.7	185.2 ± 109.2	224.0 ± 109.3	135.5 ± 163.4	332.0	242.5 ± 99.7
HCO_3^-, mg/L	149.0 ± 41.0	176.5 ± 128.2	283.3 ± 107.8	137.5 ± 77.5	143.7	285.3 ± 13.5
CO_3^{2-}, mg/L	3.8 ± 1.9	0.7 ± 0.6	2.7 ± 0.7	0.9 ± 0.9	0.3	2.2 ± 0.0
LSI	1.6 ± 0.2	0.8 ± 1.1	1.7 ± 0.1	0.7 ± 1.3	1.0	1.7 ± 0.2
RSI	5.2 ± 0.5	5.9 ± 1.9	4.5 ± 0.6	6.3 ± 2.3	5.4	4.5 ± 0.4
PSI	5.9 ± 0.9	5.7 ± 2.2	4.5 ± 1.2	6.5 ± 2.4	5.0	4.3 ± 0.4
LSCI	2.4 ± 1.1	2.4 ± 2.7	1.2 ± 0.5	2.2 ± 0.6	6.3	1.3 ± 0.0

* Only one sample

4.2 *Kinmen County*

For SWHs using tap-water in Kinmen County, the data are shown in Table 5. The values of LSI, RSI, and PSI show a slight to serious corrosion tendency for SWHs using tap-water, corresponding to a lower value in the pH value. The LSCI analysis also indicates a serious corrosion problem ($2.8 \geq LSCI \geq 1.7$), except for the Lieyu Township. Note that tap-water in Lieyu Township is mainly from the rain-water in a reservoir. Therefore, the corrosion problems should be less significant. Further, the results for SWHs using groundwater are listed in Table 6. The values of LSI, RSI, and PSI show a slight to serious corrosion tendency. In addition, the values of LSCI are higher than those of tap water ($9.1 \geq LSCI \geq 1.2$). Higher LSCI value of groundwater in Jinning is due to low alkalinity concentration but not high Cl^- concentration. Except for the Lieyu Township, the levels of Cl^- concentration are 45.2-104.5 and 69.0-167.0 mg/L for tap-water and groundwater, respectively. Although the effect of Cl^- concentration level on corrosion problem for SWHs is less significant those systems installed in Penghu County, better corrosion-resistant materials are also required.

Tab. 5: Assessment of scaling and corrosion tendency of tap-water quality in Kinmen County

Tap-water	Jincheng	Jinhu	Jinsha	Jinning	Lieyu*
Alkalinity, mg/L	35.0 ± 10.4	66.4 ± 9.7	61.5 ± 26.7	36.3 ± 14.3	56.0
pH	6.3 ± 0.5	7.1 ± 0.4	7.5 ± 0.4	6.2 ± 0.7	6.9
Cl^-, mg/L	54.3 ± 15.5	104.5 ± 28.0	101.2 ± 54.1	45.2 ± 2.9	5.5
SO_4^{2-}, mg/L	15.7 ± 15.6	72.1 ± 27.9	68.4 ± 32.9	17.5 ± 33.3	5.1
TDS, mg/L	204.2 ± 58.6	387.4 ± 45.8	355.2 ± 143.8	185.8 ± 43.4	203.0
Hardness, mg/L	36.5 ± 12.3	122.8 ± 20.3	106.4 ± 42.1	28.0 ± 6.1	36.0
HCO_3^-, mg/L	35.0 ±10.4	66.3 ± 9.7	61.3 ± 26.8	36.3 ± 14.3	56.0

CO_3^{2-}, mg/L	0.0 ± 0.0	0.1 ± 0.1	0.2 ± 0.2	0.0 ± 0.0	0.0
LSI	-1.6 ± 0.6	0.0 ± 0.3	0.2 ± 0.4	-1.8 ± 0.8	-0.8
RSI	9.5 ± 0.8	7.1 ± 0.4	7.0 ± 0.7	9.8 ± 1.0	8.4
PSI	9.0 ± 0.7	7.0 ± 0.4	7.4 ± 1.0	9.2 ± 0.7	8.2
LSCI	2.0 ± 0.4	2.8 ± 1.0	2.7 ± 0.8	1.7 ± 0.4	0.2

* Only one sample

Tab. 6: Assessment of scaling and corrosion tendency of groundwater quality in Kinmen County

Groundwater	Jincheng	Jinhu	Jinsha	Jinning	Lieyu
Alkalinity, mg/L	84.7 ± 103.7	81.2 ± 46.8	109.5 ± 68.8	11.0 ± 7.6	136.7 ± 35.5
pH	5.5 ± 1.1	6.3 ± 0.9	6.7 ± 1.0	4.8 ± 0.6	6.6 ± 0.2
Cl^-, mg/L	69.0 ± 39.8	99.6 ± 46.6	167.0 ± 20.2	75.2 ± 40.1	106.1 ± 95.7
SO_4^{2-}, mg/L	35.0 ± 43.3	49.2 ± 37.7	93.3 ± 26.2	16.7 ± 12.0	66.0 ± 30.0
TDS, mg/L	453.0 ± 233.3	425.5 ± 213.3	657.3 ± 151.1	275.5 ± 195.8	646.2 ± 223.5
Hardness, mg/L	108.6 ± 65.7	111.6 ± 69.7	176.5 ± 88.7	54.7 ± 46.5	215.3 ± 85.9
HCO_3^-, mg/L	84.6 ± 103.7	81.1 ± 46.8	109.3 ± 68.8	11.0 ± 7.6	136.6 ± 35.5
CO_3^{2-}, mg/L	0.0 ± 0.0	0.1 ± 0.1	0.2 ± 0.2	0.0 ± 0.0	0.1 ± 0.0
LSI	-1.9 ± 2.2	-0.9 ± 1.5	-0.1 ± 1.3	-3.6 ± 1.1	0.1 ± 0.3
RSI	9.3 ± 3.2	8.1 ± 2.1	7.0 ± 1.6	12.0 ± 1.7	6.5 ± 0.5
PSI	7.8 ± 3.3	7.1 ± 1.6	6.3 ± 1.2	10.8 ± 1.6	5.5 ± 0.6
LSCI	2.5 ± 2.1	1.9 ± 0.7	4.0 ± 4.0	9.1 ± 4.5	1.2 ± 0.8

4.3 *Lienchiang County*

The results for SWHs using tap-water in Lienchiang County are listed in Table 7. The values of LSI, RSI and PSI also indicate a slight to serious corrosion tendency, except for Dongju Island, which shows a slight scaling tendency. The values of LSCI range from 1.2 to 24.1. A higher rate of steel corrosion can be expected. For SWHs using groundwater, the data are shown in Table 8. In Beigan and Dongju Islands, the values of LSI, RSI, and PSI show a slight scaling tendency, while there is a slight to heavy corrosion tendency in other townships. From the analysis of LSCI, ranging from 1.4 to 4.1, the rate of steel corrosion for SWHs using groundwater is less significant than that using tap-water. Further, the levels of Cl^- concentration are also shown in Tables 7 and 8. The values are 80.9-162.5 and 121.5-199.7 mg/L for tap-water and groundwater, respectively. Thus, the level of Cl^- concentration is also a critical issue for SWHs installed in Lienchiang County.

Tab. 7: Assessment of scaling and corrosion tendency of tap-water quality in Lienchiang County

Tap-water	Nangan	Beigan	Xiju Island	Dongju Island	Dongyin
Alkalinity, mg/L	53.0 ± 1.4	40.0 ± 0.0	11.0 ± 1.4	113.0 ± 1.4	6.0 ± 0.0
pH	7.6 ± 0.0	7.9 ± 0.0	7.6 ± 0.0	7.4 ± 0.2	7.0 ± 0.2
Cl^-, mg/L	122.5 ± 6.4	162.5 ± 3.5	114.0 ± 0.0	80.9 ± 3.4	140.7 ± 8.1
SO_4^{2-}, mg/L	52.1 ± 1.9	22.8 ± 0.6	4.4 ± 2.2	26.8 ± 2.1	3.6 ± 1.5
TDS, mg/L	369.0 ± 14.1	354.5 ± 7.8	227.5 ± 12.0	379.5 ± 6.4	293.3 ± 12.6
Hardness, mg/L	107.0 ± 5.7	63.4 ± 0.0	13.9 ± 8.4	139.0 ± 0.0	11.5 ± 4.2
HCO_3^-, mg/L	52.8 ± 1.4	39.6 ± 0.0	10.9 ± 1.4	112.7 ± 1.3	6.0 ± 0.0

CO_3^{2-}, mg/L	0.2 ± 0.0	0.3 ± 0.0	0.0 ± 0.0	0.3 ± 0.1	0.0 ± 0.0
LSI	0.4 ± 0.1	0.4 ± 0.0	-1.2 ± 0.4	0.6 ± 0.2	-2.3 ± 0.4
RSI	6.8 ± 0.1	7.2 ± 0.0	10.0 ± 0.7	6.1 ± 0.2	11.7 ± 0.5
PSI	7.4 ± 0.1	8.3 ± 0.0	11.6 ± 0.8	6.0 ± 0.0	12.9 ± 0.3
LSCI	3.3 ± 0.1	4.6 ± 0.1	10.9 ± 1.2	1.0 ± 0.0	24.1 ± 1.5

Tab. 8: Assessment of scaling and corrosion tendency of groundwater quality in Lienchiang County

Groundwater	Nangan	Beigan	Xiju Island	Dongju Island	Dongyin
Alkalinity, mg/L	81.0 ± 32.5	123.0 ± 36.1	50.0 ± 31.1	122.0 ± 8.5	51.0 ± 14.8
pH	6.4 ± 0.4	6.8 ± 0.5	6.8 ± 0.4	7.6 ± 1.2	6.7 ± 0.3
Cl^-, mg/L	141.5 ± 13.4	199.7 ± 68.5	121.5 ± 3.5	131.6 ± 77.0	143.4 ± 42.1
SO_4^{2-}, mg/L	42.9 ± 7.1	58.5 ± 15.9	23.2 ± 17.7	39.2 ± 4.8	51.6 ± 13.2
TDS, mg/L	521.0 ± 35.4	731.0 ± 294.7	366.0 ± 130.1	492.5 ± 122.3	493.2 ± 92.1
Hardness, mg/L	174.5 ± 38.9	282.7 ± 141.4	85.3 ± 70.3	152.5 ± 24.7	92.5 ± 17.4
HCO_3^-, mg/L	81.0 ± 32.5	127.9 ± 36.0	50.0 ± 31.1	120.2 ± 6.0	50.4 ± 14.8
CO_3^{2-}, mg/L	0.0 ± 0.0	0.1 ± 0.1	0.0 ± 0.0	1.7 ± 2.3	0.0 ± 0.0
LSI	-0.5 ± 0.6	0.3 ± 0.6	-0.7 ± 0.3	0.9 ± 1.3	-0.9 ± 0.3
RSI	7.3 ± 0.9	6.3 ± 0.8	8.1 ± 1.0	5.8 ± 1.4	8.4 ± 0.3
PSI	6.4 ± 0.8	5.4 ± 1.0	8.0 ± 1.8	5.9 ± 0.2	8.0 ± 0.5
LSCI	2.4 ± 0.7	2.0 ± 0.4	3.5 ± 1.9	1.4 ± 0.5	4.1 ± 1.3

5. Conclusions

In Taiwan, long-term groundwater pumping has caused serious seawater intrusion in remote islands. Tap-water from desalination or groundwater re-treatment results in higher Cl^- concentration level. Therefore, water quality is a critical issue to disseminate SWHs. In this study, the samples of tap-water and groundwater in remote islands were collected and analyzed. In Penghu County, the values of LSI, RSI, and PSI for SWHs using tap-water and groundwater showed a slight scaling tendency, but all LSCI values indicated a serious corrosion tendency. In Kinmen and Lienchiang Counties, all index showed a corrosion tendency for both tap-water and groundwater. In addition, the issue of higher Cl^- concentration level in Penghu County should be addressed. Therefore, the commonly 304 stainless steel used should be replaced in order to delay pitting for SWHs and extend its service life.

Acknowledgements

This work was supported by the Bureau of Energy, the Ministry of Economic Affairs (103-D0303), Taiwan, Republic of China.

References:

Carrier Air Conditioning Company, 1965. Handbook of Air Conditioning System Design. McGraw-Hill Books. New York.

Chang, K.C., Lin, W.M., Chung, K.M., 2013. Solar thermal market in Taiwan. Energy Policy 55, 477–482

Degremont, 1991. Water Treatment Handbook. Sixth edition, distributed by Lavoisier Publishing, Paris, France.

DeZuane, J., 1997. Handbook of drinking water quality, 2nd ed., New York : Van Nostrand Reinhold

Directorate-General of Budget, Accounting and Statistics (DGBAS) Home Page, Executive Yuan, Republic of China (Taiwan). Key Economic and Social Indicators (2013) Available online: http://www.dgbas.gov.tw. Accessed 1 April 2014.

Gacem, Y., Taleb, S., Ramdani, A., Senadjki, S., Ghaffour, N., 2012, Physical and chemical assessment of MSF distillate and SWRO product for drinking purpose. Desalination 290, 107-114.

Gallegos, A.A., Martinez, S.S., Ramirez Reyes, J.L., 2005. Evaluation of Water Corrosivity Using a Corrosion Rate Model for a Cooling Water System. J. New Materials for Electrochemical Systems 8, 133-142.
Ghali, E., 2010. Corrosion resistance of aluminum and magnesium alloys understanding, performance, and testing. John Wiley & Sons, New Jersey, USA, 49-77.
Huang, X, Huang, C., 2006. Effect of Chloride Ions in Cooling Water on the Material Choice of Plates in Plate Heat Exchangers. Beijing, China, Petrochemical Design 23(2), 44-46.
Kopeliovich, D. 2012. Pitting Corrosion. SubsTech Web. http://www.substech.com/dokuwiki/doku.php?id=pitting_corrosion. Accessed 1 October 2014.
Langelier, F., 1936. The analytical control of anti-corrosion water treatment. J. American Water Works Association 28(10), 1500-1521.
Larson, T.E., Skold, R.V., 1958. Laboratory Studies Relating Mineral Quality of Water To Corrosion of Steel and Cast Iron. Corrosion 14(6), 43-46.
Liang, C.H., Zhang, W., 2006. Pitting Corrosion Mechanisms and Characteristics of Aluminum in Solar Heating Systems. J. the Chinese Chemical Society 53, 313-318.
Lin, W.M., Fan K.C., Chang, K.C., Chung, K.M., 2013. Dissemination of Solar Water Heaters in Taiwan: The Case of Remote Islands. Energies 6(10), 5101-5113.
Parrott, R., Pitt,s H., 2011. Chloride Stress Corrosion Cracking in Austenitic Stainless Steel. The Health and Safety Laboratory for the Health and Safety Executive: Buxton, UK
Prisyazhniuk, V.A., 2007. Prognosticating scale-forming properties of water. Applied Thermal Engineering 27, 1637-1641.
Puckorius, P., 1983. Getting A Better Reading on Scaling Tendency of Cooling Water. Power 127(9), 79-81.
Ryznar, J.W., 1944 A new index for determining the amount of calcium carbonate scale formed by water. J. American Water Works Association 36, 472-494.
Seneviratne, M., 2007. A Practical Approach to Water Conservation for Commercial and Industrial Facilities. Elsevier, 83-116

Conference Proceedings

Solar World Congress 2015
Daegu, Korea, 08 – 12 November 2015

DEVELOPMENT AND TESTING OF A NOVEL METHOD FOR THE DETERMINATION OF THE EFFICIENCY OF CONCENTRATING SOLAR THERMAL COLLECTORS

A. Anthrakidis[1], U. Herrmann[1], C. Schorn[1a], K. Schwarzer[2], P. Wedding[1], F. Weis[1]

[1] Solar-Institut Jülich of FH Aachen University of Applied Sciences [SIJ], Heinrich-Mußmann-Str.5, 52428 Jülich, Germany

[2] Ingenieurbüro für Energie und Umwelt [IBEU], Tuchbleiche 12, 52428 Jülich-Barmen, Germany

[a)] Corresponding author: schorn@sij.fh-aachen.de

Abstract

The objective of this research is the development, evaluation and analyzation of a new test method, called “rapid test method”, for fast and inexpensive assessment of concentrating collectors. The rapid test method aims to derive the instantaneous efficiency curve of a parabolic trough collector. Therefore, a new reference parabolic trough collector was designed and installed at a test rig in accordance with ISO 9806. The determination of the instantaneous efficiency curve according to the rapid test method was compared to the efficiency curve based on ISO 9806. The comparison shows that the rapid test method delivers reproducible and reliable values for the characteristic curve of linear concentrating collectors. The obtained results are within the limits of the measurement uncertainty of a characteristic curve based on ISO 9806. Therefore, the method can be regarded as reliable, inexpensive and easy to use alternative to the conventional measuring method.

Keywords: Rapid test method, ISO 9806, instantaneous efficiency curve, concentrating solar collector, parabolic trough collector, process heat, receiver testing

1. Introduction

The project "Development and testing of a novel method for determining the efficiency of concentrating solar thermal collectors" aims to examine, analyze and optimize the novel test method, called “rapid test method”, for small size parabolic trough collectors.

The conventional test method to evaluate the efficiency of solar thermal collectors requires high cost for the testing equipment, material and sensors. In addition, the test method requires a large number of sunny days that comply with the criteria of the standard. With the novel rapid test method the determination of performance data in the development phase of parabolic trough collectors can be conducted in a rapid, smart and inexpensive manner. Compared to the conventional measurement method in accordance to the ISO 9806:2013 standard, the application of the rapid test method can help to accelerate development steps, reduce cost and encourage small and medium-sized enterprises to tap the market segment of concentrating solar thermal collectors.

The theoretical and practical testing of the rapid test procedure is performed on a newly established test rig. Among others the test rig is equipped with a reference parabolic trough collector in order to ensure a high degree of comparability of the measurements.

2. The rapid test method

The rapid test method uses the results of two independent measurements - the stagnation temperature and the heat losses - to calculate the instantaneous efficiency curve of a parabolic trough collector. With the results of these measurements the efficiency curve can be numerically derived. Figure 1 illustrates the sequence of this approach.

The first set of measurements comprises the measurement of the stagnation temperature of a parabolic concentrator and the ambient air temperature at different levels of irradiation. The stagnation temperature is

doi:10.18086/swc.2015.10.21 Available at http://proceedings.ises.org

defined as the temperature where the system is at a steady state and in the thermal equilibrium with the environment. The irradiated energy from the sun on the collector is equal to the thermal losses, resulting in a collector efficiency of zero. The determination of the stagnation curve is carried out without water or oil as a heat transfer medium, but with air. In the absorber tube of the collector to be tested, solely air at atmospheric pressure is used, which highly reduces the complexity of test equipment. The general form of the equation for the stagnation curve is considered as: $f(G_u) = -a\ G_u^2 + b \cdot G_u$ and an example is presented in figure 2.

Secondly, the heat losses of the receiver as a function of the receiver temperature have to be determined. In this measurement a defined heat flow is transferred to the receiver pipe from the inside and the resulting wall temperature is measured. The heat can either be transferred by an electrical heating element or by a heat transfer medium that was heated up by an external heater. The application with an electrical heating element has the advantage that no closed loop for the heat transfer is required. Moreover, the application is regarded as cost effective and accurate. The general form of the equation for the heat loss curve is considered as: $f(\Delta T) = a \cdot \Delta T + b \cdot \Delta T^4$ An example for a typical heat loss curve is given in figure 3.

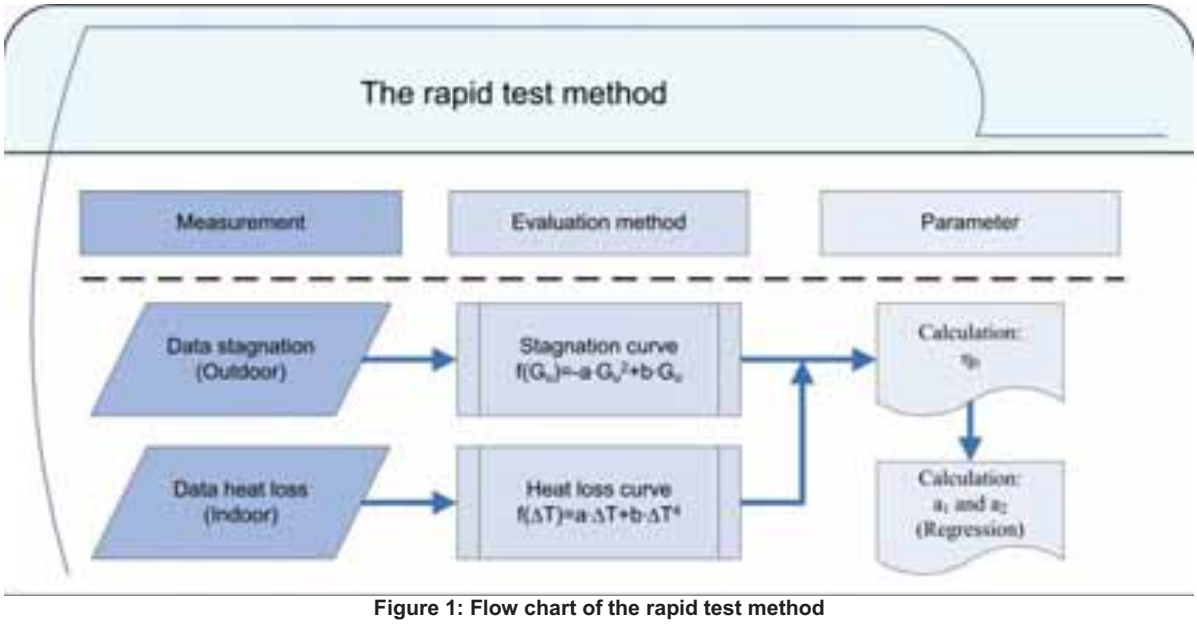

Figure 1: Flow chart of the rapid test method

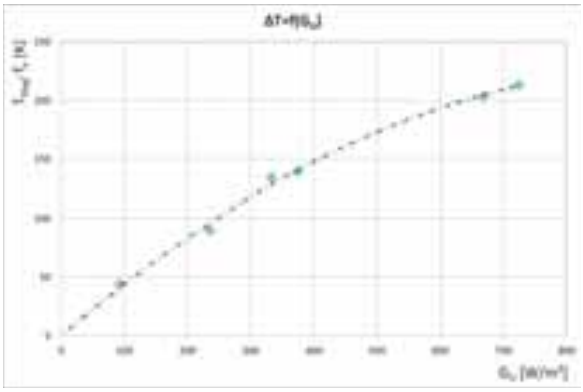

Figure 2: Example for the stagnation curve of a collector at different levels of irradiations

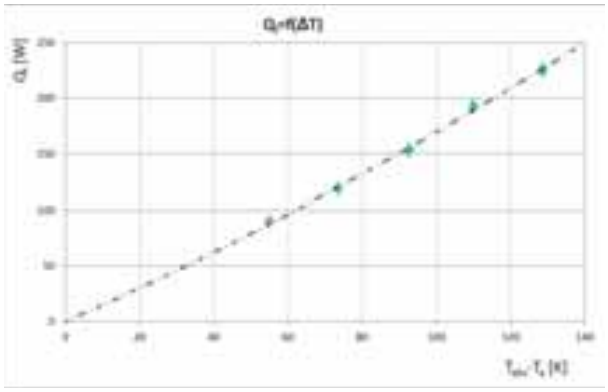

Figure 3: Example of a heat loss curve as a function of ΔT

Table 1: Nomenclature of the used indices and its description

Indices	Description	Unit	Indices	Description	Unit
η_0	Optical efficiency	[-]	G	Hemispherical solar irradiance	[W/m²]
η	Instantaneous efficiency	[-]	G_d	Diffuse solar irradiance	[W/m²]
a_1	Heat transfer coefficient	[W/(m²K)]	G_u	Usable solar irradiance	[W/m²]
a_2	Temperature dependence of the heat transfer coefficient	[W/(m²K²)]	G_b	Direct solar irradiance [DNI]	[W/m²]
ΔT	Temperature difference	[K]	Q_y	Thermal yield	[W]
$T_{fl;m}$	Mean fluid temperature	[°C]	Q_l	Thermal losses	[W]
T_a	Ambient temperature (ventilated)	[°C]	T^*_m	Reduced temperature difference	[(m²K)/W]
$T_{fl;Outlet}$	Collector outlet temperature	[°C]	T_{Stag}	Stagnation temperature	[°C]
$T_{fl;Inlet}$	Collector inlet temperature	[°C]	C	Concentration ratio	[-]
T_{Abs}	Absorber temperature	[°C]	A_p	Aperture area	[m²]
T_{corr}	Correction factor	[K]	F'	Collector efficiency factor	[-]

The way how the efficiency curve is derived from these two curves is explained below. Parameters and indices used are given in table 1.

The basic equation for the instantaneous efficiency curve is:

$$\eta = \eta_0 - \left(a_1 \cdot \frac{\Delta T}{G_u} + a_2 \cdot \frac{\Delta T^2}{G_u} \right) \qquad \text{eq.1}$$

Whereas the usable solar energy is defined as / 4 /:

$$G_u = G - G_d + \left(\frac{1}{C} \cdot G_d \right) \qquad \text{eq.2}$$

By introducing eq. 2 for G_u, the diffuse radiation that strikes the receiver's upper surface is also included in the examination. Up to a concentration ratio of approximately 50, the non-observance produces a non-negligible error. Moreover this approach allows the definition of the exact ratio between diffuse and hemispherical irradiation for different values of irradiance. For the rapid test method the temperature difference between stagnation temperature and ambient temperature is considered as ΔT:

$$\Delta T = T_{Stag} - T_a \qquad \text{eq.3a}$$

Whereas at the ISO based method the temperature difference is stated as:

$$\Delta T = \left(\frac{T_{fl;Outlet} + T_{fl;Intlet}}{2} \right) - T_a \qquad \text{eq.3b}$$

The reduced temperature difference is given by:

$$T^*_m = \frac{\Delta T}{G_u} \qquad \text{eq.3c}$$

To calculation the thermal yield of a collector at a certain irradiation and temperature level the following equation is valid:

$$Q_y = A_p \cdot G_u \cdot \eta \qquad \text{eq.4}$$

Consequently the thermal losses at an optional point can be expressed as:

$$Q_l = A_p \cdot G_u \cdot (\eta_0 - \eta) \qquad \text{eq.5a}$$

Hence, for the optical efficiency of a collector the following equation is valid:

$$\eta_0 = \eta + \frac{Q_l}{A_p \cdot G_u} \qquad \text{eq.5b}$$

For the stagnation temperatures measured during the rapid test method, the thermal losses are equal to the energy input into the system and the instantaneous efficiency is equal to zero. $\eta = 0$

From this consideration results the following formula:

$$\eta_0 = \frac{Q_l}{A_p \cdot G_u} \qquad \text{eq.6}$$

The heat loss at various radiation levels can be calculated using a combination of the stagnation curve and the heat loss curve. First, with the determined stagnation curve the temperature difference ΔT can be calculated for the corresponding irradiation. Second, the obtained temperature difference ΔT can be used in the formula of the heat loss curve to calculate the corresponding values. The numerical solution of the thermal loss at various radiation levels is then given by $Q_l = f(G_u)$. With the results obtained the optical efficiency can be calculated for each point i within the interval of the expected solar radiation G_u (0 W/m² ≤ G_u < 1000 W/m²). Resulting values for the optical efficiency at different radiation levels are presented in figure 4.

$$\eta_{0,i} = \frac{Q_{l,i}}{A_p \cdot G_{u,i}} \qquad \text{eq.7}$$

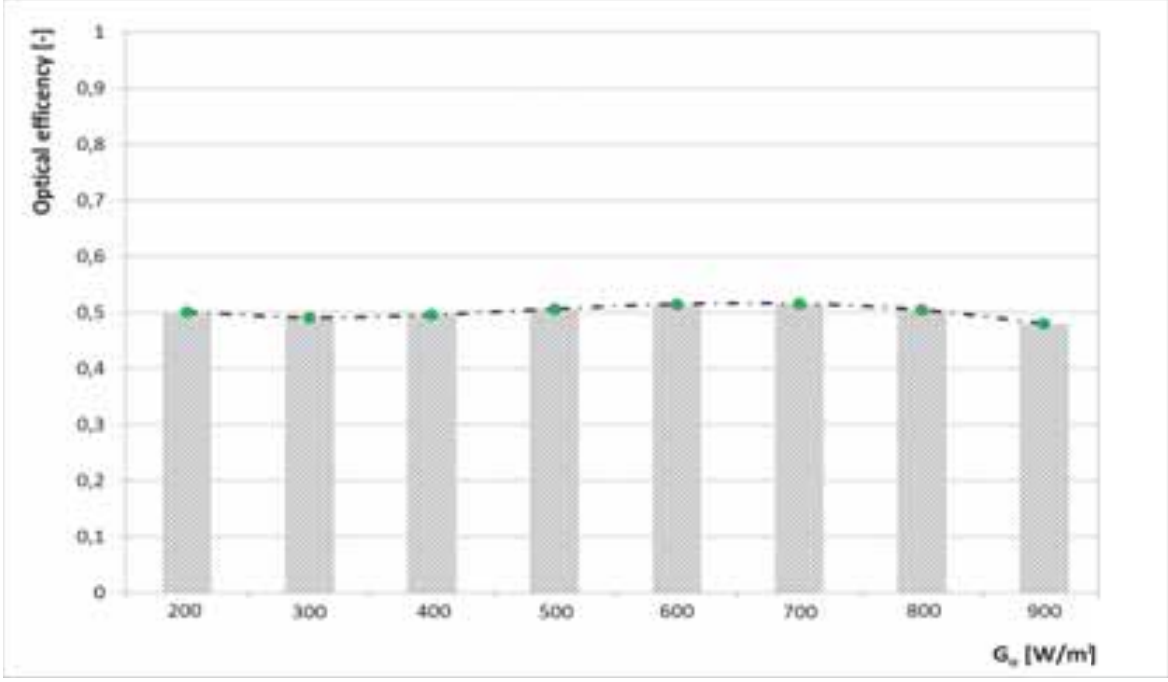

Figure 4: Example for the calculated optical efficiency at different supporting values between the lower and upper limit of the measurements

Uncertainties of measurements occur during the determination of the stagnation curve and the heat loss curve and have an effect on the value of the optical efficiency. The calculated optical efficiency varies slightly for different values of G_u, as shown in figure 4. This variation is based on the combination of two equations,

resulting in a higher-order function with a discontinuity at the saddle point of the equation. The mean value of the function of the results obtained for the optical efficiency will give a good approximation for a value η_0 for the further evaluation of the rapid test method. The limits for the integration will be set between the lowest $G_{u,low}$ and highest $G_{u,high}$ measuring point of the stagnation curve.

$$\eta_{0,mean} = \frac{1}{G_{u,high} - G_{u,low}} \cdot \int_{G_{u,low}}^{G_{u,high}} f(G_u) \cdot dG_u \qquad \text{eq.8}$$

When the optical efficiency is determined, the values for the heat loss coefficient a_1 and a_2 can be derived. The heat loss coefficient a_1 and the temperature-dependent heat transfer coefficient a_2 will be calculated by means of a regression in accordance to the least-square method. Since the instantaneous efficiency is set to zero at the stagnation point eq. 1 can be rewritten as:

$$\eta_{0,i} = \left(a_1 \cdot \frac{\Delta T_{,i}}{G_{u,i}} + a_2 \cdot \frac{\Delta T_{,i}^{\,2}}{G_{u,i}} \right) \qquad \text{eq.9}$$

To transfer the measured results of the rapid test method to real operation, the following three assumptions have to be made:

- A flow of a heat transfer medium through the absorber takes place.
- The operating point is in a steady state at a certain irradiance level and can be standardized to any irradiance level.
- The mean inner absorber tube temperature, which is measured at the rapid test method, is equal to the mean fluid temperature during a test in accordance with the standard. Otherwise a correction factor has to be determined.

$$T_{Abs} = T_{fl,m} + T_{Corr} \qquad \text{eq.10}$$

3. Test setup

At the Solar-Institut Jülich, a test bench infrastructure is operated, which allows to measure individual receiver and small parabolic trough collectors on a biaxial tracking test rig. Measurements of the solar thermal collectors are carried out based on the ISO 9806. The test rig operates with a pressurized water circuit / 1 / at temperatures up to 200 °C and at mass flows up to 200 g/s. The verification of the rapid test method was conducted with a direct comparison to the steady-state measurement method based on ISO 9806:2013. All tests were performed at the same collector with an identical receiver and insulation. The receiver openings shall be sealed to prevent free convection. Furthermore, a suitable number of measurement points in the absorber tube have to be chosen in order to determine a meaningful reference temperature. Figure 5 shows the test rig for the operation of the parabolic trough collector, which is in accordance with ISO 9806:2013. In figure 6 a reference parabolic trough collector is presented. The examined collector can biaxial tracked towards the sun during the tests and the incident angle can be checked and documented automatically by a heliosensor.

Figure 5: Test rig for conditioning of pressurized water and the data acquisition unit

Figure 6: Biaxial rotating test platform with an installed reference collector

4. Results

In July 2014 the first measurements following the rapid test method and the conventional measurements according to ISO 9806 were taken at the SIJ. Both measurements were done at the same collector prototype in order to compare the results of the rapid test method with the ISO based method.

The concentration factor of $C \sim 25$ of the tested collector refers to an absorber tube diameter $\varnothing_a$ of 35 mm. The aperture dimension is 966 mm x 1688 mm. A reflective aluminum sheet was used as reflector. The receiver of this PTC consists of a black chrome coated absorber tube and a glass envelope tube without vacuum insulation. Over the period of the measurement time a reproducible efficiency curve was determined. Efficiency curves were developed with both methods, with the rapid test and the ISO 9806 method. With both curves yearly yield calculation were performed exemplarily for a biaxial tracking collector in Würzburg / Germany using the Energy Output Calculator ScenoCalc / 10 /.The deviation between both results was below 4.0%, based on an operating temperature at 50 °C, 75 °C and 100 °C.

For the rapid test method various criteria were defined, in order to evaluate measurement points during a steady-state phase. First measurements of the collector time constant returned values up to 3 min. This means that the temperature compensation of the receiver and its components requires a comparatively long time until it is in a thermal equilibrium with the environment. In the beginning the criteria as shown below in Table 2 derived from the ISO 9806 were applied. However, this resulted in occasional deviations in the evaluation. The results are distributed over a larger interval of measurement uncertainty. Since the stability of the measured stagnation temperature over time is the most important parameter for the evaluation, a more stringent criterion for the stability of the measured temperature was introduced for further measurements. The tolerable deviation of T_{Stag} was reduced to ± 0,5 °C/min**,** in return 1 min of stable conditions is enough to get one measurement point. An analysis of the available data with the criteria of the approach 2 gave a better approximation of the characteristic curve from the rapid test method towards the characteristic curve in accordance to ISO 9806.

Table 2: Criteria for the evaluation of measurements points according to the rapid test method

Criteria	Limit value approach 1	Limit value approach 2	Comment
T_a	± 0,5 °C of mean value	± 0,5 °C of mean value	Derived from measurements
G	$G_d/G_U \leq 30\%$	$G_U \geq 100$ W/m²	Derived from measurements
T_{Stag} Stability	± 1 °C / min	± 0,5 °C / min	Derived from measurements
time mean values	4 min after stability	1 min after stability	Derived from measurements
Wind *	3 m/s ± 1 m/s	3 m/s ± 1 m/s	On the basis of ISO 9806
G_u	± 50 W/m² of mean value	± 50 W/m² of mean value	On the basis of ISO 9806

*) The dependency of the wind is in accordance with ISO 9806 only relevant, if the receiver is constructed without a glass envelope tube or if a concentration ratio <3 exists.

It is recommended to determine the time constant before applying the rapid test method in order to obtain a statement about the heating behavior and thus to identify associated conditioning times of the receiver.

In figure 7, the characteristic curve based on ISO 9806 and the curve according to the rapid test method are shown. The calculated stagnation temperature of both methods differs by 4.2 °C at G_u = 1000 W/m² and T_a = 20 °C. The determined measurement points based on the ISO procedure are set in a lower range of the reduced temperature difference, since the corresponding measurements currently limited to an outlet temperature of 200 °C. The measuring points of the rapid test method are in the higher range of the reduced temperature difference, due to the obtained stagnation temperature. For additional information the measurement uncertainty at the respective measuring points are entered. The values are calculated by the Guide of Measurement Uncertainty (GUM). The expanded uncertainty is calculated by multiplying the coverage factor k = 2 with the standard uncertainty of the particular measurement method. The measurement uncertainty is traceable to the specifications and the results from the calibration of the used sensors. The calculated measurement uncertainties are given in the table 3 below.

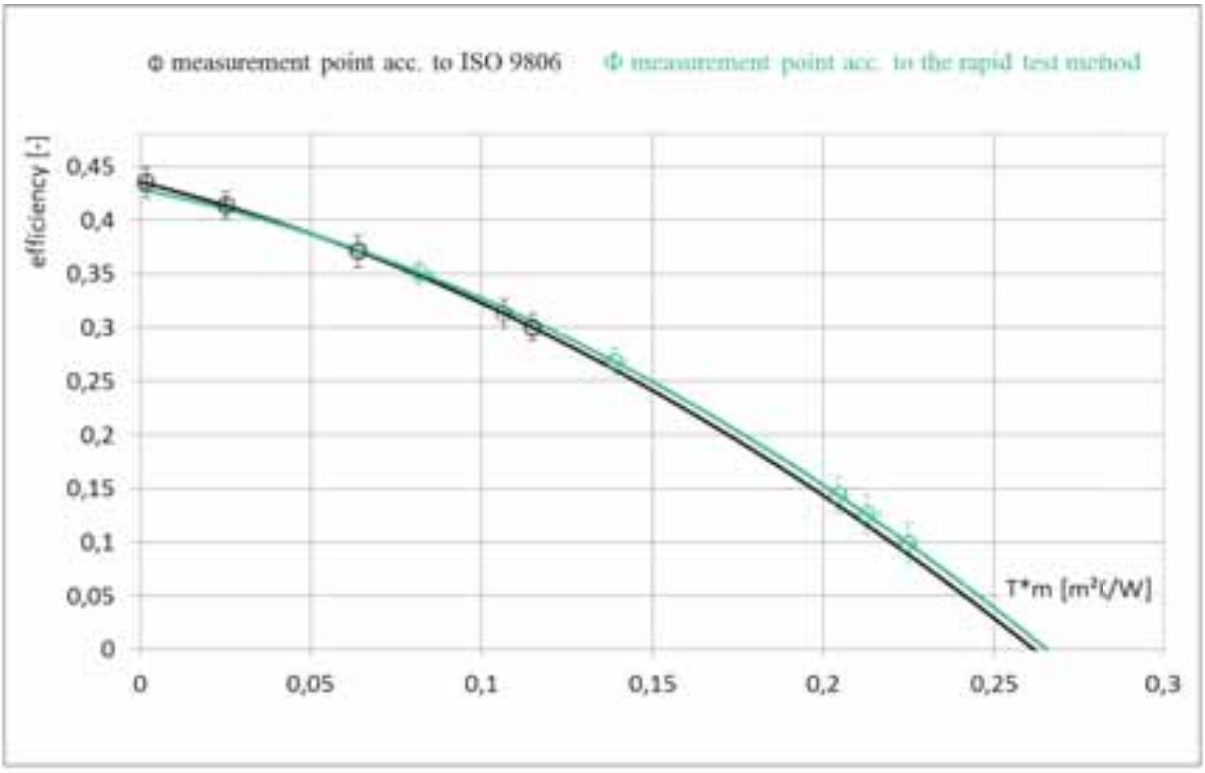

Figure 7: Diagram of the characteristic efficiency curve according to the steady state ISO 9806 method and the rapid test method at G_U of 1000 W/m²

Table 3: Values of the reduced temperature difference, the instantaneous efficiency and the values of the expanded measurement uncertainty displayed as absolute error for the selected operating points

Based on ISO 9806	T^*m [(m²K)/W]	0,00178	0,02506	0,06380	0,10651	0,11490
Absolute error		± 0,0002	± 0,0005	± 0,0014	± 0,0022	± 0,0023
	η [-]	0,435	0,414	0,371	0,313	0,300
		± 0,014	± 0,012	± 0,015	± 0,014	± 0,012
Rapid test method	T^*m [(m²K)/W]	0,08178	0,13884	0,20436	0,21263	0,22477
Absolute error		± 0,0018	± 0,0026	± 0,0037	± 0,0038	± 0,0040
	η [-]	0,351	0,268	0,144	0,126	0,099
		± 0,011	± 0,013	± 0,017	± 0,018	± 0,019

Furthermore, theoretical calculations and simulations are carried out to determine a correction factor for the rapid test method. Those calculations and simulations are necessary because of the physical conditions during the rapid test, which tend to have a higher mean temperature than the standard procedure. At the rapid test method, the mean temperature of the inner absorber tube is taken as a reference (eq.3a) whereas the ISO 9806 method considers the mean water temperature as a reference (eq.3b). By applying formula eq.10 the transformation towards the ISO curve can be conducted. In chapter 5 the determination of the correction factor is described.

5. Limitations of the rapid test method

Due to the different approach of the rapid test method and the test method based on ISO 9806, a different reference temperature for the calculation is taken into account as a basis for determining the instantaneous efficiency curve. In the rapid test method, the mean temperature inside the absorber pipe is measured during stagnation as a parameter and simultaneously treated as the average collector temperature. However, in the measuring method according to ISO 9806 the useful energy obtained from the collector is calculated by using the average fluid temperature. Owing to the differences in approach, the efficiency curve of the rapid test method is theoretically always higher than the method according to ISO 9806. To evaluate this bias theoretical calculations are performed using a receiver model with a given geometry. Further, FEM simulations to determine a correction factor for the rapid test method are carried out with COMSOL Multiphysics® Modeling Software. Moreover measurements to verify the results of the correction factor were conducted. In applying the rapid test method for absorber tubes of concentrating parabolic trough collectors there is only a slight variation of the considered average collector temperature, depending on the operation point and the mass flow rate. For the results given in figure 7 and table 3 the correction factor was determined for a mass flow of ~75 g/s, which is the mean mass flow during the measurements based on ISO 9806. The values for the correction factor at the figure 7 are between 1,5 °C to 6,5 °C, depending on the reduced temperature difference T^*m.

$$T_{Corr} = f(\dot{m}; T^*m) \qquad \text{eq.11}$$

Since the temperature correction factor is depending on the mass flow, the operating temperature, the ambient temperature and the specific receiver geometry, it must be determined for each receiver individually.

However, collector designs with low collector efficiency factor F' lead to a greater difference between the characteristics of the ISO 9806 and the rapid test. Consequently, a non-negligible error without the use of adapted correction factors will occur.

Since stagnation temperatures are measured in accordance to the rapid test method, very high thermal loads are applied on the coating of the receivers. Most absorber coatings available on the market are only stable below temperatures that are typically reached in the stagnation point at high irradiation values. The resulting thermal stress can lead to new order processes in the layers, increase reaction rates and may cause temperature-dependent diffusion processes within the layer /5/. These processes can lead to destruction, partial degradation by blistering or a change in the optical properties of the absorber coating. Table 4 gives an initial, non-exhaustive overview of different absorber coatings, which are available on the market or are currently in the research stage.

Table 4: Overview of absorber coatings and their temperature stability /3/,/5/,/9/ & /11/

Classification	Medium temperature layers						High temperature layers			
Properties	selective	selective	selective	selective	selective	selective	selective	selective	selective	selective
Product	TiNOx	Sunstrip	Black Chrystal	Chrome-Coat	Black Chrome	Solkote	Ni-Al$_2$-O$_3$	Black Cobalt	MnO_x+M^{II}Fe$_2$O$_3$	Black Moly
Functional layer	TiN_xO_y	Ni-NiO	NiSn	Cr-Cr$_2$O$_3$	Cr-CrO	Solar coating	Mo-Ni 55	Co$_3$O$_4$/Co	n.s.	Mo-MoO_2
Substrate	Cu	Al	Cu	Cu	Cu	V$_2$A, Cu	V$_2$A	n.s.	Ni-Mo alloy	n.s.
α_s	0,95	0,92 -0,97	0,93-0,98	0,97	0,95	0,88-0,94	0,94	0,96-0,92	>0,9	0,94
ε_{th} [100°C]	0,05	0,1	0,08-0,25	0,09	0,12	0,2-0,49	0,07	0,71-0,017	>0,45	0,3 [500°C]
α_s / ε_{th}	19	9,2-9,6	3,92-11,6	10,78	7,92	1,8 - 4,7	13,4		~ 2	3,13
Temperature stability/ degradation air	not specified (n.s.)	300 °C	300°C	350 °C	350°C	~73-538°C	350-400°C	400-650 °C	700 °C	350 °C
Temperature stability/ degradation vacuum	400°C	n.s.	n.s.	400°C	n.s.	n.s.	500°C	n.s.	n.s.	500 °C
Production process	PVD*	Sputtering	Sol-Gel	Elekcro-deposition	Galvano-technique	Spraying	RF-Sputtering	n.s.	Coating, Plasma	CVD**

) PVD: Physical Vapour Deposition* *) CVD Chemical Vapour Deposition*

Because of this limitation, concentrating collectors are measured during the course of the rapid test method just below the limit of their temperature stability. Measurements of stagnation temperatures takes place at lower irradiation levels in the morning or in the evening. Knowledge of the substrate layer and the functional layer with its technical specifications are thus preconditional for a careful implementation of the rapid test method. For safety reasons the receiver can be instrumented with a temperature sensor and the tracking control unit at the SIJ test rig will drive the parabolic trough out of the focus, if the temperature stability of the absorber is reached.

6. Outlook

The rapid test method delivers reproducible and reliable values for the characteristic curve of linear concentrating collectors. The obtained results are within the limits of the measurement uncertainty of a characteristic curve based on ISO 9806.

Therefore, the method can be regarded as reliable, inexpensive and easy to use alternative to the conventional measuring methods. For the testing season 2015, further comparative measurements are planned at different types of receivers and parabolic trough collectors in order to gather further experience in the implementation of the rapid test method and to check the procedure with different PTC designs.

Moreover the determination of the stagnation curve and the heating curve will be optimized in order to reduce the measurement uncertainties of the methods. Further optimization will be carried out by analyzing different regression approaches to reduce the statistical spread of the calculated optical efficiency.

7. Acknowledgement

The project is carried out within the framework of the Federal Ministry of Education and Research (BMBF) program FHprofUnt. The authors are grateful for this support.

8. References

1 A. Anthrakidis et al., 2010, Schnelltest zur Abschätzung der Wirkungsgradkennlinie von Parabolrinnenkollektoren, Tagungsbeitrag, OTTI – Symposium Thermische Solarenergie, Bad Staffelstein

2 A. Anthrakidis et al., 2012, Prüfeinrichtung zur Bestimmung der Leistungsfähigkeit von solarthermischen Kollektoren bis 200°C (PeBBLeS), Tagungsbeitrag, OTTI - Symposium Thermische Solarenergie, Bad Staffelstein

3 DGS, August 2012, Leitfaden für das SHK-, Elektro- und Dachdeckerhandwerk, Fachplaner, Architekten, Bauherren und Weiterbildungsinstitutionen, 9. Auflage

4 Stephan Fischer, 2011, Dynamische Prüfungen von Sonnenkollektoren unter besonderer Berücksichtigung der Einfallswinkelkorrektur und der Reduzierung der Prüfdauer, Dissertation Universität Stuttgart, Shaker Verlag ISBN 978-3-8440-0610-0

5 Christina Hildebrandt, 2009, Hochtemperaturstabile Absorberschichten für linear konzentrierende solarthermische Kraftwerke, Dissertation Univ. Stuttgart

6 Erwin Hölle et al., Juni 2005, Tragstruktur für solarthermische Rinnenkraftwerke, Abschlussbericht über ein Entwicklungsprojekt unter dem Az:21383-24/2 von der Deutschen Bundesstiftung Umwelt

7 ISO 9806, 2013, Solar energy – Solar thermal collectors – Test methods, First Edition 2013-11-15, Reference number: ISO 9806:2013(E)

8 Thomas Schabbach et al., 2009, Regenerative Energietechnik, Springer Verlag, 1. Auflage, ISBN 978-3-540-95881-9

9 Solar Energy Corp., Date 22.Sept.2015, Produktdatenblatt SOLEKOTE HI/SORB-IITM, http://www.solec.org

10 SP Technical Research Institute of Sweden, Date 27.Jan.2014, ScenoCalc Version No. 4.06, http://www. sp.se/en/index/services/solar/ScenoCalc/Sidor/default.aspx

11 Stieglitz et al., Thermische Solarenergie, Springer Verlag 2012, 1. Auflage, ISBN 978-3-642-29474-7

Conference Proceedings

Solar World Congress 2015
Daegu, Korea, 08 – 12 November 2015

CONCENTRATED FLUX MEASUREMENT APPARATUS FOR AN ASYMMETRICAL PARABOLIC TROUGH SOLAR CONCENTRATOR

Matteo Bortolato[1, 2], Simone Dugaria[1] and Davide Del Col[1]

[1] Department of Industrial Engineering (DII), University of Padova, Padova, Italy

[2] Interdepartmental Centre "Giorgio Levi Cases" for Energy Economics and Technology, University of Padova, Padova, Italy

Abstract

In this work, the optical performance of an asymmetrical small parabolic trough solar concentrator is experimentally characterized by adopting a direct method to define the solar flux map on the focal region. Due to the particular geometry of the optical system, the optimal plane of concentration is 45° tilted with respect to the plane containing the focal line and the vertex line. A water cooled heat flux microsensor installed on a two-axes linear handling system is used to measure the concentrated solar flux along the optimal concentration plane of the present optical system. The collected data are interpolated to obtain the flux distribution and to determine the width of the solar image over the focal line. These results together with the values of the direct normal irradiance collected during the tests and the nominal reflectance of the parabolic mirrors allow the evaluation of the intercept factor for different areas included in the concentration region.

Keywords: *solar flux mapping; heat flux microsensor; optical performance; parabolic trough, intercept factor*

1. Introduction

A parabolic trough solar collector consists of an optical system, named concentrator, that reflects the beam radiation onto a focal region, where a receiver is installed to convert the solar radiation into heat or electric energy. In order to work efficiently throughout the day, the system must be equipped with a tracking system to maintain the sun vector on the plane normal to the aperture area and containing the focal line. The ratio between the aperture area of the concentrator and the receiver area is defined as the geometrical concentration ratio and it qualitatively provides the operating temperature range of a concentrating collector. In ideal optics, parallel rays normally incident on the aperture area of a parabolic trough are concentrated along a focal line. In real applications, there is a concentration region around the focal line, whose width depends on the sunshape and on the total optical error. The sunshape represents the brightness intensity distribution across the finite angular size of the sun disc and the circumsolar aureole. The total optical error includes the shape and specular reflectance errors of the parabolic mirrors, the tracking error and the imperfect positioning and alignment of the receiver.

Experimental measurements and the development of reliable models implemented in Monte Carlo ray tracing tools become pivotal for the design and improvement of concentrating solar collectors. In the case of a parabolic trough collector, periodical monitoring the concentrated solar flux and its distribution is recommended to assess the accuracy of the tracking system, the durability of the mirror reflectance and the stiffness of the structure over time. Furthermore, the geometry and the configuration of the receiver should be designed according to the width of the concentration region and the solar flux distribution in order to optimize the performance. Once the solar map has been measured, given the aperture width of the receiver, one can calculate the intercept factor, that is the fraction of the beam radiation reflected by the mirrors and

doi:10.18086/swc.2015.10.22 Available at http://proceedings.ises.org

reaching the receiver. To ensure acceptable performance of the solar concentrating collector, the intercept factor should be higher than 90%.

The arrangement of the solar cells in a photovoltaic receiver and, if necessary, a secondary optics must be design considering that the non uniformity of the incident flux is expected to cause hot spots, current mismatch and to penalize the efficiency (Baig et al., 2013). On the other hand, in solar thermal collectors, the non uniform distribution of the concentrated solar flux on the external surface of the absorber can lead to perimetral temperature gradients. This is associated to differential thermal expansions that cause thermal stresses, whose effect can be very serious in some working conditions (Khanna et al., 2013, 2014, 2015, Eck et al., 2007). In common practice, a high mass flow rate is pumped in order to achieve a turbulent flow condition inside the tubular absorber- This approach is generally adopted in solar power plants but cannot be applied in small medium temperature concentrating collectors, especially for direct steam generation, where a certain flexibility of operation is required to maximize the working hours per day under stable conditions. The solar flux mapping is of great importance in the design of receiver with enhancement heat transfer.

In general, the measurement of the concentrated solar flux on the focal region can be performed through different techniques that can be classified as direct, indirect and measurement-supported simulation methods.

Direct methods refer to the use of a flux sensor, whose response can be directly associated with the concentrated flux. In order to get a fine spatial resolution of the measured concentrated solar flux, these sensors should have a small aperture and should be either distributed in the focal region or installed in handling systems (Röger et al., 2014). Both the techniques require the interpolation of the experimental data collected in specific points of the concentration region to get the solar flux map. In the former, several sensors are needed to obtain results with low uncertainty, but this entails that the measurement system has a very high investment cost. Furthermore, the spatial resolution may only be modest. In the latter solution, a handling system should be designed according to the geometry of the investigated concentrator; this solution allows to scan quickly the focal region and to collect much more experimental points as compared to the case of stationary and distributed sensors, thus increasing the accuracy of the results. The most common sensors employed in concentrating collectors analysis are radiometers and calorimeters (Ballestrín et al., 2012).

Radiometers deliver an electrical response that may be a voltage coming from a differential temperature sensor such as a thermocouple for the Gardon radiometer or a thermopile for the more recent heat flux microsensors (HFMs) or a current generated by a photodetector. Heat flux microsensors have been used by Ballestrin (2002) to investigate the concentrated solar flux distribution on a central volumetric receiver of a heliostat field at the Plataforma Solar de Almeria. Ferriere and Rivoire (2002) and Parretta et al. (2007) designed and realized two different radiometers arranging a photodetector respectively inside a single integrating sphere and two integrating spheres optically interconnected. Fernández-Reche et al. (2008) presented a comparative test performed in a solar furnace measuring concentrated solar flux using both a Gardon radiometer and a GaAs photovoltaic cell as photodetector. Riffelmann et al. (2006) developed the parabolic trough flux scanner (PARASCAN) to detect the solar flux on the tubular receiver of parabolic trough collectors having an aperture width of 5.76 m. The measurement system consists of two arrays of 96 photodiodes each, placed behind translucent Lambertian targets. The first array is arranged in front of the receiver tube, to detect the beam irradiance reflected by the mirrors towards the concentration region, while the second array is located behind the receiver, to measure the optical losses. The two arrays are fixed on a sliding carriage moved by a remote control. From the integrated values collected by the first and the second array, the intercept factor of the parabolic concentrator can be calculated.

When using a calorimeter mounted in the focal region of a concentrator, the solar flux can be derived from a thermal balance between the radiant power incident on the device aperture and the heat flow rate transmitted to a cooling fluid flowing through the sensor. Pérez-Rábago et al. (2006) and Estrada et al. (2007) employed calorimeters to measure the solar flux in point focus concentrators.

In indirect methods, digital cameras (CMOS cameras or, more often, CCD cameras) equipped with appropriate filters and zoom lenses are used to capture one or more images that can be related to the solar flux distribution after processing. The captured images are in gray-scale map, so they can only give qualitative information. In order to correlate the gray-scale value of each pixel to a physical irradiant flux

value, the system must be calibrated in situ. If accurately implemented and calibrated, indirect methods provide very high spatial resolution , high reliability and short measurement time.

In most cases, the digital cameras register the solar radiation reflected off a target which exhibits a diffuse reflectance very close to ideal Lambertian reflectance (camera-target method). This means that, whatever the angle of observation, the target surface appears equally bright. Ballestrín and Monterreal (2004) evaluated the concentrated solar flux on a central receiver of a heliostat fields by capturing images with a CCD camera on a moving uncooled Lambertian target. This target swings in front of the receiver aperture area and intercepts the reflected solar beam radiation in a measurement plane. Moving the target is necessary in high concentration ratio systems, where the concentrated flux may overheat and damage it. Two water-cooled Gardon radiometers placed very close to the receiver aperture are used to calibrate the CCD camera. Riffelmann et al. (2006) implemented the calibrated CCD camera-target method for flux mapping on the focal region of a parabolic trough concentrating solar collector. The Lambertian target has a notch which allows to enclose the tubular receiver and it can be moved through a telescopic arms along the focal region. On the target, higher and lower concentration areas as well as solar rays missing the absorber tube can be observed. After image processing, an approximate value of the local intercept factor can be calculated.

A new method, that has been applied to few receivers so far (Ho and Khalsa, 2012, Röger et al., 2014), regards the use of a digital camera only, without target, applied to external receivers. It is related to many sources of error that should be carefully taken into account. First, as the assumption of a perfectly diffusing material of the receiver is definitely not exact, its real reflectance should be characterized using a gonioreflectometer. Secondly, the receiver is provided with a selective coating with a high absorbance in the wavelength range of the solar spectrum and has a surface temperature much higher than the ambient air temperature. Hence, a special filter that can cut off thermal radiation emitted by the receiver in the infrared range should be adopted. Finally, the use of different filters during calibration procedure and during tests may entails error due to the difference between the actual attenuation factors and the manufacturers' specifications. Total errors associated to this method can be up to 20% - 40%, mainly because of large uncertainty in receiver reflectance and in filters' attenuation factors.

Lüpfert et al. (2008) presented a second version of PARASCAN to evaluate the flux distribution on the focal region of a parabolic trough with great accuracy. Fiber optics are arranged instead of photodiodes, behind the translucent Lambertian targets of the two parts of the moving measurement system. Each sensor part is composed by 12 segments where 16 optical fibers are mounted at distances of 2.5 mm., giving a very high spatial resolution. The optical fibers transmit the beam radiation concentrated on the focal region to a CCD camera equipped with neutral density filters, out of the hot region. A direct calibration of the system under natural sunlight is possible. From the measured flux maps, intercept factor have been calculated with an experimental uncertainty of ± 1%.

The last class of methods involves the use of ray tracing codes, which have proved to be powerful tools to model many types of solar concentrating collector and to obtain prediction of the solar flux on any surface. Nevertheless, the accuracy of the results depends on the quality of the input parameters: shape, tracking and receiver positioning errors, optical defects, optical properties of the materials and atmospheric conditions. Furthermore, the results should be validated against merely experimental measurements, in which, in this case, a high resolution and an extreme complexity is not required. Schiricke et al. (2009) developed an optical model of a parabolic trough solar concentrator by implementing in a Monte Carlo ray tracing software the photogrammetrically measured geometry of the collector, the nominal optical properties of the materials, the incidence angle of the solar rays on the aperture area, the measured values of direct normal irradiance and assuming a typical clear-sky sunshape. The model has been validated by comparing the simulated intercept factors and the flux map to those measured with an indirect method. It proved to be very accurate and reliable, hence it can be use to study the effect of different combinations of parameters on the collector performance.

In this work, a direct method based on the use of a radiometer mounted on a handling system is used to measure the solar flux map on the concentration region of an asymmetrical parabolic trough concentrator that has been designed for installing receivers with flat absorbers.

2. Experimental apparatus

The small parabolic trough concentrator considered in this work is asymmetrical since the reflective optics extends from the vertex line to the mirror rim (Fig. 1). It has been installed at the Solar Energy Conversion Lab of the Industrial Engineering Department, University of Padova. The present concentrator exhibits an aperture width of 2.9 m, a rim angle of 78°, a focal length of 1.81 m and a trough length of 2.4 m, resulting in an aperture area equal to 6.857 m^2. The reflecting optical system is made up by four back silvered glass facets arranged in two rows, which have a nominal reflectance of 96%, as provided by the manufacturer. Due to the small dimensions of the prototype, it is equipped with a two-axes solar tracking system to have the beam radiation normal to the aperture area without any cosine loss. The motion is governed by a solar algorithm when approaching the sun and by a sun sensor to achieve the best alignment. The particular geometry of the present parabolic trough concentrator is suitable to be coupled with a receiver provided with a flat geometry absorber. As an example, the receiver may be similar to some trapezoidal cavity receivers generally mounted on linear Fresnel solar collectors. In order to minimize the incidence angle of the concentrated beams on a flat receiver, the optimal concentration plane of this system is 45° tilted with respect to the plane containing the focal line and the vertex line.

Fig. 1: Prototype of the asymmetrical parabolic trough linear solar concentrator and solar flux map measuring system installed at the Solar Energy Conversion Lab of the University of Padova.

The solar flux mapping system has been designed so that the measuring plane corresponds to the optimal concentration plane. A water-cooled heat flux microsensor is mounted on a two axes (x, z) semi-automatic linear handling system. The horizontal axis (x-axis) is parallel to the trough length and the second axis (z-axis) lies on the width of the concentration region on the measuring plane. As declared by the manufacturer, heat flux microsensors have a very fast response time of 300 μs when the face is provided with a high absorptance black coating, as usual for radiant flux measurement in concentrating solar collectors. Water cooling of the sensor is necessary for applications requiring a continuous monitoring of the concentrated flux and to reduce the influence of the ambient conditions on the measurement accuracy. In fact, if the average temperature of the cooling fluid (distilled water) passing through the sensor is maintained close to the ambient air temperature, the effect of convective heat losses on the measurement of the concentrated flux can be neglected.

The horizontal x-axis is provided with a sliding carriage that can be fixed at several repeatable position along the trough length by appropriate blocking elements. On the sliding carriage, an electrical linear actuator is mounted and it allows the movement of the sensor along the z-axis to scan the concentration region. the

actuator has a stroke of 150 mm, a variable speed from 0.001 m s^{-1} to 2 m s^{-1} and a maximum positioning repeatability of 0.1 mm. On the top of the actuator, an aluminum structure supports the sensor and allows fine adjustments to make the optimal concentration plane and the measuring plane match (Fig. 2). The handling system has been mounted so that the heat flux microsensor moves on the optimal concentrating plane (Fig. 3).

Fig. 2: Electric linear actuator mounted on the sliding carriage of the x-axis and water-cooled heat flux microsensor arranged on a supporting structure.

Fig. 3: Position of the heat flux microsensor when the electric linear actuator is completely down (position 0).

The laboratory includes a first class pyrheliometer mounted on a high precision solar tracker that is used to measure the direct normal irradiance (DNI). A datalogger registers the electrical signals associated to the position of the actuator, the measured solar flux, the temperature of the heat flux microsensor's face and the direct normal irradiance with a sampling rate of 0.2 s and the collected data are reduced in Matlab® environment.

3. Experimental technique and data reduction

Before every experimental test, the reflecting facets of the parabolic trough concentrator, the sun sensor and the pyrheliometer have been cleaned. The solar flux map has been experimentally characterized on a trough length of 1200 mm along the x-axis, corresponding to a single row of parabolic mirrors. Along the investigated trough length, ten blocking elements have been arranged at a distance of 120 mm. Concentrated solar flux measurements have been performed according to the following procedure. The electrical linear actuator is brought at the first station in its zero position, in which the heat flux microsensor is 65 mm under the ideal focal line of the concentrator. The zero position of the actuator corresponds to the origin of the z-axis. Then, the working cycle of the actuator is started. It consists of a slow rise for collecting the experimental data and a quick descent to return in the zero position before being moved to the next position along the x-axis. At the end of the slow rise phase, the sensor is 65 mm above the ideal focal line, thus the investigated width on the concentration region is of 130 mm, centered on the ideal focal line. During each test, four values are registered by the data acquisition system: the position of the sensor, given by the electrical output signal of the actuator's encoder, the heat flux and the temperature signal from the heat flux microsensor and the direct normal irradiance measured by the pyrheliometer. The series of data collected during a tests are considered for data reduction in a Matlab® environment if the variations of the direct normal irradiance is within the experimental uncertainty of the pyrheliometer (± 2.5 % of the average value, with a level of confidence of 95.45 %). The number of collected data for concentrated solar flux depends on the number of measuring position along the x-axis, the actuator's speed along the z-axis and the sampling rate allowable by the data acquisition system: the higher the number of experimental data the more accurate the

resulting solar flux map. The heat flux microsensor is cooled by a flow of 0.017 kg s^{-1} of distilled water. The temperature of the cooling fluid at the inlet of the sensor is kept constant by dissipating the heat flow rate coming from the concentrated solar radiation to the ground water. Several tests have been conducted consecutively, in order to assess the repeatability of the proposed measuring technique under very similar test conditions.

The face of the sensor is coated with Pyromark 1200, a high temperature paint which has an emittance of 95 % as declared by the calibration report. According to the study by (Song et al., 2014), the total infrared spectral emittance of this coating is higher than 93% in the wavelength range between 3 μm and 14 μm. Therefore, unlike other coatings (Ballestrín et al., 2003), there is no need to introduce corrective dimensionless factors to account for the differences between the solar irradiance spectrum and the irradiance spectrum of the black body employed for the calibration of heat flux microsensors.

The procedure described in the work by Ballestrin (2002) has been adopted to evaluate the optical performance of the present asymmetrical concentrator. In order to define accurately the solar flux map and to calculate the incident power on an area of the concentration region, an interpolation of the experimental data has been performed. The interpolant should be able to predict well local trends, therefore the spline interpolants have been considered. Differently from the study by Ballestrin (2002), where an aiming strategy of 25 heliostats was set up to obtain a uniform flux distribution on the central receiver, in the present parabolic trough concentrator, a strongly non uniform flux distribution is expected. As a consequence, the spatial resolution to interpolate should be quite small to get a more accurate estimation of the incident power on an area of interest included in the focal region. In fact, the incident power is calculated by a numerical integration of the solar flux distribution, dividing the area of interest into *n* equal rectangular elements and using the tiled method, according to eq.1:

$$P_{inc} = \frac{A_{cr}}{n} \sum_{i=1}^{n} q_i'' \qquad \text{(eq. 1)}$$

where *n* is the number of data in the area of interest, A_{rc} is the surface of the area of interest and $q"_i$ is the i-th value of solar flux. Unfortunately, the spline interpolants do not allow the estimation of the uncertainty on predicted concentrated solar flux values. Therefore, in order to assess if the number of collected data is sufficient for a good definition of the solar flux map, different interpolants (linear, cubic and biharmonic) have been considered and the results of the numerical integration have been compared. If the obtained value of the power incident on an area of the concentration region does not change significantly when varying the interpolant, the accuracy in the solar flux map definition can be considered satisfactory. Once the incident power onto an area of interest has been calculated, the associated intercept factor γ can be determined as follows (eq. 2):

$$\gamma = \frac{P_{inc}}{\mathrm{DNI}\, A_{ap}\, \rho_{mir}} \qquad \text{(eq. 2)}$$

where DNI is the average value of the direct normal irradiance during the considered test run, A_{ap} is the aperture area of the row of mirrors and ρ_{mir} is the nominal reflectance of the mirrors, provided by the manufacturer.

The experimental uncertainty of the calculated power P_{inc} is derived from the combination of the integration uncertainty, the interpolation uncertainty and the uncertainties related to the handling system positioning and movement. The interpolation uncertainty has been computed as in the work by Ballestrin (2002). The interpolation uncertainty can be neglected because the chosen interpolant shall not affect the results. Furthermore, the geometry of the present asymmetrical parabolic trough concentrator allows to check that the measuring plane matches the optimal concentration plane. Finally, the uncertainty of the intercept factor has been calculated applying the law of propagation of uncertainty for uncorrelated inputs (Joint Committee

for Guides in Metrology, 2008) and neglecting the uncertainty of the nominal reflectance of the parabolic mirrors.

4. Results and discussion

Experimental measurements of the solar flux distribution on the concentration region of the asymmetrical parabolic trough concentrator have been performed consecutively during a clear sky day. The dimensions of the measuring area, which is the area scanned by the heat flux microsensor, are given by the actual stroke of the electrical linear actuator along the z-axis (130 ± 1 mm) and by the distance between the first and the last of the blocking elements along the x-axis (1082 ± 1 mm). During the presented test runs, the direct normal irradiance was around 890 W m^{-2} and the ambient air temperature was around 23°C. The water cooling of the microsensors allow to keep the temperature of its face between 19°C and 23°C during each scan of the concentration region. The speed of the electric linear actuator was set equal to 0.005 m s^{-1} in the rise phase and equal to 0.1 m s^{-1} in the descent phase. Measured data were sampled with a scan interval of 0.2 s. The resulting spatial resolution along the width of the concentration region is 1 mm and 1300 concentrated solar flux data were collected during each test. The spline interpolation has been executed over a grid with a spatial resolution of 1 mm x 1 mm, giving a set of 141873 data on the whole measuring area. A finer spacing does not entail significant variations in the calculation of the incident power on an area included in the measuring area, whatever its width.

Fig. 4 reports the 3D solar flux distribution obtained after interpolating the experimental data (blue dots) collected in a single test run through the biharmonic spline method. The origin of the z-axis corresponds to the zero position of the encoder integrated in the electrical linear actuator, while the origin of the x-axis corresponds to the projection of the external rim of the mirrors on the ideal focal line. The equation of the ideal focal line is z = 65 mm. For the sake of clarity, the solar map has been presented with a spatial resolution lower than that adopted for the calculation of the concentrated power on an area of interest included in the measuring area.

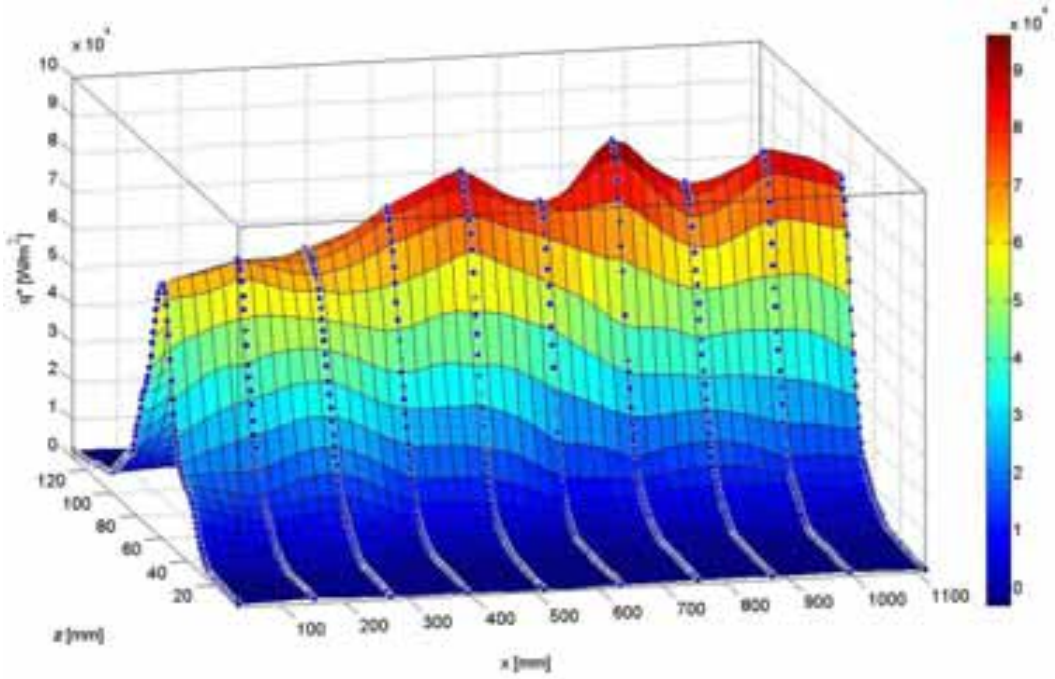

Fig. 4: Three-dimensional solar map on the measuring area defined during the experimental study of the optical performance of the asymmetrical parabolic trough installed at the University of Padova. The reported surface has been obtained after interpolating the experimental data through the biharmonic spline method.

As expected, the solar flux distribution is strongly non uniform along the width of the concentration region (z-axis). Nevertheless, there are significant variations of the solar flux even along the x-axis: the external rim of the mirrors in the considered row appears to be less efficient in concentrating the solar beam. In fact,

differently from the rest of the measuring area, the solar flux is below 80 kW m^{-2} on the first 300 mm of the investigated trough length. The maximum peak value of the measured concentrated solar flux is 96250 W m^{-2} at x = 750 mm, while the minimum peak value of 66900 W m^{-2} has been detected at the very beginning of the trough length (x = 33 mm). The isoflux contour plot related to the same test run is reported in Fig. 5: one can notice that the maximum width of the concentration region is of 100 mm and it centered on the focal line. On the central part of the mirrors composing the investigated row, the concentration of the solar beams is performed on a tighter width. According to the previous considerations, the calculation of the concentrated power and the determination of the intercept factor has been performed considering a trough length equal to the measuring area length (1082 mm) and two different widths: 100 mm and 70 mm.

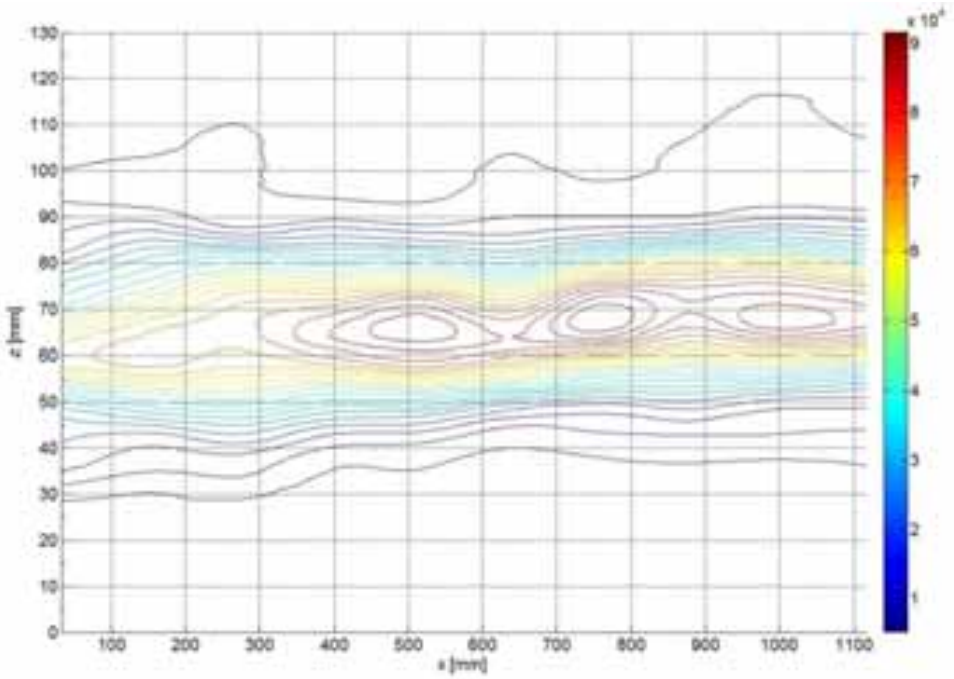

Fig. 5: Concentrated solar isoflux contour plot on the measuring area defined during the experimental study of the optical performance of the asymmetrical parabolic trough installed at the University of Padova.

Considering the solar flux map on the measuring area of Fig. 4, which has been obtained under a direct normal irradiance of 887 W m^{-2}, the concentrated power incident on an area of interest having a width of 100 mm is equal to 2705 W, while it results equal to 2604 W when the width is 70 mm. The variation of the concentrated power values is within ± 0.2 % when different spline interpolants are employed, which demonstrates that the number of experimental data collected during a single test run is high enough to get an accurate definition of the concentrated solar flux distribution on the measuring area. The experimental uncertainty of the concentrated power is between 4% and 5 % and it slightly increases when the width of the area of interest decreases. Considering these results and the nominal reflectance of the mirrors, the intercept factor is of 100% for a 100 mm width, which is consistent with the contour plot of Fig. 5, and it is of 97 % for a width of 70 mm. The shapes of the 3D surface resulting from the different test runs as well as the concentrated powers and the intercept factors on an area of interest do not vary significantly. This proves the repeatability and the reliability of the proposed experimental technique.

5. Conclusions

The solar flux map on the focal region of a prototype of an asymmetrical parabolic trough concentrator has been experimentally determined at the Solar Energy Conversion Laboratory, at the University of Padova. The solar mapping system is composed by a two-axes semi-automatic linear handling system and by a heat flux microsensor. The actual measuring area is 1082 mm x 130 mm, thus it includes a single row of mirrors of the present concentrator. During a single test run, data of the sensor position, concentrated solar flux, temperature of the sensor face and direct normal irradiance are acquired at scan interval with 0.2 s. To define

the solar flux map, the collected data have been interpolated by a spline interpolant over a grid with a spatial resolution of 1 mm x 1 mm. The obtained 3D surface for the concentrated solar flux distribution has been numerically integrated to calculate the concentrated power as a function of the width taken in the measuring area. Considering the nominal reflectance of the mirrors and the measured values of the direct normal irradiance, the intercept factor can be calculated for a certain area included in the concentration region.

According to the results, the solar flux distribution is strongly non uniform along the width of the concentration region and there are significant variations of the concentrated solar flux even along the trough length. In particular, the external part of the mirrors provide lower peak flux values near the focal line. The maximum width of the concentration region is 100 mm, whose corresponds a intercept factor of 100%. When considering a width of 70 mm, the intercept factors decreases to 97 %. The calculated value of the intercept factor varies within ± 0.2 % when different spline interpolants are considered and this entails that the number of collected data is high enough to get an accurate definition of the solar flux map. Several tests have been performed consecutively under the same test conditions and the variation of the results is negligible, proving the reliability and the repeatability of the proposed technique.

References

Baig, H., Sarmah, N., Heasman, K.C., Mallick, T.K., 2013. Numerical modelling and experimental validation of a low concentrating photovoltaic system. Solar Energy Mater. Solar Cells 113, 201-219.

Ballestrín, J., Burgess, G., Cumpston, J., 2012. 18 - Heat flux and temperature measurement technologies for concentrating solar power (CSP), in Lovegrove, K., Stein, W. (Eds.), Concentrating Solar Power Technology. Woodhead Publishing, pp. 577-e4.

Ballestrín, J., Monterreal, R., 2004. Hybrid heat flux measurement system for solar central receiver evaluation. Energy 29, 915-924.

Ballestrin, J., 2002. A non-water-cooled heat flux measurement system under concentrated solar radiation conditions. Solar Energy 73, 159-168.

Ballestrín, J., Ulmer, S., Morales, A., Barnes, A., Langley, L.W., Rodríguez, M., 2003. Systematic error in the measurement of very high solar irradiance. Solar Energy Mater. Solar Cells 80, 375-381.

Eck, M., Uhlig, R., Mertins, M., Häberle, A., Lerchenmüller, H., 2007. Thermal Load of Direct Steam-Generating Absorber Tubes with Large Diameter in Horizontal Linear Fresnel Collectors. Heat Transfer Eng. 28, 42-48.

Estrada, C.A., Jaramillo, O.A., Acosta, R., Arancibia-Bulnes, C.A., 2007. Heat transfer analysis in a calorimeter for concentrated solar radiation measurements. Solar Energy 81, 1306-1313.

Fernández-Reche, J., Sánchez, M., Alonso, M., Cañadas, I., Chenlo, F., Rodríguez, J., Ballestrín, J., 2008. Concentrating PV: An Alternative to Calorimeters for Measuring High Solar Flux Densities. Journal of Solar Energy Engineering 130, 044502-044502.

Ferriere, A., Rivoire, B., 2002. An instrument for measuring concentrated solar-radiation: a photo-sensor interfaced with an integrating sphere. Solar Energy 72, 187-193.

Ho, C.K., Khalsa, S.S., 2012. A Photographic Flux Mapping Method for Concentrating Solar Collectors and Receivers. Journal of Solar Energy Engineering 134, 041004-041004.

Joint Committee for Guides in Metrology, 2008. Evaluation of measurement data - Guide to the expression of uncertainty in measurement (JCGM 100:2008).

Khanna, S., Kedare, S.B., Singh, S., 2013. Analytical expression for circumferential and axial distribution of absorbed flux on a bent absorber tube of solar parabolic trough concentrator. Solar Energy 92, 26-40.

Khanna, S., Singh, S., Kedare, S.B., 2015. Explicit expressions for temperature distribution and deflection in absorber tube of solar parabolic trough concentrator. Solar Energy 114, 289-302.

Khanna, S., Singh, S., Kedare, S.B., 2014. Effect of Angle of Incidence of Sun Rays on the Bending of Absorber Tube of Solar Parabolic Trough Concentrator. Energy Procedia 48, 123-129.

Lüpfert, E., Riffelmann, K., Price, H., Burkholder, F., Moss, T., 2008. Experimental Analysis of Overall Thermal Properties of Parabolic Trough Receivers. Journal of Solar Energy Engineering 130, 021007-021007.

Parretta, A., Antonini, A., Armani, M., Nenna, G., Flaminio, G., Pellegrino, M., 2007. Double-cavity radiometer for high-flux density solar radiation measurements. Appl. Opt. 46, 2166-2179.

Pérez-Rábago, C.A., Marcos, M.J., Romero, M., Estrada, C.A., 2006. Heat transfer in a conical cavity calorimeter for measuring thermal power of a point focus concentrator. Solar Energy 80, 1434-1442.

Riffelmann, K., Neumann, A., Ulmer, S., 2006. Performance enhancement of parabolic trough collectors by solar flux measurement in the focal region. Solar Energy 80, 1303-1313.

Röger, M., Herrmann, P., Ulmer, S., Ebert, M., Prahl, C., Göhring, F., 2014. Techniques to Measure Solar Flux Density Distribution on Large-Scale Receivers. Journal of Solar Energy Engineering 136, 031013-031013.

Schiricke, B., Pitz-Paal, R., Lüpfert, E., Pottler, K., Pfänder, M., Riffelmann, K., Neumann, A., 2009. Experimental Verification of Optical Modeling of Parabolic Trough Collectors by Flux Measurement. Journal of Solar Energy Engineering 131, 011004-011004.

Song, X., Huan, K., Dong, W., Wang, J., Zang, Y., Shi, X., 2014. Research on infrared radiation characteristics of Pyromark 1200 high-temperature coating. Proceedings of SPIE - the International Society for Optical Engineering, 9300, 93001S-1.

Conference Proceedings

Solar World Congress 2015
Daegu, Korea, 08 – 12 November 2015

THE SEPARATED HEAT PIPE SOLAR HEATING SYSTEM

Shi liang yan [1], Niu Baolian[1] and Yu Yingying[1]

[1] School of energy and mechanical engineering, Nanjing Normal University, Nanjing(China)

Abstract

It is established a separated heat pipe solar indoor heating system .The system is divided into three parts: solar collector, separated heat pipe and indoor heating terminal. The system uses separated heat pipe as heat transfer component. It transfers solar energy from solar collector into the indoor heating terminals. So by the separated heat pipe the system will heat the indoor air with solar energy. The related experiments were carried out. The results showed that the solar thermal utilization efficiency can reach 56% when the solar radiation is at 725W/ ㎡, the evaporation and condensation temperature of heat pipe kept constant at 44.8 ℃ and 40.2℃ respectively. When the system started to run, it took three or more hours to make the indoor air temperature reach 22℃-24℃ at sunny or cloudy days. By the experimental data, it is proved that the system is a promising and feasible heating mode in the spacing heating.

Keywords: Separated heat pipe; Solar energy; Indoor air heating

1. Introduction

Solar energy is one of the renewable energy resources that hold a great potential for developed and developing countries in the future. Solar energy resources are very rich in China. Nowadays, it is being widely used for both heating and electricity generation, and has no restrictions as to the uneven distribution and the shortage of conventional resources. With the development of solar heating, the traditional heating mode has some disadvantages such as complex structure and low efficiency. It can’t keep up with the development of housing construction.

Heat pipe has been used in plenty of solar hot water system for its special thermal performance and even in the space heating system. Susheela and Sharp (2001) designed and tested a heat pipe system that could be installed on existing homes without demolishing the wall of the building. The absorber portion was mounted on the outside of a south-facing wall, with water contained in tanks as the thermal mass on the inside of the wall. Experiments were performed outdoors, and system efficiencies (defined as the ratio of power delivered to the room over incident insolation) reached as high as 60% during sunny days. Computer simulations were also performed to model the performance of the unit. Primarily based on design improvements recommended by Susheela and Sharp, Albanese et al. (2012) tested a bench-scale experimental model. Experimental variations included fluid fill levels, addition of insulation on the adiabatic section of the heat pipe, and fins on the outside of the condenser section. Filling the heat pipe to 120% of the volume of the evaporator section and insulating the adiabatic section achieved a system efficiency of 85%. Addition of fins on the condenser of the heat pipe did not significantly enhance overall performance. The heat pipe system provided substantial gains in performance relative to conventional direct and indirect gain passive solar systems and, thus,

Selection and/or peer review under responsibility of Scientific Committee
doi:10.18086/swc.2015.10.23 Available at http://proceedings.ises.org

presents a promising alternative for reducing building energy use. To better understand system performance in realistic weather conditions, in particular, the relatively cloudy and cool conditions, Robinson et al. (2013) designed, built and installed a full-scale prototype of the heat pipe system in a classroom on the University of Louisville campus in Louisville, KY. During the spring heating season of 2010 (January–April), maximum daily peak thermal efficiency was 83.7% and average daily peak thermal efficiency was 61.4%. The maximum hourly average room gain achieved during the season was 163 W/m2. On days with good solar insolation, the thermal storage was heated to temperatures sufficient to provide significant energy to the classroom – even during the coldest days of the season. During the longest period (4 days) of low insolation during the season, average hourly heat delivery to the room from storage remained positive, and was never less than 16.6 W/m2.

In these system heat pipe had shown its great heat transfer ability. In order to develop much more heat pipe solar heating system, the separated heat pipe would be introduced into the solar space heating system in this paper. Separated heat pipe solar heating system is a promising technology which has simple structure and high efficiency. It can be divided into three parts: solar collector, separated heat pipe and heating terminal. Separated heat pipe can transfer solar energy from outside to inside of the room. Solar collectors receive energy and transfer heat to the heat pipe, and heat pipe delivers heat to the indoor heating terminals. There is no other transfer medium in the system. Compared with the traditional solar heating system, it has not second heat transfer with water and reduce irreversible loss at the process of heat transfer. As separated heat pipe can extend the length of the pipe, the system has some flexible when it is designed and mounted.

Especially in rural areas and cold in northern China, the distance between buildings is far and the rainy season is short. The surrounding residential buildings have no space restricted and can get sufficient sunlight. It can provide basis for residential heating temperature and reduce fuel consumption. So separated heat pipe solar heating system has broad application prospects in these districts. In this paper, some theory analysis and experiments about the new system were carried out and the performance of the separated heat pipe solar heating system was analyzed.

2. Experimental study

2.1. System introduction

Separated heat pipe solar heating system is composed of solar collector, separated heat pipe and heating terminal as Fig. 1 shows. The evaporation section is placed in the solar collectors. When it is received the solar energy, the working fluid in the evaporator will absorb the heat and evaporate to gas, and then enters into the condensation section. The working fluid in the condensing section sends heat to the indoor air and turns into liquid, finally it returns back into the evaporator by gravity. Then the new cycle will carry on and then the solar energy was transferred from outside to inside.

In the test of separated heat pipe solar heating system, it used separated heat pipe as heat transferring component, this system is mainly composed of solar collector, the separated heat pipe evaporation section 1, the separated type heat pipe condensing section 2, the adjustment of valve 3. The solar collector is basically the same as the ordinary plate type solar collector, which mainly consisted of the solar collector, heat insulation material the separated heat pipe evaporation section, heat absorbing layer and the transparent glass cover. The evaporator section was placed in the flat panel solar collectors with 2m x 1m.The separated heat

pipe condenser is composed of copper aluminum fin tube. The condensation section of the separated heat pipe is placed in the room as the indoor terminals providing heat into the room with 0.952 ㎡. Valve 3 is designed to close the circulation channel when the system doesn't work in summer. To avoid affect the indoor lighting, the solar collector is placed on the outside wall with inclined or vertically installation. The working fluid of the separated heat pipe is R600a which is the environmental friendly. The limit on the system installation is that the height of the evaporator must be lower than that of the indoor condenser to ensure the working fluid can flow back to the evaporator. The heating room is in the fourth floor of the office building with the area 40m^2.

Compared with the traditional solar heating system, the separated heat pipe solar indoor heating system works with gravity separated heat pipe to transfer solar energy into the room without any energy consumption. It belongs to distributed system like air-conditioner installed outside wall in every room. So it is easy installation and has no effect on daylight.

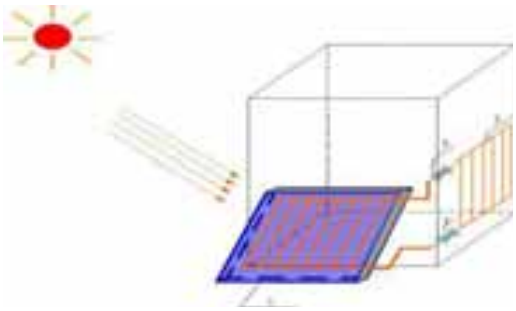

Fig. 1 the principle of the separated heat pipe solar heating system

1—flat-plate collector with separated heat pipe; 2—Control valve; 3—indoor heating terminal

2.2. Test method

The experimental apparatus was set up in the campus of Nanjing Normal University, China. Twenty J-type thermocouples were placed in the evaporator and condenser respectively, to assess temperature difference between of them at the same time. Another two J-type thermocouples were placed in the inside and outside of the room to monitor the indoor air and outside air temperature. One Hukseflux LP02 solar pyranometers was used to measure insolation values with the sensitivity is 12.13μV/(w•m^{-2}). All data was collected using Agilent 34972 a.

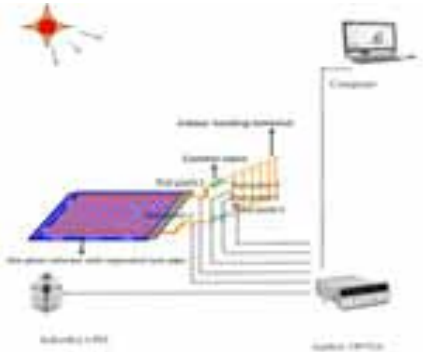

Fig.2: The experimental process of separated heat pipe solar heating system

3. Results and discussion

3.1. *Effect of solar radiation intensity on the surface temperature of indoor heating terminal and indoor air temperature at different weather conditions*

The experimental system was tested under different weather conditions including sunny and cloudy days, in the winter of 2014, in China. We counted the experimental data and chose the cloudy and sunny day as sample to analyze the performance of the system. It is the experimental data of solar radiation and surface temperature of heating terminal in the cloudy days as fig.(a) shown. When the solar radiation intensity exceeds 190W/m2 in the morning, the system starts to run. After four hours, solar radiation intensity reaches about 462W / ㎡ at noon and the system reaches stable conditions, the surface temperature of the condenser (indoor heating terminal) almost remains 29℃; the sunny day's experimental data is shown in fig.(b). When the solar radiation intensity exceeds 150W/m2 in the morning, the system starts to run. After three hours, solar radiation intensity reaches about 800W / ㎡ and the system is in the stable conditions, the surface temperature of the condenser almost remains 41℃, which is much higher than that of cloudy days. The indoor air temperature is shown in fig.(c) and fig.(d) respectively. It takes three or more hours to make the indoor air temperature reach 22--24℃ at sunny or cloudy days after the system starts to work respectively. And there is 5℃ and 9℃ temperature difference in the cloudy and sunny days respectively. So the solar radiation has great effect on the indoor air temperature. In the sunny days, according to six hours sunlight, the room temperature rising will attain 18℃, which will meet the demand of thermal comfortable temperature even the starting indoor temperature is 0℃. The better the thermal insulation of the room is, the higher the heating performance of the system is. Even in the cloudy days, the system has good thermal performance at the maximum solar radiation 462W / ㎡ and the room temperature rising 5℃ in four hours. It will be good auxiliary heating style to the electricity heating in the room, which will save much energy consumption in the south of china where is no centralized heating.

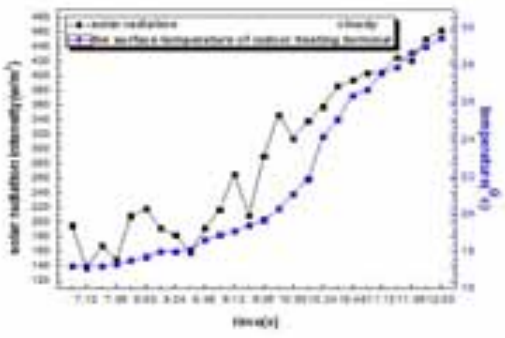

(a) Solar radiation intensity and the surface temperature of indoor heating terminal with time (cloudy)

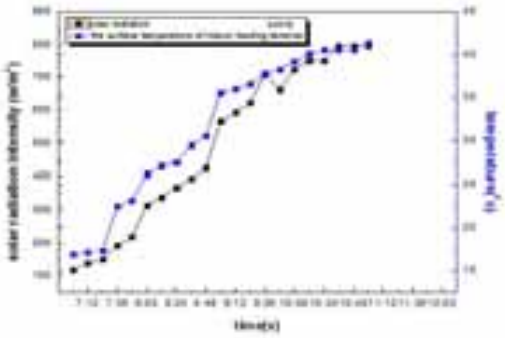

(b) Solar radiation intensity and the surface temperature of indoor heating terminal with time (sunny)

•

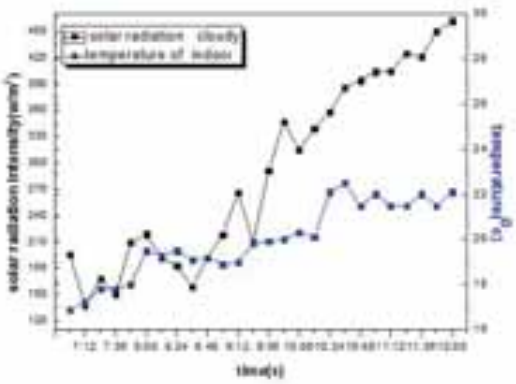

(c) Solar radiation intensity and the room temperature with time

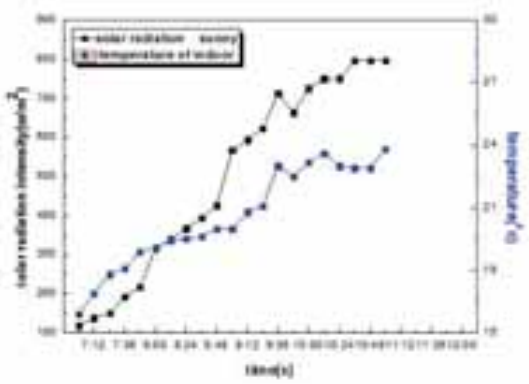

(d) Solar radiation intensity and the room temperature with time

Fig.(e) and (f) shows that solar radiation and climatic conditions have a great impact on the utilization of system thermal. It can be seen that there is 10℃ temperature difference from 8:00 to 11:00 with the large solar radiation difference. The main reason is that the amount of the working fluid at different weather days. In the sunny days, more working fluid absorbs solar energy and starts to work and transfers more heat energy to the condenser. On the other way, less working fluid transfer heat energy to the condenser and cause to the less working pressure and low working temperature in the cloudy days.

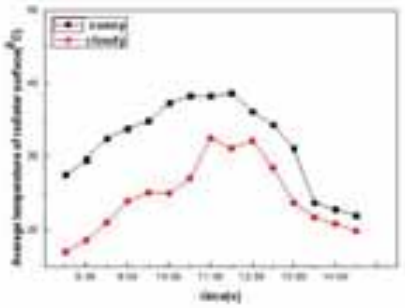

(e) Radiator surface average temperature variation at different solar radiation

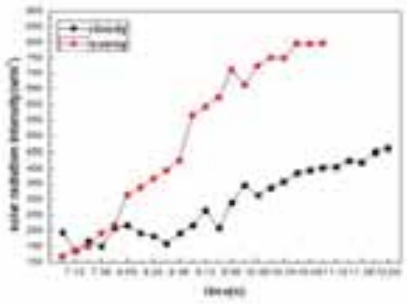

(f) Solar radiation variation at different weather condition

3.2. The profile of the radiator surface temperature at different length

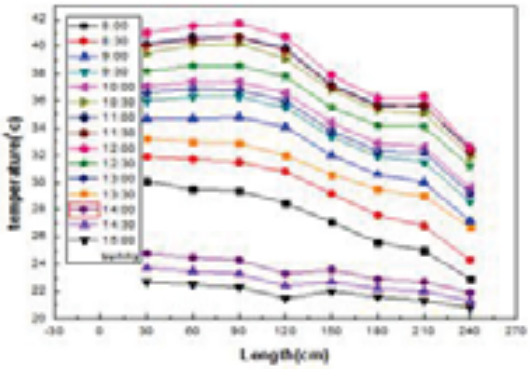

(g) The radiator surface temperature distribution at different length (sunny)

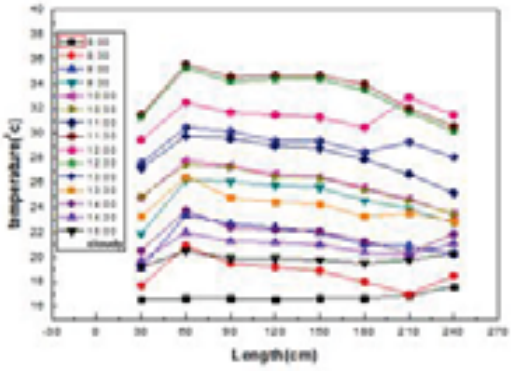

(h) The radiator surface temperature distribution at different length (cloudy)

Fig.(g).(h) shows that the radiator surface temperature distribution at different the length. 0cm represents the terminal of the radiator the nearest distance to the solar collector. And the 240cm is the length of the radiator and also the longest distance to the solar collector. In the sunny days, the surface temperature of the radiator changes from 27.5 to 41.7℃ at 8:00~12:00, and the temperature changes from 41.7 to 20.8℃ at 12.30~15:00. In the cloudy days, the surface temperature of the radiator changes from16.6 to 34.7℃ at 8:00~12:00, and the temperature changes from 34.7 to 20.2℃at 12.30~15:00. The main reason that causes the surface temperature variation is the change of the solar radiation intensity. At the same time, the surface temperature of the radiator decreases with the increase of the radiator length. This director cause is the flow resistance. The more the length of the radiator is, the more the flow resistance of the working fluid is. Then the surface temperature is the lowest at 240cm with different solar radiation.

Tab. 1: Table of heat transfer performance at different weather conditions

Weather	Solar thermal efficiency	Evaporating temperature (℃)	Condensing temperature (℃)	Solar radiation intensity (w/m^2)	Heat flow (w)
cloudy	46.5%	30.2	25.2	358	333
sunny	56%	44.8	40.2	725	820
sunny	54%	40.1	36	672	727

The table 1 shows that the solar thermal utilization efficiency can reach 56% when the solar radiation is at 725W/ ㎡ and heat flow is at 820W, and the evaporation and condensation temperature of heat pipe keep constant at 44.8 ℃ and 40.2℃ respectively. The evaporator and condenser surface temperature difference can keep 4~5℃。

4. Conclusion

This work focuses on the testing of the performance of separated heat pipe solar indoor heating system and gets the following conclusions:

(1) Compared with the traditional solar heating system, the separated heat pipe solar indoor heating system works with gravity separated heat pipe to transfer solar energy into the room without any energy consumption. With the experimental investigation, it takes three or more hours to make the indoor air temperature reach 22--24℃ at sunny or cloudy days after the system starts to work. And there is 5℃ and 9℃ temperature difference in the cloudy and sunny days respectively in four hours.

(2) The solar thermal utilization efficiency can reach 56% when the solar radiation is at 725W/ ㎡ and heat flow is at 820W, and the evaporation and condensation temperature of heat pipe keep constant at 44.8 ℃ and 40.2℃ respectively

(3) The room temperature rising can attain 9℃ in three hours in the sunny days at the solar collector only 2m2 and the room area 40m2 in Nanjing , China.

•

5. Acknowledgements

This research has been supported by National Natural Science Foundation of China (Grant No. 51208265) and the Natural Science Foundation of the Jiangsu Higher Education Institutions of China (Grant No. 12KJB560006) and the Natural Science Foundation of the Jiangsu Higher Education Institutions of China(Grant No.12KJB56006).

6. References

Susheela, N., Sharp, M.K., 2001. A heat pipe augmented passive solar system for heating of buildings. J. Energy Eng. 127 (1), 18–36.

Albanese, M.V., Robinson, B.S., Brehob, E.G., Sharp, M.K., 2012. Simulated and experimental performance of a heat pipe assisted solar wall. Solar Energy 86, 1552–1562.

Brian S. Robinson, M. Keith Sharp, .2013. Heating season performance of a full-scale heat pipe assisted solar wall. J. Solar Energy. Volume 87, 76-83.

.

Conference Proceedings

Solar World Congress 2015
Daegu, Korea, 08 – 12 November 2015

Comparison between the Experimental and the Extrapolated Stagnation Temperature – A Data Base Evaluation

Julian David Hertel[1], Víctor Martínez-Moll[1], Ramon Pujol-Nadal[1], Xabier Olano Martiarena[2], Alberto García De Jalón[2], Fabienne Sallaberry[2]

[1]Departament de Física, Universitat de les Illes Balears, Ctra de Valldemossa km 7,5, 07122 Palma de Mallorca, Illes Balears, Spain

[2]CENER (National Renewable Energy Center), Solar Thermal Energy Department, C/ Ciudad de la Innovación 7, 31621 Sarriguren, Navarra, Spain

Tel: +34 971259542, Fax: +34 971173426, julian.hertel@uib.es

Abstract

Well-designed liquid heating Flat Plate Collectors (FPC) or Evacuated Tube Collectors (ETC) could be used to provide heat at medium temperature levels for industrial processes. According to the most recent ISO 9806:2013 testing standard, the efficiency curve of a collector is constructed by a weighted least square fitting (WLS) based on at least four observations at temperatures spaced over the operating temperature range of the collector. This could lead to poor efficiency predictions at higher operating temperatures, since in this region the fit is not backed up by experimental data. To improve results in the extrapolated area without any additional experimental effort an extended observation fitting could be used, including the collector's stagnation temperature as an additional node point.

Two databases have been evaluated. One database was provided by the National Renewable Energy Centre in Spain (CENER), the other one by the Institute for Solar Technologies (SPF) in Switzerland. It has been shown that in the case of conventional FPCs the extrapolated stagnation temperature from the conventional 8-point fitting constantly underestimates the measured stagnation temperature. In the case of ETCs, on the other hand, the conventional approach leads to an overestimation.

Keywords: *IAM, Factorization, Collector testing, Medium temperature collectors, Industrial heat*

1. Introduction

The industry sector with its high and constant energy demand shows a remarkable potential for the integration of solar thermal technologies. However, beside this potential, current industrial processes still rely on conventional energy supply. Even though, in most cases, the exploitation of available solar resources is economically feasible and profitable, the unreliability and unpredictability often associated with solar energy restrict the companies from investing in new supplementary facilities. Nevertheless solar heat for industrial processes is on the rise.

The IEA task 49 created a database of operating plants to track the development of this sector. Apart from the numerous undocumented examples, the database currently counts 155 commissioned solar plants with a total capacity around 100 MW and 143,000 m^2 in size (Task 49, 2015). Projects are reported all over the world, increasing every year. Most of these plants rely on conventional flat plate and evacuated tube technology at moderate temperature levels below 100 ºC.

The temperature requirements of most industrial processes range from 60 to 260 ºC (Kalogirou, 2003). A significant share of such medium temperature processes could in theory be provided by well-insulated flat plate collectors (FPC) and evacuated vacuum tube collectors (ETC), that so far have mostly been deployed for domestic applications. Both collector types withstand operating conditions far beyond atmospheric pressure and are therefore capable of providing process heat at temperature levels above 100 ºC. Stagnation

doi:10.18086/swc.2015.10.24 Available at http://proceedings.ises.org

temperatures of conventional FPCs are around 200 ºC; those of ETC can reach even higher values, depending on the design (SPF, 2015).

According to the ISO 9806:2013 standard, the efficiency curve of the collector is based on observations at temperature levels evenly spaced over the operating temperature range of the collector. This operating range is usually below 100 ºC when operating at non-pressurized conditions. As a consequence, this approach could lead to an extrapolated area of the efficiency curve which shows larger uncertainties (see Fig. 1~~Fig. 1~~).

Con form
de fuente:

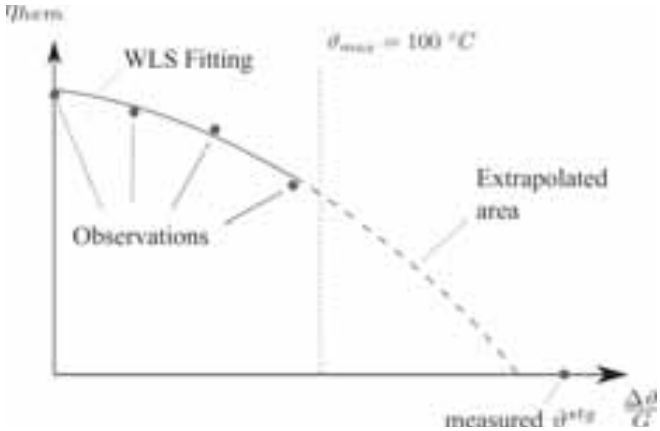

Fig. 1: Standard test procedure: At least four different experimental observations are needed to obtain the collector parameters from a WLS fitting.

One possibility to improve the accuracy of the high temperature part of a collector's efficiency curve could be to include the stagnation temperature in the fitting. The determination of the stagnation temperature forms also part of the standardized test procedure. This way, the methodology could allow improving results without any additional experimental effort.

This is meant to be a preliminary study. The feasibility of this study has been assessed by comparing both the extrapolated (not taking into account the stagnation temperature) and interpolated (taking into account the stagnation temperature) efficiency curve. To do so, three different datasets of FPCs and ETCs from two different databases have been considered. One FPC database was provided by CENER (CENER, 2015), the other two datasets consisting of FPC and ETC collectors were taken from the publicly available database of the Institute for Solar Technology (SPF, 2015). In a second step, the extrapolated stagnation temperature has been compared with the experimentally measured stagnation temperature.

Interestingly results showed a technology specific trend. It could be observed that the difference between measured and extrapolated stagnation temperature is constantly positive in the case of FPC collectors and constantly negative in the case of ETC collectors. To judge the accuracy of the new interpolated efficiency curve, experimental data is essential, which at this point is not available.

2. Collector model and standard testing regulations

In this section the collector model, the collector efficiency curve and the stagnation temperature assessment procedure are described the same way as they are defined in the standard.

2.1. Collector Efficiency Curve

The ISO 9806:2013 (ISO, 2013) is the international and currently most recent version of solar collector testing standard that includes most parts of the former European (CEN, 2006) and American standard (ANSI/ASHRAE, 2003). According to the ISO 9806:2013 standard, the performance of a collector can be characterized by its efficiency curve derived either under steady state or quasi-dynamic conditions. In the case of non-concentrating collectors that are not sensible to direct solar irradiation only, it is common practice to apply the steady state approach according to Eq. (1) (ISO, 2013).

$$\eta_{hem} = \eta_{0,hem} - a_1 \frac{\Delta\vartheta}{G} - a_2 G \left(\frac{\Delta\vartheta}{G}\right)^2 \quad (1)$$

with $\Delta\vartheta$ the temperature difference $\vartheta_m - \vartheta_a$. Where ϑ_m is the mean temperature of the heat transfer fluid (HTF) and ϑ_a is the ambient temperature. $\Delta\vartheta/G$ and $\Delta\vartheta^2/G$ are the explanatory variables of the collector efficiency curve, with G as the hemispherical solar irradiance.

Now, to characterize the collector's efficiency behavior, η_{hem} needs to be measured at least four times, each time at a different quantity $\Delta\vartheta/G$. An analytical expression according to equation (1) is then obtained by determining the characteristic constants $\eta_{0,hem}$, a_1 and a_2 applying a weighted least square fitting (WLS).

The ratio $\Delta\vartheta/G$ for different observations during the test is usually kept small to guarantee accurate fit in temperature regions the collector will most likely be operating on. This means, however, that for collectors that would possibly operate on higher $\Delta\vartheta/G$ -ratios, the fitted efficiency curve is not backed up by experimental data. Output predictions at this region could therefore be inaccurate.

Eq. (1)~~(1)~~ can be restructured to an energy output per collector area equation, when multiplying by the reference irradiance G. This form of the equation is discussed in Fig. 4~~Fig. 4~~.

$$\frac{\dot{Q}}{A} = \eta_{0,hem} G - a_1 \Delta\vartheta - a_2 \Delta\vartheta^2 \quad (2)$$

2.2. Stagnation Temperature Measurement Procedure

To overcome the problem of a lack of observations for higher temperatures without additional experimental effort, it may be useful to include the stagnation temperature as an additional node point in the fitting. For safety reasons (danger of collector over-heating), the stagnation temperature (ϑ_{stg}) is always provided alongside other collector data.

According to the ISO 9806:2013 standard, the stagnation temperature is defined as the highest temperature ϑ_{sm} that can be found on the absorber surface, while the collector is exposed to the available solar irradiance G_m and ambient temperature ϑ_{am} (outdoors, or in a solar irradiance simulator) under steady-state conditions without heat extraction from the collector (stagnation condition). To achieve these conditions with liquid heating collectors, it is recommended to drain the collector completely from all remaining heat transfer fluid and to seal all fluid pipes except for one to prevent cooling by natural circulation.

There is a standardized form of the stagnation temperature which is obtained by assuming a constant proportion of $\vartheta_s - \vartheta_a/G$. With the standard reference values $\vartheta_{as} = 30\,ºC$ and $G_s = 1000\,W/m^2$ according to Eq. (3), the standard stagnation temperature results in:

$$\vartheta_{stg} = \vartheta_{as} + \frac{G_s}{G_m}(\vartheta_{sm} - \vartheta_{am}) \quad (3)$$

Following these guidelines, the test demands that for FPCs the temperature sensor shall be positioned at two-thirds of the absorber height and half the absorber width (see Fig. 2), as it is supposed to be the point on the absorber surface where the temperature is highest during stagnation (ISO, 2013).

For ETCs the specifications are less strict. The ISO 9806:2013 states that in this case the temperature sensor should be placed at a suitable location in the collector, i.e. where the highest temperature relevant to the heat transfer fluid is to be found. Since, in the case of ETCs the absorber surface is not easily accessed, it is common practice to measure the stagnation temperature for a single tube at the tip of the pipe or copper tube respectively (see Fig. 2).

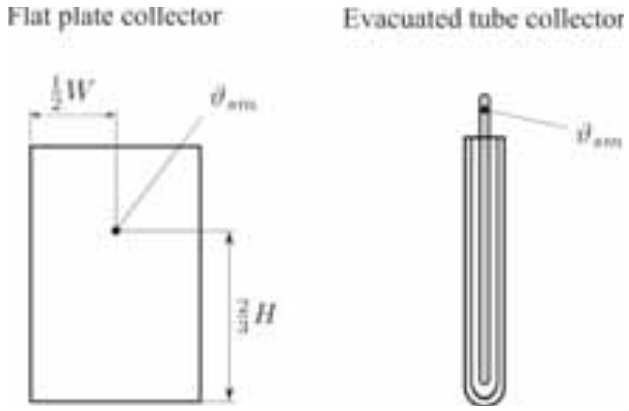

Fig. 2: Stagnation temperature measurement points according to the ISO 9806:2013, with W and H the width and the height of the flat plate collector respectively.

2.3. Collector model

When talking about using the stagnation point as an additional observation for the WLS fitting, attention should be paid to the mathematical model the efficiency curve is based on. Basically, the collector efficiency curve describes the heat transfer mechanisms within the system resulting in a fraction of useful heat and a fraction of heat losses. Fig. 3 illustrates this energy flow with the help of a resistance scheme as an analogy of an electric circuit. The scheme represents a collector with tube absorber. Q^{opt} is the energy flux in form of irradiation as it passes through the optical device. Q^{th} summarizes the heat losses consisting of radiation and convectional losses. The heat removal factor F' plays an important role in this study, as it represents the capacity of the system to transport heat from the absorber surface to the HTF. It takes into account the flow regime and absorber geometries. During stagnation the temperature ϑ_m of the absorber and ϑ_s on the absorber surface are supposed to be equal, since no heat is removed and enough time was given to reach an equilibrium of temperatures.

It is not trivial to say to what extent it is valid to assume that the stagnation point should form part of the efficiency curve. Even though heat transfer mechanisms for a drained collector differ significantly from those of an operating one with constant flow rate, the stagnation temperature measured in both cases should be the same. As Fig. 3 suggests, it is assumed that in case of stagnation there is no heat transport from the collector surface to the HTF. The absorbed energy Q^{opt} is lost completely in form of radiation and convection to the environment. It may therefore be assumed that the stagnation point should form a valid observation for the efficiency curve fitting.

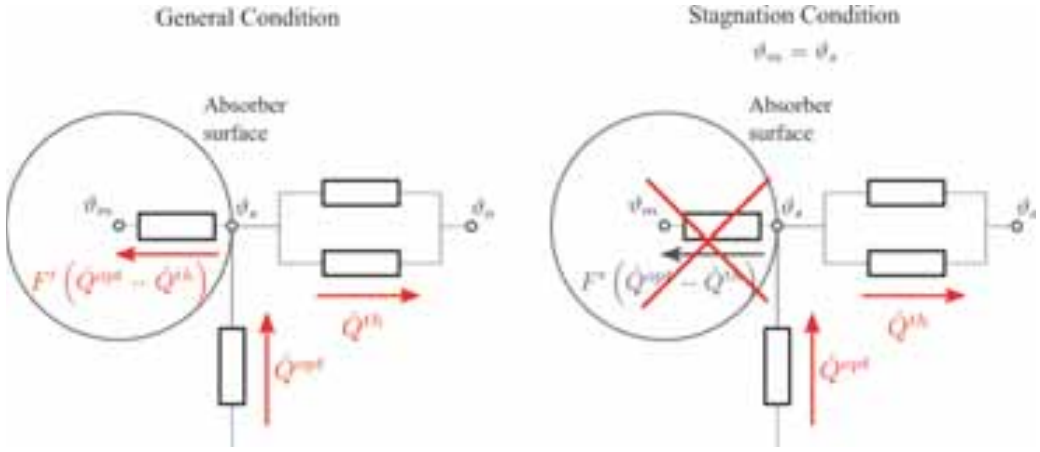

Fig. 3: General heat transfer mechanisms of a solar thermal collector during general operation and stagnation.

3. Method

Three datasets from two different databases have been evaluated. One database was provided by CENER. The database comprises 81 FPCs of different designs. Two more datasets were taken from the database of the Institute of Solar Technology in Switzerland (SPF) consisting of 24 FPCs and 23 ETCs respectively.

As for data provided by CENER, every collector was certified according to the standard regulations with eight data points at four different inlet temperatures. Apart from fitting the collector efficiency curve only to test results for the eight operational modes ($\Delta\vartheta/G$), the stagnation temperature with its typical efficiency of zero has been included as an additional observation as well.

The ISO 9806:2013 standard suggests a WLS fitting. Since uncertainty values of the temperature sensors were not available, it was applied a common multiple linear regression (MLR) fitting instead of the suggested WLS method. This will not make any difference to the outcome of the study.

The collector efficiency equation of Eq. ~~(2)(2)~~ can be converted into a multidimensional linear equation, such that it takes the form of the following general expression:

Con form
1, No revis
gramática

$$y_i = \beta_0 + \beta_1 x_{i,2} + \beta_2 x_{i,2} + \ldots + \beta_{p-1} x_{i,p-1} + \varepsilon_i \tag{4}$$

with y and x as the experimental parameters or observations, β as the regression coefficients and ε as the error. According to the MLR approach there exists a set of regression coefficients which minimizes the overall error $\sum_{i=1}^{n} \varepsilon_i$. This optimal coefficient vector is given by:

$$\widehat{\boldsymbol{b}} = (\boldsymbol{X}^T \boldsymbol{X})^{-1} \boldsymbol{X}^T \boldsymbol{Y} \tag{5}$$

where $\boldsymbol{b}$ is the vector of the regression coefficients.

$$\boldsymbol{b} = \begin{bmatrix} \beta_0 \\ \vdots \\ \beta_p \end{bmatrix} = \begin{bmatrix} \eta_0 \\ a_1 \\ a_2 \end{bmatrix} \tag{6}$$

applying this Eq. (1), the design parameters which need to be determined are the optical efficiency η_0 and the thermal coefficients $a$and a. **X** is a n × p -matrix that contains the n observations for each parameter p.

$$\boldsymbol{X} = \begin{bmatrix} 1 & x_{1,1} & \cdots & x_{1,p-1} \\ \vdots & \vdots & \ddots & \vdots \\ 1 & x_{i,1} & \cdots & x_{i,p-1} \\ \vdots & \vdots & \ddots & \vdots \\ 1 & x_{n,1} & \cdots & x_{n,p-1} \end{bmatrix} = \begin{bmatrix} 1 & \frac{\Delta\vartheta_1}{G} & \frac{{\Delta\vartheta_1}^2}{G} \\ \vdots & \vdots & \vdots \\ 1 & \frac{\Delta\vartheta_i}{G} & \frac{{\Delta\vartheta_i}^2}{G} \\ \vdots & \vdots & \vdots \\ 1 & \frac{\Delta\vartheta_n}{G} & \frac{{\Delta\vartheta_n}^2}{G} \end{bmatrix} \tag{7}$$

In the case of Eq. (1) these parameters are the constant 1 and the experimental results for $\Delta\vartheta_1/G$ and ${\Delta\vartheta_1}^2/G$. $\boldsymbol{Y}$ is also a vector of observations containing the experimental results of the collector efficiency η.

$$\boldsymbol{Y} = \begin{bmatrix} y_1 \\ \vdots \\ y_i \\ \vdots \\ y_n \end{bmatrix} = \begin{bmatrix} \eta_1 \\ \vdots \\ \eta_i \\ \vdots \\ \eta_n \end{bmatrix} \tag{8}$$

Apart from the regular fit, the 95%-confidence region has been calculated in order to analyze the accuracy of the fit and see how far the 8-point and 9-point fit are statistically apart. The 95%-confidence margin of a regression parameter is defined as

$$\beta_i^{conf} = \beta_i \pm t^*_{n-p,1-\alpha/2} \sqrt{\widehat{\boldsymbol{V}}(\boldsymbol{b})_{ii}} \tag{9}$$

with α as the confidence parameter; $\alpha = 0.05$. $t^*_{n-p,1-\alpha/2}$ is the t-value of the Student's *t*-distribution and $\widehat{\boldsymbol{V}}(\boldsymbol{b})_{ii}$ are the diagonal elements of the estimated variance-covariance matrix. The variance-covariance matrix is defined as

$$\widehat{\boldsymbol{V}}(\boldsymbol{b}) = MSE(\boldsymbol{X}^T \boldsymbol{X})^{-1} \tag{10}$$

where MSE is the mean square error of the error ε_i:

$$MSE = \sum_{i=1}^{n} (\boldsymbol{Y} - \boldsymbol{Xb})^2 \tag{11}$$

For the discussion in section 4 both efficiency curves, the 8-point fit and 9-point fit, have been plotted together with the 95%-confidence interval of the regression coefficient vector $\boldsymbol{b}$.

The SPF database already provides all efficiency curve parameters as well as the measured stagnation temperature. It was therefore not necessary to apply a MLR fitting and it was not possible to analyze the 95% confidence interval of the curve. Instead, only the difference between the measured stagnation temperature and the stagnation temperature suggested by the efficiency curve were compared with each other. This comparison also forms part of the discussion of the results obtained by the CENER data evaluation.

4. Results

4.1. CENER Database

The database comprises 81 FPCs of different design. The collectors were tested according to the ISO 9806:2013 standard regulations. Data therefore includes eight observations at four different temperature levels as well as the stagnation temperature. Based on this information one representative example has been chosen to compare two different efficiency curve fits with each other. One efficiency curve is based on the eight regular observations, while the other one also includes the stagnation point as an additional node point.

Fig. 4 shows the results for the 8-point (not including the stagnation point) and 9-point fit (including the stagnation point) of the selected collector. Beside the efficiency curves, the 95%-confidence region is indicated by dashed lines. The confidence range was determined according to Eq. (9)~~(9)~~. Interestingly, the extrapolated stagnation temperature ϑ_{fit} differs significantly from the measured stagnation temperature ϑ_{stg}. In this specific example the difference $\vartheta_{stg} - \vartheta_{fit}$ is 48.5 °C.

The 95%-confidence margin also indicates that the difference between both values is too large as to be explained by statistical accuracy of the fit. ϑ_{stg} lies far outside the 95%-confidence region. In some parts an overlap can be observed between the 95%-confidence uncertainty margins of both curves.

At this stage of research it is not possible to say which of the two curves represents the real collector behavior better. What should be noted regarding the 9-point fit is a less-realistic shape of the curve. Its curvature is opposed to the one obtained by the regular collector efficiency behavior.

The most probable solution to the real collector efficiency curve is somewhere in-between the two presented curves. In order to validate the suggested 9-point fit it is essential to obtain observations for the medium and high temperature range.

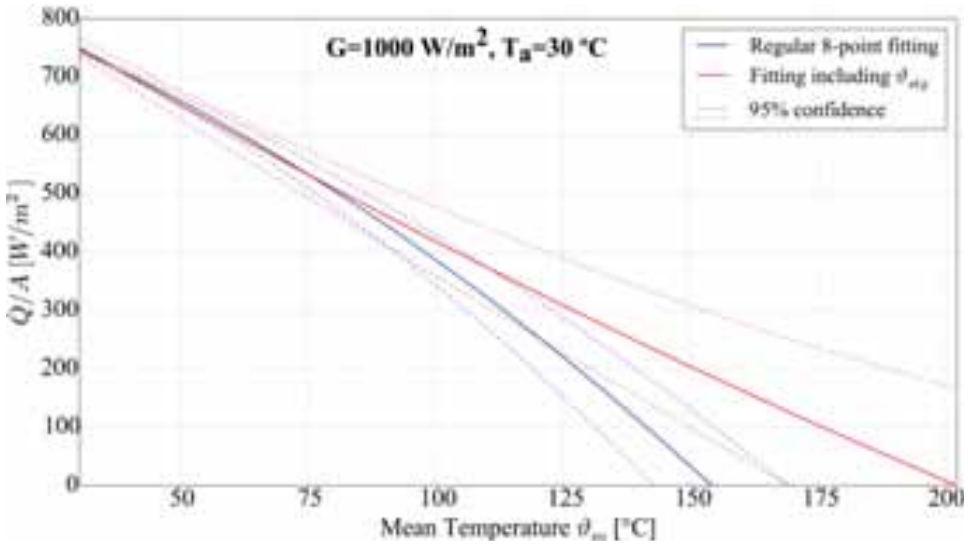

Fig. 4: Comparison of a regular 8-point fit with a 9-point fit that includes the stagnation temperature. A multiple linear regression fit (MLR) was applied to a flat plate collector with solar glass cover, aluminum plate absorber, and isolated with rock wool.

Fig 5 shows the distribution of temperature differences $\vartheta_{stg} - \vartheta_{fit}$ as they were found for all collectors of the database. Extrapolated stagnation temperature ϑ_{fit} from the 8-point fit is constantly underestimating the measured one. While the average gap is 39.47 ºC in one case it even reaches 83 ºC.

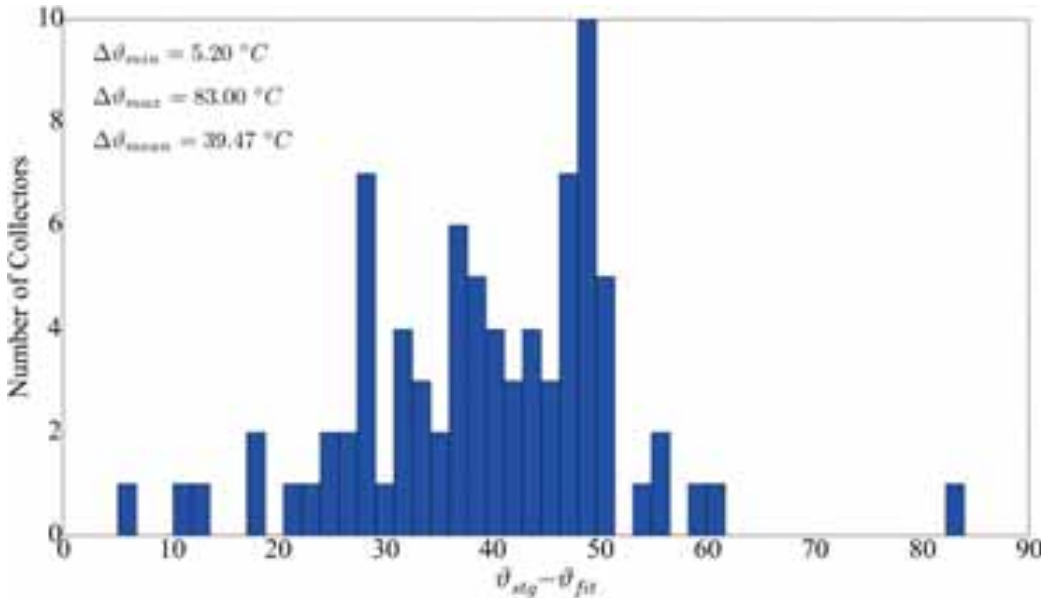

Fig. 5: Distribution of the difference between the actually measured stagnation temperature ϑ_{stg} and the estimated stagnation temperature ϑ_{fit}. The distribution represents results for 81 flat plate collectors certified by CENER.

4.2. SPF Database

SPF provides an extensive database of test results of FPCs and ETCs that is publicly available. Two datasets based on this database have been evaluated in this study. The datasets consist of 24 FPCs and 23 ETCs respectively.

As can be seen in Fig 6, results for FPCs show almost constantly positive temperature differences $\vartheta_{stg} - \vartheta_{fit}$ same as was reported for the CENER database. The maximum temperature difference found was 26.30 ºC. However, in three cases the measured stagnation temperature seems to be well represented by the extrapolated one.

As an interesting fact, it could be shown that in the case of ETCs the gap $\vartheta_{stg} - \vartheta_{fit}$ is negative in most of the cases. The extrapolated value is consequently overestimating the measured stagnation temperature. Especially in two cases a very large difference of -159.74 ºC could be found. It should be noted that one of the reasons for this negative temperature difference could be the way in which the stagnation temperature is measured for ETCs. Since it is often complicated to attach temperature sensors to the absorber surface inside the evacuated tube, the sensor is placed at the heat of the tube. Taking into consideration the temperature gradient along the tube as a result of heat transport mechanisms, a lower temperature can be expected at the tip of the tube than further down at towards the bottom.

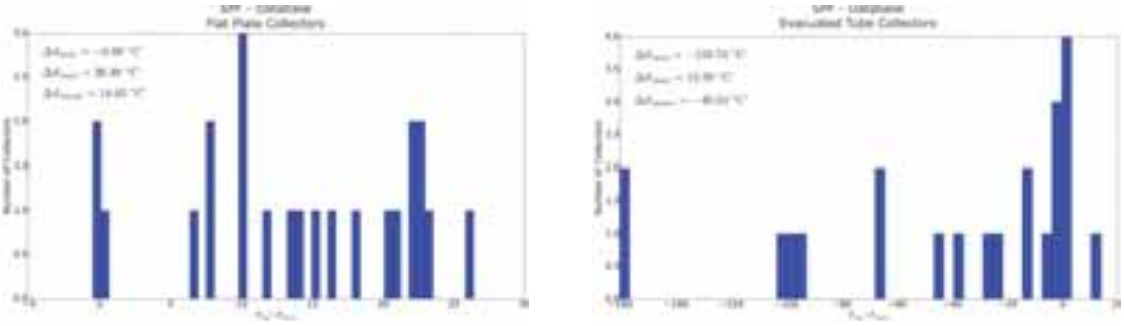

Fig. 6: Absolute distribution of the difference between the actually measured stagnation temperature ϑ_{stg} and the estimated stagnation temperature ϑ_{fit}. The distribution represents results for 24 FPCs and 23 ETCs from the SPF database.

5. Conclusion and Outlook

The conventional data fitting approach according to the ISO 9806:2013 standard constantly underestimates the actual stagnation temperature in the case of FPCs and overestimates it in the case of ETCs. The reason for these differences is most likely due to the way the stagnation temperature is measured. Stagnation temperature assessment methods differ for every type of technology. In addition, the accuracy of the measured stagnation temperature might depend on a couple of other effects such as the temperature dependency of optical properties and non-linear effects of convectional heat transfer.

An exemplary sample from the CENER database showed that since ϑ_{stg} was found outside the fit's 95-confidence interval; in this case statistical errors of the prediction could be excluded. In some parts an overlap was observed between the 95%-confidence uncertainty margins of both curves.

Whether a 9-point fit could yield more accurate results within the high temperature range of the efficiency curve is not straight forward to say. It will be necessary to validate this approach with experimental data at higher operating temperatures. This will be done in a further study. An evaluation of the results will show, whether the integration of ϑ_{stg} into WLS fitting is physically reasonable.

6. References

ANSI/ASHRAE, 2003. ASHRAE Standard 93 Methods of Testing to Determine Thermal Performance of Solar Collectors.

CEN, 2006. EN 12975-2. Thermal solar systems and components – Solar collectors – Part 2: Test methods. European Committee for Standardisation.

CENER, 2015. National Renewable Energy Centre, Spain (CENER) [WWW Document]. URL http://www.cener.com/en/ (accessed 9.27.15).

ISO, 2013. Solar energy - solar thermal collectors - test methods, ISO (Ed.) ISO 9806:2013(E).

Kalogirou, S., 2003. The potential of solar industrial process heat applications. Appl. Energy 76, 337–361. doi:10.1016/S0306-2619(02)00176-9

SPF, 2015. Institute for Solar Technology [WWW Document]. URL http://www.spf.ch/Home.44.0.html?&L=6 (accessed 9.27.15).

Task 49, 2015. SHIP database [WWW Document]. URL http://ship-plants.info/ (accessed 9.27.15).

A NEW TYPE OF SIMULATION SOFTWARE FOR DETAILED COMPONENT-BASED SYSTEM ANALYSIS

Reza Shahbazfar

rs@3optim.com

Abstract

A new type of simulation software is introduced which performs sophisticated simulations on the transient thermal, and electrical and hydraulic system behaviour. In comparison to other available software, it can simulate the sensor and controller properties, and also enables hydraulic analysis. It is possible to set or influence the component parameters throughout a simulation. In addition, several open interfaces allow the use of the software in numerous fields of application, such as in particular its implementation in other software. The software core facilitates both a fixed and a variable simulation time step.

Individual system configurations can be designed by connecting single components such as in other component-based simulation tools. The program's component library contains 15 validated components. Further components can be modelled or imported by the user if required. The software was validated using TRNSYS 17 as well as analytical considerations, and very good results have been obtained.

Keywords: *Simulation software, component based, sensor and controller properties, variable time step, hydraulic circuit analysis*

1. Introduction

The demand for renewable energy sources and their availability fluctuate over time. These variations lead to a dynamic response of the respective systems. Common dynamic system simulations can be used to analyse or predict the system's behaviour, and several simulation tools have been developed in the past Connolly, D. et al. (2009). From a technical point of view, they can be divided into system-oriented and component-based tools. Component-based simulation tools are usually used in science and for sophisticated technical applications. Depending on the desired application, the potential of commercial software tools is restricted due to a number of missing functionalities or drawbacks. This motivated the development of the new component-based and detailed simulation software (MITHRA). The aim of the new software is to integrate and combine the following (partially new) features in a single program:

- Detailed modelling of sensor, controller and data logging properties
- Detailed analysis of hydraulic circuits
- Accessibility to automatically performed simulations
- Flexibility in usage: possibility to be implemented in another software, as a stand-alone or a server-based application
- Variation of component parameters during the simulation: e.g. the variation of solar thermal collector efficiency curve parameters or the heat transfer coefficient of hot water storages U = f(…)
- A variable time step
- Fast and simple modelling of new components and features
- The flexible and combined simulation of thermal, hydraulic, electrical and if required further system behaviour in one tool

In the following sections, the software structure will be introduced briefly, and the main parts "Simulation Core" as well as the "Component Liberty" will be described more specifically with a focus on the advanced methods of MITHRA.

Selection and/or peer review under responsibility of Scientific Committee
doi:10.18086/swc.2015.10.25 Available at http://proceedings.ises.org

2. Software structure

The MITHRA software structure is shown in Fig1. It consists of a simulation core (a) and a component library (b). The simulation core processes the system information and its control strategy which are provided in two files (c). User-modelled components (d) can be simulated if necessary. The results of the simulations are dynamically written on an output file (e). Both the system file and the control file use a very simple and user-friendly syntax. However, visual interfaces like desktop or mobile apps can be applied to prepare these two files (f). The software is very well documented.

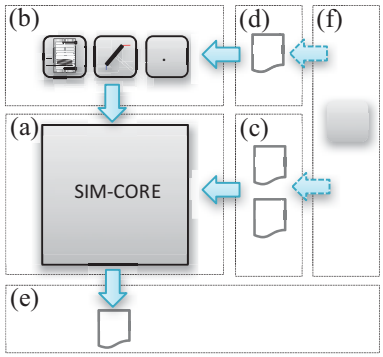

Fig. 1: Schematic structure of the software: (a) simulation core, (b) component library, (c) system file and control file, (d) user-defined components, (e) output file, (f) optional visual interfaces

Fig. 2 portrays an example of a solar thermal system which was investigated in MITHRA. It consists of a collector field with an area of 10 m^2 connected by an insulated pipe to a hot water storage with a volume of approximately 450 litre. The hot water storage has a direct temperature controlled electrical heater which is installed in the upper part. The major component details are shown in Table 1 and the measurement details are shown in Table 2. This system was modelled in MITHRA using the standard components.

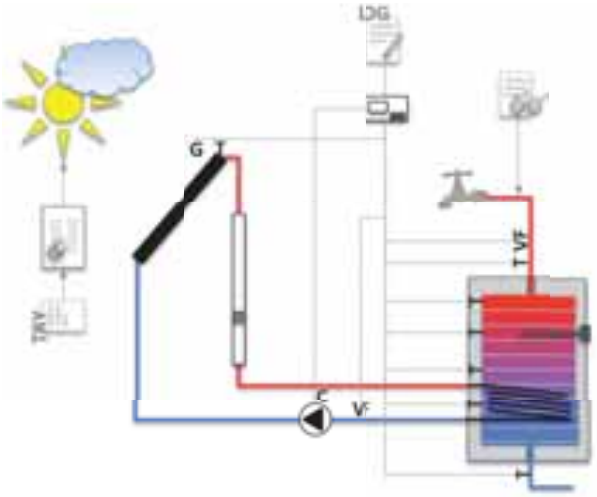

Fig. 2: Schematic structure of the exemplary solar thermal system simulated in MITHRA. The components are described in Table 1 and the sensors in Table 2

Tab. 1: Components' main information of the simulated example System shown in Fig. 2

Component	Important Parameters / Values
Test Reference Years Data , TRY-Processor, Weather data in simulation environment	Time Step = 1 min
Flat Plate Collector	Collector aperture Area = 10 m^2 η_0 = 0.8 a_1 = 3.24 $Wm^{-2}K^{-1}$ a_2 = 0.011 $Wm^{-2}K^{-2}$

Pipe	Internal Diameter (Pipe Wall) D_{in}= 0.03 m External Diameter (Insulation) D_{out}= 0.04 m Length L = 10.0 m
Pump	Set Volume Flow $\dot{V}$= 0.0001 m^3s^{-1}
Hot Water Storage	Internal Diameter (Tank) D_{in}= 0.6164 m External Diameter (Insulation) D_{out}= 1.0 m Height h = 1,5 m Number of Segments = 20 Electrical Heater Position = 70 % Electrical Heater Power P_{el}= 2 kW

Tab. 2: Sensors and control signal of the simulated solar thermal system shown in Fig. 2 from left to right and top to bottom

Abbreviations	Component	Unit
G	Solar Irradiance Sensor 1. in collector plane (G Collector)	W/m^2
T	Temperature Sensor 1. collector outlet (T Collector) 2. hot water storage internal - 99% height (T Storage 99%) 3. hot water storage internal - 70% height (T Storage 70%) 4. hot water storage internal - 50% height (T Storage 50%) 5. hot water storage internal - 30% height (T Storage 30%) 6. mains water(T Cold Water 99%)	° C
VF	Volume Flow Sensor 1. hot water withdraw (VF Hot Water) 2. solar primary loop (VF Solar Primary Loop)	m^3/s
C	Control Signal 1. solar primary loop pump (C Pump Solar Primary Loop)	1

The results obtained during a ten-day simulation, beginning on January 1 are shown in Fig. 3 and in Fig. 4 with more detailed measurement results for the exemplary day January 6. The components as well as the overall system show the expected qualitative behaviour. The quantitative evaluation is described in section 4 with the component validation with TRNSYS 17 standard library. For example, it can be observed that the upper set temperature of the electrical heater is 60 °C and the lower one is 55 °C, corresponding to the temperatures in the position of the electrical heater in 70% of the storage height (Fig. 3 and Fig.4). This is visualised in the temperature curve “T Storage 70%”. Due to stratification, mixing and several other modelled heat transfer phenomena, the upper storage temperature “T Storage 99%” is continuously influenced by the electrical heater but it remains in the desired temperature range. The system controller continuously compares the collector temperature “T Collector” with the temperature in the lower part of the storage “T Storage 30%”. In case of a (rather low) positive temperature difference of 5 K and more, the solar primary loop pump is turned on by setting the control signal “C Pump Primary Solar Loop” to “1”. The energy transport from the collector to the storage causes a temperature increase in the lower parts of the storage, as demonstrated by the temperature sensor T” Storage 50%” installed in the middle of the storage. In the weather dataset, January 5 is a sunny day with rather low hot water consumption. Thus, the solar thermal part of the system can fully heat up the water.

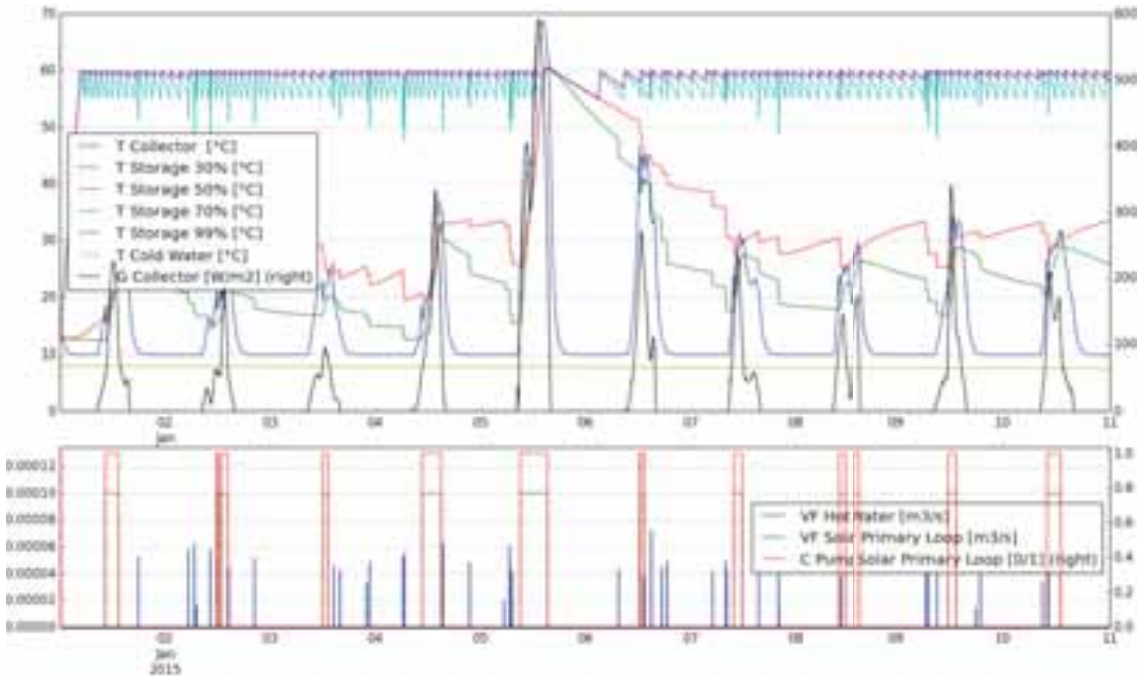

Fig. 3: Measurement results of the simulated solar thermal system shown in Fig. 2 using MITHRA. The 10 day simulation starts on January 1. The components and the sensors are described in Table 1 and Table 2.

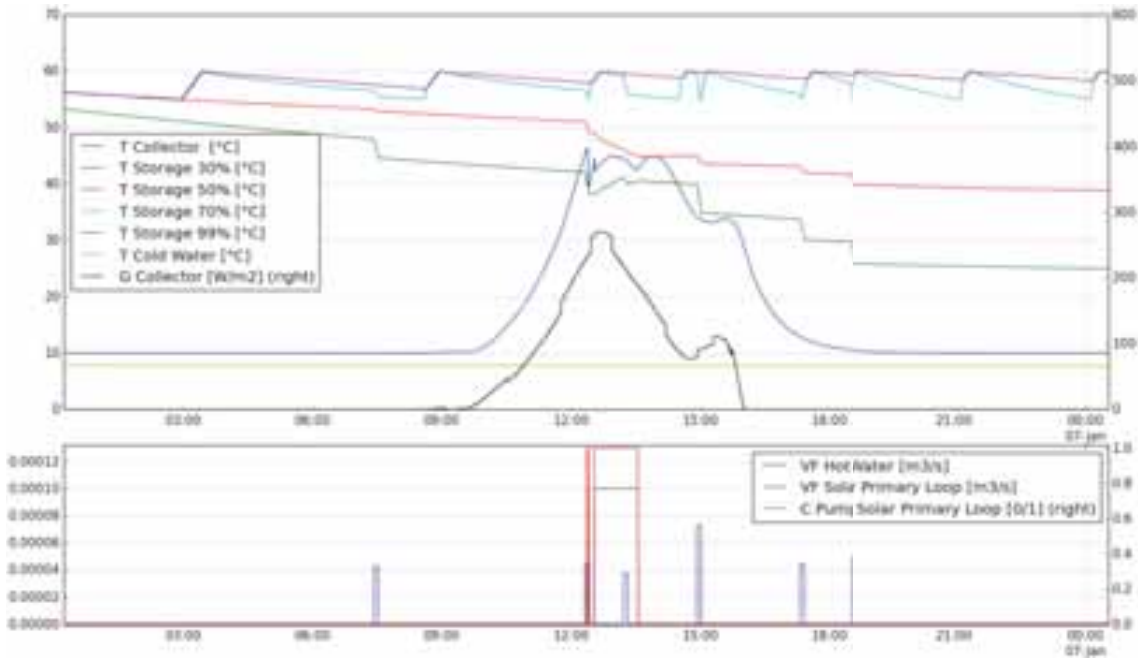

Fig. 4: Measurement results in detail for January 6 shown in Fig. 3.

3. Simulation Core

The simulation core is the most essential element of the software. In the very first step, it parses the input file, which contains the component and system description. Subsequently, a software environment is accessible where a simulation can be started manually as well as automatically by separate or wrapping software. After the simulation, an output file is generated containing the simulation results. Additionally, different implemented post processing methods for advanced plotting or data import and export are provided. In the following, the input and output files will be described before presenting the different features of the simulation core.

3.1 Input and Output Files

Figure 4 shows an example input file. The components are defined in the top of the file, and connected with each other using arrows in the bottom of the file. When defining the components, many component specific parameters can be set according to the requirements of the user. For example, to define a hot water storage tank it is possible to adjust 41 parameters, if necessary. In case the component parameters are not further defined in the input file, the component's default values will be used according to the program's manual.

An important feature is that hydraulic loops are defined (e.g. "CollectorLoop" in Fig. 5) and the components are assigned to a loop. Thereby, hydraulic circuit analysis can be performed. While some simple hydraulic analysis features are already implemented, more sophisticated features are in development.

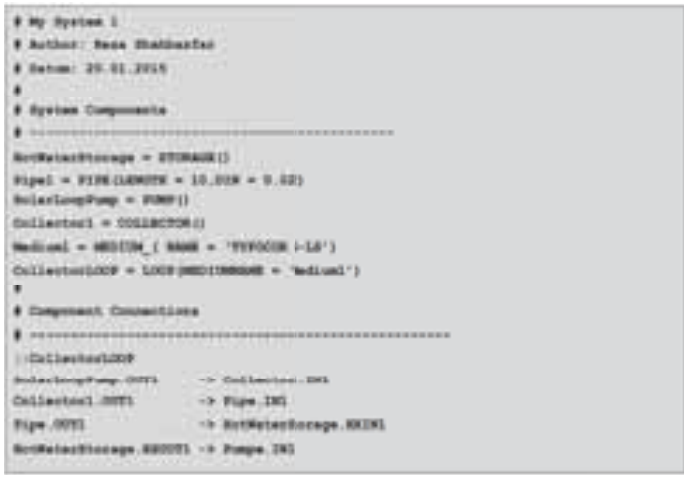

Fig. 5: Schematic structure of the simulated exemplary system in MITHRA. The components are described in Table 1 and the sensors in Table 2

The output file is generated by a data logger (see 4.9) and structured as a common csv file containing the sensor names in the first row and the time stamp in the first column (see Fig. 8). Therefore, it is easy to further process the simulation results in other programs, such as spreadsheet programs.

3.2 Port Concept

In each simulation time step, component states are linked to each other according to the system description in the input file. A port concept has been developed to enable the components to not only generate a value but also to interact with each other. Different type of ports can be distinguished:

1. Hydraulic Port
2. Energetic Port
3. Sensor Port
4. Free Port

Through a hydraulic port, energy and mass exchange including pressure is performed. The energetic port enables a non-mass-linked energetic exchange. The sensor port plays a special role since it only has a one-way interaction mode. The last category of ports is the free port, which is automatically defined by the simulation core according to the user's specific requirements; for example, when using a file reader to import different kinds of values.

3.3 Variable Simulation Time Step

Throughout system operation and respectively during simulation, there are times of high process dynamics causing highly fluctuating state values, but there are also less dynamic conditions with rather stationary conditions. In the solar thermal system (Fig. 2), one can observe typical dynamic system conditions. For example, they are caused by variations in solar radiation caused by clouds passing by, after a power-on of the solar primary pump or after a hot water withdraw. On the other hand, in the night and in the absence of a hot water withdraw the system temperatures are less dynamic.

The simulation core was designed in order to facilitate a variable simulation time step to enable the simulation to speed up under less dynamic conditions. Therefore, three different speed levels with different speedup factors can be defined at the beginning of a simulation. A suitable simulation time step is automatically chosen depending on the automatically reported component states and the required tolerance accuracy. In Fig. 6, the collector temperature and the control signal of the solar primary pump of the solar thermal system (Fig.2) are shown. The simulation was performed using a variable time step. Two short time ranges of the diagram (left dotted rectangle) are shown in Fig. 7. (left) The calculated points of the collector temperature are marked by a "+". It can be noted that the activation of the solar primary loop pump leads to more dynamic system conditions slowing down the simulation speed. Shortly after the disconnection of the solar primary loop pump, the system is less dynamic and the simulation speeds up once again (right dotted rectangle, see Fig. 7 right).

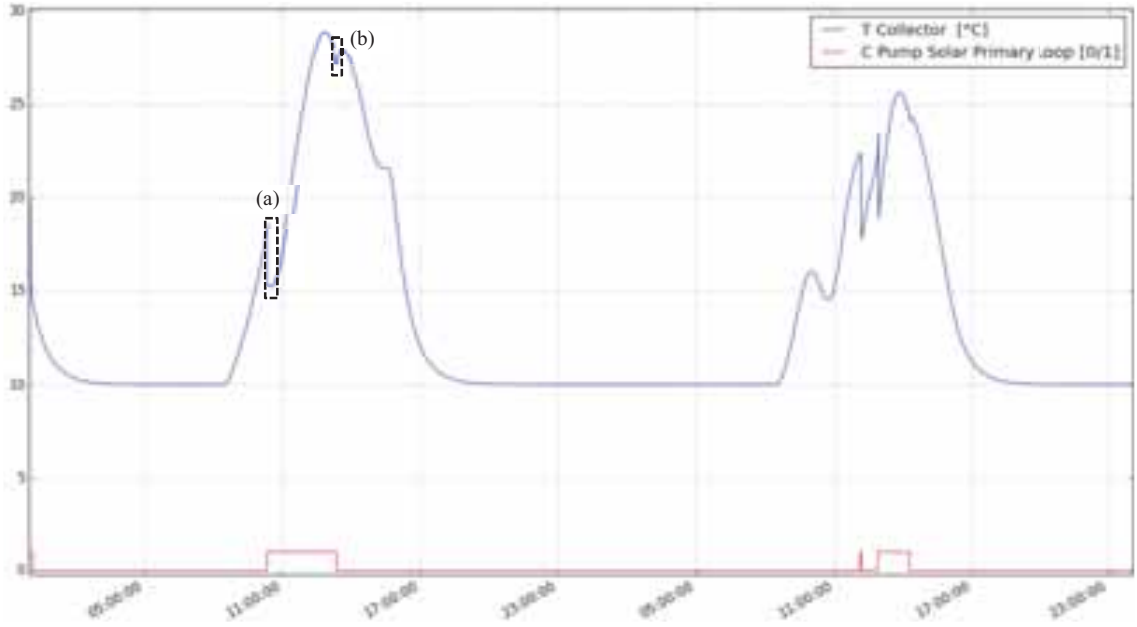

Fig. 6: Two days simulated in MITHRA using variable time steps. Two exemplary positions showing the automatic simulation speed change have been chosen (dotted rectangles) and are shown in Fig. 7 (left dotted rectangle) and Fig. 7 (right dotted rectangle).

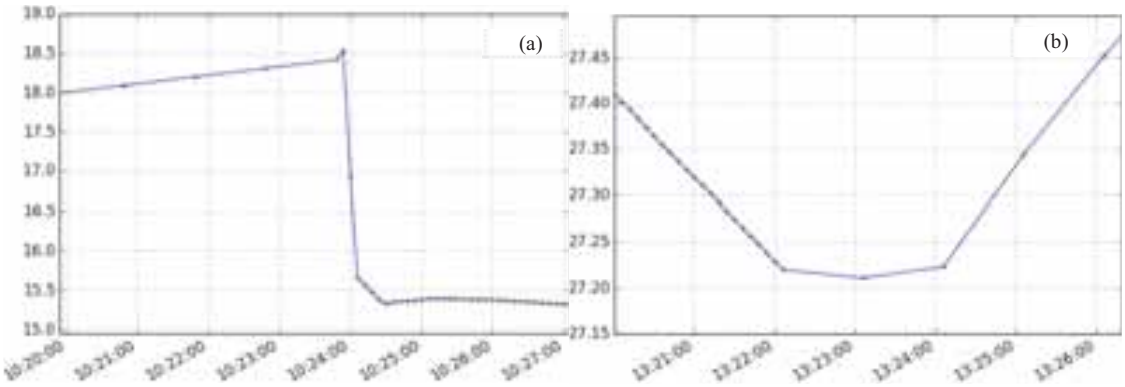

Fig. 7: X-zoom on left (a) and right (b) dotted rectangle displayed in Fig. 6. After the activation and disconnection of the primary solar loop pump the simulation time step (marked by "+") is reduced and increased, respectively.

3.4 Numerical Solver

In MITHRA, there is no global numerical solver. The numerical process is executed in the components. An explicit numerical solver has been developed to enable a fast modelling of new components. It is an automatically self-controlled solver, which reduces the simulation time on the one hand, and achieves the expected simulation accuracy on the other. This is achieved by an algorithmic manipulation of the calculated control points. It is possible to implement implicit numerical methods or to combine them.

3.6 Process Analyser

A process analyser to detect the simulation time (complexity) of each component and to plot the results if required has been developed. It detects malfunctioning components or other problems of the simulation. Additionally, warnings and errors are displayed and can be written to a file.

3.7 Hydraulic Circuit Analyser

Throughout a simulation, the hydraulic circuit analyser automatically investigates the hydraulic system behaviour. It can analyse the components of each loop and pre-calculate the pressure and the pressure drop due to a fictive volume flow. This makes it possible to automatically iterate the expected volume flow and flow direction in distribution manifolds. Therefore, the loops and the fluid within the loops are separately declared in the input file (see Fig. 5). Some components are modelled slightly different: For example, a pump can provide a pressure difference instead of a constant volume flow (see. 4.4), or new components like a safety valve and expansion vessel are modelled and can be used in loops. The hydraulic analyser works in a simple mode and its further development is possible.

4. Components

For a simulation, the system has to be described by its single components according to the input file shown in Fig. 5. While it is possible to create new components, a number of ready-to-use components are contained in the program's component library. Table 3 provides an overview of the available components. These components are quite flexible: By setting a parameter (usually called MODE), a wide range of different component constructions can be reproduced. Thus, the number of the components is not directly comparable with some existing programs. All components are validated using analytical methods or numerical methods with TRNSYS 17. A detailed mathematical and syntactical description of the components, including the validation results, is provided in the program's documentation with more than 100 pages.

Tab. 3: Component Library Overview – Ready-to-use components

Components	
Pipe	Sensor
Medium (e.g. Heat Transfer)	Equation Processor
Hot Water Storage	Numeric Function Generator
Pump	File Reader
Solar Thermal Collector	Safety Valve
Boiler	Expansion Tank
Distribution Manifold & Flow Mixer	Multi Zone Building Modell (in process)
Weather Processor / TRY	Heat Pump (in process)
Controller with Data Logger	Photovoltaic (in process)

The components are briefly described in the following sections with a focus on their advanced features.

4.*1 Pipe*

The component pipe is realized as a plug-flow-model. Additionally to the common features (for example, the calculation of the thermal losses to the environment), this component determines the hydraulic losses as well as the internal heat transfer between the single segments at different temperatures. The inlet and outlet heights can be defined. Thus, a thermal stratification in the pipe can be simulated if required. As an additional special feature, any pipe bends and a number of different hydronic components like elbows and ball or block valves can be defined and will be taken into account when the hydraulic losses are calculated.

4.2 Medium

In MITHRA, the heat transfer medium within the system hydraulics itself is considered to be a component. Therefore, the relevant required hydraulic and thermodynamic features like fluid density, viscosity, specific heat or aggregate state can be calculated dynamically with respect to the current individual system conditions. Different common mediums are already modelled, and the user can create new fluids if necessary.

4.3 Hot Water Storage

Heating applications often use hot water storage to ensure the user's thermal energy demand and to enable the system to bypass the time between energy availability on the one side and energy demand on the other. The system behaviour implies many different overlapping heat and mass transfer phenomena, which makes it rather complex to model. In MITHRA, detailed and very flexible hot water storage was modelled. In simulations, the storage medium is divided into nodes. For every node, a complex mass and energy balance is calculated. Besides the energy and mass calculations, the stratification of the storage medium including mixing effects is also considered.

It has to be underlined that in this model the number and positions of internal heat exchangers, electrical heating elements, inlets and outlets as well as the number of the nodes are not limited or restricted. The internal heat exchanger and the storage body can be described analytically by typing in the single parameters, or they can be described using overall values like U or U*A. The shape of the storage can be switched from cylindrical to cuboid.

4.4 Pump

The component pump converts electrical power into a pressure difference or to a pre-defined volume flow depending on the simulation mode and the fact whether the hydraulic circuit needs to be analysed or not. In the latter case, the pump characteristics dp = f(Vd, Pumplevel) can be defined. The pump is switched on by a control signal that is continuously variable or digital in the rage of 0…1.

The efficiency behaviour of the pump is described by two parameters: A first parameter describes the efficiency of the electromotor in terms of converting electrical energy into rotatory mechanical energy, and the latter factor describes the efficiency of the mechanical components of the pump in terms of converting the rotatory mechanical energy into a hydraulic pressure difference. Alternatively, it is possible to describe the pump's overall behaviour with a single parameter. Furthermore, the temperature increase of the fluid due to the pump inefficiency is also modelled.

4.5 Solar Thermal Collector

Several different approaches exist on how a solar thermal collector can be modelled. When performing a simulation and setting up these models, it is often problematic to get all the required parameters. Thus, many parameters need to be assumed which leads to an increase of the model uncertainty. To avoid this, a converse approach has been chosen in DSMIN for the development of the solar thermal collector model. Firstly, the data sheets of different available collectors on the market were analysed. The collector model was developed according to the identified and easily obtainable parameters. It primarily depends on the efficiency curve parameters, but also on the collector heat capacity and the incident angle of the solar irradiation. Moreover, the hydraulic collector behaviour was also taken into account. It is described by one or multiple parameters available in the collector datasheet or in the collector testing report.

4.6 Boiler

A boiler ensures that the thermal energy demand is met. Oil-fired or gas-fired boilers are two common types. Their system integration can vary as well. Usually, they are separate external devices heating up a medium in a closed loop and pumping the heated medium to the load.

In MITHRA, a flexible component model of a boiler was developed. It can convert an external energy source into thermal energy and supply it to the load using a pump. The temperature behaviour is regulated by setting an upper and lower temperature. The heat capacity, a constant or a variable efficiency function depending on the boiler's return temperature can also be taken into account in the simulation process.

4.7 Distribution Manifold / Flow Mixer

To split one inlet volume flow into multiple outlet flow rates a distribution manifold can be used. The outlet flow rates can be adjusted individually using valves. In MITHRA, a distribution manifold was modelled where the flow rate factors can dynamically be controlled by an external function during the simulation. A flow mixer is also available enabling the reverse process: Multiple inlet volume flows are mixed and provided as a single flow at the outlet.

4.8 Weather Processor

The climatic conditions play a key role for thermal or energy simulations. Thus, several methods and different sources have been developed in the past providing weather data especially for simulation purposes. Typically, solar diffuse and beam irradiance in the horizontal plane, ambient temperature, wind speed and air humidity are part of the weather information. In MITHRA, a weather processor was created as a component. It reads the weather data and is able to calculate the irradiance on the surface at any desired orientation. Therefor a complex calculation of the sun's position in the sky is internally performed and isotropic or non-isotropic sky models are utilised.

For Germany the "test reference years" (TRY) DWD (2014) is one of the most popular and free available sources for weather data used in simulations. A special "TRY mode" has been programmed in the component that enables the direct use of the TRY data without any intermediate step.

4.9 Controller and Data Logger

Energy and hydronic systems usually have a controller to ensure an appropriate operation. Usually the controller utilizes sensors, actuators and a control strategy. Common controllers provide the opportunity to log and transfer the current sensor an actuator values in a file or they analyse the data just in time. The controller in MITHRA was programmed to have these functionalities and be freely programmable.

The number of sensor inputs and actuator outputs can be chosen freely. For each input and output, the sensor type (e.g. temperature or flow sensor etc. or control signal) needs to be defined. Different simple and predefined control strategies are available, or user may define their own control strategy. An example of a control file is shown in Fig. 8. At the beginning of the file, the controller inputs are assigned to a local variable in order to be handled more easily. The solar primary loop pump is then controlled with four different if-statements using a delta-T switch-on (8 K) and switch off (4 K) including the protection of the solar loop components (100 °C) and of the storage protection at 95 °C. An example of a controller's logging file is provided in Fig. 9.

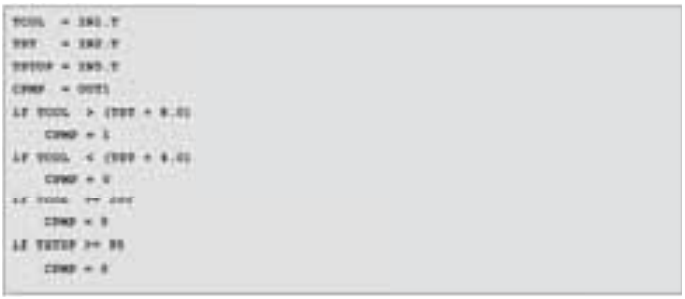

Fig. 8: Example of a simple control strategy for the controller.

Fig. 9: Example of a logging file generated by the controller. In the first column, the time stamp and the column names are provided in the first row

4.10 Sensors

As a special feature, the sensors are considered to be stand-alone components in MITHRA. Thus, it becomes easily possible to describe and numerically investigate their temporal response and measurement uncertainty in interaction with the rest of the system. In MITHRA, the measurement uncertainty is distinguished in systematic and random errors. Systematic deviation can be modelled as constant offset or can be function of the measured value or a function of simulation time. The random errors are defined by a maximum and

minimum limiting function that may also vary depending on the measured value and the simulation time. In between these two limits, a probability distribution function like a rectangular or a normal distribution function can be selected. The influence of the sensor's behaviour in terms of the logging file depends on the controller's data fetching mode (sampling or averaging and thresholding) and logging speed.

When performing detailed simulations, sometimes it can be necessary to take the sensors response behaviour into account. Hence, in MITHRA the physical sensor behaviour is provided. In Fig. 10, the overall behaviour of a simulated exemplary temperature sensor in different configurations is shown. Sensor "T_IDEAL" shows the values of the simulated system, assuming an ideal sensor. The thermal response behaviour of the sensor is modelled for the second sensor "T_SEN1". In the case of the third sensor "T_SEN2", random errors of the sensor are modelled additionally.

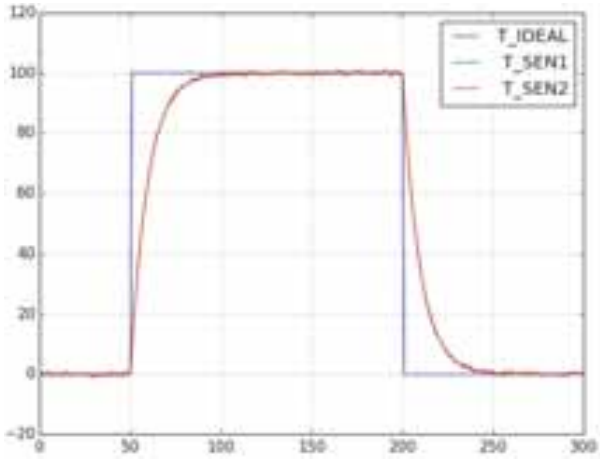

Fig. 10: Simulated temperature sensor in three different configurations: 1. Ideal ("T_IDEAL") 2. With a thermal response time (T_SEN1) 3. With thermal response time and random errors (T_SEN2)

4.11 Equation Processor

User-defined calculation can be performed using the equation processor component. The results are available at the output of the component. The number of used inputs has to be defined and the respective values must be connected in advance. It uses a similar syntax to the control file shown in Fig. 9.

4.12 Numeric Function Generator

For testing purposes or for basic control functions, it is sometimes necessary to quickly generate a value during the simulation. Thus, a value generator was modelled in MITHRA. It provides the opportunity to generate constant values, step functions or interpolations between given points and given time steps.

4.13 File Reader

The file reader makes it possible to read in external data into the simulation. The external file can contain a single value, multiple values or multiple time series provided in columns like in a csv format. In the latter case, the column separator can be defined manually. The file reader provides several mathematical and numerical functions like looping the file or using a simulation time depended or independent transfer function.

4.14 Safety Valve

A safety valve can be built into each loop to keep a maximum set pressure. In MITHRA it can be used for more sophisticated simulations including hydraulic circuit analysis. The component distinguishes an upper and a lower response pressure of the valve.

4.15 Expansion Vessels

Expansion vessels compensate the thermally caused volume variations of the fluid within the system. As expansions vessels typically have their pressure – volume characteristics, the volume compensation leads to a pressure variation in the system. To be able to simulate this behaviour, an expansion vessel has been modelled. Two different modes exist: In the first mode, a simple parametric approach is used that interpolates the "delta pressure" as a function of the "delta volume" with a predefined lookup table. The

second mode is for gas-filled membrane expansion vessels where the “delta pressure” can be calculated as a function of the “delta volume” using the ideal gas law of thermodynamics.

4.16 Component Validation

The component validation was performed by using analytical or numerical methods. For the latter, TRNSYS 17 standard library (see UW–Madison, 2009) was used to validate the component’s pipe, collector, hot water storage and weather processor. Different tests have been chosen that can isolate the component’s elementary behaviour as good as possible. For the variations within the test, a normal operation range was chosen. Additionally, two points (one extremely low and on extremely high) were considered. The component tests are described in Tab. 4.

Tab. 4: The components‘ main information of the simulated exemplary system shown in Fig. 2

Component	Variations
Pipe	Test 1: ambient temperature, Test 2: thickness of insulation , Test 3: thermal conductivity of insulation material, Test 4: inner diameter
Collector	Test 1: ambient temperature, Tests 2: irradiance, Test 3: flow rate, Test 4: collector return temperature, Test 5:incident angle, Test 6: maximum stagnation temperature (3 % max, not typical operation condition)
Hot Water Storage	Test 1: electrical heating in the upper of the storage, the vertical thermal conductivity over the time is compared, Tests 2: variations in the insulation U-Value, temperature of each node over time is compared , Test3: variation of the power of electrical heater in the bottom of the storage tank, the stratification over time is compared, Test 4: Variation of the volume flow in the internal heat exchanger, temperature over time of all nodes is compared, Test 5: hot water withdraw in the top of the tank is simulated and varied, the temperature over time of all nodes is compared
Weather Processor	Multiple test and the comparison of direct and diffuse radiation, variation of plans orientations and models anisotropic diffuse radiation calculation

In Fig. 11, an overview of the numerical validation results for typical operation ranges is shown. There are only small deviations in the range less than 0.5 percent. In very extreme situations, like a collector stagnation temperature, deviations up to 3,0 percent may occur. However, they are not of importance and the question which of the models is closer to the realty remains unanswered.

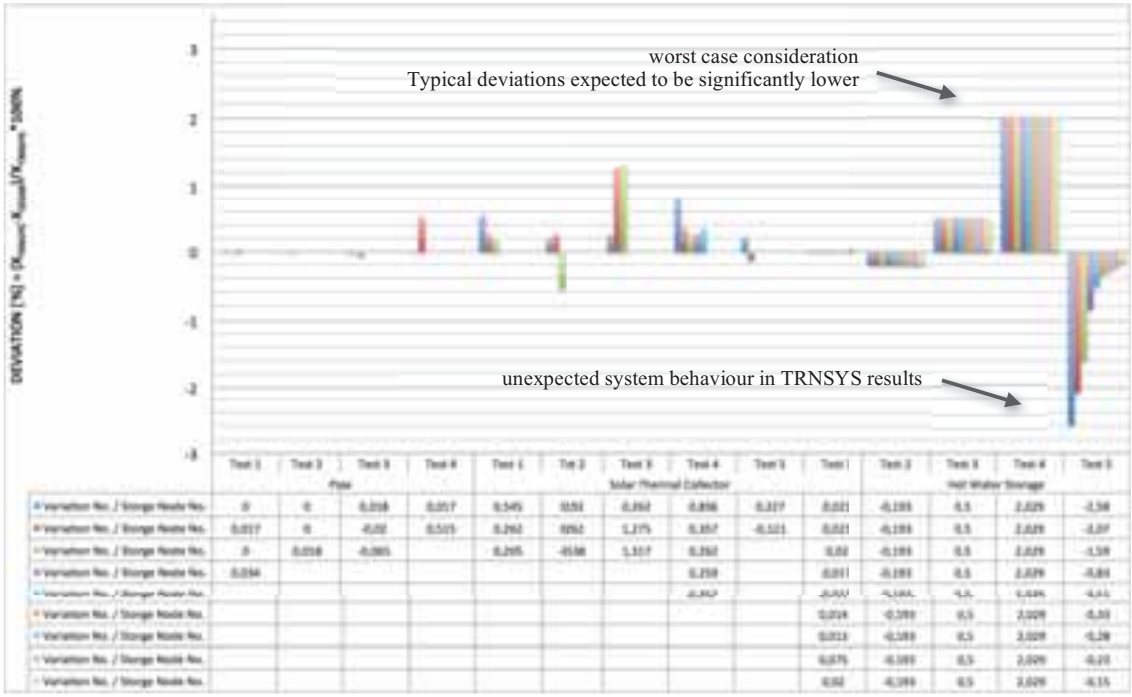

Fig. 11: Overview of the deviation in results for typical operation conditions. Tests according to Tab. 4.

5. Summary and conclusion

In this paper, a new type of flexible component-based simulation software for thermal, hydraulic and electric system simulations is introduced with many advanced methods from today's point of view. Among them, the measurement uncertainty of sensors and the controller can be modelled and investigated in interaction with the system in detail. The controller is freely programmable. Additionally, the basis for an automatic hydraulic circuit investigation is provided and can be further developed. The software can be used as stand-alone application, server-based or can even be implemented in other software. During a simulation, the component parameters can be changed. The simulation time step is variable. This tool enables a fast component or system modelling. In the software, a component library containing 15 flexible components is introduced. The components are analytically or numerically validated using TRNSYS 17 standard components. A detailed software manual containing detailed mathematical description and validation results of the components in more than 100 pages is available.

The development of this software took approximately one year of intensive programming. The experience shows that it is possible to further develop simulation tools with respect to the above named features, when considering these features from the first development steps of the simulation core and of the components. It is planned to use this software for some stand-alone and server based software applications. Three more sophisticated components will be finished by the end of spring 2016. The commercial use of MITHRA is possible but not available yet.

6. References and Acknowledgements

Connolly, D., Lund, H., Mathiesen, B. V., & Leahy, M., 2010. A review of computer tools for analysing the integration of renewable energy into various energy systems. *Applied Energy*, *87*(4), 1059–1082.

DWD Deutscher Wetterdienst, BBR Bundesamt für Bauwesen und Raumordnung, Climate & Environment Consulting Potsdam GmbH., 2014. Handbuch Testreferenzjahre von Deutschland für mittlere, extreme und zukünftige Witterungsverhältnisse. Last retrieved August 26, 2015, from http://www.bbsr-energieeinsparung.de/EnEVPortal/DE/Regelungen/Testreferenzjahre/Testreferenzjahre/TRY_Handbuch.pdf

Solar Energy Laboratory, University of Wisconsin-Madison., 2009. TRNSYS 17 a TRaNsient SYstem Simulation program - Volume 4 - Mathematical Reference. Last retrieved September 30 26, 2015, from http://web.mit.edu/parmstr/Public/TRNSYS/04-MathematicalReference.pdf

I would like to express my gratitude to **Technische Universität Darmstadt** as well as to **Professor K. U. Tichelmann** for providing TRNSYS 17 used for software validation and many thanks also to **German Academic Exchange Service DAAD** for financial support for the congress participation.

Conference Proceedings

Solar World Congress 2015
Daegu, Korea, 08 – 12 November 2015

Complex Modeling of Solar Water Heating Systems

Ilia V. Slesarenko[1]

[1] Far Eastern Federal University, Vladivostok (Russia)

Abstract

The energy balance equations describe each part of the observed solar water heating system (SWHS) with the differential equation method. The theoretical model consists of a number of such equations and compile into a system. Because all parts of the system interact, the Runge-Kutta method helps to solve it and obtain the close-to-real output parameters. Any kind of embedded modifications cause the reaction of the rest of the parameters, and can also be modeled with the referred method. Experimental data verified the reliability of the represented method, enabling modeled system optimization.

Keywords: *differential equation, heat transfer, modeling, solar collector*

1. Introduction

Experimental data verifies the average monthly production of about 0.8 kWh / m^2 in winter and about 1.85 kWh / m^2 in summer by solar water heating systems (SWHS) on territory of Far East of Russia. The experimental SWHS shown on Figure 1 gained the peak generation of about 2.8 kWh / m^2.

Fig. 1 - General view of the experimental SWHS, its solar collectors (roof of the Far Eastern Federal University, campus building)

This solar water heater is an experimental installation with medium thermal power output, up to 70 kW. It is also equipped with the remote trackable solar activity sensors, thermometers and transducers (Table 1).

Tab. 1: Main specifications of the experienced SWHS

Parameter	Value
The area of solar collectors	150 m^2
Type of solar collectors	vacuum with heat pipes
Total volume of heat storage tanks	10 m^3
Type of coolant circulation	forced

Initially, the system had a number of specific drawbacks: limited average thermal power of about 35 kW per day, insufficiently small storage tank, highly uneven supply of heat to the hot water system of the building.

doi:10.18086/swc.2015.10.26 Available at http://proceedings.ises.org

Further optimizations were considered for the initial SWHS design to make it more energy efficient and gain the best performance:

- Increase in the number of installed solar collectors to enlarge the capacity of SWHS;
- Increase the storage tank to increase the duration of the hot water supply during the peak loads;
- Apply the heat pump (HP) that takes energy from a low temperature source and supplies additional heat to the main storage tank within the period of maximum load.

The developed mathematical model enables optimization of technical characteristics of the given system taking into account all methods of improvement.

The represented model shows reliable accuracy due to the matching of transient processes curves with the obtained from the experienced SWHS curves. The model can identify the types of transition functions for the main circulation circuits required to configure the control loops of the experimental SWHS.

2. Schematic diagram of the modeled SWHS

The considered peak heating load for the designed SWHS (Figure 2) was set at 150 kW. The project of the model implies an addition of the vapor compression heat pump (VCHP) with maximum generation capacity of 55 kW and 15 kW electric drive compressor load. The temperature of filtered showers dump water is about 25°C and therefore it is acceptable to use it as the source of heat.

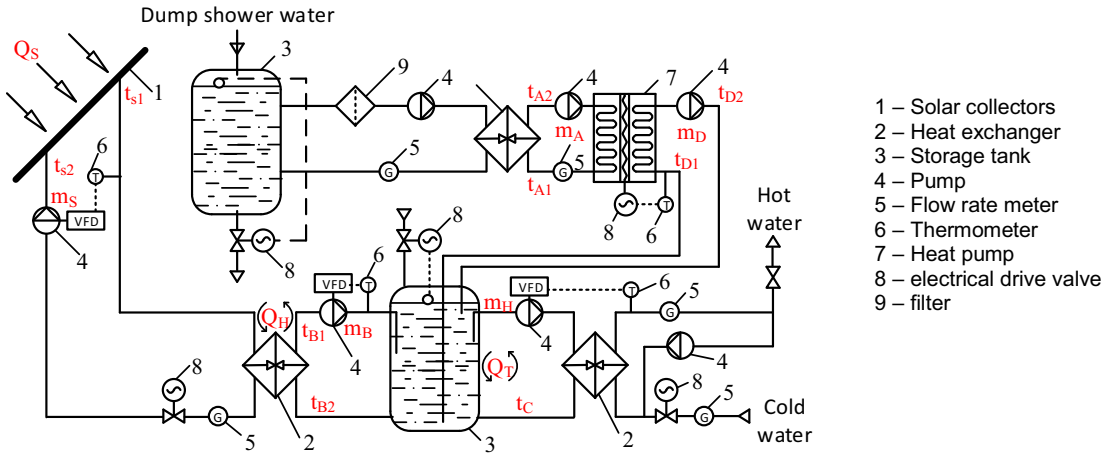

Fig. 2 – Schematic diagram of the modeled SWHS, with VCHP and dumb water heat source

Such complex solution gives the best cost effectiveness within the system lifetime. In addition, it is rather ecologically friendly because the backup source of heat is non-generated wasted energy, which supports the solar system. In addition, the proposed scheme allows the application of ventilation system in order to regenerate even more heat for the storage tank. Both the down hot water and the ventilation emissions from the facility can be the low-temperature heat sources for the HP. Inclusion of an additional buffer storage tank is highly recommended to redistribute load between SWHS and HP.

Selection of the most optimal version of scheme for the heat generating complex with reversible HP is the key issue of the described analysis. Several designs of the combined SWHS were carried out and compared with the practically modeled data. Analytical approach to the dynamic SWHS model has a number of practical advantages. The described further steps explain the performed elements analysis and ensure the necessary links between the basic units. Reflected communication between the physical parameters of different contours describe the potential problems for practical implementation. An absence of such problems in any analyzed model would therefore mean the most optimal performance within the modeled parameters.

3. System modeling

3.1 Solar collector

Solar heat absorption Q_S is changing during daylight hours, and also depending on the time of year. The equation $Q_S = f(\tau)$ represents an integral function varies with the special characteristic of the area, taking into account the specification and location of the solar collectors. The energy balance equation for the solar collector is:

$$Q_S + \dot{m}_S \cdot C_{pW} \cdot (t_S - t_S) = \dot{m}_S \cdot C_{pW} \frac{dt_{S_2}}{d\tau}, \qquad \text{(eq. 1)}$$

where $\dot{m}_1$ is the mass flow rate over the solar collectors circuit.

3.2 Recuperative heat exchanger

The following equations represent the changing of temperature of the heat transfer agent, neglecting the heat loss from the surface of the heat exchanger into the environment:

$$\dot{m}_S C_{pW}(t_{S1} - t_{S2}) - Q_H = \dot{m}_S \cdot C_{pW} \cdot \frac{dt_{A2}}{d\tau} \; ; \qquad \text{(eq. 2)}$$

$$\dot{m}_B C_{pW}(t_{B1} - t_{B2}) + Q_H = m_B \cdot C_{pW} \cdot \frac{dt_{B2}}{d\tau}, \qquad \text{(eq. 3)}$$

where Q_H is the heat transfer coefficient of the heat exchanger.

3.3 Storage tank

Water-filled tank is the heat storage system. The cold medium draws in at the bottom and accumulated in the upper zone hot water supplies the domestic demand. Overall, the model of the tank consists of two or more containers that exchange the heat through conventional stepped septum membrane.

The following energy balance equations represent the top and the bottom of the tank respectively:

$$\dot{m}_{T01} t_{T01} C_{pW} + \dot{m}_B t_{B1} C_{pW} - \dot{m}_H \cdot t_H C_{pW} - Q_T = \dot{m}_{TH} C_{pW} \frac{dt_{TH}}{d\tau}; \quad \text{(eq. 4)}$$

$$\dot{m}_{T02} t_{T02} C_{pW} - \dot{m}_B t_{B2} C_{pW} + \dot{m}_C \cdot t_C C_{pW} + Q_T = \dot{m}_{TC} C_{pW} \frac{dt_{TC}}{d\tau}. \quad \text{(eq. 5)}$$

Heat transfer within the water volume is fixed by $Q_T = V_T \cdot K_{HM}(t_{TH} - t_{TC})$, where V_T- volume of the tank, K_{HM} – heat and mass transfer coefficient. The coefficient depends on the temperature range and on the geometric characteristics of the tank.

3.4 Heat pump

The HP is the plate heat exchanger with two sections separated by an intermediate wall with simultaneous heating and cooling inside. The heat transferred from the cold section Q_C and heat transferred to the heated agent Q_{HP} is the function of the power drive of the compressor P_{HP} : $Q_{HP} = Q_C + P_{HP}$. The energy balance equations for the heat transfer inside of the HP are:

$$\dot{m}_A \cdot C_{pW}(t_{A2} - t_{A1}) - Q_{HP} = \dot{m}_A \cdot C_{pW} \cdot \frac{dt_{A1}}{d\tau}; \qquad \text{(eq. 6)}$$

$$Q_{HP} - \dot{m}_D C_{pW}(t_{D2} - t_{D1}) = \dot{m}_D \cdot C_{pW} \cdot \frac{dt_{D2}}{d\tau} \qquad \text{(eq. 7)}$$

Power to drive of the compressor is the variable parameter. The COP of the HP therefore varies due to changes in temperature of the condenser and evaporator.

3.5 Important notice for the system of equations

The simplified model can consist of only main equations mentioned above, interacting with each other. For the additional analysis, further input elements must have sufficient number of known parameters to satisfy both mathematical solution logics and thermodynamics laws.

The unified Runge-Kutta method was applied in MathLab software to conduct the approximated modeling of the observed system of equations.

4. Verification of the results

The modeled parameters were confirmed by comparison with the experimental data. The gathered data were obtained from the field tests of the combined SWHS, installed on the roof of campus building of the Far Eastern Federal University, Far East of Russia. The variation of main parameters of the observed SWHS with the given thermal generation is represented on Figure 3.

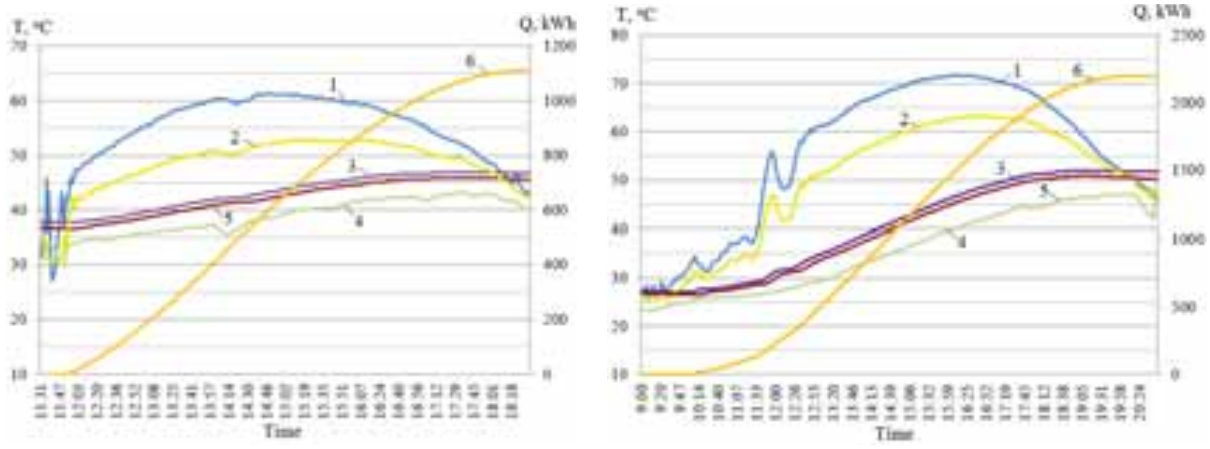

Fig. 3 - Experimental curves of the experienced SWHS from data gathered in January(a) and in July (b): 1 - temperature of the collector; 2 – temperatures of the first heat exchanger, collector agent circuit; 3 - average temperature of the tank; 4 – temperatures of the supply hot water; 5 – temperature at the bottom of the tank; 6 – cumulative solar heat gain.

The shown graphs describe the typical operaton cycle of the practical SWHS in cloudy day of summer (07/05/2012) and in snowy day of winter (01/17/2013).

In simplified view, the daily solar radiation function is an approximated sinusoidal dependence: $Q_S = Q_{S\,max} \cdot \sin(\tau)$. Also, it might be set by the parabolic function $Q_S = Q_{S\,max} \cdot (a\tau 2 + b\tau)$, where $Q_{S\,max}$ is the maximum density of solar radiation during the day.

Comparing with the modeled case, Figure 4 shows the output curves for the simulated 70 kW system with the same input data, and for the optimized system with the increased number o fsolar collectors, doubled volume of storage tank, and implemented 40 kW HP.

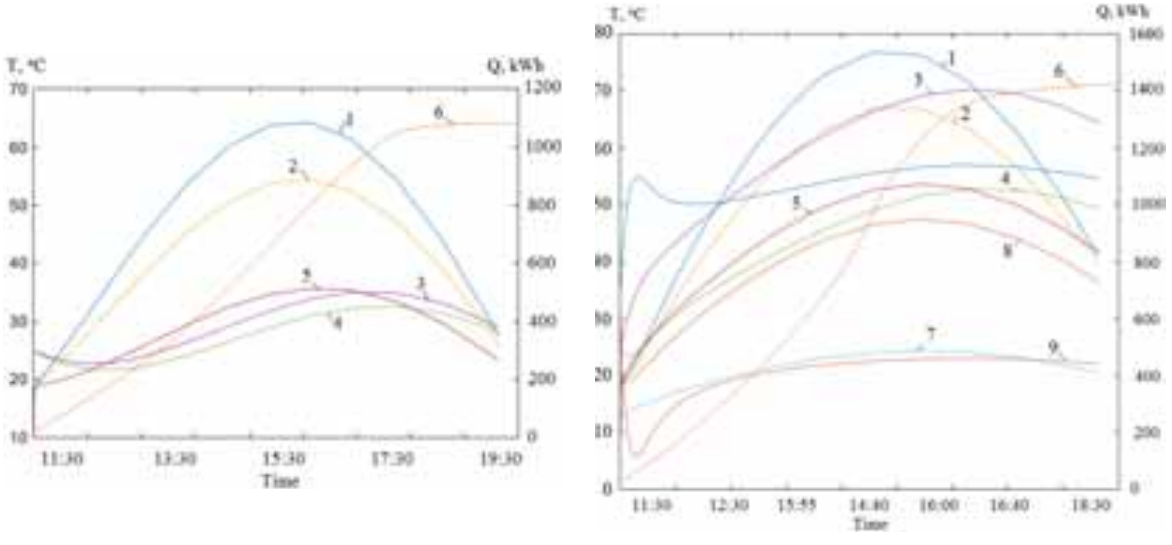

Fig. 4 - Transition functions of temperature changes in the solar collectors, heat exchangers and in main storage tank of the modeled SWHS (a – without HP, b – with the HP): 1 - the temperature of the collector; 2 – temperatures of the first heat exchanger, collector agent circuit; 3 - average temperature of the tank; 4 – temperatures of the supply hot water; 5 – temperature at the bottom of the tank; 6 – cumulative solar heat gain.

The represented model shows reliable accuracy due to the matching of transient processes curves with the obtained from the experienced SWHS curves. The model can identify the types of transition functions for the main circulation circuits required to configure the control loops of the experimental SWHS.

5. Description of the automatic control system

The modeled parameters of management actions are:

- mass flow rate regulation of the liquid in the solar circuit,
- HP power control,
- supply water flow rate control,
- water level control at the storage tank.

The operational disturbing influencers are:

- solar radiation changes at the collector surface,
- hot water demand changes,
- temperature changes of showers dumb water.

Figure 5 shows the block diagram of the control and measuring complex, which carried out the registration and recorded parameters on the main computer and automatically controlled the experimental SWHS during the tests.

Monitoring and recording environmental parameters and capacity of solar radiation incident on a horizontal and inclined surfaces produces automatic weather station Weather Station. In addition, accurate recording of direct solar radiation was carried out digital display solar radiation SOLRAD.

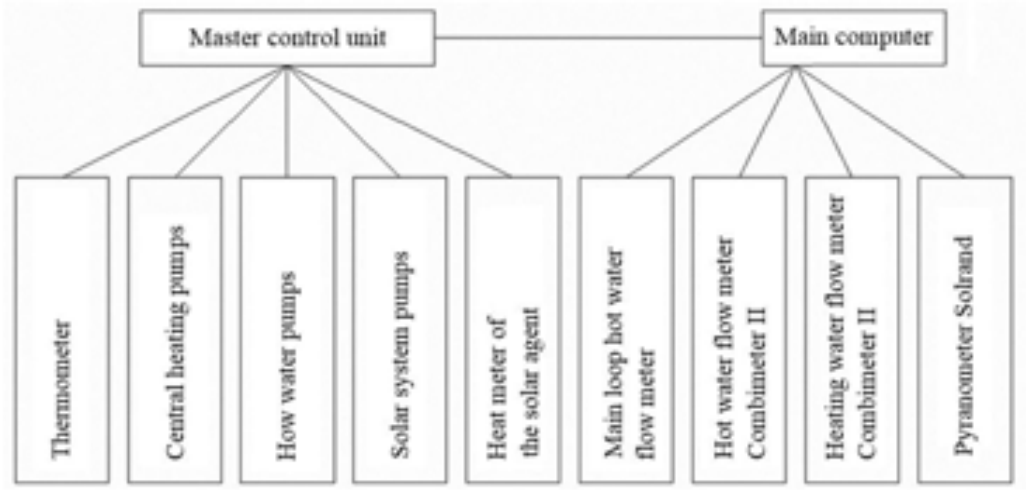

Fig. 5 - Measuring complex of the experimental SWHS

All electrical equipment for the experimental SWHS was tested and processed into the MS Excel spreadsheets.

6. Findings

1. One of the most effective and optimal scheme of SWHS is the combined solar thermal system with vapor compression heat pump (connected to two different low-temperature heat source).

2. Mathematical model improves the practical research findings. The tested method describes thermal processes of production, storage and transport of heat in the system, which can involve both series and parallel connection types, various sources of heat, and fluctuations of solar radiation intensity during the day. The model can also take into account the daily and seasonal changes in the thermal load of the consumer.

3. Comparative analysis of the experimental and calculated output characteristics data has shown the accuracy of the developed method.

References

1. Slesarenko, V.V., Slesarenko, I.V., 2014. Solar water heating systems: the analysis of schemes design, in: Abstracts 27 July - 1 August, 2014, Grand Renewable Energy 2014. - Tokyo Big Sight, Tokyo Japan.

2. Slesarenko, V.V., Bogdanovich, G.A., Slesarenko, I.V., Solar water heating systems: The analysis of schemes, in: 28 august- 2september 2011, 30th ISES Biennial Solar World Congress 2011, SWC 2011. - Kassel, Germany.

3. Burch, J., Shoukas, G., Brandemuhl, M., Krarti. M., 2016. Modeling and Test-and-Rate Methods for Innovative Thermosiphon Solar Water Heaters. July 8-13, 2006. National Renewable Energy Laboratory, University of Colorado.

4. Duffie, J.A.; Beckman, W.A. Solar Engineering of Thermal Processes; John Wiley Sons: Hoboken, NJ, USA, 1980; Chapter 12, pp. 487–497.

5. Lin, W.M.; Chang, K.C.; Liu, Y.M.; Chung, K.M. Field surveys of non-residential solar water heating systems in Taiwan. Energies 2012, 5, 258–269.

6. Jannatabadi, M.; Taherian, H. An experimental study of influence of hot water consumption rate on the thermal stratification inside a horizontal mantle storage tank. Heat Mass Transf. 2012, doi:10.1007/s00231-011-0958-6.

7. Prapas, D.E.; Veliannis, I.; Evangelopoulos, A.; Sotiropoulos, B.A. Beneficial interconnection of two thermosyphon DHW solar systems. Appl. Energy 1994, 49, 47–60.

8. Sezai, I.; Aldabbagh, L.B.Y.; Atikol, U.; Hacisevki, H. Performance improvement by using dual heaters in a storage-type domestic electric water heater. Appl. Energy 2005, 81, 291–305.

9. Chang, K.C.; Lee, T.S.; Chung, K.M. Solar water heaters in Taiwan. Renew. Energy 2006, 31, 1299–1308.

Conference Proceedings

Solar World Congress 2015
Daegu, Korea, 08 – 12 November 2015

Multi-Objective and Multi-Parameter Optimization of Solar Domestic Hot-Water Systems for Reducing On-Peak Power Consumption

Allan R. Starke[1], Theo D. M. Ruas[1], Samuel L. Abreu [2], Jose M. Cardemil[3,4] and Sergio Colle[1]

[1] LEPTEN - Laboratory of Energy Conversion Engineering and Energy Technology/Federal University of Santa Catarina (UFSC), Florianópolis, Brazil.

[2] Federal Institute of Santa Catarina (IFSC), São José, Brazil

[3] School of Industrial Engineering, Universidad Diego Portales, Santiago, Chile

[4] Fraunhofer Chile Research Foundation, Center for Solar Energy Technologies. Santiago, Chile

Abstract

Solar Domestic Hot-Water Systems can be a useful tool to reduce the energy consumption and on-peak power demand. This is particularly important in the case of Brazil where water heating in most cases is done using electrical showerheads with high installed power and low load factor. Consumers and utility companies have conflicting interests: reducing the electricity bill and shave the on-peak consumption. In the present work, these two interests were weighted and put together in the same objective function in order to find the trade-off curve with the optimized design parameters (collector area, storage volume and set point temperature) of the solar system. The analysis is carry out by considering two different policies: rebate program and time-of-use tariff (TOU). The results of the first policy show the existence of a trade-off curve between the initial investment and the yearly electricity consumption, which can be used to size the monetary incentive used for rebating the initial cost of the SDHW system. On the other hand, the results of the second policy shows a trade-off curve between the annualized life cycle cost of the system and the yearly on-peak electricity consumption, which can be used to size the TOU tariff as a function of the commitment of the utility company on reducing the on-peak electricity consumption.

Keywords: *Solar domestic hot-water systems, On-peak power consumption, Trade-off, Thermosyphon, Forced-circulation, TRNSYS.*

1. Introduction

Brazil owns one of the largest hydropower potential in the world (IEA, 2012a, 2010), because of that it currently represents the largest share on country´s electricity matrix. In fact, electricity from renewable sources currently holds a share of about 80% (70.6% hydropower, 7.6% Biomass and 1.1% wind) (EPE, 2014). This scenario of strong dependence of the hydropower makes the grid very sensitive to the seasonal rain cycles. Long periods of drought have depleted water reservoirs in 2013 and 2014, reducing the security of the system and increasing the electricity costs.

In addition, 73% of the dwellings use electric showerheads for bathing (EPE, 2012). Because of the high consumption rate, this device represents about 24% of the residential electricity consumption. As a result, roughly 5.5% (33.7 TWh/year including losses) of the electricity consumption is due to the electric showerheads (ELETROBRAS, 2007). Averaging this value on a daily basis, a daily electricity consumption of about 92.4 GWh/day is accounted. Setting this result to the statistical load profile of the residential sector (ELETROBRAS, 2007), a power load curve for this device can be estimated, as shown in Figure 1a. As depicted by this figure, electric showerheads are indicated as responsible for the two peaks on the residential electric demand profile, between 5-9 AM and 5-9 PM, with values around 11 and 14 GW, respectively. It is

Selection and/or peer review under responsibility of Scientific Committee
doi:10.18086/swc.2015.10.27 Available at http://proceedings.ises.org

worth noting that on-peak consumption to supply the electric showerheads use in Brazil is an amount equivalent to the installed capacity of Itaipu, the second largest power plant in the world. Therefore, the electricity grid must be designed for supplying this peak, implying in high transmission and distribution costs for the system operator and utility companies.

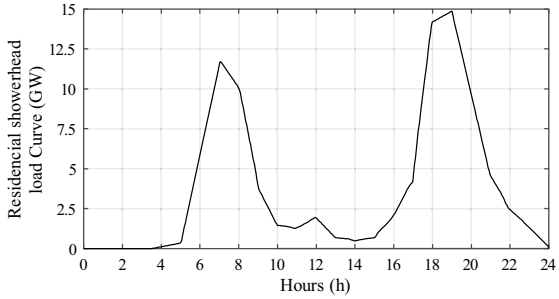

Fig. 1: Estimated showerhead load curve for Brazil.

The solar heating and cooling technologies can have an important role to play in realizing targets in energy security and economic development, especially the solar domestic hot water system, which is the most mature technology being used in a large scale since the 1960s (IEA, 2012b). This is not different for Brazil, the large-scale deployment of solar hot water system, could not only reduce the energy consumption that electric showerheads represents, but also reduce around 35 % of the on-peak power demand over the grid.

Currently, Brazil is the sixth country in total installed capacity of solar thermal collectors (IEA, 2012b). In fact, the energy supplied by solar thermal collectors currently operating in Brazil is around 4.3 GW_{th} per year, which accounts for only 3.6% of the dwellings in Brazil (EPE, 2012). As observed in other countries, a strong increase in the deployment of solar hot water heating could be achieved by introducing long-term subsidy schemes or solar obligations. According to (IEA, 2011), Brazil has a solar thermal target of 15 million m² installed in 2015, from about 7 million m² in 2011, however financial support and public policies are restricted or inexistent. In this context, this paper assesses the feasibility of thermosyphon and forced-circulation solar domestic hot-water systems (SDHWs) submitted to two different policies: a rebate program and time-based tariff. For each policy, the systems are designed in terms of the solar collector area, the thermal storage volume and the set point temperature for the in-tank heater

The main goal of these policies is to promote the use of SDHWS, considering the interest of both, consumer and energy supplier. Therefore, the system needs to be cost-effective in the point of view of the consumer (i.e. reduce the energy consumption) and for the system operator and utility companies (i.e. reduce the peak consumption).

The first policy consists of a rebate program, aiming to assist low-income consumers to acquire proper SDHWs by means of rebating or partial financing the initial cost. This will be led by the electric utilities, since they have interest in reducing on-peak consumption (Borges et al., 2005). Therefore, this case presents the optimization regarding the on-peak consumption and the acquisition cost of SDHW. This yields a Pareto frontier that is used as a tool for sizing financial incentives to acquire a solar energy system (Liu et al., 2010).

In the second policy, a time-of-use tariff for the electricity is established to discourage the consumption on-peak hours (Borges et al., 2004; Borges, 2000). Thus, the on-peak consumption and Annualized Life Cycle Costs (ALCC) are optimized to find the trade-off between paying for the electricity at on-peak hours and the increase in the ALCC due a large investing in a SDHWs. In addition, an ideal value for the time-of-use tariff can be established based on how much the distributor is committed on reducing the peak consumption (Salazar, 2004).

The proposed methods are assessed through a multi-objective optimization that considers the relevant figures in both cases, which are evaluated by a long-term transient simulation routine. A case study is presented, regarding thermosyphon and forced-circulation SDHWs for Florianopolis – Brazil, considering the two policies under different scenarios. Moreover, two levels of daily hot water consumptions were considered, 0.2 and 0.4 m^3 at 40 ºC, in order to analyze the sensitivity of the results for different hot-water demands.

2. System description

Two types of SDHWs are considered: thermosyphon and active (forced-circulation), as depicted in Figure 2. Thermosyphon systems, which work by natural circulation, are common in warm climates due the low probability of freezing, operational reliability and lower costs. This system avoids the use of pumps and dedicated control systems, however, the thermal storage needs to be placed at a higher position than the collector, and therefore is common to place it on the roof, limiting its size because of its weight and piping pressure drops.

Forced-circulation systems on the other hand, use a pump to circulate the water from the storage through the collector, allowing more flexibility on the installation of thermal storage, e.g it could be installed inside the house. Nevertheless, these systems are more complex, since they require a water pump and a differential temperature controller to ensure the proper operation of the system.

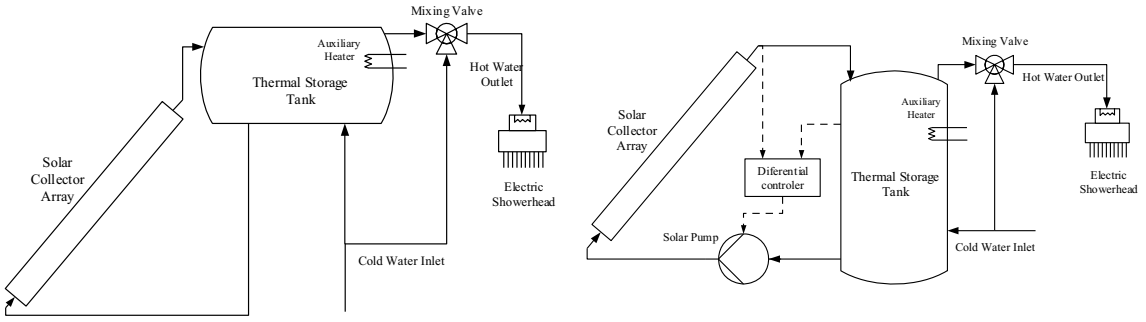

(a) (b)

Fig. 2: Schematic diagram of the solar domestic hot water; (a) thermosyphon, and (b) forced-circulation.

The solar collector and thermal storage tank considered are identical for both systems, which specifications are presented in Table 1. The specifications of the solar collector were taken from (INMETRO, 2015), considering a class A solar collector randomly chosen. Meanwhile, the configuration of the thermosyphon system are shown in Table 2, and the main features of the forced-circulation system are shown in Table 3. It is worth to mention that in both systems water is used as heat transfer fluid and no heat exchanger is considered.

Tab. 1: Specification common to both system considered.

Parameter	Values
Collector slope, β, (°)	37.6
Intercept efficiency, a_o, (-)	0.728
Efficiency slope, a_1, (W/m^2K)	6.18
Incidence angle modifier coefficient, b_0, (-)	0.1065
Tested flow rate, F_{test}, (kg/m^2h)	60
Thermal storage shape factor, S, (-)	0.5
Thermal storage insulation thickness, e_i, (m)	0.05
Thermal storage insulation conductivity, k_i, (W/mK)	0.126
Thermal storage maximum auxiliary heating rate, P_{tank}, (kW)	3
Thermal storage auxiliary heating device efficiency, η_{tank}, (-)	1
Thermal storage thermostat temperature dead band, T_{db}, $(°C)$	2
Electric showerhead maximum power, P_{aux}, (kW)	10
Electric showerhead overall loss coefficient, U_{aux}, (kJ/hK)	0
Electric showerhead efficiency, η_{aux}, (-)	0.95
Electric showerhead set point, T_{ideal}, (°C)	40

Tab. 2: Specification of the thermosyphon system considered.

Parameter	Values
Riser diameter, R_d, (m)	0.0142
Header diameter, H_d, (m)	0.027
Collector inlet diameter, d_i, (m)	0.015
Number of bends in the inlet pipeline, Nb_1, (-)	4
Inlet pipeline thermal loss coefficient, U_i, (kJ/m^2hK)	1.8
Collector outlet diameter, d_o, (m)	0.019
Number of bends in the outlet pipeline, Nb_2, (-)	4
Outlet pipeline thermal loss coefficient, U_o, (kJ/m^2hK)	1.8
Height of the solar collector, L_{col}, (m)	1.415
Vertical distance between collector's inlet and outlet, H_c, (m)	0.864
Vertical distance between collector inlet and thermal storage outlet, H_o, (m)	1.164
Thermal conductivity of the thermal storage and fluid entirety, k_w, (W/mK)	2.207

Tab. 3: Specification of the forced-circulation system considered.

Parameter	Value
Ration between utilized and test flow rate, R_{ca}, [-]	0.5
Upper temperature difference to trigger the solar pump, T_{on}, (°C)	6
Lower temperature difference to trigger the solar pump, T_{off}, (°C)	0.4

Some of the simulation parameters used in the systems are function of the design parameters (i.e. solar collector area and thermal storage volume), and need to be calculated in each iteration of the optimization process. These parameters are, thermal storage overall heat loss coefficient, thermal storage diameter and height, positions of the thermal storage thermostat and heating element, length of the solar collector and inlet piping length, number of parallel solar collector risers and maximum flow rate for the solar pump. The equations used to calculate these parameters were described in detail by Borges, (2000); Salazar, (2004)

It is worth noting that two auxiliary energy heaters were considered for both system, one inside the thermal storage and other in line to the load. The second one works as an electric showerhead and was considered in the simulation model just to ensure a comfortable water temperature for the users, in the case of the solar energy and the auxiliary heater of the tank were not able to supply the load.

The thermal performance of the SDHWs depends significantly on the domestic hot water load profile. In addition, it is impractical consider the daily and consumer variation, thus the suitable solution is to use a repetitive load profile (Kalogirou and Tripanagnostopoulos, 2006). In this paper, a statistically representative load profile was used, as depicted in Figure 3 in terms of a normalized figure. This profile was experimentally determined in a previous study (Salazar, 2004), where a group of ninety families were studied, by monitoring their electrical consumption of showerheads in one year period.

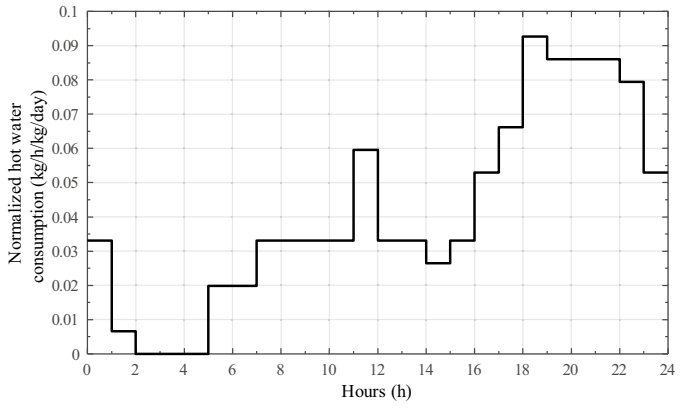

Fig. 3: Hot water daily consumption profile.

3. Methodology

The annual thermal performance and economic assessment, of both systems types, are determined by a transient simulation model. For that purpose, the Transient System Simulation Program (TRNSYS) (Klein, 2010) was used. Predicting the performance of solar systems by using simulation methods requires weather data input from the location where the system was installed. Therefore, the TMY file available from SWERA database (SWERA, 2013) for Florianopolis (27.6°S/48.5°W) was employed in this study.

The performance of the thermosyphon system was calculated through the (Morrison and Braun, 1985) model, whereas the one-tank forced-circulation system was considered as a stratified thermal storage with fixed inlet (Cooper et al., 1975). In addition, the auxiliary energy supply were simulated as electric heaters with a fixed thermal efficiency and with a maximum power (Table 1). Therefore, the actual power is modulated to meet the specified set point temperature.

Each system needs to be proper sized when submitted to two different policies that can be expressed as objective functions. Thus, an optimization routine was applied to the systems considering three design parameters as independent variables: the solar collector area, the thermal storage volume and the set point temperature for the in-tank heater. The combination of an optimization routine with a life-cycle simulation of a solar system was extensively explained by Borges et al., (2005).

Since the two used policies consider conflicting objectives between the consumer and the energy supplier, a weighted global criterion method was employed to accurately represent the behavior of these objectives in the optimization problems. With the weighted global criterion method, it is possible to solve a single objective by assigning relative weights (φ) to the conflicting ones (Borges et al., 2004, 2005; Marler and Arora, 2004)

The Generic Optimization Program (GENOPT) was used for the multi-objective and multi-parameter optimization, since it can be easily coupled with TRNSYS. This software has a large optimization algorithm library from which the hybrid algorithm of the Particle Swarm Optimization algorithm and the Generalized Pattern Search implementation of the Hooke-Jeeves algorithm (GPSPSOCCHJ) were selected. This decision is adequate for specific features of problems in which the objective function is not continuously differentiable, or it must be approximated, which is the case of the thermal simulation routines analyzed. Therefore, the design parameters can be only solved heuristically (Wetter, 2008).

3.1. Rebate program

The rebate program considers that the two conflicting objectives are the on-peak yearly energy consumption $\left(E_{peak}\right)$ and the initial investment of the solar system (IC), where the on-peak period is from 5 to 9 PM. Therefore, the optimization problem can be defined as follows,

$$\min_{\vec{x}} \left\{ f(\vec{x}) = (1 - \varphi)\frac{\mathrm{E_{peak}}(\vec{x})}{E_{peak,max}} + \varphi\frac{\mathrm{IC}(\vec{x})}{\mathrm{IC_{max}}} + \mathrm{C_1P_1}(\vec{x}) + \mathrm{C_2P_2}(\vec{x}) \right\}$$

$$\begin{aligned} &Subject\ to: \\ &\vec{x} \in S \\ &\mathrm{P_1}(\vec{x}) = \begin{cases} 0, & if\ ALCC \le ALCC_{limit} \\ \left(ALCC_{limit} - ALCC(\vec{x})\right)^2, & otherwise \end{cases} \\ &\mathrm{P_2}(\vec{x}) = \sum_t \begin{cases} 1, & if\ T_{cons}(\vec{x}) < T_{ideal} \\ 0, & otherwise \end{cases} \end{aligned} \qquad \text{(eq. 1)}$$

where S is the feasible region defined by the solar collector area (A_c), thermal storage volume (V_{tes}) and set point temperature for the in-tank heater. $E_{peak,max}$ and IC_{max} are the maximum values of the on-peak yearly energy consumption and initial cost possible on the feasible region, which were used to rewrite the two

conflicting objectives in a non-dimensional form. To do so, the optimization software was employed to find the maximum feasible values for each of the objectives, before the objective function were implemented in the simulation environment.

Two constrains were considered in this optimization problems, the first is used to guarantee that the annualize life cycle cost of the system $(ALCC)$ will be less than a specified value $(ALCC_{limit})$, and the second is used to guarantee that the system supplies water at the desired temperature (T_{ideal}). This constrained optimization problem was solved using a penalty method. (i.e. a constant value is added in the objective function when the constrained event is triggered), which are the two last terms on the right of the equation 1 ($C_1P_1(\vec{x})$ and $C_2P_2(\vec{x})$).

Since the relative importance of each conflicting function is not known, the domain of φ is divided in a series of discreet values and single objective optimizations were run for each value of φ. The results of this analysis can be presented by a curve (Pareto frontier) representing the initial cost versus on-peak yearly energy consumption. This curve is used as a tool for sizing financial incentives to acquire a system, as a solution for decreasing the on-peak power consumption. The methodology and the economic assumptions used for calculating the $ALCC$ and IC are described in the section 3.3.

3.2. Time-of-use tariff

For this policy, the two conflicting objectives considered are the on-peak yearly energy consumption and *ALCC* of the system. The period between 5 and 9 PM was considered as on-peak for applying the higher electricity tariff. In addition, the constraint used to guarantee that the system supply water is in the desired temperature to the consumers (T_{ideal}) is also considered. Therefore, the optimization problem can be defined as follows,

$$\min_{\vec{x}} \left\{ f(\vec{x}) = (1-\varphi)\frac{E_{peak}(\vec{x})}{E_{peak,max}} + \varphi\frac{ALCC_0(\vec{x})}{ALCC_{0_{max}}} + C_2P_2(\vec{x}) \right\}$$

$$Subject\ to: \quad \vec{x} \in S \qquad \text{(eq. 2)}$$

$$P_2(\vec{x}) = \sum_t \begin{cases} 1, & if\ T_{cons}(\vec{x}) < T_{ideal} \\ 0, & otherwise \end{cases}$$

where $ALCC_0$ is the annualized life cycle cost considering only the nominal value of the electricity tariff (C_e) and $ALCC_{0_{max}}$ is the maximum annualized life cycle cost possible on the feasible region. The equation 2 considers only the nominal tariff, in order to minimize the number of optimization runs. Different values of the tariff were considered in a post-processing procedure, in which the following equation was used,

$$ALCC(\vec{x}) = ALCC_0(\vec{x}) + E_{peak}(\vec{x})C_{e,TOU} \qquad \text{(eq. 3)}$$

where $ALCC$ is the total annualized life cycle cost, considering the time-of-use tariff - $C_{e,TOU}$, defined as the surcharge value added to the nominal electric tariff (C_e) during the on-peak hours. This approach removes the need of run the optimization routine for each time-of-use tariff. It is worth mention that in the case of a null value for the time-of-use tariff, the expression is reduced to $ALCC(\vec{x}) = ALCC_0(\vec{x})$.

Hence, the results of this analysis can be presented by a curve of $ALCC$ versus E_{peak}, for different values of the time-of-use tariff, showing the trade-off between paying for the electricity at on-peak hours and the increase in the $ALCC$ due a large investment on a SDHW.

3.3. Economic Figures

In order to determine the economic figures derived from the optimization processes, the life-cycle cost analysis

was considered according to (Duffie and Beckman, 2013),

$$LCC(\vec{x}) = (1 + C_{inst})IC(\vec{x})[1 + C_m PWF(N, i_m, d)] + PWF(N, 0, d)E_{aux}(\vec{x})C_e \quad \text{(eq. 4)}$$

where C_{inst} is the installation cost as a percentage of the initial cost, C_m is the annual maintenance cost as a percentage of the installed cost of the system, E_{aux} is the total auxiliary yearly energy consumption, PWF is the present-worth factor, N is the lifetime of the system, i_m is the maintenance inflation rate and d is the discount rate. In order to analyze the system on a yearly basis, the life-cycle cost can be annualized by the following equation,

$$ALCC(\vec{x}) = \frac{LCC(\vec{x})}{PWF(N, 0, d)} \quad \text{(eq. 5)}$$

Finally, the initial cost can be calculated as follows,

$$IC(\vec{x}) = (C_c A_c + C_{tes}(V_{tes}) + C_a P_{tank}) \quad \text{(eq. 6)}$$

where C_c is the solar collector cost per area, A_c is the solar collector area, C_{tes} is the thermal storage cost as a function of the storage tank volume (V_{tes}), C_a is the cost of the heating element per power and P_{tank} is the electric power of the auxiliary heater in the thermal storage.

The economic parameters considered herein are representative of the Brazilian market at the time of the study and listed in Table 4.

Tab. 4: Economic and cost considerations.

Parameter	Value
Solar system life cycle, N, $(years)$	20
Discount rate, d (%)	8
Maintenance inflation rate, i_m (%)	6.4
Solar collector cost, C_c $(€/m^2)$	119.25
Heating element cost, C_a $(€/kW)$	6.9
Annual maintenance cost, C_m $(\%\ of\ installed\ cost)$	1
Installation cost, C_{inst} $(\%\ of\ initial\ cost)$	15
Nominal value of the electric tariff, C_e $(€/kWh)$	0.1385
Exchange rates for Euro at March, 2014 , u $(BR\$/€)$	3.48

The cost, in euros, of the thermal storage (C_{tes}) was considered in the analysis by a regression model based on the prices of tanks with different volumes obtained of the main suppliers in the Brazilian market, as follows,

$$C_{tes}(V_{tes}) = \frac{1}{u}(4798.8V_{tes} - 2889.8V_{tes}^2 + 1196V_{tes}^3 - 216.9V_{tes}^4 + 14.911V_{tes}^5) \quad \text{(eq. 7)}$$

4. Results

The results of the case study are presented for Florianopolis – Brazil (27.6°S/48.5°W), considering the thermosyphon and forced-circulation SDHWs, where two levels of daily hot water consumptions were considered, 0.2 m^3 and 0.4 m^3, both at 40 ºC. These values were chosen because they can represent low-income consumers and standard consumers, respectively.

Regarding the rebate program, eight values of the $ALCC_{limit}$ were considered 130, 185, 200 and 215 €/year for low-income scenario, and 260, 370, 400 and 430 €/year for the standard consumer scenario. On the other hand, four values of the time-of-use tariff were considered in the time-based program: 0, 0.5, 1 and 2 €/kWh. Where these values are added to the nominal value of the electricity tariff in the period between 5 and 9 PM.

4.1. Rebate program

The trade-off between initial cost and yearly on-peak electricity consumption for an $ALCC_{limit}$ of 215 and 430

€/year, for the scenarios of 0.2 m³ and 0.4 m³ respectively, is depicted in Figure 4. Each point of these curves represent a result of the optimization process, with different design values that simultaneously minimize the weighted combination of the yearly on-peak electricity consumption and initial cost.

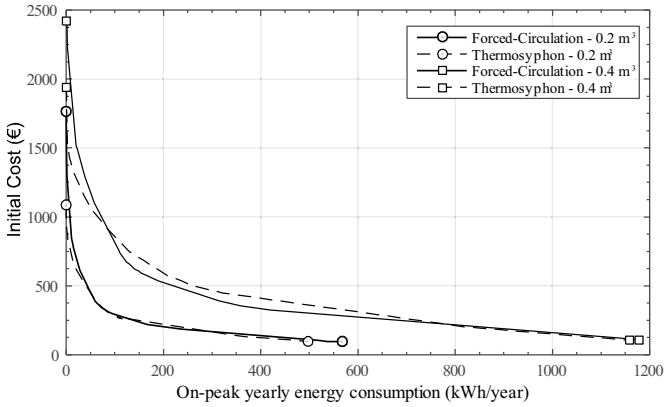

Fig. 4: Trade-off curves between initial cost and yearly on-peak electricity consumption obtained by the rebate program for an $ALCC_{limit}$ of 215 and 430 €/year for the scenarios of 0.2 m³ and 0.4 m³, respectively.

Three regions can be identified in figure 4, on the left, with high initial cost and low yearly on-peak electricity consumption there is the adverse region for the consumer, where a decrease in the on-peak electricity consumption represents a large increase on the initial cost. In contrast, on the right is observed the adverse region for the utility companies, characterized by low initial cost and high yearly on-peak electricity consumption, in this region a decrease on the initial cost represents a large increase on the on-peak electricity consumption. Finally, between these two regions, the negotiation region is observed, depicted by a small increase on the initial cost which represents a large reduction on the on-peak electricity consumption.

Within the negotiation region, systems with 0.2 m³ of daily consumption, show an increase from 150 to 250 € on the initial cost, providing a reduction from 325 to 125 kWh/year on the yearly on-peak consumption. It means that rebating 40% on the initial cost (100 € of 250 €) will provide a reduction of 62 % in the on-peak consumption, a result highly interesting for the utility companies.

Regarding the systems with 0.4 m³ of daily consumption, an increase from 300 to 400 € in the initial cost, gives a reduction between 500 to 300 kWh/year on the yearly on-peak electricity consumption. Meaning that rebating 25% on the initial cost (100 € of 400 €) will provide a reduction of 40 % on the on-peak consumption.

Finally, it is worth noting that for 0.2 m³ of daily consumption of hot water, both thermosyphon and forced-circulation systems present similar results. Moreover, for 0.4 m³, the forced-circulation system present lower values of on-peak yearly electricity consumption for the same initial cost. That result indicates that the forced-circulation system could be more effective in reducing the on-peak consumption, however, these are minor differences.

Figure 5, shows the effect of the $ALCC_{limit}$ in the trade-off curves for both the thermosyphon and forced-circulation systems, for the case of 0.2 m³ of daily consumption. It can be noticed that the limitation on the $ALCC$, reduces the domain of solutions that met the objective function, therefore, reduces the size of the trade-off curves and the negotiation region.

The proposed methodology helps defining the monetary incentive used for rebating the initial cost of the SDHWs, however, the proper size of this incentive can be only defined by the utility company and with its commitment in reducing the on-peak consumption.

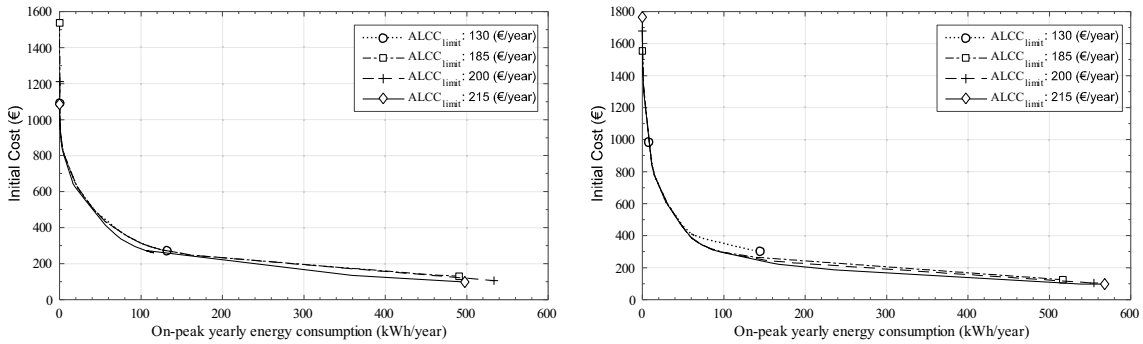

Fig. 5: Effect of the $ALCC_{limit}$ in the trade-off curves of the rebate program for thermosyphon (a), and forced-circulation (b) systems for a 0.2 m³ of hot water consumption.

4.2. Time-of-use tariff

The trade-off between the annualized life cycle cost of the system and the on-peak yearly electricity consumption are shown in Figure 6, where curves for the thermosyphon and forced-circulation are observed. The curves represented by a null value of time-of-use tariff (TOU tariff) were obtained by the optimization process using equation 2. On the other hand, the other curves were calculated as a post-processing procedure using equation 3, which allows consider different values for time-of-use tariff.

It can be seen that the results are very similar for 0.2 m³ and 0.4 m³ of hot water consumption, where the difference is due to a matter of scale. Moreover, under this policy the thermosyphon system shows better performance, being more effective on reducing the on-peak yearly electricity consumption.

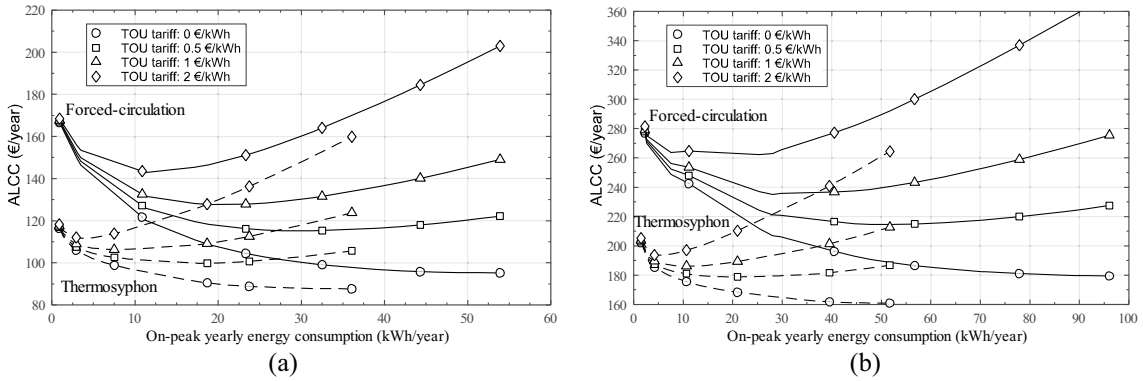

Fig. 6: The trade-off between the annualized life cycle cost of the system and the on-peak yearly electricity consumption for the thermosyphon and for-circulation system for 0.2 m³ (a), and 0.4 m₃ (b) of hot water consumption.

Regarding the different values of the TOU tariff, it can be noted that for each tariff exists a minimal value of the ALCC, indicating the optimal design for the consumer. Therefore, each minimal ALCC and its respective on-peak yearly electricity consumption can be calculated for each value of the time-of-use tariff. This is achieved by deriving the equation 3 with respect of the yearly on-peak consumption and equating to zero (minimal ALCC), as follows,

$$\frac{dALCC(\vec{x})}{dE_{peak}} = \frac{dALCC_0(\vec{x})}{dE_{peak}} + C_{e,TOU} = 0 \qquad \text{(eq. 8)}$$

where the $dALCC_0(\vec{x})/dE_{peak}$ can be calculated numerically or analytically if a regression model is applied in the $ALCC_0$ versus E_{peak} curve. Rearranging the equation 8, the intended time-of-use tariff $C^*_{e,TOU}$ can be calculated as follows,

$$C^*_{e,TOU} = -\frac{dALCC_0(\vec{x})}{dE_{peak}} \qquad \text{(eq. 9)}$$

This quantity can be plotted as a function of the on-peak yearly electricity consumption, as depicted in Figure

7. This methodology provides a tool for sizing the values of the time-of-use tariff in function of the commitment for reducing the on-peak consumption. Moreover, it is clear the existence of a negotiation region, where a small value for the TOU tariff can reduce in more than half the on-peak consumption.

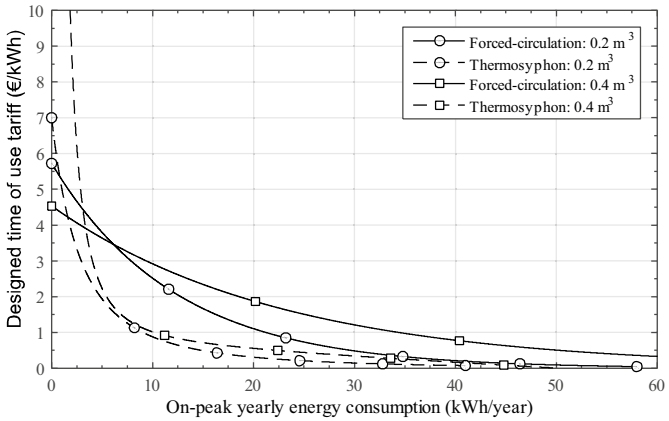

Fig. 7: Designed time-of-use tariff for the forced-circulation and thermosyphon system, considering both 0.2 m^3 and 0.4 $m^3$of hot water consumption.

Figure 7 shows that the designed values of the TOU tariff are similar for the thermosyphon system, regardless the level of hot water consumption. However, this trend is not observed for the forced-circulation system. When the system faces higher consumption, a higher TOU tariff is required to archive the same degree of reduction on the on-peak electricity consumption.

5. Conclusions

This work presented two methodologies for sizing financial policies for SDHWs, and measure its effectiveness on the reduction of on-peak electricity consumption. The approach analyzed herein considered the interest of both, consumer and energy supplier.

The first policy, rebate program, uses a trade-off curve between initial cost and yearly on-peak electricity consumption, where a clear negotiation region is identified. Therefore, it could be used as a design tool for defining the monetary incentive used for rebating the initial cost of the SDHW system, as a function of the commitment on reducing the on-peak consumption by the utility company

The second policy, time-of-use tariff, uses a trade-off curve between the annualized life cycle cost of the system and the yearly on-peak electricity consumption, for different time-of-use tariffs. This procedure shows the existence of a minimal value of the ALCC for each TOU tariff, indicating the optimal design for the consumer. Consequently, it is possible to determine the value of the on-peak yearly electricity consumption respective to the minimal ALCC, for each TOU tariff adopted. This yields a trade-off curve between the designed time-of-use tariff and the on-peak yearly electricity consumption, which helps to size the TOU tariff as a function of the commitment of the utility company on reducing the on-peak electricity consumption.

6. References

Borges, T.P.., Colle, S., Wendel, M., 2004. IMPACTOS DA ADOÇÃO DE TARIFAS DIFERENCIADAS DE ENERGIA ELÉTRICA SOBRE O PROJETO OTIMIZADO DE SISTEMAS DE AQUECIMENTO SOLAR DE ÁGUA, in: Vázquez, M., Seara, J.F. (Eds.), XII Congreso Ibérico Y VII Congreso Íbero Americano de Energía Solar. Vigo, España, pp. 14–18.

Borges, T.P.D.F., 2000. Síntese otimizada de sistemas de aquecimento solar de água. Universidade Estadual de Campinas.

Borges, T.P.F., Colle, S., Wendel, M., 2005. Multiobjective Optimization as a Decision Tool tor Financing or Rebating Domestic Solar Water Heaters, in: Solar World Congress - ISES 2005. Orlando, USA, pp. 2–6.

Cooper, P.I., Klein, S.A., Dixon, C.W.S., 1975. Experimental and Simulated Performance of a Closed Loop

Solar Water Heating System, in: ISES 1975 International Solar Energy Congress.

Duffie, J.A., Beckman, W.A., 2013. Solar Engineering of Thermal Processes, Fourth Edi. ed. Wiley, New Jersey. doi:10.1002/9781118671603

ELETROBRAS, 2007. Avaliação do Mercado de Eficiência Energética no Brasil. Pesquisa de Posse de Equipamentos e Hábitos de Uso (ano base 2005) - Classe Residencial – Relatório Brasil. Rio de Janeiro.

EPE, 2014. Brazilian Energy Balance 2014 - Year 2013. Rio de Janeiro.

EPE, 2012. NOTA TÉCNICA DEA 16/12 Avaliação da Eficiência Energética para os próximos 10 anos (2012-2021) - Série Estudos de Demanda. Rio de Janeiro.

IEA, 2012a. Technology Roadmap: Hydropower. Springer-Verlag, Paris, France.

IEA, 2012b. Technology Roadmap: Solar Heating and Cooling. Paris, France.

IEA, 2011. G-20 Clean Energy, and Energy Efficiency Deployment and Policy Progress. Paris, France.

IEA, 2010. Renewable Energy Essentials: Hydropower. Paris, France.

INMETRO, 2015. SISTEMAS E EQUIPAMENTOS PARA AQUECIMENTO SOLAR DE ÁGUA - COLETORES SOLARES. Brasília - Brazil.

Kalogirou, S.A., Tripanagnostopoulos, Y., 2006. Hybrid PV/T solar systems for domestic hot water and electricity production. Energy Convers. Manag. 47, 3368–3382. doi:10.1016/j.enconman.2006.01.012

Klein, S.A., 2010. TRNSYS: A transient systems simulation program, V. 17.

Liu, P., Pistikopoulos, E.N., Li, Z., 2010. An energy systems engineering approach to the optimal design of energy systems in commercial buildings. Energy Policy 38, 4224–4231. doi:10.1016/j.enpol.2010.03.051

Marler, R.T., Arora, J.S., 2004. Survey of multi-objective optimization methods for engineering. Struct. Multidiscip. Optim. 26, 369–395. doi:10.1007/s00158-003-0368-6

Morrison, G.L., Braun, J.E., 1985. System modelling and operation characteristics of thermosyphon solar water heaters. Sol. Energy 34, 389–405. doi:10.1016/0038-092X(86)90024-1

Salazar, J.P. de L.C., 2004. Economia de energia e redução do pico da curva de demanda para consumidores de baixa renda por agregação de energia solar térmica. Universidade Federal de Santa Catarina.

SWERA, 2013. Solar and Wind Energy Resource Assessment [WWW Document]. URL http://en.openei.org/wiki/SWERA/Data

Wetter, M., 2008. GenOpt - Generic Optimization Program - User Manual V 2.1.0.

Conference Proceedings
Solar World Congress 2015
Daegu, Korea, 08 – 12 November 2015

Performance analysis of evacuated tube solar collector for residential heating in Mongolia

Purevdalai. E [1], Amarbayar. A [2], Atsushi Akisawa [1]

[1] Graduate School of Bio Applications and System Engineering, Tokyo University of Agriculture and Technology

[2] School of Engineering and Applied Science, National University of Mongolia

Abstract

This paper presents initial result of measurement and experimental work in smoky and dusty location of Ger district, Ulaanbaatar Mongolia, as well as some problems while using the solar water heating system for residential heating in Mongolian harsh and cold climate condition. By this research, the measurement devices were placed on the forced circulation evacuated tube solar collector system installed on the top of the residential house then the measurement had been done from December to April for last two years. As a result of this study, the average collector efficiency was 65.7 % and the system efficiency was 31.5 % in real condition during for the four months of measurements.

Keywords: *Mongolian harsh and cold climate, electric heater, evacuated tube solar collector, residential house, Ger district.*

Explanation: Ger district where more than half of the capital's residents live without access to basic public services like water, sewage systems and central heating.

1. Introduction

Converting solar energy into thermal energy is useful in Mongolia where lots of thermal utilizations are. Because, thermal energy is indispensible to all residential houses due to the average ambient temperature during the most months is below +2 ^{0}C in Mongolia. On the other hand, Mongolia has much solar resource for example the annual sunshine duration is about 2900 to 3300 hours [1] and yearly solar radiation is about 1450 to 1840 kWh m^{-2} year $^{-1}$ [2].

Type of equipments that converts solar energy into thermal energy such as flat plate and evacuated tube solar collector is rarely used in Mongolia. The reasons are up to now the capacity of recent solar collectors for the whole year has not been estimated accurately in Mongolian actual condition, also high initial investment of it is not attracting consumer's interest.

In recent years, the air pollution has been evidently increasing in populated Ulaanbaatar city, because of the number of households in Ger district who burn raw coal to heat their house have been growing. It is confirmed by several studies such as The World Bank Studies [3]. This is a sign of expressing that it is time to refuse raw coal application and to use new resources of thermal energy which is harmless to the environment and productive for household's economics.

Another big concern for Ger district of Ulaanbaatar city is the deficit and improper infrastructure of electric power. As a result of it, to use an electric heater has difficulties in residential houses. But the main reason of coal burning still in use for heating in Ger district is because of expensive electric bill for long heating season. Therefore we began to seek most convenient and harmless heating system and started setting up some evacuated tube solar collector on a few objects for undergoing the operation in the winter time.

doi:10.18086/swc.2015.10.28 Available at http://proceedings.ises.org

Ultimate goals of this research work contain to research hybrid heating systems with solar water heating device in Mongolian harsh and cold climate condition for a long time, and to estimate efficiency of evacuated tube solar collector in the actual usage as well as to modify it for Mongolian climate condition and application feature. In this paper, we present a preliminary outlook of measurement and experiment that includes collector efficiency, system efficiency and some problems encountered in the real operation.

2. Methodology

2.1 System description

The measurement was done in the residential house with area of 54 square meter located in Chingeltei Ger district of Ulaanbaatar city (see **Fig. 1**). The solar water heating system combined with electric heater was installed on it in 2013. Since the end of 2013 the sytem has been used for house heating. The hybrid heating system consists of evacuated tube collector which contains four sections that have 120 pieces of heat pipe, heat storage tank that has capacity of 500 liter (see **Fig. 2**), auxiliary electric heater of 3 kW located in the heat storage tank, radiator system for heating the house, and the solar circuit pipes. The length of solar circuit pipes to supply is 11 meters (5 meters inside of the house and 6 meters outside) and the return pipe length is 12 meters (5 meters inside of the house and 7 meters outside) (see **Fig. 3**).

Fig.1: Overview of the experimental system

Fig. 2: The tank and controller of system

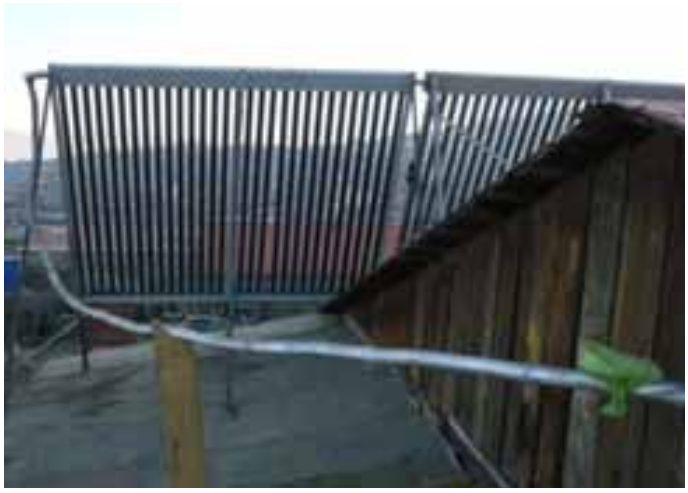

Fig. 3: Solar circuit pipe to return

2.2 Measurement and devices

Measurement was done twice in between from 2013.12.05 to 2014.04.11 and from 2014.12.03 to 2015.04.13. The following devices was used: flow meter (Ultrasonic-TDS-100), solar meter (Pyranometer-Ms-802), temperature sensors (Pt-100), power meter for measuring electrical consumption (Kyoritsu-Model-6300), data logger that stores and collects the data every 2 minute (Datamark-Ls-3000Ptv). The following temperatures such as ambient temperature (T_1), inside temperature of the house (T_2), solar fluid temperature at the collector outlet (T_3), solar fluid temperature at the collector inlet (T_4), solar fluid temperature at the tank outlet (T_5) and solar fluid temperature at the tank inlet (T_6) were measured (see **Fig. 4**).

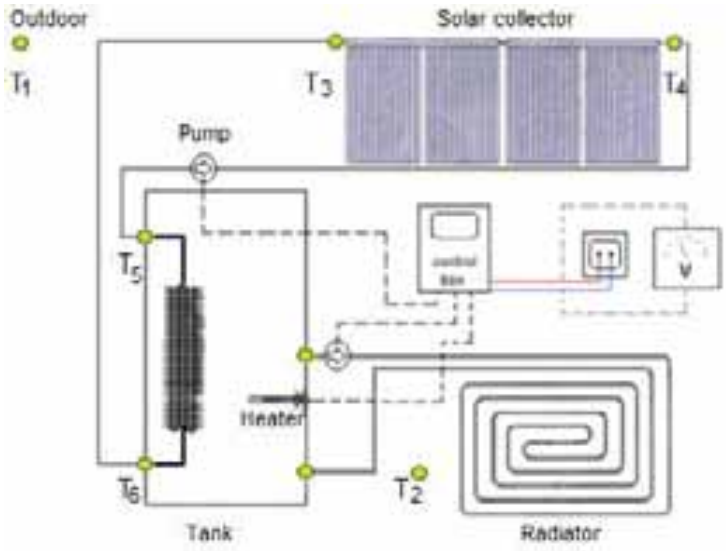

Fig. 4: The scheme of solar water heating system for house heating, and the green points indicate the temperature measurements

2.3 Calculation

Useful energy collected by the solar collector was calculated as:

$$Q_K = \dot{m}\, Cp\, (T_3 - T_4) \qquad \text{(eq. 1)}$$

To calculate the heat delivered in the tank, the solar fluid temperature data at the tank outlet and inlet was used:

$$Q_T = \dot{m}\, Cp\, (T_6 - T_5) \qquad \text{(eq. 2)}$$

The collector efficiency was calculated as:

$$\eta_K = \frac{Q_k}{A_c G} \qquad \text{(eq. 3)}$$

The system efficiency was calculated as:

$$\eta_S = \frac{Q_T}{A_c G} \qquad \text{(eq. 4)}$$

By these calculation methods above [4-6], the measurement data was processed on a specific day when the sky is more clearly. From every measured month the clearest sky day was selected. Then total daily energy collected by the solar collector and delivered to the tank was calculated on those days. As well as daily and monthly average collected and delivered energy was computed and compared. The measurement data from 2014.12.03 to 2015.04.13 used in the calculation.

3. Results and discussion

3.1 Performance of clear sky days

The days of 2014.12.13, 2015.01.21, 2015.02.15 and 2015.03.09 from every month measured were picked to compare daily energy performance. The daily global solar radiation on the collector's surface was 89 MJ day^{-1} on 2014.12.13, 110 MJ day^{-1} on 2015.01.21, 176 MJ day^{-1} on 2015.02.15 and 212 MJ day^{-1} on 2015.03.09. Daily useful energy collected by the solar collector was 64 MJ day^{-1}, 80 MJ day^{-1}, 128 MJ day^{-1} and 154 MJ day^{-1} respectively above. Daily heat energy delivered in the tank was 44 MJ day^{-1}, 43 MJ day^{-1}, 66 MJ day^{-1} and 73 MJ day^{-1}. Comparative estimate of daily energy was shown with **Fig. 5**.

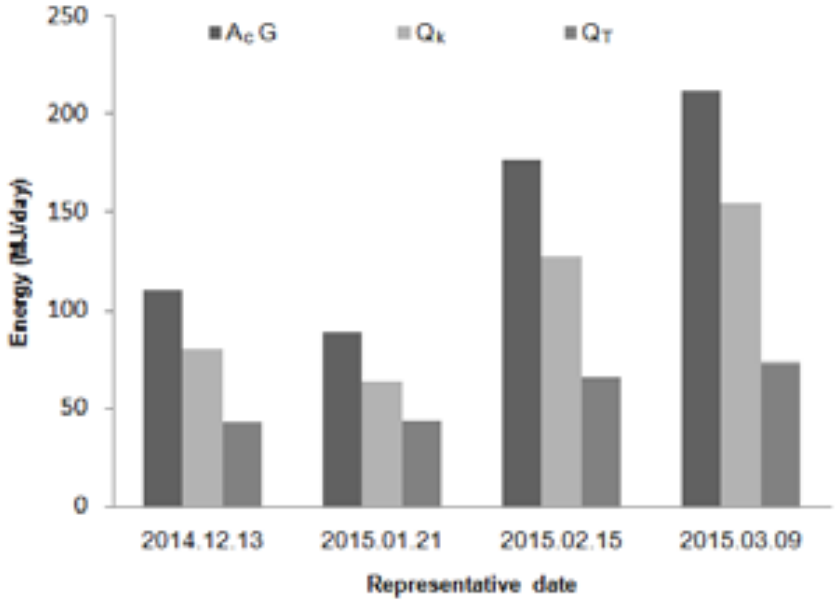

Fig. 5: Daily solar radiation on collector's total surface (Ac G), daily energy collected by solar evacuated tube collector (Q_k), daily energy delivered to the tank (Q_T)

3.2 Comparisons of the months

In this part of calculation, monthly total energy collected by the solar collector and total energy delivered to the tank wasn't computed, as we had lost some days' measurement data in February and March a few times because of capacity of data logger. In order to compare the performance of each month measured, the monthly average numbers were shown by percentage. Monthly average collector efficiencies were 64.9 % in December, 65.3 % in January, 66.1 % in February and 67.3 % in March. The reason why the collector efficiency about 65 % in December and January was, while the efficiency increased to about 67 % in February and March was connected with glass cleaning of the collector. The first half of the collector glass tube was wiped on February 11 and the rest of the part was cleaned on March 14.

Also monthly average system efficiencies were 38.5 %, 32.7 %, 27.9 %, and 26.8 % respectively. The process that collector system efficiency improves when the ambient temperature decreases during the coldest time of a year and the system efficiency reduces when the ambient temperature gets warmer was observed. It depends on water temperature in the tank. The water in the tank chills while circulating through the house heating radiator. Chilled water absorbs heat well from the solar fluid that was heated by solar collector. Thus the system efficiency in the winter time, when heat load is highest in December and January, is higher than that of the others. **Fig. 6** shows monthly average system efficiency and collector efficiency.

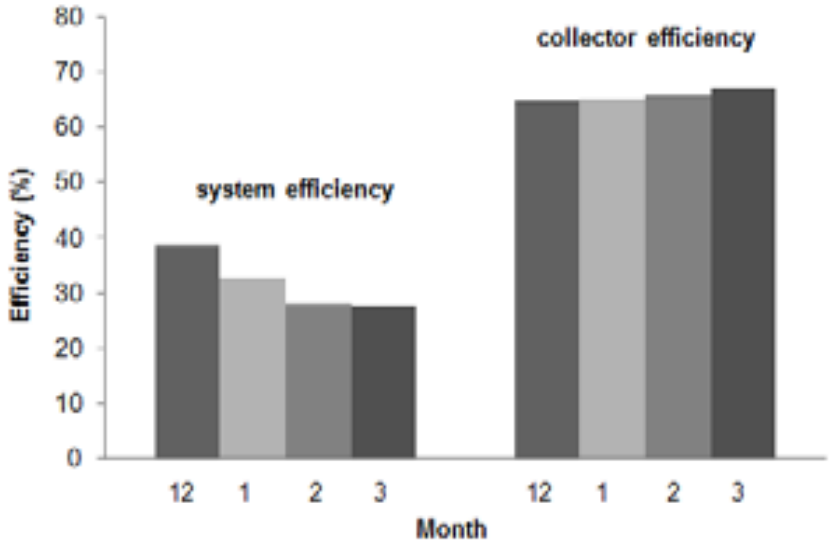

Fig. 6: Monthly average system efficiency and collector efficiency

From here, 59.3 % in December, 50.0 % in January, 42.2 % in February and 40.5 % in March of total energy collected by the solar collector were transferred into the tank, and the rest of the collected energy was lost when the energy was passing through the solar circuit pipes from the solar collector to the tank and from the tank to the solar collector.

3.3 Problems encountered

The surface of the collector glass tubes which transmits solar radiation were quite contaminated by soot and dust during the duration of experimental work (see **Fig. 7**).

Fig. 7: The glass tube contamination during the measurement (2014.01.10)

The main reason of decreasing the system efficiency is heat loss in the solar circuit pipes. During the measurement the heat insulators of the solar circuit pipes were renovated twice, but heat loss of pipes was not kept decreasing for a long time. Because material structure of the heat insulators deformed and material's body decayed and became thin due to temperature up and down during the operation time (-40 ^{0}C to +150 ^{0}C) and environmental various effects (see **Fig. 8**)

Fig. 8: Three months after heat insulator of solar circuit pipe changed (2014.01.10)

4. Conclusions

In order to estimate collector system efficiency in Mongolian actual smoky and dusty condition, the solar water heating system combined with an electric heater for heating the residential house was experimented and measured. As the result, the system efficiency was 31.5 % and the collector efficiency indicated 65.7 % averaged during the four months' measurement. Also 52 % of total energy collected by solar collector during

the four months measured was lost through the solar circuit pipes. After full cleaning of collector's glass tube, the collector efficiency increased by over 2 %.

The solar fluid was overheated by the collector during the power outage in several times, because of a solar water heating system with an evacuated tube collector uses an electrical circulation pump. Therefore, to operate the circulation pump continuously during the daytime, a small alternative resource of electric power should be used in the Ger district with electrical deficiency.

To decrease the air pollution level of Ulaanbaatar city, coal usage has to be eliminated in Ger district by finding new, convenient and harmless heating system. One of the reasonable heating systems is solar water heating systems combined with an electric heater. It is important to develop appropriate systems suitable for Mongolian climate condition and heat demand.

Nomenclature

T_i	temperature	(K)
$\dot{m}$	solar fluid mass flow rate	(kg s^{-1})
C_p	specific heat capacity	(J kg^{-1} K^{-1})
A_c	collector area	(m^2)
G	total global solar radiation at the collector's surface	(W m^{-2})

References

[1] Information and Research Institute of Meteorology Hydrology and Environment, 1988. Mongolian climate data book, second ed. Ulaanbaatar, Mongolia.

[2] Batdelger, B., Bayannasan, S., 2010. Solar radiation atlas of Mongolia, Soyombo print LLC, Ulaanbaatar, Mongolia.

[3] Air Quality Analysis of Ulaanbaatar Improving Air Quality to Reduce Health Impacts The world bank studies: Sustainable development and East Asian and Pacific region, 2011. <http://www-wds.worldbank.org/external/default/WDSContentServer/WDSP/IB/2012/01/16/000386194_20120116025654/Rendered/PDF.

[4] Duffie, J.A., Beckman, W.A., 2006. Solar engineering of Thermal Process, third ed. Wiley, New Jersey.

[5] Kaligurie, S.A., 2004. Solar thermal collectors and applications. Progress in Energy and Combustion Science 30, 231-295.

[6] Ayompe, L.M., Duffy, A., 2013. Thermal performance analysis of a solar water heating system with heat pipe evacuated tube collector using data from a field trial. Solar energy 90, 17-28.

Conference Proceedings

Solar World Congress 2015
Daegu, Korea, 08 – 12 November 2015

Experimental Investigation of the Filling and Draining processes of drainback systems (part 3)

Ruslan Botpaev, Yoann Louvet and Klaus Vajen

Kassel University, Institute of Thermal Engineering, Kassel (Germany)

Abstract

An experimental setup was constructed for the investigation of the filling and draining processes of a drainback system. Corrugated stainless steel (CSS) pipes in combination with transparent plastic hydraulic components (collector, heat storage) were applied in this study. CSS pipes are flexible, economically feasible and easy to install. However, sagging and the corrugated shape might be obstacles for a complete filling and proper draining. Therefore, several experiments with different diameters of CSS pipes (DN 12, DN 16, DN 20, DN 32) were performed. The recommended lower threshold of the flow rate for siphon establishment in hydraulics with CSS pipes has been experimentally obtained. Regarding the draining process a typical profile comprising of the emptying time and maximal draining flow rate is summarized. It is showed that the draining proceeds always in the same way (profile, emptying time) for the same hydraulics regardless of the adjusted flow rate during operation. The impact of the pumps on the draining process is also demonstrated. Finally a burst test was conducted, that proved a safe operation even by phase change of the remaining water. Conclusions are presented in details in this paper.

Keywords: *Drainback, drain-back, drain back, filling, siphon*

1. Introduction

Drainback solar thermal systems (DBS) offer failsafe freeze and overheating protections. High reliability of DBS is achieved due to three alternating stages: filling, operation and draining of the solar fluid. Each stage has its own functional purposes and requires a deep understanding of their specific peculiarities. Insignificant mistakes during design and installation might cause a fatal damage of the drainback system. Despite presence of some general recommendations towards optimal design and construction of DBS, there is a lack of publications concerning the filling and draining issues. Therefore an experimental setup was constructed for investigation of the existing knowledge gap. Different experiments were conducted and presented in the previous papers (parts 1, 2). Former both publications focused on experimental investigation of the drainback hydraulics, where smooth pipes were applied. In particular polyvinyl chloride (PVC) pipes were installed due to their transparency, which allowed the observation of the filling and draining processes. It has been shown that a siphon effect is essential for the filling process, which compensates the lift head to be overcome by the pump. The presence of an air vent at the top of the hydraulics modifies the filling and consequently the draining processes. A hydrostatic pressure difference between flow and return side is the driving force and of vital importance for a failsafe draining. In the scope of the present paper further findings on filling and draining behaviors are summarized. It is to emphasize that this paper is clearly understandable without familiarization with previous parts, despite their identical heading. The aim of the present investigation is to evaluate both operation stages (filling and draining) for the DBS with corrugated stainless steel (CSS) pipes. CSS pipes are flexible, economically feasible, compact for transportation and easy to install. However, sagging and the corrugated shape might be obstacles for a complete filling and proper draining. There are drainback systems which can be found on the market with CSS pipes, whereas some manufactures

doi:10.18086/swc.2015.10.29 Available at http://proceedings.ises.org

recommend restricting the solar piping to conventional copper pipes (Botpaev and Vajen, 2014a).

A schematic representation of both types of pipes is shown in Fig. 1, whereas the main dimensions are summarized in Tab. 1. The wave-shape of the CSS pipe is clearly visible in the longitudinal cross section of this pipe. Concerning other parameters it can be emphasized that the specific weight of CSS pipes is significantly lower, due to at least five times thinner pipe walls. Simultaneously, CSS pipes have a slightly larger top surface area and volume in comparison with copper pipes of identical sizes. It is not less important to notice, that CSS pipes obtain much higher pressure losses than copper pipes, but their cost on the market is slightly cheaper than conventional "red" pipes.

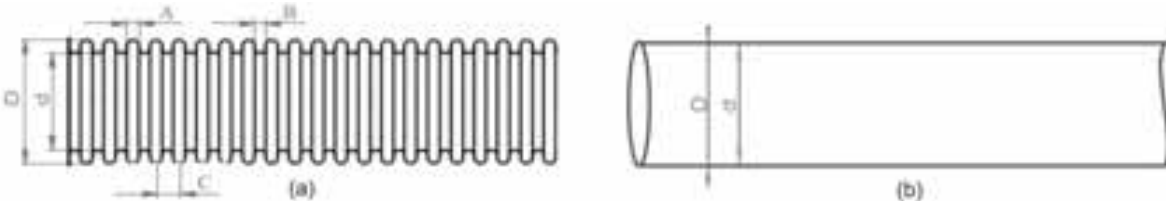

Fig. 1: Profiles of the (a) corrugated stainless steel and (b) copper pipes

Tab. 1: Dimensions of CSS and copper pipes as presented in Fig.1 (FlexxSys 2015; German pipe 2015)

DN		A	B	C	D	d	Wall thickness	Weight	Top surface area	Volume
		mm	mm	mm	mm	mm	mm	kg/m	m²/m	l/m
CSS pipes	12	2.41	1.71	4.12	16.5	12.6	0.18	0.086	0.072	0.168
	16	2.81	1.81	4.62	21.4	16.5	0.18	0.127	0.099	0.283
	20	2.51	2.31	4.82	26.2	20.5	0.18	0.174	0.138	0.437
	25	3.11	2.21	5.3	31.7	25.6	0.2	0.261	0.155	0.644
	32	3.11	1.72	4.82	41.1	34.6	0.2	0.345	0.228	1.125
Copper pipes	6				8	6	1	0.20	0.025	0.028
	15				18	16	1	0.48	0.057	0.201
	20				22	20	1	0.59	0.069	0.314
	25				28	25	1.5	1.11	0.088	0.491
	32				35	32	1.5	1.41	0.11	0.804

2. Description of experiments

The main advantage of CSS pipes is their flexibility, which allows flexible arrangement of the pipes without additional fittings and bending machine. Their competitive cost and compactness for transportation increased popularity among solar thermal system's plumbers; therefore CSS pipes have become a standard piping solution in solar thermal systems. Drainback systems however, require additional attention during design and installation due to the unique three stage operation modes. The complete hydraulics of the solar collector loop, including piping, should be completely filled after each pump activation; on the other hand the upper part of the hydraulics should be failsafe emptied when the pump is turned off. The latter is of vital importance in summer to avoid possible stagnation in collectors as well as in winter to prevent pipe failure. Can CSS pipes fulfill these specific drainback requirements?

The wave-shape profile of CSS pipes seems to be an obstacle for DBS, as the grooves inside retain water. Additionally these grooves can be a barrier for the air replacement from the hydraulics during the filling. Therefore the filling and draining properties of single samples of CSS and copper pipes were evaluated in a first step. The applied table experimental setup is shown in Fig.2. This setup consists of the following instruments and measuring devices: a "Sartorius" terminal connected to a weighing platform (accuracy ±0.1 g), a "Laserliner" digital spirit level (accuracy ±0.1° at 0° and 90°, and ±0.2° between 1° to 89°) for measurements of the tilt angle and a standard camera (not presented) to record the dynamic of the draining process. Six pipe samples: CSS pipes DN 12, DN 16, DN 20, DN 32 and copper pipes DN 6 and DN 20 of one meter each were tested. Each sample was fixed on a straight metal profile in

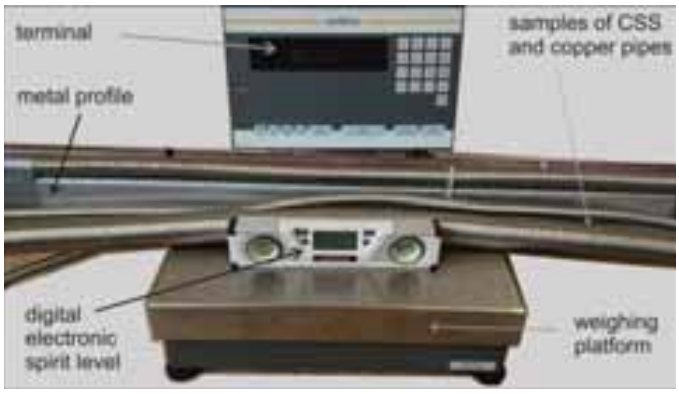

Fig. 2: Experimental setup for the filling and draining tests of CSS and copper pipes

order to maintain their linearity avoiding pipe sagging. Samples were weighed, then filled completely with water and drained at different tilt angles: 0° (horizontal), 2°, 5°, 10° and 90° (vertical). These slopes have been chosen based on a previous study summarizing the minimal recommended tilt angles for the piping in DBS (Botpaev and Vajen, 2014a). The pipes were differently filled: in vertical position from the top and from the upper edge of slightly sloped pipes. Afterward the pipes were shaken in order to test if air was still remaining in the tubes. The dynamics of the draining process was analyzed as well, through continuous weighing of the samples. Reduction of the sample's weight was recorded with a standard camera for an hour. Based on the results of this first set of experiments, quantitative draining features of CSS pipes in comparison with copper pipes were elucidated.

In a second stage the CSS pipes were integrated into an existing drainback experimental setup (Fig. 3). CSS pipes were installed in the flow side, whereas transparent PVC pipes were chosen for the return pipes. Two types of drainback systems were considered: one with heat storage as drainback reservoir and one with an additional drainback tank. Some hydraulic components were transparent for visual assesments of the processes. Pure water was colored red and used as the circulating fluid in the loop. The measuring equipment comprised magnetic-inductive flow meters, manometers and an Agilent data acquisition system. The system operated at ambient temperature during all conducted experiments.

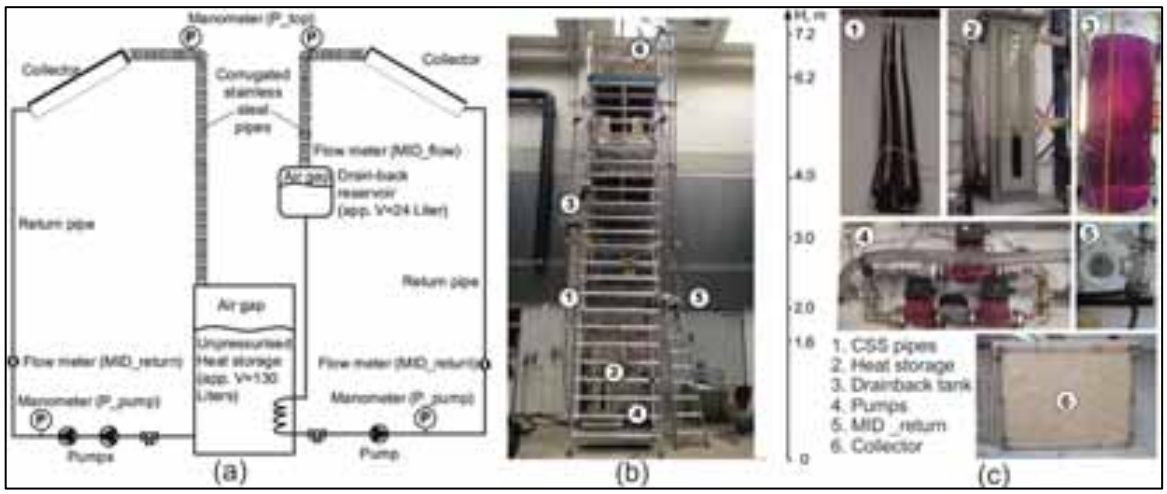

Fig. 3: Hydraulic scheme (a) of the experimental setup (b) and hydraulic components (c)

The experimental setup with a total height of 7.2 m (Fig.3, in the middle) consists of the following components:

- *Solar collector and piping.* Two parallel-connected heat-pipe collectors were hydraulically reproduced with vertical PVC (Ø38mm inside) pipes, which were mounted on a wooden board (1.7 m x 1.4 m). The tilt angle of the collector was 60° during the experiments. The piping to the collector (return side) was constructed with PVC (Ø19 mm inside) pipes, whereas CSS pipes (DN 12, DN 16, DN 20 and DN 32) were applied for the flow side. CSS pipes with a length of approx.

8.2 m were mounted in the flow side as a single piece, connected with fittings to the collector outlet and the heat storage inlet.

- *Heat storage.* Both types of drainback systems were connected to the same heat storage. The unpressurised storage was made from PP-H plastic in a cubic form. The inside dimensions are 320 mm x 320 mm x 1300 mm (LxBxH) with a total volume of about 130 litres. One centimetre of water column in the heat storage corresponds to one litre of water. On the front side of the heat storage a sight glass made of a polycarbonate plate was mounted. The heat storage has five connections - two of them connected to a heat exchanger coil located inside the tank, two others for the direct integration of the solar loop, and the last one is an air vent.
- *Drainback tank.* A drainback tank with a cylindrical form was bonded from a transparent Plexiglas pipe (Ø OD/ID 300/292 mm) and plates with an adhesive. The dimensions of this tank are 300 mm x 650 mm (BXH), which corresponds to a volume of 43 litres.
- *Pumps*. There are two possibilities to force the circulation in the solar loop of the experimental setup: either with one pump or with two pumps connected in series. Connection in series of two identical pumps doubles the head, allowing overcoming of the vertical lift head. A set of valves allows operating the solar loop either with a single pump Grundfos 25-120 or two small Grundfos Solar 15-80 pumps. The latter has two adjustable speed levels: min and max.
- *Measurements acquisition.* The data acquisition system Agilent 34970A was used for monitoring, gathering and evaluation of the measured data. Manometers and flow meters were the main sensors of the experimental setup. Muntwyler (2005) reported that some flow meters can cancel the draining proccesses, therefore magnetic-inductive flow meters (MID) were applied. The chosen MIDs - ABB Process Master 311 (accuracy ±0.4 %) are capable of measuring the flow rate in both directions. An additional advantage of MID flow meters is their ability to determine the presence of air bubbles in the flow. As long as air entrainment occurs in the stream, the sensor delivers fluctuating values of the flow rate. One flow meter was mounted in the return pipe directly above the heat storage at a height of 2 m, the second one in the flow pipe above the drainback tank at 4 m. Two digital manometers from JUMO GmbH & COKG were placed at the highest point of the hydraulics (accuracy ±0.8 kPa) and after the pumps (accuracy ±1.3 kPa). Some simple manometers were also applied for controlling purposes.

Several tests concerning the filling and draining processes were conducted and evaluated. The filling process was performed under different variations of the pump speed. The process of air replacement by water during the filling was analyzed by integrating the flow rate curve over the duration of the filling process. This test was conducted for two different hydraulic configurations, which were completely identical besides the arrangement of the CSS pipes in the flow side. The flow side piping of the first hydraulics was arranged vertically with one horizontal part at the level of the heat storage, whereas the second hydraulics had an additional horizontal part at the level between the collector and the heat storage. The length of the CSS pipes, however, was the same in both hydraulics. The course of the draining process under different operation strategies (high flow or low flow) was also analyzed. The impact of pump configuration (e.g. one pump vs. two), which are responsible for an additional pressure drop during the draining.

Finally some burst tests have been presented in order to estimate the freezing threat in CSS and copper pipes. A conventional freezing unit was applied for these experiments. In Fig. 4 is presented the interior of the

Fig. 4: The inner part of the freezer with the samples inside

mentioned freezer with the samples inside. Cables of installed NiCr-Ni thermoelements and isolating material are also shown; however they were used for other experiments which are beyond the scope of this paper. The pipe samples (CSS and copper) were filled with water and frozen, afterwards simply observed. The filling inclination was varied in accordance with obtained results from the first experiment, in order to find out its impact on the pipes while freezing.

3. Measurements and analyses

The results of the experiments are summarized in the present chapter, in the same order as they were described above. At the beginning the results of the filling and draining tests of the samples are analyzed, afterward the filling and draining processes of the setup are explained and finally the burst test is briefly described.

Experiment 1 – filling and draining properties of the CSS and copper pipe samples. Several simple experiments were performed to determine the filling and draining properties of the CSS in comparison to copper pipes. The samples were fixed on a straight metal profile to keep the linearity avoiding pipe sagging. Then the samples were filled, at the beginning in vertical position from the top, while the bottom was closed with a cap. Once the water level was close to the top, the samples were gently shaken, in order to remove the remaining air in the pipes. Observation, however, showed a full filling of the pipes without "shaking". Only copper pipes DN 6, had some difficulties by the filling due to prevailing surface tension. When the samples were filled in near horizontal position, some air was captured in the grooves, and could only be removed by placing the samples vertically. Further the filled pipe samples were adjusted to the desirable tilt angle, weighed, afterward the caps on both ends were removed, and the draining process launched. The draining profiles of the smooth copper DN 20 (Fig. 5, left) and CSS pipes DN 16 (Fig. 5, right) are presented in the Fig.5. Both graphs are scaled identically for better visual comparison of the draining dynamics of the smooth and "wave-shape" pipes. As expected the copper pipes drained completely by tilt angles steeper than 2°, whereas at a slope of 2° a small amount of water remained due to surface tension. For the same reason the copper pipe placed in horizontal position captures a considerably larger amount of water about 54 g, that represent 18 % of the water mass of the completely filled pipe sample. In CSS pipes as proposed a small amount of water always remains at all slopes range due to its special shape with grooves. It has to be emphasized that a comparable water mass remains both in horizontal as well as in vertical pipes. Moreover in vertical pipes after draining remains significantly larger amount of water than at flat slopes. This is a distinguished feature of CSS pipes, which retain water after the draining even in vertical position. Considering the dynamic of the draining for CSS and copper pipes at 0°, it can be noticed that the main volume of water flows out within 30 seconds from copper pipes, whereas about 3 minutes are required for CSS pipes.

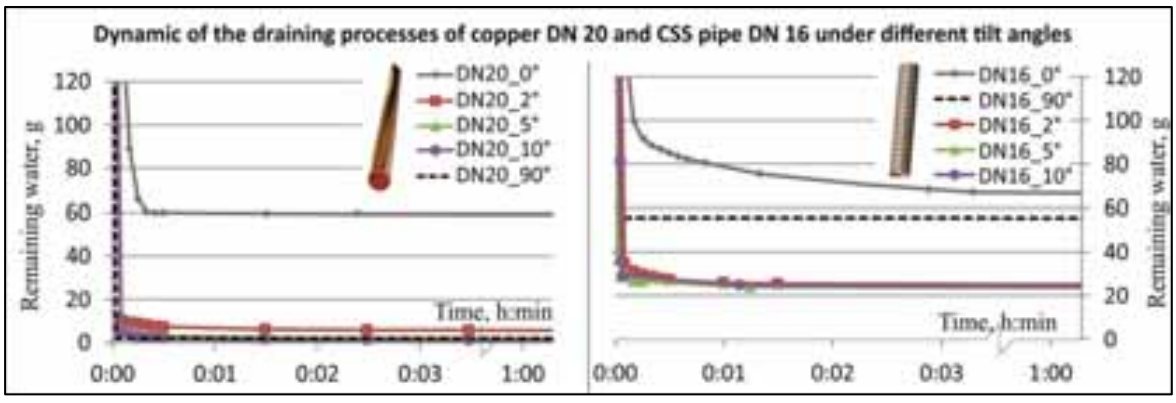

Fig. 5: Draining processes of a copper DN 20 (left) and CSS DN 16 pipe (right)

The draining processes of other samples show almost similar courses over the time, therefore only the measurements of remaining water after one hour are summarized in Tab. 2. The first columns in the table provide general information on the samples and the weighed water mass required to fill the pipes completely. This weight was considered in the next column as 100 %, in order to calculate the relative amount of remaining water after draining. The following columns present the remaining water mass after 1 hour of

draining in absolute values (gram) and in percent.

Tab. 2: Remaining water mass in copper and CSS pipes after 1 hour of draining

DN		Water content in the fully filled pipe		Remaining water mass in the pipe after 1 hour					
				0°		2°	5°	10°	90°
		g	%	g	%		g	g	g
Cu	6	33.0·(1±1%)	100	13.1±0.3	40	4.7±0.1	1.9±0.1	0.7±0.1	0±0.1
	20	310.5·(1±1%)	100	54.4±1.1	18	5.3±0.1	1.7±0.1	0.2±0.1	0±0.1
CSS	12	156.8·(1±1%)	100	90.3±1.8	58	27.5±0.6	21.9±0.4	20.5±0.4	41.4±0.8
	16	265.4·(1±1%)	100	64.5±1.3	24	24.0±0.5	23.0±0.5	22.0±0.4	55.6±1.1
	20	412.7·(1±1%)	100	53.7±1.1	13	31.7±0.6	30.4±0.6	29.6±0.6	88.9±1.8
	32	1086.6·(1±1%)	100	50.5±1.0	5	49.2±1.1	45.8±0.9	45.3±0.9	168.0±3.4

The percentage values of the remaining water, as presented in Tab.2, are illustrated in Fig.6. The graph shows the relative amount of remaining water one hour after the start of the draining process. Referring to Fig.6, it can be seen that the smaller the diameter, the more water (percentage values) remains inside. Moreover, a comparable water amount remains in the pipe regardless of the tilt angle for corrugated stainless steel pipes diameter larger than DN 16 (≥ DN 16). The latter statement is true, except in the case of a vertically positioned CSS pipe. When perpendicular to the horizontal, 15-26% of the water content remains in CSS pipes after the draining process, which should be considered during installation. On the contrary, smooth copper pipes empty completely as expected in a vertical arrangement. The "poor" emptying properties of the smooth horizontal pipes might be caused due to an insufficient initial hydrostatic pressure, which is the driving force of the draining. It is to emphasize that the draining of horizontal pipes in a real system proceeds in another way, where inertia of the flowing water and significantly larger hydrostatic pressure difference is present. Therefore, the emptying test of the presented experiment with 0° tilt angle should be considered as the worst draining case, as demonstrated in Botpaev et al. (2014) a horizontal arrangement of the smooth pipes does not affect the draining process of DBS. Similarly, better draining properties under the influence of inertia and hydrostatic pressure might be assumed for CSS pipes; however it is not possible in reality to arrange CSS pipes in such a lineal way, as it was done here by fixing them to a metal profile. Summarizing this first set of experiments, it has to be repeated that water always remains in the CSS pipes regardless of the slope. Furthermore, it should be noted that in vertical CSS pipes remains a significantly larger amount of water than in sloped one.

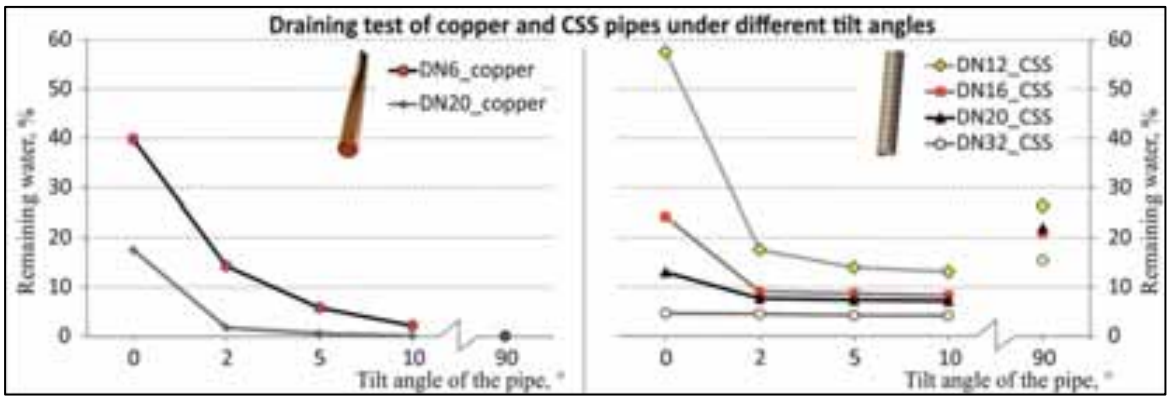

Fig. 6: Remaining water in copper and CSS pipes after one hour of draining process

Experiment 2 – filling and draining processes of a DBS with corrugated stainless steel pipes. The second set of experiments was performed with a second experimental setup, which was introduced above in Fig. 3. CSS pipes were integrated into an existing experimental setup, replacing PVC pipes in the flow side. The filling process of the system is presented in the Fig. 7, which similarly proceeds as the filling process of the same system with smooth pipes. The flow rate curve is drawn in black color, whereas the pressure is depicted in blue. The X-axis, which reflects the time in seconds was additionally split into several stages and designated with capital letters (A-C). The time interval between B and C represents the duration of the filling process with a typical spike of the flow rate at the beginning (red point). At the end of the filling process at time C all parameters such as the flow rate, the pressure after the pump and at the top are stabilized, indicating

complete air replacement by water in the hydraulics. The underpressure at the top (blue curve) shows a siphon establishment in the loop. The area under the MID_return curve over the length of the filling process, colored grey, is used to characterize the air replacement process in the solar loop (Botpaev and Vajen, 2014b). The speed of the installed pumps was varied and for each pump configuration the filling process was evaluated. Two identical but slightly modified hydraulics, the first one with one horizontal pipe arrangement of the flow side piping and the second with two (as described above) were applied.

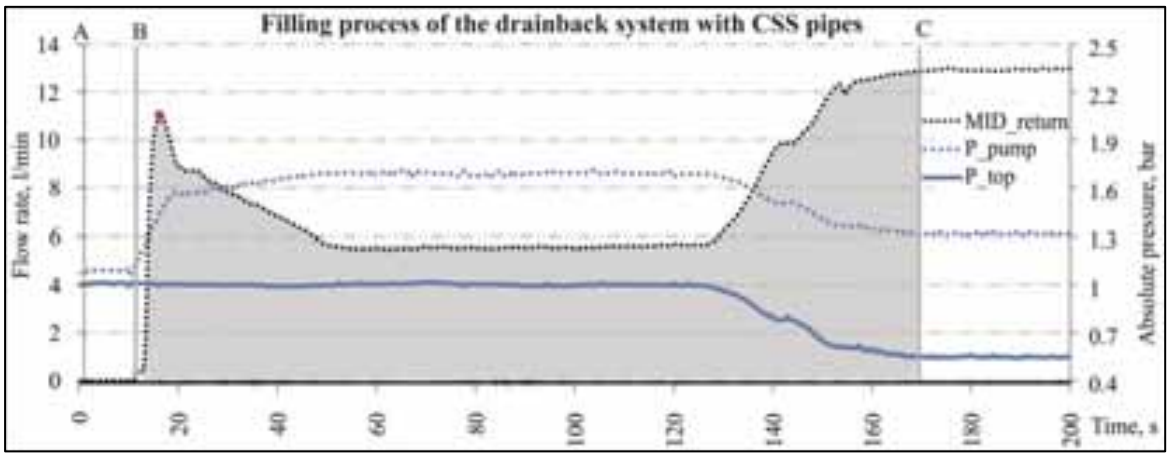

Fig. 7: The filling process of the drainback system with CSS pipes

In Fig.8 is presented the evaluation of the filling process with the above described integral method. The red point in the graph corresponds to the filling case depicted in Fig. 7, where the minimal flow rate after the spike is 5.4 l/min and the grey area under MID_return amounts to 19 l. Based on the rules for error propagation, the uncertainty of the integral is estimated and presented in the graph for two flow rates (9.7 and 25.1 l/min). The absolute uncertainties are increasing at higher flow rates, due to the impact of the uncertainty on the filling time. In spite of relatively good repeatability conditions of the experiments, there is obviously no reproducibility of the results for experiments with adjusted pump speed at minimal flow rate below 6 l/min for both hydraulic configurations (1- with one, 2- with two horizontal pipe arrangements). The filling time for these flow rates is not predictable, as the amount of water required for the filling (integral) varies significantly. The experiments with a minimal flow rate above 6 l/min show a good reproducibility of the results. It appears that a comparable amount of water should flow through the loop in order to completely remove the air in the upper part of the hydraulics independently of the flow rate. This means that the intensity of the air transport process remains identical in CSS pipe, although the filling flow rate increases. The bend of the curve (near 6 l/min) can be considered as a tipping point, a recommended lower threshold of the flow rate for a proper filling process of DBS with CSS DN 20 pipes. Above this threshold, a good reproducibility of the filling time is guaranted; the control unit of the solar thermal system can therefore be precisely adjusted. A further rise of velocity causes an increase of pressure losses in the pipes (Fig.8, right Y-axis), without intensification of the air transport process; therefore the filling around the threshold minimizes the pump energy consumption without hampering the filling process.

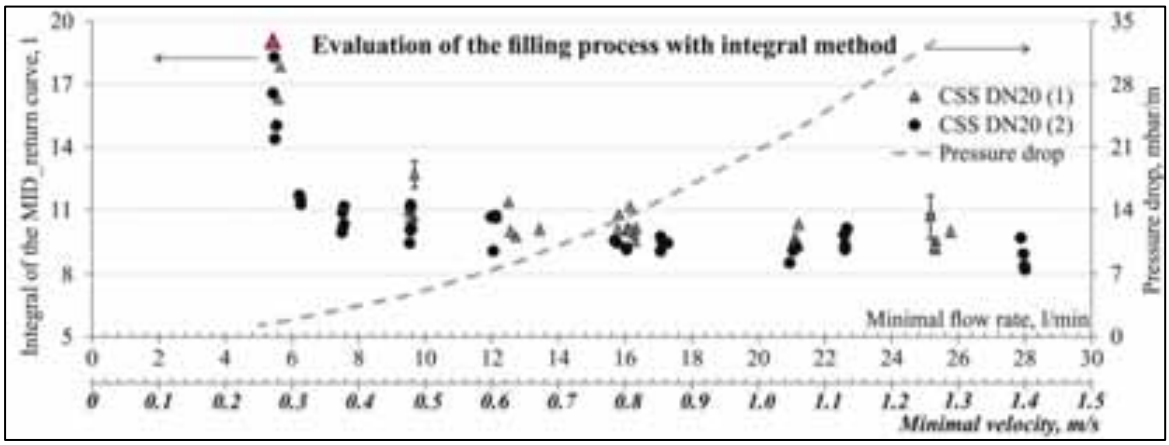

Fig. 8: Evaluation of the filling process with integral method

In Tab. 3 are summarized the values of the threshold flow rate for other CSS pipe diameters. These values were obtained based on the evaluation of two slightly modified hydraulics, as in the previous case. It is to be emphasized that the threshold for the CSS pipe DN 32 was indistinct due to lack of measurements data.

Tab. 3: Recommended lower threshold values for the filling process

CSS Pipe	DN 12	DN 16	DN 20	DN 32
Diameter of the CSS pipe, mm	12.6	16.5	20.5	34.6
Recommended lower flow rate threshold, l/min	0.85±0.01	4.00±0.04	6.00±0.06	35±2
Recommended minimum flow velocity, m/s	0.1·(1±1%)	0.3·(1±1%)	0.3·(1±1%)	0.6·(1±6%)

The minimum flow velocities in Tab.3 are calculated considering the minimal diameter (d on Fig. 1) of the CSS pipes. It should be noted that these values besides for DN 32 are smaller than the recommended minimum flow velocities in VDI 6002 (2014). This standard issued by the Association of German Engineers suggests to keep the minimum flow velocity at 0.4 m/s in order to transport the air from the hydraulics. However, this velocity is not sufficient for the filling of drainback systems with CSS pipes DN 32.

Some additional remarks about observations and calculations during the filling tests:

- There is a recommended lower flow rate threshold, which guarantees a full filling of the hydraulics. At this value occurs a predictable air replacement processes. Further growth of the flow rate lead to an increase of the pressure losses and a decrease of the filling time, but the intensity of the air transport process remains the same.
- Flow rates above 5 l/min cause vibrations in CSS pipe DN 12 followed by a strong rumble. The vibrations were observed also for other CSS pipe diameters, however without noise. It means that the distance between the bindings should be optimised also for vertical CSS pipes, in order to minimize the vibrations. In particular a transition zone vertical to horizontal and inverse have been carefully considered.
- The pressure losses in CSS pipes are approximately three times (depending on flow rate) higher than in smooth pipes.

In Fig. 9 is shown the dynamic of the flow rate during the draining process. Five experiments were carried out for the same hydraulics with different pump configurations as schematically shown at the top of the graph. For instance in experiment 1010 the draining occurred through both parallel lines, whereas in 1016 only through the large single pump, and during experiments 1102, 1006 and 1013 through the two serially connected pumps. The X-axis is a timeline of the process in seconds. The Y-axis is a flow rate measured by MID_return. Positive values correspond to the direction of the circulation during operation mode, whereas the draining process occurs in the opposite way therefore depicted in a negative range. Capital letters (C-F) at the bottom of the graph highlight the transitions between some characteristic operating stages of drainback systems. The time interval between C and D is the operating mode, at time D the pump is turned off, however due to inertia the circulation continues with a decreasing flow rate during a couple of seconds, at time E the circulation ceases, afterwards starts the draining process in opposite direction.

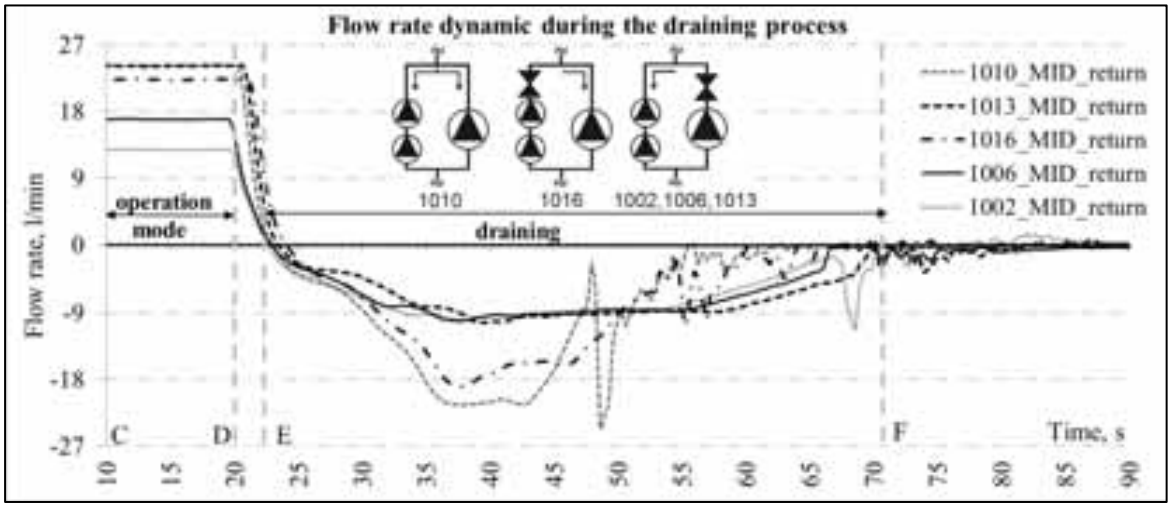

Fig. 9: Flow rate dynamic during the draining process

Pump represents a local pressure loss during the draining process. The value of the pressure loss depends on the pump(s) type and their hydraulic connection (serial or parallel). Obviously two parallel lines of pumps obtained the minimal pressure drop, whereas two pumps connected in series the maximal pressure drop. The pressure drop impacts the draining profile significantly. As presented in Fig. 9 the maximal amplitude of the flow rate during the draining process is twice larger in experiment 1010 (21.5 l/min) than for pump configuration adjusted in experiments 1002, 1006 and 1013 (9.3 l/min). Beside the maximal amplitude of the flow rate, this configuration ensures a minimal draining time which is also important. Furthermore it has to be emphasized that the draining process occurs in the same way for the same hydraulics regardless of the previous operation conditions (high flow, low flow or matched flow). It is visible that the profile of the flow rate curve (duration, amplitude) during the draining is identical for experiments 1002, 1006 and 1013, despite different flow rates during the operating mode. The flow rate during the draining even exceeded the flow rate during operation mode, as presented in the case of experiment 1016.

Some remarks about observations and calculations during the draining tests:

- The draining process proceeds always in the same profile, with identical amplitude and duration, for a certain DB hydraulics regardless of the flow rate during operation.
- The pump(s) represent(s) a relative significant pressure drop for the draining process, which impact the profile, duration of the draining process and its maximal amplitude.
- Small volumes of water always remain in CSS pipes after the draining process regardless of the tilt angle of the pipes. Furthermore in vertical pipes with large diameters more water remains than in sloped CSS pipes.
- The smaller the diameter of CSS pipes, the more water (in percentages to the full pipe) remains inside
- Vibration can occur during the draining for significantly high flow rates.

Experiment 3- burst test. In this last test, samples of different CSS pipes have been frozen in a freezing unit. Several tens of freezing and defrosting cycles have been carried out with CSS and copper pipes in horizontal position with different filling levels up to 50 %. They did not reveal any burst or visual damage of the samples. Fully filled copper pipes burst after the first freezing cycle, whereas CSS are elongated after the first freezing but are not burst. It can be concluded that remaining water in CSS pipes (partly filled) after draining does not present any danger for the pipes even after phase change of the heat transfer fluid. The only negative aspect is an energetic issue as the remaining water which transforms into ice needs to be melted at the start of the system.

4. Summary and conclusions

Experimental investigations of the filling and draining processes of drainback systems have been undertaken. The behaviour of these processes was evaluated for DBS with corrugated stainless pipes as solar collector loop piping. CSS pipes are widely used by assemblers of solar thermal systems as they are flexible, economically feasible, compact for transportation and easy to install. Because of specific design and installation requirements, the use of CSS pipe in combination with DBS was investigated in this study. In a first step, the filling and draining properties of several CSS and copper samples were investigated. The results show that CSS pipes are suited for the filling process, despite their distinguished shape with grooves. These grooves retain some fluid after the draining process, therefore water always remains in CSS pipes regardless of their tilt angle. Moreover, CSS pipes vertically positioned hold more water than identical samples with 2°, 5° or 10° slope, which is not the case for copper pipes. Indeed, Smooth pipes empty completely at angles steeper than 2°. Further experiments were conducted with a complete drainback setup. The suggested integral method was used to evaluate the filling process. The recommended lower value of the flow rate for CSS pipes with different diameters was obtained. This value is a threshold, above which a repeatable filling process with a predictable filling time is ensured. Further rise of the flow rate above this threshold during the filling is however not desirable as it causes additional pressure losses, without improvement of the air transport mechanism. Besides for DN 32 pipes, the obtained thresholds are in line with the minimum flow velocity recommended in VDI 6002. The draining experiments confirmed that the draining profile including amplitude and the draining time proceed always in the same way for a given hydraulics regardless of the flow rate during operation. The pressure drop through the pump(s) impacts the

draining profile, so it is desirable to install pump(s) allowing back flow, but also with a minimal pressure drop. Finally burst tests approved the applicability of CSS pipes for DBS, however a sufficient number of fastening points for both vertical and horizontal pipes is required, in order to avoid sagging and vibration of the pipes.

Acknowledgements

The authors would like to express their gratitude to Hessen Agentur GmbH, Germany for the financial supports of the research project "Wirtschaftlichkeit mit System: Entwicklung innovativer, kostengünstiger Komponenten und Systeme zur Erschließung neuer Marktsegmente für Solarthermie", to the Marie-Curie Actions Initial Training Network research programme of the European Union which supported the second co-author through the SolNet/SHINE project, to the company Enertracting GmbH and IdE –Institut dezentrale Energietechnologien for their helpful collaboration, and finally to the master students Mr. Ole Schöndorf, Mr. Thomas Schwander for their support during experiments.

5. References

Botpaev, R., Orozaliev, J.,Vajen, K., 2014b. Experimental investigation of the filling and draining systems (Part 1). Energy Procedia, 2013 ISES Solar World Congress 57, 2467-2476. doi: 10.1016/j.eqypro.2014.10.256.

Botpaev, R., Vajen, K., 2014a. Drainback systems: market overview. 11th Internationale Konferenz für solares Heizen und Kühlen, Gleisdorf, Austria.

Botpaev, R., Vajen, K., 2014b. Experimental investigation of the filling and draining systems (Part 2). Proceedings of the Eurosun 2014 Conference, Aix-les-Bains, France.

FlexxSys GmBH, 2015. A data sheet of corrugated stainless steel pipes.

German Pipe Industrie- und Fernwärmetechnik GmbH, 2015. http://www.germanpipe.de/domains/germanpipe_de/data/free_docs/gp_system_e-komponenten_kupfer_edelstahl_en.pdf, Nordhausen, Germany, last accessed on 30.09.2015.

Muntwyler, U.W., Drain-Back-Kompaktanlagen. Final report of BFE Project 42783/82711, 2005.

VDI 6002, 2014, Solar heating for potable water. Basic principles. System technology and application in residential buildings.

Conference Proceedings

Solar World Congress 2015
Daegu, Korea, 08 – 12 November 2015

Effect of Wide Spread Implementation of Solar Water Heaters on the Electricity Peak Load in Libya

M.J.R. Abdunnabi[1], K. M. Dadesh[2,3], O. R. Mrehel[2] and N. El-shamekh[2]

[1]Center for Solar Energy Research and Studies, Tajoura, P.O. Box 12932 Tripoli, Libya

[2]Electrical and Electronic Engineering Dept, Faculty of Engineering, Tripoli University, Libya

[3]Renewable Energy Authority of Libya (REAOL), Tripoli, Libya

Abstract

Electricity plays an important role in the contemporary life, and it has become indispensible nowadays. Reducing the peak electricity load and increasing the load factor have been considered as one of the main tasks that have to be accomplished by both electricity generation-side and demand-side managements. The residential sector of Libya consumes over 31% of the total sold electricity, and 29.8% of that is delivered to the electric water heating load. This is inefficient way of electricity utilization. Usually, the electricity supplier in Libya increases the local generation capacity or import electricity from neighboring countries. Both solutions do not resolve the problem. This work attempts to investigate the effect of replacing electric water heaters in the residential sector of Libya by solar water heaters on reducing the electricity peak load and increasing the load factor. Our results show that on average 3% of the peak load demand can be saved. This is equivalent to 149.5 MW of reduced power. The study also revealed that an annual energy savings up to 2.55 TWh, and the load factor is improved by 2% (i.e. from 65% to 67%). This saved energy is equivalent to a power plant with a nominal capacity of 448 MW considering load factor of 0.65.

Keywords: *solar water heaters, electricity peak load, hot water load pattern, Energy saving,*

1. Introduction

Libya witnessed a rapid and significant development in various sectors and economic activities during the last quarter of the previous century. This development led to the growth in electricity demand. It is reported that the energy consumption per dwelling in Libya is over five times the consumption in Morocco. This could be attributed to the fact that electricity prices in Morocco is six times electricity prices in Libya (Missaoui, 2012). The consumption per capita of energy has been multiplied more than 13 times from 1970 to 2010, where consumption per capita increased from 338 kWh in 1970 to 4651 kWh in 2010. Therefore, meeting this demand has become a significant problem of concern, and it will impact the economy of the country. Thus, it is clear that Libya will face serious challenges as it attempts to meet the apparent rising demand of energy. At the same time, it seeks to decrease the dependence on the short-lived and potentially volatile oil and natural gas to reduce the negative environmental impacts.

Although Libya possesses high installed capacity per capita compared to other developing countries, Libya has suffered severe electricity shortages. The shortages have become worse in the past few years due to the loose of a part of the generated capacity as a consequence of the turbulence in the country and the continued increased electricity demand. In the past, this shortage was reduced by importing electricity from neighboring countries. However, this is no longer the case due to the experienced shortage of the electricity in these countries as well. Many solutions have been suggested and implemented to resolve this problem. Quick solutions such as installing new gas turbine power plants and renting diesel generators did not solve the problem.

From the aforementioned high electricity consumption per capita, it is obvious that it is not an electricity generation problem, but it is a demand side management problem. It is believed that implementing energy efficiency and energy saving strategies will alleviate this issue to high extent. In Libya, almost 100% of the domestic water heaters are electric, and they consume approximately 9.3% (3028 GWh) of the total electricity generated in the country in the year 2010 (Report 2010).

doi:10.18086/swc.2015.10.30 Available at http://proceedings.ises.org

This is equivalent to a power plant with a capacity of 532 MW considering load factor of 65%. There are many studies that deal with the demand side management including domestic water heating in the literature. Moreau (2010) conducted a study to see the effect of domestic water heaters during peak periods and its impact on the demand for electricity. He suggested a shifted load control strategy to minimize such effect. The study is conducted on the province of Quebec, Canada that has a high penetration rate of water heaters, approximately 1.7GW. It is based on an experimentally validated simulation model of water heaters, and the population diversity of hot water load profile. Three scenarios of controlling the number of deactivated water heaters during the peak demand are considered. In scenario 2 the results show that the peak reduction potential is approximately 595 MW at which the pick-up is controlled according to a prioritized random function spread over a range of two hours of the peak period. However, in scenario 0, controlled reactivation case, the peak demand is 225MW.

To alleviate the effect of the domestic water heating on peak demand and energy consumption, this article attempts to investigate the influence of replacing all expected electric water heaters with solar water heaters on the Libyan grid. The investigation includes an analysis of peak load in the Libyan electricity supply, hot water load pattern of the residential sector, complete replacement scenario of electrical water heaters with solar ones, and, eventually, perform estimation of the amount of saved energy, reduced peak power, and load factor improvement.

2. Electricity Sector in Libya

Libya is a country with a large area and relatively small population spread all over the place. The state owned General Electric Company of Libya (GECOL) is solely responsible for the generation and distribution of electricity for the whole country. By law, it has the responsibility of providing electricity to every household in the nation. Libya is a rapidly developing country, and the electrical demand is expected to grow at an annual rate of 6-8 % for the next 10 years due to the economic development and increase in people level of standard 0Report, 2008). Currently, approximately 37 % of the generated electricity is using natural gas, 18% heavy oil, 34% light oil, and the rest 11% is obtained from cogeneration (Report, 2010). Apparently, all used energy resources are from fossil fuels, and there is no contribution to new and renewable energy sources.

In Libya, the generated electric energy in 2010 is 32,558 GWh, and the total installed power capacity was 8,347 MW with an available power of 6,357 MW (Report, 2010). The calculated load factor of this year is 65%. Figure 1 illustrates the average hourly power for the four seasons of the year 2010.

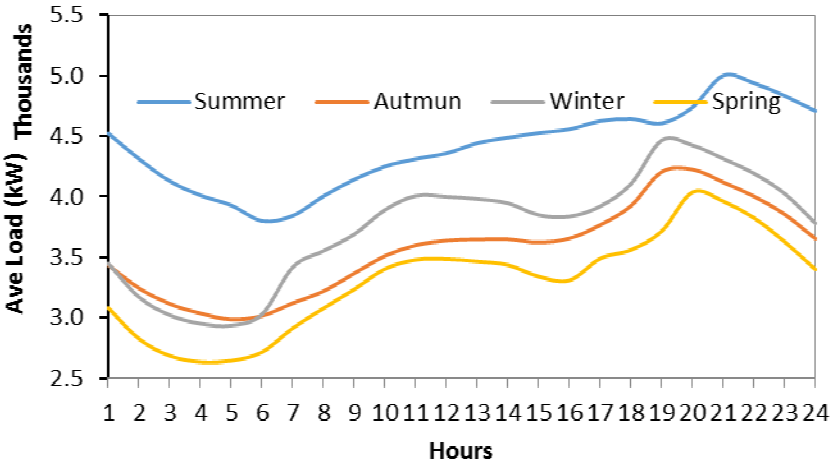

Figure 1. The average load of electricity during the four seasons of the year 2010.

It is clear that the peak power is almost after the sun set time, and, therefore, using solar energy without storage will not alleviate the peak power demand issue. However, solar water heating technology can store energy for later use, and, therefore, it can be a solution to this dilemma. Figure 2 shows the hourly maximum electricity peak during the year 2010, and it reveals that the global maximum is 5,759 MW in August month.

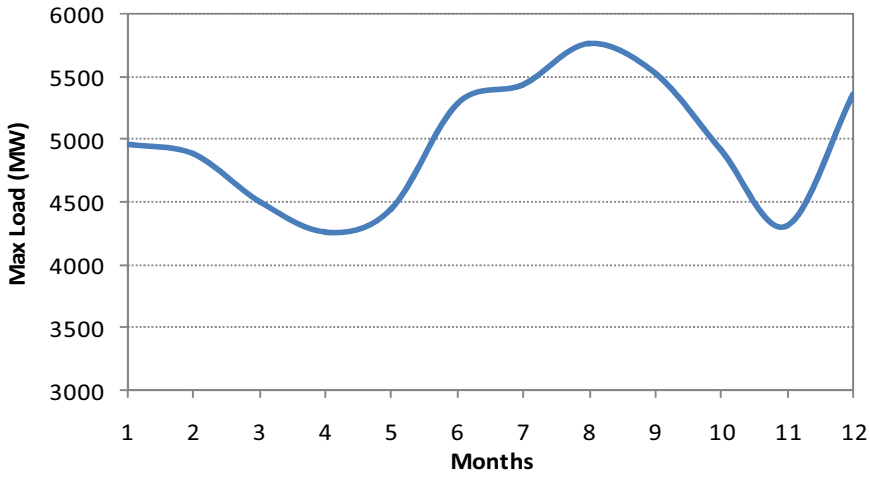

Figure 2. Monthly maximum electricity load for the year 2010

The reported incremental annual average change of the electricity peak load during the past few years is over 8% as shown in Figure 3. The year 2011 is the year of the revolution in Libya, and the supply of electricity was highly intermittent. Therefore, the years 2011 and beyond are not considered in this study.

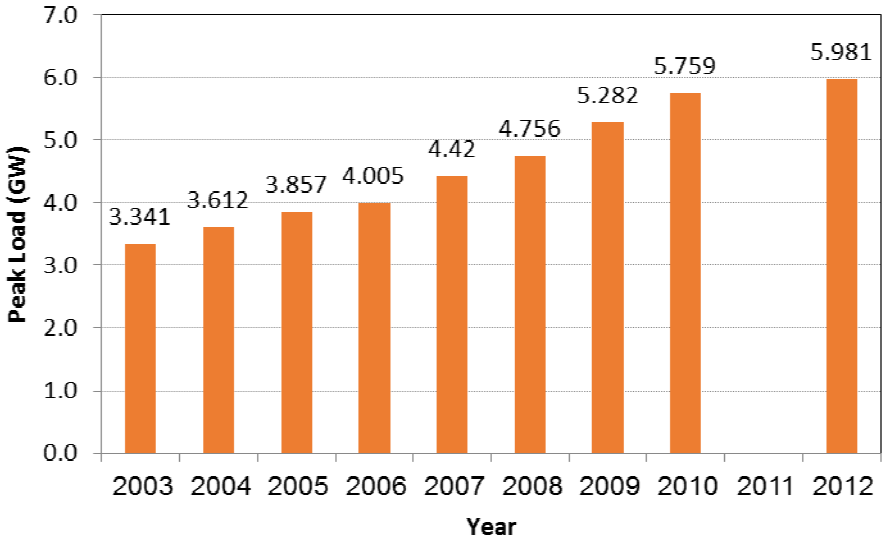

Figure 3: development of electricity load peak of Libya

Figure 4 shows the daily maximum electricity load for the year 2010. It is clear that the global peak is in the summer season with 5759 MW, and the average maximum power during the same season is 5060 MW. The second maximum occurs in the winter season with 5360 MW with the daily average maximum power of 4545 MW. The lowest maximum season power is the spring season with 4505 MW and the daily average maximum load of 4111 MW. In the autumn season, the maximum peak power is 5523 MW and the daily average maximum peak power during this season is 4333 MW. The drop in power between the summer and spring season is over 1000 MW in the maximum peak and in the daily average maximum peak. This huge difference could be attributed to the increased demand in buildings to meet the cooling load in the summer season.

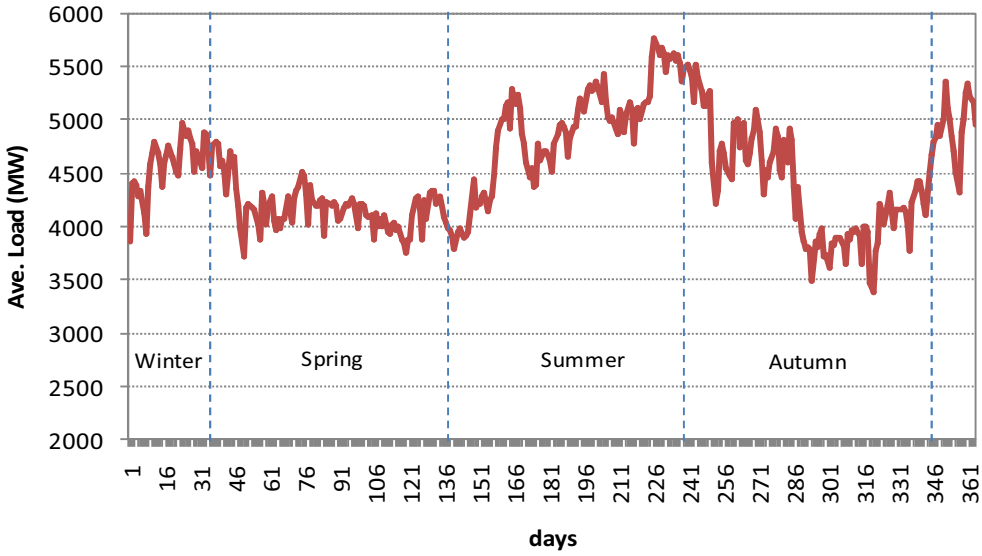

Figure 4. Daily maximum load for the year 2010

Studies made by CADMUS group (Khawaja, 2010a,b) show that the biggest demand at peak hours in the winter season is acquired by the residential sector with 34%. In the summer season the same sector demands 20% of the consumed peak energy, which comes the second after the public lighting demand as shown in Figures 5 and 6.

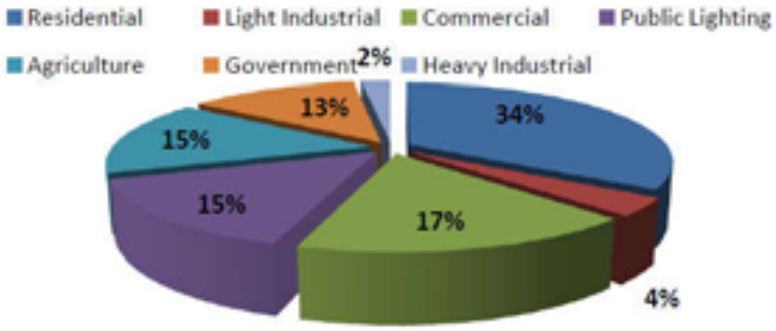

Figure 5: Winter demand at peak hours by sectors

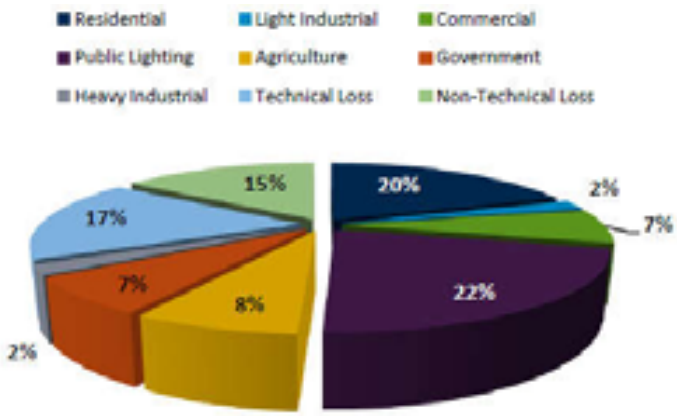

Figure 6: Summer demand at peak hours by sectors

Therefore, implementing energy conservation measures in the residential sector will highly alleviate the peak demand issue in the electricity system of Libya. Also the commercial sector composes a great share of power demand (17%) than energy consumption (13.06%). This is expected because these sectors have demand associated more with evening than daytime hours.

3. Residential Sector

According to the annual report of GECOL of the year 2010, domestic sector consumes 31.18% of the total electricity sold to different sectors of Libya as shown in Figure 7. In the meantime, a study conducted by (Ekhlat et al. 2009) shows that water heating in the domestic sector is the biggest consumer and represents about 30% as shown in Figure 8. Thus, around 9.3% of the national electricity consumption in the country is consumed by water heating for domestic purposes. In the year 2010 the total production of electric energy was about 32,558 GWh, and the amount of electricity sold was about 20,602 GWh. Therefore, the annual electricity used for domestic hot water based on generated electricity is around 3028 GWh.

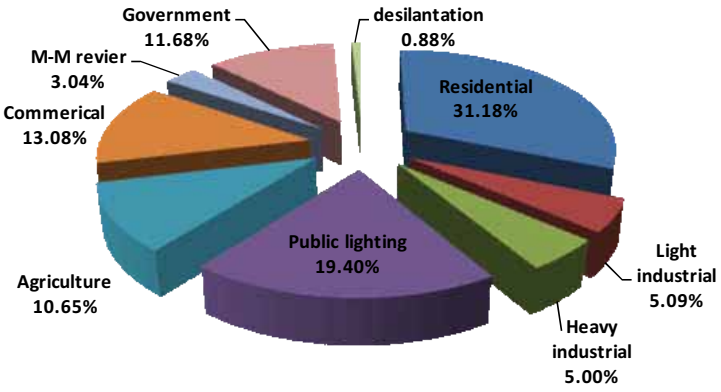

Figure 7. Sectarian distribution of electricity in Libya, 2010

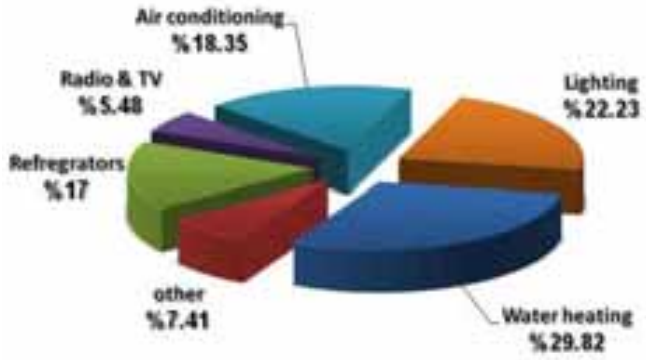

Figure 8. Electricity distribution in the Libyan houses

4. Hot water load in the Residential sector

More than a year of in-situ measurements of five solar water heaters installed in residential buildings are used to predict the average hot-water-load (HWL) pattern and quantity. The measurements were taken every 10 seconds and recorded every 30 minutes for more than a year. In this study, longer periods of measured data are used compared to the previously published data (Abdunnabi, 2005, Abdunnabi, 2012). The summary of the main results is presented in Table 1. The collected data is analyzed, and the hot water patterns for each season are obtained for the average Libyan family of 6 people. Figure 9 shows the typical seasonal hot water load pattern for the average Libyan family.

The methodology used to calculate the HWL pattern and quantity from the measured data is by unifying the different water quantities from five systems as energy, and the quantity of water is calculated at withdrawal temperature of 45°C. The results of all five systems were included in calculations as shown in Table 1. However, the summer results of the 240 liters system is excluded because the owner of this system declares that he purposely discharging large quantity of hot water daily during the summer season to protect the system from high temperature.

The study reveals that the daily quantity of hot water withdrawn at 45°C per person is about 60 litters. The estimated annual amount of energy consumed for water heating per person is about 510 kWh. For an average

Libyan family of six people, the annual amount of energy consumed per family is about 3060 kWh, which is slightly different from the previously obtained results of 2731 kWh/year/family (Abdunnabi, 2005). The study shows also that the average annual solar fraction is 70%.

Table 1: solar water heaters field study average data

Tank volume (L)	Collector area m^2	Persons/family	Ave consump. (Lit)	Ave. inlet Temp (°C)	Ave. outlet Temp (°C)	Annual energy kWh	Solar Fraction (%)
240	3.54	6	353	26.3	49.6	3450	75.2
280	4.4	4	274	24.36	47.3	2037	83.6
210	3.4	5	158	20.55	46.4	1698	57.7
240	3.54	4	319	21.82	44.44	2925	66.1
170	3	3	131	21.91	44.2	1190	58.7

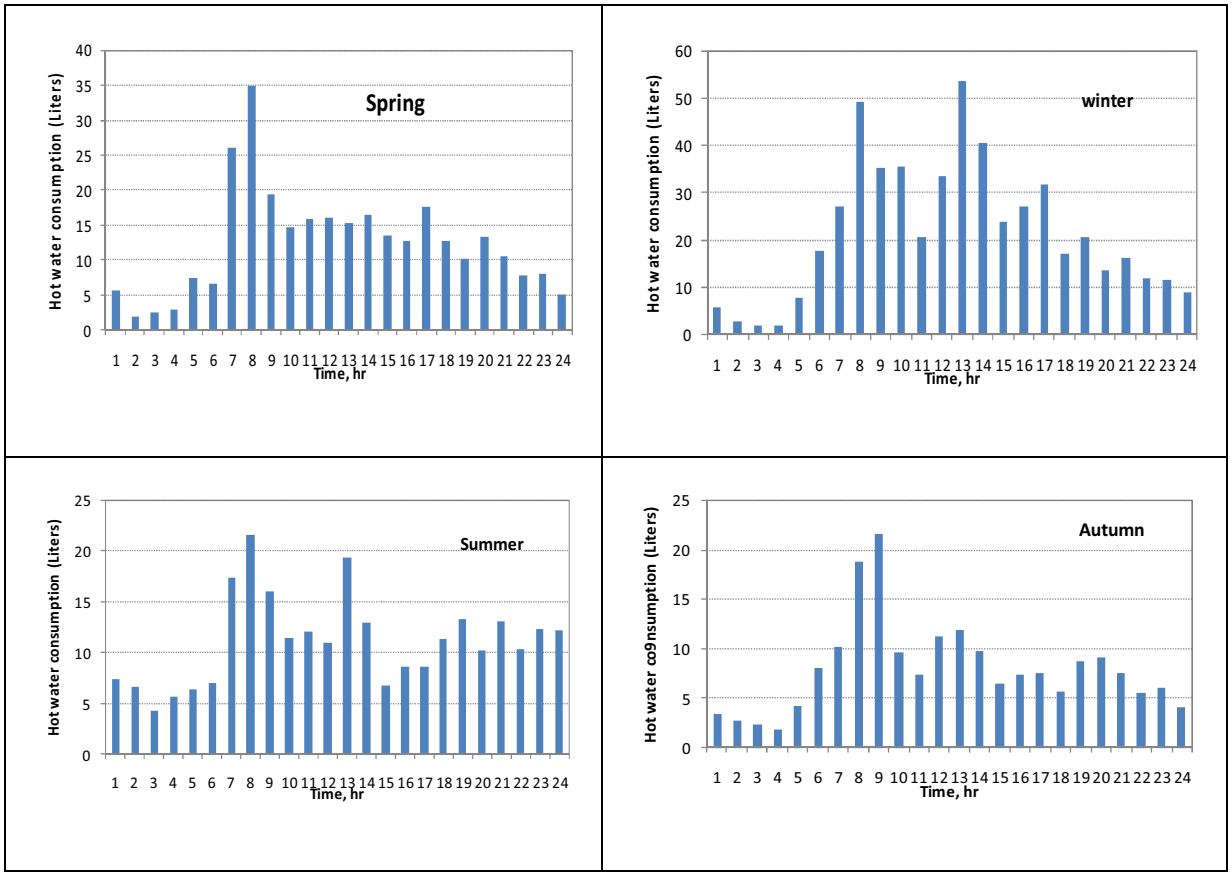

Figure 9: Typical seasonal hot water load pattern of Libyan families

To estimate the energy used for water heating in residential sector, two approaches are used: The first approach is based on the data obtained from GECOL (Report, 2010) and General Authority for information (GAI) (Report, 2007). The second approach is based on data collected from SWH field tests. The following sections will go through these two approaches in details.

First Approach

This approach will give the possible energy consumed for domestic water heating per family according to data obtained from GECOL and GAI. These data are listed in Table 2.

Table 2: Various data from GECOL and GAI

No	Category	Value	Remarks
1-	Electric Energy Sold	20,602GWh	GECOL (2010)
2-	Electric Energy Generated	32,558 GWh	GECOL (2010)
3-	Percentage of water heating in the residential sector	29.82%	Khlat, 2009
4-	Electricity consumption in the residential sector	31.18%	GECOL (Report,2010)
5-	Percentage of electricity used for water heating in domestic sector	9.3%	31.18% × 29.82%
6-	Number of Clients	889,447	GECOL (Report, 2010)
7-	Number of Houses, 2010	921,642	GAI, (Report, 2007)

From Table 2 we can calculate the maximum possible hot water energy consumption (HWEC) per family based on the generated electricity:

$$HWEC_{max} = \frac{Electric\ Energy\ Generated \times \%\ of\ water\ heating}{Number\ of\ Clients} \quad \text{(eq. 1)}$$

$$= \frac{32,558,000,000 \times 0.298}{889,447} = 3403\ kWh$$

The minimum possible HWEC per family based on electricity sold can be obtained using the same formula:

$$HWEC_{min} = 2153\ kWh \quad \text{(eq. 2)}$$

Second approach

This approach is based on the SWH field test data of HWEC and the data from GAI as given in section 4.

$$HWEC_{measured} = 3060\ kWh \quad \text{(eq. 3)}$$

Fortunately, this measured value lies between the minimum and maximum values obtained using the first approach, which makes this quantity acceptable although the number of measured samples is very small. Therefore, it is chosen to represent the typical value of HWEC for domestic sector of an average Libyan family of six people. This value is representing the useful energy of the hot water and does not represent the energy provided by the electric element in the water tank. The heat loss to the environment is not included, and it will be calculated in next section.

5. TRNSYS Simulation of EWH Performance

Commonly used electric water heaters are simulated using TRNSYS simulation program to calculate the heat loss to the environment. It is also used to assess the electric energy required to compensate the energy due to heat loss and useful energy consumed (i.e. for typical Libyan house consumption of 3060 kWh/year). Figure 10 shows the implementation of eclectic water heater in TRNSYS using a simplified electric heater model (Type 60).

The results of a single year simulation of a typical hot water load pattern of a typical Libyan house show that the consumed electric energy is increased by 8% due to the consideration of energy loss to the environment as shown in Figure 11. The calculations are made at a set point temperature of 45°C. The figure also shows the effect of increasing the set point temperature of the electric heater assuming a consumption of the same amount of useful energy (Q_useful). It is clear from the figure that increasing set point temperature from 45°C to 60°C is accompanied with an increase in the energy supplied by 4% to reach to 12%. Whereas, the heat loss to the environment is increased above 50%. In all calculations of different set point temperatures, the user temperature is maintained at 45°C.

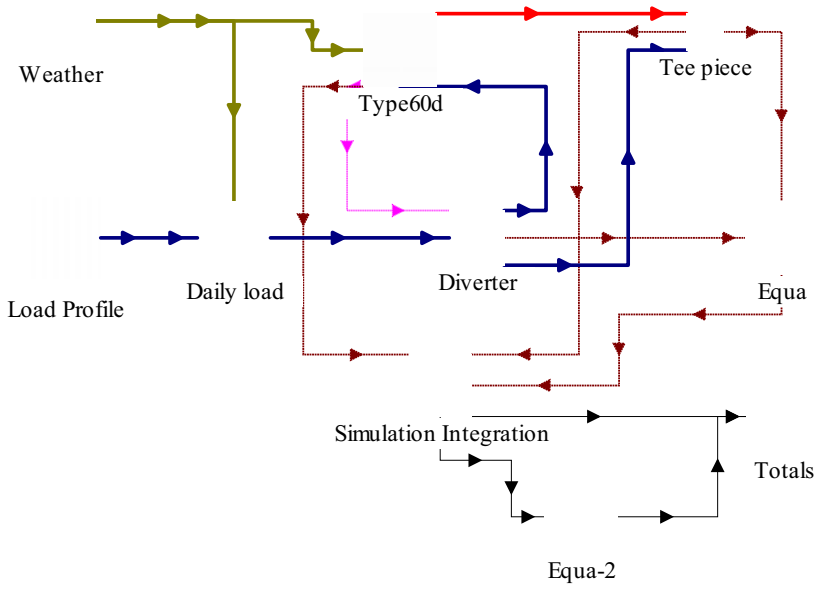

Figure 10: simulation of EWH in TRNSYS program

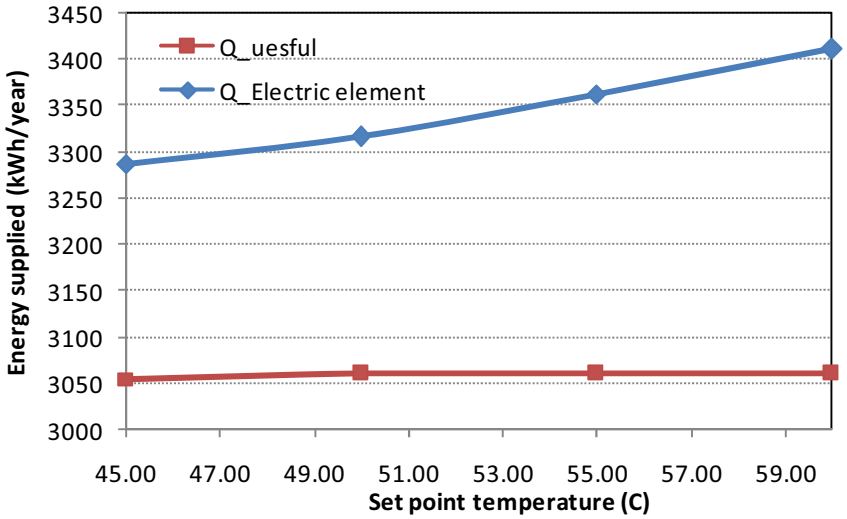

Figure 11: Effect of set point temperature on the energy supply and consumption

In This study, it is considered that the common set point temperature is 55 °C. The accompanied heat loss is about 10%. Therefore, the annual energy supplied by the electric heater per family is increased from 3060 kWh to 3364 kWh.

6. The Replacement scenario

The primarily results show that the effect of the electricity load of water heating in the residential sector on the electricity peak demand is very small. Therefore, in this study, we will investigate the maximum possible impact of a replacement scenario on the electricity peak demand without going in details of a gradual replacement. The replacement scenario is to replace the electric water heaters of the whole residential buildings by solar water heaters with an average annual solar fraction of 70%. This means that still there is 30% of the load energy demand that has to be covered by electricity.

7. Results and Discussion

The implementation of the results obtained on the residential water heating energy consumption on the electricity load for the four seasons are shown in Figures 11 to 14.

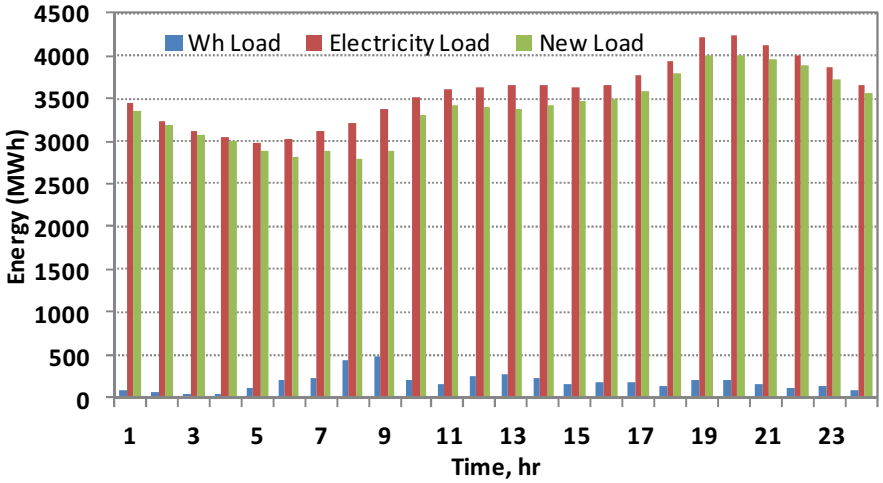

Figure 11: Energy load for autumn season

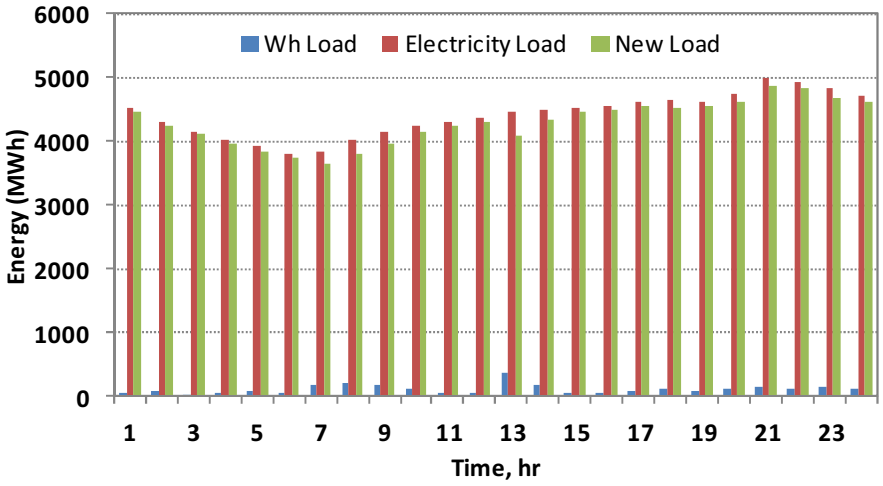

Figure 12: Energy load for summer season

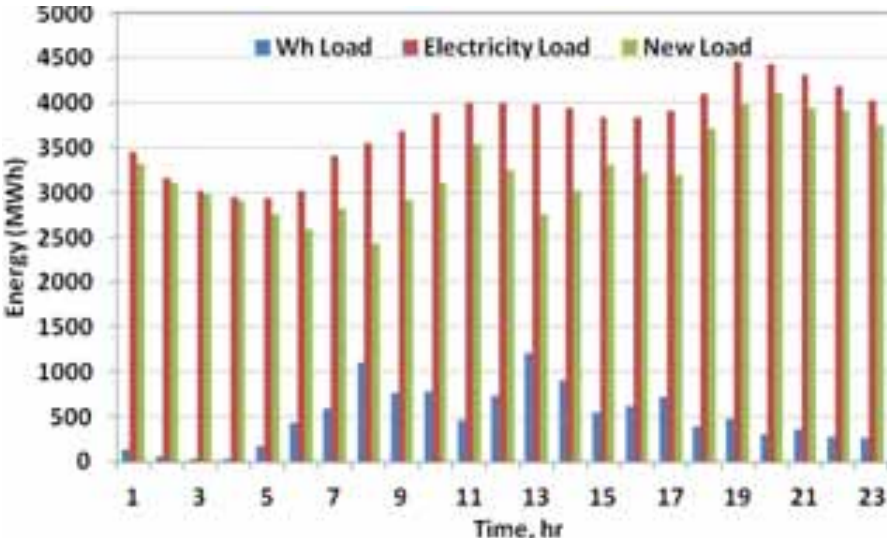

Figure 13: Energy load for winter season

In general, the obvious effect of the replacement scenario is in the winter season, so the peak load drops from 4465 MW to about 4085 MW with maximum saving in the peak load about 381 MW. Thus, the peak load is shifted one hour from 7:00 pm to 8:00 pm. Unfortunately, the maximum power capacity is needed in the

summer season where the lowest savings due to the replacement is achieved. The maximum peak load is nearly 5 GW at 9:00 pm, and the new peak load is 4.85 GW with maximum peak load savings of 149.5 MW.

In other mild seasons, autumn and spring, the maximum peak load savings are 237 and 329 MW, respectively. The peak times are at 8:00 pm for both seasons, and the new peak is shifted in spring to 9:00 pm, and in autumn it remains at the same time 8:00 pm.

The maximum peak load savings during summer, winter, autumn, and spring are 3%, 8.5%, 5.6%, and 8.1%, respectively. The average daily energy savings due to the replacement scenario in the summer, winter, autumn, and spring are 2.96 GWh, 12.8 GWh, 4.88 GWh, and 7.22 GWh, respectively. This is a considerable amount of energy that can be saved due to the suggested replacement scenario. When it comes to the reduction in the maximum capacity power installed due to the replacement scenario, it is only 149.5 MW that can be reduced. The maximum peak load of 5760 MW occurs in the summer (August) at night nearly 9:00 pm. Figure 15 shows the electricity load at the day of maximum peak load. The total energy consumption during this day is 122.45 GWh.

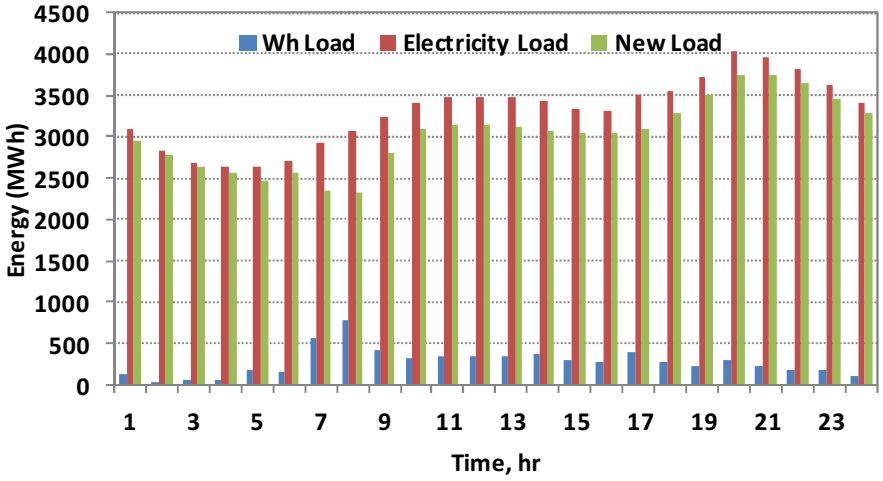

Figure 14: Energy load for spring season

The total annual saved energy using the replacement scenario of EWH with SWH is 2.55 TWh, and the load factor is improved from 65% to 67%. This saved energy is equivalent to a power plant with a capacity of 291 MW considering a load factor of 0.65, The nominal capacity will be 448 MW. This will be added to the fuel savings and huge environmental benefits due to avoiding burning fossil fuel that release harmful gaseous.

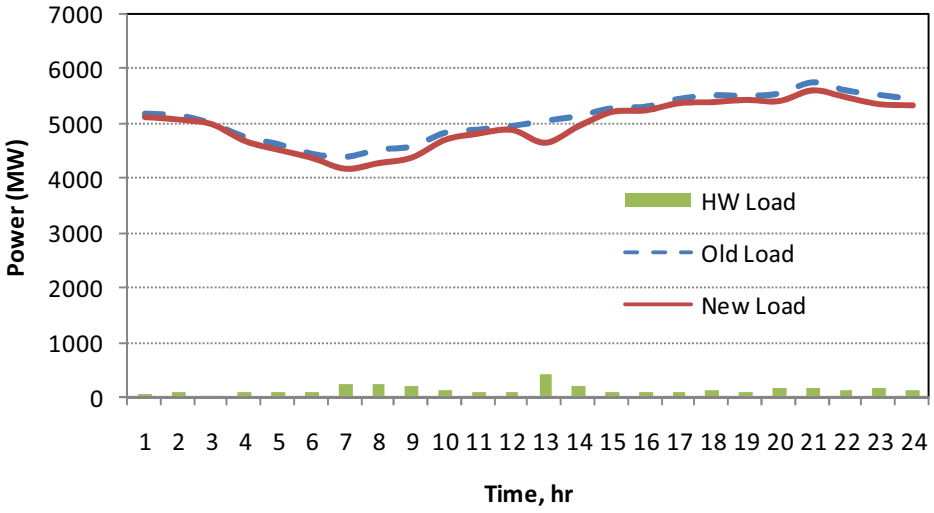

Figure 15: Effect of water heating load on summer peak load (15 August)

8. Conclusion

The Libyan electricity sector suffers from long terms intermittent for many years due to many reasons among of which bad of billing system and the high technical and non-technical losses. The total installed capacity is over 8 GW and the available operating capacity in 2010 is about 6.36 GW. The variation of the peak load among the four seasons of the year is over 1.5GW between summer and spring; this variation could be attributed to the energy consumption in buildings. On a daily basis, the maximum variation in the maximum peak load along the year is over 2.3 GW which is a very huge difference and has to be studied. Space heating/cooling, domestic water heating, and lighting are among the highest energy consumers in buildings.

Water heating for domestic purposes constitutes over 9.3% of the national electricity consumption in the country, which is equivalent to 3028GWh in 2010. The commonly utilized technology for water heating in the residential sector is the electric water heaters. This means that the most expensive along the expected life-long and the most pollutant technology used for domestic water heaters. Field study information about the hot water usage (profile and quantity) is used, and the annual hot water consumption for typical Libyan house is found 3060 kWh. The typical seasonal hot water load patterns are also obtained.

The study concluded that complete replacing of electric water heaters with solar water heaters in the residential sector will alleviate the electricity peak by 3% (149.5 MW) and improve the load factor by 2% (i.e. from 65% to 67%). However, the annual energy savings reach to 2.55TWh, and this is equivalent to a power plant with nominal capacity of 448 MW considering a load factor of 0.65. This will be added to the fuel savings and huge environmental benefits due to avoiding burning fossil fuel that release harmful gaseous.

9. References

Abdunnabi, M. and Berwian B, 2005, Economic and environmental benefits of the replacement of Solar water heaters instead of electric heaters in Libya, Scientific Journal of Science, Vol(13), July 2005 (Arabic).

Abdunnabi M, 2012, Optimum Values of Tank Volume to Collector Area Ratios of Thermosyphon Solar Water Heaters for Libyan Families, Journal of Solar Energy and Sustainable Development, JSESD, No 1, Vol,1,CSERS, 2012

Ekhlat M., Salah I. M., and Kreama N. M.,2009, " Energy Efficiency and Renewable Energy", General Electric Company of Libya "GECOL", National study, Libya, (February 2007).

Ekhlat, M., Azgalah A., and Madhon, M., 2009, Support general electric network of Libya by covering hot water load in the residential sector with solar water heaters, GECoL, internal report.

Khawaja Sami, David Korn, and Josh Keeling, 2010, Report: Winter Load Research for General electric company of Libya, The Gadums Group.

Khawaja Sami, David Korn, and Josh Keeling, 2010,Report: Summer Load Research for General electric company of Libya, The Gadums Group.

Missaoui R., Ben Hassine H., Mourtada A., 2012, Energy efficiency indicators in the Southern and Eastern Mediterranean countries, Regional report, RCREEE.

Moreau A., Control strategy for domestic water heaters during peak periods and its impact on the demand for electricity.

Report, 2007, Statistic report, General Authority for information (GAI), Libya.

Report, 2010, General Electric company annual report, 2010.

Repot, 2008, Planning electric power system studies for Libya: demand forcasting & gereation exprention planning until 2025, Final report, planning Dept. GPCoEWG and KEPCO, GECOL.

Conference Proceedings

Solar World Congress 2015
Daegu, Korea, 08 – 12 November 2015

NUMERICAL SIMULATION AND EXPERIMENTAL VALIDATION OF A SOLAR COOLING SYSTEM IN MEXICO

S. Lugo [1], O. García-Valladares [2]

[1] Posgrado en Ingeniería-Energía, UNAM, Temixco (México), sulu@ier.unam.mx
[2] Instituto de Energías Renovables, UNAM, Temixco (México), ogv@ier.unam.mx

Abstract

In this work the numerical simulation and experimental validation of a solar air conditioning to condition a 124 m^2 offices located in Jiutepec, Morelos, Mexico is presented. The model was developed and reported in a previous work, in which, using the software TRNSYS, the system is modeled for the design and sizing in order to reach the demand for air conditioning in comfort conditions for these offices. The system consists in a 8 kW adsorption air conditioning system, a thermal storage tank of 2m^3 and an area of 55.8m^2 of flat solar collectors of high efficiency, which is estimated to reach a solar fraction around 80%. The purpose of a validated model is produce a numerical tool in order to find the best operating conditions of the system and allow the study to any location where the solar cooling system can be implemented.

Keywords: *Solar cooling, TRNSYS, experimental validation, experimental analysis.*

1. Introduction

Mexico is in a privileged position to have high levels of solar radiation throughout most of the year; however this causes high temperatures in several states of Mexico and it is necessary to use cooling systems and air conditioning to have comfortable conditions. Nowadays, there are devices that can generate cold using solar energy, this is very attractive in places where cooling is required due to high ambient temperatures together with high solar radiation.

The advantages of solar cooling systems over conventional systems are mainly in the low electrical power requirement thus contributing to environmental protection, savings in energy costs and can be more easily used in remote locations away from the mains. Within the solar cooling exist two types of applications: absorption and adsorption cooling. For small capacity (<20kW) commercial absorption equipment are the following trademark: AOSOL, Pink GmbH, Robur, Sonnenklima GmbH, EAW, Yazaki, Rotartica and Climatewell. While in adsorption are: SorTech AG, InvenSor GmbH and ECN (IEA SHC-Task 38, 2010).

Among the many technologies for heat with the solar radiation, flat plate solar collectors is an option, they can reached temperatures close to 80°C with good efficiency. This range of temperature and the energy produce can be used in refrigeration equipment operating between 55°C to 95°C, the percentage of energy provided by the solar systems can be calculated (solar fraction).

The simulation program TRNSYS offers the versatility of coupling different independent models to form a solar cooling system under study. It also allows evaluate the system proposed in order to design and dimension its different components (TRNSYS, 2005).

2. Methodology

Through the program TRNSYS, the thermal behavior of offices of 124 m^2 located in Jiutepec, Morelos, Mexico has been simulated in order to show the current comfort conditions and to calculate the capacity of the refrigeration equipment necessary to achieve comfortable conditions inside the offices throughout the year (Lugo et. al., 2014).

doi:10.18086/swc.2015.10.31 Available at http://proceedings.ises.org

According to the cooling capacity required by the building, it was determined that the most appropriate system was an adsorption system trademark SORTECH model ACS 08 which has a nominal cooling capacity of 8 kW operating under the following conditions: inlet hot water temperature and flow 72°C and 1.6m^3/h, cooling water temperature and flow of 18°C and 2.0m^3/h, and an electric power required of 7W.

With SORTECH operating characteristics curves, this equipment was simulated using the TRNSYS Type 107; in this way, the interaction of this model with other components of the solar cooling system at different operating conditions was modeled.

In a second stage, the solar system was sized to provide at least 80% of the thermal energy required by the adsorption solar cooling equipment. The number and arrangement of solar collectors, size of the thermal storage tank and operating characteristics using a parametric study was obtained.

Solar technology used was flat plate solar collectors manufactured in Mexico by Modulo Solar SA de C.V. The solar collector used for this analysis is the model MS2.5 that has the following characteristics: 2.326 m^2 aperture area, mass flow rate of 3 l/min and efficiency curve according to Ec. 1 (Módulo Solar, 2013).

$$\eta = 0.7535 - 2.9132\frac{(T_{in}-T_a)}{H} - 0.0099\frac{(T_{in}-T_a)^2}{H} \quad (1)$$

The model validation is performed by comparing the results obtained using the TRNSYS simulation and experimental data collected for several days. The comparative error is expressed by the percentage mean absolute error (see Ec. 2) between the simulated and experimental data in the following form (Ayompe et. al., 2011):

$$PMAE = \frac{100}{N}\sum_{i=1}^{N}\frac{|C_i-M_i|}{M_i} \quad (2)$$

Where: *C* is the result of the value in each interval of TRNSYS

M is the result of experimentally measurement values in each interval

N is the number of data points used

In order to determine the thermal comfort in the space under study, the thermal sensation scale established by Fanger was taking account; it is based on the PMV and PPD indices divided into the levels shown in Table 1 (Fanger, 1972).

Table 1. Thermal sensation scale proposed by Fanger (Fanger, 1972)

PMV	PPD	Sensation
+3	99%	Hot
+2	77%	Warm
+1	26%	Slightly warm
0	5%	Confort (neutral)
-1	26%	Slightly cool
-2	77%	Cool
-3	99%	Cold

3. Numerical and experimental results

Daily monthly average weather conditions (Table 2) were obtained from the database generated by the UNAM, it contains meteorological information for populations in Mexico of more than 10,000 inhabitants (UNAM, 2013). These data were introduced to METEONORM software to generate a TMY format file that allows read the data in TRNSYS for short time intervals, in this case each hour (METEONORM, 2009).

Table 2. Weather conditions to Jiutepec, Morelos

Month	H MJ/m^2 day	Ht (20°) MJ/m^2 day	Ta °C	Ta_min °C	Ta_max °C	RH %
Jan	16.5	20.2	20.2	11.9	28.6	52.9
Feb	19.3	22.2	21.5	13.0	30.1	48.4
Mar	22.1	23.7	23.6	14.9	32.4	44.2
Apr	22.8	22.5	25.2	16.8	33.6	46.2
May	19.5	18.2	25.6	17.9	33.4	56.6
Jun	19.2	17.4	24.1	17.7	30.5	71.8
Jul	22.2	20.2	22.8	16.5	29.2	68.9
Aug	20.0	19.2	22.8	16.5	29.1	68.6
Sep	15.3	15.5	22.3	16.4	28.2	73.6
Oct	18.7	20.9	21.9	15.1	28.6	67.8
Nov	17.1	20.4	21.1	13.5	28.8	61.0
Dec	15.1	18.8	20.2	12.3	28.2	56.3
Average	**19.0**	**19.9**	**22.6**	**15.2**	**30.1**	**59.7**

Parametric study of solar thermal energy system was performed to obtain the area of solar collectors, the operating angle and the size of the thermal storage tank more appropriate for this case. The following conditions were considered for TRNSYS simulation: set point temperature (Tset = 72°C), difference for starting hydraulic pump (ΔT_on = 8°C) and difference to stop hydraulic pump (ΔT_off = 4°C).

Figure 1 shows the behavior of the solar fraction is shown against the area of solar collectors, with this results an area of 55.8m^2 (24 collector in an array of 4 series and 6 parallel 4Sx6P) was found in order to reach a solar fraction of around 80%.

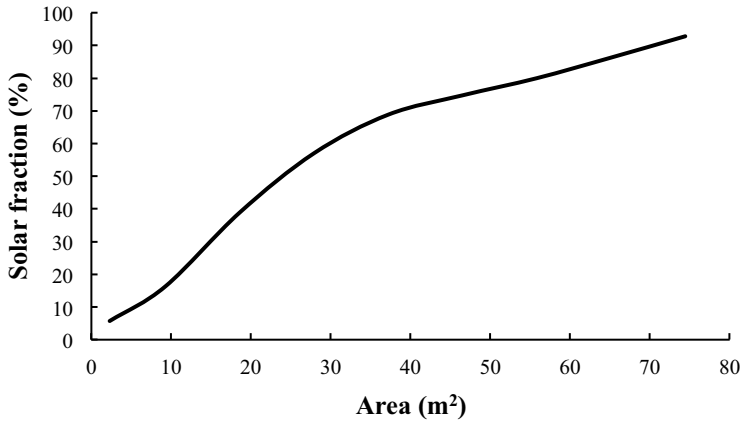

Figure 1. Sizing of flat plate solar collector arrangement

With the above arrangement (4SX6P), the solar fraction at different solar collector angles in order to find the optimum slope angle was simulated. It was obtained that 20° to the South was the best option (see Figure 2).

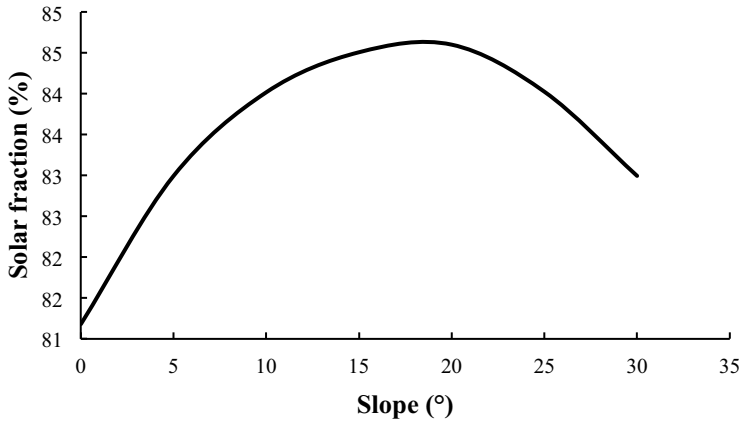

Figure 2. Slope of flat plate solar collectors

Taking into account the values found in the previous figures, the volume of the thermal storage tank was analyzed to find the better option (see Figure 3). The optimal volume of the tank found was 5 m^3, however considering the costs of it and that using a tank of 2 m^3 decreases only 1.8% the solar fraction, it was decided to use the latter one in the system installation.

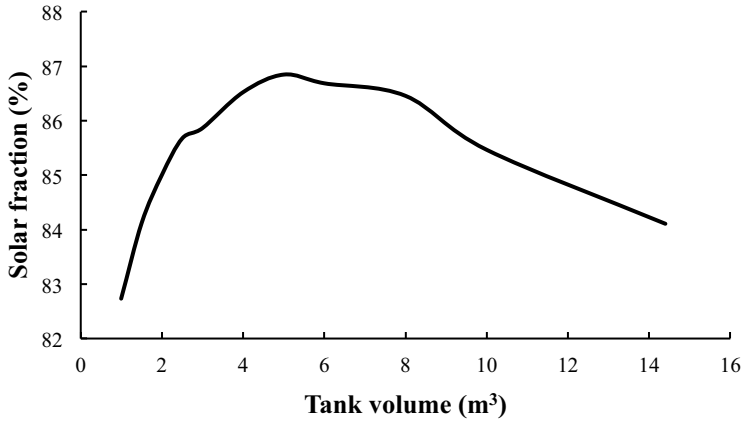

Figure 3. Volume of the thermal storage tank

According to the values obtained by the TRNSYS simulation, the final solar cooling system was designed and the selecting components are shown in Table 3 and Figure 4 shows the real components installed in the place of study in Jiutepec, Morelos.

Table 3. Components of solar cooling system

System	Trademark	Model	Quantity	Capacity
Solar cooling equipment	SORTECH	ACS08	1	8 kW
Solar collectors	Módulo Solar	MS2.5	24 (4Sx6P)	55.8 m^2
Thermal storage tank	MASS	THN-2	1	2 m^3

Figure 4. Installing components of solar cooling system

With the TRNSYS simulation of the solar cooling system, average monthly values of PMV and PPD were obtained throughout the typical year inside the offices, these range are from -0.6 to 0.07 and a maximum of 20%, respectively (see Figure 5). Therefore, according to the thermal sensation scale developed by Fanger (see Table 1), the offices under study will be in thermal comfort throughout the year.

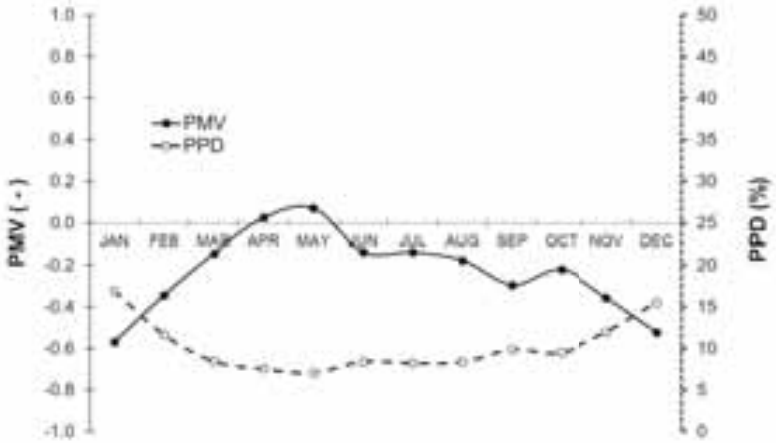

Figure 5. Comfort indices inside offices

Monthly theoretical results of this system (Figure 6) show that an annual average solar fraction of 85% is reached, surpassing the initial request. In addition, the proper functioning of equipment and comfort conditions in the offices are reached with this configuration according to the TRNSYS simulated data.

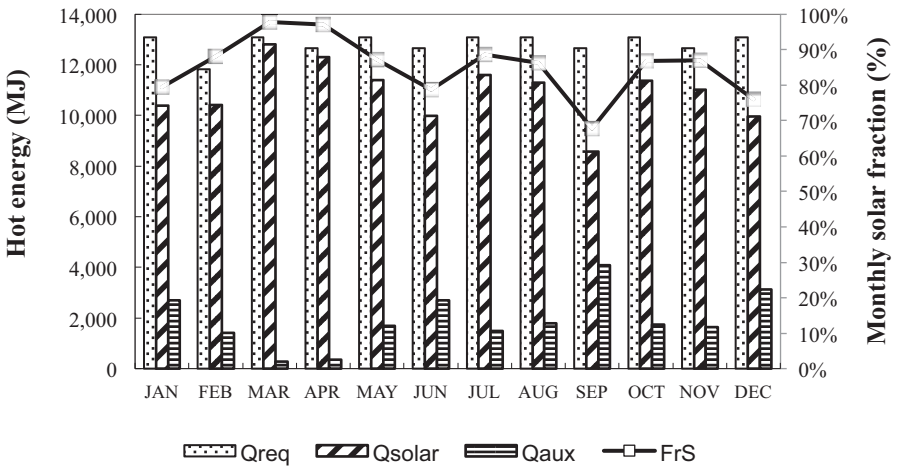

Figure 6. Thermal and energy monthly solar fraction in the solar heating system

The comparative results between the theoretical values obtained in TRNSYS and the experimental values for the outlet water temperature of the solar collector arrangement of 4Sx6P are shown in Figure 7 for a test of one day (May 25th, 2015).

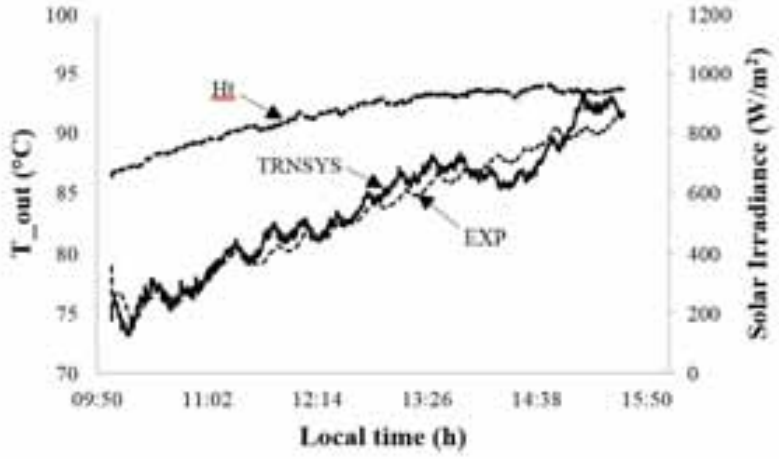

Figure 7. Comparison of outlet water temperature of the solar collector arrangement

The percentage mean absolute error (PMAE) in 10 days of testing performed for the outlet water temperature of the arrangement of flat plate solar collectors in °C is 2.75%, equivalent to ± 2.34°C. These values are within the range of uncertainty cited by Ayompe (Ayompe et. al., 2011). Due to this, the model can be considered in a good agreement with experimental data for the solar collector arrangement.

Validation of the whole solar adsorption cooling system model will be made in the near future when the coupling between the solar collector arrangement and the solar air conditioning system can be completed and experimental data can be obtained for different working conditions.

4. Conclusions

A designed solar cooling system is required to comfortably condition an office of 124 m^2 located in Jiutepec, Morelos, Mexico. The system consists in an 8 kW air conditioning system, 55.8 m^2 of flat plate solar

collectors and 2 m^3 of a thermal storage tank. The annual solar fraction reached with this system is 85%, in addition the proper functioning of equipment and comfort conditions in the offices are reached with this configuration according to the TRNSYS simulated data.

This work was carried out modeling in TRNSYS a solar air conditioning system in Mexico. The solar collector arrangement (4Sx6P) has been validated with experimental data obtained for 10 days. The percentage mean absolute error of these days of testing performed for the outlet water temperature of the arrangement of flat plate solar collectors in °C is 2.75%, equivalent to ± 2.34°C. Due to this, the model can be considered in a good agreement with experimental data for the solar collector arrangement.

Validation of the whole solar adsorption cooling system model will be made in the near future when the coupling between the solar collector arrangement and the solar air conditioning system can be completed and experimental data can be obtained for different working conditions.

The validation of this complete system provides the opportunity to have a reliable tool for the design, dimensioning and analysis of solar cooling systems in other Mexican regions with different weather and working conditions.

5. Acknowledgements

This work was partially supported by the following projects: FORDECYT No. 190603 “Estudio Sobre el Uso de la Energía Solar en Aplicaciones Residenciales, Industriales y Comerciales en Diferentes Estados del País”, project 12 “Desarrollo de captadores, sistemas solares y sistemas autocontenidos de baja temperatura con materiales novedosos para México” of CEMIE-Sol and SENER-CONACyT No. 117914 "Desarrollo de sistemas de aire acondicionado solar para zonas costeras de México". The authors also appreciate the facilities provided by Módulo Solar S.A de C.V. for the installation and experimentation of this system in its offices.

6. References

Ayompe L.M., Duffy A., McCormack S.J., Conlon M., 2011. Validated TRNSYS model for forced circulation solar water heating systems with flat plate and heat pipe evacuated tube collectors. Applied Thermal Engineering (2011); 31: 1536-1542.

Fanger P.O., 1972. Thermal comfort: Analysis and applications in environmental engineering. Mc Graw Hill, New York.

IEA SHC, 2010. Task 38 (solar air conditioning and refrigeration, 2006–2010). Consulted 08/May/2014. http://www.iea-shc-task38.org/.

Lugo-Ucán S., García-Valladares O., Rivera W., 2014. Refrigeración solar para alcanzar condiciones de confort en Jiutepec Morelos. Asociación Nacional de Energía Solar (2014). Querétaro, México.

METEONORM 6.1., 2009. Global Meteorological Database Software.

Módulo Solar, 2013. Ficha técnica de colector MS2.5. Consulted November 20th, 2014. http://www.modulosolar.com.mx/MAXOL/InformacionTecnica.php

TRNSYS, 2005. TRNSYS Manual (Version 16). U.S.A. Solar Energy Laboratory, University of Wisconsin-Madison. USA.

UNAM, 2013. Base de datos climatológicos por ciudad. Consulted January 17th, 2015. http://patox.ier.unam.mx:8080/OgvData/

7. Nomenclature and symbols

C	Calculated values
EXP	Experimental
η	Efficiency [-]
FrS	Solar fraction [%]
H	Monthly average daily horizontal irradiation [MJ/m^2 day]
M	Measured values
P	Parallel
PMAE	Percentage Mean Absolute Error [%]
PMV	Predicted Mean Vote index [-]
PPD	Predicted Percentage Dissatisfied [%]
Q	Heat energy [J]
RH	Relative humidity [%]
S	Series
T	Temperature [°C]
TMY	Typical Meteorological Year
TRNSYS	Transient Systems Simulation

Subscripts

a	Ambient
aux	Auxiliary
i	ith value
in	input
off	off
on	on
out	output
req	Required
set	Set point
t	Tilted

Conference Proceedings

Solar World Congress 2015
Daegu, Korea, 08 – 12 November 2015

Energy Consumption Estimation in Different Climates of a Solar Combisystem Combined with an Absorption Chiller

Amine Lazrak[1,2,3], Gilles Fraisse[2], Antoine Leconte[1], Bernard Souyri[2] and Philippe Papillon[1]

[1] INES/CEA, Le Bourget-du-Lac (France)

[2] LOCIE/CNRS, Le Bourget-du-Lac (France)

[3] ADEME, Angers (France)

Abstract

Currently there is no global approach to model then characterize solar thermal systems for building application. Results of the existing approaches are valid only for specific conditions (climate and thermal building properties). In a previous study a generic methodology to model solar combisystems (SCS) was developed. This methodology was applied to predict the energy consumption of two kinds of systems: SCS combined with a gas boiler and SCS combined with a heat pump. In the current paper, an extension of the methodology to SCS combined with an absorption chiller is presented. The methodology is based on the development of an artificial neural network (ANN) that models the dynamic of the system. The developed neural models were able to predict, with a good precision degree, the annual energy performance of the system in different climates based on a learning sequence of only 12 days. The satisfactory results emphasize the generic character of the methodology and show that it could be used, in the future, as an energy performance evaluation tool. Also, the proposed approach will be helpful in the context of energy performance guarantees.

Keywords: *Thermal systems, Absorption chiller, Performance estimation, Dynamic modelling, Artificial neural networks, System testing.*

Nomenclature

P_{dhw}	Heat flow rate supplied for the Domestic Hot Water (DHW)	(kW)
A	Solar collector area	(m²)
G	Global irradiance	(kW.m^{-2})
P_{sh}	Heat flow rate supplied for space heating	(kW)
P_{aux}	Power of the auxiliary system (electric back up system)	(kW)
P_{sc}	Cooling power	(kW)
TD	Time delay	
AF	Activation function	
F'	Collector efficiency factor	
$(\tau\alpha)_{en}$	Effective transmittance-absorptance product for direct solar radiation at normal incidence	
$K_{\theta d}$	Incidence angle modifier for diffuse radiation	
c_1	Linear heat loss coefficient	(W/m^{2}K)
c_2	Non-linear heat loss coefficient	(W/m^{2}K^2)
β	Collector inclination	(°)
b_0	Constant to calculate the incidence angle	

1. Introduction

Solar thermal systems combined with an auxiliary system such as a boiler, a heat pump or incorporating an absorption chiller, can play an important role in reducing energy consumption of buildings for space heating, cooling and domestic hot water production. In this sense, characterizing the energy performance of solar thermal systems is a crucial issue.

doi:10.18086/swc.2015.10.32 Available at http://proceedings.ises.org

Currently, the available methods are either based on several separate physical tests of the components of the system to be evaluated, which does not take into account the real interactions between them, or on physical models that can be complex and difficult to identify especially because today's systems are compact and prefabricated in the factory (Haller, et al., 2013), (Lazrak, Leconte, Chèze, Fraisse, Papillon, & Souyri, 2015), (Leconte, Achard, & Papillon, 2012). In the absence of a reliable method to estimate the solar thermal systems performance before their integration in the building, their market underwent major difficulties for its development (Eur'Observ'ER, 2013).

In this context it is essential to develop a generic methodology that can be applied to different types of systems which overcomes the difficulties encountered by current methods.

For this reason a generic methodology to model solar combisystems (SCS) was developed previously (Lazrak, Leconte, Chèze, Fraisse, Papillon, & Souyri, 2015), (Lazrak, et al., 2015). This methodology was applied to predict the energy consumption of two kinds of systems: SCS combined with a gas boiler and SCS combined with a heat pump.

In this paper is presented an extension of the developed methodology to SCS combined with an absorption chiller. This new methodology can be used then to characterize any system based only on a short cycle test in a semi-virtual test bench. Also, by means of this technique it will be possible to evaluate the system energy consumption that it will have when installed in the environment that it was chosen for.

2. Methodology

2.1. Overview of the proposed methodology

A more detailed description of the methodology developed could be found in (Lazrak, Leconte, Chèze, Fraisse, Papillon, & Souyri, 2015). It has been shown that the methodology developed is:

- Nonintrusive because there is no need to dismantle the system, to be tested, in order to apply the methodology.
- The method takes into account the whole system so all interactions between subsystems are modelled.
- The system procedure test is short.
- The method allows predicting the system performance for different climates.

These characteristics make the methodology relevant to overcome the weaknesses of the current methods. To show that it could be applied to several kinds of solar systems and thus investigate its generic character this method was applied to solar system combined with an absorption chiller.

The five steps to model and then to evaluate the performance of a system following the proposed approach are represented in Fig.1. Evaluating a system following the methodology developed consists on first testing the system to be characterized in a semi-virtual test bench during a short sequence of time, typically 12 days, and in a dynamic way. This short test is based on the SCSPT method developed at INES, the French solar national institute. Then, data harvested, serve to design a dynamic neural network model of the system (described in section 2.2.). Basically, the ANN learns the internal behavior of the tested system. The goal is to have a global model with good generalization ability such that it can evaluate the system energy consumption, over a year, even with unseen data. The model can then be used to estimate the system's annual performances for different conditions. As a consequence it is not required that the model reproduces faithfully the system behavior in an hourly or daily basis as long as it can estimate well enough the annual performance. The ANN developed is inherent to the system tested and thus cannot be used to replace other different system.

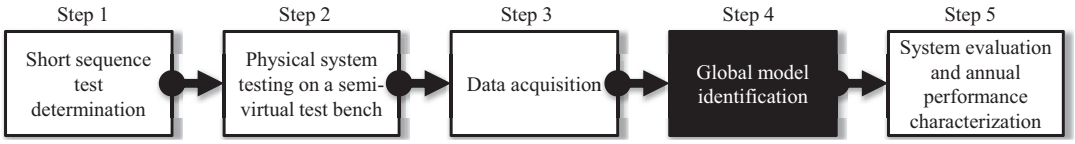

Fig. 1: Process stages of the proposed system's performance evaluation methodology

2.2. Black box modelling using ANN

Using Neural Networks seems to be the most powerful mathematic tool to solve this modelling problem. In fact, it was shown that neural networks are universal function approximators (Cybenko, 1989), so they can be used to approximate the system function. ANN were applied successfully to solve complex, non-linear, dynamic and multivariable problems. They tolerate errors, imprecisions and missing data as well (Kalogirou, 2001). Artificial neural networks were extensively used during the last decade.

The theory of ANN is clearly presented in (Dreyfus, 2005) and (Norgaard, Ravn, Poulsen, & Hansen, 2000). ANNs are parametric analytical functions whose concept takes inspiration from the human central nervous system. A neuron, the basic element of an ANN, can compute values z_l from a weighted summation of its inputs x_j. The summation coefficients ω_j^l are called synaptic weights. The subscript l denotes the neuron number. The neural operation is presented in (eq. 1). The function f_l is called the neural activation function (AF).

$$z_l = f_l\left(\sum_{j=1}^{K} \omega_j^l x_j\right) \qquad \text{(eq. 1)}$$

Inter-connected neurons constitute what is commonly called a neural network. There are several network architectures and each one is more suitable for a specific problem than others. The most common architecture for prediction and fitting problems is the class of multi-layer perceptron (MLP). An MLP is a feed-forward network built of neurons, arranged in layers. It has an input layer, one or more hidden layers and an output layer. In (fig. 2) a MLP, with E inputs, C neurons in the hidden layer and S outputs, is presented. The s^{th} output of the network can be obtained using (eq. 2).

$$y_s = f_s^S\left(\sum_{c=1}^{C} \omega_{c,s}^S f_c^C\left(\sum_{e=1}^{E} \omega_{e,c}^C u_e\right)\right) \qquad \text{(eq. 2)}$$

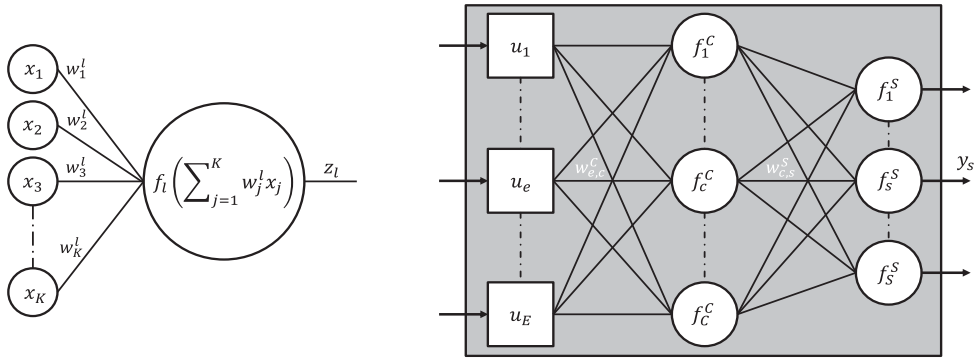

Fig. 2: Neuron formal representation (left), example of a neural network MLP with one hidden layer representation (right)

Neural network learning or training is the process of determination of an ensemble of weights so that the underlying function approximates the real system function. In fact, the objective of the training process is to minimize a cost function, with respect to weights, knowing a set of data. The short time of the system test, which is of 12 days, restricts the amount of available data for training. Therefore it is necessary to use a learning algorithm that can use a restricted data set without compromising the generalization ability of the model. For this reason it is relevant to use regularization method for the learning process. Typically, training aims to reduce the sum of squared errors see (eq. 3) with t_i the target data at the sequence time i and y_i the NN output at the same time. Regularization modifies the objective function by adding an additional term: the sum of squares of the network weights (eq. 4), q is the number of the neural network weights. By constraining the size of weights the training process produce an ANN with good generalization ability (MacKay, 1992). In fact, by keeping the weights small the ANN response will be smooth and so the over-

fitting is supposed to be prevented. In this study the objective function optimization is done using the Levenberg-Marquardt algorithm.

$$\text{sse} = \sum_{i=1}^{N} (t_i - y_i)^2 \qquad \text{(eq. 3)}$$

$$\text{ssw} = \sum_{i=1}^{q} {\omega_i}^2 \qquad \text{(eq. 4)}$$

Determination of the modelling input-output configuration is crucial to develop a generic methodology. Generally, solar thermal systems physical inputs and outputs differ from one to another. They depend on the energy sources used by the system and how this latter was designed by the manufacturer. However, energy systems can be represented in terms of power transformation between the renewable energy source, the loads and auxiliary system. This is why a compact configuration with four inputs: P_{dhw}, $A.G$, P_{sh}, P_{sc} and one output P_{aux} was selected. This open configuration, not particular to a specific system is relevant to develop a global and generic methodology. In (Lazrak, Leconte, Fraisse, Papillon, & Souyri, 2014) results concerning a solar combisystem modeling show that a dynamic ANN model (NARX model) is more efficient than a static one. The latter does not learn the dynamic of the solar system especially due to the heat storage component, for this reason dynamic neural network (fig. 3) was used.

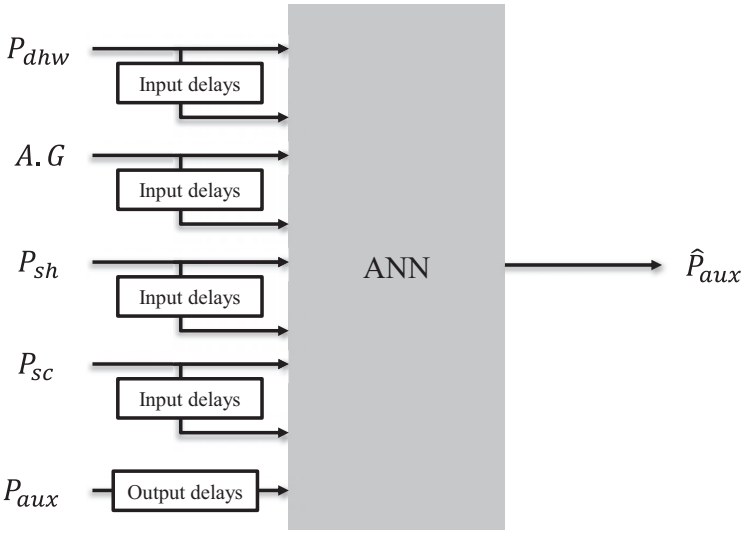

Fig. 3: NARX modelling configuration (open loop architecture), the hat "^" symbol indicates that the variable is predicted and not actual

Usually, regularization does not necessary guarantee the production of efficient networks. This is why it is essential to make some data preprocessing before training. By normalizing the input and target data vectors, the neural network training will be easier, faster and all vectors will be equally taken into account during the learning process. Equation (eq. 5) will be used to pretreat the training data in order to fall between a and b, x represent a vector of raw data through time.

$$Normalized\ variable = \frac{\mathrm{x} - x_{min}}{x_{max} - x_{min}}(b - a) + a \qquad \text{(eq. 5)}$$

The modelling time step is equal to 30 min. It was noted that the on-off cycles of the auxiliary system generate discontinuities in data. To smooth the collected data, a moving average of five time steps was applied to them.

2.3. Model Selection

During the training process, several networks are created with different number of neurons in the hidden layer, re-initializations (in order to ovoid local minima), output AF (tanh and linear functions), time delays (TD) and normalization intervals. The Bayesian information criterion (BIC) was chosen to select the most relevant network (Dreyfus, 2005), (Qia & Zhangb, 2001). It is defined by the following:

$$BIC = \ln MSE + q\frac{\ln N}{N} \qquad \text{(eq. 6)}$$

where q is the number of model weights and N the size of the learning data (number of samples).

The mean squared errors MSE (eq. 6) in BIC is calculated using the training data and in a closed loop architecture (Fig. 4) in which inputs and the initial values of the outputs, are used to predict the outputs (long-term model simulation) at future time steps.

Because the true output is available while the network is being trained, it is efficient to use it instead of feeding back the estimated output. The resulting architecture is called open loop architecture (Figs. 3 and 4). The advantage of this architecture (used only during training) is that the input to the ANN is more accurate.

The BIC selects ANNs (that have a lower BIC value) with a small number of parameters (synaptic weights). This is advantageous because ANNs with few parameters have a better generalization power, as stated in (Khosravi, Nahavandi, Creighton, & Saeid, 2013).

The whole training and selection process was developed in MATLAB R2012b.

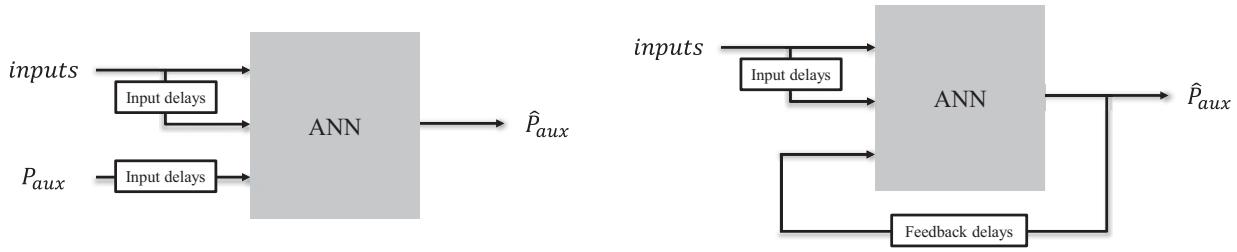

Fig. 4: Open loop architecture (left) and closed loop architecture (right)

In the following, the results of two different models for each system are presented:

- ANN1 is the model that is selected as the best model after the comparison of its performance with all the ANN models created in different boundary conditions (climate, building type).
- ANN2 is the model that would be selected based only on the BIC criterion.

2.4. The solar system evaluated

The system considered is an SCS combined with an absorption chiller. This system has been developed and designed within a national project. The goal of the project was to develop a system architecture that meets the following specifications:

- System intended for certain types of buildings of the Maghreb countries, southern Europe and the United States (Tab. 1).
- Systems with a limited number of hydraulic components (valves, circulation pumps and heat exchangers) to limit the risk of failure.
- Reduced cost
- System with good performance

The system is represented in (Fig. 5). It allows both solar discharge through the cooling tower and direct solar heating (without passing through the absorption chiller), if necessary with an electric online backup. This architecture uses only three-way valves to switch between different operating modes. This architecture uses specific units to prevent the risk of frost.

The physical characteristics of the system used to develop its TRNSYS model are given in (Tab. 2).

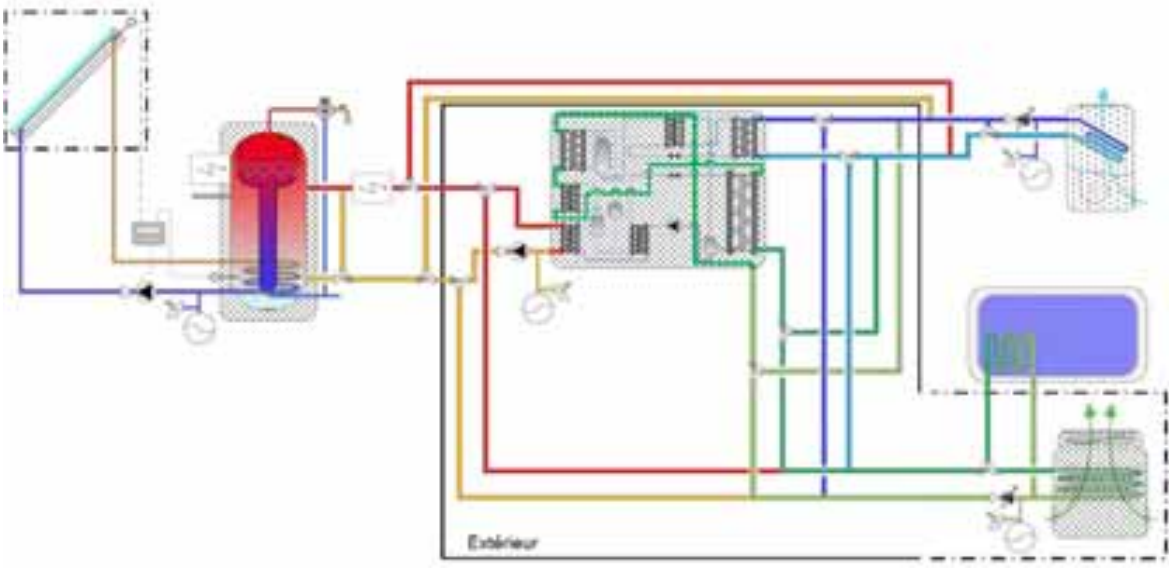

Fig. 5: Solar system combined with an absorption chiller hydraulic scheme

Training data are represented in (Fig. 6). They are the result of the system model simulation, using the Aix-En-Provence climate and a representative building of Maghreb countries, according to the SCSPT method (only 12 days).

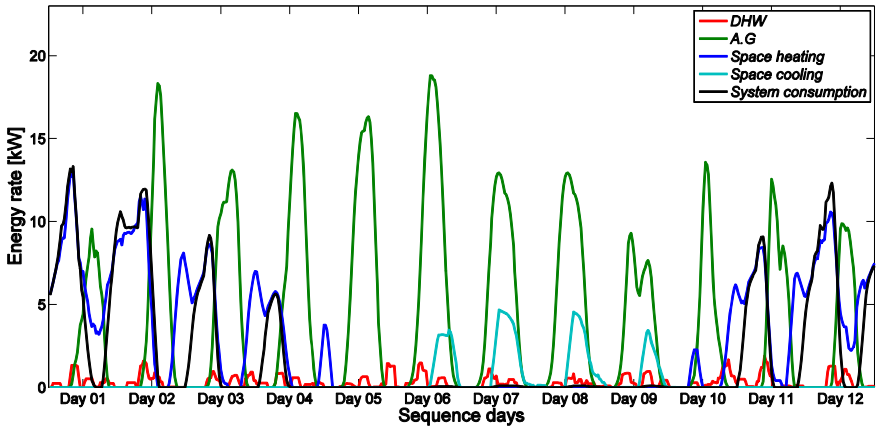

Fig. 6: Training data (SCSPT simulation results)

Tab. 1: Some characteristics of the buildings used as the boundary condition for each region

Region	Europe	USA	Maghreb countries
Area	140m²	300m²	300m²
Reference energy consumption	130 kWh/m² per year in Rennes	130 kWh/m² per year in Washington	60.7 kWh/m² per year in Marrakech
Materials of construction	Brick	Wood frame	Brick

Tab. 2: Physical characteristics of the system used in its TRNSYS model

Remarks	TRNSYS Type	Parameter values
Absorption chiller		
This type is not a standard one. It was developed based on Ziegler works (Ziegler, Hellmann, & Schweigler, 1999)	Type 881	NH_3/H_2O absorption chiller Nominal power: 7 kW.
Electric auxiliary		
Inside the storage tank	Equation bloc	Nominal power: 9 kW
Electric online backup	Equation bloc	Nominal power: 24 kW.
Dry cooler		
Heat exchanger + ventilator	Type 112 and Type 91	Nominal flow rate: 6000kg/h, Ventilator consumption: 190W
Storage		
The heat exchanger for DHW preparation is inside the storage tank	Type 340	1000l of volume 2 m height 10 cm of insulation Coefficient of lateral losses 6.76 W / K and for the upper and lower portions a value of 0.62 W / K
Solar collector		
Developed by (Haller, 2012)	Type 832	$F'(\tau\alpha)_{en}$=0.793 $K_{\theta d}$=0.9 c_1=0,749 (W/m²K) c_2=0,005 (W/m²K²) β=45° b_0=0.18 Collector area = 23 m²

3. Results and discussion

Several annual simulations were done in different boundary conditions (climates and the corresponding building type) using the TRNSYS model. The calculated energy consumptions were used to evaluate the ANN predictions (Fig. 7). The estimation results are represented in (Fig. 8).

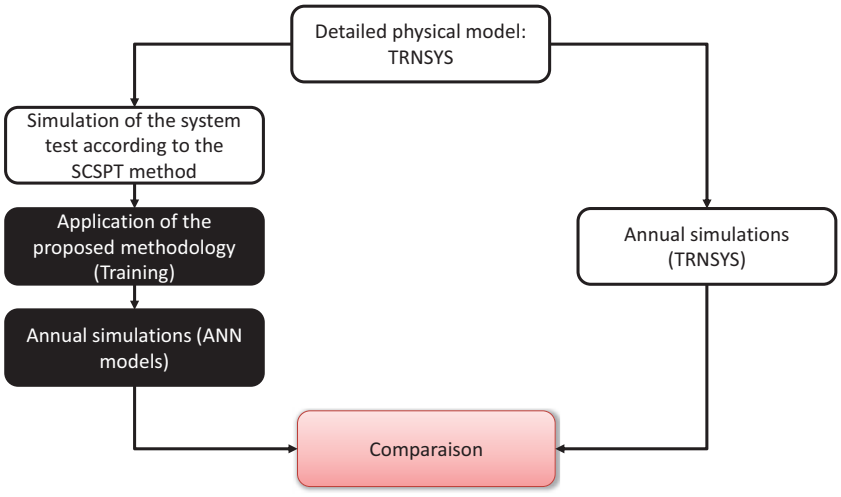

Fig. 7: Validation protocol based on the detailed TRNSYS model

Tab. 3: Characteristics of the selected ANN models

Model	Normalization interval	Number of neurons	Output TD	Input TD	AF	BIC value
ANN1	±1,0	8	3	2	tanh	-0.9946
ANN2	±1,0	12	2	1	linear	-2.2815

Each bar in the graphs represents the annual energy consumption per square meter of each system, estimated or calculated by the corresponding model in one specific environment (boundary conditions): two with ANN and one using the reference model.

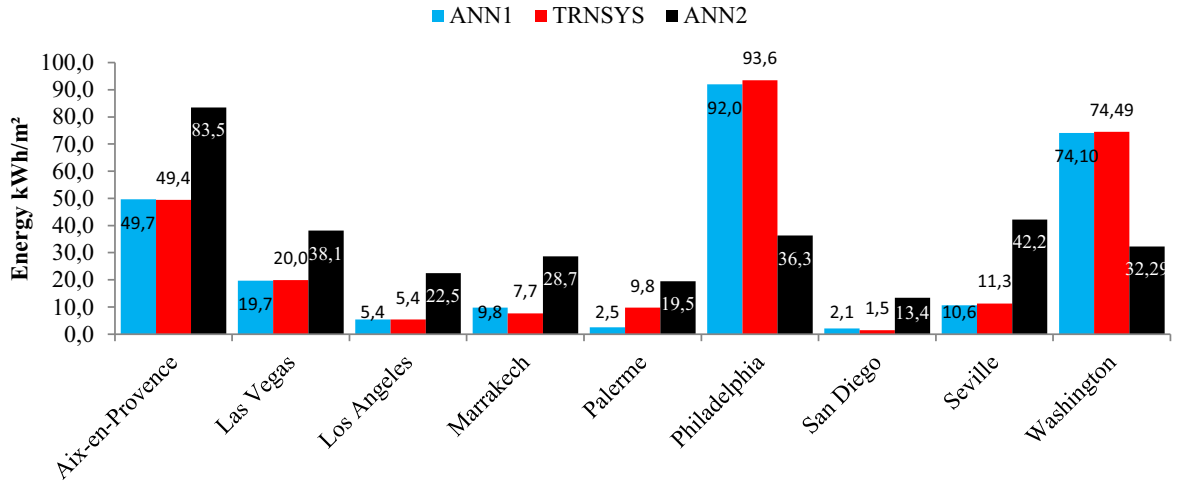

Fig. 8: Comparison of the ANN predictions and the TRNSYS calculations for annual energy consumption

Predictions of the best model ANN1 (Tab. 3) among all those created during the process of the methodology are very accurate. The errors are very low (below 5%) except for certain climates with low heat demand: Marrakech, Palermo and San Diego. However, the absolute differences are small (maximum of 7.3 kWh / m², reached in Palermo). The ANN difficulties for these conditions are due to the large differences between the learning conditions and these three climates.

ANN2 model predictions results, selected based on the BIC, reveal the mediocrity of some neural models as the statistical criterion may select. However, this model is easily detectable from the ones that must be discarded. In fact, according to the ANN2 model the annual consumption of the system in Aix-En-Provence is comparable or even greater than its consumption in Philadelphia or Washington. But this is impossible. Another ANN model that respects the trends of energy consumption depending on the climate, only among the selected models according to each configuration (normalization interval, delays and FA), was selected (Tab. 4). The results of the corresponding estimates are shown in (Fig. 9). Estimates of consumption of the system by the new neural model have greatly improved for all climates.

Tab. 4: Characteristics of the selected ANN model (2nd selection)

Model	Normalization interval	Number of neurons	Output TD	Input TD	AF	BIC value
ANN2	±0,2	7	3	2	tanh	-1.0226

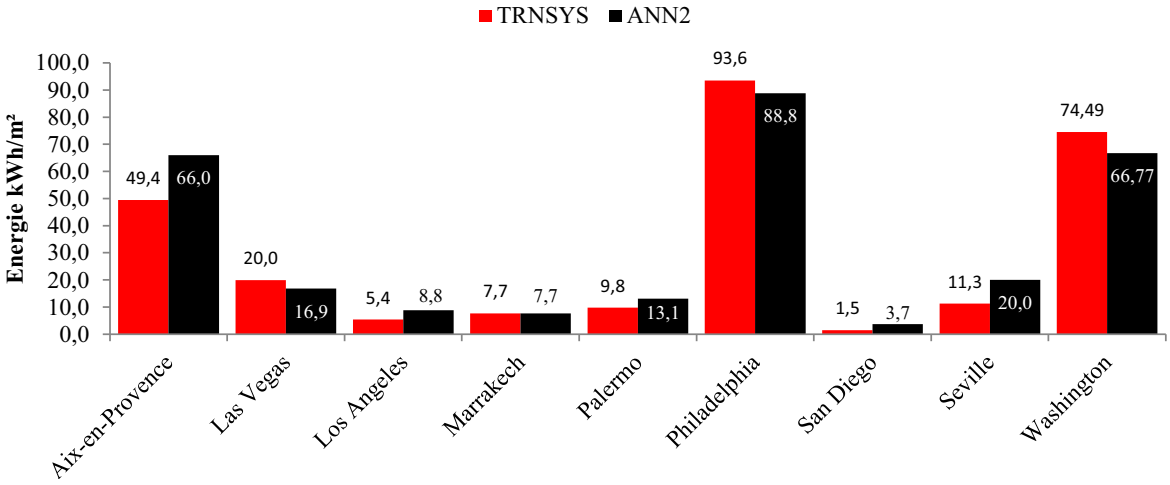

Fig. 9: Comparison of the ANN predictions and the TRNSYS calculations for annual energy consumption. Case of the ANN that has the characteristics presented in (Tab. 4)

In (Fig. 10) is given an example of the power consumption of the system in function of time during the cooling season (case of Philadelphia and ANN2). The goal of the method is to estimate the overall energy consumption and not to reproduce the exact dynamic of the system (however this is needed in the case of a control system). On the whole the model correctly follows the true evolution of the power; this shows that the differences observed in the case of certain climates occur during the heating season (winter). Creating a model per period (heating and cooling) would have probably given better results. This conclusion will be taken into account for future work.

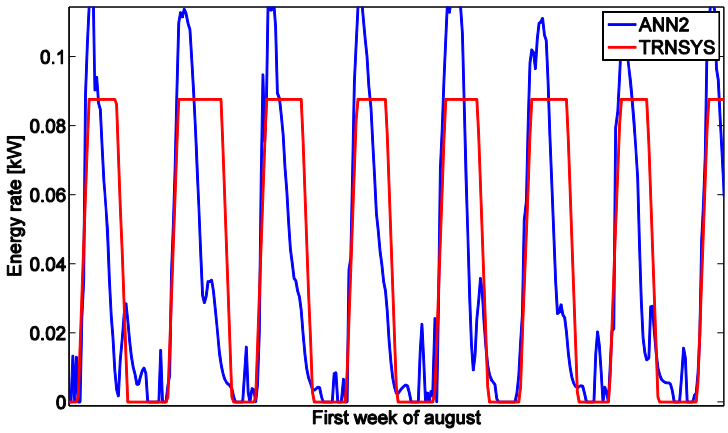

Fig. 10: ANN and TRNSYS outputs, case of the Philadelphia climate

4. Conclusion

The presented results show that the methodology developed extension to new systems such as SCS combined with absorption chillers is possible. In fact the best ANN model was able to predict with a satisfactory degree of precision, the annual energy consumption of the evaluated system, in different conditions, based on a learning sequence lasting only 12 days. In fact, the annual energy prediction errors were less than 5% in most cases. The methodology limitations appear in extreme boundary conditions compared to those used during the ANN training process. Results show also that the statistical criterion BIC is not able to select the best ANN model.

5. Acknowledgment

This work has been supported and funded by the French Agency for Environment and Energy Management (ADEME) and the National Institute of Nuclear Sciences and Techniques (INSTN).

The authors would like to greatly thank the Air Eau Environnement association which financially supported the participation to this congress.

6. References

Cybenko, G. (1989). Approximation by Superpositions of a Sigmoidal Function. *Math. Control Signals Systems, 2*, 303-314.

Dreyfus, G. (2005). *Neural networks methodology and applications.* Springer.

Eur'Observ'ER. (2013, Mai). Solar Thermal and Concentrated Solar Power Barometer. *Systèmes Solaires*.

Haller, M., Haberl, R., Persson, T., Bales, C., Kovacs, P., Chèze, D., et al. (2013). Dynamic whole system testing of combined renewable heating systems – The current state of the art. *Energy and Buildings, 66*, 667-677.

Haller, M. (2012). Dynamic Collector Model by Bengt Perers" Updated Input-Output Reference. Institut für Solartechnik, Rapperswil (Switzerland).

Kalogirou, S. (2001). Artificial neural networks in renewable in renewable energy systems application: a review. *Renewable and Sustainable Energy Reviews, 5*, 373-401.

Khosravi, A., Nahavandi, Creighton, D., & Saeid. (2013). Quantifying uncertainties of neural network-based electricity price forecasts. *Applied Energy, 112*, 120–129.

Lazrak, A., Boudehenn, F., Bonnot, S., Leconte, A., Fraisse, G., Papillon, P., et al. (2015). Development of a dynamic artificial neural network model of an absorption chiller and its experimental validation. *Renewable Energy*.

Lazrak, A., Leconte, A., Chèze, D., Fraisse, G., Papillon, P., & Souyri, B. (2015). Numerical and experimental results of a novel and generic methodology for energy performance evaluation of thermal systems using renewable energies. *Applied Energy, 158*, 142–156.

Lazrak, A., Leconte, A., Fraisse, G., Papillon, p., & Souyri, B. (2014, mai 21-22). Vers une méthodologie générique de modélisation par réseaux de neurons des systèmes énergétiques dans le bâtiment. *IBPSA*, 8. Arras, France.

Leconte, A., Achard, G., & Papillon, P. (2012). Global approach test improvement using a neural network model identification to characterise solar combisystem performances. *Solar Energy, 86*, 2001-2016.

MacKay, D. (1992). Bayesian interpolation. *Neural Computation, 4*(3), 415-447.

Norgaard, M., Ravn, O., Poulsen, N., & Hansen, L. (2000). *Neural networks for modelling and control of dynamic systems.* Springer.

Qia, M., & Zhangb, G. P. (2001). An investigation of model selection criteria for neural network time series forecasting. *European Journal of Operational Research, 132*(3), 666–680.

Ziegler, F., Hellmann, H.-M., & Schweigler, C. (1999). An approximative method for modeling the operating characteristics of advanced absorption chillers. *20th Int. congress Refrigeration.* Sydney.

Conference Proceedings

Solar World Congress 2015
Daegu, Korea, 08 – 12 November 2015

The Night Cooling Effect on a C-PVT Solar Collector

Franz Mantei[1], Mafalda Henriques[2], João Gomes[3,4],Olle Olsson[3,4] Björn Karlsson[4]

[1] Technische Universität, Berlin (Germany)

[2] University of Castelo Branco (Portugal)

[1,2,3,4] Gävle University (Sweden)

[1,2,3] Solarus Sunpower Sweden AB, Gävle (Sweden)

Abstract

Night cooling consists in running a fluid through a solar panel during the night in order to reduce the fluid temperature which can be used for cooling applications. Radiative heat losses can allow the fluid to reach temperatures below ambient while conduction and convection works to equalize the collector with the ambient temperature.

This paper analyzes the possibility of using an asymmetric concentrating photovoltaic thermal solar collector (C-PVT) for cooling applications during the night by losing heat through convection, conduction and irradiation. The cooling performance of the C-PVT collector has been measured during the night at different inlet temperatures in the interval of 13 to 38°C which corresponded to a ΔT (between the collector average and the ambient) from 6 to 28°C.

The performance of the tested C-PVT collector has been measured at different inlet temperatures in an interval of 13 to 38°C. During all performed measurements, the radiation losses did not drive the collector temperature below ambient temperature. With high ΔT (between the inlet and the ambient) of 30°C, a 1,85°C temperature decrease in the fluid was obtained. For ΔT of 14°C, the temperature decrease was only 0,88°C. The measurements showed a night U-value for the Solarus C-PVT of 4,2 W/m^{2}K This correlates well with previous papers showing measurements taken during the day.

Heat losses seem to be dominated by convection and conduction due to the existence of the glass in the collector. Despite this, a measurable relation between heat losses and cloudiness factor exists. This shows that the irradiance losses are not negligible.

Only very specific applications can be suited for night cooling with this collector design, since it is not so common to have applications that require low grade cooling during the night time or justify storing this energy. However, if the C-PVT design was made without a glass cover, the results could potentially be very different for locations with many clear nights.

Keywords: *Concentrating PVT, CPC-collector, Asymmetric Collector, Collector Testing, Night Cooling*

1. Introduction

All objects are exposed to energy flows at all times. Some flows increase the energy level of the object while others decrease and are called energy losses. Energy losses of thermal energy are called heat losses and they occur by three different processes: Conduction, Convection and Irradiation.

Any two materials that are in contact and have different temperatures transfer heat between themselves in the direction of the material with a lowest temperature. This process is called heat conduction and can be calculated with the law of Fourier:

$$\dot{q} = -k\frac{\delta T}{\delta x} \qquad \text{(equation 1)}$$

where k is the heat conductivity and $\frac{\delta T}{\delta x}$ the temperature gradient. In a flowing fluid, it also occurs an energy

doi:10.18086/swc.2015.10.33 Available at http://proceedings.ises.org

transport which depends on the velocity and the level of turbulence, thus on macroscopic movements. This transport is called heat convection and is calculated together with the heat conduction:

$$\dot{q} = \alpha \cdot (T_1 - T_2) \qquad \text{(equation 2)}$$

where α is the heat transfer coefficient which comprises fluid parameters, flow parameters and geometric parameters, and $(T_1 - T_2)$ is the temperature difference between the interacting systems.

The heat radiation denotes the electromagnetic waves which a body emits to its environment on the basis of its temperature. The maximum radiation density of a body is calculated by:

$$\dot{e}_S = \sigma \cdot T^4 \qquad \text{(equation 3)}$$

and is emitted by a so called blackbody (VDI, 2013).

1.1. The Basics behind Night Cooling

During the day, the losses described above are generally lower than the amount of incident solar radiation on the collector and, thus the collector gains energy. However, during the night, since the solar radiation is zero, the energy intake is smaller than the heat losses, which leads to a decrease of the collector temperature. This effect is called night cooling.

For being able to cool during the night two main factors are considered in this paper. One is the cooling on the basis of convectional and conductional heat losses while the other is called night sky radiative cooling.

The heat losses caused by night sky radiative cooling are done by a radiative process which can be separated in two sub processes: One is the radiation from the earth to the clear sky. This can be assumed as a black body radiation whereby the temperature of the black body is giving the surface temperature of the earth or in this case the collector. The other process is the atmospheric radiation caused by water vapor, carbon dioxide and ozone (Armenta-Déu et al., 2003).

Heat losses caused by convection and conduction will cool down the fluid in the collector to no more than the ambient temperature. On the other hand, radiative cooling is able to decrease the temperature level of the fluid below the ambient temperature, if the surface is an adequate emitter. In this way, the fluid gains heat during conductional and convectional heat exchanges (Dobson, 2005).

One final note should be made comparing PVT to standard thermal collectors. PVT panels can go below ambient temperature. This is considerably more difficult in thermal. This is because the PV cells emit much more radiation than the selective surface. Basically, a worse performance during the day by PVT collectors, leads to a better performance in cooling during the night. It is not reasonable to expect to have a panel that performs well in gaining heat during the day and, at the same time, also performs well at loosing heat during the night.

1.2. Possible Applications for Night Cooling

Since night cooling can be able to provide fluid temperatures below the ambient temperature, it can be used to decrease the temperature of materials below the ambient temperature. Three main constrains are limiting the applicability of night cooling: The first constrain is relatively small amount of cooling energy. The second constrain is the small temperature difference to the environment which significantly limit its range of applications. The third constrain is that in cloudy nights, the cooling energy gained will be at best at ambient temperature.

According to Armenta-Déu et al. (2003), possible applications for night cooling are production of fresh water, freezing and food preserving as well as building air-conditioning and energy generation. All of these applications sharing the need of cooling energy, the differences are the temperature ranges and the amount of energy required.

One way to make a night cooling system can be to, during the night, use a normal heating system but this time with the goal of losing heat. Therefore, the fluid would flow through the collector, cool down and gain

energy while passing the heat exchanger. The heat exchanger brings the low temperature energy flow to a thermal storage which will decrease its temperature level during the operation time. The lower the temperature level reached, the more possible applications can be suitable. However, the temperature level is depending on the heat losses of the module, thus if the operating temperature drops under the ambient temperature (due to night sky radiative cooling), the thermal storage could reach a rather low temperature levels.

Another possible application is to use the cooling energy for phase change of PCM (phase change materials). These materials can be used in buildings for cooling during the day. They can be mounted on the ceiling to take the heat during the day to change its phase and thereby cool down the room temperature. During the night with heat losses to the environment and without energy gain from the sun the room temperature decreases and the PCM starts to change back its phase to its previous phase. The cooling energy from the collectors could be used to cool down a bigger area of PCM increasing the potential benefit from this application.

A practical implementation of the above described could be to run the thermal cycle of the collector in the standard way and to attach a heat exchanger. The second thermal cycle could be gaseous and directly blown to the consumer, in this case, the PCM. It could also be a liquid which circulates to the PCM in a pipe system. Additionally, other applications which need space cooling, like rooms for computer servers, show potential (Armenta-Déu et al., 2003).

2. Collector Description and Method

This chapter describes the used testing equipment and system as well as the asymmetric C-PVT collector.

2.1. The Test Setup

The Solarus C-PVT collector has been placed on the rooftop of the university in Gävle, Sweden, and faced to the south with an angle of 60 degrees. The collector total surface is 2.4 m^2 divided between two throughs each with one receiver. Each receiver holds strings of cells on both sides. This strings are either 19-19-19-19 or 6-32-32-6 cell as detailed in Fig. 1 and Figure 3. The collector stand holds a Kipp & Zonen solar radiation sensor at the same tilt as the collector.

Fig. 1: Solarus C-PVT collector and solar radiation sensor

Fig. 2: Thermal system

The thermal system features two loops. In the primary loop, a fluid (water), is passed through the collectors and then to a heat exchanger. This loop is separated in two sub loops, one for each collector through. Each sub-loop has its own Kastrup flowmeter but only one pump is required to run the two sub-loops. An expansion valve is placed in the circuit for safety as shown in figure 2. At the entry and exit of the collector, four PT100 temperature sensors are installed, as show in figure 1. The primary loop also features a small tank for mixing the water and a heater which allows regulating the inlet temperature. This heater can be used

in conjunction with the secondary loop. The secondary loop is merely grid water flowing through the heat exchanger in order to reach lower inlet temperatures. Both the heater and the grid water are designed in order to keep the inlet temperature as steady as possible. A picture of the thermal system is shown in figure 2. The pumps in the thermal system in figure 2 circulate the water to the collector (shown in figure 1) and back.

2.2. Solarus C-PVT collector

The Solarus C-PVT collector design is called Maximum Reflector Concentration (*MaReCo*) and belongs to a family of stationary reflectors patented by the Swedish company Solarus. The reflector has a parabolic and circular shape and is used to concentrate the solar radiation. The reflector is made of anodized aluminum with a total solar reflectance ρ_{total} of 95% (measured according to norm ASTM891-87). A reddish brown silicone is used for electrical insulation between the mono-crystalline PV cell and the receiver core on both the upper and lower side (Gomes et al., 2013).

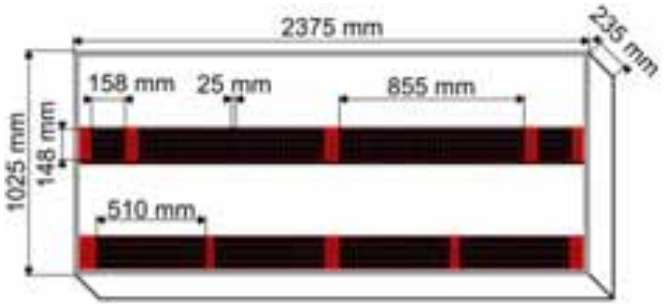

Figure 3: Test module dimensions

The module contains a glazed protection which is made of low iron tempered glass with a solar transmittance τ_{glas} of 95%, measured according to the norm ISO9050 (Giovinazzo et al., 2014) and a supporting structure manufactured out of plastic and metal (Gomes et al., 2013). The efficiency for direct light η_{direct} of the collector reaches 70%, while the efficiency for diffuse light $\eta_{diffuse}$ is 50.8%. Furthermore, the linear loss coefficient a_1 is 4.484 W/(m^{2}K) and the secondary loss coefficient a_2 is 0.0034 W/(m^{2}K) (Gomes et al., 2013).

3. Results and Discussion

For testing the performance of the Solarus C-PVT collector, measurement values from 18 nights between the 5th of September and the 2nd of November of 2014 have been analyzed. Table 1 comprises the night with the maximum (05.09. – 06.09.), average (09.09. – 10.09.) and minimum (28.10. – 29.10.) energy gain, as well as the results of a night in which an electrical heater provided a steady inlet temperature of 40°C (09.10. – 10.10.). The night time period is defined to be between 10PM and 05AM. Appendix 2 contains a wider collection of the measured night.

The following rows of the table show the cooling energy obtained, E_{cold}, in [kWh], the specific heat removal rate $\dot{e}_{cold} = \frac{\dot{E}_{average}}{A}$ in [W/m^2] (with the average energy gain during the night $\dot{E}_{average}$ and the surface area of the module A), the outlet temperature T_{out} in [°C], the ambient temperature T_{amb} [°C], the temperature difference between outlet and the inlet of the collector ΔT [°C], the temperature difference between collector average and ambient $T_{coll} - T_{amb}$ [°C], the cloudiness factor in [%] and the wind velocity v_{wind} [m/s]. The data for cloudiness and the wind velocity have been obtained from the database of the World Weather Website, which contains values for every third hour which have been taken for the time period between 10PM and 05AM and were averaged.

The measurement results show that the circulating water through the collector during the night can lose up to 2 kWh of thermal energy with an average power of more than 60 $\frac{W}{m^2}$. However these values are highly dependent on a number of conditions being met.

Table 1: Results night cooling measurement data

Night [22:00 – 05:00]	E_{cold} [kWh]	$\dot{e}_{cold}$ [W/m²]	T_{out} [°C]	T_{amb} [°C]	ΔT [°C]	$T_{coll} - T_{amb}$ [°K]	Cloudiness [%]	v_{wind} [m/s]
05.09. - 06.09.	-1,08	-63,75	23,0	10,2	-0,88	13,2	5,3	2,1
09.09. - 10.09.	-0,72	-42,23	18,7	8,6	-0,58	10,5	40,7	1,8
09.10. - 10.10.	-2,0	-117,34	35,8	8,7	-1,85	28,1	88,7	1,8
28.10. - 29.10.	-0,44	-25,79	18,6	12,74	-0,37	6,0	54,3	6,7

With a decrease in temperature of less than 1°C few applications are feasible. However, the measurement system is not made for storing the water, thus the water has been cooled down in every loop to about the same temperature.

Table 1 shows that one of the main factors in the night cooling effect of the Solarus collector is the difference between inlet and ambient temperature, as show in table 1. As expected, the larger this difference, the higher the cooling power gained during that night. This is show clearly in figure 4.

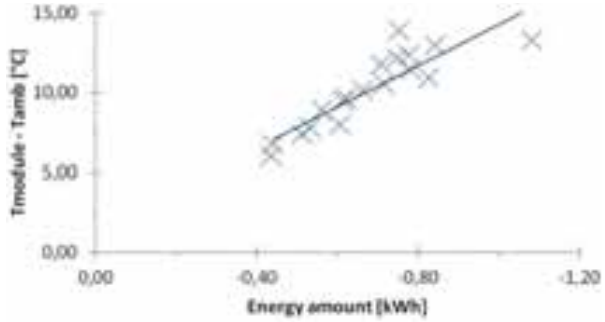

Figure 4: Cooling Energy Collected vs ΔT (Average Collector Temperature – Ambient Temperature)

During a clear night, the exchange of radiation between the collector and the sky is cooling down the collector. This way, clear nights are expected to increase heat losses. For some collector designs, this effect can be so strong that allows the collector to reach temperatures below ambient.

The measurement results listed in Table 2 in appendix can be visualized in Figure . These results show an increase in the collector heat losses when the cloudiness level is reduced. Consequently, it is not just the impact of conductional and convectional heat losses which accounts for the decrease in the fluid temperature.

The cloudiness was expected to correlate to the ambient temperature but our study in Figure **Error! Reference source not found.** did not show a clear dependency between ambient temperature and cloudiness.

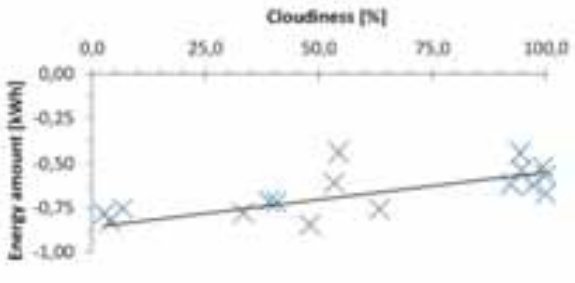

Figure 5: Impact of cloudiness on heat losses

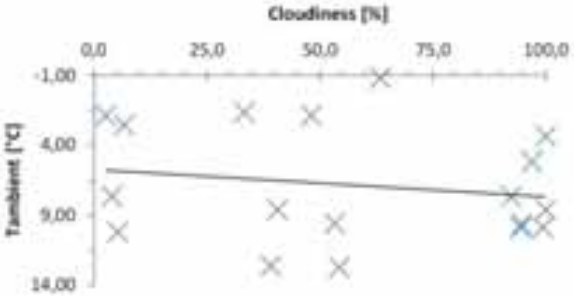

Figure 6: Impact of cloudiness on ambient temperature

In figure 7, we analyze the dependency between the cooling amount gained and the wind velocity. An

increase in wind velocity is expected to directly lead to an increase in convective heat losses. However, our measurement results shown that the heat losses are decreasing with an increasing wind velocity. This is result is an error that may be a result of the fact that the wind measurements were not done exactly in the same location where the collector night cooling power was measured. Nevertheless, these results suggest that the convectional heat losses have a lower impact on the Solarus C-PVT collector than the losses caused by conduction and radiation or, in other words, the effects of the wind velocity is less significant that other factors.

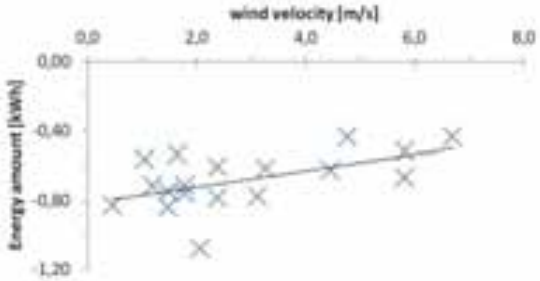

Figure 7: Impact of wind velocity on heat losses

For calculating the amount of cooling energy caused by night radiative cooling several equations are introduced for the sky temperature as well as the sky emissivity (Eicker et Dalibard, 2011). Most of these equations require temperature and pressure parameters which haven´t been measured. Two equations are just depending on the ambient temperature but Eicker et Dalibard (2011) show that the achievable results are fitting inaccurately with the measurement values and are thus not presented.

On the other hand, heat losses caused by conduction and convection can be calculated and subtracted from the entire amount of cooling energy. This method requires accurate values for the wind velocity. Previous consideration values for the wind velocity have been taken from a weather website, which is accurate enough for general statements but not for an accurate calculation of convectional heat losses.

Fig. shows the impact of cloudiness on the obtained cooling power per square meter, as well as the temperature difference between the module average and the ambient. For this graph, we have defined low cloudiness has being smaller than 7%, medium cloudiness between 40% and 60% and high cloudiness bigger than 90%. All measurements in this figure are done on an interval of the temperature difference between 7.5°C and 12.5°C where a more or less linear dependency can be seen for the impact of cloudiness. Furthermore, since many points overlap on the graph, an average of the three points (low, medium and high cloudiness) is also shown in the figure. These three points clearly show an increasing temperature difference with a decreasing level of cloudiness.

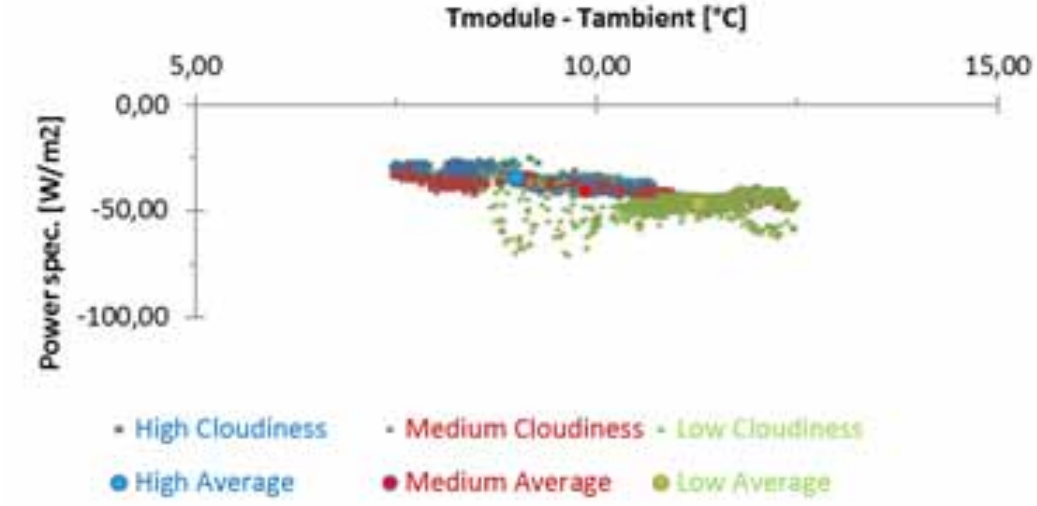

Fig. 8: Impact of cloudiness on power and temperature difference

Figure 9 shows the collector specific power loss during the night. The points measured at higher temperatures difference (inlet=40°C) display a large spread due to the fact that the available thermal test system was not able provide a sufficiently stable temperature. This factor was combined with a relatively low thermal mass of the receiver. Despite this equipment issue, it is still fair to say that the collector night U-value is close to 4.2 W/m^{2}K since there is an acceptable R^2. The U value is given by the slope of the figure 9.

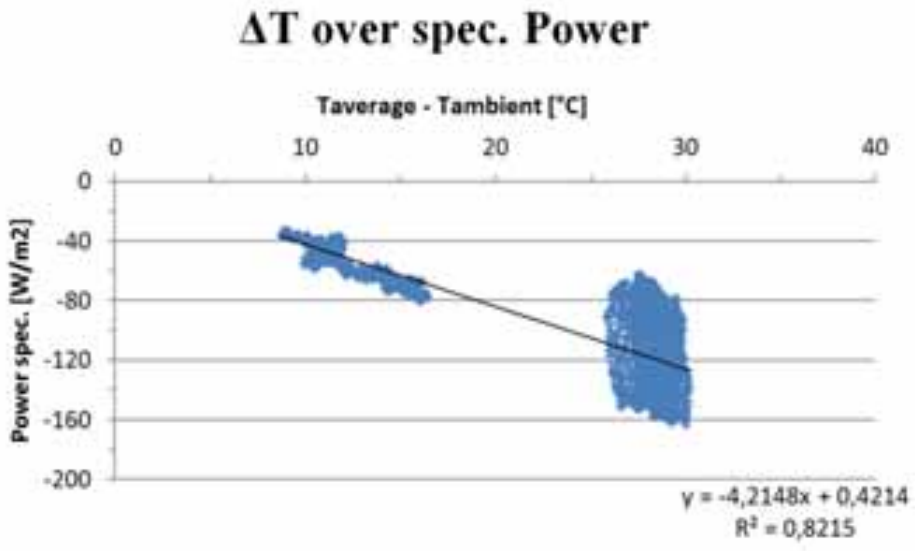

Fig. 9: Specific Power vs ΔT (Tcollector – Tambient)

Table 3 shows the result of annual simulations during the day and compares with the results of the night measurement results. It is important to note that the night cooling results are an extrapolation from an average of the nights (at 6 or 10 C above ambient temperature) to an annual output. The daily simulations were created using the Solarus simulation software. The cooling power obtained is not negligible but the issue remains how to use cooling power above ambient temperature.

Additionally, a comparison between the energy spent in pumping and the cooling gained should be performed.

Table 3: Comparison of annual output of the C-PVT in Stockholm.
Outputs in kWh/m2/day and the temperatures in °C. Tmed is the collector average temperature.

	During the Day			During the Night	
Location: Stockholm	**Tmed-Tamb**	**Heating**	**Electrical**	**Cooling**	**Tmed-Tamb**
Extracting heat at an average of 30C above Ambient	**30**	**1.06**	**0.22**	**0.20**	**6**
Extracting heat at an average of 70C above Ambient	**70**	**0.38**	**0.16**	**0.33**	**10**

4. Conclusion

The performance of the tested C-PVT collector has been measured at different inlet temperatures in an interval of 13 to 38°C.

The factor with the highest impact in the night cooling effect of the Solarus collector is the difference

between inlet and ambient temperature, as show in table 1 and 2 as well as figure 4. This implies that only very specific applications can be performed since it is not so common to have applications that require low grade cooling during the night time or justify storing this energy.

During all performed measurements, the radiation losses did not drive the collector temperature below ambient temperature. In nights, when the heater was not used to keep the inlet temperature steady, the collector temperature could be decreased by a maximum of 14°C during the whole night.

In some night, the heater was used to keep the inlet temperature steady, this leads to higher cooling energy gains being registered over the night, since we are losing energy that is provided by the heater. With high ΔT between the inlet and the ambient, as is the extreme case of a ΔT of 30°C, a 1,85°C temperature decrease in the fluid was obtained and recorded throughout the night. However, for ΔT of 14°C, the temperature decrease was only 0,88°C.

Still, the relatively low impact of cloudiness shown in figure 5 and 8 indicates that the convection and conduction heat losses are more important than the radiation heat loss for this collector design which is reasonable since the glass cover should block most of the IR radiation. Despite the dominance of conduction and convection losses, there is still a clear correlation between heat losses and cloudiness which shows that heat losses due to irradiance are occurring and are measurable.

Furthermore Figure and Figure point out that the impact of wind velocity on the cooling energy, as well as the impact of cloudiness on the ambient temperature seems smaller than expected which leads us to conclude that the dominating factor is the convectional and conductional heat losses.

Figure 9 shows an night U-value of 4,2 W/m^2K which is close to the U-value measured during the day in previous papers.

Some PVT designs can go below ambient temperature. This is much less likely to happen in standard thermal panels. This is because the PV cells emit much more radiation than the selective surface of the thermal panels. Basically, a worse performance during the day by PVT collectors, leads to a better performance in cooling during the night. It is not reasonable to expect that a panel performs well in gaining heat during the day and, at the same time, also performs well at loosing heat during the night.

When speaking about heating, it is generally accepted that energy at ambient temperature has no value. For cooling, the same is generally true. The analyses of the measurements that have been made reveal that the C-PVT collector shows little potential for cooling applications. However, if the C-PVT design was made without a glass cover the results could potentially be very different for locations with many clear nights.

5. References

[1] Armenta-Déu, C., Donaire, T., Hernando, 2003. Thermal analysis of a prototype to determine radiative cooling thermal balance, Pergamon, Renewable Energy, Grupo de Energia Solar, Universidad Complutense, Spain

[2] Dobson, R.T., 2005. Thermal modelling of a night sky radiation cooling system, Journal of Energy in Southern Africa, Vol 16 No 2, Department of Mechanical Engineering, University of Stellenbosch

[3] Eicker, U., Dalibard, A., 2011. Photovoltaic-thermal collectors for night radiative cooling of buildings, Elsevier, Solar Energy, University of Applied Science Stuttgart, Germany

[4] Giovinazzo, C., Bonfiglio, L., Gomes, J., Karlsson, B., 2014. Ray Tracing Modelling of an Asymmetric Concentrating PVT, International Solar Energy Society, Ecole Polytechnique Universitaire de Montpellier, University of Gävle, France, Sweden

[5] Gomes, J., Diwan, L., Bernardo, R., Karlsson, B., 2013. Minimizing the Impact of Shading at Oblique Solar Angles in a Fully Enclosed Asymmetric Concentrating PVT Collector, Elsevier, Energy Procedia, University of Gävle, Instituto Superior Tecnico Lisboa, Lund University, Sweden, Portugal

[6] VDI-Wärmeatlas, 2013. Grundlagen der Wärmeübertragung, 11. edition, Springer-Verlag Berlin

Heidelberg, Germany

[7] World Weather: URL: http://www.worldweatheronline.com/Gavle-weather-history/Gavleborgs-Lan/SE.aspx, 09/28/15)

6. Appendix

Table 2: Results for all considered nights

Night [22:00 – 05:00]	E_{cold} [kWh]	$\dot{E}_{cold}$ [W]	T_{out} [°C]	T_{amb} [°C]	$T_{out} - T_{in}$ [°C]	$T_{coll} - T_{amb}$ [°C]	$Cloudiness$ [%]	v_{wind} [m/s]
05.09. - 06.09.	-1,08	-154,9	22,9	10,2	-0,88	13,2	5	2,1
06.09. - 07.09.	-0,71	-101,5	24,0	12,6	-0,57	11,7	39	1,2
09.09. - 10.09.	-0,72	-102,6	18,7	8,6	-0,58	10,5	41	1,8
10.09. - 11.09.	-0,83	-118,1	18,2	7,6	-0,67	10,9	4	0,4
09.10. - 10.10.	-2,0	-285,1	35,8	8,7	-1,85	28,1	89	1,8
10.10. - 11.10.	-0,61	-86,9	17,2	9,5	-0,57	7,9	53	2,4
11.10. - 12.10.	-0,84	-120,6	14,4	1,8	-0,79	12,9	48	1,5
12.10. - 13.10.	-0,53	-76,2	17,1	9,6	-0,49	7,7	95	1,6
14.10. - 15.10.	-0,62	-88,1	16,8	7,6	-0,57	9,4	92	3,3
17.10. - 18.10.	-0,75	-107,4	14,4	2,6	-0,70	12,1	7	1,5
19.10. - 20.10.	-0,56	-80,5	17,2	8,6	-0,52	8,9	100	1,0
21.10. - 22.10.	-0,62	-89,0	14,4	5,1	-0,58	9,8	97	4,5
22.10. - 23.10.	-0,78	-111,2	13,7	1,7	-0,62	12,4	33	3,1
23.10. - 24.10.	-0,67	-95,2	13,2	3,4	-0,55	10,1	100	5,8
24.10. - 25.10.	-0,52	-73,7	16,9	9,8	-0,43	7,3	99	5,8
28.10. - 29.10.	-0,44	-62,7	18, 6	12,7	-0,37	6,0	54	6,7
29.10. - 30.10.	-0,78	-112,1	12,9	1,9	-0,68	11,4	3	2,4
31.10. - 01.11.	-0,76	-108,0	12,7	-0,9	-0,64	13,9	63	1,8
01.11. - 02.11.	-0,44	-63,1	16,4	9,9	-0,37	6,7	94	4,8

Conference Proceedings
Solar World Congress 2015
Daegu, Korea, 08 – 12 November 2015

SIMULATION OF A CONTROL FOR AIR CONDITIONING SYSTEM OPERATED BY SOLAR ENERGY

Jorge A. Cardona-Gil[1,2], C. A. Isaza-Roldan[1] and Marisol Osorio[2]

[1]Grupo de Investigación en Energía y Termodinámica

[2]Grupo de Investigación en Automática y Diseño A+D

Escuela de Ingenierías

Universidad Pontificia Bolivariana, Medellín (Colombia)

jorgeandres.cardona@upb.edu.co

Abstract

Among different strategies available technologically to reduce energy consumption and environmental impact in buildings, there is the use of new thermal-operated air conditioning systems. An available alternative is absorption refrigeration systems, which can operate with renewable energy sources such as solar energy, and use environmentally friendly refrigerant substances.

In Colombia, this type of systems have not been investigated thoroughly nor have carried out developments, because the field of solar energy is emphasized in the use of thermal energy, to be used on a refrigeration cycle that allows to condition an environment of a determined compound, and besides that, this air conditioning going to achieve through intelligent control, it has not been subject of considerable advances, neither in the part of applied research, nor its implementation. According to this, the idea is to use developments of these systems that have been simulated and implemented in other countries, including Spain, for the start in the UPB with research, development and implementation of those after making a literature review about the systems.

To develop the aforementioned system, a comprehensive literature review of the technologies has been made to be implemented in terms of automation and control. A simulation in the TRNSYS® software of the system to be implemented in a building on the campus of the UPB, which requires air conditioning for the comfort of the people who inhabit, is developed. The system will be regulated by a control system that receives information from various parts of the plant with temperature and flow sensors. To carry out the control of this system, classical control techniques are going to be use for some water systems that constitute the demonstrative installation, but for the part of chilled water and air conditioning, intelligent control techniques will be handled, which allows to meet the needs of the air conditioning system that is intended to implement, as this part is quite complex for the management of different variables. This system will operate automatically acting on valves, pumps, fans, Fan-coil and/or mats of water (they act as radiant walls) for correct operation by previously established set points.

Keywords: *Absorption cycle, Air conditioning, Control system, Renewable energy, Solar energy*.

doi:10.18086/swc.2015.10.34 Available at http://proceedings.ises.org

1. Introduction

Buildings have an impact on the lives of people and the planet's health. In developed countries, buildings use one third of the total energy, two thirds of the electricity and one eighth part water, and transform land that provides valuable ecological resources. The use of these resources and their impact on the environment may be more relevant in developing countries, such as Colombia, where the technology used for the construction and operation of most buildings is not as advanced. In this context, it has defined "sustainable building" or "green building" has been defined as a final standard that is given by an environmental performance over the life cycle of a building, which is seen and understood as a whole (LEED, 2008).

This situation has caused different institutions, associations, governments and companies to take interest in implementing measures aimed to rationalize the use of natural resources in buildings and make these important structures of society to be in harmony with the environment. The vast majority of current air conditioning systems operate on the principle of the refrigeration cycle vapor compression (El Aire Acondicionado, 2015). It has been found that these contribute significantly in an opposite direction to the concept of sustainable development.

In Latin America the main initiative was the *RIRAAS* network (*Red Iberoamericana de Refrigeración y Aire Acondicionado Solar*), which arose before 2001, with the aim of promoting and disseminating the cold production technologies with solar energy. It was financed by the program *Ciencia y Tecnología para el Desarrollo (CYTED)* and the *Consejo Nacional de Ciencia y Tecnología de México (CONACYT)* until 2004. In Latin America the main facility in solar air conditioning operation currently operates in Mexico, but besides this, there is a lot of prototypes of universities and research centers used for research and development of different technologies for solar cooling (Sparber et al., 2007).

This article aims to present an alternative to the use of air conditioning systems to reach the standard of "sustainable building" in Colombia (LEED, 2008). Under the standard of "sustainable buildings", cold production with unconventional heat sources, such as absorption cooling systems powered by solar energy, energy are potentially attractive in the tertiary sector to meet the cooling demand through air conditioning systems in buildings, important chain stores and shopping malls, among others. Such buildings include institutions such as hospitals, universities, schools, government buildings and offices, where the air conditioning systems represent a large percentage of energy consumption. In the hotel sector, absorption equipment are widely accepted as air conditioning systems, given the publicity that implies offering environmentally friendly facilities (LEED, 2008). In the literature there is not a lot information about this type of systems in which involve research and developments in Colombia.

The Artificial fluids were commercially used in systems of air conditioning in buildings, such as chlorofluorocarbons (CFC), hydrochlorofluorocarbons (HCFC) and hydrofluorocarbons (HFC) they have been considered largely as spoilage of the earth's ozone layer. Favor the greenhouse effect and to some extent, the increase in global average temperature of the planet. Since the 1987 Montreal Protocol, it have been signed international treaties to reduce emissions of these refrigerants; Colombia is part of the Montreal Protocol after the approval of Law 29 of 1992 (Wuebbles, 1994).

The conventional refrigeration cycles operated by electricity contribute significantly to the consumption of electricity and fossil fuels. The International Institute of Refrigeration (IIR) estimated that approximately 15 % of all electricity produced in the world is used in some process of cooling and air conditioning (Pérez, 2013).

Whenever there is the possibility of using thermal energy from renewable energy or effluents from industrial processes or cogeneration systems, the application of absorption systems for cold production will be competitive and interesting, which is why this article seeks to bring out the design and simulation of an air conditioning system operated by solar absorption refrigeration cycle with classic control techniques, some of which later become intelligent control techniques. This approach is intended to experiment with this type of system to find efficient ways of operation and low cost, in the future, to be competitive in the commercial field.

2. Materials and methods

The increased cost of electricity generation and environmental restrictions have strengthened in the scientific research of air conditioning systems and cooling using solar resource as a source of motive power (Vidal and Colle, 2009). The energy consumption of the world's population is constantly growing, as a result bringing the scarcity of natural resources and generate environmental problems, such as thinning of the ozone layer and the greenhouse effect. These effects generate an environmental impact hardly be solvable, therefore it becomes a matter of great concern to many countries, governments and the society. Within this reality, industries hone their processes to include control systems in order to meet the demands of energy efficient, environmentally friendly and more competitive teams. This is the case of systems operating on solar energy and absorption refrigeration cycle. The purpose of the control systems in a plant with absorption refrigeration cycle is focused on providing automatic operation where control is too complex for manual operation. These systems maintain control of the conditions that could be achieved by manual operation, providing maximum efficiency and economy in the process (Trott and T. Welch, 2000).

The process of producing cold is to reduce and maintain the temperature of a space or material below room temperature. For this to happen, it is necessary to remove heat from a low temperature source and transfer it to a high temperature source. Under the second law of thermodynamics, for the process of transfer heat from a cold to a warm body to be made, it is necessary to do a work, because spontaneously, this may not occur (Vidal and Colle, 2009). Some forms of cold production using thermal energy transfer: collection system solar energy, waste heat source, fuel (biomass or fossil) or just an electrical resistance of a transformation system and the energy received refrigeration system using solar energy are available (Vidal and Colle, 2009).

The absorption refrigeration system bases its principle in the affinity of certain substances to absorb each other on contact. Two pairs of substances are commonly used in this type of facilities: bromide water-lithium ($LiBr$-H_2O) and ammonia-water (NH_3-H_2O). The first of these combinations is mostly used for solar assisted applications due to non-toxic and non-flammable properties of water as a coolant and efficiency in terms of energy expenditure (Vidal and Colle, 2009).

The absorption refrigeration systems of single-effect (with a single generator), powered by solar energy require the union of several components for proper operation is achieved. The main components are: Solar Collectors, the Absorption Machine, the Cooling Tower, a Tank of Hot Water, an Auxiliary Heater, Chilled Water Tank and the control system. Figure 1 shows the components required for the operation of an absorption system operated by solar energy.

The use of solar energy in air conditioning systems require to test or develop new economic and efficient equipment for collection of solar radiation; thermodynamic cycles specially adapted to operate under the conditions proposed, refrigerants and refrigerant mixtures with special additives and absorbents capable of achieving high yields in the operation cycle, evaluate, simulate and improve specific cycle processes such as the operation absorption of the process itself; in addition to control systems that enable excellent integration of systems: Solar Collectors, energy storage, production of cold, heat rejection, cold storage and auxiliary or backup subsystem.

Current technology for air conditioning consumes a lot of power, so it is necessary to establish principles and strategies conducive to efficient energy use, this topic directly influence the intelligent control technique that is applied to the system. Furthermore, it is known that certain refrigerants such as Freon, produce an environmental impact when released into the environment, which affect the stratospheric ozone layer and contributes to the greenhouse effect (Edmonds et al., 1987).

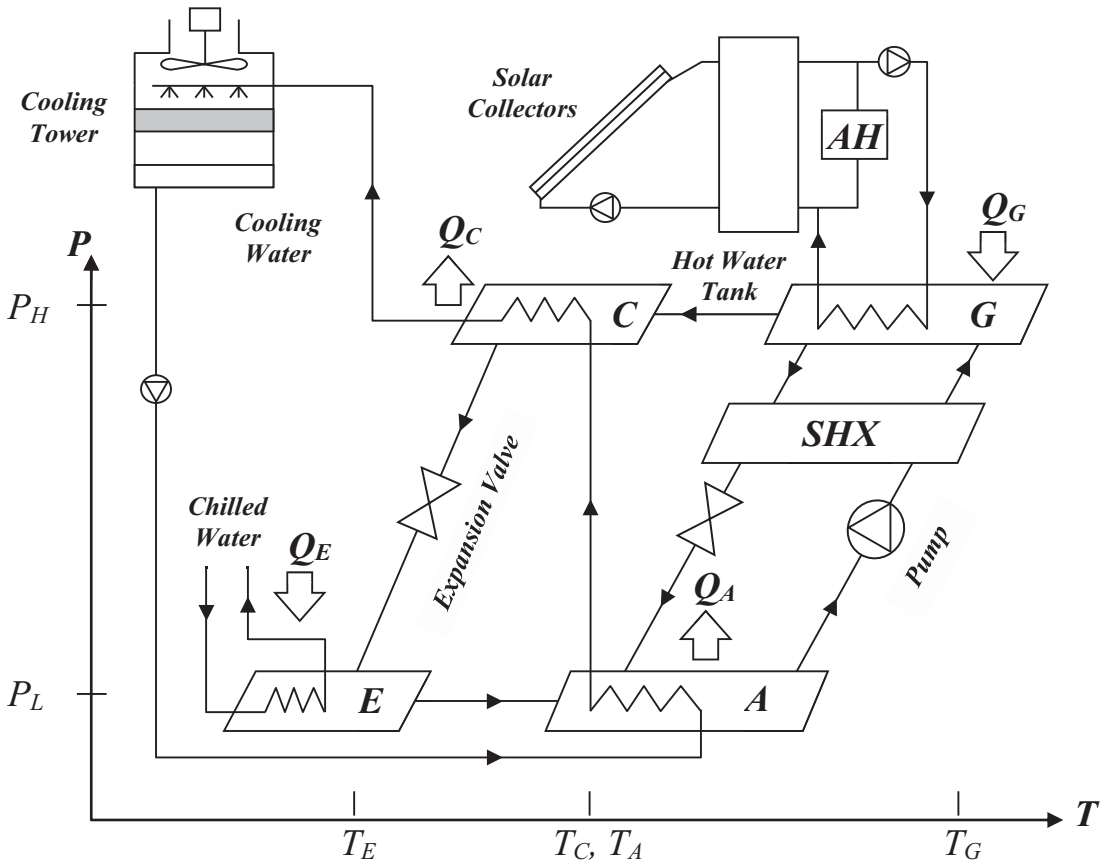

Fig. 1: Schematic diagram of a refrigeration system with single-effect absorption LiBr/H_2O, operated with solar energy

Generator (*G*).

Condenser (*C*).

System Expansion (*Expansion Valve*).

Evaporator (*E*).

Absorber (*A*).

Auxiliary Heater (*AH*)

Hydraulic pump (*Pump*).

Heat exchanger between dilute and concentrated solution (*SHX*).

In addition, the production of cold thermal energy can make future projects more attractive to be converted to natural gas, since the products of combustion of natural gas are particularly suitable (low dew point temperature) for heat recovery applications, so it is possible to integrate production processes of heat and cold with the same energy source; by including in some cases the production of electricity from diesel, gas turbines, steam cycles and even fuel cells engines; configurations that are best known as CHP (Cooling, Heat and Power) (Duarte, 2011).

The system shown in this article is intended to be implemented practically, for this reason, has been made quotes of various elements that make up the solar air conditioning system, among them are the Absorption Chiller and Solar Collectors. These components were listed in the company Shandong Lucy New Energy Technology Co., Ltd (LUCY, 2015) of China, which beside offer these products, offers to install the solar air conditioning system with absorption refrigeration cycle in any building, this structure is shown in the

Figure 2 is very similar to what is wanted to implement in the UPB, where it is noted the use of three-way valves or two-way and pump to control the flow of water from the system and to generate cooling or heating according to the configuration set you want to allow or not allow the flow of water through different circuits of the system. In this case, a heat exchanger is used, but with the kind of climate of *Medellín*, which is warm, is not need to use it.

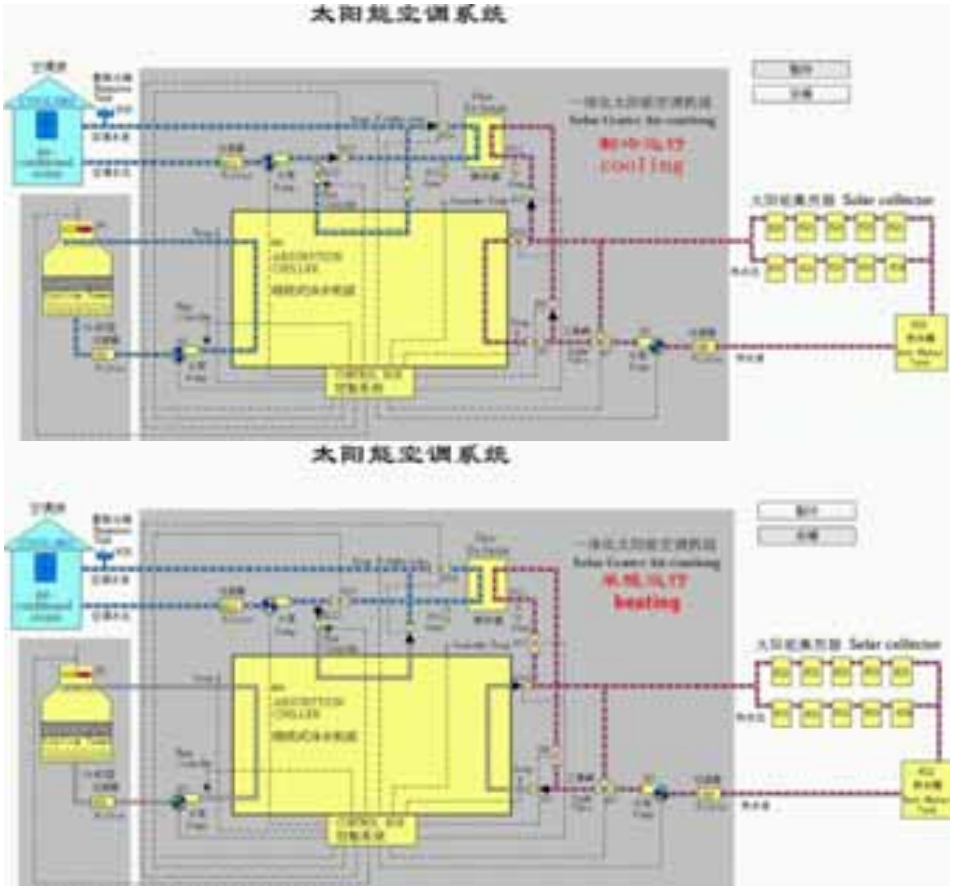

Fig. 2: Structure of solar air conditioning system for cooling and heating, installed by the Chinese company Shandong Lucy New Energy Technology Co., Ltd. Taken from LUCY (2015)

3. Results and discussion

For system simulation results of the evaluation of the thermal load integrated with the cycle of single effect absorption $LiBr/H_2O$ and subsystems Solar Collectors, Cooling Tower, chilled water distribution and accumulation of chilled water and hot; TRNSYS® using the computer program. The modeling was carried out using the parameters of the components offered by the program in the TESS library, and the following components were used: 12 modules of Solar Collectors each of 20 tubes, the area of each module is 3 m^2, they are connected in series and form a total area of 36 m^2; an Auxiliary Heater of 20 kW; two tanks of 250 l, one of hot water and other chilled water; it has several pumps and several three-way valves in the different circuits of water from the system, there are several pipes with standard parameters set; an Absorption Machine with a COP of 0.72 and cooling capacity of 11.5 kW; a Fan-coil 36000 BTU/hr (think also experiment with mats of water) and an enclosure to simulate the building of the campus of the UPB to which this system is installed.

For the meteorological data it has been processed actual data of *Medellín* through software Meteonorm® obtained in CALAIRE Laboratory by the *Universidad Nacional de Colombia*, near the UPB, TRNSYS® to understand them in the required formats.

In the simulation model that was held, the following results were obtained:

It was determined that the system will be installed in a building on the campus of the UPB, *Medellín*, air conditioning is needed for the comfort of the people who live there; installing the system in this building allow one to perform actual tests to achieve concrete results and set a starting point for the use of such systems in Colombia. The building that is selected will be used for research and laboratory purposes, it is possible that the building to be selected can be compared with a conventional system and identify pros and cons of both systems.

The simulation presented in this article (see Figure 3) of the demonstrative installation, using TRNSYS® software, shows the application of two PI controls, one for the variation of the fan speed of the cooling tower and the other for varying the flow of chilled water through a three-way valve which is connected to the handling unit (Fan-coil) of chilled water; and two ON-OFF controls, one to pump hot water from the Solar Collector, which is off at night so they are not underutilized and one for the auxiliary heater is always on to reach a temperature of 90 °C on the generator of the Absorption Chiller unless the Solar Collectors can actually reach this temperature in the day, in this case, the auxiliary heater is switched off immediately.

Tests of the preliminary simulation are done in the first week of June 2014 in *Medellín*, where high radiation was obtained, and a consumption of 14.76 kWhr in the Auxiliary Heater is produced by solar thermal energy generated in the Solar Collectors (see Figure 4), an oscillating but relatively acceptable performance air conditioning system around 22 °C (see Figure 5) and a good performance in the cooling tower, where it achieves lower cooling water temperature input 35.11 °C to 30.34 °C (see Figure 6).

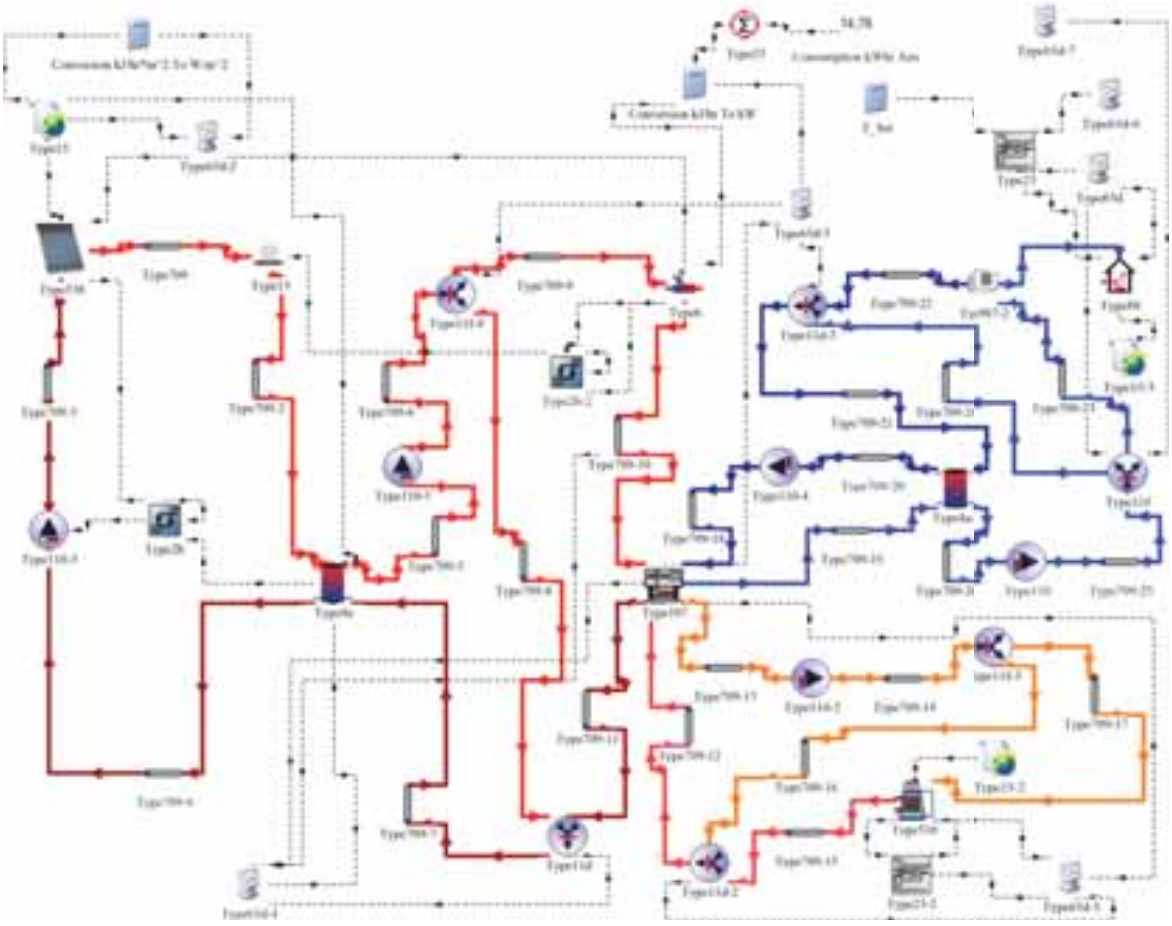

Fig. 3: Simulation of solar air conditioning system and absorption refrigeration cycle

Control techniques applied in this simulation techniques are classic control (ON-OFF and PI), and through these techniques is desired to implement intelligent control schemes. It is determined that the technique of intelligent control required to apply to the part of the air conditioning system is a control technique Fuzzy Logic, which vary PI control then PI Fuzzy control being developed will be applied using the MATLAB® software that has direct connection with TRNSYS®. To achieve this control, heuristic design experimenting with the TRNSYS® simulation software to operate in a relatively wide range model is obtained. The hot water circuit will continue with two ON-OFF controls and the cooling water with PI control in which a constant flow of water will remain. To the chilled water circuit constant water flow in the circuit pumps is maintained, but is changing the flow of water through the three-way valve installed at the inlet of the Fan-coil with PI control, the idea is to further apply a PI Fuzzy control, whether the final control element is the Fan-coil, currently used, or mats of water.

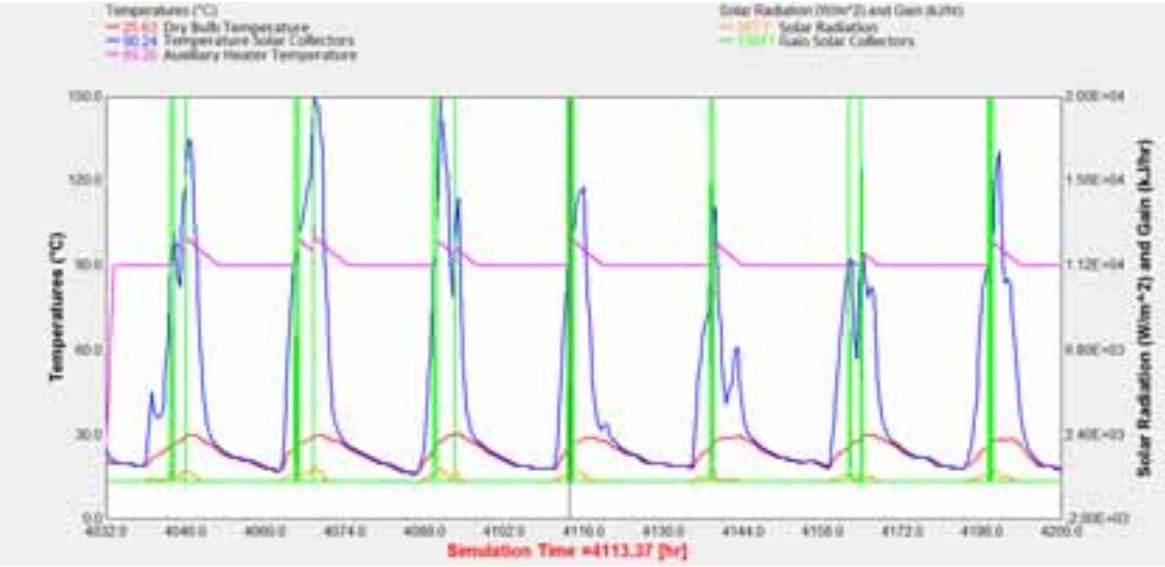

Fig. 4: Auxiliary Heater and Solar Collectors in running during the first week of June 2014 in *Medellín*

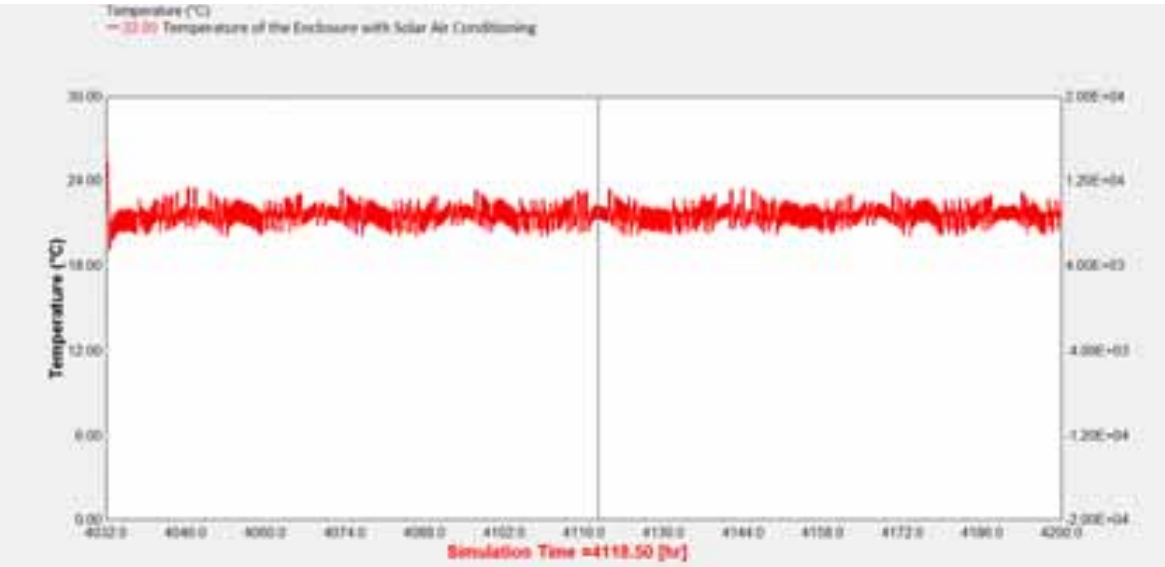

Fig. 5: Temperature of enclosure controlled by PI control

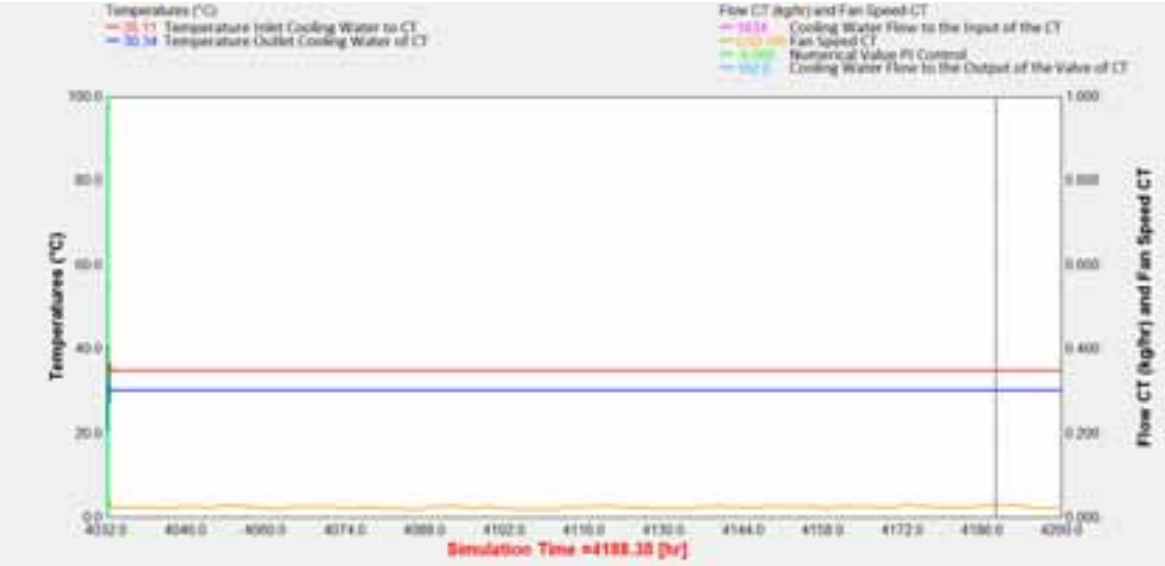

Fig. 6: Inlet and outlet water temperature of the cooling tower and fan speed controlled with PI control

In each figure can be observed the performance of the simulation previously shown in Figure 3 in the software TRNSYS®. In Figure 4, the ON-OFF control applied to the auxiliary heater operates when the Solar Collectors temperature reaches 90 °C reference and immediately turns off the auxiliary heater, this generates energy savings in the operation of the system; in Figure 5 the outlet temperature of the chilled water from the Absorption Machine and how does the PI control applied to Fan-coil to the enclosure is achieved a temperature which is around 22 °C is observed; and Figure 6 shows how does a PI control the fan speed of the cooling tower, to control the cooling water temperature from 30.34 °C to a water inlet 35.11 °C from the Absorption Machine.

4. Conclusions

Making this project generates technological breakthroughs for the industry of refrigeration and air conditioning in Colombia, as a method of renewable energy is obtained, such as solar energy, which is practically infinite and generates no pollution to the environment.

The solar air conditioning system has a nonlinear simulated behavior on the part of the air conditioning, because environmental conditions and thermal loads influence, disrupt and constantly change over time, which is why intelligent control technique (PI Fuzzy) is quite determining, since generates a lower consumption of electrical energy for soft control action applied to the actuators, furthermore it stabilizes in less time the temperature variable, which is the controlled variable.

For many applications in buildings and industrial processes can be considered that cooling through an absorption system is an environmentally responsible choice.

By using water as a coolant, mixed with salt and non-toxic chemical corrosion inhibitors, avoids the use of CFC, HCFC and HFC and management, availability and transport.

The simulation of solar air conditioning system in the TRNSYS® software, thanks to the library TESS and its focus on solar-operated systems, and meteorological data processed in Meteonorm® allow obtaining answers very close to reality and create a solid base to carry out this type of installation in reality without hesitation.

5. References

Duarte, J., 2011. «Cogeneración en Edificaciones Energéticamente Eficientes,» Noviembre. [Online]. Available: http://www.upme.gov.co/Docs/Seminarios/2011/EEE/5%20JAVIER%20DUARTE.pdf.

Edmonds, J., Wuebbles, D. and Scott, M., 1987. «Energy and radiative precursor emissions,» Diciembre. [Online]. Available: http://www.osti.gov/scitech/biblio/6468199#cite-bib.

El Aire Acondicionado, 2015. «Descripción de los diferentes tipos de Aire Acondicionado,». [Online]. Available: http://www.elaireacondicionado.com/tipos_aire_acondicionado/.

LEED, 2008. «LEED-USGBC,» Green Building Council. [Online]. Available: http://www.usgbc.org/LEED.

LUCY, 2015. «Shandong lucy new energy technology co.,ltd,». [Online]. Available: http://www.lucysolar.com/shouye.asp.

Pérez, J. P., 2013. «Experimentación de nuevas configuraciones destinadas a la mejora del COP en ciclos de compresión de vapor que utilizan CO2 como refrigerante,» Mayo. [Online]. Available: http://www.git.uji.es/investigacion/docs_investigacion/Tesis_Jorge%20Patino_UJI_2013.pdf.

Sparber, W., Napolitano, A. and Melograno, P., 2007. «Overwiew On World Wide Installed Solar Cooling Systems,» October. [Online]. Available: http://task38.iea-shc.org/data/sites/1/publications/task38-Overview.pdf.

Trott, A. R. and Welch, T., 2000. «Refrigeration and air-conditioning,». [Online]. Available: http://ezproxy.library.uwa.edu.au/login?url=http://www.engineeringvillage2.org/controller/servlet/OpenURL?genre=book&isbn=075064219x.

Vidal, H. and Colle, S., 2009. «Simulación Horaria de un Sistema de Refrigeración Combinado Eyector-Compresión de Vapor Asistido por Energía Solar y Gas Natural,» Marzo. [Online]. Available: http://www.scielo.cl/scielo.php?pid=S0718-33052009000100007&script=sci_arttext.

Wuebbles, D., 1994. «The role of refrigerants in climate change,». [Online]. Available: http://www.sciencedirect.com/science/article/pii/0140700794900825.

Conference Proceedings

Solar World Congress 2015
Daegu, Korea, 08 – 12 November 2015

SOLAR WATER HEATING FOR LIVESTOCK INDUSTRY IN TAIWAN

Yi-Mei Liu[1], Keh-Chin Chang[1], Wei-Min Lin[2] and Kung-Ming Chung[1]

[1] Energy Research Center, National Cheng Kung University, Tainan, Taiwan

[2] Department of Accounting Information, Tainan University of Technology, Tainan, Taiwan

Abstract

Solar water heating systems have been proven to be reliable and economical for producing hot water. In Taiwan, the cumulative area of solar collectors installed by the end of 2014 was approximately 2.39 million m^2, in which approximately 98% of the systems were installed in the domestic sector. Further, preheating water for livestock processing plants, where hogs are killed and processed for consumption, is potential of cost-effective application. Heated water can be used in the plants for evisceration, sanitation during processing, and the daily cleanup of the plant. In Taiwan, the number of pig farming was 8,457, and the supply for slaughtering was approximately 7.47 million heads in 2013. A livestock processing plant using combined solar thermal and heat pumps systems was chosen as the case study by the field measurements. The results showed that the hot water consumption, mass flow rate, operation of circulation pumps and heat pumps would affect the thermal efficiency, economic viability and attractiveness of a system. This study would provide useful information for all parties related to this market, manufacturers, potential users and policy-makers in Taiwan and other countries.

Keywords: *solar water heating; livestock industry; Taiwan*

1. Introduction

Besides the energy savings, applications of renewable energy technologies (e.g. solar, hydroelectric, biomass, wind, ocean and geothermal energy) have environmental benefits, like a reduction in air pollutants and greenhouse gases (Kikuchi, 2011). Therefore, tremendous efforts have been made to formulate and implement favorable policies by the governments throughout the world. In Taiwan, imported fuel accounted for 97.58% of its energy demands in 2013 (BEMOEA, 2014). Thus, renewable energy has received increasing support, particularly with the Renewable Energy Development Bill enacted in April 2010, and is projected to reach 3% of the total energy supply by 2020. Further, water heating constitutes one of the major types of energy consumption in both domestic and commercial sectors (Roulleau and Lloyd, 2008). Taiwan has a subtropical climate (latitude 22° to 25° North). The yearly global solar radiation ranges from 1200 to 1700 kWh/m^2, which is favorable for the use of solar heat. With the subsidy programs (1986–1991, 2000-present) introduced by the Bureau of Energy under the Ministry of Economic Affairs (BEMOEA) for solar water heaters (SWHs), the cumulative area of solar collectors installed was approximately 2.39 million m^2 by the end of 2014, in which approximately 0.3 million systems (or 1.6 million m^2) are in operation. Moreover, dissemination of SWHs in Taiwan was reviewed by Chang *et al.* (2009, 2015) and Lin *et al.* (2012). The major factors included system design, economic/financial considerations, degree of urbanization, and legislative support. More than 98% systems were installed in the domestic sector, and limited commercial application for industrial heat process was due to lack of experience in system design and uncertainty of expected benefits. Nevertheless, solar water heating is still the most successful account of renewable energy application in Taiwan.

Process heat generation is an unexploited application for solar heat in the sectors like food, agro-food, paper, textiles, chemicals and beverages (Karagiorgas *et al.*, 2001; Lauterbach *et al.*, 2012; Mekhilef *et al.*, 2011),

doi:10.18086/swc.2015.10.35 Available at http://proceedings.ises.org

in which the required temperatures for industrial heat processes range from 60°–260°C (Kalogirou, 2003). Lauterbach *et al.* (2014) also indicated that a solar thermal system for industrial applications under a low process temperature and constant load can result in higher system yields. However, the hydraulic setup, solar collectors and hot water consumption patterns on system performance need to be addressed. Further, livestock industry has favorable conditions to use solar heat for evisceration, sanitation during processing, and the daily cleanup of the plant. In Taiwan, pork is the major meat (≈ 40%) and its per capita consumption in average was 37.91 kg/person/year in the period of 2005–2013. The number of pig farming was 8,457, supplying approximately 7.47 million heads in 2013 (NAIF, 2013). To promote SWHs in livestock industry, it is important to analyze system performance and their financial viabilities. Also potential benefits of combined solar thermal with heat pumps for hot water production have been studied (Carbonell *et al.*, 2014). Therefore, field measurements of a combined system installed in a slaughterhouse were conducted in this study.

2. Setup of field measurements

According to the statistics by the NAIF (2013), Yunlin County (1,270 pig farms) was the top one for pig production (24.36%). As mentioned previously, solar heat can be used for evisceration, sanitation during processing, and the daily cleanup of the plant. Therefore, Yunlin meat market, located in southern Taiwan near the Tropic of Cancer, was chosen as our case study (yearly solar radiation = 6,712 MJ/m^2) for evaluating the performance of a combined solar thermal and heat pump system. Note that a boiler using low sulphur light fuel oil is also available. Figure 1 shows the two independent SWHs and heat pumps for scalding and dehairing (required temperature = 60–65°C). The A_{sc} (glazed flat-plate type) was 123.5 m^2 (system 1) and 115.8 m^2 (system 2), respectively. Note that the appropriate A_{sc} of a SWH is in the range of 130 m^2 to 160 m^2 for more reasonable energy and economic performances (Li *et al.*, 2014). The solar collectors facing south were installed on the roof with a tilt angle of 18.5^o. One 10-ton and two 7-ton storage tanks were installed. Pumps were also employed for forced circulation. The setup of mass flow rate was 0.028 and 0.019 kg/m^2/s for system 1 and system 2, respectively. The flow rate of heat pumps ranged from 105 to 118 liters per minute. The systems have been in operation since March 2013.

To evaluate the actual performance of the systems, several monitoring devices were installed. A precision spectral pyranometer (Eppley Laboratory, Inc., model PSP) was installed to measure the incident horizontal solar radiation. Seven Macnaught flow meters (Model M2SSP-1R) were located in the cold water supply line to the hot water storage tank (hot water consumption) and in the circulation line from the bottom of the storage tank to the inlet of the collectors (circulation flow rate), respectively. There were 14 platinum resistance thermometers (T_a, T_0–T_{12}, Izuder Enterprise**,** 1/10 DIN Class B) installed to monitor the ambient and local water temperature. In addition, energy consumption of the heat pumps (HP1: 38.4 kW; HP2, HP3: 40.6 kW) was recorded by the power meters. The data from the monitoring devices were sampled every 10 seconds by National Instrument (NI) data acquisition system (Model cFP-AI-110 and cFP-RTD-124) and transmitted synchronously to the host computer at the Energy Research Center, National Cheng Kung University

3. System operating performance

3.1. SWHs and heat pumps

Certifications of a solar collector or a SWH, in which the standards have been enforced by the BEMOEA, are required when filing for a rebate. The thermal efficiency η (≥ 0.5, Chinese National Standard 12558-B7277) of a SWH is calculated using the following formula. Note that the test conditions under the standard specify the daily horizontal solar radiation per square meter (≥ 7 MJ/m^2).

$$\eta = mC_p(T_f-T_i)/(A_{sc}G)$$

C_p: specific heat, MJ/(kg°C)
m: water mass flow, kg
T_i: initial temperature in the hot water storage tank, ^{o}C
T_f: final temperature in the hot water storage tank, ^{o}C
A_{sc}: effective area of solar collectors, m^2

G: daily horizontal solar radiation per square meter, MJ/m^2

In this study, the data from March 25, 2013 till June 30, 2013 were used to investigate the system's performance. Take the daily record on March 25, 2013 for example. The outdoor temperature ranged from 20 to 30 ^{o}C, and a peak solar radiation of approximately 870 W/m^2 was recorded. The daily solar radiation was approximately 5.77 kWh/m^2, and the solar energy was 712.6 kWh and 668.2 kWh for system 1 and system 2, respectively. For hot water consumption, it was in periods from 08:00 to 17:00. The daily hot water consumption was 26,045 liters. It is also noted that he daily hot water consumption in system 1 is sufficiently lower than that in system 2 in the period of March 25 to June 30, in which the peak values were 13,098 L/day and 26,573 L/day, respectively. For thermal performance of system 1, η increased with G ($\geq$ 6 MJ/m^2). The peak value was 0.476. For system 2, there was large variation of η with G while the peak value reached 0.641. Therefore, hot water usage is considered to be a critical factor for thermal efficiency of SWHs. Further, Li *et al.* (2014) indicated that the combination of SWHs and heat pumps is a very attractive option for hot water production. The COP of heat pumps varied from 2.6 to 4.9 when T_a = 18– 33°C. It is also noted that the COP of HP1 is higher than that of HP2 and HP3.

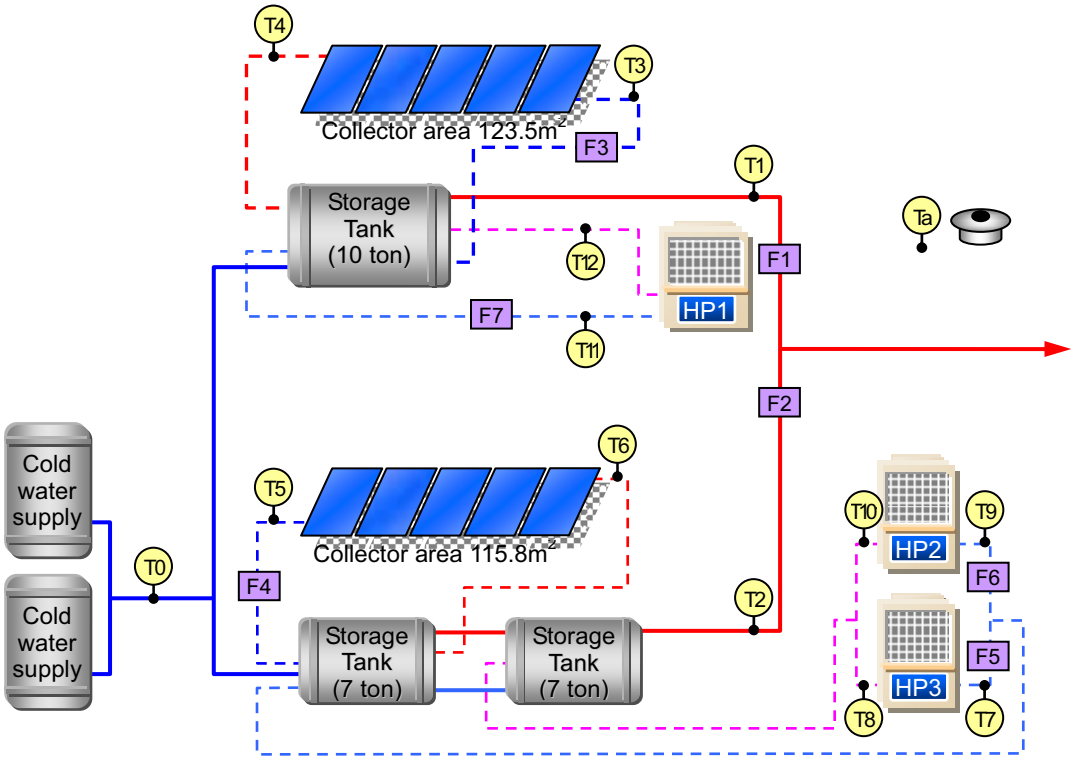

Fig. 1: A schematic drawing of SWHs and monitoring devices

3.2. Operating performance

As mentioned previously, the thermal performance of a SWH is associated with the entering water temperature and water consumption pattern. From April to June, the useful energy gain by the SWHs and HPs are shown in Table 1. For SWHs, the collected solar energy was 44,282 MJ and 58,109 MJ for system 1 and system 2, respectively. Since HP1 was least used or usually kept off in the measurement period, the ratio of collected solar energy divided by total supplied energy of the combined system is 70.8% and 27.8% for system 1 and system 2, respectively. In Table 1, it is also found that only 68% of total collected energy for system 2 was consumed. Inadequate operation of HPs is the major concern and should be taken into account to realize energy savings. Heat loss from the storage tank and piping to the environment during the night hours is also needed to be addressed. Further, the electricity consumption for the circulation pump of system 2 is sufficiently higher than that of system 1. Thus, a suitable control strategy is definitely required to ensure efficient energy savings of the system. Nevertheless, the net energy savings in the period of March 25 to June 30 was 150,655 MJ (or 1,537 MJ/day).

The monthly system operating performance from April to June is shown in Table 2. It can be seen that the solar thermal efficiency (η = 0.170–0.419) is sufficiently lower than the CNS standard, i.e. $\eta \geq 0.5$, particularly in April. This may partially corresponds to lower monthly solar radiation in April. The peak daily hot water consumption of system 1 is approximately half of that of system 2. Thus, it can postulate that a SWH with greater hot water consumption gives better system efficiency. Also, the mass flow rate was 0.028 and 0.019 kg/m^2/s for system 1 and system 2, respectively. Furbo (2005) indicated that a low mass flow rate of a SWH can result in a higher thermal efficiency. Therefore, a reduction in mass flow rate for system 1 may be required to ensure system economics. Also note that the monthly COP for HP1 (= 3.76–4.09) is slightly higher than that for HP2 (= 3.50–3.66) and HP3 (= 3.13–3.53). Further, the system economics is of interest. A simplified break-even analysis is given as below. Note that the maintenance cost and annual price change of the substituted fuel is not included. The initial cost for the SWHs and heat pumps is 2.15 and 1.15 million NT$ (1 US$ ≈ 31 NT$), respectively. The subsidies for the SWHs, based on the area of solar collectors installed, was approximately 0.7 million NT$ by the BEMOEA and Yunlin County. Further, the sales price of low sulphur light fuel oil was 22,779 NT$/kL in 2014, and its heating value is 40.19 MJ per liter (BEMOEA, 2014). Taking heating efficiency of 80%, the substituted fuel savings is estimated to be approximately 0.4 million NTD/year. Therefore, the payback period is estimated to be 6.5 years, which is less than the expected service period of a SWH (≈ 15 years). This validates the financial viability for a combined solar thermal and heat pump system for industrial heat process. As mentioned previously, the thermal performance of a SWH is associated with the entering water temperature and water consumption pattern. From April to June, the useful energy gain by the SWHs and HPs are shown in Table 1. For SWHs, the collected solar energy was 44,282 MJ and 58,109 MJ for system 1 and system 2, respectively. Since HP1 was least used or usually kept off in the measurement period, the ratio of collected solar energy divided by total supplied energy of the combined system is 70.8% and 27.8% for system 1 and system 2, respectively. In Table 1, it is also found that only 68% of total collected energy for system 2 was consumed. Inadequate operation of HPs is the major concern and should be taken into account to realize energy savings. Heat loss from the storage tank and piping to the environment during the night hours is also needed to be addressed. Further, the electricity consumption for the circulation pump of system 2 is sufficiently higher than that of system 1. Thus, a suitable control strategy is definitely required to ensure efficient energy savings of the system. Nevertheless, the net energy savings in the period of March 25 to June 30 was 150,655 MJ (or 1,537 MJ/day).

The monthly system operating performance from April to June is shown in Table 2. It can be seen that the solar thermal efficiency (η = 0.170–0.419) is sufficiently lower than the CNS standard, i.e. $\eta \geq 0.5$, particularly in April. This may partially corresponds to lower monthly solar radiation in April. The peak daily hot water consumption of system 1 is approximately half of that of system 2. Thus, it can postulate that a SWH with greater hot water consumption gives better system efficiency. Also, the mass flow rate was 0.028 and 0.019 kg/m^2/s for system 1 and system 2, respectively. Furbo (2005) indicated that a low mass flow rate of a SWH can result in a higher thermal efficiency. Therefore, a reduction in mass flow rate for system 1 may be required to ensure system economics. Also note that the monthly COP for HP1 (= 3.76–4.09) is slightly higher than that for HP2 (= 3.50–3.66) and HP3 (= 3.13–3.53). Further, the system economics is of interest. A simplified break-even analysis is given as below. Note that the maintenance cost and annual price change of the substituted fuel is not included. The initial cost for the SWHs and heat pumps is 2.15 and 1.15 million NT$ (1 US$ ≈ 31 NT$), respectively. The subsidies for the SWHs, based on the area of solar collectors installed, was approximately 0.7 million NT$ by the BEMOEA and Yunlin County. Further, the sales price of low sulphur light fuel oil was 22,779 NT$/kL in 2014, and its heating value is 40.19 MJ per liter (BEMOEA, 2014). Taking heating efficiency of 80%, the substituted fuel savings is estimated to be approximately 0.4 million NTD/year. Therefore, the payback period is estimated to be 6.5 years, which is less than the expected service period of a SWH (≈ 15 years). This validates the financial viability for a combined solar thermal and heat pump system for industrial heat process.

Tab. 1: Energy collection and consumption (March 25-June 30)

	system 1	system 2	Sum
Collected energy, SWHs, MJ	44,282	58,109	102,391

Collected energy, HPs, MJ	18,271	150,691	168,962
Total collected energy, MJ	62,523	208,800	271,353
Energy consumption, MJ	62,523	142,350	204,873
Circulation pump, kWh	195	1,129	1,323
Heat pumps, kWh	1,422	13,654	15,076

Tab. 2: System operating performance

		System 1		System 2		
Month	**G, MJ/m^2**	**η**	**COP-HP1**	**η**	**COP-HP2**	**COP-HP3**
April	10.72	0.170	3.76	0.260	3.50	3.13
May	13.81	0.272	4.22	0.419	3.51	3.35
June	14.18	0.277	4.09	0.351	3.66	3.53

4. Conclusions

The renewable energy usage is critical for its economic development and reduction in greenhouse gas emission. Also thermal uses constitute one of the major types of energy consumption. The need of raising solar thermal energy as a significant energy source is important. So far, solar water heating is the most successful account of renewable energy application for domestic hot water preparation in Taiwan. In the commercial sector, industrial process heating is a very promising application for SWHs. In addition, there are more systems with the combination of solar collectors and heat pumps available on a commercial level during the last decade. Therefore, field measurements of a combined system installed in a slaughterhouse were conducted in this study. The results identify the system as a suitable device for industrial heat process in livestock industry. A simplified break-even analysis also shows the financial viability. However, adequate operation of the system (circulation and heat pumps) is required to maximize energy savings.

Acknowledgements

This work was supported by the Bureau of Energy, the Ministry of Economic Affairs (103-D0303), Taiwan, Republic of China.

References:

Bureau of Energy, Ministry of Economic Affairs (BEMOEA), 2014. 2013 Energy Statistical Data Book, Bureau of Energy, Ministry of Economic Affairs: Taipei, Taiwan. Available online: http://web3.moeaboe.gov.tw/ (accessed on 17 March, 2015).

Carbonell, D., Haller, M.Y., Frank, E., 2014. Potential benefit of combining heat pumps with solar thermal for heating and domestic hot water preparation. Energy Procedia 57, 2656-2665.

Chang, K.C., Lin, W.M., Lee, T.S., Chung, K.M., 2009, Local market of solar water heaters in Taiwan: Review and perspectives. Renewable and Sustainable Energy Reviews 13(9), 2605-2612.

Chang, K.C., Lin, W.M., Chung, K.M., 2015. Sustainable development for solar heating systems in Taiwan. Sustainability 7, 1970-1984.

Furbo, S., Vejen, N.K., Shah, L.J., 2005. Thermal performance of a large low flow solar heating system with a highly thermally stratified tank. Journal of Solar Energy Engineering 127(1), 15-20.

Kalogirou, S., 2003. The potential of solar industrial process heat applications. Applied Energy 76, 337-361.

Karagiorgas, M., Botzios, A., Tsoutsos, T., 2001. Industrial solar thermal applications in Greece: Economic evaluation, quality requirements and case studies. Renewable and Sustainable Energy Reviews 5, 153-173.

Kikuchi, R., 2011. Environmental and socio-economic factors in carbon offsets: an approach to sustainable management and planning in climate change strategy. Journal of Environmental Planning and Management, 254(3), 355-367.

Lauterbach, C., Schmitt, B., Jordan, U., Vajen, K., 2012. The potential of solar heat for industrial processes in Germany. Renewable and Sustainable Energy Reviews 16, 5121-5130.

Lauterbach, C., Schmitt, B., Vajen, K., 2014. System analysis of a low-temperature solar process heat system. Solar Energy 101, 112-130.

Li, H., Sun, L., Zhang, Y., 2014. Performance investigation of a combined solar thermal heat pump heating system. Applied Thermal Engineering 71, 460-468.

Lin, W.M., Chang, K.C., Liu, Y.M., Chung, K.M., 2012, Field surveys of non-residential solar water heater in Taiwan. Energies 5(2), 258-269.

Mekhilef, S., Saidur, R., Safari, A., 2011. A review on solar energy use in industries. Renewable and Sustainable Energy Reviews 15, 1777-1790.

National Animal Industry Foundation (NAIF), 2013. 2013 Taiwan pig production statistics. National Animal Industry Foundation, Taipei, Taiwan.

Roulleau, T., Lloyd, C.R., 2008. International policy issues regarding solar water heating, with a focus on New Zealand. Energy Policy 36, 1843-1857.

Conference Proceedings

Solar World Congress 2015
Daegu, Korea, 08 – 12 November 2015

VALIDATION OF A SOLAR THERMAL PILOT PLANT MODEL FOR COPPER MINING PROCESSES

Alessandro Gallo[1], Martin Guillaume[1], Carlos Portillo[1] and Edward Fuentealba[1]

[1] University of Antofagasta. Centro de Desarrollo Energético Antofagasta, Chile. Avda. Angamos 601, 1270300, Antofagasta, Chile.

Abstract

In this work, the behavior of a solar thermal pilot plant installed in a copper mine in the north of Chile is investigated. The pilot plant is directly connected to the water circuit used to heat the electrolyte in the electrowinning processes. For a detailed monitoring of the system, the pilot plant counts with several measuring instruments. Recorded data are compared with results obtained in TRNSYS simulations. In addition to that, because of the high dust deposition on the solar plant, effects of soiling on the system are also investigated. Hence, this paper has the twofold objective of validating the TRNSYS model for future scale up of the solar thermal plant and at the same time to determine the effect of the dust on the collector.

Keywords: *Solar thermal plant, copper mining processes, TRNSYS simulations, soiling*.

1. Introduction

Climatic conditions and energy demand are necessary consideration for solar technology development. In that sense, Northern Chile has a high solar radiation, with an annual global horizontal irradiation of more than 2500 kWh m^{-2} (Escobar et al., 2014) and local industry, which is mainly focused on mining in deserted areas, presents an elevated energy consumption of electricity and heat. The principal activity of Chilean mining industry is extraction and production of copper. The energy demand of Chilean copper mining has reached 44.9 TWh in 2014 (including electricity and heat) and it is 60% higher than 2005 (COCHILCO, 2014).

In copper mining, two kind of process are mainly used to produce metallic cathodes, according to the extracted mineral (copper sulfides or copper oxides). Fossils fuels mostly supply the high thermal consumptions of those processes. The huge fuel consumption generated by the mines produces important quantities of greenhouse gases and it could be reduced significantly by the development of solar thermal plants to supply the heat needed in those processes.

There are two possible applications for solar thermal technology as heat source in the sulfides process: the drying and the smelting of the concentrate. In the latter, it is possible to apply the solar concentrating technologies to separate copper from other materials. Moreover, three applications are also conceivable in the oxides process: heating solutions for leach pads, electrowinning process and anodes washing (see Fig. 1).

doi:10.18086/swc.2015.10.36 Available at http://proceedings.ises.org

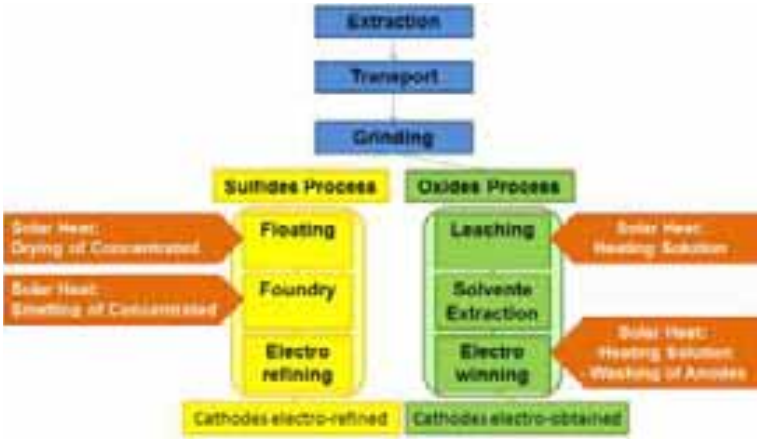

Fig. 1: Solar heat applications in copper mining processes

In Chile, the thermal energy consumption for the process of leaching (LX), solvent extraction (SX) and electrowinning (EW) is 1.5 TWh (COCHILCO, 2014) and it is obtained with fossil fuels, which involves problems for operational costs: price volatility, upward trend and uncertainty of supply. Nevertheless, solar thermal plants can obtain the same amount of heat energy and stabilizing operating costs of mining companies.

The EW process is the last step in the production of copper cathodes. To improve the efficiency of electrodeposition of copper on the plaque it is required that the electrolyte which comes from plant SX, is maintained at temperatures between 45 ° C to 55 ° C (depending on the process). Hot water is also required, at temperatures near to 90 ° C, to wash cathodes and anodes. So far, this task is achieved with a boiler, which also provides heats for the electrolyte using a heat exchanger.

In Chile, the substitution of fossil fuels with solar solutions for the production of thermal energy to the mining process has been implemented only for EW processes. To date, there are only three operating solar plants of this type. (CSP-Today Global Tracker, 2015)

The first solar plant is installed in the copper mine Constanza, and it has been operated since 2012. A surface of 404 m^2 composed of flat plane solar collectors provides energy to heat the electrolyte. The annual generation capacity of this plant is 540 MWh_t. Another solar thermal plant of this type is installed in Gaby mining company and produce 51.800 MWh_t per year, which replace 80% of fossils fuels consumption in the EW process. In this plant, flat plane solar collectors with a surface of 39.300 m^2 are used, too. The third plant has been operated since 2012 in the copper mining El Tesoro and uses parabolic trough technology. The total capacity of this plant is 10 MWt and replace 55% of diesel used in the process. (CSP-Today, 2013).

In the last years, some works have been carried out on this topic. Ushak et al. (2014) studied the behavior and the performance of a thermal solar plant to provide heat for EW process in the copper mine. It was analyzed the global efficiency during four month and the impact on the reduction of CO_2 emission. Another solar application in mining was studied by Gallo et al. (2014). They proposed the integration of thermal collectors with an absorption machine for air-conditioning of containers in mining camps of the Atacama Desert. Currently, at Energy Development Center of Antofagasta several applications for solar energy in mining are being investigated (Portillo et al., 2015).

In this paper is studied the working of a thermal solar pilot plant installed at the end of 2014, by Enermine, in the mine Lomas Bayas, in order to produce thermal energy for the EW process. The pilot plant is currently operating and it is directly connected to the heating circuit of EW system. A TRNSYS (2015) model of the pilot plant has been carried out and simulated results are being compared with operating data during the first months of working. The aim of this paper is the validation of the TRNSYS model in order to design a scaled up solar thermal plant in the near term. Furthermore, because the high rate of soiling on the solar collector can penalizes the performance of the plant (El-Nashar, 2003), simulations help to determine the loss of efficiency due to dust deposition on the collector.

2. Description of the solar thermal pilot plant

Real plant

The pilot solar thermal plant is connected to the water circuit used to heat the electrolyte in the electro-winning processes. One large size solar thermal collector is placed on the roof of a container and it has an active surface of 9.26 m^2 (see Fig. 2a). The rest of the components are protected inside of the container. The storage tank has a volume of 500 liters (see Fig. 2b).

All the elements of the pilot solar plant were installed and tested by the company Enermine. The same enterprise executed the connection between the solar module and the process with standard norms of Lomas Bayas Mining Company. Enermine also provided and disposed the instruments to measure temperatures and flow rates and to calculate the energy captured and dispatched from the solar module to the process.

In order to increase the temperature of electrolyte, the solar module is connected to the output of the main circuit of the heaters. The flow to heat by the pilot plant is obtained directly from the circulation pumps of tempering circuit. This flow is less than what comes out of the heaters (0.2% of the total flow) (Enermine, 2014), so it is possible to observe and measure the temperature rising due to the contribution of the solar module.

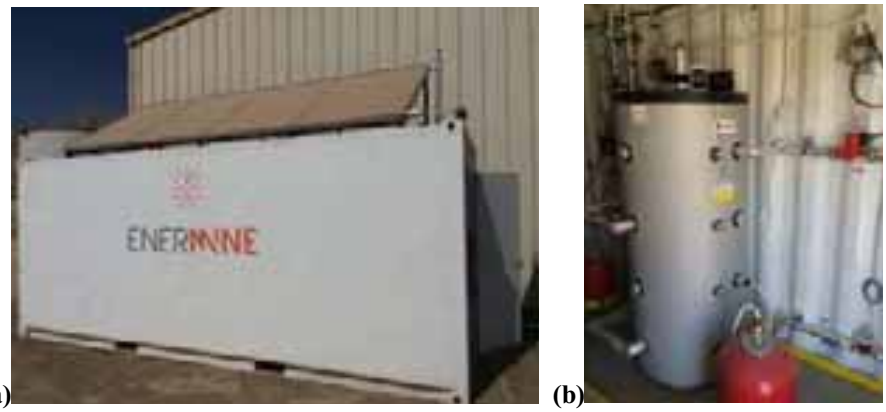

Fig. 2: Pictures of the solar thermal collectors (a) and the storage tank (b) of the pilot plant.

Figure 3 shows a schematic flow sheet of the pilot plant and measuring instruments are indicated in it. The system is composed of four hydraulic circuits: solar, storage, dispatch and process. The first circuit collects solar radiation by means of a large flat plate solar collector, disposed with an inclination of 30 degrees and an orientation of 56.6 degrees toward Northeast. The heat transfer fluid is demineralized water and it flows in the collector by the use of a circulation pump (P1) of 380 watt with a nominal mass flow of 350 kg h^{-1}. The heat is transferred by a heat exchanger (HX1) at the second loop where energy is accumulated in the storage tank (ST). In the third circuit, the water is dispatched from the accumulator to another heat exchanger (HX2). Finally, HX2 transmits the energy to the fluid of the process circuit, heating the electrolyte. In the storage circuit and in the dispatch circuit, two identical circulation pumps (P2, P3) of 100 watt move the water in their correspondent loops with two possible mass flows: 350 or 850 kg h^{-1}.

In addition to that, the system is equipped with several measuring instruments of temperature (T) and mass flow (FM). Three calorimeters (CM) calculate the energy exchanged in the circuits. Moreover, a control system (CS) is installed in the plant to activate the circulation pumps. In the solar loop, the pump is activated when the water temperature at the outlet of the collector is 6 °C higher than the temperature at the top of the storage tank. The same controller stops the circulation when the temperature difference is less than 3 °C. In the dispatch circuit, the water flows when the temperature in the tank is above 60 °C.

Because of the location and the presence of a higher building behind the plant, some shadows fall on the solar collector during the afternoon.

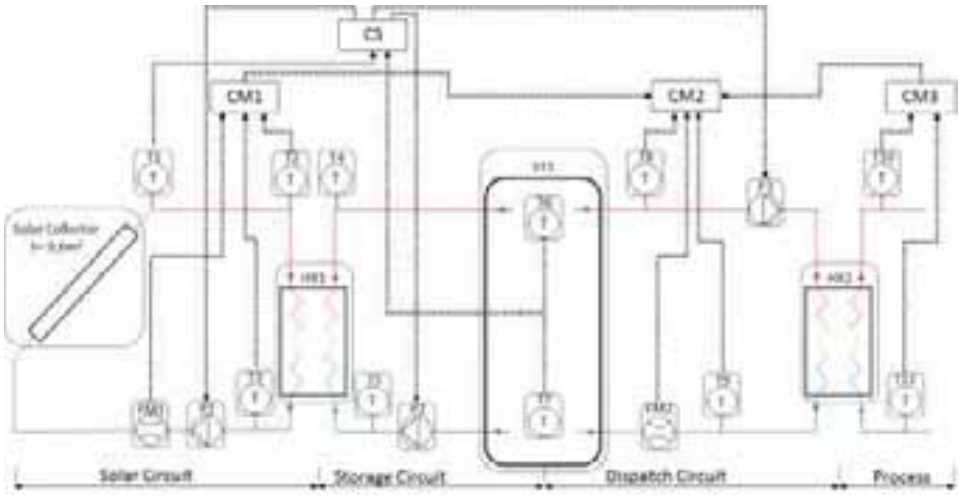

Fig. 3: Pilot plant flow sheet.

TRNSYS model

The same flow sheet of Fig. 3 was modeled in a simulation software to reproduce the pilot plant performances and to validate the model created. In particular, the plant was simulated with a simplified TRNSYS model. The flow scheme consisted in several elements called "Type", which represented the different components of the pilot plant. Table 1 resumes component characteristics. In the model, parameters referring to the size of the components were fixed; other parameters were adjusted to match simulated results with real collected data. Two inputs from collected data were introduced in the model: global radiation on the horizontal that was measured close to the collector and the temperature (T11 in Fig. 3) of the flow entering in HX2 in process circuit.

Tab. 1: summary of elements and parameters values used in simulations for the period from 19 to 31 January.

Component	TRNSYS Type	Main parameter	Value	Unit of measure	Observations
Collector	1b	Absorbing Surface	9.26	m^2 -	
		η_0	0.36	W m^{-2} K^{-1}	Optical efficiency
		K1	2.86	W m^{-2} K^{-2}	Slope efficiency
		K2	0.015		Curvature efficiency
Tank	4a	Volume	500	Liter	
		Thermal losses	2.5	W m^{-2} K^{-1}	Including pipe losses
Pumps	114	Flow P1	205	Kg/hr	
		Flow P2	350	Kg/hr	
		Flow P3	850	Kg/hr	
Heat Exchangers	5b	UA HX1	200	W K^{-1}	
		UA HX2	150	W K^{-1}	
Controllers	2b	DTmax	6	°C	Start the flow in solar circuit
		DTmin	3	°C	Stop the flow in solar circuit
	2	Tmax	59.5	°C	Start the flow in Tank load side
		Tmin	56.5	°C	Stop the flow in Tank load side
Solar Pipe	32	Thermal losses	2.36	W m^{-2} K^{-1}	
		Length	1	m	
		Internal diameter	1.905	cm	

Ambient temperature was also necessary to model thermal collector behavior and heat losses in pipes and storage tank. Because no data of ambient temperature in the site were available for the examined period, this parameter was estimated with the following method. Data of daily maximum and minimum ambient temperature in the site were available for the same period for years 2013 and 2014 and from an online database (TuTiempo, 2015) the same data for Calama, the closest city to Lomas Bayas mine (LB), were also available. Hence, an averaged ratio for the period between maximum temperature in LB and in Calama was calculated. The same operation was repeated for minimum temperature. Then, those ratios were used to estimate temperatures for 2015 in LB from Calama temperature values. Following the method of De wit et al. reported in Reicosky et al., (1989) the hourly temperature was calculated from the daily maximum and minimum values. Finally, a lineal interpolation was carried out to determine the values each minute. According to data availability, a 6-minutes time step was used in simulations. Furthermore, since collector mass flow and optical efficiency decreased in February, analyzed period was divided into four sub-periods.

3. Results

Real data

Since the pilot plant have been installed at the beginning of December, no collector cleaning was done. From data corresponding to initial weeks, a daily solar thermal production of 13.28 kWh was measured. This amount represents less than 0.1 % of energy needed to heat the electrolyte in electrowinning process and global efficiency for that period was 52%. According to information provided by Enermine (2014) maximum temperatures measured at collector outlet overcame 80 °C and effects of dust deposition were not appreciable.

For this work, data from 19 January to 20 February were available. In this period, the maximum temperatures at collector outlet were mostly below 70 °C, with the exception for the first days of February, when they reach values close to 74 °C, as it can be observed in Fig. 4a and 5. Then, a gradual decrement was registered until temperature in the tank was always less than 60 °C and no circulation to the load was observed.

Due to the presence of Andes chain at the east, the circulation inside the collector usually started after 10 a.m. and because of the shadow generated by the building behind the plant, the flow usually stopped at 3.30 p.m. Furthermore, the water circulation in the solar loop presented a minor mass flow that decreased along February.

From Fig. 4, 7, 9, 11 low collector efficiencies can be observed, due to the high dust deposition on the panel. Efficiency "Eff" for a period was calculated as the ratio between the harvested energy by the collector and the global irradiance on horizontal "$I_{g,h}$" multiplied by the collector absorbing area "A_{coll}" (see eq.1).

$$Eff = \frac{\sum_i [\dot{m}_i \cdot c_p \cdot (Tout - Tin)_i \cdot \Delta t_i]}{\sum_i (I_{g,h_i} \cdot A_{coll} \cdot \Delta t_i)} \qquad \text{(eq. 1)}$$

Where $\dot{m}$ represented the mass flow in the collector,· c_p was the specific heat, $Tout$ and Tin were the temperatures at the outlet and at the inlet of solar collector and Δt was the period length while the mass flow was considered constant.

Modeled results

Figure 4 shows results for the first period from 19 to 31 of January: the average mass flow relative error in the solar circuit for the period from 19 to 31 January was 4.3% and the average relative error in the circuit between the tank and the load was almost 6.7%. Average daily efficiency in simulations was 17.9% and it was always higher than in collected data. For real data, calculated average daily efficiency was 15%. Harvested energy by the collector in simulations was very sensible to small variation of temperature difference at collector inlet and outlet, and it causes that discrepancy in efficiency values.

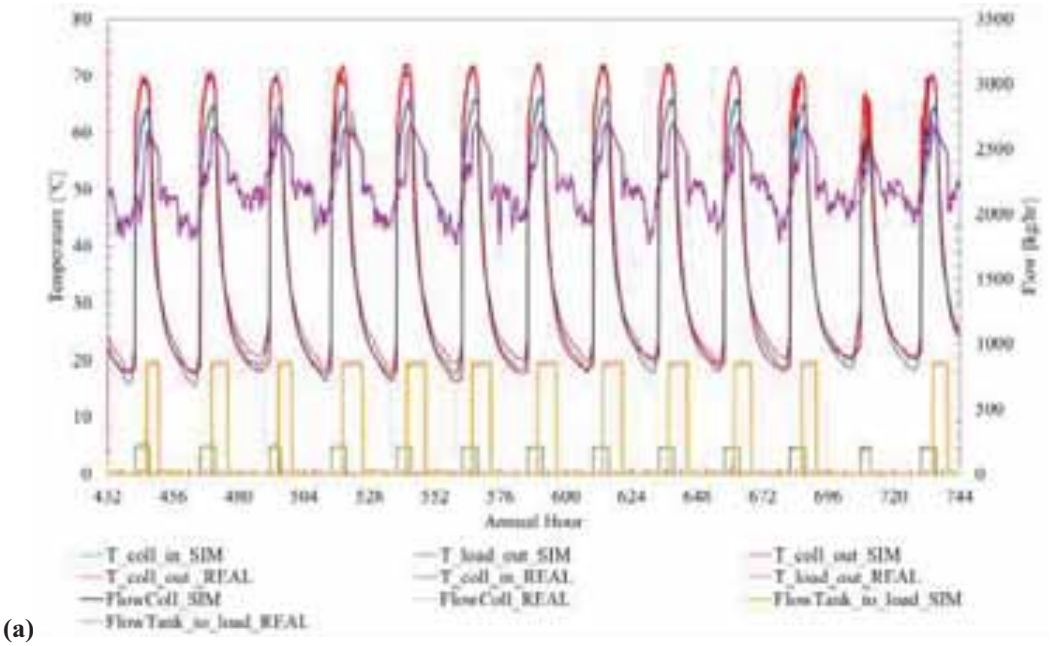

(a)

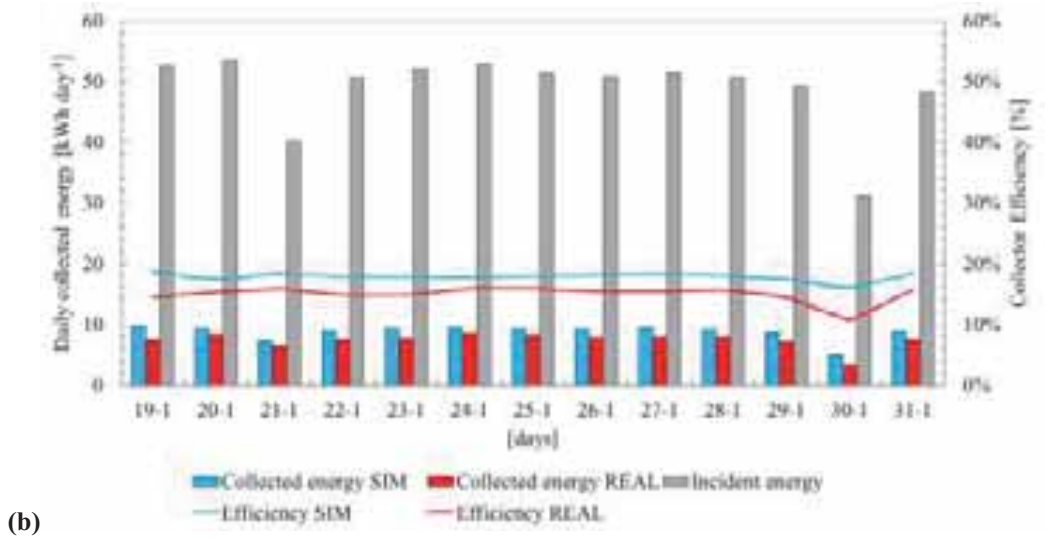

(b)

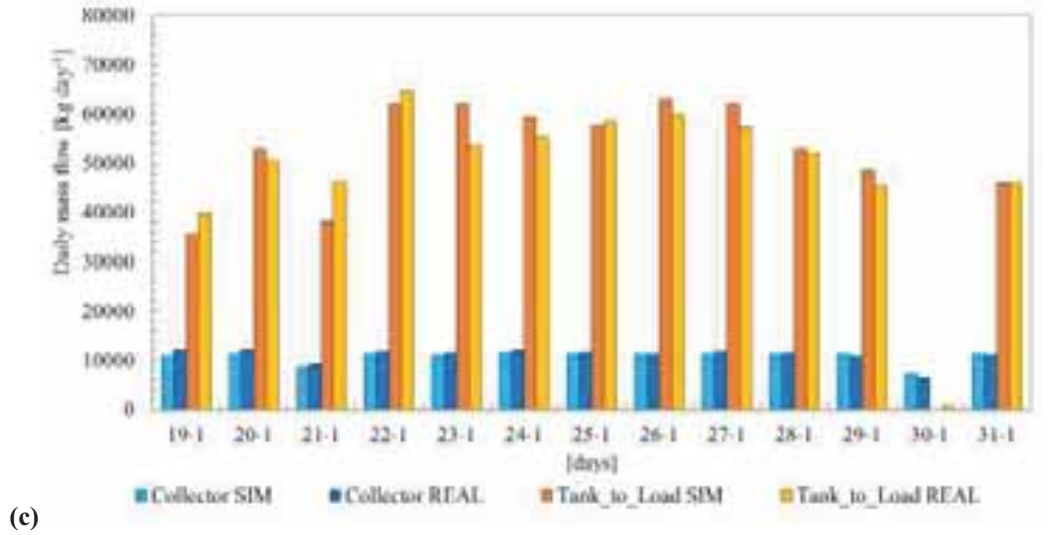

(c)

Fig. 4: Simulated and real temperature and mass flow (a), daily collected energy and collector efficiency (b) and comparison of mass flow in the collector and in the circuit tank-to-load (c) from 19 to 31 January.

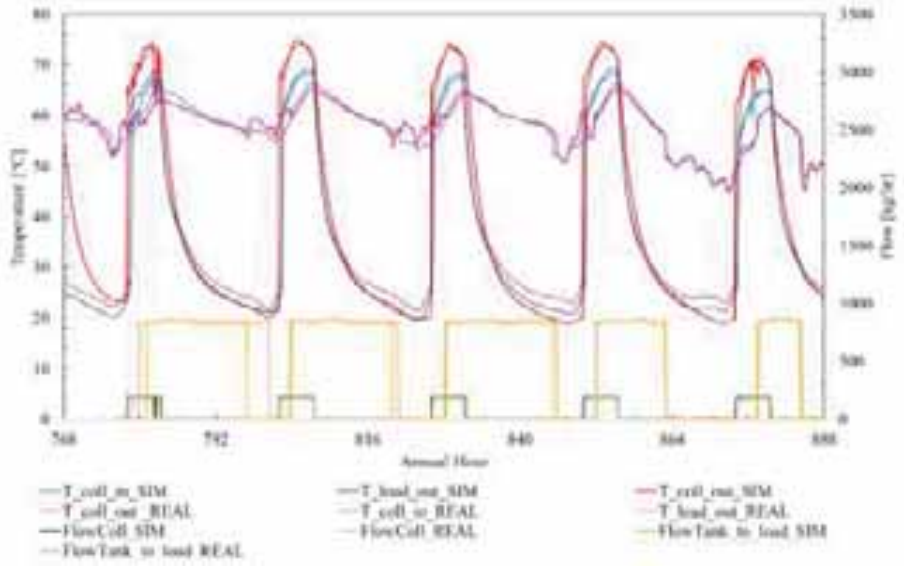

(a)

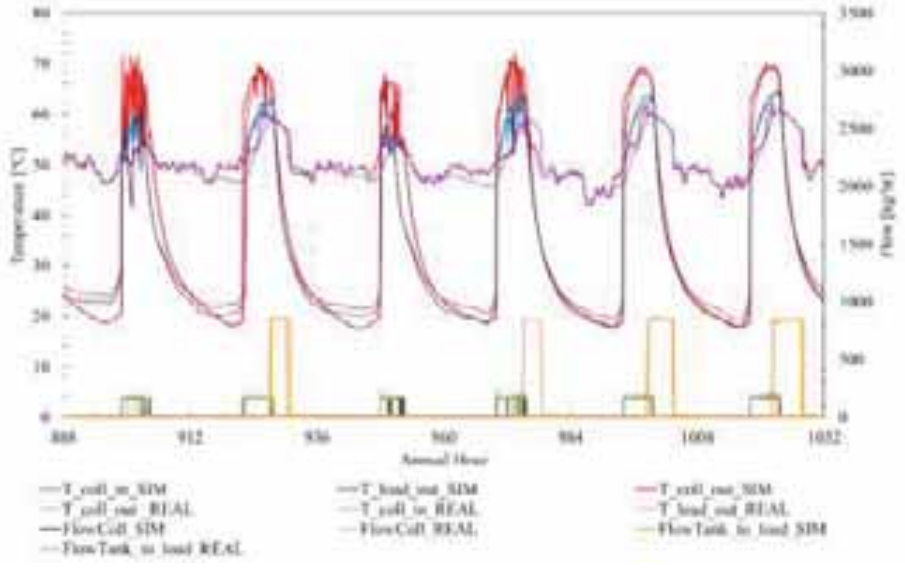

(b)

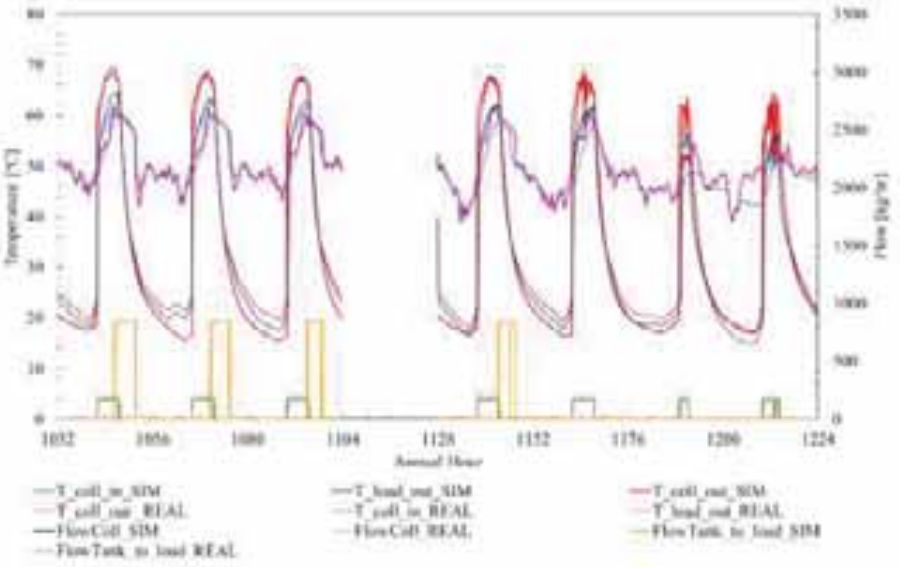

(c)

Fig. 5: Simulated and real temperature and mass flow from 2 to 6 (a), from 7 to 12 (b) and from 13 to 20 February (c).

In the second period (see fig 5a, 6) the optical efficiency was decreased to 0.355 and the mass flow was 190 kg h^{-1}. For the third (see Fig. 5b, 7) and fourth period (see Fig. 5c, 8), optical efficiency was 0.35 and 0.325 respectively and the mass flow was 170 kg h^{-1} for both. In February, results show similar trends even if accuracy is lower. This is due to the changes in some parameters and to the difficulties to find a more accurate set for the model. In general, model accuracy is lower every time a normally constant parameter (i.e. mass flow) changes its value and during partial cloudy days because of a quick variation of radiation impinging on the collector. In Fig. 5, 6, 7 and 8, 1st and 16th February are not represented because there was no data availability.

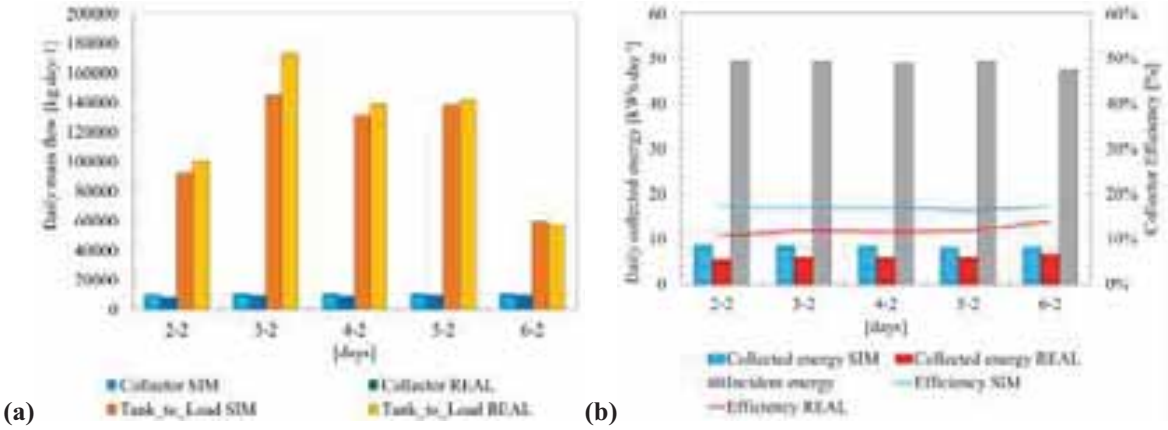

Fig. 6: Comparison of mass flow in the collector and in the circuit tank-to-load (a) and daily collected energy and collector efficiency (b) from 2 to 6 February.

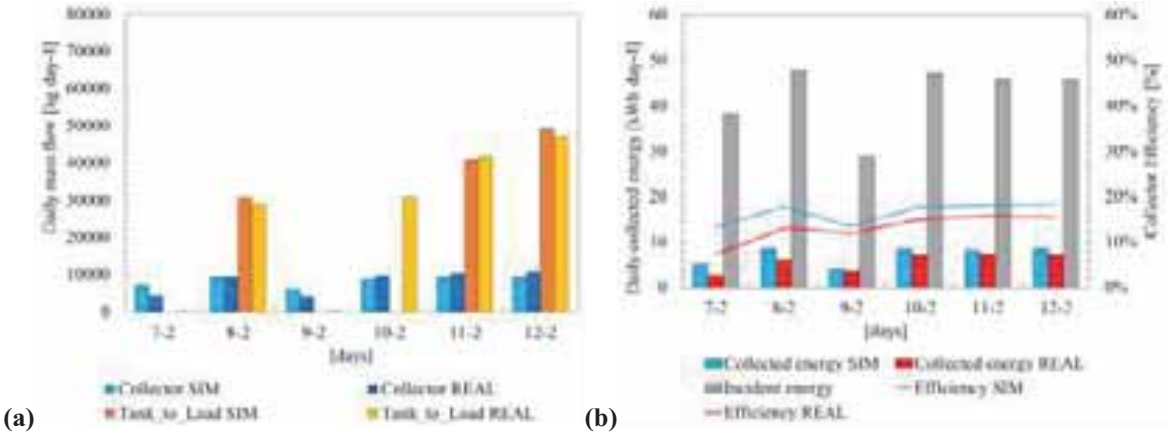

Fig. 7: Comparison of mass flow in the collector and in the circuit tank-to-load (a) and daily collected energy and collector efficiency (b) from 7 to 12 February.

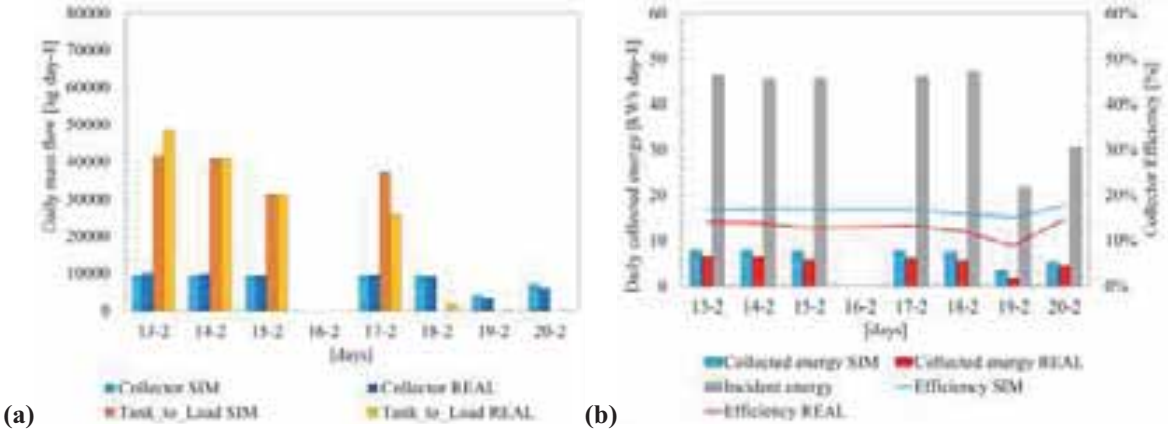

Fig. 8: Comparison of mass flow in the collector and in the circuit tank-to-load (a) and daily collected energy and collector efficiency (b) from 13 to 20 February.

4. Conclusions

In this work, a simplified model of a solar thermal pilot plant was proposed. Simulated results were compared with real data in order to validate the model and at the same time to evaluate the behavior of the plant and the effect of soling on the collector.

Because of data availability, analyzed period started on 19 January and finished 20 February 2015. In that period, daily maximum temperatures at collector outlet were mostly below 70 °C and estimated optical efficiency was 0.36 or less. Hence, outlet temperatures were approximately 10 °C lower then values recorded at the beginning of December by Enermine and optical efficiency was considerable lower than the nominal one, due to the dust deposition on the collector. During the analyzed period was also observed a gradual decrement of daily maximum temperature inside the tank until that value could not achieve 60 °C and no circulation to the load was possible.

The model was realized with TRNSYS and it can estimate the behavior of the solar plant, even if accuracy decreases for partial cloudy days and after a parameter variation (i.e. mass flow or optical efficiency). Average mass flow relative error was 4.3% for solar loop and 6.7% in load-to-tank circuit. However, calculated solar collector efficiency was always higher than the real one because the difficulties to reproduce exactly the temperature difference at collector outlet and inlet during the day.

As future work, a more detailed comparison will be conducted in order to improve achieved results and to determine the optimal frequency for collector cleaning.

Acknowledgments

Authors wish to thank Compañia Minera Lomas Bayas Mine and Enermine for the information provided and they want to thank also the Antofagasta Institutional Improvement Program (PMI ANT 120) of Chile's Ministry of Education.

References

COCHILCO Comisión Chilena del Cobre, Gobierno de Chile, 2014. Anuario de Estadisticas del Cobre y Otros Minerales 1995-2014

CSP-Today Global Tracker, http://social.csptoday.com/tracker/projects (visited last time on 28/10/2015).

CSP-Today, guía CSP Today: Chile parte 2, in CSP Today LATAM 2013

El-Nashar, A.M., 2003. Effect of dust deposition on the performance of a solar desalination plant operating in an arid desert area. Sol. Energy 75, 421–431. doi:10.1016/j.solener.2003.08.032

Enermine, 2014. Internal documents on Lomas Bayas solar thermal pilot plant and results presentation

Escobar, R. a., Cortés, C., Pino, A., Pereira, E.B., Martins, F.R., Cardemil, J.M., 2014. Solar energy resource assessment in Chile: Satellite estimation and ground station measurements. Renew. Energy 71, 324–332. doi:10.1016/j.renene.2014.05.013

Gallo, A., Alonso, E., Pulido, D., Fuentealba, E., 2014. Análisis tecno-económico de soluciones integrales de habitabilidad en emplazamientos mineros de las regiones del norte de chile basadas en envolventes modulares con acondicionamiento solar por absorción, in: XI Congreso Iberoamericano de Energía Solar.

Portillo, C., Alonso, E., Fernández, A., Ferrada, P., Gallo, A., Marzo, A., Fuentealba, E., 2015. Progress in solar energy R&D in north of Chile: Solar Platform of Atacama Desert project and ongoing activities 8–12.

Reicosky, D.C., Winkelman, L.J., Baker, J.M., Baker, D.G., 1989. Accuracy of hourly air temperatures calculated from daily minima and maxima*. Agric. For. Meteorol. 46, 193–209. doi:10.1016/0168-1923(89)90064-6

Ushak, S., Grágeda, M., Pulido, D., Oró, E., Cabeza, L.F., 2014. Application of Solar Heating on the Electrolyte Conditioning for Electrowinning Process: Thermosolar Plant Performance. Energy Procedia 57, 2930–2936. doi:10.1016/j.egypro.2014.10.328

http://www.tutiempo.net/clima/CALAMA/854320.htm (visited last time on 28/10/2015)

Conference Proceedings

Solar World Congress 2015
Daegu, Korea, 08 – 12 November 2015

Low Concentrating Solar Collectors for Economical Generation of Low-Medium Temperature Industrial Process Heat

Atul S. Jadhav and J. L. (Wikus) van Niekerk

Centre for Renewable and Sustainable Energy Studies (CRSES),

University of Stellenbosch, Stellenbosch(South Africa)

Abstract

A large fraction of the total energy consumption in the industrial sector (approximately 60%) is for direct heat/thermal applications known as Industrial Process Heat (IPH). About half of that energy is used to generate IPH, below the temperature of 300 ^{0}C. To supply this heat energy alternatively, various solar thermal technologies are being utilized. For generating heat at temp below 120 ^{0}C flat plats and evacuated tube collectors are used and for temperature above 150 ^{0}C, high concentrating technologies such as PTC, dish concentrators are used. Flat plats solar water heaters are economical and efficient in generating heat at lower temperatures. But to generate heat at temperature above 150 ^{0}C, more expensive and high concentrating solar collectors are being used. Alternative, less concentrating solar collector with zero or minimum solar tracking, can be used to generate the low-medium temperature industrial process heat. Various, more efficient low concentrating collectors are being developed and tested by researcher which can be used for such applications. These kinds of collector provide more economical solution than high concentrating collectors. In this paper we will look at some of the recently developed low concentrating solar collectors and how they can be utilized to produce low-medium temperature industrial process heat in more economical way compare to high concentrating solar collectors.

Keywords: *Industrial process heat (IPH), Solar Concentrators, Compound Parabolic Collector*

1. Introduction

Energy is the key factor contributing to economic development and quality of life worldwide. It is the basic input required to sustain economic growth. There is direct relation between the level of economic development and per capita energy consumption. Simply speaking more developed a country, higher is the per capita consumption of energy and vice-versa. But conventional energy has two major drawbacks, in the way it is produced and used. Firstly, the overall energy system has been very inefficient in the past. And secondly, major environmental and social problems are associated with the traditional energy system. According to IEA's report greenhouse gases (GHG's) emissions from the traditional energy sector will increase by 130% above 2006 levels by 2050 if new policies and practices are not implemented. (IEA, 2008) Moreover, environmental issues of conventional energy resources such as climate change and global warming are continuously forcing us for alternative sources of energy. According to the statistics released by World Health Organization (WHO), direct and indirect effects of climate change leads to the death of 160,000 people per year and the rate is estimated to be doubled by 2020. (Muneer et al., 2006) Therefore, finding clean sources of energy to satisfy the world's growing demand is one of the society's foremost challenges for the next few decades.

For last couple of decades, there is an accelerated effort, throughout the world, in R&D and implementation of various renewable energy sources i.e. solar, wind, biogas, biomass etc. Among all the renewable energy sources, solar power attracted more attentions as a greatest promising option for energy generation. Solar energy is abundance, free and clean which does not make any kind of pollution to the environment. Amount solar energy received by earth surface in a year is about 885 million terawatthours (TWh). That is 6 200 times the commercial primary energy consumed by humankind in 2008 – and 4 200 times the energy that mankind would consume in 2035 (IEA, 2011). At present consumption rate, proven fossil reserves can last for 46 years (oil), 58 years (natural gas) and almost 150 years (coal) (IEA, 2010), the energy received by the sun in one single year, if entirely captured and stored, would represent more than 6 000 years of total energy

doi:10.18086/swc.2015.10.37 Available at http://proceedings.ises.org

consumption. Capturing and distributing only one tenth of one percent of solar energy will make the energy supply problem disappear.

Presently, solar energy is being widely used for generation of electricity and heat. According to study on the world energy consumption by International Energy Agency (IEA), by 2050 around 45% of energy demand of the world will be supplied using solar energy. As electricity is the highest quality of energy it should be given priority. But energy consumption in the form of direct heat also forms a major mode of energy consumption. The importance of energy in industrial development is very crucial since major fraction of energy is used in industrial processes. It has dominated more than 50% of total energy consumption worldwide.

2. Industrial Process Heat

Industrial sector uses heat for a wide variety of applications, including washing, cooking, sterilizing, drying, preheating of boiler feed water, process heating, and much more. Three different temperature levels are used for describing the quality of the demand for heat in industries: low temperature level is defined as up to 95 °C, corresponding to the typical heat demands for space heating or industrial processes like washing, rinsing and food preparation. Temperatures between 95 ºC and 250 ºC are defined "medium". This heat is normally supplied through steam. Temperatures over 250 ºC are "high" and needed to manufacture metals, ceramics, glass etc. To estimate the potential of solar thermal technologies for industrial process heat generation, knowledge of the required different temperature levels of process heat is essential. Following table 1, gives an overview of various industrial process and their temperature levels.

Tab 1: Temperature ranges for different industrial processes (Kalogirou, 2003a)

Industry	**Process**	**Temperature (°C)**
Dairy	Pressurization	60–80
	Sterilization	100–120
	Drying	120–180
	Boiler feed water	60–90
Tinned food	Sterilization	110–120
	Pasteurization	60–80
	Cooking	60–90
	Bleaching	60–90
Textile	Bleaching, dyeing	60–90
	Drying, degreasing	100-130
	Pressing	80–100
Paper	Cooking, drying	60–80
	Boiler feed water	60–90
	Bleaching	130–150
Chemical	Soaps	200–260
	Synthetic rubber	150–200
	Processing heat	120–180
	Pre-heating water	60–90
Meat	Washing, sterilization	60–90
	Cooking	90–100
Beverages	Washing, sterilization	60–80
	Pasteurization	60–70
Timber by-products	Thermo diffusion beams	80–100
	Drying	60–100
	Pre-heating water	60–90
	Preparation pulp	120–170

Plastics	Preparation	120–140
	Distillation	140–150
	Separation	200–220
	Extension	140–160
	Drying	180–200
	Blending	120–140

These industrial sectors/processes account for a significant share of energy consumption, and currently, energy required for these processes are supplied using fossil fuels. For industrial nation like Germany about 30% of the total energy demand is consumed by industrial sector. About 65% of this energy is used for generating industrial process heat. This energy is further divided, according to temperature level of process heat. Such as, 69 % of the industrial heat is demanded at temperatures above 250 °C (Figure 1). At temperatures below 100 °C, 21 % of the heat can be provided and further 6 % between 100 and 150 °C. And remaining 4 % of the demand occurs between 150 and 250 °C. (Lauterbach et al., 2011) This data is important to understand which solar thermal technology is suitable for specific industrial process.

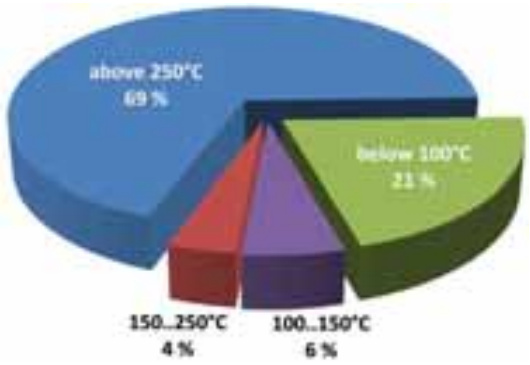

Fig 1: Industrial heat demand in Germany per temperature range. (Lauterbach et al., 2011)

Some of the sectors like steel, aluminium and ceramic have a number of processes which require high-grade heat (temperatures ranging above 800˚C), it would not be possible to provide these temperature levels with solar thermal technologies at reasonable costs. But most of the industrial processes have favourable conditions for the application solar energy. If industrial sectors actively exhibit eagerness, process heat requirement at 400 ^{0}C and below, can be successfully supplied using solar thermal technologies. Overall, an increase in solar energy in industry has the potential to contribute about 10% of all expected GHG emissions reductions in 2050. This is equivalent to the total current CO_2 emissions of France, Germany, Italy and Spain, or around one third of current emissions in the United States. (Thomas, 1995)

3. Solar thermal technologies

Among all the renewable energy sources, solar power attracted more attentions as a greatest promising option to be applied in industries. Solar energy is abundance, free and clean which does not make any kind of pollution to the environment. So far, many attempts have been made to extract solar energy by means of solar collectors, sun trackers and giant mirrors in order to utilize it for industrial purposes. To supply industrial process heat, various solar thermal technologies are being utilized. For generating heat at temp below 120 ^{0}C flat plats and evacuated tube collectors are used and for temperature above 150 ^{0}C, high concentrating technologies such as PTC, dish concentrators are used. Solar thermal technologies utilise the sun radiation to produce heat for many thermal applications. There are various solar thermal technologies available which can be utilized to supply heat at temperature between 60 ^{0}C and 250 ^{0}C. As can be seen in table 2, each technology can be characterised depending on their operating temperature, stationary or tracking etc.

Tab 2: Types of solar thermal collectors (Kalogirou, 2003b)

Motion	Collector type	Absorber type	Concentration ratio	temperature range (ºC)
Stationary	Solar pond		1	30–90
	Flat plate	Flat	1	30–80

	collector (FPC)			
	Evacuated tube collector (ETC)	Flat	1	50–150
	Compound parabolic collector (CPC)	Tubular	1–5	60–240
Single-axis tracking			5–15	60–300
	Fresnel lens collector (FLC)	Tubular	10–40	60–250
	Parabolic trough collector (PTC)	Tubular	15–45	60–300
	Cylindrical trough collector (CTC)	Tubular	10–50	60–300
Two-axes tracking	Parabolic dish reflector (PDR)	Point	100–1000	100–500
	Heliostat field collector (HFC)	Point	100–1500	150–2000

These technologies can also be differentiated by the way they use solar energy. Flat plate and evacuated tube and low concentrating collectors use direct as well as diffuse solar radiation. High concentrating and tracking collector uses only direct normal solar radiation. The main component of any solar thermal technology installation is the solar collector. Solar collector collects the heat from solar radiation and transfers it to a receiver, containing stationery/circulating fluid (usually water or thermal oil). The solar energy thus collected is carried from the circulating fluid either directly to be utilized in many different thermal applications or to a thermal energy storage tank from which can be drawn for use at night and/or cloudy days.

From figure 1, it is evident that the requirement of the low-medium temperature process heat is obvious and significant. However, for the non-concentrating solar collectors, such as evacuated tube and flat plate collector, thermal efficiency of the collector decreases with increasing temperature. Especially above 80 ^{0}C, the thermal efficiency of the solar collector falls sharply, because of which they cannot be used efficiently for these applications. Therefore, to produce process heat at temperature above 80 ^{0}C, it requires solar concentrators, as opposed to non-concentrating collectors [Sardeshpande and Pillai, 2012]. On the other hand, although the high-concentration solar collectors can generate process heat at temperature above 80 ^{0}C, they need a sun tracking system, which further escalates operation and maintenance costs. Which usually make them suitable for large-scale integrated applications, such as high-temperature solar thermal power generation. At the same time, the high-concentration solar collectors, such as tower concentration solar collector and dish concentration solar collector, can get much higher temperature, which is beyond these applications temperature above, and can cause more thermal losses. What is more, high-concentration solar collectors can lead to more diffusion loss as these systems only make use of direct normal solar radiation. Therefore, high-concentration solar collectors also do not fit economically for these low-medium temperature process heat applications.Employment of low concentrating solar collectors is necessary for generating low-medium process heat more efficiently and economically. Researchers developed various efficient and economical low concentrating collector system but very few systems are commercially available.

4. Low Concentrating Solar Collector

Compound parabolic collectors (CPC), evacuated tube collector with/without CPC and flat plate collector sometime with booster reflectors, are employed as stationery and low concentrating systems. One of the main advantages of this type of system is that they can utilise direct as well as some/ all diffuse solar radiation. This make them more efficient for solar radiation collection in a region where atmospheric pollution and dust particles, minimises direct radiation and maximizes diffuse solar radiation. Compound parabolic collector hold great promise to become alternative technology to provide industrial process heat at temperature in range of 150 ^{0}C – 250 ^{0}C. Concept design of CPC was first introduced by Winston in 1974, which is a non-imaging type of concentrator. (Winston, 1974) The basic shape of the compound parabolic concentrator (CPC) is illustrated in Figure 2. A CPC is made of two halves of symmetrical parabola with closely located focal points and their axes inclined to each other, such that rays incident within the angle between the two axes (angle of the CPC) are reflected towards the region between the two focal points and get concentrated in that region, not on a point. Thus, CPCs are non-imaging concentrators and can accept incoming radiation over a relatively wide range of angles.

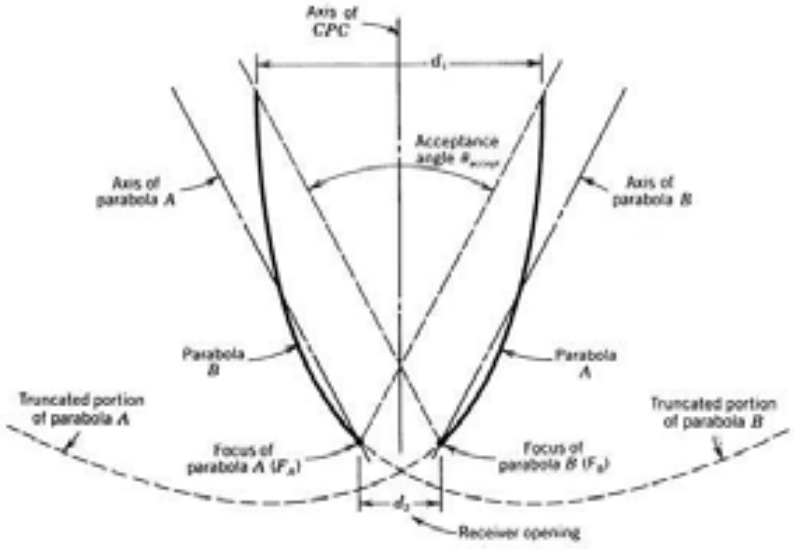

Fig 2: The geometry of conventional compound parabolic concentrator (CPC).

However, there is a trade-off, curve of a parabola has the property that its height increases very slowly as compared to its aperture, until the focal plane is reached; and it increases sharply beyond the focal plane. In the conventional design of CPC, foci of both the parabolas lie at the bottom of the CPC, and sections above the focal points of both are used. This causes rapid increase in height and a low energy concentration performance. Various designs have been proposed by several researchers to successfully overcome these limits to varying degrees.

In 2013 Jadhav et al. (Jadhav et al., 2013) proposed improved design of compound parabolic collector as compared to those reported earlier. Improved design substantially reduced the reflector height without compromising the concentration ratio. The modified design used the region below the common focus of parabolas. Based on their designed, a 100 m2 CPC system was fabricated and investigate, with aperture width 2 m, acceptance angle 3 and receiver pipe of 48 mm outer diameter had a height of around 0.5 m from base of reflector. For the same aperture width, acceptance angle and receiver dimensions, the height for conventional, untruncated CPC is around 38 m. Thus the modified CPC design needs substantially reduced support structure, and consequently, expected to be economical and easy to handle. The receiver wasn't evacuated and system generated steam at 120 ^{0}C with 43% efficiency. Cost of their 100 m^2 system was around 70 US$/m^2 and claimed that same system with few minor refinement can generate steam at around 200 ^{0}C.

Fig. 3. A photo of the experimental 100 m^{2}CPC system.

Recently, Lun Jiang et al. (Jianga et al., 2015) published performance of eXternal Compound Parabolic Concentrator (XCPC). This prototype XCPC, as seen in figure [4] is placed East-West, with pentagon absorber as cross section. Oil is used as the heat transfer fluid in the system. The absorber tube is made of a metal glass vacuum tube due to its improved heat transfer capability compared to the all glass vacuum tubes. Their test result shows that XCPC reach working temperature of 160 ^{0}C, 200 ^{0}C and 230 ^{0}C with efficiency of about 59%, 52% and 43% respectively.

Fig 4: The XCPC collector with east west axis direction. Aperture area for each collector is 4.5 m^2

Lun Jiang et al. (Jianga et al., 2015) also published performance of full size collector of Integrated Compound Parabolic Concentrator (ICPC) (Fig.6). Each of the ICPC tube is eventually fabricated at 85mm width with a absorber of 30mm height, resulting in a concentration ratio of 1.41. The aperture area is 1900mm X 85mm for each tube. A heat pipe of 8mm diameter is inserted into the absorber fin and ultrasonic welded on to the fin to ensure the heat transfer. The reflective coating is using the Flat Plate Collector with Booster Reflectors standard silver mirroring chemical process, with a protective resin to be weather proof. The optics of the ICPC is designed for a 35 degrees acceptance angle and therefore should be positioned east-west direction. But for testing purpose and the trial of the heat pipe as a heat transfer model, we implemented them as north-south aligned, and put them on a tracker to take the measurement. The result is showing a relatively lower performance compared to the XCPC model under the same temperature. However, this is mainly due to the heat pipe not functioning as ideally as a heat transfer mechanism compared to the direct flow mechanism in the XCPC array. The ICPC collectors show 42% efficiency at 200 °C based on global irradiance.

Fig 5: a) The ICPC 3.5 m^2 prototype, with full 1900mm length tube, front view. b) The cross section of the original ICPC prototype design.

Two non-tracking variation of CPC proposed by Wattana Ratismith et al. (Ratismith et al., 2014) one is more conventional double-parabolic trough, has the absorber plate perpendicular to the vertical axis of the trough cross-section. Second one is of a new flat-base shape, has the absorber plate parallel. The collectors have two novel features appropriate to non-tracking. The collectors have two novel features appropriate to non-tracking. The first is a smoothing of the power output over the day by beneficially arranging three troughs

tilted at different angles. The second salient feature in the design of these solar collectors is the use of a trough which utilises the non-focussing advantages of non-parabolic shapes in achieving high acceptance angle, high intercept factor and high concentration of diffuse sunlight.

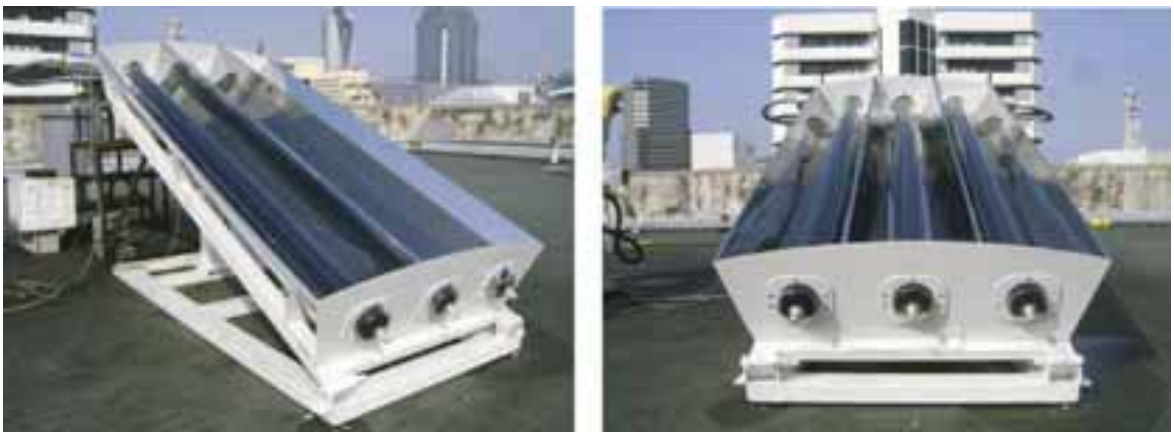

Fig 6: The non-tracking solar collector

They showed that their stationary flat base shape CPC performed better with operating temperature of 180 ^{0}C at 40% efficiency. In the experiment they used the commercially available SUNDA (SEID01) vacuum tubes of length 2.1 m with a planar absorber plate of width 9.0 cm.

Two truncated compound parabolic concentrating (CPC) solar collectors (shown in figure 7a & 7b), which combine the external CPC and the U-shape evacuated tube together, have been developed and tested by X. Li et al. (Li et al., 2013) Their CPC has concentration ratios of 3 and 6 and half-acceptance angles of 10^0 and 3^0, respectively. CPC with 3 concentration ratio will need only seasonal tracking while CPC with 10 concentration ratio will need to track sun 5 times a day. The daily thermal efficiencies of the 3X and the 6X CPC collectors can reach 40% and 46% at the collecting temperature of 200 ^{0}C, respectively. These verify that these kinds of CPC solar collectors are feasible for a wide range of intermediate industrial temperature applications.

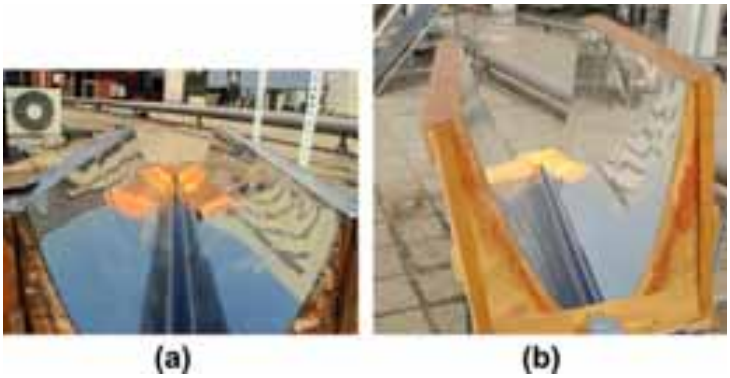

Fig 7: (a) the 3X CPC collector; and (b) the 6X CPC collector.

Last year at an international conference on solar heating and cooling, H.J. Burckhart et al. (Burckhart et al., 2013) presented results on use of novel collectors from the company SRB for heating and cooling of a building in Geneva, Switzerland. SRB Energy developed a two sided vacuum flat-plate collector, combined with CPC reflectors at the bottom side of the receiver (Figure 8a). This holds for both direct and diffuse light, which is of special importance as diffuse light amounts to about half of the total light in middle Europe. This system is stationery and according to the company, the vacuum inside the flat-plate, between 10^{-6} to 10^{-9} mbar,is expected to last for the whole service life of the collector. Figure 5b shows the collection efficiency of this system for different solar irradiations. Temperatures up to 400 °C can be reached. Figure 8b shows, that the 90 °C necessary to drive the absorption unit can easily be reached for irradiations as low as 200 W/m^2 with a reasonable efficiency. The stability and ease of operation of this solar collector has already been proven in existing installations.

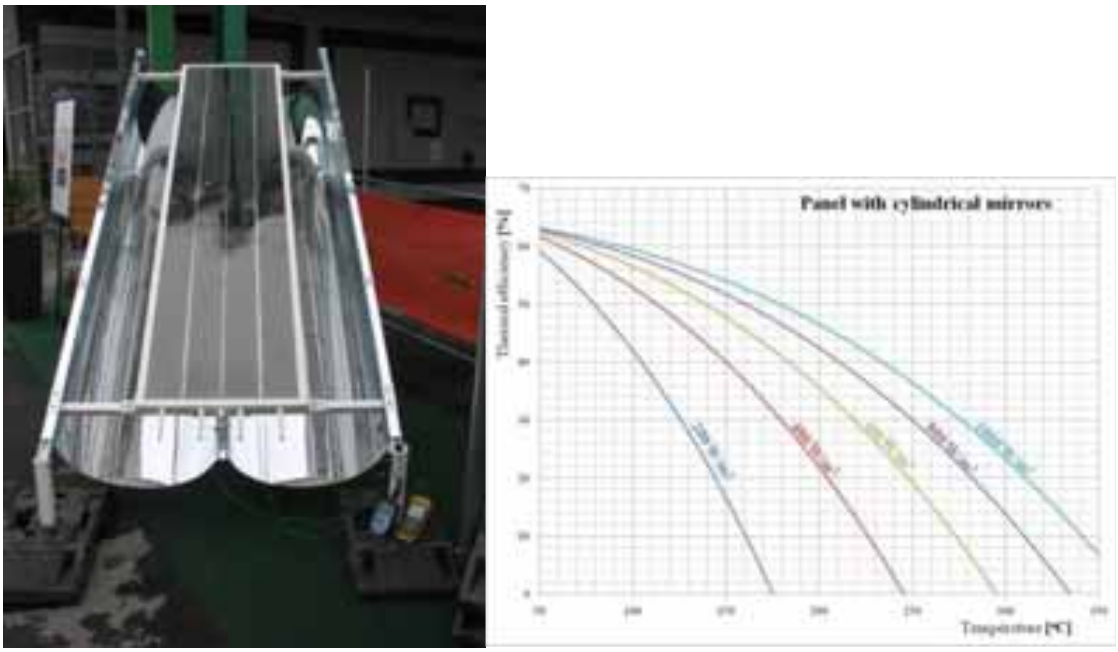

Figure 8: a) Assembly of the absorber panel and the two mirrors b) Thermal efficiency for different solar irradiation

5. Drivers for low concentrating technologies

In previous section we discussed some of stationery and low concentrating technologies, which are being developed and tested to operate at temperatures close to 250 ^{0}C. Most of these technologies, more or less are laboratory based or/and demonstration purposes only. One of the main barriers to increased deployment of solar industrial process heat systems is the high investment cost and lack of finance options. Cost plays important deciding factor for any new technology to become market ready and available to consumer. All solar process heat systems involve high initial investments in advance of a practically cost-free operating period. However, proper maintenance is required to ensure that the systems operate optimally over their full lifetime expectancy. The up-front costs particularly hamper deployment in small and medium size enterprises where financing is not available. (ESTIF, 2014)

The costs of solar thermal process heat installations in Europe range from 180 to 500 Euro / m^2 of aperture area, depending on the system concept, the size of the system, the selected components (e.g. the choice of the collector type) and on country-specific factors (e.g. salaries). Of the total costs in solar thermal technology, between 50-70% are related to the capital, while the remainder covers installation and integration. (IRENA, 2015) Table 3 provides an overview of the costs for solar concentrators: solar parabolic dish and parabolic dish are more expensive than conventional FPC and ETC but permit higher temperature ranges. Aagain these cost can vary from region to region, but for the sake of arguement Indian cost of all these technologies are taken. Comparing cost of stationery and concentrating solar collector one can easily find out that concentrating collector cost at least double than stationery solar collector. This cost difference can easily be a discouraging factor for small and medium scale industries from adopting solar process heat system.

Tab 3: Cost comparison of solar thermal collectors (IRENA, 2015)

	Stationery Solar Collectors		**Tracking Concentrating Solar Collectors**		
	FPC	**ETC**	**Parabolic Dish**	**PTC**	**Linear Fresnel**
Temperature Range ^{0}C	100 ^{0}C	120 ^{0}C	250 ^{0}C-700 ^{0}C	100 ^{0}C-400 ^{0}C	100 ^{0}C-350 ^{0}C
Cost (USD/m^2)	84-302	97-369	300-600	445	650-900
Cost (USD/kW)	216	203	600-1760	1580-2040	1160-1800

Stationery low concentrating collectors can play an important role of supplying low-medium temperature industrial process heat at a cost which can comfortably fit between the costs of stationery and tracking collectors. Theses collectors can be little expensive that stationery collector as they use reflector for concentration of solar radiation. At the same time low concentrating collectors will be less expensive that tracking collectors as they never/occasionally use more precision tracking mechanism and reflector curve. Developing and poor countries with high solar irradiation, small and medium size industries are an interesting market for such low concentrating solar thermal systems. As, these industries often rely on expensive fossil fuels for heat production and solar thermal systems reduce their dependence on fossil fuels and contribute to the reduction of operating costs. Also, the heat demands per plant are relatively small compared to the energy intensive industry, which makes the integration of solar heating systems easier. The sheer number of SMEs present could result in rapidly declining costs due to learning by doing and more effective operations by installers. This could create a virtuous circle in which, with declining costs and more experience, the deployment of solar heating systems is accelerated in this market segment. (IRENA, 2014)

6. Conclusion

A large fraction of energy used in industrial sector, is used for generating industrial process heat at temperature below 300 ^{0}C. To move away from polluting fossile fuel utilization, solar energy is succefully utilized for such applications. Presently, medium temeprature (150 ^{0}C - 300 ^{0}C) industrial process heat is supplied using solar concentrators similar to technologies used to produceconcentrated solar power (CSP). Instead of using the heat to produce power however,the heat is directly used in industrial processes. Such solar concentrators are parabolic dishes, parabolictrough concentrators and Linear Fresnel collectors. These collectors are made with efficient absorber, precision optics and tracking mechanism to produce temperature much greater that medium temperature range. Becuase these charecteristics of high concentrating collectors are expensive than the stationery solar collectors. For cost sensetive market in poor and developing counrties, for successful deplyment of solar industrial process, cost of these technologies needs to be brought down. An alternative for these expesive concentrator will be less concentrating technologies which are still under development stages. Less concentrating solar collector with zero or minimum solar tracking, can be used to generate the low-medium temperature industrial process heat. As discribed in this paper, researchers are developing more efficient low concentrating collectors which can be used for such applications. Cost comparsion of existing technologies shows that there a cost gap and market for low concentrating collectors which can be further explored. If developed further, commercialization of more efficient low concentrating technologies will further intensify the successful deployment of solar industrial process heat.

7. References

- Burckhart, H., Audinet, F., Gabassi, M., Martel, C., 2014, "Application of a Novel, Vacuum-insulated Solar Collector for Heating and Cooling." Energy Procedia, 48(0): 790-795.
- ESTIF (European Solar Thermal Industry Federation), “Solar heating and Cooling Technology Roadmap”, European Technology Platform on Renewable Heating and Cooling, June 2014, http://www.estif.org/fileadmin/estif/content/projects/ESTTP/Solar_H_C_Roadmap.pdf
- IEA (2008), Energy Technology Perspectives 2008, OECD/IEA, Paris.
- IEA (2010), World Energy Outlook 2010, OECD/IEA, Paris.
- IEA (2011), Solar Energy Perspectives 2011, OECD/IEA, Paris.
- IRENA,‘Solar Heat for Industrial ProcessesTechnology Brief’ January 2015, available at www.irena.org
- IRENA, “Renewable Energy in Manufacturing, A Technology Roadmap for REmap 2030”, June 2014, Abu Dhabi, http://irena.org/remap/REmap%202030%20Renewable-Energy-inManufacturing.pdf.
- Jadhav, A.S., Gudekar, A.S., Patil, R.G., Kale, D.M., Panse, S.V., Joshi, J.B., 2013, “Performance analysis of a novel and cost effective CPC system”,Energy Conversion and Management. 66, 56-65
- Jianga, L., Widyolara, B., Winstona, R., 2015,“Characterization of novel mid-temperature CPC solar thermal Collectors”, Energy Procedia 70, 65 – 70
- Kalogirou, S., 2003a, “The potential of solar industrial process heat applications”, Applied Energy;76(December (4)):337–61.

- Kalogirou, S., 2003b, "The potential of solar industrial process heat applications", Applied Energy; 76(December (4)):337–61.
- Lauterbach, C., Schmitt, B., Vajen, K., 2011, "Das Potential solarerProzesswärme in Deutschland", Available at: http://solar.umwelt-uni-kassel.de/downloads.de.html
- Li, X., Dai, Y., Li, Y., Wang, R., 2013, "Comparative study on two novel intermediate temperature CPC solar collectors with the U-shape evacuated tubular absorber", Solar Energy 93, 220–234.
- Muneer T, Maubleu S, Asif M., 2006, "Prospects of solar water heating for textile industry in Pakistan", Renewable and Sustainable Energy Reviews; 10(February (1)):1–23.
- Ratismith, W., Inthongkhum, A., Briggs, J., 2014, "Two non-tracking solar collectors: Design criteria and performance analysis", Applied Energy 131, 201–210.
- Sardeshpande, V., Pillai, IR., 2012, "Effect of micro-level and macro-level factors on adoption potential of solar concentrators for medium temperature thermal applications", Energy for Sustainable Development; 16:216–23.
- Thomas, A., 1995, "Solar steam generating systems using parabolic trough concentrators", Energy Conversion and Management 37, 215–245.
- Winston, R., 1974, "Principles of solar concentrators of a novel design", Solar Energy;16:89–95.

Conference Proceedings

Solar World Congress 2015
Daegu, Korea, 08 – 12 November 2015

USE OF FLAT SOLAR COLLECTORS, IN REPLACEMENT OF LPG GAS FOR WATER PRE-HEATING, TO BE USED IN ENGINES OF ELECTRIC POWER THERMAL GENERATION PLANTS

José Bione M. F.[1], Aluísio A. Medeiros Silva[2] and Carlos Salviano[2]

[1] University of Pernambuco and Institute Federal of Pernambuco, Recife (Brazil)

[2] University of Pernambuco – Escola Politécnica, Recife (Brazil)

Abstract

Energy consumption in the world has been growing every year. The industrial sector represents 27.32% of the world energy demand. Implementation of flat solar collectors (temperature > 100°C) replacing the LPG gas to preheat the water used in the electricity industry, for the three engines of the Thermal Power Plant of Electricity Energy Generation – TermoCabo with power 45 MW. Given the importance of the matter, this research project aims a technical analysis and economic evaluation of the use of flat solar collectors, including an analysis in the control system of the plant, besides an adaptation of the collectors to the charge demand and to the thermal energy storage system in order to maintain autonomy of 24 hours. The system consists of a battery of collectors associated to a complex grid of flow control and maintenance of stagnated temperature of 65°C, besides the system working independently, having the heat exchanger as a point of intersection between the primary and the secondary system. The project was planned as three closed and independent systems, because due to load operating complexity (engines) required the collectors independent worked the other parties, and the need to use glycol to increase the boiling water point, plus there a water storage system to maintain the autonomy and the third stage is the engine heating system, which is composed of thermal additive.

Keywords: *Flat Solar Collector, Solar Energy, Energy Efficiency, Heating System.*

1. Introduction

Energy consumption in the world has been growing every year. The industrial sector represents 27.32% of the world energy demand. The search for greater energy efficiency, along with policies of clean development mechanism, has encouraged the study of new techniques for power generation using renewable energy sources with lower generation of pollutants (DINIZ & BERMANN, 2012). Among the alternative energy sources, solar energy is becoming more popular, especially for residential water heating, being a cost-effective alternative to the use of electricity and natural gas (Goldemberg & Lucon, 2007; Luna et al., 2008; Oliveira et al., 2008; Altoé et al., 2012). Heating systems that use solar energy may contribute with a percentage of the total energy required by industries. Heat is often underappreciated in public policy discussions on energy, frequently overshadowed by transportation energy and electric power. However, heat accounts for 37 percent of energy consumed within most developed countries, and 47 percent of the world's energy consumption (IEA 2013). While many people associate solar energy with electricity-producing photovoltaic (PV) panels, solar can also be used for heating purposes. Solar thermal energy is most commonly used to heat outdoor swimming pools and residential water in the United States, but it can also be used for many types of industrial processes (IEA 2014). This issue brief will examine the role that solar thermal technology currently plays in industrial heating processes and outline opportunities for increased application in the world industrial sector.

The industrial sector is the leading source of energy consumption in the United States. At nearly one third of total energy use, it exceeds both the transportation and residential sectors. Within the industrial sector, nearly two thirds of energy used is consumed as heat. Some industries have even higher rates, such as the glass industry, which consumes about 80 percent of its energy for heating purposes. The remaining third can be

doi:10.18086/swc.2015.10.38 Available at http://proceedings.ises.org

attributed to electricity generation or energy lost in transmission within the grid, or by inefficient conversion within the power plant itself.

Depending on how industrial thermal energy is defined, nearly 90 percent of the energy comes from burning fossil fuels, but biomass can count for up to 11 percent.6 The remaining 10 percent of thermal industrial energy comes from electricity, which is often generated by power plants that burn fossil fuels. When including the environmental degradation from extracting fossil fuels, like mountaintop removal mining, water pollution from hydraulic fracturing of shale for natural gas, the air pollution emitted after their combustion, and large emissions of greenhouse gases, there is Environmental and Energy Study Institute a clear social incentive to find alternative sources of energy. Industry's role as the largest consumer of energy in the nation, its large heat requirements, and its heavy reliance on fossil fuels, present tremendous opportunity for application of solar thermal technology.

In Brazil, usually the use of sun energy for the generation of thermal power for industrial use is small. This issue involves the understanding of the relationship between sustainable development, modernity, freedom, market, citizenship, and especially the relationship between the lack of access to energy and technological knowledge. Given the broadness of these aspects, the attention is directed the regulatory framework of the Brazilian energy industry and the use of water heating with solar energy by national industries. Brazil receives high levels of solar radiation incidence during almost every month of the year, including in June, which corresponds to the winter solstice for the Southern Hemisphere.

The average daily distribution of global radiation per region of the country is: North 5,462 Wh/m^2; Northeast 5,688 Wh/m^2; Midwest 5,630 Wh/m^2; Southeast 5,478 Wh/m^2; South 5,015 Wh/m^2. These high solar radiation levels may provide a wide use of solar collectors for water heating, mainly in the industrial sector and can be applied in the reduction of fossil fuels, reducing also the emission of CO_2 into the atmosphere.

Given the importance of the matter, this research study aims for a technical analysis and economic evaluation of the use of solar collectors, replacing the LPG gas for water pre-heating to be used in the engines of the Termocabo plant.

1.1 Characteristics of industrial thermal demand

Industrial heating needs can be categorized into three main temperature ranges. All of them can be achieved with solar. The lowest temperature range consists of everything below 80ºC. Solar collectors are capable of meeting these temperatures and are commercially available today. The medium temperature category is between 80ºC and 250ºC. While the collectors servicing this level of heat demand are relatively limited, they do exist and are on the verge of emerging into competitive commercial production. The highest range includes everything over 250ºC and requires concentrated solar power (CSP) (see appendix) to achieve such temperatures. While CSP furnaces are rare - a few have been installed in the World for electricity production. They can achieve temperatures as high as 800ºC.

The challenge of mitigating imminent risks arising from climate change embraces not only governments, but the civil society and companies; therefore, it is necessary to develop and establish techniques that reduce the concentration of gases causing the greenhouse effect in the atmosphere. In the industry, the use of solar energy has been little explored since the energy obtained via solar collectors may be used for fluid pre-heating, what greatly reduces the amount of fuel material burnt in boilers (KALOGIROU, 2004; ABRAMOVAY, 2010).

Many industries already can take advantage of the commercially available low and mid-range temperature solar thermal collectors. They are particularly suited to meet the heating needs of the food, beverage, textiles, paper and pulp industries. Processes like sterilizing, pasteurizing, drying, hydrolyzing, distillation and evaporation, washing and cleaning, and polymerization do not require high temperatures and can easily benefit from flat plate and evacuated tube collectors (see appendix, table below). According to a study of industrial heating in European countries, 30 percent of industrial processing requires heat below 100ºC and 27 percent of industrial heating needs can be met with heat between 100-400ºC, and 43 percent requires heat over 400^{0}C.18 In the food, wine and beverage, transport equipment, textile, machinery, and pulp and paper industries, roughly 60 percent of the heating requirements can be met by temperatures below 250ºC. Despite tremendous opportunity, solar thermal heating for industrial processes has been insignificant compared to the

residential sector, and the few industrial applications that do exist have been experimental in nature, show in Table 1 different temperatures of process industry.

Tab. 1: Heating process in the different industry (Mekhilef *et al*., 2011).

INDUSTRY	PROCESS	TEMPERATURE(ºC)
Dairy	Pressurization	60-80
	Sterilization	100-120
	Drying	120-180
	Concentrates	60-80
	Boiler feed water	60-90
Tinned food	Sterilization	110-120
	Pasteurization	60-80
	Cooking	70-90
	Bleaching	70-90
Textile	Bleaching, dyeing	60-90
	Drying, degreasing	100-130
	Dyeing	70-90
	Fixing	160-180
	Pressing	80-100
Paper	Cooking, drying	60-80
	Boiler feed water	60-90
	Bleaching	130-150
Chemical	Soaps	200-260
	Synthetic rubber	150-200
	Processing heat	120-180
	Pre-heating water	60-90
Meat	Washing, sterilization	60-90
	Cooking	90-100
Beverages	Washing, sterilization	60-80
	Pasteurization	60-70
Flours and by-products	Sterilization	60-80
Timber by-products	Thermal diffusion beams	80-100
	Drying	60-100
	Pre-heating water	60-90
	Preparation pulp	120-170
Bricks and blocks	Curing	60-140
Plastics	Preparation	120-140
	Distillation	140-150
	Separation	200-220
	Extension	140-160
	Drying	180-200
	Blending	120-140
Energy Generation	Thermic	150-800

1.2 Barriers

The main barriers to the implementation of a solar heating system of high performance are the lack of data on collectors when high temperatures are employed, and its actual efficiency under different temperature conditions. In this sense, this study aimed to identify relevant parameters of fluid heating for solar power systems as well as the main process responses. In addition to tests of heat transfer, economic viability studies were performed by calculating the return time and rate on the investment.

Despite the large potential for solar energy to meet industrial thermal demand, there are several barriers to large scale implementation. The most noteworthy barriers are cost, variability of output, energy storage and process integration.

1.2.1 Cost

The economic viability of solar thermal energy depends largely on two factors: the initial cost of the installation and the price of alternatives. High upfront costs often prevent companies from investing in new technology, like solar thermal, even if the overall lifetime cost would be lower. However, while the cost of solar technologies is decreasing, the financial investment in solar remains more stable than many of the markets for fossil fuels. Thus, the largest driver of a collector's cost effectiveness is often the price of alternatives, like coal, oil and natural gas, not the cost of the collector itself. The more expensive fossil fuels become, the easier it is to justify an investment in solar thermal energy. Nevertheless, if the price of solar thermal were to drop, it would certainly enhance its economic viability. With the volatility of fuel prices, some manufacturers opt for the fixed upfront cost (see case studies) with a predictable payback period. In addition to the potential for a lower overall cost, there exists a benefit from having a predictable cost structure which is insulated from fuel market volatility. Approximately 40 percent of industrial primary energy comes from natural gas, and approximately 41 percent comes from petroleum (Kalogirou, Soteris. 2012).

Furthermore, solar thermal collectors can be made even more cost effective when tailored to the specific process heating needs of the plant (see Process Integration below). On the factory level, large-scale applications can benefit from economies of scale and lowered investment costs, increasing its economic viability. On the national level, the IEA estimates that costs can be reduced by as much as 20 percent when a country's total installed capacity doubles.

1.2.2 Variability

Solar energy, like wind energy, can be predicted to a high degree of confidence. Its availability, however, presents challenges for industries that require "24/7" demand. The reliability of the heating supply is of paramount concern to many manufacturers for whom an unanticipated disruption in production can be economically devastating. Solar thermal energy is reliable but not always available. Therefore, industries which either do not require constant production, or for whom the sunlight availability can be aligned with heating requirements, may be more confident about integrating solar thermal energy into their production. The variability of sunlight can also be mitigated by conducting statistical analyses of heating requirements vis-à-vis the regional insolation—the irradiance per square meter over a given period of time. This can be conducted as part of a procedure known as process integration (see below). Another possible solution is to store heat for later use to smooth the gaps in sunlight availability (see below).

1.2.3 Process Integration

Process integration, also known as "pinch analysis," is a field of engineering which seeks to optimize operational energy efficiency, or in other words, to reliably produce a product with the minimum energy inputs necessary. The variability of energy supply must be quantified based on daily solar radiation, ambient temperature profiles, and available storage opportunities, so that the solar collectors can be optimized to reduce economic inefficiencies. Variable energy, like solar and wind, presents a particular challenge for process integration because the supply of energy is non-continuous. Therefore, the nature of solar thermal energy supply must be addressed or it can become unaffordable in some cases.

If solar collectors supply all of the energy, the manufacturer must either align production with the energy supplied, or store the energy for later use. However, even if sunlight is not available to meet all of a factory's thermal energy needs, solar thermal can still play a role by supplying a portion of the total energy required. Under such hybrid systems, solar collectors can provide a baseline energy supply whenever it is available and the remainder can be fulfilled by a complementary fuel source. The commercially available low temperature collectors are especially effective in this strategy and are often used for pre-heating purposes.

1.2.4 Energy Storage Options

Large scale thermal energy storage is a nascent market but it can compensate for the inherent variability of sunlight. For low and medium temperatures, this can usually be performed by storing the heat in a transfer fluid like hot water or oil. Sometimes pressurized steam is used. For higher temperatures, this becomes more difficult, and costly, and requires an alternative heat transfer fluid and storage material.

The most common heat transfer fluid for CSP is molten nitrate salt, which is thermally stable within a temperature range of 220° C to 565°C, below which the salt freezes.32 The molten-salt system is currently the

only practical thermal energy system with hours-long storage potential, and has proven reliable at commercial scales.33 The National Renewable Energy Laboratory (NREL) has called on researchers to develop a heat transfer fluid that can sustain temperatures up to 1300°C and operate as low as 0°C.34 This temperature, according to NREL, is a necessary component in reaching the full potential of solar thermal applications.

1.3 Market Tends

The solar thermal industry has seen steady growth over the last few years. The global solar thermal market grew by 17 percent in 2012 and again by an estimated 42 percent in 2013, largely due to a 45-50 percent surge in the U.S. residential sector. By the end of 2014, the United States and Canada combined for 8.7 percent of the world-wide installed capacity. China led the global market with 58.9 percent of installed capacity, followed by Europe with 18.9 percent.

Excluding solar that is used mainly to heat outdoor swimming pools, the United States ranked 10th in the world in 2009 for overall installed capacity and 36th in the world for per capita capacity. Firms have begun using solar thermal for industrial process heating with a few large-scale projects in Europe and China.

1.3.1 Energy efficiency

According to the DOE's Office of Energy Efficiency and Renewable Energy, best practices in process heating, such as opportunities for heat recovery, can reduce the cost and consumption of energy by as much as 30 percent. Even plants and factories with energy management systems can improve energy efficiency from 10 percent to 15 percent by implementing best practices, thereby reducing energy costs for process heating from 5 percent to 15 percent.

2. Methodology

2.1 Analysis of types of solar thermal technology

There are two main types of solar thermal technology: stationary and concentrating (typically non-stationary). Stationary collectors do not move and can be further subdivided into flat-plate collectors and evacuated tube collectors. Stationary collectors are cheaper and require little maintenance but they can only achieve low to medium temperatures. Alternatively, concentrated solar power (CSP) collectors usually rotate to track the sun's rays and can therefore achieve much higher temperatures. However, they are also more expensive and require more maintenance.

2.1.1 Flat plate collectors

Flat plate collectors are simple, inexpensive and require little maintenance. Most commonly used to heat outdoor swimming pools and home water heating, they consist of an insulated metal box with a glass covering and an absorber plate inside. The absorber plate utilizes the sun's radiation to warm an internal heat transfer fluid (HTF), usually water, oil or air.

Flat plate collectors can be either glazed or unglazed. Unglazed collectors have no insulation over the glass which augments both heat gain and heat loss. These collectors typically reach temperatures of only 30ºC are almost exclusively used to heat outdoor swimming pools. Glazed collectors have an insulated glass covering and can typically achieve temperatures of up to 80ºC and are thus applicable to a number of the industrial heating processes in the chart above. Flat plate collectors can penetrate the medium range and achieve temperatures between 90ºC and 150ºC, but they are not yet economically efficient beyond 80ºC.

2.1.2 Evacuated tube collectors

Evacuated tube collectors are the other stationary collector and they typically consist of a row of parallel tubes which use the sun's rays to heat an absorber plate at the center of a vacuum. These collectors can achieve higher temperatures because the vacuum reduces conductive heat loss and eliminates convective heat loss. However, they are also more expensive to manufacture. Vacuum collectors have reached economically efficient temperatures between 90 oC and 150 oC, making them a useful complement to the flat plate

collectors.55 By adding reflector plates to concentrate the sunlight, these collectors have efficiently reached temperatures up to 200 oC.56

2.1.3 Concentrating Solar Power (CSP) collectors

CSP collectors can achieve the highest temperatures but they are also the most expensive to manufacture and maintain. They are extremely rare for industrial process heating and virtually nonexistent the United States, outside of utility-scale solar power plants. CSP collectors can reach extremely high temperature by rotating to follow the sun and by using arrays of reflectors to focus large amounts of sunlight onto the absorber.

2.2 Step by Step

The first step was to determine the total steam demand of the main equipments from the Termocabo plant, consisting of three generating engines, totaling installed power capacity of 48MW.

By analyzing the thermal charge on one or more items of the plant with heat transfer equations, it may be possible to obtain an estimate for the steam consumption. The mathematical model for each device uses the equations of mass balance and energy balance in control volumes, which were transcribed in an appropriate programming language for the development of applications of technical nature. The thermal charges considered in this study were: 1 Storage (1,495.0m^3), 1 Buffer (85.8m^3), 1 Day (176.0m^3), 3 Lub Oil Separators (5.0m^3), 3 Fuel Oil Separators (5.9m^3) and 3 Preheater Engines (5.5m^3). Vapor pressure is of 7 bar g at any point of the system and the boiler is capable to continuously maintain this pressure. The evaporation heat for 1 kg of steam at 7 bar is of 0.566 kW. It is known that the total heat at 7 bar of steam is 0.700kW (660.8 kcal or 2,764 kJ found in steam tables). However, the condensate still contains some heat that is not released, being completely safe ty o use the indicated value. The main equations used are:

Energy transfer equation (eq. 1).

$$Q = mC_p\left(T_f - T_i\right) \qquad \text{(eq. 1)}$$

where,

C - specific heat for water evaluated at the mean temperature, J/kg K;

m - mass flow, kg/s, and

T_f and T_i - inlet and outlet temperatures of each collector.

(Eq. 2) describes the efficiency of collectors according to local radiation:

$$\eta = \frac{Q_{absorbed}}{Q_{solar\ energy} x A_c} 100 \qquad \text{(eq. 2)}$$

The heat transfer function in the solar collectors is obtained using the Hottel--Whillier Bliss equation (Smith and Weiss, 1977) (eq. 3).

$$Q_{SC}(t) = A_{SC} f_r\left[I_r(t)(\tau\alpha) - U_{SCi}\left(T_{SCi}(t) - T_{amb}(t)\right)\right] \qquad \text{(eq. 3)}$$

The dynamics of the boiler is described by eq. (4) (Duffie and Beckman, 1980):

$$c_p \rho V_{bo} \frac{\partial T_{bo}}{\partial t} = Q_{bo}(t) + Q_{SC}(t) + Q_{cons}(t) + Q_{loss}(t) \qquad \text{(eq. 4)}$$

In Figure 1, the "cold water" of the thermal reservoirs, which due to the physical characteristics is found at the bottom part, is then pumped through the collectors, returning to the reservoir. This process is controlled by ARISTON controller as follows: When temperature T1 of the collector is higher than temperature T2 of the reservoir by a pre-adjusted constant, is actioned by a water circulation pump. The "hot water" that comes out from the thermal reservoir goes to the heat exchangers, pulled by a second pump, located after the heat exchanger, where heat is lost and returns to the thermal reservoir.

On the secondary of the heat exchanger, the mixing valve allows to adjust the temperature of the water supplied to the engine block, when the temperature of the water resulting from solar heating is sufficient to meet the needs of the engine block. In this configuration, the deviating valve controlled by a BUDERUS controller, causes the "cold water" of the engine block, pumped by a third pump, to go past the right side of the heat exchanger, receiving heat from solar heating system and returning to the engine block. If the temperature achieved with this is not sufficient, the deviating valve causes the engine block to receive water from the simulating reservoir of the boiler, where, in this case, water is heated by using electric resistance.

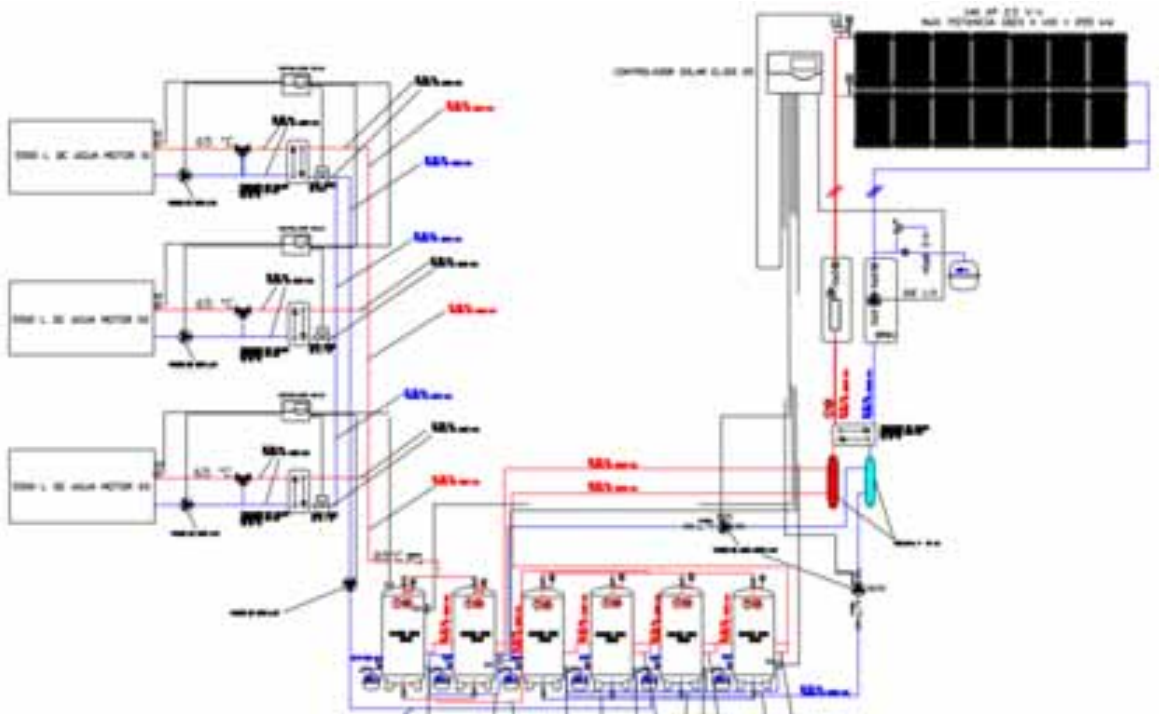

Figure 1 – Executive project

Legend: 5500L DE ÁGUA MOTOR – 5500L OF ENGINE WATER; CONTROLADOR SOLAR ELIOS – ELIOS SOLAR CONTROLLER; MÁX. POTÊNCIA – MAX. POWER.

3. Conclusion

While solar thermal use in home water heating is still extremely small, solar thermal use in other sectors of the economy is even smaller, especially in the United States. These technologies are capable of cost-effective integration into many commercial and industrial processess. However, they remain too risky for many businesses and major manufacturers due to the large upfront costs, concerns over availability of heat, and to a lack of understanding of the opportunities it provides. Despite the industrial sector consuming the largest amount of energy in the United States, and the tremendous opportunity which solar thermal technology presents, it has been largely overlooked by both manufacturers and policymakers.

Solar thermal technology is commercially available to meet demand in lower temperature ranges and already can be integrated into the food, beverage, textiles, paper, and pulp industries on a large-scale. Many of the technological barriers can be eliminated through prudent analysis of energy requirements and appropriate mechanisms for energy storage. Solar thermal's opportunity should be viewed as a way to substantially offset fossil-fueled thermal energy. A total replacement of thermal capacity could be appropriate in certain circumstances, for processes that do not require round-the-clock supply, for example, or when integration of energy storage technology to meet longer periods of demand is possible. Solar thermal integration strategies would be even more effective when coupled with energy efficiency strategies.

Incentives should do more to target the industrial heating sector specifically, and expand commercialization of medium temperature collectors and higher temperature storage technology. The economic opportunities are abundant and the environmental payoff will be much larger if policymakers focus more attention on the opportunities to reduce fossil fuel consumption in industry.

4. References

Altoé, L.; Oliveira Filho, D.; Carlo, J. C. Análise energética de sistemas solares térmicos para diferentes demandas de água em uma residência unifamiliar. *Ambiente Construído*, São Paulo, v. 12, n. 3, p. 75-87, jul./set. 2012.

Duffie, J., & Beckman, W. (1980). *Solar engineering of thermal processes*. *NASA STI/Recon Technical Report A* (Second., p. 919). New York: John Wiley & Sons.

Smith, C. C., & Weiss, T. A. (1977). Design application of the Hottel-Whillier-Bliss equation. *Solar Energy*, *19*, 109– 113. Retirado de http://www.sciencedirect.com/science/article/pii/0038092X77900470

International Energy Agency. 2013. *Co-generation and Renewables: Solution for a Low Carbon Future*. International Energy Agency. http://www.iea.org/papers/2013/CHP_Renewables.pdf (accessed December 1, 2013).

International Energy Agency, Solar Heating and Cooling Program. 2014. *Solar Heat Worldwide: Markets and Contribution to the Energy Supply 2013*. International Energy Agency. http://www.iea-shc.org/publications/downloads/Solar_Heat_Worldwide-2014.pdf .

Mekhilef, S. *et al.* 2011. A Review on Solar Energy Use in Industries. *Renewable and Sustainable Energy Reviews*. 15:1777-1790.

Kalogirou, Soteris. 2012. The potential of solar industrial process heat applications. *Applied Energy*. 76 (4): 337-361

Goldemberg, J.; Lucon, O. Energias renováveis: um futuro sustentável. *Revista USP*, São Paulo, n. 72, p. 6-15, dez./fev. 2007.

Luma, A.; Vellázquez, N.; Gallegos, R.; Bojorquez, G. Aire acondicionado solar para conjunto de viviendas en Mexicali, México. *Información Tecnológica*, México, v. 19, n. 1, p. 45-56, 2008.

Oliveira, L. F. C. de; Ferreira, R. de C.; Almeida, R. de A.; Lobato, E. J. V.; Medeiros, A. M. Potencial de redução do consumo de energia elétrica pela utilização de aquecedores solares no Estado de Goiás. *Engenharia Agrícola*, Jaboticabal, v. 28, n. 3, p. 406-416, 2008.

Conference Proceedings

Solar World Congress 2015
Daegu, Korea, 08 – 12 November 2015

Evaluation of a large solar thermal drainback system for hay bales drying

Yoann Louvet, Ruslan Botpaev and Klaus Vajen

Kassel University, Institute of Thermal Engineering, Kassel (Germany)

Abstract

In this paper, over one year of measurement data of a 127 m² drainback solar thermal system for hay drying is analysed. The study shows that high temperatures in the solar collector loop lead to partial boiling when the system starts, slowing down the filling process. More severe, due to siphon establishment, the flow rate drops and the efficiency of the field is impacted anytime the collector outlet temperature exceeds 83 °C. The existing system is then modelled with the simulation software TRNSYS 16, based on measured data. Four other hydraulic designs are as well modelled and simulated for a comparative analysis. Three use the drainback principle and one represents a "conventional" pressurized system. As expected the results demonstrate that the drainback with load-side heat exchanger has the best thermal performance and the "conventional" system the worst one. The energy yield of the drainback design with collector-side heat exchanger is comparable to the one of the "conventional" system. The parasitic electricity consumption of the solar collector loop pump is also calculated. It varies significantly depending on the system, the most demanding one being the drainback without siphon formation, with a total consumption more than doubled compared to the same system with siphon formation.

Nomenclature:

C_p	specific heat, J kg^{-1} K^{-1}	Q_{aux}	auxiliary heater energy consumption, kWh
$E(X)$	expected value, s	Q_{coll}	collector field energy production, kWh
E_{pump}	solar collector loop pump energy consumption, kWh	Q_{ref}	energy consumption for the reference system, kWh
$f_{sav,therm}$	fractional thermal energy savings	t_{fill}	filling time, s
H	pump head, m	$\dot{V}$	volume flow rate, m³ s^{-1}
h_l	head losses between two points of a piping system, Pa	ΔH	height between water surface in the storage and highest point of the hydraulics, m
P_1	power consumed by the pump, W	η_{tot}	total pump efficiency
p_{atm}	atmospheric pressure, Pa	ρ	density, kg m^{-3}
P_H	pump hydraulic power, W	g	gravitational acceleration, m s^{-2}
p_{top}	pressure at the highest point of the hydraulics, Pa	σ	standard deviation, s

Keywords: *Drainback system, Solar process heat*

1. Introduction

In order to decrease the overall costs of solar thermal systems, one option is to use the drainback configuration, which enables the reduction of both initial investment and maintenance costs (Mugnier et al., 2011). For the solar thermal branch, this target is a priority, as the growth of the solar thermal market has been flattening out during the past years, and Europe is especially stricken by this tendency (Mauthner et al., 2015). For large systems, notably dedicated to process heat or district heating, the use of the drainback technology is rarely documented in the literature and the specificities of their functioning barely addressed (Botpaev et al., in press). Bokhoven et al. (2001) and Mugnier et al. (2011) are so far the main resources dealing with large drainback systems. This paper aims at providing more knowledge on their functioning but also at highlighting their specificities compared to "conventional" pressurized glycol systems. For this purpose, extensive measurement data from an existing large drainback system for hay bales drying are analysed. After presenting the system, the focus is on the filling and draining phases, two specific features of drainback systems. The operation of the system is also studied and especially the impacts of siphon formation on the solar thermal energy yield. Finally,

doi:10.18086/swc.2015.10.39 Available at http://proceedings.ises.org

five different collector loop configurations are modelled and their energy performances compared. For smaller, single-family house systems, such detailed simulations and comparisons were already carried out by Goumaz and Duff (1981).

2. The studied system

The studied solar drainback system (DBS) is located at a farm in Frankenhausen in Germany. This DBS was built to supply heat for the drying of hay bales during the summer season. It is designed to cover the drying needs of around 300 bales per year, which corresponds to an annual load of 29 MWh. Additionally, it also covers part of the domestic hot water (DHW) and space heating demands of the farm buildings the yearlong and especially during the winter period. The collector field is showed in Fig. 1. It is composed of ten "Solar Roof" flat plate solar thermal collectors from the company Wagner GmbH. They are connected in parallel according to the Tichelmann principle. The total collector field aperture area is 127 m² (138 m² gross area).

Fig. 1: The collector field of the studied drainback system.

The collector field is connected without heat exchanger to two serially coupled heat stores constructed by the company Fsave Solartechnik GmbH. They have a total volume of 42 m³ and are made of polypropylene (PP). The use of polymers presents several advantages – ease of transport and installation, low thermal conductivity, potential for low costs – but requires the storage to remain unpressurized. This is achieved in a simple manner with the drainback configuration with load-side heat exchanger. In order to avoid any pressure variation, the system needs to be open, i.e. the storages are vented to the atmosphere. For the charge and discharge, no stratification device is installed, but horizontal lances are used to reduce the velocity of the heat transfer fluid (HTF) entering and exiting the storages. As no heat exchanger is applied in the solar collector loop and because of the drainback design, pure water is used as HTF. A single Wilo-Top-S 30/10 pump is installed and serves both as filling and circulation pump. Additionally, a motor valve connected to an air vent opens to trigger the draining phase once the pump stops. In Fig. 2 is presented a detailed hydraulic scheme of the above described system. The hay bales drying process is connected to the storage via a water-to-air heat exchanger. It enables the drying of 20 hay bales simultaneously. During a drying cycle, the relative humidity of the bales is decreased from approx. 30 % to 10 %, depending on the harvesting conditions. An auxiliary wood burner is connected to the storages with an external heat exchanger. The same heat exchanger is used for heat and DHW delivery to the farm buildings.

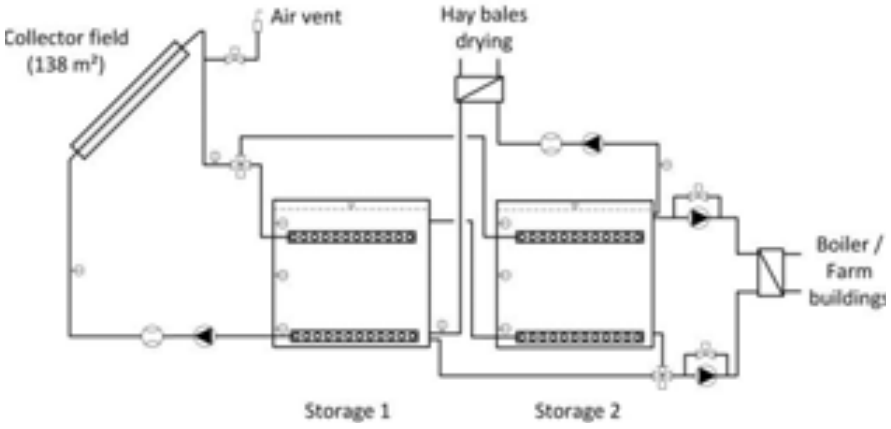

Fig. 2: Detailed hydraulic scheme of the studied system.

The system has been in operation since spring 2012. In August 2014 additional measuring devices were installed, as well as a data logging system. Calibrated temperature sensors were mounted as well as a pyranometer to measure the total irradiation on the collector plane. Fig. 3 presents the energy yield of the collector field over the previous year. In total, with a specific measured radiation of 951 kWh m^{-2} a^{-1}, the collector field delivered about 292 kWh m^{-2} a^{-1} of heat. These values are low as almost two months of data are missing over this period. If only the drying period is considered, between Mai and September, the production amounted to 218 kWh m^{-2}.

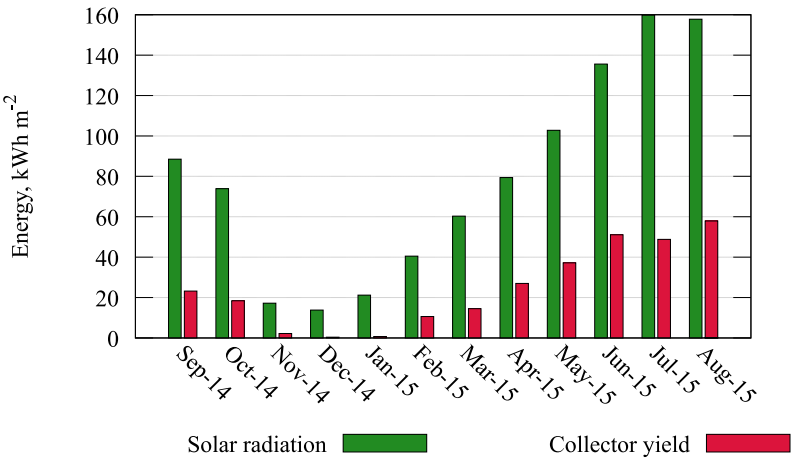

Fig. 3: Measured solar radiation in the collector plane and energy yield from the solar collector field (per m² absorber area) between September 2014 and August 2015. Due to maintenance and monitoring issues 14 days of data are missing in November, 16 between February and March, 12 in April, 12 in May and 3 in June.

3. The filling and draining processes

For a comprehensive analysis of the functioning of DBS, Botpaev et al. (2014) proposed to distinguish the filling and draining phases from the operation phase, the latter being shared by any solar thermal system. In order to better understand the specificities of these two phases in the context of large systems they are examined in detail. The previous work from Jordan et al. (2015) is here extended with additional measurement data, totalling more than 600 complete filling and 300 draining phases. The aim is to identify the phenomena which impact the filling and draining processes of large solar drainback systems.

One should also recall, as stated in Jordan et al. (2015) that the studied system is operated with a so called siphon formation (Fig. 4, left), meaning that water completely fills the flow pipe. Another design, without siphon formation (also called trickle-down design, Fig. 4, right) is also possible and its impact is simulated in section 5. Further details about these configurations can be found in Botpaev et al. (in press).

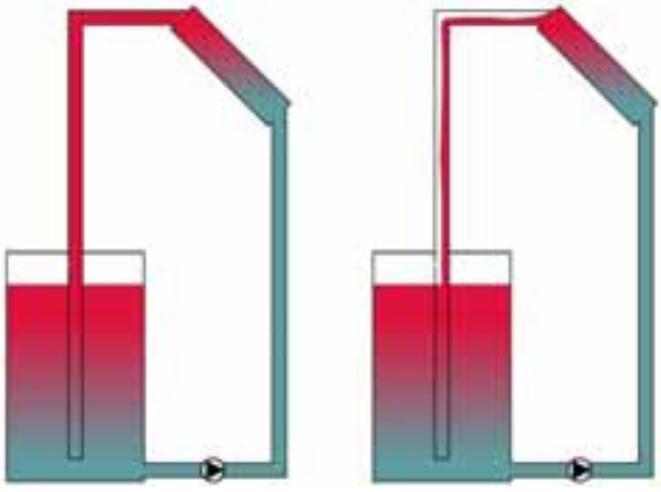

Fig. 4: DBS with siphon formation (left) and without (right). The latter is characterized by the presence of a two-phase flow (air and water) in the flow pipe.

In Fig. 5 and Fig. 6 are shown the relative frequency distribution of the studied filling and draining processes.

Each point has an accuracy of ± 10 s, due to a temporal resolution of the logging device of 10 s. Moreover, from Fig. 7 it appears that the end of the filling phase cannot always be accurately determined, as the flow rate does not always clearly stabilises as the flow rate in case (b) highlights. It was arbitrarily chosen to end a filling phase at the moment when the flow rates does not fluctuate of more than ± 5 % over the next 30 s.

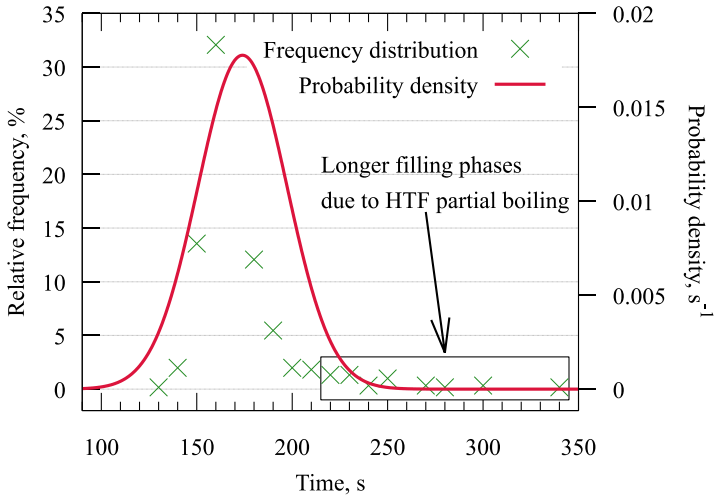

Fig. 5: Frequency distribution and probability density associated to the normal distribution for 605 filling processes. The parameters of the density curve are σ = 22.5, *E(X)* = 170.7.

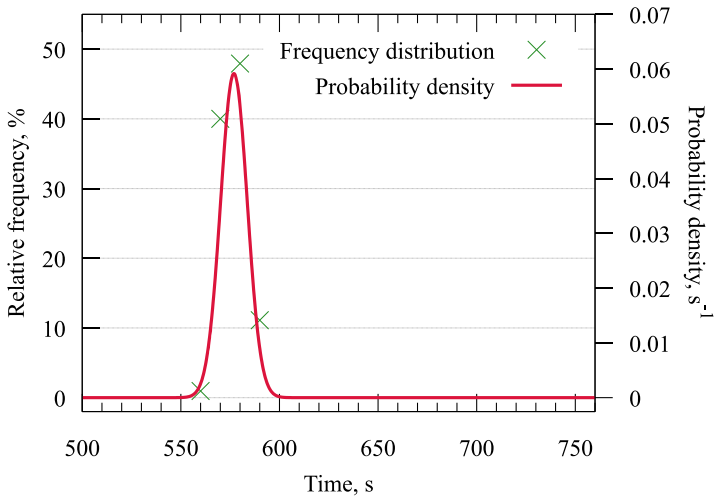

Fig. 6: Frequency distribution and probability density associated to the normal distribution for 315 draining processes. The parameters of the density curve are σ = 6.7, *E(X)* = 576.9.

From the results, it can be seen that the length of the draining phase is rather constant independently from operation conditions, with a standard deviation of 6.7 s (1.2 % of the draining time), in the range of the measurement inaccuracy (Fig. 6). Regarding the filling, the deviation is larger, at 22.5 s (13.1 % of the filling time). This can be explained by the inherent inaccuracy of the measurements as stated previously, but also by the occurrence of longer filling phases lasting up to 340 s, as shown in Fig. 5. A detailed analysis of these longer fillings reveals that they might be caused by a partial boiling of the incoming HTF when inlet temperatures and/or irradiation level are high at the moment of the filling. This conclusion is drawn from Fig. 7. Compared to a "normal" filling process (a), the longer one (b) is characterized by a quick and sharp increase of the collector field outlet temperature shortly after the start of the filling, almost reaching 100 °C. First of all one can notice that the temperature increase in the outlet pipe takes place less than 20 s after the start of the filling, the theoretical minimum time for the fluid to reach the first collector with a flow rate of 1.39 litre s^{-1} (conservative value as the flow rate is fluctuating quite fast during the filling phase). A plausible explanation is that some water should remain in the riser pipe. When the pump starts, it is pushed into the collectors and vaporizes. Secondly it demonstrates that some of the HTF boils in the collector field. This partial boiling most certainly slows down the filling process by increasing the pressure drop in the field. Each significantly longer filling phase is characterized by the same boiling phenomenon. Unfortunately, a lack of sensors did not allow

getting more details of where exactly in the field the boiling takes place.

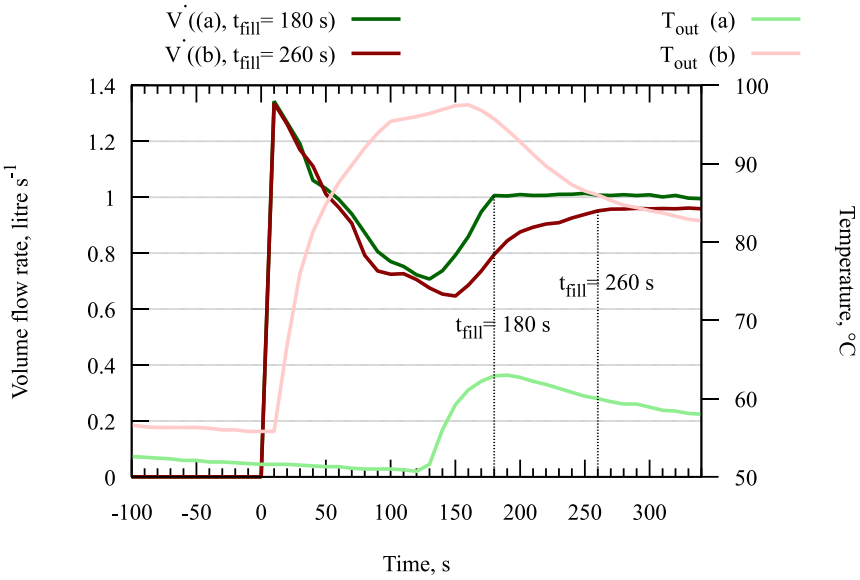

Fig. 7: Flow rate and outlet temperature profiles of two filling processes, one lasting 180 s and one 260 s. t = 0 corresponds to the start of the pump.

In the studied system, the partial boiling of the incoming HTF in the collectors does not appear to prevent the filling process. However depending on the location of the boiling in the field and the position of the collector field temperature sensor, one could imagine a situation where the threshold collector temperature is reached and detected by the sensor (in the studied system 95 °C) thus stopping the pump and causing the system to stagnate. Kratz and van Dam (1999) stated that large drainback fields are difficult to properly fill as siphon creation favours the filling of some rows at the expense of others. This effect contributes to degrade the efficiency of the system as some rows might remain non-filled. The boiling described here might enhance this uncomplete filling as rows where boiling occurs might be even more penalized.

From this analysis it can be concluded that a control strategy for the filling a DBS is always a matter of compromise. The start filling temperature difference should not be too low otherwise the first daily fillings are not stable, i.e. the collectors are cooled down by the incoming HTF which in turns stops the pump. In Frankenhausen, it often happens that the first filling of the day is shortly followed by a draining because of the cooling effect. On the contrary, if the start temperature difference is too high, there is the risk that an already quite warm incoming fluid (in case of relatively high temperatures in the storage) starts to boil. Gößlinghoff (2010) proposed in a patent to fill each parallel row of a drainback collector field successively with the use of motor-valves. Due to the boiling effect highlighted here, such a lengthy filling strategy could in practice not be very effective.

Finally, the power consumption of the pump situated in the solar collector loop was measured during the filling phase. Contrary to what is sometimes mentioned, the power required by the pump during the filling process is on average slightly lower than during operation, with 280 W against 285 W.

4. DBS and underpressure

Having a non-pressurized system vented to the atmosphere presents some advantages such as the reduction of the number of components (no expansion vessel, no safety valve) and the possibility to use of polymer materials. Nevertheless a system with siphon formation requires a careful design especially considering the risk of boiling. Indeed, from a fluid mechanics perspective, when applying an energy balance to the HTF between the highest point of the solar collector loop hydraulics and the end of the flow pipe assuming a turbulent regime, a steady flow and the fluid incompressible, one obtains the following equation (Crowe, 2009):

$$p_{top} = p_{atm} - \rho g \Delta H + h_l \qquad \text{(eq. 1)}$$

Equation 1 shows that the pressure at the top of the hydraulics might be lower than atmospheric pressure due to a siphon-like effect. It also explains that in order to reduce this potential underpressure one might either

decrease the height difference between the water level in the storage and the highest point of the hydraulics (ΔH) or increase the head losses in the flow pipe (h_l). Kratz and van Dam (1999) proposed to use a "trickling-down" flow in the flow pipe also for large solar DBS, avoiding the formation of the siphon. In the drainback configuration with load-side heat exchanger, this issue is particularly relevant as ΔH can be quite important depending on the respective location of the collectors and the storage. In Frankenhausen ΔH is equal to 6.5 m. A first approximate modelling of the pressure drops in the solar collector loop showed that with a flow rate of 0.99 litre s^{-1} (3500 kg h^{-1}) a negative pressure relatively to atmospheric pressure should occur in the solar collector loop. To examine the actual impact of this undesired phenomenon on the performance of the system, two consecutive sunny days with high collector outlet temperatures are presented in Fig. 8.

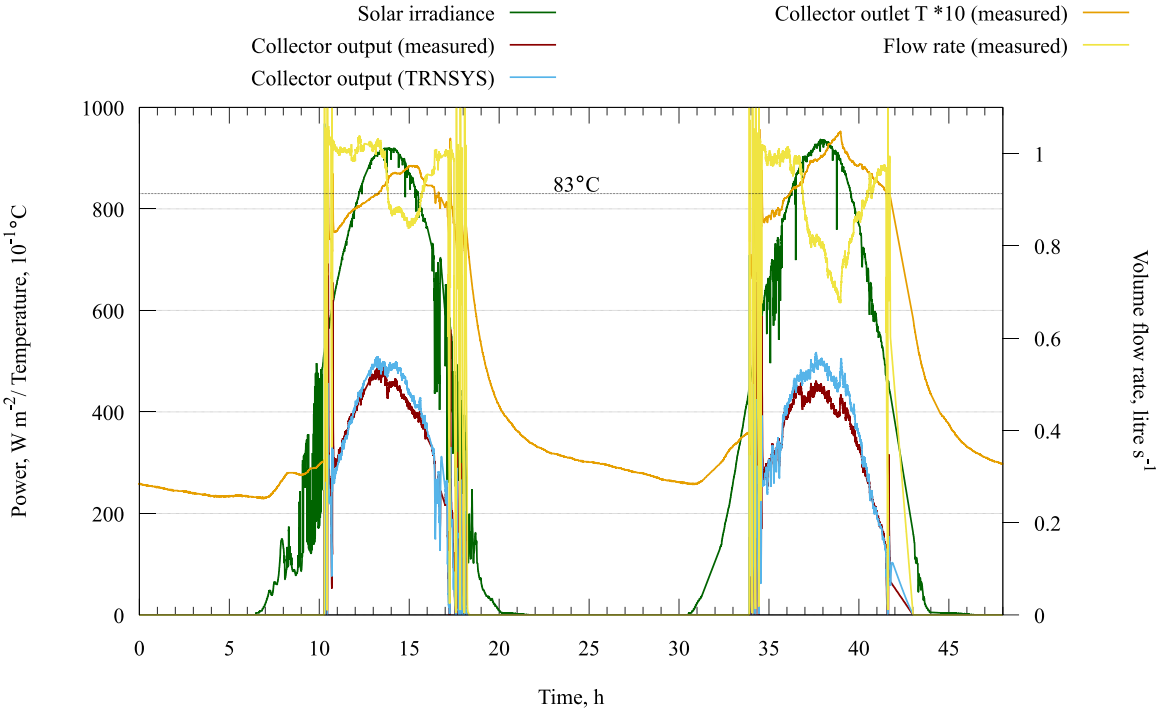

Fig. 8: Measured and calculated collector field power output over two consecutive sunny days in August 2015, with collector outlet temperatures above 83°C.

From the figure it appears that once the outlet temperature of the collector reaches a certain threshold, the flow rate sharply decreases and remains lower than during "normal" operating conditions. From Fig. 9, one can notice that this threshold temperature is around 83 °C and that after this point, the flow rate decreases linearly from 0.028 litre s^{-1} (100 litre h^{-1}) for each degree kelvin the collector field outlet temperature increases. A comparison of a TRNSYS simulation of the solar collector loop power output with actual measured data for these two days also shows that nonetheless drops the flow rate, but the efficiency of the collectors is also affected. While the relative deviation between measured and simulated power output is in a range of ± 5 % during periods when the outlet temperature is lower than the threshold temperature, this deviation reaches up to 15 % after the threshold is passed. It was however not possible to precisely determine the impact of the boiling on the collector efficiency, due to insufficient measurement data. A detailed CFD modelling would be necessary to understand how the heat transfer between the absorber and the collector HTF is affected by partial boiling. However it was not the goal of this paper.

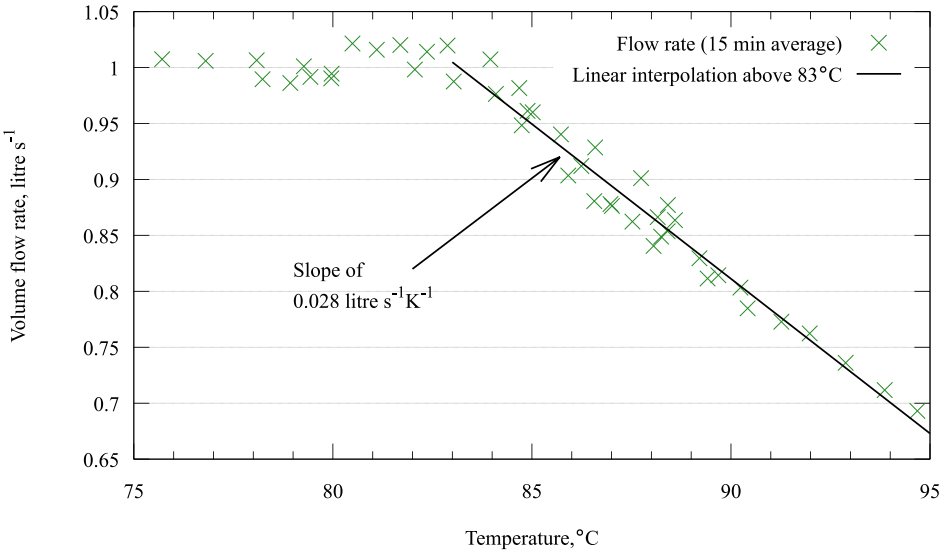

Fig. 9: Solar collector loop flow rate as a function of the collector field outlet temperature during steady irradiation periods for the two days shown in Fig. 8 (15 minutes average values).

5. System simulations

In order to compare the performance of the DBS installed in Frankenhausen with other designs, the actual system was modelled with the use of the simulation software TRNSYS 16. Some parameters were then changed in order to simulate other system designs. In Tab. 1 are summarized the five different system designs simulated. They are based on the work from Botpaev et al. (in press). The parameters of the model were configurated in order to represent as closely as possible the real system. The system was simulated over the period going from the 1st of May to the 30th of September, which corresponds to the hay drying season. The total drying load was adjusted to meet the 29 MWh required to dry 300 bales a year and the total DHW load during the period was set according to measurement data to 6.5 MWh. The load profiles were also extracted from measurement data and slightly adjusted for each simulation in order to reach the same loads in all cases. The weather data applied were extracted from hourly data for Kassel, Germany, a city located 10 km south from Frankenhausen.

Tab. 1: Description of the simulated systems and their main specificities.

System number	Description	Siphon	HTF	Pump capacity, W	Collector-side heat exchanger	Other specificity
1	Actual system: DBS with load-side heat exchanger	Yes	Water	285	No	Decreasing flow rate above 83°C outlet temperature
2	DBS with load-side heat exchanger without siphon formation	No	Water	585	No	
3	"Conventional" system	N/A	Antifreeze mixture	375	Yes	
4	DBS with collector-side heat exchanger	Yes	Water	285	Yes	Additional drainback tank (DBT)
5	DBS with collector-side heat exchanger and glycol	Yes	Antifreeze mixture	375	Yes	Additional DBT

In order to take into account some specificities of a DBS, the boiling effect described before was simulated with a flow rate decreasing above a collector outlet temperature of 83 °C, according to the profile from section 4. When a DBT is present, it was considered that it could be installed high enough to avoid a critical underpressure. Moreover, the collectors were considered with a varying heat capacity depending whether they

are or not filled with HTF. The efficiency parameters of the collector were taken from data from the manufacturer. Some studies highlighted that the type of HTF used has an impact on the efficiency coefficients of a collector (Bava et al., 2014). This effect was however not considered in the simulations, therefore the same collector coefficients were used both with water and a mixture of glycol and water as HTFs.

Concerning the flow rate and the pumping power, the pump in the solar collector loop was run at a fixed speed as in the actual system. For simplification the HTF properties were taken at a temperature of 60 °C and pumping energy needs and flow rates were also assumed constant (except for the actual system above 83 °C) and calculated for this temperature. For water, data were extracted from Verein Deutscher Ingenieure (2006). When a mixture of glycol and water was used, the data were taken from Tyforop Chemie GmbH (2009) for a volume concentration of glycol in the mixture of 40 %. In all cases, the capacity flow rate ($\dot{V}\rho C_p$) was kept constant in the solar collector loop. Moreover in systems with a collector-side heat exchanger, an overall heat transfer coefficient of 5000 W K^{-1} was considered for the heat exchanger. Given the short length of the filling phase compared to the operation phase and the minimal difference of power required by the pump between these two phases (see section 2) the power consumption difference was neglected.

In order to determine the pump capacity required in the solar collector primary loop for each case, measured values for the actual system and the total pump efficiency given by equation 2 (Grundfos, 2004) were used.

$$\eta_{tot} = \frac{P_H}{P_1} = \frac{\rho g \dot{V} H}{P_1} \qquad \text{(eq. 2)}$$

The hydraulics of system 1 was modelled in a spreadsheet and calibrated according to measurement data. In its actual working conditions the total efficiency of the pump amounts to 16 %. To estimate the pumping power required by the other systems, the same hydraulics was assumed in all cases (same pipe diameters). With the help of the model, the working point of each system was calculated. It was then assumed that for this working point a pump of 16 % overall efficiency could be found. Compared to the actual system, the results show that the systems running with glycol require 32 % more pumping power and the needs of the DBS without siphon formation are 106 % higher.

To compare the thermal performance of the systems, the fractional thermal energy savings $f_{sav,therm}$ defined in eq. 3 is used (Letz et al., 2009).

$$f_{sav,therm} = 1 - \frac{Q_{aux}}{Q_{ref}} \qquad \text{(eq. 3)}$$

Q_{aux} designates the energy supplied by the auxiliary wood boiler and Q_{ref} the sum of the different heating loads of the reference system, i.e. the hay drying load, the DHW load and the losses of the two heat stores. The auxiliary wood boiler is also assumed to be the boiler in the reference case, therefore the boiler efficiency is considered equal in both the reference and the simulated systems.

Finally, the main control strategies applied are the following:

- The control of the solar collector loop pump differs depending whether the system is drainback or not. It starts when the difference between the collector temperature and the temperature at the bottom of storage 1 (see Fig. 2) is higher than 12 K respectively higher than 7 K and stops in both cases when it drops below 3 K.
- Storage 2 has priority when the collectors are in use and is loaded as long as the collector temperature is higher than the temperature at its top. If this is not the case, storage 1 is loaded.
- The water returning from the DHW load is directed to the bottom of storage 2 as long as its temperature is higher than the temperature at the top of storage 1. Otherwise it flows at the bottom of storage 1.

The results of the simulations (Tab. 2) show that the system performing thermally the best is the DBS without siphon formation in the flow pipe (2). This is due to the fact that system 1 is penalized due to a lower boiling point in the collector field, which in return affects Q_{coll}. Over the period the collector outlet temperature of system 1 is above the threshold temperature (83 °C) during 27 hours, which corresponds to 3.4 % of the total running time of the solar pump. However to achieve this slightly better performance the energy consumption of the pump in system 2 is more than doubled (108 % increased) due to the fact that the pump continuously needs to overcome the height difference between the storage and the collector field.

The conventional system (3) is thermally performing worst as it is penalised by the presence of the heat exchanger and the use of glycol. Compared to system 1, $f_{sav,therm}$ is 3.9 % lower and the energy required by the pump to circulate the HTF is 46 % higher.

The most widespread drainback design on the market is the DBS with collector-side heat exchanger and an additional DBT (Botpaev and Vajen, 2014). Systems 4 and 5 aim at reproducing these designs, one using water as HTF (4) and the other one a mixture of glycol and water (5). It is indeed nowadays a very common trend to use glycol instead of pure water in DBS (Botpaev and Vajen, 2014). Both systems are performing very similarly to the conventional system. When comparing the two HTF, the difference in thermal performance is negligible, but the system with glycol (5) requires 32 % more electrical energy than the one with water (4) to circulate the HTF in the solar primary loop, due to higher friction losses.

Finally a configuration with a load-side heat exchanger and an additional DBT to avoid the underpressure could also be thought of but was not simulated here as such a design would increase the static pressure in the storages, which is not feasible with the PP storages used in Frankenhausen.

Tab. 2: Simulation results for the different studied systems over the drying period.

System	Q_{aux}, kWh	Q_{ref}, kWh	Q_{coll}, kWh	Q_{coll}, kWh m^{-2}	$f_{sav,therm}$, %	Solar collector loop pump running time, h	E_{pump}, kWh	E_{pump}/Q_{coll}, %
1	13137	39752	27878	219	67.0	787	223	0.8
2	12463	39754	28349	223	68.6	799	467	1.6
3	14646	39700	26082	205	63.1	876	328	1.3
4	14542	39627	26547	209	63.3	905	257	1.0
5	14512	39638	26488	208	63.4	907	340	1.3

6. Discussion and additional knowledge gained from the monitoring

The simulation results show that the two DBS without collector-side heat exchanger performs thermally slightly better than the others. They are therefore the recommended designs when the conditions are favourable, especially when the boiling risk does not exist.

When comparing other systems (notably 3, 4 and 5) the thermal performances are very similar. In these cases one decision criteria could be the pumping energy. Overall, the study showed that the pumping energy can vary quite significantly, from one system to the other. The conventional system requires 46 % more energy over the period than system 1, while the consumption of the DBS without siphon (2) is as much as 108 % higher. With today's efficient pumps sold on the European market, the relative consumption of the pumps between the different systems would not change (assuming that the same efficiency for the different working points can be achieved with actual pumps, which is in reality not the case). In terms of absolute consumption nevertheless choosing one configuration compared to the other has nowadays a much lower impact. For system 1 for instance, with a pump having a total efficiency of 35 %, which is realistic considering today's pumps, the total consumption over the period would drop from 223 kWh down to 102 kWh, which corresponds to 0.4 % of the total solar energy gain.

The results presented here are specific to the studied system and its design. It would be difficult to find a system with similar load profiles, control strategies, impact of the partial boiling on the flow rate, etc. However, they aim at showing some trends of how different DBS system designs would comparatively perform but also how DBS perform against conventional systems. Furthermore, the results might be conservative, as some authors recommend to decrease the collector efficiency when the glycol concentration in the HTF increases (Bava et al., 2014), which was not considered here. In this situation, the conventional system would be further penalized compared to DBS using water as HTF. Finally, the comparison is limited in this paper to the energy performance of the systems. One should additionally carry out a detailed cost analysis to get the whole picture of the respective advantages and drawbacks of each system against the others.

The monitoring of the field over more than a year also gave the opportunity to gain additional knowledge about the design of the system. As it was already mentioned in Jordan et al. (2015) the position in the storage of the sensor controlling the pump is very important. The tank outlet manifold and the sensor should be positioned at the same height. In Frankenhausen, the sensor is slightly lower than the outlet which causes some energy loses, as the pump is running longer as it should. Between September 2014 and August 2015, the measured losses

amount to 16.5 kWh m^{-2} a^{-1} of absorber area, which corresponds to 5.6 % of the total production of the collector field.

Finally a last issue which was encountered with the system is the deposit of lime. Its presence in the water was responsible for the blocking of the heat exchanger between the wood burner and the storage. To solve this problem, the water in the heat stores was then demineralised.

7. Conclusions

In this work several aspects of the functioning of a large drainback system for hay drying have been studied. Extensive measurement data demonstrated that the filling phase might be slowed down when the incoming HTF starts to boil in some parts of the collector field. In Frankenhausen the result is an increase of the length of the filling phase, but on even larger fields the consequences could be worse. Partial filling or early draining could result. To minimize this issue, the position of the collector field temperature sensor appears to be fundamental. The draining phase is on the contrary not significantly impacted by varying operating conditions.

Boiling is also an issue especially with the load-side heat exchanger configuration. In the studied case water starts to boil in the collector around 83 °C because of the underpressure created by the siphon formation. This phenomenon does not completely prevent the functioning of the solar collector loop but reduces the flow rate of 0.028 litre s^{-1} per degree kelvin above 83 °C and degrades the collector efficiency. The degradation is not quantified in this paper.

In a next step, different DBS designs and one “conventional” system have been simulated based on the configuration and the loads of the existing system in Frankenhausen. The simulations ran between May and September, the drying period. The results show that from a thermal point of view the fractional energy savings are 3.9 % higher with the applied drainback design compared to a “conventional” system. This improvement could reach 5.5 % if no boiling occurred in the collector field. This would however be reached at the expense of the pump electrical energy consumption, which would more than double, but still amounting to less than 2 % of the solar thermal energy gain. Overall, when considering pumping energy, resorting to water as HTF is always beneficial. If the system in Frankenhausen had a “conventional” design, the pump would require 46 % more energy. From a thermal perspective it was also shown that a DBS with collector-side heat exchanger performs very similarly to a “conventional” system.

Acknowledgments

The first author is thankful to the Marie-Curie Actions Initial Training Network research programme of the European Union which supported him through the SolNet-SHINE project. The authors are also grateful to the company Enertracting GmbH for its collaboration during this study.

8. References

Bava, F., Furbo, S., Brunger, A., 2014. Correction of collector efficiency depending on fluid type, flow rate and collector tilt. IEA-SHC Tech sheet 45.A.1.

Bokhoven, T.P., van Dam, J., Kratz, P., 2001. Recent experience with large solar thermal systems in the Netherlands. Solar Energy 71 (5), 347–352.

Botpaev, R., Louvet, Y., Perers, B., Furbo, S., Vajen, K., in press. Drainback Solar Thermal Systems: A Review. Solar Energy.

Botpaev, R., Orozaliev, J., Vajen, K., 2014. Experimental Investigation of the Filling and Draining Processes of the Drainback System (Part 1). Energy Procedia 57, 2467–2476.

Botpaev, R., Vajen, K., 2014. Drainback systems: market overview, in: Konferenzband 11. Internationale Konferenz für solares Heizen und Kühlen, Gleisdorf, Austria.

Crowe, C.T., 2009. Engineering fluid mechanics, 9th ed. Wiley, Hoboken, NJ.

Gößlinghoff, C.-H., 2010. Solaranlage mit Drain-Back-System und ein Verfahren zum Betreiben einer solchen F24J 2/46.

Goumaz, J.Y., Duff, W.S., 1981. Comparison of drain-back and dual liquid solar heating and domestic hot water systems, in: Proceedings of the International Solar Energy Society Congress, pp. 372–379.

Grundfos, 2004. Pump Handbook, Bjerringbro, Denmark.

Jordan, U., Louvet, Y., Jaradat, M., Addy, J., Fleig, D., Vajen, K., 2015. Erfahrungen mit einem offenen Sorptionskreislauf zur Trocknung von Prozessluft in Kombination mit einer Drain-Back-Solaranlage, in: 25. Symposium Thermische Solarenergie. 6. bis 8. Mai 2015, Kloster Banz, Bad Staffelstein. OTTI, Ostbayer. Technologie-Transfer-Inst, Regensburg.

Kratz, P., van Dam, J., 1999. Method for starting a system of multiple solar collectors F24J 2/42.
Letz, T., Bales, C., Perers, B., 2009. A new concept for combisystems characterization. The FSC method. Solar Energy 83 (9), 1540–1549.
Mauthner, F., Weiss, W., Spörk-Dür, M., 2015. Solar Heat Worldwide Markets and Contribution to the Energy Supply 2013. AEE Intec, IEA SHC, Gleisdorf, Austria.
Mugnier, D., Casals, L., Siré, R., Le Denn, A., 2011. Drainback systems as an efficient and safe solution for solar DHW installations: practical experience, in: Proceedings of the ISES Solar World Congress 2011, pp. 621–632.
Tyforop Chemie GmbH, 2009. Tyfocor® L. Concentrate for long-term antifreeze and corrosion protection of heating and cooling circuits, solar and heat pump systems, Hamburg, Germany.
Verein Deutscher Ingenieure, 2006. VDI-Wärmeatlas. [Berechnungsunterlagen für Druckverlust, Wärme- und Stoffübertragung], 10th ed. Springer, Berlin, Heidelberg.

Conference Proceedings

Solar World Congress 2015
Daegu, Korea, 08 – 12 November 2015

ISES SWC2015
The Integration between Solar Energy and Mining in Chile

Gustavo Díaz S.[1], Jannik Haas M[2] and Roberto Román L[2] (SWC_Author)

[1] Centro de Energía, U. de Chile (Chile) (SWC_ISES Member)

[2] Centro de Energía, U. de Chile (Chile)

Abstract

The Atacama Desert has both one of the best solar resources in the world, as well as huge mineral deposits that include copper, iron, nitrates, and lithium. In the past these resources were exploited in a non-sustainable way, which led to the burning of the scarce forests that existed and the overexploitation of water resources.

Pioneering work was done there in water desalination, the determination of solar spectra and solar constant and the utilization of solar energy in some mining processes. Today, renewable energy, and especially solar, has lowered the cost of electricity provided to the mining sector, and has also been directly applied in three cases for obtaining process heat to aid copper electrowinning production.

In this paper we present both the past, present and future of the relationship between solar energy and mining in Chile. Special emphasis is given to what is known today and further research topics that must be addressed to properly use this vast resource.

Keywords: *solar energy, process heat, solar desalination, solar electricity production, Atacama desert.*

1. Introduction

Energy and water have always been one of the largest constraints for any sort of activity in the Atacama Desert. This vast expanse of extreme aridity that lies between the Pacific Ocean and the high Andean plateau (the Altiplano region), has nearly zero average rainfall, and only a few oases and places where groundwater is found. The high Andes receive both snowfall and rainfall (concentrated mainly in the summer monsoon season); so water seeps underground to lower altitudes, but along the way picks up significant amounts of salts, boron, arsenic and other contaminants.

The first documented use of solar energy in Chile is a solar desalination plant built by the Swedish engineer Charles Wilson around 1872. It was a basin still system, with a total surface of around 5.000 m² that produced around 20.000 liters of fresh water a day from brackish water pumped from desert wells. This supplied water needs both for the miners and draft animals (mules specially) that worked at the nearby *Caracoles* silver mine district (**Fig. 1**).

This project was first widely reported by Dr. Maria Telkes and later by Prof. Julio Hirschmann (Hirschmann 1961) from Universidad Federico Santa María (Chile). It was a landmark project, and only a few years ago Historian Nelson Arellano (Arellano 2011) found original documentation and discovered that in the period from the late XIXth Century until the early XXth Century, *three* solar desalination plants were built and operated for long periods. This is quite reasonable, since solar desalination was much less expensive than coal fired desalination plants of the period, so the good results of the Wilson plant were replicated.

doi:10.18086/swc.2015.10.40 Available at http://proceedings.ises.org

The next person who did pioneering work in northern Chile was Dr. Charles G. Abbot (Abbot, 1918). This eminent researcher in the field of solar energy and solar radiation built (with the help of the Smithsonian Institution) a network of several solar observatories in different parts of the world. One of the places chosen was *Montezuma,* a mountain nearby Calama and the copper mine in Chuquicamata. This observatory operated from around 1920 until the mid 1950's, conducting systematic measurements of direct solar radiation, solar spectra and studies in the determination of the solar constant and its variability. The measurements made are quite accurate according to modern measurements and the observations of great value.

After the Second World War the low price of fossil fuels discouraged most research on the use of solar energy. A big exception was the use of solar evaporation for nitrate production.

Nitrates are produced from a mixture of naturally occurring salts called *Caliche.* Originally these salts were dissolved in hot water, and then crystallized by fractions (containing different specific salts) as the brine cooled. Since nitrates are highly soluble, this was a simple method of separating nitrate from the other salts. However huge amounts of fuel are needed for an industrial operation. And during the late XIXth Century the natural forest existing in a place called *Pampa del Tamarugal* (The flatlands of Tamarugo's, a tree species), was almost totally wiped out.

Starting in the mid 1950's the ancient method was replaced by solar evaporation of the brines and partial precipitation of the different salt fractions. This is still widely used for the production of nitrates and iodine salts, as well as the large scale production of lithium carbonate from the Atacama Salt Flats.

2. Recent uses of Solar Energy in the Mining Industry

The first oil crisis of 1973 brought renewed interest in the use of solar energy in northern Chile. Several projects went into operation. These include the following:

- A flat plate hot water system that provided up to 40 m³ of hot water a day for the showers of each shift in the El Salvador copper mine. It started operation in 1980 and is still in use (with upgrades and periodic maintenance). This project was designed by Universidad Federico Santa María (**Fig. 2**).
- Copper concentrate was dried using solar energy (250.000 Tons/year) from around 1980 to the year 2000. This simple system was later replaced by drying using mechanical presses. The new method is faster and there's less concentrate loss. There was loss in the old system due to wind blowing some of the concentrate when it was picked up from the drying ponds.
- A passive heating system for a house at the industrial water source in the high Andes in El Salvador. In operation since 1982 (**Fig. 3**).

There were other projects of varying success, but interest waned in the 1990's due to lower fuel prices. Since the early years of the XXIth century rising fuel prices, as well as environmental concerns has sparked renewed interest in the use of solar energy for the mining sector in Chile.

Today, we can divide the uses of energy for mining in Chile in the following areas:

- **Electricity production:** mining accounts for over 25% of total Chilean electrical demand. And the Energy Ministry calculates that 60% of *new* electricity demand will come from the mining sector. Electricity is used mainly in ore milling and processing, as well as conveyor belts, pumps, motors, fans and a host of other equipment.
- **Water production:** mining requires large amounts of water for leaching, flotation and evaporation processes. Water is a scarce resource and already several mines have to desalinate large amounts of seawater and then pump this up to the mines.
- **Process heat:** from an overall view, process heat is not a very large requirement, but it can be a significant amount in the plants that produce copper cathodes by the electrowinning process or the electrorefining process. Each plant requires a thermal power between 5 to 20 MW. There are over 15 plants in Chile and also plants in several other countries. Today there are two solar plants in operation

and several in the planning stages.

- **Transport:** this is a very significant energy demanding sector but, for the moment, the production of fuel for this requirement is not yet feasible.

In the following paragraphs we'll give a brief outline on how renewable energy in general, and solar energy in particular, has already had a large (and growing) impact in the Chilean energy matrix and the mining sector in particular.

3. Solar Energy and Electricity Production in Chile

Up until 2009 the conventional view in Chile was that solar energy was too expensive compared to "conventional" energy sources. Only wind power had a very modest penetration. Electrical production was concentrated in very few companies (three of them controlled over 85% of the market) and prices were very high. Contracts were over US$120/MWh and spot prices exceeded US$160/MWh.

The established companies wanted more of the same. However citizens strongly opposed large scale projects (such as very large coal fired plants or large dams) and several conventional projects were successfully blocked. At the same time several important developments took place:

- Better resource assessment proved that northern Chile had an exceptional solar resource and large scale energy needs.
- The price of solar systems, PV in particular, swiftly dropped, powering a surge in large scale projects.
- New companies decided to invest in this emerging market in Chile.

After only six years the electrical energy panorama in Chile has drastically changed. The present day situation is that over 11% of electrical energy in Chile is produced from nonconventional renewable sources (all renewables excepting large hydro), Electrical production has increased 2,9% between 2014 and 2015, but nonconventional renewables have increased 17,8% (CIFES Report). In Table 1 we show the evolution of renewable capacity generation between 2012 and 2015.

Tab. 1: Non Conventional Renewable Capacity (MW) in Chile Between 2012-2015[1]

	2012 Q1	2013 Q1	2014 Q1	2015 Q1	2015 Q2
Wind	205	205	335	836	901
Solar	0	3,6	6,7	362	741
Biomass	270	394	394	416	417
Mini Hydro	246	278	320	350	390
Geothermal	0	0	0	0	0

The incorporation of large blocks of renewable energy in the matrix, especially in the northern part of the grid, has had a very large impact in prices. Spot prices have dropped from around US$160/MWh in 2010 to less than US$60/MWh today. This is because renewables have displaced diesel fired generation at peak hours. Also overall prices have dropped. Another very important effect is that the Energy Ministry has called for renewable energy blocks to supply the electrical energy matrix, and suppliers have come forth with long term prices of around US$60/MWh.

New solar plants are being installed very quickly, and solar will tend to displace wind as the largest generator in not more than two or three years. One large CSP plant (110 MW with molten salt storage) is being built by Abengoa near Calama. It will come online early 2017. Another 3 or 4 CSP plants are under development or consideration.

So in only three or four years, the electrical energy matrix in Chile has changed significantly. The incorporation of renewables has:

[1] Table data obtained from CIFES reports 2012-2015

- Proceeded at a much faster pace than originally envisioned.
- Renewables have helped lower the price of spot energy, as they have (mostly) displaced diesel systems for peak power demand. And they have also helped lower the average energy price, since due to the excellent solar conditions in Chile, solar can be competitive today with any other energy source, including coal.
- Already provide a significant, and rapidly increasing, amount of electrical energy for the mining sector.

We must also comment that the *average* year round capacity factor of the solar plants already in operation is over 23%. This is computed comparing the nominal power of each plant, and thus the nominal yearly output with the actual energy injected to the grid on a yearly basis. Thus it takes into account of all effects, including soiling, outages, resource variability and so on. By comparison, German solar power plants have an average yearly capacity factor of less than 9%. One axis tracking plants in Chile reach capacity factors of over 30% on a yearly basis.

This panorama also has some problems. They can be summarized as follows:

- There are significant transmission capacity problems. These have resulted in that in many places there are projects that have problems injecting the power they produce. Spot prices have dropped to very low prices in these area.
- In many places there are more projects than what existing power lines can accommodate. This has led to a rethinking of the whole power grid and the interconnection of the Northern and Central power grids which should be accomplished in less than five years.

4. Solar Energy use in Process Heat in the Mining Industry

4.1. Present situation

One of the processes that use significant amounts of thermal energy is copper production by *electrowinning.* This applies mainly to copper oxide ores. The process is as follows:

- Copper ore is extracted from the mine and crushed at the mill to a diameter of around 20-30 mm. This is then conveyed to form large *leaching piles.* These typically are around 10 to 15 m high, 30 meters wide and several hundred meters in length. Under the piles there's an impermeable membrane to prevent the leaching solution from seeping into the ground.
- The leaching piles are irrigated with an acidic solution (water plus sulfuric acid). As this solution seeps through the pile, it picks up copper ore. After seeping it has a copper concentration of around 4 [g/lt].
- The solution is then piped to a *solvent extraction plant.* There, using organic solvents, a fraction is extracted with copper concentration is increased to around 20 to 27 [g/lt]. The rest, with low copper concentration is again pumped to the leaching piles.
- The high copper concentrate solution is first pumped to a special plant that removes the organic solvents, and then is pumped to the *electrowinning* production facility. In it the solution (which must be at a temperature between 55 and 60°C) is submitted to a DC current, and the copper is deposited on stainless steel cathodes. This deposition process takes several days.
- The exhausted solution is extracted from the electrowinning plant, it preheats the incoming solution, and is again incorporated into the solution that goes to the leaching piles.
- Once sufficient copper is deposited, the cathodes are removed, the copper removed, washed and packed for shipment, and the cathodes are again inserted into the electrowinning vats to repeat the process.

Heat is needed at several stages in this process. Hot water is needed to wash and clean the vats, cathodes and anodes. But most importantly to provide enough temperature to have the electrowinning vats at an optimal

point as fresh solution is added.

Normally this is done using diesel fired water heaters, which heat up the incoming solution from anywhere between 50 to 55°C (the final heating is done by the joule effect in the electrowinning vat itself). It's not a large temperature increase, since the outgoing solution preheats the incoming; but flows are very high.

Thermal requirements vary according to the size of the mine, but usually lie between 5 to 20 MWth as a nominal load. Thermal requirements increase in winter, and are higher at night. Even though the electrowinning vats have thermal insulation and systems to reduce evaporative losses, there still are significant thermal losses.

The idea of using solar energy to provide process heat for this requirement dates from the late 1990's. El Abra copper mine conducted several studies in which one of the author's participated. But, at the same time, natural gas was made available from Argentina at a price of 1/3 of diesel fuel. So the project was shelved.

Again in the early years of this century, new projects were studied. Fuel prices were again very high and there was rising concern about greenhouse gas emissions. Finally three projects were commissioned, two large scale systems and a small scale system. The main characteristics of each one is presented in **Table 2.**

Tab. 2: Solar Thermal Plants for Electrowinning Processes

Name	Operator (commissioning)	Technology	Collecting surface (m²)	Capacity factor	Comments
Pukará de Hatur	Enermine 01 Dec 2012	Flat Plate (Wagner Solar)	435	80%	Power purchase agreement
Centinela	Antofagasta Minerals 02 Jan 2013	Parabolic trough (Abengoa)	10.000	50%	Operated by Antofagasta Minerals
Gabriela Mistral	Pampa Elvira Solar 19 Aug 2013	Flat Plate (Sunmark)	39.000	80%	Power purchase agreement

We now compare the two largest plants, as regards their main characteristics:

Tab. 3: Comparison of Centinela and Pampa Elvira Solar Thermal Plants

Name	Technology	Primary circuit	Storage	Thermal delivery	Comments
Centinela	1280 single axis parabolic troughs with polymer reflector	Pressurized water with antifreeze and corrosion inhibitors	Three 120 m³ pressurized water tanks. Operate between 70 to 140°C	Up to 140°C	Can be unfocussed to prevent overheating
	Glass covered non evacuated selective surface receptor	Two collector fields		Heat exchangers for final heat delivery	
Pampa Elvira	39.000 m² flat plate collectors with selective surface	Pressurized water with antifreeze, corrosion inhibitors	4.300 m³ of nonpressurized water operates between 60 to 90°C	Up to 90°C	Tilt of collectors can be seasonally adjusted
		Backup storage for primary fluid	Active stratification control	Heat exchangers for final heat delivery	

From a technical point of view, all three plants have been successful. Only the Centinela plant had some initial

problems due to parabolic trough alignment and the need for special cleaning care due to the reflecting surface (a polymer) and the occasional deposition of acidic mist on the reflecting surface.

Two different economic models were used. In the case of Centinela Mine (Antofagasta Minerals), they called for a turnkey plant and assumed the operation. So investment was upfront, and operation and maintenance was assumed by Antofagasta Minerals. At first there were some teething difficulties, but the system has operated satisfactorily for well over a year and lives up to expectations.

In the case of Minera Gabriela Mistral and Pukará de Hatur, the developers offered a *PPA (power purchase agreement).* In essence there's a contract for selling thermal energy, and the developer takes care of day to day operation and maintenance as well as the operation of the backup fossil fuel heaters.

These authors consider that the *PPA* system has advantages, since experience has shown that this benefits optimal power production and better maintenance.

There are several other plants of this type under consideration. However the low cost of copper during the last year has caused delays in the signing of new contracts for new plants.

4.2. Technical Options and Special Issues

From a strictly technical point of view, systems that use solar tracking (i.e. parabolic troughs or linear Fresnel) should be better than flat plate systems. On a per square meter basis, costs should be lower, tracking improves output during daytime and pressurized water can be used for storage. Also these systems are more resistant to freezing and it's simple to prevent overheating.

But in fact, there's a very limited offer of both small parabolic troughs and/or Fresnel systems. And due to small production runs, the per square meter cost still tend to be high.

Large parabolic troughs are probably not very applicable because winds in excess of 5 [m/s] are common and high winds do exist.

Another problem that must be addressed is soiling. In fact this is quite a complex problem. It's very site dependent, and our experience shows that any activity near the solar fields (unpaved roads and some traffic) can influence soiling very much.

Also in the leaching and electrowinning process, very large amounts of solution that contain sulfuric acid are used. Unless the solar field is very carefully chosen, mist with some acid can affect the collectors. This can both be a problem from the point of view of soiling, as well as affect the materials of the collectors.

To better assess these problems the *Solar Energy Research Center (SERC-Chile)* project is now establishing both an experimental platform as well as specialized researchers in these problems.

4.3. New Applications

There are many other possible applications for large scale solar heat systems. Some of them are quite attractive, but demand further research. In particular:

- Solar desalination: Both the mining industry and coastal cities demand large amounts of (scarce) freshwater. Today the only option studied has been reverse osmosis (RO). However thermal desalination using MED (Multiple Effect Distillation) could be an attractive option. In theory these methods should be cost-competitive with RO. And in fact they could be less expensive, since RO plants have constant problems with membrane durability.
- Solar heating of the leaching piles: the flow of leaching solutions to the leaching piles is huge. On the order of several thousand cubic meters per hour. At the laboratory and small scale level it's been proved that copper recovery and process time are significantly improved with temperature increases of the leaching fluid of not more than 5 to 10°C. This brings significant opportunities to improve the processes and even think of *solar cogeneration.* That is install a large CSP plant near one of the mines, and cool the condensing block by rejecting the heat into the leaching piles. Many problems have to be addressed, but the opportunities for improvement are multifold.

5. Conclusions

The development of solar energy systems in Chile have evolved very rapidly, with no public subsidies. The principal existing advantages have been the need for new energy supplies at competitive costs, and an excellent solar resource.

In this atmosphere many companies have come into the country with new projects. These have had a very large impact on the energy matrix, but there are also emerging problems. These are mainly:

- High concentration of PV projects in certain areas. This has led to a very large drop in spot electricity prices. So only projects with PPA agreements become feasible.
- The shift in the energy market has shown the need for a strong improvement of the electrical transmission grid. This is now being undertaken.
- Soiling is a very variable problem, but collector field cleaning can have a significant effect on both performance and overall costs of the system.
- The (present) low price of copper and other commodities have delayed or postponed projects that are feasible from the technical and economic point of view.

Today there are two active institutions that are addressing these and other problems. These are the *Solar Energy Research Center (SERC-Chile),* a consortium of six Universities and Fundación Chile, that are devoting much manpower for research and development; and *Fraunhofer Solar Chile,* a research and development center established jointly between ISE-Fraunhofer (Germany) and the Catholic University (Chile), with the Chilean Government funding. Both institutions are working in a coordinated fashion.

Many research lines exist. Only to mention a few:

- The study of high penetration of variable renewable energy (both wind and solar) into the existing and future energy grids. These studies are being used for the planned expansion of the grids.
- Better knowledge, modelling and prediction of solar energy (beam, diffuse and global) both on a spatial and time basis for Chile.
- Measurement and effect of solar spectra on the performance and operation of solar systems. Above 2500 meter altitude in the desert, there are significant amounts of short wave UV (UV-A) and less long wave atmospheric absorptance. These are being first measured, and then we will determine if there are significant effects in the performance or durability of solar systems.
- Energy storage (especially thermal storage). The emphasis is on using low cost materials to provide thermal storage for CSP plants.
- *Solar Mining:* the intensive use of solar energy to both improve existing mining processes and reduce the carbon footprint and life cycle cost of the mines (jointly with Suttgart University).
- Other areas: these include water desalination, microgrids, legal issues and other areas

6. Acknowledgements

We must give special thanks to both the Energy Center (Centro de Energía) of Universidad de Chile; the *SERC Chile* project, CONICYT (the Chilean National Science Commission) and the *Solar Mining* project with Stuttgart University which have supported this work.

7. References

Abbot, C.G.: “The Smithsonian Solar Constant Expedition to Calama, Chile”. Proceedings of the Smithsonian Institution, 313-316 (1918).

Arellano, Nelson: “La planta solar de desalación de agua de Las Salinas (1872). Literatura y memoria de una experiencia pionera” (The solar desalination plant in Las Salinas (1872). Literature and memory of a pioneer experience). Quaderns d’Historia de l’Enginyeria, XIII, 229-251 (2011).

Julio Hirschmann: “Evaporateurs et distillateurs solaires au Chili”. Proceedings of the UN Conference of New Sources of Energy. Rome. V.6, 224-236 (1961).

R. Román, J. Haas, G. Díaz: Análisis y diagnóstico de plantas solares en Chile en Operación (Analysis and diagnostic of operating solar plants in Chile). Energy Center Technical Report for the Energy Ministry and GIZ. October 2014.

Illustrations

Fig. 1: The original Las Salinas desalination plant and a photo of the same location in 1979[1]

Fig. 2 The flat plate collector field in El Salvador (1982)

Fig. 3 The "La Ola" solar house (1982)

[1] First photo from Hirschmann, all the others by R. Román

Fig. 4 The "Amanecer Solar" plant. First 100 MW grid tied system in Chile (2014)

Fig. 5 Part of the flat plate collector field at "Pampa Elvira". The tilt mechanisms can be seen

Fig. 5 The "Centinela" parabolic trough plant. The tracking is east-west

Fig. 6 The "Centinela" parabolic system storage tanks. Each has a capacity of 120 m³

Conference Proceedings

Solar World Congress 2015
Daegu, Korea, 08 – 12 November 2015

Techno-economic comparison of solar thermal and PV for heat generation in industrial processes

Steven Meyers[1], Bastian Schmitt[1] and Klaus Vajen[1]

[1] Kassel University, Institute of Thermal Engineering, Kassel (Germany)

Abstract

The interest for renewable based water heating via electricity has increased in recent years due to the reducing costs of photovoltaics (PV) coupled with their inherent ease of installation, especially for domestic hot water applications. In larger scale solar thermal (ST) systems, namely for industrial process heat demand, solar heating has only been done by thermal collectors to date. Given the regular cost reductions for PV, this technology may one day supplant certain segments of the industrial heating market, if renewable based heating is desired. To determine if and when this may happen, a comparative analysis between PV and ST heating systems for three industrial processes operating at different temperatures was undertaken.

Results demonstrated that for applications operating below 100 °C, ST systems will still provide cheaper thermal energy as compared to PV installed between1… 2 €/W_p. To generate saturated steam at 150 °C, PV systems can provide a better economic solution when a parabolic trough ST system specific investment is more than 700 €/m^2 turnkey while being located in a region with less than 1,700 kWh/m^2a beam surface irradiation. In lower irradiation regions, the ST system cost must be even lower to compete. When PV system costs reduce to1 €/W_p, concentrating systems must reduce their costs below 400 €/m^2 to have cost superiority.

Keywords: *industrial process heat, PV, solar thermal, economic comparison*

1. Introduction

Thermal energy is the largest segment of global energy demand, accounting for nearly half of the final energy consumption (Beerepoot and Marmion, 2012). Industrial process heat comprises one third of this end use and it is estimated that solar derived thermal energy can help meet up to 5 % of global industrial demand (Lauterbach, 2014), especially when focusing on temperatures between 50 °C and 150 °C. While an interesting route to reduce fuel consumption, very few projects have been realized due to a host of factors, with high upfront project costs being a main deterrent.

With the recent and rapid improvement of PV technology, ease of installation, and its associated cost reduction, this technology is now being considered for thermal energy projects, simply by using a resistance heating element directly into a fluid stream or connected to an industrial steam boiler. Prior studies have focused mainly on small systems which provide domestic hot water (DHW). An early report (Fanney and Dougherty, 1997) shows that assuming a solar thermal DHW system costs between 4,500…6,000 USD (inflation adjusted), energy cost parity could be reached when a PV system costs between 1.65…2.85 USD/W_p (1.48…2.55 €/W_p). Current DHW systems in developed countries are estimated to cost approximately 4,500 USD turnkey, depending on local labor markets and supplies (DGS, 2012). Current PV systems for electricity generation now cost approximately 1.48 €/W_p for small commercial projects in Germany and 2.06 €/W_p in the United States, with costs reducing for larger projects (Shah and Booream-Phelps, 2015). Prices for both systems are within the range to generate thermal energy competitively. This has also been confirmed by Le Berre et al., (2014).

To date, the use of PV generated electricity to directly provide heat for industrial applications has not been rigorously studied. This is due to the more complicated nature of process integration, as industrial energy demand varies both temporally (hourly, daily and weekly) and energetically, with process temperatures ranging from 50…200 °C, and has no external grid which can be fed (which is the case with electricity). Therefore, it is imperative that an analysis be undertaken to compare both the technical and economic performance of both types of systems to determine their suitability, both now and in the future.

doi:10.18086/swc.2015.10.41 Available at http://proceedings.ises.org

2. Methodology

To determine the feasibility of different solar heating technologies in different industrial applications, three different process and temperatures were selected: from 15...60 °C or stream pre-heating (PH), from 60…90 °C or bath heating (BH), and process steam generation at 150 °C (SG). The heating demand of all three systems was constant throughout the year, which exemplifies the ideal situation for solar thermal (ST), as storage and heat exchange losses are minimized. To dimension and subsequently calculate the energy yield in such systems, a methodology described in VDI - 6002, (2014) and expanded by Lauterbach, (2014) was implemented. This approach analyzes a solar project in terms of specific collector performance, which allows for easy scalability when designing multiple systems. This method begins to size a solar field based on a "good summer day", where the highest daily yield from one square meter of collector (q_{design}), tilted to the latitude of the site, is scaled up to match the daily demand of the process. In this manner, no energy will be wasted during the annual operation of the system, as it will be undersized for the remainder of the year. For example, one process consumes 1.5 MWh/d at a temperature of 60 °C ($Q_{process,day}$). A selected solar collector, on the highest solar irradiation day, can produce 3.6 kWh/m^{2}d (determined via TRNSYS simulation in Lauterbach, 2014). By using (eq. 1), the required field size can be calculated.

$$A_{coll}^{ST} = \frac{Q_{process,day}}{q_{design}} = \frac{1.5\,\frac{MWh}{d}}{3.6\,\frac{kWh}{m^2 d}} = 416\ m^2 \qquad \text{(eq. 1)}$$

Once the collector field size is determined, it can be multiplied by the annual utilization factor (η_{sys}), generated by annual dynamic simulation (Lauterbach, 2014) and the annual irradiation incident on the collector ($H_{t,b}$ for either total or beam radiation on the collector surface) to estimate the yield of the system (eq. 2).

$$Yield_a^{ST,PV} = A_{coll}^{ST,PV} * \eta_{sys} * H_{t,b} \qquad \text{(eq. 2)}$$

Lauterbach (2014) conducted these simulations for various regions in Europe, process temperature levels, demand schedules, and storage sizes. For the PH and BH cases, results were utilized from this work to calculate the energy yields. Flat Plate and Evacuated Tube Collectors were chosen for these cases, respectively. The SG case required additional programming in MATLAB, which simulated the performance of a parabolic trough collector using the same methodology, only forgoing storage, which is rarely used while creating process steam (outside of a small buffer tank). The design yield and utilization factor for four selected regions (Würzburg, Toulouse, Madrid, and Windhoek) was calculated using a simple model with the following input parameters (Tab. 1). It was assumed that the mass flow rate of the collector could be modulated to always produce a thermal oil outlet temperature of 190 °C, required generating steam at 150 °C. Field efficiency incorporated the losses due to solar field shading, piping and heat exchanges with the boiler to generate steam. The effects of the Incident Angle Modifier (IAM) were included; however optical effects for concentrating collectors, such as end losses, were not.

Tab. 1 - Simulation parameters of the steam generation case.

Parabolic Trough Collector (NEP 1800)	η_o	0.689	
	a_1	0.36	(W/m^{2}K)
	a_2	0.0011	(W/m^{2}K^2)
Field Inlet Temperature		140	°C
Field Outlet Temperature		190	°C
Field Efficiency		90	%

Through an annual simulation, sizing parameters for steam generation case were generated. A summary of the sizing parameters used can be found in Tab. 2, Tab. 3, and Tab. 4 in Section 3.

For the PV system, it was assumed that all electrical energy will directly be consumed by the process (via resistance heating) with no storage needed. As this is a highly flexible energy source, if it could not be used directly in the process, additional resistance heaters were assumed to be installed in other processes in the factory. It is important to note that the PV generated electricity can certainly be used to decrease net demand from the electrical grid, but this is not the focus of the work. The sizing of the PV field was done to match the annual energy output of the comparative solar thermal system, as seen in (eq. 3), where the solar thermal yield is divided by the average PV system efficiency (assumed 15 %) and the incident annual irradiation (H_t).

$$A_{coll}^{PV} = \frac{Yield_a^{ST}}{\eta_{pv} * H_t} \qquad \text{(eq. 3)}$$

The financial comparison was conducted by calculating the 20 year Levelized Cost of Energy (LCOE) of both solar heating systems (eq. 4). As the energy yields were calculated in the different cases, systems costs were assumed to be directly related to their size. PV system costs are well known (Shah and Booream-Phelps, 2015) and have been assumed to be 2 €/W_p installed (or 300 €/m^2 assuming again a 15 % system efficiency), inclusive of wiring and heating equipment. ST system costs vary considerably, depending on size, balance of systems, and technology. As such, an array of LCOE calculations were conducted by varying the specific system cost from 200 €/m^2 to 1,200 €/m^2, to capture the lowest flat plate cost to the most expensive parabolic trough cost (including the effect of potential subsidies). The costs of the solar systems ($Cost_{ST,PV}$) were calculated by multiplying the calculated area of collectors or modules ($A_{coll}^{ST,PV}$) in each case by the specific cost. Other important parameters of the LCOE calculation were Discount Rate (*DR*, 5%), Operations and Maintenance (*OM*, 1.5% and 1% of system cost for ST and PV, respectively), and system degradation (*SD*, 0.5% and 1%, for ST and PV, respectively). There was assumed to be no recovery value of the systems.

$$LCOE = \frac{Cost_{ST,PV} + \sum_{n=1}^{20} \frac{OM}{(1+DR)^n}}{\sum_{n=1}^{20} \frac{Yield_a^{ST,PV} * (1-SD)^n}{(1+DR)^n}} \quad \text{(eq. 4)}$$

3. Simulation Yields

The two applications below 100 °C (PH, BH) utilized the same four regions of varying solar resource (Copenhagen, Würzburg, Toulouse, and Madrid). The SG case used the latter three and also included Windhoek, Namibia, a city with rather high direct normal insolation (DNI). Different for this case was the use of direct irradiation (H_b) on a single axis N-S tracking surface due to the parabolic trough concentrators, while the PV system yield was calculated with the global surface irradiation (H_t). The simulations assumed a daily demand of 5 MWh/day during the whole year. Storage was used for the low and medium cases, pegged at 5 kWh/m^2 of collector field size.

Tab. 2 shows the required input data, as referenced in Section 2, necessary to estimate the performance in these four locations for the PH flat plate collector case, along with the resulting annual energy yields for both the ST and PV systems, collector area, and the range of project costs. Tab. 3 depicts the same for the BH evacuated tube collector case, and Tab. 4 for the SG parabolic trough. Fig. 1 summarizes the specific yield (kWh/m^2a) for all collector types in the three cases. The PV yields are the same for the three cases, as it was assumed that the conversion efficiency for resistance heating is temperature insensitive. The results clearly show an increasing yield as a function of higher solar irradiation, and a decreasing trend as the working fluid temperature increases, even if more efficient collectors are used.

Tab. 2 - Energetic yield results from the PH case using flat plate collectors

Pre-heating (15…60 °C)		Copenhagen	Würzburg	Toulouse	Madrid
Solar Thermal	Sizing Yield (kWh/m^2d)	4.4	4.4	4.8	5
	Field Size (m^2)	1,136	1,136	1,042	1,000
	Storage Size (m^3)	110	110	101	97
	Utilization Factor (%)	54	56	59	60
	H_t (kWh/m^2a)	1191	1264	1552	1887
	Specific Yield (kWh/m^2a)	643	708	916	1,132
	Annual Yield (MWh)	731	804	954	1,132
	Project Costs (k€)	227-1,136	227-1,136	208-1,042	200-1,000
PV	Field Size (m^2)	4091	4242	4097	4000
	System Efficiency (%)	15	15	15	15
	Specific Yield (kWh/m^2a)	179	190	233	283
	Annual Yield (MWh)	731	804	954	1,132
	Project Costs (k€)	1,227	1,273	1,229	1,200

Tab. 3 - Energetic yield results from the BH case using evacuated tube collectors

Bath Heating (60…90 °C)		Copenhagen	Würzburg	Toulouse	Madrid
Solar Thermal	Sizing Yield (kWh/m²d)	3.8	4	4.2	4.4
	Field Size (m²)	1,316	1,250	1,190	1,136
	Storage Size (m³)	191	181	173	165
	Utilization Factor (%)	37	39	44	46
	H_t (kWh/m²a)	1,191	1,264	1,552	1,887
	Specific Yield (kWh/m²a)	441	493	683	868
	Annual Yield (MWh)	579	616	812	986
	Project Costs (k€)	263-1,316	250-1,250	238-1,190	227-1,136
PV	Field Size (m²)	3246	3250	3492	3485
	System Efficiency (%)	15	15	15	15
	Specific Yield (kWh/m²a)	179	190	233	283
	Annual Yield (MWh)	579	616	812	986
	Project Costs (k€)	973	975	1047	1045

Tab. 4 - Energetic yield results from the SG case using parabolic trough collectors

Steam (150 °C)		Würzburg	Toulouse	Madrid	Windhoek
Solar Thermal	Sizing Yield (kWh/m²d)	4.9	4.3	5.3	6.18
	Field Size (m²)	1,020	1,163	943	809
	Utilization Factor (%)	37	37	45	50
	H_b (kWh/m²a)	743	912	1,490	2,441
	Specific Yield (kWh/m²a)	275	337	663	1221
	Annual Yield (MWh)	320	344	626	987
	Project Costs (k€)	204-1,531	233-1,744	189-1,415	162-1,214
PV	Field Size (m²)	1,686	1,479	2,210	2,611
	System Efficiency (%)	15	15	15	15
	H_b (kWh/m²a)	1,264	1,552	1,887	2,521
	Specific Yield (kWh/m²a)	190	233	283	378
	Annual Yield (MWh)	320	344	626	987
	Project Costs (k€)	506	444	663	783

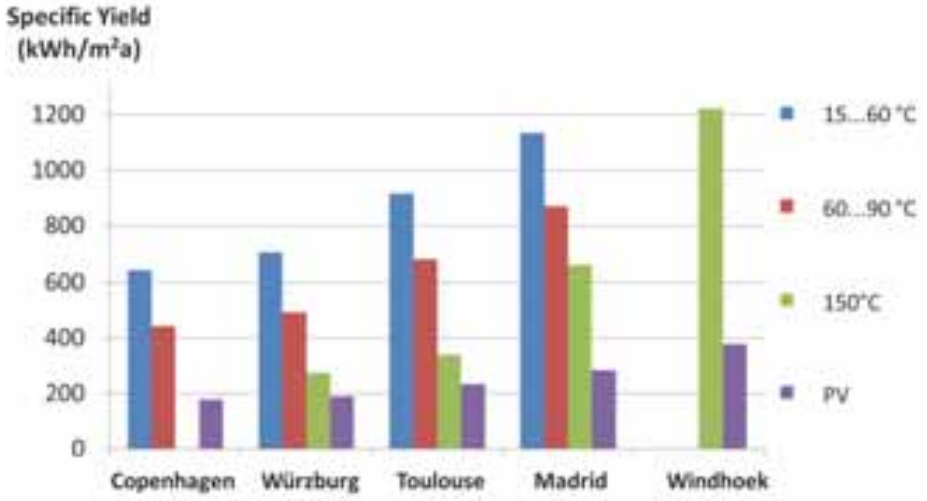

Fig. 1 - Summary of the specific collector yields in all cases

4. Comparative Analysis Results

From the previously calculated energy yields and their respective project costs, a relationship was established between them and the available solar irradiation. A metric was created to determine the better financial choice to generate thermal energy. For each financial case (solar costs, case, location), the LCOE for the ST and PV systems were calculated. The ST LCOE was then divided by the PV LCOE, yielding a ratio that if greater than one; the PV system would produce cheaper thermal energy. If less than one, the ST system would be cheaper. The results of the calculated ratio are show in Tab. 5 for the three cases. The assumed specific PV collector cost was 2 €/W_p.

Tab. 5 – Simulated LCOE Ratios for solar process heat projects. The highlighted and bold cells indicate situations where PV heating is more economically viable than ST heating. White cells with regular font show the situations where ST heating is more economically viable.

		Solar Thermal System Investment (€/m²)										
Case	Location	200	300	400	500	600	700	800	900	1000	1100	1200
15…60 °C	Copenhagen	0.19	0.28	0.37	0.47	0.56	0.65	0.75	0.84	0.94	***1.03***	***1.12***
	Würzburg	0.18	0.27	0.36	0.45	0.54	0.63	0.72	0.81	0.90	0.99	***1.08***
	Toulouse	0.17	0.26	0.34	0.43	0.51	0.60	0.68	0.77	0.86	0.94	***1.03***
	Madrid	0.17	0.25	0.34	0.42	0.51	0.59	0.67	0.76	0.84	0.93	***1.01***
60…90 °C	Copenhagen	0.24	0.35	0.47	0.59	0.71	0.83	0.94	***1.06***	***1.18***	***1.30***	***1.41***
	Würzburg	0.24	0.35	0.47	0.59	0.71	0.82	0.94	***1.06***	***1.18***	***1.30***	***1.41***
	Toulouse	0.20	0.30	0.40	0.50	0.60	0.70	0.80	0.90	***1.00***	***1.11***	***1.21***
	Madrid	0.19	0.29	0.39	0.48	0.58	0.68	0.77	0.87	0.97	***1.06***	***1.16***
150 °C	Würzburg	0.49	0.73	0.97	***1.22***	***1.46***	***1.71***	***1.95***	***2.19***	***2.44***	***2.68***	***2.92***
	Toulouse	0.37	0.55	0.74	0.92	***1.11***	***1.29***	***1.48***	***1.66***	***1.85***	***2.03***	***2.22***
	Madrid	0.26	0.39	0.52	0.65	0.77	0.90	***1.03***	***1.16***	***1.29***	***1.42***	***1.55***
	Windhoek	0.19	0.29	0.39	0.48	0.58	0.68	0.77	0.87	0.97	***1.07***	***1.16***

These results were further analyzed, generating a relationship between the LCOE ratio, ST system costs, and available solar irradiation, via multiple linear regression, with the following relationship (eq. 5). For the PH and BH cases, H_t was used and H_b for the SG case. Statistics for the curve fit are seen in Tab. 6.

$$Ratio_{LCOE} = b_0 + b_1 * ST_{Specific\ Cost} + b_2 * ST_{Specific\ Cost} * H_{t.b} \quad \text{(eq. 5)}$$

Tab. 6 - Multiple Linear Regression results

	R^2_{adj}	RMSE	F statistic	p-value	b_o	b_1	b_2
Pre-Heating	0.999	0.011	16690	0	0	0.001069	-1.26E-07
Bath Heating	0.995	0.025	5066	0	0	0.00157	-3.36E-07
Steam Generation	0.931	0.188	316	0	0	0.0027	-7.70E-07

The result of (eq. 5) coupled with an array of feasible ST system costs (200…1,200 €/m²) and incident solar irradiation values (1,000…2,600 kWh/m²a) showed the changing feasibility of ST systems to provide thermal energy as compared to PV. The results for the PH case are shown in Fig. 2, the BH case in Fig. 3, and the SG case in Fig. 4. The thick white line indicates the point where PV and ST LCOE's are the same, so parameters right of this line favor ST projects and to the left favor PV projects.

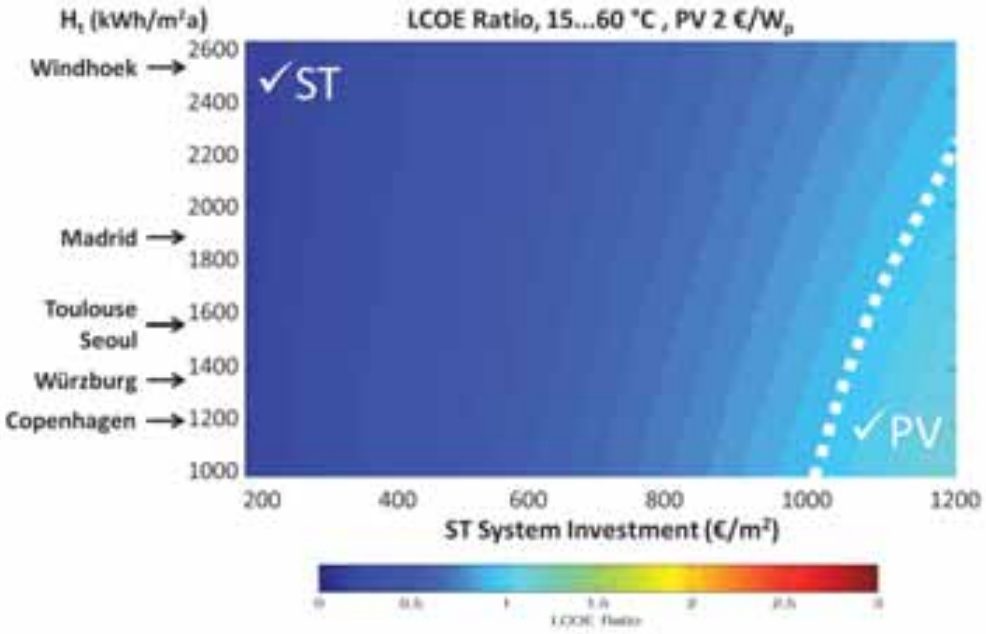

Fig. 2 – Pre-Heating LCOE comparison, where ST is the preferred choice under one, and PV over one.

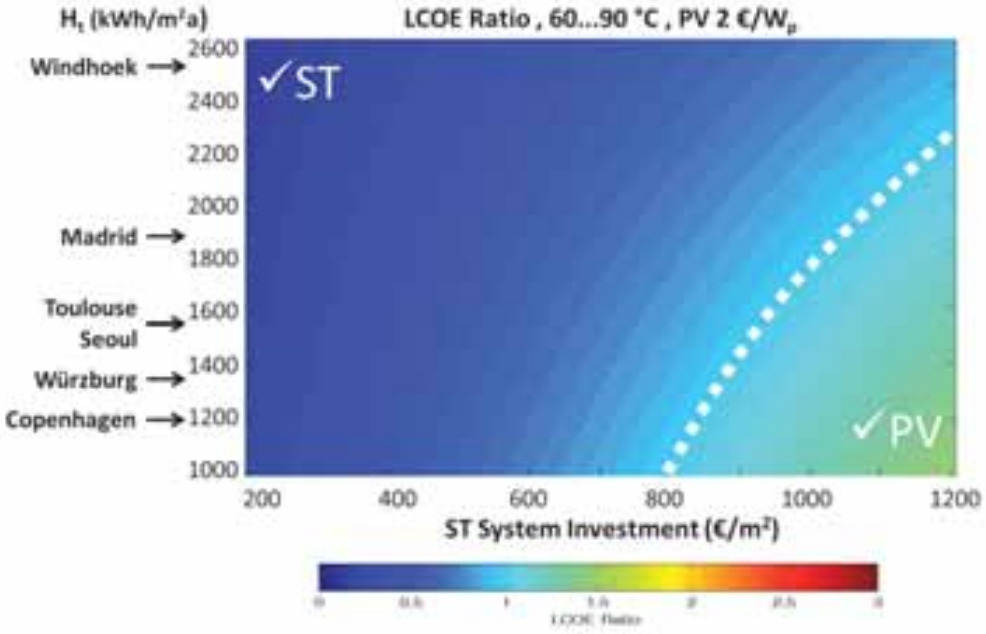

Fig. 3 – Bath Heating LCOE comparison, where ST is the preferred choice under one, and PV over one.

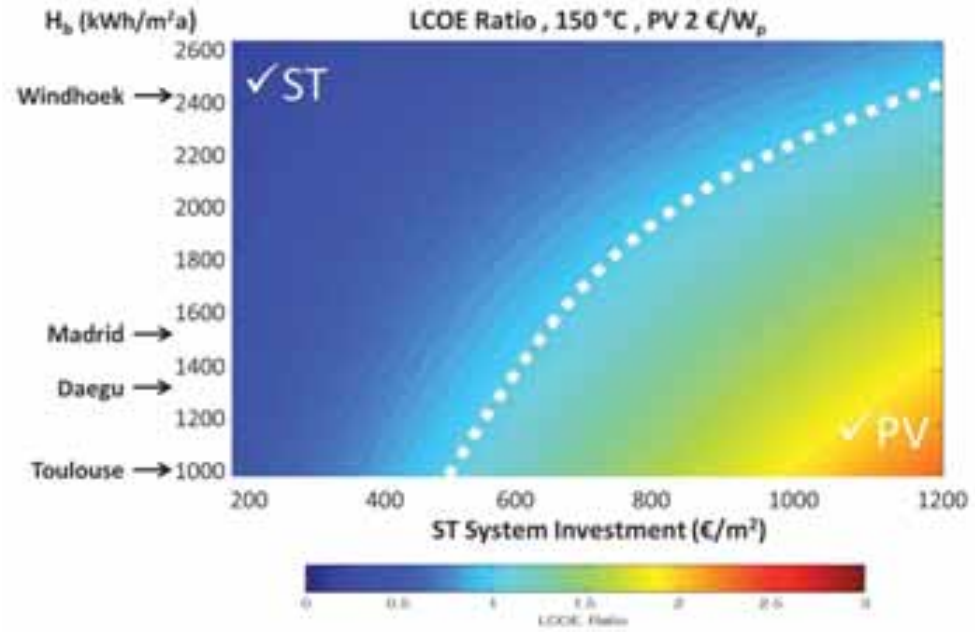

Fig. 4 – Steam Generation LCOE comparison, where ST is the preferred choice under one, and PV over one.

5. Discussion and Example Case

The tabular results in Tab. 5 clearly show that within applications and temperature levels, there are situations where PV heating is more cost effective than ST. This is most notably observed when ST system costs are significantly higher, operating at higher temperatures, and when installed in lower solar resource regions. This trend is progressively seen in Fig. 2, Fig. 3, and Fig. 4. These results are logical, as PV or electrical based heating is temperature insensitive (i.e. near constant thermal conversion efficiency), while the efficiency of a solar thermal collector decreases when operating at higher temperatures. Furthermore, PV can still produce useable energy in lower radiation, while ST struggles since there are inherent thermal losses to overcome. This helps to explain how, for example, PV may be better adapted to generate steam in most regions in Europe, as the beam irradiation is marginal at best while global irradiation is more consistent and beneficial to non-concentrating technologies. It should go without saying that steam generation with flat plate collectors would be rather challenging. Also interpreted from this table is a reason why DHW is at times being heated through PV resistance heating. In very small projects, the specific ST cost can be 900…1200 €/m^2 (DGS, 2012), making the costs very comparable with PV. Given the ease and minimal risk to install PV, this solution is gaining in popularity.

Fig. 2, Fig. 3, and Fig. 4 show a clear trend, that ST performs better compared to PV in higher irradiation regions than lower. The figures also indicate that as ST collector operating temperatures increases, so does the cost feasibility of a PV heating solution. A simple observation in all three figures again points to the fact that the area of acceptable ST projects shrinks as the collector temperature increases, while the PV area increases. This leads to the conclusion that PV heating may soon play a more important role in steam generation applications in relatively lower solar irradiation regions. This is made evident by the greater than one LCOE ratios in Fig. 4 above 700 €/m^2 ST project specific investment cost while H_b remains less than 1,700 kWh/m^{2}a. Both of these keystone values are often observed in projects within Europe.

As steam generation applications have demonstrated the nearest term situation where PV heating may be feasible, a reference case was used to assess its current state. In 2012, NEP Solar built a 627 m^2 parabolic trough collector field for a diary company in Switzerland, which generates 120 °C pressurized hot water for a cheese manufacturing facility. The specific subsidized project investment for the total system was approximately 595 €/m^2 (Frank et al., 2013), of which half was dedicated to the collector field. At this site, the annual DNI was 1,119 kWh/m^{2}a with a reported net specific steam yield of 406 kWh/m^{2}a. This value is comparable when interpreting the parabolic trough simulation results from Tab. 4 (445 kWh/m^{2}a), however operating at a higher mean plate temperature. Interpreting Fig. 4, the LCOE ratio at this point (595 €/m^2 and 1,119 kWh/m^{2}a) is 1.15, clearly indicating that a PV heating system would provide heating at a lower cost. If the solar thermal system investment could be reduced to below 550 €/m^2, it would be competitive against PV. If the incentives were removed, the project cost would increase to 990 €/m^2. To be competitive at this specific collector cost, the beam irradiation H_b must be rather high (2,200 kWh/m^{2}a). If the PV costs increased to 3 €/W$_p$, the competitive H_b changes to 1550 kWh/m^{2}a or ST system costs must be reduced to 825 €/m^2. When the PV cost is greater than 3.65 €/W$_p$, the currently designed and unsubsidized ST system becomes the preferred solution.

While PV may outperform ST in some situations, like above, it is important to point out the practicality of using PV for heating, with respect to the required land area needed to build such a project. Tab. 2, Tab. 3, and Tab. 4 display a significantly higher area required by PV to generate the same amount of thermal energy compared to ST. The multiple of land area required for the PV system relative to the ST system is shown in Tab. 7. The results indicate that PV requires relatively more space in higher solar irradiation regions, but less when operating at higher temperatures.

Tab. 7 - System size comparison between PV and ST, showing the significantly higher space needed for PV to generate thermal energy.

	Copenhagen	Würzburg	Toulouse	Madrid	Windhoek
Pre-Heating	3.6	3.7	3.9	4.0	----------
Bath Heating	2.5	2.6	2.9	3.0	----------
Steam Generation	----------	1.7	1.3	2.3	3.2

In reality, there is often limited available rooftop or land space at an industrial facility to build a solar system. This means that if a larger amount of thermal energy is desired to be displaced by solar on the same rooftop, ST

may still be chosen even if it costs more. This is one major drawback of employing PV heating for industrial heat demand. To combat the greater required PV size, a heat pump could be employed to generate the targeted energy. If the COP of the heat pump can equal the relative size difference in Tab. 7, the PV field can be sized the same as ST, generating the same thermal energy (but not necessarily at the same cost). This also assumes that there is suitable available heat from waste streams. This analysis is not pursued in this paper, but is an interest for future work.

6. Future Scenario

The results from the reference case study show that current costs for ST projects operating at higher temperatures are similar to those of PV, if not higher. While future ST costs are challenging to predict, it is well accepted that PV cost will regularly decrease in the coming years. By setting the price of PV to 1 €/W_p, an understanding can be gained as to which technology may be chosen for future projects. This will also serve as a price target for ST systems to achieve so that PV electrical heating will not supplant them as the chosen technology for thermal energy generation.

In PH applications (Fig. 5), it appears that as long as ST project costs remain under 500 €/m^2, they should be the preferred choice, no matter the available solar irradiation. Similarly in BH applications (Fig. 6), ST should be chosen if costs are below 400 €/m^2 in all irradiation conditions. However, some evacuated tube projects are currently above this cost target, emphasizing the need to still reduce costs. The motivation to reduce costs is clearly evident when using concentrating collectors (Fig. 7), as the breakeven point for concentrating ST collectors generating steam is below 300 €/m^2 for lower irradiation climates and up to 500 €/m^2 in ideal solar locations (2250 kWh/m^2a). The current project costs for SG concentrating collectors are well above this price point and significant efforts must be made to reduce costs, both with the collector and balance-of-systems, in order for ST to generate steam in the future.

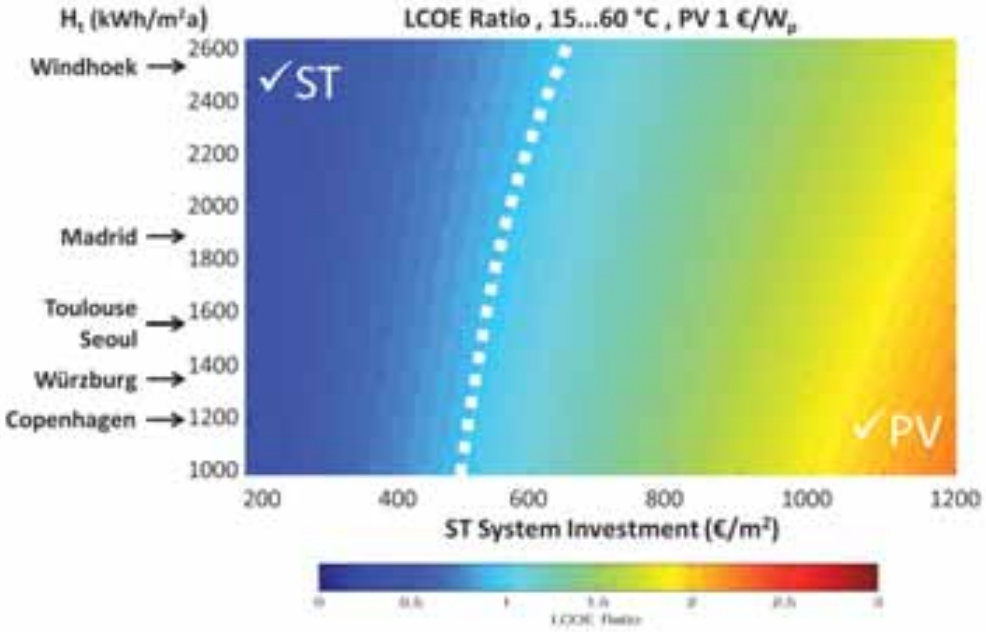

Fig. 5 – Pre Heating LCOE comparison when PV costs 1 €/W_p

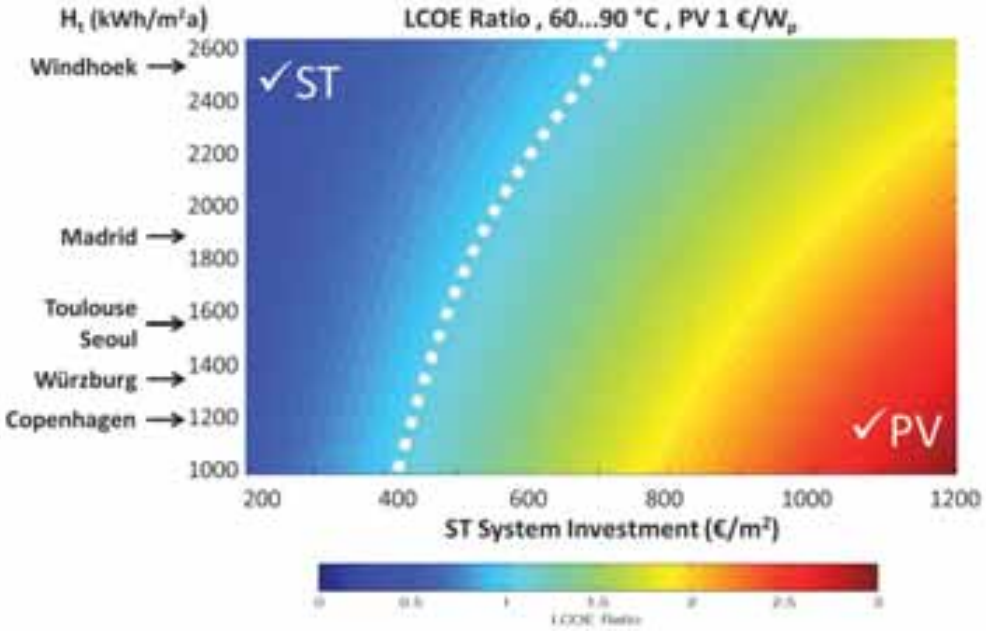

Fig. 6 – Bath Heating LCOE comparison when PV costs 1 €/W_p

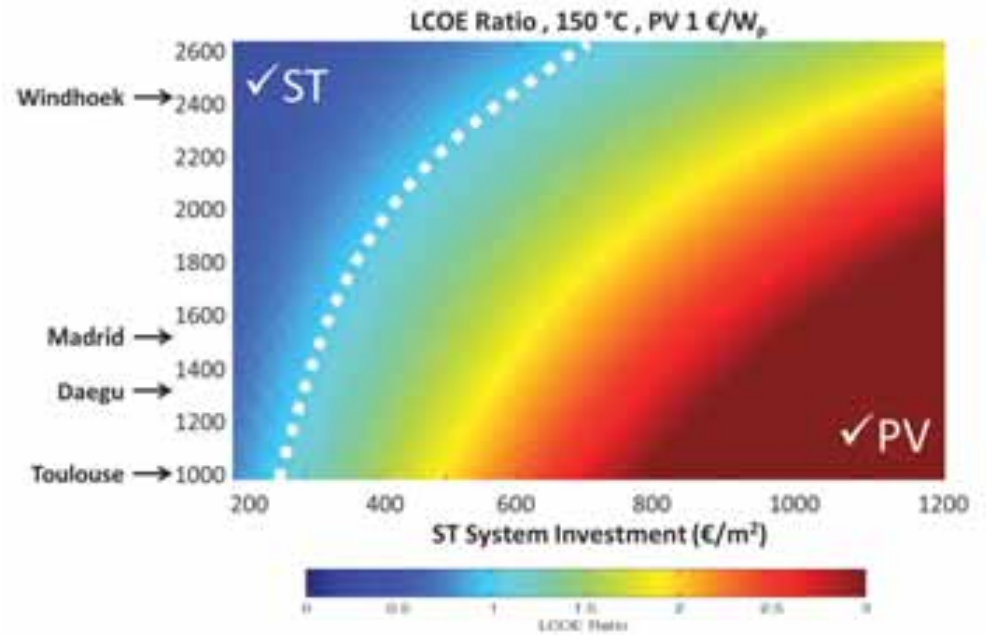

Fig. 7 – Steam Generation LCOE comparison when PV costs 1 €/W_p

7. Conclusions

The previous analysis showcased the comparison between Solar Thermal and Photovoltaics to generate thermal energy for industrial processes. At current costs, ST is still a more economic choice for applications below 100 °C, but when generating steam, PV can provide relatively lower costs when the direct solar resource is less than 1,700 kWh/m^{2}a. From the provided reference case in Switzerland, PV is already a more economical solution, mainly due to the low solar resource and high specific project cost for ST.

The 2020 specific cost goal for non-concentrating systems is 250 €/m^2, and 300 €/m^2 for concentrating, according to (Ivancic et al., 2014). These figures, especially for concentrating collectors, remain good targets to stem the competition from PV based heating. Significant efforts are still needed to realize such goals.

It is important to note that the price of fossil fuel, or its comparison with thermal energy generation, was not mentioned during this analysis. This omission was intentional, as the focus was a technical comparison between the two solar technologies.

8. Acknowledgements

The authors wish to acknowledge the European Union for funds received through the People Programme (Marie Curie Actions) of the Seventh Framework Programme FP7/2007-2013/ under REA grant agreement n° 317085 (PITN-GA-2012-317085), commonly known at the SHINE (Solar Heat INtegration Network) Program (http://www.uni-kassel.de/maschinenbau/institute/ite/solnet-shine.html), and Martin Van Well for his assistance in the LCOE model development.

9. References

Beerepoot, M. and Marmion, A.: Policies for Renewable Heat, OECD Publishing, 2012.

Deutsche Gesellschaft für Sonnenenergie: Solarthermische Anlagen: Leitfaden für das SHK-, Elektro- und Dachdeckerhandwerk, Fachplaner, Architekten, Bauherren und Weiterbildungsinstitutionen, 9. Aufl., Berlin, Losebl.-Ausg. +, 2012.

Fanney, A. H. and Dougherty, B. P.: A Photovoltaic Solar Water Heating System, J. Sol. Energy Eng, 119, 126–133, doi:10.1115/1.2887891, 1997.

Frank, E., Feuerstein, M., Minder, S., and & AG, N. S.: Parabolrinnenkollektoren für Prozesswärme in Schweizer Molkereien, 2013.

Ivancic, A., Mugnier, D., Stryi-Hipp, G., and Weiss, W.: Solar Heating and Cooling Technology Roadmap: European Technology Platform on Renewable Heating and Cooling, 2014.

Lauterbach, C.: Potential, System Analysis and Preliminary Design of Low-Temperature Solar Process Heat Systems, Kassel University Press, Kassel, Online-Resource, 2014.

Le Berre, R., Dupeyrat, P., Plotton, A., Doucet, J.-F., and Lindsay, A.: PV Domestic Hot Water System, EuroSun Proceedings, 2014.

Shah, V. and Booream-Phelps, J.: Crossing the Chasm: Solar Grid Parity in a Low Oil Price Era, 2015.

Verein Deutscher Ingenieure - 6002: Blatt 1: Solar heating for potable water - Basic Principles: System technology and application in residential buildings, 2014.

Solar heat for industrial processes in Germany – Market overview and detailed monitoring of selected systems

Dominik Ritter[1], Bastian Schmitt[2] and Klaus Vajen[1,2]

[1] Kassel University, Institute for Thermal Engineering
Kassel, Germany
[2] IdE Institute decentralized Energy Technologies
Kassel, Germany

Abstract

Since the start of the funding of solar thermal process heat systems in Germany, a growing market has begun to evolve. At the moment roughly 400 m² of collector area for solar process heat systems are submitted for approval each month; four times more than in 2012. All together about 14,000 m² were submitted since 2012 and more than half of the collector area is already in operation, delivering heat for commercial and industrial applications. Although many of these systems are within 20 m² to 40 m² and are used for very simple applications like rearing of piglets and hot water preparation for car washes, there are also bigger systems, up to 960 m², delivering heat for e.g. drying and cleaning applications of production sites and produced goods. Referring to the turnkey system costs, the average cost of nearly 800 €/m² is still quite high and differs significantly depending on the collector technology used and the application.

In addition to the funding of new solar process heat systems, a detailed monitoring of three newly installed systems is financed to gain in depth experience on solar process heat systems. These systems are a metal surface treatment facility, a bitumen production and a gas pressure regulation station. System descriptions and first results are presented.

Keywords: *industrial process heat, solar thermal, German market, monitoring*

1. Introduction

The supply of process heat has become one of the future key markets for solar thermal systems in Germany and Europe due to the significant technical potential for Germany of 130 TWh/a (Lauterbach et al. 2012). This is equivalent to more than 35 million m², with benefits such as year-long heat demand in commerce and industry, giving the opportunity to reach low solar heat generation costs. Since there were only very few systems installed in Germany until 2012, the Federal Ministry for Economic Affairs and Energy (BMWi) released a promotion for solar process heat systems within the Market Incentive Programme (MAP) in August 2012. Since then the supply of solar process heat is supported by an investment grant or subsidy on the loan redemption of up to 50 % according to the chargeable investment costs. With the latest amendment in April 2015, it was confirmed as an important component for the goal to provide 14 % of the German heat demand with renewable energies till 2020 (BMWi, 2015).

To increase the impact and quality of the new solar process heat funding, a scientific project was permitted and funded to be conducted by University of Kassel. The most important task of this scientific institution is to provide technical support and optimization measures to ensure the quality of newly installed systems. Within this scope of duties the detailed monitoring of three selected solar process heat systems is a very important issue. The aim is to gain information about the efficiency in the field of the specific applications, the effectiveness of the respective integration of solar heat, the long term reliability of the systems and possible malfunctions caused by the interaction of different heating systems.

2. Market overview and accompanying project

Since the start of the funding for solar process heat systems in August 2012 until the end of August 2015 more than 240 applications for solar thermal systems with a total gross collector area of 18,000 m² were submitted. Out of these applications only 7 % were rejected for formal reasons e.g. use of heat for domestic

Selection and/or peer review under responsibility of Scientific Committee
doi:10.18086/swc.2015.10.42 Available at http://proceedings.ises.org

hot water or the use of unglazed collectors. Additional 6 % were cancelled by the applicants themselves for unknown reasons. Nearly 90 % reached the realization phase, equivalent to an area of 13.900 m^2_{gross}. Since there is usually a larger time gap between the application for the funding and the start-up of the realized solar process heat systems, there are currently only 134 systems in operation with a collective collector area of 7,241 m^2_{gross}. Figure 1 shows a yearly breakdown based on the collector area of the application forms that were handed in, the approved applications, the systems that started operation and the systems that are still under construction. In contrast to the other values the last bar also includes the collector area of approved but not yet realized systems of previous years. In this Figure it has to be considered that the funding of solar process heat systems started at the end of August 2012 and the values for the year 2015 only represent the period from January 1st to August 31st.

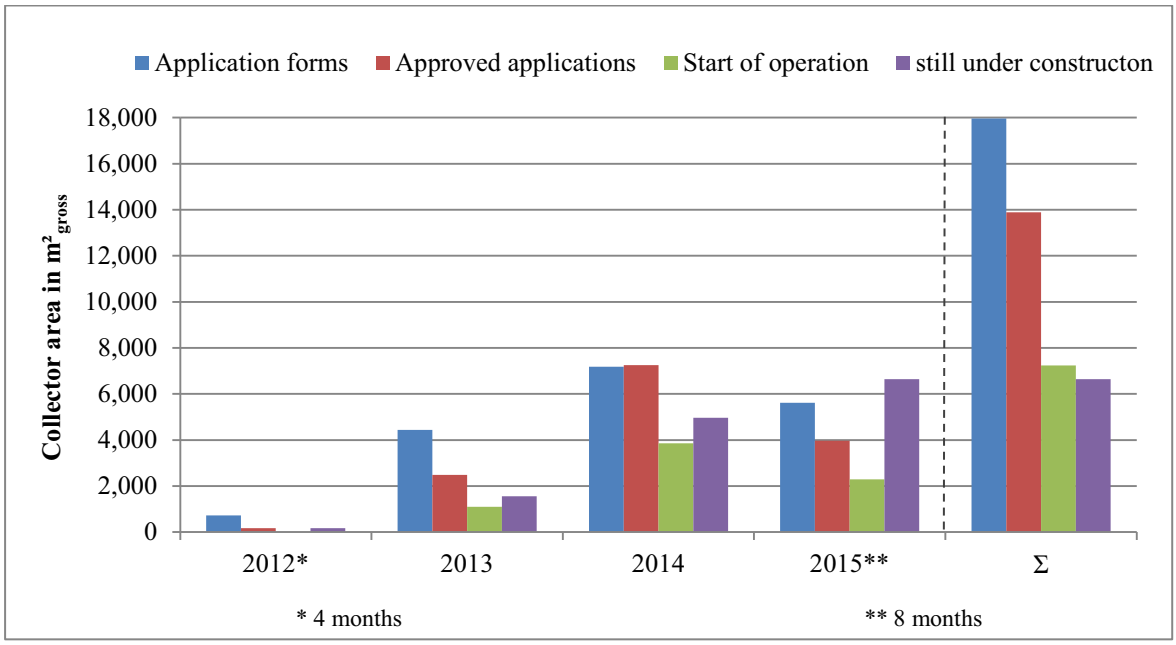

Figure 1: Overview on the German market for solar process heat

A more comparable illustration is an overview of the monthly approved applications according to the collector area as an average value for the particular year. This comparison, as it can be seen in Figure 2, shows a growth of the German market for solar process heat systems until the end of 2014. In 2015 there was a little decrease that can be explained by the restraint of applications caused by the amendment to the Market Incentive Program in April. Because of the weak start of the year 2015 and since there are still four months left, it would be too early to conclude that there is already a slowdown in growth of the German market for solar thermal process heat systems.

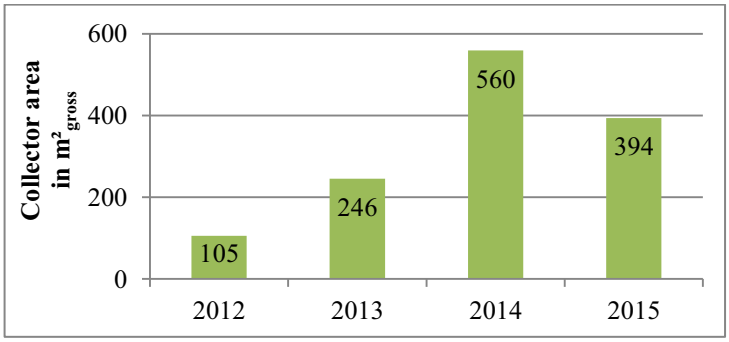

Figure 2: Average value of the monthly approved collector area in m²

At the early stage of the solar process heat funding program, the average collector field size was below 40 m^2_{gross}. Starting with the year 2013 small but constant growth of the average size was seen, reaching a peak in 2014, due to a system with 960 m^2_{gross}. However the average project size in 2015 is 66 m^2_{gross}. Although a large share of the installations is smaller than 40 m², already 22 process heat systems have a

collector field size between 100 m^2_{gross} and 960 $m^2_{gross.}$ The three largest systems that are already in operation are a 297 m² system with CPC-collectors delivering solar heat to the different baths, drying chambers and the air washer of a metal treatment company, a 507 m² air collector system for drying of wood chips and a system with 960 m² with flat plate collectors that are used to deliver heat for the dehumidification and heating of greenhouses to prevent the fouling of vegetables and to extend the growing season.

Analyzing the end use of solar heat, it becomes obvious that over 50 % of all submitted solar process heat systems are used or will be used for only two applications: rearing of piglets and car washes. Beside these two often applied systems, there is a large variety of processes heated by solar thermal systems, especially in the field of drying and cleaning of products and production sites. Other uses of the solar heat are fish farming, production of pharmaceutical goods, heating of baths for plastics testing and surface treatment, hot water production for laundries as well as bitumen processing and others.

As solar thermal systems serve as fuel savers aside from a handful of applications, it is always interesting to refer to the costs of the systems which in combination with the solar yield determine the solar heat generation cost. The breakdown of the system costs including installation and integration into the respective process but independent of the used collector technology or the application down to 1 m^2_{gross} delivers specific system costs of 789 €/m² since the start of the funding in Germany. A deviation of the system costs between the different collector technologies can be observed also varying from year to year. As it can be seen in Figure 3, the costs for solar process heat systems using flat plate collectors are in some degree stable in a range between 760 €/m² and 860 €/m² nevertheless a slight but constant increase over the years can be recognized. According to the costs for systems using air collectors or evacuated tube collectors (ETC) - including CPC - it is very conspicuous, that they are clearly higher in 2012 compared to the other years. This is caused by three systems with very high specific costs in a range between 1.500 €/m² and 2.100 €/m² that could not be compensated by the other systems. But even such expensive systems are sometimes economical feasible depending on the reference price of the conventional heating system. If it is electrical heating, this reference price can exceed 0.20 €/kWh for smaller commercial electricity consumers. On the other hand considering the 50% investment grant, some systems even reach a heat price roughly 0.03 €/kWh, being competitive with modern gas boilers delivering heat for processes. The numbers in the bars in Figure 3 are the average system size for the particular collector type and year (BAFA, 2015 and KfW Group, 2015).

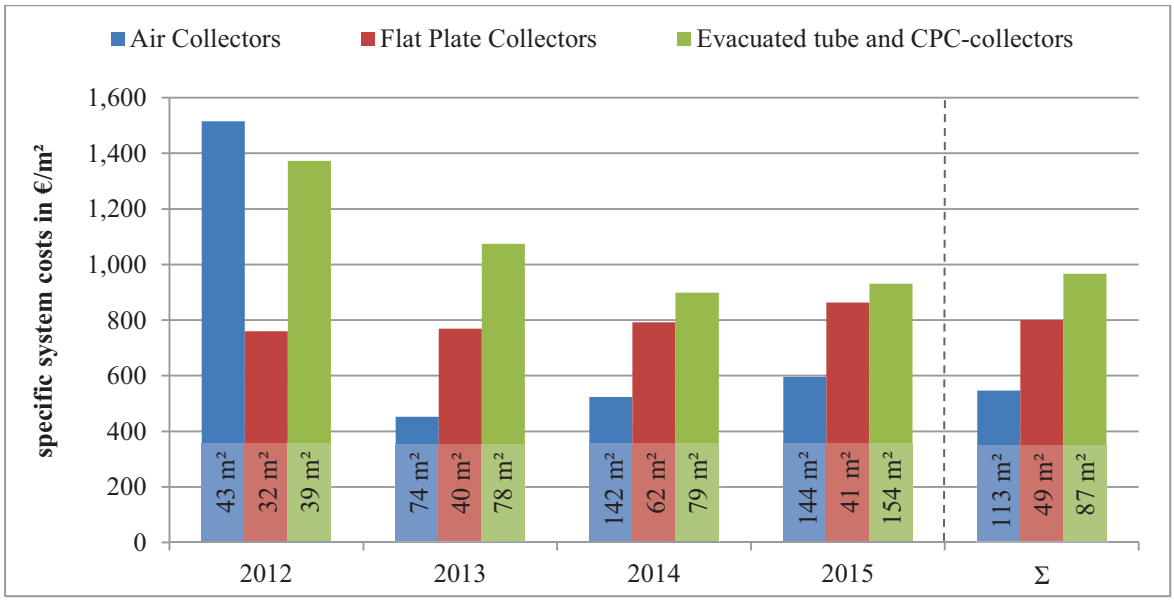

Figure 3: Average system costs for solar process heat systems in Germany according to the collector type

Since solar process heat is an emerging market in Germany and these systems are usually more complex compared to domestic applications, the BMWi is funding a scientific project to analyze and push the German market for solar process heat. As mentioned in the introduction, the University of Kassel has different tasks to ensure the quality of newly installed systems such as technical consultancy for planners, publication of technical recommendations, and identifying optimization measures. Beside this, it is also obligatory to spread the gained knowledge on the market by developing information materials and giving training courses as well

as information sessions to selected target groups. One very important task is the detailed monitoring of three selected process heat systems that were funded within the Market Incentive Program to gain information about the efficiency in the field of the specific applications, the effectiveness of the respective integration of solar heat, the long term reliability of the systems and possible malfunctions caused by the interaction of different heating systems. The requirements according to the measurement devices, the description of the systems and some first results of the monitoring can be found in the following sections.

3. Selected solar process heat systems for the monitoring

For the detailed monitoring, three applications were selected: a metal treatment company, a bitumen production facility and a gas pressure regulation station. The selection of these systems for the detailed monitoring was done using several criteria such as temperature levels, the way of integrating solar heat, the financing model as well as innovative ways of dealing with stagnation or the combination with other heat supply technologies. Table 1 gives an overview on the similarities and differences of the named systems.

Table 1: Description of solar process heat systems for the detailed monitoring

	Metal treatment	Bitumen processing	Gas pressure regulation
Collector type	CPC evacuated tube collector	Flat plate collector	Large-scale flat plate collector
Collector field	300 m^2_{gross}, roof mounted	190 m^2_{gross}, roof mounted	500 m^2_{gross}, ground mounted
Buffer storage	15 m^3	20 m^3	25 m^3
Solar assisted process(es)	Heating of baths Drying of products Heating of air washer Maintain air temperature	Hot water for bitumen emulsion process Boiler make-up water Heating of bitumen tank Steam cleaning	Heating of natural gas pipeline before decompression
Temperature level for solar system	40...70°C	20...130°C	50...60°C
Integration concept	Supply level, all heat sinks are served	Process integration, several heat sinks	Process integration, one heat sink
Combination with other heat generators	Conventional oil burner as backup that is directly loading the upper part of the buffer tank	Hydraulically separated steam boiler as backup	Gas burners as backup. Additional gas-driven heat pumps to reduce natural gas consumption
Charge / discharge of storage	Storage is directly connected to solar heating system and heating network without hydraulic disconnections	External HX for storage charging. Combination of direct hot water use and external HX to discharge the storage	Charging with internal HX, discharging with external HX
Frost prevention	Active frost protection due to water as heat transfer medium	Water glycol mixture	Water glycol mixture
Load profile	More or less constant production over the year (order related production)	Very good match between energy demand for processes and solar radiation (road building)	Highest heat demand in winter (space heating), reduced base load in summer
Financing	Self-investment	Self-investment	ESCO
Planner	Holsmölle 2014	Aschoff 2014	Heinzen 2015

Since the metal treatment facility will be explained in more detail within the following two sections, some information of the bitumen processing and gas pressure regulation station are given below.

Bitumen processing

The produced bitumen emulsion is used for road construction. As these infrastructural projects normally aren't performed in winter, the production period of the company starts around April and ends the latest in November. In addition it is not unusual that weather forecasts are used in this business determining the production output. Therefore the available solar energy and the load profile of the production site have a very good congruence and a very high solar fraction of >70 % is planned. The main energy consumer is the preparation of hot water for the emulsion process where raw bitumen and emulsifiers have to be mixed to obtain a stable product. The second consumer is the pre-heating of boiler make-up water up to 90°C for the high-pressure steam cleaning of tanks and technical equipment. On days with high solar irradiation when the solar loop reaches temperatures of at least 120°C the third consumer, the heating of a raw bitumen tank, is driven by solar thermal energy to reduce the viscosity of the raw bitumen. The internal HX of this tank is directly connected to the solar loop, so this heat sink can also be used as an active stagnation prevention device (Aschoff, 2014).

Gas pressure regulation station

Gas pressure regulation stations are used to reduce the pressure of e.g. 90 bars of the natural gas in the cross-country high-pressure pipelines to a pressure of e.g. 12 bars for the local distribution networks for the final consumers. Caused by the decompression using expansion valves the temperature would decrease below 0°C. To prevent freezing of the regulation equipment and the piping of the local network, the natural gas has to be heated. Normally this heat is provided by gas burners located in the regulation stations but as the operator has to pay market-price for the burned gas, it is possible to compete against the natural gas with solar thermal energy. The highest natural gas consumption in the local grids is always in winter when there is a huge demand for space heating. Depending on how many commercial and industrial consumers with thermal energy demand are connected to the local grid, an appreciable base load is needed to prevent the gas from freezing also in summer. The selected system for the detailed monitoring has two specialties that should be named: First there will be an additional gas-driven heat pump to reduce the natural gas consumption additionally to the heat provided by the solar thermal system. Second the whole system will be financed and operated by an ESCO selling the heat to the gas provider for a lower price compared to the conventional heating using the installed gas burners (Heinzen, 2014).

4. Solar thermal process heat for metal treatment facility

The third named solar thermal process heat system chosen for the detailed monitoring delivers heat for the surface treatment of metallic materials in a medium sized enterprise. The main business of the company is the zinc coating in two automated production lines with a high output of specified mass products. Beside this automated production there is also a manufacturing area where smaller, more individualized charges are produced in small baths that are operated by hand. Beside the main surface treatment of zinc coatings, there are also various other coatings like copper, tin, chrome, nickel or cadmium.

Conventionally the required heat is supplied by two oil burners that worked with a small storage tank. For peak loads that cannot be handled by the oil burners, there is also the possibility to heat with electrical resistant heaters. In the past approximately 15 % of the heat demand was covered by electricity. During installation of the solar thermal system, the small buffer storage was removed and replaced by a 15 m³ buffer storage heated by both heat sources (oil and solar). As mentioned in Table 1 the whole system was planned and realized as an integrated heat network, so there are no hydraulic disconnections between the solar thermal system, the buffer storage and the oil burners. They all use the same heating circuit water.

For delivering the heat to the different processes named in Table 1, there are three circuits directly connected to the storage, taking the water out of three different heights at different temperature levels. The process with the highest temperature demand is drying of coated products within two drying chambers at the production lines. Here, water to air HXs are used, requiring ta temperature up to 70°C. The medium temperature loop is mainly used for heating of different production line baths and those operated by hand. Here the required temperature reaches up to 60°C and internal tube bundles are used as heat exchangers. Additionally the heat

registers that are used for maintaining a specific temperature in the hall around the baths are supplied by the medium temperature loop as well as domestic hot water preparation and the space heating for offices and social rooms in winter. The third loop is supplying low temperature heat to an air washer that is necessary to wash pollutants out of the air. For this application a temperature around 40°C is needed. The return flows of the three heating loops are stratified into the buffer storage at different heights, depending on the temperature. Figure 4 gives an overview of the whole system of heat suppliers and heat consumers.

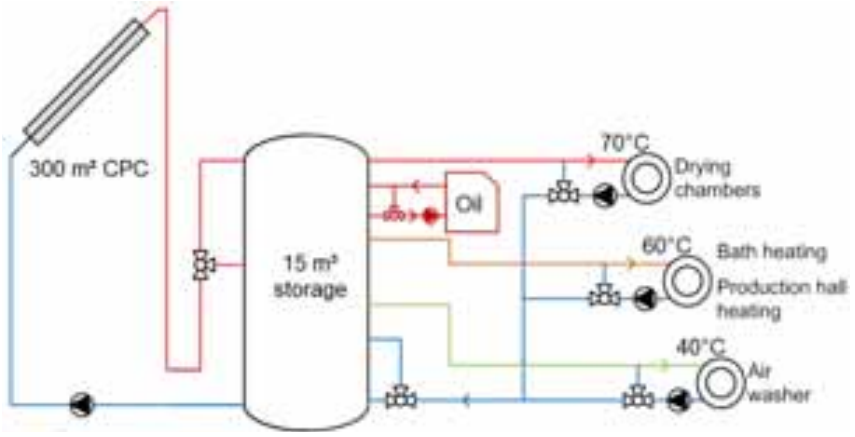

Figure 4: Hydraulic scheme of heating network supported by solar process heat system

The solar thermal process heat system consists of 63 CPC-Collectors with a total gross area of 297 m² and is installed on the roof of the production hall. The field is divided into two subfields each with an inclination of 12°, one north-east orientated with an area of 170 m^2_{gross} and the other one south-west orientated with 127 m^2_{gross}. A picture of the field can be seen in Figure 5: north-east orientated field on the left-hand side, south-west orientated field on the right-hand side.

Figure 5: CPC-collector field on metal treatment factory (Holsmölle 2015)

The control strategy is to feed the solar heat into the top of the storage at a set temperature of at least 65°C up to 100°C depending on the highest temperature of the buffer with the aim of reducing the pulsing of the oil burners. On the one hand this strategy reduces the yield of the solar loop caused by the higher temperatures, but due to the reduction of start-up times of the oil burners with poor efficiencies, a positive effect on the oil consumption can be expected. However, it was not possible so far to quantify this effect due to an increase of the production and a missing reference for the solar control strategy of pre-heating the buffer as soon as the solar flow exceeds the lowest temperature in the stratified storage (Holsmölle, 2014).

According to the detailed monitoring some important requirements were defined like the remote meter reading, the possibility to vary the interval of the data recording, the separate measurement of the heat production, heat consumption of the heat sinks connected to the solar assisted heating network, the flow distribution in every collector row, all done by the recording of the flow temperatures of each row as well as

the measurement of the stratification of the storage using at least three temperature probes (top, middle, bottom). The solar radiation is measured in the collector plane(s) using first class pyranometer(s) to calculate the system efficiency. These requirements are the same for the three systems selected for the monitoring.

5. First measuring results of the described system

As there are still some calibrations necessary to obtain reliable measurement data for the whole system, it is reasonable to present only the solar loop and storage temperatures. As an example Figure 6 depicts a Monday after a sunny weekend in July, where the buffer was nearly completely loaded. On this Monday the solar process heat system is able to cover the whole thermal energy demand of the facility.

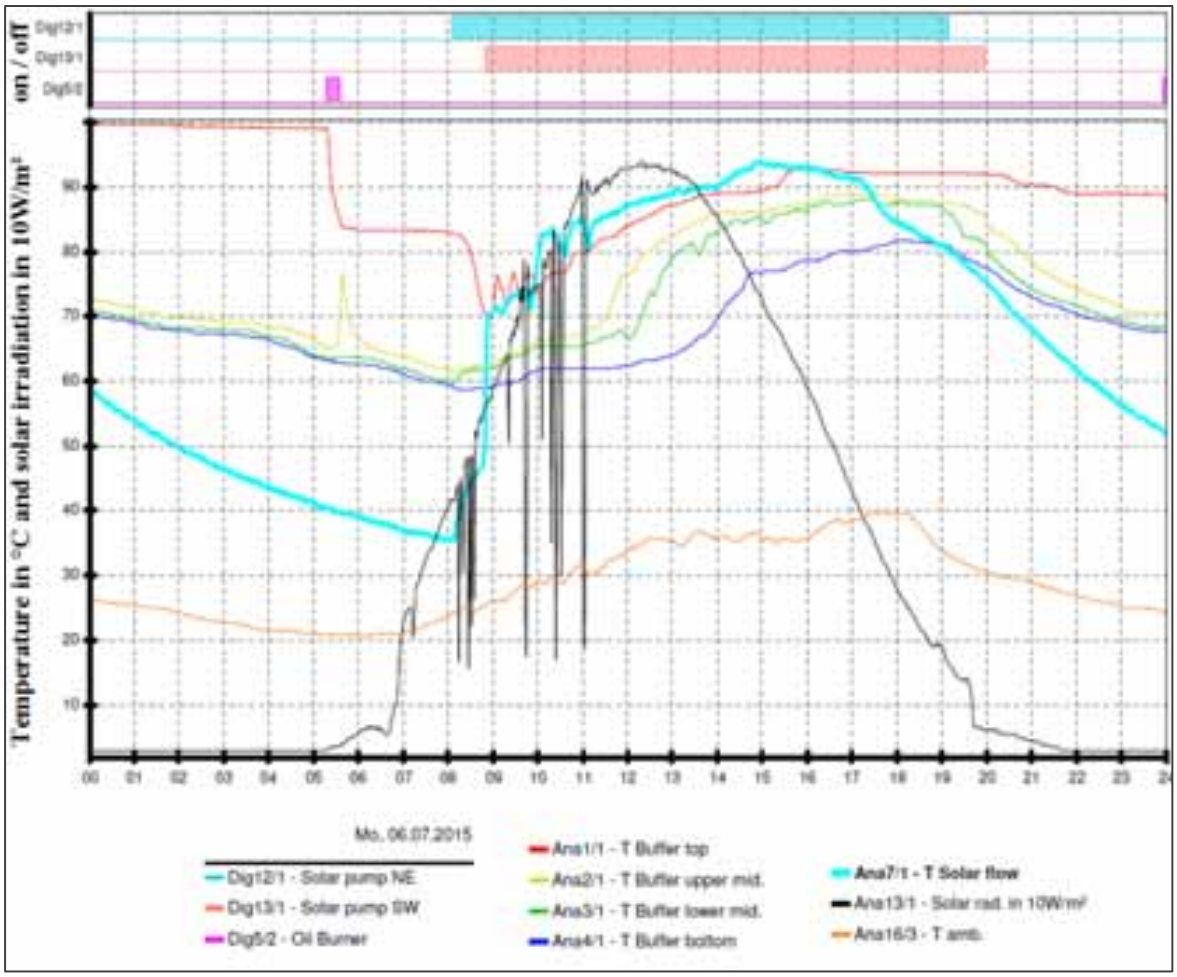

Figure 6: Temperature profiles and solar irradiation on Monday July 6th

This day, July 6th, the heating of the drying chambers and the baths started at 5:20 a.m. using solar heat from the buffer store. In Figure 6 this heating phase in the early morning can be seen with the help of the thin red line dropping from 98°C down to 83°C representing the temperature on the top of the buffer. Shortly before this temperature decrease in the storage caused by the withdrawal of the heat, the oil burners start operation because the temperature in the flow line of the higher temperature loop (not shown in Figure 6) dropped down below 65°C during the weekend.

At 8:05 a.m. the sun started to heat up the collectors and the pump driving the north-east field starts to circulate the solar loop until the temperature in the upper part of the buffer of 70°C was reached at 8:55 a.m. so the solar system started to feed in the heat. At the same time the pump for the south-west orientated field started to operate. This can be seen with the help of the turquoise line, the combined solar flow temperature, whose slope decreases immediately due to the thermal capacities of the south-west field. The maximum temperature of the combined solar flow was reached at 3 p.m. at 94°C. At this time the buffer has a temperature of 77°C at the button and 90°C at the top. After this time the solar system wasn't able to deliver

90°C anymore so it started to feed in the heat into the buffer at different heights and temperature levels until 7 p.m. As the temperature in the solar loop couldn't reach the temperature of the lower part of the storage by circulating the fluid in the collectors, the pumps for the north-east and south-west fields shut off at 7:15 p.m. resp. 8:00 p.m. The latest withdrawal of heat for the processes can be seen at 9:50 p.m. After that the temperature at the top of the storage is only slightly reduced by temperature losses over the next hours. In contrast the temperature in the middle and in the bottom of the tank decreases about 10K caused by the circulation of the medium temperature loop until 10:20 p.m. After that the temperature in the storage is nearly constant until 5:10 a.m. where the heating of the bathes started again.

Another part of the monitoring was the flow distribution in the different collector rows. This is important because if the flow in the rows is non-uniform, there is a risk of partial stagnation and for water based systems with active frost protection also a risk of freezing in single rows. Such poor flow distributions would lead to a reduced solar yield in summer and could cause damages on the collectors in winter. The described system in the metal surface treatment facility consists of 21 collector rows, each with three CPC-collectors. Figure 7 gives an overview on the two collector fields with its 12 collector rows on the north-eastern roof and 9 on the other. The piping was realized according to Tichelmann, so for each row the length of flow and return-flow pipes in sum is of equal length. This kind of piping is used to keep the pressure lost due to the piping the same for each row to ensure an evenly flow in the collectors and therefore a similar flow temperature of the rows.

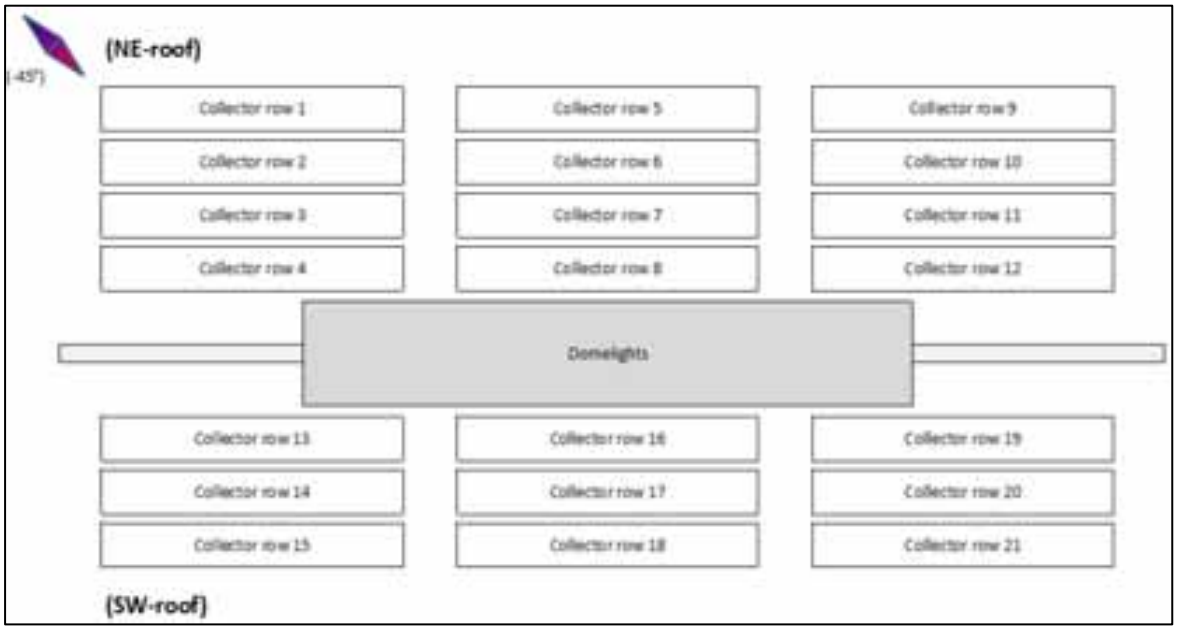

Figure 7: Scheme of the two collector fields with its 21 rows (Holsmölle 2015)

For the detailed monitoring at the end of each row a temperature probe was installed, measuring the flow temperature. In Figure 9 four temperature profiles recorded on September 21st can be seen representing four rows, two out of each field (NE, SW). They were selected because they represent the two collector rows each from the north-east and south-west field that show the largest flow temperature difference during the maximum irradiation on the collector field (760 W/m²) for the selected day.

It can be seen, that for the north-eastern field the largest temperature difference between the 12 rows is 8.2°C at 12:38 p.m. with a maximal flow temperature of 89°C for a single row and nearly half an hour later at 1:10 p.m. the largest difference in the south-west field with its 9 rows occurs with 5.6°C with a maximum temperature of 85°C. These values are reached without any additional valves. Since the working pressure is around 2.5 bars with water as heat transfer fluid, the boiling point amounts to 125...130°C. Since the maximum storage temperature is roughly 100°C and it is directly connected to the solar thermal system, there is only a small risk of stagnation due to this small temperature differences. Until now, stagnation only occurred on weekends or official holidays when the storage was fully charged with temperatures of 90...95°C at the bottom and 98...102°C at the top combined with high solar irradiation.

The breakdowns of the flow temperatures in Figure 9, for example at 12:45 p.m. and around 2:00 p.m., are caused by the controller for the solar pumps, trying to adapt the volume flow in the solar loop to meet the temperature at the top of the buffer. Therefore the volume flow at e.g. 12:45 p.m. is more than doubled from a specific volume flow of 11 l/m²h to 24 l/m²h. As this increase decreases the temperature too much, it must be reduced again. This overshooting according to the adaption of the pump speed could be optimized to obtain more constant flow temperatures.

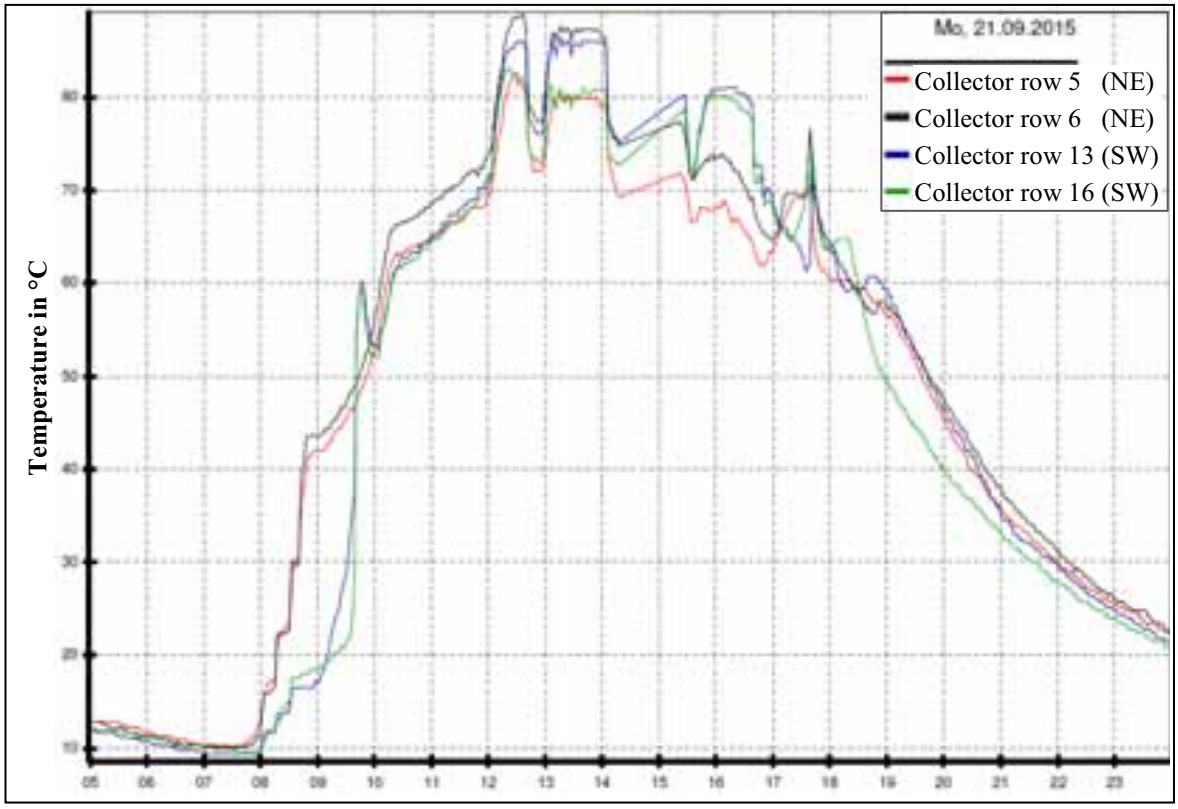

Figure 8: Comparison of the flow temperatures of the four selected collector rows

The first view on the measurement data shown in this section gives a promising first impression according the dimensioning of the solar process heat system avoiding stagnation in summer times and the flow distribution in the collector rows. Only two little optimization measures can be depicted so far: The short start-up of the oil burner shown in Figure 6 and the overshooting of the adaption of the pump speed that can be seen in Figure 9 could be optimized. As soon as the measurement data according the heat consumers and oil burners are validated, energy balances and system efficiencies will be calculated to give an overview on the whole system.

6. Conclusions and outlook

The German market for solar process heat systems is still small but with an increasing trend: Starting from a niche market for eco-minded companies, from August 2012 to August 2015 more than 7,000 m² of collector area are installed and in operation and another 7,000 m² are under construction. Meanwhile the average system size increased about 75% ending up at nearly 70 m² per installation. Although the number of new applications for approval decreased in the first half of 2015 it cannot be seen as a negative trend, because application forms were held back due to the pending novella of the German Market Incentive Programme that became effective in April. Since June the number of submitted application forms increased again, so it is still possible to achieve an increase in applied collector area compared to prior years and therefore another positive growth year for the German solar process heat market.

Although a growing market can be observed, there are still only very few planners and installers dealing with solar process heat systems, so the costs shown Figure 3 are still high due to a lack of competition and sometimes also because of missing expertise. Another fact that keeps the average costs high is the missing

economy of scale due to relatively small systems. Nevertheless 14 systems with average system costs below 500 €/m² including the costs for installation and integration are approved representing a collector area of nearly 3,000 m². These numbers show that there is significant room for cost reduction that will hopefully be exploited with the further development of the German solar process heat market, making this technology more competitive and less funding dependent.

According to the detailed monitoring, three very interesting applications depicted in Table 1 were selected to obtain significant information regarding process integration points, load profiles and combinations of different heat suppliers under real conditions. In addition there is a chance to obtain reliable long term knowledge knowing the monitoring will last for seven years after the start-up of each system. Until now, little validated data from the monitoring of the described system at the metal surface treatment facility could be collected, which is not yet sufficient provide conclusions on the systems performance. Instead, only first impressions on the flow distribution in the collector rows and temperature profiles for a 100% solar fraction working day could be seen. Assessments like the usable solar yield and the overall systems efficiency will be done as soon as the recorded data according to the oil burners and heat consumers are validated.

7. Acknowledgement

The authors gratefully acknowledge the financial support provided by the German Federal Ministry for Economic Affairs and Energy (contract no. 03MAP286) and the cooperative work with the Federal Office for Economic Affairs and Export Control and the KfW Group.

8. References

Aschoff, C., 2014. Documentation of system dimensioning and personal interviews regarding the 190 m² flat plate collector system for the bitumen factory. Aschoff Solar GmbH.

BAFA - Federal Office for Economic Affairs and Export Control, 2015. Documentation on solar thermal process heat funding. Provided within the scientific project for market analysis and development for solar thermal process heat systems. Used for statistical evaluations shown in section 2.

BMWi (Ed.): Guideline to support measures for the use of renewable energies in the heat sector (in German language), March 11th 2015.

Heinzen, R., 2015. Personal interviews regarding the 500 m² flat plate collector system for the gas pressure regulation station. Enertracting GmbH.

Holsmölle, G., 2014. Documentation of system dimensioning and personal interviews regarding the 300 m² CPC-collector system for the metal surface treatment facility. Energiebüro EGTEC.

Holsmölle, G., 2015. Pictures and scheme of collector field of the solar process heat system for the metal treatment facility. Energiebüro EGTEC.

KfW Group, 2015. Documentation on solar thermal process heat funding. Provided within the scientific project for market analysis and development for solar thermal process heat systems. Used for statistical evaluations shown in section 2.

Lauterbach, C., Schmitt, B., Jordan, U., Vajen, K., 2012. The potential of solar heat for industrial processes in Germany. Renewable and Sustainable Energy Reviews 16, 5121–5130.

Conference Proceedings

Solar World Congress 2015
Daegu, Korea, 08 – 12 November 2015

Combined Generation of Heat and Cooling for a Winemaking Process Using a Solar-Assisted Absorption Chiller

José Miguel Cardemil[1,3], Rodrigo Escobar[2], Gonzalo Quiñones[1,3], Cristian Cortés[3], Alan Pino[3], Andreas Häberle[3] and Claudio Tenreiro[4]

[1] School of Industrial Engineering, Universidad Diego Portales, Santiago, Chile.
[2] Escuela de Ingeniería, Pontificia Universidad Católica de Chile, Santiago, Chile
[3] Fraunhofer Chile Research, Center for Solar Energy Technologies, Santiago Chile
[4]Faculty of Engineering, University of Talca, Mailbox 747, Talca, Chile

Abstract

One of the key processes in winemaking is the alcoholic fermentation, an anaerobic process carried out by the metabolic action of a microorganism. During this process, temperature has an important effect on the fermentation kinetics of the process. As the fermentation is an exothermic process most of the wineries use a cooling system composed by mechanical refrigeration cycles and cooling towers in order to control the process temperature during summer and winter, when eventually additional heating might be required. Solar energy could supply both the heating and cooling demands by using an absorption chiller driven by process heat from a solar field. The aim of this study is to assess the thermal performance of the novel system composed by an absorption chiller driven by solar and biomass sources, investigating the behavior of the system in an industrial winemaking process (Miguel Torres Chile). This system consist of a lithium bromide absorption chiller, a flat plate collector solar field and a biomass-burner water heater. The results indicate that the proposed system is able to supply 48% of the cooling demand during the summer and over 90% of the heating demand during the winter

Keywords: *Winemaking industry, solar process heat, Solar cooling,*

1. Introduction

Chilean winemaking industry is worldwide renowned due to the quality of the wine and the significant annual total production. Regarding the latter, in 2013 Chile was placed as the sixth largest wine producer country and the fourth largest exporter (OIV, 2015). During this year, more than 1.3 million m^3 of wine were produced, which represents an increase of 30% with respect to 2014 (SAG, 2015). In this context, the United States and the United Kingdom are the leading importers of the Chilean wine (Vinos de Chile, 2014). As an globalized industry, the wineries needs to stay at the forefront of green technologies, reducing the carbon footprint associated to their processes, in order to maintain and/or improve the competitiveness of the industry (Christ and Burritt, 2013). In this context, during the last decade, the Chilean winemaking industry has started to adopt several sustainable solutions as an actual measure for increasing sustainability of their processes.

One of the key processes in winemaking is the alcoholic fermentation, since it is when the wine acquire its unique flavor and aroma. The fermentation occurs in the absence of oxygen (anaerobic process) and it is during the metabolic action of yeast cells, that the sugar present in the grapes is converted into ethanol, organic acids and CO_2. The yeast's life cycle and enzymatic activities are highly related to the environment conditions as sugar concentration, pH and temperature, where the latest presents higher impacts the in the process, affecting significantly the quality of the final product (Masneuf-Pomarède et al., 2006; Prusina and Herja, 2008). The

doi:10.18086/swc.2015.10.43 Available at http://proceedings.ises.org

optimal range of temperatures for winemaking fermentations depends on the type of wine, ranging from 15°C for white wines and up to 30°C for red wines (Sablayrolles, 2009). As the fermentation is an exothermic process, the temperature of the wine tends to rise and could surpass the aforementioned temperatures ranges by up to 10°C (Comfort, 2008). If that happens, other microorganism dominates the process (commonly bacteria) affecting the action of the yeast and changing the characteristics of the must. On the other hand, if the temperature is below the lower limit, the yeast's enzymatic activity decreases significantly and the fermentation periods can extend considerably (Calderón and Navascués, 2002). The fermentation typically occurs during the end of summer (March to April in the southern hemisphere). Therefore, wineries need to control the operating temperature of the fermentation vats by using conventional mechanical chillers (Torija et al., 2003). After the fermentation is completed, starts the maceration phase that gives the wine sensory characteristics, and specifically gives red wines its typical pigmentation. Additionally, this process gives wine some of the desire properties for human health, as antioxidants, antibiotics, antiviral, among others (Jackson, 2014). The maceration process occurs at an optimum temperature range between 25 to 30 °C, and it occurs commonly during the winter. Therefore, in order to keep the tanks at that temperature, wineries commonly use gas or diesel heaters.

In this context, aiming to introduce sustainable solutions in the process, several wineries in Europe have implemented absorption chillers in their production process, which allows using residual heat sources to drive the absorption machine and reducing the electricity consumption. For instance, in Austria a 100m^2 solar field was installed to feed a NH_3/H_2O absorption chiller in order to assist the fermentation process and to control and dehumidify the cooling chamber (Zeiler et al., 2000). This scheme has been also use in the sugarcane industry, for the same purposes (namely controlling the temperature of the fermentation) (Magazoni et al., 2010).

The annual global solar irradiation in the winemaking regions of Chile is about 1800 kWh/m^2, according the measurements and estimations reported in the literature (Escobar et al., 2015). This level of global irradiation allows the utilization of almost every solar thermal technology. Hence, the present study proposes a new configuration of an absorption chiller system, driven by solar energy that allow the utilization of the absorption machine as a chiller during the summer and as a heat pump during the winter, attending the energy demands of the production process all over the year. Additionally this system is integrated to a biomass heater were part of burned material is the biomass self-generated by the vineyard, which has high calorific power (Fernández-Puratich et al., 2015).Thus, the present study present the performance assessment of the system proposed through transient numeric simulations, considering the features of a pilot scale plant installed in Chilean central valley.

2. System description

The system considered herein is a pilot installation deployed in an actual industrial environment (Miguel Torres Winery). It considers an 80m^2 flat plate collectors solar field, a 5TR single effect Lithium Bromide absorption chiller and a 150 kW biomass boiler. Besides, the additional components required for integrating both systems to the existing cooling/heating circuits currently existing in the winery, such as pumps and heat exchangers. The original cooling/heating system considers three storage tanks, which one supply cold or heat to the vats at the temperature defined by the operators, depending on the season and the stage of the fermentation or maceration process. Each one of the tanks is kept at different temperature: one tank at low temperature for cooling purposes (7°C), one tank at medium temperature for heating the maceration process (30°C) and one high temperature tank (80°C) for supply heat to the previous one and for cleaning processes.

In order to facilitate the operation during both summer and winter seasons, the system proposed considered a pipe manifold and valves system, so it can operate on two different modes according the demands of the plant. Despite the fact of being a pilot scale (represents 3% of the current cooling capacity), the solar polygeneration system operates integrated directly to the productive process. Hence, in the summer mode (Fig. 1) the solar field supplies the thermal energy for driving the absorption chiller, while the chilling effect is used for reducing the temperature of the water returning from the fermentation vats cooling system. The cooling water for the absorption chiller is supplied from the mid temperature tank, which is kept at 30°C.

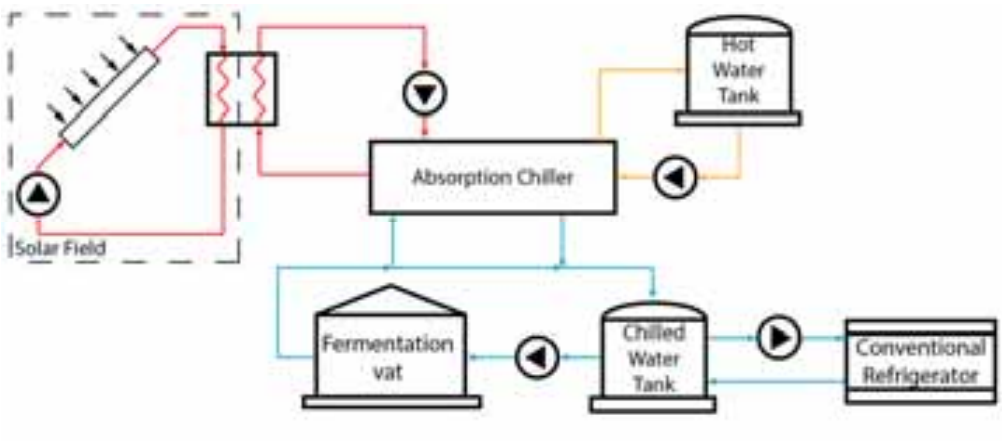

Fig. 1: System configuration in summer mode operation

In the second operation mode, during wintertime (Fig. 2), the solar radiation available is highly reduced, so the heat for driving the absorption chiller comes from the high temperature tank (80°C), which is heated by a biomass water heater. During this operation mode, the energy demanded by the process is heat at 30°C. Therefore, the returning water from the fermentation vats is used as cooling water for the absorption chiller (absorbing heat in the process) and then also absorbs the heat from the solar field. The chilling effect of the absorption machine is received by the low temperature tank, which is kept at 7°C.

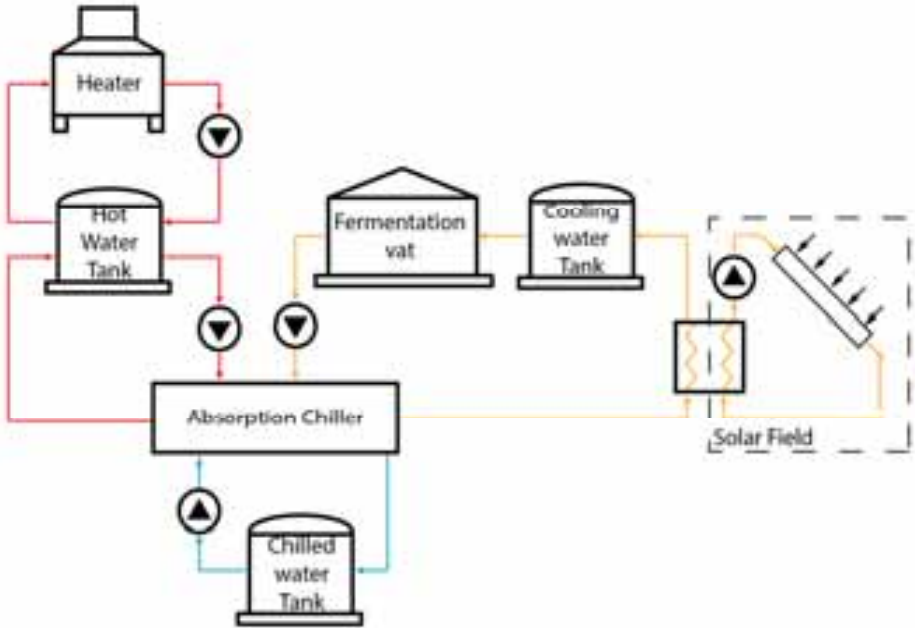

Fig. 2: System configuration in winter mode operation

3. Methodology

The methodology used in this study was adapted from the methodology developed by the Solar Energy Laboratory at the University of Wisconsin-Madison (McMahan et al., 2007). The Transient System Simulation Program (TRNSYS, 2012) was used to carry out the simulations of the complete system, where each component was simulated using a TRNSYS module (Type).

For the case of the absorption chiller, the TRNSYS Type requires the availability of a performance matrix,

which can derived from catalog data. For purpose of this study, a dedicated thermodynamic model was developed using EES software (Klein and Alvarado, 2015), and that model was validated using the datasheet of the actual absorption chiller installed in the winery, manufactured by Yazaki Energy. This approach allows the evaluation of the systems using different component capacities, allowing to optimize the configuration and to analyze the performance of the device, in operating conditions, not necessary reported by the manufactured. Therefore, thermodynamic model was developed using the methodology proposed by (Herold et al., 1996), based on balances of energy, mass and species.

Regarding the solar field, simplified models based on empirical characteristics are commonly employed to simulate transient solar collector performance. In this study, a single glazed flat plate collector was considered, considering a 2nd order incident angle modifier (IAM). Thus, the TRNSYS Type 1b module was employed. This module is based on the quadratic instantaneous efficiency equation, as indicated by (Duffie and Beckman, 2013),

$$\eta_c = F_R(\tau\alpha)_n - F_R U_L \frac{(T_i - T_{amb})}{G_T} - F_R U_{LT} \frac{(T_i - T_{amb})^2}{G_T} \qquad \text{(eq.1)}$$

where G_T is the total incident solar radiation on the collector plane, F_R is the heat removal factor, $(\tau\alpha)_n$ is the effective transmittance-absorptance product normal to the collector, U_L is the overall heat loss coefficient, U_{LT} is the correction factor of overall heat loss coefficient, T_i is the inlet water temperature in the collector, and T_{amb} is the ambient temperature. The collector considered is the FCC-1S, manufactured by Bosch. The efficiency parameters of the collector are $F_R(\tau\alpha)_n$=0.686, $F_R U_L$=3.8622 W/(m^{2}K) and $F_R U_{LT}$=0.01372 W/(m^{2}K^2) (SRCC, 2010). The mass flow rate under the test conditions was $\dot{m}_{test}$=0.0206 kg/(m^{2}s) and the solar collector has an aperture area of 1.94m^2. The solar field comprises 40 collectors in four series of 10 collectors each.

The solar field is coupled to the absorption system by a heat exchanger, which was modelled considering it as a countercurrent heat exchanger with a constant effectiveness of 0.4769, estimated at the nominal operating conditions. The temperatures of the fluids at the inlet of the heat exchanger are evaluated by TRNSYS in every timestamp simulated. Hence, the heat transferred by the solar field determined by a dedicated Type which estimates the heat transfer rate by the following equation

$$\dot{q} = \varepsilon \dot{C}_{min}\left(T_{H,out} - T_{C,in}\right) \qquad \text{(eq.2)}$$

where, $T_{H,out}$ and $T_{C,in}$ are the hot outlet and cold inlet temperatures, respectively. $\dot{C}_{min}$ is the lower capacitance rate of the flows entering the heat exchanger.

The storage tanks allows coupling the production process and the heating/cooling system, ensuring that the fermentation and maceration processes are conducted within the appropriate temperature range. Therefore, a dedicated TRNSYS type was considered in order to take into account the heat fluxes through the storage tanks surfaces as well as the stratification phenomenon. Hence, different heat transfer parameters were defined for the ceiling, floor, and wall of the tanks, depending if it is in contact with air or water, according the methodology proposed by (Kumana & Kathari, 1982).

Within the simulation, the system is controlled by a PID controller, which is simulated using a dedicated TRNSYS Type (type 23). In this simulation the proportional factor (k_p) is considered as 1000, the integral factor (k_i) is assumed as 1, and the derivative response (k_d), which determines the slope of the error is 0.1. Additionally, the mass flow rate is constrained by the operating conditions suggested by the manufacturer of the Absorption Chiller. In this context, the datasheet indicates that the mass flowrate of heat source should be between the 30% and 120% of the nominal flow rate, 1.2 kg/s. On the other hand, both Chilled water and cooling water flow rates are kept at the nominal conditions: 0.77 kg/s and 2.55 kg/s, respectively.

Considering the aforementioned conditions, the system was simulating operating in year period. The summer mode is considered from September to April; meanwhile the heating demand starts in April too. Hence, in April the system operates as summer mode and the heat released by the absorption chiller is used for heating some of the vats. Then, from May to July the system operates in winter mode, as only heating demand is present. Finally, during August neither cooling nor heating is required so the system is shut off.

4. Results

The system was simulated using TRNSYS software, considering the climatic conditions of Curicó, where the actual winery is located. The TMY considered was derived by (GeoModel-Solar, 2015). Figure 3 shows hourly totals of GHI and DNI for each day of the TMY at Curicó (34°5S, 71°1W), where the Miguel Torres Winery is located. Curicó is a small city inserted in an agricultural region where the solar resource variability is high due to its Mediterranean climate with occurrences of cloudy and clear days throughout the year with a strong summer/winter seasonality. Episodes of persistent cloud covers during several days are common during the year although less common in summer. In winter, cloud covers are more common, days are shorter, and radiation levels are highly reduced. The yearly totals are 1791 kWh/m^2 for GHI and 1952 kWh/m^2 for DNI.

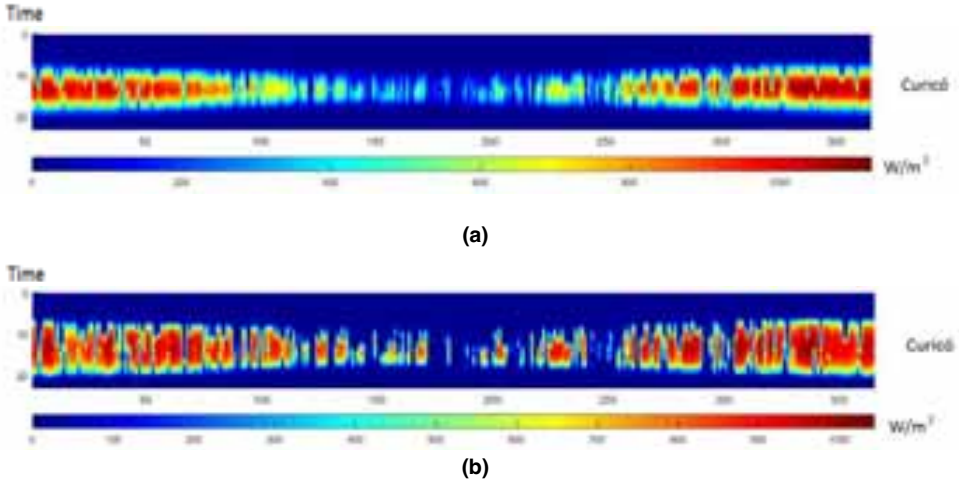

Figure 3: Hourly irradiation values for the TMY in Curicó: a) GHI, and b) DNI.

The irradiation data shows that, although the solar resource available at the site is relatively high in terms of annual totals, it is also very variable during the year and therefore a solar energy conversion system designed to operate throughout the year must include proper thermal storage capacity for acting as a buffer against the resource variability.

Figure 4 shows the hourly temperature profiles in the absorption chiller flows for a clear day in the Summer mode, where CHW corresponds to the chilled water flow temperature, CW is the cooling water flow temperature, and HW is the hot water flow temperature. It can be observed that in a clear sky day the HW inlet temperature decreases after the solar heat supply decreases at the end of the day and then increase after sunrise from approx. 45°C to slightly more than 90°C during the early afternoon when the highest solar resource is available. The HW inlet to the absorption chiller activates the cooling process, and therefore the CHW outlet temperature decreases. In turn, the CW temperature rises in proportion to the CHW temperature decrease. The CHW temperature decrease causes a reduction in the cooling demand at the cold water tank from the mechanical compression chiller, thus producing a net electricity saving. A similar situation is observed for a cloudy sky, although the HW temperature levels increase to a lower maximum level below 80°C. In such a case, the heat supplied to the system is lower, and as it generates a lower cooling effect in the absorption chiller then the electricity saving is also lower.

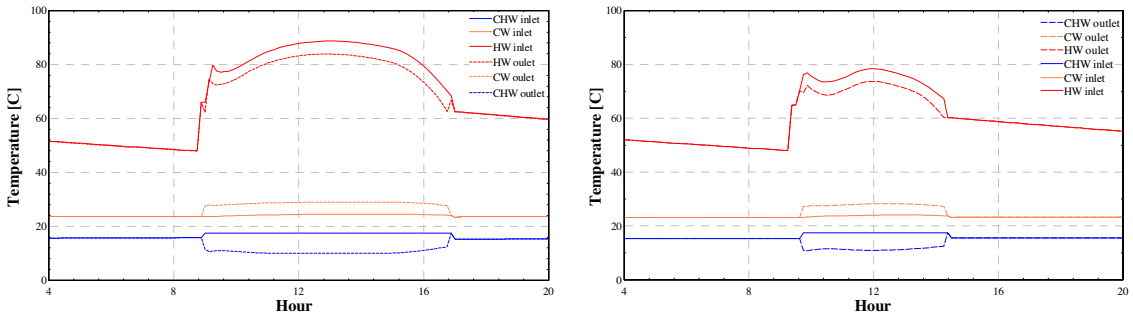

Fig. 4: Hourly temperature profiles in different components of the polygeneration system on summer mode. Left: clear sky day. Right: cloudy sky day.

Figure 5 shows the hourly heat flow rates for the three flows in the absorption chiller: hot, cooling, and chilled water. The absorption chiller is activated by means of automatic pumps that start as the HW temperature reaches a pre-determined level of 75°C. The flow rates during a clear sky day increase after the pumps start, and reach a maximum at the time of highest irradiation, to then remain relatively constant for 2 hours and then decrease until the moment in which the HW temperature reaches a value lower than 75°C when the pumps stop. In total, during a good sunny day in summer the system is capable of operating in solar mode from 9am to 5pm generating savings on LPG and electricity consumption. For a cloudy sky condition (Fig 5 right), the situation is similar to that observed for clear sky, although oscillations on the flow rates are observed as the flow temperatures also oscillate as result of variable solar irradiation. The system is capable of operating for less hours and generates lower savings.

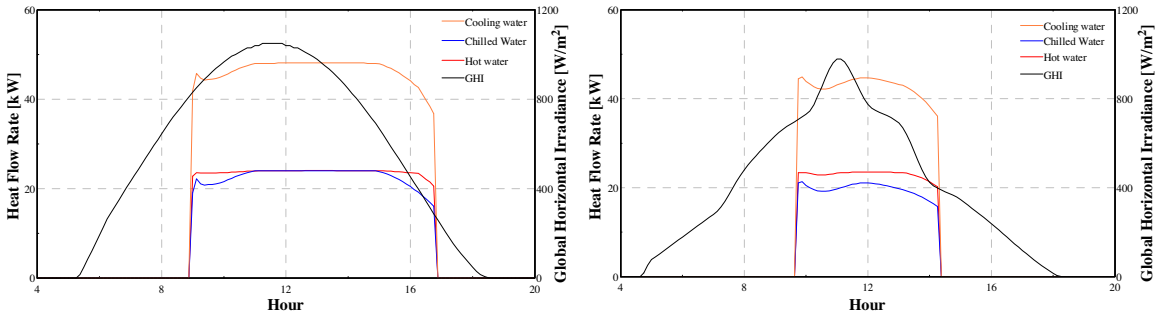

Fig. 5: Hourly heat flow rate profiles in different components of the polygeneration system in summer mode. Left: clear sky day. Right: cloudy sky day.

During winter months, the system operates in the winter mode configuration, in which the mechanical compression chiller is not used, but the absorption machine is operated as a heat pump supplying additional heat to that delivered by the solar field at 30°C water tank, thus generating a net fuel saving on the water heater. Figure 6 shows the heat flow rates in the winter mode for a clear and cloudy sky conditions. It is observed that in clear sky conditions the solar field is able to supply all heat demand, causing that the biomass heater is turn off in 3 to four hours. The operation temperatures during the winter mode operation are stable, since the operation of the absorption machine depend of the temperature of heat medium, which in this case is the biomass heater, set at 95°C. The cooling water temperature is the water returning from the vats, which do not vary significantly and the chilled water temperature is assumed constant at 15°C.

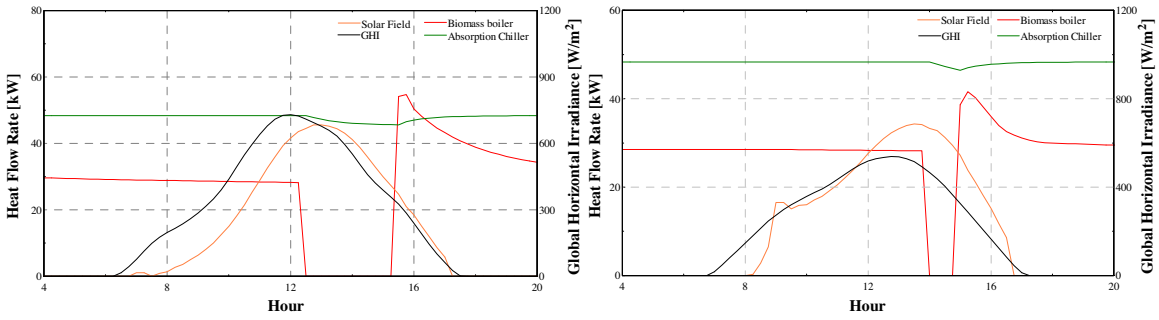

Fig. 6 Winter mode operation during clear sky (left) and cloudy sky (right) conditions. Left: clear sky day. Right: cloudy sky day.

Daily totals of heat and cooling supply for the polygeneration system are summarized in Fig. 7. As observed, the system is able to supply around 150 kWh of cooling per day, during the summer and a similar amount of thermal energy during the winter with peaks over 250 kWh in good days. However, high variability on both the heat and cooling supply are observed, since the system is highly dependent on the availability of solar radiation and the region during most of the year displays a high cloud cover variability as previously indicated. A marked seasonality also exists, with the cooling supply from the absorption chiller being higher during the summer months, decreasing during the fall and then increasing during the spring. The cooling supply from the absorption chiller is directly related to the solar heat production in the collector field. On the other hand, during the winter mode, the biomass boiler is turned on and therefore it is used as a heat source for the absorption chiller, which operates as a heat pump. Because of that, the energy delivered by the system during the winter is higher than the cooling effect supplied during the summer, since it considers the heat released by the absorption machine and the heat delivered by the solar field. Hence, since a significant part of the heat is delivered by the solar field, the high variability on the availability of solar radiation affects significantly the yield of the system.

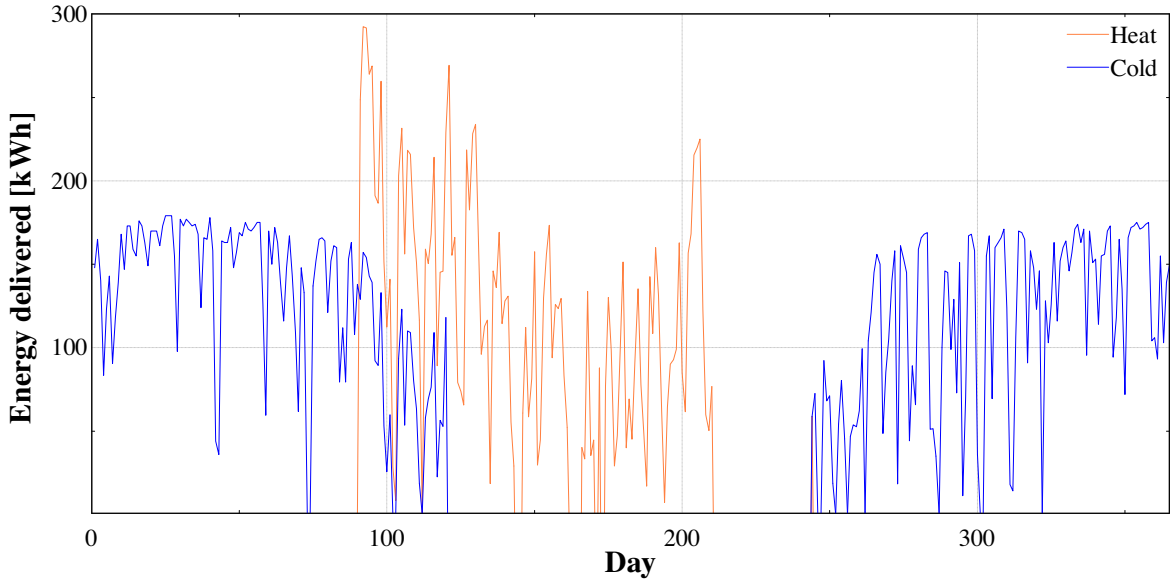

Fig. 7: Thermal energy delivered to processes in a daily basis

The thermal energy displaced by the polygeneration system represents energy savings in terms of the electricity and LPG consumption. The electricity savings are obtained as the absorption chiller cooling supply reduces the cooling supply needed from the compression chiller that keeps the low temperature water tank at 7°C, which is electrically-driven. Therefore, in order to assess the amount of electricity

savings, the simulations consider that the operation of the conventional mechanical compression chiller occurs with a coefficient of performance (COP) of 3, which is a reasonable value for a commercial mechanical compression chiller of the type used in the winery. The combustion efficiency at the gas heater is estimated at 85%, and a net heating value for LPG of 12,100 MJ/kg was considered. With these assumptions, the monthly LPG and electricity savings estimated for to the operation of the pilot system are shown in Fig. 8.

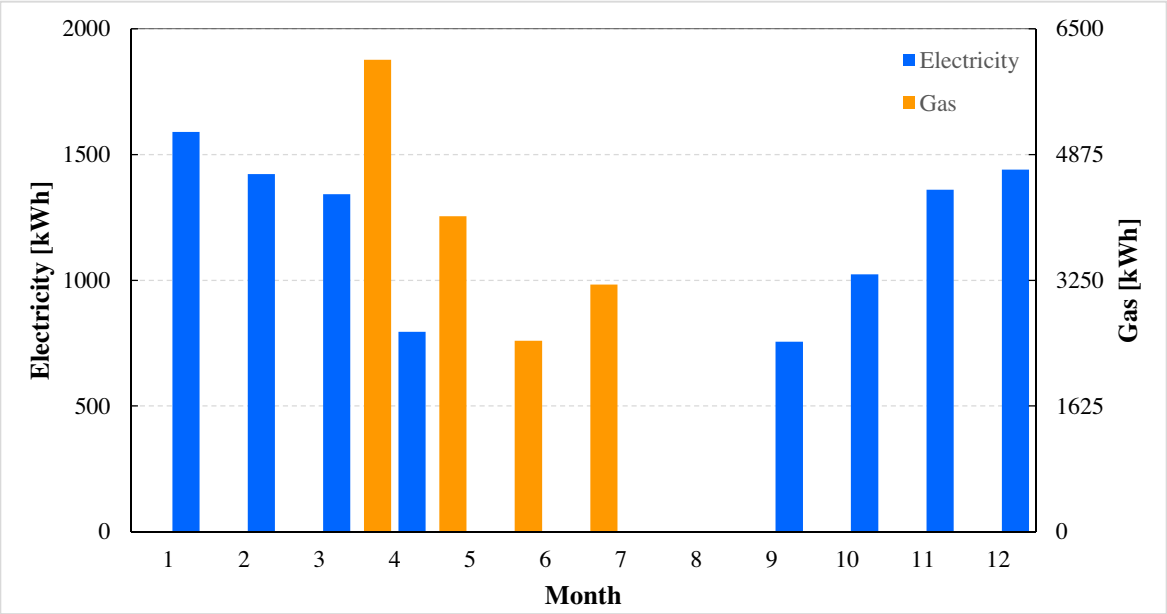

Fig. 8: Energy displaced in a monthly basis

The electricity savings reach a maximum value of 1500 kWh/month for December and January, and then decrease to slightly less than half that value, close to 750kWh/month for April and September, when the solar resource is low at the end of autumn and the beginning of spring. The solar cooling contribution is only a fraction of the available solar heat depending on the typical low value of COP for absorption chillers. From May to August, the heat delivered by the system is due to the solar field and also to the heat released by the absorption chiller. Both contributions results in the LPG savings, which range between approximately 750 kWh/month during June and almost 1400 kWh/month during august. LPG savings are produced when the solar heat is supplied as useful heat to the tank at 30°C. There is a multiplying effect on the LPG savings as the energy conversion chain is as follows: the energy supplied to the 80°C tank is given by the fuel heating value times the boiler efficiency, and then is reduced again by the heat exchanger effectiveness before reaching the 30°C tank. Thus, any heat directly supplied to the 30°C tank as is the solar heat will result in a larger saving of LPG. Additionally, when the operating conditions allow it the hot water delivered by the biomass boiler is used to drive the absorption machine, which released heat at 30°C. The COP of the absorption machine operating as a heat pump is about 1.7, so it allows to amplify the heating effect as a heat transformer, since it absorbs heat from a low temperature source.

5. Conclusions

Winemaking processes utilize heating and cooling systems in order to control the fermentation vat temperatures with variable and seasonal demand. Heating demands are supplied with LPG burning in a water boiler, while cooling demands are met by using a mechanical compression chiller electrically driven. A solar polygeneration system able to supply heat from a solar flat plate collector field and cooling water from an absorption chiller is proposed as an alternative with lower electricity and LPG consumption, thus allowing the winery to decrease its carbon footprint.

The system is composed by a solar field, an absorption chiller, three water tanks of high, medium, and low temperatures, plus the LPG water boilr and the mechanical compression chiller. Two operation modes are proposed for dealing with the high seasonality of both the solar resource and the heating and cooling demands.

The system was simulated using TRNSYS software, complemented with EES routines. Hence, the performance of the system is evaluated in terms of the reduction on the energy consumption, reduction on the carbon footprint and the exergy utilization. The results indicate that the proposed system is able to supply 48% of the cooling demand during the summer and over 90% of the heating demand during the winter, when compared to conventional systems of equivalent capacity of the pilot plant at Miguel Torres winery. This result is even more attractive when the system is scaled up, between 50 to 100% of the current cooling capacity installed at the winery. In addition, an optimization routine has been conducted in order to determine the best operation conditions for the system. Therefore, this hybrid system presents several economic advantages, enabling the possibility of an energetically autonomous winery and presents a vast potential for improvement allowing to produce a zero emissions wine.

Acknowledgement

The authors would like to acknowledge the Chilean Foundation for Agricultural Innovation (FIA) that supported this effort through Grant PYT-2013-0021 P690 with financial contributions from Miguel Torres Winery.

6. References

Calderón, F., Navascués, E., 2002. Equipos de Aplicación de la ingeniería del frío a la industria enológica, Necesidades frigoríficas en bodega. Equipos frío 23–29.

Christ, K.L., Burritt, R.L., 2013. Critical environmental concerns in wine production: an integrative review. J. Clean. Prod. 53, 232–242. doi:10.1016/j.jclepro.2013.04.007

Comfort, S.A., 2008. Guide to Red Winemaking. MoreWine 32,42.

Duffie, J. a., Beckman, W. a., 2013. Solar Engineering of thermal Processes, Fourth Edi. ed. New York.

Escobar, R. a., Cortés, C., Pino, A., Salgado, M., Pereira, E.B., Martins, F.R., Boland, J., Cardemil, J.M., 2015. Estimating the potential for solar energy utilization in Chile by satellite-derived data and ground station measurements. Sol. Energy In Press. doi:10.1016/j.solener.2015.08.034

Fernández-Puratich, H., Hernández, D., Tenreiro, C., 2015. Analysis of energetic performance of vine biomass residues as an alternative fuel for Chilean wine industry genes Hern a 83, 1260–1267. doi:10.1016/j.renene.2015.06.008

GeoModel-Solar, 2015. SolarGIS climData ©. Bratislava, Slovakia.

Herold, K.E., Radermacher, R., Klein, S.A., 1996. Absorption Chillers and Heat Pumps. Boca Raton, Florida, pp. 113 – 143.

Jackson, R.S., 2014. Wine, Food and Health, in: Wine Science: Principles and Applications. Academic Press, San Diego, pp. 908 – 939.

Klein, S., Alvarado, F., 2015. EES, Engineering Equation Solver. F-Chart Software, Box.

Magazoni, F., Monteiro, J.B., Cardemil, J.M., Colle, S., 2010. Cooling of Ethanol Fermentation Process Using Absorption Chillers. Int. J. Thermodyn. 13, 111–118.

Masneuf-Pomarède, I., Mansour, C., Murat, M.L., Tominaga, T., Dubourdieu, D., 2006. Influence of

fermentation temperature on volatile thiols concentrations in Sauvignon blanc wines. Int. J. Food Microbiol. 108, 385–390. doi:10.1016/j.ijfoodmicro.2006.01.001

McMahan, a., Klein, S. a., Reindl, D.T., 2007. A Finite-Time Thermodynamic Framework for Optimizing Solar-Thermal Power Plants. J. Sol. Energy Eng. 129, 355. doi:10.1115/1.2769689

OIV, 2015. World vitiviniculture situtation. Paris.

Prusina, T., Herja, 2008. Infl uence of Fermentation Temperature on the Quality of " Žilavka " Wines. Agric. Conspec. Sci. 73, 127–130.

Sablayrolles, J.M., 2009. Control of alcoholic fermentation in winemaking: Current situation and prospect. Food Res. Int. 42, 418–424. doi:10.1016/j.foodres.2008.12.016

SAG, 2015. Producción de Vinos 2015. Santiago, Chile.

SRCC, 2010. Test Report 2010040A. Londonderry, USA.

Torija, M.J., Rozès, N., Poblet, M., Guillamón, J.M., Mas, A., 2003. Effects of fermentation temperature on the strain population of Saccharomyces cerevisiae. Int. J. Food Microbiol. 80, 47–53.

TRNSYS, 2012. Transient System Simulation program TRNSYS.

Vinos de Chile, 2014. Estadísticas Anuales.

Zeiler, M., Podesser, E., Dermouz, H., Enzinger, P., Gunczy, S., Lauer, M., Padinger, R., Wenzel, A., 2000. Sustainable energy supply of an Austrian winery based on solar and biomass driven micro CHCP Abstract General Overview Cooling system. Contract 9001–9001.

Conference Proceedings

Solar World Congress 2015
Daegu, Korea, 08 – 12 November 2015

Analysis of solar still with nanoparticle incorporated phase change material for solar desalination application

D.Dsilva Winfred Rufuss [a], S.Iniyan[a*], L.Suganthi [b], P.A.Davies[c], Takeshi Akinaga[c]
[a] Dept. of Mechanical Engineering, Anna University, Chennai 600 025, India
[b] Department of management studies, Anna University, Chennai 600025, India
[c] School of Engineering and Applied Science, Aston University, UK
dsilva.kongu@gmail.com, iniyan777@hotmail.com [*] , suganthi2764@yahoo.com,
p.a.davies@aston.ac.uk , t.akinaga@aston.ac.uk

Abstract

In the present scenario, heat storage system started to play its role in every field including solar thermal applications. This paper mainly deals with the application of heat storage medium in solar desalination still applications. This research concerns with the theoretical analysis of latent heat energy storage with the incorporation of nano particles. In this research, paraffin wax is selected as the phase change material with 0.3 weight% of nano particles such as TiO_2, CuO and Graphene Oxide. It is found that Graphene Oxide with paraffin gives the higher results comparing with the other nano particles. The thermal conductivity increased to 0.8 W/mK for Graphene Oxide nano composite and the predicted results shows that the productivity is quite high for paraffin wax with Graphene Oxide. Mathematical modeling was carried out and the results indicate that the solar still with phase change material incorporated with nano particles gives higher results than the conventional solar stills and Graphene oxide with paraffin is found to be the best nano particle for solar desalination still application. So it is best to incorporate Graphene oxide nano particle with paraffin for the experimental setup to achieve higher productivity than conventional one.

.

Keywords: Solar still, Nano particles, latent heat energy storage, paraffin, productivity

1. Introduction

Water scarcity is a major issue that affects the world. By the year 2025, it is estimated that 1.8 billion people will be affected by water scarcity, and 2/3 of the world will experience water-stressed conditions, eventually 1/2 of the world will experience high water stress by the year 2030 (72% people will be in water stress). Presently, African regions are experiencing high water stress up to 31 %, followed by Asia, America and Europe with 25%, 7% and 2% of water stress respectively [2][3][4]. Desalination has a growing role to play in meeting the demands for fresh water.

There are various methods of desalinating sea- and brackish water. The methods includes distillation, ion exchange, membrane distillation, freezing desalination, geo-thermal desalination, solar desalination, methane hydrate crystallization, high grade water recycling, and seawater greenhouse technology [5]. The energy for desalination can be obtained from fossil fuel or alternate energy sources. Among various methods of solar desalination, solar desalination using solar stills has several advantages including simplicity, economic, ease of maintenance, and low environmental impact. However, it also disadvantages, in particular low productivity, hindering the commercial uptake of desalination based on solar stills.

In single slope solar still with heat storage, there will be heat energy storage material for absorbing and storing the heat during the peak sunshine hours and it will emit the absorbed heat when the radiation decreases, such that the temperature will be maintained inside the system. Rahim formulated a method to store the heat energy in horizontal solar desalination still. It is about 47.2% efficient during nocturnal period and no external source is required to store and recover heat [6]. Salah et al predicted the thermal performance of solar still with various absorbing materials such as coated and uncoated wiry and found that uncoated sponge has highest water collection rate [7].

doi:10.18086/swc.2015.10.44 Available at http://proceedings.ises.org

Omar et al conducted the experiment in solar still with energy storage material beneath the basin and inferred that it enhances both the productivity and efficiency of the still. It is also found that melting point of phase change material also plays a vital role in productivity yield at night [8]. Dsilva et al conducted the experiment in single slope single basin solar still with roof heat and fornd that the system gives productivity till 8 o clock in the night [9]. The incorporation of TiO_2 Nano particles with stearic acid phase change material by Harikrishnan et al, the result ended with the findings that, thermal stability and thermal conductivity of phase change material is increased with the incorporation of Nano particle [10] [11]. Additionally the research is extended to the incorporation of CuO - Nano particle with Oleic acid for cooling application and ended with the findings of improvement in cooling properties [12] [13].
The inclination angle of the glass affects the parameters such as yield rate, instantaneous efficiency. Different researchers, however, reached different conclusions about the optimal inclination. Tiwari et al made an analysis by varying inclination angle for condensing cover and also done thermal modelling of passive type solar still. It is inferred that in general, 15^o inclination angle provides maximum yield rate compared with other inclination angle. [14].Muhammed et al designed a single basin solar still for south western arid region of Pakistan and concluded that the optimum glass cover angle is 33.3 ^{o} for Islamabad [15]. Rahul Dev et al conducted experiments in solar desalination still with various inclination angles for attaining the maximum instantaneous efficiency and validated the experimental observation with modelled equation and he found that the inclination angle with 45^0 gives the maximum instantaneous efficiency [16].
The double basin solar still gives more productivity during the cooling period whereas single basin solar still gives more productivity during heating period. Elango et al performed an experiment to analyse the relation between water depth and productivity in double basin solar still. The result ends with the conclusion that double basin solar still yields more distillate only when the water depth is maintained at 1 cm [17].Hitesh conducted the experiment in double basin solar still with vacuum tube and black gravel granite attached to it. The result infers that when the still is coupled with vacuum tube and granite, the system gives higher productivity, than they are coupled individually [18]. The listed literature are some of the passive type solar stills, the active type solar stills includes the addition of collector, concentrator, air heaters, condensers etc.

The use of a collector increases the heat input to the still; therefore it may also be necessary to enhance the heat output to achieve condensation. This has been done using a humidifying tower and condensing cover. Farhad et al analysed exergy and energy for solar desalination system with a flat-plate solar collector by both experimentally and theoretically and found that there was a decrease in exergy efficiency by increasing the length of the humidification tower and that the exergy efficiency increased with decrease in inlet air temperature and tower diameter [19].Dimri conducted an experiment with effect of condensing cover with the yield of active solar still and inferred that productivity was directly proportional to the thermal conductivity of material ofthe condensing cover. Thus copper results in greater yield compared to glass and plastic since it has higher thermal conductivity [20].Tiwari et al made an analysis to relate instantaneous thermal efficiency and collector area. In this research the energy balance for each component was considered and the research ended with the formulation of equations for the various components of the still [21]. The coupling of an air heater to the solar still increased the water temperature in the basin and thus promoted the evaporation rate. Sampathkumar et al carried out a study on various active solar stillsand found that the air heater increased productivity by up to 70% [22]. This productivity is high compared with that of stills coupled with flat plate collectors, evacuated tube collectors and concentrators. Various design modifications such as heat storage, and water spraying have been done on solar stills, with air heater to achieve higher productivity. To investigate the effect of heat storage, Abdulha performed an experiment in stepped solar still solar air heater and latent heat energy storage and discussed the method for increasing the performance by adding aluminium filling. It was found that the integration gave 53% more productivity than conventional set up [23].

In active solar stills, solar collectors can be used to boost performance – including flat plate, evacuated tube, and flat plate collectors. Solar ponds and air heaters have also been used. Air heaters are effective combined with energy storage and with water spraying arrangements.

2. Mathematical Modeling

2.1 Assumptions

A solar still utilizes the heat from the sun to heat the water inside a basin. Hence evaporation takes place and the condensate is trapped by the glass cover at the top of the basin and collected through the distillate collector. The base of the still is covered by insulating material to avoid the heat loss. The productivity is about 2–5 L/m^2.day, thus more than 1 m^2 is required to supply the needs of one person. Fig. 1 gives the pictorial representation of solar still in x-y-z coordinate where as fig. 2 represents the layer wise identification of various components of solar still namely Phase change material, water, air, glass and air layers in x-y coordinate. The whole work has been carried in Institute for Energy Studies, Anna University Chennai, India and Aston University, UK.

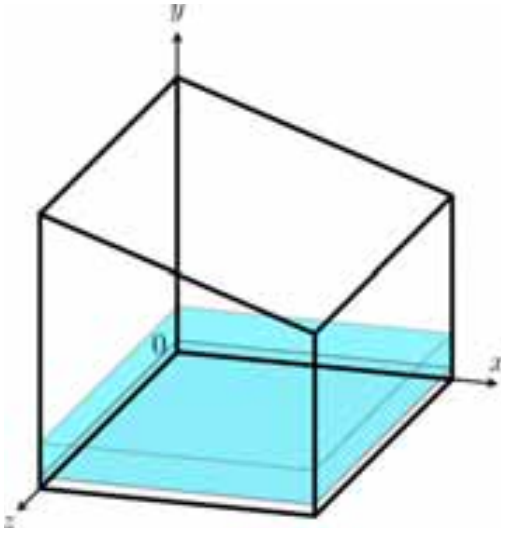

Fig. 1

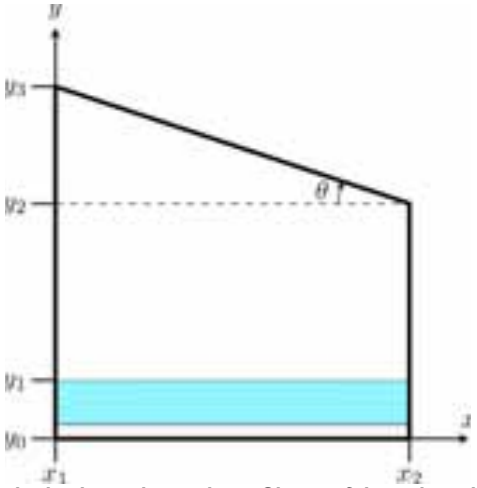

Figure 2: Solar still placed on the horizontal *z*−*x* plane. Shape of the solar still is monotonic in *z* direction.

The following assumptions are made,

a. It is assumed that the shape of the solar still is monotonic un z direction.
b. Energy input is based on only the solar energy (radiation).
c. Intensity of the solar radiation (I) and the ambient temperature (T_a) are controlling the system.
d. I changes gradually in time, I = I (tau), dI/dtau~0.
e. Temperature for water (T_w) and PCM (T_{PCM}) are same. There is no distribution for T_w and T_{PCM}, but T_w and T_{PCM} are function of time (tau). (I and T_a, implicitly, because I=I(tau) and T_a=T_a(tau)).
f. Total energy input to solar still per day, I' * area * time, yields the water production per day (via evaporation and) via condensation of water.

g. Heat capacities of basin liner and insulating material are negligible compared to those for the basin water and phase change material (PCM).
h. The system is vapour tight and the side losses are negligible.
i. PCM and basin liner are in good contact.

Using the above mentioned assumptions the mathematical modeling was carried out using vorticity transport equation, the energy equation and diffusion equation and the analysis has been conducted with respect to Chennai, India climatic condition taking the input from weather data in U.S Department of Energy. The following table represents the data taken for analysis from U.S Department of Energy.

Table.1 *IND_Chennai.432790_IWEC.stat*: Average Hourly Statistics for Global Horizontal Solar Radiation *Wh/m*^{2}.

Hours	Jan	Feb	Mar	Apr	May	Jun	Jul	Aug	Sep	Oct	Nov	Dec
0:01 – 1:00	0	0	0	0	0	0	0	0	0	0	0	0
1:01 – 2:00	0	0	0	0	0	0	0	0	0	0	0	0
2:01 – 3:00	0	0	0	0	0	0	0	0	0	0	0	0
3:01 – 4:00	0	0	0	0	0	0	0	0	0	0	0	0
4:01 – 5:00	0	0	0	0	0	0	0	0	0	0	0	0
5:01 – 6:00	0	0	0	0	1	1	0	0	0	0	0	0
6:01 – 7:00	4	6	15	40	62	58	36	26	32	29	16	9
7:01 – 8:00	96	116	176	234	251	235	179	166	200	190	147	119
8:01 – 9:00	300	350	416	446	451	424	349	337	400	375	316	303
9:01 – 10:00	497	571	647	668	649	593	498	495	577	540	471	467
10:01 – 11:00	640	732	807	836	800	710	609	616	701	656	576	572
11:01 – 12:00	707	809	873	930	887	765	669	685	765	711	616	599
12:01 – 13:00	742	862	920	963	895	775	681	709	771	709	629	616
13:01 – 14:00	703	829	875	908	830	718	633	670	704	638	571	571
14:01 – 15:00	591	713	744	772	700	599	532	571	574	508	450	464
15:01 – 16:00	420	524	559	574	510	451	407	426	412	340	291	315
16:01 – 17:00	211	291	322	329	291	269	250	248	218	153	115	137
17:01 – 18:00	34	71	90	94	88	92	93	79	47	16	9	13
18:01 – 19:00	0	1	3	3	4	7	7	4	1	0	0	0
19:01 – 20:00	0	0	0	0	0	0	0	0	0	0	0	0
20:01 – 21:00	0	0	0	0	0	0	0	0	0	0	0	0
21:01 – 22:00	0	0	0	0	0	0	0	0	0	0	0	0
22:01 – 23:00	0	0	0	0	0	0	0	0	0	0	0	0
23:01 – 24:00	0	0	0	0	0	0	0	0	0	0	0	0
Max Hour	13	13	13	13	13	13	13	13	13	12	13	13
Min Hour	1	1	1	1	1	1	1	1	1	1	1	1

2.2 Mathematical formulation

Two dimensional flow in the vertical (x-y) plane is studied for an incompressible Newtonian Boussinesq fluid. It is convenient to introduce the stream function ψ so that continuity equation is satisfied automatically, because

$$u=\frac{\partial \psi}{\partial y}, \quad v=-\frac{\partial \psi}{\partial x}. \qquad \text{(eq.1)}$$

The governing equation is the vorticity transport equation, the energy equation and diffusion equation for absolute humidity as follow:

$$\frac{\partial \omega}{\partial t}= \frac{\partial \psi}{\partial x}\frac{\partial \omega}{\partial y}-\frac{\partial \psi}{\partial y}\frac{\partial \omega}{\partial x}+\nu\left(\frac{\partial^2 \omega}{\partial x^2}+\frac{\partial \omega}{\partial y^2}\right)+\beta\frac{\partial T}{\partial x}, \quad \text{(eq.2)}$$

$$\frac{\partial T}{\partial t}= \frac{\partial \psi}{\partial x}\frac{\partial T}{\partial y}-\frac{\partial \psi}{\partial y}\frac{\partial T}{\partial x}+\frac{\lambda}{\varrho C_p}\left(\frac{\partial^2 T}{\partial x^2}+\frac{\partial T}{\partial y^2}\right), \quad \text{(eq.3)}$$

$$\frac{\partial e}{\partial t}= \frac{\partial \psi}{\partial x}\frac{\partial e}{\partial y}-\frac{\partial \psi}{\partial y}\frac{\partial e}{\partial x}+\kappa vap\left(\frac{\partial^2 e}{\partial x^2}+\frac{\partial e}{\partial y^2}\right), \quad \text{(eq.4)}$$

where z component of the vorticity (ω) is written in

$$\omega=-\left(\frac{\partial^2 \psi}{\partial x^2}+\frac{\partial \psi}{\partial y^2}\right). \quad \text{(eq.5)}$$

Transformation for general coordinates

Transformation of coordinates system: x=x(ξ,η), y=y(ξ,η).

$$\frac{\partial x}{\partial x}=\frac{1}{J}\left(\frac{\partial y}{\partial \eta}\frac{\partial x}{\partial \xi}-\frac{\partial y}{\partial \xi}\frac{\partial x}{\partial \eta}\right), \quad \frac{\partial x}{\partial y}=\frac{1}{J}\left(\frac{\partial x}{\partial \xi}\frac{\partial x}{\partial \eta}-\frac{\partial x}{\partial \eta}\frac{\partial x}{\partial \xi}\right). \quad \text{(eq.6)}$$

$$\frac{\partial^2 x}{\partial x^2}+\frac{\partial^2 x}{\partial y^2}=\frac{1}{J^2}\left(D+C_\xi\frac{\partial x}{\partial \xi}+C_\eta\frac{\partial x}{\partial \eta}\right). \quad \text{(eq.7)}$$

Herein

$$J=\frac{\partial x}{\partial \xi}\frac{\partial y}{\partial \eta}-\frac{\partial x}{\partial \eta}\frac{\partial y}{\partial \xi}, \quad C_\xi=\frac{1}{J}\left[\frac{\partial x}{\partial \eta}D\,(y)-\frac{\partial y}{\partial \eta}D\,(x)\right], \quad C_\eta=\frac{1}{J}\left[\frac{\partial y}{\partial \xi}D\,(x)-\frac{\partial x}{\partial \xi}D\,(y)\right]. \quad \text{(eq.8)}$$

A linear operator D is defined as

$$D\equiv C_{\xi\xi}\frac{\partial^2 y}{\partial \xi^2}-2C_{\xi\eta}\frac{\partial^2 y}{\partial \xi \partial \eta}+C_{\eta\eta}\frac{\partial^2 y}{\partial \eta^2}, \quad \text{(eq.9)}$$

where

$$C_{\xi\xi}=\left(\frac{\partial x}{\partial \eta}\right)^2+\left(\frac{\partial y}{\partial \eta}\right)^2, \quad C_{\xi\eta}=\frac{\partial x}{\partial \xi}\frac{\partial x}{\partial \eta}+\frac{\partial y}{\partial \xi}\frac{\partial y}{\partial \eta}, \quad C_{\eta\eta}=\left(\frac{\partial x}{\partial \xi}\right)^2+\left(\frac{\partial y}{\partial \xi}\right)^2. \quad \text{(eq.10)}$$

Tetragon $(x_1,y_1)-(x_2,y_1)-(x_2,y_2)-(x_1,y_3)-(x_1,y_1)$ (Figure: 1 and 2) in physical coordinates (x,y) is transformed onto/into a square $|\xi|\le 1$ and $|\eta|\le 1$ in the computational coordinates (ξ,η):

$$x=\frac{\xi+1}{2}\left(x_2-x_1\right)+x_1=x(\xi), \quad \text{(eq.11)}$$

$$y=\frac{\eta+1}{2}\left[\frac{\xi+1}{2}\left(y_2-y_3\right)+\left(y_3-y_1\right)\right]+y_1=y(\xi,\eta). \quad \text{(eq.12)}$$

Then,

$$\frac{\partial x}{\partial \xi}=\frac{x_2-x_1}{2}, \quad \text{(eq.13)}$$

$$\frac{\partial y}{\partial \xi}=\frac{\eta+1}{4}\left(y_2-y_3\right), \quad \text{(eq.14)}$$

$$\frac{\partial y}{\partial \eta}=\frac{\xi+1}{4}\left(y_2-y_3\right)+\frac{1}{2}\left(y_3-y_1\right), \quad \text{(eq.15)}$$

$$\frac{\partial^2 y}{\partial \xi \partial \eta} = \frac{y_2 - y_3}{4}, \quad \text{(eq.16)}$$

$$\frac{\partial x}{\partial \eta} = \frac{\partial^2 x}{\partial \xi^2} = \frac{\partial^2 x}{\partial \xi \eta} = \frac{\partial^2 x}{\partial \eta^2} = \frac{\partial^2 y}{\partial \xi^2} = \frac{\partial^2 y}{\partial \eta^2} = 0. \quad \text{(eq.17)}$$

$$\frac{\partial x}{\partial x} = \frac{1}{J}\left(\frac{\partial y}{\partial \eta}\frac{\partial x}{\partial \xi} - \frac{\partial y}{\partial \xi}\frac{\partial x}{\partial \eta}\right), \quad \text{(eq.18)}$$

$$\frac{\partial x}{\partial y} = \frac{1}{J}\left(\frac{\partial x}{\partial \xi}\frac{\partial x}{\partial \eta}\right), \quad \text{(eq.19)}$$

$$\frac{\partial^2 x}{\partial x^2} + \frac{\partial^2 x}{\partial y^2} = \frac{1}{J^2}\left(C_{\xi\xi}\frac{\partial^2 x}{\partial \xi^2} - 2C_{\xi\eta}\frac{\partial^2 x}{\partial \xi \partial \eta} + C_{\eta\eta}\frac{\partial^2 x}{\partial \eta^2} + C_{\xi}\frac{\partial x}{\partial \xi} + C_{\eta}\frac{\partial x}{\partial \eta}\right). \quad \text{(eq.20)}$$

Here,

$$J = \frac{\partial x}{\partial \xi}\frac{\partial y}{\partial \eta}, \quad \text{(eq.21)}$$

$$C_{\xi\xi} = \left(\frac{\partial y}{\partial \eta}\right)^2, \quad C_{\xi\eta} = \frac{\partial y}{\partial \xi}\frac{\partial y}{\partial \eta}, \quad C_{\eta\eta} = \left(\frac{\partial x}{\partial \xi}\right)^2 + \left(\frac{\partial y}{\partial \xi}\right)^2, \quad \text{(eq.22)}$$

$$C_{\xi} = 0, \quad C_{\eta} = \frac{1}{J}\left(-\frac{\partial x}{\partial \xi}Dy\right), \quad Dx = 0, \quad Dy = -2\beta\frac{\partial^2 y}{\partial \xi \partial \eta}. \quad \text{(eq.23)}$$

$$\frac{\partial x}{\partial \xi} = \frac{x_2 - x_1}{2}, \quad \frac{\partial x}{\partial \eta} = 0, \quad \text{(eq.24)}$$

$$\frac{\partial y}{\partial \xi} = \frac{\eta + 1}{4}\left(y_3 - y_1\right), \quad \frac{\partial y}{\partial \eta} = \frac{1}{4}\left[\xi\left(y_3 - y_1\right) + \left(-2y_1 + y_2 + y_3\right)\right], \quad \text{(eq.25)}$$

$$\frac{\partial^2 y}{\partial \xi \partial \eta} = \frac{y_3 - y_1}{4}. \quad \text{(eq.26)}$$

3. Analysis, Results and Discussion

The analyses are carried out with the codes using FORTRAN software compiler in Aston University, UK. The following results are made

The temperature profile for different layers like Phase change material (PCM), basin liner, water, air, glass, bulk are shown in figure 3 with respect to height of the still. From the figure 3, the water temperature and the basin temperature are more or less equal and the PCM temperature is found to be slightly high compared to basin temperature. Melting point of PCM plays a vital role in the selection of PCM with various applications. This gives the different melting and solidification characteristics of the PCM. Here we have incorporated Nano particles to enhance the heat transfer rate and thermal conductivity of the PCM with the insulation in side and bottom.

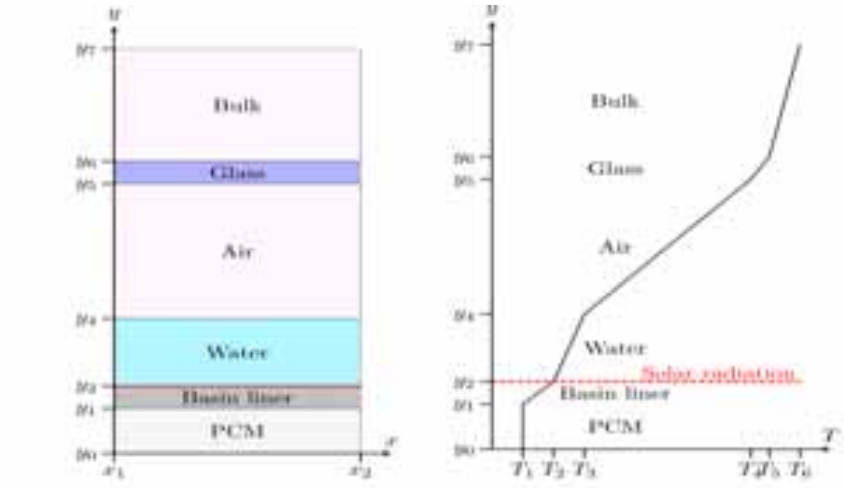

Fig : 3 Temperature profile for various layer

The work carried out with various ambient temperatures such as 20, 30, 40 C and the humidity with 0.1 and 0.2. The results for variation of water temperature and productivity with respect to solar radiation are shown in figure 4 and 5.

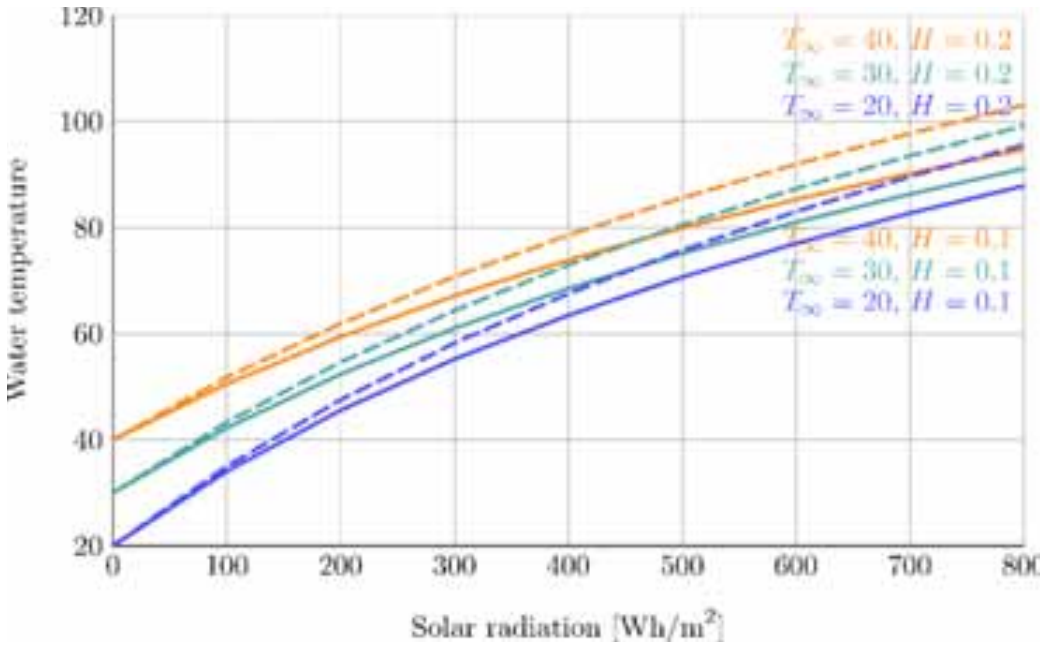

Fig:4 Water temperature Vs Solar radiation

In figure 4, the dotted line represents the water temperature variation with the relative humidity of 10% and the normal line represents the water temperature variation with the humidity of 20% and it indicates that the temperature increases with the decrease in relative humidity and decrease in moisture content. And temperature decreases with the increase in relative humidity and moisture content. From the graph, it is found that the ambient temperature and water temperature are directly proportional to each other.

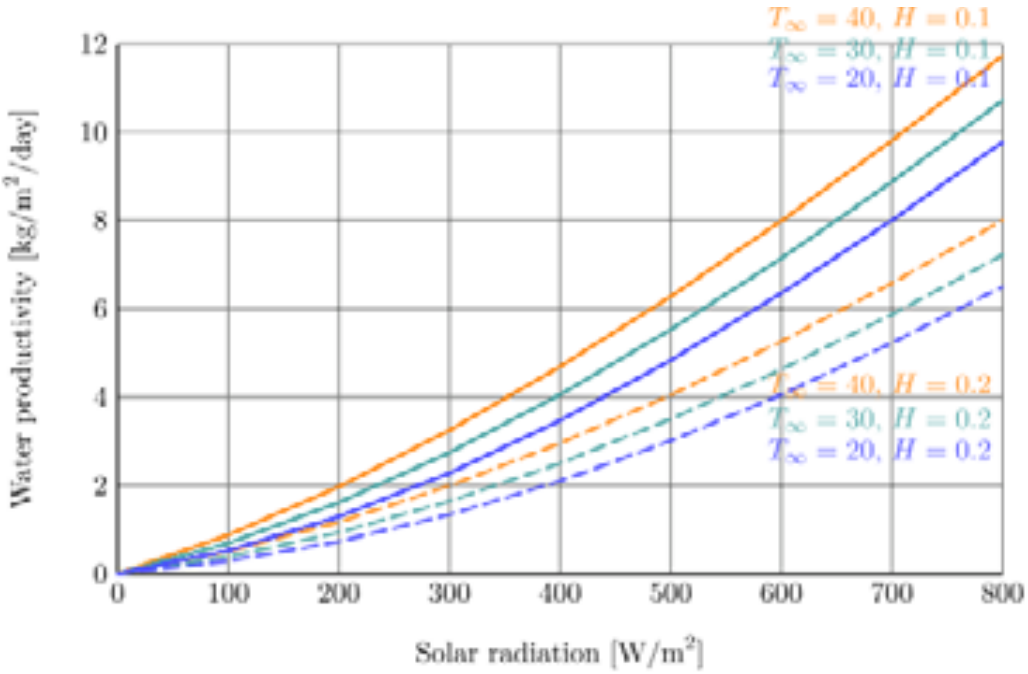

Fig .5: Water productivity Vs Solar radiation

Figure 5 represents the variation of water productivity with respect to solar radiation, Dotted line and normal line represents the variation of 10, 20% relative humidity with different ambient temperatures respectively. As the solar radiation increases, the water productivity increases gradually and there is a huge difference between 10% and 20% relative humidity. The productivity with 20% relative humidity at 40^{o}C ambient temperature was around 8 kg/m^2/day, whereas the productivity with 10% relative humidity at 40^{o}C ambient temperature was around 11.5 kg/m^2/day. The productivity is found to be comparably high for still with phase change material with nano particles, whereas the conventional still yields only 5 kg/m^2/day [9][14]. Our predicted result yields the productivity twice that of the conventional still.

From the graph, it is found that the peak productivity can be achieved during intense solar radiation, and hence the hourly productivity yield can be increased. From the single-effect and multi-effect solar stills, multi-effect solar still gives higher productivity than single-effect still. Now from the modeling result, it is quite clear that the single effect still with phase change material incorporated with nano particles yields the productivity equal to multi-effect solar still.

4. **Conclusion**.

The research aims to incorporate nano particles with phase change material for solar desalination applications. As a part, this paper provides the result of the mathematical modeling done on solar still using phase change material incorporated with nano particles. From the results, it is concluded that the addition of nano particles with phase change material enhances the productivity and the daily yield is achieved up to 12 kg/m^2/day which is quite high than the productivity of other conventional stills. So, from this paper, it is evident that the solar still using phase change materials incorporated with nano particles is superior to other conventional solar stills in all aspects. Therefore further experimental tests and optimization can be carried out as present mathematical modeling gives the concrete evidence for increased performance.

Nomenclature

A_c	Collector area, m^2
C_p	Specific heat, $Jkg^{-1}K^{-1}$
D_h	Hydraulic diameter, m
f	Friction factor, Non dimension
I	Intensity of radiation, Wm^{-2}
k	Thermal conductivity, $W\ m^{-1}K^{-1}$
k_i	Thermal conductivity of insulation material $W\ m^{-1}K^{-1}$
k_w	Thermal conductivity of the tube wall,$W\ m^{-1}K^{-1}$
L	Length of the tube, m
m	mass flow rate, kgs^{-1}
N	Number of tube, Non dimension
Nu	Nusselt number, Non dimension
Pr	Prandtl number, Non dimension
Re	Reynolds number, Non dimension
Q_{ab}	Heat absorbed, W
T_{out}	Outlet temperature of the collector, K
T_{in}	Inlet temperature of the collector, K
T_a	Atmospheric temperature, K
V	Velocity, ms^{-1}

Greek Symbol

ρ	Density, kgm^{-3}
μ	Dynamic viscosity, Nsm^{-2}
μ_w	Dynamic viscosity of tube wall, Nsm^{-2}
η	Efficiency, %

Suffix

PT	Plain tube
RT	Rod as extended surface
TT	Tube as extended surface

Reference

[1] Kabeel A E, S.A. El-Agouz. Review of researches and developments on solar stills. Desalination 2011; 276: 1–12.

[2] Bakkes J. A. Background report to the OECD environmental Outlook to 2030: overviews, details, and methodology of model-based analysis. Netherlands Environmental Assessment Agency (MNP), 2008.

[3] Arnell N. W. Climate change and global water resources: SRES emissions and socio-economic scenarios. Global environmental change, 14(1), 31-52.

[4] Barker R, Dawe D, Tuong T. P, Bhuiyan S. I., & Guerra L. C. (1999). The outlook for water resources in the year 2020: challenges for research on water management in rice production. Southeast Asia 1999; 1: 1-5.

[5] Lourdes García-Rodríguez. Assessment of most promising developments in solar desalination. Springer 2007; Solar Desalination for the 21st Century: 355-369.

[6] Rahim N.H.A. New method to store heat energy in horizontal solar desalination still. Renewable Energy 2003; 28: 419–433.

[7] Salah Abdallah ,Mazen M. Abu-Khader , Omar Badran. Effect of various absorbing materials on the thermal performance of solar stills. Desalination 2009; 242:128-137.

[8] Omar Ansari, Mohamed Asbik, Abdallah Bah, AbdelazizArbaoui, Ahmed Khmou. Desalination of the brackish water using a passive solar still with a heat energy storage system. Desalination 2013; 324: 10–20.

[9] R.Manivel, D.Dsilva Winfred Rufuss, S.Sivakumar. Experimental Investigation of Solar Desalination System with Roof Heating. International Journal of Earth Science and Engineering 2013; 7: 1459-1464

[10] Harikrishnan S, Magesh S &Kalaiselvam S. Preparation and thermal energy storage behaviour of stearic acid–TiO 2 Nanofluids as a phase change material for solar heating systems. ThermochimicaActa 2013; 565: 137-145.

[11] Harikrishnan S &Kalaiselvam S. Preparation and thermal characteristics of CuO–oleic acid Nanofluids as a phase change material. ThermochimicaActa 2012, 533, 46-55.

[12] Mettawee E. B. S &Assassa G. M. Thermal conductivity enhancement in a latent heat storage system. Solar Energy 2007; 81(7): 839-845.

[13] Kalaiselvam S, Parameshwaran R &Harikrishnan S. Analytical and experimental investigations of Nanoparticles embedded phase change materials for cooling application in modern buildings. Renewable Energy 2012; 39(1): 375-387.

[14] Anil Kr. Tiwari and G. N. Tiwari. Annual performance analysis and thermal modelling of passive solar still for different inclinations of condensing cover. International Journal of Energy Research 2007; 31: 1358-1382.
[15] Muhammad Ali Samee, Umar K. Mirza, Tariq Majeed,Nasir Ahmad. Design and performance of a simple single basin solar still. Renewable and Sustainable Energy Reviews 2007; 11: 543–549.
[16] Rahul Dev, Tiwari G.N. Characteristic equation of a passive solar still. Desalination 2009; 245: 246–265.
[17] Elango T & Murugavel K. K. The effect of the water depth on the productivity for single and double basin double slope glass solar stills. Desalination 2015; 359: 82-91.
[18] Panchal H. N. Enhancement of distillate output of double basin solar still with vacuum tubes. Journal of King Saud University-Engineering Sciences 2013.
[19] FarhadNematollahi, Amir Rahimi, TourajTavakoliGheinani. Experimental and theoretical energy and exergy analysis for a solar desalination system. Desalination 2013; 317: 23–31.
[20] Vimal Dimri, Bikash Sarkar, Usha Singh, G.N.Tiwari. Effect of condensing cover material on yield of an active solar still: an experimental validation. Desalination 2008; 227: 178–189.
[21] Tiwari G.N, Sandy Kumar, Sharma P.B, Emran Khan M. Instantaneous thermal efficiency of an active solar still. Applied Thermal Engineering 1996; 16: 189-192.
[22] Sampathkumar K, Senthilkumar P. Utilization of solar water heater in a single basin solar still—an experimental study. Desalination 2012; 297: 8–19.
[23] Abdullah A.S. Improving the performance of stepped solar still. Desalination 2013; 319: 60–65.

DESIGN, CONSTRUCTION AND TESTING OF SOLAR WATER DISTILLATION UNIT FOR RURAL WATER PURIFICATION IN NIGERIA

SAFYANU B. DANJUMA

ABUBAKAR TATARI ALI POLYTECHNIC, BAUCHI. (NIGERIA)

Abstract

This paper presents the design, testing and construction of solar water distillation unit for rural water purification in Nigeria. The construction is done purely with local and affordable materials, for rural dwellers of RafinTambari village of Bauchi, located at Latitude 10.4°N and longitude of 9.5°E. The design consists of twelve stills arrange in two rows of six, with an area of $2m^2$ for each solar still attached together. Over-head storage tank of 2000litres capacity for supplying contaminated water from the stream to the solar still, 500litre of storage tank for collecting distilled water and an output device for flushing out waste product out of the solar still. Ambient and operating conditions of the plant are assumed, the same for the twelve solar still. The overall yield at different water depth of 20, 40, 60mm were 5010ml/m^2.hr, 4465ml/m^2hr and 3776ml/$m.^2$hr respectively and the efficiency of the system at different water depth of 20, 40, 60mm were 50.1%, 44.6% and 37.7% respectively. The prevailing operating conditions were: Ambient temperature; 41°C, solar radiation; 1300W/m^2 and wind speed; 3.08m/s. Microbial load analysis of the water before and after distillations were carried out and the following were found: PH of water; 8.2, TDS of water; 100 and 10 mg/l and E.coli; 120 and 20cfu/100ml. The distilled water was certified safe and potable for human consumption

Keywords: Design, Construction, Testing, Water Analysis, Solar Distillation, and Distillate Yield

1. Introduction

Water is the basic necessity for human along with food and air. There is almost no water left on Earth that is safe to drink without purification. Only 1% of Earth's water is in a fresh, liquid state, and nearly all of this is polluted by both diseases and toxic chemicals (Alpesh et al, 2011). For this reason, purification of water supplies is extremely important. Moreover, typical purification systems are easily damaged or compromised by disasters, natural or otherwise. This results in very challenging situations that may cause for such diseases and toxic chemicals to be present in the untreated water. The need to find out the solutions to these problems needs not to be over emphasis. Fortunately there is a solution to these problems. It is a technology that is not only capable of removing a very wide variety of contaminants in just one step, but is simple, cost-effective, and environmentally friendly, that is the use of solar energy.

In addition, there are many locations where stream water is abundant but portable water is not available. Pure water is also useful for batteries and in hospitals or schools.

Green house solar still generally imitates a part of the natural hydrologic cycle in that the Sun's rays heat the saline water so that the production of water vapor (humidification) increases (Chabi, 2000). Horizontal concentric tube solar still utilizes air as working medium. Air carries the water vapor from the annular space between the clear outer and the inner tube through the inside of the inner tube where the water vapor condenses and gives up its heat of condensation directly to the seawater being sprayed on the outer surface of the inner tube. The water vapor will have the preferential tendency to condense on the inside surface of the clear outer tube (Atagunduz, 2001). Cylindrical parabolic type solar still has a parabolic reflector; the reflector is used to concentrate the incident solar radiation on the black outside surface of a tray located on the focal line of the reflector (Minasian et al, 1997).
The aim and objective of this paper is to design, construction and testing of solar water distillation unit for rural water purification and improving the efficiency and productivity of the distilled water.
A solar powered distillation device contain three basic components: a basin in which the contaminated water is contained, a surface above said feed water for the water vapor to condense onto (i.e. a glass pane), and a catch

doi:10.18086/swc.2015.10.45 Available at http://proceedings.ises.org

basin for the distilled water to drain into. During operation of the distiller, solar energy is collected by the feed water. When enough energy is absorbed by the water, the water undergoes a phase change. The water vapors then rises and comes into contact with the cooler transparent, inclined surface. Here the vapor once again goes through a phase change from vapor back to liquid. The water then condenses and runs off the transparent inclined surface into a collection bin. The distillation process rids the contaminated water of any impurities and most commonly found chemical contaminants within the environment. These contaminants are left behind in the basin (Nafey*et al*, 2000). This process is illustrated in Figure 1 below.

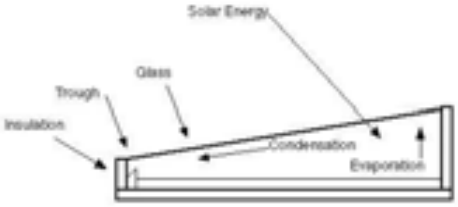

Fig. 1: Basic Solar Powered Water Distiller (Nafey*et al*, 2000).

2.0 Methodology

2.1 Principle of Solar Still Pilot Plant Design and Operation

The solar still pilot plant consists of asymmetrical solar stills arranged in two rows and each of the rows is made of six solar stills, which comprises of total of twelve solar stills. Dimension of 2m², with inclination of 10.4° (base on latitude of Bauchi), orientation of north to south and the same for the entire twelve solar stills.

The solar still consist of three basic components; (a) Basin made of galvanized iron and painted black in which the contaminated water is contained. (b) A glass pane 4mm thickness which covers the solar still and on which vapour condenses. (c) A catch basin, which collects the distilled water into the storage tank (500L).

Each of the stills has an inlet where brackish or contaminated water is fed into the still from the stream via over-head tank (2000L), mark of water depth level of 20mm, 40mm and 60mm and a drain where deposited waste water from the still is flushed after long use. A storage tank (2000L) into which distilled water is pumped from the 500L tank.

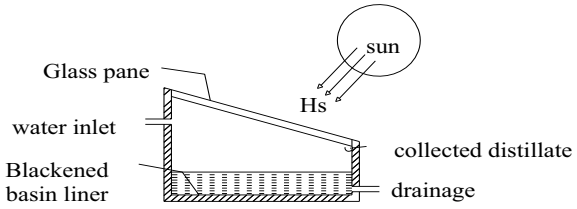

Fig. 2: Conventional solar still (Alkasim, 2012)

3.0 Energy and Mass Balance Method

The performance of a solar still is generally expressed in term of the quantity of water evaporated per unit area of the basin in one day (cubic meters of water per square meter of the basin area per day). This performance of a solar still can be predicted by writing the energy and mass balance equations on the various components of the solar still.

The energy balances for the different components of the solar still are as follows:

3.1 Glass cover

The energy balance for the glass cover can be expressed as follows (Alkasim et al 2012):

$\tau_1 H_S + [\dot{q}_{rw} + \dot{q}_{cw} + \dot{q}_{ew}] = \dot{q}_{rg} + \dot{q}_{cg}$ ……. (eq.1)

H_S – solar radiation on glass cover (W/m^2°C)

$\dot{q}_{rw}$ = internal heat transfer loss by radiation from water surface to the glass

$\dot{q}_{cw}$ = internal heat transfer loss by convention from water surface to the glass

$\dot{q}_{ew}$ = internal heat transfer loss by evaporation

$\dot{q}_{rg}$ = external heat transfer loss by radiation from glass surface to the ambient

$\dot{q}_{cg}$ = external heat transfer loss by convection from glass surface to the ambient

3.2 The Water Content (water mass)

The energy balance for water content inside the solar still is:

$\tau_2 H_S + \dot{q}_w = M_{cw} C_w \frac{dTw}{dt} + \dot{q}_{rw} + \dot{q}_{cw} + \dot{q}_{ew}$ ..... (eq.2)

3.3 The basin liner

The energy balance for the basin liner of the solar still is expressed as

$\tau_3 H_S = \dot{q}_w + \left[\dot{q}_b + \dot{q}_b \left(\frac{A_{ss}}{A}\right)\right]$ ..... (eq.3)

$\dot{q}_w$ = internal heat transfer loss from water
$\dot{q}_b$ = internal heat transfer loss from basin liner
A = still basin area (m^2)
A_{sw} − Side wall area (m^2)

3.4 The Glass Thickness

3.4.1 The External Heat Transfer.

3.4.2 Top loss Coefficient

The glass thickness in most cases is very small. Therefore, the temperature in the glass is assumed uniform. The external heat transfer loss by radiation and convention from the glass cover to ambient, $\dot{q}_g$ can be express as

$\dot{q}_g = \dot{q}_{rg} + \dot{q}_{cg}$ ..... (eq.4)

$\dot{q}_{rg} = h_{rg}(T_g + T_a)$ ..... (eq.5)

Where

$h_{rg} = \frac{\varepsilon_g \sigma[.(T_g + 273)^4 - (T_{sky} + 273)^4]}{(T_g - T_a)}$ ..... (eq.6)

And

$\dot{q}_{cg} = h_{cg}(T_g - T_a)$ ..... (eq.7)

Substituting equations (eq.5) and (eq.7) into equation (eq.4), we get

$\dot{q}_g = h_1(T_g - T_a)$ ..... (eq.8)

Where

$h_1 = h_{rg} + h_{cg}$ ..... (.eq.9)

h_1 is expressed empirically to include the effect of free convection and radiation from the glass cover (Ilaria et al, 2010). The expression is;

$h_1 = 5.7 + 3.8V \quad 0 \leq V \leq 5ms^{-1}$ ..... (eq.10)

Where V is the wind speed measured in ms^{-1}. The expression for a zero wind speed gives heat loss by natural convection.

3.4.3 Bottom and side loss coefficient

The heat loss from the water in the solar still to the ambient through the thick insulation (sawdust) and subsequently by convection and radiation from the bottom, and sides surfaces of the basin, can be written respectively as

$U_b = \left[\frac{1}{h_w} + \frac{1}{h_b}\right]^{-1} = \left[\frac{1}{h_w} + \frac{1}{\frac{K_i}{L_i}} + \frac{1}{h_{cb+h_{rb}}}\right]^{-1}$ ..... (eq.11)

$U_{sw} = U_b F_1 = \left[\frac{1}{h_w} + \frac{1}{\frac{K_i}{L_i}} + \frac{1}{h_{cb+h_{rb}}}\right]^{-1} \left(\frac{A_{ss}}{A}\right)$ ..... (eq.12)

The rate of heat loss from the basin liner to the ambient per m^2 can be written as;

$\dot{q}_b = h_b(T_b - T_a)$ ..... (eq.13)

Where

$h_b = \left[\frac{L_i}{K_i} + \frac{1}{h_{cb} + h_{rb}}\right]^{-1}$ ..... (eq.14)

3.4.4 The internal heat transfer

3.4.5RadiativeLoss Coefficient

The rate of heat transfer, $\dot{q}_{rw}$ from the water surface to the glass for infinite parallel plane is given by (Tiwari 2004, Garba and Maduekwe, 1996 and Alkasim et al, 2012)

$\dot{q}_{rw} = h_{rw}(T_w - T_g)$…… …. (eq.15)
Where h_{rw} is given by
$h_{rw} = \sigma\left[\frac{(T_w+273)^2+(T_w+273)^2}{\left(\frac{1}{\varepsilon_w}+\frac{1}{\varepsilon_w}\right)^{-1}}\right](T_w + T_g + 546)$ …….. ….. (eq.16)
With
$\varepsilon_{eff} = \left(\frac{1}{\varepsilon_w} + \frac{1}{\varepsilon_w} - 1\right)^{-1}$ ……. (eq.17)

3.4.6Convective Loss Coefficient

There is heat transfer across the humid air inside the distiller unit by free convection, which is caused by the effect of buoyancy, due to density variation in the humid fluid, which occurs due to the temperature gradient in this fluid. The rate of heat transfer from the water surface to the glass cover, $\dot{q}_{cw}$by convection in the upward direction through the humid fluid can be estimated as
$\dot{q}_{cw} = h_{cw}(T_w - T_g)$……. (eq.18)
The internal convective heat transfer coefficient, h_{cw}, from heat flow from the horizontal basin (hottest region in the still) to the water mass in the basin and vice-versa is determined from the following relations (Sodar et al, 1980, Egarievwe 1989, Tiwari, 2004, Saini and Saini, 2008 and Alkasim, et al 2012)
Nu = Co (Gr. Pr) ^{no}…….. (eq.19)
Where
$Nu = \frac{h_{cw}X_1}{K_w}$…… (eq.20)
$Gr = \frac{X_1^3\rho_w^2 g\beta\Delta T'}{\mu_w^2}$ …… (eq.21)
$Pr = \frac{C_{pw}\mu_w}{k_w}$…… (eq.22)
$\Delta T' = \left[\Delta T + \frac{(P_w - P_g)(T_w - 273)}{0.2689 - P_w}\right]$ …… (eq.23)
$\Delta T = T_w - T_g$ ……. (eq.24)
And for normal operating temperature range, say 45°C $\Delta'T$ = 17°C, expression for Gr reduces to (Tiwari, 2004)
$Gr = 2.81\times10X_1^3$ …….. (eq.25)

Table 1: values of Grashofnumber, Gr for various average spacing X_1

X1(m)	Gr	Co	no
0.15	0.948×	0.21	¼
0.2	10^5	0.21	¼
0.25	2.248×	0.075	⅓
	10^5		
	4.390×		

Source: (Tiwari, 2004)

As it can be seen from equation (eq.25) (Gr) depends on X_1 (Table 1). This Table gives the value of Gr for different X_1.
The value of *Pr* remains constant and, as given by equation (eq.22). For the normal operating temperature range and at spacing, X_1 = 0.25m; the value of the constant *Co* is: - *Co* = 0.075 and $n_o = \frac{1}{3}$. After substituting for the expressions of *Nu,* Gr and *Pr* in equation (eq.19), the convective heat transfer coefficient h_{cw} becomes
$h_{cw} = \frac{C_o K_w}{X_1}\cdot\left[\frac{X_1^3\rho_w^2 g\beta\Delta T'}{\mu_w^2}\cdot\frac{C_{pw}\mu_w}{k_w}\right]^{1/3}$ …… (eq.26)
Dunkle, (1991) also derived the following expression for h_{cw} as thus:
$h_{cw} = 0.884\left[T_w - T_{g+}\frac{(P_w - P_g)(T_w+273)}{0.2689 - P_w}\right]^{1/3}$ …….. (.eq.27)

3.4.7Evaporative Heat Loss Coefficient

The mass transfer coefficient, h_e , in terms of convective heat transfer coefficient h_{cw} , the total gas pressure, P_T, the mass of the water vapour, M_w, the air mass, M_a, the specific latent heat, L, and specific heat per unit volume at constant pressure, C_{pa} of the mixture is given by (Alkasim et al, 2012) as

$$\frac{h_e}{h_{cw}} = \frac{L}{C_{pa}}\left(\frac{M_w}{M_a}\right)\left(\frac{1}{P_T}\right) \quad \text{..... (eq.28)}$$

The expression in (eq.28) is formulated owing to the assumption that;

(i) The exchange of the water vapour with the boundary layers at both the water and glass surfaces is neglected and (ii) P_w & $P_g$are considered small compared to P_T.

The rate of heat transfer per unit area from the water surface to the glass cover is obtained by substituting the appropriate values for the parameters in equation (eq.28) thus;

$$\dot{q}_{ew} = 0.013h_{ew}(P_w - P_g) \quad \text{..... (eq.29)}$$

$$\dot{q}_{ew} = h_{ew}(T_w - T_g) \quad \text{..... (eq.30)}$$

From (eq.29) and (eq.30) we can write h_{ew} as

$$h_{ew}=1.6273\times10^{-4}h_{cw}\left(\frac{P_w-P_g}{T_w-T_g}\right) \quad \text{..... (eq.31)}$$

It is important to mention here that the value of h_{ew} can be more realistic for larger value of$(T_w - T_g)$. The values of P_W and P_g (for the range of temperature 10°C - 90°C) can be obtained from the expression (Fernandez and Chargoy, 1990).

$$P_T = \exp\left[25.317 - \frac{5144}{(T-273)}\right] \quad \text{..... (eqn.32)}$$

The total internal heat transfer coefficient $h_2$is the sum of the three internal heat transfer coefficient which can be written as:

$$h_2=\left[\frac{(T_w+273)^2-(T_g+273)}{\left(\frac{1}{\varepsilon_w}+\frac{1}{\varepsilon_g}-1\right)}\right](T_w + T_g + 546)+0.884\left[T_w + T_g + \frac{(P_w+P_g)+(T_{w+273})}{268.9\times10P_w}\right]^{1/3} + 16.273\times10^{-3} + 16.273\times10^{-3}h_{cw}\frac{P_w-P_g}{T_w-T_g}$$

4.0 Results and Discussion

In this section, average hourly solar radiation, temperature difference of ambient and still conditions and also average hourly and overall distillate yield of the solar still at water depth of 20, 40, and 60mm respectively was observed and recorded, to evaluate the design, construction and testing of the solar distillation pilot plant rural water supply.

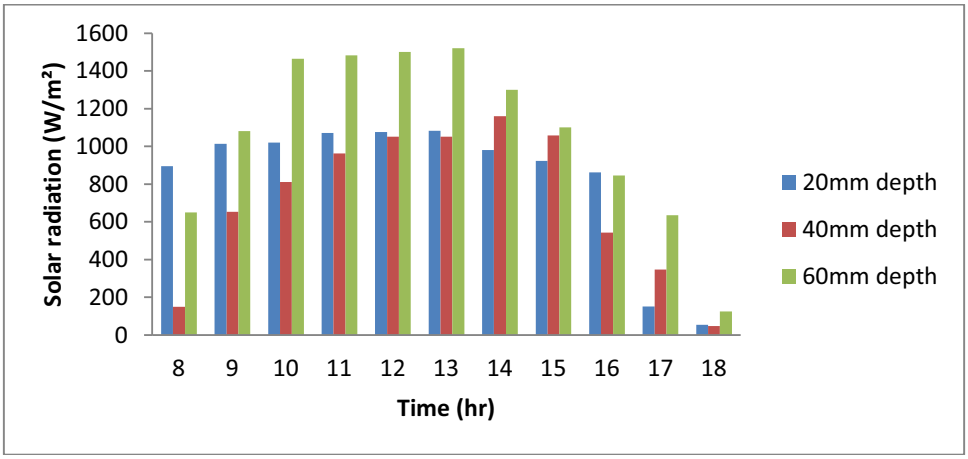

Fig.3: Average Hourly Solar Radiations

Figure 3 depicts Average hourly solar radiation at different water depth of 20, 40, and 60mm which shows highest solar radiation was recorded between 12noon to 13pm.

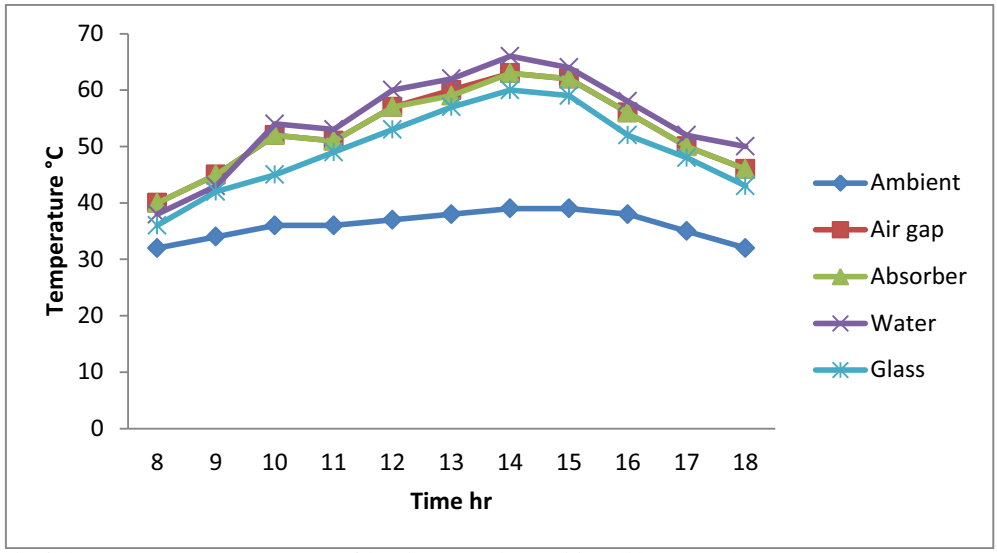

Fig. 4: Average Hourly Temperatures of Ambient and still conditions (20mm depth)

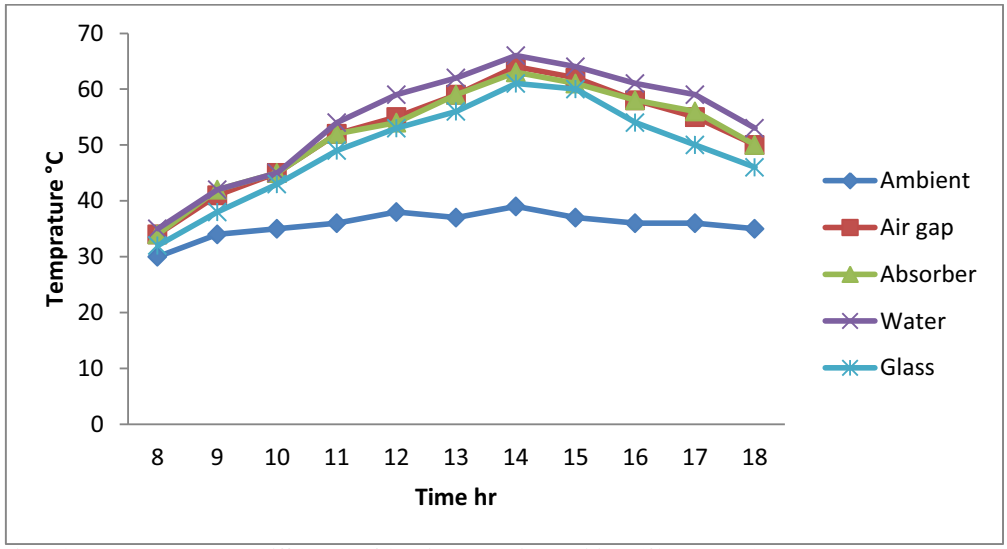

Fig.5: Average Temperature differences of Ambient and still conditions (40mm depth)

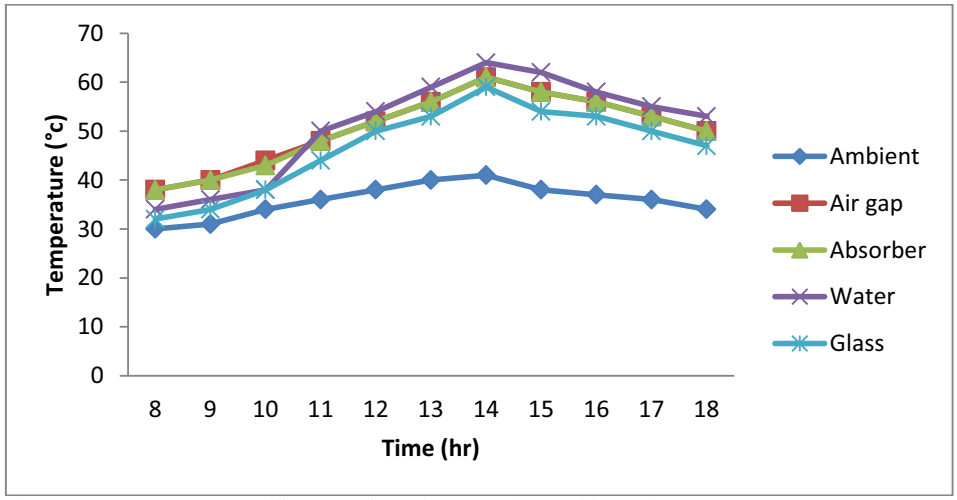

Fig.6:Average Temperature differences of Ambient and still conditions (60mm depth)

Figures (4, 5 and 6) depict Hourly temperature difference of ambient and still conditions at water depth of 20, 40 and 60mm. After observation it shows that the temperature increases with time in ascending order of highest ambient, highest glass, highest air-gap, highest water and highest absorber plate temperatures. This confirmed that the solar radiation energy is directly absorbed by the absorber plate due to high thermal conductivity as heat, which is transfer to the water, then change of state takes place from liquid to vapor as the water evaporate within the air-gap, it increases the temperature of the air-gap. As vapor makes contact with glass cover it condenses due to decrease in temperature difference. Condensations take place because the temperature of the air-gap is greater than the glass temperature and the ambient is lower than the glass temperature (Robert *et al,* 2010)

Table 1: Average Overall Hourly Distillate Yield

Time (hr)	**Yield(ml/m^{2}hr) 20mm depth**	**Yield(ml/m^{2}hr) 40mm depth**	**Yield(ml/m^{2}hr) 60mm depth**
8-9	10	8	4
9-10	17	15	11
10-11	68	60	45
11-12	160	154	123
12-13	342	256	198
13-14	403	389	287
14-15	560	423	396
15-16	602	589	476
16-17	654	603	501
17-18	680	620	512
18-19	701	625	522
19-7	813	723	701

Table 1 shows the average hourly distillate yield. It is obvious that yield of a still is affected by the water depth. The lower the water depth the greater the yield, 20mm water depth yield distillate of 5100ml/m^2.hr and the higher the water depth the lower the yield, 60mm water depth yield distillate of 3776ml/m2.hr

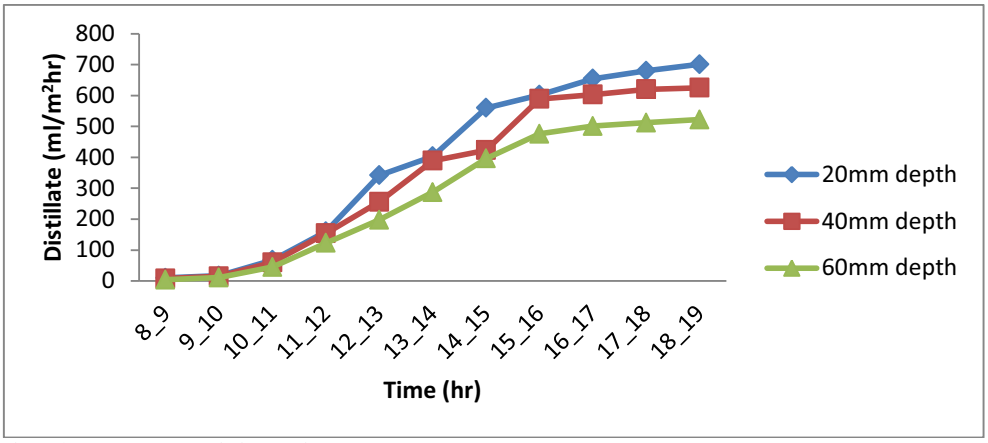

Fig.7: Average Hourly Distillate Yield

Figure 7 shows the hourly distillate yield at 20mm water depth, yield the highest distillate with time and 60mm water depth, yield the lowest distillate with time. Efficiency of the still was also affected by water depth, 20mm water depth with efficiency of 50.1%, 40mm water depth with efficiency of 44.6% and 60mm water depth with efficiency of 37.7%. The efficiency was used to evaluate the performance of the still. (Buros, 20000)

5.0 Conclusion

The design, construction and testing of solar distillation pilot plant was evaluated with water depth was set at 20, 40, and 60mm respectively. Average hourly solar radiation at different water depth mention above, which shows that highest solar radiation was recorded between 12noon to 1pm. Hourly temperature difference of ambient and still conditions were observed which shows that the temperature increases with time in ascending order of highest ambient, glass, air-gap, water, and absorber plate temperatures. Also the average hourly distillate yield was recorded and it is obvious the yield of the still is affected by water depth. Overall yield of distillate were found to be 60.12litre at 20mm water depth, 53.58litre at 40mm water depth and 45.31litres at 60mm respectively and efficiency of the system at different water depth of (20, 40, 60mm) were found to be 50.1%, 44.6% and 37.7% respectively.

Nomenclature

A - Still basin area (m^2)

A_g - Glass covers area (m^2)

A_s - Total still area (m^2)

A_{sw} – Side wall area (m^2)

B - Breadth of still (m)

C_w - Specific heat of water (J/kg°C)

F_1 - Glass area correction factor (A_s/A)

L - Length of still (m)

g -Acceleration due to gravity (m/s^2)

h_1 – Radiative heat transfer coefficient from water to glass cover ($W/m^{2}°C$)

h_2 - Convective heat transfer coefficient from glass cover to ambient ($W/m^{2}°C$)

h_3 - Heat transfer coefficient from water to the basin liner (W/m^2°C)

h_{rw} - Radiative heat transfer coefficient (W/m^2°C)

h_{cw} --Convective heat transfer coefficient (W/m^2°C)

h_{ew} - Evaproative heat transfer coefficient (W/m^2°C)

H_s - Solar radiations on the glass cover (W/m^2)

k_w - Thermal conductivity of the water in the basin (W/m^2)

ℓ - Water depth in the basin (m)

m - Distilled water production rate (kg/min)

m_t - Total distilled water production (kg)

M_w - Water content in the basin (kg)

Gr – Grashof number

Nu – Nusselt number

Pr - Prandtl number

P_g - Water vapour pressure at glass temperature (Pa)

P_w - Water vapour pressure at water temperature (Pa)

Q_{ew} - Mass of evaporated water (kg)

q̇ - Rate of energy transfer (J/s)

R_b - Basin liner reflectivity

R_g - Glass cover reflectivity

R_w - Water surface reflectivity

R.H. - Relative humidity (%)

t - Time (s)

T_a - Ambient temperature (°C)

T_b - Basin liner temperature (°C)

T_g - Glass temperature (°C)

T_w - Water temperature (°C)

U_T - Top loss coefficient (W/m^2°C)

U_B - Bottom loss coefficient (W/m^2°C)

U_{sw} - Overall heat transfer coefficient from the side wall to the ambient (W/m^2°C)

V - The wind velocity (m/s)

X_1 - Water to glass spacing (m)

Reference

AlkasimAbubakar, AdamuUsman and Ododo, J.C., (2012); A Theoretical Solar Distiller Model for Yola North-Eastern, Nigeria, Nigeria Journal for Solar Energy Vol. 23 Pp, 77- 88

Alpesh Mehta, ArjunVyas, NitinBodar, DharmeshLathiya, (2011); Design of Solar Distillation Systems. Vol.29, Pp 11 – 19.

Atagunduz, G., (2001); Solar Desalination, Ege University.

Buros , O.K., (2000); The ABC's of Desalting, TopfiedMassachusett, USA.

Chabi, M.T., (2000); An Overview of Solar Desalination for Domestic and Agriculture Water needs in Remote Arid Areas, Desalination **127**, Pp.119 – 133

Egarievwe, S.U., (1989); Solar Still for Fresh Water Production in Rural Areas- Design and Economic Consideration, Nigerian Journal of Energy, **8**(8).

Fernandez, J. and Chargoy, N. (1990), Multistage, Indirectly Heated Solar Still, Solar Energy, **4** (44): Pp. 215.

Garba, A.T. and Maduekwe, (1996); Mathematical Modelling of Some Renewable Energy Systems: A case study of Solar Cooker, Solar Still, Solar Water Heater, Saw dust and Improved Wood- Burning Stoves, Nigeria Journal of Renewable Energy, Vol. 4 (2), Pp. 1 – 11.

Ilaria B., Francesco, c., Marco, C., Matteo De, F., Biaggio Di, P., Francesca, M., Stefano, P., Giovanni, P. (2010), Ambient Temperature Modelling with Soft Computing Techniques, Solar Energy, **84:** Pp. 1264-1272.

Minasian, A.N., Al-Karaghouli, A.A. and Habeeb,S.K., (1997); Utilization of aCylindrical Parabolic Reflector for Desalination of Saline Water, Energy Conversion and Management **38** Pp 701 – 704.

Nafey, A.S., Abdelkader, M., Abdelmotalip, A.A. and Mabrouk, A.A., (2000); Parameter Affecting Solar Still Productivity, Energy Conversion and Management (41) 1797

Robert Foster, MajidGhasseni, and Alma Cota, (2010); Solar Energy (Renewable Energy and the Environment), Taylor and Francis, USA.

Saini, S.K., and Saini, R.P., (2008), Development Of Correlation For Nusselt Number And Friction Factor Solar Air-Heater With Roughened Duct Haring Arc-Shaped Wire As Artificial Roughness, Solar Energy **82** Pp 1118 – 11130.

Sodar, M.S., Nyak, J.K., Tiwari, G.N. and Kumar, A., (1980); Double Basin Water Still Energy Conversion **20** (1) m 23

Tiwari , G.N., (2004); Solar Energy Fundamentals, Design, Modelling Applications, 2nd Edition, Narosa publishing house Mumbai.

Conference Proceedings

Solar World Congress 2015
Daegu, Korea, 08 – 12 November 2015

Experimental Analysis of Solar Driven Bubble Column Humidifier for Humidification-Dehumidification (HDH) Water Desalination System

Hafiz M. Abd-ur-Rehman[1], Fahad A. Al-Sulaiman[1,2] *, and M. A. Antar[1]

[1] Mechanical Engineering Department, King Fahd University of Petroleum & Minerals (KFUPM), Dhahran (Saudi Arabia).

[2] Center of Research Excellence in Renewable Energy (CoRERE), King Fahd University of Petroleum & Minerals (KFUPM), Dhahran (Saudi Arabia).

*Corresponding author: fahadas@kfupm.edu.sa, Tel: +966(13) 860-4628.

Abstract

Humidification-dehumidification (HDH) is a carrier gas based thermal technique, which is ideal as a small scale decentralized water desalination system. An innovative design approach is to use the bubble column humidifier to enhance the performance of the HDH water desalination system. Therefore, a novel bubble column humidifier is proposed which is operated through solar thermal energy as the main source of energy input. The overall objective of this work is to develop and test the novel bubble column humidifier to identify the optimum performance operating conditions for its possible integration with a dehumidifier. The design of the bubble column humidifier is optimized in terms of perforated plate geometric features to reduce the overall pressure drop in the system. The study addresses the relation between the air pressure variation with water column height and air superficial velocity varies. The proposed bubble column humidifier is integrated with Fresnel lens to increase the water temperature as it enters the humidifier. The influence of water temperature on the vapor density is investigated at different air superficial velocities. Results indicate that the vapor density in the bubble column humidifier is significantly increased with the increase in the water temperature and air superficial velocity. One major advantages of this proposed humidifier is its ability to have a direct solar thermal heating. Subsequently, it can be located in remote areas.

Keywords: *solar thermal energy, water desalination, HDH systems, bubble column humidifier, Fresnel lens*

1. Introduction

The fresh water is the essence of life and its scarcity is the most threatening concern for mankind. The problem is more severe in developing countries where the population growth projection is much higher as compared to developed countries (Fiorenza et al., 2003). The rapid population growth resulted in higher fresh water demands for domestic and agriculture sectors to produce adequate quantities of food. While the fresh water demand is rising exponentially, the industrial revolution is making the fresh water scarcity situation more alarming by polluting the lakes and rivers by industrial waste. Given the fact that the population on earth continues to increase and industrial growth shows no signs of slowing down, it is expected that the number of people affected by clean water scarcity will escalate four times over the next 25 years (Miller, 2003). To alleviate the worries of the existing and approaching fresh water crisis, the answer for water sustainability may lie in developing the decentralized small scale water desalination system.

Solar humidification-dehumidification (HDH) is an appropriate choice for decentralized small scale water desalination system, especially in remote regions where inexpensive land and abundant solar radiations are available. The challenge is to come up with an efficient, reliable, and cost effective design approach to explore the true potential of the HDH water desalination systems. Several studies are available that explore HDH as an effective means of seawater desalination. However, the main focus of these studies is to improve the dehumidification process of the HDH system and very less attention is given towards the improvement of humidification process.

Humidification is one of the fundamental processes in the solar HDH water desalination system. There are many devices which can be used for the humidification purpose. These devices include spray tower, wetted wall tower,

Selection and/or peer review under responsibility of Scientific Committee
doi:10.18086/swc.2015.10.46 Available at http://proceedings.ises.org

packed bed tower, and bubble column (Treybal, 1980). The aim of all these devices is to raise the humidity of the air by diffusion of water into unsaturated air stream. This diffusion process is caused by the concentration difference between the water vapor in the air and air-water interface.

Several studies considered using spray tower as a humidification device in theair HDH system. In the spray tower, water is sprayed in the form of droplets that falls under the force of gravity. Air is injected from the bottom to come in a direct contact with the falling water droplets in a counterflow arrangement. These type of devices have low humidification effectiveness due to the low water holdup. Other limitations include the use of mist eliminators which are essential to avoid the water entrainment in the air at the exit of the spray tower. Furthermore, the losses in the spray nozzles caused a high pressure drop in the water stream. Younis et al. (1993), Ben-Amara et al. (2004), and Orfi et al. (2004) used spray tower as a humidification device and studied the effect of water-to-air mass flow rate ratio on the humidification efficiency. They varied the water-to-air mass flow rate ratio while keeping the absolute humidity and inlet water temperature constant. Moreover, the sprayed water temperature (60 ˚C) was kept less than the inlet air temperature (80 ˚C). The results showed that the absolute outlet humidity increased with increasing the amount of sprayed water to a certain level. However, further increase in the quantity of water initiated the air cooling and condensation of water vapor in the air. This process resulted in the decrease of absolute humidity although the outlet air is always saturated. This implies that air heated HDH cycle provides maximum air humidity at an optimum water-to-air mass flow rate ratio. Therefore, use of the multi stage air heated HDH system increases the production of fresh water.

Wetted wall towers could also be used in an HDH system for air humidification purpose. In this type, thin water film flows downward on the inner perimeter to form a wetted surface along a tower length. The air stream can either flow upward or downward to have a direct contact with the falling water thin film. These towers have a higher humidification efficiency and a lower air side pressure drop as compared to other humidification towers. However, the water flow rate is restricted to a lower capacity due to the limitation of the thin film water flow only on the inner perimeter of the tower. Wallis and Aull (1999) used polypropylene made vertically hanging fleeces for their wetted wall humidifier. The thin film of the heated water was distributed and trickled downward along the inner perimeter of the fleeces to form a wetted surface. The dry air streamed upwards and came out saturated at the outlet of the humidifier. Orfi et al. (2004) employed an improved heat and mass exchange design for a wetted wall humidifier. In their design, the water flowing velocity was reduced for better heat and mass exchange. The reduction in water flow velocity was ensured by covering the wooden vertical wetted walls with a cotton wick. The wooden vertical walls were always kept wet using capillary force. This design improvement ensued higher humidifier performance and claimed to achieve around 100 % humidification efficiency.

The packed bed tower is a widely practiced humidification device in the HDH water desalination system owing to its better performance. It is similar to the spray towers in which water is sprayed in the form of droplets that fall under the force of gravity. However, in the packed bed tower, the packing material is used to improve the humidification efficiency. The use of packing material makes the water droplets more dispersed which increases the area and time of contact between both water and air. However, this improvement leads to a higher pressure drop in the packed bed humidifier. Tab. 1 shows different packing materials. Several factors affect the choice of the packing materials and their heat and mass transfer, e.g. pressure drop, durability, cost, and quality of water. Development of packing materials in the HDH systems were reported by Mirsky and Bauthier (1993) and the performance of different packing materials in such systems were investigated by Aull and Krell (2000). Wallis and Aull (1999) showed a gradual change of fills types in packed bed towers. Introduction of film fills caused a tremendous change by providing higher thermal performance by reducing pressure drop and increasing water to air contact area. However, older splash type fill packing is being used because all these benefits are lost pertaining to high fouling potential.

1.1 Bubble Column humidifier

An innovative design approach is to use the bubble column as a humidification device for a HDH water desalination system. The choice of a bubble column as a humidifier has been inspired due to the higher rate of heat and mass transfer in the liquid-gas dispersion. In this humidifier configuration, air is passed through perforated plates to form bubbles in the hot water column. As the air bubbles propagate through the hot water column, simultaneous heat and mass transfer take place where air becomes hot and humid at the outlet of the humidifier. Heat transfer to the liquid-gas diffusion has been studied by many researchers who suggested different models to analyze the effect of heat transfer coefficient on different system parameters. Kobel et.al (1958) showed that the liquid properties and gas velocity have the main impact on the heat transfer coefficient. Kast (1962) studied the effect of rising a bubble in the fluid and indicated that the fluid element in the front of the rising

bubble moves toward the wall due to the radial momentum that it received by uprising the bubble. This radial momentum of the fluid breaks the boundary layer at the wall and the boundary layer assumption is not valid, especially in the case of high bubbles concentration. Conversely, the uprising bubble form a wake underneath sucks the fluid radially. The fast radial exchange flow due to uprising bubble results in a capacitive heat transfer. The flow around rising bubble and air humidification in the bubble column humidifier is illustrated in Fig. 1.

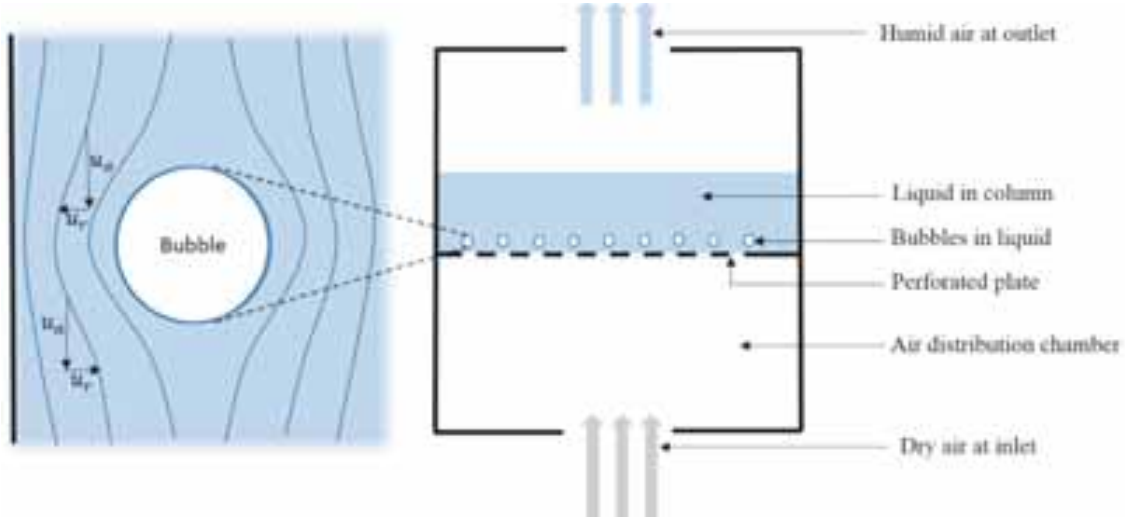

Fig. 1: Flow around rising bubble and air humidification in bubble column humidifier.

The higher rate of heat and mass transfer in a bubble column inspired the researchers to extensively practice these devices as multiphase reactor in chemical process like fisher-tropsch process, in metallurgical and many biomedical applications. However, the use of bubble column humidifier in HDH water desalination is very limited and there are very few studies that investigate the bubble column as a humidifier for HDH water desalination system. El-Agouz and Abugderah (2008) carried out an experimental investigation of a single stage bubble column humidifier. An evaporator column of 500 mm x 250 mm cross section was used in this experiment. The air stream is introduced by a 75 mm diameter PVC pipe having 32 holes of 10 mm diameter on both sides. The pipe was submerged in the water and acted as a sparger to form bubbles in the pool of water. They considered the effect of different operating parameters on the humidifier efficiency. These operating parameters include water inlet temperature, the air inlet temperature, and the air inlet velocity. Their results specified that the performance of the bubble column humidifier is considerably affected by the inlet air velocity and the inlet water temperature. The air inlet temperature has a small influence on the vapor content difference in the air. The highest efficiency achieved for the bubble column humidifier was reported as 95 % with 222 gw/kga at 75 °C of air and water temperatures. Geometrical features, such as the number of holes, holes diameter, open area ratio, and water column height were not considered in this study. El-Agouz (2010) performed another experimental study to analyze the effect of water column height, water column temperature, and air flow rate on the performance of bubble column humidifier. The effect of water column height on the efficiency of the bubble column humidifier was not significant. However, the performance of bubble column humidifier was increased with the increase in the water column temperature and air flow rate. The maximum efficiency achieved for the bubble column humidifier was reported as 98 % at air flow rate of 14 kg/hr and water temperature of 85 °C.

Zhang et al. (2011) performed an experiment on a single stage bubble column humidifier to analyze the effect of air flow rate and water level on the pressure drop and the relative humidity of air. A cylindrical column of 198 mm diameter was used as an evaporator chamber in their experiment. A sieve plate of 8 mm thickness having 91 holes of 1 mm diameter was used as sparger. Their experimental work aimed to achieve higher water vapor in the air at the exit of humidifier with less pressure drop and less blower power consumption. The results showed that the increase in the water level and air flow rate caused greater pressure drop and higher blower energy consumption. The moisture contents at the exit of the humidifier were increased with the increase of the water and air temperatures. In the range of experimental operating conditions, the experimental results showed that the air reached 100 % relative humidity.

In all the aforementioned experimental investigation of the bubble column humidifier, water is heated by an electric heater that limits the use of these devices in remote areas where electricity availability is scarce. Therefore, a novel bubble column humidifier is proposed that is operated through solar thermal energy as the main source of energy input. In this novel humidifier, the absorber plate and bubble column were incorporated in

a single frame design, as shown in Fig. 2. The absorber plate was painted black and titled to an angle equal to the latitude of Dhahran to absorb the maximum solar radiations. This design improvement has the following advantages:

- The tilted absorber plate acts as a sloped surface to create a thin film of water over the absorber plate. The minimum water depth over the absorber plate leads to better heat transfer and higher water temperature is achieved at the exit of absorber plate. It also results in minimum pressure drop in the air-side.
- The hot humid air at the exit of bubble column further passed over the thin film of hot water flowing over absorber plate to absorb more moisture and higher vapor contents are achieved at the exit of humidifier.

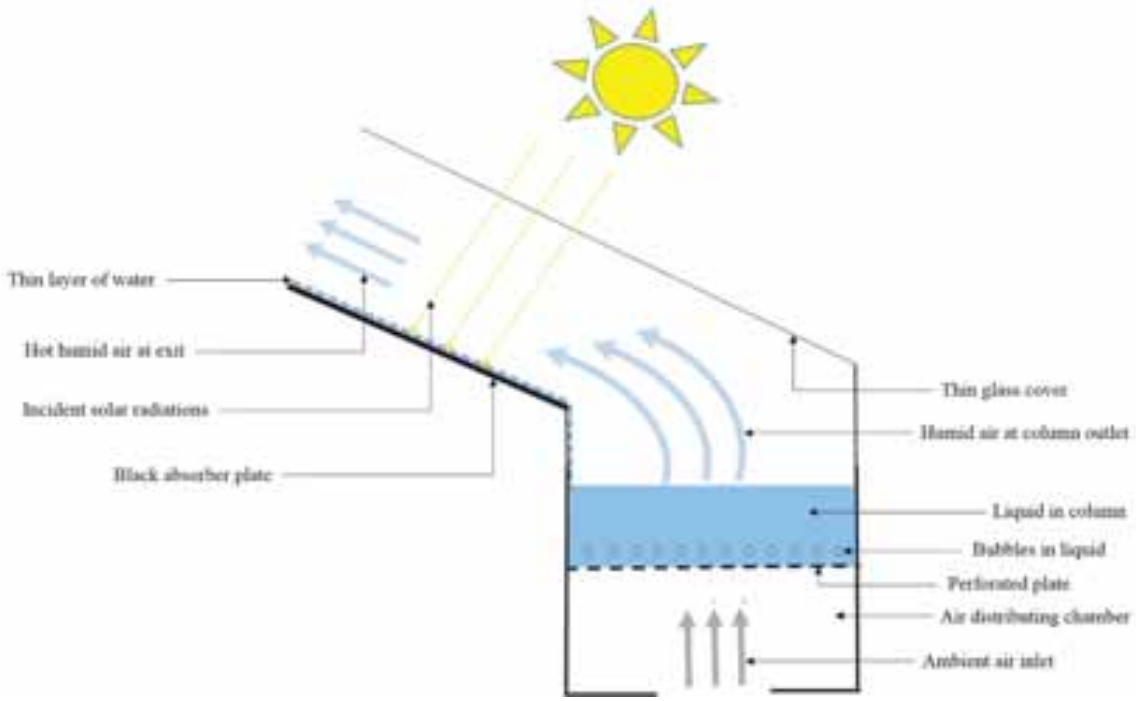

Fig. 2: Bubble column humidifier incorporated with absorber plate.

The overall objective of this work is to develop and test a new humidifier design to identify the optimum operating conditions for possible integration with a dehumidifier. Consequently, an improved HDH performance design is obtained. One major advantage of this proposed humidifier is its ability to have direct solar thermal heating. Subsequently, it can be located in remote areas.

2. Experimental Setup

A laboratory scale setup for the proposed bubble column humidifier was designed and built as shown in Fig. 3. The frame of the experimental setup was constructed of 100 mm thick Plexiglas sheet. Plexiglas is a transparent thermoplastic material that has a thermal conductivity of 0.19 W/m.K. The use of such transparent material is advantageous in a sense that it allows the observer to see what is happening inside the unit while performing the experiment. Another advantage of using the Plexiglas is its low thermal conductivity that reduces the heat loses from the system. Plexiglas sheet was also used to build the bubble column of 300 mm x 300 mm cross section and 400 mm height. A perforated plate was used as a sparger to form the bubbles in a pool of hot water in the bubble column. The perforated plate is made of a 2 mm thick black acrylic Plexiglas 300 mm x 300 mm in cross section. The perforated plate splits the bubble column into lower and upper compartments. Air ~~was~~ introduced by a 400 W adjustable blower to the lower compartment of the bubble column through a 25 mm diameter CPVC pipe. The lower compartment of the bubble column is 300 mm high. It was used to distribute the air stream uniformly through the perforated plate. The upper compartment of the bubble column is 100 mm high. It was used as a pool for hot water. Water level in the pool was measured and controlled.

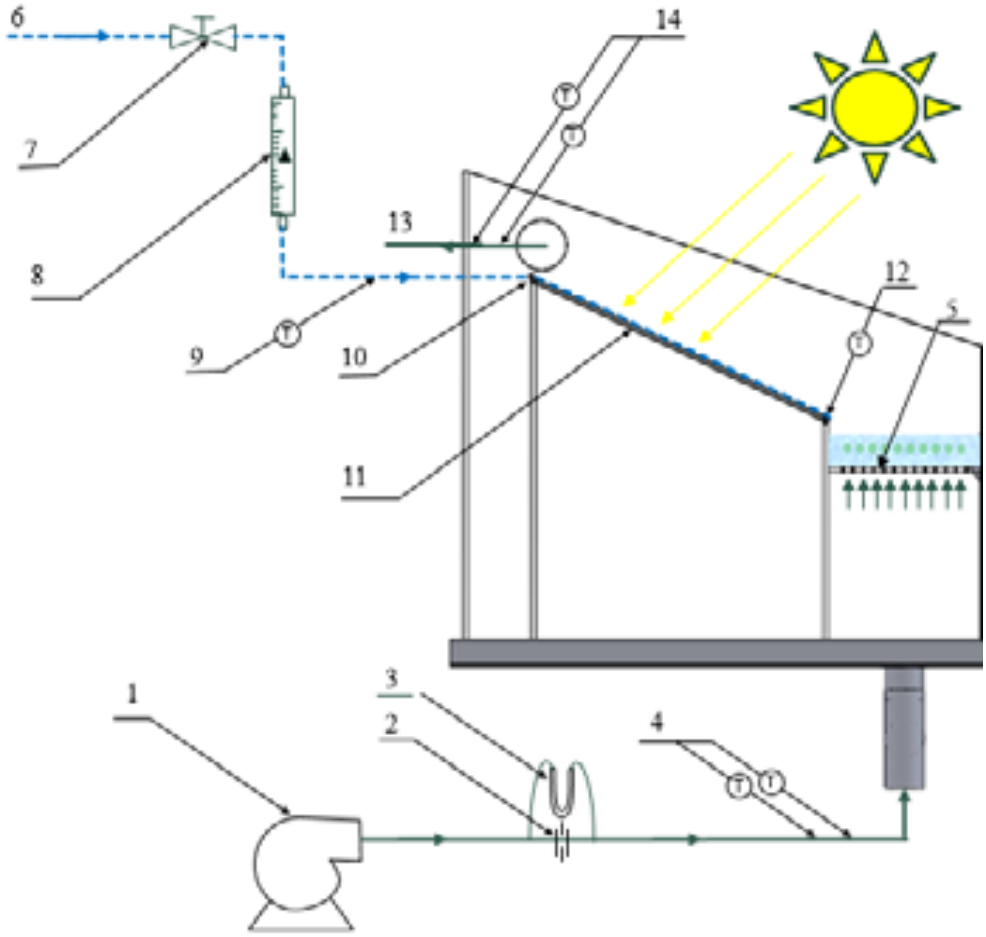

Fig. 3: Schematic diagram of experimental setup.

(1) Air blower, (2) Orifice meter, (3) Manometer, (4, 9, 12, 14) Thermocouples, (5) Perforated plate, (6) Water supply, (7) Throttle valve, (8) Rotameter, (10) Humidifier water inlet, (11) Absorber plate, (13) Humidifier air outlet

The experiment starts by blowing air using the air blower (1). The reason for blowing air first is that if the water flows first, it will penetrate down through the perforated plates (5). The blower is adjustable for the desired volumetric flow rate of the air stream that is measured by an orifice meter (2) connected to a manometer (3) to measure the pressure drop across the orifice plate and hence calculate air flow rate. The air dry-bulb / wet-bulb temperatures are measured by K-type thermocouples (4) before the air stream is admitted into the humidifier. Water supply (6) valve is then opened. The volumetric flow rate of the water was measured by a rotameter (8) adjusted to the desired value by a throttle valve (7). Water temperature is measured by a thermocouple (9) before entering the humidifier (10). A water film is distributed evenly over the black absorber plate (11) and flows by gravity. Water temperature increases as it flows over the absorber plate that is heated by solar radiations. Water temperature is measured at the exit of the absorber plate using thermocouples (12). Hot water then moves to a the bubble column chamber where air is passed through the perforated plate to form bubbles in the pool of the hot water. As the air bubbles propagate through the hot water column, simultaneous heat and mass transfer take place such that air is heated and humidified till it reaches the exit of the humidifier (13). Dry-bulb / wet-bulb temperatures of the hot and humid air are recorded using thermocouples (14) at the exit of the humidifier.

3. Data acquisition system

A data acquisition consisting of two NI 9213 thermocouple input modules installed in a NI cDAQ-9178 USB chassis is connected to a computer. Thermocouples measurements are displayed and stored using a Labview program. Real-time processed thermocouple readings are measured every 2 seconds and the average temperatures of every 5 minutes were recorded using the developed Labview program.

3.1 Instrumentation

K-type thermocouples were used to measure water temperature as well as air dry-bulb/wet-bulb temperatures. The volumetric flow rate of the water was measured by using FL5000 series rotameter of OMEGA. The

volumetric flow rate of air is measured by an orifice meter connected to a manometer to read the pressure drop across the orifice plate. The orifice meter is designed and installed according to the ISO 5167 benchmark design recommendations. Solar radiation is measured using a handheld pyranometer. The measurement devices along with their range and accuracy are summarized in Tab. 1.

Tab. 1: Measurement devices along with their range and accuracy.

Properties	Instruments	Range	Accuracy
Temperature	NI cDAQ-9178, K-Type thermocouple	-267 – 316 °C	± 0.1 °C
Relative humidity		0 - 100 % RH	± 0.1 % RH
Pressure	U-Tube manometer	0.1 - 50 cm H_2O	± 1 mm
Water flow rate	Rotameter	1 - 7 LPM	± 5 % of full scale
Water column height	Graduate level	0.1 - 20 cm	± 1 mm
Air superficial velocity	Orifice meter	10-50 cm/s	± 1 cm/s
Solar radiations	Pyranometer	0-2000 W/m2	± 5 % of full scale

Thermocouple probes are calibrated before installing them in the experimental setup. Errors in the measurement devices is calculated as the ratio of the device least count to the minimum value of the output measured by that instrument. The uncertainty in the measurements is calculated as the root sum square of the fixed error of the instrumentation and the random error observed during different measurements. The resulting uncertainties are ± 0.79 cm/s and ± 0.93 % in the air superficial velocity and vapor density, respectively.

4. Results and Discussion

4.1 Influence of geometry of the perforated plate

The optimum design consideration of the perforated plate is an important aspect in the experimental investigation of the bubble column humidifier. In the design of the perforated plate, the perforations geometric configuration should be optimized to reduce air pressure drop. Another important aspect in the perforated design is to avoid water leakage through the perforations. Keeping in mind the aforementioned aspects, three different perforated plates were designed and tested to analyze the effect of perforation geometry on the performance of the bubble column humidifier. The geometric features of the three spargers used during the experimental work are listed in Tab. 2.

Tab. 2: Geometric features of different designs of perforated plate tested during experimentation.

	Number of holes	Hole Diameter (mm)	Pitch size (mm)	Open Area Ratio (%)
Design 1	105	3	25	0.77
Design 2	105	2	25	0.33
Design 3	149	2	20	0.49

Three different designs of perforated plates were tested at different air superficial velocities. Results are shown in Fig. 4. The minimum pressure drop is achieved using design 1 due to the bigger hole diameter and higher open area ratio compared to the other two designs. However, water leakage was observed from the perforations during the experiments that showed that this design is not useful. To overcome the problem of the water leakage, design 2 was tested with the same number of holes as in design 1 but the hole diameter was reduced from 3 mm to 2 mm. Design 2 was successful in preventing water leakage from the perforations but the pressure drop was high. The high pressure drop is due to the low open area ratio in design 2. Therefore, design 3 was tested with 149 holes with 2 mm-hole diameter. The higher number of holes increased the open area ratio and reduced the pressure drop compared to design 2. Moreover, no leakage was observed with design 3 during the experiment. Therefore,

design 3 was selected as the best choice for our experimental setup. The perforated plate dimensions and hole geometry of design 3 are shown in Fig. 4. The perforated plate is 300 mm x 300 mm in cross section and it consists of 149 holes, 2 mm-diameter each. The holes are made in equilateral triangular configuration where the distance between any two adjacent holes is 20 mm. The holes are distributed 40 mm away from the boundary of the perforated plate to avoid the shear stresses near the wall of the bubble column.

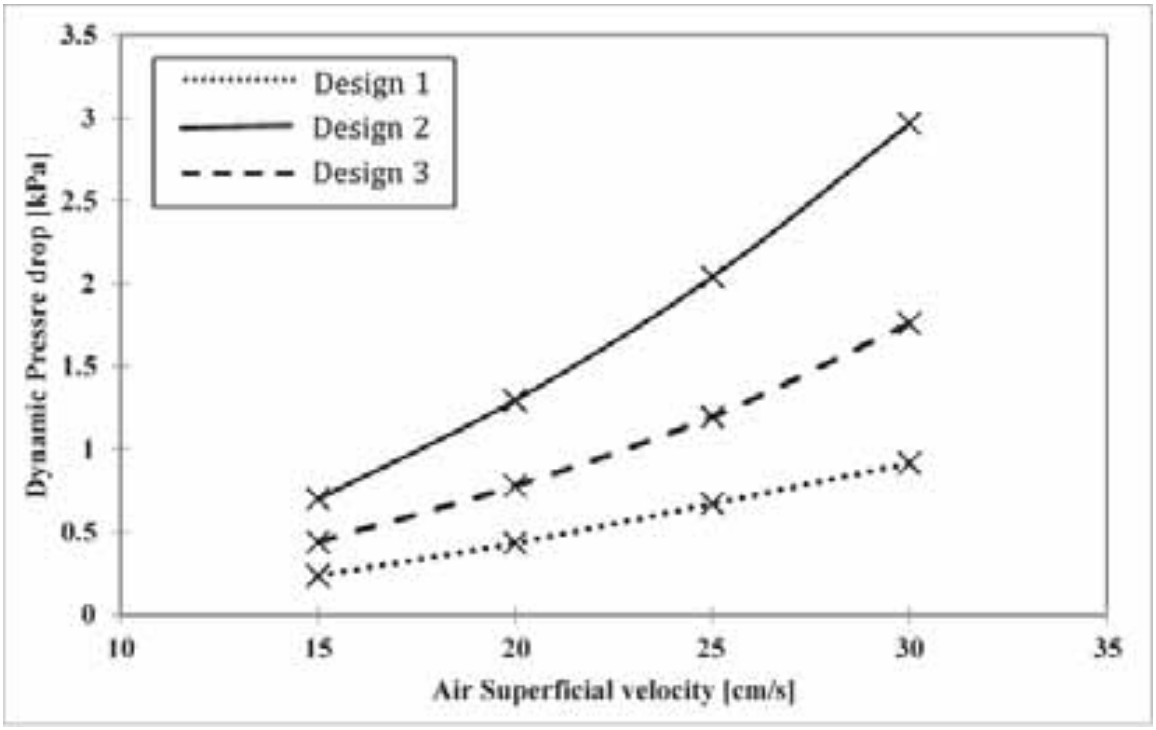

Fig. 4: Influence of air superficial velocity on the dynamic pressure drop under different design considerations of perforated plate.

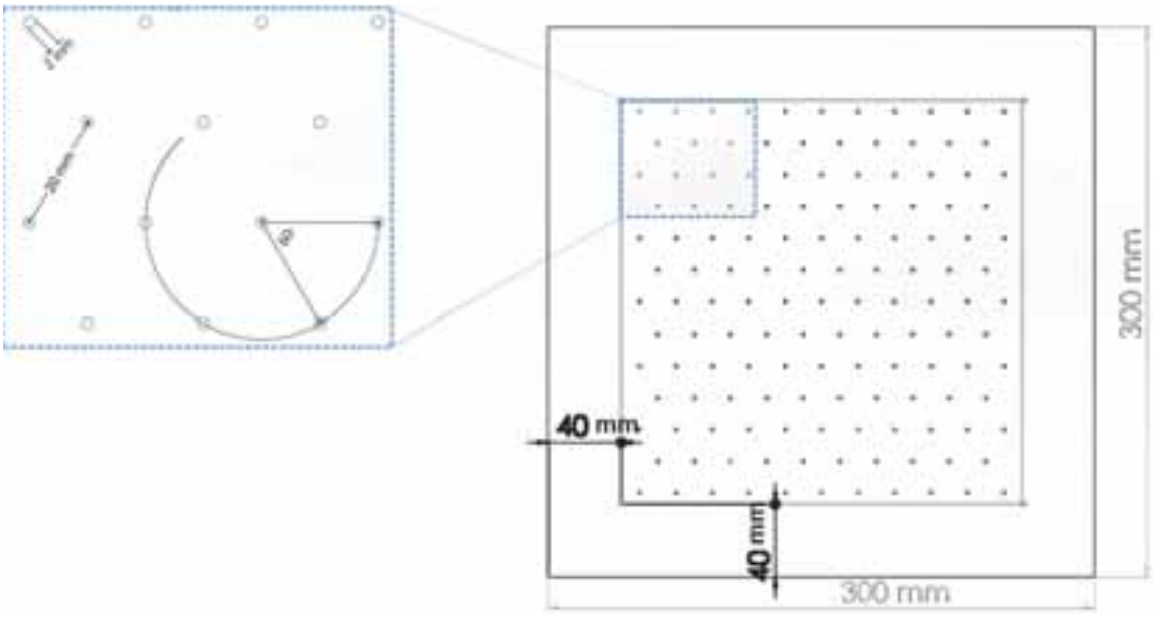

Fig. 5: Dimensioning and geometric features of the selected perforated plate.

Figure 6 shows the effect of water column height on the total air pressure drop at different air superficial velocities. The figure shows that the minimum pressure drop is attained at the lowest water column height of 1 cm and with 15 cm/s air superficial velocity. Increasing water column height to 3 cm and then to 5 cm while keeping the air superficial velocity at 15 cm/s results in a significant increase in the pressure drop. Furthermore, the air superficial velocity at 15 cm/s is not sufficient to completely overcome the static pressure head of the 5

cm water column height such that some water leaked through the perforations. Therefore, air superficial velocity at 15 cm/s is not taken into consideration for further investigations. The maximum pressure drop is monitored with a higher air superficial velocity of 30 cm/s. On contrary to the air superficial velocity of 15 cm/s, there is a slight increase in the pressure drop at higher water column heights.

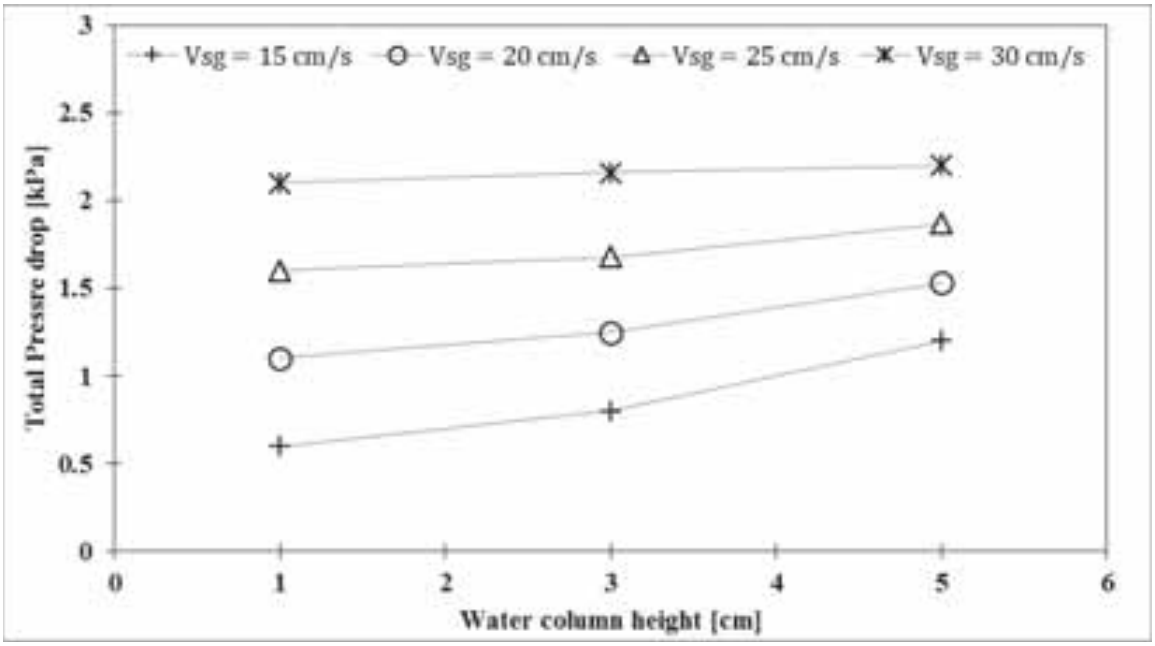

Fig. 6: Effect of water column height on the total pressure drop at different air superficial velocities.

4.2 Influence of water temperature

The major advantage of the proposed humidifier is its ability to have direct solar thermal heating for water flowing through the humidifier, the day round performance of the system was tested under climatic conditions of Dhahran, Saudi Arabia. The system was operated with and without Fresnel lens from 7 am to 5 pm in the month of June. The system performance without and with Fresnel lens was analyzed in terms of vapor density (absolute humidity) of the moist air at the exit of humidifier. Fig. 7 shows the solar heat flux, air and water inlet temperatures, and the water temperature after passing over absorber plate with and without the use of Fresnel lens. It can be seen that the solar radiation and ambient air temperature increases in the morning hours, reaching their maximum values around mid-day, and then decrease in the afternoon. Water temperature followed the same trend since it is directly influenced by the solar radiations. The black absorber plate was heated by solar radiation. Accordingly, water temperature was increased as it flows over the absorber plate. A higher water temperature was achieved by using Fresnel lens that concentrates the solar radiations on the absorber plate and, consequently, heats the water to a higher temperature.

Since the core objective of the bubble column humidifier is to effectively humidify the air, the day round performance of the proposed design is analyzed in terms of the vapor density in the moist air at the exit of humidifier. The influence of water temperature on the vapor density was investigated at different air superficial velocities. The results of the proposed design without and with Fresnel lens are presented in Fig. 8 and Fig. 9, respectively. Results indicate that the vapor density (Air humidity) in the humidifier is strongly influenced by the amount of the heat received by flowing water over the hot absorber plate. The integration of Fresnel lens increased the concentration of solar radiation on the absorber plate and heated the water to a higher temperature. The increase in the water temperature enhanced the ability of air to absorb more moisture and, consequently, higher humidity ratio is achieved at the outlet of humidifier. The increase in air superficial velocity also contributed significantly in increasing the vapor density in the moist air at the exit of humidifier. The increase in vapor density with the increase in air superficial velocity is attributed to the rise in velocity of comparatively bigger air bubbles. Moreover, the number of air bubbles increases with the increase in air superficial velocity and, consequently, provides higher interfacial area for better heat and mass transfer.

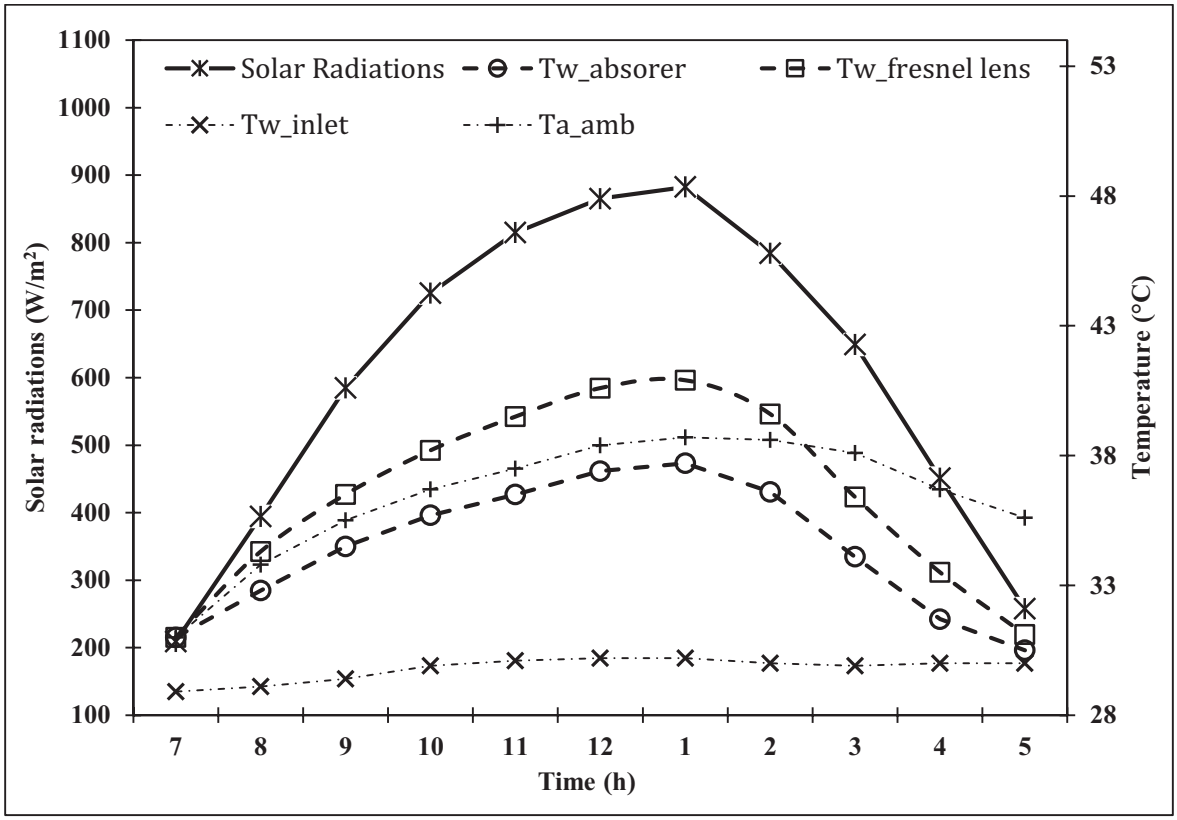

Fig. 7: The influence of solar radiations on the water temperature in the bubble column humidifier.

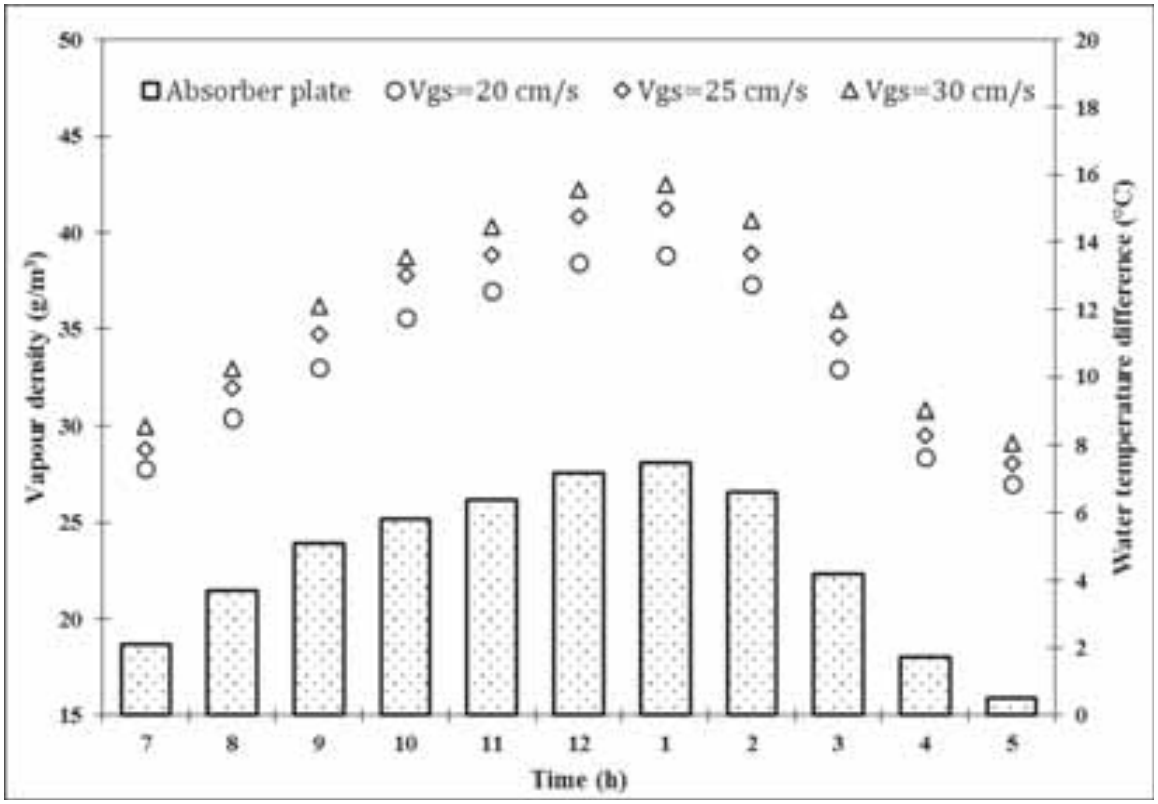

Fig. 8: Influence of water temperature and air superficial velocity on the vapor density in the moist air at the exit of humidifier.

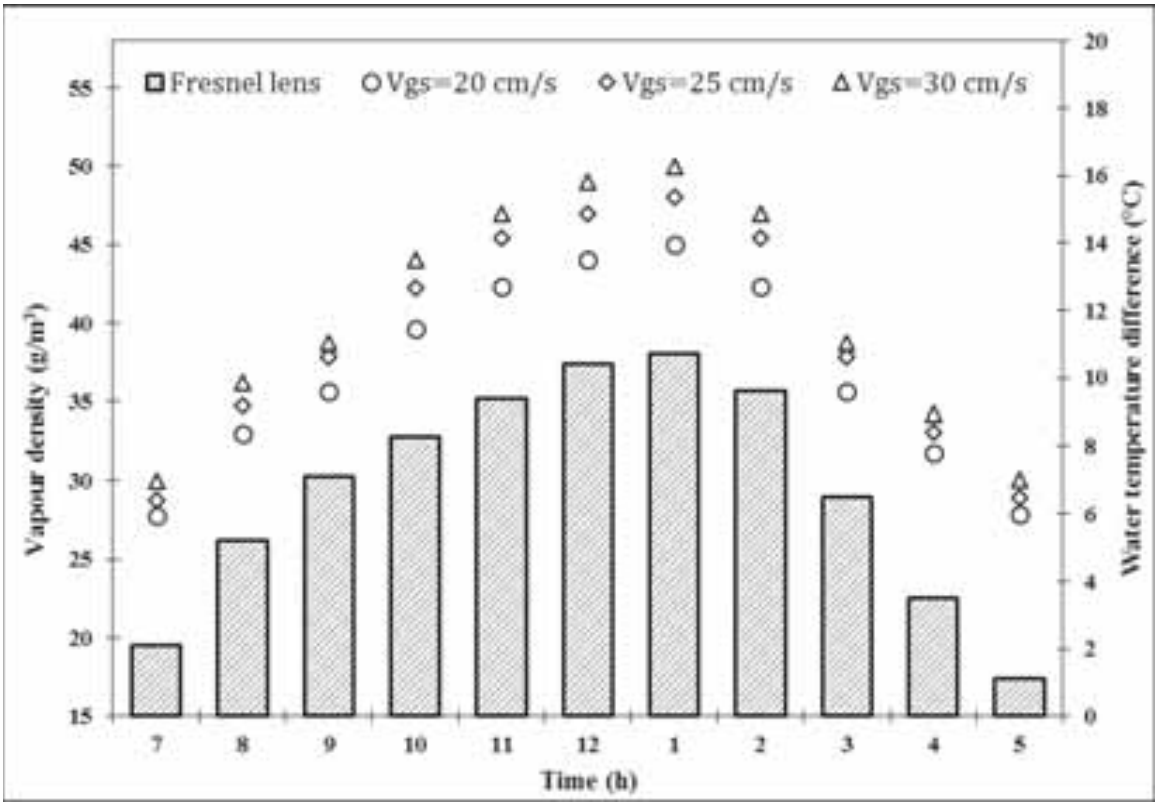

Fig. 9: Fresnel lens integration in the proposed design to increase the vapor density in the moist air at the exit of humidifier.

5. Conclusions

- The use of the bubble column humidification is an attractive option for solar humidification-dehumidification (HDH) water desalination systems. Therefore, a novel bubble column humidifier was developed and tested to identify the optimum performance operating conditions for its possible integration with a dehumidifier. One major advantage of this proposed humidifier is its ability to have a direct solar thermal heating. Subsequently, it can be located in remote areas.

- The optimum design for the perforated plate is an important aspect in the experimental investigation of bubble column humidifier. Different design configurations of the perforated plate were tested in order to achieve the lower pressure drop in the system. Findings revealed that the minimum pressure drop was experienced at a lower water column height and a lower air superficial velocity. However, the water column height and air superficial velocity should be optimized according to the geometry of the perforated plate in order to avoid water leakage through the perforations.

- The proposed design of the bubble column humidifier was integrated with the Fresnel lens in order to achieve a higher water temperature. The influence of water temperature on the vapor density was investigated at different air superficial velocities. Results indicate that the vapor density in the bubble column humidifier was significantly increased with the increase in water temperature and air superficial velocity. The increase in water temperature enhanced the ability of air to absorb more moisture and consequently higher vapor density was achieved at the outlet of bubble column humidifier.

6. Acknowledgments

The authors acknowledge the support of King Fahd University of Petroleum & Minerals (KFUPM), Dhahran, Saudi Arabia for this work through project number IN131041.

7. References

Amara, M. B., Houcine, I., Guizani, A., & Mâalej, M. (2004). Experimental study of a multiple-effect humidification solar desalination technique. Desalination, 170(3), 209-221.

Aull, R.J., & Krell, T. (2000). Design Features of Cross-Fluted Film Fill and Their Effect on Thermal Performance. CTI Journal, 21(2), 12-33.

Degaleesan, S., Dudukovic, M. and Pan, Y. (2001), Experimental study of gas-induced liquid-flow structures in bubble columns. AIChE J., 47: 1913–1931.

El-Agouz, S. A., & Abugderah, M. (2008). Experimental analysis of humidification process by air passing through seawater. Energy Conversion and Management, 49(12), 3698-3703.

El-Agouz, S. A. (2010). Desalination based on humidification–dehumidification by air bubbles passing through brackish water. Chemical Engineering Journal,165(2), 413-419.

Fiorenza, G., Sharma, V.K., & Braccio, G., 2003. Techno-economic evaluation of a solar powered water desalination plant. Energy Conversion and Management, 44, 2217-2240.

Kast, W. (1962). Analyse des wärmeübergangs in blasensäulen. International Journal of Heat and Mass Transfer, 5, 329-336.

Kolbel, H., Siemes, W., Maas, R., & Muller, K. (1958). Wärmeübergang an Blasensäulen. Chemie Ingenieur Technik, 30, 400-404. English translation: Heat transfer in bubble columns. Retrieved from http://www.fischer-tropsch.org/DOE/DOE_reports/89012412/de89012412_toc.htm.

Miller, J. E. (2003). Review of water resources and desalination technologies. Sandia National Labs Unlimited Release Report SAND-2003-0800.

Mirsky, G.R., & Bauthier, J. (1993). Evolution of Cooling Tower Fill. CTI Journal, 14(1), 12-19.

Müller-Holst, H., Engelhardt, M., Herve, M., & Schölkopf, W. (1998). Solar thermal seawater desalination systems for decentralised use. Renewable Energy, 14(1), 311-318.

Orfi, J., Laplante, M., Marmouch, H., Galanis, N., Benhamou, B., Nasrallah, S. B., & Nguyen, C. T. (2004). Experimental and theoretical study of a humidification-dehumidification water desalination system using solar energy. Desalination, 168, 151-159.

Treybal, R.E., 1980. Mass Transfer Operation, McGraw-Hill, NewYork.

Wallis, J.S., & Aull, R.J. (1999). Improving Cooling Tower Performance. Hydrocarbon Engineering, 92-95.

Younis, M. A., Darwish, M. A., & Juwayhel, F. (1993). Experimental and theoretical study of a humidification-dehumidification desalting system. Desalination, 94(1), 11-24.

Zhang, L., Cheng, G., & Gao, S. (2011). Experimental study on air bubbling humidification. Desalination and Water Treatment, 29(1-3), 258-263.

Conference Proceedings

Solar World Congress 2015
Daegu, Korea, 08 – 12 November 2015

Performance investigation of combined solar desalination and hot water system

K. S. Reddy[1*] and H. Sharon[2]

[1*] Professor, Heat Transfer and Thermal Power Laboratory, Department of Mechanical Engineering, Indian Institute of Technology Madras, Chennai – 600 036; *e-mail: ksreddy@iitm.ac.in*

[2] Research Student, Heat Transfer and Thermal Power Laboratory, Department of Mechanical Engineering, Indian Institute of Technology Madras, Chennai – 600 036

Abstract

Water treatment using solar thermal energy is more attractive for rural and remote communities as both desalination and detoxification can be carried out effectively in a single unit. In the present investigation, a hybrid solar still which has the capability to generate both potable water and hot water has been proposed and its performance has been simulated using transient mathematical modeling. The proposed still incorporates both inclined still and conventional basin type still and is ease of construction. The distillate yield from the proposed system is nearly 107 % higher than conventional inclined type solar still. The optimum gap between evaporating and condensing surface is 0.10 m. The optimum thickness of fluid film and depth of water in the basin is 0.001 m and 0.01 m. The unit is capable of generating 7.12 kg/d of distillate. The average temperature of hot water generated by the unit during summer and winter is 56.28 ° C and 45.09 ° C, respectively. The average overall efficiency of the unit is around 67.018 % and 59.61 % during summer and winter, respectively. The unit is found to meet the drinking water and hot water requirements of remote and rural communities.

Keywords: *solar distillation, hybrid still, hot water, potable water*

1. Introduction

Rapid growth in population and change in life style of human beings along side with industrialization has increased the demand for fresh water. Available limited fresh water bodies are being polluted continuously making them unfit for human consumption. The increasing demand of fresh water can be met by desalination of saline water which is available in plenty (Tabrizi et al., 2010a). Large number of desalination units fueled by conventional energy sources is being operated throughout the world but their negative impacts on atmosphere and marine environment makes their sustainability questionable (Younos and Tulou, 2005; Jijakli et al., 2012). Nearly, 40% of the mother earth's land is arid and semi-arid; supplying treated water from decentralized distillation units to these regions is found to uneconomical. But, these regions are blessed with abundant solar energy which can be used as a source to desalinate saline water for human consumption and domestic usage (Mink et al., 1998).

Solar basin type stills have been widely studied and depth of water in the evaporation basin plays a major role in their yield (Mathioulakis and Belessiotis, 2003; Khalifa and Hamood, 2009). Compared to basin stills, inclined solar stills are cheap, portable and can produce more distillate for the same absorber area (Sodha et al., 1981). Different techniques have been adopted by researchers around the globe to enhance the yield of inclined stills. Techniques like reduction of feed water mass flow rate (Aybar et al., 2005), shading of glass cover (Deniz, 2013), use of external reflectors (Tanaka and Nakatake, 2009; Tanaka, 2009), construction of weirs for increasing the residence time of water in the absorber plate (Ziabari et al., 2013) and lining of absorber plate with wicks (Hansen et al., 2015) have helped to enhance the yield of inclined stills. Phase change materials based storage units have also been integrated with inclined stills for their distillate yield

doi:10.18086/swc.2015.10.47 Available at http://proceedings.ises.org

enhancement. Phase change material based units are costly and are recommended only for cloudy weather conditions (Tabrizi et al., 2010b). It could be seen that the productivity of conventional basin type stills and vertical stills have been enhanced to large extent by making them to operate under active mode (Sampathkumar et al., 2010; Sharon and Reddy, 2015).

However, the work associated with enhancement of distillate yield from inclined stills by active mode operation is very scarce in literature and is available as a gap. Distillation units capable of producing both potable water and hot water would be of great beneficial for rural and remote locations which can be achieved by active mode operation of inclined solar stills. Omara et al., (2013) has reported that the yield from the inclined still can be enhanced by 114% by supplying the unit with preheated feed water from Evacuated Tube Collectors (ETCs). However, distillation units with low cost, simplicity and low maintenance are very important for rural based applications. Hence, in this work a hybrid solar distillation unit has been proposed which combines both inclined still and conventional still for better performance.

2. System description

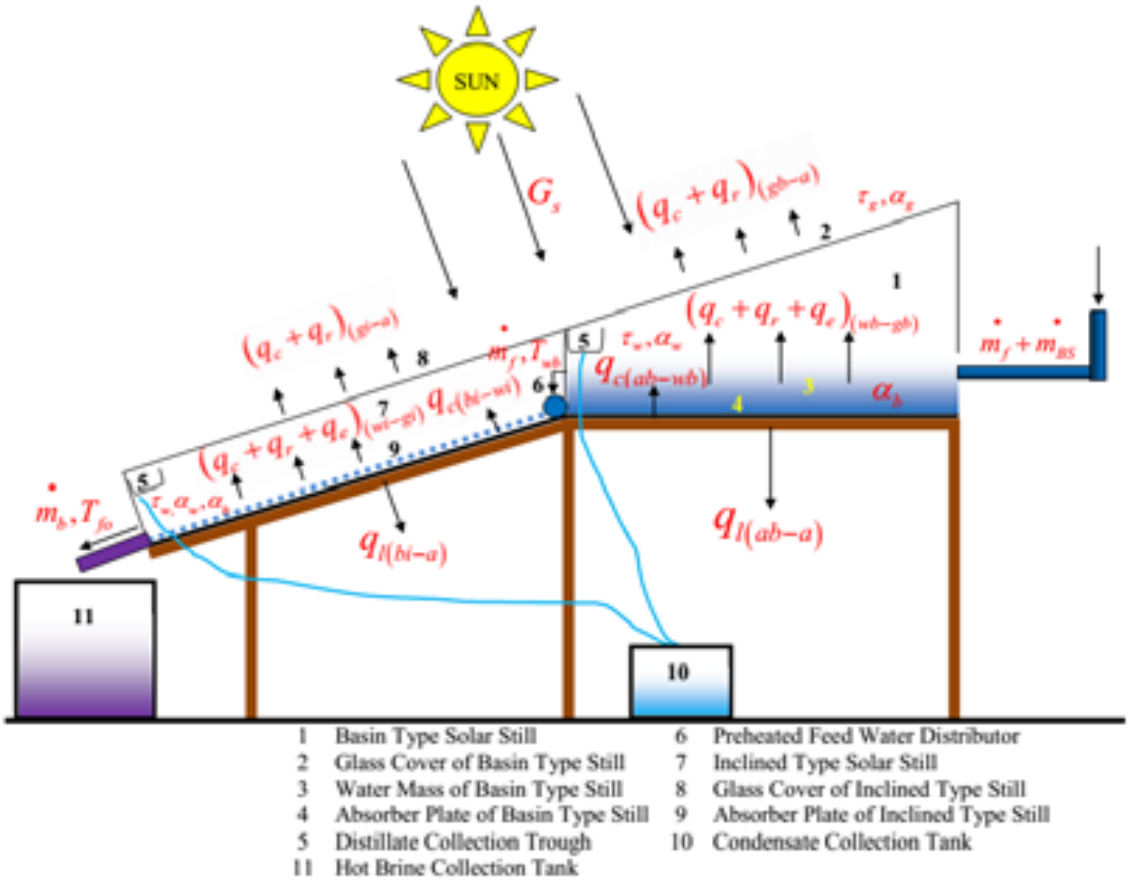

Fig. 1: Schematic represenation of the hybrid solar still along with the necessary energy transport processes

The schematic representation of the proposed hybrid solar still along with necessary energy transport processes is depicted in **Fig.1**. In the proposed system, active mode of operation of inclined still is achieved by coupling inclined still (1 m^2 area) with conventional basin type solar still (1 m^2 area). The inclination of glass cover of basin type still and inclined still is 13 $^\circ$ facing south, corresponding to the local latitude considered in this study. The integrated conventional basin type solar still acts as feed water storage and preheating unit. Preheated feed water from conventional basin type still is allowed to flow as thin over the absorber plate of inclined solar still. The absorber plate of inclined still heat ups the preheated feed water to high temperature by receiving additional solar radiation hence enhanced evaporation begins and the condensate is collected using suitable provisions. The high temperature operation of distillation unit favors efficient removal of bacteria (Sodha et al., 1981) hence the rejected hot water from inclined still can be used

for domestic purposes (Aybar, 2006). Additional distillate is also obtained from conventional basin type still. The effect of gap between condensing and evaporating surface of inclined still, thickness of fluid film, mass flow rate of feed, depth of water in the basin for summer and winter seasons on distillate yield has been simulated using the developed transient mathematical model.

3. Mathematical modeling of the proposed unit

The major assumptions that have been considered during modeling of hybrid still are given below:

a) The unit is air tight and free from vapor leakage
b) The heat capacity of glass cover, absorber plate and water mass are considered
c) There is no temperature gradient across the thickness of glass cover and water mass
d) The water level in the preheating unit (conventional still) is always maintained constant by supplying feed water
e) Heat transfer from the evaporating surface to the condensing surface is by convection, radiation and evaporation
f) Heat loss to the ambient is by convection and radiation from the glass cover and by conduction through the insulation

The energy transport process for different components of the proposed unit is given below:

Basin liner of Integrated Single Slope Still (ISSS),

$$(MC)_{ab}\frac{dT_{ab}}{dt} = G_s\tau_g\tau_w\alpha_p A_{ab} - q_{c(ab-wb)} - q_{l(ab-a)} \qquad (eq.1)$$

Water mass of Integrated Single Slope Still (ISSS),

$$(MC)_{wb}\frac{dT_{wb}}{dt} = G_s\tau_g\alpha_w A_{wb} + q_{c(ab-wb)} + \left(\dot{m}_f + \dot{m_{BS}}\right)C_{pw}T_{fi} - (q_c + q_r + q_e)_{(wb-gb)} - \dot{m}_f C_{pw}T_{wb} \qquad (eq.\ 2)$$

Glass cover of Integrated Single Slope Still (ISSS),

$$(MC)_{gb}\frac{dT_{gb}}{dt} = G_s\alpha_g A_{gb} + (q_c + q_r + q_e)_{(wb-gb)} - (q_c + q_r)_{(gb-a)} \qquad (eq.3)$$

Basin liner of Active Inclined Still (AIS),

$$(MC)_{ai}\frac{dT_{ai}}{dt} = G_s\tau_g\tau_w\alpha_p A_{ai} - q_{c(ai-wi)} - q_{l(ai-a)} \qquad (eq.4)$$

Water mass of Active Inclined Still (AIS),

$$(MC)_{wi}\frac{dT_{wi}}{dt} = G_s\tau_g\alpha_w A_{wi} + q_{c(ai-wi)} + \dot{m}_f C_{pw}T_{wb} - (q_c + q_r + q_e)_{(wi-gi)} - \dot{m}_b C_{pb}T_{fo} \qquad (eq.5)$$

Glass cover of Active Inclined Still (AIS),

$$(MC)_{gi}\frac{dT_{gi}}{dt} = G_s\alpha_g A_{gi} + (q_c + q_r + q_e)_{(wi-gi)} - (q_c + q_r)_{(gi-a)} \qquad (eq.6)$$

Convective heat transfer between the basin liner and water is given as,

For basin type still, (Zurigat and Abu-Arabi, 2004)

$$q_{c(ab-wb)} = 135.0A_{ab}(T_{ab} - T_{wb}) \qquad (eq.7)$$

For inclined type still,

$$q_{c(ai-wi)} = h_{c(ai-wi)}A_{ai}(T_{ai} - T_{wi}) \qquad (eq.8)$$

Convective heat transfer coefficient between the basin liner and flowing feed water film is given as, (El-Samadony and Kabeel, 2014)

$$h_{c(ai-wi)} = 0.664 \frac{k_f}{L} Re_L^{\frac{1}{2}} Pr_f^{\frac{1}{3}}$$

If $Re_L \leq 500000$

$$h_{c(ai-wi)} = 0.037 \frac{k_f}{L} \left(Re_L^{\frac{4}{5}} - 871 \right) Pr_f^{\frac{1}{3}}$$

If $Re_L \geq 500000$

Convective heat transfer between evaporating and condensing surface of basin type still is given as,

$$q_{c(wb-gb)} = h_{c(wb-gb)} A_{wb} \left(T_{wb} - T_{gb} \right) \quad (eq.9)$$

Heat transfer coefficient is estimated as, (Hongfei et al., 2002)

$$h_{c(wb-gb)} = 0.2 Ra'^{0.26} \frac{k_{av}}{w}$$

Evaporative heat transfer between evaporating and condensing surface of basin type still is given as,

$$q_{e(wb-gb)} = \dot{m_{BS}} h_{fg} \quad (eq.10)$$

Distillate yield is given as, (Hongfei et al., 2002)

$$\dot{m}_{BS} = \frac{h_{c(wb-gb)}}{\rho_{av} C_{pav} Le^{(1-0.26)}} \frac{M_v}{R} \left(\frac{P_{wb}}{T_{wb}} - \frac{P_{gb}}{T_{gb}} \right) A_{wb}$$

Radiative heat transfer between evaporating and condensing surface of basin type of still is given as,

$$q_{r(wb-gb)} = \frac{\sigma A_{wb} \left(T_{wb}^4 - T_{gb}^4 \right)}{\left(\frac{1}{\varepsilon_w} + \frac{1}{\varepsilon_g} - 1 \right)} \quad (eq.11)$$

Heat loss from the absorber plate to the ambient through insulation is given as,

$$q_{l(ab-a)} = k_d A_{ab} \frac{(T_{ab} - T_a)}{x_d} \quad (eq.12)$$

Convective heat transfer between the glass cover of basin type still and ambient is given as, (Zurigat and Abu-Arabi, 2004)

$$q_{c(gb-a)} = \left(2.8 + (3V) \right) A_{gb} \left(T_{gb} - T_a \right) \quad (eq.13)$$

Radiative heat transfer between the glass cover of basin type still and ambient is given as,

$$q_{r(gb-a)} = \sigma \varepsilon_g A_{gb} \left(T_{gb}^4 - T_a^4 \right) \quad (eq.14)$$

The convective, evaporative and radiative heat transfer occurring in the inclined still is found by replacing $(wb - gb)$ by $(wi - gi)$ in eq. 9 to eq. 11 and $(gb - a)$ by $(gi - a)$ in eq.12 to eq. 14.

The distillation efficiency is given as,

$$\eta_{di} = \frac{(\dot{m}_{BS} + \dot{m}_{is}) \times h_{fg} \times \Delta t}{\left(G_s \times \Delta t \times \left(A_{gb} + A_{gi} \right) \right)} \times 100 \quad (eq.15)$$

The overall efficiency is given as,

$$\eta_o = \frac{\left[\left(\dot{m}_b C_{pb} \left(T_{fo} - T_a \right) \right) + \left((\dot{m}_{BS} + \dot{m}_{is}) \times h_{fg} \right) \right] \times \Delta t}{\left[G_s \times \Delta t \times \left(A_{gb} + A_{gi} \right) \right]} \times 100 \quad (eq.16)$$

The above mentioned differential equations eq. 1 to eq. 6 were first discretized using finite difference method and were converted into algebraic equations. The obtained algebraic equations were solved using iteration method using the program written in FORTRAN language. The necessary input files were fed as separate file

for solving the equations. The time step size and convergence criteria were kept as 10 s and 0.001, respectively. The solar radiation profile for Chennai location was simulated using the method given by (Katiyar and Pandey, 2011). The monthly average wind velocity and hourly ambient temperature for the months of April and December were used for simulation.

4. Results and discussion

Effect of different parameters on the performance of the hybrid still was simulated for summer and winter months and is presented in this section. The solar radiation profile simulated for the month of April and December along with the ambient temperature is shown in **Fig. 2**. The maximum solar radiation was around 896.27 W/m^2 and 661.54 W/m^2 for summer and winter months, respectively.

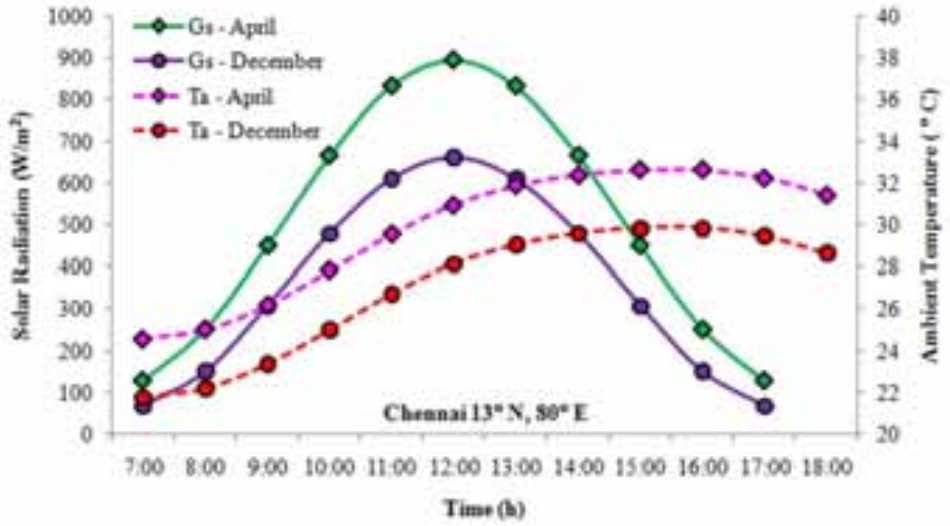

Fig. 2: Solar radiation and ambient temperature profile of Chennai during April and December

4.1. Gap between evaporating and condensing surface

The simulation was carried out for the month of April and December for 0.05 m feed water depth in basin, 0.005 kg/s feed water mass flow rate and 0.002 m fluid film thickness in inclined still. The impact of gap between the evaporating and condensing surface on the distillate yield of active inclined still during summer and winter is shown in **Fig. 3**. The yield is found to decrease from 3.11 kg/m^2-d to 2.44 kg/m^2-d with the increase in gap from 0.05 m to 0.50 m during summer. Increase in gap denotes increased air volume within the system which acts as resistance to the transfer of vapors from the evaporating surface to the condensing surface. The yield is found to decrease by 21.79 % and 25.58 %, during summer and winter with the increase in gap from 0.05 m to 0.50 m. The distillate yield during summer and winter for a gap of 0.05 m is only 6.87 % and 8.86 % higher than the yield for a gap of 0.10 m. The optimum gap can be kept as 0.10 m by considering operation and maintenance point of view.

4.2. Thickness of feed water film and mass flow rate

The simulation was carried out for the month of April and December for 0.05 m feed water depth in basin, 0.10 m gap between condensing and evaporating surface and mass flow rate of 0.005 kg/s. The impact of thickness of fluid film on the distillate yield of active inclined still during summer and winter is shown in **Fig. 4**. The yield is found to decrease from 2.94 to 2.80 kg/m^2-d while increasing the thickness of fluid film from 0.001 m to 0.01 m during summer and from 1.60 to 1.53 kg/m^2-d during winter for a mass flow of 0.005 kg/s. As the thickness increases, heat capacity of fluid film increases leading to reduced heat transfer from the absorber plate to the fluid film. Hence, it is necessary to maintain reduced fluid film thickness for the inclined still for better yield. The thin fluid film can be achieved by spreading thin metal wire mesh or porous cloth of required thickness over the absorber plate and allowing feed water to drip over these surfaces (Aybar, 2006).

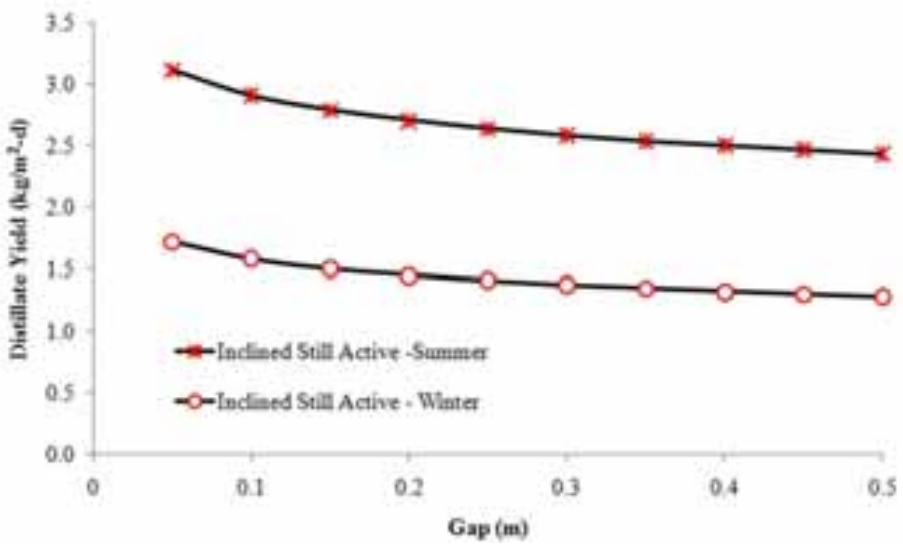

Fig. 3: Impact of gap between evaporating and condensing surface on distillate yield of active inclined still

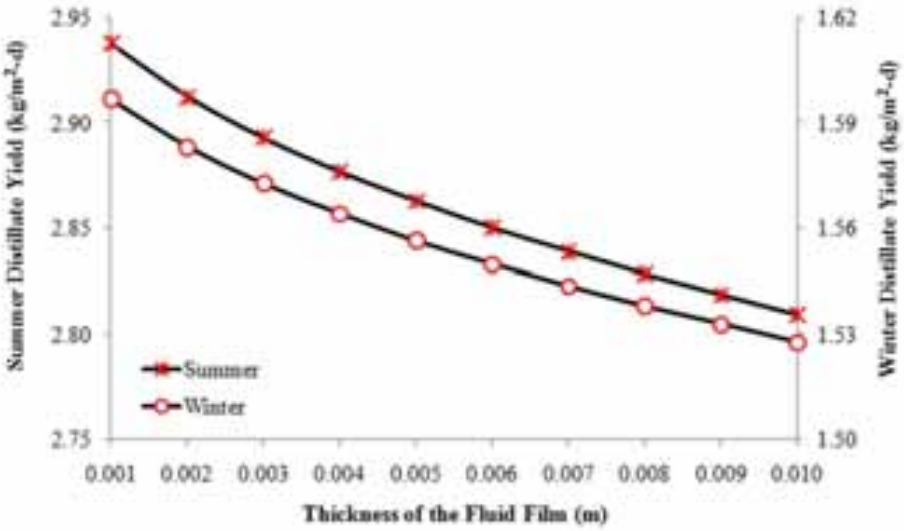

Fig. 4: Impact of thickness of fluid layer on distillate yield of active inclined still

The simulation was carried out for the month of April and December for 0.05 m feed water depth in basin, 0.10 m gap between condensing and evaporating surface and 0.001 m fluid film thickness in inclined still. The impact of mass flow rate of feed water on the distillate yield of the active inclined still is shown in **Fig. 5**. The yield is found to decrease from 9.10 kg/m^2-d to 1.24 kg/m^2-d with the increase in mass flow rate from 0.001 kg/s to 0.01 kg/s, during summer. At lower mass flow rates, the operating temperature will be higher leading to increased evaporative heat transfer and yield. At higher mass flow rates, the residence time of the feed water inside the distillation unit decreases leading to lower heat transfer from the absorber plate to water film causing reduced yield (Tabrizi et al., 2010a). The mass flow rate must be selected properly such that the feed water wets the entire absdorber plate and prevents the formation of dry patches on the surface. For a mass flow rate of 0.003 kg/s, the yield is found to be around 4.82 and 2.59 kg/m^2-d during summer and winter, respectively.

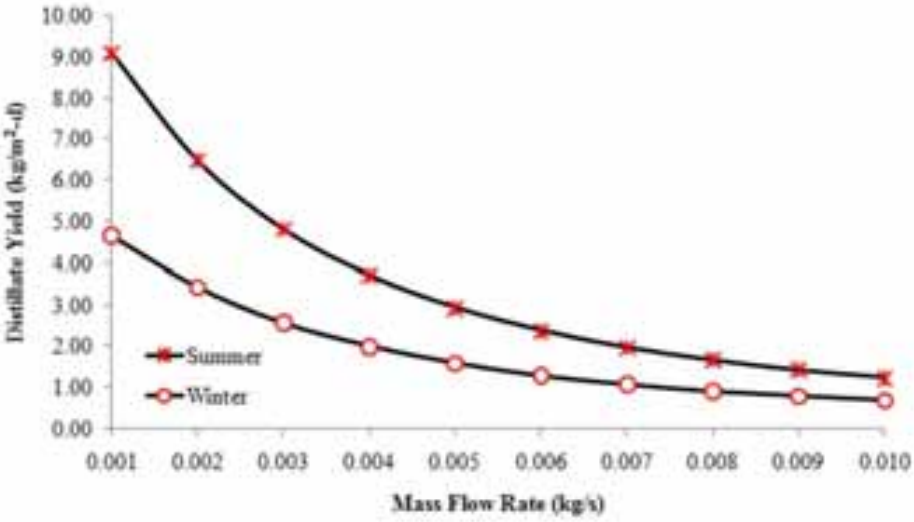

Fig. 5: Impact of mass flow rate of feed water on distillate yield of active inclined still

4.3. Depth of feed water in basin

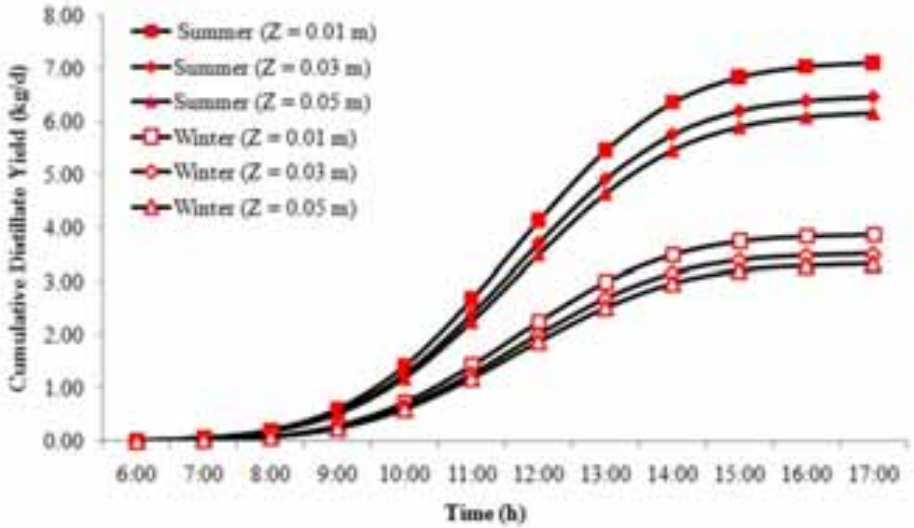

Fig. 6: Impact of depth of feed water in basin on cumulative distillate yield of the hybrid still

Feed water preheated in the basin type still is fed as input to the inclined still hence it is necessary to achieve maximum temperature using the basin type still for improved yield and hot water from inclined still. Depth of feed water in the basin type still is a major parameter which influences the yield from the hybrid still. The simulation was carried out for the month of April and December for 0.10 m gap between condensing and evaporating surface, mass flow rate of 0.003 kg/s, fluid film thickness of 0.001 m in inclined still and feed water depth of 0.01 m, 0.03 m and 0.05 m in basin. The impact of depth of feed water in basin on the distillate yield of hybrid still during summer and winter is shown in **Fig. 6**. The distillate yield is found to increase with the reduction in depth of feed water in the basin from 0.05 m to 0.01 m. Reduced yield at high depth is due to the increased mass of water in the basin which increases the heat capacity and reduces the transmissivity of the water leading to reduced radiation reaching the absorber plate of the basin type still (El-Sebaii, 2000). For a depth of 0.01 m the hybrid still produces a distillate yield of 7.12 and 3.86 kg/d during summer and winter, respectively. The yield is nearly 15.39 % and 15.91 % higher than the yield during summer and winter, respectively for a depth of 0.05 m.

4.4 Performance of the optimized hybrid distillation unit - hourly distillate and hot water productivity

The cumulative distillate yield of hybrid still is compared with passive inclined still and is shown in **Fig. 7.** Cumulative yield from passive inclined still and active inclined still is 2.54 kg/d and 5.31 kg/d, respectively. Cumulative yield of integrated single slope still (ISSS) which acts as the preheating unit for the active inclined is 1.81 kg/d. Hence, the total yield form the hybrid still (AIS +ISSS) is 7.11 kg/d. The distillate yield is found to be minimum during 6:00 to 9:00 due to reduced solar intensity and the yield increases steadily from 9:00 to 14:00, beyond 14:00 cumulative increase in yield remains nearly constant for the distillate units considered for study

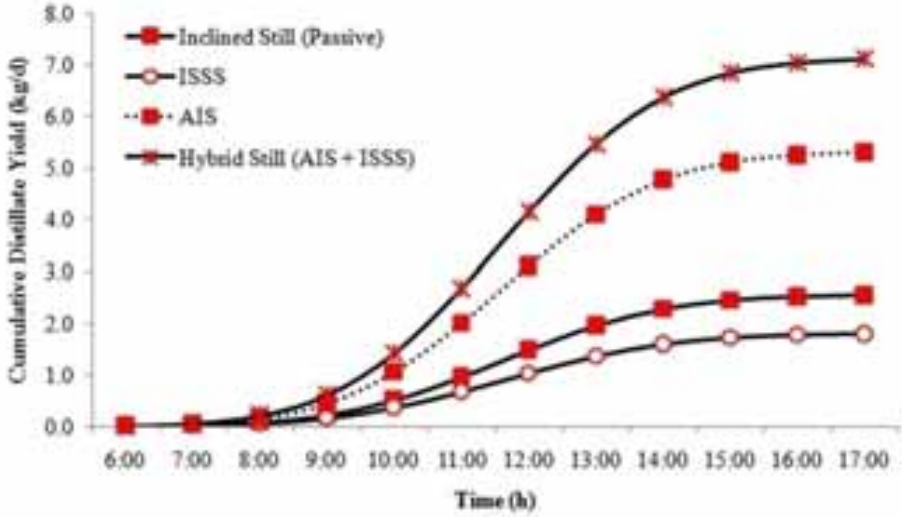

Fig. 7: Comparison of cumulative distillate yield of different distillation units

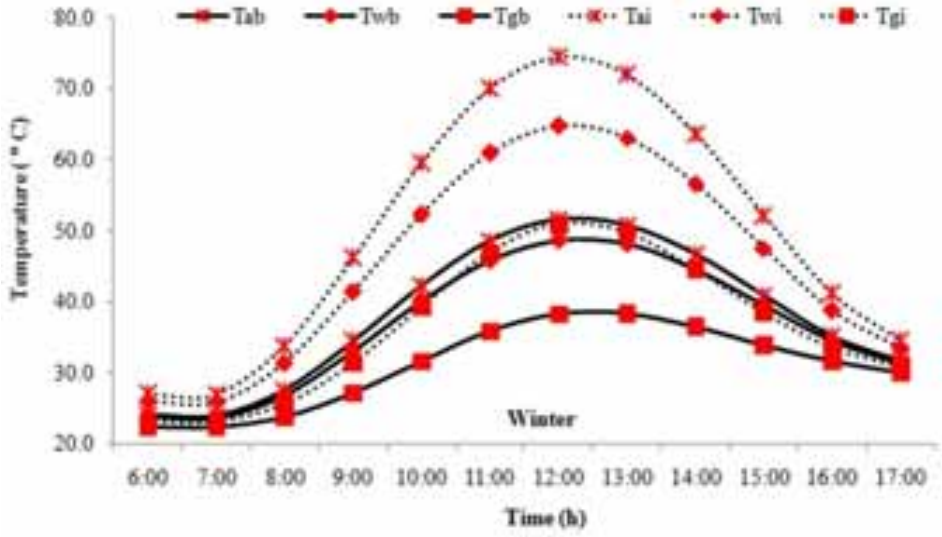

Fig. 8: Hourly variation of temperature for different components of the hybrid still

The hourly temperature profile of different components of hybrid still for the month of December is shown in **Fig. 8**. The temperature profile is found to follow the solar radiation profile for the considered day. The temperature is found to increase with the increase in solar radiation up to 12:00 and then starts decreasing beyond 12:00. The maximum temperature of the absorber plate of integrated solar still and active inclined still is 51.48 ˚C and 74.35 ˚C, respectively. Maximum temperature of the feed water while leaving basin type still is 48.59 ˚C and it reaches 64.65 ˚C while leaving the absorber plate of the inclined still. Maximum glass temperature of the basin type still and inclined still is 38.33 ˚C and 50.86 ˚C, respectively.

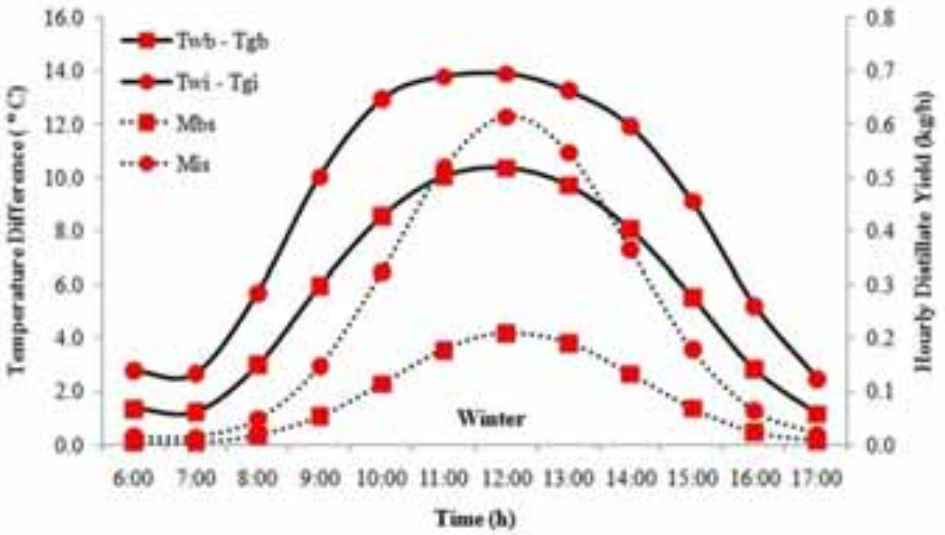

Fig. 9: Hourly distillate yield and temperature difference between evaporating and condensing surface of the hybrid still

The temperature difference between the evaporating and condensing surface of hybrid still along with its hourly distillate productivity for the month of December is shown in **Fig. 9**. The maximum temperature difference between the evaporating and condensing surface of the integrated single slope still and active inclined still is 10.35 ˚C and 13.90 ˚C, respectively. The maximum hourly productivity of the integrated single slope still and active inclined still is 0.21 kg/h and 0.61 kg/h, respectively making the total hourly productivity of the hybrid still to be around 0.82 kg/h.

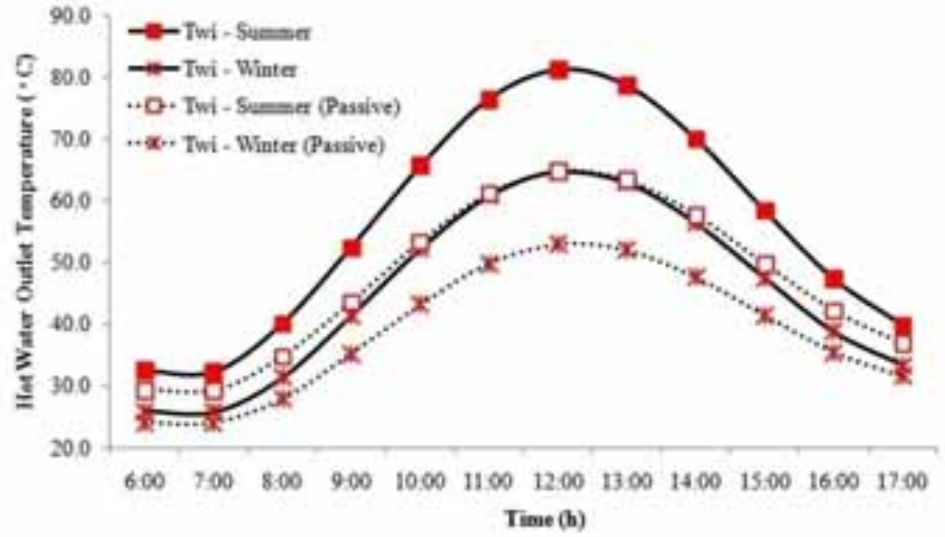

Fig. 10: Hourly temperature variation of hot water generated by the active and passive inclined still

The hourly temperature profile of the hot water generated by hybrid still during summer and winter in comparison with passive inclined still is shown in **Fig. 10.** The maximum temperature of hot water produced by passive inclined still is 64.84 ˚C and 52.91 ˚C, respectively during summer and winter. The maximum temperature of hot water produced by hybrid still is 81.29 ˚C and 64.65 ˚C during summer and winter which is higher than passive inclined still by 16.45 ˚C and 11.74 ˚C, respectively. The increase in hot water temperature of active inclined still is mainly due to preheating of feed water in the integrated single slope still of hybrid still. The average temperature of hot water generated by hybrid still is around 56.28 ˚C and 45.09 ˚C during summer and winter, respectively and the amount of hot water generated is more than 100 kg/d for both the seasons. The produced hot water can be used for domestic purposes like washing, flushing and it depends on the salinity of the feed water too (Aybar, 2006).

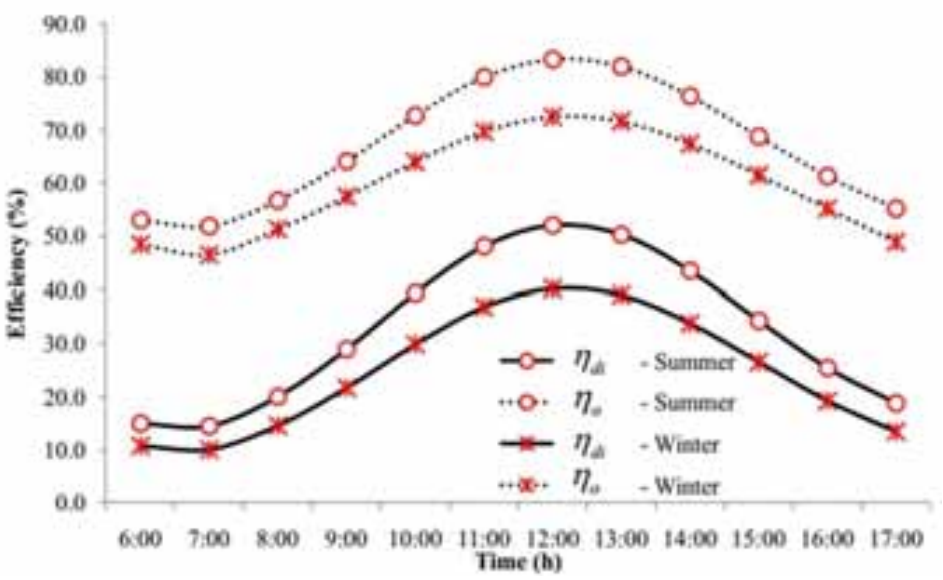

Fig. 11: Hourly variation of distillation and overall efficiency of hybrid still

The hourly variation of distillation efficiency and overall efficiency of hybrid still for summer and winter months is shown in **Fig. 11**. Distillation efficiency represents the ratio between energy content of the fresh water generated to the solar radiation input to the system. Overall efficiency represents the ratio between the energy content of the fresh water generated and useful energy of the hot water generated to the solar radiation input to the system. The efficiency varies with time due to variation in solar intensity and it reaches maximum during noon. The maximum distillation efficiency during summer and winter day is 52.14 % and 40.30 %, respectively. The maximum overall efficiency during summer and winter day is 83.40 % and 72.57 %, respectively. The average distillation efficiency and overall efficiency of the system is 32.59 % and 67.18 %, 24.73 % and 59.61 % for summer and winter, respectively.

5. Conclusion

Solar stills can carry out both desalination and detoxification in a single unit and are highly suitable for remote applications. In this study, transient simulation of hybrid solar still which has the ability to generate both potable water and hot water was carried out successfully. The distillate yield from hybrid still is found to increase with the decrease in depth of feed water in the basin type still, feed water mass flow rate and thickness of fluid film. Distillate yield from hybrid solar still is around 7.12 kg/d and 3.86 kg/d during summer and winter, respectively. Average temperature of hot water generated by the unit is around 56.28 ˚C and 45.09 ˚C during summer and winter, respectively. Overall efficiency of the hybrid unit is around 67.18 % and 59.61 % during summer and winter, respectively. The amount of hot water generated is more than 100 kg/d which is fairly sufficient for domestic activities like washing and flushing. The proposed unit will be of great benefit to rural and remote communities.

6. References

Aybar, H.S., Egelioglu, F., Atikol, U., 2005. An experimental study on an inclined solar water distillation system. Desalination 180, 285-289.

Aybar, H.S., 2006. Mathematical modeling of an inclined solar water distillation system. Desalination 190, 63-70.

Deniz, E., 2013. An investigation of some of the parameters involved in inclined solar distillation systems. Environmental Progress & Sustainable Energy 32(2), 350-354.

El-Samadony, Y.A.F., Kabeel, A.E., 2014. Theoretical estimation of the optimum glass cover water film cooling parameters combination of a stepped solar still. Energy 68, 744-750.

El-Sebaii, A.A., 2000. Effect of wind speed on some designs of solar stills. Energy Conversion and Management 41, 523-538.

Hansen, R.S., Narayanan, C.S., Murugavel, K.K., 2015. Performance analysis on inclined solar still with different new wick materials and wire mesh. Desalination 358, 1-8.

Hongfei, Z., Xiaoyan, Z., Jing, Z., Yuyuan, W., 2002. A group of improved heat and mass transfer correlations in solar stills. Energy Conversion and Management 43, 2469-2478.

Jijakli, K., Arafat, H., Kennedy, S., Mande, P., Theeyattuparampil, V.J., 2012. How green solar desalination really is? Environmental assessment using life-cycle analysis (LCA) approach. Desalination, 287, 123-131.

Katiyar, A.K., Pandey, C.K., 2011. Correlation for estimation of hourly solar radiation. International Journal of Energy and Environment, 2(1), 191-198.

Khalifa, A.J.N., Hamood, A.M., 2009. On the verification of the effect of water depth on the performance of basin type solar stills. Solar Energy, 83, 1312-1321.

Mathioulakis, E., Belessiotis, V., 2003. Integration of solar still in a multi-source, multi-use environment. Solar Energy, 75, 403-411.

Mink, G., Horvath, L., Evseev, E.G., Kudish, A.I., 1998. Design parameters, performance testing and analysis of a double-glazed, air-blown solar still with thermal energy recycle. Solar Energy, 64(4-6), 265-277.

Omara, Z.M., Eltawil, M.A., ElNashar, E.A., 2013. A new hybrid desalination system using wicks/solar still and evacuated solar water heater. Desalination 325, 56-64.

Sampathkumar, K., Arjunan, T.V., Pitchandi, P., Senthilkumar, P., 2010. Active solar distillation-a detailed review. Renewable and Sustainable Energy Reviews 14(6), 1503-1526.

Sharon, H., Reddy, K.S., 2015. Performance investiagtion and enviro-economic analysis of active vertical solar distillation units. Energy 84(1), 794-807.

Sodha, M.S., Kumar, A., Tiwari, G.N., Tyagi, R.C., 1981. Simple multiple wick solar still: analysis and performance. Solar Energy 26, 127-131.

Tabrizi, F.F., Dashtban, M., Moghaddam, H., Razzaghi, K., 2010a. Effect of water flow rate on internal heat and mass transfer and daily productivity of a weir-type cascade solar still. Desalination 260, 239-247.

Tabrizi, F.F., Dashtban, M., Moghaddam, H., 2010b. Experimental investigation of a weir-type cascade solar still with built-in latent heat thermal energy storage system. Desalination 260, 248-253.

Tanaka, H., Nakatake, Y., 2009. Increase in distillate productivity by inclining the flat plate external reflector of a tilted-wick solar still in winter. Solar Energy 83, 785-789.

Tanaka, H., 2009. Tilted wick solar still external flat plate reflector: optimum inclination of still and reflector. Desalination 249, 411- 415.

Younos, T., Tulou, K.E., 2005. Overview of desalination technologies. Journal of Contemporary Water Research & Education 132, 3-10.

Ziabari, F.B., Sharak, A.Z., Moghadam, H., Tabrizi, F.F., 2013. Theoretical and experimental study of cascade solar stills. Solar Energy 90, 205-211.

Zurigat, Y.H., Abu-Arabi, M.K., 2004. Modelling and performance analysis of a regenerative solar desalination unit. Applied Thermal Engineering 24 1061-1072.

7. Acknowledgement

The financial support provided by the Department of Science and Technology (DST, Government of India), New Delhi through the research project (Grant No: DST/TM/SERI/2k12/16(G)) is duly acknowledged.

8. Nomenclature

Nomenclature	
A	Area (m^2)
C_p	Specific heat capacity (J/kgK)
G	Solar radiation (W/m^2)
h_c	Convective heat transfer coefficient (W/m^2-K)
h_{fg}	Latent heat of evaporation (J/kg)
k	Thermal conductivity of insulation (W/m-K)
L	Length of active inclined still (m)
Le	Lewis number
M	Molecular weight (kg/kmol)
MC	Heat capacity (J/K)
$\dot{m}_{BS}$	Distillate yield from basin still (kg/s)
$\dot{m}_f$	Mass flow rate of feed water (kg/s)
$\dot{m}_{is}$	Distillate yield from inclined still (kg/s)
Pr	Prandtl number of fluid
q_c	Convective heat transfer (W)
q_e	Evaporative heat transfer (W)
q_l	Conductive heat loss (W)
q_r	Radiative heat transfer (W)
R	Universal gas constant (J/kmol-K)
Ra'	Rayleigh number
Re_L	Reynolds number
T	Temperature (◦ C)
V	Wind velocity (m/s)
x	Thickness of insulation (m)
α	absorbtivity
ε	emissivity
ρ	Density (kg/m^3)
σ	Stefan-Boltzmann constant (W/m^2 -K^4)
τ	Transmissivity
η	Efficiency (%)
Δt	Time step size (s)
Subscripts	
a	Ambient
ab	Basin liner of integrated single slope still
ai	Basin liner of active inclined still
av	Humid air
b	Brine
d	Insulation
di	Distillation
f	Fluid film
fi	Inlet feed water
fo	Outlet brine water
g	Glass
gb	Glass cover of integrated single slope still
gi	Glass cover of active inclined still
o	Overall
p	Plate
s	Global
w	Water
wb	Water mass of integrated single slope still
wi	Water mass of active inclined still

Solar Energy and Society

Conference Proceedings

Solar World Congress 2015
Daegu, Korea, 08 – 12 November 2015

Opportunities of Renewable Energies in the Mexican Legal Framework Strategy for Energy Transition in Response to International Environmental Agreements

Karla E. García García[1], María F. Sánchez Medina[1], Martha F. Mohedano Castillo[1] y Dr. Iván Galileo Martínez Cienfuegos[1]

[1] Facultad de Ingeniería, Universidad Autónoma del Estado de México (UAEMEX), Cerro de Coatepec, Paseo Universidad s/n, Toluca de Lerdo, Estado de México,C.P. 50130, México

Abstract

Electricity is one of the world´s most primary resources. Its cost and availability, have a bearing on a person´s quality of life. Mexico´s ability to satisfy the public demand for energy from renewable sources has been between 8.5% and 10.9%. As one of the undersigned countries in multilateral environmental agreements, Mexico has created laws and development initiatives in name of sustainability. In this article we will analyze data on the current energy panorama in Mexico, taken from accredited national and international sources. This will allow us to have a holistic view of the current state implementation of technology which makes good use of renewable energy. In this way, we will be able to detect investment and development opportunities in Mexico.

Key words: *Sustainable energy, energy reform, multilateral agreements, energy transition, plans for development, investment opportunities.*

1. The energy sector in Mexico

Mexico has at its disposal a vast quantity of hydrocarbons, which means that throughout history Mexico´s energy sector has come principally from fossil fuels-crude oil and natural gas. These sources provide nearly 90% of Mexico´s total energy production nationally (PROSENER, 2013).

The main task of the energy sector is to provide an energy service that will be efficient at a competitive price for the entire population. This will help the country socially and economically. In case more energy is produced than is consumed, this surplus will fall due to the decline in the production of oil and natural gas, versus the grown in consumption of energy resources nationally - around 2.7% over the last decade (PNI, 2014).

To date, more than 20% of energy generated for the public comes from fuel oil and diesel (PNASE, 2014). This is considerably more expensive than clean energy sources and natural gas. Mexico has great potential for producing gasoline, diesel, turbosine, natural gas, among many others, but this is not well financed and, as such, the necessary processes of transformation and extraction are stifled. PEMEX is a good example of the inability to produce natural gas due to the great demand. Because of this, Mexico imports natural gas; paying more than it would if it produced its own natural gas.

The energy sector in Mexico faces great challenges. The cost of electricity is high and not competitive. Compared to the US, the cost of electricity is 25% higher in Mexico, even with a government subsidy. Without which, the cost would be 73% more expensive (PNASE, 2014). This hinders the Mexican economy given that electricity is a basic need for industry, business and other services.

The slow pace of switching from fossil fuel energy centers to clean energy centers is mainly due to the monopoly which the Federal Electricity Commission has over public energy sector. Although individuals are now permitted to participate in the industry, the Federal Electricity Commission still controls all large scale energy projects which are limited by state budgets. This has become a bottle neck that impedes the speedy development of potential sources that could generate low cost electricity.[1]

The statistics for renewable energy usage in Mexico was 8.9% (around 440PJ) in 2013, as shown in figure 1. Almost 60% of which was due to traditional biomass generation.

doi:10.18086/swc.2015.09.01 Available at http://proceedings.ises.org

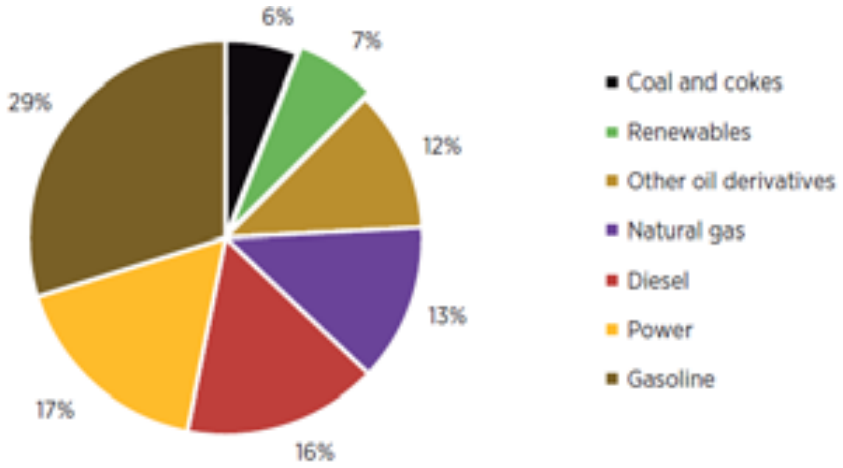

Figure 1: Total end energy consumption in Mexico, 2013 (Renewable Energy Prospects: Mexico, 2015)

2. Multilateral agreements on environmental matters

Globally, energy systems are among the biggest sources of emissions which severely compromise public health and cause global climate change.

With the aim of promoting international teamwork and implementing clean energy solutions in terms of the supply, delivery and energy demand which benefits people locally and globally, every country should implement national strategies that try to adopt production and consumption methods that protect the Earth´s ability to regenerate. Countries need to be moderate and efficient in terms of energy use and try to depend more and more on renewable energy sources such as solar energy and wind energy.

According to the United Nations Framework Convention on Climate Change (UNFCCC) we must, as a country, take control of the emission of greenhouse gases into the atmosphere in order to avoid dangerous anthropogenic interference in the climate. For this, economic development must be sustainable.

The Cancun Agreements gave a boost to international negotiations which gave the developing world the necessary technological tools, finance, adaptation and mitigation that form the basis of a greater collective effort to reduce emissions which will bear fruits for all those involved. We need officially registered projects nationally and internationally as part of the UNFCCC.

Mexico has signed bilateral agreements with Canada, US, Germany, Norway, Korea, among others in which they agree on technical cooperation and research into clean energy sources (energy efficiency, capture and storage of carbon, electrical connections, intelligent networks) and into hydrocarbons (transport and chemical treatment of heavy crude oils, unconventional gas); furthermore, we seek an interchange of experiences on the best regulatory practices and methods for designing public policy. The same is true of projects and initiatives which are created to promote the use of renewable energy, innovative technology and energy efficiency as a means of combating climate change.

2.1 Business and the Environment

Essential negotiations concerning business and the environment are being treating in all levels, including: multilateral, regional, bilateral and national. This has presented a challenge for the undersigned countries, given that taking on these commitments if which you do not fulfill, will incur fines because it is not easy to implement a manner of organizing the environment that guarantees the effective fulfillment of environmental legislation and the adequate use of natural resources.

The main multilateral environmental agreements have been signed by most countries; international development banks and agencies Inter-American Development Bank, The World Bank, International Monetary Fund, to mention a few who contribute to the subject of the environment as part of their terms and conditions by donating resources or by giving credit away. The private sector has incorporated the question of the environment in their production processes and has even imposed restrictions on business. Proactive work on the environment is increasingly common in civil organizations working alongside the government; above all in

developing countries which have had to accept the environment as an important factor in regional and bilateral agreements when such agreements are reached with countries such as Canada or the US or with the European Union. In these cases the environment is included as a legal requirement (Murillo C., 2008)

2.2 North American Free Trade Agreement (NAFTA)

The North American Free Trade Agreement is an important first step in terms of the environment as a concern for business. In this agreement environmental legislation is a priority. There is a commitment to making sure that countries respect and improve their own environmental legislation.

Despite the fact that the introduction of some topics about environment in negotiations was initially seen as an imposition, the agreement between Mexico, the US and Canada has been an important step in the development of the environmental subject in Mexico.

A notable contribution came from the promotion of public participation by means of an improved access to information, financing of public projects, public hearings for academic bodies, establishing mechanisms allowing people to report failures to follow national environmental law.

The influence of NAFTA in the institutional nature of the environment in Mexico has been unquestionable. Mexico has improved its public policies and the institutional nature of the environment and although not all changes were made to be adapted to NAFTA. To a great extent the requirements of this agreement are to enhance the process of change.

2.3 Perspectives on Renewable Energy in Mexico: REmap 2030

In 2011, SE4ALL was launched with three related objectives that need to be reached before 2030: assure universal access to energy and modern energy services, double energy efficiency and multiply the universal budget for renewable energy resources. In this context, IRENA has developed a world route for renewable energy (Remap 2030), in which Mexico has decided participate and has declared its objectives for energetic reform before 2030 in which the increase of renewable energy would put Mexico on the right track for reducing greenhouse gases significantly given that it has the potential to reduce the carbon demand in Mexico by 62%, natural gas by 21% and oil by 6% by 2030 (PNASE, 2014).

Among the challenges that Mexico faces we find the raising of consciousness, improving information about renewable energies for politicians, manufacturers, project developers and installers and users. In this way, we will be able to show an idea of how high level renewable energy generation can be incorporated into the transmission system.

According to predictions made by SENER and the Asia-Pacific Economic Cooperation, Mexico has the potential to generate 280 TW hourly of energy from renewable sources in 2030. This represents a six-fold increase on the current level of 48 TW hourly, that could be achieved with a diverse mixture of wind, solar, hydraulic, geothermic and biomass energy.

Wind and solar voltaic energy combined would represent almost 60% of renewable energy generation in Mexico and 26% of the total generation in 2030 (PNASE, 2014). Photovoltaic solar energy could contribute 30 GW in energy generation. This would be 66 TW hourly annually by 2030.

3. Reforms in Mexican legislation

In the energy sector we can identify the need to reach higher levels of production of primary energy, improve transport services, energy storage and distribution; make sure the supply is reliable; improve the efficiency and quality of the product and reduce the cost of electrical and its negative impact. The objective of this is to allow the country to make the most of its energy resources to a greater extent in order to benefit the population.

Until recently, the Mexican constitution hindered the participation of private companies in the production and extraction of energy sources from fossil fuels. This works against the development and adequate distribution of energy. Thanks to energy reforms and the secondary laws that were approved between 2013 and 2014 which allowed private companies to gain contracts the monopoly over the oil industry nationally broke, allowing PEMEX to strengthen its strategic role in the oil industry. It also acted to help competition and the implementation of a national strategy for sustainable industrial development. It also included sustainability as one of the important constitutional criteria to which private and public companies will have to adhere.

Likewise, energy reform takes into account the fact that the energy sector should act in a fashion that promotes

justice, equality, development, democracy and economic growth. In the same sense, the supply of energy should reach all the population. This will boost their potential for development in many senses. With this, we bolster the commitment to improve energy access to communities where it is not currently available. In 2011 around 20% of the population of the world didn't have access to electricity. Of this 20%, 85% were in rural areas. Also, one thousand million more only have intermittent access to electricity; their access is frequently cut (PSE, 2012).

As well as guaranteeing a good quality energy supply at competitive prices. Recent energy reforms have also sought to promote the participation of private generators and, in this way, benefit projects which allow the best use of renewable energy resources. By applying Energy Reforms we hope to gain private investment for energy generation projects and we hope that this private investment can reach 15% of the total investment in the year 2018.

While trying to promote investment into renewable energies, Mexico has worked to create and modify laws that incentivize their use and reduce the dependence on fossil fuels. In the National Plan for Energy we find an objective of 35% of electrical energy being generated with clean technology by the year 2024. The Law for Harnessing Renewable Energies and Financing the Energy Transition sets out the plans and objectives in the current availability and generation of electricity in the country. They follow the objectives set out the in National Development Plan.

Our goal as a country is to try to avoid the use of crude oil in the future. This comes from so-called unconventional resources such as shale gas and deep water. This severely damages the environment during extraction as well as increasing our dependence on fossil fuels for energy production.

3.1 General Laws on Climate Change

The objective of this law is to promote efficient energy practices and the development of low carbon technologies. According to the national objectives for emissions reduction for the year 2020, we must create a system of subsidies that promotes the main advantages of the use of non-fossil fuels, energy efficiency and sustainable public transport. We must also build up a system of incentives that promotes and permits profitable energy generation through means of renewable energies; such as wind, solar and hydraulic energy managed by the Federal Commission for Electricity. The Energy Secretary working with the Federal Commission for Electricity and the Regulatory Body for Energy will promote electrical generation from clean energy sources for at least 35% by the year 2024 (LGCC, 2012).

3.2 Energy Reform

Mexico has made substantial changes to the energy sector in an effort to increase productivity in the country. One of the main goals is to increase the level of investment and jobs available. Also, PEMEX and the Federal Commission for Electricity need to be given greater liberties to modernize. In terms of oil and gas, the reform aims to have a greater production at a lower cost. It also aims to improve competency in refining, transport and storage by involving private companies who adhere to state rules as well as the development of clean technologies.

With Energy Reform, articles 25, 27 and 28 of the constitution were all amended which opened the extraction and exploitation of hydrocarbons to private companies nationally and from abroad. This allows the state to make private service contracts which modernizes and strengthens PEMEX and the Federal Commission for Electricity without privatizing them. They remain completely Mexican companies.

Allowing the country to take full control over the planning and control of the national electricity system works to benefit a competitive system which lowers prices, provides more energy at better prices, guarantees international standards of efficiency, transparency and economic gain which will bring investment to the Mexican energy industry which will, in turn, help the country to develop. These are all other goals we hope to achieve.

In August of 2014 secondary laws on energy reform were passed. The most important of which are new laws such as: the Law on Profits Made from Hydrocarbons, the Law on Mexican Oil Reserves for Stability and Development, the Law on the Electricity Industry, the Law on Geothermic Energy, the Law on Regulatory Bodies for Energy, the National Agency's Law for Industry Safety and Environmental Protection in the Oil Sector, the Hydrocarbons Law, the Law on Mexican Oil, the Federal Commission for Electricity's Law. Other laws which were reformed include: the National Water Laws, the Law on Foreign Investment, the Mining Law,

the Law of Public and Private Associations; the Law of State Entities, Acquisition Laws, the Law of Public Sector Services, the Law of Public Building and Related Services.

3.3 Challenges for Energy Reform

In the electricity industry, clean energy generation is not always the easiest option for the development of new projects. Resources with great potential are in rural parts and to transmit this energy and interconnect the two sites, large-scale developments are required. Furthermore, clean technologies present risks and challenges in terms of use and development.

The state must guarantee the constitutional right to a healthy environment. To achieve this, we must take measures to prevent the deterioration of the environment. We must also sanction those who harm the environment and they should pay for the damage caused. This should be strictly controlled and should allow the best use be made of the available resources. This is an important step on the road to sustainability.

We must take into account that according to the Law for Harnessing Renewable Energies and the Financing of Energy Reform, energy generation from fossil fuels shouldn't exceed 65% of the total. This is a challenging target for the energy sector. This will involve new technologies for generating electricity that use renewable energy resources, such as nuclear and co-generational energy. In this way, we will be able to face up to the challenges of diversification and safety in the energy sector (PNASE, 2014).

In recent years many projects and programs have been developed with the aim of guaranteeing Mexicans' rights to basic electricity services, this idea is supported by the PND. They also want to increase electricity coverage to a greater extent. At the end of 2012, 98.11% of the population had access to electricity. This means that Mexico, on a global scale, is one of the countries with best electricity coverage. However, there are still more than 2.3 million Mexicans who do not have access to this basic service. This is around 42,945 houses (PROSENER, 2013).

4. National plan for energy reform

The national plan tries to regulate the harnessing of renewable energy resources and clean technologies for generating electricity not destined to the public. It also seeks to create a decent strategy with enough support and financing to help Mexico move along the road to energy reform. This includes the use of sustainable, low-carbon systems that help to combat the effects of climate change.

Through political incentives, programs, actions and projects that seek to increase the use of renewable energy resources and clean technology and as a response to the growing demand on energy resources and to the need to have reliable energy system, energy efficiency is highly important.

The transition to a sustainable energy system requires diversification in the energy field, a boost in the use of clean technologies and an efficient harnessing of energy resources that we have at our disposal.

Diversifying energy sources prioritizes the extended use of non-fossil technologies, bio-energies or energy produced by sustainable technologies represent a viable alternative in the process of energy diversification and sustainable development given that they substitute fossil fuels and they also contribute to reducing greenhouse gases into the atmosphere.

Within this framework and with the backing of the Law for the Promotion and Development of Bio-energy and its Control, Mexico has set itself the target of creating a policy to support bioenergy.

We need to increase efficiency in the levels of energy consumption in all sectors to reduce energy losses in the production chain which will lead to a reduction in the environmental impact. A reduction in the use of energy while providing the same level of service contributes to a more rational level of energy consumption.

To reduce the environmental impact caused by the production and consumption for which the energy sector is responsible, we need to create a series of actions focused on prevention, contention, remediation and compensation for the effects it causes. Linking these objectives within the energy and environmental sector is extremely necessary to reduce the environmental impact. Creating projects with similar goals in terms of energy reform and the harnessing sustainable energy are key factors.

Strengthening and modernizing the infrastructure in the energy sector as well as maintaining the reliability and integrity of the system involves efficiency, safety, sustainability, availability and reliability of the energy transmission and distribution lines. Projects focused on an economic infrastructure for electricity aim to create a

reliable and modern transmission network which allows for a better use to be made of Mexico's capacity for energy generation.

5. The potential to generate electricity from renewable resources

During 2013 SENER created the National Inventory of Renewable Energy in which, a geographic system provides information about the electricity generation inventory for public supply, where is possible to see the potential of renewable resources that can be used. In table 1, it is shown an example of the use of these data, in which renewable resources are classified as approved, probable and possible depending in its potential for generating electricity.

Tab 1: Potential for Generating Electricity with Renewable Resources (GWh). Source: PEAER, 2014

Resource	Geothermic	Mini-Hydraulic	Wind	Solar	Biomass
Possible	78799	N/A	87600	6500000	11485
Probable	60286	23028		N/A	391
Approved	892	2378	10513	843	592

5.1 Main projects for investment into renewable energies announce in the PNI 2014-2018

In an attempt to satisfy the increasing demand on the electricity system, we will need to develop a greater potential for generating electricity in accordance with predictions for electricity consumption nationally. In this sense, by using Energy Reform we will be able to complement the Federal Commission for Electricity's investment with the participation of individuals in electricity generation. Private investors will have the potential to generate electricity; with the exception of nuclear energy and form long term contracts with qualified experts in the area.

5.2 Wind farms in the South-East II, III, IV and V.

As a whole, they generate 1169 MW in the South-South-West region. For this project we expect an investment of around 25955 million pesos.

5.3 Small Scale Photovoltaic Solar Panel

This refers to a group of 14 plants each one with a capacity of 30MW to be developed in the north of the country. The total investment of each plant is around 884 million pesos. Together, they will generate 420MW and will require a total investment of 12378 million pesos.

5.4 Mexicali

In Mexicali there is a geothermic plant which produces 27MW. The project is designed to be built in Baja California. The total estimated cost is 267 million dollars.

6. Tenders for potential areas for development

Round Zero is an Energy Reform proposal that tries to directly assign resources for the exploitation of petroleum which guarantees a certain level of investment into PEMEX without the need to tender. This is the way it will work for private companies in later rounds.

Round one has two stages, each one with its respective tender. The first one took place on July 15 2015 where 14 areas of potential in deep waters. The second of these is planned for September 30th in which 9 plants, grouped into 5 contracts will need to be assigned. It is worth mentioning that this work will be coordinated by the National Commission for Hydrocarbons.

In round one, the committee will be made up of the following companies: Sierra Oil & Gas (Mexico), Talos Energy (USA) and Premier Oil (England). From this there were two blocks tendered on and the remaining twelve were considered deserted.

7. Conclusion

Mexico still does not have a clear idea what the implementation of renewable energy implies for the complete supply of energy. However, most laws and initiatives that have been created in the context of sustainable

energy and the substitution of fossil fuels are now considered important and almost obligatory. Possible future projects should include energy reform as something standard and obligatory to be considered.

Despite the fact that the transition to clean energy has been imperious for some years now, if it hadn't been for the international agreements in which Mexico forms part, especially the TLCAN which it signed just a year ago. Without this, Mexico would not have taken an important step on the road to energy reform. The insufficient energy supply at the Canterell Complex, among others, shows that despite having fossil fuels, we cannot continue to depend on them. This is equally true because of its cost of extraction economically as well as for the environment. We also need complex technology for their extraction.

Thanks to Mexico's fortunate location and diversity, it has enough potential to make use of different types of renewable energy. This potential is reflected in projects such as wind farms in Oaxaca and proposed projects for the Special Program for Making the Best Use of Renewable Energy. It is worth mentioning that we currently there are many available ways of gaining economic support for investors and researchers in the field of sustainability, energy efficiency and electricity from non-fossil fuels.

Allowing private investment forms part of the process of energy production and distribution opens the door to the inclusion of technological advances; this helps with efficiency and the use of renewable and fossil fuels given that it is not enough to generate energy purely from clean energies; we also need to make better use of the energy that is produced with the technology currently available. Despite the fact that energy reform was approved principally to allow technological cooperation and improve the production and distribution of energy generated from fossil fuels, it is opportune to allow private companies and national and international scientist to be part of the process. From this we will have a fair access to this service.

Mexico, to all intents and purposes is new in the field of energy from sources other than fossil fuels, it has its problems in Mexican law and the consequences of this are being lived today with unfavorable results from tenders from Round Zero and Round One. We see that there is a degree of mistrust on part of foreign and national investors. This may be the reason why expectations were not met.

As a developing country and as one of the undersigned on many international economic and environmental agreements, Mexico has to fulfill certain environmental commitments. Nevertheless, it has been shown that it is still incapable of reaching these agreements alone. There needs to be a greater role played by the population and the state to ensure that new production mechanisms can be implemented. This must also come from researchers by providing adequate conditions and support so that this task can be brought about. Also, in many international agreements on the environment we can see the role that developed countries should play in this process. This includes economic support but, more importantly, a greater level of cooperation working towards a better planet.

The bases for tenders should be changed and we should consider the conditions for their implementation by private companies that work to generate energy from different available resources. We should always keep the importance of national sovereignty in mind given that it is not easy to chain the system of energy supply so radically when the economy of the country is based largely on fossil resources. However, we need to create a decent productive reconversion program in which innovative programs for renewable energy and energy efficiency are supported.

Despite the legal deficiencies we may still be experiencing their possible future reforms, as well as economic instability, we have before us a great opportunity which we did not have previously. The opening of the market to private investors and the restructuring of the energy system which includes extraction and distribution, these tasks previously belonged exclusively to the state and are now allowing the support of third parties to reduce Mexico's technological stagnation.

Recently, it was declared that Mexico should have 35% of its electricity generated from renewable

resources. To reach this goal will require large scale legal reform. This work should be done in a team to achieve a higher percentage production from non-fossil fuels; in this way the Mexican government will be able to achieve its goals. In this regard, it is well known that Mexico has great potential and as such, it is an opportune moment to implement projects that meet current needs determined by programs designed to mitigate environmental damage and that help economically too. Investing in renewable energies is not particularly high risk given their high potential for development. In the same sense, for the proposed objective to be reached, adequate support is required for those who can help the country to reach its goals.

In conclusion, Mexico needs to improve in many areas: legislation, economy, energy supply, among others but if we do not allow and contribute to a generation of change by putting our faith in the country, it is very possible that the process of change will be severely held back.

8. References

Bibliography

Consejo Mexicano de Asuntos Internacionales,2013.Cuaderno de Trabajo México ante la Revolución Energética, D.F., México.

Consejo Mexicano de Asuntos Internacionales,2014. Apuntes sobre las Iniciativas de Leyes Secundarias de la Reforma Energética, D.F., México.

Murillo C., 2008. La Cooperación ambiental en los tratados de libre comercio,D.F., México.

Documents

BNE, Balance Nacional de Energía, 2013, Secretaría de Energía, México.

ENE, Estrategia Nacional de Energía, 2014, Secretaría de Energía, México.

ENTEASE, Estrategia Nacional de Transición Energética y Aprovechamiento Sustentable de la Energía, 2013, México.

Informe sobre la participación de las energías renovables en la generación de electricidad en México, al 31 de diciembre de 2013, 2014, Secretaría de Energía, México.

LAERFTE, Ley para el Aprovechamiento de Energías Renovables y el Financiamiento de la Transición Energética, 2013, Cámara de Diputados del H. Congreso de la Unión, México.

LANSI, Ley de la Agencia Nacional de Seguridad Industrial y de Protección al Medio Ambiente del Sector Hidrocarburos, 2014, Cámara de Diputados del H. Congreso de la Unión, México.

LASE, Ley para el Aprovechamiento Sustentable de la Energía, 2008,Cámara de Diputados del H. Congreso de la Unión, México.

LCFE, Ley de la Comisión Federal de Electricidad, 2014, Cámara de Diputados del H. Congreso de la Unión, México.

LCRE, Ley de la Comisión Reguladora de Energía, 2008, Cámara de Diputados del H. Congreso de la Unión, México.

LEG, Ley de Energía Geotérmica, 2014, Cámara de Diputados del H. Congreso de la Unión, México.

LGCC, Ley General del Cambio Climático, 2012, Cámara de Diputados del H. Congreso de la Unión, México.

LH, Ley de Hidrocarburos, 2014, Cámara de Diputados del H. Congreso de la Unión, México.

LORCME, Ley de los Órganos Reguladores Coordinados en Materia Energética, 2014, Cámara de Diputados del H. Congreso de la Unión, México.

LPDB, Ley de Promoción y Desarrollo de los Bioenergéticos, 2008, Cámara de Diputados del H. Congreso de la Unión, México.

LPM, Ley de Petróleos Mexicanos, 2014, Cámara de Diputados del H. Congreso de la Unión, México.

PEAER, Programa Especial para el Aprovechamiento de Energías Renovables, (014, Secretaría de Energía, México.

PNASE,Programa Nacional para el Aprovechamiento Sustentable de la Energía, 2014, México.

PNI, Programa Nacional de Infraestructura, 2014, Secretaría de Hacienda y Crédito Público, México.

PROSENER, Programa Sectorial de Energía, 2013, Secretaría de Energía, México.

PSE, Prospectiva del Sector Eléctrico 2012-2026, 2012, Secretaría de Energía, México.

Reforma Energética,2014, PenchynaGrub, David.Senado de la República LXII Legislatura, México.

Web references

Comission for Saving Electrical Energy, June 2015.

http://www.fide.org.mx/index.php?option=com_content&view=article&id=108&Itemid=180

International Energy Agency, August 2015.

http://www.iea.org/statistics/statisticssearch/report/?year=2012&country=MEXICO&product=Balances

http://www.iea.org/statistics/statisticssearch/report/?year=2012&country=Mexico&product=Indicators

Letter from Earth Charter in Action, , June 2015.

http://earthcharterinaction.org/contenido/pages/Lea%20la%20Carta%20de%20la%20Tierra

Memorandum of Understanding on the subject of cooperation on the environment: signed by the Republic of Korea and the Secretary for the Environment and Natural Resources in Mexico, July 2015.

http://www.semarnat.gob.mx/archivosanteriores/temas/internacional/Lists/AcuerdosInt/Attachments/142/MDE%20SEMARNAT%20-%20Corea%20-%20Protecci%C3%B3n%20ambiental%20-%20Esp.pdf

Multilateral Agreements on the Environment, SEMARNAT, Secretary for the Environment and Natural Resources,June 2015.

http://www.inecc.gob.mx/ai-convenios

Office for Diplomatic Information, June 2015.

http://www.exteriores.gob.es/documents/fichaspais/mexico_ficha%20pais.pdf

Secondary Law Initiatives, President of Mexico, Mexico, August 2015.

http://presidencia.gob.mx/reformaenergetica/#!leyes-secundarias

Secretary for Energy, August 2015.

http://www.sener.gob.mx/portal/Default.aspx?id=2918

http://sie.energia.gob.mx/bdiController.do?action=cuadro&cvecua=IE0C01

Secretary for Energy, Program for Making the Best Use of Renewable Energies, 2014.

http://vmwl1.iie.org.mx/sitioIIE/sitio/control/11/6PEAER2014-2018.pdf

The Role of Hydrocarbons in Energy Reform, June 2015.

http://sustentabilidad.energia.gob.mx/res/ProyectoFSE03.pdf

Conference Proceedings

Solar World Congress 2015
Daegu, Korea, 08 – 12 November 2015

Solar for All (Making Solar Available to Everyone), Striking a Balance for Sustainable Growth

Ignacio R. Smith[1] and Sherry Mc Millan[2]

[1] SM Solar and Wind Energy Systems Limited, Port of Spain (Republic of Trinidad and Tobago)

[2] SM Solar and Wind Energy Systems Limited, Port of Spain (Republic of Trinidad and Tobago)

Abstract

A lot of effort is being placed on bridging the gap and allowing the financially challenged sector of the population to reap the benefits of solar. However, the biggest hurdle for local and state governments is the impact that these programs may have on their treasuries. So what can regulators and decision makers do, to fund these programs efficiently.

The merging of Community Based Solar initiatives in combination with enhanced revolving funds accompanied by a change in the utility business model, can generate sustainable growth and allow everyone to enjoy cleaner forms of electricity generation.

The key is to strike a balance among all these strategies so that the subscribers will be able to access the service.

Keywords: Cash flow, Pigovian Tax, Paradigm Shift, and Community Solar.

1. Introduction

The energy requirements of the world are in a state of constant growth, this demands greater improvements in generation, transmission and distribution of electricity. The increasing demand is coupled with the need for considerable reductions in the fossil fuel bill making economic growth extremely difficult.

When faced with a reduction in their fossil fuel bill, countries also encounter challenges in areas, such as: high ratio of debt to Gross Domestic Product; low Income per Capita and absence of a legal framework for alternative generation and / or in a setting of subsidized Levelized Cost of Electricity.

Governments in developing countries seek solutions that can create jobs and job opportunities while reducing the dependency on fossil fuels, reduce its annual budget deficit that constrains its expenditure on developmental initiatives, and last offer diversification away from our predominant source of income, to overcome the boom and bust cycles to which single product economies are always exposed too.

As the countries in Latin America and the Caribbean grapple with a difficult path to economic growth with the on-going economic downturn, what can we do to bring change, what savings will it represent, how do we face these challenges, without creating additional burden to the treasury.

Opportunities and market conditions can differ from Region to Region; however, in Latin America and The Caribbean, there are several patterns that are common to most, these trends and conditions are:

— **Subsidies**. For most of Latin America and the Caribbean power generation, transmission and distribution is provided by the state at a price that gives access to the bulk of the population. This hides the true cost of the service from the subscriber promoting inefficiencies.

doi:10.18086/swc.2015.09.02 Available at http://proceedings.ises.org

- **Poverty**. For many years it was believed that Globalization was the key answer to economic growth, reduction of poverty, etc. Although this might be true, the Caribbean and Latin America has not benefit entirely from this growing trend. Poverty and growth are issues carry a high priority in governments on this side of the world.
- **Competition**. Market forces demand that companies competing in the global arena become more efficient. As they seek lower production costs, the demand more energy efficient systems.
- **Limits in Power Generation and Supply**. Generally speaking the demand for electricity expands faster than its supply. It is a fact that many developing nations experience a shortage in their supply that often threaten economic growth.
- **Environmental concerns**.

Given the current state of affairs, it is safe to say that emerging markets pose a unique opportunity to alternative energy solutions. It is in this context that it is important that governments have the vision to implement such solutions, and in so doing, improving the quality of life of their citizens.

In seizing the opportunity emerging market governments must realize that the implementation of such solutions will have to compete for financial and other resources that may be otherwise used for development projects. However, in executing their vision for the improvement of the life of the citizens, governments must make hard choices in order to guarantee the sustainability of their countries' economies.

There is a need to institute a balance between the people, time, resources and deliverables – an important aspect that it is not usually considered in economic models - a subject which has been the debate among many economists.

It is often difficult to balance economic growth models while satisfying the needs of the less fortunate. As expressed by Finn Kidland and Norman C. Prescott in their classic 1977 article "Rules vs. Discretion" which points to the fact that a:

> *"**Time-inconsistent policy may make the public happy in the short run but will ultimately fail to produce the long-run policy goal. A time-consistent policy, in contrast, nails the long-run policy goal but does not make people happy in the short run."***

Hence the reason why pondering the long term policy goals vs. the immediate goals is so important. Trinidad and Tobago is in no way different to any of its neighbors in the Caribbean and Latin America. Everyday our governments are faced with time inconsistent decisions and time consistent policy.

The renewable energy market is no different, solar power; wind generation, solar thermal and its counterparts face these crossroads. In a highly subsidized electricity generation industry responsible for dumping some fourteen million tons of carbon dioxide into the atmosphere, how is it possible to bring on stream electricity generation by means of renewable energy which have significant startup cost to the end user, way in excess to what they are currently paying.

To policy makers the answer is easy, maintain status quo – a time-inconsistent policy. Add the fact that main sources of revenue are under pressure, treaties that you are in breach of, a stagnant economy and rising unemployment, a formula for a very fragile, increasingly skeptical and hostile environment. The question must be put forward, time-consistent or time-inconsistent. Clearly, the population will favor a time-inconsistent policy. The question remains – what consequences will this policy have in the near future?

In contrast, choosing a time-consistent solution can be a cause for concern among the population making the policy an unpopular one. It then becomes a question of good governance, making a hard choice now which will benefit future generations.

This is the dilemma facing the renewable energy industry today, curb carbon dioxide emissions or hinder immediate economic growth.

2. Programs

Over the years research has shown that the development of a strong Solar Electric Generation Industry is tied three basic elements:

- Gross Domestic Product per Capita,
- Having a Legislation to Support the Industry,
- Levelized Cost of Electricity that will allow the penetration of Photovoltaic.

Figure 2.1 Elements that Support a Solar Electric Generation Industry

For Latin America and the Caribbean, we notice that one or two of the three elements are always missing, the chart below shows countries that have had a successful migration from fossil fuels to cleaner forms of electricity generation and those that are currently trying to move towards that path (Table 2.1).

Country	GPD per Capita in Real Values Expressed in US$	Energy from Renewables		
		Wind Power in Gwh	Biomas	Solar
Germany	$ 41,514.00	45,300.00	40,900.00	28,000.00
Spain	$ 29,195.00	42,400.00	9,120.00	7,280.00
Italy	$ 33,049.00	13,333	9821	18,637
Japan	$ 46,720.00	4,350.00	2,310.00	3,800.00
United States	$ 49,965.00	70,800.00	54,300.00	808.00
Trinidad and Tobago	$ 17,934.00	0.00	0.00	0.00
Venezuela	$ 12,767.00	0.00	0.00	0.00
Mexico	$ 9,742.00	86.75	823.00	9.00

Table 2.1

2.1 Paradigm Shift

A lot of ideas have been put forward to bridge the gap for solar electricity generation, notwithstanding, one model that comes to mind is the Grid Tied Utility Assisted Model, due to its nature, this paradigm shift in the way utility conducts their activities, offers a smooth transition from fossil fuel power generation systems to cleaner forms of energy, mainly solar and wind power systems in an environment of subsidized rates and in the absence of a legal framework.

This is achieved utilizing the Utility Company as the vehicle for change. Instead of being another player, the Utility acts as the supplier of the solar modules and /or other forms of alternative energy, by means of a lease agreement. The subscriber provides the space for the unit or units; the Utility provides the installation and sale of electricity power by leasing the power generating system where the homeowner pays the Utility the rate currently applied.

Because the equipment is leased to the property holder, the excess power goes back to the grid at no benefit to the homeowner. This cogeneration arrangement permits the gradual adjustment of rates, while reducing inflationary fears.

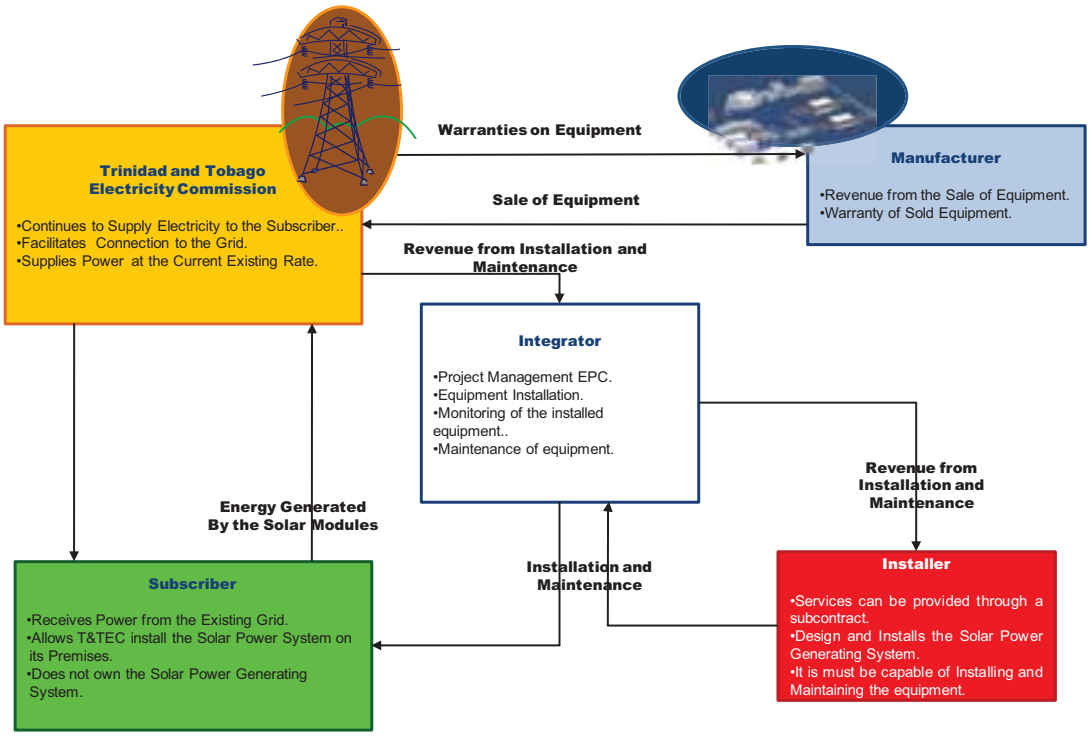

Figure 2.1.1, Inner workings of the Grid Tied Utility Assisted Model

2.2 Enhanced Revolving Fund

Unlike financial instruments such as Climate Bonds, Zero Coupon Indexed Bonds and other mechanisms used in investing in renewable energy projects, an Enhanced Revolving Fund is a mandatory contribution imposed on the industries that account for at least seventy percent (70%) of the GHG emissions released, in the form of tax. The program would mirror a trust fund that will use these contributions to finance small distributed generation projects.

An initiative such as this, is essentially a localized, downsized version of the United Nations Convention on Climate Change Clean Development Mechanism, with one fundamental difference, funding is made available to anyone who complies with the requirements.

Such schemes can operate under the supervision of Multilateral Organizations. Its primary function is the award of grants to allow organizations interested in migrating from fossil fuel electricity generation to renewable forms of electricity generation (PV and / or Wind).

The collection monies come from mandatory contributions made from the major players responsible for Carbon Dioxide Emissions and the Certificates of Emission Reductions generated in the process. This Pigouvian Tax Regime System imposed by Governments of the Region can look at: 0.5% of the total revenue of the organization and / or a ten percent 10% of the country's total carbon dioxide emissions (Table 2.2.1) at a rate of US$ 3.50 per CO_2 per ton. Similar to CDMs, guidelines for the approvals of projects must be in place. Once approved, the recipient will be in a position to give back to fund in the form of Certificates of Emission Reductions. These CERs can then be used to offset CO_2 emissions from those companies who have made payments to the fund.

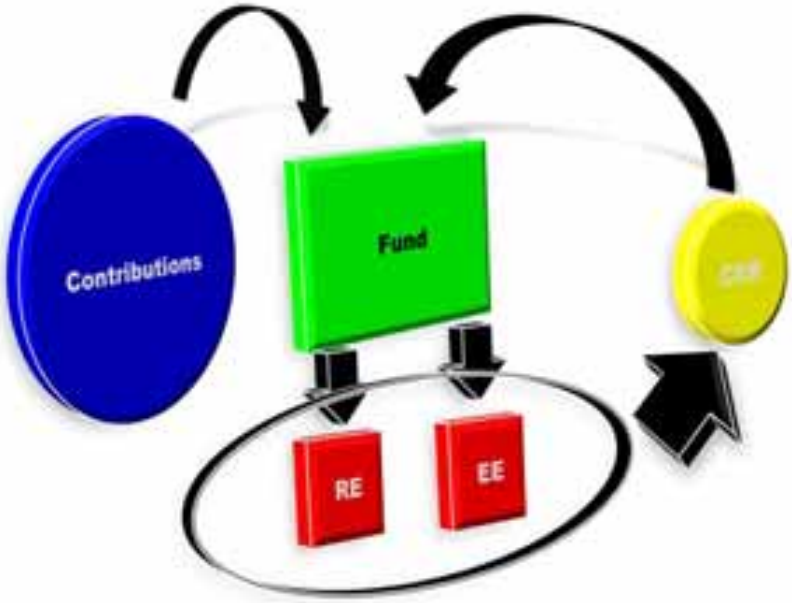

Figure 2.2.1, Enhanced Revolving Fund

The thought of using a neutral body to act the regulator and to pool the resources of the region, will move the Caribbean and Latin America closer to significantly reducing their CO_2 while democratizing renewable energy.

Country	Millions of CO2 Tons per Year
Argentina	191
Brazil	475
Venezuela	183
Trinidad and Tobago	52
Chile	80
Colombia	71
Peru	38
Puerto Rico	29
Dominican Republic	21
Ecuador	29
Total	**1,169**

Table 2.2.1

The Collection of ten percent (10%) of a total of 1,688,909,000 Tons that the Region generates at the above mentioned Carbon Dioxide per ton rate will yield US$ 590,000,000 a year, which will translate to 234 Mega Watts of Distributed Generation installed per year. At such levels the Enhanced Revolving Fund will in a position to remove from the less fortunate nations of the region their dependency of fossil fuels in a short space of time (Table 2.2.1).

2.3 Community Solar

Another model that has gained a lot of acceptance in recent years has been the creation of co-operative by communities with the purpose of using their pooled resources to provide electricity to their community members (Figure 2.3.1).

Figure 2.3.1 Graphic Representation of a Community Solar Initiative

Based on motives, the format of a community solar may vary. But undoubtedly, the most commonly used formats of this type of agreement are as follows:

- Utility Sponsored Model,
- Special Purpose Entity,
- Non – Profit "Buy a Brick" Model.

Notwithstanding, and depending on the financial benefits that the community solar format is pursuing, these alternatives can be divided as follows:

- Allocation of Cost and Benefits,
- Financial and Tax Considerations,
- Other Legal Issues.

Ultimately, when a group of people or community chooses an arrangement such as the one we have just described, they understand the complexity of the project that they are going to undertake and different elements that a venture of this nature entails.

3. Striking a Balance

Many solutions come to mind, however, the most popular and effective ones are those that we are currently considering. We begin with The Grid Tied Utility Assisted Model with roots originating from the Property Asses Clean Energy Program and the Solar Power Purchase Agreement. Then there are Community Based Solar Initiatives and last the consolidation of a Pigovian Tax System.

Bear in mind that all the proposals above mentioned qualify for Certificates of Emission Reductions, which at the end add that element that improves the returns on any of the projects that can be undertaken.

The question of striking a balance is not one that can be answered in simple terms, however, in maximizing the use of the resources, Gross Domestic Product per Capita, CO2 emission generation and society stratification play important roles.

Notwithstanding, by establishing the energy needs of the different sectors of the population, we can determine what program or combination of program works best, and therefore minimizing the levels of investment which otherwise would have been disbursed if just one solution had been considered (Figure 3.1).

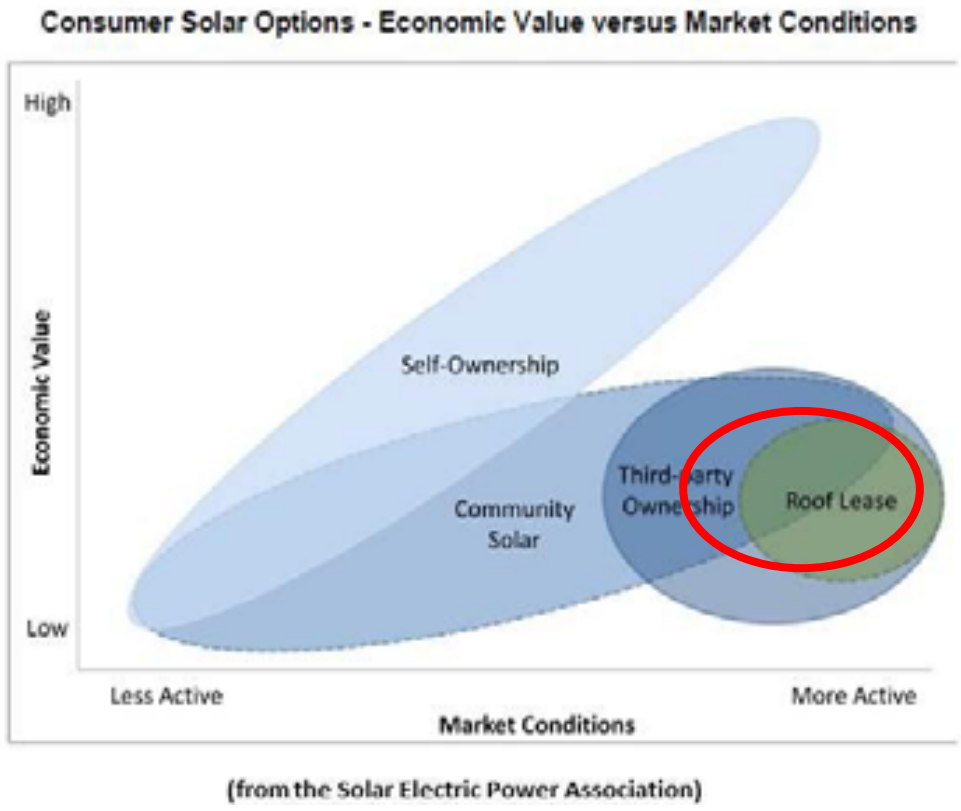

Figure 3.1

This is achieved by developing a linear model where the objective is to maximize photovoltaic penetration subject a group of constraints. Where the objective function represents what we intend to maximize or minimize and the constraints symbolize the limitation to which the model is subject to.

Our model can be expressed as follows:

Max Total PV Penetration: Max: $\sum c_i x_i = c_1x_1 + c_2x_2 + \ldots\ldots\ldots\ldots\ldots + c_nx_n$

Subject to:

$c_1x_1 + \ldots\ldots\ldots\ldots\ldots\ldots\ldots\ldots\ldots\ldots + c_nx_n < m_1$

.

.

.

$c_mx_m + \ldots\ldots\ldots\ldots\ldots\ldots\ldots\ldots\ldots\ldots + c_nx_n < m_n$

Once the model is constructed, we determine the value of our variables by applying the simplex method. After several iterations, for a population with a low GDP per capita, where the population is skewed more to low middle and low income.

The solution is weighted to a combination of an enhanced revolving with a Grid Tied Utility Assisted model.

Figure 3.2 Graphical Representation of the Results of the Model

CONCLUSIONS

The benefits of undertaking such a venture are many, however, we will limit ourselves to listing those that we consider to be the most important ones, they are as follows:

- **Reduction In Carbon Dioxide Emission**
- **Elimination of the Gas Subsidy**
- **Job Creation**
- **Export Opportunities**
- **Boost to the local assembly industry**
- **Downstream Development**

Benefits to the Nations

- **Creates permanent jobs –** nationwide and across a range of skills**.**
- **Promotes energy security** – without federal regulation or taxes that drive up energy costs.
- **Avoids costly power plants** – increasingly difficult to site.
- **No budgetary impact** - voluntary participants pay all fees and expenses.
- **Improves air quality** - reduced exhaust emissions make communities healthier.

Benefits to Property Owners

- **No upfront cost** - financing spreads costs over the life of UTILITY return on their investment.
- **Owners save money** – The absence of financing reduces the homeowner bill for the equipment that at the end of the period can be bought for residual value amount thereby allowing for the widest possible participation by the national community.
- **Assessment transfers upon sale** - new owner benefits from improvements that stay with the property.
- **Safety** - assured by best practices and guidelines established to protect all program participants.

— **Broad applicability** – residential, industrial and commercial properties. Cross border, government or privately owned Electricity Companies.
— **Voluntary** Homeowners benefit from the improvements.
— **Comfort** – efficient buildings are healthier and more comfortable.

4. References

References

1. Bloom Energy website, http://bloomenergy.com/benefits/save-money-and-the-environment/, 2010.
2. Dr. Anilla Cherian, **"Bridging the Divide Between Poverty and Climate Change Through Sustainable and Innovative Energy Technologies",** 2009.
3. Environmental Protection Agency website, Green Power Partnership, **"Solar Power Purchase Agreement"**, http://www.epa.gov/greenpower/buygp/solarpower.htm, 2008.
4. Finn Kidland and Edward Prescott, **"Rules vs. Discretion"**, 1977.
5. Friends of the Earth, **"Power Failure:** How the World Bank is Failing to Adequately Finance Renewable Energy for Development", 2005.
6. International Energy Agency, **"PV for Rural Electrification in Developing Countries - A Guide to Capacity Building Requirements"**, 2003.
7. James Crichtfield, U.S. EPA, **Solar Power Purchase Agreements"**, 2009.
8. Kristy Hamilton, **"Scaling up Renewable Energy in Developing Countries: finance and investment perspectives"**, 2010.
9. Matthew H. Brown, "**On Bill Financing, Helping Small Business Reduce Emissions and Energy Use While Improving Profitability"**,2009.
10. Murray J. Height, Department of Chemical Engineering, Massachusetts Institute of Technology, **"Sustainable Energy**", 2000.
11. National Renewable Energy Laboratories, **"Renewable Energy Cost Curve"**, 2005.
12. New York Mercantile Exchange website, **"Natural Gas Prices – Spot Henry Hub"**, http://www.naturalgasprice.net/natural-gas-price-images/natural-gas-spot-henry-hub.jpg, 2011.
13. Robert E. Marguolis, **"Solar Energy: Market Trends and Dynamics**", 2009.
14. The Rahus Institute, **"The Customer's Guide to Solar Power Purchase Agreement"**, 2008.
15. Thomas L. Chandler, **"A Greener Way To Get Electricity from Natural Gas"**, MIT News, 2009.
16. United Nations Development Program, **"HUMAN DEVELOPMENT REPORT Overcoming Barriers: Human Mobility and Development"**, 2009.
17. U.S. Department of Energy website, **"Property-Assessed Clean Energy Program (PACE)"**, http://www1.eere.energy.gov/wip/solutioncenter/financialproducts/pace. 2009.
18. Van der Geer J, Hanraads JAJ, Lupton RA. The art of writing a scientific article. *J Sci Commun* 2000;**163**:51–9.
19. Strunk Jr W, White EB. *The elements of style*. 3rd ed. New York: Macmillan; 1979.
20. Mettam GR, Adams LB. How to prepare an electronic version of your article. In: Jones BS, Smith RZ, editors. *Introduction to the electronic age*, New York: E-Publishing Inc; 1999, p. 281–304
21. http://www.weforum.org/issues/global-competitiveness
22. http//www.siteresources.**worldbank**.org/DATASTATISTICS/..
23. http://www.carbonplanet.com/country_emissions
24. http://www.eia.gov/cfapps/ipdbproject/IEDIndex3.cfm?tid=90&pid=44&aid=8
25. http://www.epa.gov/climatechange/science/indicators/ghg/**global-ghg-emissions.**html
26. http://www.energypost.eu/eu-emissions-trading-scheme-can-saved-price-band/
27. http://www.investopedia.com/terms/n/npv.asp
28. http://www.investopedia.com/terms/i/irr.asp

Conference Proceedings

Solar World Congress 2015
Daegu, Korea, 08 – 12 November 2015

Economics of global gas-to-liquids (GtL) fuels trading based on hybrid PV-Wind power plants

Mahdi Fasihi, Dmitrii Bogdanov and Christian Breyer

Lappeenranta University of Technology, Lappeenranta (Finland)

E-mails: mahdi.fasihi@lut.fi, dmitrii.bogdanov@lut.fi, christian.breyer@lut.fi

Abstract

With growing demand for transportation fuels such as diesel and concerns about climate change, this paper introduces a new value chain design for transportation fuels and a respective business case taking into account hybrid PV-Wind power plants. The value chain is based on renewable electricity (RE) converted by power-to-gas (PtG) facilities into synthetic natural gas (SNG), which is finally converted to mainly diesel in gas-to-liquid (GtL) facilities. This RE-diesel can be shipped to everywhere in the world. The calculations for the hybrid PV-Wind power plants, electrolysis and methanation are done based on annual full load hours (FLh). A combination of 5 GW_p single-axis tracking PV and wind power have been applied. Results show that the proposed RE-diesel value chain is competitive for crude oil prices within a minimum price range of about 121 - 191 USD/barrel (0.67 – 1.06 €/l of diesel production cost), depending on assumptions for cost of capital, available oxygen sales and CO_2 emission costs. RE-diesel is competitive with conventional diesel from an economic perspective, while removing environmental concerns. The cost range would be an upper limit for the conventional diesel price in the long-term and RE-diesel can become competitive whenever the fossil fuel prices are higher than the level mentioned and the cost assumptions expected for the year 2030 are achieved. A sensitivity analysis indicates that the RE-PtG-GtL value chain needs to be located at the best complemented solar and wind sites in the world combined with a de-risking strategy and a special focus on mid to long term electrolyzer efficiency improvements. The substitution of fossil fuels by hybrid PV-Wind power plants could create a PV-wind market potential in the order of terawatts.

Keywords: *Hybrid PV-Wind, Power-to-gas (PtG), SNG, Gas-to-liquids (GtL), Power-based fuels, Economics, business model, Argentina*

1. Introduction

The demand for transportation fuels is high in the world and it is growing (IEA, 2014), but fossil fuel resources are limited and we do not know how much affordable crude oil is available for transportation fuels in the long-term (EWG, 2013). Besides, it is still impossible to use electricity in some sectors, like aviation. On the other hand, our planet is facing a dramatic climate change problem (IPCC, 2014), thus even with adequate fossil fuel reserves, CO_2 emissions still would be a limiting constraint in the long-term (Carbon Tracker, 2013; 2015). Methanation (PtG) plants (Breyer et al., 2015) converting electricity into synthetic natural gas (SNG) and Gas-to-Liquids (GtL) plants (Wood et al., 2012) converting natural gas (NG) to liquid fuels (with higher heating value and easier transportation) already exist on a commercial scale.

By using solar photovoltaic (PV) and wind energy based renewable electricity (RE) for PtG and GtL plants, RE-SNG and then RE-diesel can be produced, respectively, to overcome the constraints of resource limitation and CO_2 emissions in the conventional diesel value chain. Figure 1 shows the simplified value chain of the whole process. The main components are: hybrid PV-Wind plants, electrolyzer and methanation plants, CO_2 from air scrubbing units, syngas production unit, Fischer-Tropsch synthesis plant, products upgrading plant and fuels shipping. The integrated system introduces some potentials for utilization of waste energy and by-products. This will also result in the elimination of some sub-components of the major components of the integrated system, such as gas treatment facilities and oxygen production units, which will increase the overall efficiency and will decrease the costs.

Selection and/or peer review under responsibility of Scientific Committee
doi:10.18086/swc.2015.09.03 Available at http://proceedings.ises.org

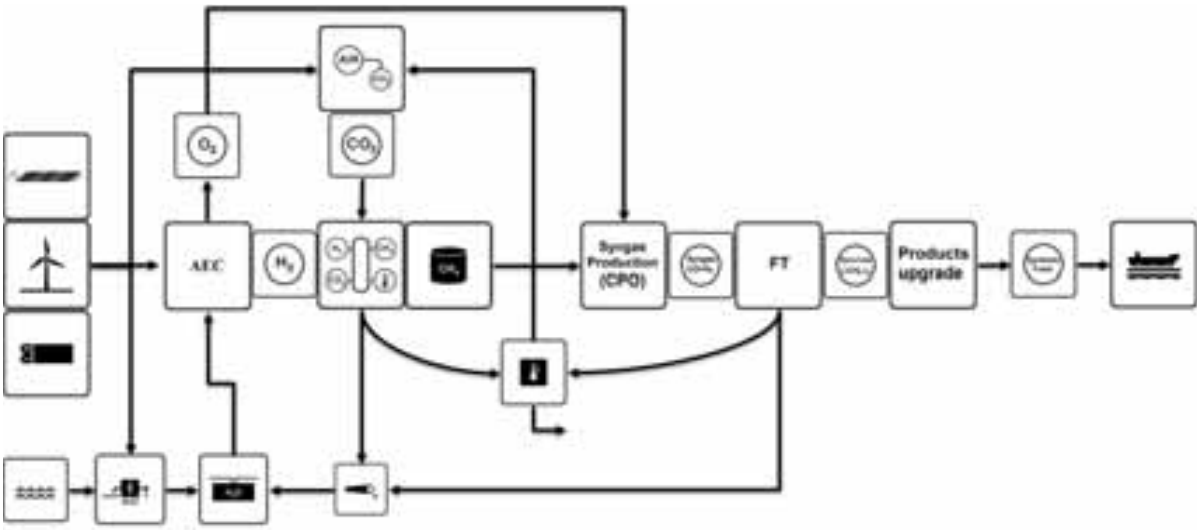

Fig. 1: The hybrid PV-Wind-PtG-GtL value chain. The main components are: hybrid PV-Wind plants, electrolyser and methanation units, CO_2 from air scrubbing units, syngas production unit, Fischer-Tropsch synthesis unit, products upgrading unit and fuels shipping. Abbreviations: alkaline electrolysis (AEC), catalytic partial oxidation (CPO), Fischer-Tropsch (FT) and reverse osmosis desalination (RO).

There are several technical options to produce hydrocarbon fuels based on hybrid PV-wind plants for the transport and mobility sector: mainly RE-PtG, RE-PtG-LNG (Fasihi et al., 2015), RE-power-to-liquids (PtL) and RE-PtG-GtL. All options can be used to buffer and store intermittent renewable electricity. This paper is focused on the RE-PtG-GtL option. Some mobility sectors like aviation, maritime transportation or heavy vehicles cannot be easily operated by batteries or natural gas (NG). Thus even in the long term, liquid hydrocarbon fuels will have a high demand. PtL is the technology to produce liquid fuels directly from renewable electricity, water and CO_2, but this technology is still under development. On the other hand, PtG and GtL technologies are well known and already run on an industrial scale. Thus, in the short term, PtG-GtL seems to be the applicatory method to produce RE-liquid fuels. This paper is an attempt to investigate the costs of this value chain.

2. Methodology

The RE-diesel production system has been divided into two main parts: RE-based SNG production and the GtL downstream value chain. In this paper, two models are used for describing the SNG production for considerations on an annual, but also on an hourly, basis.

The Annual Basis Model represents a hybrid PV-Wind power plant with 5 GW capacity for both single-axis tracking PV and Wind energy. The cost assumptions are based on expected 2030 values and that highly cost competitive components can be sourced for such very large-scale investments. No fixed tilted PV or battery is considered to be part of the plant and the produced electricity and respective calculations are based on annual full load hours (FLh) of the hybrid PV-Wind plants, which can be seen in **Table 1**. The estimate on an annual FLh basis can be surprisingly accurate if applied carefully (Breyer et al., 2011; Pleßmann et al., 2014). The annual basis plants' specification can be seen in **Table 2**. An important piece of information is the level of curtailment, or so-called overlap FLh, i.e. an equivalent of energy which cannot be used. For the special case of hybrid PV-Wind plants, a conservative estimate is 5% (Gerlach et al., 2011). This model will give a rough estimation of a system working with equal PV and wind power capacity.

The Hourly Basis Model uses the optimised combination of PV (fixed-tilted or single-axis tracking), wind power and battery capacity based on an hourly availability of the solar and wind resources to minimize the levelized cost of electricity (LCOE) and cost of SNG. Low cost batteries are added to harvest the excess electricity during overlap times to increase the FLh whenever it is beneficial. More detailed information for this approach is provided by Fasihi et al. (2015).

The full GtL value chain is only analyzed within the annual basis model because with gas storage for output SNG, the GtL plant can work on baseload conditions, which is the cost optimal solution for the GtL value chain.

The equations below have been used to calculate the LCOE of hybrid PV-Wind power plants and the subsequent value chain. Abbreviations: capital expenditures, *capex*, operational expenditures, *opex*, full load hours, *FLh*, fuel

costs, *fuel*, efficiency, η, annuity factor, *crf*, weighted average cost of capital, *WACC*, lifetime, *N*, performance ration, *PR*, overlap FLh, *overlap*.

$$LCOE_i = \frac{Capex_i \cdot \mathrm{crf} + Opex_{i,fix}}{FLh_i} + Opex_{i,var} + \frac{\mathrm{fuel}}{\eta_i} \quad \text{(Eq. 1)}$$

$$\mathrm{crf} = \frac{\mathrm{WACC} \cdot (1+\mathrm{WACC})^{\mathrm{N}}}{(1+\mathrm{WACC})^{\mathrm{N}} - 1} \quad \text{(Eq. 2)}$$

$$FLh_{PV,el} = PV_{irradiation} \cdot PR \quad \text{(Eq. 3)}$$

$$LCOE_{gross} = \frac{Wind_{FLh} \times Wind_{LCOE} + PV_{FLh} \times PV_{LCOE}}{(Wind_{FLh} + PV_{FLh})} \quad \text{(Eq. 4)}$$

$$LCOE_{net} = \frac{LCOE_{gross}}{1 - \mathrm{overlap}} \quad \text{(Eq. 5)}$$

2.1. Power-to-SNG

2.1.1. Hybrid PV-Wind power plant and battery

In this research, hybrid PV-Wind power plants are taken into account as the resource of renewable electricity. The hybrid PV-Wind power plants should be located in the regions of very high FLh to reduce LCOE of power production and subsequently the LCOE of electrolysis and methanation. **Figure 2** shows the FLh for hybrid PV-wind power plant sites in the world, where the best sites are indicated by a red colour coding. In this study, the plant is located in Patagonia, Argentina, which is among the best places in the world for solar and wind resources. The produced RE-based hydrocarbons are assumed to be shipped to Rotterdam in the European Union.

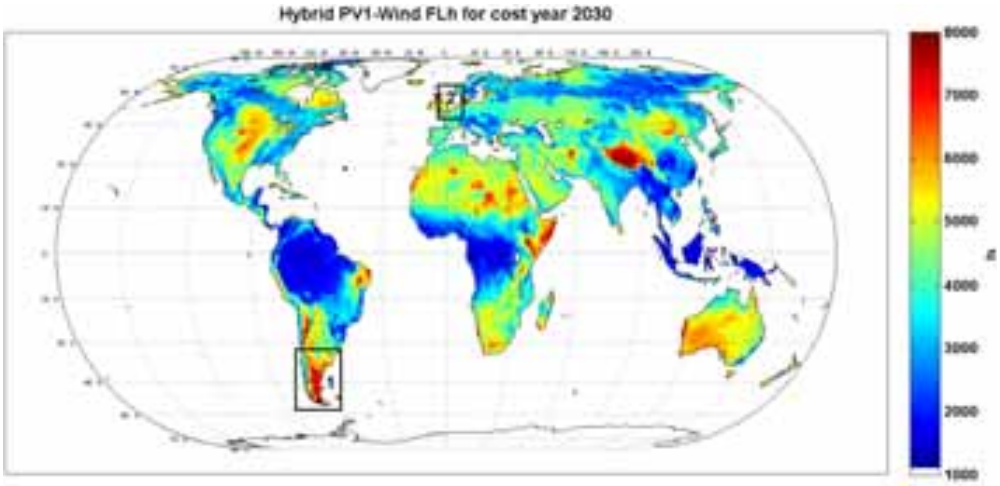

Fig. 2: World's hybrid PV-Wind power plant FLh map. The numbers refer to the place of RE-diesel production (1) and diesel demand (2).

Tab. 1: Hybrid PV-Wind power plant specification. Abbreviations: capital expenditures, *capex*, and operational expenditures, *opex*.

	Unit	Amount		Unit	Amount
PV fixed-tilted			*Wind energy*		
Capex	€/kWp	500	Capex	€/kW	1000
Opex	% of capex p.a.	1.5	Opex	% of capex p.a.	2
Lifetime	years	35	Lifetime	years	25
PV single-axis tracking			*Battery*		
Capex	€/kWp	550	Capex	€/kWh$_{el}$	150
Opex	% of capex p.a.	1.5	Opex	% of capex p.a.	6
Lifetime	years	35	Lifetime	years	10
			Cycle efficiency		90

Tab. 2: Hybrid PV-Wind power plant specification for annual analysis scenario

	Unit	Amount		Unit	Amount
Irradiation (*single-axis*)	kWh/(m²·a)	2410	PV single-axis FLh	h	2000
PV performance ratio (PR)	%	83	Wind FLh	h	5200
PV yield	kWh/kWp	2000	PV and Wind overlap	%	5
			Hybrid PV-Wind FLh	h	6840
Installed capacities					
PV single-axis installed capacity	GWp	5			
Wind installed capacity	GW	5			

2.1.2. Electrolysis and methanation

SNG production consists of two main steps: hydrogen production (Eq. 6) and methanation (Eq. 7), which are shown in **Figure 3**. Water and electricity are the inputs for the electrolysis plant, while electrical power converts water to H_2 and O_2 as products of this endothermic process. Generated H_2 and CO_2 obtained from CO_2 from ambient air capture plants are used in the exothermic process of methanation based on the Sabatier reaction to produce SNG (Bandi et al., 1995; Specht et al., 2009; Sterner, 2009).

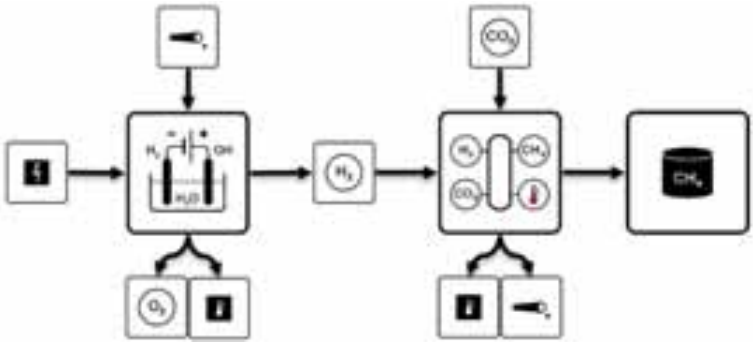

Fig 3: Power-to-Gas (electrolysis and methanation) process.

Electrolysis: $\mathrm{E} + 2H_2\mathrm{O} \rightarrow 2H_2 + O_2 + \mathrm{Q}$ (Eq. 6)

Methanation: $CO_2 + 4H_2 \rightarrow CH_4 + 2H_2\mathrm{O} + \mathrm{Q}$ (Eq. 7)

The alkaline electrolysis cell (AEC) is the well-known and a mature technology for water electrolysis (Millet and Grigoriev, 2013), while the proton exchange membrane electrolysis cell (PEMEC) (Millet and Grigoriev, 2013; Millet, 2015) and solid oxide electrolysis cell (SOEC) (Millet and Grigoriev, 2013; Elder et al., 2015) are technologies in the commercialization phase or still under development. PEMEC shows a slightly better efficiency and shorter startup time in comparison to AEC, which is an advantage while using fluctuating RE as a source of power. SOEC operates at higher temperatures and pressure. The higher temperature offers the chance to replace a part of the electricity needed for the reaction by heat. Furthermore, the produced hydrogen is at a high pressure, which decreases the required energy and cost for compressing hydrogen for the methanation process. However, the startup time of SOEC is higher than AEC and PEMEC. The reported costs for PEMEC and SOEC are higher and in a wider range than those for AEC in 2030**.** The projected specifications for these three types of electrolysers and the methanation process are shown in **Tables 3 and 4** (Agora Energiewende, 2014; Breyer et al., 2015; Energinet.dk, 2012; ETOGAS, 2015; FCH JU, 2015; Götz et al., 2015)**.** In addition, there are more uncertainties about the achievement of techno-economic targets for 2030. Therefore, alkaline high pressure electrolysis has been used in our model. Moreover, the lower capex for AEC is very important in achieving optimized SNG cost.

Tab. 3: Electrolyzers' specification. Abbreviations: electricity-to-hydrogen, *EtH_2*, efficiency, *eff.*

	Unit	AEC	PEMEC	SOEC
Capex	€/kW_{el}	319	250-1270	625-100
Opex	% of capex p.a.	3	2-5	2-5
Lifetime	years	30	20	20
EtH_2 eff. (HHV)	%	86.3	74-89	91-109
Heat demand	% of inlet E	-	-	18-20

The Sabatier reaction is applied in the methanation process and the methanation plant's specification can be seen in **Table 4**.

Tab. 4: Methanation process specification

	Unit	Amount
Capex	€/kW_{H2}	215
Opex	% of capex p.a.	3
Lifetime	years	30
H_2-to-SNG eff. (HHV)	%	77.9
H_2-to-Heat eff. (HHV)	%	14

2.1.3. CO_2 from ambient air scrubber

CO_2 can be supplied from different sources such as large power plants, or ambient air. To have a sustainable energy system with carbon neutral products, CO_2 needs to be obtained from a sustainable CO_2 source such as a biomass plants with carbon capture and utilization (CCU) or it can be captured from ambient air, which is assumed in this work. The chosen CO_2 source is independent of the location, thus carbon supply would not restrict the best places for the PtG plant.

The CO_2 capture from ambient air approach from Climeworks (Climeworks, 2015a) has been used for the energy system in this work, since between 80-90% of energy needed for this plant can be supplied by heat, rather than electricity (Wurzbacher, 2014). In this case the output heat of the methanation and electrolysis units can be used to fulfill this heat demand, which will increase the overall efficiency of the system. The output heat of alkaline electrolysis and methanation processes, via a heat exchanger with 90% efficiency, perfectly matches the heat demand of the CO_2 capture plant of the required capacity. To capture 1 ton of carbon dioxide out of ambient air, this system requires 1300-1700 kWh_{th} of thermal energy at 100-110°C and 200-250 kWh_{el} electricity (Climeworks, 2015b). The average numbers which have been used in our calculations can be seen in **Table 5**. In case of a lack of internal heat, the heat from the GtL section or heat pumps could be used to deliver the heat needed for the CO_2 capture plant.

Tab. 5: CO_2 capture plant specification

	Unit	Amount
Capex	€/(t_{CO2}·a)	356
Opex	% of capex p.a.	4
Lifetime	years	30
Electricity demand	kWh_{el}/t_{CO2}	225
Heat demand	kWh_{th}/t_{CO2}	1500

2.1.4. Water desalination

The steam output of methanation goes through the heat exchanger first, providing the heat for the CO_2 capture plant and the condensed water can be reused in electrolysis. In addition, the output water of the Fischer-Tropsch (FT) process in the GtL section can be recycled and reused in the electrolysis, but these water sources are not enough to supply all the water needed for electrolysis. Thus, a part of water needed for the electrolyzers has to be supplied from an external source. In some regions there might not be enough clean water available for electrolysis. The plant is located along a sea shore, thus seawater reverse osmosis (SWRO) desalination is used, whenever clean water demand for any other activity in the region is more than half of sustainable clean water available in the region (water stress higher than 0.5). Water desalination plant specifications can be found in **Table 6**. More details on RE-powered SWRO desalination plants are provided by Caldera et al. (2015).

PtG and liquefaction plants are built along the sea shore and electricity from hybrid PV-Wind plants is transmitted to the site. In this case, there would be no cost for water piping and pumping from the coast, where the seawater is desalinated. In addition, the GtL plant is located just beside the PtG plant and thus no SNG transportation cost has to be taken into account and the liquid fuels transportation cost to the port will be minimized as well.

Tab. 6: Water desalination and storage plants' specification (Caldera et al., 2015)

	Unit	Amount		Unit	Amount
SWRO Desalination			*Water storage*		
Capex	€/(m^3·a)	2.23	Capex	€/(m^3·a)	0.0074
Opex	% of capex p.a.	4.3	Opex	% of capex p.a.	1.5
Lifetime	years	30	Lifetime		50
Electricity consumption	kWh/m^3	3.0			
Water extraction efficiency	%	45			

2.1.5. Oxygen

Oxygen as a byproduct of electrolysis, has a very important role in the technology used in the GtL process, particularly in the syngas production. The downstream GtL plant needs about 25% of generated oxygen in the PtG plant. This is explained in more detail in Section *2.2.1. Syngas production*. In case of a potential market, it can also have a very important role in the final cost of produced SNG. The market price of oxygen for industrial purposes can be up to 80 €/t_{O2} (Breyer et al., 2015). It might be too optimistic to assume that all the produced oxygen could be sold for this price. Moreover, in case of a potential market, oxygen storage and transportation costs have to be applied. To have a rough assumption, considering all these effects, there is no benefit from oxygen in the base scenario. The projection of a maximum 20 €/t_{O2} benefit from oxygen is assumed in another study for RE-PtG-LNG (Fasihi et al., 2015), when all the produced oxygen was for sale. In the PtG-GtL case, only 75% is available for the potential market. Thus, to have the same impact by the selling of oxygen, the projection of a maximum 30 €/t_{O2} benefit from unused oxygen has been assumed in the PtG-GtL model.

2.2. Gas-to-Liquids

The GtL process provides the opportunity to convert NG or SNG to liquid fuels through a series of chemical reactions. The liquid products are easier and cheaper to transport to remote regions but also internationally, and offer new applications. The GtL process consists of three main steps: ***syngas production***, ***Fischer-Tropsch Synthesis (FTS)*** and ***products upgrading*** (Wood et al., 2012). Although these process steps are well-known, at the same time, the combined technology is complex and well-protected by limited companies developing them. GtL plants are typically capital intensive and, so far, have been affected by economies of scale which have made them viable only at large scales. Thus, the GtL plants should be built near large scale reserves of NG on a low price level. Recently some companies, such as *Velocys* (Velocys, 2015a), have developed new technologies which have made GtL viable for a lower range of capacities (1500 – 15,000 barrels of crude oil equivalent per day). Until now, there has been a limited number of actual GtL plants in operating mode, which makes it even harder to have good, publically accessible information about these systems on an industrial scale. On the other hand, the quality of input gas, selectivity of the desired products and the regional conditions have led to a development of different minor technologies.

In our model, the feedstock of the GtL plant is RE-SNG produced in a PtG system. This pure and fixed feedstock can decrease the number of determinative variables in this process. This can result in focus on a unique method, which can result in a faster improvement of the technology and decrease in the cost of the system. As an example, no gas treatment would be required in the very first step, which can decrease the cost of the system. The new companies working on affordable, small scale GtL plants can also be a big help for further applications and development of GtL plants.

2.2.1. Syngas production

SNG, as the output of the PtG plant, is the feedstock for the GtL plant. In the first step, SNG needs to be converted to syngas (mixture of CO and H_2) as the feedstock for the FT section. The desired CO:H_2 ratio for FT process is 1:2. There are different reforming technologies to produce syngas from natural gas, including catalytic partial oxidation (CPO) (Eq. 8), auto thermal reforming (ATR) (Eq. 9-11), steam methane reforming (SMR) (Eq. 12, 13) or a combination of these technologies. The main reactions of these processes are as follow (Rostrup-Nielsen, 2000):

CPO: $CH_4 + 0.5\ O_2 \rightarrow CO + 2H_2$ $\Delta H^0 = -38$ kJ/mol (Eq. 8)

ATR: $CH_4 + 1.5\ O_2 \rightarrow CO + 2H_2O$ $\Delta H^0 = -520$ kJ/mol (Eq. 9)

$H_2O + CH_4 \rightarrow CO + 3H_2$ $\Delta H^0 = 206$ kJ/mol (Eq. 10)

$CO + H_2O \rightarrow CO + H_2$ $\Delta H^0 = -41$ kJ/mol (Eq. 11)

SMR: $CH_4 + H_2O \rightarrow CO + 3H_2$ $\Delta H^0 = 206$ kJ/mol (Eq. 12)

$CO + H_2 \rightarrow CO_2 + H_2$ $\Delta H^0 = -41$ kJ/mol (Eq. 13)

Catalytic partial oxidation provides the syngas with the desired CO:H_2 ratio for the FT process, but air separation units (ASU) are needed to produce the required oxygen for this reaction. The cost of an air separation unit is reported to be at least 8% of the capital cost of GtL facilities (Maitlis and Klerk, 2013). Thus, other technologies have also been developed and used by industrial companies in syngas production from natural gas. In our model, pure oxygen is already available as the by-product of electrolysis in the PtG plants. Thus, partial oxidation is the technology that makes the most sense for syngas production within the approach of this paper. The real model would not be this simple and efficient. CO_2 would be produced in the following side reaction (Eq. 14):

$CH_4 + O_2 \rightarrow CO_2 + 2\ H_2O$ (Eq. 14)

Nothing can be done about the inherent energy loss through water made in the CPO main reaction, but there is a potential to increase the thermal energy efficiency by further advances in technologies to reduce CO_2 formation in the side reaction. This technology is used by the Shell middle distillates synthesis (SMDS) plant in Bintulu, Malaysia, and the carbon to CO conversion is reported to be 94% (Hoek, 2006). The CPO reaction happens at high temperatures, about 1000 °C, and the released heat in this reaction is used to keep it in an autothermal mode (Al-Sayari, 2013) and cannot be used for other purposes.

Table 7: GtL capital expenditures breakdown (Maitlis and Klerk, 2013)

Unit	%
Air Separation Unit	8
Syngas Unit	18
Hydrogen Unit	6
FT Synthesis Unit	24
Upgrading Units	5
Water Disposal Unit	3
Utilities	16
Offsites	20

2.2.2. Fischer-Tropsch synthesis

The Fischer-Tropsch process converts syngas to different chains of synthetic hydrocarbons $(-CH_2-)_n$, which is also known as syncrude (Eq. 15). This reaction is highly exothermic (Graves et al., 2011). In our model, the water produced in this reaction is recycled and reused in the water electrolysis at the PtG section. Also, the released heat can be used for any purpose through a heat exchanger.

Fischer-Tropsch Synthesis (FTS): $n\ CO + 2n\ H_2 \rightarrow (-CH_2-)_n + n\ H_2O$ $\Delta H^0 = -209$ kJ/mol (Eq. 15)

This reaction is mainly based on cobalt (Co) or iron (Fe) catalysts, which are operated at different temperatures. The properties of produced syncrude are mainly defined by the chosen catalyst and process conditions. Table 8 shows the different options and their specifications (Klerk, 2014; 2008).

Tab. 8: Characteristics of different types of Fischer-Tropsch synthesis practiced industrially (Klerk, 2014; 2008). Abbreviations: Low Temperature Fischer-Tropsch, *LTFT*, and High Temperature Fischer-Tropsch, *HTFT*.

Description	Fe-LTFT	Co-LTFT	Fe-HTFT
Operating temperature (°C)	200-270	170-230	320-360
Operating pressure (MPa)	2-2.5	2-2.5	2-2.5
Water gas shift active	Yes	No	No
Synthetic products composition (mass %):			
Light gas (C_1-C_2)	6	7	23
Liquid petroleum gas (C_3-C_4)	8	5	24
Naphtha (C_5-C_{10})	12	20	33
Distillate (C_{11}-C_{22})	20	22	7
Paraffin wax	50	44	-
Aromatic residue	-	-	3
Water-soluble oxygenates	4	2	10

The major products of low temperature Fischer-Tropsch (LTFT) and high temperature Fischer-Tropsch (HTFT) are mainly paraffin and olefin hydrocarbons, respectively. In addition, the products of HTFT contain aromatics which are not desired. HTFT produces a large amount of light gas (C_1-C_2) which is not favourable. In conclusion, although any FT syncrude can be refined to gasoline, jet fuel, diesel fuel and petrochemicals, LTFT seems to be a better option, when aiming for fuels with a longer chain of hydrocarbons, such as diesel.

2.2.3. Products upgrade

The syncrude contains hydrocarbons of different lengths. By adding hydrogen and hydrocracking of long chain syncrude, the hydrocarbons with a desired length can be produced as products in the upgrading unit. Equation 16 shows the simplified reaction at this step. If needed, the hydrogen used in this step can be supplied by water electrolyzer units in the PtG plant.

Products upgrade: $(-CH_2-)_n + H_2 \rightarrow C_nH_{2n+2}$ (Eq. 16)

The GtL final products can include up to 30% wax. Maximizing wax configuration in the output will increase profit, but the demand for wax is much less than diesel. Thus, in a global model, the aim is to maximize the diesel share in the output. The outputs of GtL in some publications are shown in Table 9.

Tab. 9: GtL final products composition (vol%). Abbreviations: liquefied petroleum gas, *LPG*.

Source	LPG	Naphtha	Middle distillates		Lubes & Wax	Comment
			Jet fuel / Kerosene	Diesel		
Fleisch et al. (2002)		15-25	65-85		0-30	
Brown (2013)	5	20	75			typical GtL
Velocys (2015b)		20	80			
Chedid et al. (2007)	6	26			68	
NPC (2007)		25		70	5	
Khalilpour, Karimi (2012)	5	20		75		
Bao (2010)	3	30		67		
FVV (2013)		15	25	60		Diesel mode
		25	50	25		Kerosene mode

Aiming for the maximum middle distillates share, the numbers provided by (FVV, 2013) have been used for the model of this paper, and represent naphtha, jet fuel and diesel with a share of 15%, 25% and 60%, respectively.

Considering diesel and jet fuel as the target products of this process, the potential revenue of sold by-products from the total costs and therefore the levelised cost of fuel (LCOF) of the target products in the value chain should be investigated. Paraffin wax, as a potential product of the GtL process has a higher financial value than crude oil (Jensen et al., 2013), but it is not in the slot of final products in our model. All products of the GtL process are

a function of the crude oil price, as they compete with refinery products of crude oil. Naphtha has approximately the same market value as crude oil, thus it has no additional effect than the crude oil price on the results (Globova, 2013).

GtL plants benefit a lot from economies of scale, meaning that larger plants would be lower in specific cost. The capex for a typical GtL plant with a capacity of 50,000 barrels per day (bpd) is reported to be 110,000 USD/bbl (Wood et al., 2012). The plant assumed in this paper with an approximate capacity of 26,000 bpd, is on the edge between small scale and large scale plants. *Velocys*, as a manufacturer of small scale GtL plants, reports a capex of 100,000 USD/bbl which is in the range of capex of large scale plants (Velocys, 2015a). As explained in *Section 2.2.1*., the availability of oxygen for zero marginal cost can reduce the total costs by 8%. Thus, with a USD/€ exchange rate of 1.35 (Tab. 12),, the capex of the GtL plant would be about 68 k€/bbl and it is expected to be at the same level for the year 2030.

A lifetime of 25, 25, 30 and 25 years have been reported by Udaeta et al. (2007), Velasco et al. (2010), Wood et al. (2012), (Velocys, 2015b) and FVV (2013) for GtL plants, respectively. According to the project timing (2030), and due to unfailing RE-SNG reserves as the feedstock of the GtL plant, the higher reported lifetime of 30 years should be acceptable. Table 10 shows all the assumptions for the specifications of the GtL plant in the model used in this paper.

Tab. 10: Base case specification of a hypothetical GtL plant assumed for this paper

		Unit	Amount
Capex		k€/bpd	68
Opex		% of capex p.a.	3
Lifetime		years	30
Availability		%	96
Energy efficiency		%	65
Products	naphtha	%	15
	jet fuel	%	25
	diesel	%	60
Heat release		% of inlet SNG	22

2.2.4. Products shipping

GtL products can be shipped by a product tanker fleet. The deadweight (DW) of large range vessels (LR2) is between 80,000 to 120,000 tons. The ship can carry a weight of approximately 90% of its DW (EIA, 2014b). The shipping specifications are shown in Table 11, assuming a shipping from Patagonia to Rotterdam. The data have been taken from Konovessis (2012), MAN (2013), Sea distances (2015), UNCTAD (2009) and Khalilpour (2012).

Tab. 11: Shipping specification

	Unit	Amount
Capex	m€/ship	48
Opex	% of capex p.a.	3
Lifetime	years	25
Availability	%	95
Ship type	large range 2 (LR2)	-
Ship size	ton (deadweight)	100,000
Speed	knots	14
Charge and discharge time total	days	2
Marine distance	km	13,400

3. Results

3.1. RE-PtG-GtL case study, annual basis model

Integrating all the system's elements offers some chances to increase the overall efficiency. Figure 4 shows the Sankey diagram of the entire system, depicting the energy and material flows within the entire RE-PtG-GtL value chain. The figure is the sample of a system with 1 MWh_{el} specific annual electricity input. As can be seen, the alkaline electrolyzer, at 97%, is the main electricity consuming element, while the excess heat by-product of the electrolyzer and the methanation plant is the main source of energy for the CO_2 capture plant. The heat released in the FT process accounts for 14% of initial electricity and 22% of energy content of inlet SNG to the GtL system. The overall PtG-GtL efficiency of this system, without FT heat utilization, would be 42.5%, while 65% of inlet SNG is converted to liquid fuels in the GtL plant. The 15% naphtha share is finally not available for transport fuels. However, this is no financial burden since it can be sold on the market for an attractive value which should be cost neutral.

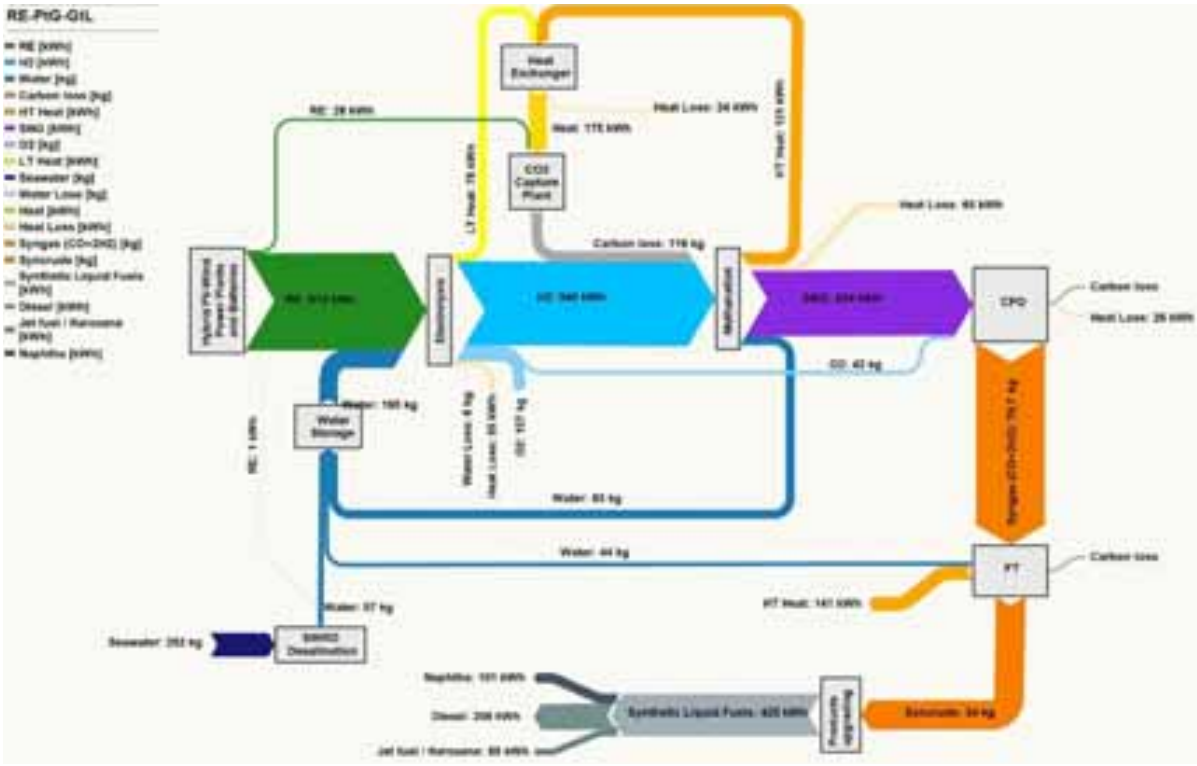

Fig. 4: RE-PtG-GtL energy and material flow diagram.

Unlike RE-SNG, RE-diesel production cost can be a function of crude oil price if there are by-products for selling on the market. All the general assumptions in the calculations of the base case can be found in **Table 12**.

Tab. 12: General assumptions in base case calculations

	Unit	Amount
WACC	%	7
Exchange rate	USD/€	1.35
Brent crude oil price	USD/bbl	80

The LCOE of wind energy and solar PV are 20.35 €/MWh and 25.36 €/MWh, respectively. The hybrid PV-Wind power plant of 5 GW produces 34,688 GWh of electricity per year and the weighted average cost is 22.89 €/MWh. The CO_2 captured from ambient air and the desalinated water cost 40.42 €/t_{CO2} and 0.52 €/m^3, respectively. A summary of all production costs for the base scenario can be found in **Table 13**.

The diesel produced in the FT-process has different characteristics than the conventional diesel produced by a

petroleum refinery. The term "FT-diesel" is used to emphasize the quality of final product. Although the quality of FT-diesel can differ from plant by plant, in this paper the density (at 20 ºC) and higher heating value (HHV) of FT-diesel are assumed to be 766 kg/m^3 and 45.471 MJ/kg, respectively (Glebova, 2013; GREET, 2010). On the other hand, the term RE-diesel is used to emphasize the source of primary energy (PE) in diesel production, while referring to the same product.

Table 13: Production cost in base scenario

	Unit	Amount
Renewable Electricity (RE)	€/MWh$_{el}$	22.89
CO_2	€/t$_{CO2}$	40.42
Desalinated water	€/m^3	0.52
RE-SNG	€/MWh$_{th,gas}$	53.31
RE-SNG	USD/MMBtu	20.85
RE-SNG	USD/bbl	120.95
RE-SNG	€/m^3	0.55
RE-PtG-GtL average product at production site	€/MWh$_{th}$	98.94
FT-diesel at destination	USD/MMBtu	39.13
FT-diesel at destination	€/MWh$_{th}$	100.03
FT-diesel at destination	€/l	0.97

Figure 5 shows the levelized costs in the RE-diesel value chain with two scenarios for the weighted average cost of capital (WACC): 7% and 5%. RE-diesel cost distribution as a share of the total is not dependent on the WACC. GtL and methanation have the highest share (45.6% and 30.4%, respectively) in the total cost. At 1.1%, shipping has the lowest share in this process. Thus, it is more important to have the plants located in regions of the highest solar and wind potential than in regions close to the target market in order to reduce the final cost.

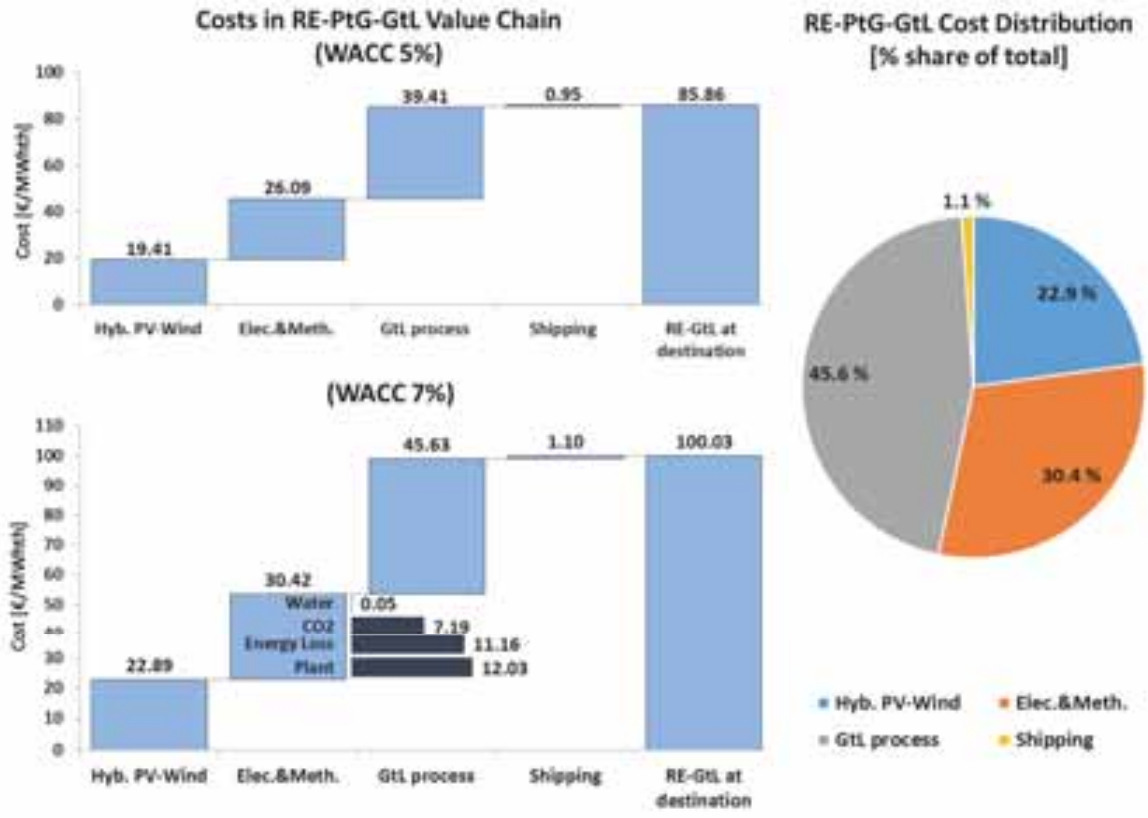

Fig. 5: RE-diesel production cost breakdown for WACC of 5% (top) and 7% (bottom).

Water and CO_2 costs are included in the electrolysis and methanation part of the value chain. With 12.03 €/MWh$_{th,gs}$, the share of the PtG plant itself in the final cost of methanation is 39.5%, while energy losses in the

electrolysis and exothermic reaction of methanation account for 36.7% of the cost of this process. At 7.19 €/$MWh_{th,gas}$, the cost of CO_2 has only a 23.6% share in the methanation plant cost, which is due to internal heat utilization for the CO_2 scrubbing process (Fig. 5).

For the assumptions of the base case scenario, the final cost of RE-diesel in Rotterdam would be 100.03 €/MWh_{th}, which is equal to 204.38 USD/bbl, 39.13 USD/MMBtu or 0.97 €/l of diesel. The RE-diesel cost is a function of the crude oil price and refining cost. **Figure 6** shows the historical trends for the crude oil price, refining cost, diesel cost and crude oil cost to diesel price ratio in percentage.

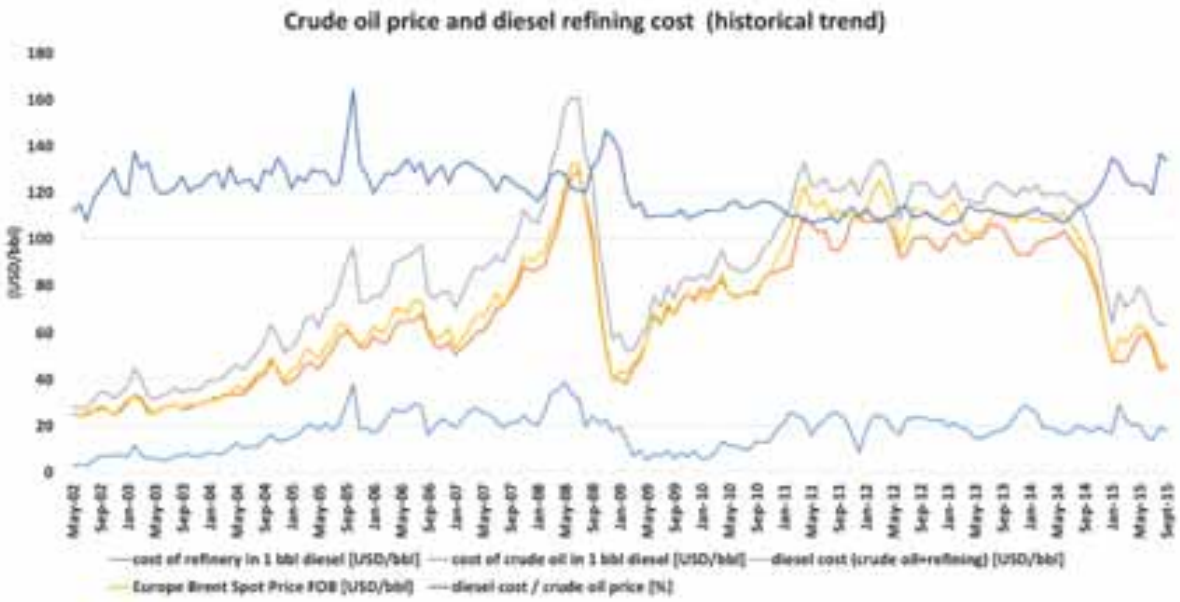

Fig. 6: Crude oil price, diesel refining cost and ratio diesel cost to crude oil price. Data taken from (EIA, 2015).

The long term (13 years) average ratio of one barrel diesel cost (crude oil consumption and refinery cost) to crude oil price is 118.76% and has been taken in this work. The ratio for the full year 2014 was 113.5%. With a crude oil price of 80 USD/bbl, the cost of conventional diesel would be equivalent to 95.01 USD/bbl, 16.38 USD/MMBtu or 0.44 €/l. Thus, the base scenario, accounting for a RE-diesel of 227 USD/bbl, is not directly competitive to the conventional diesel price, but there are some potential game changers:

A) WACC: For a WACC of 7% in the base scenario, the cost of debt and return on equity are 5% and 12%, respectively, for a debt to equity ratio of 70:30. For a WACC of 5%, the corresponding numbers would be 4% and 7%, which could be realized for a risk minimized business case. With this scenario the cost of RE-diesel in Rotterdam could be decreased by 14.2% to 85.86 €/MWh_{th}, 33.59 USD/MMBtu, 194.8 USD/bbl or 0.83 €/l of diesel equivalent. Figure 7 shows the effect of WACC on the final cost.

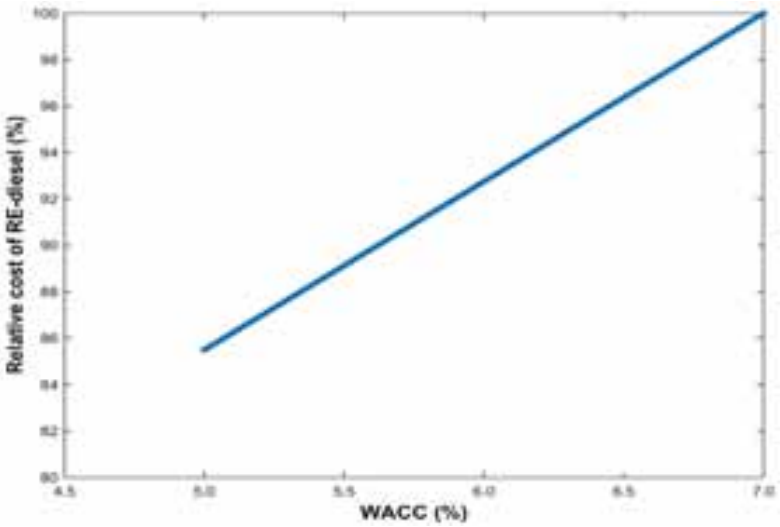

Fig. 7: Effect of WACC on final product's cost in comparison to base case scenario.

B) CO_2 emission cost: CO_2 emission cost for fossil fuels can have a huge impact on the competitiveness of RE-diesel and conventional diesel, as it increases the total cost of fossil fuels. The conventional diesel carbon emissions are 20.2 t_C/TJ (ton carbon per tera joule) (IPCC, 1996), which is equal to 74.02 t_{CO2}/TJ. The additional cost of CO_2 emissions with a maximum price of 50 €/t_{CO2} on the conventional diesel price can be seen in **Figure 8**. Assuming a crude oil price of 80 USD/bbl and 101.44 USD/bbl as the corresponding price for diesel for the base case (including the cost for refinery), a CO_2 price of up to 50 €/t_{CO2} is equivalent to a price increase of the diesel of 13.48 €/MWh_{th}, 5.27 USD/MMBtu, 30.57 USD/bbl and 0.14 €/l.

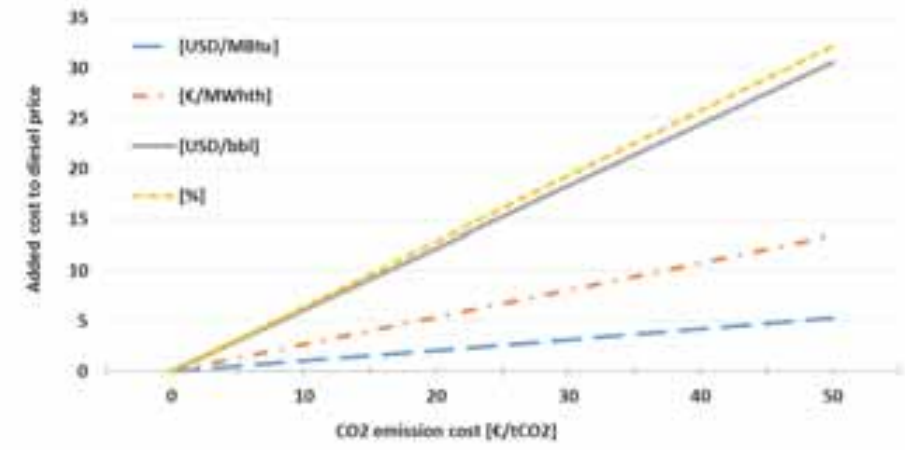

Fig. 8: The additional cost of CO_2 emissions on the conventional diesel price for a CO_2 price of up to 50 €/t_{CO2} in absolute numbers and relative for a basis crude oil price of 80 USD/bbl.

C) Oxygen: 25% of the produced oxygen by the electrolyzer units is used in the syngas production unit, but there is no financial benefit assumed from the rest of oxygen in the base scenario. The projection of a maximum average benefit of 30 €/t_{O2} is shown in **Figure 9**. An oxygen price of up to 30 €/t_{O2} is equivalent to a cost decrease of the RE-diesel of 9.00 €/MWh_{th}, 3.52 USD/MMBtu, 20.42 USD/bbl and 0.08 €/l of diesel, which is equal to a 9.00% decrease in the final cost.

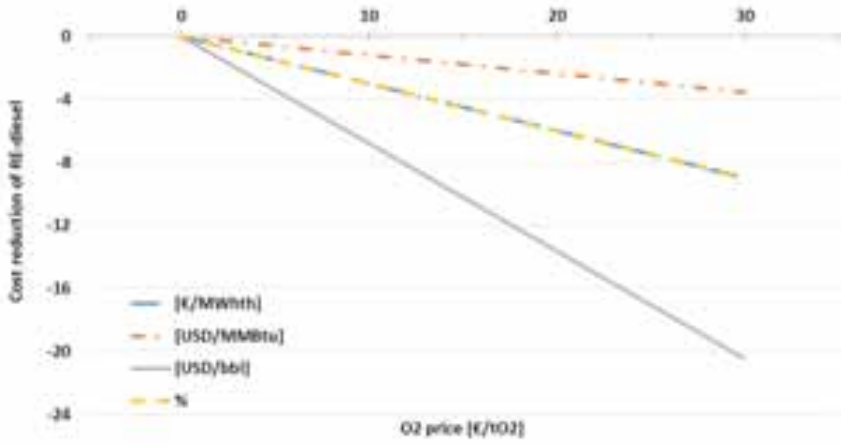

Fig. 9: Effect of oxygen benefit for an oxygen price of up to 30 €/t_{O2} on RE-diesel in absolute numbers and relative ones for the base scenario cost.

As a conclusion, an increase in crude oil price or CO_2 emission cost will increase the cost of conventional diesel, while a profitable business case for O_2 or a reliable business case at a de-risked 5% WACC level can lead to lower cost for RE-diesel cost. The effects of all these potential game changers have been summarised in **Figure 10**. The price of diesel in the EU is based on:

- the global crude oil price as depicted in Figure 10 for a price range of 40 – 200 USD/barrel,
- three scenarios for CO_2 emission cost,
- three scenarios for benefits from O_2 sales, and
- the cost of delivered RE-methane based on two different WACC levels

All projections are for the year 2030.

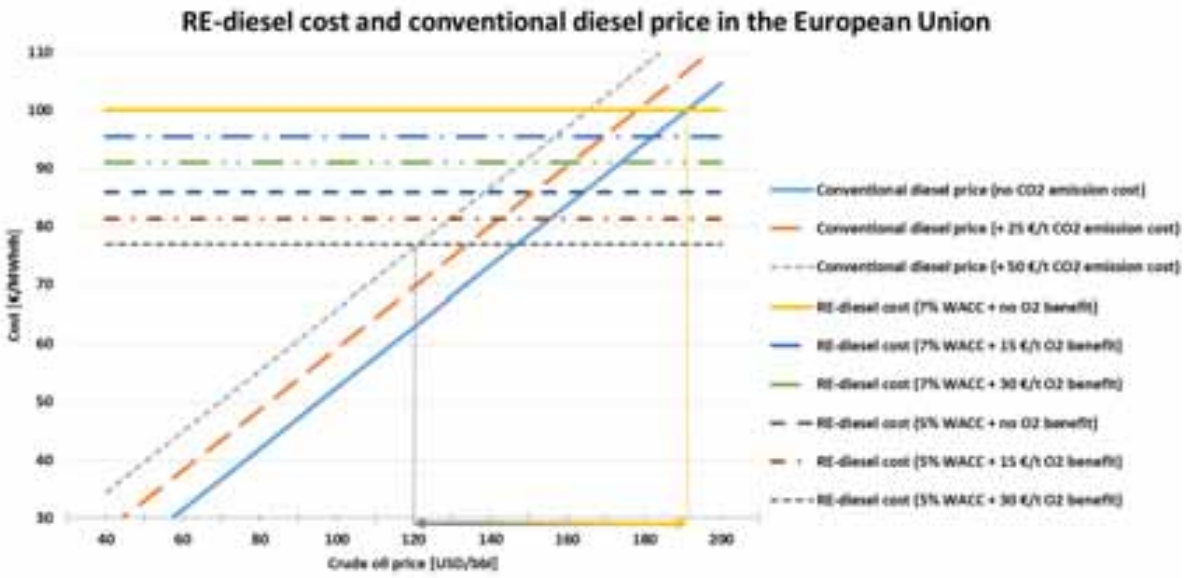

Fig. 10: All possible scenarios for the RE-diesel price in the EU based on the production costs in Patagonia. Reading example: For a crude oil price of 100 USD/bbl the conventional diesel price varies from 66 – 52 €/MWh$_{th}$ (depending on the CO_2 emission costs), while the RE-diesel cost varies from 77 – 100 €/MWh$_{th}$ (depending on WACC and O_2 benefit), i.e. for 121 USD/bbl, 50 €/t$_{CO2}$, 5% WACC and 30 €/t$_{O2}$ the RE-diesel is competitive to the conventional one without any further assumptions.

The first breakeven point can be expected for a produced RE-diesel with a WACC of 5%, CO_2 emission cost of 50 €/t$_{CO2}$, accessible oxygen price of 30 €/t$_{O2}$ and a crude oil price of about 121 USD/bbl. While RE-diesel produced under the base case (WACC of 7%, no CO_2 emission cost and no O_2 sales) can compete with conventional diesel whenever the crude oil price is higher than about 191 USD/bbl. This represents a very high difference and the base case may not easily match with market prices. But the additional assumptions are not far from reality, since a CO_2 emission cost is already applied in some countries (OECD, 2013).

To have a better understanding about the scale of the project, **Table 14** lists the physical and economic aspects of the 5 GW case assumption.

Tab. 14: The annual consumption/ production and economic aspects of the 5 GW case assumption. Abbreviations: million ton per annum, *MMTPA,* barrel per day, *bpd*.

	Unit	Amount		Unit	Amount
Hybrid PV-Wind power plant			*GtL plant*		
PV single-axis installed capacity	GW_p	5	Capacity	bpd GTL	27,720
Wind installed capacity	GW	5	Capital expenditure	bn€	1.885
Capital expenditure	bn€	7.8	Diesel production	bbl/year	5,767,900
Hybrid PV-Wind, generation	GWh_{el}	36,000	Jet fuel/ Kerosene production	bbl/year	1,442,000
Hybrid PV-Wind, used	GWh_{el}	34,670	Naphtha production	bbl/year	2,403,300
CO_2 capture plant			*Electrolysis and methanation plants*		
Capacity	MWh_{el}	131	Capacity	GWh_{el}	4.87
Capital expenditure	m€	36	Capital expenditure	bn€	2.43
CO_2 production	MMTPA	4.030	SNG production	GWh_{th}	2270
External heat utilization	GWh_{th}	6900	SNG production	MMTPA	1.47
Desalination plant			*Shipping*		
Capacity	MWh_{el}	5	Shipping volume	bbl/year	9,613,100
Capacity	m^3/h	505	number of ships	-	1.56
Capital expenditure	m€	10	Capital expenditure	m€	75
Water production	mio m^3	3.5			

The capital expenditure breakdown of the total value chain has been shown in Figure 11. The total capital cost is 13.31 bn€, while the electricity generation solely requires 59% of the capital expenditure. With 0.6% and 0.04% respectively, the capital expenditures of ships and the desalination plant are almost negligible.

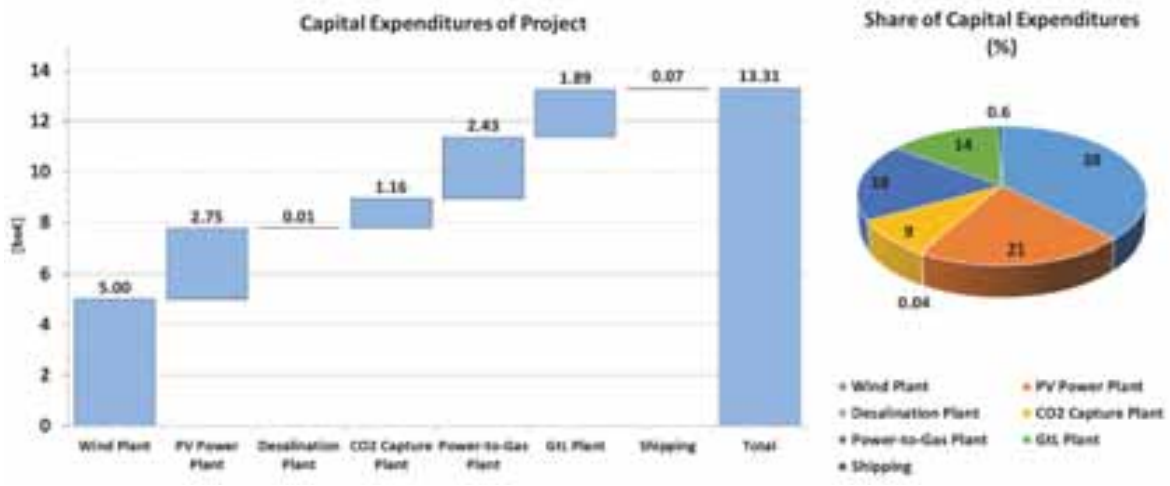

Fig. 11: The capital expenditure breakdown of hybrid PV-Wind-PtG-GtL value chain.

To have an overview on the data available to the public, one should take it into consideration that not even two GtL plants designed by one company are the same. The quality of feedstock, applied technology and desired outputs and the corresponding costs could be quite different case by case. In response to these uncertainties, a series of sensitivity analyses have been done for ±10% change in the capex, efficiency and other inputs of major elements. Figure 12 illustrate these analyses in the categories of economic changes, geographical changes and changes in plant efficiency.

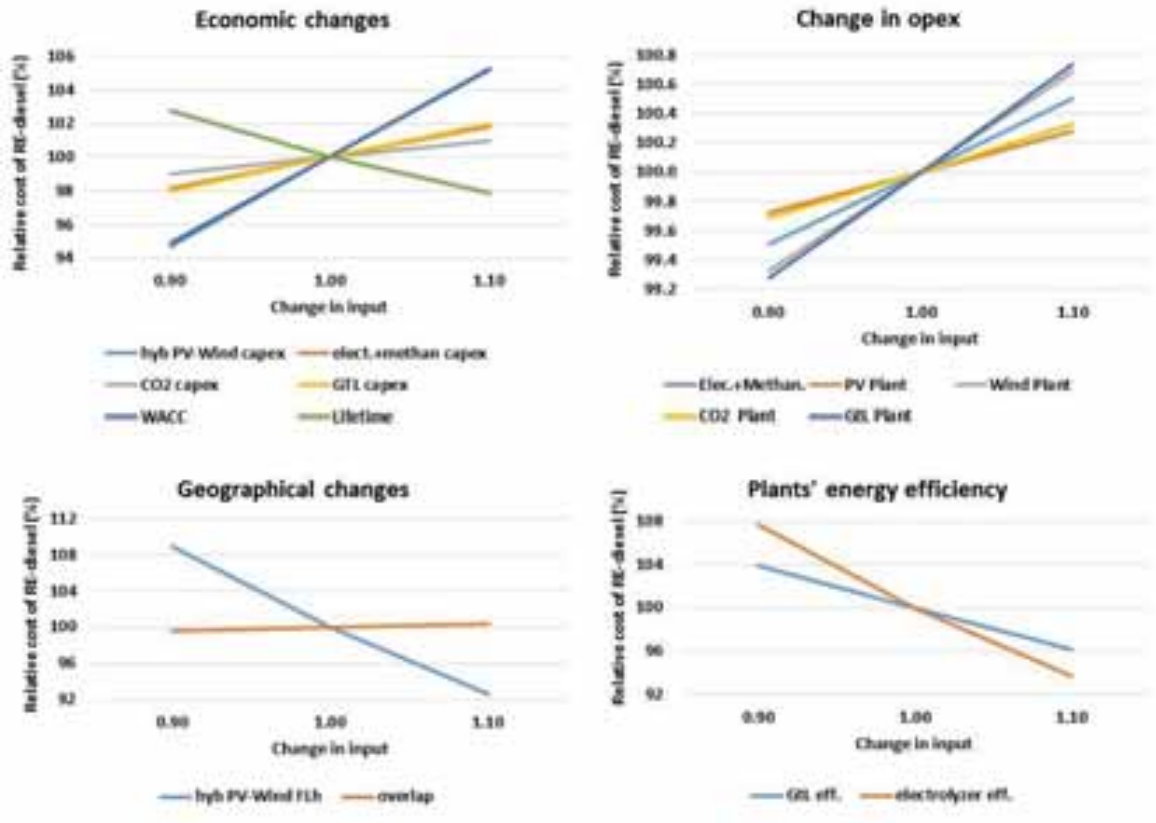

Fig. 12: Sensitivity analysis of input data based on economic changes (top, left), change in plants' opex (top, right), geographical changes (bottom, left) and plants' energy efficiency (bottom, right).

The economic changes graph illustrates that a 10% decrease in the capex of a hybrid PV-Wind power plant will result in a 5.5% decrease in the final LCOF of diesel, which is 2.5 times more than the effect of changes in the capex of the electrolysis or GtL plant. On the other hand, changes in opex shows that no single plant can cause more than a 1% change in the final production cost if the opex divergence is up to 10%. The geographical changes graph shows that a 10% decrease in the FLh of hybrid PV-Wind plant will increase the final LCOF by 9%, while a 10% increase in the efficiency will just result in a 7.5% decrease in the final products' cost. A 10% change in the amount of overlap is a very small number and it does not bring any significant change to the system. As it is expected, plants' energy efficiency analysis shows that a 10% increase in the efficiency of electrolysis and GtL plants would decrease diesel production cost by 6% and 11%, respectively. Thus, while there is no difference in the LCOF of the GtL plant, electrolysis and methanation capex, the GtL plant efficiency has a higher effect on the final product's cost. Summing up, the three final RE-diesel LCOF influencing factors are the full load hours of the hybrid PV-Wind power plant, the electrolyzer efficiency and the WACC for the entire investment. As a consequence, the RE-PtG-GtL value chain needs to be located at the best complemented solar and wind sites in the world combined with a de-risking strategy and a special focus on mid to long term electrolyzer efficiency improvements.

3.2. Optimal RE-PtG-GtL global potential, hourly basis model

The global RE-SNG generation potential has been studied by Fasihi et al. (2015) on an hourly basis. The hourly model enables the best combination of PV (fixed-tilted or single-axis tracking), wind energy and battery capacities based on an hourly availability of the solar and wind resources to minimize the levelized cost of electricity (LCOE) and cost of SNG. Low cost batteries are added to harvest the excess electricity during overlap times to increase the FLh whenever it is beneficial. Applying this approach on all regions in the world with a minimum of 6000 FLh for hybrid PV-Wind power plants and setting an upper limitation of maximum 10% area use by both PV and wind power plants, the global map of optimal electricity and SNG generation potential and the corresponding prices have been shown in Figure 13 (Fasihi et al., 2015).

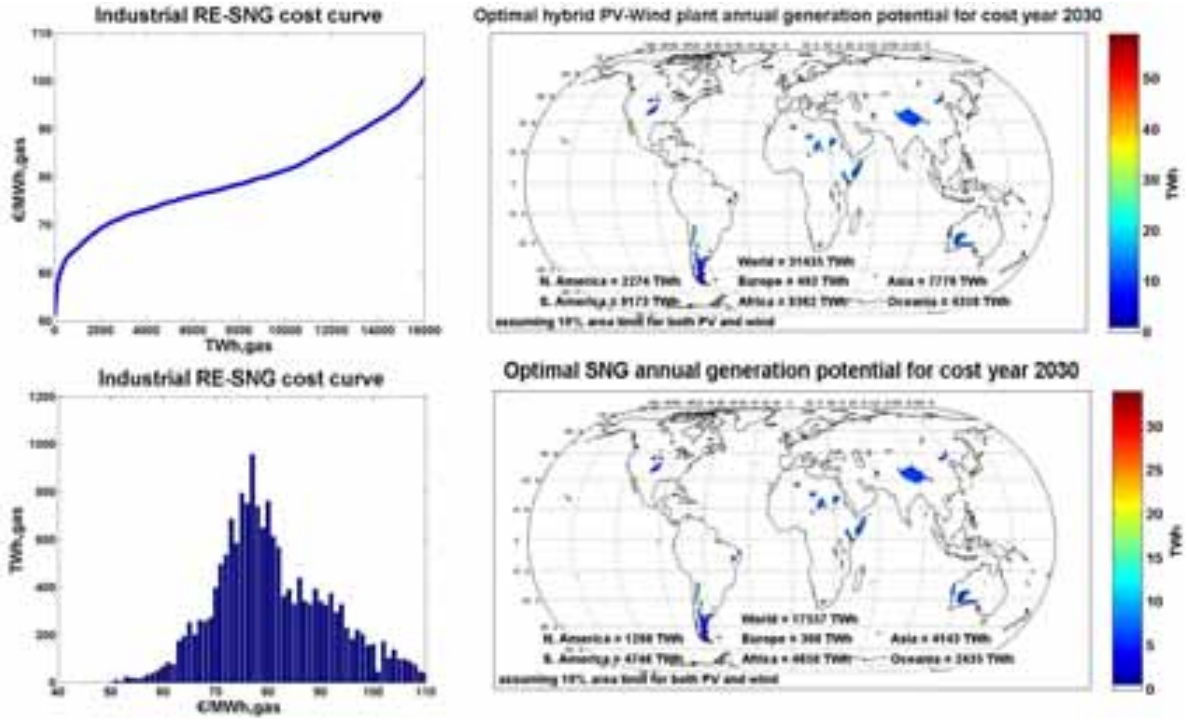

Fig. 13: Optimal hybrid PV-Wind plant annual electricity generation potential (top, right), optimal PtG plant annual SNG generation potential (bottom, right) and SNG cost curve for cost optimized SNG generation in a cumulative (top, left) and a spectral (bottom, right) distribution for the cost year 2030.

Figure 13 illustrates that the generation potential for PtG is less than the electricity generation, which is due to the electricity consumption in the desalination and CO_2 capture plant, and efficiency losses in the PtG plant and power transmission lines. The global annual optimal electricity and SNG production potential are about 31,400 TWh_{el} and 17,600 $TWh_{th,gas}$, respectively. More SNG could be produced in South America (4,750 $TWh_{th,gas}$), while the hybrid PV-Wind power plant generation in Africa (8,360 TWh_{el}) is comparable to the potential of South

America (8170 TWh_{el}). Europe has the lowest electricity and SNG production. But with 62.6%, it has the highest electricity to SNG conversion rate among all continents. With respect to global production numbers in the figure, the average electricity to SNG conversion rate can be estimated to be about 56%.

Based on Figure 13, the global optimal SNG potential is about 17,560 $TWh_{th,gas}$, which results by applying a GtL efficiency of 65% at a production of about 11,410 $TWh_{th,fuel}$ GtL products. This is equal to about 7,540 million barrel GtL products. Figure 14 illustrates the GtL industrial cost curve for global optimal SNG production as feedstock.

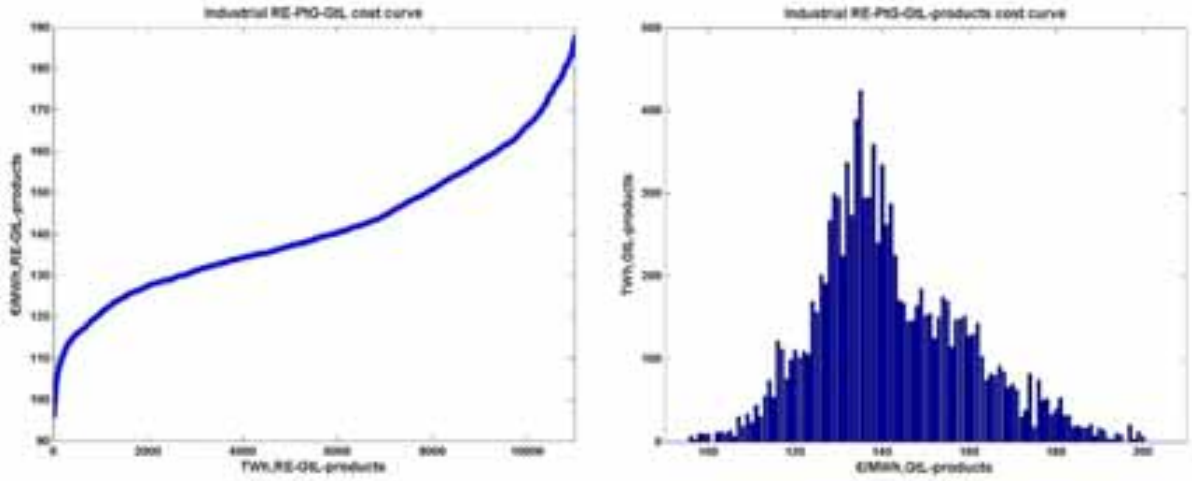

Fig. 14: GtL industrial cost curve for cost optimized GtL production based on RE-PtG in a cumulative (left) and a spectral (right) distribution for the cost year 2030.

The global GtL plants with an inlet SNG cost range of 50 to 100 €/$MWh_{th,gas}$ will result in production costs of RE-diesel in the range of 93.8 to 170.8 €/$MWh_{th,fuel}$, equal to 212.9 to 387.5 USD/bbl or 0.91 to 1.66 €/l.

4. Conclusion

Due to their emissions, there is no place for fossil fuels in a fully sustainable energy system. On the other hand, a ful substitution of fossil fuels by renewable electricity is not possible, as electricity cannot be directly used in some sectors such as aviation or heavy vehicles in all cases. Thus, renewable electricity based fuels are essential to fulfill this demand. The RE-SNG can be further converted to RE-diesel and other fuels in a liquid phase in GtL plants. Modelling an energy system without fossil fuels, the carbon source of this process cannot be from the flue gas of power plants fired by fossil fuels. Moreover, in a global scale energy system, the carbon source should be accessible wherever the renewable power is available. To have a carbon neutral product, CO_2 needed for this process should be captured from ambient air and water desalination should be applied whenever there is a certain levels of water stress in the region. All the technologies for this energy system already exist on a commercial scale and it can become operational whenever investors decide to go for it. All this being said, the system cannot run if the final product is not cost competitive.

This study shows that, with about a 191 USD per oil equivalent barrel, RE-diesel (produced in the RE-PtG-GtL chain) costs more than conventional fossil diesel in today's market. But this price difference is not like a dead end for this energy system. There are different factors which can improve the competitiveness of RE-diesel with conventional fossil diesel in the long term and not all of these factors are internal issues related to this energy system.

- The crude oil price is the very first factor. The long term change in the crude oil price is a function of production cost, production and consumption rate, reserves and political issues. On the other hand, in the short term and as long as production cost of RE-diesel is higher than the production cost of conventional fossil diesel, RE-diesel can be kept away from the market if the crude oil price is set less than RE-diesel production cost. But in the long term, when the crude oil reserves are not sufficient to cover the demand, then the market is likely to follow the RE-diesel production cost.
- Environmental concerns and fuel quality will put additional costs on the conventional fossil diesel price.

CO_2 emission cost has been already set in some countries. Moreover, the standards for fuel quality may rise to a limit at which conventional diesel cannot be produced at that quality anymore. In that case, carbon-neutral and sulphur-free RE-FT-diesel can be considered as one of the main substitutions, also for a production cost 50-100% higher than conventional fossil diesel.

- The by-products of the RE-PtG-GtL value chain can play a significant role in some regional cases, if not globally. A RE-PtG-GtL plant located in a region with high demand for oxygen can decrease the production cost of diesel by 20%. Thus, this system can still run for some special cases, if not globally.
- The other regional effect would be the risk of investment. The impact of de-risking measures have been found to be of high relevance for the economics, since reduced risks which could decrease the WACC from 7% to 5% would reduce the production cost throughout the entire value chain by about 14.2%.
- The heating value of released heat in the FT process is equal to 14% of inlet electricity to the system. A permanent (not seasonal) plan for monetizing this heat can significantly increase the overall efficiency and would decrease the costs.
- Last but not least, a revised technical system design with the same inputs and outputs might result in lower production cost. This is due to the fact that the current system cost breakdown shows that about ¾ of production cost is related to the PtG-GtL section and only 25% is related to the cost of electricity. As an example, eliminating the SNG production step in this energy system and focusing on direct production of RE-diesel from water and CO_2 will increase the efficiency, which might decrease the production cost further. But so far, PtL technology has been operating on a laboratory and pre-commercial scale only and the capex for this process is still high. Thus, it depends on the advances in the technology and the balance between increase in the efficiency and capex and their effects on the production cost. A cost comparison among these different routes is needed for a better understanding of the most promising options.

In conclusion, the external factors can have a strong impact on the competitiveness of the RE-PtG-Gtl system and in a beneficial combination they can reduce the cost of RE-diesel from the aforementioned 191 USD per oil equivalent barrel to about 121 USD, which had been a crude oil price level for already some years in the recent past (BP, 2015). These results have a significant impact on the discussions of the energy transformation towards sustainability ahead. If not concurring with the market, the hybrid PV-Wind-RE-PtG-GtL system could set an upper limit for fossil fuel prices, globally. It would also further increase the demand for solar PV systems, wind turbines, water electrolyzers, methanation plants and CO_2 capture plants. The additional market for solar PV and wind energy can be estimated to be in the terawatt scale. This potentially huge market itself would further reduce production costs and increase research and development investments in the field for more efficient technologies.

Acknowledgements

The authors gratefully acknowledge the public financing of Tekes, the Finnish Funding Agency for Innovation, for the 'Neo-Carbon Energy' project under the number 40101/14. The first author thanks the Gas Fund for the valuable scholarship. We also thank Michael Child for proofreading.

5. References

Al-Sayari S. A., 2013. Recent Developments in the Partial Oxidation of Methane to Syngas. The Open Catalysis Journal, 6, 17-28

Bandi A., Specht M., Weimer T., Schaber K., 1995. CO_2 Recycling for Hydrogen Storage and Transportation – Electrochemical CO_2 Removal and Fixation, Energy Conversion and Management, 36, 899-902

Bao B., El-Halwagi M. M., Elbashir N. O., 2010. Simulation, integration, and economic analysis of gas-to-liquid processes. Fuel Processing Technology, 91, 703-713

BP, 2015. BP Statistical Review of World Energy 2015, BP, London, 64th Edition

Breyer Ch., Rieke S., Sterner M., Schmid J., 2011. Hybrid PV-Wind-Renewable Power Methane Plants – An Economic Outlook, 6th International Renewable Energy Storage Conference (IRES), Berlin, November 28-30

Breyer Ch., Tsupari E., Tikka V., Vainikka P., 2015. Power-to-Gas as an Emerging Profitable Business through Creating an Integrated Value Chain, Energy Procedia, 73, 182-189

Brown C., 2013. Gas-to-Liquid: A Viable Alternative to Oil-Derived Transport Fuels?. Oxford Institute for Energy Studies, Oxford, May

Caldera U., Bogdanov D., Breyer Ch., 2015. Local cost of seawater RO desalination based on solar PV and wind energy: Economics, global demand and the impact of full load hours, 31st EU PVSEC, Hamburg, September 14-18, DOI: 10.4229/31stEUPVSEC2015-6AV.4.31

Carbon Tracker, 2013. Unburnable Carbon 2013: Wasted capital and stranded assets, London, www.carbontracker.org

Carbon Tracker, 2015. Carbon Asset Risk: From Rhetoric to Action, London, www.carbontracker.org

Chedida R., Kobroslya M., Ghajarb R., 2007. The potential of gas-to-liquid technology in the energy market: The case of Qatar. Energy Policy, 35, 4799-4811

Climeworks AG, 2015a. www.climeworks.com/, Zürich.

Climeworks AG, 2015b. Private communication, Zürich, September 6

[EIA] – U.S. Energy Information Administration, 2015. Gasoline and Diesel Fuel Update. EIA, Washington D.C., available at www.eia.gov/petroleum/gasdiesel/dieselpump_hist.cfm/ [accessed on 24.10.2015]

Elder R., Cumming D., Mogensen M. B., 2015. Chapter 11 - High Temperature Electrolysis, In: Styring P., Quadrelli E. A., Armstrong K. (eds.), Carbon Dioxide Utilisation, Elsevier, Amsterdam, pp. 183-209

Fasihi M., Bodanov D., Breyer Ch., 2015. Economics of Global LNG Trading Based on Hybrid PV-Wind Power Plants, 31st EU PVSEC, Hamburg, September 14-18, DOI: 10.4229/31stEUPVSEC2015-7DO.15.6

Fleisch T. H., Sills R. A., Briscoe M. D., 2002. Emergence of the Gas-to-Liquids Industry: a Review of Global GTL Developments. J. Natural Gas Chemistry, 11, 1-14

[FVV] – Forschungsvereinigung Verbrennungskraftmaschinen, 2013. Kraftstoffstudie - Zukünftige Kraftstoffe für Verbrennungsmotoren und Gasturbinen, study performed by Ludwig-BLudwi-Systemtechnik (lbst) on behalf of FVV, FVV, Frankfurt, November

Gerlach A.-K., Stetter D., Schmid J., Breyer Ch., 2011. PV and Wind Power – Complementary Technologies, 26th EU PVSEC, Hamburg, September 5-9, DOI: 10.4229/26thEUPVSEC2011-6CV.1.32

Glebova O., 2013. Gas-to-Liquid: Historical Development and Future Prospects. Oxford Institute for Energy Studies, Oxford, December

Graves Ch., Ebbesen S. D., Mogensen M., Lackner K. S., 2011. Sustainable hydrocarbon fuels by recycling CO_2 and H_2O with renewable or nuclear energy, Renewable and Sustainable Energy Reviews, 15, 1-23

[GREET] - The Greenhouse Gases, Regulated Emissions, and Energy Use In Transportation Model, 2010, developed by Argonne National Laboratory, Argonne, IL, August 26. www.greet.es.anl.gov

Hoek A., 2006. The Shell GTL Process: Towards a World Scale Project in Qatar: the Pearl Project. DGMK-Conference "Synthesis Gas Chemistry". Dresden, October 4-6

[IEA] – International Energy Agency, 2014a. World Energy Outlook 2014. IEA, Paris

[IEA] – International Energy Agency, 2014b. World Oil Transit Chokepoints. IEA, Paris

[IPCC] - Intergovernal Panel on Climate Change, 1996. Guidelines for National Greenhouse Gas Inventories, Reference Manual (Volume 3), IPCC, Geneva, www.ipcc.ch

[IPCC] – Intergovernmental Panel on Climate Change, 2014. Climate Change 2015: Synthesis Report – Summary for Policymakers, IPCC, Geneva, www.ipcc.ch

Jensen K. L., R. Jamey Menard R., and English B. C, 2013. Market Analysis for Fischer-Tropsch Waxes, Department of Agricultural and Resource Economics, University of Tennessee, available at: http://beag.ag.utk.edu/pub/WaxFinal.pdf

Khalilpour R. and Karimi I.A. 2012. Evaluation of utilization alternatives for stranded natural gas. Energy, 40, 317-328

Konovessis D., 2012. An investigation on cost-effective tanker design configurations for reduced oil outflow. Ocean Engineering, 49, 16-24

Klerk de A., 2014, Chapter 12 - Transport Fuel: Biomass-, Coal-, Gas- and Waste-to-Liquids Processes, In: Letcher T.M., Future Energy, 2nd ed., Elsevier, Boston, pp. 245-270

Maitlis P.M. and Klerk de A. (eds.), 2013. Greener Fischer-Tropsch Processes for Fuels and Feedstocks, Wiley-VCH, 1st ed., Weilheim

MAN, 2013. Propulsion Trends in Tankers MAN. MAN Diesel & Turbo – a member of the MAN Group. September, Denmark. www.dieselturbo.man.eu

Millet P., 2015. Chapter 9 - Hydrogen production by polymer electrolyte membrane water electrolysis, In: Subramani V., Basile A., and Veziroğlu T. N. (eds.), Woodhead Publishing Series in Energy, Compendium of Hydrogen Energy, Woodhead Publishing, Oxford, pp. 255-286

Millet P., and Grigoriev S., 2013. Chapter 2 - Water Electrolysis Technologies, In: Gandía L. M., Arzamendi G., Diéguez P. M. (eds.), Renewable Hydrogen Technologies, , Elsevier, Amsterdam, pp. 19-41

[NPC] – National Petroleum Council, 2007. GAS TO LIQUIDS (GTL), NPC, Washington D.C, available at: www.npc.org/Study_Topic_Papers/9-STG-Gas-to-Liquids-GTL.pdf

[OECD] - Organisation for Economic Co-operation and Development, 2013. Climate and Carbon: Aligning Prices and Policies, OECD, Paris, Environment Policy Papers, No. 1, October 9

Pleßmann G., Erdmann M., Hlusiak M., Breyer Ch., 2014. Global Energy Storage Demand for a 100% Renewable Electricity Supply, Energy Procedia, 46, 22-31

Rostrup-Nielsen J. R., 2000. New aspects of syngas production and use, Catalysis Today, 63, 159-164

Sea distances, 2015. Online tool for calculating distances between seaports, www.sea-distances.org, Accessed on 01.08.2015

Specht M., Sterner M., Stürmer B., Frick V., Hahn B., 2009. Renewable Power Methane - Stromspeicherung durch Kopplung von Strom- und Gasnetz - Wind/PV-to-SNG, Patent No: 10 2009 018 126.1, patent filed in March 9

Sterner M., 2009. Bioenergy and renewable power methane in integrated 100% renewable energy systems, Dissertation, University of Kassel

Udaeta M. E. M., Burani G. F. B., Maure J. O. A, Oliva C. R., 2007. Economics of secondary energy from GTL regarding natural gas reserves of Bolivia, Energy Policy, 35, 4095-4106

[UNCTAD] - United Nations Conference on Trade and Development, 2009. Review of Maritime Transport. UNCTAD, New York and Geneva, http://unctad.org/en/Pages/Publications/Review-of-Maritime-Transport-(Series).aspx

Velasco J. A., Lopez L., Velásquez M, Boutonnet M, Cabrera S, Järås S, 2010. Gas to liquids: A technology for natural gas industrialization in Bolivia, J. Natural Gas Science and Engineering, 2, 222-228

Velocys, 2015a. www.velocys.com/, Houston

Velocys, 2015b. Private communication, October 21

Wood D.A, Nwaoha Ch., Towler B.F., 2012. Gas-to-liquids (GTL): A review of an industry offering several routes for monetizing natural gas. J. Natural Gas Science and Engineering, 9, 196-208

Wurzbacher J., 2014. Capturing CO_2 from Air, 3rd Carbon Dioxide Utilization Summit, Bremen, October 22

Conference Proceedings

Solar World Congress 2015
Daegu, Korea, 08 – 12 November 2015

PROGRESS IN SOLAR ENERGY R&D IN NORTH OF CHILE: SOLAR PLATFORM OF ATACAMA DESERT PROJECT AND ONGOING ACTIVITIES

Carlos Portillo[1], Elisa Alonso[1], Angel Fernández[1], Pablo Ferrada[1], Alessandro Gallo[1], Martin Guillaume[1], Aitor Marzo[1] and Edward Fuentealba[1]

[1]University of Antofagasta. Centro de Desarrollo Energético Antofagasta, Chile. Avda. Angamos 601, 1270300, Antofagasta, Chile.

Abstract

Chile is now considered one of the highest potential markets for solar energy, due to the very high solar resource existing particularly in the North and the political boosting by means of becoming legislation. In the Atacama Desert highest irradiation levels in the world are achieved, over 8 kWh m^2 per day. In order to take advantage of it, the Chilean government is intended that 20% of the country's energy from renewable sources in 2025. Under this context, PV and solar thermal commercial plants, including CSP, are already operating and others under construction. In order to actively contribute to the solar resource exploitation in North of Chile, new R&D activities are being developed in the last few years by the local universities and research centers. They include the foundations of the Solar Platform of Atacama Desert (PSDA), in the Antofagasta Region, which aims to host R&D pilot-scale solar facilities for demonstrative tests under the natural environment of Atacama Desert. An overview of the related ongoing activities is presented in this work.

Keywords:*North of Chile, Solar Energy Research, Solar Platform, Atacama Desert*

1. Introduction

The Atacama Desert exhibits the highest solar radiation levels in the world with a low frequency of cloudiness in areas apart from the coast. Data showed in Fig. 1 are available in Solargis (Geomodel, 2015) and illustrate the direct normal irradiation (DNI) in the world and global horizontal irradiation (GHI) in Chile. As observed, average annual DNI of 3800 kWh/m^2 is achieved only in the Atacama Desert.

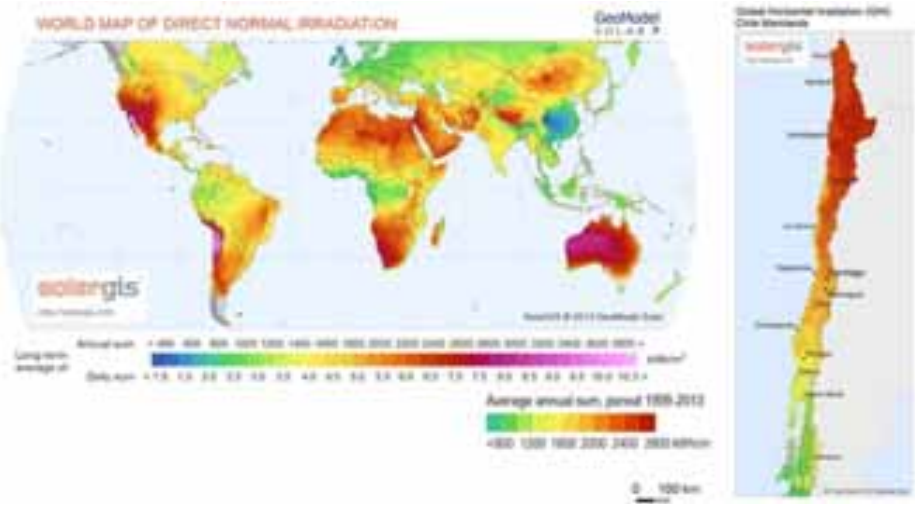

Fig. 1: World DNI and Chile GHI maps taken from Solargis.

doi:10.18086/swc.2015.09.04 Available at http://proceedings.ises.org

Despite this potential, Chile still imports the 70% of its primary energy and electricity prices have increased significantly in the last decade. Energy sources are mainly fossil fuels (coal, GNL and diesel). Moreover, Chilean industry, mostly mining, has high demands of electricity (90 % of the Northern electric system, SING) and heat (Ministerio de Energía, 2016). Although the current solar contribution to SING is yet only 1.91%, the construction of new commercial PV, solar thermal and CSP plants is ongoing since last few years. In order to contribute to this development, new local R&D activities are also being started. One of them is the PSDA, which is projected as an in-situ pilot plant to demonstrate and test solar energy technologies under the natural environment of the Atacama Desert.

2. Solar Platform of Atacama Desert Project

2.1. Objectives

Solar Platform of Atacama Desert was conceived as a technological project with the following objetives:

- To promote and carry out R&D according to the guidelines emanating from different government agencies.
- To promote collaboration with universities and national and international R&D centers in various technological areas related to solar energy.
- To provide specific knowledge opportunities that can meet the future needs of advanced human capital and technical product specialists.
- To promote collaboration with regional and national companies that allow for adequate transfer and commercialization of the developed technologies.
- To promote the productive chain and the creation of spin-offs.
- To provide technical services, including advice and consultancy services to both public and private institutions.
- To foster scientific and technological diffusion, promoting general public to aware of the advantages and benefits of the solar energy technologies.
- To become a reference center in solar energy technologies, not only in Chile but also in the whole Latin American context.

2.2. Funding and political coordination

Funds invested so far in the PSDA are contributions of the Regional Government and the University of Antofagasta which reached US $ 1.35 Million. Currently, the PSDA is considered as the Chilean Laboratory for Solar Energy Research, defined by the Corporation for promotion of production (CORFO), through the National Center for Innovation and the Sustainable Energy Development (CIFES) who is applying resources to the National Strategic Investment Fund (FIE) to cover the operating costs of the Strategic Solar Programme. It considers promoting the development of the solar industry in Chile between 2015 and 2025. For the PSDA are an approximate amount of US $ 50 Million are being evaluated for facilities, laboratories and physical adjustments. These investments are being proposed through Solar Energy Research Center (SERC Chile) and international centres based in Chile.

2.3. Current status

Currently , the land of PSDA is available and the first studies have been already carried out or are financed for the next future. Such studies are the following.

- Study on the "Structural Design and Operational Research and Development of Solar Energy in Northern Chile." STA-CDEA-UA. 2010

- Framework agreement between Centre for Energy, Environment and Technological Investigations (CIEMAT) of Spain and the University of Antofagasta. 2010
- Award of "Fourth National Competition for Centers of Excellence in Research on Priority Areas FONDAP 2013-2018." Chilean project Solar Energy Research Center (SERC-Chile).
- Award of performance agreement for higher education "Strengthening the University of Antofagasta as Regional and National Reference in Non-Conventional Renewable Energy (ERNC)." 2013-2015.
- FIC-R 2013 (Innovation Fund for Competitiveness) "Implementation, development and diffusion of the Plataforma Solar Atacama Desert inserted into the system of regional technology parks first stage". 2013 - 2014.
- FIC-R 2014 (Innovation Fund for Competitiveness) "Implementation of advanced instrumentation system as technological support of the PSDA project, first stage". 2014 – 2015
- FIC-R 2015 (Innovation Fund for Competitiveness) "Positioning of in-situ solar technology laboratory (PSDA) for the purpose of applied research, extension and training of technicians from the Region of Antofagasta. 2015 – 2017.
- Tender for design and feasibility analysis of a solar platform technology development in northern Chile funded by CORFO. It consist in an update and the business model definition of a study made in 2010

2.3. Future projection

PSDA is projected as an applied research platform in-situ , destined to test new technologies and materials considering the conditions of high radiation. In addition, it will be used to support the productive chain of the solar energy local industry, technical certificates for PV and CSP facilities and certification of products to high radiation. Complementary technologies to supply heat and miners processes of the Atacama Desert will be analyzed.

3. Current R&D Activities

3.1. Radiometry and Calibration Laboratory applied to solar technologies (RCL) and Solar resource

Due to the high levels of solar radiation and the low frequency of cloudiness in areas out from the coast, below the 10% on most sites at north (see fig. 2), the Atacama Desert rises like a promising area for solar power plants implementation.

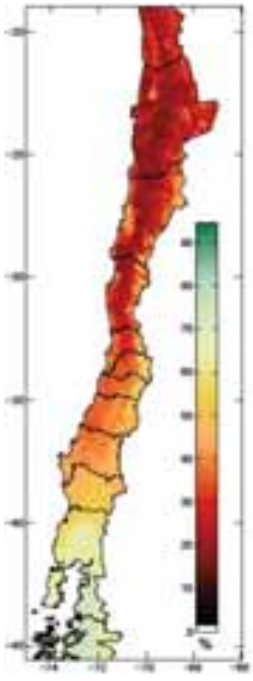

Fig. 2: Annual cloudiness in Chile (Molina Monje and Rondanelli Roias. 2012)

Accurate solar radiation measurements are necessary for the implementation of solar power plants anywhere. Especially, they are essential for centers which aim research on solar technologies. Precise solar radiation measurements are crucial to determine, e.g. the efficiency of the tested prototypes or the degradation of materials used in solar technologies. Such applications involve a series of records of terrestrial surface radiation components and other meteorological components.

The PSDA is implementing a meteorological station focused on measuring solar radiation, but also for other generic weather variables, such as temperature, atmospheric pressure and relative humidity, wind speed and direction, etc. The meteo station counts on the most advanced radiometric instrumentation. Within its equipment for solar resource, it has several types of pyranometers based on photo-cells and thermopile with individually optimised temperature compensation for measuring the Global and Diffuse Horizontal and Tilted Radiation, First Class pyrheliometers for measuring Direct Normal Irradiance, UV Radiometers to

measure the horizontal UV-A and UV-B horizontal irradiance, several two-axis solar trackers, shadow balls, etc.

Research on solar resource have shown the high radiation levels available in Atacama Desert. For example, in Fig. 3, monthly global horizontal irradiation, H_m [kWh m^{-2}], is compared with three available satellite-derived solar radiation datasets: the 22-year average data from the NASA-SSE (Surface Meteorology and Solar Energy programme) (Stackhouse, 2011), the Solar GIS (Geomodel, 2015) and the Explorador de Energía Solar (EE Solar) model (Ministerio de Energía, 2015; Ministerio de Energía et al., 2015). The total annual irradiation achieved a value of 2554 kWh m^{-2} $year^{-1}$ during the period of measurement. This is a high value that overcomes the values achieved in, e.g., Doha (Qatar) with 2048 kWh m^{-2} $year^{-1}$ (Bachour and Perez-Astudillo, 2014) or the 2190 kWh m^{-2} $year^{-1}$ achieved in Abu Dhabi, the highest one of the Arab state capitals according to Islam (Islam et al., 2010, 2009).

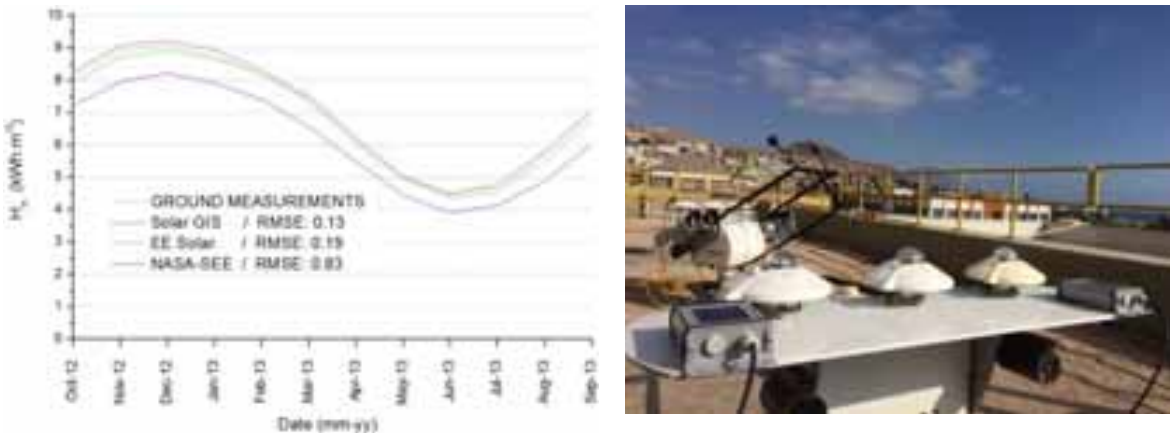

Fig. 3: Left, results of the comparison of monthly average of Global Horizontal Irradiation values derived from ground measurements against three typical years derived from satellite data: Solar GIS, EE Solar and NASA-SEE. This task was developed for a local mining company sited in Atacama Desert. Right , validation of pyranometers and pyrheliometers performance by comparison with reference instrumentetion at Universidad de Antofagasta.

The PSDA Radiometry Area tasks have been defined to provide support to the local industry in different research areas. These tasks may be summarised in four groups:

1. Instrumentation checking: testing, validation and calibration tasks to ensure the accuracy of the measurements;
2. Data evaluation: generating an accurate database and studies related to the physics of the atmosphere and the solar resource assessment;
3. Optics: optical characterisation of surfaces used in solar technologies;
4. Measurement methodologies and instrumentation development: provide tools by developing and/or adapting instrumentation with different applications to solve the measurement problems related with the new research studies to develop on solar energy area.

To achieve said goals, collaboration is ongoing with a number of national and international research centers, such as the Plataforma Solar de Almería (PSA, Spain), Universidad de Almería (UAL, Spain), and the universities belonging to the Solar Energy Research Center (SERC-Chile).

3.2. Solar PV

In collaboration with the PSDA Radiometry Area, there are also developing studies of how the Atacama environment affects the optical properties of mirrors and glasses used for solar technologies. These studies are focused on relating the surface optical degradation with the deposition rate of soiling and dust over the time. With the common aim of studying the effect of soiling on solar technologies efficiency, the

performance ratio (PR) is the most used indicator, also at the PSDA, to investigate the degradation at PV plants (IEC, 1998). The goal is to relate and correlate optical degradation of PV glass with the PR and examine the causes for this degradation. Thus, tasks within PV area include:

- Precise inspection of PV plants with current-voltage (IV) curve tracers.
- Characterization of optical properties of PV glass.
- Determination of the physical-chemical properties of accumulated dust.
- Inspection o PV plants with IV tracers, IR cameras and, in the near future, with electroluminescence.
- Study of bifacial PV modules.
- Calculation of the Levelized Cost of Electricity (LCOE)

Currently, PV plants of different technologies are being installed and will be fully operational in 2015. The technologies include mc-Si, monocrystalline Si and HIT (heterostructure with intrinsic thin layer) modules. In total, 6 plants of the size of ≈1.2 kWp each of several features such as potential induced degradation (PID) free, monofacial and bifacial glass to glass will be used to compare in situ the performance and soiling effects. The comparison goes further as the same installations will be available at the coastal zone of the Atacama Desert, in the campus of the Antofagasta University. Examples of such studies at the coastal zone of the Atacama Desert are found in Ferrada et al. (2015). It was pointed out that the maximum PR at these conditions for mc-Si modules of 230 Wp was 85% and that the rate by which PR can degrade was up to 4.5%/month. Studies regarding the resulting levelized cost of electricity (LCOE) for PV plants athe coastal zone of Atacama Desert are addressed in Fuentealba et al. (2015). Since the characteristics of the environment and solar resource may be much different at the PSDA compared to the coastal zone of Atacama Desert, detailed studies under local conditions are required.

In addition, the existing collaboration between the Centro de Desarrollo Energético Antofagasta and SERC with the International Solar Energy Research Center Konstanz (ISC Konstanz) in Germany focuses on the development of AtaMo, the solar module for the Atacama Desert. The project consists on the selection of best materials for the PV module which perform best in the Atacama Desert. Sets of solar cells based on crystalline silicon are constantly fabricated in Konstanz, and then mini modules of 1 to 4 cells are produced. The mini modules are tested in situ at the PSDA by using a current-voltage (IV) curve tracer of same technology and same measurement principle as the indoor sun simulator existing at the laboratories of ISC Konstanz. The solar cells used are monofacial on p-type mono and multi crystalline silicon substrates and bifacial on n-type monocrystalline silicon wafers, both of the size 15.6 by 15.6 cm^2. Mini modules are fabricated with PV glass of several thicknesses (from 3.2 standard down to 2 mm, 1.5 mm and 1 mm), different encapsulants such as Ethylene vinyl acetate (EVA), thermoplastic materials (TM) and low UV light cut-off (U encapsulant). The backsheets (BS) consist of standard (white), transparent and desert type sheets (optimized in terms of hardness and thickness for desert regions), as well as glass (as BS) are employed.

An AAA class solar simulator is used to measure the IV characteristics indoor at standard testing conditions (STC) before and after the lamination step to determine the cell to module losses (CTM). For the last experiment a total of 37 groups were fabricated, from which 14 groups were based on mc-Si cells for damp heat (DH), humidity freeze (HF) and ultraviolet (UV) degradation test, and 23 groups based on bifacial n-type cell for thermos cycling (TC) test and outdoor measurements at the PSDA. Fig. 4 illustrates a measurement campaign at the PSDA.

Fig. 4. Left: Set of mini modules and testing configuration at the PSDA. Right: Albedometer to quantify solar resource for mini modules.

A first evaluation of results point out to the optimum combination of materials. It consists of the use of thinner glass-glass module (1.0 to 2.0 mm thickness) showing better resistivity against thermal stress compared to glass-transparent back sheet. The encapsulant shall be used as due to its high robustness against long-term humidity exposure and higher transmissivity expected in the UV-B range. Modules with halved cells resulted to perform better in the field due to lower electrical power losses at high irradiation conditions. For full details, refer to Cabrera et al. (2015). A very preliminary estimation based on a maximum PR value of 85% for conventional mc-Si modules, bifacial AtaMo modules could generate between 29% to 32% more energy compared to mc-Si modules utilizing 23% to 33% less area, both assuming a 1 MWp PV plant.

3.3. Solar thermal and CSP systems

In the field of solar thermal technologies, several plants have been installed in the North of Chile in the last few years. Flat and parabolic trough collectors were mounted to provide heat for mining processes, mainly, where the energy consumption has reached 161.716 TJ in 2014 (including electricity and fuel). Currently, analyses of all the possible applications of solar energy in mining are being investigated. In particular, attention is paid to that processes which require the use of heat. In Fig. 5, several applications to processes sulfides and oxides are highligthed. In particular, electro-winning and anodes washing present high heat consumption and temperatures below 100°C in copper production processes.

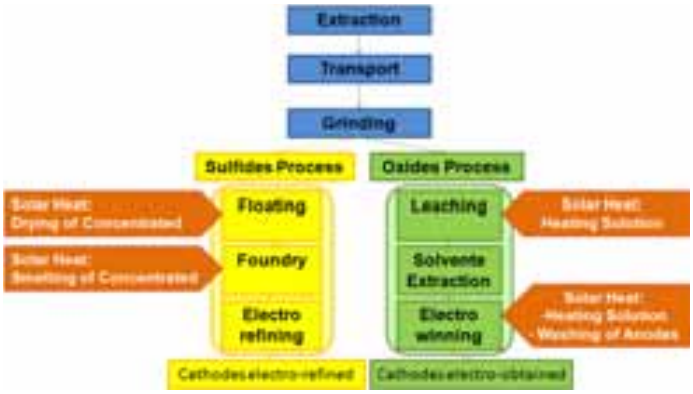

Fig. 5: Possibility for solar heat applications in copper mining processes

Researchers at University of Antofagasta are having the opportunity to collaborate with the most important local mines and to monitor the proper working of those solar facilities. Some studies have been carried out: in one case it was analysed the behaviour of the solar plant (Ushak et al., 2014) and in another one, a TRNSYS model is compared with a solar thermal pilot plant (Gallo et al., 2015). The next scheduled study concerns a parabolic trough system for heating the electrolyte in another mining company.

In Gallo et al. (2014) the integration of thermal collectors with an absorption machine was proposed for the air-conditioning of container in mining camps of the Atacama Desert. At Energy Development Center of Antofagasta, a demonstrative solar thermal plant for hot water heating is currently under installation and it is planned to install another one in the PSDA to study the effect of soiling on such systems with different environmental conditions.

A 7 kW_e solar simulator has been recently acquired in the Energy Development Center at Antofagasta University and will be shortly implemented together with a flux measurement system. Such a device will be employed as high flux radiation source until a real solar system is developed in the Solar Platform of Atacama Desert. Studies at high temperature are programmed to be addressed using the solar simulator. Most of them are focused on the solar energy usage in copper mining. Since copper extraction involves metallurgical processes at 1200 ºC they are being analysed from the point of view of their integration with concentrating solar energy systems. On the future development axis of the Solar Platform will be the proof of concept of these solar mining processes for what pre-industrial scale facilities are planned.

3.4 Thermal storage of concentrating solar energy

Chilean salt deposits have the potential to be exploited to obtain new molten fluids with the possibility to improve the properties currently associated to the solar binary salt (60% $NaNO_3$ + 40% KNO_3) used for Thermal Energy Storage (TES) in CSP plants. In this line, research and development in the solar energy sector is focussed on reducing the high cost of the operation and maintenance of these plants. One of the most important research lines in this context is the study, design and characterisation of salts that are used as energy storage fluids.

Binary mixtures of alkali molten nitrates/nitrites present phase diagrams with simple eutectic point and byadding one or more components, it is expected that the resulting mixture will have a lower melting point compared to the initial eutectic binary mixture. The design of multicomponent mixtures by the addition ofalkali/alkaline earth nitrates could extend the working temperature range of thermal energy storage (Bauer et al., 2014; Cordaro et al., 2011; Fernández et al., 2012; Gil et al., 2010; Mantha et al., 2012; Medrano et al., 2010; Olivares, 2012; Peng et al., 2010; Raade and Padowitz, 2011). The additives that present greater potential to be used for solar energy storage are $Ca(NO_3)_2$ and $LiNO_3$ as these salts decrease the melting point and improve the thermal stability, respectively.

Tab. 1: Thermophysical properties of Chilean lithium/calcium nitrate containing molten salts.

Molten salt mixture (wt.%)	Work temp. range (°C)	Viscosity at 250°C (cP)	Corrosion rate of A516 Steel at 390°C (mm/year)	Electrical conductivity at 390°C (Ω-1m-1)	Energy density (MJ/m3)	Salt Price (US$/Ton)	Two-tanks system cost/stored energy (US$/kWhth)
Solar Salt	221–589	5.51	0.97	0.37	550	893	11.67
20 $LiNO_3$ – 52 KNO_3 – 28 $NaNO_3$	130–600	6.3	0.31	0.67	513	1161	16.35
30 $LiNO_3$ – 10 $Ca(NO_3)_2$ – 60 KNO_3	134–567	5.72	0.027	0.56	607	1274	15.07
10 $LiNO_3$ – 10 $Ca(NO_3)_2$ – 60 KNO_3 – 20 $NaNO_3$	132–580	5.78	0.013	0.45	680	1038	10.98

Some researches leading by Antofagasta University (Fernández et al., 2015, 2014) have proposed the study of molten salts of more than three components as a new possibility, showing a higher energy density, based on the heat capacity, which represents an important improvement over the solar salt currently used. It is important to note that based on this parameter, a smaller amount of salt could be used to store the same amount of energy.Results obtained for the new molten salts developed at Antofagasta University were compared to baseline Solar Salt (60wt.% $NaNO_3$ – 40wt.% KNO_3) properties found in the literature (Fernández et al., 2015, 2014).

The production of $LiNO_3$ at industrial scale is the current challenge in northern Chile and could be the key for a successful development of the new generation of CSP plants but it is necessary to perform storage tests in a bigger scale and real conditions.

In this respect, the Energy Development Center at Antofagasta University is equipped with a loop of molten salts with a working range of 130-500ºC, to test the performance of new raw materials potentially suitable for its use as solar storage in the existing solar technologies using molten salt storage. In addition, the current facilities also include systems for testing the dynamic corrosion produced by the molten salts on different carbon steels, stainless steels and other coated steels, under different flow rates. Results obtained and lessons learned will be applied in the molten salt loop to be build in the Atacama Solar Platform.

A different approach to thermal storage using materials widely available in Northern Chile is based on thermochemical redox cycles of metals oxides. The interest is significant because Chile produces 34% of the global mined copper, what means that it is the larger producer in the world. The impact of copper industry in the Chilean economy is very high: it represents more than 12% of the Chilean GDP.

The redox pair CuO/Cu_2O was proposed by Wong et al. (2010, 2011) as a possible candidate for thermochemical storage of solar energy. Its viability was demonstrated in a solar rotary reactor where the reduction from CuO into Cu_2O was achieved at temperature up to 1000 ºC (Alonso et al., 2015). This study was carried out in the framework of a colaboration between the Energy Development Center at Antofagasta University and the Renewable Energy Institute of Universidad Autónoma de México (UNAM). The solar furnace at Institue of Renewable Enrgy (HoSIER) of UNAM was employed as radiation source. The progress of the reduction was monitored by recording the amount of oxygen delivered inside the solar reactor. 10 g of CuO were introduced in batch mode into the reactor as starting reactant. Gas flow was 10 Nl/min and pressure was very close to atmospheric during all the experiments. 80% of the starting CuO could be reduced into Cu_2O. Also, several cycles of reduction and oxidation were achieved. However, chemical conversion for both, reduction and oxidation was not complete. Different improvements are currently under study and development to be applied to the experimental procedure with the objective of increasing the fraction of active material. Firstly, a theoretical analysis of the operation parameters influence on the thermodynamic equilibrium was realized. As an example of this work, Fig. 6 shows the effect of the total pressure and the atmosphere composition in the equilibrium of the copper oxides system. The lower the pressure, the lower the temperature at which the reduction of CuO starts as expected according to Le Chatelier principle. The maximum conversion of CuO into Cu_2O (87.7%) occurred at 1600ºC at 1 bar of total pressure. By decreasing the pressure to 0.1 bar, the maximum conversion rises to 89.9% and it is achieved at 1400 ºC. On the contrary, the higher the pressure, the higher the temperature at which the maximum conversion is reached. At 10 bar, the maximum conversion is achieved at 1875 ºC and has a value of 84.6%. When applied for TCS, these redox processes are proposed in air because of economic reasons. However, it could be assessed to carry out the reduction stage in inert atmosphere since it would benefit the reaction. In Fig. 6b the graphs indicate that the lower the O_2 concentration the lower the equilibrium temperature. For copper oxides, the maximum conversions are 89.2% at 1575 ºC and 90.4% at 1550 ºC for 10/90 and 5/95 O_2/N_2 relations respectively. The advantages compared to air composition are not very significant in terms of conversion increasing and temperature decreasing. However, if the carrier gas is pure N_2, conversion can be increased to 93.4% at 1475 ºC, what represents an augmentation of 5.7% in the maximum conversion value at temperature 125 ºC lower than the process in air. More details can be found in Alonso et al. (2016).

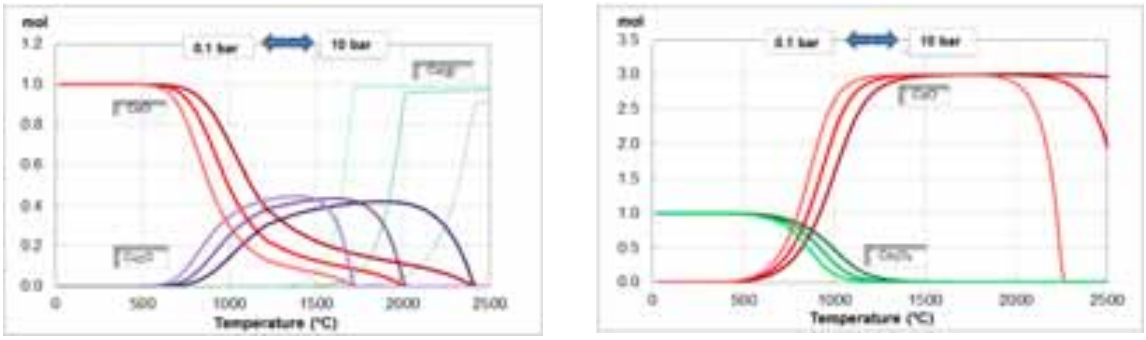

(a) (b)

Fig. 6: Effect of (a) total pressure on the thermodynamic equilibrium with a ratio air/reactant of 30. b) CuO/Cu_2O and b) gas composition in the thermodynamic equilibrium with 1 bar of total pressure and gas/solid molar ratio of 30

Experimental investigations of this system are currently under development. A lab scale facility based in a solar reactor is being constructed to be coupled with the solar simulator. The reactor consists on a rotary ceramic cavity provided with a transparent window and a gas inlet and outlet (Fig. 7). This prototype is designed to optimize the redox reactions for thermochemical storage with direct absorption of solar radiation.

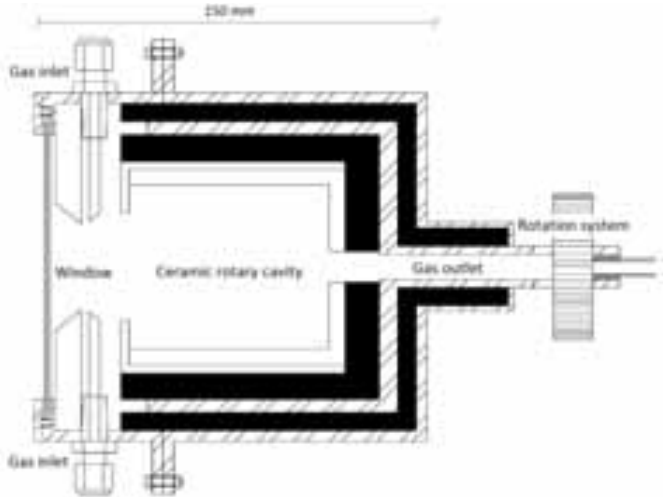

Fig. 7:Lab scale solar reactor sketch for thermochemical storage based on metal oxides based with direct radiation absorption.

In parallel to the design of the reactor, a numerical model to study the thermal behavior of the cavity was carried out. The aim of the work was to analyze how the use of different concentrators affects the cavity wall temperature. To do that, different flux distributions obtained with a ray tracing software were integrated in a CFD model. The first case was a flat profile radiation that impinged on the rear part of the reactor. Then, flux distributions generated by a solar simulator composed of an elliptical mirror and a high power lamp and by a multi-faceted concentrator was considered for the analysis. It was found a relation between the flux profile and the temperature distribution. In particular, higher temperatures were achieved at the back side of the cavity, where the most part of the radiation impinged. The most homogeneous temperature distribution was achieved for the multi-faceted concentrator case. More details can be found in Gallo et al. (2016). For the future, a more accurate model, which includes the solid phase, will be added and it will be validated with experimental tests.

With respect to the Solar Platform, future plans include the development of a scaled-up realistic facility to work under the local solar conditions. Thus current works are focused to study the performance and optimize a directly irradiated thermochemical solar energy storage system based on metal oxide particles.

4. Conclusions

Chile has a great opportunity to participate in the development and future trends of concentrated solar technology due to its potential for exploiting existing raw materials for solar energy storage and the great solar resource in the north of the country.

The proposal of new storage material using by-products and the consolidation of pilot plants in the Atacama Solar Platform, in order to obtain potential TES material is a growing trend in the institutional and private research initiatives in Chile. However, the lack of reliable and accurate data related to this topic requires a reinforcement of the relationship between Chilean institutions and solar market companies.

Due to the high demand of energy associate to mining industry, solar energy explotation in North of Chile has a special focus on this sector. In fact, mining energy demand is the most important of the country and a part of it is the form of heat. The application of solar heat is being evaluated for different stages of the cupper extraction process: floating, leaching and electrowining are examples of low temperature processes while foundry could be addressed with concentrated solar energy. R&D studies are being started in both directions and some of them count with the support of mining companies. Finally, electricy production by PV or CSP (with different types of thermal storage) is also expected to has a significant contribution to the electricity demand flat curve that characterize the mining zones of Northem Chile.

5. References

Alonso, E., Gallo, A., Pérez-Rábago, C., Fuentealba, E., 2016. Thermodynamic study of CuO/Cu_2O and Co_3O_4/CoO redox pairs for solar energy thermochemical storage. AIP Conf. Proc. 1734, 050004. doi:10.1063/1.4949102

Alonso, E., Pérez-Rábago, C.A., Licurgo, J., Fuentealba, E., Estrada, C.A., 2015. First experimental studies of solar redox reactions of copper oxides for thermochemical energy storage. Sol. Energy 115, 297–305. doi:10.1016/j.solener.2015.03.005

Bachour, D., Perez-Astudillo, D., 2014. Ground measurements of Global Horizontal Irradiation in Doha, Qatar. Renew. Energy 71, 32–36. doi:10.1016/j.renene.2014.05.005

Bauer, T., Laing, D., Tamme, R., 2014. Recent Progress in Alkali Nitrate/Nitrite Developments for Solar Thermal Power Applications, in: Molten Salts Chemistry and Technology. John Wiley & Sons, Ltd, Chichester, UK, pp. 543–553. doi:10.1002/9781118448847.ch7c

Cabrera, E., Schneider, A., Rabanal Arabach, J., Ferrada, P., Cordero, R., Fuentealba, E., Kopececk, R., 2015. Advancements in the developtment of "Atamo": A solar module adapted for the climat conditions of the Atacama Desert in Chile, in: EU PVSEC (Cod. 5EO.1.6). Hamburg.

Cordaro, J.G., Rubin, N.C., Bradshaw, R.W., 2011. Multicomponent Molten Salt Mixtures Based on Nitrate/Nitrite Anions. J. Sol. Energy Eng. 133, 011014. doi:10.1115/1.4003418

Fernández, A.G., Lasanta, M.I., Pérez, F.J., 2012. Molten Salt Corrosion of Stainless Steels and Low-Cr Steel in CSP Plants. Oxid. Met. 78, 329–348. doi:10.1007/s11085-012-9310-x

Fernández, A.G., Ushak, S., Galleguillos, H., Pérez, F.J., 2014. Development of new molten salts with $LiNO_3$ and $Ca(NO_3)_2$ for energy storage in CSP plants. Appl. Energy 119, 131–140. doi:10.1016/j.apenergy.2013.12.061

Fernández, A.G., Ushak, S., Galleguillos, H., Pérez, F.J., 2015. Thermal characterisation of an innovative quaternary molten nitrate mixture for energy storage in CSP plants. Sol. Energy Mater. Sol. Cells 132, 172–177. doi:10.1016/j.solmat.2014.08.020

Ferrada, P., Araya, F., Marzo, A., Fuentealba, E., 2015. Performance analysis of photovoltaic systems of two different technologies in a coastal desert climate zone of Chile. Sol. Energy 114, 356–363. doi:10.1016/j.solener.2015.02.009

Fuentealba, E., Ferrada, P., Araya, F., Marzo, A., Parrado, C., Portillo, C., 2015. Photovoltaic performance and LCoE comparison at the coastal zone of the Atacama Desert, Chile. Energy Convers. Manag. 95, 181–186. doi:10.1016/j.enconman.2015.02.036

Gallo, A., Alonso, E., Pérez-Enciso, R., Fuentealba, E., Pérez-Rábago, C., 2016. Numerical approach to the flux distribution effect on a solar rotary kiln performance. AIP Conf. Proc. 1734, 030016. doi:10.1063/1.4949068

Gallo, A., Alonso, E., Pulido, D., Fuentealba, E., 2014. Análisis tecno-económico de soluciones integrales de habitabilidad en emplazamientos mineros de las regiones del norte de Chile basadas en envolventes

modulares con acondicionamiento solar por absorción, in: XI Congreso Iberoamericano de Energía Solar.
Gallo, A., Guillaume, M., Portillo, C., Fuentealba, E., 2015. Validation of a Solar Thermal Pilot Plant Model for a Copper Mining Process, in: Solar World Congress. pp. 8–12.
Geomodel, 2015. Solargis [WWW Document]. URL http://solargis.info/doc/free-solar-radiation-maps-DNI (accessed 6.13.16).
Gil, A., Medrano, M., Martorell, I., Lázaro, A., Dolado, P., Zalba, B., Cabeza, L.F., 2010. State of the art on high temperature thermal energy storage for power generation. Part 1—Concepts, materials and modellization. Renew. Sustain. Energy Rev. 14, 31–55. doi:10.1016/j.rser.2009.07.035
IEC, 1998. Photovoltaic system performance monitoring – Guidelines for measurement, data exchange and analysis 1–5.
Islam, M.D., Alili, A.A., Kubo, I., Ohadi, M., 2010. Measurement of solar-energy (direct beam radiation) in Abu Dhabi, UAE. Renew. Energy 35, 515–519. doi:10.1016/j.renene.2009.07.019
Islam, M.D., Kubo, I., Ohadi, M., Alili, A.A., 2009. Measurement of solar energy radiation in Abu Dhabi, UAE. Appl. Energy 86, 511–515. doi:10.1016/j.apenergy.2008.07.012
Mantha, D., Wang, T., Reddy, R.G., 2012. Thermodynamic Modeling of Eutectic Point in the $LiNO_3$-$NaNO_3$-KNO_3 Ternary System. J. Phase Equilibria Diffus. 33, 110–114. doi:10.1007/s11669-012-0005-4
Medrano, M., Gil, A., Martorell, I., Potau, X., Cabeza, L.F., 2010. State of the art on high-temperature thermal energy storage for power generation. Part 2—Case studies. Renew. Sustain. Energy Rev. 14, 56–72. doi:10.1016/j.rser.2009.07.036
Ministerio de Energía, 2015. Campaña de medición del recurso Eólico y Solar [WWW Document]. URL http://walker.dgf.uchile.cl/Mediciones/ (accessed 6.13.16).
Ministerio de Energía, 2016. Sistema Interconectado Norte Grande [WWW Document]. Gob. Chile. URL http://antiguo.minenergia.cl/minwww/opencms/03_Energias/Otros_Niveles/Electricidad/Sistema_Electrico/sing.html (accessed 6.13.16).
Ministerio de Energía, Departamento de GeoFísica, Universidad de Chile, 2015. Explorador de Energía Solar [www. Document]. URL http://walker.dgf.uchile.cl/Explorador/Solar2/ (accessed 6.13.16).
Molina Monje, A., Rondanelli Rojas, R., 2012. Explorador del Recurso Solar en Chile - Documentación y Manual de Uso.
Olivares, R.I., 2012. The thermal stability of molten nitrite/nitrates salt for solar thermal energy storage in different atmospheres. Sol. Energy 86, 2576–2583. doi:10.1016/j.solener.2012.05.025
Peng, Q., Ding, J., Wei, X., Yang, J., Yang, X., 2010. The preparation and properties of multi-component molten salts. Appl. Energy 87, 2812–2817. doi:10.1016/j.apenergy.2009.06.022
Raade, J.W., Padowitz, D., 2011. Development of Molten Salt Heat Transfer Fluid With Low Melting Point and High Thermal Stability. J. Sol. Energy Eng. 133, 031013. doi:10.1115/1.4004243
Stackhouse, P.W., 2011. Surface meteorology and Solar Energy, NASA Technical Reports Server.
Ushak, S., Grágeda, M., Pulido, D., Oró, E., Cabeza, L.F., 2014. Application of Solar Heating on the Electrolyte Conditioning for Electrowinning Process: Thermosolar Plant Performance. Energy Procedia 57, 2930–2936. doi:10.1016/j.egypro.2014.10.328
Wong, B., 2011. Thermochemical heat storage for concentrated solar power. Phase II final report for the period September 30, 2008 through April 30, 2011. GA-C27137. General Atomics, 2011.
Wong, B., Brown, L., Schaube, F., Tamme, R., Sattler, C., 2010. Oxide based thermochemical heat storage, in: SolarPaces Conference. Perpignan, France, pp. 21–24.

On the economic effects of metering schemes in community owned residential PV systems

Nelson Sommerfeldt

KTH Royal Institute of Technology, Stockholm (Sweden)

Abstract

Community-owned, grid-connected solar photovoltaic (PV) systems in multi-family housing offer the potential for large scale installations with favorable costs as compared to single family systems. However, traditional utility metering schemes often define boundaries which result in high sales of PV generation to the grid, lowering the economic value for the cooperative. This study explores two alternative metering schemes which better represent the interests of cooperative as a single PV owner by aggregating meters within and across buildings. Measured communal load data from a cooperative in western Sweden is combined with modeled PV generation and apartment load data to calculate the net present value (NPV) of the various meter schemes under several subsidies policies. The results show that under a traditional metering scheme, 40% of the PV generation is considered sold to the network, even though only 3% of the electricity physically leaves the buildings and none leaves the estate. Reclassifying this sold electricity as self-consumed results in an increase in NPV by as much as €60,000, which is €15,000 more than the value added by subsidies. The results of this paper are useful for community organizers, PV installers, utilities, and lawmakers interested in next generation electricity markets based on distributed generation.

Keywords: *Community solar, cooperative, self-consumption, techno-economic, utility 2.0*

1. Introduction

Multi-family housing cooperatives, such as those common in Scandinavia, have the potential for procuring large, commercial scale (30-700 kW_p) solar photovoltaic (PV) systems as a single project. These types of installations can mean increased rates of PV deployment at lower costs, but coordinating many households into an economically optimal configuration presents multiple challenges. Traditional electric utility billing structures are based on a single meter per household, so when a single PV system covers the roof of many independent meters they may not be able to access the PV generated electricity. Likewise, cooperatives often consist of multiple buildings, each with their own meter, meaning buildings with PV cannot easily share it with those that do not. This internal metering division of the cooperative can lead to high volumes of PV overproduction sold to the grid, which is economically detrimental when net metering or feed-in tariffs are not present.

Using the case of a large cooperative in western Sweden, this paper quantifies the economic effects of an internally segregated metering scheme within a single PV system owner. Two integration schemes are introduced, horizontal and vertical, and are compared with the default metering conditions. The techno-economic analysis is performed using metered load data, simulated PV production, and comparisons are made using NPV. The metering schemes are also contrasted to the economic impacts of the three primary subsidy policies for distributed PV in Sweden. The results are followed with a discussion of techniques cooperatives can and have used to desegregate their metering, their limitations, and potential for improvement. The motivation for this work is to highlight the need for solutions, whether technical, political or entrepreneurial, which can lower the barriers to community owned PV systems.

2. Background

This section provides background information regarding the structure and operation of cooperative housing in Sweden, and the context of greater electricity and PV markets which investments must be considered.

2.1 Swedish cooperative housing

Swedish housing cooperatives, which make up 22% of all residences in Sweden, are non-profit associations that typically own one housing estate or multi-family dwelling (Statsitics Sweden, 2012). They are owned exclusively by the residents of the estate, who are then given the right to reside in a portion of the building (e.g. apartment) and pay an annual fee for the operational and financial management of the association. The annual

doi:10.18086/swc.2015.09.05 Available at http://proceedings.ises.org

fee is determined on a per square meter basis, meaning larger apartments pay larger fees. A well maintained building with low operations costs results in higher property values and thus higher returns for the owners. Therefore cooperatives have an incentive to invest in cost-reduction schemes, such as self-generated electricity, in order to boost market value.

An executive board elected from the members for a period of two years acts as a governing agent for the cooperative. Each member is given a single vote during the annual meeting, but it is exercised only on issues the board deems necessary to call a general vote for. Typically, investment decisions which might have a significant effect on the annual fee paid by each member, such as major energy installations, are brought to a general vote.

Electricity use in cooperatives can be split into two categories; communal and private. Communal electricity includes stairwell and exterior lighting, HVAC, and laundry rooms, while private electricity is that which is used in individual apartments. Typically, the cooperative purchases communal electricity and the costs are distributed in the annual fee, while apartments have their own meters and purchase electricity from the retailer of their choice. It is also possible for apartment electricity to be included in the communal fee, particularly if there is electric heating which dominates the load. Another structure is for the cooperative to have a single meter with the utility and for apartments to be metered and billed internally by the cooperative. This structure has the advantage of reducing fixed grid fees, which are highest for apartments due to their relatively low demand.

2.2 The Swedish electricity market

Swedish electricity supply is dominated by two sources; hydro and nuclear power, which make up 90% of the supply, with the remaining 10% being primarily biomass fueled co-generation (Swedish Energy Agency, 2015). The annual demand is typically 140-150 TWh, or 15.3 MWh per capita, and peaks during the winter months due to a high use of electric heating. Sweden has high voltage links between Norway, Finland, Denmark, Germany, and Poland, and is typically a net exporter of electricity.

The wholesale and retail electricity markets are both deregulated. The majority of electricity is traded in the Nord Pool Spot wholesale market, where hourly prices are set one day-ahead. Retailers purchase electricity from Nord Pool and resell it to end consumers, who are free to choose any retailer they wish. They can also choose the frequency to which their tariffs follow the market, from several years to hourly. The most popular and fastest growing contract type is variable price adjusted monthly (Ei, 2015).

When Sweden joined Nord Pool in 1996, the average spot that first year was 0.032 €/kWh. Immediately after prices fell to 0.015 €/kWh and stayed there until 2001, when prices rose rapidly and became more volatile. Since 2013, there has been relatively low demand and considerable oversupply such that prices are now back to the same level as 2001(Nord Pool Spot, 2015). Low price combined with unfavorable government policy, has caused two large utilities, Vattenfall and E.On to announce early retirement of four of their oldest reactors, set to close by 2020 (World Nuclear Association, 2015; World Nuclear News, 2015).

To support renewable energy development, Sweden has a quota system, known as green certificates, which is accessible by any renewable source. Demand for certificates is set by the government, and free moving prices signal potential suppliers to build. One certificate is earned for each MWh generated, and a facility is able to earn and sell its certificates for a maximum of 15 years. The green certificate program has been mostly utilized by wind and biomass based CHP (Swedish Energy Agency, 2015).

2.3 The Swedish PV market

Relative to many other countries in Europe, the Swedish market for solar PV is small. In 2014, 36.2 MW_p were installed for a cumulative total of nearly 80 MW_p (Lindahl, 2015). As shown in Figure 1, the market has been growing rapidly in recent years in conjunction with rapidly dropping in costs, which are currently 1.3–1.6[1] €/W_p (excluding VAT) for a rooftop mounted system. A well oriented, unshaded rooftop system can be expected to produce 900-1000 kWh/kW_p per year, which results in a LCOE of 0.11-0.13 €/kWh (Stridh et al., 2014).

[1] Original price figures are in Swedish crowns (SEK) and converted to Euros (€) using a 9.5 SEK/€ exchange rate throughout (Sweden Central Bank, 2015).

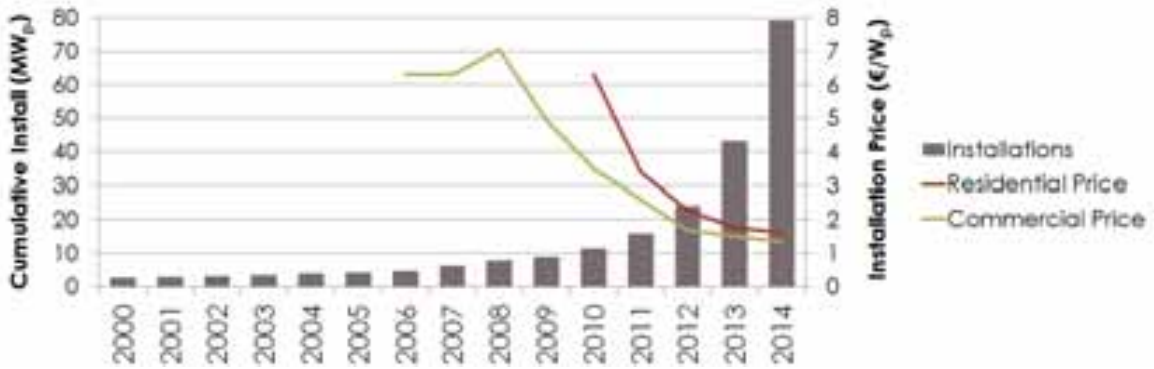

Fig. 1: Cumulative solar PV installations in Sweden (MW_p) and installation prices (excl. VAT) (€/W_p)

Another market driver has been the capital rebate subsidy which has been available at various levels from the national government since 2006. In 2009 the program was rewritten to include any micro-generation system, gave a 45% rebate on total installation cost, and was scheduled to run through 2011. This was eventually extended through 2012 and then rewritten with a new budget awarding a 35% rebate to run from 2013 to 2016 (Lindahl, 2015). The budget for this program was exhausted in 2014 and a queue of 3400 applications formed (Swedish Energy Agency, 2014). The program was modestly refunded in early 2015 (without enough to cover the queue) and the support reduced to 20% of total costs. The latest government budget proposal has once again refunded the program for the long term (2016 to 2019) and the support reduced 15%.

Building applied PV systems are subject to the same deregulated market as any other generator, so it is common for utilities to pay the wholesale market price for overproduction. One support measure allows micro-producers/prosumers (43.5 kW_p and smaller) to earn a tax rebate on overproduced electricity. This policy began in January 2015 and acts as a feed-in bonus, giving 0.063 €/kWh up to a maximum of 1900 €/year per tax payer. A small number of utilities have offered above market rates for overproduced electricity, but contracts are usually short term and it is uncertain how many will continue under the new feed-in bonus. The micro-producer subsidy will be reviewed in 2018 to determine the need for it to continue (Lindahl, 2015).

3. Methodology

The default meter configuration for this study assumes a cooperative has multiple buildings, each with its own meter on a communal electricity account. The apartments are all metered independently with separate accounts. The vertical expansion in metering occurs within a single building and combines all of apartments with the cooperative's meter. A horizontal expansion occurs between buildings, where the cooperative's individual meters can be aggregated as if they are one large meter. The two expansions are also combined, where the entire cooperative acts as a single generation source and electricity load. A graphical representation of the concepts is shown in Figure 2. In all cases, the same PV system is installed and the same load profile is present, only the way in which the boundaries for the metering are drawn changes.

Fig. 2: Diagram of the horizontal and vertical meter expansion concepts

3.1 PV production and building loads

The input values for this study are based on a cooperative in the western Swedish city of Gothenburg. There are 312 apartments divided into 13 buildings, six of which have 16 kW_p PV systems on their roofs. PV production is generated using the CEC performance model in System Advisor Model (National Renewable Energy Laboratory, 2015) using TMY2 weather data. The PV system model inputs are listed in Table 1.

Tab. 1: PV system inputs for SAM

Variable	Value	Note
Weather data	Göteborg Landvetter airport	TMY2
Modules	IBC Polysol 250 DC, p-Si	64 per array (384 total)
Inverter	SMA 15000TL-10	1 per array (6 total)
Azimuth (γ)	180°	-
Tilt (β)	30°	-
Degradation rate	0.5%	(Jordan and Kurtz, 2013)
System losses	10.0%	Annual average

Measured communal load data for 2013 and 2014 for the six PV equipped buildings has been supplied, several of which also have laundry rooms. The remaining buildings are assumed to not have laundry rooms. The load data from one of these buildings has been supplied and is multiplied to represent the remaining unsupplied meter data. The final load curve is an average of the two years of measurements. All production and building loads are considered on an hourly basis, which is necessary to determine the self-use fraction. The communal and apartment load data, along with the first year solar production is shown in Figure 3. First year solar production is 970 kWh/kW_p.

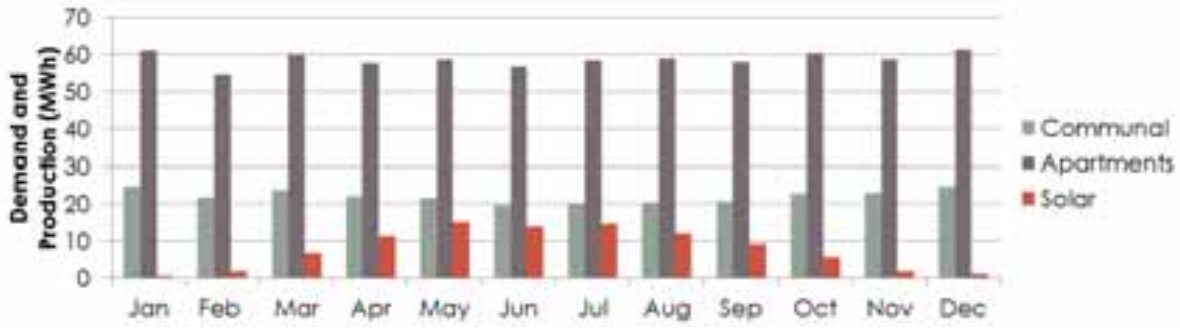

Fig. 3: Monthly data for all communal and apartment loads and solar PV production

Apartment loads are constructed using the Markov chain model developed by Widén and Wäceklgård (2010) which is based on measured plug loads of several hundred households. Since their model is stochastic and this study is deterministic, a single, unique load profile for each building is generated and used across all cases. Demand from the apartments is approximately 2260 kWh per apartment per year.

3.2 Economic calculations

Comparisons between the schemes are done with net present value (NPV, Eq. 1Eq. 1Eq. 1) using traditional deterministic engineering economics. Costs (C) can be divided into one-time and reoccurring costs, seen in Eq. 2. One-time costs include installation cost (I_0) and VAT tax (T_0), while reoccurring costs include fixed operations and maintenance (O&M, OM_t), inverter replacement (IR_t), financing interest, and taxes on the sale of electricity. This study is done assuming self-financing, and is presented before income taxes. Benefits (B) also have one-time and reoccurring components, shown in Eq. 3. The one-time capital subsidy (S_0) is assumed to be awarded in year zero, while reoccurring benefits include; the value of differed electricity purchases (self-consumption, Q_dP_r), the value of sold electricity (overproduction, Q_oP_w), and the value of meter subsidies (Q_sP_s). Inflation is not considered; therefore the discount rate (d) is real. Table 3 lists a summary of all economic input values.

$$NPV = \sum_{t=0}^{L} \frac{C_t + B_t}{(1+d)^t} \qquad \text{(Eq. 1)}$$

$$C = I_0 + T_0 + \sum_{t=0}^{L} (OM_t + IR_t) \quad \text{(Eq. 2)}$$

$$B = S_0 + \sum_{t=0}^{L} \left[(Q_d P_r) + (Q_o P_w) + \sum (Q_s P_s) \right]_t \quad \text{(Eq. 3)}$$

Tab. 3: Economic variable input values

Variable	Symbol	Unit Value	Absolute Value
Installation Cost	I_0	1.36 €/W_p	130,360 €
VAT	T_0	25% of I_0	32,590 €
Capital Subsidy	S_0	15% of I_0+T_0	24,440 €
Fixed O&M (Year 1)	OM	0.25% of I_0	325 €/yr
O&M Cost Escalation Rate	-	1%/year	-
Inverter Replacement Cost	IR	0.157 €/W_p	2525 €/inverter
Inverter Lifetime	-	15 years	-
System Lifetime	L	30 years	-
Real Discount Rate	d	3%	-
Retail Price (Year 1)	P_r	0.098 €/kWh	-
Wholesale Price (Year 1)	P_w	0.021 €/kWh	-
Green Cert. Price (Year 1)	P_s	0.016 €/kWh	-

Future electricity prices are taken from a policy comparison study for Sweden modeled with Times/Markal (Profu, 2014). The wholesale prices for the four scenarios as well as the historical annual averages are shown in Figure 4 (Nord Pool Spot, 2015). All scenarios are assumed to have an equal chance of occurring, and are therefore averaged together. Retail prices (P_r) are calculated each year based on the wholesale price, renewable support subsidies, network fee (0.021 €/kWh), electricity tax (0.030 €/kWh), retailer markup (0.005 €/kWh), and a 25% VAT applied to the sum. Network fees and electricity taxes are assumed to increase at 1% per year, which is relatively conservative compared to the historic rates (Svensk Energi, 2015). Retailer markup and VAT remain constant.

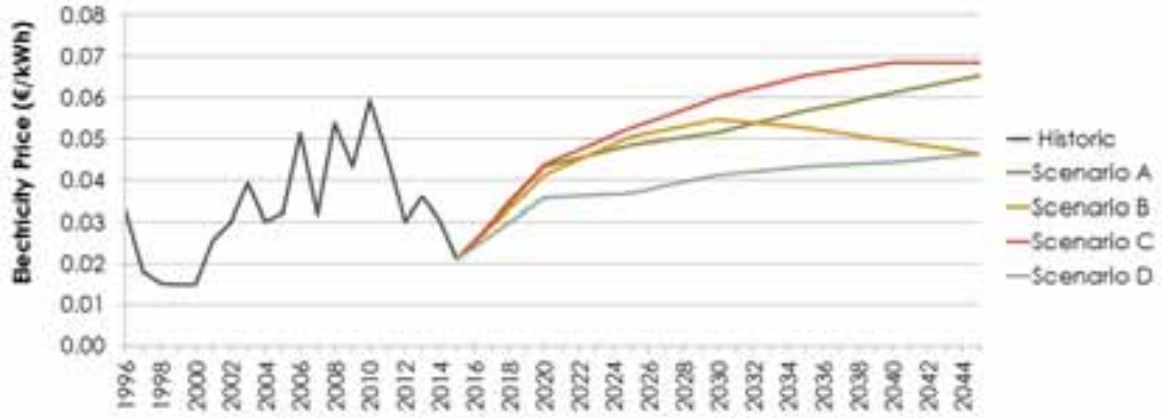

Fig. 4: Wholesale electricity price (P_w) history and future scenarios prior to averaging

3.3 Policy cases

Four policy cases are compared based on the three primary subsidies for solar PV in Sweden. The first case considers no subsidies, and the following cases are built by cumulatively adding another subsidy. The subsidies are added from the most secure (i.e. the subsidy most likely to remain long term) to the least, starting with green certificates, then the capital subsidy, and finally the feed-in bonus. Green certificates and the feed-in bonus only apply to overproduction, making $Q_s = Q_o$ in Eq. 3. The current price for green certificates is 0.016 €/kWh, which is assumed to return to the historic mean (0.022 €/kWh) by 2020 and remain at that level for the remaining 10 years which the system qualifies (Swedish Energy Agency, 2015). The feed-in bonus is assumed

to be renewed until 2020, making it a 5 year program. The capital subsidy is 15%, which matches the most recent update to the policy.

4. Results

The motivation for the alternative metering schemes is to increase the self-consumption rate, which is shown for each scheme in Figure 5. It can be seen that the vertical scheme has a greater impact on self-consumption than the horizontal, due to the apartments demanding twice as much electricity as the communal loads. It can also be seen that the combined scheme has a 100% self-consumption rate, meaning that none of the electricity generated on the cooperative's estate physically leaves it, even though the meters indicate otherwise.

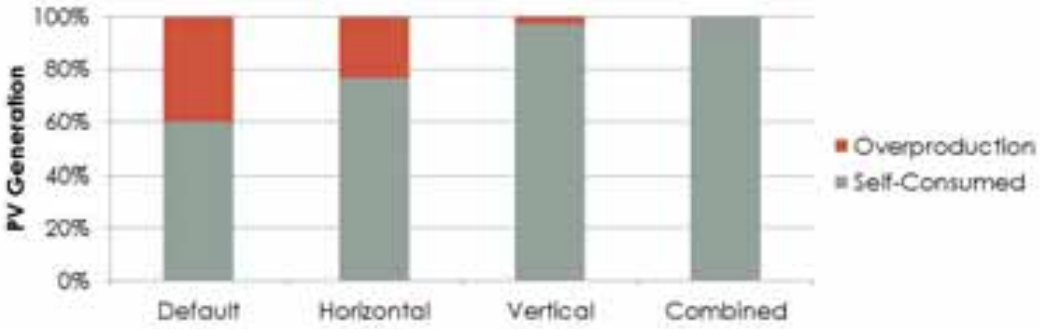

Fig. 5: Self-consumption rates between metering schemes

The effect of self-consumption on the profitability can be significant, as Figure 6 shows. The vertical scheme adds over €60,000 of value to the PV system, significantly more than any of the subsidies which only add about €44,000 put together. The horizontal scheme adds over €27,000, nearly €3000 more than the capital subsidy. As would be expected, the green certificates and feed-in bonus becomes less significant with less overproduction. In the horizontal scheme they each add about €6000, become less than €1000 in the vertical scheme, and reach zero in the combined scheme.

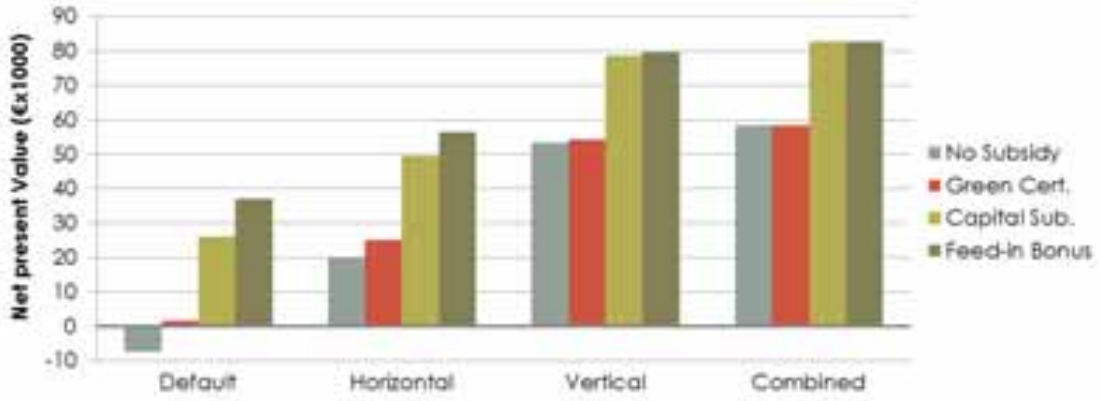

Fig. 6: Net present value of each meter scheme under the various subsidy policies

If this cooperative were to make a PV installation decision using this information only on economic rational, only the default, no subsidy case presented would be rejected. The production conditions here are relatively good, with the system oriented at nearly the optimal position and completely unshaded. Naturally these conditions do not exist everywhere. To extract these results to a more general case, the effects of a range of self-consumption and annual production values on specific NPV (€/W_p) are shown in Figure 7, without subsidies, using the same inputs presented above. The break-even line can be seen between the dark red and black contours, which will move down and to the left as installation costs decrease.

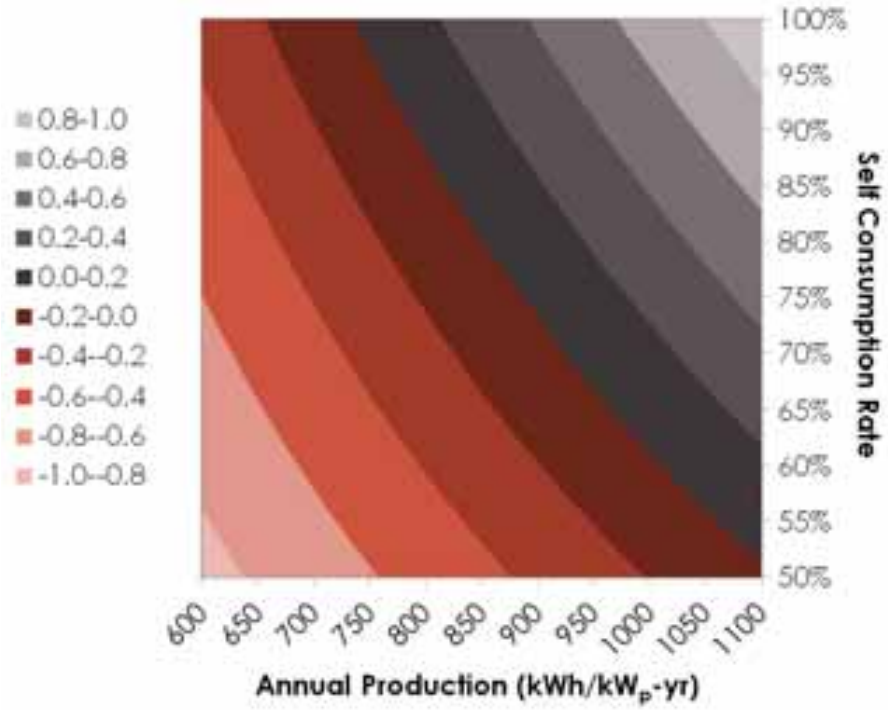

Fig. 7: Specific NPV (€/W_p) as a function of annual production and self-consumption rate

5. Discussion

The benefits of removing internal metering divides in cooperative housing can be clearly seen in the results. This is certainly known to cooperatives who have installed large scale solar PV systems, as there are examples of vertical and combined metering across Sweden (Sommerfeldt and Muyingo, 2015). However, for a cooperative which is currently using default metering, expanding the metering schemes requires overcoming some barriers.

Vertical metering schemes are actually not entirely uncommon in Sweden as mentioned in the background. However the majority of multi-family houses would need to convert, which requires replacing the utility's meters with cooperative owned versions which are then used for internal billing. The cost of this conversion would be approximately €35,000, which is nearly half of the benefit of switching to the vertical scheme, plus the cost and effort of administration over time. Also not accounted for in the results is the benefit of lower fixed network fees, since apartments typically have much higher fixed fees than high demand customers. This value varies significantly by location and should be considered on a case basis.

Expanding the metering scheme horizontally can be considerably more difficult. With the current system, the only way is to physically connect buildings behind the utility meter so that PV generation can be shared between them. Naturally, costs for this will vary depending on the current wiring and if any new wiring needs to be done internally or externally to the buildings. In one case, a large cooperative buried DC cables between the buildings. Given that this measure is taken only because of the location of the meters, one might consider the added cost and materials is unnecessary.

The results presented here indicate that there is a significant amount of PV value being captured by utilities due to the location of meters, and not because of any added service. At the same time, state sponsored subsidies are supporting PV development that may not be necessary in some cases if the meter barriers are lowered. The idea that electricity could be generated and shared between neighbors, across meters, is not particularly novel, but does go against the interests of the utilities who own those meters and the control the structure of the current system. The current technological solutions are expensive and could be considered wastefully unnecessary infrastructure. Restructuring the electricity market and tax code to enable more fluid buying and selling directly between prosumers, combined with ICT solutions, may make it possible to reduce or eliminate subsidies faster. The example presented here is within the well-defined boundaries of a cooperative, but the concept can easily be expanded to neighborhoods, districts, or even cities if the electric network can manage. Reaching a sustainable electricity market built on central and distributed generation sources, utility 2.0, should be a goal for many utilities, citizens, and politicians motivated to develop solar PV.

6. Acknowledgements

This project is funded by The Swedish Research Council Formas (no. 2012-256) and performed in conjunction with Riksbyggen and Sustainable Innovation (SUST). The author would also like to thank Johan Paradis for access to installation and meter data.

7. References

Ei, 2015. The Swedish electricity and natural gas markets 2014.

Jordan, D.C., Kurtz, S.R., 2013. Photovoltaic Degradation Rates — an Analytical Review. Prog. Photovoltaics Res. Appl. 21, 12–29. doi:10.1002/pip

Lindahl, J., 2015. National Survey Report of PV Power Applications in Sweden 2014.

National Renewable Energy Laboratory, 2015. System Advisor Model Version 2015.1.30 (SAM 2015.1.30).

Nord Pool Spot, 2015. Market Data [WWW Document]. URL http://www.nordpoolspot.com/ (accessed 9.4.15).

Profu, 2014. In-depth analysis and quantification of the NEPP scenarios, final report (Swedish). North European Power Perspectives.

Sommerfeldt, N., Muyingo, H., 2015. Lessons in community owned PV from Swedish multi-family housing cooperatives, in: 31st European Photovoltaic Solar Energy Conference and Exhibition. Hamburg.

Statsitics Sweden, 2012. Yearbook of Housing and Building Statistics 2012.

Stridh, B., Yard, S., Larsson, D., Karlsson, B., 2014. Profitability of PV electricity in Sweden, in: 40th IEEE Photovoltaic Specialist Conference. Denver, CO, USA, pp. 1492–1497.

Sweden Central Bank, 2015. Interest and Exchange Rates [WWW Document]. URL http://www.riksbank.se/en/Interest-and-exchange-rates/

Swedish Energy Agency, 2014. A basis for revision of the regulation on solar support (2014-09) (Swedish). Eskilstuna.

Swedish Energy Agency, 2015. Energy in Sweden: Facts and Figures [WWW Document]. URL http://www.energimyndigheten.se/Statistik/Energilaget1/ (accessed 9.6.15).

Svensk Energi, 2015. The Electricity Year 2014 (Swedish).

Widén, J., Wäckelgård, E., 2010. A high-resolution stochastic model of domestic activity patterns and electricity demand. Appl. Energy 87, 1880–1892. doi:10.1016/j.apenergy.2009.11.006

World Nuclear Association, 2015. Nuclear Energy in Sweden [WWW Document]. Ctry. Profiles. URL http://www.world-nuclear.org/info/Country-Profiles/Countries-O-S/Sweden/ (accessed 9.25.15).

World Nuclear News, 2015. Vattenfall confirms early closure of Ringhals units [WWW Document]. URL http://www.world-nuclear-news.org/C-Vattenfall-confirms-early-closure-of-Ringhals-units-0409154.html (accessed 9.25.15).

ISES International Solar Energy Society
Conference Proceedings
Solar World Congress 2015
Daegu, Korea, 08 – 12 November 2015

Parabolic Solar Cooker Cooking: Heat Pipes OR Spiral Copper Tubes

Omotoyosi O. Craig[1], Robert T. Dobson[1] and Wikus van Niekerk[1, 2]

[1] Department of Mechanical and Mechatronics Engineering, Stellenbosch University, Stellenbosch, 7602, South Africa

[2] Director, Centre for Renewable and Sustainable Energy Studies at Stellenbosch University, Stellenbosch, 7602, South Africa

Abstract

The idea of cooking with the sun is not new and most recently solar energy has been identified by many researchers as a solution to the challenges of poverty and hunger in the world. Solar coking is believed to be a contributor to the fight for the elimination of insufficient and or expensive energy supply for homes and industrial cooking. The parabolic types of solar cookers have been identified to cook faster at high temperatures and when they are used indirectly with the cooking section separated from the dish, they often abolish the exposure of the user to the sun and can thus be incorporated to kitchen designs. Despite this breakthrough, indirect parabolic cookers still faces a major problem, which is identifying the right cooking section type as most of the ones in existence often achieve a low utilisation efficiency as compared to their potentials. In order to analyse and predict the best cooking section type for parabolic cookers an experimental cooking was performed at Stellenbosch University, South Africa using two different types of cooker sections, the first being using coiled spiral copper tube and the other using heat pipes of 2 l volume. The cooking section was separated from the dish and was not exposed to the sun, the working fluid was transferred using high temperature flexible hose. Both types of cookers were found to be effective with the heat pipes boiling water in a record time but no heat control; the spiral copper tube also reached boiled water although at a little longer time but the flow of heat to it could be regulated. Both were seen to have their advantages and disadvantages and the selection would be based on the desired use of the cooker by the manufacturer, but base on cost, the use of spiral copper tube is recommended in this report.

Keywords: *Parabolic Solar cookers, Heat pipes, Spiral copper tube*

1. Introduction

Over one-third of the world population has been identified to be using wood as a source of energy either for general heating purpose or specifically for heating (Wentzel & Pouris 2007). This case is worse in Africa where in South Africa (which is one of the least countries with wood usage in Africa) over 84, 000 m^3 of wood is used per year (Christie & Gandar 1994). The continuous reliance on wood has led to deforestation in some communities and frustrations in many others (Diabaté et al. 2004) although over the recent years, many nations has increased their energy generation thereby reducing the over-dependency on wood and many are supporting other renewable energy alternatives. Solar cooking had been described by several authors as having the potential of leading rural industrialisation, elimination hunger and providing employment and can serve as a means of reducing the dependence on gas or electricity for cooking (Craig & Dobson 2015; Yettou et al. 2014; Al-Soud et al. 2010; Cochetel 2012), the need for its optimisation therefore is of utmost importance.

Parabolic types of solar cookers had been identified as the most efficient in terms of heat generation of all the types of solar cookers (Reddy & Ranjan 2003) and they often cook food faster than any other types of solar cooker in existence (Panwar et al. 2012). Some of the problems facing social acceptance of parabolic cookers have been identified as i) exposure to sun by the users ii) the complexity that sets up as a result of need for accurate sun tracking iii) low utilisation efficiencies among others and iv) selecting the right cooking section types.

However, the first problem identified had been overcome by the developing of indirect parabolic cooking systems (Otte 2013; Cuce & Cuce 2013; Muthusivagami et al. 2010; Schwarzer & da Silva 2008). The need for

doi:10.18086/swc.2015.09.06 Available at http://proceedings.ises.org

accurate tracking had also been overcome by development of simple dual tracking systems (Yao et al. 2014; Arbab et al. 2009; Arturo & Alejandro 2010). Effort to raise the of low utilisation efficiency of parabolic cookers are still continuous (Öztürk 2004; Kaushik & Gupta 2008; Ozturk 2007) and in this research the two popular types of cooking section used for parabolic cookers were tested and the necessary comparison was made.

2. Experimental Set Up

The experiment was performed in Stellenbosch University with location coordinates of 33˚ 55' 42.81" S, 18˚ 51'55.08" E, Elevation: 119 m. The heat transfer fluid used was shell oil S2 with maximum fil temperature of 315 °C and maximum bulk temperature of 290 °C. The experiments were carried in winter conditions in June, 2015 in South Africa. The sun path for the location of the tests are shown in figure 1 a and b which were generated from running necessary scripts on University of Oregon Solar Radiation Monitoring Laboratory (2007) online sun path calculator

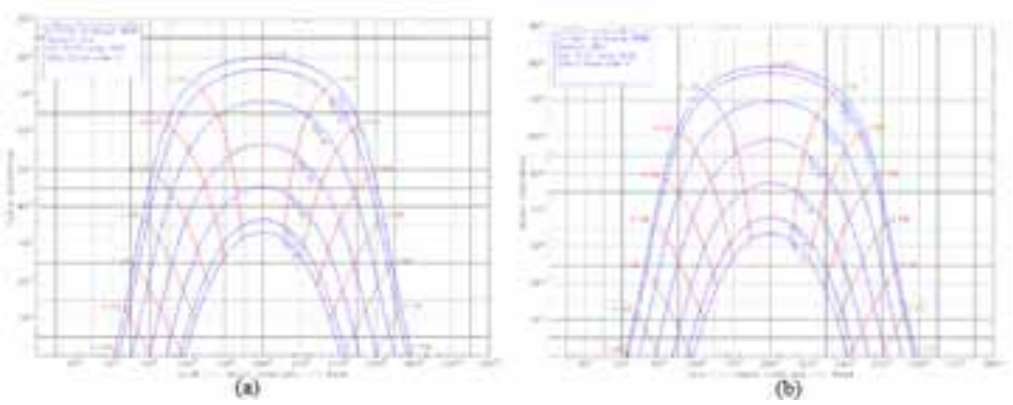

Figure 1: Stellenbosch University sun's path: December to June (a), June to December (a)

The diagram in figure 1 a shows the sun path for December to June while in figure 1 b is displayed the path of the sun for June to December for the location specified above in Stellenbosch, South Africa. The necessary angles of the sun was thus calculated using these data.

Figure 2 below is a CAD drawing of the experimental set up and how the cooking system is separated from the solar energy collection section.

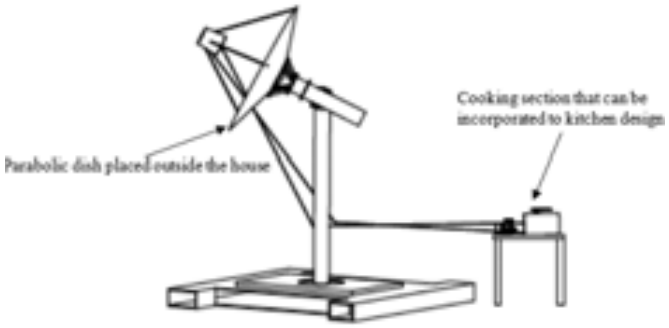

Figure 2: Complete CAD drawing of the experimental setup

A storage tank of 40 l volume was filled with the heat transfer fluid HTF, and a specially modified car pump was used to circulate the HTF throughout the system. The gasket in the automotive car pump was replaced with a high temperature Klingersil C-4430 gasket material to make the modified pump be able to withstand the temperature under which it will be functioning. High temperature hose was used to transfer the oil, the hose was insulated with a black rubber insulation clip. A depression was made inside the storage tank to allow direct cooking on in the storage and to provide a space for the two cooking section to be made. The direct placing of the cooking section in the hot oil was to reduce the heat loss between the storage tank and the cooker. A variable speed drive was connected to a three phase electric motor which was then connected to the pump to power it and also to vary the speed of the motor and ultimately vary the flow rate of the oil in the system.

The parabolic dish used was placed outside on a two axis tracker stand by Prinsloo et al. (2014) and the storage and cooking section was placed under a shade. The parabolic dish on the tracker is shown in figure 3. The two sets of cooking section manufactured is discussed in the following sections

Figure 3: Parabolic dish on tracker stand

2.1. Heat pipe cooking

The first cooking heat type was a heat pipe cooker with methanol and copper material an while the evaporator side was dipped in the storage tank, the condenser part was made to form a pot head and placed on another container beside the tank as shown in figure 4 and the heat transfer analysis is represented in figure 5

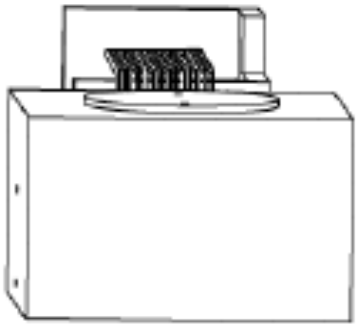

Figure 4: CAD drawing of heat pipe cooking section

The heat energy transfer analysis for the heat pipe experimental set up was performed based on the thermal resistances presented in figure 4 below.

In order to solve for the temperature and resistance in the cooking section the conservation of energy law was applied

$$\dot{Q}_{in} = \dot{Q}_{out} + \dot{Q}_{losses} \qquad (\text{eq. } 1)$$

Considering the temperature of the oil supplied by the inlet heat transfer hose in relation to the heat supplied to the oil, a balance in the thermal resistances was developed as

$$\frac{T_{in} - T_{h\_oil}}{R_{sto-in}} = \frac{T_{h\_oil} - T_{out}}{R_{sto-out}} + \frac{T_{h\_oil} - T_a}{R_{sto-amb}} + \frac{T_{h_{oil}} - T_a}{R_{sto-ck}} \qquad (\text{eq. } 2)$$

Re-arranging eq. 2 above and solving for the T_{h_oil} gives eq. 3

$$T_{h\_oil} = \left(\frac{T_{in}}{R_{sto-in}} + \frac{T_{out}}{R_{sto-out}} + \frac{T_a}{R_{sto-amb}} + \frac{T_a}{R_{sto-ck}}\right) * \left(\frac{1}{R_{sto-in}} + \frac{1}{R_{sto-out}} + \frac{1}{R_{sto-amb}} + \frac{1}{R_{sto-ck}}\right) \qquad (\text{eq. } 3)$$

Likewise, the solution for the return temperature (T_{out}) that is fed back to the heat transfer return pipe and from there carried to the receiver cavity was determined as

$$T_{out} = \left(\frac{T_{in} - T_{h\_oil}}{R_{sto-in}} - \frac{T_{h\_oil} - T_a}{R_{sto-amb}} - \frac{T_{h\_oil} - T_a}{R_{sto-ck}} - \frac{T_{h\_oil}}{R_{sto-out}}\right) * R_{sto-out} \qquad (\text{eq. } 4)$$

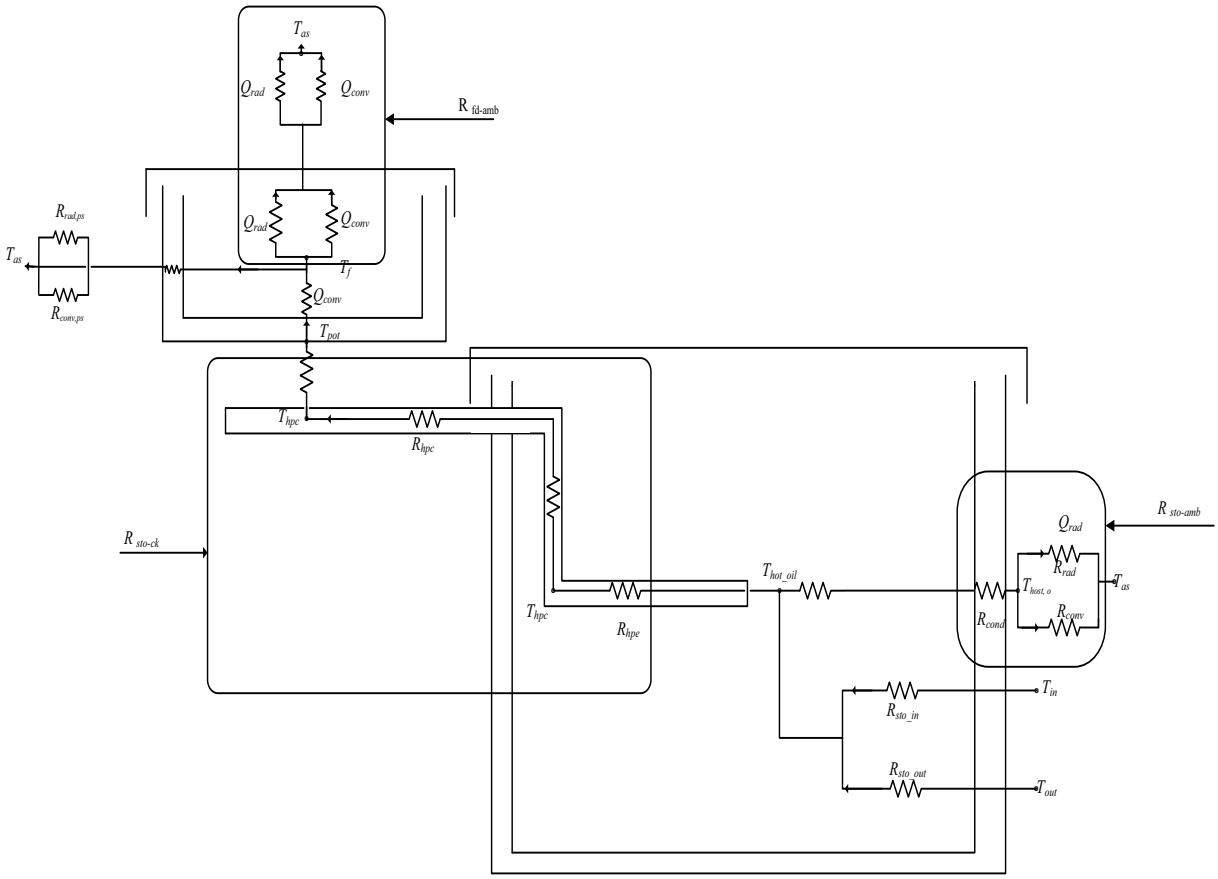

Figure 5: Thermal resistance diagram for heat pipe cooker

In order to solve for the temperature of the food item that was heated in the coking section of the solar cooker an equation for the temperature T_{fd} is developed.

The energy balance for the food can be expressed as

$$\dot{Q}_{fd} = \dot{Q}_{hp} - \left(\dot{Q}_{pot,s} + \dot{Q}_{pot,b} + \dot{Q}_{pot,cov}\right) \qquad \text{(eq. 5)}$$

When eq. 5 was expressed in terms of the temperatures and the resistances, eq. 6 was developed

$$\frac{T_{fd} - T_{hot\_oil}}{R_{ho-conv} + R_{hp} + R_{pot} + R_{sto-amb}} = \frac{T_{hp} - T_{hot\_oil}}{R_{hp} + R_{sto-amb}} - \frac{T_{fd} - T_a}{R_{pot,s}} - \frac{T_{fd} - T_a}{R_{pot,cov}} \qquad \text{(eq. 6)}$$

Rearranging the above equation, collecting the like terms and solving for T_{fd} gives

$$T_{fd} = \left[\left(R_{sto-a} + R_{ho-conv} + R_{hp} + R_{pot}\right)\left(R_{pot,s} * R_{pot,cov}\right)\left(\frac{T_{hp} - T_{hot\_oil}}{R_{hp} + R_{sto-amb}}\right)\right]$$

$$+ \left[T_a * \left(R_{ho-conv} + R_{hp} + R_{pot} + R_{sto-amb}\right)\left(R_{pot,s} * R_{pot,cov}\right)\right] \qquad \text{(eq. 7)}$$

The temperature of the food when cooked using the condenser part of heat pipe as a cooker head was thus determined using equation 7 presented above.

2.2. Spiral Copper tube

The second type of cooking section made was the spiral copper tub the diameter of the tube used is 3/8 inch and this was rolled into a flat spiral form as shown in figure 6b and this was then placed in the depression made in the cooking section as shown in figure 6a. One arm of the spiral tube enters the side wall of the depression and at a higher level than the second arm which enters the tank at a lower level, this allows hot oil to flow in freely and the cold oil flows back to the tank and the cycles repeated.

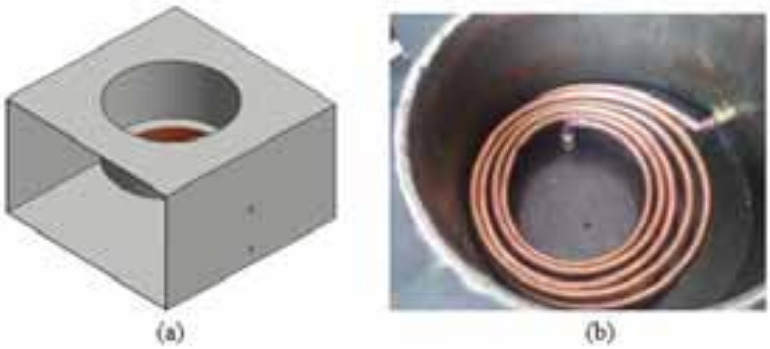

Figure 6: Thermal energy storage and cooker: cut-away 3D CAD drawing (a), spiral cook top (b)

The cooking pot was placed on the spiral head and the section was covered appropriately. The temperature of the food in the cooking pot was determined by analysing the heat transfer between the from the hot oil in the storage tank to the spiral cooker head as shown in figure 7

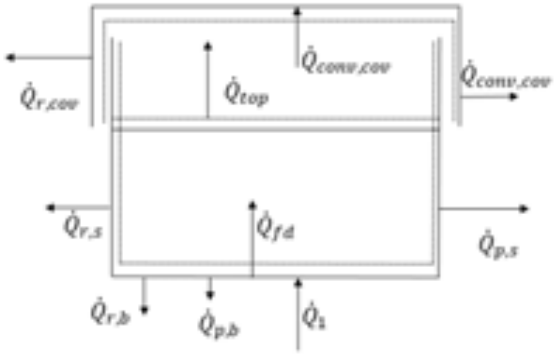

Figure 7: Heat transfer in spiral cooking section

The energy supplied the food $\dot{Q}_{fd}$ was assumed to be performing dual function, first is to overcome the internal energy of the food and the second is to balance the convection losses that occurs through the upper part of the pot and this shown in equation 8

$$\dot{Q}_{fd} = \dot{Q}_{top} + U_{fd,i} \quad \text{(eq. 8)}$$

If the mass of fluid to be cooked is taken to be m_{fd} and the temperature is considered instantaneous, then eq. 8 can be expressed explicitly as

$$\dot{Q}_{fd} = \dot{Q}_{top} + m_{fd} c_{fd} \frac{dT_{fd}}{dt} = h_{fd} A_{fd} \left(T_{pot} - T_{fd}\right) \quad \text{(eq. 9)}$$

The total heat supplied to the pot from the spiral copper tube can be taken as $\dot{Q}_1$ and it is used overcome the resistance of the pot, $\dot{Q}_{fd}$ and the convection losses through the side $\dot{Q}_{c,s}$ and the bottom of the pot $\dot{Q}_{c,b}$ as well as the radiation losses through the side $\dot{Q}_{r,s}$and bottom $\dot{Q}_{r,b}$ respectively s shown in eq. 10

$$\dot{Q}_1 = m_{pot}\, c_{pot}\, \frac{dT_{pot}}{dt} + \dot{Q}_{fd} + \dot{Q}_{c,s} + \dot{Q}_{r,s} + \dot{Q}_{c,b} + \dot{Q}_{r,b} \quad \text{(eq. 10)}$$

The various terms in eq. 10 above can be expressed shown in equation 11 to 15

$$\dot{Q}_{c,s} = h_g\, A_{side} \left(T_{pot} - T_a\right) \quad \text{(eq. 11)}$$

$$\dot{Q}_{c,b} = h_a\, A_{top} \left(T_{top} - T_a\right) \quad \text{(eq. 12)}$$

$$\dot{Q}_{r,b} = \sigma\, \varepsilon_{pot}\, A_{top} \left({T_{pot}}^4 - {T_a}^4\right) \quad \text{(eq. 13)}$$

$$\dot{Q}_{r,s} = \sigma\, A_{side} \left({T_{pot}}^4 - {T_a}^4\right)\left(1/\varepsilon_{pot} - 1/\varepsilon_{cover} - 1\right) \quad \text{(eq. 14)}$$

$$\dot{Q}_{p,s} + \dot{Q}_{top} + \dot{Q}_{p,s2} = m_a c_a \frac{dT_g}{dt} \quad \text{(eq. 15)}$$

Re-arranging the above Equations to form a first order differential Equation that can be solved numerically gives the following sets of Equation:

$$\frac{dT_{fd}}{dt} = F_{fd} \left(T_{fd}, T_{pot}, t\right) \quad \text{(eq. 16)}$$

$$\frac{dT_{pot}}{dt} = F_{pot} \left(T_{fd}, T_{pot}, T_g, t\right) \quad \text{(eq. 17)}$$

$$\frac{dT_g}{dt} = F_g\left(T_{fd}, T_{pot}, T_g, t\right) \quad \text{(eq. 18)}$$

The generated equations was then be solved numerically using Runge-Kutta fourth-order algorithm.

3. Experimental Result and Discussion

An initial experiments without any load was performed on the two types of cooking sections made. The evaporator arm of the cooker was deepen into the oil and all leaked were blocked. The electric motor was turned on using the variable speed drive and the HTF is transferred to a cavity receiver placed at the focus of the parabolic dish and the cycle continued. No cooking was performed because the aim of the experiment was to determine the variation of the heat pipe temperature with the temperature inside the tank.
The result is diagrammatically presented in figure 8 below, where the maximum difference between

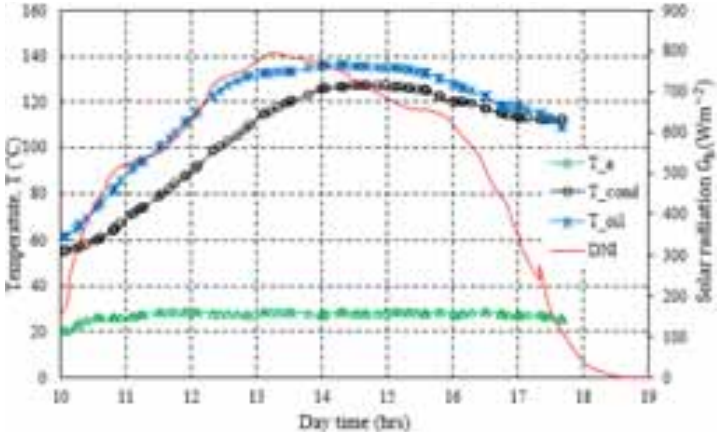

Figure 8: Condenser, oil and ambient temperature as a function of day time

the temperature of the condenser and the average oil temperature was 25 ˚C during charging of the storage system and the temperature difference reduced with time. An interesting discovery was that the temperature difference was less than 5 ˚C during discharging which predicts that the heat pipe will work well if the cooking is done in close doors or during night cooking.
Cooking experiment was done on this system by boiling 2.5 kg of water on the following day. Two sets of water was boiled by placing an aluminium pot container on the condenser part of the heat pipe and the results are displayed in figure 9. The first boiling took 2 hours 30 minutes before boiling while in the second experiment, the water boiled in 1 hour and 10 minutes, the difference can be said to be because the first experiment began when the system is still charging while the second was done when the system is fully charged.

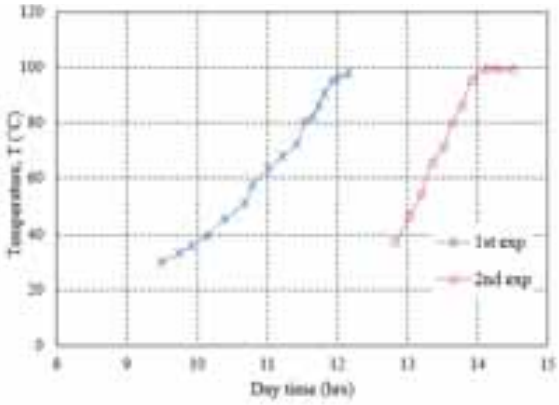

Figure 9: Water boiling Experiments on the heat pipe

The no load experiment was also performed on the spiral copper head cooking type and the result is shown in figure 10 below

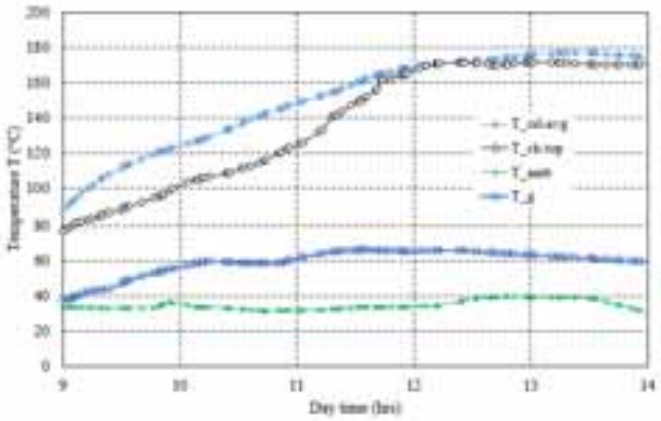

Figure 10: Cook top, oil and ambient temperature as a function of day time (08 June 2015)

The average solar radiation during the testing was 601Wm^{-2}, the storage tank became fully charged after four hours although the oil temperature was above 80 ˚C when the reading began. The initial temperature difference was less than 10 ˚C because the spiral tube was left inserted in the oil from the previous day experiment, however during the oil charging the temperature difference increased to above 20 ˚C and this temperature difference however diminished towards the time the system was almost going to be fully charged. This predict that the spiral cooker can only be effective when the system is fully charged and when the storage oil temperature fluctuation is reduced.

Cooking oil of 3 kg was used as food to be cooked on the spiral copper tube and the result is shown in figure 11 but a great temperature difference was recorded between the oil and the spiral copper tube.

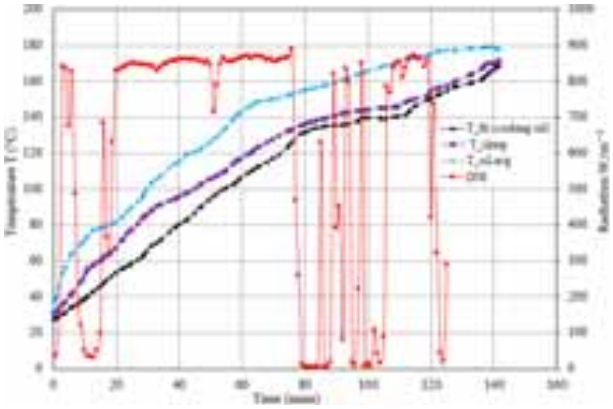

Figure 11: Cooking oil, storage oil, cook top, solar radiation as a function of experiment time

The cooking oil reached 100 ˚C after 60 minutes; the cooking oil temperature and the temperature of the spiral cooker head displayed a reduction in their temperature difference as the cooking continued and at 160 ˚C, the two temperature were almost at parity.

4. Conclusions and Recommendations

In the experiments presented in this paper, the two most popular cooking section types for indirect solar parabolic cookers had been tested under similar conditions at the same location. It can be concluded that the two types are actually a viable technology for the future. The heat pipe was noticed to transfer heat from the storage tank to the cooking section faster than the spiral cooker head and was seen to be able to work more effectively during discharging. However the spiral copper tube also performed well when the cooking was be done for a longer period, the spiral cooker head is cheap and the longer cooking time could be traced to the small surface area (single arm sucking the hot oil) of the tube inserted in the oil, as compared to the heat pipes in which several pipes were inserted into the oil. The spiral cooker is expected to perform better if an array of the tubes are combine to allow more hot oil flow to the head. Although the heat pipe cooked faster, the spiral head was preferred in this experiment because of the simplicity of its manufacturing and less complexity in its theoretical analysis. More experiments are still ongoing to use other criteria for this comparison to make necessary recommendations.

Nomenclature

Quantity	Symbol	Unit
Specific heat	c	J kg^{-1} K^{-1}
Solar radiation	G_b	W m^{-2}
Extinction coefficient^{+}	K	m^{-1}
Mass	m	kg
Emittance	ε	
Thermal resistance	R	
Density	ρ	kg m^{-3}

Subscripts

Quantity	symbol
ambient	a
food	fd
cook	ck
convection	conv
Heat pipe	hp
Hot oil	h_oil
Pot bottom part	pot,b
The side of the pot	pot,s
Storage to ambient	sto-a

References

Al-Soud, M.S. et al., 2010. A parabolic solar cooker with automatic two axes sun tracking system. *Applied Energy*, 87(2), pp.463–470

Arbab, H., Jazi, B. & Rezagholizadeh, M., 2009. A computer tracking system of solar dish with two-axis degree freedoms based on picture processing of bar shadow. *Renewable Energy*, 34(4), pp.1114–1118.

Arturo, M.M. & Alejandro, G.P., 2010. High – Precision Solar Tracking System. *Proceedings of the World Congress on Engineering 2010 Vol II*, II, pp.2–4.

Christie, S. & Gandar, M., 1994. Commercial and Social Forestry Draft Position Paper L. and A. P. C. P. in N. R. Management, ed.

Cochetel, S., 2012. *Identifying the barriers to the deployment of solar cookers in the energy-poor households of sub-Saharan Africa*. University of Exeter.

Craig, O.O. & Dobson, R.T., 2015. Stand-Alone Parabolic Solar Cookers And Rural Industrialisation In Southern Africa. , (May), pp.278–282.

Cuce, E. & Cuce, P.M., 2013. A comprehensive review on solar cookers. *Applied Energy*, 102, pp.1399–1421.

Diabaté, L., Blanc, P. & Wald, L., 2004. Solar radiation climate in Africa. *Solar Energy*, 76(6), pp.733–744.

Kaushik, S.C. & Gupta, M.K., 2008. Energy and exergy efficiency comparison of community-size and domestic-size paraboloidal solar cooker performance. *Energy for Sustainable Development*, 12(3), pp.60–64.

Muthusivagami, R.M., Velraj, R. & Sethumadhavan, R., 2010. Solar cookers with and without thermal storage—A review. *Renewable and Sustainable Energy Reviews*, 14(2), pp.691–701.

Otte, P.P., 2013. Solar cookers in developing countries—What is their key to success? *Energy Policy*, 63(0), pp.375–381. Available at:

Ozturk, H.H., 2007. Comparison of Energy and Exergy Efficiency for Solar Box and Parabolic Cookers. *Journal of Energy Engineering*, 133(1), pp.53–62.

Öztürk, H.H., 2004. Experimental determination of energy and exergy efficiency of the solar parabolic-cooker. *Solar Energy*, 77(1), pp.67–71

Panwar, N.L., Kaushik, S.C. & Kothari, S., 2012. State of the art of solar cooking: An overview. *Renewable and Sustainable Energy Reviews*, 16(6), pp.3776–3785.

Prinsloo, G.J., Dobson, R. & Schreve, K., 2014. Automatic positioner and control system for a motorized parabolic solar reflector by. , (December), pp.64–85.

Reddy, K.. & Ranjan, M., 2003. Solar resource estimation using artificial neural networks and comparison with other correlation models. *Energy Conversion and Management*, 44(15), pp.2519–2530.

Schwarzer, K. & da Silva, M.E.V., 2008. Characterisation and design methods of solar cookers. *Solar Energy*, 82(2), pp.157–163. University of Oregon Solar Radiation Monitoring Laboratory, 2007. Sun path chart program.

Wentzel, M. & Pouris, A., 2007. The development impact of solar cookers: A review of solar cooking impact research in South Africa. *Energy Policy*, 35(3), pp.1909–1919.

Yao, Y. et al., 2014. A multipurpose dual-axis solar tracker with two tracking strategies. *Renewable Energy*, 72(0), pp.88–98.

Yettou, F. et al., 2014. Solar cooker realizations in actual use: An overview. *Renewable and Sustainable Energy Reviews*, 37(0), pp.288–306.

Conference Proceedings
Solar World Congress 2015
Daegu, Korea, 08 – 12 November 2015

A simple low cost Solar Panel/Cell Characterization Experiment for Senior Undergraduate Students

Sebastian Waita*, Justus Simiyu, Alexander N. Kiragu, Vivian Imali and Bernard Aduda
University of Nairobi, Department of Physics, P.O BOX 30197-00100, Nairobi, Kenya

Abstract

A simple low cost solar cell characterization experiment has been developed for senior undergraduate students in the Department of Physics, University of Nairobi. Experiments were conducted with solar panels (also called solar modules/photovoltaic modules) rated 20 W and 40 W peak power on different sunny days on the roof top of Physics Department, University of Nairobi. It was observed that the current- voltage (I-V) curves obtained for all the measurements for each panel were comparable. The fill factor (FF), short circuit current (I_{sc}), open circuit voltage (V_{oc}), current at maximum power point (I_m) and voltage at maximum power point (V_m) were within acceptable margins when compared with the manufacturer's rated values, an indication of the reliability and accuracy of the method. The method eliminates the need for expensive characterization equipment like solar simulators, unaffordable by many developing country institutions. The experiment is recommended for senior undergraduate students with an interest in renewable energy as one way of introducing them to renewable energy. The experiment may also help in arousing the learner's interest in solar energy.

.

Key words: cost, solar cell, characterization, experiment, panel, solar panel, undergraduate, solar energy

1.0 Introduction

In 2004, the Government of Kenya through the Ministry of Energy developed the sessional paper No. 4 on energy which created the background for the energy act of 2006. The energy act in turn provided the legal framework for the enactment of the national energy policy on renewable energy in 2012 which was revised last year, 2014[1]. The action by the government was interpreted by stake holders in the renewable energy sector as an act of seriousness and commitment in promoting renewable energy, prompting them into action. As a result, there has been a lot of renewed effort and activity in the renewable energy sector in Kenya. Workshops and seminars to develop training curriculum and build Human technical capacity in renewable energy especially photovoltaic have been on the increase. Similarly, photovoltaic training centers have sprung up in large numbers in various institutions in the last two years.

The high demand in the photovoltaic training has been necessitated by the government's requirement that solar photovoltaic design and installations be done by only those licensed by the Energy Regulatory Commission (ERC), a government agency created to regulate the energy sector. Further, the government also made it compulsory for vendors, importers and contractors to employ technical people who have undergone formal training and have been licensed by ERC[2]. Currently, most training is being carried out in government institutions and by staff who work in the same intuitions after going through training. It has been observed that most of the participants (trainees) in the trainings are mainly fresh school leavers, entrepreneurs and even people working in

doi:10.18086/swc.2015.09.07 Available at http://proceedings.ises.org

other sectors of the economy[3]. It is interesting to note that the same institutions have done little if any, to develop such training or relevant laboratory experiments for their students in the institutions, especially at the University undergraduate level. There is therefore need to introduce students to these technologies at early stages. Besides, developing theoretical courses, there is need to design and develop related experiments to run parallel to the theory work. In the Department of Physics, University of Nairobi, a simple and low cost experiment for analyzing the performance of a solar panel has been developed. The experiment has been found to be useful to senior undergraduate students in creating interest as well as introducing them into solar energy. The experimental details of the set up are outlined below.

2.0 Experiment Title: Photovoltaic solar panel characterization

2.1 Objectives

The objectives of the experiment were:

1. To understand how electricity is generated from a solar cell

2. To establish the difference between a solar cell and solar panel

3. To determine the total number of solar cells in a solar panel

4. To determine the variation of current and voltage for the solar panel

5. To understand the meaning of characterization parameters: Fill Factor (FF), Short circuit current (I_{sc}), Open circuit voltage (V_{oc}), Maximum current (I_m), Maximum voltage (V_m and Maximum power (P_m).

6. To determine the: Fill Factor (FF), Short circuit current (I_{sc}), Open circuit voltage (V_{oc}), Maximum power point (P_m), Current at maximum power point (I_m), Voltage at maximum power point (V_m and compare with the rated values.

2.2 Theoretical Background

2.2.1 How a Solar Cell generates an electric current

Solar radiation consists of photons of different wavelengths and therefore with various amounts of energy. As these photons fall on a photoelectric surface, they may be reflected, absorbed or transmitted. The absorbed photons transfer their energy to electrons in the atom of the surface material. If the photons have enough energy to break the electron-atom energy bond, then the electron is dislodged from the atom and becomes a free electron, available for electric conduction. The electron leaves its normal position and becomes part of the current in the external circuit. This effect is called “photoelectric effect". The vacant site is a positive charge called a “hole”. In the process, there is separation of charges, electrons and holes and an electric field is build up providing the voltage needed to drive the current through an external load.

2.2.2 Solar Cell Characterization

A solar cell can be considered as a current generator with a diode and in cooperating series and parallel (shunt) resistances within the cell. The performance of a solar cell or solar panel (many solar cells make a solar panel) is done through characterization. Characterization mainly involves determination of the Fill Factor (FF)-a measure of how ideal the solar cell is. The variation of current (I) and voltage (V) of a solar cell in dark resembles the diode characteristics as show in Figure 1 (a) below (solid curve). On illumination, the photo voltage and photocurrent increases resulting in the broken curve[4]. However, in normal analysis and plotting, we usually translate the I-V curve to the first quadrant (Figure 1 (b)). An ideal solar cell I-V curve is also shown in Figure 1(b).

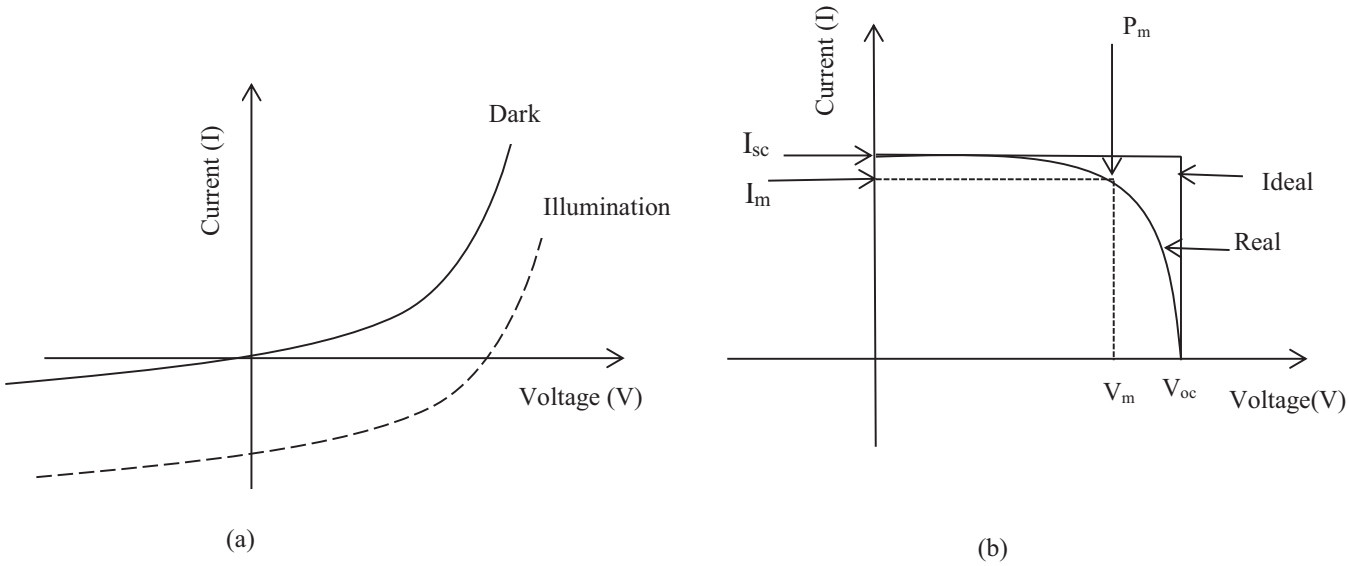

Fig. 1: The current (I)-Voltage (V) characteristics of a solar cell: in dark-solid curve and on illumination-dotted curve (a), under illumination after reflection into the first quadrant (b).

The power, P, of a solar cell is given by the product of the current and the voltage [4, 5]:

$$P = IV \quad (1)$$

Where I is the current (A) and V is the voltage (V).

The maximum power, Pm (W) is normally represented by the area of the largest rectangle that can be fitted under the curve and is defined by:

$$P_m = I_m V_m \quad (2)$$

Where I_m is the current at the maximum power point and the V_m is the voltage at the maximum power point.

The ability of a solar cell to convert incident radiation into electrical power is commonly referred to as the conversion efficiency of the solar cell. The conversion efficiency (η) of a solar cell is the maximum output power (P_m) expressed as a percentage of the input (incident) power P_{in}:

$$\eta = \frac{P_m}{P_{in}} \quad (3)$$

Thus for a practical (real) solar cell, the closer the I-V curve to the ideal case, the higher the maximum power and so is the conversion efficiency. The fitting of a solar cell I-V curve to the ideal rectangular shape is measured by the fill factor (FF) defined as:

$$FF = \frac{P_m}{I_{sc}V_{oc}} \quad (4)$$

Where I_{sc} is the short circuit current (current at zero voltage) and V_{oc} is the open circuit current (voltage when the circuit is open (no load)).

Inserting equation (2) in equation (4), we get equation 5 below:

$$FF = \frac{I_m V_m}{I_{sc}V_{oc}} \quad (5)$$

For an ideal solar cell (see Fig 1 (b)), the fill factor should be unity (1).

2.2.3 Apparatus

The following apparatus were used: A monocrystalline Silicon PSS 1220 (20 W) solar panel, a muilticrystalline Silicon PSS 1240 (40 W) solar panel, both from a local distributor company, digital multimeters (Ammeter and Voltmeter), a rheostat (0-10 KΩ), connecting wires and a Switch.

2.2.4 Experimental Procedure

The number of solar cells in each panel were counted and noted. The circuit was then connected as shown in Figure 2 below.

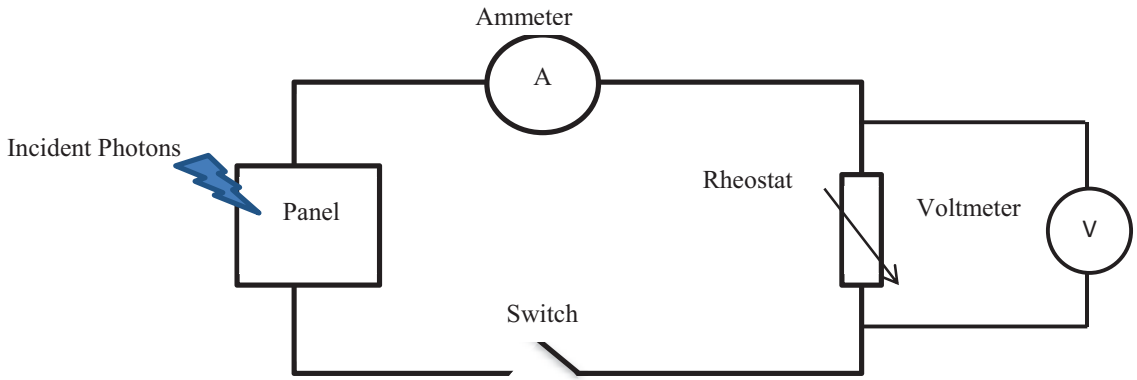

Fig. 2: The experimental set up for the solar panel characterization.

The resistance in the circuit was varied using the rheostat as the values of the current and the voltage were recorded and the data tabulated. The maximum power point was obtained from the product of current and voltage at each point. A graph of current versus voltage was plotted and the parameters FF, I_{sc},V_{oc}, I_m, V_m and P_m were obtained. The data was taken in two days that were clear and sunny.

2.2.5 Results and discussion

2.2.5.1. The 20 W solar panel

The solar panel had 36 solar cells.

Figure 3 below shows the variation of current and voltage for the 20 W solar panel (We show one curve here because all the other measurements generated similar curves). At zero voltage, the current flowing is maximum

and the circuit is shorted. As the voltage is increased (by varying the resistance), the current reduces slowly up to a voltage of about 13 V when further voltage increase leads to a large current decrease, until there is zero current at the open circuit voltage, V_{oc}.

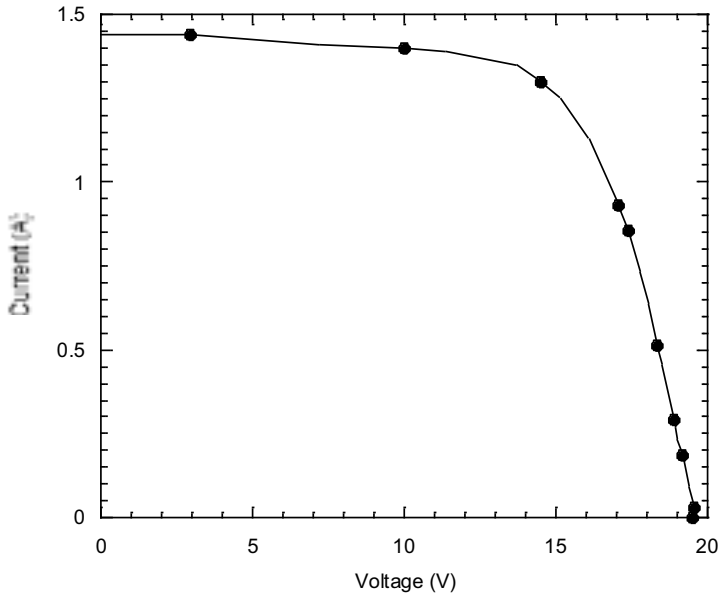

Fig. 3: Current –Voltage characteristics of the 20 W solar panel at 11.20 am of the first day.

Table 1 shows a summary of the solar cell parameters obtained from our I-V curve in Figure 3. The parameters do not show major differences from each other, because the time when measurement was done did not vary much and the weather was similar on both days and times. The manufacturer's values (rated) are shown to the extreme right of the table. As can be seen, there is quite good agreement between the experimental values obtained and the manufacturer's values.

Table 1 Summary of the measured solar Panel parameters and the manufacturer's rating.

Parameter	Day 1			Day 2		Manufacurers Rating
	11.20 am	12.00 pm	2.00 pm	12.00 pm	2.00 pm	
Im (A)	1.25	1.31	1.33	1.14	1.35	1.2
Vm (V)	15.18	14.59	13.61	15.96	13.58	16.8
Pm (W)	18.97	16.49	18.16	18.15	18.26	20
Isc (A)	1.44	1.44	1.43	1.41	1.39	1.4
Voc (V)	19.67	19.48	19.53	19.23	19.28	21
FF	0.67	0.68	0.65	0.69	0.68	0.69

2.2.5.2. The 40 W panel

The experiment was repeated with a multicrystalline 40 W solar panel of 36 solar cells.

Figure 4 shows the current -voltage spectra obtained at 12.20 pm on the first day (Again we show one curve since the other curves were similar). As can be observed, the curves are similar to those for the 20 W except for the higher values of both current and voltage. The graph can be explained in the same way as for the 20 W solar panel above.

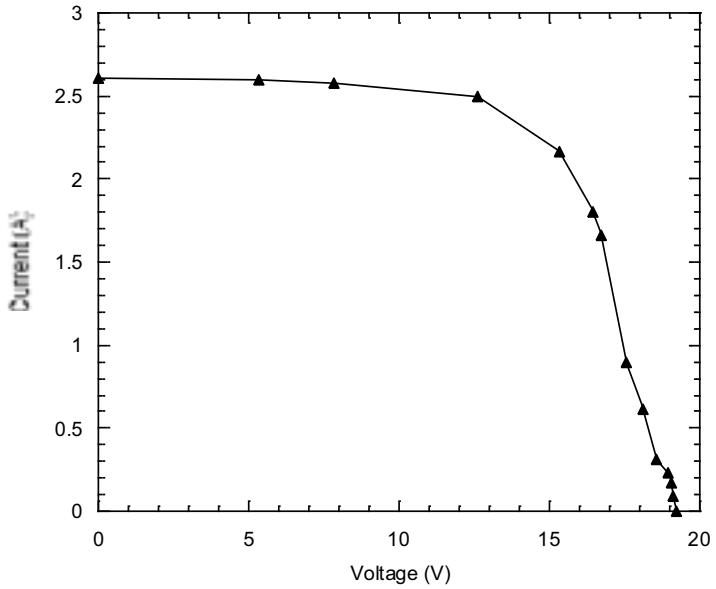

Fig 4: Current –Voltage characteristics of a 40 W solar panel: at 12.20 pm

In Table 2 below, the experimental values extracted from Figure 4 are displayed with the manufacture's rating appearing on the extreme right of the table. We notice a close relationship between our experimental values and the manufacturer's data. This consistency confirms the reliability of the experimental set up.

Table 2 Summary of the measured parameters for the 40 W solar panel and the manufacturers specifications

Parameter	Day 1			Day 2	Manufacturer's Rating
	12.20 pm	12.40 pm	2.50 pm	2.06 pm	
Im (A)	2.17	1.93	2.22	2.30	2.4
Vm (V)	15.33	15.60	13.53	13.27	16.8
Pm (W)	33.24	30.04	30.12	30.57	40
Isc (A)	2.60	2.56	2.40	2.59	2.75
Voc (V)	19.22	19.05	19.07	19.10	21
FF	0.66	0.62	0.66	0.62	0.698

3.0 Conclusion

A solar cell is the basic unit of the solar panel. A solar panel is therefore a combination of many solar cells. The solar panels used in our experiment had 36 solar cells. The current –voltage graphs obtained from the experiment were very similar in shape and values for each solar panel, though measured on different days and times, but similar climatic conditions in the sun.

The parameters obtained from the experiment for both panels were comparable to the parameters provided by the manufacturer, despite the fact that our measurements were done in real environment while the manufacturers was under STC (standard test conditions). Therefore, in Kenya and perhaps within the tropics, the experiment can be carried out successfully outdoors, eliminating the need for expensive equipment like the solar simulator. The experiment is recommended for senior undergraduate students.

References

1. www.energy.go.ke., 30th Sept 2015

2. http://www.erc.go.ke. 21st Sept 2015

3. Justus Simiyu, Sebastian Waita, Robison Musembi, Alex Ogacho and Bernard Aduda (2014),Promotion of PV Uptake and Sector Growth in Kenya through Value added Training in PV Sizing, Installation and Maintenance, Energy Procedia 57 , 817-825.

4. Martin Green (1992), Solar Cells; Operating Principles, Technology and System Applications, University of New South Wales, pge 62-84.

5. Sze S.M. (1969), Physics of semiconductor devices, Wiley - Interscience, Wiley International Edition, New York, Pg 132,640-653.

THE ROLE OF HISTORY IN REDISCOVERING THE LOST CULTURE OF SOLAR ENERGY

Cesare Silvi

Italian Group for the History of Solar Energy, Rome (Italy)

Abstract

This paper presents an update regarding the ongoing project of an Italian Archive and Museum on the History of Solar Energy, i.e. the energy contained in the direct and diffuse energy radiated every day from the Sun to Earth as well as its indirect forms of air and water currents and forests and other forms of biomass resulting from photosynthesis. The purpose of the Archive and Museum is to make available literary sources and archeological evidences of significant inventions for the use of solar energy preserved at Italian historic sites and Museums.

The focus of the Solar Archive and Museum (SAM) is on two solar ages: the primitive or ancient solar age, from antiquity up to 200 years ago, essentially based on empirical solutions, and the modern or future solar age, which has just begun, based on the knowledge and methods acquired from the scientific and technological revolutions of the last 500 years, primarily on the understanding of the composition of light and how it can be manipulated for producing steam, electricity, and fuels.

Keywords: *Solar energy, solar light, solar energy history, Italian solar energy pioneers, solar heat, solar steam, solar electricity, solar fuels, solar energy in agriculture, solar energy in architecture and urban planning, climate change, solar culture, solar education.*

1. Introduction

The 50th anniversary of the first international solar congress in 1955 in Arizona was celebrated in Florida (USA) on the occasion of the ISES SWC 2005. A book on The Fifty-Year History of the International Solar Energy Society and its National Sections was published in two volumes (Böer, 2005). This celebration emphasized an interest in the history of solar energy use, which in Italy has continued to be promoted and developed over the last ten years by the Italian Group for the History of Solar Energy (GSES, www.gses.it).

The recorded history of solar energy use by humans is a discipline that crosses many years and many disciplines. The work of GSES focuses on what it considers to be two distinct solar ages: the ***primitive or ancient solar age***, from antiquity up to 200 years ago, essentially based on empirical solutions, and the ***modern or future solar age***, which has just begun, based on the knowledge and methods acquired from the scientific and technological revolutions of the last 500 years, primarily on the understanding of the composition of light and how it can be manipulated for producing steam, electricity, and fuels.

GSES has placed special attention on research concerning discoveries and inventions that have had a great impact over centuries and millennia, which are likely to have a lasting impact on human life for much time to come.

Another important area of research for GSES has been that of the many events marking the past few decades with hopes as well as disappointment of those who expected major summits and international conferences to result in concrete programs.

The UN adopted programs, such as "Nairobi Programme of Action for the Development and Utilization of New and Renewable Sources of Energy" in the eighties and Agenda 21 following the 1992 UN Conference on Environment and Development (UNCED) held in Rio de Janeiro, are nowadays for the most part forgotten.

The cycle of major summits and international meetings continues. In 2015 there is a great deal of attention by science, business, environmental and media communities on events by international and national institutions such as the four listed below:

- Year of Light and Light-based Technologies (IYL 2015), http://www.light2015.org/Home.html
- International Year of Soils, http://www.fao.org/soils-2015/en/
- Universal Exhibition, Feeding the Planet, Energy for Life, http://www.expo2015.org/it
- 21st Session of the Conference of the Parties to the UNFCCC, http://www.cop21.gouv.fr/fr

doi:10.18086/swc.2015.09.08 Available at http://proceedings.ises.org

The topics of these four events, in principle, are all closely related and linked to solar energy. In practice, however, the lack of communication and interaction among the four events, treated as separate subjects, shows that the challenges we are facing today are not only specific, technical and scientific issues, but first and foremost cultural. Our lack of capacity to connect various topics to others, in order to understand the key problems that world faces, from climate change, to energy and scarceness of resources, to poverty, geopolitical conflicts, etc..

The use of solar energy is an age-old experience marked by fundamental discoveries in different ages, to artificially convert it into other useful forms for human beings: food, heat, fuel, mechanical energy, chemical energy, and, more recently, since the late 1800s, electricity from hydro, wind and light energy directly or indirectly coming from the Sun.

The introduction and diffusion of fossil and nuclear fuels derailed the solar energy civilizations developed over millennia, which were built on the basis of centuries old inventions that are still valuable in our lives today.

The ***primitive or ancient solar age*** was characterized by discoveries such as: fire, which enabled humans to use the solar energy stored in forest wood and other forms of biomass; agriculture and the first human settlements; solar architecture and urban planning, in which streets and buildings were oriented so as to exploit the sun's light and heat directly and naturally as well as to protect inhabitants from the sun's rays, a concept used over and over and handed down for centuries by all civilizations.

One important example of this is the Romans' discovery of transparent window-pane glass in the first century A.D., to bring daylight inside buildings and at the same time preventing cold and winds from entering them.

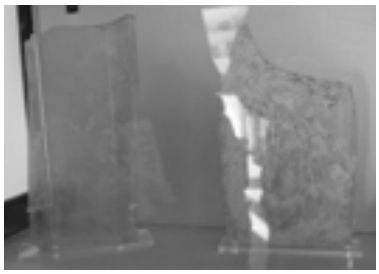

Fig. 1: Flat transparent window-pane glass from Pompeii, 1st century A.D. to capture sun's light and heat for houses and baths (Photo National Archaeological Museum, Naples, Italy)

These discoveries evolved over the ages and are still of the greatest importance in our daily lives. Think of the millions upon millions of window-panes that provide day lighting to homes and workplaces all over the world, thereby saving on artificial light from electricity generated by fossil and nuclear fuels. Think of the role of solar energy as a primary and principle source in farming. Think of solar architecture and urban planning that have shaped entire territories, from small villages to large cities, as well as the construction of buildings.

Fig. 2: An aerial view of Spello, a typical Italian small town, whose shape and relationship with the surrounding farmland is a clear reminder of its past. Ancient cities' near total dependence on solar energy set a limit on their size (Photo G. Reveane, 1993)

Prior to the discovery of fossil fuels and the beginning of the industrial revolution, human civilizations subsisted for thousands of years exclusively on solar renewable energy in its direct and indirect forms, in Italy

up to 100-150 years ago. Therefore, the importance of the sun is deeply engraved in the history of our living and working environments, in large cities and small towns, in rural areas and their landscapes.

An example is illustrated by the photograph in Fig. 2, which shows the small Umbrian town of Spello, surrounded by farmland, where the production of food and its transportation to the places of consumption depended entirely on solar energy. Spello and the hundreds of similar towns throughout Italy, show us how it was possible in the past to develop "solar energy systems" in which the built environment and the agricultural fields around it worked together as a "whole" relying exclusively on solar energy, even though in a "primitive or ancient," way, namely on an empirical basis.

This ancient renewable-solar-energy "system" still exists in our modern world. It is like an ancient "solar soul" we are used to, that we take for granted, nearly forgotten, certainly not accounted in official energy-use and economic data statistics, it is fully part of us. In fact, this solar heritage, even if widely present in modern societies and in our daily life, is often unnoticed and unknown.

In the last century people saw the rapid growth of a new energy infrastructure based on abundant use of fossil and nuclear fuels and with it, the growth of cities' in size and population. Urbanization and mega cities, and the depopulation of rural areas became the sides of the same coin.

Over the last decades, hundreds of millions of people throughout the world left their villages and moved to cities in search of new opportunities and welfare.

"With 75 per cent of Chinese expected to be living in cities within 20 years, the demand for more transport, energy, water and other vital infrastructure is set to test resources and city planners" (Simpson, 2012).

Fig. 3:The city of São Paulo, Brazil. With about 20 million inhabitants, it is one of the most populated cities in South America. We can only imagine, but we can not see the farm fields that produce food for the city as in the case of Spello in Fig.2. Photo www.scattidigusto.it (2014).

A trend that started with the discovery and diffusion of fossil fuels continues today everywhere in the world. According to experts, urbanization is an irreversible phenomena. Is it really? We will consider this question again in the Section 6 Habitat and Agriculture.

According to The United Nations Population Fund, "Urbanization has the potential to usher in a new era of well-being, resource efficiency and economic growth. But cities are also home to high concentrations of poverty. Nowhere is the rise of inequality clearer than in urban areas, where wealthy communities coexist alongside, and separate from, slums and informal settlements" (UNFPA, 2015).

Our grandparents and great-grandparents would certainly never have imagined a transition from solar energy to fossil and nuclear fuels in the proportions we see today. It's impossible to imagine what the world might look like in 2100. However, we should ask ourselves whether it's reasonable to think of an epochal transformation in which our industrially and technologically advanced societies make the switch to a ***modern or future solar age***, in which we return to the exclusive use of solar energy.

History can have an important role in helping and educating us in rediscovering the lost culture of solar energy, making it possible to power advanced societies only with solar energy.

In the following pages we treat five topics seen in a historical perspective, enriched here and there with information from The Italian National Archive and Museum on the History of Solar Energy:

- Terminology concerning energy sources on Earth;

- Earth systems and science;
- Ancient and modern solar ages;
- Solar or nuclear in the 1950s and today;
- Habitat and agriculture.

2. Terminology concerning energy sources on Earth

An important aspect in dealing with solar energy is represented by the continuous change of the terms we use when referring to it in different periods of human existence on our planet.

Energy, Solar Energy, Renewable Energy, wind energy, hydro energy, biomass etc., are common words for us today. It is very likely that they would not be understood just a few decades ago, even by the most educated people, and they were not known at all by our most recent ancestors.

What about the future? As we see it, the current terminology, though widely used, is still far from being valid for the promotion of solar energy use.

Indeed, the term “renewable energies” leads people to believe that various energy forms, such as wind, biomass, hydro, each originate from different source, with their own market niche and technology, whereas in reality they all come from the same source - the Sun. The more the solar market and technologies are integrated and promoted as a whole, the better they can be understood and defended from other proposed energy sources. There have been extraordinary developments on our understanding of how the Earth works and of its relationship with our life and the radiant light energy from the Sun. We need to develop the terminology to reflect these developments.

At the beginning of the 1900s, the Italian chemist Giacomo Ciamician (1857-1922), founder of the Institute of Chemistry of Bologna, Italy, which bears his name, in his famous speech, "The photochemistry of the future” (Ciamician, 1912), called the energy coming from the Sun *current solar energy*, i.e. the energy that the earth receives from the sun every day to distinguish it from *fossil solar energy*, i.e. solar energy accumulated by nature over centuries. Ciamician asked himself: “Is fossil solar energy the only energy source that may be used in modern life and civilization? He then concluded that it would be better to use the daily “current solar energy.”

In 1951, on behalf of the USA Atomic Energy Commission, Palmer Putnam conducted a study on the future energy for the period 1950-2050. He grouped energy sources on Earth into three broad categories: a) capital energy sources (coal, oil, gas, etc.); b) Income energy sources (direct and indirect solar energy and other forms of income energy); c) nuclear fuels. The language used by Putnam implies an economic characteristic for sources a) and b).

Fossil fuels are a "capital" created for us by the savings made by nature over millions of years. The use of “renewable energy” is an income energy that comes from the Sun and it does not undermine the consistency of our annuity that is available for us and will be for future generations. The terms used by Putnam have by now been forgotten.

The term "renewable energies" came into common use in 1981, when the United Nations organized the Nairobi Conference on New and Renewable Sources of Energy in Kenya. Its predecessor, the 1961 U.N. Conference on New Sources of Energy in Rome (Italy), presented solar, wind and geothermal energy as if they were new sources, while they had existed on Earth from the start.

Agostino Capocaccia from the University of Genoa (Italy) in 1972 reminds us that for centuries man used only *surface energies* (living beings, water, wind, wood). In the last two centuries, *energies of darkness* (coal, oil, endogenous forces, uranium), responsible for most of the pollution, have taken over. He also gathers energy resources on Earth in energies with limited supplies and energies with an unlimited supply (Capocaccia, 1972).

Most of the terms reviewed above became obsolete after the first oil shock of 1973, with the introduction of the term "alternative energy", still often used to indicate the energy from the sun, but at the time referring to all forms of energy alternatives to oil, including nuclear power.

As this brief review shows, energy forms have been referred to by different names at different times. Currently, the most prevalent terms contain the word “renewable” or “solar”.

However, drawing inspiration from "The International Year of Light and Light based Technologies,"

proclaimed by the United Nations for the year 2015, we might want to consider using more widely another word: LIGHT! Over the past five hundred years giant steps have been made in the understanding of what light is and how light works by great scientists such as Galileo, Leonardo da Vinci, Newton, Huygens, Maxwell, Planck and Einstein.

More information on these developments can be found at the web site of the International Year of Light and Light Based Technologies (www.light2015.org) and at the GSES web site www.gses.it, devoted to the Year of Light, in particular the articles in English published in Clean Technica (Perlin, 2015).

The explanation of the photoelectric effect by Einstein contributed to underscore other aspects of the structure of the atom, the nature of light and the electrical origin of the cohesive forces in molecules and matter. All this has opened fascinating prospects for the use of direct solar energy in the modern or future solar age, from solar photovoltaic cells with efficiency ratings of 50% or more to smart glass, photon solar architecture and city planning.

We might propose to gather energy sources on Earth in two categories:

- ***Light energies***, energies from the direct or indirect solar radiation: those above the surface of the Earth, that include direct and diffuse solar radiation and indirect air and water currents, naturally or artificially powered by Sun's energy, and photosynthetic phenomena which are the source of biomass. Sun's light energies can be seen by anyone, anywhere, anytime.

- ***Darkness energies***, energies stored underground, below the surface of the Earth, that include fossil fuels - coal, oil, natural gas – nuclear fuels, and the internal heat of the Earth. Until a few centuries ago we did not even know about their existence. Today we continue to discover new fossil fuels fields.

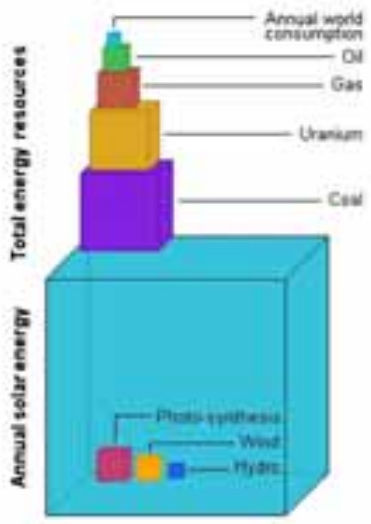

Fig. 4: Order of magnitude of energy sources on Earth (Lomborg 2001)

3. Earth systems and science

We live on Earth and need to understand how it works.

Think of it as a system made up of three subsystems, Earth's matter, Earth's energy and Earth's life, as suggested by Dr. Art Sussman in his Guide to Planet Earth (Sussman, 2000).

In terms of matter, the Earth is a closed system. It has practically the same amount of matter that it had at its origin and that cycles over and over. In terms of energy, the Earth is an open system, except for its internal heat. It receives a certain amount of energy from the sun and, after transforming it through the myriad natural processes operating on our planet, from the growth of plants to wind and water cycles, radiates that same amount back into space. As to the living world, the Earth is an interconnected system. The existence of every living being depends on a ramified network of relations with other living beings and with the matter and energy systems.

Today we're in the midst of a great new challenge: understanding that the Earth and its three subsystems work

as a whole, and that for the first time ever, their operation can be affected by human activities, partly because never before have there been so many people living on the Earth, and partly because we humans are engaged in more and more activities that can significantly affect the natural mechanisms that make our planet work.

This new awareness of how the Earth works is gaining ground through increasingly evident cultural and political processes, as in the case of climate change due to greenhouse gases as well as to the production of artificial heat on the Earth's surface, as proposed by Prof. Giovanni Francia (1911-1980) in the seventies.

Despite the scientific uncertainty that veils phenomena as complex as climate change, we can plainly no longer shut our eyes to the way the Earth works. This should be standard knowledge for everyone, just like the knowledge that the Earth is not flat but spheroid.

Once we've learned how the Earth works, it should be easier to determine the best ways to know and use its natural resources, in particular its energy resources and solar energy, so as to maintain the environmental balances on which our lives depend.

4. Ancient and modern solar ages

It often happens that we think of solar energy as an aspect of our modern world, although it had powered everything on Earth until 150-200 years ago.

We should impress in our minds that for thousands and thousands of years, light, heat and fuel from solar energy alone shaped human settlements and cities, farming and forestry, architecture and buildings, landscapes and territories, religious beliefs and cultures, social relations and lifestyles - in a word, whole civilizations. The use of renewable solar energy is thus an age-old experience and we need clearly to make a distinction between ancient and modern solar ages and understand what has been changed moving from one to the other.

Solar energy resources, at least over the last 10.000 years, have not changed. What has changed is our knowledge of them. Our ancestors had neither the scientific knowledge nor the technical means available to us today to observe, measure and monitor direct solar radiation and its indirect forms, wind, falling water, biomass and other forms over days, months, seasons and years. With a combination of satellite data and field measurements, we can estimate the amount of direct solar radiation that reaches any part of the Earth. In a word, we can find out what energy resources are available at any point on our planet.

Basic principles of solar architecture and urban planning also have not changed, nor have the basic principles used to collect, convert or store sun's heat. What has changed, and that must be underlined, is that we have learned to convert solar energy into electricity, an expression of our modern solar age.

Since the 1800s we learned first to convert power of falling water into electric energy and, more recently also that of the winds and of sun's heat and light.

The foundations of these advancements are in the many discoveries and inventions made in the last five hundred years and lie chiefly in our ever more advanced understanding of optics, light and the structure of matter, which has opened fascinating prospects for the use of solar energy in the modern age, from solar cells with efficiency ratings of 50% or more to smart glass and photon solar architecture and city planning (Perlin, 2015).

By now we know for certain that it is possible to build large and sophisticated energy infrastructure powered by solar energy to produce electricity, low-, medium- and high-temperature heat, fuels and other useful forms of energy.

It must be recalled that electricity consumption in advanced societies accounts for less than 20% of the total, while 80% is in the form of fuels and heat, the last at low temperatures, i.e. those that the Sun makes available naturally.

What we do not know today is how to build a modern solar energy system as a ***whole,*** which is something we think necessarily in order to replicate in a modern way the ancient solar energy systems. Today, the idea that the systemic aspect of the use of solar energy, which was implicit in the lives of our forebears, is overlooked. It is a cultural deficit that span all fields: science, technology, organization, sociology, economics, politics, even our terminology and ways of communicating.

A cultural deficit that regards also the recent history of modern solar energy. In 1955, on the occasion of the

first World Solar Symposium held in Arizona, the first comprehensive Directory of World Activities and Bibliography of Significant Literature on Applied Solar Energy Research was published and distributed by Stanford Research Institute for the Association for Applied Solar Energy (Stanford Research Institute, 1955).

Approximately 4000 citations relevant to 27 countries, from 1850 to 1955, are reported in this Directory. They show the human effort made to pursue solar energy in modern times, but strange to say, the prophetic visions, the inventions and the work of so many pioneers in the late 19th and early 20th century are little known today, even to solar specialists. Yet many of them, farsighted and with clear vision, anticipated problems that appear are constantly in the news today. They also anticipated the technical solutions or proposals necessary to deal with important dilemma, such as the question of favoring "Nuclear energy or Solar energy?"

5. Solar or nuclear in the 1950s and today

The solar or nuclear debate: Nuclear YES, Nuclear NO, Solar or Nuclear, continues today as did was fifty years ago.

Ahead of the Climate Change International Summit in Paris in December 2015, there are more and more voices claiming that climate change requires a technological response, and nuclear power could be an important element of that response (Guyer and Golay, 2015).

In the 1950s, solar pushed to the side with the promises of nuclear power. In fact, in the aftermath of WWII, modern solar technologies, except for hydro, and peaceful uses of nuclear energy to produce electricity were both in their infancies.

In January 1951, United States President Harry S. Truman appointed William Paley to chair the President's Materials Policy Commission to investigate the long-term availability of raw materials, making a clear distinction between those necessary for defense and those essential for the country's development. Paley thought that the United States could not afford a shortage of raw materials to jeopardize the nation's security or create a bottleneck in its economic expansion. On June 2, 1952, Paley submitted his report to the President. The committee had consulted experts in industry, academia and government, and one of the four volumes of its report on the analyses and conclusions of the study had a whole chapter devoted to what Paley called **"The possibilities of solar energy"** (Paley, 1952)**.**

The chapter summarized the results of a broader study made by Palmer Putnam in July 1951 for the US Atomic Energy Commission, in which he had reviewed all the methods for collecting solar energy and converting it into commonly used forms of energy: natural photosynthesis, heat pumps, thermal solar collectors, solar-heated homes (13 million were expected to be built in the United States by the end of 1975), water desalination, electricity generation with solar concentration systems, the exploitation of solar energy through wind and the thermal gradients of tropical waters, controlled biological photosynthesis, non-biological photosynthesis and photovoltaic.

The Paley Report concluded that up till then only tiny steps had been taken to promote solar energy, and emphasized the importance of adopting an aggressive policy to develop the entire solar-energy sector, a sector in which the United States would be able to make a huge contribution toward the well-being of the free world.

Under the Truman administration, this prospect was one of many considerations, including the idea that the development of nuclear energy to generate electricity would contribute significantly to increase the risk of proliferation of nuclear arsenals and the threat of atomic war. These fears explain Truman's decision to keep all information on nuclear energy secret. But this policy soon proved pointless, because the Soviet Union was quickly equipping itself with nuclear weapons. Truman's approach was overturned when Eisenhower won the 1952 election and entered the White House.

In a speech delivered at the United Nations General Assembly on December 8, 1953, Eisenhower announced the "Atoms for Peace" program that, according to solar energy historian John Perlin, became the ace in America's hand to win the Cold War (Perlin, 2000). With international political commitment and economic support, nuclear power took off while Paley's report was forgotten and solar energy left behind.

We wanted to recall the nuclear or solar debate in the 1950s, because nuclear energy, in spite of its technological and economic limits, which clearly emerged with great evidence during the Chernobyl and Fukushima accidents, continues to be considered a valid option to fight climate change because it does not produce greenhouse gases as do fossil fuels. Too often, nuclear energy is inappropriately considered, along with

solar energy, as a solution to the issue of climate change.

Today, unfortunately, this idea is widespread. In order to counter this misconception, in my view, we should consider Prof. Giovanni Francia's research on the Earth's thermal equilibrium, illustrated in a paper he wrote in the early 1970s titled "The Sun and the Limits of Energy on the Earth" (Francia, 1973).

Francia, a mathematician and physicist, teaching at the University of Genoa, devoted more than 20 years of his life to studying and experimenting with solar energy systems and concepts from the early sixties up to his death in 1980. He is considered by GSES the foremost Italian solar energy pioneer of the 1900s (Silvi, 2005).

In February 2005, I discovered Prof. Francia's undated paper on the Earth's thermal balance in his personal archive, donated by his heirs to the Museum of Industry and Work in Brescia (www.musilbrescia.it).

To my knowledge, the complete Italian version of Francia's paper has remained unpublished until today. We can be reasonably sure that he wrote it between late 1973 and early 1974, because a summarized French version appeared in the second half of 1974 in the Revue international d'héliotechnique, a journal published by COMPLES (Coopération Méditerranée pour l'Énergie Solaire), of which a one of a kind collection is kept at the Italian Archive and Museum on the History of Solar Energy in Brescia (Italy).

I outlined Francia's views about the thermal equilibrium of Earth in a paper about his pioneering activities that I presented in August 2005 at the World Congress organized by the International Solar Energy Society in the United States (Silvi, 2005). The interest aroused by his approach encouraged me to try to broaden knowledge of his paper.

As it was partly typewritten and partly written in longhand, it was not easy to read it. Accordingly, I transcribed it in electronic format and made a short summary of its contents that follows.

In this study, Francia focuses on the Earth's surface temperature, the point of equilibrium between the energy radiated by the Earth into space and the energy that the Earth receives from the sun. Throughout historical time, he says, the amount of thermal energy generated on Earth by natural phenomena has remained practically constant, except for changes caused by the fluctuations in solar power that occur in eleven-year cycles.

Over the last two centuries, though, energy generated artificially by human beings, above all by burning fossil fuels, has been added to the amount of naturally generated thermal energy.

Since the amount of thermal solar energy that reaches the Earth is thousands of times greater than the sum of non-solar energies, and since the uncertainties regarding its estimation are on the same order of magnitude as the latter, according to Francia the modest amount of thermal energy generated artificially by humans might seem at first sight to lead one to conclude that it has no effect at all on the Earth's thermal equilibrium.

But this is not so, as Francia explains in a few pages with a series of observations regarding the ways in which our planet's various surfaces (water, snow, soil) absorb and reflect solar radiation in different seasons and at different latitudes.

To the contrary: if in a hundred years' time this small amount of thermal energy generated continuously by humans were to reach amounts tens of times higher than those of 1974, according to Francia, it would produce phenomena of thermal instability on the Earth, triggering a chain of events with positive retrospective effects that could shift our planet into an equilibrium very far from the initial one, and at speeds much faster than living beings can adapt to.

Prof. Francia concludes that, ***"It would seem that the production of even small quantities of energy on the surface of the Earth alters the climate dramatically, and that henceforth it will be necessary to use solar energy, the only kind that does not generate thermal pollution."***

From Francia's research, which did not include the effects of greenhouse gases, one can conclude that climate change seems also to be connected to the production of artificial heat on Earth, which is added to natural thermal heat from solar radiation, by burning fossil and nuclear fuels, and by extracting the Earth's internal heat. What has not been studied, is the combined effect of the two.

6. Habitat and Agriculture

The importance of sun's energy use and human life on Earth is deeply inscribed in the history of human habitats and surrounding farmlands. Since prehistoric civilizations, habitat and farming were always based on

the same energy principles. As energy historian Vaclav Smil points out, "all agriculture was based on the conversion of solar radiation through the process of photosynthesis. Photosynthesis produced food for humans and livestock, recycled waste to fertilize the soil, and provided the fuel needed to melt the metals with which primitive farming tools were made. Traditional farming methods were thus based entirely on solar energy. Except for cutting down old forests, they did not impoverish energy stocks. The whole process was based on a virtually immediate capacity to convert solar energy flows." (Smil 1999).

Then came fossil fuels – first coal, then oil, then natural gas – and later nuclear energy. In less than a hundred years, we've built huge and efficient energy infrastructure – coal and oil shipping terminals, oil and gas pipelines, power plants and power lines, and so on – that have assured abundant energy, development and well-being, but have also had ever more obvious effects on the environment and led to profound changes in the socioeconomic geography, habitats, farming and lifestyles of whole civilizations that had grown over the centuries with the use of solar energy alone.

Mega-cities grew rapidly, as well as rural depopulated areas, altering relationships among the different functions of cities and their surroundings.

A thesis presented in Genoa in 2006 by GSES was that in order to bring the modern solar city into being we must intelligently combine and integrate the experience gained by the ancient cities – not only in terms of technical know-how, but also of art, culture, relations and communication – with the many solutions made available by the scientific discoveries and extraordinary technological developments of the past two hundred years, especially in the most recent decades (Silvi et al., 2006).

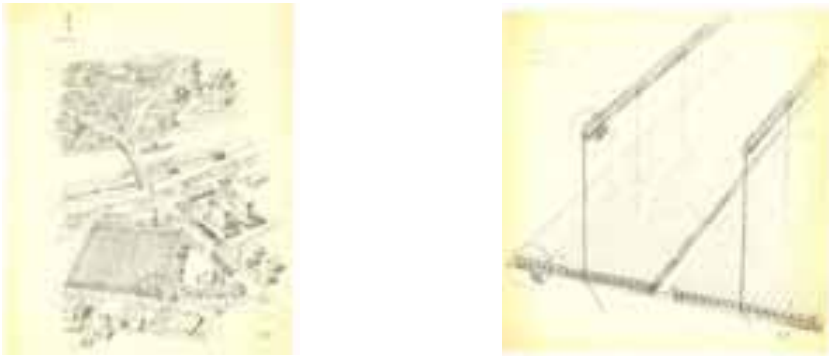

Fig. 5: Drawings of large Linear Fresnel Reflector Solar Power Plants integrated in a city designed by Francia in 1965 circa (Francia Archive donated to the Museum of Industry and Work in Brescia by his heirs in 2005)

In the "Solar City Project – Ideas for an Urban Structure", Prof. Giovanni Francia and his collaborators (Francia, 1971 et al.) discussed whether and how the discoveries, suggestions and results that solar energy science has produced in the past few decades are compatible with the new directions that architecture is taking.

They were convinced – and they believed many other people were as well – **"that in the near future scientists, architects, economists and sociologists will have to study the large-scale use of solar energy, and that (as far as they could tell at the time) for the most part their studies will focus on electricity generation and the heating and cooling of cities."**

Fig.6: Francia, right, showing a model of the solar city project, Genoa (Italy), 1978.

The Solar city exhibition held in Genoa by GSES in 2006, to honour Francia's vision of a Solar city, recounted the vicissitudes of cities, of architecture, energy and food-supply infrastructures, and the scientific discoveries

and technological developments that marked the major stages in their history, with special focus on day lighting, heating and cooling of buildings.

Gaetano Vinaccia (1889-1971), an Italian architect of the early 1900's and solar pioneer, author of more than 200 publications, most of which devoted to solar energy, in his book "The City of Tomorrow" wrote: **"To reach the city of tomorrow, we need first of all – to save time and effort – to retrieve old paths considered useless by people who think the past is a ball and chain bound to humanity's feet so as to prevent our triumphant march toward progress. The fruit of thousands of years of intelligent work, the selection that centuries of experience has contributed to, cannot be bypassed, cannot be modified, cannot be refuted except through centuries of hard and serious work. And there are absolute truths that no one can modify, much less destroy" (Vinaccia, 1939).**

Fig. 7: Front cover of Vinaccia's book "Il corso del Sole in urbanistica ed edilizia." The Course of the Sun in Urban Planning and Construction (Vinaccia, 1939).

In Genoa GSES's solar city exhibition drew inspiration from the pioneering works of two Italian important solar scientists, Francia and Vinaccia, intelligently combining our millennia experiences and principles in solar energy use with the most advanced technologies from the extraordinary scientific advancements of the last 500 years. In other words, as put by Norbert Lechner, "Use the best of the old and the best of the new" (Lechner, 2000).

Is Urbanization an irreversible phenomena? Will 75% of 10 billion people, as we are expected to become in 2015, live in cities? We do not know. For certain we might reconsider historically and scientifically what options we had in the past and what we can have in the future.

A key aspect of solar energy use is its intermittency. Until 200 years ago we knew how to use solar energy stored by nature through photosynthesis in a common fuel: fire wood.

Today there are many scientists who are working to store solar energy in a fuel that can become as commonly available as fire wood has been for centuries.

Among scientists that conquered global media attention on this possibility is Daniel Nocera. During the impact of the Arab oil embargo and other oil crises of the 70s and 80s, Nocera envisioned his scientific career as one of a humanitarian activity focused on the discovery of the "guarded secret of plants", a concept which was introduced into the scientific debate in 1912 by Italian chemist Ciamician in his paper The photochemistry of the future (Ciamician 1912, Venturi et al. 2005, Nebbia and Kauffman 2007, Nocera, 2011).

In 2011 Nocera presented a cheap coated-silicon sheet, referred to as an artificial leaf, which, when placed in a glass of tap water and exposed to sunlight, was able to split water into hydrogen and oxygen. "If there is one thing that's unique to this technological development," said Nocera, "it is that it was done with the very poor in mind."

Fig. 8: A slide by Daniel Nocera in which power lines are no longer needed. Electricity and fuel will be provided by the artificial leaf, which when placed in a glass of tap water and exposed to sunlight, is able to split water into hydrogen and oxygen

If in the last century millions moved from villages to cities, is it possible that in the future might millions move back from cities to villages? Is a modern new solar colonization of Earth thinkable and possible?

7. Italian Archive and Museum on the History of Solar Energy

The idea of Italy's Archive and Museum on the History of Solar Energy started to take shape within GSES in 2003, with the main purpose being to preserve and make widely available the Italian heritage of solar energy use in our country (Silvi, 2008).

The Archive and Museum, whose initial core has been taking shape in the past few years in Brescia, in northern Italy, at the Luigi Micheletti Foundation and the Eugenio Battisti Museum of Industry and Work (www.musilbrescia.it), is being organized around the following topics: solar pioneers and devices starting in the early years of industrialization; solar architecture and city planning; the use of solar energy in agriculture.

In this paper we have provided examples of the kind of contributions that can come from knowing the work of great Italian pioneers such as: Giovanni Francia, mathematician and physicist; Giacomo Ciamician, chemist; Gaetano Vinaccia, architect. Their stories and work are documented at the web site of GSES www.gses.it, mainly in Italian.

8. Conclusions

The "easy" and "abundant" energy provided by fossil fuels permitted architects and engineers to ignore the fundamental rules of solar architecture and city planning which had been used as guides for thirty-five hundred years – proper insolation, building orientation – and led to major changes in our society that will not be easily reversed. Perhaps, still more important, this "easy" energy resulted in the loss of the ancient culture that was necessarily sophisticated and frugal in the use of natural resources.

Today it would probably be much easier to continue, as we are doing, along the same path, continuing to build energy infrastructures based on fossil and nuclear fuels, than it would be to create an entirely new energy infrastructure that enables widespread use of solar energy.

However, human societies progress when they face difficult challenges and manage to come up with new solutions, rather than falling back on easier and conventional ones. The solar challenge is indeed a difficult one, but that's exactly why it ought to interest us and why we should work harder at advancing it.

9. References

Capocaccia A.A., 1972. Il Sole e l"Uomo – Nuove prospettive dell'Eliotecnica. Responsabilità del sapere, XXIV, vol. 101, pp 5-30, Roma.

Böer, K., 2005. The Fifty-Year History of the International Solar Energy Society and its National Sections. Publisher American Solar Energy Society, Boulder (Colorado) USA.

Ciamician, G., 1912. La photochemie de l'avenire, estrait de Scientia, vol. XII, 6ème anneé, N. XXVI-6.

Francia G. et al, 1971. Solar City Project – Hypothesis for an Urban Structure. Proceedings COMPLES meeting, Marseilles, Bulletin 19.

Francia, G., 1973. The Sun and the Limits of Energy on the Earth, in Francia's personal archive donated by his heirs to the Brescia's Museum of Work and Industry.

Lomborg, B., 2001. The Skeptical Environmentalist, Cambridge University Press, Cambridge.

Guyer, B.L., Golay, M. W., Summer 2015. Requirements for the Success of Civilian Nuclear Power in the United States. The Bridge (ISSN 0737-6278), published quarterly by the National Academy of Engineering, Washington, vol. 45, No. 2, pp. 48-54.

Lechner, N., 2007. The Future of Architecture: Sustainable Architecture, Lecture.

Lewis, N.S., Nocera, D. G., Summer 2015. The Solar Opportunity. The Bridge (ISSN 0737-6278), published quarterly by the National Academy of Engineering, Washington, vol. 45, No. 2, pp.41-47.

Nebbia G., Kauffman G.B., 2008. Prophet of Solar Energy: A Retrospective View of Giacomo Luigi Ciamician (1857–1922), the Founder of Green Chemistry, on the 150th Anniversary of His Birth, Chem. Educator 2007, 12, 362–369.

Paley, W., 1952. President's Materials Policy Commission (Paley Commission). The Promise of Technology – The Possibilities of Solar Energy. Vol. IV, United States Government Printing Office, Washington, pp. 213-220.

Perlin, John (2000) 'Nuclear or Solar? Energy Choices for the 1950's and 1960's', Workshop on "Solar Culture, History and Art to promote solar energy utilization," ISES Millennium Solar Forum Mexico 2000, Mexico City, 17-22 September 2000.

Silvi, C., 2005. The work of the Italian solar energy pioneer Giovanni Francia (1911-1980), Proceedings ISES Solar World Congress 2005, Orlando Florida, USA.

Silvi C., Los S., 2006. The Italian Solar City Travelling Exhibition. 2nd International Solar Cities Congress, Oxford, 3-6 April, 2006.

Silvi C., 2006. Solar Building Practices and Urban Planning in the Work of Gaetano Vinaccia (1889 - 1971), 2nd International Solar Cities Congress, Oxford, 3-6 April, 2006.

Silvi, C., 2008. Italy's Archive on the History of Solar Energy, Poster Presentation, Proceedings EuroSun 2008, Lisbon, Portugal.

Smil, V.,1999. Energies. An Illustrated Guide to the Biosphere and Civilization. The Mit Press. Cambridge, Massachusetts; London, England.

Simpson, P., 2012. China's urban population exceeds rural for first time ever. Report from Beijing for The Telegraph.

Stanford Research Institute for AFASE, 1955. Applied Solar Energy Research: A Directory of World Activities and Bibliography of Significant Literature, Burda E.J. (Ed), Stanford, California.

Sussman, A. (2000). Dr. Art's Guide to Planet Earth, San Francisco, CA 94107 ISBN: 1-890132-73-X, WestEd.

Venturi M., Balzani V, Gandolfi M. T, 2005. Fuels From Solar Energy. A Dream of Giacomo Ciamician, The Father of Photochemistry, Proceedings ISES SWC 2005.

Vinaccia, G., 1939. Il corso del Sole in Urbanistica ed Edilizia (The Course of the Sun in Urban Planning and Construction), Hoepli, Milano.

Vinaccia, G., 1939. Per la città di domani: Vol. 1°. Come il clima plasma la forma urbana e l'architettura. La sanità e l'igiene cittadina, Roma F.lli Palombi Editori.

Web references

UNFPA,
http://www.unfpa.org/urbanization#sthash.a4NpDjRr.dpuf (2015)

Ciamician, G. 2012. "The photochemistry of the future"
http://www.gses.it/pionieri/ciamician-photochemistry.pdf (2015)

Perlin, J., 2015. Articles by John Perlin. A contribution to GSES program for The Year of Light 2015. http://www.gses.it/incontri/annodellaluce.php#doc (2015)

Breaking The Wall to Personalised Energy @Falling Walls https://www.youtube.com/watch?v=P2QZNCNml3g (2015)

Energy Storage

Conference Proceedings

Solar World Congress 2015
Daegu, Korea, 08 – 12 November 2015

HEAT TRANSFER PEERFORMANCE RESEARCH OF HONEYCOMB CERAMIC THERMAL ENERGY STORAGE

Y. Wang[a], F.W. Bai[a], Z. F. Wang[a], Hiroaki Kiriki[b], M.X Han[b], Shuichi Kubo[b]

[a]The Key Laboratory of Solar Thermal Energy and Photovoltaic System,
IEE-CAS, No.6 Beiertiao, Zhongguancun, Bejing, 100190,China

[b]Ceramics Structure Development Project, IBIDEN CO.,LTD.,
1-1,Kitagata,Ibigawa-cho,Ibi-gun,Gifu Pref.,501-0695,Japan

Abstract

Thermal energy storage (TES) is core advantage for the concentrated solar power (CSP) technologies. A packed bed of rocks or other ceramic is especially suitable when gas is used as the heat transfer fluid. The heat transfer performance of thermal energy storage (TES) device which use the air as the heat transfer fluid and the honeycomb ceramic as the storage material was researched by experimental in this paper. The results showed that the temperature distribution was obvious thermocline distribution when charging and discharging process. The charging efficiency of the TES device was higher than 75%, and the discharging efficiency was higher than 85%.

Key words: *thermal energy storage; honeycomb ceramic thermal storage; heat transfer performance*

1 Introduction

Thermal energy storage (TES) is core advantage for the concentrated solar power (CSP) technologies. TES appears to be an important solution to correcting the mismatch between the thermal energy availability and demand of energy. Sensible heat storage is the most simply and inexpensive way of energy storage system although there are few advantage of phase change energy storage over sensible heat storage, but the technological and economical aspects make sensible heat storage superior[Sigh et al, 2010]. For CSP plants operating with air as the heat transfer fluid [Bader et al, 2011, Wang et al, 2015], TES using a packed bed of rocks has been shown to offer a simple and efficient technical solution for overcoming the intermittency of solar radiation [Zanganeh et al, 2012, Meier et al, 1991, Hänchen et al, 2011, Gross et al, 1980]. A packed bed of rocks or other ceramic is especially suitable when a gas is used as the heat transfer fluid [Sigh et al, 2010, Hanchen et al, 2011, Coutier and Faber, 1982, Hasnain 1998]. The numerical and experimental results show that the porous structure which maximize heat transfer between fluid and storage media and minimize heat transport inside the storage media [Xu et al, 2013, Zavatoni et al, 2014, Zanganeh et al, 2012]. The heat storage performance of two tanks TES and single TES had been researched by EPRI [Palo, 2010], the results showed that the cost of a single TES using fluid and solid material as the thermal storage media can reduce 33%. TES using a packed bed of sensible-latent material has been shown that a PCM volume of 1.33% of the total storage volume was sufficient to achieve stabilization of the outflow air temperature around the PCM's melting point [Zanganeh et al, 2014].

doi:10.18086/swc.2015.02.01 Available at http://proceedings.ises.org

Nomenclature

L	TES storage length
$\dot{m}$	Mass flow rate, kg/h
T	Temperature, ℃
z	Axial position
η	Efficiency
t	Time, s
c_p	Heat capacity, kJ/kg.K

Subscripts/Superscripts

i	The test section number of honeycomb ceramic of TES device
j	The thermocouple number in each test section
air	Heat Transfer fluid-air
$area$	The position of test section of TES
s	Honeycomb ceramic material
in	inlet
out	outlet
c	Charging process
d	Discharging process

In this paper, the solid thermal storage system which use the air as the heat transfer fluid and the honeycomb ceramic as the storage material was built-up and the heat transfer performance under different condition were investigated.

2 A honeycomb ceramic TES system

2.1 A honeycomb ceramic TES device

Fig.1 shows the schematic of the honeycomb ceramic TES device. The honeycomb ceramic TES device is a box which is consisted of inlet pipe, outlet pipe, cover plates and the TES materials. The size of the TES device is 1512×1412×1584mm. The air was used as the heat transfer fluid during the charging and discharging process. Honeycomb ceramics were used as the TES materials, and 4000 pieces of honeycomb ceramic were inserted into the TES device. Fig.2 is the photo of honeycomb ceramic material. The size of the honeycomb ceramic is 34.3×34.3×100mm. The property of honeycomb ceramic was shown in Table1.

Fig.1. The schematic of packed-bed TES device

Fig.2. The photo of honeycomb ceramic

Table 1 Property of honeycomb ceramic material

Aperture ratio (%)	Porosity (%)	Cell density (cell/cm^2)	Heat storage capacity (MJ/m^3)	Conductivity (W/m.k)
74	42	45	197	10.7

2.2 A honeycomb ceramic TES system

In order to analyze the heat transfer performance of the packed-bed thermal storage, an experimental system of thermal storage was built up. Fig.3 is the layout of the packed-bed thermal storage system using honeycomb ceramic as the thermal storage material.

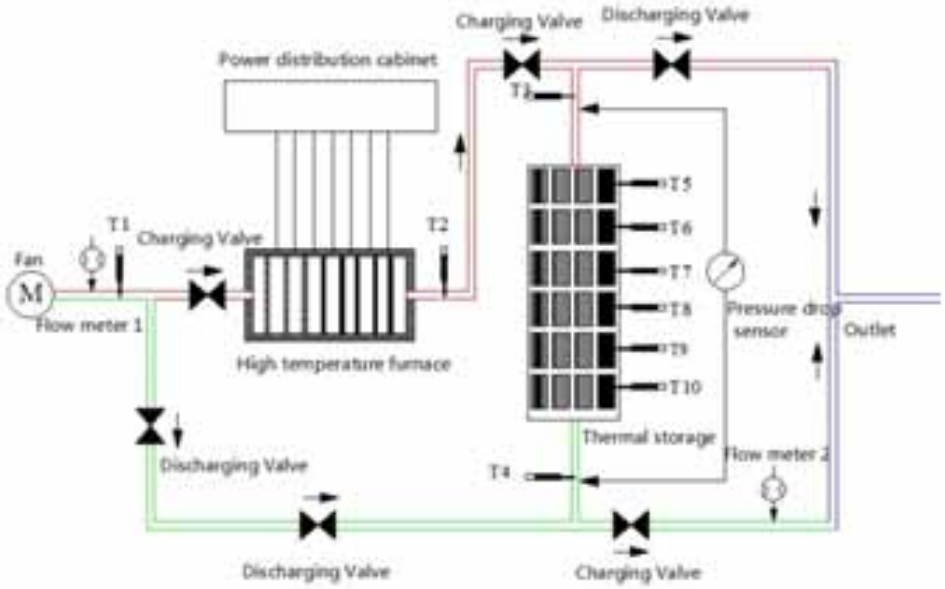

Fig.3. Schematic of packed-bed TES system

The thermal storage system is consisted of fan, high temperature air furnace, a honeycomb ceramic TES device, pressure drop sensor, thermocouple and flow meter. In the system, the fan transported air from the environment to the furnace or pipes. The high temperature furnace is the heating apparatus to heat the air.

The pressure drop when air flows through the thermal storage device were measured by the pressure drop sensor. The air temperature, honeycomb ceramic temperature and the surface temperature of the thermal storage were measured by several thermocouples. Fig.4 is the photo of the packed-bed thermal storage system.

Fig.4 The photo of the thermal storage system

In order to analyze the performance of the thermal storage device and the heat transfer between air and honeycomb ceramic, air volumetric flux, temperatures of air, honeycomb ceramic and the surface of the thermal storage device, the pressure drop of the thermal storage device were measured. The inlet air flow rate was measured by a volumetric flow meter with the range from 15 to 300m^3/h and the error is ±0.5%. The outlet air flow rate was measured by a vortex flow meter with the range from 80 to 800m^3/h and the error is ±0.5%. The pressure drop of the thermal storage was measured by the pressure drop sensor which the error is ±0.5%.

The temperatures of air, honeycomb ceramic and the surface of the thermal storage device were measured by thirty eight K-type or S-type thermocouples, which all error is ±0.1℃. The positions of the thermocouple inserted into the thermal storage device are shown in Fig.5.

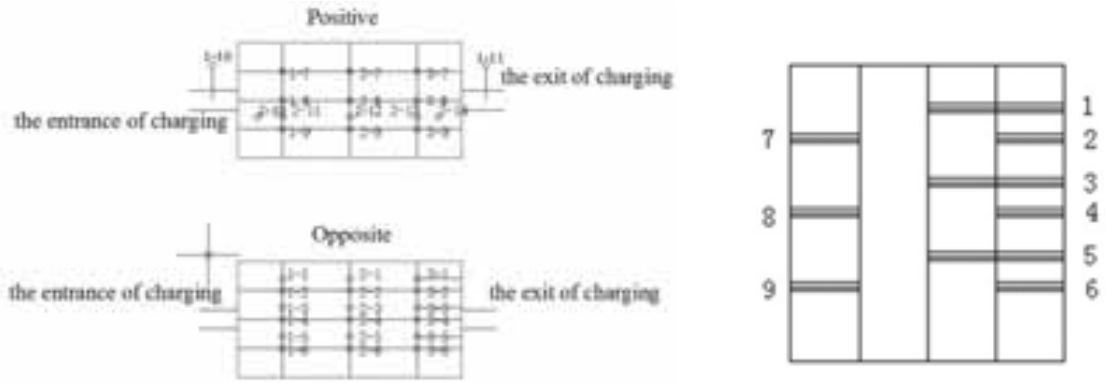

Fig.5 The position of the thermocouple in the packed bed thermal storage device

The thermocouples of 1-10 and 1-11 were measured the air inlet temperature and the air outlet temperature.

In order to measure the temperatures of honeycomb ceramic, 27 thermocouples were inserted into the thermal storage device and attached to the honeycomb ceramic surface. The thermal storage device is divided into three blocks along the length by thermocouples. The thermocouples of 1-1 to 1-9, 2-1 to 2-9 and 3-1 to 3-9 which were measured the honeycomb ceramic temperatures of the first block, the second block and the third block. The thermocouples of 2-10 to 2-14 were measured the surface temperature of the thermal storage device.

3 Experimental data analysis method

As shown in Fig.5, the arithmetic average temperature of each section is calculated as Equation (1):

$$T_{i,area} = \frac{\sum_{j=1}^{j=9} T_{i,j}}{9} \quad (i=1,2,3;\ j=1,2,\ldots 9) \qquad \text{(eq. 1)}$$

The average temperature of all the honeycomb ceramic in TES device is calculated as Equation (2):

$$T_s = \frac{\sum_{i=1}^{i=3} T_{i,area}}{3} \quad (i=1,2,3) \qquad \text{(eq. 2)}$$

The efficiency of the charging process is defined as the ratio of the net heat stored by thermal energy storage material and the total heat released by the hot air in the charging process, which can be expressed as the following equation:

$$\eta_c = \frac{M_S c_S [T_S(t_c) - T_S(0)]}{\int_0^{t_c} [T_{air,in} - T_{air,out}] c_{p_{air}} \dot{m}_{air}\, dt} \times 100\ \% \qquad \text{(eq. 3)}$$

The efficiency of the discharging process is defined as the ratio of the net heat which removed by the cold air and the total heat released by the thermal energy storage material during the whole discharging process, which can be expressed as the following equation:

$$\eta_d = \frac{\int_0^{t_d} [T_{air,out} - T_{air,in}] c_{p_{air}} \dot{m}_{air}\, dt}{M_S c_S [T_S(0) - T_S(t_d)]} \times 100\ \% \qquad \text{(eq. 4)}$$

4 Results and discussion

Several experiments under different thermal storage temperatures and air flow rates have been carried out and the thermal performance of the TES device was analyzed.

4.1 Temperature distribution

Fig.6 shows the temperature distribution in TES device during the charging process. To better compare the charging behaviour among TES, the temperature results of storage materials are reported using dimensionlesss coefficiencies for axial length, which was defined by equation (5). In this way, the L* can assume value between 0 and 1.

$$L^* = \frac{z}{L} \qquad \text{(eq. 5)}$$

As shown in Figure.6, from the inlet to the outlet, the temperature distribution is obvious thermocline distribution. At the beginning, the temperature gradient is very steep, but the temperature gradient is more and more gently during charging process. When the charging temperature is higher, the temperature difference of thermocline is greater.

Fig.7 shows the average temperature distribution of storage material under different flow rates respectively at the initial temperature of 400℃ and 500℃during discharging.

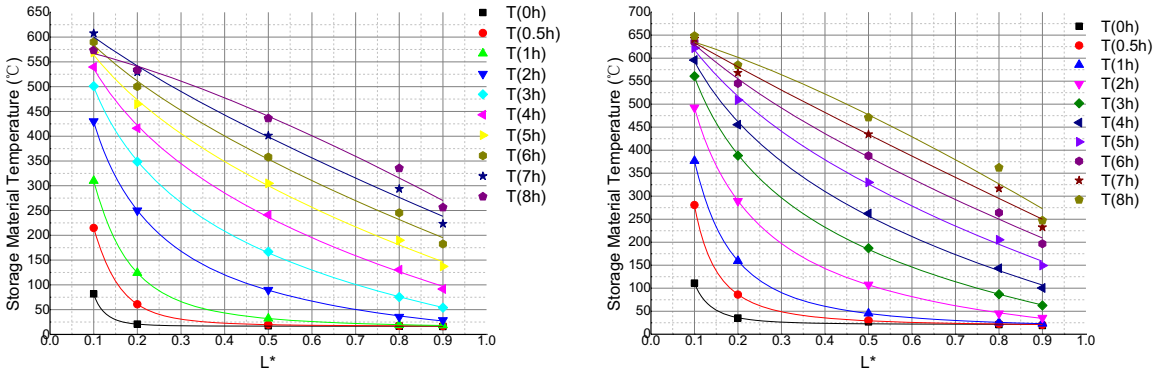

（a）400℃　　（b）500℃

Fig.6 Storage material temperature distribution of charging process

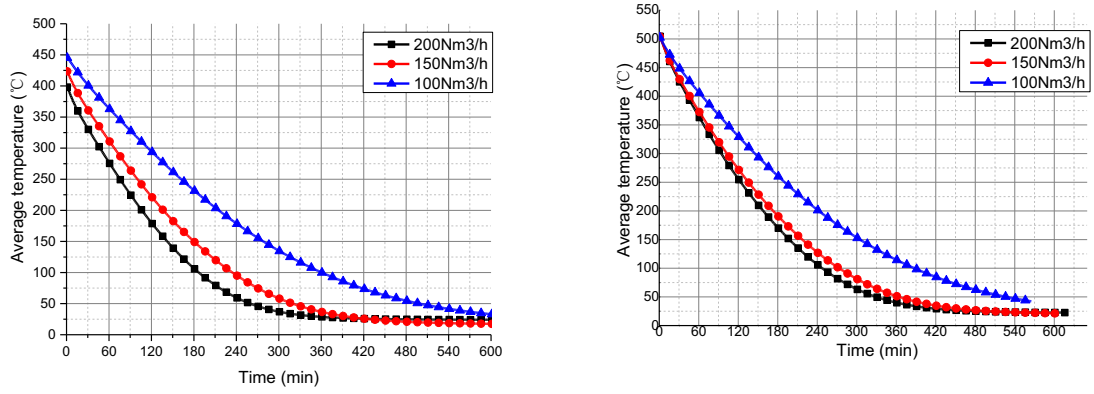

（a）400℃　　（b）500℃

Fig.7. Average temperature distribution of discharging process

From the figures, the average temperature drop of honeycomb ceramic material increases with the increasing air flow rates. The rate of temperature drop at the beginning discharging in TES device is significantly greater than the late stage of discharging. This is because the heat transfer rate between the air and the honeycomb ceramic material increases with the temperature differences increase.

Fig.8 shows the air outlet temperature variations under different air flow rates during discharging.

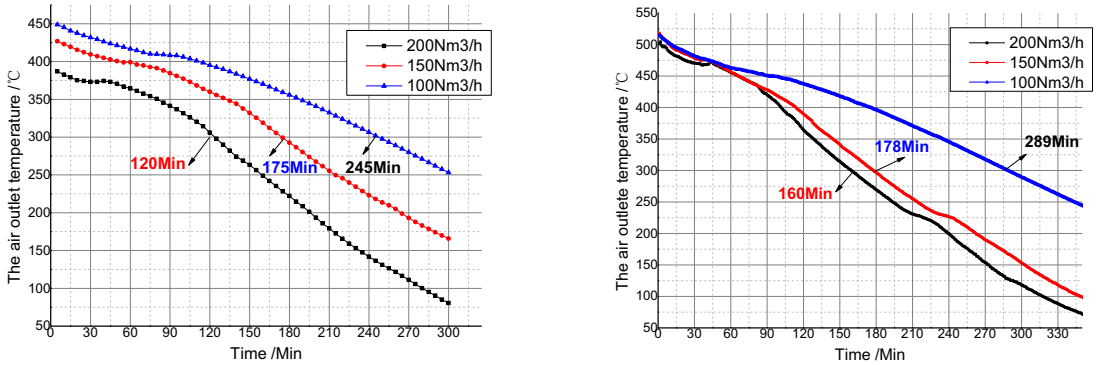

（a）400℃　　（b）500℃

Fig.8. Air outlet temperature variations of discharging process

Fig.8 indicated that the discharging time can be extended with the air flow rate decreased. The numbers in the figure mean the time that the air outlet temperature decreases from the initial temperature to 300℃. It can be seen that the time for the air outlet temperature declining to a specified value increases with the air flow rates decreases. The outlet temperature of air is higher when the temperature of honeycomb ceramic is higher at the begging of discharging.

4.2 Pressure Drop distribution

Fig.9 shows the pressure drop distribution in the TES device under different air flow rates.

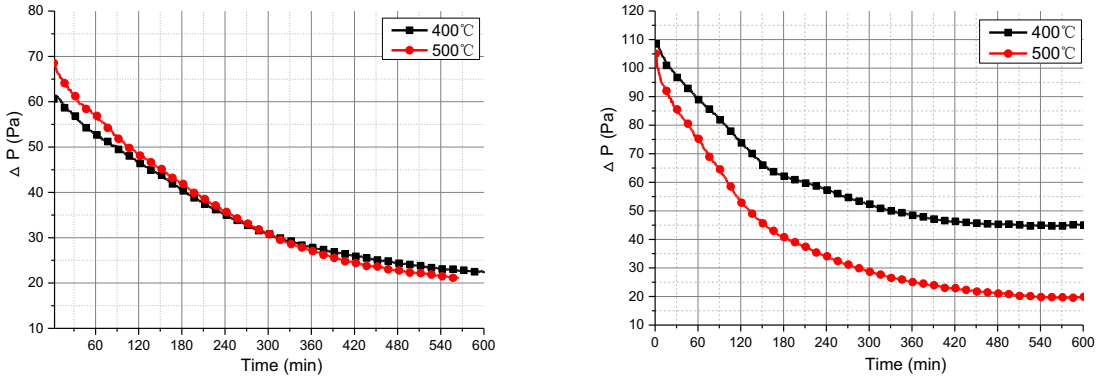

(a) 100Nm^3/h (b) 150Nm^3/h

Fig.9 Pressure drop distribution with time

The pressure drop when air flowing through the TES device was kept below 110Pa under different discharging temperature. The pressure drop increases with the increasing air flow rate, and decreases with the decreasing air outlet temperature. From the pressure drop results it can be seen that porous structure material as the thermal storage material and air as the heat transfer fluid is feasible.

4.3 The thermal storage efficiency

In order to analyze heat transfer performance of the solid thermal storage system, the charging efficiency and the discharging efficiency under different flow rates and temperature have calculated using the equation (3) and equation (4).

Fig.10 shows the charging efficiency with time of the TES device under different air flow rate. Under different flow rate the highest charging efficiency have reached about 90%, and there was a maximum efficiency within 30Min, then the charging efficiency decreased with time. The reason is that convection and conduction between air and honeycomb ceramic are weakened with the temperature difference decreased. More and more heat can be exchanged to the honeycomb ceramic.

Fig.11 shows the discharging efficiency with time of the TES under different air flow rate and initial discharging temperature. As shown in Fig.11, the discharging efficiencies of the TES are higher than 85% under different air flow rate in 300 minutes. Under the same air flow rate, even though with the different initial discharging temperature, the discharging efficiencies of the TES are nearly same in 3 hours. It clearly indicates that the honeycomb ceramic material has a good thermal stability and high heat transfer performance. Besides, the greater the air flow rate in discharging process, the higher the heat efficiency of the TES. The heat transfer rate between the air and storage material increased with the air flow rate.

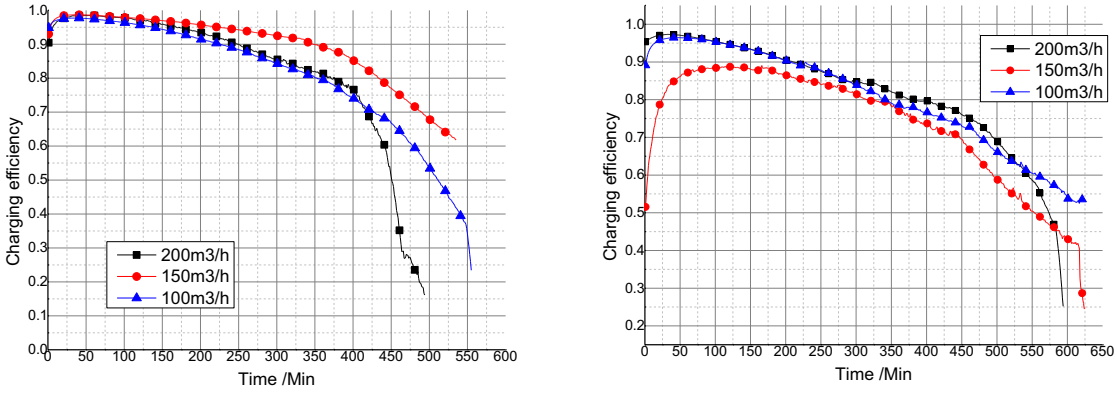

（a）400℃　　（b）500℃

Fig.10 Charging efficiency under different air flow rate

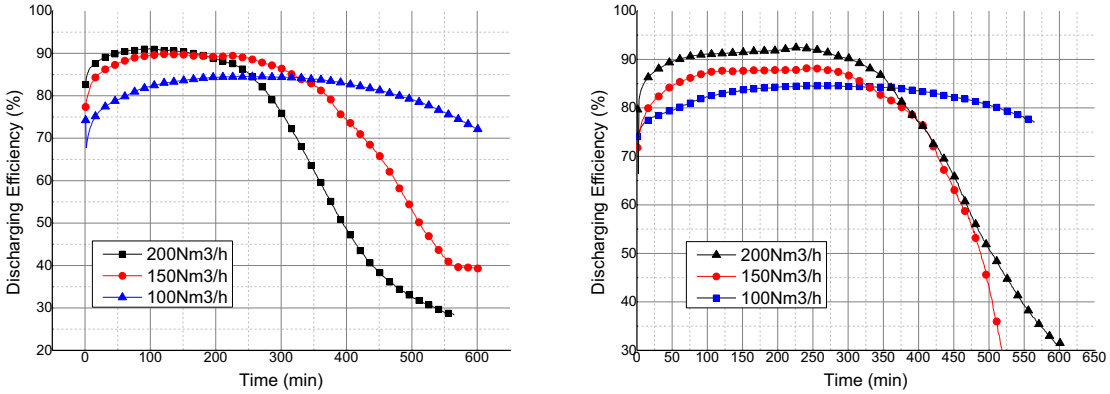

（a）400℃　　（b）500℃

Fig.11 Discharging efficiency under different air flow rate

5 Conclusions

In this paper, the heat transfer characteristic of charging and discharging were researched by experimentally.

(1) A single tank TES of packed bed using air as heat transfer fluid and honeycomb ceramic as storage material is feasible. The temperature distribution is obvious thermocline in TES when charging and discharging processes. The discharging time can be extended with the air flow rate decreased.

(2) The charging efficiency of the developed TES device was higher than 75%, and the discharging efficiency was higher than 85%.

6 Acknowledgements

This work was supported by the National Natural Science Foundation of China (No. 51306170) and the National Key Technologies R&D Programme of China (No.2014BAA01B00). This work was done by INSTITUTE OF ELECTRICAL ENGINEERING, CHINESE ACADEMY OF SCIENCES, and IBIDEN Co., Ltd., JAPAN COOPERATION. Finally, the authors thank the reviewers for their helpful comments and suggestions.

7 References

A. Meier, et al, 1991. Experiment for modeling high temperature rock bed storage, Sol. Energy Mater, 24, 255~264.

Chao Xu, et al, 2013. Effects of solid particle properties on the thermal performance of a packed-bed molten-salt thermocline thermal storage system. Appl. Therm. Eng. 57, 69-80.

Giw Zanganeh, et al, 2012. Packed-bed thermal storage for concentrated solar power e pilot-scale demonstration and industrial-scale design, Sol. Energy. 86, 3084~3098.

Giw Zanganeh, et al, 2014. Stabilization of the outflow temperature of a packed-bed thermal energy storage by combining rocks with phase change materials, Appl. Therm. Eng. 70 (1), 316～320.

Harmeet Singh, et al, 2010. A review on packed bed solar energy storage systems. Renew. Sust. Energ. Rev. 14, 1059-1069.

Hasnain SM, 1998. Review on sustainable thermal energy storage technologies, Part I: heat storage materials and techniques. Energ. Convers. Manag. 39, 1127–1138.

J.P. Coutier, E.A Faber, 1982. Two applications of a numerical approach of heat transfer process within rock beds. Sol. Energy. 29(6), 451–462.

Markus Hanchen, et al, 2011. High-temperature thermal storage using a packed-bed of rocks-Heat transfer analysis and experimental validation. Appl. Therm. Eng. 31, 1798-1806.

R. Bader, et al, 2011. A 9-m-aperture solar parabolic trough concentrator based on a multilayer polymer mirror membrane mounted on a concrete structure, J. Sol. Energy Eng. 133, 031~016.

Palo Alto, 2010. Solar Thermocline Storage Systems: Preliminary Design Study. Electric Power Research Institute. CA.

R.J. Gross, et al, 1980. Numerical simulation of dual-media thermal energy storage systems, J. Sol. Energy Eng. 102, 287~293.

S.A. Zavattoni, et al, 2014. High temperature rocked-bed TES system suitable for industrial-scale CSP plant-CFD analysis under charger/discharge cyclic conditions. Energy Proccedia, 2014, 46:124-133.

Yan Wang, et al, 2015. Experimental research of the heat transfer characteristics using a packed-bed of honeycomb ceramic for high temperature thermal storage system. Energy Procedia, 69, 1059 – 1067.

Conference Proceedings

Solar World Congress 2015
Daegu, Korea, 08 – 12 November 2015

Analysis of a silica glass based high temperature thermal energy storage unit for concentrated solar power applications

Bruno Cárdenas[1], Noel León[1], Martin H. Bremer[1] and John Pye[2]

[1] Tecnologico de Monterrey, Campus Monterrey, Monterrey (México)

[2] Australian National University, Canberra (Australia)

Abstract

The design of a directly-charged high temperature thermal energy storage (TES) unit based on molten silica-glass is presented. The 126 kWh_{th} thermal storage unit developed is aimed to operate within a solar-driven domestic scale power generation system.

The paper discusses the proposed design for the unit as well as the restrictions set by the power generation system's requirements. The transient mathematical model used to analyze the behavior and performance of the thermal energy storage unit during the different stages of the intended work cycle is thoroughly explained. An important feature of the mathematical model is that the performance of the unit is not only evaluated from an energy viewpoint, but an in-depth exergy analysis has been additionally carried out.

The results obtained through the model are exhaustively analyzed; special focus has been given to the assessment of the performance of the storage unit to guarantee that the operational requirements of the power generation system are met. The overall performance of the TES unit is satisfactory; the unit is capable of supplying the required 4 kW_{th} output throughout the 16-hour discharge while it reaches its fully charged state during the subsequent 8-hour recharge. The proposed designed for the TES unit exhibits a round trip exergy-efficiency of 59%.

Keywords: *Solar thermal energy storage, molten silica glass, high temperature heat storage, thermal storage exergy analysis*

1. Introduction

One of the major difficulties solar based electric power generation systems face is the intermittent nature of the solar resource; therefore effective methods for storing the excess thermal energy collected during periods of high solar irradiation or periods of low energy demand are needed (Hasnain,1998).

Thermal energy can be stored in three different ways: as sensible heat, as latent heat or as chemical potential through reversible chemical reactions. (Sharma et al. 2009). Latent heat storage (LHS) offer a number of benefits over sensible heat storage systems (SHS) such as higher energy densities and a nearly isothermal energy output at the phase change temperature (Zalba et al. 2003, Farid et al. 2004, Kenisarin, 2010).

An enormous amount of research has been devoted to the development of LHS systems, which are deemed as a very promising technology; however, their widespread utilization has been slowed down by the low thermal conductivity of phase change materials (PCM) and other drawbacks related to their use. (Liu et al. 2012, Cárdenas and León, 2013. Liu et al. 2015). Nowadays, large scale concentrated solar power (CSP) plants still use sensible heat materials such as rocks, synthetic oils and molten salts. A more thorough description of the state of the art of thermal energy storage for power generation can be found in the literature (Gil et al. 2010, Medrano et al. 2010, Ushak, 2015, Steinmann, 2015),

Selection and/or peer review under responsibility of Scientific Committee
doi:10.18086/swc.2015.02.02 Available at http://proceedings.ises.org

It has been broadly demonstrated that LHS has many advantages over SHS; however, there are materials whose potential as sensible storage medium has not been carefully considered yet, despite possessing outstanding properties, as is the case of soda-lime silica glass, which has high specific heat capacity, it is remarkably cheap and it is neither flammable, corrosive nor toxic.

The present research work focuses on the design and modeling of a soda-lime silica glass based high temperature thermal energy storage (TES) unit with the objective of laying the groundwork on the utilization of recycled soda-lime silica glass as a thermal energy storade medium. The unit will work in a novel solar driven micro-CHP (combined heating and power) system; however, it is thought that the concept could be scaled-up for larger CSP applications.

2. Operation within the micro-CHP system

The TES unit will operate within a solar-driven domestic distributed power generation system in which solar radiation is captured through a 30 m^2 Fresnel lens (Ramirez, 2015). Considering the solar irradiation in Monterrey, Mexico, the Fresnel Lens supplies an average power of 18.75 kW_{th} during daytime (idealized as an 8-hour period). The concentration spot of the lens strikes directly onto the reception surface of the TES unit, whose interior is filled with soda-lime silica glass (recycled from windows and bottles) that acts as the heat storage medium. As the solar radiation enters the TES unit the temperature of the storage medium increases until reaching approximately 1000°C; storing thus the incoming solar energy in the form of heat. The TES unit is connected through a heat exchanger to a 1 kW_e Stirling engine with an estimated efficiency of 30 %, which will generate electric power continuously throughout the day.

The TES unit will operate in a temperature range from 500°C to 1000°C; below 500°C the TES unit is not able to maintain the Stirling engine operating. The cyclic operation of the unit comprises two stages: an 8-hour charge (storage) period and a 16-hour discharge period . In addition to that, there is an initial charging step (not part of the cycle) in which the TES unit is brought from ambient temperature to its operating temperature of 1000°C at the heat extraction surface.

During the 16-hour (corresponding to the remaining 2/3 of the day) discharge step, the TES unit has to deliver 4 kW_{th} (defined based on the Stirling efficiency and heat exchanger losses) with no solar input. The temperature of the heat extraction surface must remain above 500 °C during the whole period. Then follows the 8-hour recharge stage in which the TES receives solar radiation once again but still maintains the 4 kW_{th} output. At the end of the recharge period, the temperature of the heat extraction surface must have reached 1000°C, so that the TES unit is fully charged and is able to undergo the subsequent 16-hour discharge period, thus maintaining a cyclic operation.

3. Concept developed for the TES unit

The TES unit proposed, shown in Figure 1, consists of a prismatic refractory concrete container whose interior is divided into smaller cavities by several equidistant vertical graphite slabs (walls), between which the approximate 82 L of glass are distributed. Two grooved rectangular graphite plaques keep the walls in vertical position and evenly spaced inside the container. The TES unit has a storage capacity of 126.3 kWh_{th} when fully charged (i.e. when the heat extraction surface is at 1000° C). The outer dimensions of the unit including insulation are: a length of 143.2 cm, a depth of 90.5 cm and a total height of 68.4 cm.

The concentrated solar radiation coming from the lens enters the TES unit through its top side (due to a system requirement) and is conducted inwards by means of the vertical walls. The walls are designed to enhance the internal heat transfer, as the soda-lime silica glass to be used has a very low thermal conductivity; facilitating thus the charge and discharge of the TES unit and helping to achieve a uniform temperature distribution throughout its interior.

The heat extraction is carried out by means of a heat transfer fluid (HTF) in contact with the bottommost graphite surface; the design of the heat exchanger design is out of the scope of the present paper and will not be discussed. In addition to the use of a heat transfer enhancement method (the vertical graphite walls), the height of the TES unit was kept to a minimum for allowing the heat stored in the upper portions of glass to

reach the discharge area rapidly and impeding it from prematurely reaching the 500°C limit.

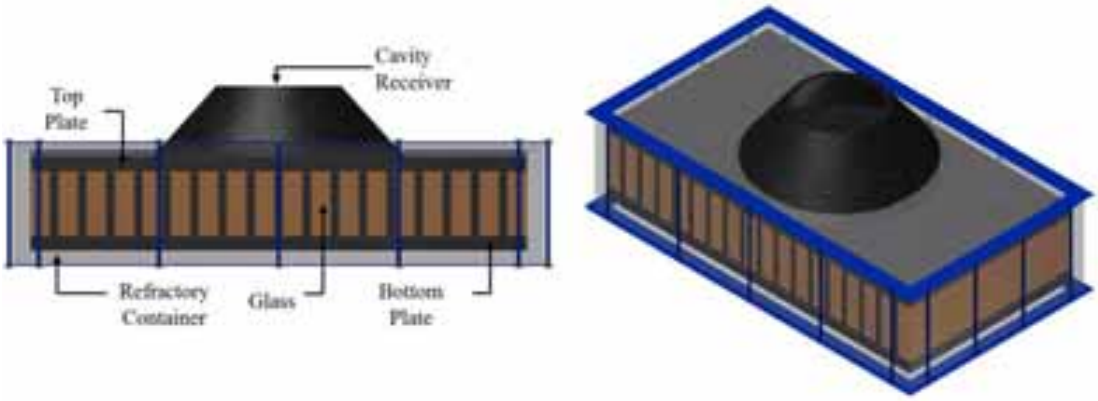

Figure 1. Views of the core of the proposed TES unit design

The cavity receiver was designed trying to emulate a blackbody, although further work is intended to refine the design. The incident solar rays are reflected many times on the interior before finally escaping from the aperture; with each reflection a fraction of the energy, is absorbed and after many reflections, the incoming radiation is mostly absorbed. The temperature of the material will increase, it will start to radiate heat and the same effect will occur; the cavity wall will absorb its own radiation and heat losses will be minimized. A radiation shape factor $F_{1\text{-}2}$ of 0.205 was achieved, which means that 20.5% of the heat that the bottom surface irradiates escapes through the aperture while 79.5 % is re-absorbed by the lateral wall of the cavity.

4. Mathematical modeling of the performance of the TES unit

4.1 Transient mathematical model developed

A transient mathematical model was developed for analyzing the thermal behavior of the TES unit throughout the cyclic operation. The model is primarily based on equations (Eq.1) and (Eq.2), the former being the one-dimensional heat conduction equation and the latter being the first law of thermodynamics for an incompressible material:

$$Q = (k \cdot A \cdot \Delta T \cdot \Delta t)/\Delta x \quad \text{(Eq.1)}$$

$$Q = m \cdot C_p \cdot \Delta T \quad \text{(Eq.2)}$$

The model originates with two main assumptions; the first one is that within a component there are no temperature gradients, meaning that the temperature is uniform over the cross-sectional area of each element. The second one is that there is no convection in the molten glass due to its elevated viscosity, which is 104 Pa·s at the flow point (920 °C) for the average composition of soda–lime silica glass. (Shand, 1958); thus, all the internal heat transfer during the complete work cycle of the TES unit is assumed to be due only to conduction.

To perform the calculations each component of the geometry of interest is divided into elements. Thereafter, an energy balance is made for each element stating that the difference between the energy entering and the energy leaving the element over a certain time-step is equal to the energy that is stored by the element.

The energy balance is performed for every element over n time-steps until a certain time or condition such as a final temperature is reached. During a given time-step a certain amount of heat is received by an element n at a temperature *T*. During the same time-step some energy leaves the element *n*, which is still at the same temperature *T*; a part of the energy leaving the element goes into the next element *n+1* while another part of it is lost to the ambient, depending the case. The difference between the energy that the element n received minus the energy conducted from the element n to the element *n+1* and the lost heat, is the energy stored by the element *n* during that particular time-step.

The energy stored by the element causes an increase in its temperature, given by Eq.2; this increase in temperature entails a change in the specific heat capacity and thermal conductivity of the material. It is

important to mention that in order for the model to have numerical stability and accurately simulate the real heat transfer phenomena a previous study (sensibility analysis) for determining the maximum time step permissible, which is a function of mesh size and temperature differences, must be carried out.

The interactions between elements are explained graphically in Figure 2. A power input of 18.75 kW_{th} (average power supplied by the Fresnel lens) is applied to the top-most surface of the top graphite plate, which conducts energy to both, glass and graphite elements in contact with its lower surface.

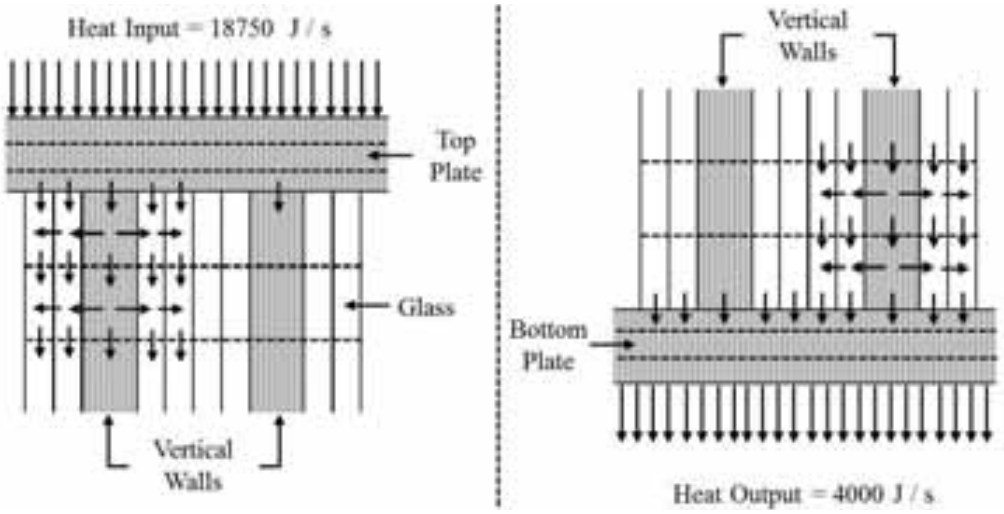

Figure 2. Thermal interactions between elements of the geometry defined for the model

The behavior of every graphite wall and the glass in the cavity next to it is assumed to be the same for every wall-cavity set; therefore only one graphite wall and the glass at one if its sides are calculated. The elements of the graphite wall conduct heat downwards to the next element of the wall and sideways to the glass next to them. The first element of glass, in a similar fashion, conducts heat to the glass element below it and to the glass element on its side; finally, the second glass element conducts heat exclusively downwards into the glass element below it. The other half of the glass in the cavity is assumed to be heated by the contiguous graphite wall; i.e. each graphite wall only interacts with half of the glass on the cavity next to it.

The bottom graphite plate receives heat from the glass and graphite elements above it, as shown in Figure 4. Except for the initial charge period, a load of 4 kW_{th} is permanently applied to its bottom-most surface to simulate the energy discharge.

The model does not calculate the temperature increase of the graphite frustum. It is assumed that the piece is able to absorb all the incident radiation that is reflected by itself; therefore, an absorptivity of 1.0 was employed for the graphite. The radiative losses were calculated based on the area of the bottom surface of the frustum and the calculated shape factor of 0.205; as aforementioned, only 20.5% of what the surface is emitting is actually lost to the surroundings.

Polynomial equations were created for the temperature dependent properties of the main materials, i.e. graphite and an average composition of soda-lime silica glass. The equations created follow the general form shown in Eq.3 and represent the average of the experimental data presented by several authors. Table 1 provides the coefficients for the calculation of the specific heat capacity (C_p) and thermal conductivity (k) of both materials.

$$C_p, k = AT^5 + BT^4 + CT^3 + DT^2 + ET + F \quad \text{(Eq.3)}$$

An important aspect of the mathematical model is the exergy analysis of the TES unit. In addition to calculating via the energy balance the energy stored by an element *n* during every time-step, the total energy accumulated by each element is also accounted for. This makes possible calculating the total exergy stored by the element through the exergy equation for an incompressible mass (Eq.4), and consequently, the exergy destroyed as well as the exergy-based efficiency of the TES unit.

$$X = (U - U_0) - T_0(S - S_0) \quad \text{(Eq.4)}$$

Tab.1: Coefficients for the calculation of the temperature dependent properties of soda-lime silica glass and graphite

Property	Coefficients		Source(s)
Glass specific heat capacity (J/g·K)	A= 9.474×10^{-15} B= -3.923×10^{-11} C= 6.221×10^{-8}	D= -4.746×10^{-5} E= 1.814×10^{-2} F= -1.833	Shand, 1958 Stebbins et al, 1984 Richet, 1987 Huang and Gupta, 1992
Glass thermal conductivity (W/m·K)	A= -1.413×10^{-14} B= 6.083×10^{-11} C= -3.120×10^{-8}	D= -2.853×10^{-5} E= 2.512×10^{-2} F= -3.668	Shand, 1958
Graphite specific heat capacity (J/g·K)	A= -4.257×10^{-16} B= 1.093×10^{-12} C= 5.638×10^{-10}	D= -4.514×10^{-6} E= 5.645×10^{-3} F= -6.034×10^{-1}	Butland and Maddison, 1974 Nihira and Iwata, 2003
Graphite thermal conductivity (W/m·K)	A= -2.370×10^{-14} B= 1.393×10^{-10} C= -3.373×10^{-7}	D= 4.429×10^{-4} E= -3.611×10^{-1} F= 209.893	Rasor and McClelland, 1960 Wagner and Dauelsberg, 1967 Bapat, 1973 Bapat and Nickel, 1973 Madelung and White, 1991

In the model, an exergy balance (Eq.5) is performed every time-step for each of the elements defined to obtain the exergy destruction at every element of the system. One of the difficulties the exergy analysis presents is quantifying the exergy content of the incident solar radiation, since the balance requires an exergy input for the calculation. Eq.6 is used as the exergy input for the balance (Petela, 2003) in which i is the amount of solar radiation, α is the absorptance of the material, and T_{sun} is considered as 5778 K.

$$X_{in} - X_{out} - X_{dest} = \Delta X_{system} \quad \text{(Eq.5)}$$

$$X_{Sun} = i\left[1 + \frac{1}{3}\left(\frac{T_0}{T_{sun}}\right)^4 - \frac{4}{3}\left(\frac{T_0}{T_{sun}}\right)\right]\alpha \quad \text{(Eq.6)}$$

The exergy transfer (X_{in}, X_{out}) comes from the heat transfer (Q) from an element at a certain temperature T to another element, for the case of conducted heat it may be accounted for as follows:

$$X_{heat} = (1 - T_0/T) \cdot Q \quad \text{(Eq.7)}$$

Evaluating a system exclusively through an energy-based efficiency could be misleading; because, even though most of the incoming energy is conserved or recovered, it will be degraded by all the internal heat transfer that occurs during the storage process causing the loss of some potential for performing work.

A notable aspect of the model developed is that it can be used for a different storage material other than soda-lime silica glass as long as the consideration of no convection is not overlooked. If it is desired to calculate the performance of a TES unit with a different storage material that undergoes a phase transition from solid to liquid, or is liquid the whole time, it is very important to evaluate if due to its viscosity and the size of the cavities in which it is contained the assumption of no convection is valid. If the storage medium is a solid material, either crystalline or amorphous, and stays solid throughout the work cycle, the model is applicable right away.

4.2 Analysis of the behavior and performance of the TES unit

Not all of the temperature profiles calculated through the mathematical model are displayed in the following Figures for the sake of an easier understanding; however, the profiles presented depict accurately the overall behavior of the TES unit. Figure 3 shows the geometric location within the unit of each of the temperature profiles shown further on in the graphs, i.e. where the temperatures are “measured”.

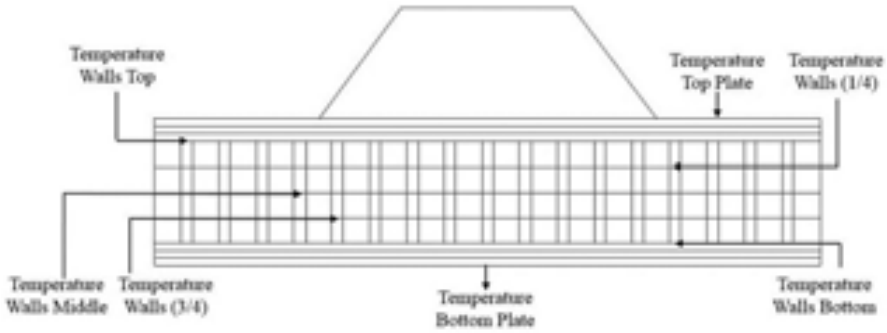

Figure 3. Geometric locations within the TES unit of some representative temperature profiles

Figure 4 shows the temperature profiles of some elements during the initial charge period, in which the 4 kW output is not present. As expected, the temperature of the first element of the top plate (where radiation strikes) is the first to increase followed by the temperatures of the rest of the elements of the different components. The temperatures, except for a short period at the beginning of the heating, increase at a very constant rate; the maximum difference between the temperature of the top plate and the temperature of the bottom plate recorded during the heating process is 87.8°C while an average difference of 76.7°C was observed throughout the heating process.

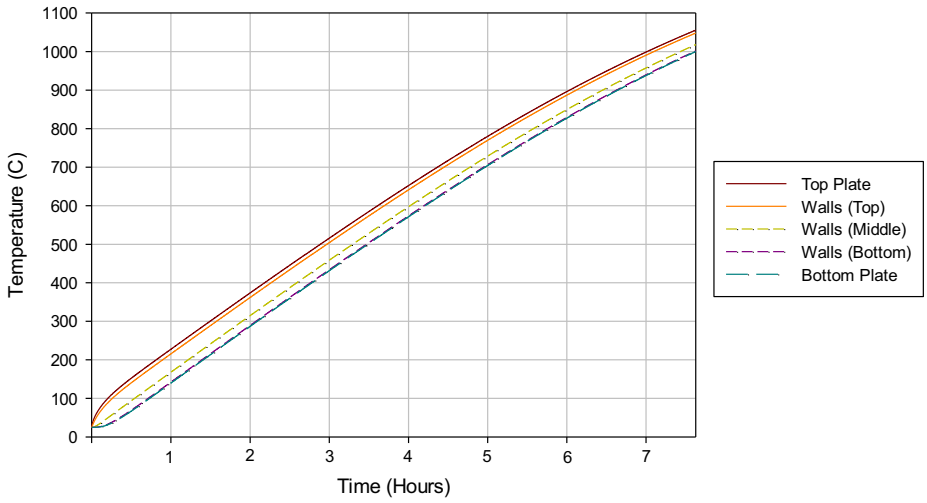

Figure 4. Representative temperature profiles during the initial charge period

The TES unit reaches its goal temperature of 1000°C in the lower surface of the bottom plate in approximately 7 hours and 38 minutes. From a micro-CHP system point of view, this is quite convenient since the TES unit could be heated up from ambient temperature to its operating temperature in 1-day time with the Fresnel lens and no external aid.

It is noteworthy that the temperature profiles of the glass elements are not included in Figure 4; the reason for this is that throughout the entire heating process the profiles of the two glass elements adjacent to each of the 30 vertical graphite wall elements maintain a very close temperature to that of their respective wall element. During the complete heating process, the difference between the temperature of the glass elements and the graphite wall element never surpassed 4°C, this rather small temperature difference suggests that the vertical graphite walls are well spaced inside the refractory container and that they are indeed facilitating the distribution of the thermal energy in the interior of the TES unit.

Figure 5 shows the temperature profiles of some representative elements of the TES unit during the discharge (or cooling) period obtained through the mathematical model. The state of the elements after the last time-step of the initial charge period is used as the starting point for the discharge stage. A load of 4 kW_{th} is applied to the bottom-most element of the bottom plate and both, the heat input and radiation losses, are set to zero; assuming that during the discharge period the cavity could be covered with insulation since there need not be an aperture for the concentrated beam from the lens.

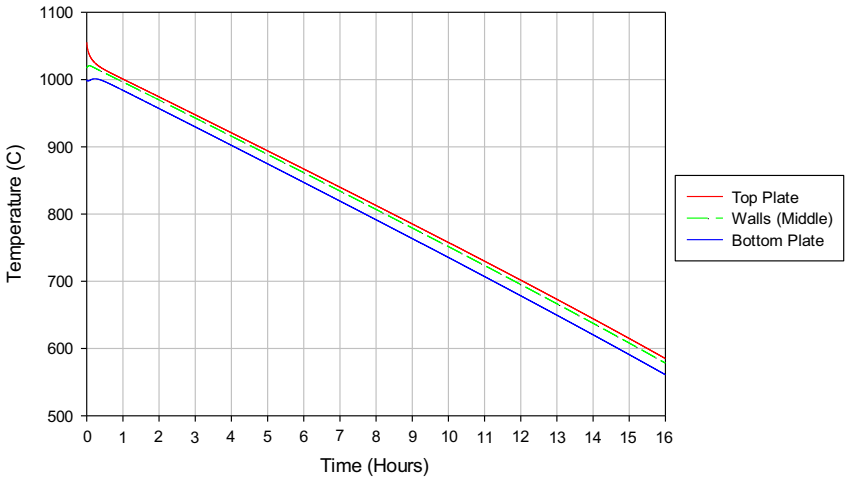

Figure 5. Representative temperature profiles during the 16-hour discharge period

As can be seen, the TES unit is capable of supplying the constant 4 kWth during the required 16-hour period, at the end of which the temperature of the bottom plate is 561°C while the temperature of the top plate is 585°C, a difference of just 24°C. The reduced height of the unit helped to minimize the temperature difference between the top and bottom plates; having such a small temperature difference at the end of the discharge period indicates a very thorough discharge of the TES unit.

Similarly to the initial charge period, the temperatures of the two glass elements adjacent to each of the 30 vertical graphite wall elements remain very similar to the temperature of their respective wall element throughout the complete discharge period. The difference between the temperature of the glass elements and the elements of the vertical wall never exceeds 2.5°C.

Figure 6 shows the temperature profiles of some representative elements during the recharge (storage) period, in which the heat input from the Fresnel is available once again but the 4 kWth output is still supplied. The last time step of the discharge process is used as the starting point for the 8-hour recharge stage. During this period, the lower surface of the bottom plate must reach 1000 °C so the TES unit is able to undergo the following 16-hour discharge period, thus maintaining a cyclic operation.

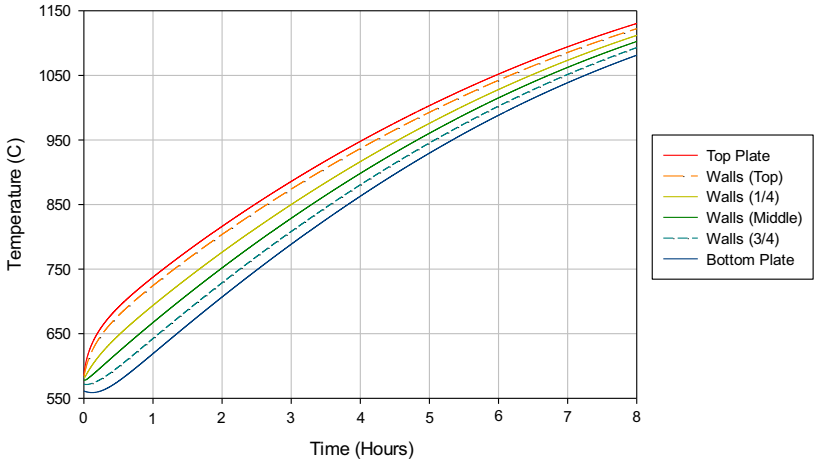

Figure 6. Representative temperature profiles during the 8-hour recharge period

The temperature profiles spread at the beginning of the heating; slightly before the first hour of heating the maximum temperature difference between the top and bottom plates of 118.8°C is reached; after this point the temperature difference between elements decreases with time. The average temperature difference between the topmost and bottommost temperature profiles throughout the complete period is 84.1°C. The temperature of the glass elements is, like in the initial charge and discharge periods, still very close to the temperature of their respective wall elements.

It may be noted that higher temperatures than those used at the starting point of the discharge are reached.

This overshoot may be eliminated, for instance, by defocusing the Fresnel lens of the micro-CHP system; however, it is not necessarily an issue. Reaching higher temperatures than necessary at the end of the recharge means that there is some tolerance in the system that would allow the TES to be fully charged in days with less-than-average conditions when the Fresnel is not capable of supplying the average 18.75 kW_{th} considered in the model. The complete work cycle of the TES unit is shown in Figure 7; the highest and lowest temperature profiles within the unit are displayed in red and blue, respectively. All the other profiles comprised between them are not presented for an easier understanding.

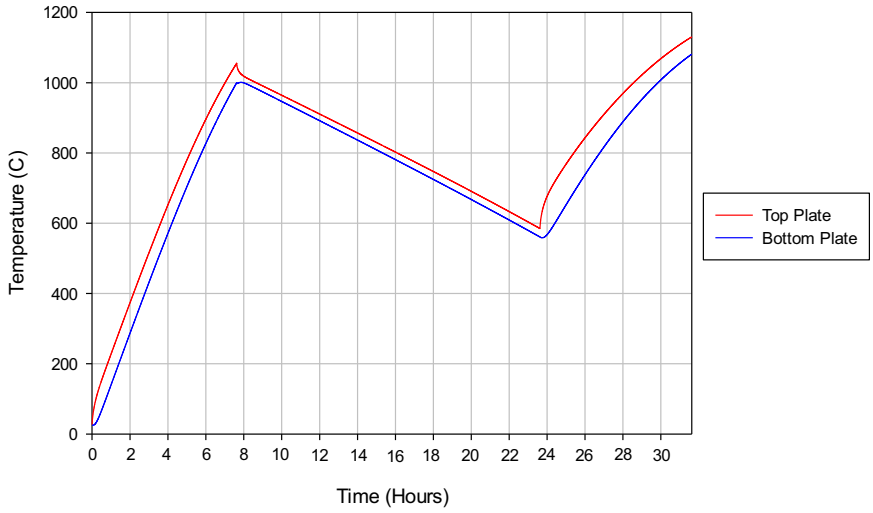

Figure 7. Highest and lowest temperature profiles throughout the complete work cycle

The change in the energy stored by the TES unit throughout the complete work cycle and its distribution in each of the components is shown in Figure 8. At the end of the initial charge period the TES unit has 454.87 MJ (126.35 kWh_{th}) of thermal energy stored, of which 51% is stored in the glass, 19.2 % in the graphite walls, 15.4 % in the top plate and 14.4 % in the bottom plate.

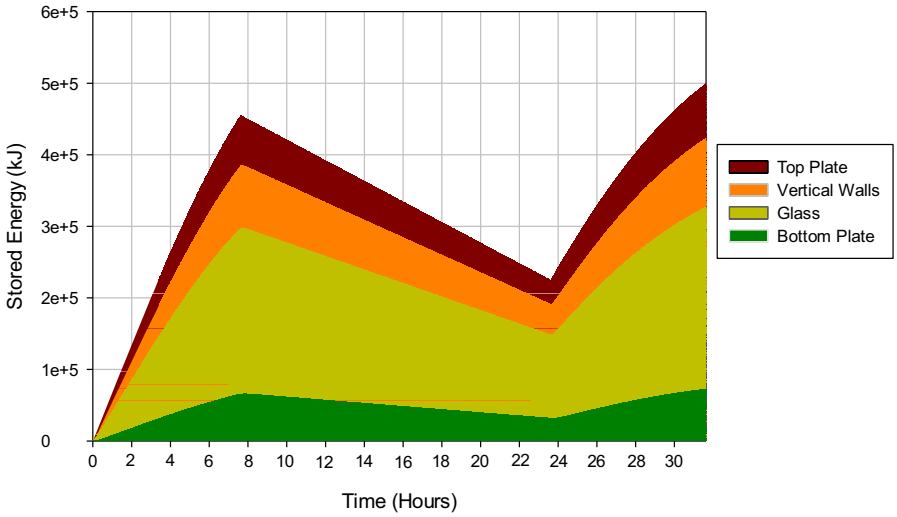

Figure 8. Energy stored in the TES unit throughout the complete work cycle

At the end of the discharge the TES unit is practically out of usable energy, only 0.964 MJ (0.26 kWh_{th}) are left in the unit, meaning that the concept developed allows a very thorough heat extraction. It is important to emphasize though, that the energy stored in the components as sensible heat from ambient temperature to 500°C, approximately 223.5 MJ (62.08 kWh_{th}), remains permanently stored in the TES unit as there is a defined minimum temperature limit for the heat extraction. Certainly those 62.08 kWh_{th} stored below 500°C could be used for low temperature applications such as heating water; however, the present modeling of the TES unit is not considering heat extraction below the established lower limit of 500°C.

Figure 9 shows the change in the exergy stored by the unit throughout the complete work cycle and its distribution in each of the components, calculated through Eq.4. At the last time-step of the initial charge (when the unit is fully charged) 268.4 MJ of exergy are stored, which is 59 % of the total energy stored. This value represents the maximum theoretical limit for the amount of the energy stored that could be transformed into work by an ideal engine or work producing device.

The exergy stored in the TES unit follows a very similar distribution than that of the energy, at the end of the initial charge period, 51.2% of the total exergy is stored in the glass, 19.1 % in the vertical walls, 15.3 % in the top plate and 14.4 % in the bottom plate. The stored exergy increase rate becomes smaller as the temperature of the elements rise because entropy becomes greater with increasing temperatures.

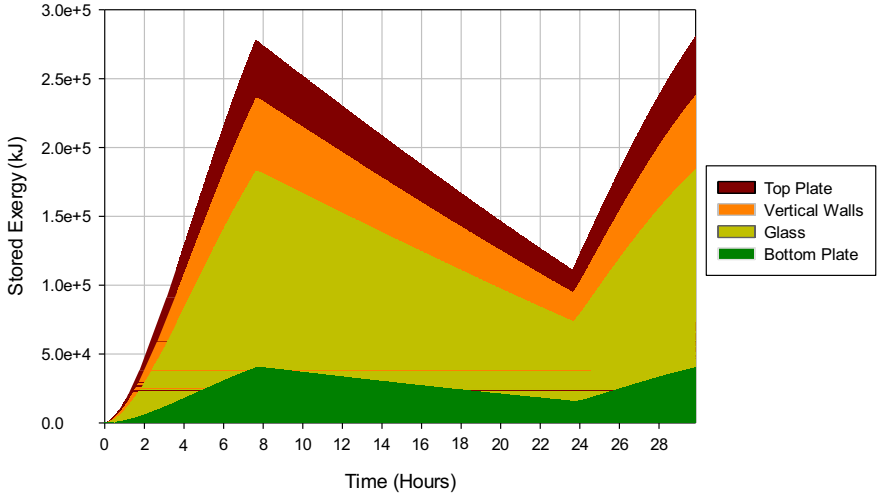

Figure 9. Exergy (work potential) stored in the TES unit throughout the complete work cycle

In order to have a proper closed cycle, the recharge period is cut before the 8 hours at the point in which the TES unit reaches its full-charge state, thus the overshoot that occurs at the end of the recharge is not considered for the round-trip exergy efficiency.

At the end of the discharge the total exergy destroyed is 0.866 MJ; which is less than 1% of the exergy stored at the beginning of the discharge. As the temperatures of the components decrease and become closer to each other the exergy destruction rate becomes smaller. Of the exergy destroyed during the discharge 50.8% occurs in the graphite walls, while the glass accounts for 26.45%, the bottom plate 22.6% and the top plate a minimal 0.14%.

During the recharge period, up to the point where the TES unit returns to the cycle initial state, the total exergy destroyed is 86.43 MJ, which represents 22.1 % of the exergy supplied by the Fresnel during that period. The amount of exergy destroyed during the discharge period is considerably smaller than during the recharge because during discharge there is only destruction due to the little heat conduction between components and the temperatures are very close to each other, while during the recharge there is a great amount of exergy input, with bigger temperature gaps and exergy is destroyed due to the actual process of storing energy.

As the temperatures of the components increase and become closer to each other the exergy destruction rate becomes smaller. Approximately 94.4% of the exergy destruction during the recharge occurs in the top plate where concentrated radiation is received, graphite walls account for 3.7 % while 1.7% is destroyed in the glass and only 0.2 % in the bottom plate.

Figure 10 presents a summary of the exergy balance of the TES unit during the discharge and recharge periods, the initial charge is not considered since it is not part of the cyclic operation, it occurs sporadically when the unit is discharged below the lower limit due to a cloudy day, for instance. Of the total 390.88 MJ (108.58 kWh_{th}) of exergy supplied by the Fresnel lens during the recharge period considered, 58.5 % is extracted from the TES for driving the Stirling engine during the discharge and recharge periods, 42.2% and 16.3% respectively, 18.7 % is lost as thermal radiation at the cavity and 22.3% is destroyed: 22.1 % during

the recharge and an almost negligible 0.22% during the discharge period.

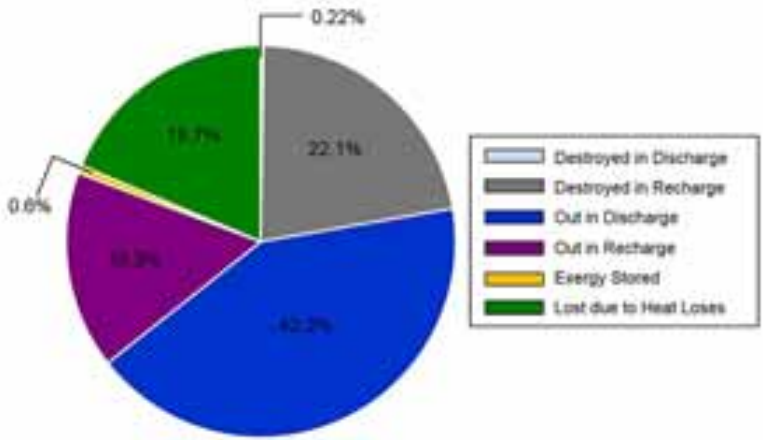

Figure 10. Exergy balance of the TES unit for the discharge and recharge periods

The TES unit has an energy-based efficiency of 72.2 % while it presents an exergy-based efficiency of 59%. In general, the energy efficiency of renewable energy systems has been found to be always greater than their exergy efficiency (Park et al. 2014), with which the analysis shown in the present paper is in agreement.

5. Shortcomings and opportunity areas in the design

This study presents a functional design for a glass-based TES unit capable of meeting the requirements of the solar driven micro-CHP system within which it will operate; nonetheless, there are still opportunity areas for the betterment of the concept, therefore optimization works should be carried out.

Preliminary tests have shown that graphite at high temperatures experiences a severe oxidation when exposed to air. The inner components are protected by contact with the molten glass; however, the issue remains for the exposed upper graphite components such as the cavity. The use of a layer of molten glass covering the interior of the receiver will be assessed, although stainless steel shields are still deemed as a good option.

The frustum-shaped receiver allows reducing radiative losses from the TES unit's inlet surface; however, its configuration has not been yet optimized. Covering the opening of the cavity with a glass plate, which is translucent to concentrated solar radiation but opaque to thermal radiation emitted by the graphite surface could help to achieve a further reduction of the radiative losses.

Although no concluding signs were found in the post-experimental assessments, devitrification of the storage medium is a latent possibility. Assuring a sufficient cooling rate for the glass in the unit is important, otherwise, it would start to devitrificate, (i.e. decompose into the elements from which it is formed). A cooling rate of approximately $8.7x10^{-3}$ Ks^{-1} is expected during the discharge of the TES unit. The critical cooling rate for silica glasses oscillates between 10^{-2} and 10^{-3} Ks^{-1} (Le Bourhis, 2008), thus the expected cooling rate of the glass in the TES unit should be sufficient for avoiding crystallization.

Theoretically, devitrification should not alter greatly the storage capacity of the TES unit. The heat capacities of silicate glasses can be closely approximated by the partial contribution of each component according to their percentage in the composition (Stebbins et al.1984, Richet, 1987), Consequently, if devitrification did occur, there would not be a significant loss in the storage capacity per unit mass of the storage medium; however, the internal thermal behavior of the TES unit could be largely modified by the different thermal conductivities of the components.

Another important area for improvement is the exergy efficiency of the storage unit. The design hereby presented attained an exergy efficiency of 59%. The internal graphite components account for a big part (~20%) of the exergy destruction. The development of a parametric model would allow improving the system in this sense by allowing exploring changes in the geometry that improve performance but don't alter much the cost of the system.

6. Concluding remarks

Soda-lime silica glass is exceedingly interesting as a sensible heat storage medium because of its elevated specific heat capacity, high chemical stability, low toxicity and flammability, and a remarkably low cost; however its use for said purpose has not been sufficiently evaluated.

A concept for a silica-glass based thermal energy storage unit for a micro-CHP system is presented. In this directly charged concept, the molten glass is enclosed in a refractory concrete container together with several narrowly spaced vertical graphite walls, whose purpose is distributing the energy uniformly throughout the storage medium. A transient mathematical model was developed for analyzing the thermal behavior of the proposed TES unit throughout the cyclic operation. The results obtained reveal a satisfactory overall performance and provide important and encouraging information. The following points may be highlighted:

- The initial charge of the unit lasts approx. 7 ⅔ hours, meaning that a unit at ambient temperature can be fully charged in 1 day time using exclusively solar power.
- Due to its effective internal design, the unit is capable of supplying the 4 kW output during the entire 16-hour discharge period maintaining a temperature superior to the 500 °C lower limit.
- During the 8-hour recharge, the unit reaches its fully charged state, whereby the continuous operation of the system is assured.

An important aspect of the mathematical modeling is the exergy analysis that was carried out. It has been found that of the total exergy (108 kWh) supplied by the solar concentrator during the recharge period, 59 % is used for driving the Stirling, 19 % is lost due to heat losses in the cavity receiver and 22 % is destroyed. The TES unit exhibits therefore an exergy efficiency of 59% while it presents an energy efficiency of 72.2%. Once the system has been further optimized, it is hoped that the combination of low-cost materials and simple fabrication could make this a cost-effective system able to meet the long term goal of $15 USD per stored kWh of heat (U.S Department of Energy, 2013).

The article presents a functional design capable of meeting the requirements of a novel solar-driven power-generation system; nonetheless, there is still a vast area of opportunity for the improvement and optimization of the proposed glass-based thermal energy storage unit.

7. Acknowledgements

The authors would like to thank the Mexican Center for Innovation in Solar Energy (CeMIE-Sol) for funding the present project through the Strategic Project #05: “Development of solar thermal storage units” and the “Energy and climate change” research group, part of the Engineering and Science School, of the Tecnológico de Monterrey for sponsoring the participation in the ISES SWC 2015.

8. References

Bapat S.G. 1973. Thermal conductivity and electrical resistivity of two types of ATJ-S graphite to 3500 K. Journal of Carbon;11: 511-514.

Bapat S.G, Nickel H. 1973. Thermal conductivity and electrical resistivity of POCO grade AXF-Q1 graphite to 3300 K. Journal of Carbon ; 11:323-327.

Butland A.T.D, Maddison R.J. 1974. The specific heat of graphite: an evaluation of measurements. Journal of Nuclear Materials ; 49: 45-56.

Cárdenas B, León N. 2013. High temperature latent heat thermal energy storage: Phase change materials, design considerations and performance enhancement techniques. Renew. Sust. Energy Rev; 27:724-737

Farid M, Khudhair A,Razack S, Al-Hallaj S. 2004. A review on phase change energy storage: materials and applications. Energy Conversion and Management; 45:1597–615

Gil A, Medrano M, Martorell I, Lazaro A, Doblado P, Zalba B, et al. 2010. State of the art on high temperature thermal energy storage for power generation. Part 1: concepts, materials and modellization.

Renew. Sust. Energy Rev; 14:31–55.

Hasnain SM. 1998. Review on sustainable thermal energy storage technologies. Part I: heat storage materials and techniques. Energy Conversion Management; 11: 1127–38.

Huang J, Gupta P.K. 1992. Temperature dependence of the isostructural heat capacity of a soda lime silicate glass. Journal of Non-Crystalline Solids; 139: 239-247.

Kenisarin M, Mahkamov K. 2007. Solar energy storage using phase change materials. Renew. Sust. Energy Rev; 11:1913–65

Le Bourhis E. Glass mechanics and technology. Wiley-VCH. Germany, 2008

Liu M, Bruno F. 2012. Review on storage materials and thermal performance enhancement techniques for high temperature phase change thermal storage systems. Renew. Sust. Energy Rev; 16:2118–32

Liu M, Gomez JC, Turchi CS, Tay NHS, Saman W, Bruno F. 2015. Determination of thermo-physical properties and stability testing of high-temperature phase-change materials for CSP applications. Solar Energy Materials & Solar Cells; 139:81–87

Madelung O, White GK. 1991. Temperature dependence of thermal conductivity of graphite. In: Thermal Conductivity of Pure Metals and Alloys, vol. 15. Springer Berlin Heidelberg. pp. 430-439

Medrano M, Gil A, Martorell I, Potau X, Cabeza L. 2010. State of the art on high- temperature thermal energy storage for power generation Part 2: case studies. Renew. Sust. Energy Rev; 14:56–72

Nihira T, Iwata T. 2003. Temperature dependence of lattice vibrations and analysis of the specific heat of graphite. Physical Review B; 68: 134305

Park S.R, Pandey A.K, Tyagi V.V, et al. 2014.Energy and exergy analysis of typical renewable energy systems. Renew. Sust. Energy Rev; 30:105-123

Petela R. 2003. Exergy on undiluted thermal radiation. Journal of Solar Energy; 74:469-88

Ramírez, Carlos. Optical design of segmented heliostat and reduced focal distance Fresnel lens for solar energy concentration. PhD thesis, ITESM, Monterrey, Mexico. 2015

Rasor NS, McClelland JD. 1960. Properties of graphite, molybdenum tantalum to their destruction temperatures. Journal of Physics and Chemistry of Solids; 15: 17-26.

Richet P. 1987.Heat capacity of silicate glasses. Journal of Chemical Geology; 62: 111-124.

Shand E.B. 1958.Glass engineering handbook. McGraw Hill.

Sharma A, Tyagi VV, Chen CR, Buddhi D. 2009. Review on thermal energy storage with phase change materials and applications. Renew. Sust. Energy Rev; 13:318–45.

Stebbins J.F, Carmichael I.S.E, Moret L.K. 1984. Heat capacities and entropies of silicate liquids and glasses. Contributions to Mineralogy and Petrology; 86:131-148.

Steinmann WD. 2015. Thermal energy storage systems for concentrating solar power technology. In: Cabeza LF (Ed.). Advances in thermal energy storage systems: Methods and applications. Woodhead Publishing, Cambridge, UK, pp.511-532.

U.S. Department of Energy, Grid energy storage. Washington, USA. 2013.

Ushak S, Fernandez AG, Grageda M. 2015. Using molten salts and other liquid sensible storage media in thermal energy storage systems. In: Cabeza LF (Ed.). Advances in thermal energy storage systems: Methods and applications. Woodhead Publishing, Cambridge, UK. pp.49-64

Wagner P, Dauelsberg LB. 1967.The thermal conductivity of ZTA graphite. Journal of Carbon, 5: 271-279.

Zalba B, Marín J, Cabeza L, Mehling H. 2003. Review on thermal energy storage with phase change: materials, heat transfer analysis and applications. Applied Thermal Engineering; 23:251–83.

Conference Proceedings

Solar World Congress 2015
Daegu, Korea, 08 – 12 November 2015

ISES SWC2015

Analysis of Fluid Flow and Heat Transfer inside a Spherical Container Encapsulated by Molten Salt

Adrián Belinchón Ovejero, Selvan Bellan, José González-Aguilar, and Manuel Romero

IMDEA Energy Institute, Ramon de la Sagra 3, 28935 Móstoles, Spain

Abstract

A mathematical model of melting process inside a spherical container, which is filled with phase change material, is developed to describe the characteristics of heat transfer and flow inside the capsule for high temperature storage systems. The finite element method is used to solve continuity, momentum and energy equations. The main intention of this investigation is to derive a dimensionless correlation for effective thermal conductivity. The correlation can be used in packed bed models to study the thermal performance of the thermal energy storage systems. The capsule is filled with sodium nitrate since its melting point is in the operation range of concentrated solar power plant. The shell of the capsule is made up of nickel, which is uniformly heated at the external surface. The enthalpy-porosity method is used to track the solid-liquid interface. The model is, validated with the reported experimental results, used to investigate the influence of pellet size and Stefan number.

Keywords: *Thermal energy storage system; Latent heat; Melting of PCM; Effective thermal conductivity*

1. Introduction

In latent heat thermal energy storage systems packed with spherical pellets, the phase change process inside the pellets plays a vital role since the overall performance of the storage tank depends on this process. Thus, it has been received great importance, considerable number of investigations on this subject has been made by both theoretically and experimentally (Assis et al., 2007; Felix et al., 2006; Hosseinizadeh et al., 2012; Ismail and Henríquez, 2000). One dimensional conduction models were developed, to study the phase change process inside a spherical capsule, by assuming the solid portion of the PCM remains at the center of the sphere, neglecting the solid core movements (e.g. Felix et al., 2006; Ismail and Henríquez, 2000). Two dimensional axisymmetric models were developed to study the flow, natural convection-dominated melting, and the movement of the solid PCM portion during melting process (e.g. Assis et al., 2007; Hosseinizadeh et al., 2012). The melting of n-octadecane in a glass spherical container was investigated numerically and experimentally by Moore and Bayazitoglu (1982) and found that the natural convection effects can be neglected at small Stefan numbers. Bareiss and Beer (1984) investigated the phase change process in cylindrical geometries; the predicted melting rate showed good agreement with the experimental data presented by Moore and Bayazitoglu (1982). Using the analysis made by Bareiss and Beer (1984), an analytical solution for the melting rate at the lower surface of the solid core in a spherical capsule was presented by Roy and Sengupta (1987).

The melting process of n-octadecane in an open spherical glass container was numerically investigated by Hosseinizadeh et al. (2012). A uniform temperature boundary condition was imposed at the outer wall of the shell. The developed model was validated with the experimental results reported by Tan (2008). Furthermore, a number of experimental and analytical investigations have been made on the heat transfer and buoyancy driven flow during melting of PCM inside spherical capsules. However, the literature survey shows that most of the past studies focused on low temperature storage applications. The literature is lack of

doi:10.18086/swc.2015.02.03 Available at http://proceedings.ises.org

melting of PCM in the closed container in high temperature range, especially in the operation range of parabolic CSP plants (300-500 °C). Accordingly, this study aims at developing a two dimensional axisymmetric model to study the natural convection dominated melting process inside a spherical container in high temperature range and, to derive the dimensionless correlation of effective thermal conductivity for packed bed models.

2. Mathematical modeling

The computational domain is shown in Fig.1. An axi-symmetric model is developed by assuming the solid and liquid phases of the PCM are homogeneous and isotropic; the flow is laminar and incompressible; the phase change process takes place in the interval between 306.3°C and 306.8°C; where the density in the mushy zone varies linearly from 2130 kg/m^3 to 1908 kg/m^3. The temperature dependent liquid phase density is defined as (Archibold et al., 2014)

$$\rho_{liq} = \rho_m / \beta(T - T_m) + 1 \qquad \text{(eq. 1)}$$

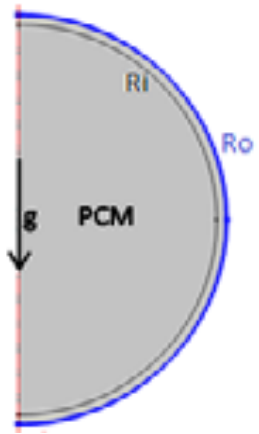

Fig.1: The computational domain

As the PCM volume changes during the phase change process, the elastic deformation takes place in the shell material (Archibold et al., 2014; Tanvir et al., 2015). The enthalpy-porosity method is used in the phase change range, by which the porosity in each element is equal to the liquid fraction in that element. Thus, the porosity is zero in solid regions. Based on the foregoing assumptions, the governing equations; continuity, momentum, and energy, are;

$$\frac{\partial \rho}{\partial t} + \nabla \cdot (\rho \vec{\mathrm{V}}) = 0 \qquad \text{(eq. 2)}$$

$$\rho \frac{\partial \vec{\mathrm{V}}}{\partial t} + \rho(\vec{\mathrm{V}}.\nabla)\vec{\mathrm{V}} = -\nabla P + \nabla.\left[\mu\left(\nabla\vec{\mathrm{V}} + \left(\nabla\vec{\mathrm{V}}\right)^T\right)\right] + \rho\vec{g} + A(\gamma)\vec{\mathrm{V}} \qquad \text{(eq. 3)}$$

$$\rho \frac{\partial h}{\partial t} + \rho\,\vec{\mathrm{V}}.\nabla h = \nabla.(k\nabla T) \qquad \text{(eq. 4)}$$

where ρ, $\vec{\mathrm{V}}$, P, μ, k, h and T are density, velocity vector, pressure, dynamic viscosity, thermal conductivity, specific enthalpy and temperature respectively. The porosity function A(γ) is defined by Eq. (5)

$$A(\gamma) = \frac{C(1-\gamma)^2}{\gamma^3 + \varepsilon} \qquad \text{(eq. 5)}$$

where the computational constant (ε), and the melting front morphology constant (C) are 0.001 and 10^5 kg/m^{3}s respectively. The specific enthalpy (h) is defined as the sum of the sensible enthalpy h_{sen} and enthalpy change due to phase change γL, where L is the latent heat of the material. The melt fraction, γ, is defined by eq. (6). Thermo-physical properties of the sodium nitrate are given in Table 1. The finite element method based commercial software COMSOL multiphysics 4.2 (2014) is used to solve the governing equations. In

order to optimize the mesh of the model, grid dependent tests were carried out for four various mesh distributions; the total number of elements was 5012, 10046, 14066 and 18506 respectively. The results given by the mesh generated with 10046 elements were, significantly deviated from the mesh with 5012 elements, analogous to the results produced by 14066 and 18506 elements. Thus, the mesh with 10046 elements was used for all calculations.

$$\gamma = \begin{cases} 0 & if\ T < T_{sol} \\ \dfrac{T - T_{sol}}{T_{liq} - T_{sol}} & if\ T_{sol} \le T \le T_{liq} \\ 1 & if\ T > T_{liq} \end{cases} \qquad \text{(eq. 6)}$$

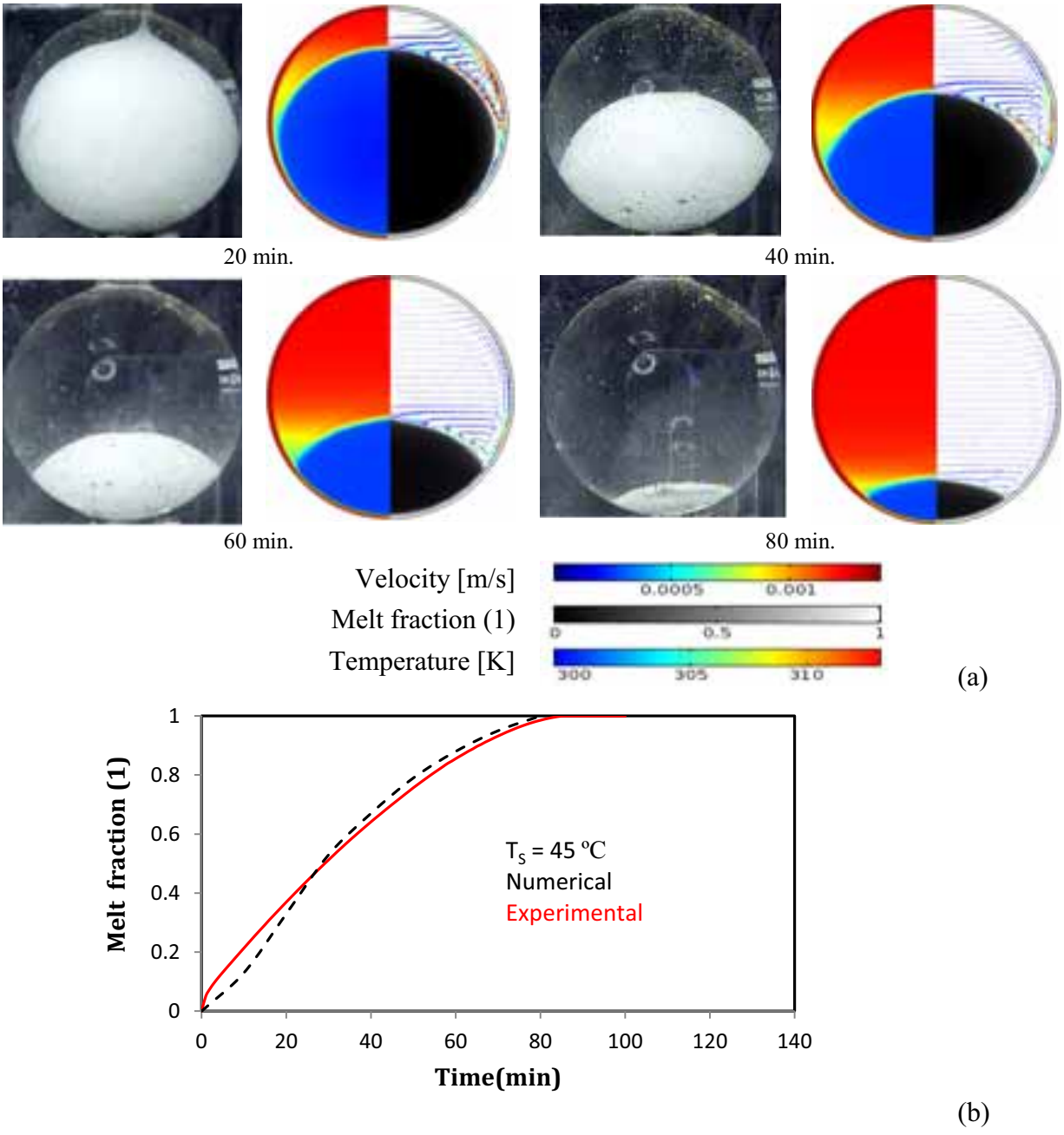

Fig. 2: Experimentally captured (Tan, 2008) and numerically predicted (a) melting front at various stages for T_s = 40ºC (b) melt fraction as a function of time for T_s = 45ºC

In order to validate the model, simulations were performed for the experimental conditions reported by Tan

(2008). In their experiments, the n-octadecane was, used as PCM, filled in a 50.83 mm inner radius capsule and 1.5 mm wall thickness. Initially, the capsule was kept at 1°C less than the melting point (29°C), when t>0 the outer surface of the capsule was fixed at 40°C. Simulation was performed for the same condition. The melting phase front, temperature and velocity distribution of the capsule during melting process are shown in Fig. 2(a) at 20 minutes intervals. Experimental photographs of melting process of the capsule are compared with the numerical results. In simulation results, the left side represents the temperature distribution and the right side represents the melt fraction and the velocity vector. Similarly, simulation was carried out for another case, where the outer surface temperature was fixed at 45°C. Fig. 2 (b) shows the comparison of experimentally measured (Tan, 2008) and numerically predicted melt fraction of the capsule. As can be seen in the figure, a good agreement is found between the numerical and experimental results.

Table 1. Thermo-physical properties of sodium nitrate

Properties	Sodium Nitrate
Density (kg/m^3)	
solid phase	2130
mushy zone	*Linear interpolation*
liquid phase	$\rho_{liq} = \rho_m / \beta(T - T_m) + 1$
ρ_m	1908
Dynamic viscosity (kg/m s)	$0.0119 - 1.53x10^{-5}T$
Latent heat of fusion (J/kg)	178000
Melting temperature (℃)	306.8
Specific heat (J/kg/K)	$444.53 + 2.18T$
Thermal expansion coef.(1/K)	$6.6x10^{-4}$
Thermal conductivity (W/m/K)	$0.3057 + 4.47x10^{-4}T$

3. Results and discussion

Using the validated model, simulation was performed to predict the melting process of a nickel spherical shell (thickness=0.5 mm) of radius 10mm, completely filled with molten salt. Initially, the capsule was kept at 301.5 °C and at t>0, the outer wall temperature was fixed at 311.5° C. Fig. 3 shows the temperature distribution and the corresponding melting process of the capsule at different stages. Each subfigure shows temperature distribution (left), melt fraction (right; black and white gradient), and natural convection flow velocity in the PCM liquid phase (right). During the initial stage of melting, the heat is transferred to the PCM through shell by conduction.

Once the melting process started at the inner surface of the shell, the natural convection starts to influences the melting process, the formed liquid PCM is heated by the inner surface of the shell. As the density changes between the solid and liquid phases, the solid part comes down due to gravity and the liquid flows upward and generates buoyancy driven flow. The heated fluid at the inner surface of the shell transfers the heat to the cold fluid close to the solid-fluid interface. Thus, an unsteady counter-clockwise circulating flow is formed above the solid part of the PCM during melting process. As a result, the melting process is faster at the top part of the solid phase and changes the spherical shape of the solid part into oblate spheroid shape as shown in the figure.

Influence of Stefan number and the capsule size on the melting process of the capsule is studied by various cases as shown in Table 2. By keeping the capsule size constant, simulations were carried out for cases 1-3 to study the effect of thermo-physical condition of the capsule (difference between the initial and outer wall temperature). Fig. 4 shows the melt fraction of the capsule as a function of time. As can be seen in the figure, an increase of temperature difference between the initial and outer wall temperature (T_S-T_0) can decrease the complete melting time. The complete melting time decreases about 8.5% and 4.5% respectively when increasing the temperature difference around 33% and 25%. The effect of pellet size on the melting rate for constant boundary conditions is presented in Fig. 5. The initial temperature and the wall temperature are

fixed and simulations were carried out for various capsule radii: 10, 15 and 20 mm. As expected, the complete melting time is decreased when the capsule size is reduced.

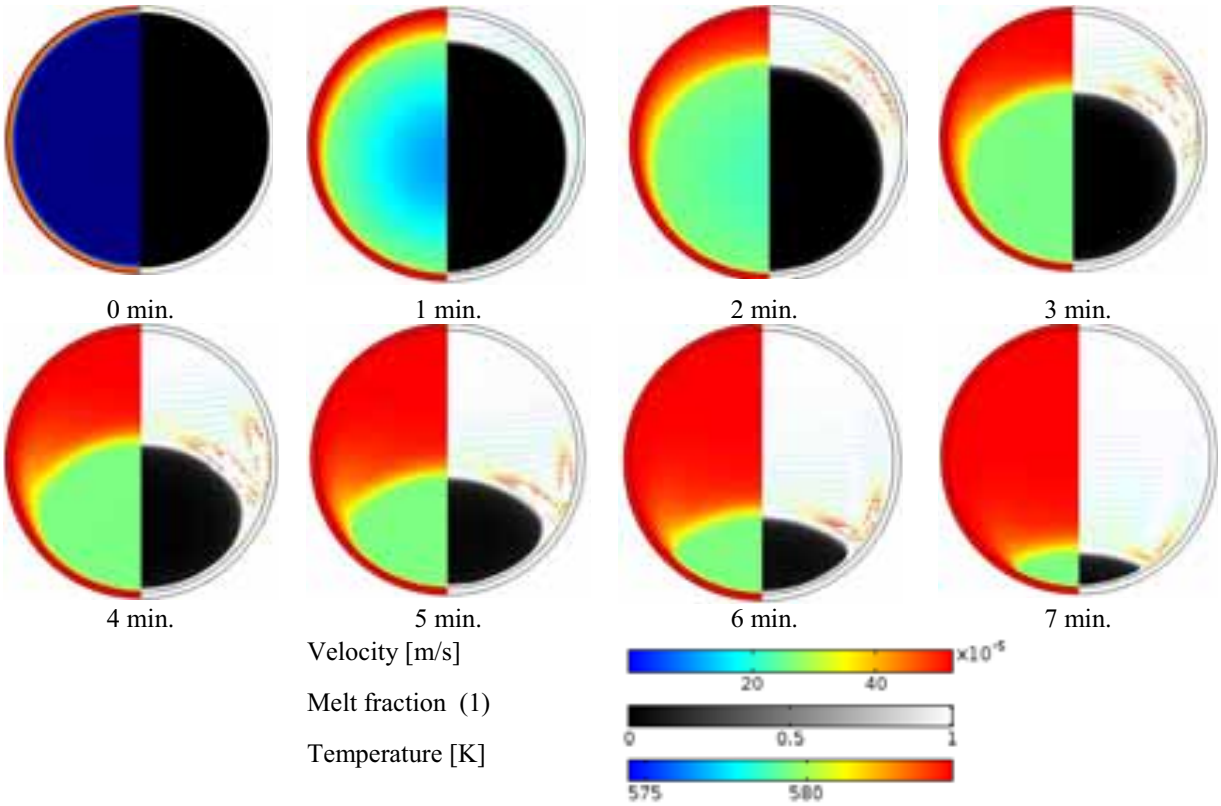

Fig. 3: Temperature distribution and the corresponding melting process of the capsule at different stages

Table 2 Analyzed cases

Case	Pellet radius (R_i) [m]	Initial Temperature (T_0) [ºC]	Surface Temperature (T_S) [ºC]	T_S-T_0 [ºC]
1	0.010	301.5	311.5	10
2	0.010	299.0	314.0	15
3	0.010	296.5	316.5	20
4	0.015	299.0	314.0	15
5	0.020	299.0	314.0	15

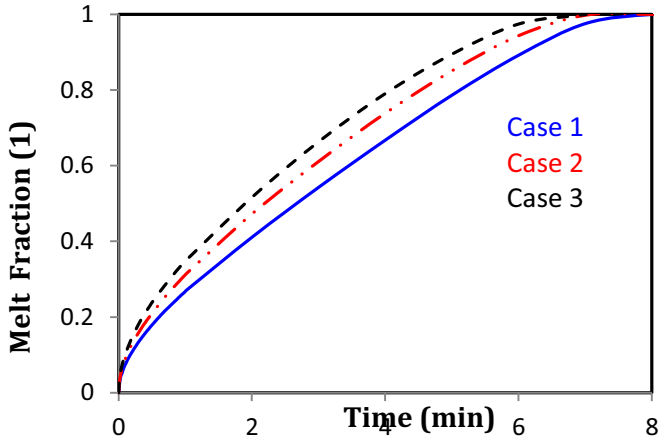

Fig.4: Melt fraction of the capsule as a function of time for various cases

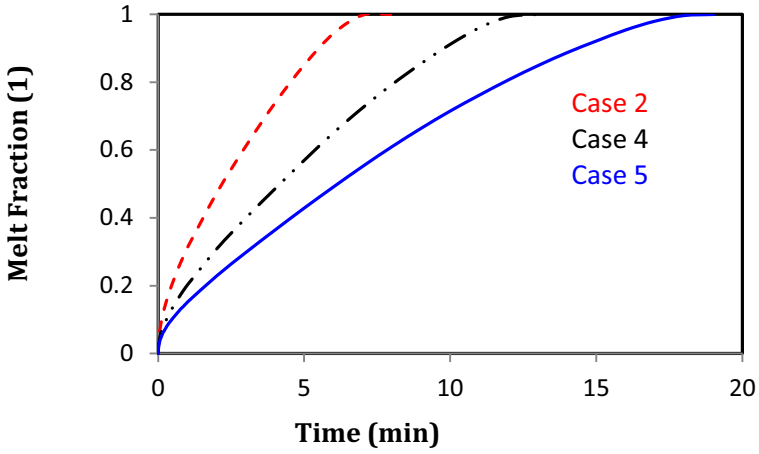

Fig. 5: Effect of pellet size on the melt fraction as a function of time.

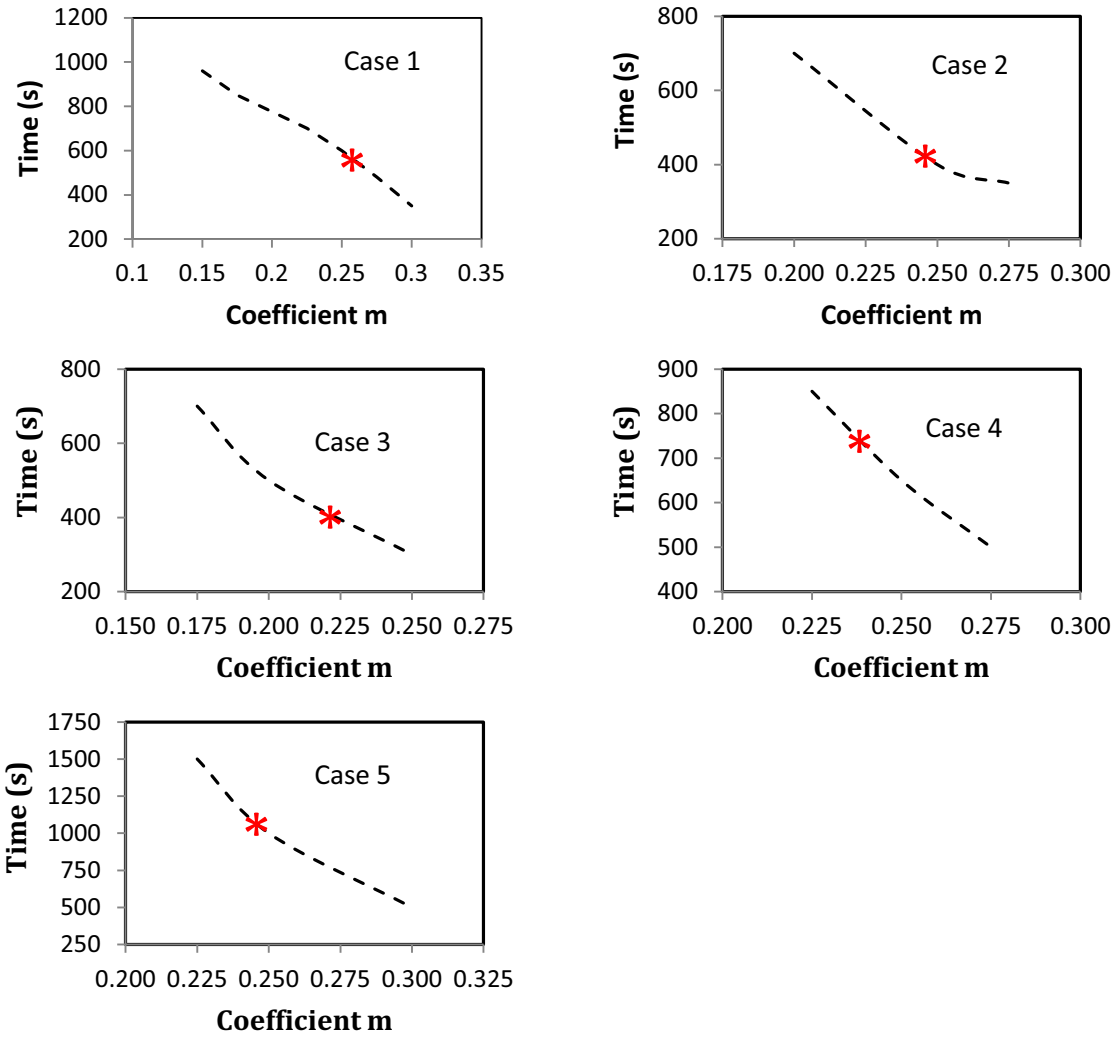

Fig.6: Complete melting time as a function of coefficient m.

In order to study the performance of the thermal energy storage system packed with spherical PCM capsules, various packed bed numerical models have been developed in the past few decades (e.g. Bellan et al., 2014a, 2015a, 2015b). As explained in the previous sections, natural convection plays vital role during melting process. However, most of the melting process models only considered the thermal conduction due to complexity in incorporating the natural convection effect during melting process. The convective effect present in the liquid region during melting can be incorporated to the packed bed system by using the effective thermal conductivity correlation. To derive that correlation for the given set of cases as shown in Table 2, one dimensional conduction model for phase change process inside a capsule has been developed by enthalpy formulation method, based on the literature models (Bellan et al., 2014b; 2014c). The correlation given in eq. (7) is used to calculate the effective thermal conductivity

$$k_{ef} = k_L C Ra^m \qquad \text{(eq. 7)}$$

In order to obtain the *C* and *m* coefficients, various values were assumed and the corresponding melt fraction evolution was predicted as a function of time. Then, the appropriate coefficients were obtained by comparing the 2D axi-symmetric model results obtained in the previous section. Initially, the coefficient of *C* was fixed at 0.18 (Bellan et al.,2015b), and calculations were made for case 1. Fig. 6 (case 1) shows the complete melting time predicted by the given correlation (Eq. 7) for various m coefficients. The complete melting time predicted by the 2D model is marked by asterisk symbol. Thus, the coefficient *m* is predicted for case 1, which is 0.26. Similarly, the coefficient *m* is predicted for other cases as shown in the figure. From this approximation, the generalized correlation is derived and given in eq. 8, which produces the same results of axisymmetric model.

$$k_{ef} = k_L 0.18 Ra^{0,243} \qquad \text{(eq. 8)}$$

4. Conclusion

An axisymmetric model has been developed to predict the heat transfer, fluid flow due to natural convection, and phase change process. The developed model has been validated with reported experimental and numerical results. Then the influence of pellet size and the Stefan number on the heat transfer characteristics and the melting process have been studied. From the axisymmetric model results, an effective thermal conductivity correlation has been derived using one dimensional model. The derived correlation can be used to simulate the charging behavior of packed bed thermal energy storage system with spherical capsules.

Acknowledgment

Authors gratefully acknowledge the Spanish Ministry of Economy and Innovation through Plan Nacional I+D+i project no. ENE2011-29293; ‘‘Comunidad de Madrid’’ and “European Social Fund” for its financial support to the ALCCONES Project through the Programme of Activities between Research Groups (S2013/MAE-2985). The research leading to these results has received funding from the European Union Seventh Framework Programme (FP7/2007-2013) under grant agreement no. 60983.

5. References

Archibold, A. R., Rahman, M.M., Goswami, D. Y., Stefanakos, E.K.., 2014. Analysis of heat transfer and fluid flow during melting inside a spherical container for thermal energy storage, Applied Thermal Engineering 64, 396-407.

Assis, E., Katsman, L., Ziskind, G., Letan R., 2007. Numerical and experimental study of melting in a spherical shell. International Journal of Heat and Mass Transfer 50, 1790–1804.

Bareiss, M., Beer, H., 1984. An analytical solution of the heat transfer process during melting of an unfixed solid phase change material inside a horizontal tube, Int. J. Heat Mass Transfer 27, 739-746.

Bellan, S., González-Aguilar, J., Romero, M., Rahman, M.M., Goswami, D. Y., Stefanakos, E.K.., 2014a. Numerical Modeling of Thermal Energy Storage System, ASME 2014 8th International Conference on

Energy Sustainability collocated with the ASME 2014 12th International Conference on Fuel Cell Science, Engineering and Technology, doi:10.1115/ES2014-6382.

Bellan, S., González-Aguilar, Archibold, A. R., J., Romero, M., Rahman, M.M., Goswami, D. Y., Stefanakos, E.K.., 2014b. Transient numerical analysis of storage tanks based on encapsulated PCMs for heat storage in concentrating solar power plants, Energy Procedia 57, 672-681.

Bellan, S., González-Aguilar, J., Romero, M., Rahman, M.M., Goswami, D. Y., Stefanakos, E.K.., David, C., 2014c. Numerical analysis of charging and discharging performance of a thermal energy storage system with encapsulated phase change material, Applied Thermal Engineering 71,481-500.

Bellan, S., Tanvir E. A., González-Aguilar, J., Romero, M., Rahman, M.M., Goswami, D. Y., Stefanakos, E.K.., 2015a. Numerical and experimental studies on heat transfer characteristics of thermal energy storage system packed with molten salt PCM capsules, Applied Thermal Engineering 90, 970-979.

Bellan, S., González-Aguilar, J., Romero, M., Rahman, M.M., Goswami, D. Y., Stefanakos, E.K.., 2015b. Numerical Investigation of PCM-based Thermal Energy Storage System, Energy Procedia, 69, 758-768

COMSOL Multiphysics Version 4.3, COMSOL AB, Stockholm, Sweden, 2013

Felix, R.A., Solanki, S.C., Saini, J.S., 2006. Experimental and numerical analysis of melting of PCM inside a spherical capsule, in: 9th AIAA/ASME Joint Thermophysics and Heat Transfer Conf. Proc., AIAA- 2006-3618.

Hosseinizadeh, S.F., Rabienataj Darzi, A.A., Tan F.L., J.M. Khodadadi., 2012. Unconstrained melting inside a sphere. 63, 55-64. Int. J. Therm. Sci. 63, 55-64.

Ismail, K.A.R., Henríquez, J.R., 2000. Solidification of pcm inside a spherical capsule. Energy Conversion and Management. 41, 173-187.

Moore, F.E., Bayazitoglu, Y., 1982. Melting within a spherical enclosure, J. Heat Transfer 104, 19-23.

Roy, S.K., Sengupta, S.,1987. The melting process within spherical enclosures, J. Heat Transfer 109 460-462.

Tan, F.L., 2008. Constrained and unconstrained melting inside a sphere. International Communications in Heat and Mass Transfer. 35, 466–475.

Tanvir E. A., Jaspreet,D., Goswami, D. Y., Stefanakos, E.K.., 2015. Macroencapsulation and characterization of phase change materials for latent heat thermal energy storage systems, Applied Energy, 154, 92-101.

Conference Proceedings

Solar World Congress 2015
Daegu, Korea, 08 – 12 November 2015

Experimental investigation of the heat performance using a packed bed of ceramic balls for high temperature thermal energy storage unit

Bei Yang[1], Yan Wang[1], Fengwu Bai[1]

[1] Key Laboratory of Solar Thermal Energy and Photovoltaic System,

Institute of Electrical Engineering, Chinese Academy of Sciences, Beijing 100190, China

Abstract

A thermal energy storage (TES) system was designed based on a packed bed of ceramic balls as storage material and air as heat transfer fluid (HTF). A series of contrast experiments were carried out under specified working conditions to analyze the heat performance of TES unit. The results showed that temperature distribution in axial direction of the packed bed and thickness of thermal stratification can be manually controlled by adjusting the air flow rate or the heating power during charging to achieve a better discharging performance. The packed bed has a good temperature uniformity along the radial direction which means a less exergy loss and smaller convective mixing radially. It was also shown that the TES unit has a highest discharging heat power of 16.5 kW, and discharging efficiency of 90%, indicating that the TES unit can achieve to store and release heat effectively.

Keywords: *Packed bed, Thermal storage, Sensible heat, Air, Ceramic balls*

1. Introduction

TES is vital for the solar thermal electricity technologies due to the random solar irradiations. The form of sensible heat storage in packed-bed of solid material is especially suitable for the system whose heat transfer fluid is air, and the cost of fabrication of tank and the heat storage material is significantly lower than other methods (Markus Hanchen et.al 2011). A wide body of publications describes numerical models for sensible heat storage in packed-beds (Antoni Gil et al., 2010; G. Zanganeh et al., 2012, 2015; Jon T. et al. , 2011; Opitz and Treffinger, 2014), but only a few include experimental investigation. The numerical results show that the porous structure maximizes heat transfer between fluid and storage media and minimizes heat transport inside the storage media.

In this paper, the design, fabrication, test of a packed-bed TES unit were described. And indicators including thermal stratification, radial temperature difference, discharge outflow temperature, discharging power output and thermal efficiency were analyzed to evaluate the heat performance.

2. Pilot-scale TES design and experimental setup

2.1. A packed-bed TES device

The packed-bed TES unit is shown schematically in Fig.1, which consists of one cylindrical shell and two conical shells. The two conical shells are arranged on the top and the bottom of the tank respectively, used to be connected with the pipes and form a raletively uniform air flow. The tank has a circular cross section with a inner diameter of 0.7 m, and a total height of 4 m. The circular tank wall is made of refractory bricks, with a thick of 100 mm. The refractory brick has a a small coefficient of thermal expansion and a raletively high strength, which can help to reduce the effect of thermal ratcheting caused by thermal expansion of the storing material; In addition, the low thermal conductivity of the refractory brick can help to reduce the heat loss as

doi:10.18086/swc.2015.02.04 Available at http://proceedings.ises.org

well. Outside the refractory bricks is a 100-mm layer of asbestos insulation, while outside which covered a 6-mm layer of stainless steel shell.

The tank is filled to the height of 2.3 m with high alumina ceramic balls with an equivalent sphere diameter of 25mm, shown as Fig.2. The physical parameters of the ceramic balls are shown in table 1. A porous metal perforated strainer is installed inside the bottom of the tank, supporting the weight of the storage materials, and avoiding the ceramic balls and debris dropping and blocking the following pipes at the same time.

Fig.1 Photo of packed-bed TES unit

Fig.2 Photo of ceramic balls

Table1. Physical parameters of ceramic ball and packed bed

Al_2O_3(%)	Packed-bed Porosity*	Density (kg m^{-3})	Specific Heat Capacity (kJ $kg^{-1}K^{-1}$)
65	0.463	2200	1.0

*Remarks: porosity is calculated as the ratio between the volume of solid material and the tank capacity in packed height.

2.2. A packed-bed TES testing system

Fig.3 shows the layout of the packed-bed TES testing system. The testing system consists of a blower, an air heating furnace, a packed-bed TES unit using ceramic balls as TES material, and regulating valves. The ambient air pumped from the blower can be heated to 600-900℃ by the 60 kW electric heating furnace, and then the hot air enters through the inlet pipe from the top, flows through the packed bed to charge the ceramic balls. Charging from the top allows the exploitation of the buoyancy effect to create and maintain thermal stratification inside the packed bed, keeping the hottest region being at the top. During discharging, the direction of the flow is reversed as cold air is circulated through the tank from the bottom.

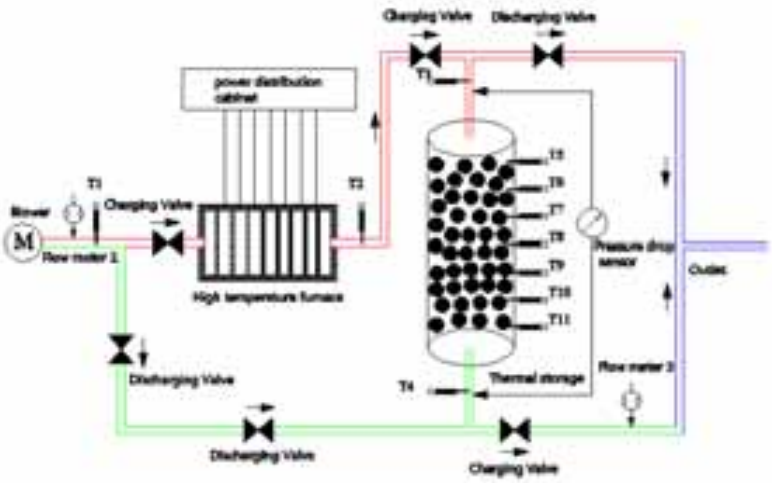

Fig.3. Schematic of packed-bed TES system

During the charging and discharging processes, the temperature is recorded by 43 K-type or S-type thermocouples throughout the system, of which 30 thermocouples are located inside the packed bed at different vertical positions. Along the height of packed bed, 5 measurement sections are arranged in every 0.5-m high, and 6 thermocouples are arranged in each section, shown as figure 4, notably that the thermocouples at the height of 2.5 m are not covered with ceramic balls; 2 thermocouples measure the temperature just above the packed bed on the tank axis and 2 in the bottom outlet pipe. In addition, other measurements include: ambient air temperature, the air flow rates at the inlet and outlet of TES system, and pressure drop when the air flowing through the packed bed. The thermocouples have an accuracy of ±0.5%. The flow meters installed at the inlet of system is a volumetric flowmeter with a measuring range of 15~300m^3/h and outlet a vortex-shedding flowmeter with range of 80~800m3/h, both of which share a common accuracy of ±0.5%.

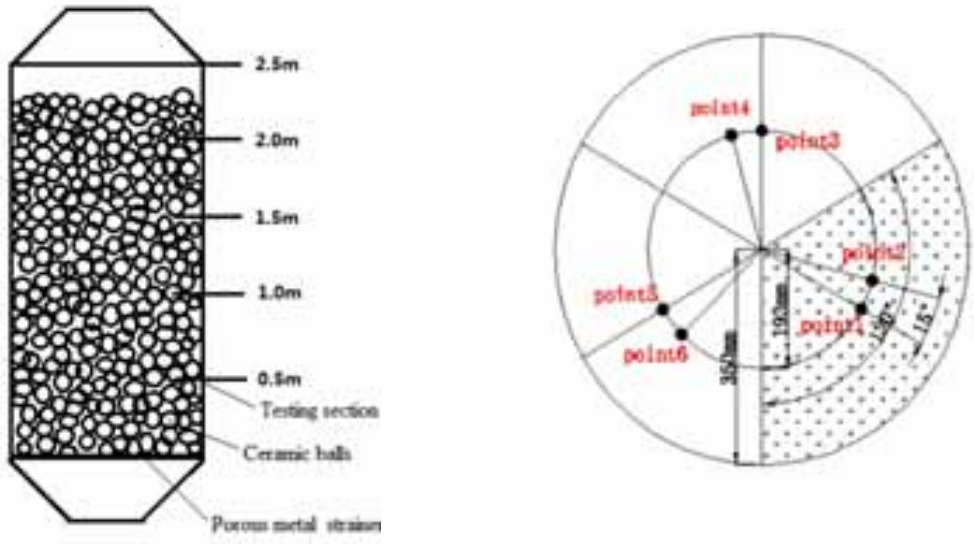

(a) (b)

Fig.4. Distribution of testing sections in packed bed (a) and testing points in each section (b)

3. Results and Discussion

In order to analyze the charging and discharging performance of the packed-bed TES system, several experiments were carried out under different working conditions with an initial discharging temperature of solid storage material about 500℃ and a discharging air flow rate of 50 Nm³/h, 100 Nm³/h, 150 Nm³/h respectively.

3.1. Temperature distribution

During the charging and discharging processes, the transient temperatures of ceramic balls were recorded by the thermocouples arranged at different heights of the packed bed. 6 thermocouples were adopted in each measuring section to ensure measurement accuracy. Thus, the average temperature at each section can be calculated as equation (1):

$$T_i = \frac{\sum_{j=1}^{j=6} T_{i,j}}{6} (\mathrm{i} = 1, 2, 3, 4) \qquad \text{(eq.1)}$$

Where, i=1,2,3,4 refers to the temperature testing section at the height of 0.5m, 1.0m, 1.5m, 2.0m respectively.

3.1.1 Transient temperature distribution of the ceramic balls

(a)

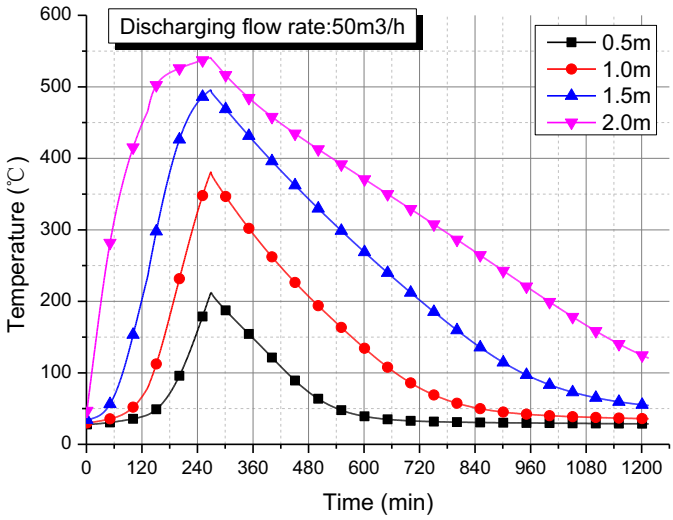

(b)

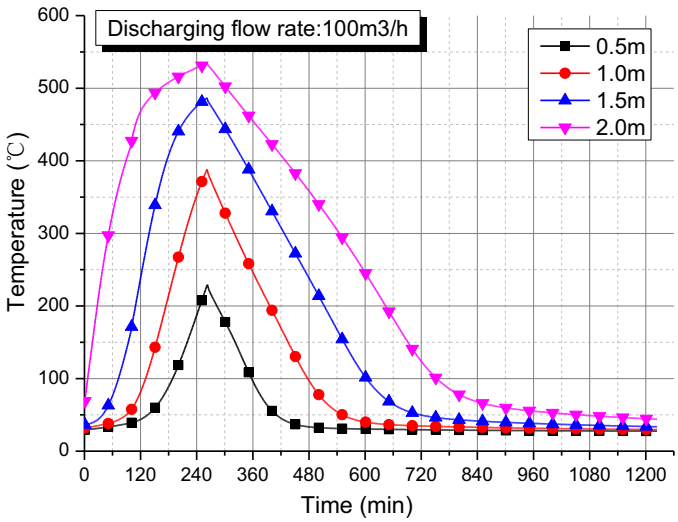

(c)

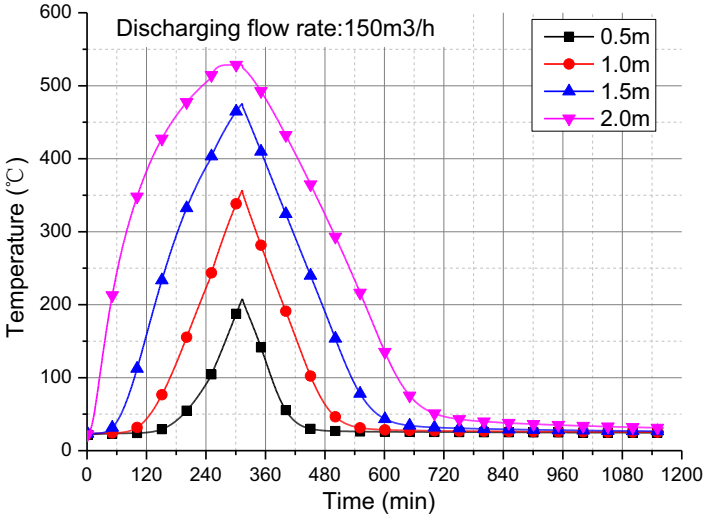

Fig.5. Transient changes of temperature distribution of ceramic balls under various conditions

(a.50 Nm³/h b. 100 Nm³/h c.150Nm³/h)

Figure 5 show the temperature distribution of ceramic balls under three different conditions. The charging conditions were not strictly controlled but manually adjusted to ensure a similar initial discharging temperature distribution of the packed bed at the end of charging. Seen from the figures, at the end of

charging temperature of ceramic balls at the height of 2.0 m is up to around 530 ℃, while at the height of 0.5 m around 210 ℃, which means the temperature difference between the top and the bottom is over 300℃. The reason for this obvious thermal stratification inside the packed bed is mainly that the air buoyancy effect was fully exploited by charging from the top and discharging reversed which keeping the hottest region being at the top and the coldest at the bottom. The experimental experience indicated that temperature distribution of packed bed and thickness of thermal stratification could be manually controlled by adjusting the air flow rate or the heating power during charging.

While during discharging the air flow rate was strictly controlled to be 50 Nm³/h, 100Nm³/h, 150Nm³/h respectively. Seen from figure 5, temperature drops of the ceramic balls increase obviously with the increasing air discharging flow rate, since the convective heat transfer between air and solid material is distinctly enhanced with a higher air velocity. After cold air enters the packed bed from the bottom, it exchanges heat with the ceramic balls from bottom to top, and the temperature of air is gradually raised while the heat energy is extracted for its further use.

It's worth noting that the air temperature rising during discharging is directly related to the thermal stratification of packed bed at the end of charging. Therefore, it is possible to match the air temperature rising and the thermal stratification of packed bed by the means of charging process control and air preheating before discharging etc., which can minimize the heat transfer temperature difference between air and solid materials, namely minimize the irreversible energy loss, and maximize the exergy efficiency of the TES system eventually.

3.1.2 Transient discharging outflow temperature

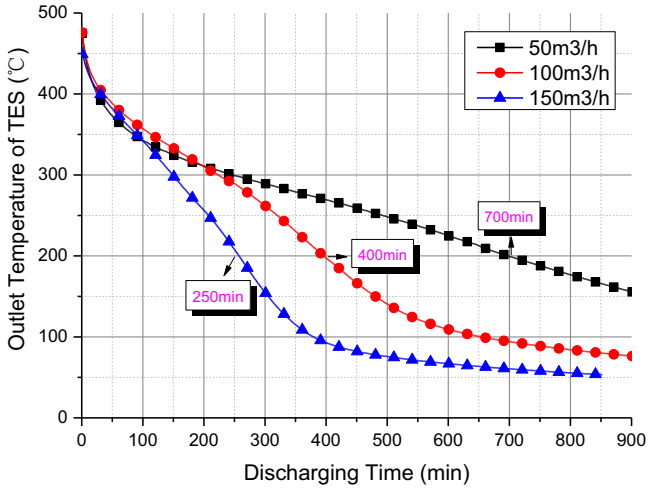

Fig.6. Transient changes of dischaging outflow temperature under different flow rates

Figure 6 shows the variation of outlet air temperature under different air discharging flow rates. Seen from it, the highest air outlet temperature is up to about 480 ℃, and it takes a period of 250min, 400min, and 700min for the outflow temperature decreasing from 480℃ to 200℃under the discharging flow rate of 50 Nm³/h, 100 Nm³/h, 150 Nm³/h respectively when the initial discharging temperature distributions are roughly the same. The results indicated that certain air outlet temperature and certain quantity of heat extracted can be obtained by controlling the discharging air flow rates, which leads the discharging process to last for various period of time, and then meets demand of various thermal storage applications.

3.1.2 Radial temperature difference in top testing section

Figure 7 shows the transient changes of radial temperature difference in the top testing section, which reflects uniformity of radial temperature distribution in the packed bed. As can be seen from the figure, the radial teperature difference is respectively about 30 ℃ and 10 ℃ during charging and discharging process when the discharging air flow rate is 100Nm³/h, showing that the packed bed has a good uniformity along the radial direction. The main reason for this phenomenon is that the packed bed has a raletively high porosity of 0.463, which makes it possible for air to flow evenly in packed bed and maximizes heat transfer between air and ceramic balls.

(a)

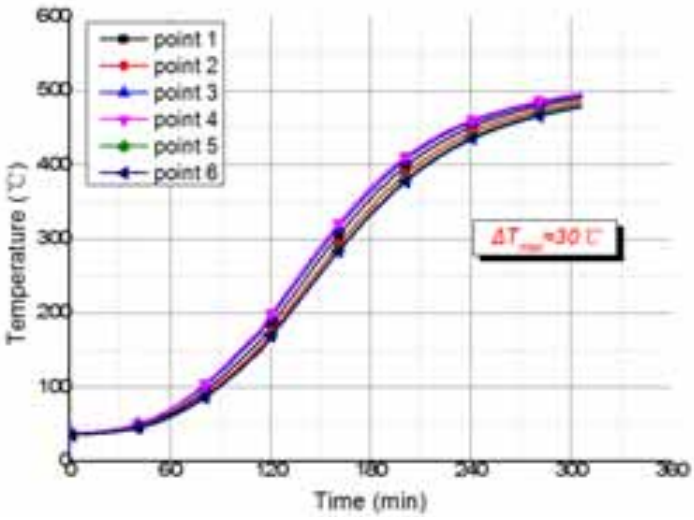

(b)

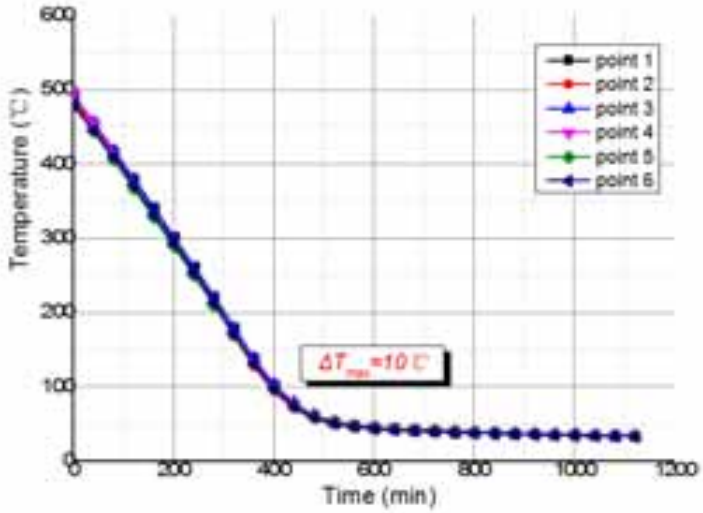

Figure 7. Radial temperature difference in top testing section
(a. Charing; b. Discharging; Discharging flow rate: 100Nm³/h)

This uniformity has advantages that exergy loss is reduced caused by heat exchanges within certain temperature ranges and radial convective mixing of air is lightened as well, resulting in a great improvement for exergy efficiency of the TES unit.

3.2 Net discharging power output

Net discharging power is defined as the heat extracted from solid materials by air in unit discharging time, which can be calculated as equation (2):

$$P_d = c\,\dot{m}\,\Delta T = c\,\dot{m}\,(T_{ao} - T_{ai}) \qquad \text{(eq.2)}$$

The temperature-dependent thermal properties of air are considered in the calculation, and density of air is determined by empirical correlation (3):

$$\rho = 0.72447e^{(-T/532)} + 0.39845e^{(-T/125.93)} + 0.16623 \qquad \text{(eq.3)}$$

Figure 8 shows variation of net discharging power under various air flow rates. As can be seen from it, the highest power can be up to 16.5 kW with a flow rate of 150 Nm³/h; and the lower the air flow rate is, the more fully heat transfer between air and ceramic balls developed, and the more stable the net discharging power output. The power curve under a certain flow rate declines slightly at the beginning of discharging, then increases to the highest value, and then continues to slowly drop eventually. The reason for this trend is that the pipe at the top of packed bed remains hot at the end of charging, while during discharging the top pipe will be cooled down at first and then heated by the discharging air, and it takes a while for the temperature difference between air outlet and inlet to reach a consistent variation.

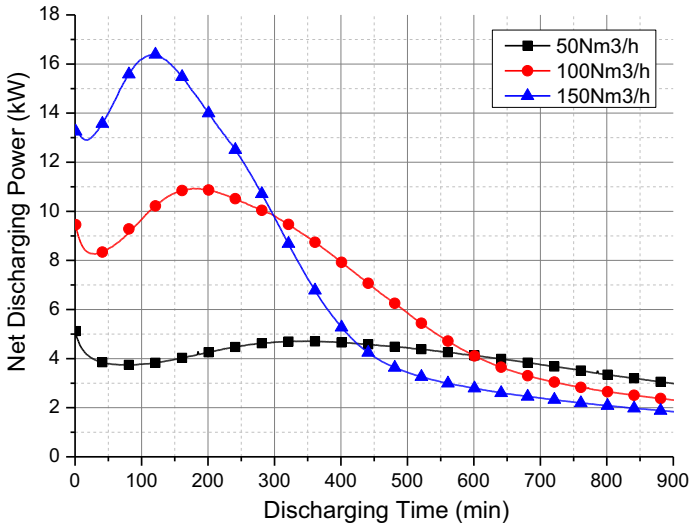

Figure 8. Transient changes of net discharging power under various air flow rates

Area between the single curve and abscissa represents the quantity of heat ectracted by air, and the results shows that the higher the air flow rate is, the larger quantity heat extracted in the first part of discharging. Therefore, it's critical to control appropriate discharging flow rate to adapt for different energy needs.

3.3 Thermal efficiency of TES unit

The heat performance of TES unit can be evaluated by the value of its thermal efficiency, including the charging and discharging efficiency. Charging efficiency is defined as the ratio of the net heat stored by solid material and the total heat released by the hot air during the charging process, which can be expressed as equation (3):

$$\eta_c = \frac{A(1-\varepsilon)\rho c_s \int_0^H [T(t_c, h) - T(t_0, h)]dh}{\int_0^{t_c} [T_{ai} - T_{ao}]\, c_a \dot{m}_a\, dt} \times 100\% \qquad \text{(eq.4)}$$

While discharging efficiency is defined as the ratio of the net heat extracted by cold air and the total heat released by the solid materials during a certain period of discharging time, which can be expressed as equation (4):

$$\eta_d = \frac{\int_0^{t_d} [T_{ai} - T_{ao}] c_a \dot{m}_a \, dt}{A(1-\varepsilon)\rho c_s \int_0^H [T(t_0, h) - T(t_d, h)] dh} \times 100\% \qquad \text{(eq.5)}$$

Figure 9 shows the charging and discharging efficiency changes of the TES unit under various working conditions, in which the discharging peirod of time is chosen as the moments before the discharging outflow temperature is not less than 100℃.

From the figure, the highest charging and discharging efficiency are respectively about 80% and 90%, which indicates that the TES unit can achieve to store and release heat effectively.

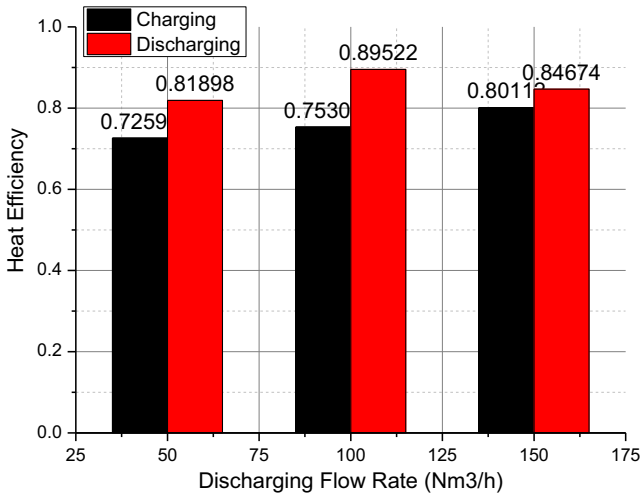

Figure 9. Charging and discharging efficiency changes of TES unit under various working conditions

Thermal efficiency of TES unit is directly related to its heat loss to the surrounding environment. Seen from the figure, the value of thermal efficiency is not so much high which indicates that the insulation measures of the TES unit remains to be further strengthened. However, it's worth noting that heat capacity of this system is limited due to a lab-scale device, and heat loss accounted for a larger proportion with a samller scale compared to the total storage heat. Therefore, the heat loss can be almost negligible and the thermal efficiency will be raised by big percentages when the heat storage system expand to the industrial scale.

4. Conclusions

A pilot-scale TES system based on a packed bed of ceramic balls with air as heat transfer fluid was designed, built, tested, and evaluated. Seris of contrast experiments under specified working conditions were carried out and the indicators including thermal stratification, radial temperature difference, discharge outflow temperature, discharging power output and thermal efficiency were analyzed to assess the heat performance of the TES unit. It was shown that temperature distribution in axial direction of the packed bed and thickness of thermal stratification can be manually controlled by adjusting the air flow rate or the heating power during charging to achieve a better discharging performance. The packed bed has a good temperature uniformity along the radial direction which means a less exergy loss and smaller convective mixing radially. The TES unit has a highest discharging heat power of 16.5 kW, and discharging efficiency of 90%, indicating that the

TES unit could achieve to storage and release heat effectively. However, good performance as the TES unit has, some optimization measures need to be further taken both in strucutres and controlling strategies optimization, such as the strengthened insulation, the expended scale and the optimally designed and controlled charging conditions etc..

5. Acknowledgments

This work was supported by the National Natural Science Foundation of China (No. 51306170) and the National Key Technologies R&D Programme of China (No.2014BAA01B00).

6. References

Antoni G., Marc M., Ingrid M., Ana L,, Pablo D., 2010. State of the art on high temperature thermal energy storage for power generation. Part 1—Concepts, materials and modellization. J. Renewable and Sustainable Energy Reviews 14 31–55.

Florian O., Peter T., 2014. Packed bed thermal energy storage model—Generalized approach and experimental validation. J. Applied Thermal Engineering 73 243-250.

G. Zanganeh, A. Pedretti, S. Zavattoni, M. Barbato, A. Steinfeld, 2012. Packed-bed thermal storage for concentrated solar power–Pilot-scale demonstration and industrial-scale design. J. Solar Energy 86 3084–3098.

G. Zanganeh, A. Pedretti, A. Haselbacher, A. Steinfeld, 2015. Design of packed bed thermal energy storage systems for high-temperature industrial process heat. J. Applied Energy 137 812–822.

Jon T., Peiwen Li et al., 2011. Analysis of heat storage and delivery of a thermocline tank having solid filler material . J. Journal of Solar Energy Engineering 133/ 021003-1.

Markus H., Sarah B., Aldo S., 2011. High-temperature thermal storage using a packed-bed of rocks-Heat transfer analysis and experimental validation. J. Applied Thermal Engineering 31:1798-1806.

Appendix

Table 1: Symbols for miscellaneous quantities

Quantity	Symbol	Unit
Area	A	m^2
Air mass flow rate	$\dot{m}$	Kg s^{-1}
Mass	m	kg
Height of packed bed	H,h	m
Temperature	T	K
Time	t	s
Power	P	kW
Specific heat	c	J kg^{-1} K^{-1}
Density	ρ	kg m^{-3}
Efficiency	η	
Porosity of pecked bed	ε	

Table 2: Subscripts

Quantity	Symbol
Air	a
Charging	c
Discharging	d
Solid material	s
Number of testing section	i
Number of testing point	j
Air flow into TES unit	ai
Air flow out of TES unit	ao

Innovative PCM Storage as Power-to-Heat Unit for Process Heat Applications

Doerte Laing-Nepustil, Ulrich Nepustil, Rameesh Sivabalan and Detlev Lodemann

Hochschule Esslingen – University of Applied Sciences, Göppingen (Germany)

Abstract

An innovative high temperature latent heat storage concept for power-to-heat application is presented. The storage is equipped with electrical heating elements, directly immerged into the phase change material to achieve best conversion efficiency. Discharging takes place by an oil cooled plate heat exchanger. For heat transfer enhancement during discharging, a new concept, using moving blades to scrape off the solidifying material, was developed. With this method, the solidified layer of phase change material on the heat exchanger surface is kept at constant thickness, allowing for constant heat flux during the major period of the discharging process. Feasibility of the concept with moving scrapers was demonstrated, showing advantages over the passive concept. First investigations on the crystal size and hardness of Sodium Nitrate were performed to improve the scraper design. A concept for separation of capacity and heat rate is described.

Keywords: *latent heat storage, PCM, high temperature, power-to-heat, process heat*

1. Introduction

The German Federal Government has set the goal to reduce greenhouse gas emissions until 2020 by 40 % compared to 1990 levels, and cut primary energy consumption by 20 % over rates for 2008. Renewables are to have a 40-45 % share in electricity production by 2025, and a 55-60 % share by 2035. By 2050, the Federal Government seeks to increase the share of renewables in the electricity mix to at least 80 %. This is a tremendous change for Germany's electricity market. The rate of surplus electricity will rise because the average load factor of renewable technologies like wind power and photovoltaic is significant lower than that of conventional power plants. Therefore the required installed capacity needs to be much higher than for the conventional electricity market. The current German electricity market, with approx. 25% of renewable electricity, has still a residual load of ca. 15 GW. In 2035, with a renewable share of 60%, the minimal residual load is expected to fall to minus 25 GW (Federal Ministry for Economic Affairs and Energy (BMWi) 2014).

The increasing share of renewables in today's generation mix and the accompanying fluctuation in generation requires large scale as well as decentralized storage capacities to secure grid stability. In the proposed power-to-heat concept, electricity, produced from PV-plants or small scale wind farms, will be used to heat up high temperature latent heat storages. The heat can be used in industrial processes, e.g. industrial bakeries.

Thermal energy storages can be differentiated into sensible, latent and thermochemical technics depending on the physical principle. The selection of storage type depends on the demands and boundary conditions of the application (temperature range, heat transfer fluid, storage duration, storage capacity, heating rates) (Laing et al. 2012).

Latent heat storage with phase change material (PCM) is using the heat of fusion and offers the possibility of efficient storage of heat with high energy density in a small temperature range. One of the main challenge of PCM storages lies in the low thermal conductivity of the phase change materials. This leads to insufficient heat transfer between the storage medium and the heat transfer fluid, resulting in an unfavorable characteristic within the discharging process. When the discharging process starts, the PCM begins to solidify first at the heat exchanger plates and forms a steadily growing insulating layer. Because of that, the heat transfer from the liquid PCM to the heat exchanger plates drops dramatically. The current state of the art is to build some kind of heat transfer structures into the storage. This can be done by using finned tubes or specially formed structures, preferably made of aluminum (Laing et al. 2013). These build in structures

Selection and/or peer review under responsibility of Scientific Committee
doi:10.18086/swc.2015.02.05 Available at http://proceedings.ises.org

improve the heat transfer but cannot solve the problem satisfactorily and they reduce the amount of PCM inside the storage and for this the thermal capacity of the storage.

The newly developed active latent heat storage concept combines three innovative aspects:

1. Electrical heating elements ("power-to-heat"), directly immerged into the phase change material to achieve best conversion efficiency.
2. Moving scrapers to improve discharge and to achieve high and near constant heat rates during discharging. The moving scrapers control the freezing front inside the latent heat storage by keeping the solidified layer of phase change material on the heat exchanger surface at constant thickness.
3. Separation of capacity and heat rate: The concept with moving scrapers requires operation in a mixture of liquid PCM with solidified PCM-particles. Therefore, in the active stage the storage cannot be discharged completely (fully discharge means total amount of PCM is solidified, thus no more movement possible). However, this concept allows for active pumping and moving of salt. During discharging the solidified PCM grains can be removed from the liquid pool and stored in an insulated "cold" tank, while liquid PCM is refilled into the heat exchanger unit from an insulated "hot" tank. During charging, the solid particles will be poured into the heat exchanger unit from the "cold" tank, while liquefied PCM is pumped into the "hot" storage tank.

The current focus lies on the first two points, to proof feasibility of the active concept.

2. Description of concept

Fig. 1 shows a scheme of the newly developed active latent heat storage concept with moving scrapers (Laing et al. 2015). For electrical heating, heating elements are used that are integrated in aluminum plates to have very good heat conduction and therefore near constant temperature over a large heat exchange surface. Discharging will take place by oil cooled flat plate heat exchangers. Here the so called "pillow plate" method was applied as a cheap design applicable to higher pressures. For heat transfer enhancement during discharging, a new concept, using moving scrapers to scrape off the solidifying material, was developed. With this method it is intended to keep the solidified layer of phase change material on the heat exchanger surface at a thin and constant thickness, allowing for constant heat flux during the major period of the discharging process.

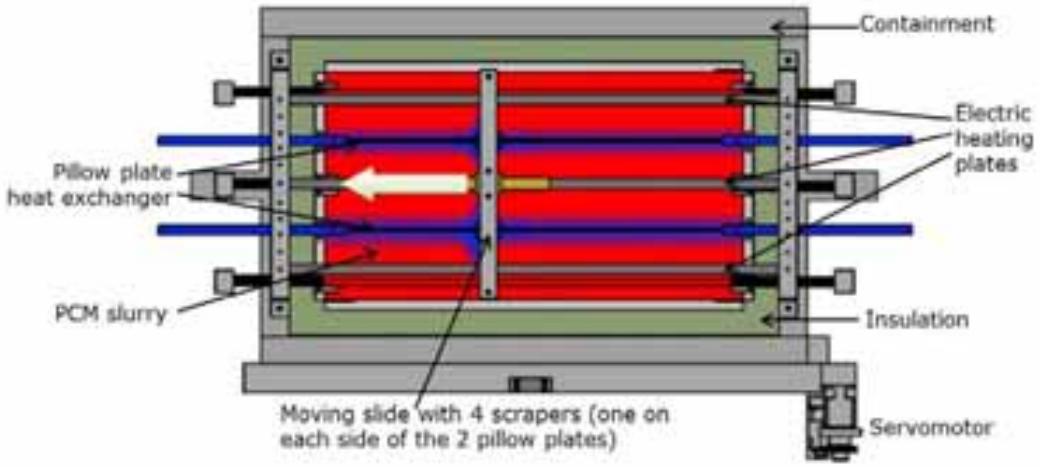

Fig. 1: Principle of the new storage concept with three heating plates, two pillow plates as heat exchanger plates and the scraper mechanic at the beginning of the discharging phase.

A first test storage unit was built and integrated in the test loop (Fig. 2). It has a total volume of 0.36 m³ and is currently filled up with ca. 375 kg of Sodium Nitrate (approx. 65% of complete filling). The storage is equipped with three specially designed electrically heated aluminum plates with an electrical heating power of 4 kW, each. For discharging, two oil cooled pillow plates are emerged into the salt. The moving scrapers are located on each side of both pillow plates, with a gap of approximately 8 mm between scraping surface and pillow plate surface. They are mounted with a metal slide on a rod, supported on the top of the storage

tank, and are moved linearly back and forth from one end to the other by a servomotor. With the current setting, the scraper takes about 14 seconds for one direction. The velocity is continuously adjustable. When the discharging process starts, the scrapers begin to move. By stirring the liquid PCM, the heat transfer on the freezing front is improved. Once the solid PCM has filled up the gap between heat exchanger surface and scraper, the thickness of the solid layer of the PCM on the pillow plates is limited to this size by the scrapers. This is the point, from which the heat rate stays almost constant, as the temperature in the liquid PCM-volume is at phase change temperature and the heat resistance is constant due to the constant thickness of the solid layer.

The storage unit is connected to a temperature control unit for heating and cooling, using synthetic thermal oil, stable up to 350°C. It has a heating rate of 20 kW and a cooling rate of 80 kW. For cycling tests, the storage unit will be heated directly through the electric heating plates immersed into the PCM. However, for preheating of the PCM close to the melting temperature, heating can be supported by the thermal oil loop to accelerate testing.

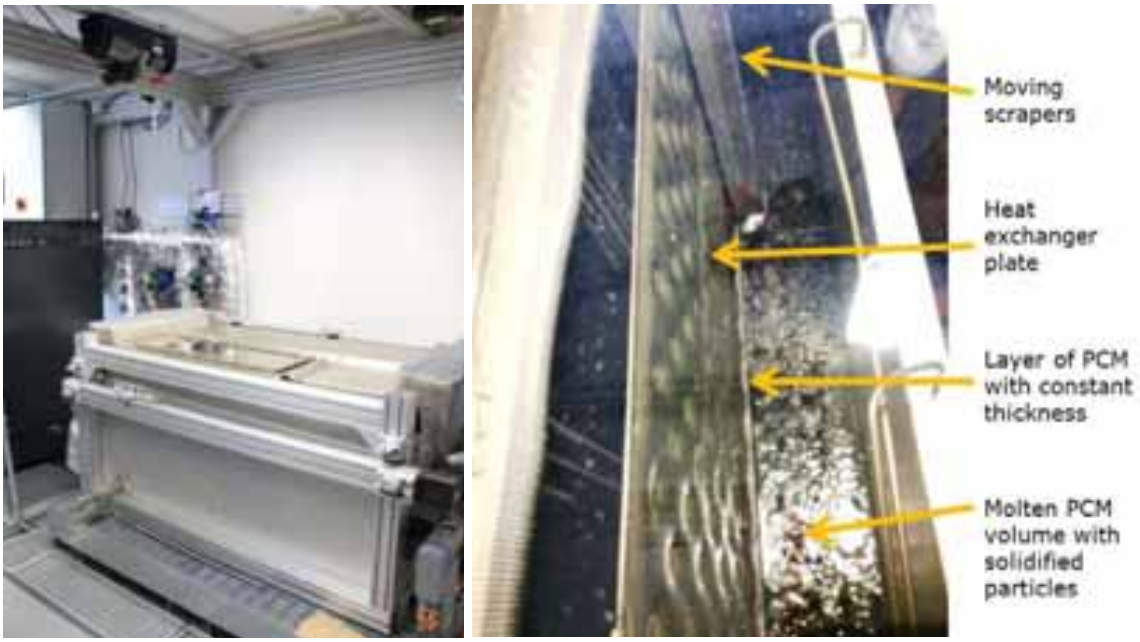

Fig. 2: Test facility with storage unit (left). Storage during commissioning, showing moving scraper that keeps frozen PCM layer at constant thickness (right).

3. Results and Discussion

3.1 Test results of storage operation

Figure 3 shows a comparison of storage discharge with and without movement of the linear scrapers. In both cases the complete storage mass was at 330 °C before discharge was started with a set temperature of 295 °C for the heat transfer fluid (HTF) at storage inlet. The dashed lines represent behavior without and full lines with scraper movement. Volume flow for the thermal oil is 20 l/min for all cases. Heat flow is calculated with the measured values and the temperature dependent density and specific heat capacity of the HTF. Apart from HTF inlet and outlet temperatures (Temp-HTF-inlet, Temp-HTF-outlet), the average temperatures of the PCM next to the cooling plates (Temp-PCM-HX) and in the middle between heating and cooling plates (Temp-PCM-liquid) are shown. To indicate the load on the scraper, the current for the scraper engine is measured (Current for scraper movement). The distance between scrapers and heat exchanger plates of the four different scrapers is not the same, due to thermal distortions of the plates and the containment. Therefore, the value of the current, shown here, is just a rough indication of the contact between scraper and solid PCM. The oscillation of the HTF temperatures and therefore the heat flow at the beginning of the discharge process is caused by the temperature control process of the cooling system.

The following advantages can be observed from the test with scraper movement (Fig. 3).

1. By stirring the hot salt, the heat transfer rate is higher than without, as long as the salt temperature is above the phase change temperature because of convection and delayed beginning of solidification. The higher heat flow in the first 45 minutes clearly proofs this statement.
2. With scraper movement, the temperature in the liquid PCM-volume reaches the phase change temperature of 306 °C after 56 minutes. Without scraper this temperature is reached only 17 minutes later.
3. Once the whole storage is at phase change temperature, the scraper movement is controlling the thickness of the solidified layer on the heat exchanger surface at constant level, resulting in a constant heat flow. This can be well observed in the last one hour of the scraper movement (scraper stopped after approx. 2 h of operation).

It can be observed that the current for scraper movement is still rising, even when there is a constant thickness of the solidified layer on all four heat exchanger surfaces and after approx. 2 hours of discharge operation the scraper movement stops. Due to the heat losses of the storage, PCM also solidifies on the containment walls. Once this layer of solidified PCM at the bottom of the storage unit reaches the front end of the scraper, there is a significant additional load on the scraper. It is assumed, that this load is the reason for the further rising current of the servomotor and that it finally causes the scrapers to stop due to overload.

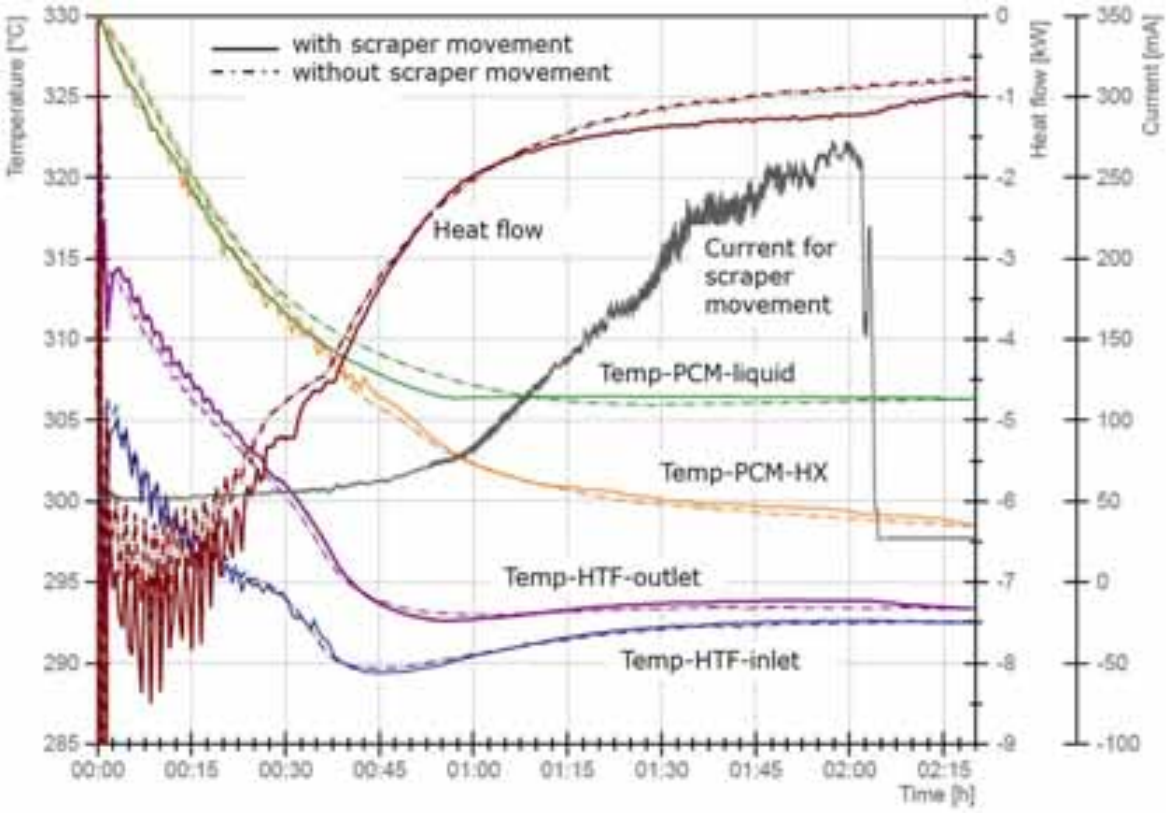

Fig. 3: Comparison of temperatures and heat flow for storage operation with and without scraper movement; current of servomotor for scraper movement.

3.2 Material aspects

In order to minimize the own power consumption of the scraper unit a more detailed knowledge of the properties of the salt is required. For this purpose, various investigations on separate samples and on samples from the storage were conducted.

The force needed to scrape off a layer of salt has been measured at ambient temperature on a sample shown in Figure 4. The sample was molten in the oven in a ceramic crucible and was left in the oven to solidify. The crystal size of the sodium nitrate changes from the surface to the inner part of the sample. On the surface, the first 3 mm have very small crystal size, followed by larger crystals. Inside the sample is a large void and the

salt can be damaged manually. Cooling on the surface occurred faster than inside the probe, therefore the crystals on the outer layer are smaller and less homogenous than inside. Fig. 4 (left) shows a cross section of the sample with the outer layer on top.

For the force measurement, the sample has been prepared with a defined edge (Fig. 4, right). Then a chisel with 6 mm width has been moved along the surface with different depths. Measurements with 0.1 mm and 0.2 mm depth are shown in Fig. 5. Two aspects can be observed. First, the force needed for the first 12 mm is higher than that needed for the second 12 mm section. Secondly, the force doubles, when the thickness of the layer is doubled. The oscillation of the signal is probably due to the inhomogeneous crystal structure.

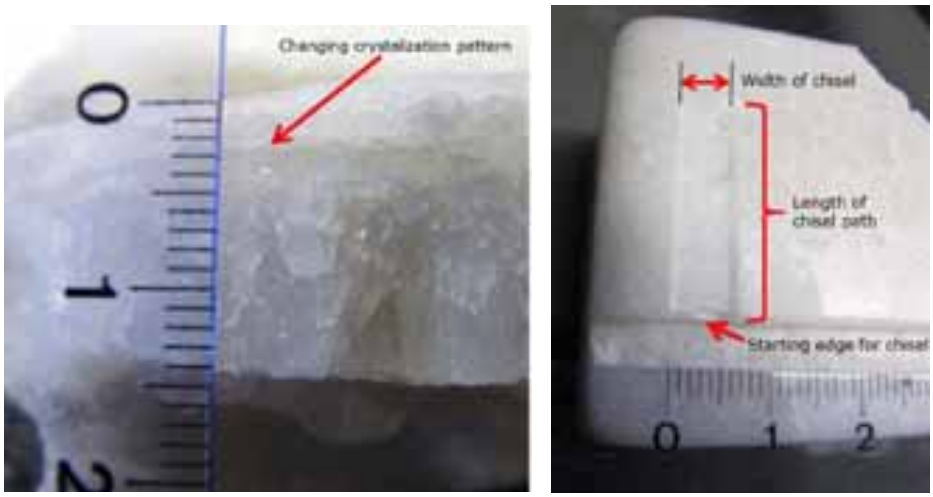

Fig. 4: Sodium Nitrate sample; left: cross section, right: chisel path.

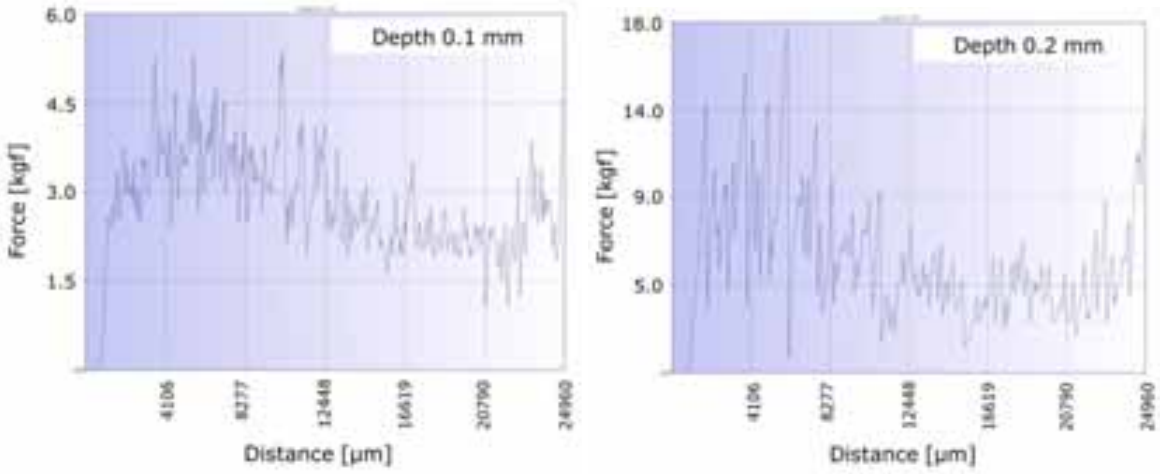

Fig. 5: Load-displacement diagram of Sodium Nitrate sample; left with 0.1 mm depth, right with 0.2 mm depth of the chisel

The examination of the sample as well as samples of the salt from inside the storage unit showed that the cooling rate affects the crystal size (see Fig. 6). As long as the scraper moves, not only a removal of the solidifying salt takes place but also a higher temperature is at the boundary layer between the solid and liquid PCM. As a result of this, the growing of the crystals is slower and it looks more homogeneous. This further improves the heat conduction in the already solidified PCM.

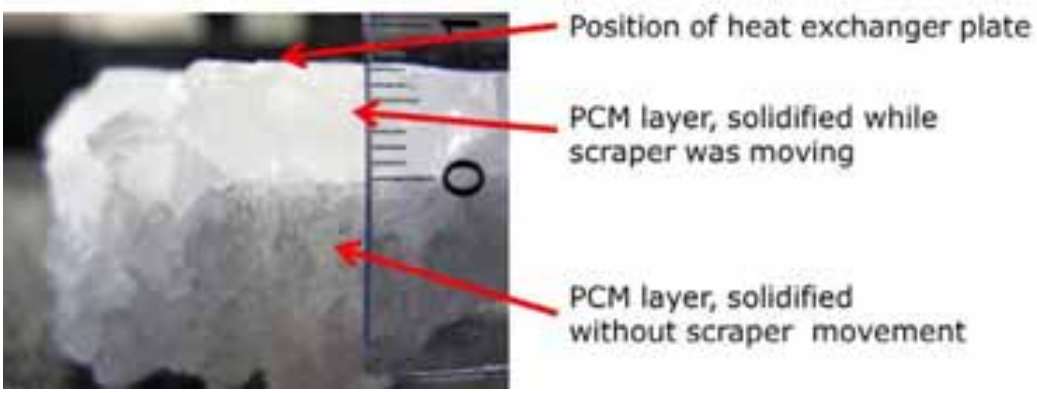

Fig. 6: Sodium Nitrate sample from inside the storage, showing the layer between heat exchanger plate and scraper on the top.

4. Conclusions and Outlook

Feasibility of the concept with moving scrapers was demonstrated, showing advantages of the active over the passive concept. With this first prototype, scraper movement stopped after approx. 2 hours of discharge operation. Due to the heat losses of the storage, PCM also solidifies on the containment walls. Once this layer of solidified PCM at the bottom of the storage unit reaches the front end of the scraper, there is a significant additional load on the scraper, which finally causes the scraper to stop. In the next generation design, the scrapers will be redesigned, to also scratch off the salt freezing at the bottom. The early limitation of the scraper movement did not allow the investigation of the maximum discharge capacity.

The cooling rate has a significant influence on the crystal size. For further design of the scrapers, a better understanding of the required forces is needed. Especially the hardness of the solid Sodium Nitrate close to melting temperature needs to be investigated.

In the second generation design it is intended to combine the electrical heating with the cooling plate to minimize the amount of components and material inside the storage and to maximize the available heat exchanger surface. With this solution, the same heat exchanger surface can be used for charging or discharging. For low temperature applications, using paraffin as phase change materials, first prototypes have been built, using resistance heating foils glued onto the heat exchanger surface. If possible, a smooth surface will be chosen, to allow a very narrow gap between scraper and heat exchanger plate. In addition investigation will be done, if the adhesion between PCM and heat exchanger surface can be reduced by nanotechnology or any other means.

The proposed concept with moving scrapers has the one disadvantage that the storage unit can never be discharged completely when using the scraper. However, it allows for a major advantage, to be able to remove solidified particles during discharge from the heat exchanger unit, while at the same time filling up the unit with liquid salt. During charging, solid particles can be refilled into the unit and liquid salt pumped back into an external storage tank. This concept (see Fig. 7) will allow for separate dimensioning of the heat exchanger unit and the storage capacity. Additional electrical charging can be easily done by immersion heaters in the “hot” tank. This would even allow for a certain power-to-heat buffer when the heat exchange unit is only charged through the heat transfer medium.

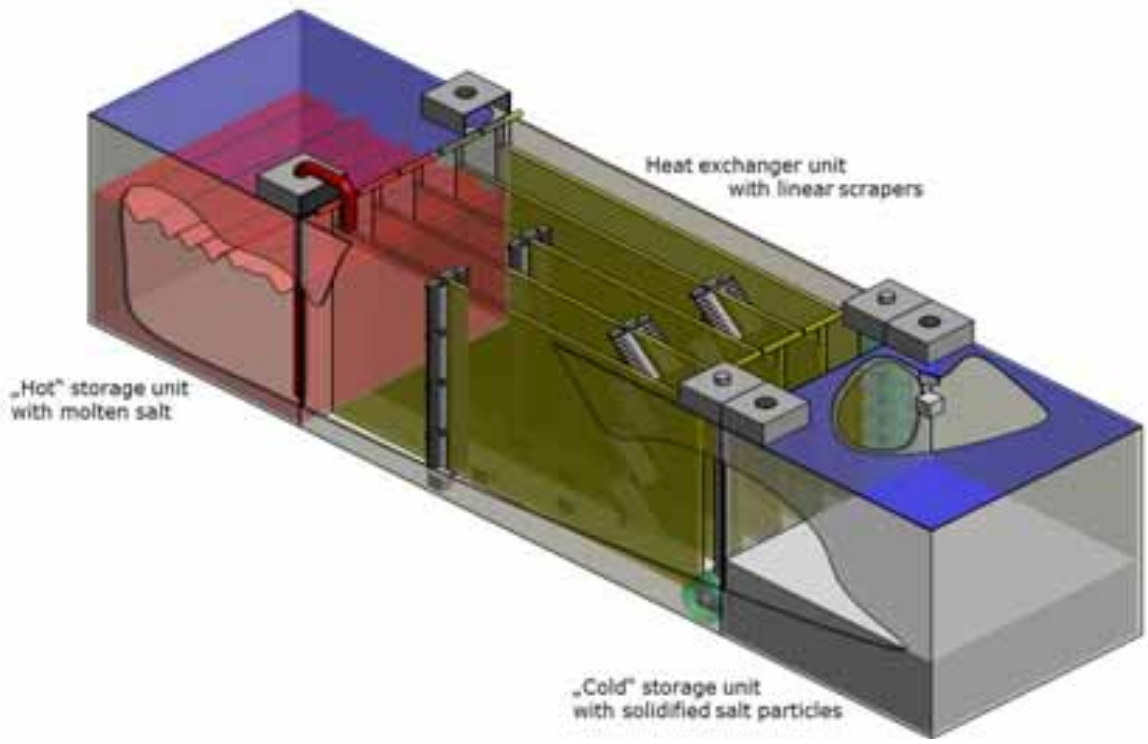

Fig. 7: Principal scheme of the storage concept with separation of capacity and heat rate

The solidified salt that is scraped off by the scraper accumulates on the bottom of the storage tank in fine granular form, due to the higher density of the solid phase. First tests with a manual slider plate showed that the grains can be easily moved to the edge of the storage. A device to remove the solidified PCM grains from the liquid volume, e.g. a conveyor screw, needs to be integrated on one side of the heat exchanger unit.

5. References

Federal Ministry for Economic Affairs and Energy (BMWi). 2014. An Electricity Market for Germany ' S Energy Transition - Discussion Paper of the Federal Ministry for Economic Affairs and Energy (Green Paper).

Laing, Doerte, Thomas Bauer, Nils Breidenbach, Bernd Hachmann, and Maike Johnson. 2013. Development of High Temperature Phase-Change-Material Storages. Applied Energy 109, pp. 497–504.

Laing, Doerte, Ulrich Nepustil, Detlev Lodemann, Konstantin Keil, and Rameesh Sivabalan. 2015. Power-to-heat - Innovative Concept for Latent Heat Storage with Direct Electrical Charging. Proceedings, 9th International Renewable Energy Storage Conference (IRES 2015).

Laing, Doerte, Wolf-Dieter Steinmann, Rainer Tamme, Antje Wörner, and Stefan Zunft. 2012. 特约文章 Advances in Thermal Energy Storage Development at the German Aerospace Center (DLR). Energy Storage Science and Technology 1 (No. 1), pp. 13–25.

Conference Proceedings

Solar World Congress 2015
Daegu, Korea, 08 – 12 November 2015

STEAM BASED CHARGING-DISCHARGING OF A PCM HEAT STORAGE

Asfafaw H. Tesfay[1], Mulu B. Kahsay[1] and Ole J. Nydal[2]

[1] School of Mechanical and Industrial Engineering, Ethiopian Institute of Technology-Mekelle, Mekelle University P.O.box 231, Mekelle, Ethiopia

[2] Department of Energy and Process Engineering, Norwegian University of Science and Technology, 7491 Trondheim, Norway

Abstract

Latent heat storage and efficient heat transport technology helps to utilize the intermittent solar energy for continuous and near isothermal applications. Nonetheless, latent heat storages face challenges of storage charging, heat retaining, and discharging the stored heat. The focus point of solar concentrators is the ideal position to collect maximum thermal power; however, this place is not convenient. Therefore, it is important to transport the concentrated heat from the focus to some place efficiently in order to utilize it safely. This paper addresses the challenges of heat transportation and storage charging-discharging issues. The heat transportation from the receiver over some distance is carried out with a pipe lines and water as heat transfer fluids. However, the charging-discharging process was carried by pipe less method with the help of fins. In addition, the stored heat was retained for a couple of days by using appropriate insulation material. The latent heat is stored in a phase change material (PCM) of nitrate salt (mixture of 60%NaNO3 and 40%KNO3), which melts at 222ºC and has 109 J/g specific heat of fusion. The storage was designed to supply nearly isothermal heat during the liquid-solid phase transition and the sensible heat stored in the solid and liquid form is used to perform additional applications that do not require uniform heat. The low thermal conductivity of the PCM is improved by using extended fins, which enhance the thermal conductivity within the storage. In this article, two-phase loop thermosyphon of steam was used to manage long distance heat transportation between the receiver and the storage. The steam in the thermosyphon flow was restricted to a maximum working temperature of 250ºC. Steam is selected for its highest heat capacity, easily availability and stable nature. The steam carries the heat from the collector focus point and condenses in a coiled pipe imbedded in aluminum plate placed on top of the storage. Many fins have solidly attached to this plate to conduct this heat down to the PCM inside the storage during charging. This design configuration avoids pressure development inside the PCM storage. The charging-discharging temperature of the storage is recorded in three zones (top, middle and bottom) of the storage. The experimental and numerical results show the heat transportation, retention and charging-discharging methods are effective.

Keywords: *solar energy, PCM storage, latent heat storage, two-phase thermosyphon,*

1. Introduction

Solar thermal energy can be stored by using sensible heat storage (SHS) or latent heat storage (LHS) using a Phase change material (PCM). The stored heat can be used for different application such as cooking, space heating, hot water supply and etc. Latent heat storage provides higher storage capacity, compact size, and nearly isothermal heat supply. However, SHS such as Rock bed, water, oil etc. are larger storage and have faster temperature decay compared to LHS of the same capacity. These characterstics SHS can be improved by combining PCM material in their design as studied by D. Okello et al. [1].]. Latent heat storage using phase change materials (PCMs) can be designed to have much higher energy storage density than the sensible heat storage [2].

doi:10.18086/swc.2015.02.06 Available at http://proceedings.ises.org

Generally, PCMs have low thermal conductivities and took longer time of charging [3]. A number of methods have been proposed to increase the thermal conductivity of PCMs [4]. The finned tube configuration [4], metal structure insertion into the PCMs [4], and dispersion of thermally conductive nano or micro particles within the PCM matrix [4] are some of the widely studied approaches. In addition to thermal conductivity, mass flow rate and inlet temperature of the heat transfer fluid (HTF) has also affected the charging-discharging process [5]. PCM charging-discharging process can be improved by designing multi stage storages with different thermo physical properties [6]. Furthermore, it can be improved by using fast flowing HTF instead of slow flowing HTF [7]. On the other hand, there is a pressure build-up concern associated with PCMs due to the expansion of air at elevated temperatures and due to volume change of PCMs. The design of this paper has tried to avoid any possible contact between the HTF and PCM and possibilities of pressure buildup by providing a 10% extra volume.

The objective of this paper was to develop thermal energy storage to store the surplus solar energy during the day and keep it for later use by supplying nearly isothermal heat during discharging. To realize this, two-phase closed loop thermosyphon based heat transfer was used to charge the PCM storage. This design provides threshold height difference between evaporator and condenser of the thermosyphon loop to initiate natural circulation by density difference. Two-phase closed loop thermosyphon was selected because it is capable of transferring heat from a heat source to a separate heat sink over some distance [8]. This heat transfer mechanism is used in many applications such as nuclear cooling and electronic cooling [9]. However, this method of charging thermal storage has rarely employed in small-scale applications such as cooking. The prime objective of this study has focused to give solutions to the alarming deforestation, energy poverty, and related ecological impacts of developing countries associated with cooking. The cooking application experiment of this paper's design has documented in an accompanied paper submitted and presented in parallel by the authors.

2. Materials and Methodology

The methodology followed in this study includes identification of appropriate PCM material that has a solid-liquid phase transition temperature of 222ºC, storage design, thermal analysis, modeling and simulation, prototype development and test.

2.1. Phase change material

The PCM used in the experiment of this study was 20 kg of solar salt (nitrate salt mixture 40% KNO_3 and 60% $NaKO_3$). For computational simplicity, the latent heat was described in terms of an effective heat capacity in a narrow temperature range of melting [10].

$$Q = \int_{T_i}^{T_f} mC_p \mathrm{dT} \tag{1}$$

$$C_P[kJ/kg] = \begin{cases} 0.75 & T < 110^0C \\ 4.2 & 110^0C \le T \le 120^0C \\ 1.4 & 120^0C < T < 210^0C \\ 12 & 210^0C \le T \le 220^0C \\ 1.6 & T > 220^0C \end{cases} \tag{2}$$

2.2. Storage design

The PCM storage is designed to be charged by a two-phase self-circulatig closed loop heat carrier, a polar mounted parabolic dish with sun tracker, a fixed receiver was designed to act as an evaporator and an aluminum casted plate with extruded fins down to the PCM was placed on top of the storage. The heat transfer fluid used was water and the receiver converts this water in to steam. Figure 1 shows a schematic and actual picture of the system.

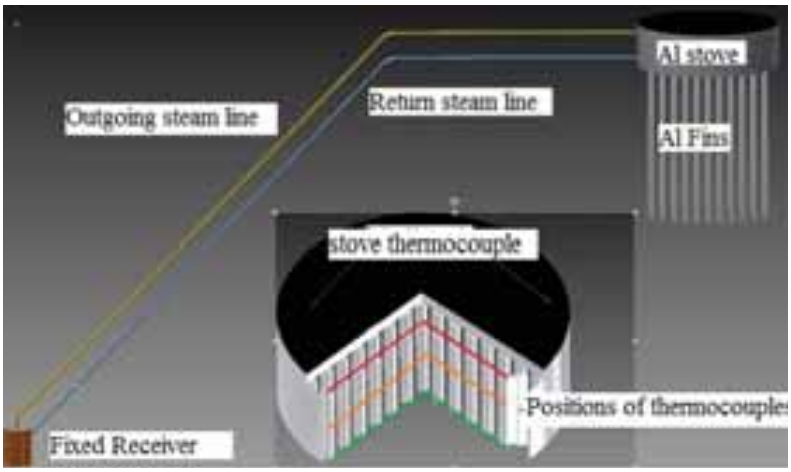

(a)

(b)

Figure 1: Design and development process of a PCM storage

The Al plate has an embedded stainless steel (SS) steam pipe that acts as heating element. The heat storage was coupled to parabolic dish filmed with 5cm glass tiles. The polar mounted technique of the concentrator's design gave a suitable platform for the fixed receiver. This concentrator is coupled to PCM storage with a thermosyphon loop. The system was tested on a real sun and artificial heating to charge the storage. In this experiment mainly K-type thermocouples, pressure gage, and photo sensors were used to measure temperature distribution, regulate steam pressure and control the tracking mechanisms of the system respectively.the complete list of items is given in Table 1.

Table 1: system instruments and sensors

Label	Description	Label	Description
A	Pressure relief valve	F	Inlet, out let and directional control valves
B	Pressure gauge	G	DC Power regulator
C	Tracking sensor	H	Parabolic dish reflector
D	Sprocket and chain drive	I	Data logger
E	DC motor	J	Thermocouples

2.3. Heat transfer mechanisms

PCM storage charging with hot water or oil utilizes the medium's sensible heat capacity, in which the amount of energy released per unit volume is relatively small. However, charging with saturated steam employs the latent heat released during its phase change. The condensate exits the PCM storage at temperatures close to the inlet steam temperature. The thermosyphon loop was first flushed to free any trapped air and filled 2/3 of its volume with water. There is no expansion tank in this loop design. A boiling-condensing mode of heat transfer technique was followed to transport the heat from the receiver to the storage. Theoretically, the mass flow rate of the fluid circulating in the loop can be found by conducting a momentum balance around the loop [11] and the heat transfer in the imbedded pipe is treated as film condensation in nearly horizontal pipes.

The mode of heat transfer between the stainless steel pipe and aluminum block is treated as a pure conduction

between composite solids as shown in Figure 2. This heat was analyzed using Fourier's conduction equations (3-5).

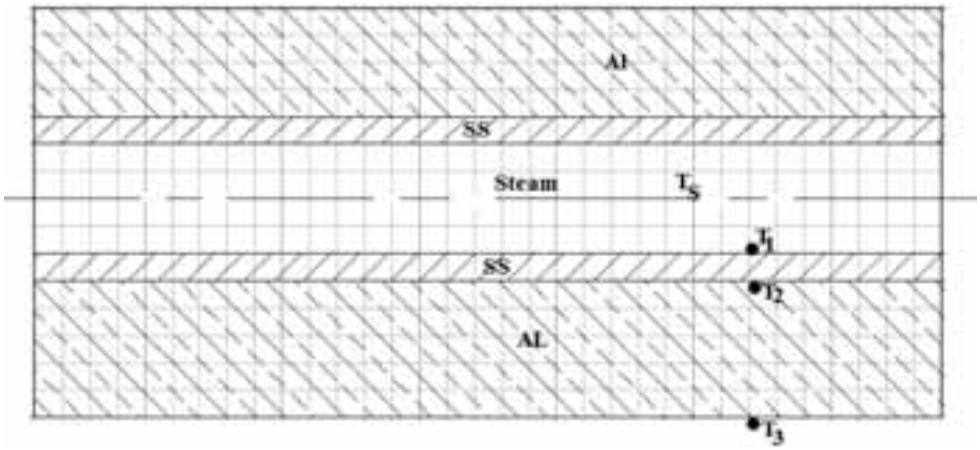

Figure 2: Composite materials of aluminum and SS

Assuming small pipe wall thickness (L) compared to pipe diameter:

$$\dot{Q}_{cond} = -kA\frac{dT}{dx} \tag{3}$$

$$\frac{\dot{Q}}{A}\int_0^L dx = -\int_{T_1}^{T_2} kdT \tag{4}$$

If the small variation of k is ignored the equation simplifies in to:

$$\dot{Q} = \frac{kA}{L}(T_1 - T_2) \tag{5}$$

Where $\frac{L}{kA}$ is the thermal resistance of the material

The overall thermal resistances of composite wall are treated in the same way as total series resistance of electric circuit. Assuming 2D geometry for simplicity: the fin and the plate temperature progress is the same and change in area (A) and thermal conductivity (k) with temperature is negligible, T_3 (fin temperature) was then calculated by:

$$T_3 - T_1 = \dot{Q}\left(\frac{L_{SS}}{k_{SS}A} + \frac{L_{Al}}{k_{Al}A}\right) \tag{6}$$

In a heating plate temperature-time profile, the analysis of the heat transfer rate from the heating plate (frying pan) to the fins and from the fins to the PCM was analyzed using eq. (7 and 8) respectively [11].

$$\dot{Q}_{p,f} = \frac{T_p - T_f}{R_{P,f}} \tag{7}$$

$$\dot{Q}_{f,PCM} = \frac{T_f - T_{PCM}}{R_{f,PCM}} \tag{8}$$

Theoretically, the temperature development of the fin is found by using eq. (9) and the heat transfer rate from the fin at temperature,T_f, to the PCM at temperature,T_{hp} , in the storage must equal to the heat transfer rate from the plate to the fin as shown in eq. (10).

$$\frac{dT_f}{dt} = \frac{\dot{Q}_{P,f} - \dot{Q}_{f,Pcm}}{m_f c_{v,f}} \tag{9}$$

$$\dot{Q}_{f,\mathrm{PCM}} = \frac{T_f - T_{PCM}}{R_{f,PCM}} = \dot{Q}_{P,f} = \frac{T_P - T_f}{R_{P,f}} \tag{10}$$

On rearranging of eq. (10), the PCM temperature simplifies to eq. (11). Figure 3 shows the COMSOL mesh of the PCM material adjacent to the fin.

$$T_{PCM} = \frac{T_f R_{PCM,f} + T_f R_{f,\mathrm{PCM},}}{R_{P,f} + R_{f,PCM}} \tag{11}$$

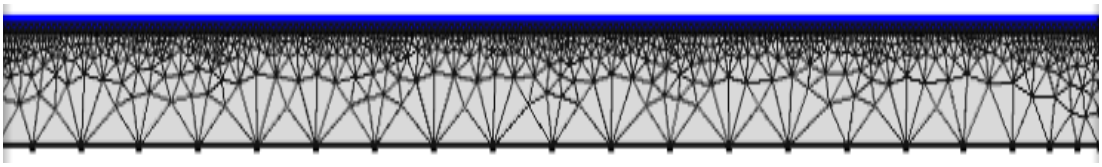

Figure 3: Mesh of PCM material during conduction charging

2.4. Thermal performance

The thermal performance of the system is given by the ratio of the useful energy stored to the energy incident at the concentrator's aperture. The storage energy is the sum of the energy stored in the PCM and in the aluminum fin. Therefore, the thermal efficiency of the system is computed by:

$$\eta_{th} = \frac{c_{Al} m_{Al} (T_f - T_i) + m \int_{T_i}^{T_f} c_p dT}{A_a I_B} \tag{12}$$

Where cp is the effective heat capacity of the PCM (eq.2)

Both normal and diffuse radiation enters the aperture area of any solar collectors. However, in concentrating collectors only the direct radiation can be focused on the receiver. In this paper, the thermal analysis of the system was performed only for its solid phase sensible heat-storing ability as it was not fully charged. The systems developed here reached 157°C of maximum temperature during the experiments of this study. Therefore, the thermal performance during these days was calculated 19%. The performance of the system was affected mainly by the heat loss from the receiver.

2.5. Insulation

Aerogel and Rockwool insulations were used to insulate the storage and the steam pipelines respectively. Although the insulations maximum working temperature is about 650°C, the maximum working temperature of the systems' was set to 250°C (by adjusting the pressure relief valve) and the design thickness of the insulation is 25mm for the storage and 50mm for the pipeline. The insulations thermal conductivity is 0.03W/Km and 0.07 W/Km respectively and they have the same surface emissivity of 0.05.

2.6. Pipe lines

The size of the steam pipeline was 10mm and 8mm with 1mm thickness. The SS pipe is used as a pipeline in the heat transfer loop and as a heating element of the Al plate respectively. The pipe has 100bar design pressure and was used for 40bar working pressure. The pipeline used Swagelok connectors and valves. A pressure gage is used to measure the pressure of the steam and regulated with the help of a safety valve that reliefs the pressure when it passed the pre-set value (40bar). The pipeline was flashed before the beginning of experiment to avoid air inclusion.

3. Results and discussion

3.1. Modelling and simulation

The storage charging process has simulated using COMSOL multiphysics 4.3. The simulation work was run for 2D and 3D models. The simulation results showed the storage is fully charged in about seven hours, when it is heated by a 250°C continuously circulating steam. The simulation considers a constant loss of 15°C from the storage. For model simplicity, the fin in the COMSOL simulation used in Figure 4 (a-c) has considered circularly rolled plate fins instead of the many cylindrical fins in the actual prototype. This fin assumption has an impact on lowering the overall charging time of the storage. The simulation shows the charging of the PCM sanduched between two fins is very quick as shown in Fig. 10(c), however, the PCM adjacent to the storage wall and bottom changes its phase very slowly. This simulation result suggests to half the dimension of the gap between the fin and the storage wall and bottom. Therefore, the PCM thickness between the fin and the wall and between the fin and the bottom should be 20mm. Moreover, it was found rolled plate fins charge the PCM quicker than rod fins. In addition to the PCM charging development, the simulation has also run to show the thermal resistance effect of the SS pipe wall on the Al plate as shown in Fig. 4(d).

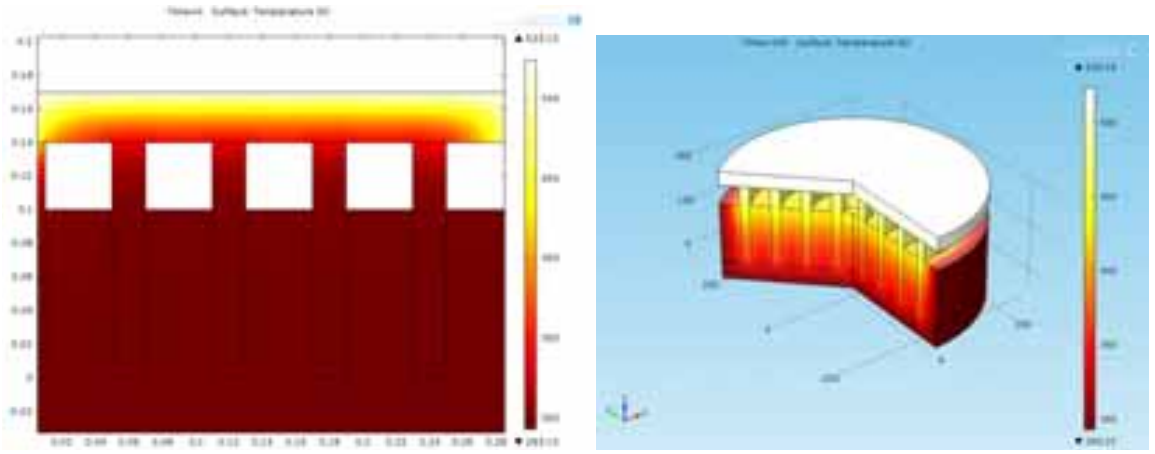

(a) (b)

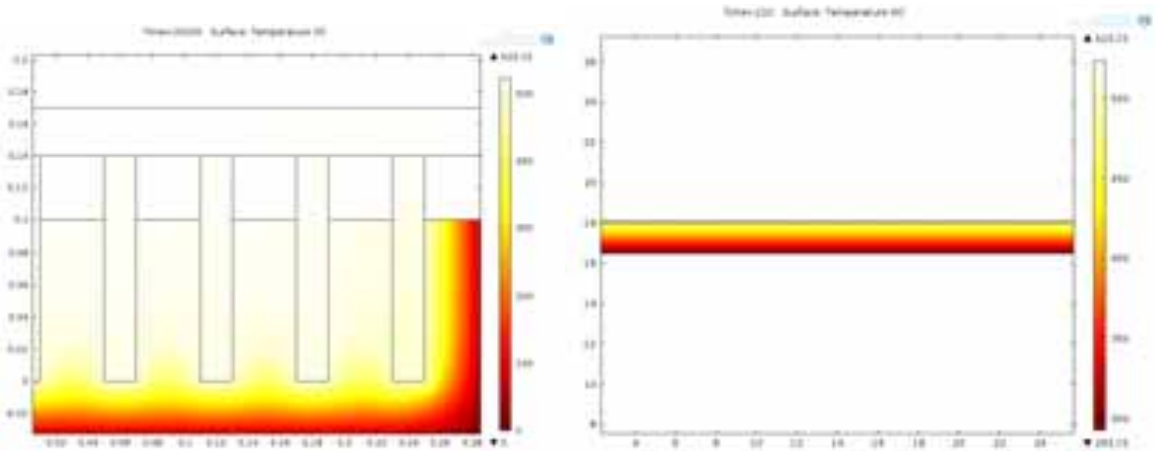

(C) (D)

Figure 4: COMSOL simulation of PCM charging and heat transfer between SS and aluminum wall

3.2. Experimental Test

The polar mounted concept eases the tracking mechanism in the secondary axis and the fixed focus receiver, was found suitable for steam generation. The steam circulates between the evaporator (receiver) and Al plate (condenser) in a closed loop naturally. The steam carries the heat from the receiver and drops it on the

aluminum plate. The fins attached to this plate in return carries this energy to the PCM storage. The test unit of this paper is shown in Figure 5.

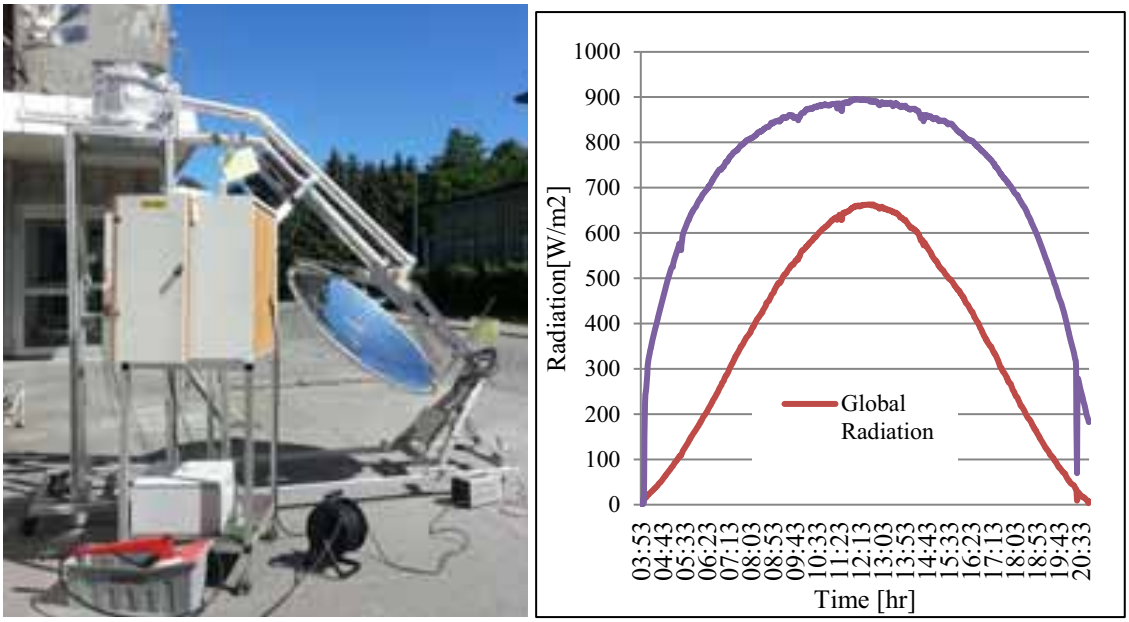

Figure 5: Parabolic dish with PCM storage Trondheim's global and normal beam radiation for 25-07-2013

a) Charging of storage on natural sun

When the solar reflector starts focusing the solar radiation on the receiver, the water inside the receiver starts boiling and a vapor at low temperature starts circulating. The stagnation temperature of this unit could not reach the melting point of the PCM. The storage was tried to be charged in successive days using the advantage of the PCM material's heat retention ability. However, this did not help to charge it fully; this was probably due to the losses at the receiver. The maximum temperature attained in the PCM storage had reached a temperature range of 130°C to157°C as shown in Figure 6.

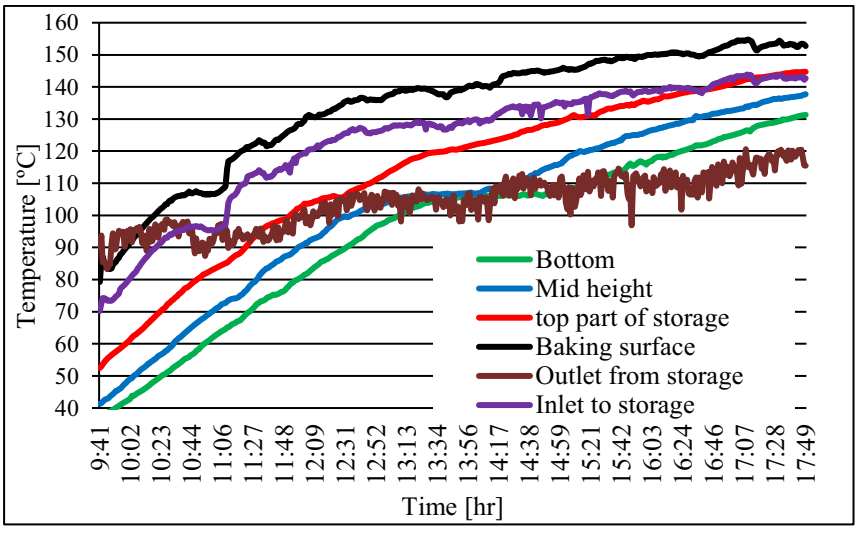

Figure 6: PCM charging practice

b) Charging of PCM storage Artificially

An artificial heating element was coiled around the receiver in order to obtain a regulated temperature at the receiver that is capable of generating steam at elevated temperature, see Figure7(b). The heating element was set to a maximum temperature of 450°C, at which it was delivering an average power of 700W to the receiver.

This power was equivalent to the solar power supply obtained from a 1.2 m parabolic dish concentrator with 80% optical efficiency and $800w/m^2$ average beam radiation. The PCM storage took about eight hours of phase change duration. The temperature development of the steam and the PCM during the charging process are shown in Figure 8.

(a) (b)

Figure 7: Receiver of a parabolic dish collector: (a) solar test and (b) heating element (before insulation)

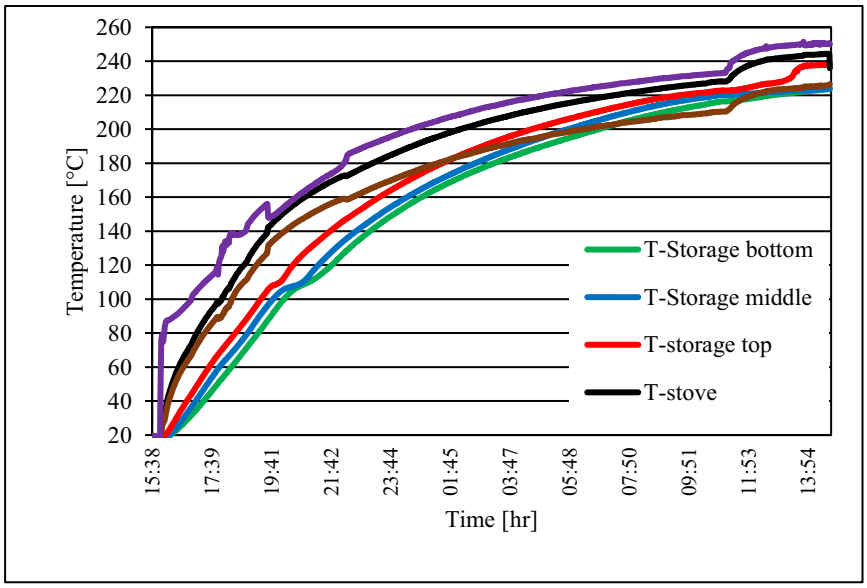

Figure 2: Artificial charging of PCM storage

The experimental result shows a close resemblance to the simulation result of charging time. This indicates the input power at the receiver is small and needs to increase it by using larger aperture area inorder to reduce the charging time.

4. Conclusion

In this paper a concept of steam based heat storage charging by using polar mounted solar concentrator has been developed and demonstrated. Heat is transfer by a thermosyphon principle, with water as the working fluid at about 35-bar pressure. Vapor is generated at the heat absorber in the focus point of the parabolic concentrator and condenses in a coiled tube, which is in Al plate. The plate has heat-conducting rods extending into latent heat storage ("solar salt", Nitrate mixture). A boiling/condensing natural circulation loop (thermosyphon) is feasible with water as the heat transfer fluid. As the water volume is small, the high pressure is manageable but requires high quality pipe and valve components. A boil-off startup procedure is operationally easy. The system can be optimized with respect to losses in the heat transfer loop, in particular

at the absorber. The absorber is a spherical boiler in a fixed position, with the solar illuminated area moving from one side to the other during the daily sun tracking

5. References

[1] Denis Okello , Ole J. Nydal and Eldad J.K. Banda, Experimental investigation of thermal de-stratification in rock bed TES systems for high temperature applications, Energy Conversion and Management, vol. 86; pp: 125–131, 2014.

[2] Kuravi S, Trahan J, Goswami DY, Rahman MM, Stefanakos EK. Thermal energy storage technologies and systems for concentrating solar power plants. Prog Energy Combust Sci, Vol.39; pp: 285–319, 2013.

[3] H.M.S. Hussein et al., Experimental investigation of novel indirect solar cooker with indoor PCM thermal storage and cooking unit, Energy Conversion and Management 49 (2008) 2237–2246.

[4] Tanvir E. Alam, Jaspreet S. Dhau, D. Yogi Goswami , Elias Stefanakos, Macroencapsulation and characterization of phase change materials for latent heat thermal energy storage systems, Applied Energy 154 (2015) 92–101

[5] Abduljalil A. Al-Abidi et al., Experimental study of melting and solidification of PCM in a triplextube heat exchanger with fins, Energy and Buildings, Vol. 68; pp: 33–41, 2014.

[6] Taha K. Aldoss and Muhammad M. Rahman, Comparison between the single-PCM and multi-PCM thermal energy storage design, Energy Conversion and Management, vol. 83; pp: 79–87, 2014.

[7] Robynne E. Murray and Dominic Groulx, Experimental study of the phase change and energy characteristics inside a cylindrical latent heat energy storage system: Part 1consecutive charging and discharging, Renewable Energy, vol. 62; pp: 571-581, 2014.

[8] Alessandro Franco and Sauro Filippeschi, Experimental analysis of Closed Loop Two Phase Thermosyphon (CLTPT) for energy systems, Experimental Thermal and Fluid Science, vol. 51; pp: 302–311, 2013.

[9] Liang Zhang et al., An indoor experimental investigation of the thermal performance of a TPLT-based natural circulation steam generator as applied to PTC systems, Applied Thermal Engineering, vol. 62; pp: 330-340, 2014.

[10] Foong Chee Who, Jørgen Løvseth, and Ole Jørgen Nydal, "Heat Capacity Measurements of NaNO3 – KNO3 Binary System", submitted paper to International journal of Thermophysics, 2011.

[11] R T Dobson and J C Ruppersberg, flow and heat transfer in a closed loop thermosyphon: part I-theoretical simulation, Journal of Energy in South Africa, Vol. 18; pp: 32-80, 2007

Conference Proceedings

Solar World Congress 2015
Daegu, Korea, 08 – 12 November 2015

Design for a Solar Thermal Energy Storage System

Ramón Gutiérrez Razo[1], Bruno Cárdenas Castañeda[1], Noel Leon Rovira[1]

Tecnológico de Monterrey - Centro de Innovación en Diseño y Tecnología, Monterrey, Nuevo León, México

Abstract

The design of a Thermal Energy Storage unit (TES) is shown to use solar energy at times where there is intermittent, shortage or lack of solar radiation. The TES unit is made of five parts: heat reservoir, heat reservoir container, heat receptor – transmitter system, thermal insulator and structural support. The TES unit material's must be abundant, be of common usage in industry, obtained either from recycling or industrial wastes. Also the materials must be non – toxic and non – flammable. Three TES designs will be shown pointing out the opportunity areas found in each one in order to achieve a TES unit with the best performance possible.

Keywords: *Solar energy, Latent heat, glass, TES*

1. Introduction

Fossil fuels domain the market to cover the world's ever growing energy demands [1]. However the extended use of fossil fuels involve environmental consequences, can cause disturbances in the global economy to sudden shortage or surplus of fossil fuels, and at one time these kind of fuels will end. Renewable energies can be a solution to the dependency of fossil fuels. Renewable energies are at the time in development, the initial investment can be high and use to be intermittent.

Currently there are solar concentration systems such as solar power towers and parabolic trough for storing heat in molten salts. However these systems require large areas of land for installation and complex piping and pumping system to withstand temperatures from 300°C to 500°C besides the corrosion caused by the salts. Both systems also require an active tracking of the sun throughout the day which increases the cost and complexity of the system [2, 3].

Solar energy has the characteristic of being abundant and clean, however the development of technologies that exploit this resource have high investments and are still under development. A disadvantage of solar energy is to be intermittent, available only in daylight and depend to weather conditions. In order to solve the aforementioned problem TES units have been developed so that solar energy can be used during periods when solar radiation is not favorable or not present.

Research of a concept of electric and mechanical energy generation has been made by the usage of stored thermal energy from the concentration of solar radiation. The search of material of common usage in industry, recyclable, or from industrial waste has been priority in the design of TES units in order to reduce costs and promote the use of solar energy.

The TES unit requires materials with good thermal conductivity, high energy density per unit of volume and mass for the heat reservoir; in the zone where energy is inserted and extracted the materials require high temperature resistance and good thermal conductivity, besides good solar radiation absorptance for the energy receptor zone; for the materials to be used as heat reservoir container and thermal insulator in order to decrease the reservoir container temperature as close to room temperature requires low thermal conductivity and high temperature resistance.

All material must be non-toxic, and non – auto ignitable at the working temperature of the TES unit.

As a first approach the research aspire to design a TES unit to supply 20 kWh of electric energy. This electricity consume is the average consume of each domestic user in Mexico.

doi:10.18086/swc.2015.02.07 Available at http://proceedings.ises.org

2. Experiment

For the development of the TES unit finite element method simulations by computer and experimental tests have been made. The finite element method takes into account the variation of the thermal conductivity and specific heat values according to changes in the temperature of the material. Three different designs of TES units will be shown pointing out the most relevant results and the opportunity areas found.

The three TES units have in common the usage of soda lime glass as a heat reservoir obtained from wastes; all the TES units use graphite obtained from industrial wastes as the energy reception – extraction system; the three heat reservoir containers are made of alumina; the thermal insulator in the three units is made of ceramic fiber and the external container is made of steel A – 36. The last three aforementioned materials are of common usage in the industry and of lower cost compared with other options.

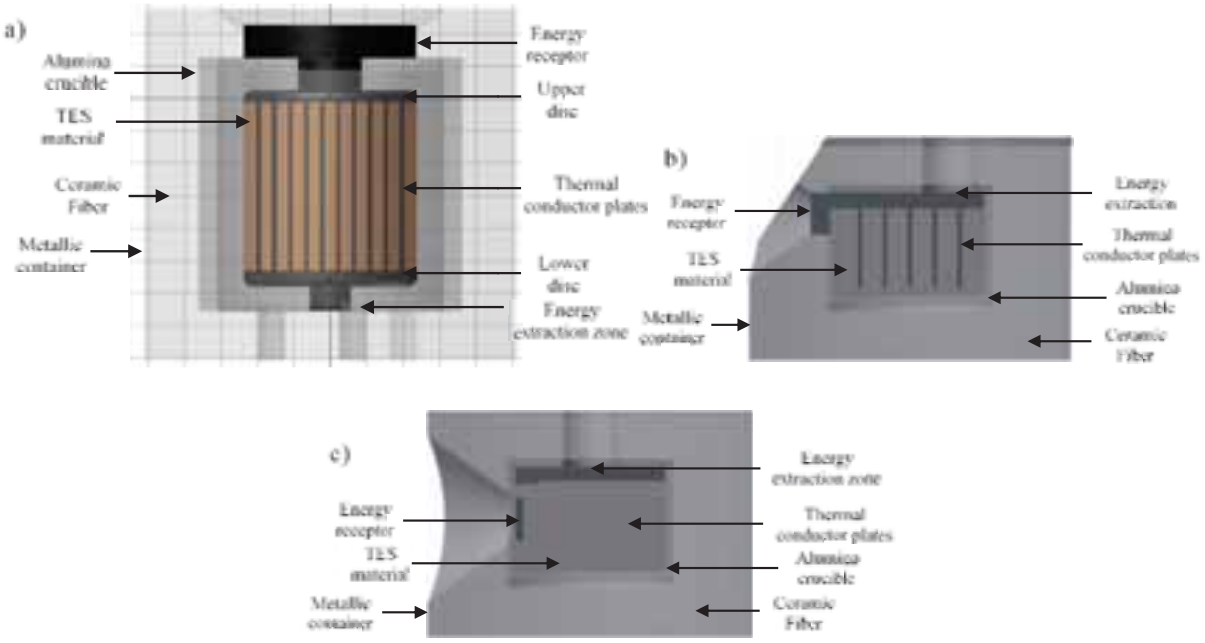

Fig. 1: TES designs. Each grid represent 4inches (around 10 cm.) The three TES drawings are at the same scale for comparative reasons.

Soda lime glass selection as a heat reservoir was based on having a good heat capacity per unit of mass. Graphite was chosen as a thermal receiver - transmitter based on its working temperature which is around 2500°C and 3000°C whenever it is protected from an oxidizing atmosphere [4], and having a good heat conductivity. Both materials share the characteristic of being abundant, and can be obtained from waste or recycled materials.
The A TES design was built and experimental tests were run. With the results obtained in the design A designs B and C were made in order to solve the shortcomings in the performance of this first design. Finite element method analysis of the TES units B and C were made in order to show the improvement in latter TES design compared with previous ones.
Designs B and C were made with 62% and 55% of the heat reservoir mass of the Design A respectively with the intention of get experimental test quicker. Designs B and C have in common the diminishing in weight and number of components of graphite and have the energy receptor as close as possible to the heat reservoir.

Tab. 1: Volume and mass of the heat reservoir of the TES units

Heat Reservoir	Volume [m³]	Mass [Kg]
Design A	0.06949	173.725
Design B	0.04303	107.575
Design C	0.0385	96.25

In the design B the thermal conductor plates made of graphite are at 90° of the direction of the incoming heat flux from the energy receptor, in the design C these plate are in the same direction of the incoming heat flux. In the

design B the energy receptor is in the upper part of the TES unit and connected to the heat reservoir by an area equivalent to the third part of the energy spot, in the design C the energy receptor is at the middle of the TES unit and is slightly inside of the heat reservoir container connected to a graphite plate non – existent in the design B.

The TES unit is designed to be connected to a Stirling Engine with a capacity of 1 kW and with a thermal efficiency of 0.25. The Stirling Engine needs a temperature of 500°C or more to operate.

For the computer simulation the Autodesk Simulation Mechanical 2014 software was used.

The following mathematical models were used to take into account the changes in the specific heat and thermal conductivity values as the temperature fluctuates.

$$C_p = 2.268 - 10.153 \times 10^{-6}T - 377.70014T^{-1} - 181791.8712T^{-2} + 6.66548856 \times 10^{7}T^{-3} - 6.011905920 \times 10^{9}T^{-4} \left[\frac{J}{g-K}\right] \quad \text{(eq. 1)}$$

$$k = \frac{418.4}{2.4 + 3.46 \times 10^{-3}T + 8.5 \times 10^{11}e^{-8.9\times10^{4}/T}} \left[\frac{w}{m-K}\right] \quad \text{(eq. 2)}$$

$$C_p = 9.474 \times 10^{-15}T^5 - 3.923 \times 10^{-11}T^4 + 6.221 \times 10^{-8}T^3 - 4.746 \times 10^{-5}T^2 + 1.814 \times 10^{-2}T - 1.833 \left[\frac{J}{g-K}\right] \quad \text{(eq. 3)}$$

$$k = -1.413 \times 10^{-14}T^5 + 6.083 \times 10^{-11}T^4 - 3.120 \times 10^{-8}T^3 - 2.853 \times 10^{-5}T^2 + 2.512 \times 10^{-2}T - 3.668 \left[\frac{w}{m-K}\right] \quad \text{(eq. 4)}$$

The specific heat of the graphite model was obtained by the fitting of two mathematical models [1]. The specific heat graphite model is useful in the range of 200K to 1000K, however the model can be expanded to temperatures of 3270K where the specific heat value almost stabilize (Eq. 1). For the thermal conductivity graphite model it was used a mathematical model made by N.S. Rasor and J.D. McClelland [8] and is useful in the range of 300K to 3270K (Eq. 2). It is assumed that the graphite used is of commercial grade quality and with isotropic properties.

The soda – lime glass store thermal energy as sensible heat. In the industry of soda – lime glass it is considered a value of 2550 kJ to bring 1 kg of soda lime glass to a working temperature [9]. The specific heat of the soda – lime glass model shown in the following section is useful in the range of 270K and 1350K (Eq. 3) [1] for higher temperature values a constant soda lime glass Cp of 1.4 kJ/kg-°C was used in the simulation. The thermal conductivity of soda lime glass model was created by the fitting of three mathematical models (Eq. 4) [1], this model is useful in the range of 270K to 1580K, for higher temperature values a constant soda lime glass thermal conductivity value of 82.4 w/m-°C was used in the simulation [6]. In the figures 2 and 3 are shown the values of the specific heat and thermal conductivity values respectively. More information about the values taken into account in the simulation for the refractory concrete, ceramic fiber and A-36 steel can be found in [6] and [13].

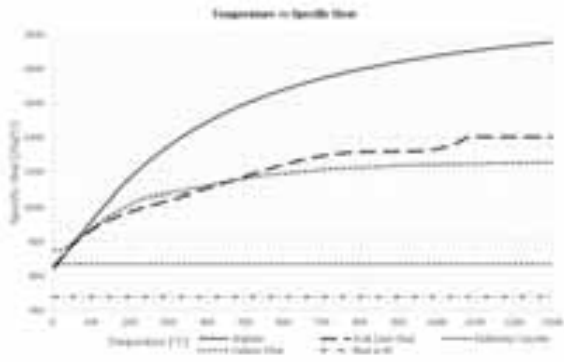

Fig. 2: Temperature vs Specific Heat

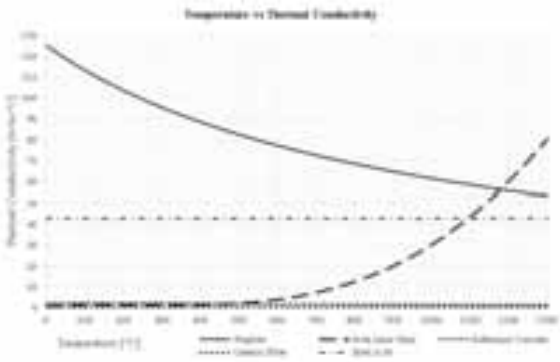

Fig. 3: Temperature vs Thermal Conductivity

Tab. 2: Material density values

Material	Density [Kg/m³]	Reference
Graphite	1700	[1]
Soda Lime Glass	2500	[1]
Refractory	2630	[10,11]
Ceramic Fiber	96	[12]
Steel A - 36	7850	[13]

A finite element method of the design B and C was made for 10 days of operation. Each TES unit will receive 5.625 kW at the energy receptor zone daily by 8 hours receiving a total of 45.0 kWh (Charge cycle) followed by 16 hours of zero entry and extraction energy (Rest cycle). The energy receptor spot had a value of emissivity of 0.95 during the charging periods and a value of zero during the rest of the day. A convection coefficient of 3.22 w/°C-m² was used over the exterior of the TES unit. At days 9 and 10 an extraction of 4.0 kW of heat over the extraction zone was applied. (Heat extraction cycle).

The central point of the energy receptor and extraction zone was taken in the finite element method simulations of the designs B and C and was assumed that the whole zone had a similar temperature. Using the Stephan Boltzmann Black Radiation (Eq. 5) [14] model for black body at the energy receptor zone was possible to calculate and estimate for the radiation heat losses. Checking at the time that the energy extraction point was above 500°C was possible to estimate how much energy was extracted by the Stirling engine.

$$Q_{RadLosses} = \varepsilon\sigma A(T_S^4 - T_{Amb}^4) \qquad \text{(eq. 5)}$$

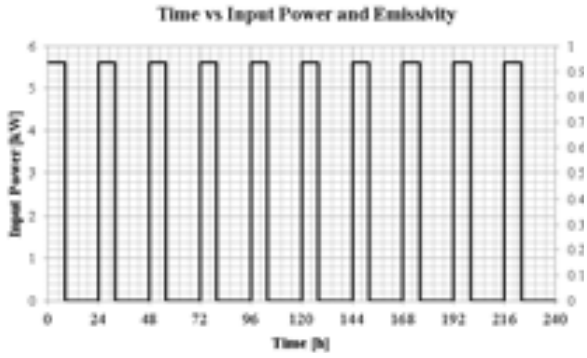

Fig. 4: Time vs Input Power and Emissivity

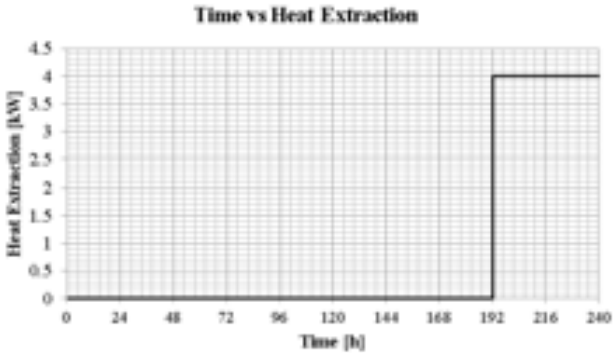

Fig. 5: Time vs Heat Extraction

All the nodes of the finite element method model started with a temperature of 20°C, the room temperature is also the same. The 10 days of simulation were divided among 1000 steps, each step represents a time of 14.4 minutes. The Autodesk Simulation Mechanical 2014 software at the end of the simulation assign a temperature for each node that compose the model. The nodes form brick, pyramidal, tetrahedral and wedges elements. Knowing the volume and density of each element can be obtained the mass. With the mass information and with mathematical models from the C_p of each material can be obtained the change in the energy stored or released.

3. Results

The solar concentrator was unavailable at the time of the A design construction, a gas furnace was built over the energy receptor. It was found that the graphite exposed at a temperature of 400°C and higher in contact with the air oxidize damaging the graphite parts until the whole part sublimates into CO_2 [17]. However, if the graphite is submerged into the heat reservoir the wear of the graphite parts use to be little to non – existent. By means of thermocouples it was found that between the energy receptor and the upper graphite disc was a temperature difference between 140°C and 200°C. This means the presence of a bottleneck to the heat flow between the aforementioned parts [1].

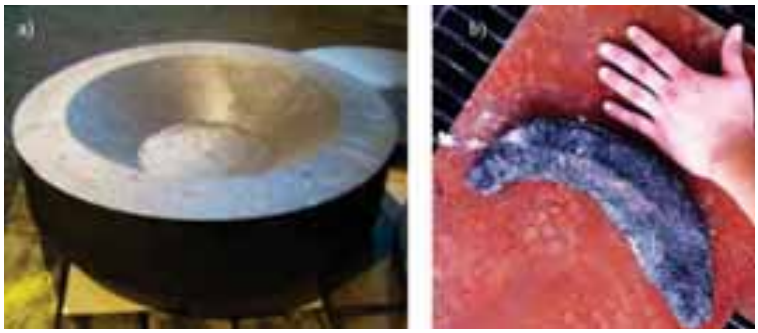

Fig. 6: Energy receptor. a) Before the charge of the TES unit b) After the charge of the TES unit.

Fig. 7: Lower graphite disc after the charge of the TES unit. a) Face of the lower disc pointing inside the crucible in direct contact with the glass melt. b) Face of the lower disc pointing outside of the crucible in contact with the atmosphere.

The TES unit was charged over a period of 6 days and 20 hours, followed this period by 9 days of cooling, with two periods of recharge of 8 hours each during the cooling stage. By using thermocouples and a data acquisition module it was possible to take and record samples of the temperature of the glass melt and the thermal insulation. The glass melt reach an average temperature between 900°C and 980°C at the end of the charge stage; the energy receptor zone reached a maximum temperature of 1200°C and the energy extraction zone reached an estimate maximum temperature of 880°C. During the charge and cooling of the TES prototype there was no device to convert the thermal energy to either mechanical or electrical energy.

Due to the aggressive degree of oxidation the following TES designs tried to diminish as much as possible the graphite parts in size and number and avoid exposing them as much as possible from the atmosphere.

The radiation reception area has a size of roughly 150 cm². In figure 9 can be seen that radiation heat losses through this area are a maximum of 72% for design B and 61% for design C from the total radiation received daily.

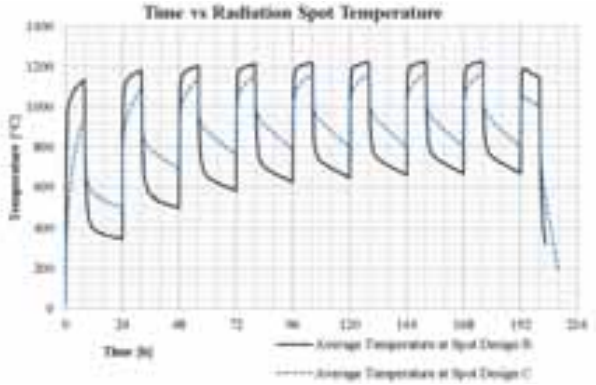

Fig. 8: Time vs Radiation Spot Temperature

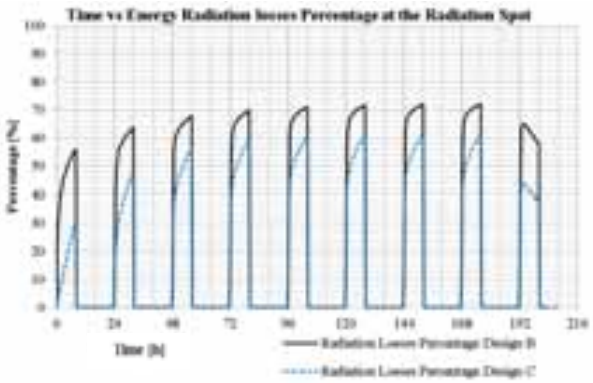

Fig. 9: Time vs Energy Radiation Losses Percentage at the Radiation Spot

The radiation losses during the charging cycle where obtained using the Eq. 5. The temperature of the central point of the energy receptor surface was taken and was assumed to be representative of the whole area. It is known that each day 45 kWh arrive at the energy receptor area. The value of 45 kWh minus the radiation losses is the energy that is stored inside the TES unit.

$$Q_{\text{Stored}} = \text{Daily Solar Energy} - \text{Radiation Losses} \qquad \text{(eq. 6)}$$

With the information from the Table 3 where energy that is stored in each material is known from the finite element method analysis, the net energy can be obtained by subtracting the total energy stored at the end of the charging state minus the total energy value at the beginning of that day.

$$Q_{\text{Net Stored}} = \text{Total Energy}_{End\ of\ Charging\ cycle} - \text{Total Energy}_{Start\ of\ the\ day} \qquad \text{(eq.7)}$$

The absolute energy losses by heat convection during the charging state can be obtained with the following equation.

$$Q_{\text{Convection losses, charging cycle}} = Q_{\text{Stored}} - Q_{\text{Net Stored}} \qquad \text{(eq. 8)}$$

The absolute energy losses by heat convection during the rest stage can be obtained with the subtraction of total energy at the end of the rest cycle to the total energy stored at the end of the charging cycle

$$Q_{\text{Convection losses ,rest cycle}} = \text{Total Energy}_{End\ charging\ cycle} - \text{Total Energy}_{End\ rest\ cycle} \qquad \text{(eq. 9)}$$

In the Figure 10 is shown the temperature in the extraction zone. If the time that the extraction zone is above 500°C is known the total energy that can be extracted from the TES unit can be obtained by multiplying the time with the heat power extracted by the Stirling Engine. The design B and C worked around 12.8 minutes and 4.2 hours respectively. The values of the total energy extracted by the Stirling Engine, the radiation and convection heat losses are shown in the summary of the Table 4.

$$Q_{\text{Extracted}} = Q_{\text{Stirlign Engine Requiered}} * t \qquad \text{(eq. 10)}$$

The Table 3 shows the total amount of energy that is stored in every material that forms the TES units. The maximum and minimum temperature of each material as a sample of how uniformly the temperature is distributed is shown as well. The figures 11 and 12 are the summarized results of the finite element method for the TES design's B and C in order to facilitate the comparison of the amount of total heat stored in the designs B and C and in which materials the heat is stored. All these results will be commented in extend in the conclusion section.

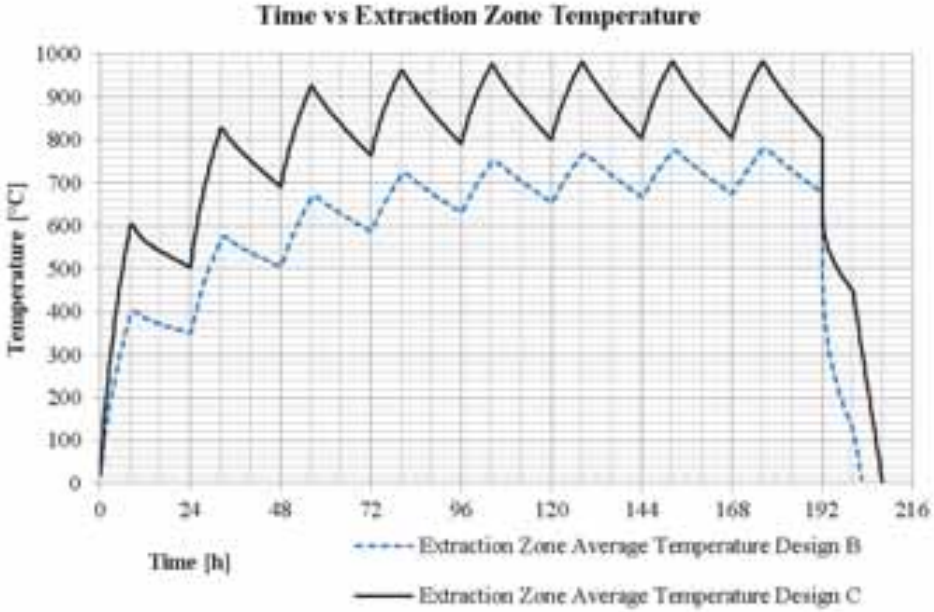

Fig. 10: Time vs Extraction Zone Temperature

Tab. 3: Stored energy in the TES units between day 8 and 9.

		Energy [kWh]		Useful Energy above 500°C [kWh]		Temp Max [°C]		Temp Min [°C]		Temp Average [°C]	
		Design B	Design C	Design B	Design C	Design B	Design C	Design B	Design C	Design B	Design C
Day 8 - Start	Graphite	8.85	11.69	2.61	5.47	674	808	662	800	673	804
	Soda lime glass	20.74	23.08	6.47	10.32	678	808	668	800	675	806
	Refractory Concrete	16.31	19.62	4.65	8.07	678	808	646	759	669	796
	Ceramic Fiber	2.85	2.93	0.13	0.32	670	799	80	46	428	499
	Metallic Container	2.18	0.69	0.00	0.00	209	121	30	52	103	76
	TOTAL	**50.93**	**58.01**	**13.85**	**24.18**						
Day 8 - End of the charging cycle	Graphite	10.28	15.48	4.96	9.27	784	1166	740	944	852	1034
	Soda lime glass	24.91	29.16	10.64	16.41	1002	1051	731	942	784	978
	Refractory Concrete	19.10	24.15	7.44	12.61	1175	1120	691	867	796	968
	Ceramic Fiber	3.24	3.56	0.32	0.66	1224	1024	82	55	500	599
	Metallic Container	2.33	0.85	0.00	0.00	209	148	30	60	111	90
	TOTAL	**59.86**	**73.21**	**23.36**	**38.94**						
Day 8 - End of the rest cycle	Graphite	7.98	11.70	2.66	5.48	678	809	666	800	677	804
	Soda lime glass	20.87	23.10	6.60	10.33	682	809	672	801	679	806
	Refractory Concrete	16.41	19.63	4.74	8.09	681	808	650	759	672	797
	Ceramic Fiber	2.87	2.93	0.14	0.32	673	799	81	46	431	499
	Metallic Container	2.20	0.69	0.00	0.00	211	121	30	52	104	76
	TOTAL	**50.34**	**58.05**	**14.14**	**24.21**						
Day 9 – Until energy extraction zone cool down	Graphite	7.98	10.46	2.66	4.24	678	1026	481	500	714	802
	Soda lime glass	20.60	20.58	6.33	7.82	815	874	549	565	674	728
	Refractory Concrete	16.31	18.10	4.65	6.55	966	962	538	557	670	717
	Ceramic Fiber	2.87	2.64	0.14	0.21	1051	861	81	43	434	451
	Metallic Container	2.20	0.60	0.00	0.00	210	115	30	49	104	68
	TOTAL	**49.96**	**52.39**	**13.77**	**18.82**						

Tab. 4: Energy gain and losses of the TES units design B and C

Summary	Design B	Design C
Radiation losses during charging stage [kWh]	30.79	24.57
Net energy stored during charging stage [kWh]	14.21	20.43
Energy stored at the end of the charging stage [kWh]	8.93	15.20
Heat losses by convection during charging stage [kWh]	5.28	5.24
Heat losses by convection during rest stage [kWh]	9.53	15.16
Total energy extracted by Stirling engine [kWh]	0.85	16.80
Useful energy remained in the TES unit [kWh]	13.77	18.82

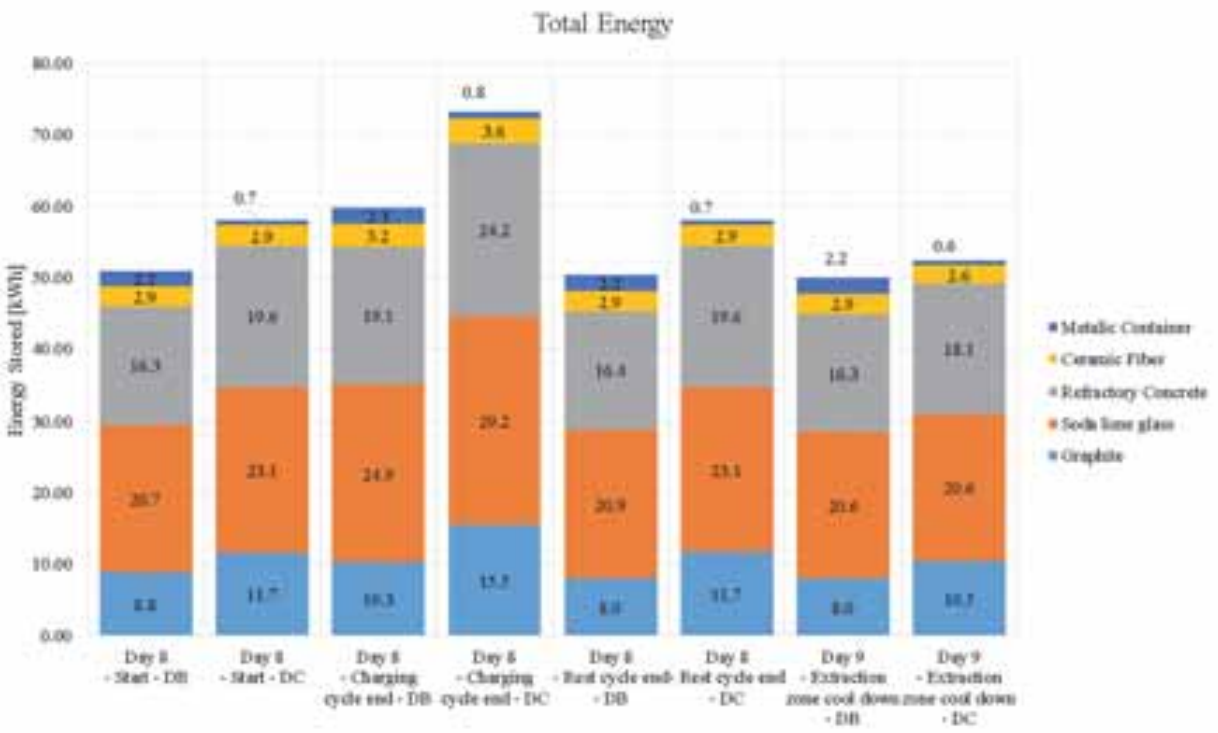

Fig. 11: Total energy stored by material between days 8 and 9 designs B and C.

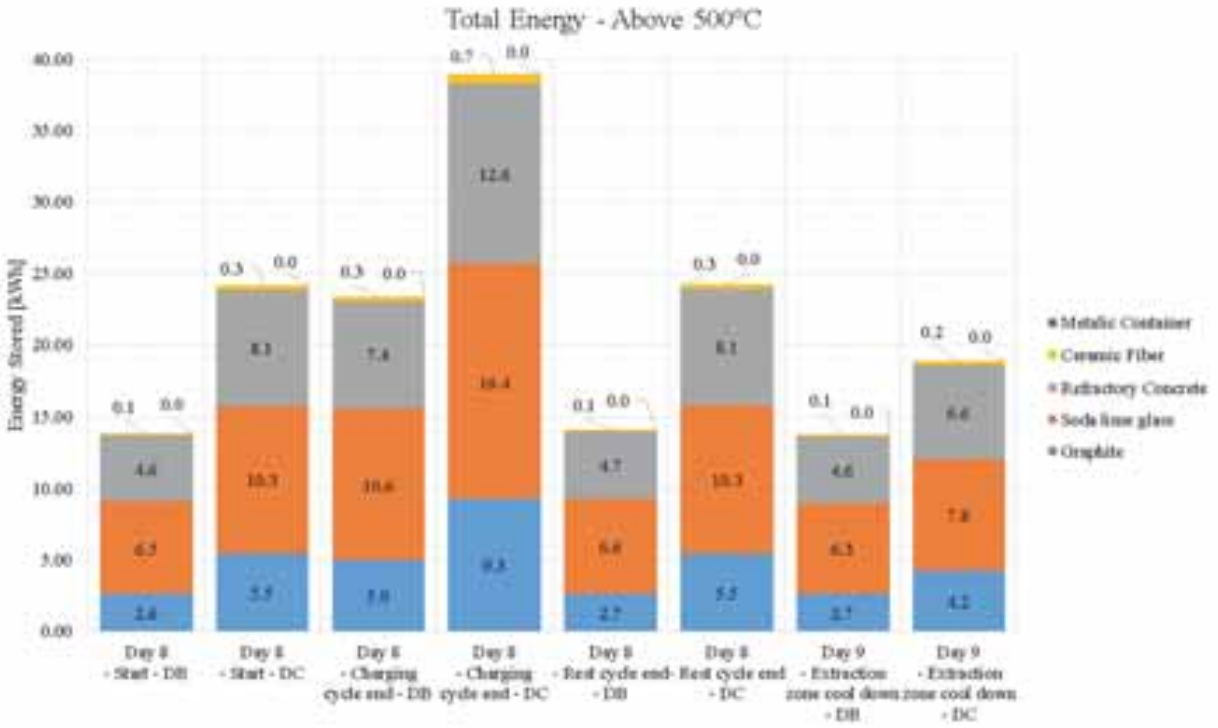

Fig. 12: Total energy above 500°C by material between days 8 and 9 designs B and C.

For the Design B four control points where taken to get an idea about the inside temperature of the reservoir heat body. Point a) and d) were taken because along the simulation they shown the highest and lowest temperature points respectively during the charging cycles. Point b) shown the highest temperature during the rest cycles, during the rest cycles point a) took the lowest temperature values. Point c) shown the lowest temperature values during the energy extraction stage.

For the Design C five control points where taken. Point a) and e) were taken because along the simulation they shown the highest and lowest temperature points respectively during the charging cycles. Point d) and b) shown the highest and lowest temperature during the rest cycles. Point c) shown the lowest temperature values during the energy extraction stage. In the figure 13b all control points are slightly off center of the model cut, just point b) is near the periphery of the crucible base normal to the TES unit cut.
This analysis consist in take the highest and lowest temperature values of the heat reservoir, any other point should lie between these two values. This should be a good approximation of the temperature of the heat reservoir and how well the heat flows through it.

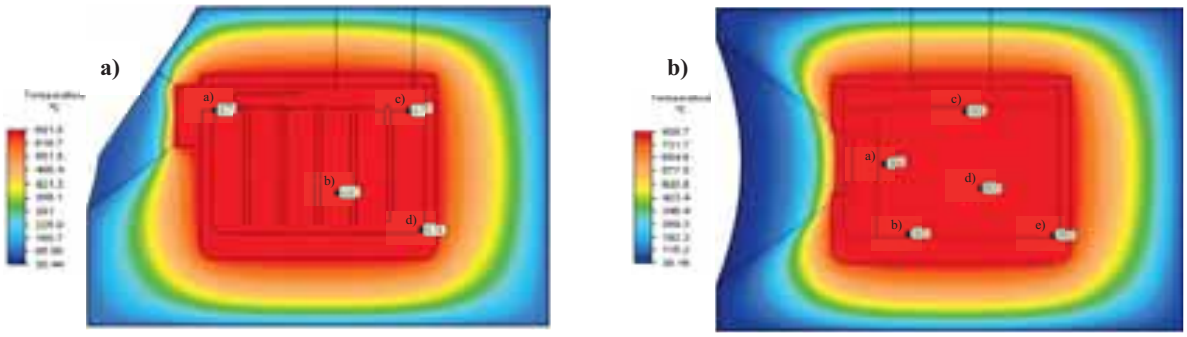

Fig. 13: Heat reservoir temperatures at the beginning of the day 9. a) Design B, b) Design C

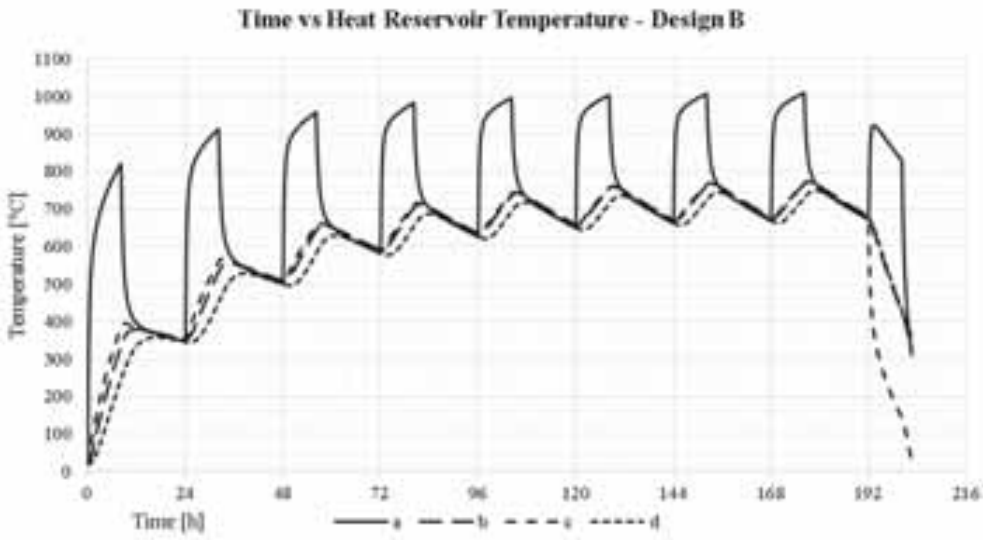

Fig. 14: Time vs Heat Reservoir Temperature - Design B

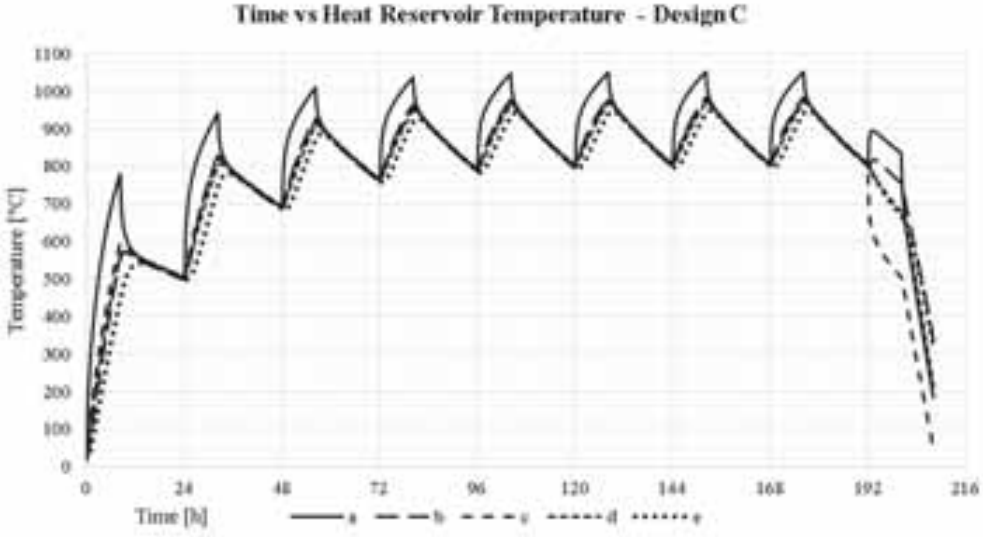

Fig. 15: Time vs Heat Reservoir Temperature - Design C

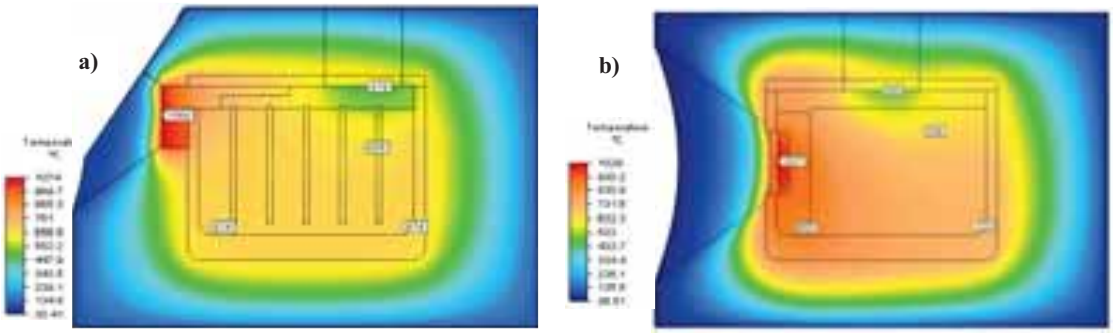

Fig. 16: Temperatures inside the TES unit at the beginning of the day 9 a) Design B after 14 minutes. b) Design C after 4.2 hours.

4. Conclusions

After many days of charging the TES units they reach a cyclical behavior, no matter how many days the system charges. The TES units shown can be consider charged after the day 4 or 5. Any gain in energy from more charge cycles are negligible (Figures 14 and 15).

The energy exchanged between the ambient and the energy receptor represent radiation heat losses from 60% to 70% of the total energy received daily. The design of a radiation cavity is a must to reduce the radiation losses. The view factor from the receptor to the environment was omitted in the equation 5 in order to get a better understanding of the radiation heat losses at their full potential, thus promoting attention to a meticulous research of the design of a radiation cavity in the near future and supporting the idea of adding an additional component to a system that tries to be has simple has possible.

The total amount of heat stored available to conversion in the TES units shown in the Figure 11 is reduced to the values shown in the Figure 12 because it must be above the working temperature of the conversion engine. For the present designs, must be above 500°C.

The design B and C both had useful energy above the 500°C after the extraction zone reached a temperature below the Stirling Engine working temperature, however the thermal conductivity of the soda lime glass is not good enough to transport the useful energy above 500°C along all its mass to the extraction point at the required heat rate.

Increase the temperature of the heat reservoir can enhance the thermal conductivity value of the glass dramatically (Fig 3) in order to increase the heat extraction rate and as a side effect improve the performance of the heat input.

Augment the area of heat extraction can uniformly consume the energy of the heat reservoir body delaying the event of reaching at the energy extraction zone a temperature below the working temperature of the conversion engine.

Shorten the length dimensions in the heat reservoir can improve the speed at which the heat spread uniformly through the heat reservoir.

In the ideal case as the heat flow cross a body mass the temperature should change homogeneously in every point of its lump in a short time, in reality this is not the case. Design C has a better spread of the heat across its heat reservoir body during the charging and rest cycles than the Design B as shown in figures 14 and 15. The sample point in both figures represent the highest and lowest temperature values inside the lump of the glass heat reservoir. In the case of the Design C the graphic lines are closer than those of the Design B. Once the TES units have achieved a cyclical behavior the maximum difference of temperature at the end of the charging cycle of the day 8 are 279°C and 110°C for the designs B and C respectively. A reason why the Design C has a better heat flow through its heat reservoir is that the energy receptor zone is slightly inside the heat reservoir container and is communicated to the inside of the TES unit through a bigger area than in the case of the Design B.
The removal of the bottlenecks between the energy receptor and heat reservoir have a great impact in the performance of the TES unit. Besides the heat flow bottle neck present in the TES unit B design, absent in the TES unit C, the graphite conductor plates in the unit B are perpendicular to the heat flow instead of being in

the same direction as in the TES unit C providing an easier path to the heat flow and increasing the amount of heat being stored inside the TES unit in this last design. The previous reasons explain why the TES unit C store more heat than the unit B.

Once the heat extraction stage begins has seen in the figures 14 and 15 the graph lines of the Design C are closer than those in the Design B. The heat flow through the heat reservoir of the Design C is more efficiently compared to the Design B. As the TES unit C store more heat, higher temperatures are achieved in the glass heat reservoir, this means that the overall glass lump thermal conductivity values will be higher in the TES unit C compared with the unit B. Once both TES units achieve a cycle behavior the glass inside the TES unit B has thermal conductivity values between 6.36 w/m-°C and 10.61 w/m-°C, meanwhile the TES unit C has thermal conductivity values between 12.92 w/m-°C and 28.30 w/m-°C. In the rest stages in designs B and C the temperature tend to homogenize uniformly in a relative short time (Figures 13, 14, 15).

The alumina crucible store a similar amount of energy compared to the main heat reservoir of soda lime glass, however the alumina has a poor thermal conduction value, so extract this energy from the crucible at the desired output power may not by viable.

The combined energy losses by radiation and by convection during the charging stage almost equals the convection heat losses during the rest stage once the system has achieve a cyclical behavior.

Even if the designed TES unit keep using graphite for the receptor and extraction heat system the number and size of these parts have diminished. To protect the graphite from the oxidation at high temperatures in the presence of air strategies like surrounding the graphite parts with an inert atmosphere or covering them with a coating of silica, silicon or silicon carbide are available[15, 16]. The designs B and C keep their graphite parts as close to the core of each design in order to avoid as much as possible the contact of the graphite parts with the atmosphere. The Design C fulfill the aforementioned requirement better than the Design B.

In a general way the TES unit B has a lower performance than the unit C due to physical flaws in its design that hinders the amount of heat rate that can be directed into the core of the TES unit B.

Work on the development of a TES unit that can work 24 hours uninterruptedly is in advance as well as new experimental tests. The research group is currently working on the design of radiation cavity to minimize the radiation heat losses and in a phase change material system to be installed on the original energy extraction zone to be in contact with the full upper area to enhance the energy extraction zone in order to extract as much a useful energy as possible before this area reach a temperature below the working temperature of the engine device.

5. Acknowledgments

The authors acknowledge Institute of Renewable Energy (IER-UNAM) through the Mexican Center of Innovation in Solar Energy (CeMIE-Sol) (Strategic Project 05 "Development of solar thermal storage tanks"), through which it was possible to develop research and support the training of human resources at postgraduate level.

6. References

[1] Cárdenas, B. 2014. Tanque de Almacenamiento de Energía Térmica. Instituto Tecnológico y de Estudios Superiores de Monterrey, Nuevo León, México.

[2] Trombe, F., & Le, A. 1973. Thousand kW solar furnace, built by the National Center of Scientific Research, in Odeillo (France). Solar Energy, 15(1), 57-61.

[3] Kronhardt, V. Alexopoulos, S. Reissel, M. Sattler, J. Hooschmidt, B. Hänel, M. Doerbeck T. High-temperature Thermal Storage System for Solar Tower Power Plants with Open-volumetric Air Receiver Simulation and Energy Balancing of a Discretized Model. Energy Procedia, 2014.

[4] Amador, B. 2012. Materiales de cambio de fase para almacenamiento de energía solar. Instituto Tecnológico y de Estudios Superiores de Monterrey, Nuevo León, México.

[5] Garcia, L. 2010. Tanque Solar de Alta Temperatura. Instituto Tecnológico y de Estudios Superiores de Monterrey, Nuevo León, México.

[6] Gutiérrez R. 2014. Diseño y Simulación de Tanque de Almacenamiento Térmico Solar. Instituto Tecnológico y de Estudios Superiores de Monterrey, Nuevo León, México.

[7] Shelby, J 2005. Introduction to glass science and technology. (2nd Ed). Cambridge: Royal Society of Chemistry.

[8] Rasor N.S, McClelland J.D. Properties of graphite, molybdenum tantalum to their destruction temperatures. Journal of Physics and Chemistry of Solids 1960; 15: 17-26.

[9] Kovacec M, Polipovic A, Stefanic N. Impact of glass cullet on the consumption of energy and environment in the production of glass packaging material. Recent Researches in Chemistry, Biology, Environment and Culture. Monteux, Switzerland, 2011.

[10] Comprit 180H M. http://www.energiaencontrol.com/ Accessed 16- September -2014

[11] Thermal Ceramics Kao-Tab 95 High Alumina Castables. http://www.matweb.com/ Accessed 16-September -2014

[12] SuperMag 1200 Spun Soluble Blanket. http://www.nutec.com/supermag1200 Accessed 9-September -2014

[13] ASTM A36 (SS400, S275) Structural Carbon Steel. http://www.makeitfrom.com/material-properties/ASTM-A36-SS400-S275-Structural-Carbon-Steel/ Accessed 28-September-2015

[14] Cengel, Y. 2011. Heat and mass transfer: Fundamentals and applications (3rd Ed.). Singapur: McGraw-Hill.

[15] Trinuruk, P., & Obara, T. 2013. Concept of prismatic high temperature gas-cooled reactor with SiC coating on graphite structures. Annals of Nuclear Energy.

[16] Zhi-qiang, F., Cheng-biao, W., Chun-he, T., Hong-sheng, Z., & Jean-Charles, R. 2013. Oxidation behaviors of SiO2/SiC coated matrix graphite of high temperature gas-cooled reactor fuel element. Nuclear Engineering and Design.

[17] Guo, W., & Xiao, H. 2007. Modeling of TG curves of isothermal oxidation of graphite. Material Science & Engineering A, 197 – 200

Conference Proceedings

Solar World Congress 2015
Daegu, Korea, 08 – 12 November 2015

De-stratification and heat loss comparison of three thermal oils in a small storage tank

Ashmore Mawire[1], Abigail Phori[1] and Simeon Taole[1]

[1] North West University, Mafikeng Campus, Private Bag X2046, Mmabatho 2745, South Africa

Abstract

An experimental comparison of de-stratification and heat loss characteristics of three different thermal oils in a storage tank is presented in this paper. The three thermal oils evaluated are Sunflower Oil, Shell Thermia C and Shell Thermia B. A small insulated 20 liter storage tank is firstly charged up with the use of an electrical heater in thermal contact with an oil circulating copper spiral coil. After charging, the storage tank is left to cool down for 24 hr cycles. Cool-down experimental thermal cycles are carried out with the three different oils. De-stratification and heat loss parameters are evaluated. The stratification number is evaluated and it signifies the degree of thermal stratification. Stratification numbers are seen to be slightly higher for Sunflower Oil as compared to the other oils at the later stages of cool-down. The heat loss factor for Sunflower Oil is lower when compared to the other thermal oils, suggesting that it is the superior oil in terms of heat retention.

Keywords: *De-stratification, heat loss, thermal oils, storage tank*

1. Introduction

In any domestic heat storage application, the rate of thermal degradation is directly related to the heat losses and the period of useful storage during cool-down thermal cycles. Heat retention or cool-down thermal cycles are essential to obtain a measure of how long the stored heat can be kept without considerable degradation which makes it un-useable. Recent work has been done to study heat losses and stratification in low temperature water storage tanks during cool-down thermal cycles (Cruickshank and Harrison, 2010; Fan and Furbo, 2012; Fernandez-Seara et al., 2011; Oliveski et al., 2003) . Limited studies have been done on heat losses during cool-down cycles using other thermal energy storage (TES) media other than water for higher temperatures (Mawire, 2013; Park et al., 2014; Okello et al., 2014; Oliveski et al., 2005; Suárez et al., 2015). According to our literature review, very little work has been done on experimental heat losses and thermal de-stratification comparisons of different TES media which operate above the boiling point of water. For small domestic scale applications during heat retention periods, it is thus necessary to do this study. In this particular paper, simplified experimental thermal de-stratification and heat loss characteristics of a small domestic oil storage tank using three different thermal oils are presented.

2. Experimental method

The schematic diagram of Fig. 1 shows the operation of the charging cycle before cooling occurs. A positive displacement charging pump (3) controlled by a variable DC power supply (4) is used to circulate oil through a copper spiral coil that is in thermal contact with an electrical heating element (1). The DC power supply is adjusted manually to vary or maintain the average charging flow-rate. An oval gear volumetric flow-meter (5) is at the bottom of a 20 litre thermal oil storage tank (6) such that it records the volumetric flow-rate during charging . The charging pump extracts oil at the bottom of the tank and pushes it through an electrical heater with an oil charging coil (1). The oil enters the charging coil at a temperature T_{in} and exits the coil at a temperature T_{out} after absorbing heat from the electrical heater controlled by a variac (2). The oil enters the top of the storage tank at a hotter temperature as compared to the bottom of the tank. The charging cycle is repeated until the bottom of the storage tank attains a relatively high temperature (~100 ^{o}C).

doi:10.18086/swc.2015.02.08 Available at http://proceedings.ises.org

For the heat retention tests, the pumps and the electrical heating elements are switched off. The storage tank is then left to cool-down naturally for 24 hrs as temperature data are recorded with a data-logger every 10 s. The storage tank is insulated with 50 cm thick rock wool that this wrapped around its walls. The insulation is placed inside an aluminium thermal shield that surrounds the storage tank.

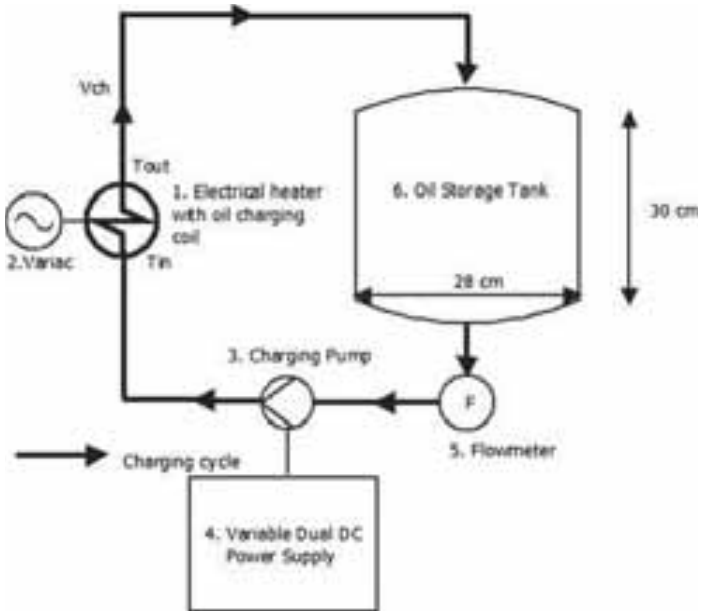

Figure 1: Experimental setup and operation (Mawire and Taole, 2013).

The temperatures in the storage tank during cool-down are monitored with 15 K-type of thermocouples placed inside the storage as shown in Fig. 2. The 15 K-type thermocouples are placed at three radial positions at five different levels along the height of the storage tank (5 axial levels). Thermocouples at Level 5 (T51, T52, T53) measure the radial temperature distribution at the top of the storage and an average temperature at this axial position is determined using these measurements. . Other average temperatures from Levels 4 - 1 are determined in a similar manner. An average storage tank temperature is thus determined from these average temperature measurements. The top thermocouples are placed at a level 50 mm below the top of the storage tank, while the bottom thermocouples (Level 1) are placed at a level 50 mm above the bottom of the storage tank.

Figure 2: The arrangements of the 15 thermocouples in the storage tank. All dimensions are in mm (Mawire and Taole, 2013).

3. Experimental thermal analysis

During the heat retention thermal cycles, the stratification number is defined by Fernandez-Seara et al. (2007) as the ratio of the mean of the thermal gradients at each time interval to that of the beginning (t = 0) and it is expressed as

$$Str = \frac{\left(\frac{\partial T}{\partial y}\right)_t}{\left(\frac{\partial T}{\partial y}\right)_{t=0}} \quad (1)$$

where

$$\frac{\partial T}{\partial y} = \frac{1}{j-1}\left[\sum_{j=1}^{j}\left(\frac{T_{j+1}-T_j}{\Delta y}\right)\right]. \quad (2)$$

where T is the average temperature at an axial level and $\Delta y = 0.05$ m is the axial distance between two adjacent thermocouple levels.

The energy lost during a 4 hr heat retention process is given as

$$E_L = \rho_{av} c_{av} V_{ST} \left(T_{iniav} - T_{finav}\right) \quad (3)$$

where ρ_{av} is the average density of the storage tank segments, c_{av} is the average specific heat capacity of the storage tank segments, V_{ST} is the total volume of the segments, T_{iniav} is the initial average temperature of the storage tank segments and T_{finav} is the final average temperature of the storage tank segments. The total rate of heat loss (which is inclusive of the insulating material, oil and tank conductivity e.t.c) during heat retention processes can be expressed as (Cruickshank and Harrison, 2010)

$$P_L = \frac{\rho_{av} c_{av} V_{ST} \left(T_{iniav} - T_{finav}\right)}{\Delta t} \quad (4)$$

where Δt is the 4 hr time interval. Heat loss to the surroundings can also be expressed as

$$P_L = U_L^{'}\left(T_{av} - T_{amb}\right) \quad (5)$$

where T_{av} is the average temperature of the segments and $U_L^{'}$ is the heat loss factor given by

$$U_L^{'} = U_L A_{ST}. \quad (6)$$

where U_L is the heat loss coefficient and A_{ST} is the overall area of the storage tank segments where the temperature is measured.

The thermal properties of the oils are temperature dependent and their temperature dependent equations are calculated from their datasheets and research papers published in literature from experimental tests (Shell Thermia B Datasheet, 2014; Shell Thermia C Datasheet, 2014; Esteban et al., 2012; Fasina and Colley, 2008; Turgurt et al., 2008). Table 1 shows the thermal properties of the different oils as a function of the temperature in ^{o}C. Sunflower Oil has the highest temperature dependent density and specific heat capacity. The thermal conductivities are seen to be within the same range. Information regarding the viscosity change with temperature of the oils was not available in literature therefore experiments need to be done.

Table 1: Temperature dependent thermal properties of the heat transfer oils

Thermal Oil	Density (kg/m^3)	Specific Heat Capacity (J/kgK)	Thermal Conductivity (W/mK)
Sunflower Oil	ρ_S = 930.62-0.65T	c_S = 2115.00+3.13T	k_S = 0.161+0.018exp(-T/26.142)
Shell Thermia C	ρ_C = 893.00-0.67T	c_C = 1798.00+3.58T	k_C = 0.121+0.132exp(-T/18.659)
Shell Thermia B	β_B = 876.00-0.65T	c_B = 1809.00+3.50T	k_S = 0.118+0.018exp(-T/168.660)

4. Results and discussion

Dimensionless thermal profiles are presented in Fig. 3, since the initial TES temperatures were slightly different for the three thermal oils due to slightly different initial charging conditions. Dimensionless temperature profiles ($T' = \frac{T}{T_{ini}}$) enable a fairer comparison of the thermal distributions during heat retention since the temperature distributions are relative to the initial conditions. The heat retention process is started when the bottom of the storage tank has reached a limiting temperature of approximately 100 ^{o}C during the charging process. This limit was set because the flow-meter could with-stand temperatures of only up to 120 ^{o}C.

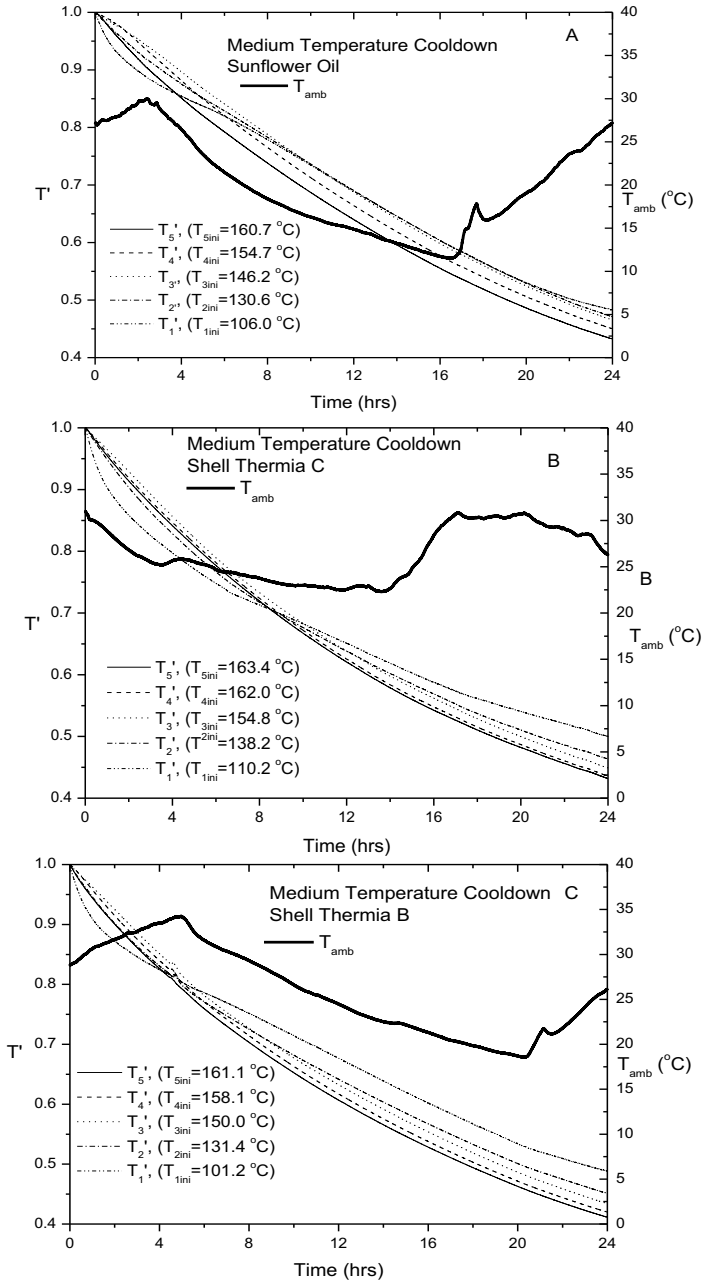

Figure 3: Dimensionless thermal profiles during 24 hr cool-down cycles for the three thermal oils.

Fig. 3 shows a general trend of similar drops in initial temperatures at a faster rate at T_5 (at the top of the storage tank) for the three thermal oils, thus implying more heat losses. T_1 has a slow rate of drop at the later

stages of heat retention when compared to T_5 for all the three thermal oils. This is because the density at the bottom of the storage tank becomes appreciably larger than at the top as time progresses because of the lower temperature at the bottom. This implies a larger thermal mass at the bottom of the storage tank at the later stages which results in a low rate of drop in the temperature. The slower rate of drop at T_1 relative to T_5 for Shell Thermia C occurs at a later time due to the higher storage temperatures. Sunflower Oil attains larger average temperatures at the end of 24 hrs suggesting that this the best oil in terms of heat retention even though its initial top storage tank temperatures are less than that of the other two oils. This suggests that the thermal mass effect is more pronounced for Sunflower Oil, the oil with the greatest density. The variations of the ambient temperatures are in accordance to the time of day when the experiments were carried out and these do not any effect on the heat loss process since the storage tank is insulated with a heat loss factor value of around 0.11 W/K.

Fig. 4 shows stratification number profiles for the three thermal oils during 24 hr heat retention cycles. The stratification number profiles decrease with time due to heat losses induced by natural convection. Shell Thermia C shows a delayed drop in stratification number as compared to the other thermal oils. This is because of the higher initial temperatures which promote a higher degree of thermal stratification. The stratification number profiles for Shell Thermia B and Sunflower Oil are almost identical during the first 4.5 hrs of cool-down possibly due to similar temperature profiles. After 4.5 hrs, Sunflower Oil shows greater values of the stratification number. This is because of the larger thermal mass due to the larger density of Sunflower Oil at the later stages. This larger thermal mass results in lower heat losses. The thermal mass effect is also evident after around 13 hrs where the stratification number profile for Sunflower Oil becomes larger than that of Shell Thermia C.

.

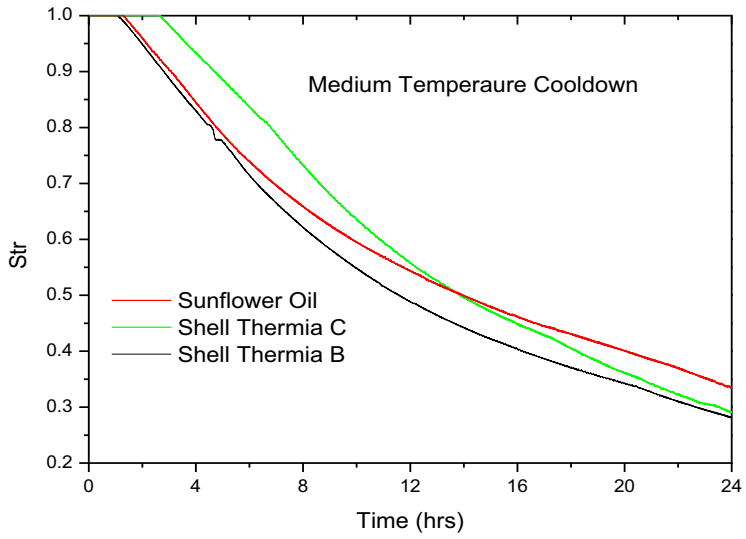

Figure 4. Stratification number profiles during 24 hr cool-down cycles for the three thermal oils.

Fig. 5 shows heat loss factors for the three thermal oils indicated by the slopes of the linear fits. Sunflower Oil is seen to have the least heat loss factor (lower gradient) as compared to the other thermal oils due to its larger thermal mass. Shell Thermia B shows the greatest heat loss factor due to its lower thermal mass. This result suggests that Sunflower Oil has better heat retention as compared to the other thermal oils.

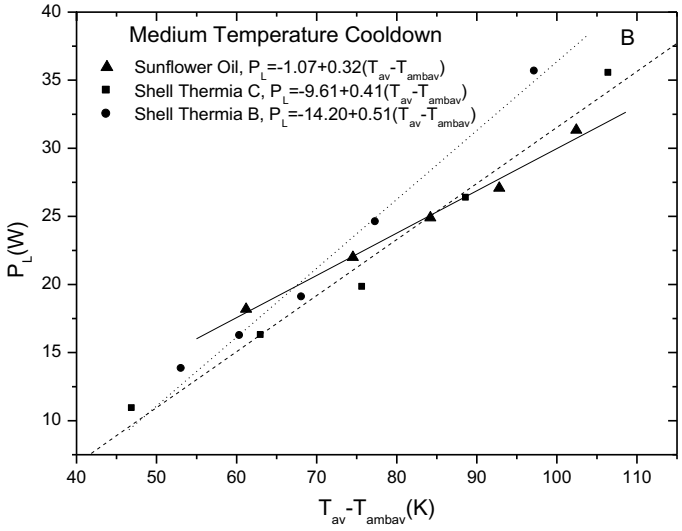

Figure 5. Heat loss factors for the three thermal oils.

5. Conclusion

Experimental results for the comparison of de-stratification and heat loss characteristics of three different thermal oils in a small storage tank were presented in this paper. The three thermal oils evaluated were Sunflower Oil (an edible oil), Shell Thermia C and Shell Thermia B. De-stratification and heat loss parameters were evaluated from cool-down thermal profiles. The stratification number was evaluated and it signified the degree of thermal stratification. Stratification numbers were seen to be slightly higher for Sunflower Oil when compared to the other oils at the later stages of cool-down due its larger thermal mass. The heat loss factor for Sunflower Oil was lower as compared to the other thermal oils, suggesting that it was the superior oil in terms of heat retention.

Acknowledgement

The authors would like to acknowledge the National Research Foundation (NRF) of South Africa for funding to carry out this research under the Incentive Funding for Rated (IFR) researchers and the Research Development grants for Y-Rated (RDYR) researchers schemes.

References

Cruickshank, C.A., Harrison, S.J., 2010. Heat loss characteristics for a typical solar domestic hot water storage. Energy and Buildings 42, 1703–1710.

Esteban. B., Riba, J.R., Baquer, G., Rius, A., Puig, R., 2012. Temperature dependence of density and viscosity of vegetable oils. Biomass and Energy 42, 1641–1671.

Fan, J, Furbo, S., 2012. Thermal stratification a hot water tank established by heat loss from the tank. Solar Energy 86, 3460–3469.

Fasina O.O, Colley, Z., 2008. Viscosity and specific heat of vegetable oils as a function of temperature 35 ^{o}C to 180 ^{o}C. International Journal of Food Properties 11, 738-746.

Fernandez-Seara, J., Uhia, F.J., Dopazo, J.A., 2011. Experimental transient natural convection heat transfer from a vertical cylindrical tank. Applied Thermal Engineering 31, 1915–1922.

Fernández-Seara J., Uhía, F.J, Sieres, .J, 2007. Experimental analysis of a domestic electric hot water storage tank Part II: dynamic mode of operation. Applied Thermal Engineering 27, 137–144.

Mawire, A., 2013. Experimental and simulated thermal stratification evaluation of an oil storage tank subjected to heat losses during charging. Applied Energy 108, 459–465.

Mawire A., Taole, S.H., 2013. Heat loss estimation in a small vertical cylindrical stratified oil storage tank. In Domestic Use of Energy (DUE) Conference 2013, South Africa, Cape Town, April 2–4, 107–113.

Okello, D., Nydal, O.J., Banda, E.K.., 2014. Experimental investigation of thermal de-stratification in rock bed TES systems for high temperature applications. Energy Conversion and Management 86, 125–131.

Oliveski, R.D., Krenzinger, A., Vielmo, H.A., 2003. Cooling of cylindrical vertical tanks submitted to natural interna convection, International Journal of Heat and Mass Transfer 46, 2015–2026.

Oliveski, R.D., Macagnan, M.H., Copetti, J.D., de La Martiniere Petroll, A., 2005. Natural convection in a tank of oil: experimental validation of a numerical code with prescribed boundary condition. Experimental Thermal and Fluid Science 29, 671–680.

Park, J.W., Park D., Ryu, D., Choi, B.H., Park, E.S., 2014. Analysis on heat transfer and heat loss characteristics of rock cavern thermal energy storage. Engineering Geology 181, 142–156.

Shell Thermia B Datasheet, 2014. http://www.lubricanthub.com/content/shell-thermia-oil-b-high-performance-heat-transfer-fluid [Accessed March 2014]

Shell Thermia C Datasheet, 2014. http://www.lubebase.com/cgi-bin/ctl/lube/Shell-THERMIA-C?id=3626 [Accessed March 2014].

Suárez, C., Iranzo, A., Pino, F.B., Guerra, J., 2015. Transient analysis of the cooling process of molten salt thermal storage tanks due to standby heat loss. Applied Energy 142, 56–65.

Turgut, A., Tavman, I., Tavman, S., 2009. Measurement of thermal conductivity of edible oils using transient hot wire method. International Journal of Food Properties 12, 741−747.concern in practice.

Conference Proceedings

Solar World Congress 2015
Daegu, Korea, 08 – 12 November 2015

Predictive Control of Thermal Storage Systems Designed for Multi-energy District Boilers: A Case Study in France

Mouchira Labidi[1], Julien Eynard[2,3], Olivier Faugeroux[2,3] and Stéphane Grieu[2,3]

[1] Cylergie, Cofely GDF-Suez, 18 avenue Tony Garnier, 69007 Lyon, France

[2] University of Perpignan Via Domitia, 52 avenue Paul Alduy, 66860 Perpignan, France

[3] PROMES-CNRS, rambla de la thermodynamique, Tecnosud, 66100 Perpignan, France

Abstract

The present work deals with improving the operation of a multi-energy district boiler by adding to the plant an optimally-designed thermal storage tank and developing a model-based predictive controller in order to manage it. The proposed architecture generates optimal command sequences dealing with the amount of thermal energy to be stored or released. In order to implement such a controller, one needs to forecast the power demand. As a consequence, a short-term forecast method, based on both a Multi-Resolution Analysis (MRA) and feedforward (multilayer) Artificial Neural Networks (ANN) is proposed. The present paper mainly focuses on the impact of Thermal Energy Storage (TES) on the functioning of a northeast France multi-energy district boiler selected as a case study. As a result, both the fossil energy consumption and CO_2 emissions are significantly reduced while the economic gain is increased.

Keywords: *multi-energy district boiler, thermal energy storage, model predictive control, artificial neural networks, power demand.*

1. Introduction

Because of the global energy crisis, the French government supports the renewable energy production. As buildings account for about 40% of total final energy consumption (more than half of this consumption is due to heating), France makes a specific effort in this sector. In addition, using biomass materials such as wood in industrial and residential heating can significantly reduce the reliance on fossil fuels and limit the CO_2 emissions (Kitzing et al., 2012). In 2000, Tanaka et al. showed that a seasonal storage system is able to decrease the consumption of energy by about 26% in a District Heating and Cooling (DHC) plant (Tanaka et al., 2000). As another interesting work, Smith et al. highlighted the benefits of storing thermal energy, in combination with CHP (Combined Heat and Power) technology (Smith et al., 2013). In 2011, Verda and Colella evaluated the effects of thermal energy storage on both the primary energy consumption and cash flows in district heating networks (Verda and Colella, 2011). Gustafsson and Karlsson showed how a thermal storage system can be used in a CHP plant for decreasing both the demand in district heating and the consumption of electricity (Gustafsson and Karlsson, 1992). In 2010, Kavvadias et al. proposed a parametric analysis as an efficient way to design CHP plants optimally (Kavvadias et al., 2010).

As a key point, advanced control techniques and management strategies are needed to improve the operation of multi-energy district boilers managed by Cofely GDF-Suez, our industrial partner. In this sense, the OptiEnR research project focuses on optimizing performance by adding thermal storage systems to the plants. First, we assessed a specific case study (Eynard et al., 2012) and we are now developing a flexible and generalized approach. It has been highlighted in a previous work that once optimally designed and managed using a sequential approach based on logical conditions, a thermal storage tank can significantly improve the overall efficiency of a plant, in particular in case of badly-sized heat generators (Labidi et al., 2014). So, the present paper deals with the optimal management of a thermal storage tank using a Model Predictive Controller (MPC). We focused on analyzing the energy savings one can achieve using such an

doi:10.18086/swc.2015.02.09 Available at http://proceedings.ises.org

advanced control approach. The power demand is forecasted using the MRA-ANN methodology. Its particularity comes from the combination of signal processing (a wavelet-based multi-resolution analysis) and artificial intelligence (multilayer artificial neural networks) tools. Lastly, a case study is selected in order to evaluate the predictive control approach.

The next section of the paper (section 2) provides a brief description of multi-energy district boiler operation. Then, the performance indicators are presented (section 3). In section 4, the design of the MPC controller allowing the thermal storage tank to be efficiently managed is carried out. Next, the developed MRA-ANN methodology is presented (section 5). Such an approach has proven to be effective in forecasting time series. It should also be noted that several other methods for power demand forecasting have been suggested and implemented (Amjady and Keynia, 2009; Dotzauer, 2002). The particularity of the proposed methodology comes from the combination of signal processing and artificial intelligence tools. Lastly, a case study is selected in order to both validate the MRA-ANN forecasting methodology and evaluate the predictive control approach (section 6). In particular, it is highlighted that the way the tank is designed and managed is a key factor in plant operation improvement. The paper ends with a conclusion and an outlook to future work.

2. Multi-energy district boiler operation

Typically, in multi-energy district boilers, the biomass units (characterized by a minimum (P_{WB}^{min}) and a maximum (P_{WB}^{max}) heat production capacity are generally sized in order to meet the major part of the power demand but they lack the capability of covering the peak loads. So, auxiliary fossil boilers are used during the coldest periods of the year, in case of shutdown maintenance activities or when the power demand is lower than P_{WB}^{min}. As stated in section 1, the main purpose of the present study is to optimize the operation of multi-energy district boilers by adding to the plants optimally-managed thermal storage tanks. Because the sequential approach we proposed initially does not take into account future power demand values, such an approach seems to be sometimes unable to optimize the whole system, in particular in case of high variability in the power demand. For this reason, we propose here an advanced strategy based on both a Model Predictive Controller (MPC) and a forecasting approach.

3. Performance indicators

In order to assess the impact of both the thermal storage system and the management strategy, energy, economic and environmental criteria are suggested as performance indicators. Because the main purpose of thermal energy storage is to decrease the consumption of gas, the gas coverage rate (C_{gas}) is proposed as an energy indicator (eq. 1). It is calculated from the thermal energy produced by the combustion of gas (E_{gas}) and wood (E_{wood}) during the considered period:

$$C_{gas} = \frac{E_{gas}}{E_{gas} + E_{wood}} \quad \text{(eq. 1)}$$

The wood coverage rate (C_{wood}) is computed in the same way than C_{gas} and is subject to contract (eq. 2):

$$C_{wood} = \frac{E_{wood}}{E_{gas} + E_{wood}} \quad \text{(eq. 2)}$$

With the aim of highlighting the economic benefits of energy savings, a criterion (Ec) is defined from E_{gas}, E_{wood}, UP_{gas} (the unitary price of gas), and UP_{wood} (the unitary price of wood) (eq. 3):

$$Ec = E_{gas} \times UP_{gas} + E_{wood} \times UP_{wood} \quad \text{(eq. 3)}$$

In order to put in perspective these economic benefits, the economic gain G is evaluated (eq. 4). It is defined as the difference between $Ec(V)$, the economic cost related to energy consumption, considering a storage

volume V, and $Ec(V = 0)$, the economic cost related to energy consumption without storage of thermal energy ($V = 0$ m^3):

$$G(V) = Ec(V) - Ec(V = 0) \quad \text{(eq. 4)}$$

The environmental impact of such a technology is evaluated thanks to criterion L_{CO2}, which is about CO_2 emissions (eq. 5). L_{CO2} is expressed from Ec_{gas}, Ec_{wood} and the Life-Cycle Assessment of CO_2 emissions from gas (U_{CO2}^{gas}) and wood (U_{CO2}^{wood}):

$$L_{CO2} = Ec_{gas} \times U_{CO2}^{gas} + Ec_{wood} \times U_{CO2}^{wood} \quad \text{(eq. 5)}$$

It should also be noted that new buildings connected to the heat network as well as future expansions of existing buildings are factors to be taken into account in order to evaluate the proposed strategy accurately. As a result, one can consider an increase in the power demand P_{net} up to 30 % and evaluate the impact of such an increase on plant operation.

4. Design of the Model-based Predictive Controller (MPC)

4.1. Principles of MPC

It is somewhat curious to note that the concept of Model-based Predictive Controller (MPC) has a long history that began during the 1970's when Engineers at Shell Oil developed their own dependent technology with an initial application in 1973 (Garcia et al., 1989). Nowadays, this concept is widely used in the control of industrial processes. Its popularity in industry is mainly due to the possibility it offers to treat operating specifications and constraints jointly during the development phase of the controller. For instance, MPC is commonly used to manage thermal comfort (Castilla et al., 2014) and energy resources (Ma et al., 2012) in buildings.

The philosophy of MPC is down to use a model to forecast the behavior of the system to be controlled and choose the best decision in the sense of an objective function while satisfying constraints. Usually, the aim is to ensure the desired set-point, regardless of disturbances with minimal effort. Constraints deal with physical limitations and are introduced for economic or security reasons. The forecast horizon is the time interval during which the objective function is minimized using an optimization algorithm (Manenti, 2011).

4.2. Structure of the controller

In this subsection of the paper, the proposed model-based predictive controller is presented. It uses a model of the multi-energy district boiler (section 4.2.1) as well as a forecast unit allowing the power demand (P_{net}) to be accurately estimated over the next 24 hours (section 4.2.2). This unit makes use of both a wavelet-based Multi-Resolution Analysis (MRA) and feedforward (multilayer) Artificial Neural Networks (ANN). The optimization problem is solved using the fmincon (*find minimum of constrained nonlinear multivariable function*) algorithm of Matlab® (sections 4.2.3 and 4.2.4). The controller's structure is depicted by Fig. 1:

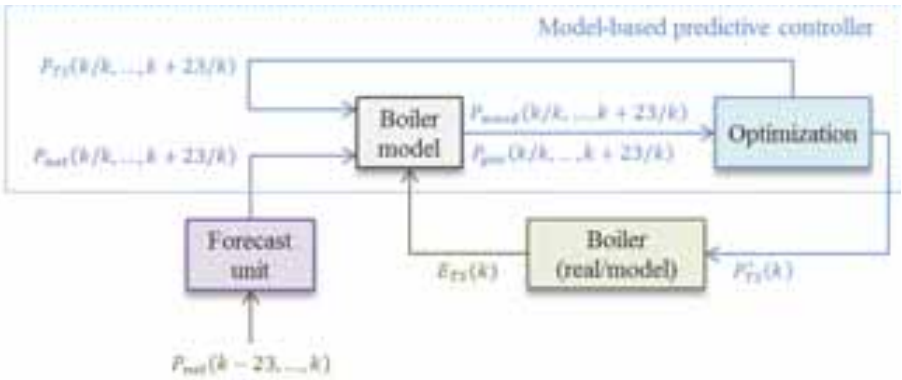

Fig. 1: Structure of the proposed controller (P_{net} is the power demand, P_{TS} is the thermal charging/discharging power, E_{TS} is the amount of energy stored or released, P_{gas} is the gas power, and P_{wood} is the wood power)

4.2.1. Model of the multi-energy district boiler

The proposed predictive controller uses the model of a multi-energy district boiler equipped with a thermal storage tank we developed and described in a previous work (Labidi et al., 2013). P_{gas} (the gas power) and P_{wood} (the wood power) are defined as functions of both the charging/discharging power of the storage tank (P_{TS}) and the power demand (P_{net}). k is the time step. The model is based on the 3 following cases, with P_{WB}^{min} and P_{WB}^{min} the wood boiler(s) minimum and maximum heat production capacities, respectively (eqs. 6 to 8):

$$\text{if } P_{WB}^{min} \leq P_{net}(k) \leq P_{WB}^{max} \text{ then } P_{wood}(k) = P_{net}(k) + P_{TS}(k) \text{ and } P_{gas}(k) = 0 \quad \text{(eq. 6)}$$

$$\text{if } P_{net}(k) \geq P_{WB}^{max} \text{ then } P_{wood}(k) = \max\left(P_{WB}^{max}, P_{net}(k) - P_{TS}(k)\right) \text{ and } P_{gas}(k) = P_{net}(k) - P_{wood}(k) \quad \text{(eq. 7)}$$

$$\text{if } P_{net}(k) \leq P_{WB}^{min} \text{ then } P_{wood}(k) = \max\left(P_{WB}^{min}, P_{net}(k) + P_{TS}(k)\right) \text{ and } P_{gas}(k) = 0 \quad \text{(eq. 8)}$$

4.2.2. Concept of time series for power demand forecasting

As it is mentioned in the previous section, P_{net} (the power demand) is a district boiler model input. So, it has to be accurately forecasted. So, a methodology based on a Multi-Resolution Analysis (MRA) and feedforward (multilayer) Artificial Neural Networks (ANN) is proposed in order to forecast time series (Brockwell and Davis, 1991, 1997). The main idea behind such a methodology is to replace the forecasting of an original signal with high variability by the estimation of its wavelet coefficients (Fig. 2). These coefficients are distinguished by specific levels of frequency as well as a variability which is lower than the variability of the original signal. As a result, the forecasting process is easier. Such an advanced approach has been developed because linear approaches like AR, ARMA or ARIMA proved to be insufficiently efficient, due to a high variability in power demand.

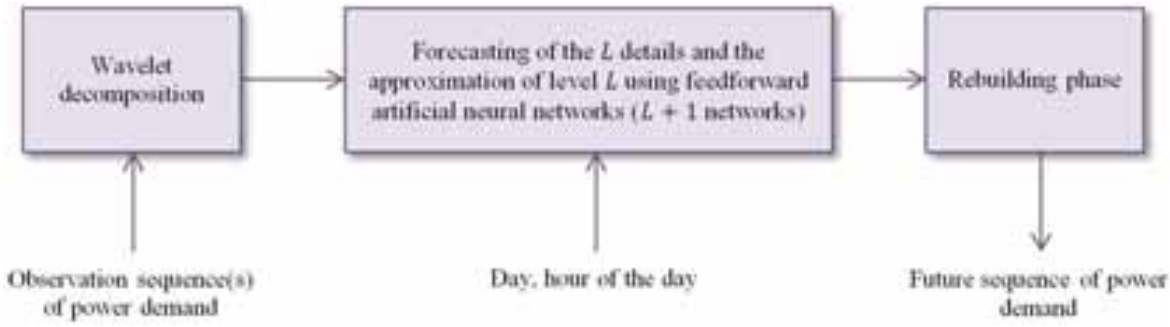

Fig. 2: MRA-ANN forecasting methodology

A time series can be defined as a sequence of numerical data points in successive order, usually occurring in uniform intervals. According to that, time series forecasting consists in using a model to estimate future values on the basis of observations. In our case, the model aims at estimating the power demand over the next 24 hours, using a set of M observation sequences whose length is also 24 hours (because of the daily cycles we observed in the data). We decided for a forecast horizon (H_f) of 24 hours as an interesting compromise between forecasting accuracy and periodicity in power demand. In addition, such horizon is well adapted to the charging and discharging cycles of the tank.

4.2.2.1. Wavelet-based multi-resolution analysis

The wavelet transform aims at decomposing a given signal into wavelets (i.e., highly localized small oscillations) (Heil and Walnut, 1989; Gubner and Chang, 1995). Unlike the Fourier transform, it offers time and frequency localization. There are two types of wavelet transforms: the Continuous Wavelet Transform (CWT) and the Discrete Wavelet Transform (DWT). We focus here on the second one. First, through Low Pass (LP) and High Pass (HP) filters, an original signal S is decomposed into low (approximations) and high (details) frequency coefficients of level 1. By decomposing successively the low frequency coefficients only,

we can produce L levels of decomposition. Fig. 3 shows the decomposition of level L of a signal x. In order to rebuild that signal, we have just to sum the L details (D_1, D_2, D_3, …, D_L) and the approximation of level L (A_L) (Mallat, 1989). It should also be noted that different families of wavelets may be chosen. Because the Daubechies wavelets (Daubechies, 1992) have the highest number of vanishing moments, this family has been chosen. Finally, the impact on performance of both the decomposition level and the wavelet order has been studied.

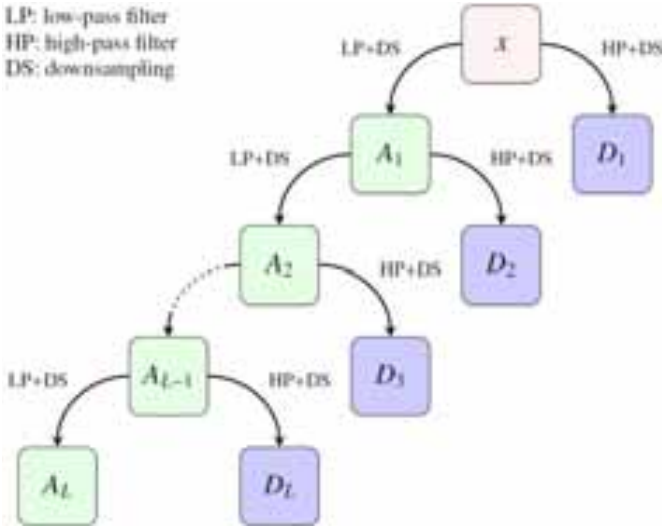

Fig. 3: Wavelet-based multi-resolution analysis leading to the decomposition of level L of a signal x

4.2.2.2. Feedforward artificial neural networks

Multilayer artificial neural networks can be used to forecast time series (Hornik et al., 1989; Kourentzes et al., 2014). Usually, each network consists in one layer of linear output neurons and one or more hidden layers of nonlinear neurons. As it is well known, the research for the adequate topology of a neural network (i.e., its number of hidden layers and neurons) is a key point. Such a research is based on a training (learning) phase during which the generalization capability of the network is controlled and its parameters are identified (Charalambous, 1992, Hagan and Menhaj, 1994).

4.2.2.3. Optimal configuration

Tab. 1: Optimal configuration and evaluation of performance

Parameter	Value
Wavelet family	Daubechies
Wavelet order	4
Decomposition level	1
Number of observation sequences	1
Number of hidden neurons	17
FIT	72.26%
MAE (Mean Absolute Error)	299.57 kW
MRE (Mean Relative Error)	5.9%

First, the time series (i.e., historical data covering a period of six months, from September 21 to April 16) is split into sequences of 24 hours, with a sampling time of 1 hour. Then, the wavelet-based multi-resolution analysis allows these sequences to be decomposed into subsequences (i.e., approximation and details coefficients). Using this database, multilayer artificial neural networks can be trained. As a key point, one network is used in order to forecast each subsequence. So, $L + 1$ networks are needed to forecast L detail coefficients and the approximation coefficient of level L. The hour of the day and the day of the year are complementary model inputs. Once all the subsequences are forecasted, they are summed to obtain the values of power demand over the next 24 hours. In order to improve forecast accuracy, we optimized the topology of the networks (note that we considered single-hidden layer structures and searched for a common

topology for all the networks so as to simplify the optimization process), the decomposition level (L) and the number of observation sequences (M). Table 1 deals with the optimal configuration and performance. Results highlight the ability of such an approach to achieve the task of prediction with accuracy.

4.2.3. Optimization problem

At each time step, the controller defines the optimal values of the charging/discharging power (P_{TS}), along the forecast horizon H_f (i.e., over the next 24 hours). Note that a positive value ($P_{TS} > 0$) stands for the charging (storage) mode whereas a negative value ($P_{TS} < 0$) is for the discharging (release) mode. So, the main goal of the control approach is to minimize the use of fossil energy by optimizing the storage process during low-demand periods and releasing the thermal energy stored when the power demand is high. Thus, the objective function J is defined as the quadratic sum of the gas power consumed at each time step, along the forecast horizon (i.e., over the next 24 hours). The optimization problem comes down to find, at each time step, the charging/discharging power (P_{TS}) such that J is minimized (eq. 9) and the constraints are met (eqs. 10 and 11):

$$\min_{[P_{TS}(k/k),\dots,P_{TS}(k+H_f-1/k)]}\left(J=\sum_{k=1}^{H_f}P_{gas}(k)^2\right) \qquad \text{(eq. 9)}$$

Two constraints ensure that thermal energy is stored or released adequately. The first one (eq. 10) is introduced in order to limit the interval of the possible values for P_{TS}. This constraint is related to the characteristics of the storage tank feed pumps. The second constraint (eq. 11) makes reference to the design of the storage system. In other words, it is related to the capacity of the tank ($E_{max} = \rho \cdot C_p \cdot V \cdot \Delta T$, with ρ the water density, C_p the specific heat of water, V the volume of the storage system and ΔT the difference in temperature between hot and cold water). E_{init} is the amount of thermal energy initially stored in the tank. So, at each time step, the amount of energy stored has to be positive and lower than E_{max}:

$$-P_{TS}^{max} \le P_{TS}(k+j/k) \le P_{TS}^{max}, \forall j \in [\![0; H_f - 1]\!] \qquad \text{(eq. 10)}$$

$$0 \le E_{init} + \sum_{i=0}^{j} P_{TS}(k+i/k) \le E_{max}, \forall j \in [\![0; H_f - 1]\!] \qquad \text{(eq. 11)}$$

4.2.4. MPC algorithm

Fig. 4 depicts the MPC algorithm used. At each time step k, a simulation over the forecast horizon based on the non-predictive (sequential) strategy (Labidi et al., 2014), the current amount of energy stored in the tank, and the forecasted values of P_{net} is performed in order for the values of $\left[P_{TS}(k/k), \dots, P_{TS}\left(k+H_f-1/k\right)\right]$ to be initialized. These values are then optimized using both the non-linear optimization algorithm "fmincon" from Matlab® and the developed model of the multi-energy district-boiler. The first optimized value is applied to the model which stands for the real system and so on until the end of the simulation process. Then, the performance indicators are computed for an off-line analysis of the results.

4.2.5. Non-predictive strategy

This strategy is based on the three following operation modes (Labidi et al., 2014):

- **Operation mode 1**: When the power demand is high (in particular during the coldest months of winter), instead of modulating the biomass power, all the (biomass) units available operate at maximum power to meet requirements and charge the tank. Once the power demand is upper than P_{WB}^{max}, the stored energy is released. In this way, the auxiliary gas unit is only switched on when the tank is empty and the power demand still exceeds P_{WB}^{max}.
- **Operation mode 2**: This second operation mode is for a moderate power demand. When $P_{net} < P_{WB}^{max}$, due to the variability in the demand, the biomass boiler (or one of the two biomass units installed at the plant) operates at minimum power (or higher) and the excees of energy produced is stored in order to be used later. If two biomass boilers are available, both can also operate at minimum power. In this way,

these units operate continuously and the number of on/off transitions is reduced. As a consequence, fossil energy can be saved.

- **Operation mode 3**: For some periods of the year (in particular during the hottest months of summer), most of the buildings connected to a heat network do not need to be heated and, as a consequence, only domestic hot water is required (low-demand periods). Instead of using the auxiliary gas unit to meet low power requirements (biomass boilers are usually oversized), the biomass unit (or the smallest boiler in case of two units being installed at the plant) and the thermal storage system can be operated as follows: first, the biomass unit runs at minimum power, what allows both the power demand to be met and the tank to be charged. Once the thermal storage system is completely filled with hot water, the boiler is shut down and the stored energy is released to afford domestic hot water. The boiler is switched on again when the tank is empty. Such a mode prevents the use of gas and favors the use of renewable energy during low-demand periods.

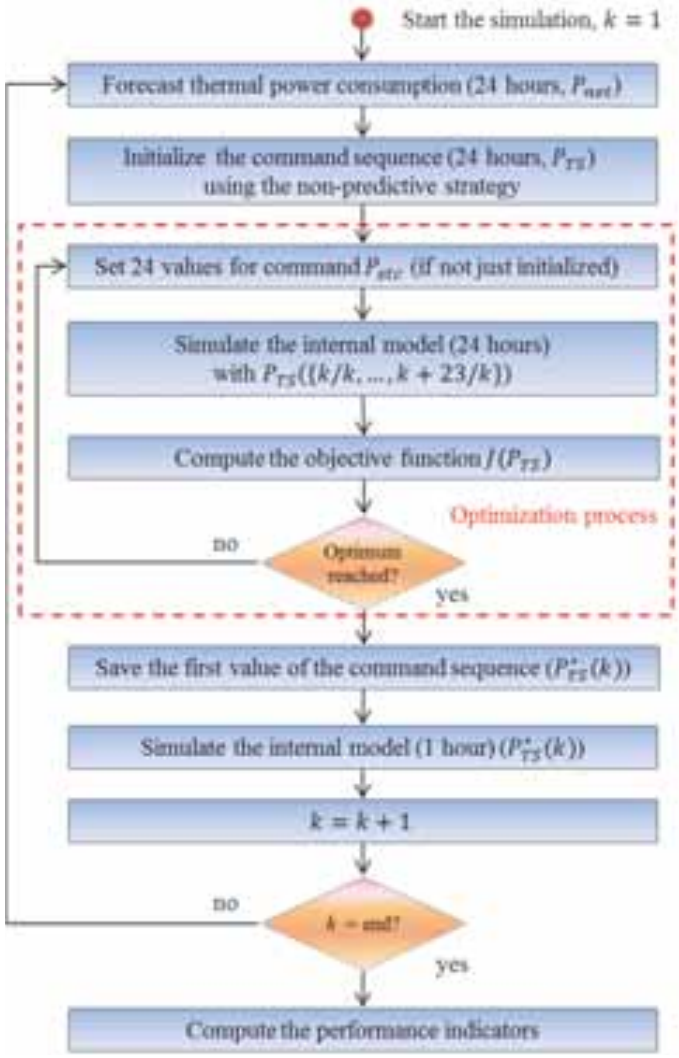

Fig. 4: MPC algorithm

5. Simulation results

5.1. Case study

We selected as a case study a multi-energy district boiler managed by Cofely GDF-Suez and located in the northeast of France, in the Alsace region (Haut-Rhin). Alsace has a semi-continental climate with cold and dry winters and hot summers. Winter starts in December and ends in February and has an average temperature of around 2 degrees Celsius across the season. January is the coldest month of the year with the

lowest average temperature of 1 degree Celsius. Winter is also the time of year with the lowest levels of precipitation. Summer starts in June and ends in August. It sees the highest levels of rainfall of the year as well as the highest temperatures with an average temperature of 18 degrees Celsius across the season. The plant is composed of three heat generators (Fig. 5).

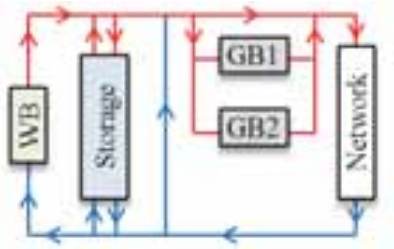

Fig. 5: Synoptic of the multi-energy district boiler

The first generator (WB) is a biomass boiler whose minimum power (P_{WB}^{min}) is 1050 kW. Its maximum power (P_{WB}^{max}) is 4200 kW. This unit is designed to ensure the basic production. A 7000 kW gas boiler (GB1) operates jointly with it during peak demand periods or alone when the power demand is lower than P_{WB}^{min}. A 9000 kW gas boiler (GB2) is switched on in case of malfunction or during maintenance phases only. Table 2 summarizes the characteristics of the boiler units.

Tab. 2: Characteristics of the boiler units

Boiler unit	Power (kW)	Efficiency (-)
WB	1050	0.70
	2100	0.75
	3150	0.88
	4200	0.95
GB1	140	0.97
	7000	0.97
GB2	180	0.97
	9000	0.97

5.2. Control results

Tab. 3: Simulation parameters

Parameter	Value
Simulation period	From September 1 to April 16
Sampling time	1 hour
Forecast horizon (H_f)	24 hours
UP_{gas}	40 € MWh^{-1}
UP_{wood}	17 € MWh^{-1}
U_{CO2}^{gas}	234 $kgCO_2$ MWh^{-1}
U_{CO2}^{wood}	13 $kgCO_2$ MWh^{-1}

Table 3 summarizes the main simulation parameters. Concerning the impact of the proposed strategy, simulation results show that the biomass boiler is sized to ensure around 85% of the power demand during the simulation period without thermal storage tank. Fig. 6 depicts the way both the gas coverage rate and the CO_2 emissions evolve according to the volume of the tank. One can clearly note that the MPC strategy allows a significant decrease in gas consumption and consequently in CO_2 emissions. Fig. 7 depicts the way the size of the tank impacts on Ec and G, respectively. One can highlight that Ec decreases with the size of the tank. Furthermore, using the proposed MPC strategy, a considerable economic gain is realized. Regarding the ability of the thermal storage tank to cope with a possible increase in power demand, one can observe (Fig. 8) that the proposed strategy allows the wood coverage rate to be 4 to 10 points higher than

when the reference scenario (RS) is considered (i.e., no thermal energy storage). In addition, on the basis of the parametric study, one can define the optimal size of the tank. For this case study, 300 m^3 can be chosen.

6. Conclusion

The present paper deals with optimizing the performance of a multi-energy district boiler. The plant is connected to a heat network for thermal energy distribution. First, a model predictive controller has been developed in order to optimize the use of the thermal storage tank. In order to implement this controller, the power demand has to be accurately forecasted. As a result, a methodology based on a Multi-Resolution Analysis (MRA) and multilayer Artificial Neural Networks (ANN) is proposed. One can highlight that the proposed control scheme allows the fossil energy consumption to be significantly reduced. The same remark applies to the functioning costs and CO_2 emissions. Future work will focus on improving the forecasted model, using self-growing artificial neural networks trained with the cascade correlation algorithm, and considering other objective functions. Finally, the proposed approach will be implemented *in situ*.

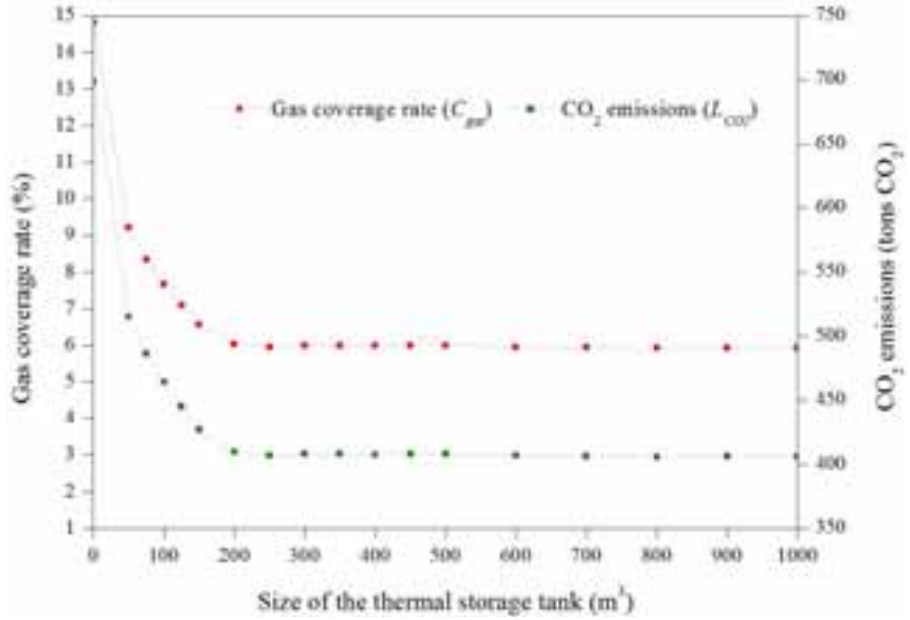

Fig. 6: Impact of the size of the thermal storage tank on the gas coverage rate (C_{gas}) and CO_2 emissions (L_{CO2})

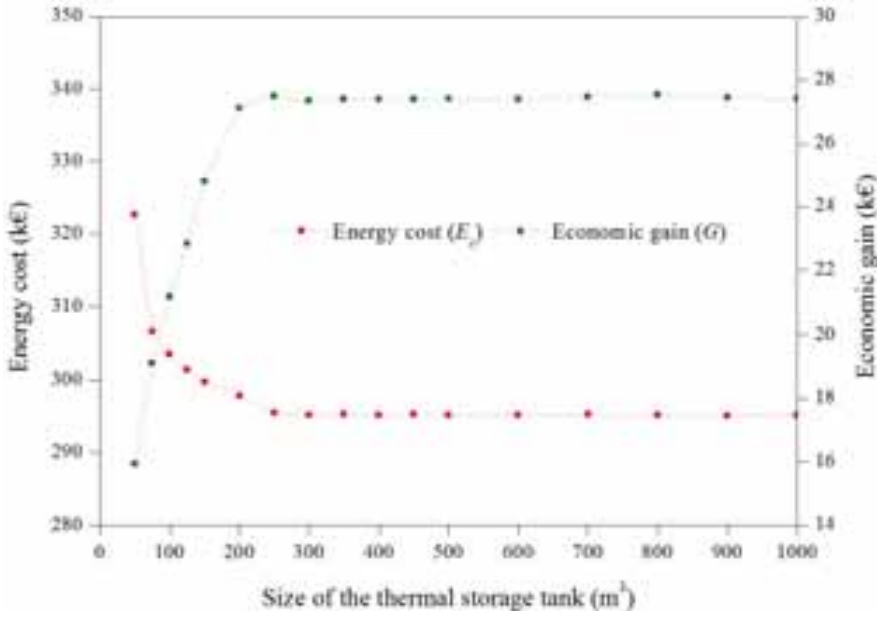

Fig. 7: Impact of the size of the thermal storage tank on the energy cost (Ec) and economic gain (G)

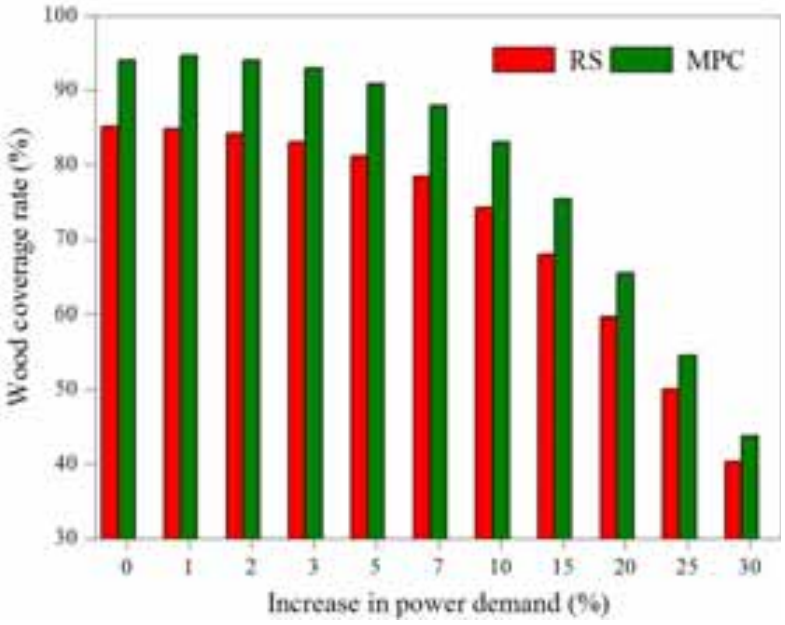

Fig. 8: Impact of an increase in power demand on the wood coverage rate (C_{wood}) (see section 3), with (MPC strategy) or without (Reference Scenario) thermal energy storage

7. References

Amjady N., Keynia F, 2009. Short term load forecasting of power systems by combination of wavelet transform and neuro-evolutionary algorithm. Energy 34 (1), 46-57.

Brockwell P.J., Davis R.A., 1991. Time series: theory and methods, 2nd ed. Springer, New York.

Brockwell P.J., Davis R.A., 1997. Introduction to time series and forecasting, Springer, New York.

Castilla M., Alvarez J., Normey-Rico J., Rodriguez F., 2014. Thermal comfort control using a non-linear MPC strategy: A real case of study in a bioclimatic building. Journal of Process Control 24 (6), 703-713.

Charalambous C., 1992. Conjugate gradient algorithm for efficient training of artificial neural networks. IEEE Proc. 139, 301-310.

Daubechies I., 1992. Ten lectures on wavelets, Society for Industrial and Applied Mathematics.

Dotzauer E., 2002. Simple model for prediction of loads in district-heating systems. Applied Energy 73 (34), 277-284.

Eynard J., Grieu S., Polit M., 2012. Predictive control and thermal energy storage for optimizing a multi-energy district boiler. Journal of Process Control 22 (7), 1246-1255.

Garcia C.E., Prett D.M., Morari M., 1989. Model predictive control: Theory and practice - A survey. Automatica 25 (3), 335-348.

Gubner J.A., Chang W.B., 1995. Wavelet transforms for discrete-time periodic signals. Signal Processing 42, 167-180.

Gustafsson S.I., Karlsson B.G., 1992. Heat accumulators in CHP networks. Energy Conversion and Management 33 (12), 1051-1061.

Hagan M.T., Menhaj M., 1994. Training feedforward networks with the Marquardt algorithm. IEEE Trans. Neural Networks 5, 989-993.

Heil C.E., Walnut D.F., 1989. Continuous and Discrete Wavelet Transforms. SIAM Review 31, 628-666.

Hornik K., Stinchcombe M., White H., 1989. Multi-layer feedforward networks are universal approximation, Neural Networks 2, 359-366.

Kavvadias K., Tosios A., Maroulis Z., 2010. Design of a combined heating, cooling and power system: Sizing, operation strategy selection and parametric analysis. Energy Conversion and Management 51 (4), 833-845.

Kitzing L., Mitchell C., Morthorst P.E., 2012. Renewable energy policies in Europe: Converging or diverging? Energy Policy 51, 192-201.

Kourentzes N., Barrow D.K., Crone S.F., 2014. Neural network ensemble operators for time series forecasting. Expert Systems with Applications 41 (9), 4235-4244.

Labidi M., Eynard J., Faugeroux O., Grieu S., 2013. Optimal design of thermal storage tanks for multi-energy district boilers. Proceedings of the 4th Inverse Problems, Design and Optimization Symposium.

Labidi M., Eynard J., Faugeroux O., Grieu S., 2014. Sequential management of optimally-designed thermal storage tanks for multi-energy district boilers. Applied Thermal Engineering 73 (1), 251-264.

Ma J., Qin J., Salsbury T., Xu P., 2012. Demand reduction in building energy systems based on economic model predictive control. Chemical Engineering Science, Dynamics, Control and Optimization of Energy Systems 67 (1), 92-100.

Mallat S., 1999. A wavelet tour of signal processing, third ed. Academic Press, Burlington.

Manenti F., 2011. Considerations on nonlinear model predictive control techniques. Computers and Chemical Engineering 35 (11), 2491-2509.

Smith A.D., Mago P.J., Fumo N., 2013. Benefits of thermal energy storage option combined with CHP system for different commercial building types. Sustainable Energy Technologies and Assessments 1, 3-12.

Tanaka H., Tomita T., Okumiya M., 2000. Feasibility study of a district energy system with seasonal water thermal storage. Solar Energy 69 (6), 535-547.

Verda V., Colella F., 2011. Primary energy savings through thermal storage in district heating networks. Energy 36 (7), 4278-4286.

Conference Proceedings

Solar World Congress 2015

Daegu, Korea, 08 – 12 November 2015

ISES SWC2015

Ageing stability of sodium acetate trihydrate with and without additives for seasonal heat storage

Weiqiang Kong, Mark Dannemand, Jakob Berg Johansen, Jianhua Fan, Janne Dragsted and Simon Furbo

Technical University of Denmark, Department of Civil Engineering, Kgs. Lyngby 2800, Denmark

Abstract

Sodium acetate trihydrate is a promising phase change material used for seasonal heat storage because it can supercool in a stable way down to ambient temperature. One challenge of this material is that it might suffer from phase separation resulting in a low utilization of the heat of fusion. Adding extra water or thickening additive has been suggested as an effective way to reduce the phase separation problem and thereby maximize the heat content of the sodium acetate trihydrate. Investigations of phase separation and heat content of supercooled sodium acetate trihydrate with and without extra water and additives were carried out under different test conditions. It was found that sodium acetate water mixtures with water contents lower than or equal to 42% would suffer from phase separation for the height of heat storage up to 8 cm. The heat content of sodium acetate trihydrate will be decreased by adding extra water. Sodium acetate trihydrate with Carboxy-Methyl Cellulose and Xanthan Gum as additives are promising heat storage materials with high heat contents and ageing stability.

Keywords: *sodium acetate trihydrate, phase change material, ageing stability, phase separation*

1. Introduction

Sodium acetate trihydrate ($NaCH_3COO \cdot 3H_2O$), consisting of 60.3% (weight %) sodium acetate and 39.7% (weight %) water, is a promising Phase Change Material (PCM) used for seasonal heat storage because of its relative high heat of fusion at the melting point of 58˚C and its long term stable supercooling ability (Furbo et al., 2010). Sodium acetate trihydrate or its water mixture is long time stable and no ageing effects are known. Experiments have shown that the salt water mixture can be stable supercooled for years. Fig. 1 shows supercooled sodium acetate water mixture samples which have been in supercooled state for approximately 3 years at indoor temperature. Even impurities such as rusty iron immersed in the supercooled sodium acetate water mixture has not influenced the stability of the supercooling, see the right sample of Fig. 1.

Fig. 1: Long term supercooled sodium acetate trihydrate water mixture samples

doi:10.18086/swc.2015.02.10 Available at http://proceedings.ises.org

In practical applications sodium acetate trihydrate might suffer from phase separation especially in the supercooled state. This is the phenomenon where anhydrous salt settles to the bottom due to its higher density compared to the density of saturated sodium acetate water solution. The heat released from the crystallization of the supercooled sodium acetate trihydrate with phase separation will be lower compared to the heat released from supercooled sodium acetate trihydrate without phase separation. Adding extra water (Furbo and Svendsen, 1977) or thickening agent (Cabeza et al., 2003) has been suggested as effective ways to reduce the phase separation and to maximize the heat content of the sodium acetate trihydrate.

This paper investigates phase separation for different heights of long term supercooled sodium acetate water mixtures by measuring the water contents in different layers, the heat content of different sodium acetate water mixtures after short and long periods with supercooling and the heat content of sodium acetate trihydrate with thickening agents CMC and X-Gum by cycle and long term tests. The test results show that sodium acetate trihydrate with CMC and with X-Gum as additives is promising heat storage materials with high heat contents and long term stability.

2. Phase separation investigations for different heights of long term supercooled sodium acetate water mixtures

The test method is described as follows:

Step 1: Prepare samples of sodium acetate water mixtures with 40%, 42%, 45%, and 46% (weight %) water with the same height in the plastic bottles shown in Fig. 2.

Step 2: Heat the samples in the oven to a temperature between 80 °C and 85 °C until the salt water mixture is fully melted.

Step 3: Take the samples out from the oven. Let them cool down to indoor ambient temperature and let them stay in a supercooled state for the desired duration.

Step 4: Initialize the crystallization of the samples, so that the salt water mixtures solidifies. The samples are left to cool down to the ambient temperature.

Step 5: Cut each sample evenly into 3 or 4 horizontal layers and put into glass bowl as shown in Fig. 3. Measure the mass of the empty glass bowls and the glass bowls with salt water mixtures before heating.

Step 6: Put the glass bowls with salt water mixtures into an oven with the temperature above 100 °C and measure the mass when all water is evaporated.

Step 7: The water percentages of each layer of the samples are determined based on the mass measurements.

Fig. 2: Plastic bottles with sodium acetate water mixtures

Fig. 3: Empty glass bowls

Experiments were carried out with 4 cm, 5 cm and 8 cm heights of the liquid sodium acetate water mixtures.

Four samples of sodium acetate water mixture of each height were made: 40% water & 60% sodium acetate, 42% water & 58% sodium acetate, 45% water & 65% sodium acetate and 46% water & 54% sodium acetate. All 12 samples was left unmoved in supercooled state for approximately 130 days and then activated by dropping seed crystals in the plastic bottle. The photos of supercooled samples of different heights before activation are shown in Figs. 4-6.

Fig. 4: 4 cm salt water mixtures after 126 days supercooling, 46%, 45%, 42%, 40% water samples from left to right

Fig. 5: 5 cm salt water mixtures after 129 days supercooling, 46%, 45%, 42%, 40% water samples from left to right

Fig. 6: 8 cm salt water mixtures after 131 days supercooling, 46%, 45%, 42%, 40% water samples from left to right

From Fig. 4 to Fig. 6 it can be seen that all the 40% and 42% salt water mixtures had visible solid segregations, while the 45% and 46% salt water mixtures remained clear and transparent after 120 days in supercooled state. The segregated salt in the 40% and 42% salt water mixtures was “soft” and “loose”. Both the 40% and 42% salt water mixtures had a clear solution layer on the top.

Table 1 to Table 3 show the water contents distribution in the layers of each sample indicated by “Top”, “Middle” and “Bottom”. The four layers used in the 8 cm samples are referred as “Top”, “Upper Middle”, “Lower Middle” and “Bottom”. The accuracy of measured mass is 0.1 g. It is assumed that if the water content in a layer is lower than the 39.7% of the trihydrate composition then phase separation is occurring. The water percentages which were lower than 39.7% are shown with red color indicating phase separation. The last row is used for checking the total water content of samples after cutting and heating by summing up evaporated water and salt water mixture of all layers.

Tab. 1 Water content distribution in 4 cm high salt water mixture samples after 126 days supercooling

4 cm samples	40% water sample (%)	42% water sample (%)	45% water sample (%)	46% water sample (%)
Top	44.7	43.5	45.4	45.8
Middle	38.6	42.1	45.3	46.0
Bottom	37.3	42.0	45.6	45.9
Water Recheck	40.2	42.5	45.4	45.9

Tab. 2 Water content distribution in 5 cm high salt water mixture samples after 129 days supercooling

5 cm samples	40% water sample (%)	42% water sample (%)	45% water sample (%)	46% water sample (%)
Top	43.9	45.0	45.4	46.4
Middle	39.4	44.9	45.6	46.4
Bottom	38.0	39.5	45.2	46.6
Water Recheck	40.0	42.4	45.4	46.5

Tab. 3 Water content distribution in 8 cm high salt water mixture samples after 131 days supercooling

8 cm samples	40% water sample (%)	42% water sample (%)	45% water sample (%)	46% water sample (%)
Top	44.7	44.9	45.9	46.5
Upper Middle	40.2	43.5	45.8	46.5
Lower Middle	38.6	40.1	45.5	46.2
Bottom	37.0	39.7	44.3	46.0
Water Recheck	39.9	42.0	45.2	46.3

From Table 1 to 3 it can be seen that the 40% water content salt water mixtures of 4 cm, 5 cm and 8 cm height all suffered from phase separation because the water content of the bottom layer was lower than 39.7% after 120 days in supercooled state which means sodium acetate trihydrate cannot be used as a stable heat storage material for container height higher than or equal to 4 cm.

All the 42% water content salt water mixtures had water contents in the lower parts of the samples of minimum 40%. The smaller the height of the salt water mixture is, the lower the difference between the water content from the bottom to the top of the sample will be. The results indicates that sodium acetate water mixtures consisting of 42% water and 58% sodium acetate won’t suffer from phase separation problems as long as the salt water mixture height is lower than 8 cm. However, conclusions on the long term stability of 42% mixtures must also include considerations of the heat content stability, see section 3.

All the 45% and 46% water content samples have relatively even water content in each layer and don't suffer from phase separation.

It can be concluded from the experiments that too low water content and a too high sample height will cause phase separation problems for long term supercooled sodium acetate water mixtures.

3. Heat content measurements of supercooled sodium acetate samples

3.1. Experimental method and test facilities

A simple heat loss method was used to determine the heat content of different supercooled sodium acetate trihydrate samples with and without additives. This was done by recording the temperature history after starting the crystallization of the supercooled samples at ambient temperature. The crystallizations were started by dropping crystals into the samples, which were placed in a glass jars. After crystallization the samples cooled down to ambient temperature again inside a well-insulated box. When the heat loss coefficient of the glass jar in the well-insulated box is determined the heat released from the samples cooling down can be calculated by Eq. (1).

$$E = \int_{t_b}^{t_e} UA(t) \cdot \left[T_s(t) - T_a(t) \right] \cdot dt / m \qquad \text{(eq.1)}$$

Where E (kJ/kg) is the measured heat content, T_s (°C) and T_a (°C) are the sample and ambient temperature. t_b (s) and t_e (s) are the begin and end time during the heat release process. m (kg) is the sample mass. UA (W/K) is the heat loss coefficient of the glass jar in the well-insulated box determined by testing the cooling process of hot water in the same glass jars with the same height as sodium acetate samples. The UA can be calculated by Eq. (2).

$$UA = \frac{mC}{t_e - t_b} ln \frac{T_e - T_a}{T_b - T_a} \qquad \text{(eq.2)}$$

Where mC (J/K) is the total heat capacity including water, glass jars and lid. T_b (°C) and T_e (°C) are the start and end sample temperature during the period from t_b to t_e.

The samples were all prepared in glass jars as shown in Fig. 7(c) with the height of 5 cm. Three thermocouples pasted outside were used to estimate the average sample temperature, see Fig. 7(b). One thermocouple was fixed outside of the box for recording the ambient temperature, see Fig. 7(a).

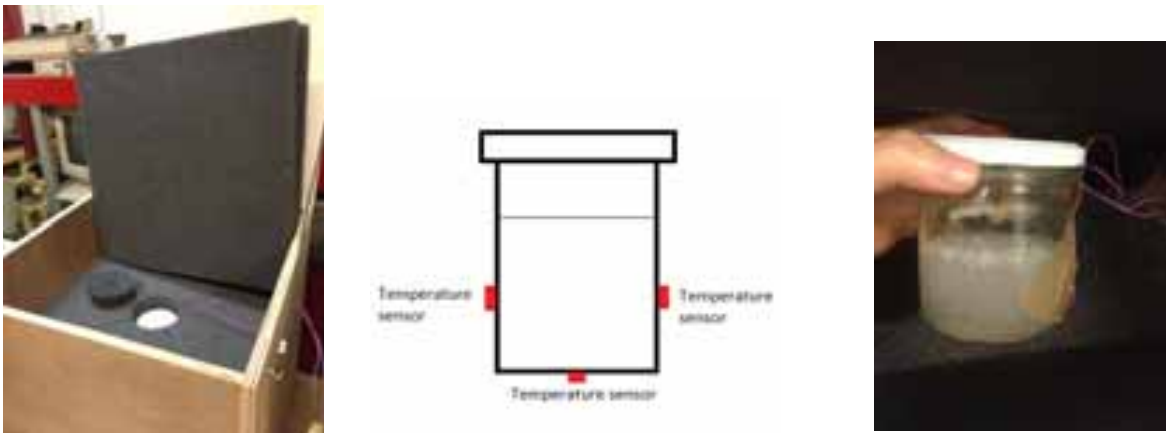

(a) (b) (c)

Fig. 7: (a) The well insulted box (b) Temperature locations (c) Glass jar

3.2. Heat content measurement of sodium acetate water mixtures with different supercooled duration

Samples of sodium acetate water mixtures with 40%, 42%, 45% and 46% water content with a sample height

of 5 cm were prepared in glass jars. Three glass jars of each sodium acetate water mixture, in total 12 glass jars were prepared. The sodium acetate water mixtures were tested with different durations of the supercooled period: short supercooled period less than 14 days, 41 days and 100 days. The tests with the short period of less than 14 days were repeated several times and the average results are given. The results are shown in Table 4 and plotted in Fig. 8 (D2.4, 2015).

It can be seen that for the short term supercooled duration tests the 42% mixture had the highest heat content. If the water content was decreased to lower values than 42% or increased to higher values than 42%, the heat content will decrease. By increasing the supercooled duration to 41 days, the heat content was only reduced for the 42% mixture. By increasing the supercooled duration to 100 days, the heat content of both the 40% and 42% mixtures were significant lower compared to the shorter supercooled duration, while the heat content of the 45% and 46% mixtures were not decreased. The reduced heat contents are marked with red color.

The results of the heat content investigations are in line with the findings of phase separation investigations in section 2. The 40% and 42% salt water mixtures with 5 cm heights suffered from phase separation problems for long term heat storage periods. Adding more extra water is an effective way to solve the phase separation problem but the heat content will be decreased.

Tab. 4 Heat content of the 40%, 42%, 45% and 46% water salt mixtures

Water content of salt water mixture	Heat content (kJ/kg)		
	Short term average	Long term (41 days)	long term (100 days)
40%	162	162	99
42%	194	162	165
45%	165	163	172
46%	159	156	150

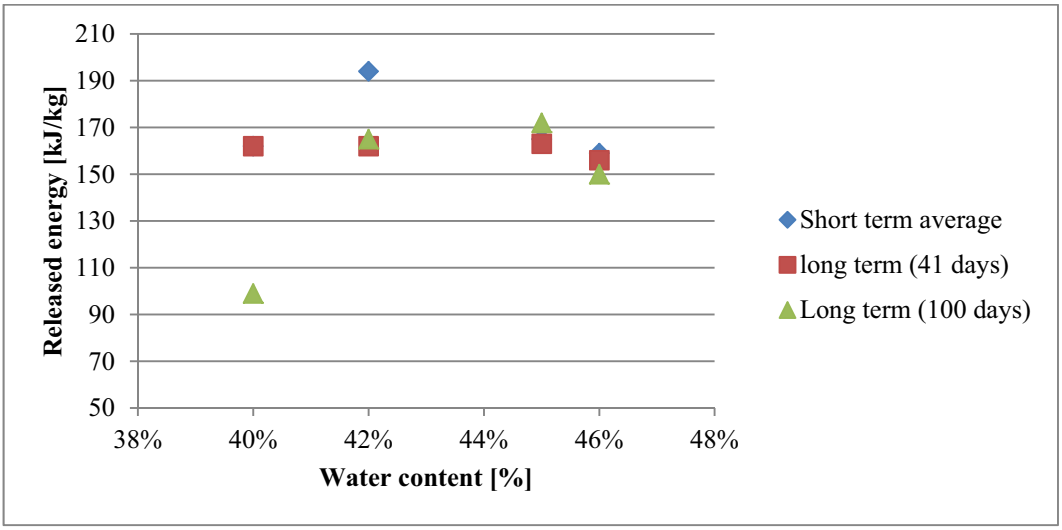

Fig. 8: Heat content of the 40%, 42%, 45% and 46% water salt mixtures

3.3 Heat content measurement of sodium acetate trihydrate with thickening additives

Carboxymethyl Cellulose (CMC) and Xanthan Gum (X-Gum) are thickening agents widely used in the food industry. The thickening effect can increase the viscosity of the liquid sodium acetate trihydrate and suspend the anhydrous salt in the container so that phase separation is reduced.

In small scale experiments, previous studies (Kong et al., 2015) showed that the heat content of sodium acetate trihydrate with 0.5% to 2% CMC or 0.3% to 0.5% X-Gum was increased typically 30% compared to pure sodium acetate trihydrate suffering from phase separation in short supercooled periods, see Fig. 9. The

green line and the purple line are the average heat contents of the 40% and 42% water content salt water mixtures. The blue and red pillars represent the results of the heat contents of sodium acetate trihydrate with different quantities of X-Gum and CMC.

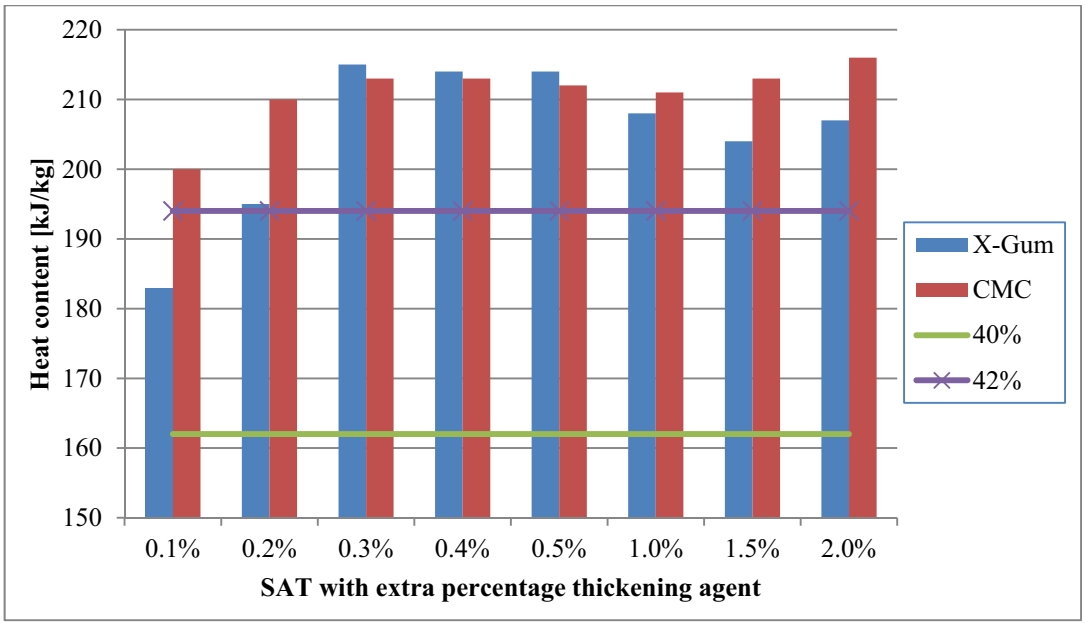

Fig. 9: Heat content of sodium acetate trihydrate with different quantities of thickening agents in short term supercooled period (Kong et al., 2015)

Ageing stability tests of sodium acetate trihydrate with extra water and with CMC were carried out through prototype modules which were designed for a demonstration seasonal heat storage system (Dannemand et al., 2015). The module was constructed by Nilan A/S as a flat plate shape. The chamber with the height of 5 cm containing PCM materials lies in the middle of module. An extension chamber is incorporated in one end at the top surface allowing for expansion of the PCMs when they are heated. An expansion bag or expansion vessel is connected to the extension chamber. Two heat exchangers with manifolds are attached on the top and bottom of the PCM chamber with the height of 4 mm. Parallel channels inside of the heat exchanger covered the entire area of the top and bottom surface of the PCM container aiming to guide a uniform flow distribution. Water is used as the heat transfer fluid running through the heat exchangers for transferring energy between PCM and test facility. The diagram and photo of the flat plate module can be seen in Figs. 10 and 11.

Fig. 10: Diagram of the prototype module (Dannemand et al., 2015)

Two flat plate modules with different PCM materials were tested. One module was filled with 199.5 kg of sodium acetate water mixture consisting of 44.8 % water and 55.2 % sodium acetate by weight. Repeating tests were carried out for 20 times with different flow rates, charge and discharge powers, temperatures settings and durations for a period of 8 month. The longest stable supercoooled duration of the module at indoor ambient temperature was two months. Then it was activated manually and the latent energy was discharged. The energy discharged of the first test cycle was 194 kJ/kg and then it dropped to 179 kJ/kg in the later test cycles. That is a 7.5 % decrease of energy released after repeating test cycles.

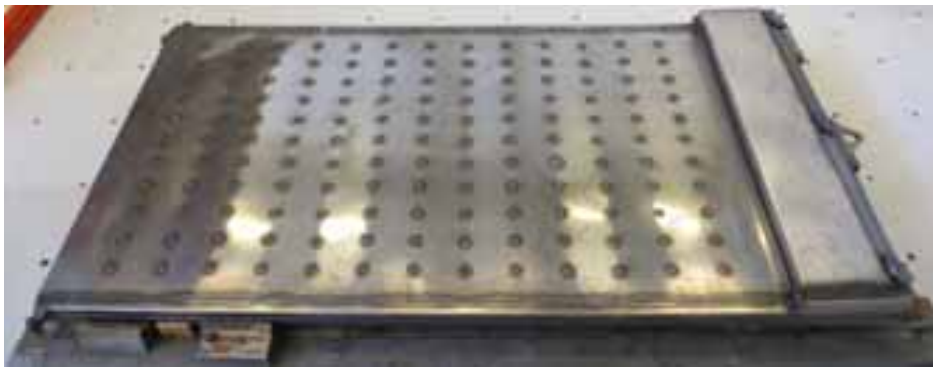

Fig. 11: Photo of the prototype module (Dannemand et al., 2015)

Another module was filled with sodium acetate trihydrate with 1% CMC, 2% graphite powder and 5 liter paraffin oil, totally 202 kg. The purpose of adding graphite and oil is to increase the heat exchange capacity rate. 10 repeating tests with similar flow rates, charge and discharge powers and temperatures settings were carried out over 2 month period. The energy discharged of the sodium acetate trihydrate with these additives was 200 kJ/kg in the first test cycle and kept stable around 201 kJ/kg in the following test cycles. The module reached stable supercooled at indoor ambient temperature for 8 days and then activated spontaneously. The energy discharged after 8 days was still 200 kJ/kg which illustrated that sodium acetate trihydrate with CMC as heat storage material had heat content stability after repeating tests and long term supercooling.

Ageing stability tests of sodium acetate trihydrate with X-Gum were carried out with another kind of prototype module which was designed as a vertical cylindrical container made of stainless steel by H.M. Heizkörper GmbH & Co. KG (Dannemand and Furbo, 2014). The module with EPP insulation is shown in Fig. 12. A plastic tube is installed with one end connecting to the top of the module and with the other end connecting to an air filter. The design can keep the same pressure of inside and outside module by allowing air exchange through the tube and the air filter. There is a heat exchanger inside the cylindrical module which consist stainless steel pipes in a circular formation with thin aluminum fins attached and manifolds located on the top and the bottom. The module is connected to a heating and cooling test facility. Water is used as the heat transfer fluid passing through the heat exchanger from bottom to top.

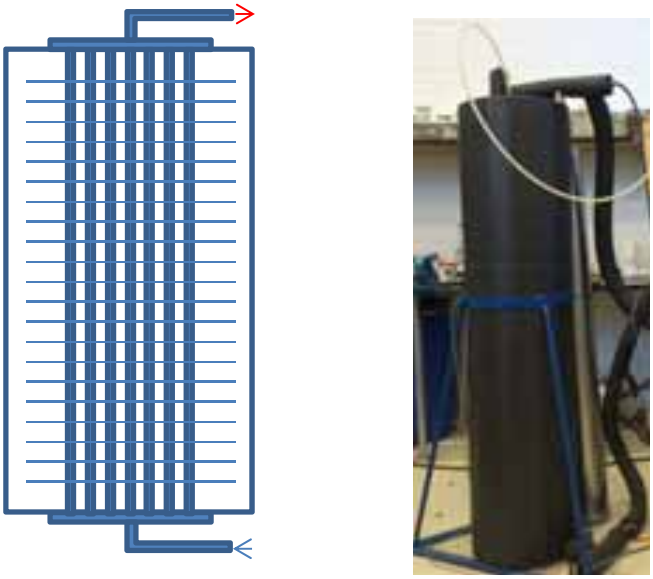

Fig. 12: Diagram and photo of cylinder module

The module contained sodium acetate trihydrate with 0.48% fine powder of Xanthan Gum (X-Gum-F) and 4.4% fine powder of graphite, totally 116.3 kg. The PCM material filled approximately 90% of the total

volume inside of the module. 20 repeating tests with similar charge and discharge flow rates, heating powers and temperature settings were carried out over four months. The module still had problems with stable supercooling possibly due to dust which caused spontaneous crystallization through the air filter and the tube into the top of the module. The longest supercooling period during these test cycles was 9 days. The energy discharged from the PCM was 205 kJ/kg at the first test cycle and stable at this level in the following test cycles.

Tab. 5 Summary of prototype module tests

PCM material	Prototype module	Heat content of the first test (kJ/kg)	Number of cycle tests	Heat content of last test (kJ/kg)	Longest supercooling duration (days)	Heat content after longest supercooled duration (kJ/kg)
44.8% water +55.2% sodium acetate	Flat plate	194	20	179	60	179
Sodium acetate trihydrate +1% CMC+2% graphite+5 liter paraffin oil	Flat plate	200	10	200	8	200
Sodium acetate trihydrate +0.48% X-Gum+4.4% graphite	Vertical cylinder	205	20	206	9	207

The prototype module test results are summarized in Table 5. It can be concluded from the laboratory prototype module tests that a sodium acetate water mixture with 44.8% water will suffer from phase separation and the energy released will decrease after repeating cycles and long term supercooled period. The sodium acetate trihydrate with CMC and X-Gum have high stability of released energy for repeating test cycles and are promising for stability for long term supercooling.

4. Conclusions

Phase separation is a key problem related to long term stability of seasonal heat storages based on stable supercooling of sodium acetate trihydrate with and without additives. Water content measurements in different layers of sodium acetate water mixtures after long term supercooled periods and heat contents measurements of sodium acetate trihydrate with additives in repeating and long term supercooled periods were investigated and presented in this paper. Based on the investigations it is concluded that:

Sodium acetate trihydrate and sodium acetate water mixtures with water contents lower than or equal to 42% will suffer from phase separation problems for the height of heat storage less than or equal to 8 cm. Sodium acetate water mixtures with water contents higher than 42% will not suffer from the phase separation if the heat storage height is lower than or equal to 8 cm. However, the heat content of the heat storage material will be decreased by adding extra water.

Sodium acetate trihydrate with the additive CMC and X-Gum are promising seasonal heat storage materials since they have high heat contents and ageing stabilities in repeating tests and long term supercooled durations.

5. References

Cabeza, L.F., Svensson, G., Hiebler, S., Mehling, H., 2003. Thermal performance of sodium acetate trihydrate thickened with different materials as phase change energy storage material. Appl. Therm. Eng. 23, 1697–1704. doi:10.1016/S1359-4311(03)00107-8

D2.4, 2015. Materials ageing stability. COMTES project - Work package 2 - Materials. Report number: D2.4 (deliverable 2.4).

Dannemand, M., Furbo, S., 2014. Test of thermobattrie heat storage module. Report number R 308. Department of Civil Engineering, Technical University of Denmark.

Dannemand, M., Kong, W., Fan, J., Johansen, J.B., Furbo, S., 2015. Laboratory Test of a Prototype Heat Storage Module Based on Stable Supercooling of Sodium Acetate Trihydrate. Energy Procedia 70, 172–181. doi:10.1016/j.egypro.2015.02.113

Furbo, S., Dragsted, J., Chen, Z., Fan, J., Andersen, E., Perers, B., 2010. Towards seasonal heat storage based on stable super cooling of sodium acetate trihydrate, in: Eorosun 2010 Congress Proceedings.

Furbo, S., Svendsen, S., 1977. Report on heat storage in a solar heating system using salt hydrates. Report no. 70. Thermal Insulation Laboratory, Technical University of Denmark.

Kong, W., Dannemand, M., Johansen, J.B., Fan, J., Dragsted, J., Englmair, G., Furbo, S., 2015. Experimental investigations on heat content of supercooled sodium acetate trihydrate by a simple heat loss method. Sol. Energy Mater. Sol. Cells Under review.

Conference Proceedings

Solar World Congress 2015
Daegu, Korea, 08 – 12 November 2015

SOLAR HOT WATER PRODUCTION BY USING LATENT HEAT STORAGE UNDER TROPICAL CONDITIONS

M.S. Naghavi[1], K.S. Ong[2], I.A. Badruddin[1], H.S.C. Metselaar[1], M. Mehrali[1], A.R. Akhiani[1]

[1] Center for advance materials, Department of Mechanical Engineering, Faculty of Engineering, University of Malaya, Kuala Lumpur (Malaysia)

[2] Department of Industrial Engineering, Faculty of Engineering and Green Technology, Universiti Tunku Abdul Rahman, Kampar (Malaysia)

Abstract

This paper reports a theoretical study about the thermal performance of the new design of solar water heater with a latent heat storage unit. The new design is a solar water heater system consisting of an array of evacuated tube heat pipe solar collectors connected to a common manifold filled with phase change material and acting as a latent heat storage tank. Solar energy incident on the evacuated tube is collected and stored in the latent heat storage tank. The stored heat is then transferred to the domestic hot water supply via a finned pipe placed inside the tank. The performance is analyzed based on an accurate set of mathematical equations. The various climatic conditions of a tropical region are considered as operating environment of the device. The thermal performance of the new design is compared with the conventional evacuated tube heat pipe solar water heater to have a better observation about the differences and advantageous of the new design. The results showed that the thermal performance of the proposed system is higher than a conventional system at certain conditions, which depend to the weather conditions and flowrates, but the sensitivity of the efficiency of the proposed system to the supply water flowrate is less than the conventional system.

Keywords: *solar water heater, evacuated tube, heat pipe, phase change material, thermal energy storage, comparative study*

1. Introduction

Many different combinations of solar thermal systems in integration with phase change material (PCM) for latent heat storage (LHS) have been developed for hot water production, air heating/cooling and power generation [1-6]. Using LHS for solar water heating (SWH) systems received many attractions by researchers. In most of the designs, the PCM was placed in the storage tank [7-13]. A general finding from the most of these researches is that under certain conditions such as system configuration, type of PCM, inlet water temperature and water flow rate, there are improvements in the performance of the SWH-PCM systems.

Al-Hinti et al. [13] experimentally investigated the performance of water-PCM for use with conventional SWH systems. PCM contained in small cylindrical aluminum containers. It was found that the use of the suggested configuration could result in a 13-14^{o}C advantage in the stored hot water temperature over extended periods of time. The hot water storage performance was also investigated when connected to flat plate collectors in a closed-loop system with conventional natural circulation. Over a test period of 24 hour, the stored water temperature remained at least 30^{o}C higher than the ambient temperature. The use of short periods of forced circulation was found to have minimum effect on the performance of the system. Nallusamy and Velraj [14] investigation on a packed bed combined sensible and latent heat storage unit integrated with solar water heating system. It was observed that the mass flow rate has a significant effect on the heat extraction rate from the collector, which in turn affects the rate of charging of the thermal energy storage (TES) tank.

Varol et al. [15] attempted to forecast the performance of a solar collector system using PCM in the hot water storage tank and compared the collector efficiency with the convectional system. In this design, PCM was placed to the bottom of the collector and hot water pipe lines were pathing under the absorber plate, through the PCM slab. It was found that the solar collector system with PCM is more effective than convectional systems. Padovan and Manzan [16] developed an algorithm to optimize a simple configuration of the SWH, which features a plane solar collector, a boiler and a PCM enhanced tank. In parallel with the optimization a sensitivity analysis was carried on in order to find out the relation between the design parameters of the tank

doi:10.18086/swc.2015.02.11 Available at http://proceedings.ises.org

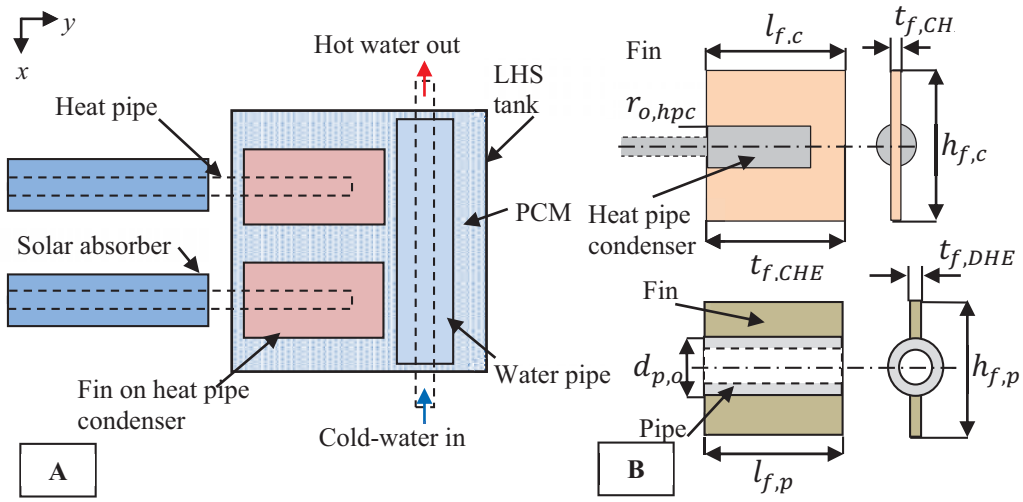

Fig. 1: A. HPSC-PCM system; B. Fin designs for condenser shell (top) and water supply pipe (bottom)

(geometry, phase change temperature of the PCM, and insulation) and the performance of the system. The main outcome of this research was that for this design, the PCM did not have major impact on the results, while other parameters play a more significant role.

To the authors' knowledge, although there are few research works on the combination of heat pipe solar collectors and PCMs in storage tanks [17, 18], there is no work done on the proposed HPSC-PCM system where there is an intermediate heat exchanger on the manifold (condenser side) of the heat pipe. A new HPSC-PCM system is described in the following section. This research plans to examine, analytically, the feasibility of this system in different climatic conditions in a tropical country (Malaysia). The charging/discharging processes during the day/night times are determined. The performance of a conventional HPSC (HPSC-C) theoretically compared with this innovative design. PCM melting/solidifying processes are determined by a one-phase Stefan problem quasi-stationary approximation method, which is one of the more widely used standard analytical solutions. Calculations are done by a computational code developed in Matlab.

2. A description of the proposed system

Fig. 1A displays the recommended HPSC-PCM system which comprises an arrangement of evacuated tube heat pipe solar collectors linked to a shared manifold loaded with PCM. This manifold functions as a LHS tank. The evaporator segments of the heat pipes are subjected to solar radiation while the condenser segments are slotted into finned sockets which have been inserted onto the manifold. The evaporator performs as an absorber of solar energy which is then conveyed to the condenser by way of heat pipe action involving evaporation and condensation. This energy is stockpiled in the PCM-filled LHS tank. Household cold water delivered by way of a finned pipe rises in temperature as it makes its way through the LHS tank. Heat transfer efficiency is raised through the welding of single-row vertical fins onto the heat pipe condenser shell and also onto the finned pipe line (Fig. 1B). Table 1 exhibits the dimensions of the LHS tank, HPSC and fins.

3. Hypothetical model

This section provides a concise presentation of equations for the arithmetical modelling of heat transfer. A comprehensive array of equations and flow charts was forwarded in a previous paper [19]. During the process of charging and discharging of heat within the PCM, three separate heat transfer developments take place. To begin with, the evaporator section of the HPSC soaks up heat from solar energy which is then conveyed to the condenser section. Subsequently, the heat transfers to the PCM through the condenser shell. The accumulated heat discharges from the PCM to the finned pipeline and warm up the water passing through it. The computations for these procedures are carried out separately and in accordance to the sequence during which they take place.

3.1. Charging mode

The main factors influencing absorbable solar radiation are ground reflectance, angle and the material employed as collector. For the purpose of assessing these factors, we harnessed the process launched by Duffie and Beckman [20]. The temperature of heat pipe segments was ascertained through an equation forwarded by Zue and Vafai [21]. Through this equation, a methodical resolution to problems related to the surface temperature along the span of a low temperature heat pipe can be realized.

Table 1, Dimensions of LHS tank, HPSC and fins

Manifold and Evacuated tube		Heat pipe	
Item	Value	Item	Value
Number of heat pipes	20	Evaporator length (mm)	1675.00
Glass tube outer diameter (mm)	58	Adiabatic length (mm)	30.00
Glass tube thickness (mm)	2	Condenser length (mm)	70.00
Absorber plate thickness (mm)	1	Evaporator outer radius (mm)	4.00
Evacuated tube length (mm)	1675	Condenser outer radius (mm)	12.00
Fin thickness on the CHE (mm)	2	Wall thickness (mm)	0.50
Storage tank height (mm)	204	Wick thickness (mm)	1.00
Storage tank width (mm)	204	Vapor core radius (mm)	3.00
Storage tank length (mm)	1725	Thermal conductivity of liquid (W/mK)	0.63
Fin height on the CHE (mm)	200	Thermal conductivity of wall (W/mK)	385
Fin length on the CHE (mm)	200	Porosity	0.5
Fin thickness on DHE (mm)	2	Permeability	1.5×10^{-9}
Fin height on DHE (mm)	91	Thickness of the fiber (mm)	2×10^{-7}
Pipe outer diameter (mm)	18	Number of meshes per unit length	4000
Length of a section (mm)	142		
Slope of solar collector (°)	20		
Glass emittance	0.88		
Plate emittance	0.95		
Reflective Index of glass	1.53		

The PCM heat equation is deemed a 2nd order linear partial differential equation with heterogeneous boundary conditions. As the transfer of heat from the condenser shell to the PCM occurs in an arrangement that is similar for both sides, computations for the PCM are ascertained based solely on one side of the condenser shell. A significant presumption regarding the quasi-stationary one-phase Stefan problem is that the hot plate (which is the finned condenser shell) is subjected to a consistent temperature. Also presumed is that heat transference from the fin on the shell to the PCM is a one-dimensional occurrence and that the temperature of the PCM at the outset is at melting point.

Expressed as $T(x,t)$, the PCM temperature is a function of position and time. At a consistent temperature, a slab of the PCM ($0 \le x \le l$) is deemed to be solid. The imposed temperature at the interface of the PCM and the HPC fin facilitates the transference of heat through the PCM. It is taken for granted that the remaining three edges are in an insulated state. The following is an expression of the mathematical model for the one-dimensional transient heating procedure.

$$\rho_s c_s \frac{\partial T}{\partial t} = k_s \frac{\partial^2 T}{\partial x^2}, \quad \text{(eq. 1)}$$

It is essential that this equation be solved in accordance to the preliminary and boundary conditions for the scale of $0 < x < X(t)$:

$$T_{pcm}(0,t) = T_{hp}(t), \quad \text{(eq. 2a)}$$

$$T_{pcm}\big(X_{pcm}(t),t\big) = T_m, \quad \text{(eq. 2b)}$$

$$\rho_l L {X_{pcm}}'(t) = -k_l \frac{\partial T_{pcm}}{\partial t}|_{x=X_{pcm}(t)}, \quad \text{(eq. 2c)}$$

$$X_{pcm}(0) = 0 \quad \text{(eq. 2d)}$$

where X(t) denotes the position of the interface. The heat equation is rendered exceedingly complex by the need to meet boundary conditions (eq. 2c). In line with the Neumann solution to the one-phase Stefan problem [22], the quasi-stationary solution for expressing the interface position and temperature dissemination in the PCM (in the context of primary physical variables related to the charging procedure) assumes the following configuration:

$$X_{pcm}(t) = \eta_{f,c}\sqrt{(2k_l St_l t)/(\rho c_l)} \quad \text{(eq. 3)}$$

$$T_{pcm}(x,t) = T_{hpc}(t) - \Delta T_l \frac{x}{X_{pcm}(t)}, 0 \le x \le X_{pcm}(t), \quad \text{(eq. 4)}$$

where, $\Delta T_l = T_{hpc}(t) - T_m$.

The heat transfer from the object to the surrounding material is accelerated by the presence of fins on the condenser shell. Consistency in terms of heat dispersal on the surface of the fin was taken as fact. For the purpose of incorporating the impact of this presupposition into the computation procedure, the effectiveness of the fin is roped in through the array of equations cited in [19].

3.2. Discharging mode

As portrayed in Figure 2, the PCM within the LHS tank is split into a fixed number of slabs (*j*). Each slab is subjected to the application of energy balance. The outlet water temperature of each slab matches that of the inlet water temperature of the neighbouring slab. The inlet water temperature determines the pace of PCM solidification for every slab. The finned pipe is positioned at the centre of the tank. This serves to partition every slab into two identical segments on both the upper and lower sides of the finned pipe. Both sides of the fin come into play during the heat transfer process.

The solidification of the PCM is attributed to the flow of cold water into the storage tank at a velocity of *v* and a temperature of $T_{w,i,i}$. Each slab's solid-liquid interface progression speed and their outlet water temperature are the undetermined variables. It is essential that the verification of these variables be carried out in unison. It is supposed that in the event the Stefan number is inconsequential ($St < 2$) during the discharging procedure, the temperature of the PCM will stay unremittingly within reach of melting point while the solid-liquid interface is advancing [22]. Hence, the supply water temperature rises in tandem with the solidification process of the slab *j*. Subsequent to complete solidification, slab *j* loses its thermal inertia, its temperature will quickly decline to match the inlet water temperature at its location, and the water will swiftly react to one fewer slab. In other words, at the outset, *N* slabs were raising the temperature of the supply water. However, upon the solidification of the initial PCM slabs, the supply water temperature elevation was attributed to *N-1* slabs. The presumptions that require contemplation for the application of this solution process are: (a) during the process of discharging, the transference of thermal energy from the PCM to the finned pipe is exclusively one-directional (i.e. on the *y* axis), (b) when the fall in the axial temperature is not excessive, the transmission of heat in the direction of x can be disregarded, (c) heat conduction within water that is thermally stable is inconsequential, (d) the latent heat of the PCM is so substantial that the surface temperature of the PCM at the fins and walls of the pipe can, for the most part, be deemed equivalent to T_m during the whole process of solidification. This presumption is believable if one takes into consideration the fact that with a raised latent temperature (insignificant Stefan number), the front will not make much headway into the PCM, while an elevated degree of conductivity will lead to the tendency to round up the temperature. In a situation where the PCM does not melt completely during charging, it follows that during the discharging process only the PCM molten mass fraction is regarded as an active mass of the PCM slab.

Heat transference to the finned pipe from the melted PCM is realized through:

$$\dot{q}(t) = \dot{q}_p(\mathrm{t}) + \dot{q}_{f,p}(\mathrm{t}) \qquad \text{(eq. 5)}$$

where $\dot{q}_p(\mathrm{t})$ denotes the heat flux to the pipe and $\dot{q}_{f,p}(\mathrm{t})$ denotes the heat flux through the fins. An array of equations for ascertaining the heat flux can be observed in [19].

Efforts to determine the solidification time of the PCM slabs necessitate a repeat solution to eq. 1 with altered initial and boundary circumstances. In such a situation, it is imperative that the heat equation be worked out in accordance with the imposed heat flux ($\dot{q} < 0$):

$$T_{pcm}(x, 0) = T_m, \qquad \text{(eq. 6a)}$$

$$\rho_s \bar{L} {Y_{pcm}}'(t) = -k_s \frac{\partial T_{pcm}}{\partial t}|_{y=Y_{pcm}(t)}, \qquad \text{(eq. 6b)}$$

$$-k_s \frac{\partial T_{pcm}}{\partial t}|_{y=0} = \dot{q}(t), \qquad \text{(eq. 6c)}$$

$$Y_{pcm}(0) = 0 \qquad \text{(eq. 6d)}$$

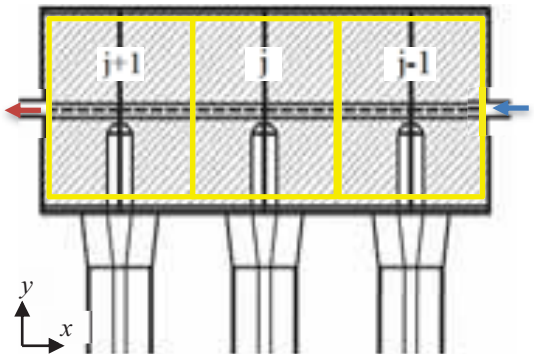

Fig. 2: Arrangement of PCM slabs

In this approach, a molten slab at its melt temperature of T_m is undergoing solidification through an imposed flux $\dot{q}(t)$ at the exteriors of the fins. In line with the Neumann solution technique for the management of a one-phase quasi-stationary Stefan problem, the inclusion of initial and boundary conditions gives rise to the following equation for the solid-liquid interface location:

$$Y_{pcm}(t) = \dot{q}(t)\, t/\rho_s\, \bar{L} \quad \text{(eq. 7)}$$

In a circumstance where the temperature of the molten PCM slabs exceeds that of the melting point, the effect of stored sensible heat can be realized by modifying the latent heat magnitude through the following equation [22]:

$$\bar{L} = L + \frac{1}{2} c_l (T_L - T_m) \quad \text{(eq. 8)}$$

where $T_L = mean\left(T_{pcm}\left(x = 0{:}\, l_{pcm}\, , t_{end}\right)\right)$ represents the mean temperature of the PCM at the culmination of the melting time.

3.3. Exploitable heated water and performance efficiency

In this segment, an evaluation is conducted on the effectiveness of the recommended scheme in comparison to a conventional scheme. In a conventional scheme (deemed a baseline system), heated water is amassed in a tank without any draining off of water in day time. The effectiveness and potential of a scheme for hot water delivery can be determined through a calculation involving the effects of stratification.

The baseline SWH system entails the passage of cold water directly across the heat pipe condenser in the manifold. The resulting hot water is then amassed in an insulated reservoir. The degree of heat transfer from the condenser to the supply water can be ascertained through equations which are also used for computing the temperature of the heat pipe surface (refer to Section 3.1). The equations for calculating heat transfer from the condenser to the supply water can be observed in [19].

Solar heat is accumulated during daylight hours and saved in the storage tank. No water is drawn out during daytime. The main purpose of the storage tank is to preserve the temperature of the heated water. It is thus essential that the degree to which heat diminishes over time be calculated. Natural thermal stratification is a significant factor in operations involving the storage of heated water in a tank[23]. Even in a circumstance where there is no water draw-off, heat convection from the hot water layer to layers of a lower temperature, and vertical conduction in the wall of the storage tank can lead to destratification [24].

Of late, a study conducted by Armstrong et al. [25], succeeded in establishing the destratification-related deficit rate of utilizable heated water in a reserve tank. This investigation revealed that a 74 litre capacity copper tank with a thickness of 0.7mm, and cladded with an outer 50mm layer of rigid polyurethane insulating foam (0.028 W/mK) [26], underwent a usable hot water volume loss rate of 2.1 litres per hour over a period of 12 hours. A division of the tank capacity by the usable volume loss rate led to the presumption that 3% of usable heated water in the tank will be done away with. An additional presumption is that the loss of heat to the environment from the wall of the tank is insignificant in comparison to the conjugate exchange with the water.

In the opinion of Armstrong [23] the utilizable heated water volume is identical to the volume of fluid from a tank that can be mixed to a favourable ultimate operational temperature (T_u.) The utilizable heated water volume can be calculated through the equation:

$$V_u(t) = m_w \times \sum_{hr=1}^{12} \frac{T_{w,t,o}(t) - T_u}{T_u - T_{w,t,i}(t)} \quad \text{(eq. 9)}$$

Bearing in mind that the tank is deemed to be in an inactive mode, and taking into consideration the usable volume loss rate percentage (*Lr*), the usable volume obliteration can be calculated through the equation below:

$$V_{u,\mathrm{d}}(t) = V_u(t) \times Lr \times (12 - t) \quad \text{(eq. 10)}$$

The expression $(12 - t)$ denotes the period that the generated heated water in the solar collector will be standing by in the tank. Thus, the volume of left over utilizable hot water after a period of 12 hours can be calculated through the equation:

$$V_{u,\mathrm{r}} = \sum_{hr=1}^{12} V_u(t) - V_{u,\mathrm{d}}(t) \quad \text{(eq. 11)}$$

As destratification does not transpire in the PCM tank, the presence of detrimental energy in this tank can be discounted ($V_{u,\mathrm{d}}(t) = 0$). In keeping with equations (9) and (11), the volume of usable hot water and total usable hot water generated by the PCM tank is calculable.

The total energy liberated by usable hot water from the water and PCM tanks can be determined through the equation:

The total delivered energy by usable hot water from the water tank and from the PCM tank can be calculated by:

$$E_d = V_{u,\mathrm{r}}\, c_{p,w}\, (T_u - T_{w,t,i}(t)) \quad \text{(eq. 12)}$$

The systems' energy efficiency is computed through:

$$\eta_{tot} = \frac{E_d}{S} \quad \text{(eq. 13)}$$

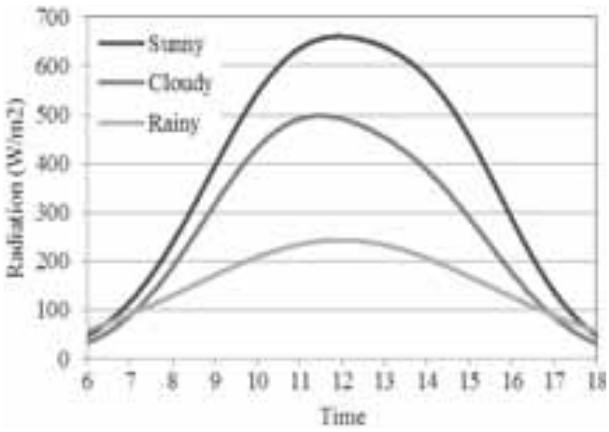

Fig. 3: Solar radiation

4. Results and discussion

The predominant objective of this endeavour is to hypothetically assess the thermal capacity of the combined HPSC-LHS systems for storage in various climate conditions and compare it with the baseline system. In this investigation, water does not flow across the manifold during the day. It is only after sunset, when the system controller allows water to flow through the inbuilt pipe in the tank, then the system is in discharging mode. The precision of this hypothetical approach is examined in [19].

Authentic meteorological data stretching over a time span of two years (2008-2009) was acquired from the Kuala Lumpur International Airport meteorological station (Lat. 2.44^{o}& Long. 101.42^{o}) to assess the twelve-monthly solar radiation concentration. As for the daily solar radiation, the days were classified as sunny (I>18 MJ/m^2/day), cloudy (18>I>13 MJ/m^2/day) and rainy (13>I MJ/m^2/day) days. The average solar radiation level for each classification is displayed in Figure 3.

4.1. PCM charging and discharging processes

At the outset, the PCM is in a solid form. The liquefaction process of the PCM is triggered upon its arrival at the melting temperature. Table 2 displays the features of the paraffin utilized as the PCM and copper fin properties. The temperature of the melted fraction climbs unremittingly on condition that the supply of heat is uninterrupted. The rise and fall of the temperature gradient is directly linked to heat flux discrepancies. The efficiency of the finned shell on the heat pipe condenser is approximately 90% for copper materials. As previously stated, the system involves the employment of 20 steel pipes. During charging mode, the storage tank remains on standby and no supply water flows through the pipe. As such, for all 20 slabs, the PCM thermoclines and interface growth designs are identical. Figure 4 portrays the progressions of the liquid-solid interfaces for the three distinct weather conditions. At the conclusion of a sunny day, it was observed that melting of roughly 60mm of the PCM thickness had occurred at each side of the finned shell. As for a cloudy and rainy day, the level of melting was approximately 52mm and 43mm, respectively. It is apparent that during the morning hours, the interface progression rate is accelerated. The two explanations for this circumstance are (a) the elevated temperature gradient between the condenser and the PCM during the morning heating up period and (b) the attendance of liquid PCM surrounding the fin with its intrinsic depleted convective heat transfer coefficient. As heat transmission through the heat pipe takes place purely in one direction, specifically from the evaporator section to the condenser section (resembling a one-way valve [27]), energy wastage from the storage tank is averted.

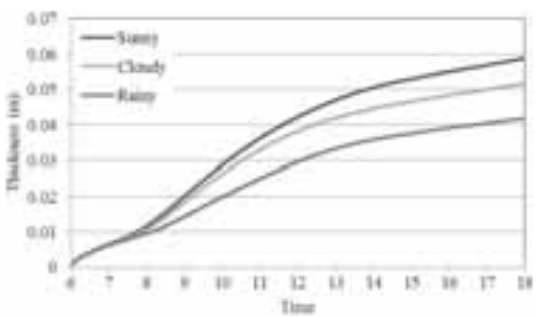

Fig. 4: Liquid-solid interface in charging mode

Tab. 2: Physical properties of paraffin wax and copper fins [28, 29]

Property	PCM	Fin (Solid)
Melting point (°C)	64	-
Density solid / liquid at 15/70°C (kg/m^3)	990 / 916	2713
Thermal conductivity of solid / liquid (W/mK)	0.349 / 0.167	380
Specific heat solid / liquid (kJ/kgK)	2.76 / 2.48	0.96
Volume expansion at ΔT=20°C (%)	0.293	-
Heat storage capacity (kJ/kg)	174	-
Dynamic viscosity (kg/ms)	0.00385	-

While the heat transfer route in the charging mode runs parallel to the *x* axis, in the discharging mode it runs parallel to the *y* axis (Figure 1). It is taken for granted that the discharge procedure begins subsequent to sunset as soon as the controller permits the flow of supply water through the finned pipe. Due to the fact that in the discharging mode, the transference of convective heat within the pipe is paired to heat deletion from the PCM, the most significant parameters to scrutinize in the storage reservoir are the outlet water temperature and solid-liquid interface progression of the various slabs.

As described in Section 3.2 and Figure 2, as a result of the elevation in water temperature while flowing through the finned pipe during discharging mode, the phase alteration performance of the PCM fluctuates across the span of the storage tank. In both rectangular slabs, heat transfer from the molten PCM to the finned pipe is symmetrical. The progression of the solid-liquid interface in relation to three slabs of the PCM tank for two flow rates and three weather conditions is exhibited in Figure 5. The outcomes imply that former PCM slabs experience solidification quicker than latter ones. This is attributed to the greater temperature disparity of the inlet supply water and PCM.

Owing to the elevated temperature of the molten PCM at the extremity of the charging mode (refer to Equation 8), a customized latent heat value of 229*kJ/kg* was utilized to ascertain the interface progression.

4.2. Temperature of supply water

The simulation outcomes for the outlet supply water temperature after 18:00 at flow velocities of 50 litres and 70 litres per hour (lph) are displayed in Figure 6. The inlet cold water temperature is maintained at 29ºC. An elevation in the flow rate brings about a decrease in the system's operating time. The proposed operational temperature for household usage is between 38ºC and 41ºC [30]. For this study, the operational temperature was presumed to be 40ºC. As such, the system's operating time with an outlet water temperature in excess of 40ºC is downgraded from more than four hours to just about three hours. The maximum outlet supply water temperature on days that are sunny was recorded as 53ºC for a flow rate of 50 lph, and close to 47ºC for a flow rate of 70 lph.

The HPSC-C system equipped with 20 heat pipes was simulated at two flow rates for three weather conditions to evaluate the outlet water temperature. According to the graphs, the peak usage period is during noontime, and the highest hot water temperatures in the HPSC-C system in various circumstances are below

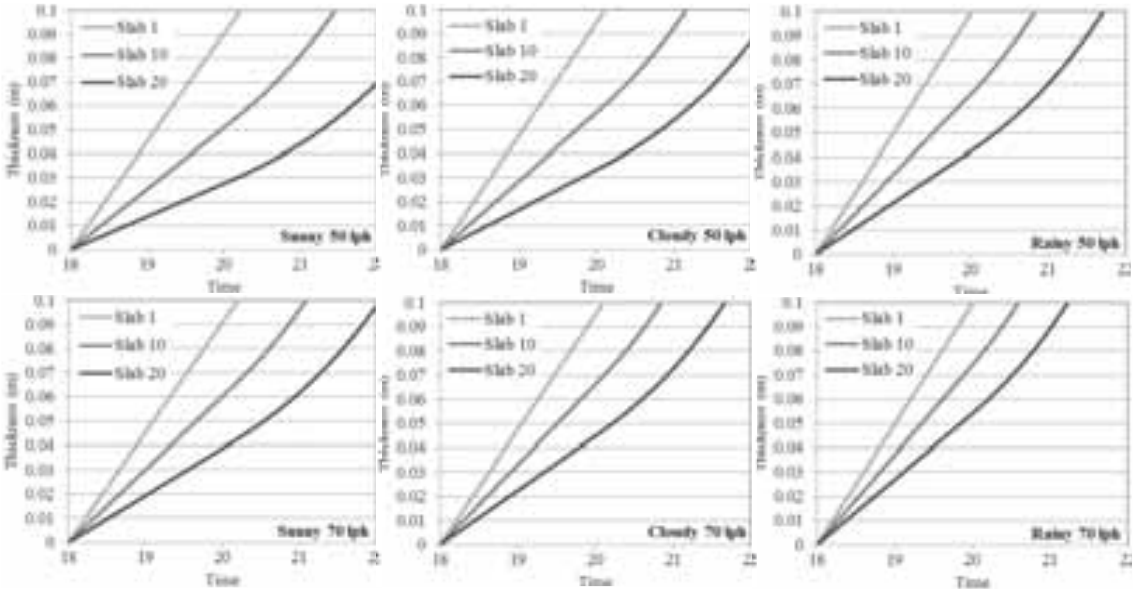

Fig. 5: Progression of solid-liquid interface in slabs 1, 10 and 20 of PCM tank

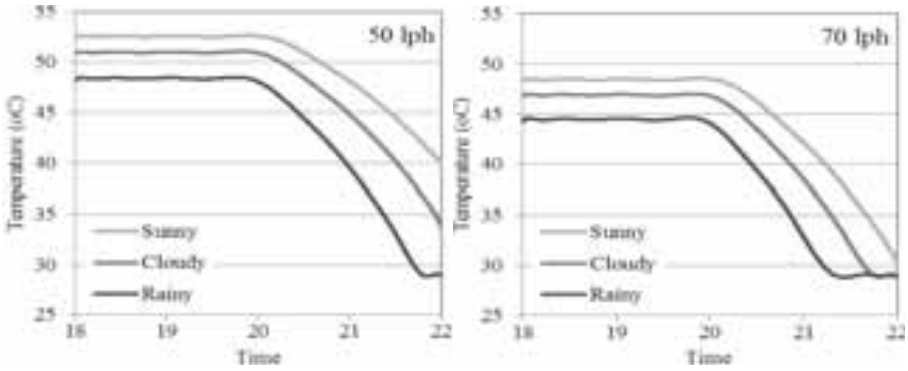

Fig. 6: Outlet supply water temperature ($T_{w,i,o}$) for ETHPSC-PCM system

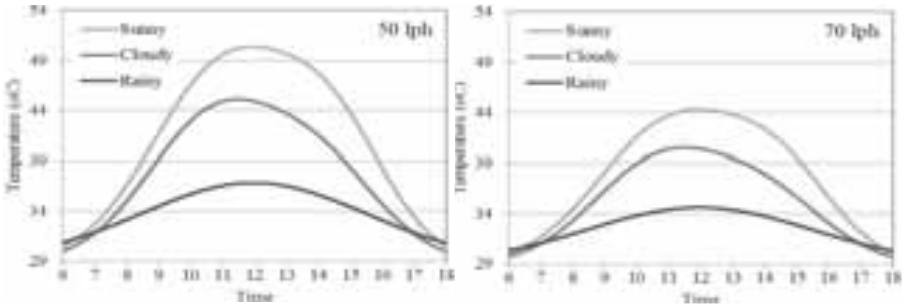

Fig. 7: Outlet water temperature ($T_{w,b,o}$) for ETHPSC-C system

those in the HPSC-PCM system. As the demand for domestic heated water is at its highest at sundown, the usefulness of the recommended system is enhanced by the moving of the peak time to this period.

4.3. Comparative investigation

In order to compare the baseline and proposed systems, it is presumed that the produced hot water in the storage tank of the baseline system remains in the storage tank until evening. The releasing water from the hot water storage tank and the LHS tank start at the same time. As the temperature of the outlet water from the tank is above that of the operating temperature (39°C), it is essential that it be mixed with cold water (29°C).

The scale of generated heated water at operating temperature as well as the total effectiveness of the systems can be approximated through the equations presented in Section 3.3. A comparison between the HPSC-PCM system and the HPSC-C system in terms of efficiency (η_{tot}) and usable volume (V_u) for two flow rates and

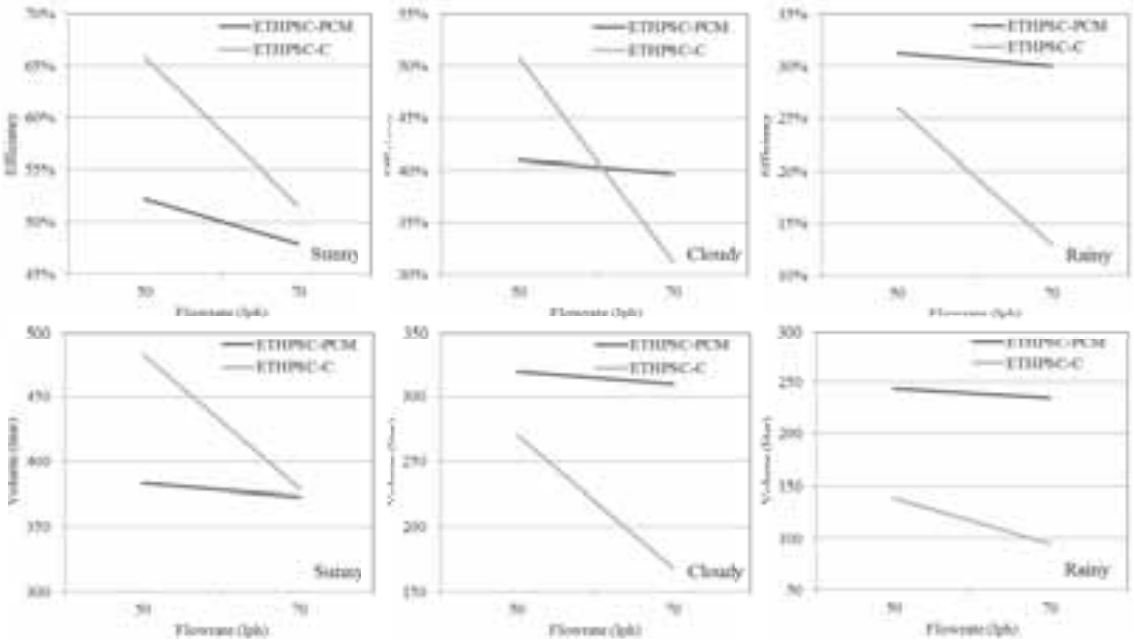

Fig. 8: Comparison of efficiency and usable hot water volume

three weather conditions are shown in Figure 8. As the thermal operational level of the HPSC-C system plunges drastically upon elevations in the draw-off flow rates, it follows that the volume of usable heated water also plummets. As for the proposed system, by increasing the flowrate, although a decrease in thermal efficiency is unavoidable, this decrease is not as rapid as in the conventional system. On a sunny day, the efficiency of the HPSC-PCM system ranges between 53% and 48% upon an elevation in the flow rate from 50 lph to 70 lph. Under a similar circumstance, the efficiency level of the HPSC-C fluctuates between 61% and 52%. During harsh (rainy) weather conditions, the effectiveness of the HPSC-C system ranges from 26% at 50 lph, to below 13% at 70 lph. In a similar situation, the efficiency of the HPSC-PCM system varies between 32% and 30%. Generally, the efficiency range of the HPSC-PCM system extends between 53% and 30%, while that of the HPSC-C system stretches between 65% and higher to 14% and below. This is an indication that the innovative system is superior to the conventional system in terms of stability. A similar efficiency trend was observed in the context of water capacity. The most outstanding revelation is the fact that the innovative system is capable of offering at least 200 litres of heated water under the harshest of weather conditions, while the conventional system is unable to meet the demand for domestic hot water on rainy, and perhaps even on cloudy days.

To be able to have a more detailed view about the effectiveness of the performance of the HPSC-PCM in a tropical climate, the available data of three meteorological stations in Malaysia for two years were studied. The number of days in a year with different weather conditions are shown in Table 3 and Figure 9. It is observed that averagly 45% of the days in a year are mostly sunny and rests are in mostly cloudy or rainy conditions. According to Figure 9, the ratio of sunny days could be even as low as ~32% in a year. Refer to the Figure 8, both designs have suffiecent performance in sunny days. However, in non-sunny days the new design provide more hot water volume and more stable operation, which this illustrates the advantageous of the new design in comparison with the conventional model.

Tab. 3: Number of the sunny, cloudy and rainy days in a year

Station	Location (Lat./Long.)	Sunny	Cloudy	Rainy
Mersing (2007)	2° 27' N / 103° 50' E	164	121	80
Mersing (2008)	2° 27' N / 103° 50' E	145	136	84
Subang (2008)	3° 07' N / 101° 33' E	188	121	56
Subang (2009)	3° 07' N / 101° 33' E	202	116	47
KLIA (2008)	2° 44' N / 101° 42' E	121	165	79
KLIA (2009)	2° 44' N / 101° 42' E	169	129	67
	Average	**45%**	**36%**	**19%**

5. Conclusion

A hypothetical study was conducted on the feasibility of integrating an evacuated tube heat pipe solar collector and a latent heat storage tank. This study was based on authentic meteorological data as regards to

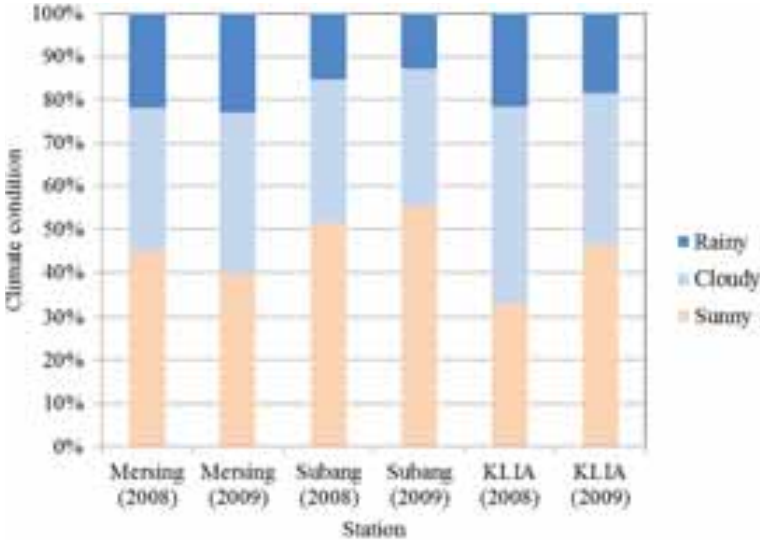

Fig. 9: The ratio of climatic condition during a year

three Malaysian weather conditions. An examination of the HPSC-PCM charging/discharging procedures revealed that under certain circumstances, the thermal performance of the recommended system is superior to that of a standard system. While the HPSC-C system and the HPSC-PCM function are in satisfactory level on sunny days, at a certain flow rate on cloudy and rainy days the HPSC-PCM system exhibited a higher level of effectiveness. This investigation also uncovered that the degree of sensitivity to the supply water flow rate is lower for the recommended system than the conventional system.

6. References

[1] S. Wu, G. Fang, Dynamic performances of solar heat storage system with packed bed using myristic acid as phase change material, Energy and Buildings, 43 (2011) 1091-1096.
[2] H. Benli, A. Durmuş, Performance analysis of a latent heat storage system with phase change material for new designed solar collectors in greenhouse heating, Solar Energy, 83 (2009) 2109-2119.
[3] W. Saman, F. Bruno, E. Halawa, Thermal performance of PCM thermal storage unit for a roof integrated solar heating system, Solar Energy, 78 (2005) 341-349.
[4] G. Serale, F. Goia, M. Perino, Numerical model and simulation of a solar thermal collector with slurry Phase Change Material (PCM) as the heat transfer fluid, Solar Energy, 134 (2016) 429-444.
[5] Z. Liao, A. Faghri, Thermal analysis of a heat pipe solar central receiver for concentrated solar power tower, Applied Thermal Engineering, 102 (2016) 952-960.
[6] S. Esakkimuthu, A.H. Hassabou, C. Palaniappan, M. Spinnler, J. Blumenberg, R. Velraj, Experimental investigation on phase change material based thermal storage system for solar air heating applications, Solar Energy, 88 (2013) 144-153.
[7] N. Nallusamy, S. Sampath, R. Velraj, Experimental investigation on a combined sensible and latent heat storage system integrated with constant/varying (solar) heat sources, Renewable Energy, 32 (2007) 1206-1227.
[8] A.J.N. Khalifa, K.H. Suffer, M.S. Mahmoud, A storage domestic solar hot water system with a back layer of phase change material, Experimental Thermal and Fluid Science, 44 (2013) 174-181.
[9] M. Ibáñez, L.F. Cabeza, C. Solé, J. Roca, M. Nogués, Modelization of a water tank including a PCM module, Applied Thermal Engineering, 26 (2006) 1328-1333.
[10] T. Kousksou, P. Bruel, G. Cherreau, V. Leoussoff, T. El Rhafiki, PCM storage for solar DHW: From an unfulfilled promise to a real benefit, Solar Energy, 85 (2011) 2033-2040.
[11] M. Esen, A. Durmuş, A. Durmuş, Geometric design of solar-aided latent heat store depending on various parameters and phase change materials, Solar Energy, 62 (1998) 19-28.
[12] S. Canbazoğlu, A. Şahinaslan, A. Ekmekyapar, Ý.G. Aksoy, F. Akarsu, Enhancement of solar thermal energy storage performance using sodium thiosulfate pentahydrate of a conventional solar water-heating system, Energy and Buildings, 37 (2005) 235-242.
[13] I. Al-Hinti, A. Al-Ghandoor, A. Maaly, I. Abu Naqeera, Z. Al-Khateeb, O. Al-Sheikh, Experimental investigation on the use of water-phase change material storage in conventional solar water heating systems, Energy Conversion and Management, 51 (2010) 1735-1740.
[14] N. Nallusamy, R. Velraj, Numerical and experimental investigation on a combined sensible and latent heat storage unit integrated with solar water heating system, Journal of Solar Energy Engineering, Transactions of the ASME, 131 (2009) 0410021-0410028.
[15] Y. Varol, A. Koca, H.F. Oztop, E. Avci, Forecasting of thermal energy storage performance of Phase Change Material in a solar collector using soft computing techniques, Expert Systems with Applications, 37 (2010) 2724-2732.
[16] R. Padovan, M. Manzan, Genetic optimization of a PCM enhanced storage tank for Solar Domestic Hot Water Systems, Solar Energy, 103 (2014) 563-573.
[17] H.S. Xue, Experimental investigation of a domestic solar water heater with solar collector coupled phase-change energy storage, Renewable Energy, 86 (2016) 257-261.
[18] A. Papadimitratos, S. Sobhansarbandi, V. Pozdin, A. Zakhidov, F. Hassanipour, Evacuated tube solar collectors integrated with phase change materials, Solar Energy, 129 (2016) 10-19.
[19] M.S. Naghavi, O.K. Seng, I.A. Badruddin, M. Mehrali, M. Silakhori, H.S.C. Metselaar, Theoretical model of an evacuated tube heat pipe solar collector integrated with phase change material, Energy, (2015).
[20] J.A. Duffie, W.A. Beckman, Solar Engineering of Thermal Processes, Wiley, 2013.
[21] N. Zhu, K. Vafai, Analysis of cylindrical heat pipes incorporating the effects of liquid–vapor coupling and non-Darcian transport—a closed form solution, International Journal of Heat and Mass Transfer, 42 (1999) 3405-3418.
[22] V. Alexiades, A.D. Solomon, Mathematical Modeling of Melting and Freezing Processes, Taylor & Francis Group, 1993.

[23] P. Armstrong, D. Ager, I. Thompson, M. McCulloch, Domestic hot water storage: Balancing thermal and sanitary performance, Energy Policy, 68 (2014) 334-339.
[24] J. Fernandez-Seara, F.J. Uhía, J. Sieres, Experimental analysis of a domestic electric hot water storage tank. Part I: Static mode of operation, Applied thermal engineering, 27 (2007) 129-136.
[25] P. Armstrong, D. Ager, I. Thompson, M. McCulloch, Improving the energy storage capability of hot water tanks through wall material specification, Energy, 78 (2014) 128-140.
[26] B. Standard, In-situ formed dispensed rigid polyurethane and polisocyanurate foam products, in: British Standard BS EN 14318-1 2013, British Standards Institute, 2013.
[27] A. Faghri, Review and advances in heat pipe science and technology, Journal of Heat Transfer, 134 (2012).
[28] N. Ukrainczyk, S. Kurajica, J. Šipušić, Thermophysical comparison of five commercial paraffin waxes as latent heat storage materials, Chemical and Biochemical Engineering Quarterly, 24 (2010) 129-137.
[29] P. Lamberg, K. Siren, Analytical model for melting in a semi-infinite PCM storage with an internal fin, Heat and mass transfer, 39 (2003) 167-176.
[30] T.M.V.M. Association, Recommended Code of Practice for Safe Water Temperatures, in, BEAMA, London, England, 2013.

Nomenclature

Symbols

A_p	Pipe inner surface area	t_{CHE}	PCM thickness in CHE mode
$A_{c,c}$	Cross section area of the fin on HPC	t_{DHE}	PCM slab thickness in DHE mode
$A_{f,c}$	Face area of the fin on the HPC	$t_{f,CHE}$	Thickness of fin on heat pipe
$c_{p,l}$	Specific heat of liquid PCM	$t_{f,DHE}$	Thickness of fin on water pipe
$c_{p,s}$	Specific heat of solid PCM	t_{hp}	Thickness of the heat pipe wall
$c_{p,w}$	Specific heat of water	t_{wck}	Thickness of the wick
$d_{i,p}$	Pipe inner diameter	T_{amb}	Ambient temperature
d_w	Mesh wire diameter	T_{hp}	Heat pipe surface temperature
d_t	Glass tube outer diameter	T_m	PCM melting temperature
E_d	Total delivered energy	T_{pcm}	PCM temperature
g	Gravity	T_s	Cold water temperature
$h_{f,c}$	Fin height on the condenser	T_u	Water operating temperature
$h_{f,p}$	Fin height on pipe	$T_{w,b,i}$	Inlet water temperature in baseline system
h_{pcm}	Heat transfer coefficient in PCM	$T_{w,b,o}$	Outlet water temperature in baseline system
h_{st}	Storage tank height	$T_{w,i,i}$	Inlet water temperature in innovative system
h_w	Heat transfer coefficient in water	$T_{w,i,o}$	Outlet water temperature in innovative system
k_{eff}	Effective thermal conductivity of wick	$T_{w,t,i}$	Inlet water temperature to water storage tank
$k_{f,c}$	Thermal conductivity of fin on condenser	$T_{w,t,o}$	Outlet water temperature from water storage tank
$k_{f,p}$	Thermal conductivity of fin on pipe	V_u	Usable volume of hot water
k_l	Thermal conductivity of liquid PCM	$V_{u,\mathrm{d}}$	Destroyed usable volume of hot water
k_s	Thermal conductivity of solid PCM	$V_{u,\mathrm{r}}$	Remained usable volume of hot water
k_w	Thermal conductivity of heat pipe wall	w_{st}	Storage tank width
l_a	Length of heat pipe adiabatic region	X_{pcm}	Liquid-solid location in PCM slab
l_c	Length of heat pipe condenser region	Y_{pcm}	Solid-liquid location in PCM slab
l_e	Length of heat pipe evaporator region	**Greek**	
$l_{f,c}$	Fin length on the condenser	α_s	Thermal diffusivity $[= k_s/\rho_s c_s]$
$l_{f,p}$	Fin length on pipe	β_s	Slope of solar collector
l_p	Length of solar absorber plate	β_e	Expansion coefficient of the PCM
l_{st}	Storage tank length	ε	Porosity
$l_{st,s}$	Length of a section of the storage tank	θ	Angle of incidence
L	Latent heat of PCM	ρ_i	Diffuse reflectance of that surface
Lr	Usable volume loss rate percentage	ρ_g	Diffuse reflectance of the ground
$\dot{m}$	Water mass flow rate	ρ_l	Liquid PCM density
m_w	Mass of the stored hot water in water storage tank	ρ_s	Solid PCM density

N_a	Number of apertures per unit length of wick	ρ_w	Water density
N_f	Number of the fins	μ_{pcm}	Dynamic viscosity of the PCM
$P_{f,c}$	Perimeter of the fin on HPC	μ_w	Dynamic viscosity of the water
q	Heat flux	v_w	Mean velocity of water inside the pipe
S	Absorbed solar energy	ϕ	Latitude
St	Stefan number [$=c_l \Delta T_l / L$]	η	Efficiency

Conference Proceedings

Solar World Congress 2015
Daegu, Korea, 08 – 12 November 2015

Combined heat and power generation of the hydrogen chain based on MYRTE platform

Auline Rodler, Pierrick Haurant, Ghjuvan-Antone Faggianelli , Guillaume Pigelet , Philippe Poggi

University of Corsica, UMR SPE CNRS 6134, F-20000 Ajaccio, France

Abstract

The objective of this paper is to present the thermal recovery system of the MYRTE hydrogen chain. This system recaptures the thermal energy produced by the proton exchange membrane (PEM) fuel cell (100 kW) and a PEM electrolyzer (10 Nm^3/h). The recovery system must insure to maintain the set point temperature of the inlet cooling water to the facilities. In that view, the heat is collected and stored in a water storage tank and the rest is dissipated using a turbofan. In this paper, the power dissipated and stored in the recovery system is evaluated based on measurements. The results show that the fuel cell generates at its maximal electrical power an equivalent amount of thermal power. Finally, a model coupling the fuel cell and the heat recovery system is implemented in TRNSYS®, showing a good agreement to the measurements.

Keywords: Co-generation**,** Hydrogen, Fuel cell, Electrolyzer, Solar energy

1. Introduction: Energy Context in Corsica

Corsica Island is located in the Genova golf in the Mediterranean Sea and therefore exposed to the Mediterranean climate, characterized by hot and dry summers and mild and humid winters. Its solar energy potential is one of the most important of France. As Corsica is very hilly in the centre, we can find different climates via the island. The solar resource distribution is very heterogeneous and the solar radiation can be very fluctuating.

Besides, the Corsican electrical grid is typical of an insular electrical network: it is weakly connected to the mainland grid, small-sized and sensitive to variations in electrical production. The threshold of maximum 30% of integration of fatal intermittent production, fixed by the French law to insure the insular grid's stability, was overpassed in 2012[1]. However, photovoltaic plants projects are still considered.

Therefore, storage systems to smooth the intermittency of the solar production seem necessary. Hydrogen production and consumption can help to manage electrical power fluctuations of intermittent renewable energy sources integrated into the electrical grid.

In this context, the hybrid MYRTE (mission hydrogen for the integration of renewable into the electrical grid) demonstration platform has been built: it combines a photovoltaic array and a hydrogen chain used as a storage solution.

2. The hydrogen solution: MYRTE project

The first aim is to test hydrogen storage solutions as an alternative to the peak shaving of electrical demand (Darras, 2010). Another aim of this platform is to monitor the photovoltaic power output smoothing and to reduce the PV fluctuations (Darras et al., 2012). Finally, the development of algorithms and optimal strategy

[1] http://corse.edf.com/edf-en-corse/nos-energies/nos-energies-48454.html

doi:10.18086/swc.2015.02.12 Available at http://proceedings.ises.org

management coupling the processes (PV production – Hydrogen chain) is another target.

2.1 Presentation of the experimental platform

The experimental MYRTE platform is a technological platform dedicated to the coupled studies between PV/hydrogen chains. This platform has been inaugurated on January 2012.

MYRTE platform is composed of the following sub systems (Fig. 1):

- A photovoltaic array of 560 kW_p (3700 m^2 covered by 2240 PV TENESOL TE2200 modules);
- 28 DC/AC three-phase 17 kW inverters (SMA SUNNY TRIPOWER 17000TL);
- The fuel cell subsystem (SSPAC), composed of a PEM (proton exchange membrane) fuel cell with a power of 100 kW supplied by AREVA ;
- The subsystem electrolyser (SSEL), composed of a PEM electrolyzer of a nominal power of 50 kW with a H_2 flowrate which can reach 10 Nm^3/h, developed by AREVA ;
- The storage subsystem, composed of drying and purification systems of gases as well as two H_2 storage tanks and one O_2 tank (GLI ETS Citergaz) each with a volume of 28 m^3, under a maximal pressure of 35 bars (1400 Nm^3 d'H_2 and 700 Nm^3 d'O_2) ;
- A 800 kVA transformer to inject electrical production on the high voltage network ;
- The thermal recovery subsystem to recover heat from the electrolyzer and the fuel cell to maintain the operative temperature of both systems.

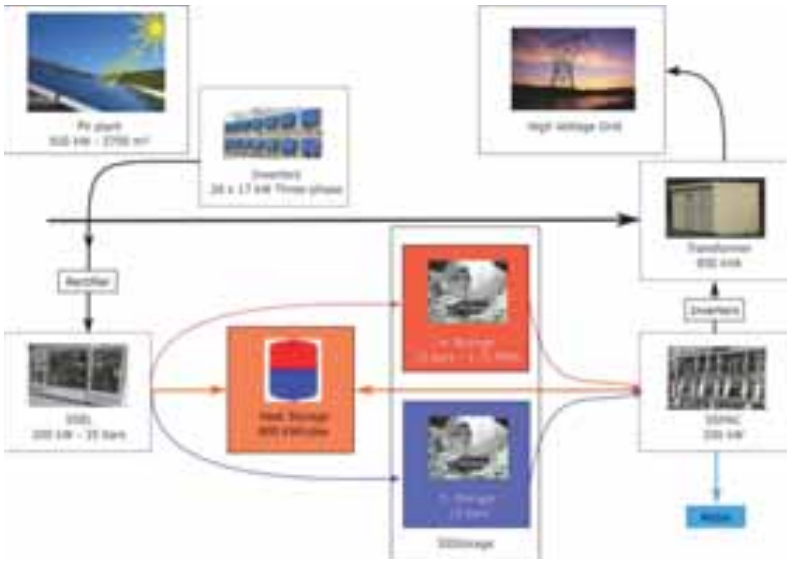

Figure 1: Operating of MYRTE

The electrical mean efficiency of the hydrogen chain is of about 23 – 25 %. The facilities as the fuel cells release heat when they generate electricity and are therefore interesting for combined heat and power (CHP) applications, also known as cogeneration. CHP hydrogen system time-averaged electrical, thermal and global (combining both heat and electrical powers) efficiencies have been evaluated by Hwang et al. (2013) to about 37 %, 24 % and 61 % respectively. To conclude, recovering the thermal heat of fuel cell systems strongly increases the overall energy efficiency of the global system.

2.2 Heat recovery

To increase the global efficiency of the hydrogen chain, the heat recovery system is composed of a thermal energy storage system to store the heat produced by the fuel cell (FC) and electrolyzer (EL). This heat can then be used in a secondary loop, for example for a residential application.

The cooling loop will systematically act on both electrolyzer and fuel cell, that is, the water passes through their heat exchangers to guaranty the operating temperature which is 60 °C for the electrolyzer and 70 °C for the fuel cell. The maximal overall operating temperature not to overpass is fixed to 75 °C, for security reasons. The absorbed heat is then stored or dissipated by turbofans (Fig 2). The glycolic liquid is kept in movement

by a pump (KQ500) and goes to the heat exchanger of the tank where the heat can be stored. The maximal temperature of the water which will go back to the electrolyzer and fuel cell is fixed in between 35 – 40 °C. This set point temperature is ensured by turbofans which will dissipate the heat if the sensor KT501 indicates a temperature above the set point temperature. The cooling overall flow rate depends on the electrolyzer or fuel cell system working order and depends on the opening percentage of the regulation valves. For the moment, the experimental set up is not connected to any secondary loop which could allow exploiting the heat. As seen on the schematic drawing of the thermal recovery system (Fig.2), the water can follow different paths in the circuit. It is possible to cool down the electrolyzer and fuel cell systems, to recover the heat from them and exploit it or absorb the heat without recovering it.

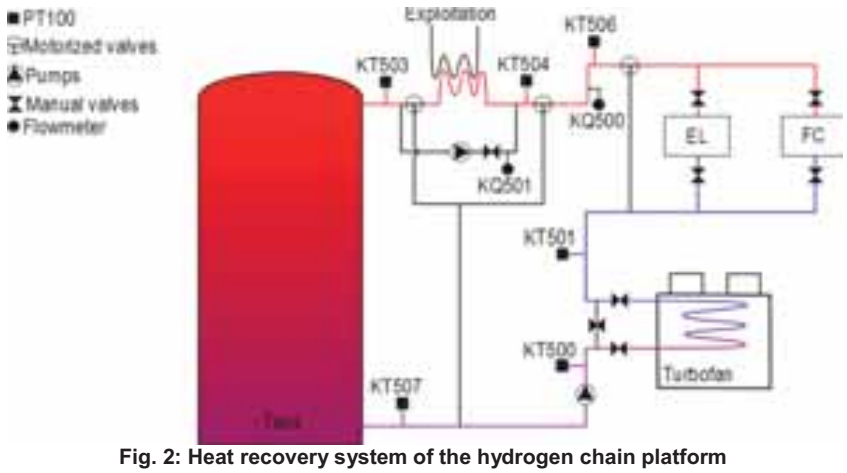

Fig. 2: Heat recovery system of the hydrogen chain platform

Different modes in the circuit are possible:

- **Mode to cool down the system** which is ordered by the control system. Different cases are possible depending if the storage is full and depending on the water temperature of the sensor KT501 placed before electrolyzer and fuel cell heat exchangers:
    1. If the storage is not full and KT501 < set point temperature (35 °C): we will store the heat;
    2. If the storage is not full and KT501 > set point temperature: we will store the heat and dissipate the heat by the two turbofans;
    3. If the storage is full and KT501 > set point temperature: the turbofan is used (frequency of the fan is function of the overtaking of the set point temperature);
    4. If the storage is full and KT501 < set point temperature: the turbofan is used (at its minimal working).
- **Mode to recover the heat to a second water circuit:** the system would allow the water to go to a second circuit. The water would be in between 45 and 55°C for the heating system of a building. Until now, this mode is not possible as there is no connection to a building.
- **Mode to take out the heat without recovering the heat:** the heat is transferred to the storage tank and to the turbofan.
- **Stopping mode or manual mode.**

3. Modelling

3.1 Presentation of the measurements feedback

In this paper, we present results for a three day period in May 2014, when the platform was working in a peak shaving mode: each day, the electrolyzer consumed 46 kW during the day and the fuel cell produced a maximum of 95 kW between 08.30 pm and 10.30 pm (Fig. 3). The peak shaving mode consists in using additional sources of energy at moments when the electricity demand is important. That is, the MYRTE platform is used at moments of peak shaving: the fuel cell is used to supply electricity to the grid. The heat recovery system is turned on only when the electrolyzer or fuel cell is operating. The set point temperature of the KT501 was fixed to 35°C.

The heat recovery system is turned on only when the electrolyzer or fuel cell are used. The set point temperature of the KT501 was fixed to 35°C. For the moment, the experimental set up is not connected to any secondary loop which could allow exploiting the heat.

The electrical power generated by the fuel cell and the power consumed by the electrolyzer were measured (Fig. 3) as well as different temperatures (KT506, KT507 and KT501 show in Fig. 3). The outside temperature was also measured and a flowmeter gave the flowrate in the recovery loop. All measures are given at a minute time step.

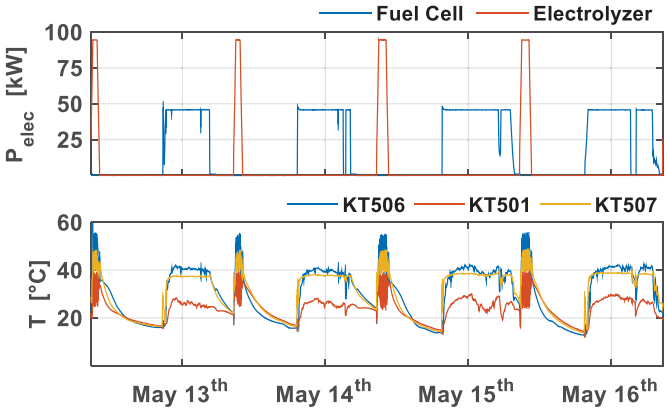

Figure 3: Electrolyzer and fuel cell electrical power

We can observe in Fig. 3 that the inlet fluid temperature in the thermal recovery system, measured by sensor KT506:

- reaches 40°C to 42°C when the electrolyzer works;
- varies between 41°C and 53°C when the fuel cell works.

Whatever the time considered, these temperatures are below the optimal temperatures of both systems, and far from their maximal operating temperatures: the hydrogen systems seem to be cooled down too much.

Besides, these fluid temperature ranges indicate that the heat recovered could be used for residential applications, as for the heating or pre-heating systems.

The fluid temperature decreases from 2 to 3 °C when the electrolyzer works and from 5 to 7 °C when the fuel cell works when it passes through the storage tank. Then, the water circulates through the turbofan and its temperature decreases strongly whatever its input temperature. When the electrolyzer works, the glycolic water temperature drops always below 30°C when measured on KT501. It oscillates between 32°C and 38°C when the fuel cell is on. The turbofan dissipates too much heat since it is oversized or not well controlled, so that the heat recovery system overcools the systems.

3.2 Sub-system parametrisation

A transient model adapted to the case study MYRTE, and particularly to the heat recovery system, is being developed using TrnSys® (TRNSYS, 1996). It is a software with a modular structure dedicated to dynamical simulation of complex energy systems. It aims at considering the global system composed by a set of interconnected subsystems modelled in 'types'. The thermal behaviour of the sub-systems has been modelled thanks to 'types' stemming from TRNSYS library (Tab. 1).

Table 1 Elements of TRNSYS model

Elements	Type	Comment
Data reader	9	Flowrate, ambiant temperature, fuel cell control signal and electrolyzer control signal
Pipe	31	Hypothesis on the sizes and the thermal losses
Turbofan	Macro	Pipe and forced convection simulated
Water Tank	60d	With internal exchangers and taken into account the stratification (20 nodes)
Electrolyzer	Macro	Only the thermal aspect of the electrolyzer is considered
Fuel cell	170 k	FC O_2/H_2 controlled with the intensity

The inputs of the model are:

1. the outdoor temperature ;
2. the flowrate of the glycolic fluid (KQ500);
3. heat generated by the electrolyzer.

The outputs of the model are:

1. the water temperature before, in and after the storage tank ;
2. the inlet and outlet temperature of the turbofan ;
3. the power and energy dissipated by the turbofan ;
4. the power and energy stored by the tank.

3.2.1 Tank

The water storage tank was modelled by using the Type 60d, which is a dynamical model for thermal stratified storage. It includes heat exchangers and auxiliary heaters. In this model, the tank is divided in N volumes or nodes. The water temperature for node i is evaluated according to the energy balance (Eq.1):

$$m_{w,i}c_p\frac{dT_{w,i}}{dt} = Q_{HEX,i} + Q_{AUX,i} + Q_{loss,i} + Q_{cond,tank,i} + Q_{conv,tank,i} + Q_{fconv,inout,i} \quad \text{(eq. 1)}$$

where

- $Q_{HEX,i}$ and $Q_{AUX,i}$ are the heat from the exchanger and auxiliairies
- $Q_{loss,i}$ is the thermal losses to the outside
- $Q_{cond,tank,i}$ is the thermal exchanges by conduction of the fluid in the tank between node i and nodes $i+1$ and $i-1$
- $Q_{conv,tank}$ is the thermal exchanges due to convection in the tank
- $Q_{conv,inout}$ is the bleedoff exchanges and the exchanges of the water supply in the tank to the N inputs/outputs of the tank.

This model is dynamic and zonal as it calculates the thermal transfers between control volumes, so it considers the stratification in the tank. The parametrization of the tank is sensitive as the geometry of its heat exchanger is particular. The tank is composed of 4 connected metal plates filled in with water and in contact with the exterior surface of the tank. The water tank is 4m high and has a 2m diameter, with a total volume reaching 14 m^3.

The circulation of the fluid for this type of exchanger and the heat exchanges by conduction with the water of the tank differ from the exchanges of a tank with a coil. The circulation speed is smaller whereas the contact surfaces are more important. This is why we have considered a very long exchanger and we have overestimated the thermal exchange coefficients.

3.2.2 Electrolyzer

In TrnSys we do not have a ‘type’ modelling the electrolyzer PEM so that in this study the electrolyzer has

been considered as a constant heating source when operating. The heat has been evaluated from differences between the measured KT501 and KT506 temperatures.

This first very simple modelling does not allow simulating the thermal dynamic behaviour of the heat recovery system of MYRTE in a reliable way. The model validation will have a critical sense only when the fuel cell is operating. It is necessary that the model evaluates several levels of temperatures and heat supply. However, this simple modelling is necessary so that the global model can evaluate the average heat generated by the electrolyzer and can insure a continuity through the simulations between each operating period of the fuel cell.

3.2.3 Fuel cell

The fuel cell model implemented in the type 170 is composed of an electrochemical, a thermodynamic and a thermal model. Different outputs are calculated: the stack temperature, the electrical production and the gas consumption.

The electrochemical model is based on different works (Amphlett et al., 1996; Ulleberg 1998). The voltage of a single cell is:

$$U_{cell} = E + \eta_{act} + \eta_{\Omega} \qquad \text{(eq. 2)}$$

where E is the thermodynamic potential given by Nernst equation, η_{act} is the anode and cathode activation over-voltage and η_{Ω} the ohmic over-voltage, quantifying the transport losses due to the proton conductivity.

The thermodynamical model has been set up to establish the inlet flowrates for the oxygen $\dot{n}_{O_2,in}$ and hydrogen $\dot{n}_{H_2,in}$, according to Faraday's law. With this law the real consumption of the gas considering the stoichiometrical coefficients S_{H_2} et S_{O_2} are calculated:

$$\dot{n}_{H_2,in} = S_{H_2} \frac{N_{cell} I_{FC}}{n.F} \text{ and } \dot{n}_{O_2,in} = S_{O_2} \frac{1}{2} \dot{n}_{H_2,cons} \qquad \text{(eq. 3)}$$

The stack temperatures T_{stack} are evaluated according to the thermal model where c_t is the thermal capacity of the stacks:

$$c_t \frac{dT_{FC}}{dt} = Q_{gen} - Q_{loss} - Q_{cool} - Q_{evap} \qquad \text{(eq. 4)}$$

Q_{gen} is the heat generated by the fuel cell, Q_{loss} the heat dissipated in the environment, Q_{evap} the heat dissipated by evaporation at the cathode and Q_{cool} the heat dissipated thanks to an auxiliary.

The principal parameters used for one stack are listed in the table below (Tab. 2) where the eventual connections between parameters and other types are indicated.

Table 2: Elements of the model

Characteristic elements /parameters			**Inputs**			**Outputs**		
Number of cells per stack	N_{cell}	100	Control signal	δ	$\delta = (P_{FC} > 0)$	Power per stack	P_{stack}	Graph (Type 65)
Number of stacks	N_{stack}	4	Intensity of the cell	I_{FC}	$I_{FC} = f(V, P_{FC})$	Current (stack)	U_{stack}	Graph (Type 65)
Electrodes surface	A_{PEM}	400 cm²	Input pressure	$p_{gaz,in}$	1.5 Bars	Gas consumption	$\dot{n}_{H_2,in}$	H_2 tank
Ambient temperature	T_{amb}	Inputs (Type 9)	Stochiometric coefficients	S_{gaz}	1.15 (H2) ; 2.5 (O2)		$\dot{n}_{O_2,in}$	O_2 tank
Connexion to TrnSys Types			Input fluid temperature	T_{cool}	Inputs (Type 9)	Heat	Q	$T_{out} = f(T_{in}, Q)$
Constants			Set point temperature in the stack	T_{stack}	Macro Fan			
Connexion to Calculators			Set point temperature in the stack	T_{stack}	70 °C			

3.2.4 Turbofan

The turbofan has been modelled associating it to a dissipating cooling system. This system depends on an all or nothing controller. The heat dissipated by the fan is a function of the set point temperature and the flowrate.

The turbofan in composed of a very long heat exchanger of 500 m of 13 mm of diameter with a fin and two fans. There is no existing model in the TrnSys library able to model this kind of turbofan, so that a macro has been developed composed of a pump (Type 3b), managing the water flowrate in the pipe (Type 31) where the sizes are the one of the heat exchanger. The effect of the fins allows increasing the contact area, and therefore increasing the conduction transfer. In the model, the thermal loss coefficient of the pipe is increased so that the conduction transfers due to the fins are well modelled. The cooling of the fluid is accelerated by using fans. This phenomenon is modelled by using a resulting temperature: it corresponds to the outside air temperature adjusted with a negative offset. The resulting temperature is used only when the set point temperature (T_{sp} = 35 °C) is overpassed by at least 2°C ($\Delta T_+ = 2$ °C) and is not used when the temperature is under the set point temperature by 3 °C: $T = T_{sp} - \Delta T_-$ where $\Delta T_- = 3$ °C

The parameters ΔT_+ and ΔT_- are the dead-bands of the fans regulator which is at the origin of the oscillations seen on the temperatures measured by the sensors when the fuel cell operates.

4. Simulation Results

4.1 Electrical outputs

The electrical characteristics of the fuel cell and its sizes are implemented in the Type 170 (Tab. 2). With these parameters we have plot the current–voltage (I–U) characteristics of the PEM fuel cell (Fig 4). This simulation has been compared to the measurements. The measurements stem from a test (blue curve) while the fuel cell was operating in a dynamic mode during 8 hours. We have also represented the I-U curve of this stack, initially characterized (red curve). We can notice that the voltage simulated is always higher than the measured one. Around the nominal operation of the fuel cell, for a current of 333 A, the measured voltage of a stack was initially of 75.1 and of 74.8 V during the test, whereas it is of 79.5 V in the simulations. The curves $P_{FC} = f(I_{FC})$ around the nominal power of the fuel cell are very close to each other. For I = 333 A, the electrical measured powers are of 100 kW, against 105 kW for the simulated powers.

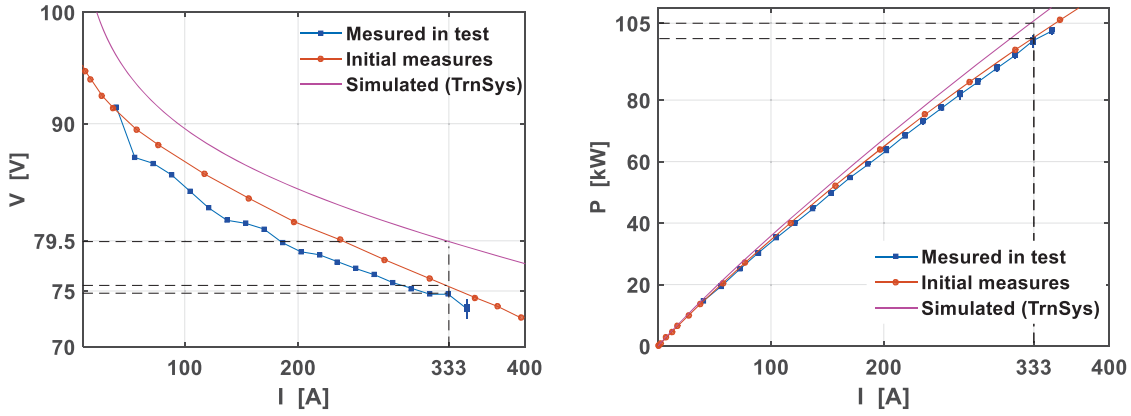

Figure 1: Measured current-voltage curve (blue), current-voltage curve obtained of a stack during the initial characterization (red) and current-voltage curve generated by TrnSys (pink). b.) Current-power characterisation of the fuel cell.

The electrical simulated and measured powers generated by the fuel cell during the period studied are represented on Fig. 5. For both cases, the powers are lower than the powers provided by the curves $P_{FC} = f(I_{FC})$ of Fig. 4 for I = 333 A. This means that during this period the fuel cell was not used exactly at its nominal capacity. The simulation tends to overestimate the electrical power generated by the fuel cell by 5 to 7 kW: the simulated power is of 100 kW whereas the measured power is of 94 kW. These differences are due to the fact that the measured power is the active power whereas the simulated power is the DC power.

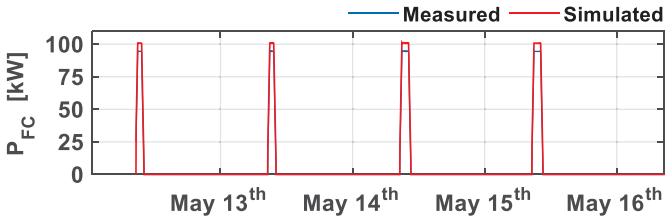

Figure 2: Measured and simulated electrical fuel cell powers

To conclude, the fuel cell type seems correctly parametrized.

4.2 Simulated fluid temperatures

The thermal model and its outputs are the specificity of this model and paper. The outlet water temperatures evaluated by the model after the hydrogen systems, the tank and the turbofan are going to be compared to the measurements with the use of the sensors: KT506, KT507 and KT501 (Fig 6). Whatever the fluid temperature, we focus on if the trends of the simulations are correctly calculated:

1. The simulated temperature increases when one of the hydrogen systems operates. When the fuel cell is on, we can observe oscillations on the KT501 which are due to the turbofan and the valves operation. These oscillations are reproduced by the model but their frequency and phasing are not respected. These results could be improved by characterizing more in detail the control of the turbofan and implementing it in the model. The fluctuations on the simulated temperatures are under evaluated:

   - for KT501: local maximal and minimal temperatures are reproduced with root mean square errors of respectively 1.96 °C and 1.77 °C. These fluctuations are linked to the turbofan regulator bandwidth. These differences show that the limits of the band have to be improved;
   - for KT506, these temperatures are evaluated with root mean square errors of 3.46 °C and 1.77 °C. The heat generated by the model tends to smoothen the inlet temperature;
   - for KT507, the root mean square maximal and minimal errors are respectively of 1.0 °C and 1.71 °C.

2. We see that the temperature decreases due to the thermal losses when no hydrogen system is operating, that is when the water stagnates. These losses are slightly under evaluated by the model. Indeed, concerning the measurements done by KT506, the temperature difference between a moment when the fuel cell starts and a moment when it ends up is of 19.7°C for the first day, of 20.3°C for the second, of 21.5°C for the third and finally of 23°C for the last day. The simulated temperatures show respectively differences of 14.0 °C, 17.2 °C, 11.3 °C and 12.4 °C. When the fuel cell stops operating we can see differences of 8 – 10 °C between simulation and measurement at the KT501 sensor. These differences are mainly explained by the phase shift of the fluctuations produced by the turbofan regulation. At given moments, the measured temperature is at its maximum of the oscillation whereas the simulated temperature is at the minimal.

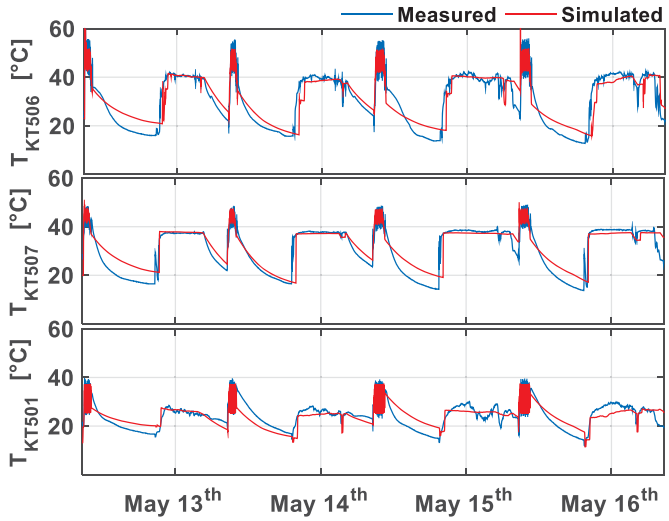

Figure 3: Measured (KT506, KT507 and KT501) and simulated temperatures

4.3 Thermal power

The thermal behaviour of the different elements of the heat recovery system, when the fuel cell operates, is presented on Figs. 7 and 8. Fig. 8 is a boxplot summing up the statistical weights of the heat evaluated: on each box, the horizontal line represents the median, the points is the mean, the vertical line links up the maximum and minimum values, and the horizontal bottom and upper edges of the box are respectively the 25th and 75th percentiles. Thus the spacing between the edges of the box indicates the degree of dispersion of the values.

We can notice that the heat produced by the fuel cell is correctly evaluated: the mean heat produced is of about 70 kW (Fig. 8). However, the fluctuations observed on the measurements are not reproduced by the model when the fuel cell operates at its nominal power. The heat calculated at its nominal power is of about 86 kW whereas the measured power is between 82 and 101 kW.

When the fuel cell reaches its nominal power, the thermal simulated exchanges in the tank are of 15.2 kW against 14.5 kW with the measures (Fig. 8). We notice that the simulated power fluctuates less compared to the measured (between 0-20 kW for the simulation against 0-46 kW for the measurements). This is due to the simulated temperature located after the fuel cell, which is less varying. The simulated heat generated by the fuel cell seems too smooth and stable.

Finally, the thermal dissipated power by the turbofan is slightly under evaluated but acceptable. In average the turbofan model dissipates 54.2 kW whereas the measurements show 55.6 kW. Here, the fluctuations are suitably evaluated.

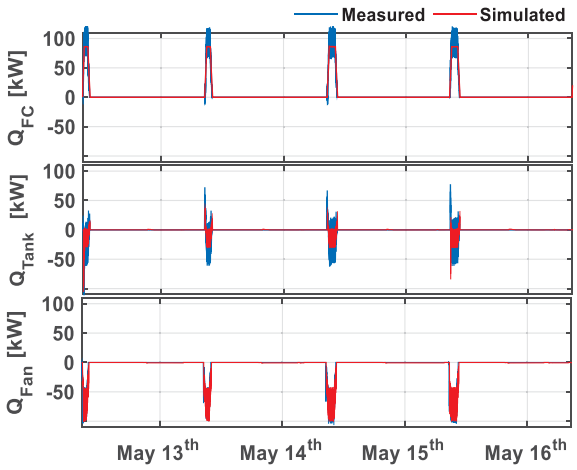

Figure 4: Temporal simulated and measured thermal powers when the fuel cell operates

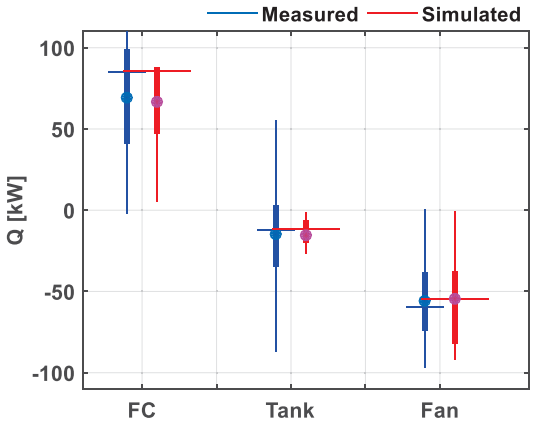

Figure 5 : Thermal measured and simulated boxplot powers when the fuel cell operates

To conclude, the model tends to agree with the measurements for both transient temperature and thermal exchanges simulations. Certain aspects need to be improved: the thermal losses on the pipes as well as the tank thermal exchanges. When looking at the transient evolution of the temperatures and heat exchanges we have often noticed that the fluctuations are less well represented with the model.

5. Conclusion

The experimental MYRTE platform is dedicated to PV/ hydrogen studies. It is composed of a 560 kW_p PV array, of a fuel cell with a nominal power of 100 kW, an electrolyzer with a nominal power of 50 kW and a hydrogen flowrate reaching 10 Nm^3/h. It is composed of hydrogen and oxygen tanks for the storage. The heat generated by the electrolyzer and fuel cell is recovered via the heat recovery system in order to maintain a set point temperature.

This paper focusses on the transient modelling of the heat recovery system. The different sub-models are introduced and the global electrical and thermal performances are presented. First the PEM fuel cell is modelled using type 170 of TrnSys. The model seems to be correctly parameterized: the electrical and thermal outputs agree and are correlated to the measurements. The turbofan seems to reproduce the heat dissipated though its regulation needs to be improved. The losses in the pipes are under estimated by the model but the

global trend is acceptable. Finally, the TrnSys type 60d used for the tank is acceptable but we know that our tank has a particular geometry so further measurements need to be done to characterize the tank model and to know whether we can improve type 60d. The heat generated by the electrolyzer has been measured and the average measured heat generated has been used in the model as an input.

The next step is to model the thermal exchanges in the electrolyzer and to transform it in a TrnSys Type. This model will be based on (Agbli et al., 2011, Gorgun, 2006) works and further measurements will be required to set the current-voltage curves for different operating temperatures. If a more detailed performance of the global model is expected then we will need to work on the regulation of some sub-models in order to increase the transient responses accuracy.

The final aim of this work is to be able to exploit the heat generated by the platform in order to recover it for residential applications. A future study, coupling an efficient building's behaviour and this experimental platform will be done in order to quantify the global energy saving which could be achieved. Also, for the moment, this platform is used for electrical demands, whereas we have seen that the heat generated can be as important as the electricity produced. A future application will be to prioritize the heat and consider electricity as a residual power. Finally, a technical and economic analysis will lead to be able to propose the best application to increase the global platform's energy and exergy efficiency.

6. References

Agbli, K.S., Péra, M.C., Hissel, D., Rallières, O., Turpin, C., Doumbia, I., 2011. Multiphysics simulation of a PEM electrolyser: Energetic Macroscopic Representation approach. International Journal of Hydrogen Energy 36, 1382–1398. doi:10.1016/j.ijhydene.2010.10.069

Amphlett J. C., Mann R. F., Peppley B. A., Roberge P. R., Rodrigues A. and Salvador J. P. (1996) A model predicting transient responses of proton exchange membrane fuel cells. J. Power Sources 61(1-2): 183-188

Darras, C., 2010. Modélisation de systèmes hybrides photovoltaïque/hydrogène: applications site isolé, micro-réseau et connexion au réseau électrique dans le cadre du projet PEPITE (ANR PAN-H). (PhD, « French »). Università di Corsica Pascal Paoli.

Darras, C., Muselli, M., Poggi, P., Voyant, C., Hoguet, J.-C., Montignac, F., 2012. PV output power fluctuations smoothing: The MYRTE platform experience. Int. J. Hydrog. Energy 37, 14015–14025. doi:10.1016/j.ijhydene.2012.07.083

Gorgun, H., 2006. Dynamic modelling of a proton exchange membrane (PEM) electrolyzer. International Journal of Hydrogen Energy 31, 29–38. doi:10.1016/j.ijhydene.2005.04.001

Hwang, J.-J., 2013. Transient efficiency measurement of a combined heat and power fuel cell generator. Journal of Power Sources 223, 325–335. doi:10.1016/j.jpowsour.2012.09.086

TRNSYS Mathematical Reference, 1996. Solar Energy Laboratory Madison, United States, University Wisconsin.

Ulleberg Øystein, 1998. Stand-alone power systems for the future: optimal design, operation & control of solar-hydrogen energy systems. Norwegian University of Science and technology, Norway.

Conference Proceedings

Solar World Congress 2015
Daegu, Korea, 08 – 12 November 2015

DIRECT ILLUMINATED ROCK-BED HEAT STORAGE A POTENTIAL COMPONENT OF A SOLAR THERMAL SYSTEM FOR FOOD PRESERVATION AND SPACE HEATING IN RURAL AREAS OF MOZAMBIQUE

Amos Veremachi[1], Boaventura C. Cuamba[1], Ole J. Nydal[2], Jorgen Lovseth[2] and Azer Zia[3]

[1] Eduardo Mondlane University, Maputo-Mozambique

[2] Norwegian University of Science and Technology, Trondheim-Norway

[3] Department of Physics, Uppsala University-Sweden.

Abstract

Sun drying is a well known method of food preservation in countries with high level of solar irradiation and one of the ancient applications of solar energy. This method is widely applied for drying different agricultural products, meat and fish in rural areas of Mozambique. However, sun drying is ineffective method for food preservation and lead to poor product quality and post harvest losses. A more effective method of solar radiation deployment for food preservation is solar drying, which involves solar dryers. But many of them are direct solar dryers. Therefore they exhibit the same intermittent nature as the source of radiation does, which turn them useless devices during off-sun conditions. In order to extend the usefulness of solar dryers even in off-sun conditions, heat storage must be incorporated. In this study, in an in-door test, the potential of a direct illuminated rock-bed heat storage based on natural convection of air is experimentally investigated. The results show a good potential of rock-bed heat storage to supply thermal energy for low-to-medium temperature applications.

Keywords: *Direct illumination, heat storage, solar drying, space heating, sun drying, natural convection and food preservation*.

1. Introduction

Mozambique is a Southern African country and share common characteristics with the other African countries in that the majority of its population lives dispersed in rural areas, far from the national electricity grid. In fact only 18 % of Mozambican population is connected to national electricity grid (IRENA, 2012). The major fraction of population has biomass as major source of energy for different domestic needs. According to IRENA (2012), biomass contributes with more than 78 % of primary energy.

A source of growing concern, however, is the fact that one of the major sources of biomass is increasingly becoming scarcer due to unsustainable use of forest resources, land use change and also desertification (Cuamba et al, 2006; Chikukwa, 2008). While the burning of biomass has become a common practice among the emerging small commercial farmers in Mozambique for drying tobacco, the gains from this agricultural crop may be reduced if this trend remains as it is.

Fortunately, the country is among those possessing high levels of solar radiation (Nijegorodov et al, 2003; Cuamba et al; 2006). Therefore, solar thermal energy may be useful for drying different agricultural products including tobacco and other foodstuff either used as a solely source or used in a complementary way with the other sustainable sources of thermal energy.

Sun drying is well known method of food preservation in countries with high level of solar radiation and one

doi:10.18086/swc.2015.02.13 Available at http://proceedings.ises.org

of ancient applications of solar energy. However, sun drying as it is done under environmental conditions is ineffective method of food preservation due to constraints it presents and lead to poor product quality and spoilage leading thereby to postharvest losses, as discussed in Weiss & Buchinger (2012) and also by Raman et al. (2012).

Some of the pitfalls imposed by sun drying can be removed by the adoption of solar drying techniques. Solar drying involves the use of solar dryers and leads to more heat supply to the products than that available in natural conditions thereby turning the use of solar radiation into a more effective process (Weiss & Buchinger, 2012; Bala & Debnath, 2012: Raman et al. 2012).

Solar dryers can be natural convection and forced convection based. But many solar dryers enable the drying activity while solar radiation is present and are not useful during off-sun conditions. For this to happen, heat storage must be integrated.

The integration of heat storage enables the collection of solar thermal energy during day light and its storage for later use. The stored thermal energy can be used either to supply heat to the dryer or to be used for the space comfort in winter in absence of solar radiation, enabling this way overnight drying process of the products and space heating.

There are different ways to charge the storage. In one of the ways, the absorbing material and the storage are separate units; in this case a carrier medium is needed to transport heat from the absorber and charge the storage. In the other, in which the need of a carrier medium is bypassed, the absorber is an integrated part of the storage, in which case the storage is directly illuminated.

Although, in general, forced convection solar drying is an advantageous process as compared to natural convection solar drying, the requirements of forced convection solar dryers are not affordable to many rural families in Mozambique due to additional costs the forced convection generator brings. In fact, the cost associated with the forced convection generator is pointed as a constraint to implementation of forced convection solar dryers in low income families (Bala & Debnath, 2012).

Thus, despite the limitations of indirect natural convection solar dryers when applied to commercial and industrial scales as argued by (Bala & Debnath, 2012), some of them may be suitable to domestic applications for drying agricultural products and space heating. Thus, in this study, the potential of a side illuminated Rock-bed heat storage with natural convection as heat transfer mechanism to enable off-sun indirect solar drying of food and space heating is experimentally investigated.

2. Background Information

Solar drying of agricultural crops and different foodstuff is recognized as a midterm between the expensive and environmental damaging process of burning wood and fossil fuels and the traditional and vulnerable process of sun drying (Raman et al, 2012). In its extensive and comprehensive review Raman et al (2012) provides the state of art in solar drying technologies in developing countries, giving more emphasis to technologies enabling off-sun drying, and recognizes the benefits arising from its adoption from financial and environmental point of view.

Off-sun drying requires integration of heat storage. Then solar thermal energy must be collected during day light and carried to the storage; from which it can be extracted when needed. At some point in this paper two modes of charging the storage were mentioned: one that requires a heat carrier medium from the collector to the storage, and the other where the need of a heat carrier medium is bypassed. In the later, the storage is directly illuminated and heat is absorbed by the storage material.

During heat extraction, a fluid must be heated in interaction with the storage material. Then, the fluid carries the heat to the dryer. Again, the process can be carried out through two different modes of heat transfer namely natural convection which depends entirely on buoyancy force, and forced convection which require the forced convection generator.

Some studies devoted their attention in reviewing different types of dryers and discussing their performances and applicability in developing countries. In addition, they presented the current status of solar dryers and discussed the potentials of solar drying technology by revisiting their experimental performance in tropic and sub tropic regions as well as simulation of some of the types of dryers (Weiss & Buchinger, 2012) and others

designed, developed and tested a forced/ Natural convection solar vegetable dryer with heat storage (Babagana et al., 2012).
It is widely recognized that forced convection is an advantageous process over natural convection. In fact, (Babagana et al. 2012) found that forced convection mode was more efficient in that it enabled higher air flow and control in addition to reduced drying time. Due to additional costs that the forced convection generator brings, it may be suitable for commercial and industrial dryers**,** but not adequate for low income rural families, in which case the natural convection based solar dryers may be useful as a tool for drying agricultural products and other kinds of food at small scale applications and also for space heating applications. In fact in Raman et al. (2012) review, one of the focuses was on indirect natural convection based solar dryers with heat storage. Several studies referred in this review paper related to this type of dryers recognize the suitability and benefits of indirect natural convection based solar dryers to be applied in small farms in rural areas of developing countries. Bergman et al. (2011) also recognize that whenever and wherever heat transfer and operating costs have to be minimized, then natural convection based systems is the recommended choice.

Natural convection dryers are more popular for drying agricultural products owing to their low cost, simplicity in operation and maintenance; but presents lower drying rates, hence longer drying time than their counterpart (Babagana et al., 2012; Bala & Debnath, 2012). However, solar dryers regardless of their category are more effective than sun drying, because they lead to reduced drying time and good quality product.
In their turn Othman et al. (2006) devoted their attention to solar dryers with heat storage, that also integrate auxiliary sources of energy and controlling structure to allow off-sun drying activity of agricultural products.

With the similar purpose and recognition of the need to supplant the pitfalls brought about by the intermittent nature of the solar radiation, five years later after Othman's paper, Bal et al.(2011) published a review paper that focused to solar dryers with PCM heat storage.

2.1. The Physics of Natural Convection

The extent to which natural convection of a fluid occurs is dependent on buoyancy force. The driving force of this agent is density gradient which in turn is caused by temperature gradient within the fluid (Bergman et al. 2011). In most of the cases, the ultimate driving force of a natural convection of a fluid is the interaction between temperature gradient and gravitational field.

The arising motion of the fluid must be determined by considering heat and mass transfers coupled with the fluid flow mechanisms.

The density of the fluid is a function of its temperature and their dependence at constant pressure can be expressed through the volumetric expansion coefficient β:

$$\beta = -\frac{1}{\rho}\left(\frac{\partial \rho}{\partial T}\right)_P \qquad \text{(eq.1)}$$

For the finite variation of temperature at constant pressure, the following approximation can be used:

$$\beta \approx -\frac{1}{\rho}\left(\frac{\Delta \rho}{\Delta T}\right) \Rightarrow \Delta \rho \approx -\beta.\rho.\Delta T \qquad \text{(eq.2)}$$

Buoyancy force is proportional to density difference.

Whenever there is a relative motion between two bodies in contact, a friction forces arise at their interface; opposing to the motion.

Under steady state conditions, air flow rates driven by buoyancy are established by balancing buoyancy and frictional forces. Then, the ratio of the buoyancy force to the viscous force acting on the fluid, define the Grashof number:

$$Gr = \frac{g.\Delta\rho.V}{\rho.\nu^2} = \frac{g.\beta.\Delta T.V}{\nu^2} = \frac{g.\beta.(T_s - T_\infty).\delta^3}{\nu^2} \qquad \text{(eq.3)}$$

Natural convection over a surface, besides depending on its temperature variation and thermophysical properties of the fluid, is also geometry and surface orientation dependent.

Simple analytical relations are difficult to obtain in natural convection regimes due to the complex nature of the fluid flow. Therefore, most of the relations used to describe natural convection are experiment based

correlations:

In our case, during the illumination of the storage, heated air at the entrance of the cavity rise carrying with it thermal energy; and as it goes through the voids of storage material it releases the heat to the rocks. Thus, we assume non-local equilibrium case. Then, the source of heat is interrupted.

Now we have the rocks, at the cavity entrance, at higher temperature. Therefore, the air at the vicinity of the cavity interacts with hot rocks from which it absorbs heat. Again as it goes through the voids, thermal interaction occurs and emerges at the top at temperature suitable for drying food products or space heating.

The pressure drop within the packed bed can be given by Carman-Kozeny equation:

$$\frac{\Delta p}{\Delta z} = -\frac{180.\mu.v_o.(1-\varepsilon)^2}{{d_s}^2.\varepsilon^3} \quad \text{(eq.4)}$$

Where μ is fluid viscosity, v_o is the superficial velocity, ε is the bed void fraction and Δz, the bed height.

The pebble rock particles are assumed as of spherical form having a diameter d_s. Thus, characteristic length δ will be given by:

$$\delta = \frac{\pi.d_s}{2} \quad \text{(eq.5)}$$

Then, heat transfer coefficient between rock pebbles and air is a function of Nusselt number, thermal conductivity of rocks and characteristic length: $h = \frac{k.N_u}{\delta}$ (eq.6)

In this equation Nusselt number expression for external convection between air and spherical rock surface is adopted. Thus, (eq.7)

$$N_u = 2 + \frac{0.589.Ra^{\frac{1}{4}}}{\left[1+\left(\frac{0.469}{\Pr}\right)^{\frac{9}{16}}\right]^{\frac{4}{9}}}$$

Where Ra is the Rayleigh Number and $\Pr$, the Prandlt number.

The Rayleigh number is defined as the product of the Grashof and Prandtl numbers:

$$Ra = Gr.\Pr = \frac{g.\beta.(T_s - T\infty).\delta^3}{\nu^2}.\Pr \quad \text{(eq.8)}$$

The Nusselt Number in natural convection is also given by:

$$Nu = \frac{h.\delta}{k} = C.Ra^n \quad \text{(eq.9)}$$

Where n and C are constants that depend on the geometry of the surface and the flow regime.

3. Material and Methods

In this study a 400 mm diameter and 1000 mm height stainless steel cylinder, was adopted as a container for the storage material. Then, a cavity with same dimensions as the concentrator opening was made at its bottom side and a steel grid was welded at the cavity to hold the storage material.

The storage material comprises 257.5 kg of pebble rocks with 28 mm equivalent diameter. Afterwards two layers, of 50 mm thick, rock wool were used as thermal insulation for the heat storage.

The test was done using a solar simulator comprising a set of 7 halogen lamps and a concentrator to focus the light flux on the cavity located at the bottom side of the storage.

Experiments were performed in two different situations: At first with unglazed cavity and then with glazed

cavity using borosilicate glass. In each experiment, lamps were left on for almost 4 hours and then turned off.

To monitor temperatures at different levels along the storage and also to monitor heat front progression, three thermocouples were used. Then, the sensors were connected to a dataloger interfaced to a PC through labview program to read temperatures each second.
A thermografic camera was also used to scan temperatures at the cavity.

Table 1. *Thermophysical properties of pebble rocks*

Property	Density, $\rho\left[\frac{kg}{m^3}\right]$	Specific Heat, $c_P\left[\frac{J}{kg.K}\right]$	Thermal Conductivity, $k\left[\frac{W}{m.K}\right]$	Volumetric Heat capacity, $\rho.c_P\left[\frac{MJ}{m^3K}\right]$	Void Fraction	Average diameter, m
Magnitude	2630	830	2.79	2.183	0.38	0.028

The schematic representation of the storage and the measuring points is given in the figure below.

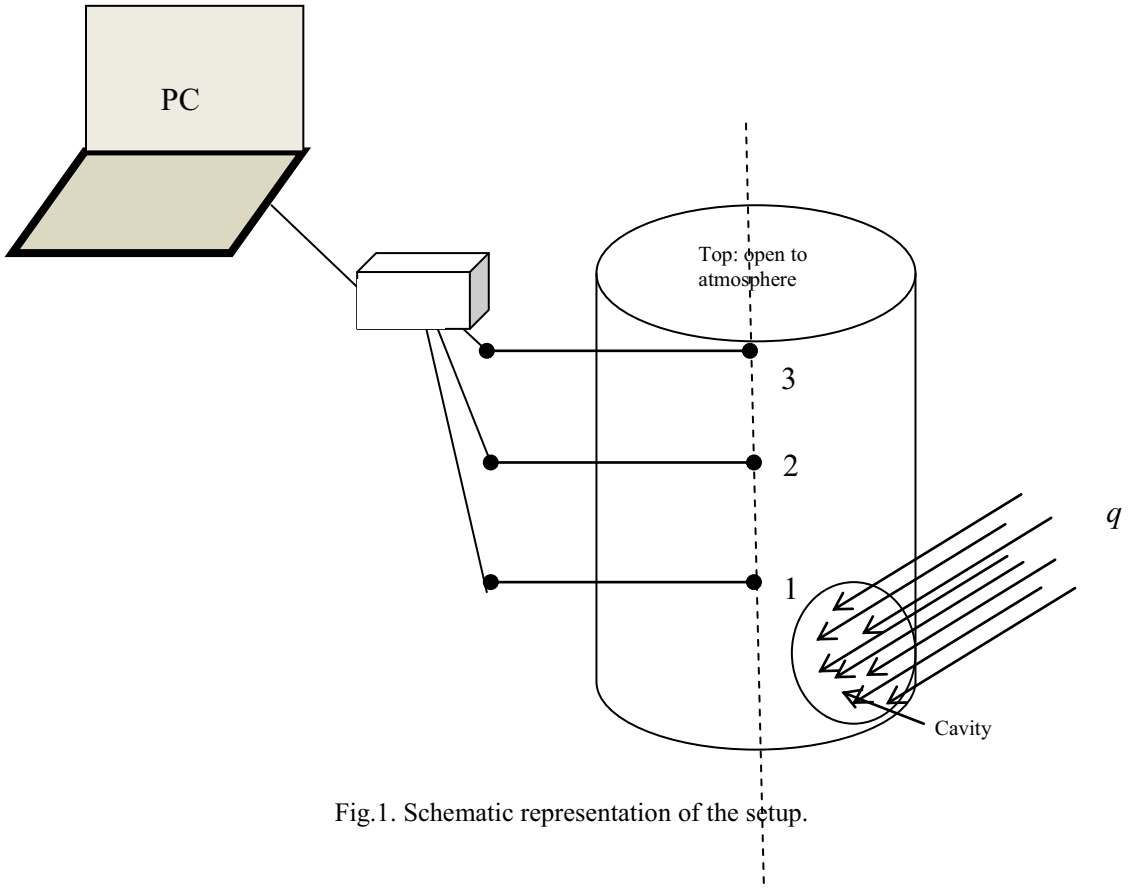

Fig.1. Schematic representation of the setup.

4. Results and Discussion

The following charts in figs.2 and 3 show temperature profiles at different levels of the HS for the unglazed and glazed cavity setup, respectively.

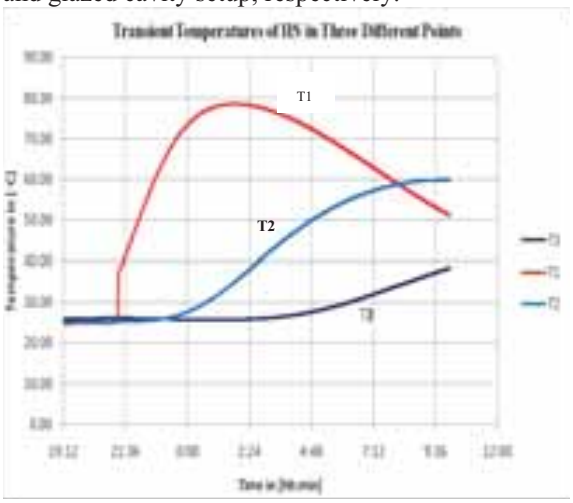

Fig.2. Chart showing temperature profiles at three different levels of HS for the unglazed cavity setup.

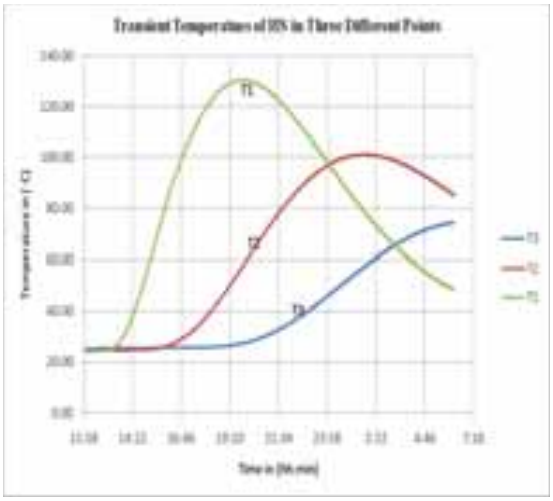

Fig.3. Chart showing temperature profiles at three different levels of HS for the glazed cavity setup.

The experiment that is referred in fig.2, was done with unglazed cavity. As can be seen from fig.2 the highest temperature registered by the first thermocouple, located 20 cm above the cavity, at the end of charging process was about 80 ^{o}C. Readings from the sensor located at the top of the HS show that until the time reading process was interrupted, temperature went from 25^{o}C to around 40^{o}C in about 13.5 hrs and was still in rise. This represents 15^{o}C above initial temperature and almost 20^{o}C above ambient temperature.

The experiment related to the chart in fig.3 was done with the cavity covered with borosilicate glass. In order to allow the air to go through the cavity a slit of about 5 cm was left at the bottom side of the cover. From the chart in fig.3 it can be seen that the first thermocouple went until 130 ^{o}C by the end of the charging process. The topmost sensor went until 75 ^{o}C by the end of measurement process. This represents almost 55^{o}C above ambient temperature. After about 13.5 hrs temperature at the top was above 60^{o}C.

The fact that temperature rise at the top of the storage is observed long after the charging process is particularly important in this case because the purpose of integrating the heat storage would be fulfilled. That is, it will allow the collection of thermal energy during sunlight and its storage to enable drying of the products or space heating in the absence of sunlight (overnight or cloudy day food drying/space heating). In either case the top of the storage needs to be connected to a drying chamber or to a house through appropriate channel to allow the hot air to go through.

It is reasonable to affirm that in both cases (with or without borosilicate glass cover at the cavity) the levels of temperatures registered is consistent with drying temperatures of many agricultural products and also suitable for space heating in the regions of Mozambique presenting cold winter. However, the performance of the heat storage needs to be tested through its integration with solar thermal collection system and a drying chamber or a house in order to assure the temperature of the air delivered to the final application its indeed appropriate for the purpose.

By integrating solar thermal energy collection, thermal storage and a drying system/or a house it is possible to achieve a fairly natural convection based efficient system. Then, the updraft driving pressure difference in the system may be given by:

$$\Delta p = \rho . \frac{\Delta T}{T} . g . \Delta z \qquad \text{(eq.10)}$$

Δz is the height difference between the air input and air exit levels (bed height)

This pressure difference will be balanced against flow friction to determine the air flow through the system.

By locating the drying and transport volumes above the solar collection and storage systems it is possible to increase the draft through the system owing to the fact that friction per unit height difference is normally smaller for the drying and transport regions than for the solar collection. In fact, Phueakphun & Fuenkajorn (2010) used a similar setup for space heating and their reasoning may be adapted in the present context to describe system‘s behavior and performance.

In our case, the storage is directly illuminated through a cavity at its bottom side by a concentrated radiation thereby being charged with thermal energy. In an outdoor experiment, a Scheffler reflector can be used to direct solar radiation to the storage’s cavity. In its turn, the storage may be connected to the drying chamber or a house, accordingly.

It should be noted that the glazed cavity setup leads to an increase of at least 62 % on the temperatures of the HS in different levels as compared to unglazed cavity setup. This difference may be attributed to the fact that the glazing decreased convective and radiactive heat loss from the cavity.
The storage is a biphasic system comprising rock pebbles and air.

Some assumptions can be adopted here, namely one-dimensional heat flow, no temperature gradients within rock particles and air is only heated by thermal energy from the rocks either reflected or by convection. The heat absorbed by the container is also neglected and the walls of the storage, but the open parts, are adiabatic.

During the performed tests in the present system, two stages can be distinguished:

1. The Storage is being illuminated by the system of lamps:

During this stage, it can be said that, heat flux impinges directly on the rocks surrounding the cavity (directly or after is transmitted by borosilicate glass cover) and is absorbed by the rocks..Then, as a consequence of heat absorption the temperature of rocks is raised. From there, heat is transferred to the flowing air at the cavity by convection. The air is heated as it goes through the voids in the bed thereby interacting with hot rock pebbles. Then, it is cooled when it faces the uppermost rock pebbles, which are at relatively low temperature, by convection. Thus, energy is gained by the rock pebble system by absorbing heat flux and is lost to the air by convection through the top open side of the storage. Energy balance equation can be written as:

$$m_{rP} c_{rP} \frac{dT_{rP}}{dt} = \alpha_{rP} q A_{cav} - h_{rP} A_r \left(T_{rP} - T_{airb}\right) \quad \text{(eq.11)}$$

The air in the storage gain heat from heat reflected at rock pebbles, radiation and convection heat transfer from rock particles and loses energy to the surrounding at the open top of the storage by convection:

$$m_{air} c_{air} \frac{dT_{airb}}{dt} = f_{ab}\left(1-\alpha_{rP}\right) q A_{cav} + h_r A_r \left(T_{rP} - T_{airb}\right) - \dot{m}.c_{air}\left(T_{airb} - T_{sur}\right) \quad \text{(eq.12)}$$

2. System of lamps is turned-off:

In this stage, cold air enters the storage through the cavity and absorbs heat from the rock pebbles:

$$m_{rP}.c_{rP} \frac{dT_{rP}}{dt} = -h_{rP} A_r \left(T_{rP} - T_{airb}\right) \quad \text{(eq.13)}$$

$$m_{air} c_{air} \frac{dT_{airb}}{dt} = h_{rP} A_r \left(T_{rP} - T_{airb}\right) - \dot{m} c_{air}\left(T_{airb} - T_{sur}\right) \quad \text{(eq.14)}$$

5. Conclusion

The potential of a natural convection based and direct illuminated rock bed heat storage has been experimentally investigated. A solar simulator comprising 7 halogen lamps and a solar concentrator coupled to the lamp system to focus the light flux to a storage cavity located at the bottom side of the storage have been used during the experiment.

The experiments were done in two different conditions. In one setup the cavity was not covered and the concentrated light flux went through the cavity and thermally interacted with the rock pebbles. In the other, the storage cavity was covered with a borosilicate glass, with 5 cm gap left to let the air go through.

Temperatures at three different positions within the storage were monitored using type-k thermocouples.

In both setups temperatures at the top part of the storage (air exit) are suitable for the intended applications, with even good performance with the borosilicate cover at the cavity, representing 62 % increase as compared to the levels of temperature achieved with uncovered cavity. However, further experiments need to be done with the heat storage integrated to the solar concentrator and a drying system or space to be heated in order to assure the performance of the system.

References

Babagana, G; Silas, K & Mustafa, B.G (2012). Design and Construction of Forced/Natural Convection Solar Vegetable Dryer with Heat storage. ARPN Journal of Engineering and Applied Sciences.7, 10; ISSN 1819-6608.

Bala, B.K & Debnath, N. (2012). Solar Drying Technology: Potential and Developments. Journal of Fundamentals of Renewable Energy and Applications. Vol.2. Article ID R:120302, Ashdin Publishing.

Bal et.al (2011). Review of Solar Dryers with latent Heat Storage Systems for Agricultural Products. Renewable and Sustainable Energy Reviews.15, 876-880.

Chikukwa, A. (2008). Modelling of a Solar Stove: Small Scale Concentrating System with Heat Storage. NTNU.

Cuamba, B. et al. (2006). A Solar Energy Resources assessment in Mozambique. Journal of Energy in Southern Africa. Vol.17, nr 4, November 28.

IRENA Mozambique (2012). Renewables Readness Assessment. www.irena.org.

Nijegorodov, N.I et al.(2003). Comprehensive Study of Solar Conditions in Mozambique: The Effect of Trade Winds on Solar Components. Renewable Energy..28, 1963-1983. Elsevier Science LTD.

Othman et al. (2006). Development of Advanced Solar Assisted Drying Systems. Renewable Energy. 21, 703-709/

Phueakphum, D. & Fuenkajorn, K. (2010). A rock Fills Based Solar Thermal Energy Storage System for Housing. ScienceAsia. 36, 237-243.

Raman, S.V; INiyan, S. & Goic, R. (2012). A Review of Solar Drying Technologies. Renewable and Sustainable Energy Reviews. 16, 2652-2670.

Weiss, W. & Buchinger, J. (2012). Solar Drying. Institute of Sustainable Technologies. Austria.

List of Symbols:

Symbol	Quantity
c_{rP}	Specific heat of rock pebbles
α_{rP}	Absorptance of rock pebbles
A_{cav}	Area of Cavity
A_r	Area of rocks
c_{air}	Specific heat of air
h_{rP}	Heat transfer coefficient rock-air
T_{rP}	Temperature of rock pebbles
T_{airb}	Temperature of the air in the rock bed
T_{sur}	Temperature of the surrounding
q	Heat Flux
m_{rP}	Mass of rock pebbles
m_{air}	Mass of air
Δz	Height difference between air input and air output points

Conference Proceedings

Solar World Congress 2015
Daegu, Korea, 08 – 12 November 2015

PERFORMANCE ANALYSIS OF A NEW THERMAL STRATIFICATION DEVICE FOR HOT WATER STORAGE TANK HEATED AT THE BOTTOM

Jianhua Fan[1], Vaclav Ptacek[1], Simon Furbo[1], Janne Dragsted[1] and Pengjie Sun[2]

[1] Department of Civil Engineering, Technical University of Denmark, Denmark

[2] Beijing Computing Center, Beijing, China

Abstract

Thermal stratification in heat storage tank has a major influence on the thermal performance of the heating system. For heat storage tank heated from the bottom, the whole tank is heated in order to provide hot water for the consumer. A new stratification device has been developed to place the heated water at the top of the tank, therefore allowing the energy usage to be reduced since the whole tank does not need to be heated to provide hot water. The aim of the paper is to investigate the performance of the newly developed thermal stratification device by means of experiments and computational fluid dynamics (CFD) simulations. Experiments have been carried out to measure water temperatures at different levels of the tank during charging by a vertical heating element integrated in the stratification device. A simplified CFD model of the cylindrical heat storage tank with the stratification device and a heating element at the bottom of the tank is created in Ansys Fluent 15.0. Transient fluid flow and heat transfer in the tank during charging are calculated. The CFD calculated water temperatures are compared to the measured temperatures. A parametric study has been carried out to investigate how thermal stratification in the tank is influenced by the design of the stratifier such as pipe thickness, material type, diameter of the pipe, by dimensions of the tank and by power of the heating element, etc.

The investigations elucidate how well a hot water tank heated at the bottom with a vertical heating element can be stratified by using the new stratifier design. Based on the CFD calculations, design of the stratification device is optimized.

Keywords: Heat storage tank, thermal stratification, stratification device, Computational fluid dynamics (CFD), Experiments

1. Introduction

Thermal stratification in heat storage tanks has a major influence on the thermal performance of solar heating systems. A high degree of thermal stratification in the storage tank increases the thermal performance of a solar heating system because the return temperature to the solar collector is lowered (Furbo 1984, van Koppen C 1979, Furbo 1987). A lower inlet temperature to the solar collector will increase the efficiency and operating hours of the solar collector. Further, the temperature at the top of the storage will be closer to the desired load temperature. Therefore the auxiliary energy consumption will be decreased which increases the solar fraction (Hollands 1989, Furbo 2006). Thermal stratification and natural convection flow in a vertical cylindrical hot water tank during standby periods were investigated in previous investigations (Andersen 2007, Fan 2012a, 2012b). Transient, three-dimensional CFD models of hot water storage tanks were developed and validated against thermal measurements. The results show that the CFD calculation predicts satisfactorily the water temperatures in the tank during cooling of the tank. The natural convection flow along the tank sides is strongly influenced by the thermal stratification in the tank.

A tank heated from the bottom could be used as heat storage in a solar heating system, or as heat storage for PV heating. Compared to conventional tank, it is more difficult to ensure high degree of thermal stratification in the tank heated from the bottom as natural convection in the tank created by the heating element will mix water in the tank therefore destroying thermal stratification in the tank. Typically the whole tank is heated in order to provide hot water for the consumer. A new stratification device has been developed to place the

Selection and/or peer review under responsibility of Scientific Committee
doi:10.18086/swc.2015.02.14 Available at http://proceedings.ises.org

heated water at the top of the tank, therefore allowing the energy usage to be reduced since the whole tank does not need to be heated to provide hot water for the consumer.

The aim of the paper is to analyze performance of the newly developed thermal stratification device by means of experiments and computational fluid dynamics (CFD) simulations.

2. The investigation methods

Experiments have been carried out to investigate thermal performance of the newly developed stratification device. Fig. 1 shows test setup a cylindrical heat storage tank of 110 liters installed with a stratification device. The tank is made of 2 mm steel. The stratification device is mounted at the bottom of the cylindrical tank, see Fig. 1A. The stratification device consists of two parts: A steel pipe with a diameter of 115 mm at the bottom and a plastic pipe with a diameter of 20 mm at the top, see Fig. 1B. Inside the steel pipe of the stratification device there is a vertical electrical heating element of 2.91 kW installed. When heated by the heating element, water in the stratification device rises up and enters in the tank though an opening at the top of the plastic pipe, while there are gaps at the bottom of the stratification device, allowing water from the tank to enter into the inlet stratification device. This forms a circulation of water flow driven by natural convection. Photo of the tank is shown in Fig. 1C. Experiments have been carried out to measure water temperatures at different levels of the tank during charging at different operation conditions.

(A) design of the tank (B) photo of the stratification device (C) photo of the tank

Fig. 1: Experimental setup of a heat storage tank with a stratification device

A simplified CFD model of the cylindrical heat storage tank charged with a heating element at the bottom of the tank is created in Ansys Fluent 15.0, see Fig. 2. The tank has a diameter of 394 mm and a height of 841 mm, resulting in a volume of 110 liters. The stratification device is placed in the middle of the tank, stretching from the bottom to the top of the tank. The bottom part of the device is a steel pipe with a diameter of 115 mm and a thickness of 4.3 mm, while the upper part of the device is a plastic pipe with a diameter of 20 mm and a thickness of 2.3 mm, see Fig. 2. The parabolic top end and bottom end of the tank are made flat in order to facilitate good meshing. The water volume above the opening of the plastic pipe and the dead volume at the bottom of the tank were kept the same as the tank in experiment, therefore influences on thermal stratification by the simplification is minimized. The 3D tank model includes the steel tank wall as a solid region and the hot water volume of the tank as a fluid region while the insulation materials are not directly modelled. The effect of the insulation materials is considered by the heat loss coefficients measured by the experiment. The heat loss coefficient of the tank is divided into three parts: heat loss coefficient of the top surface, of the side surface and of the bottom surface. The heat loss coefficients measured by the experiments are used as input to the model. The following equations are used to calculate temperature

dependent heat loss coefficients of the tank:

$$K_{top} = 0.24 + 0.00015 * t \quad [W/K] \quad \text{(eq. 1)}$$

$$K_{side} = 1.75 + 0.00148 * t \quad [W/K] \quad \text{(eq. 2)}$$

$$K_{bottom} = 0.41 + 0.00034 * t \quad [W/K] \quad \text{(eq. 3)}$$

$$K_{total} = 2.4 + 0.00198 * t \quad [W/K] \quad \text{(eq. 4)}$$

where t is the water temperature in the tank, [˚C].
Mean average ambient air temperature during the experiment is used as the free stream temperature of the tank surfaces. The tank wall material, steel, has a thermal conductivity of 60 W/K/m and a density of 7850 kg/m^3.

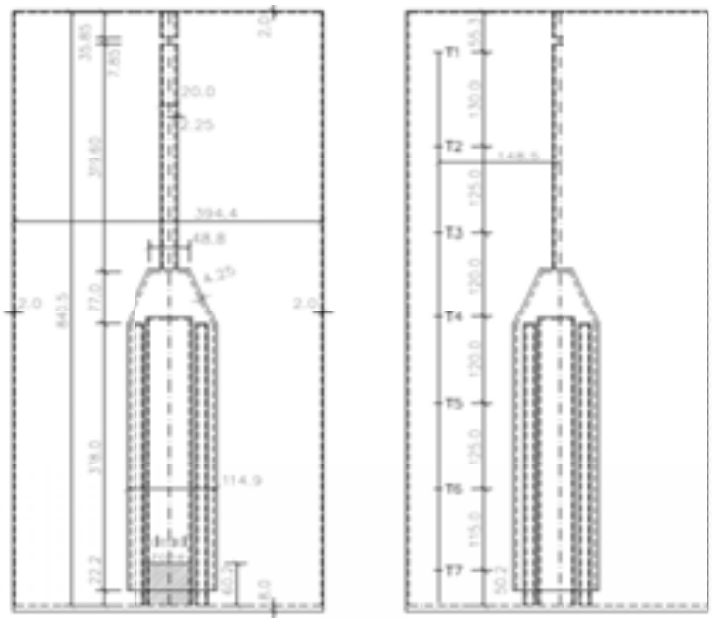

Fig. 2: Simplified CFD model of the tank with a stratification device

The mesh on the vertical cut-plane of the tank is shown in Fig. 3A. In order to better resolve the heat transfer and fluid flow in the region adjacent to the tank wall, a boundary layer mesh is applied so that there is a fine and dense mesh in the area close to the wall, see Fig. 3B and 3C.

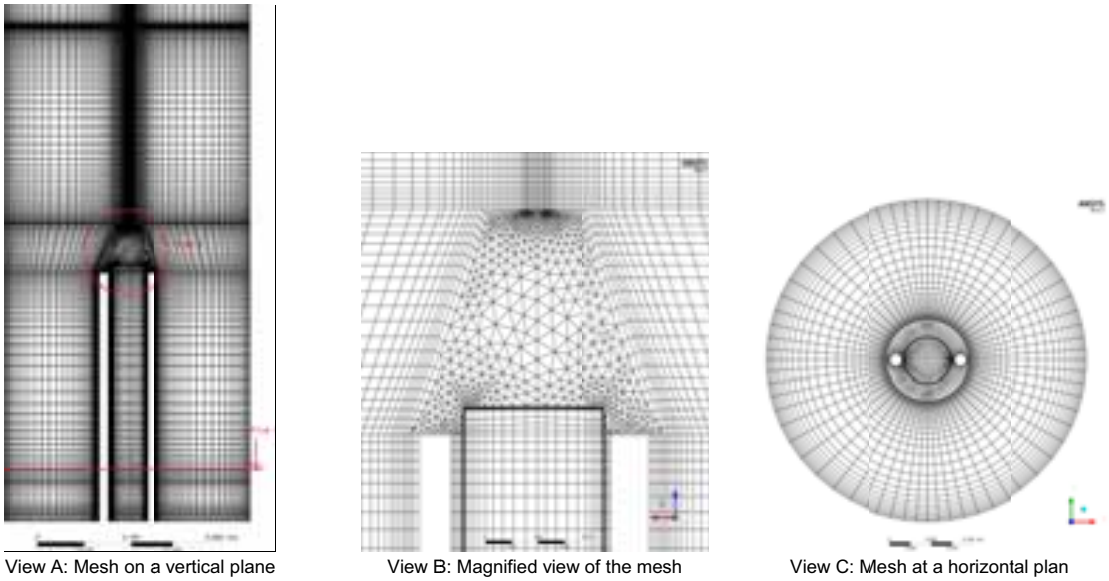

View A: Mesh on a vertical plane | View B: Magnified view of the mesh | View C: Mesh at a horizontal plan

Fig. 3: Mesh of the CFD model of the tank

Calculation of Rayleigh number shows that the flow in the tank is turbulent, therefore the k-ε turbulent model is used in the calculation. Transient CFD calculations are performed with Boussinesq approximation. The PRESTO and second order upwind method are used for the discretization of the pressure and the momentum/energy equations respectively. The SIMPLE algorithm is used to treat the pressure-velocity coupling. The transient simulations start with a cold tank with temperature close to the ambient air temperature. A zero velocity field is assumed at the start of all simulations. The calculation is considered convergent if the scaled residual for the continuity equation, the momentum equations and the energy equation are less than 10^{-3}, 10^{-3} and 10^{-6} respectively. The simulation runs with a time step of 1 s and a duration of 1 h. One simulation takes approximately 24 hours for a quad-core processor computer with 4 X 3 GHz CPU frequency and 8G memory.

3. Validation of the CFD model

Transient fluid flow and heat transfer in the tank during charging are calculated. The CFD calculated water temperatures are compared to the measured temperatures. Fig. 4 shows measured and calculated temperatures in the tank at 7 different levels of the tank after 1 hour of charging from a cold tank. Locations of the temperature sensors are illustrated in Fig. 1A. Measured temperatures are shown with a title 't_e*' while CFD calculated temperatures are shown with a title 't_c*'. The last number in the title '*' indicates the location of temperature sensor. The charging power is 2.91 kW. At the start of the charging, the measured temperature at the top of the tank was 5 K higher than the temperature used in the CFD model. This difference in temperatures will influence the difference between measured and calculated temperature as water at the top of the tank will slowly flow towards the bottom of the tank during charging.

The difference between the measured and the calculated temperatures is within the range of 0-4 K at the end of the charging. It can be seen that there is a good agreement between the measured and the CFD calculated temperatures through the whole tank, therefore the CFD model is considered reliable. The validated CFD will then be used to investigate how thermal stratification in the tank is influenced by different designs of the stratification device.

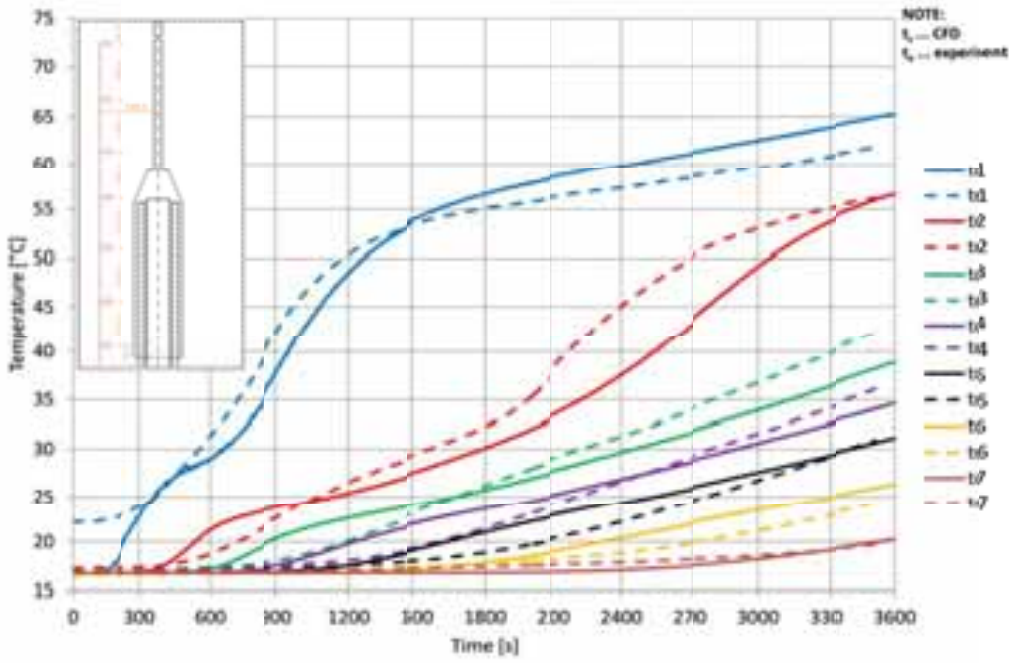

Figur 4. Measured and calculated temperatures in the tank during a 1h charge (t_c.., CFD; t_e…, experiment).

4. Parametric analysis

The validated CFD model is used to calculate water temperatures in the 110 l Metro tank after 1 hour of charging. At the start of the charging, the tank has a uniform tank temperature of 16.5°C. Calculations are carried out to investigate the influence of the design of the stratification device on thermal stratification in the tank. The investigations focuses on diameter and wall thickness of the PEX pipe, opening area of the PEX pipe, diameter of the hole separating the plastic pipe and the steel pipe as well as dimeter, wall thickness for the steel pipe around the heating element. Also calculations with a PP pipe around the heating element were carried out. The charging power is 2.91 kW in the calculations.

4.1 Diameter and wall thickness of the PEX pipe

Fig. 5 shows calculated temperatures in the tank during a 1 hour charge with different diameters of the PEX pipe. The PEX pipe in the experiments has an outer diameter of 20 mm and an inner diameter of 15.5 mm, therefore 20/15.5 mm is used as a reference. In Fig. 5, 'tb*', 't* 16mm' and 't* 25mm' represent the reference pipe of 20/15.5 mm, a pipe of 16/12 mm and a pipe of 25/20.4 mm respectively. The last number in the title '*' indicates the location of temperature sensor. It can be seen that the diameter of the PEX pipe has almost no influence on water temperatures in the tank, therefore it can be concluded that thermal stratification is not influenced by diameter of the PEX pipe if pipe diameter lies within the range from 16-25 mm. It indicates that the investigated pipe diameters are sufficient large so that they will not create significant friction loss for the natural convection flow in the pipe during charging.

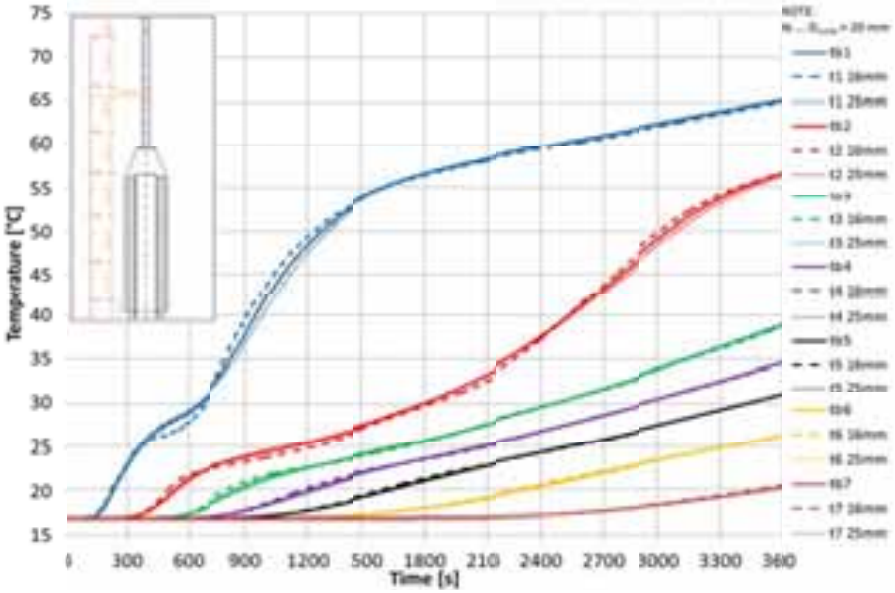

Figur 5. Calculated tank temperatures during a 1 (h) charge for different PEX pipe diameters.

Fig. 6 shows calculated water temperatures during a 1 hour charge with different wall thicknesses of the PEX pipe. The PEX pipe in the experiments has a wall thickness of 2.25 mm, which is shown as reference in Fig. 6. The text 'tb*', 't* 1mm' and 't* 3mm' represent respectively wall thickness of 2.25 mm, 1 mm and 3 mm. The last number in the title '*' indicates the location of temperature sensor. It shows that the wall thickness has insignificant influence on water temperatures in the tank. The tank with a PEX pipe wall thickness of 2.25 mm has almost the same temperature as the tank with a pipe wall thickness of 3 mm while with a wall thickness of 1 mm, there is a larger temperature difference. The largest temperature difference between the three tanks is smaller than 1 K. It means that further increase of wall thickness will not make any influence on thermal stratification in the tank while the thermal stratification tends to get worse with a decrease of wall thickness to be below 1 mm. This could be explained by a larger heat transfer from the hot water in the pipe to water in the tank through the pipe wall.

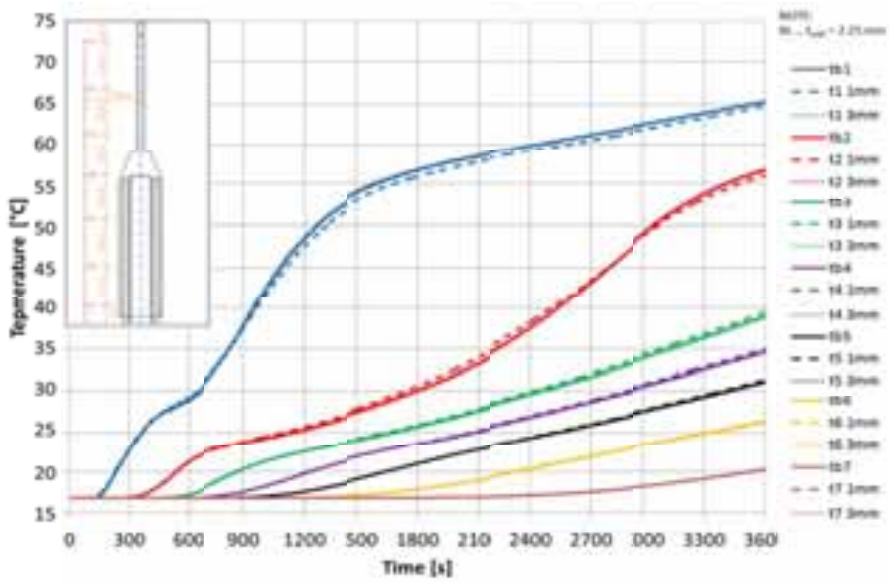

Figur 6. Calculated tank temperatures during a 1 (h) charge for different PEX pipe wall thicknesses.

4.2 Opening area at the top of the PEX pipe

Water heated by the heating element will rise up and enter into the PEX pipe. At the top of the PEX pipe, there are holes in the pipe that allow heated water enter into the tank. With an increase of the number of holes, the opening area increases. Fig. 7 shows calculated water temperatures after 1 (h)s of charging with different opening areas at the top of the PEX pipe. The reference number is 12 holes, represented by 'tb*', where * represents an integral number from 1 to 7. 't* 6' and 't* 24' show the result for 6 holes and 24 holes respectively. It is shown that thermal stratification in the tank is not influenced by varying the number of holes from 6 to 24.

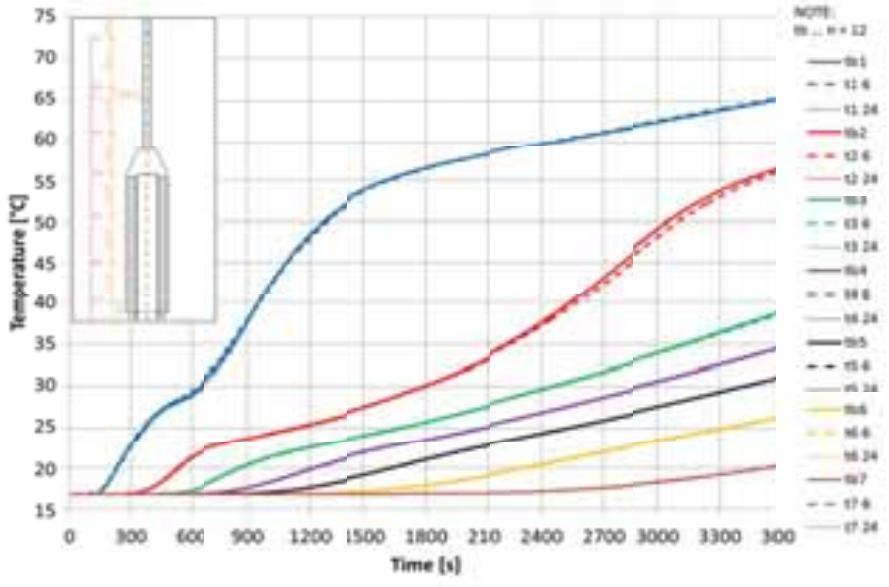

Figur 7. Calculated tank temperatures during a 1 (h) charge for different opening areas at the top of the PEX pipe.

4.3 Opening area between the steel pipe and the PEX pipe

In between the conic top of the steel pipe and the PEX pipe, there is a hole with smaller diameter than both the steel pipe and the PEX pipe. In the experiment, the opening area is 21.3% of the PEX cross section area. Investigations were carried out to study the influence of diameter of the opening area on calculated temperatures. The following opening areas were calculated: 5%, 10%, 15%, 30% and 40% of the PEX cross section area. The results of the calculation with different opening areas are shown in Fig. 14, 15 and 16. It

can be seen that the opening area influences significantly water temperatures in the tank. After 1 hour of charging the water temperature at the top of the tank is the highest for the tank with an opening area of 10% in between the steel pipe and the PEX pipe.

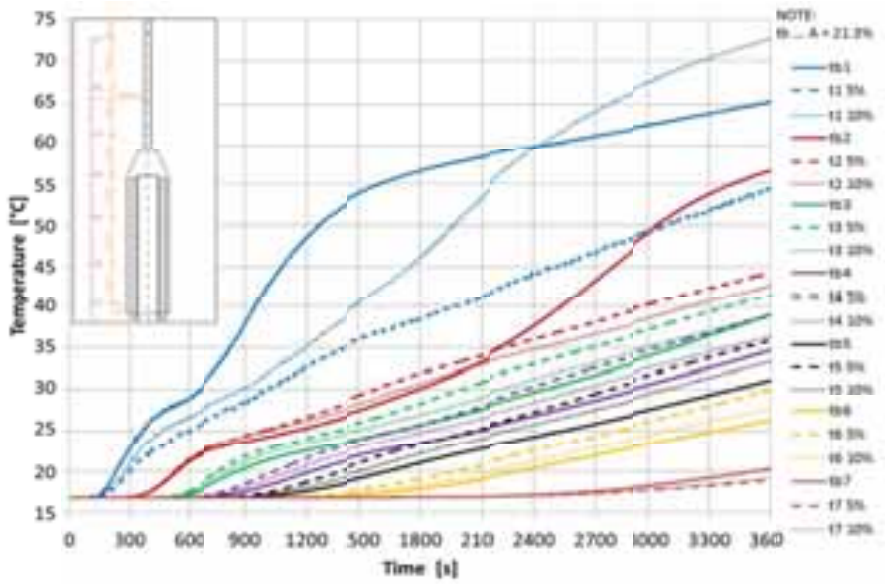

Figur 8. Calculated tank temperatures during a 1h charge for different opening areas between the conic steel pipe and the PEX pipe.

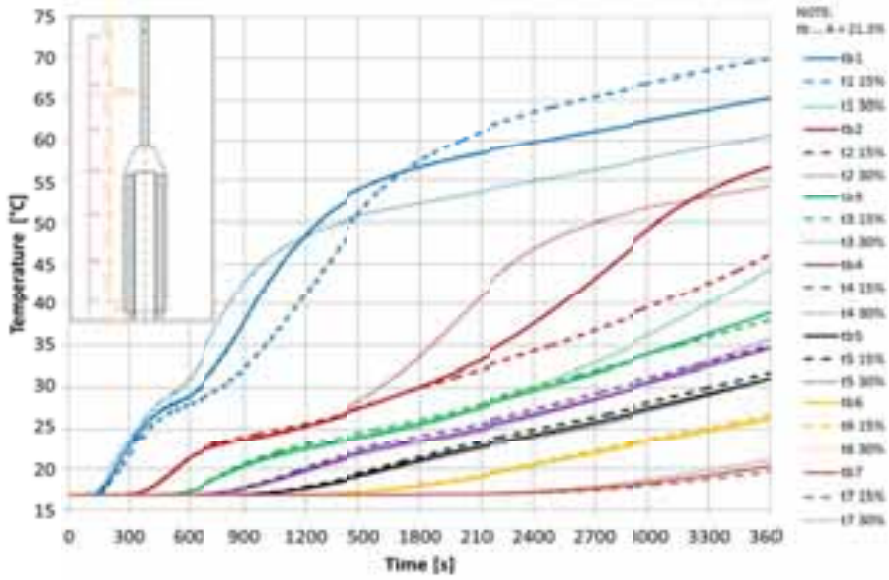

Figur 9. Calculated tank temperatures during a 1 (h) of charge for different opening areas between the conic steel pipe and the PEX pipe.

The reason of the best thermal stratification for an opening area of 10% could be explained by the buoyancy driven flow due to charging. For a slower movement of the buoyancy driven flow, water will have adequate time to be heated to a higher temperature. On the other hand, if the flow is too slow, heat will be lost from the heated water to water in the tank through the pipe walls. Therefore a decrease of the opening area from 10% to 5% will result in a lower water temperature at the top of the tank, see Fig. 8, while with an increase of the opening area from 10% to 15% or larger, the buoyancy driven flow in the pipe will be increased therefore resulting in a lower water temperature at the top of the tank.

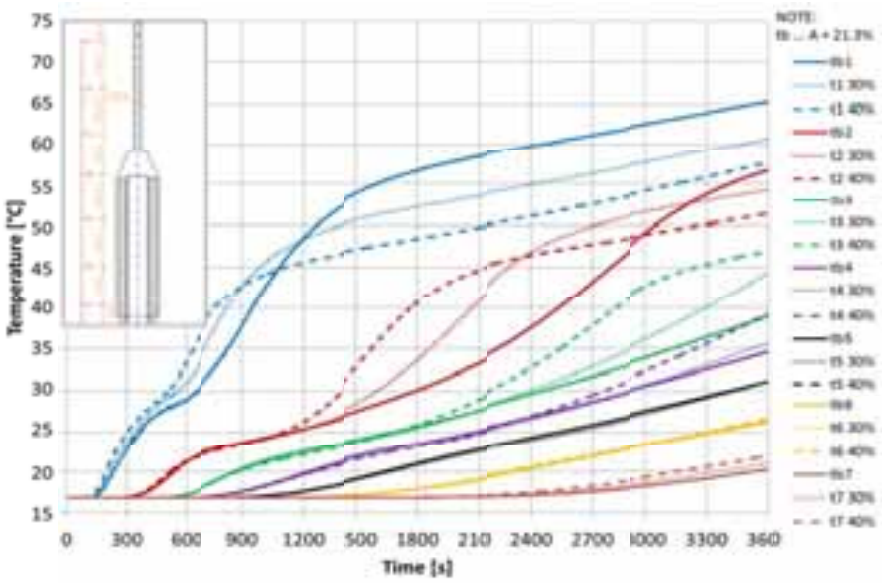

Figur 10. Calculated tank temperatures during a 1 (h) of charge for different opening areas between the conic steel pipe and the PEX pipe.

Fig. 11 shows calculated effective energy content of the tank for different opening areas between the conic steel pipe and the PEX pipe. The effective energy of the tank is obtained by summing up energy content of water in the tank with a temperature higher than 50°C. Therefore it determines the useful energy of the tank after charging. It shows that the opening area has a significant influence on the effective energy content of the tank. Charging of a tank with an opening area in between 21.3% and 30% of the cross section area of the PEX pipe will result in the largest effective energy content. It means that although an opening area of 10% will result in the highest water temperature in the tank but the effectively energy content of the tank is not the largest because the relative slower fluid flow in the pipe means smaller water volume heated to 50°C at the end of charging.

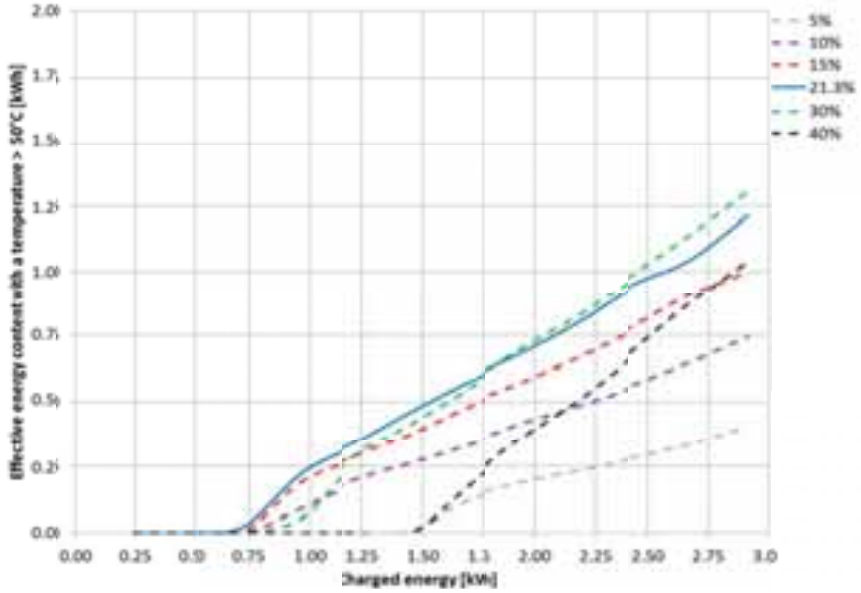

Figur 11. Calculated effective energy content of the tank for different opening areas between the conic steel pipe and the PEX pipe.

4.4 Diameter and wall thickness of the steel pipe

Fig. 12 shows calculated water temperatures in the tank for different diameters of the steel pipe. In the experiment the steel pipe has a diameter of 114.9 mm and a wall thickness of 4.25 mm, therefore it is used as reference. A diameter of 110 mm and 125 mm are used in the investigations. It can be seen in Fig. 12 that

the diameter of the steel pipe has insignificant influence on water temperature in the tank after 1 hour of charging.

Calculations were carried out for a wall thickness of 1 mm and 2 mm. The results show that there is almost no difference in temperatures with a decrease of wall thickness from 4.25 mm to 1 mm and 2 mm.

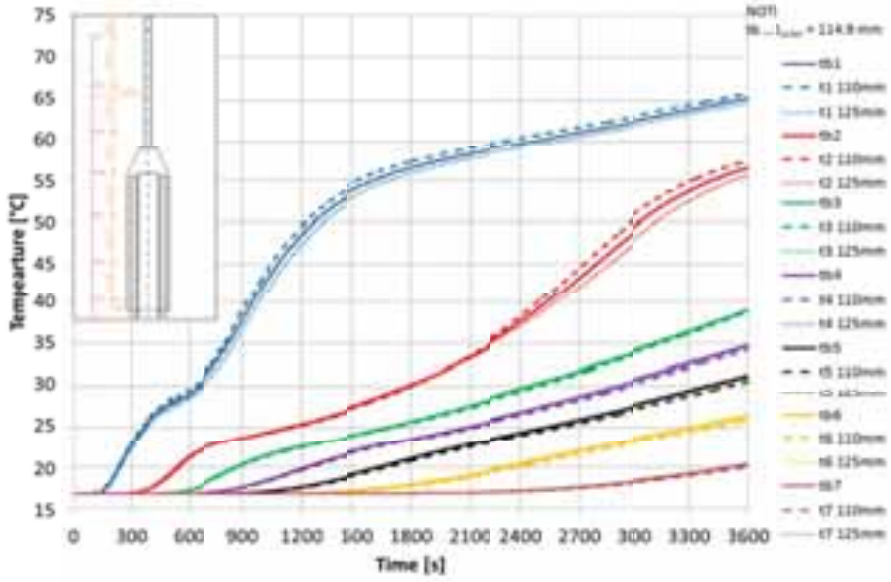

Figur 12. Calculated tank temperatures during a 1 (h) of charge for different diameters of the steel pipe.

4.5 Different materials of the pipe around the heating element

In the experiment the pipe around the heating element is made of steel. Investigations were carried out to study the influence of material of the pipe on water temperature in the tank. In addition to steel as a reference, PEX and PP are used as pipe materials. The results are shown in Fig. 13. It can be seen that pipe material has a strong influence on water temperature in the tank. The lower the thermal conductivity of the pipe material, the better the thermal stratification in the tank is. For a pipe made of material with a higher thermal conductivity for example steel, the water temperature at the bottom part of the tank will be higher due to heating by horizontal heat transfer across the pipe. On the other hand, the lower the thermal conductivity of the pipe around the heating element, the higher the water temperature at the top of the tank will be, for example, when PP is used as pipe material.

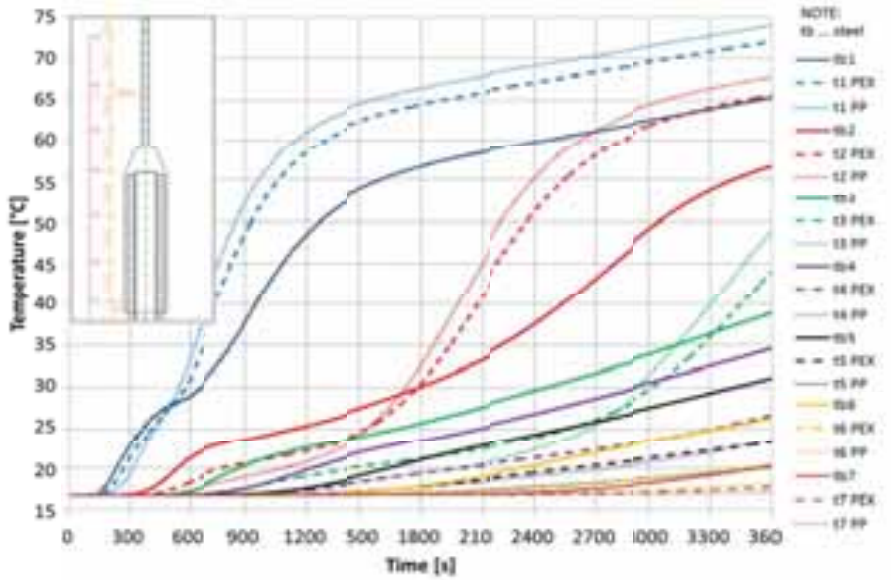

Figur 13. Calculated tank temperatures during a 1 (h) of charge for different pipe materials.

Fig. 14 and 15 show velocity vectors around the heating element with steel and with PP as pipe material respectively. As shown in Fig. 14, there is a dominant upward flow around the heating element due to heating of water in the stratification device, while along the pipe wall there is an apparent downward flow caused by heat loss from the steel pipe wall in the horizontal direction. The uprising flow collides with the downward flow, creating flow circulations in the conic top.

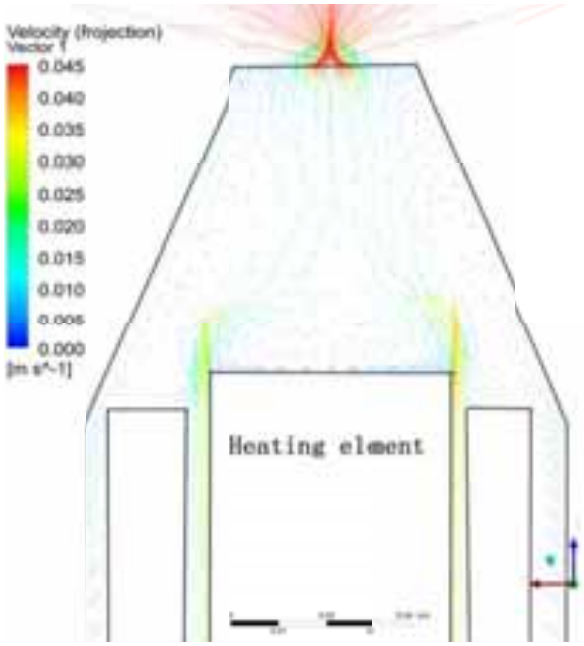

Figur 14. Velocity vectors around the heating element with steel as pipe material.

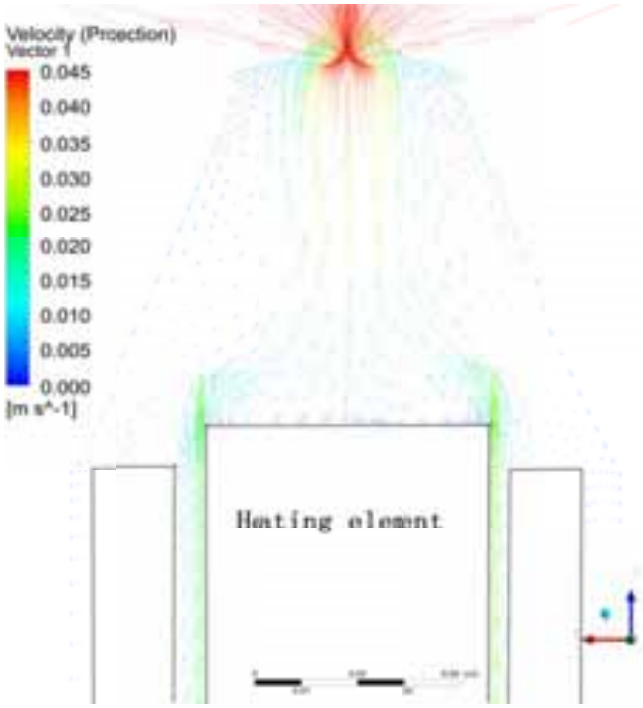

Figur 15. Velocity vectors around the heating element with PP as pipe material.

When PP is used as pipe material, the downward flow along the pipe wall is minimized, which can be explained by lower thermal conductivity of PP compared to steel. Since heat loss from the pipe is significantly reduced, the driving force of the downward flow becomes smaller. As a result water flow around and above the heating element is more regular, resulting in a higher water temperature when it enters the plastic pipe. Therefore it can be concluded that use of a material with lower thermal conductivity for the pipe around the heating element has the following advantages:

(1) increased temperature at the top of the tank

(2) decreased heat transfer between the stratification device and the bottom of the tank

(3) better thermal stratification in the tank and thus higher effective energy content of the tank after charging.

5. Conclusions

A newly developed thermal stratification device was investigated by means of experiments and computational fluid dynamics (CFD) simulations. Experiments have been carried out to measure water temperatures at different levels of the tank during charging by a vertical heating element integrated in the stratification device. Transient fluid flow and heat transfer in the tank during charging are calculated by a simplified CFD model. The CFD calculated water temperatures are compared to the measured temperatures. The results show that the CFD model can satisfactory predict thermal stratification in the tank during charging.

A parametric study has been carried out to investigate how thermal stratification in the tank is influenced by design of the stratifier such as pipe thickness, material type, diameter of the pipe, opening area etc. The investigations elucidate how well a hot water tank heated at the bottom with a vertical heating element can be stratified by using the new stratifier design. The results show that diameter and wall thickness of the PEX pipe have minor influence on thermal stratification in the tank if the diameter of the pipe is in the range of 16-25 mm and the wall thickness is in the range of 1-3 mm. Opening area at the top of the PEX pipe has insignificant influence on water temperature in the tank during charging while opening area in between the PEX pipe and the conic pipe has a significant influence. The calculations show that an opening area of 10% of the cross section area of the PEX pipe gives the highest water temperature at the top of the tank but the effective energy content of the tank is the largest if an opening area in between 21.3% and 30% is used.

Concerning the pipe around the heating element, diameter and wall thickness has almost no influence on water temperature in the tank if steel is used as pipe material. Use of a material with lower thermal conductivity for the pipe around the heating element will result in a higher temperature at the top of the tank and an increased degree of thermal stratification in the tank.

Acknowledgements

This research was supported by the Danish ELFORSK Research Program and by the Special fund for the development of small and medium enterprises (EU China Cooperation Program) SQ2013Z0G100002.

6. References

Andersen E, Furbo S, Theoretical comparison of solar water/space heating combi systems and stratification design options. Journal of Solar Energy Engineering 2007; 129: 438-448.

Fan J, Furbo S. Buoyancy driven flow in a hot water tank due to standby heat loss. Solar Energy 2012; 86:3438-3449.

Fan J, Furbo S. Thermal stratification in a hot water tank established by heat loss from the tank. Solar Energy 2012; 86:3460-3469.

Furbo S. Varmelagring til solvarmeanlæge, PhD report, No. 162, Thermal Insulation Laboratory, Technical University of Denmark, 1984.

Furbo S, Mikkelsen S. Is low flow operation an advantage for solar heating systems? Proceedings of the ISES Solar World Congress Hamburg, Germany, Bloss, W. H. and Pfisterer, F., Pergamon Press, Oxford, 1987;962-966.

Furbo S, Knudsen S. Improved design of mantle tanks for small low flow SDHW systems. International Journal of Energy Research 2006; 30: 955-965.

Hollands K, Lightstone M. A review of low-flow stratified-tank solar water heating system. Solar Energy 1989;43: 97-105.

van Koppen C, Thomas J, Veltkamp W. The actual benefits of thermally stratified storage in a small and medium size solar systems. Proceedings of the ISES Solar World Congress, 1979, Atlanta, USA, 1979; 579-580.

Conference Proceedings

Solar World Congress 2015
Daegu, Korea, 08 – 12 November 2015

DEVELOPMENT OF A PERFORMANCE CALCULATION PROGRAM FOR SOLAR DOMESTIC HOT WATER SYSTEMS WITH IMPROVED PREDICTION OF THERMAL STRATIFICATION

Jianhua Fan[1], Simon Furbo[1] and Zhe Li[2]

[1] Department of Civil Engineering, Technical University of Denmark, Denmark

[2] Beijing Computing Center, Beijing, China

Abstract

The transient fluid flow and heat transfer in a hot water tank during cooling caused by standby heat loss were investigated by computational fluid dynamics (CFD) calculations and by thermal measurements in previous investigation. It is elucidated how thermal stratification in the tank is influenced by the natural convection and how the heat loss from the tank sides will be distributed at different levels of the tank at different thermal conditions.

A heat loss removal factor is introduced to characterize the effect of the buoyancy driven flow on exchange of heat loss between tank layers by natural convection. Based on results of the CFD calculations, a generalized equation of the heat loss removal factor is obtained by regression which calculates the heat loss removal factor for a given temperature gradient in the tank. The equation takes into account the influences of tank volume, height to diameter ratio, tank insulation, thickness and material property of the tank wall and initial thermal conditions of the tank. The equation is validated for a tank volume in the range of 150 l and 500 l and a height to diameter ratio of 1-5. The equation is implemented in a simulation program for a solar domestic hot water (SDHW) system with a hot water tank charged by a built-in heat exchanger spiral. The program can calculate thermal performance of a SDHW system. Thermal performance calculated by the program will be compared to the measurements. The investigations elucidate accuracy and reliability of the program for calculation of temperatures and thermal performance of a solar domestic hot water system.

Keywords: Hot water tank, thermal stratification, performance calculation program, Computational fluid dynamics (CFD), Heat loss removal factor

1. Introduction

Thermal stratification in solar storage tanks has a major influence on the thermal performance of solar heating systems. A high degree of thermal stratification in the storage tank increases the thermal performance of a solar heating system because the return temperature to the solar collector is lowered (Furbo 1984, van Koppen C 1979, Furbo 1987, Haller 2009, Haller 2010). A lower inlet temperature to the solar collector will increase the efficiency and operating hours of the solar collector. Further, the temperature at the top of the storage will be closer to the desired load temperature. Therefore the auxiliary energy consumption will be decreased which increases the solar fraction (Hollands 1989, Furbo 2006).

Heat loss from the tank sides helps to build up thermal stratification in the tank. Due to heat loss to the surroundings, the fluid close to the tank wall has a lower temperature than the fluid at the centre of the tank. The relative colder fluid flows downwards along the tank wall while the fluid with higher temperature rises up in the centre of the tank.

Thermal stratification and natural convection flow in a vertical cylindrical hot water tank during standby periods were investigated in the literature (Andersen 2007, Fan 2012a). Transient, three-dimensional CFD models of hot water storage tanks were developed and validated against thermal measurements. Zachar carried out a numerical analysis of flow distributors to improve temperature stratification in storage tanks (Zachar 2007). Neural network modelling was used for calculation of thermal stratification in a solar DHW storage (Geczy-Vig 2010).

The aim of the investigation is to elucidate how thermal stratification in the tank is influenced by the natural

doi:10.18086/swc.2015.02.15 Available at http://proceedings.ises.org

convection and how the heat loss from the tank sides will be distributed at different levels of the tank at different thermal conditions. The ultimate goal of the investigation is to improve an existing program for performance calculation of solar domestic hot water systems in terms of prediction of thermal stratification in the tank.

2. The experimental and numerical investigations

Experimental investigations were carried out on a slim 150 l tank with a diameter of 0.34 m and a height of 1.68 m in order to evaluate the effect of heat loss on thermal stratification in a tank. The height to diameter ratio of the tank is 5.0. The tank is made of steel with a thickness of 5 mm and is insulated with 5 cm mineral wool. Temperature distribution of the tank is measured with 14 copper/constantan thermocouples (type TT) equally placed from the bottom to the top of the tank. The heat loss coefficient from different parts of the tank is measured with the setup shown in Fig. 1. During the measurements, the tank is heated by an electric heating element to a uniform constant temperature. The electric heating element is placed at the very bottom of the tank. The heat loss from the tank is therefore equal to the power consumption of the electric heating element under steady state conditions. Measurement of the heat loss coefficient from different parts of the tank is possible with help of the iso-temperature box which is kept at the same temperature as the water temperature in the tank. A uniform temperature of the air in the box is achieved as the air is fully mixed by means of a fan inside the box. Therefore there is no heat loss from the part of the tank covered by the box. Air temperature in the box and ambient air temperature are measured by copper/constantan thermocouples, type TT. By means of measurements with different positions of the box and with two temperature levels of 76.0˚C and 36.5˚C, the distribution of the heat loss coefficient for the different parts of the tank is determined for different temperature levels. The measurement accuracy of temperatures is 0.5 K. For the temperature level of 36.5ºC, the total heat loss coefficient of the tank is measured. The heat loss coefficients for the different parts of the tank are obtained by assuming the same distribution of the heat loss coefficients among the different tank parts as with a hot water temperature of 76 ºC. Since the distribution of the heat loss coefficient for different parts of the tank is mainly dependent on the tank design and insulation, the assumption will not introduce significant errors in the analysis. Linearly temperature dependent heat loss coefficients for different parts of the tank are then obtained, see Equation 1-4.

$$K_{top} = 0.24 + 0.00015*(T - 273.15) \quad [W/K] \quad \text{(eq. 1)}$$

$$K_{side} = 1.75 + 0.00148*(T - 273.15) \quad [W/K] \quad \text{(eq. 2)}$$

$$K_{bottom} = 0.41 + 0.00034*(T - 273.15) \quad [W/K] \quad \text{(eq. 3)}$$

$$K_{total} = 2.4 + 0.00198*(T - 273.15) \quad [W/K] \quad \text{(eq. 4)}$$

where T is the water temperature in the tank, [K].
The measured heat loss coefficients of the tank are used as inputs to the numerical investigations.

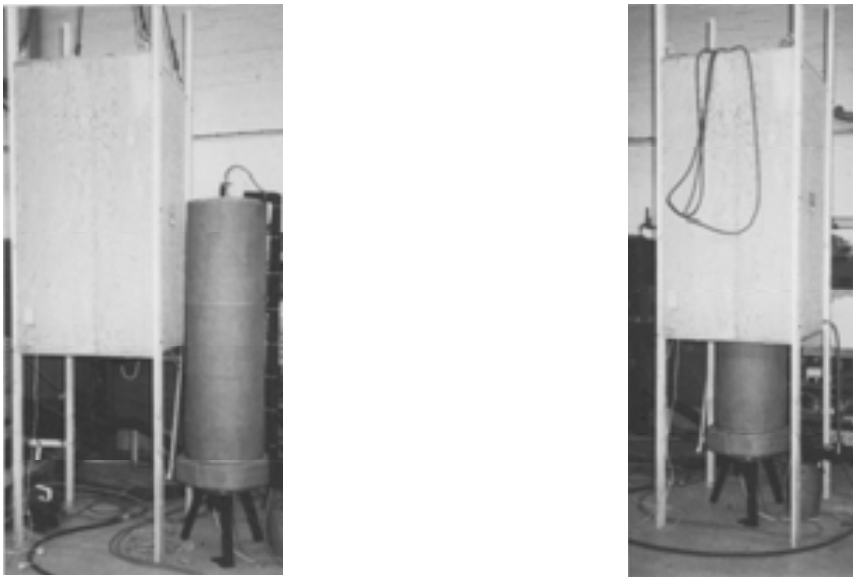

A. The Iso-temperature box and the tank B. Measurement of tank heat loss coefficient

Figure 1. Experimental setup

A tank simulation program (SpiralSol) has been developed to calculate water temperatures in a tank with a built-in heat exchanger spiral (Furbo 1984). Thermal stratification in the tank under different operating conditions is considered. The program is able to determine the thermal performance of a solar heating system taking into consideration thermal stratification in the tank. The program is improved in this paper in the term of prediction of thermal stratification by considering the influence of buoyancy driven flow along the tank side wall.

In the program, the tank is equally divided into a number of layers (N=10), numbered sequentially from the bottom to the top of the tank, see Fig. 2. Heat loss from the side of the layer I is defined as $Q_{loss}(I)$ calculated based on conventional heat transfer theory while the heat loss moving from the layer above (I+1) to the layer (I) due to the buoyancy driven flow is defined as $Q_{flow}(I)$. A heat loss removal factor $a(I)$ for interface I is defined as the ratio between the heat loss moved down by natural convection and the total amount of heat loss of the layer. The heat loss of the layer includes both heat loss from the side of the tank and the heat loss moved down from the layer above.

$$a(I) = \frac{Q_{flow}(I)}{Q_{flow}(I+1) + Q_{loss}(I+1)} \qquad \text{(eq. 5)}$$

For the top layer N, the heat loss moving from the layer above is replaced by the heat loss from the top of the tank.

$$a(N-1) = \frac{Q_{flow}(N-1)}{Q_{\text{top loss}} + Q_{loss}(N)} \qquad \text{(eq. 6)}$$

Thermal stratification in the tank is characterized by a temperature gradient Gr(I).

$$Gr(I) = \frac{T_{layer}(I+1) - T_{layer}(I)}{H_{layer}(I+1) - H_{layer}(I)} \qquad \text{(eq. 7)}$$

where T_{layer} (I) is the average fluid temperature of layer I in K, while H_{layer} (I) is the average height of layer I in m measured from the bottom of the tank.

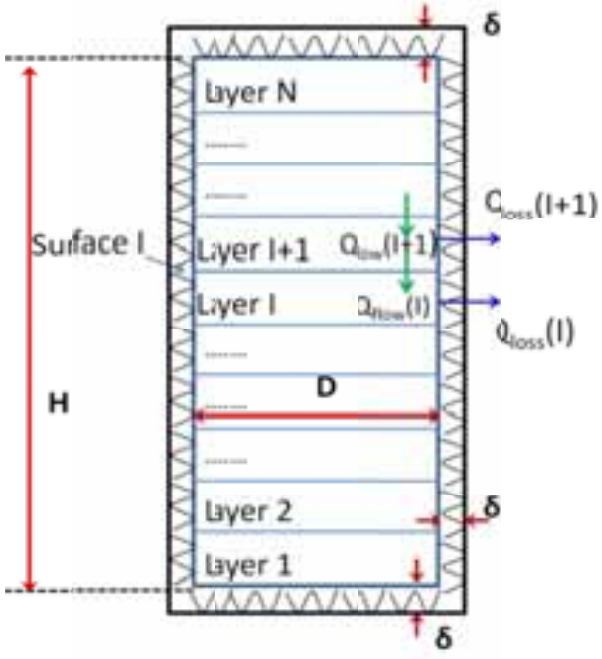

Fig. 2 Schematic illustration of a tank consisting of N layers.

3. The downwards flow along tank wall due to heat loss from the tank

3.1 The initial conditions of the tank

CFD model of the slim hot water tank has been developed and validated against measurements (Fan 2012a). Calculations have been made using the validated CFD models to investigate the influence of the downward flow along the tank wall due to heat loss from the tank. The initial condition of the tank was either a fully charged tank with a uniform water temperature of 80 ˚C or a stratified tank after a hot water draw-off. In the stratified tank, the water temperature at the upper part of the tank is 80 ˚C while it is 17 ˚C at the bottom of the tank. Fig. 3 shows the temperature profile of the stratified tank after a hot water draw-off. The stratified tank corresponds to a tank after a hot water draw-off of 75 liters.

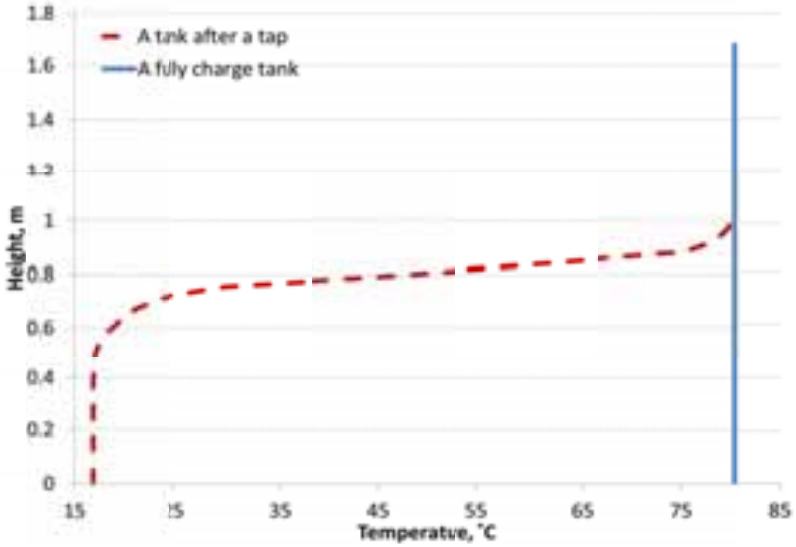

Fig. 3 Temperature profile of a fully charged tank and of a stratified tank after a hot water draw-off

3.2 The dependence of downward velocity on temperature gradient during standby period of a fully charged tank

Fig. 4A shows water temperatures in the tank after 24 hours standby of a fully charged tank. Due to heat loss from the tank, water temperature at the upper part of the tank drops by 14 K, while at the bottom of the tank water temperatures decreases by 27 K. In the tank with a height 0.24 m-1.68 m from the bottom of the tank, there is a temperature of 64-66˚C, indicating a small temperature gradient. In the lower 24 cm of the tank there is a larger temperature difference.

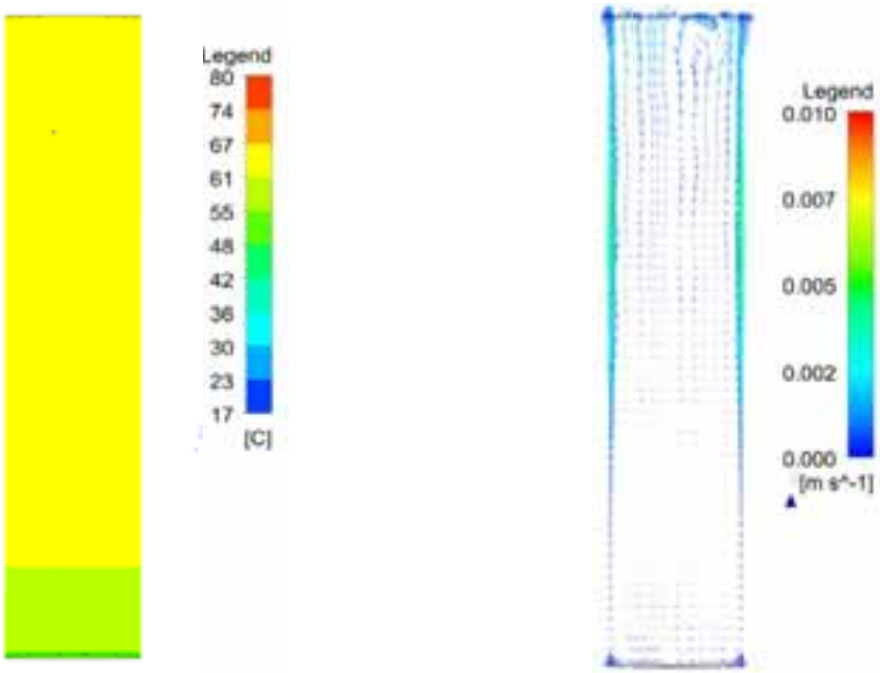

A. Temperature distribution B. Velocity vectors

Fig. 4 CFD calculated velocity vectors and temperature distribution in the tank after a 24 hours standby period with an originally fully charged tank.

Fig. 4B shows velocity vectors of fluid flow in the tank after a 24 hours standby period starting with a fully charged tank. Due to heat loss from the tank side, water close to the tank side has a lower temperature than water in the center of the tank at the same height. The colder water tends to flow downwards along the tank side wall as its density is higher, while in the center of the tank warmer fluid tends to flow upwards, creating a water circulation in the tank. The buoyancy induced flow will drive fluid with lower temperature from the upper part of the tank to the bottom part of the tank, consequently establishing thermal stratification during standby period of the tank. Temperature gradient in the tank has a significant influence on the downward flow along the tank side wall. Fig. 5 shows dependence of downward velocity on temperature gradient in the tank after 24 hours standby cooling of a fully charged tank. It is shown that the larger the temperature gradient, the lower the downward flow is. At height in the range of 0.7-1.68 m where the temperature gradient is as low as 0-2 K/m, the average downward flow velocity is 1 mm/s-7 mm/s. While at the bottom of the tank (at height 0-0.6 m) where there is a larger temperature gradient in the range of 3-25 K/m, the downward flow is significantly reduced to be lower than 1 mm/s.

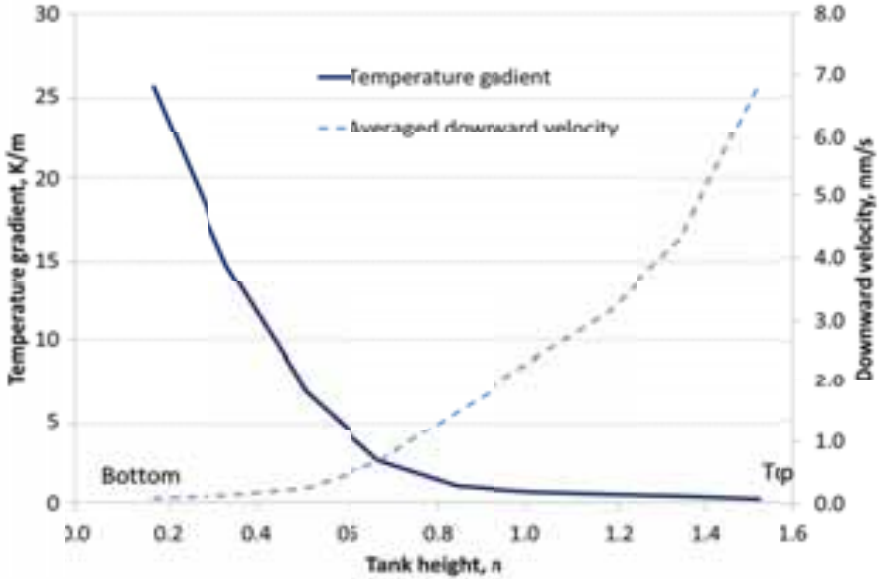

Fig. 5 Dependence of downward velocity on temperature gradient in the tank after a 24 hours standby period starting with a fully charged tank.

3.3 The dependence of downward velocity on temperature gradient during standby period of a stratified tank

The buoyancy driven flow in a stratified tank is investigated as well. Fig. 6A shows the temperature distribution in the tank at 5 hours standby of a stratified tank. At the upper part of the tank there is a water temperature of 70-75˚C while the water temperature at the bottom of the tank is almost constant at 17˚C. Fig. 7 shows temperature gradient versus water temperatures in the tank. In the middle part of the tank there is a strong thermal stratification with a temperature increase of 47 K from 0.5 m to 1.2 m height of the tank, corresponding to a temperature gradient in the range from 44 K/m to 99 K/m. At the top of the tank with a height in the range from 1.2 to 1.68 m, the temperature gradient is smaller than 20 K/m. The temperature gradient is small as well at the bottom of the tank with a height from 0 to 0.4 m.

From Fig. 6B it can be seen that there is a downward flow along the tank wall at the height of 1.4 m or higher due to the absence of stratification. Water in the central parts of the tank water is flowing upwards as water in the center of the tank is relatively warmer. At the height of 1.1 m, the downward flow is reduced significantly, which can be explained by the presence of strong stratification at that part of the tank. At the bottom of the tank there is a small temperature gradient but the downward buoyancy driven flow is not present. However a small uprising flow along the tank wall can be observed. The rising flow has the magnitude of approx. 0.4 mm/s. This can be explained by a warmer steel tank wall at the bottom of the tank caused by heat gain from the upper part of the tank due to thermal conduction through the tank wall and from the ambient air which has a slightly higher temperature. The heat gain heats up the fluid adjacent to the wall, creating upward flow.

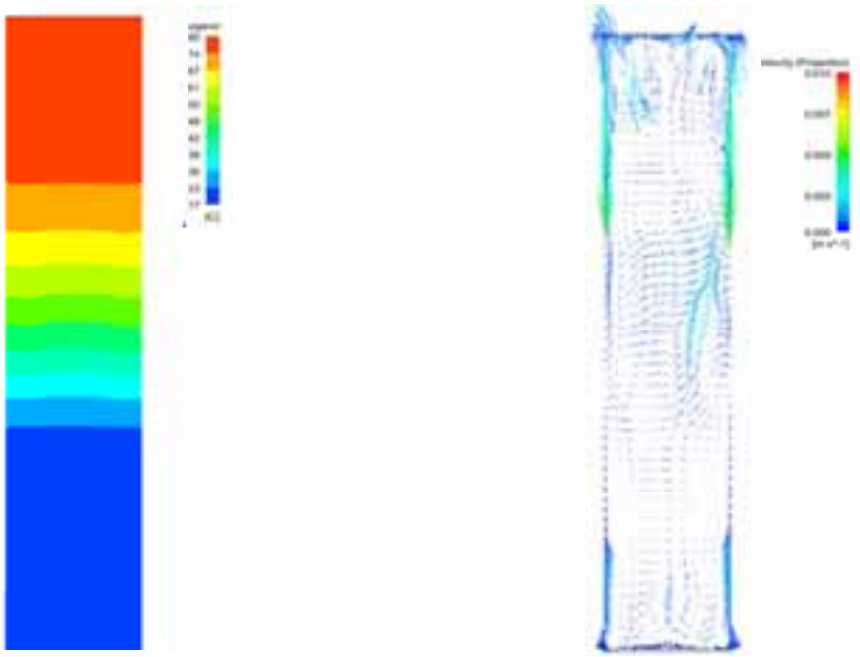

A. Temperature distribution B. Velocity vectors

Fig. 6 CFD calculated velocity vectors and temperature distribution in the tank after 5 hours of standby with an originally stratified tank.

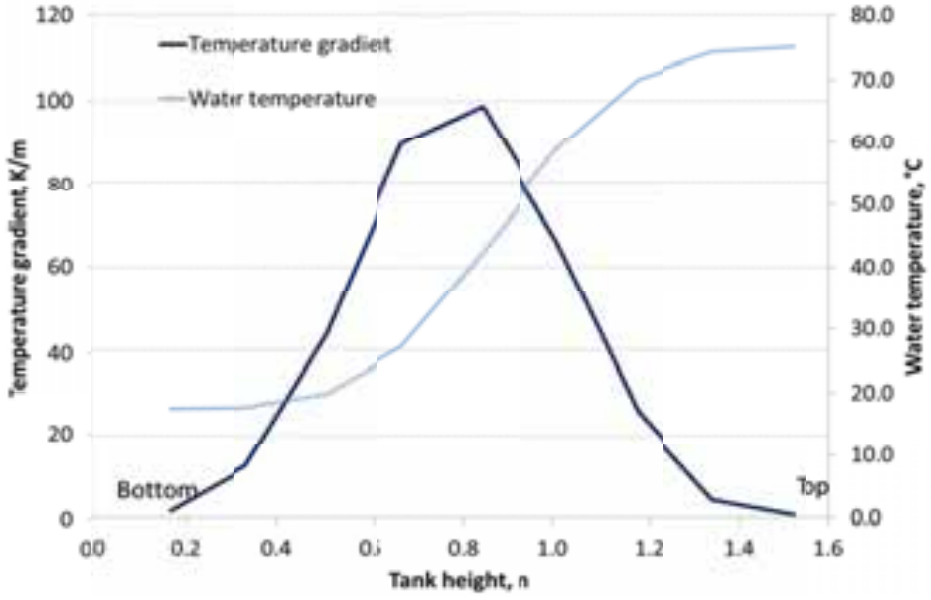

Fig. 7 Temperature gradient in the tank after 5 hours of standby for a stratified tank.

Fig. 8 shows the dependence of downward flow along the tank side wall on temperature gradient in the tank. At the top of the tank where there is a small temperature gradient, the downward flow has an average speed of 1 mm/s- 4.5 mm/s. While the flow is significantly reduced in the middle part of the tank with a height from 0.4 m to 1.2 m where there is a temperature gradient higher than 20 K/m.

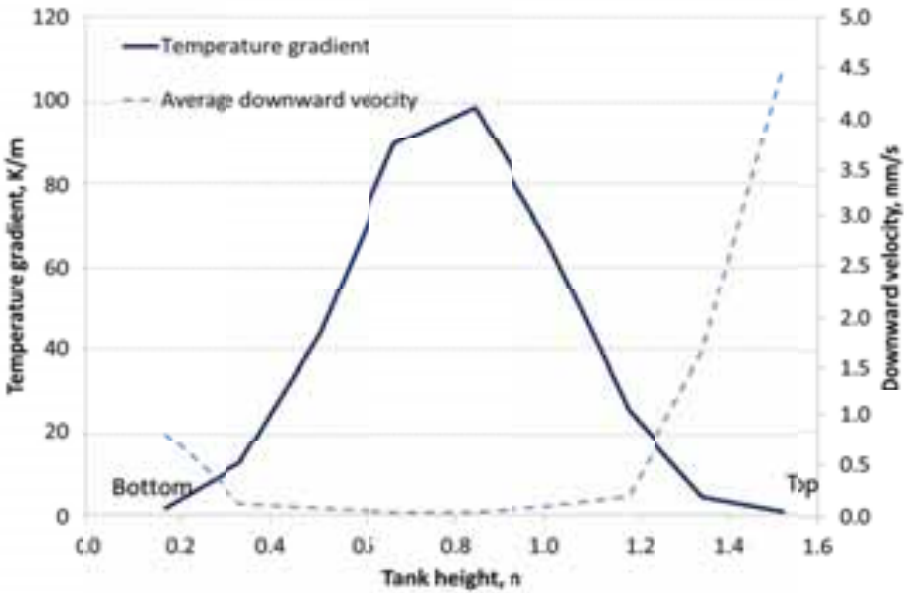

Fig. 8 Dependence of downward velocity on temperature gradient in the tank after 5 hours of standby for a stratified tank.

4. The heat loss removal factor

4.1 Equation of the heat loss removal factor

In order to quantify the effect of the buoyancy driven flow on exchange of heat loss between tank layers by natural convection, a heat loss removal factor is introduced. Based on the results of previous CFD investigations, a simple equation is obtained by regression that calculates the heat loss removal factor for a given temperature gradient in the tank (Fan 2012b). The equation takes into account the influences of tank volume, tank height to diameter ratio, tank insulation, thickness and property of the tank wall and initial conditions of the tank, see equation (8).

$$Gr(I) \le 0.25: \quad a(I) = 0.65 - Gr(I)$$

$$Gr(I) > 0.25: \quad a(I) = \frac{1}{2.32 + 1.39D^2H + 0.116H/D} \ln\left(\frac{Q_{loss}(I+1)}{8.12H + 2.23D + 4.71/H/D}\right) Gr(I)^{\frac{T_{layer}(I+1) - T_a}{85.8 + 39.5D^2H + 18.3H/D} - 1}$$

(eq. 8)

where $a(I)$ is the heat loss removal factor of the ith tank layer;

H is the tank height in m;

D is the tank diameter in m;

$Q_{loss}(I+1)$ is the heat loss from the side of the tank layer $I+1$ in W/m^2.

$T_{layer}(I+1)$ is the average water temperature in the tank layer I+1, ºC;

T_a is the ambient air temperature, ºC;

$Gr(I)$ is temperature gradient of the ith tank layer in K/m.

Fig. 9 shows the heat loss removal factor as a function of temperature gradient. In the calculation a tank with a volume of 150 l and a height to diameter ratio of 5 is used. Water temperature in the tank and ambient air temperature is assumed to be 80ºC and 20ºC respectively. It is clearly shown that when there is almost no temperature gradient (< 5 K/m), the heat loss removal factor lies in the range from 0.1 to 0.7, meaning that 10-70% of the heat loss accumulated in the layer will be transported downwards. In the region where there is a temperature gradient larger than 5 K/m, the heat loss removal factor is smaller than 0.1, which means that

only an insignificant part of the heat loss is transported downward.

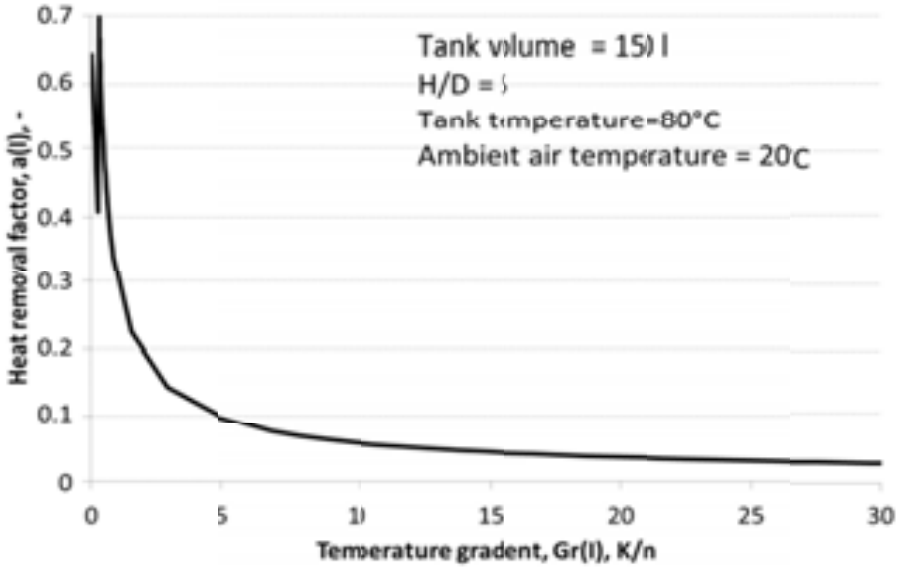

Fig. 9 Heat loss removal factor as a function of temperature gradient in the tank.

4.2 Comparison between the measured and the simulated water temperatures

The equation (eq. 8) is implemented in the tank simulation program SpiralSol. Water temperatures calculated by the program is compared to the measured temperatures. Fig. 10 shows a comparison between the measured water temperatures and the simulated water temperatures by the programs with and without using the heat removal factor. The initial condition of the tank is a fully charged tank with a uniform water temperature of 80ºC. The measured water temperatures are shown in curves while the simulated water temperatures are shown by dots and crosses. After one hour of standby cooling, the water temperature at the bottom of the tank is decreased to 75ºC while there is a temperature decrease of 0.5 K in the rest of the tank. After 24 hours standby cooling of the tank, the water temperature at the top of the tank was measured to be 66.4 ºC. Water at the bottom of the tank was cooled down to 54.6 ºC. The program without the heat removal factor predicts water temperatures of 65.7 ºC and 55.7 ºC at the top and at the bottom of the tank respectively. The disagreement between the measured and the simulated temperatures is -0.7 K at the top of the tank and 0.9 K at the bottom of the tank. With the heat loss removal factor considered in the program, the prediction accuracy of the program is improved slightly. The error of prediction is decreased to -0.4 K at the top of the tank and to 0.6 K at the bottom of the tank. The existing disagreement could be explained by the numerical method of the program. As the tank is divided into 16 layers in the simulation, there is a uniform temperature in each layer. This is not true in reality. The error could be decreased by increasing the number of layers in the calculation but it will significantly increase simulation time. The error could also be due to measurement uncertainty of the heat loss coefficients which are used as inputs in the program.

Fig. 11 shows comparison between simulated water temperatures with and without using the heat loss removal factor. It is shown that there is a similar improvement after 12 hour, 24 hour, 36 hour and 48 hour of natural cooling by using the heat loss removal factor.

A comparison between the measured and the simulated water temperatures is presented in Fig. 12 for an initially stratified tank. There is a good agreement between the simulations and the measurements. Consideration of the heat loss removal factor in the program makes only insignificantly improvement. This could be explained by the fact that the heat loss removal factor will be small for a tank with a large temperature gradient, therefore for a majority part of the tank the difference with and without considering the heat loss removal factor is marginal.

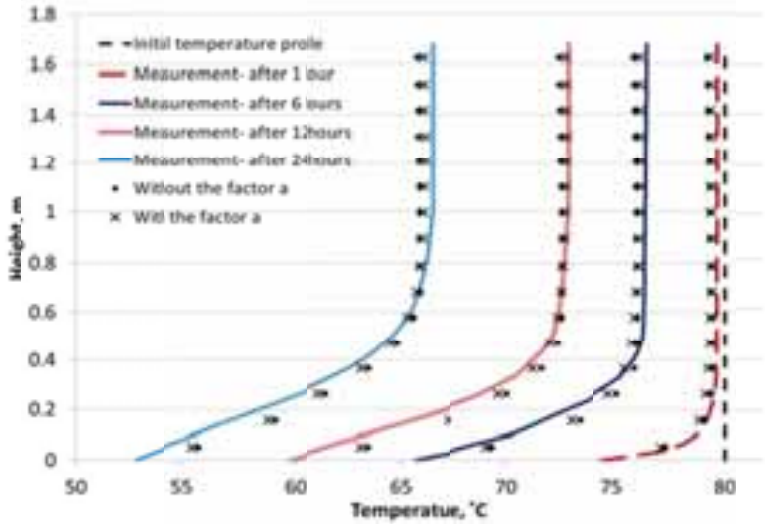

Figure 10. Comparisons between measured and simulated temperatures starting with a fully charged tank.

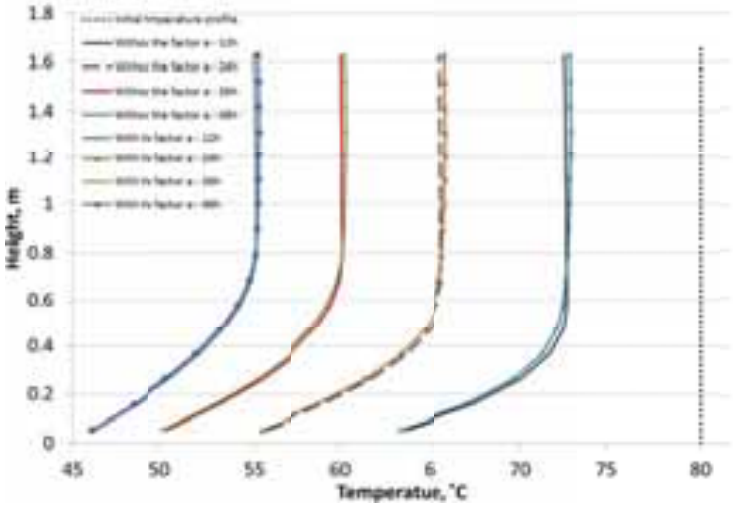

Figure 11. Comparisons between simulated temperatures starting with a fully charged tank.

It can be concluded that for a fully charged tank the prediction accuracy of the program is improved by taking into consideration the heat loss removal factor, while the improvement is marginal for an already stratified tank. Generally there is a good agreement between the simulated and the measured water temperatures, which documents credibility of the program.

The program is then used to calculate thermal performance of a solar heating system with a solar collector of 2 m^2, a tank volume of 150 l and a daily tapping of 100 liters. The results show that there is a marginal difference between thermal performance calculated by the program with and without using the heat loss removal factor. This could be explained by the fact that the tank in most of the time is stratified due to 3 times of hot water tapping per day. In a stratified tank the removal of heat loss between layers is minimized due to the presence of temperature gradient in the tank.

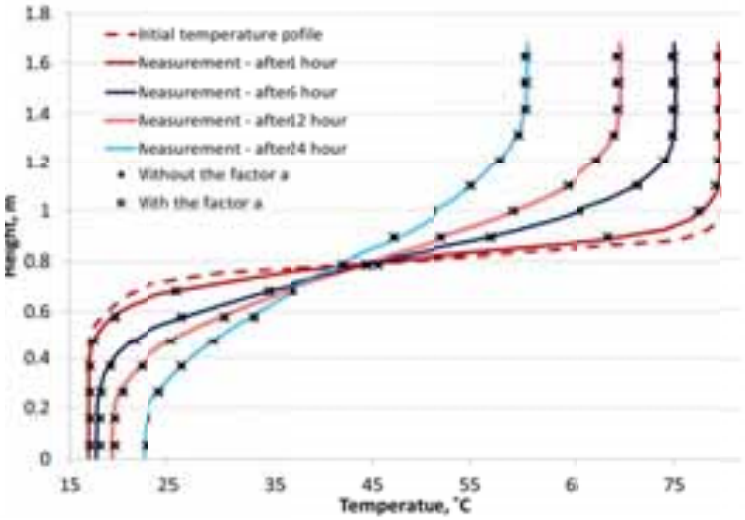

Figure 11. Comparisons between measured and simulated temperatures starting with a stratified tank.

5. Conclusions

The downward flow along the tank side wall caused by natural cooling of the tank is investigated by means of validated CFD models. The results show that the downward flow moves water with colder temperature down to a lower level of the tank, thus helping to establish thermal stratification in the tank. The magnitude of the downward flow is significantly influenced by the temperature gradient in the tank. The higher the temperature gradient in the tank, the lower the downward fluid velocity is. For a fully charged tank there is a strong downward flow in most of the tank where the temperature gradient is smaller than 5 K/m. For a stratified tank the downward flow is only apparent in the upper part of the tank where there is a high water temperature and a low temperature gradient. In the rest of the tank there is limited flow along the tank side wall.

A heat loss removal factor is introduced in the tank simulation program Spiralsol to quantify the effect of the buoyancy driven flow on exchange of heat loss between tank layers by natural convection. A generalized equation of the heat loss removal factor is implemented in the program. The simulated water temperatures in the tank are compared to the measured ones. The results show that for a fully charged tank the prediction accuracy of the program is improved by taking into consideration the heat loss removal factor, while the improvement is marginal for an already stratified tank. Generally there is a good agreement between the simulated and the measured water temperatures, which documents credibility of the program.

The program is then used to calculate thermal performance of a solar heating system with a solar collector of 2 m^2, a tank volume of 150 l and a daily tapping of 100 liters. The results show that there is a marginal difference between thermal performance calculated by the program with and without using the heat loss removal factor. This could be explained by the fact that the tank in most of the time is stratified due to 3 times of tapping per day. In a stratified tank the removal of heat loss between layers is minimized due to the presence of temperature gradient in the tank.

Acknowledgements

This research was supported by the Special fund for the development of small and medium enterprises (EU China Cooperation Program) SQ2013Z0G100002.

6. References

Andersen E, Furbo S, Theoretical comparison of solar water/space heating combi systems and stratification design options. Journal of Solar Energy Engineering 2007; 129: 438-448.

Fan J, Furbo S. Buoyancy driven flow in a hot water tank due to standby heat loss. Solar Energy 2012; 86:3438-3449.

Fan J, Furbo S. Thermal stratification in a hot water tank established by heat loss from the tank. Solar Energy 2012; 86:3460-3469.

Furbo S. Varmelagring til solvarmeanlæge, PhD report, No. 162, Thermal Insulation Laboratory, Technical University of Denmark, 1984.

Furbo S, Mikkelsen S. Is low flow operation an advantage for solar heating systems? Proceedings of the ISES Solar World Congress Hamburg, Germany, Bloss, W. H. and Pfisterer, F., Pergamon Press, Oxford, 1987; 962-966.

Furbo S, Knudsen S. Improved design of mantle tanks for small low flow SDHW systems. International Journal of Energy Research 2006; 30: 955-965.

Geczy-Vig P, Farkas I. Neural network modelling of thermal stratification in a solar DHW storage. Solar Energy 2010; 84: 801-806.

Haller MY, Yazdanshenas E, Andersen E. A method to determine stratification efficiency of thermal energy storage processes independently from storage heat losses. Solar Energy 2010; 84: 997-1007.

Haller M, Cruickshank C, Streicher W, Methods to determine stratification efficiency of thermal energy storage processes–Review and theoretical comparison. Solar Energy 2009; 83: 1847-1860.

Hollands K, Lightstone M. A review of low-flow stratified-tank solar water heating system. Solar Energy 1989;43: 97-105.

van Koppen C, Thomas J, Veltkamp W. The actual benefits of thermally stratified storage in a small and medium size solar systems. Proceedings of the ISES Solar World Congress, 1979, Atlanta, USA, 1979; 579-580

Zachar A, Aszodi A. Numerical analysis of flow distributors to improve temperature stratification in storage tanks. Numerical Heat Transfer Part A-applications 2007; 51: 919-940.

Conference Proceedings

Solar World Congress 2015
Daegu, Korea, 08 – 12 November 2015

Value of Energy Continuity for Commercial Photovoltaic Systems with Battery Storage

Sasha Merigan and Deborah Sunter, Ph. D.

Johns Hopkins University, Washington, DC (USA)

Abstract

This paper presents a model that computes the payback period of photovoltaic systems with battery storage (PVBS). The model, termed SPPEEDI (SAIDI Payback Period Evaluation for Extended Duration Interruption), incorporates savings from avoided business interruption with utilization of PVBS. While the PVBS system can produce clean energy and maintain energy continuity, its prohibitive cost of installation is a barrier to widespread adoption. By using the SPPEEDI model and incorporating avoided business interruption in evaluating PVBS payback periods, the model allows for a more accurate estimate of the return on investment for PVBS. This analysis identifies key grid outage thresholds where commercial PVBS could be a better investment than conventional photovoltaic systems.

Keywords: *Commercial battery storage, photovoltaics, energy continuity, SAIDI, electric grid interruption,*

1. Introduction

Business continuity should be considered when analyzing the value of photovoltaic systems with battery storage (PVBS). Grid interruption can be very costly to businesses and PVBS can maintain electricity throughout an outage, preventing potential business interruptions and related financial losses. Accurate evaluation of payback periods requires that the value of energy continuity during grid outages be taken into account. This paper introduces a model, termed SPPEEDI (SAIDI Payback Period Evaluation for Extended Duration Interruption), that more accurately evaluates payback periods of PVBS by taking avoided lost revenue from grid outages into consideration. By comparing investments in PVBS to investments in PV, this paper identifies grid outage levels necessary for PVBS to surpass PV as an investment opportunity.

To account for grid outages, the SPPEEDI model uses the System Average Interruption Duration Index (SAIDI), an international standard used to quantify reported outage duration. SAIDI represents the annual cumulative amount of grid interruption experienced by the average customer. It is calculated by dividing the total minutes of sustained customer interruption (interruptions over 1-5 minutes, depending on the local definition) (CPUC 2015, NERC 2010) in a given year by the number of total customers served by the utility (eq. 1). Thus, this measure provides an estimate of the average number of minutes of sustained grid downtime a single customer would experience in a given year. Outages shorter than "sustained customer interruptions" are defined as momentary outages and are not considered in this analysis.

$$\frac{\text{Sum of annual sustained interruption durations for all customers}}{\text{Total number of customers served}} = \text{SAIDI} \qquad \text{(eq. 1)}$$

SAIDI is useful for estimating losses to individual customers and can be translated into the additional value of PVBS as avoided losses. Many commercial entities track these statistics themselves for internal use. For application in analyzing investments in PVBS for a single business, internally collected data is often more reliable than utility provided data and can provide customized estimates of PVBS payback periods when applied to the SPPEEDI model. Although the quality of reported SAIDI data is inconsistent and often incomplete (LaCommare & Eto, 2004), it can be useful as a broad average. Readers can replace SAIDI figures and financial loss estimates used in this analysis directly with internally collected data for more accurate estimates of PVBS payback periods on a case-by-case basis. In this analysis, the SPPEEDI model is applied to a broad range of reported SAIDI values reflecting 12-years of reported outage data covering 150

doi:10.18086/swc.2015.02.16 Available at http://proceedings.ises.org

US utilities (Larsen et al. 2014). A range of 0-15,000 minutes of SAIDI was chosen for this analysis to reflect the content of this data set.

2. Methodology

2.1. Case Study Specifications

This analysis uses a commercial sector case study because commercial losses from grid interruption far outpace losses in the residential and industrial sectors, making up 72% of total losses in the US in 2004 (LaCommare & Eto, 2004). Since Walmart has already introduced PV installations on a large scale to existing stores to cut energy costs and was ranked #1 in installed solar capacity among commercial entities in the US in 2014 (SEIA 2014), it is reasonable to assume Walmart would continue to invest in solar, specifically PVBS if it becomes a more attractive investment than PV. Hence, a typical Walmart Supercenter will serve as the analysis case study. For this case study, nine scenarios are considered, taking into account variability in solar insolation and total installed system costs. These scenarios can be seen in Table 1.

Table 1: Walmart Superstore Case Study Scenarios

Current costs, Low Insolation	Current costs, Medium Insolation	Current costs, High Insolation
Near-term costs, Low Insolation	Near-term costs, Medium Insolation	Near-term costs, High Insolation
Long-term costs, Low Insolation	Long-term costs, Medium Insolation	Long-term costs, High Insolation

Solar insolation levels of 4.5 kWh/m^2/d, 6.0 kWh/m^2/d and 7.5 kWh/m^2/d are used for this study. These values were chosen by creating a histogram of the continental US solar insolation data (NREL 2015b). It was determined that 63% of the data points fall between 4.5-7.5 kWh/m^2/d, with a mean of 5.1 kWh/m^2/d and a standard deviation of 1.2 kWh/m^2/d. To calculate the total installed system costs of silicon solar panels and lithium ion battery systems, three investment levels are analyzed using current cost estimates (2014 values, NREL 2015a, DOE 2013c), near-term (2020 values, NREL 2015a, DOE 2013b) and long-term (2035 values, NREL 2015a, DOE 2013b) cost projections. The values are compared using real 2015 dollars.

The analysis also takes into account annual operation and maintenance costs (SAM 2015), increasing cost of electricity over time (SAM 2015), panel degradation (SAM 2015), and discount and inflation rates (SAM 2015). To calculate the value of energy produced, the average cost of commercial electricity in the US (EIA 2015) is used. The value of avoided grid interruption is quantified by the amount of revenue that would have been lost had the business been forced to close due to grid outage. Model input values can be found in Table 2.

2.2. Analysis Calculations

The SPPEEDI model executes the following equations in Excel in order to calculate payback periods in all nine scenarios with grid outages varying between 0 –15000 minutes at intervals of 10 minutes.

The SPPEEDI model calculates the avoided revenue losses from using PVBS systems for energy and business continuity during grid outages. Before the losses can be calculated, the average revenue per minute is calculated by dividing Walmart's annual total sales by the total number of Walmart stores (SBRI 2015, eq. 2). This analysis doesn't take into account that this average includes Walmart stores of different sizes. The current average is assumed to be sufficient for use in the case study.

$$\frac{\text{Walmart annual total sales}\left(\frac{\$}{\text{year}}\right)}{\text{\# of Walmarts}\times 365\left(\frac{\text{days}}{\text{year}}\right)\times 24\left(\frac{\text{hours}}{\text{day}}\right)\times 60\left(\frac{\text{minutes}}{\text{hour}}\right)} = \text{Revenue per minute}\ \left(\frac{\$}{\text{min}}\right) \quad \text{(eq. 2)}$$

Table 2: Model Inputs (real 2015 dollars)

		References
Battery Storage Installed Costs		
Current Installed Costs (2014)	$1025/kWh	DOE 2013c
Near-term Installed Costs (2020)	$256/kWh	DOE 2013b
Long-term Installed Costs (2035)	$154/kWh	DOE 2013b
Photovoltaics Installed Costs		
Current Installed Costs (2014)	$2760/kW	NREL 2015a
Near-term Installed Costs (2020)	$2500/kW	NREL 2015a
Long-term Installed Costs (2035)	$1750/kW	NREL 2015a
Insolation Values		
Low	4.5 kWh/m^2/d	NREL 2015b
Medium	6 kWh/m^2/d	NREL 2015b
High	7.5 kWh/m^2/d	NREL 2015b
Other Model Inputs		
Walmart Supercenter Revenue per Minute	$181	Eq. 2
Installed PV Capacity	2600 kW	Eq. 5
Installed Battery Storage	17,400 kWh	Eq. 7
PV Energy Density	148.5 W/m^2	SPR 2015
Walmart Supercenter Average Square Footage	18,300 m^2	SBRI 2015
Walmart Annual Total Sales	$405 billion	SBRI 2015
Number of Walmart Stores	4255	SBRI 2015
Annual Average Energy Use of Retail Buildings	231.4 kWh/m^2	EIA 2006
Cost of Electricity ($/kWh)	$0.1075	EIA 2015
Annual Increase in Cost of Electricity	5%	SAM 2015
Annual PV Degradation Rate	0.5%	SAM 2015
PVBS System Lifetime	25 years	SAM 2015
PV System Lifetime	25 years	SAM 2015
Annual O & M Costs	$20/yr/kW	SAM 2015
Discount Rate	5.5%	SAM 2015
Inflation Rate	2.5%	SAM 2015

Average revenue per minute for the case study is then multiplied by total annual duration of grid outage experienced, using SAIDI, to find annual avoided revenue losses (eq. 3). The annual avoided revenue losses represent the revenue that would have been lost if PVBS had not been installed. This value will later be applied directly towards paying back the initial cost of the system as savings. This value is calculated for each year throughout the lifetime of the system, in this case 25 years, adjusting for net present value by incorporating inflation and the discount rate. This equation is not applied to PV systems without battery storage because they stop functioning in the case of grid interruption due to safety regulations common throughout the world (IEA 2009), and therefore do not provide energy continuity during grid outage. Net present value was also taken into account by incorporating annually compounding inflation and the discount rate.

$$\text{Revenue per minute } \left(\frac{\$}{\text{min}}\right) \times \text{Annual SAIDI } \left(\frac{\text{minutes of outage}}{\text{year}}\right) = \text{Annual avoided revenue losses } \left(\frac{\$}{\text{year}}\right) \quad \text{(eq. 3)}$$

Sullivan et al. (2009) explores the financial losses incurred during grid outages, finding a range of $8.1-$93.3/kWh for electrical interruption cost at multiple outage durations for medium and large commercial and industrial customers, with an average cost per kWh across all outage durations of $28.04/kWh. The Walmart Superstore case study under consideration assumes an electrical interruption cost of $22/kWh, a value consistent with the results from Sullivan et al. The interruption cost per unit energy ($/kWh) is found by dividing the average revenue per minute (eq. 2) by the energy use per minute (eq. 4). The energy use per minute is calculated directly from annual energy use from the Walmart case study (Table 2), assuming that energy use is evenly distributed throughout each day and throughout the year. These values are taken from the first year after investment, with subsequent years being impacted by a discount rate and inflation.

$$\frac{\text{Average revenue per minute}}{\text{Average energy use per minute}} = \text{Interruption cost per unit energy } \left(\frac{\$}{\text{kWh}}\right) \quad \text{(eq. 4)}$$

It is important to note the large range for electrical interruption costs found by Sullivan et al. Depending on the commercial activities, the vulnerability to grid outages can vary by an order of magnitude. The analysis shown in this paper explores an average risk. However, the SPEEDI model can easily be modified to analyze any electrical interruption costs by simply modifying the input parameters in Table 2. This is particularly attractive to businesses that already have estimates for revenue losses during grid outages.

The installed PV capacity for both PVBS and PV is calculated by dividing the annual average energy use by the average annual solar insolation (eq. 5). The annual average energy use is found by multiplying the annual average energy use of retail buildings in the US per m^2 (EIA 2006) by the average Walmart Supercenter floor space (SBRI 2015). The insolation level of 4.5kWh/m^2/d was chosen for sizing the system because it is the lowest insolation included in this analysis and ensures that all systems considered produced enough electricity to supply the Walmart Supercenter case study's needs. The roof space requirements of the system are calculated by multiplying the system size by the average energy density of a range of common solar panels (SPR 2015, eq. 6). The result requires a capacity of at least 2578 kW, with a 2600 kW PV system used for this analysis covering 17,372 m^2, fitting within typical Walmart Supercenter rooftop constraints (SBRI 2015). System losses beyond the photovoltaic efficiency, such as losses in the inverter and wiring, are not considered in this analysis for simplicity.

$$\frac{Annual\ average\ energy\ use\left(\frac{kWh}{year}\right)}{Solar\ insolation\left(\frac{kWh}{m^2 day}\right)\times\frac{365\ days}{year}\times\frac{1\ m^2}{1\ kW}} = Installed\ PV\ Capacity\ (kW) \quad \text{(eq. 5)}$$

$$\frac{\text{Installed PV capacity (kW)}}{Energy\ density\ \left(\frac{kW}{m^2}\right)} = PV\ system\ roof\ space\ requirements\ (m^2) \quad \text{(eq.6)}$$

The installed battery storage for the PVBS system is calculated based on surviving a 36-hour break in grid access, the average time of cloud cover during a hurricane (NOAA 2015), at normal electricity consumption levels without losing power. This is done by multiplying the average hourly energy use by a 36-hour break in grid access (eq. 7). Battery discharge factors are not included in this analysis for simplicity.

$$\frac{\text{Annual average energy use}\left(\frac{\text{kWh}}{\text{year}}\right)}{\frac{365\ \text{days}}{\text{year}}\times\frac{24\ \text{hours}}{\text{day}}}\times 36\ \text{hours} = \text{Installed battery storage (kWh)} \quad \text{(eq. 7)}$$

The annual electricity production by the PV and PVBS systems is then calculated by multiplying the installed capacity by the selected insolation levels, taking panel degradation into account (eq. 8). Without battery storage, revenue flow is assumed to cease during periods of outage. It was also assumed that the PV system without battery storage would stop functioning during grid downtime, as is the current practice in the United States and around the world (IEA 2009). Although the battery-connected PVBS would continue to operate during grid interruption, demonstrating "islanding" capability, production during grid outage was also assumed to be zero because heavy cloud cover during extreme weather would severely limit production. The solar production during outage needs to be subtracted from annual production of both PV and PVBS for this reason (eq. 9).

$$\left(\text{PV installed capacity(kW)} - \text{Degradation (kW)}\right)\times\text{solar insolation}\left(\frac{\text{kWh}}{\text{m}^2\text{d}}\right)\times\frac{1\ \text{m}^2}{1\ \text{kW}}\times\frac{365\ \text{days}}{1\ \text{year}} = \text{Uncorrected annual electricity production}\left(\frac{\text{kWh}}{\text{year}}\right) \quad \text{(eq. 8)}$$

$$\text{Uncorrected annual solar production}\left(\frac{\text{kW}}{year}\right) - \text{Average energy production}\left(\frac{\text{kWh}}{\text{min}}\right)\times\text{Annual SAIDI}\left(\frac{\text{minutes of outage}}{\text{year}}\right) = \text{Annual electricity production}\left(\frac{\text{kWh}}{\text{year}}\right) \quad \text{(eq. 9)}$$

The value of the PV electricity production is then calculated by multiplying the average cost of electricity from the grid by the Annual PV electricity production (eq. 10). Annual PV savings can be viewed as profit from electricity that is sold into the grid or savings from electricity not purchased from the grid. Depending on local net metering regulations, prices for electricity purchased from the grid and sold to the grid may differ and should be accounted for when considering other case studies. In this case, they are assumed to be

equal. Net present value is also taken into account by incorporating annually compounding inflation and the discount rate, as well as annual predicted increases in electricity cost.

$$\text{Annual electricity production } \left(\frac{\text{kWh}}{\text{year}}\right) \times \text{grid electricity cost } \left(\frac{\$}{\text{kWh}}\right) = \text{Annual PV savings } \left(\frac{\$}{\text{year}}\right) \quad \text{(eq. 10)}$$

The annual avoided revenue losses (eq. 3) and annual PV savings (eq. 10) are then added to find annual total savings (eq. 11). This sum represents the total amount of value received from PV solar production and avoided grid outage each year. The annual avoided revenue losses and annual PV savings are assumed to be evenly distributed throughout the year. Please note that companies can substitute annual avoided revenue losses with their own internally collected figures on outage losses at this point to tailor the SPPEEDI model to analyzing PVBS investments in their own particular situation.

$$\text{Annual avoided revenue losses } \left(\frac{\$}{\text{year}}\right) + \text{Annual PV savings } \left(\frac{\$}{\text{year}}\right) = \text{Annual total savings } \left(\frac{\$}{\text{year}}\right) \quad \text{(eq. 11)}$$

The initial cost of the PVBS system is calculated by multiplying the cost of PV panels per kW by the capacity to be installed, multiplying the cost of battery storage by the capacity to be installed, and adding these two products (eq. 12). For conventional PV systems, the installed battery storage capacity is set to zero.

$$\text{PV panel cost per kW } \left(\frac{\$}{\text{kW}}\right) \times \text{Installed PV capacity (kW)} +$$
$$\text{Battery cost per kWh } \left(\frac{\$}{\text{kWh}}\right) \times \text{Installed battery storage capacity (kWh)} = \text{Initial system cost (\$)} \quad \text{(eq. 12)}$$

The cumulative total savings is then calculated for each year of system operation for each SAIDI value. The whole year payback periods are found with a LOOKUP function that identifies how many years there are before the cumulative total savings exceeds the initial investment cost of the system (eq. 13).

$$\sum_{\text{year}=1}^{\text{Payback period (years)}} \text{Annual total savings (\$)} > \text{Initial system cost (\$)} \quad \text{(eq. 13)}$$

To find payback periods with greater resolution, linear interpolation is used.

2.3. Model Limitations

The SPPEEDI model is based on losses from sustained grid outage, which despite being a large part of costs caused by grid outage, has less total financial impact nationwide in the US than momentary outage. Momentary outages are responsible for 67%, while sustained interruptions account for only 33% of total losses from outages in the US (LaCommare & Eto 2004). In its present form, the SPPEEDI model may underestimate outage losses by not incorporating losses from momentary outages. The SPPEEDI model may also underestimate grid outage losses because extended loss may be compounding, yielding higher loss as duration increases (NARUC 2013b).

A number of other potential financial losses from grid outage are not considered in SPPEEDI, although their financial impact is likely to be smaller than that of either momentary outages or revenue losses (LaCommare & Eto 2004). Lost product, food spoilage, damage to equipment, lack of productivity, restart costs, and data loss can add additional financial loss from grid outages. Furthermore, labor costs could add to losses, if overtime pay is necessary for made-up time, or deduct from losses if worker hours are cut as a result. In calculating financial loss, the SPPEEDI model also does not take into account high-resolution variations, such as season, day of the week, and time of day of outages. The value of supply management optimization (e.g. storing energy at times of low energy prices and selling energy to the grid at time of high energy prices) is also not incorporated into the model and may have an impact on payback periods of PVBS. Opportunity cost of investments in PVBS over competing energy continuity technologies, such as diesel generation, could impact payback period as well. Although the diesel generator is the current standard backup power system for commercial applications, Hotchkiss et al. (2013) showed that microgrids are less likely to survive an outage relying on diesel generators than on PVBS and can create significant costs from both installation and fuel consumption (NARUC 2013a).

The inputs used in this analysis present uncertainty. Future cost projections of PV and battery storage, electricity, and annual operation and maintenance could be effected by many economic or technological factors. Current cost estimates are also averages that may not apply accurately in all regions and in all applications.

While including all of these dimensions in future iterations of the SPPEEDI model could improve accuracy, it is likely to complicate calculations and may decrease broad applicability as companies would have to collect more extensive data for analysis. The current model allows for ease of use and functions with minimal inputs. By inputting data that many companies may already have at hand, this model can easily be applied to investments in PVBS based on the reader's needs.

3. Results

To show the impact of incorporating grid disruption on payback periods, the results compare the payback periods for conventional grid-attached solar systems (PV), PVBS omitting SAIDI, and PVBS including SAIDI. Next, to provide context to the model, PVBS and PV payback periods are compared based on US national SAIDI statistics (Larson 2014). Lastly, the relationship between SAIDI and payback period is explored by showing percent change in payback period for investments in PVBS as a function of SAIDI.

Figure 1: The payback period of PVBS decreases with increases in SAIDI, surpassing the payback period of PV at a SAIDI of 2640 minutes for near-term costs, and medium insolation.

3.1. The Value Of Incorporating Grid Outage

Figure 1 illustrates the change in payback periods by incorporating SAIDI when analyzing the value of PVBS. Without SAIDI (green line), the payback period of PVBS is always higher than that of PV (red line) because of its higher initial investment cost. However, when incorporating SAIDI (blue curve), the payback period for PVBS decreases with additional avoided outage duration, improving on the investment potential in places vulnerable to grid interruption. At the point where the blue curve crosses the red line, PVBS becomes a better investment than PV and has a shorter payback period with SAIDI being taken into account. Current evaluations do not account for SAIDI and are represented by the green curve. The valuation represented by the blue curve internalizes the value of energy continuity and more accurately portrays the investment potential of PVBS. The two PVBS curves diverge significantly as SAIDI continues to increase, showing that PVBS investment analyses in areas vulnerable to extreme weather will be strongly impacted by this novel evaluation.

Table 3: Investments in PVBS vs PV (These are the amounts of SAIDI minutes required for PVBS to become a better investment than PV in different cost scenarios and at different levels of solar insolation)

	Low Insolation	Medium Insolation	High Insolation
Current Cost	7750 minutes	10820 minutes	11690 minutes
Near-term Cost	2090 minutes	2640 minutes	3200 minutes
Long-term Cost	1640 minutes	2120 minutes	2590 minutes

Figure 2: Although high solar insolation decreases payback periods, PVBS financially outperforms PV better in areas of low insolation. Values shown are derived from near-term cost projections.

Table 3 shows the minimum annual SAIDI values required for an investment in PVBS to outperform conventional PV financially. In all scenarios, PV systems without battery storage have the shortest payback period assuming a SAIDI of 0 minutes, where there is no grid interruption throughout the year or SAIDI is not considered. However, at higher levels of SAIDI, PVBS has a shorter payback period than PV. With system costs decreasing, as is predicted in the near and long- term, investments in PVBS outperform PV with increasingly lower SAIDI values. Higher insolation values favor PV systems relative to PVBS (Figure 2). PV systems rely solely on energy production for revenue; whereas, PVBS revenues also incorporate avoided revenue losses from grid interruption. Note the slight upward slope of the PV payback period lines (dark red). This is because PV systems cease functioning during periods of grid outage, losing revenue and increasing payback periods. The effect of this on payback periods is weak compared to that of grid downtime, mainly because the value of electricity production per minute is much lower than the value of avoided revenue losses from grid downtime per minute, as can be seen in Table 4.

Table 4: Value of 1 Minute of Grid Interruption (For each minute of grid interruption, the value of avoided lost revenue from business continuity due to PVBS far exceeds losses from the PV system not producing electricity)

PV Production	-$1.06
Avoided Lost Revenue	$181

Figure 3 shows payback periods in current, near-term, and long-term cost conditions at medium insolation levels. PVBS becomes more competitive at predicted long-term cost levels, because the price of batteries is expected to drop faster than the price of PV. As the cost of batteries continues to account for a smaller portion of the total cost, PVBS becomes competitive with PV at even lower levels of SAIDI.

Figure 3: As prices decrease in the near- and long-term cost scenarios, PVBS becomes competitive with PV at much lower levels of SAIDI. Values shown are derived from medium insolation scenarios.

3.2. Payback Periods With US National SAIDI Values

In a study containing 12 years of data from over 150 utilities nationwide in the United States, Larsen et al. (2014) reported that SAIDI including outages resulting from extreme weather averaged 372.2 minutes in the US. The minimum, maximum, median, and mean of this data set are run through the SPPEEDI model to find nationally relevant payback periods based on actual conditions (Tables 5-7). The "Impact of SAIDI on Payback Period" column in Tables 5-7 shows the percent change in payback periods at each level of grid interruption relative to the base case with no grid interruption. This impact is calculated in eq. 14. The mean, while at the lower end of the SAIDI scale used in this analysis, shows an impact of SAIDI on payback periods between 6.0% and 9.5%. Although the reported maximum value has very short payback periods, this is representative of only a single year at a single utility and does not represent the data as a whole, as shown by the median being lower than the mean. This also points to the fact that although adoption of the SPPEEDI model would accelerate PVBS's progress towards achieving grid parity even at low levels of SAIDI, it will have the most impact on businesses in areas that experience higher SAIDI values, such as those vulnerable to extreme weather or located in regions with unreliable grid access.

$$\left(1-\frac{\text{PVBS payback period with SAIDI (years)}}{\text{PVBS payback period base case (years)}}\right)\times 100\% = \text{Percent change in PVBS payback period (\%)} \quad \text{(eq. 14)}$$

Table 5: At low insolation (4.5 kWh/m^{2}d), including SAIDI in evaluating PVBS investment decreases the payback period by 8% on average based on near-term cost projections, but could have an impact as high as 84% in regions vulnerable to extreme weather and grid outages.

US National SAIDI Statistics (2000-2012) at Low Insolation	SAIDI (outage minutes)	Payback period (years)			Percent Change in Payback Period		
		Current Costs	Near-term Costs	Long-term Costs	Current Costs	Near-term Costs	Long-term Costs
PVBS Base Case	0	>25	22.1	15.5	NA	0	0
Minimum	1.2	>25	22.1	15.5	NA	~0	~0
Median	173.0	>25	21.3	14.8	NA	-3.8%	-4.5%
Mean	372.2	>25	20.4	14.0	NA	-8.0%	-9.5%
Maximum	14,437.6	9.1	3.8	2.4	NA	-83.0%	-84.3%
PV Base Case	0	15.363	14.084	10.222	0	0	0
PV Mean	372.2	15.377	14.097	10.231	+0.093%	+0.093%	+0.096%

Table 6: At medium insolation (6.0 kWh/m²d), including SAIDI in evaluating PVBS investment decreases the payback period by 6.9% on average based on near-term cost projections, but could have an impact as high as 80% in regions vulnerable to extreme weather and grid outages.

US National SAIDI Statistics (2000-2012) at Medium Insolation	SAIDI (outage minutes)	Payback Period (years)			Percent Change in Payback Period		
		Current Costs	Near-term Costs	Long-term Costs	Current Costs	Near-term Costs	Long-term Costs
PVBS Base Case	0	>25	17.0	11.7	0	0	0
Minimum	1.2	>25	17.0	11.7	~0	~0	~0
Median	173.0	>25	16.5	11.3	NA	-3.2%	-3.8%
Mean	372.2	>25	15.9	10.8	NA	-6.9%	-7.9%
Maximum	14,437.6	9.5	3.6	2.3	NA	-79.1%	-80.3%
PV Base Case	0	11.641	10.639	7.647	0	0	0
PV Mean	372.2	11.650	10.646	7.653	+0.071	+0.071%	+0.073%

Table 7: At high insolation (7.5 kWh/m²d), including SAIDI in evaluating PVBS investment decreases the payback period by 6% on average based on near-term cost projections, but could have an impact as high as 75% in regions vulnerable to extreme weather and grid outages.

US National SAIDI Statistics (2000-2012) at High Insolation	SAIDI (outage minutes)	Payback Period (years)			Percent Change in Payback Period		
		Current Costs	Near-term Costs	Long-term Costs	Current Costs	Near-term Costs	Long-term Costs
PVBS Base Case	0	>25	13.8	9.4	0	0	0
Minimum	1.2	>25	13.8	9.4	NA	~0	~0
Median	173.0	>25	13.4	9.1	NA	-2.8 %	-3.2%
Mean	372.2	>25	13.0	8.8	NA	-6.0%	-6.8%
Maximum	14,437.6	8.1	3.4	2.2	NA	-75.5%	-76.7
PV Base	0	9.360	8.538	6.104	0	0	0
PV Mean	372.2	9.366	8.543	6.107	+0.056%	+0.057%	+0.057

Figure 4 shows the percent change of payback periods for PVBS at different costs and levels of grid outage at medium insolation. This figure draws from the same data as Tables 5-7 and is also calculated using eq. 14. The current cost curve (blue) is set apart from the near- and long-term cost curves because at this cost, the PVBS system does not pay itself off within its 25-year lifetime at SAIDI levels below 2770 minutes.

Fig. 4: The percent change in payback periods from additional SAIDI increases dramatically with additional grid interruption, making investment in PVBS particularly attractive to potential customers in areas vulnerable to grid outage.

4. Conclusion

The model developed for this study incorporates avoided revenue losses from grid outages in evaluating payback periods of investments in PVBS. Grid outages, measured as minutes of SAIDI, can significantly affect payback periods of PVBS and should, therefore, be considered in valuation and investment decisions. Such valuation of investments in PVBS more accurately portrays pertinent financial considerations by internalizing impacts on business continuity of such an investment. Including SAIDI in PVBS valuation also inevitably improves prospective investment in this technology, as grid outages are a consistent challenge of doing business in a grid-connected environment. PVBS can be a better financial investment than PV as well as a more reliable energy continuity measure than backup diesel generators. PVBS investment evaluations are impacted most by including SAIDI in regions vulnerable to extreme weather, as these are the areas that experience the greatest benefits from bolstered energy continuity. Payback periods of PVBS are effected between 6.0-9.5% by incorporating average US national SAIDI values, with outliers experiencing as much as 84% shorter payback periods. As climate change continues to increase the severity and frequency of storms throughout the world (Fischer and Knutti 2015; IPCC 2013), investments in these systems may become even more attractive. The SPPEEDI model, although applied in this study to the United States, can be applied internationally as well. Countries with unreliable grid service or vulnerability to extreme weather would particularly benefit from this model. This model is also very applicable for private industry, allowing businesses to input their own company-specific internal data to calculate the value of an investment in PVBS for themselves. This robust analysis of the value of PVBS can help investors make more informed decisions regarding solar energy and battery storage systems.

5. References

1. B. Hojjati & S. Wade (Hojjati & Wade 2012), U.S. Commercial Buildings Energy Consumption and Intensity Trends: A Decomposition Approach. November 2012. http://www.usaee.org/usaee2012/submissions/Presentations/Hojjati%20USAEE_IAEE%20Final_Nov_4_2012.pdf
2. California Public Utilities Commission (CPUC 2015), Reliability Standards. July 2015. http://www.cpuc.ca.gov/PUC/energy/ElectricSR/Reliability/rel_stand.htm
3. Energy Information Administration (EIA 2006), Commercial Buildings Energy Consumption Survey, Table C21. Electricity Consumption and Conditional Energy Intensity by Building Size for Non-Mall Buildings, 2003. December 2006. http://www.eia.gov/consumption/commercial/data/2003/pdf/c21.pdf
4. Energy Information Administration (EIA 2015), Electric Power Monthly, Table 5.3. Average Retail Price of Electricity to Ultimate Customers: Total by End-Use Sector, 2005 - April 2015 (Cents per Kilowatthour). http://www.eia.gov/electricity/monthly/epm_table_grapher.cfm?t=epmt_5_03
5. Executive Office of the President (EOP 2013a), Economic Benefits of Increased Resilience to Weather Outages. August 2013. http://energy.gov/sites/prod/files/2013/08/f2/Grid%20Resiliency%20Report_FINAL.pdf
6. Gabriele Villarini and Gabriel A. Vecchi (Villarini and Vecchi 2013). Projected Increases in North Atlantic Tropical Cyclone Intensity from CMIP5 Models. J. Climate, 26, 3231–3240. May 2013. doi: http://dx.doi.org/10.1175/JCLI-D-12-00441.1
7. International Energy Agency (IEA 2009), Overcoming PV Grid Issues in the Urban Areas. October 2009. http://www.iea-pvps-task10.org/IMG/pdf/rep10_06.pdf
8. K. LaCommare, J. Eto (LaCommare & Eto 2004), Understanding the Cost of Power Interruptions to U.S. Electricity Consumers. September 2004. http://emp.lbl.gov/sites/all/files/REPORT%20lbnl%20-%2055718.pdf
9. M. Sullivan, M. Mercurio, J. Schellenberg (Sullivan et al 2009), Estimated Value of Service Reliability for Electric Utility Customers in the United States. June 2009. http://certs.lbl.gov/pdf/lbnl-2132e.pdf

10. National Association of Regulatory Utility Commissioners (NARUC 2013a), Cost-Benefit Analysis of Various Electric Reliability Improvement Projects from the End Users' Perspective. November 2013. http://www.naruc.org/Publications/FINAL%20MD%20SERCAT%202013_for%20posting.pdf

11. National Association of Regulatory Utility Commissioners (NARUC 2013b), M. Keogh and C. Cody, Resilience in Regulated Utilities. November 2013. http://www.naruc.org/Grants/Documents/Resilience%20in%20Regulated%20Utilities%20ONLINE%2011_12.pdf

12. National Oceanic and Atmospheric Administration (NOAA 2015), Tropical Cyclone Observations. April 2015. http://www.prh.noaa.gov/cphc/pages/FAQ/Observations.php

13. National Renewable Energy Laboratory (NREL 2015a), D. Feldman, G. Barbose, R. Margolis, M. Bolinger, D. Chung, R. Fu, J. Seel, C. Davidson, and R. Wiser, Photovoltaic System Pricing Trends: Historical, Recent, and Near-Term Projections 2015 Edition. August 2015. http://eetd.lbl.gov/sites/all/files/pv_system_pricing_trends_presentation.pdf

14. National Renewable Energy Laboratory (NREL 2015b), Solar Data. April 2015. http://www.nrel.gov/gis/data_solar.html

15. National Renewable Energy Laboratory (Hotchkiss et al. 2013), E. Hotchkiss, I. Metzger, J. Salasovich, and P. Schwabe. Alternative Energy Generation Opportunities in Critical Infrastructure. November 2013. http://www.nrel.gov/docs/fy14osti/60631.pdf

16. North American Electric Reliability Corporation (NERC 2010), State of Reliability 2013. May 2013. http://www.nerc.com/pa/RAPA/PA/Performance%20Analysis%20DL/2013_SOR_May%2015.pdf

17. P. Larsen, J. Sweeney, K. Hamachi-LaCommare, and J. Eto (Larsen et al 2014), Exploring the Reliability of U.S. Electric Utilities. April 2014. http://www.usaee.org/usaee2014/submissions/OnlineProceedings/IAEE_ConferencePaper_01Apr2014.pdf

18. Statistic Brain Research Institute (SBRI 2015), Wal-Mart Company Statistics. April 2015. http://www.statisticbrain.com/wal-mart-company-statistics/

19. Solar Energies Industry Association (SEIA 2014), Solar Means Business 2014: Top US Commercial Users. 2014. http://www.seia.org/research-resources/solar-means-business-2014-top-us-commercial-solar-users

20. Solar Power Rocks (SPR 2015), October 2015. http://www.solarpowerrocks.com/square-feet-solar-roof/

21. System Advisor Model (SAM 2015). National Renewable Energy Laboratory. Version 1.30.2015. https://sam.nrel.gov/

22. US Department of Energy (DOE 2013a), US Energy Sector Vulnerabilities to climate change and Extreme Weather. July 2013. http://energy.gov/sites/prod/files/2013/07/f2/20130716-Energy%20Sector%20Vulnerabilities%20Report.pdf

23. US Department of Energy (DOE 2013b), Grid Energy Storage. December 2013. http://energy.gov/sites/prod/files/2013/12/f5/Grid%20Energy%20Storage%20December%202013.pdf

24. US Department of Energy (DOE 2013c), V. Viswanathan, M. Kintner-Meyer, P. Balducci, C. Jin, National Assessment of Energy Storage for Grid Balancing and Arbitrage, Phase II, Volume 2: Cost and Performance Characterization. September 2013. http://energyenvironment.pnnl.gov/pdf/National_Assessment_Storage_PHASE_II_vol_2_final.pdf

Conference Proceedings

Solar World Congress 2015
Daegu, Korea, 08 – 12 November 2015

Novel Encapsulation Technique to Upscale Latent Heat Storage Capacity in Steam Accumulators

Hakeem Niyas, P. Muthukumar

Department of Mechanical Engineering, Indian Institute of Technology Guwahati, Assam, India

Abstract

Cylindrical latent heat storage (LHS) capsules are used in steam accumulators for reducing the pressure drop in the vessel. Due to the high thermal resistance offered by the phase change material (PCM) in capsules with a higher diameter, more number of less diameter capsules need to be used for a particular storage capacity. In the present study, a novel encapsulation technique is proposed for effective heat transfer in cylindrical LHS capsules. With this technique, less number of capsules can yield the similar or higher storage capacity in a comparatively lesser charging time. A numerical model is developed to study the performance characteristics of the proposed novel encapsulation technique. In the numerical model, the effective heat capacity method is applied to consider the latent heat of the PCM and Boussinesq approximation is used to include the natural convection of the molten layer of the PCM. Darcy law's source term is added in the momentum equation to deduce the velocities of the PCM in its actual form in the mushy zone.

Keywords: *Heat transfer enhancement, Latent heat storage, Novel encapsulation, Phase change material.*

1. Introduction

Steam accumulators are applied as buffer storage devices between steam generators and consumers in case of a mismatch between the steam production and consumption (Stevanovic et al., 2012). During discharge in a steam accumulator, the steam pressure drops. Two viable techniques such as incorporating a flash evaporator or an encapsulated latent heat storage (LHS) capsule are preferred to avoid the pressure drop. Due to the exergy loss by mixing in the flash evaporator system, encapsulated LHS capsule is advantageous (Steinmann and Eck, 2006). Cylindrical capsules were being used normally in commercial steam accumulators (Medrano et al., 2010). Several experimental and numerical studies were carried out to study the LHS characteristics of cylindrical capsules during both charging and discharging processes (Bourdillon et al., 2015; Himeno et al., 1988; Steinmann and Tamme, 2008). Certain reviews encompass the major research works on encapsulated systems (Farid et al., 2004; Su et al., 2015). Despite of several advantages like reduction of temperature transients in steam accumulator, high volume-specific storage capacity, etc. (Medrano et al., 2010), the major disadvantage of encapsulated LHS capsule is the limitation in the diameter of the cylindrical capsules. With an increase of diameter, the resistance to heat transfer also increases due to the low thermal conductivity of the phase change material (PCM). In the present study, a novel encapsulation technique is proposed to alleviate this. The novelty proposed here is to use a shell-and-tube LHS system with a very small inner tube. With this, the heat transfer would be enhanced due to lesser thickness of PCM and increased heat transfer area when compared to the LHS capsule having basic encapsulation. For comparing the performance characteristics of the basic and proposed novel technique, capsules having a LHS capacity of 0.25 MJ are considered. Sodium nitrate and SS304 are selected as the PCM and encapsulating material. The thermo-physical properties of sodium nitrate are given in Tab. 1. Figure 1 shows the schematic of the cylindrical capsule and novel encapsulated cylindrical capsule. The diameter of the LHS capsules having basic and novel encapsulation for storing the corresponding LHS capacity are 63.5 mm and 64.3 mm. A small tube of diameter 6 mm is used as the inner tube for the novel capsule. The design of capsules is made in such a way that the volume of PCM in both the capsules are same.

doi:10.18086/swc.2015.02.17 Available at http://proceedings.ises.org

Tab. 1: Thermo-physical properties of sodium nitrate

Properties	Values	References
Density (ρ, kg m^{-3})		Bauer et al., 2012
Solid phase	2130	
Mushy zone	Linear interpolation	
Liquid phase	1908	
Latent heat of fusion (ΔH_f, J kg^{-1})	178,000	
Dynamic viscosity (μ, Pa s)	$0.0119 - 1.53 \times 10^{-5} T$	Janz et al., 1979
Melting point (T_m, K)	579.95	
Specific heat (c, J kg^{-1} K^{-1})	$444.53 + 2.18 T$	Lan and Kou, 1991
Thermal expansion coefficient (β, K^{-1})	6.6×10^{-4}	
Thermal conductivity (k, W m^{-1} K^{-1})	$0.3057 + 4.47 \times 10^{-4} T$	White and Davis, 1967

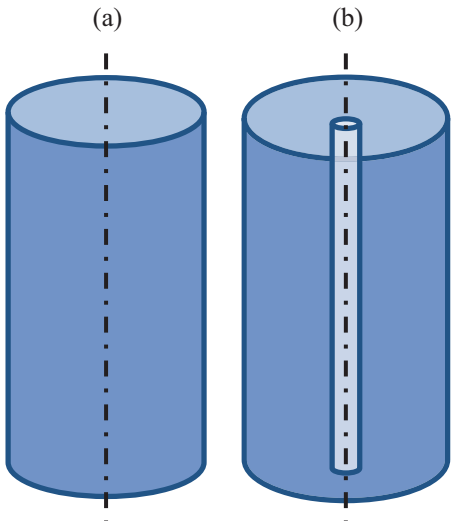

Fig. 1: Schematic diagram of encapsulated capsules (a) basic (b) novel

2. Numerical model

Three physical processes are to be simulated to study the LHS behavior of encapsulated LHS capsules, i.e. conduction, phase change and convection. A 2-D axisymmetric model is developed in view of the symmetry of flow and heat transfer around the vertical axis. Molten PCM movement due to natural convection heat transfer within the capsules is assumed to be laminar, Newtonian and incompressible. The major difficulty in the modeling of LHS system is the inclusion of latent heat and this is implemented using effective heat capacity method wherein a single term called effective heat capacity is used to consider both sensible and latent heat. The simulation is modelled using COMSOL Multiphysics software and the discontinuous effective heat capacity is applied using a Heaviside function. Buoyancy effect of the molten PCM is incorporated using Boussinesq approximation. To properly interpret the velocities in mushy zone, Darcy law's source term is added in the momentum equation. The governing equations and their corresponding sub-equations are given in Eqs. (1-8). Capsules are initially kept at 564.95 K and 594.95 K during charging and discharging processes. At any time ($t > 0$), the boundaries are given a temperature of 594.95 K and 564.95 K during charging and discharging processes thereby making a temperature swing of 30 K. The major performance parameter used in LHS is melt fraction. Melt fraction of the PCM can be calculated based on the lever rule applied between the solidus and liquidus temperatures and it is given by Eq. (8). During charging / discharging, melt fraction of the PCM possess a value of 0 / 1 initially and when it reaches a value of 1 / 0, it is said to be completely charged / discharged.

$$c = \begin{cases} c_{ps} & for\ T < T_S \\ c_{p,eff} & for\ T_S \le T \le T_L \\ c_{pl} & for\ T > T_L \end{cases} \quad \text{(Eq. 1)}$$

$$c_{p,eff} = \frac{c_{ps} + c_{pl}}{2} + \frac{\Delta H_f}{2\Delta T_m} \quad \text{(Eq. 2)}$$

$$\nabla . \vec{V} = 0 \quad \text{(Eq. 3)}$$

$$\frac{\partial \vec{V}}{\partial t} + (\vec{V} . \nabla)\vec{V} = \frac{1}{\rho}\left(-\nabla P + \mu \nabla^2 \vec{V} + F + \vec{S}\right) \quad \text{(Eq. 4)}$$

$$\rho c \frac{DT}{Dt} = k \nabla^2 T \quad \text{(Eq. 5)}$$

$$F = \rho \vec{g} \beta \left(T - T_m\right) \quad \text{(Eq. 6)}$$

$$\vec{S} = \frac{(1-\theta)^2}{(\theta^3 + \varepsilon)} A_{mush} \vec{V} \quad \text{(Eq. 7)}$$

$$\theta = \frac{T - T_S}{T_L - T_S} = \frac{T - T_m + \Delta T_m}{2\Delta T_m} = \begin{cases} 0 & for\ T < T_S \\ 0-1 & for\ T_S \le T \le T_L \\ 1 & for\ T > T_L \end{cases} \quad \text{(Eq. 8)}$$

3. Results and discussions

3.1. Grid Independency Test

Free triangular mesh is adapted in the developed numerical model. In order to test the dependency of numerical results on the mesh element size, a simulation is ran with the novel cylindrical capsule for charging process. The LHS capsule is initially at 564.95 K. At any time t > 0, the boundaries of the capsule are given 594.95 K. The average temperature of the capsule is compared for different element sizes viz. 10408, 12031 and 14410 elements. It is observed from Fig. 2 that the model with 12031 elements is found to be grid independent. Similarly, grid independency test carried out for the basic cylindrical capsule yields an optimum mesh size with 11672 elements.

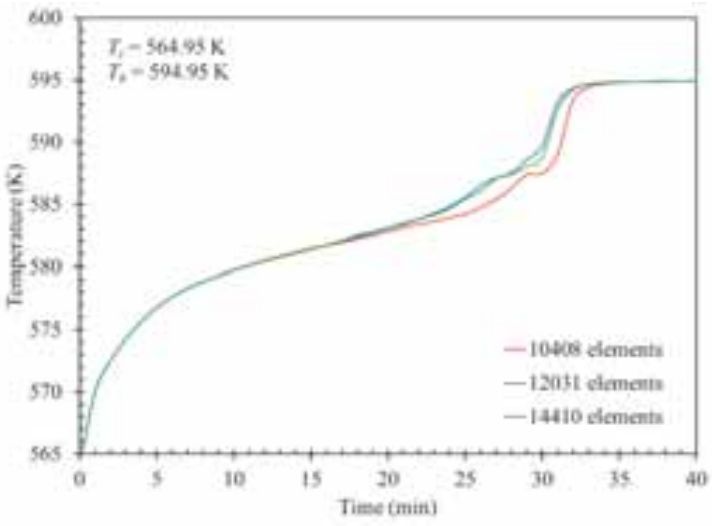

Fig. 2: Grid independent test

3.2. Temperature Distribution – Charging

Figure. 3 shows the comparison of the average temperature variation of the basic and novel LHS capsules during charging process. PCM kept in the capsules during charging is initially in the solid state at 564.95 K. When an uniform high temperature of 594.95 K is given on the boundary of the capsule, heat is transferred from periphery of the capsules and stored in the form of sensible and latent heat. It is inferred from Fig. 3 that the increase in average temperature is faster in LHS capsule having novel encapsulation than basic encapsulation. This is due to 2 reasons viz., increased surface area available for heat transfer and reduced thickness of the PCM layer.

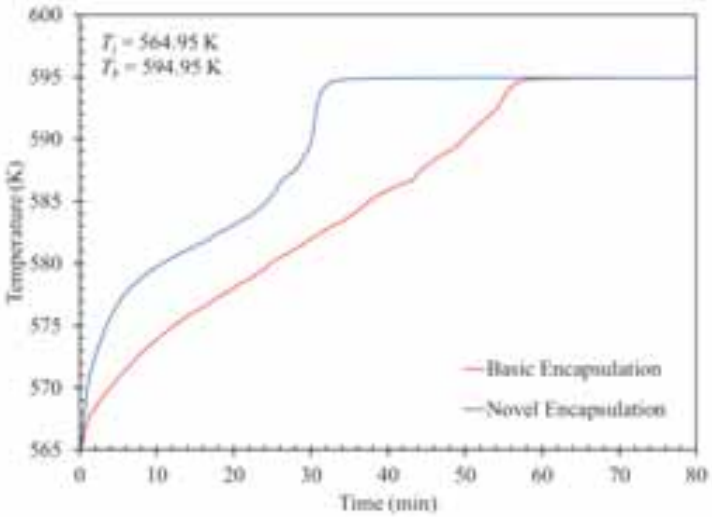

Fig. 3: Temperature distribution during charging

3.3. Charging Time

Charging time of the LHS capsule is defined with respect to the melt fraction of the PCM. The LHS capsule is said to be fully charged when the melt fraction of the PCM reaches unity. Figure. 4 shows the comparison of average melt fraction variation of basic and novel LHS capsules. It can be noted from Fig. 4 that the charging time of novel capsules is lesser than the basic capsule. It takes about 57 min and 32 min for complete charging of the PCM in LHS capsules having basic and novel encapsulation. There is a charging time reduction of 44 % in capsule having novel encapsulation when compared with the basic encapsulation. Screenshots of melt fraction variation of LHS capsules during charging are given in Fig. 5. The effect of natural convective heat transfer can be seen from the asymmetric temperature variation in the capsules at 15, 30, 45 min (basic encapsulation) and 30 min (novel encapsulation).

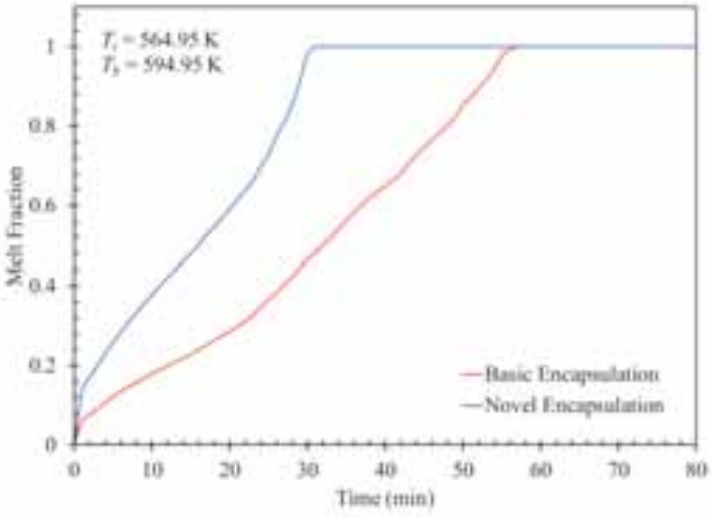

Fig. 4: Melt fraction distribution during charging

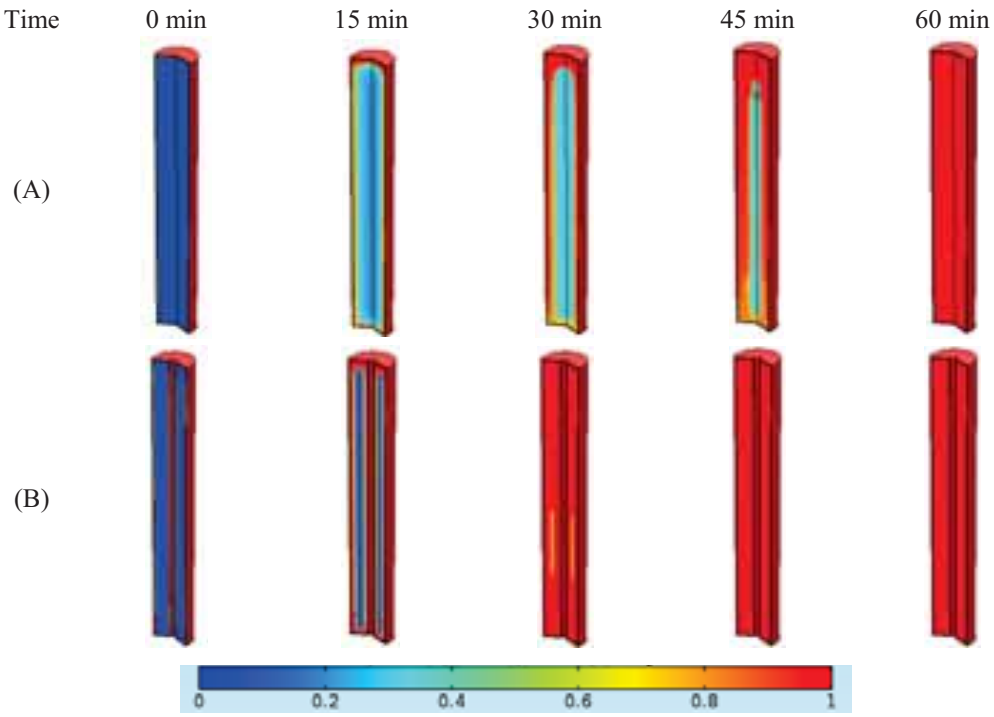

Fig. 5: Melt fraction distribution during charging (A) Basic encapsulation (B) Novel encapsulation

3.4. Temperature Distribution – Discharging

Figure. 6 shows the comparison of the average temperature variation of the LHS capsules having basic and novel encapsulation during discharging process. PCM kept in the capsules during discharging is initially in the liquid state at 594.95 K. When an uniform low temperature of 564.95 K is given on the boundary of the capsule, heat is transferred from the capsules and gets discharged in the form of sensible and latent heat. It is inferred from Fig. 6 that the decrease in average temperature is faster in LHS capsule having novel encapsulation than the basic encapsulation similar to the charging process.

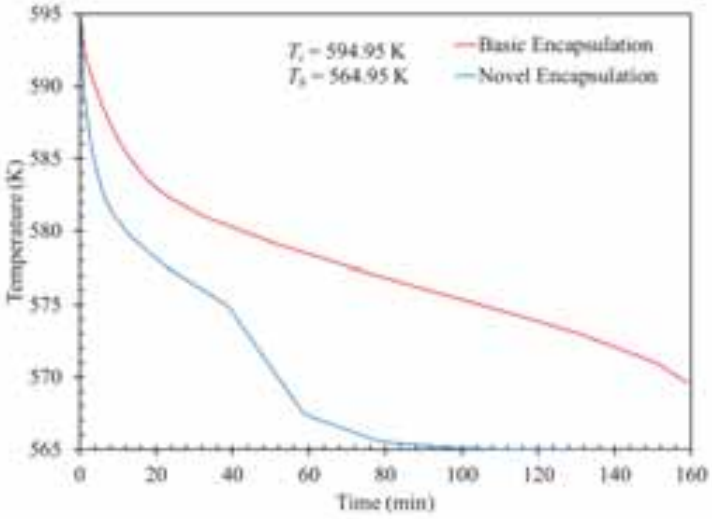

Fig. 6: Temperature distribution during discharging

3.5. Discharging Time

Discharging time of the LHS capsule is defined similarly with respect to the melt fraction of the PCM. The LHS capsule is said to be fully discharged when the melt fraction of the PCM reaches zero. Figure. 7 shows the comparison of average melt fraction variation LHS capsules having basic and novel encapsulation. It can

be noted from Fig. 7 that the discharging time of novel capsules is much lesser than the basic capsule. It takes about 158 min and 48 min for complete discharging of the PCM in LHS capsules having basic and novel encapsulation. There is a discharging time reduction of 70 % in capsule having novel encapsulation when compared with the basic encapsulation. Screenshots of melt fraction variation of LHS capsules during discharging are given in Fig. 8. It can be understood from Fig. 8 that solidification of PCM is highly dominated by conductive heat transfer and less or no influence by natural convection heat transfer.

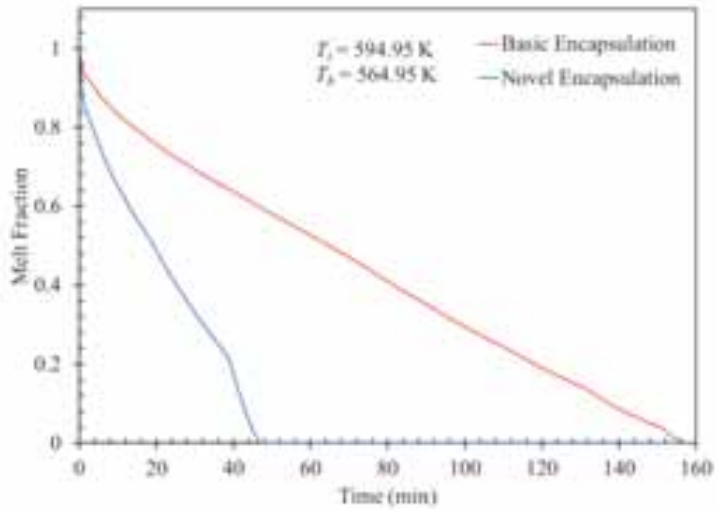

Fig. 7: Melt fraction distribution during charging

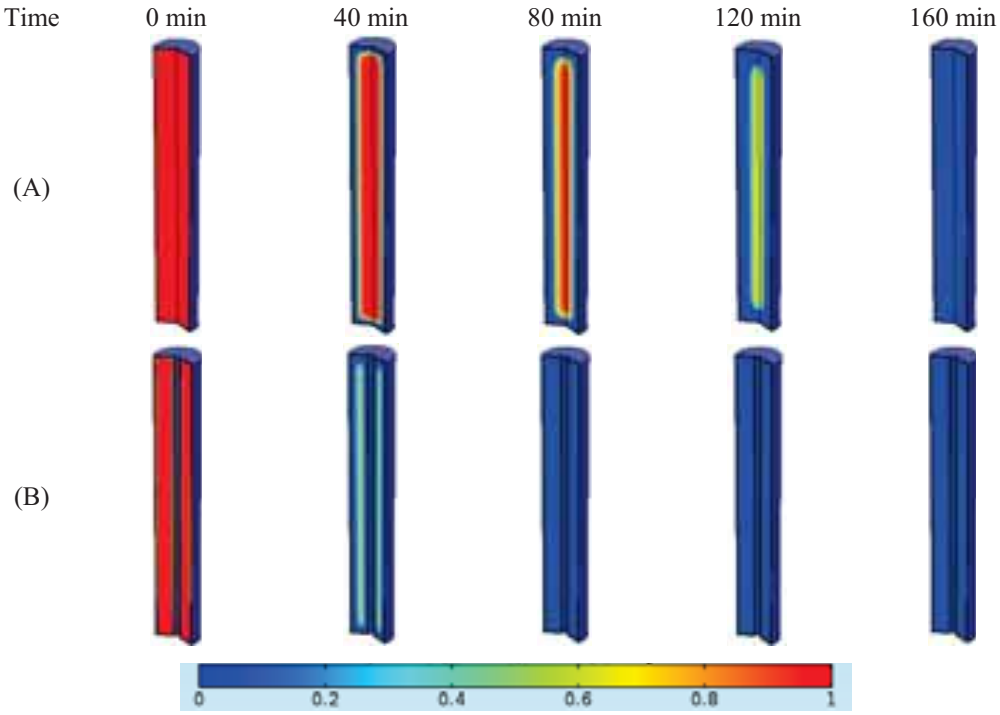

Fig. 8: Melt fraction distribution during charging

4. Conclusions

A thermal model was developed to compare the performance of LHS capsules having basic and novel encapsulation during charging and discharging processes. It was found that the charging of PCMs in both the models was dominated by natural convection. Numerical results shown that for the same mass of PCM, LHS capsules with novel encapsulation yields lesser charging and discharging time than the capsule with basic

encapsulation. This is due to 2 reasons viz., increased surface area available for heat transfer and reduced thickness of the PCM layer. It took about 57 min and 32 min for complete charging and 158 min and 48 min for complete discharging in the LHS capsules with basic and novel encapsulation. It can be noted that the charging and discharging time of the LHS capsule with novel encapsulation shown a reduction of about 44 % and 70 % respectively when compared with the LHS capsule with basic encapsulation. The results of the current study will be useful in the design of compact and efficient LHS encapsulated capsules.

5. Acknowledgements

The authors sincerely thank the Department of Science and Technology (DST), Government of India, for their financial support (Project No: DST/TM/SERI/2K10/53(G)).

6. References

Bauer, T., Laing, D., Tamme, R., 2012. Characterization of sodium nitrate as phase change material. Int. J. Thermphys. 33, 91-104.

Bourdillon, A.C., Verdin, P.G., Thompson, C.P., 2015. Numerical simulations of water freezing processes in cavities and cylindrical enclosures. Appl. Therm. Eng. 75, 839-855.

Farid, M.M., Khudhair, A.M., Razack, S.A.K., Al-Hallaj, S., 2004. A review on phase change energy storage: materials and applications. Energy Convers. Manage. 45, 1597-1615.

Himeno, N., Hijikata, K., Sekikawa, A., 1988. Latent heat thermal energy storage of a binary mixture-flow and heat transfer characteristics in a horizontal cylinder. Int. J. Heat Mass Transfer. 31 (2), 359-366.

Janz, G.J., Allen, C.B., Bansal, N.P., Murphy, R.M., Tomkins, R.P.T., 1979. Physical Properties Data Compilations Relevant to Energy Storage. II. Molten Salts: Data on Single and Multi-component Salt Systems, NSRDS-NBS-61 (Pt. 2), U.S. National Bureau of Standards. <http://www.nist.gov/data/nsrds/NSRDS-NBS61-II.pdf> (Last accessed 01.11.2015)

Lan, C.W., Kou, S., 1991. Effects of rotation on heat transfer, fluid flow and interfaces in normal gravity floating-zone crystal growth. J. Cryst. Growth. 114, 517-535.

Medrano, M., Gil, A., Martorell, I., Potau, X., Cabeza, L.F., 2010. State of the art on high-temperature thermal energy storage for power generation. Part 2—Case studies. Renewable Sustainable Energy Rev. 14, 56-72.

Steinmann, W.D., Eck, M., 2006. Buffer storage for direct steam generation, Sol. Energy. 80, 1277-1282.

Steinmann, W.D., Tamme, R., 2008. Latent heat storage for solar steam systems. J. Sol. Energy Eng. 130, 011004:1–5.

Stevanovic, V.D., Maslovaric, B., Prica, S., 2012. Dynamics of steam accumulation. Appl. Therm. Eng. 37, 73–79.

Su, W., Darkwa, J., Kokogiannakis, G., 2015. Review of solid–liquid phase change materials and their encapsulation technologies. Renewable Sustainable Energy Rev. 48, 373-391.

White, L.R., Davis, H.T., 1967. Thermal conductivity of molten alkali nitrates. J. Chem. Phys. 47, 5433-5439.

Conference Proceedings

Solar World Congress 2015
Daegu, Korea, 08 – 12 November 2015

Novel Fin for Effective Heat Transfer in Shell-and-Tube Latent Heat Storage System

Hakeem Niyas, P. Muthukumar

Department of Mechanical Engineering, Indian Institute of Technology Guwahati, Assam, India

Abstract

Due to the low thermal conductivity of phase change materials (PCMs), latent heat storage (LHS) technology has not yet commercialized to its fullest capability. Many heat transfer enhancement techniques were studied by several researchers and each of the techniques put forward has its own pros and cons. In the present study, a novel fin is proposed for effective heat transfer in shell-and-tube LHS devices. A numerical model is developed to study the performance characteristics of the proposed novel fin and to compare it with no fin and standard fin configurations. Effective heat capacity method is used to simulate the phase change mechanism. Sodium nitrate is used as the PCM and air is used as the heat transfer fluid. Performance parameters such as melt fraction and charging time are evaluated. Axial temperature variation of PCM in the LHS models is also studied.

Keywords: *Heat transfer enhancement, Latent heat storage, Novel fin, Phase change material.*

1. Introduction

The most intensely examined LHS system is the shell-and-tube system. This is due to the fact that many engineering systems employ cylindrical pipes and also heat loss from the shell-and-tube system is minimal (Agyenim et al., 2010). Several techniques were reported to improve the overall heat transfer effectiveness of the LHS system (Kurnia et al., 2013; Li et al., 2013; Rathod and Banerjee, 2015). Extensive reviews in this context were also published (Fan and Khodadadi, 2011; Kenisarin and Mahkamov, 2007; Liu et al., 2012). Every heat transfer enhancement technique has certain disadvantages:

- Sprinkling of high thermal conductivity metallic particles – the metallic particles settle down due to its high density after repeated charging and discharging cycles.
- Extended heat transfer surfaces (Fins) – materials having a high corrosion resistance and high/moderate thermal conductivity are suitable for heat transfer media in LHS systems. Materials having these properties (eg: stainless steel) are denser and hence the total weight of the system becomes high.

To increase the overall heat transfer in the LHS devices, a novel fin is proposed in the present study. Figure 1 shows the schematic of the shell-and-tube LHS module and the inner tube with and without novel/standard fins. The novel fin proposed here is half of the standard fin cut diagonally. This will reduce the weight and cost of the fin material by a factor of 0.5 and hence making the LHS system, light weight and cost-effective. For comparing the performance characteristics of the basic and proposed novel technique, capsules having a LHS capacity of 0.5 MJ are considered. Sodium nitrate and air are selected as the PCM and heat transfer fluid (HTF). SS 304 is selected as the HTF tube. The thermo-physical properties of sodium nitrate are given in Tab. 1. Figure 1 shows the schematic of the no fin, standard fin and novel fin configurations. The length of the LHS models is 0.5 m. The height and width of the fin is 10 mm and 2 mm in the standard fin configuration. The design of LHS models is made in such a way that the volume of PCM in all the configurations are same.

doi:10.18086/swc.2015.02.18 Available at http://proceedings.ises.org

Tab. 1: Thermo-physical properties of sodium nitrate

Properties	Values	References
Density (ρ, kg m^{-3})		Bauer et al., 2012
Solid phase	2130	
Mushy zone	Linear interpolation	
Liquid phase	1908	
Latent heat of fusion (ΔH_f, J kg^{-1})	178,000	
Dynamic viscosity (μ, Pa s)	$0.0119 - 1.53 \times 10^{-5}\ T$	Janz et al., 1979
Melting point (T_m, K)	579.95	
Specific heat (c, J kg^{-1} K^{-1})	$444.53 + 2.18\ T$	Lan and Kou, 1991
Thermal expansion coefficient (β, K^{-1})	6.6×10^{-4}	
Thermal conductivity (k, W m^{-1} K^{-1})	$0.3057 + 4.47 \times 10^{-4}\ T$	White and Davis, 1967

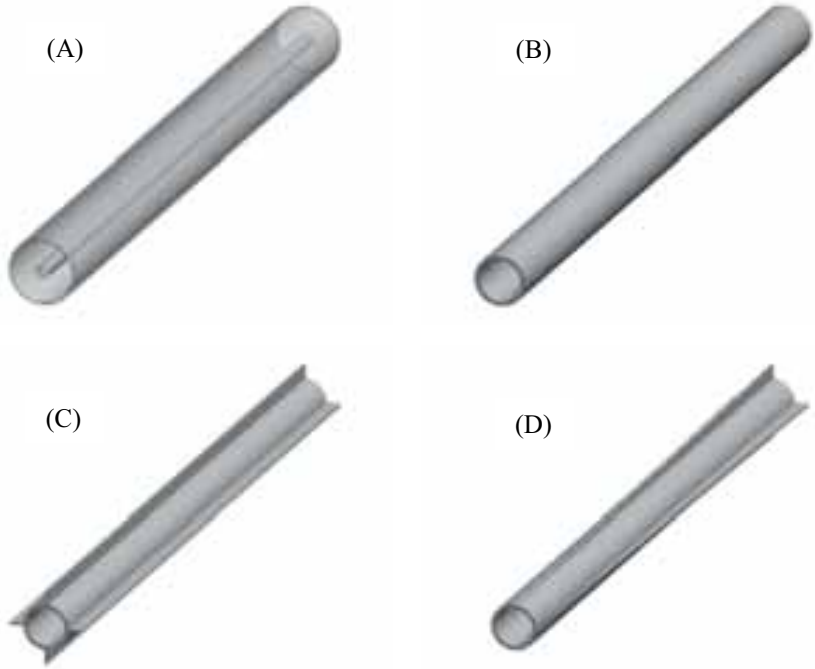

Fig. 1: Schematic of (A) shell-and-tube LHS module (B) inner tube without fin (C) inner tube with standard fin (D) inner tube with novel fin

2. Numerical Model

A 3-D conjugate heat transfer model is developed to simulate the flow characteristics of HTF and heat transfer characteristics of PCM. The major difficulty in the modeling of LHS system is the inclusion of latent heat and this has been implemented using effective heat capacity method. The simulation is modelled using COMSOL Multiphysics software. Buoyancy effect has been incorporated using Boussinesq approximation. To properly interpret the velocities in mushy zone, Darcy law's source term was added in the momentum equation. The governing equations and their corresponding sub-equations are given in Eqs. (1-8). LHS models are initially kept at 564.95 K during the charging process. At any time ($t > 0$), the inlet of the model is given a temperature of 594.95 K and a constant velocity of 2 m/s. The major performance parameter used in LHS is melt fraction. Melt fraction of the PCM can be calculated based on the lever rule applied between the solidus and liquidus temperatures and it is given by Eq. (8). During charging, melt fraction of the PCM possess a value of 0 initially and when it reaches a value of 1, it is said to be completely charged.

$$c = \begin{cases} c_{ps} \ \ for\ T < T_S \\ c_{p,eff}\ for\ T_S \le T \le T_L \\ c_{pl} \ \ for\ T > T_L \end{cases} \quad \text{(Eq. 1)}$$

$$c_{p,eff} = \frac{c_{ps} + c_{pl}}{2} + \frac{\Delta H_f}{2\Delta T_m} \quad \text{(Eq. 2)}$$

$$\nabla . \vec{V} = 0 \quad \text{(Eq. 3)}$$

$$\frac{\partial \vec{V}}{\partial t} + (\vec{V}.\nabla)\vec{V} = \frac{1}{\rho}\left(-\nabla P + \mu \nabla^2 \vec{V} + F + \vec{S}\right) \quad \text{(Eq. 4)}$$

$$\rho c \frac{DT}{Dt} = k \nabla^2 T \quad \text{(Eq. 5)}$$

$$F = \rho \vec{g} \beta (T - T_m) \quad \text{(Eq. 6)}$$

$$\vec{S} = \frac{(1-\theta)^2}{(\theta^3 + \varepsilon)} A_{mush} \vec{V} \quad \text{(Eq. 7)}$$

$$\theta = \frac{T - T_S}{T_L - T_S} = \frac{T - T_m + \Delta T_m}{2\Delta T_m} = \begin{cases} 0 \ \ for\ T < T_S \\ 0-1\ for\ T_S \le T \le T_L \\ 1 \ \ for\ T > T_L \end{cases} \quad \text{(Eq. 8)}$$

3. Results and discussions

3.1. Temperature Distribution

Figure. 2 shows the comparison of the average temperature variation of the single tube shell-and-tube LHS model with no fin, standard fin and novel fin during charging process. PCM kept in the capsules is initially in the solid state at 564.95 K. When an uniform high temperature of 594.95 K and velocity of 2 m/s are given on the inlet of the LHS model, heat is transferred from the fluid and gets stored in PCM in the form of sensible and latent heat. It is inferred from Fig. 2 that the increase in average temperature is faster in LHS model having standard fin than that of no fin and novel fin, initially. This is due to the higher surface area available for heat transfer. But after a certain period of time, say t = 360 min, the increase in average temperature is faster in LHS model having novel fin than that of other two cases. The reason for this is the configuration of the novel fin, wherein the heat transfer area is more in the less heat transfer potential region, i.e. near the outlet portion of the model. Screenshots of temperature variation at different times are given in

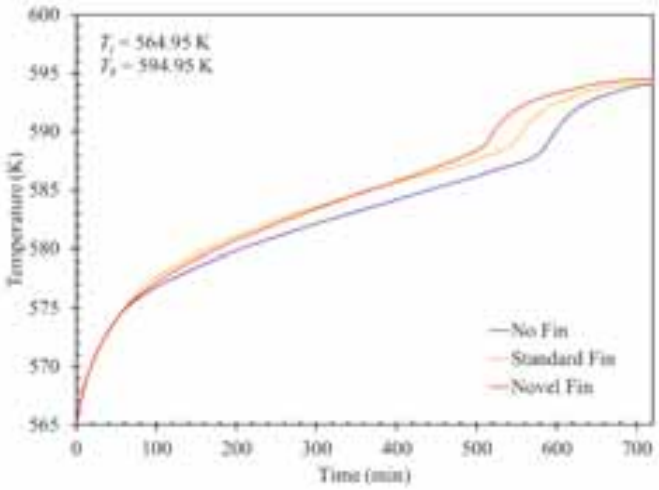

Fig. 2: Temperature distribution

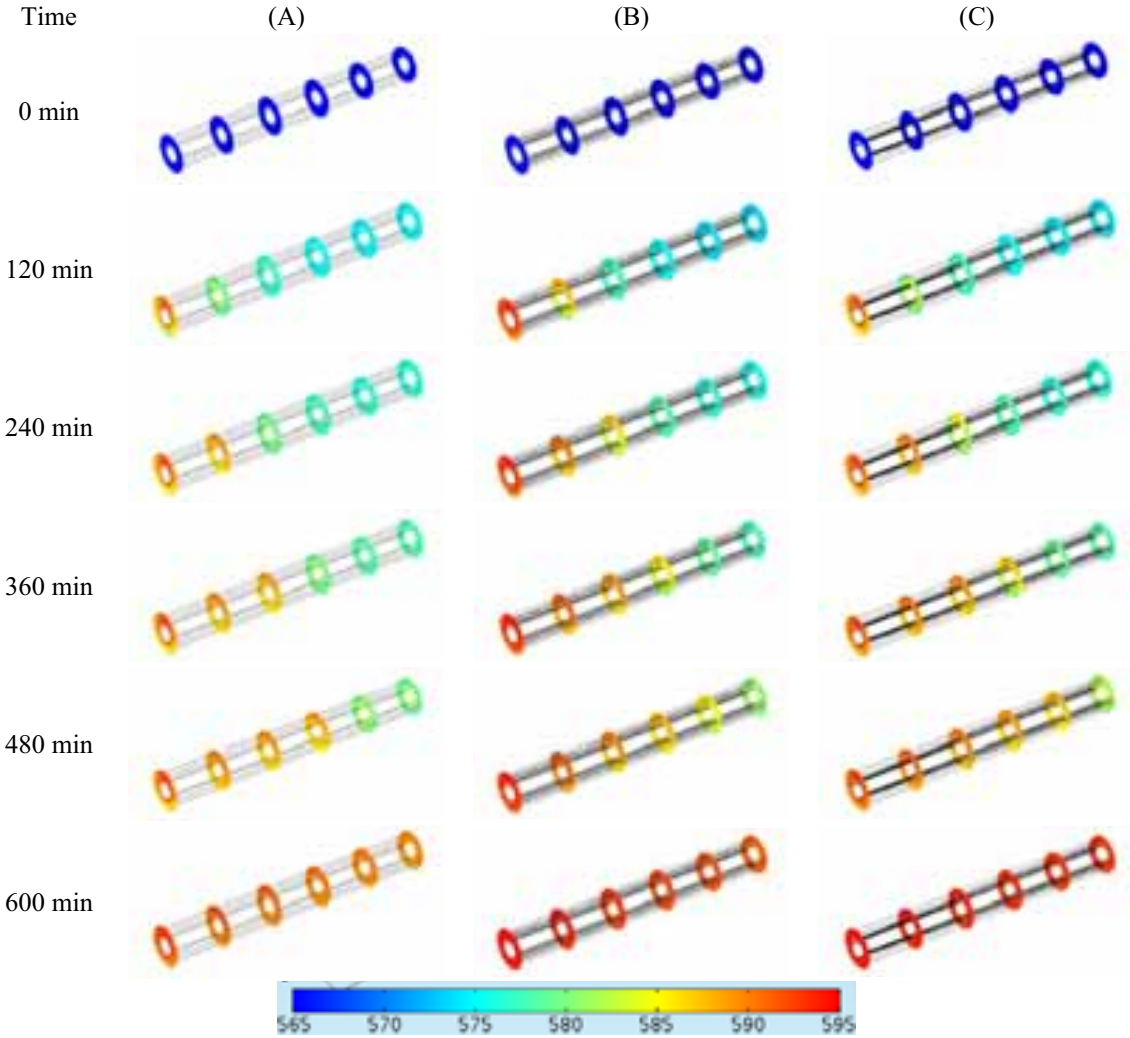

Fig. 3: Temperature distribution at different times

Fig. 3. It can be noted from Fig. 3 that the standard fin configuration dominates in temperature rise of PCM than the other two configurations, initially (t = 120 min, 240 min, 360 min) and novel fin configuration dominates in temperature rise of PCM during the last period (t = 480 min, 600 min).

3.2. Charging Time

Charging time of the LHS model is defined with respect to the melt fraction of the PCM. The LHS model is said to be fully charged when the melt fraction of the PCM reaches unity. Figure. 4 shows the comparison of average melt fraction variation of LHS model with no fin, standard fin and novel fin during charging process. It can be noted from Fig. 4 that the charging time of novel fin configuration is lesser than the no fin and standard fin configurations. It takes about 597 min, 551 min and 518 min for complete charging in the LHS model with no fin, standard fin and novel fin. It can be noted that the charging time has decreased by about 13.2 % and 6 % when using novel fin configuration with respect to no fin and standard fin configurations.

3.3. Axial Temperature Variation

Figure. 5 shows the axial temperature variation of the PCM in the LHS model. Surface average temperature of LHS model at x/L = 0, 0.1, 0.2, 0.3, 0.4 and 0.5 are plotted with respect to time. It can be noted from Fig. 5 that temperature of PCM in the inlet side of the LHS module increased faster in all the three configurations than that of the outlet side which is due to the presence of high temperature difference between the PCM and HTF at the inlet side. It is also noted from Fig. 5 that in both no fin and standard fin configurations, the difference between the temperature of PCM in the inlet and outlet portion is more than that of the novel fin configuration.

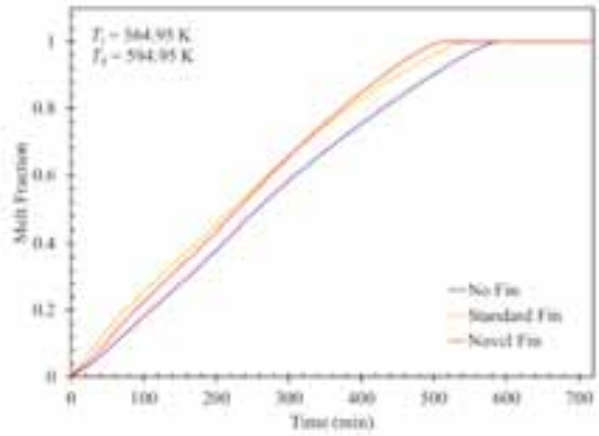

Fig. 4: Melt fraction distribution

(A)

(B)

(C)

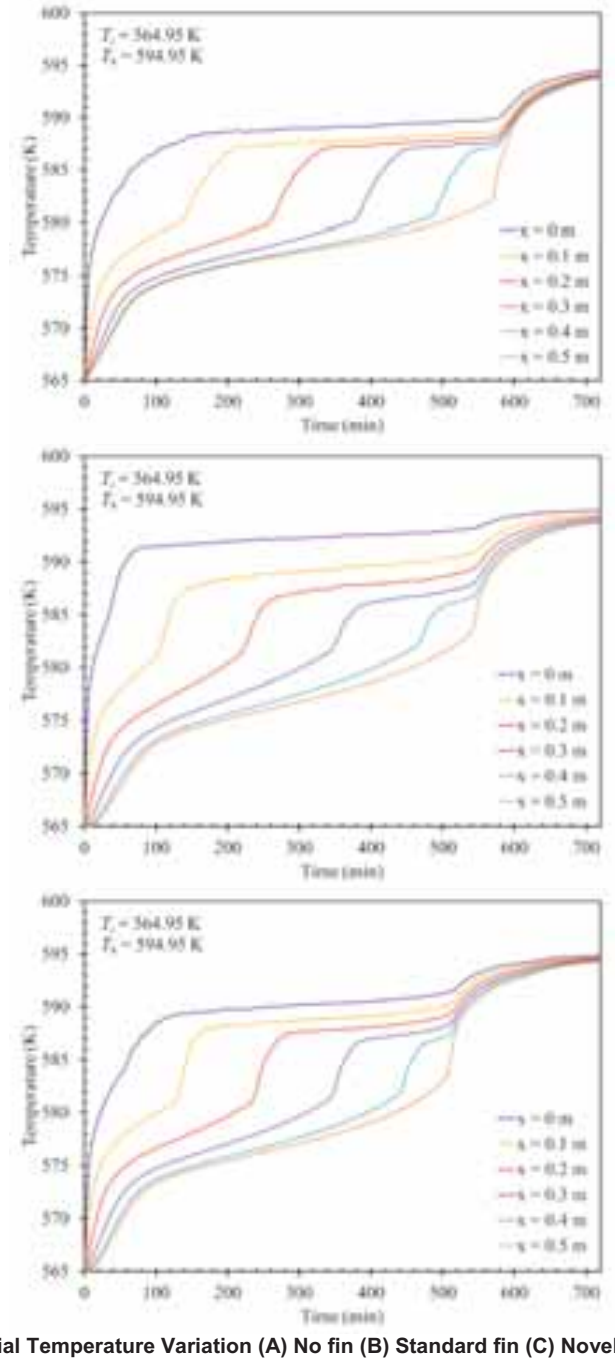

Fig. 5: Axial Temperature Variation (A) No fin (B) Standard fin (C) Novel fin

4. Conclusions

A novel fin is proposed for effective heat transfer in shell-and-tube LHS devices. A numerical model is developed to study the performance characteristics of the proposed novel fin and compare it with no fin and standard fin configurations. It is found from the numerical study that it takes about 597 min, 551 min and 518 min for complete charging in the LHS system with no fin, standard fin and novel fin. It can be noted that the charging time has decreased by about 13.2 % and 6 % when using novel fin system with respect to no fin and standard fin configurations. The novel fin proposed has also an additional advantage of weight and cost reduction by a factor of 0.5.

5. Acknowledgements

The authors sincerely thank the Department of Science and Technology (DST), Government of India, for their financial support (Project No: DST/TM/SERI/2K10/53(G)).

6. References

Agyenim, F., Hewitt, N., Eames, P., Smyth, M., 2010. A review of materials, heat transfer and phase change problem formulation for latent heat thermal energy storage systems (LHTESS). Renewable Sustainable Energy Rev. 14, 615–628.

Bauer, T., Laing, D., Tamme, R., 2012. Characterization of sodium nitrate as phase change material. Int. J. Thermphys. 33, 91-104.

Fan, L., Khodadadi, J.M., 2011. Thermal conductivity enhancement of phase change materials for thermal energy storage: A review, Renewable Sustainable Energy Rev. 15, 24-46.

Janz, G.J., Allen, C.B., Bansal, N.P., Murphy, R.M., Tomkins, R.P.T., 1979. Physical Properties Data Compilations Relevant to Energy Storage. II. Molten Salts: Data on Single and Multi-component Salt Systems, NSRDS-NBS-61 (Pt. 2), U.S. National Bureau of Standards. <http://www.nist.gov/data/nsrds/NSRDS-NBS61-II.pdf> (Last accessed 01.11.2015)

Kenisarin, M., Mahkamov, K., 2007. Solar energy storage using phase change materials, Renewable Sustainable Energy Rev 11, 1913-1965.

Kurnia, J.C., Sasmito, A.P., Jangam, S.V., Mujumdar, A.S., Improved design for heat transfer performance of a novel phase change material (PCM) thermal energy storage (TES). Appl. Therm. Eng. 50, 896-907.

Lan, C.W., Kou, S., 1991. Effects of rotation on heat transfer, fluid flow and interfaces in normal gravity floating-zone crystal growth. J. Cryst. Growth. 114, 517-535.

Li, T., Lee, J.H., Wang, R., Kang, Y.T., 2013. Enhancement of heat transfer for thermal energy storage application using stearic acid nano composite with multi-walled carbon nanotubes. Energy. 55, 752-761.

Liu, M., Saman, W., Bruno, F., 2012. Review on storage materials and thermal performance enhancement techniques for high temperature phase change thermal storage systems, Renewable Sustainable Energy Rev. 16, 2118-2132.

Rathod, M.K., Banerjee, J., 2015. Thermal performance enhancement of shell and tube Latent Heat Storage Unit using longitudinal fins. Appl. Therm. Eng. 75, 1084-1092.

White, L.R., Davis, H.T., 1967. Thermal conductivity of molten alkali nitrates. J. Chem. Phys. 47, 5433-5439.

Renewable Energy Grid Integration & DistributionTheme

Eurasian Super Grid for 100% Renewable Energy power supply: Generation and storage technologies in the cost optimal mix

Dmitrii Bogdanov and Christian Breyer

Lappeenranta University of Technology, Lappeenranta (Finland)

E-mail: Dmitrii.Bogdanov@lut.fi, Christian.Breyer@lut.fi

Abstract

Increasing ecological problems provoked by human activities, including the fossil fuel based energy sector, emerge the development of a renewable energy (RE) based system as the way to stop pollution and global warming but also to reduce total energy system cost. Small population density and availability of various types of RE resources in Eurasian regions including solar, wind, hydro, biomass and geothermal energy resources enables the very promising project of building a Super Grid connecting different Eurasian regions' energy resources to reach synergy effects and make a 100% RE supply possible. For every sub-region it is defined a cost-optimal distributed and centralized mix of energy technologies and storage options, optimal capacities and hourly generation. Charge and discharge profiles of storages are computed for regions interconnected by high-voltage direct current (HVDC) power lines. System cost and levelized cost of electricity (LCOE) for each sub-region are computed. The results show that a 100% RE-based system is lower in cost than nuclear and fossil carbon capture and storage (CCS) alternatives.

Keywords: *100% Renewable Energy, Eurasia, Russia, energy system optimization, storage, grid integration, Economic Analysis.*

1. Introduction

Installation of distributed small-scale and centralized PV plants is already profitable in numerous regions in the word and PV electricity generation cost tends to decrease further (Breyer and Gerlach, 2013; Vartiainen et al., 2015). However, the share of PV generation is bound by the need to install storage systems in order to reach a high PV share of more than about 30% in total energy supply. Interconnection of various regions with different demand and renewable energy (RE) resource profiles can decrease the need for storage solutions and increase the reliability of the RE-based system for reaching a 100% RE supply in the very end. A cost competitive 100% RE system can be reached in case of optimal design and wise utilization of all available RE resources in order to reach maximum synergy between various resources and different regions.

The idea of a global Super Grid for power supply was already discussed some years ago (Komoto et al., 2009) and again recently (State Grid Corporation of China, 2015), but attracted new attention by the Gobitec and North-East Asian Super Grid initiative, which considers the eastern parts of Eurasia as part of the North-East Asian Super Grid (Mano et al., 2014; Komoto et al., 2009; Taggart et al., 2012; Song, 2012; Song, 2014; Komoto et al., 2013; Breyer et al., 2015), influenced by the EU-MENA Desertec (Dii, 2012; Knies, 2009). Bridging technologies such as power-to-heat and heat storage (Böttger et al., 2014) will convert electricity generation losses and electricity curtailment to valuable heat for residential and industrial needs. Power-to-water in the form of seawater reverse osmosis (SWRO) desalination starts to play a major role for the clean water targets. Power-to-Gas (PtG) technology based on water electrolysis, CO_2 from air, and methanation reactors will provide 100% renewable synthetic natural gas supply for chemicals, fertilizers, other industries, transportation and other non-power sectors (Sterner, 2009; Agora Energiewende, 2014a). All these technologies and high renewable energy potentials of Eurasia makes the installation of a RE-based system in the region possible. However, a cost competitive 100% RE system can be reached in case of optimal design and wise utilization of all available RE resources in order to reach a maximum synergy between various resources, different regions and the integration of energy sectors. Design of optimal energy system is the main

doi:10.18086/swc.2015.06.01 Available at http://proceedings.ises.org

aim of this paper.

2. Methodology

In order to define a cost optimal 100% RE system we have created a model based on linear optimization of energy system parameters under given constrains. The energy system model includes various power generation and storage technologies, as well as water desalination and synthetic gas generation sectors, which operate as flexible demand.

2.1 Model overview

The energy system optimization model is based on a linear optimization of the system parameters under a set of applied constraints with the assumption of a perfect foresight of RE power generation and power demand. A multi-node approach enables the description of any desired configuration of sub-regions and power transmission interconnections, i.e. not all the sub-regions have to be interconnected, but a grid configuration can be defined in scenario assumptions or can be chosen close to an existing grid configuration. The main constraint for the optimization is the matching of the demand and generation of every sector for every hour of the applied year. The hourly resolution of the model significantly increases the computation time; however, it guarantees that for every hour of the year the total generation within a sub-region covers the local demand from all the sectors and enables a more precise system description including synergy effects of different system components for the power system balance.

The target of the system optimization is the minimization of the total annual cost of the system including the power sector and additional flexible electricity demand sectors (water desalination and gas synthesis sectors). System cost is calculated as the sum of the annual costs of installed capacities of the different technologies, costs of energy generation and generation ramping. The system also includes distributed generation and self-consumption of residential, commercial and industrial electricity consumers (prosumers) by installing respective capacities of rooftop PV systems and batteries. For these prosumers, the target function is minimal cost of consumed energy calculated as the sum of self-generation, annual cost and cost of electricity consumed from the grid, minus benefits from the sale of excess energy.

2.2 Input data

The model uses several types of input datasets and constraints:

- historical weather data for direct and diffuse solar irradiation, wind speed and precipitation amounts,
- historical daily water flow data in the major rivers and water reservoirs,
- synthetic geothermal energy potential data,
- synthetic load data for every sub-region,
- non-energy sector natural gas consumption for every sub-region,
- projected water desalination demand for every sub-region,
- technical characteristics of used energy generation, storage and transmission technologies, such as power yield, energy conversion efficiency, power losses in transmission lines and storage roundtrip efficiency,
- technical characteristics of used SWRO desalination,
- capital expenditures, operational expenditures and ramping costs for all technologies,
- electricity costs for residential, commercial and industrial consumers,
- limits for minimum and maximum installed capacity for all energy technologies,
- configuration of regions and interconnections.

The datasets for solar irradiation components, wind speed and precipitation are taken from NASA databases (Stackhouse and Whitlock, 2008; Stackhouse and Whitlock, 2009) and partly reprocessed by the German Aerospace Center (Gerlach et al., 2011; Stetter, 2012). The spatial resolution of the data is 0.45˚x0.45˚. The time resolution is hourly for wind speed and solar irradiation, and monthly for precipitation. The feed-in time series for fixed optimally tilted solar photovoltaic (PV) systems is computed in accordance to Gerlach et al. (2011), based on Huld et al. (2008) and for single-axis north-south oriented continuous horizontal tracking, on

Duffie and Beckmann (2013). The feed-in time series for wind power plants is computed in accordance to Gerlach et al. (2011) for standard 3 MW wind turbines (E-101) for hub height conditions of 150 meters (Enercon, 2014).

Geothermal data are evaluated based on existing information on the surface heat flow rate (IASPEI, 2015; AAPG, 2015) and surface ambient temperature for the year 2005 globally. For areas where surface heat flow data are not available, the extrapolation of existing heat flow data were performed. Based on that, temperature levels and available heat of the middle depth point of each 1 km thick layer, between depths of 1 km and 10 km (Chamorro et al., 2014a,b; Huenges, 2012) globally with 0.45˚x0.45˚ spatial resolution, are derived.

Water demand is calculated based on water consumption projections and future water stress (Luck et al., 2015). It is assumed that water stress greater than 50% shall be covered by seawater desalination. Transportation costs are also taken into account; calculations are described in Caldera et al. (2015). Industrial gas consumption is based on consumption and distribution data from central statistical database of the Federal State Statistics Service of Russia (2015), BP gas consumption data (BP, 2014) and IEA gas consumption projections to the year 2030 (IEA, 2014; IEA, 2013).The synthetic load data are based on public available hourly load data on a national level, e.g. for Japan but also European countries, and takes into account local data such as gross domestic product, population, temperature and power plant structure.

2.3 Applied technologies

The technologies applied in the Eurasian energy system optimization can be grouped into three main categories: conversion of RE resources into electricity, energy storage, and electricity transmission.

The technologies for converting RE resources into electricity applied in the model are ground-mounted (optimally tilted and single-axis north-south oriented horizontal continuous tracking) and rooftop solar PV systems, concentrating solar thermal power (CSP), wind onshore, hydro power (run-of-river and dams), biomass plants (solid biomass and biogas), waste-to-energy power plants and geothermal energy.

The energy storage technologies used in the model are battery storage, pumped hydro storage (PHS), adiabatic compressed air energy storage (A-CAES), thermal energy storage (TES) and power-to-gas (PtG) technology. PtG includes synthetic natural gas (SNG) synthesis technologies: water electrolysis, methanation, CO_2 scrubbing from air, gas storage, and both combined and open cycle gas turbines (CCGT, OCGT). SNG synthesis process technologies have to be operated in synchronization because of hydrogen and CO_2 storage absence. Additionally, there is a 48-hour biogas buffer storage and a part of the biogas can be upgraded to biomethane and injected to the gas storage.

The electricity transmission technologies are represented on two levels: power distribution and transmission within the sub-regions are assumed to be based on standard alternating current (AC) grids and inter-regional transmission grids are modelled on high voltage direct current (HVDC) technology. Power losses in the HVDC grids consist of two major components: length dependent electricity losses of the power lines and losses in the converter stations at the interconnection with the AC grid. The full model block diagram is presented in Figure 1.

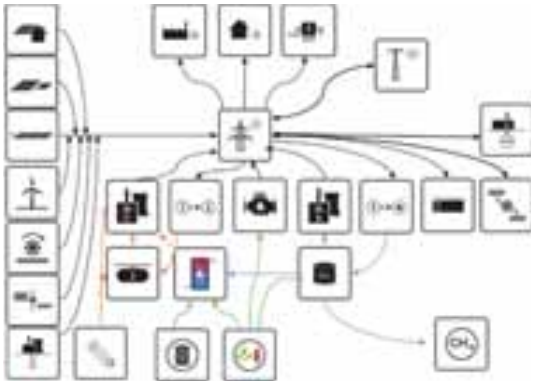

Fig. 1. Block diagram of the energy system model for Eurasia.

3. Scenario assumptions

3.1 Regions subdivision and grid structure

The Eurasian region is divided into 13 sub-regions. These are seven Federal Districts of Russia, Belarus, Kazakhstan, Uzbekistan, Turkmenistan, Caucasus regions including Armenia, Azerbaijan and Georgia, and Pamir including republics of Kirgizstan and Tajikistan. In this paper we discuss four scenarios of energy system development options:

- Region-wide energy systems, in which all the regions are independent (no HVDC grid interconnections) and the electricity demand has to be covered by the respective region's own generation;
- country-wide energy system, in which the regional energy systems are interconnected by HVDC grids within the borders of nations;
- area-wide energy system, in which the country-based energy systems are interconnected;
- integrated scenario: area-wide energy system with water desalination and industrial gas demand, in which the PtG technology is used not only as a storage option within the system, but also covering the industrial gas demand.

The Eurasian region's subdivision and grid configuration are presented in Figure 2. Structure of HVDC grid based on existing configuration of Integrated Power System (IPS) grid.

Fig.2. Eurasian sub-regions and HVDC transmission lines configuration.

3.2 Financial and technical assumptions

The model optimization is carried out on an assumed cost basis and technological status for the year 2030 and the overnight building approach. The investment cost (capex) and operation and maintenance (opex) numbers refer in general to a kW of electrical power, in case of water electrolysis to a kW of hydrogen thermal combustion energy, and for CO_2 scrubbing, methanation and gas storage to a kW of methane thermal combustion energy. Efficiencies of water electrolysis, CO_2 scrubbing and methanation refer to the higher heating value of hydrogen and methane, respectively. The financial assumptions for the energy system components including HVDC transmission lines for the 2030 reference year are provided in the Supplementary Material (Table I). The financial assumptions for storage systems refer to a kWh of electricity, and gas storage refers to a thermal kWh of methane at the lower heating value. Financial numbers for HVDC transmission lines and converter stations are given for the net transmission capacity (NTC). Assumptions are mainly taken from Pleßmann et al. (2014) but also other sources (Komoto et al., 2009; Hoffmann, 2014, Fraunhofer ISE, 2014; Urban et al., 2009; European Commission, 2014a). The technical assumptions concerning power to energy ratios for storage technologies, efficiency numbers for generation and storage technologies and power losses in HVDC power lines and converters are provided in the Supplementary Material (Tables II, III and IV, respectively). Electricity prices for residential, commercial and industrial consumers in Russia for the year 2030 are taken from Gerlach et al. (2014) and applied for all other regions. Prices are provided in the Supplementary Material (in Table V). Excess generation, which cannot be self-consumed by the prosumers, is assumed to be fed into the grid for a transfer price of 2 €cents/kWh. Prosumers cannot sell to the grid more power than their own annual consumption.

3.3 Feed-in for solar and wind energy

The feed-in profiles for solar CSP, optimally tilted, single-axis tracking PV and wind energy are calculated based on NASA data on direct and diffuse solar irradiation, wind speed, temperature and surface roughness for the year 2005 reprocessed by the German Aerospace Center. The assumed wind power plants consist of 3 MW wind turbines at 150 meters hub height. The dataset is used in a 0.45˚x0.45˚ spatial and hourly temporal resolution for the real weather conditions of the year 2005. Feed-in full load hours for sub-regions are computed on the basis of the 0.45˚x0.45˚ spatially resolved single sub-area data using a weighted average formula. The sub-regions' numbers are calculated using the rule: 0%-10% best sub-areas of a region are weighted by 0.3, 10%-20% best sub-areas of a region are weighted by 0.3, 20%-30% best sub-areas of a region are weighted by 0.2, 30%-40% best sub-areas of a region are weighted by 0.1 and 40%-50% best sub-areas of a region are weighted by 0.1. The computed average full load hours for CSP, optimally tilted, single-axis tracking PV systems and wind power plants are provided in the Supplementary Material (Table VI).

The aggregated profiles of solar PV generation (optimally tilted, single-axis tracking), CSP solar field and wind energy power generation, normalized to maximum capacity averaged for Eurasia, are presented in Figures 3.

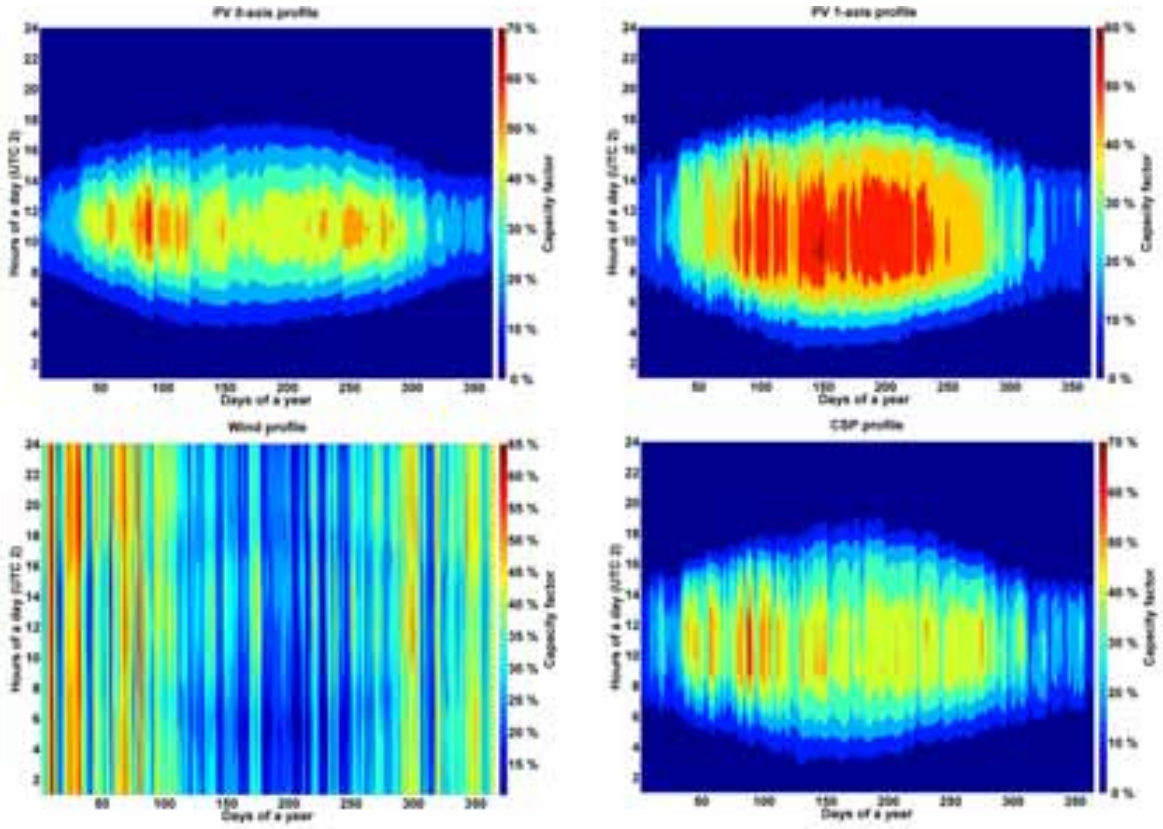

Fig.3. Aggregated feed-in profiles for optimally tilted PV (top left), single-axis tracking PV (top right), 3 MW 150 m hub height wind turbine (bottom left) and CSP solar field (bottom right).

3.3 Biomass and geothermal heat potentials

Biomass and waste resource potentials are mainly taken from DBFZ (2009). All bio-waste is divided in three components: solid waste, solid biomass and biogas sources. Solid waste is comprised of municipal and industrial used wood; solid biomass includes straw, wood and coconut residues; biogas sources are excrements, municipal bio-waste and bagasse. Costs for biomass are calculated using data from the International Energy Agency (IEA, 2012) and Intergovernmental panel on climate change (IPCC, 2011). For municipal solid waste a 50 €/ton gate fee is assumed for waste incineration. Calculated solid biomass, biogas, solid waste and geothermal heat potentials are provided in the Supplementary Material (Table VII). Prices for biomass fuels are provided in the Supplementary Material (Table VIII), and price differences between countries are explained

by various waste and residue component shares.

Regional geothermal heat potentials are calculated based on spatial data for available heat, temperature and geothermal plants for depths from 1 km to 10 km. For each 0.45˚x0.45˚ area and depth, geothermal LCOE is calculated and optimal well depth is determined. It is assumed that only 25% of available heat will be utilised as an upper resource limit. The total available heat for the region is calculated using the same weighed average formula as for solar and wind feed-in, except for the fact that areas with geothermal LCOE exceeding 100 €/MWh are excluded.

3.4 Upper and lower limitations on installed capacities

Lower and upper limits are applied to renewable energy sources (PV, wind onshore, and hydro power) and pumped hydro storage. For CSP, biomass, biogas, waste-to-energy power plants, gas turbines, battery and gas storage, and units of the power-to-gas process, the lower limit is set to zero. For lower limitations of PV systems, wind power plants, hydropower plants and PHS storage systems, data of existing installed capacities in Eurasian sub-regions have been taken mainly from the GlobalData (2015) database and the Platts (2012) database . Lower limits on already installed capacities in Eurasian sub-regions are provided in the Supplementary Material (Table IX).

Upper limits for CSP, PV systems (optimally tilted, single-axis tracking) and wind power plants are based on land use limitations and the density of capacity. The maximum area covered by solar systems is set to 6% of the total sub-regions' territories and for wind power plants to 4%, respectively. The capacity densities are 225 MW_{th}/km^2 for the CSP solar field, 75 MW/km^2 for PV systems (optimally tilted, single-axis tracking) and 8.4 MW/km^2 for wind onshore power plants. For hydro power plants and PHS storage, upper limits are set to 150% and 200% of already installed capacities by the end of 2013. All upper limits of installable capacities in Eurasian sub-regions are summarized in the Supplementary Material (Table X). For all other technologies, upper limits are not specified. However, for biomass residues, biogas and waste-to-energy plants it is assumed, due to energy efficiency reasons, that the available and specified amount of the fuel is used during the year.

3.5 Load

The demand profiles for sub-regions are computed as a fraction of the total country demand based on synthetic load data weighted by the sub-regions' populations. Figure 4 represents the area-aggregated demand of all sub-regions in Eurasia. Electricity demand increase by year 2030 is estimated using IEA data (IEA, 2014), numbers for Kazakhstan and Belarus are based on GlobalData assumptions (GlobalData, 2010; GlobalData, 2013).

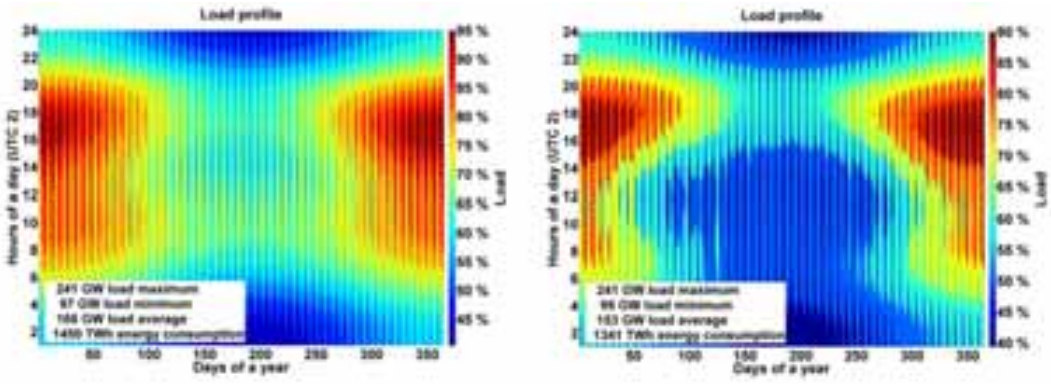

Fig. 4. Aggregated load curve (left) and system load curve with prosumers influence (right) for the year 2030.

Industrial gas demand values (gas demand excluding electricity generation and residential sectors) and desalinated water demand for Eurasia sub-regions are presented in the Supplementary Material (Table XI), gas demand values are based on the IEA data and the Federal State Statistics Service of Russia. Desalination demand numbers are based on water stress and water consumption projection.

4. Results

To analyze the cost structure of the different scenarios, a set of fundamental parameters are computed according to methodology described in Breyer et al. (2015).

4.1 Main findings on the optimized energy system structure and costs

For all scenarios optimized electrical energy system configurations are derived and characterized by optimized installed capacities of RE electricity generation, storage and transmission for every modelled technology, leading to respective hourly electricity generation, storage charging and discharging, electricity export, import and curtailment. The average financial results of the different scenarios for the total system (including PV self-consumption and the centralized system) are expressed as levelized cost of electricity (LCOE), levelized cost of electricity for primary generation (LCOE primary), levelized cost of curtailment (LCOC), levelized cost of storage (LCOS), levelized cost of transmission (LCOT), total annualized cost, total capital expenditures, total renewables capacity and total primary generation, as presented in Table I. Weighted average cost of capital (WACC) is set to 7% for all scenarios, but for residential PV self-consumption WACC is set to 4%.

From Table I it can be easily seen that the installation of HVDC transmission lines has a positive impact on the electricity cost and annual expenditures of the system; electricity cost of the entire system in the case of area-wide open trade power transmission decreases 6.0% and 14.6% compared to the country-wide and region-wide scenarios, respectively. Grid utilization decreases the primary energy conversion capacities and generation by 10.0% and 21.0% in terms of installed capacities and by 4.0% and 8.9% in terms of generated electricity in reference to country-wide and region-wide scenarios, respectively. Grid utilization leads to a significant decrease of storage utilization, whereas cost of transmission is relatively small in comparison to the decrease in primary generation and storage costs. Curtailment costs do not decrease as much as storage cost in the case of broader grid utilization; however, the impact of excess energy on total cost is rather low. The rather small difference between area-wide and country-wide scenarios can be explained by the dominant share of Russia in the total electricity demand.

The integration of water desalination and industrial gas synthesis sectors results in a further decrease in LCOE of 18.9% compared to the area-wide open trade scenario. This cost reduction is mainly explained by a reduction of storage cost by 82% due to additional flexibility provided by the gas synthesis and desalination sectors decreasing the need of storage utilization. Primary electricity generation cost decreased by 5.3%, mainly because of increased flexibility of the system. Flexible demand simplifies utilization of low-cost wind and solar electricity, and that leads to a decrease of flexible geothermal and biomass power plants capacities, as can be seen in Table II. For the case of biogas a substantial fraction is re-allocated from the electricity sector to the industrial gas demand for efficiency reasons. The share of hydro dam power plants does not change since flexibility provided by this source is still needed and the upper limit is reached for most of the regions, even interregional electricity trade decreases, which leads to a 40% fall in electricity transmission cost.

Whereas the total installed capacity of RE decreases with an increase of grid utilization, the installed capacity of wind turbines increases the more the energy system is interconnected and integrated. For Eurasia wind is the least cost RE source, thus wind energy imports displace a part of higher cost inland solar PV generation. Optimally tilted PV share is close to zero in almost all regions. However, for the region-wide and country-wide scenarios in the Caucasus region the installed capacity of optimally tilted PV exceeds single-axis tracking PV capacity and is 77.5% of total power system PV capacities in the region due to the less favorable solar irradiation conditions, which decrease the benefits of the single-axis tracking PV technology. Obviously, transmission lines decrease the need for energy storage options; installed capacities of batteries, PHS, A-CAES, heat storage, Power-to-Gas and gas turbines decrease with the grid expansion. PHS capacity stays the same for all scenarios and equal to lower limit of installation.

Table I: Financial results for the four scenarios applied in Eurasian regions.

	Total LCOE	LCOE primary	LCOC	LCOS	LCOT	Total ann. cost	Total CAPEX	RE capacities	Generated electricity
	[€/MWh]	[€/MWh]	[€/MWh]	[€/MWh]	[€/MWh]	[b€]	[b€]	[GW]	[TWh]
Region-wide	62.6	42.7	3.2	16.8	0.0	91	837	739	1771
Country-wide	56.9	41.8	2.2	10.5	2.4	82	758	648	1681
Area-wide	53.5	41.0	1.5	7.1	3.9	77	713	583	1613
Integration scenario	43.4	38.8	0.9	1.3	2.3	125	1166	981	2654

Table II: Overview on installed RE technologies and storage capacities for the four scenarios.

		Region-wide	Country-wide	Area-wide	Integration scenario
PV self-consumption	[GW]	91.5	91.5	91.5	91.5
PV optimally tilted	[GW]	6.0	6.0	6.5	0.2
PV single-axis tracking	[GW]	109.4	49.0	15.5	170.9
PV total	[GW]	206.9	146.5	113.4	262.6
CSP	[GW]	0	0	0	0
Wind energy	[GW]	327.2	317.9	300.0	559.8
Biogas power plants	[GW]	15.2	15.1	13.8	10.4
Biomass power plants	[GW]	17.3	16.7	16.4	14.5
MSW incinerator	[GW]	1.3	1.3	1.3	1.3
Geothermal energy	[GW]	2.7	2.7	2.7	2.4
Hydro Run-of-River	[GW]	0.2	0.2	0.1	6.4
Hydro dams	[GW]	88.4	87.8	90.9	91.2
Battery PV self-consumption	[GWh]	0	0	0	0
Battery total	[GWh]	15.2	15.2	8.7	0.5
PHS	[GWh]	9.0	9.0	9.0	9.0
A-CAES	[GWh]	1783.5	497.4	0.3	0.0
Heat storage	[GWh]	0	0	0	0
PtG electrolyzers	[GW_{el}]	32.5	21.7	15.8	105.2
CCGT	[GW]	48.4	33.5	27.2	0.6
OCGT	[GW]	40.3	37.1	28.6	33.3
Steam Turbine	[GW]	0.8	0.8	0	0

In the case of the region-wide open trade scenario, all sub-regions of Eurasia need to match their demand using only their own RE resources. In the case of the country-wide and area-wide open trade scenarios, a division of regions into net exporters and net importers can be observed. An annual import and export diagram for area-wide open trade is presented in Figure 5. Differences in generation and demand are mainly due to export and import, but in a minor quantity also due to storage losses, and for the area-wide integrated sector scenario (not shown in Fig. 5) due to energy consumption for SNG production. Figure 5 also gives a good overview on regions' RE resources; net exporters are sub-regions with the best renewable resources and net importers are sub-regions with moderate ones.

Fig. 5. Annual generation and demand diagrams for area-wide open trade scenario.

Figure 5 reveals the net exporter regions: North-West Russia and Pamir regions. Net importers are Central Russia and Belarus. Hourly resolved profiles for regional generation in Importer region (Central Russia), Balancing region (Kazakhstan) and Exporting region (North-West Russia) are presented in the Supplementary Material (Fig. 1, 2 and 3, respectively). For the integrated scenario a drastically increased electricity demand for the desalination and SNG producing sectors changes the picture dramatically; SNG producing regions tend to increase the intra-regional electricity generation to fulfill the increased demand.

PV self-consumption overview is given in the Supplementary Material (Table XII). Self-generation does not play a significant role due to low electricity price and covers only 37.3% of residential prosumers' demand, 30.7% and 31.8% of demand for commercial and industrial prosumers. An overview of installed capacities for the sub-regional energy system structures is presented for three different scenarios (region-wide, area-wide and integrated scenario) in Figure 6.

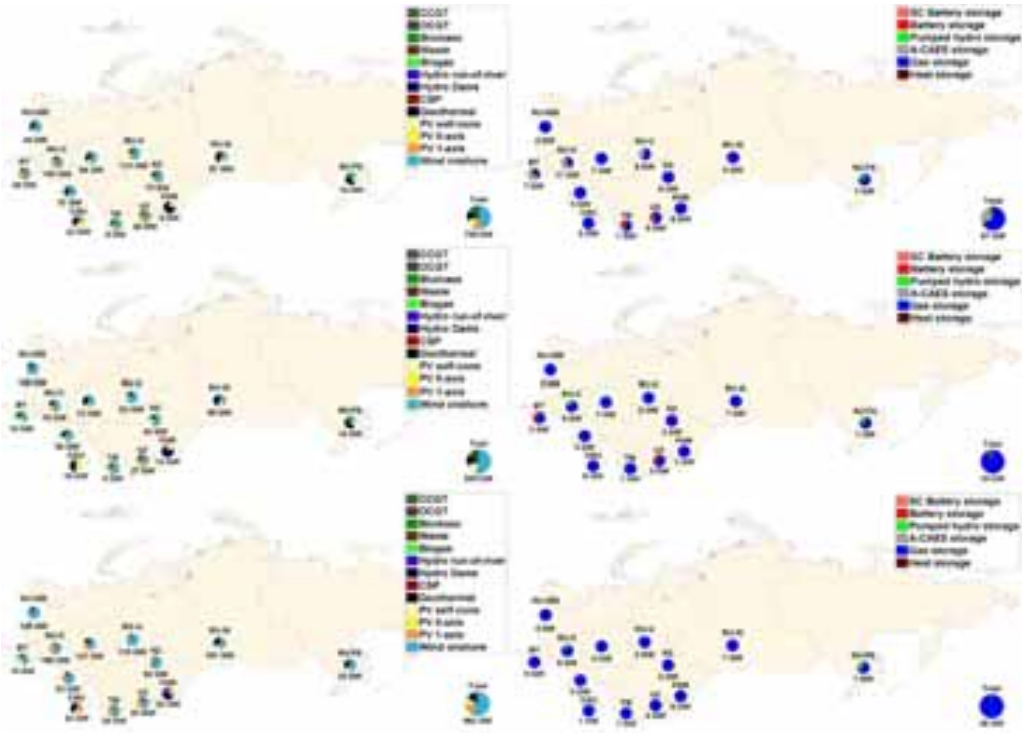

Fig. 6. Installed capacities of RE generation (left) and storages (right) for region-wide (top), area-wide (center) open trade and integrated (bottom) scenarios.

From Figure 6 we can see that in the case of region-wide open trade in the sub-regions of Belarus, Central

Russia and Caucasus, the solar PV capacities exceed 30% of all installed power capacities despite the fact that wind power FLH in these regions are better or comparable to PV FLH. Upper limit for wind is not reached as well, but optimal mix of capacities in these regions includes high share of PV. The interconnected HVDC transmission grid significantly decreases total installed capacities (Fig. 6 and Tab. II) and especially solar PV capacities, whereas installed capacities are increased in wind resource rich regions, such as North-West Russia.

For the integrated scenario the installed capacities of PV increase again because of a higher electricity demand and increased system flexibility. Additional demand in the case of a RE-based energy system can change the entire system structure because of shifting optimal cost structure parameters and areas being confronted with their upper resource limits.

The structure of HVDC power lines and utilized RE resources strongly influences the total storage capacity needed, but also interferes with the composition of different storage technologies for the energy system in the same area. Data of storage systems discharge capacities, annual energy throughput and full load cycles per year are summarized in the Supplementary Material (Table XIII). The generation capacities of storage technologies decrease with integrations of the HVDC grid. However, for the integrated scenario capacities of storage technologies increase in absolute numbers. State-of-charge profiles for the area-wide scenario for battery, PHS, A-CAES and Gas storages are provided in the Supplementary Material (Fig. 4)

The findings for the aggregated area integrated scenario can be summarized in an energy flow diagram comprised of the primary RE resource converters, the energy storage technologies and the HVDC transmission grid. The difference of primary power generation and final electricity demand is subdivided into potentially usable heat and ultimate system losses. Both are comprised of curtailed electricity, heat produced by biomass, biogas and waste-to-energy power plants, heat of transforming power-to-hydrogen in the electrolyzers, hydrogen-to-methane in methanation and methane-to-power in the gas turbines, and the efficiency loss in A-CAES, PHS, battery storage, as well as by the HVDC transmission grid. This energy flow for the integrated system is presented in Figure 7; diagrams for the region-wide and area-wide scenarios are presented in the Supplementary Material (Fig. 5).

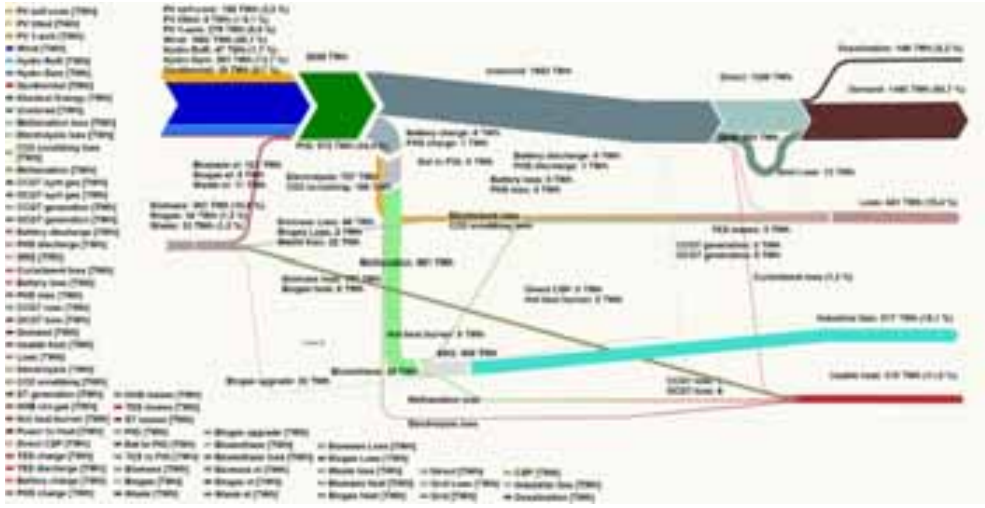

Fig. 7. Energy flow of the system for the integrated scenario.

The numeric values for LCOE components and the import/export share in all regions and scenarios are summarized in the Supplementary Material (Table XIV). The share of export is defined as the ratio of net exported electricity to the generated primary electricity of a sub-region and the share of import is defined as the ratio of imported electricity to the electricity demand. The area average is composed of sub-regions' values weighted by the electricity demand.

5. Discussion

The installation of a HVDC transmission grid enables a significant decrease in the cost of electricity in the RE-based system. The total levelized cost of electricity in the region decreased from 62.6 €/MWh for the region-wide open trade scenario to 56.8 €/MWh for the country-wide open trade scenario and 53.5 €/MWh for the area-wide open trade scenario. The total annualized cost of the system decreased from 91 b€ to 77 b€. In parallel the capex requirements are reduced from 837 b€ for the region-wide open trade to 758 b€ and 713 b€ for the country-wide and area-wide open trade scenarios, respectively. Additional costs of HVDC transmission lines (annual cost 5.6 b€, capex 61 b€ for area-wide scenario) are compensated by a substantial decrease in generation and storage capacities enabled by lower losses and costs of energy transmission compared to energy storage, and access to low cost electricity generation in other regions. In addition, the HVDC transmission grid enables additional benefits due to the large spatial east-west dimension of the Eurasian region.

PV self-consumption influences the power sector in an interesting way. The region-wide, country-wide and area-wide open trade scenarios are also calculated without PV self-consumption and the total demand is assumed to be covered by a more centralized system. The annualized costs for the more centralized 100% RE system is 1.7% lower for the region-wide scenario (89.5 b€ against 91 b€ base scenario), and 2.2% lower for the country-wide scenario, and 2.4% lower for the area-wide open trade scenario. PV self-consumption provokes additional costs because of a different target function of prosumers. Prosumers tend to reach their minimum annual cost of electricity consumption. The LCOE of PV self-consumption then must be lower than the grid electricity selling price, but can be higher than the total system LCOE. In addition to higher generation cost, prosumers' electricity generation provokes some positive and negative distortion in the system demand profile, i.e. the system reacts by installing more flexibility granting capacities, such as low cost RE or further storage capacities, which increases the system costs as well. The peak load in the system is not reduced due to the fact that peaks occurs in the winter time, when solar PV generation is negligible in the major parts of Eurasia, however the load gradients in the system are reduced from spring to autumn during daylight hours. For the region-wide scenario a comparable low cost increase due to the decentralized generation can be explained by the fact that additional disturbance cost in the system (provoked by prosumers) is compensated by access to low cost residential electricity (for residential consumers WACC is assumed to be 4%). Finally, PV self-consumption is in particular valuable in area constraint regions, since zero impact areas on rooftops can be utilized for local electricity generation, which in turn reduces the requirement of imports. This may be in some regions a policy option for reaching higher local value creation and less foreign policy risk, induced by higher electricity imports.

The fourth scenario, integration, represents the possibility to cover projected natural gas demand (except the gas demand for power generation and residential purposes), and clean water demand by SNG generation and SWRO desalination, respectively. In parallel with supplying demand, such an integration gives the system additional flexibility, especially for seasonal fluctuation compensation. The availability of RE in Eurasia is sufficient to cover additional electricity demand for producing 517 TWh_{th} (49 bcm) of SNG and 18.3 billion m^3 of clean water. Adding 1100 TWh_{el} for gas synthesis and SWRO desalination induces an additional installation of RE generation capacities of 150 GW of PV and about 260 GW of wind energy. As well, former long-term gas storage is partly substituted by short-term battery storage. Next, there is a significant increase in electrolyzer units of about 90 GW and substantially reduced gas turbines and biomass powered plants capacities.

The system generates excess heat as a byproduct of biogas and biomass CHP plants, waste-to-energy incinerators, gas turbines, electrolyzers and methanation units. In addition, there is excess electricity, which can be curtailed or converted to heat, stored in heat storage and used finally in the heat sector. The usable heat amount varies from 223 TWh_{th} per year for the area-wide scenario up to 301 TWh_{th} for the region-wide scenario. The waste heat from biomass and gas power plants is evenly distributed over the year. At the same time, excess electricity is generated mainly during the period from October to April, when heat is most valuable. Cooling demand is included in electricity demand numbers and therefore does not generate an additional demand. For the integrated scenario the amount of usable heat is even higher, at 315 TWh_{th}, due to higher curtailment, whereas the heat profile distribution is mainly the same. In total the integration benefit for the electricity, water and industrial gas sectors is estimated to be about 37.7 b€ of the annual system cost. There

are also decreases in the electricity demand by 355 TWh and the curtailed electricity by 46.6 TWh. These benefits account to 23%, 12% and 41%, respectively, compared to the non-integrated, separate systems. Further, the cost of clean water seems to be quite affordable at 1.49 €/m^3 and the cost of electricity decreases by 18.9% to 43 €/MWh for the integrated scenario compared to the area-wide open trade scenario without sector integration. However, the cost of synthetic gas, at 112.5 €/MWh, appears to be significantly higher than the current price.

The findings for the Eurasian 100% renewable resource-based energy system can be compared to recent insights in Europe about non-renewable options, such as nuclear energy, natural gas and coal carbon capture and storage (CCS) alternatives (Agora Energiewende, 2014). These alternatives could also lead to a low carbon energy system, which is of highest relevance for a climate change mitigation strategy. The LCOE of the alternatives are as follows (Agora Energiewende, 2014): 112 €/MWh for new nuclear (assumed for 2023 in the UK and Czech Republic), 112 €/MWh for gas CCS (assumed for 2019 in the UK) and 126 €/MWh for coal CCS (assumed for 2019 in the UK). However, a report published by the European Commission (European Commission, 2014b) concludes that CCS technology is not likely to be commercially available before the year 2030. The findings for Europe are assumed to be also valid for Eurasia in the mid-term. The 100% renewable resource-based energy system options for Eurasia presented in this work are considerably lower in cost (about 44 - 61%) than the higher risk options, which have still further disadvantages. These include nuclear melt-down risk, nuclear terrorism risk, unsolved nuclear waste disposal, remaining CO_2 emissions of power plants with CCS technology, a diminishing conventional energy resource base and high health cost due to heavy metal emissions of coal fired power plants. Dittmar (2012) also emphasizes the mentioned limitations on nuclear fission, but also points out that the financial and human research and development resources spent for nuclear fusion are no help either for the energy problems in the world and even worse these resources are not available for research of pathways towards a low cost energy future.

6. Conclusion

Existing RE technologies can generate enough energy to cover all electricity demand for the year 2030 on a significantly lower price level of 43 - 61 €/MWh_{el}, compared to non-renewable options, depending on geographical and sectoral integration. It is also possible to cover the gas demand of the industrial and transportation sectors with PtG technology, however for a gas price which is substantially higher than today. Heat generated as a byproduct of electricity, synthetic natural gas generation and curtailed electricity conversion can cover up to 300 TWh_{th} of heat demand. For the region-wide scenario PV plays the role of the main energy supply in some regions, however, with integration of the HVDC grid, the role of PV decreases in a first step, but it is increased again for a broader sectoral integration in a second step. The HVDC transmission grid plays a key role since the established Super Grid enables a significant cost decrease within the renewable resource-based energy system. The utilization of a HVDC transmission grid leads to a cut-off of storage utilization and significantly reduces primary generation capacities. At the same time, PV self-consumption induces a moderate increase of total electricity costs of 1.5 - 2.5%. This is due to the fact that consumers tend to utilize solar energy at a higher cost level and the excess electricity from prosumer generation provokes additional disturbances in the system. In turn, this increases the system need for flexibility.

For the integrated scenario it was found that industrial SNG generation displaces SNG storage as seasonal storage for the electricity sector. Instead of gas turbine utilization in case of an energy deficit, the system curtails the SNG generation in that system set-up as a major source of flexibility to the system.

More research is needed for a better understanding of a fully integrated renewable energy system in Eurasia. However, this research work clearly indicates that a 100% renewable resources-based energy system is a real low cost and low risk policy option.

Acknowledgements

The authors gratefully acknowledge the public financing of Tekes, the Finnish Funding Agency for Innovation,

for the 'Neo-Carbon Energy' project under the number 40101/14. The authors would like to thank Svetlana Afanasyeva, Arman Aghahosseini, Javier Farfan and Michael Child for helpful support.

Supplementary Material

Supplementary data associated with this article can be found, in the online version, at www.researchgate.net on the profiles of the authors.

7. References

AAPG, 2015. Global Heat Flow Database. American Association of Petroleum Geologists, Tulsa, USA, Available at: [http://www.datapages.com/gis-map-publishing-program/gis-open-files/global-framework/global-heat-flow-database].

Agora Energiewende, 2014a. Stromspeicher in der Energiewende, Berlin. Available at: www.agora-energiewende.de/themen/optimierung/detailansicht/article/studie-die-energiewende-muss-nicht-auf-stromspeicher-warten/ [accessed: 30.01.2015] [in German]

Agora Energiewende, 2014b. Comparing the cost of low-carbon technologies: what is the cheapest option? report by Prognos AG on behalf of Agora Energiewende, p. 10-13.

Böttger D., Götz M., Lehr N., Kondziella H., Bruckner T., 2014. Potential of the power-to-heat technology in district heating grids in Germany. Energy Procedia 46, 246-253.

BP, 2014. BP statistical review of world energy 2014. BP, London.

Breyer Ch., Gerlach A., 2013. Global Overview on Grid-Parity, Prog. Photovoltaics Res. Appl. 21, 121-136.

Breyer Ch., Bogdanov D., Komoto K., Ehara T., Song J., Enebish N., 2015. North-East Asian Super Grid: Renewable energy mix and economics, Jap. J. of Appl. Phys. 54, 8S1.

Caldera U., Bogdanov D., Breyer Ch., 2015. Local cost of seawater RO desalination based on solar PV and wind energy: Economics, global demand and the impact of full load hours. 31th EU PVSEC, Hamburg, September 14-18, DOI: 10.4229/31stEUPVSEC2015-6AV.4.31, [available online at: www.researchgate.net/publication/281745784_Local_cost_of_seawater_RO_desalination_based_on_solar_PV_and_wind_energy_Economics_global_demand_and_the_impact_of_full_load_hours]

Chamorro C.R., García-Cuesta J.L., Mondéjar M.E., Pérez-Madrazo A., 2014a. An estimation of the enhanced geothermal systems potential for the Iberian Peninsula. Renewable Energy 66, 1-14

Chamorro C.R., García-Cuesta J.L., Mondéjar M.E., Pérez-Madrazo A., 2014b. Enhanced geothermal systems in Europe: An estimation and comparison of the technical and sustainable potentials. Energy 65, 250-263

DBFZ, 2009. Regionale und globale räumliche Verteilung von Biomassepotenzialen. German Biomass Research Centre. [in German]

Dii, 2012. 2050 Desert power – perspectives on a sustainable power system for EUMENA. Dii, Munich.

Dittmar M., 2012. Nuclear energy: Status and future limitations, Energy, 37, 35-40

Duffie J.A., Beckmann W.A., 2013. Solar engineering of thermal processes. John Wiley & Sons, Hoboken.

Enercon, 2014. Enercon product overview, Enercon GmbH, Aurich.

European Commission, 2014a. ETRI 2014 - Energy technology reference indicator projections for 2010-2050. EC Joint Research Centre Institute for Energy and Transport, Petten, Netherlands

European Commission, 2014b. Integration of renewable energy in Europe. study prepared by KEMA Consulting, DNV GL – Energy, Imperial College and NERA Economic Consulting on behalf of DG

Energy, Brussels, p. 7-8 and 54.

Fraunhofer ISE, 2014. PV cost vision 2050 – scenarios on the future cost development of photovoltaics. Fraunhofer Institute for Solar Energy Systems.

Gerlach A.-K., Stetter D., Schmid J., Breyer Ch., 2011. PV and Wind Power – complementary technologies. 26th EU PVSEC, Hamburg, September 5-9. DOI: 10.4229/26thEUPVSEC2011-6CV.1.32, [available online at: www.researchgate.net/publication/261172609_PV_and_Wind_Power__Complementary_Technologies]

Gerlach A., Werner Ch., Breyer Ch., 2014. Impact of Financing Cost on Global Grid-Parity Dynamics till 2030, 29th EU PVSEC, Amsterdam, September 22-26, DOI: 10.4229/29thEUPVSEC2014-7DO.15.4, [available online at: www.researchgate.net/publication/266558306_Impact_of_Financing_Cost_on_Global_Grid-Parity_Dynamics_till_2030]

GlobalData, 2010.Belarus Power Market Outlook to 2030. GlobalData, London.

GlobalData, 2013. Kazakhstan Power Market Outlook to 2030: Market Trends, Regulation and Competitive Landscape. GlobalData, London.

GlobalData, 2015. Power database, GlobalData, London, [online] http://power.globaldata.com/default.aspx

Hoffmann W., 2014. Importance and evidence for cost effective electricity storage. 29th EU PVSEC, Amsterdam, September 22-26.

Huenges E., 2012. Geothermal Energy Systems, Exploration, Development and Utilization, 2nd edition, Weinheim, Germany.

Huld T., Šúri M., Dunlop E. D., 2008. Geographical variation of the conversion efficiency of crystalline silicon photovoltaic modules in Europe. Prog. Photovoltaics Res. Appl. 16, 595–607.

IASPEI, 2015. International Association of Seismology and Physics of the Earth's Interior, The International Heat Flow Commission, Colorado, USA. IHFC database Available at: [http://www.heatflow.und.edu/index2.html].

IEA, 2012. Technology roadmap – bioenergy for heat and power. IEA Publishing, Paris.

IEA, 2013. Medium-term gas market report 2013. IEA Publishing, Paris.

IEA, 2014. World Energy Outlook 2014. IEA Publishing, Paris.

IPCC, 2011. Special report on Renewable Energy sources and Climate Change mitigation. Intergovernmental panel on climate change, Geneva.

Knies G. (ed.), 2009. Clean power from deserts – the Desertec concept for energy, water and climate security. Whitebook 4th Ed. DESERTEC Foundation, Hamburg.

Komoto K., Ito M., Van der Vleuten P., Faiman D., Kurokawa K. (eds.), 2009. Energy from the desert – very large scale photovoltaic systems: socio-economic, financial, technical and environmental aspects. Earthscan, London.

Komoto K., Enebish N., Song J., 2013. Very large scale PV systems for North-East Asia: preliminary project proposals for VLS-PV in the Mongolian Gobi desert. 39th PVSC, Tampa, June 16-21.

Luck M., Landis M., Gassert F., 2015. Aqueduct Water Stress Projections: Decadal projections of water supply and demand using CMIP5 GCMs, Washington DC, World Resources Institute

Mano S., Ovgor B., Samadov Z., Pudlik M., Jülich V., Sokolov D., Yoon J.Y., 2014. Gobitec and Asian Super Grid for Renewable Energies in Northeast Asia report prepared by Energy Charter Secretariat, Energy Economics Institute of the Republic of Korea, Energy Systems Institute of the Russian Federation, Ministry of Energy of Mongolia, Japan Renewable Energy Foundation.

Platts, 2012. UDI world electric power plants data base (WEPP). Platts – a division of The McGraw-Hill, Washington.

Pleßmann G., Erdmann M., Hlusiak M., Breyer Ch., 2014. Global energy storage demand for a 100% renewable electricity supply. Energy Procedia 46, 22-31.

Song J., 2012. Cooperation with neighboring countries for super-grid in Gobi desert (SG-Gobi Project). International conference on Renewable Energy Cooperation and Grid Integration in North-East Asia, Ulaanbaatar, Mongolia, November 11-12.

Song J., 2014. Super grid in North-East Asia through renewable energy. Asia-Pacific Tech Monit. 31, 24-27.

Stackhouse P.W., Whitlock C.H., (eds.), 2008. Surface meteorology and solar energy (SSE) release 6.0, NASA SSE 6.0, Earth Science Enterprise Program. National Aeronautic and Space Administration (NASA), Langley. Available at: http://eosweb.larc.nasa.gov/sse/ [accessed: 28.05.2015]

Stackhouse P.W., Whitlock C.H., (eds.), 2009. Surface meteorology and solar energy (SSE) release 6.0 Methodology, NASA SSE 6.0. Earth Science Enterprise Program, National Aeronautic and Space Administration (NASA), Langley. Available at: http://eosweb.larc.nasa.gov/sse/documents/SSE6Methodology.pdf [accessed: 28.05.2015]

State Grid Corporation of China, 2015. Global Energy Internet, China Electric Power Press

Sterner M., 2009. Bioenergy and renewable power methane in integrated 100% renewable energy systems. Dissertation, University of Kassel.

Stetter D., 2012. Enhancement of the REMix energy system model: global renewable energy potentials optimized power plant siting and scenario validation. Dissertation, Faculty of Energy-, Process and Bio-Engineering, University of Stuttgart.

Taggart S., James G., Dong Z.Y., Russell C., 2012. The future of renewable linked by a transnational asian grid. Proc. of the IEEE 2012 100, 348-359.

Urban W., Lohmann H., Girod K., 2009. Abschlussbericht für das BMBF-Verbundprojekt Biogaseinspeisung. Fraunhofer UMSICHT. [in German].

Vartiainen E., Masson G., Breyer Ch., 2015. PV LCOE in Europe 2015-2050, 31th EU PVSEC, Hamburg, September 14-18; 10.4229/31stEUPVSEC2015-7DO.15.1, [available online at: www.researchgate.net/publication/281939918_PV_LCOE_in_Europe_2015-2050]

Conference Proceedings

Solar World Congress 2015
Daegu, Korea, 08 – 12 November 2015

Real-time Simulations of 15,000+ Distributed PV Arrays at Sub-Grid Level using the Regional PV Simulation System (RPSS)

Nicholas A. Engerer[1], James Hansard[2]

[1] The Fenner School of Environment and Society, The Australian National University (Australia)

[2] College of Engineering and Computer Science, The Australian National University

Abstract

The Regional PV Simulation System (RPSS), recently jointly developed by The Australian National University and National ICT Australia (NICTA), has been created to assist in the integration of high penetrations of small-scale, distributed solar PV energy systems. This system is capable of simulating many thousands of small-scale PV systems with input from only a small number (~1%) of the total installed fleet. This distributed solar PV simulation system is the first step towards delivering forecasts of their collective power output, and will serve as a very useful tool to electrical utilities and energy markets. Through cooperation with the local distribution network service provider, ActewAGL, the RPSS has been deployed in the Canberra, Australia region delivering real-time simulations of distributed PV power output as grouped by transformer. Canberra, the capital city of Australia, and has some of the highest penetrations of solar PV in the country, and has set a renewable energy target of 90% by 2020, making it a prime candidate for the application of these real-time simulations. Herein, the methodology used in this real-time version of the RPSS are presented, as well as a case study which highlights its usefulness under strong variability in distributed PV system power output.

Keywords: *Solar Energy, Distribution, Grid Integration, Simulation, Solar PV*

1. Introduction

As the number of distributed photovoltaic arrays installed worldwide continues to grow, so does the need for real-time simulations systems that are capable of assessing their impact on the electrical grids to which they connect. In the case of micro-generators, which are defined here as small-scale PV systems with rated capacities less than 100 kW, this is often extraordinarily challenging, due to the lack of information available about their instantaneous power output. In Australia, over 1.4 million individual systems have been installed, the vast majority of which are unmonitored, and therefore their interval-level contributions to the electrical grid are unknown. Their total installed PV capacity now exceeds 4.5 GW as of June 2015, with an average system size of 4.5 kW (APVI 2015). This represents substantial growth from only 41 kW of capacity at the start of 2009. As a result of this impressive uptake, 20% of Australian households now have a solar PV system installed at their residence (ABS 2014). Looking forward, the installed cost of PV is approximately $1.75/W for systems >10 kW, and thus continued strong uptake is anticipated, particularly in commercial site applications (APVI 2015). Moderate uptake scenarios from Australian solar analytics company SunWiz project installed distributed PV capacity to exceed 7 GW by 2020 (SunWiz 2015). For perspective, Australia's largest electricity market, the National Electricity Market (NEM), has a total large-scale generation capacity of approximately 50 GW.

What these statistics represent is that distributed small-scale solar installations represent a fast growing and increasingly robust energy generation source in Australia. Its penetrations of PV are among the highest in the world, with cost parity being reached throughout the continent (Chen and Franklin 2011). However,

Selection and/or peer review under responsibility of Scientific Committee
doi:10.18086/swc.2015.06.02 Available at http://proceedings.ises.org

these developments place Australia on the forefront of the challenges associated with high-penetration distributed PV integration into the electricity grid. At the time of writing, Australian utilities had already begun to ban grid export or limit the total installed capacity permitted per individual system (Ergon Energy 2015, Horizon Power 2012). This represents a reactive, rather than proactive response to the intermittency challenges faced by distributed solar resources, which have been documented to induce intolerable voltage fluctuations within Australian distribution networks (Noone 2013).

One of the key barriers to increasing the penetrations of distributed PV in these areas is lack of information regarding the real-time power output of these distributed PV generators. Without this information, utilities will remain unable to impose mitigative solutions via emerging technologies such as distributed energy storage systems, because they will remain naïve on where and when large changes in solar power output will occur. This has necessitated the creation of a simulation system that is able to produce real-time estimates of the contributions of distributed PV systems to the electrical grid, entitled the Regional PV Simulation System (RPSS), whose initial version was developed in the doctoral thesis of the first author (Engerer 2015a).

The RPSS is a real-time capable, scalable, robust computational system that is capable of producing power output estimates from many thousands of distributed small-scale PV systems. This is accomplished through use of monitored PV system power output as the sole operational input, using the K_{PV} methodology of Engerer and Mills (2014). This methodology has been demonstrated to produce excellent results (Tan et. a. 2014; Engerer and Mills 2014; Engerer 2015b). The initial version of the RPSS was shown to produce accurate city-scale simulations across the Canberra region with active reporting from less than 1% of the total PV generators (Engerer 2015a). These simulations were generated for 12,000+ PV systems using suburb-level PV data provided by local distributor ActewAGL, and presented under several different strong collective ramp events.

A further iteration of the RPSS is the subject of this manuscript. Whereas, the previous system computed only aggregate estimates using suburb-level data, version 2 applies these same methods to simulation of 15,000+ micro-generators installed in Canberra, Australia, as organized by transformer (referred to interchangeably herein as a "node"). A beta version of this product will run in real-time from November 2015, with its official launch coinciding with the delivery of this manuscript. The remainder of this paper will detail its data sources and methodology, as well as explore a case study highlighting its usefulness.

2. Data

There are two primary sources of data used within this simulation system. Firstly, the local distribution network service provider, ActewAGL, has provided system information for 15,638 installed micro-generators. This includes the locations of each PV system, the nominal rated capacity and the node on which these systems are installed within ActewAGL's network. Together, these 15,000+ systems comprise 45 MW of distributed generation capacity. Secondly, five-minute interval PV system power output is now available from over 200 sites across Canberra, which are actively reporting on the webpage PVOutput.org in near real-time. These data are actively collected every five minutes by this simulation system through the PVOutput.org Application Programming Interface (API), before being quality controlled and ingested into the simulation system. PVOutput.org users also provide system meta-characteristics, including the module and inverter types, array system layout (e.g. numbers of modules, parallel strings) and the system tilt and azimuth. The collected data are processed through a quality control algorithm, which extracts the exact orientation of each array and removes any erroneous data (Engerer 2015b).

Fig. 1: PV systems in Canberra which are actively reporting their power output every five minutes to PVOutput.org, before being ingested into the Regional PV Simulation System. The black lines are the boundaries of Canberra suburbs

3. Methods

3.1. Modelling PV system characteristics

Given that only the rated capacity, suburb level location and node of each unmonitored PV system is provided, there is a built-in uncertainty in the simulation data. PV systems can have a wide-variety of azimuths and orientations, module and inverter types and system layouts. They are also subject to many different soiling and shading conditions. The lack of availability of the meta-characteristics data (or, rather, its lack of provision) necessitates that the azimuth, tilt and array layouts be selected statistically, requires that the system layouts be assigned randomly and means the de-ratings are simulated.

Before delving into the uncertainty issues at hand, it is worth noting that these issues will not necessarily be present in future modelling studies. Plans for these limitations to be removed in future versions of the RPSS are in place through continued cooperation from ActewAGL, and therefore it is completely possible to know these characteristics with certainty and remove these constraints on the modelling process.

3.1.1 PV system orientations

For the systems' orientation in space, the uncertainty was reduced significantly by sampling the PV systems installed throughout the Canberra region. This was accomplished through a partnership with SolarHub, a local solar installer, who provided extensive detail about 535 PV arrays that they installed in Canberra. Through this information, and that from an additional 74 unique locations gathered from PVOutput.org, it is possible to extract a distribution of tilts and azimuths that are common for Canberra rooftops, and use these as the basis for making assumptions about the remaining 15,000+ sites.

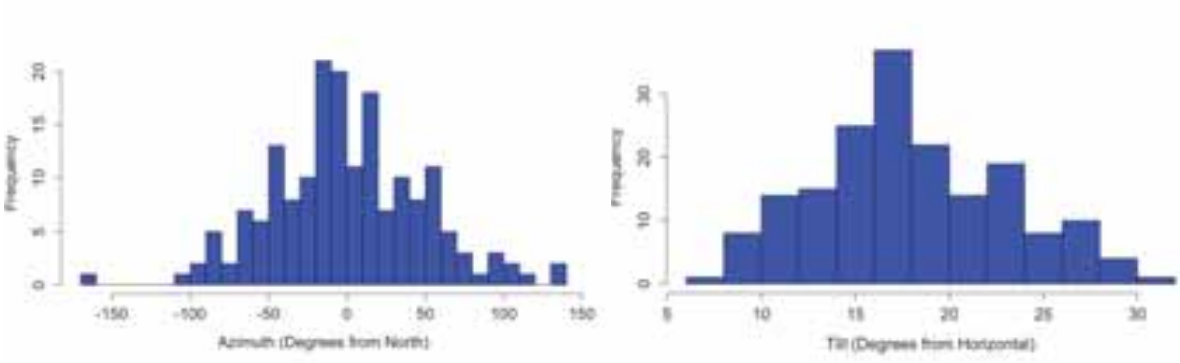

Fig. 2: Histogram of observed azimuths (left) and tilts (right) from over 600 Canberra homes

Figure 2 demonstrates a decidedly Gaussian distribution in the observed tilts and azimuths. This provides a solid statistical basis from which to model the azimuth and tilts of the remaining unmonitored PV systems. These data demonstrate a mean of 0.85° with a standard deviation of 48.5° for the azimuth and a mean of 18.3° and standard deviation of 4.9° for the tilts. From this, a Gaussian distribution of azimuths and tilts is modelled, from which the uncertain PV systems can be assigned an estimated pair of values through a probability weighted, random selection. This process allows for significant removal of uncertainty in system orientation from the modelling process.

3.1.2 PV system layouts

System layouts are more complicated, but are ameliorated indirectly through the limitations of the PV and inverter modelling software, and, again, through statistical sampling. The Sandia Performance and Inverter models are limited to databases of approximately 520 different PV modules and 460 inverter types, which cover a wide array of rated capacities. It is therefore possible, at this time, to simulate only modules that are present in these databases. The modules and inverters chosen from these databases in representation of each system were selected randomly with several constraints. First, only module combinations that were able to satisfy the reported rated capacity were permitted. This means, for example, a 1.4 kW array could not be simulated using 250 W modules, as no combination of 250W modules can create an array of 1.4 kW capacity. Second, from the possible combinations, a random solution was selected from a modelled Gaussian distribution based on the observed installed modules. This is to ensure that it is more likely to select 7 x 200 W modules to build the 1.4 kW array rather than to use 20 x 70 W modules, as the observed dataset has a mean module rating of 245 W and a standard deviation of 27 W. Inverters were chosen randomly from those whose ratings equalled or exceeded the installed capacity, but were limited to a doubling of the installed capacity.

3.1.3 PV system locations

Lastly, the locations of the PV systems were assigned randomly about each transformer node and constrained to lie within the reported suburb. Suburbs in Canberra have an average area of approximately 3 km^2, but can reach as large as 11 km^2 or as small as 0.4 km^2 in some cases. The suburbs of Canberra are outlined by the polygons in Figure 1 above. There will some sensitivity to this random assignment of site locations, particularly within the timing of ramp events, however, these issues have not been quantified, based on the rationale that this limitation will be removed once the exact locations of the installed systems are known as will be the case in future collaborative data provided by ActewAGL.

3.2. Application of the K_{PV} Methodology

The primary input data to the simulation system is the recorded power output from the sub-set of monitored PV systems within the modeled network. The power output from the monitored sub-set of PV systems can be used to simulate the performance of all the nearby PV systems on the modeled network via the clear-sky index for photovoltaics, K_{PV} (Engerer and Mills 2014):

$$K_{PV} = \frac{PV_{meas}}{PV_{clr}} \qquad \text{(eq. 1)}$$

where PV_{meas} is the reported power output and PV_{clr} is the simulated clear sky power output.

If two sites are close enough to one another (nearby), the KPV values between sites can be assumed to be equivalent. This means that the estimation of a nearby PV system's performance can be computed via:

$$PV_{est_2} = \frac{PV_{meas_1}}{PV_{clr_1}} \bullet PV_{clr_2} \quad \text{(eq. 2)}$$

where site 1 is the monitored site and site 2 is the nearby un-monitored site.

In order to apply this method at scale, each simulated system requires the computation of its clear-sky performance. These can be populated using the system level information provided by ActewAGL, following the clear sky simulation procedure outlined in Engerer and Mills (2014).

In order to estimate the power output of each simulated site, a K_{PV} value must be assigned based on the performance of nearby monitored systems. Rather than simply use a single nearby site, an average of the nearby K_{PV} values is used, computed using η closest sites.

$$PV_{est_2} = \frac{1}{\eta}\sum_{i=1}^{\eta} K_{PV_i} \bullet PV_{clr_2} \quad \text{(eq. 3)}$$

Where η is chosen on-the-fly, in a manner that maximizes the simulation accuracy. This is determined by using the sub-set of monitored sites to estimate one another at each time step, to determine which number of neighboring sites (η) minimizes the RMSE error.

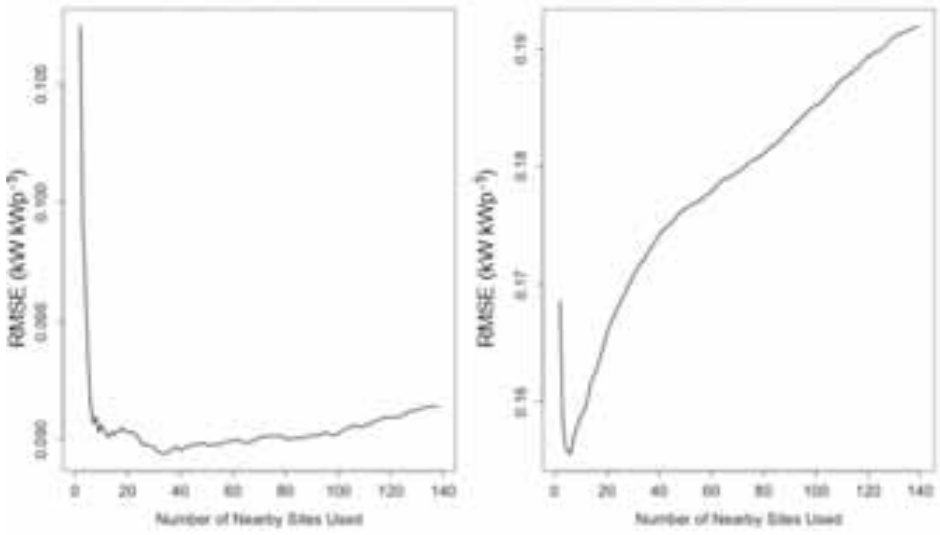

Fig. 3: RMSE values plotted against the number of neighbouring sites used in the K_{PV} based estimate. At left, an example from a clear sky day, at right, that from a partly cloudy day.

3.2.1 Simulated De-rating

An important step in the simulation process is the inclusion of de-rating from soiling, shading and other inefficiencies. These values are very difficult to quantify for non-monitored PV systems. Herein, the simulated behavior of the unmonitored sites will be based on the observed de-ratings of the monitored sites. This is based on the K_{PV90} calculation (Engerer 2015b), which is the running 90th percentile of K_{PV} from the past 30 days. Each unmonitored site is randomly assigned a K_{PV90} profile from one of the monitored sites for a given day. This allows for de-rating to be partially accounted for. At the time of writing, there is not any available research on this topic in the literature, and thus how to simulate PV system de-rating at this scale is not presently well understood. Future research work extending from this manuscript will explore this topic through a sensitivity analysis, simulating many thousands of possible shading scenarios to better quantify these uncertainties

4. Result: Real-time Operations

Through combination of the above data sources and methodologies, city-wide simulations of distributed PV power output across Canberra can now be created in real-time. The result is a live, operational version of the RPSS, which is now hosted and displayed in real-time at http://rpss.info. This online system produces city-wide simulations of PV system power output, mapped to ActewAGL's distribution network by transformer. This result, made possible by an up-scaling of the K_{PV} methodology, represents a significant, unique and promising tool for scientific, engineering and operational purposes. For the first time, it is now possible to quantify the power production of unmonitored distributed PV assets in near real-time, as grouped by distribution asset. The usefulness of this tool can be demonstrated through the following case study, from a particularly high variability day from 5 March 2014.

3.1 Operational Example: 5 March 2014

The meteorological conditions of 5 March 2014 were dominated by passing convective cloud embedded in westerly wind flow, which consequently produced large solar variability throughout the daylight period. The day began with partly cloudy conditions that persisted through 10:00 AEDT. At this time, there was a brief, but significant clearing of cloud cover, with a corresponding 12 MW increase in collective power output over only 10 minutes. From 10:20 AEDT, a very rapid drop in collective power output is observed as a uniform, opaque cloud deck moved in from the southwest, resulting in a 16 MW fall in collective power output over the 60 minute period to 11:20 AEDT. During the period between 10:05 AEDT and 11:00 AEDT, the apparent leading edge of the cloud shadow can be observed within the simulation (Figure 4).

Here, three nodes with particularly high penetrations (>40%) have been selected and highlighted, in order to demonstrate the temporal separation in ramp events across the geographic region (Figures 4 and 5). Node 2498 experiences the negative ramp event first, followed by node 2440, which is part-way through the negative ramp event, as can be seen in the right hand image of Figure 4. Node 2078, however, still experiences relatively clear conditions at this time, and has not yet ramped down its power output. This separation in the timing of these negative ramp events can be observed more clearly in Figure 5, which displays a 20 minute difference between the negative ramp at node 2498 and 2078. Given the separation distance of 20 km this implies a cloud speed of approximately 16.5 m s^{-1} (60 km $h^{-1)}$. Additionally, a strong positive ramp follows at approximately 12:05 AEDT through 1:15 AEDT. Again, a sequential pattern is observed, with node 2498 reaching a peak first, followed by node 2440 and then 2078.

This transformer level breakdown is also useful for comparing the ramp rates experienced by these individual nodes to that experienced collectively across the network. Using the most extreme 10 minute negative ramp events for the 10:00 - 11:00 time period, the collective ramp rate across all sites was 0.03 kW kWp^{-1} min^{-1}, while the three nodes experienced ramp rates of 0.04 kW kWp^{-1} min^{-1}, 0.072 kW kWp^{-1} min^{-1} and 0.057 kW kWp^{-1} min^{-1}. So, perhaps unsurprisingly, the ramps experienced by individual nodes can be shown to be more extreme than that experience by the collective system. We expect that by tracking these types of events over time, the most extreme events can be characterised, and the distribution systems engineered to withstand them. Plausibly, this simulation system could also be used to test the theoretical limits of distribution networks, by adding additional simulated PV systems to transformer nodes under strong ramp events like this one until the variability exceeds the capability of the given transformer to respond.

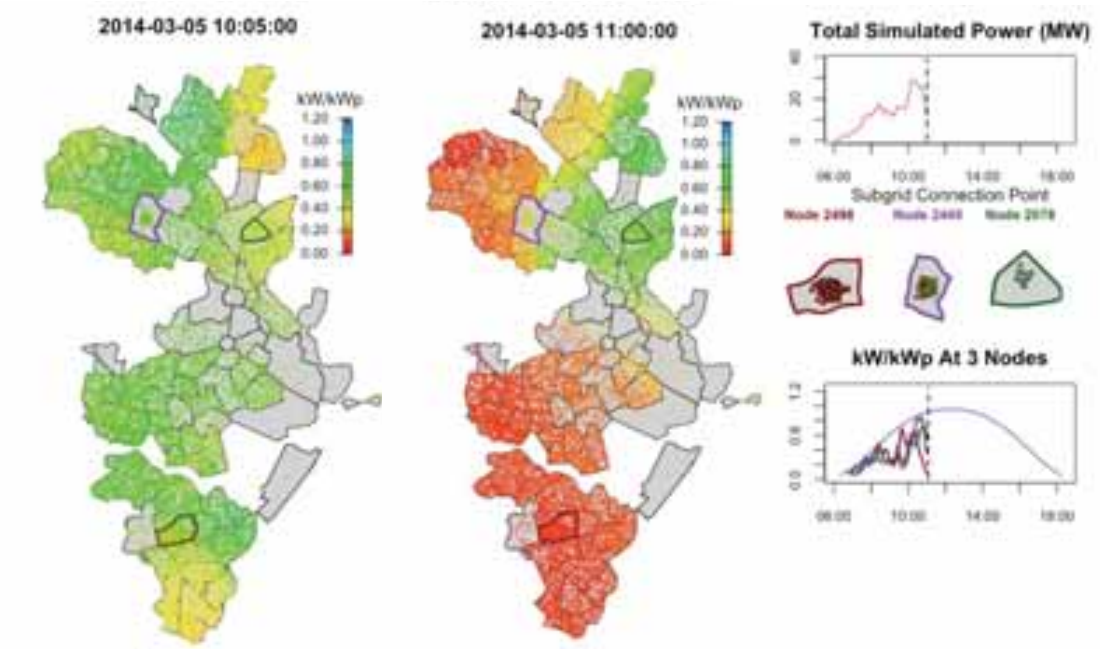

Fig. 4: These two images display the simulated power output from 15,000+ PV systems at two different times (10:05 and 11:00 AEDT) during a high variability day on 5 March 2014. Each point on the map represents a simulated PV system, with colour varying from red through to blue as power output (kW kW_p^{-1}) increases. Grey polygons display the boundaries of the major Canberra suburbs. At right, the power output is displayed as a time series, in both total power (MW) output and by three selected transformers (kW kW_p^{-1}). In the top time series plot, the blue line depicts the clear-sky curve for the collective output from all simulated PV systems. This simulation can be viewed online at bit.ly/ARENA_DNSPs.

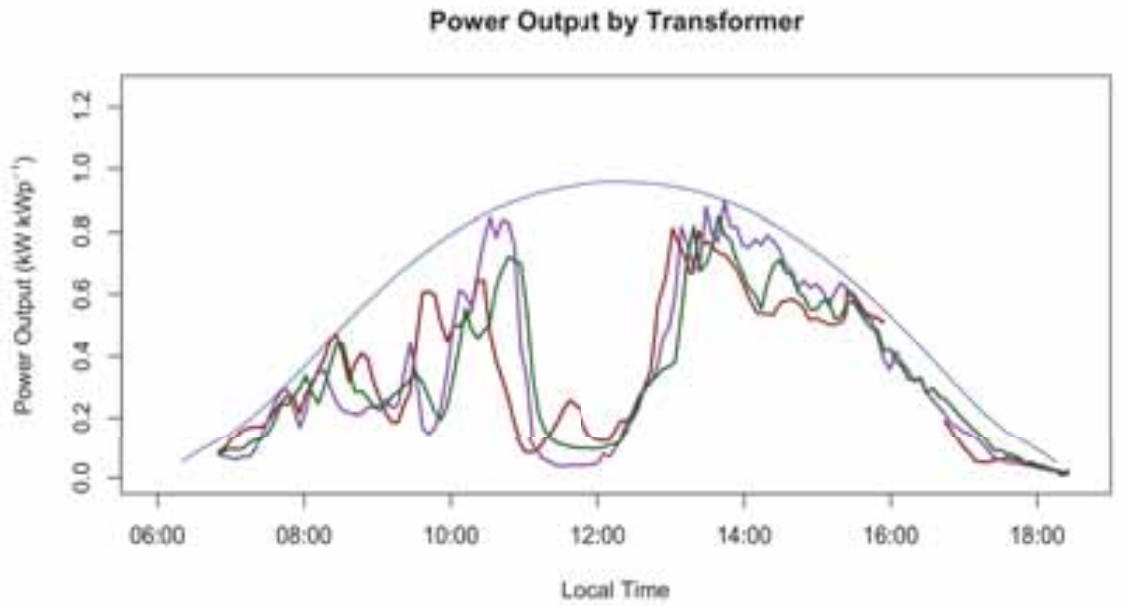

Fig. 5: The simulated power output (kW kW_p^{-1}) is presented for each of the three selected transformers (red 2498, purple 2440 and green 2078) during the high variability day of 5 March 2014.

5. Future Work

With the presented version of the RPSS in place, future efforts will work to increase the amount of monitored PV data ingested into the system, blend this surface data with satellite inputs and incorporate short-term forecasting methods to bring the system to true real-time status. Efforts are currently underway, which will double the current monitoring network, through deployment of tens of data-logging devices through funding from the Australian Renewable Energy Agency (ARENA), as well as to include data from inverter companies SMA and Fronius. Through these cooperative efforts, we expect to increase the total number of monitored sites in Canberra to 500-700 over the next two years. This will allow for more extensive validation of the present modeling methods.

Additionally, Australia has recently begun to receive 1 km^2 satellite data every 10 minutes from the new Himawari 8 satellite, which is a substantial improvement over the 4 km^2 hourly data from its predecessor. This will create the opportunity to develop model blending techniques which will be used to combine the K_{PV} and satellite derived irradiances, as well as cross-validate these two methods. Recent advances in solar PV analytics technology have even shown that PV systems can be used to extract the diffuse and beam components of radiation (Engerer and Xu 2015), raising the prospect of satellite derived irradiance validation or spatio-temporal analyses of solar radiation using large PV monitoring networks like the one being used by the RPSS.

Furthermore, this system, despite the inclusion of additional sites and the satellite data, will still only operate in near real-time, without the inclusion of short-term solar forecasting. This is due to the inherent time-lagged nature of the reporting data and the time taken to complete the modeling process and deliver the result. For this tool to truly provide proactive decision making capability, it must be incorporate short-term solar forecasting technologies. In the near future, we intend to apply the latest in short-term, distributed solar forecasting technology to this problem, thereby advancing the RPSS to true real-time operational status.

6. Conclusions

This version of the Regional PV Simulation System, which is now capable of simulating 15,000+ PV systems at transformer level in Canberra, Australia, is a unique and promising tool for distribution network service providers and energy markets in Australia. For the first time, the contributions of small-scale, monitored solar PV assets can be quantified for distribution networks, as organised by distribution asset. This information will be a key enabler for future scenarios that increase the allowable penetrations of solar PV via combinations of accurate distributed PV forecasting and energy storage technologies. With the information provided by this simulation system, distribution networks will no longer be naïve with respect to the real-time behaviour of their distributed PV assets, removing one of the most significant sources of uncertainty within Australian electrical grids. This tool, made possible through an up-scaling of the K_{PV} methodology, is now running in real-time, and can be located at http://rpss.info. Soon, this operational system will begin delivering near real-time information to local utility ActewAGL, with plans to incorporate short-term solar forecasting and high-resolution satellite imagery into its operations. Future work will aim to increase the accuracy and robustness of the modelling methods, with emphasis on increasing the number of ingested monitoring sites and blending surface based K_{PV} estimates with those based on satellite-derived irradiance.

7. References

[ABS] Australian Bureau of Statistics, 2014. One in five households now use solar energy. 2014. Web. Accessed 20 July 2015.

Chen, L. and Franklin, E., 2011. Mapping the onset of solar grid-parity in Australia. Proceedings of the 49th Annual Conference of the Australian Solar Energy Society. Sydney, November 2011.

Engerer, N.A., 2015a. City-wide simulations of distributed photovoltaic array power output. Ph.D. thesis, The Australian National University. Submitted August 2015.

Engerer, N.A, 2015b. QCPV: A quality control algorithm for distributed photovoltaic array power output. Submitted to IEEE Transactions on Sustainable Energy. August 2015.

Engerer, N.A. and Mills, F.P., 2014. K_{PV}: a clear-sky index for photovoltaics. Solar Energy, 105, pp. 679–

693.

Engerer, N.A. and Xu, Y., 2015. A simple model for estimating the diffuse fraction of solar irradiance from photovoltaic array power output. 21st International Congress on Modelling and Simulation (MODSIM2015). Gold Coast, Australia, December 2015.

Ergon Energy. PV Industry Alert. Issue 20. 23 June 2015

Horizon Power, 2012. Technical requirements for renewable energy systems. Technical Report HPC-9FJ-12-0001-2012.

Noone, B., 2013. "PV integration on Australian distribution networks." The Australian PV Institute, UNSW, Australia.

[APVI] Pv-map.apvi.org.au. Australian Photovoltaic Institute Market Analyses, 2015. Web. Accessed 21 July 2015.

SunWiz, 2012. Solar PV forecast for AEMO 2012-2022. Technical Report.

Tan, J., Engerer, N .A., and Mills, F.P., 2014. Estimating hourly energy generation of distributed photovoltaic arrays: a comparison of two methods. Proceedings of the 52nd Annual Conference of the Australian Solar Energy Society. Melbourne, May 2014.

Conference Proceedings

Solar World Congress 2015
Daegu, Korea, 08 – 12 November 2015

PROTECTION OF ELECTRICAL DISTRIBUTION SYSTEMS BY SMART GRID, CONSIDERING SOLAR PHOTOVOLTAIC GENERATION

José Bione de Melo Filho[1] and José Aderaldo Lopes[2]

[1] Federal Institute of Education, Science and Technology of Pernambuco and University of Pernambuco

[2] Companhia Energética de Pernambuco, Recife (Brasil)

Abstract

According to resolution 482 of the Brazilian National Electric Energy Agency (ANEEL), connection of micro and mini generation directly on power distribution grids are now possible in Brazil, in both cases only from renewable sources. This resolution provides that each customer can have a photovoltaic system producing energy to complement the own consumption and can inject the excess energy in the power grid, establishing a power compensation cycle, with credits valid for some months (net metering). Massive connections of distributed micro and mini generation demands a centralized control and an intelligent management system that only will be possible with use of smart grid technologies, including telecommunications infrastructure, computing facilities, smart metering and advanced protection/automation. This paper presents an assessment of impacts on the protection in electrical power distribution systems when micro and mini generators are connected on grid, considering solar photovoltaic and smart grid concepts.

Keywords: Smart Grid, Protection Grid, PV connect on Grid, Solar Energy, Distributed Generation,

1. Introduction

Power generation by photovoltaic panels, is a widely used technology in Europe and the United States. The great motivation for use of this technology is the reduction of environmental impacts, as well as, the attractiveness of generation systems using distributed, low voltage, as shown in research carried out by Angelopoulos (2004) and Guan, et al. (2009) on the integration of distributed generation in low voltage circuits and their impact on power systems, analyzing power quality and the technical and economic feasibility of the connection.

As the resolution 482, it is possible to micro and mini connection generation distributed electricity from renewable sources, with the low voltage electrical grid. The publication of this resolution is a regulatory framework in Brazil. This resolution states that each client, whether residential, commercial or industrial, may have on the roof or other location of your unit consuming a photovoltaic central producing energy to complement the own consumption. The excess energy is injected into the grid and through the power compensation system used in the subsequent months, the consumer unit or other consumer property. So with the established regulations is underway in Brazil the development of a market with the implementation of various plants, micro and mini generation distributed in consumer units connected to electrical grids of distributors.

According Toledo et al. (2012), the massive connections of micro and mini generation distributed require a control and an intelligent management, which will be possible with the use of smart grid technologies, such as

doi:10.18086/swc.2015.06.03 Available at http://proceedings.ises.org

telecommunications infrastructure, computing, smart metering and protection and automation advanced. According to Toyama et al. (2010), the connection and protection of small generators to operate in parallel with the utility grid present some significant challenges, especially in relation to security and protection of persons and facilities. There are therefore a number of technical concerns about small connected generation systems, such as risks to grid security and other consumers, provided power quality, islanding, frequency variation, harmonic distortion, power factor and influence in action the grid protection systems. The departure from the standards set by rules and procedures characterizes an abnormal condition of operation, and the connection of protection to be able to identify this gap and isolate the systems ceasing the mains power supply.

Before the described scenario, this paper presents an assessment of impacts on the protection of electrical distribution systems by generation micro and mini connection, considering solar photovoltaic generation and smart grid concepts. Article make a contribution to consolidating the micro central connection and mini generation to the electrical distribution grid with reliability and safety of people and facilities, contributing important insights for consumers, equipment manufacturers, installers and electric utilities in Brazil. The article is a master's thesis summary developed / directed by the authors at the University of Pernambuco and Federal Institute of Pernambuco, Recife, Brazil.

2. Overview of smart grids in Brazil

In Brazil, the practical initiatives for implementation of smart grids (REI) are still timid, limited to a number of pilot projects. The implementation of motivation of smart grids in Brazil are: improving grid reliability, improved quality of supply, reduction of non-technical losses of energy, energy efficiency and renewable energy deployment. However, the regulatory framework is being prepared to receive the new technology in the distribution system. Several studies have been and are being conducted by government agencies and the private sector.

The research and development projects in the area of smart grids that are being carried out by partnerships between electric utilities, universities, research centers, laboratories and manufacturers have been important in assessing the performance and benefits resulting from the implantation of REI in Brazil. Including quotes to the strategic project and call cooperated No 011/2010, ANEEL, "Brazilian Program for Electric Smart Grid" which was proposed by CEMIG, with participation of other thirty-six companies and six research institutions, and the coordination of implementation carried out by the Institute of the Brazilian Association of Electricity Distributors (IABRADEE).

According to the Ministry of Science report, Technology and Innovation (MCTI) (2014) and according to data released by the Brazilian Agency for Industrial Development (ABDI) in partnership with the Owning Companies Association Institute for Infrastructure and Private Systems telecom (iAptel), in Brazil there are more than 200 ongoing projects on the KING theme. These initiatives involve about 450 institutions, covering more than 300 suppliers, 126 research centers and 60 concessionaires in the electricity sector, as well as ministries, regulatory agencies and universities. It is estimated that the amount of investments of these types of projects will reach R $ 1.6 billion considering initiatives in the generation, transmission and distribution.

Application of R & D resources in demonstration projects or pilots, ie projects that evaluate the concept of KING on the whole, has given up in the distribution segment, considering that is the most affected sector by the changes arising from the implementation of the REI. Among these projects, according to data from the first half of 2013, more than half of the investments made and planned the projects were part of the stage of the innovation chain: experimental development, showing the importance given by the concessionaires to real trials of the concept of REI.

Figure 1 shows eight of the main statements designs or REI pilots in Brazil. These projects make up an investment made / provided over R $ 200 million, according to 2013 data.

Fig. 1 - Main Projects of REI in Brazil

The first pilot projects have been conducted by Light and Cemig, being followed by others in the industry. Light within the Inova Energy program is developing an REI project with the installation of about one million smart meters, whose main objective is to reduce non-technical losses. So this is the first step to implement the large-scale project in Brazil smart grids.

3. Micro and Mini generation distributed in Brazil

In April 2012, the National Electric Energy Agency (ANEEL) published the resolution in 482 (2012), which establishes the general conditions for access of micro and mini generation distributed to power distribution systems in Brazil.

With the advent of this Resolution was revised module three (3) of the Electricity Distribution Procedures in the National Electricity System (ANEEL) (2013), introducing the section 3.7, guidelines for micro access and mini generation distributed where the requirements are indicated minimum required for generating central connection point. The proposed protection system must be assessed and studied, to identify whether its implementation ensures the sensitivity requirements, reliability and selectivity of the protection of the interconnected distribution system, utilities and micro or mini generation as well as the safety of installations and operating personnel and maintenance.

The resolution in the 482 states that distributed micro (Micro GD) are electric power generating plants, with lower installed power than or equal to 100kW, using sources based on hydropower, solar, wind, biomass or qualified cogeneration, connected to the distribution grid through plants consuming units (RU). Already distributed mini generation (Mini GD) are the power plants with the same characteristics, however, with installed power greater than 100kW and 1MW or less.

In order to enable the micro and mini generation, the resolution in the 482 also established the power compensation system (metering net), in which the surplus active energy injected into the grid, generated by consumer unit with micro or mini generation distributed, compensate the consumer active electricity. The implementation of micro power plants and photovoltaic solar mini generation provides the technical basis for developing the use of solar energy, and build skills to assess the technical and commercial arrangements of small distributed generation with grid-connected photovoltaic systems.

However, by injection directly into electric energy distribution systems, because of the existence of micro central and distributed minigeneration, these become active systems, may generate energy consumption and at the same time. As is the case for most distribution systems, these were not designed for two-way flow of energy, and, therefore, are likely to have problems with the growth of distributed generation.

According Thong, et al. (2005), the connection of distributed generation (DG) in distribution systems can impact various parameters of these systems, for example, power flow (which now becomes bidirectional), the voltage profile, voltage stability , current imbalances, protective systems and, finally, as a result of these changes, the quality of electricity.

The inclusion of micro and / or mini generation distributed impacts in many processes of a company that distributes electricity, for example: planning, operation, protection study, among others, thus presenting great challenges and requiring new techniques to optimize and operate these systems. According to Cabello and Pompermayer (2013), in Brazil, the legislation only allows access to the electrical system of the central distributors of micro and renewable mini generation and not allowed these plants operate in isolation, but in an integrated way, reason in which shall be automatic devices which prevent "islanding" ie when the automated system of micro and mini generation detecting a power failure from the grid should automatically disconnect and interrupt the supply of power from generation of the consumer unit to the grid distribution. Brazilian law also does not allow the direct sale of the energy generated, just compensation through credits, the slaughter of consumption. The production of electricity from solar photovoltaic systems today is among the generation of alternatives, the most viable technical and economically, to the core of micro and mini generation, as a direct result of the fall in the price of photovoltaic modules, good availability, speed and ease of installation.

It should be noted that the deployment, operation and maintenance of micro centers and distributed mini generation as well as their connection to the electrical systems of distributors must meet the requirements of standards and regulatory regulations issued by the competent bodies, since they dictate rules to be followed by those involved, party accessing (owner of consumer micro or mini generation) and accessed (electricity distribution), so that the interconnected micro or mini system generation x distributor to operate safely and reliably meeting all the technical requirements.

4. Assessment of Impacts on the Protection of Electrical Systems Distribution Micro Centers connection and Mini generation Solar Photovoltaic

This topic assess the impacts on the protection of electrical distribution systems of micro central connection and photovoltaic solar mini generation considering the security aspects and operation of facilities as well as the operation and maintenance personnel involved and the concepts of electrical smart grid.

4.1 Initial considerations

The increasing penetration of micro plants and mini generation brings new challenges for the planning, operation, maintenance, protection and control of electrical distribution systems. Currently, most electrical distribution systems in Brazil, operates radial configuration, that is, energy flows in one direction. The implementation of micro centers and distributed mini generation changes the system topology, passing the energy to flow in several directions, impacting the protection of electrical distribution systems. The current distribution protection systems use simple schemes based on switches and fuses, sectionalizers, reclosers line and substation, associated with overcurrent and automatic reclosing relays. These simple schemes may require adjustments and upgrades to support the connection of micro and minigeneration centers. According to the Institute of Electrical and Electronics Engineers (IEEE) (2004), advanced protection schemes that can adapt to changes in the distribution system configuration can be essential for distributed generation plants connection. They will depend on the data collection in strategic locations and communication of data between intelligent relays for distribution system protection, through the protection to be an integral part of the automation of distribution systems. Great micro central numbers and mini generation can bring problems of stability and frequency control, just a few issues that are relevant in the generation and transmission systems

become relevant also in the electric distribution system. However, new automation technology, protection, control, communication and information systems, applied to electrical distribution systems will bring many benefits to the operation, supervision and monitoring system, improving the quality of power supply to customers.

Next is to assess the impacts on the protection of electrical distribution systems micro central connection and photovoltaic solar minigeneration, using inverters to transform the direct current generated in PV modules into alternating current. It makes up the assessment comparing the distribution system with and without the central considering the topology, currently adopted by the distributors, specifically the Energy Company of Pernambuco (CELPE), distributor of electricity in the state of Pernambuco. For example, using distribution transformers with delta connection, in 13.8kV, the side of the distributor and grounded wye, 380 / 220V, the side of the consumer units (loads). All evaluations are carried out considering the distribution of figure 2 circuit, the data presented in Table 1.

Figure 2 shows the Jordan River substation Celpe 69 / 13.8kV-10 / 12,5MVA three feeders, be simulated in the feeder 2, the connection of a central microgeneration 71,91kWp and mini generation center 989, 82kWp. The central micro and mini generation were designed based on the maximum values adopted by CELPE (2013 and 2014) for micro connection and mini generation, based on the resolution at 482. The maximum values were chosen to simulate the extremes of micro connection and distributed mini generation.

For simulations we considered the central microgeneration 71,91kWp made up of eighteen (18) photovoltaic series in parallel, each series with seventeen (17) Solar modules from Bosch. The connection to the grid is performed by a three-phase central inverter with an output of 75kW. For simulations it considered the center of mini generation 989,82kWp formed by 234 (two hundred thirty-four) photovoltaic series in parallel, each set with 18 (eighteen) modules from Bosch Solar. The connection to the grid is performed by a three-phase central inverter with an output of 1000kW.

Tab. 1: The electrical distribution system data

Components of the Distribution System	Impedances (pu base of 100 MVA and voltage system)		
	Positive sequence (Z_1)	Negative sequence (Z_2)	Zero sequence (Z_0)
Equivalent system equivalente 69kV – SE Rio Jordão	0,0331+j0,1222 pu	0,0331+j0,1222 pu	0,0610+j0,5221 pu
Transformer 69/13,8kV -10/12,5MVA	j0,6716 pu	j0,6716 pu	j0,6716 pu
Transformer 13,8/0,38kV -1,0MVA	j7,5 pu	j7,5 pu	j7,5 pu
Transformador 13,8/0,38kV -0,15MVA	j23,33 pu	j23,33 pu	j23,33 pu
Cable 185mm^2 -AL	0,1107+j0,1359(pu/km)	0,1107+j0,1359(pu/km)	0,2041+j1,3623(pu/km)
Cable 70mm^2 -AL	0,2984+j0,1559(pu/km)	0,2984+j0,1559(pu/km)	0,3914+j1,4022(pu/km)

It is noteworthy that the distribution grid shown in Figure 4 has aluminum cable protected in the primary, and the trunk line in the 185mm2 section and the lead in the 70mm2 section. The secondary grid has aluminum multiplexed cable in the 120mm2 section.

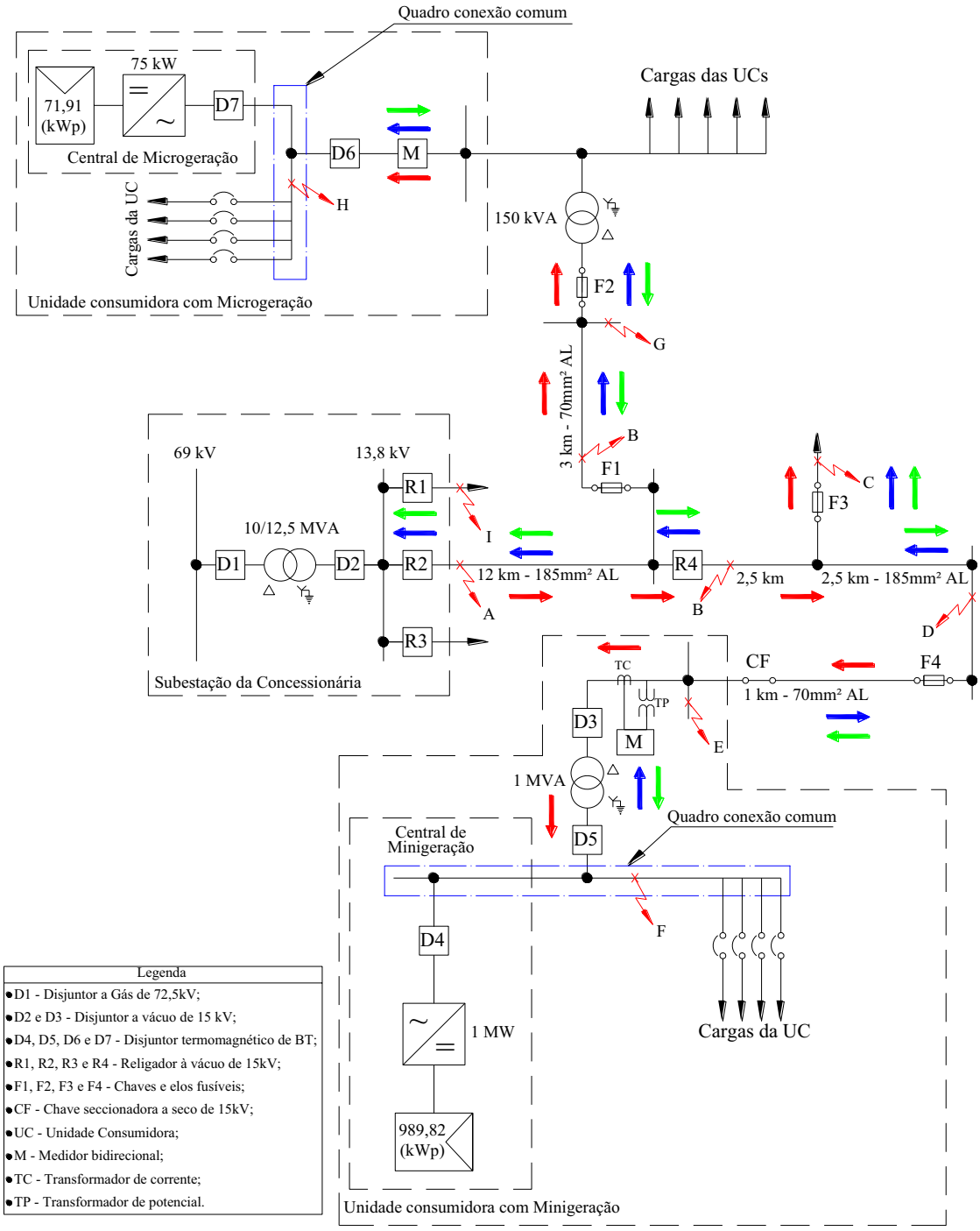

Fig. 2 - Distribution system - ways of short-circuit currents

4.2 Evaluation of short circuit of the electrical distribution system with connection of micro and mini generation.

When you have central micro and / or mini generators connected to the distribution gridsnetwork, their short-circuit levels have changes due to redistribution of possible fault current sources in the feeder. This change may cause undesirable effects in the operation and coordination of protection of the electrical distribution system, considering that proper coordination of relays, reclosers, fuses, sectionalizers is based on contribution to current lack of available sources that feed the defect. It is desirable to maintain a good coordination of relays, reclosers and fuses on the utility system with and without the core of micro and mini generation connected to the network.

According Sidhu and Bejmert (2012), the central micro and / or mini generation can be represented by a Norton equivalent circuit, where it has an ideal current source, a diode, and a resistor connected in parallel with the current source and resistor in series.

To calculate the short-circuit fault point of current, whereas the central micro and / or mini generation there is shown the system of distributing the Thevenin equivalent circuit at the point and the sources of micro and / or mini generation the equivalent circuit Norton and through the superposition theorem obtaining the total fault current.

For the circuit of Figure 2 were calculated short-circuit currents in given points, using the program: Analysis of simultaneous faults (ANAFAS) developed by Cepel. The ANAFAS is a interactive and friendly tool for analyzing faults in electrical systems, allowing the modeling system (prefault loading, representing the capacitance of the lines and loads, etc.) and the simulation of different types of defect that can be defined for compounds of simultaneous faults.

In Tables 2 and 3 show the results of simulation of a short circuit, three-phase, two-phase, open and single-phase single phase with 40Ω of contact resistance, showing the contributions of the Celpe system, Central micro and Central mini generation. It is noteworthy that the contributions of micro GD and mini GD were calculated considering that at the time of short circuit they are injecting all power on the network.

According Katiraei, et al. (2012), the central contribution of micro and / or mini generation to lack depends on the inverter design, and in most models can reach up to 120% of rated drive current. For the simulations presented considered for contribution of micro plants and mini generation this maximum value, é 120% of rated current of inverter 75kW and 1000kW.

The results shown in Tables 2 and 3 show that the contributions of the central micro GD and mini GD and for the current total short circuit, at various points of simulated faults when they occur in the medium voltage (13.8 kV) is very small and to zero if the defect is phase-ground due to the delta connection on the high side of the transformer Celpe and the high side of the transformer consuming unit mini GD, given that due to the transformer connection, there zero sequence component. The results also show that the system Celpe source of contributions are significant, especially when the short circuit is three-phase or two-phase and occurs in low voltage on the AC side.

It is noteworthy that in the medium voltage contributions of the central micro and / or mini generation for short circuits and three-phase two-phase currents are small due to the same are connected to the low voltage side; therefore, the values should be reflected for medium voltage using the transformer turns ratio, as shown in Table 2. To short-circuit the low voltage on the DC side of photovoltaic solar plant, do not have Celpe source contribution, given that the drive does not work as a rectifier.

Tab.2: Results of short circuit current, three-phase and two-phase

Point of Short Circuit	Short Circuit Current (A)							
	Three-phase				Two-phase			
	Celpe	MicroGD	MiniGD	Total	Celpe	MicroGD	MiniGD	Total
A	5.270	3,77	50,21	5.324	4.568	3,77	50,21	4.622
B	1.500	3,77	50,21	1.554	1.300	3,77	50,21	1.354
C	1.300	3,77	50,21	1.354	1.127	3,77	50,21	1.181
D	1.150	3,77	50,21	1.204	997	3,77	50,21	1.051
E	1.060	3,77	50,21	1.114	919	3,77	50,21	973
F	13.830	137	1.823	15.790	11.986	137	1.823	13.946
G	1.140	3,77	50,21	1.194	988	3,77	50,21	1.042
H	5.770	137	1.823	7730	5.001	137	1.823	6961
I	5.270	3,77	50,21	5.324	4.568	3,77	50,21	4.622

Tab. 3: Results of short-circuit currents, single-phase frank and single-phase with 40Ω of contact resistance.

	Short Circuit Current (A)	
	Single phase frank (Ro = 0)	Single phase with contact (Ro = 40Ω)

Point Short Circuit	Celpe	MicroGD	MiniGD	Total	Celpe	MicroGD	MiniGD	Total
A	5.550	0,00	0,00	5.550	199	0,00	0,00	199
B	560	0,00	0,00	560	175	0,00	0,00	175
C	470	0,00	0,00	470	170	0,00	0,00	170
D	410	0,00	0,00	410	164	0,00	0,00	164
E	380	0,00	0,00	380	161	0,00	0,00	161
F	15.530	137	1.823	1.7490	5	137	1.823	1.965
G	440	0,00	0,00	440	165	0,00	0,00	165
H	6.000	137	1.823	7.960	5	137	1.823	1.965
I	5.550	0,00	0,00	5.550	199	0,00	0,00	199

According to Sidhu and Béjart (2012), when the PV plant is well protected (overcurrent, overvoltage, anti ilhamento) their contribution to fault current is also limited in time. For this reason there is no problem with the coordination of protection when a high-powered photovoltaic power plant is connected to the distribution grid. However, the distributor of the operation should be careful when the photovoltaic penetration level is high; in this case it is recommended to conduct special studies for the feeder and some coordination with directional relays may be required.

When the short circuit occurs in the low voltage from the point of view of the concessionaire, independent of whether or not central micro and / or connected min Generation for the micro and / or mini generadores acessantes, it is recommended to check the suitability of the breaking capacity of their protective equipment, circuit breakers and fuses.

4.3 Evaluation of Micro and Mini generadores connection in relation to the Coordination and Selectivity Protection

The evaluation of micro central connection and mini generation, regarding the coordination and selectivity of protection of electrical distribution systems, is performed based on the circuit of Figure 2. It is considered that without the plants, the protection is set, serving the criteria established by the concessionaires, according to the settings in Table 4.

Tab. 4: Settings of protection devices

Substation or Grid/ Equipament	Voltage (kV)	RTC (A)	Phase Protection		Neutal Protection	
			Manufacturer and type	Setting	Manufacturer and type	Setting
SE Rio Jordão Recloser 21J1	13,8	800-5	ZIV 8IRV	Tap: 480 A Eq: 480 A Cur: I0,14 Inst: 3200A	ZIV 8IRV	Tap: 48 A Eq: 48 A Cur: M0,4 Inst: 1600A
SE Rio Jordão Recloser 21J2	13,8	800-5	ZIV 8IRV	Tap: 480 A Eq: 480 A Cur: I0,14 Inst: 3200A	ZIV 8IRV	Tap: 48 A Eq: 48 A Cur: M0,4 Inst: 1600A
SE Rio Jordão Recloser 21J3	13,8	800-5	ZIV 8IRV	Tap: 480 A Eq: 480 A Cur: I0,14 Inst: 3200A	ZIV 8IRV	Tap: 48 A Eq: 48 A Cur: M0,4 Inst: 1600A
REDE Recloser R_4	13,8	600-1	Arteche Smart RC P500	Tap: 240 A Eq: 240 A Curva: 0,10 Inst: 1440A	Arteche Smart RC P500	Tap: 30 A Eq: 30 A Curva: 0,2 Inst: 480A

Reclosing relays (79) and the fuses are set as follows:

- ✓ number of apertures (NA): 3;

- ✓ number of reclosing(NR): 2;
- ✓ intervals reclosing: 1o 7s e 2o 7s;
- ✓ time of reset: 120s
- ✓ fuse link F1: 40k
- ✓ fuse link F2: 8k
- ✓ fuse link F3: 50k
- ✓ fuse link F4: 80k

In Figure 2 the arrows in red color represents the Celpe substation contribution to short circuits and arrows in blue and green colors represent the contribution of the central mini generation and micro respectively. With the micro connection and / or distributed mini generation feeders, the values of short circuit currents considered fuse and recloser operation will be changed. Then, to the circuit of Figure 2 analyzes the coordination and selectivity of network protections for short circuit in the various points shown in the figure.

4.3.1 Short-circuit at point A or AB grid

In the short-circuit point A or AEB grid must be eliminated by R2 recloser, whose performance conditions do not change with micro central connection and mini generation. However, it has been contributing to the short circuit of micro and mini generation plants, until the R2 recloser open and plants are disconnected for lack of tension. Thus, one should assess whether the fuses F1 and F2 keys support the short-circuit current from Central micro and R4 recloser settings and the key fuse link F4 support the short-circuit current from the central mini generation, thereby avoiding the undue opening of these protection devices. By evaluating the values of short-circuits shown in Tables 2 and 3, and R4 recloser settings and the nominal values of links, it can be stated, for the example given, which does not have any problem, but for a greater amount of core It may need to make some adjustments in these protective devices.

4.3.2 Short-circuit at point B and BDE grid

Short circuits at point B, after R4 recloser or BDE network must be eliminated by R4 recloser, whose performance conditions do not change with micro central connection and mini generation and may even improve as short chain passing the R4 recloser is the sum of the Celpe contribution to the Central microgeneration. However, it has been contributing to the short circuit Central mini generation until the R4 recloser open and the center is disconnected for lack of tension. Thus, one should assess whether the F4 key fusible link supports the short-circuit current from the central mini generation, thereby avoiding the undue opening of these protection devices. Assessing the short-circuit values shown in Tables 2 and 3 and the nominal value of the bond, it can be said, for our example, there would be no problem, but for a larger number of plants can be necessary to make some adjustment in this protection device.

4.3.3 Short-circuit at point C

Short circuits in C must be disposed of by the key fusible link F3, so be selective with the R4 recloser, to test if the defects are temporary or permanent. With the connection of micro power plants and minigeneration has contributions from central to short circuits, however, while the micro central contribution through the R4 recloser contributing to improve the sensitivity of protection, the central contribution of minigeneration no more R4 in recloser, which may cause the selectivity between the fuse F3 key and R4 recloser is lost. With the connection of power stations, utilities must well evaluate the selectivity of the protections of extensions with fusible link and reclosers. Due to the small contribution minigeneration center for short, as shown in Tables 2 and 3, it can be stated, for the example given, which does not have any problem, but to a larger number of plants and to a system with low currents short circuits, rural feeders may be necessary to change settings of reclosers or replace the extension of fuses for seccionalizador or recloser.

4.3.4 Short-circuit at point B and BG grid

Short circuits at point B after the fuse F1 key or BG network must be eliminated by F1 recloser, so be selective with the R2 recloser, to test if the defects are temporary or permanent. With the connection of the central micro and mini generation has contributions from central to short circuits until the R2 recloser open and plants are disconnected for lack of tension. Thus, one should assess whether the F2 key fusible link supports short-circuit

current from Central micro and R4 recloser settings and the key fuse link F4 support the short-circuit current from Central mini generation, thereby avoiding the undue opening of these protection devices. The mini generation central contribution fails the recloser R2, which may cause the selectivity between the fuse F1 key and the recloser R2, is lost. As noted above, with the connection of power stations, utilities must well evaluate the selectivity between protections extensions with fusible link and reclosers. Due to the small contribution minigeneration center for short, as shown in Tables 2 and 3, it can be stated, for the example given, which does not have any problem, but to a larger number of plants and to a system with low currents short circuits, rural feeders may be necessary to change settings of reclosers or replace the extension of fuses for seccionalizador or recloser.

4.3.5 Short-circuit at point I

Short circuits in point they must be eliminated by the recloser R1, whose performance conditions do not change with micro central connection and minigeneration. However, it has been contributing to the short circuit of plants and micro minigeneration until the open recloser R1. In this situation, the central remain connected, because the short-circuit occurs in an adjacent tray. However, it has short-circuit current passing in the opposite direction R2 and R4 reclosers. Thus, one should assess whether the currents flowing in the opposite direction to normal load flow, by R2 and R4 are enough to make the protection work by turning off all or part of the load feeder 2, which characterizes lack of selectivity protection. To solve this problem you should use directional overcurrent relays in the protection of reclosers substations that have a high amount of core micro and minigeneration. It should be noted that the opening of R2 or R4, and stop the service consumers or cause undesirable ilhamentos hampers the fault location, increasing the time of the interruption and the cost of maintenance.

4.3.6 Short-circuit at point F and H

Short circuits in F and H points are defects that occur in consumer units, where the plants are installed, and must be eliminated by D6 and D7 Breakers to the central micro and D5 and D4 to the central minigeneration. For those short, the contribution of Celpe for short is added to the central contribution; therefore, should be assessed to the new situation the breaking capacities of circuit breakers remain adequate. The influence of the central contributions to the defect, circulating on the medium voltage grid.

5. Conclusion

In the assessments it was observed that the micro central connection and / or minigeneration in distribution system designed to feed the radially load may bring a number of problems with the coordination of the protective devices, because the actual distribution system It has several load leads over the circuits may have more than one protective device on the line between the substation and the central connection.

The example showed that for connecting small amount of core micro and / or mini generation the influence in protection systems is not significant, but for mass connection, the protection system of distribution and transformer feeders should be well assessed through coordination studies of protection. Micro connections and / or distributed mini generation should take the utilities to make adjustments in the distribution protection systems, so that system performance is not reduced, which will probably lead to the implementation of smart grid technologies.

The assessments also show that the addition of plants and micro mini generation distributed to a distribution system has the potential to impact protection and beyond the point of common coupling. The greatest concern are the effects on the protection systems traditionally designed for radial operation. Among the issues that must be considered has two-way flows, increased fault levels, safety, voltage control, equipment capacity, automatic restart, islanding and coordination and selectivity. These effects are not limited to grids in which the control panel is connected, and can affect the relay protection in adjacent grids as well. Thus, careful studies to identify and solve these problems are needed whenever a plant is added in order to ensure continued safe and reliable operation of the system.

The implementation of smart grid technologies that enable communication between protection devices, enabling the control and supervision of the interconnected utility system with the center of the party accessing,

enabling direct disarm distributor breaker Central micro or mini generation, will bring greater reliability and security for system operation and maintenance.

6. Bibliographical reference

Agência Nacional de Energia Elétrica (ANEEL). Resolução normativa nº 482. Brasília-DF, abril, 2012.

Agência Nacional de Energia Elétrica (ANEEL). Procedimentos de Distribuição de Energia Elétrica no Sistema Elétrico Nacional (PRODIST)- módulo 3. abril de 2012. Disponível na Internet em: http://www.aneel.gov.br/area.cfm?idArea=82. Acessado em: 15 de março, 2013.

Angelopoulos, K. Integration of distributed generation in low voltage grids: power quality and economics. Master Thesis, University of Strathclyde in Glasgow, Glasgow, 2004.

Cabello, A. F. e Pompermayer, F. M. Energia Fotovoltaica Ligada à Rede Elétrica: Atratividade para o Consumidor Final e Possíveis Impactos no Sistema Elétrico. Instituto de Pesquisa Econômica Aplicada (IPEA). Brasília, fevereiro, 2013. Disponível em: http://www.ipea.gov.br/portal/index.php?option=com_content&view=article&id=17110&catid=337&Itemid=1, Acessado em: 16 de novembro, 2014.

Companhia Energética de Pernambuco (CELPE). Conexão de Microgeradores e Minigeradores ao Sistema de Distribuição de Média Tensão - VM02.00-00.005. Recife, novembro, 2013.

Companhia Energética de Pernambuco (CELPE). Norma de Conexão de Microgeradores ao Sistema de Distribuição de Baixa Tensão - VM02.00-00.004. Recife, agosto, 2014.

Guan, F. H., et al. Research on Distributed Generation Technologies and its Impact on Power Systems. IEEE, 2009.

Institute of Electrical and Electronic Engineers (IEEE). Impact of Distributed Resources on Distribution Relay Protection. Report to the Line Protection Subcommittee of the Power System Relay Committee, prepared by working group D3, agosto, 2004.

Katiraei, F., et al. Investigation of Solar PV Inverters Current Contributions during Faults on Distribution and Transmission Systems Interruption Capacity. Western Protective Relay Conference, Quanta Technology, outubro, 2012.

Ministerio da Ciência, Tecnologia e Inovação (MCTI) e Joint Research Centre (JRC). Redes Elétricas Inteligentes - Diálogo Setorial Brasil-União Europeia (2014). Brasília, novembro de 2014.

Sidhu, T. S. e Bejmert, D. Short-circuit Current Contribution from Large Scale PV Power Plant in the Context of Distribution Power System Protection Performance. University of Western Ontario, Canada, maio, 2012.

Thong,V.V., et al. Power quality and voltage stability of distribution system with distributed energy resources. International Journal of Distributed Energy Resources. ISSN 1614-7138, Volume 1 Number 3. Editora: Technology & Science Publishers, 2005.

Toledo, F.O., et al. Desvendando as Redes Elétricas Inteligentes. São Paulo-SP: 1a Ed. Brasport, 2012.

Toyama, J. et al. Conexão e Proteção de Geração Distribuída no Sistema de Distribuição. IEEE/PES 2010 T&D Transmission and Distribution Conference and Exposition Latin América, São Paulo, 2010.

Conference Proceedings
Solar World Congress 2015
Daegu, Korea, 08 – 12 November 2015

An Impact of Artificial Intelligence Control on Photovoltaic/Thermal (PVT) – Ground Source Heat Pump (GSHP) Hybrid System

Kwang Seob Lee[1], Andrew Putrayudha S.[1], Evgueniy E.[2], Libing Y[2], Eun Chul Kang[3] and Euy Joon Lee[3]

1 University of Science and Technology (UST), Daejeon (South Korea)

2 CanmetENERGY, Ottawa (Canada)

3 Korea Institute of Energy Research (KIER), Daejeon (South Korea)

Abstract

Hybrid renewable energy utilization in residential and commercial building become an important issue in the world. IEA policy on renewable heat says that expanding the use of modern biomass, geothermal energy, solar energy and ambient energy to produce heat and power could contribute substantially to meet energy security objectives and mitigate climate change. Based on that background, in this study, two different renewable energy systems, which are photovoltaic/thermal (PVT) and ground source heat pump (GSHP) were combined together to produce heating, cooling and electricity simultaneously so-called tri-generation. This hybrid technology has been introduced and analyzed in terms of energy savings compared to the conventional system which uses a boiler and chiller to produce heating, cooling and electricity from the grid. For one house and one office, conventional system consumed 276.7kWh/m2-yr of energy and the combination of three renewable energy systems save the primary energy up to 97.9kWh/m2-yr or 35.4% energy reduction. An impact of Advance control system by using artificial neural network and fuzzy logic control system will be explained and analyze in order to achieve better energy savings. By these two techniques, it showed that for one single residential house, 11%-36% primary energy reduction by using ANN and 11%-23% primary energy reduction by using Fuzzy Logic control could be achieved.

Keywords: *artificial control system, ground source heat pump, photovoltaic/thermal, renewable energy, Trigeneration.*

1. Introduction

The urge of renewable energy utilization in the world become higher and higher as the new policy scenario of energy in the world published. The share of renewables in primary energy use in the New Policies Scenario rises to 18% in 2035, from 13% in 2011. This resulting from the rapidly increasing demand for modern renewables to generate power, produce heat and make transport fuels based on world energy outlook 2013[1]. Power generation from renewables increases by over 7000 TWh from 2011 to 2035, making up almost half of increase in total generation. Renewables become second-largest source of electricity before 2015 and approach coal as the primary source by 2035, with continued growth of hydropower and bioenergy, plus rapid expansion of wind and solar PV as shown in Fig.1.

Selection and/or peer review under responsibility of Scientific Committee
doi:10.18086/swc.2015.06.04 Available at http://proceedings.ises.org

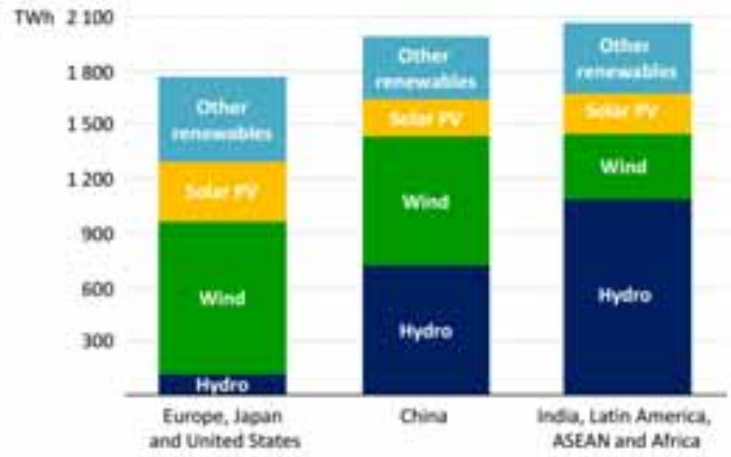

Fig. 1 Growth in electricity production from renewable sources 2011-2035[2]

Based on those background, utilization of renewable energy technologies will be explained not only one source of renewable energy but combination of two renewable energies will be covered and the impact of the advance control system on energy saving. Combination of Photovoltaic/Thermal or known as PVT and Ground Source Heat Pump (GSHP) or Geothermal Heat Pump have been chosen as the system that will be covered in this paper. Photovoltaic/Thermal or PVT is a combination of photovoltaic (PV) and solar thermal components/system which produce both electricity and heat from one integrated component system [3]. Typically, commercially available PV modules are only able to convert 6-18% of the incident radiation falling on them into electricity, with the remainder lost by reflection or as heat [4]. One of the characteristics of photovoltaic is that as the surface temperature of the panel goes up, the efficiency of the system itself decreasing [5]. Ground Source Heat Pump (GSHP) is one of the promising technologies for space heating and cooling applications A GSHP extracts heat energy stored below the ground during the winter for heating applications. As the ground temperature at which heat is absorbed is higher than the ambient temperature, the coefficient of performance of GSHP becomes higher than the system that would operate directly taking heat from the ambient which very low during winter [6]. As what have mentioned before, an impact of advance control system such as Artificial Neural Network and Fuzzy Logic will be analyzed here. Fuzzy logic is a logical system, which is an extension of multivalued logic. However, in a wider sense, fuzzy logic (FL) is almost synonymous with the theory of fuzzy sets, a theory that relates to classes to objects with unsharp boundaries in which membership is a matter of degree. On the other hand, ANN is a type of artificial intelligence that mimics the behavior of human brain and is famous for its robustness due to the use of a generalization technique instead of memorization. By using these two artificial intelligence control, an improvement in energy saving can be achieved. These two intelligence control were chosen because of their capability to deal with lots of dynamic variable of the systems.

2. System Modeling

Two renewable energy system was chosen as the subject of this study which is the combination of the PVT and GSHP system for the single residential house of 200m2 as its described on Fig. 2 and it's component on Table 1:

Table 1 Main Component of PVT-GSHP system

#	1	2	3	4	5	6	7	8	9	10
Main component	House/ Office	Fan coil unit	Main pump	GSHP	GSHP pump	GS-Tank pump	PVT pump	Solar-tank pump	Hot water tank	Cold water tank
Quantity	n/m	n+m	1	1	1	1	1	1	1	1

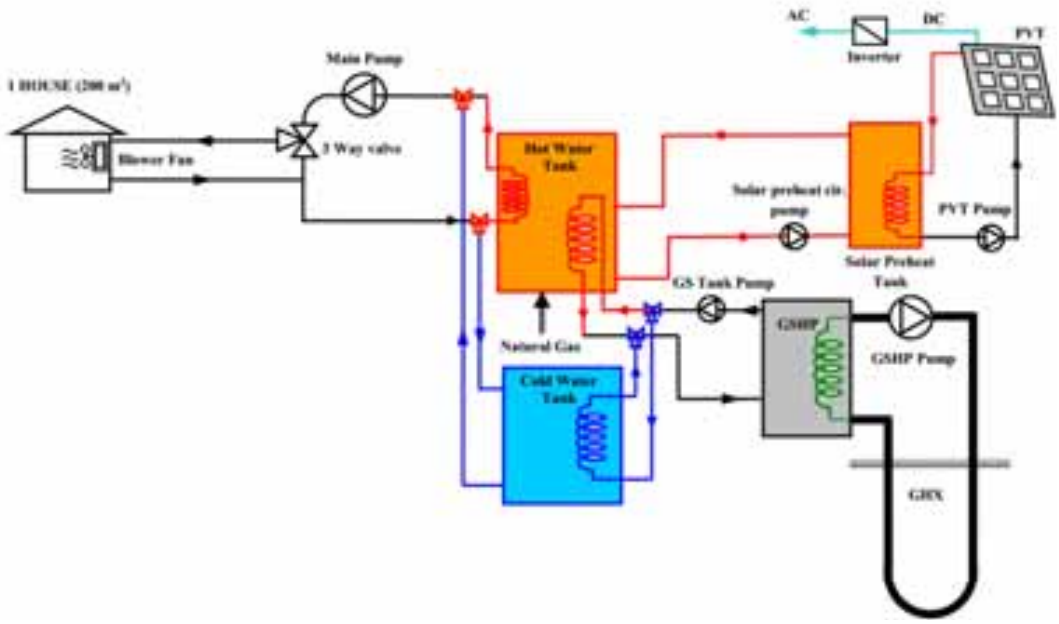

Fig.2 Schematic Diagram of PVT-GSHP system

GHSP system and PVT module that used on the simulation are based on the TRNSYS 17 library. Ground heat exchanger was modelled as a vertical, single U-tube heat exchanger that interacts thermally with the ground. Type 557 ground heat exchanger model was considered to be the state-of-the-art in dynamic simulation of ground heat exchanger and is most commonly used in ground heat exchanger application. It is a water-to water heat pump with 5 ton rated heating capacity and 2.5 ton rated cooling capacity. For the PVT part, TRNSYS17 provides three major model in the library which are Type 50, Type 555 and type 56(mode). All the models are largely theoretical based. These TRNSYS PVT models were reviewed under IEA, Solar Heating and Cooling Program, Task 35. The electrical output for PVT is 295W and the thermal output is 1.5kW

The simulation models were run in Incheon, South Korea weather data over a year to simulate and analyze the energy system's performance while satisfying the building heating and cooling demands. The control and management of microgeneration systems is very important for their optimal operation. Simple On-Off control strategy is often used, but its major disadvantage is not being able to allow part load operation of devices. The efficient operation of the microgeneration systems, especially for single dwellings, has the following attributes: nonlinear behavior uncertainties of electrical and thermal demands; and vagueness of the performance of the microgeneration system. Due to these attributes, an intelligent approach is required. Fuzzy Logic (FL) control approach was chosen because FL linguistic rules can simplify the control of the PVT-GHSP system given its complexity. MATLAB Fuzzy Logic Toolbox was used for the implementation of the FL controller and then integrated to the system models. Also another advance control system called Artificial Neural Network (ANN) will be implemented on this systems. Comparative study was conducted to see the impact of the artificial intelligence control to the possibility energy and cost savings compare to the conventional On-Off strategy.

3. METHODOLOGY

Two artificial control system were introduced (Fuzzy Logic and ANN). Fuzzy Logic system that applied on this study consist of two control strategies, FL for GSHP and FL for PVT.

The operation of the heat pump is controlled by two input variables: the storage tank temperature and the temperature difference between the actual room temperature and the thermostat set-point. The output of the fuzzy logic controller is the fractional state of operation of the ground source heat pump with a number ranging from 0 to 1 with 0 turning the device OFF and 1 representing full load operation. On the other side, the operation of PVT system is controlled by 2 input variables: the electrical demand and the temperature

difference between panel and the bottom of the tank. The fuzzy logic if-then rules for GSHP and PVT control signal are presented in Table 2 and Table 3 for heating and cooling period respectively. The rules are chosen intuitively based on the research team's experiences.

Table 2 If then rules for GSHP operational state

Hot Water Storage Tank Temp.	dT=Troom-Tset				
	Lg Neg.	Sm Neg.	None	Sm Pos.	Lg Pos.
L	H	H	M	L	L
M	H	M	L	Off	Off
H	M	L	Off	Off	Off
VH	Off	Off	Off	Off	Off
Cold Water Storage Tank Temp.	dT=Troom-Tset				
	Lg Neg.	Sm Neg.	None	Sm Pos.	Lg Pos.
VL	Off	Off	Off	Off	Off
L	Off	Off	Off	L	M
M	Off	Off	L	M	H
H	L	L	M	H	H

Table 3 If then rules for PVT operational state

Electrical Demand	dTtank = Tpanel – Tbottom			
	Vlow	Low	Medium	High
L	Off	L	L	M
M	Off	L	M	H
H	Off	L	M	H

The control strategies using artificial neural network investigated in this study consist with 1 input layer with 11 inputs, 2 hidden layers with 20 neurons each and 1 output layer with 1 output as it described in Table 4. Matlab® Neural Network Toolbox was used to train and test the ANN models. The hyperbolic tangent sigmoid transfer function was used in the hidden layers and the linear transfer function was applied in the output layer because of the two-layer sigmoid/linear network usually can represent any functional relationship between inputs and outputs if the sigmoid later has enough neurons. The simulation was done for both heating and cooling season.

Table 4 ANN layers in PVT-GSHP system

1 Output	T_{room} (+3h)	T_{room} (+4h)	T_{room} (+5h)	T_{room} (+6h)
11 Inputs	Current ambient temperature			
	Ambient temperature 7.5 minutes before			
	Ambient temperature 3 hours later	Ambient temperature 4 hours later	Ambient temperature 5 hours later	Ambient temperature 6 hours later
	Current solar irradiance			
	Solar irradiance 7.5 minutes before			
	Solar irradiance 3 hours later	Solar irradiance 4 hours later	Solar irradiance 5 hours later	Solar irradiance 6 hours later
	Current internal gains			
	Internal gains 7.5 minutes before			
	Internal gains 3 hours later	Internal gains 4 hours later	Internal gains 5 hours later	Internal gains 6 hours later
	Current room temperature			
	Room temperature 7.5 minutes before			

The control algorithms were made based on the output variables on the ANN simulations for heating and cooling. 6 logics for heating and cooling were introduced in this control system as those can be seen in Table 5 and Table 6.

Table 5 ANN based control for heating period

		System components controlled by the ANNs based controller	Input variables used by the ANNs based controller	Condition to be satisfied	Output of ANN controller in case of the previous condition is satisfied
Heating period	ANN_LOGIC H1	Blower Fan, Main Pump	$T_{coll}(+3h)$, $T_{coll}(+4h)$, $T_{coll}(+5h)$, $T_{coll}(+6h)$	At least 2 of $T_{coll}(+3h)$, $T_{coll}(+4h)$, $T_{coll}(+5h)$, $T_{coll}(+6h)$ greater than 21.5 °C	Blower Fan & Main Pump: OFF
	ANN_LOGIC H2	Blower Fan, Main Pump			
	ANN_LOGIC H3	Blower Fan, Main Pump, GSHP, GSHP Pump, GS Tank Pump, Auxiliary heater	$T_{coll}(+3h)$, $T_{coll}(+4h)$, $T_{coll}(+5h)$, $T_{coll}(+6h)$, Hot Water Tank Temperature at levels 2 & 5	At least 1 of $T_{coll}(+3h)$, $T_{coll}(+4h)$, $T_{coll}(+5h)$, $T_{coll}(+6h)$ greater than 21.5 °C	Blower Fan & Main Pump: OFF; GSHP & GSHP Pump & GS Tank Pump: ON if T2≥45 °C, OFF if T5≥50 °C; Auxiliary heater: ON if T2≥40 °C, OFF if T5≥45 °C
	ANN_LOGIC H4		$T_{coll}(+3h)$, $T_{coll}(+4h)$, $T_{coll}(+5h)$, $T_{coll}(+6h)$		Blower Fan & Main Pump: OFF; GSHP & GSHP Pump & GS Tank Pump: OFF; Auxiliary heater: OFF
	ANN_LOGIC H5	Blower Fan, Main Pump, GSHP			Blower Fan & Main Pump: OFF; GSHP: operation at lower heating capacity (2 ton)
	ANN_LOGIC H6	GSHP			GSHP: operation at lower heating capacity (2 ton)

Table 6 ANN based control for cooling period

		System components controlled by the ANNs based controller	Input variables used by the ANNs based controller	Condition to be satisfied	Output of ANN controller in case of the previous condition is satisfied
Cooling period	ANN_LOGIC C1	Blower Fan, Main Pump	$T_{coll}(+3h)$, $T_{coll}(+4h)$, $T_{coll}(+5h)$, $T_{coll}(+6h)$	At least 2 of $T_{coll}(+3h)$, $T_{coll}(+4h)$, $T_{coll}(+5h)$, $T_{coll}(+6h)$ lower than 20.5 °C	Blower Fan & Main Pump: OFF
	ANN_LOGIC C2	Blower Fan, Main Pump			
	ANN_LOGIC C3	Blower Fan, Main Pump, GSHP, GSHP Pump, GS Tank Pump	$T_{coll}(+3h)$, $T_{coll}(+4h)$, $T_{coll}(+5h)$, $T_{coll}(+6h)$, Cold Water Tank Temperature at levels 2 & 9	At least 1 of $T_{coll}(+3h)$, $T_{coll}(+4h)$, $T_{coll}(+5h)$, $T_{coll}(+6h)$ lower than 20.5 °C	Blower Fan & Main Pump: OFF; GSHP & GSHP Pump & GS Tank Pump: ON if T2≥15 °C, OFF if T9≤12 °C
	ANN_LOGIC C4		$T_{coll}(+3h)$, $T_{coll}(+4h)$, $T_{coll}(+5h)$, $T_{coll}(+6h)$		Blower Fan & Main Pump: OFF; GSHP & GSHP Pump & GS Tank Pump: OFF;
	ANN_LOGIC C5	Blower Fan, Main Pump, GSHP			Blower Fan & Main Pump: OFF; GSHP: operation at lower cooling capacity (1.5 ton)
	ANN_LOGIC C6	GSHP			GSHP: operation at lower cooling capacity (1.5 ton)

On-off control strategy of GSHP is controlled by an aquastat in hot water and cold-water tank for both heating and cooling season. PVT panels that are controlled by on-off strategy, use the temperature difference between tank top and hot water storage tank bottom as the control variable. Table 7 and Table 8 describe the control strategy of on-off control system:

Table 7 On-off control strategy for GSHP

GSHP		Aux. heater	
ON	OFF	ON	OFF
T2[a](HT[b]) ≤ 50 °C T9[a](CT[b]) ≥ 12 °C	T9[a] (HT[b]) ≥ 55 °C T9[a] (CT[b]) ≤ 8 °C	T2[a](HT[b]) ≤ 45 °C	T9[a](HT[b]) ≥ 55 °C

[a] T2, T5, T9 are the temperature sensors in tank node 2, 5 and 9 respectively. Each storage tank is divided into 10 isothermal nodes, 1 at the tank top and 10 at the tank bottom.
[b] HT: hot water storage tank; CT: cold water storage tank (when GSHP in cooling mode operation).

Table 8 On-off control strategy for PVT

PVT circulation pump		Solar preheat tank circulation pump	
ON	OFF	ON	OFF
$\Delta T^a \geq 10°C$	$\Delta T^a \leq 3°C$	$\Delta T^b \geq 7°C$	$\Delta T^b \leq 2°C$

[a] ΔT is the temperature difference between the PVT panel and solar preheat tank bottom.
[b] ΔT is the temperature difference between the solar preheat tank top and hot water storage tank bottom.

4. RESULT AND DISCUSSION

The impact of artificial intelligence, fuzzy logic control and ANN control system on PVT-GSHP are explained below:

The result of the usage of fuzzy logic compared to the on-off control system for PVT-GSHP can be seen in Fig.7 and Fig. 8:

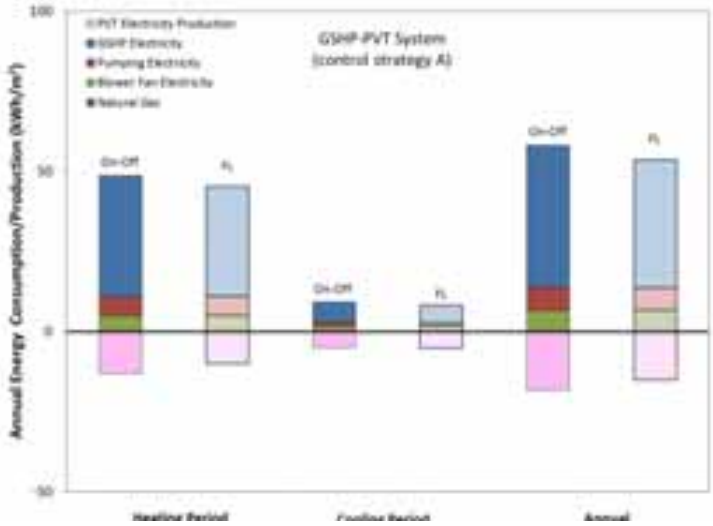

Fig. 7 (A) GSHP and PVT system with FL control

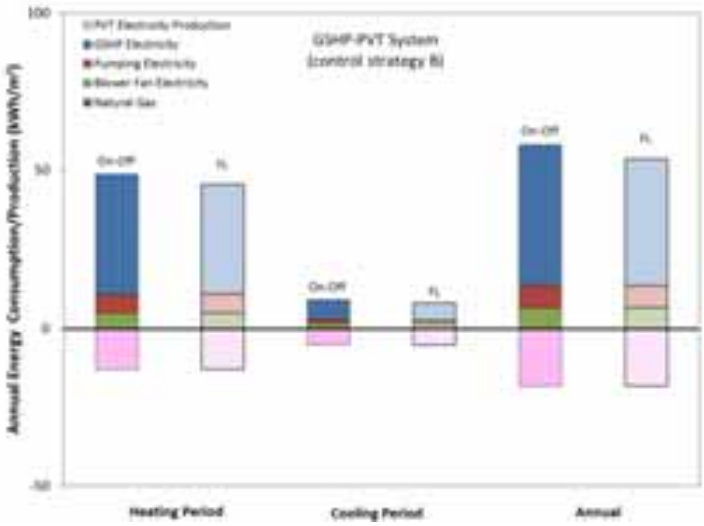

Fig. 8 (B) GSHP with FL control and PVT system with On-off control

The result shown in Fig. 7 and Fig. 8, indicate that the GSHP and blower fan electricity consumption are approximately the same and the pumping energy is slightly higher for the system with control strategy B. The main difference resulted from the two control for the PVT system resulted in higher electricity production, since all PVT panels are circulated with glycol fluid which reduces panel surface temperature and subsequently increases electric efficiency (production). Conversely, in the case of PVT system is controlled with FL strategy (strategy A), a fraction of total installed PVT panels is circulated with fluid to provide thermal energy depending on solar pre-heat tank temperature and electric demand. This causes the panel surface temperature and subsequently increases for PVT panels without circulation fluid and

consequently reduces electric efficiency and overall electricity production.

In Artificial Neural Network Part, TRNSYS software is used for the system models development and the MATLAB® Neural Networks Toolbox is used for the implementation of the ANN controllers. The result shows that control logic H4, H5, C4 and C5 shows the best energy saving compared to the on-off control system among all the other control logic strategies. Fig. 9 shows the result of ANN control on PVT-GSHP system.

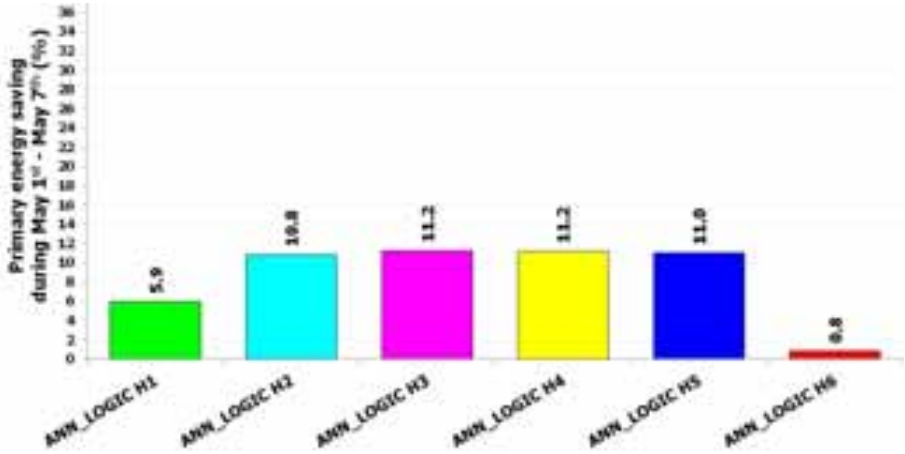

Fig. 9 Primary energy saving on ANN control during heating season

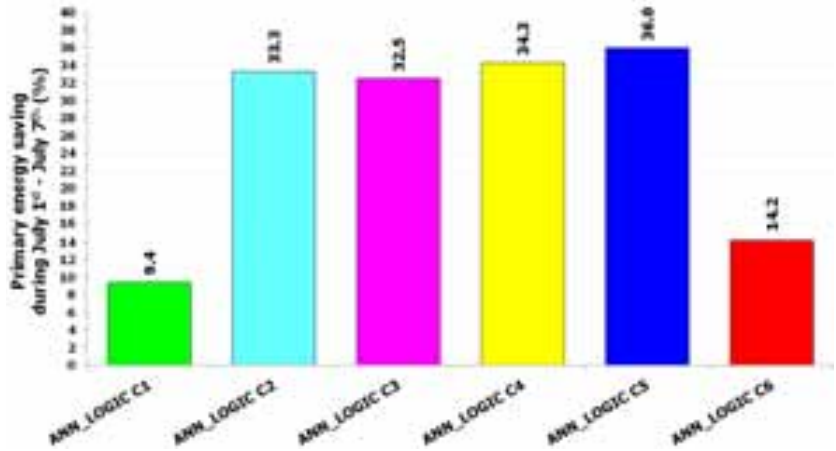

Fig. 10 Primary energy saving on ANN control during cooling season

The result show that the GSHP-PVT system with the ANN based strategies has low primary energy consumption if compared to the On-Off logic in particular, the strategies ANN_LOGIC H4 and ANN_LOGIC H5 result in approximately 11% total primary energy saving while ANN_LOGIC C4 and ANN_LOGIC C5 allow to reduce the primary energy consumption approximately 35% during a week.

5. Conclusion

In this study, as the main objectives, PVT-GSHP was developed, analyzed and optimized by using Fuzzy Logic control system, artificial neural network and on-off control system for application in residential buildings with 200m2 size. Energy consumption by utilize GSHP and PVT system analysis had been done on the previous research and showed a significant energy reduction. By using artificial intelligence control (fuzzy logic, artificial neural network and on-off control), system was calculated using TRNSYS 17 and MATLAB software and these are the conclusions:

- With the application of the FL control strategy and Artificial Neural Network instead of conventional On-Off control, the GSHP and GSHP-PVT systems are able to show a promising result in reduction of energy consumption in residential building with 200m2 size compared to the

building (residential)

- Energy reduction of PVT-GSHP system while using fuzzy logic controller is quite significant for FL(A) is 15.8% and FL (B) with 18.3%. FL(B) strategy has the better energy reduction because of all the PVT works which reduce the surface panel temperature and increase the efficiency of the system.
- With the utilization of ANN control to the system, system could save energy up to 11% during heating period (May 1st – May 7th) and 36% during the cooling period (July 1st – July 7th)

It is expected that in future study, cost analysis also will be performed in the future research to see the effect of the system cost, fuel cost, control cost and also payback period of the system. Comparison with the another advance control systems also will be done to see the effect of Fuzzy Logic and ANN control compared to another control system such as PID controller. Also with the application of advanced control strategies and system optimization, a microgeneration system will be able to achieve further energy and cost savings.

6. ACKNOWLEDGEMENT

This research was supported by a grant (16CTAP-CO096424-02) from Technology Advancement Research Program (TARP) funded by Ministry of Land, Infrastructure and Transport of Korean government.

7. REFERENCES

[1] IEA (International Energy Agency), 2013, World Energy Outlook 2013-Renewable energy outlook, OECD/IEA, Paris

[2] Van der Hoeven, Maria, 2013, World Energy Outlook 2013, London

[3] T.T. Chow, 2010, A Review on photovoltaic/thermal hybrid solar technology, Applied Energy, 87,365-379

[4] T.N. Anderson et al.,2009, Performance of a building integrated photovoltaic/thermal(BIPVT) solar collector, Solar Energy, 83,445-455

[5] L.R. Katherine, 2010, Photovoltaic Cell Efficiency at Elevated Temperatures, Massachusetts Institute of Technology, USA

[6] T Sivasakthivel, K Murugesan, PK. Sahoo, 2014, Optimization of ground heat exchanger parameters of ground source heat pump for space heating applications, Energy, 78,573-586

[7] Minister of Natural Resources Canada, 2001-2005, Clean Energy Project Analysis: RETScreen Engineering & Cases Textbook Ground-Source Heat Pump Project Analysis Chapter, Minister of Natural Resources, Canada

Maximizing the benefits of Solar Energy in Smart Energy Communities

Susan Roaf[1], Julie Tubia[2], Andrew Peacock[1], Edward Owens[1] and Monica Oliphant[3]

[1] Heriot Watt University, Edinburgh (Scotland)

[2] Institut National des Sciences Appliquées, Toulouse (France)

[3] University of South Australia, Adelaide (Australia)

Abstract

The first decades of phenomenal growth in the solar industry the focus was on getting more systems installed. Today, with the plummeting costs of photovoltaics, the emphasis in many projects has shifted towards getting as much economic, social and environmental value as possible from the installed systems, and this is increasingly made possible by installations at the community scale. Increasingly individuals, communities and cities are looking to utilize the ability to balance supply and demand with energy storage and controls in local energy micro-grids to maximize the use of locally generated energy within the generating communities. This paper review a range of European projects that aim to manage the production and the consumption of electricity within communities that generate their own energy with renewable energy resources and compares the approaches and results of these projects and discusses what appears to work best at motivating and engaging communities in the orchestration of local energy demand and supply. Building on experiences of community energy projects in South Australia it then provides a summary of the real world market constraints with the related issues of writing lease agreements, models and IP agreements and concludes with a short discussion of the drivers and barriers encountered in the market led model in Australia and in the European research domain of funded research.

Keywords: *Smart grid, Demand Response, Load energy management, Energy storage.*

1. Introduction

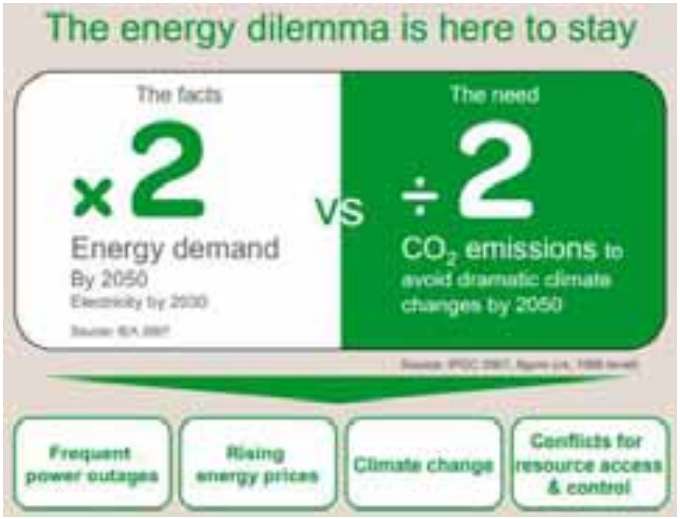

Fig.1: Diagram simplifying the universal Energy Dilemma

doi:10.18086/swc.2015.06.05 Available at http://proceedings.ises.org

Globally nations are caught in the same energy dilemma, with multiple and complex drivers pushing consumers away from the use of large scale, fossil fuel derived power sources to more regionally sourced, secure and renewable energy supplies. However it is increasingly appreciated that it is not only a modal shift in energy sourcing but also a step change approach to the yield that can be harvested from different energy sources that is needed to meet the ever more stringent ghg emissions reductions targets mooted to deal with the rapidly evolving climate threats. The European union, under its FP7 research funding round, has financed over two dozen community energy projects with a view to exploring the relative merits of different approaches to the orchestration of local energy supply and demand models. This paper outlines these projects and characterizes their properties and rationales. In order to start on the path of orchestration of supply and demand it is important to understand the nature of energy demand patterns in a region.

1.1 Electricity consumption in European households

Despite the fact that the production of construction materials emits CO_2 which increases the ecological footprint of buildings, the bulk of the CO_2 emissions from a building stem from use throughout its service life, proportionally depending on the life of the building. Energy and CO2 emissions, however, are not limited to our housing and transport needs. Higher living standards lead to a rising demand for goods such as computers, phones, music systems etc. that require regular re-charges of energy, particularly in the high tech, electric loads dominated lifestyles of many in Western Europe. The growing peak loads associated with such lifestyles have stimulated a plethora of European research projects by research centers, universities, product suppliers and electric power companies, often working together to explore the extent to which the orchestration of local renewable energy supply and local energy demand can be achieved in micro-grid systems and communities. The objectives of these European projects are largely driven by pressing need to meet climate change targets, the need to integrate a bigger share of renewable energies sources in the electricity generation to reduce carbon footprint, greenhouse gas emissions and dependence on fossil fuels and the desire to grow and flourish in the burgeoning markets for related products. The new markets promise not only profits from new product ranges and environmental benefits but also stimulation of local economy, new jobs, the ability to develop locally 'self-repairing' systems and in turn a degree of energy resilience and security which explains why there are high levels of support for investment in such projects by some politicians.

A major challenge is seen to be the turning of a generation of entrenched energy 'consumers' into the next generation of people involved also in the generation of their own electricity generation and consumption, turning consumers into 'prosumers'. Whether this goal can be achieved by raising environmental awareness, reducing power bills or helping consumers to install innovative technologies in their homes to participate actively in the process is explored in many of the local micro-grid projects outline below.

While across Europe there has been a decline in space heating consumption (-25 Mtoe) , water heating figures remain fairly constant (13% of load), while the share of load for electrical appliances from rose from 9 percent to 11 per cent between 2004 and 2012. Average dwelling sizes across Europe increased by c. 4 per cent since 2000 being now around 87 m2 per dwelling on average and consequently energy consumption per dwelling decreased slightly less, at 2 percent per year, than consumption per m2 at 2.4 per cent per year. This means that almost 20% of the energy efficiency progress for thermal uses has been offset, all things being equal, by the larger size of dwellings.

A major part of the story has been the soaring use of energy in appliances and in 2012 EU house-holds consumed around 40% more for small appliances than in 2000 (~ 990 kWh/year up from 700 kWh/year) although there has been a slight decreases of the annual consumption per dwelling for large appliances (- 142 kWh). Refrigerators, freezers and washing machines' consumption decreased, mainly due to substantial electricity savings with the diffusion of efficient new equipment.

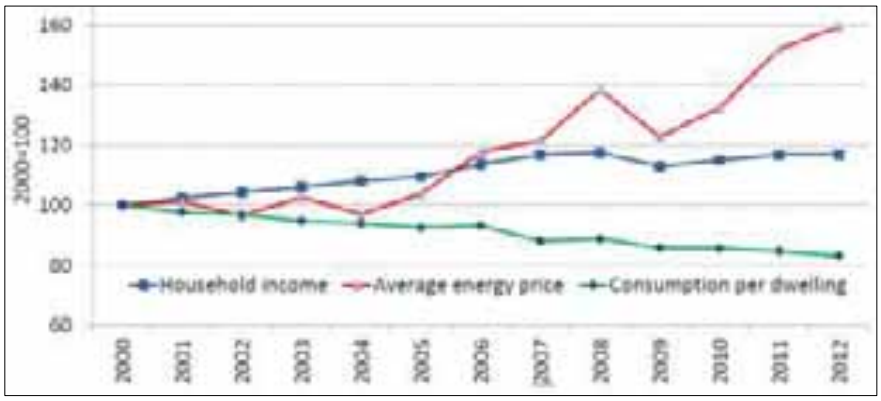

Fig. 1: Specific consumption per European dwellings, energy price and income. The figure shows the average price of gas, electricity and heating oil weighted with energy market shares (at constant prices). Income capture by private household consumption. Energy prices in Europe for households have increased by 64% between 2004 and 2012[1] (6.4%/year).

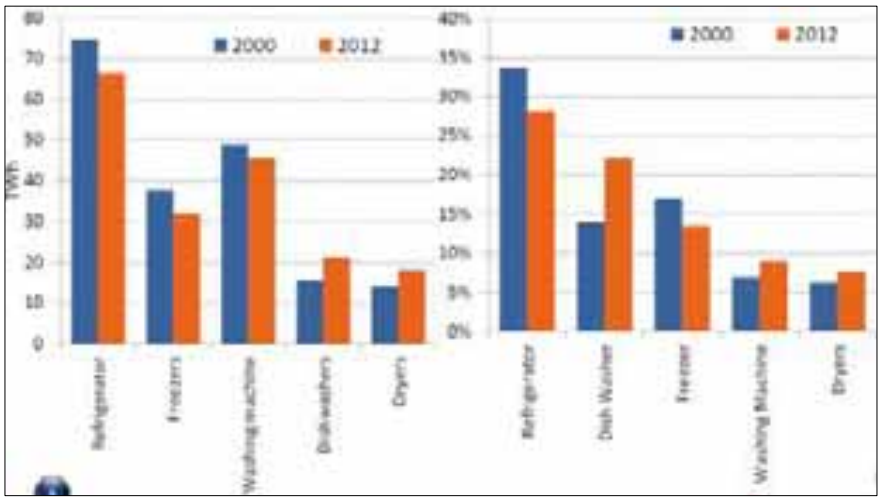

Fig. 2: Consumption of large electrical appliances by type (EU 27). Average number of appliance per dwelling in the EU shown here.

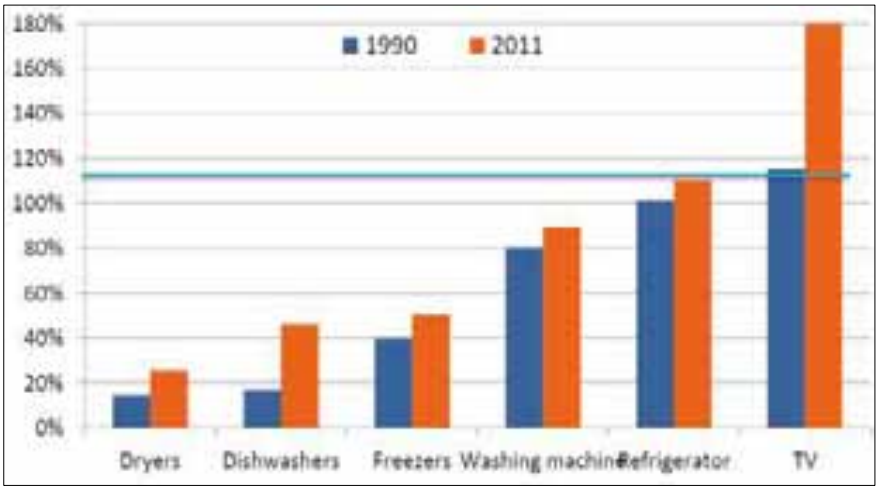

Fig. 3: Average number of appliance per dwelling in the EU

[1] http://www.odyssee-mure.eu/publications/efficiency-by-sector/household/

Energy efficiency improved for EU households by 21 percent over the period 2000-2013, ie by 1.8 per cent per year. The efficiency improvement for heating reaches 20 per cent since 2000, 15 per cent for water heating, and 14 per cent for large electrical appliances.

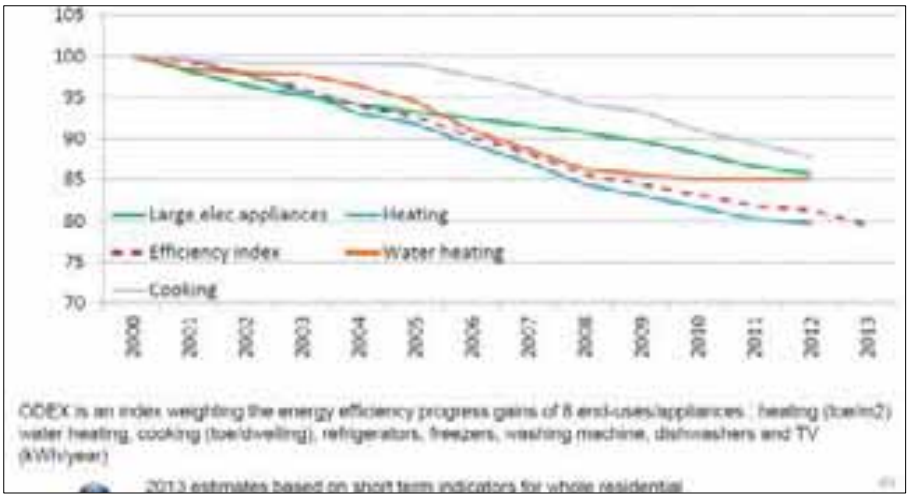

Fig. 4: Energy efficiency progress for households in the EU: ODEX

However, set again the overall trends for increased space size of households and increased use of appliances the equipment efficiency gains in themselves do not offer the hope of any radical reduction energy consumption per household and hence the widescale interest in more radical schemes to effect major emissions reductions from the energy sector and the growing interest in renewable energy micro-grids structured at a community level where the benefits of the final emissions reductions achieved can be accrued by the local users in the form of reduced costs per household in imported fossil fuel, or nuclear generated electricity.

Within the EU countries are required to develope National Energy Efficiency Action Plans (NEEAPs) set out estimated energy consumption, planned energy efficiency measures and the improvements individual EU countries expect to achieve. Under the Energy Efficiency Directive, they must draw up these plans every three years and also provide annual reports. Central to new thinking here is the idea of the Smart Grid.

2. European Initiatives: The Smart Grid

A Smart grid is defined in the report about Smart Grids by Felix Covrig et al. (2014) for the Joint Research Center of the European Commission as “an electricity network that can intelligently integrate the behavior and actions of all users connected to it in order to deliver sustainable economic and secure electricity supplies” and is an emerging concept for electricity networks across Europe[2].

The development of electric utilities and generation from renewable energy creates new constraints on electrical systems. These trends, together with the high price of primary energy sources and an awareness of climate issues at a national level, make a better management of electricity demand, a better pilotage and better efficiency of the whole electrical system necessary. Issues for the consumer and the citizen are three: improvement of the quality and continuity of the electrical supply necessary to allow the supply of the required services to the consumer, guarantee the safety of supply and the management of energy billing.

According to the International Energy Agency (IEA), European electricity consumption is projected to

[2] http://ec.europa.eu/research/energy/pdf/smartgrids_en.pdf

increase at an average annual rate of 1.4 percent up to 2030 and the share of renewables in Europe's electricity generation will double; from 13 percent now to 26 percent in 2030. Smart Grids do not represent a simple product development step and cannot be developed 'in-house'. Their supply chains are not the same as their procurement chains which brings risks with it that have to be managed. New grid technology cannot be fully proven in the laboratory or on a simulator but needs real world pilot operations, in a controlled situation on a real grid as a prerequisite for adoption. However there is little value in one-off new technology installations and as wide area adoption, through commercial mechanisms, is needed to attain its benefits the EU instituted a large funded trench of projects under its FP7 research programme to explore and develop such pilot schemes.

3. 12 European Micro-Grid Research Pilot Projects Described

The 12 demonstration sites reviewed here are located in different climate zones and are characterized by different energy generation and consumption habits. Their characteristics are review in Table 1. With their project titles, locations and climates summarised. They are grouped by types of project under headings covering projects that cover distributed renewable energy systems, district energy management, user participation of users in the projects, scoping different approaches to the challenge of engaging users in managing demand.

3.1 Electricty generation: distributed RES.

EEPOS

Energy management and decision support systems for Energy POSitive neighborhoods

The EEPOS system shows a semi-centralized structure where energy management is carried out on two levels: neighborhood (centralized) and building (decentralized). The main aims of the neighborhood level energy management system are described by **Klebow et al. (2013)**, and they are: matching of local electricity generation and consumption, congestion management in local electricity grids and power balancing on electricity market level. These objectives will be achieved by shifting of controllable electrical loads. Additional functions of the EEPOS system are statistical data analysis and end-user involvement in energy management processes.

At high RES penetration, in times of low renewable energy production, energy shortages can occur, whereas in times of high wind or PV power production, electricity production rates may even exceed those of consumption. Without proper energy management, grid instabilities can occur, and generated energy may be lost. **Automation of low voltage distribution grids** is one of the steps towards smart grids and successful integration of RES.

Bidirectional energy management systems can, for instance, help to cope with the mentioned challenges by the automated exploitation of load shifting or virtual storage potentials. Additionally, bidirectional data communication allows smart meters to send information on current electricity prices to the end-user. In this way, the end-user obtains the opportunity to manually maintain energy consumption in a cost effective and grid supporting way.

http://eepos-project.eu/eepos/eepos-project/energy-management-on-the-neighbourhood-level/

Project	N.	Sites	Climate	Average T°C (Summer)		Average T°C (Winter)	
				MIN	MAX	MIN	MAX
AMBASSADOR	1	INES, Chambery, FRANCE	Temperate Cfb	15	28	-1	9
	2	Lavrion, GREECE	Continental Csa	23	28	10	15
	3	BedZED, Wallington, UNITED KINGDOM	Temperate Cfb	12	23	2	9
CoSSMic	1	Konstanz GERMANY	Oceanic Cfb	13	25	-1	4
	2	Caserta ITALY	Temperate Csa	20	31	4	13
DIMMER	1	Turin ITALY	Humid subtropical Cfa	17	28	-2	8
	2	Manchester UNITED KINGDOM	Moderate Cfb	12	21	2	8
e-balance	1	Park Bronsbergen Zutphen, THE NETHERLANDS	Oceanic temperate Cfb	15	21	1	6
	2	Region of Batalha, PORTUGAL	Mediterranean Cfb	19	29	8	15
EEPOS	1	Helsinki, FINLAND	Humid continental Dfb	12	22	-7	1
	2	Langenfeld, GERMANY	Temperate Cfb	14	24	0	7
EINSTEIN	1	Building level Bilbao, SPAIN	Oceanic Cfb	17	24	6	14
	2	District level Warsaw, POLAND	Humid continental Dfb	14	25	-4	2
EPIC-HUB	1	Port of Genoa, ITALY	Temperate Csa	20	29	3	13
	2	Belgrade airport, SERBIA	Humid subtropical Cfa	17	28	-2	6
	3	Bilbao exhibition, SPAIN	Oceanic Cfb	17	24	6	14
NEXT-Buildings	1	Amsterdam, HOLLAND	Oceanic Cfb	13	23	1	6
	2	Lyon, FRANCE	Oceanic Cfb	17	28	1	7
	3	Helsingborg, SWEDEN	Oceanic Cfb	13	22	-1	5
Nice Grid	1	Carros, FRANCE	Mediterranean Subtropical Csa	20	28	6	14
NRG4Cast	1	Municipality of Miren, SLOVENIA	Humid subtropical Cfa	18	29	2	10
	2	Athens, GREECE	Mediterranean Subtropical Csa	22	28	7	13
	3	Turin, ITALY	Humid subtropical Cfa	17	28	-2	8
	4	Reggio nell Emillia, ITALY	Mediterranean Cfa	19	30	-1	7
	5	Aachen, GERMANY	Temperate Cfb	14	24	1	7
ORIGIN	1	The Findhorn Community, SCOTLAND	Temperate Cfb	10	19	0	7
	2	The Damanhur Community, ITALY	Warm and temperate Cfb	17	28	-2	8
	3	Tamera Healing Biotope, PORTUGAL	Temperate Csa	17	26	8	15
RESILIENT	1	Ebbw Vale, UNITED KINGDOM	Temperate Cfb	10	19	1	6
	2	Cordium, BELGIUM	Oceanic temperate Cfb	12	22	2	6
	3	Savona, ITALY	Temperate Csa	20	29	3	13

Table 1. Characteristics of the 12 reviewed FP7 micro-grid projects

One of the subsystems of the Information and Decision Support System is the end-user collaboration tool that engages and motivates end-users to decrease their energy consumption and to shift energy appliances from peak hours to off-peak hours of the day. To achieve this, the main functions of the tool are end-user energy performance reporting, benchmarking and guidance, neighbourhood discussion forums, energy saving games or contests in the neighbourhood, and targeted energy saving group actions trough **crowdsourcing**[3].

NEXT-buildings project:

Next zero energy buildings at lowest cost using competitive sustainable technology.

The innovative technologies[4] developed in Next-Buildings are some dual function building elements (insulation/photovoltaic), innovative windows, and ICT solutions. The first one will be applied cost-effectively and will improve aesthetics and easiness of handling. Then the second one will enable daulight steering based on micro-lamellas in the glass. Finally the third one will optimize the use of locally produced electricity, heat and cooling, and will provide inhabitant feedback based on smart metering and near real time data gathering. This project shows the next generation of low energy buildings. However, the scope goes beyond low energy buildings only. At the demonstration sites also smart technologies and ICT are applied, to enable efficient integration of locally generated renewable energy. Solutions will reduce CO_2 at negative or no cost.

Nice Grid

NICE Grid in the south of France has been developed with a consortium of 10 companies and with funding from the European Commission (FP7 scheme) and the French Agency ADEME also this larger is dealing with PV integration within a 10,500 inhabitant city with the objectives of: 1) PV integration, load shedding and islanding in 7 identified district called “solar districts”; 2) energy storage and the shift of residential appliances consumption allows for reducing the grid constraints due to PV. Load shedding consists in reducing the peak demand in winter by 3.5 MW at the primary substation level, by combining residential and commercial demand side management and 3) disconnecting for a limited duration a commercial district from the main grid, and supplying it only with PV generation and grid batteries.

3.2 Electricty generation: district energy management

Demand Response (DR) is defined as: “Changes in electric usage by customers from their normal consumption patterns in response to changes in the price of electricity over time, or to incentive payments designed to induce lower electricity use at times of high wholesale market prices or when system reliability is jeopardised.”

AMBASSADOR project

Real-time optimization **strategies**[5] at district level by combining ecosystem awareness (models, usages, prediction), flexibility (through horizontal energy flows), resources sharing (centralized and mutualized) and energy management strategies (advanced analytics, ICT, anticipation).

[3] Definition : it is the process of obtaining needed services, ideas, or content by soliciting contributions from a large group of people, and especially from an online community, rather than from traditional employees or suppliers (from https://en.wikipedia.org/wiki/Crowdsourcing).
[4] http://next-buildings.com/images/next-buildings%20d7.3%20v1.0.pdf
[5] http://ambassador-fp7.eu/wp-content/uploads/2013/01/AMBASSADOR_ICT4SusPlaces.pdf

EPIC-HUB project

The Energy-Hub model identifies and optimises the interactions between different input energy sources in order to satisfy electricity and heating/cooling demands. In the energy hub model, you consider a given load (or loads, electricity, heating or cooling demands); the system will optimise the hub's inputs (energy imports, from the grids or RES) by using the consumption forecasts (future demand in a given time horizon). In addition to these data, in this model, you know the hub nodes (e.g. CHP, batteries, boilers, and so on) where each of them has its own configuration parameters.

The optimisation process will state which the best configuration of the "battery element" (node of the hub) by selecting/suggesting: a) the best technical solution if you are planning investments in your facility or b) the best strategy to manage/control that energy system (i.e. batteries) at operation time in the given time horizon of the optimisation process. In this last case, you have to consider that the strategy optimises the overall energy behaviour of the hub (facility or district) without any specific optimisation of the usage related to the specific energy system (e.g. battery or boiler).

3.3 Participation of users in the projects: surveys

In many countries, the transition to sustainable energy supply and the emergence of smart grids are in progress. The deployment of distributed Renewable Energy Sources (RES) for the energy supply for buildings and residential areas has been increasing significantly in the recent years. Many people living in residential areas have already begun to produce electricity locally, e. g. through the installation of photovoltaic (PV) panels on the roofs of their houses. Their role has thus evolved from being only consumers of energy to becoming prosumers, not only consuming but also producing energy.

e-balance project

The project has been created to develop solutions for residential customers by taking into account technical and non-technical aspects, with the goal of improving the energy efficiency in small scale communities. The moto is to involve participants to offer innovative technologies that suit them most. Therefore e-balance project collects participants' views through online survey. By assessing users' feedback it can know what is appreciated about the energy management system (EMS). Among their three demonstration sites in Portugal, the Netherlands and Poland, with respectively 1661, 1632 and 1647 participants, they discovered what the habitants like most about the system was to save money (reduction of the power bills), although for Dutch habitants the benefits from energy consumption monitoring and data analyses made by the system are more appreciated than the savings. On the other hand, 71% of Polish people want free installation be encouraged joining the project and a 50% share of them will enjoy free maintenance of the system. Finally half of the Portuguese are very interested in forecasting of their monthly energy consumption.

Moreover, they have questioned the habitants about their enthusiasm to join the project to be aware of the factors that could discourage them to enable the EMS be implemented in their houses. Generally people are afraid of losing control of their home appliances and that frequent failures will appear that require repairs too expensive for them. One third of the respondents think that they will not get any return on the initial investment they have made. The last factor discouraging from using the system is about privacy reasons.

ADDRESS project

In this project the incentives of participants[6] on the French demonstration site of the ADDRESS project in Houat and Hoëdic are for 30% about the protection of the environment and the same share for their attraction

[6] More than 7% of the consumers participate in the field tests (among the 373 consumers of the two islands).

to the new technologies. And then, 20% of the respondents' motivation is about saving money and also an equal part of them desire to obtain a secured electrical supply.

ORIGIN project

In the ORIGIN concept, a behavioral study has been made among two of its communities, Tamera and Findhorn, with respectively 19 and 40 participants. On a five-step scale from strongly agree to strongly disagree, when it is asked how much they feel concerned about data protection there is an average value for Tamera of 3.8 and only 2.9 for Findhorn. Both communities agree on an average of 4.2 to have access to personal historical consumption data. They are also mostly interested in the forecast on the availability of renewable energy with a total average of 4.3. Finally it is asked what should be the main aim of the project. In average, the optimization of CO2 emissions and protection of the environment is seen as most important. And then economic benefits for the community are rated second highest.

3.4 Participation of users in the projects: variable tariffs

CoSSMic project

"In the CoSSMic concept the user leaves to the control system to decide exactly when an appliance is used, for example the user readies the washing machine in the evening and states when it should be finished, for example the next afternoon. Then the control system will start it when at the most optimal times taking into account both the output from local (to the neighborhood) PV system and the grid price."

"Yes, the users must provide constraints on that are adhered to by the control system, and the control system take into account predicted variation in prices. In the trial site only static price schemes are available, where the variation over the day is known in advance, but we plan to do simulations with more dynamic market driven pricing."

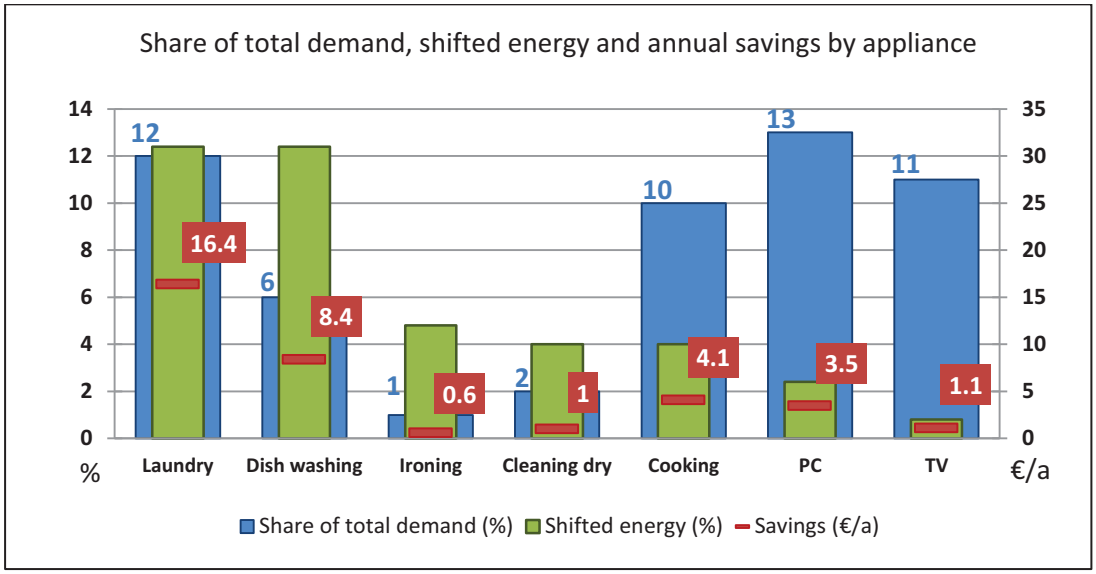

Figure 5. ORIGIN project Chart based on Fischer et al. (2015)'s paper (see references).

EEPOS project
Energy management and decision support systems for Energy POSitive neighbourhoods.

It was aimed at developing a new system for energy management and automated load control on the neighbourhood level, the EEPOS Neighbourhood Energy Management System. With the new system, designed to use automated load shifting of controllable electrical loads and active end-user envolvement in energy management processes to:

- Match of local electricity generation and consumption
- Management congestion in local electricity grids
- Increase energy efficiency within the system

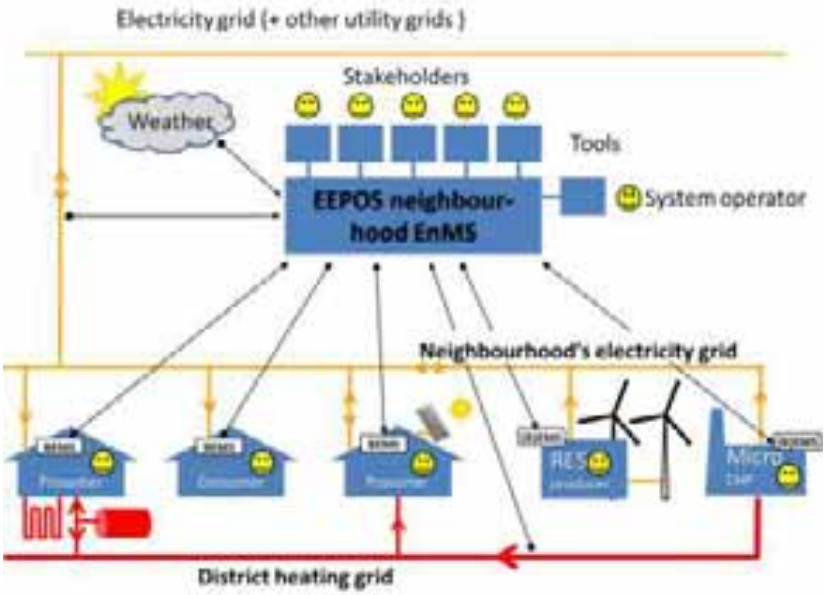

Figure 6. System diagram for the EEPOS project
http://eepos-project.eu/eepos/eepos-project/an-eepos-neighbourhood/

4 Thermal and Electrical storage in the projects

A range of different kinds of energy storage are described by Mohd et al. (2008), and they discuss the difficulty of their integration into a smart grid, not least because of it expense. However due to the pressing need to integrate increasing shares of renewable energy generation in future power supply systems and to shave ever growing peak loads on energy supply systems energy storage is expected to take place at all grid levels in the electrical network in future. Some projects within the twelve reviewed have no storage at all like the EPIC-HUB project while others like **Nice Grid** have storage media and strategies integrated at every stage of the project. The AMBASSADOR project includes 30 kWh Zebra batteries (sodium), 25 kWh Li-ion batteries and 50kWh Lead acid batteries.

RESILIENT incorporates both thermal and electrical storagewith two differnt storage media being both sodium nickel molten salts (sonick fiamm - 470 ah, voltage: 278 v so 104,5 kwh - total charge/discharge maximum time: 2 hours an inverter maximum power 70 kw) and hitachi li-on batteries with a 25 kwh capacity (c. 30 minutes charging/discharging time). This demosite is deemed to be a polygenerative site where Electrical and Thermal Energy production are constantly monitored and managed in an optimal way that enables them to respond to demand (over which they have no control) in with optimal energy responses.

The EU EINSTEIN project was implemented to reduce the consumption of primary energy in buildings

using solar thermal energy in combination with heat pumps and Seasonal Thermal Energy Storage (STES) for space heating and domestic hot water requirements[7]. The research is turned to existing building which have particular requirements and constraints that requires new developments and adaptation of existing technologies. Two pilot plants have been build, one at building level in Bilbao, Spain, and the other at district level in Warsaw, Poland. The decision for a certain type of storage mainly depends on the local requisites like the geological and hydro-geological situation in the underground of the respective construction site. Above all an economical rating of possible storages according to the costs for a kWh of thermal energy that can be used from the storage allows the choice of the best storage technology for every single project. The installation of solar panels is not the main objectives of the project, this is why there is no electrical storage created on the demonstration sites: the electricity is entirely fed back in the main grid when it is not consumed.

5 Legal and Fiscal Frameworks for Community Energy

What is not being funded within such European projects is research into the legal and fiscal mechanisms that will be essential for locally owned micro-grid and other distributed energy supply and generation systems including legal frameworks for the drafting of lease agreements, company models and IP agreements, such as are being pursued currently in the South Australian solar community movement. Monica Oliphant Research, in collaboration with Finlaysons and Solar Wind Systems has been developing one such model is being developed for the City of Campbelltown in South Australia[8].

The Model has been designed to lower energy use costs across the community through the application energy efficiency strategies and embedded solar installations. Electricity pricing will be locked in for life of the project which is between 7-10 years depending on the site, paid for in part by the capital raised through sale of $600 shares. Shareholders are given a return on investment annually for life of the project. Governance is through a new Trading Cooperative or through an existing organization whose constitution allows them to raise capital. Approval of a prospectus needs to be gained from the Office of Consumer and Business Affairs and at the end of the project (7-10 years) shareholders have their $600 returned and the installed equipment is transferred to the building owner providing fee electricity for the remaining life of the equipment. All measures are tailored to suit each building/site and are 'behind the meter' to avoid having to operate as an electricity retailer. An initial audit determines the current energy usage and identifies energy efficiency options. This provides sufficient preliminary data to enable building owners to determine if they wish to go to next step. The cost of this preliminary audit is $1,500. A full audit costs between $5,000 and $10,000 depending on size and complexity of the facility. This will provide accurate costing and data for input into the model to verify 'return on investment' to shareholders. The prospectus is prepared and approval sought from OCBA (Office of Business and Community Affaires) and voted on at a local public with a local board of directors. The lease agreement is signed with building owner and at that point the capital raising commences and the fully subscribed Community Energy Project is launched. In South Australia the Bendigo Bank is supporting the project and will maintain bank records and provide advice on engagement, capital raising etc.

6 Conclusions

Much research in Europe is currently being funded through the strategic European research mechanisms and within the 'Big Energy' industry on mechanisms for maximizing the growing contribution of distributed renewable generation through the use of energy demand and supply orchestration, through the exploitation of changing behaviors and local energy controls and management, with or without energy storage integrated into local distributed energy micro-grids. The South Australian case study has been included to emphasize the multiply complex nature of not only optimizing the value of distributed energy within national grids in theory and reality, but also enabling them to happen locally in practice, in the emerging energy revolution.

[7] EINSTEIN's leaflet: http://www.einstein-project.eu/fckeditor_files/D_9_2_EINSTEIN_leaflet_English.pdf
[8] https://www.lga.sa.gov.au/webdata/resources/files/Campbelltown_Final_Report_October_2012_-_Case_Studies.pdf

7 References

About ORIGIN

Fischer, D., Flunk, A., Kreifels, N., Lindberg, K., Wille-Haussmann, B., 2015. Modelling the Effects of Variable Tariffs On Household's Electric Load Profiles by Use of Occupant Behaviour Submodels. http://www.origin-energy.eu/system/files/Origin_DSM_DaF.pdf

Peacock, A.D., Owens, E.H., Roaf, S., Corne, D.W., Dissanayake, M., Tuohy, P.G., Stephen, B., Galloway, S., 2014. Autarkic energy systems: balancing supply and demand with energy storage and controls in local energy micro-grids, in: 2014 Asia-Pacific Solar Research Conference.

About EEPOS

Klebow, B., Purvins, A., Piira, K., Lappalainen, V., Judex, F., 2013. EEPOS automation and energy management system for neighbourhoods with high penetration of distributed renewable energy sources: A concept, in: Intelligent Energy Systems (IWIES), 2013 IEEE International Workshop on. IEEE, pp. 89–94. http://ieeexplore.ieee.org/stamp/stamp.jsp?tp=&arnumber=6698567

About Nice Grid

Lannez, S., Foggia, G., Muscholl, M., Passelergue, J.C., Lebosse, C., Mercier, K., 2013. Nice grid: Smart grid pilot demonstrating innovative distribution network operation, in: PowerTech, 2013 IEEE Grenoble. IEEE, pp. 1–5.

Michiorri, A., Girard, R., Kariniotakis, G., Lebossé, C., Albou, S., 2012. A local energy management system for solar integration and improved security of supply: The Nice Grid project, in: Innovative Smart Grid Technologies (ISGT Europe), 2012 3rd IEEE PES International Conference and Exhibition, pp. 1–6.

About storage

Mohd, A., Ortjohann, E., Schmelter, A., Hamsic, N., Morton, D., 2008. Challenges in integrating distributed energy storage systems into future smart grid. IEEE International Symposium. 1627–1632. http://ieeexplore.ieee.org/stamp/stamp.jsp?tp=&arnumber=4676896

About consumers

Darby, S.J., McKenna, E., 2012. Social implications of residential demand response in cool temperate climates. Energy Policy 49, 759–769. http://ac.els-cdn.com/S0301421512006076/1-s2.0-S0301421512006076-main.pdf?_tid=c569bc64-4a6f-11e5-9975-00000aab0f27&acdnat=1440428141_31d195ad11a96c0f3f9d079fbd302af9

Darby, S.J., 2013. Load management at home: advantages and drawbacks of some active demand side options. Procs. of the Institution of Mechanical Engineers, Part A: Journal of Power and Energy 227, 9–17. http://pia.sagepub.com/content/early/2012/10/30/0957650912464623.full.pdf+html

About EUROPE – General papers

Felix Covrig, C., Ardelean, M., Vasiljevska, J., Mengolini, A., Fulli, G., Amoiralis, E., Sánchez Jiménez, M., Filiou, C., European Commission, Joint Research Centre, Institute for Energy and Transport, 2014. Smart grid projects outlook 2014. Publications Office, Luxembourg. http://www.researchgate.net/profile/Eleftherios_Amoiralis/publication/269763242_Smart_Grid_Projects_Outlook_2014/links/5495ab8c0cf29b94482411d5.pdf

Boughen, N., Castro, Z.C., Ashworth, P., 2013. Understanding the residential customer perspective to emerging electricity technologies: Informing the CSIRO Future Grid Forum. Brisbane, Queensland: CSIRO.

Albadi, M.H., El-Saadany, E.F., 2008. A summary of demand response in electricity markets. Electric Power Systems Research 78, 1989–1996.

Downing P. Understanding consumer attitudes to 'sustainable community infrastructure'. Icaro Consulting Report for the UK Green Building Council and the Zero Carbon Hub (2009).

Belhomme, R., Tranchita, C., Vu, A., Maire, J., Huet, O., 2011. Overview and goals of the clusters of smart grid demonstration projects in France, in: Power and Energy Society General Meeting, IEEE, 1–8.

Off-Grid & Rural Energy Access

Conference Proceedings

Solar World Congress 2015
Daegu, Korea, 08 – 12 November 2015

RURAL ELECTRIFICATION AT THE ECUADORIAN JUNGLE A NEW MANAGEMENT MODEL, PREPAID SYSTEM

Robert Peñaranda Loayza

Empresa Eléctrica Quito. Quito, Ecuador.

Abstract

A new management model for rural electrification with off grid photovoltaic systems is presented. This management model is based in a prepaid meter for each house that has a photovoltaic kit, where the electrical distribution company sells days of energy to the client. This model requires that the user visits an agency at least once every two months to recharge more days. The prepaid system allows to monitoring in a better way how the systems are working and how the clients interact with the new photovoltaic kits. The advantages of this management model are on the one hand that the electrical distribution company is closer to the client and achieves a better monitoring; on the other hand the system is implemented without additional communication equipment. This is made possible by the use of a prepaid key to recharge days of energy. The system is analyzed, data about clients is presented, and the future of the project is discussed

Keywords: *Rural electrification, prepaid meter, solar home system, solar energy, off grid system*.

1. Introduction

Ecuador has 4 regions: The Sierra, The Coast, Amazonia, where the jungle is, and the Galapagos Islands. The project is developed in two provinces of Amazonia: Sucumbíos and Orellana. These provinces are some of the ones with the least access to electrical energy. Indeed, according to the last census from 2010, 73,43% [1] of the people have access to electrical energy in Sucumbíos and Orellana. Consequently the object of the present program is to increment the access to electrical energy in order to reach the government plan of 96% of the population with access to electrical energy in the rural area.

To achieve this ambitious objective a new management model for rural electrification has been developed with individual isolated "Photovoltaic Systems" (PVS) including a prepaid meter. The main objective is to be able to monitor the PVS systems without additional communications equipment and without needing anybody to travel to the houses where the PVS have been installed. Trying to avoid old practices where the systems are installed, but no proper maintenances is given to the equipment. This causes some consequences like that the photovoltaic systems get broken and people lose trust in solar energy.

The aim is to reduce cost in maintenance and give a better service to the systems that are being installed in really remote communities, some accessible only by boat or small aircraft.

One additional objective is to encourage people to be responsible for the PVS. The prepaid meter system makes people think that the electric company is monitoring them and this will help to avoid the misuse of the equipments.

doi:10.18086/swc.2015.03.01 Available at http://proceedings.ises.org

2. System Overview

The new photovoltaic systems which are being installed in communities of the Ecuadorian jungle (Sucumbíos and Orellana) have two circuits, one for the DC lighting and the other for the AC part including the inverter. It is composed of the following elements:

- 3 Solar Panels (130 Wp)
- 1 Charge Controller + Prepaid System
- 1 Inverter (700W)
- 2 LED lamps (7W DC)
- 4 LED lamps (11W DC)
- 1 Portable lamp/ cell phone charger.
- 2 AGM Batteries (300Ah 6V)

The system is based in older systems to which some improvements have been added. One of them is the LED lighting, which permits illumination without depending on the inverter as well as being more efficient. The other significant improvement is the addition of a controller and a prepaid meter, which cut the energy in the house if there are no remaining days of energy. The meter helps to have a better control of the PVS, so people paid for consumption and also functions as a data logger. The following graph shows the schematic of the Photovoltaic systems.

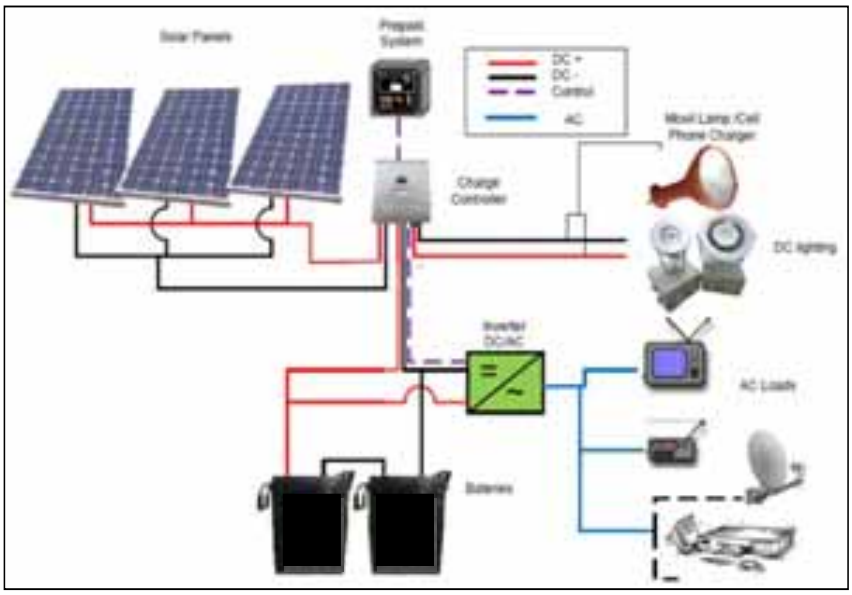

Figure 1: Photovoltaic system with prepaid meter scheme

3. Prepaid System

The prepaid system allows users to have energy for a given number of days, depending on the credit acquired. All the information of the PVS as the operation of the solar systems, how much credit is available, is saved in the prepaid system and a prepaid key. This small key permit to buy days of energy and to download the information of the PVS when it is connected to a recharge center, then new data is downloaded and additional energy days are sold to the client.

One special feature is if the user, for any reason, has no credit in the system. He could request a maximum of

10 more days until he could go to a recharge center with only pressing a button on the prepaid equipment. The credit can be acquired in any authorized recharge center. In case the prepaid key is remove from the prepaid systems, all the equipment continues to work.

The prepaid system methodology forces the people to bring the key to an authorized recharge center in order to get more days of energy. In case the prepaid system does not have days, the controller shuts down the DC lights and the inverter. A maximum of 60 days of energy can be charged in this management model. This allows the energy company to get data on the PVS at least every 2 months for better monitoring. The recharge centers are usually in the main town where people from the communities go at least one time per month for trade, medical assistance and other activities.

The main requirement for the recharge centers is to have access to internet. Indeed, it enables to save data of the different prepaid keys and send it to a main database, where it could be used for further analysis.

Among the advantages that the prepaid system presents are:

- To be able to know the production of the solar panels
- State of the batteries, voltage of battery.
- Alarms in the system, low battery, over charge, days without energy.
- How many days of energy the client has left and when was his last recharge.

3.1. Prepaid system implementation.

This new management model is already implemented in some areas around Quito and it has been installed in the Ecuadorian jungle. After the installation of some photovoltaic systems, the distribution company observes that the users come to the recharge centers at least once per month to acquire credit for their PVS. The data obtained permits us to know how the system is working and monitor the systems, consequently the customer feels more responsible with the solar equipment and the electrical distribution company has a bigger income for future maintenance and most importantly, the change of batteries after 5 years.

One of the major challenges that the project is facing is the interconnectivity of the recharge centers with the database. This is due to the fact that some of the recharge centers are in remote cities and consequently the internet connections are poor, which can prohibit getting the data from PVS. Recharge centers must have a secure internet connection for these kinds of projects to be successful.

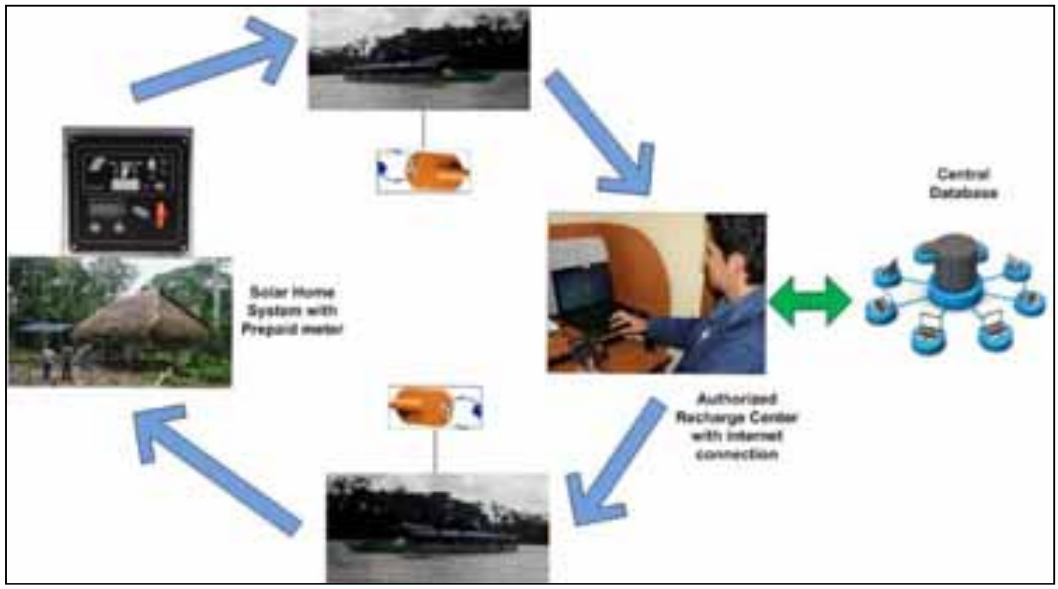

Figure 2: Prepaid system management model schematic

Figure 3: Typical installation of prepaid system and inverter.

4. The Overall Cost

The investment for each individual photovoltaic system with the prepaid meter is around $ 2400.00 which includes all the components of figure 1 and installation.

At the provinces of Sucumbíos and Orellana 500 new prepaid photovoltaic systems and 500 prepaid meters for repowering old systems, will be installed. The investment for the first phase of the project is $1,575,152.80 for the installation and purchase of the 500 new PVS and 500 prepaid systems for repowering.

The project has social interests, such as an understanding of the social costs of not having electrical energy as well as the benefits that the project will produce like:

- Savings in the cost of transportation to bring diesel for gen sets.

- Prevent migration to big cities

-Access to information and communication

-Improve the service of utilities, education, health and drinking water.

The PVS systems have an expected life time of 20 years and the batteries will be changed 3 times in the life time of the system.

5. Results

The project developed in the surroundings of Quito permit us to evaluate how the system will work in the Ecuadorian jungle. The data is obtained when the client goes to charge days on the prepaid key, the data from the PVS is downloaded to the database and we obtained the basic information to evaluate the system as shown below:

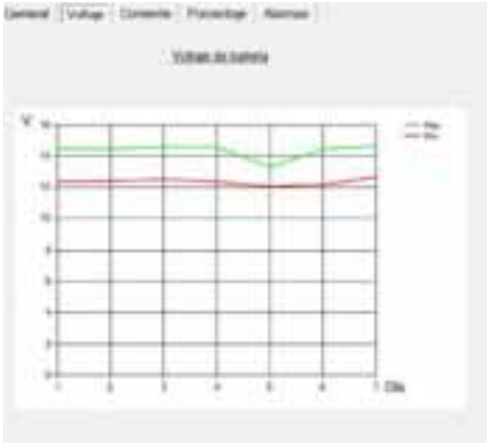

Figure 4: Battery voltage of a PVS, actual data download from a prepaid key. [2]

Figure 5: General Data of the PVS, downloaded from the prepaid key. [2]

This information allows to know if the system is operating properly, giving us an idea of the consumption and the production of solar panels. Some important information is how many times the user acquires credit for the prepaid system, which could show if the system was manipulated by the user. For example if the user does not recharge the prepaid key in more than two months, perhaps they are taking energy directly from the batteries.

The expected result in the jungle is to have a power of 195kW installed with solar power and a daily production of 780kWh. The new individual solar systems will provide electricity to around 500 families and repower 500 more systems in the Ecuadorian jungle, which are going to be monitored by the prepaid meter.

6. Conclusions and Outlook

This article presents the implementation of the prepaid system in individual photovoltaic systems for rural electrification and the expectations for monitoring in the Ecuadorian jungle.

By the end of the project 500 new PVS will be installed in the provinces of Sucumbios and Orellana, and 500 more will be repowered.

One of the advantages of the present project is that it is being carried out without additional communication lines or communication devices for monitoring. The prepaid meter and its key permit to obtain data of the PVS, when the users acquire more days of energy.

A recommendation for this type of projects is that the recharge centers should have a secure internet

connection in order to send data to the servers and the database. Additionally one person should be in charge of the database to monitor the data and observe for inconsistencies of the system.

These new photovoltaic systems allow access to electrical energy to people who live in communities at the middle of the jungle, the access to communication, a better education and an improvement in their economy.

As complement of the project new hybrid (solar-genset) microgrids will be developed in some communities, installation of solar water pumpers and solar public lighting as part of a big plan to provide electrical energy service to communities in the Ecuadorian jungle.

7. References

[1] INEC, 2010. Censo nacional. Ecuador

[2] PHOCOS, 2014. Program PREPCOM.

[3] M. Balseca, 2012. Programa Luz para el Sumak Kawsay. Quito, Ecuador.

[4] PHOCOS, 2014. Manual operación sistema prepago prepcom. Bolivia.

Conference Proceedings

Solar World Congress 2015
Daegu, Korea, 08 – 12 November 2015

Rural Electrification Initiatives in Fiji – A Case Study of Solar Home Systems

Ravinesh Tendra Nand[1] and Atul Raturi[2]

[1]Department of Energy, Suva, Fiji

[2] The University of the South Pacific, Suva, Fiji

Abstract

Fiji is striving towards to provide its entire population with access to modern forms of energy, especially access to electricity. In 2007, 89% of the population had access to electricity which comprised 82% of rural and 96% of urban dwellers. Although access to electricity in rural areas is still significantly low compared with urban areas , it represents a marked improvement from 69 % in 2003. The current (2014) estimates of overall national electrification rate are 92- 95% .The progress in rural electrification can mainly be attributed to a number of on-going initiatives including main grid extensions, solar home systems, diesel mini-grids and pico-hydro schemes but the solar home systems (SHS) program is the most popular and preferred option in remote rural and maritime regions.

Keywords: *Electrification rate, Solar Home System (SHS), Fiji*

1. Introduction

The challenges of providing electricity services to communities in smaller islands and remote rural areas of Fiji are multi-faceted and are further compounded by their geographical distances from the main electrical grids. Also, as the infrastructure developments for electricity supply are capital intensive, the typically lower power demands and low returns in these areas do not generally encourage investments from the power utility or any other private investors. Thus, the members of the public in such localities mainly rely on State assistance for their electricity needs.

In addition to grid extension wherever feasible, there are two common options for electrification in Fijian rural communities are (i) village diesel generator based mini-grid systems and (jj) Solar Home Systems (SHS). The main criterion underpinning the preferred option includes utilization of clean energy resources, affordable and reliable power system and more importantly, the least-cost option.

The SHS initiative has been found to be the most cost-effective and affordable to the end users. By the end of 2014, the Department of Energy (DoE) under its Rural Electrification initiative had installed over 5,700 SHS, directly assisting over 28, 000 people across the country (DoE, 2014 II).

2. Policy Frameworks

The overarching policy guideline for national development in Fiji is the Green Growth Framework (GGF) of 2015 (PIDF,2014). The GGF has ten thematic focus areas which include Energy Security as well as Technology and Innovation respectively. The GGF is closely aligned to the National Sustainable Energy for All (SE4All) Initiative and the National Energy Policy. The main targets are that all households be electrified by 2020 and the share of renewable energy in electricity generation will be 80 % by 2020. Long term targets are to double the share of renewable energy in the overall energy mix to up to 25 % by 2030. Moreover, energy supplies should be clean, affordable, environmentally friendly and sustainable.

doi:10.18086/swc.2015.03.02 Available at http://proceedings.ises.org

Government also has a Rural Electrification Policy through which the costs for energy infrastructure are largely subsided in order to provide electricity to the rural, remote and maritime communities (DoE, 2014 I). The SHS program is one of the major programs under the Rural Electrification initiatives. The Department of Energy (DoE) manages the rural electricity programme which is heavily subsidised by the government. This has resulted in the establishment of 500 diesel generator based mini-grids and more than 1500 grid extensions since the programme began in 1994(DoE, 2014 III).

3. Quasi-RESCO Model

The SHS project implementation, maintenance and management approach is an extension of the Renewable Energy Service Company (RESCO) model. The SHSs are fully funded, maintained and owned by the Government, which partners with RESCOs through formal contracts for servicing and maintenance works. The end-users are levied a reasonable and affordable service fee per month, which is paid 6 monthly in advance. The table below summarizes the details of the SHS program.

Table 1: Details of Government funded Solar Home Systems

Project Type	SHS Type I (2009 – 2013)	SHS Type II (2014 to present)
Major components	Solar Panels 2 x 50Wp Battery 100Ah DC LED lights: 1 x 1W DC CFL lights: 3 x 11W & 1 x 7W Charge Controller 1 x 10A	Solar Panels 2 x 135 Wp Battery 200Ah DC LED lights: 3 x 9 W, 1 x 7W, 1 x 1W Charge Controller 1 x 20A, Inverter 300 W
No. Installed (2014)	3460	2346
Refundable End User Contribution (FJD)	84	108
Monthly service fee (FJD)	14	18

However, there are only a small number of RESCOs operating in Fiji and even fewer in rural and maritime areas. Usually, either two or at most three RESCOs are contracted on an annual basis through DoE's tendering process to carry out servicing and maintenance works. Each household with SHS is assigned to one of the six Service Zones, where each RESCO has a defined non-overlapping geographical boundary as its area of operations.

Table 2: Summary of SHS servicing and maintenance plan – 2015 (source: DoE)

Service Zone	1	2	3	4	5	6
Service Areas	Bua	Macuata	Cakaudrove	Lomaiviti, Kadavu, Rewa	Yasawa, Rotuma, Viti Levu	Lau
No. of SHS	992	1078	1640	802	873	421

Basically, service zones 1, 2, 3 and part of zone 5 are SHS on rural and remote mainland's predominantly on second largest island of Vanualevu and the other zones cover the maritime islands. At the end of 2015, a total of 5806 SHS were on ground.

The DOE SHS programme has been rolled out in 10 phases with the pilot phase implemented in 2002 when 259 systems were installed in Vanua Levu. As fig.1 shows, by the end of current 11th phase, a total of 9,000 SHS systems would be in existence across Fiji.

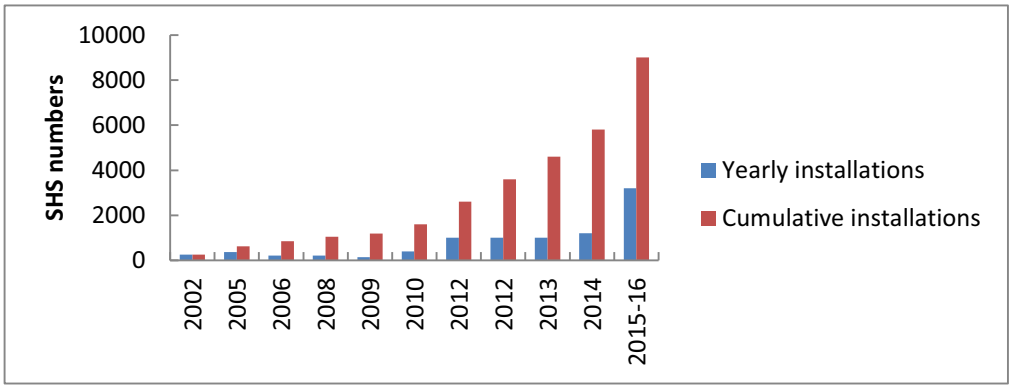

Figure 1: Yearly and cumulative SHS installations (source: DoE)

4. SWOT Analysis of Quasi-RESCO Model

Table 3: SWOT analysis of the Government funded Solar Home Systems

Strengths	Weaknesses
• Provision of clean and affordable electricity services. • Sustainability of the projects is guaranteed as SHS is maintained by a government entity(DoE). • Rural and remote communities are not burdened with maintenance and servicing costs. • In some communities, village solar managers collect monthly rental from individual households and handover to designated Revenue collectors from DoE.	• Rural market for SHS maintenance and backup support is restricted to Government contracted service providers. • Accumulating arrears due to defaulting SHS customers. • Limited transfer of Technical knowledge to SHS households. • Recurring annual cost to Government for procurement of replacement equipment and costs for payments of maintenance contractors. • Irresponsible use of SHS by households; battery misuse and system overloading impacts battery life. • Not all households could be visited by DoE officials during the scheduled revenue collection trips, given the geographical spread of SHS customers and transport logistics.
Opportunities	**Threats**
• To open up the market for RESCOs for SHS service and maintenance works, enabling business opportunities for more companies, SME's and individuals that would generate economic activities in rural areas. • Upgrade of system sizes/capacity to cater for growing electricity demand by households. • Training and knowledge transfer to communities on SHS technical aspects. • Government to transfer the ownership of SHS to individual households and the savings from the	• Lack of care for SHS by individual households. • Misuse of the SHS by households reduces project components lifetime. • Non-payment for maintenance jeopardise the whole initiative.

avoided costs of service and maintenance can be diverted to other projects.	

5. Impacts of SHS Program

Most SHS recipients have directly benefitted through having improved basic lighting in their homes and consequently reducing their dependence on expensive fuels like kerosene, benzene and diesel which were previously used for lighting. Also, the time spent and transportation costs to reach the usually distant commercial centers to purchase fuels are now utilized for other income generation activities including farming.. The extended lighting hours in these households as a result of SHS has enabled improved night time study facilities for school children and also assist the women with their daily household chores/weaving etc. Similarly, the introduction of Type II SHS with inverters has provided the supporting infrastructure for better communications and entertainment such as radios/TVs, and use of computers. With the spread of cellular network in remote areas, phone charging has become a daily need for most of the remote population. Moreover, fuel supply chain issues with associated logistical challenges of transportation to remote rural and maritime locations from the main business centers is of much lesser concern to the recipients of SHSs. The families assisted through the SHS are relieved of their former regular financial costs of repair and periodic maintenance of their kerosene and/or benzene lamps and in few cases diesel generator systems. In addition, the numerous health and environmental benefits of the use of clean, affordable, renewable solar energy has catalyzed positive social changes into these communities. Above all, the avoided dependence on fossil fuels for lighting purposes in these communities, contributes towards the national goal of reducing fuel imports and increasing the share of renewable energy into our national energy mix. Furthermore, the SHS program has had significant impacts on improving Fiji's national electrification rate.

A 2012 study (Urmee and Harries, 2012) surveyed one hundred and five SHS using households in Fiji and found that 84% of the respondents had an increase in their quality of life. They did not report any significant income-generation activities emanating from this initiative. However, a similar study conducted in Bangladesh (Urmee and Harries,2011) reported that SHS can be used productively to create extra income. Some of the driving factors for a successful SHS programme were identified as systems designed to fulfil user's needs and a sense of ownership.

Figure 2: A typical Solar Home System in rural Fiji (Photo: DoE)

Figure 3: SHS lighting for income generation: an example from Tonga (Photo: IUCN/Atul Raturi)

6. Challenges

The main challenge is ensuring the sustainability of these solar projects and improving the overall management of the SHS program. The current practice of managing the SHSs entails the government issuing short-term service and maintenance contracts to RESCOs for specific project localities. However, the RESCOs are not necessarily the same as the ones that initially designed and installed the SHSs. This discontinuation of services from RESCOs does not guarantee a commitment from their end to see successful operation of the SHSs for the expected project lifetime. Also there are no incentives for the RESCOs to make every SHS work properly because it could be perceived as limiting future business opportunities for the RESCOs. As such, there is high possibility that standards of service and maintenance works carried out by RESCOs could be compromised compared with if there was some system of direct financial reward to the RESCOs for ensuring continued operations of SHSs.

The current practice of SHS maintenance requires RESCOs to visit their designated service areas at least once every 3 months and any requests to attend to technical issues that arise after the RESCOs scheduled visit usually takes considerably longer period of time to respond. This warrants a significant shift in the current practice.

Another significant challenge is the recovery of arrears (maintenance fee) as a result of defaulting customers, which was around 1000 SHS customers in 2015. However, this challenge is mostly a result of those SHS where the pre-payment meters were either non-functional and households had to pay a standard monthly fee or where pre-payment meters and/or cut-off switches were not part of the SHS installed. However, the DoE through a dedicated consultations program targeting such defaulting SHS customers can improve the situation if not solved completely. On the other hand, although relatively expensive but upgrading the SHS with technical features such as cut-off switches as part of charge controller would be better.

Another area of concern for the rural electrification projects including SHSs is the absence of private sector investments in electricity generation for the rural and maritime areas. The numerous incentives provided by the Government including supportive national policies for uptake of renewable energy projects, have failed to materialize into a truly RESCO model for electricity supply at community level. The greatest challenge faced by the Government is to find ways to reduce its direct role in the RESCO process and focus on a regulatory framework for anexpanded RESCO model.

7. Way Forward for SHS program

SHS program has not been operating under a true RESCO model because Governmenet is still financing the servicing and maintaemanace as well as having absolute control over the projects. Moreover, most of the SHS

capital financing is donor-funded . Thus, there is a need to open the market and let the SHS households and RESCOs to operate freely. This will result in fewer blackout periods for customers as they will not have to wait for the periodic visit by Government contracted service providers and the Government can concentrate on other energy projects since the DoE will not be involved in maintenance and revenue collections. This presents an opportunity for Government to become more strategic and focus more on its core role in the energy sector of providing access to electricity rather than managing energy projects. Overall, the removal of government control over the SHS will enhance the sense of ownership for SHS customers.

Alternatively, in view of the present system of contracting RESCOs by Government, there is a need for long term contracts with RESCOs which bundles together; system design, supply, installation and service & maintenance contracts, which could bring about more RESCOs to participate through competitive tender process, conducted periodically by government. This would also encourage more genuine commitments from RESCOs leading to enhancement in their standards of service delivery as well. Either way, the monitoring system for SHS program within DoE needs strengthening and timely evaluations for continuous improvements.

Furthermore, Government needs to come up with other options to enable financing for SHS rather than people just waiting for DoE to roll out SHS projects annually, where households have to wait on average between 14 to 18 months from the time of payment of their contribution to DoE and the time they get a SHS installed. With alternative financing options, people can still benefit from a reasonable level of subsidy from Government for their capital costs and hence can have other arrangements for regular system servicing and maintenance with their preferred RESCO. This would not only open up the market for more RESCOs to participate in SHS program but provide options for households to acquire different sizes of SHS, usually slightly larger than the Type II systems supplied by DoE, depending on the energy needs of households. With the above, the DoE can provide standard designs and technical requirements for a range of SHS sizes that the people can choose from. However, the Government needs to ensure at the same time, that the alternative financing mechanism(s) is accessible, affordable and reliable to ordinary Fijians.

Moreover, some changes to policies and regulations governing the energy sector is necessary. Especially, the review of national rural electrification policy and its limitations on SHS program beneficiaries. Likewise, regulations need reconsiderations to allow some level of flexibility and inclusivity with regards to registartion and licencing of electricians and RESCOs, in view of potential solar technicians and smaller RESCOs that could participate in SHS program from a broader spectrum of the society. In addition, the abovementioned regulatory changes would enable more choices for SHS customers and provide certainity and confidence to all stakeholders. Similarly, enforcement of technical standards for SHS installations including for servicing and maintenance works and ensuring compliance by all stakeholders through a more responsive regulatory framework can contribute immensely to the sustainability of SHS program in Fiji.

8. Conclusions

The SHS program has over the years provided affordable lighting solutions to many Fijian households in rural, remote and maritime communities. It has helped bring positive changes to the lifestyles of the common people enabling better environment for children's education, connecting people with modern means of communication through cell phones, televisions etc. In short, SHS program is a critical factor towards Fiji achieving its Sustainable Energy for All goals and hence supporting SDG goal seven. Cutting down the use of kerosene for lighting will also have an immediate impact on black-carbon emissions which is considered a potent short-lived climate pollutant.

Fiji could consider provision of electricity to the remaining rural and maritime communities by grouping all such SHS projects into a single national comprehensive project and possibly make submissions to the Green Climate Fund (GCF) for financing. This comprehensive SHS program could be part of a broader national Green House Gas (GHG) mitigation program. Training and capacity building are of paramount importance to make the SHS programme a sustainable initiative.

9. References

DOE (2014 I) :Rural Electrification Policy, 2014 edition. Department of Energy, Suva, Fiji. (unpublished)

DOE (2014 II) :Solar Home System Inspection Reports, 2009-2014. Department of Energy, Suva, Fiji. (internal report)

DOE (2014 III) :Sustainable Energy for All: Rapid Assessment and Gap Analysis Report, 2014. Department of Energy, Suva, Fiji. http://www.se4all.org/wp-content/uploads/2015/05/Fiji_RAGA.pdf Accessed 15/06/2015

PIDF, 2014, Green Growth Framework For Fiji, 2014. Ministry of Strategic Planning, National development and Statisitics, Suva, Fiji. http://pacificidf.org/wp-content/uploads/2014/08/Pesentation-Fiji-Green-Growth-Framework-PIDF-Slideshow.pptx Accessed 10/06/2015

Urmee ,T. and Harries ,D. , 2011, Determinants of the success and sustainability of Bangladesh's SHS program, Renewable Energy,36,2822-2830

Urmee ,T. and Harries ,D. , 2012, The solar home PV program in Fiji – A successful RESCO approach?, Renewable Energy, 48 , 499-506

Conference Proceedings

Solar World Congress 2015
Daegu, Korea, 08 – 12 November 2015

SWC_ Off-grid rural electrification approaches – Lesson learnt from ASEAN

Badariah Yosiyana[1] and Susy Simarangkir[2]

[1, 2] ASEAN Centre for Energy, Jakarta (Indonesia)

Abstract

The Association of Southeast Asian Nations (ASEAN) has a population of approximately 625 million people, of which around 50% live in rural areas. More than 20% of ASEAN Member States's (AMS) population still does not have access to reliable, affordable and sustainable sources of electricity that impede economic development and an improved standard of living. Providing their citizens with electricity access and increasing their respective electrification ratio has been a constant effort and become high priority over the last decades. The challenges to improve electricity access are diverse including institutional, governance barriers, financial and technical.

Successful examples of rural electrification based on renewable energy can be found all over ASEAN. However, less successful examples are equally widespread since renewable energy utilization often lacked a sound long term strategy or feasible business models which are crucial to ensure the sustainability. The lessons learnt from these rural electrification projects prove that the ASEAN region is still facing many challenges.

This paper presents the rural electrification situation at the regional as well as country level in ASEAN. The paper also does comparative analysis- based on the literature review, survey, interview and workshop- to explore cross learning potential and give recommendation that could serve as input for policy review, evaluation and improvement to assist future electrification efforts in the region.

The paper focuses on six aspects of off-grid rural electrification in ASEAN: (1) Policy framework; (2) Financing mechanisms and required support policies; (3) Project setup and business models; (4) Appropriate technology solutions; (5) Socio-economic aspects and community involvement; and (6) Capacity building and training. For each aspect, a number of successful approaches and lessons learnt were analysed.

Keywords: *Rural electrification, off-grid, renewable energy, ASEAN*

1. Introduction

Access to energy must be assured for development of a region, a process in which living standard (e.g. electricity, heat, mobility) of its people improves. Energy consumption in ASEAN has grown rapidly especially in megacities. However, energy (electricity) distribution to rural area remains as a challenge due to geographic and demographic characteristic of the region spread widely across southeast Asia. Rural electrification was therefore high on political agenda of the countries over the last decades and continues to be an important issue for a number of countries in the region, especially in Cambodia, Lao PDR, Indonesia and Myanmar. The reasons for low electrification rates differ from country to country: high generation costs and low income as well as adverse topographic conditions and high transportation costs are potential obstacles to successful rural electrification in those countries.

Nevertheless, the ASEAN region and its member countries are endowed with vast renewable energy resources. Hydropower, biomass, solar or wind power are feasible and often cost-efficient alternatives to conventional means of rural electrification, in particular in areas with high grid extension costs or a sparse density of population.

doi:10.18086/swc.2015.03.03 Available at http://proceedings.ises.org

There are many examples of successful and sustainable rural electrification utilizing renewable energy in the ASEAN region. Less successful examples, however, are equally existed and lead to a waste of financial resources and;/ an unnecessary high number of households without access to modern energy services. Lack of knowledge and technical skills, ineffective and unsustainable project design and the absence of financial resources undermine the long term impact of many rural electrification efforts.

This paper presents the current rural electrification trends at the regional level and at the same time review the development and lesson learnt in Cambodia, Indonesia, Lao PDR and Myanmar. These countries were selected since the electrification rate are relatively low, therefore the rural electrification activities has been significant. This work makes use of both preliminary and secondary data in presenting the current status of rural electrification in ASEAN. The data are collated from past and recent studies on rural electrification in ASEAN. A stakeholder surveys, interviews and workshop with related stakeholders and experts were also conducted for this study.

The categories studied include policy framework, financing mechanism and required support policies, project setup and business model, appropriate technology solution, socio-economic aspects and community involvement and capacity building and training.

2. Rural Electrification in ASEAN

The current level of electrification rate in the region is around 81.2% (ACE, 2015a). Wide disparity in electrification rate exists in ASEAN. Singapore, Brunei Darussalam and Malaysia has reached (almost) 100% of electrification rate, while only 33% of the population in Myanmar have access to electricity. With high priority putting by AMS to provide access to electricity, the percentage of population with electricity access has increased during the last decade. Constant effort to increase their respective electrification rate resulting the number of people without access to electricity has went down from an estimated 190 million in 2015 (IEA, 2006) to 118 million in 2013 (ASEAN Secretariat, 2015) (Table 1).

Despite the efforts and important improvements in some of the countries, to date more than 18% of ASEAN's population still does not have access to affordable, reliable and sustainable sources of electricity. The absent of electricity access hampers economic development and an improved standard of living in entire regions. The region without access to electricity usually locate in isolated communities, such as islands, forests fringes and hilly settlements. These communities are generally small, consisting of low income households – with characteristic that may be economically less attractive to electricity distribution companies or even government electrification program that usually prioritizes the allocation of the scarce resources.

Tab. 1 Rural electricity access in ASEAN (as of 2013)

Country	Total Population (Thousand)[1]	Population without Electricity (Thousand, approx.)	Electrification Rate (%)[2]	GDP Per Capita at Current Market Prices in USD[1]
Brunei Darussalam	406	1	99.8	39,679
Cambodia	14,963	9,876	34	1,037
Indonesia	248,818	48,520	80.5	3,460
Lao PDR	6,644	841	87.34	1,548
Malaysia	29,948	180	99.4	10,420
Myanmar	61,568	41,251	33	888
Philippines	99,385	9,442	90.5	2,707
Singapore	3,845	0	100	55,182
Thailand	68,251	7,030	89.7	5,679
Vietnam	89,709	1,794	98	1,909
ASEAN	623,536	118,933	81.2	3,832

Sources: 1. ASEAN Secretariat, 2015. ASEAN Statistical Year Book 2014.
2. ACE, 2015a

2.1 Cambodia

Electrification rate of Cambodia is very low with only 34% of the population have access to electricity (ACE, 2015a). The Royal Government of Cambodia has set an ambitious target to reach 100% of the village with certain type of electricity by 2020 (including battery power) and 70% of household connected with grid-quality electricity by 2030. This target is further detailed in the National Strategic Development Plan Update 2009-2013 and Rural Electrification Master Plan (REMP) with Ministry of Mines and Energy as the focal point.

According to REMP, the total cost to electrify all village is about US$ 427 million or US$ 490 per household with 872,000 households to be connected. A total of 272,000 households will be electrified in the off-grid areas by decentralized mini-grids and solar battery chargings by the target year 2020. The gross investment costs will amount to about $147 million. While the remaining villages will be connected to the grid through grid extension. Electricity Authority of Cambodia or EAC (2014) reported that all the licenses issued covered 11,218 villages which was 79.716% of the number of villages in Cambodia. However, the distribution network developed until 2013 covered only 7,187 villages amounting to 51.07% of the total villages. Electricity prices in Cambodia are among the highest in the region between US$ 0.14 in urban areas to almost US$ 1 per kWh in rural areas (ACE, 2015b). It is mainly due to small diesel fuelled isolated generation system completely dependent on high-cost fuel imported from foreign countries, and not having interconnected system and high power losses in the distribution network (EAC, 2007).

The Royal Government of Cambodia has issued a Royal Decree to establish a public institution the Rural Electrification Fund (REF). The objectives of the REF are to facilitate access to electricity infrastructure and provide a secure, reliable, environmentally safe, and sustainable energy supply of various types, at reasonable and affordable price. The funding for REF shall be through donations and grants whose sources and terms shall be acceptable to the Ministry of Industry, Mines and Energy and to the Ministry of Economy and Finance and other sources from the government. The REF has received funds from Government of Cambodia through loan from World Bank and grant from Global Environment Facility Trust Fund (GEF). The funds provided grant assistance to licensees for new connections to households and for installation of mini and micro hydro projects and renewable energy projects, including solar home system. During 2012, REF, which was working as an independent organization was transferred to the control of Electricite Du Cambodge (EDC), the state own electricity company.

Over the years, a number of REF programs (such as Power to the Poor (P2P) Program, Program for Providing Assistance to Develop Electricity Infrastructure in Rural Areas, and Expansion of Grid Networks) attempted to enhance electricity access either as part of overall rural development or specifically targeting rural electrification. At present around 12,000 Solar Home System and about 60 Rural Electricity Enterprises (REE) that run biomass gasifier and numerous small mini hydro sites have been implemented under REF (Sovanna, 2012). P2P program provided interest free loan for: (i) costs for the connection fees of the electricity supplier, (ii) costs for deposit to be deposited with the electricity supplier, (iii) costs for purchase of materials and labour for the installation of wires from the connection point to its house, and (iv) costs for purchase of materials and labour for the installation of in-house wiring. The loan was disbursed through the licensee who is responsible to pay back to REF by collecting from the Borrower in easy monthly instalments within a specific period (EAC, 2014).

2.2 Indonesia

Rural electrification has been one of the development program priorities set by the Government of Indonesia since mid-1980s given that electrification and village electrification ratio was low at that time. In spite of difficult geographical and financial barriers, Indonesia continues to make measured progress towards providing access to electricity to the majority of its rural population. According to Indonesia Central Bureau of Statistic (BPS, 2014), in 2013, number of village in Indonesia was 74,093 that covered around 59 million households. The number of village with electricity has reached 62,682 or 80.5% percent of total village (Ministry of Energy and Mineral Resources, 2014).

On a regional basis, the electrification rate varies from below 30% in very isolated areas (e.g. Papua and East Nusa Tenggara) to over 99% in the urban centers of Java (e.g. Jakarta, Bandung and Surabaya). The successful

electrification program has increased both electrification and village electrification ratio tremendously in the last 20 years. The lack of a unified land, low population densities particularly in the eastern part of Indonesia and low average consumption per capita makes economies of scale difficult to achieve. In this case, utilization of local energy resources that predominantly renewable energy are the best option to cope with this situation.

The government categorizes rural electrification in two stages, namely pre-electrification and rural electrification (Ministry of Energy and Mineral Resources, 2010). The pre-electrification was program that provide minimum electricity supply for lightning and other minimum use of appliances (such as radio) for the household with power limited up to 100 W, powered by photovoltaic (typically Solar Home System) and micro-hydro power plant. The rural electrification was considered as full electrification program where household is connected to 220 VA or 450 VA. The electricity could be generated by diesel generator and/or hybrid power plant that combining diesel generator and renewable energy technologies such as centralized photovoltaic and wind turbine.

As rural development and its energy service provision are one of key development priorities, there are various government agencies and ministries that involve in rural electrification, i.e. Ministry of Finance, National Planning Agencies, Ministry of Home Affairs, Ministry of Rural Area and Development of Disadvantage Region, Ministry of Cooperative and Small Medium Enterprise, Ministry of Public Work and Housing, and State Electricity Company. Most of these ministries implementing renewable-based rural electrification projects through different model of delivery: directly carry out project procurement, channeling special allocation fund through provincial government, or by carrying research and development project in the beginning, followed by handing over the system to local government and State Electricity Company after the research project completed. Funding for rural electrification project comes from various sources: annual national budget, annual regional budget, multilateral and bilateral grant/technical assistance, international donor organization/NGOs, CSR and others.

2.3 Lao PDR

In 2006, electrification rate of Lao was only 47 percent (Malaykham, 2006), significantly improve to 87 percent in 2013 (ACE, 2015). Rural electrification was set as power sector priority with clear target of 70% by 2010 and 90% by 2020, as stated in Rural Electrification Master Plan (REMP) (Institute of Renewable Energy Promotion, Ministry of Energy and Mines, 2013). According to Ministry of Energy and Mines (MEM, 2004), the electrification rate expansion are conducted in two methods: (i) to expand the grid to comparatively easily accessible areas and (ii) provide off-grid supplies to remote areas where it is difficult to expand the present grid due to environment or cost reasons. Development of off-grid renewable energy sources such as SHP, solar, wind, biomass increases the energy self-sufficiency and security as well as sustainability. Currently, more than 20,000 households have been connected to solar home systems and Small Hydropower (SHP) have been providing electricity to people living in rural and remote area (MEM, 2011).

Vongsay and Bounsou (2014) mentioned that electric power system of Lao PDR is separated into three parts by regions (Northern, Central and Southern region) because there is no national grid connected from north to south. The extensions of electric power grids to remote households are either prohibitively expensive or economically unjustified. The main problems to implement off-grid renewable energy technology for rural electrification are: high initial investment cost with low rate of return and unavailability of tools for management and technical standards.

The Law on Electricity, first published in 1997 and revised in 2009 then later in 2011, appointed Ministry of Energy and Mines (MEM) for framing policies and strategies for the energy sector including developing Laws and Regulation on electricity business. The responsibility of MEM included supervision of electricity companies and assisting the government in deciding the tariff. The Institute of Renewable Energy Promotion (IREP) under MEM oversees the implementation of renewable energy, energy efficiency and rural electrification programs in Lao PDR. The Law on Electricity has recommended the utilization of RE-based power plants for rural electrification, either in grid tied or off-grid mode. The law also has provision for generating funds for rural electrification.

The Lao government has successfully implemented few off-grid renewable energy-based rural electrification

Programs with the help of international funding (World Bank, JICA). The public-private partnership models like those of Provincial Energy Service Companies (PESCOs) and Sunlabob (100% Lao owned company engaged in selling hardware and providing commercially viable energy services for remote areas), have been successfully implemented. However, these programs have not resulted in large scale deployment of off-grid renewable energy technologies for rural electrification due to dependence on subsidy.

2.4 Myanmar

Myanmar has one of the lowest electrification rate in ASEAN. According to Ministry of Livestock, Fisheries and Rural Development (2014), there are 63,899 villages in Myanmar, of which only 36% of the villages having access to electricity. The remaining of 40,865 villages need to be electrified. The disparity of electricity access between rural and urban area is huge. Yangon and Mandalay, the biggest cities in Myanmar, have the electrification rate of 75%; while the rural areas have electrification rate as low as 16 percent. In fact, most of rural communities in border areas have no access to the grid-based electricity at all, while some regions and states with a high share of rural population (e.g. Ayeyarwady and Magway Regions and Rakhine State) have access to grid-based electricity below 10 percent (World Bank, 2014).

The main mode of electrification has been the utilization of diesel generator followed by the extension of national grid. The utilization of renewable energy has been constantly promoted, such as single house solar system (SHS), solar lamp charging system, small scale hydropower and biogas system. Government of Myanmar has appointed several ministries to boost the electrification rate. Ministry of Livestock, Fisheries and Rural Development (MoLFRD) is the main implementer for rural electrification, both off-grid and on-grid; Ministry of Electrical Power (MoEP) is responsible for national grid, which mainly electrifies urban areas; Ministry of Industry is helping and encouraging small and medium enterprises to invest on electricity supply; Ministry of Science and Technology undertakes researches for rural electrification especially on biomass and biogas in cooperation with Ministry of Agriculture and Irrigation.

In order to escalate the rural development and poverty reduction activities, on August 2013, Ministry of Livestock and Fisheries was reorganized as the MoFLRD, and assigned as the Focal Ministry for rural development. Under MoFLRD, Department of Rural Development (DRD) is responsible for all rural infrastructures, including electricity access. To promote the off-grid rural electrification, DRD has organized rural development and electrification committee in village and township, surveyed the community needs, allocated budget according to parliament's decision and cooperate with private sectors, UN agencies, and NGO to achieve the electrification target.

Myanmar National Electrification Plan (NEP) 2015 – 2030 is being formulised by MoEP and MoLFRD with the help from the global Sustainable Energy for All (SE4All) initiatives, led by the World Bank and the United Nations. The NEP is envision to be a comprehensive action plan for developing, financing, and implementing electricity access scale-up program in the whole country, with the target of achieving universal access by 2030. Its aims to align support from different stakeholders with the implementation program for achieving national access targets and syndicates financing on a timely, ongoing and programmatic basis. NEP also proposed institutional reforms required to ensure alignment of funding sources and accountabilities for effective and timely implementation of the electrification program.

3. Off-grid Rural Electrification Approaches

The success (or failure) of off-grid rural electrification approaches with Renewable Energy Technology (RET) depends not only on a broad range of influencing factors: geography, availability of natural resources, reliability of technical solutions, financial feasibility; but also human capacity and dedication of individuals to name only few of them. These factors vary greatly from country to country and framework conditions are comparable only to a limited extent.

However, there are certain factors which are considered to be indispensable for successful rural electrification approaches which shall be carefully considered for planning and implementation of such projects. These factors comprise: (i) a stable and predictable policy framework; (ii) reliable support policies and a feasible

financing mechanism; (iii) a sustainable project setup and business models; (iv) the application of appropriate technology; (v) the due consideration of socio-economic aspects and community involvement; and (vi) continuous training and capacity building.

3.1 Policy Framework for Off-grid Rural Electrification

Most of the countries in the region have established rural electrification bodies or formulated schemes with supportive legislation to extend the rural electrification. However, there has been no separate policy framework for off-grid rural electrification. Provisions regarding off-grid electrification are usually included in the policies and plans for rural electrification in general, which most often focus on grid extension as the least-cost solution for many rural areas.

The REF in Cambodia started a pilot project in Kampong Speu with the first US$ 10,000 repaid from the 12,000 SHS rent-to-own programme. The target of this pilot project was 1,000 households. REFs were identifying the families and managing the loans with customers. The similar project has been very successful in Lao PDR. The REMP in Lao PDR set a National Electrification Target of 94.7% on household basis by 2020, which will be achieved by on-grid system, i.e. grid extension (90.9%) and by off-grid system using mini/micro hydropower and SHS (3.8%) (MEM, 2010). REMP considered affordability as the most important criterion. At initial stage, the project developers were required to visit the village with a sample of SHS kit and explains its technical features and application as well as the payment schemes to the villagers in detail prior to list potential customers. If the percentage of candidates that was able to pay less than 50% of total households, this village would not be selected for SHS-based electrification.

While in Indonesia, the enactment of Law No.30/2007 on Energy affirmed the right of citizen to the access to energy. The law made improving access of energy for the poor and community lives in remote area as one of the key objectives of national energy management. Energy access could be achieved through providing assistance/support to the poor to improve access to energy and developed energy infrastructure in the underdeveloped region to reduce regional disparities (Government of Indonesia, 2007).

Table 2 presents common key policies to promote off-grid rural electrification prevalent in the ASEAN region.

Tab. 2 Key policies for promoting off-grid rural electrification in the ASEAN

Key Policies	Main content of the policy
Strategies	- Long term objectives and strategic goals; - Transparent overall rules and guidance regarding development plans and financial; - Roles and responsibilities among the relevant institutions and stakeholders.
Development plans	- Review of energy access in the country (i.e. detailed electrification rates in different areas); - Criteria for the selection of target areas/communities; - Resource mapping for target areas/communities (i.e. water course, biomass, wind, solar, etc.); - Action plans including prioritization of areas/communities to be electrified; - Data collection on location, socio-economic conditions, electricity demand, etc. for the targeted villages.
Financial incentives	- Specification on types and amounts of financial incentives for off-grid electrification projects (e.g. investment subsidies, VAT exemption, import duty exemption, income tax holidays, etc.); - Criteria for the entities eligible for financial incentives (e.g. power producers, project owners, end-user, community, etc.); - General pricing principles for off-grid electrification (i.e. tariff structure for off-grid applications).
Financing mobilization	Mechanism for mobilizing funds for off-grid rural electrification (including domestic as well as international sources).

3.2 Financing Mechanism and Required Support Policies

There are several possibilities that can be applied to finance off-grid rural electrification projects. The option most commonly applied in the ASEAN are private financing, financing through the public power utility, government financing, and Public Private Partnerships (PPP)[1]. Table 3 summarizes the financing mechanism and required support policies in ASEAN.

Tab. 3 Financing mechanisms and required support policies

Financing mechanisms	Financing sources	Key support policies required
Private financing	• Equity • Commercial and/or soft loans	• Market-based electricity pricing policy in target areas; • Clear legal framework on private financing in off-grid rural electrification; • Indirect subsidies (e.g. technical assistance, free land use, VAT and import duty exemption, income tax holidays, etc.); • Soft loan policy for RET-based rural electrification projects.
Public power utility financing	• Equity • Commercial and/or soft loans	• Inclusion of off-grid electrification into the utility's work program (e.g. through regulation); • Policy on cross-subsidized tariffs; • Indirect subsidies (e.g. technical assistance, free land use, VAT and import duty exemption, income tax holidays, etc.); • Soft loan policy for RET-based rural electrification projects.
Government financing	• Government budget • International/local grant (ODA) • Local/international long-term soft loans	• Policy on off-grid rural electrification; • Institutional setup to implement off-grid rural electrification programs; • Financial incentives including direct and indirect subsidies.
Public Private Partnership (PPP) financing	• Private financing • Government budget • Grants and loans	• Grants (e.g. project preparation, seed investment, etc.); • Soft loans policy for RE-based rural electrification projects; • Financial incentives including direct and indirect subsidies.

The public power utilities (e.g. PLN in Indonesia and EDL in Lao PDR) are investing in off-grid rural electrification projects using their equity capital and (soft) loans from local and/or international financing institutions, thereby cross-subsidizing rural electrification activities and – in some cases – creating business cases for private developers. Subsidies are regularly provided by the government or international partners in order to ensure financial viability for the project developers/investors and affordability for the customers at the same time. In a SHS project in Cambodia with 12,000 planned installations, US$ 100 were granted for each supplied household. The subsidy made the rental fee payment to the developer affordable for the customers at US$ 4.86 per month for a 50-Wp SHS and US$ 3.35 per month for a 30-Wp SHS over a 4-year period without interest (ACE, 2012).

3.3 Project Setup and Business Models

One of the big hurdles for off-grid rural electrification is the fact that private investments are not economically viable or the return on investment is comparably low. Thus, a sound project setup including a feasible business model indispensably ensures effectiveness and sustainability of rural electrification projects

[1] The term "PPP" is widely used in different contexts. Within this paper, PPP refers to a project where the public and the private sector cooperate and both parties provide investments.

The lack of organizational structures, high levels of initial capital investments, and lack of ability or willingness to pay by rural customers are some of the major issues that make it challenging to develop a business model for off-grid rural electrification.

A large variety of business models for off-grid rural electrification exist in the ASEAN region, depending largely on local conditions and political objectives. Table 4 summarizes the successful business model applied in AMS. In reality, however, a hybrid types of these models are often applied, combining the advantages of different approaches.

Tab. 4 Project types and business models

Business model	Key features
	Market-based models
Fee-for-service model	A project investor/developer invests in and owns the off-grid power generating system and supplies electricity to rural customers. The investor/developer ensures operation, maintenance and replacement of the power system. The customers pay for the electricity they use either based on metering (kW/h) or a fixed (monthly) charge. The electricity tariffs are usually set at a financially viable level (cost covering) and are relatively high compared to other approaches.
Dealer model	Customers/end-users purchase the power system either with own cash and/or loans. The customer is normally a household or a facility owner (e.g. rice miller). Beyond warranty service, the customer assumes responsibility for all operational and replacement costs. There is no payment for consumed electricity, only consumables and spare parts required for the operation and maintenance of the power system have to be purchased.
Lease model	In contrast to the dealer model, the equipment is owned by the lessor (e.g. ESCO) and transferred to the customer only at the end of the leasing period. The lessor remains responsible for maintenance and repair, while the customer pays a (monthly) rental fee during the leasing period.
	Government induced community-based business models
Fully grant-based model or Partially grant-based model	An off-grid power system is 100% grant-financed, usually by government or international partners, while the projects implemented under the partially grant-based business model will be financed by a mix of grant and long-term soft loans and/or local contributions (e.g. from the government budget or the community). The power system is usually owned, operated and maintained by a community- based entity such as village committee, community cooperative, etc.
	Public Private Partnership (PPP) models
Operation-Maintenance PPP model	The Operation-Maintenance model is a partnership, in which a public partner invests in an off-grid power generating system and contracts a private partner to operate and maintain the system. The public partner retains ownership and overall management of the power system.
Operation-Maintenance-Management PPP model	Under the Operation-Maintenance-Management model, a public partner enters a contract with a private partner to operate, maintain and manage the off-grid power system. The public partner remains the owner of the system, but the private partner may invest own capital in the system.

Fee-for-service business models helped attract the private sector to invest in off-grid rural electrification. This model applied in Shwe Hlay Chaung village in Myanmar which was implemented in 2008 to replace diesel-based battery charging system by a rice husk gasification power using a dual-fuel engine. The system included a rice husk gasifier, a 30 HP dual gas engine, a 20 kV electric generator, power distribution to supply electricity

to 50 households and a battery charging system and also free of charge electricity supply to a pagoda and monastery. The project was owned by a private developer who operated and maintained the system. Total investment was around US$ 6,100 financed by a commercial loan with 7% interest rate per annum. The total income was around US$ 500. Taking into account the cost of equipment maintenance, the investment was paid back in 2 years (ACE, 2012).

3.4 Appropriate Technology Solutions

Technology choice is one of the most critical factors that affect the success and sustainability of an off-grid rural electrification project. There are several types of technologies that can be utilized for off-grid rural electrification: diesel generators, hydro power (mini, micro or pico system), biomass gasification power system, biogas-based power system, wind power (home-scale system), solar PV (mini, home-scale or pico systems), hybrid power system. However, the most common technologies used are solar photovoltaic (PV) – both SNS as well as mini grids- and mini/micro hydro systems.

Typical SHS includes a 10 to 130 Wp PV array, a rechargeable battery for energy storage, one or more high efficiency lamps and an outlet for television or radio. The mini/mico/pico-grids are typically in the range of 5 to 1,000 kW and provide water pumping and in-house appliances. Almost all the countries reviewed have used SHS as a means for extending lighting to areas that could not be reached by the grid. A key factor of the success of the solar PV programme in different countries is due to quality standards ensured for PV panels, batteries and other components as approved by the technical standards committees in respective countries.

Two steps should be carried out in order to select an appropriate technology for an off-grid rural electrification project:

- A technical analysis to preliminarily identify the appropriate technologies; and
- Economic and financial analysis of different possible technologies.

The technical analysis includes the collection and assessment of the main input data such as local renewable energy resources, population, dispersion of customers, energy consumption, income level, willingness to pay, requirement on reliability of electricity supply, productive use of energy, etc. The technical analysis should also take into account the efficiency, reliability and expected lifetime.

The economic and financial analysis includes the capital costs, O&M costs, and other related costs (e.g. O&M training cost, environmental protection cost) of each technology, the tariff system proposed and the subsidies offered. These assessments are usually conducted technology neutral and are not pre-determined by choosing a particular technology.

3.5 Socio-Economic Aspects and Community Involvement

Socio-economic and environmental aspects as well as potential impacts on the community need to be taken into consideration in off-grid project planning and implementation. It is observed from the rural electrification efforts in all the study countries, the benefits of electricity increased standard of living, productive activities and social institutions. Environmental benefits include positive impacts on soil, water and air pollution.

In addition, local community involvement is an essential aspect in rural electrification projects. If a project is not well explained, accepted or appreciated by the community beneficiaries, sustainability can be hampered. Community involvement is therefore important at all stages of the project cycle, from planning and project development to project implementation and long- term operation. It is crucial to understand the community's needs and potential before starting with the actual planning of a project. For example the chosen project design (e.g. business model) will only work, if gain acceptance from the villagers. The communities and their representatives play furthermore a crucial role in supporting the construction works (especially for hydropower projects) as well as in operating and maintaining the power system in case this task is not carried out by a private entity.

A close monitoring and evaluation of the socio- economic and environmental impacts of off- grid rural electrification are particular interest in order to asses and understand the long-term impacts and benefits of

the measure. Since rural electrification programs most often have a political and development objective, the monitoring of economic progress, social and welfare impacts as well as environmental consequences of a particular off-grid electrification program is essential.

3.6 Capacity Building and Training

Capacity Building and Training (CB&T) is fundamental for all involved stakeholders to ensure that they can fulfil their roles and responsibilities in an off-grid rural electrification project. The Mini Hydro Power Project for Capacity Development (MHPP) in Indonesia promotes the dissemination and exchange of know-how on mini hydropower, as well as the sharing of best practices in the building of sustainable facilities (MHPP, 2011). Typically, the following stakeholders are eligible for targeted CB&T measures:

- Policy makers and government officials (central and local level);
- Project developers;
- Financial institutions and private investors;
- Equipment manufacturers and construction companies;
- Power plant operators and managers;
- Local communities/end-users

General information on aspects such as policy, technology, financing, project impacts and benefits, etc. are to be provided to most of the stakeholders in order to raise awareness and general knowledge on off-grid rural electrification. Various formats of CB&T measures such as seminars, workshops, study tours, site visits, classroom and on-site training were applied in ASEAN region. The selection of an appropriate type of CB&T depends on the target stakeholders as well as the topics presented.

4. Conclusion and recommendations

Rural electrification is one of the keys to rural development and gaining high priority in ASEAN region to meet the economic and social development goals, as well as political priority. Though all countries reviewed here have developed policy frameworks and envisage bringing more areas under electrification, some countries have no specific policy framework for off-grid rural electrification and have not shown specific initiatives to improve the overall household connection level.

Further, source of funding for rural electrification programs were in the form of private financing, government financing and PPP. Private financing is used for commercially viable projects. Government financing can offer low, affordable electricity tariffs to rural villagers, however the investment are hardly paid back while PPP combines the advantages of the private and the government financing mechanism. Subsidy component either to improve the infrastructure or through cross subsidization of tariffs for poor customers are observed in all rural electrification program in the region.

The off-grid technologies prioritized seem to fit to a large extent with the geographical characteristics of the demand, resources potential and distribution system. The distribution system and technological performance are relatively better placed for solar PV than for micro hydro and biomass gasifier.

This paper shared the rural electrification experiences and lesson learnt from four selected countries of ASEAN for cross learning potential across the region as well as other developing countries. This review presents a number of recommendations for the planning and implementation of off-grid rural electrification:

- Policy makers shall develop the key policies for promoting off-grid rural electrification which shall include a development strategy and concrete action plans, a suitable electricity pricing policy, financial incentives and a framework on funding mobilization;
- A clear legal framework for private investment in off-grid rural electrification needs to be established in order to mobilize the private sector to become actively involved in this market;
- A central institution/agency shall be created to coordinate the planning and implementation of all off-grid rural electrification activities in a country;
- The public sector should use its resources to finance off-grid projects in poor rural areas where business

models can hardly be established and projects are less or not profitable. Wherever possible and economically viable, priority should be given to the private sector to get engaged for investment and project development;

- The business model selected for an off- grid rural electrification project shall have some degree of flexibility and fit the specific conditions of the community implementing the project. The business model may have to be modified along the way in order to cater to the actual developments and changes in the project structure during project implementation;
- Whatever is the selected business model, maintenance should be taken to ensure that end-users have access to quality electricity services at affordable prices;
- The project design must not be technology driven. Technology choices are to be based on practical considerations. A cost-benefit analysis of different technology options (including grid extension) should be carried out to determine the least-cost solution;
- Productive and institutional applications of electricity not only help to improve standards of living (e.g. job creation, better health care) but also increase the economic attractiveness of the off-grid power project. The project developers therefore must consider initiating or enhancing productive activities as they significantly increase the sustainability of the project;
- Maximizing the awareness and involvement of the benefitting community in the early stages of the project cycle, especially during the project assessment phase, is vital to the success of off-grid project implementation. Key activities include public awareness campaign, regular meetings with community leaders and focus-group meetings;
- Capacity building and training to develop local capacities in design, implementation, management and O&M is essential for the success of off-grid rural electrification projects. Therefore, adequate resources should be devoted to developing local capacities.

5. Acknowledgements

The article is based on a review of the off-grid rural electrification approach in ASEAN, conducted as part of Renewable Energy Support Programme in ASEAN (ASEAN-RESP) Phase I, from 2010 – 2013. The ASEAN-RESP Phase I was a joint programme between Deutsche Gesellschaft für Internationale Zusammenarbeit, GmbH (GIZ) and ASEAN Centre for Energy (ACE).

6. References

Akhomdeth Vongsay and Xayphone Bounsou. Sustainable Management of Small Hydropower for Rural Electrification in Lao PDR by Economic, Social and Environment Blueprint Perspective. Journal of Automation and Control Engineering Vol. 2, No. 2, June 2014.

ASEAN Centre for Energy (ACE). 2012. Report on Survey and Study on Innovative Rural Electrification Approaches. Jakarta.

ASEAN Centre for Energy (ACE). 2015a. Report on Survey and Study on Renewable Energy Development 2006-2013. ASEAN Centre for Energy. Jakarta.

ASEAN Centre for Energy (ACE). 2015b. Cambodia Country Profiles. http://aseanrenewables.info/country-profile/cambodia/electricity-tariff-rate-of-electrification/ [last accessed 24 October 2015]

ASEAN Secretariat. 2015. ASEAN Statistical Yearbook 2014. http://www.asean.org/images/2015/July/ASEAN-Yearbook/July%202015%20-%20ASEAN%20Statistical%20Yearbook%202014.pdf. [last accessed 20 October 2015]

Badan Pusat Statistik. 2014. Jumlah Desa Menurut Provinsi dan Letak Geografi 2003 – 2014. http://www.bps.go.id/linkTableDinamis/view/id/906. [last accessed 29 October 2015]

Bouathep Malaykham. 2006. Renewable energy in Lao PDR. http://www.sunlabob.com/data/documents/energy_issues/LG-06-10-Renewable_Energy_Lao_PDR.pdf [last accessed 09 September 2015]

Department of Rural Development, Ministry of Livestock, Fisheries and Rural Development. 2015. Rural

Electricity Access. Paper presented at the meeting of ACE mission.Yangon.

Electricity Authority of Cambodia. 2007. Report on Power Sector for the Year 2006. Phnom Penh.

Electricity Authority of Cambodia. 2014. Report on Power Sector for the Year 2013. Phnom Penh.

Government of Indonesia, 2007. Law No.30/2007 on Energy. Jakarta

Institute of Renewable Energy Promotion, Ministry of Energy and Mines. 2013. Rural Electrification in Lao PDR, Paper presented at Rural Electrification Workshop, Yangon.

Mini Hydro Power Project for Capacity Development.2011. Best Practices Guideline on Off-grid Micro Hydro Power Schemes for Rural Electrification. Ministry of Energy and Mineral Resources and GIZ. Jakarta

Ministry of Planning and Investment. 2004 National Growth and Poverty Eradication Strategy, Vientiane, Lao PDR, 2004.

Ministry of Energy and Mines of Lao PDT. 2010. Rural Electrification Master Plan and Hydro Assessment Study in Lao PDR, Vientiane, Lao PDR.

Ministry of Energy and Mines of Lao PDR. 2011. Renewable Energy Development Strategy of the Lao PDR. Vientiane, Lao PDR.

Ministry of Energy and Mineral Resources, 2010, "Rencana Pembangunan Jangka Menengah Kementerian ESDM" (*MEMR Medium Term Development Program 2010-2014*), MEMR, Jakarta.

Ministry of Energy and Mineral Resources, 2014, "Indonesia's Country Report on Renewable Energy", Paper presented at the meeting of Renewable Energy Sub Sector Network, Kuala Lumpur.

Ministry of Industry, Mines and Energy. 2006. The Master Plan Study on Rural Electrification by Renewable Energy in the Kingdom of Cambodia. Cambodia.

Toch Sovanna. 2012. The Potential of Renewable Energy in Cambodia, Paper presented at the 2nd EAS Energy Efficiency Conference, Phnom Penh.

World Bank. 2014. *Myanmar - Development of a Myanmar national electrification plan towards universal access 2015-2030*. Washington, DC: World Bank Group. http://documents.worldbank.org/curated/en/2014/01/20187855/myanmar-development-myanmar-national-electrification-plan-towards-universal-access-2015-2030 [last accessed 29 October 2015]

Conference Proceedings

Solar World Congress 2015
Daegu, Korea, 08 – 12 November 2015

Solar Water Pumping: Kenya and Nepal Market Acceleration

Emily Kunen[1], Bikash Pandey[1], Robert Foster[1], Jennifer Holthaus[1], Binod Shrestha[2] and Bernard Ngetich[3]

[1] Winrock International, Arlington, Virginia (United States)
[2] Winrock International, Kathmandu (Nepal)
[3] Winrock International, Nairobi (Kenya)

Abstract

Solar water pumping is a mature, reliable, and economically attractive solution for off-grid irrigation, livestock water, and community water supply. With increasing reliance on water pumping for food security needs, and limited access to conventional energy sources for many communities most in need of water pumping, development programs around the world are accelerating market development for solar powered water pumping systems. Financial, managerial, technical, market access, and educational challenges exist. However, examples from Kenya and Nepal demonstrate how successful initiatives have developed to overcome such barriers. These examples demonstrate that challenges can be overcome through public-private partnerships that take advantage of relative cost savings, increased reliability of both solar power and irrigation systems, and improved technology access through innovative financing models. These interventions help accelerate solar water pumping adoption in Kenya, Nepal, and elsewhere.

Keywords: *Photovoltaics, solar water pumps, renewable energy*

1. Introduction

Solar photovoltaic water pumping (PVWP) is one of the most economically attractive solar energy applications with installed systems proven to provide 20 or more years of reliable service. There is an excellent match between seasonal solar resource and seasonal water needs (Foster, 2009). A wide range of water supply needs can be met by PVWP, from livestock and community water supply, to small and even large-scale irrigation needs. PVWP system costs have declined significantly, from over US$25 per peak watt over 15 years ago (Foster, 1998), to total PVWP system costs under US$5 a peak Watt possible today (Foster and Cota, 2013).

Irrigation is a critical tool in addressing food security challenges; however, conventional grid or fossil fuel energy sources are not adequate to meet global irrigation needs. There are new opportunities emerging in the transition from diesel to solar powered pumps to reach farmers who cannot access traditional energy sources. A significant shift has begun in the rural water pumping industry where previous diesel pump dealers now provide solar powered pumping systems that are outpacing diesel systems sales due to lower life cycle costs. Some vendors in South Asia that previously sold only diesel/gas pumps, have expanded their product lines to include PVWPs and now report selling more PVWPs than diesel pumps. Ambitious targets for PV water pumps in South Asia are indicative of the promise of this technology. Bangladesh's Infrastructure Development Company Limited aims to finance 50,000 PVWPs by 2025 (Rahman, 2015), the Alternative Energy Promotion Center of Nepal plans 500 PVWPs by 2017, and India's Ministry of New and Renewable Energy target is 100,000 PVWPs by 2015 and one million installations by 2021 (International Centre for Integrated Mountain Development, 2015).

Key challenges faced in markets where PVWP development has been implemented, as well as in those areas where it has not yet materialized, illuminate several challenges, including financial, managerial, technical, and market access challenges. A key challenge for PV water pumping systems is the upfront cost. The lifetime cost of irrigation varies depending on the system, its maintenance, and inputs. Analyses have shown PV water pumping systems have payback times of two to three years (Foster and Cota, 2013). PV capital costs require financing schemes that can help farmers realize financial savings in a few years and over the lifetime of the

doi:10.18086/swc.2015.03.04 Available at http://proceedings.ises.org

system. Many existing PVWP projects are subsidy driven, funded by grants, or financed through loans that farmers obtain from banks. The overall challenges are not just related to PVWP technologies, but the entirety of the system that the energy is a part of, including for irrigation, agriculture, and community systems.

2. Solar Water Pumping Advances

A PVWP system is similar to any other conventional water pumping system except that the power source is solar energy. PVWP systems have, as a minimum, a PV array, a motor, a pump, and normally a water storage tank. The PV arrays are sometimes mounted on passive trackers (which use no motors) to follow the sun throughout the day for increasing pumping time and water volume. Alternating current and direct current motors are used to power centrifugal, displacement like piston or helical rotor pumps. Water is more cheaply and effectively stored in a tank rather than storing electro-chemical energy with batteries. Pump motors are normally direct drive from the PV array using a maximum power point tracking (MPPT) controller, thus eliminating batteries, decreasing system costs while increasing reliability (Foster, 2009).

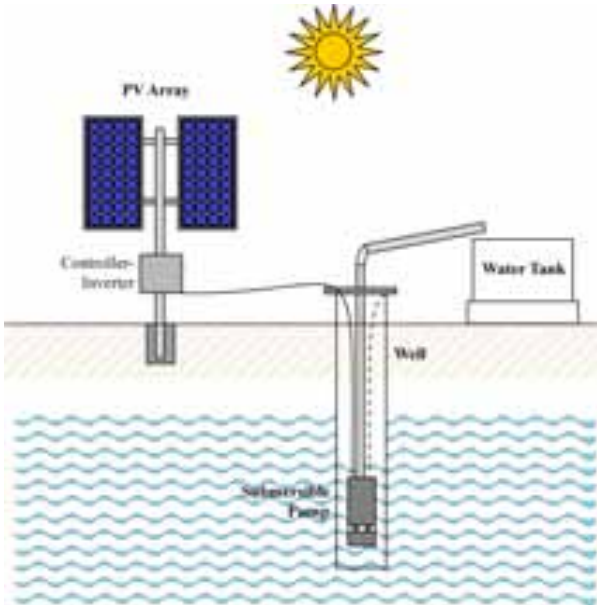

Fig. 1: Typical PV water pumping system components.

General size categories of PV water pumping systems are based on motor power output (Watts or kW):

- *Small* >50 W to < 1 kW
- *Medium* 1 to 5 kW
- *Large* >5 to 100 kW

The size categories tend to correlate with the differing technologies used for solar pumping. Small PVWPs have the longest history for commercial application and show the most technology diversity. Small, low-power systems can provide large amounts of water by pumping throughout the entire day, which provides affordable water pumping solutions for even poor, smallholder farmers in remote regions.

2.1 Helical rotor water pumps

One of the most important developments to advance PV water pumping over the past 15 years has been the development of helical rotor submersible pumps. The helical rotor is a positive displacement pump mechanism that is mounted to a submersible motor. The motor is similar to that used for centrifugal submersible pumps. Like the centrifugal submersible pump, the helical rotor submersible pump can last for many years with no regular maintenance required. Most new PVWPs use this type of design. Table 1 provides a comparison of basic advantages and disadvantages for different pump types.

Fig. 2: Example helical rotor pump end commonly used for solar water pumping.

Tab. 1: Typical operational characteristics of different PV water pump types.

Type of PV Water Pump	Advantages	Disadvantages
Submersible centrifugal	•Simple, with one moving part. •Regular maintenance not required. •Efficient at high flow rates or low lift. •Good tolerance for moderate amounts of sand and silt. •Most conventional, widely available.	•Poor efficiency at low volumes (<30 liters per minute) or high lift. •Capacity is reduced disproportionately at low speeds (in low-sun conditions). •Impellers can fill with sediments and may require periodic cleaning.
Helical rotor, submersible or surface	•Simple, with one moving part. •Regular maintenance not required. •Highly efficient at low flow rates (4-50 liters per minute). •Maintains full lift capacity at all speeds. •Good tolerance for moderate amounts of sand and silt.	•No major disadvantages.
Diaphragm, submersible or surface rotary vane	•Relatively low initial cost. •Efficient at very low flow rates (4-20 liters per minute). •Maintains full lift capacity at all speeds.	•Requires preventive maintenance. •Poor tolerance for sand and silt. •Requires filtration (rotary vane pump).
Surface centrifugal	•Relatively low cost. •Efficient for low lift and high flow rates. •Easy to inspect and maintain due to surface location. •Good tolerance for moderate amounts of sand and silt.	•Suction limit is about 6 meters or less. •Requires priming (filling the intake). •May be damaged by running dry if it loses prime.

2.2 Affordable solar water pumps

PVWP system costs have rapidly declined due to the decreasing cost of PV modules. PVWP system costs are now one quarter of what they were 20 years ago (Foster, 1998). PV module prices have dropped by over 80 percent over the past 8 years, and are expected to drop about another 50 percent in the next five years or so. This cost decrease has made it possible to obtain small-scale PVWP systems for only a few hundred dollars. These systems are cheaper to install than competing diesel systems or often even electric grid options if no power is already on site.

Typical mid-size PVWP systems range from 1-2 kWp and cost about US$4,000-7,000 installed depending on location. Payback for many PVWP systems is typically only two to three years, with expected lifetimes of over 25 years for alternating current pumps, while direct current pumps need replacement every five to seven years, depending on water quality.

One example of an affordable small PVWP is the Futurepump manufactured in India, shown in Figures 3 and 4. This is an inexpensive piston pump that sells for about US$400 and operates on only an 80 Wp solar module. It is very simple to operate and can replace treadle pumps. Futurepump provides 900 liters per hour at six meter total dynamic head (TDH), or 2,000 liters per hour at one meter TDH. This pump is limited to about eight meter TDH.

Fig. 3: The Futurepump piston water pumping system manufactured in India retails for US$400 with the PV module.

Fig. 4: SunFlower 80 Wp module name plate used for the Futurepump PV water pumping systems.

3. Kenya Smallholder Solar Irrigation

Agriculture makes up the largest share of Kenya's GDP (25%), but only 6% of agricultural land is irrigated. With a labor force of almost 18 million, 75% of which are engaged in the agricultural sector, Kenya has huge potential to increase its agricultural output if irrigation can be accessed for smallholder farmers. However, "[irrigation-based farming] is developed under large-scale irrigation schemes for crops like rice, a few farmers have their own irrigation systems for export crops like horticultural produce, and a limited number of smallholders practice small scale irrigation farming" (Aila and Atieno, 2006).

The U.S. Agency for International Development (USAID) funded Kenya Smallholder Solar Irrigation Project (KSSI) is being implemented by Winrock International (WI), in partnership with DuPont Kenya, SunCulture, Futurepump Ltd, the USAID-funded Kenya Agricultural Value Chains Enterprises Project (KAVES), and others. KSSI is part of the Renewable Energy Leader with Associates (RELWA) program, which aims to scale up access to, and adoption of, renewable energy globally, with a focus on increasing farmer access to renewable energy technologies that can improve agricultural productivity, sustainability, and income.

KSSI aims to improve quality of PVWP systems in Kenya while facilitating an increase in commercial sales of PVWPs to smallholder farmers who benefit by either eliminating use of costly diesel fuel or by converting from rain-fed to irrigated farming in arid areas that have never used pumps. KSSI is setting up PVWP demonstration sites around the country. Although the Government of Kenya is implementing an expanded rural electrification program, over two-thirds of the country does not have access to grid power. KSSI targets farmer groups that will not be reached by the grid in the next 5-10 years. As of September 2015, some farmers choose to buy the less expensive PVWPs even in areas where the grid is nearby. Some success factors of PVWP market acceleration in Kenya under KSSI are illustrated through the following examples.

3.1 Kenya PVWP market dynamics

The market for PVWPs in Kenya is changing rapidly. In January 2015, a WI survey of PVWP retailers with products affordable to smallholder farmers identified several companies present in the Kenyan market. SunCulture sells a 300 Wp pump kit that retails for US $2,200. Futurepump Ltd has an 80 Wp SunFlower pump kit that retails for US $400. Davis and Shirtliff is the PVWP national leader and sells a small Shurflo direct current diaphragm pump for US$400 (pump only). This company has sold over 4,000 units and is now developing a 120 Watt solar pump kit to retail for US $700. A new company, KickStart, recently entered the market with a 120Wp MoneyMaker solar pump that retails for US $395. PVWP vendors in Kenya vary greatly in numbers of sales and maintenance staff, ability to respond to increasing demand for their products, and ability to reach smallholder farmers to raise awareness about their products.

3.2 Overcoming educational barriers to commercialization of PVWPs in Kenya

WI found that the key barriers to increased commercialization of PVWPs are not technological but instead center around the need to directly reach thousands of smallholder farmers with information on cost, performance, installation, and maintenance of PVWPs. In this regard, WI functions as a neutral intermediary between farmers and PVWP companies. Working in partnership with large agricultural initiatives, such as the USAID-funded KAVES project and its 500,000 participating farmers, WI ensures that two or three PVWP companies attend farmer field days so that farmers can compare products and choose one that best suits particular farm needs. WI also set up PVWP demonstration sites for early adopter farms in several counties and is arranging for farmer groups affiliated with KAVES and DuPont to attend demonstrations at these sites. WI reaches out to banks and cooperative savings organizations to ensure that farmers have financing options for PVWP purchases and technical trainings for PVWP companies to ensure they can provide high-quality products, installation, and maintenance. Some example KSSI cases of PVWP in Kenya are provided in the following sections.

Fig. 5: Winrock invited PVWP retailers Futurepump (at left, with green hose) and KickStart to display their mobile units at a KAVES Field Day in Kenya, October 2015.

3.3 PVWP for drip irrigation in Nyahururu

Patrick Mwendwa is a typical farmer in Nyahururu who owns five acres, one of which is for his homestead. He uses one acre for apiculture, two acres for onions under drip irrigation, and one acre for various vegetable crops for domestic use. Before installing a PVWP, Mr. Mwendwa hand watered his vegetable crops using a water can, which was cumbersome. Prior to the PVWP, he could not grow onions because of the high water requirements of the crop.

After attending a training facilitated by WI at a SunCulture (KSSI partner) demonstration plot, Mr. Mwendwa purchased a complete PVWP system with a one acre drip kit to improve his farm productivity. He financed the PVWP from his savings for a total cost of US$3,320, including the drip irrigation system. The SunCulture PVWP is set in a 20 meter hand dug well and fills a 10 cubic meter water storage tank at a height of four meters in about five hours.

Mr. Mwendwa planted onions, a high value crop, using the one acre drip irrigation system. He found ready markets for his produce and realizes high returns on his investment. He plans to expand his drip-irrigated acreage by another acre since the PVWP has additional capacity that he is not using.

Fig. 6: One acre drip irrigation system using a PVWP on the Mwendwa farm in Nyahururu, Kenya.

3.4 PVWP for drip irrigation in Bogoria

The Noroloro Women's Group in Bogoria (Baringo County) was formed in 2006. This Group initially worked with livestock and later transitioned to fruit and vegetable production, which needed irrigation to be productive during the dry seasons. This Group began using an NGO-donated SunCulture pump in August 2014 to irrigate two acres through drip tape irrigation. The SunCulture PVWP pumps about 10,000 liters per day from a five foot depth pond which obtains water from a diverted canal.

Fig. 7: The SunCulture 300 Wp PVWP, owned by the Noroloro Womens Group, provides 10,000 liters per day for two acres of drip irrigation.

3.5 PV water pumping for aquaculture and irrigation in Kendu Bay

WI is collaborating with Futurepump at a demonstration site in Kendu Bay and nearby farms, where farmer Joshua Okundi purchased a SunFlower PVWP. Mr. Okundi owns five acres of farmland, which he uses to grow corn, passion fruit, tomato, banana, French beans, sweet pepper, kale, carrot, potato, peanut, avocado, and mango. He also has two fishponds, with 1,000 and 1,500 fish each, in which he grows tilapia. Mr. Okundi uses the 80 Wp Sunflower PVWP for the following activities at his farm:

- Pump water from the canal to the elevated tank for later use irrigate his crops.
- Pump water from the canal to the tilapia fishponds for oxygenation.
- Furrow irrigate passion fruit, avocado, banana, and a mango tree nursery.
- Pump water from the canal for domestic use.

The PVWP has enabled Mr. Okundi to save about US$20 per day from avoided fuel costs for a diesel pump he used to run. The SunFlower pump was purchased for US$400, achieving payback in about one month. The PVWP also allowed Mr. Okundi to start four new money-generating farming activities at his farm, hence improving his income. WI is conducting a detailed cost-benefit analysis at these demonstration sites to document the income benefits of PVWPs.

Fig. 8: Mr. Joshua Okundi with his Futurepump PVWP, used to recirculate water for a tilapia pond for oxygenation and also to irrigate a banana grove. The farm is located near Kendu Bay on Lake Victoria in Kenya.

3.6 PV water pumping for drip irrigation in Thika

A SunCulture demonstration site near Thika irrigates two acres of land that is not connected to a grid. The SunCulture submersible helical rotor pump (from China) sits one meter below the water surface in a pond. The head is about 20 meters to reach the 10 cubic meter tank at the top of a hill. The tank is filled twice a week and takes about four hours to fill. The community uses water from the tank daily to drip irrigate two acres and a nursery. The PVWP was installed in July, 2015 for US$2,200 and was a more inexpensive option compared with connecting to the nearby electric grid which was quoted at US$3,700 along with an energy consumption charge of US$0.19/kWh. This cost is more than the amortized cost of a direct drive PVWP over 20 years (estimated at about US$0.12/kWh).

Fig. 9: Thika solar water pumping system used for drip irrigation.

4. Accelerated Commercialization of PV Water Pumping in Nepal

Nepal is an agriculturally dependent country with a majority of its people involved either directly or indirectly in agriculture. Traditional agriculture in Nepal is rain-fed and depends on rainfall during the summer monsoon season. Farmers generally grow cereal crops like rice and wheat during the monsoon season. In the dry season, from November to March, many farmers leave their land barren due to lack of water, while more wealthy farmers can grow high value vegetables using either diesel or grid powered electric pumps for irrigation. With the high cost of fossil fuel along with maintenance costs, farmers have to bear huge financials burden for operation and maintenance of diesel pumps. Nepal suffers from severe electric power shortages, which causes frequent power cuts and load-shedding, so grid powered electric pumps are often unreliable. PVWPs are a reasonable irrigation solution for the dry season to increase farmer incomes. PVWPs also provide opportunity for high value horticulture farming in the off-season, which can generate even higher incomes for farmers.

Market challenges in Nepal include: limited PVWP products options; relatively few PVWP suppliers; limited access to finance; inadequate information and understanding about PVWP among farmers hesitant to change farming practices; and lack of coordination between government agencies, the solar power industry, promoters and organizations working to improve agriculture and irrigation efficiencies. USAID funds the Accelerated Commercialization Solar Photovoltaic Water Pumping (AC-PVWP) project, implemented by WI, that focuses on capacity building and market development activities to expand commercialization and adoption of PVWP systems for irrigation, livestock watering, and community water supply. There is a large demand for water pumping, but due to the high initial capital costs, many Nepalese farmers are unable to afford the technology. WI is working with SunFarmer Nepal and local cooperatives for investment capital to provide equity and loans to farmers so they can obtain PVWPs and increase their farm productivity. Some example AC-PVWP cases of PV water pumping in Nepal are described below.

Fig. 10: Winrock International demonstration PVWP unit at Khajura, Banke, Nepal.

4.1 SunFarmer financial loan model for PVWP installations in Nepal

The SunFarmer loan model is aimed at creating access to PVWP irrigation services for the farmers of Nepal through innovation in technology, finance, and long-term service commitments. The model serves as a platform to converge multiple stakeholders to accelerate commercialization of PVWP. Under this model, SunFarmer invests up to 50% of the initial capital for PVWP system installation and farmers pay off the loan in installments through the designated cooperative within the Power Purchase Agreement (PPA) period (e.g., two years). With this financing scheme, more farmers can install PVWP systems for irrigation. In addition to financing, SunFarmer performs technical and financial assessments to ensure that the system is properly

installed and guarantees free repair and maintenance, to ensure system performance within the PPA period. SunFarmer supports farmers to identify the most affordable and reliable systems tailored their needs. Upon successful completion of the agreement period, SunFarmer hands over ownership of the project and PVWP system to the farmers.

4.2 *PV water pumping for vegetable farming in Pokharikada*

A demonstration PVWP unit with the Pokharikada Village Development Committee in Surkhet district was installed by Suryodaya Urja Private Ltd., irrigating 4.4 acres of land for a group of 20 farmers. The system consists of a 1.4 kW Grundfos submersible helical rotor pump, 1,260 Wp PV array, grounding system, and accessories as shown in Figures 11 and 12. The submersible pump is placed in an 8 m^3 water tank in a spring box. The system is designed to lift 10,000 liters of water 60 meters up to a 20 m^3 collection tank. The water is then fed to drip and sprinkler system and the farmers use the water in queue. The total cost of the system was US$4,988 and the civil component was US$4,260, which included the water tank, reservoir tank, and the distribution pipes. The demonstration system was financially supported by the Government of Nepal, the Village Development Committee, the Raising Income of Small and Medium Farmers Project (RISMFP), USAID's Knowledge-based Integrated Sustainable Agriculture and Nutrition (KISAN) Project, and AC-PVWP.

Figs. 11 & 12: PVWP system and water storage tank used for vegetable farming at Pokharikada, Surkhet, Nepal.

4.3 Cooperative loan for PVWP installation at Chinchu

Suryodaya Urja installed a PVWP demonstration unit in Chinchu, Surkhet to irrigate 2.8 acres of land for 10 farmers. The 1.4kW Grundfos submersible helical rotor pump, much like the Pokharikada system, is placed in a 5 m^3 water tank serving as a spring box. The system is designed to lift 10,000 liters of water 60 meters up to a 24 m^3 collection tank. The water is then fed to a drip and sprinkle system and the farmers use the water in queue. The total cost of the system was US$4,988 excluding the civil components. Small Farmer Saving and Credit Cooperative, a local cooperative in the village, financed US$3,000 for the PVWP system at an interest of 18%. In addition, the Municipality Office, USAID's KISAN project, and WI through the AC-PVWP also provided financial support. This system is able to irrigate several crops, such as tomatoes, cauliflower, cabbage, black eyed beans, string beans, potatoes, chile, cucumber, and bitter gourd. With PV water pumping, the farmers group is now able to irrigate throughout the year, have produced their first crop of vegetables, and have paid the first loan installment. It is expected that farmers will fully repay their loan within two years.

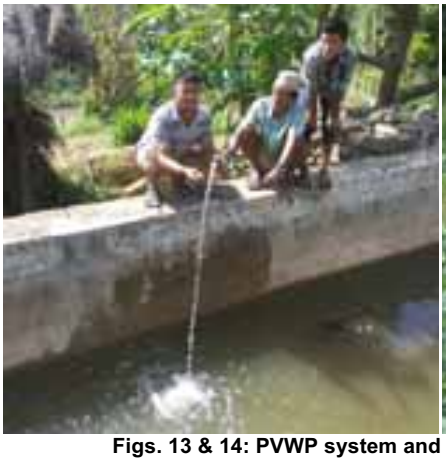


Figs. 13 & 14: PVWP system and vegetable farming at Chinchu, Surkhet, Nepal.

Demonstration projects in Surkhet have attracted other stakeholders, projects, and organizations working in the agricultural and irrigation sectors. Government agencies, including the District Development Committee, Village Development Committee, and Municipalities, as well as projects like RISMFP and High Value Agriculture Project (HVAP) have also shown interest in the PVWPs and plan to integrate PV water pumping technology in their projects.

4.4 PVWP for poultry farming in Chitwan

A PVWP is used for pumping water for a poultry farm in Madi, Chitwan. The system was installed by Madi Saurya Urja, a local agent of the Rural and Alternative Energy Service Centre. The PVWP can provide 4,000 liters per day of water, as required by the poultry farm. The system consists of a 300 Wp PV array with battery storage using a 150 AH deep cycle lead-acid battery. The 0.5 kW alternating current pump operates from a 1 kVA inverter connected to the battery. The total cost of the PVWP system was US$830, excluding civil works and was purchased directly by the farmer from his operational profits.


Figs. 15 & 16: PVWP system using a battery and inverter used at a Madi, Chitwan poultry farm in Nepal.

5. Conclusions

The solar water pumping examples in Kenya and Nepal, along with others around the world demonstrate overcoming barriers for commercial sales of solar water pumps by taking advantage of relative cost savings, increased reliability of PV and irrigation, increased technical access through innovative financing models, and educating farmers on pump choices. These successes have been possible through technical and market advances that have lowered costs and increased market access for PVWP. The real challenges now for wide-scale adoption of PVWP are not technological in nature, but rather pertaining to market and educational barriers. When compared to diesel or grid-electricity powered pumps, solar water pumping systems offer better returns on investments and more reliable electricity and water supplies.

Efforts to commercialize PVWP technology for irrigation are on-going. By embedding the technologies in value chain productive use projects that support farmers to increase income by growing and selling off-season produce, there are increased opportunities to demonstrate financial benefits. Current commercialization barriers are overcome through public-private partnerships that emphasize quality systems, education and demonstrations, and linkages with innovative micro-finance institutions, and partnerships with technology providers.

The challenges and successes of PVWP initiatives demonstrate lessons learned that can be applied in other regions, such as Sub-Saharan Africa, where only four percent of land area is irrigated, despite having areas with potentially sustainable water supplies (Giordano et al., 2012). With continued expansion of irrigated land, and demand further still for irrigation solutions in food insecure regions, there is great potential for accelerating and commercializing PVWP systems for irrigation. The scalability and cross regional applicability of these technologies though will depend on the water resources, market linkages, financing options, and management systems.

6. References

Aila, P., Atieno, R., 2006. Agricultural policy in Kenya: Issues and Processes. Presented at Future Agricultures Consortium Workshop, Institute of Development Studies, University of Nairobi.

Foster, R., Cisneros, G., Hanley, C. J., 1998. Life-Cycle Cost Analysis for Photovoltaic Water Pumping Systems in Mexico, in: Proceedings of the 2nd World Conference on Photovoltaic Energy Conversion, Volume III, 15th European PV Solar Energy Conference, 27th US IEEE Photovoltaics Specialists Conference, 10th Asia/Pacific PV Science and Engineering Conference, Vienna, Austria, July 6-10, 1998, pp. 3021-3025.

Foster, R., Cota, A., 2013. Solar Water Pumping Advances and Comparative Economics, Presented at Solar World Congress, International Solar Energy Society (ISES), Quintana Roo, Mexico.

Foster, R., Ghassemi, M., Cota, A., 2009. Solar Energy, Renewable Energy and the Environment Series, 1st edition. Volume 2, Taylor and Francis Publishing, CRC Press, A. Ghassemi (Ed.), Boca Raton, Florida.

Giordano, M., de Fraiture, C., Weight, E., van der Bliek, J. (Eds.), 2012. Water for wealth and food security: supporting farmer-driven investments in agricultural water management, Synthesis Report of the AgWater Solutions Project. International Water Management Institute (IWMI), Colombo, Sri Lanka.

International Centre for Integrated Mountain Development, 2015. Solar Powered Pumps for Irrigation Purposes (SPIP): Experiences from India and Bangladesh. Presentation at the Launch Workshop for the Project "Reviving Springs and Providing Access to Solar Powered Irrigation Pumps (SPIP) Through Community Based Water Use Planning," Kathmandu, Nepal.

Rahman, F., 2015. IDCOL Solar Irrigation Projects, Presented at the Launch Workshop for the Project "Reviving Springs and Providing Access to Solar Powered Irrigation Pumps (SPIP) Through Community Based Water Use Planning," Kathmandu, Nepal.

Conference Proceedings

Solar World Congress 2015
Daegu, Korea, 08 – 12 November 2015

Solar Milk Cooling: Smallholder Dairy Farmer Experience in Kenya

Robert Foster[1], Brian Jensen[2], Brian Dugdill[1], Bruce Knight[1b], Abdul Faraj[3], Johnson Kyalo Mwove[3], and Wendy Hadley[1]

[1] Winrock International, Arlington, Virginia ([1] USA and [1b] Kenya)

[2] SunDanzer, Inc., Tucson, Arizona (USA)

[3] Egerton University, Njoro (Kenya)

Abstract

The USAID Photovoltaics for Sustainable Milk for Africa through Refrigeration Technology *(PV-SMART)* project is a new and creative concept of providing on-farm solar milk refrigeration for off-grid dairy farmers in Kenya. It uses a modified off the shelf direct drive photovoltaic refrigerator (PVR) technology, coupled with innovative cooling and energy storage approaches to chill evening milk on the farm for later transport the next morning to dairy collection centers. The battery-free PVR unit is designed to work optimally in locations with at least 4 average peak sun-hours per day. Farmers can receive a premium price for providing higher quality, refrigerated evening milk to dairy processors that would otherwise spoil. Dairy processors can also charge a premium for better quality and tasting dairy products from better quality milk that is maintained chilled from farm to factory. These solar farm milk coolers (FMC) are the first of their kind anywhere in the world and are a unique refrigeration system that uses thermal ice storage in lieu of electrochemical batteries and can operate directly on dc power from a PV module powering a variable speed dc compressor. The initial 40 pilot Solar FMC units have performed well in Kenya and lab and field assessments are discussed.

Keywords: *photovoltaics, direct drive solar refrigeration, milk chilling, Kenya*

1. Kenyan Dairy Sector

The ***Photovoltaics for Sustainable Milk for Africa through Refrigeration Technology (PV-SMART)*** project aims to tackle off-grid milk cooling under the United States Agency for International Development (USAID) Powering Agriculture Energy Grand Challenge Program (PAEGC). In collaboration with Winrock International (WI), SunDanzer Refrigeration Inc. (SDZR), a leading US solar refrigeration technology company, was awarded a highly competitive USAID grant to implement the project. The 3-year project began in 2014 and is implemented in collaboration with the County Governments and Agriculture Ministries of Baringo and Nakuru, and the Department of Dairy and Food Science and Technology at Egerton University located at Njoro, and various partner dairy cooperatives all in Kenya

There are over 850,000 small holder dairy farmers in Kenya, about 85 percent of whom do not have access to the national electric power grid. Diesel fuel is expensive and logistics difficult to deliver to small rural dairy farmers. Thus, there has not been an economical method available for on-farm milk chilling for the vast majority small holder dairy farmers in Kenya and other less developed regions globally. The typical Kenyan dairy farmer has about 3 to 5 cows, producing an average of about 8 liters per day of milk per cow (typically ~60% as morning milk and ~40% as evening milk). Dairy cooperatives have an organized morning milk collection system, but normally do not accept evening milk since by morning it has a high bacteriological count. Due to the lack of on-farm refrigeration, evening milk for which there is no milk collection has to be

doi:10.18086/swc.2015.03.05 Available at http://proceedings.ises.org

either forced consumed, sold cheaply to nearby neighbors or hawkers, or is lost. In Kenya, only about 40% of milk produced is processed nationally.

This failing in upstream milk production causes milk spoilage and lost farm earnings. It also causes poor quality milk and further losses in earnings along the downstream dairy value chain. Of the milk that does arrive, much of it still has a high bacterial count due to lack of refrigeration, resulting in poor quality dairy products. Farmers could receive a premium price for better quality, refrigerated milk; dairy processors could charge a premium for better quality products if milk can be kept cool all the way from cow to consumer; especially during the all-important first four hours after milking that determine quality.

In order to enhance the value of milk from remote producers, *PV-SMART* has developed an affordable solar powered farm milk cooler (FMC) so these producers can deliver cool milk rather than warm to the central collection stations. The farmers also use FMCs on the farm to preserve other produce such as eggs, meat, fruits and vegetables. Besides demonstrating the technology proof of concept, *PV-SMART* is also working with stakeholders to open up financing for solar technologies like PVRs that can increase on-farm productivity and increase incomes. Farmers need access to technology and credit on reasonable terms to finance the initial purchase of solar power systems, which have higher capital costs but lower operating costs when compared to traditional remote generation energy technologies like diesel gen-sets.

PV-SMART has a three-phase implementation strategy for developing, disseminating, and financing FMCs in Kenya as follows:

- **Pilot Phase 1 (Year 1):** Develop a FMC by enhancing an established off the shelf PVR model adapted as a Solar FMC and field tested on 40 farms in Baringo and Nyandarua Counties, and at Egerton University. A small wire basket for perishable household food is included, as well as two 5V USB ports for daytime cell phone charging.

- **Prototype field testing Phase 2 (Year 2):** A second generation prototype Solar FMC will be further tested on another 40 farms and with milk transporter-collectors and other potential dairy users.
- **Commercial roll-out Phase 3 (Year 3):** Based on feedback from field testing the final prototype design will be: (i) adapted, (ii) a local dealer network established and (iii) the Solar FMC commercially launched on to the Kenyan market and other countries in the region; and further afield.

PV-SMART initial pilots are underway with the Mogotio and Ngorika Dairy Cooperatives near Nakuru working in collaboration with a local Kenyan dairy processor experimenting with a milk quality payment system for the very first time in Kenya.

The project is also collaborating with established financial service associations such as the Savings and Credit Cooperative Societys (SACCOS) that already work with dairy cooperatives. The SACCOS can easily provide affordable financing for farmers for solar FMC systems. The estimated return on investment for the dairy farmer is from 1 to 3 years, depending on farm milk production levels. In March, 2015, the first 40 pilot units were deployed to the dairy cooperatives, as well as with the Egerton university dairy research unit. Performance of these units and farmer feedback on the early pilot systems are being used to make further design refinements.

2.0 Direct Drive Photovoltaic Refrigeration

The PVR has thermal storage (ice storage) instead of electro-chemical battery storage, and a direct connection is made between the cooling system and the PV panel. The embodied technologies were originally developed in support of NASA's future planetary mission's refrigeration requirements about a decade ago (Foster et al., 2001). This is accomplished by integrating water as a phase-change material into a well-insulated refrigerator cabinet and by developing a microprocessor-based control system that allows

direct connection of a PV panel to a variable-speed dc compressor. By storing ice in the walls of the refrigerator, it eliminaes the needs of battery storage. The refrigerator uses a vapor compression cooling cycle with an integral thermal storage liner, PV modules, and a controller. The refrigerator employs a variable-speed dc compressor.

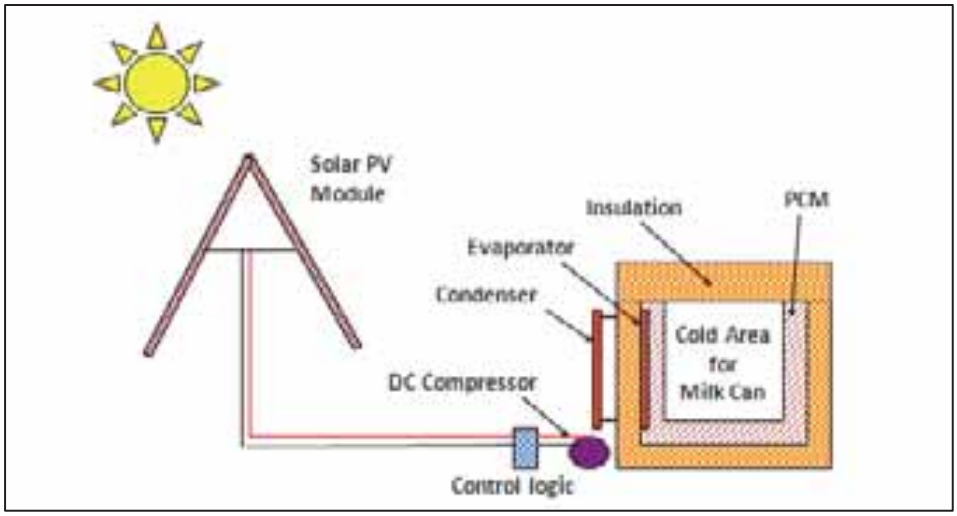

Fig. 1: Solar direct drive refrigerator with variable speed DC compressor and E-W "fixed tracking" array.

The PVR uses a fixed axis East-West tracker. This allows the variable speed dc compressor to start to spin earlier and until much later in the day, providing additional hours of refrigeration over a traditional equatorial facing fixed array. PV prices have come down sufficiently that "fixed tracking" is a viable economic option over tracking without the future maintenance concerns. This type of approach works especially well in lower latitudes like Kenya. This innovative simple approach provides superior performance.

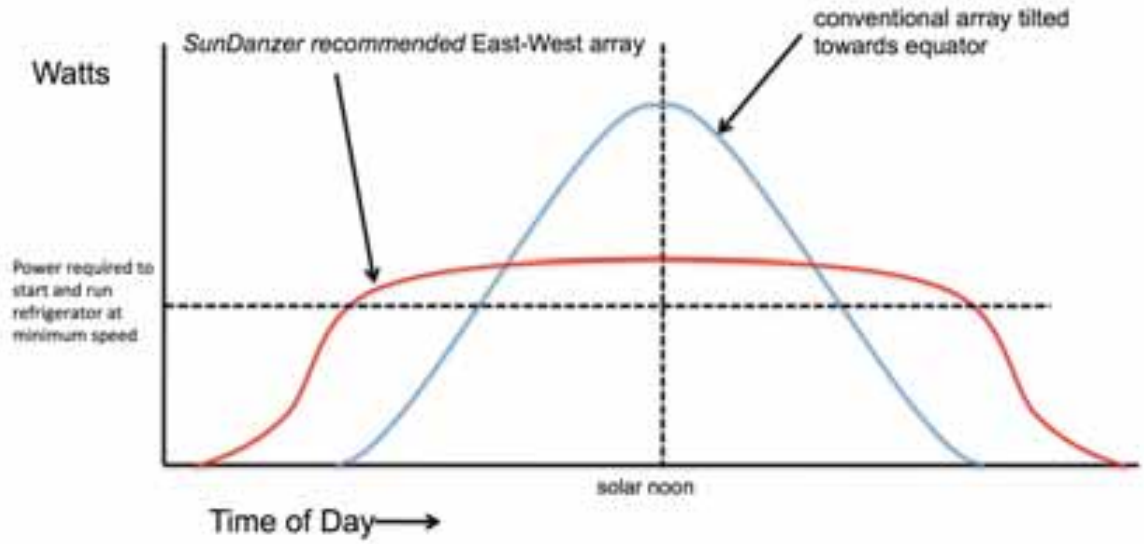

Fig. 2. E-W "fixed tracking" array designed to maximize compressor run time rather than energy capture.

With the compressor running most of the daylight hours due to the E-W "fixed tracking" array (the array is not actually moving like a conventional tracker, but is fixed with half the array facing East and the other half facing West to maximize daily compressor run time). Ice is formed and stored into the walls of the PVR. Thus, there is no need for expensive battery storage and replacements. Ice does not wear out. Testing at New Mexico State University for NASA and SDZR on an early prototype PVR with ice storage was successful for over a decade (Foster et al., 2001), which led to the development 5 years ago of direct drive vaccine PVRs using ice storage. The proven PVR technology is now expanded to FMCs.

In order to maximize heat transfer, the FMC incorporates brine bags which do not freeze at 0°C that are placed around the milk cans to increase heat transfer and cool milk quickly. As well as providing a complete and well-balanced diet for the newborn calf, kid or human baby, milk also contains antibacterial agents to protect the suckling young from potential infectious diseases; these antibacterial agents also slow bacteriological growth – the cause of milk souring. This effective natural protection is called the lactoperoxidase system, and has both bacteristatic and bactericidal effects against some milk spoilage microflora for about the first four hours after milking. Bacteriological growth is futher retarded when mik temperatures fall below 10°C and is essentially halted at 4°C. The FMC chills 25 liters of milk down to 10°C in a couple of hours, and the milk temperature in the morning is about 4°C as shown in Fig. 4.

Fig. 3: PV using thermal ice storage and brine bags to chill evening milk.

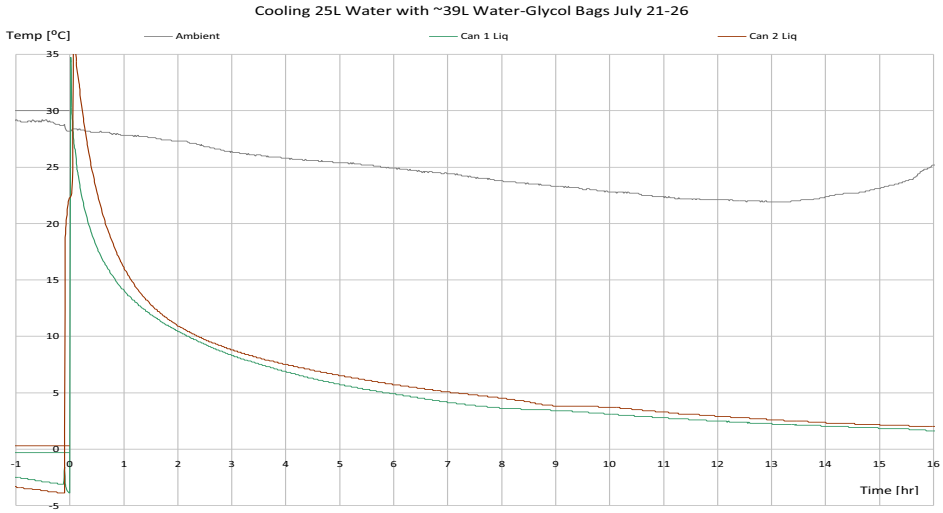

Fig. 4: Solar milk chilling lab test temperature reduction results for 2 milk cans. Bacteriological growth in milk largely becomes inactive below about 7°C. There is about a 4 hour window before significant bacterial growth starts in milk. The FMC unit successfully meets this threshold for 25 liters of milk.

Fig. 5: Dairy farmer from Ngorika shown with his E-W fixed tracking array for a Solar FMC.

3.0 Preliminary FMC field Operational and Technical Findings

WI in collaboration with Egerton University (Kenya's leading agricultural university) has been monitoring and evaluating (M&E) the performance and benefits of the Solar FMCs installed on the Mogotio and Ngorika Cooperative dairy farms. The WI team developed a '*PVSMART* Milk Chillers User Satisfaction Survey' form that Egerton has been using to survey half of the farmers with FMCs as of Oct. 1, 2015 after 5 to 6 months of operation.

PV-SMART team is also monitoring solar irradiance at Ngorika and Egerton sites. A few selected milk cans have a Hobo data logger installed on them to monior milk can temperature data. The temperature probe is installed on the can with foam over it so that it measures true milk can temperature only, see Figure 6.

Fig. 6: Brian Jensen of SDZR and Bruce Knight of WI install a temperature probe and small datalogger on a 10 liter milk can at Egerton University Dairy Lab.

The preliminary findings are based on meetings with users, milk can temperature data, and field observations by the WI and Egerton University team. All solar milk chillers visited are functioning properly except one unit which had a refrigerant leak upon delivery probably due to some of the extremely rough roads traversed for delivery; easily repaired by a local refrigeration technician.

Fig. 7: Johnson Mwove of Egerton University dairy lab surveying a dairy farmer with a solar FMC near Mogotio.

Installation: The units are all very well-installed. However installation costs were somewhat high for the Phase 1 pilot and will decrease in subsequent phases with the normal learning curve.

User operation: No major issues were found with user operation. Most users were not cooling milk to full capacity (25 liters), while two farmers were exceeding capacity and successfully cooling 40 liters a night. There was one farm where the woman operator had no prior experience operating a refrigerator before and had misunderstood the sign on top of the refrigerator to keep the chest lid open when "not in use" as to leave the lid open during the day when there was no milk. Her misinterpretation was corrected and the unit now operates correctly.

Milk temperature: The FMCs work well to chill 25 liters of evening milk to 4^{O}C and lower. If some milk is not removed the next morning and left throughout the day, small quantities of milk can freeze, indicating the prototype FMC may have 'spare' cooling capacity for Kenya. Figure 8 below shows daily milk cooling cycle for one of the farmers, milk temperature is repeatedly cooled to about 5°C. Note that the farmer puts the milk can outside for drying after cleaning representing the daily peak temperatures.

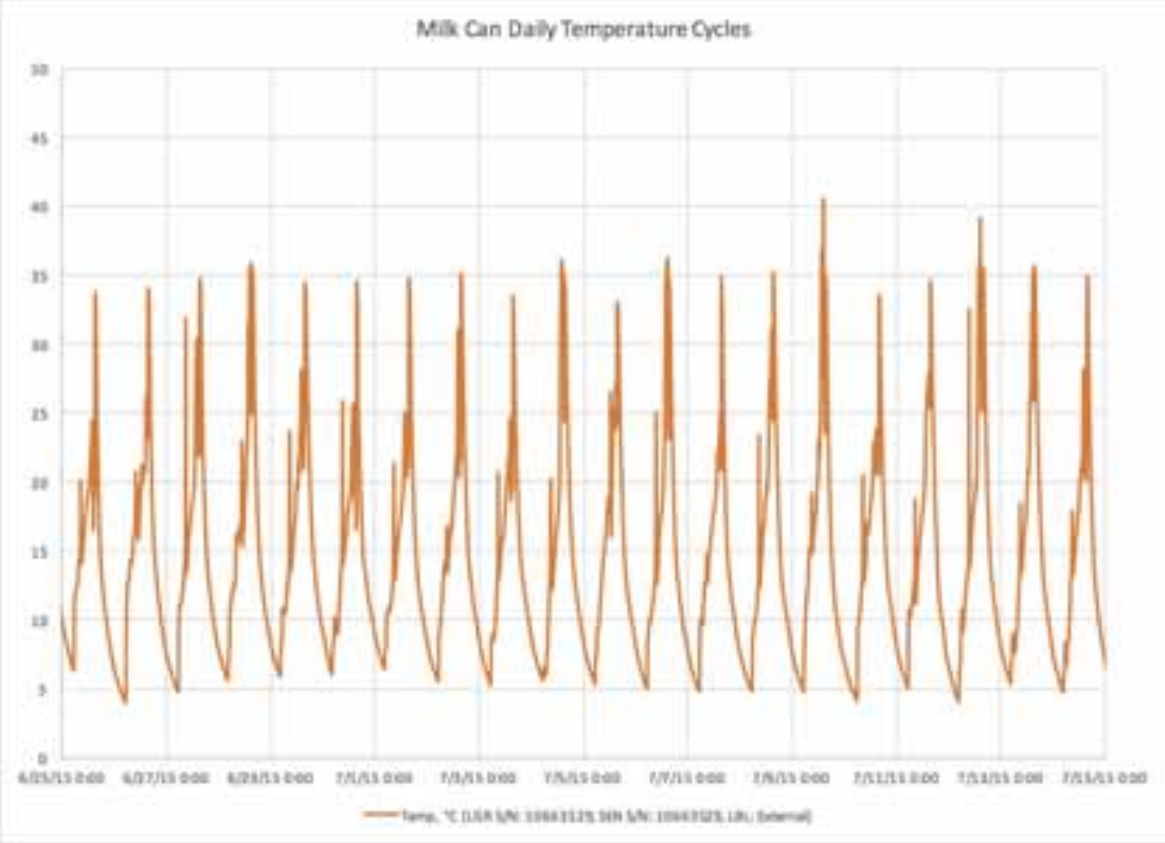

Fig. 8: Daily milk cooling cycles at a farmer's location: milk can temperatures. Note they clean and put the milk can outside in the sun to dry during the day.

Cooling Capacity: About half the users did not have enough evening milk to fill the pilot FMC. About ¼ of users utilize full capacity at 25 liters either from their own production or by also combining production with that of their neighbors, thus earning extra income for milk handling/bulking. Another user also earns extra income from charging cell phones from the two USB ports installed on the refrigeration unit, as much as US$1 per day (rate of US$0.10 per phone charge).

About ten percent of users have too much evening milk, i.e. more than 25 liters. These users and the cooperative managements want the FMC to be able to chill 50 liters milk in the standard 50 liters can. Some users are storing/cooling milk in plastic containers in the FMC and already exceeding the original design capacity. One cooler in Ngorika is chilling 40 liters milk in a food grade plastic water barrel, achieving overnight cooling to 'below 10^{O}C, indicating the potential of the unit to chill more milk adequately.

Other uses: Dairy value chain actors have been innovative in finding novel and remunerative uses for their prototype FMCs including:

- Standard cooling of evening milk by individual farmers;
- Bulk cooling of milk assembled from a number of local farmers by a farmer-collector;
- Bulk cooling of milk assembled from a number of local farmers by a collector-transporter;
- Keeping pasteurized milk chilled prior to sale in the immediate locality;
- Cold storage of perishable fresh foods; and,
- Cell phones charging.

3.1 Ngorika Dairy Association Observations

The Ngorika dairy farmers are overall satisfied with the cooling capacity of the FMCs and consider that the pilot project is going well. One farmer noted that small quantities of milk left in for longer time periods rather than just overnight sometimes might freeze. Since Ngorika is much higher (>2,500 meters above sea level) and thus much cooler due to the altitude, they have historically been able to sell some excess evening milk. The Ngorika farmers using the Solar FMCs have had no milk rejections whatsoever, so there is still an additional income increase due to quality. One farmer actually cools 40 liters of evening milk to $4^{O}C$ overnight in a 40 liter food grade plastic container rather than a traditional milk can. Their potential incremental gross earnings gain at current milk price was about KES51,300 (US$488) per month. This farmer produces more milk and is interested in increasing cooling capacity, or obtaining a second unit. Another farmer was found to have a potential incremental gross earnings gain at current milk price through the Solar FMC of about (US$564) per month (for own farm & farms serviced by collector).

Fig. 9: Satisfied Ngorika dairy farmer is happy with the Solar FMC and is actually exceeding recommended design cooling capacity by successfully cooling 40 liters of evening milk overnight.

3.2 Mogotio Dairy Cooperative Observations

The Mogotio dairy farmers have 18 Solar FMCs, as well as one unit at the dairy cooperative headquarters. The Co-op considers the Solar pilot as 'going very well' and they are interested in more units. Mogotio farmers are seeing significant increased income by selling evening milk stored overnight in the Solar FMCs, more so than Ngorika. This is due to the much hotter climate. Some users are even buying their neighbors evening milk and refrigerating to sell the next morning. The Solar FMCs benefit farmers because they can: (i) sell more milk; (ii) boost farmer earnings by collecting milk from neighbors, (iii) charge a cooling fee;

and (iv) keep drinks and perishable food cool and fresh for longer periods. For example one farmer was able to sell an extra ~8.5 liters of milk daily. Another farmer, besides chillng milk, also charges cell phones for 10 neighbors daily at US$0.10 each; the earnings are used to hire a 'Boda-Boda' (motor-cycle taxi) to transport her 2 teenage daughters to and from school. Her potential incremental gross earnings gain at the current milk price is about US$125 per month (including cell phone charging). Other smaller dairy farmers not utilizing the Solar FMC to full capacity (e.g, 5 lpd) had a potential incremental gross earnings gain at current milk price as low as US$23 per month.

So hotter climates are better as far as payback. But everyone surveyed likes and wants the Solar FMCs. The neighboring dairy cooperative next to Mogotio now wants their own Solar FMCs after seeing the successful results of their neighbors.

Fig. 10: Mogotio dairy farmer with his fixed E-W tracking array powering the Solar FMC.

4.0 Cost Benefit

Milk quantity and potential incremental gross earnings gain at current milk prices is already quite good for these pilot units, with simple payback ranging anywhere from one to three years depending on user milk production. From the initial surveys users sell between 2 and 45 liters of extra evening milk each day, indicating gross incremental income gains ranging from US$23 to $650 per month. These figures factor in gains by users bulking milk or charging cell phones on behalf of neighbors.

A complete cost benefit analysis will be done after one year of operation during Phase 2 to determine an acceptable/optimum Solar FMC price for SDZR and farmers. For Phase 2, SDZR plans to distribute units with end user cost share; for the initial pilot, farmers were not asked to cost share the Solar FMC price (only their time and milk cans); USAID PAEGC funded the units to buy down the technology risk for demonstrating a completely new concept with relatively poor rural small holder dairy farmers.

5.0 Conclusions

The key technical and operational take aways from the preliminary assessment of the *PV-SMART* Phase 1 pilot PVR units are that Solar FMCs offer small off-grid dairy farmers and milk collector/transporters the affordable opportunity for a value adding route to market that delivers better quality milk attracting premium

prices, especially for evening milk. All units are working well with no complaints from farmers. A couple of farmers already are chilling 40 liters of evening milk with success. Consideration may be given to increasing the cooling capacity to cool a 40 or 50 liter milk can. From the initial surveys users sell between 2 and 45 liters of extra evening milk each day, indicating gross incremental income gains ranging from US$23 to $650 per month with expected paybacks ranging from 1 to 3 years for the Solar FMCs. A cost benefit analysis will be done during Phase 2 to determine an acceptable/optimum Solar FMC price for users and SDZR. There is also huge market potential in other countries in Africa, Asia, and Latin America; there are from 3 to 5 million off-grid small dairy farmers in the African Tripartite Free Trade Area (TFTA). The project is now planning to leverage the technical and operational achievements achieved during first phase and apply lessons learned to the upcoming Phases 2 and 3.

6.0 References

Foster, R., L. Estrada, D. Bergeron, 2001. Photovoltaic Direct Drive Refrigerator with Ice Storage: Preliminary Monitoring Results, Presented at “ISES Solar World Congress,“ Adelaide, Australia.

Conference Proceedings

Solar World Congress 2015
Daegu, Korea, 08 – 12 November 2015

Ray Tracing for Evaluation of the SK14 Solar Concentrator as a Solar Fryer

Ole Jorgen Nydal[1] and Asfafaw Tesfay[2]

[1] Norwegian University of Science and Technology, Trondheim (Norway)

[2] Ethiopian Institute of Technology – Mekelle, Mekelle, (Ethiopia)

Abstract

SK14 is a well known solar dish reflector which is made for cooking in a pot positioned at the focal point. The reflector consists of aluminium sector sheets which are attached to a light frame designed for manual solar tracking. The SK14 is here evaluated as a reflector for frying of the Ethiopian injera bread. Ray tracing shows that the reflected rays spread more evenly on the pan, but also gives higher losses compared with an ideally smooth reflector. A test on heating a frying pan which was custom made for the SK14 showed that frying temperatures for injera baking can be reached with the SK14 reflector. High thermal losses and illumination of the pan at an angle results in quite long heating time for the pan.

Keywords: *Solar fryer, SK14, ray tracing, solar cooker, concentrating solar heat*

1. Introduction

The SK14 (Seifert EG-Solar 2007) is a parabolic dish, made up of sector shaped elements of reflecting aluminium. The light weight frame has a support structure for a cooking pan in the focal point of the dish. SK14 offers a low cost solution for cooking in the sun, using manual solar tracking.

Baking of the injera bread is common in Ethiopia, most often with firewood as the energy source. Electrical stoves for injera baking is available, but most households in Ethiopia are not connected to the electrical grid. As the deforestation is severe, and as Ethiopia has very good solar potentials, solar powered injera baking could be an attractive solution.

Solar baking of the injera bread has been considered earlier with direct methods (Gallagher 2011, Asfafaw et.al 2014) and with indirect methods by positioning the pan on top of a heat storage charged by steam from a solar concentrator (Asfafaw at al 2014). Systems with integrated storage units offer flexibility for the user, but tend to become more complex requiring solar tracking, heat transfer systems and storage methods.

The SK14 reflector has been designed for solar cooking. This work explores the use of SK14 for frying of injera. Ray tracing is applied for evaluation of differences between an ideal reflector and the SK14. Some tests have also been made on the heating time for an aluminium frying pan designed for the SK14.

2. Experiment

Figure 1 shows a photo of the SK14 reflector, with a cooking pot and a frying pan in the focal area. The sun tracking is made by manually turning the parabola every few minutes.

doi:10.18086/swc.2015.03.06 Available at http://proceedings.ises.org

Fig. 1: SK14 with a pot and a frying pan

Two aluminum plates have been constructed (2 cm thickness each) to fit with the standard holder for the SK14 (hexagonal shape). One is anodized black, the other has no surface treatment.

A feasibility experiment was made to see if frying temperatures could be reached at non-ideal conditions, as experienced with a low solar angle in Norway (see Figure 1). Thermocouples are inserted into the plates from the side and logged during the charging of the plate in the reflector. After the baking plate is heated, the reflector is turned, giving easy access to the baking plate. The pan should have sufficient energy for 1-3 injera bakings, depending on the pan thickness.

Figure 2 shows the temperature rise of the pan in two tests. The stagnation temperatures in these tests are quite low, about 130 degrees C in the first one. The sun angle in this test was low, and midway in the first test a cold Norwegian wind started blowing, effectively halting the further temperature rise. In the second test, the response to spraying the pan with water was included. Earlier work has shown that injera can be baked on a metal surface at temperatures down to 150 degrees. Using SK14 for injera frying is therefore expected to be feasible under the more favourable conditions of the Ethiopian sun (about 13 degrees latitude).

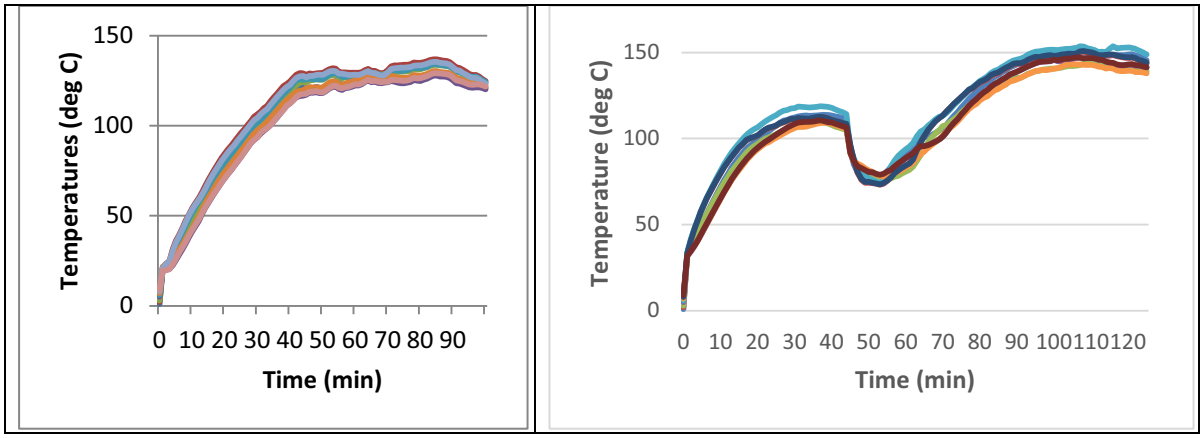

Fig. 2: Temperature rise on a hexagonal frying pan heated in the SK14 concentrator. Left: The temperature rise halted when a cold wind started blowing. Right: Water spraying of the pan after 40 minutes

3. Ray tracing

The illumination of the plates is investigated with a ray tracer, in order to optimize the position of the pan. The ray tracer is described in (Nydal, 2013, 2015). The tracer is programmed in C++, with the Qt library for the GUI and with OpenGL for the visualization. The tracer gives the user the options to assemble different kinds of reflectors and absorbers (trough, dish, plate, sphere, pipe, Scheffler reflector) for analysis with a user specified sun (density of sun points and direction). Each element can be assemblies of discretized mirror tiles or smooth mathematical surfaces. A screen shot with a 1D sun is shown in Figure 3.

The basic equation solved in a ray tracer is to find the intersectionsbetween a line and a surface and then to compute the reflected ray from the incoming ray and the surface normal vector at the intersection point. An intersected point (P) on the surface is u units in length from the origin point (S) of a ray having vector (d) as

the direction.

$$\vec{P} = \vec{S} + u\vec{d} \quad (1)$$

A surface (flat plate, sphere, cylinder, paraboloid etc.) can be described by an algebraic relation

$$p(x, y, x) = 0 \quad (2)$$

Eq.1 on component form is then substituted into Eq. 2 (for the coordinates x,y,z) which gives an equation for u. With the normal vector (n) computed at the resulting intersection point (P), the reflected ray has the direction (r):

$$\vec{r} = \vec{d} - 2(\vec{d} \cdot \vec{n})\vec{n} \quad (3)$$

The ray tracing is then the management of the rays, taking also into account shading effects

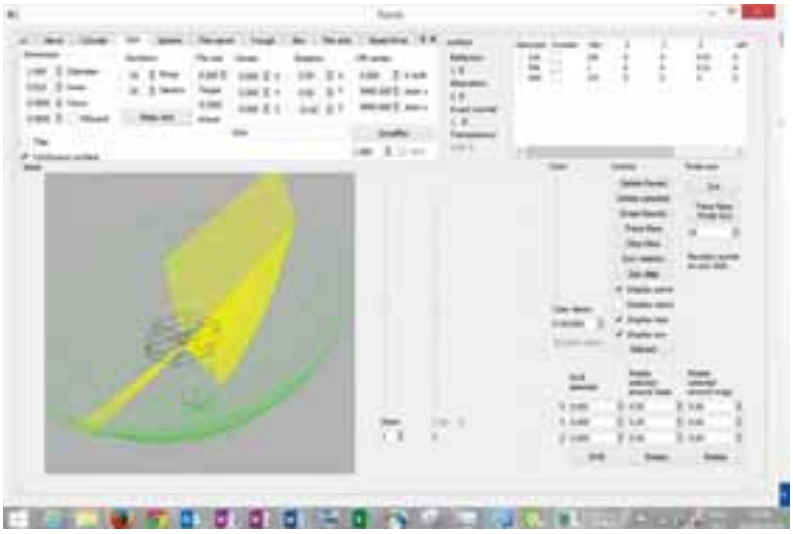

Fig. 3: Screen capture of the ray tracer program

Figure 3 shows screen captures of a case with 40 degrees sun inclination (morning or afternoon sun). The frying pan is positioned with the focal point of the concentrator at the centre point of the pan. At low solar angles, the plate will be illuminated from both sides, giving a non-symmetric heating of the plate. With an ideal reflector, all rays are captured by the plate. With a sector tiled reflector (the SK14 geometry is approximated with tiles generated from 16 sectors and 16 rings), the illumination is more spread out on the plate and the losses increases, depending on the vertical positioning of the plate (20-30% in this case).

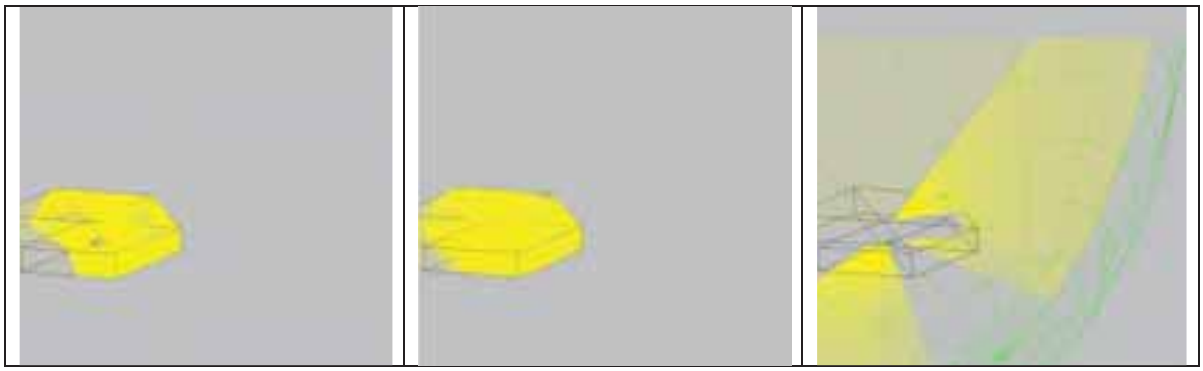

Fig. 4: Screenshots of the pan illumination at 40 degrees solar angle. Left: ideal concentrator. Centre: SK14 concentrator. Right: Test with a 1 dimensional sun (sun rays on a line)

Figures 5 and 6 show sensitivities to the vertical positioning of the pan by adjusting the height such that the focal point is at the bottom, centre and top of the pan. The simulations are made with a sun covering half of the concentrator.

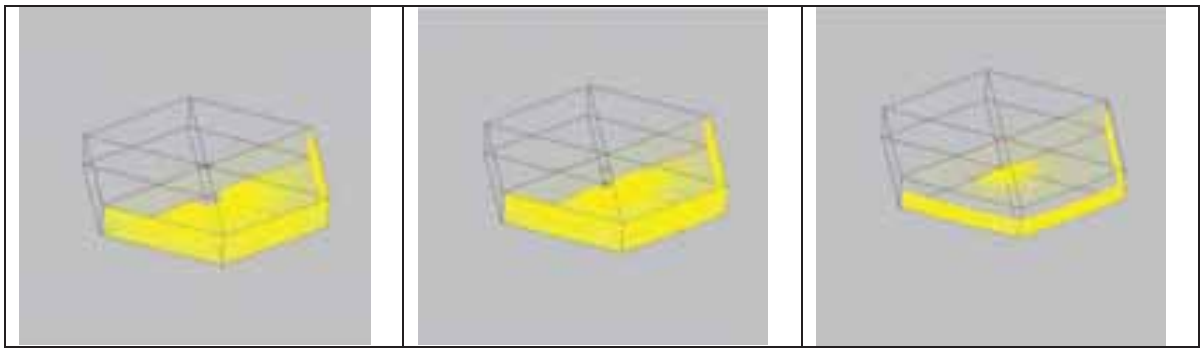

Fig. 5: Screenshots of the pan illumination at different vertical positions. Smooth concentrator, half illuminated Left: Focal point on top. Centre: focal point in the centre of the pan. Right: focal point at the bottom

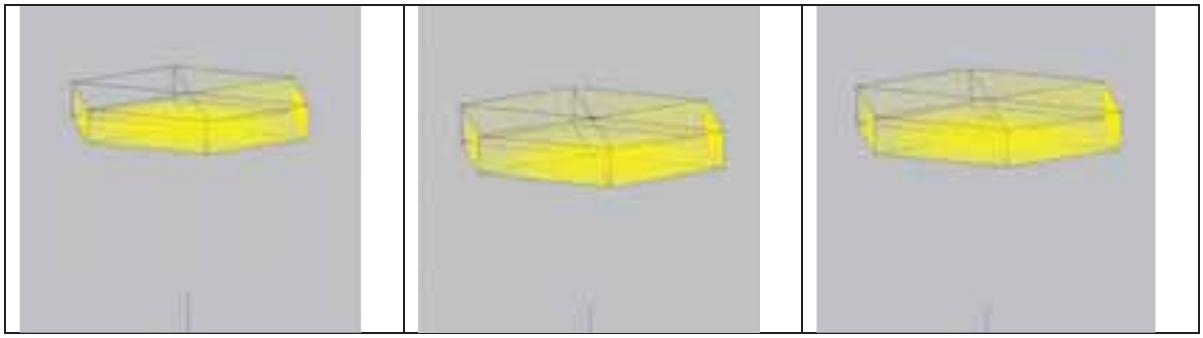

Fig. 6: Screenshots of the pan illumination at different vertical positions. SK14 concentrator, half illuminated Left: Focal point on top. Centre: focal point in the centre of the pan. Right: focal point at the bottom

The SK14 concentrator spreads the reflected rays significantly more than the ideal smooth reflector. This gives less sensitivity to the positioning of the pan, but does also give higher losses. The ideal reflector shows a more critical sensitivity to the positioning of the pan, with also a higher risk of generating hot spots on the pan.

4. Discussion

Figure 7 shows the temperature time recordings of Figure 2 plotted with a time shift to allow for comparisons of trends. The temperature measurements in Figure 2 do show some variations for the different thermocouples. The illumination is not uniform across the plate, nor at the different sides of the plate. Figure 7 includes the band of the measurements.

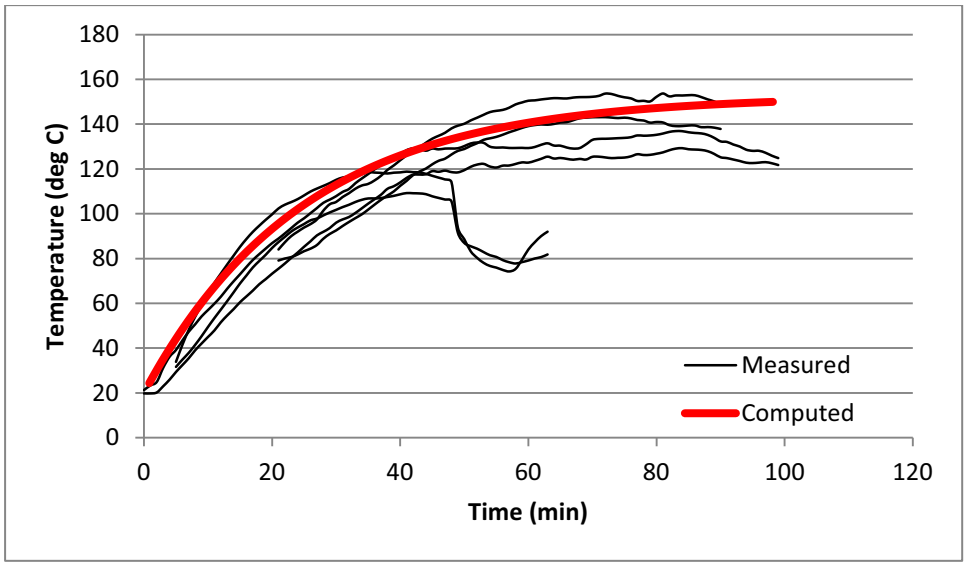

Fig. 7: Overlapped temperature measurements from Figure 2 (thin lines) and computational estimates (thick line)

A simple computational estimate can be made by neglecting the internal heat transfer dynamics (heat conduction) and consider the pan to have uniform temperature. The temperature evolution can then be computed from estimates of the solar radiation and of the losses. Figure 7 shows the integrated temperature from the energy balance:

$$\frac{\partial \rho A d c T}{\partial x} = \rho C_r A - h A_i (T - T_a) \qquad (4)$$

The definition of the variables and the numbers which have been applied are given in Table 1.

Table 1 Values for the temperature computations

Variable	Value	Comments
ρ - density	2800 kg/m^3	The temperature dependency is neglected
A - plate area	0.0706 m^2	The plate is hexagonal, but the area is for simplicity estimated from a circle with a diameter of 30 cm
A_l- area for heat losses	2A m^2	The plate is hexagonal, but the loss area is for simplicity estimated from the top and bottom surfaces, sides neglected
d - plate thickness	0.02 m	
c - heat capacity	910 J/KgK	The temperature dependency is neglected
T - temperature		
h - heat transfer coefficient	9 W/m^{2}K	This value is tuned based on the experiments
T_a - ambient temperature	20 degrees C	
q - solar radiation	900 W/m^2	This is a typical value measured in Trondheim on a clear and sunny day. The solar intensity was not measured at the day of the experiments, so the value is an estimate
C_r- effective concentration ratio	5	This value is tuned based on the experiments, and includes all optical losses

From Figure 7 it can be seen that the uncertainty in the heating and loss conditions of the plate in the SK14 concentrator can be quite large. The solar tracking is manual and the ambient conditions can change during the heating – wind has a strong effect on the heat losses from the plate. This rough estimate, based on tuning of the heat supply (the effective concentration ratio) and the losses (the effective heat transfer coefficient for the top and bottom surfaces) indicates that the stagnation temperature will in this Norwegian case be quite low. Frying temperatures can be reached, but after considerable time.

If one side of the pan could be insulated, the losses could potentially be reduced. Figure 8 shows ray tracer results for two latitude cases: Trondheim in Norway (about 60 degrees) and Mekelle in Ethiopia (about 13 degrees).

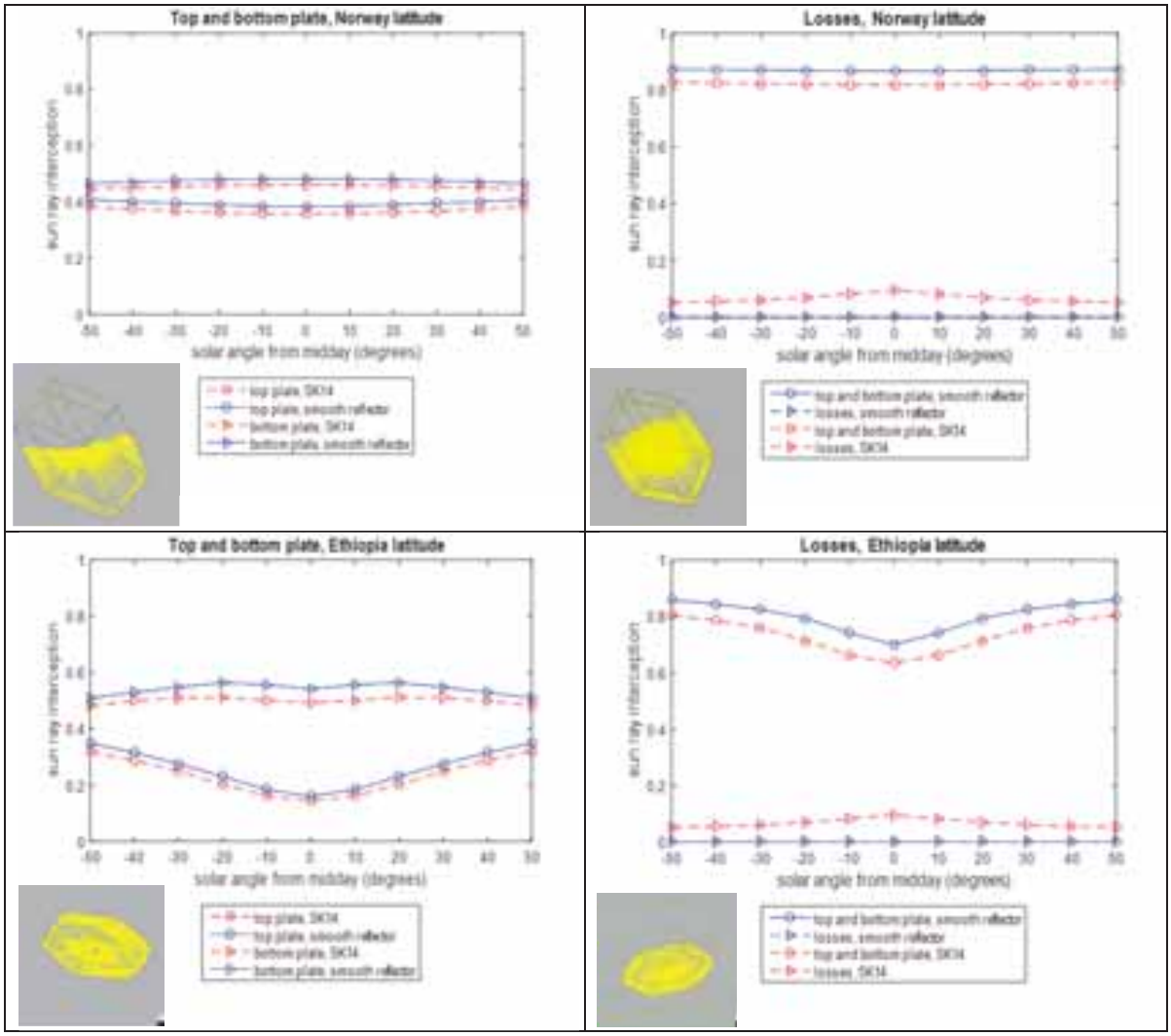

Fig. 8 Ray tracing results for solar tracking during a day in Norway and in Ethiopia

With the frying pan kept in a horizontal position the angle with the concentrator will be larger in Norway than in Ethiopia. This means that both sides of the pan will be illuminated more in the Norwegian case than in the Ethiopian case. Insulating the top plate during heating of the plate may not provide a strong benefit even for the Ethiopian case, as the top illumination is still quite large also at Ethiopian latitudes. The illumination of the sides of the plate is also significant (about 10%).

5. Conclusions

From previous tests, it has been demonstrated that the Ethiopian injera bread can be baked on an aluminium surface. The tests made in this work shows that frying temperatures can be reached in an SK14 concentrator, fitted with a custom made aluminium pan. The SK14 can then be a low cost alternative for direct solar injera baking.

The pan is exposed to the ambient, so the thermal losses will reduce the performance of the fryer. The sector tiled geometry of the SK14 spreads the reflected sun rays more on the pan, but also gives higher losses due to rays missing the pan, compared with an ideal concentrator. An ideal reflector surface can, however, give a too concentrated illumination of the pan depending on the positioning in relation to the focal point.

The direct frying system can be optimized by using a concentrator with a smaller rim angle. If only one side

of the pan is illuminated, it can open for insulation of the other side, and similarly during frying.

References

1. Alan Gallagher A solar fryer Solar Energy 2011; 85(3):496-505
2. Dieter Seifert EG-Solar (2007). Solartechnologie 2007, EG Solar http://www.eg-solar.de/produkte/solartechnologie2007.pdf
3. Asfafaw Tesfay, Mulu Bayray, Ole Jorgen Nydal Design and development of solar thermal injera baking: steam based direct baking Energy Procedia, volume 57, pp. 2946-2955, 2014
4. Asfafaw Tesfay, Mulu Bayray, Ole Jorgen Nydal Storage integrated solar stove: A case of solar injera baking in Ethiopia IEEE GHTC conference, San Jose, California, October 2014
5. Ole Jorgen Nydal Ray tracing for optimization of a double reflector system for direct illumination of a heat storage 2013 ISES Solar World Congress, Cancun Mexico, 3-8 November 2013
6. Ole Jorgen Nydal Ray tracing for simulation of a light guide efficiency. SASEC2015, Third Southern African Solar Energy Conference. Kruger National Park, South Africa, 11 – 13 May 2015 example given below.

Clean Transportation Technologies & Strategies

Conference Proceedings

Solar World Congress 2015
Daegu, Korea, 08 – 12 November 2015

Performance of a Solar EV Charger in the Pacific Island Countries

Alvin. A. Datt, Aman Singh and Atul Raturi

University of the South Pacific, Suva (Fiji)

Abstract

The unsustainable dependence of the Pacific Island Countries (PICs) on imported fossil fuels and climate change concerns have made the region to look for alternative sources for energy. A major portion of fossil fuels goes towards transportation and it is imperative that other options such as biofuels and hybrids/ EVs are seriously explored. Considering the small distances involved, EVs can be profitably deployed in urban areas and also within the myriad tourist resorts spread across the Pacific islands. Solar PV based charging stations can play a major role in this endeavor. This paper describes the design and performance of first solar electric vehicle (EV) charging station in the Pacific Island Countries. The actual performance of this 2.6 kW_P station is compared with the simulated results obtained using HOMER. Finally, the paper also looks at the way forward for development of electric mobility in the region.

Keywords: Pacific Island Countries (PICs), Electric Vehicles, Solar PV

1.0 Introduction

1.1 Energy situation in Fiji and the Pacific Island Countries

The Pacific Island Countries (PICs) are heavily dependent on the imported fossil fuels for their day to day energy needs. These countries end up spending huge amount of their budget on fossil imports. For instance, the petroleum imports for Fiji have increased from about $400million in 2004 to over $1.2billion in 2008 which tends to account for a quarter of country's total imports[1]. The dominance of transportation sector in the imported fuel usage in Fiji is quite evident from the figs.1 & 2:

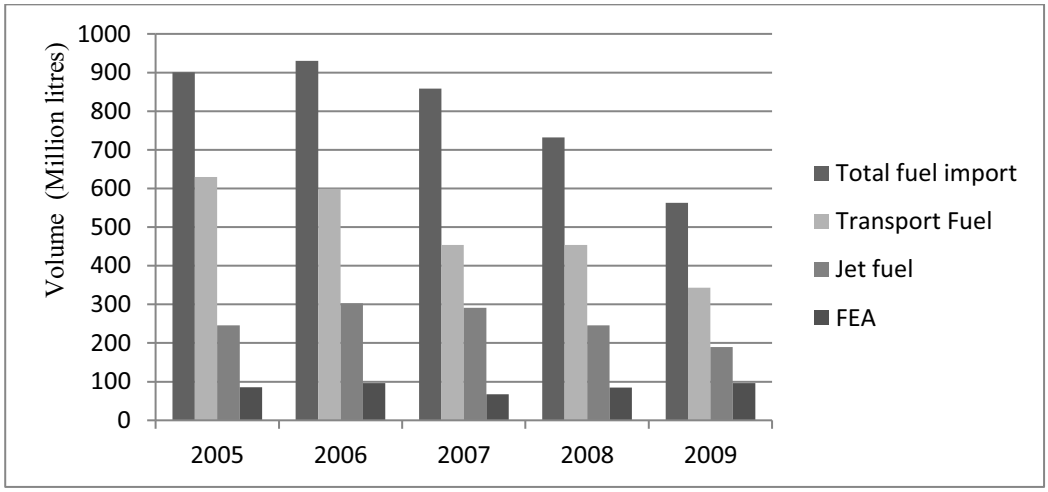

Figure 1: Fuel Import Levels in Fiji
(Source: http://www.irena.org)

doi:10.18086/swc.2015.01.01 Available at http://proceedings.ises.org

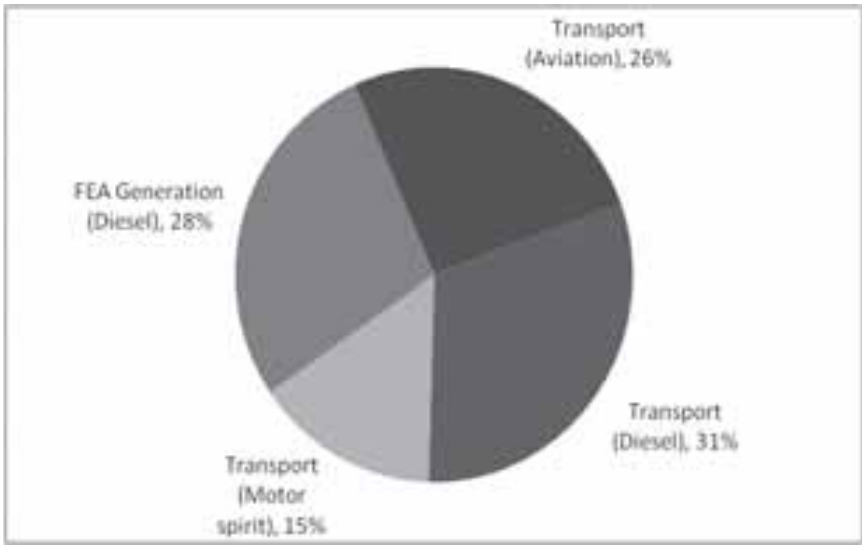

Figure 2: Oil Imports – RBF Estimates (2008 – 2011)
(Source: National Energy Forum - Reserve Bank of Fiji)

The Asian Development Bank's report launched in 2013, projects that under the present scenario, Fiji's energy demand will increase at an annual rate of 1.7 percent through the year 2035[2]. It also highlights the fact that the price of fuel in the Pacific is one of the highest in the world and only about 30% of households have access to electricity on average. Hence, the dependency of the PIC's on imported fuels for power generation hinders economical development since energy is a major driving force for the industrial and transportation sectors.
The PICs' heavy dependence on the fossil fuels can also be noticed by the figures discussed in International Renewable Energy Associations policy report where it estimates that 80 percent of regions primary energy consumption is based on oil of which 75 percent is used by the transportation sector and more than 20 percent is being used for electricity generation [3]..

1.2 The Development of Solar Electric Vehicles

An important development in terms of photovoltaic technology has been the introduction of solar charging stations for the charging of electric plug – in vehicles. The whole idea to use solar powered electric vehicles is to increase the use of renewable energy, and provide electric vehicle owners with a greener charging option. According to [4] "Electric cars are already among the cleanest-running vehicles on the road—charging them on solar makes them that much better".Obviously, if a EV charging station uses electricity mostly from burning fossil fuels, then the EV is simply outsourcing the pollution to the power plant.. But using electricity from solar panels erases this predicament [5].

A plug-in electric vehicle (PEV) is defined as any motor vehicle that can be recharged from any external source of electricity and the electricity is stored in rechargeable battery packs. PEV is a subcategory of electric vehicles that includes all-electric or battery electric vehicles (BEVs), plug-in hybrid vehicles, (PHEVs), and electric vehicle conversions of hybrid electric vehicles[6]. In the recent years, environmental and climate-change impacts of the petroleum-based transportation infrastructure, along with the uncertain oil prices, have led to renewed interest in an electric transportation infrastructure.

A recent study investigated the question of which alternative energy (Photovoltaic or biofuel) would be best for powering electric vehicles. The study explored the impacts of biofuels and PV on direct land use, greenhouse gas emissions, and lifecycle greenhousegas emissions. In all three categories Photovoltaic technology was found to bemore efficient and beneficial [7].

A number of companies like Ford, Toyota, Nissan, and of course Tesla to mention a few, have been quite active in the development of electric vehicles and more car manufacturers are now developing their electric

versions [8,9] However with the widespread implementation of electric vehicle networks within large cities, such as those provided by POD Point [6] in the UK and Europe, EV users can plug in their cars while at work and leave them to charge throughout the day for charging, hence solving the problem of driving range of the EV as enough charge would be available all the time.

Furthermore, Electric car maker Tesla has installed its "Supercharger" rapid car charging network at different locations throughout California. Superchargers are powered by solar technology, developed by solar installer Solar. The Superchargers can charge the Model S cars with 100 kilowatts of power and provide three hours of driving at 60 mph in about half an hour [9].

The solar-assisted charging stations use solar photovoltaic (PV) arrays to generate electricity to charge the electric vehicles. The Oak Ridge National Laboratory (ORNL) conducted a demonstration project involving solar assisted charging stations for EVs (2009-2014) . The project objective were to install 125 solar EV chargers and study their impact on the grid . The systems were grid-connected to enable charging at all times .and an external battery was employed to offset grid demand if needed.. The installed PV power per parking space was sufficient to support 10,000 miles driving per year.. One of the project collborators, Nissan North America, installed 30 solar powered carging stations.[10].

After going through the developments in the sector of electric vehicles and the solar charging stations globally, it can be realized that the potential for such a development is high but there are certain factors like the availability of enough solar charging stations, and the driving range of the electric vehicles that need to be considered. The idea of battery swapping at stations located on regular distance can prove to be a solutionfor the driving range problem of EV's considering that installing solar charging stations on a number of locations would become an expensive course. According to [11] instead of recharging EVs from electric socket, their batteries could be mechanically replaced on special stations in a few minutes.

1.0 The Solar Charging Station

2.1An Overview

An important aspect of any solar charging station is the installation of the panel and other components such as battery and the charge controller of the system.

Solar Panel –A solar panel is made up of a number of series and parallel combinations of identical individual cells to generate the desired power output (current and voltage). Panels are assigned a power rating in watts based on the maximum power they can produce under ideal sun and temperature conditions. The rated power output is used to help determine how many panels are needed to meet the electrical load demands. Multiple panels combined together are called solar arrays [11]. PV solar array is normally mounted on a canopy above the solar-assisted EV parking spaces. In addition to providing a mounting structure for the solar PV array, the canopy provides shading and protection for the components and also helps to keep the vehicle cool during charging. The canopy solar PV modules are electrically connected in a parallel/series arrangement to supply the optimal direct current (DC) voltage to the inverter. The inverter converts direct current from the array to alternating current to feed to the power grid through a transformer [10]**.**

Battery – electrical utility supplying power for the charging stations and is concerned about surge loads on the grid from vehicle charging. The function of the battery banks is to store energy on site, charging the batteries during periods of low charging demand, and discharging the batteries back into the electrical grid during high demand to minimize the surge load on the grid [10].

Charge Controller - a device that is very important because it blocks reverse current, prevents overcharging and discharging of the batteries and protects battery from overloading [12].Hence it prevents the battery from reduced lifespan. Charge controllers come in all sizes, and protection and monitoring features. The selection depends on the size of installed solar panel(s) and the complexity of loads and future expansion possibility. Different charging and maintenance algorithms are used depending on the type of the battery [11].

2.1.1 An Overview of the Project

The project of solar charging station at The University of the South Pacific was funded by the French Government under the Pacific Funding Programme. The major aim of the project is demonstrate one of the the climate change mitigation strategies in the region by moving towards a more sustainable form of energy for the transportation sector, help the students at the university with research in the field area and create awareness of the solar charging stations for electric vehicles..

Figure 3.The solar charging station roof mounted panels with two supports to allow for vehicle parking and charging area

2.1.1.1 The Technology Overview

Table 1.Power System details

	Description
Solar Panels (2.625kWp)	BP Solar BP4175
Array Frame	Roof mount array aluminiumUnirac module mounting rack
Batteries	Haze – HZYSL6 – 225, 6V @C100 (Gel)
Solar regulator	Outback FM60 60A MPPT
Inverter (240V, 50H)	Outback GFX1424, 1400W, 24V
Monitoring & Control	Outback Mate3, FlexNet DC

2.1.1.2 Station Design

The solar array is mounted on the roof on top of the equipment hut using Unirac rails and clips. The roof of the hut is tilted at latitude angle (18 degrees) and faces due north for the best annual performance of the

panels. Four Haze (Gel) batteries , a charge regulator and an inverter are mounted inside the hut.

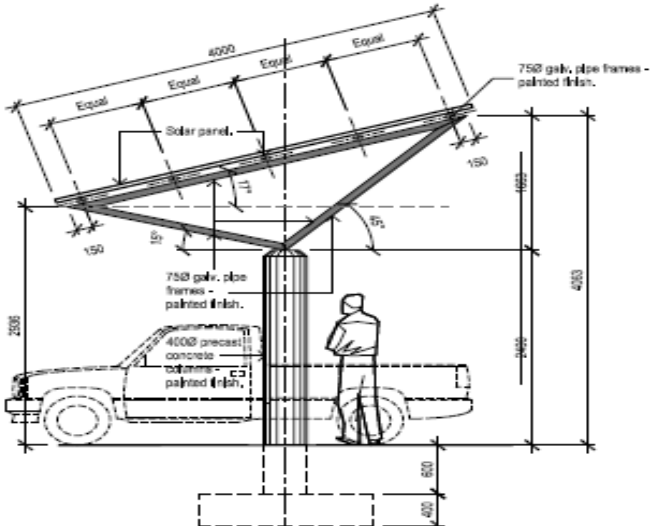

Figure 4. Construction plan for the charging station

2.1.1.3 System Features

A fully integrated and automated monitoring Outback system is installed to monitor the performance of the system. The FlexNET DC coupled with MATE3 provides advanced monitoring and control features. The MATE3 has an integrated data logger which can record system readouts for up to a year and hence allows for remote access and control. FlexNET DC collects, monitors and records time based battery amp, watt and voltage data for display on Outback MATE components. This provides data for precise battery recharging. There are five LEDs on the FlexNET DC that act as state of charge indicator bar. The advanced recording features of the system allows for the remote access of data for PV array performance, battery usage and load parameters.

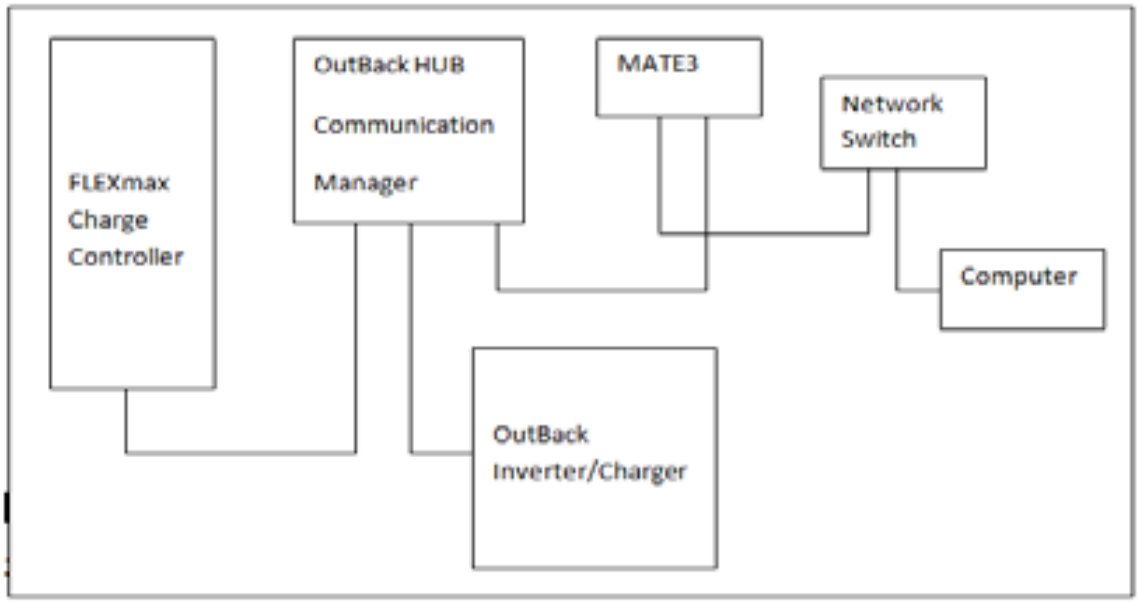

Figure 5.System Diagram

2.1.1.4 Solar Panel

Table 2.Electrical Characteristics of solar panel

	STC 1000W/m²	**NOCT 800W/m²**
Maximum power (P_{max})	175W	126W
Voltage at P_{max}(V_{mpp})	35.4V	31.5V
Current at P_{max} (I_{mpp})	4.94A	3.95A
Short circuit current (I_{sc})	5.45A	4.41A
Open circuit voltage (V_{oc})	43.6V	39.7V
Module efficiency	14.0%	
Tolerance P_{max}	3/+5%	
Nominal voltage	24V	
Efficiency reduction at 200W/m²	<5% reduction (efficiency 13.3%)	
Limiting reverse current	5.45A	
Temperature coefficient of I_{sc}	0,105%/ ºC	
Temperature coefficient of V_{oc}	-0,360%/ ºC	
Temperature coefficient of P_{max}	-0,45%/ ºC	
(3) NOCT	47±2°C	
Maximum series fuse rating	20A	
Application class (according to IEC 61730:2007)	Class A	
Maximum system voltage	600V (U.S. NEC) 1000V (IEC 61730:2007)	

[Source: http://www.wfsenate.co.uk/media/uploads/88bb977f0e91a4459c7ee5108e61552f2570c6dd.pdf]

2.1.1.5 I – V Characteristics

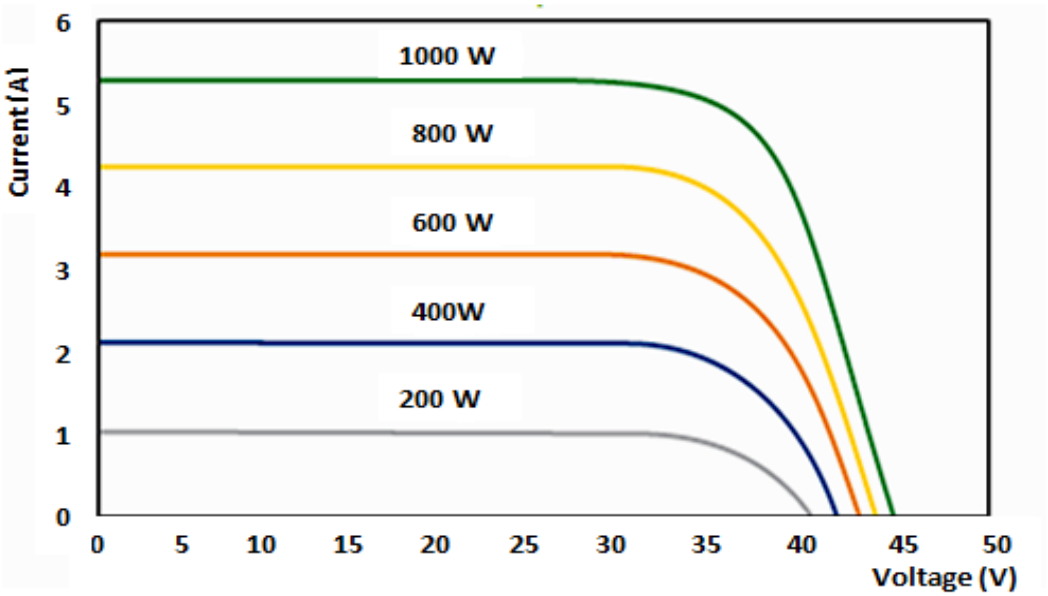

Figure 6.Dependence of the Performance of the Panel on Irradiance
[Source: http://www.wfsenate.co.uk/media/uploads/88bb977f0e91a4459c7ee5108e61552f2570c6dd.pdf]

2.1.1.6 Battery

Haze – HZYSL6 – 225 Gel series is lead acid type batteries. Advanced Gel design is used in these batteries and is highly suitable of cyclic solar Photo voltaic applications [13]. Some of the important Features of the battery includes**;** repeat cycling for daily usage, good performance over long discharges, good tolerance to high temperature applications, less self discharge, good charge acceptance due to low internal resistance and it can be discharged even when not fully charged without the loss of battery capacity [13].

2.1.1.7 Solar Regulator

The FLEXmax (OutBack FM60-150 MPPT Solar Controller) Maximum Power Point Tracking (MPPT) is continuous and active and helps increase the photovoltaic power yield to about 30 percent more compared to non – MPPT controllers [14]. It is able to function at ambient temperature of as high as 40° C. It also has the ability to step-down a higher voltage solar array for the recharging of a lower voltage battery bank and is able to display the current status and logged performance data for past 128 days.

2.1.1.8 Inverter

The OutBack inverter (GFX 1424, 1400W, 24V) is designed for applications to lower power demands. It comprises of a DC to AC sine wave inverter, battery charger and an AC transfer relay. It provides power back up in the event of an outage through the in- built transfer relay which acts by disconnecting the loads from the grid and powers them from the inverter [15]. Hence it helps reduce disruption in power supply in times of usage.

Results and Discussions

2.0 Solar Resource

3.1 Solar Resource at the Charging Station Site

Panel Orientation: Tilt=18° -- Azimuth=0° (Due North) -- **Skyline Heading=0°**
GPS Location: Latitude=18.14996°S -- Longitude=178.44655°E
Solar Access: Annual: 95% -- winter (May-Oct): 94% -- summer (Nov-Apr): 95%

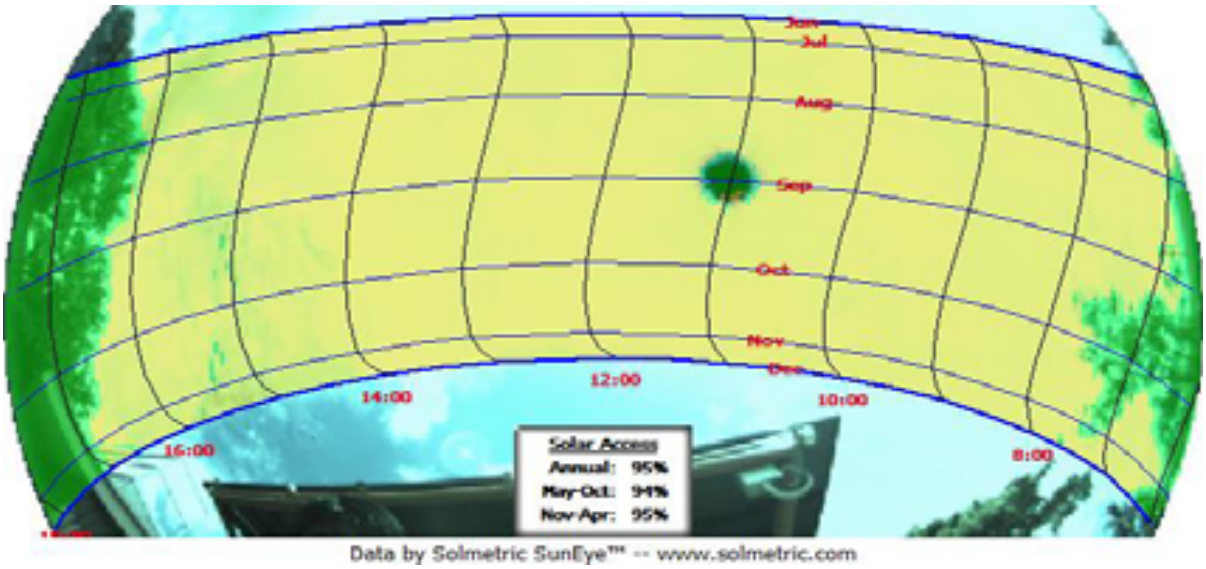

Figure7. Sunpath close to the charging station ataround 11:00 a.m

The view in fig. 7 shows the annual sunpaths drawn on top of the captured skyline. The open sky is shown in yellow and the detected shade-causing obstructions are indicated in green. Fig. 8 shows the solar access percentages at the site.

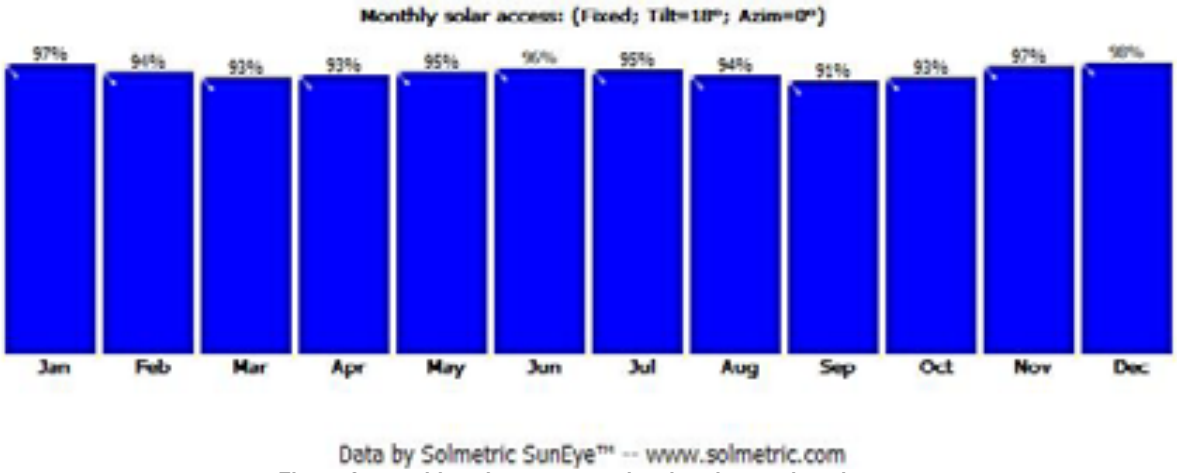

Figure 8. monthly solar access at the charging station site

4.0 Performance of Solar Charging Station

4.1

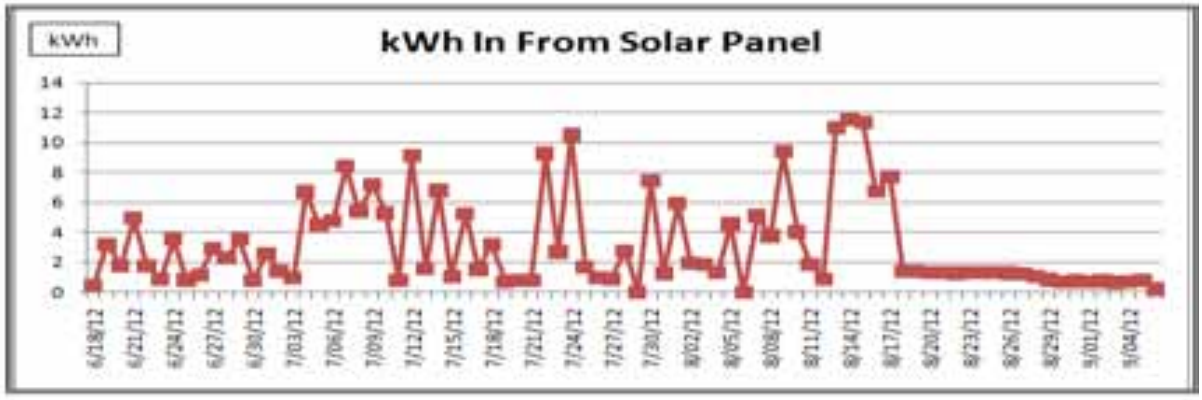

Figure 9

Fig. 9 shows the energy generation by the solar panel in kWh. The fluctuation in the production is dependent on the charging/discharging activities at the solar charging station.

The graphs in fig.10 and fig. 11 showthe relationship between the energy supplied and the stste-of-charge of the system battery.

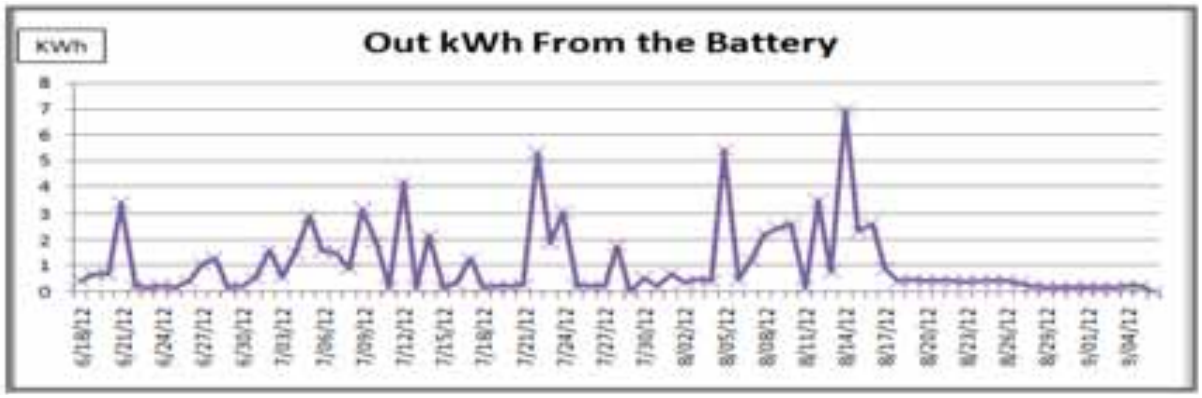

Figure 10

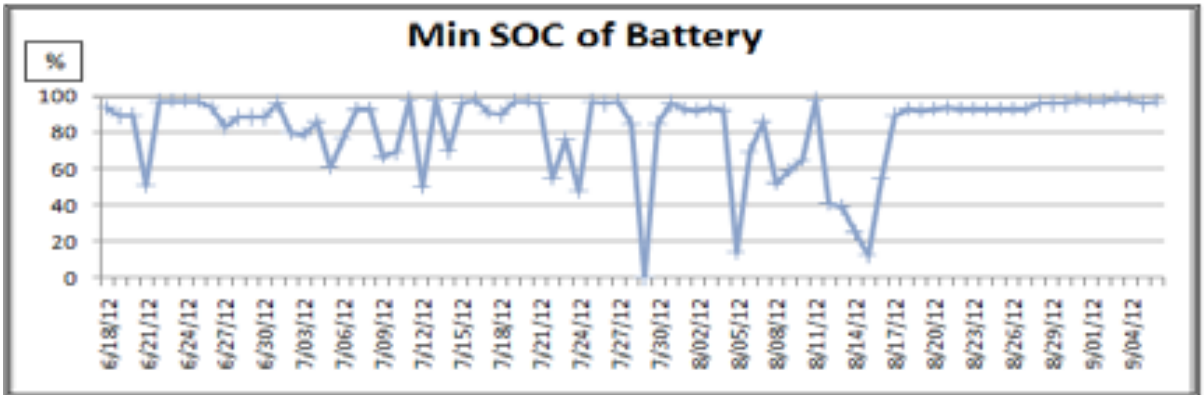

Figure 11

From the three sets of graphs above, it can be noticed that whenever there is low usage of power from the station, the state of charge of the battery is maintained above 90% and hence there is low input from the panels. However when the charging activity is high, the state of charge drops and the energy supply by the panels increases. For example, at 8/14/12, the usage is about 7 kWh, state of charge decreases below 20% and the panel produces about 12 kWh to maintain the charge status of the battery. Moreover, after 8/20/12 the charging activity is almost zero, state of charge is seen to be very close to 100% and hence the power production from the panel is also close to zero.

4.2 The Projected Output Simulations for the Charging Station

The EV charging PV system was also simulated using HOMER Software. The simulated results were given through the analysis of the input data of the system components of the solar charging station and the solar radiation data available at the location of the station. The scaled annual average horizontal solar radiation at the station location was 5.21 kWh/m^2/day.

From the PV Output graph and simulation result it can be seen that an average system value of around 0.47 kW can be taken on a monthly basis. However, there are times when the panel is capable of producing around 2 kW and even higher during peak months. This result campares well with the actual production witha mean out put of around 11 kWh/day.

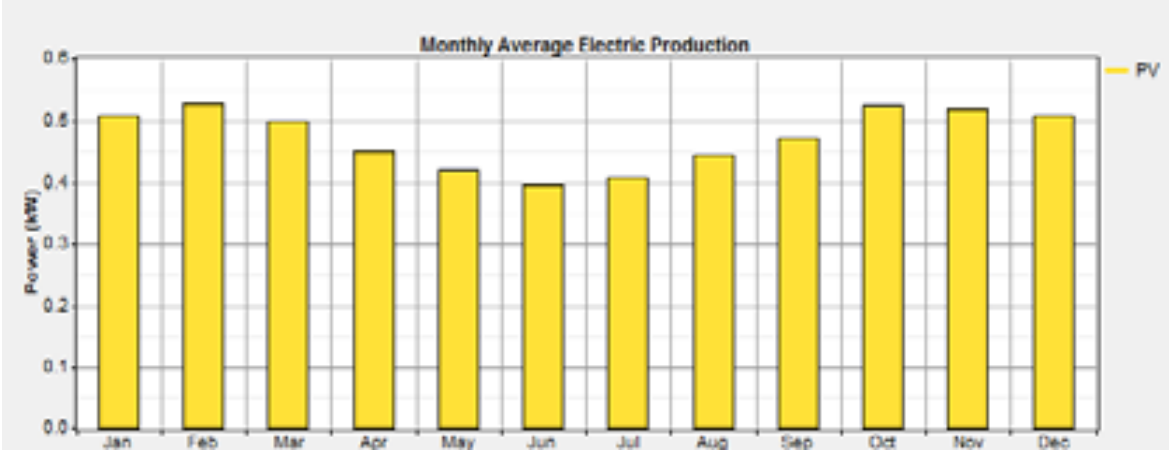

Figure 12: Monthly Average Electric Production

Table 3. The Charging Station Projected Performance

Quantity	Value	Units
Rated capacity	2.65	kW
Mean Output	0.47	kW
Mean energy Output	11.3	kWh/d
Capacity Factor	17.8	%

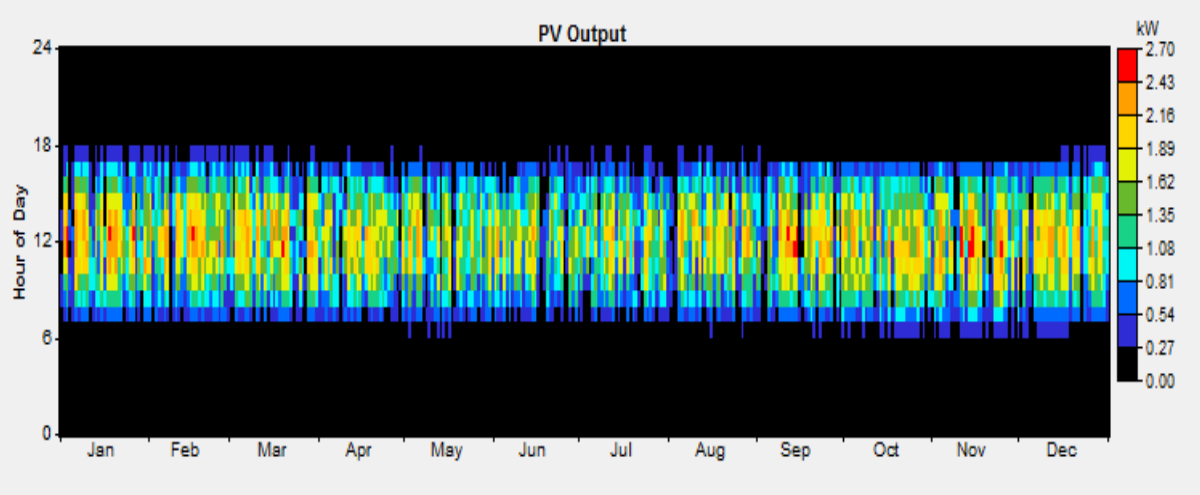

Figure 13: Ouput projection of the solar panel

5.0 The Scope of Solar Charging Station and Electric Vehicles in Fiji and Pacific Island Countries

The solar charging stations have a good potential in the Pacific island countries due to the availability of high solar radiation in the region. The geographical location of the PIC's gives them an advantage as they are located near the equator. For this reason charging stations can be erected at a number of places around the Pacific.
The charging stations and solar electric vehicles would be of great use to the resorts around the islands. It would provide them with an opportunity to help minimize pollution by using green energy like solar while cutting down their electrcity bills and crabon footprint.. The only cost involved is in the setting up of the charging station and purchasing of electric vehicle. Most of the resorts operate electric buggies/carts to transport gusets and also for their golf courses. Deploying solar chargers on the myriad of resorts in the region will reduce their dependence on fossil fueled utility power or thier own generators.

Moreover, the private transport companies and government can also invest in the charging stations and develop a solar EV charging car park. For example, some of the parking lots of Suva City Council and the government can be turned into solar charging stations.Most of the office/factory workers travel short distances and hence they can plug in their vehicles in the car park while they attend to their routine work.. The main business districts are quite small and electric three-wheelers can be efficiently utilized for delivery etc. The government and companies can also think on the line for use of the vehicles for business purposes. Recently, electric three- wheelers have been launched in Fiji and a transport company is introducing all electric buses. The car dealers in Fiji have also started importing plug-in vehicles like Nissan Leaf and with the Fijian govenment's zero tax policy on Evs/hybrids, theier populariity market is quickly grwing. The need for developing sustainable transport solutions inthe Pacific cannot be overemphasised and solar-charged EVs present a great way forward

6.0 Conclusion

Solar charged EVs present a significant potential for moving the Pacific Island Countries towards a sustainable transportation sector. The devployment of solar charging stations similar to the one presented here would help the EV market grow and protect vehicle owners from the rising fuel prices. It would also help to the issue of climate change mitigation by reducing the GHG emissions in the land transpaortation section.. The analysis of the performance of the solar charging station indicate that a 2.65kW system at the University of the South Pacific is capable of producing a between 10-12 kWh/day. It is envisaged that in not too distant future the EV numbers would increae sizably and the solar chargers will play an important role in expanding their reach. The recent drastic reduction in solar panel pricesmeans decreasing installation cost of charging stations and establishing solar PV as a major contributor to suatinable transport solutions. .

Web References

1. "Islands discuss energy challenges", http://www.pacifictradeinvest.com/wp/?p=4861. Date accessed 10/10/2014
2. http://www.fijisun.com.fj/2013/10/16/report-warns-fiji-on-dependence-on-imported-fuel/. Date accessed 12/10/2014
3. http://www.irena.org/DocumentDownloads/Publications/Policy_Challenges_for_Renewable_Energy_Deployment_PICTs.pdf. Date accessed 13/9/2014
4. "The Business Model for Solar-Powered Electric Car Charging". David Herron. Available on http://www.plugincars.com/solar-powered-electric-car-charging-business-model-127710.html , date accessed - 15/08/14
5. "Plug-in Electric Vehicles (PEVs)". Center for Sustainable Energy, California. Retrieved 10/08/2014
6. http://energy.gov/articles/history-electric-car" Date accessed - 12/11 /2014
7. "Photovoltaics beat biofuels at converting sun's energy to miles driven http://phys.org/news/photovoltaics-biofuels-sun-energy-miles.html. Date accessed 10/10/2014
8. "New and Used Nissan Leafs" Available on: http://www.thecarconnection.com/cars/nissan_leaf. Date accessed - 02/03/2014
9. "Tesla unveils free solar-powered car charging stations for Model S owners" http://gigaom.com/2012/09/24/tesla-unveils-free-solar-powered-car-charging-stations-for-model-s-owners/. Date accessed – 15/08/2014
10. http://energy.gov/sites/prod/files/2014/07/f18/vss138_lapsa_2014_o.pdf . Accessed 10/09/2015
11. Assessment of Solar Home Systems (SHS) for Isolated Rural Communities in Vanuatu Using Project Lifecycle/Sustainability Framework (Chow .J.T, 2010),Michigan Technological University. https://www.mtu.edu/peacecorps/programs/civil/pdfs/jack-chow-thesis-final.pdf date accessed 15/05/15
12. Blue Sky Energy. http://www.blueskyenergyinc.com/reviews/article/what_is_a_charge_controller. Date accessed - 19/08/2014.
13. http://www.acalbfi.com/uk/Power-supplies/Batteries/p/HZY-SL-Series/00000058GM . Date accessed - 19/08/2014.
14. OutBack FM60 – 150 Charge Controller with MPPT FLEXmax 60 http://store.oynot.com/mpptmx60.html . Date accessed - 20/08/2014.
15. GFX International Series-Sealed True SinewaveInverter/Charger. Available on; http://www.dcbattery.com/outback_gfx_inverters.pdf. Date accessed – 19/08/2014

Conference Proceedings

Solar World Congress 2015
Daegu, Korea, 08 – 12 November 2015

The Battery Energy Storage System (BESS) Design Option for On-Campus Photovoltaic Charging Station (PV-CS)

Ayda Esfandyari[1], Brian Norton[1], Michael Conlon[1], Sarah.J McCormack[2]

[1] Dublin Energy Lab/Dublin Institute of Technology, Dublin (Ireland)

[2] Trinity College Dublin, Dublin (Ireland)

Abstract

As the application of Light weight Electric Vehicles (LEVs) increase in communities, Dublin Institute of Technology (DIT) uses these small vehicles for short distance journeys around its 78 acre campus of "Grangegorman" located in inner Dublin city, Ireland. This paper presents an introduction to the campus Photovoltaic Charging Station (PV-CS) that generates clean electricity from the sun and charges the LEVs batteries which can lead to reduction of CO_2 emissions, along with fulfillment of national and international green sustainability targets. Based on the evaluation of possible options for PV-CS design, the optimal design configuration was chosen as a "Battery Energy Storage System (BESS)". The PV generated electricity that is stored in battery banks will serve as the primary source for charging the campus vehicles, with any surplus demand being met by the utility grid. Batteries have been included in the design due to intermittent nature of Irish sunshine and the charge time requirements of campus load. This paper concentrates on the detailed sizing of the BESS via two approaches: BESS with DC generation and BESS with LEV load demand. In the first approach the outputs were normalized and grouped into specified generation categories in MATLAB. To establish the accurate BESS capacity the load demand variations of the LEVs were monitored. Based on DC generation and demand profile, the optimal capacity of BESS was chosen to be in the range of 6-8 kWh, which can accommodate up to 6 LEVs.

Keywords: *Renewable Energy Resources (RES), Battery Electric Vehicle (BEV), Light weight Electric Vehicle (LEV), Battery Energy Storage System (BESS), Greenhouse Gases (GHG),*

1. Introduction

Transport is the second biggest emission intensive sector in Europe, accounting for nearly a quarter of Greenhouse Gases (GHG) pollutions (European Commission, 2013). Since the energy consumption of transport heavily depends on fossil fuels, Battery Electric Vehicle (BEV), an alternative to conventional vehicles, can help to minimize emission levels at the usage point. Moreover, with the trends encouraged by governments and political parties, strong commitments have been made on both European and International levels to increase the penetration of Renewable Energy Resources (RES) (Da Graça Carvalho, 2012). BEVs have significant benefits in an urban context, mainly due to shorter trips, lower speed and power requirements (Smith, 2010). As shown in Table 1, BEVs capacity and technology can vary and subsequently are influenced by the size of the vehicle (SEI, 2007; World Electrified Vehicle Sales, 2013). Applications of small utility vehicles are gaining interest in both public and local sectors such as: night time deliveries, airports, in parks and golfing facilities (Standford, 2007; Heathrow Airport, 2011). Our focus is on CarryAll 13.76 kWh vehicles, which throughout this paper is referred to as Light weight Electric Vehicle (LEV).

doi:10.18086/swc.2015.01.02 Available at http://proceedings.ises.org

Table. 1: Various BEV Battery Capacities

Vehicle	EV Type	Battery Technology	Battery Capacity
Nissan Leaf	BEV	Lithium-ion	24 kWh
Tesla Model S	BEV	Lithium-ion	60/85 kWh
Renault Zoe	BEV	Lithium-ion	22 kWh
Renault Kangoo ZE	BEV	Lithium-ion	22 kWh
Small Utility	BEV	Lead-Acid	13.76 kWh

Solar energy in particular has emerged as one of the prominent sources of alternative energy, with significant potential for reducing CO_2 emissions at the generation point (SEAI, 2010). Furthermore, Photovoltaic (PV) panels can be used in charging stations to accommodate the BEV's batteries charge demand (Hamilton, et al., 2010; Abella & Chenlo, 2003). This research proposes an application, where the PV-CS is used to supply the required charge of the campus LEVs. The campus fleets are adopted for short distance commutes at day/night time around Grangegorman's expanding campus allowing the generation of reliable green electricity, thus fulfilling campus's sustainability targets.

2. Solar Climate and Potential (in Ireland) :

PV systems use the photovoltaic effect to convert solar radiation directly into electricity. Solar radiation reaching the Earth's surfaces includes both direct and diffuse insolation, where the most common measurement for quantifying solar radiation is the total radiation on a horizontal surface, often referred to as global radiation (Duffie & Beckman, 2013). PV generation is directly related to the solar radiation intensity, i.e., higher solar radiation levels provide greater electricity output. Figure 1(a) from Met Éireann data (Irish Meteorological Service, 2011), illustrates the sunshine profile of Ireland. Based on this information, the annual sunshine hours for the temperate region of Ireland is between 1100-1600, where May and June are the sunniest periods during the year with average sunshine durations of 5 and 6.5 hours per day. During the month of December, the average sunshine values can be extremely low and available for only one hour (Flood, et al., 2011).

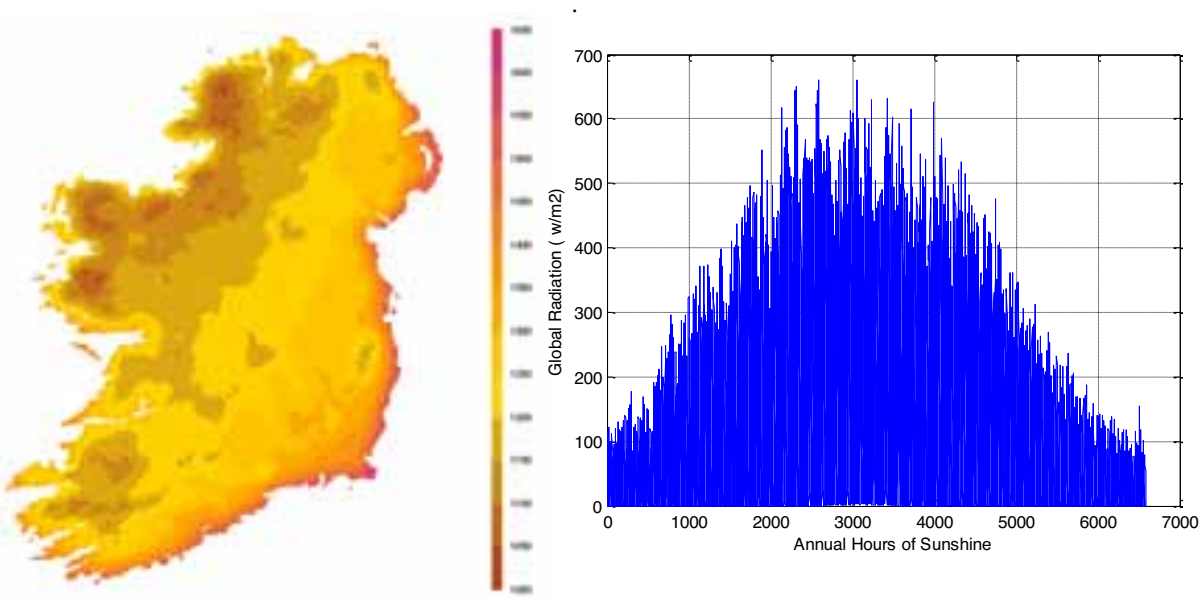

Figure. 1: Met Éireann Data: (a) Annual Hours, (b) Averaged out Global Radiation (W/m^2) of 10 years

Figure 1(b) signifies the "annual averaged global solar radiation" profile of Dublin, using 10 years of measured data by Met Éireann. The irradiance data (W/m^2) accounts for seasonal (monthly) sunshine variations and has been captured hourly every day from 04:00 – 21:00 at Dublin airport meteorological

station. As can be observed from the graph, the insolation levels are greater during the summer period, reaching a maximum level of 660 W/m^2/day, while the mean value of the global radiation is ~ 140W/m^2/day. These fluctuations in solar radiation levels, and DIT campus's expansion targets, will require a sizable PV covered roof area that can harvest sufficient electricity for the campus LEVs demand.

The PV system will be installed on the Orchard-House building; it is shown along with the building plan in Figure 2 (a) & (b). This is the current charging point for the campus LEVs the CarryAll 500 which is illustrated in Figure 2 (c). The vehicle specification is summarized in Table 2. Since Orchard house is situated near the main access point of university, it is a favourable location for deploying PV-CS. The total available roof area is 3700 m^2 but the dedicated south facing area of this roof (highlighted with red-lines in figure 2(a)), is ~ 69 m^2 at an inclination of ~ 36 degrees. When considering a regular 250 W monocrystalline PV panel of 1.63 m^2, the purposed area can accommodate a 10.5 kW system composed of 42 panels.

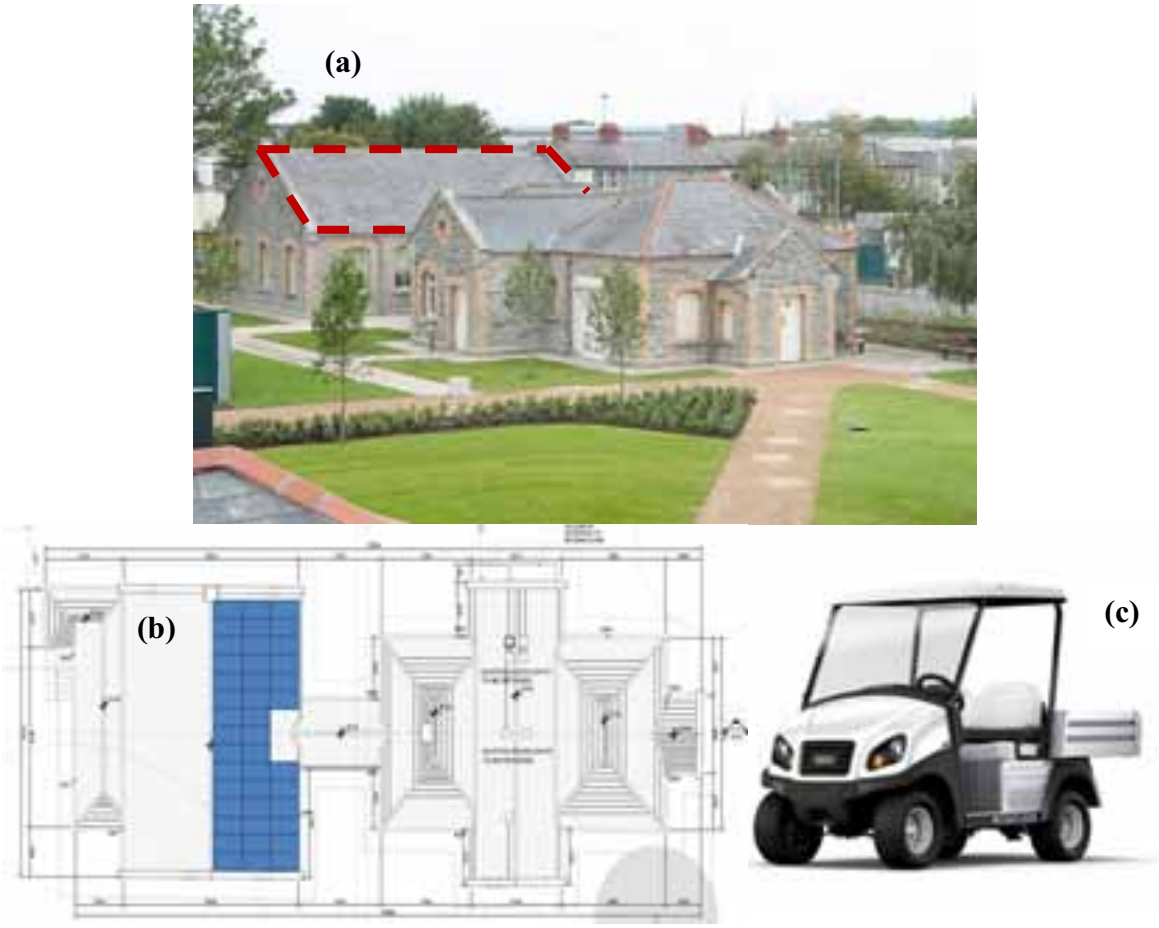

Figure.2: Orchard-House Building site (a), Roof schematic plans (b), CarryAll 500 LEV (c)

Table. 2: Specifications of the CarryAll 500 LEV

Motor Type	48 V DC
Horse Power Rated	3.7 hp (2.7 kW) rated; Peak 20 hp (14.9 kW)
Transmission	Direct/ Drive Double Reduction
Speed	15 mph (~ 25 km/h)
Battery Model	Trojan (T-145) with Flip-Flops x 8Units
Battery Voltage	48 Volts (6 Volts x 8Units)
Battery Capacity	13.76 kWh (1.72 kWh Each Unit)
Battery Capacity	260 Ah kWh (Each Unit)

3. PV-CS Design Options

In order to advance the PV-CS design, it is vital to identify the optimal design option, which has the potential to deliver electricity in a sufficient, reliable and cost effective manner. Sizing and deployment of the PV installation tends to be an iterative process, in which numerous design factors need to be examined, such as: solar potential of the site, array size, available cost, nature of the load, demand profile, operating voltage, choice of the storage unit and or grid integration (Lee, et al., 2012; Esfandyari, et al., 2015). PV-CS can be divided into a number of segments (Esfandyari, et al., 2014) such as PV and system components, cabling, protection and mounting elements, charge controller, inverter, battery storage unit and the load. Integration of each of these components can lead to a distinct system design arrangement. (Esfandyari, et al., 2015) determined the hypothetical design set-ups for the campus PV-CS and grouped the outcomes into five possible options; (i): decoupled grid (AC); (ii): decoupled direct PV (DC); (iii): decoupled PV with storage (DC); (iv): coupled PV-grid without storage and (v): coupled PV-grid with storage. These configurations are summarized in Figure 3. Furthermore, the average cost for each system component and various installation categories is presented in Table 3. These figures are quoted from PV suppliers and data reported by Sustainable Energy Authority of Ireland (SEAI, 2013).

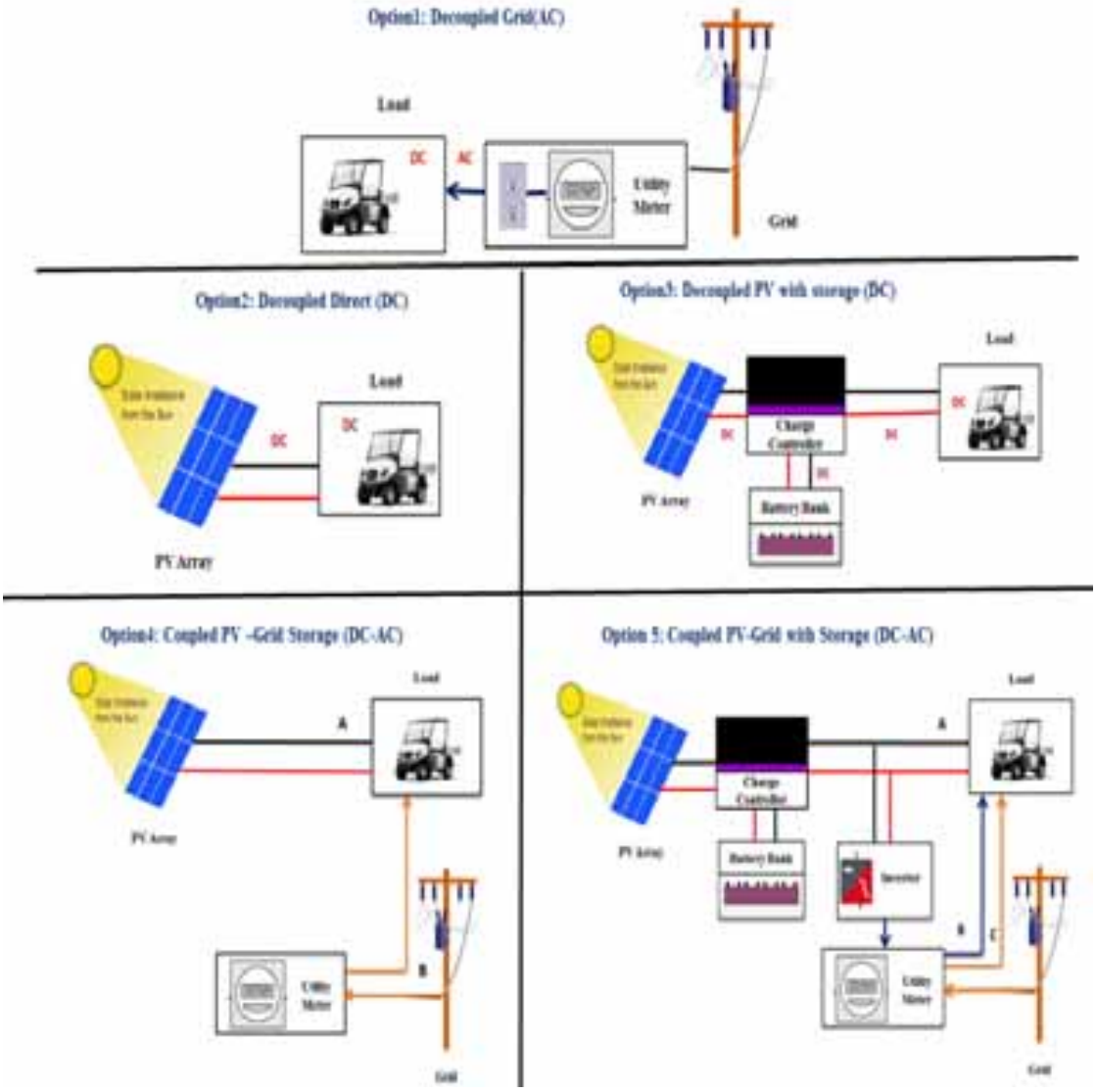

Figure. 3: Detailed Schematic for Design Options of Campus PV-CS

Table. 3: Cost breakdown for PV-CS system components and installation (SEAI, 2013)

Component	Average Cost
Solar Photovoltaic Panels	€854 per kW
Inverter	€619 per kW
Instrumentation and Control	€177
Battery (Lead Acid)	€350 (400 Ah)
Installation-Electrical	€543
Installation-Civil	€904
Installation-Mechanical	€191
Maintenance	€109
Other	€88

From Figure 3, option 1 "decoupled grid (AC);" is the existing scheme for charging the cars, where LEVs are directly fed by the grid. In this case the electricity is supplied to the load in the form of AC, via standard three pin plug sockets at 230 Volts/13 Amps. Since the LEV batteries run on the DC voltage, and each vehicle is comprised of 8 Trojan lead acid batteries at a total of 48 Volts, the AC quantities must be converted into their DC equivalent. This is achieved through the internal inverter of the vehicles. However this is not a sustainable way for energy generation, as ~76% of Ireland's primary energy is generated from fossil fuels (SEAI, 2014). In order to address sustainability targets of: self-sufficiency in energy, improvements of security of supply and reduction of amount of GHG, solar energy was proposed as a method of green electricity generation.

Option 2, considered the possibility of synchronized design, where LEVs are directly charged using PV. In this case, solar panels are used as the primary and only source of power. The PV panels will need to be arranged on the roof of the vehicle, where DC electricity directly fed to the Trojan batteries and/or DC brushed motor. While the capital cost of system components for the case "decoupled direct PV (DC)", will be at the lower end of spectrum (due to incorporation of minimum ancillary elements), the fluctuation in solar radiation and absence of any secondary generation will require a large LEV roof coverage. In other words, with particularly low average winter sunshine durations, (only for one hour), and the demand profile of Trojan batteries (Esfandyari, et al., 2015) that can be as high as 13.76 kWh, the installed PV capacity needs be substantial for the vehicle's rooftop (at least 1.75 kW which will take up ~ 11.4 m^2). Thus, this option was not a viable choice.

Option 3 examined a set-up where the PV panels are installed in a standalone configuration. The "decoupled PV with Storage (DC)" will operate on DC voltage only, where the electricity generated from the fitted panels on the roof of Orchard house will be regulated through the charge controller and stored in a number of battery banks. The storage unit will serve as the primary source of energy, which will accommodate the vehicles load requirements. However, due to the absence of any back-up generator, the reliability of this set-up will be poor. Where in the event of lower sunshine hours, the depleted charge of the storage unit might not be restored leaving the LEVs batteries exhausted, unless the of the PV-array and subsequently the battery banks can be oversized to guarantee meeting the maximum load requirement but this can increase the capital cost significantly. As the result, this option was not identified as a practical choice.

Option 4 considered the possibility of running a coupled configured system. Coupled PV-grid without storage allows the load to be charged on both DC-AC voltages, depending on the available sunshine levels. The coupled possibilities are labelled as A and B in Figure 3 option 4. 'A' is the daytime scenario where the solar radiation is utilized as the primary source for charge generation. This means parking the LEVs during the hours of sunlight and recharging the batteries directly via the DC voltage. In the case of low solar radiation and/or higher demands, the load could be supplied by the utility grid as shown by in 'B'. However, as the LEVs are normally used during the day and charged at night time, this option was also not appropriate.

The choice of "coupled PV-grid with storage"/Option 5 completed the design scenarios, by combining all the

system configurations retrieved from the previous options. In this case the practicable methods for charge restoration of LEVs are described in sections: A, B and C. In 'A' PV will be used during daylight to generate electricity and this electricity will be stored in the battery storage unit. The storage unit charge could be used afterwards to charge the LEVs, thus it will not pose any limitations on user's driving needs. In 'B', any surplus in PV generation where the storage batteries are full is sent to the grid. Finally 'C' includes the grid as the back-up generation for the load, in the event of low solar radiation and consequently resulting in no charge in the storage batteries. This design option was chosen to be the most viable choice for Grangegorman PV-CS.

4. Battery Energy Storage System (BESS) Design Option

To consistently utilize the solar generated electricity in Grangegorman where solar radiation and charging habits of the users fluctuate, the designated PV-CS design will incorporate a battery storage unit. As described in the earlier section Option 5 the "Battery Energy Storage System (BESS) design option will be examined further. Since the storage component is the predominant module of this configuration, the accurate sizing of this unit is imperative. Previously, (Esfandyari, et al., 2015) applied a methodology which was adapted from (Lee, et al., 2012 ; Masters, 2004). In this manner, the battery capacity was altered with respect to: maximum daily load demand, days of autonomy, Depth of Discharge (DOD), efficiency and voltage level. The days of autonomy which accounted for the number of the days that the storage batteries need to accommodate the load, were calculated based on Peak Sunshine Hours (PSH) of 2.83 hours for a typical day in Dublin (Ayompe, et al., 2011). Thus, the selected lead acid batteries were settled to the capacity value of ~ 390-400 Ah as advised by the battery suppliers., with 40% DOD and 85% efficiency and a voltage level similar to voltage level of LEVs Trojan Lead acid batteries, i.e., 8 batteries with at 6 volts-260 Ah. Based on this methodology and with 95% system availability, the recommended storage days for the PV-CS was estimated as 4.93 days, which resulted in 72 or 32 batteries for summer and winter load profiles respectively. Yet, as stated by the authors, due to auxiliary issues associated with: efficiency, cost, sheltering and maintenance of the estimated batteries, the work required further justifications and a more pragmatic capacity value for BESS.

As mentioned earlier, BESS will be exploited as the preeminent energy source, for storing the available PV generated DC output and subsequently dispatching the charge to the load. Inappropriate sizing of the batteries, (over-sizing or under-sizing the BESS unit), will have ramifications on the cost and or reliability of the campus PV-CS. In exchange, optimization of BESS capacity will depend on a number of constraints such as: obtainable solar resource, mandatory LEV demand, available budgets and cumulative project size. The adopted approach here has examined the first two constraints; DC generation and LEV load demand, where the proposed storage size was formulated.

4.1. BESS with DC generation

Hourly recorded meteorological insolation data at Dublin airport station is presented in figure 4 where the seasonal variations in solar intensity are clear. The roof plan of the chosen building and its accessible area as illustrated in figure 4, acts as a constraint for PV deployment. The total daily horizontal insolation values (kW/m^2) were scaled to correspond to the roof area of 69 m^2. Moreover, as the designated panels are 15.4% efficient, the DC generated output was calculated (gray cross line) and is presented in Figure 4. As displayed in figure 4, the magnitude of total daily DC output varies between the minimum of 3.56 kWh/day which occurred on the 31th of December to the maximum value of ~ 63 kWh/day occurred on 15th of June. Due to the overcast climate of Ireland, the total numbers of the days with high output and close to the maximum point are quite low (especially from November-March). Previously statistical tools were adopted (Arthur, et al., 1988; Lee, et al., 2012; Ibrahim, et al., 2012), such as curve fitting, regression model and probability density distributions, for analyzing the solar radiation distribution. The approach adopted in this study was essentially based on investigating the DC generation and determining the distribution of specified generation categories in MATLAB. After inspection of several groups, case 1 and 2 were designated as the best representative scenarios.

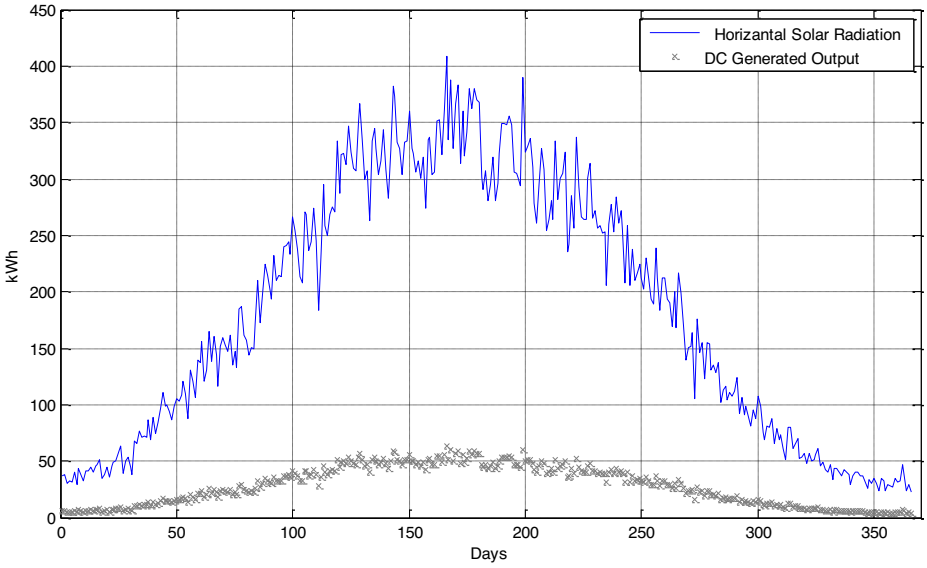

Figure. 4: Orchard House Horizontal Solar Radiation (Blue), DC Generated Output (Gray Cross Line)

The bin interval for the first case was selected as 1kW which resulted in 60 incremental generation groups. Furthermore, the bin intervals were extended to 2 kW for the second category, which reduced the incremental generation groups to 30. This was merely to examine the population density of each group profile with respect to the count of intervals. These two cases are illustrated in Figure 5, where x axis represents the generation bins and y axis depicts the population or number of occurrence for generation days.

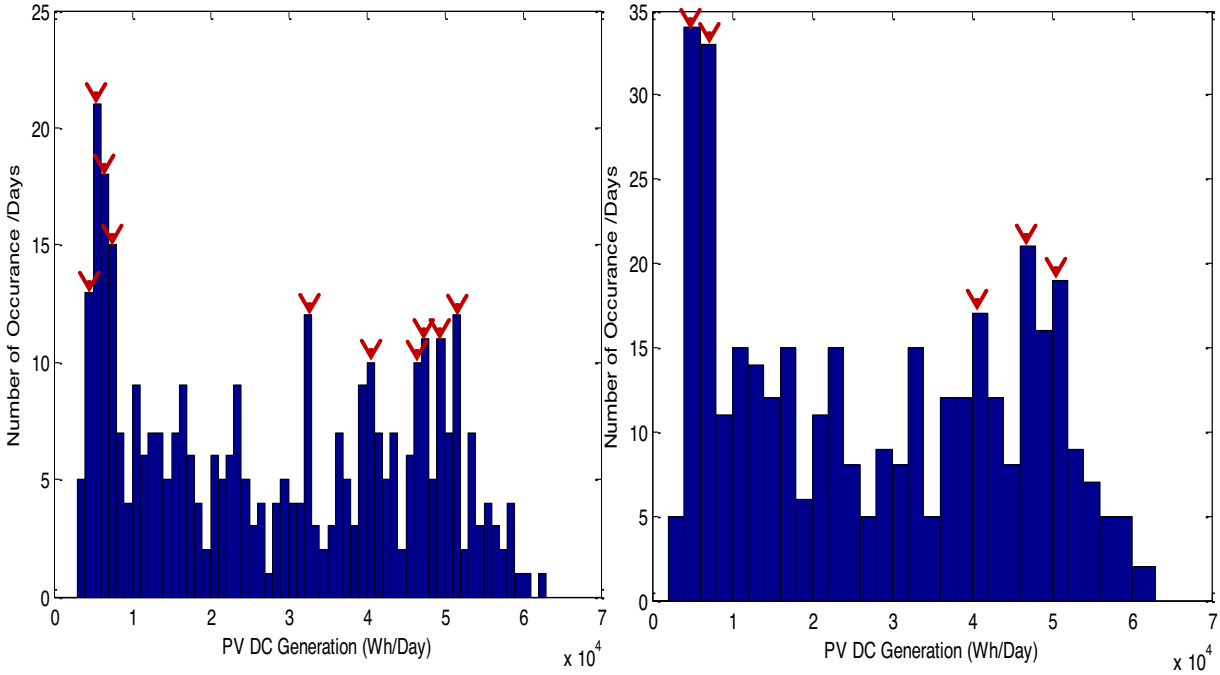

Figure. 5: PV DC Generation: (a) 1000 Watts group segmentations, (b) 1000 Watts group segmentations

In order to identify the most applicable generation band for BESS sizing, the maximum peak values in each category were extracted, tabulated and is presented in Table 4. Table 4 reports on the number of the occurrence (population intensity) of the individual peak values, the associated bin range and percentage of divergence from the potential maximum day of generation. There were 10 chosen peaks for the first case, and the peak numbers were reduced to 5 for the second case. Nevertheless the population intensity of the second category peaks contains more days of occurrence.

Table. 4: DC Generation Normalised Peak Density

Peak	Number of Occurrence /Days (Case 1 = 1k)	Bin Range (Case 1 = 1k)	Deviation from the Max (Case 1= 1k)	Percentage Of generation	Number of Occurrence /Days (Case 1 = 2k)	Bin Range (Case 1 = 2k)	Deviation from the Max (Case 1= 2k)
1	13	4-5 kWh	92%	8%	-	-	-
2	21	5-6 kWh	90.5%	9.5%	34	4-6 kWh	90.5%
3	18	6-7 kWh	88.89%	11.11%	33	6-8 kWh	88.89%
4	15	7-8 kWh	87.3%	12.7%	-	-	-
5	12	32-33 kWh	48%	52%	-	-	-
6	10	40-41 kWh	35%	65%	17	40-42 kWh	35%
7	10	46-47 kWh	26%	74%	-	-	-
8	11	47-48 kWh	24%	76%	21	46-48 kWh	24%
9	11	49-50 kWh	22.3%	77.7%	-	-	-
10	12	51-52 kWh	17.5%	82.5%	19	50-52 kWh	17.5%

As it can be seen from the table, over the course of the year the generation bands which had the higher distribution densities were between 4-6 kWh, 6-8 kWh 40-42 kWh, 46-48 kWh and 50-52 kWh. Thus, the battery size/days of autonomy would need to be matched to the most appropriate generation band.

4.2. BESS with LEV Load Demand

In order to determine the prospective PV-CS BESS unit, the second technique inspected the daily load profile of the campus vehicles. This was to quantify the accurate demand band of the LEVs as well as average and maximum demand bands. The demand profile was measured using a designated power meter "Hawk5000". The Hawk meter with its capability to monitor the electricity supply and consumption by means of Current Transformers (CTs), was wired up to the current charging point. The energy meter captured: current, voltage, real power, power factor, and energy at a specified sampling interval.

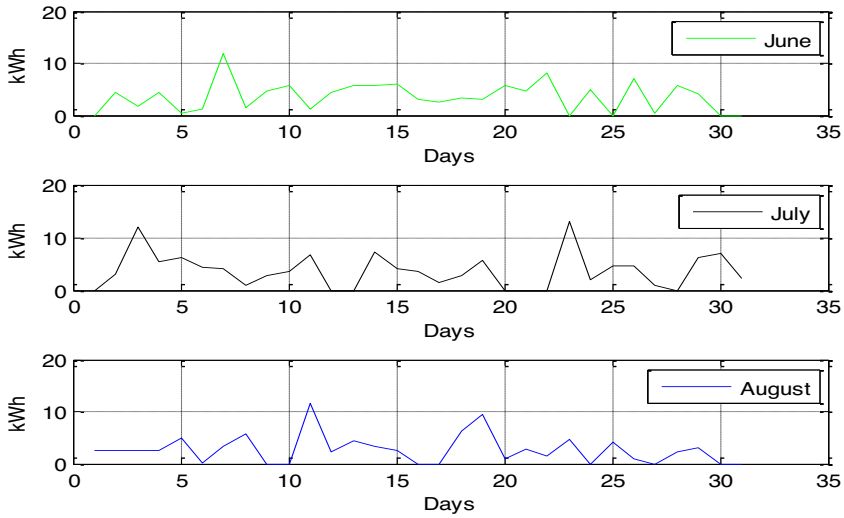

Figure. 6: Load Demand Profile of two LEVS (June-July-August 2015)

The desired sampling rate in this case was selected and varied between 1 to 5 minutes. Every time a load was plugged in to the charging point, the variations of measurement signals were sensed by CTs and stored in the data logger. Figure 6 presents the daily energy requirements of the two LEVs. The data was collected for

over 3 months (June - July - August 2015). It is summarized in Table 5, the maximum load demand of the LEVs was on 23th of July (13.03 kWh/day - close to the total capacity of one vehicle). The average demand of the total load was 2.11 kWh/day. This value emphasises the variation of the rate of charge.

Table. 5: Load Demand profile of Two LEVs (Maximum and Average)

Generation	Maximum DC Generation Output	Maximum Load Demand	Average DC Generation Output	Average Load Demand
10.5 kW (STC)	62 kWh/day	13.03 kWh	28 kWh/day	2.11 kWh/day

In order to identify the most appropriate size of BESS, generation potential and demand profiles were measured. As the average load demand of each vehicle is limited (2.11 kWh/day for the total campus load), when the cost factor of the batteries were considered the generation ranges of 4-6kW, 6-8kW were viable. Moreover, with the new battery technologies in the market, for example the Tesla Powerwall (Tesla, 2015), which are lightweight rechargeable batteries offering reliable operation and security at 7 kWh per unit, the 6-8 kW range was perceived as a better option. In other words, if the BESS unit was matched to 6-8kW, it could accommodate almost 6 campus vehicles.

5. Conclusion

Introduction of a PV-CS in DIT Grangegorman campus, Dublin, Ireland that generates clean electricity from the sun and charges the campus LEVs batteries, can substitute a portion of the charge supplied from the conventional utility grid, and further help to achieve suitability targets. In this paper design options for PV-CS were discussed. Due to intermittent nature of Irish sunshine and user's charging habit, the choice of coupled PV-Grid with storage unit/ BESS was identified as the most viable solution. Yearly averaged values of solar insolation for Dublin were examined and appropriately scaled to represent the DC generated output of 10.5 kW PV array with 15.4% efficiency. In order to size the BESS unit accordingly BESS was investigated in conjunction with generation and demand requirements. Since the load demand of the two LEVs was, within the DC generation ranges of 4-6kW, 6-8k, these ranges were selected for BESS sizing. With reference to the new technologies in the battery industry for example Tesla Powerwall at 7kWh, the 6kw-8kW range was recognised as possibly a better option. This capacity band with reference to the average load demand of 2.11 for two LEVs could accommodate up to 6 cars. .

6. Acknowledgment

Authors would like to thank Dr Agata Świerc Dublin Energy Lab (DEL) Visiting Assistant Professor for her enormous level of support and advice. Also authors would like to acknowledge the Fiosraigh scholarship (DIT), Grangegorman Development Agency, Dublin Institute of Technology, and Trinity College Dublin for all the support and facilities. Finally authors wish to thank, Mr Paul McDunphy, Mr Terry Maher, Mr Eamonn Murphy, Mr Alan Keyes as well as all the porters and night time securities in Grangegorman.

7. References

Abella, M.A., Chenlo, F., (2003). Photovoltaic charging station for electrical vehicles. 3rd World Conference on Photovoltaic Energy Conversion, Pages 2280-2283,

Arthur, Y.D., Gyamfi, K.B., Appiah, S.K., (1988). Probability Distibutional Analysis of Hourly Solar Irradiation in Kumasi-Ghana, Pages 63-75,

Ayompe, L.M., Duffy, A., McCormack,S.J., Conlon, M., (2011). Measured performance of a 1.72 kW rooftop grid connected PV system in Ireland, Energy Conversion and Management, Vol 52, Issue 2, Pages 816-825,

Da Graça Carvalho (2012), EU energy and climate change strategy, Energy, Vol. 40, Issue , Pages 19-22,

Duffie, J.A., Beckman, W.A., (2006). Solar Engineering of Thermal Processes, Hoboken, NJ Wiley,

Esfandyari, A., O'Farell, K., Norton, B., .McCormack, S.J., (2014). Electric bike PV Charging Station Station (PV-CS): Experimental design for Electrical fault investigations. Irish Transport Research Network, Limerick, Ireland,

Esfandyari, A., Norton, B., Conlon, M., .McCormack, S.J., (2015). Essentails for on-campus Photovoltaic Charging Station(PV-CS):Grangegorman. Irish Transport Research Network, Galway, Ireland,

European Commission., (2013). A 2030 framework for climate and energy policies, Available at: http://ec.europa.eu/energy/consultations/doc/com_2013_0169_green_paper_2030_en.pdf.

Flood, E., McDonnell, K., Murphy, F., Devlin, G., (2011). A Feasibility Analysis of Photovoltaic Solar Power for Small Communities in Ireland, The Open Renewable Energy Journal, 4(1), Pages 78-92,

Hamilton, C., Gamboa, G., Elmes, J, Kerley, R., Arias, A., Pepper, M., Shen, J., Batarseh, I., (2010). System architecture of a modular direct-DC PV charging station for plug-in electric vehicles, IECON - 36th Annual Conference on IEEE Industrial Electronics Society , Pages 2516-2520,

Heathrow Airport Unveils Driverless Electric Car Transport System., (2011). Available at: http://laughingsquid.com/heathrow-airport-unveils-driverless-electric-car-transport-system/. [Accessed: 01-Sep-2015],

Ibrahim, S., Daut, I., Irwan, Y.M., Irwanto, M., Gomesh, N., Farhana, Z., (2012), Linear Regression Model in Estimating Solar Radiation in Perlis. *Energy Procedia*, 18, Pages1402-1412, Available at: http://dx.doi.org/10.1016/j.egypro.2012.05.156

Lee, I.E., Sim, M.L., Kung, F.W L., Ghassemlooy, Z., (2012). Statistical analysis and modelling of one-minute global solar irradiance for a tropical country. 2nd International Symposium on Environment Friendly Energies and Applications, EFEA, Pages 243-248,

Lee, K.H., Malmedal, K., Sen, P.K., (2014). Conceptual Design and Cost Estimate for a Stand-Alone Residential Photovoltaic System, Green Technologies Conference, IEEE, Pages.1-6,

Masters, G. M., (2004), Renewable and efficient electric power systems. Hoboken, NJ Wiley,

Smith, W.J. (2010). "Can EV address Ireland's CO2 emissions from transport?" Energy Vol 35, Issue 12, Pages 4514-452,

Standford University, (2007). Use of Golf Cart-Type Vehicles at Standford University, Avaiable at: https://transportation.stanford.edu/parking_info/carts.shtml,

Sustainable Energy Ireland (SEI), (2007), Hybrid Electric and Battery Electric Vehicles (Technology, Costs and Benefits),

Sustainable Energy Authority of Ireland, Best Practice Guid. Photovoltaics., (2010). http://www.seai.ie/Publications/Renewables_Publications_/Solar_Power/Best_Practice_Guide_for_PV.pdf

Sustainable Energy Authority of Ireland., (2013). Small- and Micro-scale Generation Pilot Field Trials : Technical Report,

Sustainable Energy Authority of Ireland., (2014). Energy in Ireland 1990 – 2013, Avaiable at: http://www.seai.ie/Publications/Statistics_Publications/Energy_in_Ireland/Energy-in-Ireland-1990-2013 report.pdf

The Irish Meteorological Service Online., (2011), Available at: http://www.met.ie/climate-ireland/sunshine.asp

Tesla,. (2015). Tesla Powerwall, Available at: http://www.teslamotors.com/powerwall. [Accessed: 02-Aug-2015],

World Electrified Vehicle Sales, (2013), Available: http://evobsession.com/world-electrified-vehicle-sales-2013/. [Accessed: 02-Aug-2015].

ISES International Solar Energy Society

Conference Proceedings

Solar World Congress 2015

Daegu, Korea, 08 – 12 November 2015

Comparison & Verification of Program for Deducting Optimal Ratio of New Renewable Energy System

Hye-Min, Jang[1], Jun-Ho Hong [2] , Yong-Ho Lee [3] , Young-Hum Cho[4] And Jung-Ha Hwang[5]

1 School of Architecture, Civi, Environmental and energy Engineering, Kyungpook National University, Daegu, Korea

2 School of Architecture, Civi, Environmental and energy Engineering, Kyungpook National University, Daegu, Korea

3 School of Architecture, Civi, Environmental and energy Engineering, Kyungpook National University, Daegu, Korea

4 Department of Architecture, Yeungnam University, Gyeongsan, Korea

5 School of Architecture, Kyungpook National University ,Daegu, Korea

Abstract

To fight weather anomaly affected by greenhouse gases due to rapid industrialization, the Korean government enforced the Act on the Promotion of the Development, Use and Dissemination of new renewable Energy since 2004, according to which 15% of the energy (as of 2015) that is expected to be used in a public building whose total floor area is at least 1,000 ㎡ should be provided with new renewable energy system when the building is constructed, reconstructed, or extended.

However, this act just presents an obligatory provision ratio of new renewable energy system and do not provide an optimal installation ratio of the system optimal to characteristics of energy use of building and demands of building users. In this context, the purpose of this study is to develop a program for deducting an optimal ratio of a new renewable energy system and to verify the program′s validity when compared to a simulation.

As for comparison and verification, the researcher compared the coefficient of determination values of factors related to economic, environmental and technical aspects to determine higher or lower correlation.

Keywords*: New &Renewable-energy, Economy Analysis, Technical Analysis, Environment Analysis, Optimize the ratio*

1. Introduction

1.1. Background and purpose

To fight severe environmental problems such as weather accidents and ozone layer destruction due to greenhouse gases, the Korean government enforced the Act on the Promotion of the Development, Use and Dissemination of new renewable Energy since 2004, according to which a new public building whose total floor area is at least 3,000 ㎡ should be applied by a new renewable energy system to the amount of 5% of the total construction expenses. Later the act was so revised that it was applied to construction, reconstruction and extension of a public building whose total floor area is at least 1,000 ㎡ and the expected amount of energy used (not the total construction expenses). However, the act just presents an obligatory provision ratio of new renewable energy system and do not provide an optimal installation ratio of the system optimal to characteristics and use of building and demands of building users. Thus, in case of lack of professional knowledge, it is difficult to select a new renewable energy system for a building and to deduce an optimal ratio of installing the system for complex application.

In this context, the researcher in this study developed a program for selecting a new renewable energy system and deducing an optimal ratio of installing during planning and designing a building (KRESS) and compared & verified reliability of the program for deducing an optimal ratio with which various systems are enabled to be

doi:10.18086/swc.2015.01.03 Available at http://proceedings.ises.org

combined and designed by selecting an appropriate source of new renewable energy and then calculating capacity of the system in the phase of initial designing.

1.2 Methods and scope

As a study of comparison and verification of a program for deducing an optimal ratio of a new renewable energy system, the methods and scope of this study are as follows.

The researcher compared and verified the validity of the developed program by using a developing tool (KRESS) and a simulation tool (Energy Plus) for selecting an optimal ratio of installing a new renewable energy system for public office buildings.

For comparison & verification of validity, the researcher assessed correlations of sub-items based on economic, environmental and technical aspects, a data that was used to compare and verify optimal application by evaluation priority for designing a new renewable energy system and optimal ratio of installing the system.

2. Overview of the developed program and buildings for comparison and verification

2.1 Overview of the developed program

The KRESS program developed in this study was developed by using of the MS-Excel VBA. As seen in the flow chart in Figure 1, the program can deduce an optimal ratio of installing a new renewable energy system on the expected amount of energy use of a building when considering solar power, solar collector, and heat pump, sources that can be easily applied to buildings among the 11 sources of new renewable energy designated domestically.

Fig 1. Develop program's Flow Chart & User Interface

When basic data such as building use and area are entered, the program calculates the energy consumption of the building based on the database, estimates the obligatory energy supply and the capacity of a new renewable energy system based on the calculation, and then presents application methods and optimal ratio of installing for evaluation items including economic, environmental and technical aspects based on evaluation priority of the energy.

2.2 Selection of buildings for comparison and verification

For verifying the validity of the developed program, the researcher performed a simulation analysis in which variables such as capacity of air conditioning and heating, number of occupants, and lighting equipment were applied by zone-based schedules based on weather data according to the current state of buildings (as seen in Table 1), by using the KRESS and the Energy Plus tools.

Table. 1 Overview of the subject building.

Area (㎡)	Construction area	2,929.27
	Total floor area	10,320.48
	Parking area	1,533.98
Thermal perfusion (W/㎡.K)	Exterior wall	0.47
	Windows	2.7
Internal heating value (W/㎡)	Person	0.15
	lighting	20
	Electrical equipment	22
direction	East	

According to the results of the simulation (see Table 2), the total energy requirement was 2,806,648 kWh by the KRESS and 3,232,935 kWh by the Energy Plus, with the deviation of 13.2%. In the Energy Plus, changes in daily air conditioning & heating and amount of electricity used were applied because of application of local weather data, while the KRESS uniformly calculated amount demanded based on the unit equation presented by legislation. This is the reason that the energy requirement deduced by the KRESS was less than that by the Energy Plus, requiring further examination Tables, figures, equations, and lists

Table. 2 Estimated energy consumption of the subject building

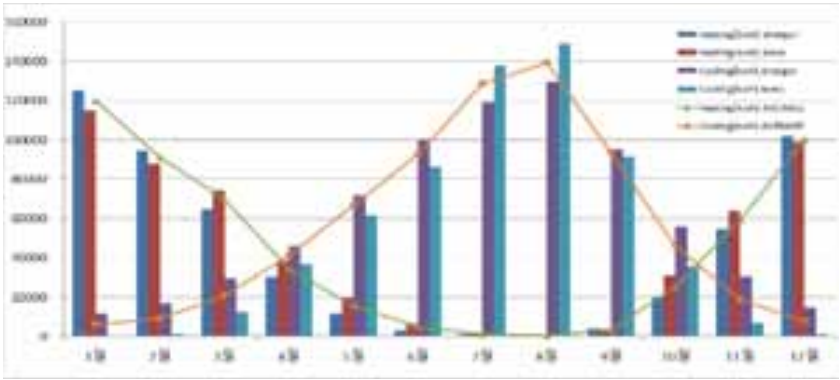

End Uses Energy	KRESS	Energy plus	measuring efficiency
Heating	464,623 (kwh)	538,793 (kwh)	13.8 %
Cooling	514,935 (kwh)	619,694 (kwh)	16.9 %
Hot water	132,893 (kwh)	154,227 (kwh)	13.8 %
Electronic Equipment	1,694,197 (kwh)	1,920,224 (kwh)	11.8 %
Total End Uses	2,806,648 (kwh)	3,232,935 (kwh)	13.2 %

3. Comparison & verification and optimal ratio of new renewable energy system

3.1 Comparison & verification of new renewable energy system

For comparison & verification of new renewable energy system, the researcher classified methods of application of [C01～66] (see Figure 2) so that at least 671.157kWh of new renewable energy could be produced when the ratio of obligatory installation was 12 % based on the Act (as of 2014), investigating the reliability of the developed program via comparison & verification of correlations based on the KRESS and the Energy Plus. For comparison & verification of correlations, higher or lower correlation was determined via comparing the coefficient of determination (R^2) values of the factors of economic, environmental and technical aspects of the KRESS and the Energy Plus.

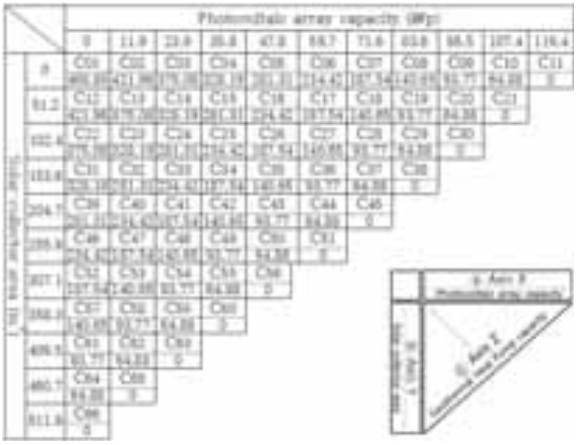

Fig 2. Categories of application plans of a new and renewable energy system

As for the correlations of economic aspects by the KRESS and the Energy Plus, among the sub-items of the economic aspects (see Figure 3), the R^2 value of initial investment costs used for installing and applying a new renewable energy system was 1.0 [Eic], that of maintenance and management cost used for maintaining and managing the system for certain period was 1.0 [Emrc], and that of energy cost that could be reduced by the system was 0.92 [Eec]. As for the correlations of technical aspects (see Figure 4), the R^2 value of supply reliability for safe supply of energy was 0.97 [Tesr] and that of energy efficiency as a rate of energy production on initial investment cost was 0.95 [Tee]. For the correlations of environmental aspects (see Figure 5), the R^2 value of CO2 emission for reducing greenhouse gases was 0.81 [Ecey].

As for correlations based on economic and technical aspects, the R^2 values were consistent as the entered values of the main items in the KRESS and the Energy Plus. However, the environmental aspects showed deviations in the correlation R^2 due to difference in the total energy demands between the KRESS and the Energy Plus.

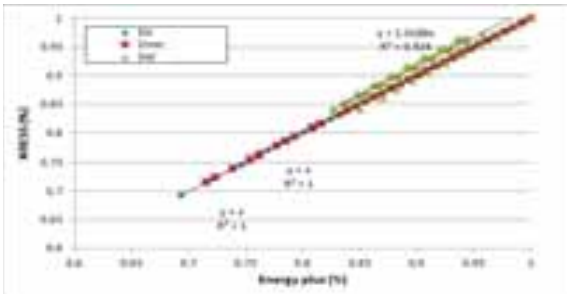

Fig 3. Comparison and testing of correlations according to economy

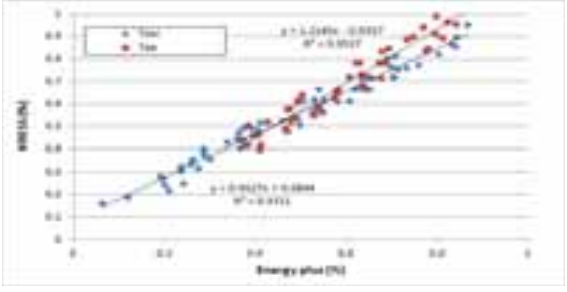

Fig 4. Comparison and testing of correlations according to technicality

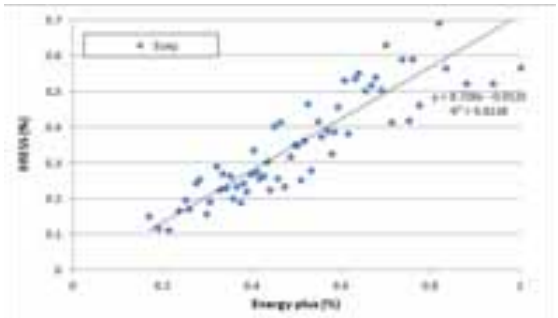

Fig 5. Comparison and testing of correlations according to environmentality

3.2 Optimal ratio of installing a new renewable energy system

Via analysis of economic, environmental and technical aspects per each alternative [$C_{01\sim66}$], an optimal ratio of installment was analyzed (see Table 3).

As for an optimal system based on the economic aspects of a building, C_{11} : PV (100%) was assessed as an optimal system both by the KRESS and the Energy Plus. For an optimal system based on technical aspects, the KRESS assessed only C_{11} : PV (100%) as optimal one, while the Energy Plus assessed C_{11} : PV (100%) and C_{21} : PV (90%)+SC(10%) as optimal ones. For an optimal system based on environmental aspects, both the KRESS and the Energy Plus assessed C_{21} : PV (90%)+SC(10%) as an optimal system. As for an optimal ratio of installment based on complexity, the KRESS assessed C_{11} : PV (100%) as an optimal system, while the Energy Plus assessed a (complex) C_{21} : PV (90%)+SC(10%) as an optimal system reflecting characteristics of building use and zone-based energy use schedule. As mentioned above, in the simulation of subject building for comparison and verification by the KRESS and the Energy Plus, a system was assessed as an optimal one as the PV was more applied in a single or complex system. For the subject building, thus, at least 90% of PV in a system may be most efficient ratio for a new renewable energy system.

Table. 3 Optimal installation percentage of multiple applications of new renewable energy by the programs

[unit:%]

	KRESS	Energy plus
Optimal installation percentage		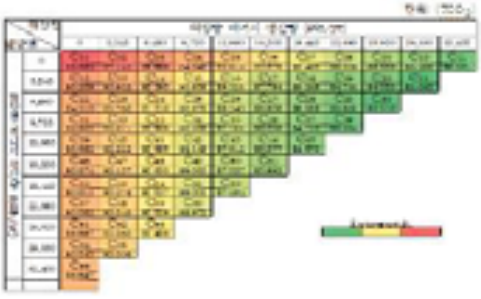
The Economy Analysis	C_{11}	C_{11}
	PV (100%)	PV (100%)
The technical Analysis	C_{11}	C_{11}, C_{21}
	PV (100%)	PV (100%), PV (90%) +SC (10%)
The Environment Analysis	C_{21}	C_{21}
	PV (90%) +SC (10%)	PV (90%) +SC (10%)
The Optimize Analysis	C_{11}	C_{21}
	PV (100%)	PV (90%) +SC (10%)

*[SC]:Solar Collector ,[PV]:Photo Voltaic, [GH]:Ground Heat`

4. Conclusion

As a study of comparison and verification of a program for deducing an optimal ratio of a new renewable energy system, the results of this study are as follows.

1) The researcher investigated verification of the developed program by calculating the total amount of energy use using the KRESS and the Energy Plus; the amount simulated by the Energy Plus was 13.2% higher than that by the KRESS because the former reflected characteristics of energy consumption based on building use, energy production based on surrounding weather, and requirements by users.

2) The R^2 values of economic and technical aspects by application methods [$C_{01\sim66}$] in the KRESS and the Energy Plus were 0.97 and 0.96, respectively, indicating that the deviation of coefficient of determination in the A Study of Optimal Design Techniques for the Application of Renewable Energy Combination Systems in School Facilities correlation was slight because the main items entered for the two simulations were consistent. The R2 value based on the environmental aspects was relatively lower, or 0.81, due to the difference in total energy requirement between the KRESS and the Energy Plus. However, the overall R^2 value was 0.91, indicating a favorable correlation.

3) As for an optimal sy stem of new renewable energy assessed by analysis of technical & environmental aspects per each alternative [$C_{01\sim66}$] for the subject building, both the KRESS and the Energy Plus assessed a system in which PV was more applied among the new renewable energy sources as an optimal one. For application methods of a new renewable energy system appropriate for the subject building, C_{11} : PV (100%) (A single system) and C_{21} : PV (90%)+SC(10%) (A complex system) may be optimal ones.

In developing a program for deducing an optimal ratio of a new renewable energy system for public buildings, selecting an appropriate energy source and calculating energy capacity & combining various systems, the comparison & verification of the results by the KRESS and the Energy Plus simulations was determined to be favorable. Improvements in reliability are required through further verification of various variables and consistent supplementation.

Acknowledgement

This Work was supported by basic research through the national research foundation of Korea(NRF) funded by the ministry of education, science and technology (NRF-2011-0012071)

References

1. Yong-Ho Lee, Sang-Hyun Seo, Hyung-Jin Kim, Young-Hum Cho, Jung-Ha Hwang., 2013, A Study on the Optimization of a Renewable Energy System in Fire Station Buildings, Journal of the Korean Solar Energy Society, Vol. 33, No. 1, pp. 79-88.

2 Jun-ho Hong, Yong-Ho Lee, Young-Hum Cho, Jung-Ha Hwang, 2014, A Study on the Development of a Proper Installation Ratio Determination Program for Each New and Renewable Energy System in Public Buildings, Architectural Institute of Korea, Spring Proceedings, Vol. 34, No. 1, pp. 256-260.

3. Hyun-Woo Lee, Min-Su Chae., 2011, A CO Emission Reduction Method through Correlation Analysis of Design Parameters in Buildings, Journal of the Korean Solar Energy Society, Vol. 31, NO. 1, pp100-106.

4. Sung-Rag Lee, Nam-Gee Jeung, Kun-Ki Lee, Seung-Hoon Lee, Myung-Do Oh., 2010, Life Cycle Cost Analysis of Energy Saving Performance for Apartment, Architectural Institute of Korea, Winter Annual Conference, pp254-259.

5. Ji-Yeon Kim, 2010, A Study of Optimal Design Techniques for the Application of Renewable Energy Combination Systems in School Facilities, Ph.D. thesis, Inha University, Incheon, Korea.

6. Sang-Hyun, Jun-ho Hong, Yong-Ho Lee , Young-Hum Cho, Jung-Ha Hwang,2013, A Study on the Analysis of the Efficiency of New and Renewable Energy Applied to Complex Government Office Buildings, Korean Solar Energy Society, Spring Proceedings, Vol.2013 No.4

7. Jun-ho Hong, Yong-Ho Lee, Young-Hum Cho, Jung-Ha Hwang, 2013, A Study on the Planning of Hybrid Renewable Energy Systems Optimization Apply in the general hospital building, Proceedings of the SAREK Summer Annual Conference

Author Index

A

B

C

D

E

F

G

H

I

J

K

L

M

N

O

P

Q

R

S

T

U

V

W

Y

Z